# Echocardiography in Pediatric and Congenital Heart Disease

*Echocardiography in Pediatric and Congenital Heart Disease: From Fetus to Adult*
Edited by Wyman W. Lai, Luc L. Mertens, Meryl S. Cohen and Tal Geva
 ISBN: 978-1-405-17401-5

### Video clips on DVD-ROM

This book is accompanied by a **DVD with over 300 video clips** showing anatomy and conditions described in the text.

- All the clips are fully referenced in the text, where you see this symbol: 
- The database of videos is fully searchable.
- The DVD is suitable for PC and Mac computers.

Additional supplementary video clips are also available on a **companion website** for downloading at:

**www.wiley.com/go/lai/echocardiography**

# Echocardiography in Pediatric and Congenital Heart Disease

## From Fetus to Adult

EDITED BY


**Wyman W. Lai, MD, MPH**
Director, Non-Invasive Cardiac Imaging
Division of Pediatric Cardiology
Morgan Stanley Children's Hospital of New York Presbyterian
New York, NY, USA

**Luc L. Mertens, MD, PhD**
Section Head, Echocardiography
The Hospital for Sick Children
Associate Professor of Pediatrics
University of Toronto
Toronto, ON, Canada

**Meryl S. Cohen, MD**
Associate Professor of Pediatrics
University of Pennsylvania School of Medicine;
Director, Echocardiography Laboratory
Co-Director, Cardiology Fellowship Training Program
The Children's Hospital of Philadelphia
Philadelphia, PA, USA

**Tal Geva, MD**
Professor of Pediatrics
Harvard Medical School;
Chief, Division of Non-Invasive Cardiac Imaging
Department of Cardiology
Children's Hospital Boston
Boston, MA, USA



WILEY-BLACKWELL
A John Wiley & Sons, Ltd., Publication

This edition first published 2009, © 2009 by Blackwell Publishing Ltd

Blackwell Publishing was acquired by John Wiley & Sons in February 2007. Blackwell's publishing program has been merged with Wiley's global Scientific, Technical and Medical business to form Wiley-Blackwell.

*Registered office:* John Wiley & Sons Ltd, The Atrium, Southern Gate, Chichester, West Sussex, PO19 8SQ, UK

*Editorial offices:* 9600 Garsington Road, Oxford, OX4 2DQ, UK
The Atrium, Southern Gate, Chichester, West Sussex, PO19 8SQ, UK
111 River Street, Hoboken, NJ 07030-5774, USA

For details of our global editorial offices, for customer services and for information about how to apply for permission to reuse the copyright material in this book please see our website at www.wiley.com/wiley-blackwell



*Library of Congress Cataloging-in-Publication Data*

Echocardiography in pediatric and congenital heart disease : from fetus to adult / [edited by] Wyman Lai . . . [et al.].

p. ; cm.

Includes bibliographical references and index.

ISBN 978-1-4051-7401-5 (alk. paper)

1. Electrocardiography. 2. Congenital heart disease. 3. Congenital heart disease in children. 4. Pediatric cardiology. I. Lai, Wyman.

[DNLM: 1. Echocardiography—methods. 2. Heart Defects, Congenital—diagnosis. WG 141.5.E2 E186 2009]

RC683.5.E5E258 2009

616.1'207547—dc22

2009013413

ISBN: 978-1-4051-7401-5

A catalogue record for this book is available from the British Library.

Set in 9/12pt Meridien by Graphicraft Limited, Hong Kong
Printed and bound in Singapore

01 2009

# Contents

**Video clips on DVD-ROM**

This book is accompanied by a **DVD with over 300 video clips** showing anatomy and conditions described in the text.

- All the clips are fully referenced in the text, where you see this symbol: 
- The database of videos is fully searchable.
- The DVD is suitable for PC and Mac computers.

Additional supplementary video clips are also available on a **companion website** for downloading at:

**www.wiley.com/go/lai/echocardiography**

# List of Contributors


**Catherine Barrea MD**
Assistant Professor
University of Louvain Medical School;
Staff Physician
Pediatric Cardiology
Cliniques Universitaires Saint-Luc
Brussels, Belgium

**Annemien van den Bosch MD, PhD**
Erasmus MC Rotterdam
Department of Cardiology;
Cardiologist in Training
Erasmus MC Rotterdam – Thoraxcenter
Department of Cardiology
Rotterdam, The Netherlands

**David W. Brown MD**
Assistant Professor of Pediatrics
Harvard Medical School;
Staff Physician
Pediatric Cardiology
Children's Hospital Boston
Boston, MA, USA

**Piet Claus PhD**
Post-Doctoral Researcher
Division of Cardiovascular Imaging and Dynamics
Department of Cardiovascular Diseases
Catholic University of Leuven;
Medical Imaging Research Center
University Hospital Gasthuisberg
Leuven, Belgium

**Meryl S. Cohen MD**
Associate Professor of Pediatrics
University of Pennsylvania School of Medicine;
Director, Echocardiography Laboratory
Co-Director, Cardiology Fellowship Training Program
The Children's Hospital of Philadelphia
Philadelphia, PA, USA

**Steven D. Colan MD**
Professor of Pediatrics
Harvard Medical School;
Associate Director of Clinical Operations
Department of Cardiology
Children's Hospital Boston
Boston, MA, USA

**Julie De Backer MD, PhD**
Senior Clinical Investigator (Cardiology and Medical Genetics)
Ghent University;
Head of Clinic, Cardiology
University Hospital Ghent
Ghent, Belgium

**Ann De Paepe MD, PhD**
Professor in Medical Genetics
Ghent University;
Head of Department of Medical Genetics
University Hospital Ghent
Ghent, Belgium

**Jan D'hooge PhD**
Associate Professor
Division of Cardiovascular Imaging and Dynamics
Department of Cardiovascular Diseases
Catholic University of Leuven;
Medical Imaging Research Center
University Hospital Gasthuisberg
Leuven, Belgium

**Harry C. Dietz MD**
Victor A. McKusick Professor of Medicine and Genetics
Institute of Genetic Medicine
Department of Pediatrics, Medicine and Molecular Biology and Genetics;
Investigator
Howard Hughes Medical Institute
Johns Hopkins University
School of Medicine
Institute of Genetic Medicine
Baltimore, MD, USA

**Benedicte Eyskens MD, PhD**
Assistant Professor of Paediatrics
University of Leuven
Leuven, Belgium

**Matthew Fenton MB, BS, BSc**
Consultant Paediatric Cardiologist
Great Ormond Street Hospital for Children
NHS Trust
London, UK

**Geoffrey A. Forbus MD**
Assistant Professor of Pediatrics
Medical University of South Carolina;
Director, Pediatric Cardiology Outpatient Clinics
Medical University of South Carolina
Charleston, SC, USA

**Michele A. Frommelt MD**
Associate Professor of Pediatrics
Division of Pediatric Cardiology
Medical College of Wisconsin;
Director of Fetal Echocardiography
Children's Hospital of Wisconsin
Milwaukee, WI, USA

**Peter C. Frommelt MD**
Professor of Pediatrics
Medical College of Wisconsin;
Director of Echocardiography
Children's Hospital of Wisconsin
Milwaukee, WI, USA

**Javier Ganame MD, PhD**
Scientist
University of Leuvens;
Staff Cardiologist
Department of Pediatric Cardiology
University Hospitals Leuven
Leuven, Belgium

**Tal Geva MD**
Professor of Pediatrics
Harvard Medical School;
Chief, Division of Non-Invasive Cardiac Imaging
Department of Cardiology
Children's Hospital Boston
Boston, MA, USA

**David J. Goldberg MD**
Assistant Professor
University of Pennsylvania School of Medicine;
Staff Physician
Pediatric Cardiology
The Children's Hospital of Philadelphia
Philadelphia, PA, USA

**J. René Herlong MD**
Assistant Professor of Pediatrics
Duke University School of Medicine;
Medical Director of Non-Invasive Imaging
Duke University Medical Center
Durham, NC, USA

**Lisa K. Hornberger MD**
Professor of Pediatrics and Obstetrics and Gynecology
University of Alberta;
Director of the Fetal and Neonatal Cardiology Program
Stollery Children's Hospital and Royal Alexandra Hospital
Edmonton, AB, Canada

**James C. Huhta MD**
Medical Director
Non-Invasive Imaging
All Children's Hospital
St. Petersburg, FL, USA

**Richard A. Humes MD**
Professor of Pediatrics
Wayne State University;
Chief, Division of Cardiology
Department of Pediatrics
Children's Hospital of Michigan
Detroit, MI, USA

**Sachine Khambadkone MBBS, DcH, MD, DNB, MRCP**
Honorary Senior Lecturer
Institute of Child Health
University College London;
Consultant Paediatric Cardiologist
Great Ormond Street Hospital for Children NHS Trust
London, UK

**Mary Etta E. King MD**
Associate Professor of Pediatrics
Harvard Medical School;
Director
Massachusetts General Hospital
Boston, MA, USA

**H. Helen Ko BS, RDMS, RDCS, FASE**
Technical Director/Operations Manager
Pediatric Echocardiography
Pediatric Cardiology
Mount Sinai Medical Center
New York, NY, USA

**Wyman W. Lai MD, MPH**
Associate Professor of Clinical Pediatrics
Columbia University;
Director
Non-Invasive Cardiology Imaging
Morgan Stanley Children's Hospital of New York Presbyterian
New York, NY, USA

**Matthew S. Lemler MD**
Professor of Pediatrics
University of Texas Southwestern Medical Center at Dallas;
Division of Cardiology
Children's Medical Center of Dallas
Dallas, TX, USA

**Jami C. Levine MS, MD**
Assistant Professor of Pediatrics
Harvard Medical School;
Associate in Cardiology
Children's Hospital, Boston
Boston, MA, USA

**Mark B. Lewin MD**
Professor of Pediatrics
University of Washington School of Medicine;
Chief, Pediatric Cardiology
Director of Echocardiology Laboratory
Seattle Children's Hospital
Seattle, WA, USA

**Bart Loeys MD, PhD**
Associate Professor in Genetics
Ghent University;
Assistant-Chief of Clinic
Ghent University Hospital
Ghent, Belgium

**Leo Lopez MD**
Associate Professor of Clinical Pediatrics
Albert Einstein College of Medicine;
Director of Pediatric Cardiac Non-Invasive Imaging
Children's Hospital at Montefiore
New York, NY, USA

**Irene D. Lytrivi MD**
Assistant Clinical Professor of Pediatrics
Mount Sinai School of Medicine;
Staff Physician
Pediatric Cardiology
Mount Sinai Medical Center
New York, NY, USA

**Jackie McGhie**
Congenital Cardiac Ultrasound Specialist
Erasmus University Medical Center Rotterdam
Rotterdam, The Netherlands

**Colin J. McMahon MB, MRCPI**
Consultant Paediatric Cardiologist
Department of Paediatric Cardiology
Our Lady's Hospital for Sick Children
Dublin, Ireland

**Jan Marek MD, PHD**
Associate Professor of Cardiology
Institute of Child Health
University College London;
Director of Echocardiography
Consultant Pediatric and Fetal Cardiologist
Great Ormond Street Hospital for Children
London, UK

**Folkert Jan Meijboom MD, PhD**
Lecturer in Pediatric Cardiology and Adult Congenital Heart Disease
University of Utrecht
Academic Medical Centre Utrecht;
Staff Physician
Department of Pediatrics and Cardiology
Academic Medical Centre Utrecht
Utrecht, The Netherlands

**Luc L. Mertens MD, PhD**
Section Head, Echocardiography
The Hospital for Sick Children;
Associate Professor of Pediatrics
University of Toronto
Toronto, ON, Canada

**Erik C. Michelfelder MD**
Associate Professor of Pediatrics
University of Cincinnati College of Medicine;
Director, Fetal Heart Program
Cincinnati Children's Hospital Medical Center
Cincinnati, OH, USA

**Stéphane L.J. Moniotte MD, PhD**
Assistant Professor
University of Louvain Medical School;
Staff Physician
Pediatric Cardiology
Cliniques Universitaires Saint-Luc
Brussels, Belgium

**James C. Nielsen MD**
Associate Professor of Pediatrics
Mount Sinai School of Medicine;
Director, Non Invasive Imaging
Mount Sinai Medical Center
New York, NY, USA

**Sharon E. O'Brien MD**
Assistant Professor of Pediatrics
Boston University;
Director of Pediatric Cardiology
Boston Medical Center
Boston, MA, USA

**Erwin Oechslin MD**
Associate Professor of Medicine
University of Toronto;
Director, Toronto Congenital Cardiac Centre for Adults;
Staff Physician, Cardiology
University Health Network
Peter Munk Cardiac Centre
Toronto General Hospital
Toronto, ON, Canada

**Ira A. Parness MD**
Professor of Pediatrics
Mount Sinai School of Medicine;
Chief, Division of Pediatric Cardiology
Mount Sinai Medical Center
New York, NY, USA

**Christina Phelps MD**
Senior Fellow, Children's Hospital Denver
The Children's Hospital
University of Colorado Health Sciences Center at Denver
Aurora, CO, USA

**Andrew J. Powell MD**
Associate Professor of Pediatrics
Harvard Medical School;
Director, Cardiovascular MRI
Children's Hospital Boston
Boston, MA, USA

**Claudio Ramaciotti MD**
Professor of Pediatrics
University of Texas Southwestern Medical Center;
Director of Echocardiography Laboratory
Children's Medical Center of Dallas
Dallas, TX, USA

**Jack Rychik MD**
Professor of Pediatrics
University of Pennsylvania School of Medicine;
Director, Fetal Heart Program at the Cardiac Center
The Children's Hospital of Philadelphia
Philadelphia, PA, USA

**Jack C. Salerno MD**
Associate Professor of Pediatrics
University of Washington School of Medicine;
Staff Physician
Pediatric Cardiology
Seattle Children's Hospital
Seattle, WA, USA

**Ulrike E. Salzer-Muhar MD**
Associate Professor of Pediatrics
Medical University of Vienna;
Division of Pediatric Cardiology
Department of Pediatrics and Adolescent Medicine
Vienna General Hospital
Vienna, Austria

**Girish S. Shirali MBBS**
Professor of Pediatrics and Obstetrics/Gynecology
Vice-Chair for Fellowship Education
Department of Pediatrics, Medicine and Molecular Biology and Genetics
Medical School of South Carolina;
Director, Echocardiography Laboratory
Medical University of South Carolina
Charleston, SC, USA

**John M. Simpson MD, FRCP**
Honorary Senior Lecturer in Heart Disease
King's College;
Consultant in Pediatric and Fetal Cardiology
Director of Paediatric Echocardiography
Evelina Children's Hospital
Guy's and St Thomas' NHS Foundation Trust
London, UK

**Tajinder P. Singh MD, MSc**
Assistant Professor of Pediatrics
Harvard Medical School
Harvard University;
Staff Physician
Pediatric Cardiology
Children's Hospital Boston
Boston, MA, USA

**Thierry Sluysmans MD, PhD**
Professor of Pediatrics
Université Catholique de Louvain;
Director, Cliniques Universitaires Saint Luc
Brussels, Belgium

**Jeffrey F. Smallhorn MBBS, FRACP, FRCP(c)**
Professor of Pediatrics
University of Alberta;
Director, Echocardiography Laboratory
Program Director, Pediatric Cardiology
Stollery Children's Hospital
Edmonton, AL, Canada

**Carolyn T. Spencer MD**
Assistant Professor of Pediatrics
Department of Cardiology
Harvard Medical School;
Staff Cardiologist
Children's Hospital Boston
Boston, MA, USA

**Shubhika Srivastava MBBS**
Associate Professor of Pediatrics
Director, Echocardiography Laboratory
Mount Sinai Medical Center
New York, NY, USA

**J. Geoffrey Stevenson MD**
Professor of Pediatrics
University of Washington
Director, Cardiac Ultrasound
Children's Hospital and Regional Medical Center
Seattle, WA, USA

**Theresa A. Tacy MD**
Associate Professor of Pediatrics
Lucile Packard Children's Hospital
Stanford University;
Director, Echocardiography Laboratory
Lucile Packard Children's Hospital
Stanford University
Stanford, CA, USA

**Elif Seda Selamet Tierney MD**
Instructor in Pediatrics
Harvard University;
Assistant in Cardiology
Department of Cardiology
Children's Hospital Boston
Boston, MA, USA

**Cecile Tissot MD**
Research Associate at the Children's Hospital Denver
The Children's Hospital
University of Colorado Health Sciences Center at Denver
Aurora, CO, USA;
Attending Cardiologist
The Children's Hospital
Geneva, Switzerland

**Manfred Otto Vogt MD, PhD**
Consultant Pediatric Cardiologist
Technical University Munich
German Heart Center Munich
Clinic for Pediatric Cardiology and Congenital Heart Disease;
Head of Echo-Lab
Pediatric Cardiology and Congenital Heart Defects
German Heart Center Munich
Munich, Germany

**Luciana T. Young MD**
Associate Professor of Pediatrics
Northwestern University Feinberg School of Medicine;
Director, Echocardiography Laboratory
Children's Memorial Hospital
Chicago, IL, USA

**Adel K. Younoszai MD**
Assistant Professor
University of Colorado;
Director, Echocardiography Laboratory
The Children's Hospital
University of Colorado Health Sciences Center at Denver
Aurora, CO, USA

# Preface

The genesis of this book was motivated by our recognition that it has been well over a decade since the publication of a textbook of pediatric echocardiography. Indeed, the field has since witnessed many technological advances as well as dramatic growth in clinical applications. We were encouraged to pursue this work mostly by our trainees and colleagues, who repeatedly told us that the field lacks a comprehensive, contemporary source of information that describes the integration of cardiac ultrasound into clinical practice in patients with congenital and acquired pediatric heart disease. We debated the merits of a printed textbook in this era of electronic information and instant access to the latest literature over the web. After much discussion we concluded that although the latest research papers and review articles are indeed readily available, they do not substitute for a source of information that systematically covers the field topic-by-topic, and educates the reader about all aspects related to echocardiography in patients with congenital heart disease, from the fetus to adult.

Our aim was to provide a comprehensive, integrated approach to pediatric cardiac ultrasound that incorporates all contemporary technologies. We feel it is important to include detailed information about the anatomy and pathophysiology of each lesion and to describe the goals and techniques of the echocardiographic examination before, during, and after treatment. Although still images are helpful in highlighting certain anatomic and functional features of many conditions, they do not substitute for visualizing the heart in cine loops. Therefore, the book includes a DVD with hundreds of examples of key anatomic and functional issues mentioned in the text. We hope that future editions will be fully electronic and accessible on the internet. As with any medical textbook, the rapid advances in our field will soon require that new information be added to maintain its relevance. It is, therefore, important to us to hear from our readers on how to improve the next edition.

This book is the product of many excellent contributions from the best experts in the field, both from Europe and from North America. We are indebted to their hard work, dedication, and exceptional talents. We also wish to express immense gratitude to our mentors who have inspired us, to our colleagues who have encouraged and supported us throughout this project, to the many talented sonographers who produced most of the excellent images used in this work, and to our trainees whose questions and quest for knowledge provided the primary motivation for this book. We are also grateful to the staff at Wiley-Blackwell for their support and professionalism with the production of this book. Finally, and most importantly, we wish dedicate this book to our families, whose unwavering support has made this work possible.

Wyman W. Lai, MD, MPH
Luc L. Mertens, MD
Meryl S. Cohen, MD
Tal Geva, MD

# Dedications

To my parents, CheToo and SoFa Lai; my wonderful wife, Lydia; and my children, Justin and Amanda.

*Wyman W. Lai*

To my wife Benedikte, my daughter Virginie and my son Francis. For all the time I could not spend with them.

*Luc L. Mertens*

To my husband Bruce Randazzo and my children Jake, Isabel and Ethan for supporting me always.

*Meryl S. Cohen*

To my wife Judith and sons Omri and Alon.

*Tal Geva*

# 1 Introduction to Cardiac Ultrasound Imaging

*Echocardiography in Pediatric and Congenital Heart Disease: From Fetus to Adult*
Edited by Wyman W. Lai, Luc L. Mertens, Meryl S. Cohen and Tal Geva
 ISBN: 978-1-405-17401-5

# 1 Ultrasound Physics

**Piet Claus and Jan D'hooge**

Department of Cardiovascular Diseases, Catholic University of Leuven; Medical Imaging Research Center, University Hospital Gasthuisberg, Leuven, Belgium

## Physics and technology of echocardiography

Echocardiography is the discipline of medicine in which images of the heart are created by making use of ultrasound waves. Knowledge of the physics of ultrasound helps us to understand how the different ultrasound imaging modalities operate, including two dimensional (2D) and Doppler imaging.

This section describes the essential concepts of how ultrasound waves can be used to generate an image of the heart. Certain technological developments will also be discussed. For more detailed treatment of ultrasound physics and imaging there is dedicated literature, to which readers should refer [1,2].

### How the ultrasound image is created

#### The pulse–echo experiment

The essential principle of ultrasonic imaging, as used in echocardiography, is the so-called acoustic "pulse–echo" experiment. Such an experiment can be described as follows:

**1** A short electric pulse is applied to a piezoelectric crystal. This electric field will induce a shape change of the crystal through reorientation of its polar molecules. In other words, due to application of an electric field the crystal will momentarily deform.

**2** The deformation of the piezoelectric crystal induces a local compression of the tissue with which the crystal is in contact: i.e., the superficial tissue layer is briefly compressed resulting in an increase in local pressure; this is the so-called acoustic pressure (Fig. 1.1).

**3** This local tissue compression (with subsequent decompression, i.e., rarefaction) will propagate away from the piezoelectric crystal at a speed of approximately 1530 m/s in soft tissue (Fig. 1.2). This is the so-called acoustic wave. The rate of compression/decompression determines the frequency of the wave and is typically 2.5–10 MHz (i.e., 2.5–10 million cycles per second) for diagnostic ultrasonic imaging. As these frequencies cannot be perceived by the human ear, these waves are said to be "ultrasonic."

**4** Spatial inhomogeneities in tissue density or tissue elasticity will result in a disturbance of the propagating wave. They will cause part of the energy in the wave to be scattered, i.e., retransmitted in all possible directions. The part of the scattered energy that is retransmitted back into the direction of origin of the wave is called *backscatter*. Moreover, at the interface between different types of tissue (e.g., blood and myocardium), part of the acoustic wave is reflected (i.e., specular reflections) similar to the reflections of optic waves on a water surface. Both the specular and backscattered reflections propagate back towards the piezoelectric crystal.

**5** When the reflected (compression) waves impinge upon the piezoelectric crystal, the crystal deforms. This results in relative motion of its (polar) molecules and generation of an electric field, which can be detected. The amplitude of this electric signal is directly proportional to the amount of compression of the crystal, i.e., the amplitude of the reflected/backscattered wave. This electric signal is called the radio-frequency (RF) signal and represents the amplitude of the reflected ultrasound wave as a function of time (Fig. 1.3).

The total duration of the above described "pulse–echo" experiment is about 100 μs when imaging at 5 MHz. The reflected signal in Fig. 1.3 is referred to as an A-mode image ("A" referring to "Amplitude").

#### Grayscale encoding

A single "pulse–echo" measurement as described above will result in a single line in the ultrasound image. In order to reconstruct a single image line, the RF signal resulting from a pulse–echo experiment is processed in the following manner:

**1** *Envelope detection:* The high-frequency information of the RF signal is removed by detecting the envelope of the signal (Fig. 1.4).

**2** *Grayscale encoding:* The signal is subdivided as a function of time in small intervals (i.e., pixels). Each pixel is attributed a number, defined by the local amplitude of the signal, ranging between 0 and 255 ($2^8$ or 8-bit image). "0" represents "black;" "255" represents "white;" a value in between is

*Echocardiography in Pediatric and Congenital Heart Disease: From Fetus to Adult*
Edited by Wyman W. Lai, Luc L. Mertens, Meryl S. Cohen and Tal Geva
 ISBN: 978-1-405-17401-5

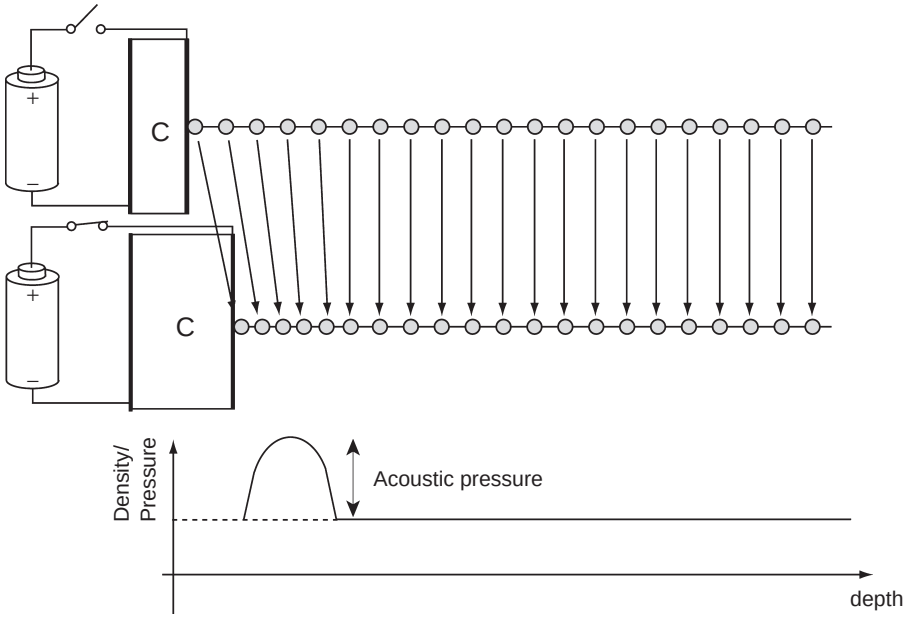


**Figure 1.1** Local tissue compression due to deformation of the piezoelectric crystal when applying an electric field.

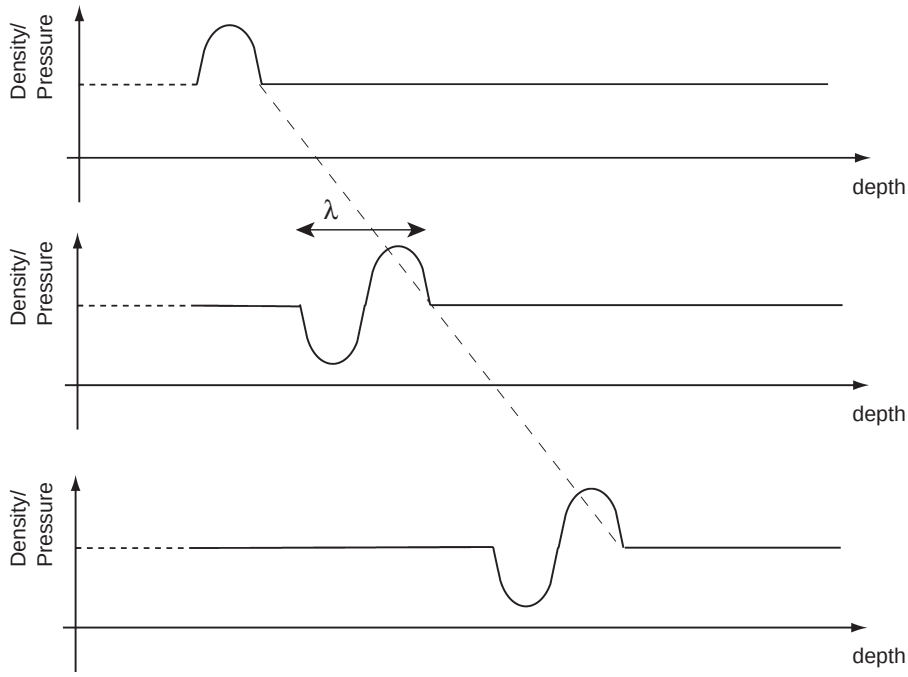


**Figure 1.2** The local tissue compression/decompression propagates away from its source at a speed of approximately 1530 m/s in soft tissue.

represented by a grayscale. By definition, bright pixels correspond to high-amplitude reflections. This process is illustrated in Fig. 1.4.

**3** *Attenuation correction*: As wave amplitude decreases with propagation distance due to attenuation (mostly due to conversion of acoustic energy to heat), reflections from deeper structures are intrinsically smaller in amplitude and therefore show less bright. In order to give identical structures located at different distances from the transducer a similar gray value (i.e., reflected amplitude), compensation for this attenuation must occur. Thus, an attenuation profile as a function of distance from the transducer is assumed, which allows for automatic amplification of the signals from deeper regions – the so-called automatic time-gain compensation (TGC), also referred to as depth-gain compensation. As the pre-assumed attenuation profile might be incorrect, sliders on the ultrasound scanner (TGC toggles) allow for manual correction of the automatic compensation.

**4** *Log-compression*: In order to increase the image contrast in the darker (i.e., less bright) regions of the image, gray values in the image are redistributed according to a logarithmic curve (Fig. 1.5).

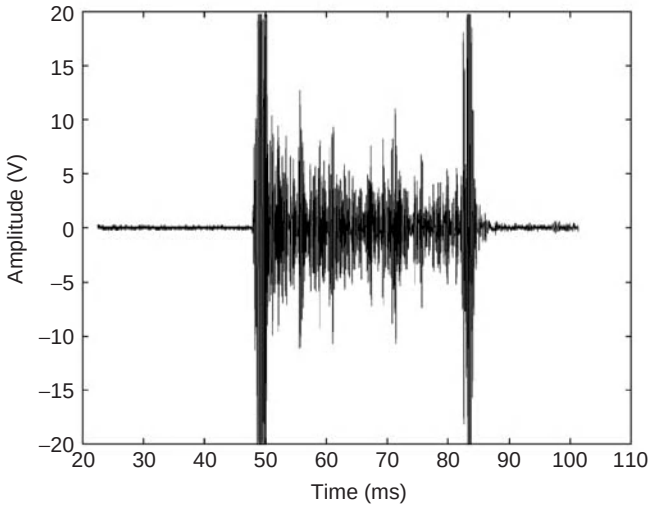


**Figure 1.3** The reflected amplitude of the reflected ultrasound waves as a function of time after transmission of the ultrasound pulse is called the radio-frequency (RF) signal.

### Image construction

In order to obtain an ultrasound image, the above procedures of signal acquisition and post-processing are repeated.

For conventional B-mode imaging ("B" referring to "brightness" mode), the transducer can either be translated (Fig. 1.6a) or tilted (Fig. 1.6b) within a plane between two subsequent "pulse–echo" experiments. In this way, a conventional 2-D cross-sectional image is obtained. The same principle holds for 3-D imaging by moving the ultrasound beam in 3-D space between subsequent acquisitions.

Alternatively, the ultrasound beam is transmitted into the same direction for each transmitted pulse. In that case, an image line is obtained as a function of time, which is particularly useful to look at motion. This modality is therefore referred to as M-mode (motion-mode) imaging.

## Image artifacts

### Side lobe artifacts

In the construction of an ultrasound image, the assumption is made that all reflections originate from a region directly in front of the transducer. Although most of the ultrasound energy is indeed centered on an axis in front of the transducer,

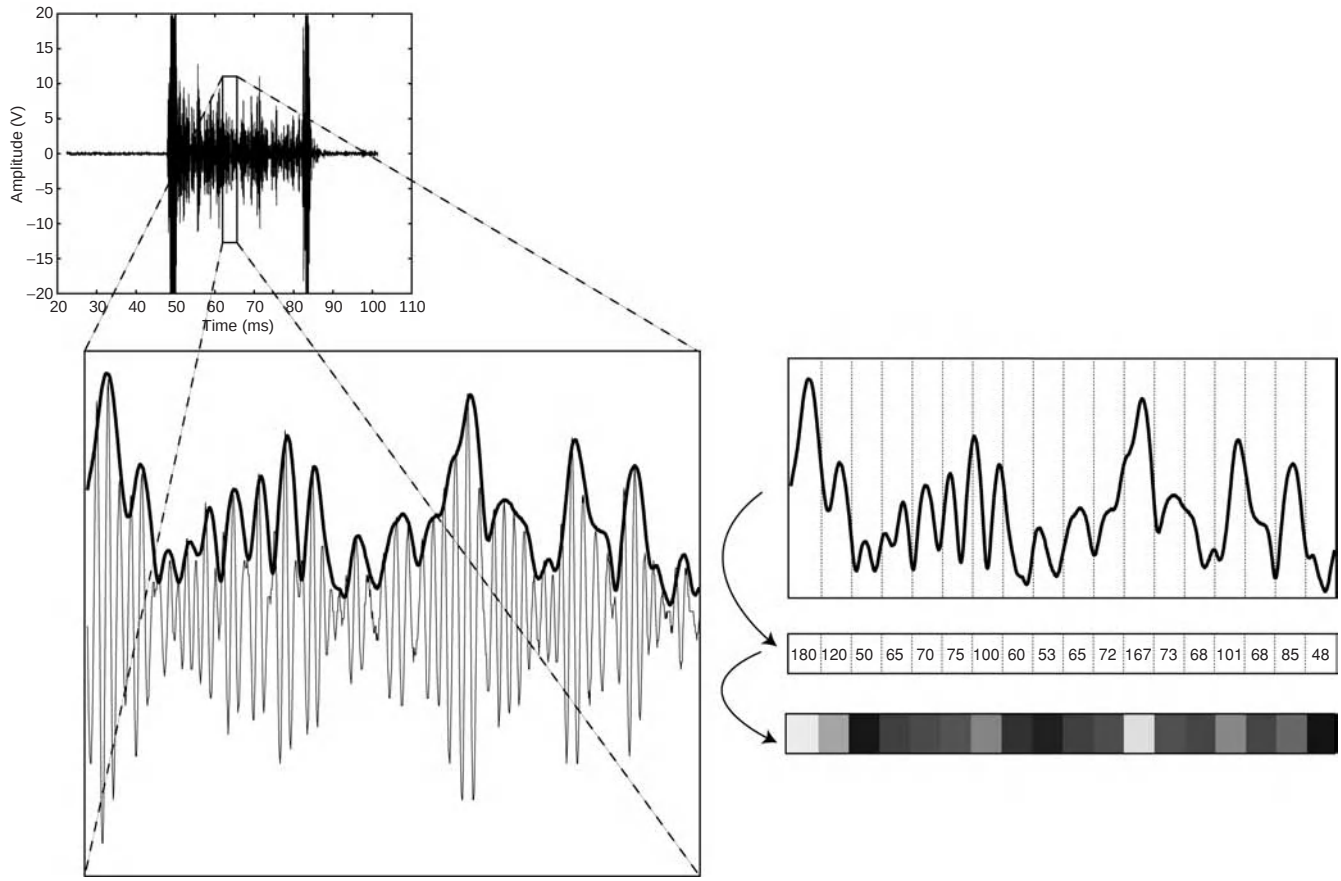


**Figure 1.4** The RF signal is demodulated in order to detect its envelope. This envelope signal (bold) is color encoded based on the local signal amplitude.

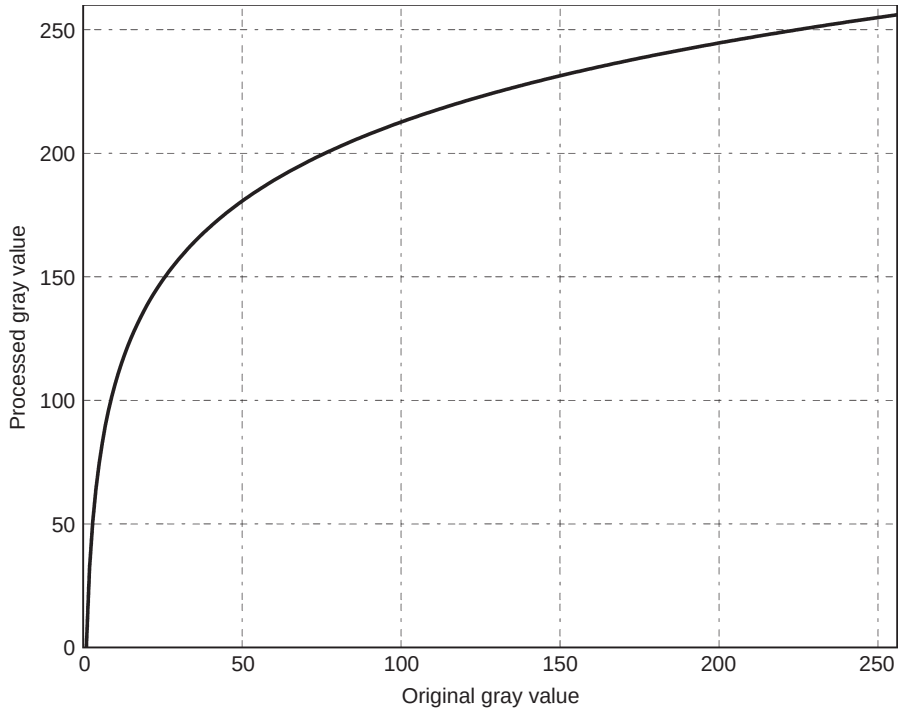


**Figure 1.5** The logarithmic compression curve.

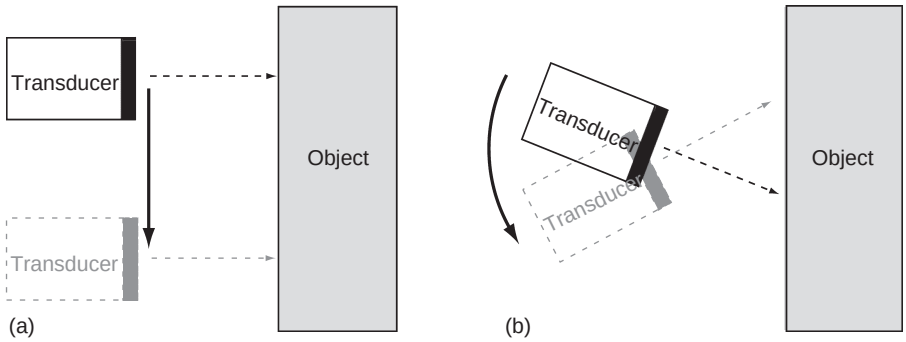


**Figure 1.6** Translation of the ultrasound source results in a linear image format **(a)** whereas pivoting results in sector images **(b)**.

in practice part of the energy is also directed sideways (i.e., directed off-axis). The former part of the ultrasound beam is called the main lobe whereas the latter is referred to as the side lobes (Fig. 1.7).

Because the reflections originating from these side lobes are much smaller in amplitude than the ones coming from the main lobe, they can typically be neglected. However, image artifacts can arise when the main lobe is in an anechoic region (i.e., a cyst or inside the left ventricular cavity) causing the relative contribution of the side lobes to become significant.

### Reverberation artifacts

When the reflected wave arrives at the transducer, part of the energy is converted to electrical energy as described in the previous section. However, another part of the wave is simply reflected on the transducer surface and will start propagating away from the transducer as if it were another ultrasound transmission. This secondary "transmission" will propagate in a way similar to that of the original pulse, which means that it is reflected by the tissue and detected again (Fig. 1.8).

These higher-order reflections are called reverberations and give rise to ghost structures in the image. They typically occur when strongly reflecting structures such as ribs or the pericardium are present in the image.

## Ultrasound technology and image characteristics

### Ultrasound technology

#### Phased array transducers

Rather than mechanically moving or tilting the transducers, as in machines of the previous era, modern ultrasound devices make use of electronic beam steering. For this purpose, an

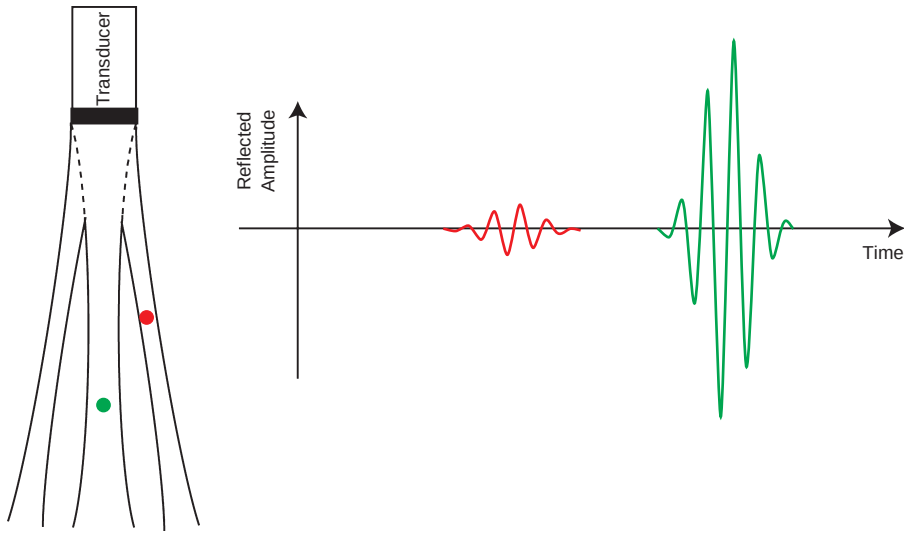


**Figure 1.7** Reflections caused by side lobes (red) will induce image artifacts because all reflections are assumed to arrive from the main ultrasound lobe (green).

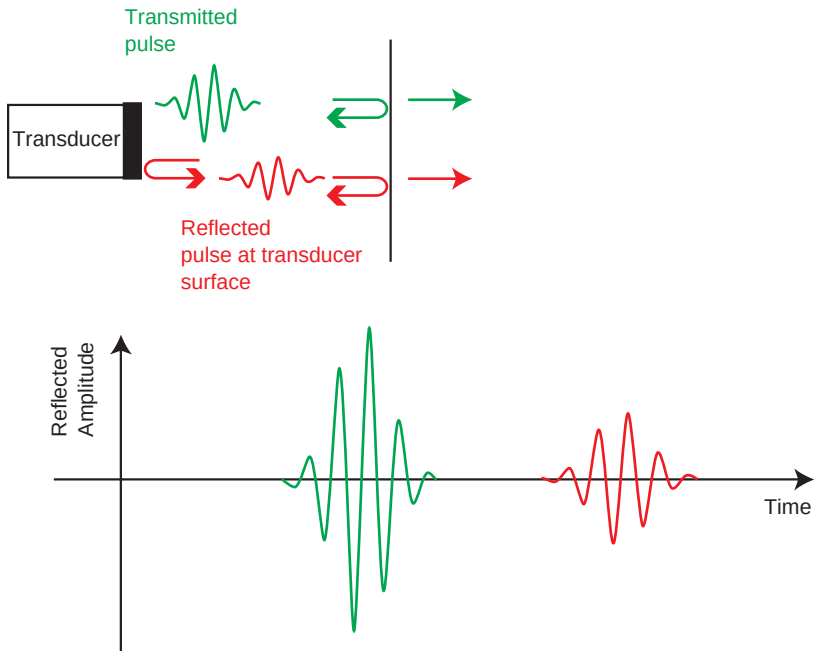


**Figure 1.8** A transmitted wave (green) will reflect and result in an echo signal (green). The reflected wave will, however, partially reflect at the transducer surface (red) and generate secondary signals (red).

array of piezoelectric crystals is used. By introducing time delays between the excitation of different crystals in the array, the ultrasound wave can be sent in a particular direction without mechanical motion of the transducer (Fig. 1.9). The RF signal for a transmission in a particular direction is then simply the sum of the signals received by the individual elements. These individual contributions can be filtered, scaled and time-delayed separately before summing. This process is referred to as *beam-forming* and is a crucial aspect for obtaining high-quality images. The scaling of the individual contributions is typically referred to as *apodization*.

This concept can be generalized by creating a 2D matrix of elements that enables steering of the ultrasound beam in three dimensions. This type of transducer is referred to as a matrix array or 2D array transducer. Because each of the individual elements of such an array needs electrical wiring, manufacturing such a 2D array remained technically challenging for many years. Nevertheless, 2D arrays are now readily available.

### Second harmonic imaging

Wave propagation as illustrated in Fig. 1.2 is only valid when the amplitude of the ultrasound wave is relatively small (i.e., the acoustic pressures involved are small). Indeed, when the amplitude of the transmitted wave becomes significant, the shape of the ultrasound wave will change during propagation,

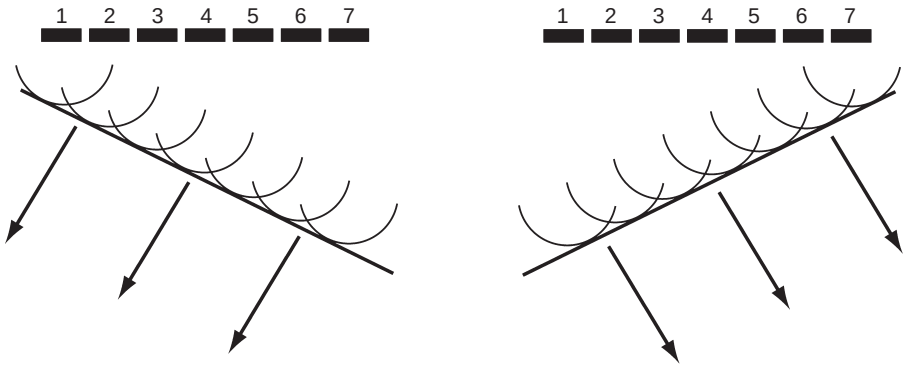


**Figure 1.9** An array of crystals can be used to steer the ultrasound beam electronically by introducing time delays between the activation of individual elements in the array.

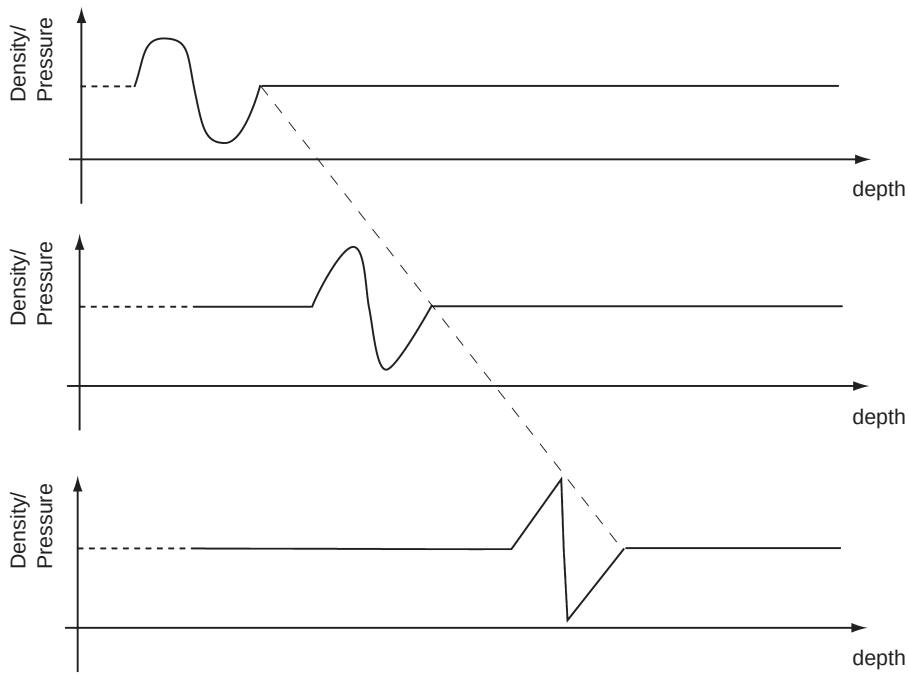


**Figure 1.10** Nonlinear wave behavior results in changes in shape of the waveform during propagation.

as illustrated in Fig. 1.10. This phenomenon of wave distortion during propagation is referred to as nonlinear wave propagation. It can be shown that this wave distortion implies that harmonic frequencies (i.e., integer multiples of the transmitted frequency) are generated. Transmitting a 1.7-MHz ultrasound pulse will thus result in the spontaneous generation of frequency components of 3.4, 5.1, 6.8, 8.5 MHz, and so on, and these harmonic components will grow stronger with propagation distance. The rate at which the waveform distorts for a given amplitude of the wave is tissue dependent and characterized through a nonlinearity parameter, $\beta$ (or the so-called "B/A" parameter).

The ultrasound scanner can be set up in such a way as to receive only the second harmonic component through filtering of the received RF signal. If further post-processing of the RF signal is done in the exact same way as described above, a second harmonic image is obtained. Such an image typically has a better signal-to-noise ratio by avoiding clutter noise due to (rib) reverberation artifacts. This harmonic image is often used in patients with poor acoustic windows. Although harmonic imaging increases signal-to-noise, it has intrinsically poorer axial resolution.

### Contrast imaging

As blood reflects little ultrasound energy it shows dark in the image. For some applications (such as myocardial perfusion assessment) it might be useful to increase artificially the reflectivity of the blood. This can be achieved by means of an ultrasound contrast agent. Indeed, air is an almost perfect reflector of ultrasound energy. As such, the injection of small air bubbles (of diameter similar to that of red blood cells) will increase blood reflectivity. Modern ultrasound contrast agents encapsulate these air bubbles in order to limit diffusion of the air (or a heavier gas) in blood.

## Image resolution

The spatial resolution of an ultrasound image varies, and depends on the position of the structure relative to the

transducer. Moreover, the resolution along the image line (*axial resolution*) is different from the one perpendicular to the image – within the 2D image plane (azimuth or *lateral resolution*), which is different again from the resolution in the direction perpendicular to the image plane (*elevation resolution*).

### Axial resolution

In order to obtain an optimal axial resolution, a short ultrasound pulse needs to be transmitted. The length of the transmitted pulse is mostly determined by the characteristics of the transducer. Indeed, the more frequencies the transducer can generate (in other words, the more broadband the transducer), the shorter the pulses it can generate. Transducer bandwidth is typically proportional to the mean transmission frequency. A higher frequency transducer will thus produce images with a better axial resolution. Unfortunately, higher frequencies are attenuated more by soft tissue. As such, a compromise needs to be made between image resolution and penetration depth (i.e., field of view). In pediatric and neonatal cardiology, most often 5- to 10-MHz transducers are used resulting in a typical axial resolution of the order of 500 to 250 μm respectively.

Note that in order to enable second harmonic imaging, a longer ultrasound pulse needs to be transmitted. As a result, the intrinsic axial resolution of the second harmonic image is worse despite improvement of the signal-to-noise ratio. Therefore, some of the cardiac structures appear thicker, especially valve leaflets. This should be considered when interpreting the images.

### Lateral resolution

The lateral resolution is determined by the width of the ultrasound beam (i.e., the width of the main lobe). The narrower the ultrasound beam, the better the lateral resolution. In order to narrow the ultrasound beam, several methods can be used but the most obvious one is focusing. This is realized by introducing time delays between the firing of individual array elements (similar to what is done for beam steering) in order to make sure that the transmitted wavelets of all individual array elements arrive at the same position at the same time and will thus constructively interfere (Fig. 1.11). Similarly, time delaying the reflections of the individual crystals in the array will make sure that reflections coming from a particular point in front of the transducer will sum in phase and therefore create a strong echo signal (Fig. 1.11). Because the sound velocity in soft tissue is known, the position from which reflections can be expected is known at each time instance after transmission of the ultrasound pulse. As such, the time delays applied in receive can be changed dynamically in order to move the focus point to the appropriate position. This process is referred to as *dynamic (receive) focusing*.

The easiest way to improve focusing performance of a transducer is by increasing its size (i.e., aperture). Unfortunately, the aperture needs to fit between the patient's ribs, thereby limiting the size of the aperture and thus limiting lateral resolution of the imaging system. For an 8-MHz pediatric transducer, realistic numbers for the lateral resolution of the system are depth dependent and are approximately 0.3 mm at 2 cm going up to 1.2 mm at 7 cm depth.

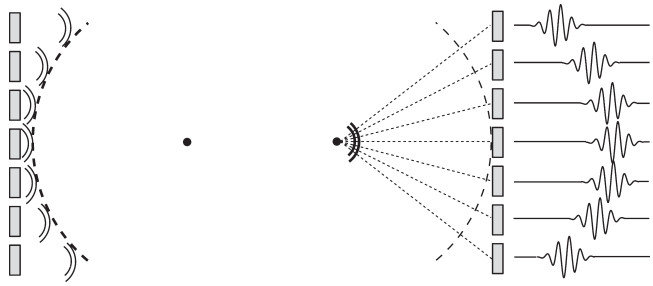

**Figure 1.11** Introducing time delays during transmission of individual array elements (left) allows for all wavelets to arrive at a particular point (focus) simultaneously. Similarly, received echo signals can be time delayed so that they constructively interfere (receive focus).

### Elevation resolution

For elevation resolution, the same principles hold as for lateral resolution in the sense that the dimension of the ultrasound beam in the elevation direction will be determinant. However, most ultrasound devices are still equipped with 1-D array transducers. As such, focusing in the elevation direction needs to be done by the use of acoustic lenses, which implies that the focus point is fixed in both transmit and receive (i.e., dynamic focusing is not possible in the elevation direction). This results in a resolution in the elevation direction that is worse than the lateral resolution. Moreover, most often, transducer aperture in the elevation direction is somewhat smaller (in order to fit in between the ribs of the patient) resulting in a further decrease of resolution compared to the lateral component. Newer systems with 2-D array transducer technology have more similar lateral and elevation image resolution.

### Temporal resolution

Typically, a 2D pediatric cardiac image consists of 300 lines. The construction of a single image thus takes about 300 × 100 μs (the time required to acquire one line) or 30 ms. Therefore, about 33 images can be produced per second, which is sufficient to look at motion (e.g., standard television displays only 25 frames/second). With more advanced imaging techniques such as parallel beam forming, higher frame rates can be obtained (70–80 Hz).

## Doppler imaging

### Continuous-wave Doppler

When an acoustic source moves relative to an observer, the frequencies of the transmitted and the observed waves are

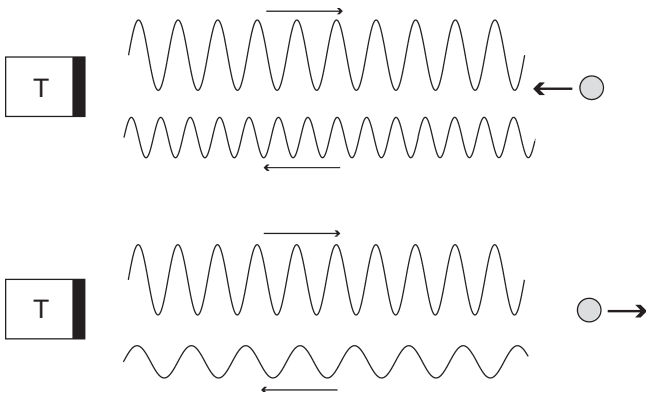


**Figure 1.12** The Doppler effect will induce a frequency shift of the transmitted ultrasound wave when the reflecting object is in motion.

different. This phenomenon is known as the Doppler effect. A well-known example is that of a whistling train passing a static observer: the observed pitch of the whistle is higher when the train approaches than when it moves away.

The Doppler phenomenon can be used to measure tissue velocities by comparing the transmitted to the received ultrasound frequency. Indeed, when ultrasound scattering occurs at stationary tissues, the transmitted and reflected frequencies are identical. This statement is only true when attenuation effects are negligible. In soft tissue there will be intrinsic frequency shift due to frequency-dependent attenuation. When scattering occurs at tissue in motion (Fig. 1.12), a frequency shift – the Doppler shift ($f_D$) – will be induced that is directly proportional to the velocity ($v$) by which the tissue is moving:

$$f_D = -2v \cos \theta \, f_T / c$$

where $f_T$ is the transmit frequency, $\theta$ is the angle between the direction of wave propagation and the tissue motion, and $c$ is the velocity of sound in soft tissue (i.e., 1530 m/s). Note that for motion orthogonal to the image line, $\theta = 90°$ and the Doppler shift is zero regardless of the amplitude of the tissue velocity $v$. The Doppler phenomenon thus only allows measuring the magnitude of the velocity along the image line – motion orthogonal to the line is not detected. In practice, an angle up to 20° is considered acceptable in order to obtain clinically relevant measurements.

In order to make a Doppler measurement, one piezoelectric crystal is used for transmitting a continuous wave of a fixed frequency and a second crystal is used to record continuously the reflected signals. Both crystals are embedded in the same transducer, and the frequency difference, that is, the Doppler shift, is continuously determined. The instantaneous shift is displayed as a function of time in a so-called *spectrogram*. However, because different velocities are present within the ultrasound beam for any given time instance during the cardiac cycle, a range of Doppler frequencies is typically detected. There is thus a spectrum of Doppler shifts measured and displayed in the spectrogram (Fig. 1.13) – hence the name "spectral Doppler" often encountered in literature. Finally, as typical blood velocities cause a Doppler shift in the sonic range (20 Hz to 20 kHz), the Doppler shift itself can be made audible to the user. A high pitch (large Doppler shift) corresponds to a high velocity whereas a low pitch (small Doppler shift) corresponds to a low velocity. As such, the user gets both visual (spectrogram) and aural

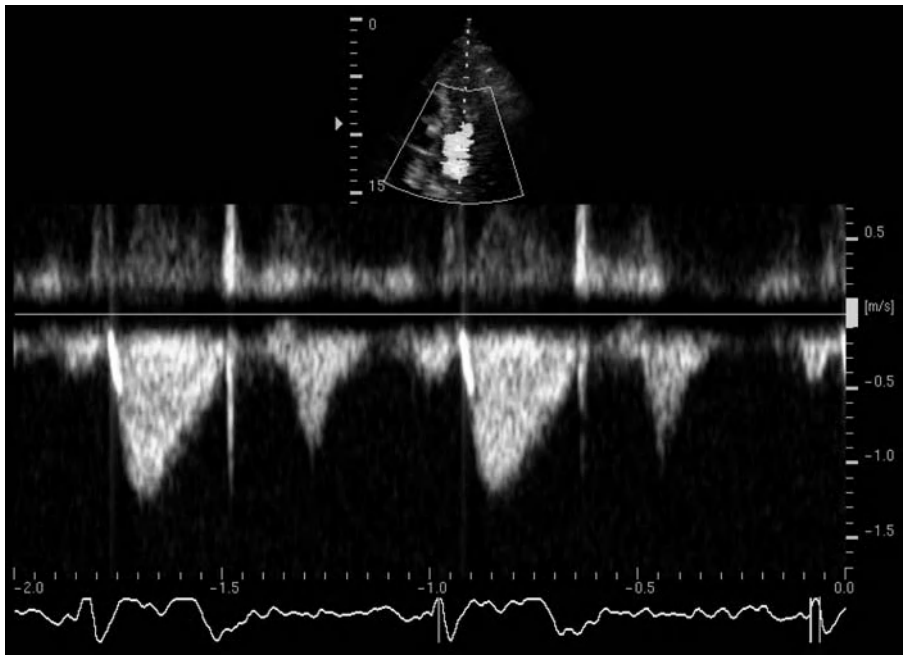


**Figure 1.13** Example of a continuous-wave Doppler spectrogram of the left ventricular outflow tract.

information on the velocities instantaneously present in the ultrasound beam.

The system described above is referred to as the continuous-wave (CW) Doppler system. As an ultrasound wave is transmitted continuously, no spatial information is obtained. Indeed, all velocities occurring anywhere within the ultrasound beam (i.e., on the selected ultrasound line of interrogation) will contribute to the reflected signal and appear in the spectrogram. In fact, as the ultrasound signal weakens with depth due to attenuation, velocities close to the transducer will intrinsically contribute more than the ones occurring further away.

## Pulsed-wave Doppler

The "pulse–echo" measurement described previously can be repeated along a particular line in the ultrasound image at a given repetition rate (referred to as the "pulse repetition frequency," or PRF). Rather than acquiring the complete RF signal as a function of time, in pulsed-wave Doppler mode, a single sample of each reflected pulse is taken at a fixed time after the transmission of the pulse (the so-called range gate or sample volume). In case the position of the scattering sites relative to the transducer remains constant over time, all reflections will be identical and therefore all samples taken at the range gate as well. However, when the tissue is moving relative to the transducer, the ultrasound wave will have to travel further (motion away from the transducer) or less far (motion toward the transducer) between subsequent acquisitions. As a result, the reflected signal will shift in time and the sample taken at the range gate will change (Fig. 1.14). Note that motion orthogonal to the direction of wave propagation will not induce a significant change in propagation distance for the ultrasound wave; it will not result in a significant time shift of the reflected signal and will thus not be detected by the system.

It can be demonstrated that the frequency of the signal constructed in this way is directly proportional to the velocity

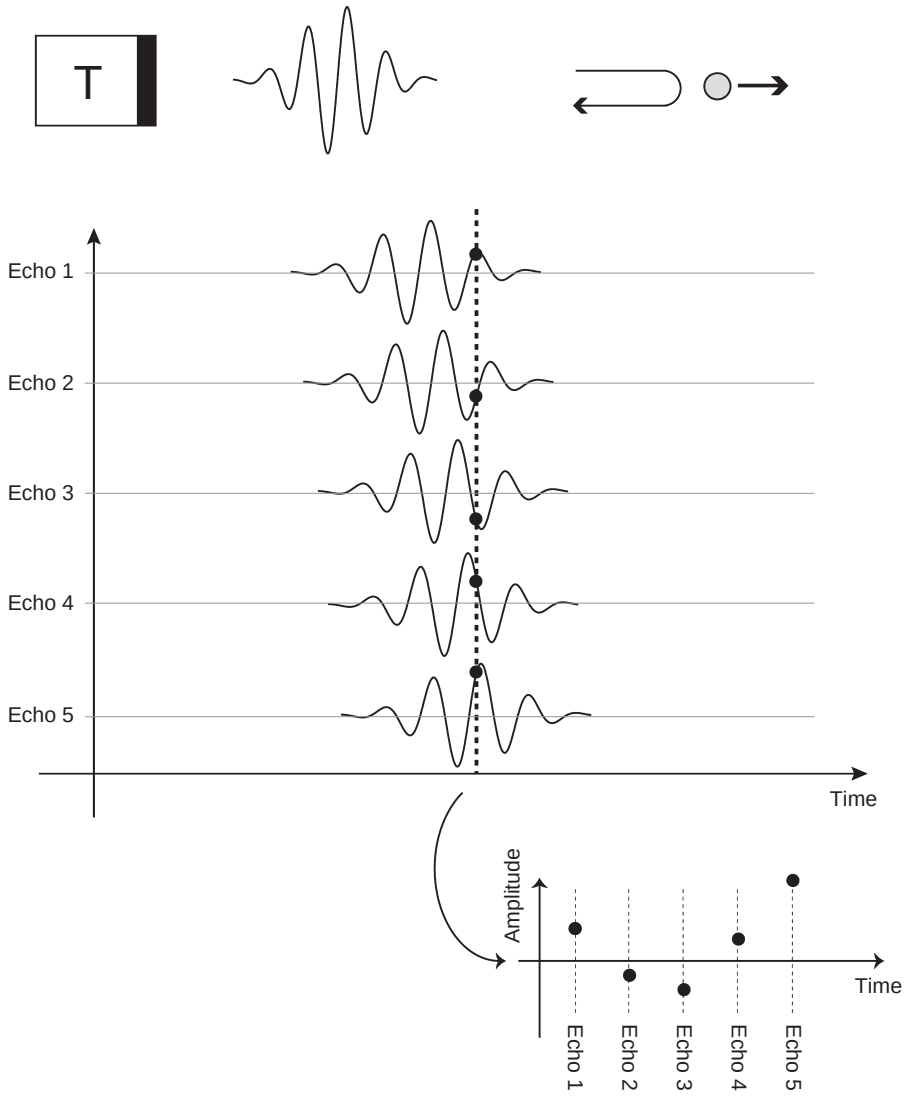


**Figure 1.14** Schematic illustration of the principle of the pulsed-wave Doppler system.

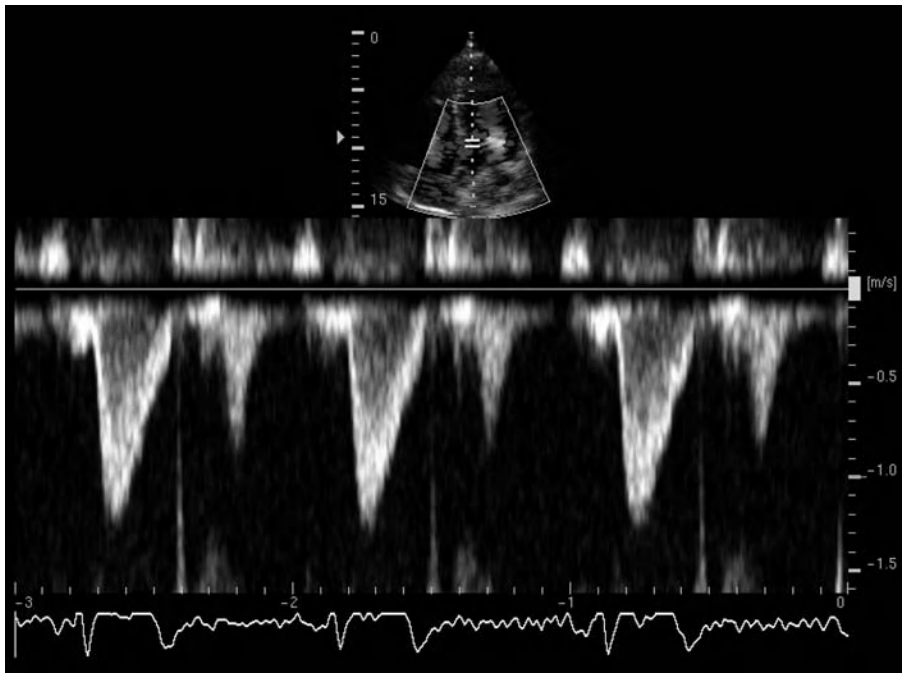


**Figure 1.15** Example of a pulsed-wave Doppler spectrogram of the left ventricular outflow tract.

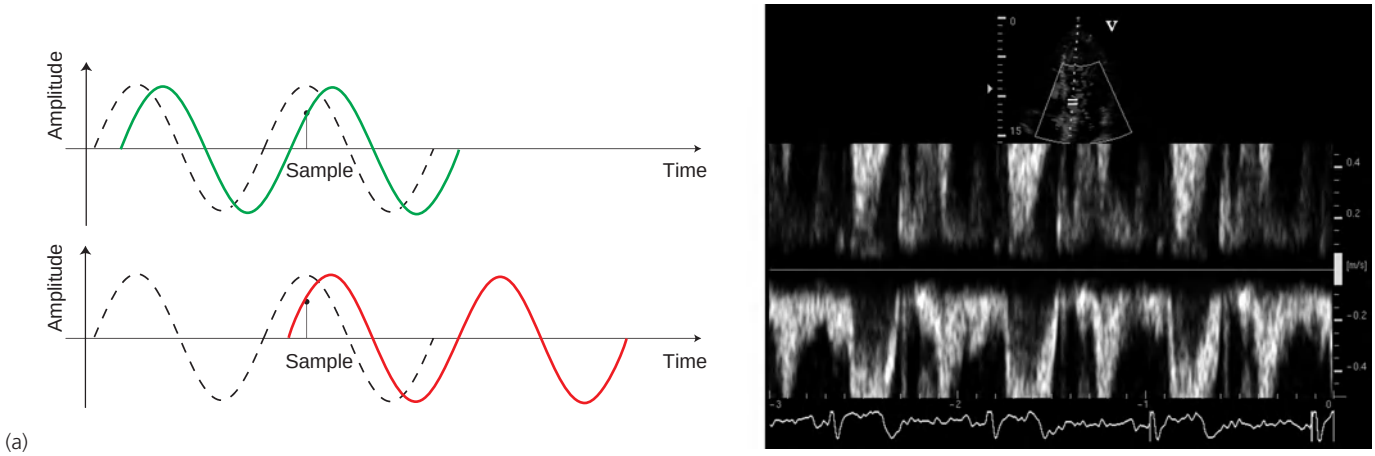


(a) (b)

**Figure 1.16** Principle of aliasing in Doppler acquisitions **(a)** and a practical example **(b)**.

of the reflecting object following the same mathematical relationship that is given in the Doppler equation. For this reason, this imaging mode is referred to as pulsed-wave (PW) *Doppler* imaging despite the fact that the Doppler phenomenon as such is not exploited.

For a PW Doppler system, velocities are displayed as a function of time in a spectrogram similar to what is done for the continuous-wave (CW) Doppler system (Fig. 1.15). However, the velocities displayed in a PW spectrogram are occurring within a specific region (the sample volume) within the 2-D image.

## Aliasing

If the velocity of the scattering object is relatively large and the shift between two subsequent acquisitions is larger than half a wavelength, the PW Doppler system cannot differentiate this high velocity (Fig. 1.16a – red signal) from a low velocity (Fig. 1.16a – green signal) because the extracted samples at the range gate are identical. This effect is known as aliasing, and a clinical example is given in Fig. 1.16b. In order to avoid aliasing, either the PRF needs to be increased or the transmit frequency decreased. The latter option is not commonly used in practice.

## Velocity resolution

A high PRF will ensure that aliasing will not occur when the maximal detectable velocity is high. However, as the ultrasound system can only measure a fixed number of velocity amplitudes, the smallest difference between two velocity amplitudes detectable by the system will decrease with

increasing PRF. As such, a compromise needs to be made between velocity resolution and maximal detectable velocity. For this reason, it is important in practice to keep the PRF as small as possible while still avoiding aliasing in order to have maximal accuracy of the velocity measurement. When the maximum velocity is high, PW Doppler will not be able to detect the highest velocity and CW Doppler will be required.

## Color flow imaging

The PW Doppler measurement can be implemented for several range gates along the image line and can be repeated for each image line in order to obtain velocity information within a 2D region of interest. However, many ultrasound pulses need to be transmitted to reconstruct a single image line (as explained above), therefore the temporal resolution of such a system is extremely poor (a maximal frame rate of a few hertz is obtained). In order to overcome this problem, color flow (CF) imaging has been developed because it allows estimation of the velocity based on only two ultrasound transmissions in the same direction. Although in theory two pulses are indeed sufficient, in practice more pulses are used to improve the quality of the measurement. Indeed, similar to PW Doppler, motion of the scattering sites between acquisitions will result in a time delay between both reflected signals if motion of the tissue is present (Fig. 1.17). By measuring this time delay between both reflections, the amount of tissue displacement between both acquisitions is obtained. The local velocity is then simply calculated as this displacement divided by the time interval between both acquisitions (= 1/PRF).

This procedure can be applied along the whole RF line in order to obtain local velocity estimates along the line (from close to the transducer to the deepest structures). Moreover, it is repeated between subsequent image lines within the 2D image. In this way, CF imaging can visualize the spatial distribution of the velocities by means of color superimposed onto the grayscale image. By convention, red represents velocities toward the transducer and blue represents velocities away from the transducer. The CF technique can also be applied to data acquired along a single image line. In that case the M-mode grayscale image can be displayed together with the estimated local velocities. This is known as color flow M-mode.

Similar to the PW Doppler technique, aliasing can occur with CF imaging and can be reduced by increasing PRF (allowing less time for motion between the two acquisitions) or reducing the transmission frequency. However, PRF settings are linked to the velocity resolution in the same way as for the PW Doppler system. An important difference with the PW Doppler technique is that the local average velocity rather than the local spectrum in velocities is measured. Peak velocity values measured with both techniques will thus be different with CF imaging giving lower peak values.

## Myocardial velocity imaging

### Doppler myocardial imaging

The exact same Doppler systems as described above can be used to measure myocardial velocities rather than blood velocities. The only difference is related to filtering: when imaging blood velocities the goal is to filter out slowly moving, strongly reflecting structures (i.e., velocities originating from the myocardium) whereas myocardial velocity imaging requires filtering structures that are moving at high velocity and that have low scattering power (i.e., the blood). On occasion, Doppler myocardial imaging displays slowly moving blood; blood aggregation also makes the structures stronger reflectors.

### Estimation of motion in 2D: speckle tracking

A limitation of the conventional Doppler techniques (CW, PW and CF) is that they only detect motion along the image

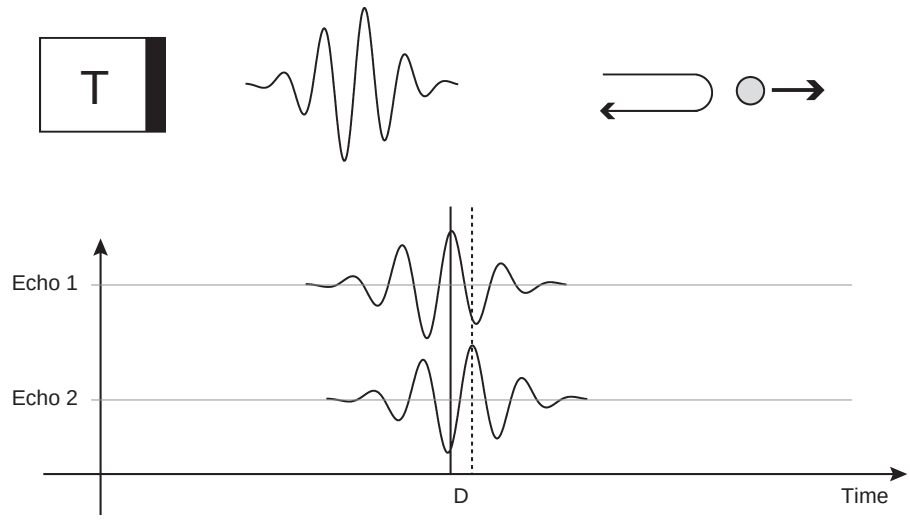


**Figure 1.17** Principle of color flow imaging.

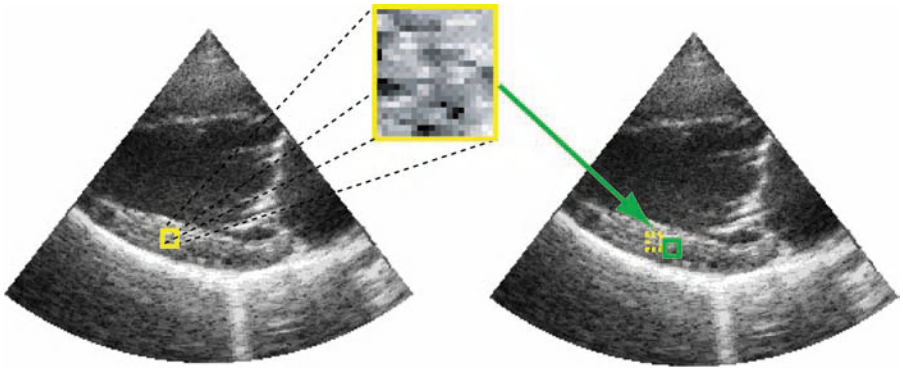

**Figure 1.18** A particular segment of soft tissue (i.e., the heart) results in a specific spatial distribution of gray values (i.e., speckle pattern) in the ultrasound image. This pattern can be used as an acoustic marker of the tissue.

line. Indeed, motion perpendicular to the image line will not be detected.

In order to overcome this limitation several methods have been proposed, but a very popular one is a technique commonly referred to as "speckle tracking." The principle of "speckle tracking" is very simple: a particular segment of tissue is displayed in the ultrasound image as a pattern of gray values (Fig. 1.18). Such a pattern, resulting from the spatial distribution of gray values, is commonly referred to as a "speckle pattern." This pattern characterizes the underlying myocardial tissue acoustically and is (assumed to be) unique for each tissue segment. It can therefore serve as a fingerprint of the tissue segment within the ultrasound image.

If the position of the tissue segment within the ultrasound image changes, we can assume that the position of its acoustic fingerprint will change accordingly. Tracking of the acoustic pattern during the cardiac cycle thus allows detection of the motion of this myocardial segment within the 2D image. The same approach can be taken when 3D datasets are available. Fundamental to this methodology is that speckle patterns are preserved between image frames. It can be shown that this is indeed the case if tissue rotation, deformation and out-of-plane motion between subsequent image frames is limited. An obvious way to achieve this is by acquiring grayscale data at a sufficiently high frame rate in order to make the time interval between subsequent image acquisitions short and as such avoid the above effects.

Although these methods were initially proposed to measure 2D myocardial velocities, they have more recently also been applied to measure 2D blood flow patterns using ultrasound contrast agents [3]. More information on ultrasound velocity estimation methodologies can be found in ref. [4].

## References

1. Suetens P. *Fundamentals of Medical Imaging.* Cambridge University Press, Cambridge, 2002; Chapter 7: Ultrasonic Imaging, pp. 145–83.
2. Szabo T. *Diagnostic Ultrasound Imaging: Inside Out*. Elsevier Academic Press, London, 2004.
3. Zheng H, Liu L, Williams L et al. Real time multicomponent echo particle image velocimetry technique for opaque flow imaging. *Appl Phys Lett* 2006;88;261915.
4. Jensen JA. *Estimation of Blood Velocities Using Ultrasound*. Cambridge University Press, Cambridge, 1996.

# 2 Laboratory Function, Instrumentation, Patient Preparation and Patient Safety

**Richard A. Humes**

Department of Pediatrics, Wayne State University; Division of Cardiology, Department of Pediatrics, Children's Hospital of Michigan, Detroit, MI, USA

## Introduction

This chapter provides a description of the working features of the pediatric echocardiography laboratory. The component parts of the laboratory exist ultimately to perform the echocardiographic procedure in a safe, effective and diagnostically accurate fashion. Attention to the details presented in this chapter will aid the clinician and laboratory manager in the development and maintenance of laboratory construction and operation. There are few references for the design and functioning of a modern pediatric echocardiography laboratory. In the 1990s, societies and organizations interested in echocardiography began to see the need for unifying the operations of echocardiography laboratories, and uniform guidelines and standards were developed [1]. The formation of a collaborative group to develop guidelines resulted in the development of standards for the performance of pediatric echocardiography [2]. These standards were developed to provide a framework that was inclusive of most pediatric echocardiography laboratories, yet rigid enough to focus the activities of these laboratories toward this common standard.

## Laboratory function

An echocardiographic laboratory may be defined as an area of physical space with an ultrasound machine designed for echocardiography that is operated by trained personnel in a safe and effective fashion. A pediatric echocardiography laboratory primarily examines pediatric (below 18 years of age) patients but may also serve patients of all ages with congenital cardiac disease as well as mothers carrying fetuses with potential cardiac disease.

*Echocardiography in Pediatric and Congenital Heart Disease: From Fetus to Adult*
Edited by Wyman W. Lai, Luc L. Mertens, Meryl S. Cohen and Tal Geva
 ISBN: 978-1-405-17401-5

### Personnel and training

Operation of ultrasound equipment to produce cardiac images is a difficult task that requires trained personnel. Most commonly this task is performed by sonographers who are trained to obtain the images, which are then interpreted by physicians. Physicians may also perform echocardiograms primarily, and physician training must include performance as well as interpretation of these studies.

It is recommended that sonographers receive instruction in institutions accredited for this training [3]. In an attempt to encourage as well as monitor this training, related ultrasound societies have promoted the development of formal training programs. The quality and amount of training found in sonographer training programs may vary greatly from region to region. Such programs may include college-, university- or community college-based training facilities, usually offering an associates degree in the field. Additionally, some for-profit schools also offer training with a certificate of completion. On-the-job training of other allied health personnel is discouraged as it usually lacks the formal technical training that characterizes established training programs. Any ultrasound school curriculum should also include didactic instruction in cardiac anatomy, physiology and pathophysiology, and ultrasound physics. Sonographer training programs should include at least 12 months of clinical training in echocardiography and an additional 6 months dedicated to pediatric echocardiography. This clinical training should include the performing of 40 echocardiograms per month, plus observation and review of an equal number during that same time period. A credential in diagnostic cardiac sonography is highly recommended for each sonographer. In pediatric echocardiography laboratories, a credential in pediatric cardiac sonography is highly desirable. The ongoing competence of the sonographer will be enhanced by continued performance of studies. A minimum of 100 studies per year is required for continued competence. Additionally, continuing education credits totaling at least 15 over 3 years is recommended, with 10 of those credits in pediatric echocardiography.

Physicians who perform and interpret pediatric echocardiograms should have formal training in pediatric cardiology

and pediatric echocardiography. Echocardiography training is a requirement of fellowship training in pediatric cardiology. As a basic requirement, cardiology fellowship training should involve the performance of at least 300–400 echocardiograms as part of the 3-year training program [4,5]. Advanced training, such as training to become a laboratory director, may involve an extra year of training and performance of an additional 700 echocardiographic studies in pediatric patients. The minimum continuing competence of the interpreting physician should also include yearly interpretation of at least 300 echocardiograms and ongoing continuing medical education credit of 15 hours of American Medical Association (AMA) category 1 credit in echocardiography over 3 years.

Ancillary laboratory personnel should also be present for the scheduling of tests and distribution of echocardiogram reports to referring physicians. The number and training of these personnel may vary with the size and study volume of the laboratory. Computerized echocardiography management systems can be extremely useful in managing the workflow and reporting in any echocardiography laboratory. Information technologists trained to manage digital echocardiography systems may also be required, particularly in large laboratories.

Transesophageal and fetal echocardiographic studies may also be done in the pediatric laboratory and are an important part of the pediatric echocardiography laboratory. Training, experience and ongoing quality assurance should include these efforts within the framework of laboratory operations as appropriate to the particular laboratory setting. Transesophageal echocardiography is most frequently performed in the operating room setting in most pediatric cardiology practices. The most common use of transesophageal echocardiography in pediatric practice is in the evaluation of the pre- and postoperative patient undergoing repair of congenital heart disease. In these cases, general anesthesia is used and anesthetic concerns are managed by the anesthesiology team. A smaller proportion of transesophageal examinations are done in an outpatient arena. In this setting, a proper facility and protocol for the conduct of these studies, as well as arrangements for proper sedation and postprocedural monitoring need to be in place. Physician training in transesophageal probe insertion should include 25–30 supervised insertions, and image capture and probe manipulation should include 30–50 supervised training examinations before establishing competency. It is suggested that ongoing competency be maintained with continued performance of at least 50 studies per year in this area [6]. Care and training in probe insertion must be emphasized. The smaller diameter of the esophagus encountered in pediatric patients makes experience a critical consideration [7]. The role of the sonographer in transesophageal studies is highly variable among different laboratory settings. In some, the sonographer is actively involved in probe manipulation and image acquisition, just as seen in transthoracic examinations. When the sonographer is involved at this level, the training and ongoing competence issues mirror those of physicians.

Fetal echocardiography also requires a developed skill set that is different from that utilized in standard pediatric and congenital echocardiography. Whereas transthoracic and transesophageal imaging requires the operator to generate many "standard" views in established imaging planes, fetal echocardiographic images are frequently nonstandard and obtained at the whim of fetal position. The ability to recognize and interpret these nonstandard and off-plane images places a premium on the experience and training of the operator in pediatric echocardiography. Additional knowledge about maternal–fetal physiology must supplement the understanding of congenital heart disease and echocardiographic imaging. Fetal echocardiographic training may take place in several settings depending upon the expertise available and the volume of studies done. A shared experience in obstetrical imaging or maternal fetal medicine offers a possible route for intensive training in obstetrical imaging techniques [8,9].

## Working environment

The echocardiographic laboratory should have adequate space to perform pediatric echocardiograms. A recommendation of 150 square feet (~14 $m^2$) has been outlined in previous position papers [1]. Privacy of patients must be maintained in this environment, and a sink and antiseptic soap must be available for proper hand washing. Space must be available for the data evaluation and interpretation of the studies, a process that may interface with the laboratory reporting system. Space must also be available for the storage of records and supplies. A system must be developed within the laboratory for record keeping and archival storage of the echocardiographic data and images in accordance with applicable state or federal guidelines and the facility's policies for medical record storage. Emergency resuscitation equipment should be available, recognizing the potentially serious nature of the diseases frequently seen in pediatric cardiology.

## Protocols

Each laboratory should develop a written protocol for the laboratory operation. These protocols should include the details and sequence of performing the transthoracic, transesophageal and fetal examinations. The protocols may be specific and unique to the individual laboratory. However, common standard imaging views and reporting formats should be present in all laboratory settings. Protocols should also be in place for routine laboratory functions such as ultrasound machine maintenance, laboratory safety, quality assurance and sedation.

## Quality assurance

The efficient and well-run pediatric echocardiography laboratory should develop a program for continuing assurance

and evaluation of laboratory quality. Quality assurance programs may take many forms and have been identified as an essential part of an accredited laboratory. A necessary part of any quality assurance program is the simple and ongoing documentation of laboratory activities in concert with periodic review of these data by all laboratory personnel. Items that are suggested for quality assurance review include equipment maintenance, procedure volumes, continuing medical education credits, ongoing peer review of study performance and interpretation, and correlation and confirmation of echocardiogram results by comparison with other related procedures such as surgery, cardiac catheterization or magnetic resonance imaging as appropriate [2].

Quality assurance efforts can be time consuming and laborious, particularly during the development phase. Efforts should be made to keep the data collection meaningful to ongoing laboratory operations and quality, and manageable such that excessive time is not spent in collecting quality data at the expense of regular laboratory operations. This can seem like a contrary process at its inception. The early efforts at laboratory quality assurance submitted to the Intersocietal Commission for the Accreditation of Echocardiography Laboratories (ICAEL) demonstrated a frequent temptation to be overinclusive in the first quality assurance effort. The extra work that this brings to the day-to-day function of the laboratory can seem overwhelming. The items reviewed in any quality assurance effort should focus on the collection of a stratified sample of the laboratory efforts. For example, the correlation of Doppler estimation of aortic stenosis gradients may be compared with catheter-derived values from the same patient over a period of time. When the laboratory is satisfied that enough data have been collected to assure good correlation or to rectify errors, another point of anatomy may be reviewed and compared. Periodically, correlations done previously may be revisited to update their current accuracy. Similarly, reviewing small, but representative samples of sonographers' and physicians' work for peer review may prove meaningful in identifying consistent errors or omissions, while not overburdening the individuals concerned.

It is extremely important for any quality assurance effort that the collected data are written down and tabulated in a concise format that is then presented regularly to the laboratory group for review. This should happen in an informational format that is intended to educate, not punish, individuals for their efforts.

### Accreditation

Echocardiography laboratory accreditation was established in 1998 by the Intersocietal Commission for the Accreditation of Echocardiography Laboratories (ICAEL). The original participating societies were the American Society of Echocardiography, the American College of Cardiology and the Society of Pediatric Echocardiography. This was intended to be a voluntary educational process for establishing uniformity in laboratory practices by the participating organizations. With the guidance of the societies and establishment of practice guidelines, standards documents were constructed to outline basic echocardiography laboratory practice. Many of these standards did not exist prior to their development by ICAEL. Third-party insurance carriers across the country have been examining the utility of laboratory accreditation practices in enhancing the uniform quality of each echocardiography laboratory and have begun writing accreditation requirements into their own individual payment guidelines. This trend is still evolving and subject to the ever-changing climate in medical payment policy.

## Instrumentation

### Echocardiography equipment

The echocardiographic machine must have the capabilities required to perform the standard pediatric echocardiogram (Chapter 4). These capabilities must include two-dimensional imaging, M-mode, pulsed-wave and continuous-wave Doppler, and color flow Doppler mapping. Electrocardiogram (ECG) gating and a color monitor are also required. A hard-copy paper printout capability is often desirable, but not required, particularly in the current age of digital storage and the electronic medical record. The system must also have the ability to store moving images and to make measurements of cardiac structures and Doppler velocities. Tissue Doppler analysis and three-dimensional probes and software packages are suggested but not required for the diagnosis of congenital heart disease.

An echocardiographic system used in the pediatric echocardiography laboratory must be capable of imaging a wide variety of patient sizes with different depths of penetration. This is generally accomplished by using multiple transducers with different transmitted frequencies (Chapter 1). The available transmitted frequencies of these transducer probes should range from 12 to 2.5 MHz; this is usually achieved with three separate probes. The ultrasound system should also contain a dedicated continuous-wave Doppler probe.

In addition to frequency differences, these probes commonly have physical and functional differences that are important to echocardiography and pediatric patients. Cardiology transducer probes are designed to fit between rib spaces with an overall smaller "footprint". This design differs significantly from probes used for abdominal or obstetrical ultrasound, where larger linear or curvilinear probes are preferred. The display of the cardiology transducer is also different than that produced by a linear probe as it displays the image within an 80–90 degree "sector" shown as a pie-shaped wedge on the viewing screen. Transducers with a high frequency (12–8 MHz) have higher resolution but less depth of penetration than low-frequency transducers. The beam focuses at a very short (4–5-cm) depth. These probes

are appropriate for use in the neonate or small infant but have limited use beyond this age group. By comparison, low-frequency transducers (2–4 MHz) have a much greater depth of penetration, longer focal length (12–16 cm), larger footprint but lower resolution and are more suitable for larger children and adults. This leaves the need for a mid-range frequency transducer (4–6 MHz) for examination of the toddler or smaller child, one with technical capabilities in between the other probes. Improvement in transducer technology has broadened the range of these transducers by allowing variable rather than fixed transmitted frequencies. These technological advancements have allowed improved imaging over a broad range of patient sizes, without having to frequently change transducers. Ideally these improvements will continue until a single transducer is acceptable for all patients. However, the fundamental properties of ultrasound physics currently constrain this effort, and the operator should be prepared to change transducers for different areas of interest in some patients.

Not all ultrasound machines may be appropriate for cardiac imaging. The motion of the heart requires the use of inherently greater frame rates, which are additionally enhanced by beam focusing. Static abdominal imaging rarely requires these same frame rates. Cardiac color flow Doppler is also processed differently because of the cardiac motion, with smaller packet sizes, more able to handle the inherently higher velocity flow signals found in both normal and, especially, pathological conditions. For digital acquisition, the cardiac ultrasound machine requires longer captured loops than is required for static abdominal imaging. A cardiac ultrasound machine requires ECG gating for analysis of cardiac event timing, which can also serve as a methodology for the capturing and timing of digital images. Echocardiography, particularly in pediatrics, requires a machine that is mobile and may be used at the bedside so as to provide patient care at the point of service.

The motion of the heart in cardiac imaging, as well as the type of clinical information that is desired, has driven the development of newer technologies that do not currently have wide application in non-cardiac ultrasound, including real-time three-dimensional imaging. Moreover, novel techniques such as tissue Doppler, speckle tracking and myocardial strain determination are examples of applications that have been derived to answer specific questions of cardiac function.

Specialized imaging may also occur within the pediatric echocardiography laboratory, particularly one that is hospital- or institution-based. These special studies include transesophageal and fetal imaging. Both of these techniques require attention to equipment and personnel. Transesophageal probes are currently available for small pediatric patients as well as larger children and adults. In order to obtain a full and complete transesophageal study, it is desirable to have a transesophageal probe for which the imaging plane can be electronically steered in an arc of 180° so that areas of interest can be viewed from a multitude of imaging planes. Older biplane transesophageal echocardiography (TEE) probes, which allow two fixed, 90° orthogonal planes, are still used for very small infants but do not have the same range of images.

## System settings

Echocardiograms done in children generally are more conducive to good image quality than images seen in larger patients and adults. Although not all children will produce excellent images just by virtue of their being smaller, the imaging quality problems are far fewer than seen in large adult patients. Despite the relative ease of imaging, care should be taken to adjust the ultrasound machine to optimize the image. The degree to which the operator can currently adjust the image has changed over the years because of technical improvements. Current machines control much of the image and signal processing. Differences exist between manufacturers with respect to how much operator control is allowed. Indeed, several major manufacturers have developed a single button to adjust and optimize images. Manufacturers may identify control functions by names that differ from other manufacturers. This may confound the operator when working with equipment from a variety of vendors. There remain some simple adjustments that can help to optimize image acquisition, and each operator should be familiar with the technical aspects of the major machine adjustment controls.

The choice of transducer, as mentioned above, is the first and perhaps most important decision for enhancing image quality. Choosing a low-frequency transducer (2.5–3 MHz) for a small infant will result in a grainy picture, lacking in detail. A high-frequency transducer (7–10 MHz) will not provide enough ultrasound energy at greater depths to enable proper imaging of older children or adults due to attenuation of the ultrasound signal. The initial selection of transducer at the onset of the examination should be based on the usual practice determined by the patient's age and size. However, the operator should be ready to change transducers as the situation dictates. For example, excellent parasternal images may be obtained from a mid-range transducer in a toddler, but subxiphoid images require greater depth of penetration, which may be accomplished by switching to a lower frequency probe. Conversely, a larger child or adult may be best imaged with a low-frequency transducer, but certain areas of interest in the near field may be better imaged with a high-frequency probe. The trained operator doing a pediatric examination should expect to be continually changing systems settings or transducers to optimize the image as the situation dictates.

System presets should be initially adjusted in a standard, laboratory-specific manner to produce a uniform appearance of studies within a given laboratory. Most manufacturers have developed "pediatric" settings that optimize the image

for smaller patients. These preset functions most often adjust the preprocessing settings. Although these are certainly subjective in the ultimate image quality, they usually represent very useful starting points that have been developed by multiple pediatric users for each manufacturer's machine. Beginning an examination using presets not designed for the particular imaging can produce suboptimal images and is sometimes overlooked as a source of imaging difficulties. It is particularly important to choose appropriate presets for color flow Doppler maps. Color flow imaging preferences may be very subjective for different laboratories. Doppler color flow maps in cardiology differ significantly from obstetrical or abdominal imaging, with higher wall filters and lower or absent persistence.

The image depth should be adjusted so that the heart or area of interest fills the viewing screen, thus minimizing the depth of interest. Controlling this feature will minimize the power that is needed, improve the frame rate of both imaging and Doppler signals, and focus the observer on the area of interest. Controls that enlarge or "zoom in" on a particular area of interest are vital when looking at both normal and pathological structures.

The transmit power of the system adjusts the amplitude of the transmitted ultrasound wave. Many terms are used to refer to transmit power, such as acoustic power, output power, transmit gain and power gain, among others. The image is produced by the returning echoes, which are related to this power or amplitude squared, so this setting is adjusted to allow the ultrasound to penetrate the tissue to the maximum depth. The receiver gain setting (or 2D gain) is used to adjust the strength of the returning echoes and may be controlled in two ways. Overall receiver gain may be changed to enhance the brightness of the returning signals. Additionally, time-gain compensation allows the operator to adjust the returning gain by virtue of the time that it took for the returning signal to reach the transducer [10]. This effectively changes the gain at various depths of interest. This function is controlled on most machines by a set of horizontal slide bars, which are usually set to minimize the gain in the near field (where returning signals are strongest and can overwhelm the image) and enhance the weaker returning signals from greater depth. In order to discern structures of different acoustic impedance, the contrast image must be adjusted. What we perceive as contrast is usually changed by adjusting the compression or dynamic range. This is the range (in decibels) between the weakest and strongest returning signals. Controlling the dynamic range can improve the image that is received by the monitor [11]. Newer echocardiogram machines also allow the operator to adjust the beam focus dynamically. Concentrating the beam width at a certain depth of interest will help to enhance the returning echoes from that specific level and can be particularly effective in fetal imaging, where the target image of the fetal heart is small and at a given short depth range.

In color flow Doppler mapping, the sector must be adjusted to the area of interest. If the sector is too large, the frame rate decreases significantly resulting in an uninterpretable image. Adjustment to assure that the area of interest is seen but the frame rate is acceptable is a part of echocardiographic training.

### Storage format and reporting

Echocardiographic storage must occur in a format that allows playback of moving images. In echocardiography it is unacceptable to store only static images on media such as film or paper. Acceptable media include videotape or digital formats. The evolution of storage media has paralleled the development of modern computer systems. It is clear that digital image storage is quickly becoming the medium of choice for most institutions Confidentiality of data should be maintained in any system. For videotape, this means storage in an area without patient access. For digital systems, a password should be required to access the images on the computer system. The length of storage of pediatric imaging data should comply with institutional protocols as well as applicable state and federal guidelines [2]. Manufacturers of ultrasound and other medical imaging equipment have attempted to unify digital storage formats within the "Digital Imaging and Communications in Medicine," or DICOM, standard. This combined effort of vendors and medical users has produced an evolving standard that has been incorporated into most current medical imaging equipment so that digital output from multiple systems may be interpreted and incorporated into large databases or hospital electronic medical records.

The echocardiogram report should be in a clear and consistent format for the laboratory. Information including patient identification, operator, date of study, date of birth, height and weight, referring physician and the indication for the examination should be clearly noted on a typewritten report that contains a physician's signature. Report formats may vary between laboratories, but should not vary within a laboratory. Required fields for a complete echocardioraphic examination have been outlined in published recommendations and standards and are detailed in Chapter 4 [2,14].

## Patient preparation

### Environmental issues

An adequate amount of time should be allocated for each study according to the procedure type. The performance time of an uncomplicated, complete (imaging and Doppler) pediatric transthoracic examination is estimated to be approximately 45 to 60 minutes (from patient encounter to departure) [1,2]. An additional 15 to 30 minutes may be required for complicated studies. The performance time of an uncomplicated, limited study is 15 to 45 minutes. All procedures should be explained to the patient and/or parents or

guardian prior to the onset of the study. The patient should be placed in a reclining position in a comfortable, ambient environment. Appropriate pillows and blankets should be utilized for patient comfort and privacy. Adjustable beds are available for echocardiography with ergonomically engineered mobility and cut-outs that can help to facilitate the examination. A darkened room should be used for all echocardiographic exams. Ideally, the room lighting should be made adjustable with a dimmer switch. The sonographic gel should be warmed to body temperature prior to the start of the examination. It is recommended that appropriate distractions be provided in echocardiographic laboratories performing echocardiographic studies on preschool children. These may include toys, games, television or movies. Ideally, each study is performed in a separate room to limit distractions and noise from other studies or patients as well as to ensure patient privacy. A television hooked to a cable TV provider or a DVD/VCR can provide entertainment for the children during the study. Small treats such as lollipops or distraction with bubble blowing or stuffed animals have also been very successful in calming frightened toddlers. With adjustment of the examination bed, a parent can often lie back with the infant in her or his arms, providing security and comfort (Fig. 2.1). The dedicated use of distracters such as these can considerably reduce the need for, and inherent cost of, sedation and sedation personnel. In all cases, an appropriate parent or guardian should accompany children during the echocardiographic study except where privacy issues supersede.

## Sedation

Most pediatric echocardiography laboratories offer patient sedation to obtain an adequate examination. Sedation is generally required in the age range 1 month to 3 years. Written policies should exist for the use of conscious sedation in children including, but not limited to, the type of sedatives, appropriate dosing for age and size, and proper monitoring of children during and after the examination [12,13]. Since the publication of the sedation guidelines, there have been many changes in pediatric sedation practice across the United States. Each hospital or facility must follow its own guidelines regarding sedation.

There are many acceptable protocols that can produce the necessary sedative effect on patients for this procedure. Echocardiography is generally not a painful procedure. Sedation is most frequently required to calm a frightened infant or toddler. Many laboratories have developed different sedation protocols depending upon experience and comfort with different agents. Chloral hydrate given orally in a dose of 50–100 mg/kg (maximum 500 mg) produces somnolence in most toddlers. The bitter taste, even in syrup, can make delivery of this drug difficult in the uncooperative patient. In addition, some children have a reaction to chloral hydrate and become combative. There are alternative sedatives including midazolam. Intranasal administration of midazolam (in the intravenous formulation) in a dose of 0.4 mg/kg (maximum dose 4 mg) administered as half of the dose in each nostril appears to be quite effective [15]. This short-acting drug may be delivered rapidly, is never rejected and acts quickly to produce anxiolysis. It has not been associated with oversedation at these doses and children recover quickly, requiring little post-sedation monitoring. A second dose, often at half the original rate, may be administered as needed if the sedation time is not long enough or if the first dose is not as effective as needed. Other institutions have turned to cardiac anesthesia to help in the management of

**Figure 2.1** During her echocardiogram a toddler is perfectly calm without sedation in her mother's lap with a sucker and cartoons.

echocardiography sedation. Face-mask anesthesia, usually requiring no intravenous line, can be used, with cardiac anesthesiologists managing the patient through the entire study. This is a safe and effective method and the child is only anesthetized for the time of the study. The post-sedation recovery time can be significantly shortened using this method.

## Patient safety

### Protocols

Organization of the laboratory should include protocols to ensure patient safety, including infection control and machine and transducer cleaning. Each laboratory should have a written procedure in place for handling acute medical emergencies in children. Pediatric dosing information and/or appropriate pediatric doses of emergency medications must be available. A fully equipped cardiac arrest cart (crash cart) should be on the premises in any echocardiography laboratory. Appropriately sized oxygen masks for pediatric patients and oxygen delivery systems should also be available.

## Conclusion

In summary, the organization of the pediatric echocardiography laboratory offers a unique set of challenges because of the tremendous variety in patient sizes and disease processes. The laboratory functions should follow established guidelines to ensure successful operation. Ongoing issues of personnel qualifications, training, continuing education and quality assurance outlined in this chapter may form a basis for this organization.

## References


1. Kisslo J, Byrd BF, Geiser EA et al. Recommendations for continuous quality improvement in echocardiography. *J Am Soc Echocardiog* 1995;8:S1–S28.
2. ICAEL Standards for Pediatric Transthoracic Echocardiography Testing Part 1. Pediatric Echocardiography Laboratory Operations. Columbia, MD: Intersocietal Commission for the Accreditation of Echocardiography Laboratories, 2007 (http://www.intersocietal.org/icael/pdfs/standards/Pediatric_Org.pdf).
3. Ehler D, Carney DK, Dempsey AL et al. Guidelines for cardiac sonographer education: recommendations of the American Society of Echocardiography Sonographer Training and Education Committee. *J Am Soc Echocardiog* 2001;14:77–84.
4. Meyer R, Hagler D, Huhta J et al. Guidelines for physician training in pediatric echocardiography: recommendations of the Society of Pediatric Echocardiography committee on physician training. *Am J Cardiol* 1987;60:164–5.
5. Silverman NH, Sklansky MS, Weinberg PM et al. ACC/AHA/AAP Recommendations for Training in Pediatric Cardiology, Task Force 2: Pediatric Training Guidelines for Noninvasive Cardiac Imaging endorsed by the American Society of Echocardiography and the Society of Pediatric Echocardiography. *J Am Coll Cardiol* 2005;45:1384–8.
6. Fyfe DA, Ritter SB, Snider AR et al. Guidelines for transesophageal echocardiography in children. *J Am Soc Echocardiog* 1992;5:640–4.
7. Fleischer DE, Goldstein SA. Transesophageal echocardiography: What the gastroenterologist thinks the cardiologist should know about endoscopy. *J Am Soc Echocardiog* 1990;3:428–34.
8. Rychik J, Ayres N, Cuneo B et al. American Society of Echocardiography Guidelines and Standards for Performance of the Fetal Echocardiogram. *J Am Soc Echocardiog* 2004;17:803–10.
9. Meyer R, Hagler D, Huhta J et al. Guidelines for physician training in fetal echocardiography: Recommendations of the Society of Pediatric Echocardiography Committee on Physician Training. *J Am Soc Echocardiog* 1990;3:1–3.
10. Vermilion RP. Technology and instrumentation. In: Snider AR, Serwer GA, Ritter SB (eds) *Echocardiography in Pediatric Heart Disease*, 2nd edn. St Louis: Mosby-Year Book, 1997;1–21.
11. Geva T. Echocardiography and Doppler ultrasound. In: Garson A, Bricker JT, Fisher DJ, Neish SR (eds) *The Science and Practice of Pediatric Cardiology*, 2nd edn. Baltimore: Williams & Wilkins, 1998;845–74.
12. Lai WW, Geva T, Shirali GS et al. Guidelines and Standards for Performance of a Pediatric Echocardiogram: A report from the Task Force of the Pediatric Council of the American Society of Echocardiography *J Am Soc Echocardiog* 2006;19:1413–30.
13. American Academy of Pediatrics: Committee on Drugs. Guidelines for monitoring and management of pediatric patients during and after sedation for diagnosis and therapeutic procedures. *Pediatrics* 1992;89:1110–15.
14. American Academy of Pediatrics: Committee on Drugs. Guidelines for monitoring and management of pediatric patients during and after sedation for diagnosis and therapeutic procedures: addendum. *Pediatrics* 2002;110:836–8.
15. Kauffman RE, Morrow WR, Anderson MR et al. Intranasal absorption of midazolam (abstract). *Clin Pharmacol Ther* 1995;209.

# 3 Nomenclature and Segmental Approach to Congenital Heart Disease

**Tal Geva**

Harvard Medical School; Division of Noninvasive Cardiac Imaging, Department of Cardiology, Children's Hospital Boston, Boston, MA, USA

Before the advent of surgical treatment for patients with congenital heart disease (CHD), physicians generally regarded these conditions as hopeless. For example, in *Holt's Diseases of Infancy and Childhood: A Textbook for the use of Students and Practitioners*, which was published in 1933, the chapter on congenital anomalies of the heart concluded with the following paragraph on treatment: "This is unsatisfactory. As a rule, nothing can be done to treat patients symptomatically; in some instances digitalis may be of help. Quiet is essential in those with dyspnea" [1]. In 1936, Dr Maude Abbott, who worked at McGill University, published the first systematic classification of CHD based on a study of 1000 heart specimens [2]. Two years later in 1938, Dr Robert Gross performed the first successful cardiovascular operation – ligation of a patent ductus arteriosus in a 7.5-year-old girl [3]. This was followed by Blalock and Taussig's successful establishment of a systemic-to-pulmonary artery shunt to alleviate cyanosis in tetralogy of Fallot [4]; resection of aortic coarctation by Gross and Hufnagel and by Crafoord and Nylin; and the first open heart surgery to close an atrial septal defect by Gibbon in 1953 [5]. These and other landmark advances in the treatment of patients with CHD during the 1940s and 1950s inspired interest in the study of CHD morphology and stimulated the development of several taxonomies for its classification.

The highly variable spectrum of congenital anomalies of the cardiovascular system presents a challenge for those who care for these patients. A comprehensive classification scheme of CHD based on clear and internally consistent nomenclature is, therefore, essential for diagnosis, management, research, and education. The goals of any CHD taxonomy are:
**1** to provide a consistent nomenclature based on anatomic-morphologic features of the cardiac chambers;
**2** to devise a systematic analytical approach that produces a specific and unique set of diagnoses for each cardiac malformation;
**3** to be applicable to all forms of CHD, including cardiac malformations that have not yet been described;
**4** to promote understanding and exchange of data among clinicians and researchers.

This chapter describes a segment-by-segment approach, known as the *segmental approach to congenital heart disease*, to the classification and nomenclature of congenital anomalies of the heart and great vessels. Van Praagh and his colleagues originally proposed this classification system in the 1960s and early 1970s [6–8] and have since refined it [9,10]. Importantly, notable modifications and alternative taxonomies have been proposed by pathologists, geneticists, embryologists, cardiologists, cardiovascular surgeons, radiologists and others [10–23]. In particular, many practitioners favor the nomenclature advocated by Anderson and colleagues [24]. However, despite numerous efforts by individuals and professional groups to advocate the use of a single classification system, none has achieved uniform acceptance. A potentially more successful approach, currently being developed, is to acknowledge the major taxonomies and to create a system that cross-links individual malformations and therapeutic procedures to common codes [25,26]. Although this chapter emphasizes the taxonomy advocated by Van Praagh et al., readers should also familiarize themselves with Anderson's nomenclature and, most importantly, maintain a clear and consistent method of communication within their institutions.

## Segmental analysis of congenital heart disease

Analysis of CHD is based upon an understanding of the developmental, morphologic and segmental anatomy of the heart and great vessels. The cardiac segments are the anatomic and embryologic "building blocks" that form the mammalian heart (Fig. 3.1). The three main segments are: (i) veins and atria; (ii) ventricles; and (iii) great arteries. There are two connecting segments between the main segments: (i) the atrioventricular (AV) canal; and (ii) the conus or infundibulum. The AV canal consists of the AV valves (the

*Echocardiography in Pediatric and Congenital Heart Disease: From Fetus to Adult*
Edited by Wyman W. Lai, Luc L. Mertens, Meryl S. Cohen and Tal Geva
 ISBN: 978-1-405-17401-5

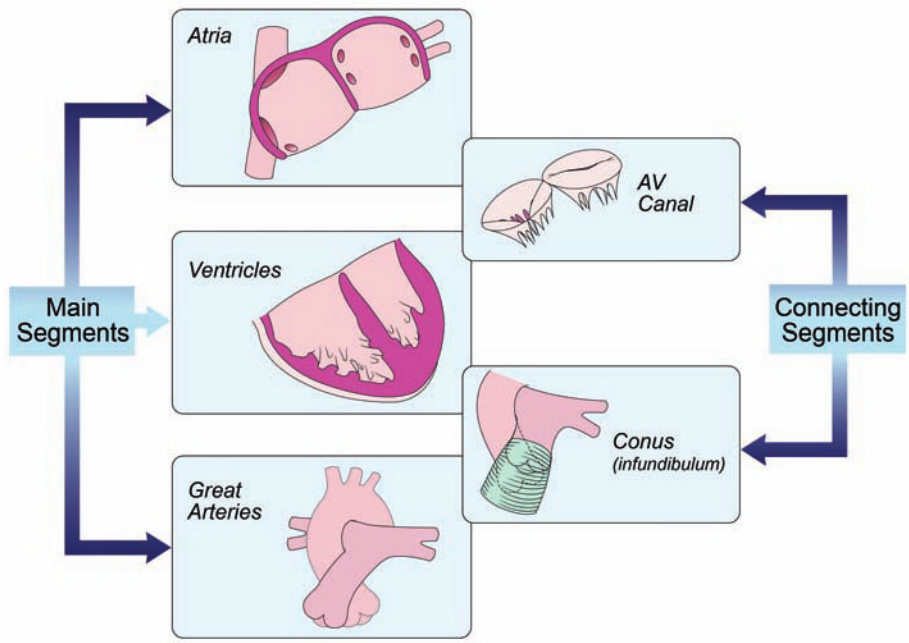


**Figure 3.1** Anatomic segments of the heart. The three main cardiac segments are the atria, ventricles and great arteries. There are two connecting segments: the atrioventricular (AV) canal (including the AV valves, the interatrial and interventricular components of the AV canal septum), and the conus (or infundibulum). The connecting segments may be viewed as multidirectional joints between the main cardiac segments allowing infinite possibilities of atrioventricular and ventriculo-arterial alignments. In the segmental approach to congenital heart disease it is essential that each cardiac segment is analyzed separately and independent of adjacent segments.

mitral and tricuspid valves in normally formed hearts) and the atrioventricular septum. The infundibulum (or conus) is the connecting segment between the ventricles and the great arteries. In normally formed hearts, the infundibulum consists of a circumferential subpulmonary myocardium shaped like a prolate cone (as viewed externally; hence conus) or a funnel (as viewed internally; hence infundibulum). The normal subpulmonary infundibular myocardium separates the pulmonary and tricuspid valves. The normal subaortic infundibulum consists only of a conal septum (the myocardium that separates the left and right ventricular outflow tracts). The subaortic infundibular free wall is normally absent, resulting in fibrous continuity between the left and noncoronary aortic valve leaflets and the anterior leaflet of the mitral valve.

The fundamental principle of segmental analysis of CHD is to analyze each component of the heart in a sequential step-by-step fashion. First, the anatomic pattern (i.e., situs) of the abdominal and thoracic organs is defined and the position of the heart is described. Then, each of the main cardiac segments is examined, described and assigned a designation based upon its unique morphologic features, independent of neighboring segments (Fig. 3.2). For example, each ventricle is defined according to its intrinsic morphology and not by the entering atrioventricular valve or the exiting great artery. Analysis of the main cardiac chambers – veins and atria, ventricles and great arteries – involves two steps. First, the *identity* of the chamber or great vessel is determined based upon its morphology and intrinsic myocardial architecture. Second, the *situs* of the cardiac segment is determined. In the case of the atria, their situs may be solitus (normal), inversus (mirror image of solitus) or ambiguous (indeterminate). Once the three main cardiac segments are characterized according to their unique morphologic features, the connecting segments are analyzed and defined. Finally, a complete set of diagnoses is formulated by combining the five cardiac segments and all associated cardiovascular anomalies as described in the following section.

## Step-by-step segmental analysis

The following 10 steps are taken as part of the segmental analysis of CHD:

**1. Thoraco-abdominal situs** (Fig. 3.3). Before analyzing intracardiac anatomy, the situs of the thoracic and abdominal organs is determined to provide an "anatomic framework" for further analysis. Normally, the visceral organs are "lateralized." In other words, the pattern of anatomic organization of the abdominal organs, tracheo-bronchial tree and lungs is asymmetric. In *situs solitus* (normal arrangement), the spleen, pancreas, stomach and sigmoid colon are left-sided, and the liver, cecum and appendix are right-sided. The left lung comprises two lobes and the left mainstem bronchus is longer, more horizontal and hyparterial (courses inferior to the left pulmonary artery). The right lung comprises three lobes and the right mainstem bronchus is shorter and eparterial (courses posterior to the right pulmonary artery). In visceral *situs inversus*, the spatial organization of the abdominal and thoracic organs is the mirror image of normal. In other words, there is complete left–right reversal of the position and orientation of the organs. It is worth noting that in visceral situs inversus the pattern of anatomic organization is asymmetric similar to situs solitus but in mirror image. In

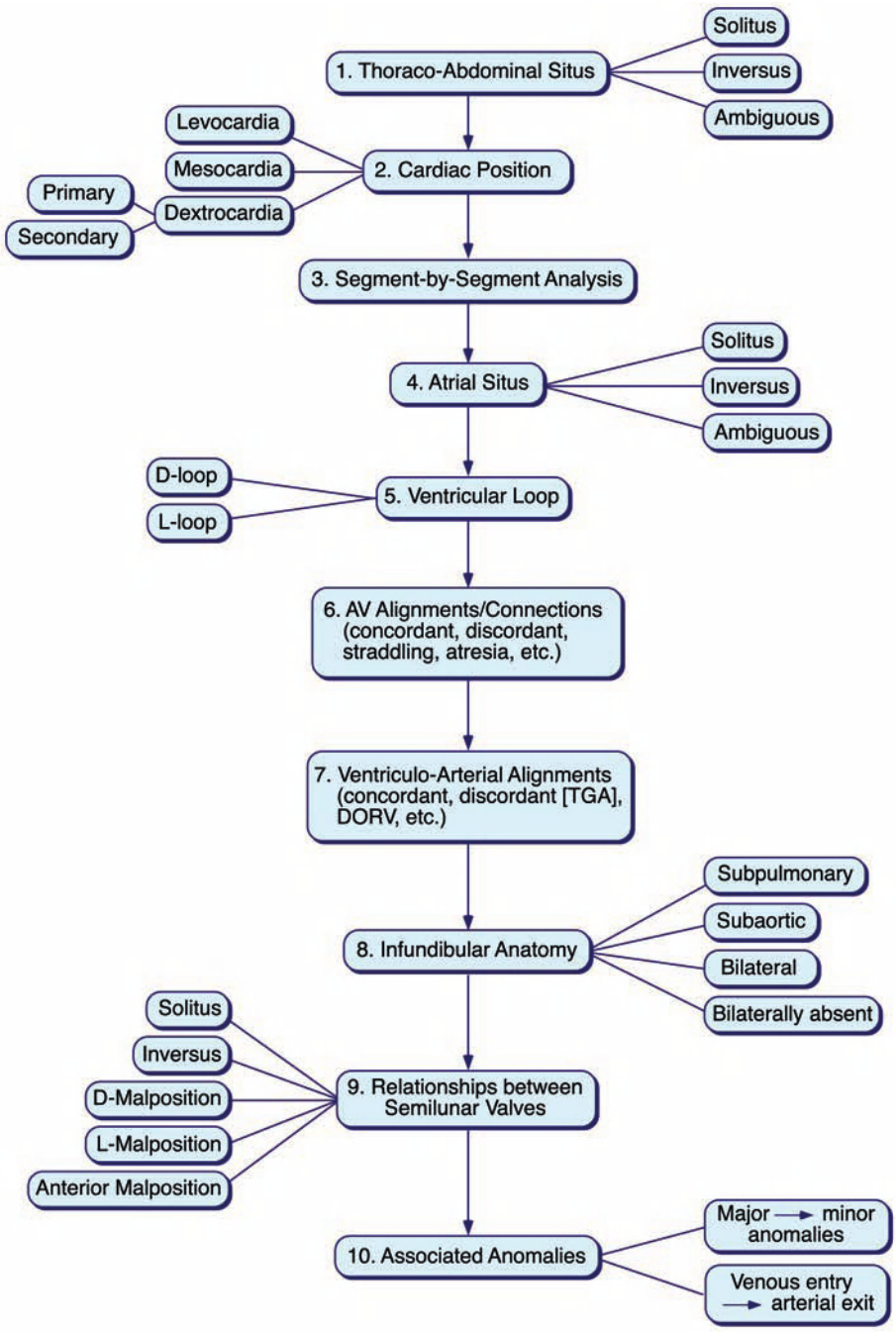


**Figure 3.2** The 10 steps of the segmental approach to diagnosis of congenital heart disease. Before analyzing intracardiac anatomy, the situs of the thoracic and abdominal organs and cardiac position within the thorax must be determined to provide an "anatomic framework" for further analysis (steps 1 and 2). When describing cardiac anatomy, the following principles apply. (i) Each cardiac segment must be described in terms of its own unique anatomic features and not according to those of adjacent segments (steps 3–9). For example, the left ventricle is determined according to its internal morphology, particularly its smooth superior septal surface, and not according to the AV valve that connects it with the atria (usually it is the mitral valve but it may be both mitral and tricuspid valves, as in double-inlet left ventricle, or it may be a common AV valve or even a tricuspid valve). (ii) For each cardiac segment, both its situs and connections must be described specifically and not inferred from each other. (iii) Associated malformations (step 10) may be described in order of their hemodynamic importance or in an anatomic order (progressing from the venous entry to the arterial exit of the heart). DORV, double-outlet right ventricle; TGA, transposition of the great arteries.

*situs ambiguous*, the spatial position and orientation of the abdominal and thoracic organs are abnormally symmetric and inconsistent. For example, the spleen may be absent, the liver may be midline, both lungs may have two or three lobes, and the bronchi may be similar to each other in length and orientation. Situs ambiguous is typically associated with heterotaxy syndrome, a condition characterized by partial or complete lack of lateralization of the visceral organs, splenic anomalies, congenital heart disease, and extracardiac anomalies [27,28]. In many patients with heterotaxy syndrome, visceral situs cannot be clearly designated as solitus or inversus, hence the term *situs ambiguous* is used. However, the anatomic organization of the visceral organs in these patients is often partially lateralized, allowing for determination of a "predominant situs." For example, when the stomach is right-sided and the inferior vena cava is left-sided, the predominant abdominal situs is inversus even though the liver may be midline.

**2. Cardiac position** (Fig. 3.4). The position of the heart within the thorax can be described as levocardia, mesocardia or dextrocardia based on the spatial location of the majority of the cardiac mass relative to the sternum. In addition, the

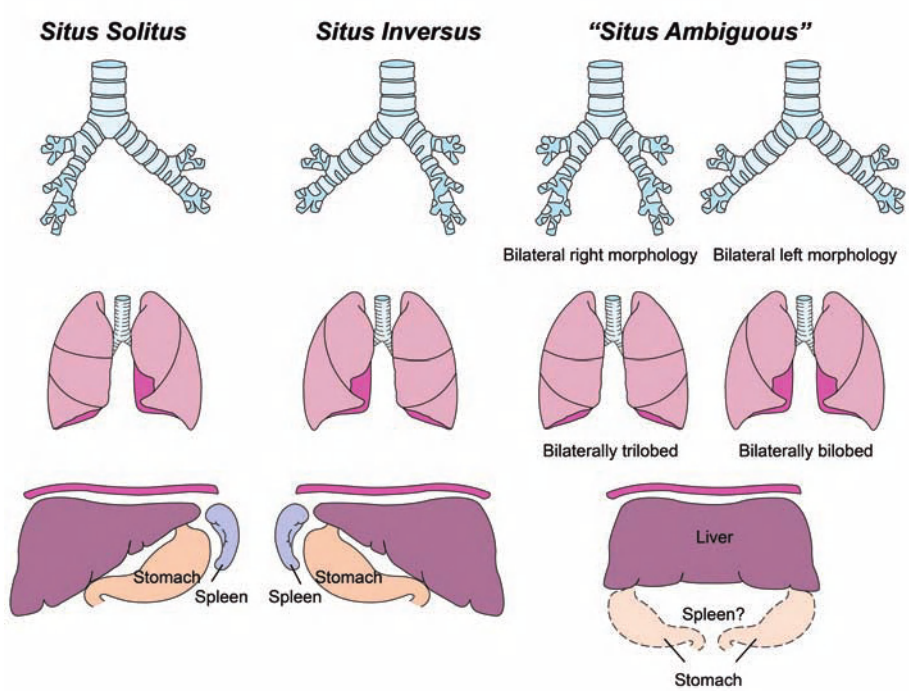


**Figure 3.3** Thoraco-abdominal situs. Top panel: The morphology of the tracheo-bronchial tree can be helpful in predicting atrial situs. In situs solitus, the right mainstem bronchus is short and eparterial (its branch for the right upper lobe is over the second branch of the right pulmonary artery) and the left mainstem bronchus is longer and hyparterial (it courses underneath the left pulmonary artery). In situs inversus, there is mirror-imaging of the anatomy seen in situs solitus. In situs ambiguous the bronchi can have a bilaterally right or bilaterally left morphology. Bilaterally hyparterial left bronchial morphology can be seen in patients with heterotaxy syndrome and polysplenia, whereas bilaterally eparterial right bronchial morphology is seen in patients with heterotaxy syndrome and asplenia. Middle panel: Lung lobation also correlates with atrial situs. A bilobed left lung and a trilobed right lung are typical in situs solitus. In situs inversus, the right lung is bilobed and the left lung is trilobed. As with the tracheo-bronchial tree, in situs ambiguous the lungs may be bilaterally bilobed or bilaterally trilobed. Lower panel: In visceral situs solitus the liver is right-sided and the stomach and spleen are left-sided. Incomplete lateralization of the abdominal organs with a midline liver and stomach may be seen in patients with heterotaxy syndrome. Splenic anomalies (asplenia, polysplenia, hyposplenia and a single right-sided spleen) and complex cardiac anomalies are frequent. In patients with heterotaxy syndrome and visceral situs ambiguous, the disposition of the abdominal situs predicts atrial situs less reliably then bronchial anatomy.

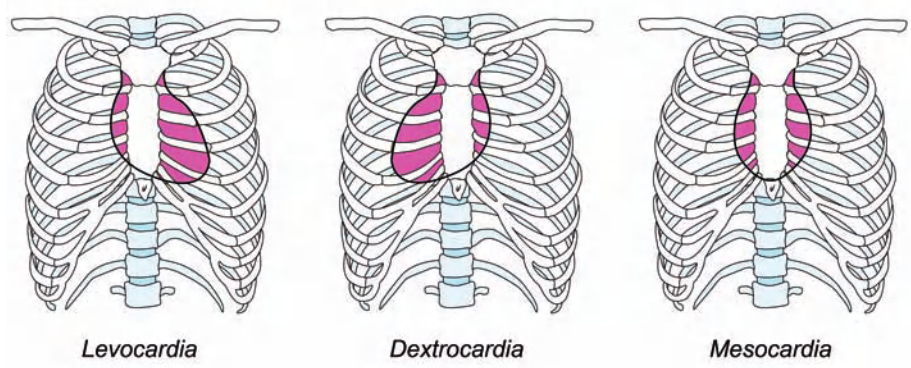


**Figure 3.4** Cardiac position within the thorax. In levocardia, the heart is predominantly in the left hemithorax. In dextrocardia, the heart is predominantly in the right hemithorax. In mesocardia, the heart is midline and the apex typically points anteriorly or inferiorly. The orientation of the apex should be explicitly described because the position of the heart within the thorax and the orientation of the apex may not be concordant (e.g., dextrocardia with a leftward pointing apex).

orientation of the long axis of the heart (the orientation of the axis connecting the AV junction and the apex) should be described. Although the position of the heart within the thorax and the orientation of the base-to-apex axis are often concordant (e.g., levocardia and a leftward pointing apex), occasional exceptions occur.

In levocardia, the heart is positioned predominantly in the left hemithorax. In dextrocardia, the heart is predominantly in the right hemithorax. In mesocardia, the heart is midline with approximately equal proportions of the cardiac mass on each side of the sternum. The base-to-apex axis in mesocardia is usually oriented anteriorly or sometimes inferiorly. The terms *primary* and *secondary* dextrocardia are used to distinguish between cardiac malposition related primarily to cardiac anomalies and secondary to noncardiac anomalies. *Primary dextrocardia* is defined as a condition in which the

heart is in the right hemithorax due to a structural congenital heart defect. In primary dextrocardia the apex usually points to the right. *Secondary dextrocardia* is a condition in which the heart is either "pushed" or "pulled" toward the right hemithorax due to extracardiac abnormalities. Examples of circumstances where the heart is "pushed" to the right hemithorax include left-sided tension pneumothorax, left congenital lobar emphysema, and left-sided diaphragmatic hernia. Conditions where the heart is pulled toward the right hemithorax include hypoplasia or agenesis of the right lung. In secondary dextrocardia the cardiac apex may point to the left or anteriorly. Leftward malposition of the heart occurs in patients with right diaphragmatic hernia or hypoplasia or agenesis of the left lung. In the latter condition, the heart is displaced toward the left superior hemithorax and the base-to-apex orientation points toward the left axilla.

In addition to malposition of the heart within the thorax, the heart can rarely be partially or completely exteriorized, a condition termed *ectopia cordis*. The extent of the midline defect that allows the heart to be partially or completely outside the thoracic cavity varies. A known association of anomalies, of which ectopia cordis is a component, is termed *pentalogy of Cantrell*. This group of defects includes: deficiency of the anterior diaphragm; a midline supra-umbilical abdominal wall defect; a defect in the diaphragmatic pericardium; congenital cardiac abnormalities; and a defect of the lower sternum [29].

**3. Segment-by-segment analysis of cardiac anatomy** (Fig. 3.2). At this stage, the three main segments and the two connecting segments are analyzed individually (steps 4–9 below).

**4. Atrial situs** (Fig. 3.5). The first step in determining atrial situs is to identify the atria according to their morphologic characteristics (Table 3.1; Fig. 3.5a,b). The atria are not designated based on systemic and/or pulmonary venous connections because these can be variable. Instead, the atria are defined by their intrinsic anatomy. The right atrial myocardium includes the crista terminalis and tinea sagittalis (Fig. 3.5a). The septal surface of the right atrium features the superior and inferior limbic bands of the fossa ovale. The right atrial appendage is typically broad-based, has a triangular shape, and its position is anterior relative to the left atrial appendage. The pectinate muscles of the right atrial appendage extend toward the AV valve annulus and the Eustachian valve. The left atrium is characterized by an elongated narrow appendage (Fig. 3.5b). The left atrial appendage is located posterior relative to the right atrial appendage. In

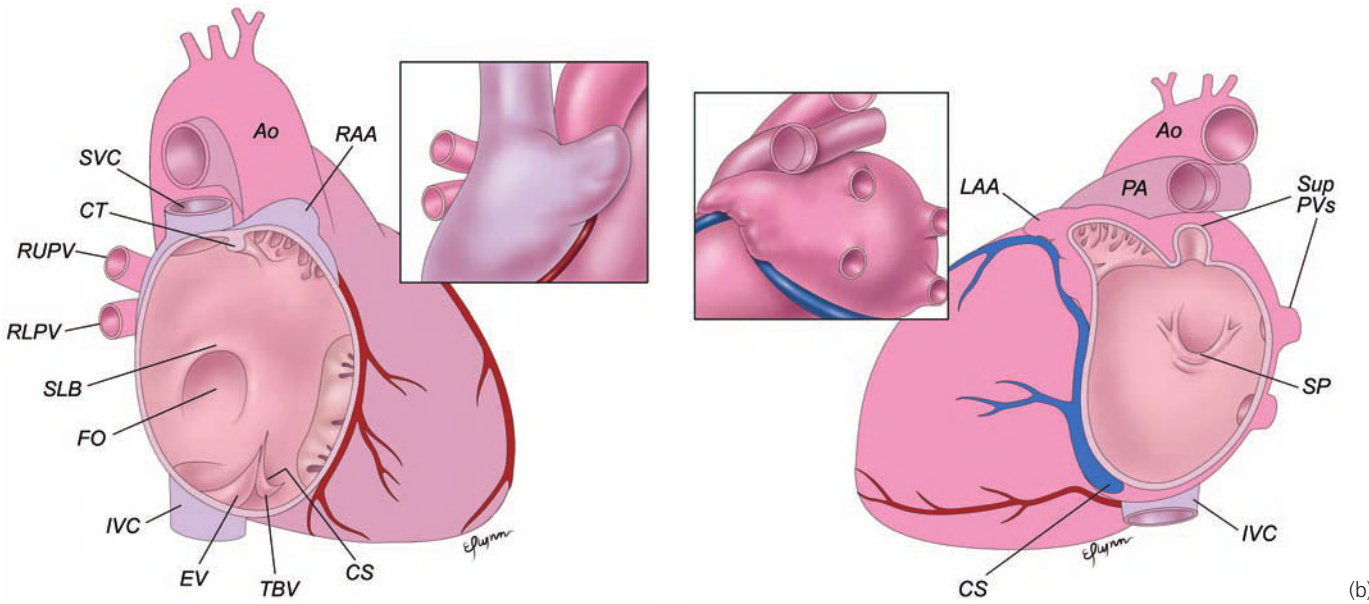


**Figure 3.5** Atrial morphology and situs. **(a)** Right atrial morphology: The right atrium (RA) can be divided into three components. (i) The *sinus venosus* includes the orifices of the inferior vena cava (IVC), superior vena cava (SVC) and coronary sinus (CS), and is characterized by its smooth surface (absence of muscular trabeculations). The sinus venosus is separated from the other components of the right atrium by remnants of the embryonic right venous valve system, which includes the Thebesian valve (TBV) and the Eustachian valve (EV). (ii) The *right atrial appendage* (RAA) is characterized by a broad-based triangular shape and coarse trabeculations (pectinate muscle). The crista terminalis (CT) is a prominent muscle bar that separates the sinus venosus component of the RA from the trabeculated right atrial appendage and is the site of the sinoatrial node. (iii) The *interatrial portion of the AV canal* includes the base of the atrial septum and the tricuspid valve annulus. The fossa ovale (FO) forms the interatrial septum and is characterized by an oval-shaped muscular boundary (termed *septum secundum* or *limbus of the fossa ovale*) whereas the floor of the fossa is covered by septum primum. **(b)** Left atrial morphology. Similar to the right atrium, the left atrium can also be divided into three components: (i) a pulmonary venous component; (ii) a left atrial appendage (LAA), which is narrow-based and elongated; and (iii) the AV canal region, which is bordered distally by the mitral valve annulus. Note the attachments of septum primum (SP) on the left atrial septal surface.

(c)

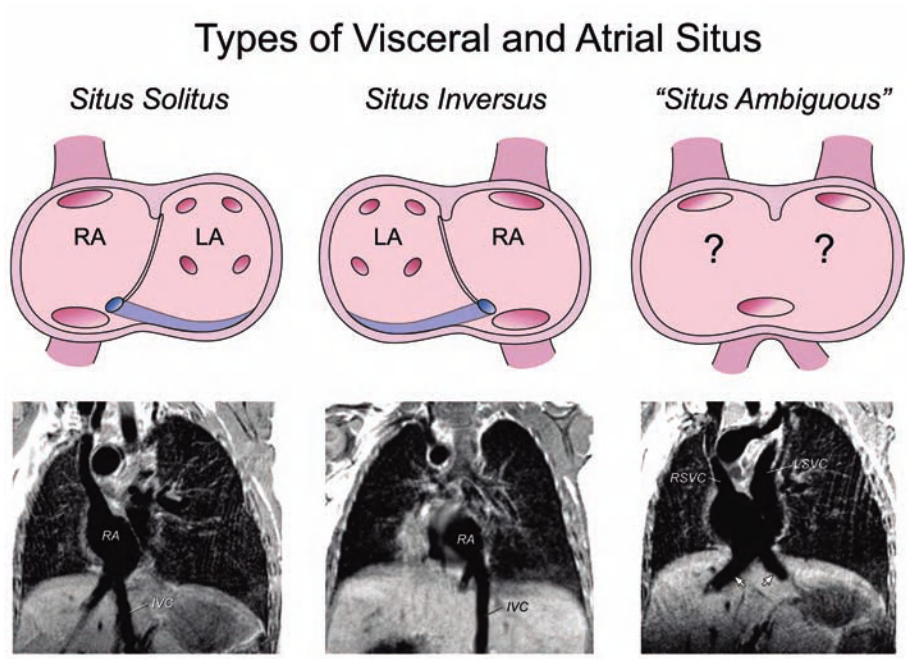


**Figure 3.5 (c)** Diagram of atrial situs. Upper panel: In *atrial situs solitus*, the right-sided right atrium (RA) receives the major horn of the sinus venosus, including the superior vena cava, inferior vena cava and the orifice of the coronary sinus. The left-sided left atrium (LA) normally receives the pulmonary veins; its septum features septum primum (the flap valve of the foramen ovale) and a narrow-based, elongated and posterior appendage (Table 3.1). In *atrial situs inversus*, the right atrium is left-sided and the left atrium is right-sided. In *atrial situs ambiguous,* typically seen in patients with heterotaxy syndrome, the anatomic landmarks characteristic of the right and left atria are not sufficient to determine situs (either situs solitus or situs inversus). Commonly in this situation, the atria are in common with absence (or presence of only remnants) of the atrial septum, the inferior vena cava may be interrupted between the renal and hepatic segments, there may be bilateral superior venae cavae and the coronary sinus may be unroofed. The atrial appendages may be quite similar to each other. Lower panel: Coronal plane spin-echo magnetic resonance imaging (MRI) images in patients with heterotaxy syndrome and atrial situs solitus (left panel), atrial situs inversus (central panel), and atrial situs ambiguous (right panel). Ao, aorta; LSVC, left superior vena cava; PA, pulmonary artery; RLPV, right lower pulmonary vein; RSVC, right superior vena cava; RUPV, right upper pulmonary vein; SLB, superior limbic band of fossa ovale; Sup PVs, superior pulmonary veins.

**Table 3.1** Morphologic criteria for identification of right atrium and left atrium

| | Right atrium | Left atrium |
|---|---|---|
| **Myocardial features** | Crista terminalis, tinea sagittalis, extension of pectinate muscles toward AV valve | Pectinate muscles confined to appendage* |
| **Appendage** | Broad-based, triangular, anterior | Long and narrow (finger-like), posterior |
| **Septum** | Septum secundum (limbus of the fossa ovale) | Septum primum (valve of the foramen ovale) |
| **Veins** | Receives the major horn of the sinus venosus: IVC†, SVC‡, CS§. | Normally receives all pulmonary veins** |

CS, coronary sinus; IVC, inferior vena cava; SVC, superior vena cava.
*When a persistent left superior vena cava (LSVC) drains directly into the left atrium a muscle bar similar to a crista terminalis may be present in the LSVC–LA junction.
†In cases with interrupted IVC, the right atrium receives the CS.
‡The SVC is not a reliable marker of the right atrium because a persistent left superior vena cava may drain directly into the left atrium [38].
§When the coronary sinus is unroofed, the drainage site of the IVC may incorrectly identify the right atrium. In such a circumstance, drainage of the IVC to the unroofed coronary sinus creates the appearance of IVC-to-left atrium connection. When the CS is unroofed and the IVC is interrupted, the shape, size and location of the atrial appendages may be used for identification of atrial situs.
**The pulmonary veins are not a reliable marker of the left atrium due to their potential for variable connections.

contrast to the right atrial appendage, the pectinate muscles of the left atrium are confined to the appendage. The left atrial septal surface features septum primum (the valve of the foramen ovale).

In atrial situs solitus (Fig. 3.5c) the right atrium is right-sided, whereas in atrial situs inversus it is left-sided. In individuals with normal anatomy, the right atrium receives the major horn of the sinus venosus, including the superior vena

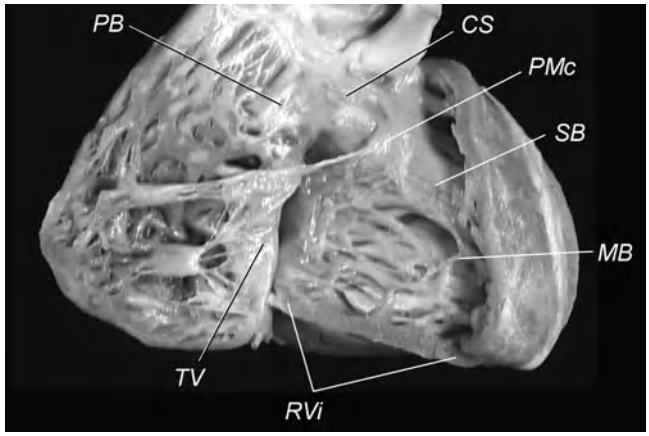


(a)

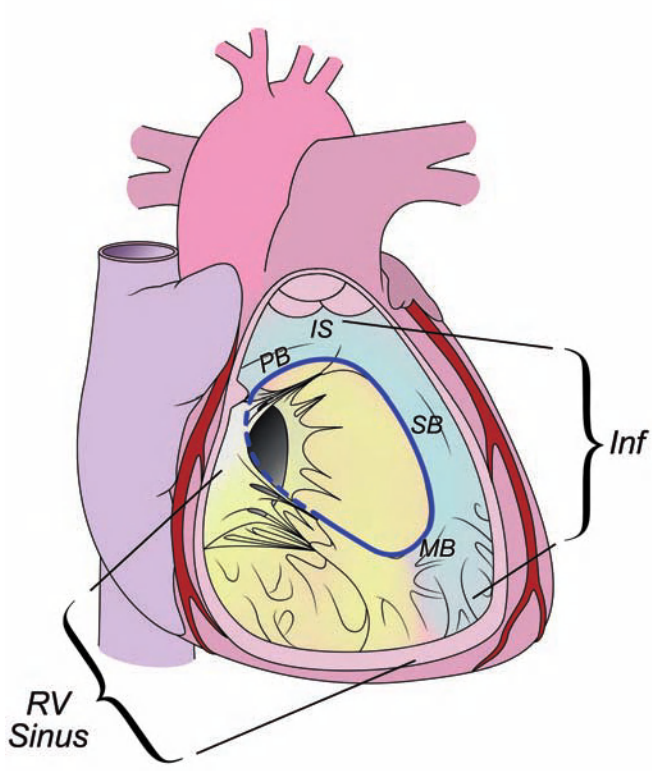


(b)

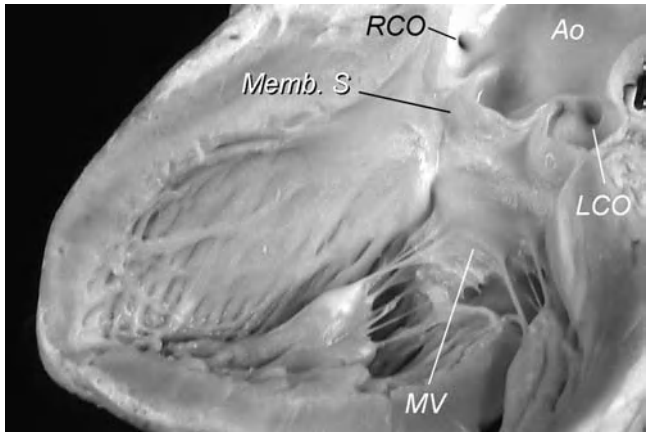


(c)

cava, inferior vena cava and the orifice of the coronary sinus (the cardiac termination of the left horn of the sinus venosus). The left atrium normally receives the pulmonary veins. In atrial situs ambiguous, typically seen in patients with heterotaxy syndrome, the anatomic landmarks characteristic of the right and left atria are not sufficient to determine situs (either situs solitus or situs inversus). Variations of anatomy may include a common atrium with absence (or presence of only remnants) of the atrial septum, interruption of the inferior vena cava between the renal and hepatic segments, bilateral superior venae cavae and an unroofed coronary sinus. The atrial appendages can be similar to each other; however, in most cases of heterotaxy syndrome the atrial appendages are not identical (i.e., they are not "isomeric"). Although the distribution of the pectinate muscles has been proposed as a useful marker of atrial identity [30], imaging of the pectinate muscle in living patients has not been consistently achieved.

**5. Ventricular loop** (Fig. 3.6). The first step in determining the ventricular loop (situs) is to identify the left and right ventricles. It is important to recognize that between the atrioventricular and the semilunar valves (what is generally considered the ventricular mass of the heart) there are three distinct chambers: the left ventricle, the right ventricular sinus and the infundibulum (or conus) [7,8,31,32]. The normal right ventricle comprises two distinct chambers,

**Figure 3.6** (*left*) Ventricular morphology and situs. **(a)** Right ventricular (RV) morphology. Note the coarse trabeculations and the chordal attachments of the tricuspid valve (TV) to the trabeculated septal surface. **(b)** The normal right ventricle comprises two distinct chambers, which are well incorporated into each other: the right ventricular (RV) sinus, and the infundibulum (Inf). The boundary between the RV sinus and the infundibulum is termed the *proximal os infundibulum* (shown as a dark ring) and comprises the parietal band (PB), infundibular septum (IS), septal band (SB), moderator band (MB) and the anterior papillary muscle of the tricuspid valve. The RV sinus may be subdivided into an atrioventricular (AV) canal portion (underneath the septal leaflet of the tricuspid valve) and the trabecular portion, which extends to the RV apex. The infundibulum may be subdivided into a distal (subpulmonary) portion – which includes the distal portion of septal band, infundibular septum and parietal band – and the proximal infundibulum, which is typically trabeculated and has its own apex adjacent to the RV sinus apex. **(c)** Left ventricular morphology. The most reliable morphologic feature of the left ventricle is its smooth superior septal surface. In the normal left ventricle, the finely trabeculated apex (trabeculae carneae) are quite characteristic. However, in a markedly hypertrophied left ventricle, or in double- or common-inlet left ventricle, the apical trabeculations may be prominently hypertrophied (similar to the trabeculations seen in the right ventricle). In the normal left ventricle, the mitral valve (MV) attaches to two large groups of papillary muscles, which attach to the left ventricular free wall. The aortic valve is in fibrous continuity with the mitral valve due to absence of an intervening conal musculature in this region. More anteriorly, under the right coronary cusp of the aortic valve, conal musculature comprises the infundibular septum. Ao, aorta; CS, coronary sinus; LCO, left coronary orifice; Memb. S, membranous septum; PMc, papillary muscle of the conus; RCO, right coronary orifice; RVi, right ventricular inflow (sinus).

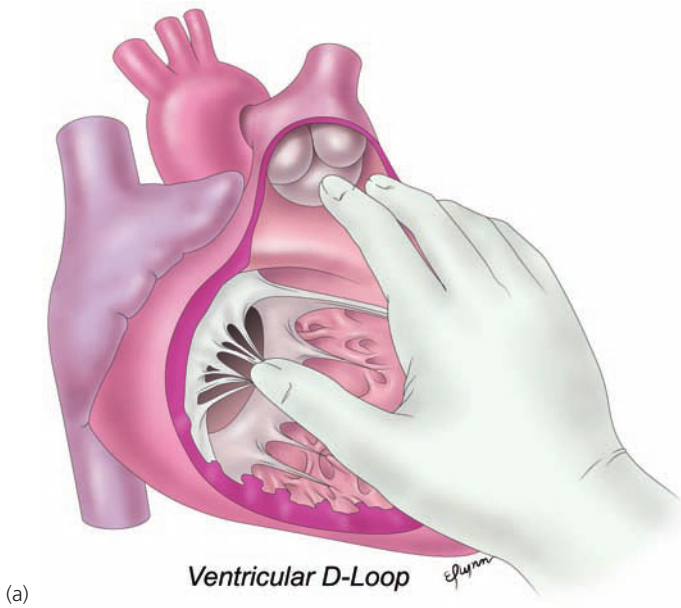


(a)

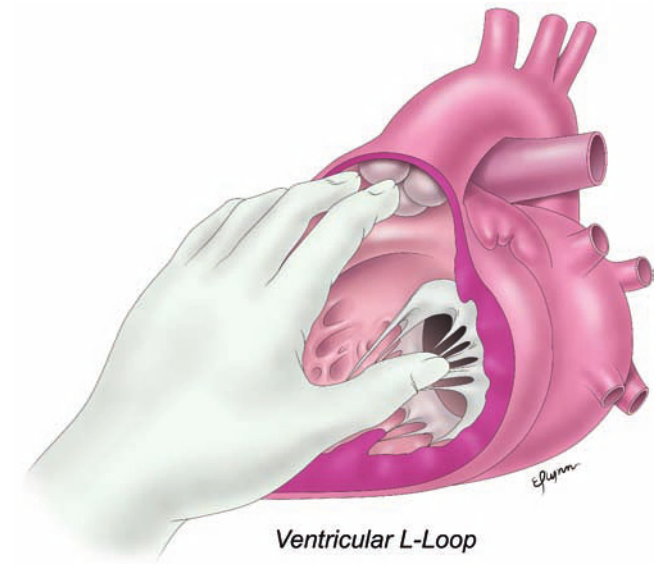


(b)

**Figure 3.7** Determination of ventricular situs. **(a)** In ventricular D-loop the palmar aspect of the right hand is placed over the right ventricular septal surface with the thumb in the tricuspid valve, the fingers in the right ventricular outflow and the dorsum of the right hand facing the right ventricular free wall. **(b)** In ventricular L-loop the palmar aspect of the left hand faces the right ventricular septal surface with the thumb in the tricuspid valve (or inflow), the fingers in the right ventricular outflow and the dorsum of the left hand facing the right ventricular free wall. Using this principle, ventricular situs can be determined regardless of ventricular position in the chest. The same principle also applies to the left ventricle. When using the left ventricle, a right-handed left ventricle will be L-looped and a left-handed left ventricle will be D-looped.

which are well incorporated into each other: the right ventricular sinus and the infundibulum. Externally, the normal right ventricle is triangular in shape and the diaphragmatic (inferior) wall makes an acute angle with the anterior wall. Internally, the normal right ventricle is characterized by septal attachments of the tricuspid valve, coarse trabeculations, and a distinct septal surface that includes the septal and moderator bands (Fig. 3.6a). The infundibulum is normally well incorporated with the right ventricular sinus, such that their separate identities may be obscured (Fig. 3.6a,b). However, these chambers have different embryologic and developmental origins. Moreover, in several congenital cardiac anomalies the infundibulum is either poorly incorporated with the right ventricular sinus (e.g., double-chambered right ventricle [33]) or is completely dissociated from the right ventricular sinus and completely associated with the left ventricle (e.g., anatomically corrected malposition of the great arteries and transposition of the great arteries with posterior aorta [31,34]). The anatomic features of the normal left ventricle are illustrated in Fig. 3.6c. Externally, the shape of the normal left ventricle approximates that of a cone. Internally, the myocardial architecture exhibits fine apical trabeculations, attachments of the mitral valve to two distinct papillary muscles that attach to the left ventricular free wall without attachments to the interventricular septum. The aortic valve is in fibrous continuity with the mitral valve due to absence of an intervening conal musculature in this region. It is important to recognize, however, that variations in anatomy and physiology can greatly alter left ventricular morphology, and many of the morphologic characteristics of the normal left ventricle can be altered. For example, in a markedly hypertrophied left ventricle, or in double or common inlet left ventricle, the apical trabeculations may be prominently hypertrophied, similar to the trabeculations of the right ventricle. Also, the normal attachments of the mitral valve to the left ventricular free wall papillary muscles are usually altered in common AV canal defects, straddling mitral valve, and other malformations. Therefore, the most reliable morphologic feature of the left ventricle is its smooth superior septal surface.

Once ventricular identity has been established based on morphologic criteria, the type of ventricular loop can be determined (Fig. 3.7a,b). The type of ventricular loop is clinically relevant in that it determines the pattern of coronary artery distribution, the disposition of the conduction system, and the internal organization of the ventricular myocardium. Furthermore, L- (or levo-)ventricular loop is associated with increased risks of atrioventricular block (either congenital or acquired), Ebstein-like malformation of the left-sided tricuspid valve, and hypoplasia of the left-sided right ventricular sinus. Because the spatial position of the ventricles varies widely, a right–left location relative to each other cannot be used reliably to determine the ventricular loop [35,36]. Instead, the principle of *chirality* is used. This

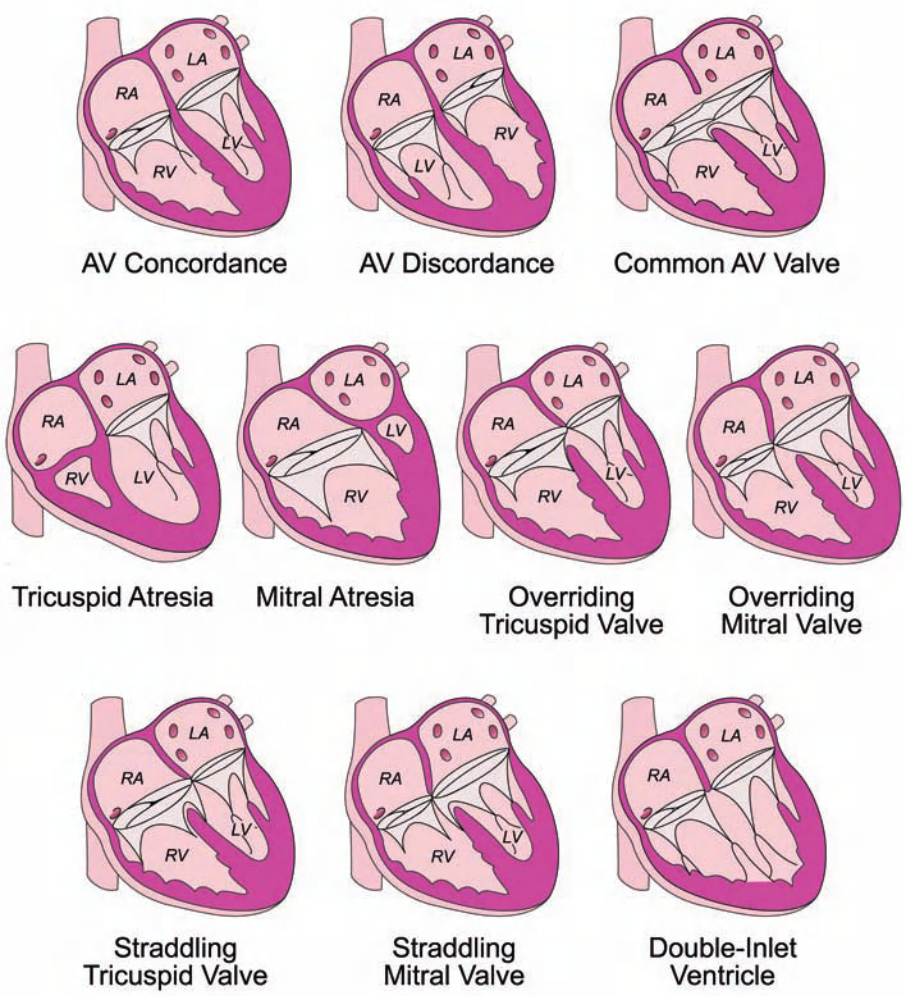


**Figure 3.8** Diagram illustrating some of the possible atrioventricular (AV) alignments and connections. This step in the segmental approach to congenital heart disease follows identification of atrial and ventricular morphology and situs. RA, right atrium; LA, left atrium; RV, right ventricle; LV, left ventricle.

method can be applied regardless of the spatial position of the ventricles and requires only the identification of the inflow, outflow and septal surface of one of the ventricles (Fig. 3.7a,b). The only circumstance where the type of ventricular loop cannot be reliably determined is in anatomically single right ventricle without a recognizable left ventricle or an interventricular septum.

**6. Atrioventricular alignments and connections** (Fig. 3.8). Once the identity and situs of the atria and the ventricles have been established, attention is then focused on the first connecting segment, the AV canal. Figure 3.8 illustrates several representative types of AV alignments and connections. However, it is important to recognize that these examples are only samples of an anatomic continuum.

**7. Ventriculo-arterial alignments** (Fig. 3.9). Next, the outflow of the heart is examined to determine from which cardiac chamber each great artery originates. Ventriculo-arterial alignment describes how the semilunar valves and their respective great vessels align with the underlying ventricles. Figure 3.9 illustrates several representative types of ventriculo-arterial alignments. However, it is important to recognize that the spectrum of possible alignments between the great arteries and the underlying ventricles is a continuum. Any classification of ventriculo-arterial alignment into discrete groups requires drawing sharp borders within transition zones, which inevitably leave certain anatomic variations straddling between categories. The preferred approach is to assign a great vessel to an underlying ventricle when it completely or nearly completely relates to that chamber. In cases where a semilunar valve significantly overrides the ventricular septum the preferred approach is to describe the anatomy (e.g., right ventricular origin of the aorta and biventricular origin of the main pulmonary artery). Specifically, the so-called "50% rule" is not practicably applicable in vivo due to complex three-dimensional relations between the ventricles and the great arteries, the curved geometry of the ventricular septum, and rotational and translational cardiac motion. It is important to note that determination of ventriculo-arterial alignment is based on the spatial relationships between the semilunar valves and the underlying ventricles and is not based on the type of infundibulum present (see next paragraph).

**8. Type of infundibulum (conus)** (Fig. 3.10). The infundibulum is the connecting segment between the ventricles and

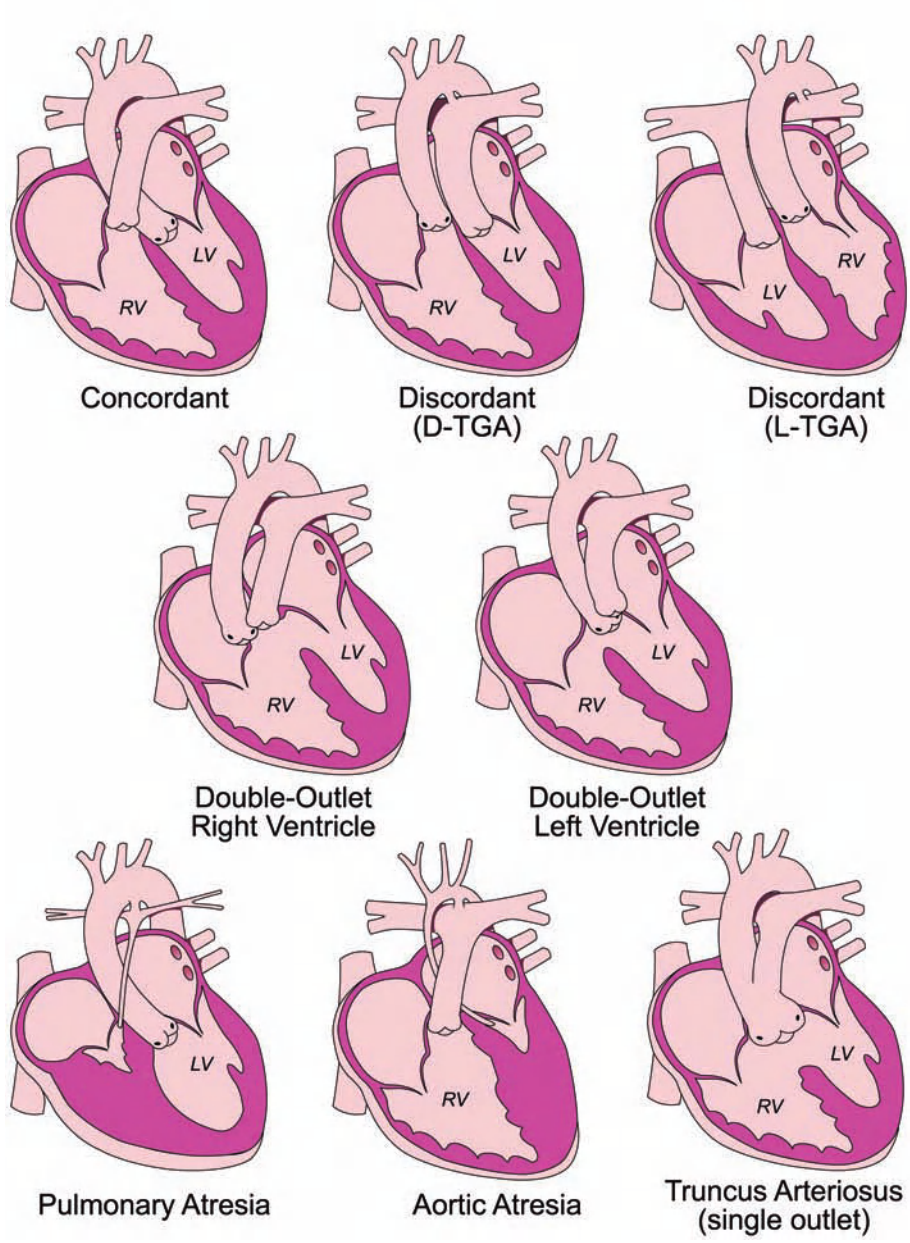


**Figure 3.9** Diagram illustrating some of the possible ventriculo-arterial (VA) alignments and connections. Note that the type of ventriculo-arterial alignment is determined by which great artery arises entirely or predominantly from which ventricle. It is clinically impractical accurately and reproducibly to determine great arterial origin from either ventricle in terms of percent origin. Specifically, the so-called "50% rule" is not applicable in vivo. This is due to complex three-dimensional relations between the ventricles and the great arteries, the complex geometric nature of the ventricular septum and cardiac motion in systole and diastole and with respiration. D-TGA, D-loop transposition of the great arteries; L-TGA, L-loop transposition of the great arteries; RV, right ventricle; LV, left ventricle.

the great arteries. In normal anatomy, there is a complete *subpulmonary conus* with muscular separation between the pulmonary and the AV valves (Fig. 3.6a,b), whereas the subaortic conus is incomplete, allowing fibrous continuity between the left and noncoronary cusps of the aortic valve and the anterior leaflet of the mitral valve (Fig. 3.6c). Part of the subaortic conus is normally present in the form of a conal septum represented by the myocardium that separates the anterolateral aspect of the left ventricular outflow (the myocardium under the right coronary cusp of the aortic valve) and the right ventricular outflow tract. In some patients, there is an increased distance between the left coronary cusp and the anterior mitral leaflet due to elongation of the intervalvular fibrosa. In this circumstance, the aortic and mitral valves are said to have fibrous contiguity as opposed to fibrous continuity.

Normal conal anatomy is termed *subpulmonary conus* indicating presence of a complete subpulmonary infundibular myocardium and partial absence of the subaortic infundibular free wall. Abnormal conal anatomy includes complete subaortic conus, bilateral conus and bilaterally absent conus. A *subaortic conus* is present when the aortic valve is supported by infundibular myocardium completely separating it from the AV valve(s). The subpulmonary conus is incomplete with absence of infundibular myocardium between the pulmonary and AV valve(s). A subaortic conus is often found in transposition of the great arteries. However, it is important to recognize that: (i) transposition of the great arteries is a specific type of ventriculo-arterial alignment (which great artery originates from which ventricle?) and is not defined by the type of conus; and (ii) any type of conus may be present

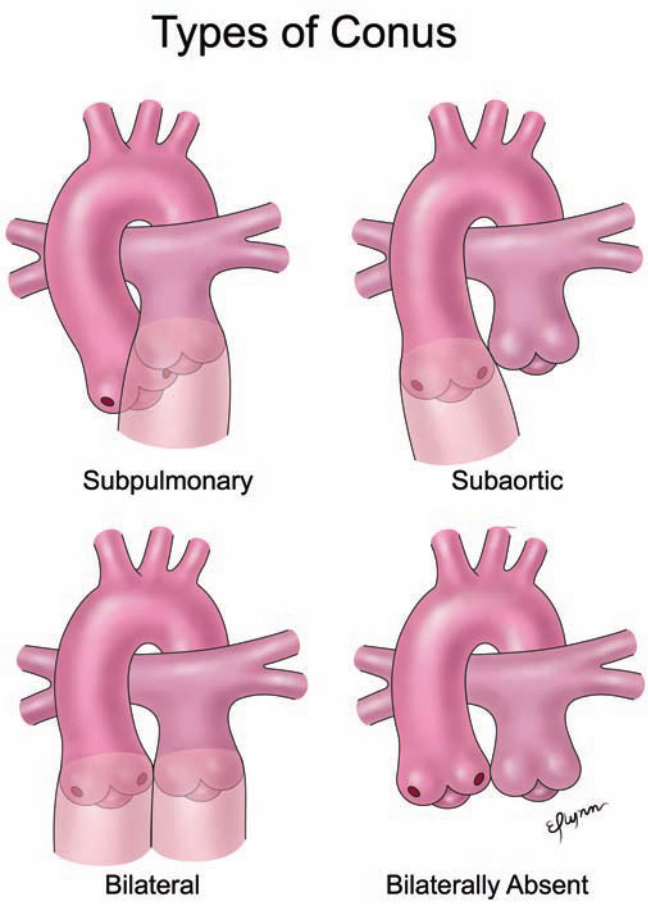


**Figure 3.10** Type of infundibulum. In general, there are four types of conus (or infundibulum): (i) *subpulmonary* with absence of subaortic infundibular free wall (found in the normal heart); (ii) *subaortic* with absence of subpulmonary infundibular free wall (often found in transposition of the great arteries); (iii) *bilateral conus* (commonly found in patients with double-outlet right ventricle, but can be rarely found in patients with transposition of the great arteries (TGA) and even in patients with normally related great arteries); (iv) *bilaterally absent* (found in some patients with double-outlet left ventricle).

in transposition of the great arteries or in any other type of ventriculo-arterial alignment [37].

*Bilateral conus* is present when both semilunar valves are completely separated from the AV valve(s) by infundibular myocardium. Although a bilateral conus is commonly associated with double-outlet right ventricle, it is important to recognize that, similar to transposition, (i) double-outlet right ventricle is a specific type of ventriculo-arterial alignment (which great artery originates from which ventricle?) and is not defined by the type of conus; and (ii) any type of conus may be present in double-outlet right ventricle.

*Bilaterally absent conus* is the least common type of infundibular anatomy. It is present when both semilunar valves are in direct fibrous continuity with the AV valve(s) as a result of absence of infundibular myocardium. It is most commonly seen in double-outlet left ventricle.

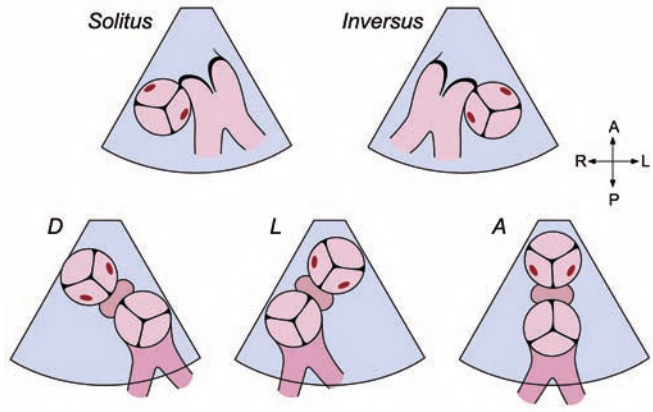


**Figure 3.11** Relationships between semilunar valves. The diagram illustrates several common interrelations between the semilunar valves as seen by a transthoracic echocardiographic parasternal short-axis view. It must be recognized, however, that the interrelations between the semilunar valves form an anatomic continuum. D, dextro (rightward); L, levo (leftward); A, anterior; P, posterior; R, right; L, left.

**9. Relationship between semilunar valves** (Fig. 3.11). This step in the segmental approach to congenital heart disease describes the spatial relationships between the aortic and pulmonary valves. Although the spatial relationships between the semilunar valves are often associated with predictable patterns of ventriculo-arterial alignments, there are many exceptions to these rules. Moreover, it is important to recognize that the designation of "D" and "L" to describe the spatial relationships between the semilunar valves does not provide information regarding the anterior–posterior and the superior–inferior orientation. Therefore, it is important to provide that information as part of comprehensive description of the anatomy.
**10. Associated anomalies**. Once the three main cardiac segments and the two connecting segments have been evaluated and categorized, all associated cardiovascular anomalies are systematically examined and described. To provide a logical and consistent description of all associated anomalies, they can either be described in order of their hemodynamic importance (from major to minor anomalies) or in an anatomic order (progressing from the venous entry to the arterial exit of the heart) (Fig. 3.2).

## Conclusion

The above-described segmental approach to anatomic analysis of congenital heart disease allows accurate description of all known forms of cardiac anomalies and can be applied to patients of all ages using diagnostic imaging modalities such as angiography, echocardiography, computed tomography and magnetic resonance imaging. In rare circumstances when the morphology does not conform to a clearly defined diagnostic category, it is essential to provide an accurate detailed description of the anatomy using tools provided by the segmental approach to CHD.

## References


1. Holt L, McIntosh R. Congenital anomalies of the heart. In: Holt L, McIntosh R (eds) *Holt's Diseases of Infancy and Childhood: A Textbook for the use of Students and Practitioners*. New York: D. Appelton-Century Co., 1933;501–10.
2. Abbott ME. *Atlas of Congenital Cardiac Disease.* New York: The American Heart Association, 1936.
3. Gross RE. Surgical management of the patent ductus arteriosus: with summary of four surgically treated cases. *Ann Surg* 1939; 110:321–56.
4. Blalock A, Taussig HB. Landmark article May 19, 1945: The surgical treatment of malformations of the heart in which there is pulmonary stenosis or pulmonary atresia. By Alfred Blalock and Helen B. Taussig. *JAMA* 1984;251:2123–38.
5. Gibbon JH Jr. Application of a mechanical heart and lung apparatus to cardiac surgery. *Minn Med* 1954;37:171–85, passim.
6. Van Praagh R. The segmental approach to diagnosis of congenital heart disease. In: *Birth Defects: Original Article Series*. Baltimore: Williams & Wilkins; 1972, 4–23.
7. Van Praagh R, Van Praagh S, Vlad P, Keith JD. Anatomic types of congenital dextrocardia: diagnostic and embryologic implications. *Am J Cardiol* 1964;13:510–31.
8. Van Praagh R, Van Praagh S. Isolated ventricular inversion. A consideration of the morphogenesis, definition and diagnosis of nontransposed and transposed great arteries. *Am J Cardiol* 1966; 17:395–406.
9. Van Praagh R, Santini F, Geva T. Segmental situs in congenital heart disease: a fundamental concept. *G Ital Cardiol* 1990;20:246–53.
10. Van Praagh R. The segmental approach clarified. *Cardiovasc Intervent Radiol* 1984;7:320–5.
11. Lev M. Some newer concepts of the pathology of congenital heart disease. *Med Clin North Am* 1966;50:3–14.
12. Lev M, Liberthson RR, Golden JG et al. The pathologic anatomy of mesocardia. *Am J Cardiol* 1971;28:428–35.
13. de la Cruz MV, Nadal-Ginard B. Rules for the diagnosis of visceral situs, truncoconal morphologies, and ventricular inversions. *Am Heart J* 1972;84:19–32.
14. Stanger P, Rudolph AM, Edwards JE. Cardiac malpositions. An overview based on study of sixty-five necropsy specimens. *Circulation* 1977;56:159–72.
15. Rao PS. Dextrocardia: systematic approach to differential diagnosis. *Am Heart J* 1981;102:389–403.
16. Freedom RM. The "anthropology" of the segmental approach to the diagnosis of complex congenital heart disease. *Cardiovasc Intervent Radiol* 1984;7:121–3.
17. Shinebourne EA, Macartney FJ, Anderson RH. Sequential chamber localization – logical approach to diagnosis in congenital heart disease. *Br Heart J* 1976;38:327–40.
18. Tynan MJ, Becker AE, Macartney FJ et al. Nomenclature and classification of congenital heart disease. *Br Heart J* 1979;41: 544–53.
19. Anderson RH, Becker AE, Freedom RM et al. Sequential segmental analysis of congenital heart disease. *Pediatr Cardiol* 1984;5:281–7.
20. Anderson RH, Becker AE, Tynan M et al. The univentricular atrioventricular connection: getting to the root of a thorny problem. *Am J Cardiol* 1984;54:822–8.
21. Weinberg PM. Systematic approach to diagnosis and coding of pediatric cardiac disease. *Pediatr Cardiol* 1986;7:35–48.
22. Van Praagh R. Diagnosis of complex congenital heart disease: morphologic-anatomic method and terminology. *Cardiovasc Intervent Radiol* 1984;7:115–20.
23. Van Praagh R. The importance of segmental situs in the diagnosis of congenital heart disease. *Semin Roentgenol* 1985;20:254–71.
24. Anderson RH, Razavi R, Taylor AM. Cardiac anatomy revisited. *J Anat* 2004;205:159–77.
25. Beland MJ, Franklin RC, Jacobs JP et al. Update from the International Working Group for Mapping and Coding of Nomenclatures for Paediatric and Congenital Heart Disease. *Cardiol Young* 2004;14:225–9.
26. Jacobs JP, Franklin RC, Jacobs ML et al. Classification of the functionally univentricular heart: unity from mapped codes. *Cardiol Young* 2006;16(Suppl. 1):9–21.
27. Geva T, Vick GW 3rd, Wendt RE, Rokey R. Role of spin echo and cine magnetic resonance imaging in presurgical planning of heterotaxy syndrome. Comparison with echocardiography and catheterization. *Circulation* 1994;90:348–56.
28. Van Praagh R, Van Praagh S. Atrial isomerism in the heterotaxy syndromes with asplenia, or polysplenia, or normally formed spleen: an erroneous concept. *Am J Cardiol* 1990;66:1504–6.
29. Cantrell JR, Haller JA, Ravitch MM. A syndrome of congenital defects involving the abdominal wall, sternum, diaphragm, pericardium, and heart. *Surg Gynecol Obstet* 1958;107:602–14.
30. Uemura H, Ho SY, Devine WA, Anderson RH. Analysis of visceral heterotaxy according to splenic status, appendage morphology, or both. *Am J Cardiol* 1995;76:846–9.
31. Van Praagh R, Van Praagh S. Anatomically corrected transposition of the great arteries. *Br Heart J* 1967;29:112–19.
32. Geva T, Powell AJ, Crawford EC et al. Evaluation of regional differences in right ventricular systolic function by acoustic quantification echocardiography and cine magnetic resonance imaging. *Circulation* 1998;98:339–45.
33. Wong PC, Sanders SP, Jonas RA et al. Pulmonary valve-moderator band distance and association with development of double-chambered right ventricle. *Am J Cardiol* 1991;68:1681–6.
34. Van Praagh R, Perez-Trevino C, Lopez-Cuellar M et al. Transposition of the great arteries with posterior aorta, anterior pulmonary artery, subpulmonary conus and fibrous continuity between aortic and atrioventricular valves. *Am J Cardiol* 1971; 28:621–31.
35. Geva T, Van Praagh S, Sanders SP et al. Straddling mitral valve with hypoplastic right ventricle, crisscross atrioventricular relations, double outlet right ventricle and dextrocardia: morphologic, diagnostic and surgical considerations. *J Am Coll Cardiol* 1991;17:1603–12.
36. Geva T, Sanders SP, Ayres NA et al. Two-dimensional echocardiographic anatomy of atrioventricular alignment discordance with situs concordance. *Am Heart J* 1993;125:459–64.
37. Pasquini L, Sanders SP, Parness IA et al. Conal anatomy in 119 patients with d-loop transposition of the great arteries and ventricular septal defect: an echocardiographic and pathologic study. *J Am Coll Cardiol* 1993;21:1712–21.
38. Van Praagh S, Geva T, Lock JE et al. Biatrial or left atrial drainage of the right superior vena cava: anatomic, morphogenetic, and surgical considerations – report of three new cases and literature review. *Pediatr Cardiol* 2003;24:350–63.

# 4 The Normal Pediatric Echocardiogram

**Wyman W. Lai[1] and H. Helen Ko[2]**

[1]Columbia University; Noninvasive Cardiology Imaging Laboratory, Division of Pediatric Cardiology, Morgan Stanley Children's Hospital of New York Presbyterian, New York, NY, USA
[2]Mount Sinai Medical Center, Pediatric Cardiology, New York, NY, USA

## Examination principles

The basic elements of a standard examination are two-dimensional images supplemented by Doppler and color Doppler information in multiple orthogonal imaging planes [1]. In the current era, the use of M-mode echocardiography is reserved primarily for the assessment of ventricular function [2]. Any laboratory performing a pediatric echocardiogram should have a written examination protocol that outlines the views to be obtained, the imaging modalities to be deployed for each view, and the preferred methods for recording and display. Whenever possible, the initial pediatric echocardiogram should be a complete study. A list of the structures to be examined with each view is helpful, and the required versus optional measurements should be clearly defined. A complete examination should include a qualitative or quantitative assessment of ventricular function.

The pediatric echocardiogram is organized by acoustic "windows" from which the heart is examined. Many pediatric echocardiography laboratories begin the examination with subxiphoid, or subcostal, imaging instead of left parasternal views. This allows for the determination and display of visceral situs (site or location) at the beginning of an examination. Regardless of where the examination starts, the segmental approach is used to describe all of the major cardiovascular structures in sequence [3–5].

Complete sweeps of the heart should be made during the examination to rule out abnormalities at its base or apex or on one of its surfaces. The study information may be recorded as complete sweeps, multiple selected single planes, or with a combination of both techniques [6–8]. Most ultrasound systems are configured so that a notch, or some other marking, on the side of a transducer corresponds to the side of a symbol displayed at the top of the image sector, usually to the right side of the screen. Therefore, when the transducer is positioned with the notch to the patient's left (at the 3 o'clock position), the left side of the patient will be displayed on the right of the screen. When the transducer is clockwise rotated so that the notch is directed inferiorly (at 6 o'clock), the inferior structures are displayed on the right side of the screen. In the course of a routine sweep, the transducer notch position is held in a fixed position, and the transducer is angled to obtain a series of images in the desired imaging plane.

Because of the wide range of complex pathology that may be seen on a pediatric echocardiogram, images should be shown in their correct spatial, or "anatomically correct," position on the display screen. Therefore, the anterior and superior structures are displayed at the top of the screen, and the rightward structures are generally placed on the left side of the image display (with the exception being the parasternal long-axis view where the cardiac apex is displayed on the left of the screen by convention).

The diagnostic accuracy of an examination depends greatly on the image quality. Technical adjustments must be made by the operator to improve signal-to-noise ratio and image resolution. The appropriate probe and optimal transducer frequency are selected to image the structures in question, and adjustments of the electronic (acoustic) focus depth are made throughout the study as necessary. Centering of structures of interest, using an appropriate degree of magnification, and optimizing of windows for imaging and Doppler interrogation are critical for image quality. The optimal window should allow the ultrasound beam to be directed perpendicularly to structures of interest for imaging and parallel to flow jets for Doppler interrogation and color flow mapping. Patient position, comfort, and level of anxiety are important considerations throughout the examination.

In the usual performance of an echocardiogram, the goals from each view should be: (i) imaging of cardiovascular structures; (ii) color and/or spectral Doppler interrogation of each valve and other major cardiovascular structures; and (iii) a complete evaluation of any suspicious chamber, vessel or flow jet identified during the course of the examination. Tables 4.1–4.5 list the structures that should be visualized

*Echocardiography in Pediatric and Congenital Heart Disease: From Fetus to Adult*
Edited by Wyman W. Lai, Luc L. Mertens, Meryl S. Cohen and Tal Geva
 ISBN: 978-1-405-17401-5

from the standard examination views. As a pediatric echocardiogram is progressing, the sonographer or echocardiographer must keep in mind the indications for the study and the need to address, as they arise, issues that may affect treatment. A complete examination may require that custom, or "in-between," planes be used to investigate or display an abnormality.

Extracardiac structures are also visualized during a standard transthoracic examination. Mediastinal abnormalities such as masses or cysts, if present, should be noted [9,10]. The presence or absence of the thymus may be seen in young children. Careful attention to symmetry and amplitude of diaphragm motion and screening for pleural effusions from subxiphoid and flank windows is particularly important in postoperative cardiac patients.

## Standard orthogonal imaging views

The five standard views of a pediatric echocardiogram, as defined by the American Society of Echocardiography, are all employed as part of a routine examination: subxiphoid (subcostal), apical, parasternal (left parasternal), suprasternal notch and right parasternal [11]. These imaging planes provide unique information regarding cardiovascular malformations that are often seen in childhood. A complete examination requires that the cardiovascular structures be imaged from multiple orthogonal planes. This practice minimizes artifacts due to false "dropout" of structures imaged parallel to the beam of interrogation, or "shadowing" from reflective structures proximal to the area of interest.

The imaging planes are identified by transducer location (subxiphoid, apical, parasternal, suprasternal notch and right parasternal) and by the plane of examination relative to the heart (4-chamber, 2-chamber, long-axis and short-axis) (Fig. 4.1). In addition, imaging planes may be described as anatomic planes (sagittal, parasagittal, transverse or coronal). The views and structures presented below are described as seen in a patient with normal or near-normal cardiovascular anatomy.

### Subxiphoid (subcostal) views

Subxiphoid imaging [12–14] begins with the determination of abdominal visceral situs in the transverse plane. The transducer is positioned with the notch at the 3 o'clock position, and anterior structures are displayed at the top of the screen. In addition to visualization of the liver and stomach, the spleen should be sought in patients with suspected abnormal abdominal visceral situs. The location of the hepatic segment of the inferior vena cava and descending aorta in relation to the midline and one another are then determined (Fig. 4.2). The patency of the inferior vena cava should be documented in its long axis (the transducer is rotated clockwise so that the notch is at the 6 o'clock position), and the abdominal descending aorta should also be demonstrated

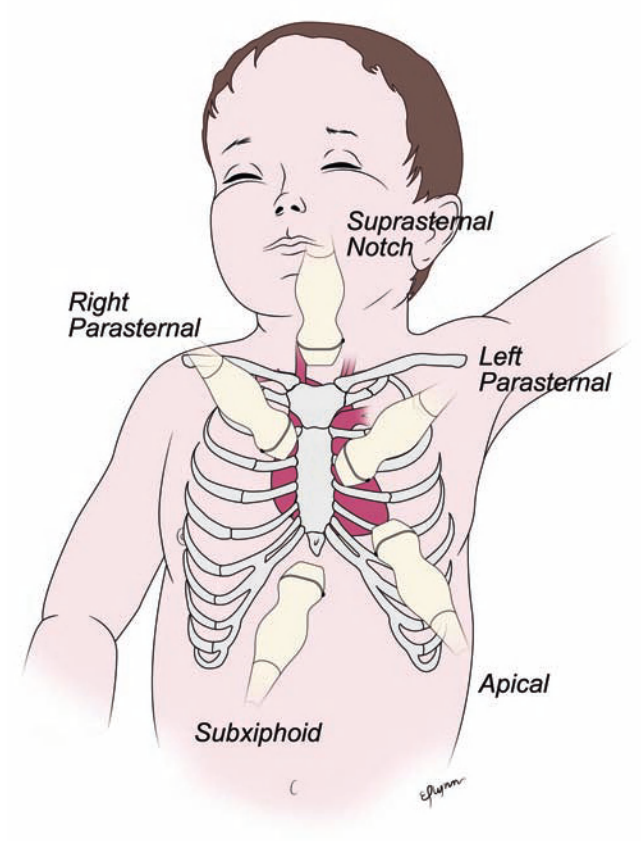


**Figure 4.1** Transducer locations for standard imaging windows. (1) Subxiphoid, (2) Apical, (3) Left parasternal, (4) Suprasternal notch, and (5) Right parasternal.

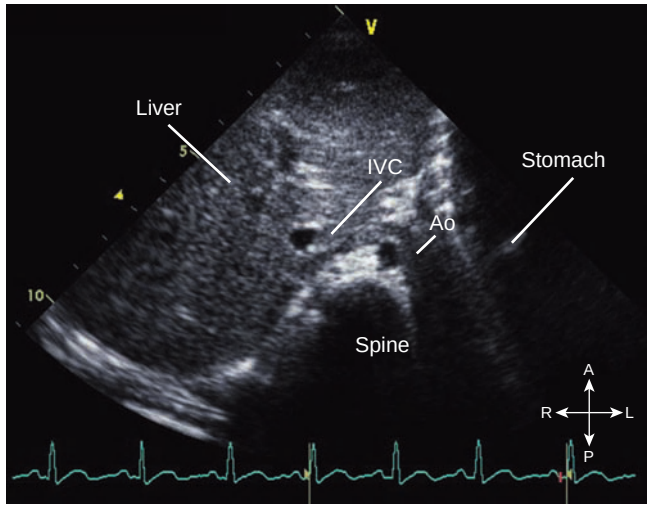


**Figure 4.2** Axial image of a child with normal abdominal visceral situs. Ao, aorta; IVC, inferior vena cava.

(Fig. 4.3). If a dilated azygos vein is seen posterior to the descending aorta, interruption of the inferior vena cava should be suspected. Inadvertent compression of the inferior vena cava, mimicking interruption, may be avoided by reducing the amount of abdominal pressure used to obtain the image.

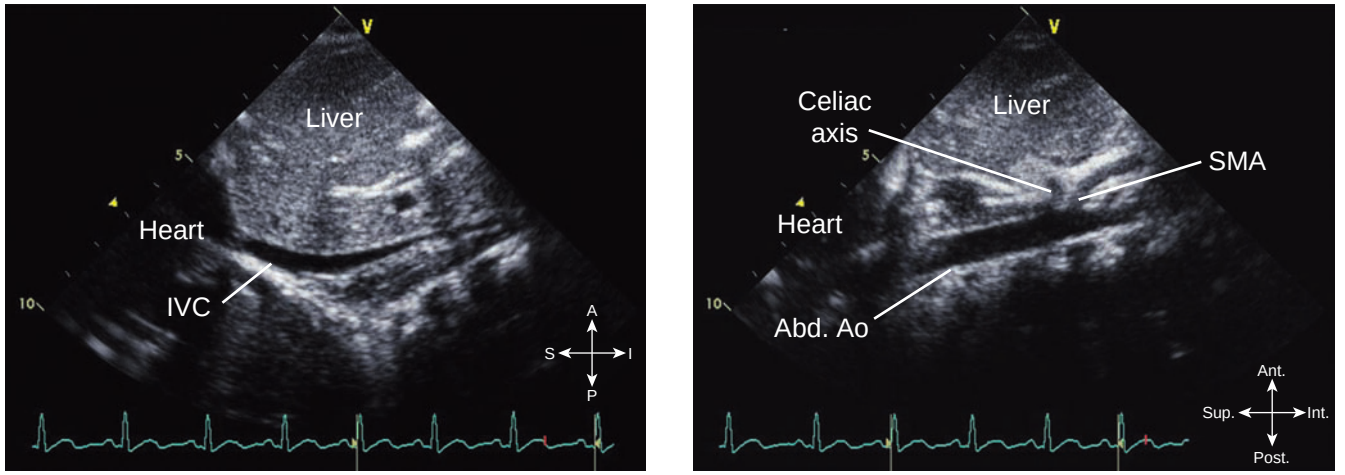


(a) (b)

**Figure 4.3** Long-axis composite image of uninterrupted inferior vena cava and descending aorta. **(a)** IVC, inferior vena cava. **(b)** Abd. Ao, abdominal aorta; SMA, superior mesenteric artery.

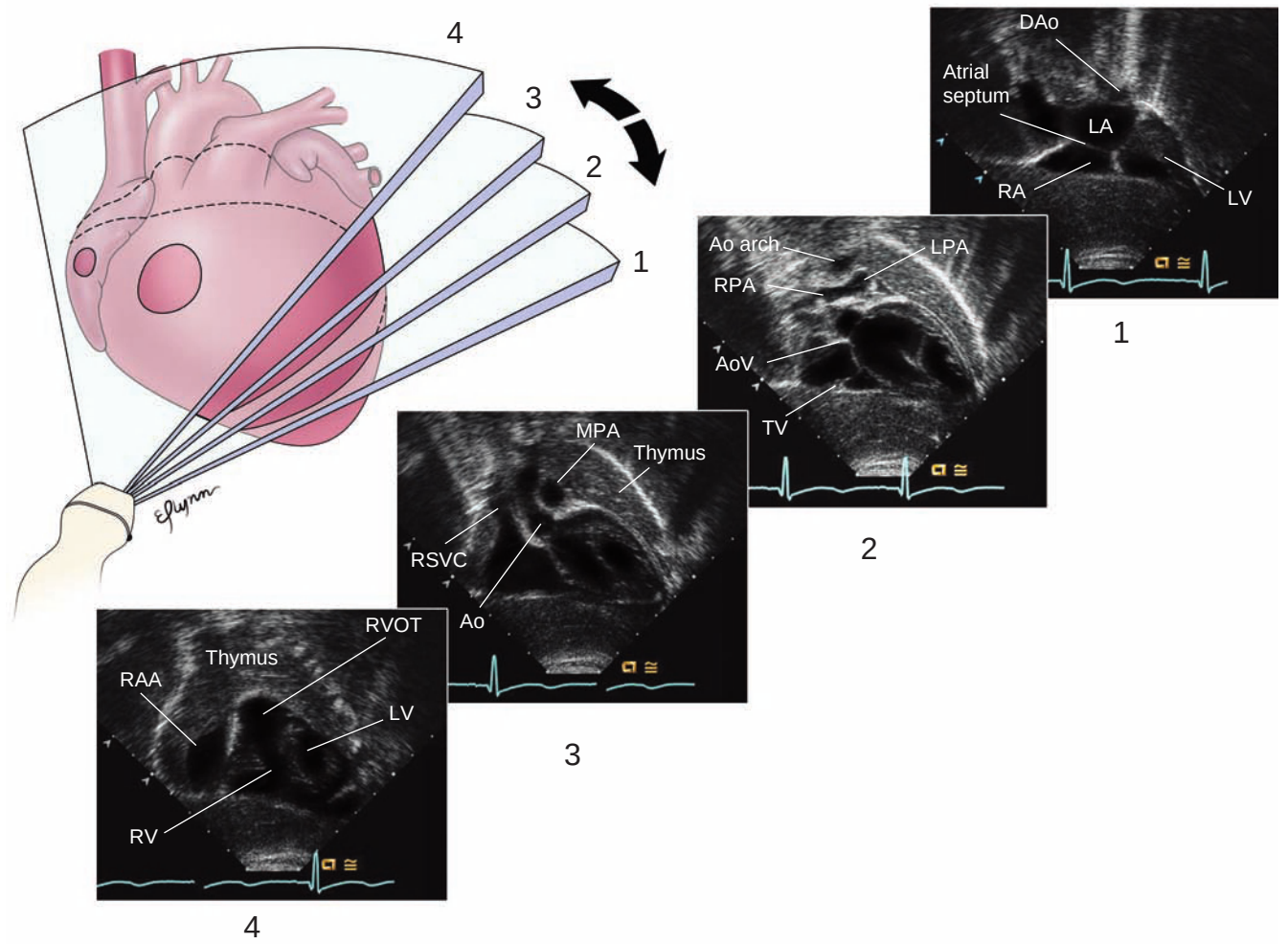


**Figure 4.4** Serial images of subxiphoid long-axis sweep. **(1)** DAo, descending aorta; LA, left atrium; LV, left ventricle; RA, right atrium. **(2)** Ao arch, aortic arch; AoV, aortic valve; LPA, left pulmonary artery; RPA, right pulmonary artery; TV, tricuspid valve. **(3)** Ao, aorta; MPA, main pulmonary artery; RSVC, right superior vena cava. **(4)** LV, left ventricle; RAA, right atrial appendage; RV, right ventricle; RVOT, right ventricular outflow tract.

The imaging plane is then inverted so that the superior structures are displayed at the top of the screen. As the plane of imaging is angled from the abdomen to the thorax, the connections of the hepatic veins to the inferior vena cava are visualized, followed by the connection of the inferior vena cava to the right atrium. The descending aorta at the level of the diaphragm should be identified, and any additional vascular structures crossing the diaphragm should be fully investigated.

The subxiphoid long-axis (coronal) sweep begins in the transverse plane and utilizes the liver as an acoustic window to the heart (Fig. 4.4 and Videoclip 4.1). The connections of the hepatic veins to the inferior vena cava should be documented, as well as the entrance of the inferior vena cava to the right atrium. As the sweep passes the inferior/posterior surface of the heart, the coronary sinus is often well visualized along the right posterior atrioventricular groove, and the posterior descending coronary artery may be seen in the posterior interventricular groove. The long-axis view allows for good visualization of the atrial septum and characterization of right versus left atrial and ventricular morphology. As imaging transitions into a nearly coronal plane, the ventricular outflow tracts are well displayed, as is the right atrial appendage and the normal right superior vena cava to the right of the ascending aorta. The position of the left coronary ostium may be well visualized as the ascending aorta and sinuses of Valsalva are imaged. The bifurcation of the main pulmonary artery into the branch pulmonary arteries should be documented during the sweep. Color flow mapping in the subxiphoid long axis may be advantageous for interrogation of the atrial septum and the anterior muscular septum.

The subxiphoid short-axis (sagittal) sweep (Fig. 4.5 and Videoclip 4.2(a,b)) starts in a parasagittal plane with the transducer notch positioned inferiorly (6 o'clock). The short-axis "reference view" includes the atria (including the right atrial appendage), the atrial septum, and the superior and inferior

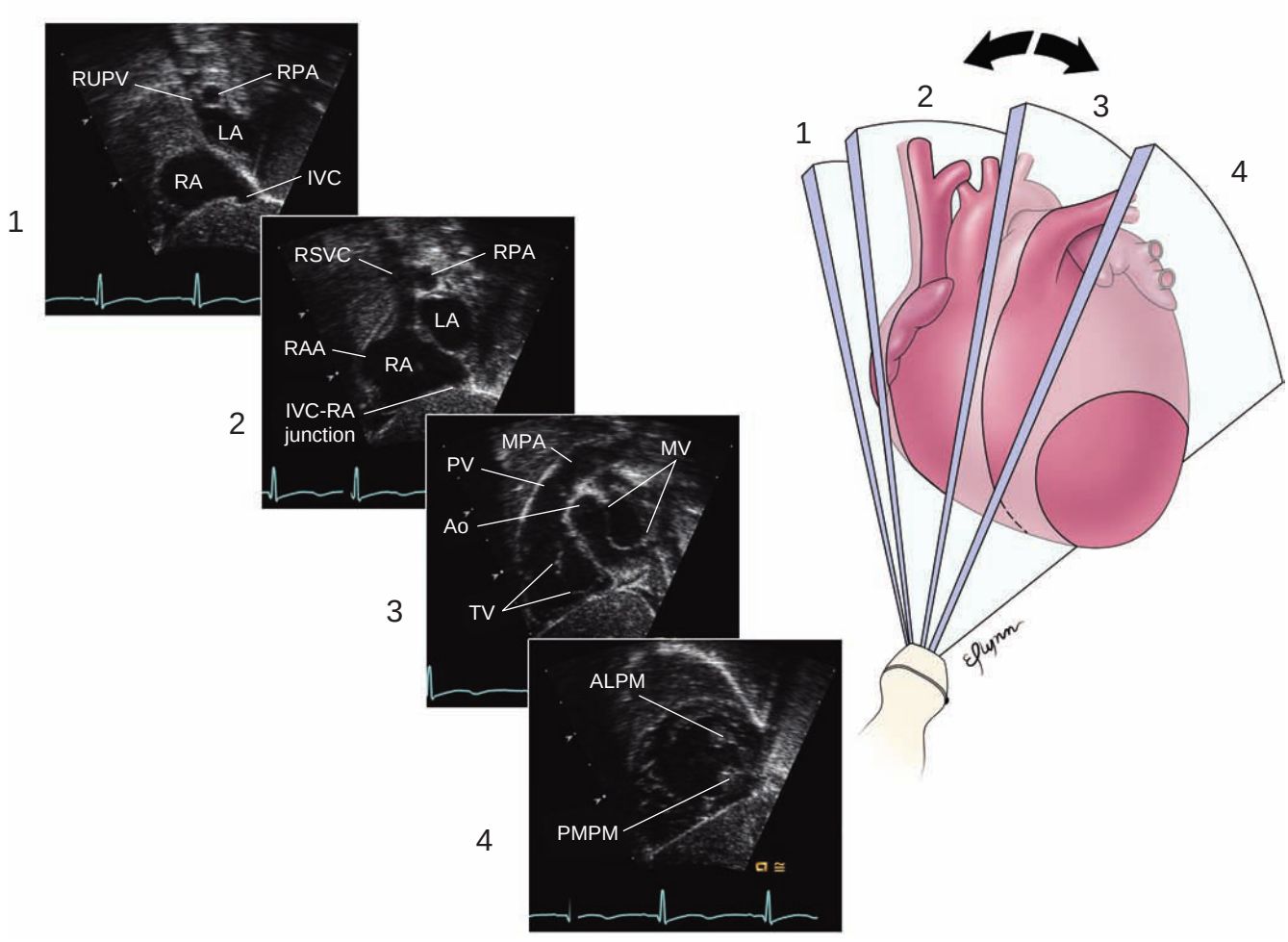


**Figure 4.5** Serial images of subxiphoid short-axis sweep. **(1)** IVC, inferior vena cava; LA, left atrium; RA, right atrium; RPA, right pulmonary artery; RUPV, right upper pulmonary vein. **(2)** IVC-RA junction, inferior vena caval–right atrial junction; LA, left atrium; RA, right atrium; RAA, right atrial appendage; RPA, right pulmonary artery; RSVC, right superior vena cava. **(3)** Ao, aorta; MPA, main pulmonary artery; MV, mitral valve; PV, pulmonary valve; TV, tricuspid valve. **(4)** ALPM, anterolateral papillary muscle; PMPM, posteromedial papillary muscle.

venae cavae. The Eustachian valve – the venous valve of the inferior vena cava – is frequently seen in this view as an extension of the anterior wall of the inferior vena cava [15]. The imaging sweep normally begins to the right, allowing visualization of the right upper pulmonary vein as it passes lateral and posterior to the superior vena cava and then proceeds from the base to the apex of the heart. The right pulmonary artery is seen in cross-section posterior to the superior vena cava and above the roof of the left atrium. The arch of the azygos vein above the right pulmonary artery and into the superior vena cava may be well visualized. Atrial septal morphology, including the apposition of septum primum and septum secundum, is often well seen in the short-axis plane. The tricuspid valve is imaged before the mitral valve as the transducer passes from right to left. The morphology of the atrioventricular valves, including fibrous continuity between the atrioventricular and aortic valves, can be identified as the imaging plane passes the atrioventricular canal region. The transducer position may need to be repositioned during the sweep (generally more rightward on the abdomen, taking advantage of the right-sided liver as an acoustic window) to maintain a short-axis imaging plane as the apex of the heart is visualized. A list of structures that should be identified on the subxiphoid views is provided in Table 4.1. Color flow mapping of the atrial and ventricular septa, particularly in smaller children, is often best visualized in the subxiphoid short-axis sweep. Doppler interrogation of the descending aorta at the level of the diaphragm is recommended as part of a complete examination in all patients.

**Table 4.1** Structures viewed from subxiphoid (subcostal) views

| |
|---|
| Inferior vena cava |
| Hepatic veins |
| Abdominal aorta |
| Diaphragm |
| Superior vena cava |
| Left atrium |
| Right atrium |
| Atrial septum |
| Coronary sinus |
| Pulmonary veins |
| Mitral valve |
| Tricuspid valve |
| Left ventricle |
| Right ventricle |
| Ventricular septum |
| Left ventricular papillary muscles |
| Aortic valve |
| Pulmonary valve |
| Ascending aorta |
| Coronary arteries |
| Main and branch pulmonary arteries |
| Pericardium |

## Apical views

Standard apical [16] 4-chamber and long-axis ("3-chamber") – as well as, in some laboratories, apical 2-chamber – views are obtained. The child is placed in a partial left lateral decubitus position with the left arm raised to bring the apex of the heart closer to the chest wall, and the apical impulse may be palpated for transducer placement. The notch of the transducer is directed toward the left axilla, at the 2–3 o'clock position as viewed from the apex. The apical 4-chamber reference view allows for the spectral and color Doppler interrogation of the atrioventricular valves and characterization of ventricular morphology. With the proper adjustments, the apical displacement of the normal tricuspid annulus relative to the mitral annulus, ventricular trabeculations and the moderator band may be well visualized. The 4-chamber sweep (Fig. 4.6 and Videoclip 4.3(a,b)) begins posteriorly to demonstrate the coronary sinus [17], the entrance of the inferior vena cava into the right atrium bordered anteriorly/inferiorly by the Eustachian valve, and the thoracic descending aorta posterior to the left atrium in the nearly transverse plane. The sweep covers the anterior surface of the heart after passing through the "5-chamber view," which demonstrates the left ventricular outflow tract and ascending aorta (Table 4.2). The ventricular apex may be magnified in the 4-chamber view for careful color Doppler mapping of the apical muscular septum. This view should not be used to interrogate the atrial septum as it is parallel to the ultrasound beam and false dropout can occur.

At the end of the 4-chamber sweep, repositioning of the transducer medially toward the lower left sternal border and moving up one or two rib spaces brings the right ventricular inflow and right ventricular free wall more into alignment with the beam of interrogation. Superior and anterior angulation from this position brings the right ventricular outflow tract into alignment and often offers an optimal angle for Doppler interrogation of the right ventricular outflow tract and color flow mapping of the pulmonary valve (Fig. 4.7).

The apical long-axis ("3-chamber") view is obtained by rotation of the transducer clockwise approximately 60° from the 4-chamber view (Fig. 4.8), with the transducer notch at 4 o'clock. Imaging of the left ventricular outflow tract from the apex allows for visualization of subaortic structures oriented perpendicular to the plane of insonation [18]. The long-axis view allows for optimal Doppler interrogation of the left ventricular outflow tract and ascending aorta as well as color flow mapping of the aortic valve. Modified views foreshortening the left ventricle may allow clearer visualization of the left ventricular outflow tract.

The 2-chamber view is utilized primarily for quantification of global left ventricular function [19] and assessment of regional wall motion. It might not be performed as a standard view in all laboratories. This view is obtained by rotation of the transducer counterclockwise approximately

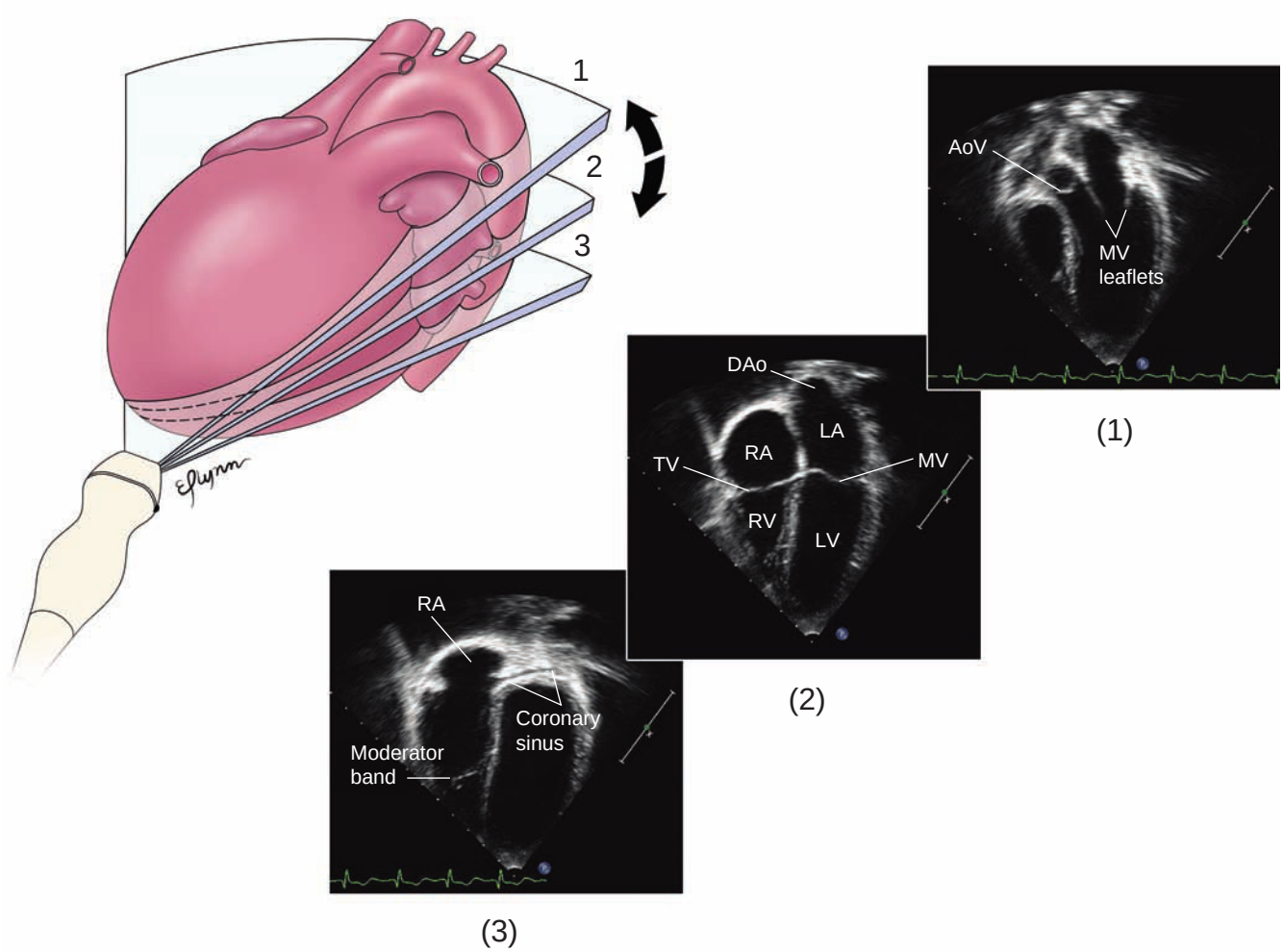


**Figure 4.6** Serial images of apical four-chamber sweep. **(1)** AoV, aortic valve; MV leaflets, mitral valve leaflets. **(2)** DAo, descending aorta; LA, left atrium; LV, left ventricle; MV, mitral valve; RA, right atrium; RV, right ventricle; TV, tricuspid valve. **(3)** RA, right atrium.

**Table 4.2** Structures viewed from apical views

| |
|---|
| Inferior vena cava |
| Left atrium |
| Right atrium |
| Atrial septum |
| Coronary sinus |
| Selected pulmonary veins |
| Mitral valve |
| Tricuspid valve |
| Left ventricle |
| Right ventricle |
| Ventricular septum |
| Left ventricular papillary muscles |
| Aortic valve |
| Pulmonary valve |
| Ascending aorta |
| Main and branch pulmonary arteries |

60–90° from the 4-chamber view, with the transducer notch at 12–1 o'clock. The anterior wall is displayed on the right side of the screen and inferior wall on the left (Fig. 4.9).

### Parasternal (left parasternal) views

With the child still in a partial left lateral decubitus position, the transducer is placed on the upper to mid left sternal border with the transducer notch directed toward the right shoulder (10 o'clock) to provide a parasternal [17,20] long-axis view. The long-axis reference view is obtained with the transducer positioned over the left ventricular outflow tract (Fig. 4.10 and Videoclip 4.4(a,b)), allowing visualization of the aortic valve, mitral valve and the basal walls of the left ventricle. The fibrous continuity between the mitral and aortic valves is easily demonstrated, and the phasic motion of the valve leaflets is well visualized. The transducer is tilted toward the right hip to visualize the tricuspid valve and right ventricular inflow. The coronary sinus ostium may also

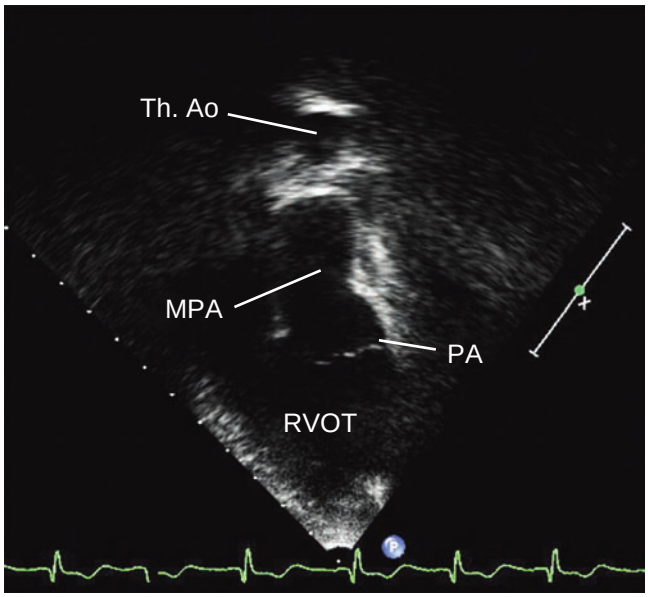


**Figure 4.7** Image of modified apical view demonstrating the right ventricular outflow tract. MPA, main pulmonary artery; RVOT, right ventricular outflow tract; PV, pulmonary valve; Th. Ao, thoracic aorta.

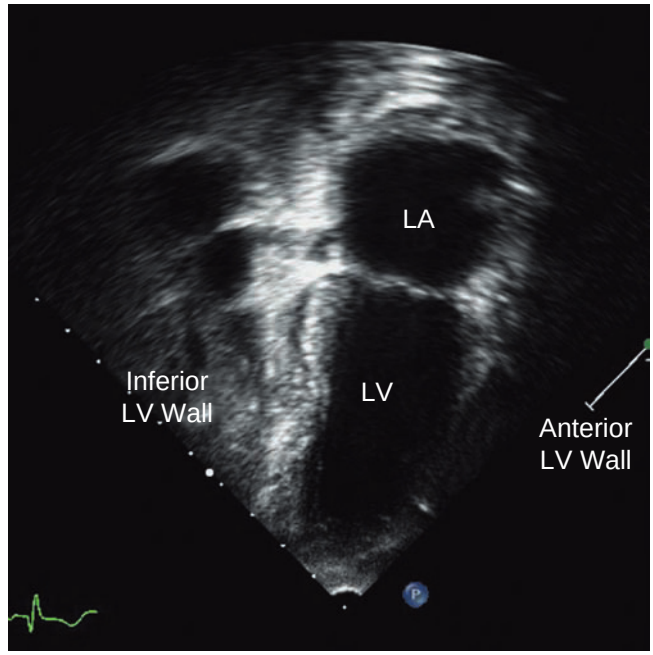


**Figure 4.9** Image of apical two-chamber view. LA, left atrium; LV, left ventricle.

be visualized with this posterior sweep. The transducer is then tilted anteriorly toward the left shoulder to visualize the right ventricular outflow tract, pulmonary valve and main pulmonary artery. Color flow mapping of each of the valves should be performed from the parasternal window. Repositioning of the transducer superiorly may be required to provide a long-axis or modified parasagittal view of the aorta, which best demonstrates the ascending aorta and the location of the right coronary artery ostium relative to the sinotubular junction.

The parasternal short-axis view (Fig. 4.11 and Videoclip 4.5) at the base of the heart can provide detailed imaging of aortic valve morphology [21] as well as views of the right ventricular infundibulum and pulmonary valve. From the long-axis

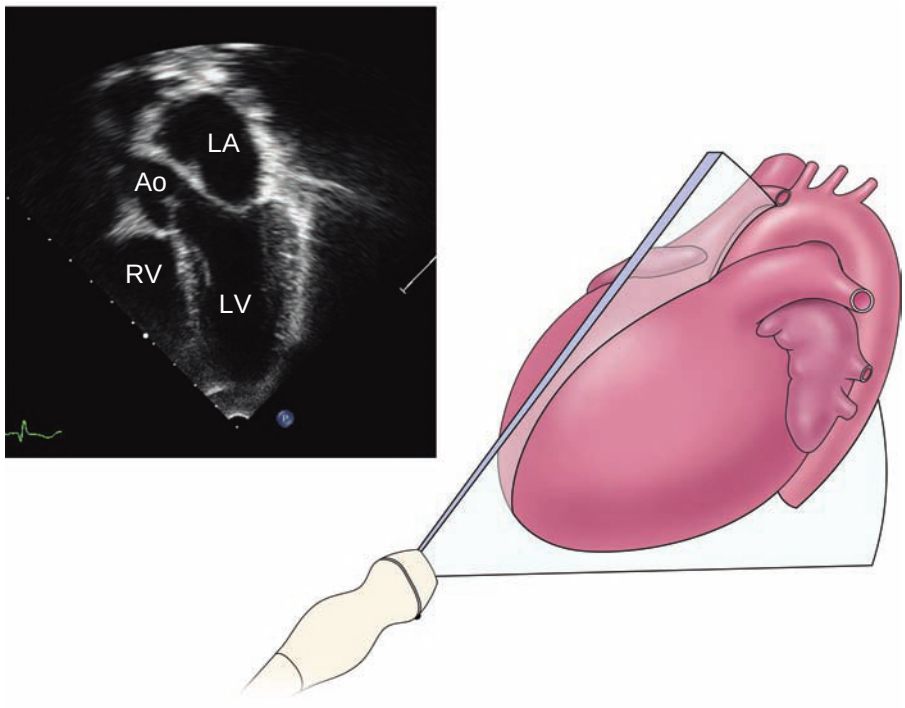


**Figure 4.8** Image of apical long-axis view. Ao, aorta; LA, left atrium; LV, left ventricle; RV, right ventricle.

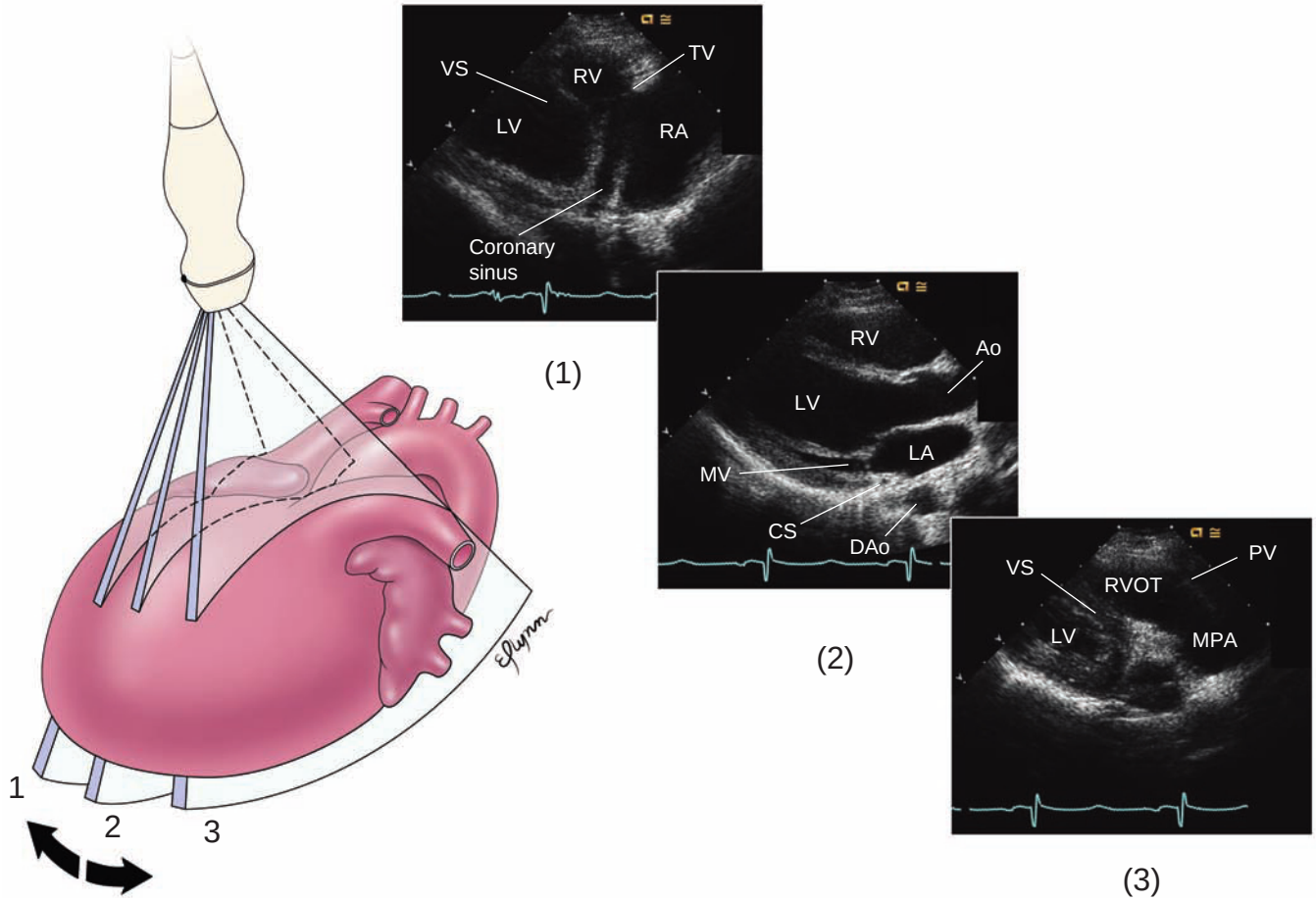


**Figure 4.10** Serial images of parasternal long-axis sweep. **(1)** LV, left ventricle; RA, right atrium; RV, right ventricle; TV, tricuspid valve; VS, ventricular septum. **(2)** Ao, ascending aorta; CS, coronary sinus; DAo, descending aorta; LA, left atrium; LV, left ventricle; MV, mitral valve, RV, right ventricle. **(3)** LV, left ventricle; MPA, main pulmonary artery; PV, pulmonary valve; RVOT, right ventricular outflow tract; VS, ventricular septum.

view, the transducer is clockwise rotated so that the transducer notch is directed toward the left shoulder (2 o'clock). The short-axis reference view consists of: the aorta centered in the imaging sector; the right ventricular inflow; the right ventricular outflow tract and main pulmonary artery; and the atria. Although relatively parallel to the beam of insonation, the atrial septum may be visualized in a modified short-axis view obtained by slight clockwise rotation (3 o'clock) and repositioning the transducer one or two rib notches inferiorly; this view may be especially useful in larger children with poor subxiphoid windows. Examination of the coronary artery ostia should be obtained from the short-axis views, as well as imaging and color flow mapping of the proximal coronary arteries (Figs 4.12 and 4.13) [22–24]. Clockwise rotation of the transducer (also 3 o'clock) into a transverse view elongates the left main and anterior descending coronary arteries, and often demonstrates the bifurcation of the left main coronary artery. The great cardiac vein may also be well visualized from this transverse left parasternal window [25]. Slight counterclockwise rotation (1 o'clock) may elongate the right coronary artery and improve its visualization.

The parasternal short-axis sweep begins with the transducer tilted toward the right shoulder to demonstrate better the main and branch pulmonary arteries. Detailed imaging of the pulmonary valve and proximal main pulmonary artery may require repositioning of the transducer inferiorly, as well as tilting and clockwise rotation (to 3 o'clock) to provide a nearly coronal plane of imaging directed superiorly. The parasternal short-axis sweep progresses from the base of the heart to the apex. On the left border of the heart at the base, the sweep shows the branch pulmonary arteries, followed by the left atrial appendage positioned anterior to the left upper pulmonary vein, and then the left lower pulmonary vein proximal to the atrioventricular groove. Color and spectral Doppler are often helpful in distinguishing the left atrial appendage from the left upper pulmonary vein. The morphology of the mitral leaflets and valve apparatus, including the position of the left ventricular papillary muscles, is often best seen on short-axis views of the ventricles. In larger

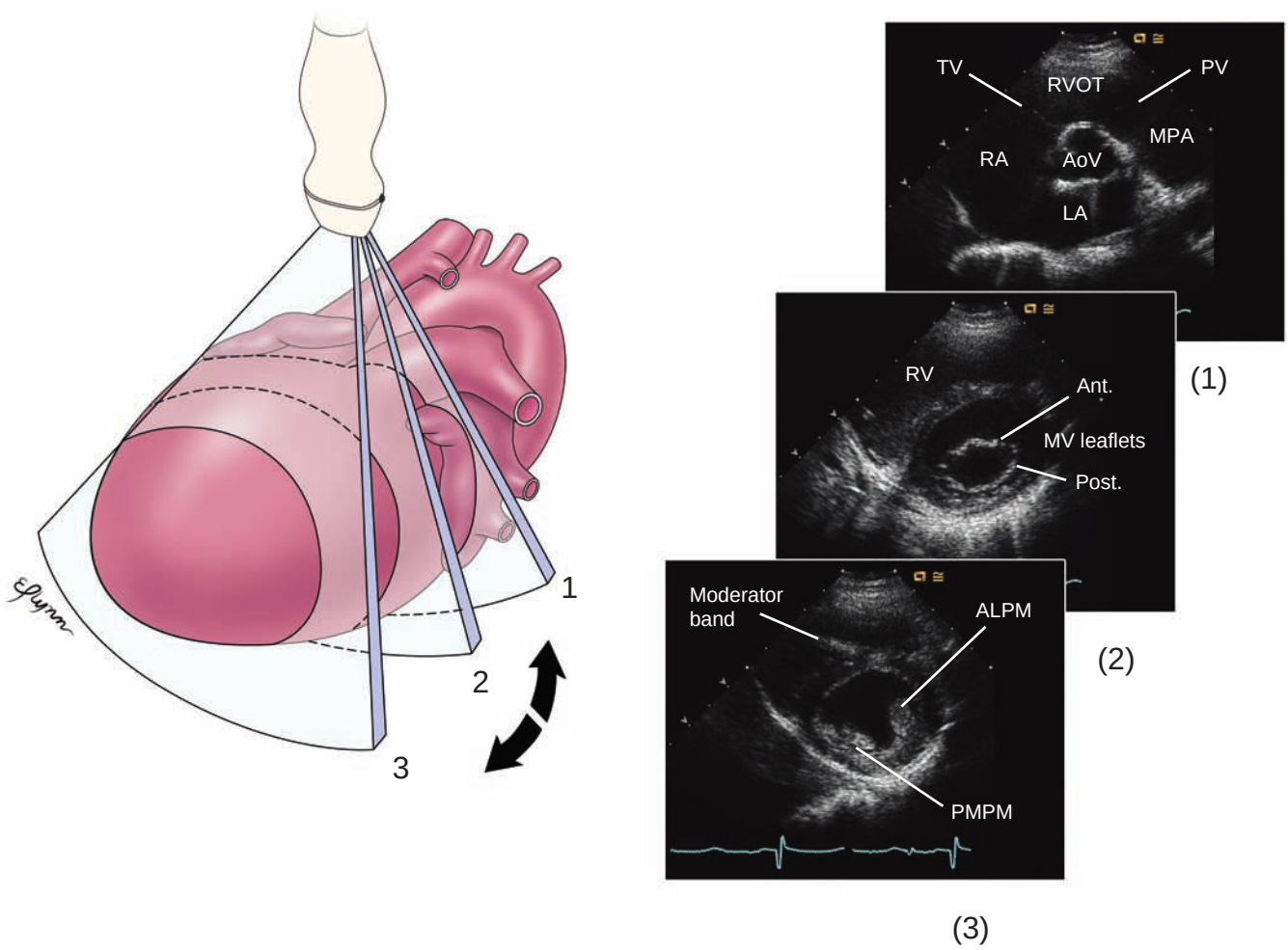


**Figure 4.11** Serial images of parasternal short-axis sweep. **(1)** AoV, aortic valve; LA, left atrium; MPA, main pulmonary artery; PV, pulmonary valve; RA, right atrium; RVOT, right ventricular outflow tract; TV, tricuspid valve. **(2)** ant., anterior; post., posterior; MV, mitral valve; RV, right ventricle. **(3)** ALPM, anterolateral papillary muscle; PMPM, posteromedial papillary muscle.

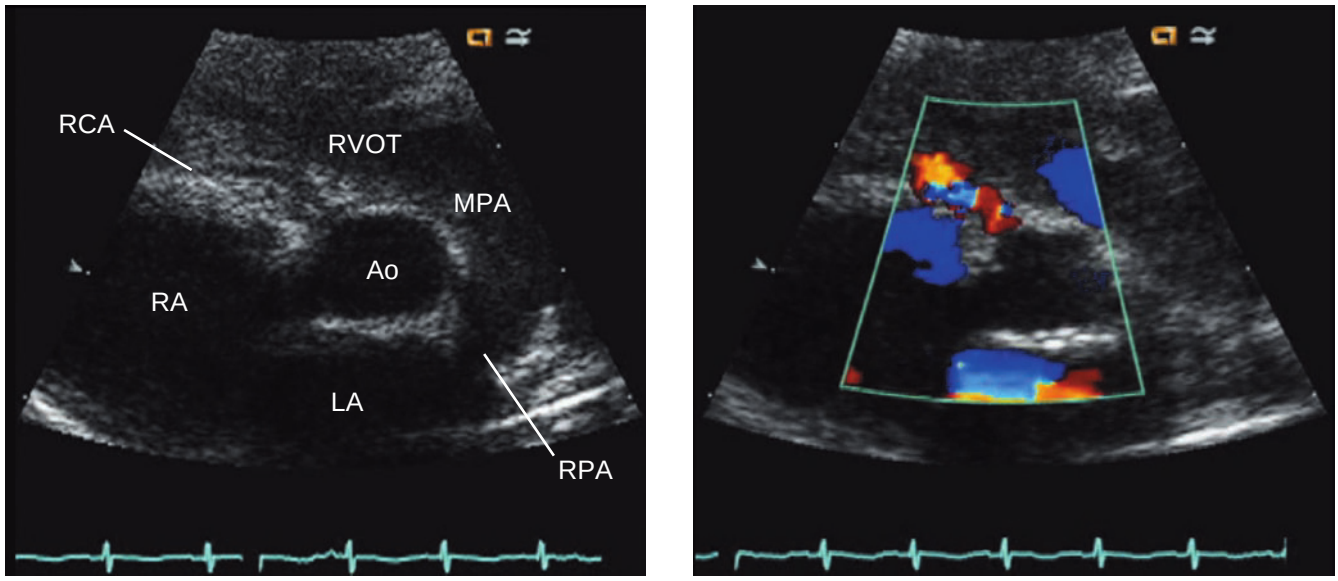


(a) (b)

**Figure 4.12** **(a)** Short-axis 2D and **(b)** color Doppler images of axial right coronary artery. (a) Ao, aorta; LA, left atrium; MPA, main pulmonary artery; RA, right atrium; RCA, right coronary artery; RPA, right pulmonary artery; RVOT, right ventricular outflow tract.

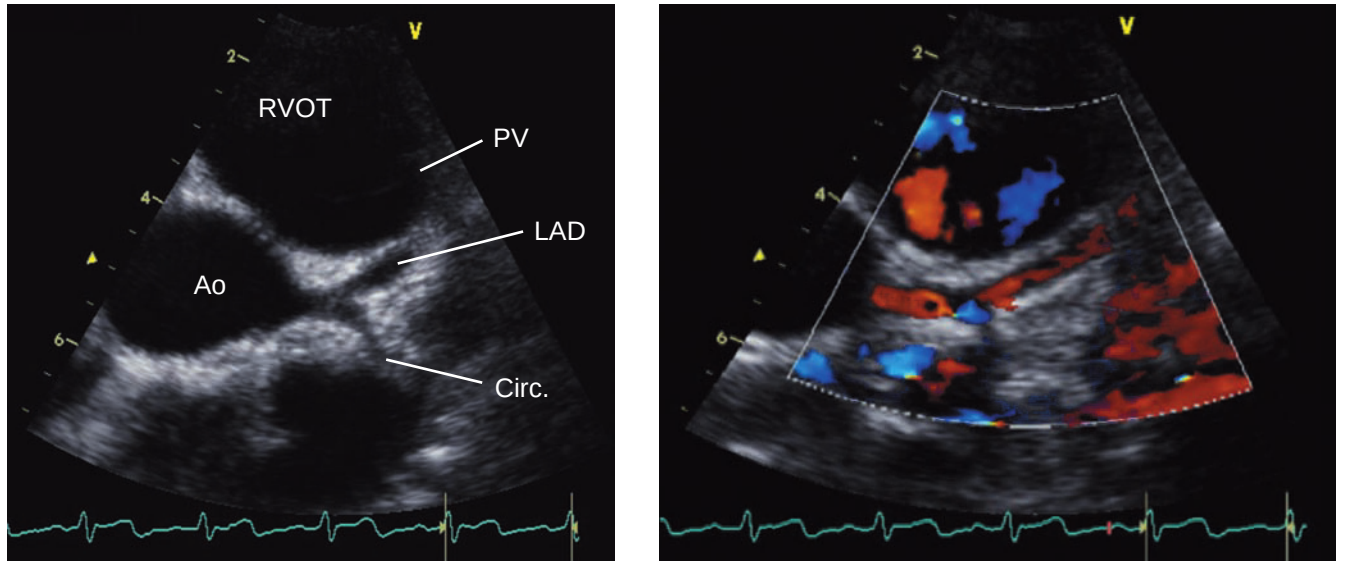


(a) (b)

**Figure 4.13 (a)** Short-axis 2D and **(b)** color Doppler images of axial left coronary artery. (a) Ao, aorta; Circ., circumflex; LAD, left anterior descending; PV, pulmonary valve; RVOT, right ventricular outflow tract.

hearts, color flow mapping of the ventricular septum may require separate sweeps of the anterior and posterior portions of the septum to assess for muscular ventricular septal defects. Examination of the apical muscular septum may require repositioning of the transducer toward the apex during the short-axis sweep. A list of structures that should be identified on the left parasternal views is provided in Table 4.3.

A "ductal view" is obtained from imaging in a parasagittal plane from a high left parasternal window, with the transducer notch at 12 o'clock. This window lines up the ultrasound beam with the main pulmonary artery–ductus–descending aorta continuum and allows for exclusion of a normally located small patent ductus arteriosus (Fig. 4.14 and Videoclip 4.6). The distal aortic arch and superior thoracic aorta may also be visualized through the heart and the main pulmonary artery, and, in larger individuals, the aortic isthmus is sometimes best seen from this position. The heart may be used as an acoustic window for the rest of the thoracic descending aorta.

**Table 4.3** Structures viewed from left parasternal views

| | |
|---|---|
| Inferior vena cava | Right ventricle |
| Superior vena cava | Ventricular septum |
| Left atrium | Left ventricular papillary muscles |
| Right atrium | Aortic valve |
| Atrial septum | Pulmonary valve |
| Coronary sinus | Ascending aorta |
| Pulmonary veins | Coronary arteries |
| Mitral valve | Main and branch pulmonary arteries |
| Tricuspid valve | Pericardium |
| Left ventricle | |

Clockwise rotation of the transducer to a high left sternal border transverse plane (transducer notch at 3 o'clock) may better demonstrate the left pulmonary veins in some larger individuals.

## Suprasternal notch views

The child is placed in a supine position, and the neck and upper back may be arched with the assistance of a rolled towel or pillow. Imaging from the suprasternal notch [26–28] includes positioning of the transducer in the right supraclavicular region and occasionally in the left supraclavicular region. In the coronal, or short-axis, plane with

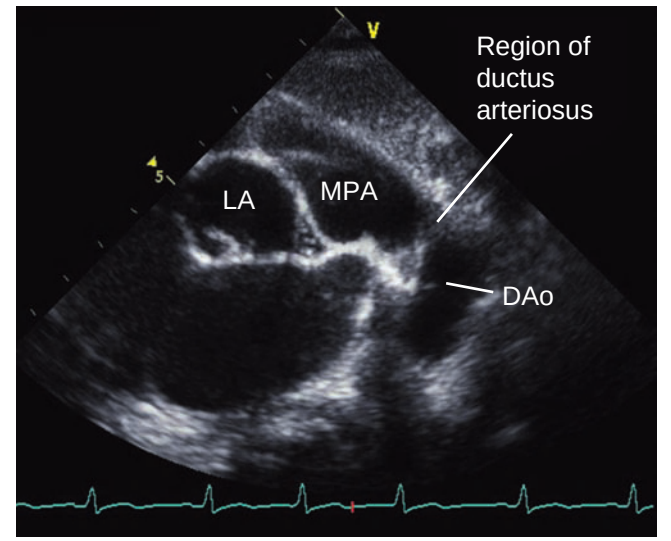


**Figure 4.14** Parasternal image of "ductal" view. DAo, descending aorta; LA, left atrium; MPA, main pulmonary artery.

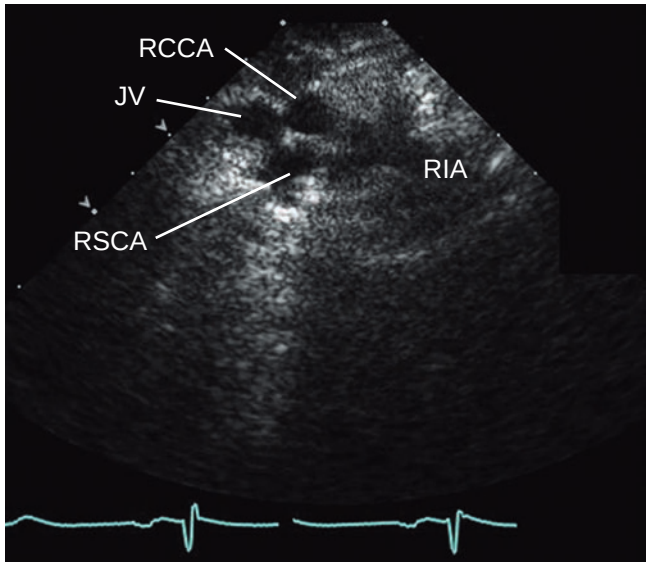


**Figure 4.15** Image of superiorly (cranially) angulated view of branching pattern of the aorta. JV, jugular vein; RCCA, right common carotid artery; RIA, right innominate artery; RSCA, right subclavian artery.

the transducer notch at 3 o'clock, the connection or absence of the left innominate vein to the right superior vena cava may be visualized. The leftward extent of the left innominate vein should be examined by color flow mapping to exclude a left superior vena cava or an anomalous pulmonary venous connection. Infrequently, small tributaries of the left innominate vein, such as the left superior intercostal vein or left internal thoracic vein, may be seen draining normally by color flow mapping.

From the suprasternal notch short-axis view, superior (cranial) angulation of the transducer demonstrates the branching pattern of the aorta (Fig. 4.15 and Videoclip 4.7(a,b)) [29]. The sidedness of the aortic arch may be determined as opposite of the direction, or sidedness, of the first brachiocephalic artery. Visualization of the aorta relative to the trachea or acoustic shadowing from the tracheal air column may help confirm arch sidedness. A normal branching pattern of the aortic arch should be documented by demonstration of a normally bifurcating first brachiocephalic artery; if the first branch does not bifurcate normally and/or the first and second branches are the same size, an aberrant origin of the subclavian artery should be suspected.

Demonstration of the left aortic arch in its long axis (Fig. 4.16 and Videoclip 4.8) is achieved by counterclockwise rotation, resulting in a transducer notch position of 1–2 o'clock from the coronal plane in the suprasternal notch window. The axis is from left shoulder to right anterior hip. As noted above, the distal aortic arch and aortic isthmus are sometimes best seen from a "ductal view." Further counterclockwise rotation and leftward angulation often best demonstrates the left pulmonary artery (Fig. 4.17). A list of structures that should be identified on the suprasternal notch views is provided in Table 4.4.

With the transducer in a nearly coronal plane (transducer notch at 3 o'clock) using an increased depth of field, the right pulmonary artery is demonstrated in its long axis. In smaller individuals, both the right and left pulmonary venous

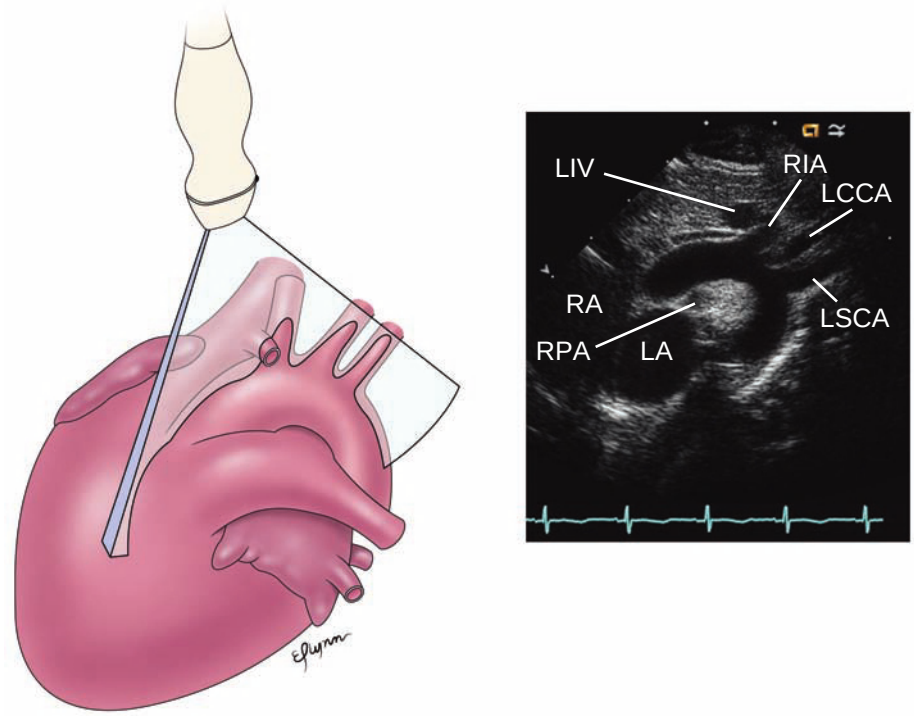


**Figure 4.16** Image of suprasternal notch aortic arch view. LA, left atrium; LCCA, left common carotid artery; LIV, left innominate vein; LSCA, left subclavian artery; RA, right atrium; RIA, right innominate artery; RPA, right pulmonary artery.

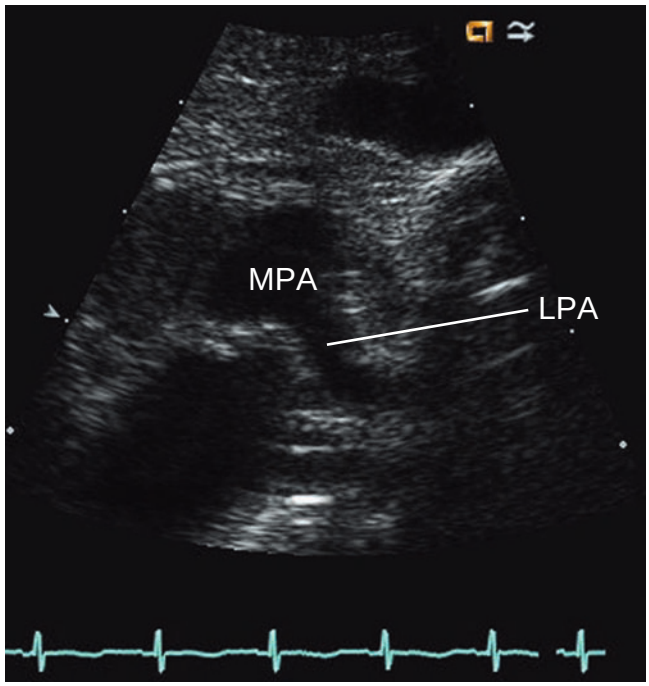


**Figure 4.17** Image of suprasternal notch left pulmonary artery view. LPA, left pulmonary artery; MPA, main pulmonary artery.

connections to the left atrium are well visualized in the far field of the suprasternal notch or left infraclavicular transverse view ("crab view") (Fig. 4.18 and Videoclip 4.9). Repositioning the transducer over the right supraclavicular or infraclavicular regions may better reveal the right pulmonary artery or right pulmonary veins. Flow in the superior vena cava may also be best seen in this plane.

**Table 4.4** Structures viewed from suprasternal notch views

| | |
|---|---|
| Superior vena cava | Main and branch pulmonary arteries |
| Left atrium | Aortic arch |
| Pulmonary veins | Proximal brachiocephalic arteries |
| Ascending aorta | Left innominate vein |
| Superior thoracic aorta | |

## Right parasternal views

The rightward extent of the atrial septum and nearby structures may be well visualized in a parasagittal imaging plane from the right parasternal border with the transducer notch at 12 o'clock (Table 4.5) [30]. Positioning of the patient in a right lateral decubitus position is often helpful. From a window at the mid to upper right sternal border (Fig. 4.19), the structures imaged are similar to the subxiphoid short-axis reference view: the atria, the atrial septum, and the superior and inferior venae cavae. The unique feature of the right parasternal window is that the atrial septum is oriented perpendicular to the plane of insonation, resulting in less "dropout" artifact. This view is therefore useful to assess for a sinus venosus defect. A sweep is made initially toward the right to demonstrate the rightward extent of the atrial septum and the right upper pulmonary vein. The azygos vein is often seen by imaging and color flow mapping as it arches over the right pulmonary artery and connects to the superior vena cava. The sweep then is directed leftward to image and color flow map the overlapping septum primum and septum secundum (Videoclip 4.10(a,b)). Doppler interrogation of the left ventricular outflow tract should also be performed from the

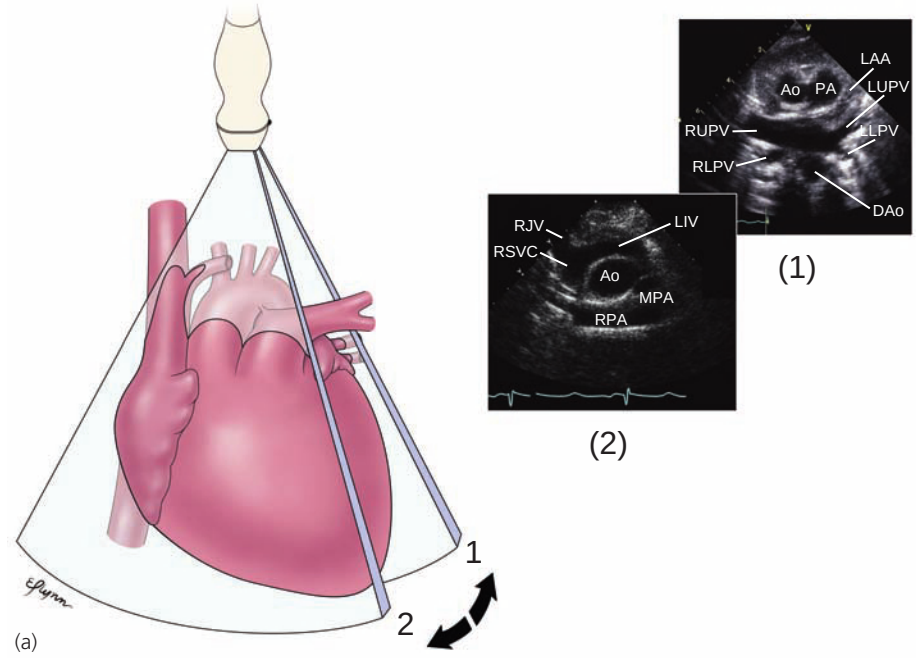


**Figure 4.18** **(a)** Serial images of suprasternal notch short-axis sweep. **(1)** Ao, aorta; LAA, left atrial appendage; LLPV, left lower pulmonary vein; LUPV, left upper pulmonary vein; PA, pulmonary artery; RLPV, right lower pulmonary vein; RUPV, right upper pulmonary vein; DAo, descending aorta. **(2)** Ao, aorta; LIV, left innominate vein; MPA, main pulmonary artery; RPA, right pulmonary artery; RJV, right jugular vein; RSVC, right superior vena cava.

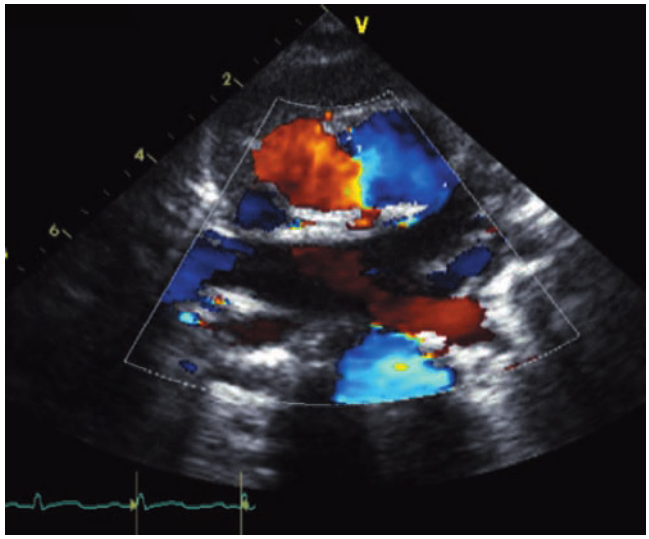


(b)

**Figure 4.18** **(b)** Color Doppler image of pulmonary veins to left atrium.

**Table 4.5** Structures viewed from right parasternal views

| |
|---|
| Inferior vena cava |
| Superior vena cava |
| Right atrium |
| Atrial septum |
| Right pulmonary veins |
| Ascending aorta |
| Right pulmonary artery |

superior right upper parasternal window if indicated. In larger children, a separate inferior window one or two rib spaces lower may be utilized to demonstrate the more inferior structures at the rightward extent of the heart.

Rotation into a short-axis (transverse) imaging plane from a superior right parasternal window, with the transducer notch then positioned at 3 o'clock, allows visualization and color flow mapping of the right upper pulmonary vein. Sweeping from cranial to caudal, the relative positions of the right superior vena cava and ascending aorta are seen, followed by the right pulmonary artery in its long axis. The right upper pulmonary vein is visualized just below the right pulmonary artery bifurcation. Frequently, three separate right pulmonary veins are demonstrated by imaging or color flow mapping (Fig. 4.20 and Videoclip 4.11(a,b)).

## Additional or supplemental imaging views

There are two "in-between" imaging views that are performed as part of a normal echocardiogram in some pediatric echocardiography laboratories. These "in-between" views are described as analogs of the right anterior oblique and the left anterior oblique, or long axial oblique, angiographic views used in cardiac catheterization procedures. The performance

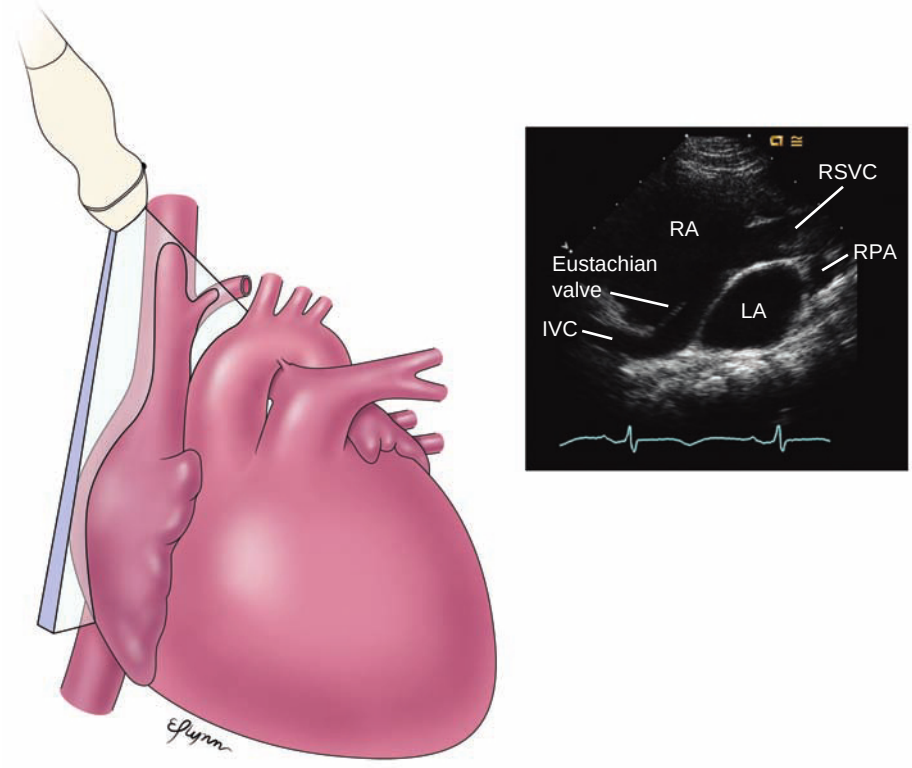


**Figure 4.19** Image of right parasternal longitudinal view. IVC, inferior vena cava; LA, left atrium; RA, right atrium; RPA, right pulmonary artery; RSVC, right superior vena cava.

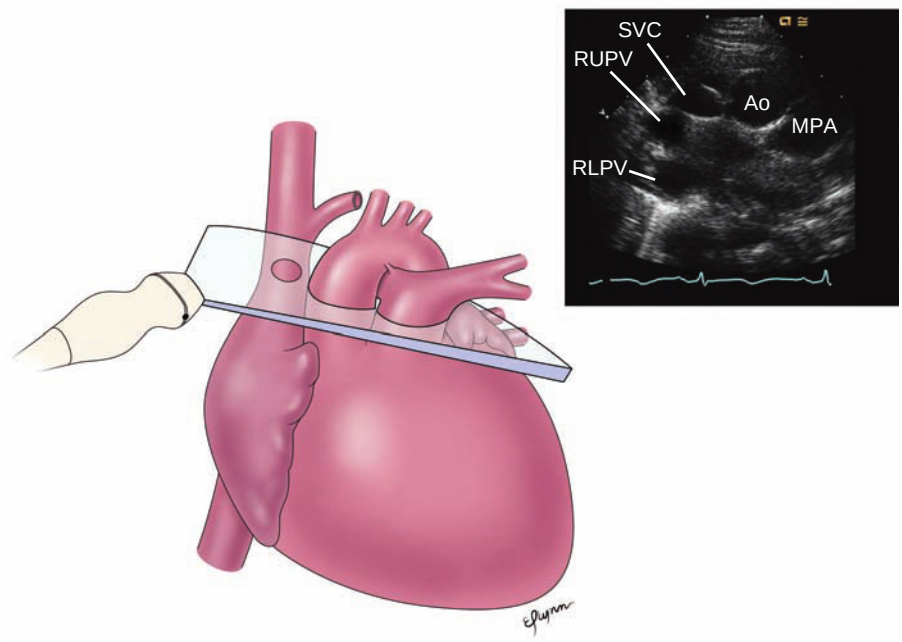


**Figure 4.20** Image of right parasternal short-axis view. Ao, aorta; MPA, main pulmonary artery; RLPV, right lower pulmonary vein; RUPV, right upper pulmonary vein; SVC, superior vena cava.

of these views is particularly important when cardiovascular malformations are suspected in the regions of interest.

## Right anterior oblique view

The right anterior oblique view [31,32] is acquired by rotation of the transducer approximately 45° counterclockwise from the standard subxiphoid long-axis view, resulting in the transducer notch being positioned at 1–2 o'clock (Fig. 4.21). This plane simultaneously images the inflow and outflow portions of the right ventricle and highlights abnormalities of conal septum, particularly when there is anterior malalignment. It also demonstrates the right ventricular outflow tract and the connection to the branch pulmonary arteries.

## Left anterior oblique view

The left anterior oblique view [33–35] is a sweep acquired by rotation of the transducer 30–45° clockwise from the standard subxiphoid long-axis view, resulting in the transducer notch being positioned at 4–5 o'clock, and scanning from base to apex (normally from right hip to left shoulder) (Fig. 4.22). This plane produces an en face view of the atrioventricular valves that best demonstrates any abnormal attachment of the atrioventricular valve leaflets and the chordal and papillary muscle positions. It also highlights the left ventricular outflow tract and can be used to perform Doppler interrogation of this region.

## "Flank" views

Supplemental imaging from the "flanks" is indicated when early postoperative examinations are performed. These views are obtained along the right and left posterior axillary lines near the level of the diaphragm with the transducer notch at 12 o'clock, resulting in a coronal imaging plane (with the superior structures to the right of the display screen and the inferior structures to the left) (Fig. 4.23). Whenever possible, the liver or the spleen should be used as an acoustic window in order to visualize the costophrenic margin and beyond to observe diaphragmatic motion as well as to rule out pleural effusion.

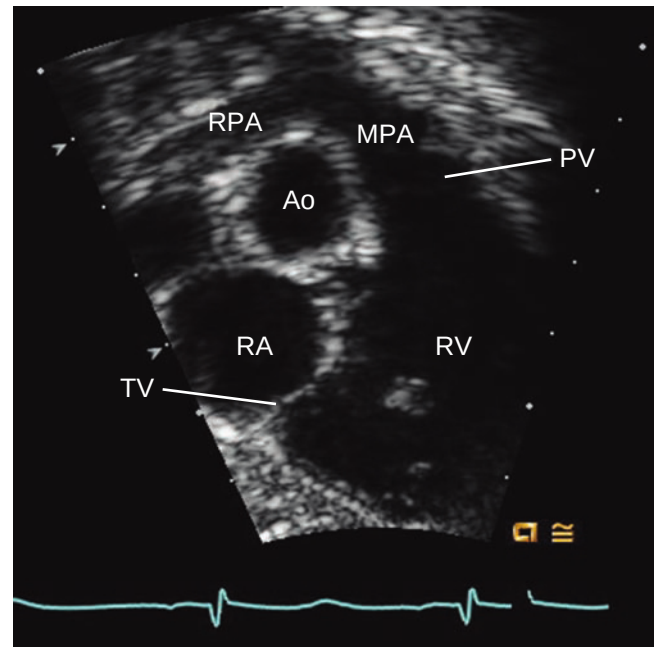


**Figure 4.21** Image of right anterior oblique view. Ao, aorta; MPA, main pulmonary artery; PV, pulmonary valve; RA, right atrium; RPA, right pulmonary artery; RV, right ventricle; TV, tricuspid ventricle.

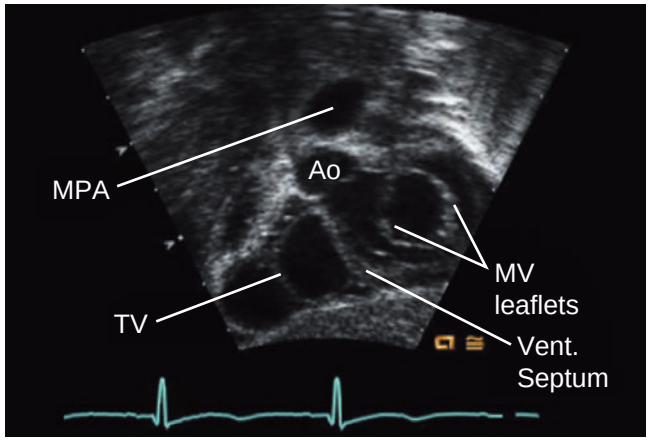


**Figure 4.22** Image of left anterior oblique view. Ao, aorta; MPA, main pulmonary artery; MV leaflets, mitral valve leaflets; TV, tricuspid valve; Vent. Septum, ventricular septum.

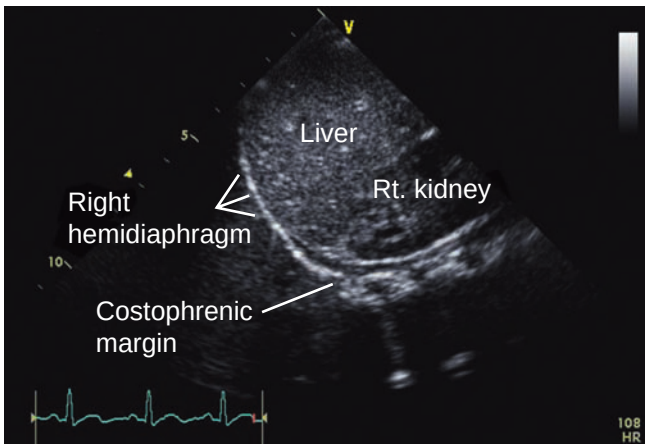


**Figure 4.23** Flank view. Rt., right.

## Measurements

The measurement of cardiac structures and flows is critical to the interpretation of a pediatric echocardiogram. An abnormally small or large structure can be a clue to otherwise silent pathology, and is important to the planning of surgical procedures. Mild forms of obstruction can be diagnosed only by accurate measurement of flow velocities.

In general, it is recommended that all relevant measurements be made as part of a complete pediatric echocardiogram, as outlined in Chapters 5–8 on quantitative methods. In addition, guidelines have been published for the echocardiographic assessment of valvar regurgitation [36] and the quantification of chamber size, ventricular mass and function in adult patients [19]. The measurements that are "relevant" in pediatric patients, however, will vary depending upon the specifics of their cardiovascular anatomy. The examination protocol of a laboratory should specify which measurements to perform and the laboratory procedure for obtaining each measurement.

Recommended measurements may be grouped into measurements of cardiovascular structures, ventricular size and function measurements, hemodynamic measurements, and miscellaneous/pathology-related measurements. The reader is referred to the appropriate sections of this textbook for a discussion of each of these measurement categories.

## Reporting

The minimal elements of a pediatric echocardiography report have been defined in guidelines published by the American Society of Echocardiography [11], and an adapted version is provided in Table 4.6. Basic identifier information should be listed, and a statement relating to the indication for study is required. Appointment information, including the indications for the study, should be provided. The patient's height and weight should be recorded for body surface area calculation. Conveyance of the echocardiographic findings in a clear and cogent manner is important. Abbreviations should be generally avoided or, when used, should be clearly noted and/or unambiguous.

The report findings section can be configured in a variety of ways but should include information on: (i) structural findings; (ii) measurements of cardiovascular structures made; (iii) Doppler echocardiographic data; and (iv) ventricular

**Table 4.6** Minimal elements for a pediatric echocardiography report

| |
|---|
| **Patient identifier data** |
| Name |
| Date of birth |
| Medical record identifier |
| **Appointment information** |
| Date of study |
| Location of study |
| Referring physician |
| Sedation used |
| Study indications |
| **Patient height and weight** (for body surface area calculation) |
| **Findings section** |
| Structural features (morphologic diagnoses) |
| Measurements of cardiovascular structures (with z-scores for comparison with normal data) |
| Doppler (hemodynamic) findings |
| Ventricular function assessment (quantitative or semiquantitative) |
| **Summary section** |

function assessment. Positive findings and pertinent negative findings should be listed.

Information pertaining to cardiovascular anatomy and structure can be conveyed utilizing the segmental approach. In addition to reporting the absolute values, it is useful to report quantitative measures within the context of age- or size-appropriate norms (e.g., z-score values) [37–39].

The important hemodynamic and ventricular function measurements are discussed in other sections of this textbook. Relevant Doppler information concerning the atrioventricular valves, semilunar valves and any shunt sites should be provided. Quantitative or semiquantitative Doppler and ventricular function information, when appropriate, should be included in the report.

A summary section should be provided. If possible, pertinent changes from the previous study should be noted. Any technical or other limitations – such as lack of patient cooperation – that might compromise the diagnostic accuracy of the echocardiographic examination should be specified in the report. Examples include suboptimal acoustic windows, heart rate constraints, and excessive patient motion during the examination.

## Conclusion

The normal pediatric echocardiogram includes multiple orthogonal views using two-dimensional, M-mode, Doppler and color Doppler techniques to document structural and hemodynamic findings. Written protocols for each pediatric echocardiography laboratory are useful to standardize the approach to these studies. A systematic approach to assessment using the segmental method will help assure completeness of the study. Structures should be imaged and displayed in their correct spatial, or "anatomically correct," position. A comprehensive report, including the indication for the study, positive findings, pertinent negative findings, and limitations to imaging should be provided.

## References


1. Henry WL, DeMaria A, Gramiak R et al. Report of the American Society of Echocardiography Committee on Nomenclature and Standards in Two-dimensional Echocardiography. *Circulation* 1980;62:212–17.
2. Snider AR, Serwer GA, Ritter SB. *Echocardiography in Pediatric Heart Disease*, 2nd edn. St Louis: Mosby, 1997.
3. Lev M. Pathologic diagnosis of positional variations in cardiac chambers in congenital heart disease. *Lab Invest* 1954;3:71–82.
4. Van Praagh R. Diagnosis of complex congenital heart disease: morphologic-anatomic method and terminology. *Cardiovasc Intervent Radiol* 1984;7:115–20.
5. Anderson RH, Becker AE, Freedom RM et al. Sequential segmental analysis of congenital heart disease. *Pediatr Cardiol* 1984;5:281–7.
6. Thomas JD, Adams DB, Devries S et al. Guidelines and recommendations for digital echocardiography. *J Am Soc Echocardiog* 2005;18:287–97.
7. Frommelt PC, Whitstone EN, Frommelt MA. Experience with a DICOM-compatible digital pediatric echocardiography laboratory. *Pediatr Cardiol* 2002;23:53–7.
8. Mathewson JW, Dyar D, Jones FD et al. Conversion to digital technology improves efficiency in the pediatric echocardiography laboratory. *J Am Soc Echocardiog* 2002;15:1515–22.
9. Chandraratna PA, Littman BB, Serafini A et al. Echocardiographic evaluation of extracardiac masses. *Br Heart J* 1978;40: 741–9.
10. O'Laughlin MP, Huhta JC, Murphy DJ Jr. Ultrasound examination of extracardiac chest masses in children. Doppler diagnosis of a vascular etiology. *J Ultrasound Med* 1987;6:151–7.
11. Lai WW, Geva T, Shirali GS et al. Guidelines and standards for performance of a pediatric echocardiogram: a report from the Task Force of the Pediatric Council of the American Society of Echocardiography. *J Am Soc Echocardiog* 2006;19: 1413–30.
12. Bierman FZ, Williams RG. Subxiphoid two-dimensional imaging of the interatrial septum in infants and neonates with congenital heart disease. *Circulation* 1979;60:80–90.
13. Lange LW, Sahn DJ, Allen HD, Goldberg SJ. Subxiphoid cross-sectional echocardiography in infants and children with congenital heart disease. *Circulation* 1979;59:513–24.
14. Sanders SP, Bierman FZ, Williams RG. Conotruncal malformations: diagnosis in infancy using subxiphoid 2-dimensional echocardiography. *Am J Cardiol* 1982;50:1361–7.
15. Limacher MC, Gutgesell HP, Vick GW et al. Echocardiographic anatomy of the Eustachian valve. *Am J Cardiol* 1986;57: 363–5.
16. Silverman NH, Schiller NB. Apex echocardiography. A two-dimensional technique for evaluating congenital heart disease. *Circulation* 1978;57:503–11.
17. Tajik AJ, Seward JB, Hagler DJ et al. Two-dimensional real-time ultrasonic imaging of the heart and great vessels. Technique, image orientation, structure identification, and validation. *Mayo Clin Proc* 1978;53:271–303.
18. DiSessa TG, Hagan AD, Isabel-Jones JB et al. Two-dimensional echocardiographic evaluation of discrete subaortic stenosis from the apical long axis view. *Am Heart J* 1981;101:774–82.
19. Lang RM, Bierig M, Devereux RB et al. Recommendations for chamber quantification: a report from the American Society of Echocardiography's Guidelines and Standards Committee and the Chamber Quantification Writing Group, developed in conjunction with the European Association of Echocardiography, a branch of the European Society of Cardiology. *J Am Soc Echocardiog* 2005;18:1440–63.
20. Tanaka M, Neyazaki T, Kosaka S et al. Ultrasonic evaluation of anatomical abnormalities of heart in congenital and acquired heart diseases. *Br Heart J* 1971;33:686–98.
21. Zema MJ, Caccavano M. Two dimensional echocardiographic assessment of aortic valve morphology: feasibility of bicuspid valve detection. Prospective study of 100 adult patients. *Br Heart J* 1982;48:428–33.
22. Jureidini SB, Marino CJ, Waterman B et al. Transthoracic Doppler echocardiography of normally originating coronary arteries in children. *J Am Soc Echocardiog* 1998;11:409–20.

23. Zeppilli P, dello Russo A, Santini C et al. In vivo detection of coronary artery anomalies in asymptomatic athletes by echocardiographic screening. *Chest* 1998;114:89–93.
24. Clouse M, Cailes C, Devine J et al. What is the feasibility of imaging coronary arteries during routine echocardiograms in children? *J Am Soc Echocardiog* 2002;15:1127–31.
25. Harada K, Tamura M, Toyono M, Takada G. Noninvasive visualization and measurement of great cardiac vein flow by transthoracic Doppler echocardiography in normal children. *Am J Cardiol* 2001;88:710–13.
26. Allen HD, Goldberg SJ, Sahn DJ et al. Suprasternal notch echocardiography. Assessment of its clinical utility in pediatric cardiology. *Circulation* 1977;55:605–12.
27. Sahn DJ, Allen HD, McDonald G, Goldberg SJ. Real-time cross-sectional echocardiographic diagnosis of coarctation of the aorta: a prospective study of echocardiographic-angiographic correlations. *Circulation* 1977;56:762–9.
28. Snider AR, Silverman NH. Suprasternal notch echocardiography: a two-dimensional technique for evaluating congenital heart disease. *Circulation* 1981;63:165–73.
29. Murdison KA. Ultrasonic imaging of vascular rings and other anomalies causing tracheobronchial compression. *Echocardiography* 1996;13:337–56.
30. McDonald RW, Rice MJ, Reller MD, et al. Echocardiographic imaging techniques with subcostal and right parasternal longitudinal views in detecting sinus venosus atrial septal defects. *J Am Soc Echocardiog* 1996;9:195–8.
31. Marino B, Ballerini L, Marcelletti C et al. Right oblique subxiphoid view for two-dimensional echocardiographic visualization of the right ventricle in congenital heart disease. *Am J Cardiol* 1984;54:1064–8.
32. Isaaz K, Cloez JL, Danchin N et al. Assessment of right ventricular outflow tract in children by two-dimensional echocardiography using a new subcostal view. Angiocardiographic and morphologic correlative study. *Am J Cardiol* 1985;56:539–45.
33. de Leva F, Caso P, Calabro R et al. Tetralogy of Fallot. Subcostal approach in bidimensional echocardiography. *G Ital Cardiol* 1984;14:113–20.
34. Chin AJ, Yeager SB, Sanders SP et al. Accuracy of prospective two-dimensional echocardiographic evaluation of left ventricular outflow tract in complete transposition of the great arteries. *Am J Cardiol* 1985;55:759–64.
35. Cohen MS, Jacobs ML, Weinberg PM, Rychik J. Morphometric analysis of unbalanced common atrioventricular canal using two-dimensional echocardiography. *J Am Coll Cardiol* 1996;28:1017–23.
36. Zoghbi WA, Enriquez-Sarano M, Foster E et al. Recommendations for evaluation of the severity of native valvular regurgitation with two-dimensional and Doppler echocardiography. *J Am Soc Echocardiog* 2003;16:777–802.
37. Fisher SD, Easley KA, Orav EJ et al. Mild dilated cardiomyopathy and increased left ventricular mass predict mortality: the prospective P2C2 HIV Multicenter Study. *Am Heart J* 2005;150:439–47.
38. Daubeney PE, Blackstone EH, Weintraub RG et al. Relationship of the dimension of cardiac structures to body size: an echocardiographic study in normal infants and children. *Cardiol Young* 1999;9:402–10.
39. Sluysmans T, Colan SD. Theoretical and empirical derivation of cardiovascular allometric relationships in children. *J Appl Physiol* 2005;99:445–57.

# 2 Quantitative Methods

*Echocardiography in Pediatric and Congenital Heart Disease: From Fetus to Adult*
Edited by Wyman W. Lai, Luc L. Mertens, Meryl S. Cohen and Tal Geva
 ISBN: 978-1-405-17401-5

# 5 Structural Measurements and Adjustment for Growth

**Thierry Sluysmans[1] and Steven D. Colan[2]**

[1]Universite Catholique de Louvain; Cliniques St Luc, Brussels, Belgium
[2]Department of Cardiology, Children's Hospital Boston, Boston, MA, USA

## Introduction

Observations of the developing cardiovascular system date from antiquity, with Aristotle's description of the beating heart in a chicken egg. However, quantitative description of the cardiovascular system, an essential part of William Harvey's method, was an essential step on the path of modern cardiology. The development of measurement techniques, beginning in the 19th century, combined with the ability to treat heart lesions beginning in the mid-20th century, spurred interest in accurate diagnosis and in methods correlating physiology with clinical outcome.

Determination of the dimensions of the heart and great arteries is mandatory for adequate diagnosis and treatment of congenital heart diseases [1]. For many cardiac disorders, these quantitative variables are highly predictive of outcome and provide critical information about response to therapy, timing of intervention and, most importantly, which type of intervention is likely to have the optimum outcome. Invariably, changes in the size and shape of cardiovascular structures can be secondary to factors other than the disease process, and methods are therefore required to differentiate these potential confounders from the disease process. These issues are particularly evident in children, where diagnostic evaluation is subject to the need to differentiate between disease or treatment effects and the effects of age and somatic growth. Because all cardiovascular structures increase in size in conjunction with growth, comparison of subjects whose body size is not identical requires some method of adjusting for this effect.

Of equal importance is the need for standardization of the methods by which these measurements are performed. Recommendations for standardization of measurements in adults have been published by the American Society of Echocardiography [2], but their relevance for pediatrics is limited due to a failure to include the full range of relevant measurements and the failure to consider the impact of body size and growth on the size of cardiovascular structures. These recommendations assume that the normal range and degree of abnormality of cardiovascular structures are independent of body size. Although this assumption is of questionable validity in adults, it is clearly invalid in children. In addition, due to both historical factors and because measurements are being performed for the management of a different spectrum of disorders, the manner in which the measurement is performed for the evaluation of congenital heart disease may not be the same.

Appendix 1 to this textbook contains a set of normative data for echocardiographic measurements that are derived from data collected at Children's Hospital Boston. The methods of data collection and analysis have been previously published [3,4]. The valid use of these normative data requires an understanding of the method of measurement to comprehend the circumstances under which these normative values can be employed, and these methods are presented in the appendix in conjunction with the data. Here we present a discussion of the general issues surrounding adjustment of cardiovascular structures for age and body size and the methods that were used in the derivation of the models that are provided in the appendix.

## Allometric modeling

Many disease processes result in a change in the size of cardiovascular structures, and these changes are often diagnostically and prognostically useful. For example, the magnitude of left ventricular (LV) dilation in patients with aortic regurgitation is useful in determining the severity of regurgitation and is also useful in predicting outcome after surgery. However, the usefulness of this variable is limited by the confounding effects of other factors that influence left ventricular size. In general, cardiovascular structures are highly plastic, remodeling in response to sustained changes in the hemodynamic state related to many interacting factors

*Echocardiography in Pediatric and Congenital Heart Disease: From Fetus to Adult*
Edited by Wyman W. Lai, Luc L. Mertens, Meryl S. Cohen and Tal Geva
 ISBN: 978-1-405-17401-5

including growth, development, exercise participation, genetics, body composition, basal metabolic rate and hematocrit, in addition to many environmental factors such as altitude and ambient temperature. Adjustment for these confounders improves the utility of these measurements. Body size and age are two of the most potent confounders, particularly in children, and considerable effort has been devoted by many investigators to identification of the relationship between body size and the size of cardiovascular structures. The relative growth of a part of an organism in relation to the growth of the entire organism is known as allometry, and therefore here we are concerned with cardiovascular allometry.

In addition to the implications of allometry for patient care, adjustment for the effects of changes in body size also has important implications for clinical research. Although many clinical trials attempt to avoid potential confounders by selection of a properly matched control group, if the disease or the therapeutic intervention can impact growth then detection of beneficial effects due to the therapeutic intervention can still be confounded by differential growth in the treated and untreated groups. For example, consider a study undertaken to determine if a novel medical therapy can favorably alter the severity of left ventricular dilation in infants with dilated cardiomyopathy. The typical study design would include active and placebo treated cohorts matched for age and body surface area at the time of study enrollment, thereby in theory permitting direct comparison of ventricular size between groups without the need to account for differences in body size. If growth during the treatment period was similar in children in both cohorts, comparison of the change in size of the LV between groups would address the study question. However, if active treatment influences somatic growth either directly or secondary to improved cardiovascular status, the increase in left ventricular size related to growth would confound the interpretation of the direct effects of treatment on left ventricular size. A method of directly adjusting for the effects of growth would improve the ability to accurately detect therapeutic effects.

## The fallacy of indexing for BSA: the so-called "per-BSA method"

Historically, the most common approach to the problem of adjusting cardiovascular structures for body size has been to express them as their ratio relative to body surface area (BSA). For example, "cardiac index" is usually calculated as cardiac output (CO) divided by BSA, and "ventricular mass index" is calculated as ventricular mass divided by BSA. The continued common reliance on such "per-surface area standards" [5] despite their lack of validity [6–8] justifies a critical discussion of the deficiencies in this method prior to an exploration of alternative approaches to this problem.

The per-BSA method was based on the observation that in numerous intra- and inter-species studies, body heat production and CO was documented to be linearly related to BSA over a broad range of body size [9,10]. Consequently, cardiac index (CO/BSA) was adopted as a reasonably valid method of comparing the CO of individuals of varying BSA. Next, based on regression models that found a nearly linear relationship between CO and the size of other cardiac and vascular structures, the per-BSA method was extrapolated and adopted by many as a general method for adjusting for the effects of growth on all cardiovascular structures.

Unfortunately, although the relationship between two variables can often be described as linear, this does not mean that this is the best descriptor of their relationship. Virtually any curve can be modeled as a line over a sufficiently short interval. However, the mathematical inadequacy of this method can be readily recognized by a simple example. There are many studies documenting a statistically significant linear relationship between left ventricular volume and BSA, and a statistically significant linear relationship between left ventricular dimension and BSA. However, volume and dimension are related by a cubic function, and it is therefore mathematically impossible for both volume and dimension to have a true linear relationship to BSA. The delusion that the per-BSA provides an adequate method of adjusting for the effects of body size is based on excess reliance on simple regression analysis performed over short ranges of the independent variable in the absence of critical examination of how well the mathematical model actually describes the data, particularly in the absence of any meaningful theoretical basis [11].

There is, in fact, a relatively simple statistical method by which to test whether an allometric model provides an adequate description of the relationship between body size and the size of the body part. The purpose of "indexing" or "normalizing" a variable such as CO for BSA is to permit valid comparisons between individuals of differing BSA by eliminating any residual dependence of the indexed variable on BSA. Therefore, if the method of indexing or adjusting for body size fully accounts for the effect of body size on the cardiovascular measurement, then the indexed variable will have the same mean value and the same distribution regardless of body size. From a statistical point of view, a variable indexed to BSA should have the same mean and distribution regardless of BSA.

It is worth considering a concrete example of how easily one can be misled by a high correlation coefficient obtained by linear regression. Figure 5.1 presents the strong linear relationship ($r = 0.92$) between the diameter of the aortic valve annulus (AoV) and BSA in 550 normal children varying in age from newborn to 18 years of age [3]. Such observations, in the absence of careful testing for whether this linear model eliminates residual dependence of AoV on BSA, has led to the common method of a per-BSA standard approach where "indexed AoV" is calculated as AoV divided by BSA.

What happens if we critically test whether the per-BSA method fully accounts for the effect of body size? As noted

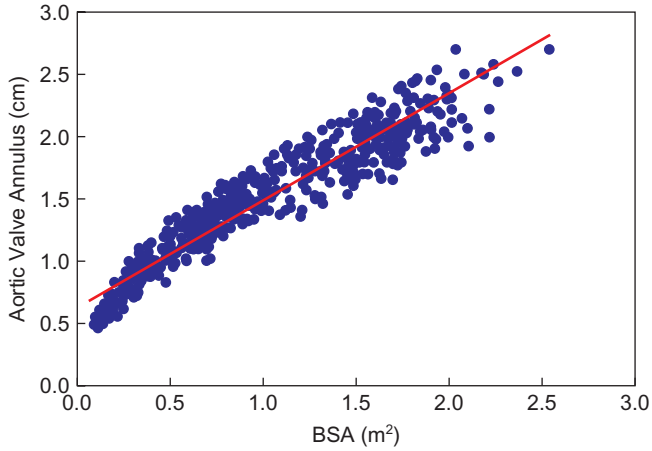


**Figure 5.1** Graph of aortic valve annulus dimension versus body surface area (BSA) in 550 normal children. The linear regression line is also shown.

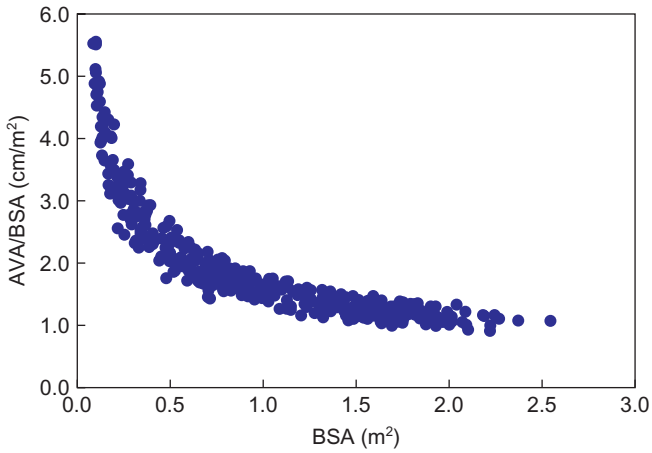


**Figure 5.2** Graph of AVA/BSA versus BSA in 550 normal children. AVA, aortic valve annulus dimension; BSA, body surface area.

above, this would imply that firstly, there should be no significant correlation between BSA and BSA-adjusted AoV, and secondly, BSA-adjusted AoV should have the same distribution regardless of BSA. Thus, if the normal range for AoV for an adult who is 1.8 $m^2$ is 1.2 ± 0.2 $cm/m^2$, then this same mean and standard deviation should be correct regardless of BSA. Figure 5.2 presents the relationship of AoV/BSA ("indexed aortic valve annulus diameter") to BSA. If this method of "indexing" were successful, AoV/BSA would have no correlation and no significant variance with respect to BSA. Instead, the relationship illustrated in Fig. 5.2 is curvilinear, the linear fit has a significantly non-zero slope value, and the data distribution around the mean value is not constant with BSA. Because, as shown in Fig. 5.2, the mean ± standard deviation (SD) of the "indexed aortic valve annulus diameter" for a BSA of 1.8 $m^2$ is 1.2 ± 0.2 $cm/m^2$, whereas for a BSA of 0.2 $m^2$ the mean ± SD is 3.5 ± 0.75 $cm/m^2$, this method clearly does not come close to meeting the requirements for an adequate method of normalization.

For the mathematically inclined, it is relatively easy to determine the circumstances under which the per-BSA method will fail. In order for the per-BSA method of indexing to work, three assumptions must be met. The relationship to BSA must be linear, the intercept of the regression line must be zero, and the variance must be constant over the range of BSA. The first two assumptions arise mathematically as follows. For any variable such as AoV, if the "indexed AoV" (AoVi) is calculated as AoVi = AoV/BSA, then this relationship can be rearranged as AoV = AoVi × BSA. This rearrangement reveals that the relationship has the equation of a line ($y = mx + b$) where the intercept ($b$) is zero and the line has a slope ($m$) equal to AoVi. If we look back at Fig. 5.1, the regression line does not pass through the intercept (AoVi = 0.65 when BSA = 0) and although the regression has a high correlation, the data deviate from the regression line such that at low and high BSA values the data points are skewed below the regression line whereas in the mid-range the data are skewed above the regression line, indicating that the relationship is not truly linear. The failure of the linear fit adequately to describe the data is best demonstrated by examining the residuals of the linear regression, shown in Fig. 5.3. Indeed, a significantly better fit ($r = 0.96$) can be achieved with a nonlinear curvefit of the form $y = mx^a + b$, as shown in Fig. 5.4. The superiority of the nonlinear regression is shown in Fig. 5.5, where the residuals of the nonlinear regression are seen to have no significant residual relationship to BSA. The failure to meet the third assumption (constant variance) is also shown in Figs 5.1 and 5.3, where the data spread around the regression line is seen to increase as BSA increases, which is to say the variance is not constant over the range of BSA. This pattern of having the variance rise as a function of BSA (nonconstant variance, or

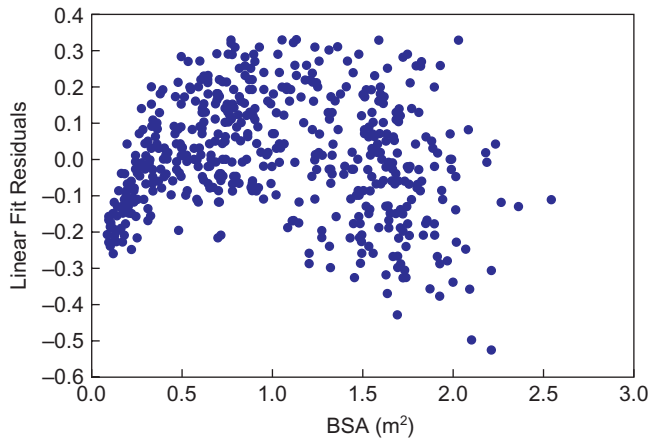


**Figure 5.3** Graph of the residuals of the linear regression of aortic valve annulus dimension versus body surface area (BSA) in 550 normal children. The residuals of the linear regression deviate from zero such that for low and high BSA values the residuals are skewed below zero whereas in the mid-range the data are skewed above zero, indicating that the relationship is not truly linear.

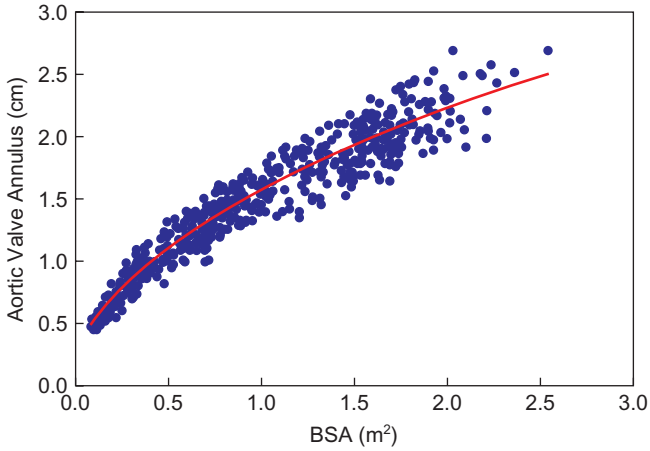


**Figure 5.4** Nonlinear regression of the form $y = ax^b + c$ for aortic valve annulus dimension versus body surface area (BSA) in 550 normal children.

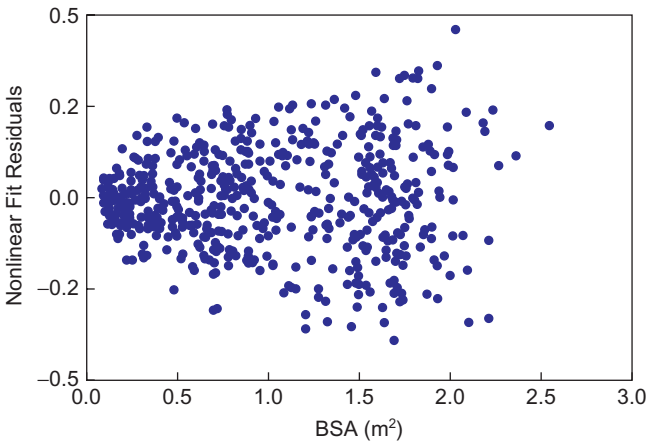


**Figure 5.5** Graph of the residuals of the nonlinear regression of aortic valve annulus dimension versus body surface area (BSA) in 550 normal children. The residuals of the nonlinear regression have no significant residual relationship to BSA, although the magnitude of the residuals clearly varies as a function of BSA (heteroscedasticity).

heteroscedasticity) is observed for virtually all cardiovascular parameters [11–15] and, as shown in Fig. 5.5, it is not eliminated by the nonlinear regression. Heteroscedasticity is a common statistical observation in almost all growth models in biology and economics [11] and can be explained by the BSA- and age-related increase in the interindividual variation in other factors that influence the size of these structures, such as blood pressure, adiposity, and habitual activity level.

## Alternative "indexing" methods

The inadequacy of the per-BSA method has led investigators to evaluate other approaches to adjusting for the effect of body size on the size of cardiovascular structures. The first and simplest is to attempt to linearize the relationship by transforming either the cardiovascular structure or the BSA.

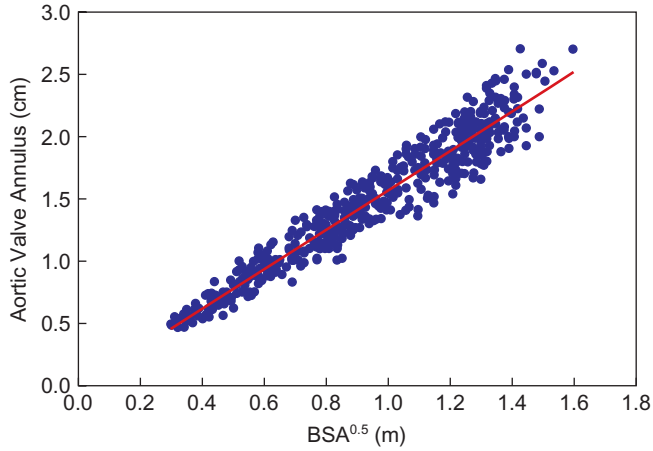


**Figure 5.6** Graph of aortic valve annulus dimension versus the square root of body surface area ($BSA^{0.5}$) in 550 normal children.

Several authors have noted that the areas of cardiovascular structures relate linearly to BSA, whereas their diameters relate linearly to the square root of BSA ($BSA^{0.5}$). It has in fact been suggested that this approach can be generalized [3] such that linear measurements should be normalized to $BSA^{0.5}$, area measurements should be normalized to BSA, and volume measurements should be normalized to $BSA^{1.5}$. In general, fully normalized variables should be dimensionless, and this method indeed results in dimensionless normalized variables because $cm/(m^2)^{0.5}$, $cm^2/m^2$ and $cm^3/(m^2)^{1.5}$ all reduce to cm/m.

If we explore this option with regard to the relationship of AoV versus $BSA^{0.5}$ (Fig. 5.6), the regression is indeed highly linear with a zero intercept, meeting two of the requirements for an adequate method of "indexing." The graph of $AoV/BSA^{0.5}$ versus BSA is shown in Fig. 5.7, and there is no significant relationship between the two. However, examination

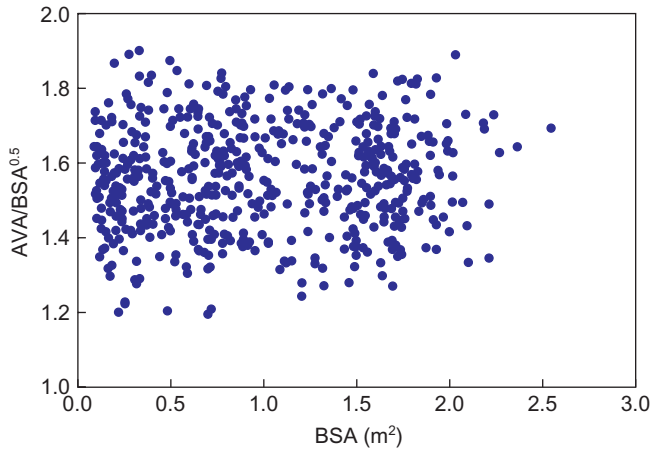


**Figure 5.7** Graph of the relationship between $AVA/BSA^{0.5}$ versus BSA in 550 normal children. AVA, aortic valve annulus dimension; BSA, body surface area; $BSA^{0.5}$ = square root of BSA.

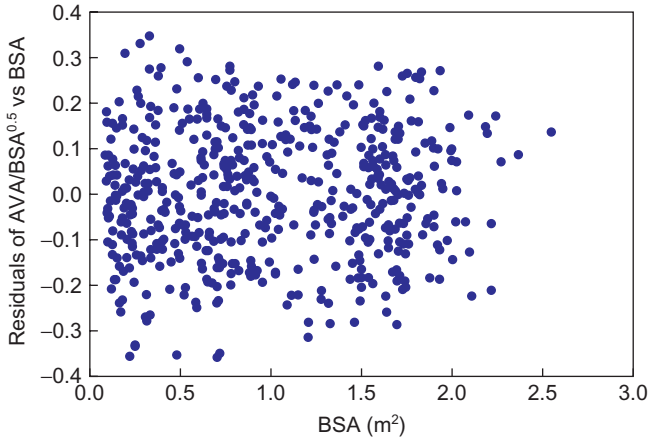


**Figure 5.8** Graph of residuals of the regression shown in Fig. 5.7 (AVA/$BSA^{0.5}$ versus BSA) in 550 normal children. AVA, aortic valve annulus dimension; BSA, body surface area; $BSA^{0.5}$ = square root of BSA.

of the residuals of the relationship between $AoV/BSA^{0.5}$ and BSA (Fig. 5.8) demonstrates that the data spread still varies as a function of BSA, thereby failing to meet the third criterion for an adequate method of "indexing." Besides failing to deal with heteroscedasticity, the approach of indexing to fixed (0.5, 1, 1.5) powers of BSA has not been uniformly successful in fully eliminating residual variance between BSA and certain cardiovascular structures, such as left ventricular dimension, volume and mass [4]. Similarly, the annuli of the tricuspid and mitral valves are usually elliptical such that the annulus area indeed relates to BSA but the major and minor diameters do not relate to $BSA^{0.5}$ [3].

## Z-score methods

The failure of these simpler methods has resulted in the growing dependence of the pediatric community on the use of z-scores, also known as normal deviates, to adjust for the effect of age and/or body size on the size of cardiovascular structures [16]. The z-score of a variable is the position, expressed in standard deviations, of the observed case relative to the mean of the population distribution. For cardiovascular structures, the calculation of z-scores is performed relative to the distribution of the structure in the normal population in order to adjust for the normal relationship to age or body size. Again, an example helps to illustrate this approach. For a given variable such as AoV the relationship versus BSA must first be determined directly in a large population of normal subjects and both the mean and standard deviation of the normal distribution are obtained as functions of BSA. For any new observation, the position of the variable within the normal distribution for that patient's BSA is then determined as the number of standard deviations from the normal population mean. For a patient who has an observed $AoV = AoV_O$, the mean value ($AoV_N$) of the parameter that would be expected for that body size in the normal population and the standard deviation ($SD_N$) of the parameter that would be expected for that BSA are used to calculate the z-score as $(AoV_O - AoV_N)/SD_N$.

Z-scores are normalized variables, which means that a z-score of zero represents a value at the normal population mean and a z-score of 1 or −1 represents a value that is 1 standard deviation above or below the normal mean. The interpretation of z-scores is exactly parallel to the use of percentiles to express age-adjusted height and weight relative to the normal population. In the case of height and weight, calculation of percentiles adjusts for the normally expected age-related change in height or weight, permitting comparison of subjects at varying ages. Although z-scores can be readily converted to percentiles, their use is preferable as they avoid range compression in the higher and lower ranges. For example, a z-score of 4 (4 standard deviations above the normal population mean) has a percentile of 99.8, whereas a z-score of 10 (10 standard deviations above the population mean) has a percentile of 99.9. At values outside of the normal range, it is much easier to appreciate the magnitude of abnormality of a structure when it is expressed as a z-score. The z-score approach represents the most powerful and flexible approach to normalizing cardiovascular parameters for the effects of age and BSA and has therefore become the standard approach in pediatric cardiology [16].

Several caveats concerning the application of z-scores should be discussed. Obviously, an appropriate population for determination of "normal" values must be selected, including an appropriate range for BSA and age as well as consideration of other potential confounders such as sex and race. The method of measurement must also be the same for the normal population and new cases. This implies that z-scores derived by echocardiography cannot be assumed to be applicable to measurements obtained using magnetic resonance imaging. The method of calculating BSA must also be the same as that used in the derivation of the z-scores, a requirement that is often neglected. There are a number of published methods for calculating BSA from height and weight, and the formulas do not yield the same results, particularly at lower values. Unfortunately, many publications do not indicate which of the several formulas has been used, making it impossible to compare results. Several of the older formulas continue to be used, despite their poor methodology. For example, the 1916 formula published by DuBois and DuBois [17] continues to be used by many authors despite the fact that measurements in only five subjects were used to derive the formula, no children were included, and the subjects most certainly were not normal because the smallest subject included in the study was a 34-year-old cretin dwarf!

For purposes of reference, the published formulas in most common use are:

The formula of Du Bois and Du Bois [17]:

$$BSA = 0.00718 \times height^{0.725} \times weight^{0.425}$$

The method of Dreyer and Ray [18]:

$$BSA = 0.1 \times weight^{0.6666}$$

The two methods published by Boyd [19]:

$$BSA = 0.0004688 \times (1000 \times weight)^{0.8168 - 0.0154 \log(1000 \times weight)}$$

$$BSA = 0.0003207 \times (1000 \times weight)^{0.7285 - 0.0188 \log(1000 \times weight)} \times height^{0.3}$$

The formula of Haycock et al. [20]:

$$BSA = 0.024265 \times height^{0.3964} \times weight^{0.5378}$$

The formula of Gehan and George [21], based on Boyd's data:

$$BSA = 0.02350 \times height^{0.42246} \times weight^{0.51456}$$

The formula of Mosteller [22]:

$$BSA = ((height \times weight)/3600)^{0.5}$$

For each of these formulas, height is in centimeters, weight is in kilograms and body surface area is in square meters. The formula with the soundest experimental basis is that of Haycock et al. [20]. In a systematic analysis of the normative data at Children's Hospital Boston, in which we compared the amount of variance of the cardiovascular structures relative to BSA that could be explained by each of these formulas, we found the Haycock formula to have the best performance [3].

## Choice of normalizing variable

The selection of which parameter of body size – height, weight or BSA – is optimal for the purposes of normalizing the size of cardiovascular structures has been controversial [23,24]. We found that in normal children, BSA performed better than height or weight [3]. The controversy concerning which variable is appropriate has arisen primarily in the discussion surrounding the correct method of adjusting for the effect of body size on left ventricular mass [25,26]. Concern has been expressed that use of BSA as the normalizing variable can result in underdetection of left ventricular hypertrophy in the presence of obesity. Physiologically, adipose tissue is less metabolically active than other tissues and therefore has a lower level of blood flow [27], implying that the normal relationship between BSA and CO is disrupted in the presence of obesity. The recommendation has therefore been put forward that left ventricular mass should be adjusted for height. However, there are substantial differences in lean body mass between individuals, and obesity is associated with an increase in lean body mass as well as adipose tissue. Adjustment for height alone ignores these differences. Alternatively, stroke volume and CO have been reported to relate more closely to fat-free mass [28], and therefore fat-free mass has been suggested as a potential allometric scaling variable [24]. However, fat-free mass is not generally measured in clinical practice and normative data relative to this variable are not available. Furthermore, although the blood flow requirements of adipose tissue are reduced, adipose tissue is not inert and therefore the impact of adipose tissue on cardiac output should not be totally neglected. It is likely that some adjustment for the relative amounts of fat-free mass versus adipose tissue will provide the most accurate method of incorporating body mass into the allometric scaling process, but more work is required to settle this issue.

## Heteroscedasticity

Another caveat concerning the application of z-scores is that a nonconstant variance of error has been demonstrated for virtually all echocardiographic measurement. As shown in Figs 5.4 and 5.5, the data range increases as the absolute value of BSA increases. This phenomenon, known as heteroscedasticity or nonconstant variance, has received considerable attention, as discussed in some detail by Abbott and Gutgesell [11]. There are several statistical methods that can be used to reduce nonconstant variance when constructing confidence and prediction intervals. These methods include multiple regression techniques [29], variance stabilizing transformations [11,16,29–31] and weighted least squares analysis [32]. Such statistical methods, although improving the accuracy of prediction intervals, are invariably ad hoc and lack a sound physiologic basis for choosing one method over another. In heart growth, data are skewed to the right, and logarithmic transformation is probably the most common type of transformation used in medical research for correcting heteroscedasticity and right skewed data [11]. For residuals that demonstrate a reasonably regular relationship to the independent variable, the method of Altman [33] has particular appeal of simplicity both in terms of calculation and interpretation. Regardless of the method that is selected, the end result must be tested to confirm that the final model results in an equal and constant distribution around the mean value over the full range of the independent variable, and that 96% of all data are included in the interval going from –2SD to +2SD.

## Analytic versus statistical derivation of z-scores

The methods described in the foregoing are based on the assumption that it is possible to define a continuous mathematical model, such as $y = ax^b + c$, that adequately describes the relationship between the size of the cardiovascular structure and either age or a parameter of body size over the full range of the independent variable. This approach has the unique advantage of permitting some conclusions to be reached concerning the nature of the physiologic relationships between these parameters. This is discussed in more

detail below, but briefly, the fact that the cross-sectional areas of the central arteries and cardiac valves are highly correlated with BSA, and that BSA is a primary determinant of CO, supports the concept that flow is a primary and reproducibly constant determinant of the growth of these structures. An alternative approach that has also been pursued is a purely statistical description of the data, which permits derivation of z-scores but does not provide any physiologic implications. Perhaps the best known of these approaches is the LMS (lambda-mu-sigma) method that has been used to calculate the z-scores and percentiles for height and weight data [34–37]. This method evaluates the population distribution over discrete intervals of the independent variable and then applies a smoothing function to the derived ranges to yield a continuous description of the data that is nevertheless not a single function over the full range. The variable nature of height and weight data relative to age lend themselves well to this approach. This technique is most advantageous when the determinates of growth are sufficiently heterogeneous that a single relationship that adequately describes the data over the full range of the independent variable cannot be identified. However, the other advantage is that the variance of the data does not have to follow a regular equation. That is, even if an adequate parametric model can be identified to describe the mean behavior of the population, the alternatives to the LMS method that were described above to deal with the problem of heteroscedasticity may still be inadequate. For example, we found that although an exponential growth model of the form $y = ax^b + c$ is adequate to describe the relationship between BSA and left ventricular mass over the full range of BSA, it was not possible to identify a method of calculating the standard deviation as a function of BSA that resulted in confidence intervals that adequately described the data at both the upper and lower ends of the data range. The LMS method overcomes this issue [38], albeit at the cost of eliminating any physiologic implications of the regression model. Nevertheless, for the explicit purposes of calculating normative data ranges, this approach appears to represent the best approach for those variables for which an explicit parametric approach fails to describe the data adequately.

## Principles underlying cardiovascular dimensions

The relation of cardiovascular dimensions and body size can be observed empirically and analyzed statistically, as described from echocardiographic measurements of cardiac and vascular dimensions. The relation can also be predicted theoretically from one or more basic physical principles or design characteristics. These two approaches can be used for purposes of reciprocal verification. That is, a higher level of confidence can be attached to conclusions that are achieved through both theoretical and empirical methods. We performed such a comprehensive analysis [3] and present the results in brief here.

The development and maintenance of optimum geometric properties of the vascular pathways is essential to provide adequate blood flow over a wide range of body activities, and simultaneously to avoid excess hemodynamic stress. Optimized design of biological structures as a result of the environmental pressure exerted by natural selection is an established principle of biology that explains the curvilinear relation of the weight of a tree and the size of its branch [39], the relation between the diameters of pulmonary bronchi and bronchial air flow [40,41] or the shape of eggs [42]. It is believed that the driving principle underlying the optimization of vascular dimensions is to minimize the energy required to propel blood in the vascular system by optimizing the interrelation between vessel radius and flow rates. Theoretical foundations of the principle of minimum work [43,44] and theoretical studies of optimality of the vascular system [45–50] have been validated by the quantitative studies of coronary [51] and cerebral artery dimensions [52]. The theoretical aspects and details of the calculations have been presented [45,51,52].

### The principle of minimum work

The energy cost of phasic blood flow is determined by two components. Viscous energy loss [53,54] is related to friction at the vessel–blood interface and decreases with increasing vessel radius. This is a geometric relationship related to the fact that the volume of contained blood increases as the cube of the radius whereas the surface area increases in proportion to the square of the radius. Therefore, the proportion of the blood that encounters a viscous interface decreases as the radius increases, which means there is proportionally less resistance to flow in large vessels. The second component of energy loss is due to the oscillatory nature of blood flow in the central vasculature. The oscillatory component of energy loss, related to the need to accelerate flow with every beat, increases as the blood column and the vessel radius gets larger and the inertia of the blood increases. The optimal vascular dimension is that at which the sum of these two energy demands is minimized, that is, when the vessel is not too big and not to small (Fig. 5.9). The viscous energy loss and the energy content of blood volume were calculated for the aorta and the main pulmonary artery over the entire range of body size (0.2–1.8 $m^2$ BSA) and over the whole range of CO corresponding to all physical activities (from 3.5 L/min/$m^2$ to 17.5 L/min/$m^2$ CO) in order to determine the optimal vessel size [3]. We found that the size of the aorta that we observed in our normal population corresponded to the theoretical optimal value in terms of energy dissipation for CO up to two times the resting CO in infants, increasing to values that were optimal for three to four times the resting CO for older children (Fig. 5.10). Data obtained from athletes and

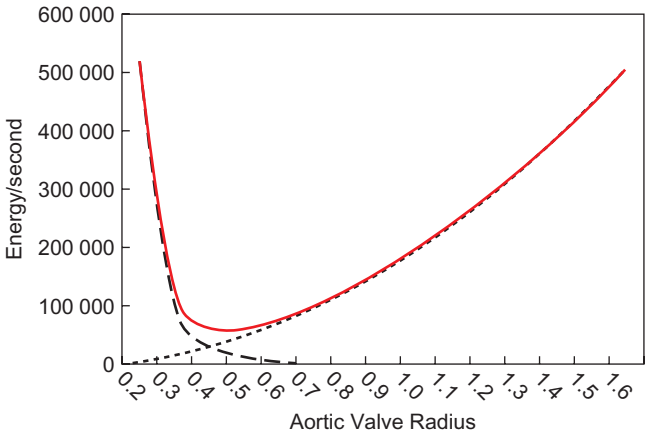


(a)

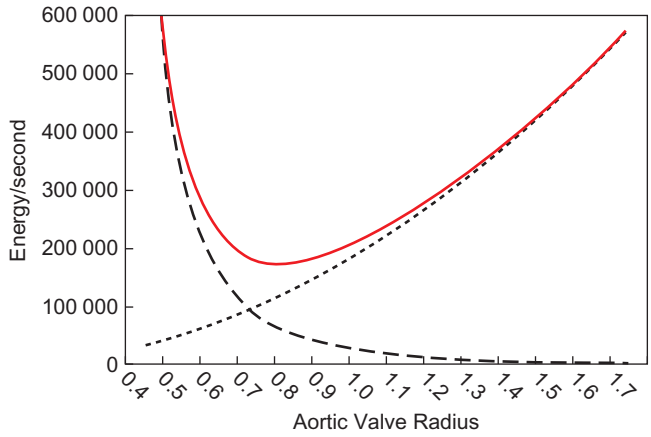


(b)

**Figure 5.9** Optimal aortic valve radius calculated according to the principle of minimal work for two levels of cardiac output. Energy loss per second (erg/s) because of viscous friction (long-dashed line) is plotted against the radius of the aortic valve (cm). On the same scale, the inertial energy content of blood (short-dashed line) and total energy loss calculated as the sum of viscous energy loss and inertial energy content loss (continuous line) are plotted for theoretical cardiac outputs of 3.5 L/min **(a)** and 17.5 L/min **(b)**, representing the theoretical cardiac output at rest and at maximal exercise of a normal subject with a body surface area (BSA) of 1 $m^2$. The least amount of total energy loss per unit time corresponds to the minimum of the total energy loss curve. The corresponding radius for 3.5 L/min flow is 0.45 cm, whereas it is 0.8 cm for 17.5 L/min. These values represent the theoretical range of normal optimal aortic valve radius for this BSA. Reproduced from Sluysmans T, Colan SD. Theoretical and empirical derivation of cardiovascular allometric relationships in children. *J Appl Physiol* 2005;99:445–57, with permission from the American Physiologic Society.

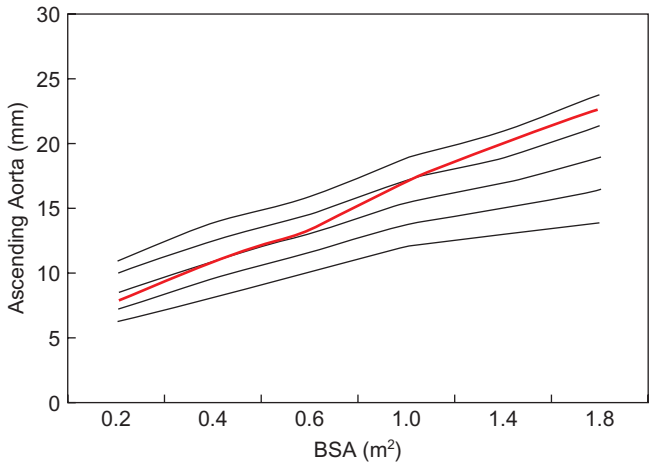


**Figure 5.10** Principle of minimum work: comparison of optimal dimensions and observed dimensions of vascular pathways. Comparison of the optimal valve and vascular diameters derived from the theoretical principle of minimal work and calculated for cardiac output of 1 × 3.5, 2 × 3.5, 3 × 3.5, 4 × 3.5 and 5 × 3.5 L/min, respectively (thin lines, from low to high values) with the mean observed values (thick line) of the ascending aorta in normal subjects. The normal mean diameters are optimal in terms of energy dissipation for cardiac output equivalent to twice the cardiac output at rest in infants and approximately four times the cardiac output at rest for older children, corresponding to the progressively higher peak activity level and heart rate reserve associated with growth. Vascular dimensions appear optimized to accommodate the cardiac output associated with peak normal activity. Reproduced from Sluysmans T, Colan SD. Theoretical and empirical derivation of cardiovascular allometric relationships in children. *J Appl Physiol* 2005;99:445–57, with permission from the American Physiologic Society.

hypertensive subjects indicate that cardiac structures adapt to peak or mean 24-h levels of pressure and volume demand. Heart rate response is the primary determinant of CO increase with exertion, and infants have an approximate 2-fold magnitude of heart rate reserve, a value that increases to 3–4-fold in older children and young adults. Thus the difference between observed diameters that are optimal in terms of energy dissipation in infants versus children corresponds to the expected difference in CO associated with age-appropriate physical activity and range of intensity of exertion.

## Adjustment of ventricular size for growth

In contrast to the finding that the cross-sectional area of the cardiac valves and vessels related most closely to BSA, and that valve and vessel diameters relate most closely with $BSA^{0.5}$, our empiric observation was that LV volume varies as a function of $BSA^{1.4}$ [3]. This observation was found to relate to the nonlinear decrease in heart rate (HR) that is seen with an increase in body size, where HR is proportional to $BSA^{-0.4}$ in normal human subjects [3]; and in various series evaluating different species of mammals with a 1800- to 500 000-fold increase of body weight, HR was proportional to $BSA^{-0.38}$ [55,56]. Cardiac output is equal to the product of heart rate (HR), end-diastolic ventricular volume (EDV) and ejection fraction (EF). If we combine the known linear relationship between CO and BSA ($CO \approx BSA^{1.0}$) [9,10] with our findings that $HR \approx BSA^{-0.4}$ and that EF is independent of BSA, the predicted relationship between ventricular volume and BSA is $EDV \approx BSA^{1.4}$. Left ventricular EDV, determined according to several different algorithms, related most closely to $BSA^b$ where mean $b = 1.38$ (range 1.343–1.398). This value is not

significantly different from the predicted value of 1.4, confirming the validity of the predictive model. It is also clear that when factors other than BSA influence basal heart rate, the relationship between BSA and ventricular size can be expected to change. Two examples of this are complete heart block and training-induced bradycardia, both of which are associated with ventricular volumes larger than would be predicted for BSA. Less well-investigated and outside the scope of this discussion is whether the normal age-related fall in heart rate in adults similarly influences the relationship between heart rate and ventricular size, creating a need for indexing ventricular size for both age and BSA.

## Conclusion

The progress in therapeutic options available to the pediatric cardiology community has made it requisite that we identify meaningful risk and outcome variables for evaluating our interventions, which often requires the ability to differentiate between the effects of body size and the effects of disease. Echocardiographic imaging techniques have made this information available on an unprecedented scale, enabling analyses that permit both improved understanding of the control mechanisms in the growth of cardiovascular structures and the routine application of normative data to clinical practice.

## References


1. Lipshultz SE, Miller TL. Establishing norms for echocardiographic measurements of cardiovascular structures and function in children. *J Appl Physiol* 2005;99:386–8.
2. Lang RM, Bierig M, Devereux RB et al. Recommendations for chamber quantification: a report from the American Society of Echocardiography's Guidelines and Standards Committee and the Chamber Quantification Writing Group, developed in conjunction with the European Association of Echocardiography, a branch of the European Society of Cardiology. *J Am Soc Echocardiog* 2005;18:1440–63.
3. Sluysmans T, Colan SD. Theoretical and empirical derivation of cardiovascular allometric relationships in children. *J Appl Physiol* 2005;99:445–57.
4. Colan SD, Parness IA, Spevak PJ et al. Developmental modulation of myocardial mechanics: age- and growth-related alterations in afterload and contractility. *J Am Coll Cardiol* 1992;19:619–29.
5. Tanner JM. Fallacy of per-weight and per-surface area standards, and their relation to spurious correlation. *J Appl Physiol* 1949;2:1–15.
6. Graham TP Jr, Jarmakani JM, Canent RV Jr et al. Left heart volume estimation in infancy and childhood. Reevaluation of methodology and normal values. *Circulation* 1971;43:895–904.
7. Gutgesell HP, Rembold CM. Growth of the human heart relative to body surface area. *Am J Cardiol* 1990;65:662–8.
8. Henry WL, Ware J, Gardin JM et al. Echocardiographic measurements in normal subjects. Growth-related changes that occur between infancy and early adulthood. *Circulation* 1978;57:278–84.
9. Grollman A. Physiologic variations in the cardiac output in man. *Am J Physiol* 1929;90:210–17.
10. Lange PE, Onnasch DG, Schaupp GH et al. Size and function of the human left and right ventricles during growth. Normative angiographic data. *Pediatr Cardiol* 1982;3:205–11.
11. Abbott RD, Gutgesell HP. Effects of heteroscedasticity and skewness on prediction in regression: modeling growth of the human heart. *Methods in Enzymology* 1994;240:37–51.
12. El Habbal M, Somerville J. Size of the normal aortic root in normal subjects and in those with left ventricular outflow obstruction. *Am J Cardiol* 1989;63:322–6.
13. King DH, Smith EO, Huhta JC et al. Mitral and tricuspid valve annular diameter in normal children determined by two-dimensional echocardiography. *Am J Cardiol* 1985;55:787–9.
14. Gutgesell HP, French M. Echocardiographic determination of aortic and pulmonary valve areas in subjects with normal hearts. *Am J Cardiol* 1991;68:773–6.
15. Lester LA, Sodt PC, Hutcheon N et al. M-mode echocardiography in normal children and adolescents: some new perspectives. *Pediatr Cardiol* 1987;8:27–33.
16. Kirklin JW, Blackstone EH, Jonas RA, Kouchoukos NT. Anatomy, dimensions, and terminology. In: Kirklin JW, Barrat-Boyes BG (eds) *Cardiac Surgery*. New York: Churchill Livingstone, 1993;21–60.
17. Du Bois D, Du Bois EF. A formula to estimate the approximate surface area if height and weight be known. *Arch Intern Med* 1916;17:863–71.
18. Dreyer G, Ray W. Further experiments upon the blood volume of mammals and its relation to the surface area of the body. *Philos T Roy Soc Lond* 1912;202:191–212.
19. Boyd E. *The Growth of the Surface Area of the Human Body*. Westport: Greenwood Press, 1935.
20. Haycock GB, Schwartz GJ, Wisotsky DH. Geometric method for measuring body surface area: a height-weight formula validated in infants, children, and adults. *J Pediatr* 1978;93:62–6.
21. Gehan EA, George SL. Estimation of human body surface area from height and weight. *Cancer Chemother Rep* 1970;54:225–35.
22. Mosteller RD. Simplified calculation of body-surface area [letter]. *N Engl J Med* 1987;317:1098.
23. Winter EM, Brooks GA. From Euclid to molecular biology and gene expression: where now for allometric modeling? *Exerc Sport Sci Rev* 2007;35:83–5.
24. Batterham AM, George KP, Whyte G et al. Scaling cardiac structural data by body dimensions: A review of theory, practice, and problems. *Int J Sports Med* 1999;20:495–502.
25. De Simone G, Daniels SR, Devereux RB et al. Left ventricular mass and body size in normotensive children and adults: Assessment of allometric relations and impact of overweight. *J Am Coll Cardiol* 1992;20:1251–60.
26. Daniels SR, Kimball TR, Morrison JA et al. Indexing left ventricular mass to account for differences in body size in children and adolescents without cardiovascular disease. *Am J Cardiol* 1995;76:699–701.
27. Frayn KN, Karpe F, Fielding BA et al. Integrative physiology of human adipose tissue. *Int J Obes Relat Metab Disord* 2003;27:875–88.

28. Collis T, Devereux RB, Roman MJ et al. Relations of stroke volume and cardiac output to body composition: the strong heart study. *Circulation* 2001;103:820–5.
29. Bates DM, Watts DG. *Nonlinear Regression Analysis and its Applications.* New York: John Wiley & Sons, 1988.
30. Zar JH. *Biostatistical Analysis.* Englewood Cliffs: Prentice-Hall, 1974.
31. Montgomery DC, Peck EA. *Introduction to Linear Regression Analysis.* New York: John Wiley & Sons, 1992.
32. Theil H. *Principles of Econometrics.* New York: John Wiley & Sons, 1971.
33. Altman DG. Construction of age-related reference centiles using absolute residuals. *Stat Med* 1993;12:917–24.
34. Ward R, Schlenker J, Anderson GS. Simple method for developing percentile growth curves for height and weight. *Am J Phys Anthropol* 2001;116:246–50.
35. Flegal KM. Curve smoothing and transformations in the development of growth curves. *Am J Clin Nutr* 1999;70:163S–5S.
36. Cole TJ, Freeman JV, Preece MA. British 1990 growth reference centiles for weight, height, body mass index and head circumference fitted by maximum penalized likelihood. *Stat Med* 1998;17:407–29.
37. Cole TJ, Green PJ. Smoothing reference centile curves: the LMS method and penalized likelihood. *Stat Med* 1992;11:1305–19.
38. Foster BJ, Mackie AS, Mitsnefes M et al. A novel method of expressing left ventricular mass relative to body size in children. *Circulation* 2008;117: 2769–75.
39. Murray CD. A relationship between circumference and weight in trees and its bearing on branching angles. *J Gen Physiol* 1927;11:431–41.
40. Weibel ER. *Morphometry of the Human Lung.* New York: Springer-Verlag, 1963.
41. Horsfield K. Diameters, generation, and orders in the bronchial tree. *J Appl Physiol* 1990;68:457–61.
42. Thompson DW. On the shape of eggs and on certain other hollow structures. In: Bonner JT (ed.) *On Growth and Form.* New York: Macmillan, 1943;935–57.
43. Murray CD. The physiologic principle of minimal work applied to the angle of branching arteries. *J Gen Physiol* 1926;6:835–41.
44. Murray CD. The physiologic principle of minimum work: I. The vascular system and the cost of blood volume. *Proc Natl Acad Sci U S A* 1926;12:207–14.
45. Pollanen MS. Dimensional optimization at different levels of the arterial hierarchy. *J Theor Biol* 1992;159:267–70.
46. Kamiya A, Togawa T. Optimal branching structures of the vascular tree. *Bull Math Biophys* 1972;34:431–8.
47. Kamiya A, Togawa T. Theoretical relationship between the optimal models of the vascular tree. *Bull Math Biophys* 1974; 36:311–23.
48. Zamir M. The role of shear forces in arterial branching. *J Gen Physiol* 1976;67:213–22.
49. Uylings HBM. Optimization of diameters and bifurcation angles in lungs and vascular tree structures. *Bull Math Biol* 1977;39: 509–20.
50. Sherman TF. On connecting large vessels to small: the meaning of Murray's law. *J Gen Physiol* 1981;78:431–53.
51. Seiler C, Kirkeeide RL, Gould KL. Basic structure-function relations of the epicardial coronary vascular tree: Basis of quantitative coronary arteriography for diffuse coronary artery disease. *Circulation* 1992;85:1987–2003.
52. Rossitti S, Löfgren J. Vascular dimensions of the cerebral arteries follow the principle of minimum work. *Stroke* 1993;24:371–7.
53. Caro CC, Pedley TJ, Schroter RC, Seed WA. Flow in pipes and around objects. In: Caro CG, Pedley TJ, Schroter RC, Seed WA (eds) *The Mechanics of the Circulation.* New York: Oxford University Press, 1978;44–78.
54. Yoganathan AP, Cape EG, Sung H-W et al. Review of hydrodynamic principles for the cardiologist: Applications to the study of blood flow and jets by imaging techniques. *J Am Coll Cardiol* 1988;12:1344–53.
55. Holt JP, Rhode EA, Kines H. Ventricular volumes and body weight in mammals. *Am J Physiol* 1968;215:704–15.
56. Rihl J. Die frequenz des herzschlages. In: *Handbuch der normalen und pathologischen physiologie.* Berlin: Springer, 1926;449–57.

# 6 Hemodynamic Measurements

**Steven D. Colan**
Department of Cardiology, Children's Hospital Boston, Boston, MA, USA

## Introduction

Hemodynamics refers to the physiology of blood flow and the forces responsible for blood flow. The discussion of hemodynamics is generally limited to pressure, flow and their complex interrelationship in the circulatory system. A complete understanding of hemodynamics requires knowledge of both blood flow and pressure throughout the cardiovascular system. Unfortunately, neither pressure nor flow can be directly measured using echocardiography. Instead, image and Doppler data are used to provide estimates of pressure and flow. An understanding of the strength and weakness of the echocardiographic methods used to assess hemodynamics is therefore critically important in avoiding misdiagnosis. The ensuing discussion is focused on the principles of fluid mechanics that underlie the hemodynamic assessment and the relationship between these principles and estimation of pressure and flow from ultrasound data.

The assessment of hemodynamics is fundamentally a quantitative process and it is tightly interwoven with fluid mechanics. The reliance on mathematical formulas to describe the mechanical behavior of the cardiovascular system is therefore necessarily intrinsic to assessing hemodynamics. This has the effect of intimidating many people who are not mathematically or quantitatively predisposed. This is unfortunate, because in most instances the important principles of fluid mechanics can be understood without the use of complex mathematics. The formulas are clearly necessary for the quantification of hemodynamics, and are therefore included in the presentation. However, insofar as possible the fluid mechanical principles will also be explained conceptually.

The study of mechanics in general is all about energy and forces acting on matter. The three primary forms of matter are solids (which have a definite shape and volume), liquids (which have a definite volume but no shape) and gases (which have neither a definite shape nor a definite volume). Fluids are substances that do not have a defined shape, and include both liquids and gases. Fluid mechanics is therefore specifically about the effects of forces acting on a gas or a liquid. Understanding hemodynamics is entirely dependent on the ability to measure and understand the forces acting on the circulatory system, and the primary mission of this chapter is to communicate the nature of these interactions and the echocardiographic methods available to measure them.

Issac Newton, amongst his manifold accomplishments, is perhaps best remembered for inventing the science of mechanics. Newton's second law states that changes in momentum of a body occur in proportion to the net forces acting upon it. Momentum is the product of mass × velocity, and therefore for situations where the mass is invariant, a change in momentum only occurs when there is a change in velocity. The equation that expresses this relationship is force = mass × acceleration. In addition to gravity, there are two other primary forces that act on liquids. Pressure is an omnidirectional force that acts perpendicular to all surfaces of the liquid and is the force that is most commonly measured when assessing hemodynamics. The other primary force acting on fluid that is in motion is shear stress, the viscous force that arises when elements of fluid move past each other or past a solid surface. Shear stress is conceptually equivalent to friction, and represents a form of kinetic energy. In contrast to pressure, shear stress is very difficult to measure and the role it plays in hemodynamics is far less familiar to students of hemodynamics. Newton's second law states that the net balance of forces must account for any observed changes in momentum of blood flow. Although this concept is often referred to as conservation of momentum, it does not imply strict conservation of momentum but rather that changes in momentum imply a proportional response to force. The secret to understanding hemodynamics is to follow the energy. This chapter includes a number of examples of how these sometimes unapparent energy fluxes arise and how they are hemodynamically important. Box 6.1 lists the abbreviations used in this chapter to represent certain variables and other parameters that are used in hemodynamics.

*Echocardiography in Pediatric and Congenital Heart Disease: From Fetus to Adult*
Edited by Wyman W. Lai, Luc L. Mertens, Meryl S. Cohen and Tal Geva
 ISBN: 978-1-405-17401-5

**Box 6.1 Symbols and abbreviations for hemodynamic variables and other parameters**

$m$ = mass
$v$ = velocity
$g$ = gravitational constant
$h$ = height
$E$ = energy
$P$ = pressure
ρ = density of blood
CSA = cross-sectional area
TVI = time–velocity integral
$Qp/Qs$ = ratio of pulmonary to systemic flow
PISA = proximal isovelocity surface area
EOA = effective orifice area
AOA = anatomic orifice area
$C_c$ = coefficient of contraction
ROA = regurgitant orifice area
RF = regurgitant flow

## Relationship between pressure and flow

Estimation of pressure differences between one anatomic location and another is one of the most common operations performed during the hemodynamic evaluation. The physical principles behind the relationship between pressure and flow are well defined but are complex. Pressure is a form of potential energy that can be converted to kinetic energy in the form of flow, and the conversion can also take place in the opposite direction, as the kinetic energy of flow gets converted into pressure. This process parallels that occurring with a roller coaster. An initial energy input is supplied to the coaster to elevate it to a position of high gravitational (potential) energy at the top of a steep descent. The gravitational energy ($E_G$) is calculated from the mass ($m$), the gravitational constant ($g$) and the height ($h$) as $E_G = mgh$. During the descent, potential energy is converted to the kinetic energy of high-velocity movement, and potential energy falls to zero at the nadir of the descent. Kinetic energy ($E_K$) is calculated from mass and velocity ($v$) as $E_K = {}^1/_2 mv^2$. The kinetic energy then propels the roller coaster up the next incline, and the kinetic energy is progressively converted to potential energy as velocity decreases and height is gained. The conversion is not perfect, as some energy is lost to heat (mechanical friction and wind resistance), so each subsequent hill must be a bit lower for the coaster to reach the top. The nature of the relationship between pressure and flow in the vascular system is exactly parallel, where pressure energy can be reversibly converted to the kinetic energy of flow, with invariably some loss of energy in the form of heat due to viscous friction.

### The Bernoulli equation

The Dutch mathematician Daniel Bernoulli (1700–82) described the mathematical relationship between pressure and velocity in steady laminar flow. The derivation of the Bernoulli equation is based on the conservation of energy principle, which states that the energy at all points within a closed system must be constant. For a fluid, the energy density (energy per unit volume) can be calculated from the pressure ($P$), density of the fluid (ρ), velocity of flow ($v$), the gravitational constant ($g$) and the height ($h$) as:

$$\text{energy density} = P + {}^1/_2\rho v^2 + \rho gh.$$

These three energy components are the pressure energy, the kinetic energy per unit volume, and the potential (gravitational) energy per unit volume. When comparing this calculation with the formulas presented above for gravitational and kinetic energy for the coaster, mass in this case is replaced by mass per unit volume (density). Based on conservation of energy, the energy density will be the same at any two points in the fluid, which means that:

$$P_1 + {}^1/_2\rho v_1^2 + \rho gh_1 = P_2 + {}^1/_2\rho v_2^2 + \rho gh_2.$$

If the measurement is performed at two points close to the same height, the gravitational components can be assumed to be equal and this relationship yields the familiar form:

$$P_1 - P_2 = {}^1/_2\rho(v_2^2 - v_1^2).$$

Although this formula is correct for steady flow, flow in the cardiovascular system is pulsatile in many locations, and therefore two components must be added to accommodate the inertial and viscous effects of flow, yielding what is generally known as the complete Bernoulli equation (Fig. 6.1). Although mathematically complex, the complete Bernoulli equation can be understood in a conceptual fashion that renders it both accessible and useful. The three terms in the complete Bernoulli equation account for convective (kinetic) acceleration, flow acceleration and viscous friction, and the nature and importance of each of these components can be considered independently because, as seen in the equation, their contributions to the net pressure difference are independent and additive.

$$\Delta P = \underbrace{\frac{1}{2}\rho(v_2^2 - v_1^2)}_{\text{Convective Acceleration (Kinetic) Component}} + \underbrace{\rho\int_1^2 \frac{dv}{dt}\,ds}_{\text{Local Acceleration (Inertial) Component}} + \underbrace{R(\mu,v)}_{\text{Viscous (Sheer Stress) Component}}$$

**Figure 6.1** The complete Bernoulli equation. $P$ = pressure, ρ = fluid density, $v$ = velocity, $t$ = time, $s$ = distance, and $R(\mu,v)$ is shear force expressed as a function of velocity ($v$) and position ($\mu$).

The first component in the complete Bernoulli equation quantifies convective acceleration, which is the acceleration of particles over a distance and describes the increase in velocity of a particle as it travels from point A to point B. This represents the change in kinetic energy and therefore this component is known as the convective or kinetic component. The kinetic component is obtained by measuring the velocity at the two locations and represents the simplified Bernoulli equation that is most commonly used for estimating the pressure drop across valves. For large pressure differences, the starting velocity ($v_1$) is generally small compared with the distal velocity ($v_2$), and is therefore generally ignored, reducing the equation representing the pressure drop to $^1/_2\rho v_2^2$, where ρ is the density of blood, which is approximately 1050 kg/m$^3$. So how does this formula get turned into $4v_2^2$, the commonly used formula in clinical practice, instead of $525v_2^2$? The formula in clinical use is used to report the pressure difference in units of mm Hg, but the right-hand side of the equation is in units of kg/ms$^2$. The conversion factor between mm Hg and kg/ms$^2$ is 133.3, and 525/133.3 = 3.94, which is rounded to 4, and hence we end up with pressure change in mm Hg = $4v_2^2$.

The second component in the complete Bernoulli equation, flow acceleration or local acceleration, is the acceleration at a point in phasic flow, and arises as a consequence of the inertial effects of oscillatory flow, that is, the need phasically to accelerate and decelerate the column of flow. This term is known as the inertial or local acceleration term. The difference between convective and local acceleration can be confusing, but it is important. At those positions of the cardiovascular system where flow is phasic, the velocity of flow at any given location will increase and decrease with each heartbeat. This is local acceleration. However, when matched for phase, the velocity at this location varies little from beat to beat. In contrast, if acceleration occurs between points A and B, the velocity is higher at point B even when matched for phase due to convective acceleration. Convective acceleration can be seen even in steady (nonphasic) flow, but local acceleration is seen only with phasic flow.

The periodic nature of the cardiac cycle has a number of implications for blood flow in the heart and central vasculature. The onset of a rise in pressure generates the force that accelerates the blood and generates flow. Because of inertial effects, the increase in flow velocity invariably lags behind pressure. In the arterial system this is readily seen when pressure and flow waveforms are viewed simultaneously. The effect can also be seen by evaluating flow across the mitral valve using Doppler while simultaneously recording pressure in the left atrium and ventricle (Fig. 6.2). When pressure in the left ventricle falls below that in the left atrium, the pressure difference between the left atrium and ventricle provides the force that accelerates flow into the left ventricle. The flow accelerates as long as pressure is higher in the atrium. Peak velocity occurs at the instant in time when

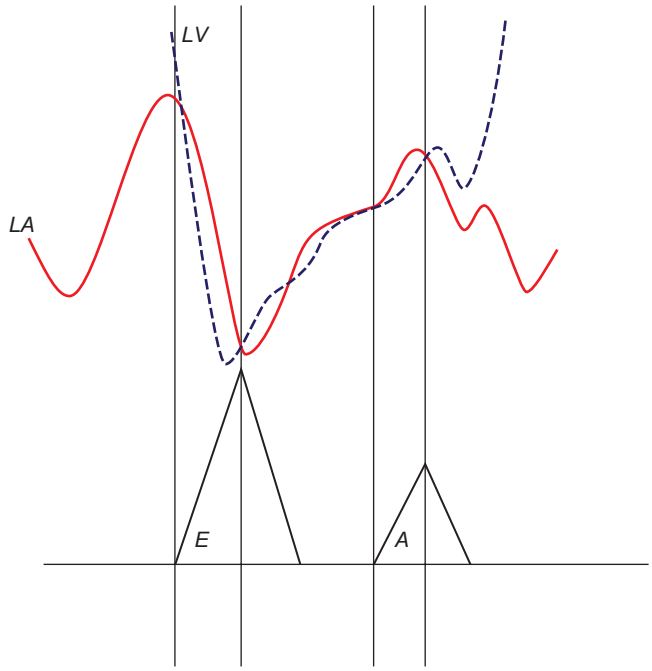


**Figure 6.2** The relationship between the mitral inflow velocity and the pressure difference between the left atrium (LA) and left ventricle (LV). Flow acceleration of the E-wave on the mitral inflow Doppler tracing begins with the first pressure crossover and corresponds with a period when LV pressure is higher than pressure in the LA. Peak velocity of the E-wave corresponds to the second pressure crossover and the deceleration phase of the E-wave corresponds to flow against the pressure gradient when LA pressure is higher than LV. This pattern is repeated during the A-wave.

the pressure is the same in both chambers, and the entire deceleration phase occurs when the pressure is lower in the atrium, and the reversed pressure difference acts as the force that decelerates the flow. The inertial forces account for the fact that blood flows against the pressure difference. This sequence of pressure differentials is repeated during atrial contraction. The local acceleration component accounts for the phase lag between the pressure wave and the flow wave. In the absence of obstruction, the inertial term of the complete Bernoulli equation dominates the convective (kinetic energy) term. This means that the simplified Bernoulli equation cannot be used to quantify intraventricular flow or flow across the unobstructed left ventricular inflow or outflow tracts [1]. However, because the phase lag is approximately symmetric during acceleration and deceleration phases, local acceleration has no significant impact on the calculation of mean pressure differences. Similarly, because acceleration is zero at peak pressure, this component also does not contribute to the calculation of the peak pressure drop. Therefore, although this component is important in understanding instantaneous pressure–velocity differences in the circulation, in the presence of obstruction we are usually more interested in mean and peak pressure differences between different anatomic locations in the circulation, and

when used for this purpose the inertial component of the complete Bernoulli equation can be ignored.

The third component in the complete Bernoulli equation relates to viscous forces. Viscous friction is a concept introduced previously and refers to the resistance to motion within a liquid. For blood flowing within a tube, the layer adjacent to the wall is immobile and acts as a brake on the adjacent layer, and so forth to the center of the tube. Smaller tubes exert more resistance to flow because the circumference is large relative to the contained area, whereas larger vessels have smaller surface areas acting on the fluid relative to the contained volume. For blood flowing through an orifice, the flow profile is nearly flat, that is, all the blood is flowing at the same velocity through the orifice. The issue of flow profiles is discussed in more detail in the next section, but the uniform velocity of flow means that although there is shear stress at the boundary with the valve, there are no significant viscous effects between adjacent layers. The net result is that, in general, the viscous friction component is negligible across valves, modest in large vessels, and quite important in small or stenotic vessels. For purposes of estimation of pressure losses across stenotic valves, this component can also generally be neglected. However, it is important to understand the circumstances under which viscous friction does contribute substantially, such as in the Blalock–Taussig shunt, and therefore the simplified Bernoulli equation does not perform well.

## Flow, velocity and acceleration

Flow refers to the quantity of fluid that passes a point during a specified length of time, and is expressed as units of volume per unit of time, for example liters/minute. Although the term "instantaneous flow" is sometimes encountered, this still represents the estimation of flow over some arbitrarily short interval and the units remain volume/time. Velocity is the rate of change in position of a mass, and in this case velocity of flow refers to the rate at which the liquid changes position; it therefore has units of distance per unit time, for example, meters/second. Acceleration is the rate of change in velocity, and has units of distance per time, for example meters/second$^2$.

Velocity of blood flow can be estimated noninvasively using the Doppler principle, but both flow and acceleration must be calculated and cannot be directly measured echocardiographically. There are two methods in common use for echocardiographic evaluation of blood flow. Image data can be used to calculate change in volume of a chamber, yielding the volume per beat. For example, left ventricular stroke volume, calculated as the difference between end-diastolic and end-systolic volume, represents the total volume of flow exiting the left ventricle over the course of a single cardiac cycle. This method cannot differentiate between forward flow across the aortic valve versus mitral regurgitation or flow through a ventricular septal defect.

Alternatively, blood flow can be quantified by multiplying flow velocity by the cross-sectional area (CSA) of flow. This important relationship is commonly used to derive flow, as flow = velocity × CSA, or to derive the area, as CSA = flow/velocity. Calculating the flow through a blood vessel or through an orifice is complicated by the need to measure the average velocity of flow across the cross-sectional area. To obtain the measure of flow equivalent to that obtained using the volumetric method described above, that is, as volume per beat, the flow must be calculated as the integration over the time period of interest of the average velocity multiplied by the cross-sectional area (CSA). There are several technical aspects of assessing orifice area and velocity that are of importance to Doppler measurements in general but are worth briefly mentioning prior to discussing the specific use of Doppler-based estimates of flow.

### Importance of angle of insonation for Doppler samples

The vector nature of velocity data dictates that the ultrasound sample beam must be oriented as closely as possible to the direction of flow. The Doppler shift that is induced in the reflected ultrasound is a direct manifestation of the motion of the reflector relative to the transducer. Motion directly toward or away from the transducer results in a maximum Doppler shift, whereas motion perpendicular to the ultrasound beam results in no Doppler shift. When the direction of flow is not parallel to the angle of insonation, the magnitude of underestimation of flow velocity varies as a function of the cosine of this angle. Although it is theoretically possible to calculate the true velocity of flow if both the measured velocity and the angle of insonation are known, in practice the accuracy of this calculation is suboptimal and it is far preferable to align the ultrasound beam with the direction of flow, a process that is considerably facilitated by use of color Doppler flow mapping.

### Flow profile

The velocity that is relevant to calculation of flow is the average velocity over the CSA, that is, the spatial average. Average or mean velocity can be a significant source of confusion because the average can be calculated with respect to either time or space. The term 'average velocity' is used here to differentiate the spatial average from the mean value over the course of the cardiac cycle, that is, the temporal mean. The temporal mean velocity is commonly measured clinically to determine the mean pressure drop across valves. Whereas the temporal mean velocity can be calculated from the spectral Doppler time–velocity tracing, the spatial mean is more difficult to measure. This difficulty is encountered because velocity varies across the cross-section of the vessel or orifice whereas spectral Doppler measurements are made

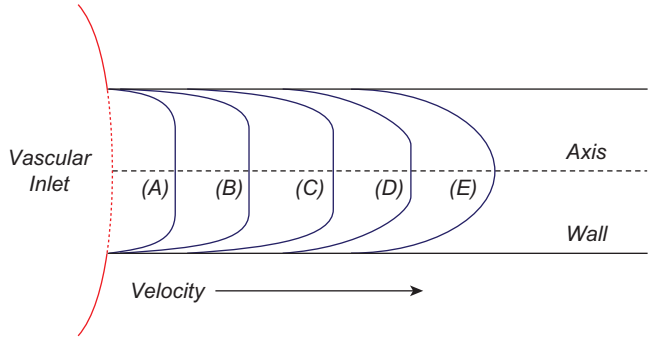


**Figure 6.3** Steady laminar flow in a straight tube has a nearly flat velocity profile at the inlet; the profile becomes progressively more parabolic (A–E) as it travels into the vessel. The peak velocity increases progressively during this transition.

*A. Cross-sections at which axial velocity profiles are presented.*

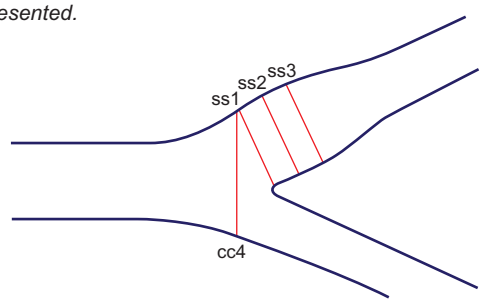


*B. Axial velocity profiles for the common and internal carotid arteries in the symmetry plane.*

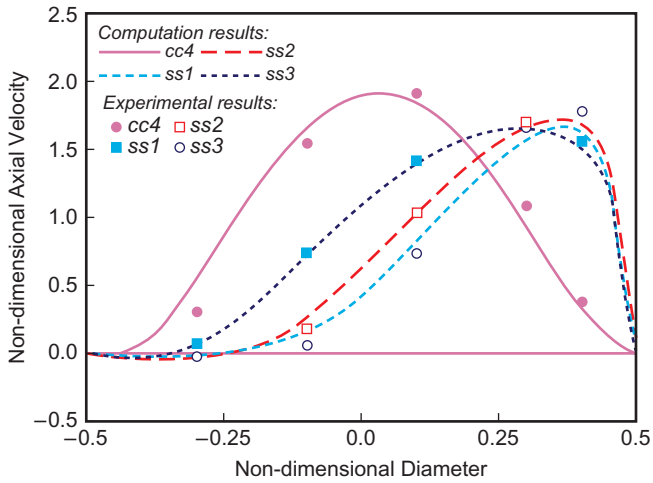


**Figure 6.4** Flow profile at the carotid bifurcation. The flow profile proximal to the bifurcation is parabolic, but is skewed toward the side of bifurcation within the internal carotid with a marked reduction in axial velocity. Reprinted from Hyun S, Kleinstreuer C, Archie JP Jr. Computational particle-hemodynamics analysis and geometric reconstruction after carotid endarterectomy. *Comput Biol Med* 2001;31:365–84, with permission from Elsevier.

over a small sample volume that may or may not be representative of the average velocity. The variation in velocity across the flow stream is known as the flow profile, and in a straight, rigid tube with steady laminar flow the velocity profile is parabolic, with zero velocity near the wall and the highest velocity in the center of the tube (Fig. 6.3). Mathematically, parabolic flow has an axial (peak) velocity that is twice the mean spatial velocity. In contrast, flow entering a tube from a reservoir has a flat velocity profile at the inlet and gradually becomes parabolic as flow propagates through the tube (Fig. 6.3). This transition relates to the viscous drag between the wall and the adjacent fluid. The area over which this interaction affects the rate of flow is known as the boundary layer. As flow in the boundary area is slowed by viscous drag between the wall and the fluid, the effect of viscous drag between adjacent areas of fluid progressively increases the thickness of the boundary area. Because net flow remains constant, the fall in velocity in the periphery of the vessel is accompanied by acceleration of central flow. Consequently, when the velocity profile is parabolic, the maximum velocity significantly overestimates the mean velocity. Because the velocity profile at the vessel inlet is flat, spectral Doppler measurement of the peak velocity at this level provides a valid estimate of average velocity, and valid estimates of flow can therefore be calculated. Elsewhere in the circulation, for example if an estimate of relative flow volume into the left and right pulmonary arteries is required, a three-dimensional assessment of velocity is required to derive the spatial average velocity for flow calculations [2,3]. The three-dimensional echocardiographic methods of measuring flow are relatively new, are not widely available, and have had limited validation to date.

Vascular flow profiles have other important implications, which are often insufficiently appreciated. At vascular bifurcations, such as the carotid artery bifurcation [4], the greater central velocity in the carotid artery results in a skewed velocity profile in the internal carotid artery, with greater velocity flow along the aspect of vessel adjacent to the bifurcation (Fig. 6.4). For flow in a curved tube, the flow profile in the curved segment depends on the flow profile at the entrance to the curve. If the flow profile at the entrance is parabolic, the location of the maximum axial velocity is shifted toward the outer wall and flow velocity along the inner wall slows and may develop vortices or flow reversal [5]. In contrast, if the flow profile is flat at the entrance to the curve, centrifugal forces produce higher pressure in the outer aspect of the curve, and according to the Bernoulli principle the lower pressure at the inner curvature results in higher velocity along the inner aspect of the vessel. The flow profile in the ascending aorta is generally flat, and therefore the aortic arch manifests greatest velocity of flow along the inner curvature.

## Doppler flow quantification

The most commonly used location for flow assessment is the aortic valve. In the normal aortic valve, the diameter of the

orifice can be measured at the level of the annulus with a high degree of accuracy and reproducibility, and the CSA can then be calculated as a circle, $CSA = \pi \cdot (\text{diameter}/2)^2$. The time–velocity curve of a pulsed Doppler sample placed at the same anatomic position at which the diameter was measured is digitized to obtain the time–velocity integral (TVI). The per-beat flow across the valve (stroke volume) is calculated as the product of CSA and TVI. Finally, multiplication of stroke volume by heart rate provides cardiac output. The use of pulsed Doppler ensures that the velocity sample is obtained at the vascular inlet, where the flow profile is flat. If continuous-wave Doppler is used, the peak velocity may be erroneous due to sampling of more distal flow profiles where onset of a parabolic flow profile results in mid-vessel flow acceleration (Fig. 6.3).

In theory, other locations can be sampled in a similar fashion, but in each case there are additional factors that reduce the accuracy of the method. For example, estimation of volume of flow across the pulmonary valve in addition to flow across the aortic valve should in theory permit calculation of the relative magnitude of pulmonary versus aortic flow ($Qp/Qs$). In practice, measurement of the pulmonary valve orifice area is subject to greater error than the aortic valve due to technical factors such as the need to rely on lower-resolution lateral measurements instead of axial resolution, and poorer images of the pulmonary valve. Because the annulus diameter is squared in the calculation of CSA, a 10% error in measurement of the diameter results in a 19% error in CSA. Furthermore, because $Qp/Qs$ is a ratio, if a pulmonary valve diameter of 10 mm is mis-measured as 9 mm, the resulting error in $Qp/Qs$ is 25%. Clearly, relatively small measurement errors can have an unexpectedly large impact.

Flow across either of the atrioventricular valves can in theory be measured as well, but both measurement of annulus area and flow across the annulus present additional problems. The atrioventricular valve annuli are often elliptical, and hence area calculation requires measurement of both the major and minor diameters. The atrioventricular valve annulus is also more compliant than the semilunar valve annulus and varies dynamically over the course of diastole. Measurement of flow velocity across the atrioventricular valves must also take into consideration the motion of the valve over the course of the cardiac cycle, an issue that is not commonly appreciated. In order to calculate flow across the mitral valve, the flow velocity relative to the mitral annulus is the required datum. However, the blood velocity that is obtained when the Doppler sample volume is positioned at the mitral annulus is actually the velocity of flow *relative to the transducer*, not relative to the annulus. This is true for the aortic annulus as well, but the motion of the aortic valve relative to the transducer is small. By contrast, there is significant motion of the mitral annulus. During systole, the apex remains fixed while the mitral annulus is pulled toward the apex, and this motion is reversed in diastole. Long-axis shortening in the normal heart is 20 ± 5%. Although many textbooks of echocardiography state that transmitral flow can be calculated by multiplication of TVI × CSA, failure to incorporate annular motion into the calculation of mitral flow results in an underestimation of transmitral flow of about 20%. In theory, the motion of the mitral annulus relative to the annulus can be measured and can be incorporated into the calculation, but the accuracy of such an approach has not been validated.

### Continuity equation

Because the vasculature is a closed system, the principle of conservation of mass predicts that flow at various points in the circulation will be equal, a concept expressed quantitatively in the continuity equation. For example, in the absence of intracardiac shunts or valve regurgitation, the flow across all four cardiac valves will be equal. For the aortic and mitral valves, this can be expressed quantitatively:

$$CSA_{aortic} \times FVI_{aortic} = CSA_{mitral} \times FVI_{mitral}$$

The continuity equation has been used extensively in the calculation of flow orifice size. In this example, if the mitral valve is stenotic, measurement of the aortic CSA and the FVI across both valves permits calculation of the orifice of the stenotic mitral valve as:

$$CSA_{mitral} = (CSA_{aortic} \times FVI_{aortic})/FVI_{mitral}$$

The continuity equation is commonly used to estimate regurgitant volumes. In the absence of an interventricular communication, the difference in antegrade flow volume across the aortic and mitral valves represents additional flow secondary to aortic or mitral regurgitation. The continuity equation also forms the basis of the calculations involved in estimating the volume of regurgitant flow using the proximal isovelocity area (PISA) method. This method is discussed in more detail below.

## Flow through a stenotic orifice

Flow through a stenotic orifice is an important source of hemodynamic disturbances and therefore a focal point of cardiovascular evaluation. Flow can be either antegrade, such as flow across a stenotic aortic valve, or retrograde, as is seen in aortic regurgitation. Although these two situations are generally discussed as completely distinct phenomena, the two situations have identical physics of flow, which therefore underpins the methods of assessing the physiologic significance of either stenosis or regurgitation. Despite their similarities from a hydrodynamic perspective, there is a fundamental difference in the nature of the hemodynamic burden associated with each of these lesions. Antegrade flow

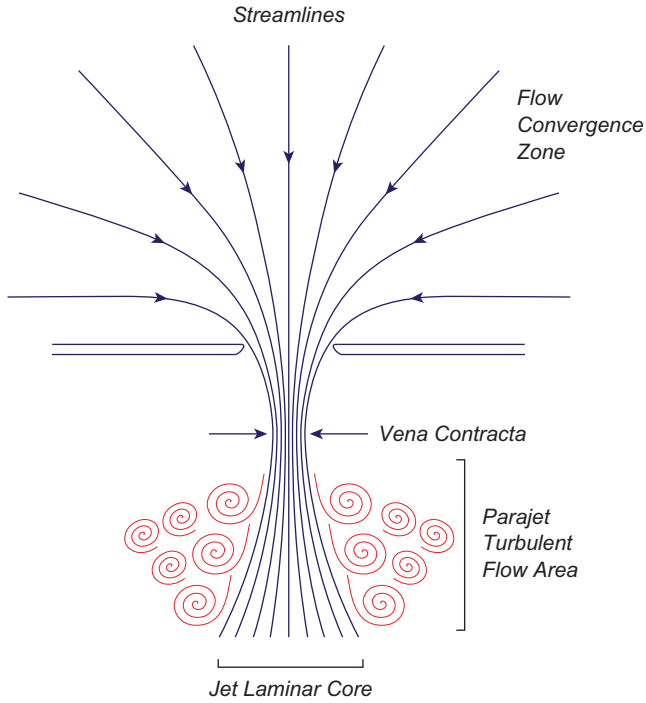


**Figure 6.5** Flow through an orifice in a flat surface. The flow convergence area is characterized by nonturbulent flow that follows streamlines converging in a symmetric pattern. The inertial forces of the peripheral streamlines are directed toward the center of the orifice and exert forces in a direction that narrows the jet to a minimum cross-sectional area at the level of the vena contracta; the streamlines then diverge in the jet laminar core. The parajet area is characterized by turbulent flow eddies.

across a stenotic valve represents a situation where the delivery of a fixed volume of flow across a stenotic orifice creates a variable pressure load in the originating chamber. We are therefore interested in assessing the magnitude of the pressure load associated with antegrade flow across a stenosis. By contrast, regurgitation through a stenotic orifice represents a situation where a fixed pressure results in a variable magnitude of retrograde flow. The regurgitant volume therefore represents the primary hemodynamic burden associated with valve regurgitation, and as such represents the primary parameter of interest in assessing the clinical importance of valve regurgitation.

Doppler assessment of stenotic orifices represents one of the more crucial advances in the noninvasive assessment of hemodynamics. There are many limitations to these methods, and an understanding of the physics of flow through a vascular or valve stenosis is critical to comprehension of these limitations. Figure 6.5 illustrates the manner in which the flowing liquid converges as it approaches and enters an orifice. The equal force that is present throughout a liquid results in flow from all directions moving directly toward the orifice, following flow streamlines as indicated in Fig. 6.5. As the streamlines approach the orifice they converge and enter the orifice. The inertia of the peripheral streamlines pushes the streamlines even closer together than the size of the true orifice. The minimum area of narrowing of the flow stream distal to its discharge from the orifice is known as the *vena contracta*, which represents the narrowest CSA of the flow stream. Distal to the vena contracta, the streamlines begin to diverge, forming a central core of laminar flow that persists for a variable distance. The high-velocity edges of the central core shear against the stagnant flow in the parajet region, creating turbulent eddies that gradually engulf the central core and the surrounding stagnant area. Each of these areas of flow (flow convergence area, vena contracta, jet laminar core and turbulent parajet zone) has important properties that affect the hemodynamic importance of the stenosis.

## Flow convergence area

Figure 6.5 depicts continuous flow from a large chamber through a relatively small circular orifice with sharp boundaries in a flat surface. The flow emerges as a jet into a large receiving chamber. Under these conditions the characteristics of the discharging or receiving chamber have little or no impact on the jet properties. As flow converges toward the orifice from all directions, the laminar streamlines are pushed closer together, progressively narrowing the CSA across which the flow passes.

## Vena contracta

The vena contracta represents the smallest CSA through which the flow passes and is therefore also known as the *effective orifice area* (EOA), distinguishing it from the actual CSA of the physical orifice, which is known as the *anatomic orifice area* (AOA). The vena contracta can be identified on color Doppler images [6–8], and the color Doppler derived values have been found to correlate closely with EOA [9] and severity of valve regurgitation [10]. The relative magnitude of jet narrowing that occurs at the level of the vena contracta is calculated as the ratio of the EOA to the AOA, known as the coefficient of contraction ($C_c$). Because the EOA represents the point of minimum CSA for the jet, velocity of flow achieves a maximum and pressure achieves a minimum at this point. The constriction of flow that occurs at the level of the EOA means that for a specific AOA, the net flow across a regurgitant orifice is less than would be predicted at any given driving force, and the net pressure fall across a stenotic orifice is more than would be predicted for any give volume of flow. The impact of the vena contracta formation is compounded by viscous losses secondary to the shear stresses as the flow crosses the orifice. The net impact of the combination of the viscous forces and the contraction of flow area is that the hemodynamic effect of a stenosis can be significantly greater than would be predicted on the basis of the actual orifice size. The net impact of these effects can be calculated as the *coefficient of discharge*, a very useful engineering concept that represents the ratio of the actual flow through an orifice compared with the flow that is predicted in the absence of

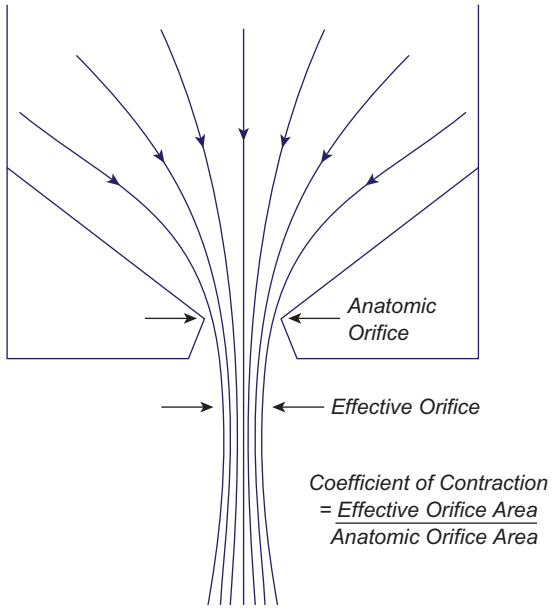


**Figure 6.6** Impact of the inlet configuration on the coefficient of contraction. Compare the pattern of flow in Fig. 6.5 with this illustration of flow through a similar circular orifice but having a conical inlet. Because the direction of flow in the lateral streamlines is less angulated relative to the central axis of flow, the conical inlet results in less flow contraction at the level of the vena contracta, that is, a coefficient of contraction that is closer to 1.

| | *Domed* | *Intermediate* | *Flattened* |
|---|---|---|---|
| *Anatomic area* |  |  |  |
| 1.0 $cm^2$ | 0.9 | 0.85 | 0.76 |
| 0.75 $cm^2$ | 0.88 | 0.83 | 0.74 |
| 0.5 $cm^2$ | 0.85 | 0.81 | 0.71 |

**Figure 6.7** The coefficient of contraction for various valve configurations and valve orifice areas. The coefficient of contraction is directly related to anatomic valve area but is more dependent on inlet geometry. A flatter valve shape is associated with more marked contraction at the level of the vena contracta. Reprinted from Gilon D, Cape EG, Handschumacher MD et al. Effect of three-dimensional valve shape on the hemodynamics of aortic stenosis: Three-dimensional echocardiographic stereolithography and patient studies. *J Am Coll Cardiol* 2002;40:1479–86, with permission from Elsevier.

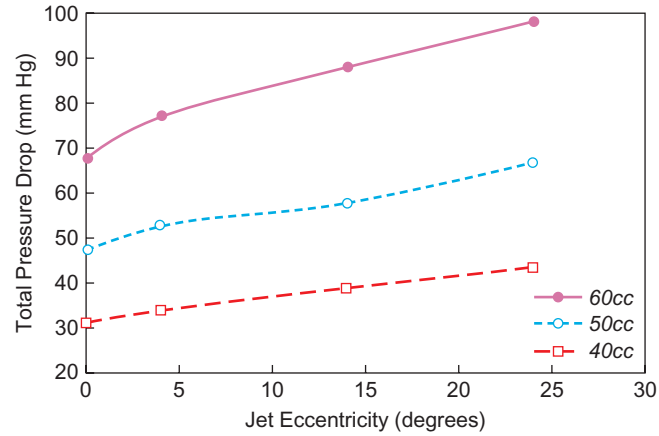


**Figure 6.8** Effect of jet eccentricity (expressed as degrees of angulation of the jet with respect to the axis of the vessel) and flow rate on the pressure drop across a stenotic orifice. The three curves represent flows of 40, 50 and 60 cc/min. Reproduced from Richards KE, Deserranno D, Donal E et al. Influence of structural geometry on the severity of bicuspid aortic stenosis. *Am J Physiol-Heart C* 2004;287:H1410–16, with permission from the American Physiologic Society.

viscous losses and flow stream contraction. The discharge coefficient is commonly used to express the overall efficiency of mechanical valves.

It is the EOA and not the AOA that determines the hemodynamic importance of a stenosis. The $C_c$ represents the magnitude of flow stream compression, and as shown in Fig. 6.6, this is dependent on the geometry of both the orifice and the inlet area. The magnitude of the narrowing of the flow stream at the level of the vena contracta depends on the geometry of the area proximal to the orifice because the streamlines exert this compressive force in proportion to the angle of flow of the streamline relative to the direction of flow in the central axis, with streamlines perpendicular to the axis of flow exerting the highest compressive forces. Gilon et al. [11] evaluated the impact of valve geometry on the $C_c$ in stenotic aortic valves and found that, as would be predicted from the principle illustrated in Fig. 6.6, domed valves have a much smaller impact on the reduction in valve area at the level of the vena contracta than flat valves (Fig. 6.7). In addition, jet eccentricity, which refers to angulation of the jet relative to the central axis of the vessel, also results in a smaller than expected effective orifice area [12]. With an eccentrically oriented jet, pressure drop is more than expected for the anatomic orifice size (Fig. 6.8). This additional pressure loss is secondary to increased energy loss due to viscous effects. The increase in viscous effects relates to the fact that the surface area of an eccentric jet is larger, relative to the cross-sectional area, than for a circular jet, and the amount of viscous friction increases in proportion to the surface area that is in contact with the flow.

## Jet laminar core

Laminar flow is present as the jet emerges through the orifice, and it persists for a variable distance distal to the orifice. For a free jet, the theoretical length of this central laminar core is four times the diameter of the orifice [13]. Bounded jets may have much longer laminar cores, and in theory turbulence may be absent. The presence of a laminar cylinder of flow distal to the valve is often misunderstood because of the appearance of these jets on color

Doppler. The velocity of the jet is generally sufficiently great to result in aliasing, and the appearance of aliasing is presumed to represent turbulence. This is not correct, and in fact it is not possible to determine on the basis of color Doppler where the laminar core ends and the turbulent zone begins.

## Parajet stagnant area

The viscous forces between the jet and the stagnant flow between the jet and the wall of the receiving chamber create eddies (circular flow or areas of flow reversal), which may be turbulent. Turbulent flow is characterized by local random fluctuation in the magnitude and direction of velocity. Laminar flow and turbulent flow represent the two ends of a spectrum, and the exact line separating them is undefined. A number of available color Doppler machines include a variance mapping mode, which displays the variance in the Doppler shift within the sample volume, as an imprecise index of turbulence. A common clinical error is to assume that aliasing of the color Doppler signal implies turbulence. The primary hemodynamic importance of turbulent flow is the energy loss that occurs due to the increased amount of viscous shear related to adjacent areas of flow with nonuniform velocity and direction. The kinetic energy of the flowing blood is lost as heat as the velocity of flow is slowed by the shear stress, in much the same fashion as the kinetic energy of a moving automobile is converted into heat by the friction of the brake pads.

## Pressure recovery

The Bernoulli equation implies that the conversion of pressure to velocity is reversible, and that velocity can be converted to pressure. The concept of the reversibility of conversion between potential and kinetic energy was explained earlier. When blood flows across a stenotic orifice, velocity rises and pressure falls, with the lowest pressure associated with the narrowest portion of the jet (the vena contracta). As the flow stream widens and the flow velocity diminishes, the pressure rises, a phenomenon known as pressure recovery [14]. Pressure recovery is always incomplete, because some energy is lost due to viscous effects as turbulence forms along the boundaries of the outflow jet (Fig. 6.9). The amount of energy lost in this transition depends on the shape of the outlet chamber. If the shape is optimized to eliminate the parajet stagnant area, as illustrated in Fig. 6.10, the streamlines follow the chamber walls and the flow remains laminar. The physiologic impact of this effect can be clinically significant. For aortic stenosis, there is an inverse relationship between the size of the aortic root and the amount of pressure recovery that takes place across a stenotic aortic valve [12]. Similarly, pressure recovery is less in eccentric jets [12]. For any given orifice size, the functional severity of stenosis is therefore greater in eccentric jets both because of a greater pressure loss (smaller effective orifice area), as discussed above, and due to the reduced pressure recovery.

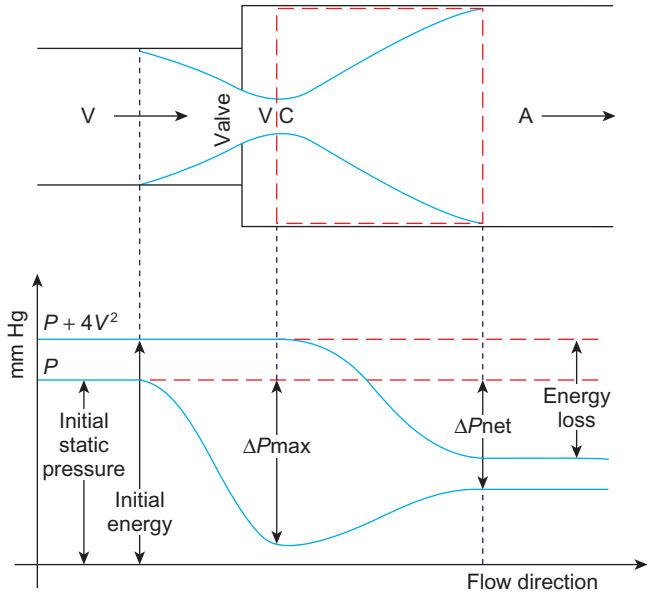


**Figure 6.9 Upper panel:** Schematic representation of a system composed of left ventricle outflow tract (V), stenotic aortic valve (valve) and ascending aorta (A). Flow narrows as it crosses the valve to a minimum at the vena contracta (VC). **Lower panel:** Corresponding changes in pressure ($P$) and total energy (pressure + kinetic energy, $P + 4V^2$). Initially the kinetic component of energy is small and static pressure dominates. As flow accelerates across the valve, static pressure reaches a minimum value at the level of the vena contracta ($\Delta P$max) and subsequently rises to a final level ($P$net) that is below the level that was initially present. Total energy ($P + 4V^2$) is maintained as long as laminar flow is present, due to a rise in kinetic energy, which is maximum at the level of the vena contracta. Distal to the vena contracta, parajet turbulence results in a loss of kinetic energy that is not fully compensated by the pressure recovery and there is a net loss of energy. Modified from Garcia D, Pibarot P, Dumesnil JG et al. Assessment of aortic valve stenosis severity – A new index based on the energy loss concept. *Circulation* 2000;101:765–71, with permission from Lippincott, Williams and Wilkins.

## Coanda effect

The Coanda effect (after Henri Marie Coandă, 1886–1972), also known as "boundary layer attachment," is the tendency of a stream of fluid to follow a convex surface, rather than follow a straight line in its original direction (Fig. 6.11). The Coanda effect is commonly encountered in daily life and is familiar to anyone who has had fluid run down the outside of a pitcher when trying to pour! In the heart, the Coanda effect accounts for the observation that jets adjacent to solid boundaries tend to adhere to the wall; for example, aortic regurgitation jets that track along the valve cusp or the ventricular septal surface. The Coanda effect is also a manifestation of the Bernoulli principle, where the more rapid reduction in velocity of flow along the unbounded aspect of the jet creates a pressure differential that pushes the jet toward the surface (Fig. 6.12).

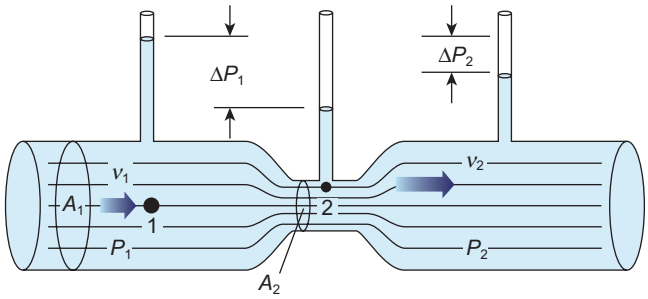


**Figure 6.10** The Venturi tube (after Giovanni Venturi, 1746–1822) is a cylindrical pipe with a streamlined constriction designed to minimize energy losses in the fluid flowing through it. The pressure drop between the inlet and area of greatest constriction ($\Delta P_1$) can be used to calculate flow and is the basis of the Venturi meter. The shape of the outlet is optimized to avoid turbulence. With optimal geometry of the tube, pressure recovery can lead to a net loss of pressure as small as 10% ($\Delta P_2$) if turbulent flow is avoided and the only energy loss is due to the viscous effects at the walls of the chamber. $A_1$ and $A_2$ are the initial and minimum cross-sectional areas, $v_1$ and $v_2$ are the initial and final velocities, and $P_1$ and $P_2$ are the initial and final pressures.

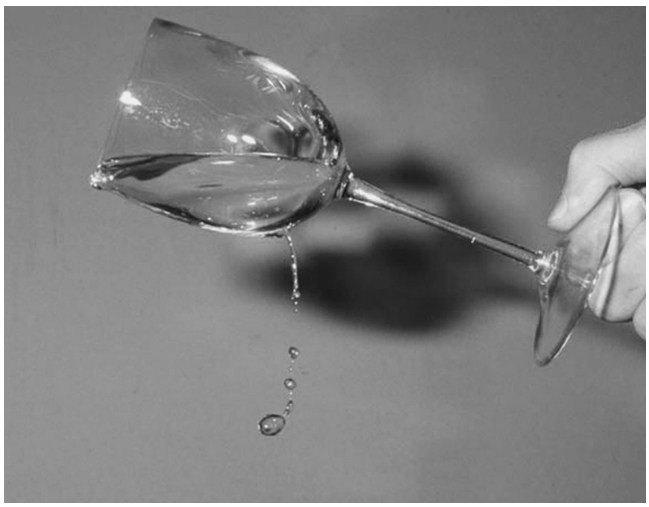

**Figure 6.11** The Coanda effect. The fluid emerging from the glass adheres to the glass and appears to defy gravity by following the glass in a horizontal and even transiently upward stream.

## Pressure differences versus Doppler velocity

The ability to calculate pressure differences based on velocity of flow measurements performed using the Doppler shift of reflected ultrasound has become a staple of patient care. However, these methods are evaluating fundamentally different properties and as a result there is substantial variability between the results of the two methods. A number of important sources of variance have been identified, not all of which can be eliminated.

**1** *Velocity measurement error*. Doppler techniques do not measure velocity, but only the component of velocity in the direction of the ultrasound beam. An off-angle Doppler sample results in underestimation of the true velocity.

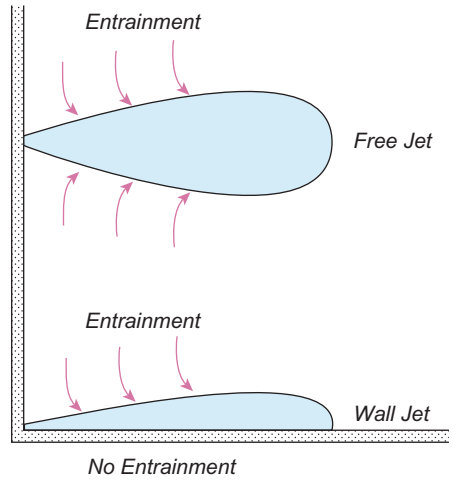


**Figure 6.12** Explanation for the Coanda effect. The shear stress between the boundary of the jet and the parajet stagnant area is symmetric in free jets but asymmetric in jets that are adjacent to solid boundaries. The pressure is greater along the free edge where velocity falls more rapidly compared with the bounded, nonturbulent aspect of the jet. The greater pressure on the free side pushes the jet toward the solid boundary. Because the proportion of the jet exposed to energy loss is smaller, the high velocity flow is maintained for a longer distance.

**2** *Pressure measurement error*. Inadequately synchronized pressure transducers, catheter disturbance of the flow being measured, and measurement of stagnation pressure can each lead to catheter pressure measurement errors.

**3** *Physiologic variance*. There can be considerable differences in the hemodynamic state of a sedated patient in the catheterization laboratory compared with the awake and sometimes uncooperative patient having an echocardiogram. Although the correlation between simultaneous Doppler and catheter measurements is much higher than can be achieved with nonsimultaneous samples [15], simultaneous samples are fundamentally irrelevant to clinical practice.

**4** *Peak-to-peak versus peak pressure differences*. Catheter calculations are generally based on the difference between the peak pressure difference between two chambers even though these occur at different times, whereas Doppler measurements provide an estimate of peak instantaneous pressure drop. This difference is primarily an issue in mild stenosis.

**5** *Pressure recovery*. Because Doppler techniques do not detect pressure recovery, they may overestimate functional severity [16]. A catheter pressure sample downstream from a stenotic valve measures recovered pressure, but measuring the maximum pressure drop within the vena contracta is generally not possible [17]. Similarly, catheter pressure differences may overestimate the net pressure loss if the distal pressure sample is taken close to the vena contracta because pressure recovery can continue for 5–10 cm downstream. Smaller peak velocities are associated with a greater degree of pressure recovery, resulting in greater relative differences between catheter and Doppler estimates of pressure

differences even though the absolute differences tend to be small.

**6** *Failure of assumptions concerning the use of the simplified Bernoulli equation.* Use of the simplified Bernoulli equation assumes that the proximal velocity is negligible and that viscous effects are small. The proximal velocity assumes greater importance when the change in velocity is small. Tunnel-like stenoses, eccentric jets and prosthetic valves are all subject to greater viscous effects.

## Measurement of orifice area

The continuity equation is often used to derive an estimate of valve area. When mean spatial velocity can be measured at two locations in continuity ($V_1$ and $V_2$) and CSA is known at one of these locations ($A_1$), the CSA at the second location ($A_2$) can be calculated as $A_2 = (A_1 \times V_1)/V_2$. This calculates the EOA, not the true orifice, and as such is a more important predictor of hemodynamic burden. The assumption that $V_1$ represents the mean spatial velocity is important, because it limits the location at which flow is calculated to those anatomic locations where the flow profile is flat. The Gorlin equation, which is generally used for the invasive estimate of valve area, is a special case of the continuity equation where flow velocity is replaced by the square root of the pressure drop according to the Bernoulli equation for steady flow. The Gorlin equation for valve area (VA) is:

$$VA = CO/(FT \times HR \times VF \times \Delta P^{0.5})$$

where CO = cardiac output (mL/min), FT = the period of flow across the valve (s), HR = heart rate (beats/min), $\Delta P^{0.5}$ = square root of the pressure drop across the valve (mm Hg), and VF = valve factor. The valve factor is an empirically derived constant that was obtained through direct measurement of the anatomic valve areas of aortic and mitral valves; the derived values are 44.5 for the aortic and 38.0 for the mitral valves. Although valve areas derived using the continuity equation are often compared with those obtained invasively using the Gorlin equation, this comparison is not entirely correct because the Gorlin calculation, in contrast to the calculation based on the continuity equation, provides an estimate of AOA, not EOA.

Although the standard approach to assessment of the hemodynamic significance of an obstructive discrete orifice (valve, vessel or other communication) in adults is assessment of valve area, this is not the usual practice in pediatrics, where most clinical decisions are based on measurement of pressure gradients alone. Arguments can be made in favor of either approach. Direct measurement of anatomic orifice area is often not possible and in any case it always, to an unpredictable extent, underestimates the severity of obstruction because it does not provide effective orifice area, which is always smaller than the true orifice area. The indirect calculation of orifice area using methods based on the Bernoulli principle (such as the Gorlin equations) rely on measurement of pressure and flow. If there is a normal amount of flow across an orifice, the pressure gradient provides an accurate measure of orifice area. Due to the limitations of current instrumentation, measurement of pressure is far more accurate than measurement of flow. Although variation in flow can contribute substantially to variation in gradient, the variation in flow has to exceed the error in the measurement of flow in order for measurement of flow to contribute to diagnostic accuracy of the test. This latter observation appears to be the primary factor contributing to the difference in practice between adult and pediatric evaluation. Although marked reduction in cardiac output is common in adults with valvar heart disease, it is very unusual in children. Hence, the assumption is generally made in pediatrics that incorporation of measurement of flow across the valve orifice is more likely to increase rather than decrease the error in the estimate of hemodynamic severity.

Clinically, peak pressure gradient is generally used to assess the hemodynamic significance of ventricular outflow obstruction, whereas mean gradient is usually used to assess the significance of ventricular inflow obstruction. For virtually all types of obstruction, peak velocity and peak gradient are poorly related to valve area whereas mean gradients are elemental to the calculation of valve area (note that the Gorlin formulas are based on mean catheterization pressure gradient and transvalvar flow) and in practice are highly correlated with orifice area. The hemodynamic importance of mitral stenosis relates to the severity of reduction in mean transmitral flow or elevation of mean left atrial pressure, both of which are directly related to effective orifice area, which accounts for the dependence on mean gradients for assessing severity of mitral stenosis. By contrast, the hemodynamic importance of ventricular outflow obstruction generally relates to the impact this has on the ventricle, and the ventricular response is more closely related to peak pressure than to mean pressure. Specifically, the risk for subendocardial ischemia, arrhythmias and sudden death relate more closely to peak ventricular pressure. In addition, the myocardial hypertrophic response to pressure overload relates more closely to peak than to mean pressure, because the primary mechanical stimulant to hypertrophy is peak wall stress, not mean wall stress [18].

## Measurement of flow across regurgitant orifices

Flow through the orifice itself is nonturbulent [13], and direct calculation of flow is therefore possible if the CSA of the regurgitant orifice is known. Two of the hemodynamic

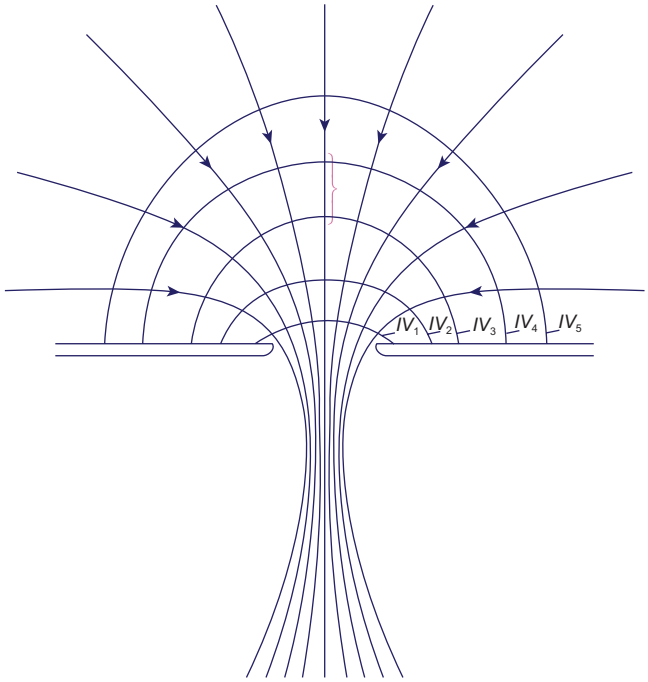


**Figure 6.13** Flow acceleration proximal to an orifice proceeds along streamlines such that flow velocity is similar at adjacent points between streamlines, resulting in isovelocity boundaries of increasing velocity as the flow approaching the orifice is distributed across a progressively smaller cross-sectional area. The isovelocity surfaces are hemispheroidal at some distance from the orifice ($IV_5$), become hemispheric in the region 1–2 times the orifice diameter ($IV_4$ and $IV_3$), and flatten as they approach the flow orifice ($IV_1$ and $IV_2$), becoming completely flat at the orifice. The distance from the orifice to the isovelocity profile can be used to calculate the area of the isovelocity surface only in the area in which the isovelocity profile has a hemispheric configuration (indicated in the figure by the curly bracket). This hemispheric zone has been shown to be restricted to a distance that is between one and three times the orifice area.

principles discussed above can be combined to enable estimation of this regurgitant volume using the proximal isovelocity surface area (PISA) method. First, the continuity equation predicts that flow across the area proximal to an orifice must equal the flow through the orifice. Second, the pattern of flow convergence proximal to an orifice can be used to calculate the volume of flow across a surface proximal to the regurgitant orifice. The PISA method is based on the observation that the flow convergence area is characterized by a series of isovelocity lines of progressively higher velocity (Fig. 6.13). For a circular orifice, these isovelocity lines are hemispheric in shape for a portion of the flow convergence area, permitting relatively simple calculation of the PISA. The surface area of a sphere with radius $r$ is $4\pi r^2$, and therefore the surface area of the hemispheric PISA is $2\pi r^2$. When this is combined with measurement of the flow velocity at the level of the isovelocity hemisphere, flow is calculated as flow velocity × PISA. The PISA method has been used to estimate regurgitant flow volume in aortic and mitral regurgitation with reasonable correlation with other methods. The specifics of the method are:

**1** align the transducer insonation angle in color Doppler mode with the central axis of flow into the regurgitant orifice;
**2** adjust the velocity scale to produce an aliasing boundary near to the flow orifice;
**3** measure the distance between the aliasing boundary and the flow orifice, which represents the radius ($r$) of the hemisphere;
**4** calculate the PISA as $2\pi r^2$;
**5** calculate peak regurgitant flow (RF) as PISA × aliasing velocity;
**6** calculate the ROA as RF/$V_{max}$, where $V_{max}$ represents the maximum velocity of flow through the regurgitant orifice;
**7** calculate the regurgitant volume as ROA × TVI, where TVI is the time–velocity integral of the flow across the regurgitant orifice.

There are a number of factors that limit the applicability of the PISA method. In a significant number of patients, aliasing boundaries cannot be identified within the flow field proximal to the regurgitant orifice, either because the required flow conditions are not present or secondary to inadequate echocardiographic images. In those subjects in whom an aliasing boundary is identified, it is often difficult to identify the position of the regurgitant orifice in order to measure the distance between the orifice and the PISA. One of the assumptions that underlies the PISA calculation is that of a hemispheric PISA. There are several factors that can alter the shape of the PISA. The isovelocity contours can be distorted by encroachment of proximal structures on the flow field [19]. For example, if a regurgitant jet emerges from the mural aspect of a valve commissure, the presence of the wall within the proximal convergence area prevents formation of full hemispheric contours. Even in unbounded flow, the PISA is hemispheric only for a specific portion of the flow convergence area [20,21], as illustrated in Fig. 6.13. Using laser Doppler anemometry, Shandas et al. [22] found the formation of hemispheric isovelocity contours to be limited to the region between one and three times the orifice diameter. This restriction is difficult to apply because the size of the regurgitant orifice is often not known and, indeed, the PISA calculation is being performed to ascertain the orifice diameter. Nozaki et al. [21] found that a hemispheric isovelocity contour is present at a distance of 1 cm from the orifice for most clinically relevant regurgitant orifice sizes, and they recommend adjustment of the aliasing velocity until a boundary forms at about 1 cm from the regurgitant orifice. Finally, the regurgitant orifice is not always constant. For example, patients with mitral valve prolapse may have substantial variation in ROA over the course of systole. It is not uncommon to find that the tricuspid valve has a large ROA in early systole that nearly disappears by end-systole. If there is significant variation in ROA over the cardiac cycle,

the calculation of regurgitant volume using this method will be inaccurate.

### Relative impact of pressure and CSA on the volume of flow across a regurgitant orifice

The observation that the velocity of flow from a chamber is proportional to the square root of the pressure in the chamber is known as the Torricelli principle after Evangelista Torricelli (1608–47). This principle allows derivation of the hydraulic determinants of flow through an orifice, because flow = velocity × CSA. The Torricelli principle predicts that flow through an orifice is proportional to the product of the orifice area and the square root of the pressure difference across the orifice. This principle can be used to predict the regurgitant volume in aortic or mitral regurgitation as:

$$RV = ROA \times CT(P_2 - P_1)^{0.5}$$

where RV = regurgitant volume, ROA = regurgitant orifice area, $C$ = constant, $T$ = duration of regurgitation, and $P_1$ and $P_2$ = mean pressure in the originating ($P_1$) and receiving ($P_2$) chambers, respectively, over the regurgitant time. The primary implication of this relationship is that changes in the size of the regurgitant orifice have far more impact on the severity of regurgitation than do the changes in the pressure difference across the orifice. In fact, the physiologically tolerated change in arterial pressure is generally sufficiently small that manipulation of blood pressure has minimal effect on regurgitant volume. For example, it is unusual for afterload reduction therapy to induce a fall of more then 10% in mean arterial pressure, and yet even this hemodynamic response would result in only a 3% fall in regurgitant volume.

## References


1. Thomas JD, Popovic ZB. Intraventricular pressure differences – A new window into cardiac function. *Circulation* 2005;112: 1684–6.
2. Poulsen JK, Kim WY. Measurement of volumetric flow with no angle correction using multiplanar pulsed Doppler ultrasound. *IEEE Trans Biomed Eng* 1996;43:589–99.
3. Shiota T, Jones M, Aida S et al. Calculation of aortic regurgitant volume by a new digital Doppler color flow mapping method: An animal study with quantified chronic aortic regurgitation. *J Am Coll Cardiol* 1997;30:834–42.
4. Hyun S, Kleinstreuer C, Archie JP Jr. Computational particle-hemodynamics analysis and geometric reconstruction after carotid endarterectomy. *Comput Biol Med* 2001;31:365–84.
5. Myers LJ, Capper WL. Analytical solution for pulsatile axial flow velocity waveforms in curved elastic tubes. *IEEE Trans Biomed Eng* 2001;48:864–73.
6. Tribouilloy CM, Enriquez-Sarano M, Bailey KR et al. Assessment of severity of aortic regurgitation using the width of the vena contracta – A clinical color Doppler imaging study. *Circulation* 2000;102:558–64.
7. Ishii M, Jones M, Shiota T et al. Quantifying aortic regurgitation by using the color Doppler-imaged vena contracta – A chronic animal model study. *Circulation* 1997;96:2009–15.
8. Mascherbauer J, Rosenhek R, Bittner B et al. Doppler echocardiographic assessment of valvular regurgitation severity by measurement of the vena contracta: an in vitro validation study. *J Am Soc Echocardiog* 2005;18:999–1006.
9. Tribouilloy C, Shen WF, Quéré J-P et al. Assessment of severity of mitral regurgitation by measuring regurgitant jet width at its origin with transesophageal Doppler color flow imaging. *Circulation* 1992;85:1248–53.
10. Evangelista A, Del Castillo HG, Calvo F et al. Strategy for optimal aortic regurgitation quantification by Doppler echocardiography: Agreement among different methods. *Am Heart J* 2000;139, 773–81.
11. Gilon D, Cape EG, Handschumacher MD et al. Effect of three-dimensional valve shape on the hemodynamics of aortic stenosis: Three-dimensional echocardiographic stereolithography and patient studies. *J Am Coll Cardiol* 2002;40:1479–86.
12. Richards KE, Deserranno D, Donal E et al. Influence of structural geometry on the severity of bicuspid aortic stenosis. *Am J Physiol-Heart C* 2004;287:H1410–16.
13. Diebold B, Delouche A, Delouche P et al. In vitro flow mapping of regurgitant jets – Systematic description of free jet with laser Doppler velocimetry. *Circulation* 1996;94:158–69.
14. Garcia D, Pibarot P, Dumesnil JG et al. Assessment of aortic valve stenosis severity – A new index based on the energy loss concept. *Circulation* 2000;101:765–71.
15. Vlahos AP, Marx GR, McElhinney D et al. Clinical utility of Doppler echocardiography in assessing aortic stenosis severity and predicting need for intervention in children. *Pediatr Cardiol* 2008;29:507–14.
16. Gjertsson P, Caidahl K, Svensson G et al. Important pressure recovery in patients with aortic stenosis and high Doppler gradients. *Am J Cardiol* 2001;88:139–44.
17. Heinrich RS, Fontaine AA, Grimes RY et al. Experimental analysis of fluid mechanical energy losses in aortic valve stenosis: importance of pressure recovery. *Ann Biomed Eng* 1996;24: 685–94.
18. Colan SD. Ventricular function in pressure overload lesions. In: Fogel MA (ed.) *Ventricular Function and Blood Flow in Congenital Heart Disease*. Malden, MA: Blackwell Publishing, 2005;187–204.
19. Anayiotos AS, Fan P, Perry GJ et al. Analysis of the proximal orifice flowfield under pulsatile flow conditions and confining wall geometry: Implications in valvular regurgitation. *Echocardiogr J Cardiovasc Ultrasound Allied Tech* 1998;15:219–32.
20. Rodriguez L, Anconina J, Flachskampf FA et al. Impact of finite orifice size on proximal flow convergence: Implications for Doppler quantification of valvular regurgitation. *Circ Res* 1992; 70:923–30.
21. Nozaki S, Shandas R, DeMaria AN. Requirement for accurate measurement of regurgitant stroke volume by the combined continuous-wave Doppler and color Doppler flow convergence method. *Am Heart J* 1997;133:19–28.
22. Shandas R, Gharib M, Sahn DJ. Nature of flow acceleration into a finite-sized orifice: Steady and pulsatile flow studies on the flow convergence region using simultaneous ultrasound Doppler flow mapping and laser Doppler velocimetry. *J Am Coll Cardiol* 1995;25:1199–212.

# 7 Echocardiographic Evaluation of Systolic Function

**Luc L. Mertens[1], Javier Ganame[2] and Bénédicte Eyskens[2]**

[1]The Hospital for Sick Children, Toronto, Canada
[2]Department of Pediatric Cardiology, University Hospitals Leuven, Leuven, Belgium

Assessment of ventricular function is an essential part of every echocardiographic study performed in children with congenital and acquired heart disease. Evaluation of systolic function is challenging due to the confounding effect of different factors such as ventricular geometry and variable loading conditions associated with congenital heart disease. In order to understand the uses and limitations of the different echocardiographic techniques in pediatrics, you must be familiar with some physiologic concepts of ventricular function. In this chapter we will furnish the essential physiologic background before giving an overview of the different echocardiographic techniques used in the evaluation of systolic function in children.

## Background: the mechanics of cardiac systolic function

The performance of the ventricle as a pump depends on the contraction of the sarcomeres as well as on the chamber geometry, valvular function, loading conditions and heart rate. When studying systolic function, one should distinguish between intrinsic myocardial function or contractility and ventricular pump function or performance. At both levels two different components can be distinguished, namely force development resulting in the generation of pressure and deformation resulting in the ejection of blood. At the level of fiber mechanics, active myocardial force development results in fiber shortening. At the level of the entire ventricle, force development results in pressure development and deformation, which causes volume changes. Both force development and deformation interact and their relationship is influenced by wall properties (such as tissue composition or elasticity, fiber structure and global geometry) and loading conditions (preload and afterload). Ventricular pump function can be studied from a global perspective (pressure–volume relationship) or from a regional perspective, where the contributions of individual wall segments are taken into account (regional stress–strain relationship). This is illustrated in Fig. 7.1[1].

Based on this model, cardiac function can be evaluated at various levels of integration: (i) myocardial function; and (ii) global and regional left ventricle (LV) pump performance. The different levels should be taken into account when evaluating cardiac function using imaging techniques. Looking at volumetric changes, such as calculating ejection fraction, is different from measuring intrinsic contractility.

In the normal heart, sarcomere shortening is about 15%. This percentage of shortening results in a 35–40% wall thickening and the ejection of 55–60% of the blood volume contained in the left ventricle at each systole [2,3]. In contrast to skeletal muscle fibers, cardiac fibers do not assemble in parallel arrays but bifurcate and recombine to form a complex three-dimensional network in different directions and layers. Myofibers in the epicardium are predominantly left-handed longitudinally oriented; their orientation changes gradually to circumferential in the mid-wall, and to right-handed longitudinally oriented in the endocardium. This complex three-dimensional (3D) orientation and separation in layers results in fiber interaction while shortening. When myofibers shorten, thicken and twist, they compress each other in three directions. This process, called cross-fiber shortening, is responsible for the amplification of the individual components of shortening, thickening and twisting by a squeezing effect on neighboring fibers. This fiber organization causes the ejection of 60–70% of blood volume despite only 15% fiber shortening. For a detailed overview of the basics of cardiac mechanics related to echocardiography, we refer readers to two recent sources [4,5].

## Cardiac function at the ventricular level

Global ventricular performance is the ability of the heart to develop force and deform so that it can eject blood. Ventricular performance can be assessed by measuring the

*Echocardiography in Pediatric and Congenital Heart Disease: From Fetus to Adult*
Edited by Wyman W. Lai, Luc L. Mertens, Meryl S. Cohen and Tal Geva
 ISBN: 978-1-405-17401-5

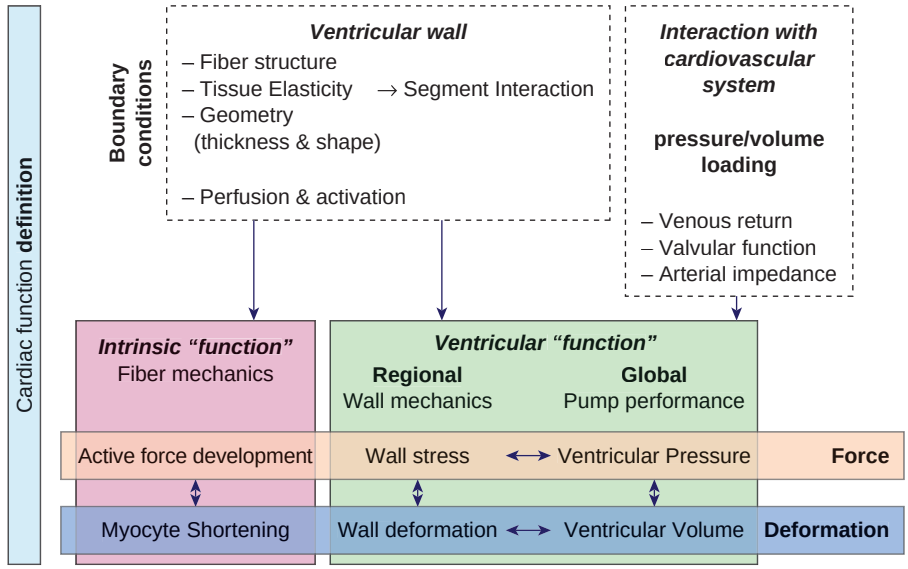


**Figure 7.1** An integrated view of cardiac function at different levels showing mechanisms involved in and influencing cardiac function. Reproduced from Sutherland G, Hatle L, Claus P et al. *Doppler Myocardial Imaging. A Textbook*. Hasselt: BSWK, 2006, with permission of BSWK.

*stroke volume*, which is the blood volume ejected by the heart with every heartbeat. The resulting *cardiac output* is the product of stroke volume and heart rate. Cardiac output depends on: preload, afterload, heart rate and intrinsic contractility. *Preload* is the load present at the end of diastole before cardiac contraction starts. It is best defined in the isolated muscle strip model as end-diastolic fiber length. According to the Frank–Starling relationship, up to a certain maximum, greater preload results in greater force generation. In the intact organ end-diastolic fiber length cannot be measured and usually LV end-diastolic volume is used as a surrogate for fiber length. However, in patients with chronic volume load this is an inaccurate measurement for preload as ventricular remodeling with eccentric hypertrophy changes the resting length of the myofibers. Also end-diastolic pressure is taken as a surrogate measurement for preload. This does not accurately reflect fiber length as influenced by ventricular compliance. Congenital heart disease is often associated with chronic volume overload. Examples of left ventricular volume overload are chronic mitral or aortic regurgitation, ventricular septal defects and patent ductus arteriosus. Examples of chronic right ventricular volume are chronic pulmonary and tricuspid regurgitation and atrial septal defects. Increased preload leads to increased systolic performance and increased stroke volume, whereas reduced preload leads to lower stroke volume and ejection fraction. This should be taken into account when evaluating systolic function with volumetric techniques.

*Afterload* in an isolated muscle strip is the force resisting shortening after the onset of systole. In the intact organ it is best defined as the resistance against which the ventricle contracts, or wall stress [6]. This is determined by intracavitary pressure, cavity dimension and wall thickness (Laplace's law):

$$\text{wall stress} = \text{pressure} \times \text{radius}/(2 \times \text{wall thickness})$$

Wall stress varies throughout systole. Peak systolic wall stress is the highest wall stress during systole and is the trigger for the development of concentric hypertrophy. Increased wall thickness reduces wall stress. Total systolic wall stress (time–stress integral) determines oxygen consumption. End-systolic wall stress is the afterload at the end of systole (at the moment of aortic valve closure). This determines the degree of systolic shortening. Important determinants of afterload are peak arterial pressure, arterial compliance, and vascular resistance. Wall stress is a force, which means that it can be considered as a vector with components in different directions, taking into consideration a cardiac coordinate system: circumferential stress (short axis), meridional stress (long axis) and radial stress (transmural). The best representation of myocardial stress would be to calculate fiber stress, which is the stress exerted on the fibers. Due to the organization and orientation of the fibers, stress on the fibers is not identical to stress in the direction of the cardiac coordinate system [6]. Ideally, one should determine fiber stress, and for determination of afterload, end-systolic fiber stress can be considered to be the best index. Excess afterload diminishes myocardial shortening and elevates myocardial oxygen consumption. This should be taken into account when interpreting most of the systolic function indices. In congenital and acquired pediatric heart disease a lot of conditions are associated with changes in afterload. Aortic stenosis, aortic coarctation and arterial hypertension are examples of conditions in which ventricular afterload is increased. The chronic increase in wall stress results in concentric hypertrophy with increased wall thickness, which reduces wall stress. This implies that when studying patients with chronic increased pressure loading, ventricular remodeling can normalize wall stress and thus pressure loading should not be confused with increased afterload. Above a certain threshold, ventricular hypertrophy can cause ventricular dysfunction [7]. Wall

stress or afterload is also increased in patients with dilated cardiomyopathy, who have thin myocardial walls and a dilated ventricular cavity [8,9]. The diminished mass/volume ratio increases fiber stress throughout systole. As such a depressed contractility increases afterload even when blood pressure is normal or reduced. It is important to realize that blood pressure is not a reliable surrogate for afterload.

Apart from preload and afterload, *heart rate* is an important factor for cardiac performance. An increased heart rate progressively enhances the force of ventricular contraction up to a certain limit. This phenomenon is called the "force–frequency relation." This relationship is thought to be due to increased myocardial calcium concentrations at higher heart rates [10]. When heart rate becomes too high (>180 beats/min for the adult heart), contractile force decreases again. In isolated muscle strips obtained from failing ventricles the force–frequency effect is blunted [11]. In the intact heart, the influence of the decreased duration of ventricular filling at elevated heart rates opposes the force–frequency effect.

*Intrinsic contractility* refers to the ability of the cardiac muscle to generate force and shorten independently of preload, afterload and heart rate. In the isolated myocardial fiber, increased contractility results in a higher velocity of muscle shortening and total amount of shortening. In the past, several attempts have been made to transfer this physiologic concept of contractility, expressed in the isolated myocardial fiber, to the intact beating heart in vivo. To disconnect the intrinsic contractile state from loading conditions and heart rate turned out to be extremely difficult. Most indices of cardiac function are indeed indices of contractility, but most are also responsive to changes in load and do not give an accurate measurement of contractile function. True load-independent assessment may be impossible in a clinical context. The gold standard for assessing ventricular contractility is the invasive recording of pressure–volume loops [12]. The need to manipulate the loading conditions and the requirement for invasive monitoring with high-fidelity catheters limit the clinical usefulness of this technique [13,14].

## Echocardiographic assessment of left ventricular function

Echocardiography and Doppler ultrasound are the main tools used to evaluate LV function noninvasively in children with heart disease. Different techniques have been proposed to assess myocardial function. A distinction can be made between techniques that measure global function and techniques that look at regional myocardial function. A further distinction can be made between measurements based on dimensional changes (like fractional shortening, ejection fraction and myocardial deformation) and techniques based on Doppler measurements (like maximal d*P*/d*t*, myocardial performance index and tissue velocities). The techniques can also be distinguished based on the exact timing within the cardiac cycle: ejection fraction and systolic strain are ejection phase parameters, whereas maximal d*P*/d*t* and the isovolumetric acceleration are pre-ejection phase indices.

### Systolic function derived from dimensional changes

Fiber shortening during ejection results in displacement of blood caused by dimensional changes within the myocardium and the myocardial wall. Traditionally, the assessment of global systolic function has been based on changes in ventricular size and volume (Videoclips 7.1–7.4). The three measurements most commonly used to express global ventricular function are percent shortening fraction, ejection fraction and cardiac output.

The *percent fractional shortening* (%FS) is defined as the percentage change in left ventricular dimension from end-diastole to end-systole. In most laboratories LV dimensions are measured from the M-mode echocardiograms obtained at the level of the papillary muscles using the parasternal short- or long-axis views. Two-dimensional (2-D) imaging is used to optimize the M-mode cut through the left ventricular cavity (Fig. 7.2). Measuring %FS involves measuring the degree of apposition of the inferolateral wall of the left ventricle to the ventricular septum. The left ventricular cavity is measured at the end of diastole, defined by the onset of the QRS-complex (left ventricular end-diastolic dimension, LVEDD), and at peak systole, which is the closest point of apposition between the septum and the inferolateral wall (left ventricular end-systolic dimension, LVESD). The %FS is defined as:

$$\%FS = (LVEDD - LVESD)/LVEDD \times 100$$

This measurement normally varies between 28% and 38%. Values below 28% suggest reduced systolic function (Fig. 7.2). Values above 38% indicate hyperdynamic function. The popularity of this measurement is due to the ease and rapidity with which it can be performed. There are, however, important limitations. A first one is that regional motion of the septum and posterior wall are used as parameters for global function. This assumes that there are no regional wall motion abnormalities. The measurement becomes inaccurate or impossible when regional septal hypokinesia or dyskinesia is present. This occurs in different circumstances, such as in the context of right ventricular volume overload (atrial septal defects), which can be associated with dyskinetic (paradoxical) septal motion in which the septum moves away from the inferolateral wall during systole (Fig. 7.3). Septal hypokinesia or dyskinesia commonly occurs in the immediate postoperative (post-bypass) period and in case of bundle branch block or dyssynchrony where the maximal

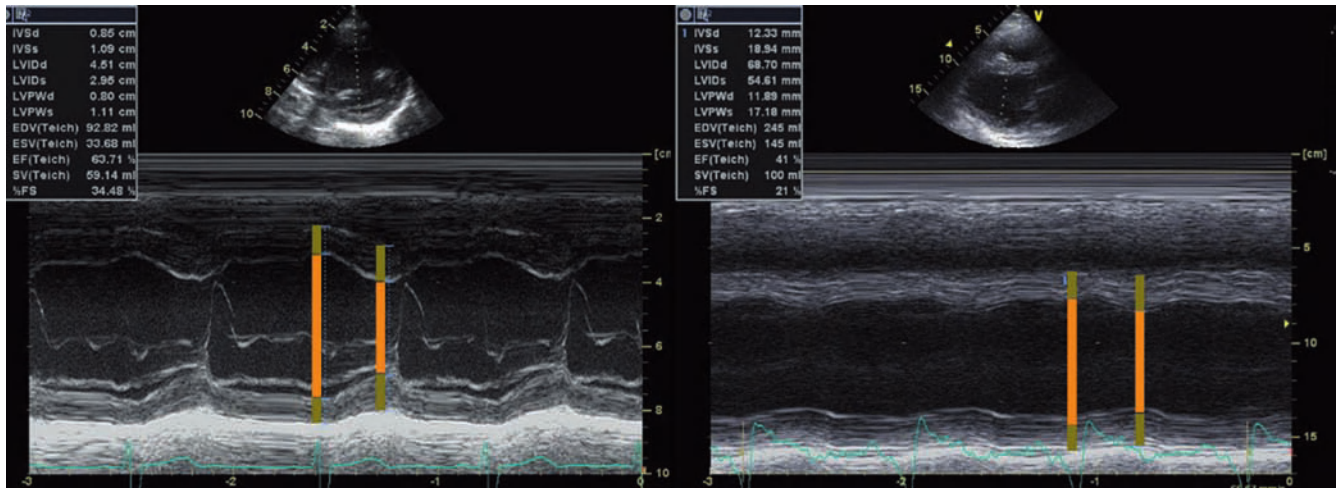


(a) (b)

**Figure 7.2** Left ventricular fractional shortening is calculated by measuring end-diastolic and end-systolic dimensions using M-mode echocardiography from parasternal short-axis or long-axis views. **(a)** Normal subject. **(b)** Patient with dilated cardiomyopathy and reduced fractional shortening.

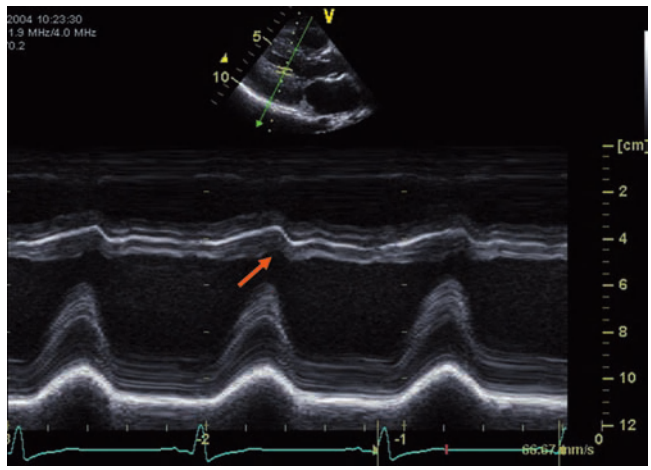


**Figure 7.3** Ultrasonogram showing that the measurement of percent fractional shortening is not applicable when paradoxical septal motion is present, as in patients with atrial septal defects, because the interventricular septum (IVS) moves away from the inferolateral wall in systole. The red arrow indicates the paradoxical motion of the IVS.

systolic motion of the inferolateral wall and septum do not occur at the same moment. These conditions affect the measurement of %FS and overestimate the reduction in global systolic function. Conversely, when regional function is preserved in the septum and posterior wall but reduced in other regions, calculated %FS overestimates global LV function. Also %FS only reflects circumferential fiber shortening. As such it is only looking at radial deformation (wall thickening) and inward motion of the septum and inferolateral wall. It does not take into account longitudinal and circumferential deformation, or torsion of the ventricle. A second important limitation of %FS is its load-dependency. The technique is influenced by changes in both preload and afterload and does not only reflect intrinsic myocardial function. Increased preload will increase LVEDD and will thus affect the measurement. Increased afterload will influence LVESD as it may result in earlier closure of the aortic valve thus resulting in a lower %FS. These effects of loading should be taken into account when interpreting the measurement. A final important limitation is the dependency of the calculation on LV geometry. With volume loading the shape of the LV ventricle becomes more spherical, affecting measurements and dimensional changes. When hypertrophy of the wall occurs, as in the context of arterial hypertension or hypertrophic cardiomyopathy, endocardial dimensional changes are influenced by the effect of the thickened wall resulting in an overestimation of systolic function.

*Ejection fraction* is the percentage change in LV volume from end-diastole to end-systole. Its calculation requires determination of left ventricular volumes:

$$EF = (LVEDV - LVESV)/LVEDV \times 100$$

where LVEDV is the LV volume at end-diastole and LVESV is the LV volume at end-systole.

Left ventricular volumes can be calculated using M-mode echocardiography, 2-D echocardiography and 3-D echocardiography. Quinones et al. [15] proposed a simplified formula to calculate EF by measuring internal dimensions of the LV using M-mode. It is obvious that this method includes a lot of assumptions and has all the limitations of M-mode. A better estimate of left ventricular volume is given by 2D echocardiography. The method most commonly used and also recommended by the American Society of Echocardiography is the modified Simpson's method or disk summation method [16,17]. In this method two orthogonal planes

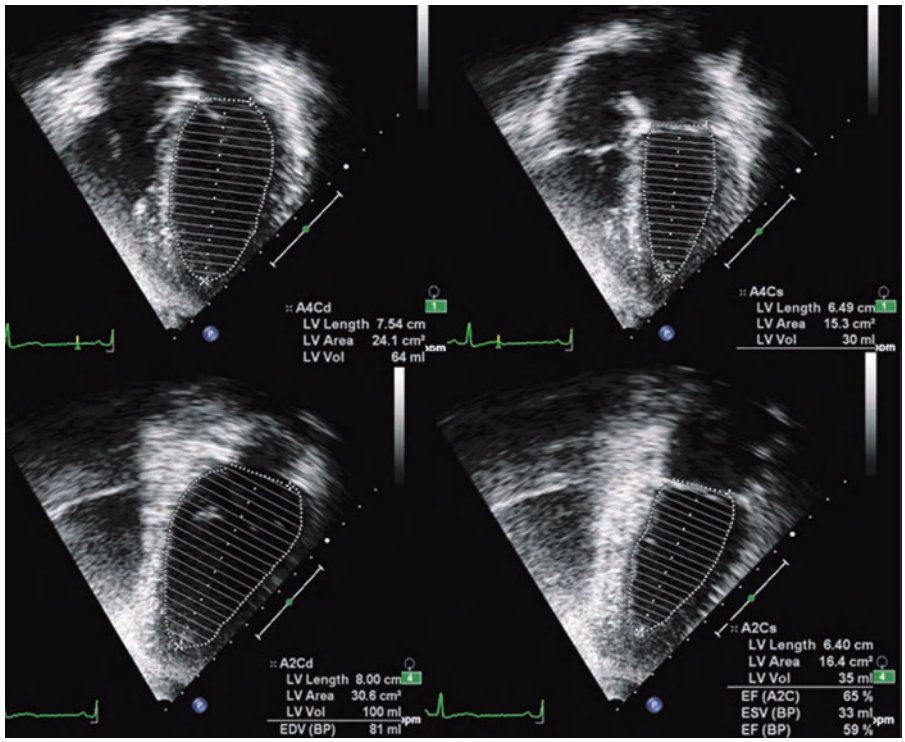


**Figure 7.4** With the modified Simpson method, left ventricular ejection fraction is calculated by delineating end-diastolic and end-systolic volumes in the apical apical 4-chamber and 2-chamber views.

from the apical view are used (apical 4-chamber and apical 2-chamber view). The LV is divided into a number ($n$) of cylinders or disks of equal height. The height of each cylinder is determined by dividing the total length of the LV cavity ($L$) by the number of cylinders ($L/n$). The volume of each cylinder is calculated from the diameters of the cylinders, $a$i and $b$i, obtained in the two planes. The left ventricular volume ($V$) is the sum of the volumes of the individual cylinders:

$$V = \pi/4 \sum(a\text{i} \times b\text{i}) \times L/n$$

This summation of disks method is probably the most reliable one for calculating ejection fraction but also the most time-consuming in daily clinical practice because it requires LV endocardial delineation at end-diastole and end-systole in two apical views (Fig. 7.4). Therefore alternative more simplified methods for calculating LV volumes, like the Bullet method or area–length method, have been developed. The problem with these methods is that they assume a particular geometrical shape of the left ventricle and can therefore only be used for a normally shaped ellipsoidal left ventricle.

The different methods require tracing the endocardial borders defining the blood–tissue interface. For this purpose optimal 2D images of the left ventricle are required and foreshortening of the left ventricular cavity should be avoided. Automatic border detection algorithms have been developed based on integrated backscatter methods to improve the accuracy of endocardial border detection, even allowing automation of the calculation of ejection fraction [18,19]. These methods use the differences in reflective properties between blood and tissue. Kimball et al. [20] and also Mahle et al. [21] have shown that this method can be used in children with hypoplastic left heart syndrome to evaluate right ventricular function through different stages of palliation. Three-dimensional echocardiography has recently been introduced, and the new high-frequency matrix transducers allow acquisition of full volumetric datasets even in children [22]. This is further discussed in Chapter 41. Like %FS, measurement of EF has limitations: it is certainly more time consuming compared to calculation of %FS but the advantage is that it takes into account regional dysfunction in the assessment of global function. Like fractional shortening, the method is load-dependent and dependent on ventricular geometry. This explains why the calculation of ejection fraction is more difficult to apply to the right ventricle which has a complex three-dimensional structure [23–26]. Despite this, 2D techniques to determine RV EF have been shown to correlate reasonably well with EF calculated with magnetic resonance imaging (MRI) [27]. Three-dimensional echocardiography can also be used to calculate

RV ejection fraction but imaging the whole RV cavity in a single 3D volumetric dataset with sufficient spatial resolution to delineate the endocardial borders remains challenging [28]. Analysis of RV function is, further hampered by the extensive RV trabeculations. Similar problems occur when dealing with even more complex geometry like the univentricular heart.

As fractional shortening is mainly assessing circumferential fiber shortening, a separate assessment of longitudinal fiber shortening could provide additional information on LV function. The longitudinal fibers are mainly located in the subendocardium and the epicardium. In a normal heart circumferentially oriented fibers predominate over longitudinal fibers, and short-axis shortening exceeds long-axis shortening. This means that the sphericity of the ventricle normally decreases during contraction as the short-axis diameter decreases more than the long-axis diameter. As longitudinal function might be affected differently from radial/circumferential function due to the different fiber orientation in the different layers of the myocardium, it makes sense to evaluate longitudinal function separately from short-axis function. A measurement that is easy to calculate is *displacement of the atrioventricular (AV)-valve annulus.* This is obtained using an apical 4-chamber or 2-chamber view. An M-mode line can be drawn through the lateral or septal annuli (Fig. 7.5) [29]. Also the tricuspid annular displacement can be measured using M-mode (Fig. 7.6). This measurement is sometimes referred to as tricuspid annular systolic excursion (TAPSE) [30–32]. From the M-mode through the annulus, the total displacement and timing of displacement of the AV valve plane can be measured. Because the apex is relatively fixed, the annulus moves in the direction of the apex during systole mainly due to fiber shortening within the different wall segments. Like ejection fraction AV-displacement is load-dependent and influenced by valve regurgitation. It is also influenced by global cardiac motion as the heart translates in the chest during cardiac contraction. Measuring annular displacement is easy to perform and gives additional information on ventricular function. Its use has been proposed for the evaluation of right ventricular systolic function, where longitudinal shortening is an important component of contraction due to the longitudinal fiber orientation in the right ventricular wall. Different conditions affect longitudinal function. Diseases associated with an increase in mass/volume ratio (such as arterial hypertension, aortic stenosis or hypertrophic cardiomyopathy) are associated with an increased short-axis shortening and decreased long-axis function. In conditions with a decreased mass/volume ratio (as in volume overload and dilated cardiomyopathy), increased long-axis function and decreased short-axis shortening can be observed.

To overcome some of the problems associated with load-dependency of %FS and EF, methods were developed to try to correct for loading. The *velocity of circumferential fiber shortening* (*V*cf) measures the velocity of dimensional changes during ejection. Fiber shortening only occurs during ejection, and based on this the mean velocity of fiber shortening (*V*cf) is calculated by dividing %FS by ejection time. The value *V*cf is an estimate of the average rate of change of the LV diameter per unit of time. It is calculated as:

$$V\text{cf} = \%\text{FS}/\text{ejection time}$$

This index has the advantage over %FS in that it not only looks at the amount of shortening but also incorporates the speed at which shortening occurs. It can be corrected for heart rate variability by dividing by the square root of the preceding R-R interval (Bazett's correction). This corrected *V*cfc is relatively insensitive to preload changes but highly

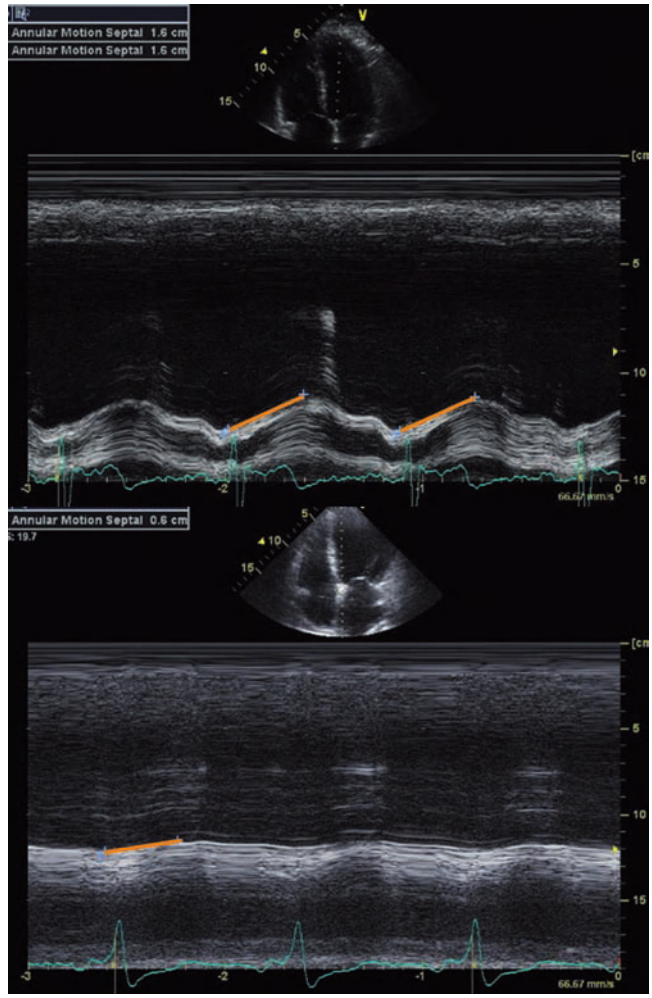


(a)

(b)

**Figure 7.5** The amount of displacement of the base toward the apex in systole assesses left ventricular longitudinal function. It can be quantified by drawing an M-mode perpendicular to the annuli from the apical 4-chamber view. **Panel A:** Subject with normal septal motion. **Panel B:** Reduced longitudinal motion in a patient with dilated cardiomyopathy.

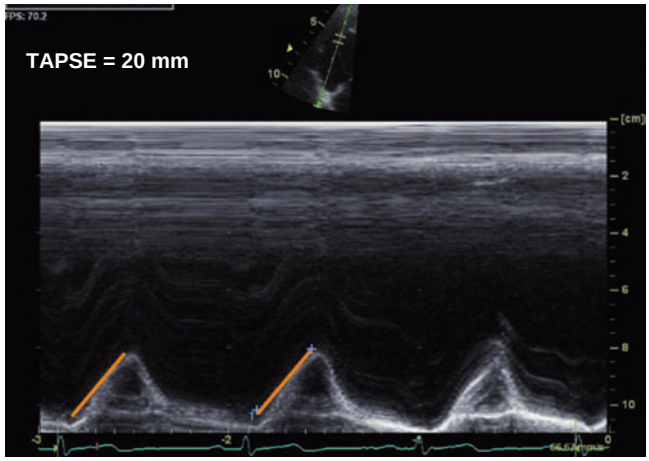


**Figure 7.6** Tricuspid annular systolic excursion (TAPSE) gives an estimate of right ventricular longitudinal systolic function. Note that longitudinal shortening of the right ventricle exceeds that of the left ventricle.

sensitive to changes in contractility and afterload [33]. The preload-independency is a big advantage, and if corrected for afterload, *V*cfc can be used as a parameter for contractility. It is, however, only valid when the LV shape is elliptical and short-axis geometry is circular. As based on %FS measurement, *V*cf is a global LV systolic parameter derived from only two myocardial segments. This index can be misleading if there is regional myocardial dysfunction. Also *V*cf does not directly measure the velocity of fiber shortening but measures the velocity of endocardial inward motion in systole. This, combined with some geometrical assumptions, is thought to reflect fiber shortening. Measurement of *V*cf also assumes that transmural myocardial wall thickening is uniform. This is incorrect as there are transmural differences within the walls, with the endocardial shortening exceeding epicardial shortening. This is due to geometrical constraints and implies that endocardial indices such as %FS and EF misrepresent mean fiber shortening throughout the wall. When the wall hypertrophies this misrepresentation of endocardial indices increases.

To overcome this problem, the measurement of *mid-wall fractional shortening* was developed [34,35]. For this technique the left ventricle is represented by an ellipsoidal model with uniform wall thickness. The LV wall is then divided into an inner and an outer shell, thus defining a concentric two-shell geometry. Mid-wall fractional shortening has been proposed as a sensitive index of myocardial function that is independent of wall thickness, making it particularly suitable when LV hypertrophy is present (Fig. 7.7). Using a mid-wall fractional shortening calculation, patients with hypertensive heart disease, coarctation and aortic stenosis were shown to have abnormal myocardial function despite the presence of normal or supranormal indices of endocardial shortening [36–38]. The calculation of mid-wall shortening uses geometric assumptions, such as uniform wall thickness, and models the LV as an ellipsoid. It cannot be used in case of abnormal geometry. Moreover, like endocardial fractional shortening, it is preload- and afterload-dependent. The limitations are similar to endocardial parameters, the only

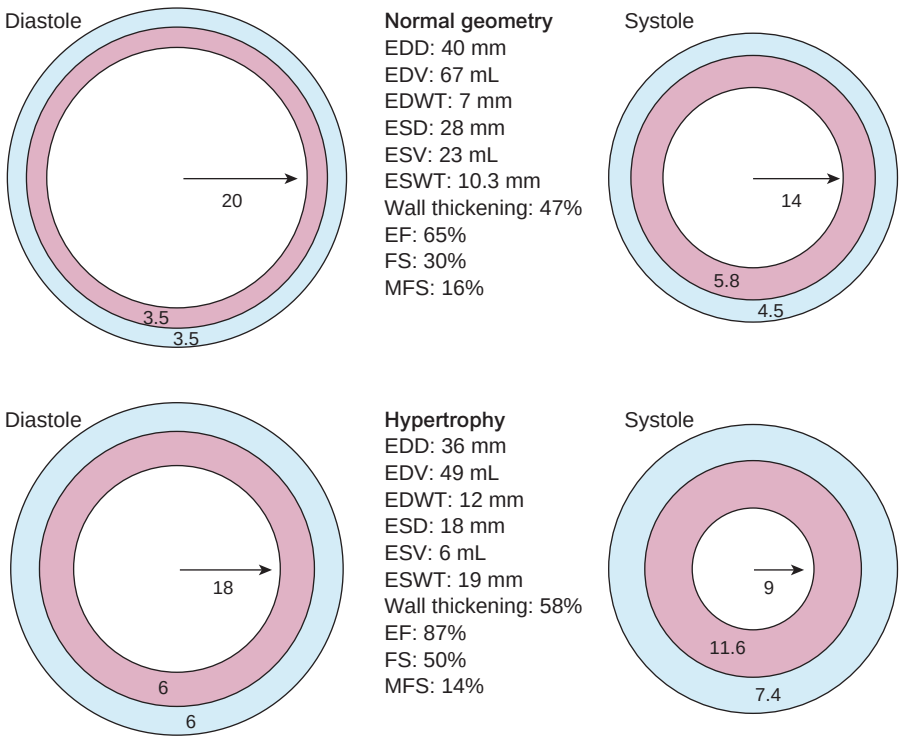


**Figure 7.7** In systole, wall thickening is accompanied by greater inward motion of the subendocardial myocardium than of the subepicardial myocardium. If hypertrophy is present, this difference is even greater, leading to overestimation of transmural myocardial function if endocardial indices of function are used. EDD, end-diastolic dimension; EDV, end-diastolic volume; EDWT, end-diastolic wall thickness; EF, ejection fraction; ESD, end-systolic dimension; ESV, end-systolic volume; ESWT, end-systolic wall thickness; FS, fractional shortening; MFS, mid-wall fractional shortening.

advantage being that these parameters are independent of wall thickness.

As mentioned above, *V*cfc is relatively preload-independent and mainly dependent on afterload and contractility. Therefore it is logical to use *V*cfc corrected for afterload as an index for contractility. Colan et al. [33] adopted this principle and used calculated end-systolic meridional wall stress as a measure for afterload. This technique requires definition of end-systolic stress values. Ventricular dimensions are obtained using an M-mode echocardiogram. Forearm blood systolic and diastolic pressures are measured, and using a tonometry device the carotid pulse tracing can be recorded. Using the dicrotic notch at aortic valve closure, end-systole can be defined and end-systolic blood pressure can be extrapolated on the indirect arterial pressure waveform by measuring the height from the baseline to the dicrotic notch. A phonogram-derived signal is superimposed on the M-mode image and the end-systolic LV dimension and posterior wall thickness are measured at the point of aortic valve closure (first component of the second heart sound). Based on these measurements end-systolic meridional wall stress ($WS_M$) can be calculated using the formula:

$$WS_M = \frac{1.35 \times P \times D}{h(h + h/D) \times 4} \text{ (expressed in g/cm}^2\text{)}$$

where $P$ is end-systolic pressure (in mm Hg), $D$ is the LV end-systolic internal diameter (in cm) and $h$ is the end-systolic posterior wall thickness (cm).

Colan et al. [33] found a direct negative correlation between *V*cfc and end-systolic meridional wall stress. This seems intuitively logical as one can understand that increasing afterload will reduce the velocity of fiber shortening in the absence of any change in myocardial contractility. If contractility increases (for instance by giving positive inotropic drugs) it can be expected that *V*cfc will increase if afterload does not increase. The relationship between *V*cfc and end-systolic wall stress within the normal range has been published. Abnormal LV contractility is defined as values for wall stress versus *V*cfc falling below the normal expected range. The linearity of the relationship was questioned especially in younger children [39,40]. Moreover, it was shown that wall stress as calculated in the formula misrepresents afterload in children and young adults with abnormal left geometry [41]. In this study wall stress was compared with fiber stress, and the authors were able to demonstrate that the relationship between both only holds with a normal wall thickness-to-chamber dimension. When this ratio is increased (e.g. hypertrophic cardiomyopathy), meridional wall stress underestimates fiber stress, whereas when the ratio is decreased (e.g. dilated cardiomyopathy) meridional wall stress overestimates fiber stress. This index has never become widely used in clinical practice because it is complex to perform, requiring the simultaneous recording of a phonocardiogram and a carotid or axillary arterial pulse tracing to calculate end-systolic wall stress. A simplified method was proposed using mean arterial pressure instead of end-systolic wall stress as a measure of afterload [40]. This facilitates clinical applicability but reduces the accuracy of the method. The method has been applied in a number of different clinical conditions. It has become a very useful tool for the evaluation of cardiac contractility in pediatric patients exposed to anthracyclines. Lipshultz et al. [42–44] could demonstrate that the velocity of fiber shortening versus wall stress is a useful index for following patients with anthracycline cardiotoxicity. They demonstrated a progressive deterioration in contractility with time. In these patients it is important to use methods that correct for afterload as one of the common findings in these patients is a decrease in wall thickness, which will increase wall stress.

## Blood pool Doppler indices of ventricular function

In the previous section we discussed methods for evaluating systolic function based on measurements of ventricular dimensional changes. These methods all have limitations but are commonly used in daily clinical practice because of their ease. One of the main problems with these methods is their geometry dependency, which limits their use in congenital heart disease. To overcome the influence of geometry in the assessment of ventricular function, blood pool Doppler measurements can be used. Different Doppler parameters have been proposed in the evaluation of ventricular function.

One of the most commonly used is the measurement of *maximal dP/dt* The maximal rate of rise in LV pressure during the isovolumic contraction period ($dP/dt_{max}$) is an invasive index that is derived from pressure traces obtained in the ventricle. It reflects the pressure-generating capacity of the cardiac muscle. This measurement can indirectly be derived from a continuous-wave Doppler tracing of a mitral regurgitation jet (Fig. 7.8). During the isovolumetric contraction period there is no significant rise in LA pressure and therefore the rise in mitral regurgitant velocity during this period reflects $dP/dt$. The time interval is measured between 1 m/s and 3 m/s. Between those two measurements the pressure difference as calculated by the Bernoulli equation is 32 mm Hg. Calculation of $dP/dt$ can be accomplished by measuring the time difference on the velocity spectrum and using the equation $dP/dt$ = 32 mm Hg/time in seconds. For the normal LV, $dP/dt$ is 1200 mm Hg/sec or more. The same calculation can be applied to the RV using the tricuspid regurgitation jet.

As the presence of mitral regurgitation is a prerequisite to measure $dP/dt$, it cannot be considered a real isovolumetric measurement because there is some volume change in the

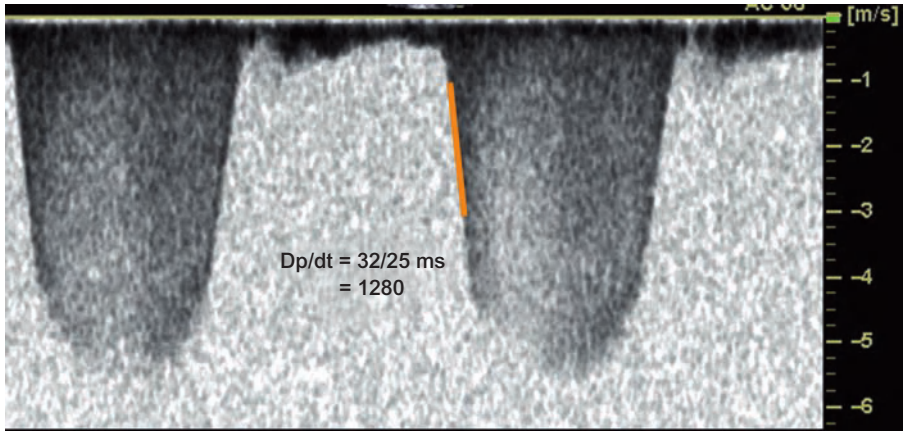


**Figure 7.8** The mean rate of pressure rise during isovolumic contraction is measured from a continuous-wave Doppler of the mitral regurgitation jet as the time it takes the left ventricle to increase its pressure from 1 m/s to 3 m/s. Applying the Bernoulli equation, the d*P*/d*t* is calculated as follows: 32 mm Hg/time (s).

ventricle due to the regurgitant volume. Morever, the regurgitation can increase LA pressure. The advantage is that this method is geometry-independent and very sensitive to changes in contractility. Because it is measured before aortic valve opening, it is also relatively independent of changes in afterload. The measurement is, however, preload-dependent, which is a problem when you have significant mitral regurgitation. Its measurement requires an excellent Doppler trace, which might not be easy to obtain in the context of mild to moderate mitral regurgitation and the low-velocity tricuspid regurgitant jet.

*Aortic/pulmonary blood flow velocities* can be measured using pulsed or continuous wave Doppler signals through the ascending aorta/pulmonary artery. Systolic time intervals can be measured and used to assess ventricular function [45]. One of the indices that gained some interest is the ratio of pre-ejection period (PEP) to left ventricular ejection time (ET). This method is rather cumbersome, is poorly validated in children and, moreover, is extremely afterload-dependent as PEP and ET are very sensitive to afterload changes. Another problem is the influence of conduction delays, which will prolong PEP. Finally, ejection time is heart rate-dependent.

The *myocardial performance index* (MPI) was introduced by Tei et al. as a nongeometrical index that incorporates systolic and diastolic time intervals in expressing global ventricular function [46–48]. Systolic dysfunction results in prolonged isovolumic contraction time (ICT) and shortened ET, whereas diastolic dysfunction results in prolongation of isovolumic relaxation time (IRT). The MPI can easily be calculated using Doppler echocardiography measuring simple time intervals from mitral and aortic Doppler traces (Fig. 7.9). MPI is defined as:

$$\text{MPI} = (\text{ICT} + \text{IRT})/\text{ET}$$

Normal values for the left ventricle are 0.35 ± 0.03 and for the right ventricle 0.28 ± 0.04. The larger the MPI, the more abnormal is ventricular function. The main advantage of this index is that it does not use any geometric assumptions and thus can be used in children with abnormal geometry [49,50]. One of the main limitations is that MPI does not differentiate between systolic and diastolic dysfunction. If it is abnormal, it indicates that "something" is wrong with ventricular function that needs further definition using other techniques. Another problem is the load-dependency of the MPI, as shown by Cheung et al. [51]. This is not surprising because both ICT and IRT are influenced by changes in preload and afterload. In children this load-sensitivity did not seem to affect measurements importantly when acute load changes were evaluated [49]. Theoretically MPI should be very sensitive to almost any change or abnormality in contractility, loading and relaxation. It is also distorted in the case of conduction abnormalities. For this reason it should be used with caution, for instance, in patients after correction for tetralogy of Fallot, who often have right bundle branch block [52,53].

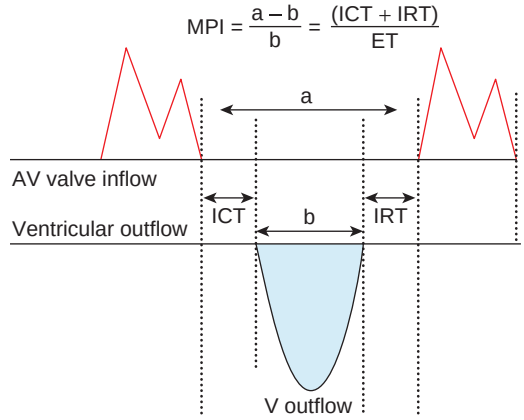


**Figure 7.9** Diagram illustrating how to measure the myocardial performance index (MPI). Isovolumic contraction time (ICT), isovolumic relaxation time (IRT) and ejection time (ET) are measured with Doppler echocardiography. Also the time from mitral valve closure to mitral valve opening minus ET can be used to calculate MPI. Reproduced from Eidem BW, O'Leary PW, Tei C, Seward JB. Usefulness of the myocardial performance index for assessing right ventricular function in congenital heart disease. *Am J Cardiol* 2000;86: 654–8 with permission.

## Assessment of regional myocardial function

Apart from evaluating global myocardial function, the assessment of regional differences in myocardial function is an important issue. This is obvious for the assessment of patients with coronary artery disease where decreased regional myocardial perfusion will result in decreased regional function. It is still uncertain and debatable how important regional functional analysis is for children with acquired and congenital heart disease, where in most cases ventricular function seems to be globally affected. Few studies have actually been perfomed in children quantifying regional myocardial function in different diseases. It might be that regional differences precede more global changes in myocardial function.

Regional wall motion analysis is based on assessing the function of individual segments. This requires a definition of the segments to be studied. Different segmental methods have been proposed historically, but in 2002 a consensus document on myocardial segmentation was published [54]. In this document a 17-segment model of the LV was proposed. For the purpose of analysis, the LV is subdivided into three levels (basal, mid and apical) and 17 segments. The basal and mid segments are each subdivided into six segments, the apical level is subdivided into four segments + the actual apex. The 17 segments can be displayed in a circumferential polar plot (Figs 7.10 and 7.11). A numeric scoring system has been developed based on the evaluation of the contractility of each segment. In this system, higher scores indicate more severe wall motion abnormality:

**1** normal
**2** hypokinesis
**3** akinesis
**4** dyskinesis
**5** aneurysm

The interpretation of the individual segments is largely based on subjective scoring and not on accurate quantification. Segmental function can be assessed at rest as well as during exercise or pharmacologic stress (such as dobutamine stress echocardiography). To improve the quantification of regional myocardial function, new techniques such as tissue Doppler echocardiography and strain rate imaging have been introduced.

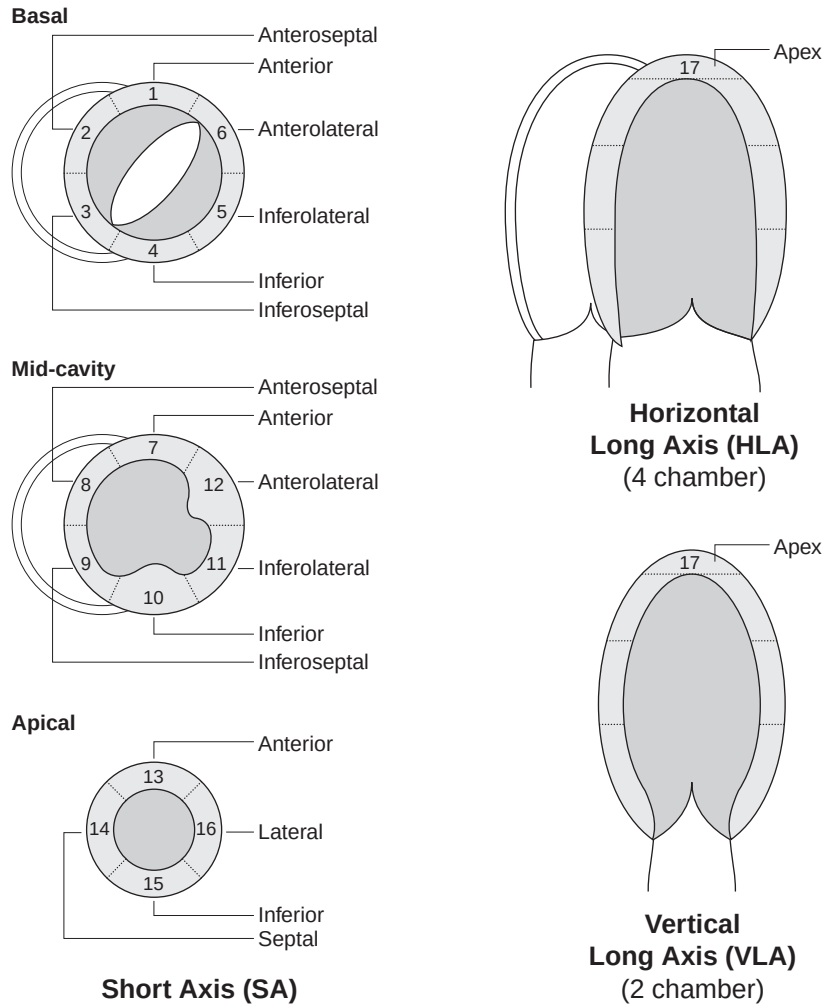


**Figure 7.10** Diagram of the 2-chamber view, the 4-chamber view and short-axis (SA) planes showing the name, location and anatomic landmarks for selection of the basal (tips of the mitral valve leaflets), mid-cavity (papillary muscles) and apical (beyond papillary muscles but before cavity ends) short-axis slices for the recommended 17-segment system. Reproduced from Cerqueira MD, Weissman NJ, Dilsizian V et al. Standardized myocardial segmentation and nomenclature for tomographic imaging of the heart: a statement for healthcare professionals from the Cardiac Imaging Committee of the Council on Clinical Cardiology of the American Heart Association *Circulation* 2002;105:539–42 with permission.

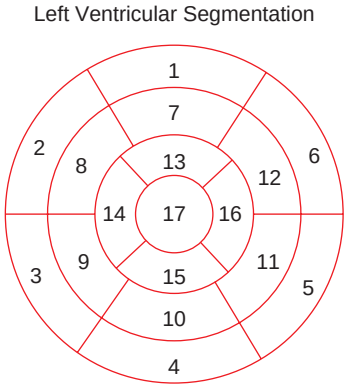


1. basal anterior
2. basal anteroseptal
3. basal inferoseptal
4. basal inferior
5. basal inferolateral
6. basal anterolateral
7. mid anterior
8. mid anteroseptal
9. mid inferoseptal
10. mid inferior
11. mid inferolateral
12. mid anterolateral
13. apical anterior
14. apical septal
15. apical inferior
16. apical lateral
17. apex

**Figure 7.11** Display, on a circumferential polar plot, of the 17 myocardial segments and the recommended nomenclature for tomographic imaging of the heart. Reproduced from Cerqueira MD, Weissman NJ, Dilsizian V et al. Standardized myocardial segmentation and nomenclature for tomographic imaging of the heart: a statement for healthcare professionals from the Cardiac Imaging Committee of the Council on Clinical Cardiology of the American Heart Association. *Circulation* 2002;105:539–42 with permission.

## Tissue Doppler imaging for the evaluation of myocardial function

Most of the previously discussed methods indirectly assess myocardial function by looking at dimensional changes or at blood pool data during the ejection period. It is tempting to try to look directly into the myocardium using echocardiography and measure regional function by quantifying myocardial properties such as velocity and deformation. Tissue Doppler imaging (TDI), also known as Doppler myocardial imaging or myocardial velocity imaging, is a technique that allows one to measure regional myocardial properties such as myocardial motion and deformation [55]. In the late 1980s and early 1990s, the use of adapted thresholds and clutter filters made it possible to distinguish between the poorly reflective and rapidly moving blood (range 50–150 cm/s) and the highly reflective and slow-moving myocardium (3–25 cm/s). These technical adaptations allowed measurement of myocardial velocities within a segment [56,57]. After the initial description of tissue velocities, experimental studies confirmed that, for normal myocardium, changes in segmental systolic velocities are closely linked to changes in contractility [58]. This resulted in numerous clinical studies investigating the value of regional myocardial velocities in various diseases such as ischemic heart disease, aortic insufficiency and hypertrophic cardiomyopathy [59,60]. The introduction of TDI into the comprehensive echocardiographic evaluation of children with acquired or congenital heart disease has also been received with much enthusiasm. Because of the unusual ventricular geometries often present in patients with congenital heart disease, quantitative noninvasive methodologies to evaluate ventricular performance, either global or regional, have been lacking. Tissue Doppler imaging affords the echocardiographer a nongeometric quantitative measure of both systolic and diastolic ventricular function that is easily obtained, reproducible and clinically valid [61]

Myocardial velocities can be measured with either pulsed-wave or color Doppler methodologies. With *pulsed-wave TDI*, a pulsed Doppler sample volume of 4–8 mm is placed within the myocardium and the myocardial wall is aligned as parallel as possible to the ultrasound beam. The resulting velocity waveform represents the peak instantaneous velocity in that area throughout the cardiac cycle. It provides a real-time display with high temporal resolution (250–300 frames/s) of myocardial velocities. The spatial resolution is limited because the myocardial wall moves whereas the sample volume remains fixed. Another limitation is that myocardial velocities in each myocardial segment need to be acquired separately and no post processing is possible.

A normal pulsed-wave TDI trace obtained in the basal septum (Fig. 7.12) is characterized by first a short and sharp isovolumic contraction peak, followed by a longer systolic peak that corresponds to base-to-apex motion of the myocardium during systole. This is followed by another short-lived isovolumic relaxation peak. Later, the early diastolic and the late-diastolic waves occur; they represent the opposite motion of the AV valve plane toward the base in diastole when the left ventricle fills. By convention, motion toward

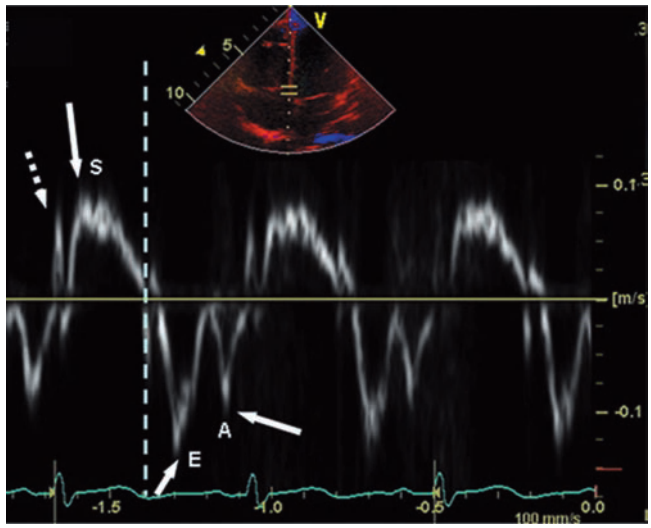


**Figure 7.12** Typical pulsed-wave-derived myocardial velocity profile in the basal septal segment. The high temporal resolution of the technique allows the discrimination of short-lived events like isovolumic contraction time (ICT; dotted arrow). Dashed line indicates aortic valve closure. S, peak systolic myocardial velocity; E, peak early diastolic myocardial velocity; A, peak late diastolic myocardial velocity.

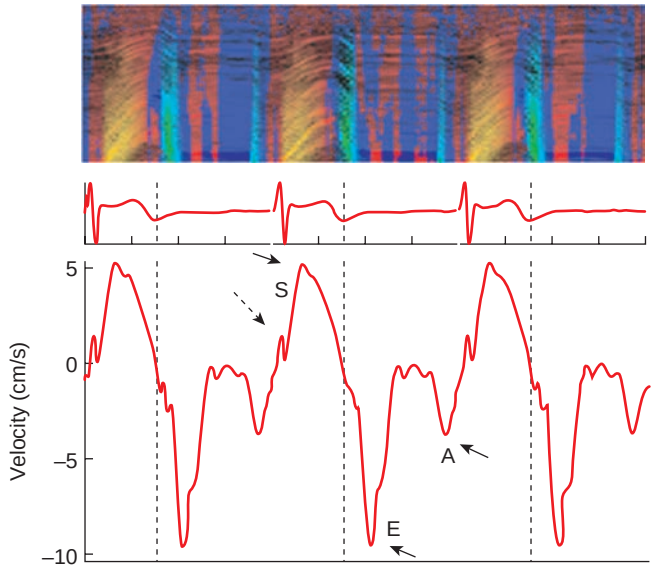


**Figure 7.13** Myocardial velocity profile derived from color Doppler myocardial imaging. Note that peak values are lower than when using pulsed-waved velocities (see Fig. 7.12). Dashed lines indicate aortic valve closure. S, peak systolic myocardial velocity; E, peak early diastolic myocardial velocity; A, peak late diastolic myocardial velocity.

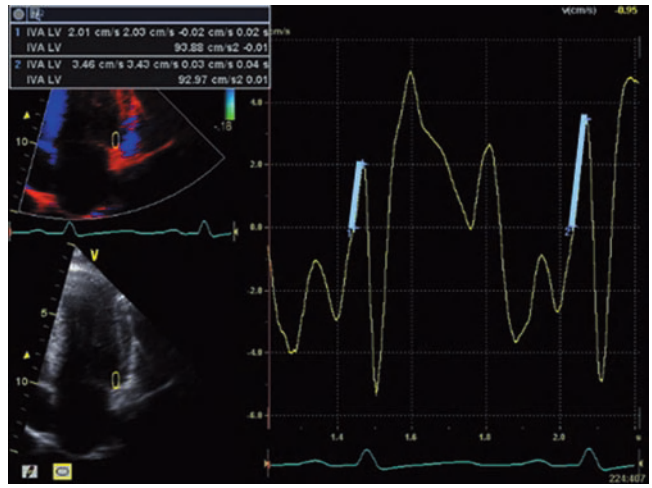

**Figure 7.14** The myocardial acceleration during isovolumic contraction is calculated as the peak velocity divided by time during isovolumic contraction. The thick blue lines highlight the isovolumetric velocity curve from which the mean accerleration is calculated. Reproduced with permission of Leuven University Press.

the transducer is represented as positive waves and motion away from the transducer as negative waves.

With *color Doppler myocardial imaging* (CDMI), the regional mean velocities, instead of peak velocities, are measured using autocorrelation techniques. The difference in measurement technique explains why CDMI-derived myocardial velocities are on average 15–20% lower compared with pulsed-wave-derived myocardial velocities [62]. With CDMI, the mean velocities can be displayed as a velocity curve by indicating a region of interest at any point on the myocardial wall in the 2D image or as a color-coded M-mode map (Fig. 7.13). As in blood pool Doppler imaging, myocardial velocities toward the transducer are coded in red, whereas motion away from the transducer is coded in blue. One advantage of CDMI is that it combines a good temporal resolution (>180 frames/s) with a high spatial resolution in the axial direction, thus making it possible to calculate myocardial velocity gradients. Secondly, velocities are recorded simultaneously in different myocardial segments. This allows the comparison of regional wall motion in the different myocardial segments simultaneously. Thirdly, a cineloop containing velocity information can be stored digitally and off-line analysis can later be performed.

*Myocardial acceleration during isovolumic contraction* (IVA) is a recently described index of contractility. Isovolumic acceleration is calculated as the average rate of myocardial acceleration during isovolumic contraction (Fig. 7.14) expressed in centimeters per second [63]. As isovolumic contraction is a short-lived event (30–40 ms), calculation of IVA requires images obtained at high temporal resolution (>200 frames/s). In experimental studies IVA has been validated as a sensitive noninvasive index of RV and LV contractility that is unaffected by preload and afterload within a physiologic range. Subsequently the value of IVA has been evaluated in clinical conditions. In patients with repaired tetralogy of Fallot, IVA was reduced indicating a reduced contractile function related to the degree of pulmonary regurgitation [64]. It has also been shown to be a useful noninvasive marker of allograft rejection in pediatric heart transplant patients [65]. The value of IVA as a regional functional parameter was questioned by Lyseggen et al. [66]. In their experimental animal study they showed that IVA is preload-dependent when left ventricular end-diastolic pressures are elevated. Moreover, there was no consistent relationship between regional IVA measurements and regional myocardial contractility in ischemic heart segments. When calculated from longitudinal velocities near the LV base, IVA should only be used as a global functional parameter. An important aspect in the use of IVA is its heart rate dependency [67]. This explains partly the relatively large variability in baseline measurements; however, its relationship with heart rate means that this methodology could be used to study the force–frequency relationship. This was applied by Cheung et al. [68] in the perioperative period in patients following surgery for congenital heart conditions. These authors demonstrated that the force–frequency relationship, as measured by IVA, is preserved in patients after atrial septal closure but is severely blunted in patients immediately after the arterial switch operation. The same principle could be used during stress echocardiography, as demonstrated by Pauliks et al. [69]. Further data are certainly required regarding the applicability of this technique in children with congenital heart disease.

## Current clinical applications of tissue velocities

Multiple experimental and clinical studies have been performed to characterize the myocardial velocity profile in normal subjects. In the longitudinal direction, systolic and diastolic myocardial velocities are greater at the base of the heart and decrease toward the apex, which remains almost stationary [70]. When analyzing radial myocardial function, myocardial velocities are higher at the endocardium than at the epicardium [71]. For these reasons, a gradient in myocardial velocities exists between the base and the apex (in the longitudinal direction), and between the endo- and epicardium. Tissue Doppler velocities have been used for the assessment of systolic and diastolic ventricular function. In this chapter we will focus mainly on the systolic velocities as a parameter for systolic function.

### Use of systolic tissue Doppler velocities in children

The first step was to establish normal values for tissue velocities in children. A number of studies of children have been published to establish normal reference values of tissue Doppler velocities [72–75]. These demonstrated that tissue velocities vary with age, heart rate, myocardial segment and myocardial layer. A very large study published by Eidem et al. included 325 children of different ages [70]. They showed that pulsed-wave tissue Doppler velocities are also correlated with parameters of cardiac growth, especially the left ventricular end-diastolic dimension and left ventricular mass. This means that tissue velocities are not entirely geometry independent and that ventricular geometry influences wall mechanics. This has important implications when applying this methodology in children with congenital heart disease. Another issue is the load-dependency of tissue velocities. In initial adult studies, tissue velocities were reported to be relatively load-independent [76], whereas later studies demonstrated the load-dependency of tissue velocities. In this context a distinction has to be made between acute load changes and the chronically adapted ventricles where preload and afterload can normalize due to the hypertrophic response. Acute preload changes clearly affect tissue velocities whereas this is less clear for the effect of chronic loading conditions. Studies in children with congenital heart disease having chronic increases in left ventricular preload have documented minimal changes in tissue Doppler velocities compared with normal pediatric controls. In a large study by Eidem et al. the effect of different congenital abnormalities on tissue Doppler velocities was studied [77]; Kiraly and colleagues [78] performed a similar study. All the data seem to indicate that load changes affect systolic tissue velocities and that the latter should be used with care under these conditions.

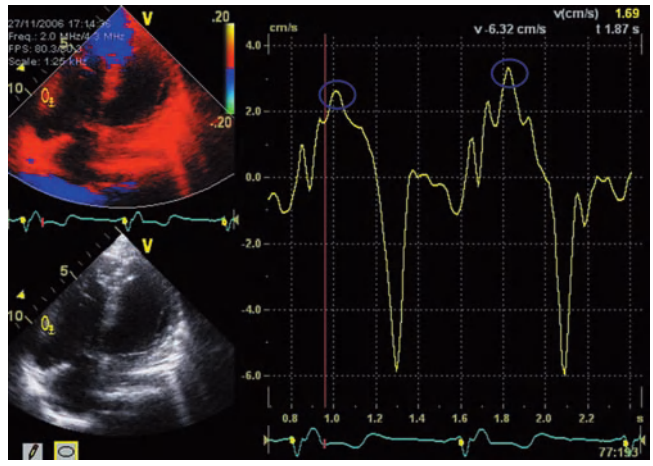


**Figure 7.15** Myocardial velocity profile in the basal right ventricular myocardial segment of a patient after repair of tetralogy of Fallot. Systolic and diastolic myocardial velocities are reduced.

Data on right ventricular systolic velocities have also been published. It has been shown that right ventricular systolic velocities were elevated in patients with atrium septal defects before closure of the defect [79,80]. These values normalized within 24 hours after closure of the defect. Quantitative assessment of right ventricular performance after repair of tetralogy of Fallot has also been the subject of considerable investigation. Tissue Doppler velocities are decreased in tetralogy patients following repair, with some regional wall motion abnormalities detectable in the right ventricle [81].

Apart from their dependency on age, heart rate, geometry and load, tissue Doppler velocities have additional inherent limitations. Like other Doppler modalities employed in echocardiography, tissue velocities are angle-dependent and currently unidimensional, relying on a one-dimensional assessment of myocardial velocity (typically in either the longitudinal or radial direction). An intrinsic problem of tissue velocities is that when measuring velocities, the movement of the heart within the thorax (*cardiac translation*) is also measured. So the measurement is influenced by regional myocardial events as well as global cardiac motion within the chest. Additionally the motion and velocity of a myocardial segment are influenced not only by its own intrinsic contractility but also by adjacent myocardial segments (defined as *tethering*). The identification of regional myocardial dysfunction by tissue Doppler echocardiography is therefore significantly limited when regional disease exists (e.g., a localized myocardial infarction) because these diseased segments may continue to move relatively normally due to the influence of healthy adjacent myocardium. These and other limitations in tissue Doppler echocardiography are beginning to be overcome by the continued development and clinical application of strain imaging in adults and children with acquired or congenital cardiac disease.

## Deformation imaging in pediatric and congenital heart disease

### Ultrasonic strain rate/strain imaging: the principles

Uematsu et al. proposed to look at gradients in myocardial velocities within a myocardial wall [71]. These authors demonstrated that in the left ventricular posterior wall, the endocardium moved faster than the epicardium in the radial direction. The myocardial velocity gradient was shown to be reduced in patients with dilated cardiomyopathy and ischemic heart disease. This concept was further explored by Heimdal et al., and the technique of ultrasound-based strain rate and strain imaging (deformation imaging) was developed [82]. Regional strain rate corresponds to the rate of regional myocardial deformation and can be calculated from the spatial gradients in velocities between two neighboring points in the myocardium (Fig. 7.16). The underlying principle is that instantaneous differences in tissue velocity between two adjacent segments reflect either expansion or compression of the tissue in between. Regional strain rate is the rate of deformation (per second) and can be measured from the velocity difference between two segments of myocardium divided by the distance between them (= area of computation). For pediatrics we use computational distances of 4–5 mm in the radial direction and 8–9 mm for the longitudinal direction. Regional strain represents the amount of deformation (%), or the fractional change in length, caused by an applied force and is calculated by integrating the strain rate curve over time during the cardiac cycle. Strain measures the amount of deformation, and strain rate the velocity of shortening, two measurements that reflect different aspects of myocardial function and provide complementary information (Fig. 7.17).

Deformation can be compression, that is, shortening in the longitudinal direction (systole) and thinning in the radial direction (diastole), or expansion, that is, lengthening in the longitudinal direction (diastole) and thickening in the radial direction (systole). Shortening is either active contraction or passive recoil after stretching. Similarly, elongation can be relaxation after contraction or passive stretching. Conventionally compression is characterized by a negative strain rate, and strain and expansion by a positive strain rate and strain (Figs 7.18 and 7.19). In contrast to myocardial

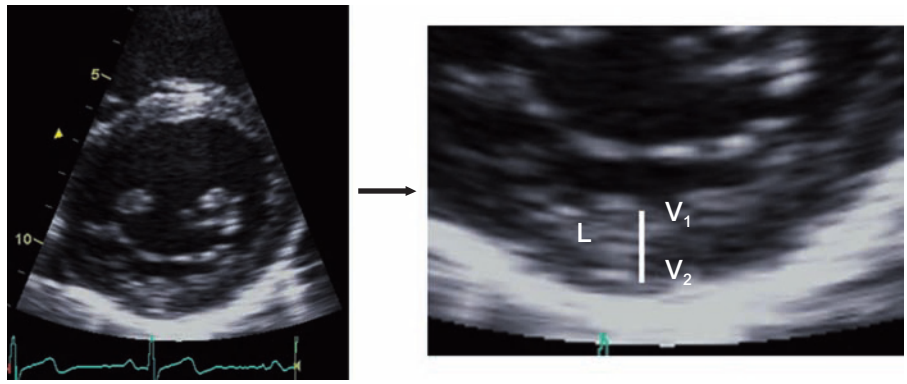


**Figure 7.16** Strain rate is calculated as the difference in myocardial velocity ($V_2 - V_1$) between two points of a predetermined region of interest divided by its initial length (L).

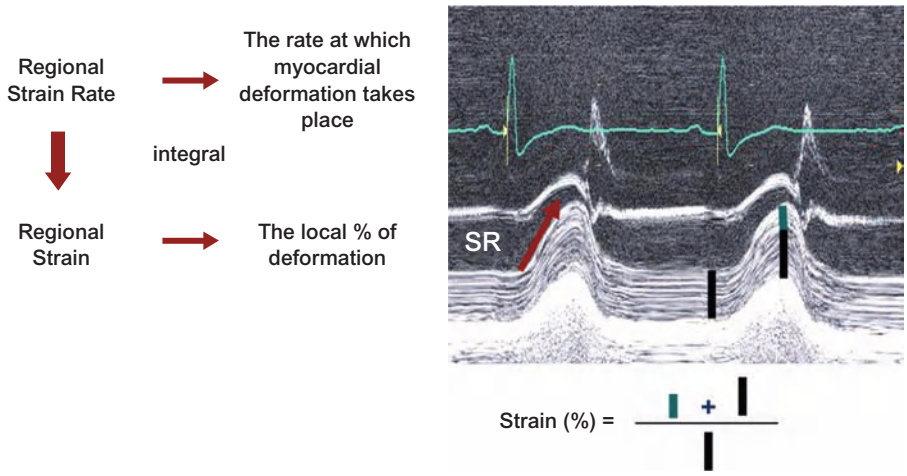


**Figure 7.17** Strain rate (SR) represents the rate at which myocardial deformation takes place and peaks in early systole. Strain is the total amount of regional myocardial deformation and peaks at the end of systole. This highlights the fact that they reflect different aspects of myocardial function.

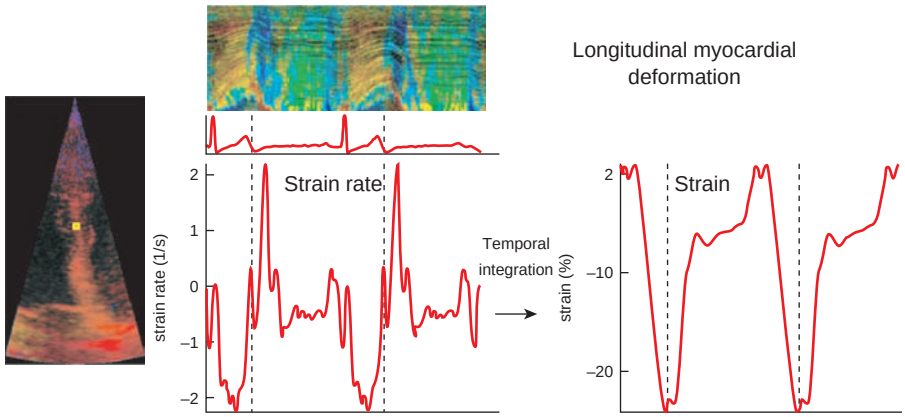


**Figure 7.18** Longitudinal myocardial deformation in the interventricular septum from an apical 4-chamber view. Shortening in systole is displayed as negative values, whereas lengthening in diastole is displayed as positive values. Dashed lines indicate aortic valve closure. Reproduced with permission from Leuven University Press.

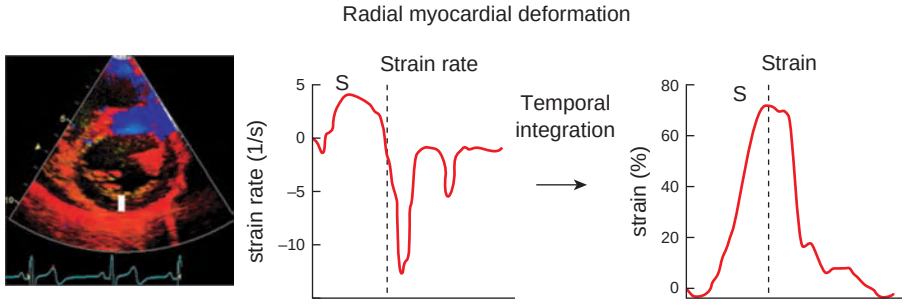


**Figure 7.19** Radial myocardial deformation of the inferolateral wall. The radial strain rate is calculated from a short-axis view containing myocardial velocity data. Wall thickening in systole is displayed as positive values, whereas wall thinning in diastole is displayed as negative values. Temporal integration of the strain rate curve results in the local strain profile. Note strain rate peaks early in systole whereas strain peak late in systole. S, systole; dotted lines indicate aortic valve closure. Reproduced with permission from Leuven University Press.

velocities, the new indices of deformation strain rate and strain are not influenced by global heart motion and motion in adjacent segments, and are therefore better indices of true regional myocardial function.

## Normal data in children

The first paper on normal strain rate and strain data in children was published by Weidemann et al. [83]. They obtained normal strain and strain rate measurements in 33 healthy children (aged 4–16 years). Boettler et al. looked at the values in different age groups and demonstrated that strain and strain rate values are influenced by heart rate [84].

## Clinical applications in pediatric patients

### Regional right ventricular deformation in congenital heart disease

One of the most important challenges in congenital heart disease is the assessment of right ventricular function. In current clinical practice there is no good easily accessible technique that allows quantification of right ventricular function. The complex geometry of the RV makes the evaluation of RV function extremely difficult. In daily practice echocardiographers often resort to eyeballing for assessing RV systolic function. Quantitative assessment of RV function using strain and strain rate imaging has been performed in a number of congenital malformations. Data have been published for patients after tetralogy of Fallot correction [85–87] and in patients with a systemic right ventricle such as in Senning or Mustard patients. A study published by Eyskens et al. showed that regional peak systolic strain and strain rate values were reduced in the basal, mid and apical segments of the RV free wall and correlated well with global ejection fraction [88].

### Regional left ventricular function in pediatric heart disease

In ischemic heart disease in adults, there is obvious importance in studying regional left myocardial function. The importance is less obvious for children with acquired or congenital heart disease, where it is thought that only global function is affected. Nevertheless there is some evidence that looking at regional myocardial function using deformation imaging might give additional information for patients with left ventricular dysfunction. In routine clinical practice often only fractional shortening or ejection fraction based on M-mode echocardiography is assessed in pediatric cardiology. This basically only looks at radial ventricular function in the basal part of the LV and assesses only geometric changes of the LV cavity, not what is happening within the LV wall. There have been a number of publications looking at LV function in children using deformation imaging. This technique has been applied to patients after abnormal left coronary artery originating from the pulmonary artery (ALCAPA) repair

[89], hypertrophic cardiomyopathy [90,91], Friedreich ataxia [90], Duchenne muscular dystrophy [92], and anthracycline toxicity [93,94].

### Current shortcomings of deformation imaging and future perspectives

As deformation imaging derived from velocity imaging is based on Doppler technology, it is an angle-dependent technique. Langeland et al. [95] validated a two-dimensional technique that is independent of the insonation angle allowing both radial and longitudinal deformation measurement in single datasets. Other new techniques such as Speckle-tracking allow quantification of two-dimensional LV mechanics using echocardiography [96,97]. Another limitation of deformation imaging is that it is a load-dependent technique. Both preload and afterload changes affect the measurements. The clinical relevance of this certainly needs further study.

## Conclusion

Different techniques are available for assessing systolic ventricular function in children. However, no technique allows easy quantification of intrinsic myocardial contractility. Most techniques used in daily clinical practice are load-dependent and/or geometry-dependent.

## References


1. Sutherland G, Hatle L, Claus P et al. *Doppler Myocardial Imaging. A Textbook*. Hasselt, Belgium: BSWK, 2006.
2. MacGowan GA, Shapiro EP, Azhari H et al. Noninvasive measurement of shortening in the fiber and cross-fiber directions in the normal human left ventricle and in idiopathic dilated cardiomyopathy. *Circulation* 1997;96:535–41.
3. Rademakers FE, Rogers WJ, Guier WH et al. Relation of regional cross-fiber shortening to wall thickening in the intact heart. Three-dimensional strain analysis by NMR tagging. *Circulation* 1994;89:1174–82.
4. Sengupta PP, Korinek J, Belohlavek M et al. Left ventricular structure and function: basic science for cardiac imaging. *J Am Coll Cardiol* 2006;48:1988–2001.
5. Sengupta PP, Krishnamoorthy VK, Korinek J et al. Left ventricular form and function revisited: applied translational science to cardiovascular ultrasound imaging. *J Am Soc Echocardiog* 2007; 20:539–51.
6. Regen DM. Calculation of left ventricular wall stress. *Circ Res* 1990;67:245–52.
7. Hein S, Arnon E, Kostin S et al. Progression from compensated hypertrophy to failure in the pressure-overloaded human heart: structural deterioration and compensatory mechanisms. *Circulation* 2003;107:984–91.
8. Hara Y, Hamada M, Hiwada K. Left ventricular end-systolic wall stress is a potent prognostic variable in patients with dilated cardiomyopathy. *Jpn Circulation J* 1999;63:196–200.
9. Laskey WK, Sutton MS, Zeevi G et al. Left ventricular mechanics in dilated cardiomyopathy. *Am J Cardiol* 1984;54:620–5.
10. Piot C, Lemaire S, Albat B et al. High frequency-induced upregulation of human cardiac calcium currents. *Circulation* 1996;93: 120–8.
11. Meyer M, Keweloh B, Guth K et al. Frequency-dependence of myocardial energetics in failing human myocardium as quantified by a new method for the measurement of oxygen consumption in muscle strip preparations. *J Mol Cell Cardiol* 1998;30:1459–70.
12. Suga H, Sagawa K, Shoukas AA. Load independence of the instantaneous pressure–volume ratio of the canine left ventricle and effects of epinephrine and heart rate on the ratio. *Circ Res* 1973;32:314–22.
13. Kass DA, Maughan WL, Guo ZM et al. Comparative influence of load versus inotropic states on indexes of ventricular contractility: experimental and theoretical analysis based on pressure–volume relationships. *Circulation* 1987;76:1422–36.
14. Suga H. Paul Dudley White International Lecture: cardiac performance as viewed through the pressure-volume window. *Jpn Heart J* 1994;35:263–80.
15. Quinones M, Waggoner A, Reduto LA et al. A new, simplified and accurate method for determining ejection fraction with two-dimensional echocardiography. *Circulation* 1981;64:744–53.
16. Schiller NB, Shah PM, Crawford M et al. Recommendations for quantitation of the left ventricle by two-dimensional echocardiography. American Society of Echocardiography Committee on Standards, Subcommittee on Quantitation of Two-Dimensional Echocardiograms. *J Am Soc Echocardiog* 1989; 2:358–67.
17. Lang R, Bierig M, Devereux R et al. Recommendations for chamber quantification. *Eur J Echocardiogr* 2006;7:79–108.
18. Hashimoto I, Ichida F, Miura M et al. Automatic border detection identifies subclinical anthracycline cardiotoxicity in children with malignancy. *Circulation* 1999;99:2367–70.
19. Kuhl HP, Schreckenberg M, Rulands D et al. High-resolution transthoracic real-time three-dimensional echocardiography: quantitation of cardiac volumes and function using semi-automatic border detection and comparison with cardiac magnetic resonance imaging. *J Am Coll Cardiol* 2004;43:2083–90.
20. Kimball TR, Witt SA, Khoury PR, Daniels SR. Automated echocardiographic analysis of systemic ventricular performance in hypoplastic left heart syndrome. *J Am Soc Echocardiog* 1996; 9:629–36.
21. Mahle WT, Coon PD, Wernovsky G, Rychik J. Quantitative echocardiographic assessment of the performance of the functionally single right ventricle after the Fontan operation. *Cardiol Young* 2001;11:399–406.
22. Riehle TJ, Mahle WT, Parks WJ et al. Real-time three-dimensional echocardiographic acquisition and quantification of left-ventricular indices in children and young adults with congenital heart disease: comparison with magnetic resonance imaging. *J Am Soc Echocardiogr* 2008;21:78–83.
23. Silverman NH, Hudson S. Evaluation of right ventricular volume and ejection fraction in children by two-dimensional echocardiography. *Pediatr Cardiol* 1983;4:197–203.
24. Trowitzsch E, Colan SD, Sanders SP. Two-dimensional echocardiographic estimation of right ventricular area change and ejection fraction in infants with systemic right ventricle

(transposition of the great arteries or hypoplastic left heart syndrome). *Am J Cardiol* 1985;55:1153–7.
25. Trowitzsch E, Colan SD, Sanders SP. Two-dimensional echocardiographic evaluation of right ventricular size and function in newborns with severe right ventricular outflow tract obstruction. *J Am Coll Cardiol* 1985;6:388–93.
26. Friedberg MK, Rosenthal DN. New developments in echocardiographic methods to assess right ventricular function in congenital heart disease. *Curr Opin Cardiol* 2005;20:84–8.
27. Helbing WA, Bosch HG, Maliepaard C et al. Comparison of echocardiographic methods with magnetic resonance imaging for assessment of right ventricular function in children. *Am J Cardiol* 1995;76:589–94.
28. Vogel M, Gutberlet M, Dittrich S et al. Comparison of transthoracic three dimensional echocardiography with magnetic resonance imaging in the assessment of right ventricular volume and mass. *Heart* 1997;78:127–30.
29. Stoylen A, Skjaerpe T. Systolic long axis function of the left ventricle. Global and regional information. *Scand Cardiovasc J* 2003;37:253–8.
30. Saxena N, Rajagopalan N, Edelman K, Lopez-Candales A. Tricuspid annular systolic velocity: a useful measurement in determining right ventricular systolic function regardless of pulmonary artery pressures. *Echocardiogr-J Card* 2006;23: 750–5.
31. Lopez-Candales A, Rajagopalan N, Gulyasy B et al. Comparative echocardiographic analysis of mitral and tricuspid annular motion: differences explained with proposed anatomic-structural correlates. *Echocardiography* (Mount Kisco, NY) 2007;24:353–9.
32. Hammarstrom E, Wranne B, Pinto FJ et al. Tricuspid annular motion. *J Am Soc Echocardiog* 1991;4:131–9.
33. Colan SD, Borow KM, Neumann A. Left ventricular end-systolic wall stress-velocity of fiber shortening relation: a load-independent index of myocardial contractility. *J Am Coll Cardiol* 1984;4: 715–24.
34. Shimizu G, Hirota Y, Kita Y et al. Left ventricular midwall mechanics in systemic arterial hypertension. Myocardial function is depressed in pressure-overload hypertrophy. *Circulation* 1991;83:1676–84.
35. de Simone G, Devereux RB, Koren MJ et al. Midwall left ventricular mechanics. An independent predictor of cardiovascular risk in arterial hypertension. *Circulation* 1996;93:259–65.
36. de Simone G, Devereux RB. Rationale of echocardiographic assessment of left ventricular wall stress and midwall mechanics in hypertensive heart disease. *Eur J Echocardiog* 2002;3: 192–8.
37. de Simone G, Devereux RB, Celentano A, Roman MJ. Left ventricular chamber and wall mechanics in the presence of concentric geometry. *J Hypertens* 1999;17:1001–6.
38. Gentles TL, Sanders SP, Colan SD. Misrepresentation of left ventricular contractile function by endocardial indexes: clinical implications after coarctation repair. *Am Heart J* 2000;140: 585–95.
39. Banerjee A, Brook MM, Klautz RJ, Teitel DF. Nonlinearity of the left ventricular end-systolic wall stress-velocity of fiber shortening relation in young pigs: a potential pitfall in its use as a single-beat index of contractility. *J Am Coll Cardiol* 1994;23: 514–24.
40. Rowland DG, Gutgesell HP. Noninvasive assessment of myocardial contractility, preload, and afterload in healthy newborn infants. *Am J Cardiol* 1995;75:818–21.
41. Gentles TL, Colan SD. Wall stress misrepresents afterload in children and young adults with abnormal left ventricular geometry. *J Appl Physiol* 2002;92:1053–7.
42. Lipshultz SE, Colan SD, Gelber RD et al. Late cardiac effects of doxorubicin therapy for acute lymphoblastic leukemia in childhood. *N Engl J Med* 1991;324:808–15.
43. Lipshultz SE, Grenier MA, Colan SD. Doxorubicin-induced cardiomyopathy. *N Engl J Med* 1999;340:653–4; author reply, 5.
44. Lipshultz SE, Lipsitz SR, Sallan SE et al. Chronic progressive cardiac dysfunction years after doxorubicin therapy for childhood acute lymphoblastic leukemia. *J Clin Oncol* 2005;23:2629–36.
45. Ahmed SS, Levinson GE, Schwartz CJ, Ettinger PO. Systolic time intervals as measures of the contractile state of the left ventricular myocardium in man. *Circulation* 1972;46:559–71.
46. Tei C, Dujardin KS, Hodge DO et al. Doppler index combining systolic and diastolic myocardial performance: clinical value in cardiac amyloidosis. *J Am Coll Cardiol* 1996;28:658–64.
47. Tei C, Ling LH, Hodge DO et al. New index of combined systolic and diastolic myocardial performance: a simple and reproducible measure of cardiac function – a study in normals and dilated cardiomyopathy. *J Cardiol* 1995;26:357–66.
48. Tei C, Nishimura RA, Seward JB, Tajik AJ. Noninvasive Doppler-derived myocardial performance index: correlation with simultaneous measurements of cardiac catheterization measurements. *J Am Soc Echocardiog* 1997;10:169–78.
49. Eidem BW, O'Leary PW, Tei C, Seward JB. Usefulness of the myocardial performance index for assessing right ventricular function in congenital heart disease. *Am J Cardiol* 2000;86: 654–8.
50. Eidem BW, Tei C, O'Leary PW et al. Nongeometric quantitative assessment of right and left ventricular function: myocardial performance index in normal children and patients with Ebstein anomaly. *J Am Soc Echocardiogr* 1998;11:849–56.
51. Cheung MM, Smallhorn JF, Redington AN, Vogel M. The effects of changes in loading conditions and modulation of inotropic state on the myocardial performance index: comparison with conductance catheter measurements. *Eur Heart J* 2004;25: 2238–42.
52. Abd El Rahman MY, Abdul-Khaliq H, Vogel M et al. Value of the new Doppler-derived myocardial performance index for the evaluation of right and left ventricular function following repair of tetralogy of fallot. *Pediatr Cardiol* 2002;23:502–7.
53. Norozi K, Buchhorn R, Bartmus D et al. Elevated brain natriuretic peptide and reduced exercise capacity in adult patients operated on for tetralogy of fallot is due to biventricular dysfunction as determined by the myocardial performance index. *Am J Cardiol* 2006;97:1377–82.
54. Cerqueira MD, Weissman NJ, Dilsizian V et al. Standardized myocardial segmentation and nomenclature for tomographic imaging of the heart: a statement for healthcare professionals from the Cardiac Imaging Committee of the Council on Clinical Cardiology of the American Heart Association. *Circulation* 2002;105:539–42.

55. Sutherland GR, Di Salvo G, Claus P et al. Strain and strain rate imaging: a new clinical approach to quantifying regional myocardial function. *J Am Soc Echocardiogr* 2004;17:788–802.
56. McDicken WN, Sutherland GR, Moran CM, Gordon LN. Colour Doppler velocity imaging of the myocardium. *Ultrasound Med Biol* 1992;18:651–4.
57. Isaaz K, Thompson A, Ethevenot G et al. Doppler echocardiographic measurement of low velocity motion of the left ventricular posterior wall. *Am J Cardiol* 1989;64:66–75.
58. Gorcsan J 3rd, Strum DP, Mandarino WA et al. Quantitative assessment of alterations in regional left ventricular contractility with color-coded tissue Doppler echocardiography. Comparison with sonomicrometry and pressure-volume relations. *Circulation* 1997;95:2423–33.
59. Derumeaux G, Ovize M, Loufoua J et al. Doppler tissue imaging quantitates regional wall motion during myocardial ischemia and reperfusion. *Circulation* 1998;97:1970–7.
60. Vinereanu D, Ionescu AA, Fraser AG. Assessment of left ventricular long axis contraction can detect early myocardial dysfunction in asymptomatic patients with severe aortic regurgitation. *Heart* 2001;85:30–6.
61. Mertens L, Ganame J, Eyskens B. What is new in pediatric cardiac imaging? *Eur J Pediatr* 2008;167:1–8.
62. Kukulski T, Voigt JU, Wilkenshoff UM et al. A comparison of regional myocardial velocity information derived by pulsed and color Doppler techniques: an in vitro and in vivo study. *Echocardiography* (Mount Kisco, NY) 2000;17:639–51.
63. Vogel M, Schmidt MR, Kristiansen SB et al. Validation of myocardial acceleration during isovolumic contraction as a novel noninvasive index of right ventricular contractility: comparison with ventricular pressure-volume relations in an animal model. *Circulation* 2002;105:1693–9.
64. Frigiola A, Redington AN, Cullen S, Vogel M. Pulmonary regurgitation is an important determinant of right ventricular contractile dysfunction in patients with surgically repaired tetralogy of Fallot. *Circulation* 2004;110(11 Suppl. 1):II153–7.
65. Pauliks LB, Pietra BA, DeGroff CG et al. Non-invasive detection of acute allograft rejection in children by tissue Doppler imaging: myocardial velocities and myocardial acceleration during isovolumic contraction. *J Heart Lung Transplant* 2005;24(7 Suppl.): S239–48.
66. Lyseggen E, Rabben SI, Skulstad H et al. Myocardial acceleration during isovolumic contraction: relationship to contractility. *Circulation* 2005;111:1362–9.
67. Vogel M, Cheung MM, Li J et al. Noninvasive assessment of left ventricular force-frequency relationships using tissue Doppler-derived isovolumic acceleration: validation in an animal model. *Circulation* 2003;107:1647–52.
68. Cheung MM, Smallhorn JF, Vogel M et al. Disruption of the ventricular myocardial force-frequency relationship after cardiac surgery in children: noninvasive assessment by means of tissue Doppler imaging. *J Thorac Cardiov Sur* 2006;131: 625–31.
69. Pauliks LB, Vogel M, Madler CF et al. Regional response of myocardial acceleration during isovolumic contraction during dobutamine stress echocardiography: a color tissue Doppler study and comparison with angiocardiographic findings. *Echocardiography* (Mount Kisco, NY) 2005;22:797–808.
70. Eidem BW, McMahon CJ, Cohen RR et al. Impact of cardiac growth on Doppler tissue imaging velocities: a study in healthy children. *J Am Soc Echocardiogr* 2004;17:212–21.
71. Uematsu M, Miyatake K, Tanaka N et al. Myocardial velocity gradient as a new indicator of regional left ventricular contraction: detection by a two-dimensional tissue Doppler imaging technique. *J Am Coll Cardiol* 1995;26:217–23.
72. Kapusta L, Thijssen JM, Groot-Loonen J et al. Tissue Doppler imaging in detection of myocardial dysfunction in survivors of childhood cancer treated with anthracyclines. *Ultrasound Med Biol* 2000;26:1099–108.
73. Rychik J, Tian ZY. Quantitative assessment of myocardial tissue velocities in normal children with Doppler tissue imaging. *Am J Cardiol* 1996;77:1254–7.
74. Hiarada K, Orino T, Yasuoka K et al. Tissue doppler imaging of left and right ventricles in normal children. *Tohoku J Exp Med* 2000;191:21–9.
75. Roberson DA, Cui W, Chen Z et al. Annular and septal Doppler tissue imaging in children: normal z-score tables and effects of age, heart rate, and body surface area. *J Am Soc Echocardiog* 2007;20:1276–84.
76. Sohn DW, Chai IH, Lee DJ et al. Assessment of mitral annulus velocity by Doppler tissue imaging in the evaluation of left ventricular diastolic function. *J Am Coll Cardiol* 1997;30:474–80.
77. Eidem BW, McMahon CJ, Ayres NA et al. Impact of chronic left ventricular preload and afterload on Doppler tissue imaging velocities: a study in congenital heart disease. *J Am Soc Echocardiog* 2005;18:830–8.
78. Kiraly P, Kapusta L, Thijssen JM, Daniels O. Left ventricular myocardial function in congenital valvar aortic stenosis assessed by ultrasound tissue-velocity and strain-rate techniques. *Ultrasound Med Biol* 2003;29:615–20.
79. Eyskens B, Ganame J, Claus P et al. Ultrasonic strain rate and strain imaging of the right ventricle in children before and after percutaneous closure of an atrial septal defect. *J Am Soc Echocardiog* 2006;19:994–1000.
80. Pauliks LB, Chan KC, Chang D et al. Regional myocardial velocities and isovolumic contraction acceleration before and after device closure of atrial septal defects: a color tissue Doppler study. *Am Heart J* 2005;150:294–301.
81. Vogel M, Sponring J, Cullen S et al. Regional wall motion and abnormalities of electrical depolarization and repolarization in patients after surgical repair of tetralogy of Fallot. *Circulation* 2001;103:1669–73.
82. Heimdal A, Stoylen A, Torp H, Skjaerpe T. Real-time strain rate imaging of the left ventricle by ultrasound. *J Am Soc Echocardiog* 1998;11:1013–19.
83. Weidemann F, Eyskens B, Sutherland GR. New ultrasound methods to quantify regional myocardial function in children with heart disease. *Pediatr Cardiol* 2002;23:292–306.
84. Boettler P, Hartmann M, Watzl K et al. Heart rate effects on strain and strain rate in healthy children. *J Am Soc Echocardiog* 2005;18:1121–30.
85. Weidemann F, Eyskens B, Mertens L et al. Quantification of regional right and left ventricular function by ultrasonic strain rate and strain indexes after surgical repair of tetralogy of Fallot. *Am J Cardiol* 2002;90:133–8.

86. Abd El Rahman MY, Hui W, Yigitbasi M et al. Detection of left ventricular asynchrony in patients with right bundle branch block after repair of tetralogy of Fallot using tissue-Doppler imaging-derived strain. *J Am Coll Cardiol* 2005;45:915–21.
87. Abd El Rahman MY, Hui W, Dsebissowa F et al. Quantitative analysis of paradoxical interventricular septal motion following corrective surgery of tetralogy of fallot. *Pediatr Cardiol* 2005;26: 379–84.
88. Eyskens B, Weidemann F, Kowalski M et al. Regional right and left ventricular function after the Senning operation: an ultrasonic study of strain rate and strain. *Cardiol Young* 2004;14: 255–64.
89. Di Salvo G, Eyskens B, Claus P et al. Late post-repair ventricular function in patients with origin of the left main coronary artery from the pulmonary trunk. *Am J Cardiol* 2004;93:506–8.
90. Weidemann F, Eyskens B, Mertens L et al. Quantification of regional right and left ventricular function by ultrasonic strain rate and strain indexes in Friedreich's ataxia. *Am J Cardiol* 2003;91:622–6.
91. Ganame J, Mertens L, Eidem BW et al. Regional myocardial deformation in children with hypertrophic cardiomyopathy: morphological and clinical correlations. *Eur Heart J* 2007;28: 2886–94.
92. Mertens L, Ganame J, Claus P et al. Early regional myocardial dysfunction in young patients with Duchenne muscular dystrophy. *J Am Soc Echocardiog* 2008;21:1049–54.
93. Ganame J, Claus P, Eyskens B et al. Acute cardiac functional changes after subsequent anthracycline infusions in children. *Am J Cardiol* 2007;99:974–7.
94. Ganame J, Claus P, Uyttebroeck A et al. Myocardial dysfunction late after low-dose anthracycline treatment in asymptomatic pediatric patients. *J Am Soc Echocardiog* 2007;20;1351–8.
95. Langeland S, D'Hooge J, Wouters PF et al. Experimental validation of a new ultrasound method for the simultaneous assessment of radial and longitudinal myocardial deformation independent of insonation angle. *Circulation* 2005;112:2157–62.
96. Helle-Valle T, Crosby J, Edvardsen T et al. New noninvasive method for assessment of left ventricular rotation: speckle tracking echocardiography. *Circulation* 2005;112:3149–56.
97. Notomi Y, Lysyansky P, Setser RM et al. Measurement of ventricular torsion by two-dimensional ultrasound speckle tracking imaging. *J Am Coll Cardiol* 2005;45:2034–41.

# 8 Diastolic Ventricular Function Assessment

**Peter C. Frommelt**
Medical College of Wisconsin, Children's Hospital of Wisconsin, Milwaukee, USA

## Introduction

Echocardiography is the primary tool in the diagnosis and assessment of pediatric heart disease, including abnormalities of ventricular function. The initial focus when assessing myocardial function has traditionally centered on systolic function. Diastolic dysfunction, although recognized as a component of pediatric heart disease, has been less well understood and investigated. There are several reasons for this: (i) diastolic disease is felt to be relatively rare in pediatric patients; (ii) there is no single measure that adequately describes diastolic function (in contrast to ejection fraction, which is a simple method to characterize systolic function); (iii) echocardiographic techniques that help understand diastolic disease are not routinely applied in children; and (iv) Doppler patterns that characterize diastolic function vary significantly with age and heart rate in children in the absence of diastolic disease. Despite these challenges, there has been a recent evolution in diastolic assessment of children using echocardiography, and this chapter will focus on the techniques of diastolic function assessment. Appendix 2 is available on the accompanying DVD that includes a review of the diseases in which diastolic dysfunction has been identified in children.

## Definition and physiology of diastole

Diastole is the phase of the cardiac cycle during which ventricular filling occurs (Fig. 8.1). It is defined as the time period beginning at end-ejection (closure of the semilunar valves) and extending until the atrioventricular (AV) valves are closed. Diastole can be further divided into four components:
**1** Isovolumic relaxation – defined as the time from semilunar valve closure to onset of flow across the AV valve.

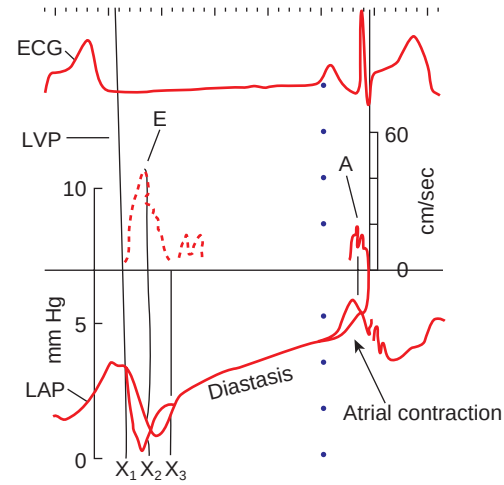


**Figure 8.1** Simultaneous recordings of left atrial pressure (LAP), left ventricular pressure (LVP) and mitral valve Doppler inflow tracings in open chested dogs. When left ventricular pressure decreases to a value equal to left atrial pressure (the first crossover point shown as $X_1$), the mitral valve opens and the onset of flow occurs on the mitral valve Doppler trace. Both pressures decrease rapidly after mitral valve opening, with a short duration of transvalvular pressure difference. The peak E velocity (E) occurs at the second crossover point $X_2$, which corresponds closely in time with the left ventricular minimum pressure. Deceleration from the peak E velocity begins with the onset of the increase in left ventricular diastolic pressure (the rapid filling wave) and ends at the third crossover point $X_3$. In mid-diastole, the two pressures appear to be equal, increasing slowly together (diastasis), and there is no flow across the mitral valve. Left atrial pressure increases and exceeds left ventricular pressure with atrial contraction, producing flow across the mitral valve at the A wave of the Doppler trace. ECG, electrocardiogram. Reprinted from Courtois M, Kovacs S, Ludbrook P. Transmitral pressure-flow velocity relation. Importance of regional pressure gradients in the left ventricle during diastole. *Circulation* 1988;78:661–71, with permission from Wolters Kluwer.

**2** Rapid filling – starts when ventricular pressure after systolic contraction decreases to a value less than atrial pressure. As ventricular pressure continues to fall during early diastole, a pressure difference is generated between the atrium and ventricle. Blood flows across the AV valve because of this pressure difference and ventricular filling begins. This early diastolic flow, which can be detected by pulsed Doppler in

*Echocardiography in Pediatric and Congenital Heart Disease: From Fetus to Adult*
Edited by Wyman W. Lai, Luc L. Mertens, Meryl S. Cohen and Tal Geva
 ISBN: 978-1-405-17401-5

the AV valve orifice, is called the early filling, or "E" velocity, wave. The E velocity peaks in early diastole, generally at the time of ventricular pressure minimum, and decelerates as ventricular pressure begins to increase with continued ventricular filling.

**3** Diastasis – occurs in mid-diastole when atrial and ventricular pressures equalize after early filling, so that little flow passes across the AV valve.

**4** Atrial contraction – in late diastole atrial pressure suddenly increases and again exceeds ventricular pressure, generating a second wave of flow across the AV valve. This late diastolic velocity profile is called the atrial contraction or "A" wave.

Many factors influence ventricular diastolic filling, including ventricular systolic function, AV valve function, rate of ventricular relaxation, the passive compliance or stiffness of the atrial and ventricular muscle, atrial systolic function, the loading or volume conditions of the two chambers, intrathoracic pressure changes with respiration, and heart rate and rhythm. All of these factors influence the observed diastolic velocity profile, and so must be considered in the analysis of these Doppler waveforms.

Atrial filling has also been analyzed using Doppler echocardiography. Systemic and pulmonary venous inflow is pulsatile and can generally be separated into systolic and diastolic phases. The systolic phase occurs during ventricular systole when atrial pressure drops as the atria relax after atrial contraction. In addition, there is active apical displacement of the AV valve annulus during ventricular systole, which creates a suction effect in the atria, with resultant augmentation of venous emptying into the atria. As atrial filling continues in later systole against a closed AV valve, atrial pressures rise and venous inflow decelerates. The diastolic phase of venous inflow is initiated with AV valve opening in early diastole, as this causes a sudden decrease in atrial pressure. During this phase, the atria act as a conduit from the veins to the ventricles. Diastolic venous inflow begins to decrease with increasing ventricular pressure as the ventricular chambers fill. With atrial contraction, there is a sudden increase in atrial pressure and cessation of venous inflow. If atrial pressures are elevated at the time of atrial contraction, significant reversal of flow from the atria into the veins can be seen and has been described as the atrial reversal phase of venous inflow. The same factors that influence ventricular filling are important in atrial filling as well; in addition, AV valve competence and venous vessel compliance play a significant role.

## Echocardiographic techniques for assessing diastolic function

### Doppler echocardiography

Doppler echocardiography measures blood flow velocities noninvasively with both spatial and temporal orientation. The current understanding of diastolic function and characterization of diastolic disease have mostly developed through investigation of intracardiac diastolic blood flow patterns using Doppler echocardiography [1]. The majority of work done on both adults and children has involved analysis of mitral and pulmonary venous inflow Doppler patterns [2–5], although interest in right ventricular diastolic function has grown recently.

### Mitral inflow

#### *Technique*

Pulsed Doppler analysis of mitral inflow velocities is straightforward and easily incorporated into a routine complete echocardiographic study. The best position for Doppler analysis is the apical 4-chamber view, where the Doppler signal can be aligned nearly parallel to mitral inflow, allowing accurate quantitation of peak velocities. Sample volume position is also critical, with the peak velocities generally best recorded distal to the mitral annulus near the tips of the valve leaflets [6–8]. Both peak E and peak A velocities are significantly decreased as the sample volume is moved into the left atrium. The use of color Doppler can help better align both the Doppler cursor and sample volume positions.

#### *Measurements*

Several different indices of left ventricular diastolic function can be derived from the mitral valve Doppler inflow trace (Fig. 8.2) [9]. These include diastolic time intervals, peak velocities during early filling and with atrial contraction, area filling fractions, velocity and area ratios, and peak filling rate. The most commonly used diastolic time interval is the isovolumic relaxation time (IVRT), which is the time from aortic valve closure to the initiation of diastolic flow across the mitral valve. It can be measured from the aortic closure component of the second heart sound as recorded on a phonocardiogram to the onset of diastolic flow velocity from

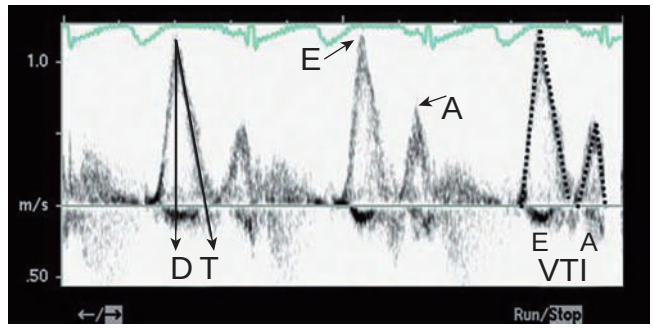


**Figure 8.2** Typical mitral inflow Doppler during childhood. Note the dominant peak E and smaller peak A velocities. The velocity time integrals of the E wave (E VTI) and A wave (A VTI) are outlined. Deceleration time (DT) is measured from the peak E velocity to cessation of early diastolic flow (arrows).

the mitral valve Doppler tracing. It is also possible to measure this interval using continuous-wave Doppler positioned at the apex with the Doppler cursor angled to record both left ventricular outflow tract velocities in systole and left ventricular inflow velocities simultaneously from a 5-chamber view. The time from cessation of aortic forward flow to the onset of diastolic mitral inflow is the IVRT. This index is regarded as relatively heart rate independent. In patients with impaired left ventricular relaxation, IVRT is prolonged; conversely, in patients with abnormal left ventricular compliance and elevated left atrial pressures, it may be shortened. The deceleration time during early filling from peak E velocity to cessation of flow has also been used to describe the time course of relaxation, with more prolonged deceleration correlating with delayed relaxation. The duration of diastolic flow varies with heart rate, however, so deceleration time shortens with increasing heart rate irrespective of the diastolic properties of the heart [10] and is generally not a clinically useful measure in tachycardic infants and children.

Measurements of peak velocities during early filling (peak E velocity) and during atrial contraction (peak A velocity) are simple to obtain from the Doppler trace, and the ratio of these two velocities has been used to describe the pattern of left ventricular diastolic filling. In a similar way, the patterns of left ventricular filling can also be described by the area under the velocity curve, or velocity time integral (VTI), during E and A-wave filling. E area and A area fractions can be compared with the total Doppler area under the diastolic curve. In addition, the area or filling fraction in the first 33% ($^1/_3$ filling fraction) and first 50% ($^1/_2$ filling fraction) of diastole have also been used to characterize the pattern of mitral inflow. Finally, peak left ventricular filling rates can be measured from the mitral valve inflow Doppler [11,12]. The Doppler peak filling rate can be calculated as the peak E velocity multiplied by the mitral annulus cross-sectional area (calculated as $\pi d/4$, where $d$ = the annulus diameter measured from the two-dimensional echocardiogram). Because this filling rate may vary with cardiac output, it is more useful to calculate the peak filling rate normalized to mitral stroke volume using the following equation:

peak filling rate (stroke volumes/s)
= peak E velocity (cm/s)/mitral valve VTI (in cm)

## Pulmonary venous inflow

### *Technique*

Studies using pulsed-wave Doppler to assess pulmonary venous inflow have described a variety of patterns in different disease states; information obtained using this technique appears complementary to mitral inflow Doppler analysis and has added to the understanding of left ventricular diastolic function [13–16]. To obtain pulmonary venous inflow Doppler measurements, the pulsed-wave sample volume is placed in the right or left upper pulmonary vein from an apical 4-chamber window. From this view, flow as it enters the left atrium can be aligned parallel to the Doppler beam using color Doppler. The sample volume should be placed as far distally into the vein as possible, preferably 1–2 cm distal to the orifice, for the most accurate and reproducible data. The closer the sample volume is placed to the orifice of the vein, the more turbulent and less distinct the Doppler signal becomes. In the uncommon pediatric patient with a suboptimal apical 4-chamber view, the parasternal, subcostal and/or suprasternal views may provide visualization and alignment with pulmonary venous inflow. Transesophageal imaging also provides an excellent window for evaluation of pulmonary venous inflow.

### *Measurements*

Measurements performed on the pulmonary venous inflow Doppler trace include peak systolic velocity, peak diastolic velocity, the velocity time integral during the systolic and diastolic phases compared with the total area under the curve, and systolic/diastolic velocity and velocity time integral ratios (Fig. 8.3). The systolic pulmonary venous flow is frequently biphasic in infants and young children and likely represents dissociation between atrial relaxation and mitral annular displacement (Fig. 8.4). The highest systolic velocity is usually measured. Finally, the velocity and duration of atrial reversal have been measured and found to be important in differentiating diastolic Doppler patterns in the face of elevated left atrial and left ventricular end-diastolic pressure (see "Patterns of diastolic dysfunction" below).

### *Caveat*

Pulmonary vein compliance also likely plays a role in the pulmonary venous Doppler pattern seen in pediatric patients. The young healthy infant has continuous phasic forward flow through the pulmonary veins with rare reversal of flow with atrial contraction [17]. The finding of atrial reversal

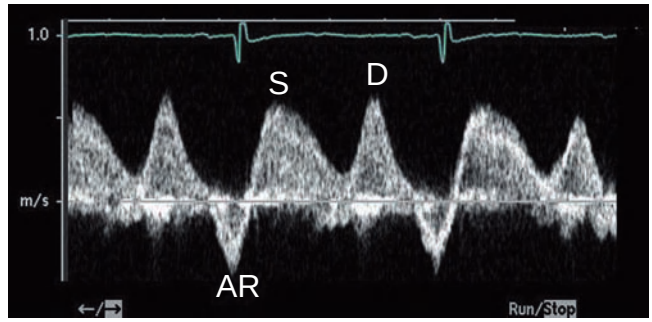


**Figure 8.3** Pulmonary venous inflow Doppler. Phasic flow is characteristically seen with peaks in diastole (D) and systole (S) and deceleration of flow at end-systole and end-diastole. Atrial reversal of flow (AR) can be seen in late diastole with atrial contraction and may reflect elevated left ventricular end-diastolic filling pressure.

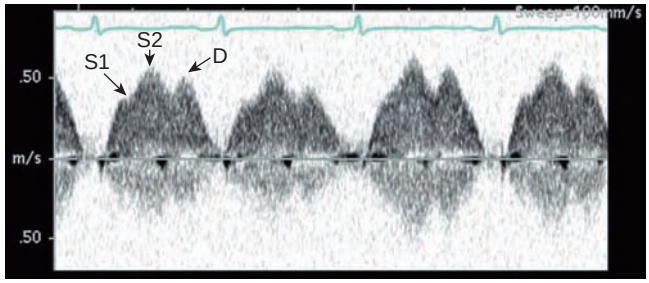


**Figure 8.4** Pulmonary venous inflow Doppler in an infant with triphasic peaks during left atrial filling. There are two peaks in systole and one peak in diastole (D). The initial systolic peak (S1) likely represents atrial relaxation in early systole, whereas the second systolic peak (S2) is associated with augmented atrial filling secondary to mitral annular displacement toward the apex during ventricular contraction; this pattern is a normal variant and not characteristic of diastolic disease.

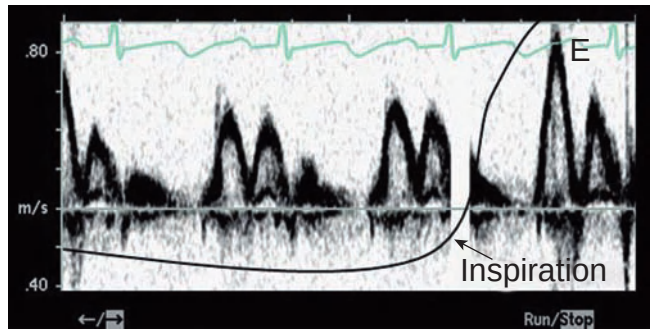


**Figure 8.5** Tricuspid inflow Doppler and the effect of respiration on patterns of inflow. Inspiration decreases intrathoracic pressure and augments venous return to the right atrium and across the tricuspid valve; this is seen with the increase in the E-wave velocity (E) and the altered Doppler pattern compared with the tracings during exhalation.

flow in any neonate should be cause for concern as a sign of abnormally elevated left atrial pressure. This probably reflects the poor compliance of the pulmonary veins in neonates because of the limited flow through the pulmonary vascular bed in utero. In the healthy child, however, reversal of flow is common and likely reflects the more compliant nature of the proximal pulmonary veins rather than abnormalities in left ventricular diastolic function. The duration of reversal of flow in the pulmonary veins with atrial contraction is a more sensitive indicator of abnormal diastolic function, particularly when the reversal duration exceeds A-wave velocity duration on the mitral inflow Doppler.

## Tricuspid and systemic venous inflow

Right heart filling can also be assessed by Doppler echocardiography. Indices of diastolic function used for mitral and pulmonary vein inflow can be applied to the tricuspid and systemic venous inflow Doppler patterns, and appropriate positioning of the Doppler cursor remains important [18]. Right ventricular diastolic function can be difficult to assess by inflow Doppler analysis of tricuspid and systemic venous inflow, however, because of variable preload with normal respiration (Fig. 8.5). There can be dramatic variations in right ventricular filling with changes in intrathoracic pressure during the respiratory cycle. Inspiration lowers intrathoracic pressure and augments systemic venous emptying into the right atrium, and this alters the patterns of both systemic venous emptying and tricuspid inflow that are unrelated to the diastolic properties of the right ventricle. Forward systemic vein inflow is augmented and tricuspid inflow velocities increased with inspiration, and these flows are decreased with exhalation/positive-pressure ventilation when intrathoracic pressure increases. The tricuspid inflow peak E velocity increases by 26% and peak A by 20% with inspiration in normal children [19].

Superior vena cava inflow velocities have a characteristic pattern in normal children as observed in our laboratory; they are always biphasic with dominant systolic right atrial filling. Interestingly, reversal of flow in the superior vena cava during atrial contraction is not seen. This likely implies that right atrial compliance is increased compared with the left atrium, where brief reversal of pulmonary venous inflow with atrial contraction is frequently seen in normal children. There is no age-related variability in superior vena cava inflow patterns when comparing infants and children, unlike other inflow Doppler patterns. This suggests that there is less alteration in right atrial dynamics with age, and it may also be related to the fact that superior vena cava inflow patterns are a less sensitive technique in the assessment of right atrial and right ventricular filling dynamics.

Systemic venous Doppler patterns are influenced by right atrial hypertension, tricuspid valve dysfunction, pericardial disease and arrhythmias. Marked reversal of systemic vein flow with atrial contraction reflects right atrial hypertension or tricuspid stenosis. Decreased or reversed systolic flow suggests significant tricuspid insufficiency, loss of atrioventricular synchrony or restrictive disease. Large pericardial effusions can limit diastolic filling with absence or reversal of diastolic systemic vein flow during exhalation. This is associated with a marked decrease in tricuspid E-wave velocities with onset of exhalation and reciprocal changes in mitral E-wave velocities (>25% decrease with onset of inspiration) [20–24]. Additional important caveats about inflow Doppler indices are discussed below:

### *Abnormalities that affect inflow Doppler analysis*

*AV valve stenosis*

With AV valve stenosis, there is atrial hypertension with restricted flow across the AV valve and a prolonged pressure gradient decay from the atrium to the ventricle [25–28]. This results in an increased peak E velocity with marked prolongation of E-wave deceleration and variable A-wave velocities. Because the inflow pattern is influenced predominantly by the stenosis and heart rate, assessment of the diastolic

properties of the ventricle becomes impossible. Venous Doppler patterns in AV valve stenosis reflect the elevation in diastolic atrial pressure and delay in diastolic emptying so that venous diastolic inflow is reduced with mild to moderate stenosis and can be absent in patients with severe stenosis. Atrial pressure can be markedly elevated with atrial contraction, and so prolonged and high-velocity reversal of flow is commonly seen on venous inflow Doppler at end-diastole.

*AV valve insufficiency*

AV valve insufficiency will also affect venous inflow patterns, as the regurgitant jet flow increases systolic atrial pressures abnormally. This is best identified by systolic reversal of venous flow, which is generally only seen with severe insufficiency [29–33]. With moderate insufficiency, systolic forward flow is decreased, whereas patients with mild insufficiency generally have normal biphasic flow patterns. An important caveat in venous assessment of AV valve insufficiency is the direction of the insufficiency jet, as the location of the jet relative to the vein interrogated may alter the pattern significantly [34]. Jets directed into the atrial wall are less likely to alter vein flow than free jets that are directed toward the vein being interrogated.

*Pulmonary/systemic venous obstruction*

Pulmonary or systemic vein stenosis as it enters the heart can be seen in many congenital cardiac defects, both preoperatively and following surgical repair. The pulsed Doppler pattern with vein obstruction is characterized by continuous high-velocity turbulent flow with loss of the biphasic pattern seen normally. This is most easily apparent by the loss of end-systolic and end-diastolic deceleration to baseline, which again is a hallmark of normal venous inflow Doppler tracings. Newborns, particularly with significant left-to-right shunt lesions, can have a more continuous pattern of pulmonary vein flow, but the biphasic systolic and diastolic peaks are maintained with Doppler velocities that approach the baseline at end-systole and end-diastole. Color Doppler interrogation is helpful as an initial screen, because stenosis is likely when aliasing of vein flow is seen into the atrium when using the maximum color Nyquist limits.

*Arrhythmias*

Arrhythmias can alter both AV valve and venous inflow patterns, and the changes seen can be useful in identifying or confirming an arrhythmia. Junctional ectopic rhythms are frequently seen after congenital heart repair and can be difficult to identify by the surface electrocardiogram (Fig. 8.6). It is critical that these are identified and differentiated from late diastolic reversal of flow, as the etiology and treatment of diastolic reversal (diastolic disease or AV valve stenosis) is quite different than systolic reversal (rhythm abnormality) [35]. This assessment can also be complicated by severe AV valve insufficiency, as this will also cause

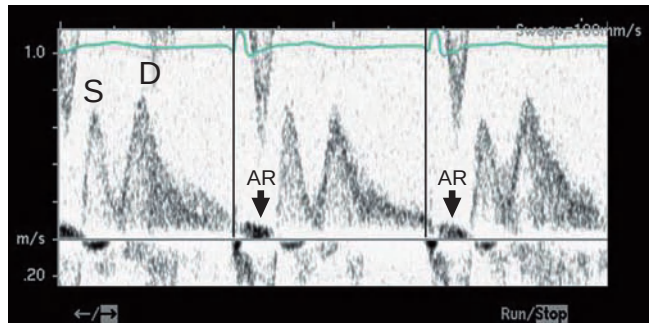


**Figure 8.6** Pulmonary venous inflow Doppler in a patient with junctional rhythm and loss of atrioventricular (AV) synchrony. With this rhythm abnormality the atria are activated retrograde from the AV node simultaneously with the ventricle during ventricular systole, and so the left atrium is contracting against a closed mitral valve. This results in systolic elevation in atrial pressure with a prominent atrial reversal (AR) wave during ventricular systole; this is easily identified as systolic because the wave occurs *after* the QRS deflection on the ECG tracing (line). Phasic systolic (S) and diastolic (D) inflow is seen with a shortened duration of systolic inflow because of the AR wave and no evidence of diastolic reversal of flow.

systolic reversal of flow. With complete heart block, there is loss of regular A-wave velocities on the inflow Doppler and variable flow reversal waves in the veins during the different phases of the cardiac cycle that correlate with each atrial contraction; these reversal waves are accentuated when they occur during ventricular systole as the atrium is contracting against a closed AV valve. Premature atrial beats frequently result in one large E-wave secondary to augmented early diastolic filling by the premature atrial contraction. Conversely, premature ventricular beats interrupt early diastolic filling and close the AV valve prior to atrial contraction, resulting in decreased E-wave velocity and duration, absent A-wave velocities, and significant systolic reversal of flow in the veins during atrial contraction (Fig. 8.7). Finally,

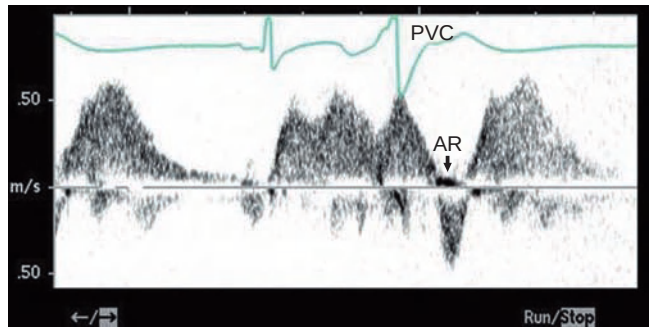


**Figure 8.7** Pulmonary venous inflow Doppler in a patient with a premature ventricular beat (PVC). With the premature ventricular activation as seen on the ECG tracing (PVC), diastolic pulmonary venous inflow is interrupted and a prominent atrial reversal of flow (AR) wave is appreciated, reflecting retrograde activation of the atria with the premature beat. This results in systolic atrial contraction against a closed mitral valve, sudden elevation in left atrial pressure, and reflux of blood back into the pulmonary veins.

with atrial flutter/fibrillation, A-wave velocities again may be difficult to identify and systolic vein forward flow is diminished because of frequent atrial contractions during ventricular systole with poor atrial relaxation.

## Doppler tissue imaging

Changes in inflow Doppler tracings may not reflect alterations in the intrinsic diastolic properties of the ventricular muscle, as they are frequently influenced by myocardial loading conditions. The development of ultrasonic quantitative imaging of myocardial motion has improved understanding of myocardial diastolic function in both normal children and children with heart disease. The technique that has been the focus of the majority of investigation, called Doppler tissue imaging (DTI), allows regional assessment of myocardial wall velocities throughout the cardiac cycle. Specifically, pulsed Doppler assessment of longitudinal mitral, septal and tricuspid annular motion has yielded important new observations in both children and adults, and has become a complementary technique to standard diastolic indices of function using echocardiography. Application of this technique in the analysis of mitral annular motion has provided additional insight in the noninvasive assessment of left ventricular diastolic function [36–51]. Similarly, tricuspid annular motion as an assessment tool for diastolic right ventricular function has been described [51–57]. Importantly, there is no significant variation in tricuspid annular motion with respiration, suggesting that this technique, unlike tricuspid inflow, is relatively preload independent [52]. The mitral early diastolic annular velocity also appears to be relatively preload independent, so that changes in intravascular volume have little effect on that velocity [58–62]. This is in striking contrast to mitral inflow velocities, which can change dramatically with changes in intravascular volume [45,59]. Given the variable volume loads that return to the heart in children with congenital heart disease, it appears that pulsed DTI may be a helpful load-independent technique in assessing ventricular diastolic function in pediatric echocardiography.

Ventricular myocardial contraction and expansion occur along the major (apex to base) and minor (anterior to posterior) axes. AV valve annular motion occurs along the long axis of the ventricle as the annulus is displaced toward the apex in systole and away from the apex in diastole. Early diastolic motion of the annulus appears to reflect recoil of the ventricle from a contracted state and has correlated well with other indices of relaxation in clinical studies [36,42,48,49], whereas late diastolic annular motion is likely affected by both ventricular diastolic and atrial systolic function. The apical echocardiographic window appears to be an ideal view to assess annular motion because the motion is parallel to the apex, allowing well-aligned Doppler interrogation throughout the cardiac cycle. In addition, the apex and crux of the heart are relatively fixed in position with little translational (i.e. rocking) motion of the heart throughout the cardiac cycle.

### *Technique*

Doppler assessment of annular motion requires a modified wall filter and decreased overall gains to display the low-velocity, high-amplitude signals of the myocardium while avoiding blood flow detection. This modification is available from most commercial ultrasound vendors. Annular pulsed DTI recordings are best obtained from an apical 4-chamber view with the patient in the left lateral decubitus position (Fig. 8.8). Transducer angulation and position changes to maximize parallel alignment of the Doppler cursor with the plane of maximal annular motion are frequently required. The pulsed Doppler cursor generally provides the best annular velocity signals when the sample volume gate is 3–5 mm in children. In order to visualize clearly the low-velocity spectral Doppler patterns, the Nyquist limits should be decreased to 15–30 cm/s while using the lowest wall filter settings. It also is helpful to lower the dynamic range to 30–35 dB and decrease overall gains to minimize noise around the signal. Recordings should be made with a simultaneous ECG display to correlate timing of annular motion with cardiac electrical events. Doppler tracings should be displayed at a sweep speed of 100–150 mm/s better to separate waveforms and assess temporal changes in myocardial wall motion.

The mitral and tricuspid annuli have circumferential attachments to the ventricular myocardium. Mitral annular motion at the septal–annular junction is easily obtained because the transducer can be best maintained parallel to annular motion at the septum. It may not completely reflect

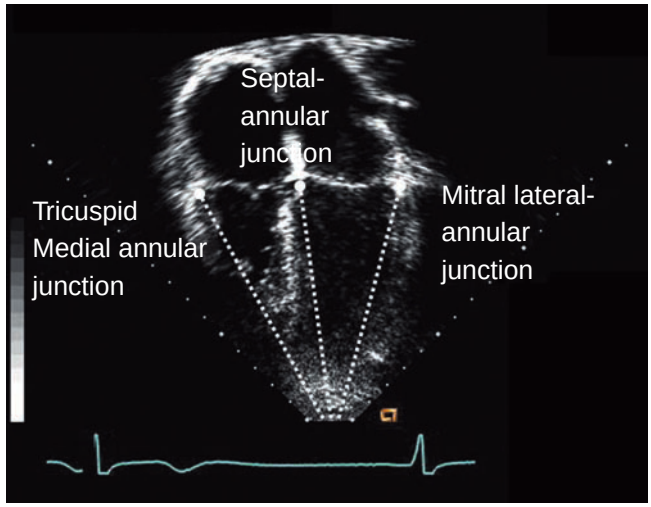


**Figure 8.8** Apical 4-chamber image of Doppler cursor position to obtain pulsed Doppler tissue imaging (DTI) recordings from the mitral septal–annular and mitral lateral–annular junctions and the tricuspid medial annular (nonseptal) junction.

left ventricular dynamics, however, because of the influence of right ventricular function on septal motion. Lateral–annular motion probably provides a better assessment of left ventricular myocardial function, but it is harder to maintain a parallel transducer position when assessing the lateral–annular junction because of translational shifts in cardiac position during the cardiac cycle. Tricuspid annular motion, as a reflection of right ventricular longitudinal function, is best assessed at the medial–annular (i.e., nonseptal) junction. All three positions can provide high-quality spectral Doppler tracings that can be easily recorded and interpreted.

### *Measurements*

Several diastolic measurements can be obtained from the pulsed DTI tracings of annular motion (Fig. 8.9). Two diastolic waveforms are usually seen, much like the E- and A-waves on inflow Doppler, that represent the early diastolic annular velocity (called the $E_a$-, or E′-wave) and diastolic velocity with atrial contraction (called $A_a$-, or A′-wave). These waveforms are seen below the baseline as the annulus moves away from the apex in diastole. A third distinct waveform is seen above the baseline during systole and represents systolic mitral annular motion toward the apex (called $S_a$-wave). Diastolic time intervals can also be measured. Isovolumic relaxation, the time from the end of systolic motion to the initiation of early diastolic motion, can frequently be identified. It may be associated with very low-velocity signals that likely represent translational shifts in heart position with the transition from systole to diastole. Finally, early diastolic deceleration time (DT) can be measured as the time from peak early diastolic velocity to return of the diastolic velocity to baseline prior to annular motion with atrial contraction.

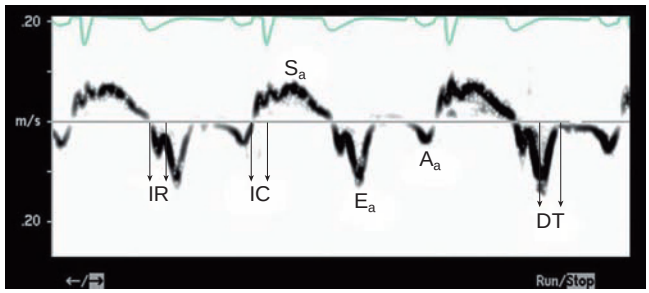


**Figure 8.9** A typical pulsed Doppler tissue imaging (DTI) tracing from the mitral annulus showing the different measures that can be obtained. Two diastolic waveforms are usually seen below the baseline: the annular velocity during early diastole ($E_a$), and the annular velocity during atrial contraction ($A_a$). The deceleration time (DT) is the interval from the peak $E_a$ velocity until cessation of early diastolic annular motion. The systolic annular velocity ($S_a$) is the dominant waveform above the baseline, starting shortly after the QRS complex. The isovolumic relaxation time (IR, measured as the time from the end of the systolic waveform to the beginning of the early diastolic velocity) and the isovolumic contraction time (IC, measured as the time from the end of the diastolic waveform with atrial contraction to initiation of the systolic velocity) are identified with arrows. Small, low-velocity waveforms are commonly seen during isovolumic relaxation and likely represent translational changes in annular position.

### Limitations

Although pulsed DTI of both tricuspid and mitral annular motion have been found to be clinically useful, some caveats are important to remember when applying this technique. DTI velocities, just like blood flow velocities, are dependent on the angle of insonation; it is critical to interrogate the myocardial segment parallel to the wall motion in order to obtain the true peak velocities. Some myocardial segments have very low-velocity motion, and it sometimes can be difficult to separate this motion from translational shifts in the cardiac mass during the cardiac cycle. Finally, it is important to remember that segmental wall motion patterns may not reflect global myocardial function.

## Color M-mode flow propagation

The pattern of ventricular filling can be visualized by M-mode assessment of early diastolic flow propagation velocity from AV valve to apex using color Doppler. The color M-mode tracing is obtained from the apical 4-chamber view with the cursor aligned parallel with diastolic inflow. The area of color Doppler interrogation is manipulated to obtain the longest column of flow from the AV annulus to the apex of the ventricle. The M-mode cursor is positioned through the center of the color signal. This index can be useful in the routine clinical evaluation of LV diastolic function as it provides an estimate of ventricular filling that appears to correlate well with the time constant of LV relaxation (τ) [63–65]. Studies have found that color M-mode Doppler is not affected by preload alterations and is most strongly influenced by LV relaxation both in experimental models during varying lusitropic conditions [66,67] and in humans with heart disease [68–70]. As relaxation becomes abnormal, the rate of early diastolic flow propagation into the ventricle slows. This decrease in flow propagation can be measured as the slope (described as the flow propagation velocity, or $V_p$) of the line drawn from apex to base on the color tracing (Fig. 8.10). The slope of flow propagation can be best seen by decreasing the color Nyquist limit to display the first color aliasing velocity (usually at Nyquist velocity about 75% of the peak E-wave velocity). The higher the slope, the faster the flow propagation and more rapid the ventricular relaxation.

## Myocardial deformation imaging

### Strain rate/strain imaging

Strain rate and strain imaging appear to be important new methods for the quantification of both left ventricular and right ventricular function. Assessment of myocardial mechanics is now available echocardiographically for quantification of regional myocardial function. Importantly, myocardial strain

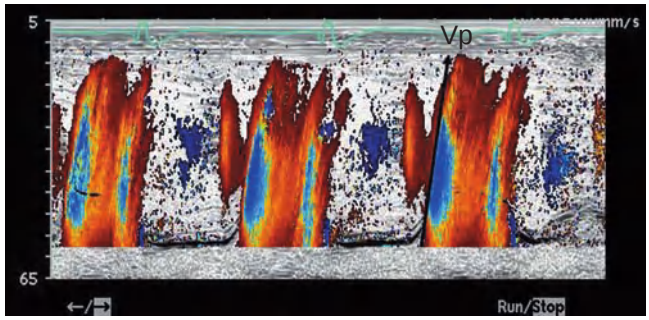


**Figure 8.10** M-mode color Doppler image of the flow propagation velocity of mitral inflow. The M-mode cursor is directed apex to base through the left ventricular inflow from a 4-chamber view, and the color Doppler Nyquist limit is dropped until a clear linear aliasing envelope is seen in the color Doppler tracing. The propagation velocity (*Vp*) is the slope of the line drawn parallel to the aliasing envelope (arrow). Steeper slopes correlate with more rapid diastolic relaxation in the ventricle.

and strain rate quantify myocardial deformation while negating the effects of cardiac translational motion and local tethering effects that complicate pulsed Doppler analysis of annular motion [71–80]. Regional strain rate corresponds to the rate of deformation of a specific segment of the myocardium. Strain rate curves are calculated from tissue velocity data, where the strain rate is the difference of two velocities in the segment of interest divided by the distance between those two velocity points. Strain is calculated by integrating strain rate over time and is expressed as a percentage. Limitations related to angle dependence as well as signal noise have compromised the clinical acceptance of DTI-derived strain and strain rate measurements, and therefore a Doppler-independent technique is attractive. Ultrasonic speckle tracking is a Doppler-independent technique to derive directionally unconstrained imaging of the myocardial motion [81]. Speckles are ultrasound reflectors within tissue and are highly reproducible. This technique computes and displays multiple derivative parameters of diastolic function, including diastolic velocities, diastolic strain rate, and times to peak for these parameters from the tracked endocardial contour by advanced analyses (Fig. 8.11) [72]. The load dependency [59] and influence of heart rate [82] on strain and strain rate have also been investigated, but application of this technology in the assessment of diastolic function in children has been limited.

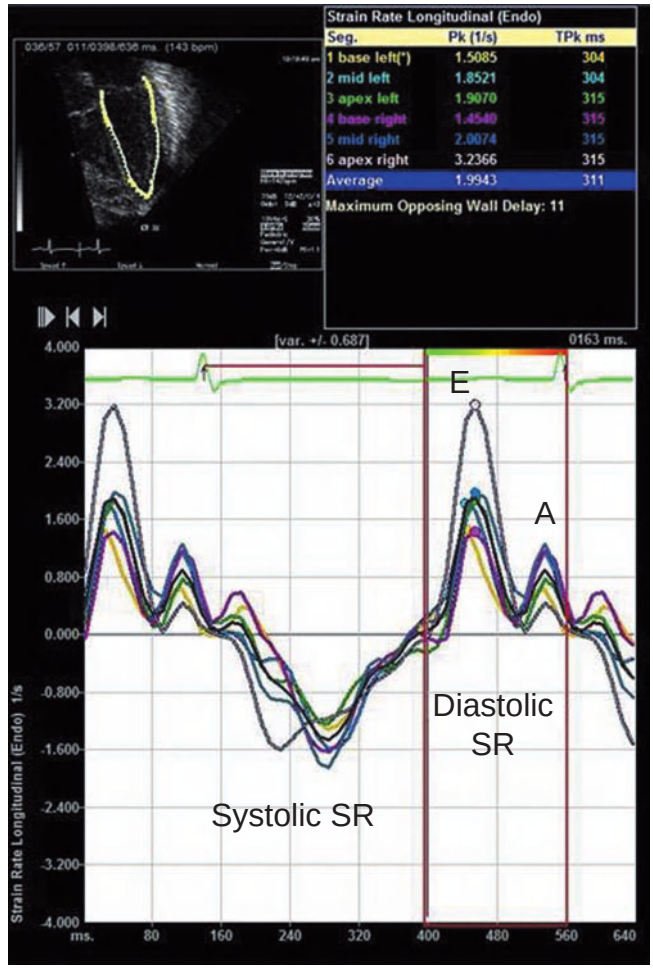


**Figure 8.11** Longitudinal strain rate graph from the endocardium of the left ventricle in a child with normal intracardiac anatomy and function. The ventricle is divided into six segments as described in the table above the graph (base left, mid left, apex left, base right, mid right and apex right), and strain rate from the different segments is calculated using speckle tracking. The linear graph colors correspond to the segments represented, and the strain rate (SR) throughout the cardiac cycle is displayed. Systolic SR is negative because the distance between the two points interrogated is shortening, whereas diastolic SR is positive as the distance is lengthening in the normal heart. Two distinct diastolic curves are seen, representing early (E) filling and filling with atrial contraction (A). Notice that the E and A diastolic SR peaks occur at similar intervals from QRS activation of the ventricle, and the time to peak (TPk) for diastolic SR from the different segments is provided in the table as a gauge of synchrony. Pk, peak.

### Left atrial volume

Left atrial (LA) volume appears to be a reliable marker of duration and severity of left ventricular diastolic disease. It is attractive because whereas Doppler indices describe diastolic function at one moment in time, LA volumes reflect chronic cumulative filling pressures over time. LA volume has been well correlated with the severity of diastolic dysfunction as estimated by Doppler echocardiographic methods in the elderly; only 9% of the population with evidence of normal diastolic function had LA enlargement (defined as ≥30 $cm^3/m^2$ in women and ≥33 $mL/m^2$ in men) whereas 100% of those with estimated severe dysfunction had a significantly enlarged LA [83]. LA enlargement, as evidenced by an indexed volume of ≥32 $cm^3/m^2$, has also been shown to be a risk factor for a first cardiovascular event (atrial fibrillation, stroke, heart failure) in elderly adults [84]. Finally, LA enlargement has been correlated with survival in the elderly, with those patients with the largest atria having the poorest

survival [85–88]. This measure has not been routinely utilized in children, although normal values have been established and appear to vary with patient size. Healthy children and young adults were divided into five groups according to body surface area: 0.5–0.75 $m^2$, 0.75–1.0 $m^2$, 1.0–1.25 $m^2$, 1.25–1.5 $m^2$ and >1.5 $m^2$; mean left atrial maximum volume/body surface area as estimated by three-dimensional echocardiography was 19.6, 21.7, 22.0, 24.5 and 27.4 mL/$m^2$, respectively [89]. Unfortunately, normal values for right atrial volumes in children have not been established.

The size of the LA varies during the cardiac cycle and only maximum LA volume is routinely measured in clinical practice. This is best assessed at mitral valve opening. The minimum volume can also be measured and is best estimated at mitral valve closure at end-diastole. The left atrium can be assessed by the phasic functions of the chamber during diastole: these can be described by the total LA emptying volume as an estimate of reservoir volume, which is calculated as the difference between maximum and minimum LA volumes; the LA passive emptying volume (calculated as the difference between maximal LA volume and the LA volume preceding atrial contraction); LA active emptying (contractile) volume (calculated as the difference between pre-atrial contraction LA volume and minimum LA volume); and LA conduit volume (calculated as the difference between LV stroke volume and the total LA emptying volume). Not surprisingly, phasic contributions vary with the degree of diastolic dysfunction, with the relative contribution of the reservoir, conduit and contractile function of the LA to the filling of the LV in normal adults estimated at 40%, 35% and 25%, respectively [90]. With abnormal LV relaxation, the relative contribution of LA reservoir and contractile function increases and conduit function decreases. However, as LV filling pressure progressively increases with advancing diastolic dysfunction, the LA serves predominantly as a conduit.

Many methods exist to estimate LA size, including M-mode assessment of diameter. The American Society of Echocardiography has recommended quantification of LA size by biplane two-dimensional (2D) echocardiography using either the method of disks (by Simpson's rule) (Fig. 8.12) or the area–length method (Fig. 8.13) [91]. Both methods have been validated and appear to be more accurate than M-mode estimates of LA size. Both techniques underestimate LA volume compared with MR and CT methods. It is important to remember certain caveats to improve accuracy of the measure:

- the LA can be foreshortened by inappropriate transducer position; the length measure of the two orthogonal planes utilized should not differ by more than 5 mm;
- the maximal LA volume should be measured; this is the frame immediately before mitral valve opening; and
- the LA border should be consistently measured; the inferior border of the LA is the mid-point of the mitral annulus (not the leaflet tips), and the tracing of the border should exclude the appendage and pulmonary venous confluence.

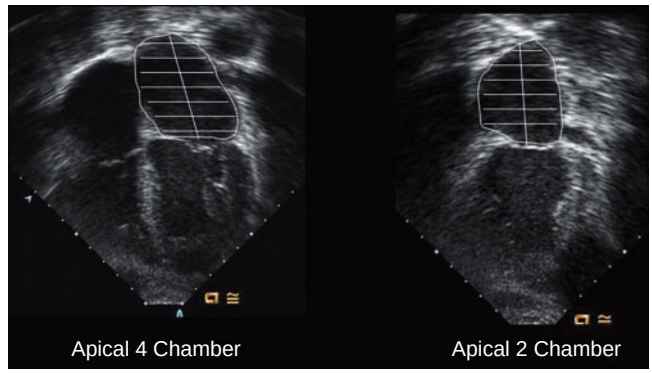


**Figure 8.12** Calculation of left atrial volume using the biplane method of disks (modified Simpson's rule) from orthogonal apical 4-chamber and 2-chamber images with the left atrium traced at its maximum volume at end-systole immediately before mitral valve opening.

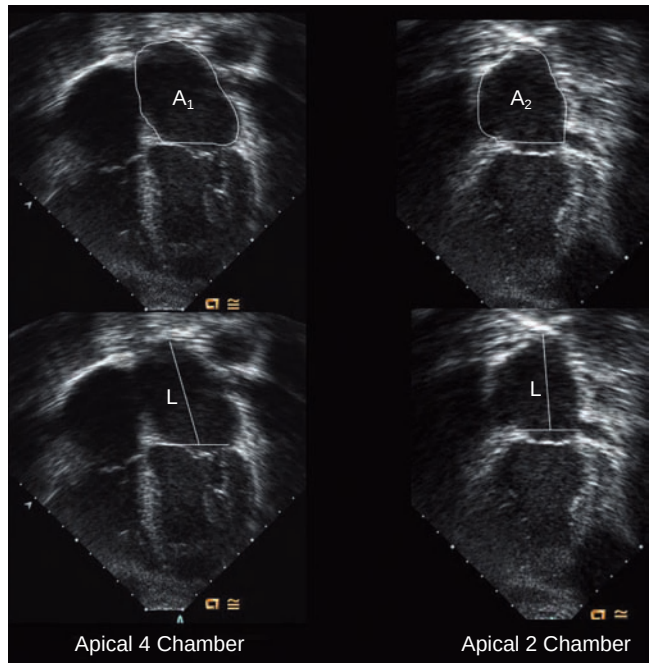


**Figure 8.13** Calculation of left atrial volume using the biplane area–length method from orthogonal apical 4-chamber and 2-chamber images with the left atrium traced at its maximum volume at end-systole immediately before mitral valve opening. The formula for LA volume is $8/3\pi[(A_1)(A_2)/(L)]$ where L is the shortest of either the apical 4- or 2-chamber length. Note that the length is measured from the back wall to the hinge point of the mitral annulus, not the mitral leaflets.

## Diastolic disease

### Patterns of diastolic dysfunction

Because of the many physiologic variables that determine atrial and ventricular filling, simple analysis of pulmonary venous and mitral inflow Doppler patterns as the sole means of diagnosing diastolic dysfunction can be limited. Elegant

**Table 8.1** Classification of left ventricular diastolic function

| | Mitral inflow | Pulmonary venous flow | DTI septal |
|---|---|---|---|
| **Normal** | E/A 2.3 ± 0.6<br>109 ms ≤ DT ≤ 216 ms | S < D<br>$MVA_{dur}$ > $PVA_{dur}$ | $E/E_a$ <10 |
| **Abnormal relaxation** | E/A ≤1.0<br>DT age/HR dependent | S > D<br>$MVA_{dur}$ > $PVA_{dur}$ | $E/E_a$ <10 |
| **Pseudo-normal** | E/A similar to normal<br>DT similar to normal | S < D<br>$MVA_{dur}$ < $PVA_{dur}$ | $E/E_a$ >10 |
| **Restrictive physiology** | E/A >1.5<br>DT <150 ms | S < D<br>$MVA_{dur}$ < $PVA_{dur}$ | $E/E_a$ >10 |

E, mitral inflow E-wave velocity; A, mitral velocity at atrial contraction; DT, mitral deceleration time; S, pulmonary venous systolic velocity; D, pulmonary venous diastolic velocity; $E_a$, mitral early diastolic septal annular velocity; $MVA_{dur}$, duration of mitral A-wave velocity; $PVA_{dur}$, duration of pulmonary venous atrial reversal velocity.

studies by Appleton and colleagues, however, have provided significant insight into the etiology of commonly identified Doppler patterns seen in a variety of disease states [92,93]. They identified Doppler patterns of mitral and pulmonary venous inflow that appear to correlate more with myocardial function and hemodynamic status than the disease process itself. They proposed a dynamic continuum of abnormal Doppler patterns that varied with changes in left atrial pressure, rate of relaxation of the left ventricle and compliance of the ventricle (Table 8.1).

### Abnormal relaxation with normal atrial pressure

The mildest form of diastolic dysfunction is abnormal ventricular relaxation, when the active uncoupling of the ventricular muscle after systolic contraction is delayed. Diastolic dysfunction is initially manifested by impaired left ventricular relaxation; because ventricular compliance is unaffected, normal left atrial pressure is maintained. In this pattern, a slower rate of ventricular pressure fall after ventricular contraction results in later AV valve opening and a longer isovolumic relaxation time. Delayed relaxation also causes a reduced early diastolic pressure gradient across the AV valve so that the peak E velocity is decreased. Relaxation continues during early diastole and delays the ventricular pressure rise during rapid filling, prolonging the E-wave deceleration time. With less filling in early diastole, the percentage of filling with atrial contraction will likely be increased as a compensatory mechanism to maintain cardiac output, resulting in an increased A-wave velocity, decreased early filling fractions and decreased E-wave/A-wave velocity and VTI ratios (Fig. 8.14). In addition, atrial emptying is slower during early diastole in these patients with a resultant decrease in diastolic venous inflow and dominant systolic

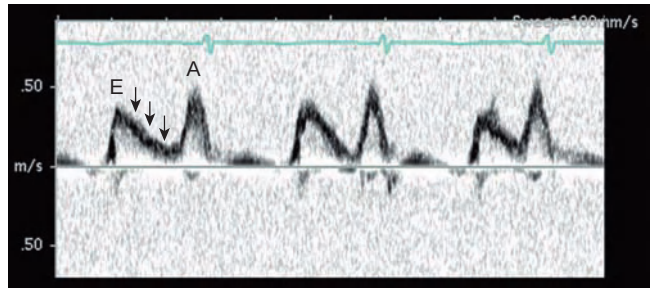


**Figure 8.14** Mitral inflow Doppler in a child with abnormal relaxation. Note the decreased early diastolic (E) velocities and increased velocities with atrial contraction (A). Deceleration time of the E-wave velocity is also prolonged (arrows) and reflects the delay in relaxation into mid-diastole.

venous velocities (Fig. 8.15)[94,95]. Because atrial pressures are generally not significantly elevated in these patients, there is little reversal of vein flow with atrial contraction. The presence of a mid-diastolic filling wave is occasionally seen in patients with abnormal relaxation and slower heart rates; this "L" wave (as characterized by Keren [96]) appears to reflect markedly delayed relaxation that creates a mid-diastolic pressure gradient across the mitral valve with resultant additional filling during the diastasis phase between the E- and A-waves (Fig. 8.16) [1,97].

### Abnormal relaxation with elevated atrial pressure

As diastolic disease progresses, an intermediate or "pseudo-normal" inflow pattern is seen in patients with abnormal ventricular relaxation in association with a moderate increase in atrial pressure [92,93]. Worsening diastolic disease results in reduced ventricular compliance and an increase in atrial diastolic pressure, which normalizes the

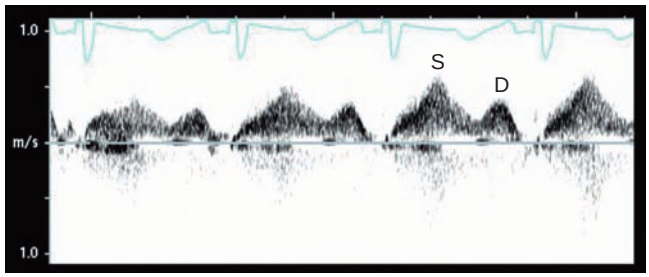


**Figure 8.15** Pulmonary venous inflow Doppler in a child with abnormal relaxation. Note the decreased diastolic (D) velocities compared with the systolic (S) velocities. No reversal of flow with atrial contraction is seen, suggesting that end-diastolic left ventricular pressure is not increased.

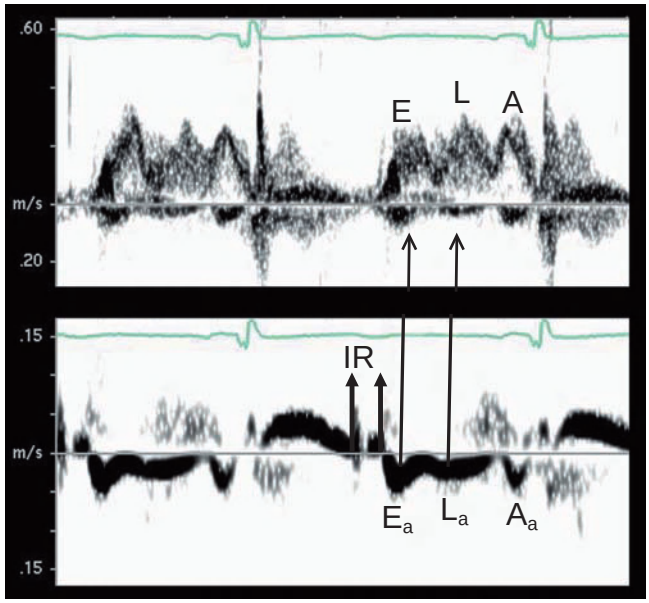


**Figure 8.16** Mitral inflow Doppler (top panel) and septal annular pulsed Doppler tissue imaging (DTI; bottom panel) recordings from a child with abnormal left ventricular relaxation. The mitral inflow is unusual with decreased early diastolic velocities (E) and a prominent mid-diastolic filling wave (L). The mitral annular DTI tracing mimics this pattern with significantly decreased early annular ($E_a$) velocities and mid-diastolic annular motion ($L_a$); these waves appear to initiate the early and mid-diastolic inflow waves on the mitral inflow trace (arrows) and likely represent delayed and prolonged ventricular relaxation. Not surprisingly, isovolumic relaxation (IR) is also prolonged. Annular motion with atrial contraction ($A_a$) and inflow with atrial contraction (A) appear unaffected.

early diastolic gradient from atrium to ventricle with resultant normalization of the E-wave velocity and E/A velocity ratio. In these patients, the increase in atrial pressure masked relaxation abnormalities by normalizing the early diastolic pressure gradient across the AV valve. An inflow tracing which is indistinguishable from normal results (the "pseudo-normal" pattern). This limits the utility of inflow Doppler as an effective screen for diastolic disease. Because of this, it has been recognized that analysis of pulmonary venous inflow patterns is a useful adjunct in the assessment of left ventricular diastolic disease in children and adults. Most importantly, prolonged reversal of pulmonary vein flow with atrial contraction (AR-wave) has been identified as a sensitive and specific sign of elevated left ventricular filling pressure. Because normal children and adults can have some reflux of blood into the pulmonary veins with atrial contraction, the key feature of the AR-wave is that its duration is prolonged compared with the duration of A-wave filling on the mitral inflow Doppler tracing. A pediatric study from the Mayo Clinic documented a sensitivity and specificity of approximately 90% for elevated LV end-diastolic pressure when the ratio of the pulmonary AR-wave duration to the mitral A-wave duration is greater than 1.2, and when the difference between the pulmonary venous AR-wave duration and the mitral inflow A-wave duration exceeds 29 ms [10]. Identification of prolonged atrial reversal in the pulmonary veins appears to be the most sensitive indicator of LV diastolic disease available from Doppler inflow analysis (Fig. 8.17).

The utility of diastolic annular DTI patterns as a marker of abnormal relaxation has been well demonstrated. The early diastolic mitral DTI velocity ($E_a$-wave) has also been found to

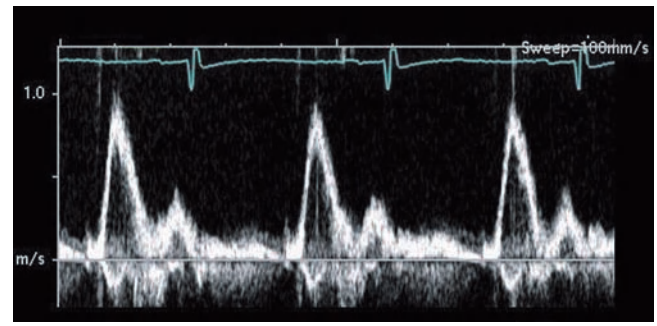


(a)

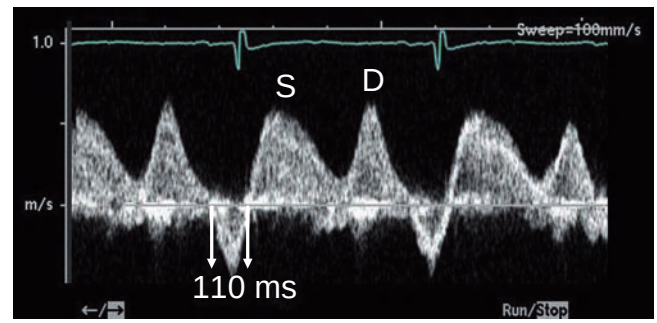


(b)

**Figure 8.17** Mitral inflow Doppler **(a)** and pulmonary venous inflow Doppler **(b)** tracings from a child with diastolic disease characterized by pseudo-normal left ventricular filling. The mitral inflow tracing appears normal because the early diastolic filling (E) velocity has been "pseudo-normalized" by elevated left atrial pressures with poor left ventricular (LV) compliance. The pulmonary venous inflow tracing shows prolonged atrial reversal (AR) with atrial contraction, and the AR duration (120 ms) exceeds the A duration (80 ms) from the mitral tracing. This finding correlates with elevated end-diastolic ventricular pressure and helps to discriminate that the mitral pattern is "pseudo-normal." D, diastolic velocities; S, systolic velocities.

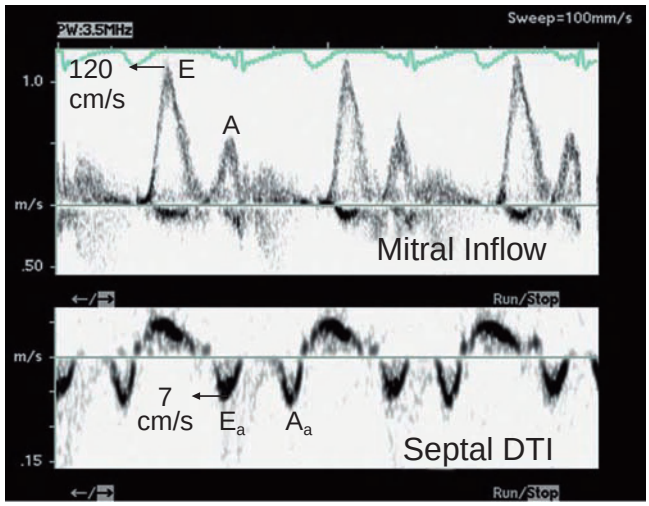


**Figure 8.18** Mitral inflow Doppler (top panel) and septal annular pulsed DTI (bottom panel) recordings from a child with pseudo-normal left ventricular filling. The mitral inflow tracing appears normal because the early diastolic filling (E) velocity has been "pseudo-normalized" by elevated left atrial pressures with altered LV compliance. The mitral annular DTI tracing shows a significantly decreased early annular (Ea) velocity, however, reflecting abnormal diastolic relaxation that is unaffected by the elevation in filling pressure. Because the E wave velocity normalizes with increasing filling pressure while the $E_a$ velocity remains decreased as diastolic disease progresses, the $E/E_a$ ratio can be used to identify diastolic disease. In this example, the $E/E_a$ ratio is 120/7=17.1, which is clearly above the normal range of 7.0±1.9 in children.

be significantly lower in patients with abnormal relaxation compared with normal subjects. Importantly, however, this decrease in $E_a$ persisted in patients with a pseudo-normal mitral inflow Doppler pattern and elevated left atrial pressure [46,48–50]. These findings suggest that the early diastolic annular velocity may be a more sensitive indicator of abnormal relaxation, and invasive studies have shown a good inverse correlation between $E_a$ and the time constant of left ventricular pressure decay, tau. The early diastolic annular velocity also appears to be relatively preload independent, with no significant change during volume loading [58–62]. This contrasts with mitral inflow velocities, which have been shown to vary significantly with changes in volume status and preload. Because mitral inflow E-wave velocity increases whereas mitral annular $E_a$-wave velocity remains low with increasing left atrial pressure in patients with diastolic dysfunction, the $E/E_a$ ratio appears be a useful noninvasive predictor of increased left atrial pressure (Fig. 8.18). A hemodynamic study correlated an $E/E_a$ ratio >10 with pulmonary capillary wedge pressure >12 mm Hg in adults [49].

Color M-mode assessment of LV flow propagation has been used to differentiate patients with normal from those with "pseudo-normal" filling [98], and to estimate the effect of LV filling pressure when combined with pulsed Doppler indices [63,99,100]. Decreased rates of flow propagation ($V_p$) correlate with delayed relaxation, and this persists in the face of increasing left atrial pressure [101]. A study in children used color M-mode Doppler to assess diastolic function and found that the ratio of the mitral inflow E-wave velocity to $V_p$ was a good predictor of elevated LV end-diastolic pressure. A ratio of $E/V_p$ >2.0 predicted an LV end-diastolic pressure ≥15 mm Hg with a sensitivity of 100% and a specificity of 77% [63]. In addition, color M-mode flow propagation, like early annular diastolic velocities, appears to be preload independent [66]. This is another tool for the identification of "pseudo-normal" LV filling.

### Abnormal ventricular compliance

The most severe form of diastolic disease is seen in patients with poor ventricular compliance and markedly elevated atrial pressures. Because of increased ventricular stiffness to filling, atrial pressures are elevated and generate an increased early pressure gradient across the AV valve. An increase in peak E-wave velocity results as blood rapidly fills the ventricle. Because of abnormal ventricular compliance, however, ventricular pressure rises rapidly with small changes in volume. This abrupt increase in ventricular diastolic pressure during rapid filling causes premature cessation of E-wave flow and a short deceleration time (Fig. 8.19). Ventricular pressures are markedly elevated in late diastole, resulting in a decreased or absent peak A-wave velocity because only a slight additional pressure gradient can be generated across the AV valve with atrial contraction. High atrial pressure also results in early AV valve opening during ventricular relaxation, and this can be identified by a shortened isovolumic relaxation time. Venous inflow Doppler shows rapid atrial filling in early diastole with AV valve opening as the high-pressure atrium empties; this flow decelerates in mid-diastole as ventricular pressures rise abruptly with filling (Fig. 8.20). There frequently is prolonged reversal of venous inflow with atrial contraction

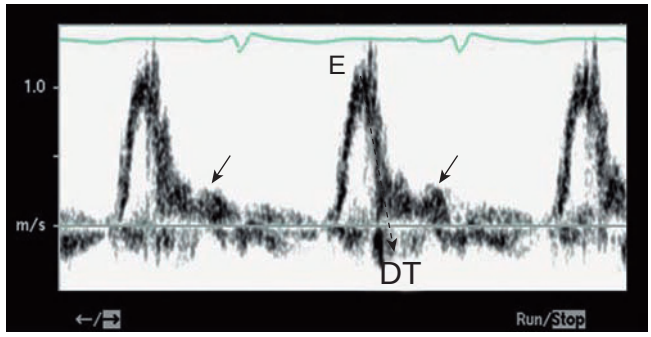


**Figure 8.19** Mitral inflow Doppler in a child with abnormal ventricular compliance. Note the increased early diastolic (E) velocities and rapid deceleration time (DT) of the E-wave velocity secondary to the poor compliance as ventricular pressure rises rapidly during early filling, abolishing the early transvalvar gradient across the mitral valve. In late diastole, ventricular pressures have risen to the point where very little additional filling occurs with atrial contraction (arrows).

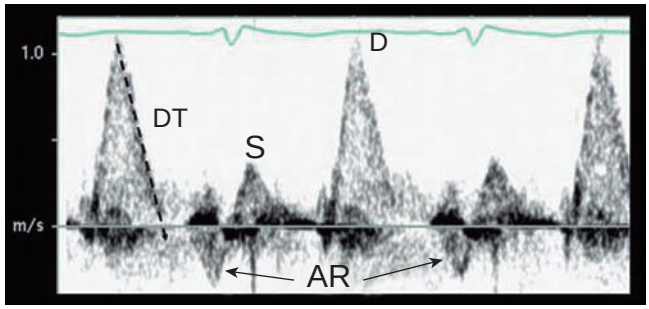


**Figure 8.20** Pulmonary venous inflow Doppler in a child with abnormal ventricular compliance. Note the increased diastolic (D) velocities compared with the systolic (S) velocities, with rapid deceleration of the diastolic wave in mid-diastole (DT), reflecting the rapid increase in left ventricular pressure during early filling with a resultant increase in diastolic left atrial pressure and abrupt cessation of pulmonary venous emptying. Atrial reversal of flow with atrial contraction is seen (AR), reflecting the marked increase in end-diastolic left ventricular pressure as an additional sign of poor compliance. Systolic venous inflow is blunted because of the chronic left atrial hypertension and distension.

because of the dramatic increase in both atrial and ventricular pressure at end-diastole. Systolic venous inflow is blunted because of chronic atrial hypertension and distension.

As with pulmonary venous inflow, identification of high-velocity reversal of inferior vena cava inflow with atrial contraction suggests poor right ventricular compliance and has been used to identify elevated right atrial filling pressures in adults. Specifically, reversal velocities during atrial contraction that exceed forward velocities have been correlated with central venous pressures greater than 15mm Hg (Fig. 8.21) [102]. This finding has not been corroborated in children and is likely to be invalid when positive-pressure ventilation or airway disease is present secondary to the associated dramatic changes in intrathoracic pressure.

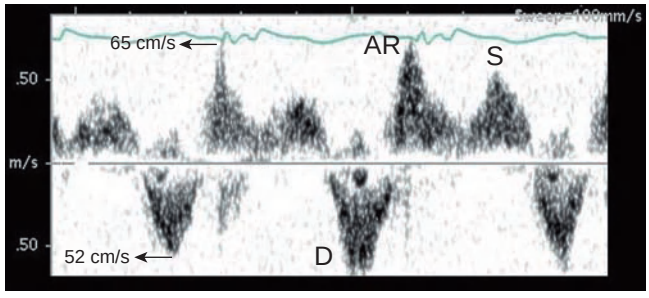


**Figure 8.21** Hepatic venous inflow Doppler in a child with abnormal ventricular compliance. Early diastolic (D) velocities are seen below the baseline, reflecting forward flow into the right atrium. However, there is marked reversal of flow with atrial contraction (AR), with a peak velocity that exceeds the forward diastolic peak velocity (65 vs 52 cm/s), reflecting markedly elevated right atrial end-diastolic pressure. In addition, there is significant tricuspid insufficiency in the patient, with resultant reversal of flow during systole as well (S).

## Diastolic function in pediatric patients without heart disease

### Age-related changes in diastolic filling

Doppler patterns of left atrial and left ventricular filling have identified variable pulmonary venous and mitral inflow patterns that appear to correlate and change with increasing age in the pediatric patient. The greatest change appears to occur during infancy, when both fetal and neonatal Doppler patterns show predominant ventricular filling during atrial contraction with decreased peak E-wave velocity and decreased E-wave/A-wave velocity and velocity time integral ratios compared with older children. The infant mitral pattern is consistent with altered ventricular relaxation/compliance and a decreased early transmitral pressure gradient. This is also reflected in the pulmonary venous Doppler patterns seen in young infants, with increased peak systolic velocities, decreased peak diastolic velocities, and increased systolic/diastolic velocity and velocity time integral ratios compared with older children. These patterns of altered filling seen in infancy likely reflect differences in the diastolic properties of immature myocardium, but they are also influenced by changes in heart rate and loading conditions. With increasing age, there is a shift in left ventricular filling from late to early diastole, and a shift in left atrial filling from systole to diastole during the first year of life; in general, older children and adolescents have pulmonary venous and mitral inflow Doppler patterns that are similar to patterns seen in healthy young adults. Characterization of inflow Doppler (Table 8.2) and annular DTI velocities (Table 8.3) in normal neonates, children and adults has provided reference values for future investigations in children and adults with congenital and acquired heart disease. Interestingly, the patterns of filling described in infants recur in the elderly adult as part of the "normal" process of myocardial aging. Findings related to age are summarized below.

#### Infants

It has been recognized that the diastolic properties of immature myocardium are different from more mature myocardium, so there has been significant interest in characterizing the diastolic properties of infants without heart disease. Using standard inflow Doppler techniques that assess left ventricular filling across the mitral valve [103–105], new insights into the pattern of maturation of left ventricular diastolic function have been revealed. It appears that the relaxation properties of the left ventricle at birth are significantly impaired, characterized by prolongation of the isovolumic relaxation time [103,106] and limited early diastolic inflow with predominant left ventricular filling in late diastole with atrial contraction. This pattern rapidly changes during the first 2 months of life, with mitral early filling velocities increasing by 80% from baseline newborn values. After 2 months of age, the early filling

**Table 8.2** Normal inflow Doppler values in infants and children

| Demographics | <1 year | 1–5 y | 6–9 y | 10–13 y | 14–18 y | Total |
|---|---|---|---|---|---|---|
| *N* | 63 | 68 | 55 | 58 | 81 | 325 |
| Male | 29 | 39 | 27 | 38 | 44 | 177 |
| Age (y) | 0.40 ± 0.30 | 3.05 ± 1.51† | 7.91 ± 1.12† | 11.99 ± 1.11† | 16.0 ± 1.40† | 78 ± 6.0 |
| Weight (kg) | 6.6 ± 2.7 | 15.1 ± 5.4† | 33.8 ± 14.9† | 47.2 ± 16.3† | 66.1 ± 15.5† | 33.3 ± 25.2 |
| BSA ($m^2$) | 0.34 ± 0.08 | 0.62 ± 0.14† | 1.07 ± 0.27† | 1.37 ± 0.29† | 1.73 ± 0.25† | 1.0 ± 0.6 |
| HR (bpm) | 124 ± 16 | 105 ± 17† | 80 ± 11† | 75 ± 12 | 69 ± 16 | 90 ± 26 |
| **Echocardiographic** | | | | | | |
| LV EDD (cm) | 2.3 ± 0.3 | 3.1 ± 0.4† | 3.9 ± 0.4† | 4.3 ± 0.4† | 4.7 ± 0.4† | 3.6 ± 1.0 |
| LV ESD (cm) | 1.4 ± 0.2 | 1.9 ± 0.3† | 2.4 ± 0.3† | 2.7 ± 0.3† | 3.0 ± 0.4† | 2.3 ± 0.6 |
| LV PWT (cm) | 0.4 ± 0.1 | 0.6 ± 0.1† | 0.7 ± 0.1* | 0.8 ± 0.1* | 0.9 ± 0.2 | 0.7 ± 0.2 |
| LV SWT (cm) | 0.5 ± 0.1 | 0.6 ± 0.1† | 0.8 ± 0.1† | 0.8 ± 0.2 | 1.0 ± 0.2† | 0.7 ± 0.2 |
| LV mass ($g/m^2$) | 18.9 ± 6.5 | 43.6 ± 16.4† | 82.3 ± 28.3† | 110.1 ± 32.9† | 158.4 ± 48.5† | 81.8 ± 58.9 |
| Mitral E velocity | 79.7 ± 18.8 | 95.2 ± 19.5† | 94.4 ± 14.8 | 94.5 ± 16.0 | 90.3 ± 17.8 | 90.8 ± 18.5 |
| Mitral A velocity | 65.3 ± 13.3 | 61.3 ± 12.1 | 49.4 ± 12.5† | 49.5 ± 13.8 | 45.5 ± 13.2 | 54.4 ± 15.0 |
| Mitral E/A ratio | 1.24 ± 0.30 | 1.60 ± 0.46† | 1.99 ± 0.51† | 2.02 ± 0.58 | 2.13 ± 0.65 | 1.79 ± 0.61 |
| PV S-wave velocity | 44.6 ± 10.3 | 48.0 ± 8.9 | 50.7 ± 11.3 | 49.0 ± 11.1 | 47.7 ± 7.3 | 48.7 ± 9.2 |
| PV D-wave velocity | 46.0 ± 9.5 | 54.5 ± 11.0† | 53.3 ± 11.4 | 58.4 ± 12.1 | 57.9 ± 15.0 | 54.6 ± 12.9 |
| PV A-reversal velocity | 16.4 ± 6.3 | 20.6 ± 4.3† | 20.2 ± 3.8 | 21.2 ± 4.9 | 20.0 ± 5.2 | 20.5 ± 5.1 |
| Tricuspid E velocity | 53.3 ± 12.3 | 61.6 ± 12.5* | 60.5 ± 13.9 | 59.6 ± 11.4 | 60.4 ± 10.9 | 59.2 ± 12.4 |
| Tricuspid A velocity | 53.2 ± 13.0 | 48.3 ± 12.3* | 42.4 ± 10.8* | 39.2 ± 11.3 | 34.5 ± 11.2* | 43.3 ± 13.5 |
| Tricuspid E/A ratio | 1.01 ± 0.38 | 1.27 ± 0.31† | 1.49 ± 0.40† | 1.61 ± 0.47* | 1.88 ± 0.56† | 1.47 ± 0.53 |
| SF (%) | 38.9 ± 4.1 | 38.0 ± 3.6 | 37.4 ± 3.8 | 37.4 ± 4.2 | 36.4 ± 4.3 | 37.6 ± 4.1 |
| LV MPI | 0.33 ± 0.08 | 0.34 ± 0.07 | 0.32 ± 0.06 | 0.34 ± 0.06 | 0.34 ± 0.08 | 0.33 ± 0.08 |
| RV MPI | 0.29 ± 0.09 | 0.28 ± 0.07 | 0.29 ± 0.08 | 0.28 ± 0.08 | 0.29 ± 0.08 | 0.28 ± 0.08 |

A, atrial; BSA, body surface area; D, diastolic; E, early diastolic velocity; EDD, end-diastolic dimension; ESD, end-systolic dimension; HR, heart rate; LV, left ventricular; MPI, myocardial performance index; PV, pulmonary venous; PWT, posterior wall thickness; S, systolic; SF, shortening fraction; SWT, systolic wall thickness.

*P < 0.05, †P < 0.01 compared with preceding column.

Data expressed as mean ± SD.

Doppler velocities expressed as cm/s.

Reprinted from Eidem BW, McMahon CJ, Cohen RR et al. Impact of cardiac growth on Doppler tissue imaging velocities: a study in healthy children. *J Am Soc Echocardiogt* 2004;**17**:212-21, with permission from Elsevier

velocities do not appear to change dramatically [103]. These differences do not appear to be related to any heart rate effect, as the impact of heart rate on early peak filling rates appears negligible in infants younger than 3 months [103]. This suggests that the changes identified using these echo indices are related to rapid improvement in the diastolic myocardial properties of the maturing heart. Neonatal studies have also documented a shift in right ventricular filling to late diastole, consistent with altered diastolic function and similar to the pattern seen across the mitral valve in newborns [104]. Pulmonary venous inflow Doppler also reflects altered diastolic function in the neonate, with predominant systolic pulmonary venous emptying that fits with the pattern of delayed ventricular relaxation [107].

Doppler tissue imaging has also provided additional insight into the maturational properties of the infant myocardium [108–111]. The shift in left ventricular filling from late to early diastole with increasing age during infancy is associated with a similar age-related shift in mitral annular velocities, so that E/A and $E_a/A_a$ velocity ratios correlated well for all mitral inflow patterns during childhood. There is gradual improvement in early diastolic mitral annular motion and inflow velocities during the first 7 days after birth, suggesting improvement in diastolic function consistent with more rapid relaxation of the left ventricle in early diastole [109]. By contrast, there is no change in tricuspid diastolic annular motion or inflow velocities, suggesting that the right ventricle may have delayed and different adaptive improvement in diastolic function compared with the left ventricle in the young neonate. These findings are crucial in characterizing the normal infant, so that abnormal (versus appropriate maturational) diastolic patterns can be appreciated. In addition, they suggest that the young infant may be less tolerant of preload changes than the older infant, who has more mature myocardium and improved diastolic function. This is important in understanding and developing management

**Table 8.3** Normal annular Doppler tissue imaging values in infants and children

| Age group | N | E′-wave velocity | A′-wave velocity | S′-wave velocity | ICT | IRT | E/E′ratio |
|---|---|---|---|---|---|---|---|
| Mitral annular | | | | | | | |
| <1 y | 63 | 9.7 ± 3.3 | 5.7 ± 1.8 | 5.7 ± 1.6 | 77.4 ± 18.4 | 57.0 ± 14.8 | 8.8 ± 2.7 |
| | | (8.8–10.5) | (5.3–6.2) | (5.3–6.1) | (72.7–82.0) | (53.1–60.8) | (8.1–9.5) |
| 1–5 y | 68 | 15.1 ± 3.4† | 6.5 ± 1.9 | 7.7 ± 2.1† | 76.9 ± 15.9 | 62.1 ± 13.2 | 6.5 ± 2.0† |
| | | (14.3–15.4) | (6.1–7.0) | (7.2–8.2) | (72.8–80.9) | (58.9–65.4) | (6.0–7.0) |
| 6–9 y | 55 | 17.2 ± 3.7† | 6.7 ± 1.9 | 9.5 ± 2.1† | 77.9 ± 18.9 | 62.9 ± 11.9 | 5.8 ± 1.9 |
| | | (16.2–18.3) | (6.2–7.3) | (8.9–10.1) | (72.4–83.4) | (59.5–66.3) | (5.3–6.4) |
| 10–13 y | 58 | 19.6 ± 3.4† | 6.4 ± 1.8 | 10.8 ± 2.9* | 76.6 ± 16.2 | 62.6 ± 12.4 | 4.9 ± 1.3 |
| | | (18.7–20.5) | (5.9–6.9) | (10.0–11.5) | (72.4–80.9) | (59.4–65.9) | (4.6–5.2) |
| 14–18 y | 81 | 20.6 ± 3.8 | 6.7 ± 1.6 | 12.3 ± 2.9† | 78.9 ± 15.4 | 69.5 ± 15.5* | 4.7 ± 1.3 |
| | | (19.7–21.4) | (6.3–7.1) | (11.6–12.9) | (75.4–82.3) | (66.1–73.0) | (4.4–5.0) |
| Total | 325 | 16.5 ± 5.3 | 6.4 ± 1.9 | 9.3 ± 3.4 | 77.5 ± 16.7 | 63.2 ± 14.4 | 6.1 ± 2.4 |
| | | (16.0–17.1) | (6.2–6.6) | (8.9–9.7) | (75.7–79.5) | (61.7–64.9) | (5.9–6.4) |
| Septal | | | | | | | |
| <1 y | 63 | 8.1 ± 2.5 | 6.1 ± 1.5 | 5.4 ± 1.2 | 77.5 ± 17.5 | 53.0 ± 11.7 | 10.3 ± 2.7 |
| | | (7.5–8.7) | (5.7–6.4) | (5.1–5.7) | (73.0–82.0) | (50.0–56.0) | (9.7–11.0) |
| 1–5 y | 68 | 11.8 ± 2.0† | 6.0 ± 1.3 | 7.1 ± 1.5† | 80.1 ± 15.5 | 59.8 ± 12.0 | 8.1 ± 1.8† |
| | | (11.3–12.3) | (5.7–6.4) | (6.8–7.5) | (76.3–83.9) | (56.9–62.7) | (7.7–8.5) |
| 6–9 y | 55 | 13.4 ± 1.9† | 5.9 ± 1.3 | 8.0 ± 1.3 | 82.8 ± 15.3 | 65.6 ± 10.7 | 7.2 ± 1.6 |
| | | (12.8–13.9) | (5.5–6.3) | (7.6–8.4) | (78.4–87.2) | (62.5–68.7) | (6.8–7.7) |
| 10–13 y | 58 | 14.5 ± 2.6 | 6.1 ± 2.3 | 8.2 ± 1.3 | 87.9 ± 16.4* | 72.5 ± 12.3 | 6.6 ± 1.4 |
| | | (13.8–15.2) | (5.6–6.7) | (7.9–8.5) | (83.6–92.2) | (69.3–75.8) | (6.3–7.0) |
| 14–18 y | 81 | 14.9 ± 2.4 | 6.2 ± 1.5 | 9.0 ± 1.5 | 88.4 ± 15.6 | 77.5 ± 14.5 | 6.4 ± 1.5 |
| | | (14.3–15.4) | (5.9–6.6) | (8.7–9.3) | (84.9–91.9) | (74.3–80.8) | (6.1–6.8) |
| Total | 325 | 12.6 ± 3.4 | 6.1 ± 1.6 | 7.6 ± 1.9 | 83.5 ± 16.5 | 66.1 ± 15.3 | 7.7 ± 2.3 |
| | | (12.2–13.0) | (5.9–6.3) | (7.4–7.8) | (81.7–85.4) | (64.4–67.9) | (7.5–8.0) |
| Tricuspid annular | | | | | | | |
| <1 y | 63 | 13.8 ± 8.2 | 9.8 ± 2.4 | 10.2 ± 5.5 | 68.7 ± 18.2 | 52.0 ± 12.9 | 4.4 ± 2.3 |
| | | (11.7–15.9) | (9.1–10.5) | (8.8–11.7) | (63.9–73.5) | (48.5–55.4) | (3.8–5.0) |
| 1–5 y | 68 | 17.1 ± 4.0† | 10.9 ± 2.7 | 13.2 ± 2.0† | 77.7 ± 15.0 | 59.0 ± 13.9 | 3.8 ± 1.1 |
| | | (16.1–18.1) | (10.2–11.6) | (12.7–13.7) | (73.9–81.5) | (55.4–62.5) | (3.5–4.1) |
| 6–9 y | 55 | 16.5 ± 3.0 | 9.8 ± 2.7 | 13.4 ± 2.0 | 91.8 ± 21.5† | 58.5 ± 17.5 | 3.6 ± 0.8 |
| | | (15.7–17.4) | (9.0–10.6) | (12.8–14.0) | (85.5–98.0) | (53.4–63.6) | (3.4–3.9) |
| 10–13 y | 58 | 16.5 ± 3.1 | 10.3 ± 3.4 | 13.9 ± 2.4 | 98.1 ± 21.7 | 61.7 ± 19.9 | 3.5 ± 1.4 |
| | | (15.7–17.4) | (9.3–11.2) | (13.2–14.5) | (92.2–103.9) | (56.4–67.1) | (3.2–3.9) |
| 14–18 y | 81 | 16.7 ± 2.8 | 10.1 ± 2.6 | 14.2 ± 2.3 | 101.9 ± 20.4 | 62.9 ± 18.9 | 3.7 ± 1.0 |
| | | (16.0–17.3) | (9.5–10.7) | (13.7–14.7) | (97.2–106.6) | (58.5–67.3) | (3.5–3.9) |
| Total | 325 | 16.1 ± 4.7 | 10.2 ± 2.8 | 13.0 ± 3.4 | 88.2 ± 23.1 | 59.0 ± 17.2 | 3.8 ± 1.4 |
| | | (15.6–16.7) | (9.9–10.5) | (12.6–13.4) | (85.6–90.8) | (57.0–60.9) | (3.6–4.0) |

A, Late diastolic velocity; A′, late diastolic annular velocity; ICT, isovolumic contraction time; E, early diastolic inflow Doppler velocity; E′, early diastolic annular velocity; IRT, isovolumic relaxation time; S, systolic velocity; S′, systolic annular velocity.

*$P < 0.05$; †$P < 0.01$ compared with procceeding age group.

Data expressed as mean ± SD (95% confidence interval). Doppler tissue imaging velocities are expressed in cm/s. Time intervals are expressed in milliseconds.

From Eidem BW, McMahon CJ, Cohen RR et al. (2004) Impact of cardiac growth on Doppler tissue imaging velocities in healthy children. *J Am Soc Echocardiogr* **17**, 212–221.

techniques for the infant with congenital heart disease, both prior to and after surgical intervention.

The premature infant has also been studied using echocardiography to assess diastolic function [110], and again abnormalities in relaxation were identified. It appears that the evolution of diastolic maturation is prolonged in preterm infants, with persistent dominant diastolic filling with atrial contraction during the first 2 months after birth, in contrast to term infants, in whom there is a progressive decrease in the atrial contraction filling fraction during that time. This

delay may be at least partially related to the dramatic increase in stroke volume in the preterm infant, which doubles during the first 2 months of life, again in contrast to the term infant, who has only a 37% increase in stroke volume. Altered diastolic performance limits tolerance to preload stressors, which was emphasized in a review of preterm infants with a patent ductus arteriosus (PDA) [111]. Those patients who had persistent patency of the ductus arteriosus showed patterns of inflow Doppler velocities across the mitral valve that were consistent with an elevation in left atrial and left ventricular filling pressures, which obviously would then have an adverse effect on pulmonary venous pressure and pulmonary capillary physiology. The ductal left-to-right shunt alters left atrial preload, leading to the left atrial hypertension. These changes rapidly reversed to the normal range after closure of the PDA, and this likely helps to explain why a PDA is frequently poorly tolerated in the preterm infant.

### Healthy children/athletes

Diastolic properties of the left ventricle and right ventricle have been recently characterized in healthy children using inflow Doppler [10,116] and pulsed annular Doppler tissue imaging [51,52,112–118]. Mitral inflow parameters are remarkably stable from age 3 years through 17 years, with similar E-wave velocities, A-wave velocities, E-wave/A-wave velocity ratio and isovolumic relaxation time; only deceleration time changes significantly, and this most likely is related to the effect of decreasing heart rate with age. DTI measures correlated significantly with age and parameters of cardiac growth [116], but were not influenced by gender, heart rate or respiration. Research studies have also focused on the influence of diastolic function with exercise in healthy adolescents and young adults. Diastolic function appears well preserved in elite female and male athletes [119,120] despite significant changes in left ventricular wall thickness and ventricular dimensions. It appears that diastolic function has a significant impact on peak exercise oxygen uptake [121], with a strong correlation identified between diastolic flow propagation into the left ventricle using color M-mode and peak oxygen consumption with exercise. In fact, it appears that assessment of diastolic function measured at rest using echocardiography may be a useful predictor of better adaptation of myocardial performance during exercise with a positive impact on peak oxygen consumption. Finally, a study has identified pathologic alterations in left ventricular diastolic relaxation following marathon running in recreational runners independent of the predicted change in preload, suggesting the phenomenon of exercise-induced cardiac fatigue [122]. In some of the runners, these changes correlated with elevations in cardiac troponin-T, suggesting exercise-induced cardiac damage. It certainly raises the question of how much is too much when considering exercise as a good thing.

### The right ventricle

Right ventricular (RV) regional function has been well characterized and found by multiple modalities to be clearly different than left ventricular function [123–130]. Regional right ventricular function in the normal heart has greater longitudinal regional velocities, more displacement of the free tricuspid annulus toward the apex, and reduced circumferential shortening velocities compared with the left ventricle. In fact, right ventricular longitudinal shortening is the dominant mode of systolic contraction in healthy young subjects. This is likely explained by the fact that longitudinal/oblique fibers are dominant within the right ventricular free wall, whereas circular mid-wall fibers are dominant in the left ventricular lateral wall, with a mixture of both types found in the ventricular septum. Longitudinal right ventricular free wall velocities are greatest at the base, with a progressive decrease in velocities at the mid-wall and apex. Regional contractility along the longitudinal axis appears accurately to reflect global function of the RV, even with varying inotropic state and loading conditions. This observation has been substantiated in both experimental and clinical settings that have documented the strong association between right ventricular longitudinal deformation and global right ventricular function [124–126]. Understanding these differences in myocardial mechanics between the two ventricles is critical in the analysis of right ventricular diastolic function, because early RV diastolic motion also appears to be predominantly longitudinal (Fig. 8.22). Total early diastolic excursion and rate of early diastolic excursion of the tricuspid annulus correlated significantly with assessment of right ventricular peak filling rate calculated by magnetic resonance imaging (MRI) [131].

## Strategy for the echocardiographic assessment of diastolic function in children

The discussion above suggests that a new paradigm is needed to better assess diastolic function in pediatric patients echocardiographically (Fig. 8.23). This approach must include the routine screening of mitral, tricuspid, pulmonary and systemic vein inflow in all children. In addition, all children should have DTI assessment of tricuspid annular motion as well, because tricuspid inflow Doppler patterns can vary so dramatically with respiration. Left atrial volumes and mitral DTI assessment should be obtained in all children who have abnormal mitral/pulmonary venous inflow patterns and/or have known heart disease. Similarly, right atrial volumes and main pulmonary artery Doppler assessment should be obtained in all children who have abnormal tricuspid inflow/DTI patterns and/or have known heart disease. Serial evaluations, additional echocardiographic techniques and/or invasive testing should be done in those identified with diastolic disease.

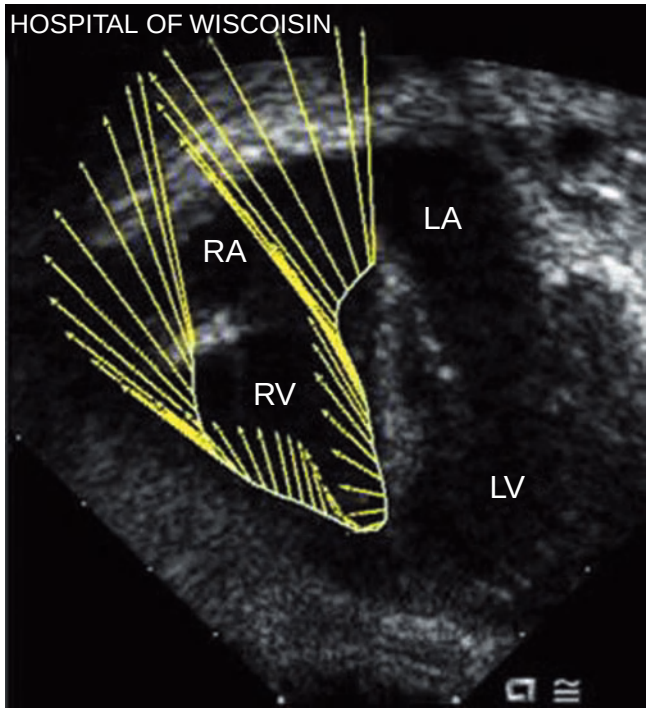


**Figure 8.22** Apical 4-chamber image with velocity vector characterization of right ventricular (RV) motion. The arrows denote the direction and amplitude of regional myocardial velocities, and this frame from early diastole shows dominant longitudinal motion of the right ventricular base away from the apex, reflecting the importance of longitudinal motion in right ventricular diastolic mechanics. LA, left atrium; LV, left ventricle; RA, right atrium.

## Conclusions

Diastolic function can be assessed by Doppler echocardiography in pediatric patients and should be part of the routine echocardiographic exam.

- Mitral and pulmonary venous inflow Doppler patterns can identify abnormal left ventricular relaxation and compliance as well as an elevation in left atrial pressure.
- Age-related differences in inflow Doppler patterns are important to recognize in the pediatric patient, because a shift in ventricular filling from late to early diastole is expected during infancy in normal children.
- Doppler tissue imaging analysis of mitral and tricuspid diastolic annular motion can significantly augment the identification of diastolic disease in children.
- Ventricular hypertrophy from any cause, cardiomyopathies, children with single ventricle physiology, children with tetralogy of Fallot after repair, children with right ventricles under abnormal volume or pressure load, and children after cardiac transplantation are at significant risk for diastolic disease and should be assessed carefully.
- Newer techniques, including color M-mode Doppler, myocardial deformation imaging and assessment of atrial volumes, may add to the echocardiographic assessment of diastolic disease and should also be applied in children.

As noted above, an appendix is available on the accompanying DVD that includes a review of the diseases in which diastolic dysfunction has been identified in children. The diseases covered are divided into three categories:

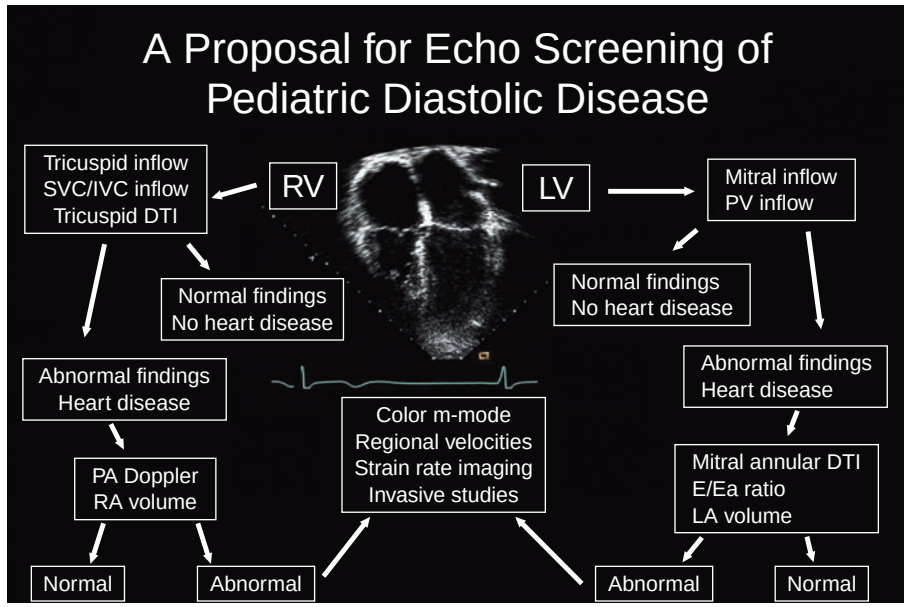


**Figure 8.23** Proposed schematic flowchart for the assessment of diastolic function in pediatric patients using echocardiography. DTI, Doppler tissue imaging; E, early diastolic filling velocity; $E_a$, early annular velocity; IVC, inferior vena cava; LA, left atrium; LV, left ventricle; PA, pulmonary artery; RA, right atrium; RV, right ventricle; SVC, superior vena cava.

**1** Primary myocardial disease/transplantation
**2** Acquired heart disease/systemic disease states
**3** Congenital heart disease.

## References


1. Courtois M, Kovacs S, Ludbrook P. Transmitral pressure-flow velocity relation. Importance of regional pressure gradients in the left ventricle during diastole. *Circulation* 1988;78:661–71.
2. Snider AR, Serwer GA, Ritter SB. Methods for obtaining quantitative information from the echocardiographic examination. In: *Echocardiography in Pediatric Heart Disease*. Missouri: Mosby, 1997;133–234.
3. Oh JK, Appleton CP, Hatle LK et al. The noninvasive assessment of left ventricular diastolic function with two-dimensional and Doppler echocardiography. *J Am Soc Echocardiog* 1997; 10:246–70.
4. Nishimura RA, Housamans PR, Hatle LK et al. Assessment of diastolic function of the heart: Background and current applications of Doppler echocardiography. Part I. Physiology and pathophysiologic features. *Mayo Clin Proc* 1989;64:71–81.
5. Nishimura RA, Abel MD, Hatle LK et al. Assessment of diastolic function of the heart: Background and current applications of Doppler echocardiography. Part II. Clinical studies. *Mayo Clin Proc* 1989;64:181–204.
6. Gardin JM, Dabestani A, Takenaka K et al. Effect of imaging view and sample volume location on evaluation of mitral flow velocity by pulsed Doppler echocardiography. *Am J Cardiol* 1986;57:1335–9.
7. Jaffe WM, Dewhurst TA, Otto CM et al. Influence of Doppler sample volume location on ventricular filling velocities. *Am J Cardiol* 1991;68:550–2.
8. Ding ZP, Oh JK, Klein AL et al. Effect of sample volume location on Doppler-derived transmitral inflow velocity values. *J Am Soc Echo* 1991;4:451–6.
9. Snider A, Serwer G, Ritter S. *Echocardiography in Pediatric Heart Disease*, 2nd edn. St Louis, Missouri: Mosby Year Book, 1997.
10. O'Leary PW, Durongpisitkul K, Cordes T et al. Diastolic ventricular function in children: A Doppler echocardiographic study establishing normal values and predictors of increased ventricular end-diastolic pressure. *Mayo Clin Proc* 1998;73: 616–28.
11. Rokey R, Kuo LC, Zoghbi WA et al. Determination of parameters of left ventricular diastolic filling with pulsed Doppler echocardiography: Comparison with cineangiography. *Circulation* 1985;71:543–50.
12. Bowman LK, Lee FA, Jaffe CC et al. Peak filling rate normalized to mitral stroke volume: A new Doppler echocardiographic filling index validated by radionuclide angiographic technique. *J Am Coll Cardiol* 1988;12:937–43.
13. Keren G, Sherez J, Megidish B et al. Pulmonary venous flow pattern – its relationship to cardiac dynamics. *Circulation* 1985;71:1105–12.
14. Smallhorn H, Freedom R, Olley P. Pulsed Doppler echocardiographic assessment of extraparenchymal pulmonary vein flow. *J Am Coll Cardiol* 1987;9:579–9.
15. Klein A, Tajik A. Doppler assessment of pulmonary venous flow in healthy subjects and in patients with heart disease. *J Am Soc Echocardiogr* 1991;4:379–92.
16. Adurrahman L, Hoit B, Banerjee A et al. Pulmonary venous flow Doppler velocities in children. *J Am Soc Echocardiogr* 1998;11:132–7.
17. Agata Y, Hiraishi S, Oguchi K et al. Changes in pulmonary venous flow pattern during early neonatal life. *Br Heart J* 1994;71:182–6.
18. Berman GO, Reichek N, Brownson D et al. Effects of sample volume location, imaging view, heart rate and age on tricuspid velocimetry in normal subjects. *Am J Cardiol* 1990;65:1026–30.
19. Riggs TW, Snider AR. Respiratory influence on right and left ventricular diastolic function in normal children. *Am J Cardiol* 1989;63:858–61.
20. Leeman DE, Levine MJ, Come PC. Doppler echocardiography in cardiac tamponade: exaggerated respiratory variation on transvalvular blood flow velocity integrals. *J Am Coll Cardiol* 1988;11:572–8.
21. Appleton CP, Hatle LK, Popp RL. Cardiac tamponade and pericardial effusion: respiratory variation in transvalvular flow velocity studied by Doppler echocardiography. *J Am Coll Cardiol* 1998;11:1020–30.
22. Gonzalez MS, Basnight MA, Appleton CP. Experimental pericardial effusion: relation of abnormal respiratory variation in mitral flow velocity to hemodynamics and diastolic right heart collapse. *J Am Coll Cardiol* 1991;17:239–48.
23. Gonzalez MS, Basnight MA, Appleton CP. Experimental cardiac tamponade: a hemodynamic and Doppler echocardiographic reexamination of right and left heart ejection dynamics to the phase of respiration. *J Am Coll Cardiol* 1991;18:243–52.
24. Byrd BF III, Linden RW. Superior vena cava Doppler flow velocity patterns in pericardial disease. *Am J Cardiol* 1990; 65:1464–70.
25. David D, Lang RM, Marcus RH et al. Doppler echocardiographic estimation of transmitral pressure gradients and correlation with micromanometer gradients in mitral stenosis. *Am J Cardiol* 1991;67:1161–4.
26. Gonzalez MA, Child JS, Krivokapich J. Comparison of two-dimensional and Doppler echocardiography and intracardiac hemodynamics for quantification of mitral stenosis. *Am J Cardiol* 1987;60:327–32.
27. Braverman AC, Thomas JD, Lee RT. Doppler echocardiographic estimation of mitral valve area during changing hemodynamic conditions. *Am J Cardiol* 1991;68:1485–90.
28. Pearlman AS. Role of echocardiography in the diagnoses and evaluation of severity of mitral and tricuspid stenosis. *Circulation* 1991;(Suppl. 1):1–193.
29. Castello R, Pearson AC, Lenzen P et al. Effect of mitral regurgitation on pulmonary venous velocities derived from transesophageal echocardiography color-guided pulsed Doppler imaging. *J Am Coll Cardiol* 1991;18:1499–506.
30. Klein A, Obarski TP, Stewart WJ et al. Transesophageal Doppler echocardiography of pulmonary venous flow: A new marker of mitral regurgitation severity. *J Am Coll Cardiol* 1991;18:518–26.
31. Klein A, Stewart WJ, Bartlett J et al. Effects of mitral regurgitation on pulmonary venous flow and left atrial pressure: an

intraoperative transesophageal echocardiographic study. *J Am Coll Cardiol* 1992;20:1345–52.
32. Kamp O, Huitink H, van Eenige MJ et al. Value of pulmonary venous flow characteristics in the assessment of severity of native mitral valve regurgitation: an angiographic correlated study. *J Am Soc Echo* 1992;5:239–46.
33. Lai L-P, Shyu KG, Chen JJ et al. Usefulness of pulmonary venous flow pattern and maximal mosaic jet area detected by transesophageal echocardiography in assessing the severity of mitral regurgitation. *Am J Cardiol* 1993;72:1310–13.
34. Klein AL, Shyu KG, Chen JJ et al. Importance of sampling both pulmonary veins in grading mitral regurgitation by transesophageal echocardiography. *J Am Soc Echo* 1993;6:115–23.
35. Brown MD, Frommelt PC. Intraoperative rhythm analysis using pulmonary venous Doppler: Importance of atrioventricular interval. *Pediatr Cardiol* 2006;27:128–30.
36. Nagueh S, Sun, H, Kopelen H et al. Hemodynamic determinants of the mitral annulus diastolic velocities by tissue Doppler. *J Am Coll Cardiol* 2001;37:277–85.
37. Frommelt PC. Pulsed Doppler tissue imaging of mitral annular motion: a new technique in the non-invasive assessment of diastolic function. *Prog Pediatr Cardiol* 1999;10:75–82.
38. Alam M, Hoglund C. Assessment by echocardiogram of left ventricular diastolic function in healthy subjects using the atrioventricular plane displacement. *Am J Cardiol* 1992;69:565–8.
39. Kuklinski T, Voigt JU, Wilkenshoff UM et al. A comparison of regional myocardial velocity information derived by pulsed and color Doppler techniques: an in vitro and in vivo study. *Echocardiography* 2000;17:639–51.
40. Donovan CL, Armstrong WF, Bach DS. Quantitative Doppler tissue imaging of the left ventricular myocardium: validation in normal subjects. *Am Heart J* 1995;130:100–4.
41. Garcia MJ, Rodriguez L, Ares M et al. Myocardial wall velocity assessment by pulsed Doppler tissue imaging: Characteristic findings in normal subjects. *Am Heart J* 1996;132:648–56.
42. Ramdas GP, Kanwaljit SG. Amplitudes, durations, and timings of apically directed left ventricular myocardial velocities: I. Their normal pattern and coupling to ventricular filling and ejection. *J Am Soc Echocardiogr* 1998;11:105–11.
43. Ramdas PG, Kanwaljit SG. Amplitudes, durations, and timings of apically directed left ventricular myocardial velocities: II. Systolic and diastolic asynchrony in patients with left ventricular hypertrophy. *J Am Soc Echocardiogr* 1998;11:112–18.
44. Przemyslaw P, Lange A, Fleming AD et al. Doppler tissue imaging: myocardial wall motion velocities in normal subjects. *J Am Soc Echocardiogr* 1995;8:659–68.
45. Bach DS, Armstrong WF, Donovan CL et al. (1996) Quantitative Doppler tissue imaging for assessment of regional myocardial velocities during transient ischemia and reperfusion. *Am Heart J* 1996;132:721–5.
46. Rodriguez L, Garcia M, Ares M et al. Assessment of mitral annular dynamics during diastole by Doppler tissue imaging: comparison with mitral Doppler inflow in subjects without heart disease and in patients with left ventricular hypertrophy. *Am Heart J* 1996;131:982–7.
47. Garcia MJ, Rodriguez L, Ares M et al. Differentiation of constrictive pericarditis from restrictive cardiomyopathy: assessment of left ventricular diastolic velocities in longitudinal axis by Doppler tissue imaging. *J Am Coll Cardiol* 1996;27:108–14.
48. Oki T, Tabata T, Yamada H et al. Clinical application of pulsed Doppler tissue imaging for assessing abnormal left ventricular relaxation. *Am J Cardiol* 1997;79:921–8.
49. Nagueh SF, Middleton KJ, Kopelen HA et al. Doppler tissue imaging: a noninvasive technique for evaluation of left ventricular relaxation and estimation of filling pressures. *J Am Coll Cardiol* 1997;30:1527–33.
50. Sohn DW, Chai IH, Lee DJ et al. Assessment of mitral annulus velocity by Doppler tissue imaging in the evaluation of left ventricular diastolic function. *J Am Coll Cardiol* 1997;30:474–80.
51. Rychik J, Tian ZY. Quantitative assessment of myocardial tissue velocities in normal children with Doppler tissue imaging. *Am J Cardiol* 1996;77:1254–7.
52. Frommelt PC, Ballweg JA, Whitstone BN et al. Usefulness of Doppler tissue imaging analysis of tricuspid annular motion for determination of right ventricular function in normal infants and children. *Am J Cardiol* 2002;89:610–13.
53. Nikitin NP, Witte KKA, Thackray SDR et al. Longitudinal ventricular function: normal values of atrioventricular annular and myocardial velocities measured with quantitative two-dimensional color Doppler tissue imaging. *J Am Soc Echocardiogr* 2003;16:906–21.
54. Kukulski T, Hubbert L, Arnold M et al. Normal regional right ventricular function and its change with age: a Doppler myocardial imaging study. *J Am Soc Echocardiogr* 2000;13:194–204.
55. Mammarstrom E, Wranne B, Pinto FJ et al. Tricuspid annular motion. *J Am Soc Echocardiogr* 1991;4:131–9.
56. Nakagawa Y, Fujimoto S, Mizuno R *et al*. Assessment of the normal adult right ventricular diastolic function using M-mode echocardiographic measurement of tricuspid ring motion. *Int J Cardiac Imag* 1998;14:391–5.
57. Ueti OM, Camargo EE, Ueti AA et al. Assessment of right ventricular function with Doppler echocardiographic indices derived from tricuspid annular motion: comparison with radionuclide angiography. *Heart* 2002;88:244–8.
58. Eidem B, McMahon C, Ayres N et al. (2005) Impact of chronic left ventricular preload and afterload on Doppler tissue imaging velocities: a study in congenital heart disease. *J Am Soc Echogardiogr* 2005;18:830–8.
59. Abali G, Tokgozoglu L, Ozcebe OI et al. Which Doppler parameters are load independent? A study in normal volunteers after blood donation. *J Am Soc Echocardiogr* 2005;18:1260–5.
60. Gomez CA, Ludomirsky A, Ensing GJ et al. Effect of acute changes in load on left ventricular diastolic function during device closure of atrial septal defects. *Am J Cardiol* 2005;95:686–8.
61. Giardini A, Moore P, Brook M et al. Effect of transcatheter atrial septal defect closure in children on left ventricular diastolic function. *Am J Cardiol* 2005;9:1255–7.
62. Pascotto M, Caso P, Santoro G et al. Analysis of right ventricular Doppler tissue imaging and local dependence in patients undergoing percutaneous closure of atrial septal defect. *Am J Cardiol* 2004;94:1202–5.

63. Border WL, Michelfelder EC, Glascock BJ et al. Color M-mode and Doppler tissue evaluation of diastolic function in children: simultaneous correlation with invasive indices. *J Am Soc Echocardiogr* 2003;16:988–94.
64. Brun P, Tribouilloy C, Duval AM et al. Left ventricular flow propagation during early filling is related to wall relaxation: a color M-mode Doppler analysis. *J Am Coll Cardiol* 1992; 20:420–32.
65. Takatsuji H, Mikami T, Urasawa K et al. A new approach for evaluation of left ventricular diastolic function: spatial and temporal analysis of left ventricular filling flow propagation by color M-mode Doppler echocardiography. *J Am Coll Cardiol* 1996;27:365–71.
66. Garcia MJ, Smedira NG, Greenberg NL et al. Color M-mode Doppler flow propagation velocity is a preload insensitive index of left ventricular relaxation: animal and human validation. *J Am Coll Cardiol* 2000;35:201–8.
67. Ogawa T, Scotten LN, Walker DK et al. What parameters affect left ventricular diastolic flow propagation velocity? In vitro studies using color M-mode Doppler echocardiography. *Cardiovasc Ultrasound* 2005;3:24.
68. Stugaard M, Smiseth OA, Risoe C et al. Intraventricular early diastolic filling during acute myocardial ischemia: assessment by multigated color M-mode Doppler. *Circulation* 1993;88: 2705–13.
69. Stugaard M, Brodahl U, Torp H et al. Abnormalities of left ventricular filling in patients with coronary artery disease: assessment by color M-mode Doppler technique. *Eur Heart J* 1994;15:318–27.
70. Djaiani GN, McCreath BJ, Ti LK et al. Mitral flow propagation velocity identifies patients with abnormal diastolic function during coronary artery bypass graft. *Anesth. Analg* 2002;95: 524–30.
71. Sutherland GR, Di Salvo G, Claus P et al. Strain and strain rate imaging: a new clinical approach to quantifying regional myocardial function. *J Am Soc Echocardiogr* 2004;17:788–802.
72. Marwick TH. Measurement of strain and strain rate by echocardiography: ready for prime time? *J Am Coll Cardiol* 2006;47:1313–27.
73. Hayashi S, Linda B, Seeberger A et al. Analysis of mitral annulus motion measurements derived from M-mode, anatomic M-mode, tissue Doppler displacement, and 2-dimensional strain imaging. *J Am Soc Echocardiogr* 2006;19:1092–101.
74. Stoylen A, Slordahl S, Skjelvan G et al. Strain rate imaging in normal and reduced diastolic function: Comparison with pulsed Doppler tissue imaging of the mitral annulus. *J Am Soc Echocardiogr* 2001;14:264–74.
75. Weidemann F, Eyskens B, Sutherland GR. New ultrasound methods to quantify regional myocardial function in children with heart disease. *Pediatr Cardiol* 2002;23:292–306.
76. Pellerin D, Sharma R, Elliott P et al. Tissue Doppler, strain, and strain rate echocardiography for the assessment of left and right systolic ventricular function. *Heart* 2003;89(Suppl. 3):iii9–17.
77. Kapusta L, Thijssen JM, Cuypers MH *et al*. Assessment of myocardial velocities in healthy children using tissue Doppler imaging. *Ultrasound Med Biol* 2000;26:229–37.
78. Swaminathan S, Ferrer PL, Wolff GS et al. Usefulness of tissue Doppler echocardiography for evaluating ventricular function in children without heart disease. *Am J Cardiol* 2003;91:570–4.
79. Weidemann F, Eyskens B, Jamal F et al. Quantification of regional left and right ventricular radial and longitudinal function in healthy children using ultrasound-based strain rate and strain imaging. *J Am Soc Echocardiogr* 2002;15:20–8.
80. Jamal F, Bergerot C, Argaud L et al. Longitudinal strain quantitates regional right ventricular contractile function. *Am J Physiol Heart Circ Physiol* 2003;285:H2842–7.
81. Cho GY, Chan J, Leano R et al. Comparison of two-dimensional speckle and tissue velocity based strain and validation with harmonic phase magnetic resonance imaging. *Am J Cardiol* 2006;97:1661–6.
82. Boettler P, Hartmann M, Watzl K et al. Heart rate effects on strain and strain rate in healthy children. *J Am Soc Echocardiogr* 2005;18:1121–30.
83. Tsang TS, Barnes ME, Gersh BJ et al. Left atrial volume as a morphophysiologic expression of left ventricular diastolic dysfunction and relation to cardiovascular risk burden. *Am J Cardiol* 2002;90:1284–9.
84. Pritchett AM, Mahoney DW, Jacobsen SJ et al. Diastolic dysfunction and left atrial volume: A population-based study. *J Am Coll Cardiol* 2005;45:87–92.
85. Beinart R, Boyko V, Schwammenthal E et al. Long-term prognostic significance of left atrial volume in acute myocardial infarction. *J Am Coll Cardiol* 2004;44:327–34.
86. Tsang TSM, Abhayaratna WP, Barnes ME et al. Prediction of cardiovascular outcomes with left atrial size: is volume superior to area or diameter? *J Am Coll Cardiol* 2006;47:1018–23.
87. Rossi A, Cicoira M, Bonapace S et al. Vassanelli left atrial volume provides independent and incremental information compared with exercise tolerance parameters in patients with heart failure and left ventricular systolic dysfunction. *Heart* 2007;93:1420–5.
88. Moller JE, Hillis GS, Oh JK et al. Left atrial volume: a powerful predictor of survival after acute myocardial infarction. *Circulation* 2003;107:2207–12.
89. Pearlman JD, Triulzi MO, King ME et al. Left atrial dimensions in growth and development: normal limits for two-dimensional echocardiography. *J Am Coll Cardiol* 1990;16:1168–74.
90. Abhayaratna WP, Seward JB, Appleton CP et al. Left atrial size: physiologic determinants and clinical applications. *J Am Coll Cardiol* 2006;47:2357–63.
91. Lang RM, Bierig M, Devereux RB, et al. Recommendations for chamber quantification. *J Am Soc Echocardiogr* 2005;18: 1440–63.
92. Appleton CP, Hatle LK, Popp RL. Relation of transmitral flow velocity patterns to left ventricular diastolic function: new insights from a combined hemodynamic and Doppler echocardiographic study. *J Am Coll Cardiol* 1988;12:426–40.
93. Appleton CP, Hatle LK. The natural history of left ventricular filling abnormalities: Assessment by two-dimensional and Doppler echocardiography. *Echocardiography* 1990;9:453–62.
94. Rossvoll O, Hatle LK. Pulmonary venous flow velocities recorded by transthoracic Doppler ultrasound: Relation to left ventricular diastolic pressures. *J Am Coll Cardiol* 1993;21:1687–95.
95. Iuchi A, Takashi O, Satoru O et al. Evaluation of pulmonary venous flow pattern in hypertrophied and dilated hearts: A

study with transesophageal pulsed Doppler echocardiography. *J Cardiogr* 1991;21:75–88.
96. Keren G, Meisner JS, Sherez J et al. Interrelationship of mid-diastolic mitral valve motion, pulmonary venous flow, and transmitral flow. *Circulation* 1986;74:36–44.
97. Frommelt PC, Pelech AN, Frommelt MA. Diastolic dysfunction in an unusual case of cardiomyopathy in a child – insights from Doppler and Doppler tissue imaging analysis. *J Am Soc Echocardiogr* 2003;16:176–81.
98. Moller JE, Sondergaard E, Poulsen SH et al. Pseudo-normal and restrictive filling patterns predict left ventricular dilation and cardiac death after a first myocardial infarction: a serial color M-mode Doppler echocardiographic study. *J Am Coll Cardiol* 2000;36:1841–6.
99. Moller JE, Sondergaard E, Seward JB et al. Ratio of left ventricular peak E-wave velocity to flow propagation velocity assessed by color M-mode Doppler echocardiography in first myocardial infarction: Prognostic and clinical implications. *J Am Coll Cardiol* 2000;35:363–70.
100. Gonzalez-Vilchez F, Ares M, Ayuele J et al. Combined use of pulsed and color M-mode Doppler echocardiography for the estimation of pulmonary capillary wedge pressure: an empirical approach based on an analytical relation. *J Am Coll Cardiol* 1999;34:515–23.
101. Larrazet F, Bouabdallah K, Le Bret E et al. Tissue Doppler echocardiographic and color M-mode estimation of left atrial pressure in infants. *Crit Care Med* 2005;6:496–7.
102. Ommen SR, Nishimura RA, Hurrell DG et al. Assessment of right atrial pressure with 2-dimensional and Doppler echocardiography: a simultaneous catheterization and echocardiographic study. *Mayo Clin Proc* 2000;75:24–9.
103. Schmitz L, Xanthopoulos A, Koch H et al. Doppler flow parameters of left ventricular filling in infants: how long does it take for the maturation of the diastolic function in a normal left ventricle to occur? *Pediatr Cardiol* 2005;25:482–91.
104. Riggs TW, Rodriguez R, Snider AR et al. Doppler echocardiographic evaluation of right and left ventricular filling in normal neonates. *J Am Coll Cardiol* 1989;13:700–5.
105. Harada K. Role of age on transmitral flow velocity patterns in assessing left ventricular diastolic function in normal infants and children. *Am J Cardiol* 1995;76:530–6.
106. Schmitz L, Xanthopoulos A, Lange PE. Isovolumic relaxation time shortens significantly during the three months after birth. *J Am Soc Echocardiogr* 2004;17:275–6.
107. Harada K, Suzuki T, Tamura M et al. Effect of aging from infancy to childhood on flow velocity patterns of pulmonary vein by Doppler echocardiography. *Am J Cardiol* 1996;77: 221–4.
108. Iwashima S, Seguchi M, Ohzeki T. Left ventricular diastolic performance in neonates. *Circulation* 2005;69:1094–8.
109. Mori K, Nakagawa M, Edagawa T et al. Pulsed wave Doppler tissue echocardiography assessment of the long axis function of the right and left ventricles during the early neonatal period. *Heart* 2004;90:175–80.
110. Schmitz L, Stiller B, Pees C et al. Doppler-derived parameters of diastolic left ventricular function in preterm infants with a birth weight <1500 g: reference values and differences to term infants. *Early Hum Dev* 2004;76:101–14.
111. Schmitz L, Stiller B, Koch et al. Diastolic left ventricular function in preterm infants with a patent ductus arteriosus: a serial Doppler echocardiography study. *Early Hum Dev* 2004;76:91–100.
112. Hiarada K, Orino T, Yasuoka J et al. Tissue Doppler imaging of left and right ventricles in normal children. *Tohoku J Experimental Med* 2000;191:21–9.
113. Kapusta L, Thijssen JM, Cuypers MH et al. Assessment of myocardial velocities in healthy children using tissue Doppler imaging. *Ultrasound Med Biol* 2000;26:229–37.
114. Mori K, Hayabuchi Y, Kuroda Y et al. Left ventricular wall motion velocities in healthy children measured by pulsed wave Doppler tissue echocardiography: normal values and relation to age and heart rate. *J Am Soc Echocardiogr* 2000;13: 1003–11.
115. Roberson D, Cui W, Chen Z et al. Annular and septal Doppler tissue imaging in children: Normal z-score tables and effects of age, heart rate and body surface. *J Am Soc Echocardiogr* 2007;20:1276–84.
116. Eidem BW, McMahon CJ, Cohen RR et al. Impact of cardiac growth on Doppler tissue imaging velocities: a study in healthy children. *J Am Soc Echocardiogr* 2004;17:212–21.
117. Ayabakan C, Ozjutlu S. Left ventricular myocardial velocities in healthy children: quantitative assessment by tissue Doppler echocardiography and relation to the characteristics of filling of the left ventricle. *Cardiol Young* 2004;14:156–63.
118. Watanabe M, Ono S, Tomomasa T et al. Measurement of tricuspid annular diastolic velocities by Doppler tissue imaging to assess right ventricular function in patients without congenital heart disease. *Pediatr Cardiol* 2003;24:463–7.
119. Palmieri V, Palmieri EM, Arezzi E et al. Peak exercise oxygen uptake and left ventricular systolic and diastolic function and arterial mechanics in healthy young men. *Eur J Appl Physiol* 2004;91:664–8.
120. Nottin S, Nguyen L-D, Terbah, M et al. Left ventricular function in endurance trained children by tissue Doppler imaging. *Med Sci Sports Exerc* 2004;36:1507–13.
121. Naylor LH, Amolda LF, Deague JA et al. Reduced ventricular flow propagation velocity in elite athletes is augmented with the resumption of exercise training. *J Physiol* 2005;563:957–63.
122. Whyte G, George K, Shave R et al. Impact of marathon running on cardiac structure and function in recreational runners. *Clin Sci* 2005;108:73–80.
123. Davlouros PA, Niwa K, Webb G et al. The right ventricle in congenital heart disease. *Heart* 2006;92(Suppl. 1):i27–i38.
124. Haber I, Metaxas DN, Geva T et al. Three-dimensional systolic kinematics of the right ventricle. *Am J Physiol Heart Circ Physiol* 2005;289:1826–33.
125. Xia L, Huo M, Wei Q et al. Analysis of cardiac ventricular wall motion based on a three-dimensional electromechanical biventricular model. *Phys Med Biol* 2005;50:1901–17.
126. Leather HA, Ama R, Missant C et al. Longitudinal but not circumferential deformation reflects global contractile function in the right ventricle with open pericardium. *Am J Physiol Heart Circ Physiol* 2006;290:2369–75.
127. Nikitin NP, Witte KKA, Thackray SDR et al. Longitudinal ventricular function: normal values of atrioventricular annular and myocardial velocities measured with quantitative

two-dimensional color Doppler tissue imaging. *J Am Soc Echocardiogr* 2003;16:906–21.

128. Kukulski T, Hubbert L, Arnold M et al. Normal regional right ventricular function and its change with age: a Doppler myocardial imaging study. *J Am Soc Echocardiogr* 2000;13: 194–204.
129. Mammarstrom E, Wranne B, Pinto FJ et al. Tricuspid annular motion. *J Am Soc Echocardiogr* 1991;4:131–9.
130. Nakagawa Y, Fujimoto S, Mizuno R et al. (1998) Assessment of the normal adult right ventricular diastolic function using M-mode echocardiographic measurement of tricuspid ring motion. *Int J Cardiac Imag* 1998;14:391–5.
131. Ueti OM, Camargo EE, Ueti AA et al. Assessment of right ventricular function with Doppler echocardiographic indices derived from tricuspid annular motion: comparison with radionuclide angiography. *Heart* 2002;88:244–8

# 3

# Anomalies of the Systemic and Pulmonary Veins, Septa and Atrioventricular Junction

*Echocardiography in Pediatric and Congenital Heart Disease: From Fetus to Adult*
Edited by Wyman W. Lai, Luc L. Mertens, Meryl S. Cohen and Tal Geva
 ISBN: 978-1-405-17401-5

# 9 Pulmonary Venous Anomalies

**David W. Brown**
Pediatric Cardiology, Children's Hospital Boston, Boston, MA, USA

## Definition

Pulmonary venous anomalies include many anatomic variations, with a wide range of clinical presentations and outcomes. The anomalies may be grouped into four categories:

- *abnormal numbers* of pulmonary veins
- normal pulmonary venous connections with *anomalous drainage*
- *stenotic connections*
- *anomalous connections*.

The presentation ranges from normal, in those with variations on the normal number of pulmonary veins, to life-threatening disease in the neonate with obstructed total anomalous pulmonary venous connection. Fortunately, the vast majority of pulmonary venous anomalies may now be readily and rapidly diagnosed by echocardiography.

## Incidence

The incidence of pulmonary venous anomalies varies widely according to the particular anomaly observed. An abnormal number of pulmonary veins is commonly encountered; anatomic studies show a single right or single left pulmonary vein in nearly 25% of the population, and a third pulmonary vein is present on either side in 1.6–2% [1]. Cor triatriatum, an example of stenotic pulmonary venous connection due to incomplete incorporation of the common pulmonary vein into the left atrium, occurs in 3 in 100 000 of the population [2]. Partial anomalous pulmonary venous connection (PAPVC) has been described in autopsy series in 400–700 in 100 000 specimens [1], with isolated PAPVC in 160 of 100 000. Total anomalous pulmonary venous connection (TAPVC) has been described in 9 in 100 000 of the population [3,4].

*Echocardiography in Pediatric and Congenital Heart Disease: From Fetus to Adult*
Edited by Wyman W. Lai, Luc L. Mertens, Meryl S. Cohen and Tal Geva
 ISBN: 978-1-405-17401-5

## Etiology

Most cases of pulmonary venous anomalies are sporadic. However, there are known syndromic associations for PAPVC, most notably Turner and Noonan syndromes [5,6]. TAPVC similarly has syndromic associations, including cat-eye, Holt–Oram and the asplenia syndromes. Numerous case reports of non-syndromic familial cases suggest a heritable genetic cause, with heterogeneous genetic loci reported; one gene for familial total anomalous pulmonary venous return in a large Utah kindred was mapped to chromosome 4p13-q12 [7].

## Morphology and classification

### Developmental considerations

The classification of pulmonary venous anomalies is based on an understanding of the embryologic development of the pulmonary veins, and the relationships between the pulmonary veins, systemic veins and the atria. The lungs and tracheobronchial tree are derived from the foregut, and the pulmonary vascular bed is formed by a portion of the splanchnic plexus; as such, the pulmonary vascular bed shares venous drainage with the splanchnic bed, the umbilicovitelline and cardinal venous systems, and thus early in gestation it is not connected to the developing heart. At 32–33 days of gestation, the pulmonary veins subsequently establish a communication with the common pulmonary vein, which becomes incorporated into the posterior aspect of the developing left atrium.

The precise site of development of the common pulmonary vein is controversial, with some believing that the vein derives from an evagination in the sinoatrial region of the heart [8], and others that the common vein arises from the pulmonary venous plexus confluence [1]; a third theory holds that it originates from a confluence of capillaries growing into the mesocardium between the lung buds and the heart. Regardless, as this communication is established with the left atrium, the connections of the pulmonary venous system to the systemic venous system are typically obliterated. The common pulmonary vein becomes incorporated into the

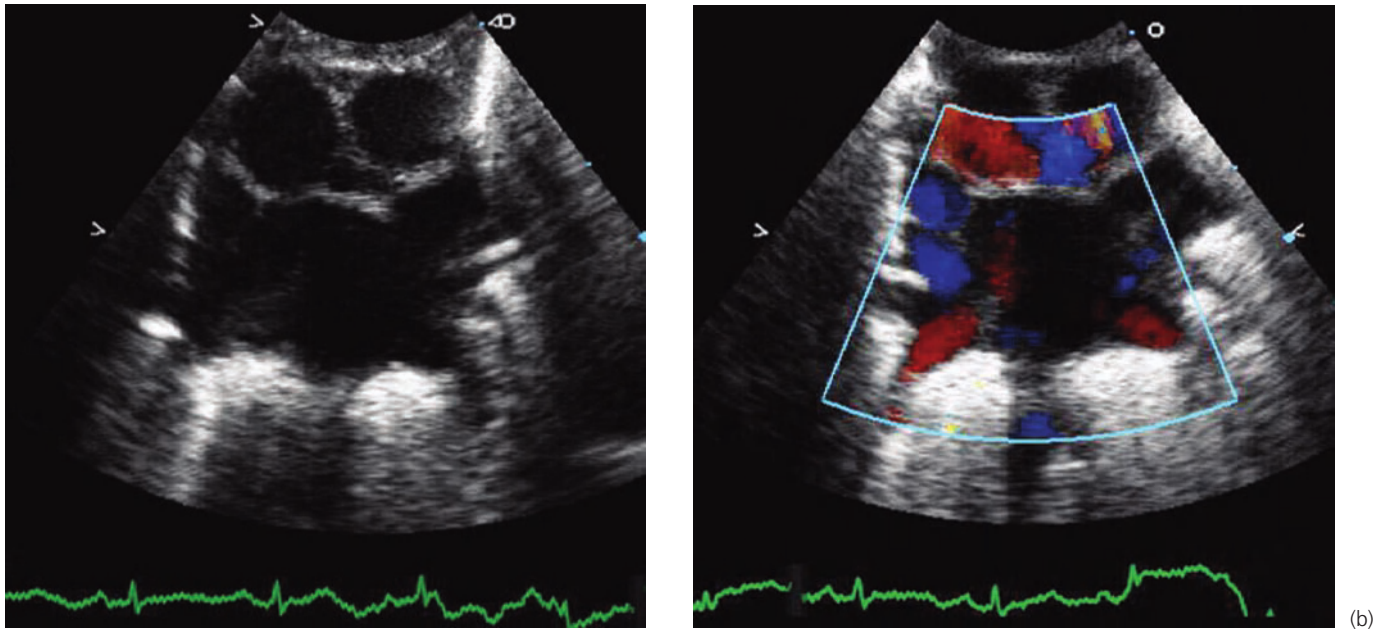

(a) (b)

**Figure 9.1** Normal pulmonary venous connection. Suprasternal notch view of the pulmonary veins and left atrium with two-dimensional imaging **(a)** and color Doppler flow mapping **(b)** showing the "crab" view. Two left and two right pulmonary veins drain normally into the left atrium – the "legs" of the crab; the right superior vena cava and left atrial appendage are the "claws."

posterior aspect of the left atrium, between the left and right horns of the sinus venosus, superior to the coronary sinus, and leftward of septum primum; ultimately two right and two left pulmonary veins connect directly to the left atrium. Nearly all of the pulmonary venous anomalies considered in this chapter may be seen as a result of abnormal development of the common pulmonary vein.

## Anatomy

### Abnormal number of pulmonary veins

An abnormal number of pulmonary veins results from irregular incorporation of the common pulmonary vein into the left atrium. With normal incorporation of the common pulmonary vein, two right and two left pulmonary veins connect directly and separately to the left atrium (Fig. 9.1). When incomplete incorporation of either the right or left side occurs, a single pulmonary vein may drain that lung; a single left pulmonary vein is more frequently observed than a single right [1]. More rarely, a common pulmonary vein accepts veins from both sides and then drains into the left atrium – an arrangement seen most often in those with asplenia forms of heterotaxy [1]. When more than typical incorporation occurs, a third pulmonary vein on either the right or left side is observed [1].

### Normal pulmonary venous connections with anomalous drainage

This results when the common pulmonary vein incorporates normally into the left atrium, resulting in normally positioned pulmonary venous connections, but due to interatrial anatomy the pulmonary venous inflow is directed into the morphologic right atrium. Most commonly this is due to anatomically leftward *malposition or malattachment of septum primum*, which can result in partial or total anomalous pulmonary venous drainage, depending upon the degree of malposition and number of veins affected (Fig. 9.2). This

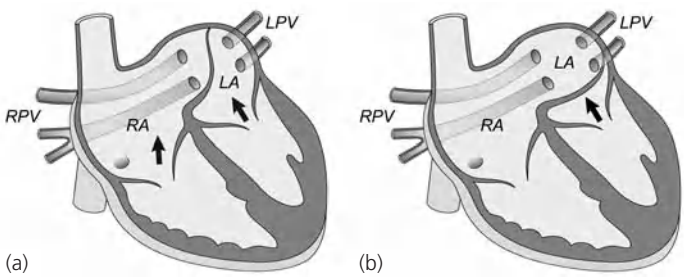


(a) (b)

**Figure 9.2** Malposition of septum primum. **(a)** Mild leftward malposition with normal pulmonary venous connections results in anomalous drainage of the right upper and lower pulmonary veins to the right atrium. **(b)** With more severe malposition of septum primum, drainage of all four pulmonary veins is directed anomalously into the right atrium. Note the absence of a well-developed septum secundum; this is common in patients with the polysplenia forms of heterotaxy syndrome. LA, left atrium; LPV, left pulmonary veins; RA, right atrium; RPV, right pulmonary veins.

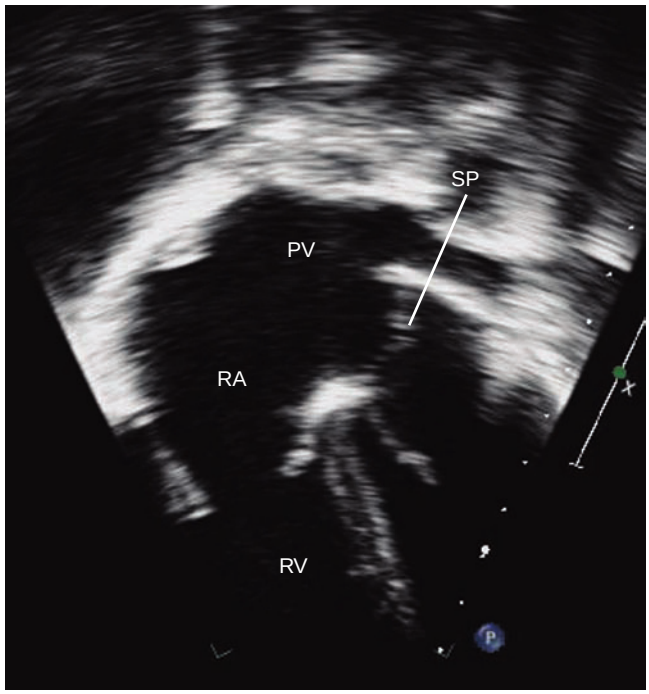


**Figure 9.3** Total anomalous pulmonary venous drainage. Apical two-dimensional image in this patient with severe leftward malposition of septum primum (SP) shows the lack of septum secundum superiorly, normal pulmonary venous connections to the posterior aspect of the left atrium, and leftward malposition of SP resulting in total anomalous pulmonary venous drainage. PV, pulmonary veins; RA, right atrium; RV, right ventricle.

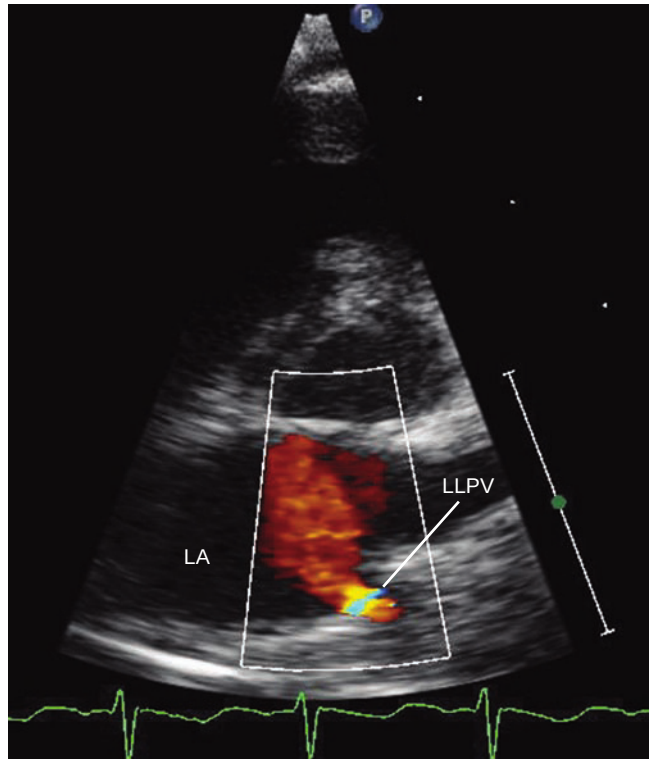


**Figure 9.4** Pulmonary vein stenosis. Parasternal short-axis view of the left atrium (LA) in a patient with an otherwise structurally normal heart demonstrates discrete stenosis of the left lower pulmonary vein (LLPV) at its junction with the left atrium.

is commonly encountered in those with polysplenia syndrome due to absence of septum secundum and resulting anatomic leftward malposition of septum primum (Fig. 9.3) [9]. Another frequently encountered example is *common atrium* as also observed in the heterotaxy syndromes, where virtual absence of the atrial septum results in ipsilateral drainage of the pulmonary veins into respective sides of the common atrium.

### Sinus venosus defect (SVD)

Sinus venosus defect is a type of anomalous pulmonary venous drainage with normal connections that occurs due to "unroofing" or absence of the sinus venosus tissue between the right pulmonary veins and the superior vena cava or right atrium [10,11]. This topic is covered in detail in Chapter 11. It is important to note that despite the absence of sinus venosus septum, the pulmonary veins remain normally connected to the left atrium.

### Stenotic connections

Stenotic connections may be seen in individual pulmonary veins with normal connections to the heart, in anomalously connecting veins, or as stenosis of the common pulmonary vein, which manifests as *cor triatriatum sinister*. Stenosis of the individual pulmonary veins is a rare disorder that may result from abnormal incorporation of the common pulmonary vein into the left atrium [12]; trauma or manipulation provoking inflammation may be antecedent events. Pulmonary vein stenosis can be found in otherwise structurally normal hearts, or in association with congenital heart defects, commonly atrial or ventricular septal defects [13], or less often with complex heart disease such as the heterotaxy syndromes [14]. The stenosis can be extraparenchymal, with obstruction at the pulmonary vein–left atrial junction (Fig. 9.4), intraparenchymal, with diffuse involvement of the smaller pulmonary veins in the lung, or both. Investigations have implicated intimal proliferation of abnormal myofibroblasts in the pathology of this disease [15,16]. Finally, stenosis of anomalously connecting pulmonary veins is commonly encountered, particularly in those with total anomalous pulmonary venous connection below the diaphragm.

### Cor triatriatum sinister

This results from incomplete incorporation of the common pulmonary vein into the posterior aspect of the left atrium. Cor triatriatum has many variations, the classic form consisting of a membranous partition that divides the left atrium into a chamber that receives the pulmonary veins posteriorly, and a chamber that communicates with the mitral valve anteriorly and inferiorly (Fig. 9.5). A communicating orifice of varying size is typically present, the atrial septum is usually

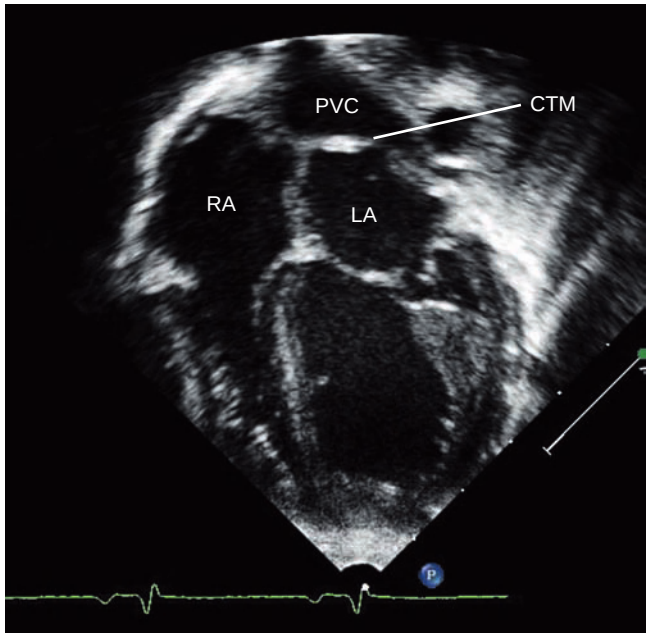


**Figure 9.5** Classic cor triatriatum sinister. Apical 4-chamber view example of the "classic" form of cor triatriatum, with a discrete "membrane" (CTM) seen between the pulmonary venous confluence (PVC) and the anatomic left atrium (LA). The only egress for pulmonary venous blood is through the membrane orifice. RA, right atrium.

intact, and the left atrial appendage is on the distal side of the cor triatriatum membrane as a feature of the anatomic left atrium [17]. Variations include the presence of an atrial septal defect, which communicates between the right atrium and either the pulmonary venous chamber or the distal true left atrial chamber; decompressing anomalous venous connections; "subtotal" cor triatriatum, which can involve the veins from only one side of the lung; and atresia of the dividing membrane, termed "complete" cor triatriatum (Fig. 9.6).

### Atresia of the common pulmonary vein

This is a rare disorder, with functionally no communication between the pulmonary venous confluence and the heart or the systemic veins; a blind-ending pouch is present at the confluence of the pulmonary veins with no outlet to flow [18].

### Partial anomalous pulmonary venous connection (PAPVC)

This involves one or more (but not all) pulmonary venous connections to the systemic venous circulation, with a wide anatomic spectrum of variations possible (Fig. 9.7). As mentioned previously, PAPVC must be considered distinct from cases of partial anomalous pulmonary venous *drainage*. Left-sided pulmonary veins typically form anomalous connections to left cardinal vein derivatives (such as the left innominate vein and coronary sinus), and right-sided veins typically connect to derivatives of the right cardinal system (superior and inferior venae cavae), although crossed drainage across the midline is possible as the splanchnic venous plexus is a midline structure. With reclassification of many cases previously considered PAPVC to the superior vena cava and right atrium as sinus venosus defects or malposition of septum primum, the most common form of PAPVC is connection of the left pulmonary veins to the left innominate vein, with the second most common form being right pulmonary venous connections to the inferior vena cava (IVC).

With left-sided pulmonary venous connection to the left innominate vein, one or more left pulmonary veins connect to the innominate vein by a persistent embryologic vein, named a *vertical vein* due to its orientation (Figs 9.7a and 9.8); an atrial septal defect is commonly present. Other less common left-sided connections include ones to a persistent left superior vena cava, to a coronary sinus (Fig. 9.7b) or to right-sided venous structures such as the superior vena cava, the azygous vein and the IVC [19].

Anomalous right pulmonary venous connection of all or some of the right pulmonary veins to the IVC is frequently encountered as part of a malformation termed *scimitar syndrome* (Fig. 9.7c). This term was coined to describe the crescent-shaped (or "sword-like," resembling a Turkish scimitar) shadow seen on X-ray in the right lower lung field, projected by the right pulmonary vein as it courses to join the IVC at or just below the diaphragm [20]. This syndrome is frequently associated with other anomalies of right lung development, including hypoplasia of the right lung and right pulmonary artery, secondary dextrocardia, bronchial abnormalities, anomalous arterial connection to the right lung from the aorta, and pulmonary sequestration [20,21].

### Total anomalous pulmonary venous connection (TAPVC)

This occurs when all pulmonary veins have connections to the systemic venous circulation. Embryologically, TAPVC results from failure to establish a normal connection between the pulmonary venous plexus and the common pulmonary vein before the connections with the splanchnic venous system have regressed. The most commonly used anatomic classification [22] of TAPVC is based on the site of connection(s) between the pulmonary and systemic veins:

Type I – with anomalous connections at the *supracardiac* level.
Type II – the *cardiac* type, with anomalous connections to the coronary sinus.
Type III – the *infradiaphragmatic* type, with anomalous connections below the diaphragm.
Type IV – with *mixed* types of connections.

With all types, an interatrial communication to allow blood to enter the systemic circulation is necessary to sustain life, so that a patent foramen ovale or atrial septal defect is considered part of the malformation.

Supracardiac TAPVC (Fig. 9.9a) is the most common type (47% in the largest published series [23]), and among this group the most common site of connection is to the leftward aspect of the innominate vein (36% of all cases of TAPVC

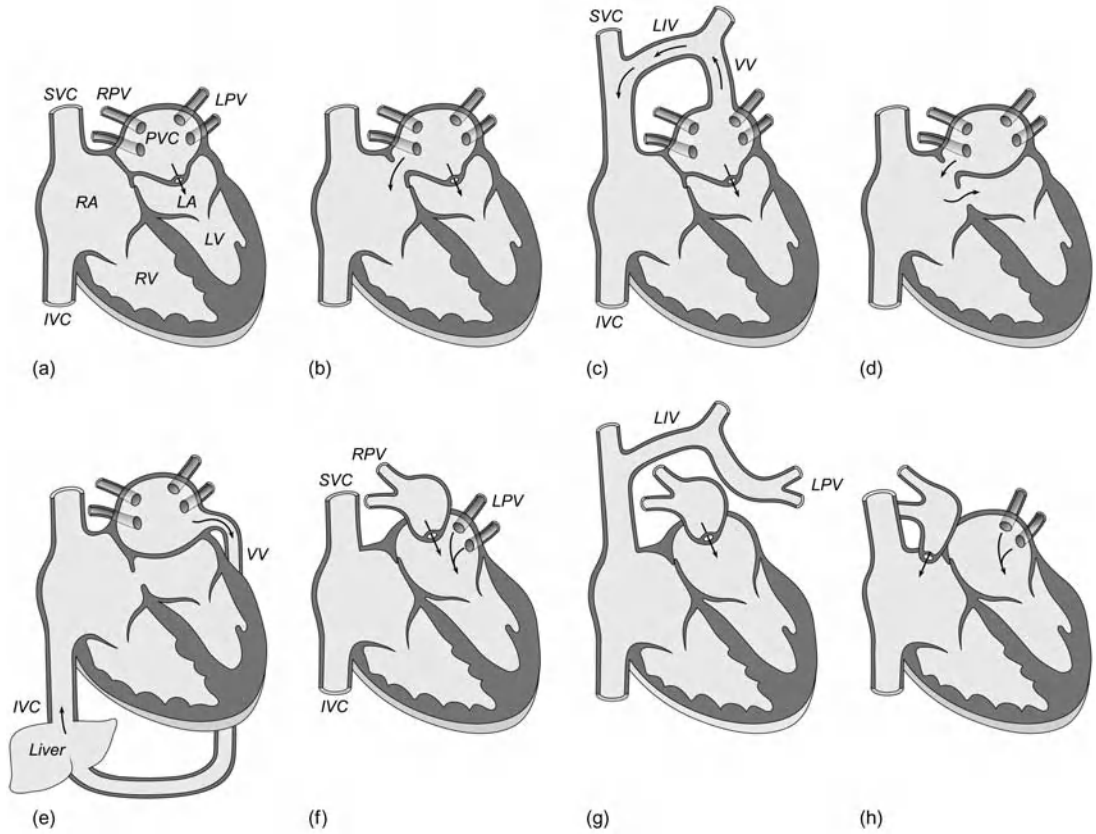


**Figure 9.6** Cor triatriatum variants. **(a)** Classic cor triatriatum. Right and left pulmonary veins (RPV, LPV) drain to the pulmonary venous confluence (PVC), with a discrete membrane between the PVC and true left atrium (LA); the only egress for blood is through the opening in the membrane. **(b)** Cor triatriatum with defect between the PVC and the right atrium (RA), which allows for decompression of pulmonary venous blood. **(c)** Cor triatriatum with decompressing vertical vein (VV) to the left innominate vein (LIV), which allows for decompression of the PVC. **(d)** Pulmonary venous return decompresses via a communication between the PVC and right atrium, and then crosses to the true left atrium via a patent foramen ovale. **(e)** Decompressing vertical vein that descends below the diaphragm to connect to the systemic venous circulation via the hepatic or portal veins. **(f)** "Partial" or subtotal cor triatriatum with normally draining left pulmonary veins; the right pulmonary veins communicate with the true left atrium via a stenotic orifice. **(g)** Subtotal cor triatriatum of the right pulmonary veins along with partial anomalous venous return of the left pulmonary veins via the left innominate vein. **(h)** Subtotal cor triatriatum of the right pulmonary veins to the right atrium with normal drainage of the left pulmonary veins to the left atrium. SVC, superior vena cava; IVC, inferior vena cava; RV, right ventricle; LV, left ventricle.

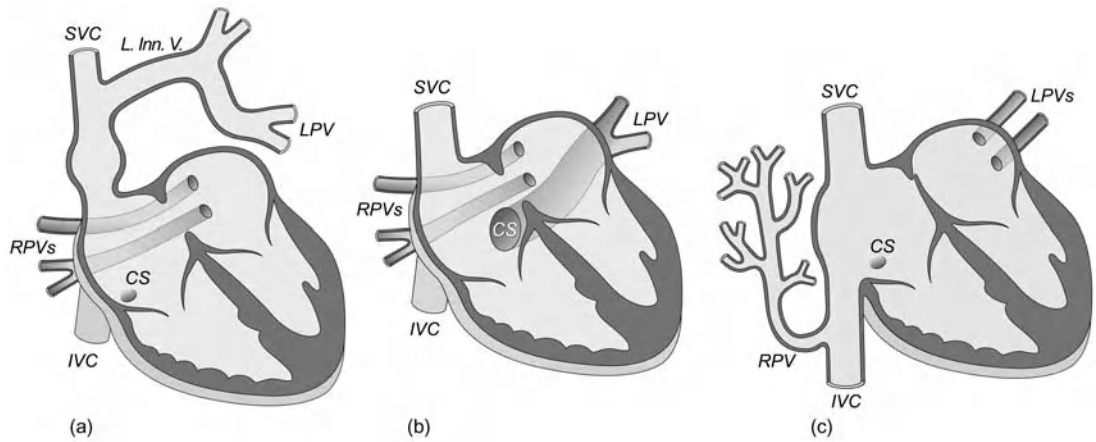


**Figure 9.7** Variants of partial anomalous pulmonary venous connection. **(a)** Anomalous connection of the two left pulmonary veins (LPV) to the left innominate vein (L. Inn. V.) to the superior vena cava (SVC); the right pulmonary veins (RPVs) connect normally to the left atrium. **(b)** Anomalous connection of the left pulmonary veins to the coronary sinus (CS). **(c)** Anomalous connection of the right pulmonary veins to the inferior vena cava (IVC) to right atrium junction; in association with right lung hypoplasia this is termed "scimitar syndrome." See text for more details.

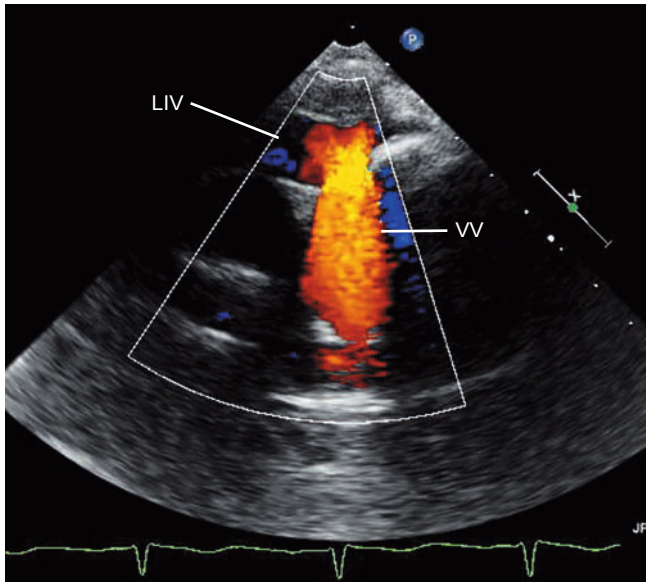


**Figure 9.8** Partial anomalous pulmonary venous connection (PAPVC): left upper pulmonary vein to innominate vein. High parasternal short-axis view with color Doppler flow mapping in this patient with PAPVC of the left upper pulmonary vein to the left innominate vein (LIV) shows a large vertical vein (VV) connecting with the caudal aspect of the dilated LIV (Videoclip 9.1).

[23]). Typically a pulmonary venous confluence is present posterior to the left atrium, and this drains via a left-sided ascending vertical vein to the innominate vein (Fig. 9.10). This vertical vein usually passes anterior to the left pulmonary artery and mainstem bronchus, although occasionally this will pass *between* these structures, which usually results in clinically significant obstruction to pulmonary venous flow. Supracardiac TAPVC with right-sided connections to the right superior vena cava or azygous vein occurs, but is less common; a similar but right-sided vertical vein is observed, which typically courses anterior to the hilum of the right lung.

Cardiac TAPVC (Fig. 9.9b) occurs in 16% of cases [23,24], and involves anomalous connection between the pulmonary venous confluence and the coronary sinus, with a venous vessel connecting typically in the region of the left atrioventricular groove. The coronary veins drain normally into the proximal end of the coronary sinus, and the typically severely dilated coronary sinus drains normally into the right atrium; the coronary sinus septum is usually intact (Fig. 9.11).

Infradiaphragmatic TAPVC (Fig. 9.9c) occurs in 13–23% [23,24], with anomalous connection typically to the umbilicovitelline system below the diaphragm. A descending vertical vein typically originates from the confluence of pulmonary veins to course below the diaphragm (just anterior to the esophagus in the esophageal hiatus) to form connections with the portal venous system (most common), the ductus venosus, hepatic vein or IVC (Fig. 9.12). Obstruction is frequently present with infradiaphragmatic forms of TAPVC for a number of reasons, most commonly due to intrinsic narrowing of the connecting vessel, the interposition of the hepatic sinusoids between the pulmonary venous drainage and the heart for those that drain via the portal vein, and constriction of the ductus venosus.

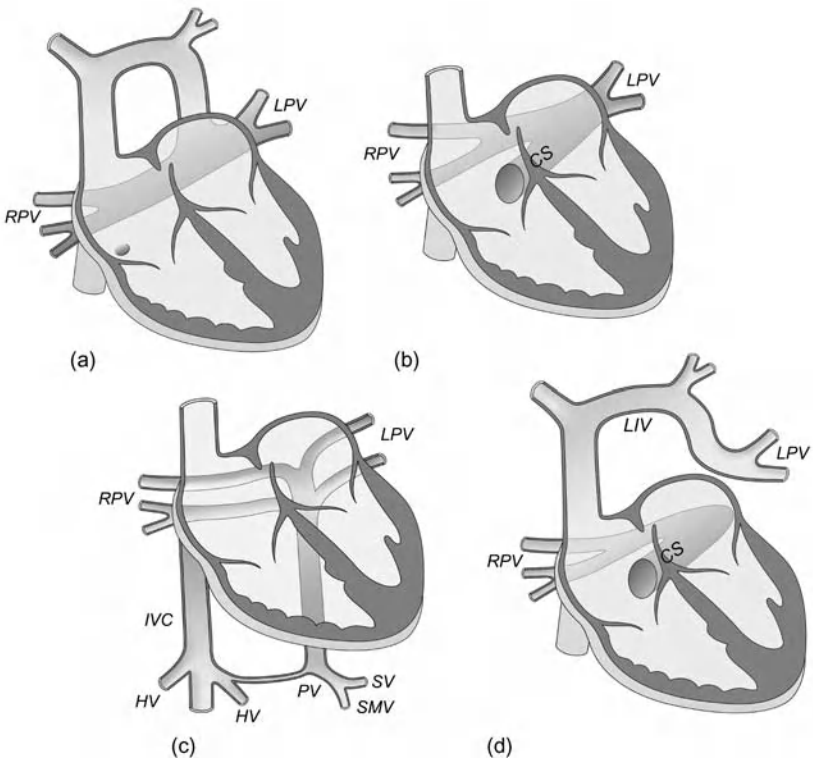


**Figure 9.9** Variants of total anomalous pulmonary venous connection (TAPVC). **(a)** Supracardiac: both right (RPV) and left (LPV) pulmonary veins join a common pulmonary venous confluence behind the heart, which drains via a vertical vein to the undersurface of the left innominate vein, and thence to the right atrium. **(b)** Cardiac: the pulmonary venous confluence connects to the coronary sinus (CS), and thence to the right atrium via the coronary sinus ostium. **(c)** Infradiaphragmatic: the pulmonary venous confluence drains inferiorly via a vertical vein to the portal vein (PV) or hepatic veins (HV) and thence to the right atrium. **(d)** Mixed connections: left pulmonary veins drain to the left innominate vein (LIV), and right pulmonary veins to the coronary sinus in this example. IVC, inferior vena cava; SMV, superior mesenteric vein; SV, splenic vein.

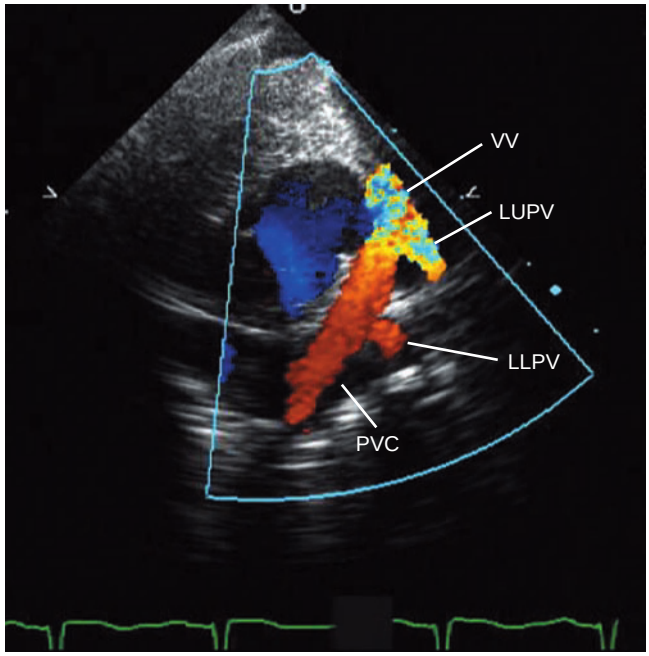


**Figure 9.10** Supracardiac total anomalous pulmonary venous connection (TAPVC). Parasternal short-axis view with color Doppler flow mapping in this patient with supracardiac TAPVC to the left innominate vein shows the pulmonary venous confluence (PVC) that courses leftward and superiorly; the left upper pulmonary vein (LUPV) joins more superiorly in this example and courses via the vertical vein (VV) toward the leftward aspect of the innominate vein. LLPV, left lower pulmonary vein (Videoclip 9.2).

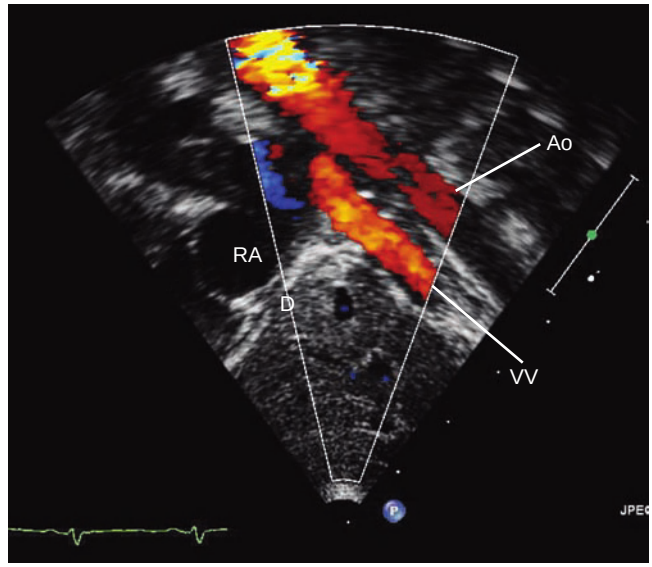


**Figure 9.12** Infradiaphragmatic total anomalous pulmonary venous connection (TAPVC). Subxiphoid short-axis imaging with color Doppler mapping in this patient with infradiaphragmatic TAPVC shows a large vertical vein (VV) coursing inferiorly from behind the heart through the diaphragm (D); this is anterior to the aorta (AO). Flow is toward the probe (red) in both vessels. RA, right atrium.

Mixed TAPVC (Fig. 9.9d) is the least common type (7–10% [23,24]), with often complex variations of the above forms of venous connections represented.

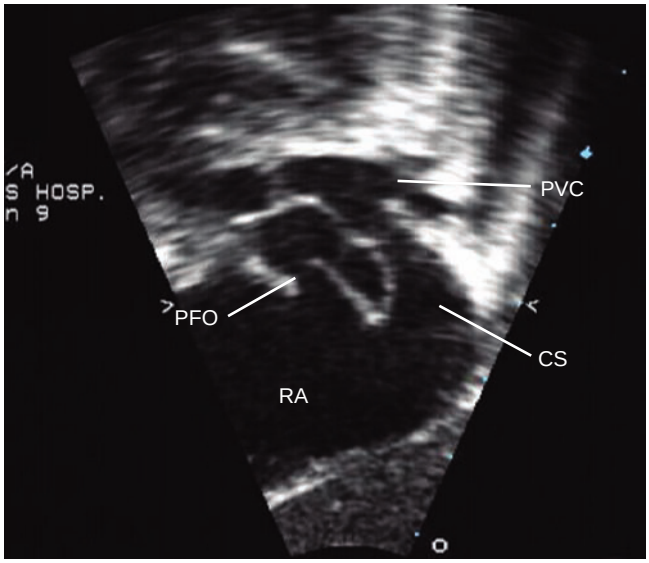


**Figure 9.11** Cardiac total anomalous pulmonary venous connection (TAPVC). Subxiphoid short axis two-dimensional view in this patient with TAPVC to the coronary sinus shows the pulmonary venous confluence (PVC) draining via a communicating vein to the severely dilated coronary sinus (CS). Note the relative hypoplasia of the left atrium and the obligate open position of the patent foramen ovale (PFO), which allows filling of the left heart. RA, right atrium.

## Pathophysiology

The pathophysiology of the various forms of pulmonary venous anomalies depends entirely upon the nature of the anomaly, the degree of mixing of systemic and pulmonary venous blood, and the presence or absence of obstruction to pulmonary venous flow.

Anomalies that result in pulmonary venous obstruction cause pulmonary venous hypertension in the affected lobe or lobes. With an increase in the number of lobes affected and worsening obstruction, the pulmonary venous hypertension is transmitted back through the vascular bed of the lung, resulting in pulmonary capillary and pulmonary artery hypertension. A cascade of effects on the pulmonary vasculature results, from acute changes such as pulmonary edema and reflex pulmonary vasoconstriction, to chronic alterations in pulmonary vascular resistance, vessel reactivity and vascular remodeling. The effects of this dramatic increase in afterload on the right side of the heart include initially compensatory right ventricular hypertrophy, subsequent chamber enlargement, contractile dysfunction and eventual right heart failure.

The pathophysiology of most of the various forms of PAPVC is similar to that of an atrial septal defect, with

increased pulmonary blood flow due to recirculation of oxygenated blood through the lungs; this is dependent upon the extent of the pulmonary vascular bed drained by the anomalously connecting vein(s), as well as the status of the atrial septum. The excess flow through the right heart and lungs leads to dilation of the right atrium, right ventricle and pulmonary vascular bed. With PAPVC of a single pulmonary vein and an intact atrial septum, typically the anomalous blood flow is 20–25% of total pulmonary blood flow [25], which is rarely clinically apparent. With PAPVC of an entire lung with an intact atrial septum, due to the greater compliance of the right atrium and right ventricle relative to the left side of the heart, the anomalously draining blood usually represents 66% rather than 50% of pulmonary venous drainage. When encountered with forms of scimitar syndrome (Fig. 9.7c), the net shunt tends to be lower (24–32% of pulmonary blood flow) due to abnormalities of the right lung parenchyma and pulmonary vasculature [26]. The subsequent development of pulmonary vascular disease with PAPVC is rare, but has been reported [27].

If a small atrial septal defect is present with PAPVC, the pathophysiology is similar to that discussed above; if a large atrial septal defect is present, the degree of left-to-right shunt is often significantly increased, with pulmonary recirculation not only of blood from the anomalously draining lung but also half or more of the normally connecting lung's blood via the atrial septal defect. Partial anomalous pulmonary venous *drainage* shares similar pathophysiology to PAPVC, with the degree of left-to-right shunt dependent upon the number of pulmonary veins redirected to the right atrium by the malpositioned septum.

The pathophysiology seen with TAPVC depends greatly upon the presence or absence of pulmonary venous obstruction, as well as the adequacy of the interatrial defect to allow flow to the systemic circulation. In the absence of pulmonary venous obstruction, there is complete mixing of systemic and pulmonary venous blood in the right atrium; as the resistance to pulmonary blood flow is significantly lower than that of the systemic circulation, there is significant pulmonary overcirculation (often 3–5 times normal) and the systemic saturation may be 90% or higher (resulting often in clinically inapparent cyanosis). Right ventricular dilation and hypertrophy frequently occur, along with varying degrees of pulmonary hypertension.

The size of the interatrial communication with TAPVC plays a critical role; with worsening restriction to flow across the atrial septum, there is not only a dramatic increase in pulmonary overcirculation (and worsening pulmonary hypertension) but also diminished systemic output. Similarly, with extrinsic or intrinsic obstruction to pulmonary venous flow, the cascade of pulmonary vascular changes discussed above may occur. Infants with obstructed TAPVC typically present in the first month of life, with a rapid and fulminant progression of dyspnea to cardiorespiratory failure [28].

## Imaging

Any detailed assessment of the pulmonary venous connections and drainage must by necessity include an assessment of the systemic venous anatomy, right and left atria, and the atrial septum. These structures are imaged from multiple acoustic windows, including the subcostal, apical, left parasternal, high right parasternal and suprasternal notch. Two- and three-dimensional imaging along with careful color and spectral Doppler techniques are used to render complete imaging of these structures. As the majority of pulmonary venous anomalies are diagnosed in infants and children, transthoracic echocardiography is the preferred modality and can yield a diagnosis in the vast majority of cases; however, transesophageal echocardiography (TEE) may be a helpful adjunct diagnostic modality in the older patient with poor transthoracic acoustic windows. Cardiac magnetic resonance imaging (MRI) with angiography is an excellent alternative modality for delineation of both systemic and pulmonary venous anatomy in those in whom a complete diagnosis cannot be obtained with echocardiographic techniques [29,30].

### Goals of the examination

The goals of the echocardiographic examination in this setting can be summarized as follows:

- Determination of number of pulmonary veins
- Determination of pulmonary venous connections
- Determination of pulmonary venous drainage
- Position and status of the atrial septum
- Systemic venous connections
- Hemodynamic assessment:
  - flow direction (by color and spectral Doppler);
  - presence or absence of pulmonary venous obstruction;
  - presence or absence of atrial septal restriction (by color and spectral Doppler);
  - evidence of hemodynamic load (right atrial and right ventricular enlargement, diastolic septal flattening associated with right ventricular volume load, increased pulmonary blood flow);
  - evidence of right ventricular or pulmonary artery hypertension by tricuspid regurgitation jet;
  - evidence of right ventricular dysfunction or failure.

### Imaging of abnormal number of pulmonary veins

The subcostal window is ideal for the evaluation of pulmonary veins in infants and young children. The parasternal, subclavicular and suprasternal windows are more useful in older patients. In older patients, the right parasternal and subcostal windows are often better than the left parasternal view for imaging the connection of the right upper pulmonary vein. In both long- and short-axis subcostal views the right upper pulmonary vein can be imaged entering the left atrium superiorly and just posterior to the right superior

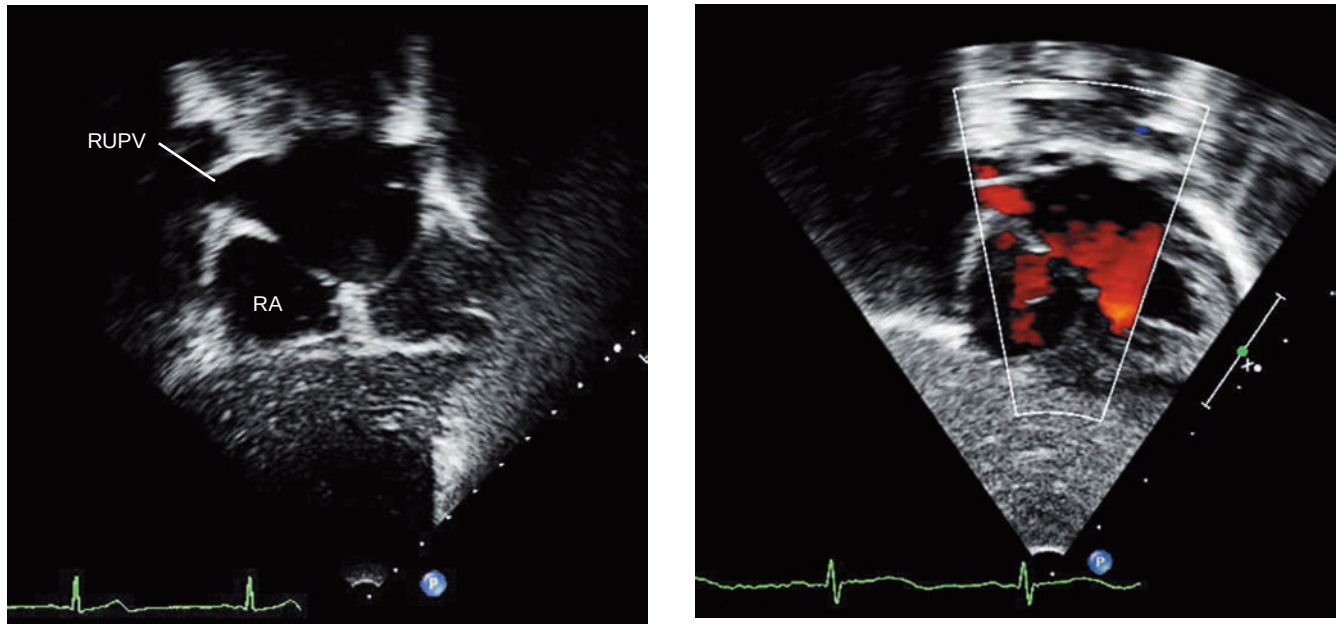


(a) (b)

**Figure 9.13** Normal subxiphoid long-axis view: right upper pulmonary vein. Subxiphoid long-axis view with two-dimensional **(a)** and color Doppler flow mapping **(b)** in this patient with normal pulmonary venous anatomy. RUPV, right upper pulmonary vein; RA, right atrium.

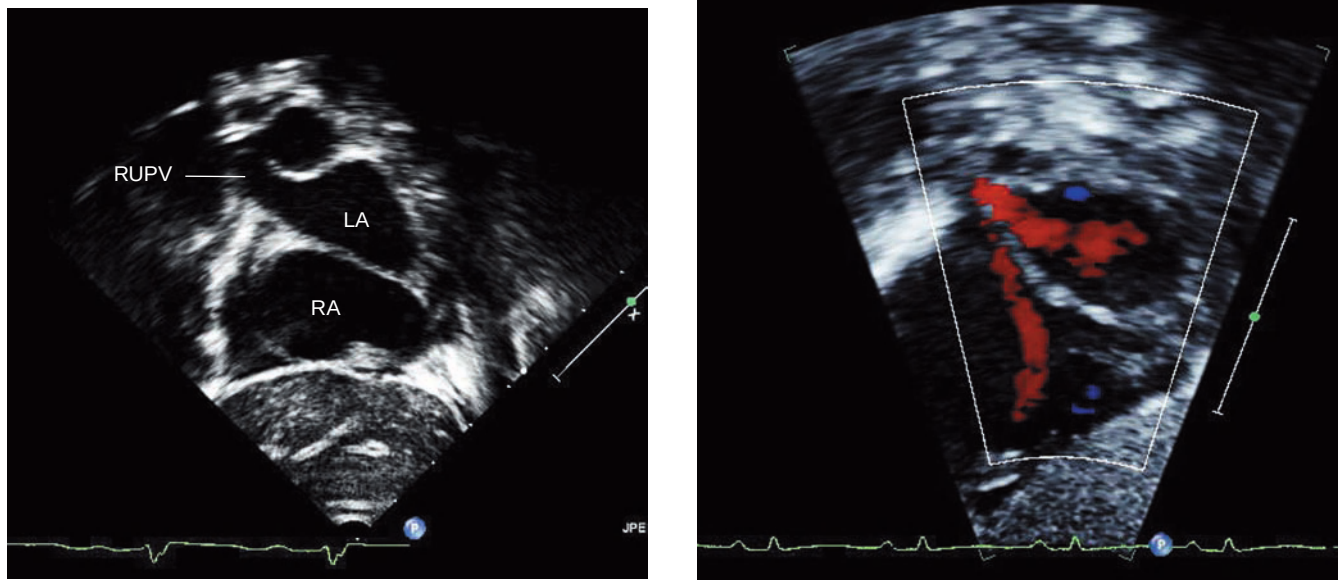


(a) (b)

**Figure 9.14** Normal subxiphoid short-axis view: right upper pulmonary vein. Subxiphoid short-axis view with two-dimensional **(a)** and color Doppler flow mapping **(b)** in this patient with normal pulmonary venous anatomy. The right pulmonary artery is seen in cross-section above the right upper pulmonary vein (RUPV). RA, right atrium; LA, left atrium.

vena cava (Figs 9.13 and 9.14). The suprasternal notch view is particularly helpful in infants, where the so-called "crab view" can frequently demonstrate the drainage of all four pulmonary veins (Fig. 9.1). Transesophageal echocardiography can be helpful in patients with suboptimal transthoracic acoustic windows.

### Imaging of normal pulmonary vein connections with anomalous drainage

The typical acoustic views for establishing this diagnosis are the subxiphoid, apical (Fig. 9.3), and high parasternal short-axis views, all of which can demonstrate the site of connection of the pulmonary veins to the posterior aspect of

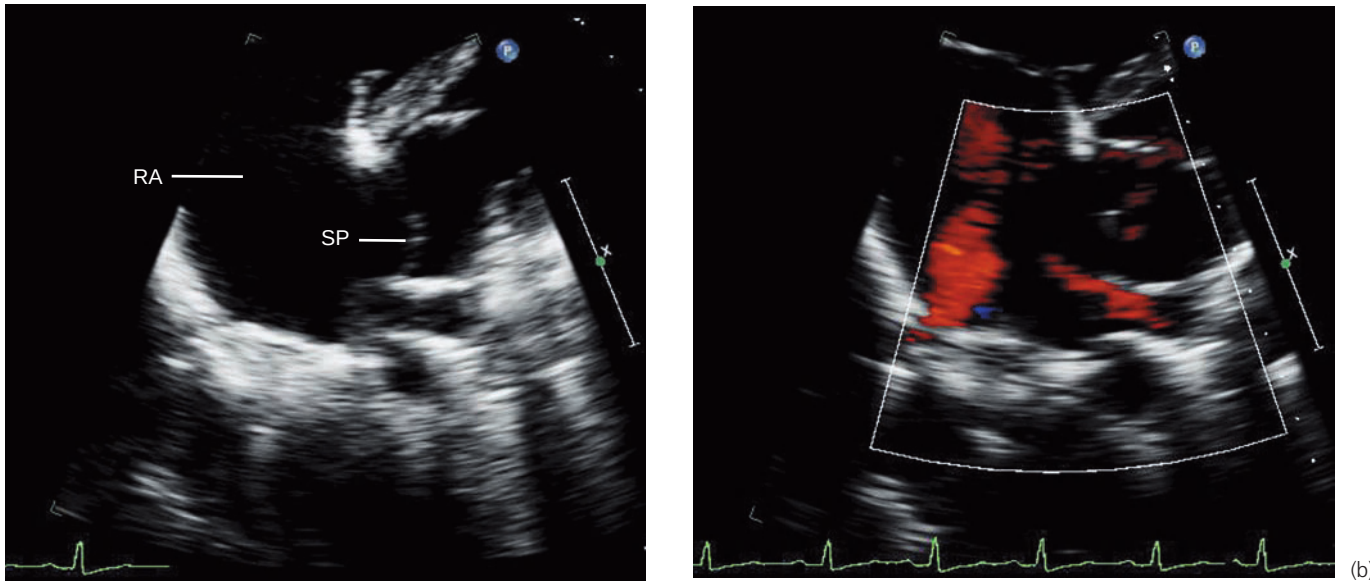


(a) (b)

**Figure 9.15** Total anomalous pulmonary venous drainage: parasternal short-axis view. Parasternal short-axis image with two-dimensional **(a)** and color Doppler flow mapping **(b)** in this patient with severe leftward malattachment of septum primum (SP). Note the normal connection of the pulmonary veins posteriorly, with flow directed to the right atrium (RA).

the anatomic left atrium, as well as establish the plane of septum primum and demonstrate any attachments to the wall of the left atrium. In older patients, a low parasternal short-axis window (Fig. 9.15) is frequently the most helpful, as the views from subxiphoid and suprasternal notch are typically not adequate to demonstrate the position of septum primum. In addition to two-dimensional imaging, color Doppler is critical in demonstrating the anomalous drainage toward the anatomic right atrium. Due to the absence of septum secundum encountered in patients with polysplenia syndrome, establishing the landmarks of the anatomic left atrium is important to distinguish this entity from "ipsilateral" pulmonary veins, in which true anomalous connection of the right pulmonary veins occurs to the anatomic right of the right horn of the sinus venosus. Pulsed- and continuous-wave spectral Doppler may be helpful in demonstrating any restriction to flow of the anomalously draining pulmonary veins due to restricting attachments of septum primum, although this is rarely encountered clinically.

### Imaging of pulmonary vein stenosis

Stenosis of individual pulmonary veins is best imaged from high parasternal windows, and in younger patients from suprasternal and subxiphoid views. Careful evaluation of all four pulmonary veins and their respective orifices is required by two-dimensional imaging. Color Doppler and pulsed- and continuous-wave spectral Doppler techniques are necessary to evaluate the presence and severity of obstruction (Figs 9.4 and 9.16). Normal pulmonary venous Doppler flow patterns are typically laminar, low-velocity and phasic, with a short flow reversal during atrial systole (the retrograde "A"-wave,

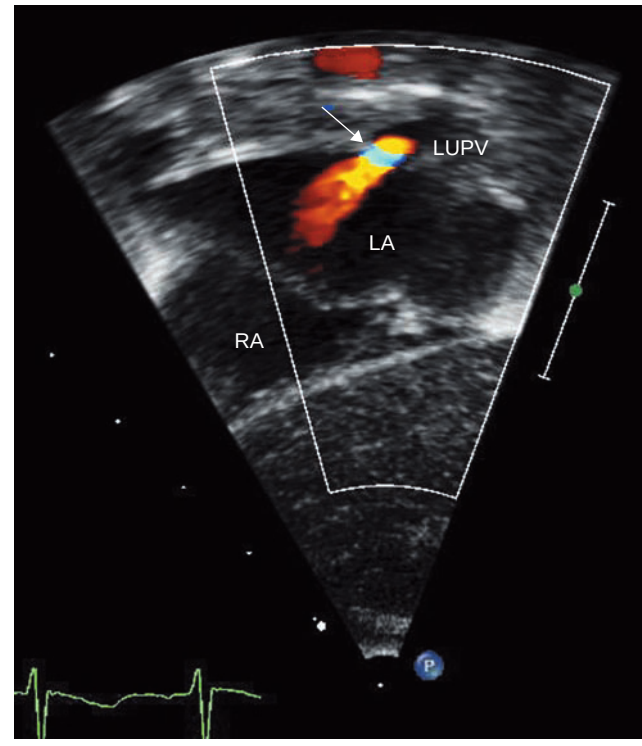


**Figure 9.16** Pulmonary vein stenosis: subxiphoid view. Subxiphoid long-axis image of the left atrium (LA) with color Doppler flow mapping shows discrete stenosis of the left upper pulmonary vein (LUPV) at its junction with the LA (arrow). Note the dilation of the vein proximal to the obstruction. RA, right atrium.

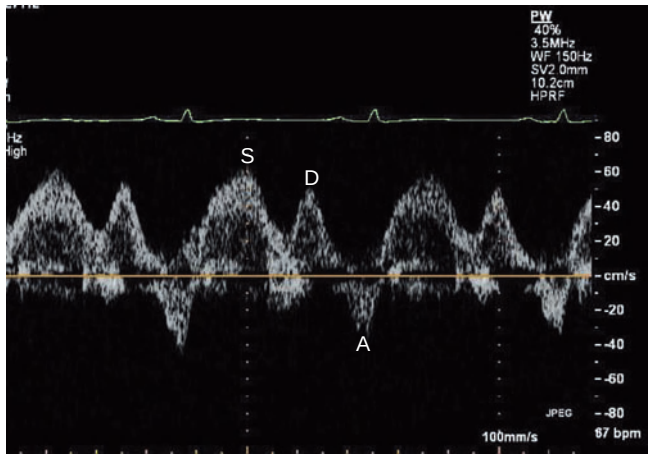


**Figure 9.17** Normal pulmonary vein Doppler pattern. Spectral Doppler pulsed-wave interrogation of the right upper pulmonary vein from apical imaging demonstrates the normal phases of pulmonary venous flow. Flow is laminar and low velocity, with retrograde flow noted in atrial systole (A-wave, A). S, systolic wave; D, diastolic wave.

Fig. 9.17). With increasing degrees of obstruction, the retrograde A-wave is absent, velocities increase and phasicity of flow is lost (Fig. 9.18). In practice, care must be taken to obtain accurate spectral Doppler tracings, which is made more difficult by the fact that the direction of inflow from the pulmonary vein orifices is rarely parallel to the interrogating transducer from any of the usual views; modified or off-axis views are frequently required.

Due to acoustic dropout from lung tissue, typically only stenoses of the distal pulmonary veins and their respective orifices can be imaged by echocardiography; more long-segment stenosis that extends back into the hilum of the lungs is better imaged by other modalities such as cardiac MRI, cardiac computed tomography (CT) or by catheter angiography. Other clues to the diagnosis of pulmonary vein stenosis include evidence from parasternal short-axis views of pulmonary hypertension in response to pulmonary venous inflow obstruction – such as dilation of the right atrium, right ventricle and pulmonary artery – along with systolic flattening of the interventricular septum indicative of right ventricular hypertension.

### Imaging of cor triatriatum

The cor triatriatum membrane is often easily demonstrated from apical views as a curvilinear membrane in the mid-portion of the left atrium, separating the pulmonary venous portion of the left atrium from the true anatomic left atrium (Figs 9.5 and 9.19). The membrane is often thin, and may move throughout the cardiac cycle in response to changes in atrial filling pressures and flows. Parasternal short-axis and subxiphoid imaging is important in demonstrating the relationship of the cor triatriatum membrane to the left atrial appendage, as well as the position of septum primum. Malposition and/or malattachment of septum primum can be easily confused with cor triatriatum from some views; one of the keys in establishing the diagnosis of cor triatriatum is that the left atrial appendage is invariably on the distal or "low-pressure" side of the membrane, and the position of septum primum is often normal. A supramitral stenosing ring, by contrast, is located on the immediate atrial side of the mitral annulus, does not encompass the left atrial appendage, is frequently more immobile, and may cause restriction of mitral leaflet excursion due to valvar attachments.

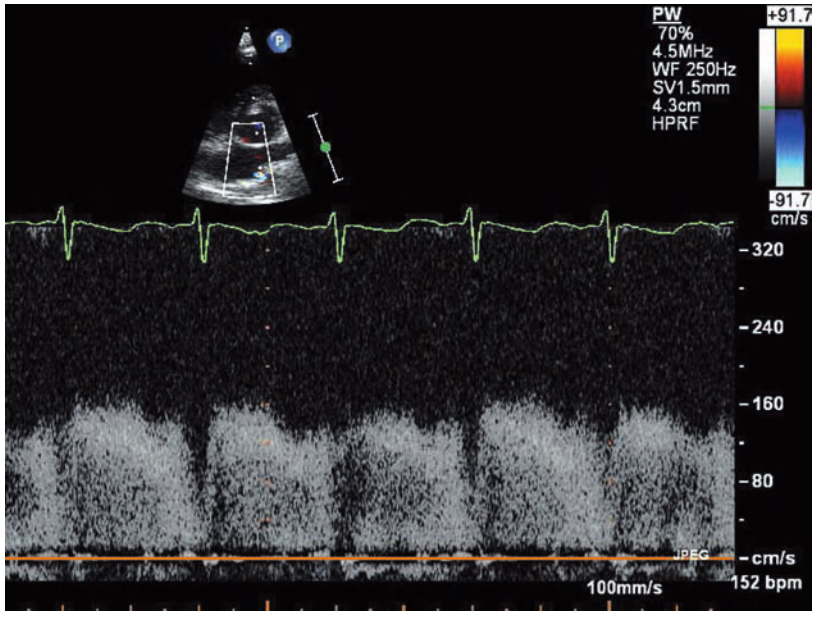


**Figure 9.18** Pulmonary vein stenosis Doppler pattern. Spectral Doppler pulsed-wave interrogation of the left lower pulmonary vein (LLPV) from parasternal short-axis view in a patient with discrete stenosis of the LLPV at its junction with the left atrium. Note the high velocity and increased turbulence of venous flow, loss of phasic variation and absence of the retrograde "A"-wave relative to the normal pattern (see Fig. 9.17).

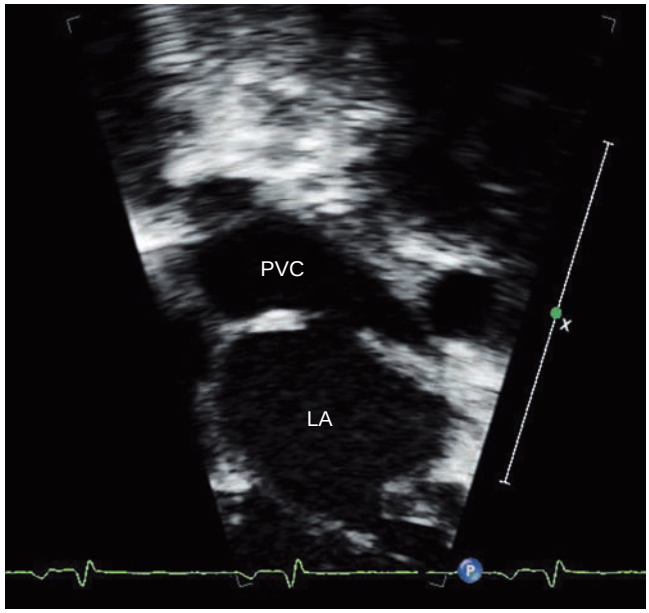


**Figure 9.19** Apical view of "classic" cor triatriatum. Apical two-dimensional image of a typical classic cor triatriatum "membrane" with a large orifice allowing pulmonary venous inflow from the pulmonary venous confluence (PVC) and the true left atrium (LA) (Videoclip 9.3).

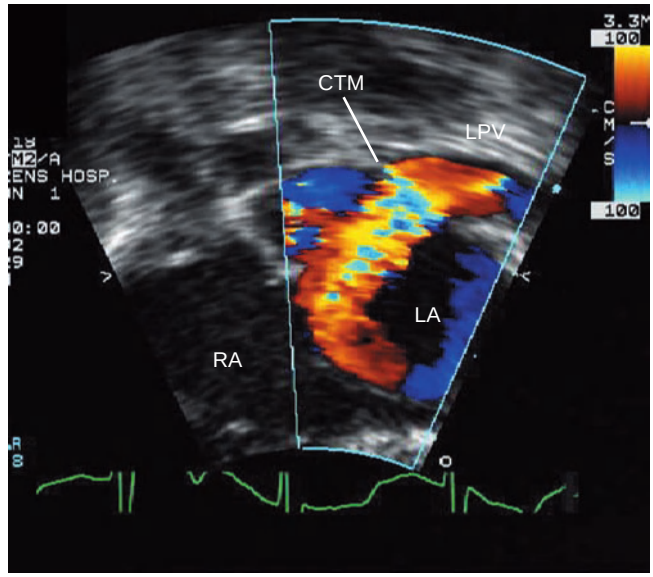


**Figure 9.21** Partial cor triatriatum. Off-axis apical view of the left atrium (LA) with color Doppler flow mapping shows a left-sided partial cor triatriatum, with a "membrane" (CTM) between the confluence of left pulmonary veins (LPV) and the LA. Note the obstruction by color Doppler flow. RA, right atrium.

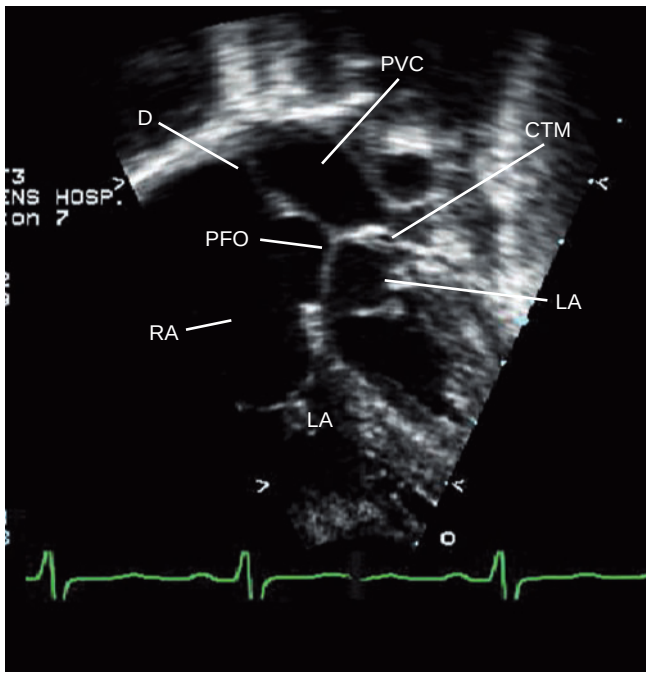


**Figure 9.20** Cor triatriatum with patent foramen ovale (PFO) in hypoplastic left heart syndrome (HLHS). Off-axis apical two-dimensional image in an infant with HLHS and cor triatriatum. Note the defect (D) between the pulmonary venous confluence (PVC) and the right atrium (RA) superiorly, as well as the flap of septum primum inferiorly that allows a patent foramen ovale communication with the true left atrium (LA). CTM, cor triatriatum membrane.

Careful evaluation of the atrial septum from subxiphoid and parasternal short-axis views is necessary to elucidate the nature of an interatrial communication, if present (Fig. 9.20). In addition, the course and drainage of each of the pulmonary veins should be evaluated, because partial forms of cor triatriatum can occur (Fig. 9.21), as well as anomalous pulmonary venous connection in some variants (Fig. 9.6) [31,32]. The presence or absence of obstruction across the cor membrane is often best confirmed from the apical view, even in older patients, as the flow jet is often directed toward the mitral valve (Fig. 9.22). Color Doppler interrogation along with pulsed- and continuous-wave spectral Doppler can provide information regarding direction of flow and degree of obstruction, along with estimates of the peak and mean pressure gradient across a stenotic orifice.

### Imaging of PAPVC

The diagnosis of PAPVC is established through careful assessment of the pulmonary venous connections as well as the systemic venous anatomy. The systemic vein distal to the connection of the pulmonary vein is often dilated, which is frequently the first clue that PAPVC may be present (Figs 9.23 and 9.24). Anomalous connection of pulmonary veins to the innominate vein or superior vena cava (SVC) is best evaluated from high parasternal views (Fig. 9.8), both short- and long-axis, as well as the suprasternal notch; in infants and young children, PAPVC may be imaged even from subcostal windows. Care must be taken to distinguish normal

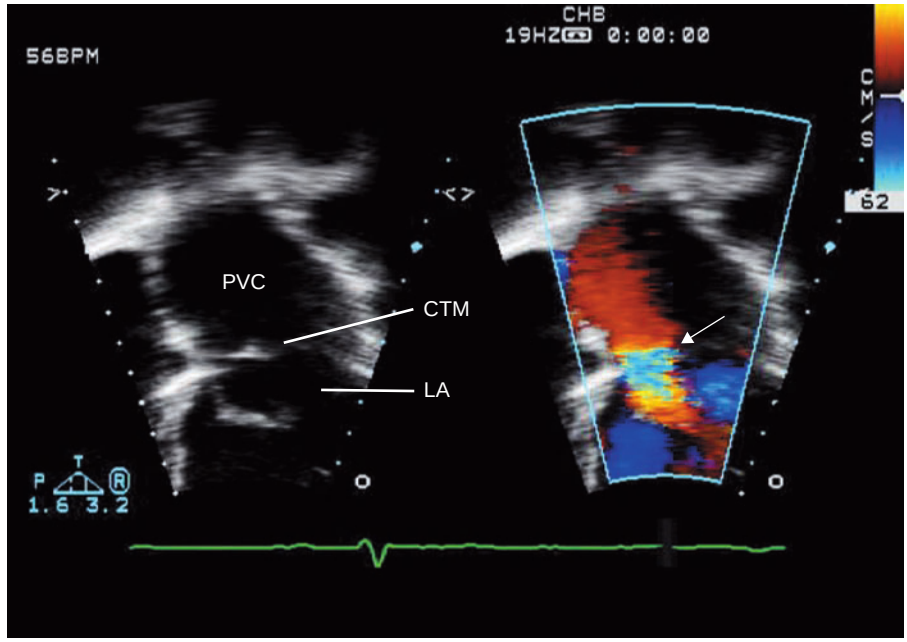


**Figure 9.22** Classic cor triatriatum with obstruction. Apical view with two-dimensional and color Doppler mapping shows an example of a more "distal" cor triatriatum membrane (CTM) in an adult patient with pulmonary hypertension. The orifice that allows pulmonary venous inflow is medial in this case, with flow acceleration by color Doppler (arrow). PVC, pulmonary venous confluence; LA, left atrium.

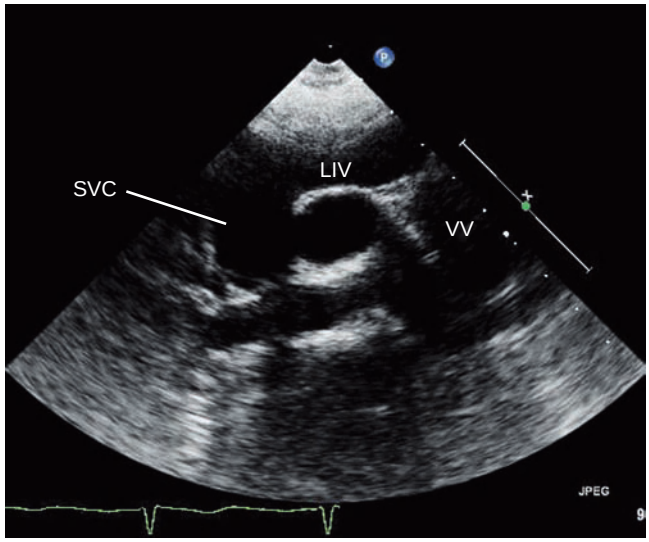


**Figure 9.23** Partial anomalous pulmonary venous connection (PAPVC): left upper pulmonary vein to innominate vein. Suprasternal notch short-axis two-dimensional image in this patient with PAPVC of the left upper pulmonary vein to the innominate vein shows the dilated left innominate vein (LIV) and right superior vena cava (SVC). VV, vertical vein. (Videoclip 9.1).

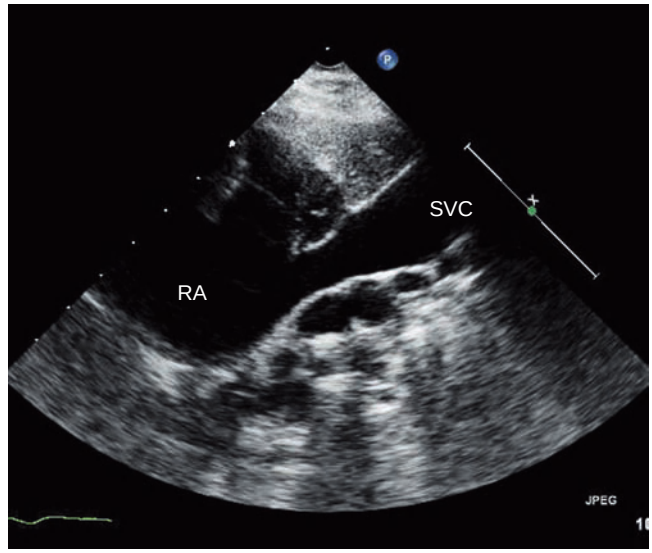


**Figure 9.24** Partial anomalous pulmonary venous connection (PAPVC): dilated superior vena cava (SVC). High right parasternal long-axis image in this patient with PAPVC of the left pulmonary veins to the innominate vein demonstrates marked dilation of the SVC, consistent with significantly increased venous return through this vessel. RA, right atrium.

systemic venous structures (e.g., azygous vein, superior intercostal vein) from PAPVC; helpful clues in establishing the diagnosis include the absence of normally connected pulmonary veins to the left atrium (Fig. 9.25), dilation of the innominate vein and SVC, and evidence of right ventricular volume overload by diastolic septal flattening (Fig. 9.26).

PAPVC to the coronary sinus is best imaged from subcostal (particularly in infants and children) and parasternal views, but also from apical views (Fig. 9.27). The coronary sinus is typically severely dilated, necessitating an evaluation of the presence or absence of a persistent left SVC.

PAPVC to the IVC, which usually establishes the diagnosis of scimitar syndrome, is most easily imaged from the subcostal window. Both short- and long-axis imaging of the IVC is naturally best accomplished through this window, and frequently two-dimensional (2D) and color Doppler show

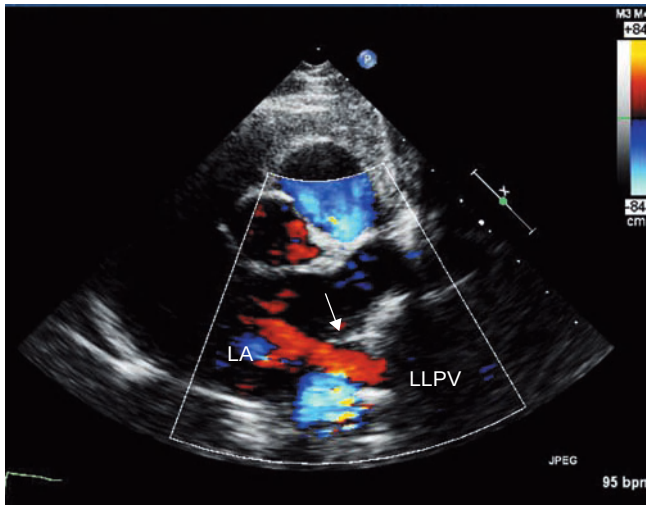


**Figure 9.25** Partial anomalous pulmonary venous connection (PAPVC): left atrium. Left parasternal short-axis image of the left atrium with color Doppler flow mapping in this patient with PAPVC of the left upper pulmonary vein to the innominate vein. Only a single left pulmonary vein (left lower pulmonary vein, LLPV) is noted connecting normally to the left atrium (LA), with absence of a vessel where the left upper pulmonary vein normally connects (arrow).

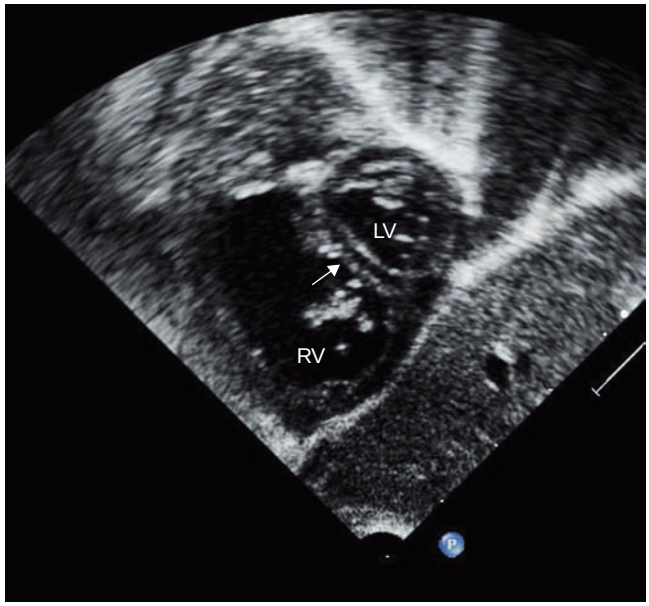


**Figure 9.26** Partial anomalous pulmonary venous connection (PAPVC): right heart dilation. Subxiphoid short-axis view of the ventricles in this patient with PAPVC of the left pulmonary veins to the innominate vein demonstrates significant right ventricular (RV) dilation and diastolic septal flattening (arrow). LV, left ventricle.

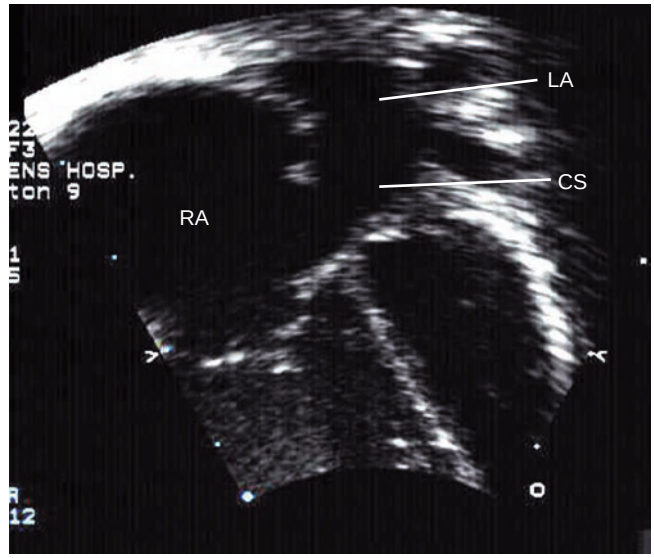


**Figure 9.27** Partial anomalous pulmonary venous connection (PAPVC): left pulmonary veins to coronary sinus. Apical two-dimensional view in this patient with PAPVC of the left pulmonary veins to the coronary sinus (CS) shows a severely dilated coronary sinus ostium, which was the first clue to the diagnosis in this patient. Note the dilation of the right-sided heart structures relative to the left. RA, right atrium; LA, left atrium.

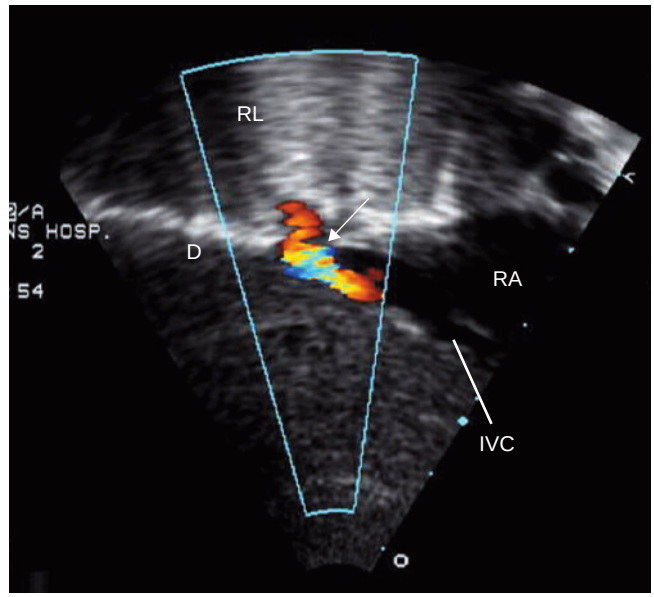


**Figure 9.28** Partial anomalous pulmonary venous connection (PAPVC): scimitar syndrome. Subxiphoid image with color Doppler flow mapping in this patient with scimitar syndrome demonstrates PAPVC of right pulmonary veins to the inferior vena cava (IVC) at its junction with the right atrium (RA). Note the mild flow acceleration by color Doppler (arrow). D, diaphragm; RL, right lung (Videoclip 9.4).

veins anomalously connecting to the IVC just proximal to the junction with the right atrium (Fig. 9.28). Careful evaluation with pulsed- and continuous-wave spectral Doppler can establish the presence or absence of stenosis of the anomalously connecting pulmonary veins. The rightward border of the left atrium typically has an abnormally "blunted" contour consistent with the diagnosis. Abnormal cardiac position (mesocardia or dextrocardia) and hypoplasia of the right pulmonary artery are often further clues to the diagnosis.

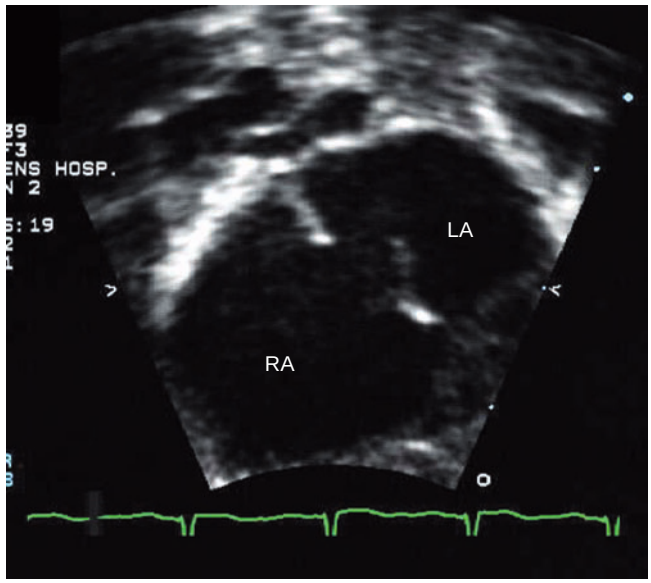


**Figure 9.29** Total anomalous pulmonary venous connection (TAPVC): atrial septum, apical view. Apical imaging shows septum primum deviated far into the left atrium in this patient with supracardiac TAPVC. Note the hypoplasia of the left atrium (LA) relative to the right atrium (RA) and the smooth contour of the superior aspect of the left atrium consistent with absent normal pulmonary venous connections.

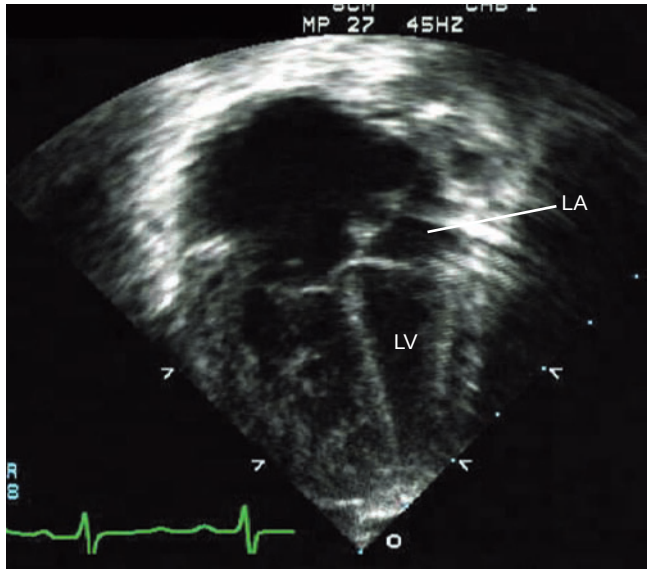


**Figure 9.31** Total anomalous pulmonary venous connection (TAPVC): left heart hypoplasia. Apical view in this patient with supracardiac TAPVC demonstrates the relative hypoplasia of the left atrium (LA), mitral valve and left ventricle (LV) relative to the corresponding right heart structures.

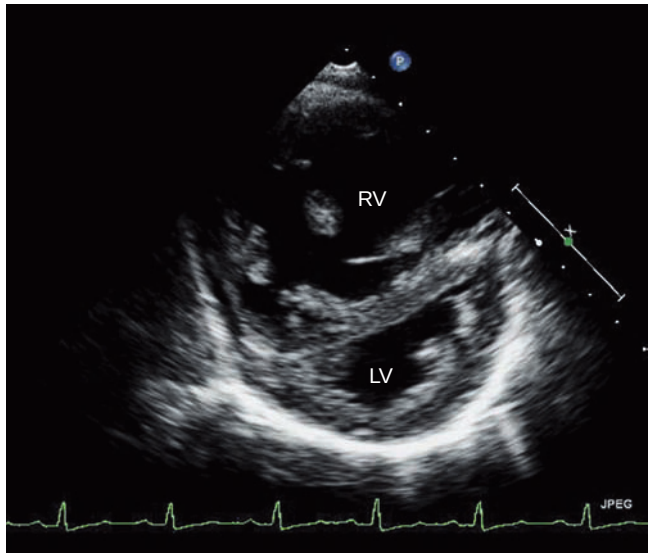


**Figure 9.30** Total anomalous pulmonary venous connection (TAPVC): right ventricular hypertension. Left parasternal short-axis image of the ventricles shows the dilation of the right ventricle (RV) relative to the left ventricle (LV), as well as the flat septal position in systole consistent with systemic right ventricular pressures in this patient with TAPVC.

## Imaging of TAPVC

As with PAPVC, the echocardiographic assessment of TAPVC requires a careful step-by-step analysis of the anatomy from multiple imaging views. The right atrium is frequently dilated, and the atrial septum bows into the left atrium (Fig. 9.29). The right ventricle is dilated, and in addition to volume overload, right ventricular hypertension is often present; the ventricular septum often bows into the left ventricle (Fig. 9.30). Concomitantly, the left-sided heart structures are frequently mildly hypoplastic (although rarely too hypoplastic to support a two-ventricle circulation for isolated forms of TAVPC; Fig. 9.31). The first clue to the diagnosis is the inability to image the pulmonary veins draining into the left atrium, along with a hypoplastic left atrial chamber. Typically the pulmonary venous confluence is noted as an echo-free space behind the left atrium.

The challenge with cases of TAPVC is to image each of the four major pulmonary veins and to determine the size, course and drainage of each of these veins. This is particularly important as "mixed" forms of TAPVC occur and can significantly complicate the surgical management. The size of the individual pulmonary veins has been determined to be an independent risk factor for the development of recurrent obstruction in TAPVC following surgical repair [33], and thus this should be one of the goals of the evaluation. The most helpful views are typically the subxiphoid, parasternal and suprasternal notch views; evaluation includes both 2D imaging and color Doppler flow mapping. The size, orientation (horizontal or vertical) and position of the pulmonary venous confluence relative to the left atrial chamber represent crucial information for the surgeon, as well as the course and ultimate connection of the venous channel draining the pulmonary venous blood into the systemic circulation.

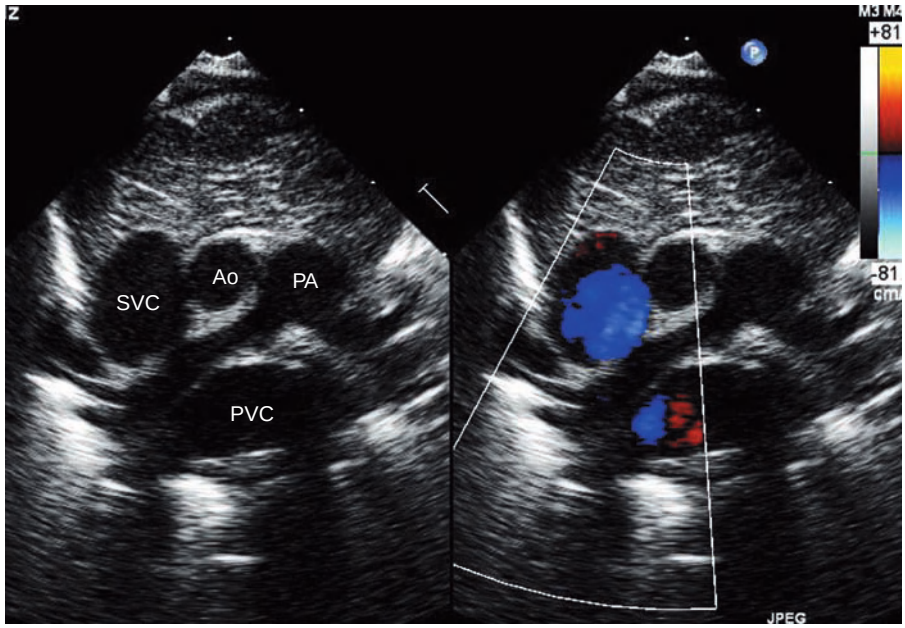


**Figure 9.32** Supracardiac total anomalous pulmonary venous connection (TAPVC): high parasternal short-axis view. High parasternal imaging in the short axis in this patient with supracardiac TAPVC shows the severely dilated right superior vena cava (SVC), the first clue to the diagnosis from this view. Note the pulmonary venous confluence (PVC) appears relatively normally positioned in this plane posterior to the pulmonary artery bifurcation. AO, ascending aorta; PA, pulmonary artery.

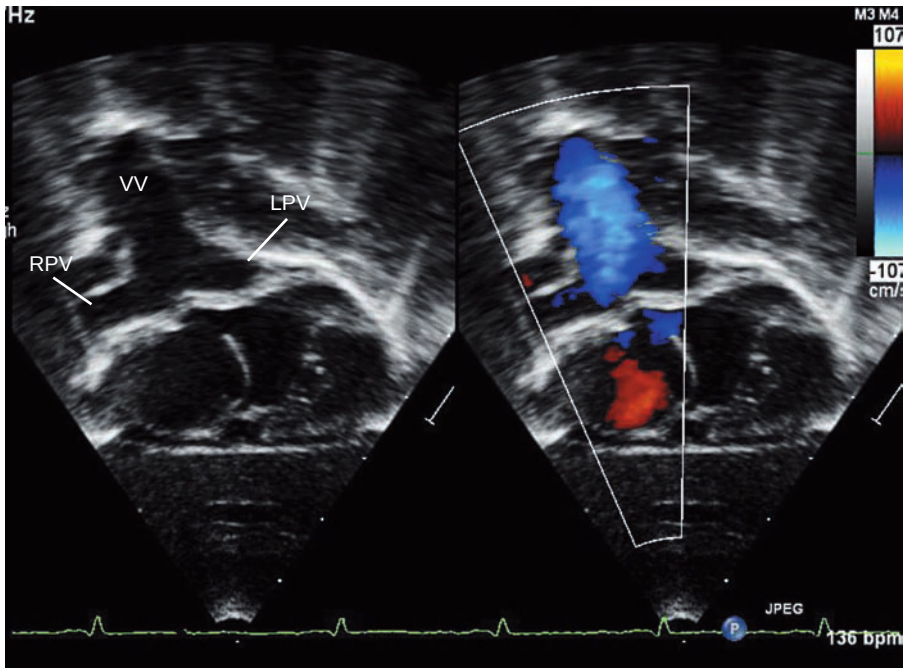


**Figure 9.33** Supracardiac total anomalous pulmonary venous connection (TAPVC): subxiphoid long-axis view. Subxiphoid two-dimensional and color Doppler flow mapping in this patient with supracardiac TAPVC shows flow from both right (RPV) and left pulmonary veins (LPV) into a large, superiorly draining vertical vein (VV). Note the obligate right-to-left shunt across the secundum atrial septal defect.

With supracardiac TAPVC, the vertical vein is frequently imaged to the left of the midline, with venous flow ascending to join most commonly into the leftward aspect of the innominate vein. The innominate vein and SVC are usually severely dilated (Fig. 9.32). Despite the venous connections that are typically high in the chest, the individual pulmonary veins and location and course of the vertical vein in supracardiac TAPVC are often well imaged from subxiphoid views in infants (Fig. 9.33). The connection between the vertical vein and the systemic venous system is frequently easily imaged from high parasternal short-axis and suprasternal notch views, with color Doppler flow mapping important to ascertain the direction of venous flow and the presence of any degree of obstruction (Figs 9.10 and 9.34). The vertical vein most commonly ascends anterior to both the left pulmonary artery and the left mainstem bronchus; however, this vessel may pass *between* the left pulmonary artery and the bronchus, which results in extrinsic compression of the vessel and obstruction to pulmonary venous return (Fig. 9.35). In addition to color Doppler, pulsed- and continuous-wave spectral Doppler from high parasternal and suprasternal notch views are crucial in demonstrating the

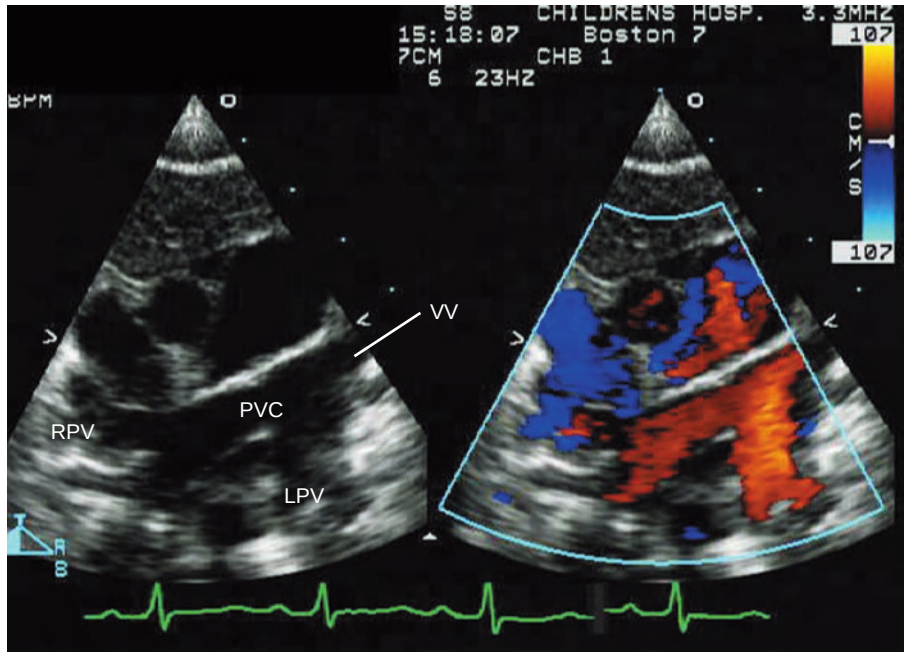


**Figure 9.34** Total anomalous pulmonary venous connection (TAPVC): supracardiac to the left innominate vein. Parasternal short-axis imaging in this patient with TAPVC via a left-sided vertical vein (VV) to the left innominate vein. Note the horizontal configuration of the pulmonary venous confluence (PVC). RPV, right pulmonary veins; LPV, left pulmonary veins.

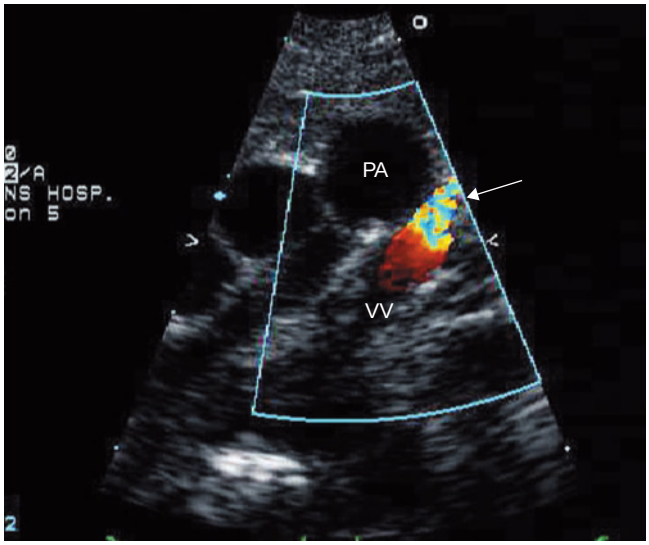


**Figure 9.35** Total anomalous pulmonary venous connection (TAPVC): supracardiac to the left innominate vein. Parasternal short-axis imaging with color Doppler flow mapping in a patient with supracardiac TAPVC and obstruction of the left-sided vertical vein (VV) as it courses in between the left pulmonary artery and the left mainstem bronchus (arrow). This patient had a mean gradient of ~14 mm Hg at this site by Doppler and suprasystemic right ventricular pressure. PA, pulmonary artery (Videoclip 9.5).

presence and severity of obstruction; severe obstruction to pulmonary venous flow is considered an urgent if not emergent indication for surgical repair. Other evidence of pulmonary hypertension, such as dilation of right-heart structures and systolic flattening of the interventricular septum as noted from short-axis views, is frequently present (Fig. 9.30). Other forms of supracardiac connections that may be present include right-sided connections to the right SVC or azygous vein (Fig. 9.36); obstruction can occur in these forms as well, if the ascending vertical vein passes between the right pulmonary artery and the trachea or right mainstem bronchus.

"Cardiac" TAPVC is typically associated with a severely dilated coronary sinus, which can be noted from multiple views along the posterior left atrioventricular groove; this structure is best imaged from subcostal (particularly in infants and children) and parasternal views (Figs 9.11, 9.37 and 9.38), but also easily noted from apical views even in larger adult patients (Fig. 9.39). Two-dimensional and color Doppler imaging of each of the pulmonary veins is best performed from high parasternal short-axis views, suprasternal notch imaging and subxiphoid long-axis imaging when possible (Fig. 9.40). Other causes of a dilated coronary sinus include a persistent left SVC and partial anomalous pulmonary venous connection to the coronary sinus, and these must be confirmed or excluded. The orifice of the coronary sinus is typically quite large. Obstruction to pulmonary venous flow in this form of TAPVC, either at the venous channel draining into the coronary sinus or at the level of the coronary sinus ostium, is rare, but can be excluded with color and pulsed-Doppler assessment of these structures (Fig. 9.41). As with other forms of TAPVC, other evidence of the presence of this defect includes dilation of the right-heart structures and evidence of some degree of pulmonary and right ventricular hypertension.

Infradiaphragmatic TAPVC is associated with a high incidence of obstruction to pulmonary venous drainage. The pulmonary venous confluence is often positioned posterior to the left atrium, with a draining vertical vein that descends through the esophageal hiatus of the diaphragm (just anterior to the esophagus; Fig. 9.12) to connect with the portal

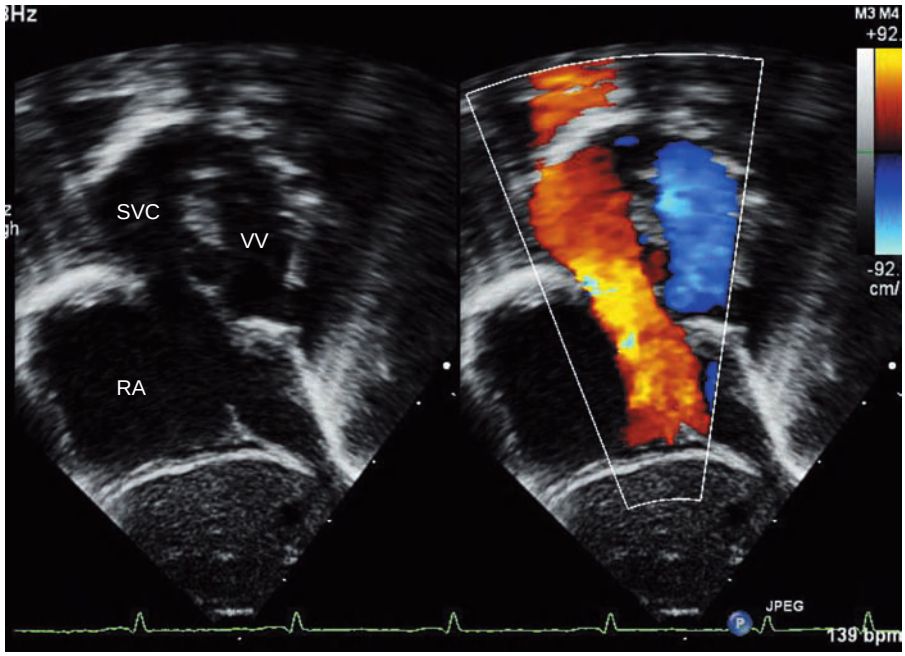


**Figure 9.36** Total anomalous pulmonary venous connection (TAPVC): supracardiac to the right superior vena cava. Subxiphoid short-axis two-dimensional and color Doppler flow mapping in this patient with TAPVC to the right superior vena cava (SVC) shows the large vertical vein (VV) that courses posterior to the right pulmonary artery and mainstem bronchus, to arch and join the right SVC at the level of the azygous vein. RA, right atrium (Videoclip 9.6).

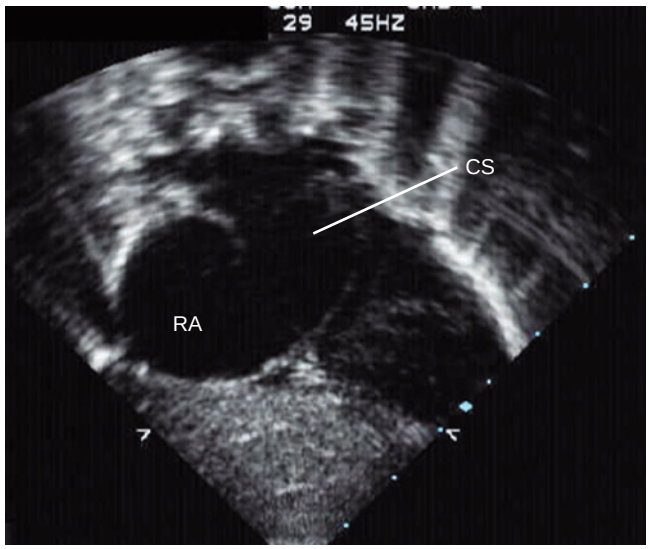


**Figure 9.37** Cardiac total anomalous pulmonary venous connection (TAPVC): subxiphoid long-axis view. Subxiphoid long-axis view of the atria in this patient with TAPVC to the coronary sinus (CS) shows a severely dilated CS, often the first indication that this type of TAPVC may be present. RA, right atrium.

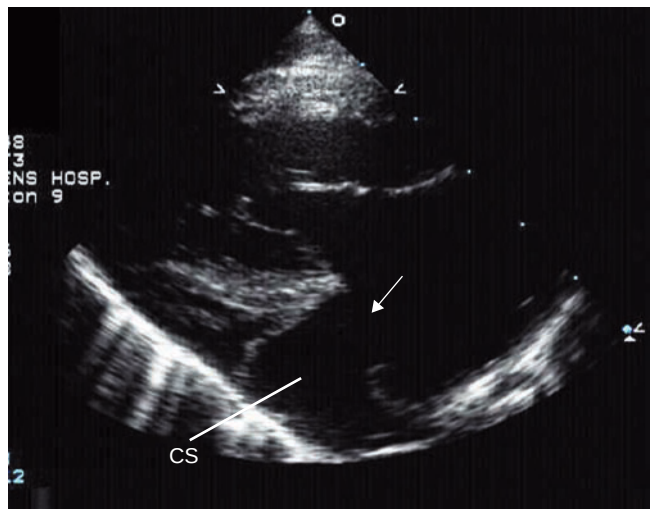


**Figure 9.38** Cardiac total anomalous pulmonary venous connection (TAPVC): parasternal long-axis view. Parasternal long-axis two-dimensional imaging in this patient with TAPVC to the coronary sinus (CS) shows a severely dilated CS and coronary sinus ostium (arrow).

venous system (most common), the ductus venosus, hepatic vein or IVC (Fig. 9.42). The individual veins joining the confluence may be imaged from high parasternal and suprasternal notch views (Fig. 9.43), although subxiphoid imaging is crucial in demonstrating the location, size and course of the draining vertical vein, as well as the ultimate connection(s) to the systemic venous system below the diaphragm. Careful color, pulsed-wave and continuous-wave Doppler evaluation are mainstays in determining the site of connection as well as the presence and degree of venous obstruction. Obstruction most often occurs at the junction between the vertical vein and the portal vein, ductus venosus or hepatic vein, and Doppler tracings are characterized by an increase in absolute venous velocities and a loss of phasicity (Fig. 9.44). Pulmonary hypertension in this setting is the rule and is often severe; evaluation of other structures such as the patent ductus arteriosus (if present) can assist in assessing the degree of pulmonary hypertension (Fig. 9.45).

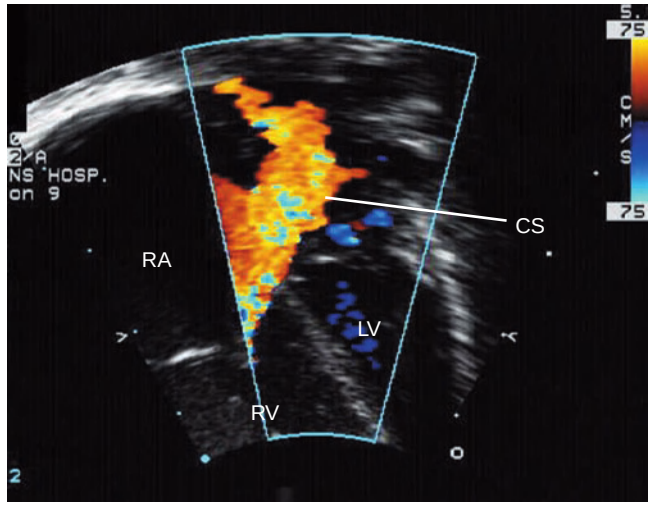


**Figure 9.39** Cardiac total anomalous pulmonary venous connection (TAPVC): apical view. Apical view with color Doppler flow mapping in this patient with TAPVC to the coronary sinus (CS) demonstrates all pulmonary venous flow directed via the dilated CS into the right atrium (RA). RV, right ventricle; LV, left ventricle.

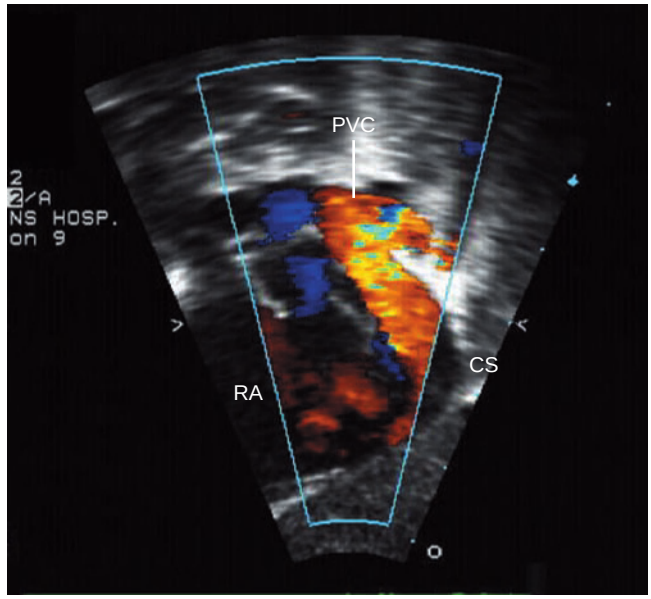


**Figure 9.40** Cardiac total anomalous pulmonary venous connection (TAPVC): subxiphoid short-axis view. Subxiphoid short-axis view in this patient with TAPVC to the coronary sinus (CS) demonstrates the typical "whale's tail" of pulmonary venous flow directed into the right atrium via the severely dilated CS. PVC, pulmonary venous confluence; RA, right atrium.

As the interatrial communication is life-sustaining in TAPVC, a thorough evaluation of the atrial septum is necessary to determine the type and size of the communication, and the presence or absence of obstruction to flow. The most helpful views of the atrial septum are obtained from subxiphoid long- and short-axis views, as the plane of the atrial septum is typically en face to the interrogating probe.

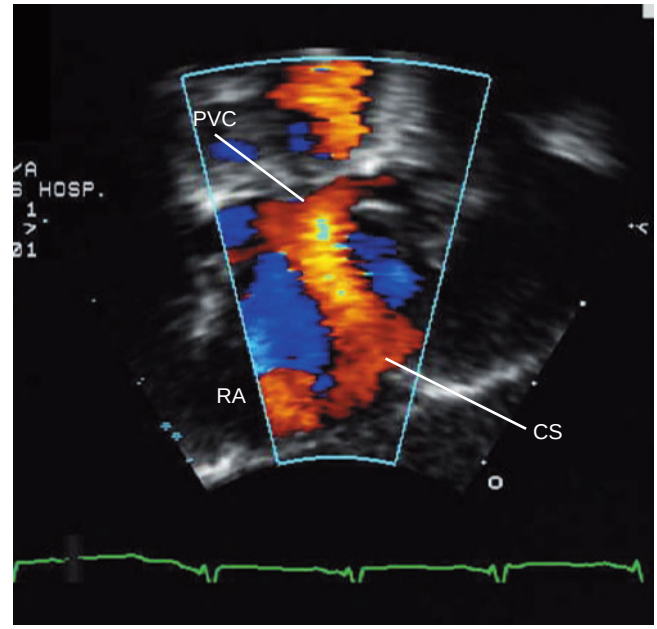


**Figure 9.41** Cardiac total anomalous pulmonary venous connection (TAPVC): subxiphoid long-axis view with obstruction. Subxiphoid long-axis imaging in this patient with TAPVC to the coronary sinus (CS) shows mild flow acceleration in the connecting vein between the pulmonary venous confluence (PVC) and the CS. The mean gradient in this patient as estimated by spectral Doppler was only ~3 mm Hg. RA, right atrium.

Parasternal short-axis views are also helpful; color Doppler and spectral Doppler techniques are helpful in determining the size of the flow jet and any degree of obstruction to flow.

## Prenatal assessment

Due to the small amount of pulmonary blood flow and resulting pulmonary venous return to the left heart in utero (roughly 7% of fetal combined ventricular output [34]), the diagnosis of pulmonary venous anomalies by fetal echocardiography is challenging, particularly partial anomalous pulmonary venous return, which is infrequently diagnosed in utero [35,36]. Indirect clues that suggest the diagnosis of partial or total anomalous pulmonary venous connections, such as dilation of the right-heart structures, disproportion of the great arteries or mild hypoplasia of the left atrium [37], should prompt an evaluation of pulmonary venous return that is as complete as possible, although such clues are nonspecific and can also be associated with coarctation of the aorta, other left-sided obstructive lesions or arteriovenous malformation. Visualization of a venous confluence behind the left atrium, as well as the visualization of a vertical vein, are common findings associated with fetal cases of TAPVC; obstruction to pulmonary venous flow has also been reported [36]. Findings suggestive of scimitar syndrome with PAPVC include dextrocardia and hypoplasia of the right pulmonary artery [36]. Some diagnoses, such as malposition of the atrial septum with anomalous pulmonary venous drainage, are

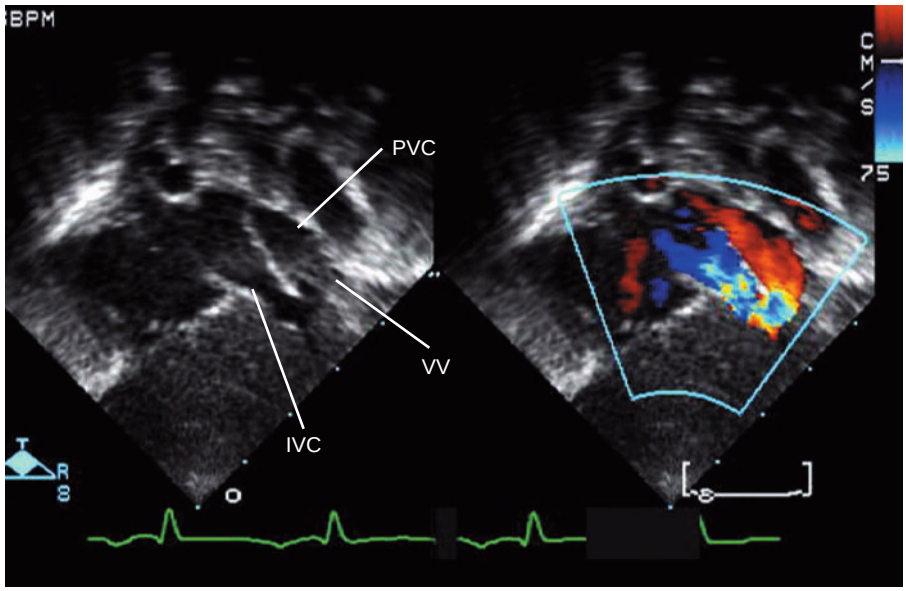


**Figure 9.42** Infradiaphragmatic total anomalous pulmonary venous return (TAPVC): subxiphoid short-axis view. The subxiphoid short-axis view with two-dimensional and color Doppler flow mapping in this patient with infradiaphragmatic TAPVC shows the vertical vein (VV) descending just below the level of the diaphragm, and then coursing directly anteriorly to drain directly into the inferior vena cava (IVC). Note the color flow acceleration at the connection to the IVC. PVC, pulmonary venous confluence.

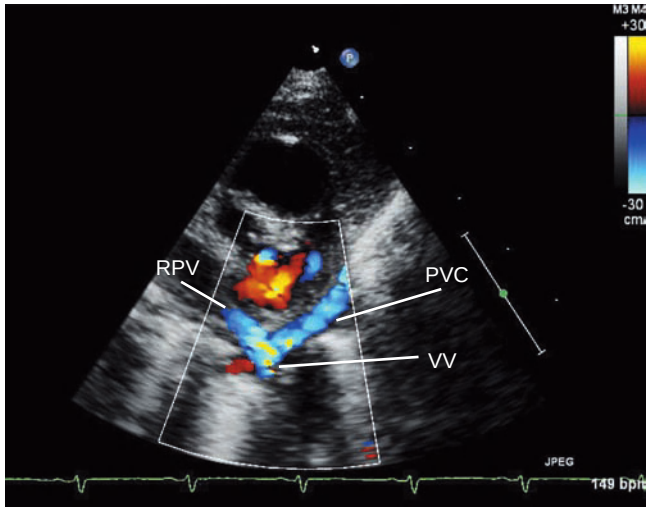


**Figure 9.43** Infradiaphragmatic total anomalous pulmonary venous connection (TAPVC): parasternal short-axis view. A parasternal short-axis view with color Doppler flow mapping in this patient with infradiaphragmatic TAPVC shows right (RPV) and left (LPV) pulmonary veins coursing posteriorly to meet and descend via a vertical vein (VV) below the diaphragm.

extremely difficult to establish in utero due to the normal deviation of septum primum into the left atrium, although other findings suggestive of heterotaxy syndrome with polysplenia would heighten the suspicion of this potential diagnosis. Pulmonary veins are seen best from the fetal 4-chamber view as well as short-axis views; color and pulsed-wave Doppler mapping is of great utility in confirming the presence of normal or abnormal pulmonary venous drainage.

## Imaging of the adult

The diagnosis of pulmonary venous anomalies in the adult patient is difficult due to technical limitations. Adequate 2D imaging and Doppler signals are difficult to obtain from subcostal and suprasternal views due to increased distance from the probe. For larger patients, the high parasternal short-axis view is often the most helpful, which allows assessment of the atrial septum as well as the lower pulmonary veins and frequently the left upper pulmonary vein as well. The right upper pulmonary vein is difficult to image from this vantage point in larger patients, although the high right sternal border view is often helpful in these situations to exclude a sinus venosus defect. Indirect evidence of anomalous pulmonary venous drainage may be seen in even the largest patients, including enlargement of the right heart chambers and diastolic flattening of the interventricular septum, typically from parasternal short-axis views.

Transesophageal echocardiography provides an excellent alternative in these situations; TEE allows for clear imaging of the atria, atrial septum, pulmonary veins and the venae cavae from multiple imaging planes. Nearly all pulmonary venous anomalies, including cor triatriatum, sinus venosus defect and partial anomalous pulmonary venous return, may be readily diagnosed by TEE [38–40]. A potential drawback, however, is the inability to image completely the connections between the pulmonary and systemic venous system, which may be high in the mediastinum or below the diaphragm. Cardiac MRI is an excellent alternative to TEE in children and adults with suspected pulmonary venous anomalies, allowing clear visualization of the atria, atrial septum and pulmonary and systemic veins, and accurate quantification of right ventricular size, function and pulmonary to systemic venous flow ratio [30,41,42].

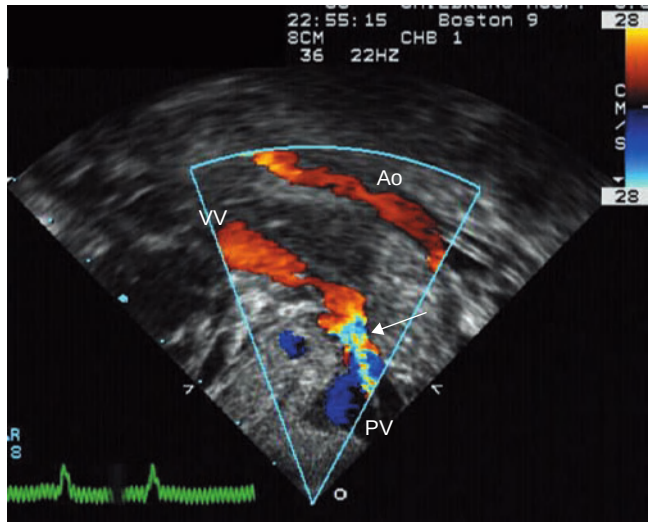


(a)

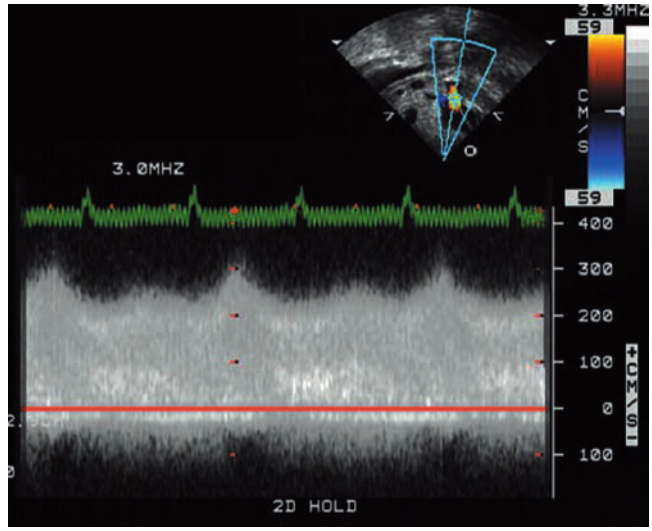


(b)

**Figure 9.44** Infradiaphragmatic total anomalous pulmonary venous connection (TAPVC) with obstruction. **(a)** Subxiphoid short-axis image with color Doppler flow mapping in this patient with infradiaphragmatic TAPVC shows severe obstruction of the vertical vein (VV) at the site of entry (arrow) into the portal vein (PV), which is markedly dilated. **(b)** Continuous-wave spectral Doppler tracing from the same patient, demonstrating continuous high-velocity flow with complete loss of phasic variation. The mean gradient estimate across this region of obstruction was ~28 mm Hg. AO, descending aorta.

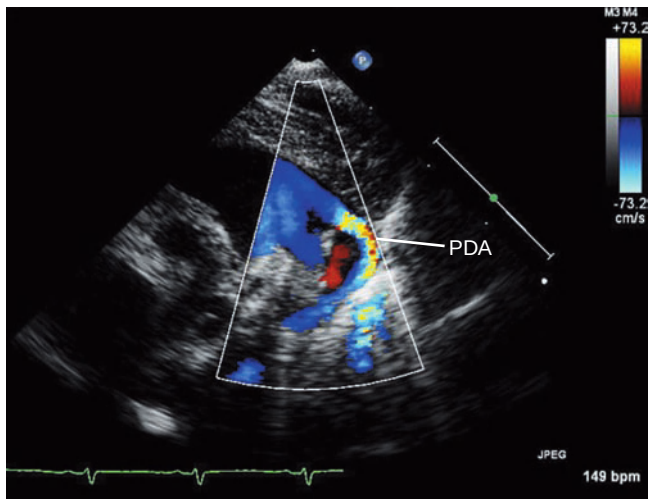


(a)

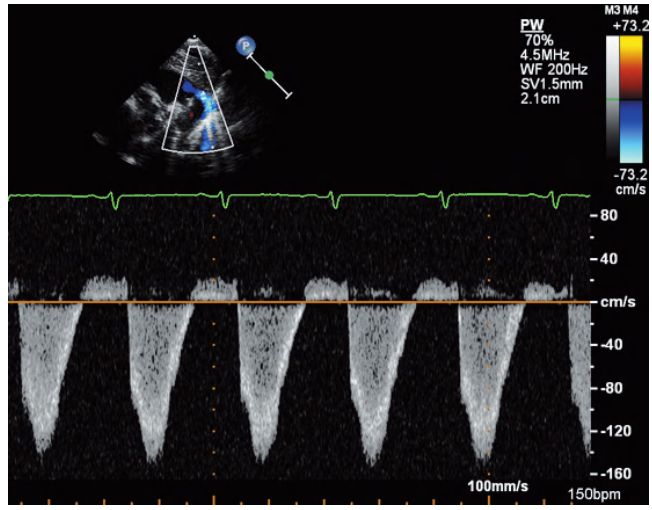


(b)

**Figure 9.45** Total anomalous pulmonary venous connection (TAPVC): pulmonary hypertension with obstructed veins. **(a)** Parasternal imaging with color flow Doppler shows the patent ductus arteriosus (PDA) in this patient with obstructed infradiaphragmatic TAPVC. **(b)** Spectral Doppler pattern of the ductus arteriosus in the same patient. Pulmonary artery pressure is suprasystemic in systole (below the baseline).

## Echocardiographic guidance of transcatheter and surgical treatment

The treatment of the vast majority of pulmonary venous anomalies, where treatment is indicated, is surgical. For congenital or acquired pulmonary vein stenosis, transcatheter techniques have been described, with treatment options varying from simple balloon dilation [43,44], to cutting balloon dilation [45,46], stent placement [47,48] and even drug-eluting stents. Although such transcatheter interventions have proven helpful in acutely relieving obstruction in congenital pulmonary vein stenosis, the disease tends to be progressive and frequently recurs (Fig. 9.46). Surgical intervention, similarly, has been largely unsuccessful in the long term, although more recently the "sutureless" operative technique has had perhaps more success at reducing the recurrence of pulmonary vein stenosis [49]. As this disease tends to affect the young infant and the intervention is typically a vascular procedure, intraprocedural imaging in the catheterization laboratory is typically by angiography, and echocardiography has been more often used for following the status of the pulmonary veins noninvasively in follow-up after the procedure, along with the degree of right

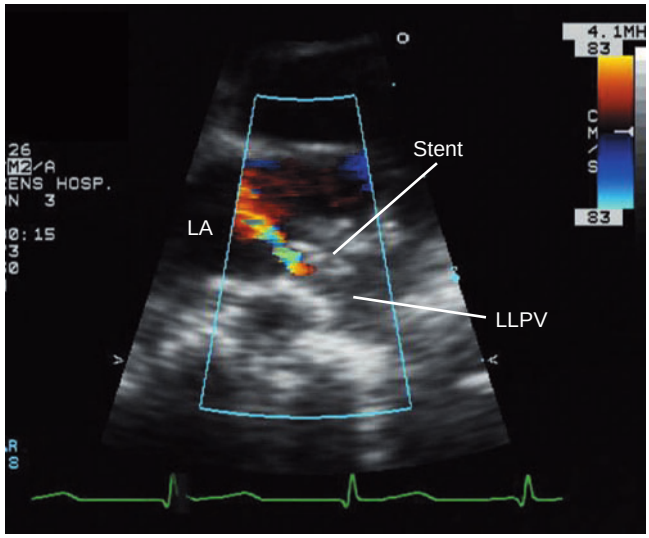


**Figure 9.46** Pulmonary vein in-stent restenosis. Parasternal short-axis image with color Doppler flow mapping in this patient with severe recurrent pulmonary vein stenosis shows a small jet of accelerated pulmonary venous inflow in the left lower pulmonary vein (LLPV). Note the gap between the color flow jet and the edges of the stent consistent with in-stent restenosis. LA, left atrium.

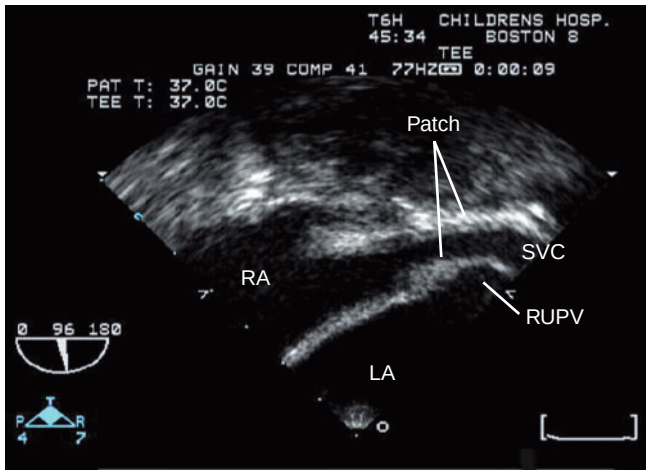


**Figure 9.47** Postoperative transesophageal echocardiography (TEE) after superior sinus venosus repair. Long-axis (bicaval) TEE view following "two-patch" repair of the unroofing defect between the right upper pulmonary vein (RUPV) and the superior vena cava (SVC), as well as patch augmentation of the SVC anteriorly. The SVC is mildly narrowed but unobstructed. RA, right atrium; LA, left atrium (Videoclip 9.7).

ventricular and pulmonary artery hypertension by Doppler assessment. The surgeon may find TEE helpful in demonstrating the acute relief of pulmonary vein stenosis in the operating room, and TEE is the mainstay of noninvasive surveillance for recurrence over the weeks and months following repair.

Intraoperative TEE is considered helpful during repair of sinus venosus defects or other forms of partial anomalous

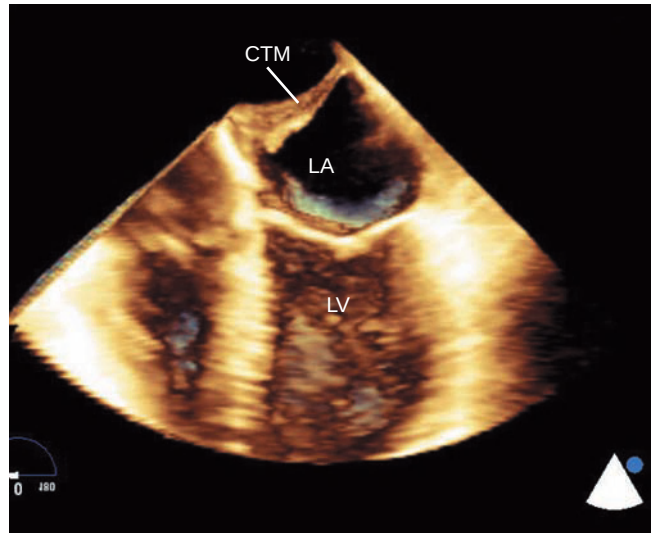


**Figure 9.48** Three-dimensional transesophageal echocardiogram. Preoperative image with 3D probe demonstrates a thick cor triatriatum "membrane" (CTM) within the left atrium (LA). LV, left ventricle (Videoclip 9.8).

venous return, cor triatriatum and total anomalous pulmonary venous return (Fig. 9.47) [50,51]. Three-dimensional TEE probes are now becoming available to assist with intraoperative evaluation as well (Fig. 9.48). Complex venous baffling may be required for repair of partial anomalous pulmonary venous return, and TEE is excellent for evaluating the patency of the pulmonary and systemic venous pathways as well as residual leaks. TEE evaluation of repair of TAPVC, however, may be more challenging as the surgical anastomosis is often directly anterior to the esophagus, at times too close to the interrogating probe to allow for complete color and pulsed Doppler interrogation. In small infants, moreover, the possibility of probe-related distortion or compression of the pulmonary venous pathway must be considered. In this situation epicardial intraoperative imaging is an option that allows for imaging of the venous anastomosis without the potential for such distortion; this is also a good option for infants weighing less than 3 kg, for whom the passage of even the most miniaturized TEE probe is difficult. Regardless of the technique, the goals of post-cardiopulmonary bypass imaging include evaluation of the repair, exclusion of residual lesions, and functional assessment including the AV valves, right heart pressures by Doppler estimate, and ventricular function.

## Postoperative assessment

The goals of longer-term postoperative imaging are determined in many respects by the nature of the repaired lesion. Congenital or acquired pulmonary vein stenosis is discussed in some detail in the preceeding section. Resection of cor triatriatum has a high success rate, with excellent survival and long-term results [52]; follow-up evaluation includes

comprehensive imaging of the left atrium and any residual membrane tissue, color and spectral Doppler evaluation of flow in the pulmonary veins and left atrium, evaluation of any residual interatrial defects, and assessment of right heart pressure, size and function.

Following repair of sinus venosus defect, obstruction of both the pulmonary venous pathway and the SVC have been described [53]. In repaired partial anomalous pulmonary venous return, echocardiographic follow-up evaluation should include assessment for any stenosis of the venous baffle to the left atrium, residual leaks, presence of any stenosis of the systemic vein, and assessment of right heart pressure, size and function.

Repair of total anomalous pulmonary venous return is associated with a significant risk of recurrent pulmonary venous obstruction, both at the level of the anastomosis of the confluence to the left atrium, as well as at the level of the individual pulmonary veins. The risk of recurrence of obstruction across all types of TAPVC repair is ~11% [54]. Goals for the echocardiographic assessment of these patients must include careful assessment, by both color and spectral Doppler, of the dimensions and flow characteristics of the pulmonary venous confluence anastomosis as well as the individual pulmonary veins. Subxiphoid imaging in conjunction with high parasternal and suprasternal notch imaging is helpful for the delineation of the individual pulmonary veins; frequently the apical view is best for evaluation of the pulmonary venous confluence, as the orifice is usually directed at the left atrial outlet and parallel to the interrogating transducer in this view (Fig. 9.49). Evaluation of the right heart size, pressure and function are important to exclude pulmonary hypertension and ventricular dysfunction in this setting.

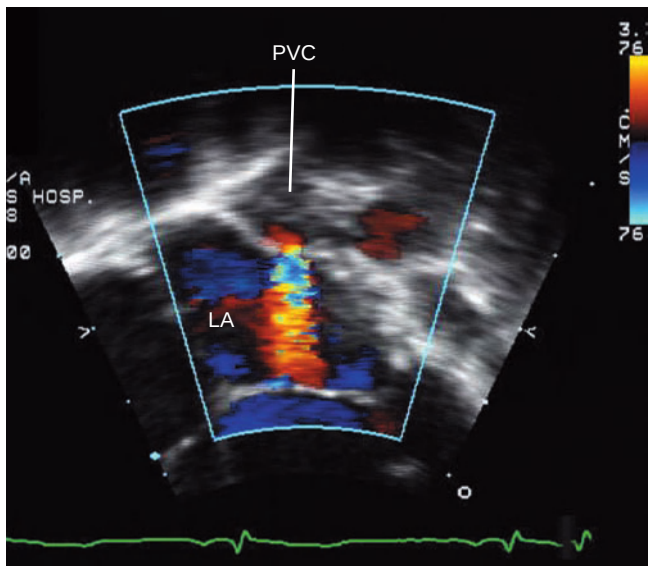


**Figure 9.49** Recurrent obstruction after repair of total anomalous pulmonary venous connection (TAPVC). Apical view with color Doppler flow mapping in this patient after repair of infradiaphragmatic TAPVC shows severe obstruction at the anastomosis between the pulmonary venous confluence (PVC) and the left atrium (LA).

## References


1. Healy J Jr. An anatomic survey of anomalous pulmonary veins: their clinical significance. *J Thorac Cardiovasc Surg* 1952;23: 433–44.
2. Ostman-Smith I, Silverman NH, Oldershaw P et al. Cor triatriatum sinistrum. Diagnostic features on cross sectional echocardiography. *Br Heart J* 1984;51:211–19.
3. Ferencz C, Rubin JD, McCarter RJ et al. Congenital heart disease: prevalence at livebirth. The Baltimore-Washington Infant Study. *Am J Epidemiol* 1985;121:31–6.
4. Hoffman JI, Kaplan S. The incidence of congenital heart disease. *J Am Coll Cardiol* 2002;39:1890–900.
5. Moore JW, Kirby WC, Rogers WM et al. Partial anomalous pulmonary venous drainage associated with 45,X Turner's syndrome. *Pediatrics* 1990;86:273–6.
6. van Wassenaer AG, Lubbers LJ, Losekoot G. Partial abnormal pulmonary venous return in Turner syndrome. *Eur J Pediatr* 1988;148:101–3.
7. Bleyl S, Nelson L, Odelberg SJ et al. A gene for familial total anomalous pulmonary venous return maps to chromosome 4p13-q12. *Am J Hum Genet* 1995;56:408–15.
8. Neill CA. Development of the pulmonary veins; with reference to the embryology of anomalies of pulmonary venous return. *Pediatrics* 1956;18:880–7.
9. Moller JH, Nakib A, Anderson RC et al. Congenital cardiac disease associated with polysplenia. A developmental complex of bilateral "left-sidedness". *Circulation* 1967;36:789–99.
10. Van Praagh S, Carrera ME, Sanders SP, et al. Sinus venosus defects: unroofing of the right pulmonary veins – anatomic and echocardiographic findings and surgical treatment. *Am Heart J* 1994;128:365–79.
11. Blom NA, Gittenberger-de Groot AC, Jongeneel TH et al. Normal development of the pulmonary veins in human embryos and formulation of a morphogenetic concept for sinus venosus defects. *Am J Cardiol* 2001;87:305–9.
12. Edwards JE. Congenital stenosis of pulmonary veins. Pathologic and developmental considerations. *Lab Invest* 1960;9:46–66.
13. Sade RM, Freed MD, Matthews EC et al. Stenosis of individual pulmonary veins. Review of the literature and report of a surgical case. *J Thorac Cardiovasc Surg* 1974;67:953–62.
14. Rubino M, Van PS, Kadoba K et al. Systemic and pulmonary venous connections in visceral heterotaxy with asplenia. Diagnostic and surgical considerations based on seventy-two autopsied cases. *J Thorac Cardiovasc Surg* 1995;110:641–50.
15. Sadr IM, Tan PE, Kieran MW et al. Mechanism of pulmonary vein stenosis in infants with normally connected veins. *Am J Cardiol* 2000;86:577–9, A10.
16. Riedlinger WF, Juraszek AL, Jenkins KJ et al. Pulmonary vein stenosis: expression of receptor tyrosine kinases by lesional cells. *Cardiovasc Pathol* 2006;15:91–9.
17. Niwayama G. Cor triatriatum. *Am Heart J* 1960;59:291–317.
18. Dudell GG, Evans ML, Krous HF et al. Common pulmonary vein atresia: the role of extracorporeal membrane oxygenation. *Pediatrics* 1993;91:403–10.

19. Juraszek AL, Cohn H, Van PR et al. Isolated left-sided scimitar vein connecting all left pulmonary veins to the right inferior vena cava. *Pediatr Cardiol* 2005;26:846–7.
20. Neill CA, Ferencz C, Sabiston DC. The familial occurrence of hypoplastic right lung with systemic arterial supply and venous drainage: "scimitar syndrome." *Johns Hopkins Med J* 1960;107:1–21.
21. Gao YA, Burrows PE, Benson LN et al. Scimitar syndrome in infancy. *J Am Coll Cardiol* 1993;22:873–82.
22. Craig JM, Darling RC, Rothney WB. Total pulmonary venous drainage into the right side of the heart; report of 17 autopsied cases not associated with other major cardiovascular anomalies. *Lab Invest* 1957;6:44–64.
23. Burroughs JT, Edwards JE. Total anomalous pulmonary venous connection. *Am Heart J* 1960;59:913–31.
24. Lucas RV Jr, Adams P Jr, Anderson RC. Total anomalous pulmonary venous connection to the portal venous system: A cause of pulmonary venous obstruction. *AJR Am J Roentgenol* 1961;86:561–75.
25. Tajik AJ, Gau GT, Ritter DG, et al. Echocardiographic pattern of right ventricular diastolic volume overload in children. *Circulation* 1972;46:36–43.
26. Fiandra O, Barcia A, Cortes R et al. Partial anomalous pulmonary venous drainage into the inferior vena cava. *Acta Radiol* 1962;57:301–10.
27. Saalouke MG, Shapiro SR, Perry LW et al. Isolated partial anomalous pulmonary venous drainage associated with pulmonary vascular obstructive disease. *Am J Cardiol* 1977;39:439–44.
28. Delisle G, Ando M, Calder AL et al. Total anomalous pulmonary venous connection: Report of 93 autopsied cases with emphasis on diagnostic and surgical considerations. *Am Heart J* 1976;91: 99–122.
29. Geva T, Greil GF, Marshall AC et al. Gadolinium-enhanced 3-dimensional magnetic resonance angiography of pulmonary blood supply in patients with complex pulmonary stenosis or atresia: comparison with x-ray angiography. *Circulation* 2002; 106:473–8.
30. Greil GF, Powell AJ, Gildein HP et al. Gadolinium-enhanced three-dimensional magnetic resonance angiography of pulmonary and systemic venous anomalies. *J Am Coll Cardiol* 2002; 9:335–41.
31. Geggel RL, Fulton DR, Rockenmacher S. Nonobstructive cor triatriatum in infancy. *Clin Pediatr (Phila)* 1999;38:489–91.
32. Wolf WJ. Diagnostic features and pitfalls in the two-dimensional echocardiographic evaluation of a child with cor triatriatum. *Pediatr Cardiol* 1986;6:211–13.
33. Jenkins KJ, Sanders SP, Orav EJ et al. Individual pulmonary vein size and survival in infants with totally anomalous pulmonary venous connection. *J Am Coll Cardiol* 1993;22: 201–6.
34. Rudolph AM, Heymann MA. The circulation of the fetus in utero. Methods for studying distribution of blood flow, cardiac output and organ blood flow. *Circ Res* 1967;21:163–84.
35. Driggers RW, Spevak PJ, Crino JP, et al. Fetal anatomic and functional echocardiography: a 5-year review. *J Ultrasound Med* 2003;22:45–51.
36. Valsangiacomo ER, Hornberger LK, Barrea C et al. Partial and total anomalous pulmonary venous connection in the fetus: two-dimensional and Doppler echocardiographic findings. *Ultrasound Obstet Gynecol* 2003;22:257–63.
37. Allan LD, Sharland GK. The echocardiographic diagnosis of totally anomalous pulmonary venous connection in the fetus. *Heart* 2001;85:433–7.
38. Sunaga Y, Hayashi K, Okubo N et al. Transesophageal echocardiographic diagnosis of coronary sinus type atrial septal defect. *Am Heart J* 1992;124:1657–9.
39. Watanabe F, Takenaka K, Suzuki J et al. Visualization of sinus venosus-type atrial septal defect by biplane transesophageal echocardiography. *J Am Soc Echocardiogr* 1994;7:179–81.
40. Jean D, Girard F, Couture P et al. Transesophageal echocardiographic diagnosis of sinus venosus-type atrial septal defect associated with partial anomalous venous connections during cardiac surgery in adults. *J Cardiothorac Vasc Anesth* 1995;9:438–41.
41. Valente AM, Sena L, Powell AJ et al. Cardiac magnetic resonance imaging evaluation of sinus venosus defects: comparison to surgical findings. *Pediatr Cardiol* 2007;28:51–6.
42. Powell AJ, Tsai-Goodman B, Prakash A et al. Comparison between phase-velocity cine magnetic resonance imaging and invasive oximetry for quantification of atrial shunts. *Am J Cardiol* 2003;91:1523–5, A9.
43. Driscoll DJ, Hesslein PS, Mullins CE. Congenital stenosis of individual pulmonary veins: clinical spectrum and unsuccessful treatment by transvenous balloon dilation. *Am J Cardiol* 1982; 49:1767–72.
44. Singh H, Singh C, Aggarwal N et al. Angioplasty of congenital pulmonary vein stenosis. *Indian Heart J* 2005;57:709–12.
45. Seale AN, Daubeney PE, Magee AG et al. Pulmonary vein stenosis: initial experience with cutting balloon angioplasty. *Heart* 2006;92:815–20.
46. Bromberg-Marin G, Tsimikas S, Mahmud E. Treatment of recurrent pulmonary vein stenoses with endovascular stenting and adjuvant oral sirolimus. *Catheter Cardiovasc Interv* 2007;69:362–8.
47. Tomita H, Watanabe K, Yazaki S, et al. Stent implantation and subsequent dilatation for pulmonary vein stenosis in pediatric patients: maximizing effectiveness. *Circ J* 2003;67:187–90.
48. Cook AL, Prieto LR, Delaney JW et al. Usefulness of cutting balloon angioplasty for pulmonary vein in-stent stenosis. *Am J Cardiol* 2006;98:407–10.
49. Spray TL, Bridges ND. Surgical management of congenital and acquired pulmonary vein stenosis. *Semin Thorac Cardiovasc Surg Pediatr Card Surg Annu* 1999;2:177–88.
50. Stevenson JG, Sorensen GK, Gartman DM et al. Transesophageal echocardiography during repair of congenital cardiac defects: identification of residual problems necessitating reoperation. *J Am Soc Echocardiogr* 1993;6:356–65.
51. Rosenfeld HM, Gentles TL, Wernovsky G et al. Utility of intraoperative transesophageal echocardiography in the assessment of residual cardiac defects. *Pediatr Cardiol* 1998;19:346–51.
52. Alphonso N, Norgaard MA, Newcomb A et al. Cor triatriatum: presentation, diagnosis and long-term surgical results. *Ann Thorac Surg* 2005;80:1666–71.
53. Stewart RD, Bailliard F, Kelle AM et al. Evolving surgical strategy for sinus venosus atrial septal defect: effect on sinus node function and late venous obstruction. *Ann Thorac Surg* 2007;84:1651–5.
54. Hancock Friesen CL, Zurakowski D, Thiagarajan RR et al. Total anomalous pulmonary venous connection: an analysis of current management strategies in a single institution. *Ann Thorac Surg* 2005;79:596–606.

# 10 Systemic Venous Anomalies

**Leo Lopez[1] and James C. Huhta[2]**

[1]The Children's Hospital at Montefiore, New York, NY, USA
[2]Noninvasive Imaging, All Children's Hospital, St. Petersburg, Florida, FL, USA

The development of and variations in the normal human venous system have been the object of study for many years [1,2]. Abnormalities in systemic venous return can occur in isolation, often with little hemodynamic significance, or in association with other congenital heart diseases. With the increasing utility of diagnostic catheterization and corrective surgery in patients with congenital heart disease, prior identification and analysis of systemic venous anomalies can prevent significant morbidity and mortality, and echocardiography has become an essential tool in the diagnosis and management of these patients [3–6]. Because of the wide variability within this class of abnormalities, evaluation of the systemic venous return must involve a systematic approach with a comprehensive description of each individual segment: the superior vena cava (SVC), the inferior vena cava (IVC), the azygos and hemiazygos veins, the hepatic veins, the coronary sinus (CS) and the innominate vein.

Atrial situs is a key variable in any understanding of the systemic veins [7]. If there is lateralized situs (situs solitus or situs inversus), the CS is usually present, and systemic venous anomalies are few, rare and fairly predictable. The most common abnormality in situs solitus is a persistent left SVC connecting to the CS. The systemic venous return in situs inversus is usually a mirror image of the normal pattern. If there is abnormal situs, as in heterotaxy syndrome with isomeric atrial appendages (right isomerism or left isomerism), there is often a common atrium with fundamentally flawed venous segments [8–12]. The abnormalities are complex and frequent, but they can be predictable based on the type of isomerism (or on whether the heterotaxy syndrome is of the asplenia type or the polysplenia type) [3,13]. In right isomerism, the CS is almost always absent, and there are usually bilateral superior venae cavae (SVCs) connecting to bilateral morphologically right atria without a connecting vein. In left isomerism, many abnormalities coexist, but anomalous hepatic venous connection is quite common. The IVC is frequently interrupted with azygos continuation. There may be bilateral SVCs connecting directly to the atria bilaterally, or the left SVC may connect to a CS if present. Systemic venous anomalies, such as bilateral SVCs, anomalous hepatic venous connection, or IVC interruption with azygos continuation, can have important implications in the management of patients with single ventricle circulation, thereby requiring complete identification and characterization prior to surgical intervention.

*Echocardiography in Pediatric and Congenital Heart Disease: From Fetus to Adult*
Edited by Wyman W. Lai, Luc L. Mertens, Meryl S. Cohen and Tal Geva
 ISBN: 978-1-405-17401-5

## Prevalence

Systemic venous anomalies are rare in isolation, although their frequency is higher when associated with other congenital heart diseases. For example, a persistent left SVC, the most common systemic venous anomaly, occurs in 0.3–0.5% of the general population [14–16], whereas its frequency in patients with congenital heart disease is as high as 2–10% [17–19]. In the setting of heterotaxy syndrome, which has an incidence of 10/100 000 livebirths [20] and a frequency of 0.8% in patients with congenital heart disease [13], systemic venous anomalies occur in more than 70% of cases [13,21].

## Embryology and etiology

The embryologic origins of the major systemic veins are outlined in Table 10.1, and the embryologic origins of common systemic venous anomalies are outlined in Table 10.2. Early development of the venous system includes bilateral venous structures in the (i) umbilical; (ii) vitelline; and (iii) cardinal areas. The paired umbilical veins from the chorionic villi and the more medial and also paired vitelline veins from the yolk sac appear during the third week of gestation (13-somite stage). Each pair drains into the caudal aspect of the developing common atrium, thereby forming the right and left horns of the sinus venosus. The paired cardinal veins appear during the fourth week of gestation (20-somite stage), and this system includes (i) the anterior cardinal veins from the cranial end of the embryo; (ii) the posterior cardinal veins from the caudal end; and (iii) the convergence of both sets into the

**Table 10.1** Embryologic origins of the major systemic veins

| Systemic vein | Embryologic origin |
|---|---|
| Superior vena cava | Right anterior cardinal vein |
| Left innominate vein | Persistent connection between the anterior cardinal veins after regression of the left anterior cardinal vein |
| Coronary sinus | Left common cardinal vein (left sinus horn) |
| Inferior vena cava | Right vitelline vein, right hepatocardiac vein, right subcardinal vein, caudal segment of the right supracardinal vein |
| Hepatic veins | Vitelline veins, omphalomesenteric veins |
| Azygos vein | Right supracardinal vein |
| Hemiazygos vein | Left supracardinal vein |

common cardinal veins, which, in turn, are incorporated into the respective horns of the sinus venosus. Lateralization in systemic venous return appears to occur during the fourth week of gestation by two processes: (i) leftward invagination of the junction between the left sinus horn and the common atrium; and (ii) rightward shift of the sinus venosus. These events lead to isolation of the left sinus horn from the developing left atrium (LA) and commitment of all the systemic venous return to the right atrium (RA). The anterior cardinal system produces the SVCs. Normally the left anterior cardinal vein regresses by the sixth month of gestation with the following morphologic consequences:

**1** the connection between the anterior cardinal veins enlarges, ultimately becoming the left innominate vein;
**2** the left common cardinal vein drains only the coronary circulation via the CS;
**3** the remnant of the left anterior cardinal vein becomes the ligament of Marshall and the left superior intercostal vein.

The hepatic veins develop during the fourth and fifth weeks of gestation from the confluence of the left and right omphalomesenteric veins, a network of sinusoids that evolves from and between the vitelline veins and eventually forms one right-sided hepatocardiac confluence in the lateralization of the sinus venosus to the right. Between the sixth and eighth weeks of gestation, the venous return from the bilateral posterior cardinal veins gradually shifts to the more medial subcardinal and supracardinal veins (the supracardinal veins provide a connection between the subcardinal veins and the distal cranial segment of the posterior cardinal vein). As the caudal segment of the posterior cardinal veins regresses, anastomoses between the right and left subcardinal veins develop. Right-sided dominance develops from regression of the left subcardinal vein and coalescence of the right subcardinal and hepatic veins. The right subcardinal system eventually becomes the suprarenal segment of the IVC, and the supracardinal system eventually becomes the subrenal segment of the IVC as well as the azygos and hemiazygos veins.

**Table 10.2** Embryologic origins of common systemic venous anomalies

| Systemic venous anomaly | Embryologic origin |
|---|---|
| Left SVC | Persistence of the left anterior cardinal vein |
| Connecting vein between bilateral SVCs | Formation of connection between anterior cardinal veins |
| Atretic right SVC | Regression of right anterior cardinal vein |
| Left SVC to LA | Failure of infolding between left sinus horn and LA (absent CS), persistence of left anterior cardinal vein versus extensive unroofing of the CS |
| Levoatrial cardinal vein | Persistent connection between primordial common pulmonary vein and cardinal veins |
| Right SVC to LA or to both atria | Leftward superior displacement of right sinus horn versus unroofed right pulmonary veins near SVC–RA junction |
| Interrupted IVC | Failure of connection between right hepatocardiac veins and right subcardinal veins; prominent right supracardinal vein becomes azygos continuation or prominent left supracardinal vein becomes hemiazygos continuation |
| Bilateral IVCs | Persistence of caudal segment of left supracardinal vein |
| Left IVC to RA | Persistence of left supracardinal vein and regression of right supracardinal vein |
| Retroaortic innominate vein | Formation of alternate connection between anterior cardinal veins |

CS, coronary sinus; IVC, inferior vena cava; LA, left atrium; RA, right atrium; SVC, superior vena cava.

If the genetic code for bilateral isomeric atrial appendages is predetermined, the embryologic development of the venous system is altered and cannot be compared with normal development. With increasing knowledge of the development of abnormal visceroatrial situs, systemic venous anomalies represent one component of the morphologically diverse lesions that comprise heterotaxy syndrome. There is a trend toward persistence of the bilateral venous return, which is present early in gestation. Whether the regularity of venous anomalies in isomerism is due to local effects after differentiation or to a separate but related early genetic signal is not known.

## Superior vena caval anomalies

The right SVC, a valveless derivative of the anterior cardinal venous system formed from the two brachiocephalic or innominate veins, drains blood from the upper half of the body. It receives the azygos vein and several small veins from the pericardium and other mediastinal structures. The lower half is within the pericardium, and it is covered in front and on each side by serous pericardium.

### Left SVC to the coronary sinus (bilateral SVC)

The most common systemic venous anomaly is a persistent left SVC, with a prevalence of 0.3–0.5% in the general population and a frequency of 2–10% among patients with congenital heart disease [14–19]. In fact, it occurs in 20% of patients with tetralogy of Fallot and in 8% of those with Eisenmenger syndrome [22]. A persistent left SVC drains via the CS into the RA in 92% of cases and into the LA (Fig. 10.1a), either directly because of absence or unroofing of the CS or via a left pulmonary vein (partially persistent left SVC), in the other 8% [23,24].

Embryologically, failure of regression of the left anterior cardinal and left common cardinal veins results in this anomaly. If a connection forms between the right and left anterior cardinal veins, it can persist as a connecting vein, as seen in 60% of cases with bilateral SVCs [18]. In general, the size of the connecting vein is inversely proportional to the size of the persistent left SVC [17,18]. A persistent left SVC normally courses (i) in front of the left pulmonary artery and aortic arch; (ii) between the left atrial appendage and the left pulmonary veins; and (iii) into the CS as it traverses along the left atrioventricular groove. Occasionally it courses behind the left pulmonary artery with potential for obstruction as it traverses between the left pulmonary artery and the left bronchus, an area that has been referred to as the "anatomic vise."

#### Pathophysiology and clinical significance

In bilateral SVCs with the left SVC to an intact CS, there is normal systemic venous return to the RA. From a practical standpoint, identification of bilateral SVCs prior to surgical intervention in the setting of congenital heart disease can have a significant impact on the cannulation approach during initiation of cardiopulmonary bypass support [25]. In addition, identification of a well-developed connecting vein can allow for surgical ligation of the left SVC in the operating room if necessary. In the setting of a functionally single ventricle, staged surgical intervention involves a bidirectional superior cavopulmonary anastomosis (bidirectional Glenn procedure). Bilateral SVCs without a connecting vein may require bilateral bidirectional superior cavopulmonary anastomoses or, occasionally, surgical ligation of the left SVC [26].

#### Imaging

The anomalous vein can be detected by echocardiography with a sensitivity of 95–100% [3]. A high left parasagittal view in a nearly vertical orientation can delineate most of the left SVC and its continuity with the CS (Fig. 10.2). A suprasternal short-axis view can display both SVCs and their relationship to the ascending aorta (Fig. 10.3 and Videoclip 10.1). In addition, a connecting vein, if present, can usually be visualized in this view, particularly with the use of low-scale color mapping. Color mapping sweeps in a subcostal short-axis (sagittal) view can also show the supero-inferior flow from both SVCs into the heart. A persistent left SVC is the most common cause of a dilated CS, which can be seen during the posterior sweep of an apical 4-chamber view (Fig. 10.4 and Videoclip 10.2) and along the posterior atrioventricular groove in a parasternal long-axis view [27] (Fig. 10.5) (other causes of a dilated CS will be discussed later in this chapter). If the left SVC cannot be delineated easily by imaging and/or color mapping, injection of saline contrast into the left arm will result in the presence of contrast in the dilated CS. Prenatal diagnosis of a persistent left SVC usually results from identification of a dilated CS as seen during the posterior sweep in 4-chamber views and in the long-axis view of the left ventricle in the area of the left atrioventricular groove [28]. A persistent left SVC can also be identified in cross-section as an additional vessel to the left of the pulmonary artery on a prenatal three-vessel view [29]. The length of the left SVC can usually be shown in leftward sagittal sweeps of the heart.

### Left SVC to the coronary sinus with an atretic right SVC

Rarely a persistent left SVC occurs without a right SVC secondary to regression of the right anterior cardinal vein [30,31]. In this arrangement, the right-sided head and neck vessels drain via the right innominate vein into the left SVC, which in turn drains via a dilated CS into the RA (Fig. 10.1b). This rare anomaly can usually be delineated in a suprasternal short-axis view (Fig. 10.6 and Videoclip 10.3).

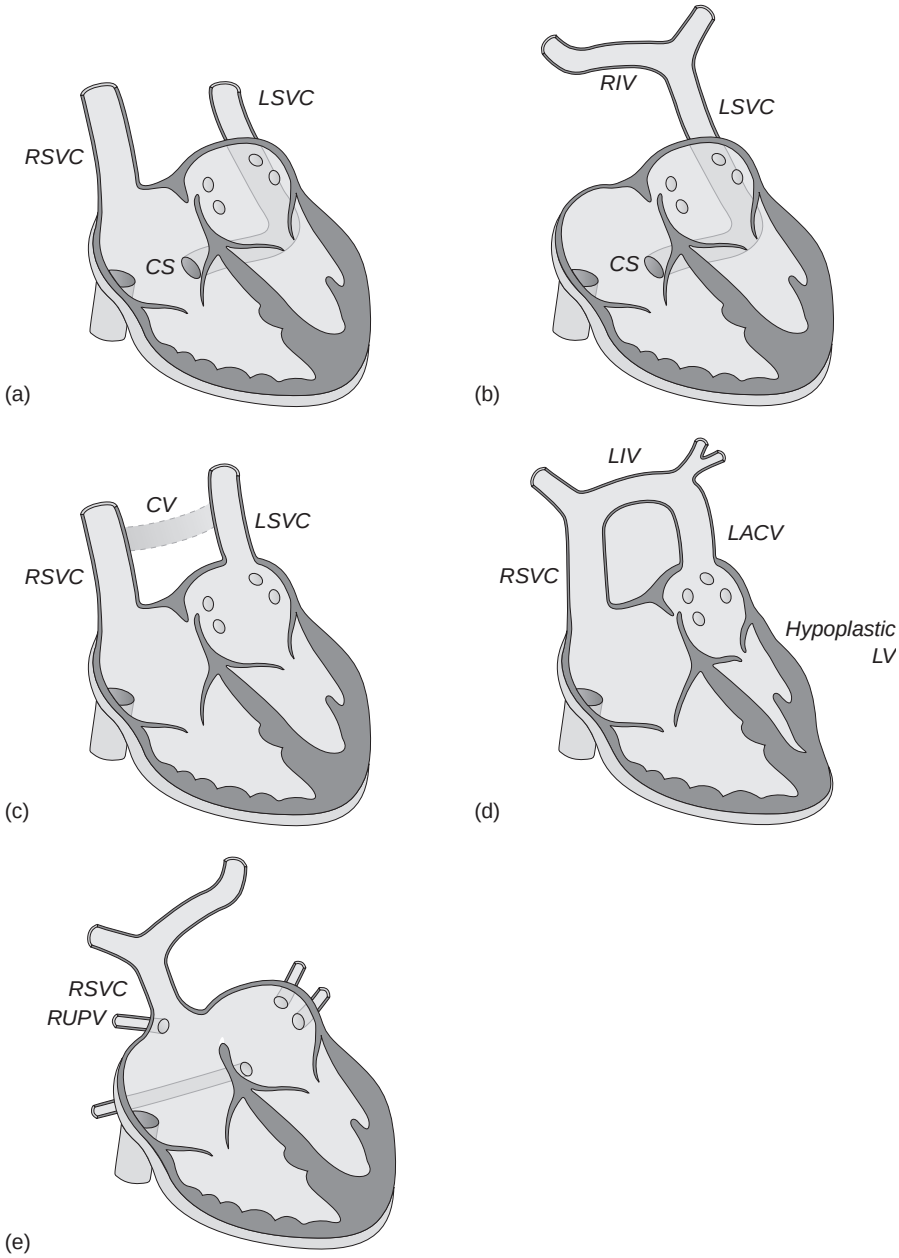


**Figure 10.1** Anomalies of the superior vena cava. **(a)** Persistent left superior vena cava (LSVC) draining into a dilated coronary sinus without a connecting vein between the bilateral superior venae cavae. **(b)** Atretic right superior vena cava (RSVC) with a persistent LSVC draining into a dilated coronary sinus. **(c)** LSVC draining directly into the left atrium, occasionally with a connecting vein between the bilateral superior venae cavae. **(d)** Hypoplastic left heart syndrome with a restrictive patent foramen ovale and a levoatrial cardinal vein connecting from the left atrium into the left innominate vein (LIV). **(e)** Biatrial connection of the RSVC in a sinus venosus defect with partially anomalous drainage of the right upper pulmonary vein (RUPV) into the right atrium. CS, coronary sinus; CV, connecting vein; LACV, levoatrial cardinal vein; LV, left ventricle; RIV, right innominate vein.

## Left SVC to the left atrium

When the left SVC drains directly into the LA (Fig. 10.1c) (as seen in 8% of patients with a left SVC) [23], it usually courses in front of the left pulmonary artery and connects directly to the LA between the left upper pulmonary vein and the left atrial appendage [32,33]. Because it occurs as a rare, isolated defect, some have suggested that a left SVC draining directly into the LA results from failure of the infolding between the left sinus horn and the LA (with consequent failure of development or absence of the CS) and from persistence of the left anterior cardinal vein (Raghib anomaly) [34]. Others, however, suggest that the defect results from extensive unroofing of the CS [35,36]. Nevertheless, the most common scenario for direct connection of a left SVC to the LA is in isomeric atrial appendages with bilateral right or left atria wherein the bilateral SVCs drain into both sides of the atrial mass. In this setting, the CS is usually absent, and an embryologic explanation may not be relevant because the situs is abnormal.

## Pathophysiology and clinical significance

When there is no communication between the right and left atria, patients with a left SVC to the LA will present early in infancy with cyanosis and no heart murmur. When there is a connecting vein between the bilateral SVCs, however, the left SVC and connecting vein can provide decompression of

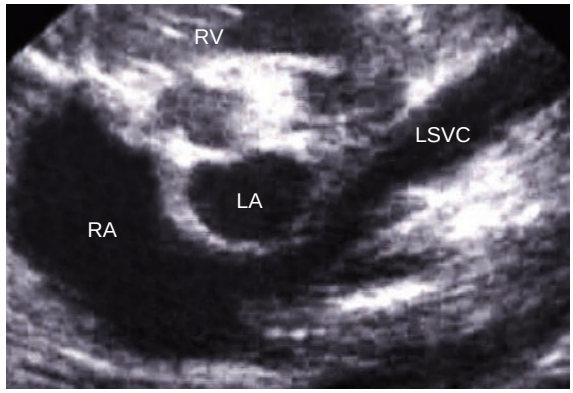


**Figure 10.2** High left parasagittal view of a persistent left superior vena cava draining via a dilated coronary sinus into the right atrium. LA, left atrium; LSVC, left superior vena cava; RA, right atrium; LA, left atrium.

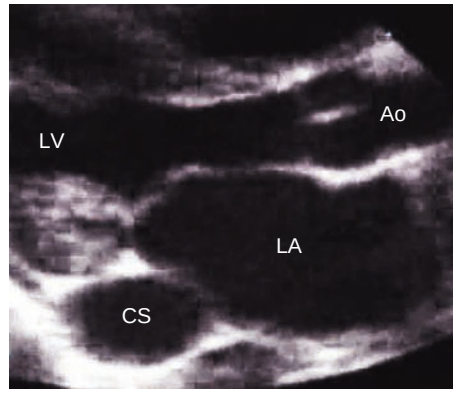


**Figure 10.5** Parasternal long-axis view of a dilated coronary sinus in cross-section as it traverses along the posterior left atrioventricular groove. Ao, aorta; CS, coronary sinus; LA, left atrium; LV, left ventricle.

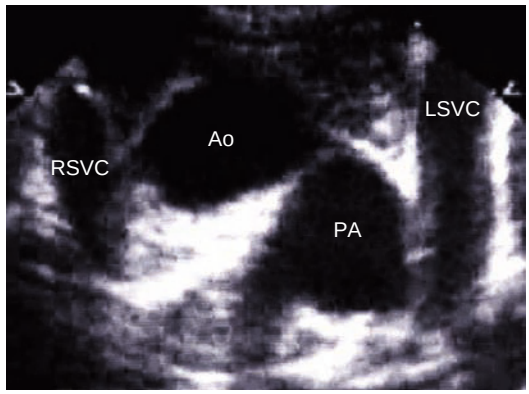


**Figure 10.3** Suprasternal short-axis (transverse) view of bilateral superior venae cavae without a connecting vein. Ao, aorta; LSVC, left superior vena cava; PA, pulmonary artery; RSVC, right superior vena cava.

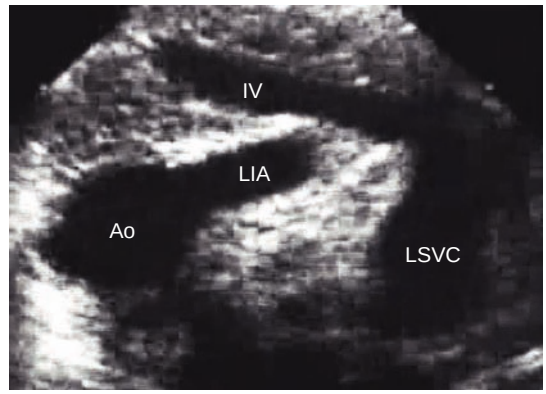


**Figure 10.6** Suprasternal short-axis (transverse) view of an atretic right superior vena cava with drainage of the right innominate vein via the left superior vena cava (LSVC) and coronary sinus into the right atrium; the patient also has a right aortic arch whose first branch is the left innominate artery (LIA). Ao, aorta; IV, innominate vein.

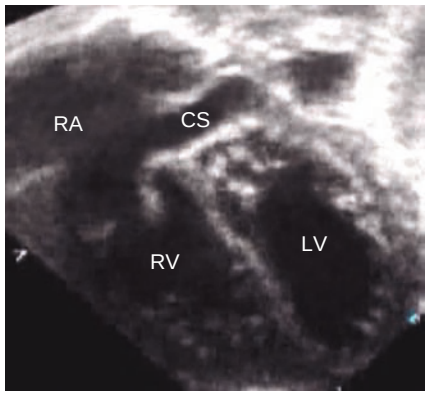


**Figure 10.4** Posterior sweep in an apical 4-chamber view reveals a dilated coronary sinus. CS, coronary sinus; LV, left ventricle; RA, right atrium; RV, right ventricle.

left atrial blood into the right SVC, and color mapping will reveal retrograde flow along the left SVC (Fig. 10.7). Surgical treatment of this anomaly involves ligation of the left SVC if there is a connecting vein or if the upper venous pressure is less than 15 mm Hg with test occlusion of the left SVC [26]. Alternatively, the left SVC can be reimplanted into the RA or the pulmonary artery [37,38]. More recently, the surgical approach has favored creation of an intra-atrial baffle [39]. A persistent left SVC to the LA can cause cyanosis after a Fontan procedure, and interventional catheterization with coil occlusion of the vein can be lifesaving and preclude the need for another operation.

### Imaging

The diagnosis of a persistent left SVC with direct connection to the LA can be made by echocardiography using the same high left parasagittal and suprasternal short-axis views discussed previously. In the absence of a connecting vein between the bilateral SVCs, there is obligate flow from the left SVC into the LA, and color mapping will reveal antegrade flow along the left SVC. Injection of saline contrast into the left arm will result in the appearance of contrast in the LA.

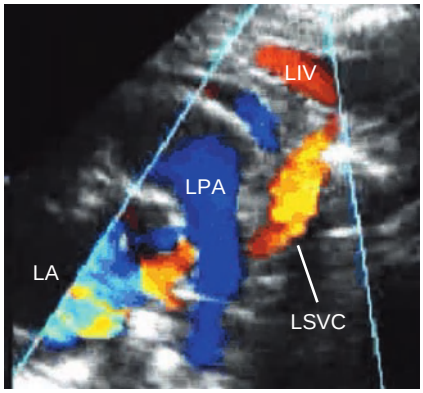


**Figure 10.7** Suprasternal short-axis (transverse) view with color mapping of a left superior vena cava (LSVC) connecting directly to the left atrium (LA). In the setting of a connecting (left innominate) vein between the bilateral superior venae cavae, there is retrograde flow along the LSVC from the LA. LIV, left innominate vein or connecting vein between the bilateral superior venae cavae; LPA, left pulmonary artery.

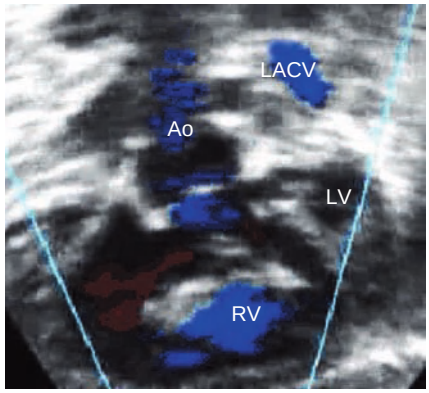


**Figure 10.8** Subcostal short-axis (sagittal) view with color mapping of a levoatrial cardinal vein in a patient with small restrictive atrial septal defects, mitral atresia, left ventricular hypoplasia, ventricular septal defect, and double-outlet right ventricle. The flow in the levoatrial cardinal vein is away from the heart into the left innominate vein. Ao, aorta; LACV, levoatrial cardinal vein; LV, left ventricle; RV, right ventricle.

Radionuclide studies can also be used to detect the early appearance of systemic venous blood in the LA [40,41].

## Levoatrial cardinal vein

Elevated left atrial pressures in the setting of left atrial outlet obstruction early in gestation may result in persistence of the levoatrial cardinal vein, a vessel that decompresses the LA into the left innominate vein or right SVC (Fig. 10.1d) [42]. The levoatrial cardinal vein is an embryologic connection between the capillary plexus of the embryonic foregut (the origin of the pulmonary veins) and the cardinal venous system.

### Pathophysiology and clinical significance

Unlike the normal course of a persistent left SVC, a levoatrial cardinal vein usually courses behind the left pulmonary artery and in front of the left bronchus, the "anatomic vise," which can cause compression or obstruction of the vessel as it traverses the area. Left atrial outlet obstruction occurs when there is mitral stenosis or atresia and a restrictive atrial septal defect or intact atrial septum with or without hypoplastic left heart syndrome (Fig. 10.8 and Videoclip 10.4).

### Imaging

When this constellation of problems is diagnosed by echocardiography, suprasternal short-axis views can show the retrograde flow within the decompressing vessel from the LA or left pulmonary vein into the left innominate vein or right SVC (Fig. 10.9).

## Right SVC to the left atrium or to both atria

Direct connection of the right SVC to the LA is a rare anomaly and has been attributed to leftward and superior displacement of right sinus horn [43–45]. However, the superior sinus venosus defect has also been attributed to this

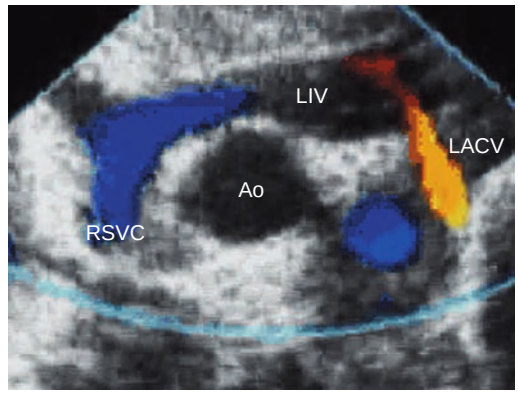


**Figure 10.9** Suprasternal short-axis (transverse) view with color mapping of a levoatrial cardinal vein (LACV) in a patient with small restrictive atrial septal defects, mitral atresia, left ventricular hypoplasia, ventricular septal defect, and double-outlet right ventricle. The flow in the LACV is away from the heart into the left innominate vein (LIV). Ao, aorta; RSVC, right superior vena cava.

embryologic event, and biatrial connection of the right SVC (Fig. 10.1e) is a hallmark finding of a superior sinus venosus defect, suggesting that the two lesions are variants of one anomaly. More recent reports suggest that both variants result from unroofing of the right pulmonary veins at or above the junction between the right SVC and the RA [46]. In other words, the usual partition between the posterior aspect of the right SVC and the anterior aspect of the right pulmonary veins is absent. Hemodynamically, cyanosis results from the first variant and right ventricular volume overload results from the second. By echocardiography, the relationship of the right SVC to both atria can be delineated in subcostal short-axis (sagittal) views (Fig. 10.10) or right sternal border long-axis views (Fig. 10.11 ).

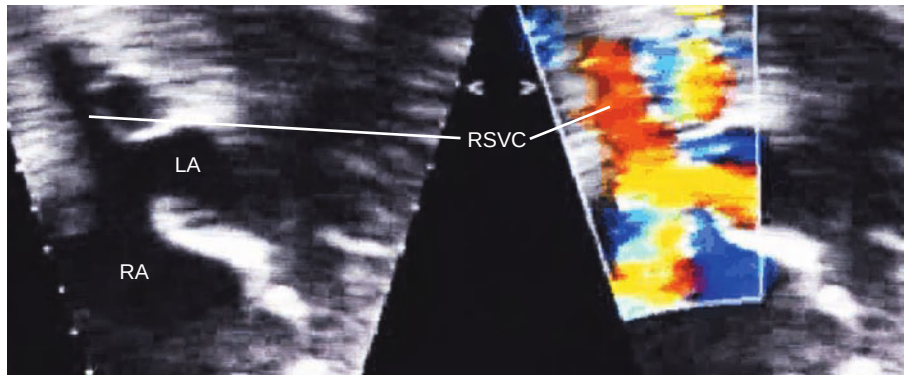


**Figure 10.10** Subcostal short-axis (sagittal) view with color mapping of a right superior vena cava with biatrial connection. LA, left atrium; RA, right atrium; RSVC, right superior vena cava.

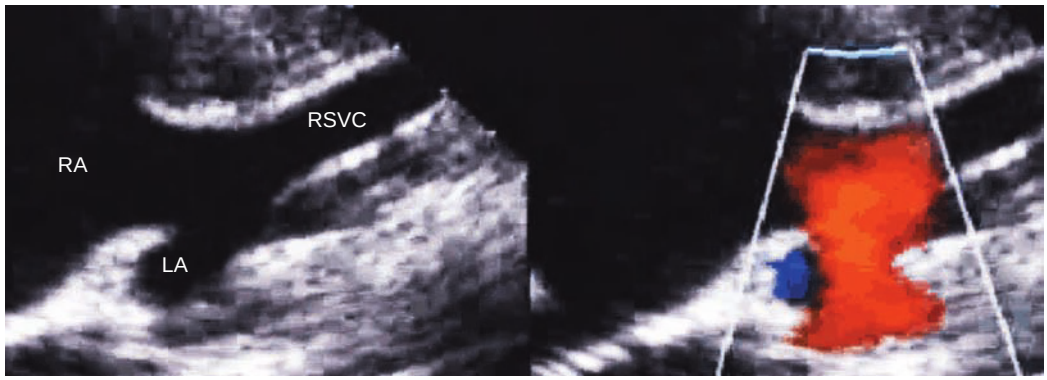


**Figure 10.11** Right sternal border long-axis view with color mapping of a right superior vena cava (RSVC) with biatrial connection. LA, left atrium; RA, right atrium.

### Other superior vena caval anomalies

Obstruction of the SVC in isolation is extremely rare. Occasionally it results from compression by a tumor or from thrombus formation. In the setting of congenital heart disease, postoperative SVC obstruction can occur after an atrial switch procedure for transposition of the great arteries and after repair of a sinus venosus defect with partially anomalous return of the right upper pulmonary vein. Management of these patients sometimes involves balloon dilation during cardiac catheterization [47]. Echocardiographic diagnosis of SVC obstruction usually involves subcostal, right sternal border, and suprasternal imaging and color mapping, although occasionally a transesophageal echocardiogram is necessary because prior surgery often results in poor transthoracic echocardiographic windows.

## Inferior vena caval anomalies

There is a broad spectrum of variations in inferior systemic venous return below the level of the renal veins. However, the progressively anterior location of the ascending IVC as it receives the hepatic veins and connects to the RA is fairly constant. Although embryologists have suggested that the IVC segment connecting to the heart is independent of the hepatic segment, there is no evidence to support this concept in humans. On the contrary, direct hepatic connection to the heart in left isomerism argues against such a segment above the liver. The spectrum of inferior systemic venous return in 1000 consecutive patients seen in a pediatric cardiology clinic revealed a completely normal pattern in 97%, and separate connection of the IVC and hepatic veins occurred only in left isomerism [3]. Evaluation of the IVC and its spatial relationship to the descending aorta may be useful in the diagnosis of atrial situs, particularly in patients with heterotaxy syndrome [48]. Echocardiography is useful when imaging the IVC [5], and subcostal views can display its lateral and anterior relationship to the aorta in these patients [7] (Fig. 10.12).

### Interrupted IVC with azygos/hemiazygos continuation

The common azygos trunk (i) is formed from paravertebral drainage of the right ascending lumbar vein, subcostal vein and lumbar azygos vein if present; (ii) ascends along the rightward posterior aspect of the mediastinum to the level of the fourth thoracic vertebra; (iii) arches anteriorly at this level above the root of the right lung; and (iv) drains into the SVC just before it pierces the pericardium. At this site the azygos vein is joined by the right superior intercostal vein,

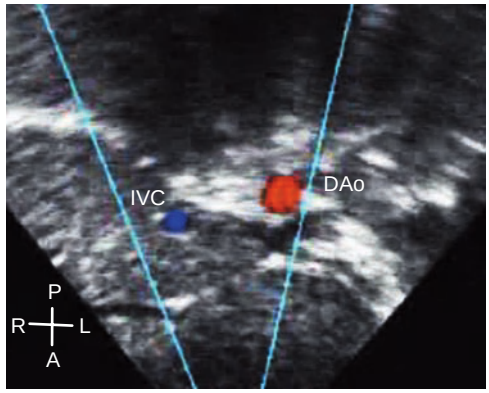


**Figure 10.12** Subcostal long-axis (transverse) view with color mapping displaying the spatial relationship between the inferior vena cava (IVC) and the descending aorta (DAo) just below the level of the diaphragm; the IVC is rightward and anterior in location with respect to the DAo. A, anterior; L, left; P, posterior; R, right.

which represents the confluence of the second, third and fourth posterior intercostal veins. The hemiazygos vein (i) drains the left renal vein, lumbar azygos, lumbar veins and the lower three posterior intercostal veins; (ii) ascends along the left side of the vertebrae (similar to the azygos vein); (iii) crosses the midline across the anterior surface of the eighth vertebral body; and (iv) connects to the azygos vein on the right at this level.

Interruption of the IVC with azygos continuation (also known as absence of the hepatic segment of the IVC with azygos continuation) (Fig. 10.13a) occurs in up to 84% of patients with left isomerism or polysplenia syndrome [49], but it may also occur in patients with situs solitus [3] and rarely in patients with right isomerism or asplenia syndrome [50]. It has a prevalence of approximately 0.6% among patients with congenital heart disease [51] and less than 0.3% among those without other heart defects [15,16]. Embryologically, failure of the right subcardinal vein to connect to the right vitelline and right hepatocardiac veins results in absence of the hepatic segment of the IVC. The right supracardinal vein enlarges and ultimately becomes the azygos continuation to the right SVC. In the setting of a left SVC, the left supracardinal vein becomes the hemiazygos continuation of an interrupted IVC. In either arrangement, the hepatic veins maintain their connection to the floor of the atrial mass. Both the azygos and

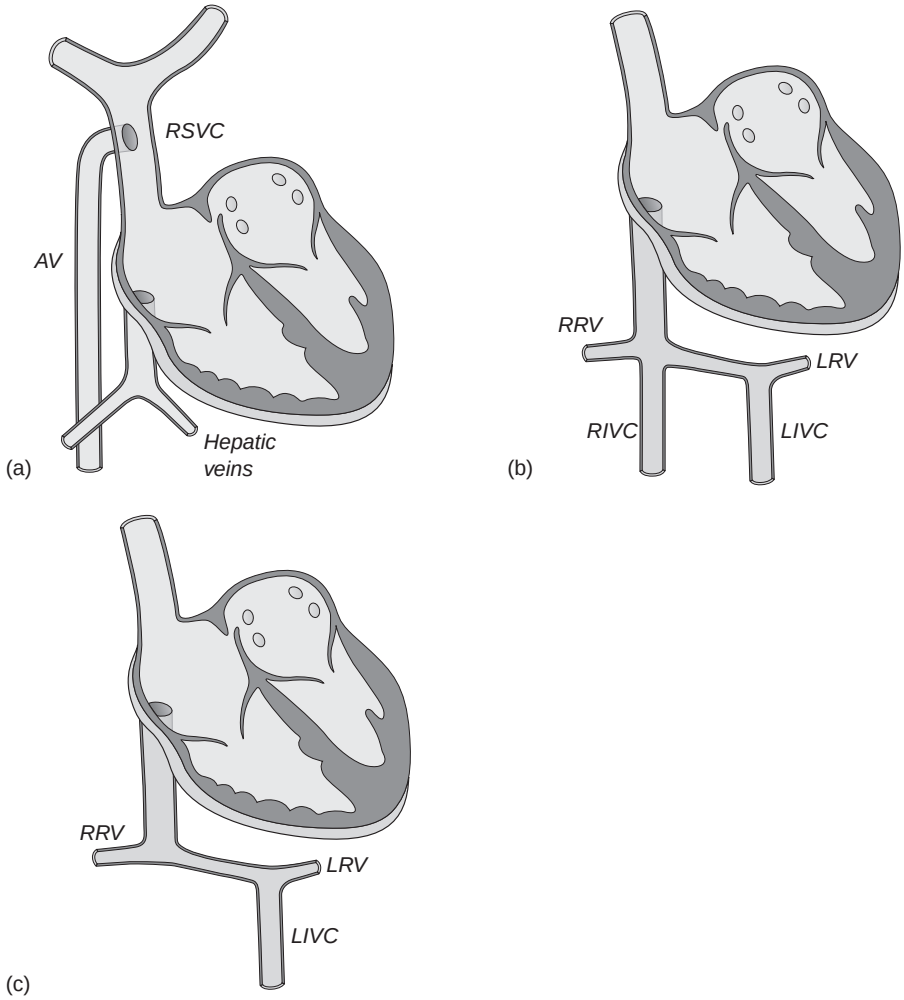


**Figure 10.13** Anomalies of the inferior vena cava (IVC). **(a)** Interrupted IVC with azygos continuation to the right superior vena cava (RSVC). **(b)** Bilateral IVCs converging into a common right-sided IVC at the level of the renal veins. **(c)** Left inferior vena cava (LIVC) connecting to the right IVC at the level of the renal veins with an atretic subrenal segment of the right IVC. AV, azygos vein; LRV, left renal vein; RIVC, right inferior vena cava; RRV, right renal vein.

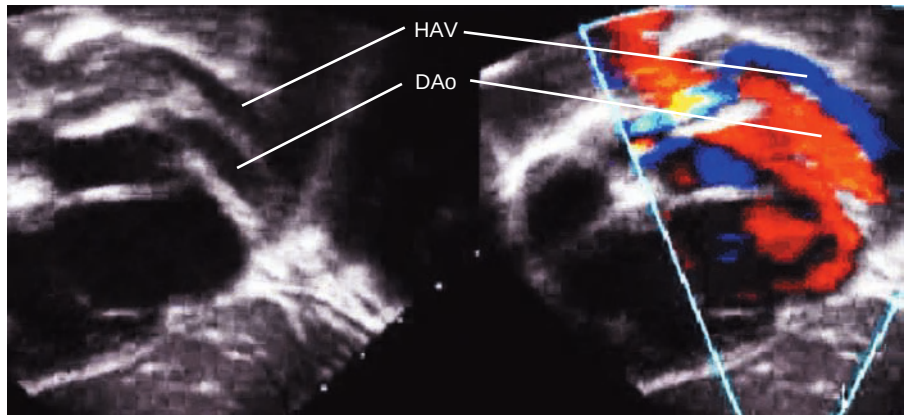


**Figure 10.14** Subcostal short-axis (sagittal) view with color mapping of an interrupted inferior vena cava with hemiazygos continuation into the left superior vena cava; the hemiazygos vein (HAV) is parallel and posterior to the descending aorta (DAo).

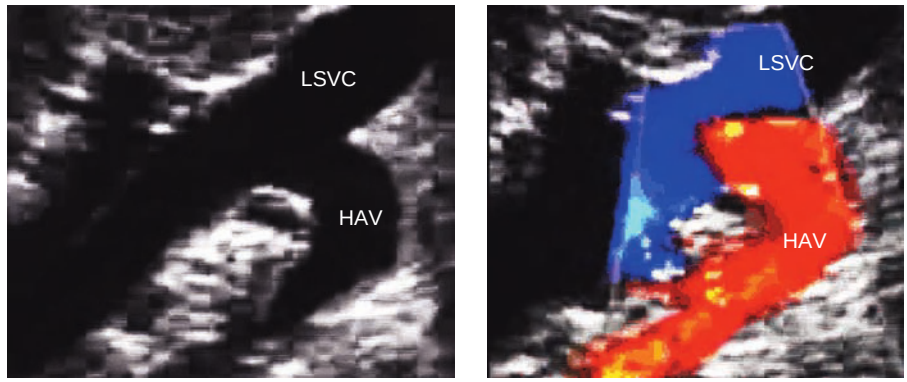


(a) (b)

**Figure 10.15** Modified high left parasagittal view **(a)** without and **(b)** with color mapping of an interrupted inferior vena cava with hemiazygos continuation into the left superior vena cava (LSVC). HAV, hemiazygos vein.

hemiazygos veins may be patent with azygos continuation [3,52,53].

### Pathophysiology and clinical significance

Because an interrupted IVC is usually seen in the setting of heterotaxy syndrome, the hemodynamic significance of abnormal systemic venous connections is frequently determined by the associated intracardiac anomalies. It is important to diagnose azygos continuation of the IVC by echocardiography because cardiac catheterization and intraoperative venous cannulation may be difficult in these patients [25,54,55]. In addition, patients with left isomerism and this anomaly are at increased risk for complete heart block, and emergency placement of a pacemaker can be difficult via an azygos vein.

### Imaging

Subcostal short-axis (sagittal) and long-axis (transverse) views with posterior angulation usually demonstrate hepatic venous drainage without an IVC connection to the RA. Occasionally a prominent hepatic vein is erroneously identified as the IVC in subcostal short-axis (sagittal) views, and displaying the length of the IVC from its more posterior location at the level of the kidneys to its more anterior location before it joins the RA can help to avoid this error. Subcostal short-axis (sagittal) imaging can also demonstrate a prominent azygos vein as a venous vessel coursing parallel to the descending aorta along its rightward and posterior aspect (a prominent hemiazygos vein courses along the leftward and posterior aspect of the descending aorta). Color mapping reveals opposite direction of flow in the azygos or hemiazygos vein and the descending aorta (Fig. 10.14 and Videoclip 10.5). Right sternal border long-axis (parasagittal) and suprasternal long-axis views can also demonstrate the arch of the azygos vein as it connects to the posterior aspect of the right SVC (Fig. 10.15). Echocardiography usually reveals absence of the full length of the IVC during sagittal sweeps of the fetal chest and abdomen. Identification of the prominent azygos vein behind and to the right of the descending aorta is often the first clue to an interrupted IVC in utero [28].

## Bilateral IVCs (duplication of the IVC)

Bilateral inferior venae cavae (IVCs) occur in 0.2–0.3% of the general population [56] and results from persistence of both supracardinal veins. Persistence of both subrenal IVCs occurs rarely in patients with and without abnormal situs [57]. Normally, the left IVC ends at the renal veins, crosses in front of the descending aorta, and joins the right IVC at the

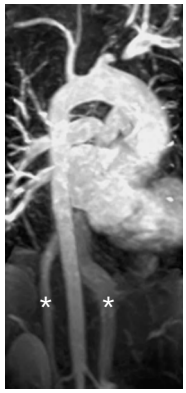


**Figure 10.16** Magnetic resonance angiogram of bilateral inferior venae cavae (asterisks) converging into a common inferior vena cava just below the diaphragm. Reproduced by courtesy of Dr Tal Geva, Children's Hospital Boston.

level of the kidneys (Fig. 10.13b). Connection of bilateral IVCs may occur at other levels, and the practical significance of this rare anomaly depends on exactly where the two IVCs join (Fig. 10.16). Echocardiographic diagnosis of this defect is extremely difficult.

### Left IVC to the right atrium (absent right IVC)

A left IVC connecting to the RA is a rare anomaly that occurs in 0.2–0.5% of the general population [56]. It results from regression of the right supracardinal vein and persistence of the left supracardinal vein. In this arrangement, the hepatic segment of the right IVC (including the hepatic veins) maintains its connection to the RA. The caudally located left IVC can cross in front of the descending aorta at or above the level of the renal veins before connecting to the right IVC (Fig. 10.13c) or it can drain into a prominent hemiazygos vein. Subcostal long-axis (transverse) imaging and color mapping sweeps (at a low color mapping scale) can sometimes display the left IVC as it crosses the midline in front of the descending aorta before connecting with the hepatic segment of the right IVC (Fig. 10.17 and Videoclip 10.6).

### Right IVC to the left atrium

There have been a few reports of anomalous drainage of the IVC into the LA with an intact atrial septum [58–60], although others have suggested that these cases are related to persistence of the embryonic valves of the sinus venosus in the setting of an atrial septal defect [61] or to errors in pathologic description [62]. In any case, a complete embryologic explanation for direct connection of an IVC to the LA is not currently available. Preoperative diagnosis of these lesions is especially important to prevent iatrogenic diversion of IVC flow to the LA during surgical closure of an atrial septal defect [63]. Echocardiographic evaluation involves careful color mapping of IVC flow in subcostal and right sternal border views. Injection of saline contrast into a lower extremity systemic vein can confirm the diagnosis, with the immediate appearance of contrast in the LA. In the absence of a communication between the RA and LA, these patients have an obligatory right-to-left shunt and are therefore cyanotic. In the presence of an interatrial communication, biatrial connection of the IVC may be a result of an inferior secundum atrial septal defect that is confluent with the IVC or an inferior sinus venosus defect (Fig. 10.18).

## Hepatic vein anomalies

Normal hepatic venous drainage occurs from both hepatic lobes directly into the IVC, and abnormal drainage can involve some or all of the hepatic veins. Anomalous hepatic venous connection directly to the heart occurs in up to 28% of patients with right isomerism or asplenia syndrome [13],

(a)

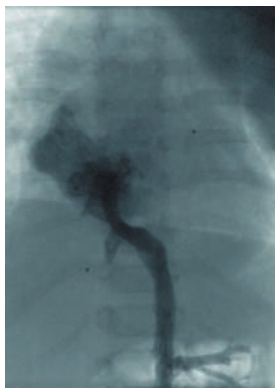

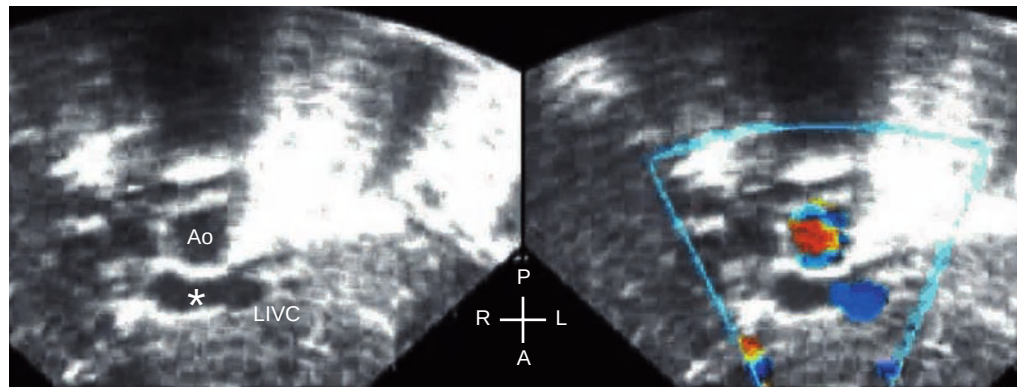


(b)

**Figure 10.17** **(a)** Angiogram of a left inferior vena cava that crosses the midline just below the diaphragm before draining into the right atrium. **(b)** Subcostal long-axis (transverse) view with color mapping of a left inferior vena cava (LIVC) at the level where it crosses in front of the descending aorta (asterisk) before draining into the right atrium. A, anterior; Ao, aorta; L, left; P, posterior; R, right.

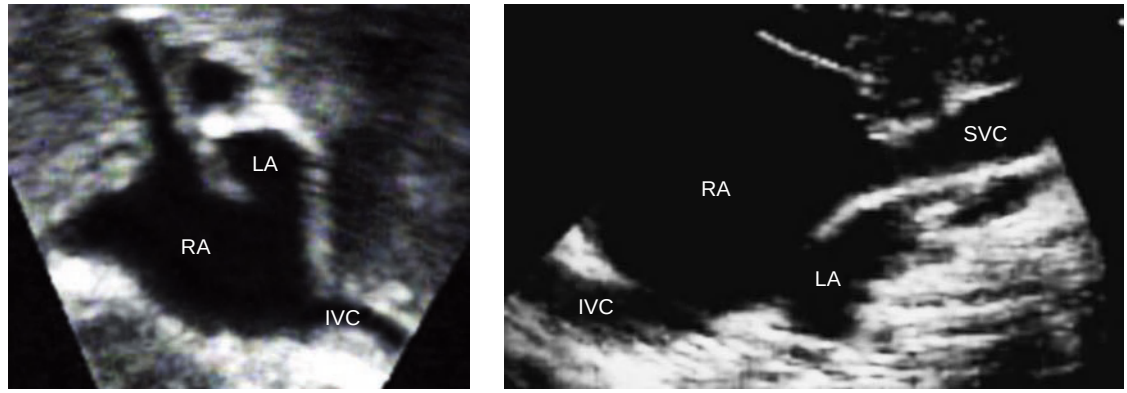


(a) (b)

**Figure 10.18** Biatrial connection of an inferior vena cava (IVC) secondary to an atrial septal defect that is confluent with the IVC in **(a)** a subcostal short-axis (sagittal) view, and **(b)** a right sternal border long-axis view. LA, left atrium; RA, right atrium; SVC, superior vena cava.

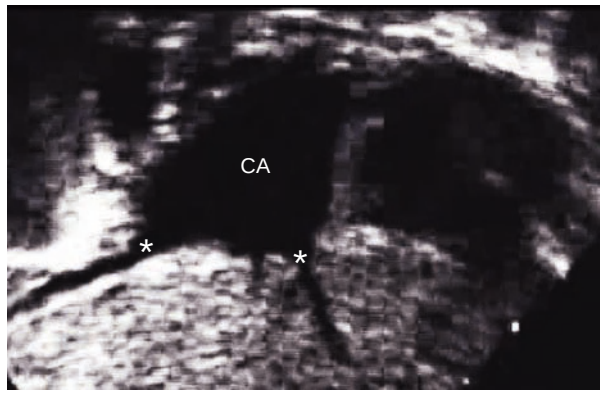


**Figure 10.19** Subcostal long-axis (transverse) view of separate hepatic venous connections (asterisks) into the common atrium (CA) of a patient with heterotaxy syndrome and a functionally single ventricle.

although it may also occur in situs solitus or situs inversus [3,64,65]. Anomalous hepatic venous connection to the atrial mass via a single trunk also occurs in left isomerism, although occasionally there are two or more separate venous connections. Recognition of anomalous hepatic venous drainage in patients with single ventricle anatomy and in patients undergoing liver transplantation is critical in determining the appropriate surgical intervention. For example, failure to identify a separate accessory hepatic vein prior to a Fontan procedure can result in the inadvertent exclusion of this vessel with decompression from the Fontan pathway via the accessory hepatic vein into the atrial mass; this, in turn, results in significant progressive cyanosis after the operation [66,67]. Echocardiographic evaluation of the IVC and hepatic veins should be performed during the posterior sweep in subcostal long-axis (transverse) views, apical views and parasternal long-axis views (Fig. 10.19 and Videoclip 10.7).

## Coronary sinus anomalies

Although the CS drains into the RA, some consider it a left atrial structure as it courses along the posterior aspect of the left atrioventricular groove, accounting for its absence in right isomerism with its bilateral morphologically right atria. It represents the left horn of the sinus venosus after leftward invagination of the junction between the left sinus horn and the common atrium. Aside from a dilated CS, other anomalies of the CS are rare [68].

### Dilated coronary sinus

The CS becomes dilated as a result of abnormally increased flow or pressure. Some causes of the former include: (i) a persistent left SVC; (ii) a coronary sinoseptal defect; (iii) partially or totally anomalous pulmonary venous drainage into the CS; (iv) a coronary arteriovenous fistula; and (v) partially or totally anomalous hepatic venous drainage into the CS. Increased pressure in the CS results primarily from right atrial hypertension, particularly in the setting of the classic Fontan procedure involving direct anastomosis of the right atrial appendage to the pulmonary artery. As discussed previously, a dilated CS can be seen by echocardiography during the posterior sweep of an apical 4-chamber view (Fig. 10.4 and Videoclip 10.2) and along the posterior atrioventricular groove in a parasternal long-axis view [27] (Fig. 10.5). When a dilated CS is seen, a systematic approach should include evaluation of the left innominate vein, the individual pulmonary veins, the coronary arteries, the hepatic veins, and the roof of the CS. It is especially important to evaluate the CS with views wherein the roof is perpendicular to the ultrasound beam, and these include the posterior sweep of an apical view as well as a high left parasagittal view in a nearly vertical orientation. When a coronary sinoseptal

defect is associated with a left SVC and is located along the superior aspect of the CS as it passes behind the LA, it can present like a left SVC to the LA and may or may not be associated with an additional interatrial communication. Injection of saline contrast into the left arm may result in the appearance of contrast in the LA.

### Coronary sinus ostium atresia or stenosis

Atresia or stenosis of the CS ostium is extremely rare, with usually little hemodynamic significance. The obstruction is thought to result from a prominent Thebesian valve. In cases with a benign clinical course, the myocardial venous blood usually decompresses via a persistent left SVC, although occasionally decompression occurs via prominent Thebesian veins or a coronary sinoseptal defect. The absence of adequate decompression is generally associated with poor outcome, emphasizing the critical importance of even a small left SVC in these cases. Suprasternal short-axis views with color mapping can demonstrate retrograde flow from the left SVC into the connecting vein in most of these cases. It is important to distinguish this anomaly from the normal drainage of a prominent superior intercostal vein or internal thoracic vein into the left innominate vein in the setting of a small CS. It is especially critical to identify this anomaly prior to surgical intervention because ligation of a left SVC in the setting of CS ostium atresia or stenosis will lead to severe myocardial ischemia and/or sudden cardiac arrest [69,70].

### Other coronary sinus anomalies

Absence of the CS is common in the setting of abnormal atrial situs with isomerism and is distinctly uncommon in the setting of lateralized atrial situs [3]. Rarely the coronary sinus connects to the IVC instead of the RA [71].

## Innominate vein anomalies

The left innominate vein (i) originates from the persistent connection between the anterior cardinal veins after regression of the left anterior cardinal vein; (ii) represents the systemic venous drainage from the left subclavian and left common jugular veins; and (iii) courses in front of the aortic arch and ascending aorta before draining into the right SVC.

### Retroaortic innominate vein

In this rare anomaly, the innominate vein courses behind the ascending aorta and below the aortic arch before draining into the right SVC at a level below the connection of the azygos vein. It occurs in 1% of patients with congenital heart disease [72] and in at most 0.008% of the general population [62]. It is most commonly seen in patients with tetralogy of Fallot or truncus arteriosus and a right aortic arch [72–74]. Embryologically, some have suggested that this anomaly results from failure of development of the usual connection between the anterior cardinal veins and formation of an alternative connection in a different location [74].

#### Pathophysiology and clinical significance

Although there is no hemodynamic significance to this lesion, it can have an effect during venous cannulation [25] and during a bidirectional superior cavopulmonary anastomosis procedure. When the innominate vein is absent, it usually represents the presence of bilateral SVCs without a connecting vein. However, a retroaortic innominate vein may also occur in this setting.

#### Imaging

Echocardiographic evaluation involves suprasternal short-axis and long-axis views. Short-axis imaging of a normal left innominate vein reveals its course in front of the ascending aorta, usually just below the origin of the first aortic arch branch. With a retroaortic innominate vein, short-axis sweeps can reveal two separate and parallel vessels (representing the right pulmonary artery and the retroaortic innominate vein) coursing behind the ascending aorta (Fig. 10.20 and Videoclip 10.8). Occasionally, the right pulmonary artery is small, and the problem may not be recognized if the retroaortic innominate vein is erroneously identified as a normal-sized right pulmonary artery. In long-axis views, two circles are seen below the transverse aortic arch, the superior one representing the cross-section of the retroaortic innominate vein and the inferior one representing the cross-section of the right pulmonary artery (Fig. 10.21).

### Other innominate vein anomalies

Other extremely rare anomalies of the innominate vein include duplication of the left innominate vein [62] and absent left innominate vein (Fig. 10.22 and Videoclip 10.9).

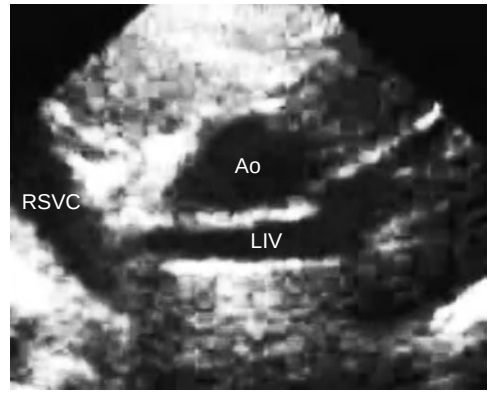


**Figure 10.20** Suprasternal short-axis view of a retroaortic innominate vein. Ao, aorta; LIV, left innominate vein; RSVC, right superior vena cava.

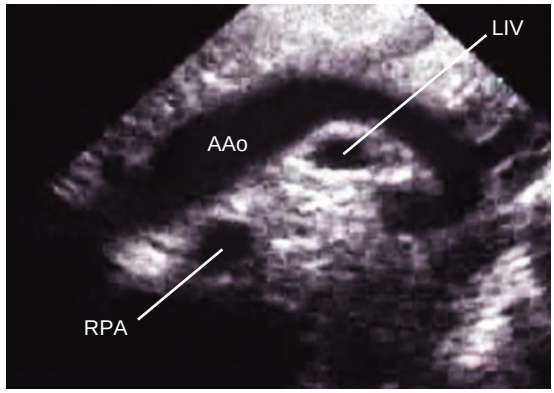


**Figure 10.21** Suprasternal long-axis view of a retroaortic innominate vein as it courses below the aortic arch and above the right pulmonary artery. AAo, ascending aorta; LIV, left innominate vein; RPA, right pulmonary artery.

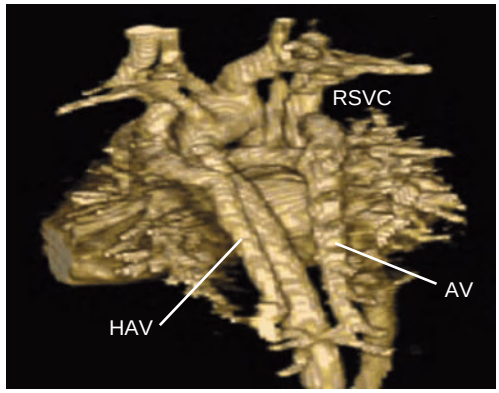


**Figure 10.22** Posterior view during magnetic resonance 3D reconstruction of an absent left innominate vein. The left head and neck vessels drain into the hemiazygos vein (HAV), which in turn connects to the azygos vein (AV) below the diaphragm with subsequent drainage via the azygos vein into the right superior vena cava (RSVC). Reproduced by courtesy of Dr Tal Geva, Children's Hospital Boston.

## References


1. McClure CFW, Butler EG. The development of the vena cava inferior in man. *Am J Anat* 1925;35:331–83.
2. Seib GA. The azygos system of veins in American whites and American negroes, including observations on the inferior caval venous sytem. *Am J Phys Anthropol* 1934;19:29.
3. Huhta JC, Smallhorn JF, Macartney FJ et al. Cross-sectional echocardiographic diagnosis of systemic venous return. *Brit Heart J* 1982;48:388–403.
4. Foale R, Bourdillon PD, Somerville J, Rickards A. Anomalous systemic venous return: recognition by two-dimensional echocardiography. *Eur Heart J* 1983;4:186–95.
5. Slovis TL, Clapp SK, Farooki ZQ. Noninvasive evaluation of the inferior vena cava. The value of sonography. *Am J Dis Child* 1984;138:277–80.
6. Tacy TA, Silverman NH. Systemic venous abnormalities: embryologic and echocardiographic considerations. *Echocardiography (Mount Kisco, NY)* 2001;18:401–13.
7. Huhta JC, Smallhorn JF, Macartney FJ. Two dimensional echocardiographic diagnosis of situs. *Brit Heart J* 1982;48:97–108.
8. Ivemark BI. Implications of agenesis of the spleen on the pathogenesis of conotruncus anomalies in childhood; an analysis of the heart malformations in the splenic agenesis syndrome, with fourteen new cases. *Acta Paediatrica* 1955;44(Suppl. 104):7–110.
9. Ongley PA, Titus JL, Khoury GH et al. Anomalous connection of pulmonary veins to right atrium associated with anomalous inferior vena cava, situs inversus and multiple spleens: a developmental complex. *Mayo Clin Proc* 1965;40:609–24.
10. Rastelli GC, Rahimtoola SH, Ongley PA, McGoon DC. Common atrium: anatomy, hemodynamics, and surgery. *J Thorac Cardiovasc Surg* 1968;55:834–41.
11. Van Mierop LHS, Gessner JH, Schiebler GL. Asplenia and polysplenia syndromes. *Birth Defects* 1972;8:36–44.
12. Krayenbuhl CU, Lincoln JC. Total anomalous systemic venous connection, common atrium, and partial atrioventricular canal. A case report of successful surgical correction. *J Thorac Cardiovasc Surg* 1977;73:686–9.
13. Van Praagh S. Cardiac malpositions and the heterotaxy syndromes. In: Keane JF, Lock JE, Fyler DC (eds) *Nadas' Pediatric Cardiology*. Philadelphia, PA: Saunders Elsevier, 2006;675–95.
14. Abbott ME. *Atlas of Congenital Cardiac Disease*. New York: AHA, 1936.
15. Papez JW. Two cases of persistent left superior vena cava in man. *Anat Rec* 1938;70:191–8.
16. Sanders JM. Bilateral superior vena cava. *Anat Rec* 1946;94:657.
17. Campbell M, Deuchar DC. The left-sided superior vena cava. *Brit Heart J* 1954;16:423–39.
18. Winter FS. Persistent left superior vena cava: survey of world literature and report of thirty additional cases. *Angiology* 1954; 5:90–132.
19. Cha EM, Khoury GH. Persistent left superior vena cava. Radiologic and clinical significance. *Radiology* 1972;103:375–81.
20. Fyler DC, Bucklet LP, Hellenbrand WE, Cohn HE. Report of the New England Regional Infant Cardiac Program. *Pediatrics* 1980; 65(Suppl.):375–461.
21. Rubino M, Van Praagh S, Kadoba K et al. Systemic and pulmonary venous connections in visceral heterotaxy with asplenia. Diagnostic and surgical considerations based on seventy-two autopsied cases. *J Thorac Cardiovasc Surg* 1995;110:641–50.
22. Wood P. *Diseases of the Heart and Circulation*, 2nd edn. Philadelphia: JB Lippincott, 1956.
23. Meadows WR, Sharp JT. Persistent left superior vena cava draining into the left atrium without arterial oxygen unsaturation. *Am J Cardiol* 1965;16:273–9.
24. Looyenga DS, Lacina SJ, Gebuhr CJ, Stockinger FS. Persistent left superior vena cava communicating with the left atrium through a systemic–pulmonary venous malformation. *J Am Coll Cardiol* 1986;8:621–6.
25. Bosher LH Jr. Problems in extracorporeal circulation relating to venous cannulation and drainage. *Ann Surg* 1959;149: 652–63.
26. Freed MD, Rosenthal A, Bernhard WF. Balloon occlusion of a persistent left superior vena cava in the preoperative

evaluation of systemic venous return. *J Thorac Cardiovasc Surg* 1973;65:835–9.
27. Snider AR, Ports TA, Silverman NH. Venous anomalies of the coronary sinus: detection by M-mode, two-dimensional and contrast echocardiography. *Circulation* 1979;60:721–7.
28. Hornberger LK. Abnormalities of systemic and pulmonary venous connections. In: Allan L, Hornberger LK, Sharland G (eds) *Textbook of Fetal Cardiology*. London: Greenwich Medical Media, 2000;103–14.
29. Galindo A, Gutierrez-Larraya F, Escribano D et al. Clinical significance of persistent left superior vena cava diagnosed in fetal life. *Ultrasound Obstet Gynecol* 2007;30:152–61.
30. Karnegis JN, Wang Y, Winchell P, Edwards JE. Persistent left superior vena cava, fibrous remnant of the right superior vena cava and ventricular septal defect. *Am J Cardiol* 1964;14:573–7.
31. Choi JY, Anderson RH, Macartney FJ. Absent right superior caval vein (vena cava) with normal atrial arrangement. *Brit Heart J* 1987;57:474–8.
32. Horwitz S. Clinical diagnosis of persistent left superior vena cava draining into left atrium. *Jpn J Thorac Surg* 1974;27:647–51.
33. Taybi H, Kurlander GJ, Lurie PR, Campbell JA. Anomalous systemic venous connection to the left atrium or to a pulmonary vein. *Am J Roentgenol RA* 1965;94:62–77.
34. Raghib G, Ruttenberg HD, Anderson RC et al. Termination of left superior vena cava in left atrium, atrial septal defect, and absence of coronary sinus; a developmental complex. *Circulation* 1965;31:906–18.
35. Davis WH, Jordaan FR, Snyman HW. Persistent left superior vena cava draining into the left atrium, as an isolated anomaly. *Am Heart J* 1959;57:616–22.
36. Fischer DR, Zuberbuhler JR. Anomalous systemic venous return. In: Anderson RH, Baker EJ, Macartney FJ et al. (eds) *Paediatric Cardiology*, 2nd edn. London: Churchill Livingstone, 2002;851–65.
37. Shumacker HB Jr, King H, Waldhausen JA. The persistent left superior vena cava. Surgical implications, with special reference to caval drainage into the left atrium. *Ann Surg* 1967;165:797–805.
38. Foster ED, Baeza OR, Farina MF, Shaher RM. Atrial septal defect associated with drainage of left superior vena cava to left atrium and absence of the coronary sinus. *J Thorac Cardiovasc Surg* 1978;76:718–20.
39. de Leval MR, Ritter DG, McGoon DC, Danielson GK. Anomalous systemic venous connection. Surgical considerations. *Mayo Clin Proc* 1975;50:599–610.
40. Konstam MA, Levine BW, Strauss HW, McKusick KA. Left superior vena cava to left atrial communication diagnosed with radionuclide angiocardiography and with differential right to left shunting. *Am J Cardiol* 1979;43:149–53.
41. Park HM, Smith ET, Silberstein EB. Isolated right superior vena cava draining into left atrium diagnosed by radionuclide angiocardiography. *J Nucl Med* 1973;14:240–2.
42. Bernstein HS, Moore P, Stanger P, Silverman NH. The levoatriocardinal vein: morphology and echocardiographic identification of the pulmonary-systemic connection. *J Am Coll Cardiol* 1995;26:995–1001.
43. Kirsch WM, Carlsson E, Hartmann AF Jr. A case of anomalous drainage of the superior vena cava into the left atrium. *J Thorac Cardiovasc Surg* 1961;41:550–6.
44. Braudo M, Beanlands DS, Trusler G. Anomalous drainage of the right superior vena cava into the left atrium. *Can Med Assoc J* 1968;99:715–9.
45. Shapiro EP, Al-Sadir J, Campbell NP et al. Drainage of right superior vena cava into both atria. Review of the literature and description of a case presenting with polycythemia and paradoxical embolization. *Circulation* 1981;63:712–7.
46. Van Praagh S, Geva T, Lock JE et al. Biatrial or left atrial drainage of the right superior vena cava: anatomic, morphogenetic, and surgical considerations – report of three new cases and literature review. *Pediatr Cardiol* 2003;24:350–63.
47. Ali MK, Ewer MS, Balakrishnan PV et al. Balloon angioplasty for superior vena cava obstruction. *Ann Int Med* 1987;107:856–7.
48. Elliott LP, Cramer GG, Amplatz K. The anomalous relationship of the interior vena cava and abdominal aorta as a specific angiocardiographic sign in asplenia. *Radiology* 1966;87:859–63.
49. Van Praagh S. Cardiac malpositions and the heterotaxy syndromes. In: Keane JF, Lock JE, Fyler DC (eds) *Nadas' Pediatric Cardiology*, 2nd edn. Philadelphia: Saunders Elsevier, 2006;675–95.
50. Ruscazio M, Van Praagh S, Marrass AR et al. Interrupted inferior vena cava in asplenia syndrome and a review of the hereditary patterns of visceral situs abnormalities. *Am J Cardiol* 1998;81:111–16.
51. Anderson RC, Adams P Jr, Burke B. Anomalous inferior vena cava with azygos continuation (infrahepatic interruption of the inferior vena cava). Report of 15 new cases. *J Pediatr* 1961;59:370–83.
52. Haswell DM, Berrigan TJ Jr. Anomalous inferior vena cava with accessory hemiazygos continuation. *Radiology* 1976;119:51–4.
53. Floyd GD, Nelson WP. Developmental interruption of the inferior vena cava with azygos and hemiazygos substitution. Unusual radiographic features. *Radiology* 1976;119:55–7.
54. Huhta JC, Smallhorn JF, Macartney FJ. Cross-sectional echocardiographic diagnosis of azygos continuation of the inferior vena cava. *Catheter Cardio Diag* 1984;10:221–32.
55. Wolfhard U, Splittgerber FH, Gocke P, Reidemeister JC. Bilateral inferior vena cava with azygos continuation but without congenital heart disease complicates routine venous cannulation for cardiopulmonary bypass in an adult. *Thorac Cardiovasc Surg* 1997;45:40–2.
56. Bass JE, Redwine MD, Kramer LA et al. Spectrum of congenital anomalies of the inferior vena cava: cross-sectional imaging findings. *Radiographics* 2000;20:639–52.
57. Gladstone RJ. Development of the inferior vena cava in the light of recent research, with especial reference to certain abnormalities, and current descriptions of the ascending lumbar and azygos veins. *J Anat* 1929;64:70–93.
58. Meadows WR, Bergstrand I, Sharp JT. Isolated anomalous connection of a great vein to the left atrium. The syndrome of cyanosis and clubbing, "normal" heart, and left ventricular hypertrophy on electrocardiogram. *Circulation* 1961;24:669–76.
59. Gardner DL, Cole L. Long survival with inferior vena cava draining into left atrium. *Brit Heart J* 1955;17:93–7.
60. Black H, Smith GT, Goodale WT. Anomalous inferior vena cava draining into the left atrium associated with intact interatrial septum and multiple pulmonary arteriovenous fistulae. *Circulation* 1964;29:258–67.

61. Lucas RV, Krabill KA. Abnormal systemic venous connections. In: Emmanoulides GC, Rreimenschneider TA, Allen HD, Gutgesell HP (eds) *Moss and Adams' Heart Disease in Infants, Children, and Adolescents: Including the Fetus and Young Adult*, 5th edn. Baltimore: Williams & Wilkins, 1995;874–902.
62. Geva T, Van Praagh S. Abnormal systemic venous connections. In: Allen HD, Driscoll DJ, Shaddy RE, Feltes TF (eds) *Moss and Adams' Heart Disease in Infants, Children and Adolescents: Including the Fetus and Young Adult*, 7th edn. Philadelphia: Lipincott Williams & Wilkins, 2007;792–817.
63. Mustard WT, Firor WB, Kidd L. Diversion of the venae cavae into the left atrium during closure of atrial septal defects. *J Thorac Cardiovasc Surg* 1964;47:317–24.
64. Georghiou GP, Erez E, Bruckheimer E et al. Anomalous hepatic venous drainage. *Ann Thorac Surg* 2005;80:1113–15.
65. Stoller JK, Hoffman RM, White RD, Mee RB. Anomalous hepatic venous drainage into the left atrium: an unusual cause of hypoxemia. *Respir Care* 2003;48:58–62.
66. Fernandez-Martorell P, Sklansky MS, Lucas VW et al. Accessory hepatic vein to pulmonary venous atrium as a cause of cyanosis after the Fontan operation. *Am J Cardiol* 1996;77:1386–7.
67. Yoshimura N, Yamaguchi M, Oshima Y et al. Intrahepatic venovenous shunting to an accessory hepatic vein after Fontan type operation. *Ann Thorac Surg* 1999;67:1494–6.
68. Mantini E, Grondin CM, Lillehei CW, Edwards JE. Congenital anomalies involving the coronary sinus. *Circulation* 1966;33: 317–27.
69. Prows MS. Two cases of bilateral superior vena cava, one draining a closed coronary sinus. *Anat Rec* 1943;87:99–106.
70. Edwards JE. Malformations of the thoracic veins. In: Gould SE (ed) *Pathology of the Heart*, 2nd edn. Charles C Thomas Publishers, Springfield, 1960.
71. Brickner ME, Eichhorn EJ, Netto D et al. Left-sided inferior vena cava draining into the coronary sinus via persistent left superior vena cava: case report and review of the literature. *Catheter Cardiovasc Diag* 1990;20:189–92.
72. Choi JY, Jung MJ, Kim YH et al. Anomalous subaortic position of the brachiocephalic vein (innominate vein): an echocardiographic study. *Brit Heart J* 1990;64:385–7.
73. Smallhorn JF, Zielinsky P, Freedom RM, Rowe RD. Abnormal position of the brachiocephalic vein. *Am J Cardiol* 1985;55: 234–6.
74. Gerlis LM, Ho SY. Anomalous subaortic position of the brachiocephalic (innominate) vein: a review of published reports and report of three new cases. *Brit Heart J* 1989;61:540–5.

# 11 Anomalies of the Atrial Septum

**Tal Geva**

Harvard Medical School; Division of Noninvasive Cardiac Imaging, Department of Cardiology, Children's Hospital Boston, Boston, MA, USA

## Definition

Defects that allow interatrial communication can result from openings in the atrial septum (defined as *atrial septal defect*, or ASD), or from defects in the sinus venosus septum (defined as *sinus venosus defect*) or in the tissue that separates the coronary sinus from the left atrium (defined as *coronary sinus septal defect*). Patent foramen ovale is an interatrial communication that exists normally in the fetus and in most newborns, but because of its clinical importance in certain congenital heart defects and in older patients with paradoxical emboli and stroke, it is discussed in this chapter. Atrial septal defects are further classified into secundum and primum defects. The latter – defects that result from abnormal formation of the embryonic endocardial cushions – are discussed in Chapter 15.

## Incidence

Defects of the atrial septum comprise the third most common type of congenital heart disease, with an estimated incidence of 56 per 100 000 live births [1]. This estimate represents the median incidence based on analysis of 43 published articles spanning many decades. With improved recognition of clinically silent defects by echocardiography, recent estimates are approximately 100 per 100 000 live births [2].

## Etiology

Most cases of secundum ASD are sporadic; however, several investigators reported familial clusters with different modes of inheritance as well as an association with conduction defects. Examples include mutations in the cardiac transcription factor gene *NKX2-5* [3–5], a mutation in the myosin heavy chain 6 gene located on chromosome 14q12 [6], as well as other mutations [7–9]. Secundum ASD is also frequently associated with genetic syndromes such as Holt–Oram, Noonan, Down, Budd–Chiari and Jarcho–Levine, to mention just a few [10–16].

## Morphology and classification

### Developmental considerations

The classification of interatrial communications is based on understanding of atrial septation and the relationships between the pulmonary veins, the systemic veins and the atria. Atrial septation involves the following structures:

- septum primum
- septum secundum
- atrioventricular (AV) canal septum
- sinus venosus septum
- coronary sinus septum.

Detailed description of atrial septation can be found in several publications [17–20]. Briefly, septum primum – the first septum to appear in the developing atria at approximately 28 days of development – grows as a crescent-shaped structure toward the developing endocardial cushions (Fig. 11.1a). Its leading edge is covered by a layer of mesenchymal cells (mesenchymal cap) [20]. The space between the developing septum primum and the closing endocardial cushions is termed *foramen primum* or the *primary foramen*. Septum secundum, also called the *limbus of the fossa ovale*, is a crescent-shaped muscular infolding of the atrial wall that develops to the right of septum primum (Fig. 11.1b). Foramen primum closes as a result of fusion between the mesenchymal cap of septum primum and the now fused superior and inferior endocardial cushions (Fig. 11.1c). Foramina secundi (secondary foramens) form at the same time as coalescing fenestrations within septum primum (Fig. 11,1b,c).

The AV canal septum is formed, at least in part, by the superior and inferior endocardial cushions and contributes to septation of the outlet portion of the atria and the inlet portion of the ventricles (Fig. 11.1). Normal development of

*Echocardiography in Pediatric and Congenital Heart Disease: From Fetus to Adult*
Edited by Wyman W. Lai, Luc L. Mertens, Meryl S. Cohen and Tal Geva
 ISBN: 978-1-405-17401-5

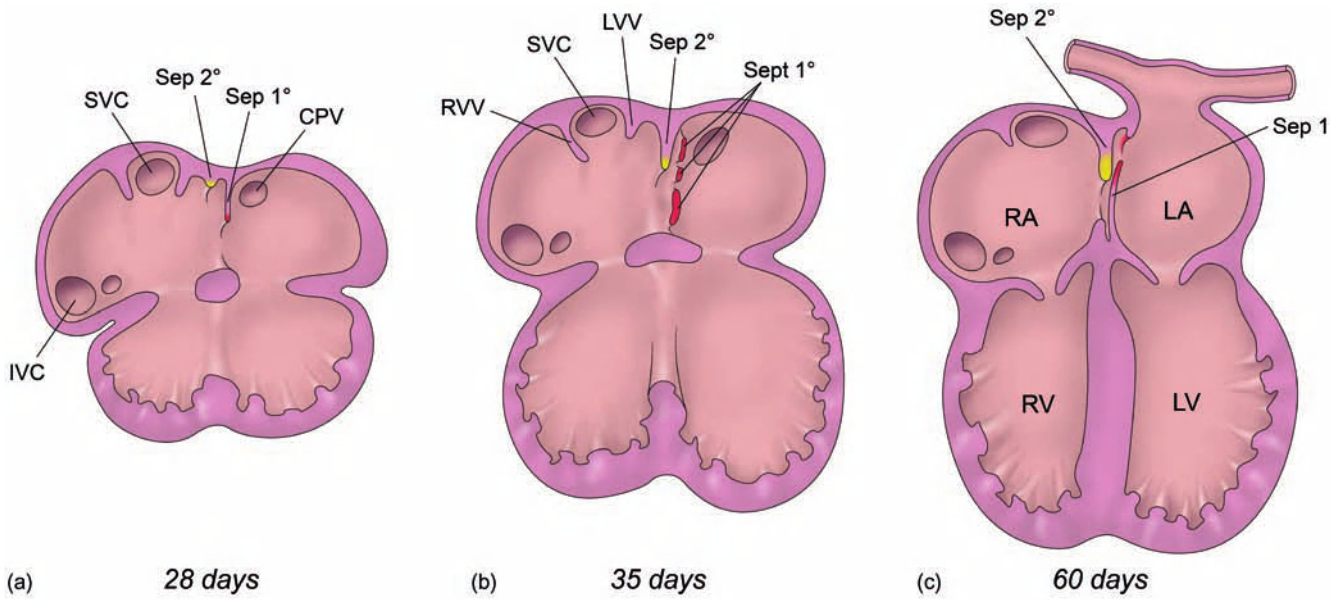


**Figure 11.1** Diagram showing development of the atrial septum. **(a)** At 28 days after gestation, septum primum (Sep 1°) develops as a crescent-shape structure with a layer of mesenchymal cells at the leading edge (red color). The space between the developing septum primum and the developing endocardial cushions is called *foramen primum* or *ostium primum*. Septum secundum (Sep 2°) appears shortly thereafter to the right of septum primum. **(b)** At 35 days, both septum primum and septum secundum continue to develop. The openings within septum primum are called *foramina secundi*. **(c)** At 60 days, the atrial septum is nearly fully formed and the foramina secundi close by way of coalescing fenestrations within septum primum. The foramen ovale remains patent throughout pregnancy. CPV, common pulmonary vein; IVC, inferior vena cava; LA, left atrium; LV, left ventricle; LVV, left venous valve; RA, right atrium; RV, right ventricle; RVV, right venous valve; SVC, superior vena cava.

the atrial septum results in formation of the fossa ovalis, which includes the following anatomic elements: (i) muscular boundaries contributed by *septum secundum;* (ii) the valve of the fossa ovalis, which attaches on the left atrial aspect of the septum – *septum primum;* and (iii) a muscular septum between the inferior aspect of the fossa ovalis and the tricuspid and mitral valve annuli – the *AV canal septum* (Fig. 11.2). The tissue that separates the right pulmonary veins from the

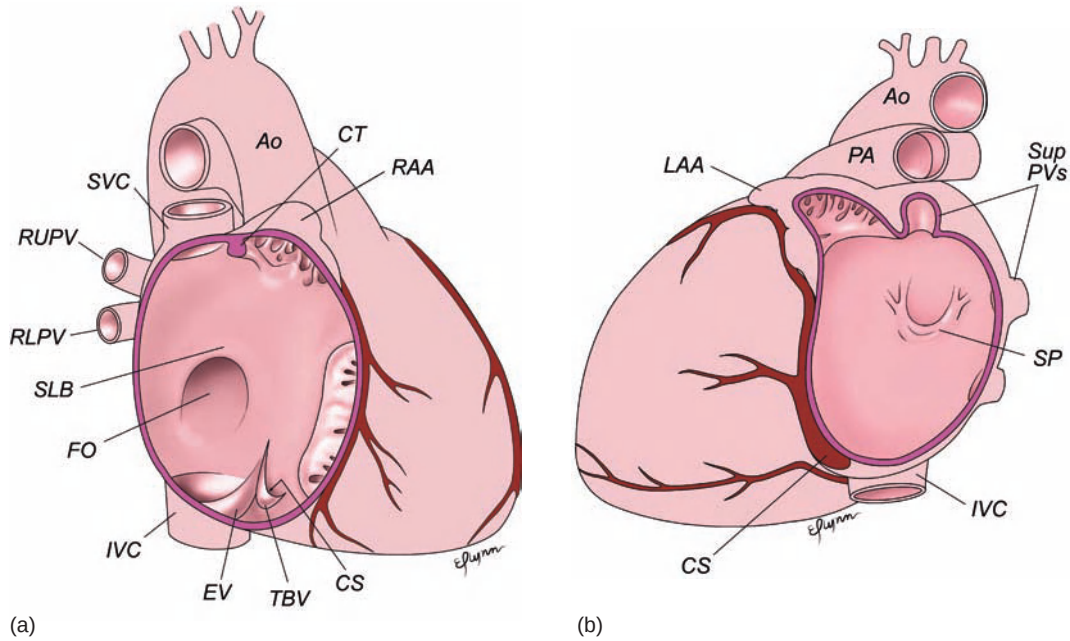


**Figure 11.2** Diagram showing the anatomy of the atrial septum. **(a)** Right atrial aspect. **(b)** Left atrial aspect. Ao, aorta; CS, coronary sinus; CT, crista terminalis; EV, Eustachian valve; FO, foramen ovale; IVC, inferior vena cava; LAA, left atrial appendage; PA, (main) pulmonary artery; RAA, right atrial appendage; RLPV, right lower pulmonary vein; RUPV, right upper pulmonary vein; SLB, superior limbic band (septum secundum); SP, septum primum; Sup PVs, superior pulmonary veins; SVC, superior vena cava; TBV, Thebesian valve.

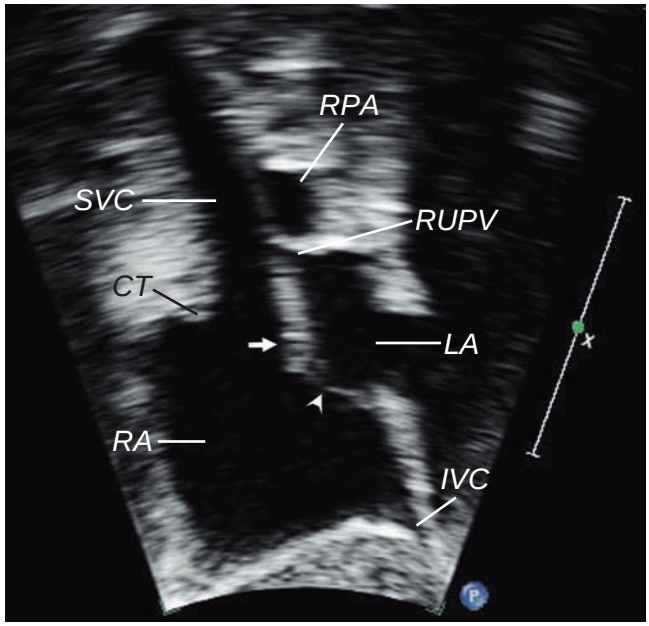


**Figure 11.2 (c)** Echocardiographic view.

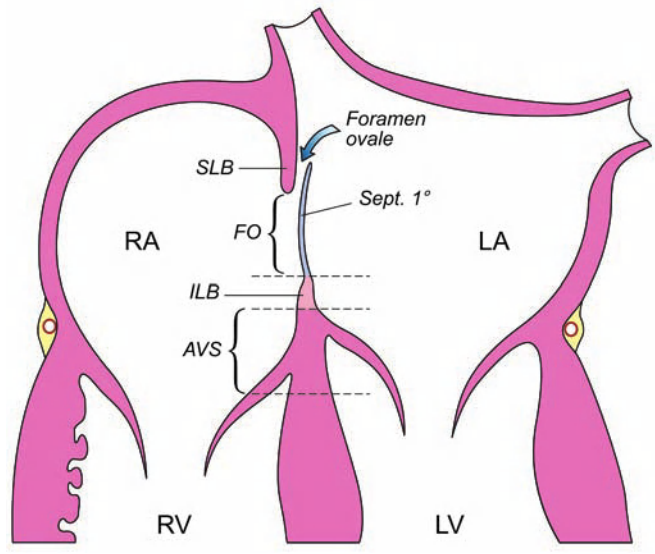


**Figure 11.3** Diagram of atrial septal components showing patent foramen ovale (PFO; arrow). AVS, atrioventricular septum; FO, foramen ovale; ILB, inferior limbic band; LA, left atrium; LV, left ventricle; RA, right atrium; RV, right ventricle; Sept. 1°, septum primum; SLB, superior limbic band (septum secundum).

superior vena cava (SVC) and from the posterior aspect of the right atrium is termed *sinus venosus septum* [21,22]. The tissue that separates the coronary sinus from the left atrium is termed *coronary sinus septum*.

## Anatomy

### Patent foramen ovale (PFO)

This is the space between a well-developed (valve-competent) septum primum and a normally formed septum secundum (Fig. 11.3). PFO is a normal interatrial communication during fetal life, characterized by streaming of flow from the ductus venosus and, to a lesser extent, from the inferior vena cava, through the foramen ovale to the left atrium (Fig. 11.4a). After birth, left atrial pressure normally exceeds right atrial pressure and, as a result, septum primum apposes septum secundum (the superior limbic band of the fossa ovalis) and the foramen ovale narrows (Fig. 11.4b; Videoclips 11.1 and 11.2). A PFO is seen in almost all newborns, and with a decreasing frequency in older individuals [23–25]. Complete anatomic closure of the foramen ovale occurs in 70–75% of adults [26].

### Secundum atrial septal defect

This is a defect within the fossa ovale, usually due to a single or multiple defects within septum primum (Fig. 11.5). Septum secundum is usually well formed. Most secundum ASDs are not confluent with the venae cavae, right pulmonary veins, coronary sinus or the AV valves. With the exception of PFO, secundum ASD is the most common cause of an atrial-level shunt. The size of secundum ASDs varies from several millimeters to 2–3 centimeters. Large defects are usually associated with marked deficiency, or even complete absence, of septum primum. Rarely, a secundum ASD results from deficiency of septum secundum (the muscular limb of the fossa ovalis). In such cases, the superior border of the defect can reach the SVC–right atrial junction ("high" secundum defect) but, in contrast to sinus venosus defect, does not involve the right upper pulmonary vein.

### Primum atrial septal defect

Primum ASD is an endocardial cushion defect with an interatrial communication located between the anterior-inferior margin of the fossa ovalis and the AV valves. It is considered a form of partial AV canal defect with two separate AV valve annuli and no ventricular septal defect of the AV canal type (Fig. 11.1 and Chapter 15).

### Sinus venosus defect (SVD)

This is a communication between one or more of the right pulmonary veins and the cardiac end of the SVC and/or the posterior wall of the right atrium (Fig. 11.5) [21]. SVDs comprise approximately 4–11% of ASDs [27]. From an anatomic standpoint, SVD is not an atrial septal defect because it does not allow direct communication between the left and right atria. Instead, the interatrial communication is through one or more of the pulmonary veins. The most common location of a SVD (approximately 87% [21]) is between the right upper pulmonary vein and the superior vena cava, below the

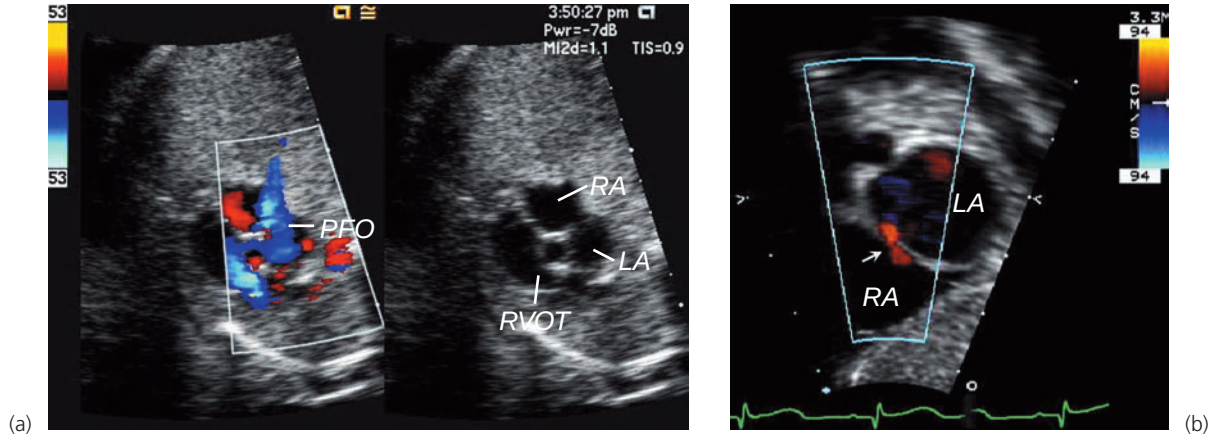


(a) (b)

**Figure 11.4** Patent foramen ovale. **(a)** Fetal echocardiogram at 18 weeks' gestation showing flow from the ductus venosus to the left atrium (LA) through a patent foramen ovale (PFO). **(b)** Patent foramen ovale (arrow) in a newborn. LA, left atrium; RA, right atrium; RVOT, right ventricular outflow tract.

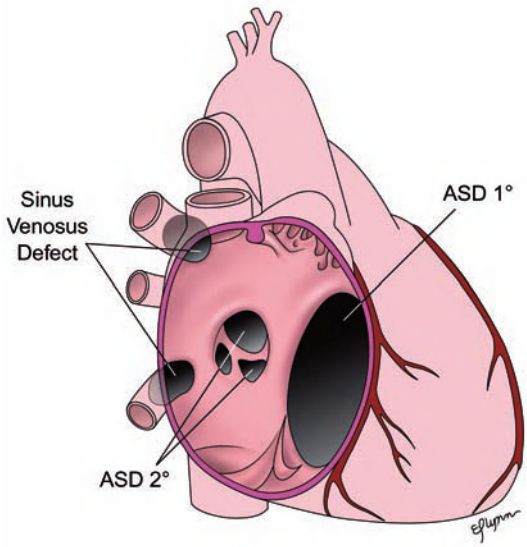


**Figure 11.5** Diagram showing types of interatrial communications. ASD 1°, primum atrial septal defect; ASD 2°, secundum atrial septal defect.

insertion of the azygos vein (SVC-type SVD). The defect results from partial or complete absence of the sinus venosus tissue that separates the anterior aspect of the right upper pulmonary vein from the posterior wall of the SVC [21,22]. The deficiency of the sinus venosus septum can extend peripherally to involve secondary branches of the right pulmonary veins, resulting in drainage of several pulmonary veins to the SVC. The left atrial orifice of the right upper pulmonary vein is usually widely patent, allowing for a communication between the left atrium and the cardiac end of the SVC. The combination of an interatrial shunt through the left atrial orifice of the right upper pulmonary vein (left atrium-to-SVC-to-right atrium) and drainage of right upper pulmonary vein blood to the right atrium through the SVC typically results in a large left-to-right shunt and marked right ventricular volume overload [28].

Less frequently, the defect also involves the right lower and/or middle pulmonary veins and the middle or inferior aspects of the right atrium. This type of sinus venosus defect has been called IVC-type although direct involvement of the inferior vena cava is either extremely rare or not present. For that reason, the term *sinus venosus of the right atrial type* is preferred [21]. In many patients with the right atrial-type SVD, the entire sinus venosus septum is absent, resulting in anomalous drainage of all right pulmonary veins to the right atrium.

It is important to recognize that although the right pulmonary veins in SVD almost always drain anomalously, their anatomic connections with the left atrium are usually normal, through their native orifices. In the rare circumstance when the left atrial orifice of the right upper pulmonary vein is atretic, there is no interatrial communication and the anatomic appearance is that of partially anomalous pulmonary venous connection of the right upper pulmonary vein to the SVC.

### Coronary sinus defect

This is an uncommon anomaly that results from partial or complete unroofing of the tissue separating the coronary sinus from the left atrium, allowing the right and left atria to communicate through the defect and the coronary sinus orifice (Fig. 11.6). The orifice of the coronary sinus in this anomaly is usually large as a result of the left-to-right shunt, resulting in a sizeable defect in the inferior aspect of the atrial septum near the entry of the inferior vena cava. The association of a coronary sinus septal defect and persistent left superior vena cava is termed *Raghib syndrome* [29]. When the coronary sinus is completely unroofed, the left superior vena cava enters the left superior corner of the left atrium, anterior to the orifice of the left upper pulmonary vein and posterior to the left atrial appendage.

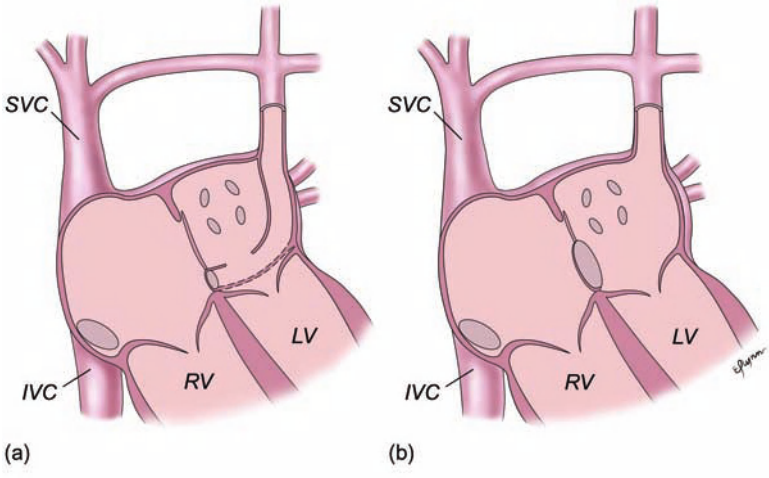


**Figure 11.6** Diagram of coronary sinus septal defect. **(a)** Small coronary sinus septal defect associated with left superior vena cava-to-coronary sinus. **(b)** Unroofed coronary sinus associated with left superior vena cava (Raghib syndrome). Note the large interatrial communication through the coronary sinus ostium. IVC, inferior vena cava; LV, left ventricle; RV, right ventricle; SVC, superior vena cava.

### Common atrium

Common atrium is present when septum primum, septum secundum and the AV canal septum are absent (usually in patients with heterotaxy syndrome). Remnants of atrial septal tissue can sometimes be recognized in these patients, such as a fibromuscular strand that crosses the inferior aspect of the common atrium (inferior limbic band of the fossa ovale) or remnants of venous valve tissue.

## Pathophysiology

Regardless of the specific anatomic type and assuming no AV valve stenosis or hypoplasia, the amount of shunting through an interatrial communication is determined by the defect size and relative compliance of the right and left ventricles. Over the first few months of life, right ventricular compliance typically rises leading to an increasing left-to-right shunt. In adults, left ventricular compliance normally decreases, further augmenting the left-to-right flow. Shunt flow through the right heart and lungs leads to dilation of the right atrium, right ventricle, pulmonary arteries and pulmonary veins. Most young children tolerate this increased pulmonary blood flow well and are asymptomatic; a few develop dyspnea or growth failure [30,31]. Defects in this age group are typically detected after auscultation of a heart murmur or incidentally when a chest radiogram, an electrocardiogram or an echocardiogram is obtained for other indications. Up to 5–10% of patients with significant left-to-right shunts may develop pulmonary vascular disease by adulthood leading to pulmonary hypertension. Adults with unrepaired ASDs are also at risk for exercise intolerance, atrial arrhythmias and paradoxical emboli [32,33]. Small secundum ASDs (≤5–8 mm) may close spontaneously or become smaller in the first few years of life; thereafter, defects tend to become larger with time [34,35]. By contrast, primum ASDs, sinus venosus septal defects and coronary sinus septal defects almost never become smaller with time.

## Imaging

The atrial septum is imaged from multiple acoustic windows, including the subcostal, apical, left parasternal and high right parasternal. Two- and three-dimensional imaging as well as color and spectral Doppler techniques are used in concert for comprehensive evaluation of the fossa ovalis, sinus venosus and coronary sinus septa. If a defect is seen from one acoustic window, its presence must be confirmed from other windows. Transesophageal echocardiography (TEE) – often used during surgical and transcatheter closure of ASDs (see below) – is also performed as a diagnostic procedure in patients with suboptimal transthoracic windows and inconclusive diagnosis. In such cases, cardiac magnetic resonance imaging (MRI) can be considered as a noninvasive alternative [28,36,37]. Contrast echocardiography is another helpful technique in certain patients (e.g., poor acoustic windows, diagnosis of left superior vena cava associated with coronary sinus septal defect [Raghib syndrome]) [38].

### Goals of the examination

- Determination of defect location and size.
- Relationships with neighboring structures (e.g., mitral and tricuspid valves, systemic and pulmonary veins).
- Measurement of defect margins (for assessment of suitability for transcatheter closure).
- Hemodynamic assessment:
  - flow direction (by color and spectral Doppler);
  - mean transseptal pressure gradient (when flow velocity is increased and the flow pattern is turbulent);
  - evidence of hemodynamic load (right atrial and right ventricular enlargement, diastolic septal flattening associated with right ventricular volume load, increased pulmonary blood flow);

- estimation of right ventricular systolic pressure based on tricuspid regurgitation jet velocity and/or the systolic configuration of the ventricular septum.
- Biventricular function.
- Detection of associated lesions.

### Imaging of secundum ASDs

The subcostal acoustic window is ideally suited for evaluation of the fossa ovale because the normally oriented septum is relatively echo-reflective from that position (Fig. 11.7). This minimizes the likelihood of false dropout of acoustic signals,

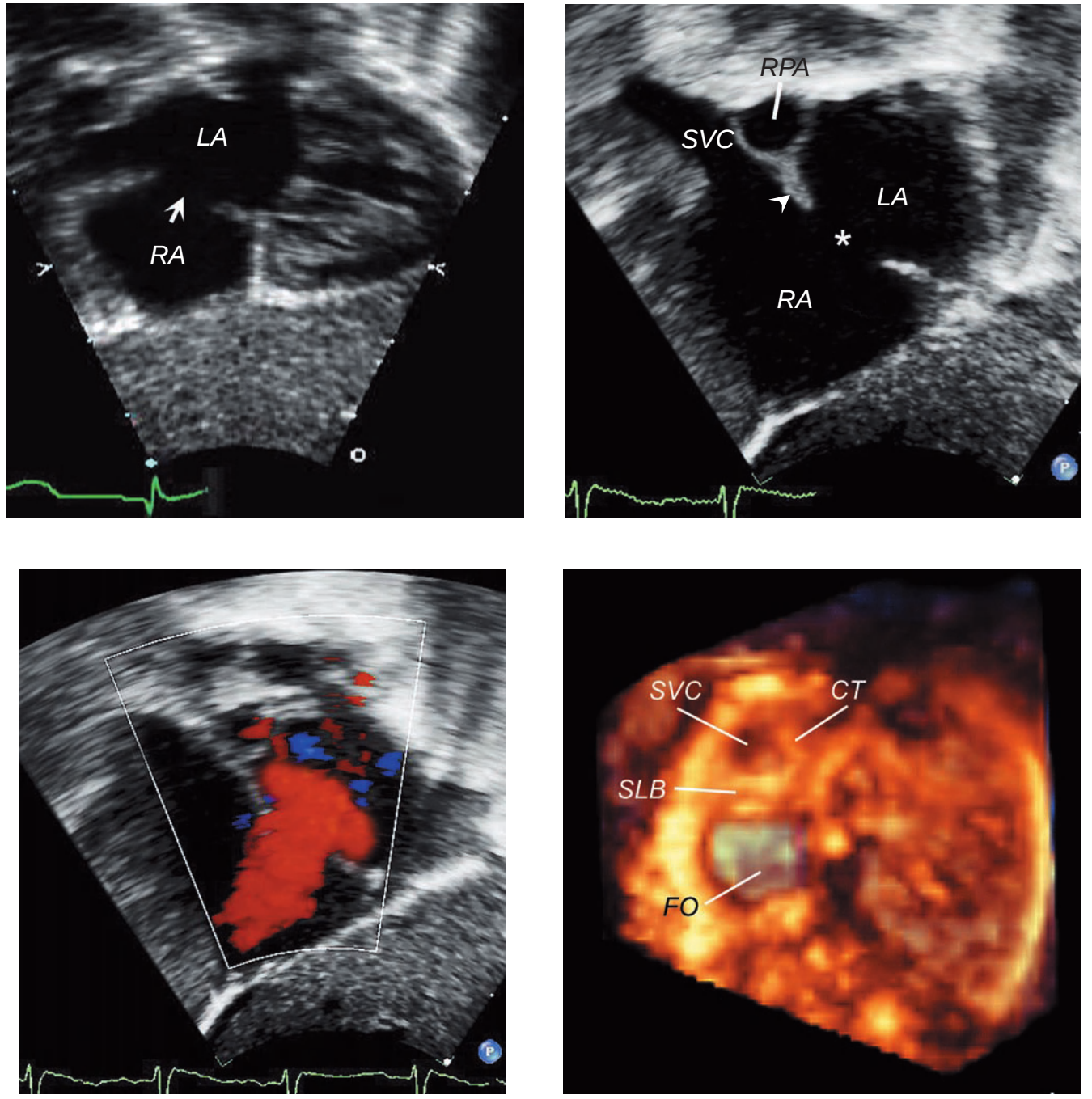


**Figure 11.7** Imaging of secundum atrial septal defect (ASD) from the subxiphoid window: **(a)** Long-axis view. The arrow points to the secundum atrial septal defect. **(b)** Short-axis view. The asterisk indicates secundum atrial septal defect; arrowhead denotes superior limbic band (septum secundum). **(c)** Color Doppler flow mapping from the short-axis view. **(d)** Real-time 3D imaging (right atrial view). CT, crista terminalis; FO, fossa ovale; LA, left atrium; RA, right atrium; RPA, right pulmonary artery; SLB, superior limbic band; SVC, superior vena cava.

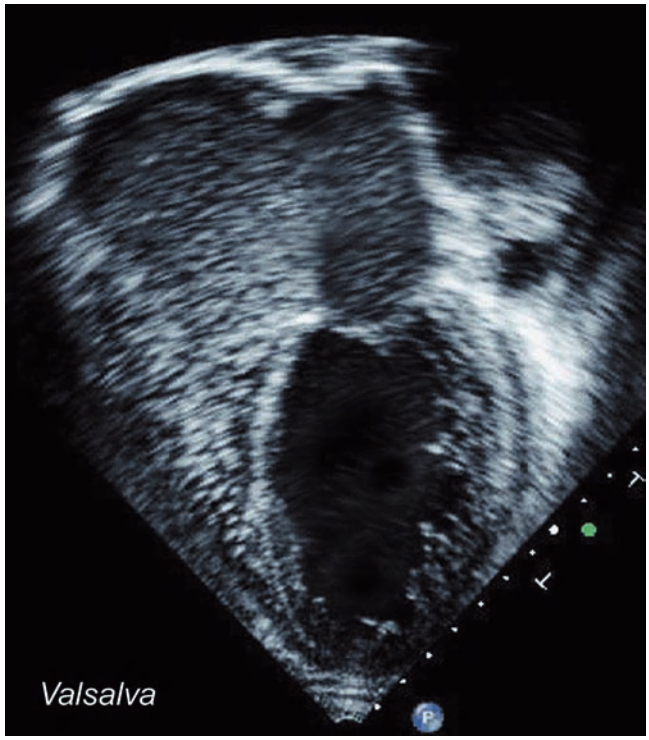


**Figure 11.8** Contrast echocardiogram in a patient with secundum atrial septal defect (ASD). During a Valsalva maneuver, contrast crosses the atrial septum and appears in the left heart.

which can lead to erroneous diagnosis of an ASD. Imaging is performed in the long- and short-axis views, and the use of "in-between" transducer angles is encouraged. A secundum ASD is seen as a defect within the fossa ovale, confirmed by evidence of transseptal flow by color Doppler (Fig. 11.7a–d; Videoclips 11.3 and 11.4). In the subcostal long-axis view, a secundum ASD is not contiguous with the posterior right atrial free wall or with the right pulmonary veins. Such findings are suggestive of a SVD of the right atrial type. In the subcostal short-axis view, the superior limbic band of the fossa ovale separates a secundum ASD from the SVC and the right upper pulmonary vein. The subcostal short-axis view is also optimal for assessment of right ventricular volume load (right ventricular dilation and diastolic septal flattening) and right ventricular hypertension (systolic septal flattening).

The apical window is not ideally suited for evaluation of the fossa ovale due to the risk of false dropout of acoustic signal as a result of the parallel orientation of the ultrasound beam relative to the atrial septum. However, this view is helpful for measurement of the tricuspid regurgitation jet velocity for estimation of right ventricular systolic pressure. The apical window is also helpful for detection of acoustic signals during a contrast echocardiogram (Fig. 11.8). The imager is looking for the appearance of acoustic reflective signals ("bubbles") in the left atrium and left ventricle (representing right-to-left flow) or a negative jet effect in the right atrium representing left-to-right flow.

The parasternal window is helpful, especially in the short-axis plane, for imaging of the atrial septum. A low left parasternal short-axis view can often provide adequate imaging of the atrial septum, even in patients with suboptimal subcostal windows (Fig. 11.9). This view is helpful for measurement of the antero-posterior diameter of the defect. The presence or absence of right ventricular volume and pressure loads is also evaluated from the parasternal short-axis view.

The high right parasternal window is also ideally suited for assessment of the fossa ovale and the superior sinus venosus septum as a result of the perpendicular orientation of these

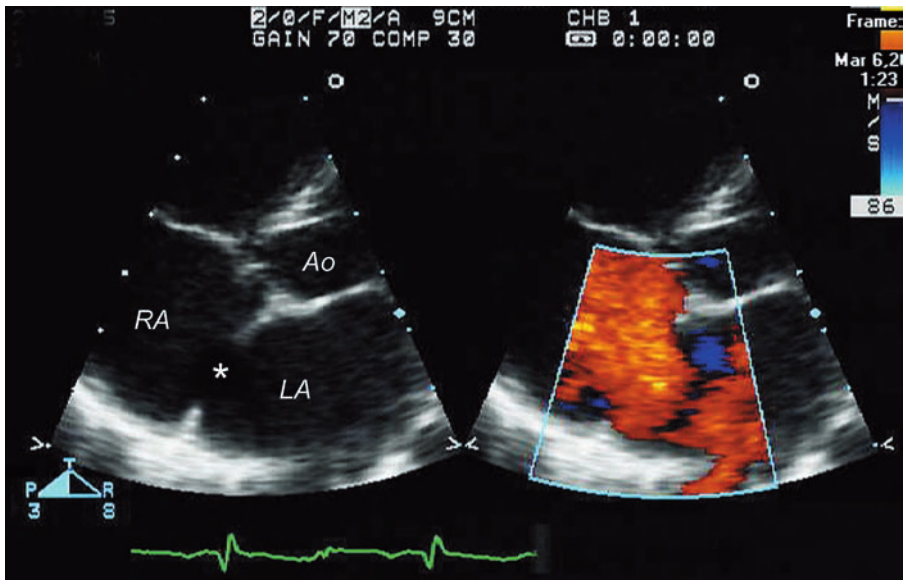


**Figure 11.9** Imaging of secundum atrial septal defect (ASD) from the parasternal short-axis view. Left panel depicts a 2D image of the defect (*). The right panel shows flow from the left atrium to the right atrium through the defect. Ao, aorta; LA, left atrium RA, right atrium.

structures relative to the ultrasound beam. Placing the patient in the right lateral decubitus position facilitates imaging from this acoustic window.

### Imaging of sinus venosus defects

SVC-type SVD is seen best from the subcostal short-axis and high right parasternal views as a communication between the right upper corner of the left atrium at the usual location of the right upper pulmonary vein and the SVC just above its right atrial junction (Fig. 11.10; Videoclip 11.5(a,b)). The cross-section of the right pulmonary artery is seen in these views as an oval-shaped vessel crossing just above the defect, behind to the SVC. Color-coded Doppler flow mapping shows flow from the left atrium through the SVC to the right atrium and confirms the pulsatile nature of the flow in the right pulmonary artery (Videoclip 11.5a). Imaging

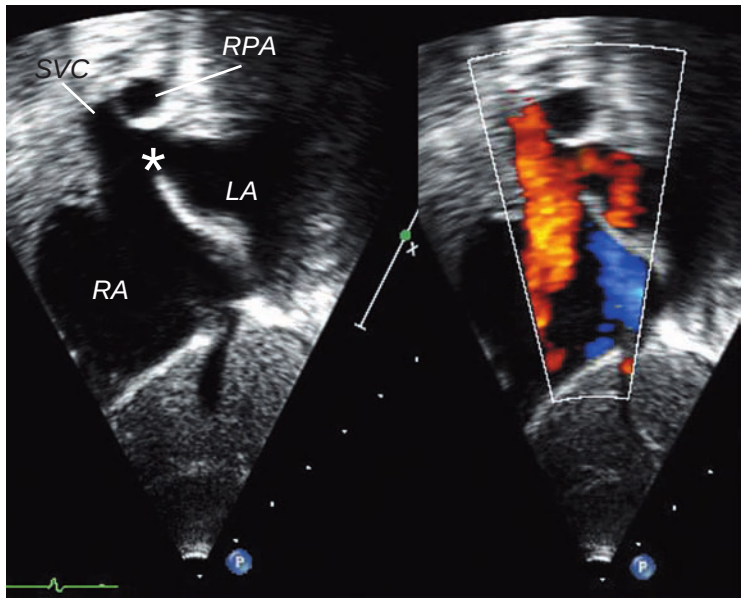


(a)

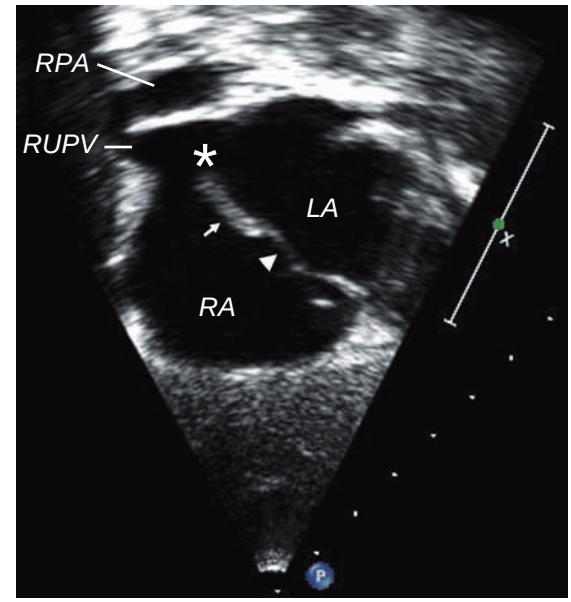


(b)

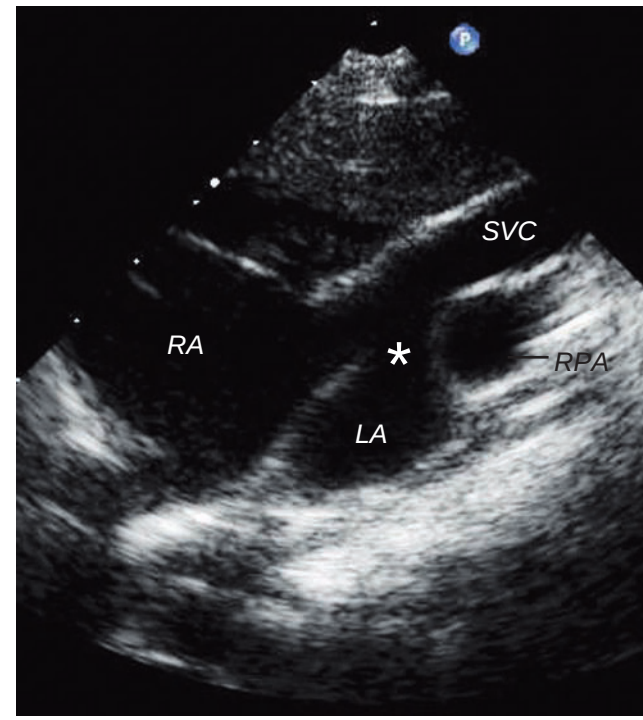


(c)

**Figure 11.10** Imaging of superior vena cava (SVC)-type sinus venosus defect. **(a)** Imaging from the subxiphoid short-axis view. Note the location of the defect (*) cranial to the superior limbic band of the fossa ovale and its communication with the cardiac end of the SVC. Blood flows from the left atrium (LA) to the SVC through the left atrial orifice of the right upper pulmonary vein and sinus venosus defect. Note the absence of direct interatrial communication; hence, sinus venosus defect is NOT an atrial septal defect. **(b)** Imaging from the subxiphoid long-axis view. The arrowhead points to the fossa ovale, which is covered by septum primum. The full arrow points to the superior limbic band of the fossa ovale. Note the interatrial communication (*) via the enlarged left atrial orifice of the right upper pulmonary vein (RUPV). **(c)** Imaging from the high right parasternal view. Note the location of the defect (*) just below the right pulmonary artery (RPA). RA, right atrium.

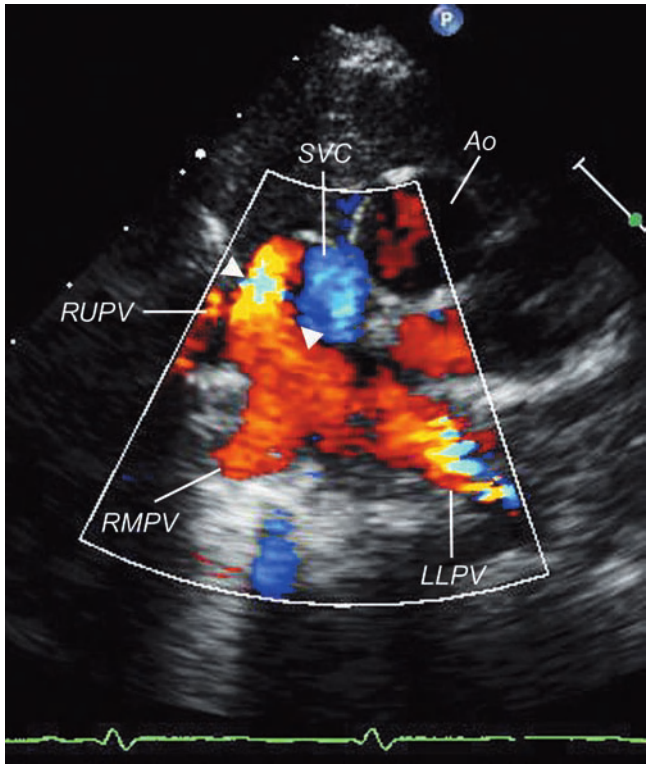


**Figure 11.11** Imaging of superior vena cava-type sinus venosus defect from the parasternal short-axis view. The arrowheads mark the margins of the defect, which results from deficiency in the tissue that separates the posterior wall of the superior vena cava (SVC) from the anterior wall of the right upper pulmonary vein (RUPV). Flow from the left atrium into the superior vena cava (and then to the right atrium) is through the left atrial orifice of the right upper pulmonary vein (RUPV). Ao, ascending aorta; LLPV, left lower pulmonary vein; RMPV, right middle pulmonary vein.

in the transverse plane of the chest from either left or right parasternal windows at the level of the cardiac end of the SVC is helpful in showing the unroofed sinus venosus septum, seen as absence of the tissue separating the right upper pulmonary vein from the SVC (Fig. 11.11; Videoclip 11.6). This view also shows the communication between the left atrium and the SVC, the site of the left atrial orifice of the right upper pulmonary vein. Evaluation of the hemodynamic burden associated with SVD defect is similar to that of secundum ASD.

Right atrial-type SVD is seen best from the subxiphoid long-axis and from the parasternal short-axis views, appearing as a posterior-inferior atrial defect with no posterior margins (Fig. 11.12; Videoclip 11.7). In other words, the defect is flushed with the posterior atrial free wall, which, in fact, comprised the back wall of the right lower and middle pulmonary veins. The left atrial orifices of the right pulmonary veins form the interatrial communication, and the pulmonary veins drain directly into the right atrium. The anomalous drainage of the right pulmonary veins is best seen from the parasternal short-axis view.

### Imaging of coronary sinus defects

The diagnosis of a coronary sinus septal defect is often first suspected in a patient with ASD physiology and an enlarged coronary sinus ostium (Fig. 11.13). The dilated coronary sinus ostium is seen as an inferior interatrial communication, just above and slightly anterior to the inferior vena cava–right atrial junction. The defect might be confused with an ostium primum ASD, except for the intact anterior mitral leaflet and absence of other features of AV canal defect. Once the enlarged coronary sinus ostium is recognized, the coronary sinus is imaged in detail from multiple views. Absence of a visible coronary sinus indicates complete lack of sinoatrial septal tissue (the wall separating the coronary sinus from the left atrium) – a condition known as completely unroofed coronary sinus. In a partially unroofed coronary sinus, part of the sinoatrial septal tissue is seen and the coronary sinus is recognizable. The presence or absence of a persistent left superior vena cava must be ascertained. When present (Raghib syndrome), the left atrial termination of the left superior vena cava is anterior to the left upper pulmonary vein and posterior to the left atrial appendage. Remnants of coronary sinus septum might be visualized within the left atrium at the entrance of the left superior vena cava. Injection of agitated saline through an intravenous cannula placed in the left arm, while imaging from the apical 4-chamber window, demonstrates the appearance of the contrast in the left upper corner of the left atrium with subsequent appearance in the right atrium. Rarely, the ostium of the coronary sinus is stenotic or atretic, in which case the interatrial shunt is small or absent and the coronary sinus septal defect allows drainage of cardiac venous return directly to the left atrium. In patients with typical Raghib syndrome, the fossa ovale is usually small and displaced superiorly. An associated secundum ASD is unusual.

### Prenatal assessment

Detailed evaluation of the atrial septum is integral to a comprehensive fetal echocardiogram. Two-dimensional and Doppler (spectral and color flow mapping) ultrasound are used to evaluate the anatomic components of the septum – septum primum and septum secundum – and the pattern of interatrial blood flow. In the normal fetus, oxygenated blood from the placenta flows through the umbilical vein to the ductus venosus, streaming through the foramen ovale to the left atrium. The direction of flow is in a caudal–cephalad direction, which is best imaged in the sagittal plane of the fetus (Fig. 11.4). A restrictive septum or intact atrial septum are important fetal cardiac abnormalities often associated with other congenital heart defects (e.g., transposition of the great arteries, hypoplastic left heart syndrome, tricuspid atresia) and are discussed in their respective chapters.

Prenatal diagnosis of an atrial septal defect is challenging. In contrast to primum ASD, which can be reliably diagnosed

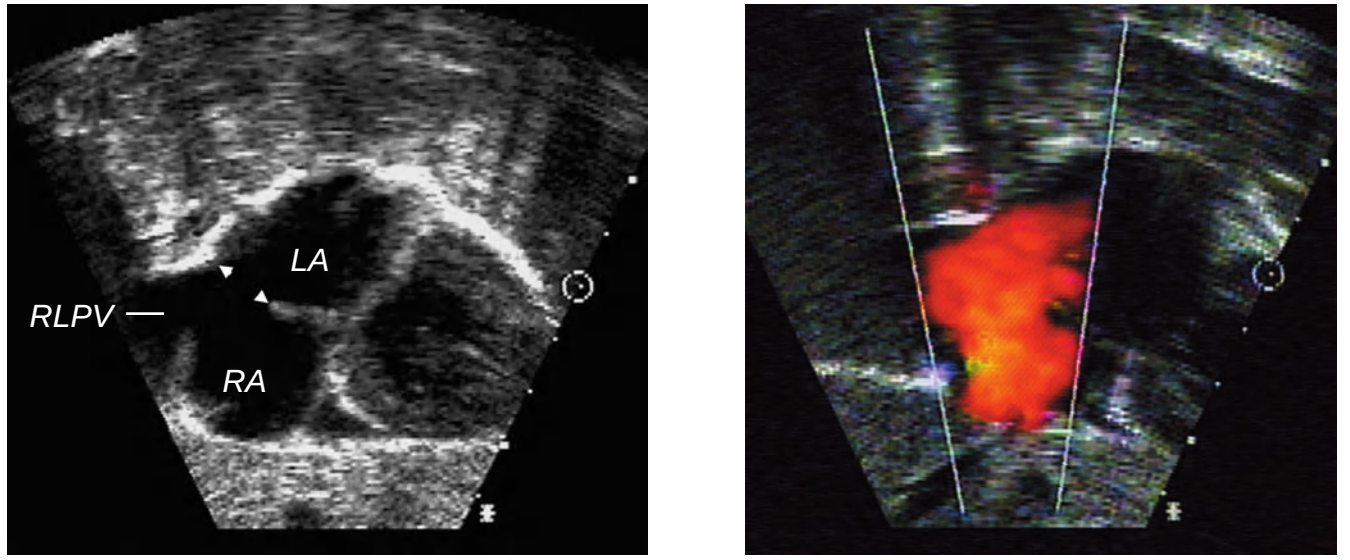


(a) (b)

**Figure 11.12** Right atrial-type sinus venosus defect. **(a)** Subxiphoid long-axis view showing a large defect between the posterior wall of the right atrium (RA) and the anterior wall of the right lower pulmonary vein (RLPV). The interatrial communication (arrowheads) is via the left atrial (LA) orifice of the right lower pulmonary vein. This illustrates anomalous drainage of the RLPV to the RA but with normal connection. Note the absence of any septal tissue along the posterior wall of the RA. **(b)** Color Doppler flow mapping demonstrates flow into the right atrium from the right lower pulmonary vein and from the left atrium.

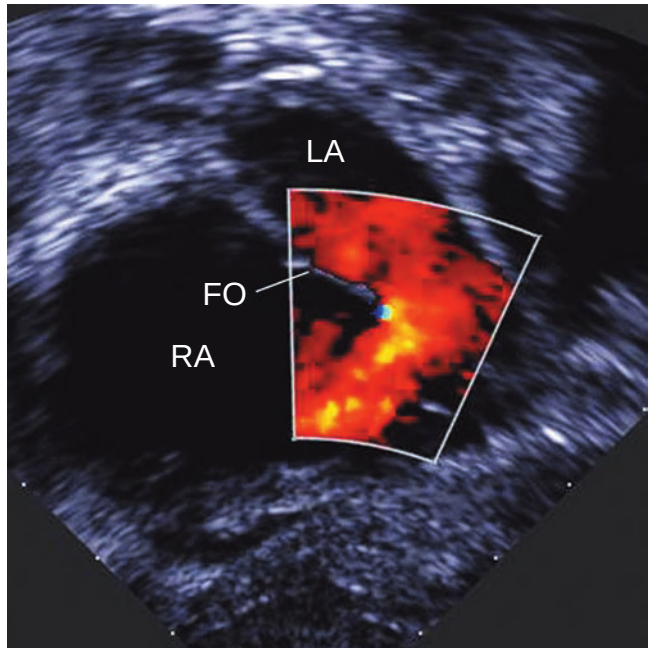


**Figure 11.13** Coronary sinus septal defect. Blood flows from the left atrium (LA) through the unroofed coronary sinus into the right atrium (RA) through the enlarged coronary sinus ostium. Note the inferior-posterior location of the coronary sinus ostium and its relation to the intact fossa ovale (FO).

in most cases, the diagnosis of a secundum ASD is less reliable, especially in the absence of associated congenital heart defects. For example, Driggers et al. found that the agreement between pre- and postnatal echocardiograms for diagnosing secundum ASDs was only modest (kappa = 0.6) [39]. This known limitation of fetal echocardiography is due to the difficulty in distinguishing small-moderate secundum ASDs from the normal flow through a patent foramen ovale. With regard to prenatal diagnosis of sinus venosus or coronary sinus septal defects, the data published to date are scant. However, it is worth noting that the study of Driggers and colleagues demonstrated a weak ability to diagnose partially anomalous pulmonary venous connections by fetal echocardiography [39].

## Imaging of the adult

The main challenge in the evaluation of the atrial septum in the adult is technical, relating to difficulties in obtaining clear images and a Doppler signal from subcostal or transthoracic acoustic windows. The ability of transthoracic echocardiography (TTE) to diagnose sinus venosus defect in adults is even poorer, with only one in four cases correctly diagnosed [40]. Enlargement of right heart chambers associated with flattening of the interventricular septum during diastole indicative of right ventricular volume should prompt suspicion of atrial-level shunting. Therefore, when clinical, electrocardiographic, radiographic and/or echocardiographic evidence suggests an intracardiac shunt and TTE is inconclusive, further evaluation is warranted. Transesophageal echocardiography (TEE) provides an excellent alternative to transthoracic imaging, allowing for clear imaging of the fossa ovale, sinus venosus septum, cardiac ends of the pulmonary veins, and the coronary sinus [40–51]. Cardiac MRI provides

a noninvasive alternative to TEE in adults with suspected ASDs, allowing clear visualization of the anatomic elements of the atrial septum as well as accurate quantification of right ventricular size and function and the ratio of pulmonary-to-systemic flow ratio [28,52–54].

## Echocardiographic guidance of transcatheter ASD closure

The limited ability of X-ray fluoroscopy to image the atrial septum renders echocardiographic guidance essential for transcatheter closure of secundum ASD and PFO. Transesophageal echocardiography has been used to guide transcatheter device placement since the 1980s [43,55–59]. Technological advances, including miniaturization and development of high-resolution multiplane probes, have greatly enhanced the clinical utility of TEE in patients with congenital heart disease. More recently, intracardiac echocardiography (ICE) has been advocated as an alternative to TEE (Fig. 11.14) [60–66]. Although extensive experience with TEE during transcatheter closure of ASDs has demonstrated its usefulness [43], the procedure is usually performed under general anesthesia with endotracheal intubation to protect the airways and to provide adequate ventilation. An expert echocardiographer usually performs the imaging, and this adds to the cost and personnel associated with the procedure. Although ICE requires the use of an expensive disposable imaging catheter, which increases the cost of the procedure, the imaging can be performed by the catheterization team. In a study that compared the hospital charges and costs of 20 TEE-guided ASD closures with 20 ICE-guided procedures, Alboliras and Hijazi found that on average, ICE was more expensive than TEE [67]. Therefore, the choice of transesophageal versus intracardiac echocardiographic guidance of transcatheter closure of ASDs depends on institutional experience, availability of resources (e.g., anesthesia support and expert echocardiographers), and future technological advances (e.g., miniaturization of real-time 3D imaging probes).

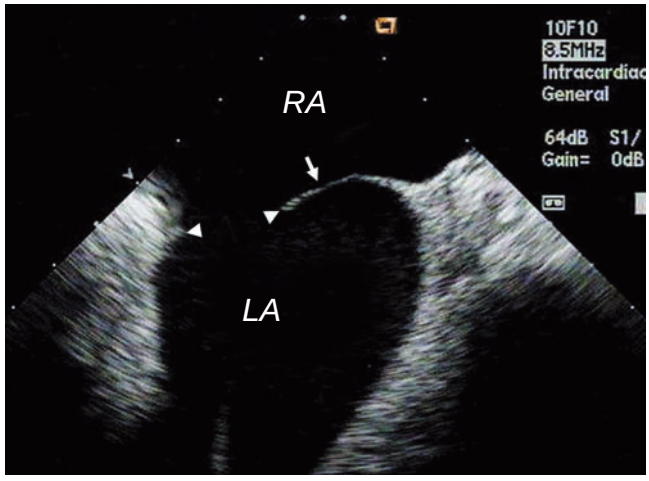


(a)

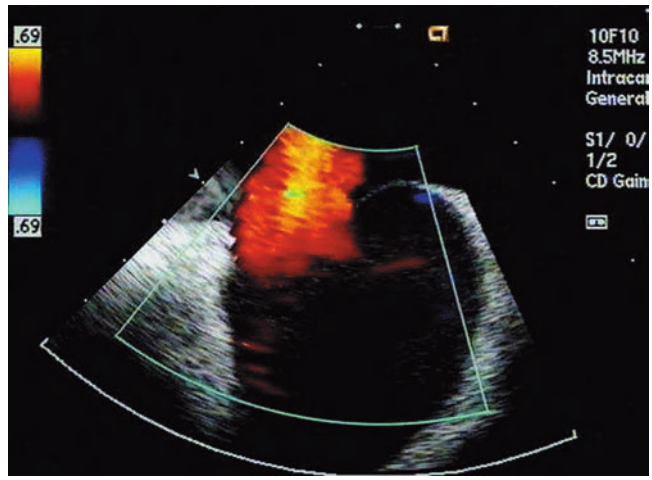


(b)

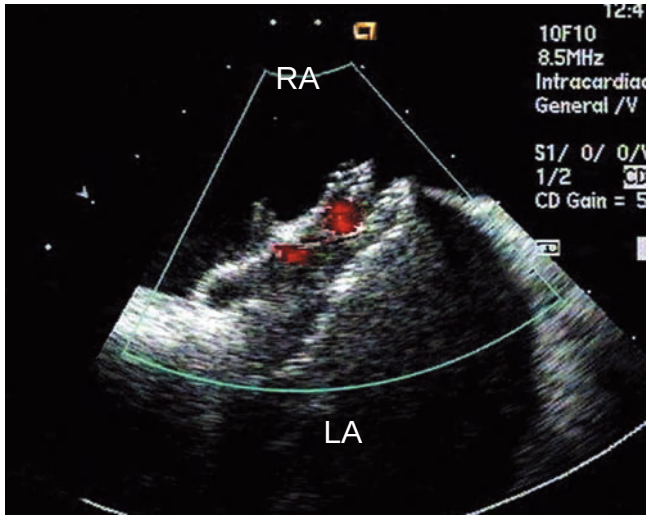


(c)

**Figure 11.14** Intracardiac echocardiographic imaging of secundum atrial septal defect (ASD). **(a)** The arrowheads point to the margins of the defect. The white arrow points to septum primum. **(b)** Color Doppler flow mapping showing flow from the left atrium to the right atrium. **(c)** After deployment of an atrial septal defect occluding device, no left-to-right flow is seen. LA, left atrium; RA, right atrium.

Echocardiographic support for transcatheter ASD or PFO closure can be divided into 3 phases – before, during and after device deployment.

**1. Before device deployment:** Imaging of the location and size of the defect(s) and its relationships with neighboring structures, including the AV valves, venae cavae and right pulmonary veins (Fig. 11.15). Identification of multiple defects is particularly important for planning the procedure. The margins (rims) of the defect are measured as well as the total septal length. Many centers also measure the stretched diameter of the defect based on echocardiographic and fluoroscopic measurements of a balloon inflated across the defect (Fig. 11.16). Color and spectral Doppler are used to evaluate the transseptal shunt. The pulmonary veins are imaged to exclude partially anomalous pulmonary venous connection, and the degree of AV valve regurgitation is evaluated as baseline for comparison after device deployment. In patients with associated congenital heart disease, a comprehensive TEE is recommended before device deployment.

**2. During device deployment:** First, the course and position of the sheath are ascertained. Next, the left atrial arms or disc are released. The catheter and device are then retracted to approximate the left atrial arms/disc against the left atrial septal surface with particular attention to the orientation of

(a)

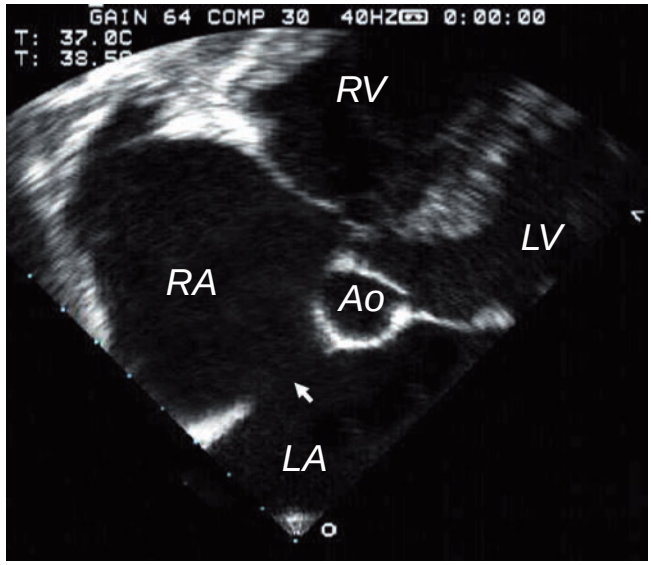


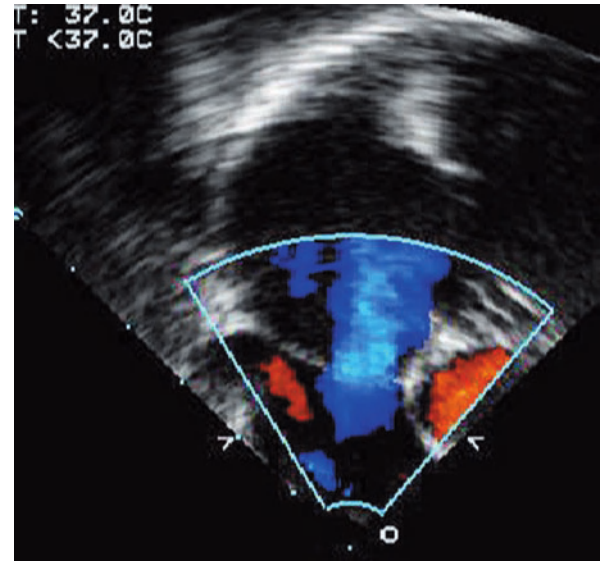


(b)

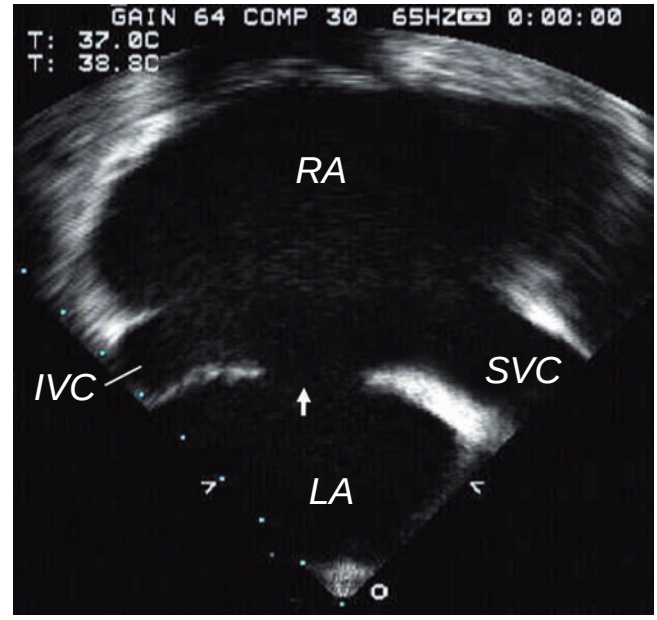


(c)

**Figure 11.15** Transesophageal echocardiographic imaging of secundum atrial septal defect. **(a)** Horizontal plane image showing a moderate-sized secundum atrial septal defect (arrow). Note the retroaortic (Ao) location of the defect. **(b)** Color Doppler flow mapping showing flow from the left atrium to the right atrium. **(c)** Vertical plane image showing the superior-inferior dimension of the secundum defect (arrow). IVC, inferior vena cava; LA, left atrium; LV, left ventricle; RA, right atrium; RV, right ventricle; SVC, superior vena cava.

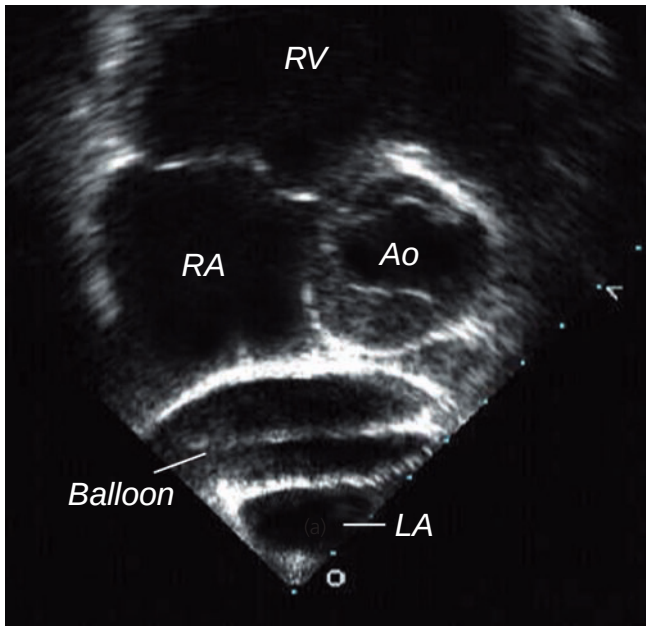


**Figure 11.16** Balloon sizing of secundum atrial septal defect. Ao, aortic root; LA, left atrium; RA, right atrium; RV, right ventricle.

the device relative to the atrial septal plane (Fig. 11.17a). Once the device is in proper position, the right atrial arms/disc are released (Fig. 11.17b). Again, proper position is ascertained before the device is released (Fig. 11.17c; Videoclip 11.8).

**3. After deployment:** Imaging aims to evaluate the proper and stable device position across the atrial septum; the presence, location and extent of residual transseptal flow; device impingement on neighboring structures (SVC, IVC, coronary sinus, pulmonary veins, AV valves); and any adverse change that might be related to the procedure.

Key to a successful procedure is effective communication between the imaging, catheterization and anesthesia teams. The echocardiographic images should be clearly available to the catheterization team, preferably through a dedicated high-resolution screen mounted beside the fluoroscopy and the physiologic monitoring screens.

## Intraoperative assessment

Although intraoperative echocardiography can be used during surgical closure of ASD, its utility varies according to defect type and associated anomalies. Randolph et al. demonstrated a low rate of major findings before and after surgical closure of secundum ASD [68]. However, intraoperative TEE is considered helpful during repair of sinus venosus defects, coronary sinus septal anomalies and complex intra-atrial baffles, the use of a minimal access approach and primum ASD surgery [68–74]. The transesophageal approach is generally preferred because it does not interfere with the surgical field, provides a wider field of view, and often yields superior image quality compared with epicardial imaging. Miniaturization of multiplane TEE probes has allowed transesophageal imaging in most infants weighing ≥3 kg. Epicardial imaging should be considered in patients in whom TEE is contraindicated or considered hazardous [75], and in circumstances where real-time 3D imaging is desirable. Development of a real-time 3D TEE imaging capability has recently become possible. Goals of the pre-cardiopulmonary bypass examination include confirmation of the preoperative diagnosis and refinement of surgical planning. After cardiopulmonary bypass, imaging is performed to evaluate the integrity of the repair, for the exclusion of residual lesions, and for functional assessment (e.g., ventricular function, AV valve regurgitation).

## Follow-up assessment

Continued echocardiographic surveillance is important after transcatheter and surgical treatment of all forms of interatrial communications. Although residual transseptal shunts are commonly seen by TEE or ICE immediately after device deployment, their frequency decreases substantially over time, with reports indicating 1–2% residual leaks [76–78]. It is worth noting, however, the lower sensitivity of transthoracic color Doppler echocardiography in detecting residual atrial-level shunts as compared with TEE or agitated saline contrast studies [79,80]. A key element of echocardiographic surveillance after transcatheter closure of ASDs is monitoring of the device for late complications, including obstruction of neighboring structures [81], fractures and change in device configuration [82], late migration or embolization of the device [83,84], thrombus formation [85,86], inflammatory reaction leading to abscess formation or local erosion [87,88], and perforation or rupture of cardiac structures [89–91].

Detailed echocardiographic assessment should be performed after surgical repair of ASD to exclude residual shunts, confirm remodeling of the right ventricle and resolution of right heart volume load, and rule out pericardial effusion in the early postoperative period. In patients after repair of sinus venosus and coronary sinus septal defects, the evaluation also includes assessment of the systemic and pulmonary venous pathways. Assessment of biventricular function and valve function, and noninvasive assessment of right ventricular systolic pressure are integral to the echocardiographic follow-up of all patients with repaired ASDs, regardless of the closure technique.

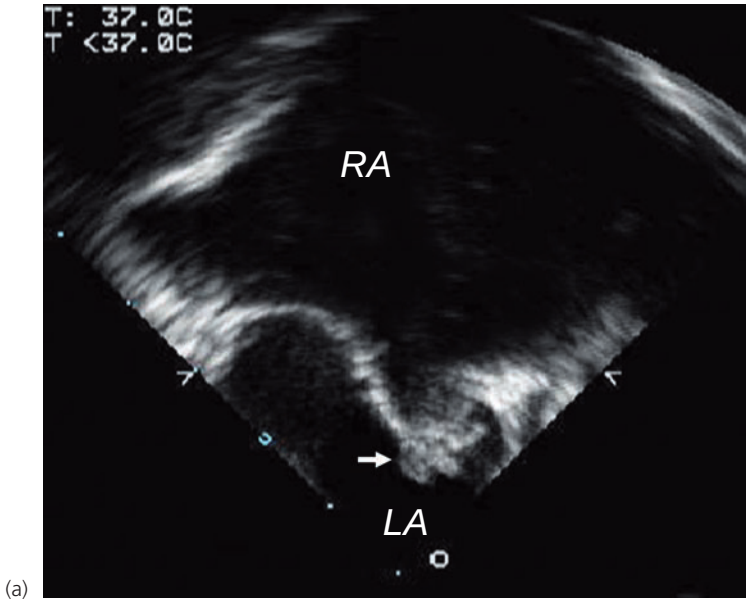


(a)

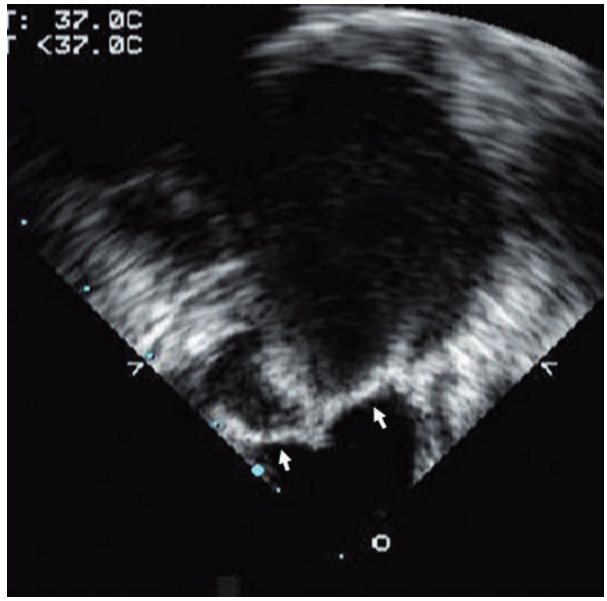


(b)

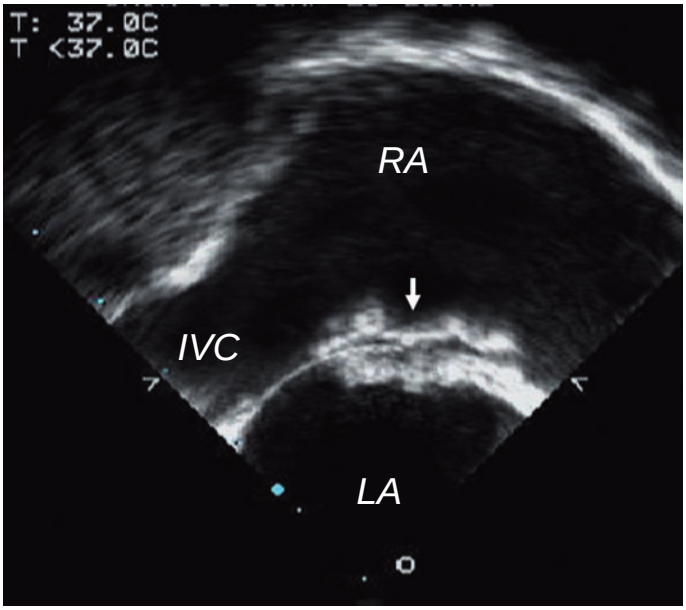


(c)

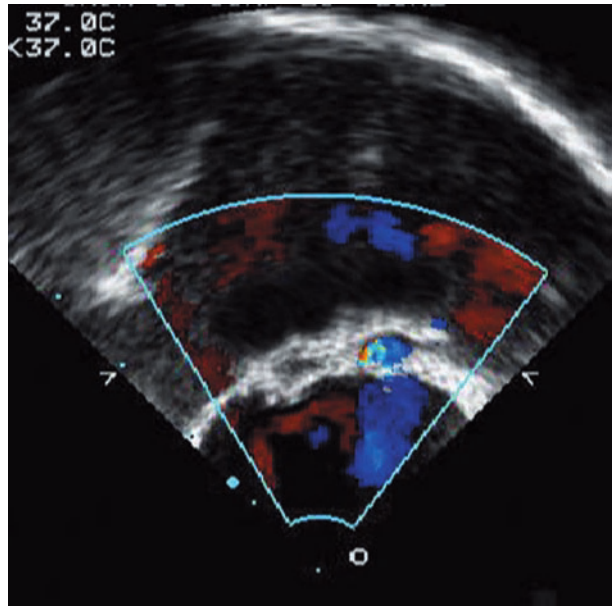


(d)

**Figure 11.17** Transesophageal echocardiographic guidance of transcatheter device closure of secundum atrial septal defect. **(a)** The device (arrow) is advanced into the left atrium (LA). **(b)** The left atrial arms are opened (arrows) and the device is retracted until the arms are flushed against the left atrial septal surface. **(c)** Vertical plane image showing the deployed device with the left and right atrial arms flushed against the atrial septum. **(d)** Color Doppler flow mapping shows a small amount of flow between the arms of the device but no residual atrial septal defect. IVC, inferior vena cava; RA, right atrium.

## References


1. Hoffman JI, Kaplan S. The incidence of congenital heart disease. *J Am Coll Cardiol* 2002;39:1890–900.
2. Botto LD, Correa A, Erickson JD. Racial and temporal variations in the prevalence of heart defects. *Pediatrics* 2001;107:E32.
3. Schott JJ, Benson DW, Basson CT et al. Congenital heart disease caused by mutations in the transcription factor NKX2-5. *Science* 1998;281:108–11.
4. Benson DW, Silberbach GM, Kavanaugh-McHugh A et al. Mutations in the cardiac transcription factor NKX2.5 affect diverse cardiac developmental pathways. *J Clin Invest* 1999;104:1567–73.
5. McElhinney DB, Geiger E, Blinder J et al. NKX2.5 mutations in patients with congenital heart disease. *J Am Coll Cardiol* 2003;42:1650–5.
6. Ching YH, Ghosh TK, Cross SJ et al. Mutation in myosin heavy chain 6 causes atrial septal defect. *Nat Genet* 2005;37:423–8.

7. Okubo A, Miyoshi O, Baba K et al. A novel GATA4 mutation completely segregated with atrial septal defect in a large Japanese family. *J Med Genet* 2004;41:e97.
8. Ikeda Y, Hiroi Y, Hosoda T et al. Novel point mutation in the cardiac transcription factor CSX/NKX2.5 associated with congenital heart disease. *Circ J* 2002;66:561–3.
9. Hosoda T, Komuro I, Shiojima I et al. Familial atrial septal defect and atrioventricular conduction disturbance associated with a point mutation in the cardiac homeobox gene CSX/NKX2-5 in a Japanese patient. *Jpn Circ J* 1999;63:425–6.
10. Strauss RM, Ferguson AD, Rittey CD, Cork MJ. Microcephaly-lymphoedema-chorioretinal-dysplasia syndrome with atrial septal defect. *Pediatr Dermatol* 2005;22:373–4.
11. Yoshihara K, Ozawa T, Sakuragawa H et al. [Noonan syndrome associated with atrial septal defect, pulmonary stenosis, and completely unroofed coronary sinus without LSVC: a case report]. *Kyobu Geka* 1999;52:134–7.
12. Cunningham ET Jr, Eliott D, Miller NR et al. Familial Axenfeld-Rieger anomaly, atrial septal defect, and sensorineural hearing loss: a possible new genetic syndrome. *Arch Ophthalmol* 1998; 116:78–82.
13. Diegeler A, Van Son JA, Mohr FW. Budd-Chiari syndrome as late complication of secundum atrial septal defect closure. *Eur J Cardiothorac Surg* 1997;12:501–3.
14. Shimizu K, Arai H, Sakamoto T et al. Jarcho-Levin syndrome associated with atrial septal defect and partial anomalous pulmonary venous return: a case report. *J Card Surg* 1997;12: 198–200.
15. Aynaci FM, Ozdemir M, Isik Y. Atrial septal defect in Hallermann Streiff syndrome. *Genet Couns* 1997;8:145–6.
16. Holt M, Oram S. Familial heart disease with skeletal malformations. *Br Heart J* 1960;22:236–42.
17. Anderson RH, Brown NA, Webb S. Development and structure of the atrial septum. *Heart (British Cardiac Society)* 2002;88: 104–10.
18. Dalgleish AE. The development of the septum primum relative to atrial septation in the mouse heart. *J Morphol* 1976;149: 369–82.
19. Mommersteeg MT, Soufan AT, de Lange FJ et al. Two distinct pools of mesenchyme contribute to the development of the atrial septum. *Circ Res* 2006;99:351–3.
20. Wessels A, Anderson RH, Markwald RR et al. Atrial development in the human heart: an immunohistochemical study with emphasis on the role of mesenchymal tissues. *Anat Rec* 2000; 259:288–300.
21. Van Praagh S, Carrera ME, Sanders SP et al. Sinus venosus defects: unroofing of the right pulmonary veins – anatomic and echocardiographic findings and surgical treatment. *Am Heart J* 1994;128:365–79.
22. Blom NA, Gittenberger-de Groot AC, Jongeneel TH et al. Normal development of the pulmonary veins in human embryos and formulation of a morphogenetic concept for sinus venosus defects. *Am J Cardiol* 2001;87:305–9.
23. Hagen PT, Scholz DG, Edwards WD. Incidence and size of patent foramen ovale during the first 10 decades of life: an autopsy study of 965 normal hearts. *Mayo Clinic Proc.* 1984;59:17–20.
24. Connuck D, Sun JP, Super DM et al. Incidence of patent ductus arteriosus and patent foramen ovale in normal infants. *Am J Cardiol* 2002;89:244–7.
25. Fisher DC, Fisher EA, Budd JH et al. The incidence of patent foramen ovale in 1,000 consecutive patients. A contrast transesophageal echocardiography study. *Chest* 1995;107:1504–9.
26. Schneider B, Zienkiewicz T, Jansen V et al. Diagnosis of patent foramen ovale by transesophageal echocardiography and correlation with autopsy findings. *Am J Cardiol* 1996;77:1202–9.
27. Attenhofer Jost CH, Connolly HM, Danielson GK et al. Sinus venosus atrial septal defect: long-term postoperative outcome for 115 patients. *Circulation* 2005;112:1953–8.
28. Valente AM, Sena L, Powell AJ et al. Cardiac magnetic resonance imaging evaluation of sinus venosus defects: comparison to surgical findings. *Pediatr Cardiol* 2007;28:51–6.
29. Raghib G, Ruttenberg HD, Anderson RC et al. Termination of left superior vena cava in left atrium, atrial septal defect, and absence of coronary sinus; a developmental complex. *Circulation* 1965;31:906–18.
30. Phillips SJ, Okies JE, Henken D et al. Complex of secundum atrial septal defect and congestive heart failure in infants. *J Thorac Cardiov Surg* 1975;70:696–700.
31. Weinberg M Jr, Miller RA, Hastreiter AR et al. Congestive heart failure in children with atrial septal defect. *J Thorac Cardiov Surg* 1966;51:81–7.
32. Saxena A, Divekar A, Soni NR. Natural history of secundum atrial septal defect revisited in the era of transcatheter closure. *Indian Heart J* 2005;57:35–8.
33. Shah D, Azhar M, Oakley CM et al. Natural history of secundum atrial septal defect in adults after medical or surgical treatment: a historical prospective study. *Br Heart J* 1994;71:224–7; discussion 228.
34. Hanslik A, Pospisil U, Salzer-Muhar U et al. Predictors of spontaneous closure of isolated secundum atrial septal defect in children: a longitudinal study. *Pediatrics* 2006;118:1560–5.
35. Cockerham JT, Martin TC, Gutierrez FR et al. Spontaneous closure of secundum atrial septal defect in infants and young children. *Am J Cardiol* 1983;52:1267–71.
36. Holmvang G, Palacios IF, Vlahakes GJ et al. Imaging and sizing of atrial septal defects by magnetic resonance. *Circulation* 1995; 92:3473–80.
37. Durongpisitkul K, Tang NL, Soongswang J et al. Predictors of successful transcatheter closure of atrial septal defect by cardiac magnetic resonance imaging. *Pediatr Cardiol* 2004;25: 124–30.
38. Rosenzweig BP, Nayar AC, Varkey MP, Kronzon I. Echo contrast-enhanced diagnosis of atrial septal defect. *J Am Soc Echocardiogr* 2001;14:155–7.
39. Driggers RW, Spevak PJ, Crino JP et al. Fetal anatomic and functional echocardiography: a 5-year review. *J Ultrasound Med* 2003;22:45–51; quiz 52–3.
40. Kronzon I, Tunick PA, Freedberg RS et al. Transesophageal echocardiography is superior to transthoracic echocardiography in the diagnosis of sinus venosus atrial septal defect. *J Am Coll Cardiol* 1991;17:537–42.
41. Tempe DK, Sharma S, Banerjee A et al. The utility of transesophageal echocardiography for detecting residual shunt in a patient undergoing atrial septal defect repair. *Anesth Analg* 2007;104:777–8.
42. Trinca M, Caeiro A, Fernandes R et al. Sinus venosus atrial septal defect in an adult, diagnosed by transesophageal echocardiography. *Rev Port Cardiol* 2006;25:369–70.

43. Kleinman CS. Echocardiographic guidance of catheter-based treatments of atrial septal defect: transesophageal echocardiography remains the gold standard. *Pediatr Cardiol* 2005;26: 128–34.
44. Pascoe RD, Oh JK, Warnes CA et al. Diagnosis of sinus venosus atrial septal defect with transesophageal echocardiography. *Circulation* 1996;94:1049–55.
45. Oh JK, Seward JB, Khandheria BK et al. Visualization of sinus venosus atrial septal defect by transesophageal echocardiography. *J Am Soc Echocardiogr* 1988;1:275–7.
46. Mehta RH, Helmcke F, Nanda NC et al. Transesophageal Doppler color flow mapping assessment of atrial septal defect. *J Am Coll Cardiol* 1990;16:1010–16.
47. Hausmann D, Daniel WG, Mugge A et al. Value of transesophageal color Doppler echocardiography for detection of different types of atrial septal defect in adults. *J Am Soc Echocardiogr* 1992;5:481–8.
48. Lin SL, Ting CT, Hsu TL et al. Transesophageal echocardiographic detection of atrial septal defect in adults. *Am J Cardiol* 1992;69:280–2.
49. Sunaga Y, Hayashi K, Okubo N et al. Transesophageal echocardiographic diagnosis of coronary sinus type atrial septal defect. *Am Heart J* 1992;124:1657–9.
50. Watanabe F, Takenaka K, Suzuki J et al. Visualization of sinus venosus-type atrial septal defect by biplane transesophageal echocardiography. *J Am Soc Echocardiogr* 1994;7:179–81.
51. Jean D, Girard F, Couture P et al. Transesophageal echocardiographic diagnosis of sinus venosus-type atrial septal defect associated with partial anomalous venous connections during cardiac surgery in adults. *J Cardiothor Vasc An* 1995;9:438–41.
52. Durongpisitkul K, Tang NL, Soongswang J et al. Cardiac magnetic resonance imaging of atrial septal defect for transcatheter closure. *J Med Assoc Thai* 2002;85(Suppl. 2):S658–66.
53. Taylor AM, Stables RH, Poole-Wilson PA, Pennell DJ. Definitive clinical assessment of atrial septal defect by magnetic resonance imaging. *J Cardiovasc Magn Reson* 1999;1:43–7.
54. Holmvang G. A magnetic resonance imaging method for evaluating atrial septal defects. *J Cardiovasc Magn Reson* 1999;1:59–64.
55. Ishii M, Kato H, Inoue O, et al. Biplane transesophageal echo-Doppler studies of atrial septal defects: quantitative evaluation and monitoring for transcatheter closure. *Am Heart J* 1993; 125:1363–8.
56. Hellenbrand WE, Fahey JT, McGowan FX et al. Transesophageal echocardiographic guidance of transcatheter closure of atrial septal defect. *Am J Cardiol* 1990;66:207–13.
57. Hijazi Z, Wang Z, Cao Q et al. Transcatheter closure of atrial septal defects and patent foramen ovale under intracardiac echocardiographic guidance: feasibility and comparison with transesophageal echocardiography. *Catheter Cardiovasc Interv* 2001;52:194–9.
58. Latiff HA, Samion H, Kandhavel G et al. The value of transesophageal echocardiography in transcatheter closure of atrial septal defects in the oval fossa using the Amplatzer septal occluder. *Cardiol Young* 2001;11:201–4.
59. Figueroa MI, Balaguru D, McClure C et al. Experience with use of multiplane transesophageal echocardiography to guide closure of atrial septal defects using the amplatzer device. *Pediatr Cardiol* 2002;23:430–6.
60. Baglini R. Intracardiac echocardiography in monitoring atrial septal defect percutaneous closure: initial experience in an adult laboratory. *Int J Cardiol* 2007;114:274–6.
61. Zanchetta M, Rigatelli G, Pedon L et al. Transcatheter atrial septal defect closure assisted by intracardiac echocardiography: 3-year follow-up. *J Interv Cardiol* 2004;17:95–8.
62. Zanchetta M. On-line intracardiac echocardiography alone for Amplatzer Septal Occluder selection and device deployment in adult patients with atrial septal defect. *Int J Cardiol* 2004; 95:61–8.
63. Earing MG, Cabalka AK, Seward JB et al. Intracardiac echocardiographic guidance during transcatheter device closure of atrial septal defect and patent foramen ovale. *Mayo Clinic Proc* 2004; 79:24–34.
64. Zanchetta M, Pedon L, Rigatelli G et al. Intracardiac echocardiography evaluation in secundum atrial septal defect transcatheter closure. *Cardiovasc Interv Radiol.* 2003;26:52–7.
65. Zanchetta M, Onorato E, Rigatelli G et al. Intracardiac echocardiography-guided transcatheter closure of secundum atrial septal defect: a new efficient device selection method. *J Am Coll Cardiol* 2003;42:1677–82.
66. Butera G, Chessa M, Bossone E et al. Transcatheter closure of atrial septal defect under combined transesophageal and intracardiac echocardiography. *Echocardiography (Mount Kisco, N.Y.)* 2003;20:389–90.
67. Alboliras ET, Hijazi ZM. Comparison of costs of intracardiac echocardiography and transesophageal echocardiography in monitoring percutaneous device closure of atrial septal defect in children and adults. *Am J Cardiol* 2004;94:690–2.
68. Randolph GR, Hagler DJ, Connolly HM et al. Intraoperative transesophageal echocardiography during surgery for congenital heart defects. *J Thorac Cardiov Surg* 2002;124:1176–82.
69. Muhiudeen Russell IA, Miller-Hance WC, Silverman NH. Intraoperative transesophageal echocardiography for pediatric patients with congenital heart disease. *Anesth Analg* 1998;87:1058–76.
70. O'Leary PW, Hagler DJ, Seward JB et al. Biplane intraoperative transesophageal echocardiography in congenital heart disease. *Mayo Clinic Proc* 1995;70:317–26.
71. Rosenfeld HM, Gentles TL, Wernovsky G et al. Utility of intraoperative transesophageal echocardiography in the assessment of residual cardiac defects. *Pediatr Cardiol* 1998;19:346–51.
72. Stevenson JG. Role of intraoperative transesophageal echocardiography during repair of congenital cardiac defects. *Acta Paediatr Suppl* 1995;410:23–33.
73. Stevenson JG. Utilization of intraoperative transesophageal echocardiography during repair of congenital cardiac defects: a survey of North American centers. *Clin Cardiol* 2003;26:132–4.
74. Bichell DP, Geva T, Bacha EA et al. Minimal access approach for the repair of atrial septal defect: the initial 135 patients. *Ann Thorac Surg* 2000;70:115–18.
75. Ayres NA, Miller-Hance W, Fyfe DA et al. Indications and guidelines for performance of transesophageal echocardiography in the patient with pediatric acquired or congenital heart disease: report from the task force of the Pediatric Council of the American Society of Echocardiography. *J Am Soc Echocardiogr* 2005;18:91–8.
76. Nugent AW, Britt A, Gauvreau K et al Device closure rates of simple atrial septal defects optimized by the STARFlex device. *J Am Coll Cardiol* 2006;48:538–44.

77. Hijazi ZM, Cao Q, Patel HT, et al. Transesophageal echocardiographic results of catheter closure of atrial septal defect in children and adults using the Amplatzer device. *Am J Cardiol* 2000;85:1387–90.
78. Spies C, Timmermanns I, Schrader R. Transcatheter closure of secundum atrial septal defects in adults with the Amplatzer septal occluder: Intermediate and long-term results. *Clin Res Cardiol* 2007;96:340–6.
79. Belkin RN, Pollack BD, Ruggiero ML, et al. Comparison of transesophageal and transthoracic echocardiography with contrast and color flow Doppler in the detection of patent foramen ovale. *Am Heart J* 1994;128:520–5.
80. Waggoner AD, Davila-Roman VG, Hopkins WE et al. Comparison of color flow imaging and peripheral venous saline contrast during transesophageal echocardiography to evaluate right-to-left shunt at the atrial level. *Echocardiography (Mount Kisco, N.Y.)* 1993;10:59–66.
81. Soo AW, Healy DG, Walsh K, Wood F. Inferior vena cava and coronary sinus obstruction after percutaneous atrial septal defect device closure requiring surgical revision. *J Thorac Cardiovasc Surg* 2006;131:1405–6.
82. Spence MS, Qureshi SA. Complications of transcatheter closure of atrial septal defects. *Heart (British Cardiac Society)* 2005; 91:1512–14.
83. Hsiao JF, Hsu LA, Chang CJ et al. Late migration of a sideris septal occluder device for closure of atrial septal defect into the left atrium with mitral valve obstruction. *Am J Cardiol* 2007;99:1479–80.
84. Cotts T, Strouse PJ, Graziano JN. Late migration of a Sideris buttoned device for occlusion of atrial septal defect. *Catheter Cardiovasc Interv* 2006;68:754–7.
85. Clarke AC, Hirsch KJ, Kells CM, Howlett J. Thrombus formation on an atrial septal defect closure device. *Can J Cardiol* 2005;21:68–70.
86. Divchev D, Schaefer A, Fuchs M et al. Thrombus formation on an atrial septal defect closure device: a case report and review of the literature. *Eur J Echocardiogr* 2007;8:53–6.
87. Divchev D, Podewski EK, Mengel M et al. Inflammatory, abscess-forming foreign body reaction mimics a thrombus formation on an atrial septal defect closure device: A commented case report. *Eur J Echocardiogr* 2006;8:298–302.
88. Meier B. Iatrogenic atrial septal defect, erosion of the septum primum after device closure of a patent foramen ovale as a new medical entity. *Catheter Cardiovasc Interv* 2006;68:165–8.
89. Baykut D, Doerge SE, Grapow M et al. Late perforation of the aortic root by an atrial septal defect occlusion device. *Ann Thorac Surg* 2005;79:e28.
90. Divekar A, Gaamangwe T, Shaikh N et al. Cardiac perforation after device closure of atrial septal defects with the Amplatzer septal occluder. *J Am Coll Cardiol* 2005;45:1213–18.
91. Amin Z, Hijazi ZM, Bass JL et al. Erosion of Amplatzer septal occluder device after closure of secundum atrial septal defects: review of registry of complications and recommendations to minimize future risk. *Catheter Cardiovasc Interv* 2004;63:496–502.

# 12 Anomalies of the Ventricular Septum

**Geoffrey A. Forbus and Girish S. Shirali**

Department of Pediatrics, Medical University of South Carolina; Medical University of South Carolina, Charleston, SC, USA

## Definition

A ventricular septal defect (VSD) is defined as a hole (or defect) between the right and left ventricles. This defect may occur in isolation or, less commonly, may be part of a complex cardiac malformation.

## Incidence

The reported incidence of congenital heart disease (CHD) in general, and VSD in particular, has varied widely, due at least in part to varying ascertainment methodologies and the variable natural history of VSD. Large population-based studies provide sufficient live births (denominators) at the expense of an inability to detect all with CHD (numerators), whereas intensive, sensitive studies usually cannot be done on very large populations [1]. Given the high propensity of VSDs to close spontaneously, starting as early as in utero, the incidence of VSD would be much higher if all fetuses were examined, somewhat lower if all newborns were examined, lower again if only those newborns with murmurs were examined, and lower still if these subjects were first evaluated at 1 year of age [2]. Prior to the wide availability of echocardiography, the incidence of VSD was reported between 30 and 240 per 100 000 births [3–5]. More recently, a higher incidence of VSD has been reported, particularly in premature infants [6–10]. Utilizing screening echocardiography in neonates, a muscular ventricular septal defect was diagnosed in 5320 and 5660 per 100 000 term and preterm babies, respectively [8,9]. Groups reporting a high incidence have also reported high rates of spontaneous closure of these defects. The perceived increase in the incidence of VSD may be due to increased sensitivity of perinatal and neonatal surveillance rather than to a true increase in incidence. Between 10 000 and 11 000 infants with an isolated VSD are diagnosed annually in the United States [5,11,12]. Between 15% and 20% of these patients (1500–2200 patients) require surgery annually [13].

*Echocardiography in Pediatric and Congenital Heart Disease: From Fetus to Adult*
Edited by Wyman W. Lai, Luc L. Mertens, Meryl S. Cohen and Tal Geva
 ISBN: 978-1-405-17401-5

## Etiology

The developmental etiology of VSDs is felt to be multifactorial. Certainly, VSDs are quite prevalent in association with genetic abnormalities, especially in trisomies 13, 18 and 21 as well as other less common syndromes. Most of these defects are large, associated with increased right-to-left shunting [14,15]. Children with Down syndrome have a higher incidence of inlet VSD when compared with children without Down syndrome [16]. In the autosomal dominant Holt–Oram syndrome, both atrial and ventricular septal defects are inherited in association with limb deformity as a result of mutations in the gene encoding the transcription factor TBX5 [17].

The Baltimore-Washington Infant Study has revealed an association between paternal use of marijuana and cocaine, paternal occupation such as jewelry making and paint stripping, and the occurrence of membranous and muscular VSD in the offspring [18,19].

## Morphology and classification

### Development

The availability of in vivo labeling of cells has facilitated the science of establishing the origin and fate of major components of the developing heart [20]. The current description is based primarily on an understanding of cardiac septation that has developed over the past decade [21]. The linear heart tube is formed by fusion of the paired mesodermal heart fields. This tube consists of two concentric layers of cells – the outer myocardium and the inner endocardium – separated by acellular cardiac jelly [22]. During cardiac looping, myocardium is formed by local differentiation, and proliferation occurs at the myocardium at the outer curvature of the heart, lining the atria and ventricles [23,24]. Cardiomyocyte

differentiation is more advanced in these chambers than it is in the midline of the atria, the atrioventricular (AV) junction, the inner curvature of the heart loop, and the outflow tract. During looping of the straight heart tube, acellular cardiac jelly disappears from the developing atria and ventricles, and starts to accumulate in the AV junction and the outflow tract. The AV cushions consist of mesenchymal cells that are derived from endocardium, whereas the outflow-tract ridges incorporate a substantial contribution of neural crest-derived mesenchymal cells.

Between 4 and 7 weeks' gestation in humans, the heart is septated by the fusion of several tissues including AV and outflow cushion-derived mesenchyme, the mesenchymal cap of the primary atrial septum, and the muscular components of the atrial and ventricular septa [21,25–27]. These mesenchymal septa become largely myocardial in later stages of development [22,28–31]. Septation of the ventricles involves a complex series of events. The transitional zone between the embryonic left and right ventricles (LV and RV) is characterized by the expression of "neuromuscular" markers, and forms a ring around the primary interventricular foramen, termed the "primary ring" [26,32–34]. This ring separates the upstream portion (the atrium and LV) from the downstream portion (the RV and outflow tract) of the heart. Myocardialization of the endocardial cushions in the outflow tract (outflow-tract ridges) leads to the formation of a muscular outlet septum [35]. At 5 weeks, a muscular septum is identifiable between the trabecular portions of both ventricles. Eventually, the muscular interventricular septum is formed from three components: (i) the primary, or trabecular, component that develops from the septum separating the trabeculated cavities of the developing RV and LV; (ii) the inlet component that develops from the AV cushions; and (iii) the outlet portion that develops from the outflow-tract ridges. The fused major (superior and inferior) AV cushions and the mesenchymal cap of the primary atrial septum eventually form the membranous septum. The bifurcation of the ventricular conduction system is the landmark that separates the contribution of the AV cushions and the outflow-tract ridges to septation, and divides the muscular ventricular septum into inlet, trabecular and outlet portions [21]. The recent availability of ultra-high-resolution echocardiography technology, coupled with the newly created supply of gene knock-out mice with predictable cardiac phenotypes, promises to provide accurate insights into abnormal cardiac development.

## Anatomy

In the contemporary era, where much is known of the prognosis and associated lesions that accompany VSD in specific locations, and treatment choices are expanding to include transcatheter options, a thorough understanding of the anatomy of the ventricular septum is important. Several schemes for nomenclature and classification have been proposed. The scheme proposed in this chapter is based on schemes provided by Anderson, Soto and Van Praagh, and conforms with the Congenital Heart Surgery Nomenclature and Database Project [36–39]. For each structure, an attempt is made to provide several of the names that are in common usage.

This discussion begins with a description of the normal ventricular septum. The right and left ventricular aspects of the septum do not correspond (Figs 12.1 and 12.2). Viewed from the RV, the septum may be divided into four zones: inlet, trabecular, outlet and membranous. The smooth-walled inlet septum extends inferiorly and posteriorly from the hinge of the septal leaflet of the tricuspid valve to the distal septal attachments of the tricuspid valve papillary muscles. Inferior to this and extending anteriorly is the trabecular septum, which is characterized by coarse trabeculations

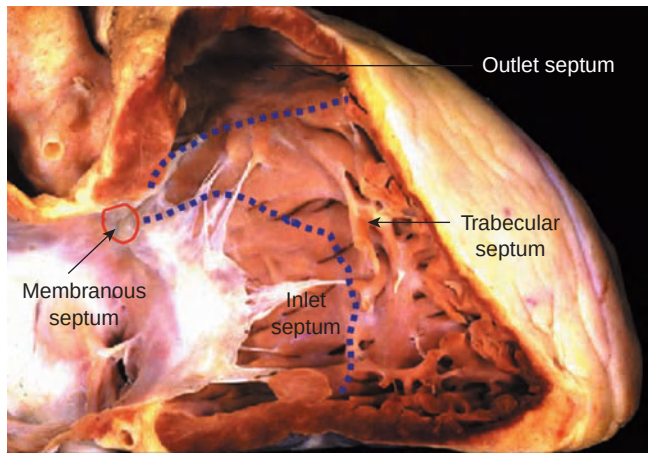


**Figure 12.1** Right ventricular aspect of the ventricular septum. The free wall of the right ventricle has been removed. Reproduced with permission of Professor Robert H. Anderson.

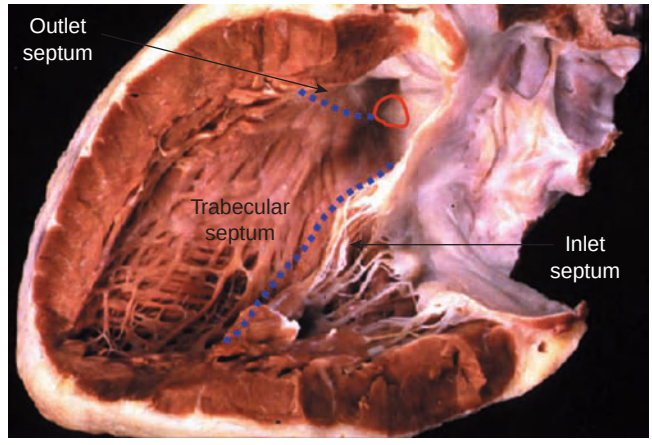


**Figure 12.2** Left ventricular aspect of the ventricular septum. The free wall of the left ventricle has been removed. Reproduced with permission of Professor Robert H. Anderson.

on the RV aspect. The trabecular septum is separated from the smooth-walled outlet septum by the septal band (septo-marginal trabeculation), which courses superiorly and posteriorly from the mid-portion of the ventricular septum. The septal band divides into an antero-superior limb, which courses superiorly toward the pulmonary valve and blends into the subpulmonary infundibulum, and a postero-inferior limb, which courses towards the RV free wall, where it merges with the parietal band (septo-parietal trabeculation). The pulmonary valve is elevated above these muscle bands by the subpulmonary infundibulum. This latter structure consists of a circumferential free-standing cylindrical sleeve of muscle immediately below the hinges of the pulmonary valve. Inferiorly and posteriorly, this sleeve merges imperceptibly with the outlet (conal, infundibular) septum. The aortic outflow tract and valve are located posterior to and rightward of the outlet septum. The inlet, trabecular and outlet zones of the ventricular septum radiate postero-inferiorly, antero-inferiorly and antero-superiorly, respectively, from the membranous septum, which lies adjacent to the antero-septal commissure of the tricuspid valve on the right side and is adjacent to the right coronary–noncoronary commissure on the left side. In the normal heart, the membranous septum is a small, translucent area that has two components, an interventricular and an AV component, which are separated by the septal leaflet and antero-septal commissure of the tricuspid valve. The "AV septum" accounts for the offset between the septal hinges of the mitral and tricuspid valves. It is defined by right atrial myocardium (superiorly and to the right) and left ventricular (LV) myocardium (inferiorly and to the left) [40]. The interventricular component of the membranous septum is bounded superiorly by the AV portion of the membranous septum, anteriorly by the subaortic outlet septum, inferiorly by the trabecular septum and posteriorly by the inlet septum. The conduction tissues, consisting of the AV conduction bundle, the branching bundle and left bundle branch, course in the posterior-inferior border of the membranous septum.

VSDs that extend to the membranous septum have been variously described as membranous, perimembranous or paramembranous VSDs; we retain the latter term. These defects account for 80% of surgical and autopsy series of VSDs [37,41]. By definition, all such defects are "roofed" by the tricuspid valve, resulting in fibrous continuity between the tricuspid and mitral valves. They are located between the outlet (conus) and inlet (ventricular) portions of the RV, and have been termed "conoventricular." They are directly beneath the commissure between the right and noncoronary cusps of the aortic valve. A paramembranous VSD may extend inferiorly to the trabecular (muscular) septum, or posteriorly to the inlet septum, or anteriorly toward the outlet septum. In the latter instance, it may be associated with hypoplasia or absence of the outlet septum. Paramembranous defects frequently exhibit tricuspid valve abnormalities consisting of redundant fibrous tissue, varying degrees of tethering of the anterior leaflet of the tricuspid valve and fused chordae. Accessory fibrous (so-called aneurysmal) tissue may lie along the posterior or superior margin of the VSD. The proximity of paramembranous VSD to the antero-septal commissure of the tricuspid valve may lead to adherence of these leaflets to the edges of the defect, causing shunting directly from the LV into the right atrium [42,43].

Muscular VSDs account for 5–20% of all VSDs. These are classified, based on their location, into anterior, midmuscular, apical and posterior defects [44,45]. Large trabecular VSDs may be clearly identifiable as single defects on the LV surface, but they may be covered by dense and coarse trabeculations on their RV aspect, giving the appearance of multiple defects – the so-called "Swiss-cheese" septum [46]. Muscular defects may also be serpiginous, with some distance between their LV and RV orifices. Large apical VSDs may exhibit communication between the apex of the LV and RV sinus, or between the LV apex and that of the RV apical infundibular recess [47].

The outlet septum may exhibit one of several abnormalities. It may be completely absent, as with a subarterial (conal septal, doubly committed, juxta-arterial, subpulmonary) VSD, or it may be malaligned relative to the trabecular septum ("malalignment" VSD). Subarterial VSDs usually occur in isolation. They account for 5–7% of surgical and autopsy series in Western populations, and up to 30% in Asian populations [41,48]. The absence of the outlet septum leads to fibrous continuity (in the form of a raphe) between the adjacent cusps of the aortic and pulmonary valves; these two valves lie at the same level. This defect is characterized by absence of not only the outlet septum but also of the free-standing subpulmonary sleeve of infundibulum that characterizes the normal heart. The postero-inferior rim of these defects may be either muscular (if the defect extends inferiorly to the trabecular septum) or fibrous (if the defect extends posteriorly to the membranous septum). Due to the close proximity of these defects to the right coronary cusp of the aortic valve, the lack of support to the aortic valve from below and the Venturi effect of flow across these defects, there is a strong tendency for the right coronary cusp of the aortic valve to prolapse into a subarterial VSD [49]. The prolapsing right coronary cusp may close off the defect partially or completely.

VSDs that exhibit malalignment of the outlet septum are usually not isolated malformations; they typically comprise one component of complex malformations such as tetralogy of Fallot or interrupted aortic arch. If the outlet septum is malaligned anteriorly and leftward, the "floor" of the RV outflow tract is elevated, creating the substrate for subpulmonary obstruction. Conversely, if the outlet septum is malaligned posteriorly and rightward, the "roof" of the LV outflow tract is lowered, thus creating the substrate for subaortic obstruction. Whether a defect exhibits malalignment of the outlet

septum is a separate issue from whether it extends to the membranous septum: not all malalignment defects are paramembranous, and the converse is also true.

Defects that are located posterior and inferior to the septal leaflet of the tricuspid valve have been designated as "inlet" or as VSD of the AV canal type. However, these isolated defects are not considered part of the spectrum of AV canal defects. Such defects account for 5–8% of all VSDs. Viewed from the LV, they remain in the LV outlet. Inlet VSDs may be associated with straddling chordal and papillary muscle attachments of the septal leaflet of the tricuspid valve across the VSD into the LV. Hearts with straddling tricuspid valves characteristically exhibit malalignment between the interatrial and interventricular septum, and varying degrees of hypoplasia of the RV [50–53].

## Pathophysiology

A VSD may have two closely related adverse consequences: altered hemodynamics due to a left-to-right shunt and alteration of the pulmonary vascular bed.

### Left-to-right shunt

Left-to-right shunting across a VSD provides greater blood flow to the pulmonary circulation than to the systemic circulation [54]. The magnitude of the left-to-right shunt depends on VSD size and the resistance in the pulmonary vascular bed. Based on both these factors, VSDs are broadly divided into three categories: small, moderate and large [55–58]. A small defect restricts flow, thus preventing equalization of pressure between the ventricles and preserving normal RV pressure. A moderate-sized defect usually provides some resistance to pressure but little resistance to flow. As a result, this defect leads to variable elevation of RV pressure, and impressive left-to-right shunting. A large defect offers little resistance to flow or pressure. This defect leads to RV hypertension and a large left-to-right shunt.

Left-to-right shunting across a VSD may lead to three adverse hemodynamic consequences: (i) LV volume overload; (ii) pulmonary overcirculation; and (iii) potentially compromised systemic cardiac output. The increased volume load on the LV leads to LV dilation, which produces elevation of end-diastolic pressure via the length–tension relationship [59]. LV hypertrophy develops as a compensatory mechanism to minimize increase in wall tension, but it also decreases ventricular compliance, thus further aggravating the increase in end-diastolic pressure [60]. This elevation in end-diastolic pressure is reflected in increased left atrial and pulmonary venous pressure. This increases the hydrostatic pressure in the pulmonary capillary bed, leading to increased pulmonary interstitial fluid and possibly pulmonary edema [61]. Pulmonary compliance and gas exchange may be altered as a result [62].

### The pulmonary vascular bed

A hemodynamically significant VSD leads to a "common ejectile force," where RV and pulmonary arterial systolic pressure is systemic [63]. Increased pulmonary blood flow and increased pulmonary arterial pressure may alter the normal maturation of the pulmonary vascular bed [64]. As the pulmonary resistance drops over the first few weeks after birth, left-to-right shunting of blood increases, leading to pulmonary overcirculation. Left alone, this scenario gradually evolves into one characterized by increasing pulmonary vascular resistance (PVR) and decreasing symptoms [65]. The pulmonary arteriole transitions from having a reactive muscular wall to potentially irreversible structural changes consisting of medial hypertrophy and intimal proliferation, which manifests as increased PVR. Eventually, PVR exceeds systemic vascular resistance, leading to right-to-left shunting across the VSD, and cyanosis.

### Associated defects

VSDs most frequently occur in isolation. However, in surgical series, nearly 50% of all patients with a VSD have an additional cardiac anomaly [66,67]. A moderate-sized or large patent ductus arteriosus (PDA) is more commonly encountered in infants in heart failure. Atrial septal defects, pulmonary stenosis and a persistent left superior vena cava are seen in up to 13%, 15% and 8% of VSD patients, respectively, in surgical series [68]. Double-chambered RV and subaortic stenosis, either separately or in combination, have been reported in up to 10% of VSD patients in surgical series [69–73].

Aortic regurgitation (AR) is an acquired and frequently progressive lesion in some patients with VSD [74–78]. It develops in association with subarterial and paramembranous VSD, but is more likely to develop with the former than with the latter [75]. Competence of the aortic valve requires three main levels of support for the valve apparatus: support from above by well-developed commissures, support at the level of the leaflets by apposition during diastole, and support from below by the outlet septum [79]. Deficiencies at any of these levels may constitute the substrate for the development of AR. The subarterial VSD lies directly below the entire length of the right coronary cusp of the aortic valve, accounting for the strong tendency of this cusp to prolapse into the VSD. Prolapse of the right coronary cusp of the aortic valve leads to defective apposition of the leaflets. In addition, absence of the outlet septum leads to deficient support for the valve apparatus from below. This constitutes the substrate for AR, almost always due to prolapse of the right coronary cusp of the aortic valve [75].

By contrast, the paramembranous VSD lies below both the right and noncoronary cusps of the aortic valve. AR in this setting has been attributed to prolapse of the right or noncoronary cusp(s) of the aortic valve [74]. Leaflet deformities include elongation, and thickened and rolled edges [80]. The

left coronary cusp of the aortic valve is distant from the ventricular septum, and prolapse of this leaflet into a VSD is quite uncommon.

## Imaging

### Goals of the examination

The goals of echocardiography in the context of VSD can be summarized as follows:

- Determination of defect location and size.
- Relationships with neighboring structures (e.g., tricuspid, aortic and pulmonary valves).
- Measurement of defect margins (for assessment of suitability for transcatheter closure).
- Hemodynamic assessment.
- Flow direction (by color and spectral Doppler).
- Estimation of right ventricular systolic pressure based on VSD flow and tricuspid regurgitation jet velocities (peak pressure gradients with a simultaneous measurement of systemic systolic blood pressure), and/or the systolic configuration of the ventricular septum.
- Mean transseptal pressure gradient.
- Evidence of hemodynamic load (left ventricular enlargement, systolic septal flattening associated with right ventricular pressure load, increased pulmonary blood flow).
- Biventricular function.
- Detection of associated lesions.

### Transthoracic imaging

Historically, echocardiographic techniques such as M-mode were utilized to assess indirect – albeit unreliable – measures of left-to-right shunting [81,82]. In the mid-1970s real-time two-dimensional (2D) echocardiography became clinically useful and was rapidly applied to the evaluation of children with CHD [83]. Greater experience and improving technology contributed to the increasing accuracy of the technique [84,85]. The introduction of pulsed-wave and color flow Doppler led to dramatic improvements in the ability of echocardiography accurately to diagnose VSD in situations that had posed a challenge, such as identifying muscular or multiple VSDs (Videoclip 12.1), and differentiating between the flow profiles of RV outflow tract obstruction and subarterial VSD [86–88]. Today, 2D echocardiography has evolved into a universally applicable modality for the comprehensive diagnosis of VSD [89,90]. Available techniques include M-mode, 2D, and pulsed-wave and continuous-wave Doppler. These provide for accurate identification of VSD location, number, size and margins, and also provide physiologic information including RV and pulmonary arterial pressure [91,92]. Indirect and some direct information regarding shunt volume may also be derived.

Two-dimensional echocardiography, utilizing a combination of multiple windows, planes and sweeps, is the mainstay for complete examination of the ventricular septum. The subxiphoid long-axis sweep starts inferiorly at the base of the heart. As it progresses superiorly, it profiles the inlet septum and both the AV and interventricular components of the membranous septum. Advancing superiorly and anteriorly, this sweep demonstrates the trabecular septum. The subxiphoid short-axis sweep demonstrates anterior or posterior malalignment of the outlet septum (Videoclip 12.2). Subarterial VSDs are well seen, with flow directed from the LV directly to the pulmonary valve and main pulmonary artery. As this sweep progresses leftward, it demonstrates the boundary between the RV inflow-sinus and outflow portions.

The apical 4-chamber sweep starts posteriorly in the plane of the coronary sinus and the AV valves. This view demonstrates the posterior septum – the inlet septum above, and the trabecular septum below – quite well. As the plane of this sweep proceeds anteriorly, the membranous septum comes into view immediately inferior to the septal leaflet of the tricuspid valve. Medial repositioning and clockwise rotation of the transducer help to examine the subaortic outflow tract for posterior malalignment of the outlet septum. Anterior malalignment VSDs typically cannot be demonstrated from this view. In the presence of an inlet (canal-type) VSD, straddling of the tricuspid valve septal leaflet may be seen from this view (Fig. 12.3).

The parasternal long-axis view transects the aorta and the LV in their long axis. It enables evaluation of anterior VSDs. Subarterial VSDs are best seen from this view; these are characterized by the absence of any muscle between the superior margin of the VSD and the hinge of the right coronary cusp of the aortic valve. Prolapse of the right coronary cusp of the aortic valve into subarterial or paramembranous VSD is well

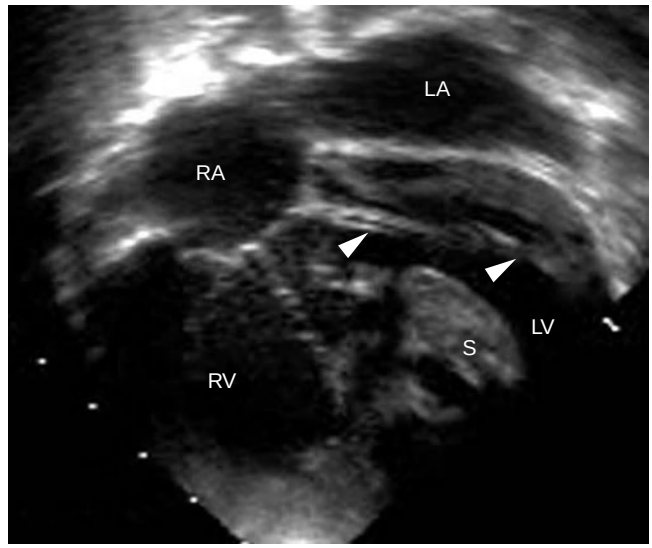


**Figure 12.3** Apical 4-chamber view of an inlet ventricular septal defect (VSD) with straddling of the septal leaflet of the tricuspid valve (arrows). S, septum; RA, right atrium; RV, right ventricle; LA, left atrium; LV, left ventricle.

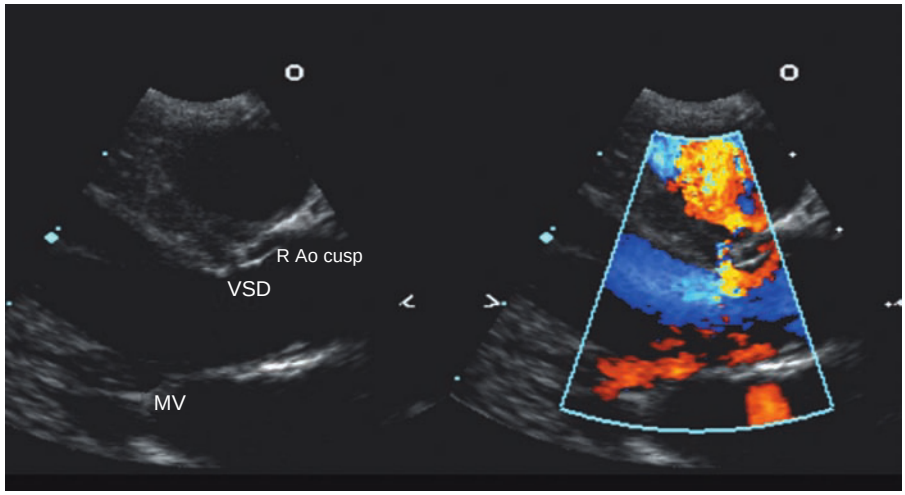


**Figure 12.4** Parasternal long-axis view of a paramembranous ventricular septal defect (VSD) with aortic cusp prolapse. R Ao cusp, right aortic cusp; MV, mitral valve.

seen (Fig. 12.4). Aortic cusp prolapse may partially or completely close off a VSD, making it difficult to determine the location of the original defect from this view. Posterior malalignment of the outlet septum, which "lowers the roof" of the subaortic outflow tract, is well seen (Fig. 12.5). Inferiorly, the parasternal long-axis view demonstrates anterior muscular VSDs. Tilting the transducer to the tricuspid inflow and the pulmonary outflow tract demonstrates paramembranous and anterior malalignment VSDs, respectively (Fig. 12.6).

The parasternal short-axis view is of great utility in demonstrating VSD location. Beginning at the base of the heart, paramembranous VSDs are seen between 9 o'clock and 11 o'clock positions (Videoclip 12.3). Tricuspid valve aneurysmal tissue may shroud the VSD, leading to underestimation of its size by 2D echocardiography; this is unmasked by color flow Doppler (Fig. 12.7). Anterior (outlet) extension of these defects is seen between 11 and 12 o'clock. A subarterial VSD is seen between 12 o'clock and the hinge of the pulmonary valve (2 o'clock; Fig. 12.8; Videoclip 12.4). Anterior malalignment VSDs appear as dropout between 11 and 1 o'clock; the outlet septum itself is seen more anteriorly and leftward than normal, thus "raising the floor" of the subpulmonary outflow tract. As this sweep progresses down the septum, muscular VSDs are profiled well (Fig. 12.9). Posterior muscular VSDs appear between 7 and 10 o'clock, midmuscular VSDs appear between 10 and 12 o'clock, and anterior muscular VSDs appear between 12 and 2 o'clock. Inlet (AV-canal type) VSDs appear between 7 and 9 o'clock in the course of this sweep.

Echocardiography must include careful examination for additional VSDs. All of the margins of the defect must be examined for any evidence of substrate that might complicate VSD closure, such as straddling AV valve apparatus (Videoclip 12.5), and prolapse of aortic valve cusps into the VSD (Videoclip 12.6).

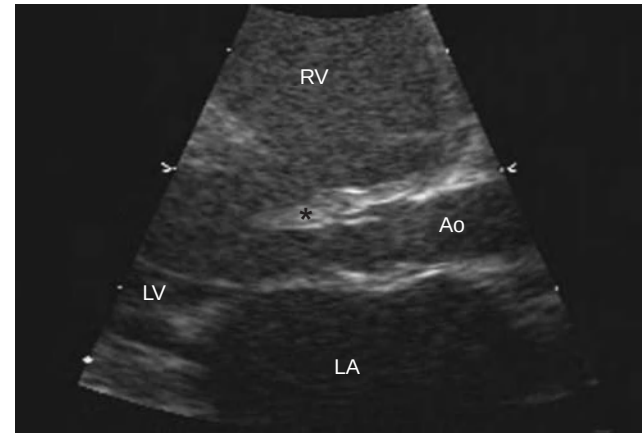


**Figure 12.5** Parasternal long-axis view of a posterior malalignment ventricular septal defect (VSD). Asterisk (*) denotes outlet septum. RV, right ventricle; LV, left ventricle; Ao, aorta; LA, left atrium.

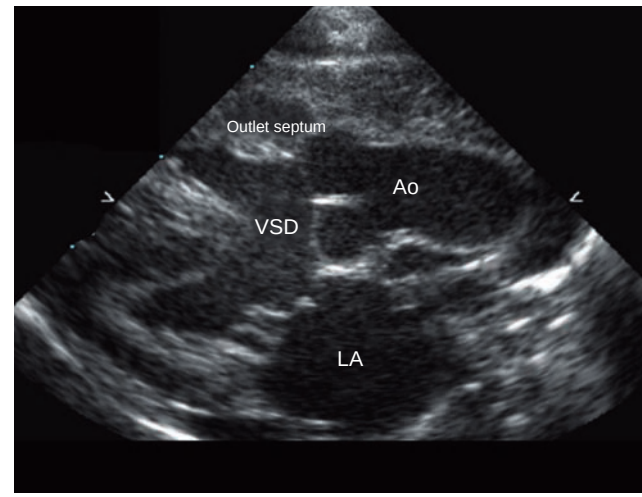


**Figure 12.6** Parasternal long-axis view of an anterior malalignment ventricular septal defect (VSD). Ao, aorta; LA, left atrium.

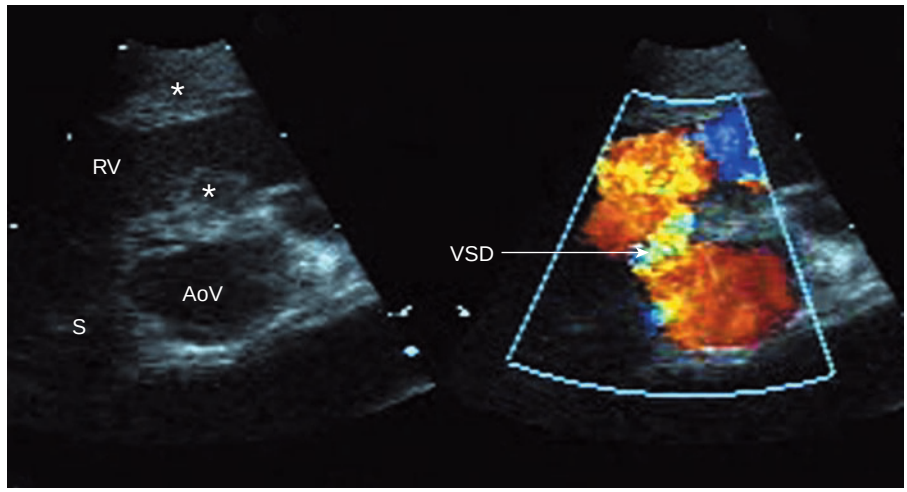


**Figure 12.7** Parasternal short-axis view of a paramembranous ventricular septal defect (VSD) with tricuspid valve (TV) aneurysmal tissue. Asterisk (*) denotes sleeve of infundibulum. RV, right ventricle; S, septal leaflet of the TV; AoV, aortic valve.

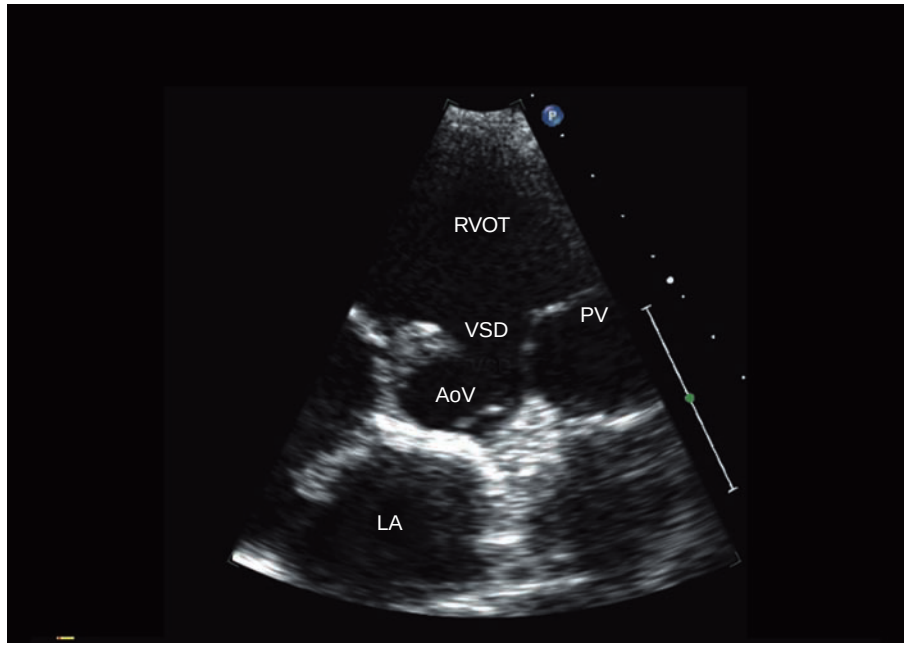


**Figure 12.8** Parasternal short-axis view of a subarterial ventricular septal defect (VSD). AoV, aortic valve; RVOT, right ventricular outflow tract; VSD, ventricular septal defect; PV, pulmonary valve; LA, left atrium.

Combined color flow and pulsed-wave Doppler assessments provide adequate reliable information about the magnitude of left-to-right flow as well as RV and pulmonary arterial pressure, obviating the need for catheterization in all but a miniscule minority of patients [92–95]. The combination of these modalities is used to evaluate not only the defect itself, but also associated hemodynamic perturbations such as left atrial and LV dilation, and RV and pulmonary arterial hypertension.

## Prenatal assessment

Although VSD is the most common CHD diagnosed during the first year of life, its detection in the fetus can be challenging [96]. Nevertheless, prenatal echocardiographic detection of VSDs in isolation is quite possible albeit with less frequency than the identification of other abnormalities such as AV septal defects [97]. Identifying the number and location of the defects is as important in the fetus as it is postnatally. Detection in the fetus can be more problematic due in part to fetal movement and the challenge of obtaining standard transthoracic-equivalent views. Defects of the ventricular septum can be identified from a 4-chamber view by 2D imaging with the ultrasound beam parallel to the septum, and are distinguished from dropout by the appearance of a "T" artifact (echo-dense areas at the blood–tissue interface of a true VSD; Fig. 12.10) [85]. Care must be taken when interrogating the membranous septum because dropout can create the appearance of a defect – this structure is exceptionally

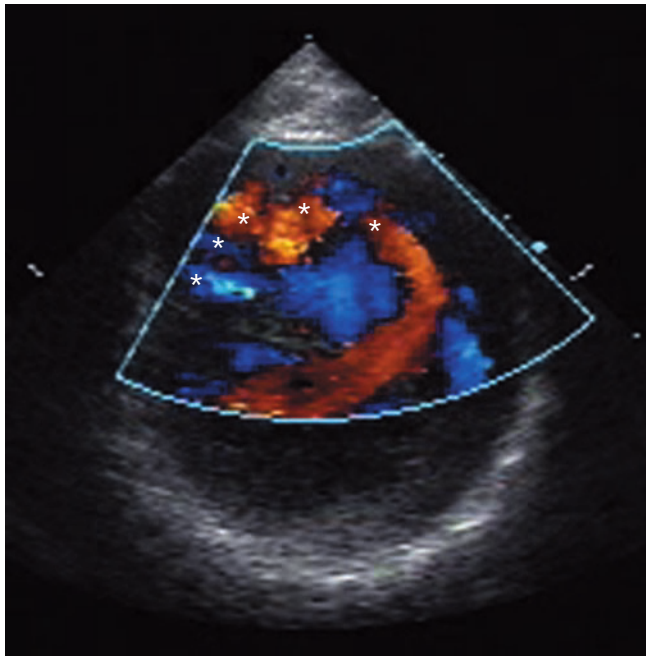

**Figure 12.9** Parasternal short-axis view of multiple muscular ventricular septal defects (VSDs) denoted by asterisks.

thin in both the fetus and neonate. Aligning the septum in a perpendicular orientation allows the use of color Doppler to assist in the detection of true defects. The ventricular pressures are similar in the fetus; decreasing the color scale is helpful in detecting this low-velocity ventricular shunting. The association of chromosomal abnormalities such as trisomies 18 and 21 should increase the level of suspicion of associated VSDs, especially malalignment and inlet types, respectively [2].

## Imaging of the adult

Imaging of the adult with a VSD can be problematic, as a larger body habitus and adult-specific lung disease (such as emphysema) often contribute to poor acoustic windows. Adequate visualization of the defect is paramount in the surveillance of this growing patient population for the development of potential hemodynamically associated lesions, such as aortic insufficiency in perimembranous VSDs with aortic cusp prolapse, double-chambered right ventricle, and subaortic membrane development, in addition to progressive left ventricular dilation and endocarditis [98–100]. TEE can be of extreme importance in detecting these lesions when TTE images are suboptimal. Often in the adult, TEE can be performed with moderate sedation obviating the need for the general anesthesia that is frequently necessary in the pediatric population.

## Preoperative imaging

Preoperative assessment of VSDs includes both TTE and TEE. The goals and techniques of transthoracic imaging are described in detail above. Transesophageal echocardiography is used in the operating room to evaluate further the ventricular septum preoperatively (Fig. 12.11); but this imaging modality is also implemented in the postoperative evaluation following surgical repair and prior to closure of the chest. Bettex et al. found that preoperative TEE findings resulted in an alteration in the planned surgical approach in 18 of 865 (2.1%) pediatric patients undergoing cardiothoracic surgery [101]. Postoperatively, TEE findings have been shown

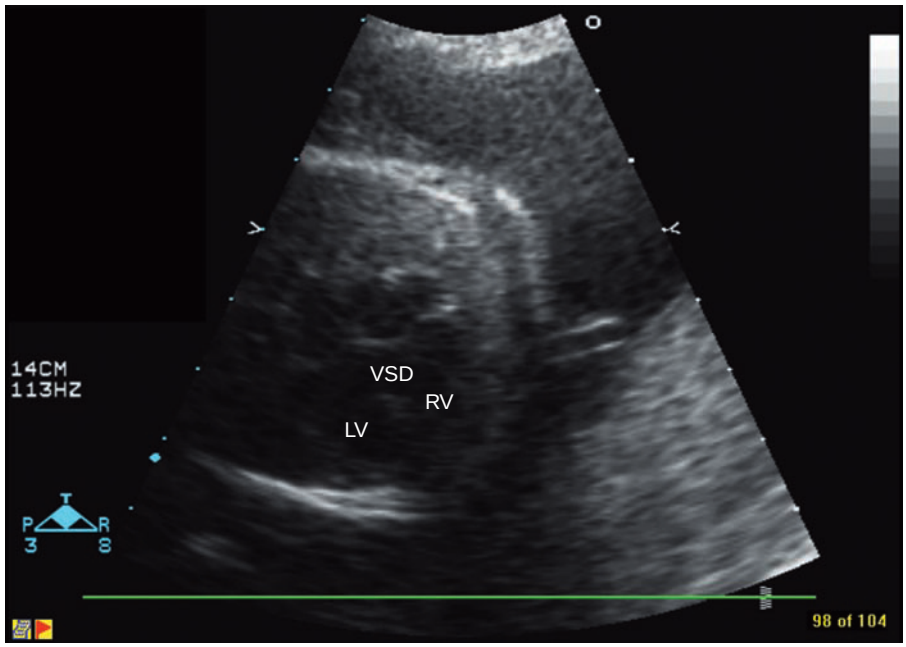


**Figure 12.10** Fetal apical 4-chamber view of a moderate muscular ventricular septal defect (VSD). LV, left ventricle; RV, right ventricle.

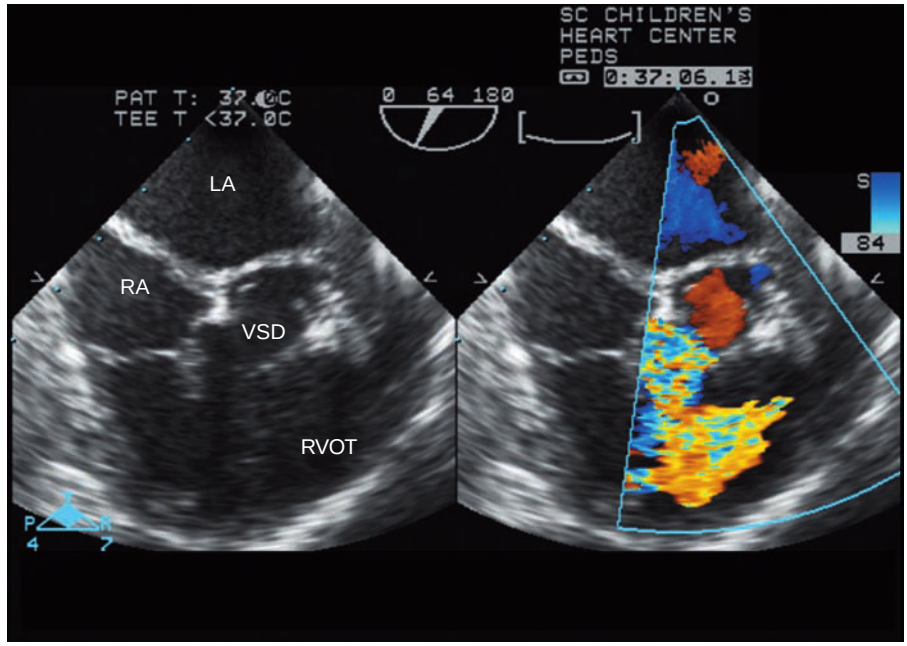


**Figure 12.11** Transesophageal echocardiography (TEE) imaging of a moderate paramembranous ventricular septal defect (VSD) preoperatively. LA, left atrium; RA, right atrium; RVOT, right ventricular outflow tract.

to change the surgical management, including the return to cardiopulmonary bypass (CPB) for repair of significant residual lesions, in as many as 7.5% of cases where this imaging modality was implemented [102]. Further, medical management of the patient immediately post-CPB can be altered based on TEE findings, such as the need for additional inotropes, the identification of intracardiac air and the assessment of ventricular filling [101]. This modality has been shown to be safe in regards to ventilation in babies as small as 2 kg, the patient population at highest risk of having residual postoperative defects [103].

## Echocardiographic guidance of transcatheter techniques

In addition to assisting in the management of VSDs in the operating room, TEE is used to guide transcatheter device closure of VSDs – an application that has growing clinical relevance. Surgical closure of muscular VSDs can be challenging due to the dense trabeculations of the right ventricular aspect of the septum. Device occlusion of congenital muscular defects and certain perimembranous defects has been shown to be safe and effective with the implementation of TEE to guide catheter position and proper deployment of the device [104]. TEE is used for sizing of the defect to ensure selection of the appropriate device as well as for the assessment of residual defects or impingement on AV or aortic valves upon deployment [105]. More recently, intracardiac echo (ICE) has been shown to be effective in the guidance of VSD occluder devices. Although the catheters are expensive, require a fairly large sheath (8–10.5 Fr) and have a learning curve secondary to novel imaging planes, ICE offers the possibility of performing the procedure without subjecting the patient to general anesthesia [106].

## Postoperative assessment

The primary objective in the echocardiographic assessment of the postoperative patient following isolated VSD closure is the evaluation for residual ventricular-level shunts. Residual defects can be detected along the margins of the VSD patch. Rychik et al. found that 38% of patients had echocardiographic evidence of residual ventricular-level shunting at the peripatch area (Fig. 12.12; Videoclip 12.7) [107]. Sixty-five percent of these patients with VSD, where jet diameter measured by color Doppler was less than 4 mm, exhibited spontaneous resolution of the residual shunt by 10 months post-repair. Also, defects remote from the repair site can become manifest following repair of a large VSD, certainly if ventricular pressures were similar preoperatively.

Further, the thorough evaluation of structures adjacent to the surgical site or through which the repair was performed is paramount. In the current era, the preferred route for repair of most VSDs is via a right atriotomy. A subset of these patients will require detachment of the tricuspid valve anterior leaflet, septal leaflet, or both for better defect exposure, with subsequent resuspension of the leaflets after VSD closure [108]. Although the documented incidence of stenosis and/or regurgitation is low following this approach, interrogation of the tricuspid valve is important. Repair via a ventriculotomy, either right or left, is rarely required save for specific circumstances, such as repair of apical or otherwise inaccessible muscular VSDs. However, ventricular dysfunction and aneurysm development following this approach should be sought via serial echocardiograms indefinitely.

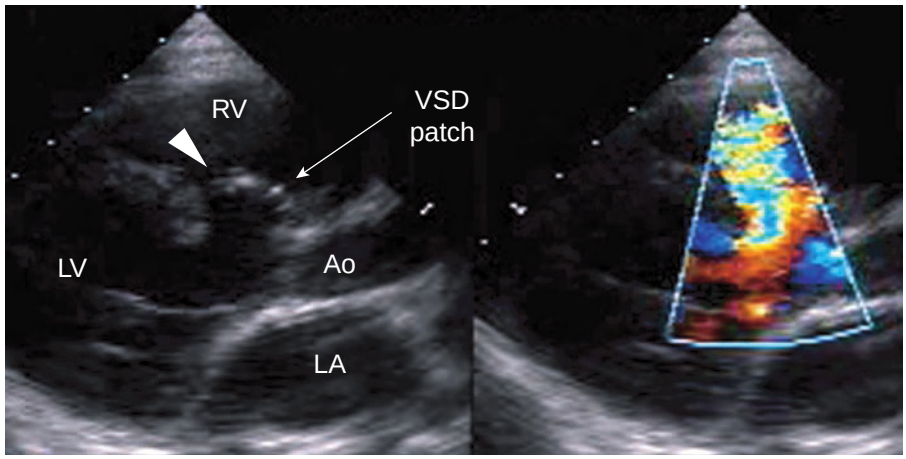


**Figure 12.12** Parasternal long-axis view of a peripatch residual ventricular septal defect (VSD) shown with color compare mode. Ao, aorta; RV, right ventricle; LV, left ventricle.

The postoperative evaluation of patients following repair of paramembranous or subarterial VSDs with aortic cusp prolapse and resultant aortic insufficiency should involve a thorough evaluation of the valve for residual incompetence either as a result of the surgical repair or from preexisting damage to the valve. Even when valvuloplasty is performed at the time of VSD closure, aortic insufficiency may progress postoperatively. Predictors of the need for subsequent aortic valve replacement following initial surgical closure of a VSD with aortic cusp prolapse include patient age greater than 15 years and at least moderate insufficiency preoperatively [109]. This subset of patients should be followed serially with specific scrutiny of the aortic valve.

## References


1. Hoffman JIE, Kaplan S. The incidence of congenital heart disease. *J Am Coll Cardiol* 2002;39:1890–900.
2. Paladini D, Palmieri S, Lamberti A et al. Characterization and natural history of ventricular septal defects in the fetus. *Ultrasound Obstet Gynecol* 2000;16:118–22.
3. Fyler DC, Buckley LP, Hellenbrand WE et al. Report of the New England Regional Infant Care Program. *Pediatrics* 1980;65 (Suppl.):375–461.
4. Dickinson DF, Arnold R, Wilkinson JL. Ventricular septal defect in children born in Liverpool 1960 to 1969. *Br Heart J* 1981;46:47–54.
5. Mitchell SC, Korones SB, Berendes HW. Congenital heart disease in 56,109 births. *Circulation* 1971;43:323–32.
6. Mehta AV, Chidambaram B. Ventricular septal defect in the first year of life. *Am J Cardiol* 1992;70:364–366.
7. Meberg A, Otterstad JE, Froland G et al. Increasing incidence of ventricular septal defects caused by improved detection rate. *Acta Paediatr* 1994;83:653–700.
8. Du ZD, Roguin N, Barak M et al. High prevalence of muscular ventricular septal defect in preterm neonates. *Am J Cardiol* 1996;78:1183–5.
9. Roguin N, Du ZD, Barak M et al. High prevalence of muscular ventricular septal defect in neonates. *J Am Coll Cardiol* 1995;26:1545–8.
10. Sands AJ, Casey FA, Craig BG et al. Incidence and risk factors for ventricular septal defect in "ow risk" neonates. *Arch Dis Child-Fetal* 1999;81:F61–F63.
11. Arias E, MacDorman MF, Strobino DM et al. Annual summary of vital statistics – 2002. *Pediatrics* 2003;112:1215–30.
12. Hoffman JIE, Christianson R. Congenital heart disease in a cohort of 19,502 births with long-term follow-up. *Am J Cardiol* 1978;42:641–7.
13. Keith JD. Ventricular septal defect. In: Keith JD, Rowe RD, Vlad P (eds) *Heart Disease in Infancy and Childhood*. New York: Macmillan, 1978;320–79.
14. Nora JJ, Fraser FLC. *Medical Genetics*. Philadelphia: Lea & Febiger, 1974:334.
15. Musewe NN, Alexander DJ, Teshima I et al. Echocardiographic evaluation of the spectrum of cardiac anomalies associated with trisomy 13 and trisomy 18. *J Am Coll Cardiol* 1990;15:673–7.
16. Marino B, Papa M, Guccione P et al. Ventricular septal defect in Down syndrome. Anatomic types and associated malformations. *Am J Dis Child* 1990;144:544–5.
17. Vaughan CJ, Basson CT. Molecular determinants of atrial and ventricular septal defects and patent ductus arteriosus. *Am J Med Genet* 2000;97:304–9.
18. Correa-Villasenor A, Ferencz C, Loffredo C et al. Paternal exposures and cardiovascular malformations. The Baltimore-Washington Infant Study Group. *J Expo Anal Environ Epidemiol* 1993;3(Suppl. 1):173–85.
19. Ewing CK, Loffredo CA, Beaty TH. Paternal risk factors for isolated membranous ventricular septal defects. *Am J Med Genet* 1997;71:42–6.
20. De la Cruz MV, Markwald RR. *Living Morphogenesis of the Heart.* Boston: Birkhäuser, 1998.
21. Lamers WH, Moorman AFM. Cardiac septation. A late contribution of the embryonic primary myocardium to heart morphogenesis. *Circ Res* 2002;91:93–103.
22. de Jong F, Virágh S, Moorman AFM. Cardiac development: A morphologically integrated molecular approach. *Cardiol Young* 1997;7:131–46.

23. Christoffels VM, Habets PEMH, Franco D et al. Chamber formation and morphogenesis in the developing heart. *Dev Biol* 2000;223:266–78.
24. Moorman AFM, Schumacher CA, de Boer PAJ et al. Presence of functional sarcoplasmic reticulum in the developing heart and its confinement to chamber myocardium. *Dev Biol* 2000; 223:279–90.
25. Moorman AFM, Lamers WH. Development of the conduction system of the vertebrate heart. In: Harvey RP, Rosenthal N (eds) *Heart Development*. San Diego: Academic Press, 1999; 195–207.
26. Wessels A, Markman MWM, Vermeulen JLM et al. The development of the atrioventricular junction in the human heart. *Circ Res* 1996;78:110–17.
27. Wessels A, Markwald RR, Webb S et al. Atrial development in the human heart: An immunohistochemical study with emphasis on the role of mesenchymal tissues. *Anat Rec* 2000; 259:288–300.
28. Mjaatvedt CH, Yamamura H, Wessels A et al. Mechanisms of segmentation, septation, and remodeling of the tubular heart: Endocardial cushion fate and cardiac looping. In: Harvey RP, Rosenthal N (eds) *Heart Development*. San Diego: Academic Press, 1999;159–77.
29. Moorman AFM, van den Hoff MJB, de Jong F et al. Myocardialization: A novel mechanism of cardiac septation. In: Clark EB, Nakazawa M, Takao A (eds) *Etiology and Morphogenesis of Congenital Heart Disease: Twenty Years of Progress in Genetics and Developmental Biology*. Armonk: Futura, 2000; 131–5.
30. Kruithof BPT, van den Hoff MJB, Wessels A et al. Cardiac muscle cell formation after development of the linear heart tube. *Dev Dyn* 2003;227:1–13.
31. Van den Hoff MJB, Kruithof BPT, Moorman AFM et al. Formation of myocardium after the initial development of the linear heart tube. *Dev Biol* 2001;240:61–76.
32. Ikeda T, Iwasaki K, Shimokawa I et al. Leu-7 immunoreactivity in human and rat embryonic hearts, with special reference to the development of the conduction tissue. *Anat Embryol* 1990;182:553–62.
33. Lamers WH, Wessels A, Verbeek FJ et al. New findings concerning ventricular septation in the human heart. Implications for maldevelopment. *Circulation* 1992;86:1194–205.
34. Wessels A, Vermeulen JL, Verbeek FJ et al. Spatial distribution of "tissue-specific" antigens in the developing human heart and skeletal muscle. III. An immunohistochemical analysis of the distribution of the neural tissue antigen GlN2 in the embryonic heart: implications for the development of the atrioventricular conduction system. *Anat Rec* 1992;232:97–111.
35. Lamers WH, Virágh SS, Wessels A et al. Formation of the tricuspid valve in the human heart. *Circ Res* 1995;91:111–21.
36. Anderson RH, Wilcox BR. The surgical anatomy of ventricular septal defect. *J Card Surg* 1992;7:17–35.
37. Soto B, Ceballos R, Kirklin JW. Ventricular septal defects: a surgical viewpoint. *J Am Coll Cardiol* 1989;14:1291–7.
38. Van Praagh R, Geva T, Kreutzer J. Ventricular septal defects: how shall we decribe, name and classify them? *J Am Coll Cardiol* 1989;14:1298–9.
39. Jacobs JP, Burke RP, Quintessenza JA et al. Congenital Heart Surgery Nomenclature Database Project: ventricular septal defect. *Ann Thorac Surg* 2000;69:S25.
40. Ho SY, McCarthy KP, Rigby ML. Morphology of perimembranous ventricular septal defects: implications for transcatheter device closure. *J Interven Cardiol* 2004;17:99–108.
41. Lincoln C, Jamieson S, Shinebourne E et al. Transatrial repair of ventricular septal defects with reference to their anatomic position. *J Thorac Cardiovasc Surg* 1977;74:183–90.
42. Braunwald E, Morrow AG. Ventriculo-right atrial communication: diagnosis by clinical, hemodynamic, and angiographic methods. *Am J Med* 1960;28:913–20.
43. Leung MP, Mok CK, Lo RN et al. An echocardiographic study of perimembranous ventricular septal defect with left ventricular to right atrial shunting. *Br Heart J* 1986;55:45–52.
44. Kirklin JK, Castaneda AR, Keane JK et al. Surgical management of multiple ventricular septal defects. *J Thorac Cardiovasc Surg* 1980;80:485–93.
45. Ramaciotti C, Vetter JM, Bornemeier RA et al. Prevalence, relation to spontaneous closure, and association of muscular ventricular septal defects with other cardiac defects. *Am J Cardiol* 1995;75:61–5.
46. Kirklin JW, McGoon DC, DuShane JW. Surgical treatment of ventricular septal defect. *J Thorac Cardiovasc Surg* 1960;40: 763–75.
47. Van Praagh S, Mayer JE Jr, Berman NB et al. Apical ventricular septal defects: follow-up concerning anatomic and surgical considerations. *Ann Thorac Surg* 2002;73:48–56.
48. Tatsuno K, Ando K, Takan A et al. Diagnostic importance of aortography in conal ventricular-septal defect. *Am Heart J* 1975;89:171–7.
49. Schmidt KG, Cassidy SC, Silverman NH et al. Doubly committed subarterial ventricular septal defects: echocardiographic features and surgical implications. *J Am Coll Cardiol* 1988;12: 1538–46.
50. Liberthson RR, Paul MH, Muster AJ et al. Straddling and displaced atrioventricular orifices and valves with primitive ventricles. *Circulation* 1971;43:213–26.
51. Milo S, Ho SY, Macartney FJ et al. Straddling and overriding atrioventricular valves: morphology and classification. *Am J Cardiol* 1979;44:1122–34.
52. Rastelli GC, Ongley PA, Titus JL. Ventricular septal defect of atrioventricular canal type with straddling right atrioventricular valve and mitral valve deformity. *Circulation* 1968;37: 816–25.
53. Bharati S, McAllister HA Jr, Lev M. Straddling and displaced atrioventricular orifices and valves. *Circulation* 1979;60: 673–84.
54. Mas MS, Bricker JT. Clinical physiology of left-to-right shunts. In: Garson A Jr, Bricker JT, McNamara DG (eds) *The Science and Practice of Pediatric Cardiology*. Philadelphia: Lea and Febiger, 1990;999–1001.
55. Van Hare GF, Soffer LJ, Sivakoff MC et al. Twenty-five-year experience with ventricular septal defect in infants and children. *Am Heart J* 1987;114:606–14.
56. Weidman WH, Gersony WM, Nugent EW et al. Indirect assessment of severity in ventricular septal defect. *Circulation* 1977;56(I Suppl.):I24–I33.

57. Fyler DC. Ventricular septal defect. In: Fyler DC (ed.) *Nadas' Pediatric Cardiology*. Philadelphia: Hanley and Belfus, 1992;435–57.
58. Graham TP, Gutgesell HP. Ventricular septal defect. In: Emmanouillides GC, Riemenschneider TA, Allen HD (eds) *Heart Disease in Infants, Children and Adolescents*. Baltimore: Williams & Wilkins, 1995;724–46.
59. Braunwald E, Ross J Jr, Sonnenblick EH. Mechanisms of contraction of the normal and failing heart. *N Engl J Med* 1967; 227:853–62.
60. Jarmakani MM, Graham TP Jr, Canent RV Jr et al. Effect of site of shunt on left heart volume characteristics with ventricular septal defect and patent ductus arteriosus. *Circulation* 1969; 40:411–18.
61. Vincent RN, Lang P, Elixon EM et al. Extravascular lung water in children immediately after operative closure of either isolated atrial septal defect or ventricular septal defect. *Am J Cardiol* 1987;56:536–9.
62. Davies H, Williams J, Wood P. Lung stiffness in states of abnormal pulmonary blood flow and pressure. *Br Heart J* 1962;24:129–38.
63. Edwards JE, Helmholz HF Jr, DuShane JW et al. Pathologic study of hearts previously catheterized. *Mayo Clinic Proc* 1952; 28:113–20.
64. Dammann JF Jr, Ferencz C. The significance of the pulmonary vascular bed in congenital heart disease. III. Defects between the ventricles or great vessels in which both increased pressure and blood flow may act upon the lungs and in which there is a common ejectile force. *Am Heart J* 1956;52:210–31.
65. Lucas RV Jr, Adams P Jr, Anderson RC et al. The history of isolated ventricular septal defect. A serial physiologic study. *Circulation* 1961;24:1372–87.
66. Blackstone EH, Kirklin JW, Bradley EL et al. Optimal age and results in repair of large ventricular septal defects. *J Thorac Cardiovasc Surg* 1976;72:661–79.
67. Barratt-Boyes BG, Neutze JM, Clarkson PM et al. Repair of ventricular septal defect in the first two years of life using profound hypothermia-circulatory arrest techniques. *Ann Surg* 1976;184:376–90.
68. Kouchoukos NT, Blackstone EH, Doty DB et al. *Kirklin/Barratt-Boyes Cardiac Surgery. Ventricular Septal Defect*. Philadelphia: Churchill Livingstone, 2003:850–909.
69. Simpson WF Jr, Sade RM, Crawford FA et al. Double-chambered right ventricle. *Ann Thorac Surg* 1987;44:7–10.
70. Leichter DA, Sullivan I, Gersony WM. "Acquired" discrete subvalvular aortic stenosis: natural history and hemodynamics. *J Am Coll Cardiol* 1989;14:1539–44.
71. Lauer RM, DuShane JW, Edwards JE. Obstruction of left ventricular outlet in association with ventricular septal defect. *Circulation* 1960;22:110–25.
72. Baumstark A, Fellows KE, Rosenthal A. Combined double chambered right ventricle and discrete subaortic stenosis. *Circulation* 1978;57:299–303.
73. Kitchiner D, Jackson M, Malaiya N et al. Morphology of left ventricular outflow tract structures in patients with subaortic stenosis and a ventricular septal defect. *Br Heart J* 1994;72: 251–60.
74. Keane JF, Plauth WH, Nadas AS. Ventricular septal defect with aortic regurgitation. *Circulation* 1977;56(Suppl. I):72–7.
75. Rhodes LA, Keane JF, Keane JP et al. Long follow-up (to 43 years) of ventricular septal defect with audible aortic regurgitation. *Am J Cardiol* 1990;66:340–5.
76. Sakakibara S, Konno S. Congenital aneurysm of the sinus of Valsalva associated with ventricular septal defect. *Am Heart J* 1968;75:595–603.
77. Nadas AS, Thilenius OG, LaFarge CG et al. Ventricular septal defect with aortic regurgitation: medical and pathologic aspects. *Circulation* 1964;29:862–73.
78. Plauth WH, Braunwald E, Rockoff SD et al. Ventricular septal defect and aortic regurgitation. *Am J Med* 1965;39:552–67.
79. Van Praagh R, McNamara JJ. Anatomic types of ventricular septal defect with aortic insufficiency. Diagnostic and surgical considerations. *Am Heart J* 1968;75:604–19.
80. Leung MP, Beerman LB, Siewers RD et al. Long-term follow-up after aortic valvuloplasty and defect closure in ventricular septal defect with aortic regurgitation. *Am J Cardiol* 1987;60: 890–4.
81. Gutgesell HP, Paquet M. *Atlas of Pediatric Echocardiography*. Hagerstown: Harper & Row, 1978.
82. Lester LA, Vitullo D, Sodt P et al. An evaluation of left atrial/aortic root ratio in children with ventricular septal defect. *Circulation* 1979;60:364–72.
83. Henry WL, Maron BJ, Griffith JM. Cross-sectional echocardiography in the diagnosis of congenital heart disease. *Circulation* 1977;56:267–73.
84 Hagler DDJ, Edwards WD, Seward JB et al. Standardized nomenclature of the ventricular septum and ventricular septal defects, with applications for two-dimensional echocardiography. *Mayo Clin Proc* 1985;60:741–52.
85. Canale JM, Sahn DJ, Allen HD et al. Factors affecting real-time, cross-sectional echocardiographic imaging of perimembranous ventricular septal defect. *Circulation* 1981;63:689–97.
86. Ludomirsky A, Huhta JC, Vick GW III et al. Color Doppler detection of multiple ventricular septal defects. *Circulation* 1986;74:1317–22.
87. Houston AB, Lim MK, Doig WB et al. Doppler assessment of the interventricular pressure drop in patients with ventricular septal defects. *Br Heart J* 1988;60:50–6.
88. Ludomirsky A, Tani L, Murphy DJ et al. Usefulness of color-flow Doppler in diagnosing and in differentiating supracristal ventricular septal defect from right ventricular outflow tract obstruction. *Am J Cardiol* 1991;67:194–8.
89. Cheatham JP, Latson LA, Gutgesell HP. Ventricular septal defect in infancy: detection with two-dimensional echocardiography. *Am J Cardiol* 1981;47:85–9.
90. Sharif DS, Huhta JC, Marantz P et al. Two-dimensional echocardiographic determination of ventricular septal defect size: correlation with autopsy. *Am Heart J* 1989;117:1333–6.
91. Silbert DR, Brunson SC, Schiff R et al. Determination of right ventricular pressure in the presence of a ventricular septal defect using continuous wave Doppler ultrasound. *J Am Coll Cardiol* 1986;8:379–84.
92. Murphy DJ, Ludomirsky A, Huhta JC. Continuous wave Doppler in children with ventricular septal defect: noninvasive estimation of pressure gradient. *Am J Cardiol* 1986;57:428–32.
93. Sommer RJ, Golinko RJ, Ritter SB. Intracardiac shunting in children with ventricular septal defect: evaluation

with Doppler color flow mapping. *J Am Coll Cardiol* 1990;6: 1437–44.

94. Moises VA, Maciel BC, Hornberger LK et al. A new method for noninvasive estimation of ventricular septal defect flow by Doppler color flow mapping: imaging of the laminar flow convergence region on the left septal surface. *J Am Coll Cardiol* 1991;3:824–32.
95. Ge Z, Zhang Y, Kang W et al. Noninvasive evaluation of interventricular pressure gradient across ventricular septal defect: a simultaneous study of Doppler echocardiography and cardiac catheterization. *Am Heart J* 1992;1:176–82.
96. Allan LD, Sharland GK, Milburn A et al. Prospective diagnosis of 1,006 consecutive cases of congenital heart disease in the fetus. *J Am Coll Cardiol* 1994;23:1452–8.
97. Stoll C, Garne E, Clementi M, Euroscan study group. Evaluation of prenatal diagnosis of associated congenital heart disease by fetal ultrasonographic examination in Europe. *Prenat Diagn* 2001;21:243–52.
98. Hoffman P, Wojcik AW, Rozanski J et al. The role of echocardiography in diagnosing double chambered right ventricle in adults. *Heart* 2004;90:789–93.
99. Neumayer U, Stone S, Somerville J. Small ventricular septal defects in adults. *Eur Heart J* 1998;19:1573–82.
100. Minette MS, Sahn DJ. Ventricular septal defects. *Circulation* 2006;114:2190–7.
101. Bettex DA, Schmidlin D, Bernath M-A et al. Intraoperative transesophageal echocardiography in pediatric congenital cardiac surgery: a two-center observational study. *Anesth Analg* 2003;97:1275–82.
102. Muhiudeen IA, Roberson DA, Silverman NH et al. Intraoperative echocardiography for evaluation of congenital heart defects in infants and children. *Anesthesiology* 1992;76:165–72.
103. Andropoulos DB, Ayres NA, Stayer SA et al. The effect of transesophageal echocardiography on ventilation in small infant undergoing cardiac surgery. *Anesth Analg* 2000;90:47–9.
104. Holzer R, Balzer D, Cao Q-L et al. Device closures of muscular ventricular septal defects using the Amplatzer muscular ventricular septal defect occluder. *J Am Coll Cardiol* 2004;43: 1257–63.
105. Carminati M, Gianfranco B, Chessa M et al. Transcatheter closure of congenital ventricular septal defect with Amplatzer septal occluders. *Am J Cardiol* 2005;96:52L–58L.
106. Cao Q-L, Zabal C, Koenig P et al. Initial clinical experience with intracardiac echocardiography in guiding transcatheter closure of perimembranous ventricular septal defects: feasibility and comparison with transesophageal echocardiography. *Catheter Cardiovasc Interv* 2005;66:258–67.
107. Rychik J, Norwood WI, Chin AJ. Doppler color flow mapping assessment of residual shunt after closure of large ventricular septal defects. *Circulation* 1991;84(5 Suppl.):III153–61.
108. Bol-Raap G, Weerheim J, Kappetein AP et al. Follow-up after surgical closure of congenital ventricular septal defect. *Eur J Cardiothoracic Surg* 2003;24:511–15.
109. Chiu S, Wang JK, Lin MT et al. Progression of aortic regurgitation after surgical repair of outlet-type ventricular septal defects. *Am Heart J* 2007;153:336–42.

# 13 Tricuspid Valve and Right Atrial Anomalies

**Ulrike E. Salzer-Muhar**

Division of Pediatric Cardiology, Department of Pediatrics and Adolescent Medicine, Vienna General Hospital, Vienna, Austria

## Anomalies of the tricuspid valve

Morphologic anomalies of the tricuspid valve (TV) result from hypoplasia and thickening of the valve leaflets with a reduced valve orifice (*tricuspid stenosis*); from displacement of part of the origin of the valve leaflets from the atrioventricular junction into the cavity of the right ventricle (*Ebstein anomaly*); or from malformed but not displaced valve leaflets (*tricuspid dysplasia*). An additional anomaly is *double-orifice tricuspid valve*, a TV exhibiting two valve orifices.

### Definitions

*Tricuspid stenosis* (TS) is a condition producing obstruction to right ventricular filling due to abnormalities of the TV in respect of its form, annular dimension and/or function. Rarely, the obstruction is found at the subvalvar or supravalvar level.

*Ebstein anomaly* – termed after Wilhelm Ebstein, who described this entity in 1866 [1] – is a malformation of the TV defined by the displacement of part of the origin of its leaflets from the atrioventricular junction into the cavity of the right ventricle. This displacement is accompanied by varying degrees of valvar dysplasia and abnormal distal attachments [2]. The TV itself is usually regurgitant, but may be also stenotic or even imperforate. Another feature is variable ventricular myocardial dysfunction [3].

*Tricuspid valve dysplasia* is defined as a spectrum of congenital malformations of valve leaflets, chordae and papillary muscles. It frequently leads to tricuspid regurgitation.

*Double-orifice tricuspid valve (DOTV)* is defined as an anomalous tricuspid valve exhibiting two orifices. It is also termed "duplication of the TV" [4,5]. *DOTV* with one orifice straddling is discussed in the section on double-outlet right atrium (DORA) under "Anomalies of the right atrium".

*Echocardiography in Pediatric and Congenital Heart Disease: From Fetus to Adult*
Edited by Wyman W. Lai, Luc L. Mertens, Meryl S. Cohen and Tal Geva
 ISBN: 978-1-405-17401-5

### Incidences

Isolated TS is a very rare condition with an unknown incidence. Tricuspid stenosis associated with annular hypoplasia, however, has been identified in various forms of congenital heart disease such as tetralogy of Fallot, pulmonary atresia with intact ventricular septum, D-transposition of the great arteries, congenitally corrected transposition, double-outlet right or left ventricle, as well as superior-inferior ventricles with or without twisted atrioventricular connection [6]. Functional obstruction of the TV by tumors is also well documented [7].

Ebstein anomaly is an uncommon disorder occurring in about 3–5 in 100 000 live births [8,9], thereby accounting for 0.38–0.50% of congenital heart disease [9,10]. Males and females are equally affected. The incidence in the fetus is higher. TV dysplasia, first described in 1971 [11], is an uncommon disorder and its incidence is not known. It is generally more frequently described in fetal series. Detected fetuses with either Ebstein anomaly or TV dysplasia usually exhibit the severe end of the spectrum [12], whereas milder forms may only be detected in adolescence or even in adulthood. Ebstein anomaly of varying expression is also an intrinsic lesion in congenitally corrected transposition of the great arteries, and is found in up to 90% of autopsies [1,13].

Double-orifice tricuspid valve is an extremely rare anomaly and is reported to be associated with atrioventricular septal defect, tetralogy of Fallot and several TV anomalies such as Ebstein anomaly, tricuspid dysplasia, TV prolapse and straddling TV [14,15].

### Etiology

The majority of reported cases of isolated TS are sporadic. TS has been reported in congenital polyvalvular disease, and is associated with trisomy 13, 15 and 18 [6,16].

Although the majority of reported cases of Ebstein anomaly are sporadic, familial occurrence has been observed [17,18]. Only recently, Ebstein anomaly and duplication of the distal arm of chromosome 15 was reported [19]. Canine TV malformation, a model of human Ebstein anomaly, was found to map to dog chromosome 9 [20]. The association with

syndromes, such as Down, Marfan, Noonan and Cornelia de Lange syndromes, is rare [21]. Twenty years ago, a linkage between maternal use of lithium and Ebstein anomaly was reported, but this linkage could not be confirmed by further studies [12,22].

Reported cases of TV dysplasia are also sporadic, although association with Down syndrome is reported [12]. The etiology of DOTV is not known.

## Developmental considerations

Although TV differentiation in isolated TS has received little attention, studies have shown that chordae and leaflets originate from the endocardial cushions [23]. Ebstein anomaly is thought to occur as a result of incomplete undermining of the right ventricular myocardium, which itself is also abnormal [21]. The late-forming septal and posterior TV leaflets remain adherent to the underlying ventricular wall, with disturbance of their chordal and papillary muscle development. The anterior TV leaflet forms much earlier than the septal and posterior leaflets. Although it is not adherent, it becomes elongated, redundant and fenestrated and exhibits abnormally formed chordae tendineae [21]. As a result, the orifice of the Ebstein valve – the functional tricuspid annulus – is rotated rightward and anteriorly, instead of simply "displaced" downward [24].

By analogy with Ebstein anomaly, TV dysplasia is thought to occur as a result of incomplete undermining of the right ventricular myocardium resulting in abnormal development of valve leaflets, chordae and papillary muscles [21]. The late-forming septal leaflet is most often involved.

Double-outlet tricuspid valve can be considered to be the result of imperfect valve formation by the endocardial cushions, thus explaining its frequent association with arioventricular septal defect [25].

## Anatomy

The normal TV has three leaflets, which are located in the septal, anterior and posterior (inferior, mural) position. The medial papillary muscle supports the zone of apposition between septal and anterior leaflets, the larger anterior papillary muscle supports the zone between anterior and inferior leaflets, and the smaller inferior muscle (or multiple muscles) supports the zone of apposition between the inferior and septal leaflets. A characteristic feature of the normal TV is the presence of chordae from the septal leaflet to the ventricular septum [24].

In the rare form of congenital isolated TS, the reduced valve orifice is mainly due to thickening of the TV leaflets and abnormal chordal attachments [6]. Congenital TS associated with annular hypoplasia, as found in several forms of congenital heart disease, is usually characterized by annular hypoplasia with abnormalities of all parts of the TV including leaflets, commissures, chordae and papillary muscles [6]. Congenital supravalvular TS is caused by a membrane attached either at the level of the tricuspid annulus or at the midportions of the leaflets [26].

The distinguishing anatomic features of Ebstein anomaly include (1) displacement of septal and posterior leaflets; (2) possibly restricted motion of the anterior leaflet; (3) an atrialized right ventricle with true tricuspid annulus dilation; and (4) potential myocardial dysfunction.

A characteristic feature of the normal TV is the so-called "offsetting" of the septal tricuspid leaflet relative to the anterior mitral valve leaflet. Adjusting for body surface area (BSA), the normal distance between the septal hingepoints of the tricuspid and the mitral valve is usually <0.8 cm/m$^2$ [27]. A value >0.8 cm/m$^2$ is diagnostic for Ebstein anomaly [28]. In mild forms of Ebstein anomaly, only the septal leaflet is mildly displaced. In moderate to severe cases, the displaced septal and posterior leaflets are thickened, dysplastic and focally muscularized with only few or even absent chordae tendineae. The septal leaflet is sometimes missing. In the most severe forms all three leaflets are adherent to the ventricular wall, forming a tricuspid sac, which may even lack an orifice (for details see also Carpentier´s classification of Ebstein anomaly) [27].

The anterior leaflet in Ebstein anomaly is not displaced. Its proximal hingepoints are at the true tricuspid annulus, but it is usually elongated and malformed. Its distal attachments are either (1) the anterior papillary muscle ("focal attachment"), then the septal leaflet, will be completely absent or represented by cauliflower-like remnants [29]; (2) short and poorly formed chordae inserting at the right ventricular wall ("tethering" if they are three or more in number) [26]; or (3) a muscular shelf situated between the inlet and the trabecular part of the right ventricle ("linear attachment"), with the anterior leaflet exhibiting a curtain-like appearance. Tethering and linear attachment will cause restricted motion of the anterior leaflet [21,29]. In general, the anterior leaflet contains not only a true orifice but also several accessory orifices (fenestrations) that direct blood toward the pulmonary valve [21]. Rarely the anterior leaflet forms an atretic membrane [29].

Tricuspid valve function will depend on (1) the degree of displacement and dysplasia of septal and posterior leaflets; (2) the size and mobility of the anterior leaflet and its fenestrations; and (3) dilatation of the true tricuspid annulus [21]. Small fenestrations will usually make the valve stenotic and regurgitant; large fenestrations will cause varying degrees of regurgitation.

The portion of the right ventricle between the true tricuspid annulus and the functional annulus is called the atrialized portion of the right ventricle. At the severe end of the spectrum, the functional right ventricle consists only of trabecular and outflow components. The right ventricle may exhibit thinning and aneurysmal dilation of both the diaphragmatic wall and the outflow component; the left ventricle has an abnormal geometry due to leftward bowing of the ventricular septum [21].

In Ebstein anomaly, associated mitral valve anomalies include prolapse, cleft, parachute valve deformity, and double-orifice mitral valve [2,21]. As the tricuspid annulus is an incomplete fibrous ring, direct muscular connections between atrium and ventricle may provide the anatomic substrate for ventricular pre-excitation (Wolff–Parkinson–White syndrome) [21].

The spectrum of TV dysplasia ranges from minimal changes with mildly dysplastic, thickened leaflets but normal chordae and papillary muscles, through short chordae and underdeveloped papillary muscles, to severe changes including agenesis of entire leaflets and subvalvar structures [11]. In contrast to Ebstein anomaly there is no displacement of both the septal and mural leaflets. This is important for discriminating the extreme variant of TV dysplasia – unguarded orifice TV, exhibiting only rudimentary valve tissue at the atrioventriclar junction – from Ebstein anomaly. In tricuspid dysplasia, and its extreme variant, the leaflet will be absent, not displaced [30]. In the rare case of unguarded orifice, ruling out displacement of the posterior leaflet will confirm the diagnosis.

Three variants of DOTV have been described: (1) the commissural variant with the accessory ostium lying within the commissure; (2) the central variant or bridge type, with a fibrous bridge dividing the orifice into two ostia; and (3) the hole variant, with the accessory ostium lying within a leaflet [4]. In all of these variants each of the two orifices exhibits a subvalvular tensor apparatus.

## Pathophysiology

Isolated TS will cause diastolic obstruction of flow from the right atrium into the right ventricle. The increase of right atrial and central venous pressure will depend on right ventricular compliance, the effective size of the TV orifice, and the possibility of a right-to-left shunt through a patent foramen ovale (PFO) or an atrial septal defect (ASD). The pathophysiology of TS associated with other forms of congenital heart disease, mainly right heart hypoplasia, will depend on the underlying lesion and the size of an associated atrial septal defect.

In the symptomatic neonate with Ebstein anomaly, the TV is usually regurgitant, but rarely may be stenotic or even atretic [31]. Due to high postpartum pulmonary vascular resistance, tricuspid regurgitation (TR) and right heart failure will be even more pronounced, thereby leading to a markedly reduced or even absent pulmonary blood flow. Functional pulmonary atresia must be differentiated from anatomic pulmonary atresia, which is present in about 20% [31]. Functional pulmonary atresia improves with falling pulmonary resistance; the goal of medical therapy is to reduce pulmonary hypertension.

In the older child, adolescent and adult with Ebstein anomaly, the degree of TR and impairment of right ventricular function will determine the degree of right heart failure with venous congestion. The size of a concomitant atrial septal defect (ASD) determines the amount of cyanosis. As already mentioned above, Ebstein anomaly predisposes to tachyarrhythmias, which are poorly tolerated.

Depending on its degree, TR associated with TV dysplasia will cause progressive dilation of the right atrium and right ventricle; it may also trigger arrhythmias. In the fetus and neonate, right ventricular pressure is systemic due to physiologic conditions. Hence, TV dysplasia will have a major impact on TV closure and the degree of TR. Therefore, with appropriate management and falling pulmonary resistance, postnatal improvement in isolated TV dysplasia is to be expected [32,33]. By analogy to Ebstein anomaly, a wide foramen ovale will be beneficial in utero to prevent development of hydrops. Associated lesions such as pulmonary stenosis and pulmonary atresia will require postnatal intervention and surgery.

Usually DOTV is considered as benign, and its pathophysiology is determined by associated lesions.

## Imaging

### Goals of the examination

The main objectives of echocardiography in the setting of anomalies of the tricuspid valve can be summarized as follows:

- Visualization of the TV:
  - morphology and movement of leaflets;
  - searching for dysplastic thickened-rolled leaflets, short chordae, adherence of leaflets, underdeveloped papillary muscles (Figs 13.1 and 13.2; Videoclip 13.1);
  - chordae;
  - papillary muscles.
- size of the TV annulus (Figs 13.3 and 13.4; Videoclip 13.2):
  - calculation of z-score [34];
  - comparison with size of mitral valve annulus;
  - ruling out TV clefts;
  - visualization of multiple orifices and their size.
- Characterization of TS:
  - thickened, rolled TV leaflets may also dome in diastole, further shortening chordae with abnormal attachments;
  - a stenosing membrane may be detected within the funnel of the TV thus restricting the opening of the leaflets [26];
  - measurement of maximal velocity ($V_{max}$) across TV:
    – normal value <0.8 m/s; $V_{max}$ >1.3 m/s in absence of left-to-right shunt indicates significant TS [35] (Note: take into account that flow may be also increased because of concomitant regurgitation).
  - calculation of maximal and mean diastolic transvalvular pressure gradient.
- Assessment of tricuspid regurgitation (TR):
  - hemodynamic assessment of TR by spectral Doppler and color flow mapping:

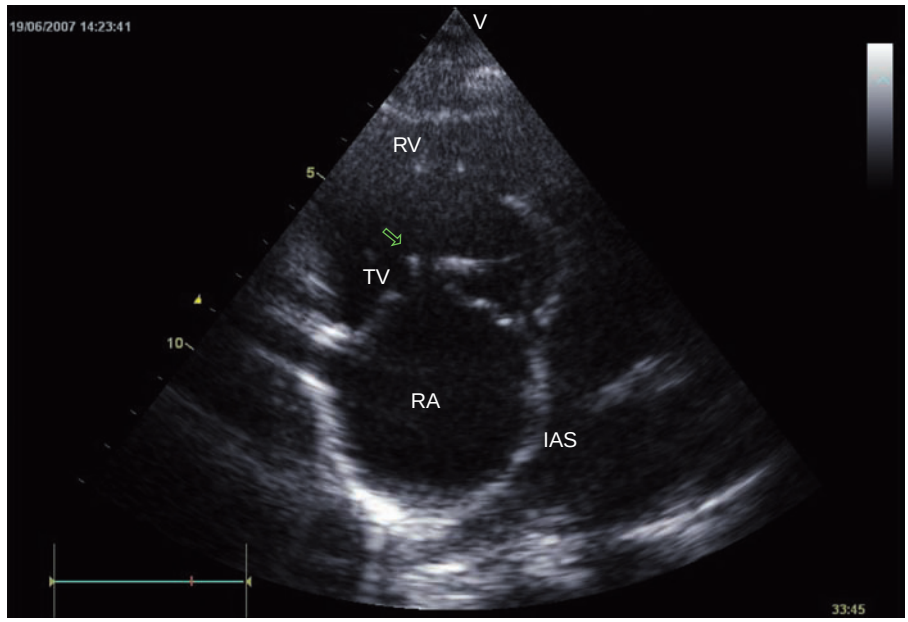


**Figure 13.1** Parasternal long-axis right ventricular inflow demonstrating tethering of both anterior and septal tricuspid valve leaflets, annulus dilation with failure of central leaflet coaptation (arrow), and dilation of the right atrium (note the position of the interatrial septum) in a child after dilation of critical pulmonary stenosis in infancy. IAS, interatrial septum; RA, right atrium; RV, right ventricle; TV, tricuspid valve.

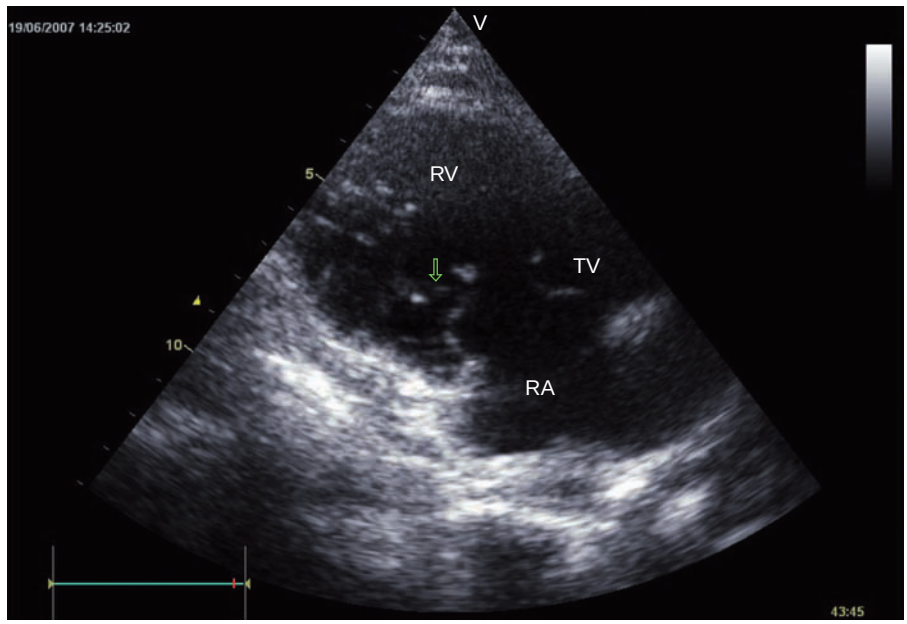


**Figure 13.2** Parasternal long-axis right ventricular inflow showing adherence of the posterior tricuspid valve leaflet, shortened chordae (arrow), and dysplastic posterior and anterior leaflets. RA, right atrium; RV, right ventricle; TV, tricuspid valve.

grading of TR (Fig. 13.5) (Note: use low pulse repetition frequency [PRF] and Nyquist limits to optimize visualization and measurement of low-velocity regurgitation jets. Look also for valve regurgitation jets from fenestrations.)
direction and origin of the jet;
calculation of systolic right ventricle (RV)–right atrium (RA) gradient and right ventricular pressure (Note: in right heart failure mean atrial pressure will be increased.)
flow profile in inferior vena cava (IVC), superior vena cava (SVC), hepatic veins (HV), and coronary sinus (CS) (Note: may not provide an estimation of the degree of TR if the jet is directed to the posterior wall of the right atrium.)

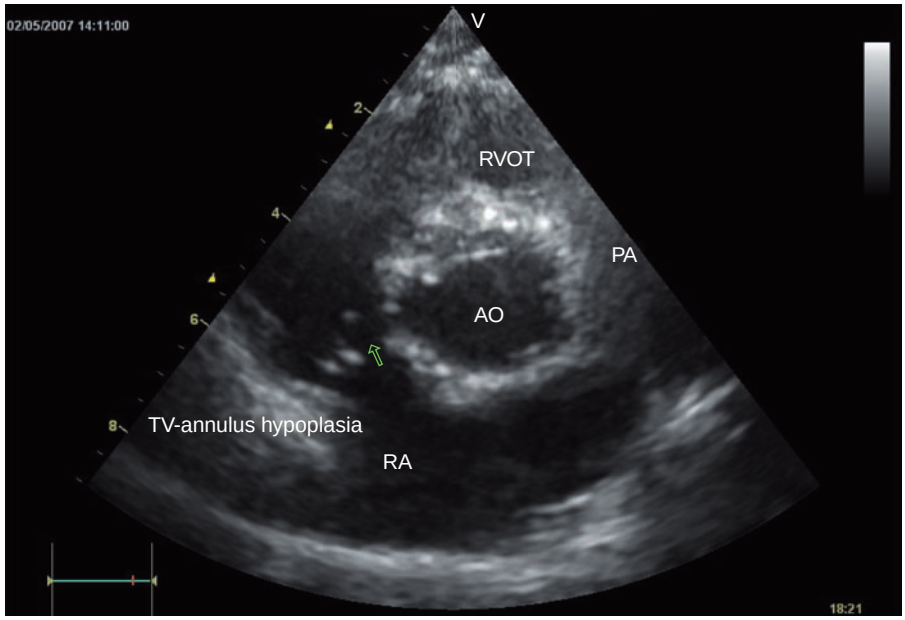


**Figure 13.3** Modified parasternal short-axis view of tricuspid stenosis associated with annular hypoplasia (arrow) and a small ventricular septal defect leak. AO, aorta; PA, pulmonary artery; RA, right atrium; RVOT, right ventricular outflow tract; TV, tricuspid valve.

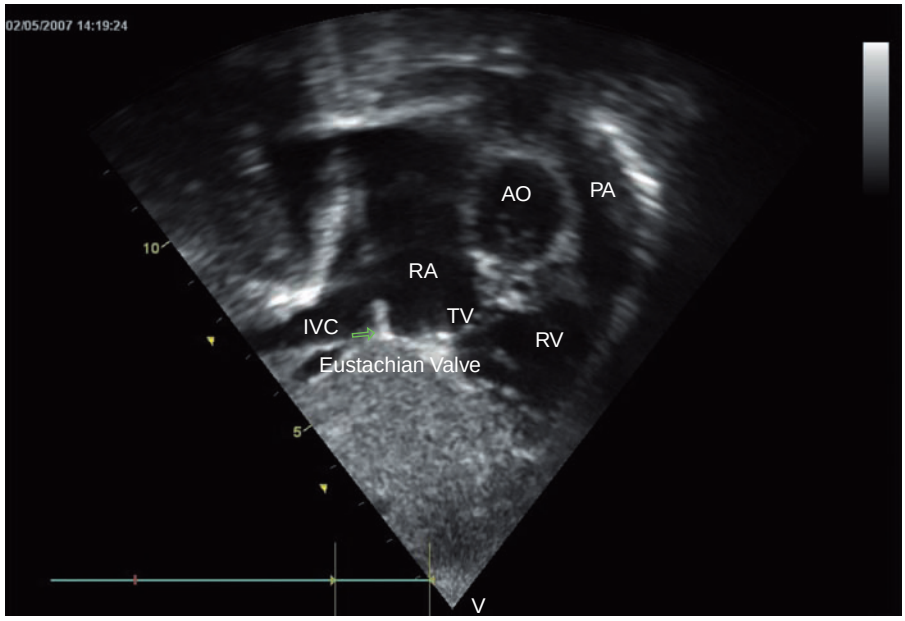


**Figure 13.4** Subcostal short-axis view of tricuspid stenosis associated with annular hypoplasia and atrial septal defect. Note the prominent Eustachian valve (arrow). AO, aorta; IVC, inferior vena cava; RA, right atrium; RV, right ventricle; PA, pulmonary artery; TV, tricuspid valve.

Dilatation of right heart chambers and veins (IVC, SVC, HV and CS)

- Ebstein anomaly – diagnosis and description:
  Displacement of the septal TV leaflet by a value >0.8 cm/m$^2$ BSA (Fig. 13.6) (Note: if this is not feasible, search for displacement of the posterior TV leaflet.)
  Septal and posterior leaflets – degree of displacement, dysplasia (Fig. 13.7; Videoclip 13.3), tethering, absence

Anterior leaflet:
elongation, redundancy and/or sail-like appearance (Fig. 13.8);
distal attachments (focal, tethering and/or linear)
mobility (Videoclip 13.4);
fenestrations.

Measurement of the size of the true (i.e., original) tricuspid annulus z-score [10], comparison with the size of the mitral valve annulus

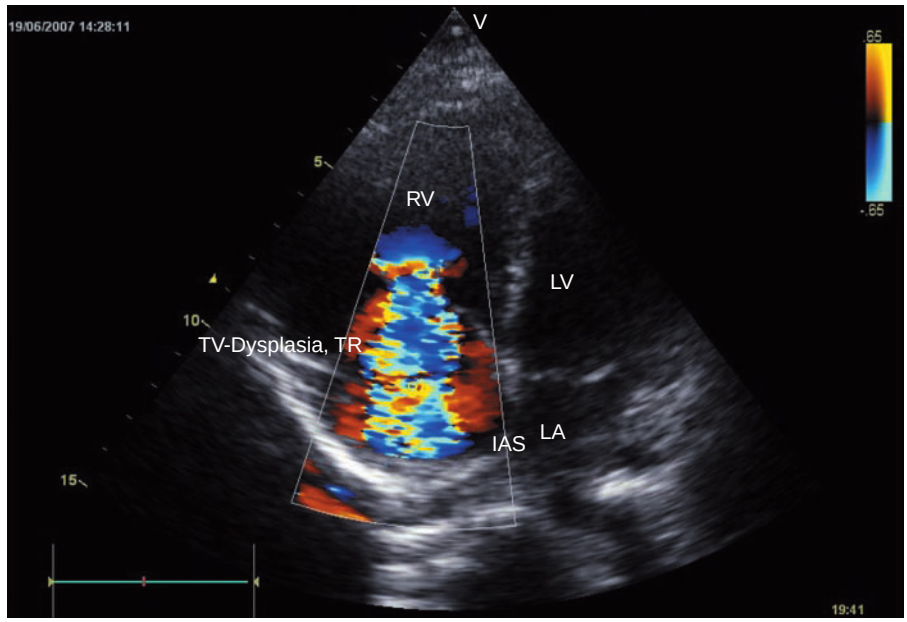


**Figure 13.5** Apical 4-chamber view of color flow mapping of tricuspid regurgitation due to tricuspid dysplasia. IAS, interatrial septum; LA, left atrium; LV, left ventricle; RA, right atrium; RV, right ventricle; TR, tricuspid regurgitation; TV, tricuspid valve.

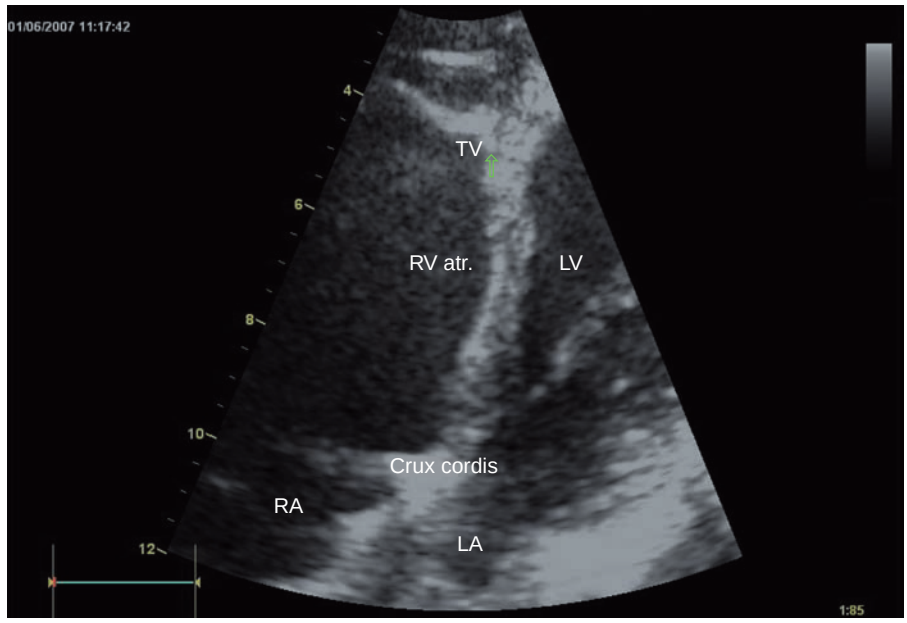


**Figure 13.6** Modified 4-chamber view of tricuspid valve septal displacement from the crux cordis and the atrialized right ventricle (RV atr.). LA, left atrium; LV, left ventricle; RA, right atrium; TV, tricuspid valve.

Assessment of anatomic severity (Fig. 13.9), including calculation of the chamber area ratio in the 4-chamber view at end-diastole [36], using (RA + aRV)/(RV + LA + LV), where RA = area of the right atrium; aRV = area of the atrialized portion of the right ventricle; RV = area of the right ventricle; LA = area of the left atrium; and LV = area of the left ventricle; a ratio ≥1 in a neonate indicates a very poor prognosis.

- Direction of shunt in presence of a PFO or ASD:
  - left-to-right shunt – additional right ventricular overload?
  - right-to-left shunt (Videoclip 13.5).
- Pulmonary stenosis: usually mild hypoplasia of the pulmonary valve, pulmonary artery and branches
- Assessment of ventricular function:
  - right ventricle:
    - fractional area change, Tei index [24,37];

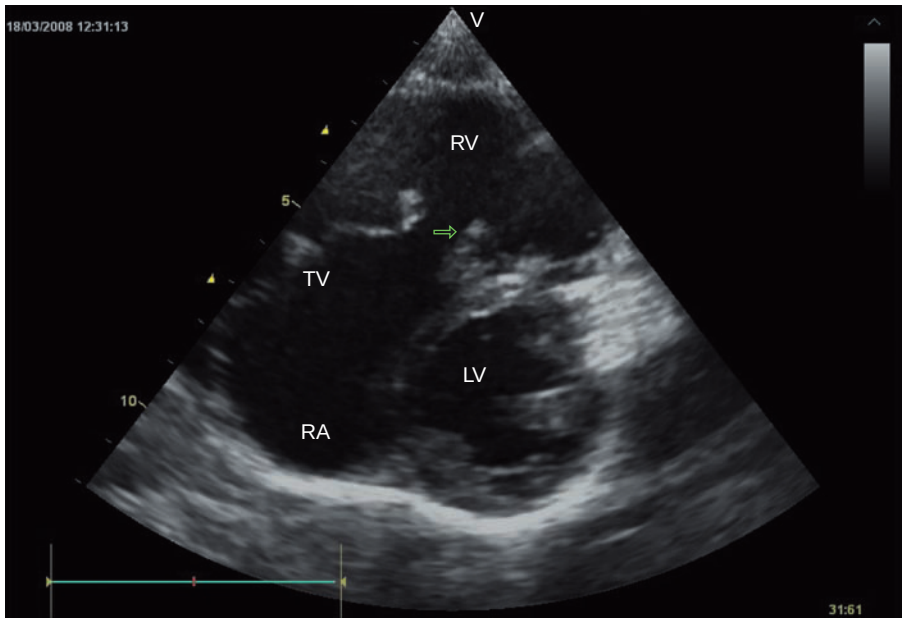


**Figure 13.7** Parasternal short-axis view of displaced and dysplastic septal leaflet in Ebstein anomaly. LV, left ventricle; RA, right atrium; RV, right ventricle; TV, tricuspid valve.

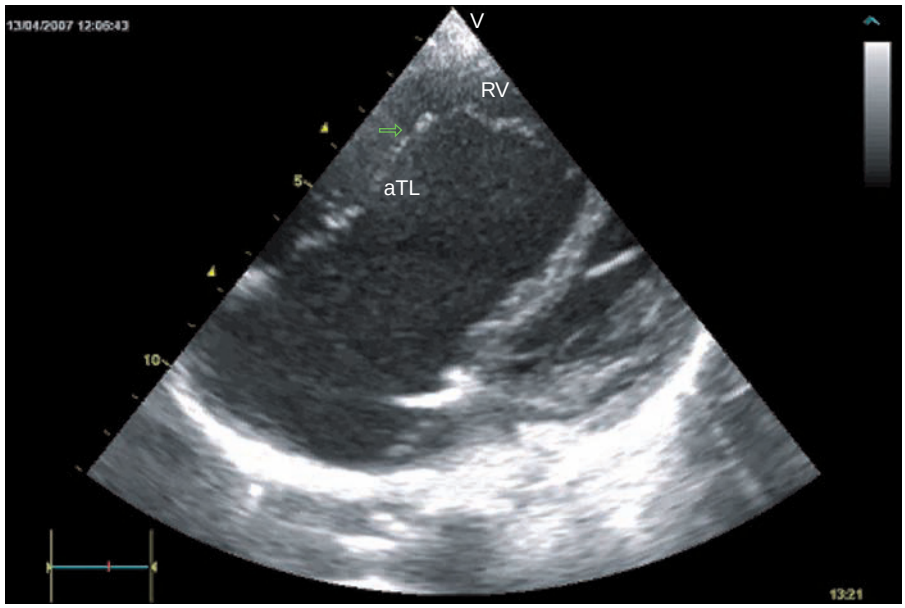


**Figure 13.8** Modified 4-chamber view of an elongated and redundant anterior tricuspid valve leaflet in Ebstein anomaly. aTL, anterior tricuspid leaflet; RV, right ventricle.

– aneurysmal dilation of the outflow tract, defined as twice the diameter of the aortic root [27] (Fig. 13.10);
– right ventricular thinning, dyskinesis.

- left ventricle (Fig. 13.11 and Videoclip 13.6):
  – M-mode: shortening fraction, end-systolic and end-diastolic diameters (often below normal range).

• Detection of associated lesions (see above)
• Ruling out alternative conditions causing TR: Ebstein anomaly, tricuspid dysplasia, unguarded orifice, TV prolapse, tricuspid annular dilation, secondary tricuspid annular dilation (due to pulmonary hypertension, cardiomyopathy or infarction), right ventricular dysplasia, rheumatic TV disease, carcinoid heart disease, connective tissue disease, endocarditis, traumatic TV disease) [38]:

Note: an important entity to be ruled out in a critically ill newborn is critical TR in the presence of a flail leaflet due to ischemic myocardial necrosis and rupture of a papillary muscle [39].

The basic morphology and functional aspects of the TV in both Ebstein anomaly and TV dysplasia can be assessed by

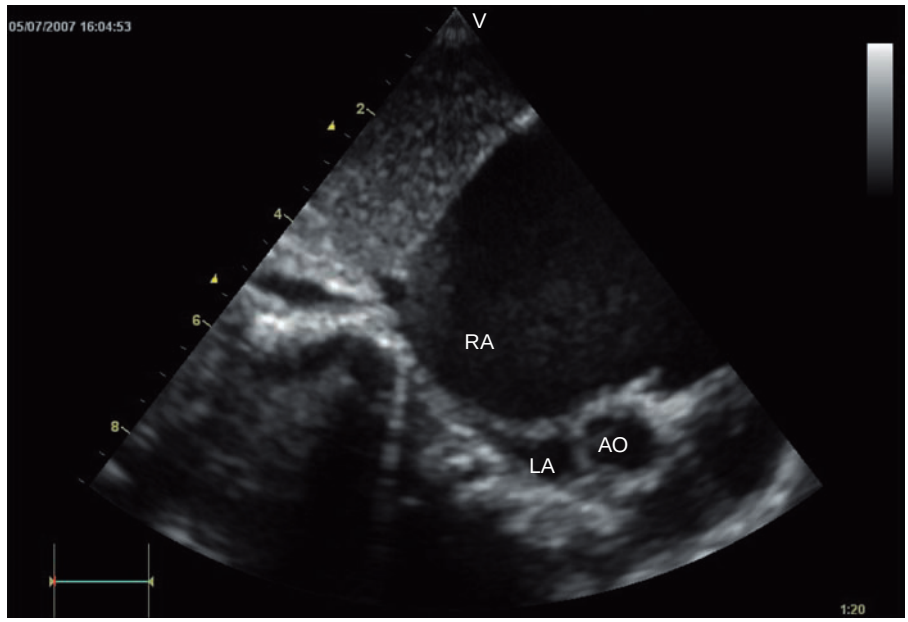


**Figure 13.9** Subcostal short-axis view of massive dilation of right atrium. AO, aorta; LA, left atrium; RA, right atrium.

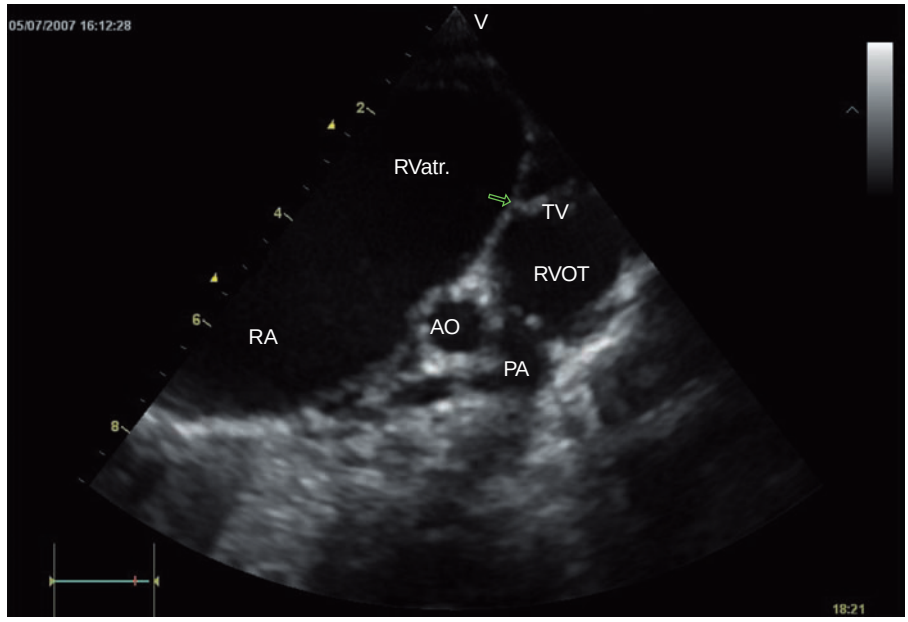


**Figure 13.10** Modified subcostal short-axis view showing massive dilation of right atrium, atrialized right ventricle, and aneurysmal dilation of right ventricular outflow tract. AO, aorta; RA, right atrium; RVatr., atrialized right ventricle; RVOT, right ventricular outflow tract; PA, pulmonary artery; TV, tricuspid valve.

two-dimensional (2D) transthoracic echocardiography (TTE) from apical, parasternal and subcostal windows. Color and spectral Doppler are useful for assessment of the TV and the atrial septum.

The apical 4-chamber view best displays the displacement of the septal TV leaflet downwards to the apex. Frequently, the septal leaflet is thickened and dysplastic and exhibits an impaired movement due to abnormally short chordae tendineae. It may be also absent or represented by cauliflower-like remnants on the ventricular septum (Videoclip 13.7) [26,29].

The parasternal long-axis view through the right ventricular inflow tract will be useful for visualization of the anterior and posterior (also named inferior or mural) leaflets [24,26]. The posterior leaflet – mainly its hingepoint and the degree of tethering – can be imaged from the parasternal view through the right ventricular inflow tract or from subcostal coronal/sagittal views. Rarely this leaflet may be

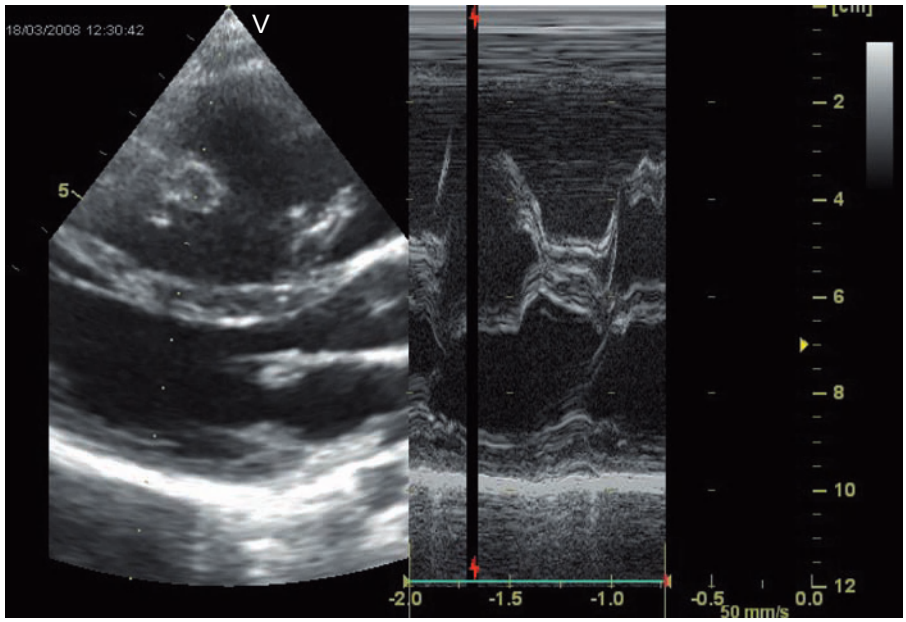


**Figure 13.11** Parasternal long-axis 2D and M-mode images demonstrating reduced left ventricular diameters, paradoxical septal movement, and excursion of the anterior tricuspid valve leaflet.

also absent [26]. The proximal hingepoint of the anterior leaflet is assessed in the parasternal long-axis view through the right ventricular inflow tract. Its sail-like movement and bulging into the right ventricular outflow tract are best imaged in parasternal short-axis views.

The subcostal 4-chamber (coronal) and short-axis (sagittal) views demonstrate the anterior and septal leaflets. In addition, the subcostal en face view, achieved by rotating the transducer 30–45° clockwise from the standard subcostal coronal view, provides insight to all three leaflets [24]. The distal attachments of the anterior leaflet, as well as fenestrations, are best visualized in subcostal coronal/sagittal views [26].

With TEE, the subvalvar apparatus can be extensively studied in transgastric views, which allow imaging of all three leaflets in their short axis [24,40]. TEE may be of particular importance for patients who are in the mid-portion of the anatomic spectrum or who have inadequate acoustic transthoracic windows [41].

Three-dimensional TTE appears useful for the visualization of the posterior leaflet and the degree of tethering [42]. Computerized tomography (CT) and MRI have been used to study anterior leaflet motion and right ventricular volumes [43–46].

In DOTV, 2D echocardiography can demonstrate duplication of the ostium on parasternal short-axis, apical 4-chamber and parasternal long-axis views through the right ventricular inflow tract. Imaging of the two orifices can best be achieved from subcostal short-axis and en face views.

## Prenatal assessment

The TV is best assessed in the 4-chamber view. Isolated TS is rarely found in the fetus. If present, acceleration of flow across the thickened valve is generally seen. The right atrium, although usually increased in size, will be able to decompress across the foramen ovale.

Ebstein anomaly is more common in prenatal reports about congenital heart disease than could be expected from postnatal series. This is because the severe end of the spectrum – with severe TR, marked cardiomegaly, possible arrhythmia and fetal hydrops – is likely to be detected during screening of the fetal heart [12].

Tricuspid valve dysplasia is likely to be detected during screening of the fetal heart as it may cause significant cardiomegaly (Fig. 13.12 and Videoclip 13.8) [12]. TV dysplasia may be associated with pulmonary atresia and intact ventricular septum. In the fetus, DOTV may also be diagnosed in association with tricuspid dysplasia.

The following findings are important for prognosis in Ebstein anomaly and TV dysplasia [32]:

- Degree of TR (Videoclip 13.9).
- Presence of right ventricular outflow tract obstruction (may progress during pregnancy) (Videoclip 13.10), flow pattern in the main pulmonary artery and the ductus arteriosus in longitudinal views.
- The ratio of fossa ovale diameter over the length of the atrial septum on a horizontal 4-chamber view: a ratio >0.3 has been reported to be beneficial (Fig. 13.13) [47].
- Maximal velocity across aortic valve (as an estimate for left ventricular output).
- Presence of arrhythmia.
- Presence of Uhl anomaly [48,49].
- Exclusion of functional TR (e.g., in presence of fetal hyperthyroidism, other conditions causing fetal heart failure with secondary tricuspid annulus dilation).

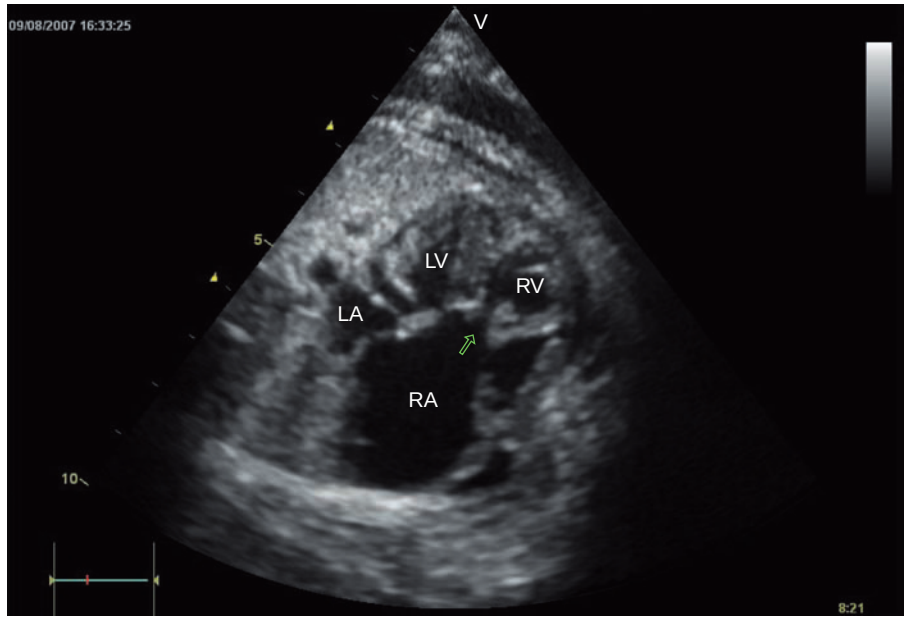


**Figure 13.12** Fetal 4-chamber image of dysplastic septal and anterior leaflets (arrow); dilation of the right atrium and right ventricle; and a small pericardial effusion. LA, left atrium; LV, left ventricle; RA, right atrium; RV, right ventricle.

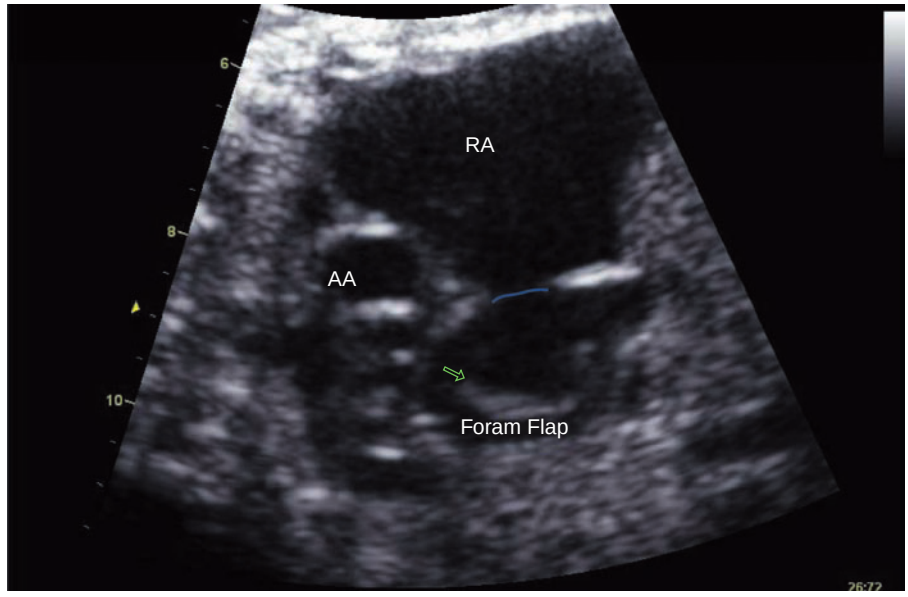


**Figure 13.13** Fetal sagittal view of dilation of right atrium with a beneficial ratio (>0.3) of foramen ovale (line) to length of atrial septum (arrow). AA, ascending aorta; RA, right atrium; Foram, foraminal.

- Cardiothoracic ratio.
- Presence of venous pulsations in the umbilical vein and venous duct.
- Pericardial effusion.
- Fetal hydrops.

Usually serial assessments are performed, the interval depending on the degree of fetal heart failure. In the fetus with Ebstein anomaly, both TR and stenosis will cause dilation of the right atrium and the atrialized right ventricle. Antegrade flow through the pulmonary valve will depend on the degree of TR, the size of the true right ventricle and concomitant pulmonary stenosis [32]. With diminishing antegrade flow through the pulmonary valve the retrograde flow from the ductus arteriosus will increase. In the presence of severe TR, the size of the foramen ovale is crucial, as it will allow decompression of the right heart, right-to-left shunt at atrial level, and maintenance of the combined cardiac output by increasing left ventricular stroke volume [47]. A restrictive foramen ovale, however, is likely to be associated with fetal heart failure, hydrops and intrauterine death [32].

### Imaging of the adult

Due to the enlargement of the right heart, the lungs are often displaced, so that transthoracic images are usually of high quality. If difficulties are encountered in obtaining clear images of the TV leaflets, number of orifices and the subvalvar apparatus, TEE is recommended [24]. The mid-esophageal 4-chamber view will allow imaging of the anterior and septal leaflets; the right ventricular inflow-and-outflow view is especially useful for Doppler assessment. The transgastric views allow identification of all three leaflets, and the best image of the chordae tendineae and papillary muscles is provided in the transgastric right ventricular inflow view [24,40]. In addition to echocardiography, preoperative magnetic resonance imaging (MRI) is promising for assessment of ventricular volumes and function, whereas 3D echo has been able to visualize myocardial abnormalities as spongy myocardium [44,45].

### Preoperative assessment

Successful TV repair, particularly in Ebstein anomaly, depends mainly on the presence of a mobile and free leading edge of the anterior leaflet, short papillary muscles and chordae, as well as fenestrations generally not precluding a satisfactory repair. If the posterior leaflet is large enough it will permit a bifoliate repair. Rarely, if all three leaflets are large enough, a trifoliate repair will be possible.

### Intraoperative assessment

Intraoperative TEE will be helpful during surgery of isolated TS and the other above-mentioned conditions, mainly with respect to the evaluation of the degree of postoperative valve regurgitation. A finding of DOTV, for example, in tetralogy of Fallot may hamper transatrial repair [14].

In Ebstein anomaly and TV dysplasia, the aim of the prebypass examination is confirmation of preoperative findings as well as refinement of diagnosis (e.g., by detecting an ASD) [50]. Intraoperative examination after TV repair allows rapid determination of the degree of residual TR and/or stenosis, and also assessment of both the integrity of the repair of the ASD and ventricular function. After right ventricular plication, the territory of the right coronary artery should be assessed [28,41,43]. In case of TV replacement, significant paravalvular leaks and an iatrogenic membranous ventricular septal defect (VSD) must be ruled out [41].

### Postoperative assessment

Early postoperative follow-up imaging must rule out pericardial effusion, document biventricular function, determine the gradient across the TV, and assess the degree of TV regurgitation [41]. Long-term follow-up will again focus on TV function as well as on right atrial and right ventricular size. In experienced, high-volume centers freedom from reoperation for recurrent TR at 10 years was 80–88% [3,43].

## Anomalies of tricuspid valve alignment

Examples of rare anomalies of TV alignment include *straddling TV*, in which the tensor apparatus arises from both the right and the left ventricle, and *overriding TV*, in which the annulus is committed to both chambers.

### Definitions

The tricuspid valve is termed as *straddling* when its chordae tendineae and papillary muscles are attached on both sides of the ventricular septum so that the right atrium may empty into both ventricles [51]. It is termed as *overriding* when its annulus is connected to both ventricles. The degree of overriding will determine whether this connection is truly biventricular (override <50%), with two ventricles of comparable size present, or whether this connection is univentricular, with one dominant and one rudimentary ventricle (override >50%) [51]. Straddling and overriding may coexist [6]. Colloquially spoken, straddling TV creates an intermediate heart between a normal heart and double-inlet left ventricle [52,53].

### Incidences

The exact incidence of straddling/overriding TV per se is not known. The condition of a straddling TV is of importance in univentricular hearts [54], but crucial in decision-making for biventricular repair as it may be present in 3% of lesions as ventricular septal defect, tetralogy of Fallot, double-outlet right ventricle, and transposition of the great arteries [55]. Although certainly underdiagnosed in univentricular hearts, straddling TV is a rare condition, found in only 0.71% of autopsies in the Cardiac Registry of the Children's Hospital in Boston [56].

### Etiology

The etiology of straddling and/or overriding TV must be regarded in the context of the etiology of the associated lesion.

### Morphology and classification

#### Developmental considerations

The proposed morphogenesis for a straddling TV is not as a primary anomaly. Straddling or overriding of the TV, instead, is thought to be secondary to embryologic events leading to hypoplasia of the right ventricular inflow tract and as a consequence to malposition of the ventricular septum with ventriculoatrial septal malalignment [53,56].

#### Anatomy

##### *Straddling tricuspid valve in biventricular hearts*

In straddling TV in biventricular hearts, there is marked malalignment between the ventricular and the atrial septum.

The right ventricular inflow tract is usually smaller than the left ventricular inflow tract. The nonstraddling part of the TV opens into the right ventricle, whereas the straddling part opens into the left ventricle [51]. In order to avoid surgically induced heart block, it is important to know that the position of the penetrating atrioventricular bundle reflects the degree of malalignment [57]. In the above-mentioned post-mortem study the pathomorphology of lesions associated with straddling TV included the following: ventricular septal defect (80%; 68% involving the inlet septum); attachments of the TV to the posteromedial papillary muscle group of the left ventricle (95%); either normal attachments of the mitral valve (50%) or mitral stenosis if chordae inserted only into the anterolateral papillary muscle group (25%). Further findings were situs solitus with D-looped ventricles (84%) and L-looped ventricles (16%). The great arteries were either normally related (42%, complicated in the majority by tetralogy of Fallot) or abnormally related (58%, transposition of the great arteries, double-outlet right ventricle, or double-outlet left ventricle) [56].

### *Double-orifice tricuspid valve with one orifice straddling*

The distinct anatomic features of this condition, which is characterized by marked hypoplasia of the right ventricle, are discussed in the respective sections on DOTV (see above) and DORA (see below) [6].

## Pathophysiology

The pathophysiology of straddling TV in biventricular hearts is determined by the pathophysiology of the above-described associated lesions. Mitral stenosis, if present, results in an increase in left atrial pressure.

## Imaging

### Goals of the examination

The main objectives of echocardiography in the setting of anomalies of TV alignment can be summarized as follows:

- Imaging of the TV: (Fig. 13.14)
  - morphology and movement of leaflets; chordae and papillary muscles
  - determination of degree of straddling [58,59]:
    - classification of abnormal chordal insertions of the valve in the left ventricle: (A) near the crest of the ventricular septum; (B) at some distance from the midline and inferior to the ventricular septal defect; or (C) into the endocardial surface of the free wall or into a papillary muscle of the left ventricle;
    - diastolic movement of the affected leaflet through the ventricular septal defect into the left ventricle indicates straddling of major degree [60].
- Determination of associated overriding TV as less than or greater than 50% (Fig. 13.15)
- Imaging of the mitral valve with respect to papillary muscles, chordal insertion (straddling mitral valve) and morphology of leaflets (cleft or parachute mitral valve)
- Determination of the degree of atrioventricular malalignment
- Assessment of size and type of ventricular septal defect
- Assessment of size of right ventricular inflow tract with respect to the possibility of either biventricular or one-and-a-half repair
- Detection of associated lesions
- Assessment of biventricular function
- Assessment of hemodynamics by conventional Doppler and color flow mapping (CFM) with respect to:

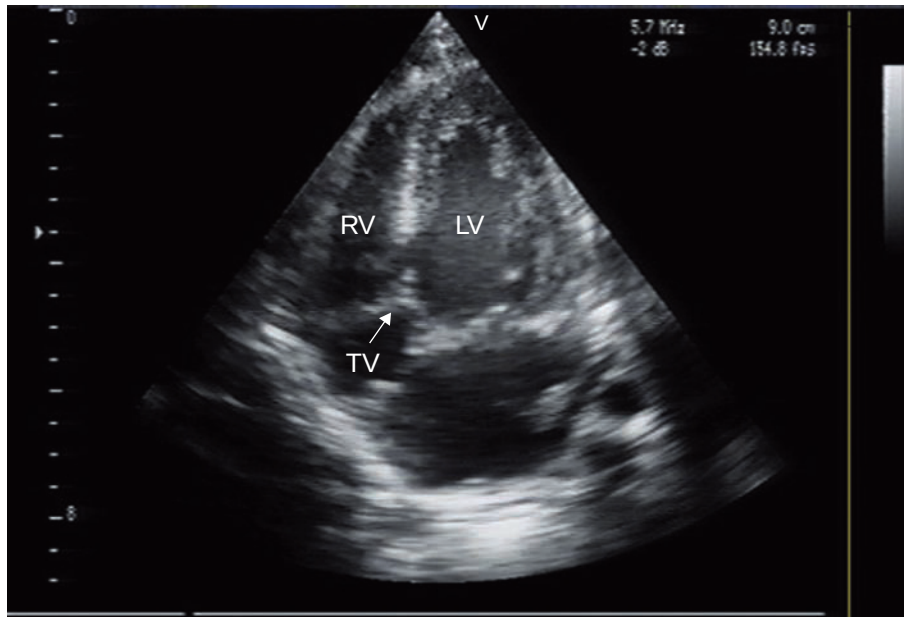


**Figure 13.14** Apical 4-chamber view of a straddling and overriding tricuspid valve (TV), mild hypoplasia of right ventricular inflow tract, and inlet ventricular septal defect. LV, left ventricle; RV, right ventricle.

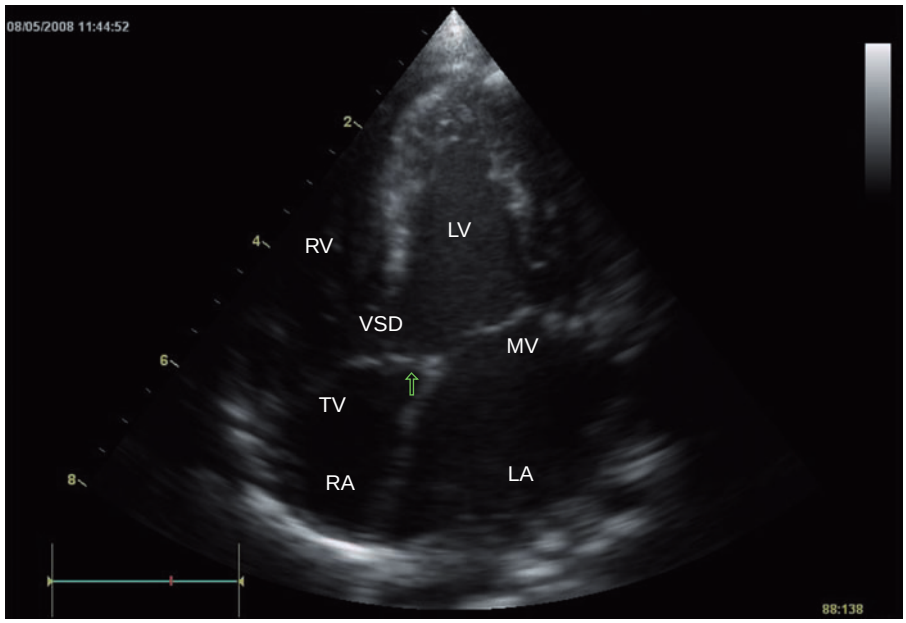


**Figure 13.15** Apical 4-chamber view of a perimembranous/inlet ventricular septal defect, malalignment of interatrial and interventricular septum, and overriding tricuspid valve with high offsetting (arrow) and smallish right ventricular inflow. LA, left atrium; LV, left ventricle; MV, mitral valve; RA, right atrium; RV, right ventricle; TV, tricuspid valve; VSD, ventricular septal defect.

TR and its degree; calculation of systolic RV–RA gradient.

Mitral valve function.

In the apical 4-chamber view the malalignment between atrial and ventricular septum is characterized by rightward deviation of the ventricular septum. The ventricular septal defect usually is located in the inlet septum and does not reach the crux of the heart [60]. The normal offsetting of the atrioventricular valves is not present [60]. The inlet ventricular septal defect and the atrioventricular malalignment can also be imaged in parasternal short-axis views.

In the apical 4-chamber view a straddling tricuspid valve is characterized by abnormal chordal insertions of the valve [60]. For the classification of the exact type of straddling (A, B or C), additional views, especially subcostal 4-chamber and short-axis views, might be necessary. If chordae and papillary muscle disposition are not clearly identified, the finding of the movement of a tricuspid valve leaflet through the ventricular septal defect in diastole can be taken as a reliable diagnostic sign [60].

When imaging the straddling tricuspid valve in the 4-chamber view, the additional presence of overriding is only obvious when overriding of the valve exceeds 50% of its annual diameter. In case of a lesser degree of overriding, a right ventricular inlet view, with the transducer rotated anticlockwise by approximately 90° from the 4-chamber view and angled posteriorly, is useful [61].

### Prenatal assessment

There are no reports in the literature on diagnosis of tricuspid valve straddling in the fetus. The goals of fetal examination, however, will not differ from the above-mentioned goals of postnatal examination.

### Imaging of the adult

By TEE, the mid-esophageal 4-chamber view is especially helpful in demonstrating the crux of the heart. Classification of type of straddling by TEE will necessitate transgastric views [60].

### Intraoperative assessment

As surgical techniques of closure of ventricular septal defect (VSD) will depend on the degree of straddling [62–64], the objective of pre-bypass TEE is the reassessment of tricuspid and mitral chordal attachments and valve function. In cases of biventricular repair, the various demanding procedures for VSD closure are monitored. In cases of one-and-a-half ventricular repair, the partial biventricular repair and bidirectional Glenn anastomosis are monitored [65]. Post-bypass TEE is directed at ruling out a significant residual shunt across the ventricular septum and atrioventricular valve dysfunction, mainly TV regurgitation.

### Postoperative assessment

Postoperative follow-up in the early postoperative period must rule out pericardial effusion and document biventricular function and the degree of TV incompetence. Long-term follow-up will focus on TV function as well as on the residuae common after repair of the associated lesions.

## Systemic venous valve anomalies

Systemic venous valve anomalies in the right atrium result from remnants (*Eustachian valve*, *Thebesian valve* or *Chiari network*) or, at the extreme end of the spectrum, persistence of the fetal right sinus venosus valve (*cor triatriatum dextrum*).

## Definitions

Remnants of the fetal right sinus venosus valve involve two venous valves: the valve guarding the orifice of the inferior vena cava at its connection to the right atrium – the *Eustachian valve* – and the valve guarding the orifice of the coronary sinus – the *Thebesian valve*. Persistence of the fetal right sinus valve in its original dimension can result in (1) a fenestrated membrane, frequently described as a *Chiari network* [66]; (2) a membranous sac protruding into the right ventricle through the TV; or (3) complete septation of the right atrium, defined as *cor triatriatum dextrum*.

## Incidences

Both the Eustachian and Thebesian valves are normal structures within the right atrium. Due to the polymorphism of the Thebesian valve, the true incidence at autopsy is not 100% but only 80% [67]. The incidence of a Chiari network is about 2–3% at autopsy [68]. Its incidence detected by transthoracic echocardiography is reported to be low (<0.6%), but by TEE is comparable with that at autopsy [69]. Membranous sacs protruding into the right ventricle [70–72] and cor triatriatum dextrum [73–75] are very rare conditions based on the scarcity of case reports on infants, children, and adults.

## Etiology

The majority of reported cases are sporadic. Prominent Eustachian and Thebesian valves and cor triatriatum dextrum have been found to be associated with tricuspid stenosis, tricuspid atresia, Ebstein anomaly [76] and right ventricular hypoplasia [77,78]. Interestingly, when the Eustachian valve was studied in patients with hypoplastic left heart syndrome, it was found to be absent in 61% of patients with mitral and aortic atresia [79].

## Morphology and classification

### Developmental considerations

After the right horn of the sinus venosus is incorporated into the right atrium, the valve of the right sinus venosus divides the right atrium almost into two chambers. The valve usually regresses between weeks 9 and 15 of gestation. The cranial portion of the valve forms the crista terminalis, whereas the caudal portion forms the valves of the inferior vena cava (Eustachian valve) and coronary sinus (Thebesian valve). If the right sinus venosus valve fails to reabsorb completely, either a fenestrated membrane (Chiari network) or a membranous sac will remain. Persistence of the right sinus venosus valve with either a complete or incomplete membrane results in separation of the right atrium into anterolateral ("primitive atrial") and posteromedial ("sinus venosus") components (cor triatriatum dextrum) [75,80]. It has been speculated that prominence and persistence of venous valves may alter fetal blood flow and cause diminished flow across the TV, thus leading to underdevelopment of right heart structures [77,78].

### Anatomy

The Eustachian and Thebesian valves are fibromuscular webs attached to the crest in the regions of the opening of the inferior vena cava and the coronary sinus, respectively. A Chiari network usually consists of fine fibers, 1–2 mm thick, extending from the atrial septum (usually the limbus of the fossa ovalis) to the Eustachian and Thebesian valves [67]. Notably, an association of Chiari network with a PFO and atrial septal aneurysm has been described [69,81]. As benign variants, very prominent Chiari networks [82], as well as fenestrated and unfenestrated membranes [83], should be considered. Spinnaker-like [84] or parachute-like [85] membranous sacs are anatomically described as saccular membranes anchored to the Eustachian valve, the lower border of the foramen ovale, and the tricuspid annulus [70]. They may obstruct right ventricular inflow and outflow [84,85].

Cor triatriatum dextrum is characterized by anatomic division of the right atrium by a membrane, which separates the right atrium into two components: (1) a posteromedial venous component receiving both caval veins and the coronary sinus; and (2) an anterolateral part consisting of the right atrial appendage and the vestibule of the TV [76,80]. The membrane itself may exhibit defects allowing blood flow between the two components of the right atrium. The size of a concomitant atrial septal defect within the fossa ovalis is variable.

## Pathophysiology

Three levels of systemic venous valve pathophysiology exist. First, prominent systemic venous valves may occur without functional significance. A prominent Eustachian valve or Chiari network, however, may be associated with endocarditis [86], right atrial thrombus and embolic stroke [87], the latter related to the relatively high association with PFO and atrial septal aneurysm [69,81].

Second, valves of considerable prominence may divide the right atrium and result in obstruction of flow into the right heart. Spinnaker- and parachute-like membranous sacs in otherwise normal hearts may protrude into the orifices of both the tricuspid and pulmonary valves, thereby causing episodes of cyanosis [70,84]. With cor triatriatum dextrum in otherwise normal hearts, variable obstruction of blood flow through the membrane is present depending on the size and number of its perforations. There is also a variable shunt to the left atrium depending on the size of the defect within the fossa ovalis. The degree of peripheral venous congestion, including protein-losing enteropathy, and cyanosis will thus depend on the severity of obstruction and the size of the interatrial communication.

Third, persistent venous valves and cor triatriatum dextrum may occur in hearts with either atresia or stenosis of right-sided valves [88]. The pathophysiology of the underlying lesion is not altered.

## Imaging

### Goals of the examination

Echocardiographic examination in the context of systemic venous valve anomalies should focus on the following:

- Visualization of the Eustachian valve
- Visualization of other conditions:
  - chiari network;
  - spinnaker- and parachute-like membranous sacs with/without protrusion into the right ventricle.
  - cor triatriatum dextrum:
    - location and attachments of membrane (Fig. 13.16);
    - identification of the two parts of the right atrium: the anteriorly located true right atrium exhibits the atrial appendage;
    - connections of the superior vena cava and coronary sinus to the two parts;
    - size of the TV annulus, calculation of z-score [34].
- Hemodynamic assessment by spectral Doppler and CFM:
  - ruling out obstruction of flow:
    - flow profile in superior and inferior venae cavae, hepatic veins, and at the orifice of the coronary sinus;
    - assess for turbulent (diastolic) flow across membranes, thus defining the higher and lower pressure parts of the right atrium.
  - direction of shunt in presence of an ASD, PFO and/or atrial septal aneurysm: contrast-echocardiography might be helpful.
- Detection of associated lesions:
  - atrial septal defect, tricuspid and pulmonary valve abnormalities, and/or right heart hypoplasia.
- Note: the following conditions may present as mobile structures within the right atrium [82]:
  - thrombi, vegetations, tumors (myxoma or rhabdomyoma)

  Flail TV leaflet, ruptured chordae tendineae.

With 2D echocardiography, the conditions described above are usually easily visualized using standard views. The right atrium and its lateral wall are best imaged from the parasternal short-axis view and from both parasternal and subcostal 4-chamber views. In addition, subcostal short-axis views and parasternal long-axis views through the right ventricular inflow tract will be useful for visualization of both the superior and inferior venae cavae.

Color and spectral Doppler are useful for the assessment of intracavitary membranes, atrial septum, tricuspid valve and pulmonary valve. TEE is especially useful for better delineation of membranes within the right atrium and also for guiding interventions, such as surgical closure of ASD and PFO, as it will avoid inadvertent "closure" of a prominent Eustachian valve mistaken for an ASD (Fig. 13.17). As the cavo-tricuspid isthmus – the part of the right atrium bordered by the orifice of the inferior vena cava, the Thebesian valve and the TV – is of great interest for electroanatomic mapping and catheter ablation, 3D reconstruction of this region by MRI has been reported [89]. Although sometimes very prominent and redundant, membranous sacs may not obstruct flow into the right ventricle [83].

### Imaging of the Eustachian valve

Angulating the transducer posteriorly from the subcostal 4-chamber view will allow visualization of the Eustachian valve as a thin linear structure crossing the floor of the right atrium from its origin at the orifice of the inferior vena cava to its insertion at the inferior limbus of the fossa ovalis [90]. It may also be visualized in the subcostal short-axis view (Fig. 13.18)

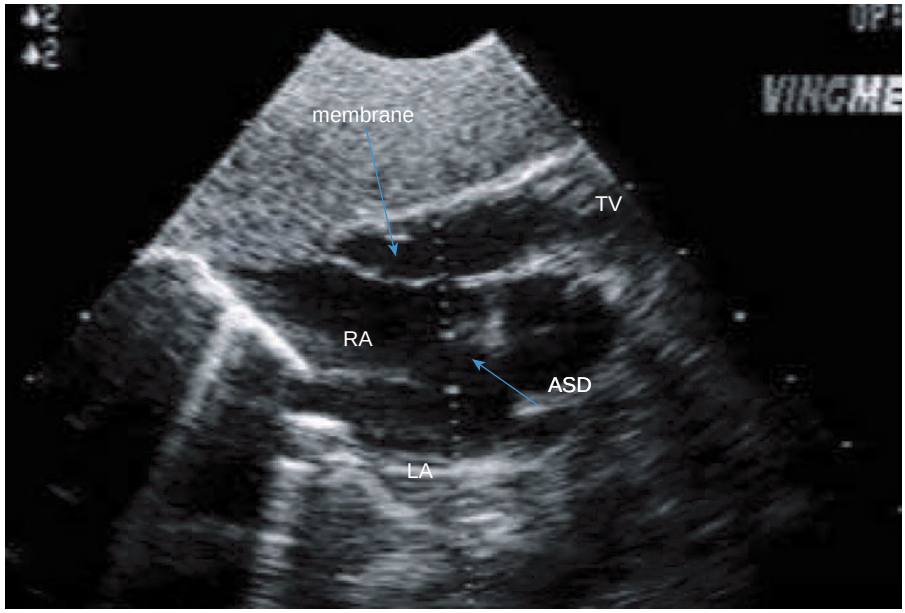


**Figure 13.16** Subcostal 4-chamber view of a membrane in the right atrium obstructing the inflow to the right ventricle. ASD, atrial septal defect; LA, left atrium; RA, right atrium; TV, tricuspid valve.

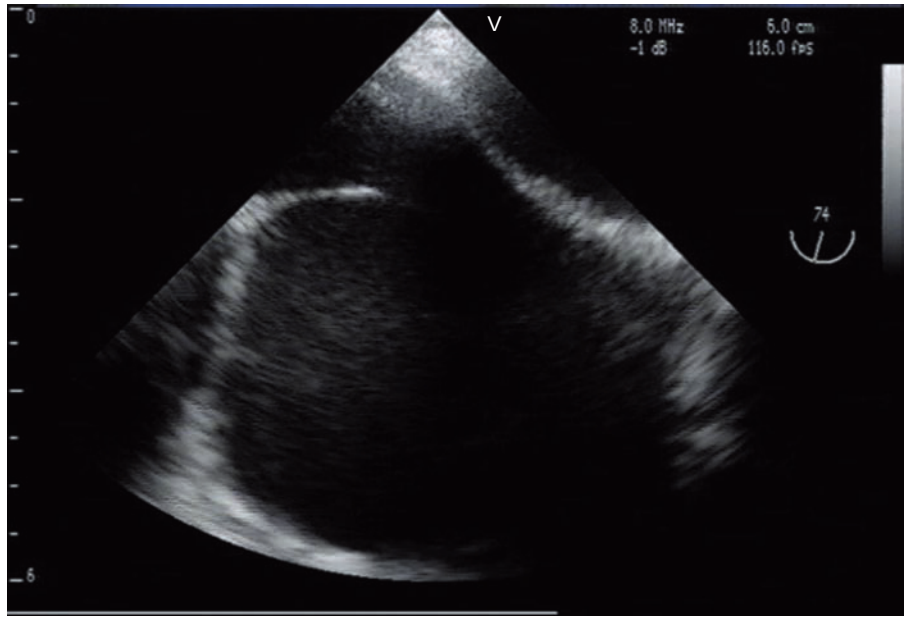


**Figure 13.17** Bicaval view of a Eustachian valve guarding the orifice of the inferior vena cava. The "defect" seen is *not* an atrial septal defect.

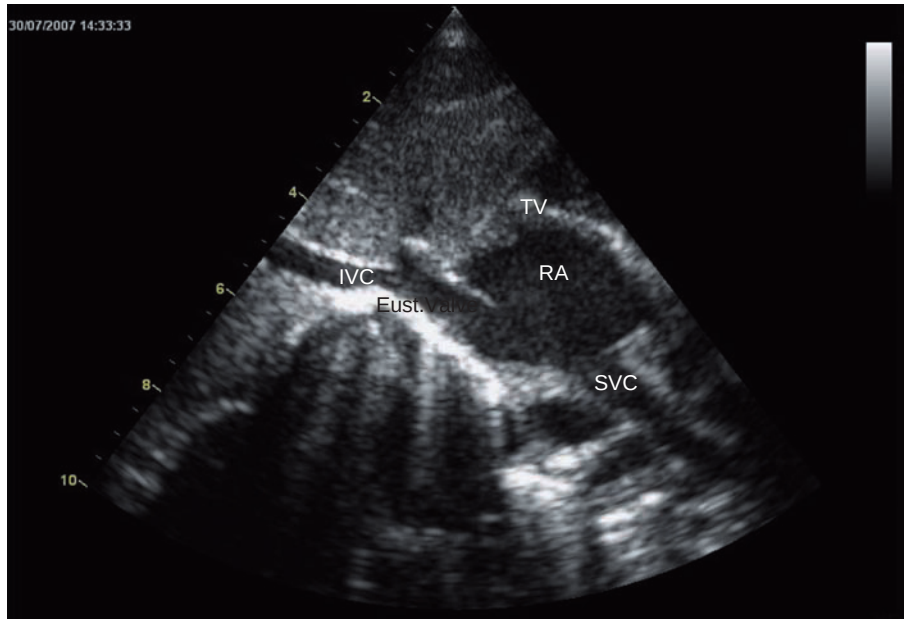


**Figure 13.18** Subcostal sagittal (short-axis) bicaval view of the Eustachian valve guarding the orifice of the inferior vena cava. Eust., Eustachian; IVC, inferior vena cava; RA, right atrium; SVC, superior vena cava; TV, tricuspid valve.

and the parasternal long-axis view through the right ventricular inflow tract (Videoclip 13.11). Daily echocardiographic experience tells us that, unless the valve is very prominent, its origin at the orifice of the vena cava, but generally not its atrial insertion, can be visualized by TTE in almost every healthy infant and in the vast majority of healthy children studied. By TEE the valve can be visualized in the bicaval view thus demonstrating the same level of incidence in the adult population as in children. Prominent Eustachian valves, even if they are mobile and fenestrated, should not be termed a Chiari network.

### Imaging of the Thebesian valve

Unless very prominent, the Thebesian valve – a thin linear structure at the entrance of the coronary sinus – can only be visualized by TEE in the 4-chamber view by angling the plane of view posteriorly.

### Imaging of a Chiari network

Visualization is best achieved via the parasternal long-axis view through the right ventricular inflow, the parasternal short-axis view and the apical 4-chamber view (Fig. 13.19 and Videoclip 13.12). A Chiari network is imaged as a serpentine

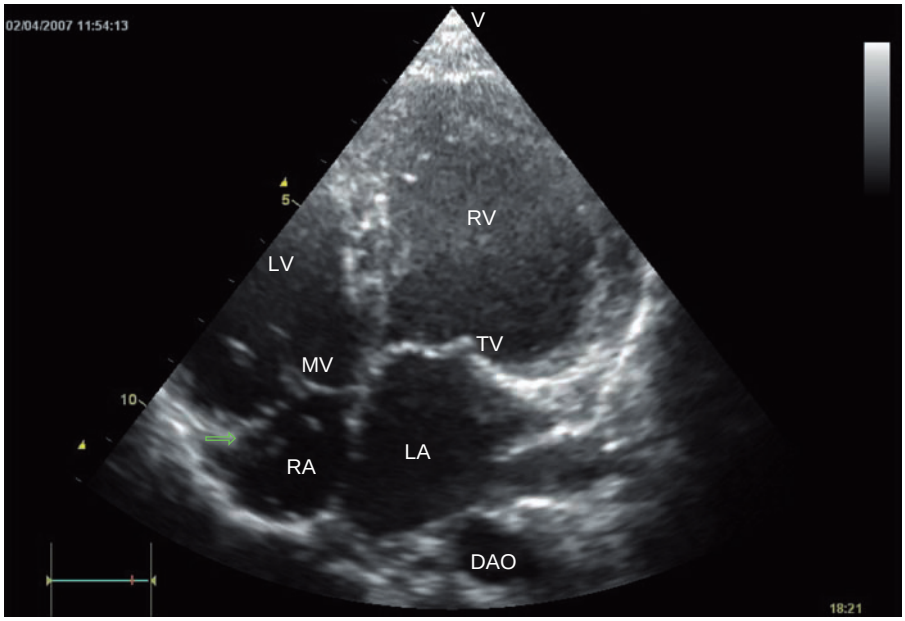


**Figure 13.19** Apical 4-chamber view of Chiari network (arrow) in atrioventricular discordance. The right-sided valve is a mitral valve. DAO, descending aorta; LA, left atrium; LV, left ventricle; MV, mitral valve; RA, right atrium; RV, right ventricle; TV, tricuspid valve.

fenestrated membrane or a honeycomb-like, highly mobile reflective structure within the right atrium [87], whipping toward the posterior aspect of the right atrium during systole and sometimes even prolapsing into the TV orifice during diastole. Timely assignment of its cyclic motion can be achieved by the concomitant use of M-mode echocardiography. A Chiari network may be seen to originate from either the Eustachian or the Thebesian valve and attached to the upper wall of the right atrium or the atrial septum [87].

### Imaging of spinnaker- and parachute-like membranous sacs

In the same views as used for imaging a Chiari network, these large, membranous, highly mobile and reflective structures are seen originating from the Eustachian valve with attachments to the atrial septum. Movement into the right ventricle may result in tricuspid and pulmonary valve obstruction. The membranous sacs may even herniate through the foramen ovale into the left atrium [70].

### Imaging of isolated cor triatriatum dextrum

In the subcostal short-axis (sagittal) view a perforate membrane is seen running from the inferior vena cava toward the interatrial septum, separating the right atrial appendage and the TV from both venae cavae, thus creating a true double-chambered right atrium. The drainage of the coronary sinus is variable, but is more often seen into the upstream chamber. An atrial septal defect as additional outlet from the upstream chamber may be visualized. If it is small and the obstruction between the upstream and downstream chamber is severe, then enlargement of both venae cavae may be taken as a diagnostic hallmark [91].

### Prenatal assessment

The Eustachian valve can be visualized in short-axis views (sagittal planes) mostly as a mobile, curvilinear and thin structure directing the blood from the inferior vena cava through the valve of the foramen ovale into the left atrium. Prenatal diagnosis of a persistent and redundant Eustachian valve simulating an atrial tumor [92] and of a Chiari network in association with fetal cardiac arrhythmia has been reported [93]. There are no reports in literature concerning the prenatal diagnosis of cor triatriatum dextrum, although this diagnosis should be added to the various cardiac diseases causing fetal congestive heart failure and hydrops.

### Imaging of the adult

By TEE, the Eustachian valve can be imaged in short-axis views in every adult. Sometimes the fibrous bands at the opening of the coronary sinus, the Thebesian valve, are noted [93]. A Chiari network can be visualized by TEE in modified bicaval, short-axis and 4-chamber views [94]. Rarely, thrombi [95,96] and vegetations in right-sided endocarditis [97] may be visualized on a Eustachian valve. In the presence of a Chiari network, contrast echocardiography is recommended to rule out patency of the foramen ovale [69]. Entrapment of catheters or pacemaker leads can be occasionally seen [87,98]. In cor triatriatum dextrum, the exact locations of the membrane in the right atrium along with the morphology of the TV can be clearly visualized by TEE [91].

### Intraoperative assessment

During the planning and echocardiographic guidance stages of both surgical and transcatheter ASD closure, the presence of a prominent Eustachian valve should be noted, with documentation in the report. Many centers have painfully reported that intraoperatively a prominent Eustachian valve was misinterpreted as atrial septum [99]. Closure of this alleged atrial septal defect will result in postoperative cyanosis as blood from the inferior vena cava will be directed via the true atrial septal defect to the left atrium. This condition of inadvertent closure can be easily demonstrated by peripheral venous contrast echocardiography using veins of the legs. In order to avoid such a situation before ASD device deployment, the echocardiographer has to identify clearly the location and size of the defect and, in addition to its rims, its relationship with the Eustachian valve and the inferior vena cava.

Successful surgical resection of membranous sacs and division of cor triatriatum dextrum membranes have been described in neonates, children and adults. Transluminal balloon therapy has been performed with only short-term success in a single patient [100]. Goals of the pre-cardiopulmonary bypass examination include confirmation of diagnosis. The post-bypass examination aims at demonstrating unobstructed flow through the right atrium, closure of ASD, and functional assessment of the TV and ventricles.

### Postoperative assessment

In the early postoperative period echocardiographic evaluation has to rule out pericardial effusion and a residual shunt across the atrial septal defect. In the long term, echocardiographic evaluation aims at assessing both venous and tricuspid flow, as well as ventricular function. There is no evidence from literature that recurrence of intra-atrial membranes occurs.

## Anomalies of the right atrium

### Definitions

*Double-outlet right atrium* (DORA) is a condition in which the right atrium empties into both the right and left ventricles as the result of leftward deviation of the atrial septum [101]; it is generally associated with complex congenital heart disease. Conditions promoting DORA include atrioventricular septal defect (AVSD) with atrial septum malalignment [102] and straddling tricuspid valve (TV).

*Giant right atrium* (GRA) is defined as an isolated disproportionate enlargement of the right atrium in the absence of other cardiac lesions known to cause right atrial dilation [103]. Other terms in use for this entity are idiopathic dilation of the right atrium and congenital enlargement of the right atrium [104]. There is evidence from literature that there has always been some difficulty in differentiating GRA from a right atrial diverticulum [105] or aneurysm.

### Incidences

Double-outlet right atrium is a rare condition, and its true incidence is not known. A retrospective review of the surgical treatment of DORA associated with AVSD in a high-volume pediatric cardiac center revealed only 12 patients over a period of 19 years [106]. As DORA is also a distinct but often underdiagnosed feature in complex congenital heart disease with straddling TV, its true incidence is likely to be higher than reported. DORA is also a descriptive term that is not universally used, even when the condition is recognized.

Giant right atrium is another rare anomaly, first described in a surgical patient in 1955 [107], but defined as an entity only in 1965 [103]. Usually it is diagnosed in the second to fourth decade [108–110], sometimes in children [111–113], and occasionally in infancy [104,111,114–116] and during prenatal life [104,111,114,117–120]. Its true incidence is not known. The largest analysis in the literature summarizes case reports of 103 patients [108], aged from 32 weeks of pregnancy to 79 years, of whom almost half were asymptomatic and were only diagnosed incidentally from cardiomegaly on chest X-ray. Obviously symptomatic fetuses and infants seem to represent the more severe end of the spectrum [104]. The inconsistency of descriptive terms in literature, as mentioned above, explains the difficulty in estimating the true incidence of this entity.

### Etiology

Most cases of DORA are sporadic. In the presence of AVSDs, DORA has also been associated with Ellis–van Creveld syndrome, Turner syndrome, Raghib syndrome and right lung agenesis [106]. The majority of reported cases of GRA are also sporadic.

### Morphology and classification

#### Developmental considerations

##### *DORA associated with AVSD*

In a small number of hearts later showing the distinct characteristics of an AVSD, leftward lateral direction of the downgrowing septum primum may cause fusion with the left lateral endocardial cushion, instead of with the superior and inferior cushions as usual. This abnormal development of the septum primum with consequential atrial septal malalignment and DORA may be accompanied by abnormal development of both the coronary sinus septum, leading to a persistent left superior vena cava with unroofed coronary sinus, and the sinus venosus septum, with anomalous pulmonary drainage [106,121,122]. Depending on the division of the atrioventricular orifice during embryologic development, DORA in AVSD will be associated with either a common atrioventricular valve or two separate valve orifices, one of which may be a straddling TV (see below).

### *Giant right atrium*

Cases of GRA are mainly congenital in origin, although inflammation and ischemia may also play a role [123]. Histologic evaluations of excised tissue reveal an abnormal atrial wall exhibiting muscular degeneration and fibrosis [104,113] but occasionally demonstrate also focal lymphocytic infiltration [115].

## Anatomy

### *DORA associated with AVSD*

The distinct features of this condition are the leftward deviation of the atrial septum and its malalignment with the ventricular septum. The true left atrium, characterized by a normally located left atrial appendage, is posteriorly located and receives all four pulmonary veins. Rarely, an incomplete supravalvular membrane, situated above the commissures of the mural leaflet with the superior and the inferior bridging leaflet, may be present [124]. A persistent left superior vena cava draining into an unroofed coronary sinus (Raghib syndrome) is found in association in 25% of cases [106]. The AVSD is more likely to exhibit two separate atrioventricular valve orifices than a common atrioventricular valve orifice. The latter variant was found only when the AVSD was associated with tetralogy of Fallot [125].

### *DORA with double-orifice TV with one orifice straddling*

This extremely rare condition comprises the originally described variant: the ventricular septum is intact although the muscular inlet septum is shortened (as in AVSD); a right-sided non-straddling TV opens from the right atrium into the small right ventricle, a more left-sided TV opens from the right atrium into the larger left ventricle, and a mitral valve opens from the left atrium into the left ventricle, with or without mitral stenosis. In this "true" original variant of DORA three atrioventricular valves are present in a single patient [126]. This condition should not be confused with double-orifice TV, in which each of the orifices opens into the right ventricle.

The distinct anatomic feature of GRA is an isolated disproportionate dilation of the right atrium. The related lesion of right atrial diverticulum may be singular or multiple saccular structures, which are usually located either at the free or at the lateral wall [108]. So-called right atrial appendage aneurysms exhibit a paper-thin wall [108].

## Pathophysiology

Double-outlet right atrium allows blood to flow from the right atrium to the left ventricle, which will cause arterial oxygen desaturation. The pathophysiology of DORA associated with AVSD will depend on the size of the secundum ASD. If the defect is large, the oxygenated blood from the pulmonary veins will flow easily into the right atrium, with the hemodynamics resembling that in an ASD (see Chapter 11). A secundum ASD as the only outlet from the left atrium, however, will lead to pulmonary venous hypertension, and the hemodynamics will resemble those seen in patients with cor triatriatum (see Chapter 14). An isolated persistent left superior vena cava with drainage via a normal coronary sinus into the right atrium will have no effect; however, with an unroofed coronary sinus, an admixture of venous blood to the oxygenated left atrial blood will occur [106]. In DORA with double-orifice TV with one orifice straddling, the pathophysiology is similar to other forms of right heart hypoplasia.

In GRA, compression of adjacent structures may cause chest pain, fatigue and dyspnea [104,108]. The abnormal tissue of the right atrial wall has arrhythmic potential giving rise to both ectopic pacemakers causing ectopic atrial tachycardia or macroreentry circuits causing atrial flutter [116]. Further more, atrial arrhythmias may cause thrombus formation with pulmonary and/or paradoxical systemic embolization [127]. Rarely, long-standing ectopic tachycardia may also induce congestive heart failure related to impaired systolic function [104,116]. Secondary dilation of the tricuspid annulus may occur followed by secondary TR [112].

## Imaging

With 2D echocardiography, the alignment of atrial and ventricular septa, the junction between the atrial septum or interatrial groove and the atrioventricular sulcus, and the size of the right atrium are best imaged from the 4-chamber views (both by TTE and TEE).

The right atrium and the right atrial appendage are usually easily visualized using parasternal, subcostal and suprasternal standard views. In case of extensive dilation, however, additional unconventional acoustic windows (low right parasternal and low right axillary windows) will be needed to optimize assessment (Fig. 13.20). Color and spectral Doppler are useful for evaluation of the atrial septum and the TV. TEE is especially useful for detection of thrombi and spontaneous echo contrast inside the right atrium and diverticula, whereas MRI [110,128] and multislice CT [128,129] will allow not only the visualization of wall thickness (thereby ruling out constrictive pericarditis, pericardial defects and cysts) but complete delineation of the intrapericardial malformation and its topographic relation to adjacent structures.

### Goals of the examination

In the context of anomalies of the right atrium, echocardiographic examination has the following objectives.

#### *DORA associated with AVSD*

- Determination of the size of the secundum ASD and degree of atrial septal malalignment
- Confirmation of all four pulmonary veins entering the left atrium

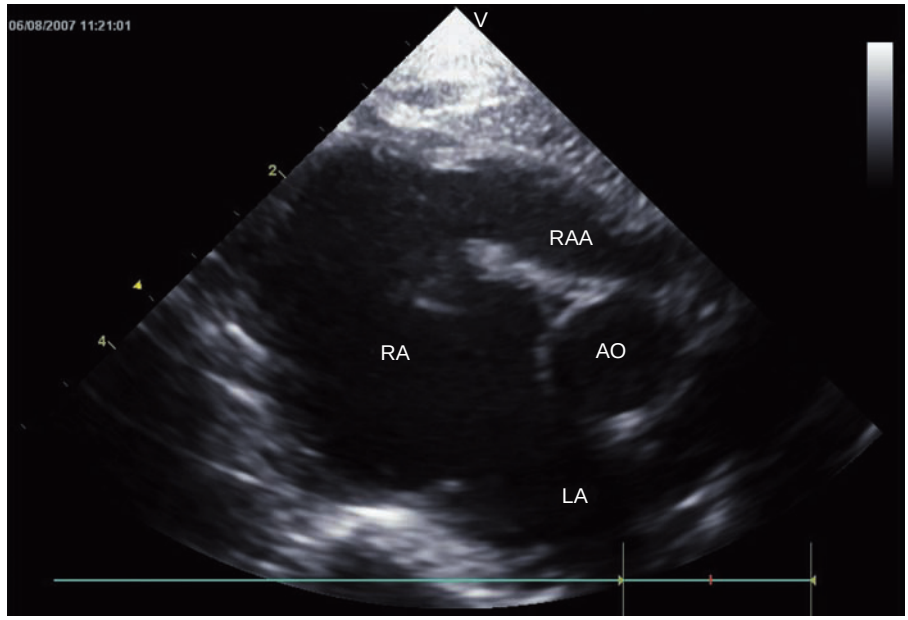


**Figure 13.20** High right parasternal short-axis view demonstrating impressive dilation of the right atrium and the right atrial appendage in an infant. AO, aorta; LA, left atrium; RA, right atrium; RAA, right atrial appendage.

- Ruling out supramitral membrane
- Ruling out left persistent vena cava
- Specific hemodynamic assessment (by spectral Doppler and CFM):
  - assessment of pulmonary venous flow;
  - flow direction through ASD and mean transseptal pressure gradient;
  - calculation of systolic RV–RA gradient based on TR.
- Morphology of AVSD (one versus two orifices; left-sided atrioventricular valve)
- Biventricular function
- Detection of associated lesions such as tetralogy of Fallot and coarctation of the aorta [106].

***DORA with straddling TV without ventricular septal defect (i.e., true DORA, not DOTV)***

- Assessment of diameter of the right-sided, nonstraddling part of TV and the size of the inflow tract of the right ventricle
- Assessment of the left-sided straddling part of the TV and the mitral valve (with respect to mitral stenosis).

***Giant right atrium***

- Establishment of the diagnosis:
  - measurement of size, planimetric size of the right atrium;
  - differentiation from right atrial diverticulum and aneurysm.
- Ruling out other cardiac lesions known to cause right atrial dilation, of which the most important are Ebstein anomaly, tricuspid dysplasia, sinus venosus defect, intracardiac tumors and restrictive cardiomyopathy [130]
- Ruling out potential secondary sequelae:
  - spontaneous intracardiac contrast and thrombi;
  - dilation of tricuspid annulus and TR;
  - tachycardia-induced cardiomyopathy; assessment of biventricular function;
  - displacement and/or compression of cardiac structures such as the right coronary artery, superior vena cava, right ventricle, etc.
- Detection of associated lesions.

### Imaging of DORA with AVSD

In the apical 4-chamber view the malaligned septum primum is characterized by an extreme leftward deviation of the lower part of the atrial septum (Fig. 13.21 and Videoclip 13.13) From both the apical and subcostal 4-chamber views, the secundum ASD can be imaged as a defect above the level of the left-sided valve orifice and confirmed by color Doppler. Further imaging of the valve in the subcostal coronal view with clockwise rotation 30° to 45° until the valve is seen en face will allow differentiation between AVSD with two orifices and AVSD with one common valve orifice, as well as diagnosis of unbalanced forms of AVSD (see Chapter 15).

### Imaging of giant right atrium

The giant right atrium and its lateral wall are best imaged from the parasternal short-axis view and from both parasternal and subcostal 4-chamber views. In addition, subcostal short-axis views and parasternal long-axis views through the right ventricular inflow tract will be useful for visualization of both the superior and inferior venae cavae.

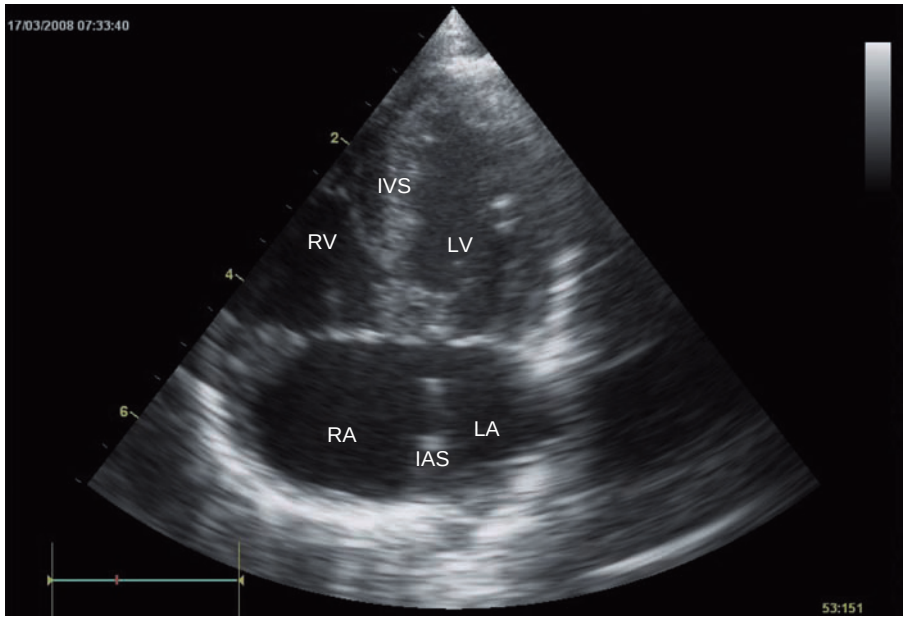


**Figure 13.21** Apical 4-chamber view of atrioventricular septal defect, secundum atrial septal defect, common atrioventricular valve orifice, and malalignment of interatrial and ventricular septum creating double-outlet right atrium. IAS, interatrial septum; IVS, interventricular septum; LA, left atrium; LV, left ventricle; RA, right atrium; RV, right ventricle.

### Prenatal assessment

As DORA is a rare condition there are no reports on prenatal diagnosis. AVSD with severe leftward deviation of the septum primum is sometimes associated with unbalanced AVSD with right ventricular dominance.

Antenatal diagnosis of GRA has been described [104,108], and is challenging because the investigator may be also confronted with concomitant fetal tachyarrhythmia and even fetal hydrops [104]. As mentioned above, symptomatic fetuses obviously represent the severe end of the spectrum of this entity.

In the presence of congestive heart failure serial assessment of hemodynamics and not only measurement of cardiothoracic circumference and ratio – which will give abnormal values due to the malformation per se – has to aim at documenting response to medical therapy or to contribute to decision-making for preterm delivery.

### Imaging of the adult

Transesophageal echocardiography and MRI will allow clear imaging of DORA either associated with AVSD or with straddling TV as well as associated lesions (e.g., Raghib syndrome). Visualization of malalignment will be possible in the 4-chamber view [64]. Venous contrast injected into the left arm will help to rule out Raghib syndrome.

According to the literature for GRA, a combined approach using TEE, electrocardiogram (ECG)-gated MRI, and occasionally also multislice CT is used for complete assessment [110,128,129]. The latter imaging techniques have almost completely replaced angiography, which nowadays is only performed when ectopic pacemakers and reentry circuits are treated with catheter ablation [108,116].

### Preoperative and intraoperative assessment

In DORA associated with AVSD, monitoring of the surgical procedure by TEE has to confirm a wide septectomy and atrial septal defect patch closure as well as complete repair of AVSD [131] and, if present, rerouting of the left persistent vena cava to the right atrium.

The decision to proceed with surgical resection of GRA should be made on an individual basis [104]. Atrial resection along with a modified right atrial Cox maze procedure could be considered in the presence of life-threatening atrial tachyarrhythmias refractory to medical treatment [104]. Surgical scarring may again trigger atrial arrhythmias and, as there are also concerns regarding recurrent right atrial dilation, special operative techniques, such as pericardial reinforcement, have been introduced [115]. Preoperatively, special attention should be given to the course of the right coronary artery [104]. The distorted right coronary artery can be usually imaged at 11 o'clock in the parasternal short-axis view by rotating the transducer counterclockwise. In case of severe right atrial enlargement, modifications of that acoustic window will be necessary.

In GRA, pre-cardiopulmonary bypass examination by TEE includes confirmation of the preoperative diagnosis and will focus on morphology and function of the TV, as significant dysfunction may necessitate refinement of surgical planning.

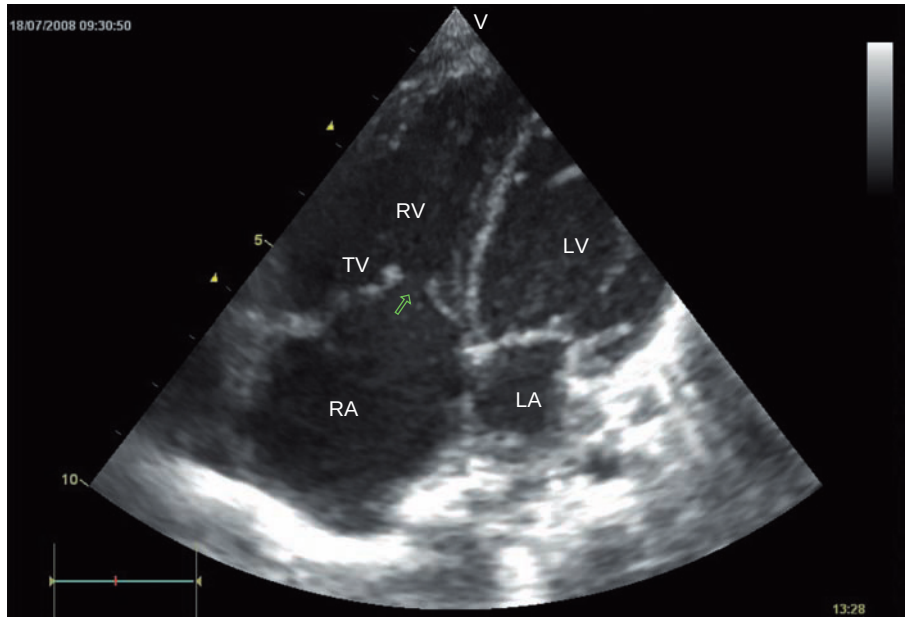


**Figure 13.22** Apical 4-chamber view demonstrating secondary dilation of tricuspid annulus and severe tricuspid regurgitation in giant right atrium (arrow pointing toward failure of central leaflet coaptation). LA, left atrium; LV, left ventricle; RA, right atrium; RV, right ventricle; TV, tricuspid valve.

### Postoperative assessment

In DORA associated with AVSD, a complete postoperative examination must rule out pericardial effusion and postoperative pulmonary venous obstruction, as well as document the integrity of AVSD repair [132].

In GRA, the early postoperative echocardiographic evaluation must rule out pericardial effusion originating either post-bypass or due to reduction of right atrial size (i.e., ex vacuo origin – empty-space-filling effusion). Long-term assessment should include searching for recurrent progressive right atrial dilation, thrombus formation and dysfunction of the TV (Fig. 13.22) [104,108].

## References


1. Ebstein W. Über einen sehr seltenen Fall von Insufficienc der Valvula tricuspidalis, bedingt durch eine angeborene hochgradige Missbildung derselben. *Arch Anat Physiol* 1866; 238–54.
2. Freedom RM, Mawson JB, Yoo SJ, Benson LN. Ebstein's malformation of the TV. In: *Congenital Heart Disease: Textbook of Angiocardiography*. Armonk, NY: Futura Publishing Co, 1997;349–66.
3. Dearani JA, O'Leary PW, Danielson GK. Surgical treatment of Ebstein's malformation: state of the art in 2006. *Cardiol Young* 2006;16(Suppl. 3):12–20.
4. Cascos AS, Rabago P, Sokolowski M. Duplication of the tricuspid valve. *Br Heart J* 1967;29:943–9.
5. Yoo SJ, Hode C, Moes CAF et al. A case report of double-orifice tricuspid valve. *Int J Cardiol* 1993;39:85–7.
6. Freedom RM, Mawson JB, Yoo SJ, Benson LN. Abnormalities of the tricuspid valve. Straddling, stenosis, or congenital regurgitation. In: *Congenital Heart Disease: Textbook of Angiocardiography*. Armonk, NY: Futura Publishing Co, 1997;367–81.
7. Togo T, Hata M, Sai S et al. Tricuspid valve myxoma in a child with coronary occlusion and aneurysms. *Cardiovasc Surg* 1994; 2:418–19.
8. Perry LW, Neill CA, Ferencz C et al. Infants with congenital heart disease: the cases. In: Ferencz C, Rubin JD, Loffredo CA, Magee CA (eds) *Epidemiology of Congenital Heart Disease. The Baltimore Washington Infant Study 1981–1989. Perspectives in Pediatric Cardiology*, Vol. 4. Mt Kisco, NY: Futura Publishing Co, 1993;33–62.
9. Samanek M, Voriskova M. Congenital heart disease among 815,569 children born between 1980 and 1990 and their 15-year survival: a prospective Bohemia survival study. *Pediatr Cardiol* 1999;20:411–17.
10. Rowe RD, Freedom RM, Mehrizi A. *The Neonate with Congenital Heart Disease*, 2nd edn. New York: WB Saunders Company, 1981;515–28.
11. Becker AE, Becker MJ, Edwards JE. Pathologic spectrum of dysplasia of the tricusid valve: features in common with Ebstein's malformation. *Arch Pathol* 1971;91:167–78.
12. Sharland G. Abnormalities of the atrioventricular junction. In: Allan L, Hornberger L, Sharland G *Textbok of Fetal Cardiology*, 1st edn. London: Greenwich Medical Media, 2000; 131–47.
13. Freedom RM. Congenitally corrected transposition of the great arteries: definitions and pathologic anatomy. *Progr Pediatr Cardiol* 1993;10:3–16.
14. Oppido G, Napoleone CP, Ragni L et al. Double orifice tricuspid valve in an infant with tetralogy of Fallot. *Ann Thorac Surg* 2006;81:1121–3.

15. Eberhardt L, Chetaille P, Kreitmann B. A very unusual combination of straddling and overrding of the tricuspid valve associated with clefting of the mitral valve. *Cardiol Young* 2005;15:422–4.
16. Balderston SM, Shaffer EM, Washington RL. Congenital polyvalvular disease in trisomy 18: echocardiographic diagnosis. *Pediatr Cardiol* 1990;11:138–42.
17. McIntosh N, Chitayat D, Bardanis M, Fouron JC. Ebstein anomaly: report of a familial occurrence and prenatal diagnosis. *Am J Med Genet* 1992;42:307–9.
18. Uyan C, Yazici M, Uyan AP et al. Ebstein's anomaly in siblings: an original observation. *Int J Cardovasc Imaging* 2002;18:435–8.
19. Miller MS, Rao PN, Dudovitz RN, Falk RE. Ebstein anomaly and duplication of the distal arm of chromosome 15: report of two patients. *Am J Med Genet* 2005;139:141–5.
20. Andelfinger G, Wright KN, Lee HS et al. Canine tricuspid valve malformation, a model of human Ebstein anomaly, maps to dog chromosome 9. *J Med Genet* 2003;40:320–4.
21. Edwards WD. Embryology and pathologic features of Ebstein's anomaly. *Progr Pediatr Cardiol* 1993;2:5–15.
22. Sipek A. Lithium and Ebstein's anomaly. *Cor Vasa* 1989;31: 149–56.
23. Oosthoek PW, Wenink ACG, Vrojlik BC et al. Development of the atrioventricular valve tension apparatus in the human heart. *Anat Embryol* 1998;198:317–29.
24. Martinez RM, O'Leary PW, Anderson RH. Anatomy and echocardiography of the normal and abnormal tricuspid valve. *Cardiol Young* 2006;16(Suppl. 3):4–11.
25. Radermecker MA, Chauvaud S, Carpentier A. Double-outlet right atrium with restrictive ostium primum and incomplete supravalvular ring presenting as congenital mitral valve stenosis. *J Thorac Cardiovasc Surg* 1995;109:804–5.
26. Snider AR, Serwer GA, Ritter SB (eds). Abnormalities of ventricular inflow. In: *Echocardiography in Pediatric Heart Disease*. Mosby-Year Book Inc, 1997;385–9.
27. Carpentier A, Chauvaud S, Mace L et al. A new reconstructive operation for Ebstein's anomaly of the TV. *J Thorac Cardiovasc Surg* 1988;96:92–101.
28. Shiina A, Seward JB, Edwards WD et al. Two-dimensional echocardiographic spectrum of Ebstein's anomaly: detailed anatomic assessment. *J Am Coll Cardiol* 1984;3:356–70.
29. Ho SY, Rigby M, Anderson RH (eds). Ebstein malformation. In: *Echocardiography in Congenital Heart Disease Made Simple*. Imperial College Press, 2005;214–18.
30. Anderson RH, Silverman NH, Zuberbühler JR. Congenitally unguarded tricuspid orifice: its differentiation from Ebstein's malformation in association with pulmonary atresia and intact ventricular septum. *Pediatr Cardiol* 1990;11:86–90.
31. Freedom RM, Benson LL. Neonatal expression of Ebstein's anomaly. *Prog Pediatr Cardiol* 1993;2:2–27.
32. Fouron JC. Anomalies of the right heart. In: Yagel S, Silverman NH, Gembruch U (eds) *Fetal Cardiology*, 1st edn. London/New York: Martin Dunitz, Taylor & Francis Group, 2003;183–200.
33. Misu Y, Hiraishi S, Oguchi K, Amano K. Successful management of severe tricuspid regurgitation associated with hydrops fetalis in a case of dysplastic TV. *Pediatr Cardiol* 1999; 20:435–7.
34. Daubeney PE, Blackstone EH, Weintraub RG et al. Relationship of the dimension of cardiac structures to body size: an echocardiographic study in normal infants and children. *Cardiol Young* 1999;9:402–10.
35. Perez JE, Ludbrook PA, Ahumada GG. Usefulness of Doppler echocardiography in detecting tricuspid valve stenosis. *Am J Cardiol* 1985;55:601–3.
36. Celermajer D, Cullen S, Sullivan I. Outcome in neonates with Ebstein's anomaly. *J Am Coll Cardiol* 1992;19:1041–6.
37. Eidem BW, Tei C, O'Leary PW et al. Non-geometric quantitative assessment of right and left ventricular function: myocardial performance index in normal children and patients with Ebstein's anomay. *J Am Soc Echocardiogr* 1998;11:849–56.
38. Ammash NM, Warnes CA, Connolly HM et al. Mimics of Ebstein's anomaly. *Am Heart J* 1997;134:508–13.
39. Donnelly WH, Bucciarelli RL, Nelson RM. Ischemic papillary muscle necrosis in stressed newborn infants. *J Pediatr* 1980; 96:295–300.
40. Sreeram GM, Mark JB. Right ventricle, right atrium, tricuspid valve, and pulmonary valve. In: Perrino AC, Reeves ST (eds) *A Practical Approach to Transesophageal Echocardiography*. Philadelphia: Lippincott Williams & Wilkins, 2003;218–32.
41. Hagler DJ. Echocardiographic assessment of Ebstein's anomaly. *Progr Pediatr Cardiol* 1993;2:28–37.
42. Patel V, Nanda NC, Rajdev S et al. Live, real time three-dimensional transthoracic echocardiographic assessment of Ebstein's anomaly. *Echocardiography* 2005;22:847–54.
43. Chauvaud S, Berrebi A, d'Attelis N et al. Ebstein's anomaly: repair based on functional analysis. *Eur J Cardiothorac Surg* 2003;23:525–31.
44. Betrian Blasco P, Gallardo Agromayor E. Ebstein's anomaly and left ventricular noncompaction association. *Int J Cardiol* 2007;119:264–5.
45. Arslan S, Gurlertop HY, Gundogdu F, Senocak H. Left ventricular noncompaction and mid-cavity narrowing associated with Ebstein's anomay: Three-dimensional transthoracic echocardiographic image. *Int J Cardiol* 2007;115:E52–E55.
46. Abrams DJR, Kilner P, Till JA et al. Prolapse of the anterosuperior leaflet of the TV secondary to congenital anomalies of the valvar and sub-valvar apparatus: a rare cause of severe tricuspid regurgitation. *Cardiol Young* 2005;15:417–21.
47. Pavlova M, Fouron JC, Drblik SP et al. Factors affecting the prognosis of Ebstein's anomaly during fetal life. *Am Heart J* 1998;135:1081–5.
48. Uhl HSM. Previously undescribed congenital malformation of the heart: almost total absence of the myocardium of the right ventricle. *Bull Johns Hopkins Hosp* 1952;91:197–205.
49. Azhari N, Assaquat M, Bulbul Z. Succesful repair of Uhl's anomaly. *Cardiol Young* 2002;12:192–5.
50. Randolph GR, Hagler DJ, Connolly H et al. Intraoperative transesophageal echocardiography during surgery for congenital heart defects. *J Thorac Cardiovasc Surg* 2002;124:1176–82.
51. Ho SY, Rigby M, Anderson RH. Straddlng and overriding atrioventricular valves. In: *Echocardiography in Congenital Heart Disease Made Simple*. Imperial College Press, 2005;209.
52. Eberhardt L, Chetaille P, Kreitmann B. A very unusual combination of straddling and overriding of the tricuspid valve

associated with clefting of the mitral valve. *Cardiol Young* 2005; 15:422–4.
53. Lamers WH, Wessels A, Verbeek FJ et al. New findings concerning ventricular septation in the human heart. Implications for maldevelopment. *Circulation* 1992;86:1194–205.
54. Kiraly L, Hubay M, Cook AC et al. Morphologic features of the uniatrial but biventricular connection. *J Thorac Cardiovasc Surg* 2007;133:229–34.
55. Kirklin JW, Baratt Boyes BG. *Cardiac Surgery*. New York: Churchill Livingstone, 1993;811–17.
56. Pesotto R, Padalino M, Rubino M et al. Straddling tricuspid valve as a sign of ventriculoatrial malalignment: A morphometric study of 19 postmortem cases. *Am Heart J* 1999;138:1184–95.
57. Anderson RH. Surgical repair of straddling and overrding valve. *Cardiol Young* 1997;7:122–8.
58. Rice MJ, Seward JB, Edwards WD et al. Straddling atrioventricular valve: two-dimensional echocardiographic diagnosis, classification and surgical implications. *Am J Cardiol* 1985;55: 505–13.
59. Tabry IF, McGoon DC, Danielson GK et al. Surgical management of straddling atrioventricular valve. *J Thorac Cardiovasc Surg* 1979;77:191–201.
60. Sutherland G, Sreeram N. Congenital anomalies of the atrioventricular valves. In: Stümper O, Sutherland GR (eds) *Transesophageal Echocardiography in Congenital Heart Disease*. London: Edward Arnold, 1994;89–106.
61. Smallhorn JF, Tommasini G, McCartney FJ. Detection and assessment of straddling and overriding atrioventricular valves by two dimensional echocardiography. *Br Heart J* 1981;46: 254–62.
62. Reddy VM, Liddicoat JR, McElhinney DB et al. Biventricular repair of lesions with straddling tricuspid valves using techniques of cordal translocation and realignment. *Cardiol Young* 1997;7:147–52.
63. Serraf A, Nakamura T, Lacour-Gayet F et al. Surgical approaches for double-outlet right ventricle or transposition of the great arteries associated with straddling atrioventricular valves. *J Thorac Cardiovasc Surg* 1996;111:527–35.
64. Pacifico AD, Soto B, Bargeron LM. Surgical treatment of straddling tricuspid valves. *Circulation* 1979;60:655–664.
65. Reddy M, McElhinney DB, Silverman NH et al. Partial biventricular repair for complex congenital heart defects: an intermediate option for complicated anatomy or functionally borderline right complex heart. *J Thorac Cardiovasc Surg* 1998; 116:21–7.
66. Chiari H. Ueber Netzbildungen im rechten Vorhofe des Herzens. *Beitr Path Anat* 1897;22:1–10.
67. Pejkovic B, Krajnc I. Anatomical peculiarities of the cavotricuspid isthmus in the human heart. *Wien Klin Wochenschr* 2006;118(Suppl. 2):43–7.
68. Ralston L, Wasdahl W. Chiari's network. *Am J Med* 1958; 25:810–13.
69. Schneider B, Hofmann T, Justen MH, Meinertz T. Chiari's network. Normal anatomic variant or risk factor for arterial embolic events? *J Am Coll Cardiol* 1995;26:203–10.
70. Moreno F, Castro C, Borches D et al. Persistent sinus venosus valve mimicking pulmonary stenosis and atrial tumor. *Ann Thorac Surg* 2006;81:1123–6.
71. Sutherland RD, Stanger P, Climie ARW et al. Large anomalous fibrous sac in the right side of the heart. *Circulation* 1969; 29:837–40.
72. Thomka I, Bendig L, Szente A, Arvay A. Cor triatriatum dextrum simulating right ventricular myxoma and pulmonary stenosis. *Thorac Cardiovasc Surg* 1983;31:114–16.
73. van Ledden-Klok M, de Mol A, Backx A. Symptomatic divided right atrium in a newborn. *Cardiol Young* 2007;17:110.
74. Alkhulaifi AM, Serraf A, Planche C. Ascites and weight loss in a child: due to congenital division of the right atrium. *Cardiol Young* 1999;9:335–7.
75. Hansing CE, Young WP, Rowe GG. Cor triatriatum dexter. Persistent right sinus venosus valve. *Am J Cardiol* 1972;30: 559–64.
76. Gerlis LM, Anderson RH. Cor triatriatum dexter with imperforate Ebstein's anomaly. *Br Heart J* 1976;38:108–11.
77. Bharati S, McAllister HA Jr, Tatooles CJ et al. Anatomic variations in underdeveloped right ventricle related to tricuspid atresia and stenosis. *J Thorac Cardiovasc Surg* 1976;72: 383–400.
78. Schutte DA, Rowland DG, Allen HD, Bharati S. Prominent venous valves in hypoplastic right hearts. *Am Heart J* 1997; 134:527–31.
79. Remmel-Dow DR, Bharati S, Davis JT et al. Hypoplasia of the Eustachian valve and abnormal orientation of the limbus of the foramen ovale in hypoplastic left heart syndrome. *Am Heart J* 1995;130:148–52.
80. Kauffmann S, Anderson DH. Persistent venous valves, maldevelopment of the right heart, and coronary artery–ventricular communications. *Am Heart J* 1963;6:664–9.
81. Pearson AC, Nagelhout D, Castello R et al. Atrial septal aneurysm and stroke: A transesophageal echocardiographic study. *J Am Coll Cardiol* 1991;18:1223–9.
82. Akcaboy MI, Ekici F, Tutar E. Unusually redundant Chiari network. *Pediatr Cardiol* 2006;27:525–6.
83. Lanzarini L, Luca E, Fontana A, Foresti S. Cor triatriatum dextrum resulting from the persistence of embryonic remnants of the right valve of the sinus venosus: prevalence and echocardiographic aspects in a large consecutive non-selected patient population. *Ital Heart J* 2001;2(Suppl.):1209–16.
84. Heydarian M, Siewers RD, Zuberbuhler JR. Persistent right sinus venosus valve producing right ventricular outflow tract obstruction. *Pediatr Cardiol* 1997;18:133–5.
85. Smith NM, Byard RW, Vigneswaran R et al. Parachute-like sinus venosus remnant: echocardiographic and pathological appearance. *Pediatr Cardiol* 1993;14:82–5.
86. Gil DS, Birchley S. Eustachian valve endocarditis. *Echocardiography* 2006;23:256–7.
87. Pellett AA, Kerut EK. Echo rounds. The Chiari network in an echocardiography student. *Echocardiography* 2004;21: 91–3.
88. Trento A, Zuberbuhler JR, Anderson RH et al. Divided right atrium (prominence of the Eustachian and Thebesian valves). *J Thorac Cardiovasc Surg* 1988;96:457–63.
89. Ector J, De Buck S, Adams J et al. Cardiac three-dimensional magnetic resonance imaging and fluoroscopy merging: a new approach for electroanatomic mapping to assist catheter ablation. *Circulation* 2005;112:3769–76.

90. Snider AR, Serwer GA, Ritter SB (eds). The normal echocardiographic examination. In: *Echocardiography in Pediatric Heart Disease*, 2nd edn. Mosby-Year Book, 1997;22–67.
91. Mühler EG, Franke A, Messmer B. Divided right atrium (cor triatriatum dexter) with azygous drainage of the superior caval vein. *Cardiol Young* 1996;6:80–3.
92. Arenas Ramirez J, Fernandez Castro C, Otero Chouza M et al. Persistent and redundant Eustachian valve simulating atrial tumor: prenatal diagnosis. *Ultrasound Obstet Gynecol* 2007;29: 704–7.
93. Clements J, Sobotka-Pojhar M, Exalto N, van Geijn HP. A connective tissue membrane in the right atrium (Chiari network) as a cause of fetal cardiac arrhythmia. *J Obstet Gynecol* 1982;142:709–12.
94. Cujek B, Mycyk T, Khour M. Identification of Chiari's network with transoesophageal echocardiography. *J Am Soc Echocardiogr* 1992;5:96–9.
95. Barriales V, Tamargo JA, Aguado MG et al. Floating thrombi on the Eustachian valve as a complication of venous thromboembolic diseases. *Int J Cardiol* 2004;93:289–91.
96. De Keyser JL, Herregods MC, Dujardin K, Mullens W. The Eustachian valve in pulmonary embolism. rescue or perilous? *Eur J Echocardiogr* 2006;7:336–8.
97. Pellicelli AM, Pino P, Terranova A et al. Eustachian valve endocarditis: a rare localization of right-sided endocarditis. A case report and review of the literature. *Cardiovasc Ultrasound* 2005;3:30.
98. Butera G, Montinaro A, Carminati M. The pull-push technique to deal with a redundant Eustachian valve interfering with placement of a PFO occluder. *Catheter Cardiovasc Interv* 2006; 86:961–4.
99. Yang MW, Wenig ZC, Lin SL, Lin CY. Congenital atrial septal defect with prominent Eustachian valve: contrast echocardiographic study in a child. *J Med Ultrasound* 1996;4:89–91.
100. Savas V, Samyn J, Schreiber TL et al. Cor triatriatum dexter. Recognition and percutaneous transluminal correction. *Cathet Cardiovasc Diagn* 1991;23:183–6.
101. Van Mierop LHS. Pathology and pathogenesis of endocardial cushion defects. Surgical implications. In: Davila JC (ed.) *Second Henry Ford Hospital International Symposium on Cardiac Surgery*. New York: Appleton-Century-Crofts, 1977;201–7.
102. Ahmadi A, Mocellin R, Spillner G, Gildein HP. AVSD with double-outlet right atrium. *Pediatr Cardiol* 1989;10:170–3.
103. Sumner RG, Phillips JH, Jacoby WJ Jr, Trucker DH. Idiopathic enlargement of the right atrium. *Circulation* 1965;32:985–91.
104. Forbes K, Kantoch MJ, Divekar A et al. Management of infants with idiopathic dilatation of the right atrium and atrial tachycardia. *Pediatr Cardiol* 2007;28:289–96.
105. Morishita Y, Kawashima S, Shimokawa S et al. Multiple diverticula of the right atrium. *Am Heart J* 1990;120:1225–7.
106. Brancaccio G, Amodeo A, Rinelli G et al. Double outlet right atrium: anatomic and clinical considerations. *Ann Thorac Surg* 2007;83:619–21.
107. Bailey CP. *Surgery of the Heart.* Philadelphia: Lea & Febiger, 1955;403–20.
108. Binder TM, Rosenhek R, Frank H et al. Congenital malformations of the right atrium and the coronary sinus: an analysis based on 103 cases reported in the literature and two additional cases. *Chest* 2000;117:1740–8.
109. Sajeev CG, Francis J, Sankar V et al. Idiopathic dilatation of right atrium with atrial standstill presenting as stroke. *Echocardiography* 2006;23:50–2.
110. Guaricci AI, Tarantini G, Basso C et al. Images in cardiovascular medicine. Giant aneurysm of the right atrial appendage in a 39-year-old woman. *Circulation* 2007;115:e194–6.
111. Blaysat G, Villain E, Marcon F et al. Prognosis and outcome of idiopathic dilatation of the right atrium in children. A cooperative study of 15 cases. *Arch Mal Coeur Vaiss* 1997;90:645–8.
112. Chatrath R, Turek O, Quivers ES et al. Asymptomatic giant right atrial aneurysm. *Tex Heart Inst J* 2001;28:301–3.
113. Imren Y, Halit V, Kula S, Olgunturk R. Giant right atrial aneurysm: care report. *Int J Cardiol* 2006;112:e66–68.
114. Divekar A, Soni R, Ross D. Rapidly progressive idiopathic dilation of the right atrium in infancy associated with dynamic obstruction of the airways. *Cardiol Young* 2002;12:491–3.
115. Kalangos A, Ouaknine R, Hulin S et al. Pericardial reinforcement after partial atrial resection in idiopathic enlargement of the right atrium. *Ann Thorac Surg* 2001;71:737–8.
116. Mizui S, Mori K, Kuroda Y. Ectopic atrial tachycardia due to aneurysm of the right atrial appendage. *Cardiol Young* 2001; 11:229–32.
117. Rutledge J, Robertson MA, Kantoch M, Dyck J. Idiopathic dilation of the right atrium: case report and survey of the literature. *Can J Cardiol* 1997;13:855–7.
118. Kozelj M, Angelski R, Pavcnik D, Zorman D. Idiopathic enlargement of the right atrium. *Pediatr Cardiol* 1998;19: 420–1.
119. da Silva AM, Witsemburg M, Elzenza N, Stewart P. Idiopathic dilatation of the right atrium diagnosed in utero. *Rev Port Cardiol* 1992;11:161–3.
120. Reinhardt-Owlya L, Sekarski N, Hurni M et al. Idiopathic dilatation of the right atrium simulating Ebstein's anomaly. Apropos of a case diagnosed in utero. *Arch Mal Coeur Vaiss* 1998;91:645–9.
121. Nunez L, Aguado MG, Sanz E, Perez Martinez V. Surgical repair of double-outlet right atrium. *Ann Thorac Surg* 1984; 37:164–6.
122. Perez-Martinez VM, Garcia-Fernandez F, Oliver-Ruiz J, Nunez-Gonzalez L. Double-outlet right atrium with two atrioventricular valves and left atrial outlet atresia. *J Am Coll Cardiol* 1984;3:375–80.
123. Habara M, Fujieda H, Nakamura Y. Images in cardiology. Atrial myocarditis: a possible cause of idiopathic enlargement of bilateral atria. *Heart* 2006;92:842.
124. Radermecker MA, Somerville J, Li W et al. Double orifice right atrioventricular valve in atrioventricular septal defect: morphology and extension of the concept of fusion of leaflets. *Ann Thorac Surg* 2001;71:358–60.
125. Westerman GR, Norton JB, Van Devanter SH. Double-outlet right atrium associated with tetralogy of Fallot and common atrioventricular valve. *J Thorac Cardiovasc Surg* 1986;91:205–7.
126. Isomatsu Y, Kurosawa H, Imai Y. Straddling tricuspid valve without a ventricular septal defect. *Br Heart J* 1989;62:222–4.
127. Suedkamp M, Horst M, Mehlborn U et al. Surgical repair of right-atrial aneurysm. *Thorac Cardiovasc Surg* 2000;48:35–7.

128. Hasdemir C, Gurgun C, Yavuzgil O et al. Giant right atrial diverticulum associated with Wolff–Parkinson–White syndrome. *J Cardiovasc Electrophysiol* 2006;17:443.
129. Kühn A, Schreiber C, Hausleiter J, Vogt M. Giant right atrial aneurysm in a symptomatic adult – a rare congenital malformation. *Eur Heart J* 2006;27:2375.
130. Hager S, Mahrholdt H, Goldfarb LG et al. Giant right atrium in the setting of desmin-related restrictive cardiomyopathy. *Circulation* 2006;113:e53–e55.
131. Alivizatos P, Anderson RH, Macartney FJ et al. AVSD with balanced ventricles and malaligned atrial septum: double-outlet right atrium. Report of two cases. *J Thorac Cardiovasc Surg* 1985;89:295–7.
132. Starc TJ, Bierman FZ, Bowman FO Jr et al. Pulmonary venous obstruction and atrioventricular canal anomalies: role of cor triatriatum and double outlet right atrium. *J Am Coll Cardiol* 1987;9:830–3.

# 14 Mitral Valve and Left Atrial Anomalies

**James C. Nielsen[1] and Sharon E. O'Brien[2]**

[1]Mount Sinai Medical Center, New York, NY, USA
[2]Boston Medical Center, Boston, MA, USA

## Introduction

Anomalies of the mitral valve may involve one or more of its components: the mitral annulus, valve leaflets, chordae tendineae or papillary muscles. Mitral valve anomalies are commonly associated with additional cardiovascular anomalies. This chapter will focus on isolated congenital mitral valve and left atrial anomalies. Acquired mitral stenosis and the "classic" giant left atrium seen with rheumatic heart disease are discussed in Chapter 38. Cor triatriatum, which results from incomplete absorption of the common pulmonary vein, is discussed in Chapter 9.

## Definitions

*Mitral valve prolapse* (MVP) is systolic extension of a leaflet segment beyond the annular plane. Historically, the definition of what constitutes true MVP has varied resulting in diagnostic confusion [1]. Defining MVP as classic or nonclassic forms is supported by adult outcome studies [1,2]. Classic MVP exists when systolic displacement is >2 mm and diastolic leaflet thickness >5 mm; nonclassic MVP exists when the displacement is >2 mm with leaflet thickness <5 mm. Borderline displacement <2 mm is considered a normal variant and is not associated with morbidity or progression [1].

*Cleft mitral valve* is present when the anterior leaflet is cleft (split) into two separate leaflet components, each of which attach to a separate papillary muscle group. *Isolated cleft MV* (ICMV) is a cleft not associated with an ostium primum defect and is the subtype addressed in this chapter. *ICMV* frequently coexists with other congenital heart lesions – the term "isolated" refers only to the lack of an ostium primum defect. *Straddling mitral valve* (SMV) is defined as the presence of chordal attachments on both sides of the ventricular septum, and by definition can only occur in the presence of a ventricular septal defect (VSD) [3–5]. In SMV the anterior leaflet is frequently divided [6], leading to a separate commissure and thus a trileaflet MV; this arrangement, however, is not, strictly speaking, a cleft because chordae tendineae from two separate leaflets join a single (or closely spaced) papillary muscle group(s). It is appropriately termed a commissure. *Double orifice mitral valve* (DOMV) is defined as two separate orifices each supported by its own chordae and papillary muscles. *Congenital mitral stenosis* (MS) is defined as an abnormality at any level of the mitral valve apparatus that results in restriction of diastolic filling. Isolated *congenital giant left atrium* (GLA) is defined as left atrial enlargement out of proportion to the hemodynamic load on the left atrium in the absence of rheumatic heart disease. It is frequently referred to as congenital left atrial aneurysm or left atrial appendage aneurysm [7,8].

## Incidence

Initial reports of MVP prevalence were hindered by selection bias and the lack of a clear definition of prolapse resulting in high prevalence rates of 5–10% [9]. More recent studies in unselected individuals [1,10] report a much lower prevalence of 0.6 to 2.4%. The true incidences of ICMV, DOMV and SMV are yet to be determined [11,12]. Pathologic studies from large congenital cardiac registries have reported ICMV in 41/3369 (1.2%) [12], DOMV in 28/2733 (1.0%) [13] and SMV in 8/2200 (0.4%) [4]. Congenital MS is an equally rare condition that occurs in approximately 0.4% of patients with congenital heart disease [14]. Worldwide, the prevalence of acquired rheumatic mitral stenosis exceeds that of congenital MS; however, in developed nations congenital MS is more common. Congenital GLA is very rare, with less than 10 pediatric cases reported in the literature [7,8,15–19].

## Etiology

In primary classic MVP there is myxomatous degeneration of the valve without an identifiable connective tissue disorder.

*Echocardiography in Pediatric and Congenital Heart Disease: From Fetus to Adult*
Edited by Wyman W. Lai, Luc L. Mertens, Meryl S. Cohen and Tal Geva
 ISBN: 978-1-405-17401-5

Familial inheritance can be present in an autosomal dominant fashion [20]. Secondary MVP is histologically identical to primary, but is present with connective tissue disease (e.g., Marfan or Ehlers–Danlos syndromes). ICMV with normally related great arteries (NRGA) and DOMV have in common abnormal development of the embryonic endocardial cushions and, therefore, can be seen with increased frequency in trisomy 21 [12,13]. The rarity of SMV [4] and its association with other complex anatomic lesions [6] makes it difficult to ascribe a specific etiology to SMV. Similarly, congenital MS typically involves disruption of several components of the valve apparatus, hypoplasia of additional left-sided structures and other complex cardiac lesions, which makes the determination of specific etiology equally challenging. In contrast to idiopathic giant right atrium (see Chapter 13) [21], which is by definition truly "isolated," congenital GLA has most frequently been reported in the setting of some degree of mitral valve disease [22]. The exact etiology of congenital GLA is obscure. Surgical and histological examinations have demonstrated extremely thin atrial wall and fibrosis [8,18,19]. Authors have proposed fetal viral infection or focal developmental error leading to lack of myoblasts and loss of wall integrity [16,17].

## Morphology and classification

### Developmental considerations

The atrioventricular (AV) valve leaflets, chordae tendineae and the myotendinous junction are derived from the endocardial cushions, with some contribution of myocardial cells [23–25]. The complex process of normal morphogenesis of the AV junction and AV valve is under investigation [26,27]. The rarity of SMV, DOMV, ICMV and congenital MS, together with their frequent association with other abnormalities, makes defining their developmental basis extremely challenging. On a basic level the lower aspect of the endocardial cushions, through a poorly understood interaction with myocardial cells, forms freely mobile "mature" leaflets through delamination (detachment) from the myocardial wall, eventually leaving only the chordae tendineae attached to both leaflet and papillary myocardium [26]. How interruption of this process leads to these complex anomalies is yet to be defined. For ICMV it is generally recognized that failure of fusion of the left ventricular aspect of the superior and inferior endocardial cushions results in a cleft in the anterior leaflet [28]. Of note, the portion of the endocardial cushions that participates in the final step of ventricular septation eventually leads to the formation of both the membranous septum and the anterior MV leaflet [26,28], which fits with the anatomic observation (see "Anatomy" below) that the cleft attachments in ICMV with NRGA are always near the membranous septum [12]. SMV in the setting of crossed AV inflows, superior-inferior ventricles and right ventricular (RV) sinus hypoplasia is thought to be related to a post-looping abnormal clockwise rotation (twisting) that brings the infundibular chamber in close proximity to the leftward aspect of the developing AV canal, which allows the MV to straddle into the infundibular chamber [5]. Congenital MS can develop from an abnormality of one or more of the components. The narrowing of the supravalvular area, annulus and valve leaflets often extends distally with additional subvalvar obstruction from hypertrophied or misplaced papillary muscles and abnormal chordae. Four common anatomic subtypes have been described: typical congenital MS, parachute MV, supravalvar mitral ring and hypoplastic MS. The last subtype will be addressed in Chapter 20 [29]. By limiting flow to distal structures during embryologic development, MS may play a role in the hypoplasia or stenosis of downstream structures [30].

### Anatomy

#### Mitral valve prolapse

The MV annulus is nonplanar with a morphology that resembles a "saddle" (Fig. 14.1) [31]. The inferior borders of the annulus (closer to the LV apex) are adjacent to the commissures, with the superior edge of the annulus located approximately 90° orthogonal to this plane (Fig. 14.2). This morphology has been shown to reduce stress on the leaflets [32] and has implications for design of annuloplasty rings [33,34]. In addition, the nonplanar morphology is particularly important to appreciate when imaging and defining what constitutes MVP [2,31]. In a normal MV the leaflet edges are thrust together during ventricular systole, which involves papillary muscle contraction and tensing of the chordae, along a 2–4-mm coaptation zone (zona coapta) at the leaflet tips. MVP results when a leaflet edge slips past this coaptation zone. More significant MVP (classic) usually

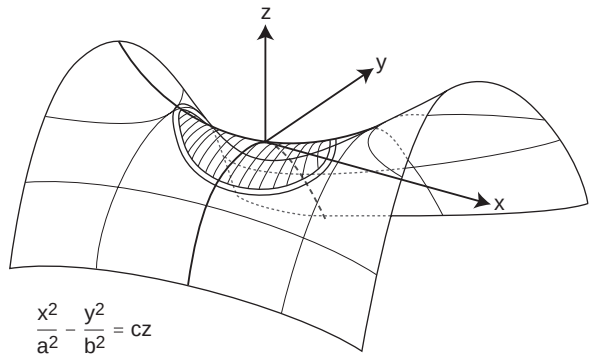


**Figure 14.1** Schematic of an idealized "saddle shaped" surface – hyperbolic paraboloid – which is concave downward in one direction (parallel to the *yz* plane) and upward in a perpendicular direction (parallel to the *xz* plane). The symbols *a*, *b* and *c* denote constants that determine the shape of the structure. Reproduced with permission from Levine RA, Triulzi MO, Harrigan P, Weyman AE. The relationship of mitral annular shape to the diagnosis of mitral valve prolapse. *Circulation* 1987;75(4):756–67.

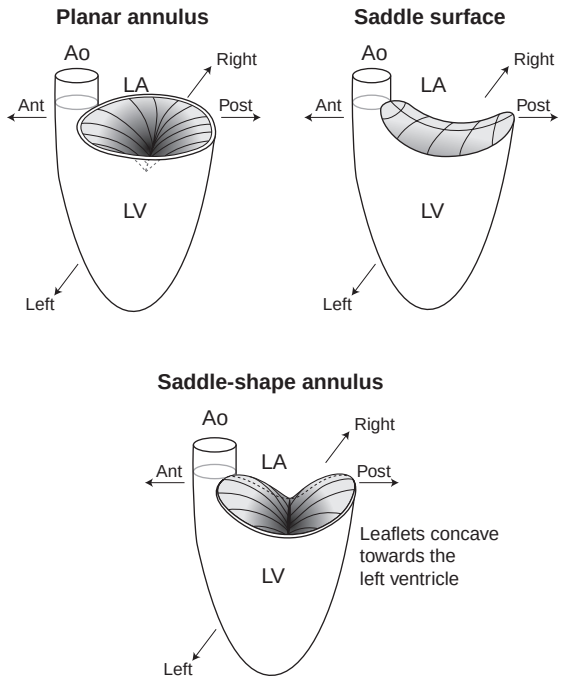


**Figure 14.2 Top left:** Diagram of the model in vitro with a planar annulus and leaflets curving downward toward the zone of coaptation. Adjacent cardiac structures are also diagrammed. Ant., anterior; Ao, aorta; LA, left atrium; LV, left ventricle; Post., posterior. Top right: Diagram of the model in vitro with the leaflets and annulus shaped to lie on a saddle surface. Bottom: The model restructured with leaflets concave toward the left ventricle, reflecting its systolic pressure, but not protruding above the anterior and posterior high points of the saddle-shaped annulus. Reproduced with permission from Levine RA, Triulzi MO, Harrigan P, Weyman AE. The relationship of mitral annular shape to the diagnosis of mitral valve prolapse. *Circulation* 1987;75(4):756–67.

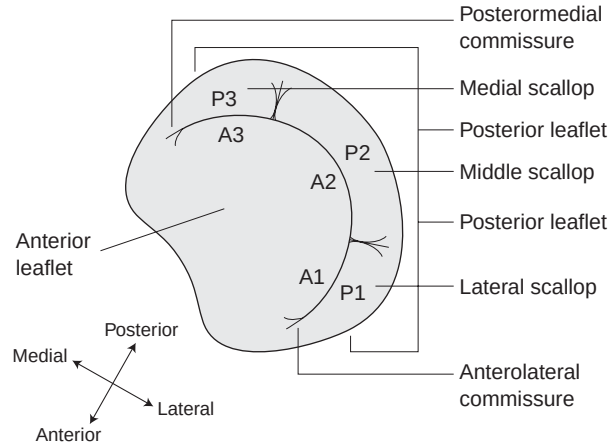


**Figure 14.3** Nomenclature used to describe the anatomy of the mitral valve leaflet segments and commissures (surgical view from the left atrium). A1, lateral segment; A2, middle segment; A3, medial segment; P1, lateral scallop; P2, middle scallop; P3, medial scallop. Reproduced from Shanewise JS, Cheung AT, Aronson S et al. ASE/SCA guidelines for performing a comprehensive intraoperative multiplane transesophageal echocardiography examination: recommendations of the American Society of Echocardiography Council for Intraoperative Echocardiography and the Society of Cardiovascular Anesthesiologists Task Force for Certification in Perioperative Transesophageal Echocardiography. *J Am Soc Echocardiogr* 1999 Oct;12(10):884–900, with permission from Elsevier.

results from excessive leaflet tissue (redundancy), myxomatous proliferation of the spongiosa and elongation of the chordal apparatus [35]. These abnormalities lead to a more fundamental failure of MV function, significant prolapse, mitral regurgitation (MR) and rarely chordal rupture.

A standard nomenclature of leaflet segments provides consistency when describing the location of isolated prolapsing segments (Fig. 14.3). Posterior and bileaflet prolapse are more common than anterior, with an incidence of 52% and 33%, respectively, versus 15% reported with a large adult surgical series on isolated MVP [36].

## Isolated cleft mitral valve

By definition, this exists without an ostium primum defect. Within this definition, there are two separate categories, which were characterized in a large anatomic investigation [12]. When ICMV coexists with an abnormal conotruncus the cleft attachments are to the subarterial left ventricular (LV) myocardium, in a more vertical location. This morphology is important to define and recognize because it can lead to LV outflow tract obstruction [12,37,38]. In addition, ICMV with an abnormal conotruncus is notable for having no features similar to AV canal defects – namely a normal ventricular inlet/outlet ratio [39] and no association with trisomy 21. This differs from the ICMV with normally related great arteries (NRGA) subgroup, where the cleft attachments are more horizontal to the ventricular septum. In ICMV with NRGA, trisomy 21 is more frequent and a reduced inlet/outlet ratio is present [12,40]. Prior to this insight there had been debate about whether ICMV was related in some manner to AV canal defects [41–43]. To sort this out, investigators had examined the location of the cleft attachments, papillary muscle location and inlet/outlet ratio, producing different conclusions [38–44]. The recognition of two distinct groups – NRGA and abnormal conotruncus – was key to explaining the vertical location of the cleft attachment [12]. In ICMV with NRGA the cleft attachments are to the membranous septum (when intact) or to the crest of the ventricular septum when a VSD is present. Functionally, the attachment appears to "migrate" superiorly when the membranous septum is intact resulting in a cleft location that is in between horizontal and vertical.

## Straddling mitral valve

MV chordal attachments in the right ventricle constitutes SMV. This lesion is always associated with a VSD and an abnormal conotruncus, either double outlet right ventricle

(DORV) or transposition of the great arteries (TGA) [6]. Straddling is across the anterior (outlet) aspect of the septum and differs from a straddling tricuspid valve, which crosses the inlet septum [45]. The attachments of a SMV are to a single papillary muscle or closely spaced papillary muscle groups within the infundibulum to either the conal septum, septal band or the free wall, and can involve the anterior leaflet or both MV leaflets. When SMV is present in the setting of {S,D,L} or {S,L,D} segmental sets there are invariably crossed AV valve inflows, superior-inferior ventricles and hypoplasia of the RV sinus [5]. Major straddling occurs when greater than one-half of the MV is related to the infundibulum. Typically the MV orifice is adequately sized and rarely more than mildly incompetent. In addition, outflow obstruction from the attachments is rare, with risk factors for survival related to the presence of multiple or noncommitted (remote) ventricular septal defects [37].

### Double-orifice mitral valve

In its most frequent form this exists with two discrete orifices each with its own chordal support and papillary muscles. The orifices are frequently divided by a "fibrous ridge," which is actually normal MV leaflet tissue separating the orifices [46,47]. This separation can either be limited to the tips of the respective orifices, sparing the more basal aspects, or extend along the entire length of the leaflets [47]. Another much less common anatomic variation is a muscular separation of the orifices associated with papillary muscle abnormality [13]. The size of the papillary muscles varies directly with the size of the orifice that they subtend. At one end of the spectrum is a tiny anterolateral orifice (chordal ring) without papillary support inserting directly into the LV wall. More typically, the valves are relatively equal in size. When DOMV is present with an AV canal defect it is often characterized by a smaller posteromedial orifice.

### Mitral stenosis

Typical congenital MS involves thickened and rolled leaflets, shortened chordae tendineae with absence of the interchordal spaces, and underdeveloped papillary muscles, which may be closely spaced [29]. Typical MS has also been termed "symmetric" [48], implying equal distribution of chordae to each papillary muscle and equal papillary muscle size. Asymmetric papillary muscle location, size and distribution of chordal attachments is common (found in approximately 30% of a large cross-sectional study) [49], and in the extreme results in a true parachute MV [50] with all chordae inserting into a single papillary muscle – typically the anterolateral papillary muscle is absent [29,50]. Congenital MS is strongly associated with obstructive left-sided lesions including pulmonary vein stenosis, supravalvar and valvar aortic stenosis, parachute mitral valve, supravalvar mitral ring, subaortic membrane and coarctation of the aorta – the last four lesions together were originally described by Shone et al. [14]. Supravalvar mitral ring is an important subtype of MS characterized by a membranous tissue growth from the left atrial side of the mitral leaflets that results in a variable degree of stenosis. This lesion can be progressive and is optimally treated surgically [48, 49].

### Congenital giant left atrium

The morphology of congenital GLA is fairly consistent [7,8,51], with a globally enlarged left atrial cavity and more focal aneurysmal enlargement of the atrial wall adjacent to the appendage. Typically the atrial cavity extends apically along the anterior and lateral left ventricular wall (Fig. 14.4). The mass effect can lead to compression of the left ventricular free wall, right atrium and adjacent thoracic structures, including the esophagus, left bronchus and recurrent laryngeal nerve.

## Pathophysiology

The pathophysiology associated with either abnormal MV development (cleft, straddling, parachute or double orifice) or abnormal MV apparatus function (MVP) is predominantly

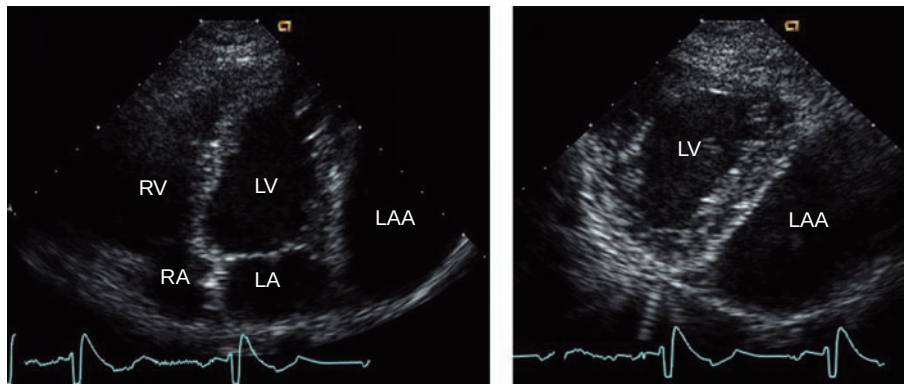


**Figure 14.4** **(a)** Systolic frame from an apical view of a congenital giant left atrium. Note the extension of the grossly enlarged left atrium leftward and laterally extending toward the cardiac apex. **(b)** Parasternal short-axis view demonstrating the enlarged left atrium compressing the left ventricular free wall. RV, right ventricle; RA, right atrium; LV, left ventricle; LA, left atrium; LAA, left atrial aneurysm. Reproduced with permission from Park JS, Lee DH, Han SS et al. Incidentally found, growing congenital aneurysm of the left atrium. *J Korean Med Sci* 2003;18:262–6.

a function of the competence of the valve (regurgitation) and the adequacy of the flow orifice (stenosis). An additional factor specific to ICMV with abnormal conotruncus and SMV is the location of the attachments relative to the potential pathway from LV to the outflow and whether this pathway is adequate for a biventricular repair [37,52,53].

Chronic MR can develop in classic MVP and in general is well tolerated with minimal symptoms. The indications for surgical MV plasty are related to the exact mechanism and location of prolapse, the integrity of the MV apparatus, the degree of MR, age and the LV size. Preservation of long-term LV function is the rationale behind early surgical intervention [36]. Acute chordal or papillary muscle rupture, resulting in a flailed leaflet, and acute MR is poorly tolerated, producing acute left atrial and pulmonary artery hypertension. In general, flail involving the posterior leaflet is more amenable to surgical repair.

Isolated cleft mitral valve frequently results in MR due to the lack of adequate coaptation zone along the cleft. The outcome following plasty, which basically involves suture plasty of the cleft to improve coaptation, is a trade-off between better coaptation and adequacy of the flow orifice with good mid-term outcomes [54,55].

Double orifice mitral valve without associated lesions occurs rarely (7% of all DOMV cases) [46], which is likely an underestimate because when DOMV is present in isolation, the valve typically is functioning well and is clinically silent. The pathophysiology is generally not related to the dysfunction of the DOMV, but rather the morbidity of the associated lesions – frequently AV canal defects, stenosis of the aggregate flow orifice or obstructive left-sided lesions [13,46]. In DOMV with an AV canal defect, if regurgitation is present the posteromedial orifice is frequently the culprit. Significant mitral stenosis of a DOMV is often present and is amenable to balloon valvuloplasty in selected patients [49].

The hemodynamic burden of mitral stenosis, and therefore symptoms, depends upon the flow orifice size and the cardiac output. As heart rate increases, diastole is shortened more than systole and the mean gradient across the valve increases, even at a fixed cardiac output. To maintain a given cardiac output a greater mean pressure gradient is required. For severe stenosis a small increase in flow rate necessitates a large increase in the pressure gradient [56]. The elevated left atrial pressure results in left atrial dilation, elevated pulmonary venous pressures, pulmonary edema and dyspnea. Pulmonary hypertension in moderate or severe MS is secondary to transmission of pressure to the pulmonary bed, reactive vasoconstriction and vessel wall changes [57]. Severe pulmonary hypertension can in turn lead to right ventricular dysfunction and tricuspid regurgitation. Left atrial dilation is a powerful substrate for atrial fibrillation, which increases the risk of thromboembolic events.

## Imaging

### Goals of the examination

The goals of echocardiographic examination in the setting of mitral valve anomalies can be summarized as follows:

- Assessment of mitral valve apparatus morphology and function, including:
  - the integrity of chordal and leaflet support structures;
  - length of the chordae;
  - chordal attachments and papillary muscle – location and number;
  - careful definition of the annular plane;
  - identification of MVP;
  - localization of the prolapsing leaflet segment (Fig. 14.3);
  - identification of MV cleft attachment location;
  - identification of SMV – major versus minor;
  - identification of associated conotruncal and atrioventricular canal lesions;
  - feasibility of biventricular repair by visualizing the pathway from LV to outflow as it relates to the ICMV or SMV attachments.
- Full interrogation of all MR jets:
  - localize the regurgitation orifice;
  - assess the degree of MR using multiple methods to overcome limitations of each:
    - color flow mapping (spatial distribution);
    - width of the jet at the vena contracta;
    - continuous-wave Doppler with analysis of the spectral pattern;
    - pulse-wave spectral Doppler of pulmonary veins;
    - consider quantification of the regurgitant volume.
- Anatomic and hemodynamic assessment of the MV flow orifice:
  - annulus size – dimensions in two orthogonal planes;
  - assessment of anatomic flow orifice by two-dimensional (2D) imaging;
  - recognize physiology that leads to reduced orifice flow – ASD and/or reduced cardiac output;
  - doppler interrogation.
- Left atrial size
- Left ventricular size
- Estimation of right ventricular pressure by tricuspid regurgitation jet and/or by ventricular septal configuration
- Ventricular function

As the above goals highlight, imaging of the MV is an involved process, which is best accomplished within the framework of a normal thorough congenital examination utilizing slow sweeps of the cardiac anatomy from multiple acoustic windows. Imaging tips specific to each lesion and the details of the hemodynamic assessment of stenosis are discussed below.

### Mitral valve prolapse (MVP)

In its more subtle form, this can be erroneously missed, or diagnosed when not present. This is mainly due to failure to

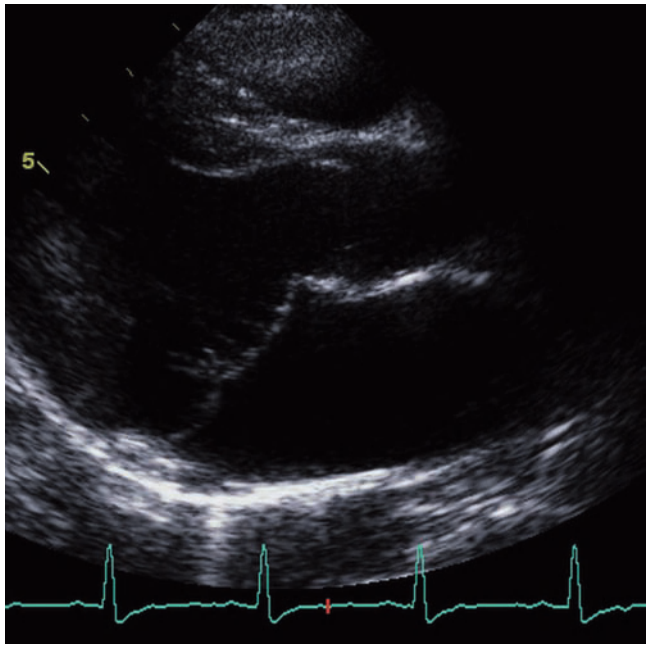

**Figure 14.5** Systolic frame from a standard parasternal long-axis view showing mild mitral valve prolapse. Note the displacement of both the anterior and posterior leaflets beyond the annular plane (Videoclip 14.1).

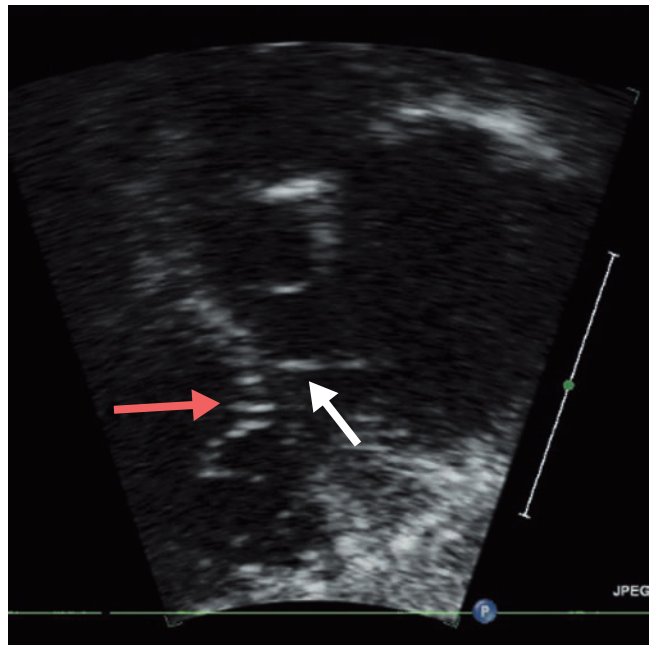

**Figure 14.6** Systolic frame from a modified short-axis view obtained from a subxiphoid window profiling an isolated cleft of the mitral valve in a young child. From the subxiphoid window the chordae of the cleft (white arrow) are perpendicular to the plane of interrogation, which provides better visualization compared with the parasternal short-axis window. Note the characteristic location of the attachments near the membranous septum – which is marked by the anteroseptal commissure of the tricuspid valve (arrow) Videoclip 14.2).

account for the nonplanar anatomy of the annulus [31]. The leaflets of a normal MV move beyond the annular level in standard two- and four-chamber views where the annular edge extends more inferiorly (closer to the LV apex) and can be mistaken for MVP; therefore MVP should be diagnosed from ventricular long-axis views (Fig. 14.5; Videoclip 14.1). Isolated MVP of the posterior leaflet is best seen from long-axis views (P2) and two-chamber views (P1 and P3). Isolated posterior leaflet prolapse is particularly important to recognize because the outcome of surgical plasty is excellent [36], which may alter the threshold for recommending repair.

### Isolated cleft mitral valve with NRGA

Visualization of the cleft attachments is best from a subxiphoid short-axis view (Fig. 14.6; Videoclip 14.2). ICMV with an abnormal conotruncus has more vertically positioned cleft attachments near the LV outflow. Examination of ICMV is focused on determining if outflow tract obstruction is present and if the cleft interferes with the potential pathway from the LV to the great artery (either aorta or pulmonary); it is best accomplished from modified subxiphoid windows (Fig. 14.7) that profile each respective structure of interest. One often needs to rotate the transducer from standard long- and short-axis views to visualize these pathways better [6]. In addition, sweeping this anatomy once the modified view is found is crucial to understanding the adequacy of the pathway and degree of potential outflow obstruction.

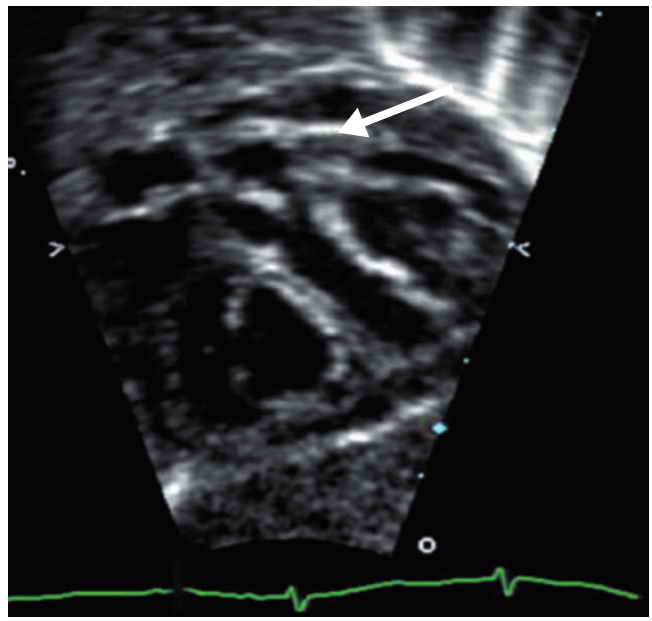

**Figure 14.7** Diastolic frame from a modified view obtained from a subxiphoid window profiling an isolated cleft of the mitral valve (ICMV) in an infant with D-transposition of the great arteries {S,D,D}. Note the vertical orientation (arrow) of the cleft attachments, typical for ICMV with transposition or double-outlet right ventricle (see text). The cleft attaches to the leftward aspect of the left ventricular outflow.

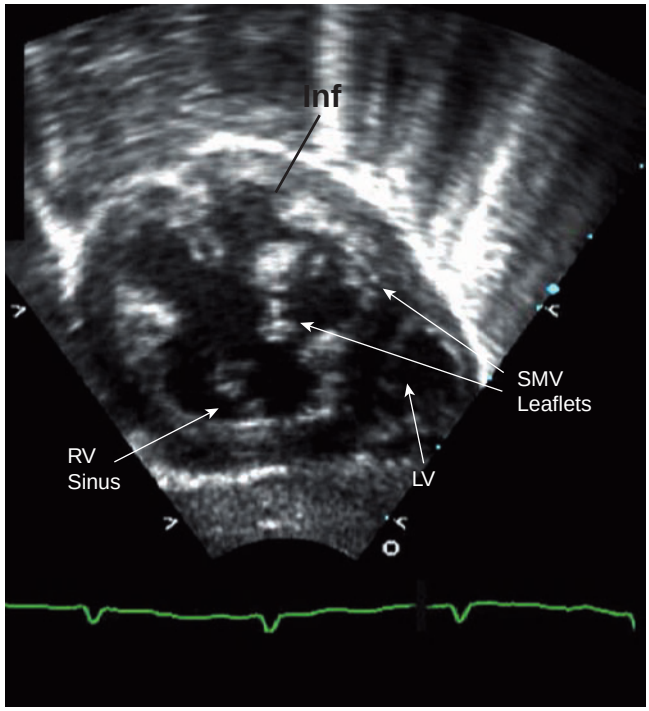


**Figure 14.8** Diastolic frame from a modified long-axis view obtained from a subxiphoid window profiling major straddling of the mitral valve in an infant with double-outlet right ventricle (DORV) {S,D,D}. Note the commissure of the straddling valve with attachments within the infundibulum and the marked degree of straddling that would preclude biventricular repair. Inf, infundibulum; RV, right ventricular; LV, left ventricle; SMV, straddling mitral valve.

## Straddling mitral valve

Imaging is focused on first identifying major straddling (Figs 14.8 and 14.9; Videoclip 14.3), which usually precludes biventricular repair. When straddling is minor, similar to ICMV, standard and modified subxiphoid views provide visualization of the straddling chordae and papillary muscles, their exact attachment location and the feasibility of VSD closure or baffle repair. Parasternal imaging provides enhanced visualization of the chordal attachments within the infundibulum (free wall, septal band or conal septum) in SMV or within the LV outflow in ICMV (Fig. 14.10).

## Double-orifice mitral valve

This is best visualized from an apical view, rotating the transducer counterclockwise to image each orifice in its long-axis plane. Standard short-axis views from either parasternal or subxiphoid windows (Fig. 14.11; Videoclip 14.4) provide imaging of the double orifice en face, and sweeping the MV in this plane defines the extent of the fibrous ridge, the adequacy of each orifice and competency of the valve [47].

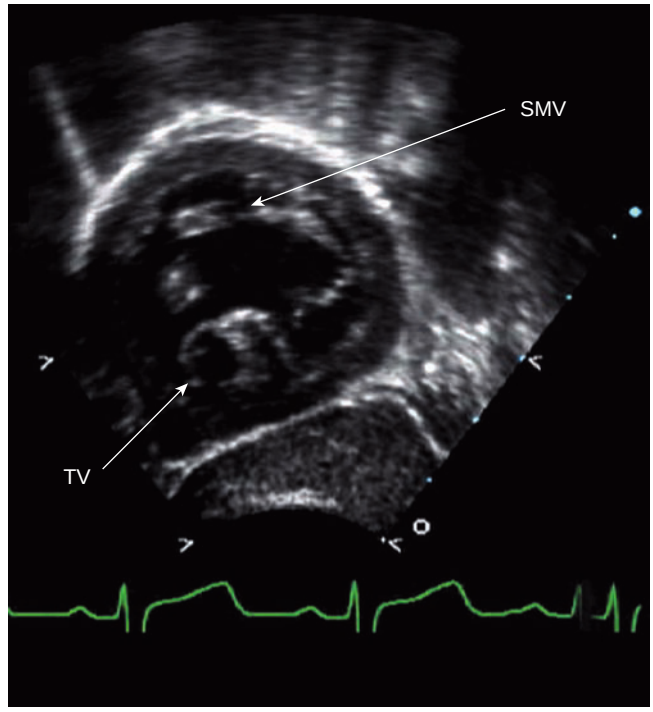


(a)

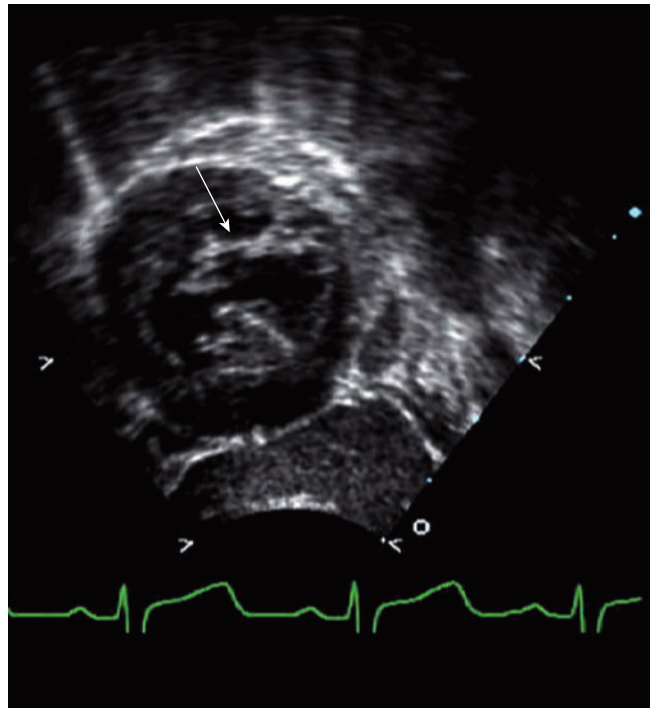

(b)

**Figure 14.9** Diastolic **(a)** and systolic **(b)** frames from a modified short-axis view obtained from a subxiphoid window profiling major straddling of the mitral valve (SMV) in an infant with transposition of the great arteries (TGA) {S,D,D} pulmonary stenosis. Note the inferiorly positioned tricuspid valve (TV) inflow and the straddling via the anterior (outflow) aspect of the ventricular septum. The systolic frame (b) shows the coapting commissure (arrow) of the straddling valve. (Videoclip 14.3).

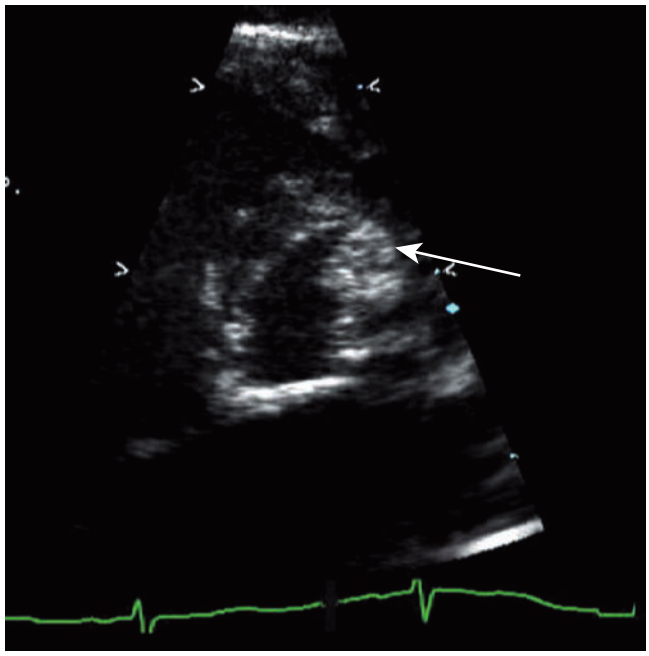

**Figure 14.10** Systolic frame from a standard short-axis plane profiling the exact location (arrow) of the cleft attachments to the leftward aspect of the left ventricular outflow tract in the same infant as shown in Fig. 14.9 with D-transposition of the great arteries {S,D,D} and isolated cleft of the mitral valve.

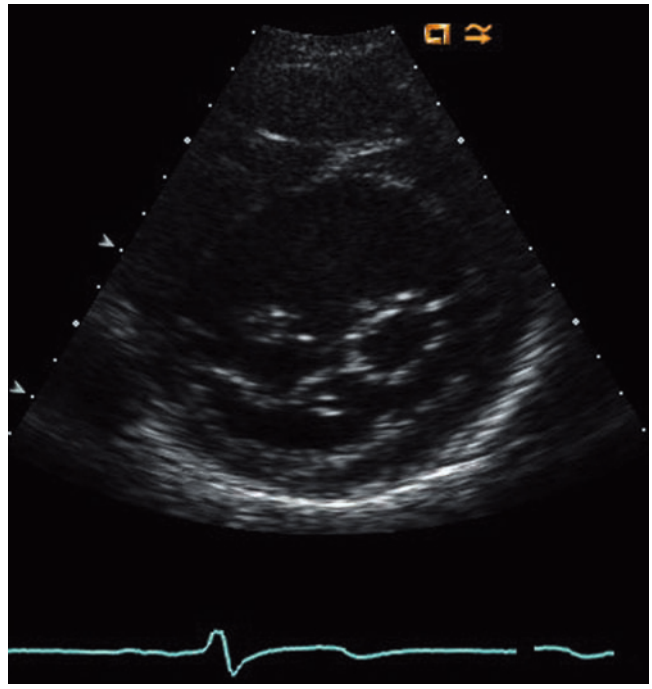

**Figure 14.11** Diastolic frame from a parasternal short-axis plane demonstrating a double-orifice mitral valve. Note the equal size of each orifice and their location above their respective papillary muscle groups. (Videoclip 14.4).

### Supravalvar mitral ring

This is a challenging lesion to image [58] and requires a high index of suspicion and diligence on the part of the imager. One should suspect this lesion in the setting of congenital MS with an increasing degree of stenosis over time. The membrane is thin and adherent to the atrial side of the leaflet with frequently only its edge visible. The four-chamber apical views provide an interrogation angle perpendicular to the membrane, thereby enhancing visualization. Careful sweeps utilizing appropriate gain and compression settings, transducer selection and targeted magnification of the leaflets is key (Fig. 14.12; Videoclip 14.5(a,b)). Any uncertainty about the presence or absence of this diagnosis following a thorough transthoracic examination should prompt a transesophageal echocardiogram (Fig. 14.13).

### Typical congenital MS and parachute mitral valves

These are best imaged in the apical (Fig. 14.14; Videoclip 14.6), and ventricular long- and short-axis planes. The subxiphoid window in infants and younger children typically gives a higher yield than the parasternal window. Slow, targeted sweeps of the mitral apparatus utilizing magnification mode provide optimal visualization to differentiate subtypes of mitral stenosis (Fig. 14.15; Videoclip 14.7(a,b)).

### Congenital giant left atrium

Imaging is focused on assessing the overall size of the left atrium, distortion of other cardiac structures including the atrial septum and ventricular septum, and narrowing of the inferior vena cava (IVC) or superior vena cava (SVC). The left atrial size is best assessed from the apical four-chamber view. It is important to image the full extent of the left atrial cavity with slow sweeps. Measurements of size should be performed in similar imaging planes for a given patient to limit intertest variability. The morphology and function of the mitral and aortic valves should be thoroughly examined given the frequent association with rheumatic heart disease.

### Mitral stenosis – flow orifice assessment

In general, the challenge of defining and grading the degree of stenosis is a significant one that is best addressed utilizing all available clinical (signs and symptoms), hemodynamic and imaging data. Similar to other congenital lesions, a single (or multiple combined) echocardiographic parameter(s) that accurately characterize(s) the degree of stenosis does not exist. Flow orifice area (valve area) is the best available measure of stenosis. In many types of congenital MS, however, defining the minimal flow orifice is not possible due to the complex anatomy of the flow orifice, which is often not the mitral valve annulus [29]. This is particularly true of lesions addressed in this chapter – MS that is not associated with annular hypoplasia. Nevertheless, annular dimensions appropriately adjusted for body surface area (see Chapter 5)

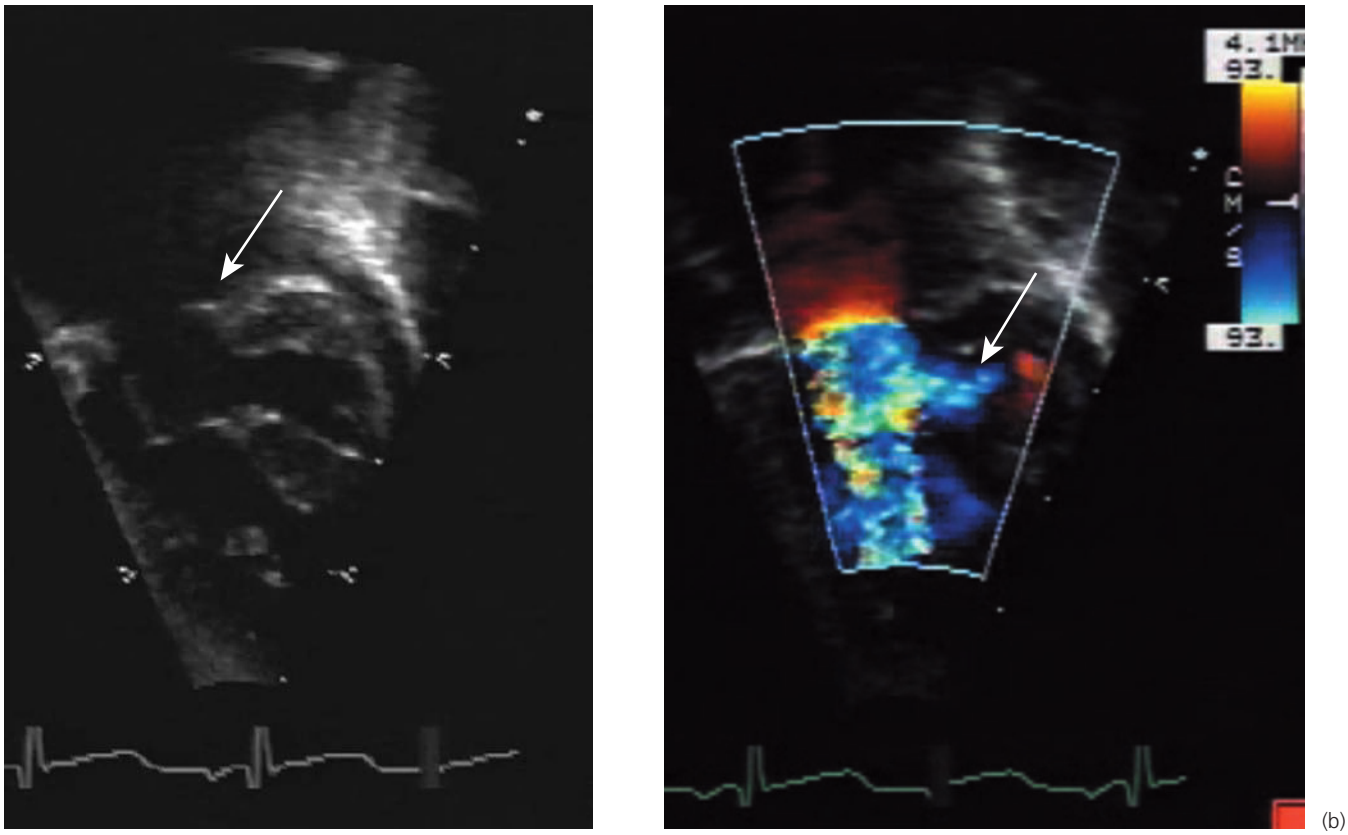


(a) (b)

**Figure 14.12** **(a)** Diastolic frame from an apical window demonstrating congenital mitral stenosis and a supravalvar mitral ring (SVMR). Note the prominent papillary muscle that extends further toward the annulus than in a normal apparatus, the accompanying shortened chordae and hypoplasia of the annulus. The membranous SVMR (arrow) is seen as a thin projection from the atrial side of the leaflet, extending from the annulus into the supravalvar flow orifice. **(b)** Color Doppler in the same imaging plane demonstrating flow acceleration beginning just prior to the annulus – a characteristic finding in SVMR. When present this should prompt the imager to undertake an extensive search for an unrecognized SVMR. Note the additional egress from the inflow (arrow) directed laterally via an abnormal intrachordal space. This type of complex inflow orifice makes accurate measurement of the flow orifice area particularly challenging (see text). (Videoclip 14.5(a,b)).

and expressed as a z-score have been shown to predict outcome [59] and should be obtained using magnified diastolic frames from the apical four-chamber (lateral dimension) and parasternal long-axis views (antero-posterior dimension). Calculation of the mitral valve area using planimetry is a well-established technique in adults [60,61] and has shown good agreement with anatomic measurements from explanted intact mitral valves [62]. The valve is imaged in the parasternal short-axis view and the maximal orifice is planimetered to calculate the area; again, indexing to body surface area is critical. It is crucial that careful attention is given to the acoustic window that profiles the mitral inflow cone in its short axis, which may be off-angle relative to the left ventricular short axis, and then defining the smallest flow orifice with careful sweeping. Figure 14.16 demonstrates the potential limitations of this technique in congenital MS. Although three-dimensional (3D)-echocardiography promises better definition of the minimal flow orifice [63] in adults and older children, the underlying complex anatomy and the high heart rates of infants challenge the spatial and temporal resolution of current 3D technology.

Surrogate parameters to flow orifice area can be divided into two main categories:

**1** those based on the continuity principle (flow orifices in continuity with one another must handle equal total flow in a given short time interval) – this includes Doppler-derived continuity equation and flow convergence zone analysis (proximal isovelocity surface area; see Chapter 6);

**2** the pressure response to flow across a narrowed orifice – which includes Doppler-obtained pressure gradient and pressure half-time (PHT).

Both categories require obtaining an accurate instantaneous peak velocity by continuous-wave spectral Doppler. Proper alignment of the range-gated Doppler beam (cursor) with the MV inflow is the first step accurately to characterize the velocity. This is achieved by interrogation of the mitral valve flow orifice from an acoustic window that provides adequate spectral Doppler signal at the optimal angle of interrogation;

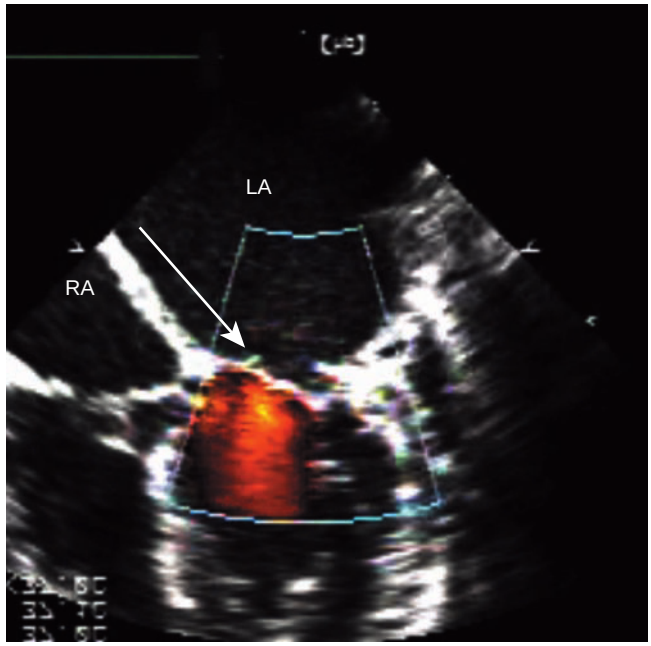


**Figure 14.13** Systolic frame from a transesophageal echocardiogram (TEE), mid-esophageal four-chamber view in the same patient as seen in Fig. 14.12. Note the enhanced visualization of the supravalvar mitral ring provided by TEE. The membrane is now conspicuous, extending from both the lateral aspect of the atrial side of the leaflet and the medial aspect (arrow).

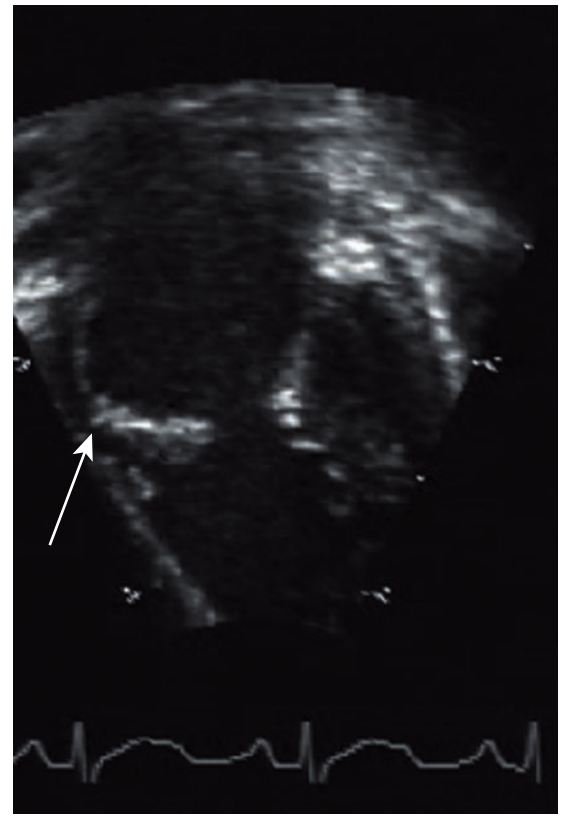

(b)

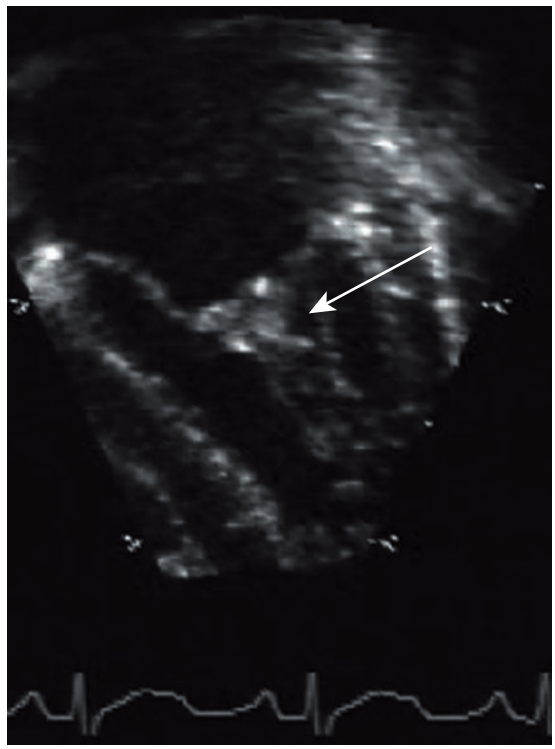

(a)

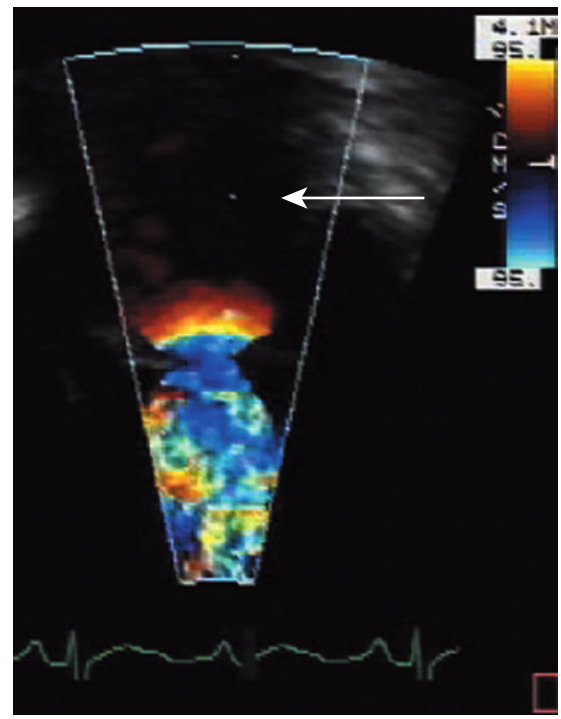

(c)

**Figure 14.14** **(a)** A late-systolic frame in typical congenital mitral stenosis from an apical four-chamber view. Note the thickened and short chordae (arrow). **(b)** An early diastolic frame – note the rolled and thickened leaflet tips, the reduced orifice size and doming of the middle aspect of the anterior leaflet (arrow). **(c)** Color Doppler with flow acceleration in the distal aspect of the inflow (arrow indicates the annulus level). Note the proximal isovelocity surface area (PISA) aliased lines representing increasing velocity "shells" as the flow approaches the small orifice.

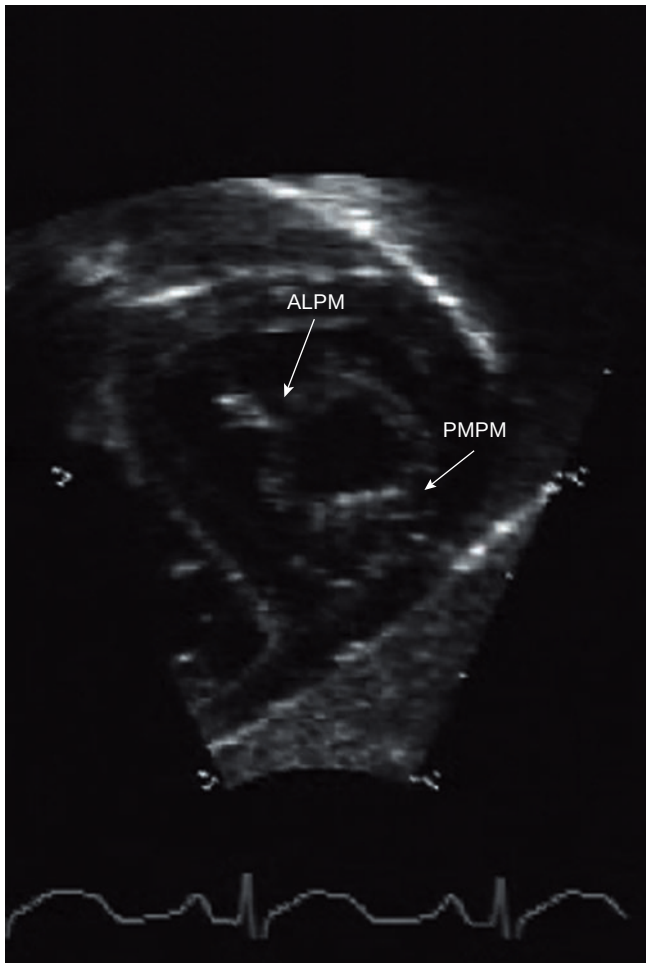


(a)

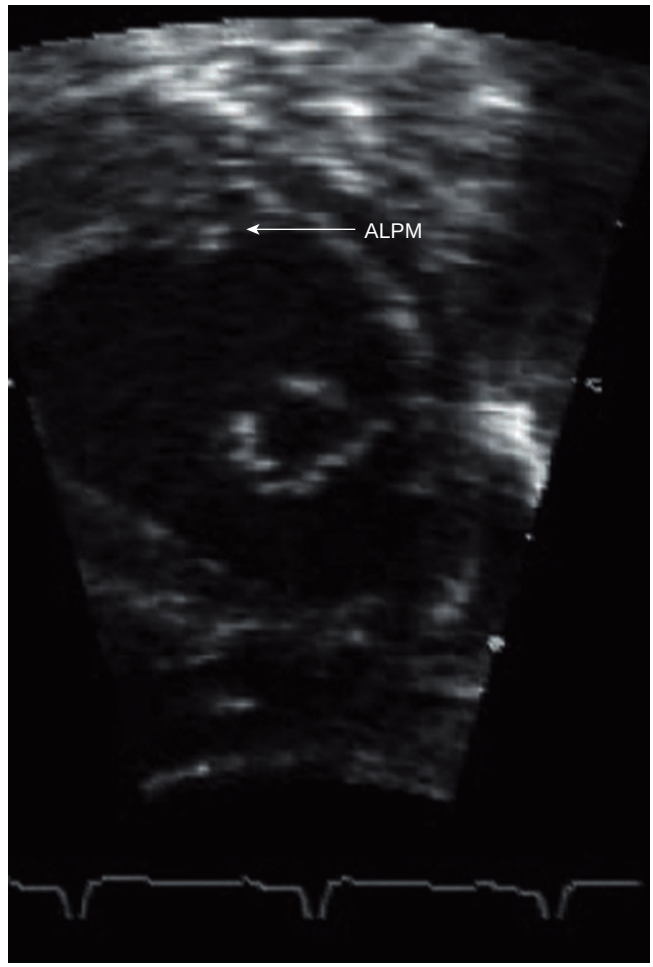


(b)

**Figure 14.15 (a)** Diastolic frame short-axis plane from a subxiphoid window in typical congenital mitral stenosis. Note separate well-spaced papillary muscle groups (arrows). **(b)** Diastolic frame, short-axis plane from a subxiphoid window demonstrating a parachute mitral valve. Note the presence of a hypoplastic anterolateral papillary muscle (arrow) that receives no chordae, which is the most common arrangement in the parachute lesion (see text). ALPM, anterolateral papillary muscle group; PMPM, posteromedial papillary muscle group.

this acoustic window is optimal for Doppler interrogation, and may be different than the optimal acoustic window for 2D visualization of anatomy and measurement of structures. Typically, this is a modified apical window, but restricting oneself to a standard view is a mistake that can lead to a misrepresentation of the gradient.

The mean MV gradient is a useful surrogate to mitral valve area [64,65]. It is obtainable in most patients, even in those with poor acoustic windows. When compared with simultaneous catheterization, the mean Doppler gradient shows good agreement [66], with a mean difference of 0.2 ± 1.2 mm Hg. As detailed previously, the dependence of gradient on cardiac output is strong and explains why nonsimultaneous comparison with invasive gradient yields poor agreement, both in large studies of adult subjects [67] and in smaller pediatric cohorts [48,49,68]. Recording the heart rate as a measure of cardiac output is useful for serial comparison. The presence of less than a full systemic cardiac output (ASD or low cardiac output state) needs to be recognized when using flow-based measures of mitral stenosis. Limited published data exist on what level of gradient constitutes significant stenosis. A mean gradient >3 mm Hg [59] or peak >12 mm Hg [48] has been used as the definition of significant mitral stenosis in native valves; and a peak >19 mm Hg as severe MS following MV replacement [69].

Doppler-derived pressure half-time (PHT) is based on the principle that the rate of pressure gradient decline varies with the degree of obstruction. With increasing obstruction the pressure gradient across the valve is maintained for a longer time. The PHT is the time needed for the initial peak pressure gradient to decrease by half. The relationship proposed by Hatle et al. [70] is MV area ($cm^2$) = 220/PHT (ms). The constant 220 is empirically derived based on adults using the Gorlin [71,72] method of value area as the reference standard. Many studies in adults have examined this correlation [61]; however, only one investigation utilized the more

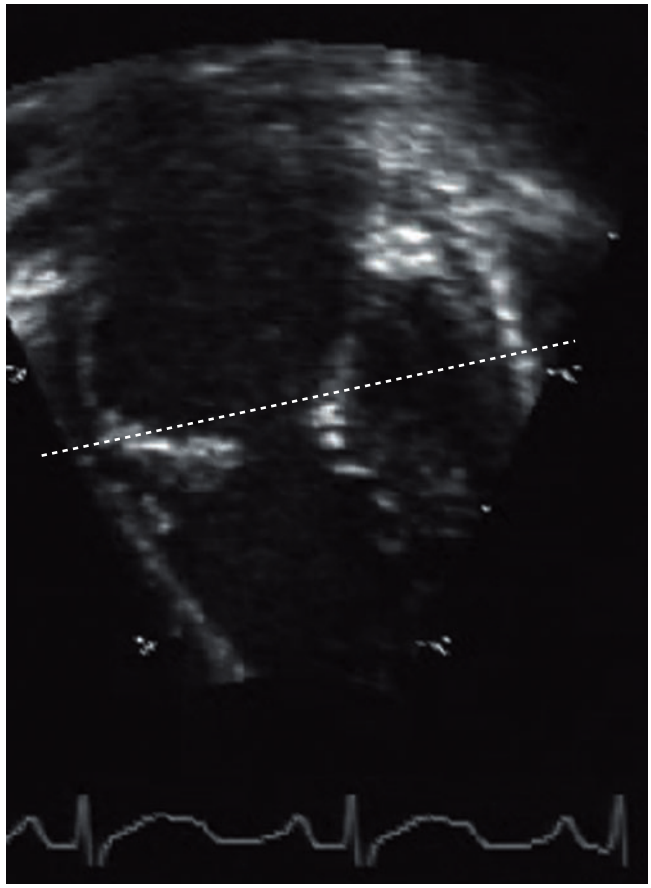

(a)

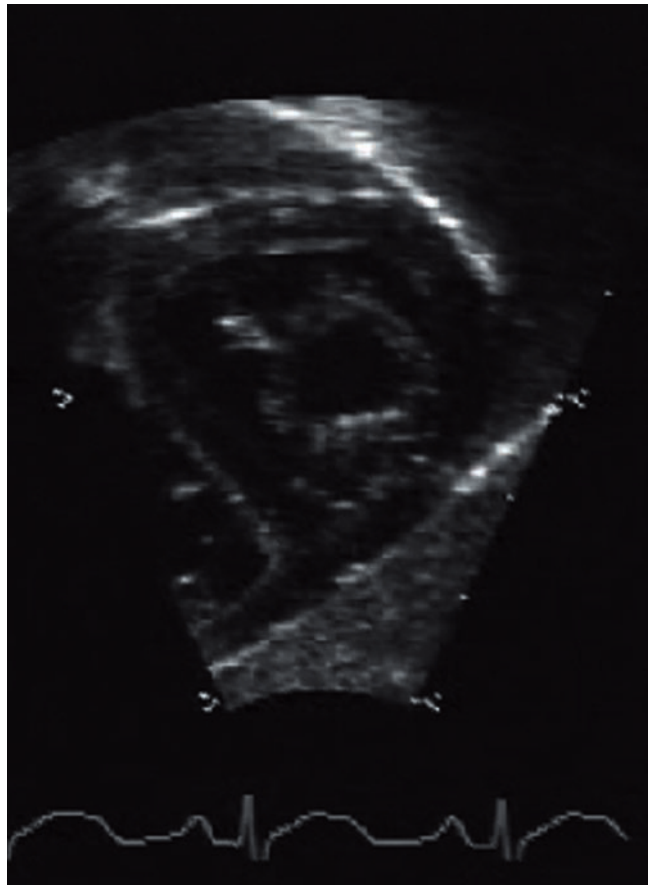

(b)

**Figure 14.16** Diastolic frames in an apical four-chamber plane **(a)** and subxiphoid short-axis plane **(b)** in the same patient as seen in Fig. 14.15a. Note that the orifice appears falsely adequate in the short-axis view, due to the relationship of the distal aspect of the leaflets to the orifice – the leaflet adjacent to the orifice runs nearly parallel to the orifice (a). When imaging in the orthogonal plane (white dashed line) it is difficult to locate this exact plane, thus the orifice is inadequately characterized and appears larger.

robust reference standard of direct anatomic measurement of explanted valves [62,73]. In that study, PHT showed reasonable correlation ($r = 0.80$) with explanted MV areas. Of note, the same investigation showed 2D-echocardiographic planimetry had significantly better correlation ($r = 0.95$), with a mean difference near zero and limits of agreement of −0.21 to +0.29 $cm^2$ [73]. PHT is also dependent on both atrial and ventricular compliance, the initial transmitral pressure gradient and the heart rate [74,75], all of which are dynamic variables in normal growing children and markedly altered in congenital heart disease. In addition, as shown in a Doppler study on newborns [76], diastolic filling is shifted to later in diastole with increasing heart rate, which alters the PHT independent of the flow orifice area. Given the above, PHT has little role in congenital MS and its use should be reserved for adult-sized pediatric patients, and always assessed in the context of other measures of stenosis.

## Prenatal assessment

Typically, only severe cases of MVP (as in neonatal Marfan syndrome) will be diagnosed prenatally. However, it is possible to diagnose ICMV, SMV, mitral stenosis and DOMV (Fig. 14.17; Videoclip 14.8) by fetal echocardiography. In general, these rare lesions are diagnosed by interrogating the MV apparatus from all available acoustic windows, which allows identification of the chordal and papillary muscle positions, leaflet number, presence of a cleft, and valve size and integrity. When an abnormal conotruncus is found a diligent search for ICMV and SMV in the context of an assessment of possible biventricular repair is critical. Given the current spatial and temporal resolution of fetal imaging, subtle forms of the above lesions, such as non-classic MVP, ICMV with NRGA and no VSD, and DOMV with a chordal ring, may go undetected. As with any fetal examination, the impact of missing these lesions needs to be appreciated, but in the context of their overall favorable prognosis. The hemodynamic significance of mitral stenosis can be difficult given the redundancy of the fetal circulation at the atrial septal and ductal levels, which can lead to less than full cardiac output traversing the mitral valve. Defining the MV apparatus as above, including careful measurement of the annulus and a thorough Doppler interrogation of ascending aorta, transverse

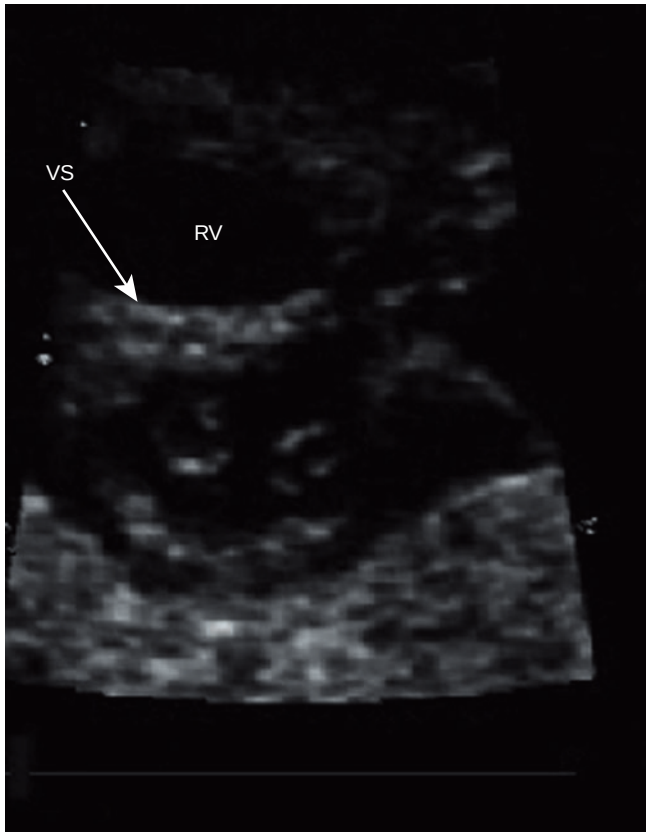


**Figure 14.17** Diastolic frame in a short-axis plane in a fetus of 31-weeks gestation, demonstrating a double-orifice mitral valve. RV, right ventricle; VS, ventricular septum; (Videoclip 14.8).

arch, ductus and foramen ovale, provides insight into the physiology and aids in characterizing the degree of stenosis.

## Echocardiographic guidance of transcatheter and surgical treatment

The surgical advances made in the last two decades in MV plasty [36] have added considerable complexity to the perioperative transesophageal echocardiographic (TEE) interrogation of MV anatomy and function [77,78]. Critical to this success is an accurate assessment of the exact mechanism underlying the MV dysfunction, which requires a systematic, thorough interrogation of the MV apparatus and, importantly, effective communication between the imaging team and surgeon. This interchange is dynamic and ongoing during surgical MV plasty. The en face view of the valve (Fig. 14.3) provides a foundation for the nomenclature as well as a vantage point for systematic interrogation. Briefly, the esophageal four-chamber view is obtained with minimal transducer angulation (0–15°); the mitral valve is then scanned from the superior, mid and lower esophageal locations, which typically profiles the A1–P1, A2–P2 and A3–P3 segment coaptation, respectively. The commissural view from the mid-esophagus with 45–70° of angulation and the transgastric en face view (0–10° of angulation with anteflexion) provide additional views to verify which leaflet segments are dysfunctional. This interrogation method provides a foundation that can be modified to evaluate the more complex lesions of ICMV, SMV, DOMV and congenital MS.

Balloon valvuloplasty for congenital mitral stenosis is utilized when the mitral disease is the predominant lesion (i.e., not hypoplastic left heart syndrome), other surgically correctable lesions are absent and the anatomy of the valve narrowing is favorable [48,49,79]. Importantly, a supravalvar mitral ring must be definitively excluded as balloon valvuloplasty of this lesion has poor outcomes compared with surgery [49]. Typical (symmetric) MS and parachute valves can be palliated with valvuloplasty in selected patients, thereby delaying surgical plasty or valve replacement, with good medium-term improvement of the stenosis and relief of congestive heart failure symptoms. As the long-term morbidity following mitral valve replacement in growing children is significant [69], palliative valvuloplasty is an option in selected patients. Guidance of the procedure using TEE involves a systematic interrogation of the valve as described above, with a diligent search for a supravalvar ring and confirmation of the exact annulus dimensions; this is critical for appropriate balloon sizing. Because the therapeutic mechanism involves tearing of the leaflets and fused chordal tissue [48], post-procedure imaging is focused on assessing the new flow orifice and characterizing the presence and degree of MR. The balance between relieving MS without creating excessive MR is vital, and imaging should be focused on this issue, by confirming the anatomy of the valve, establishing a baseline MS gradient, noting the physiology (cardiac output), assessing MR, and repeating this evaluation as needed by the interventionalist during serial dilations. Given the tearing mechanism of balloon mitral valvuloplasty the resulting effective flow orifice is by definition complex and is seldom accurately characterized direct measurement (planimetry).

## Imaging of the adult and postoperative assessment

Transthoracic echocardiography (TTE) in adults with SMV, DOMV and ICMV is typically limited by poor acoustic windows – especially from the subxiphoid views, which are critical in ICMV and SMV. As the ventricular long-axis views are standard in adult imaging and MVP is diagnosed from this plane, the previously discussed issues around MVP and imaging approach to evaluate MVP is well suited to the adult patient. TTE assessment of the hemodynamic severity of MS using color and spectral Doppler in adults is typically achievable, even in those with poor acoustic windows; however, the details of the morphology and exact mechanism of the mitral valve apparatus dysfunction are often incompletely characterized with TTE alone. Transesophageal echocardiography (discussed above) is, in general, ideally suited to image

the MV due to the close proximity of the probe to the MV apparatus. Surgical repair has been advocated for congenital GLA due to the frequent morbidities of atrial tachycardia [16,80,81] and compressive effects [7,17,18]. Imaging following resection is straightforward as therapy is generally curative [8,18].

Postoperatively, there are numerous potential issues surrounding the above lesions, but the basic aspects of valvular competence (regurgitation) and the adequacy of the flow orifice (stenosis) are central. Following mitral valve repair or replacement, a thorough evaluation of residual MS, mitral regurgitation, paravalvar leaks and normal motion of prosthetic valves is performed. Serial mean gradients from appropriately obtained spectral Doppler interrogation provide a repeatable, consistent and simple means of follow-up. As mentioned previously, the limitation of gradient should be noted and heart rate during interrogation recorded.

## References


1. Freed LA, Levy D, Levine RA et al. Prevalence and clinical outcome of mitral-valve prolapse. *N Engl J Med* 1999;341:1–7.
2. Levine RA, Handschumacher MD, Sanfilippo AJ et al. Three-dimensional echocardiographic reconstruction of the mitral valve, with implications for the diagnosis of mitral valve prolapse. *Circulation* 1989;80:589–98.
3. Liberthson RR, Paul MH, Muster AJ et al. Straddling and displaced atrioventricular orifices and valves with primitive ventricles. *Circulation* 1971;43:213–26.
4. Freedom RM, Bini R, Dische R, Rowe RD. The straddling mitral valve: morphological observations and clinical implications. *Eur J Cardiol* 1978;8:27–50.
5. Geva T, Van Praagh S, Sanders SP et al. Straddling mitral valve with hypoplastic right ventricle, crisscross atrioventricular relations, double outlet right ventricle and dextrocardia: morphologic, diagnostic and surgical considerations. *J Am Coll Cardiol* 1991;17:1603–12.
6. Fraisse A, del Nido PJ, Gaudart J, Geva T. Echocardiographic characteristics and outcome of straddling mitral valve. *J Am Coll Cardiol* 2001;38:819–26.
7. Hougen TJ, Mulder DG, Gyepes MT, Moss AJ. Aneurysm of the left atrium. *Am J Cardiol* 1974;33:557–61.
8. Morales JM, Patel SG, Jackson JH et al. Left atrial aneurysm. *Ann Thorac Surg* 2001;71:719–22.
9. Levy D, Savage D. Prevalence and clinical features of mitral valve prolapse. *Am Heart J* 1987;113:1281–90.
10. Flack JM, Kvasnicka JH, Gardin JM et al. Anthropometric and physiologic correlates of mitral valve prolapse in a biethnic cohort of young adults: the CARDIA study. *Am Heart J* 1999; 138:486–92.
11. Hoffman JI, Kaplan S. The incidence of congenital heart disease. *J Am Coll Cardiol* 2002;39:1890–900.
12. Van Praagh S, Porras D, Oppido G et al. Cleft mitral valve without ostium primum defect: anatomic data and surgical considerations based on 41 cases. *Ann Thorac Surg* 2003;75:1752–62.
13. Bano-Rodrigo A, Van Praagh S, Trowitzsch E, Van Praagh R. Double-orifice mitral valve: a study of 27 postmortem cases with developmental, diagnostic and surgical considerations. *Am J Cardiol* 1988;61:152–60.
14. Shone JD, Sellers RD, Anderson RC et al. The developmental complex of "parachute mitral valve," supravalvular ring of left atrium, subaortic stenosis, and coarctation of aorta. *Am J Cardiol* 1963;11:714–25.
15. Zimand S, Frand M, Hegesh J. Congenital giant left atrial aneurysm in an infant. *Eur Heart J* 1997;18:1034–5.
16. Varghese PJ, Simon AL, Rosenquist GC et al. Multiple saccular congenital aneurysms of the atria causing persistent atrial tachyarrhythmia in an infant. Report of a case successfully treated by surgery. *Pediatrics* 1969;44:429–33.
17. Mansour E, Aldousany A, Arce O et al. Recurrent congenital left atrial aneurysm in a newborn. *Pediatr Cardiol* 1998;19: 165–7.
18. Kadowaki MH, Berger S, Shermeta DW et al. Congenital left atrial aneurysm in an infant. *J Pediatr Surg* 1989;24:306–8.
19. Fountain-Dommer RR, Wiles HB, Shuler CO et al. Recognition of left atrial aneurysm by fetal echocardiography. *Circulation* 2000;102:2282–3.
20. Devereux RB, Brown WT, Kramer-Fox R, Sachs I. Inheritance of mitral valve prolapse: effect of age and sex on gene expression. *Ann Intern Med* 1982;97:826–32.
21. Sumner RG, Phillips JH, Jacoby WJ Jr, Tucker DH. Idiopathic enlargement of the right atrium. *Circulation* 1965;32:985–91.
22. Apostolakis E, Shuhaiber JH. The surgical management of giant left atrium. *Eur J Cardiothorac Surg* 2008;33:182–90.
23. Kanani M, Moorman AF, Cook AC et al. Development of the atrioventricular valves: clinicomorphological correlations. *Ann Thorac Surg* 2005;79:1797–804.
24. De la Cruz MV, Gimenez-Ribotta M, Saravalli O, Cayre R. The contribution of the inferior endocardial cushion of the atrioventricular canal to cardiac septation and to the development of the atrioventricular valves: study in the chick embryo. *Am J Anat* 1983;166:63–72.
25. Oosthoek PW, Wenink AC, Vrolijk BC et al. Development of the atrioventricular valve tension apparatus in the human heart. *Anat Embryol (Berl.)* 1998;198:317–29.
26. Wessels A, Sedmera D. Developmental anatomy of the heart: a tale of mice and man. *Physiol Genomics* 2003;15:165–76.
27. Lincoln J, Alfieri CM, Yutzey KE. Development of heart valve leaflets and supporting apparatus in chicken and mouse embryos. *Dev Dyn* 2004;230:239–50.
28. Wessels A, Markman MW, Vermeulen JL et al. The development of the atrioventricular junction in the human heart. *Circ Res* 1996;78:110–17.
29. Ruckman RN, Van Praagh R. Anatomic types of congenital mitral stenosis: report of 49 autopsy cases with consideration of diagnosis and surgical implications. *Am J Cardiol* 1978;42: 592–601.
30. Rudolph AM, Heymann MA, Spitznas U. Hemodynamic considerations in the development of narrowing of the aorta. *Am J Cardiol* 1972;30:514–25.
31. Levine RA, Triulzi MO, Harrigan P, Weyman AE. The relationship of mitral annular shape to the diagnosis of mitral valve prolapse. *Circulation* 1987;75:756–67.
32. Salgo IS, Gorman JH 3rd, Gorman RC et al. Effect of annular shape on leaflet curvature in reducing mitral leaflet stress. *Circulation* 2002;106:711–17.

33. Tibayan FA, Rodriguez F, Langer F et al. Annular remodeling in chronic ischemic mitral regurgitation: ring selection implications. *Ann Thorac Surg* 2003;76:1549–54; discussion 1554–5.
34. Gorman JH 3rd, Gorman RC, Jackson BM et al. Annuloplasty ring selection for chronic ischemic mitral regurgitation: lessons from the ovine model. *Ann Thorac Surg* 2003;76:1556–63.
35. Marks AR, Choong CY, Sanfilippo AJ et al. Identification of high-risk and low-risk subgroups of patients with mitral-valve prolapse. *N Engl J Med* 1989;320:1031–6.
36. Suri RM, Schaff HV, Dearani JA et al. Survival advantage and improved durability of mitral repair for leaflet prolapse subsets in the current era. *Ann Thorac Surg* 2006;82:819–26.
37. Fraisse A, Massih TA, Vouhe P et al. Management and outcome of patients with abnormal ventriculo-arterial connections and mitral valve cleft. *Ann Thorac Surg* 2002;74:786–91.
38. Moene R. Congenital mitral valve anomalies in transposition of the great arteries. *Am J Cardiol* 1982;49:1972.
39. Penkoske P. Further observations on the morphology of atrioventricular septal defects. *J Thorac Cardiovasc Surg* 1985;90: 611.
40. DiSegni E. Cleft anterior leaflet of the mitral valve with intact septa. A study of 20 cases. *Am J Cardiol* 1983;51:919.
41. Sigfusson G, Ettedgui JA, Silverman NH, Anderson RH. Is a cleft in the anterior leaflet of an otherwise normal mitral valve an atrioventricular canal malformation? *J Am Coll Cardiol* 1995; 26:508–15.
42. Smallhorn JF, de Leval M, Stark J et al. Isolated anterior mitral cleft. Two dimensional echocardiographic assessment and differentiation from "clefts" associated with atrioventricular septal defect. *Br Heart J* 1982;48:109–16.
43. Anderson R. Of clefts, commissures, and things. *J Thorac Cardiovasc Surg* 1985;90:605.
44. Disegni E. Two-dimensional echocardiography in detection of endocardial cushion defect in families. *Am J Cardiol* 1985;55: 1649.
45. Pessotto R, Padalino M, Rubino M et al. Straddling tricuspid valve as a sign of ventriculoatrial malalignment: A morphometric study of 19 postmortem cases. *Am Heart J* 1999;138:1184–95.
46. Zalzstein E, Hamilton R, Zucker N et al. Presentation, natural history, and outcome in children and adolescents with double orifice mitral valve. *Am J Cardiol* 2004;93:1067–9.
47. Trowitzsch E, Bano-Rodrigo A, Burger BM et al. Two-dimensional echocardiographic findings in double orifice mitral valve. *J Am Coll Cardiol* 1985;6:383–7.
48. Moore P, Adatia I, Spevak PJ et al. Severe congenital mitral stenosis in infants. *Circulation* 1994;89:2099–106.
49. McElhinney DB, Sherwood MC, Keane JF et al. Current management of severe congenital mitral stenosis: outcomes of transcatheter and surgical therapy in 108 infants and children. *Circulation* 2005;112:707–14.
50. Oosthoek PW, Wenink AC, Macedo AJ, Gittenberger-de Groot AC. The parachute-like asymmetric mitral valve and its two papillary muscles. *J Thorac Cardiovasc Surg* 1997;114:9–15.
51. Park JS, Lee DH, Han SS et al. Incidentally found, growing congenital aneurysm of the left atrium. *J Korean Med Sci* 2003; 18:262–6.
52. Serraf A, Nakamura T, Lacour-Gayet F et al. Surgical approaches for double-outlet right ventricle or transposition of the great arteries associated with straddling atrioventricular valves. *J Thorac Cardiovasc Surg* 1996;111:527–35.
53. Anderson R. Which hearts are unsuitable for biventricular correction? *Ann Thorac Surg* 1998;66:621.
54. Perier P, Clausnizer B. Isolated cleft mitral valve: valve reconstruction techniques. *Ann Thorac Surg* 1995;59:56–9.
55. Tamura M, Menahem S, Brizard C. Clinical features and management of isolated cleft mitral valve in childhood. *J Am Coll Cardiol* 2000;35:764–70.
56. Rahimtoola SH, Durairaj A, Mehra A, Nuno I. Current evaluation and management of patients with mitral stenosis. *Circulation* 2002;106:1183–8.
57. Otto CM, Davis KB, Reid CL et al. Relation between pulmonary artery pressure and mitral stenosis severity in patients undergoing balloon mitral commissurotomy. *Am J Cardiol* 1993;71: 874–8.
58. LaCorte M, Harada K, Williams RG. Echocardiographic features of congenital left ventricular inflow obstruction. *Circulation* 1976; 54:562–6.
59. Schwartz ML, Gauvreau K, Geva T. Predictors of outcome of biventricular repair in infants with multiple left heart obstructive lesions. *Circulation* 2001;104:682–7.
60. Nichol PM, Gilbert BW, Kisslo JA. Two-dimensional echocardiographic assessment of mitral stenosis. *Circulation* 1977;55: 120–8.
61. Gonzalez MA, Child JS, Krivokapich J. Comparison of two-dimensional and Doppler echocardiography and intracardiac hemodynamics for quantification of mitral stenosis. *Am J Cardiol* 1987;60:327–32.
62. Faletra F, Pezzano A Jr, Fusco R et al. Measurement of mitral valve area in mitral stenosis: four echocardiographic methods compared with direct measurement of anatomic orifices. *J Am Coll Cardiol* 1996;28:1190–7.
63. Chen Q, Nosir YF, Vletter WB et al. Accurate assessment of mitral valve area in patients with mitral stenosis by three-dimensional echocardiography. *J Am Soc Echocardiogr* 1997;10: 133–40.
64. Hatle L, Brubakk A, Tromsdal A, Angelsen B. Noninvasive assessment of pressure drop in mitral stenosis by Doppler ultrasound. *Br Heart J* 1978;40:131–40.
65. David D, Lang RM, Marcus RH et al. Doppler echocardiographic estimation of transmitral pressure gradients and correlations with micromanometer gradients in mitral stenosis. *Am J Cardiol* 1991;67:1161–4.
66. Nishimura RA, Rihal CS, Tajik AJ, Holmes DR Jr. Accurate measurement of the transmitral gradient in patients with mitral stenosis: a simultaneous catheterization and Doppler echocardiographic study. *J Am Coll Cardiol* 1994;24:152–8.
67. Otto CM, Davis KB, Holmes DR Jr et al. Methodologic issues in clinical evaluation of stenosis severity in adults undergoing aortic or mitral balloon valvuloplasty. The NHLBI Balloon Valvuloplasty Registry. *Am J Cardiol* 1992;69:1607–16.
68. Banerjee A, Kohl T, Silverman NH. Echocardiographic evaluation of congenital mitral valve anomalies in children. *Am J Cardiol* 1995;76:1284–91.
69. Beierlein W, Becker V, Yates R et al. Long-term follow-up after mitral valve replacement in childhood: poor event-free survival in the young child. *Eur J Cardiothorac Surg* 2007;31:860–5.

70. Hatle L, Angelsen B, Tromsdal A. Noninvasive assessment of atrioventricular pressure half-time by Doppler ultrasound. *Circulation* 1979;60:1096–104.
71. Gorlin R, Gorlin SG. Hydraulic formula for calculation of the area of the stenotic mitral valve, other cardiac valves, and central circulatory shunts. I. *Am Heart J* 1951;41:1–29.
72. Cohen MV, Gorlin R. Modified orifice equation for the calculation of mitral valve area. *Am Heart J* 1972;84:839–40.
73. Flachskampf FA, Klinghammer L. Determination of stenotic mitral valve area: new, old, and gold standards. *Eur J Echocardiogr* 2008;9:321.
74. Karp K, Teien D, Bjerle P, Eriksson P. Reassessment of valve area determinations in mitral stenosis by the pressure half-time method: impact of left ventricular stiffness and peak diastolic pressure difference. *J Am Coll Cardiol* 1989;13:594–9.
75. Thomas JD, Weyman AE. Doppler mitral pressure half-time: a clinical tool in search of theoretical justification. *J Am Coll Cardiol* 1987;10:923–9.
76. Harada K, Takahashi Y, Shiota T et al. Effect of heart rate on left ventricular diastolic filling patterns assessed by Doppler echocardiography in normal infants. *Am J Cardiol* 1995;76:634–6.
77. Stewart WJ, Currie PJ, Salcedo EE et al. Intraoperative Doppler color flow mapping for decision-making in valve repair for mitral regurgitation. Technique and results in 100 patients. *Circulation* 1990;81:556–66.
78. Kawano H, Mizoguchi T, Aoyagi S. Intraoperative transesophageal echocardiography for evaluation of mitral valve repair. *J Heart Valve Dis* 1999;8:287–93.
79. Kveselis DA, Rocchini AP, Beekman R et al. Balloon angioplasty for congenital and rheumatic mitral stenosis. *Am J Cardiol* 1986;57:348–50.
80. Wagshal AB, Applebaum A, Crystal P et al. Atrial tachycardia as the presenting sign of a left atrial appendage aneurysm. *Pacing Clin Electrophysiol* 2000;23:283–5.
81. Tanabe T, Ishizaka M, Ohta S, Sugie S. Intrapericardial aneurysm of the left atrial appendage. *Thorax* 1980;35:151–3.

# 15 Common Atrioventricular Canal Defects

**Meryl S. Cohen**

Department of Pediatrics, University of Pennsylvania School of Medicine, The Children's Hospital of Philadelphia, Philadelphia, PA, USA

## Definition

The term "common atrioventricular canal" describes a group of cardiac defects characterized by abnormalities of the structures derived from the endocardial cushions during embryologic development of the heart. In these lesions, both atria are connected to a common (single) atrioventricular valve. Typically there are deficiencies in the atrial and ventricular septa as well as abnormalities of the atrioventricular valves. There is a spectrum of disease from an exclusive atrial communication to a large ventricular communication that usually dictates the physiology and the clinical course. There is also a range of abnormalities of the common atrioventricular valve, and incompetence of the valve is the norm. Common atrioventricular canal defects are frequently associated with Down syndrome. At least 40% of children with Down syndrome have congenital heart disease, and of those, common atrioventricular canal is one of the most frequent lesions seen along with isolated ventricular septal defect (VSD) [1]. Of note, there are several different terms used to describe the atrioventricular canal defect including endocardial cushion defect, atrioventricular septal defect, common atrioventricular orifice and atrioventricularis communis. For the remainder of this chapter the term *common atrioventricular canal defect* (CAVC) will be used because it is anatomically correct and is inclusive of abnormality of the atrioventricular valve.

## Incidence

Congenital heart disease occurs in approximately 5–12 per 1000 live births [2]. The incidence of CAVC is approximately 34.8 per 100 000 live births (range 24.2 to 39.6 per 100 000 live births), representing the ninth most common congenital heart lesion. The incidence is likely higher in the fetal population because termination of pregnancy is sometimes performed if Down syndrome or congenital heart disease is detected before birth.

## Etiology

A strong link exists between CAVC and Down syndrome (trisomy 21): in fact, the risk of CAVC is increased 1000-fold compared with subjects having normal chromosomes. Despite this known association, the responsible gene on chromosome 21 has yet to be identified. The gene encoding DSCAM (Down syndrome cell adhesion molecule) has been proposed as a possible candidate gene [3]. CAVC can also have an autosomal dominant pattern of inheritance or occur sporadically [4]. An association with chromosome 8p deletion and familial clusters with different modes of inheritance have also been reported [5,6]. CAVC is also seen frequently in association with the heterotaxy syndrome, particularly the asplenia type.

## Morphology and classification

### Developmental considerations

Prior to the formation of the endocardial cushions, cardiac jelly expands in the region between the atria and the primitive ventricles, the so-called atrioventricular canal. The endocardial cushions are the primordia of the valves and septa of the developed heart, and form as a result of epithelial-to-mesenchymal transformation [7]. Embryos that fail to develop these cushions experience demise once a fully functional heart is required in late gestation. The endocardial cushions are made up of mesenchymal tissue and are divided into superior, inferior, right and left cushions. The atrioventricular canal septum is formed, at least in part, by the superior and inferior endocardial cushions, which contribute to septation of the outlet portion of the atria and the inlet portion of the ventricles. If the endocardial cushions fail to fuse, likely as a result of abnormal migration of mesenchymal

*Echocardiography in Pediatric and Congenital Heart Disease: From Fetus to Adult*
Edited by Wyman W. Lai, Luc L. Mertens, Meryl S. Cohen and Tal Geva
 ISBN: 978-1-405-17401-5

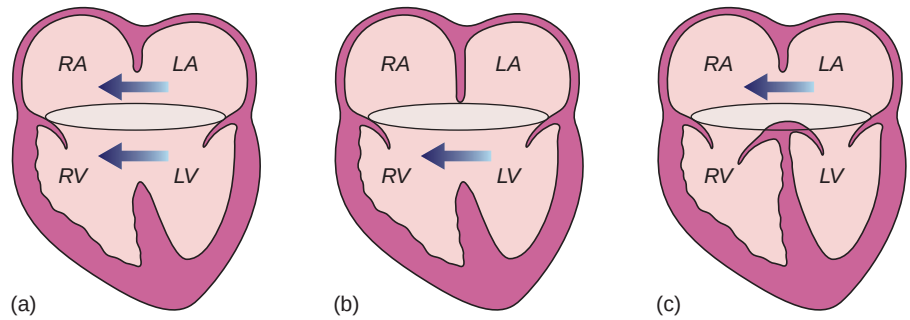


**Figure 15.1** **(a)** Diagrammatic representation of the complete form of common atrioventricular canal (CAVC) defect with a large atrial and large ventricular communication and a common atrioventricular valve orifice over both ventricles. **(b)** Diagrammatic representation of the rare form of CAVC with no atrial communication but a large ventricular septal defect. The atrioventricular valve sits more superiorly in the defect closing off the atrial communication. **(c)** Diagrammatic representation of the incomplete form of CAVC with a large atrial communication, no ventricular communication and two atrioventricular valve orifices. The atrioventricular valve sits more inferiorly and adheres to the ventricular septum, thereby closing off the ventricular communication.

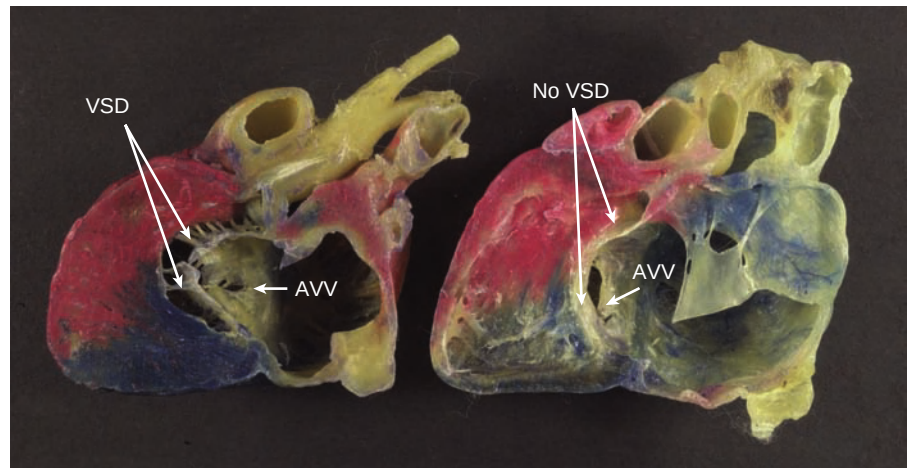


**Figure 15.2** **(a)** Waxed anatomic specimen of a left ventricular view of the ventricular septum in the complete form of common atrioventricular canal (CAVC) demonstrating the scooped out appearance of the ventricular septum from the ventricular septal defect (VSD) with some chordal attachments of the atrioventricular valve (AVV) to the crest of the septum. **(b)** The same view in a waxed anatomic specimen of incomplete CAVC demonstrating that the AVV is adherent to the crest of the ventricular septum with no VSD component. The scooped out appearance of the ventricular septum is still present despite no ventricular level shunting.

cells, the canal portion of the atrial and ventricular septum do not develop. In addition, abnormalities of atrioventricular valve development occur, particularly affecting the septal leaflet of the tricuspid valve and the anterior leaflet of the mitral valve. Detailed description of development of the endocardial cushions can be found in several publications [7–9].

## Anatomy

CAVC is categorized in several ways. The deficiency in the atrioventricular septum is the same in all forms, but the relationship of the atrioventricular valve within that defect is variable. Indeed, if the atrioventricular valve leaflets are removed in a heart specimen with CAVC, it is impossible to distinguish between the various subtypes. The *complete* form of CAVC (Figs 15.1a and 15.2a) is characterized by an interatrial communication antero-inferior to the margin of the fossa ovalis and adjacent to the atrioventricular valves, along with a large posterior VSD along the septal leaflet of the atrioventricular valve extending into the vicinity of the membranous septum, giving the ventricular septum a scooped out appearance (Figs 15.2a and 15.3). Instead of two distinct atrioventricular valves, there is a common atrioventricular valve with a common annulus. Typically there is at least one mural or lateral leaflet positioned exclusively over the right ventricle and one mural leaflet positioned exclusively over the left ventricle; these mural leaflets can be variable in size [10]. Moreover, in contrast to the normal tricuspid and mitral valves, there are two leaflets that bridge the crest of the ventricular septum in the superior and inferior position

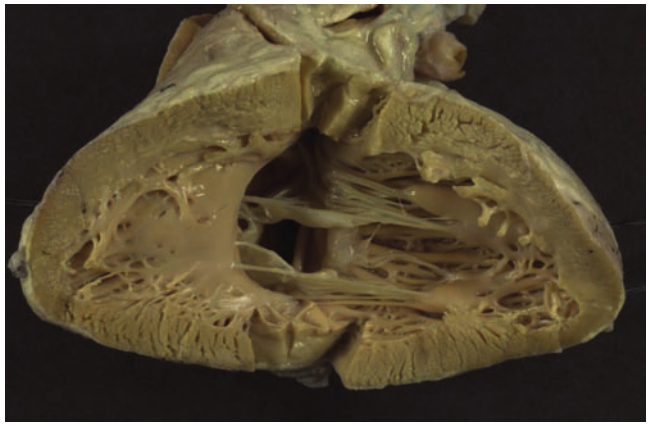

**Figure 15.3** An anatomic specimen of complete common atrioventricular canal (CAVC) in the left ventricular view of the ventricular septum shows the superior and inferior bridging leaflets crossing the ventricular septum into the left ventricle and the scooped out appearance of the ventricular septum.

(Figs 15.3 and 15.4a,b). The superior bridging leaflet distorts the atrioventricular junction and subsequently causes superior displacement ("unwedging") of the aortic outflow tract, the aortic annulus no longer being able to sit between the normal tricuspid and mitral valves (Fig. 15.4b). As a result, the length of the left ventricle from the atrioventricular valve annulus to the apex is foreshortened and the length from the apex to the aortic valve annulus is elongated (typically these measures are equal in length in the normal heart) (Fig. 15.5) [11]. The inferior bridging leaflet has extensive chordal attachments to the crest of the ventricular septum whereas the chordal attachments of the superior leaflet are variable; the latter have been subclassified by Rastelli and colleagues (Fig. 15.6) [12]. In Rastelli type A, the superior bridging leaflet is divided at the level of the ventricular septum (Fig. 15.7). In the type B arrangement, the rarest form, division of the superior bridging leaflet occurs to a right ventricular papillary muscle. In type C, the superior bridging leaflet is undivided or "free floating;" this is the most rudimentary form of CAVC and is common in Down syndrome (Fig. 15.8). Rastelli type A is more commonly associated with preoperative left ventricular outflow obstruction, in part because of increased elongation of the outflow tract [13]. The complete form of CAVC is typically seen in children with Down syndrome. In a more unusual form of complete CAVC, the atrioventricular valve leaflets sit superiorly in the atrioventricular defect such that the atrial communication is

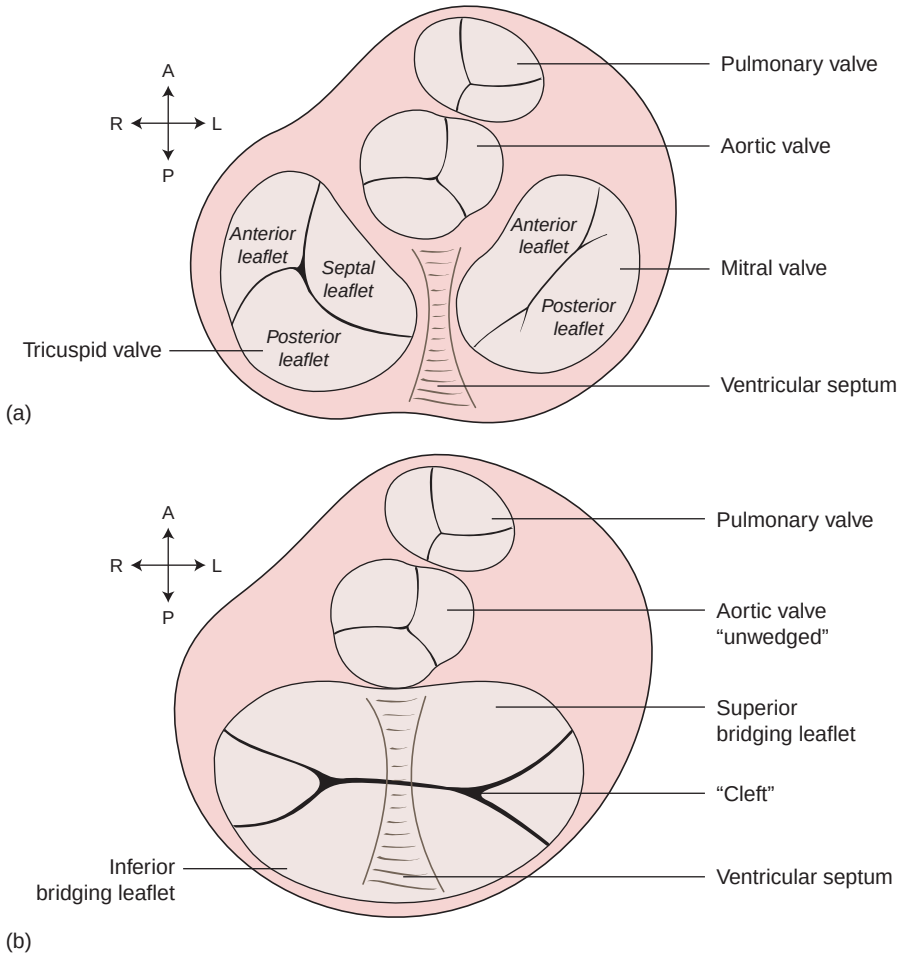


**Figure 15.4** **(a)** Diagram depicting the relationship of the mitral and tricuspid valves to the aortic valve in a normal heart. The aortic valve sits wedged between the two atrioventricular valves. **(b)** The same view is depicted in this diagram of common atrioventricular canal (CAVC). The superior and inferior bridging leaflets are demonstrated with the "cleft" where the two bridging leaflets come together at the ventricular septum. The aortic valve is unwedged anteriorly as a result of the superior bridging leaflet.

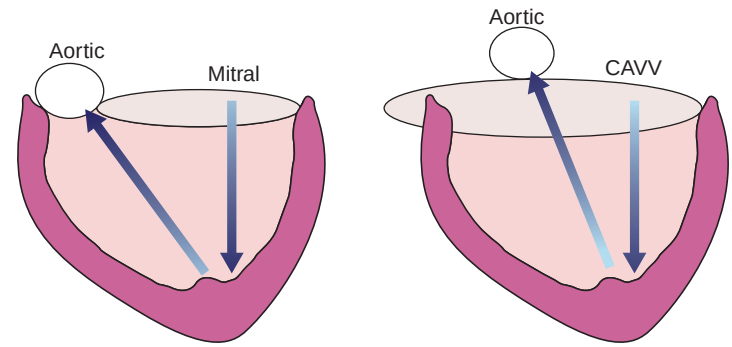


**Figure 15.5** Diagram showing that the length of inflow and outflow are the same in the left ventricle of the normal heart **(left)**. In common atrioventricular canal (CAVC), the outflow length is elongated because of the unwedged aortic valve **(right)**.

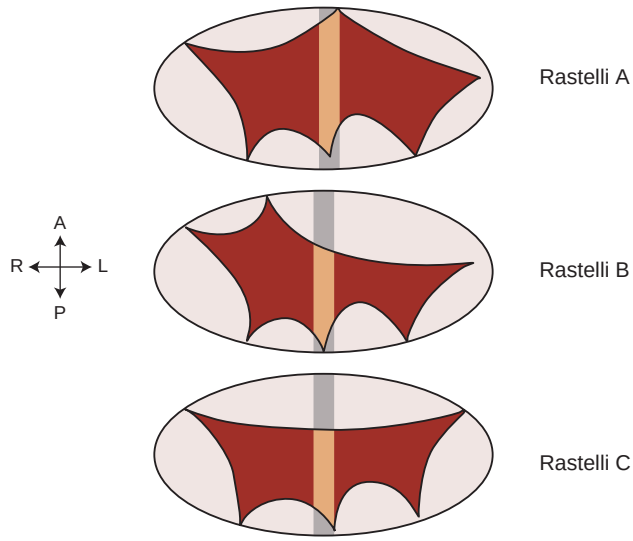


**Figure 15.6** Rastelli classification. In type A **(top)** the superior bridging leaflet is divided at the level of the ventricular septum. In type B **(center)** division of the superior bridging leaflet occurs to a right ventricular papillary muscle. In type C **(bottom)** the superior bridging leaflet is undivided or "free floating."

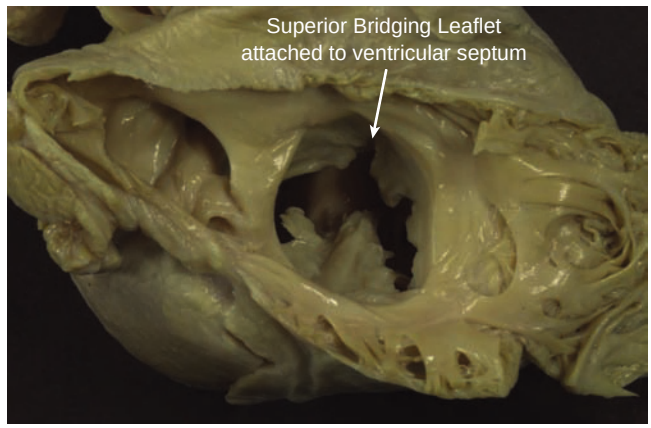


**Figure 15.7** Anatomic specimen showing the right atrial view looking down toward the common atrioventricular valve. This view demonstrates Rastelli type A anatomy with division of the superior bridging leaflet at the ventricular septum.

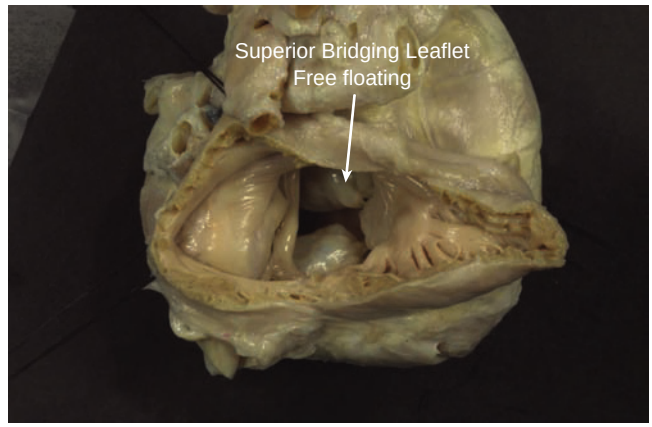


**Figure 15.8** Anatomic specimen showing the right atrial view looking down toward the common atrioventricular valve. This view demonstrates Rastelli type C anatomy with a free-floating superior bridging leaflet.

trivial or absent and the ventricular communication is large (Fig. 15.1b). Even rarer is the CAVC defect where atrioventricular valve tissue fills in the atrial and ventricular communications and there is no shunting whatsoever.

The *incomplete* (or *partial*) form of CAVC is characterized by an interatrial communication in the canal portion of the atrial septum (located between the antero-inferior margin of the fossa ovalis and the atrioventricular valves), with a common atrioventricular annulus in association with two atrioventricular valve orifices (Fig. 15.1c). This form is often called ostium primum atrial septal defect (ASD). However, this term does not describe the atrioventricular valve abnormality or the fact that the defect in the atrioventricular septum is the same as in the complete form of CAVC. The distinction is that the atrioventricular valve tissue is adherent to the crest of the ventricular septum forming a connecting tongue, thus allowing no ventricular level shunt (Figs 15.2b and 15.9). Although the two orifices are separate, the valves do not resemble normal tricuspid and mitral valves and thus the term mitral valve "cleft" is a misnomer. In fact the so-called "cleft" is the deficit of atrioventricular valve tissue where the superior and inferior bridging leaflets meet at the ventricular septum (Fig. 15.10). Atrioventricular valve regurgitation through this deficit in CAVC is the norm.

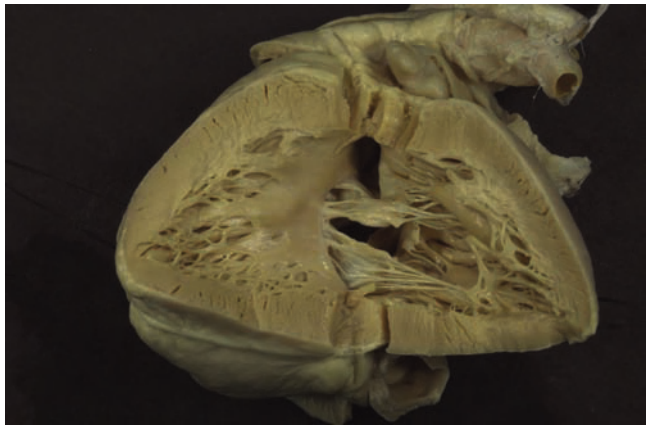

**Figure 15.9** Anatomic specimen of incomplete common atrioventricular canal (CAVC) in the left ventricular view of the ventricular septum, demonstrating the scooped-out appearance of the ventricular septum with the atrioventricular valve adherent to the septum and no ventricular septal defect (VSD) component. This view highlights the "cleft" of the left-sided atrioventricular valve.

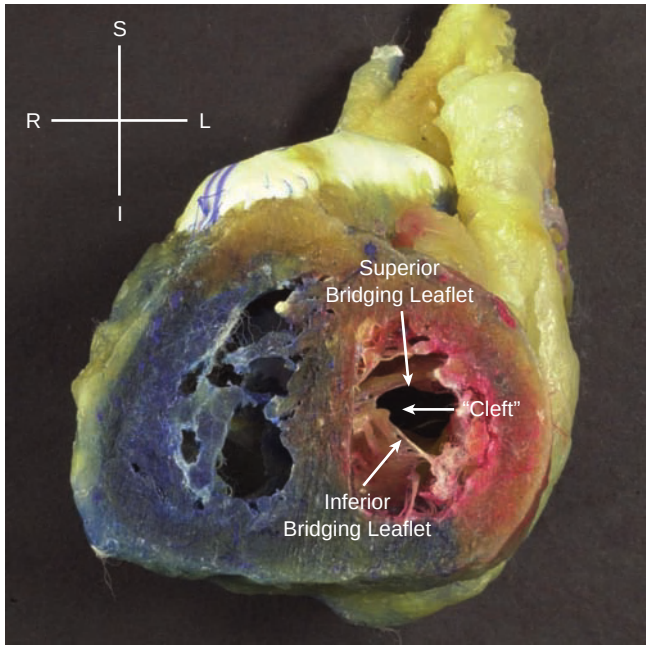


**Figure 15.10** Waxed specimen cut in the subcostal sagittal echocardiographic view showing that the orientation of the "cleft" is perpendicular to the ventricular septum. The normal anterior leaflet is more parallel to the ventricular septum.

There is an intermediate form in the spectrum of CAVC known as *transitional* type, characterized by significant chordal attachments of the superior bridging leaflet to the ventricular septum with some shunting through these chordae at the ventricular level. The VSD component is typically restrictive with subsystemic pulmonary artery pressure.

In CAVC, the relationship of the atrial septum to the common atrioventricular valve may be balanced or unbalanced. In the balanced form, the atrial septum sits over the ventricular septum with equal distribution of atrial inflow to the right and left side of the atrioventricular valve. Rarely, the atrial septum is unbalanced or malaligned (also known as "double outlet atrium") such that the atrial septum is deviated predominantly over the left atrial inflow (double-outlet right atrium) or the right atrial inflow (double-outlet left atrium) (Fig. 15.11a,b). Inflow into the contralateral ventricle can be obstructed in some cases.

Maldistribution of the atrioventricular valve over the ventricles occurs much more commonly than atrial unbalance and accounts for 10% of all cases of CAVC [14]. When the atrioventricular valve sits more over one ventricle than the other, the contralateral ventricle is typically hypoplastic (Figs 15.11c,d and 15.12a,b). Unbalance to the right (with left ventricular hypoplasia) is more common and is often associated with other levels of left-sided obstruction including coarctation of the aorta. In its most extreme form, unbalance to the right is a variant of hypoplastic left heart syndrome, sometimes with no left ventricular cavity seen. Unbalance to the left (with right ventricular hypoplasia)

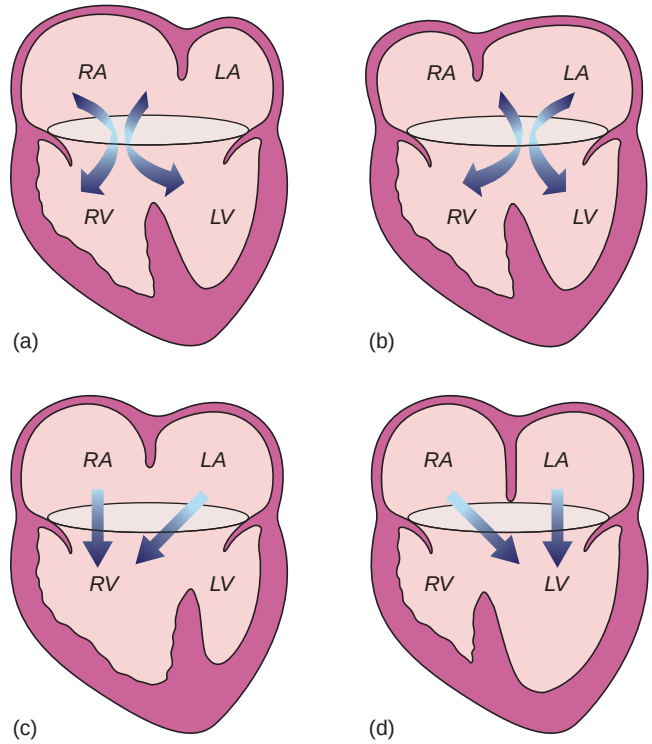


**Figure 15.11** **(a)** Diagram showing double-outlet right atrium with malalignment of the atrial septum toward the left atrium. **(b)** Diagram showing double-outlet left atrium with malalignment of the atrial septum toward the right atrium. **(c)** Diagram showing unbalanced common atrioventricular canal (CAVC) to the right with concomitant left ventricular hypoplasia. **(d)** Diagram showing unbalanced CAVC to the left with concomitant right ventricular hypoplasia.

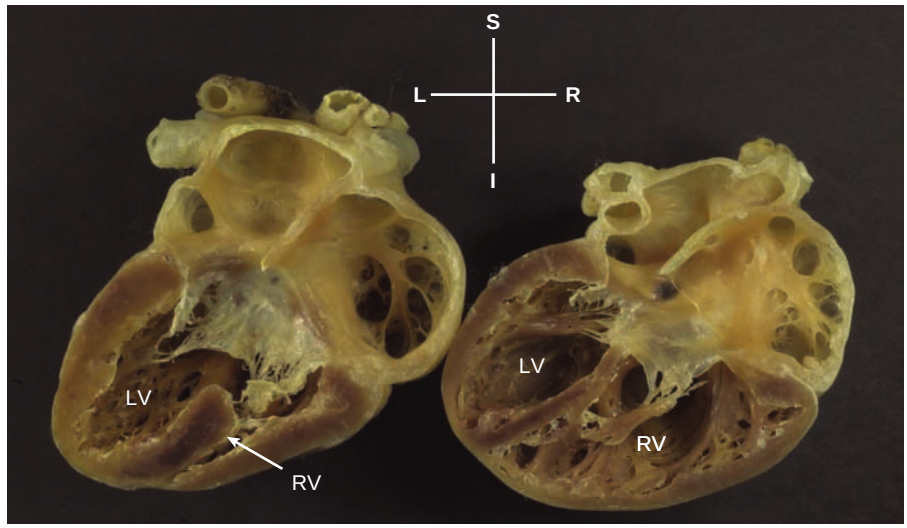


(a) Unbalanced CAVC to Left (b) Balanced CAVC

**Figure 15.12** Anatomic wax specimens cut in the apical 4-chamber view. **(a)** Looking toward the superior bridging leaflet, the specimen demonstrates unbalance of the atrioventricular valve to the left with right ventricular hypoplasia. **(b)** A specimen in the same view with a common atrioventricular valve that is well balanced over both ventricles. LV, left ventricle; RV, right ventricle.

can exhibit pulmonary outflow obstruction. Unbalance of the atrioventricular valve in relationship to the ventricular septum can occur in all forms of CAVC.

In CAVC, the left ventricular anterolateral papillary muscle is often displaced posteriorly compared with normal [15]. Left atrioventricular valve abnormalities can also be seen in approximately 5% of CAVC cases, most typically double-orifice or single papillary muscle (parachute) [15–17]. These lesions are more common in incomplete CAVC and can also be seen in association with unbalanced defects to the right with concomitant left ventricular hypoplasia. Such valve abnormalities may complicate surgical repair with possible residual left atrioventricular valve regurgitation, stenosis or both [17,18].

CAVC frequently has associated lesions including tetralogy of Fallot (usually seen in children with Down syndrome), patent ductus arteriosus, coarctation of the aorta, and left ventricular outflow tract obstruction. Secundum type ASDs and additional VSDs can also be seen. In heterotaxy syndrome, CAVC is common particularly in the asplenia type.

Atrioventricular canal type VSD (otherwise known as inlet-type VSD) can exist as an entity without a common atrioventricular junction. These are defects along the septal leaflet of the tricuspid valve, often with straddling of the tricuspid valve chordae into the left ventricle. These defects are frequently seen in association with complex congenital heart disease. Further detail about this type of VSD can be found in Chapter 12.

## Pathophysiology

The clinical course of a patient with CAVC defect is variable and depends on the magnitude of atrial- and ventricular-level shunting, the severity of atrioventricular valve regurgitation, the degree of unbalance at the level of the ventricles if present, and other associated lesions. In the balanced form of CAVC, ventricular-level left-to-right shunting is determined almost exclusively by the pulmonary vascular resistance because the defect is large and unrestrictive with right ventricular and pulmonary artery pressure at systemic levels. In the early newborn period, symptoms are few but as the pulmonary vascular resistance decreases over 6–8 weeks, the amount of left-to-right ventricular shunting increases, with a concomitant increase in pulmonary blood flow and volume overload to the left atrium and ventricle. If left uncorrected, this defect will result in symptoms of congestive heart failure including growth failure, respiratory symptoms and tachycardia.

When the predominant lesion is a significant ASD, the left-to-right shunt is determined by the relative compliance of the right and left ventricles. Shunting increases over the first few months of life as right ventricular compliance improves. Atrial-level shunting causes dilation of the right atrium, right ventricle and pulmonary arteries. If atrial-level shunting occurs in isolation, most young children tolerate well this increased pulmonary blood flow and are asymptomatic, but dyspnea and/or growth failure can occur in some cases [19]. In those with transitional-type CAVC, restrictive ventricular-level shunting is seen in combination with the atrial-level shunt. Depending on the magnitude of the ventricular-level shunting, some will have evidence of heart failure whereas others with smaller shunts will not. Atrioventricular valve regurgitation, particularly of the left atrioventricular valve, can also cause an undue volume burden on the left atrium and ventricle resulting in cardiomegaly and symptoms of heart failure.

If CAVC is not surgically addressed, pulmonary vascular disease may ensue. This will occur earlier (within the first

year of life) in those with large ventricular communications but can also occur in those with exclusively atrial communication in later decades of life. Although the restrictive VSD in the transitional type of CAVC can close with more atrioventricular valve tissue, the ostium primum ASD and the large CAVC-type VSD typically do not close spontaneously.

Those children with Down syndrome and CAVC are at greater risk for the development of pulmonary vascular obstructive disease within the first year of life [16]. Studies of children with and without Down syndrome have demonstrated that those with Down syndrome are more likely to have elevated pulmonary vascular resistance at the time of surgical repair [16]. Noncardiac issues may come into play in Down syndrome, including chronic airway obstruction and central hypoventilation, which may increase pulmonary vascular resistance.

## Imaging

CAVC is imaged from multiple acoustic windows. Two-dimensional imaging provides excellent visualization of the anatomy in CAVC and is utilized along with color and spectral Doppler techniques to perform a comprehensive anatomic and physiologic evaluation of the defect. Three-dimensional echocardiography is emerging as a tool that augments two-dimensional imaging by demonstrating details of atrioventricular valve anatomy and in assessment of the left ventricular outflow tract. Transesophageal echocardiography (TEE), often used to assess surgical repair of CAVC, can also be utilized as a diagnostic tool in patients with suboptimal transthoracic windows and/or inconclusive diagnosis. Rarely, cardiac catheterization is required before surgery to augment the information provided by the echocardiogram.

### Goals of the examination

The objectives of echocardiographic examination in the context of CAVC can be summarized as follows:

- Determination of ASD size, and additional defects.
- Determination of ventricular septal defect size, and additional defects.
- Anatomy of atrioventricular annulus, valve(s) and chordal attachments:
  - relationship of valve to atrioventricular septum;
  - Rastelli classification;
  - assessment of atrioventricular valve leaflets;
  - assessment for left and right (Ebstein's anomaly) atrioventricular valve anomalies;
  - assessment of spacing of the left ventricular papillary muscles.
- Assessment for atrial or ventricular level unbalance:
  - relationship of atrial septum to inlet;
  - distribution of atrioventricular valve over the ventricles (subcostal view);
  - assessment of atrioventricular valve annulus and inflow into the ventricle by color in unbalanced CAVC (apical 4-chamber view);
  - determination of severity of ventricular hypoplasia.
- Assessment of etiology of left ventricular outflow tract obstruction if present.
- Hemodynamic assessment:
  - flow direction of atrial and ventricular septal defect (by color and spectral Doppler);
  - peak instantaneous pressure gradient across the VSD (if present) to estimate right ventricular pressure by continuous-wave Doppler;
  - assessment of severity of atrioventricular valve regurgitation by color flow mapping;
  - evidence of hemodynamic load to the left and right ventricles (dilation, increased flow across pulmonary outflow and left atrioventricular valve inflow);
  - estimation of right ventricular systolic pressure based on tricuspid regurgitation jet velocity by continuous-wave Doppler (in cases of restrictive or no VSD);
  - assessment of severity of left ventricular or right ventricular outflow tract obstruction if present.
- Measures of biventricular function.
- Detection of associated lesions, particularly patent ductus arteriosus, coarctation of the aorta, secundum-type ASD, additional VSD, tetralogy of Fallot.

### Imaging of complete CAVC

Subcostal imaging provides excellent windows to evaluate the atrial septum and the relationship of the common atrioventricular valve to the septum. In particular, the subcostal frontal (long-axis) (Videoclip 15.1) view and the "in between" left anterior oblique (LAO) acoustic sweep demonstrate the size of the ostium primum-type ASD (Fig. 15.13a). Additional atrial communications are seen in these planes as well. Color Doppler in a subcostal frontal or LAO view shows the atrial-level shunt direction (Fig. 15.13b; Videoclip 15.2). The subcostal frontal view also demonstrates the unwedging of the aortic outflow and abnormal elongation of the left ventricular outflow tract with the resultant curve in the ascending aorta, the so-called "goose-neck deformity" (Figs 15.14 and 15.15; Videoclip 15.1). The subcostal LAO view is ideal to image the common atrioventricular valve "en face" to assess how much is apportioned to each ventricle (i.e., determination of balance; Fig. 15.16 and Videoclip 15.3) [20]. The subcostal sagittal (short-axis) view can also be utilized to assess the anatomy of the atrioventricular valve; chordal attachments of the atrioventricular valve to the ventricular septum can be seen in this view and can determine Rastelli classification. In addition, this view differentiates between normal tricuspid and mitral valves and the atrioventricular valve associated with CAVC (Fig. 15.17a,b). Often, the size of the VSD is difficult to determine in subcostal imaging because the probe sweeps through

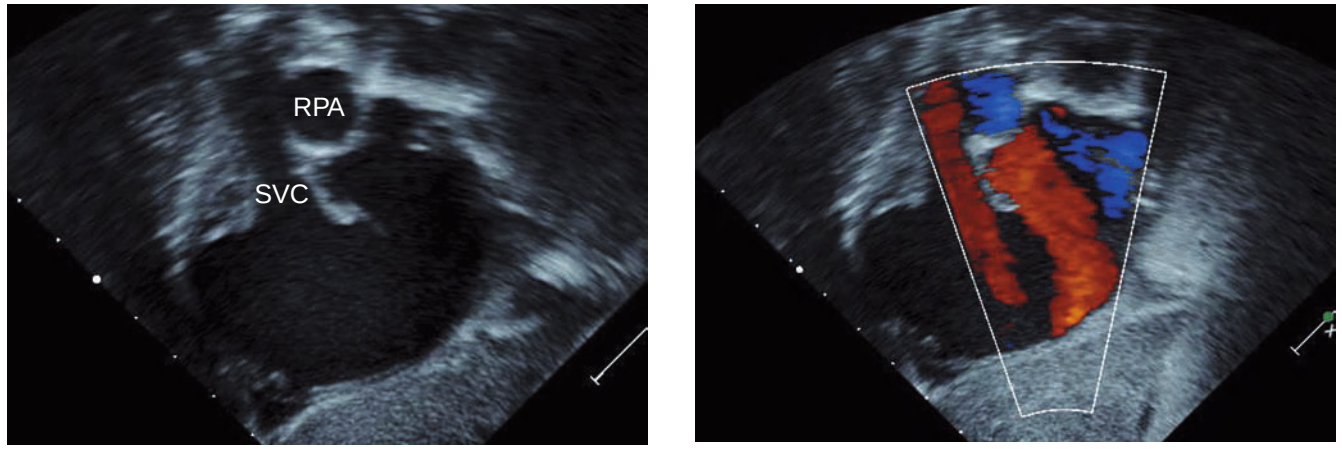


(a) (b)

**Figure 15.13 (a)** Subcostal left anterior oblique view demonstrating a large ostium primum atrial septum defect (ASD). **(b)** Same view with color flow mapping showing left-to-right shunting at the atrial level. RPA, right pulmonary artery; SVC, superior vena cava.

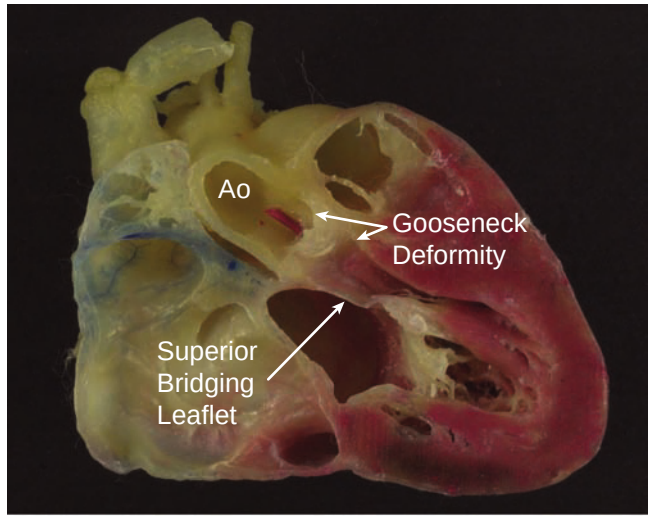


**Figure 15.14** Anatomic specimen cut in subcostal frontal view demonstrating how the superior bridging leaflet in common atrioventricular canal (CAVC) causes the displacement of the left ventricular outflow tract This anatomic finding has been called a "gooseneck deformity", pathognomonic for this lesion. Ao, aorta.

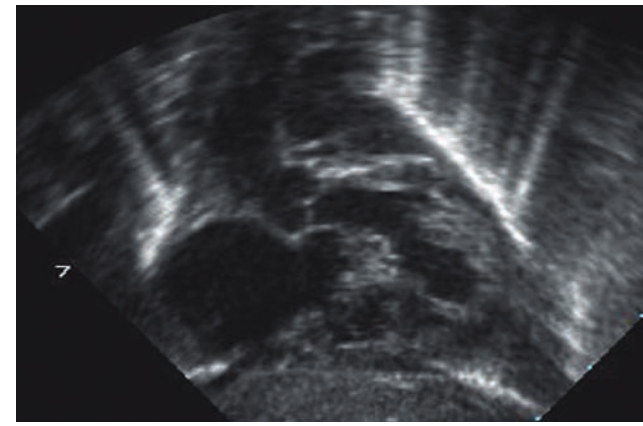

**Figure 15.15** Subcostal frontal view demonstrating the "gooseneck deformity" of the left ventricular outflow tract in common atrioventricular canal (CAVC).

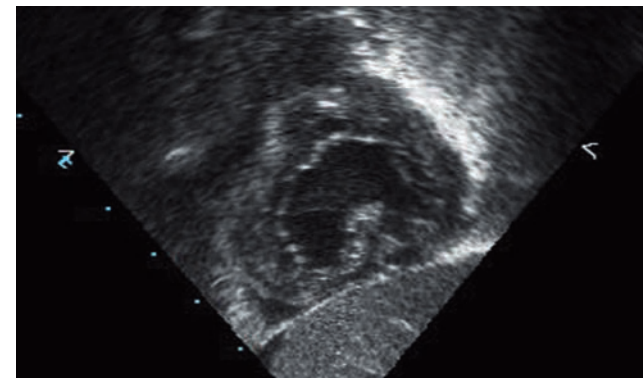

**Figure 15.16** Subcostal left anterior oblique view of the common atrioventricular valve seen "en face" in the open position. This view can be used to assess the severity of unbalance of the valve over the ventricles.

the defect without highlighting its edges. The papillary muscles can be identified in the subcostal sagittal view and are often located counterclockwise to their position in a normal heart. The presence of a solitary papillary muscle should be highlighted as a complicating factor for the repair of the mitral valve [15].

The apical window is not ideally suited for evaluation of the atrial septum because of false dropout of the acoustic signal from the parallel orientation of the ultrasound beam relative to the atrial septum. However, the 4-chamber view is extremely useful when imaging CAVC because it displays the orientation of the atrioventricular valve within the atrioventricular septal defect, thus helping to determine the size of

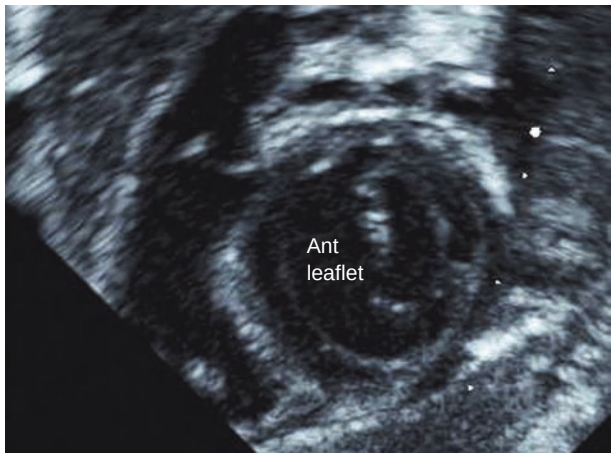


(a)

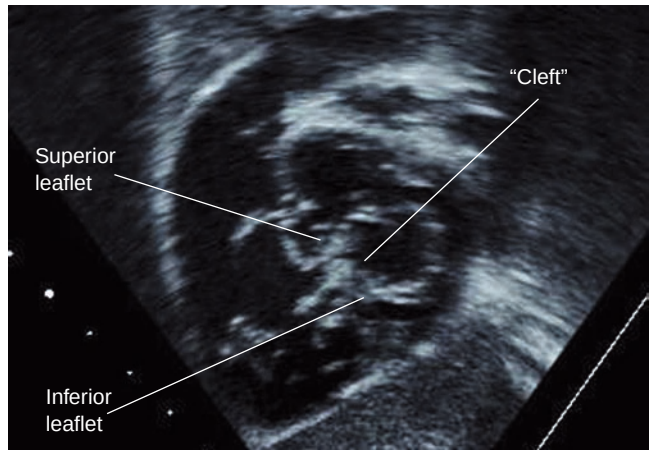


(b)

**Figure 15.17 (a)** Subcostal sagittal view in a normal heart exhibiting the anterior leaflet (Ant leaflet) in parallel with the ventricular septum. **(b)** The same view in common atrioventricular canal (CAVC) demonstrates that the superior and inferior bridging leaflets are perpendicular to the ventricular septum.

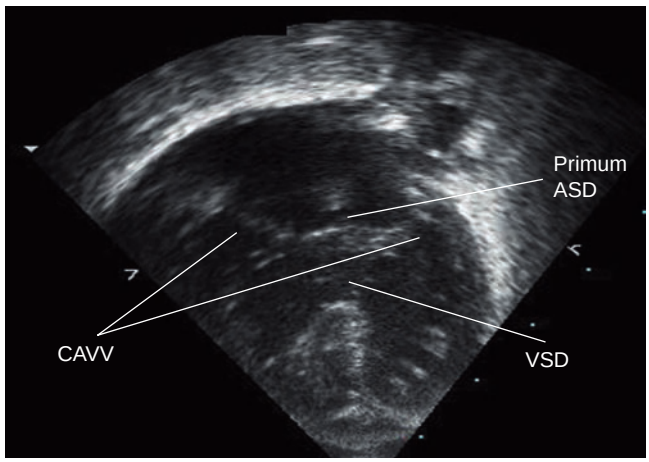


**Figure 15.18** Apical 4-chamber view of complete common atrioventricular canal (CAVC) showing the relationship of the common atrioventricular valve (CAVV) within the atrioventricular septal defect. A more superior or inferior location of the valve alters the size of the atrial and ventricular communications. ASD, atrial septal defect; VSD, ventricular septal defect.

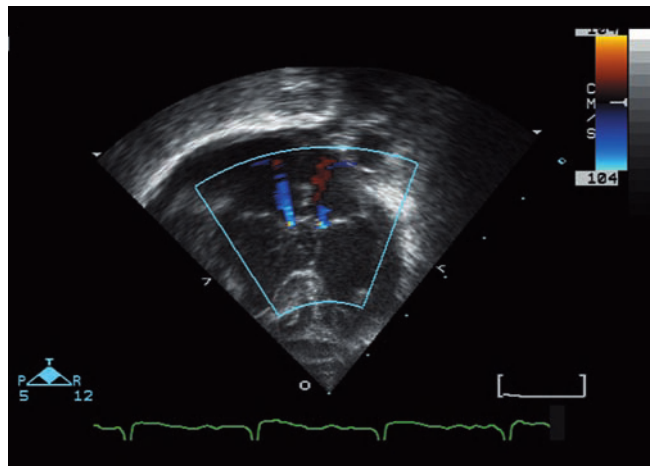

**Figure 15.19** Apical 4-chamber view of complete common atrioventricular canal (CAVC) with color Doppler demonstrating atrioventricular valve regurgitation in systole. Chordal attachments of the atrioventricular valve to the crest of the ventricular septum are also seen.

the ventricular communication (Fig. 15.18 and Videoclip 15.4). Chordal attachments in relation to the ventricular septum can also be demonstrated in this plane. Tilting of the transducer from posterior to anterior in this view often reveals the full scope of the VSD and helps diagnose additional septal defects (Videoclip 15.5) [21]. In addition, this view best demonstrates atrioventricular valve inflow and valve regurgitation (Fig. 15.19 ). Subjective and quantitative measures of atrioventricular valve regurgitation can be performed using this view as well. The apical 5-chamber view helps to identify left ventricular outflow tract obstruction with quantitation of severity by pulsed-wave and continuous-wave Doppler.

The parasternal long-axis view helps in estimation of the severity of atrioventricular valve regurgitation. A low left parasternal short-axis view can often provide additional imaging of the atrial septum, particularly in patients with suboptimal subcostal windows. The parasternal short-axis plane at the level of the ventricular septum highlights the VSD. It also identifies additional muscular defects (Fig. 15.20). The superior and inferior bridging leaflets of the left atrioventricular valve are also demonstrated, often with atrioventricular valve regurgitation through the "cleft" (Fig. 15.21 and Videoclip 15.6). Papillary muscle orientation is also seen in this view.

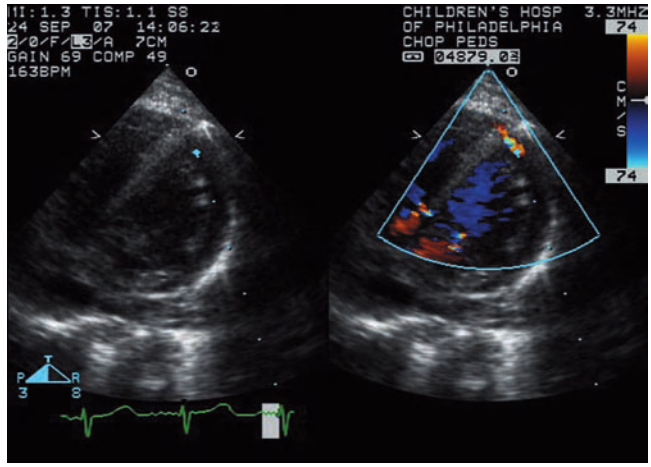


**Figure 15.20** Dual image in parasternal short-axis view highlighting the ventricular septum. Sweep of the ventricular septum demonstrates a small additional anterior muscular VSD seen only with color Doppler.

### Imaging of incomplete and transitional CAVC

Imaging goals are similar for the incomplete and transitional forms of CAVC. Subcostal LAO and sagittal views are particularly useful to demonstrate that the two atrioventricular valves are anatomically abnormal with bridging of the superior leaflet across the ventricular septum. In fact, the subcostal sagittal view often helps to clinch the diagnosis of CAVC because a normal mitral valve anterior leaflet is in a perpendicular orientation to the left atrioventricular valve in CAVC (Fig. 15.17a,b). The LAO view highlights the ostium primum ASD well (Fig. 15.13a,b; Videoclip 15.2). Double-orifice mitral valve and other left atrioventricular valve abnormalities are more common in the incomplete form and therefore should be ruled out in all cases.

The apical 4-chamber view demonstrates nicely the position of the atrioventricular valve in association with the ventricular septum (Fig. 15.22; Videoclip 15.7) and helps to identify atrioventricular valve regurgitation (usually through the "cleft") (Fig. 15.23). Ventricular-level shunting, if identified, can often be seen in this view, including shunting from the left ventricle to the right atrium (Fig. 15.24). In transitional CAVC, the amount of ventricular-level shunting may be minimal; color Doppler is useful to detect a small defect (Fig. 15.25). The parasternal short-axis view can be used to align the VSD jet for quantitative estimate of right ventricular pressure.

### Imaging of the left ventricular outflow tract

With the left ventricular outflow tract elongation of CAVC, obstruction can occur both before and after surgical intervention. Outflow obstruction is more common in the incomplete form and in Rastelli subtype A. The etiology of outflow tract obstruction varies and includes abnormal chordal attachments to the left ventricular side of the septum (Videoclip 15.8), discrete subaortic membrane, septal hypertrophy, and anomalous or prominent anterolateral papillary muscle [22]. The apical 5-chamber view displays the left ventricular outflow tract well. It also allows for an appropriate angle of interrogation to identify obstruction by Doppler. The parasternal long-axis view also displays the left ventricular outflow tract well and identifies the cause of obstruction at this level.

### Imaging of unbalanced CAVC

Unbalance at the level of the atria is quite rare. When suspected, it is best seen in the apical 4-chamber view (Videoclip 13.13). Atrial inflow can be evaluated with color Doppler. Pulsed-wave and continuous-wave Doppler performed in this view can help determine if there is obstruction across the atrioventricular valve inlet and the severity of that obstruction (by measurement of the mean inflow gradient). The contralateral atrium may appear hypoplastic.

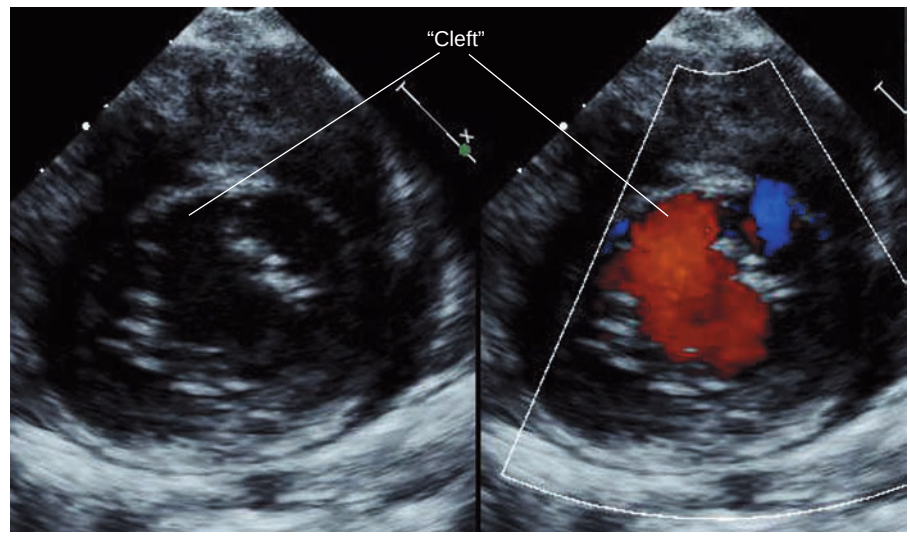


**Figure 15.21** Dual image in parasternal short-axis view demonstrating the superior and inferior bridging leaflets in the open position with the "cleft" highlighted.

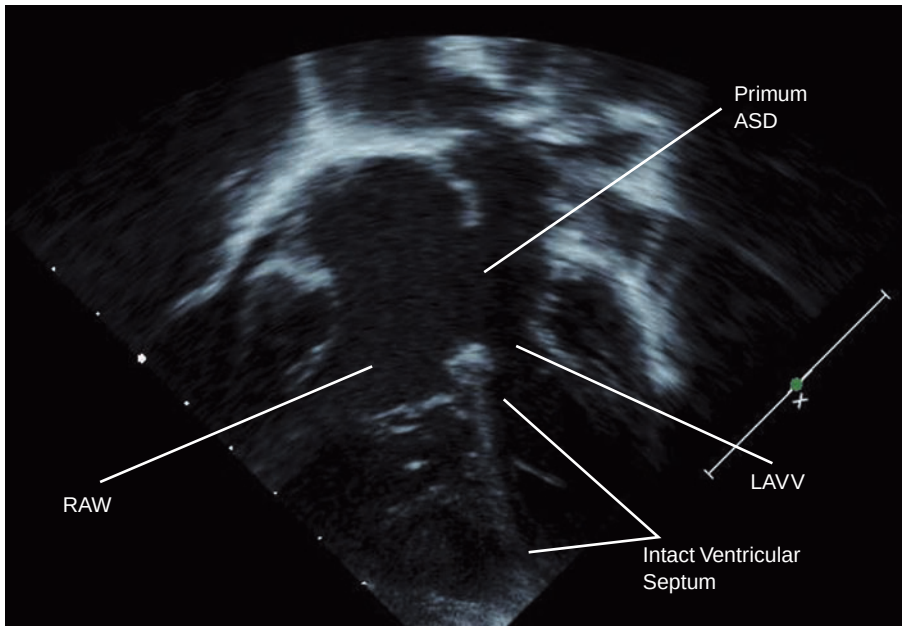


**Figure 15.22** Apical 4-chamber view of incomplete common atrioventricular canal (CAVC) with two atrioventricular valve orifices and no ventricular septal defect (VSD) component. RAVV, right atrioventricular valve; LAVV, left atrioventricular valve. ASD, atrial septal defect.

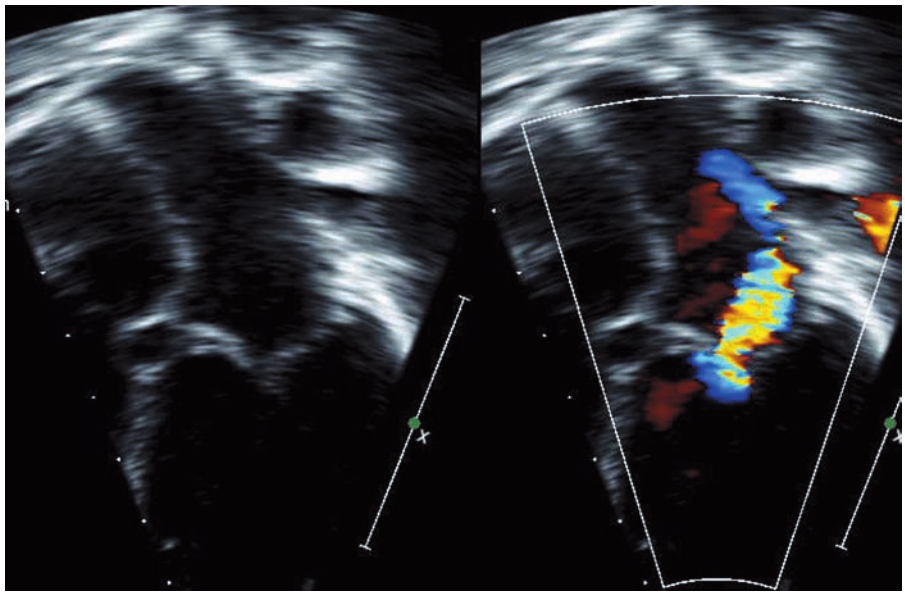

**Figure 15.23** Dual image of apical 4-chamber view of incomplete common atrioventricular canal (CAVC) with atrioventricular valve in the closed position (systole) shows regurgitation through the "cleft."

When there is unbalance at the level of the ventricle, the subcostal left anterior oblique or sagittal view help to determine how much of the valve is apportioned to each ventricle (Fig. 15.26; Videoclip 15.9) [20]. The apical 4-chamber view provides additional information because the severity of ventricular hypoplasia is usually best exhibited in this plane (Fig. 15.27(a,b)). In addition, color flow in diastole can demonstrate how much inflow crosses into the hypoplastic ventricle by measuring the secondary color Doppler inflow diameter (Fig. 15.28). In unbalanced CAVC to the right, limited inflow into the left ventricle is a risk factor for poor outcome of biventricular repair [23]. Other markers of left ventricular adequacy can also be used to determine whether biventricular repair can be successfully performed, including direction of flow at the VSD in systole (right-to-left flow is a risk factor) and direction of flow in the transverse aortic arch (retrograde flow is a risk factor) [20]. Assessment for distal levels of obstruction, particularly at the outflow tract and the arch (unbalance to the right), is an important component of the echocardiographic assessment of unbalanced CAVC.

## Additional defects

Defects commonly associated with CAVC are discussed in other chapters. However, certain lesions deserve mention

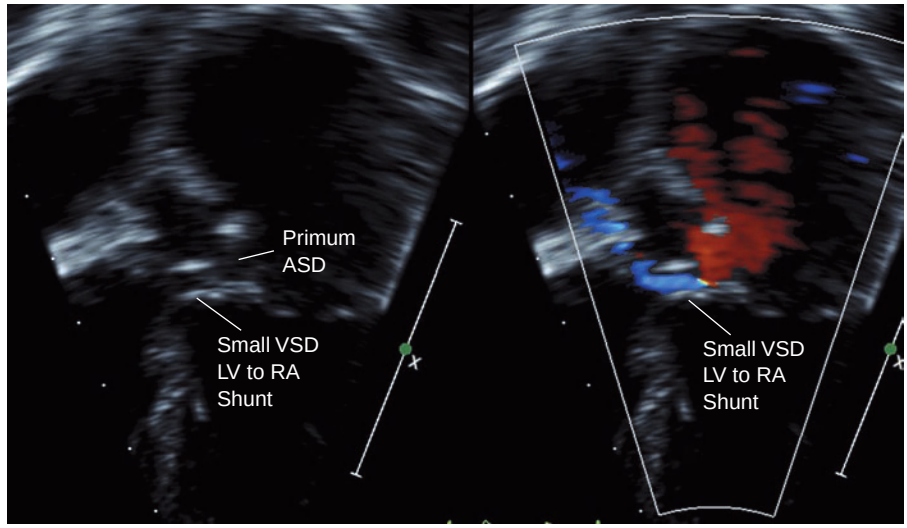


**Figure 15.24** Dual image of apical 4-chamber view of transitional common atrioventricular canal (CAVC) demonstrating a left ventricle-to-right atrial shunt through the atrioventricular valve. ASD, atrial septal defect; LV, left ventricle; RA, right atrium.

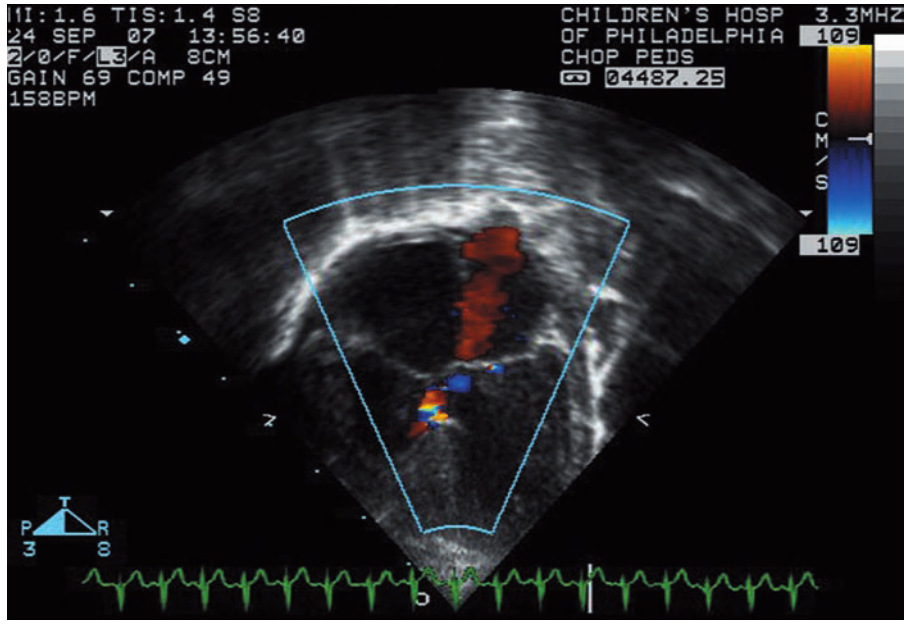


**Figure 15.25** Apical 4-chamber view with color Doppler of a transitional common atrioventricular canal (CAVC) showing a restrictive ventricular septal defect (VSD) component as evidenced by aliased color flow. Chordal attachments to the crest of the ventricular septum limit the blood flow across the ventricular septal defect.

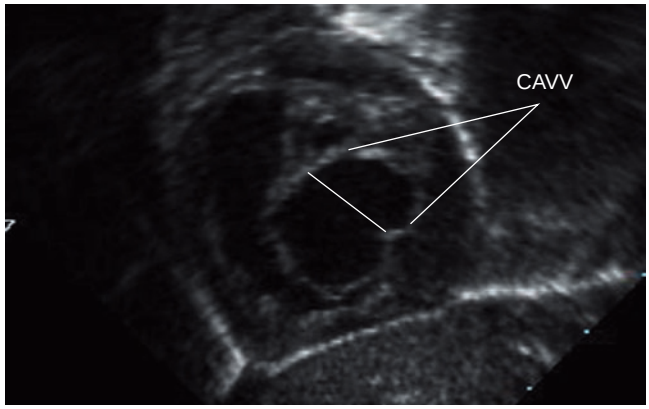


**Figure 15.26** Subcostal left anterior oblique view demonstrating mild unbalance of the common atrioventricular valve (CAVV) to the right. More of the valve opens into the right ventricle than the left ventricle.

here. Subcostal imaging, apical 4-chamber and parasternal views help to confirm the association of CAVC with tetralogy of Fallot (Fig. 15.29). In this combination of defects, anterior malalignment of the conal septum is seen in association with the features of complete CAVC (Rastelli subtype C).

A patent ductus arteriosus should always be ruled out in CAVC, particularly in children with Down syndrome. A high parasternal view (the "ductal" view) is used to confirm its presence. Suprasternal imaging is used to determine arch sidedness, to rule out coarctation of the aorta and to confirm normal systemic and pulmonary venous connections (of particular importance in those with heterotaxy syndrome).

## Prenatal assessment

In fetal echocardiography, the 4-chamber view readily identifies most of the anatomic features of CAVC, including

(a)

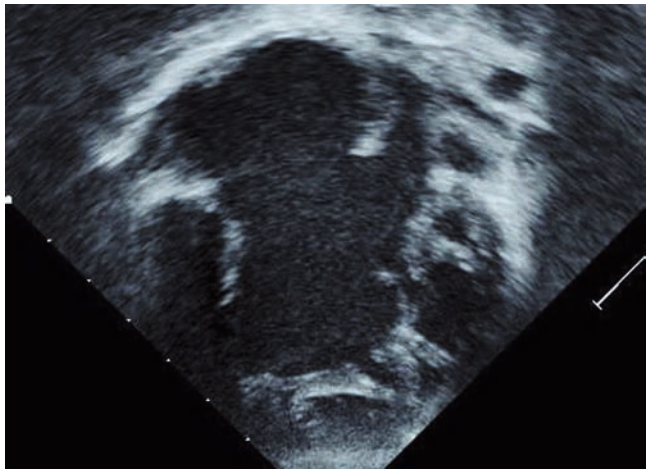

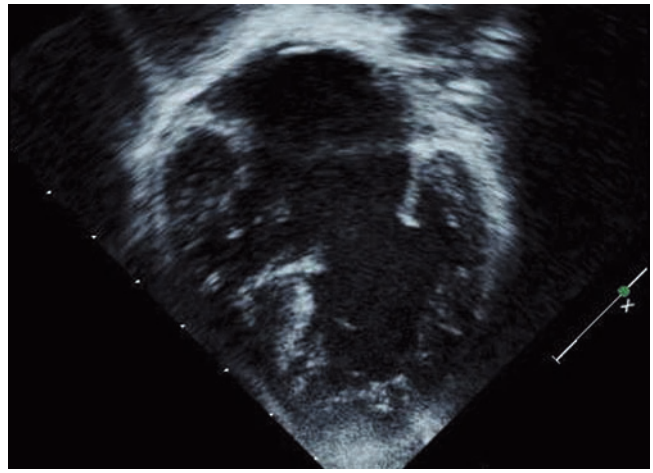

(b)

**Figure 15.27 (a)** Apical 4-chamber view showing severe unbalanced common atrioventricular canal (CAVC) to the right with left ventricular hypoplasia. The atrioventricular valve sits almost entirely over the right ventricle. **(b)** The same view showing unbalanced CAVC to the left with marked right ventricular hypoplasia.

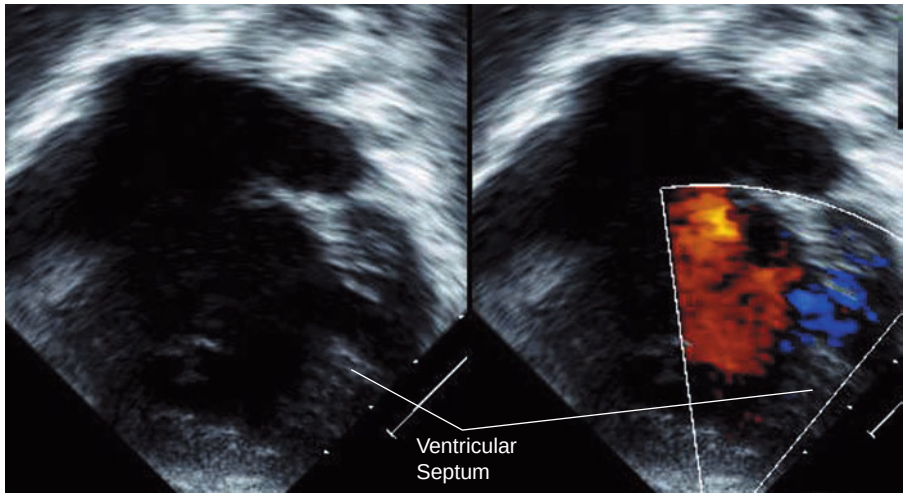


**Figure 15.28** Dual image of severe unbalanced CAVC to the right with the common atrioventricular valve emptying almost exclusively into the right ventricle. Color Doppler inflow (in red) enters exclusively into the right ventricle with no inflow seen into the left ventricle because the common AV valve obstructs flow into the left ventricle in the open position.

the common atrioventricular valve and its position within the atrioventricular defect, the size of the atrial communication and the size of the VSD (Fig. 15.30 and Videoclip 15.10). Gooseneck deformity can be seen on fetal echocardiography as well (Fig. 15.31 and Videoclip 15.11). A short-axis sweep of the heart may demonstrate the common atrioventricular valve straddling the ventricular septum, similar to the postnatal view. This is especially useful in fetuses with a small or no VSD. Color Doppler is used to identify direction of flow in the defects but is dependent on the angle of interrogation. Fetal flow patterns are demonstrated, including right-to-left atrial-level shunting and bidirectional flow at the VSD. Common atrioventricular valve regurgitation, if present, can also be seen (Videoclip 15.12). Severe atrioventricular valve regurgitation is poorly tolerated by the fetus and can result in heart failure and hydrops fetalis. Unbalance of the atrioventricular valve over the ventricles can also be seen with concomitant hypoplasia of the contralateral ventricle. CAVC with heterotaxy syndrome is suspected in prenatal diagnosis if the associated findings are identified such as significant conotruncal abnormalities or total anomalous pulmonary venous connection [24]. Complete heart block is sometimes seen in association with CAVC in the fetus, and outcome in this group of patients is poor [24]. If the diagnosis of CAVC is made before birth, serial fetal echocardiography is suggested to observe for progression of disease. When counseling families about this fetal diagnosis, amniocentesis is suggested because there is a significant association with Down syndrome.

## Imaging of the adult

Imaging the adult with CAVC can be challenging, particularly in those with Down syndrome. The subcostal acoustic window is typically not feasible in the adult patient because

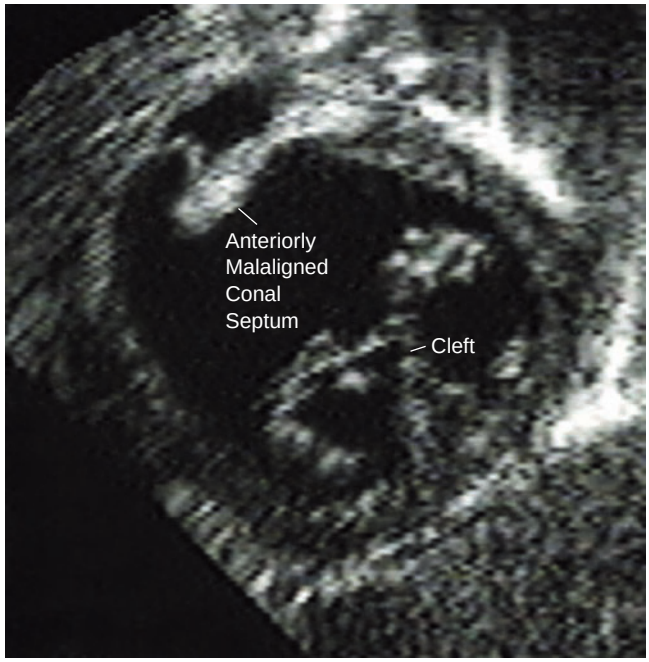


**Figure 15.29** Subcostal sagittal view demonstrating two atrioventricular valve orifices in an incomplete common atrioventricular canal (CAVC) with anterior malalignment of the conal (infundibular) septum causing subpulmonary stenosis (tetralogy of Fallot).

of limited ultrasound penetration at that distance from the heart. Thus, accurate assessment of the atrial communication (ostium primum defect) may be difficult. In contrast, the apical window provides much information in the adult with CAVC, including relative size and dilation of the ventricles, subjective assessment of biventricular shortening, the relationship of the atrioventricular valve within the defect and severity of atrioventricular valve regurgitation. Importantly, a right ventricular pressure estimate can be performed in this view to help determine if pulmonary vascular disease has developed. Most adults with unrepaired complete CAVC will have evidence of pulmonary vascular disease and may even demonstrate signs of Eisenmenger syndrome with right-to-left shunting at the ventricular level. Incomplete CAVC is occasionally diagnosed in adulthood because symptoms may not occur until the third or fourth decade of life. Similar views to those used for complete CAVC are required to make the diagnosis. The full extent of the ostium primum atrial communication may not be appreciated on transthoracic imaging. Transesophageal echocardiography (TEE) provides an excellent alternative to transthoracic imaging, particularly in adults with poor acoustic windows. The probe is in close proximity to the atrial septal structures and atrioventricular valves, and imaging of these regions is improved. Cardiac magnetic resonance imaging (MRI) can offer a noninvasive alternative to TEE in adults with suspected CAVC.

## Intraoperative assessment

Intraoperative imaging to assess the CAVC repair is typically performed using TEE. Epicardial imaging should be considered in patients in whom TEE is contraindicated or considered hazardous (i.e., very small infants, subjects with esophageal disease). Preoperative TEE imaging, if performed, confirms the diagnosis and may enhance or alter surgical planning. Although transthoracic imaging provides most of the information required for surgical intervention, preoperative TEE

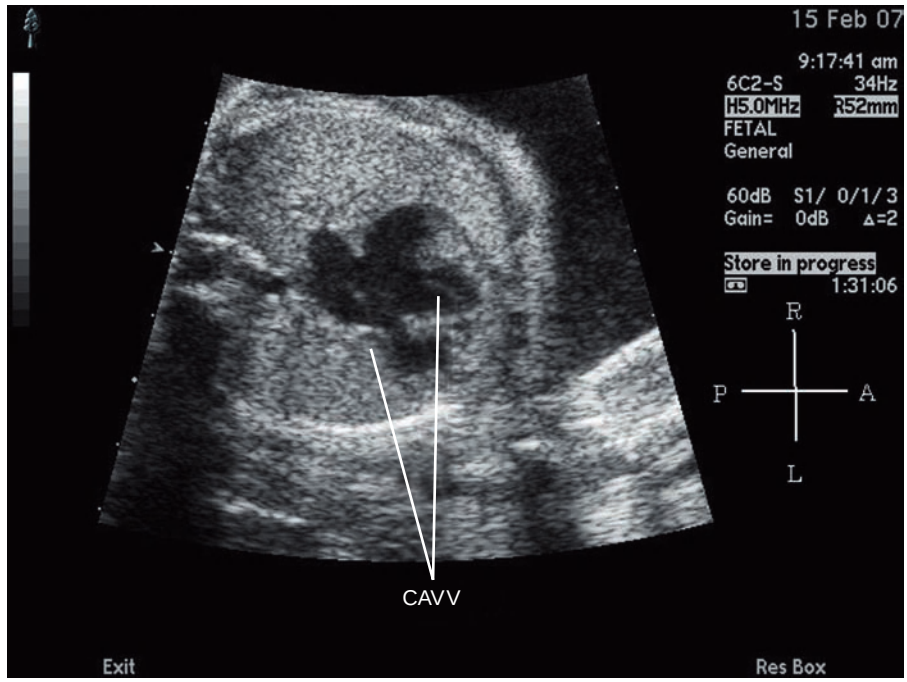


**Figure 15.30** Fetal echocardiogram in 4-chamber view showing complete common atrioventricular canal (CAVC) with a large ostium primum atrial septal defect component.

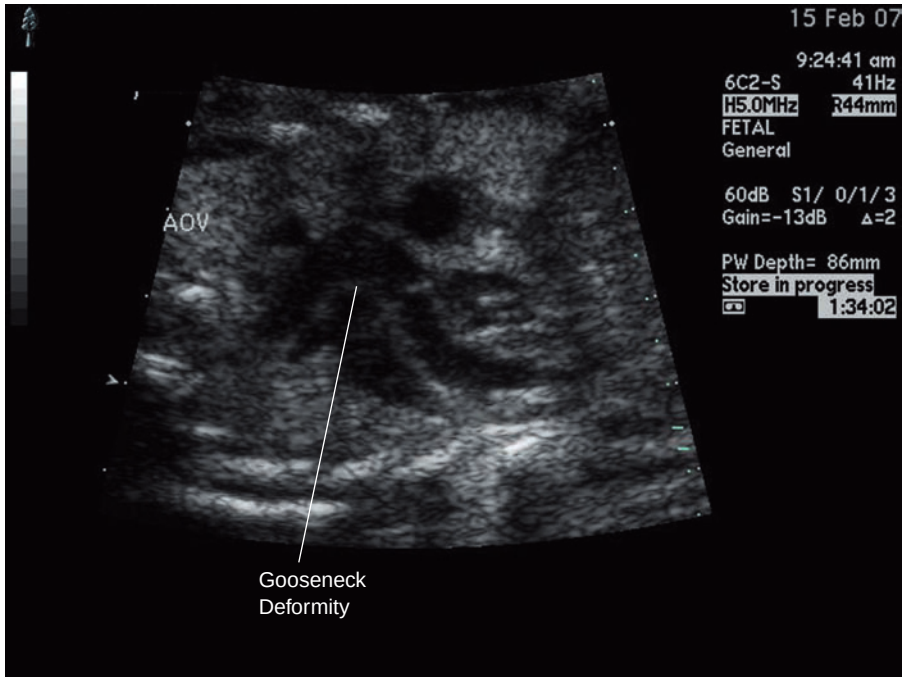


**Figure 15.31** Fetal echocardiogram highlighting the gooseneck deformity of the left ventricular outflow tract in common atrioventricular canal (CAVC).

can help to identify atrioventricular valve morphology and the etiology of atrioventricular valve regurgitation. Postoperative TEE imaging is performed as the patient is weaned from cardiopulmonary bypass to assess adequacy of the repair (Fig. 15.32 and Videoclip 15.13). The procedure identifies residual atrial and ventricular septal defects, and assesses the severity of residual atrioventricular valve regurgitation and the potential for development of atrioventricular valve stenosis. Global assessment of ventricular function is also performed. Determination of the significance of residual VSDs can be challenging. In general, a residual defect measuring less than 3 mm at its greatest diameter will not require surgical reintervention, whereas defects greater than 4 mm will require immediate reoperation. In borderline cases or in very small infants, intraoperative hemodynamic assessment of the residual shunt – by measuring the ratio of pulmonary blood flow to systemic blood flow (Qp:Qs) via oxygen saturation measurements – can help in the decision-making process [25].

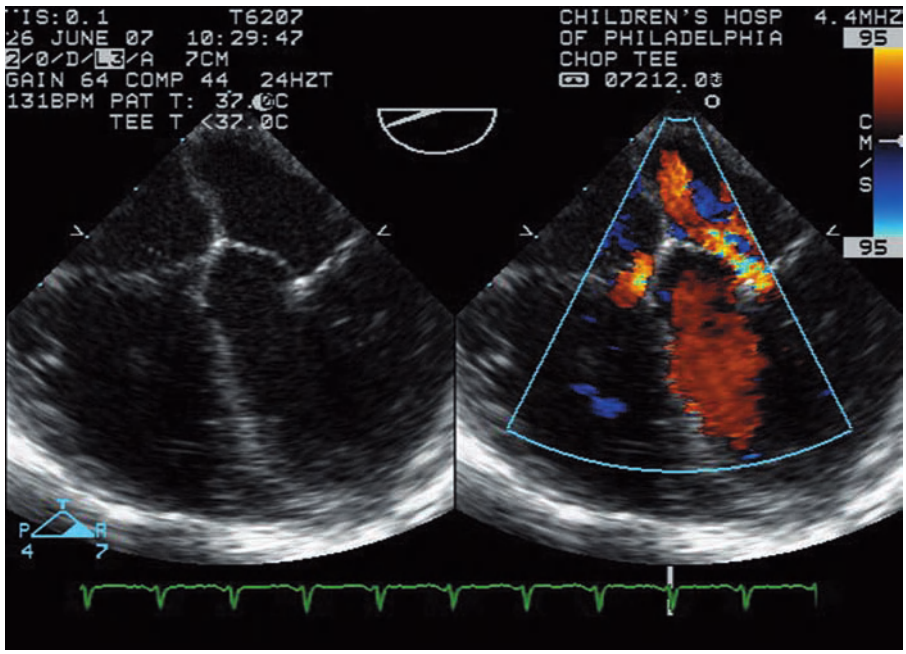


**Figure 15.32** Dual image of a postoperative transesophageal echocardiogram in the 4-chamber view showing mild left and right atrioventricular valve regurgitation with no residual atrial or ventricular septal defects.

Underestimation of the severity of atrioventricular valve regurgitation on intraoperative TEE compared with postoperative transthoracic assessment is common [26–28]. These differences are likely related to alterations in preload, afterload and inotropic support from the immediate post-bypass period to the more stable postoperative state. Moreover, color Doppler may be interpreted slightly differently with TEE in comparison with transthoracic echocardiography. Despite these limitations, intraoperative TEE is a useful screening tool to determine whether immediate reintervention is necessary.

## Follow-up assessment

Follow-up echocardiographic assessment is an important component in the long-term care of the patient with CAVC. Except in unusual circumstances, surgical intervention is almost always recommended for this defect. At present, there are no viable medical or catheter-directed therapeutic options for this lesion. Repair of CAVC generally involves patch closure of the atrial and ventricular communication (if present) using a one-patch or two-patch technique with suture approximation of the superior and inferior bridging leaflets on the left ventricular side (Fig. 15.33 and Videoclip 15.14) [29].

Surveillance soon after repair includes assessment for residual atrial and ventricular communications, and for residual atrioventricular valve regurgitation as well as assessment for pericardial effusion. Residual ASDs are unusual but can occur. Small residual VSDs are common [25,30]. Color Doppler is a very sensitive technique to assess for residual shunts. VSDs <2 mm in diameter will often close spontaneously after CAVC repair [31]. Continuous-wave Doppler can be used to measure the peak velocity of the VSD jet and help to estimate right ventricular pressure, particularly when there is no right atrioventricular valve regurgitation. Assessment for resolution of pulmonary hypertension by estimation of right ventricular pressure is also important, particularly in those with complete CAVC, Down syndrome or late diagnosis.

Assessment of left atrioventricular valve function is one of the most important components of the postoperative evaluation of CAVC. This evaluation includes assessment of the degree of atrioventricular valve regurgitation. Most repairs of CAVC include at least partial closure of the left atrioventricular valve "cleft" to improve left atrioventricular valve regurgitation (Fig. 15.34 and Videoclip 15.14). Left-sided atrioventricular valve regurgitation is the primary indication for reoperation in patients with repaired CAVC (Fig. 15.35). Significant atrioventricular valve regurgitation seen on the preoperative echocardiogram is a risk factor for severe regurgitation on postoperative study [32,33]. Residual or recurrent left atrioventricular valve regurgitation typically occurs at the interface of the superior and inferior bridging leaflets but can occur at the other commissures as well. Three-dimensional echocardiography is emerging as a useful tool to help determine the location and etiology of left atrioventricular valve regurgitation [34]. Early primary repair, before significant atrioventricular valve regurgitation develops, may help prevent reoperation in some cases [35,36].

Postoperative assessment for left atrioventricular valve stenosis is important as well. Left atrioventricular valve leaflet motion may be limited by cleft closure (Figs 15.36, 15.37 and Videoclip 15.15). More severe stenosis can occur with suture closure of the cleft in those with smaller valves

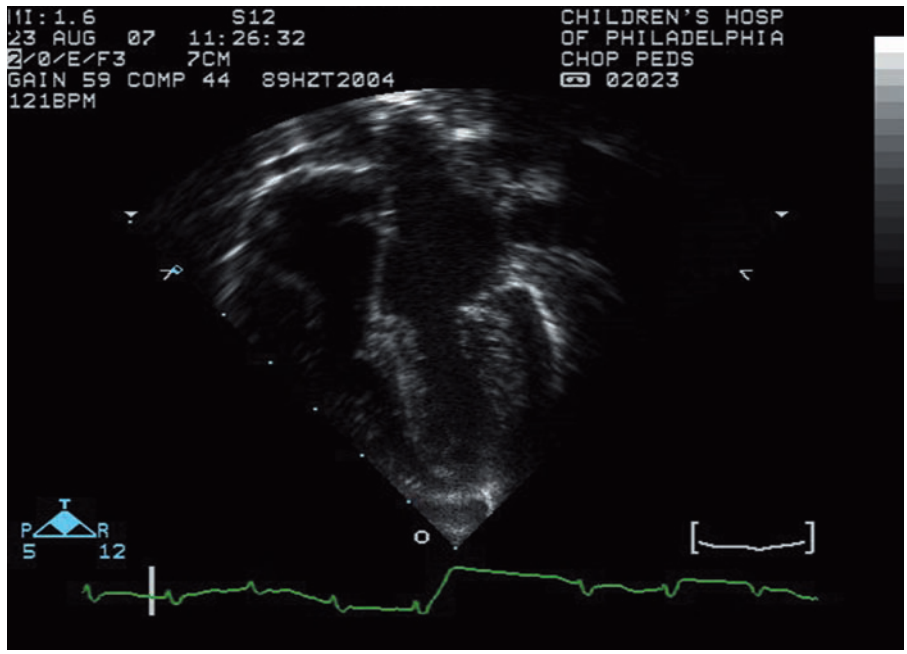


**Figure 15.33** Apical 4-chamber view in a postoperative patient with complete common atrioventricular canal (CAVC) demonstrating a single patch closing the atrial and ventricular septal defects. The patch also divides the common atrioventricular valve into a right and left atrioventricular valve.

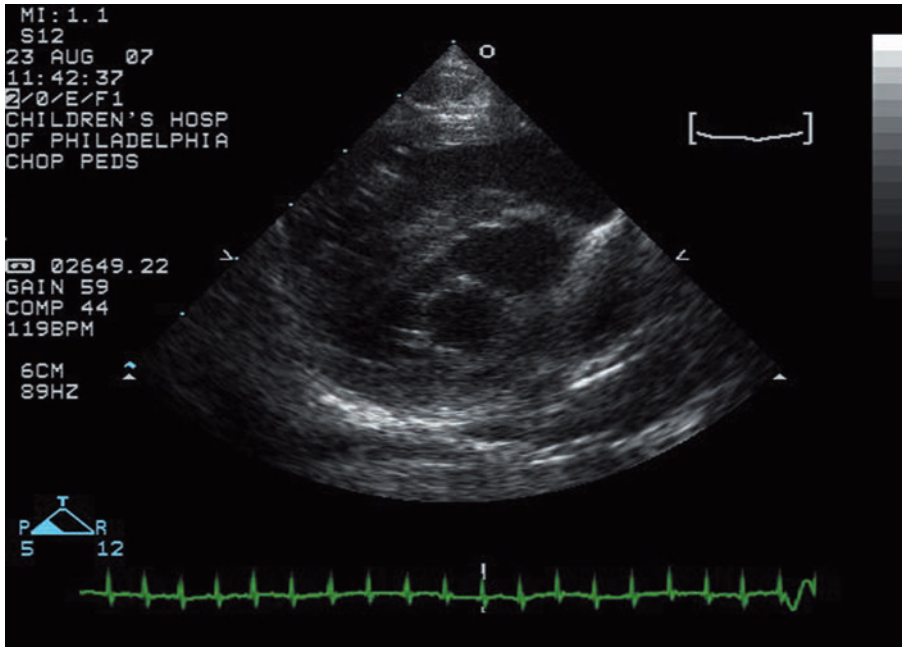


**Figure 15.34** Parasternal short-axis view showing partial suture closure of the "cleft" of the left atrioventricular valve in a postoperative patient. Cleft closure can sometimes result in the development of left-sided atrioventricular valve stenosis.

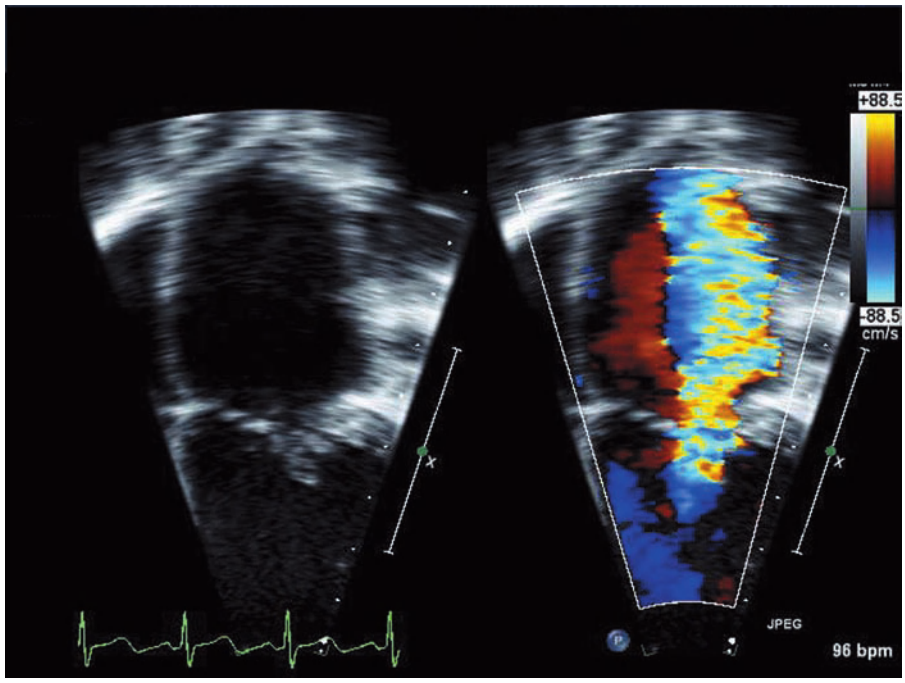


**Figure 15.35** Dual image of apical 4-chamber view demonstrating severe left atrioventricular valve regurgitation through a residual "cleft" with a markedly dilated left atrium. The regurgitant jet occupies more than 50% of the atrial area.

preoperatively. It can also be seen after surgical division in those with single papillary muscles or maldistribution of the common atrioventricular valve.

Long-term assessment of CAVC repair includes surveillance for progression of left atrioventricular valve regurgitation and/or stenosis. In addition, evaluation of ventricular function and estimation of pulmonary artery pressure remain important. Left ventricular outflow tract obstruction, if present preoperatively, may progress in the long term and may impact aortic valve function.

Many techniques have been developed to assess left atrioventricular valve regurgitation. Importantly, no method is the gold standard, especially in the pediatric population. Both qualitative and quantitative methods exist and all have limitations. The majority of echocardiographers continue to utilize the qualitative method of estimating the left

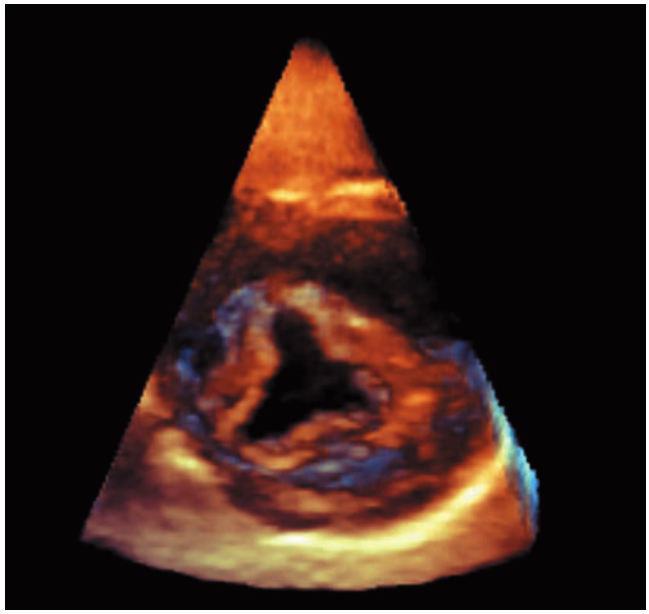

**Figure 15.36** 3D image highlighting the left atrioventricular valve "cleft" of AVC.

atrioventricular valve regurgitation jet area compared with the left atrium area [37]. This method has been reported in correlation with angiographic grading in children [38]. It does not require complicated calculation and can be performed serially in the same patient to assess for progression over time. The hemodynamic impact of valve regurgitation can also be assessed. Left atrial and left ventricular dilation are common when atrioventricular regurgitation is severe (Fig. 15.35 and Videoclip 15.14). Other quantitative methods include proximal isovelocity surface area (PISA), vena contracta (regurgitant jet area), and assessment of the severity of pulmonary venous flow reversal [39]. Discussion of these methods can be found in Chapter 6.

Echocardiography demonstrates most of the important characteristics of all forms of CAVC defects. Diagnostic cardiac catheterization for these lesions is usually not required unless there is concern for increased pulmonary vascular resistance. Postoperative echocardiographic surveillance helps diagnose residual or recurrent abnormalities that may require intervention.

## Acknowledgements

I would like to acknowledge and thank Dr Paul M. Weinberg for his assistance and guidance in the writing of this chapter and for the contribution of his photographs of the pathologic specimens.

## References

1. Marx GR, Fyler DC. Endocardial cushion defects. In: Keane JF, Lock JE, Fyler DC (eds) *Nadas' Pediatric Cardiology*. Philadelphia, PA: Saunders Elsevier, 2006;663–74.
2. Hoffman JI, Kaplan S. The incidence of congenital heart disease. *J Am Coll Cardiol* 2002;39:1890–900.
3. Barlow GM, Chen XN, Shi ZY et al. Down syndrome and congenital heart disease: a narrowed region and a candidate gene. *Genet Med* 2001;3:91–101.

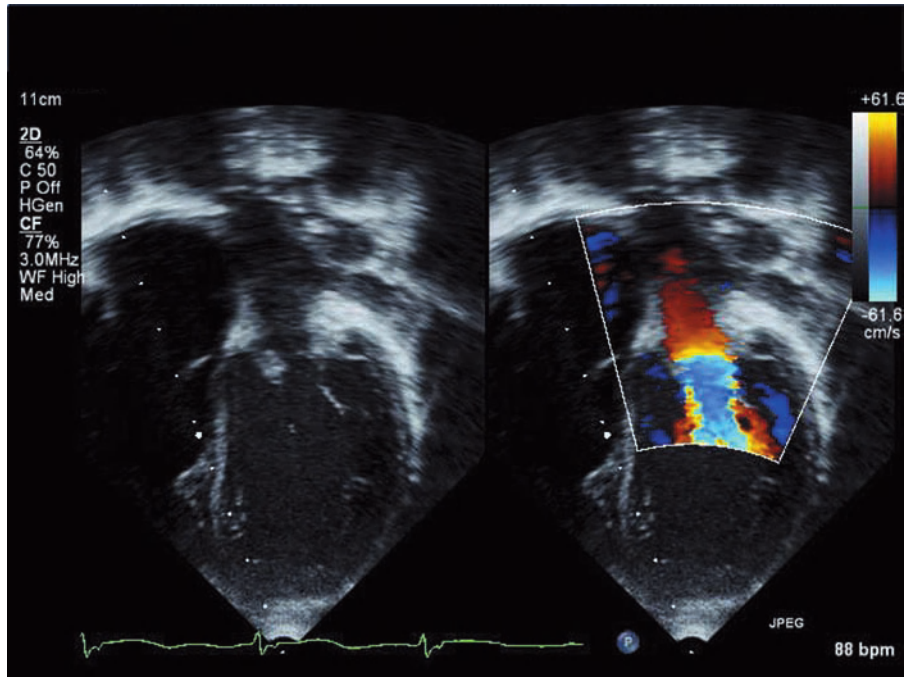


**Figure 15.37** Dual image of apical 4-chamber view. The two-dimensional image shows limited excursion of the atrioventricular valve leaflets. Color Doppler demonstrates inflow acceleration and mild left atrioventricular valve stenosis after "cleft" closure.

4. Maslen CL. Molecular genetics of atrioventricular septal defects. *Curr Opin Cardiol* 2004;19:205–10.
5. Kumar A, Williams CA, Victorica BE. Familial atrioventricular septal defect: possible genetic mechanisms. *Br Heart J* 1994;71: 79–81.
6. Devriendt K, Van Schoubroeck D, Eyskens B et al. Prenatal diagnosis of a terminal short arm deletion of chromosome 8 in a fetus with an atrioventricular septal defect. *Prenat Diagn* 1998; 18:65–7.
7. Loewy Kirby M. *Endocardium, Cardiac Cushions, and Valve Development in Cardiac Development*. New York: Oxford University Press, 2007;119–31.
8. Butcher J, Markwald RR. Valvulogenesis: The moving target. *Phil Trans R Soc B* 2007;2130:1–15.
9. Eisenberg LM, Markwald RR. Molecular regulation of atrioventricular valvuloseptal morphogenesis. *Circ Res* 1995;77:1–6.
10. Barrea C, Levasseur S, Roman K et al. Three-dimensional echocardiography improves the understanding of left atrioventricular valve morphology and function in atrioventricular septal defects undergoing patch augmentation. *J Thorac Cardiovasc Surg* 2005;129:746–53.
11. Anderson RH, Ho SY, Falcao S et al. The diagnostic features of atrioventricular septal defect with common atrioventricular junction. *Cardiol Young* 1998;8:33– 49.
12. Rastelli GC, Ongley PA, Kirklin JW, McGoon DC. Surgical repair of complete form of persistent common atrioventricular canal. *J Thorac Cardiovasc Surg* 1968;55:299–308.
13. Mahle WT, Shirali GS, Anderson RH. Echo-morphological correlates in patients with atrioventricular septal defect and common atrioventricular junction. *Cardiol Young* 2006;16 (Suppl. 3):43–51.
14. Bharati S, Lev M. The specturm of common atrioventricular orifice (canal). *Am Heart J* 1973;86:553–61.
15. Chin AJ, Bierman FZ, Sanders SP et al. Subxiphoid 2-dimensional echocardiographic identification of left ventricular papillary muscle anomalies in complete common atrioventricular canal. *Am J Cardiol* 1983;51:1695–9.
16. Clapp S, Perry BL, Farooki ZQ et al. Down syndrome, complete atrioventricular canal and pulmonary vascular obstructive disease. *J Thorac Cardiovasc Surg* 1990;100:115–21.
17. Ilbawi MN, Idriss FS, DeLeon SY et al. Unusual mitral valve abnormalities complicating surgical repair of endocardial cushion defects. *J Thorac Cardiovasc Surg* 1983;85:697–704.
18. Michielon G, Stellin G, Rizzoli G et al. Left atrioventricular valve incompetence after repair of common atrioventricular canal defects. *Ann Thorac Surg* 1995;60(6 Suppl.): S604–9.
19. Weinberg M Jr, Miller RA, Hastreiter AR et al. Congestive heart failure in children with atrial septal defect. *J Thorac Cardiovasc Surg* 1966;51:81–7.
20. Cohen MS, Jacobs ML, Weinberg PM, Rychik J. Morphometric analysis of unbalanced common atrioventricular canal using two-dimensional echocardiography. *J Am Coll Cardiol* 1996;28: 1017–23.
21. Silverman NH, Zuberbuhler JR, Anderson RH. Atrioventricular septal defects: cross-sectional echocardiographic and morphologic comparisons. *Int J Cardiol* 1986;13:309–31.
22. Draulans-Noe H, Weinink ACG. Anterolateral muscle bundle of the left ventricle in atrioventricular septal defect: left ventricular outflow tract and subaortic stenosis. *Pediatr Cardiol* 1991;12:83–8.
23. Szwast A, Marino BS, Rychik J et al. The LV inflow index: a novel echocardiographic parameter for predicting biventricular repair success in unbalanced atrioventricular canal. *J Am Soc Echocardiogr* 2008;21:605 [abstr.].
24. Cohen MS. Clarifying anatomical complexity: diagnosing heterotaxy syndrome in the fetus. *Prog Pediatr Cardiol* 2006;22: 61–70.
25. Yang SG, Novello R, Nicolson SC et al. Evaluation of ventricular septal defect repair using intraoperative transesophageal echocardiography: frequency and significance of residual defects in infants and children. *Echocardiography* 2000;17:681–4.
26. Lee HR, Montenegro LM, Nicolson SC et al. Usefulness of intraoperative transesophageal echocardiography in predicting the degree of mitral regurgitation secondary to atrioventricular defect in children. *Am J Cardiol* 1999;83:750–3.
27. Kim HK, Kim WH, Hwang SW et al. Predictive value of intraoperative transesophageal echocardiography in complete atrioventricular septal defect. *Ann Thorac Surg* 2005;80:56–9.
28. Honjo O, Kotani Y, Osaki S et al. Discrepancy between intraoperative transesophageal echocardiography and postoperative transthoracic echocardiography in assessing congenital valve surgery. *Ann Thorac Surg* 2006;82:2240–6.
29. Castaneda AR, Jonas RA, Mayer JE, Hanley FL. Atrioventricular canal defect. In: *Cardiac Surgery of the Neonate and Infant*. Philadelphia, PA: W.B. Saunders, 1994;167–86.
30. Rychik J, Norwood WI, Chin AJ. Doppler color flow mapping assessment of residual shunt after closure of large ventricular septal defects. *Circulation* 1991;84:153–61.
31. Dodge-Khatami A, Knirsch W, Tomaske M et al. Spontaneous closure of small residual ventricular septal defects after surgical repair. *Ann Thorac Surg* 2007;83:902–5.
32. Ten Harkel AD, Cromme-Dijkhuis AH, Heinerman BC et al. Development of left atrioventricular valve regurgitation after correction of atrioventricular septal defect. *Ann Thorac Surg* 2005;79:607–12.
33. Murashita T, Kubota T, Oba J et al. Left atrioventricular valve regurgitation after repair of incomplete atrioventricular septal defect. *Ann Thorac Surg* 2004;77:2157–62.
34. Takahashi K, Guerra V, Roman KS et al. Three-dimensional echocardiography improves the understanding of the mechanisms and site of left atrioventricular valve regurgitation in atrioventricular septal defect. *J Am Soc Echocardiogr* 2006;19: 1502–10.
35. Suzuki K, Tatsuno K, Kikuchi T, Mimori S. Predisposing factors of valve regurgitation in complete atrioventricular septal defect. *J Am Coll Cardiol* 1998;32:1449–53.
36. Boening A, Scheewe J, Heine K et al. Long-term results after surgical correction of atrioventricular septal defects. *Eur J Cardiothorac Surg* 2002;22:167–73.
37. Helmcke F, Nanda NC, Hsiung M et al. Color Doppler assessment of mitral regurgitation with orthogonal planes. *Circulation* 1987;75:175–83.
38. Wu YT, Chang AC, Chin AJ. Semiquantitative assessment of mitral regurgitation by Doppler color flow imaging in patients aged < 20 years. *Am J Cardiol* 1993;71:727–32.
39. Khanna D, Miller AP, Nanda NC et al. Transthoracic and transesophageal echocardiographic assessment of mitral regurgitation severity: Usefulness of qualitative and semi-quantitative techniques. *Echocardiography* 2005;22:748–69.

# 4

# Anomalies of the Ventriculoarterial Junction and Great Arteries

*Echocardiography in Pediatric and Congenital Heart Disease: From Fetus to Adult*
Edited by Wyman W. Lai, Luc L. Mertens, Meryl S. Cohen and Tal Geva
 ISBN: 978-1-405-17401-5

# 16 Anomalies of the Right Ventricular Outflow Tract and Pulmonary Valve

**Matthew S. Lemler and Claudio Ramaciotti**

University of Texas, Southwestern Medical Center at Dallas; Division of Cardiology, Children's Medical Center of Dallas, Dallas, TX, USA

Diseases of the right ventricular (RV) outflow tract result in either obstruction to flow into the pulmonary arteries, or regurgitation across the pulmonary valve. The latter can occur either as the primary manifestation of disease, as is the case in absent pulmonary valve syndrome, or as a consequence of either surgical or catheterization management of obstructive lesions. This chapter focuses on isolated abnormalities of the RV outflow tract. RV outflow tract abnormalities associated with other complex conditions will be discussed in other parts of this book. Pathology of the RV outflow tract is divided into the following headings: pulmonary valve stenosis, subpulmonary stenosis, absent pulmonary valve (nonconotruncal) and main pulmonary artery stenosis.

## Pulmonary valve stenosis

Pulmonary valve stenosis is defined as an obstruction of the RV outflow at the level of the pulmonary valve. It is the fourth most common congenital heart lesion, occurring in approximately 53 (range 35–83) per 100 000 live births [1]. Depending on severity, presentation can range from in utero diagnosis to discovery in the older patient evaluated for an asymptomatic murmur. Pulmonary valve stenosis is usually found in isolation. However, when the valve is dysplastic, there is an increased incidence of additional cardiac and noncardiac malformations [2]. Syndromes that are commonly associated with pulmonary valve stenosis include Noonan, congenital rubella, Williams and Alagille syndromes [3–5].

### Morphology and classification

The normal pulmonary valve consists of three leaflets supported in a semilunar fashion within the sinuses of the pulmonary trunk. The free edges of each leaflet are appreciably longer than the chord of the sinus that supports it. This arrangement permits the leaflets to fit snugly together in the closed position [6]. Morphologic types of pulmonary valve stenosis can be divided into three categories:

**1** The most common form is the dome-shaped valve. Fusion or absence of the commissures results in a small central opening. The degree of fusion determines the size of the orifice. The valve leaflets remain mobile in this type of stenosis [2,6].

**2** Thickened and mucoid leaflets with poor mobility are typical of dysplastic pulmonary valves. The thickened, dysplastic leaflets are characteristically associated with a narrowed sinotubular junction [6,7].

**3** Unicuspid and bicuspid pulmonary valves rarely occur in isolated pulmonary valve stenosis. They classically occur with more complex lesions such as tetralogy of Fallot [7]. Only 4% of quadricuspid pulmonary valves result in clinically important pathology; of these 33% result in stenosis and 67% cause regurgitation [8].

Poststenotic dilation of the main pulmonary artery is common in patients with pulmonary valve stenosis. However, it does not occur in patients with dysplastic pulmonary valves. Additionally, the degree of stenosis does not correlate with the size of the main pulmonary artery.

### Pathophysiology

The clinical consequences of pulmonary valve stenosis are directly related to the degree of obstruction caused by the valve. Normal or only mild RV hypertrophy occurs in response to mild or moderate pulmonary valve stenosis. Marked RV hypertrophy develops as a consequence of high-pressure work associated with severe pulmonary valve stenosis (Fig. 16.1a,b; Videoclip 16.1). The infundibular region of the RV is easily affected by hypertrophy and can give rise to dynamic and/or anatomical subvalvar obstruction. Severe RV hypertrophy can lead to reduced end-systolic deformation of the right ventricle (RV), diminished elastic recoil in early diastole and elevated RV pressure in early diastole [9]. Significant elevation of RV systolic and diastolic pressures results in the elevation of right atrial pressure and dilation of the right atrium. Right-to-left shunting may then occur in the presence of an atrial septal defect (ASD) or a patent foramen ovale (PFO) (Fig. 16.1d).

*Echocardiography in Pediatric and Congenital Heart Disease: From Fetus to Adult*
Edited by Wyman W. Lai, Luc L. Mertens, Meryl S. Cohen and Tal Geva
 ISBN: 978-1-405-17401-5

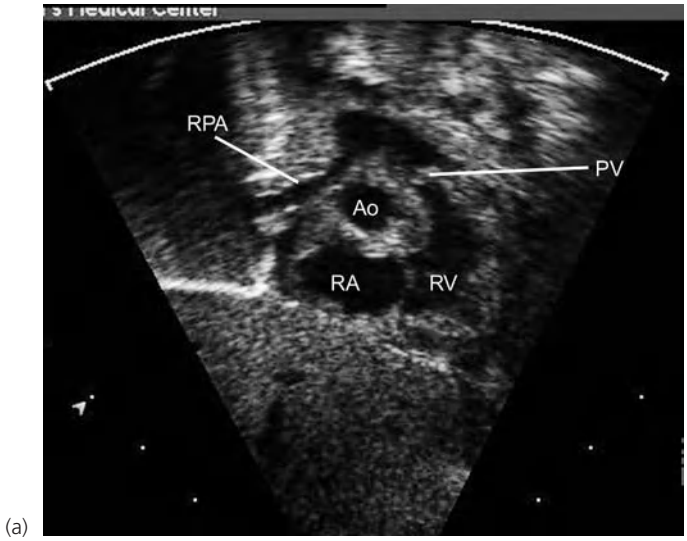


(a)

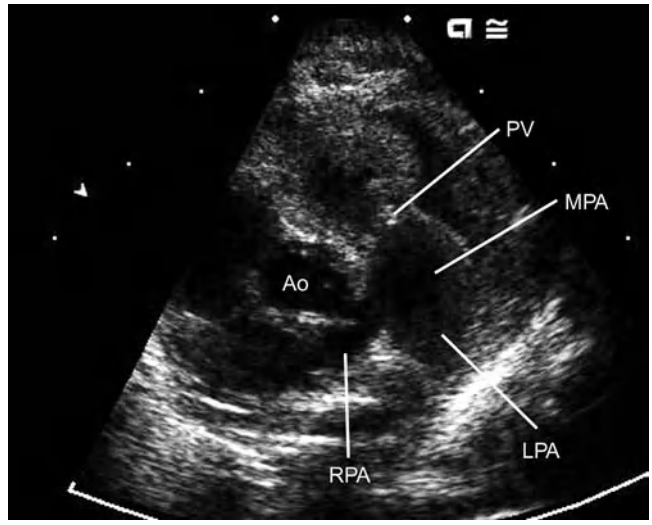


(c)

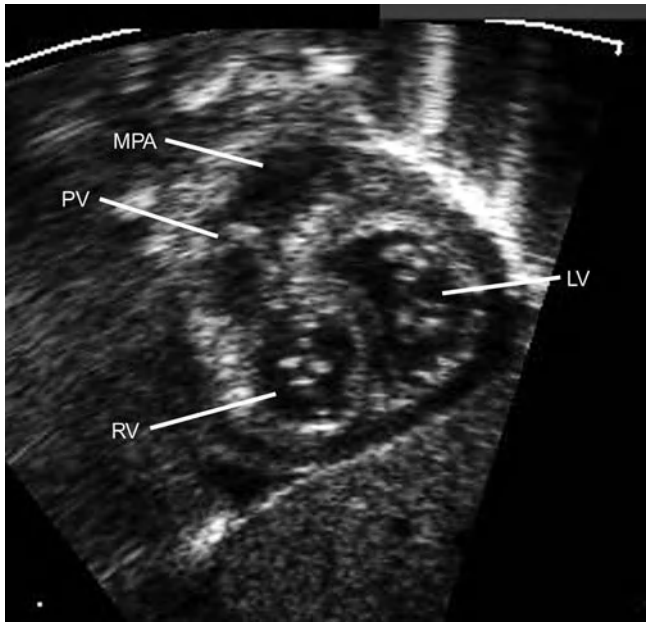


(b)

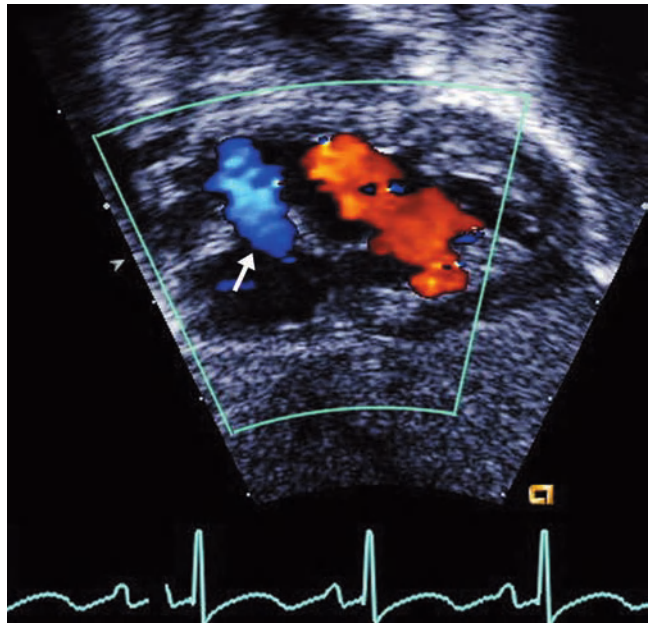

(d)

**Figure 16.1** Term infant with critical pulmonary valve stenosis prior to intervention. **(a)** Subcostal long-axis view: dysplastic pulmonary valve with systolic doming. **(b)** Subcostal short-axis view: systolic frame showing subvalvar narrowing secondary to dynamic compression of hypertrophied muscle bundles, the intraventricular septum deviates toward the left ventricle indicative of supra-systemic right ventricular systolic pressure. **(c)** Parasternal short-axis view: dilated main and proximal left pulmonary arteries. **(d)** Subcostal long-axis view: right-to-left flow across a patent foramen ovale (arrow). Ao, aorta; LV, left ventricle; RA, right atrium; RV, right ventricle; PV, pulmonary value; MPA, main pulmonary artery; RPA, right pulmonary artery; LPA, left pulmonary artery.

Critical pulmonary valve stenosis represents the most severe form of RV outflow obstruction. It is separated from severe stenosis in the neonate by the inability of the RV to maintain systemic arterial saturations above 90% in the absence of a patent ductus arteriosus (PDA) [10]. Adequate pulmonary blood flow becomes dependent on left-to-right shunting across the PDA. As this places an extra volume load on a left ventricle (LV) already facing the increased afterload present during the neonatal transitional period, poor biventricular function ensues. RV end-diastolic pressure increases, causing right-to-left shunting across the PFO, with decreased flow through the RV outflow tract to the pulmonary arteries. Although the right-to-left atrial shunting results in cyanosis, it also maintains cardiac output by providing preload to the LV.

Progression of pulmonary stenosis commonly occurs in neonates, but is rare after the first few months of life. Rowland et al. showed that 29% of patients who were evaluated at less than 1 month of age increased their gradient

more than 20 mm Hg. By contrast, only 8% of patients initially evaluated past 1 month of age showed progression of their stenosis gradient by 20 mm Hg or more. No patients over 2 years of age with a gradient <50 mm Hg developed severe stenosis [11]. The rapid progression of pulmonary stenosis in the neonate is at least partially the result of normal hemodynamic changes, including an increase in cardiac output [12] and drop in pulmonary vascular resistance [13].

## Imaging

### Goals of examination and transthoracic imaging

In the setting of pulmonary valve stenosis, the objectives of echocardiographic examination can be summarized as follows:

- Define the morphology of the pulmonary valve with particular attention to leaflet mobility and thickness.
- Measure the diameter of the pulmonary annulus.
- Measure the diameters of the main and branch pulmonary arteries.
- Measure the Doppler estimated peak and mean gradients across the valve from multiple views (Fig. 16.2).
- Identify any additional levels of obstruction (e.g., infundibular, supravalvar).
- Determine the presence of a PDA; if present, determine the size and direction of flow.
- Determine the degree of pulmonary valve regurgitation.
- Evaluate the degree of RV hypertrophy and dilation.
- Assess RV function.
- Estimate RV systolic pressure based on the peak velocity of the tricuspid regurgitation jet.
- Assess size and morphology of the tricuspid valve.
- Evaluate the degree of tricuspid valve regurgitation.
- Assess size of the right atrium.
- Evaluate the atrial septum for a shunt: if present, measure the defect's size and determine the direction of flow by color and spectral Doppler.
- Determine the presence of associated defects.

### Prenatal assessment

Isolated pulmonary valve stenosis can be reliably diagnosed in the fetus. In patients with mild or moderate pulmonary valve stenosis the cardiac chambers tend to be normal in size. In addition, the PDA demonstrates normal antegrade flow. Therefore, the examiner must rely on the size, morphology and flow acceleration across the pulmonary valve [14]. In fetuses with severe or critical pulmonary valve stenosis the morphology of the RV is often determined by the degree of tricuspid valve regurgitation. In patients with severe tricuspid valve regurgitation, the RV is dilated and the ventricular wall is normal or thinned, whereas in patients without tricuspid regurgitation, the RV is hypertrophied (Fig. 16.3) [15,16]. The degree of enlargement of the right atrium correlates with the degree of tricuspid valve regurgitation [15]. In patients with critical pulmonary valve stenosis, flow across the PDA is retrograde into the pulmonary arteries. Serial evaluations of the fetus diagnosed with pulmonary stenosis are important because progression from mild to critical pulmonary stenosis or even atresia has been well documented [15,17].

It is important to assess flow across the PFO, as fetuses with severe pulmonary stenosis and obstruction to flow across the PFO are at high risk of developing hydrops [18]. As a result of decreased preload, the LV is unable to generate adequate cardiac output. However, restrictive right-to-left shunting across the foramen ovale is difficult to diagnose because the investigator cannot rely on a significant increase in velocity to identify the restriction [19]. Therefore, it is important also

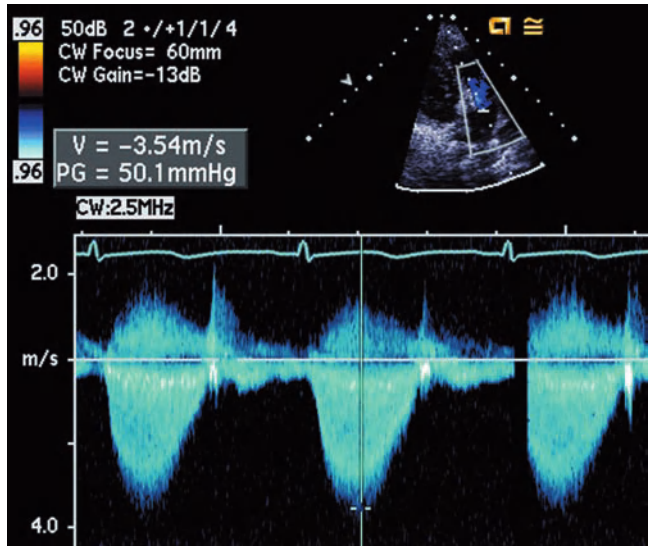


**Figure 16.2** Pulmonary valve stenosis: continuous-wave Doppler showing increased flow velocity with a predicted maximum instantaneous gradient of approximately 50 mm Hg.

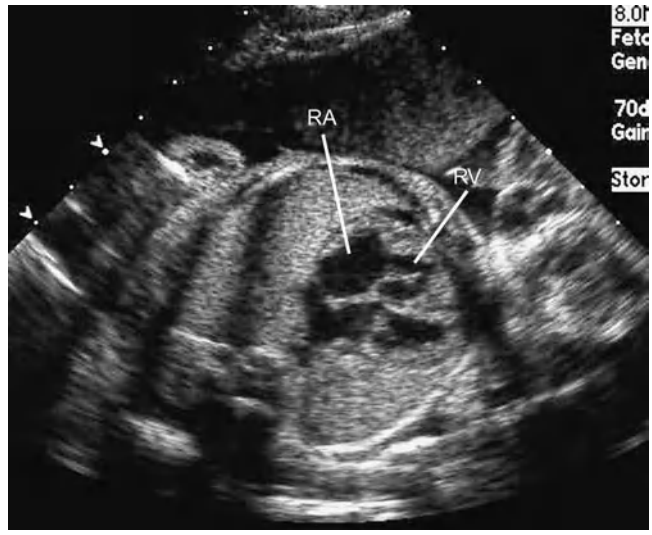


**Figure 16.3** 27 week gestation fetus with critical pulmonary valve stenosis. The four-chamber view demonstrates severely hypertrophied right ventricle (RV) with right atrial (RA) enlargement.

to look for signs of impending hydrops fetalis, including increased cardiothoracic ratio, pericardial effusion, holosystolic tricuspid valve regurgitation and abnormal venous Doppler flow [18].

### Preoperative and precatheterization assessment

The anatomy of the pulmonary valve is determined by two-dimensional (2D) imaging. The pulmonary valve is appreciated in the parasternal long-axis view by tilting the transducer toward the patient's left shoulder, and in the parasternal short-axis view at the base of the heart. In addition to the morphology of the valve, the subcostal sagittal (short-axis) and right anterior oblique views provide an excellent opportunity to assess additional levels of obstruction. Using standard echocardiography views, the pulmonary valve is imaged in its longitudinal axis. However, using a high-parasternal view, a cross-sectional image of the pulmonary valve can be obtained by visualizing the short axis of the aortic valve and rotating the transducer clockwise ~10–20° (Fig. 16.4 and Videoclip 16.2(a,b)) [20].

Indirect methods to quantitate the degree of pulmonary valve stenosis include assessments of RV thickness and the degree of systolic flattening of the ventricular septum. Although these findings are helpful adjuncts, the most reliable measurements of RV obstruction employ pulsed- and continuous-wave Doppler. When evaluating a patient with pulmonary valve stenosis by Doppler it is important to understand that pressure gradients depend on the amount of flow across the valve [21]. Conditions that reduce the flow across the valve will underestimate the degree of obstruction. For example, in patients with severe RV dysfunction the ventricle is unable to generate enough pressure to overcome the increased afterload caused by the stenotic valve and maintain an adequate stroke volume. Additionally, in patients with pulmonary artery hypertension or a PDA, the distal pulmonary artery pressure is elevated, thus masking the true impediment to flow caused by the narrowed valve. However, conditions that cause intracardiac left-to-right shunting such as an ASD, and, therefore, increase blood flow across the pulmonary valve will falsely elevate the gradient. The Bernoulli equation is most accurate in patients with discrete stenosis. The equation becomes less reliable in patients with long-segment stenosis or multiple stenoses in series. Although the peak instantaneous gradient obtained by Doppler is often higher than the peak-to-peak gradient obtained in the cardiac catheterization laboratory [22], the literature supports the accuracy of Doppler-derived peak instantaneous gradients to predict catheter-derived maximum instantaneous gradients [22–24]. In contrast, Silvilairat

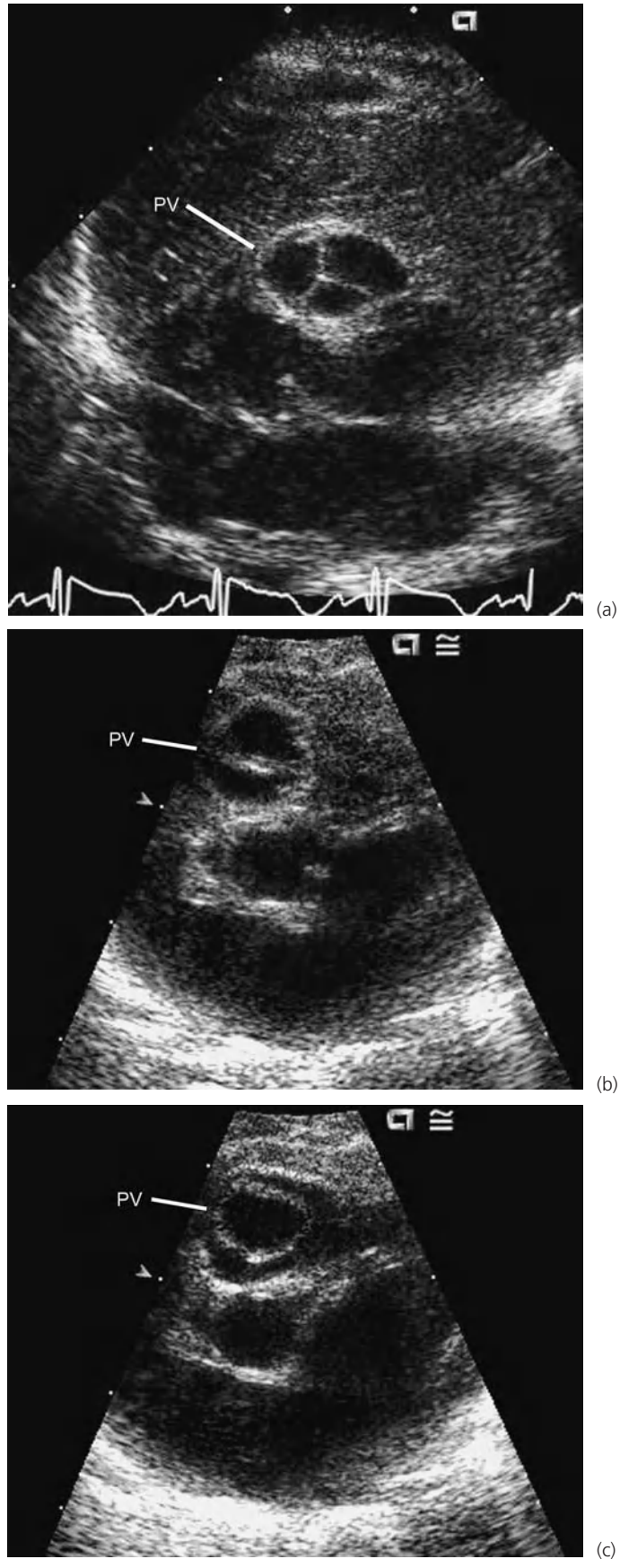


**Figure 16.4** (*right*) High parasternal view showing a cross-section of the pulmonary valve (PV). **(a)** Normal trileaflet pulmonary valve seen in diastole. **(b)** Bicuspid pulmonary valve in diastole. **(c)** Bicuspid pulmonary valve in systole.

et al. reported that outpatient mean Doppler gradients more accurately predicted catheter peak-to-peak gradients in both isolated pulmonary valve stenosis [25] and complex pulmonary outflow stenosis [26]. Because echocardiography is now the primary diagnostic and monitoring modality, whereas natural history studies and thresholds for intervention are determined by catheter-obtained gradients, it is important to understand the fundamental differences between these modalities in order to reconcile differences between Doppler-estimated and catheter-measured gradients (see Chapter 2 for further details) [27–29].

### Transcatheter and surgical treatment

Catheter balloon dilation is now the primary modality for treatment of pulmonary valve stenosis. However, surgical intervention is still occasionally required for patients with infundibular stenosis or supravalvar stenosis, and for patients with dysplastic pulmonary valves without poststenotic dilation. Echocardiography is the main diagnostic modality for planning catheterization and surgical interventions. Indications for balloon dilation of pulmonary valve stenosis remain controversial. The excellent results and low morbidity of the procedure have led to use of balloon valvuloplasty even in patients with mild obstruction. Mullins has recommended balloon valvuloplasty for patients with Doppler-measured peak instantaneous gradients as low as 35 mm Hg, along with other objective signs of RV hypertrophy by echocardiography or electrocardiography [30]. Others feel that the RV systolic pressure should exceed 55–60 mm Hg [6]. Patients with critical pulmonary valve stenosis are almost uniformly treated in the cardiac catheterization laboratory with balloon valvuloplasty. Measurement of the diameter of the pulmonary annulus is required to plan adequately for the catheterization procedure. Typically the balloon size is 1.1–1.3 times the size of the pulmonary annulus, with a maximum balloon-to-annulus diameter ratio of 1.4.

### Post-procedure assessment and long-term sequelae

Since its original description in 1982, balloon valvuloplasty has become the treatment of choice for patients with congenital pulmonary valve stenosis [31]. However, some patients are still repaired by surgery. Comparing surgical and catheter results, O'Connor et al. found no hemodynamically significant difference in post-procedural pulmonary valve gradients between balloon valvuloplasty and surgical repair (24 mm Hg versus 16 mm Hg) at 5-year follow-up. However, there were no patients with moderate or severe regurgitation in the catheter group, compared with 45% in the surgical cohort [32]. In a similar study, moderate pulmonary valve regurgitation occurred in 44% of patients after surgery compared with 11% in the catheterization group [33]. Long-term investigations document the occurrence of both restenosis and regurgitation after both surgery and balloon dilation. In a comparative study with mean follow-up of almost 10 years, restenosis developed in 5.6% of patients in the surgical arm compared with 14.1% of patients who underwent balloon valvuloplasty [33].

Long-term follow-up studies of patients treated with surgical pulmonary valvotomy show significant sequelae. Roos-Hesselink et al. reported 37% of patients with moderate or severe pulmonary regurgitation at follow-up of 22–33 years. Reoperation was required in 9% of the cohort [34]. Earing et al., at a median follow-up of 34 years, found that 53% of patients required reintervention; 75% had valve replacement for severe pulmonary regurgitation [35].

It is important to identify the site and type of residual obstruction in patients after balloon valvuloplasty. Studies have documented an increase in infundibular gradients immediately after intervention. These gradients will decrease in both the short and long term [36,37]. By contrast, patients with residual gradients across the valve do not show resolution with time [36]. Suboptimal long-term results are related to older age at procedure, dysplastic valve morphology and greater baseline transpulmonary gradients [36]. Patients with Noonan syndrome have higher residual gradients compared with nonsyndromic patients [38], leading some physicians to advocate surgical repair of pulmonary valve stenosis in patients with Noonan syndrome.

Patients with critical pulmonary valve stenosis can undergo pulmonary valve balloon dilation in the cardiac catheterization laboratory (Fig. 16.5). However, some patients with a diminutive pulmonary annulus require a transannular patch and a systemic-to-pulmonary artery shunt [39]. After balloon dilation the tricuspid valve, pulmonary valve and RV have all been documented to increase in size at or

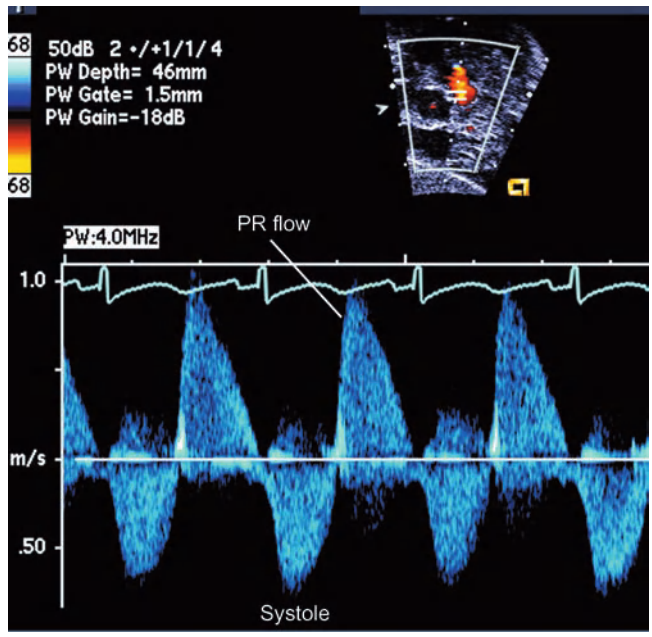


**Figure 16.5** Critical pulmonary valve stenosis status post successful balloon dilation. Continuous wave Doppler shows no residual gradient (systole) with free pulmonary regurgitation (PR flow).

above the rate of somatic growth [40,41]. Most patients have adequate systemic oxygen saturations after balloon valvuloplasty. However, patients with hyperdynamic RV outflow tracts can develop infundibular obstruction (so-called "suicide" RV), causing inadequate flow across the RV outflow tracts. Other patients remain cyanotic secondary to right-to-left shunting across the PFO due to poor RV compliance or RV hypoplasia [42]. It is important to recognize these physiologic states by echocardiography, because both require resumption of prostaglandin therapy. Although the dynamic infundibular stenosis usually resolves within several days, a poorly compliant RV might take several weeks to resolve. Therefore, surgical creation of a systemic-to-pulmonary artery shunt should be entertained.

### Pulmonary valve regurgitation

Mild pulmonary valve regurgitation is common before intervention and is considered a normal variant (Videoclip 16.1b). However, it is important to follow the progress of pulmonary regurgitation in patients who have undergone either surgical valvotomy or balloon valvuloplasty. Many studies analyzing the long-term effects of pulmonary regurgitation have used either subjective or semiquantitative methods to evaluate the degree and the consequences of pulmonary regurgitation [34,36]. Detection of pulmonary regurgitation is performed primarily with color flow Doppler. Retrograde flow can be seen in the distal pulmonary arteries in patients with a significant degree of regurgitation. Quantification of pulmonary regurgitation by color Doppler has been poorly validated, mainly because of comparison with other unreliable techniques. Methods include determination of overall jet size, depth of penetration of color flow Doppler into the RV, width of the vena contracta, or overall width of the jet in relation to the width of the RV outflow tract [43]. Spectral Doppler can be used to measure the end-diastolic pressure difference between the RV and the pulmonary artery. Silversides et al., using cardiac magnetic resonance imaging (MRI) as a reference method, found in patients with repaired tetralogy of Fallot that pressure half time <100 ms is associated with hemodynamically significant pulmonary regurgitation [44]. Yang et al. determined that a "no flow time" (diastolic period – duration of pulmonary regurgitation) >80 ms and a pressure half-time <100 ms distinguished angiographic severe pulmonary regurgitation from milder forms of disease [45].

RV dilation secondary to volume overload should be sought as indirect evidence of significant regurgitation. Williams et al. used a ratio of the pulmonary regurgitation color jet width to the pulmonary valve annulus of 0.4 (measured in early diastole in the parasternal short-axis plane) to differentiate between ≤1+ and ≥2+ angiographic grade pulmonary regurgitation. In the same study, indexed RV end-diastolic diameter correlated with angiographic pulmonary regurgitation. Nonetheless, there was significant overlap between angiographic grades. Retrograde diastolic flow in the branch pulmonary arteries was also statistically significant in separating the degrees of pulmonary regurgitation [46].

## Subpulmonary stenosis, including double-chambered right ventricle

Subvalvular pulmonary stenosis includes infundibular pulmonary stenosis and double-chambered right ventricle (DCRV). Infundibular stenosis can be primarily caused by a discrete fibromuscular obstruction or hypertrophic cardiomyopathy. Secondary forms include an aneurysm of the ventricular septum, an aneurysm of the sinus of Valsalva, accessory tricuspid valve tissue, cardiac tumors and RV hypertrophy secondary to pulmonary valve stenosis. Hypertrophic cardiomyopathy and the secondary forms will not be discussed in this chapter. Discrete fibromuscular subpulmonary obstruction is described as a ring or fibromuscular diaphragm with an orifice located at the infundibular ostium or within the RV infundibulum. DCRV encompasses conditions in which the muscular structures comprising the proximal infundibular ostium create a division within the right ventricle, resulting in muscular narrowing between the RV sinus (inflow) and the infundibulum (outflow). Patients with this abnormality are also categorized as having anomalous RV muscle bundles. The progressive obstruction divides the right ventricle into a proximal high-pressure RV sinus chamber and a low-pressure infundibular chamber distal to the muscular structures.

The incidence of discrete fibromuscular obstruction has been reported to vary between 0.2% and 8% of all cases of pulmonary stenosis [47,48]. The incidence of DCRV is not accurately known. Due to its progressive nature, this lesion is more easily detected after the first months of life. It has been suggested that 3–7% of patients with a ventricular septal defect (VSD) will acquire pulmonary outflow obstruction [49,50]. Among all patients with a VSD seen at the Children's Hospital Boston between 1973 and 2002, 0.04% developed a double-chambered right ventricle [51]. Simpson et al. [52] reported a 10% prevalence in children undergoing VSD repair, and Moran et al. noted development of DCRV in 3.1% of patients undergoing tetralogy of Fallot repair before the age of 2 years [53]. In a series from Spain, 0.75% of all cardiac defects repaired in childhood included DCRV [54].

The embryologic mechanism suggested for the development of discrete fibromuscular obstruction is a defect in absorption of the anterolateral conus or pulmonary infundibulum [55]. There is no consensus about the origin of the anomalous muscle bundles that make up a DCRV. Some have suggested that the anomaly arises from hypertrophy of the moderator band, whereas others have implicated a higher than usual takeoff of the trabecula septomarginalis, or that it is the result of hypertrophy of an abnormally located moderator band in patients with a VSD. It has also been proposed that the anomaly is due to persistence of prominent septal-parietal

trabeculations [56–60]. Possible relationships between DCRV and Down syndrome [61] and Noonan syndrome [62] have been proposed. In addition, Lougheed et al. have reported the development of RV outflow tract obstruction in almost 10% of recipients of fetal twin-to-twin transfusion [63].

## Morphology and classification

In its more common form, the obstruction caused by anomalous RV muscle bundles is not present in the first months of life. The muscle bundles become more prominent as the patient grows, and the obstruction is usually progressive [59]. However, rates of progression vary considerably [52,64]. In addition, several authors have described various forms of obstruction within the RV that are different from typical DCRV. These include an anomalous apical shelf with or without an associated Ebstein anomaly; an apical shelf confluent with the outlet septum that can give the impression of double-outlet LV; and a circumferential muscular diaphragm in the presence of tetralogy of Fallot [65–67].

Subpulmonary obstruction caused by a discrete fibromuscular ridge usually begins at the lower portion of the infundibulum. RV cavity division by anomalous muscle bundles usually occurs at the junction between the sinus (inlet) and the infundibular (outlet) components of the RV. DCRV due to anomalous muscle bundles can occur in isolation, but is more commonly associated with a VSD, with or without LV outflow obstruction. The anomalous muscle bundles have also been described to develop proximal to the usual RV outflow obstruction found in tetralogy of Fallot [53]. It may also occur in patients with other conotruncal lesions such as D- or L-loop transposition of the great arteries or double-outlet RV [68]. Membranous VSD is the cardiac anomaly most commonly associated with DCRV, although muscular and malalignment defects are also found. In the majority of cases, the LV communicates with the proximal high-pressure RV sinus. Another common association is between DCRV with or without a membranous VSD and discrete subvalvar aortic stenosis [69]. The development of left ventricular outflow tract obstruction has been reported to occur before, concomitant with, or even years after surgical repair of DCRV.

## Pathophysiology

In the majority of patients the obstruction caused by anomalous muscle bundles is progressive [59], but rates of progression vary considerably [52,64]. Progressive RV outflow obstruction causes an increase in the pressure gradient measured within the RV cavity. In our experience, in most cases the VSD communicates with the proximal high-pressure RV sinus chamber [70]. The progression of obstruction in such patients causes a decrease in the amount of left-to-right shunting. In the most severe cases of DCRV the shunt across the VSD can reverse. In the past, these patients have been considered to have a form of tetralogy of Fallot, due to the similar physiology and clinical features. In fact, the two conditions are part of a continuum. However, although spontaneous closure of the VSD and left ventricular outflow abnormalities are more frequently associated with DCRV, pulmonary annular hypoplasia, right aortic arch, and pulmonary artery abnormalities are typical in patients with tetralogy of Fallot.

In some patients with DCRV the VSD may undergo spontaneous closure. It is widely believed that cases that present with an intact ventricular septum may actually have had spontaneous closure of a VSD. Right ventricular dysfunction, a late finding, is more commonly seen in patients with restrictive or even closed VSD and markedly elevated RV pressure.

## Imaging

### Goals of examination and transthoracic imaging

The goals of echocardiographic examination in the setting of subpulmonary stenosis can be summarized as follows:

- Define the site and severity of obstruction(s) within the RV cavity.
- Define the type of subpulmonary stenosis.
- Determine the morphology of the anomalous muscle bundle/subpulmonary obstruction in relation to the tricuspid and pulmonary valves.
- Determine the presence of an associated VSD, its relation to the obstruction site, and the pressure gradient across the defect.
- Determine the presence of associated left ventricular outflow tract abnormalities.
- Assess the degree of tricuspid regurgitation and determine proximal chamber pressure.
- Evaluate RV function.

### Prenatal assessment

DCRV is rarely present in newborns, and the diagnosis is infrequently made in utero [71,72]. RV outflow tract obstruction has been associated with twin-to-twin transfusion. The recipient twin may develop infundibular or valvar stenosis in utero with the potential to progress to pulmonary atresia [63].

### Preoperative assessment

The anatomy of subpulmonary obstruction can be thoroughly determined by a complete echocardiographic examination. In patients with discrete subpulmonary stenosis, a nonmobile, thick ridge is seen at the level of the proximal infundibular ostium (Fig. 16.6). This structure is best visualized in subcostal short-axis, long-axis and oblique views as well as the parasternal short-axis view. Similar views are used to demonstrate anomalous muscle bundles in DCRV (Fig. 16.7 and Videoclip 16.3(a,b)). Color Doppler flow mapping helps to highlight their existence even in the presence of a mild gradient. In the subcostal oblique view a complete image of the RV cavity is seen (Fig. 16.7b). This view also permits measurement of the distance from anomalous muscle bundles to tricuspid and pulmonary valves. Subcostal views usually provide optimal angles for measurement of flow velocities within the RV cavity. Useful anatomic information

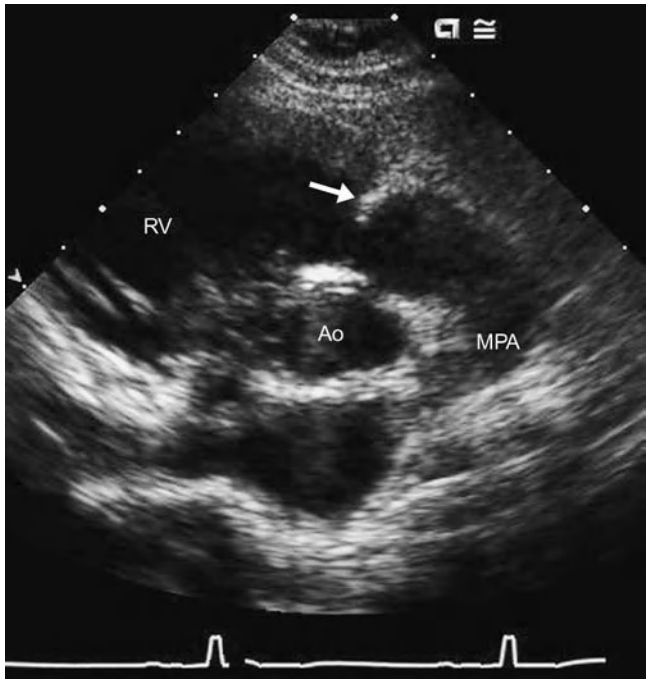


**Figure 16.6** Discrete subvalvar pulmonary stenosis seen from the parasternal short-axis view. Note the nonmobile ridge (arrow) in the right ventricular outflow tract. Ao, aorta; LA, left atrium; RA, right atrium; RV, right ventricular inflow; Inf, infundibulum; LV, left ventricle.

and gradient estimation of the RV outflow obstruction can also be obtained by anteriorly angling the transducer from a modified apical view. This view can be obtained by sliding the transducer rightward and superior from the apical four-chamber view. Subcostal and parasternal short-axis sweeps from apex to base allow similar assessment of the RV. Obstruction caused by a fibromuscular ridge located immediately below the pulmonary valve may be difficult to differentiate from isolated valvar stenosis. Therefore, special attention should be paid to leaflet motion, presence of leaflet fluttering and presence of early valvar closure.

Complete evaluation of the ventricular septum by 2D imaging and color flow mapping is important to evaluate the presence and location of a VSD. Special attention to the relationship of the defect to the anomalous muscle bundles is required. In the presence of a high-pressure proximal RV chamber, a low gradient across the VSD is expected even in the presence of significant restriction. Imaging of the left ventricular outflow tract from apical and parasternal views, in addition to a subcostal approach, should focus upon the possible presence of discrete subaortic stenosis.

Estimation of RV pressure based on the tricuspid regurgitation jet velocity confirms the elevated systolic pressure in the proximal chamber. Agreement of pressure estimation in the RV proximal and distal chambers based on measurement of flow velocities across the VSD, RV outflow and tricuspid regurgitation jet solidifies understanding of hemodynamic status.

Wong and colleagues [73] suggested that the degree of superior displacement of the moderator band could identify patients at risk for development of DCRV. The distance from the pulmonary valve to the moderator band was measured from subcostal views and normalized for the size of the tricuspid valve annulus. Alva et al. [60] challenged the prognostic value of the moderate band displacement

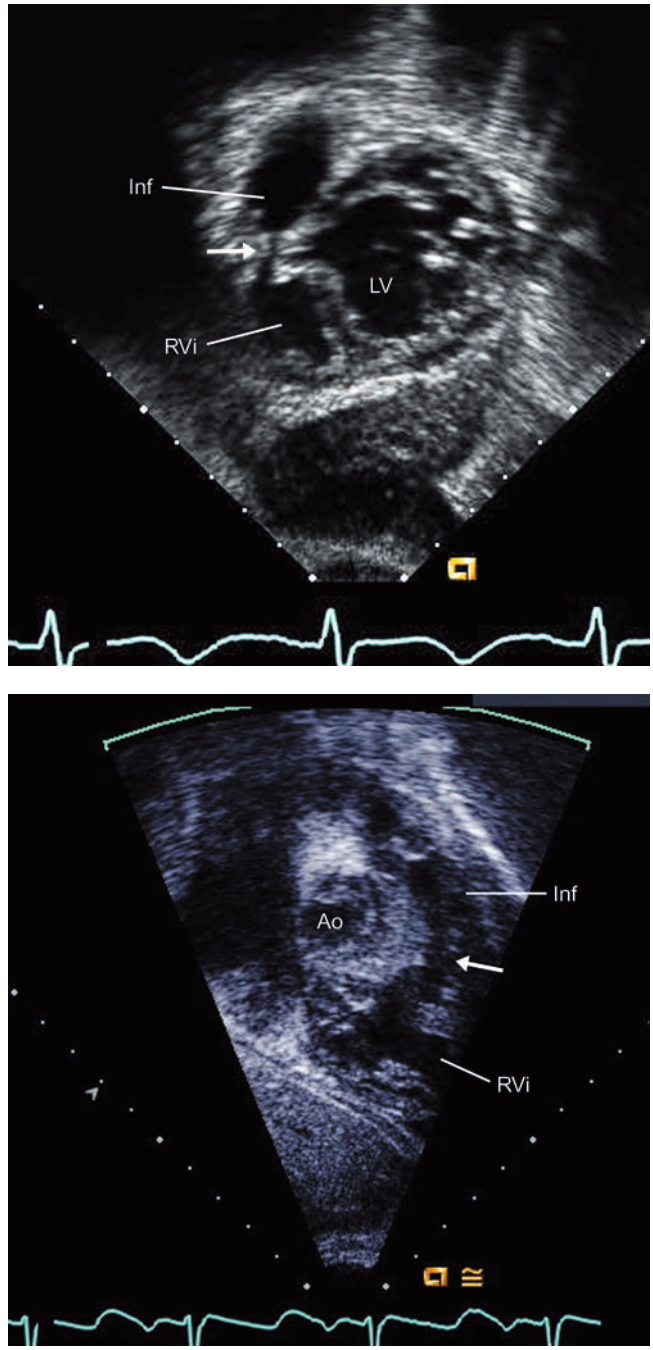


**Figure 16.7** Double-chambered right ventricle with a prominent anomalous muscle bundle producing severe narrowing of the proximal os infundibulum (arrow). **(a)** Subcostal short-axis view. **(b)** Subcostal oblique coronal view.

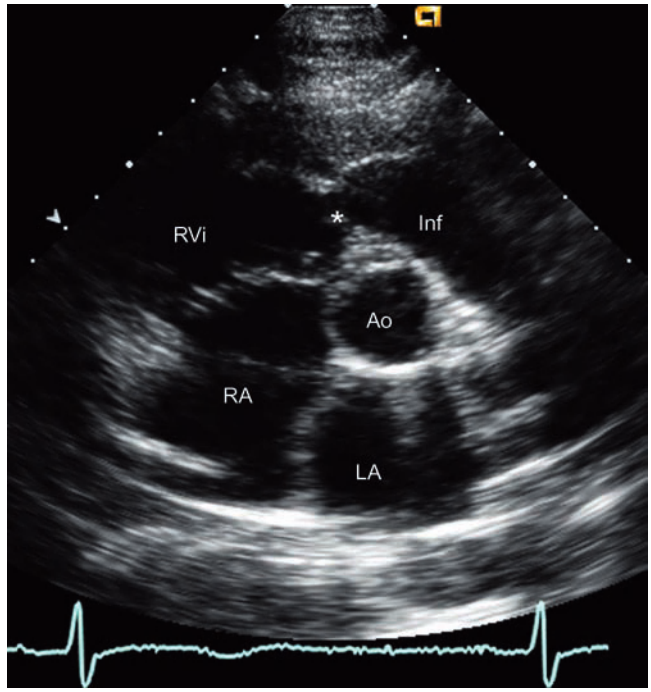


(c)

**Figure 16.7 (c)** Parasternal long-axis view (asterisk denotes proximal os infundibulum). Ao, aorta; LA, left atrium; RA, right atrium; RV, right ventricular inflow; Inf, infundibulum; LV, left ventricle.

measurements, as they believed that the abnormal muscle bundle probably represents accentuated septal-parietal trabeculations, rather than an abnormal moderator band.

### Echocardiographic guidance of surgical treatment

Treatment of discrete subpulmonary obstruction and DCRV is surgical. Operations are usually performed beyond infancy, with low mortality and good results. Most patients are referred for surgery based only on echocardiographic findings. The details about location of obstruction, its relation to tricuspid and pulmonary valves, and relative position of the VSD are helpful for safe surgical planning. Preoperative transesophageal echocardiography can confirm these details, particularly in larger patients. The RV cavity with the anomalous muscle bundles and the relationship to the ventricular septal defect are usually best demonstrated in a 45–80° "RV inflow-outflow view." The subpulmonary ridge can be viewed from 30 to 90° depending on the spatial orientation of the RV outflow tract.

### Postoperative assessment

Echocardiographic assessment starts in many cases as the patient is weaned from cardiopulmonary bypass. Evaluation of residual obstruction within the RV cavity in the early postoperative period should take into consideration intravascular volume status and inotropic support. A decrease in RV volume caused by low intravascular volume and a hyperdynamic ventricle will exaggerate the residual gradient. Follow-up of patients with DCRV should include assessment of the left ventricular outflow tract, as Vogel et al. have demonstrated that the subaortic obstruction can develop after surgical correction of DCRV [69].

RV dysfunction that is present preoperatively usually improves after relief of the obstruction. In 1984, Kveselis et al. [74] reported the long-term follow-up of 20 patients. After a mean follow-up of 19 years, five developed aortic regurgitation and two had mild RV outflow tract obstruction. In 2000, Galal and colleagues reported follow-up of 73 patients after repair of DCRV [75]. A small residual VSD was present in seven, and there were no other residual lesions. Recurrent obstruction related to anomalous muscle bundles has not been reported as a significant long-term complication.

### Imaging of the adult

The best views to evaluate subpulmonary obstructions are the subcostal long-axis, short-axis and oblique views as well as the parasternal short-axis view. However, in adult patients subcostal images are more difficult to acquire, and the relevant anatomy is usually seen best from the parasternal approach. Adult patients with DCRV commonly present with high gradients and either a restrictive VSD or intact ventricular septum. Therefore, color Doppler flow mapping is particularly helpful even in the presence of poor echocardiographic windows.

## Absent pulmonary valve with intact ventricular septum

Absent pulmonary valve is a rare lesion characterized by absence or severe dysplasia of the pulmonary valve leaflets resulting in an unguarded and usually narrowed junction between the RV outflow and the main pulmonary artery. Absent pulmonary valve occurs in two distinct morphologies. The more common variant occurs as part of tetralogy of Fallot, with a typical malalignment conoventricular septal defect, whereas the much less common lesion is associated with an intact ventricular septum. Although these two abnormalities are often grouped together, it has been proposed that the pathology is the result of two different embryologic pathways [76]. When absent pulmonary valve presents with a VSD it reflects a conotruncal anomaly. This lesion is rarely associated with a patent ductus arteriosus, and often occurs with chromosomal abnormalities, including 22q deletion. A severe malformation of the pulmonary valve that results in pulmonary stenosis and regurgitation is the primary defect in patients with absent pulmonary valve and intact ventricular septum. These patients typically have a PDA when diagnosed in utero, and are rarely affected with chromosomal abnormalities.

Secondary to the high fetal lethality of absent pulmonary valve, especially when associated with a VSD, the incidence

of the two lesions is significantly different depending on the age of diagnosis. Razavi et al. reported absence of the pulmonary valve in 1% of 2000 fetuses diagnosed with congenital heart disease [77]. Of these patients, 10% had an intact ventricular septum and 90% had an associated VSD. Elective termination was performed in 30% of the fetuses diagnosed with absent pulmonary valve, and a further 15% of the pregnancies ended in intrauterine death. At the other end of the spectrum, Zucker et al. reported 18 patients with absent pulmonary valve recognized after birth; 60% were associated with a VSD and 40% had an intact ventricular septum [78]. Unlike patients with a VSD, who universally presented before 3 days of age, 43% of patients with an intact ventricular septum presented after age 8 years. The clinical manifestations are highly disparate, ranging from fetal heart failure and hydrops to patients who are asymptomatic [79–81].

### Pathophysiology

The primary physiologic consequences of absent pulmonary valve syndrome are pulmonary regurgitation and pulmonary stenosis. The right ventricle, main pulmonary artery and branch pulmonary arteries become dilated from the increased volume and pressure load. Patients with an intact ventricular septum characteristically develop less severe dilation of the branch pulmonary arteries. This is thought to be related to the presence of a patent ductus arteriosus in utero, which provides a pathway for runoff into the systemic circulation [82,83]. When the branch pulmonary arteries are significantly dilated, patients will often present with airway obstruction [83].

### Imaging

Echocardiography should provide all the essential information necessary to manage patients with absent pulmonary valve. An echo-bright fibrous ring occupying the location of the pulmonary valve can be identified in the parasternal short- and long-axis views and in the subcostal coronal, short-axis and oblique views. Thickened, dysplastic valve remnants can sometimes be identified as part of the lesion (Fig. 16.8 and Videoclip 16.4(a,b)). The degree of stenosis depends on the size of the valve annulus. Subvalvar obstruction is rarely part of this lesion, but must be excluded. The right ventricle is characteristically dilated and hypertrophied. RV size and function are difficult to measure using standard 2D imaging. Therefore, it is important to evaluate the ventricle from multiple views. It is also important to measure the diameters of the main and distal pulmonary arteries. This can be accomplished in the parasternal short-axis and suprasternal views. Size discrepancies between the right and left pulmonary arteries have been reported [80]. With the exception of a PDA, additional abnormalities are rare. Serial examinations are important to follow the degree of RV outflow tract obstruction, size and function of the RV, and growth of the main and distal pulmonary arteries.

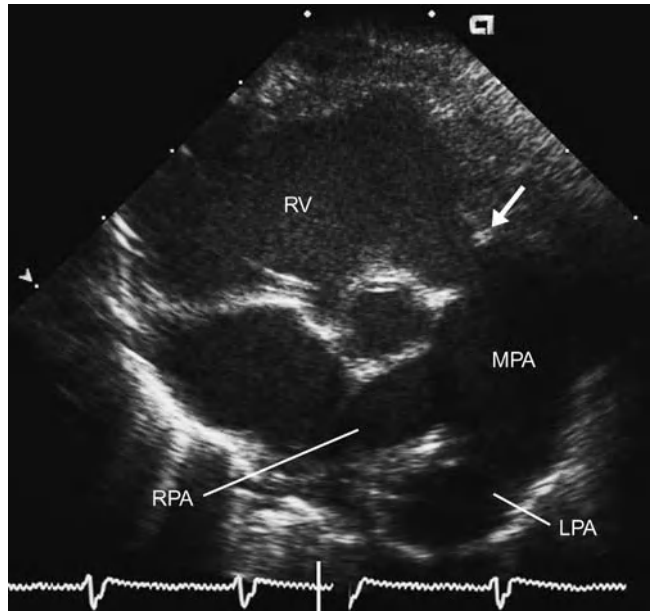


**Figure 16.8** Absent pulmonary valve with intact ventricular septum seen from the parasternal short-axis view. Note the unguarded pulmonary valve, dilated right ventricle, and severely dilated main pulmonary artery and proximal right and left pulmonary arteries.

### Prenatal assessment

Several series have documented the ability correctly to diagnose absent pulmonary valve with and without the presence of a VSD in the fetus [82–84]. The characteristic findings of enlargement of the central pulmonary arteries and dilated RV are uncommon until gestation reaches 22 weeks. Prior to 22 weeks' gestation, the diagnosis can still be made by the finding of severe pulmonary regurgitation [85]. It is important to determine the presence of a VSD or a PDA, which rarely occur together. The high degree of fetal and neonatal loss associated with absent pulmonary valve makes it imperative to perform frequent follow-up examinations and to arrange delivery at a center with the ability to perform cardiovascular surgery. Serial measurements of the cardiothoracic ratio, diameters of the pulmonary trunk and branches, and Doppler velocities across the RV outflow and main pulmonary artery are important as well as frequent assessments for signs of hydrops fetalis.

## Main pulmonary artery stenosis

Obstruction distal to the pulmonary valve can occur at the level of the main pulmonary artery and/or pulmonary artery branches. These lesions are found in 2–3% of patients with congenital heart disease in association with various cardiovascular anomalies [86]. In this chapter we will only discuss lesions of the main pulmonary artery. Lesions of the branch pulmonary arteries are discussed in Chapter 18.

The embryologic mechanisms involved in the development of supravalvar pulmonary stenosis are not known. This

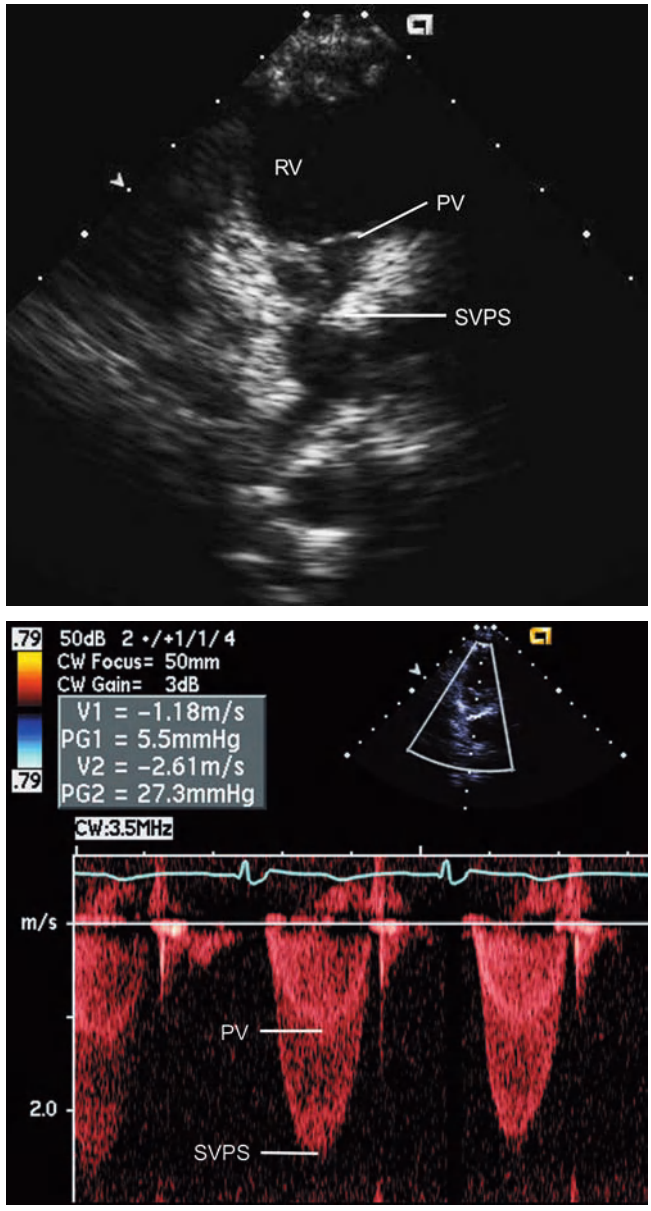


(a)

(b)

**Figure 16.9** Supravalvar pulmonary stenosis. **(a)** Parasternal short-axis view showing a membranous diaphragm causing narrowing between the pulmonary valve (PV) and the pulmonary bifurcation. **(b)** Continuous wave Doppler demonstrating a double envelope caused by two velocities; the first is flow across the pulmonary valve and the second represents increased velocity across the supravalvar obstruction. SVPS, supravalvar pulmonary stenosis.

anomaly has been associated with Williams, DiGeorge, Alagille, Keutel and congenital rubella syndromes. Congenital obstruction at the level of the main pulmonary artery can be caused by a discrete ridge or by a diffusely hypoplastic segment. The ridge can be located immediately distal to the pulmonary valve, at the mid-portion of the main pulmonary artery, or close to the bifurcation. Acquired lesions are seen after surgical intervention. Surgical banding of the main pulmonary artery is a palliative therapeutic option used to prevent pulmonary overcirculation and detrimental alteration of the pulmonary vasculature. In patients who have undergone main pulmonary artery banding, a poststenotic dilation can be seen. Imaging at regular intervals is needed for early diagnosis of migration of the surgical band, which can cause encroachment on the branch pulmonary arteries. The encroachment can interfere with branch pulmonary artery growth and cause stenosis and hypoplasia. Obstruction at the level of the neo-main pulmonary artery has also been reported after the arterial switch operation, due to manipulation and positioning for the LeCompte maneuver.

## Imaging

Stenosis of the main pulmonary artery can be visualized from parasternal long- and short-axis views (Fig. 16.9). The anatomy can be demonstrated in young patients by anteriorly angling the transducer from a modified apical view and from subcostal short-axis and right anterior oblique views. Maximum instantaneous and mean gradients across the main pulmonary artery are determined by pulsed-wave and continuous-wave Doppler interrogation of flow from each view. When using continuous-wave Doppler, jets originating at other levels of obstruction can mask the actual gradient across the main pulmonary artery.

## References


1. Hoffman JIE, Kaplan S. The incidence of congenital heart disease. *J Am Coll Cardiol* 2002;39:1890–900.
2. Freedom RM, Benson L. Congenital pulmonary stenosis and isolated congenital pulmonary insufficiency. In: Freedom RM, Yoo SJ, Mikailian H, Williams WG (eds) *The Natural and Modified History of Congenital Heart Disease*, 1st edn. New York: Blackstone Publishing, 2004;107–18.
3. Bertola DR, Kim CA, Sugayama SMM et al. Cardiac findings in 31 patients with Noonan's syndrome. *Arq Bras Cardiol* 2000;75:409–12.
4. Almeda FQ, Kavinsky CJ, Pophal SG, Klein LW. Pulmonic valvular stenosis in adults: Diagnosis and treatment. *Catheter Cardio Interv* 2003;60:546–57.
5. Dore A. Pulmonary stenosis. In: Gatzoulis MA, Webb GD, Daubeney PEF (eds) *Diagnosis and Management of Adult Congenital Heart Disease*. Edinburgh: Elsevier, 2003;299–303.
6. Tynan M, Anderson RH. Pulmonary stenosis. In: Anderson RH, Baker EJ MacCartthy FJ et al. (eds) *Pediatric Cardiology*, 2nd edn. London: Harcourt, 2002;1461–79.
7. Bashore TM. Adult congenital heart disease: Right ventricular outflow tract lesions. *Circulation* 2007;115:1933–47.
8. Hurwitz LE, Roberts WC. Quadracuspid semilunar valve. *Am J Cardiol* 1973;31:623–6.
9. Vermilion RP, Snider AR, Bengur R, Meliones JN. Long-term assessment of right ventricular diastolic filling in patients with pulmonic valve stenosis successfully treated in childhood. *Am J Cardiol* 1991;68:648–52.
10. Artman M, Mahony L, Tietel DF. *Neonatal Cardiology*. New York: McGraw-Hill, 2002.

11. Rowland DG, Hammill WW, Allen HD, Gutgesell HP. Natural course of isolated pulmonary valve stenosis in infants and children utilizing Doppler echocardiography. *Am J Cardiol* 1997;79:344–9.
12. Mandelbaum VH, Alverson DC, Kirchgessner A, Linderkamp O. Postnatal changes in cardiac output and haemorrhology in normal neonates born at full term. *Arch Dis Child* 1991;66:391–4.
13. Emmanouilides GC, Moss AJ, Duffie ER, Adams FH. Pulmonary arterial pressure changes in human newborn infants from birth to 3 days of age. *J Pediatr* 1964;65:327–33.
14. Fouron JC. Anomalies of the right heart. In: Yagel S, Silverman N, Gembruch U (eds) *Fetal Cardiology*. London: Martin Dunitz, 2003.
15. Todros T, Paladini D, Chiappa E et al. Pulmonary stenosis and atresia with intact ventricular septum during prenatal life. *Ultrasound Obstet Gynecol* 2003;21:228–33.
16. Davignon AL, Greenwold WE, DuShane JW et al. Congenital pulmonary atresia with intact ventricular septum Clinicopathologic correlation of two anatomic types. *Am Heart J* 1961;62:591–602.
17. Todros T, Presbitero P, Gaglioti P. Pulmonary stenosis with intact ventricular septum: Documentation of development of the lesion echocardiographically during fetal life. *Int J Cardiol* 1988;19:355–62.
18. Huhta J, Quintero RA, Suh E, Bader R. Advances in fetal cardiac intervention. *Curr Opin Pediatr* 2004;16:487–93.
19. Giardina A, Schmitt B, Azakie A, Tacy TA. Effect of chamber capacitance on Doppler flow pattern across restrictive defects in obligatory atrial-level shunts. *J Am Soc Echocardiogr* 2004;17:1286–91.
20. McAleer E, Kort S, Rosenzweig BP et al. Unusual echocardiographic views of bicuspid and tricuspid pulmonic valves. *J Am Soc Echocardiogr* 2001;14:1036–8.
21. Snider AR, Serwer GA, Ritter SB. *Echocardiography in Pediatric Heart Disease*, 2nd edn. St Louis: Mosby-Year Book, 1990.
22. Aldousany AW, DiSessa TG, Dubois R et al. Doppler estimation of pressure gradient in pulmonary stenosis: Maximal instantaneous vs peak-to-peak, vs mean catheter gradient. *Pediatr Cardiol* 1989;10:145–9.
23. Frantz EG, Silverman NH. Doppler ultrasound evaluation of valvar pulmonary stenosis from multiple transducer positions in children requiring pulmonary valvuloplasty. *Am J Cardiol* 1988;61:844–9.
24. Lima CO, Sahn DJ, Valdes-Cruz LM et al. Noninvasive prediction of transvalvular pressure gradient in patients with pulmonary stenosis by quantitative two-dimensional echocardiographic Doppler studies. *Circulation* 1983;67:866–71.
25. Silvilairat S, Cabalka AK, Cetta F et al. Echocardiographic assessment of isolated pulmonary valve stenosis: Which outpatient Doppler gradient has the most clinical validity? *J Am Soc Echocardiogr* 2005;18:1137–42.
26. Silvilairat S, Cabalka AK, Cetta F et al. Outpatient echocardiographic assessment of complex pulmonary outflow stenosis: Doppler mean gradient is superior to the maximum instantaneous gradient. *J Am Soc Echocardiogr* 2005;18:1143–8.
27. DeGroff C. Response to: Echocardiographic assessment of isolated pulmonary valve stenosis: Which outpatient Doppler gradient has the most clinical validity? *J Am Soc Echocardiogr* 2006;19:364.
28. DeGroff C. Doppler echocardiography. *Pediatr Cardiol* 2002;23:307–33.
29. Lemler MS, Valdes-Cruz LM, Shandas RS, Cape EG. Insights into catheter/Doppler discrepancies in congenital aortic stenosis. *Am J Cardiol* 1996;83:1447–50.
30. Mullins CE. *Cardiac Catheterization in Congenital Heart Disease*. Oxford: Blackwell Futura, 2006.
31. Kan JS, White RI, Mitchell SE, Gardner TJ. Percutaneous balloon valvuloplasty: A new method for treating congenital pulmonary valve stenosis. *N Engl J Med* 1982;307:540–2.
32. O'Connor BK, Beekman RH, Lindauer A, Rocchini A. Intermediate-term outcome after pulmonary balloon valvuloplasty: Comparision with a match surgical control group. *J Am Coll Cardiol* 1992;20:169–73.
33. Peterson C, Schilthuis JJ, Dodge-Khatami A et al. Comparative long-term results of surgery versus balloon valvuloplasty for pulmonary valve stenosis in infants and children. *Ann Thorac Surg* 2003;76:1078–83.
34. Roos-Hesselink JW, Meijboom FJ, Spitaels SEC et al. Long-term outcome after surgery for pulmonary stenosis (a longitudinal study of 22–33 years). *Eur Heart J* 2006;27:482–8.
35. Earing MG, Connolly HM, Dearani JA et al. Long-term follow-up of patient after surgical treatment for isolated pulmonary valve stenosis. *Mayo Clin Proc* 2005;80:871–6.
36. Gupta D, Saxena A, Kothari SS, Juneja R. Factors influencing late course of residual valvular and infundibular gradients following pulmonary valve balloon dilation. *Int J Cardiol* 2001;79:143–9.
37. Jarrar M, Betbout F, Farhat MB et al. Long-term invasive and non-invasive results of percutaneous balloon pulmonary valvuloplasty in children, adolescents, and adults. *Am Heart J* 1999;138:950–4.
38. Masura J, Burch M, Deanfield JE, Sullivan ID. Five-year follow-up after balloon pulmonary valvuloplasty. *J Am Coll Cardiol* 1993;21:132–6.
39. Hanley FL, Sade RM, Freedom RV et al. Outcomes in critically ill neonates with pulmonary stenosis and intact ventricular septum: A multiinstitutional study. *J Am Coll Cardiol* 1993;22:183–92.
40. Kovalchin JP, Forbes TJ, Nihill MR, Geva T. Echocardiogrphic determinants of clinical course in infants with critical and severe pulmonary valve stenosis. *J Am Coll Cardiol* 1997;29:1095–101.
41. Gildein HP, Kleiner S, Goh TH et al. Pulmonary valve annulus grows after balloon dilation of neonatal critical pulmonary valve stenosis. *Am Heart J* 1998;136:276–80.
42. Sommer RJ, Rhodes JR, Parness IA. Physiology of critical pulmonary valve obstruction in the neonate. *Catheter Cardio Interv* 2000;50:473–9.
43. Feigenbaum H, Armstrong WF, Ryan T. *Echocardiography*, 6th edn. Philadelphia: Lippincott Williams & Wilkens, 2005.
44. Silversides CK, Veldtman GR, Crossin J et al. Pressure half-time predicts hemodynamically significant pulmonary regurgitation in adult patients with repaired tetrology of Fallot. *J Am Soc Echocardiogr* 2003;16:1057–62.
45. Yang H, Pu M, Chambers CE et al. Quantitative assessment of pulmonary insufficiency by Doppler echocardiography in patients with adult congenital heart disease. *J Am Soc Echocardiogr* 2008;21:157–64.
46. Williams RV, Minich LL, Shaddy RE et al. Comparison of Doppler echocardiography with angiography for determining the severity of pulmonary regurgitation. *Am J Cardiol* 2002;89:1438–40.
47. Castaneda-Zuniga WR, Formanek A, Ampaltz K. Radiologic diagnosis of different types of pulmonary stenoses. *Cardiovasc Radiol* 1978;1:45–57.
48. Rowe RD. Pulmonary stenosis with normal aortic root. In: Keith JD, Rowe RD, Vlad P (eds) *Heart Disease in Infancy and Childhood*, 3rd edn. New York: Macmillan, 1978;761–88.

49. Weidman WH, Blount SG, DuShane JW et al. Clinical course in ventricular septal defect. *Circulation* 1977;56(1 Suppl.):I56–69.
50. Corone P, Dovon F, Gaudeau S et al. Natural history of ventricular septal defect. A study involving 790 cases. *Circulation* 1977; 55:908–15.
51. Keane JF, Fyler DC. Ventricular septal defect. In: Keane JF, Lock JE, Fyler DC (eds) *Nadas' Pediatric Cardiology*, 2nd edn. Philadelphia: Saunders Elsevier, 2006;527–47.
52. Simpson WF Jr, Sade RM, Crawford FA et al. Double-chambered right ventricle. *Ann Thorac Surg* 1987;44:7–10.
53. Moran AM, Hornberger LK, Jonas RA, Keane JF. Development of a double-chambered right ventricle after repair of tetralogy of Fallot. *J Am Coll Cardiol* 1998;31:1227–33.
54. Cabrera A, Martinex P, Rumoroso JR et al. Double-chambered right ventricle. *Eur Heart J* 1995;16:682–6.
55. Valdes-Cruz LM, Cayre RO. Anomalies of the right ventricular outflow tract and pulmonary arteries. In: Valdes-Cruz LM, Cayre RO (eds) *Echocardiographic Diagnosis of Congenital Heart Disease. An Embryologic and Anatomic Approach*. Philadelphia: Lippincott-Raven, 1999;325–48.
56. Hartman AF Jr, Goldring D, Carlsson E. Development of right ventricular obstruction by aberrant muscle bands. *Circulation* 1964;30:679–85.
57. Lintermans JP, Roberts DB, Gunteroth WG, Figley MM. Two-chambered right ventricle without outflow obstruction in ventricular septal defect. *Am J Cardiol* 1968;21:582–7.
58. Rowland TW, Rosenthal A, Castaneda AR. Double-chamber right ventricle: experience with 17 cases. *Am Heart J* 1975;89:455–62.
59. Pongiglione G, Freedom RM, Cook D, Rowe RD. Mechanism of acquired right ventricular outflow tract obstruction in patients with ventricular septal defect: an angiocardiographic study. *Am J Cardiol* 1982;50:776–80.
60. Alva C, Ho SY, Lincoln CR et al. The nature of the obstructive muscular bundles in double-chambered right ventricle. *J Thorac Cardiovasc Surg* 1999;117:1180–9.
61. Eltohami EA, Hajar HA, Folger GM. Double-chambered right ventricle and Down's syndrome: a proposed new association. *Angiology* 1994;45:119–23.
62. Ozkutlu S, Cil E, Pasaoglu I, Saraclar M. Noonan syndrome with double-chambered right ventricle. *Pediatr Cardiol* 1996;17:251–3.
63. Lougheed J, Sinclair BG, Fung Kee Fung K et al. Acquired right ventricular outflow tract obstruction in the recipient twin in twin-twin transfusion syndrome. *J Am Coll Cardiol* 2001;38:1533–8.
64. Oliver JM, Garrido A, Gonzalez A et al. Rapid progression of midventricular obstruction in adults with double-chambered right ventricle. *J Thorac Cardiovasc Surg* 2003;126:711–17.
65. Restivo A, Cameron AH, Anderson RH, Allwork SP. Divided right ventricle: a review of its anatomical varieties. *Pediatr Cardiol* 1984;5:197–204.
66. Yoo S-J, Kim YM, Bae EJ et al. Rare variants of divided right ventricle with sequestered apical trabecular component. *Int J Cardiol* 1997;60:249–55.
67. Karczenski K. Double-chambered right ventricle. *Perspect Pediatr Pathol* 1988;12:115–27.
68. Freedom RM, Mawson J, Yoo S-J, Benson LN. The divided right ventricle; anomalous right ventricular muscle bundles and other entities. In: Freedom RM, Mawson J, Yoo S-J, Benson LN (eds) *Congenital Heart Disease: Textbook of Angiocardiography*. Armonk, NY: Futura, 1997;389–407.
69. Vogel M, Smallhorn JF, Freedom RM et al. An echocardiographic study of the association of ventricular septal defect and right ventricular muscle bundles with a fixed subaortic abnormality. *Am J Cardiol* 1988;61:857–60.
70. Hubail Z, Ramaciotti C. Spatial relationship of the VSD to the anomalous muscle bundle in double-chambered right ventricle. *Congenital Heart Dis* 2007;2:421–3.
71. Leandro J, Dyck JD, Smallhorn JF. Intra-utero diagnosis of anomalous right ventricular muscle bundle in association with a ventricular septal defect: a case report. *Pediatr Cardiol* 1994;15: 46–8.
72. Marton T, Hajdu J, Papp Z. A rare case of non-immune hydrops fetalis: double-chambered right ventricle. A case report. *Fetal Diagn Ther* 2001;16:251–3.
73. Wong PC, Sanders SP, Jonas RA et al. Pulmonary valve-moderator band distance and association with development of double-chambered right ventricle. *Am J Cardiol* 1991;68:1681–6.
74. Kveselis D, Rosenthal A, Ferguson P et al. Long-term prognosis after repair of double-chamber right ventricle with ventricular septal defect. *Am J Cardiol* 1984;54:1292–5.
75. Galal O, Halees Z, Solymar L et al. Double-chambered right ventricle in 73 patients: spectrum of the disease and surgical results of transatrial repair. *Can J Cardiol* 2000;16:167–74.
76. Podzimkova J, Hickey MS, Slavik Z et al. Absent pulmonary valve syndrome with intact ventricular septum: Role of ductus arteriosus revisited. *Int J Cardiol* 1997;61:109–12.
77. Razavi RS, Sharland GK, Simpson JM. Prenatal diagnosis by echocardiogram and outcome of absent pulmonary valve syndrome. *Am J Cardiol* 2003;91:429–32.
78. Zucker N, Rozin I, Levitas A, Zalzstein E. Clinical presentation, natural history, and outcome of patients with the absent pulmonary valve syndrome. *Cardiol Young* 2004;14:402–8.
79. Bearman W, Fripp RR, Rowe SA, Yabek S. Congenital isolated pulmonary valve incompetence: Neonatal presentation and early natural history. *Am Heart J* 1992;124:248–51.
80. Marek J, Skovranek J, Povysilova V. Congenital absence of aortic and pulmonary valve in a fetus with severe heart failure. *Heart* 1996;75:98–100.
81. Grotenhuis HB, Nijveld A, Backx A. Absent pulmonary valve syndrome with intact ventricular septum and patent ductus arteriosus: Report of two cases and a short review of the literature. *Ann Thorac Surg* 2003;75:280–2.
82. Volpe P, Paladini D, Maasini M et al. Characteristics, associations and outcome of absent pulmonary valve syndrome in the fetus. *Ultrasound Obstet Gynecol* 2004;24:623–8.
83. Yeager SB, Van Der Velde ME, Waters BL, Sanders SP. Prenatal role of the ductus arteriosus in absent pulmonary valve syndrome. *Echocardiography* 2002;19:489–93.
84. Nørgaard MA, Alphonso N, Newcomb AE et al. Absent pulmonary valve syndrome. Surgical and clinical outcomes with long-term follow-up. *Eur J Cardio-thorac Surg* 2006;29:682–7.
85. Galindo A, Gutieree-Larray F, Martinez JM et al. Prenatal diagnosis and outcome for fetuses with congenital absence of the pulmonary valve. *Ultrasound Obstet Gynecol* 2006;28:32–9.
86. Trivedi KR, Benson LN. Peripheral pulmonary artery stenosis. In: Freedom RM, Yoo SJ, Mikailian H, Williams WG (eds) *The Natural and Modified History of Congenital Heart Disease*, 1st edn. New York: Blackstone Publising, 2004;119–34.

# 17 Pulmonary Atresia with Intact Ventricular Septum

**Jami C. Levine**
Children's Hospital Boston, Boston, MA, USA

## Definition

Pulmonary atresia with intact ventricular septum (PA/IVS) is a relatively uncommon congenital heart disease characterized by luminal discontinuity between the right ventricular outflow tract and the main pulmonary artery in the absence of a ventricular septal defect.

## Historical background

Peacock published the first case series of patients with PA/IVS in 1869 [1]. This included a historical review in which he credits John Hunter for the first description of this anomaly in 1783. Grant first described the associated coronary artery abnormalities in 1926 [2]. There were anecdotal case reports in the mid-1900s, including a series of 10 cases described by Maude Abbot in her seminal atlas of congenital heart disease [3]. Glaboff et al. published the first detailed description of PA/IVS with a dilated right ventricle (RV) in 1950 [4]. From 1955 through 1970, a number of reports described the anatomic features of PA/IVS [5–12]. The first attempts at surgical palliation were reported in the 1960s [6,8,13]. Initially, surgical therapy was technically successful but did not significantly improve outcome. Over the ensuing decades, the diagnostic evaluation has become more refined and the treatment plans more tailored to the anatomic variants, resulting in dramatically improved prognosis for infants with PA/IVS [14,15].

## Incidence

In the New England Regional Infant Cardiac Program, 75 of 2251 infants (3.3%) had PA/IVS, and 85% of these were diagnosed in the first week of life [16]. Estimates of the incidence of PA/IVS vary from 1 in 8000 live births [17] to 1 in 144 000 live births [16]. Without treatment 50% of infants die within 2 weeks, and 85% die by 6 months of age [7,17–20]. Death is typically due to complications of cyanosis secondary to insufficient pulmonary blood flow.

## Etiology

Both genetic and environmental factors have been implicated in the etiology of PA/IVS, but little is known about specific contributing factors. It is likely that genetic factors, when important, are multifactorial. From empiric data, it appears that PA/IVS is not one of the more heritable forms of heart disease [21] and is only occasionally associated with specific chromosomal anomalies. There are, however, anecdotal reports of pedigrees that include more than one family member with PA/IVS, including a few reports of affected siblings [22,23].

The role of environmental factors in the etiology of PA/IVS is also unknown. Evidence that environmental factors can directly influence the development of the right heart comes from a report by Baetz-Greenwalt et al. [24]. This paper described 14 infants with right heart hypoplasia, all diagnosed within a 2-year period in a small area of Ohio. Of this group, 79% had extracardiac anomalies, prompting speculation that an environmental exposure in the second month of pregnancy may have produced a new syndrome, which included abnormalities of right heart growth.

There are several theories about the morphogenesis of pulmonary valve atresia [9,25–27]. Most popular is the flow theory, which assumes that an anatomic abnormality early in development decreases blood flow through the right heart, resulting in diminished growth of right heart structures. The lack of growth leads to further decrease in flow through the right heart. Eventually, this cycle ends in acquired atresia of the pulmonary valve. Several structural defects have the potential to disrupt flow through the right ventricle, including primary abnormalities of the foramen ovale, Eustachian valve, tricuspid valve and pulmonary valve. It is likely that

*Echocardiography in Pediatric and Congenital Heart Disease: From Fetus to Adult*
Edited by Wyman W. Lai, Luc L. Mertens, Meryl S. Cohen and Tal Geva
 ISBN: 978-1-405-17401-5

the timing of valve atresia is important and that infants with the smallest right heart structures are the ones who experienced the earliest progression to atresia, whereas those with dilated right hearts may have had antegrade flow for a longer period, thus allowing for more in utero growth of the right heart.

## Morphology

There is significant morphologic heterogeneity among patients with PA/IVS [7,9,11,14,25–32]. Initial anatomic studies suggested that patients could be divided into two relatively distinct groups depending on the size of their right heart structures [5,7–9,25–31]. Those with pulmonary atresia and hypoplasia of the RV were designated as type I, whereas those with pulmonary atresia and normal or enlarged right heart structures were designated as type II. Type I patients had small, abnormal tricuspid valves, severe right ventricular hypertrophy and coronary artery fistulae, whereas type II patients were more likely to have severe tricuspid regurgitation, a thin-walled and dilated right ventricle, and a massively enlarged right atrium, but no significant coronary artery fistulae. It is clear from more contemporary anatomic studies that there is a continuum with respect to right heart disease, yet the majority of patients tend to have features that grossly fit into one of these two subtypes.

### Pulmonary atresia with RV hypoplasia

#### Right atrium

The vast majority of patients have a patent foramen ovale, although ~20% of patients have a secundum atrial septal defect (ASD) [9]. The right atrium and its associated caval connections may be dilated and hypertrophied, although this is probably dependent on the amount of tricuspid regurgitation, the size of the foramen ovale and the length of time that the hemodynamic abnormalities were present.

#### Right ventricle and tricuspid valve

The size of the tricuspid valve correlates with the size of the right ventricle [25–27,30–33]. Studies suggest that 70–90% of patients with PA/IVS have hypoplasia of both tricuspid valve and right ventricle, with up to 60% of patients having severe right ventricular hypoplasia [14,26,28,30,33]. Hypoplasia typically involves all segments of the right ventricle, although some portions may be so underdeveloped as to be absent [34]. The right ventricular sinus (inlet) is often foreshortened (Figs 17.1 and 17.2). The moderator band and tricuspid valve papillary muscles may be poorly defined, although when present they can be severely hypertrophied. The infundibular portion is frequently hypoplastic, and in about 10–25% of patients it is atretic [31,32,34]. The ventricular endocardium is typically fibrotic and in some cases there

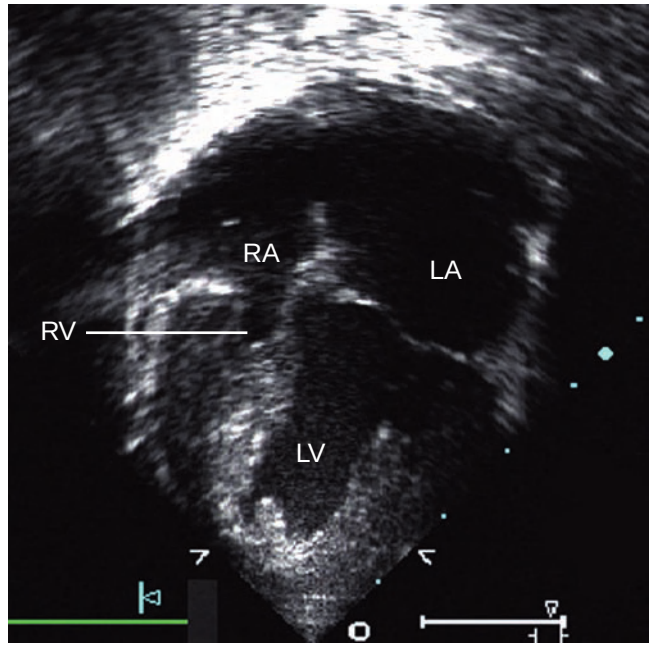


**Figure 17.1** Severely hypoplastic right ventricle (RV) in pulmonary atresia with intact ventricular septum. Four-chamber view from the apical window demonstrates a diminutive right ventricular cavity and a hypoplastic tricuspid valve annulus. LA, left atrium; LV, left ventricle; RA, right atrium.

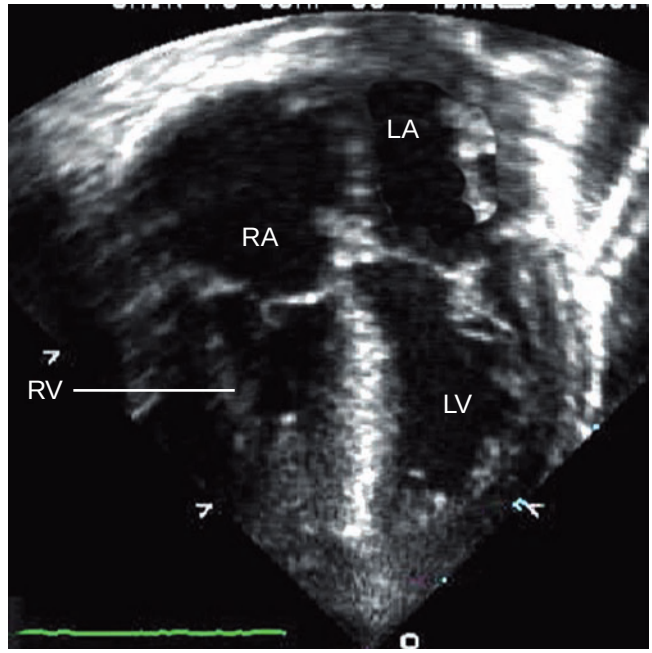


**Figure 17.2** Moderately hypoplastic right ventricle in pulmonary atresia with intact ventricular septum seen from the apical 4-chamber view. Note the nearly normal-sized tricuspid valve annulus. The right ventricle is about two-thirds the length of the left ventricle. LA, left atrium; LV, left ventricle; RA, right atrium; RV, right ventricle.

may be diffuse endocardial fibroelastosis as well as myocardial fiber disarray [25,35–38].

Typically, the valve annulus is small and the leaflets and supporting apparatus are morphologically abnormal. The Congenital Heart Surgeons Society (CHSS) multicenter study found that the tricuspid valve annulus diameter z-score is less than –2 in 50% of patients and less than –5 in 10% of patients [14]. In addition to annular hypoplasia, the leaflets are often thickened, especially at their edges, the chordae tendineae are short and the papillary muscles are small. These abnormalities often result in tethered leaflets with reduced mobility [6,7,9,15,25,32,39].

### Coronary arteries

Abnormalities of the coronary arteries and the presence of RV sinusoids are common in PA/IVS [14,25,27,32,40–43]. Right ventricular sinusoids are endothelial-lined channels within the myocardium that communicate with the cavity. These are remnants of the sinusoidal spaces that nourish the myocardium in early fetal life. When they persist in postnatal life, they can be a site of communication between the right ventricular cavity and the coronary arteries. These fistulous communications are found in as many as 50% of patients with small, hypertensive RVs and may provide the only source of egress of blood from the RV [14,28,40–45]. Their prevalence increases with increased RV pressure and correlates inversely with the size of the tricuspid valve and RV cavity.

The epicardial coronary arteries may also be abnormal, exhibiting intimal proliferation, nodularity or endarteritis [28,37,45,46]. Stenotic lesions within the coronary arteries or atresia of the coronary artery ostium at the aortic root can be present. These abnormalities disrupt the flow of oxygenated blood from the aortic root to the myocardium. The myocardium that does not receive antegrade flow from the epicardial coronary arteries may be perfused entirely with blood from the right ventricle through persistent fistulous communications [42,43,47]. This condition is known as a *right ventricular-dependent coronary circulation* (Figs 17.3–17.5) and is present in 10–20% of patients with PA/IVS [14,31,40,42,45,48–50].

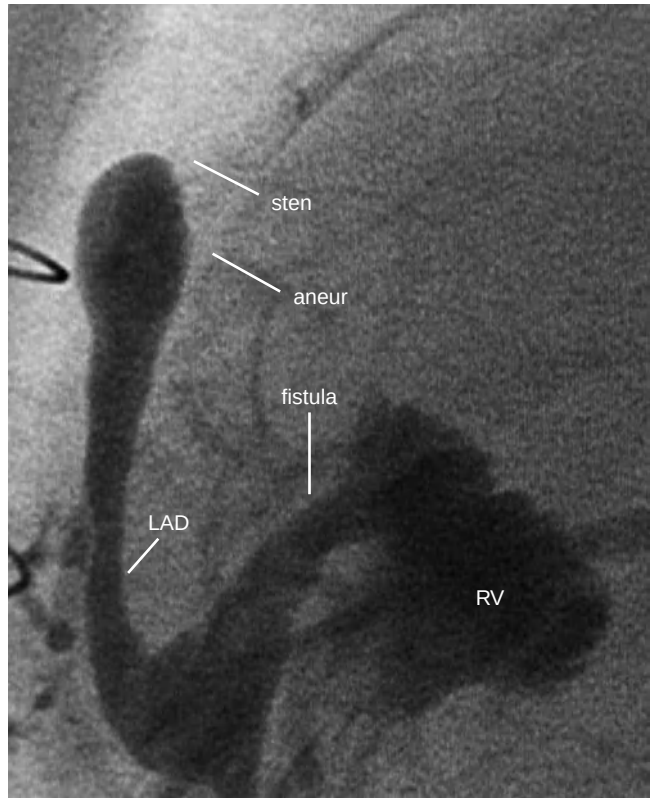


**Figure 17.3** Moderate right ventricular hypoplasia with coronary artery fistulae. This angiogram illustrates a large fistula from the right ventricle to the left anterior descending coronary artery. The injection into the ventricle opacifies the distal two-thirds of the coronary artery. The contrast ends at an aneurysmal dilation. There is stenosis of the "true" coronary artery just above this. LAD, left anterior descending; RV, right ventricle; aneur, aneurysm; sten, stenosis.

### Pulmonary valve and arteries

By definition, there is luminal discontinuity between the right ventricle and the main pulmonary artery. In almost all cases the pulmonary valve is atretic. Approximately 70–80% of the patients have a small but patent infundibulum and membranous atresia of the valve, often with recognizable pulmonary valve tissue and definable commissures [20,25,27] (Figs 17.6 and 17.7). The remainder have muscular infundibular atresia with or without overlying fibrous valve tissue [14,18] (Fig. 17.8). Rarely, the infundibulum is atretic and the pulmonary valve is patent [51]. The atretic pulmonary valve annulus diameter may be normal or mildly hypoplastic. The main and branch pulmonary arteries are usually normal in size [9,18]. In the CHSS database, only 6% of patients had significant pulmonary artery hypoplasia [14]. Rarely, the main pulmonary artery is absent. Pulmonary blood flow is almost always through a patent ductus arteriosus [45,46].

### Pulmonary atresia with RV dilation

The right ventricle is dilated in ~5–10% of patients with PA/IVS [14,28,31,32]. Right heart enlargement may be mild, but patients in this group can have massive cardiac enlargement.

### Right atrium

In contrast to the patients with right ventricular hypoplasia, patients in this group typically have severe tricuspid regurgitation. The right atrium is often severely dilated and there may be associated dilation of the venae cavae. The patent foramen ovale is often stretched with right-to-left atrial-level shunt.

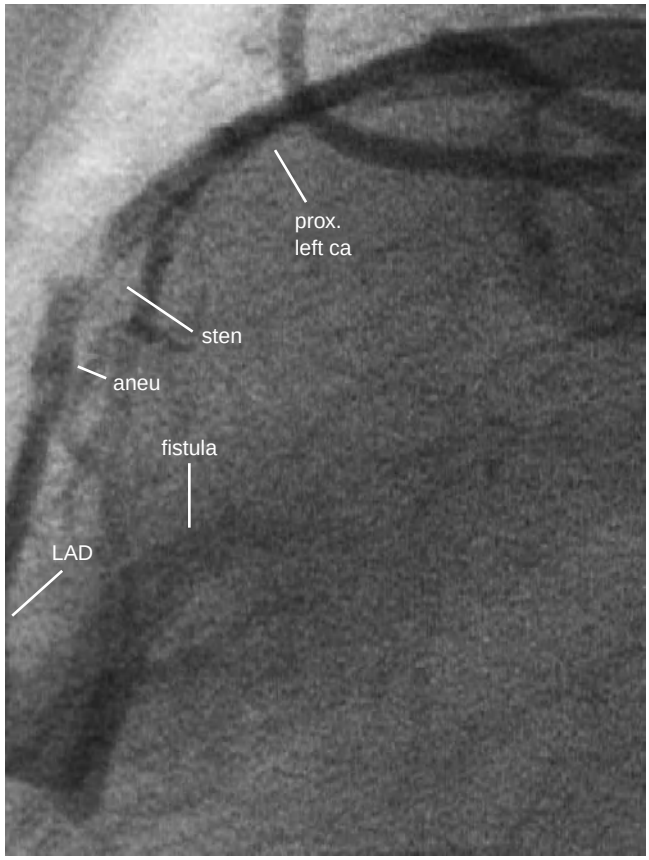


**Figure 17.4** Coronary fistula in right ventricular dependent coronary circulation. This image is from the same patient as seen in Fig. 17.3, but the angiography is done in the aortic root. The "true" left coronary can be seen proximally, but the stenosis is not seen well and the aneurysm is not obvious. LAD, left anterior descending; aneur, aneurysm; prox. left ca, proximal left coronary artery; sten, stenosis.

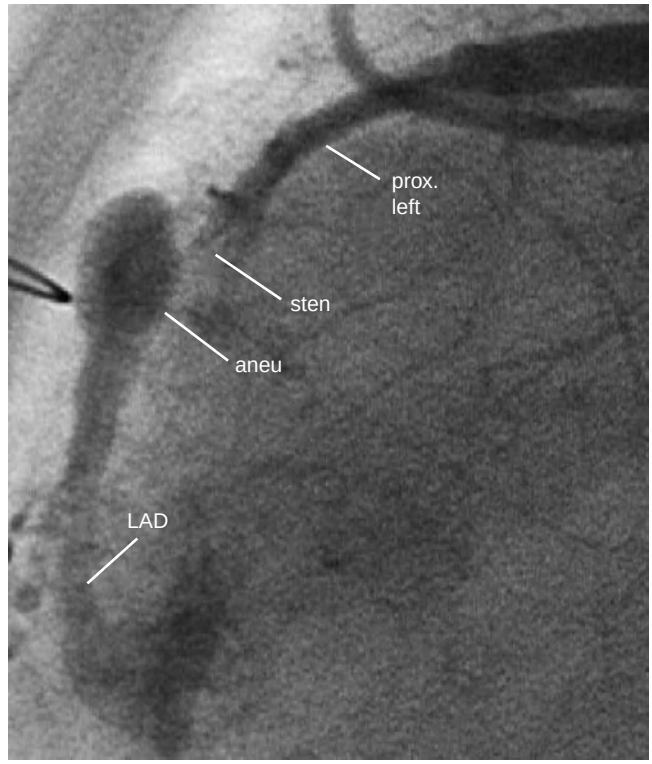


**Figure 17.5** Coronary fistula in right ventricular dependent coronary circulation. This image is identical to that in Fig. 17.4, but depicts a different phase of the cardiac cycle. Now the aneurysm and the associated stenosis of the coronary artery are easily visualized. LAD, left anterior descending; aneu, aneurysm; prox. left, proximal left coronary artery; sten, senosis.

### Right ventricle and tricuspid valve

The tricuspid valve annulus and RV are both larger than normal. In many, the right heart becomes so dilated that it compresses the left heart, compromising cardiac output (Fig. 17.9). The heart may have a "wall-to-wall" appearance on chest radiography, similar to severe Ebstein anomaly (Fig. 17.10). In some of these patients, Ebstein anomaly coexists with significant apical displacement of the septal leaflet, leading to poor coaptation and severe tricuspid regurgitation [29,32,34,52,53]. In others, the tricuspid valve is hinged normally at the annulus but the leaflets are redundant, dysplastic and sail-like. Because of the tricuspid regurgitation, the right ventricle is unlikely to be hypertensive and endocardial fibroelastosis is uncommon. The right ventricle tends to be thin-walled and dilated. Uhl anomaly of the right ventricle is uncommon, but has been reported [54]. Patients with a dilated right ventricle typically have true membranous atresia of the pulmonary valve, although rarely they may have an associated muscular atresia of the infundibulum.

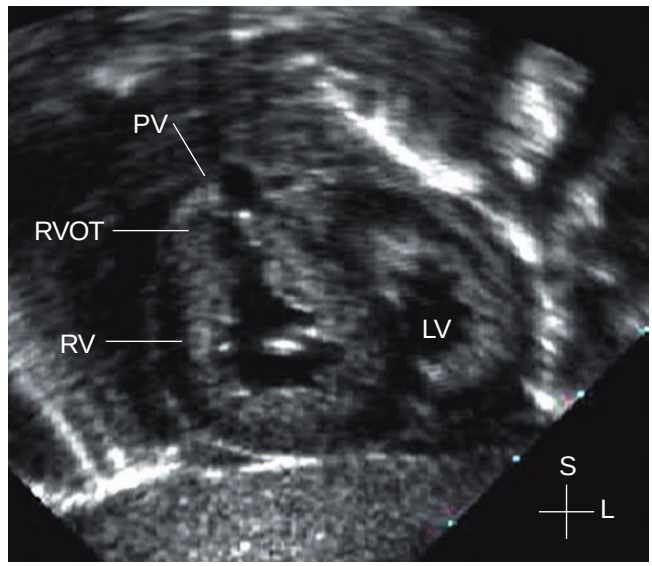


**Figure 17.6** Right ventricular outflow tract (RVOT) in membranous pulmonary atresia seen from the subcostal short-axis view of the outflow tract. Note the small but well-formed right ventricular outflow with a good-sized pulmonary valve (PV) annulus. Inf, infundibulum; LV, left ventricle; RV, right ventricle.

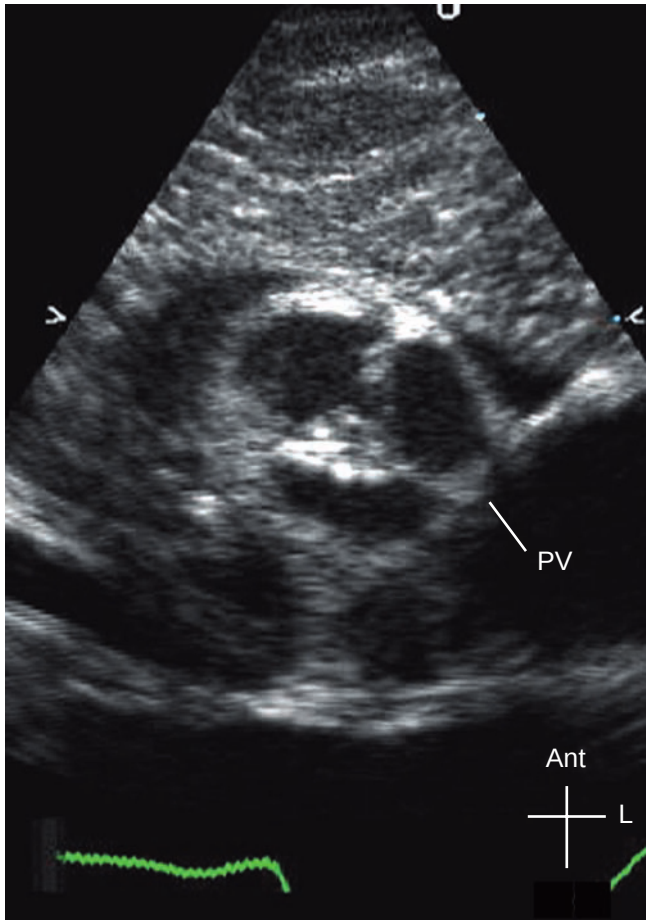


**Figure 17.7** Pulmonary valve anatomy in pulmonary atresia with intact ventricular septum. This "en face" image is taken from the high left parasternal window with the marker pointing straight left. The main pulmonary artery sinuses appear essentially normal. The commissures are well delineated, but thickened. This morphology is often seen in patients with membranous valve atresia. PV, pulmonary valve.

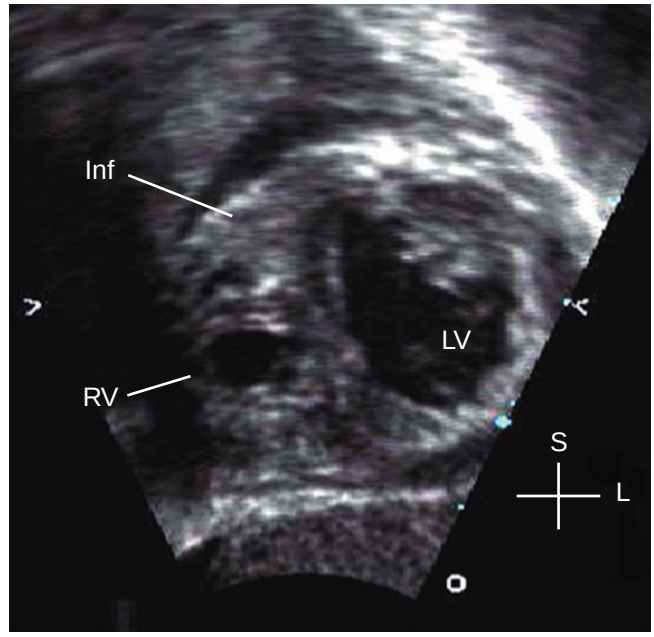


**Figure 17.8** Right ventricular outflow tract in muscular pulmonary atresia. This subcostal short-axis view demonstrates a short right ventricular outflow tract with no obvious infundibular cavity. Instead there is a muscular obliteration of the outlet and no identifiable pulmonary annulus. Inf, infundibulum; LV, left ventricle; RV, right ventricle.

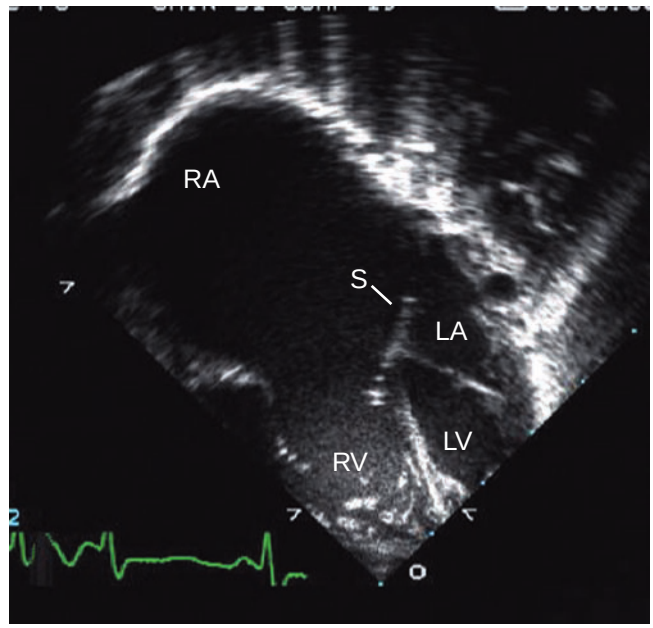


**Figure 17.9** Severely dilated right ventricle and right atrium in pulmonary atresia with intact ventricular septum seen from the apical window. The tricuspid valve annulus and right atrium are severely dilated. The tricuspid valve leaflets are elongated and the right ventricle is significantly larger than the left. The atrial septum deviates leftward, making the left atrium look much smaller than usual. LA, left atrium; LV, left ventricle; RA, right atrium; RV, right ventricle; S, septum.

### Coronary arteries

Because the right ventricle in this group of patients decompresses during systole through tricuspid regurgitation, right ventricular hypertension is uncommon or mild and anomalies of the coronary arteries are rare.

### Pulmonary valve and arteries

Similar to the right ventricular hypoplasia group, the pulmonary valve annulus, main pulmonary artery and branch pulmonary arteries are likely to be normal in size or mildly undersized. It is unusual for them to be diminutive, discontinuous or absent.

## Associated structural heart disease

Normal cardiac position and segmental anatomy are present in ~98% of patients with PA/IVS. There have been reports of associated morphologic abnormalities of the left heart, but hemodynamically significant left heart disease is rare [31,55,56].

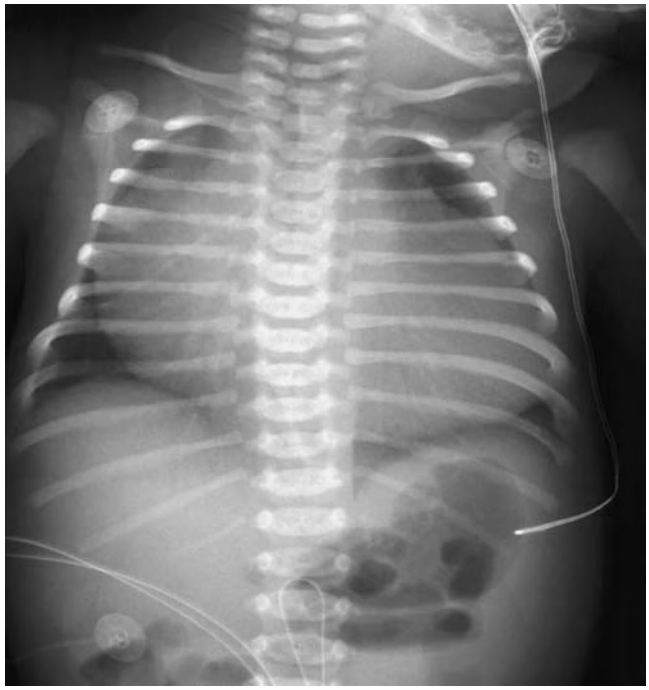

**Figure 17.10** Chest radiograph in newborn with severe right heart dilation and pulmonary atresia with intact ventricular septum. Note that the borders of the cardiac silhouette extend from the right chest wall to the left chest wall.

## Pathophysiology

### Preoperative

Before birth, PA/IVS with severe tricuspid regurgitation and massive dilation of the right heart can result in low cardiac output, hydrops and intrauterine death. Fetuses with PA/IVS and normal-sized or hypoplastic right ventricles usually survive pregnancy.

After birth, the systemic venous return crosses the atrial septum through the foramen ovale and mixes with the pulmonary venous return in the left atrium, which results in cyanosis. The ductus arteriosus remains the only source of pulmonary blood flow, and survival depends on maintaining ductal patency.

The systolic pressure in the right ventricle depends on the pathways available for blood to exit the chamber. In the presence of a competent tricuspid valve the systolic pressure is usually very high, whereas in those with severe tricuspid regurgitation the pressure may be normal or only mildly elevated. In the postnatal circulation, coronary artery abnormalities can become important in a number of ways. In those with RV-dependent coronary artery circulation, oxygen delivery to the myocardium depends on the perfusion pressure and oxygen content in the right ventricle. If either of these falls significantly, myocardial ischemia can result. With or without RV-dependent coronary circulation, increased intracavitary pressure may lead to chronic subendocardial ischemia. Finally, the presence of RV-to-coronary artery communications can allow for a right-sided circular shunt [46]. Blood can go from RV to coronary artery to coronary vein to coronary sinus to right atrium to RV without passing through the systemic capillary bed. Any or all of these factors can cause chronic and/or intermittent ischemia, which can adversely affect both systolic and diastolic myocardial properties [55,57–60].

### Postoperative

Postoperative physiology varies greatly depending on the operation performed. The most dramatic changes are those occurring after decompression of the RV. As right ventricular pressure falls, myocardium that was perfused through sinusoids may experience at least a transient decrease in blood flow, leading to myocardial ischemia. The degree of ischemia depends on the extent to which blood from the aortic root can reach those myocardial segments through the epicardial coronary arteries. If there are significant coronary artery stenoses, the myocardial segments distal to those stenoses may become profoundly ischemic and severe ventricular dysfunction may ensue [48,49]. Even without coronary stenoses, ischemia can occur as right ventricular pressure falls if there are large coronary–cameral fistulae, as these may cause "steal" of blood flow from the coronary arteries [57,58]. Ventricular dysfunction can be transient, although for some patients it is profound and irreversible.

## Treatment

### Prenatal

Accurate early diagnosis offers parents the option to consider fetal therapy. Evidence from prenatal studies indicates that early atresia of the pulmonary valve is associated with an arrest of right heart growth in utero. This observation has led to speculation that in utero restoration of antegrade pulmonary blood flow may stimulate growth of the right ventricle and tricuspid valve. Although successful prenatal balloon dilations of the pulmonary valve have been reported, experience is too limited to evaluate the efficacy of this fetal intervention [61]. As the instruments and techniques used for in utero balloon valvuloplasty continue to improve [61–66], further investigations of the risks, benefits and criteria for patient selection are warranted.

### PA/IVS with RV hypoplasia

The goal of treatment is to achieve a two-ventricle repair in as many infants as possible without compromising myocardial perfusion [14,67–96].

Patients with RV-dependent coronary circulation are at risk for myocardial ischemia and death if the right ventricle is decompressed. Therefore, a single ventricle management strategy is pursued. The first step is to create a stable source of pulmonary blood flow by a systemic-to-pulmonary artery

shunt. Eventually, palliation is achieved with Fontan-type circulation in the first few years of life [14,97,98]. Without establishment of antegrade pulmonary blood flow, there is no growth of the right ventricle and it usually remains hypoplastic and hypertensive. There is a paucity of long-term outcome data in these patients, but medium-term follow-up data suggest that the overall survival in patients with PA/IVS and a single ventricle circulation is ~80% [14,97,98].

For the majority of infants, coronary flow is not dependent on the right ventricle and a biventricular repair can be considered. The first step is creation of antegrade pulmonary blood flow. This can be achieved by placement of a right ventricular outflow tract patch, surgical valvotomy, or by transcatheter perforation and balloon dilation of the valve [67,72,90,91, 99]. The hope is that restoring antegrade pulmonary blood flow can stimulate right heart growth, ultimately giving the patient a right ventricle that can carry a full cardiac output.

If antegrade flow is established and significant cyanosis persists, an alternate source of pulmonary blood flow such as a Blalock–Taussig shunt may be required. Once stable pulmonary blood flow is established, patients are followed with noninvasive imaging to assess tricuspid valve and RV growth. If the RV grows sufficiently, then an attempt is made to occlude or ligate any accessory sources of pulmonary blood flow and close any existing atrial level shunts, either surgically or with an implantable occlusion device.

In many series, there is a subset of patients who thrive after a right ventricular outflow tract procedure and a shunt, yet fail attempts to remove the shunt from the circulation and close the atrial communication(s). In some of these patients a strategy has been pursued in which the atrial communication is closed and a bidirectional Glenn shunt is performed (called *1.5-ventricle repair*). This allows inferior vena caval flow to be carried by the right ventricle while flow from the superior vena cava is delivered directly to the pulmonary vascular bed [100–102].

### PA/IVS with RV dilation

Management of patients with PA/IVS and massive RV dilation is challenging. This group has higher rates of in utero demise, newborn morbidity and postoperative mortality. There have been some successful attempts at creating a biventricular circulation by performing tricuspid valvuloplasty in addition to placement of a right ventricular outflow tract patch. In some cases, this may be done in association with a surgical reduction in the size of the RV and/or right atrium. Rarely, pulmonary valvotomy or a right ventricular outflow tract patch alone is sufficient.

## Imaging

PA/IVS was first diagnosed by M-mode echocardiography in the late 1970s [103,104]. By the mid-1980s, two-dimensional (2D) echocardiography had supplanted M-mode, increasing the available anatomic detail [105,106]. With the addition of color and spectral Doppler technology, noninvasive evaluation has become more detailed and increasingly important for diagnosis and assessment of prognosis.

### Prenatal assessment

Increasingly, the diagnosis of PA/IVS is being made in utero [107–117]. Because this lesion frequently causes a change in chamber size, it is relatively easy to identify on an obstetrical screening exam. Unfortunately, right ventricular hypoplasia may not be obvious early in the second trimester, and screening ultrasound at 14–18 weeks of gestation may only identify the most severe cases. Early diagnosis can be made more often if color Doppler is used to evaluate tricuspid valve function, flow through the right ventricular outflow tract and pulmonary valve, and the direction of ductal flow.

Fetal evaluation includes detailed assessment of the right heart structures, including tricuspid valve size and function; right ventricular morphology, size and function; presence of coronary artery fistulae; morphology of the RV outflow tract and the pulmonary arteries as well as the direction of flow through the ductus arteriosus. Evaluation of the tricuspid valve includes measurements of the annulus diameter in the 4-chamber and long-axis planes and depiction of the valvar and subvalvar apparatus anatomy (Figs 17.11–17.13). Color

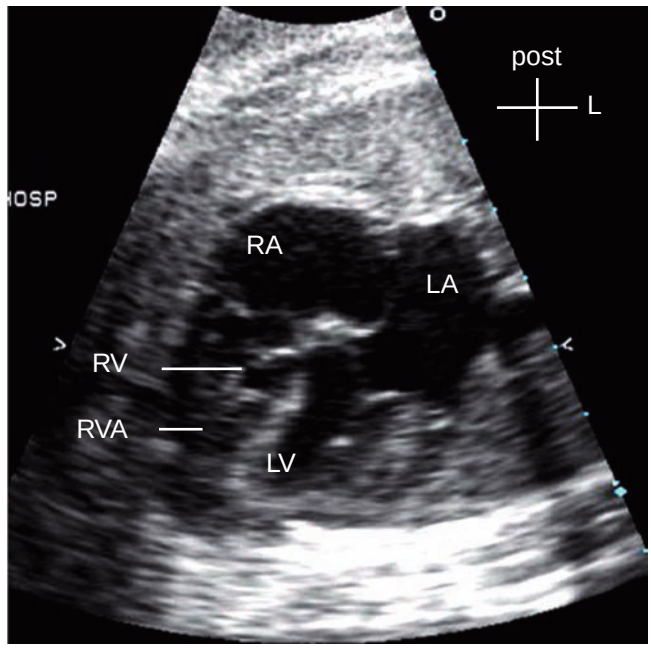


**Figure 17.11** Fetal heart in pulmonary atresia with intact ventricular septum and right ventricular hypoplasia. Note the markedly hypoplastic right ventricular cavity and that the apex does not reach the left ventricular apex. The tricuspid valve annulus diameter is roughly half that of the mitral valve and the atrial septum deviates into the left atrium. LA, left atrium; LV, left ventricle; RA, right atrium; RV, right ventricle; RVA, right ventricular apex.

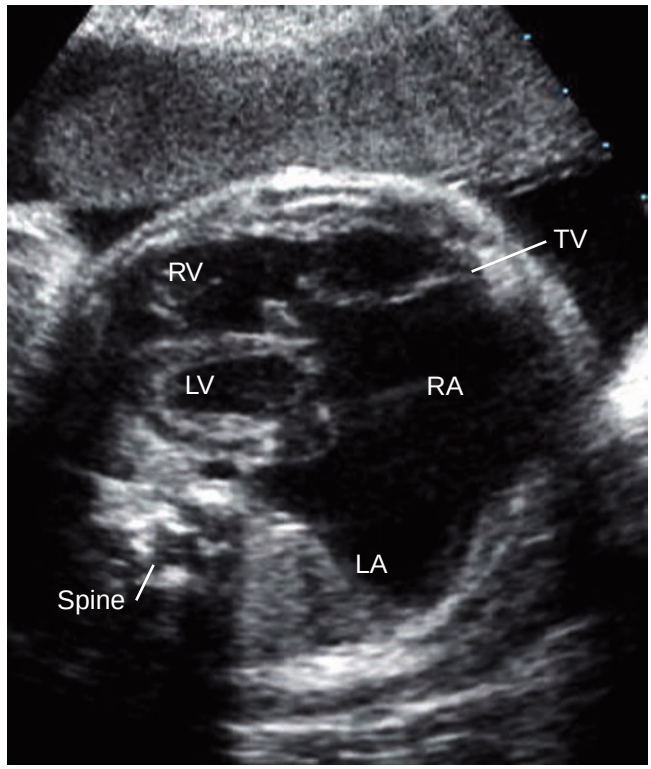


**Figure 17.12** Fetal heart in pulmonary atresia with intact ventricular septum and right ventricular dilation. The image illustrates that the heart spans the entire width of the chest. It also extends posteriorly, although one can see small amounts of lung tissue behind the left atrium and left ventricle. The tricuspid valve annulus is dilated and the leaflets are redundant. LA, left atrium; LV, left ventricle; RA, right atrium; RV, right ventricle; TV, tricuspid valve.

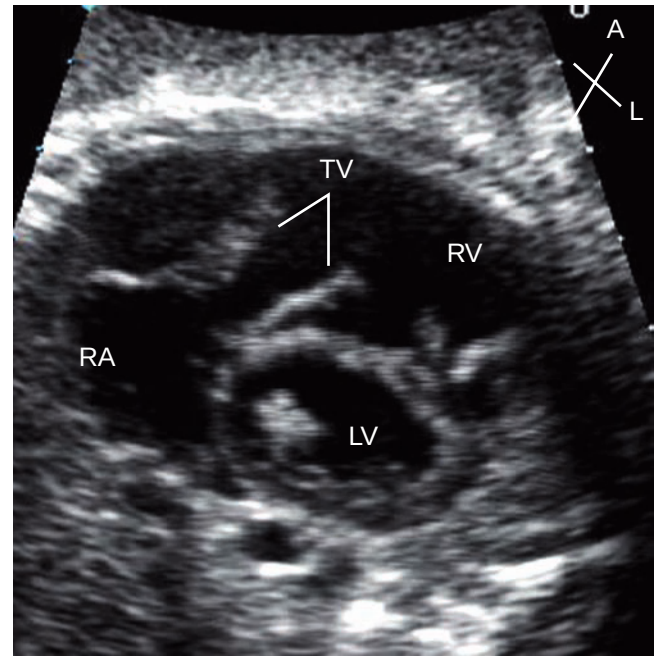


**Figure 17.13** Tricuspid valve in fetus with pulmonary atresia and intact ventricular septum. This coronal view shows massive dilation of the right ventricle as well as the redundant, sail-like tricuspid valve leaflets. LV, left ventricle; RA, right atrium; RV, right ventricle; TV, tricuspid valve leaflets.

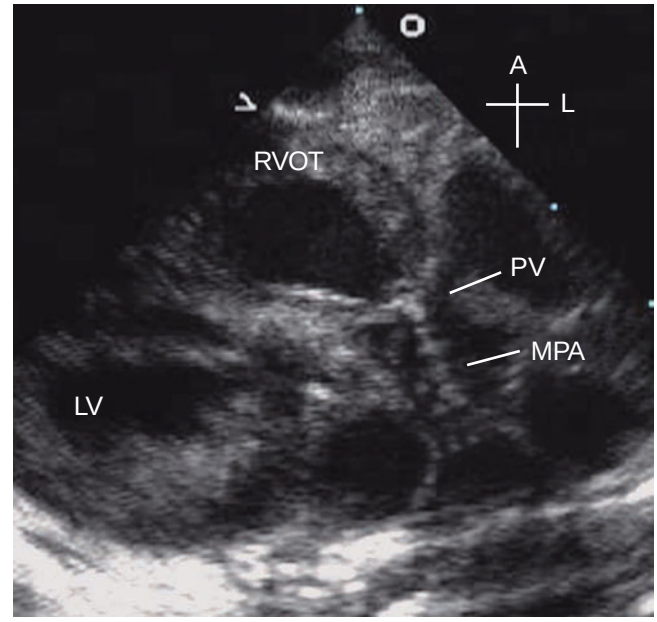


**Figure 17.14** Right ventricular outflow tract evaluation in a fetus with membranous pulmonary atresia. This long-axis view of the right ventricular outflow tract demonstrates a patent infundibulum, an atretic pulmonary valve, and a good sized main pulmonary artery. LV, left ventricle; MPA, main pulmonary artery; PV, pulmonary valve; RVOT, right ventricular outflow tract.

Doppler is used to assess valve inflow and regurgitation. Spectral Doppler should be used to assess the inflow pattern and to estimate right ventricular systolic pressure when a regurgitation jet is present. The right ventricle should be evaluated in all views with attention to length, degree of hypertrophy and degree of systolic dysfunction. Color Doppler is used to screen for coronary artery fistulae [112,117]. Magnifying the right ventricle and interrogating the cavity and myocardium by color Doppler with a low Nyquist limit allows visualization of coronary artery fistulae in some fetuses. Fistulae are seen as streams of color signals within the myocardium and jets into the cavity during diastole. The right ventricular outflow tract and main pulmonary artery are imaged to evaluate pulmonary annulus size and outflow tract patency (Fig. 17.14). Color Doppler is used to determine presence or absence of flow across the pulmonary valve. In the presence of flow from the aorta to the pulmonary artery through the ductus arteriosus, the pulmonary valve may not open even when it is not anatomically atretic (functional atresia). In this case, detection of pulmonary regurgitation excludes pulmonary valve atresia. The main and branch

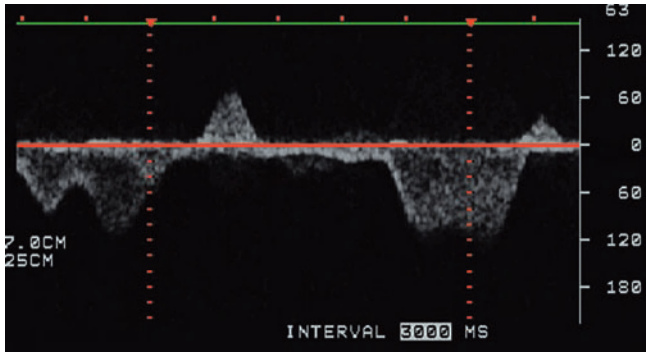


**Figure 17.15** Spectral Doppler in the hepatic veins in a fetus with pulmonary atresia and intact ventricular septum. Flow below the baseline is toward the heart and flow above the baseline is away from the heart. This tracing shows a prolonged period of no flow in the hepatic veins as well as a short period of retrograde flow (away from the heart). Typically, hepatic venous flow is toward the heart, occasionally with very short periods of no flow. This tracing is consistent with severe tricuspid regurgitation.

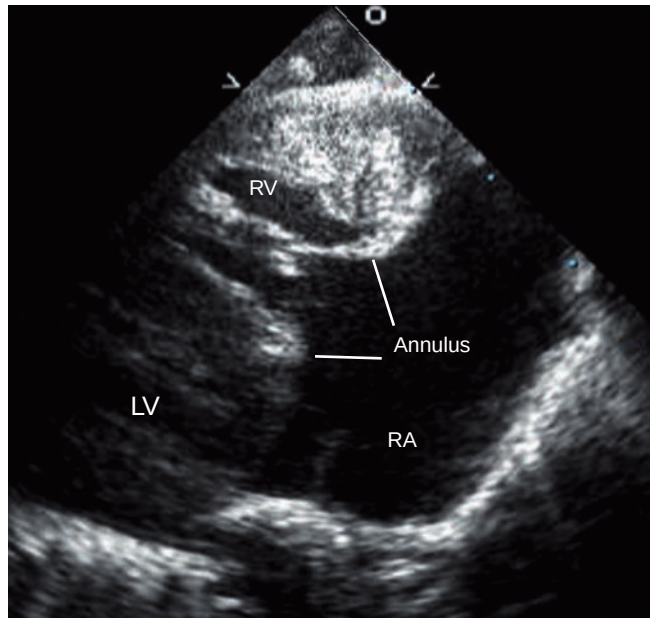


**Figure 17.16** Parasternal long-axis view of the tricuspid valve and right ventricular inflow. The transducer is angled toward the right. This is a standard view for measuring the tricuspid valve annulus (in addition to the 4-chamber view). The hinge points of the tricuspid valve are noted. The valve annulus is measured at the hinge points of the leaflets, not at the functional orifice. LV, left ventricle; RA, right atrium; RV, right ventricle.

pulmonary artery anatomy and size are documented. The ductus arteriosus is evaluated with 2D imaging and color Doppler. In PA/IVS, flow is from the aorta to the pulmonary arteries, the reverse of normal flow direction. The atrial septum is evaluated to document unrestrictive right-to-left flow at the atrial level. As with all fetuses, the echocardiogram includes an evaluation of left heart anatomy and function as well as Doppler evaluation of the umbilical vessel, ductus venosus and inferior vena cava. The flow profile in the umbilical vessels and hepatic veins can be markedly abnormal in the presence of significant tricuspid regurgitation (Fig. 17.15).

Studies in fetuses with PA/IVS show that a smaller tricuspid valve diameter and right ventricular size are predictive of worse hypoplasia of the right heart at birth, and are associated with a lower likelihood of achieving a biventricular outcome [113–116]. Sequential prenatal echocardiograms also add important prognostic information about growth velocity of the tricuspid valve and right ventricle, as well as progression of tricuspid regurgitation [113]. Although no studies have documented that prenatal diagnosis of PA/IVS leads to improved postnatal outcome, some studies of other duct-dependent congenital heart disease have suggested decreased morbidity and neurologic sequelae in prenatally diagnosed patients [118–121].

## Preoperative imaging

Similar to the prenatal evaluation, the postnatal echocardiogram includes a comprehensive anatomic survey with particular attention to the right-sided structures. Every effort should be made to optimize conditions for high-quality imaging, including adjustment of lighting, use of high-frequency transducers and minimization of patient movements.

The ability of the right ventricle to fill and, therefore, to grow depends on the size of the tricuspid valve and on the size and compliance of the inflow portion. Numerous studies have demonstrated that tricuspid valve annulus diameter predicts outcome after catheter-based or surgical treatment of PA/IVS [14,114–116,122,123]. Therefore, it is of upmost importance to obtain clear images of the tricuspid valve and its supporting apparatus and to measure the annulus diameters in orthogonal views. The apical 4-chamber view depicts the lateral diameter (Figs 17.1 and 17.2) and the parasternal long-axis shows the anterior–posterior diameter (Fig. 17.16). An annulus diameter z-score of less than −3 is associated with a lower likelihood of tolerating right ventricular decompression as the sole intervention [14]. The subvalvar apparatus can be difficult to image due to right ventricular hypertrophy (Fig. 17.17). It is often best seen in the short-axis sweeps from the parasternal and the subcostal acoustic windows. Three-dimensional imaging of the subvalvar apparatus can help clarify the anatomy in some patients. Color and spectral Doppler are used to assess inflow and regurgitation (Fig. 17.18 and Videoclip 17.2).

The right ventricular inflow is best imaged in the 4-chamber and subcostal long-axis views (Figs 17.1 and 17.2), allowing measurements of chamber length. The outflow portion of the right ventricle is visualized from the subcostal short-axis view (Figs 17.7 and 17.8; Videoclip 17.2), from the parasternal long-axis view with the transducer angled toward the left shoulder, and from the parasternal short-axis view with the transducer focused on the area anterior to the

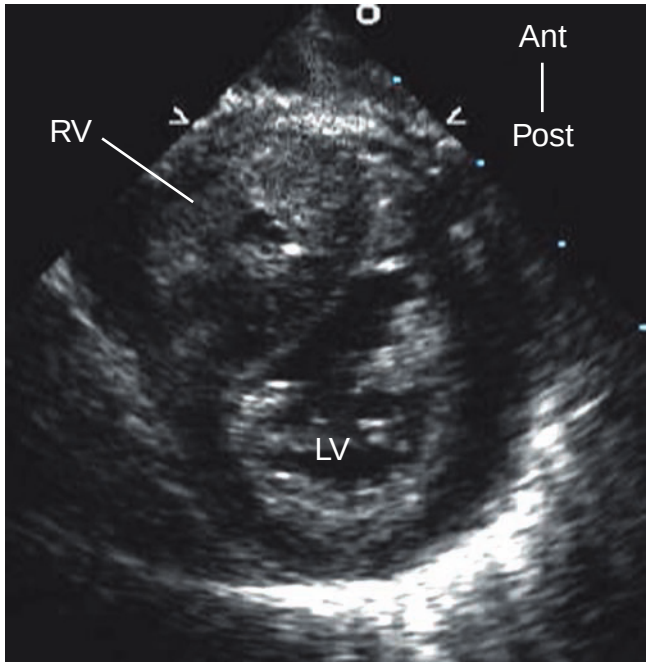


**Figure 17.17** Parasternal short-axis imaging of the ventricles during systole at the level of the left ventricular papillary muscles. Note that only a small amount of right ventricular cavity is visualized at this level. There is severe hypertrophy of the right ventricular wall as well as septal bowing toward the left ventricle, consistent with suprasystemic right ventricular pressure. LV, left ventricle; RV, right ventricle.

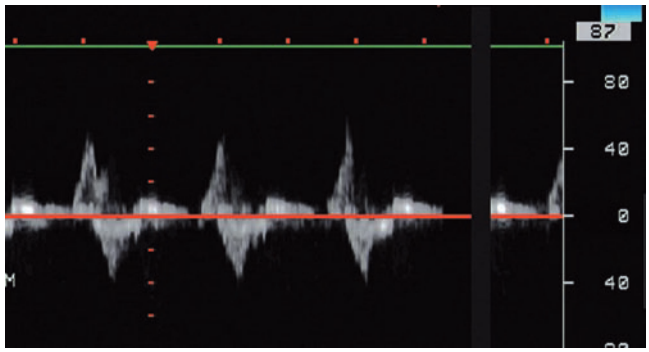


**Figure 17.18** Doppler tracing of the tricuspid valve inflow recorded from the apical 4-chamber view in patient with pulmonary atresia and intact ventricular septum. Note the very short period of low-velocity antegrade flow across the valve (above the baseline). The flow below the baseline will vary depending on the amount of tricuspid regurgitation.

aortic root (Fig. 17.19 and Videoclip 17.3). These views are excellent for evaluating the anatomy of the infundibulum and for color Doppler interrogation evaluating flow in the area of the pulmonary valve. As with the prenatal echocardiogram, detection of a tiny antegrade jet through the pulmonary valve might be difficult to visualize in the presence of retrograde ductal flow into the main pulmonary artery.

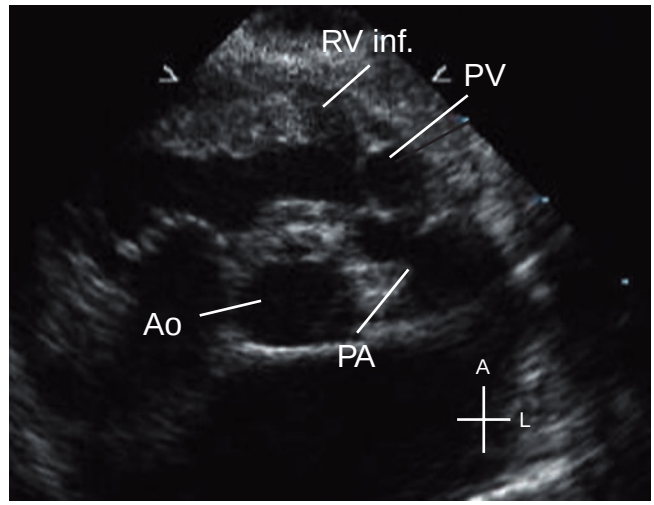


**Figure 17.19** Parasternal short-axis image of the right ventricular outflow tract demonstrating a patent infundibulum. The pulmonary valve tissue is clearly seen but there is no functional orifice. The pulmonary valve annulus is well developed. Ao, aorta; PA, main pulmonary artery; PV, pulmonary valve; RV inf., right ventricular infundibulum.

Therefore, detection of even the smallest jet of pulmonary regurgitation indicates that the pulmonary valve is not atretic.

The diameters of the pulmonary valve annulus and main and branch pulmonary arteries are measured from the parasternal images, although sometimes they are also clearly seen from an apical 4-chamber view with the transducer angled superiorly. The pulmonary artery branches are best seen from a high parasternal short-axis view with the transducer placed just below the left clavicle (Figs 17.20 and 17.21). The main pulmonary artery is evaluated in this view as well as from the parasternal long- or lower short-axis views.

The presence and size of an atrial-level shunt are evaluated from the subcostal long- and short-axis views (Fig. 17.22). One expects to see predominantly right-to-left shunting at the atrial level. In the rare event of a restricted atrial shunt, it manifests as turbulent flow demonstrated by color and spectral Doppler of the right-to-left flow jet. The mean gradient is recorded.

The ductus arteriosus is imaged from a high left parasternal view. In most patients, the pulmonary arteries are supplied by a patent ductus arteriosus. Rarely aorto-pulmonary collateral vessels are present and a thorough evaluation of the mid-thoracic descending aorta to detect these vessels should be done. The mid-thoracic aorta can be imaged from the subcostal view, but parasternal windows can be used as well.

Detailed evaluation of the coronary arteries is particularly important in patients with PA/IVS. Right ventricular sinusoids and coronary artery fistulae are evaluated by color Doppler [124–126]. The ventricular cavity and myocardium are interrogated by color Doppler with a low Nyquist limit from

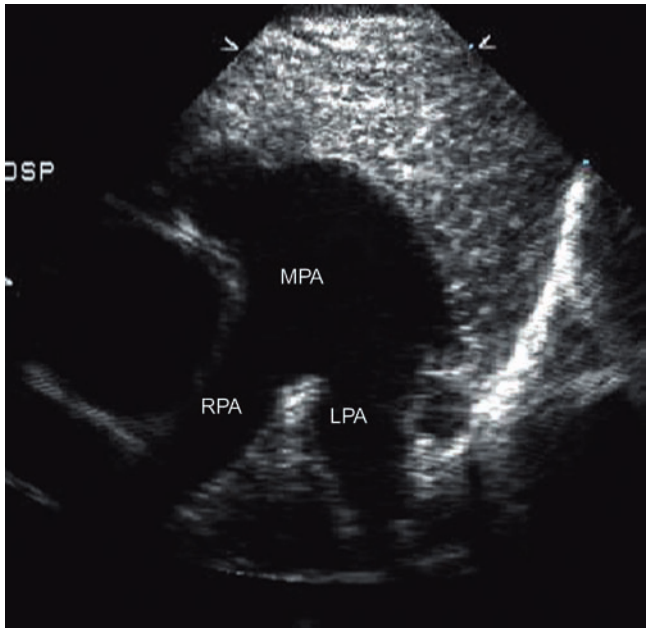


**Figure 17.20** Branch pulmonary arteries in a patient with membranous pulmonary atresia. The image is from a high left parasternal imaging window with the marker oriented to the left. The main and branch pulmonary arteries are normal in size and appearance. Lpa, left pulmonary artery; Main PA, main pulmonary artery; Rpa, right pulmonary artery.

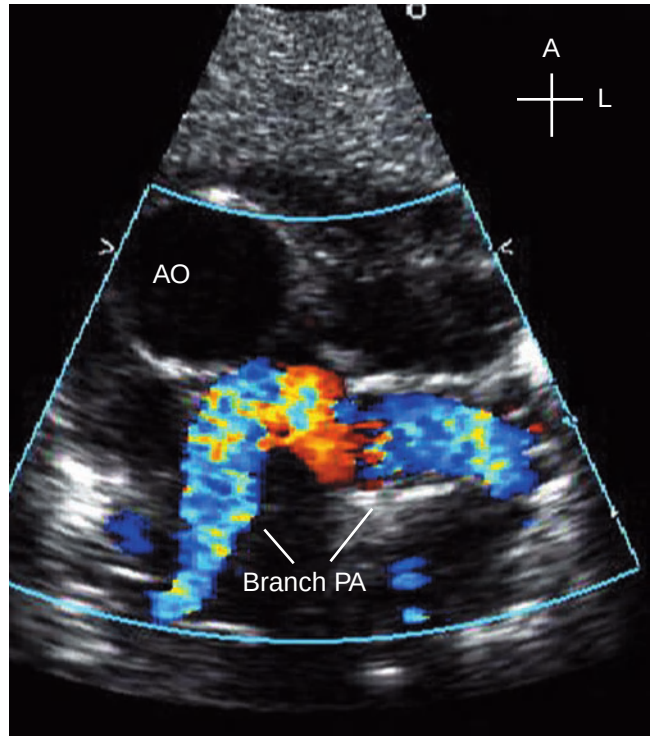


**Figure 17.21** Branch pulmonary arteries in a patient with muscular pulmonary atresia. The image is from a high left parasternal imaging window with the marker oriented to the left. The pulmonary arteries are confluent and normally located, but no main pulmonary artery is present. AO, aorta; PA, pulmonary artery.

the 4-chamber, parasternal and subcostal views (Fig. 17.23 and Videoclips 17.4–17.6). Coronary–cameral fistulae manifest as flow signal within the myocardium, communicating with the right ventricular cavity. The ostia and proximal segments of the left and right coronary arteries are evaluated from the parasternal short-axis view. The coronary artery origins are identified by 2D imaging and, importantly, flow from the root into the coronary arteries is then documented by color Doppler. Rarely, coronary ostial atresia can be present [127]. Although echocardiography can document the presence of coronary fistulae and/or sinusoids, cardiac catheterization and angiography remain the gold standard for the assessment of a right ventricular-dependent coronary circulation.

For those with a dilated right ventricle, the echocardiogram proceeds in a similar fashion but with more attention directed toward the anatomy and function of the tricuspid valve and the subvalvar apparatus. Three-dimensional (3D) echocardiography can be helpful in evaluating the tricuspid valve in these patients. Finally, detailed assessment of left ventricular size and function is important, with particular attention to the presence of any regional wall motion abnormalities.

## Intraoperative imaging

The role of imaging in the operating room varies depending on the operation performed. In the setting of shunt placement, there is usually little need for imaging support,

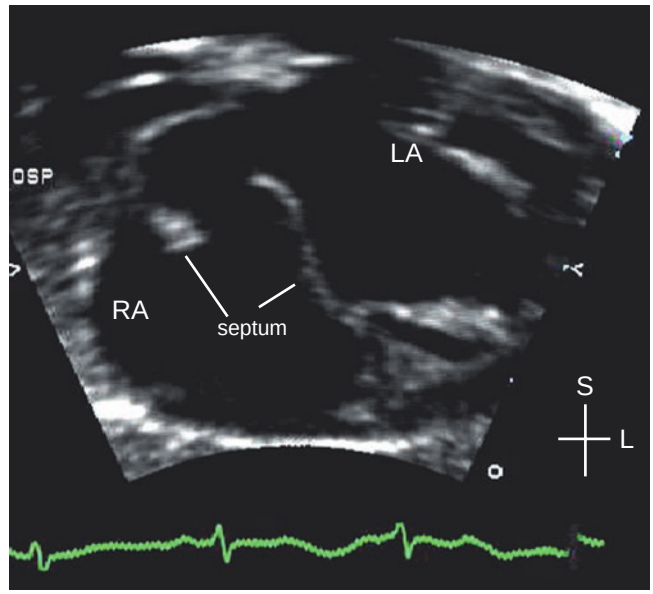


**Figure 17.22** Patent foramen ovale in newborn with pulmonary atresia and intact ventricular septum imaged from the subcostal long-axis window. The image shows the widely sprung foramen ovale with the basal portion of the septum swung toward the left atrium. This appearance is typical in all forms of pulmonary atresia with intact ventricular septum. LA, left atrium; RA, right atrium.

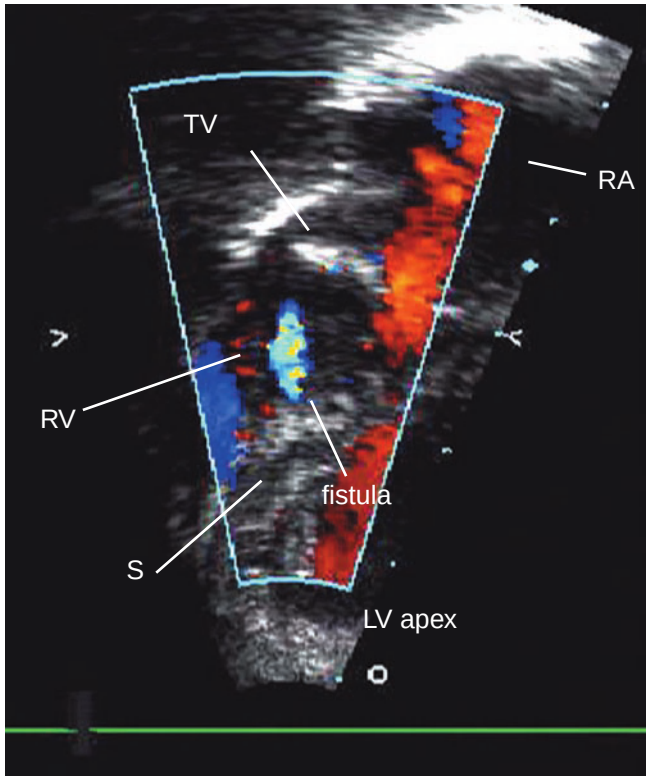


**Figure 17.23** Fistula from the coronary artery to the right ventricle. This is a magnified image of the small right ventricle taken from the apical 4-chamber view. Note the prominent color jet in the middle of the right ventricle. This represents flow from an apical sinusoid into the right ventricle. LV, left ventricle; RA, right atrium; RV, right ventricle; S, septum; TV, tricuspid valve.

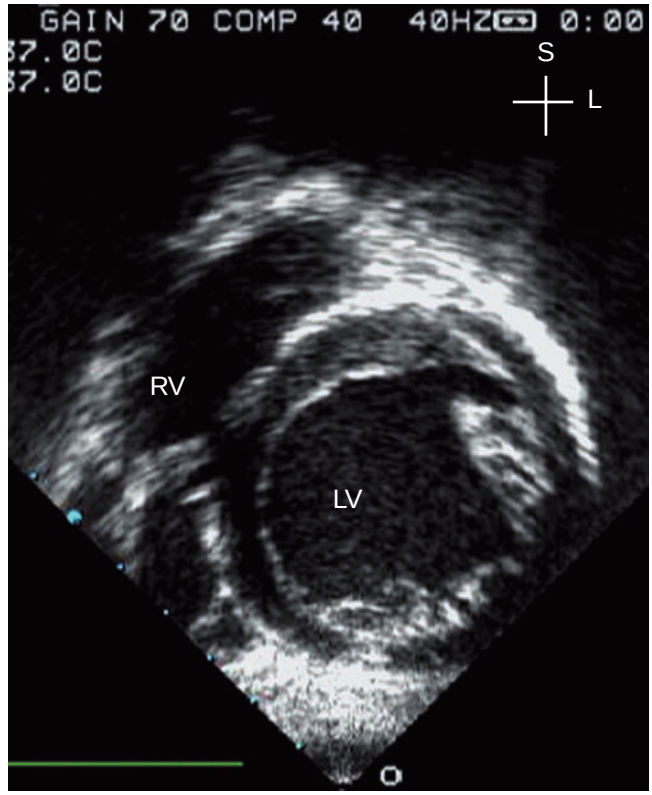


**Figure 17.24** Transgastric view of the ventricles. The esophageal probe is in the stomach and anteflexed maximally to achieve this view. It should be possible to sweep from right to left and visualize most of the left ventricle. The anterior portion of the right ventricle is seen as well, but other segments may be difficult to image. LV, left ventricle; RV, right ventricle.

although some surgeons request an evaluation of ventricular function once shunt flow commences. In patients undergoing right ventricular decompression, imaging is useful for assessing both right and left ventricular function after the procedure. In addition, echocardiography can document patency of the right ventricular outflow tract. The right ventricle and the outflow can be evaluated by epicardial imaging techniques, but transesophageal echocardiography (TEE) is preferred because of the wider field of view and because it avoids interference with the surgical field. Ventricular function can be assessed by TEE from all views, but is often best demonstrated from transgastric views (Fig. 17.24). In these views, the ventricles can be imaged in short-axis with a sweep from the base of the heart to the apex. Further assessment is done in the 4-chamber view with attention to both global function and regional wall motion abnormalities.

In patients with PA/IVS and dilated RV, the first operation often involves right ventricular decompression, tricuspid valve plasty, and a procedure to decrease the size of the right heart chambers. In these patients, TEE can be used to assess tricuspid valve and right ventricular function in addition to left ventricular function. In general, the tricuspid valve is best imaged from the 4-chamber view and from short-axis views obtained from the mid-esophagus. This is done with the imaging plane at a 90–110° orientation with the probe turned toward the patient's right. Three-dimensional imaging can be helpful in both pre- and postoperative imaging of the tricuspid valve and right ventricle.

## Postoperative imaging

Goals for follow-up echocardiography vary with the surgical strategy being pursued. In children with a systemic-to-pulmonary artery shunt, the shunt can be imaged from the high parasternal views (Figs 17.25 and 17.26). The shunt can also be imaged from the subcostal views. If shunt occlusion is suspected, the descending aorta is interrogated by Doppler for evidence of diastolic flow reversal due to runoff through the shunt (Fig. 17.27).

After a procedure to decompress the RV, follow-up echocardiography is used to evaluate the right ventricular outflow tract and pulmonary valve for obstruction and regurgitation (Fig. 17.28). Echocardiography is also important for assessing tricuspid valve size and function, RV size

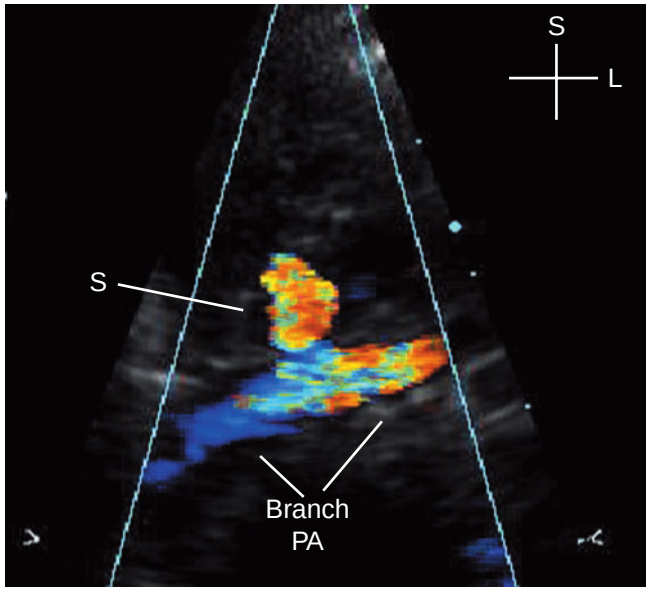


**Figure 17.25** Blalock–Taussig shunt. Image of the distal end of a right Blalock–Taussig shunt taken from a high left parasternal view. The marker is pointed to the left and the transducer is angled slightly toward the right chest to find the distal end of the shunt. PA, pulmonary arteries; S, shunt.

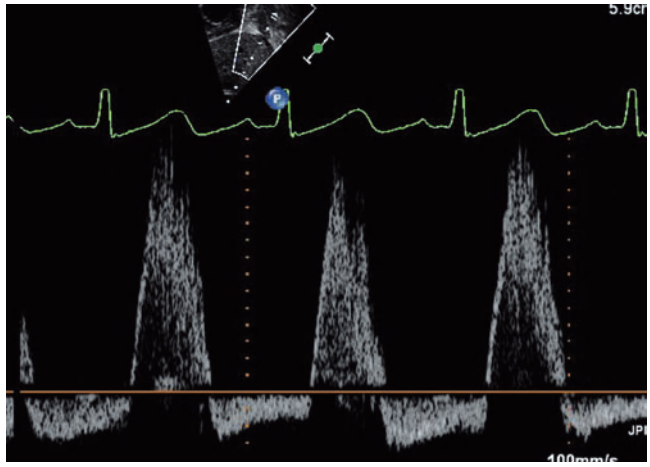

**Figure 17.27** Spectral Doppler in the descending aorta recorded from the subcostal window with the cursor aligned with the descending aorta. Note the normal systolic flow profile toward the diaphragm as well as holodiastolic flow going away from the diaphragm. This diastolic flow is typical for a patient with an aorto-pulmonary shunt.

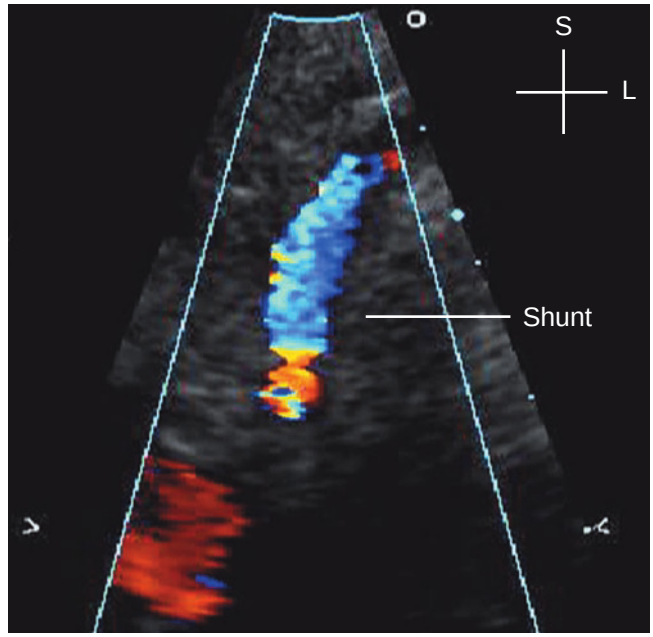


(a)

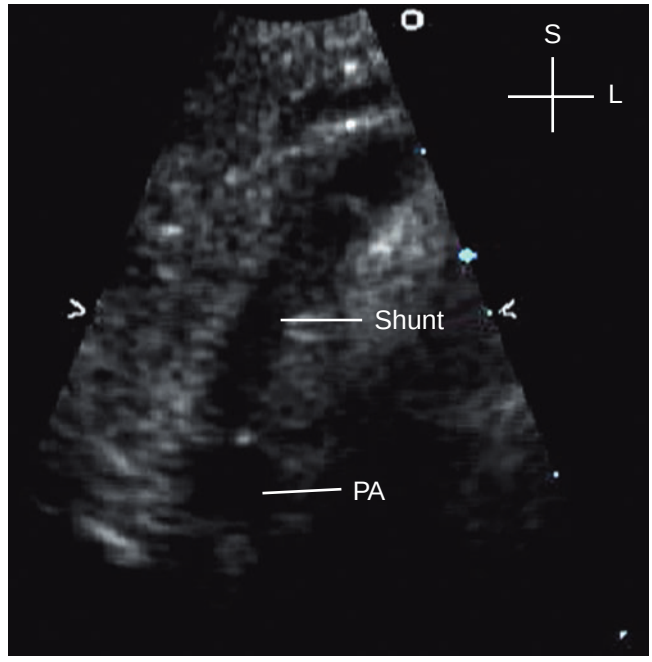


(b)

**Figure 17.26** Long-axis views of the Blalock–Taussig shunt. The transducer is positioned just to the left of the upper sternum with the marker oriented superiorly or slightly to the left. The examiner sweeps toward the right to get into the plane of the shunt. **(a)** The shunt with color Doppler. **(b)** The shunt by 2D imaging. The entire length of the shunt is visualized. These views are used to evaluate the shunt for thrombus or focal stenosis. PA, pulmonary artery.

and function, the direction of flow across the atrial septum, and global and regional LV function. RV systolic pressure is evaluated based on the tricuspid regurgitation jet velocity. In some patients, abnormalities of the RV myocardial architecture persist despite adequate chamber growth (Fig. 17.29). Similarly, persistent structural abnormalities of the tricuspid valve are common and may be the substrate for hemodynamically important stenosis and/or regurgitation. Diastolic flattening of the interventricular septum is a common finding and suggests right ventricular volume overload from pulmonary and/or tricuspid valve regurgitation (Fig, 17.30).

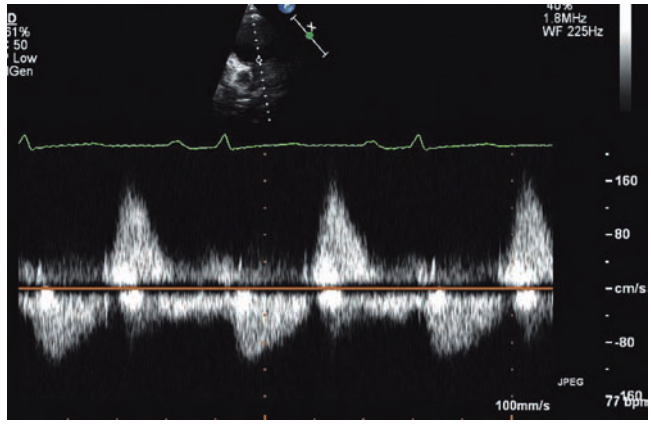


**Figure 17.28** Spectral Doppler of the right ventricular outflow tract. The signal below the baseline represents antegrade systolic flow across the pulmonary annulus. The signal above the baseline represents retrograde diastolic flow in the right ventricular outflow tract from pulmonary regurgitation.

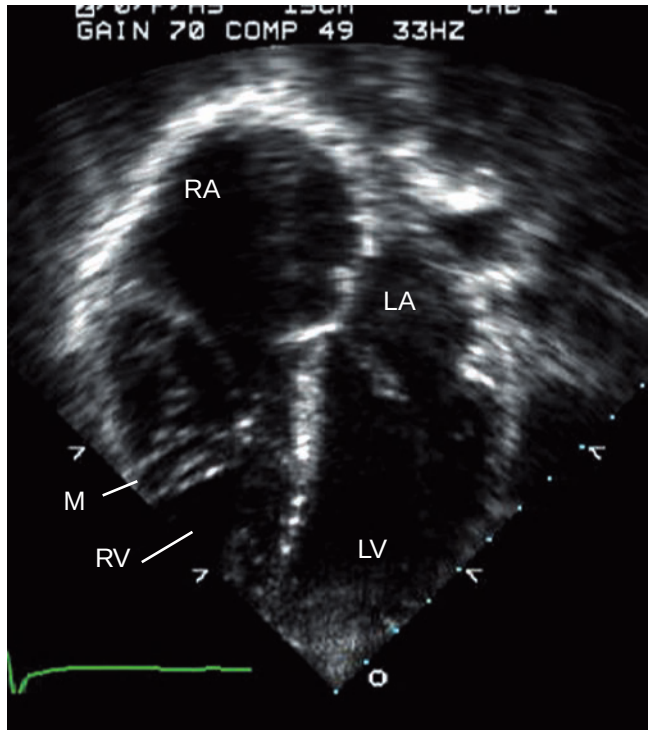


**Figure 17.29** Right ventricular growth, 6 years after biventricular repair. This is a 4-chamber view in a patient with pulmonary atresia with intact ventricular septum status post-pulmonary valve dilation and placement of a Blalock–Taussig shunt followed by shunt ligation and atrial septal defect closure at age 1 year. The right ventricle is nearly normal in length, but still has abnormal myocardial architecture. Note the large mid-ventricular muscle bar. LA, left atrium; LV, left ventricle; M, muscle bar; RA, right atrium; RV, right ventricle.

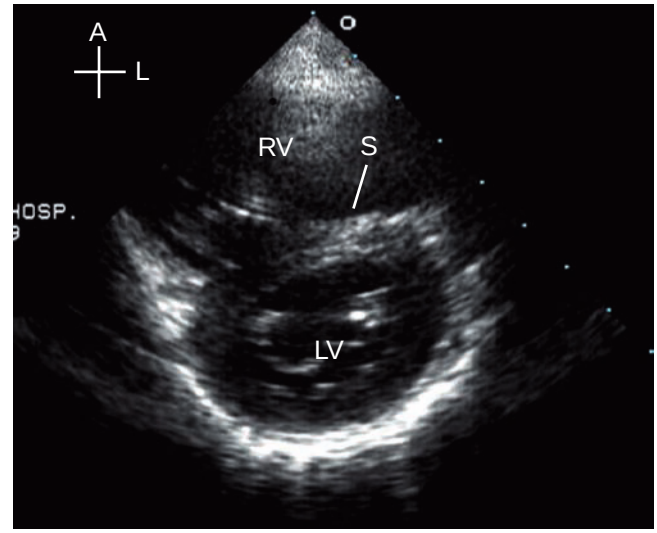


**Figure 17.30** Right ventricle after pulmonary valve dilation. This is a parasternal short-axis image showing the right ventricle several years after pulmonary valve dilation. Compared with the newborn period, the right ventricle is less hypertrophied and the cavity is larger. There is diastolic septal flattening consistent with right ventricular volume load from pulmonary regurgitation. LV, left ventricle; RV, right ventricle; S, septum.

In patients managed with a single ventricle strategy, echocardiography focuses on the elements relevant to a successful Fontan operation. Follow-up echocardiography includes detailed evaluation of LV size and function, atrioventricular valve regurgitation and pulmonary artery growth. Each follow-up study should document unrestrictive flow across the atrial septum. In patients undergoing a modified Fontan operation, the right ventricle usually remains hypoplastic and hypertensive and the septum bows into the left ventricle (Figs 17.31 and 17.32).

In patients with PA/IVS and abnormal coronary arteries (e.g., fistulae, stenoses), long-term follow-up of myocardial function is warranted. In addition to standard assessment of global and regional left ventricular function at rest, stress echocardiography can provide information about myocardial segments at risk for ischemia. To date, experience with this patient group is limited and the optimal strategy for evaluating myocardial ischemia in this population (e.g., stress echocardiography, nuclear techniques, magnetic resonance perfusion and viability) awaits further studies.

Cardiac magnetic resonance imaging (MRI) can be used during follow-up of patients with PA/IVS when quantification of antegrade blood flow into the pulmonary artery is important in deciding treatment strategy. In older patients in whom echocardiography cannot adequately image the right ventricle or pulmonary arteries, this modality offers a noninvasive alternative.

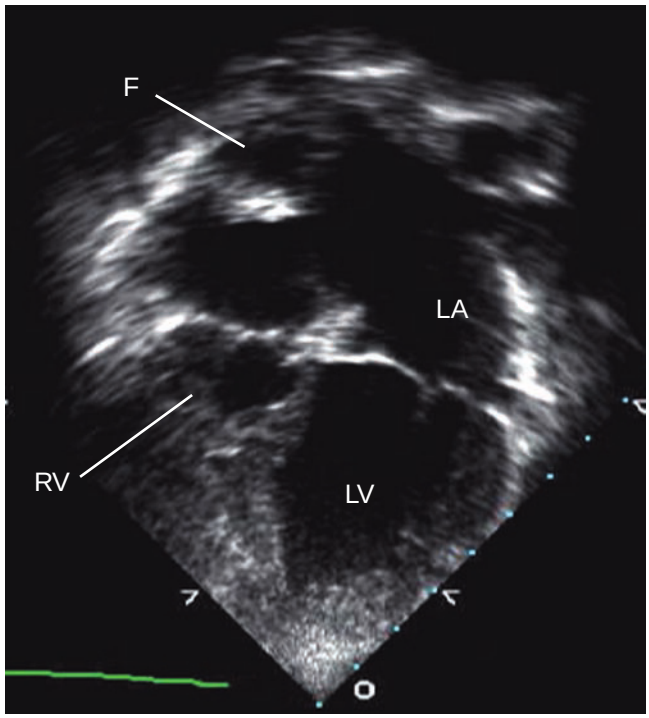


**Figure 17.31** Lateral tunnel style of Fontan operation seen from the apical 4-chamber view in a patient with moderate right ventricular hypoplasia. The hypoplastic tricuspid valve and right ventricle are seen. As expected without antegrade flow through the right ventricular outflow tract, no right ventricular growth has taken place. The Fontan tunnel is identified in the posterior portion of the right atrium. F, Fontan pathway; LA, left atrium; LV, left ventricle; RV, right ventricle.

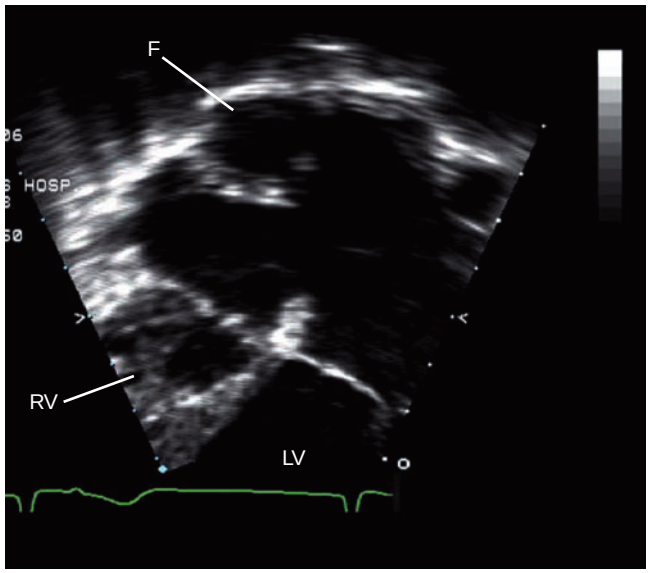


**Figure 17.32** Fontan pathway. This is a magnified image from the 4-chamber view of the right atrium in a patient with a lateral tunnel style of Fontan pathway. This is an excellent view for evaluating the tunnel, any fenestrations in the tunnel, right-sided pulmonary venous flow around the tunnel and the tricuspid valve function. F, Fontan pathway; LV, left ventricle; RV, right ventricle.

## References

1. Peacock TB. Malformation of the heart, atresia of the orifice of the pulmonary artery, aorta communicating with both ventricles. *Trans Pathol Soc London* 1869;20:61–86.
2. Grant RT. An unusual anomaly of the coronary vessels in the malformed heart of a child. *Heart* 1926;13:273–83.
3. Abbott ME. *Atlas of Congenital Cardiac Disease.* New York: American Heart Association, 1936.
4. Glaboff J, Gohmann J, Little J. Atresia of the pulmonary artery with intact ventricular septum. *J Pediatr* 1950;37:396–9.
5. Greenwold W, DuShane J, Burchell H et al. Congenital pulmonary atresia with intact ventricular septum: Two anatomic types. In: *Proceedings of the 29th Scientific Session*. American Heart Association, 1956;51.
6. Paul MH, Lev M. Tricuspid stenosis with pulmonary atresia, a cineangiographic pathologic correlation. *Circulation* 1960;22: 198–203.
7. Davignon AL, Greenwold WE, DuShane JW, Edwards JE. Congenital pulmonary atresia with intact ventricular septum: clinicopathologic correlation of two anatomic types. *Am Heart J* 1961;62:591–602.
8. Benton JW, Elliott LP, Adams P et al. Pulmonary atresia and stenosis with intact ventricular septum. *Am J Dis Child* 1962; 104:161–8.
9. Elliott LP, Adams P, Edwards JE. Pulmonary atresia with intact ventricular septum. *Brit Heart J* 1963;25:489–501.
10. Morgan BC, Stacy GS, Dillard DH. Pulmonary valvular and infundibular atresia with intact ventricular septum. *Am J Cardiol* 1965;16:746–50.
11. Cole RB, Alexander JM, Lev M, Paul MH. Pulmonary atresia with intact ventricular septum. *Am J Cardiol* 1968;21:23–31.
12. Bowman FO, Malm JR, Hayes CJ et al. Pulmonary atresia with intact ventricular septum. *J Thorac Cardiovasc Surg* 1971;61:85–95.
13. Gersony WM, Bernhard WF, Nadas AS, Gross RE. Diagnosis and surgical treatment of infants with critical pulmonary outflow obstruction: Study of thirty four infants with pulmonary stenosis or atresia, and intact ventricular septum. *Circulation* 1967;35:765–76.
14. Hanley FL, Sade RM, Blackstone EH et al. Outcomes in neonatal pulmonary atresia with intact ventricular septum. A multi-institutional study. *J Thorac and Cardiovasc Surg* 1993;105: 406–23.
15. Reddy M, Ungerleider R, Hanley F. Pulmonary valve atresia with intact ventricular septum. In: Garson A, Bricker TJ, Fisher DJ, Neish SR (eds) *Science and Practice of Pediatric Cardiology*, 2nd edn. Baltimore: Williams and Wilkins, 1998;1563–77.
16. Fyler DC, Buckley LP, Hellenbrand WE et al. Report of the New England Regional Infant Cardiac Program. *Pediatrics* 1980;65: 375–461.
17. Mitchell SC, Korones SB, Berends HW. Congenital heart disease in 56,109 births. *Circulation* 1971;43:323–32.
18. Buckley LP, Dooley KJ, Fyler DC. Pulmonary atresia and intact ventricular septum in New England. *Am J Cardiol* 1976;37:124.
19. Dhanavaravibul S, Nora JJ, McNamara DG. Pulmonary atresia with intact ventricular septum: problems in diagnosis and results of treatment. *J Pediatr* 1970;77:1010–16.

20. deLeval M, Bull C, Hopkins R et al. Decision making in the definitive repair of the heart with a small right ventricle. *Circulation* 1985;72(Suppl. 2):52–60.
21. Nora JJ, Nora AH. Update on counseling the family with a first-degree relative with a congenital heart defect. *Am J Med Genet* 1988;29:137–42.
22. Chitayat D, McIntosh N, Fouron JC. Pulmonary atresia with intact ventricular septum: a single gene disorder. *Am J Med Genet* 1992;42:304–6.
23. Erikson NL, Buttino LJ, Juberg RC. Congenital pulmonary atresia and patent ductus arteriosus in two sibs. *Am J Med Genet* 1989;32:187–8.
24. Baetz-Greenwalt B, Ratliff NB, Moodie DS. Hypoplastic right-sided heart complex: a cluster of cases with associated congenital birth defects: a new syndrome? *J Pediatr* 1983;103: 399–401.
25. Zuberbuhler JR, Anderson RH. Morphological variations in pulmonary atresia with intact ventricular septum. *Br Heart J* 1979;41:281–8.
26. Kutsche LM, van Mierop LHS. Pulmonary atresia with and without ventricular septal defect: a different etiology and pathogenesis for the atresia in the 2 types? *Am J Cardiol* 1983; 51:932–5.
27. Freedom RM, Mawson JB, Yoo S-J, Benson LN. Pulmonary atresia and intact ventricular septum. In: Freedom RM, Mawson JB, Yoo S-J, Benson LN (eds) *Congenital Heart Disease Textbook of Angiography.* New York: Futura Publishing, 1997; 617–62.
28. Van Praagh R, Ando M, van Praagh S et al. Pulmonary atresia: Anatomic considerations. In Kidd BSL, Rowe RD (eds) *The Child with Congenital Heart Disease after Surgery.* New York: Futura, 1976;103.
29. Freedom RM, Dische MR, Rowe RD. The tricuspid valve in pulmonary atresia and intact ventricular septum: a morphological study of 60 cases. *Arch Pathol Lab Med* 1978;102:28–31.
30. Bull C, de Leval MR, Mercanti C et al. Pulmonary atresia and intact ventricular septum: A revised classification. *Circulation* 1982;66:266–72.
31. Daubeny PE, Delaney DJ, Anderson RH et al. Pulmonary atresia with intact ventricular septum. Range of morphology in a population-based study. *J Am Coll Cardiol* 2002;39:1670–9.
32. Freedom RM. The morphological variations of pulmonary atresia and intact ventricular septum: Guidelines for surgical intervention. *Pediatr Cardiol* 1983;4:183–8.
33. Choi YH, Seo JW, Choi JY et al. Morphology of tricuspid valve in pulmonary atresia with intact ventricular septum. *Pediatr Cardiol* 1998;19:381–9.
34. Dyamenahalli U, McCrindle B, McDonald C et al. Pulmonary atresia with intact ventricular septum: management of, and outcomes for, a cohort of 210 consecutive patients. *Cardiol Young* 2004;12:299–308.
35. Bryan CS, Oppenheimer EH. Ventricular endocardial fibroelastosis. Basis for its presence or absence in cases of pulmonic or aortic atresia. *Arch Pathol* 1969;87:82–6.
36. Essed CE, Klein HW, Kredict P. Coronary and endocardial fibroelastosis of the ventricles in the hypoplastic left and right heart syndromes. *Virchows Arch* 1975;368:87–97.
37. O'Connor WN, Cottril CM, Johnson CL et al. Pulmonary atresia with intact ventricular septum and ventriculocoronary communications: surgical significance. *Circulation* 1982;65: 805–9.
38. Bulkley BH, D'Amico B, Taylor AL et al. Extensive myocardial fiber disarray in aortic and pulmonary atresia. Relevance to hypertrophic cardiomyopathy. *Circulation* 1983;67:191–8.
39. Silver MD, Lam JHC, Ranganathan N, Wigle ED. Morphology of the human tricuspid valve. *Circulation* 1971;43:333–48.
40. Lauer RM, Fink HP, Petry EL et al. Angiographic demonstration of intramyocardial sinusoids in pulmonary valve atresia with intact ventricular septum and hypoplastic right ventricle. *N Engl J Med* 1964;271:68–72.
41. Williams RR, Kent GB, Edwards JE. Anomalous cardiac blood vessel communicating with the right ventricle. Observations in a case of pulmonary atresia with an intact ventricular septum. *Arch Path* 1951;52:480–7.
42. Freedom RM, Harrington DP. Contribution of intramyocardial sinusoids in pulmonary atresia and intact ventricular septum to a right sided circular shunt. *Br Heart J* 1974;36:1061–5.
43. Lenox CC, Briner J. Absent proximal coronary arteries associated with pulmonic atresia. *Am J Cardiol* 1972;30:666–9.
44. Cornell SH. Myocardial sinusoids in pulmonary valvular atresia. *Radiology* 1966;86:421–4.
45. Patel RG, Freedom RM, Moes CA et al. Right ventricular volume determinations in 18 patients with pulmonary atresia and intact ventricular septum. Analysis of factors influencing right ventricular growth. *Circulation* 1980;61:428–40.
46. Oppenheimer EH, Esterly JR. Some aspects of cardiac pathology: eleven unusual coronary endarteritis with congenital cardiac malformations. *Bull Johns Hopkins Hosp* 1966;119:343.
47. Selamet SE, Hsu DT, Thaker HM, Gersony WM. Complete atresia of coronary ostia in pulmonary atresia and intact ventricular septum. *Pediatr Cardiol* 2004;25:67–9.
48. Giglia TM, Mandell VS, Connor AR et al. Diagnosis and management of right ventricular dependent coronary circulation in pulmonary atresia with intact ventricular septum. *Circulation* 1992;86:1516–28.
49. Tanoue Y, Kado H, Maeda T et al. Left ventricular performance of pulmonary atresia with intact ventricular septum after right heart bypass surgery. *J Thorac Cardiovasc Surg* 2004; 128:710–17.
50. Gittenberger-De Groot AC, Sauer U, Bindl L et al. Competition of coronary arteries and ventriculocoronary arterial communications in pulmonary atresia with intact ventricular septum. *Int J Cardiol* 1988;18:243–58.
51. Geva T, Van Praagh S, Van Praagh R. Thoracoabdominal ectopia cordis with isolated infundibular atresia. *Am J Cardiol* 1960;66:891–3.
52. Newfeld EA, Cole RB, Paul MH. Ebstein's malformation of the tricuspid valve in the neonate. Functional and anatomic pulmonary outflow tract obstruction. *Am J Cardiol* 1967;19: 727–31.
53. Freedom R, Anderson R, Perrin D. The significance of ventriculo-coronary arterial connections in the setting of pulmonary atresia with an intact ventricular septum. *Cardiol Young* 2005;15:447–68.
54. Cote M, Davignon A, Fouron JC. Congenital hypoplasia of the right ventricular myocardium Uhl's anomaly associated with pulmonary atresia in a newborn. *Am J Cardiol* 1973;31: 658–61.

55. Akiba T, Becker AD. Disease of the left ventricle in pulmonary atresia with intact ventricular septum. *J Thorac Cardiovasc Surg* 1994;108:1–8.
56. Sholler GF, Colan SD, Sanders SP. Effect of isolated right ventricular outflow obstruction on left ventricular function in infants. *Am J Cardiol* 1988;62:778–84.
57. Gentles TL, Colan SD, Giglia TG et al. Right ventricular decompression and left ventricular function in pulmonary atresia with intact ventricular septum. The influence of less extensive coronary anomalies. *Circulation* 1993;88:183–8.
58. Akagi T, Benson LN, Williams WG et al. Ventriculo-coronary arterial connections in pulmonary atresia with intact ventricular septum, and their influences on ventricular performance and clinical course. *Am J Cardiol* 1993;72:586–90.
59. Hausdorf G, Gravinghoff L, Deck EW. Effects of persisting myocardial sinusoids on left ventricular performance in pulmonary atresia with intact ventricular septum. *Eur Heart J* 1987; 8:291–6.
60. Sideris EB, Olley PM, Spooner E et al. Left ventricular function and compliance in pulmonary atresia with intact ventricular septum. *J Thorac Cardiovasc Surg* 1982;84:192–9.
61. Tulzer G, Arzt W, Franklin RC et al. Fetal pulmonary valvuloplasty for critical pulmonary stenosis or atresia with intact septum. *Lancet* 2002;360:1567–8.
62. Maxwell D, Allan L, Tynan MJ. Balloon dilatation of the aortic valve in the fetus:a report of two cases. *Br Heart J* 1991; 65:256–8.
63. Kohl T, Sharland G, Allan L et al. World experience of percutaneous ultrasound-guided balloon valvuloplasty in human fetuses with severe aortic valve obstruction. *Am J Cardiol* 2000;85:1230–3.
64. Tworetzky W, Marchall AC. Fetal interventions for cardiac defects. *Pediatr Clin N Am* 2004;51:1503–13.
65. Tworetzky W, Wilkins-Haug L, Jennings RW et al. Balloon dilation of severe aortic stenosis in the fetus: potential for prevention of hypoplastic left heart syndrome: Candidate selection, technique and results of successful intervention. *Circulation* 2004;110:2125–31.
66. Marshall AC, van der Velde ME, Tworetzky W et al. Creation of an atrial septal defect in utero for fetuses with hypoplastic left heart syndrome and intact or highly restrictive atrial septum. *Circulation* 2004;110:253–8.
67. Hawkins JA, Thorne JK, Boucek MM et al. Early and late results in pulmonary atresia and intact ventricular septum. *J Thorac Cardiovasc Surg* 1990;100:492–7.
68. Leung MP, Mok CK, Lee J et al. Management evolution of pulmonary atresia and intact ventricular septum. *Am J Cardiol* 1993;71:1331–6.
69. Mainwarning RD, Lamberti JJ. Pulmonary atresia with intact ventricular septum. Surgical approach based on ventricular size and coronary anatomy. *J Thorac Cardiovasc Surg* 1993;106: 733–8.
70. Lewis AB, Wells W, Lindesmith GG. Evaluation and surgical treatment of pulmonary atresia and intact ventricular septum in infancy. *Circulation* 1983;67:1318–23.
71. McAffrey FM, Leatherbury L, Moore HV. Pulmonary atresia and intact ventricular septum. Definitive repair in the neonatal period. *J Thorac Cardiovasc Surg* 1991;57:551–6.
72. Milliken JC, Laks H, Hellenbrand W et al. Early and late results in the treatment of patients with pulmonary atresia and intact ventricular septum. *Circulation* 1985;72(Suppl.):61–9.
73. Shaddy RE, Sturtevant JE, Judd VE, McGough EC. Right ventricular growth after transventricular pulmonary valvotomy and central aortopulmonary shunt for pulmonary atresia and intact ventricular septum. *Circulation* 1990;82(Suppl. 4): 157–63.
74. Steinberger J, Berry JM, Bass JE et al. Results of a right ventricular outflow patch for pulmonary atresia with intact ventricular septum. *Circulation* 1992;86(Suppl. 3):67–75.
75. Billingsley AM, Laks H, Boyce SW et al. Definitive repair in patients with pulmonary atresia and intact ventricular septum. *J Thorac Cardiovasc Surg* 1989;97:746–54.
76. Foker JE, Braunlin EA, St Cyr JA et al. Management of pulmonary atresia with intact ventricular septum. *J Thorac Cardiovasc Surg* 1986;92:706–15.
77. Aborilas ET, Julsrud PR, Danielson GK et al. Definitive operation for pulmonary atresia with intact ventricular septum: results in twenty patients. *J Thorac Cardiovasc Surg* 1987;93: 454–64.
78. Luckstead EF, Mattioli L, Crosby I et al. Two-stage palliative surgical approach for pulmonary atresia with intact ventricular septum (Type I). *Am J Cardiol* 1972;29:490–6.
79. Weldon CS, Harmann AF Jr, McKnight RC. Surgical management of hypoplastic right ventricle with pulmonary atresia or critical pulmonary stenosis and intact ventricular septum. *Ann Thorac Surg* 1984;37:12–24.
80. Sano S, Ishino K, Kawada M et al. Staged biventricular repair of pulmonary atresia or stenosis with intact ventricular septum. *Ann Thorac Surg* 2000;70:1501–6.
81. Yoshimura N, Yamaguchi M Ohashi H et al. Pulmonary atresia with intact ventricular septum: Strategy based on right ventricular morphology. *J Thorac Cardiovasc Surg* 2003;126:1417–26.
82. Pawade A, Capuani A, Penny DJ et al. Pulmonary atresia with intact ventricular septum. Surgical management based on right ventricular infundibulum. *J Cardiac Surg* 1993;8:371–83.
83. Latson LA. Nonsurgical treatment of a neonate with pulmonary atresia and intact ventricular septum by transcatheter puncture and balloon dilation of the atretic valve membrane. *Am J Cardiol* 1991;68:277–9.
84. Agnoletti G, Piechaud JF, Bonhoeffer P et al. Perforation of the atretic pulmonary valve: long-term follow-up. *J Am Coll Cardiol* 2003;41:1399–403.
85. Wang J-K, Wu M-H, Chang C-I et al. Outcomes of transcatheter valvotomy in patients with pulmonary atresia and intact ventricular septum. *Am J Cardiol* 1999;84:1055–60.
86. Alwi M, Geetha K, Bilkis A et al. Pulmonary atresia with intact ventricular septum: percutaneous radiofrequency-assisted valvotomy and balloon dilation versus surgical valvotomy and Blalock Taussig shunt. *J Am Coll Cardiol* 2000;35:468–76.
87. Humpl T, Soderberg B, McCrindle B et al. Percutaneous balloon valvotomy in pulmonary atresia with intact ventricular septum: impact on patient care. *Circulation* 2003;108:826–32.
88. Ovaert C, Qureshi SA, Rosenthal E et al. Growth of the right ventricle after successful transcatheter pulmonary valvotomy in neonates and infants with pulmonary atresia and intact ventricular septum. *J Thorac Cardiovasc Surg* 1998;115:1055–62.

89. Weber H. Initial and late results after catheter intervention for neonatal critical pulmonary valve stenosis and atresia with intact ventricular septum: A technique in continual evolution. *Cathet Cardiovasc Intervent* 2002;56:394–9.
90. Graham TP, Bender HW, Atwood GF et al. Increase in right ventricular volume following valvulotomy for pulmonary atresia or stenosis with intact ventricular septum. *Circulation* 1974;49(Suppl. 11):69–79.
91. Rychik J, Levy H, Gaynor JW et al. Outcome after operations for pulmonary atresia with intact ventricular septum. *J Thorac Cardiovasc Surg* 1998;116:924–31.
92. Squittieri C, di Carlo D, Giannico S et al. Tricuspid valve avulsion or excision for right ventricular decompression in pulmonary atresia with intact ventricular septum. *J Thorac Cardiovasc Surg* 1989;97:779–84.
93. Laks H, Gates RN, Grant PW et al. Aortic to right ventricular shunt for pulmonary atresia with intact ventricular septum. *Ann Thorac Surg* 1995;59:342–7.
94. Williams WG, Burrows P, Freedom RM et al. Thrombo-exclusion of the right ventricle in children with pulmonary atresia and intact ventricular septum. *J Thorac Cardiovasc Surg* 1991;101:222–9.
95. Jahangiri M, Zurakowski D, Bichell D et al. Improved results with selective management in pulmonary atresia with intact ventricular septum. *J Thorac Cardiovasc Surg* 1999;118: 1046–55.
96. Ekman Joelsson BM, Sunnegardh J, Hanseus K et al. The outcome of children born with pulmonary atresia and intact ventricular septum in Sweden from 1980 to 1999. *Scand Cardiovasc J* 2001;35:192–8.
97. Najm HK, Williams WG, Coles JG et al. Pulmonary atresia with intact ventricular septum: results of the Fontan procedure. *Ann Thorac Surg* 1997;63:669–75.
98. Powell AJ, Mayer JE, Lang P, Lock JE. Outcome in infants with pulmonary atresia, intact ventricular septum and right ventricle-dependent coronary circulation. *Am J Cardiol* 2000; 86:1272–4.
99. Giglia TM, Jenkins KJ, Matitiau A et al. Influence of right heart size on outcome in pulmonary atresia with intact ventricular septum. *Circulation* 1993;88(Suppl. 1):2248–56.
100. Miyaje K, Shimada M, Sekiguchi A et al. Pulmonary atresia with intact ventricular septum: long term results of "one and a half ventricular repair". *Ann Thorac Surg* 1995;60: 1762–4.
101. Takayama H, Sekiguchi A, Chikada M. Update: Pulmonary atresia with intact ventricular septum: long-term results of "one and a half ventricular repair". *Ann Thorac Surg* 2001; 72:2178–9.
102. Muster AJ, Zales VR, Ilbawi MN et al. Biventricular repair of hypoplastic right ventricle assisted by pulsatile bidirectional cavopulmonary anastomosis. *J Thorac Cardiovasc Surg* 1993; 105:112–19.
103. Meyer RA, Kaplan S. Echocardiography in the diagnosis of hypoplasia of the left or right ventricles in the neonate. *Circulation* 1972;46:55–64.
104. Lewis, BS, Amitai N, Simcha A et al. Echocardiographic diagnosis of pulmonary atresia with intact ventricular septum. *Am Heart J* 1979;97:92–5.
105. Trowitsch E, Colan SD, Sanders SP. Two-dimensional echocardiographic evaluation of right ventricular size and function in newborns with severe right ventricular outflow tract obstruction. *J Am Coll Cardiol* 1985;6:388–93.
106. Silove ED, DeGiovanni JV, Shiu MF, Myint YM. Diagnosis of right ventricular outflow tract obstruction in infants by cross sectional echocardiography. *Br Heart J* 1983;50:416–20.
107. Sharland GK, Chita SK, Allan LD. Tricuspid valve dysplasia or displacement in intrauterine life. *J Am Coll Cardiol* 1991;17: 944–9.
108. Daubeny PEF, Sharland GK, Cook AC et al. Pulmonary atresia with intact ventricular septum. Impact of fetal echocardiography on incidence at birth and postnatal outcome. *Circulation* 1998;98:562–6
109. Todros T, Paladini D, Chiapppa E et al. Pulmonary stenosis and atresia with intact ventricular septum during prenatal life. *Ultrasound Obstet Gynecol* 2003;21:228–33.
110. Allan LD, Crawford DC, Tynan MJ. Pulmonary atresia in prenatal life. *J Am Coll Cardiol* 1986;8:1131–6.
111. Allan LD, Cook A. Pulmonary atresia with intact ventricular septum in the fetus. *Cardiol Young* 1992;2:367–76.
112. Maeno YV, Boutin C, Hornberger LK et al. Prenatal diagnosis of right ventricular outflow tract obstruction with intact ventricular septum and detection of ventriculo-coronary connections. *Heart* 1999;81:661–8.
113. Peterson R, Levi D, Williams R et al. Echocardiographic predictors of outcome in fetuses with pulmonary atresia with intact ventricular septum. *J Am Society of Echocardiogr* 2006; 19:1393–400.
114. Salvin J, Colan SD, McElhinney DB et al. Fetal tricuspid valve annulus as a predictor of single vs. biventricular outcome in pulmonary atresia with intact ventricular septum. *Pediatrics* 2006;118:415–20.
115. Satou GM, Perry SB, Gauvreau K, Geva T. Echocardiographic predictors of coronary artery pathology in pulmonary atresia with intact ventricular septum. *Am J Cardiol* 2000;85:1319–24.
116. Minich LL, Tani LY, Ritter S et al. Usefulness of the preoperative tricuspid/mitral valve ratio for predicting outcome in pulmonary atresia with intact ventricular septum. *Am J Cardiol* 2000;85:1325–8.
117. Tworetzky W, Reddy VM, Brook MM et al. Improved surgical outcome after fetal diagnosis of hypoplastic left heart syndrome. *Circulation* 2001;103:1269–73.
118. Sandor G, Cook A, Sharland G et al. Coronary arterial abnormalities in pulmonary atresia with intact ventricular septum diagnosed during fetal life. *Cardiol Young* 2002;12:436–44.
119. Mahle WT, Clancy RR, McGaurn SP et al. Impact of prenatal diagnosis on survival and early neurologic morbidity in neonates with the hypoplastic left heart syndrome. *Pediatrics* 2001;107;1277–82.
120. Verheijen PM, Lisowski LA, Stoutenbeek P et al. Prenatal diagnosis of congenital heart disease affects preoperative acidosis in the newborn patient. *J Thorac Cardiovasc Surg* 2001;123: 798–803.
121. Bonnet D, Coltri A, Butera G et al. Detection of transposition of the great arteries in fetuses reduces neonatal morbidity and mortality. *Circulation* 1999;99:916–18.

122. Daubeny P, Wand D, Delany D et al. Pulmonary atresia with intact ventricular septum: predictors of early and medium-term outcome in a population-based study. *J Thorac Cardiovasc Surg* 2005;130:1071–8.
123. Odim J, Laks H, Plunkett M, Tung T. Successful management of patients with pulmonary atresia with intact ventricular septum using a three tier grading system for right ventricular hypoplasia. *Ann Thorac Surg* 2006;81:678–84.
124. Sanders SP, Parness IA, Colan SD. Recognition of abnormal connections of coronary arteries with the use of Doppler color flow mapping. *J Am Coll Cardiol* 1989;13:922–6.
125. Velvis H, Schmidt KG, Silverman NH, Turley K. Diagnosis of coronary artery fistula by two-dimensional echocardiography, pulsed Doppler ultrasound and color flow imaging. *J Am Coll Cardiol* 1989;14:968–76.
126. Garcia J, Zellers TM, Weinstein EM, Mahoney L. Usefulness of Doppler echocardiography in diagnosing right ventricular coronary arterial communications in patients with pulmonary atresia and intact ventricular septum and comparison with angiography. *Am J Cardiol* 1998;81:103–4.
127. Wald R, Juraszek A, Pigula F, Geva T. Echocardiographic diagnosis and management of bilateral coronary ostial atresia in a patient with pulmonary atresia and intact ventricular septum. *J Am Soc Echocardiogr* 2006;19:939.e1–e3.

# 18 Abnormalities of the Ductus Arteriosus and Pulmonary Arteries

**Theresa A. Tacy**
Lucile Packard Children's Hospital, Stanford University, Stanford, CA, USA

## Anomalies of the ductus arteriosus

### Definition

The ductus arteriosus is a normal vascular structure in mammalian embryos that connects the main pulmonary artery (MPA) with the descending aorta or a subclavian artery. In left aortic arch the ductus arteriosus inserts into the proximal descending aorta at its junction with the aortic isthmus, distal to the origin of the left subclavian artery. In right aortic arch the ductus arteriosus can connect the right descending aorta with the MPA (right-sided ductus arteriosus), the proximal left subclavian artery with the MPA (left-sided ductus arteriosus), or both (bilateral ductus arteriosus). In the fetus, the ductus arteriosus carries blood from the right ventricle (RV) to the aorta, bypassing the high-resistance pulmonary vascular bed. Normally, the ductus arteriosus closes during the first day of life. Persistent ductal blood flow beyond the newborn period is termed patent ductus arteriosus (PDA).

### Incidence

The incidence of PDA varies considerably depending on the postnatal age of subjects and their degree of prematurity. PDA is common in preterm infants and is considered a functional abnormality as opposed to a structural congenital cardiac anomaly. In term infants the normal ductus arteriosus may stay open for several days after birth. Echo-Doppler studies in healthy newborns have shown functional closure of the ductus arteriosus in almost all subjects by 4–7 days after birth [1,2]. Based on analysis of 40 published articles spanning several decades, Hoffman and Kaplan estimated the median incidence of PDA in term infants at 56.7 per 100 000 live births [3].

### Etiology

The etiology of isolated PDA in full-term infants older than 1 week is not known. Recent investigations have identified the genes affecting the development of the fourth and sixth pharyngeal arches, and noted their association with cardiovascular defects similar to those observed in DiGeorge syndrome [4].

### Morphology

#### Developmental considerations

The normal anatomy and congenital malformations of the ductus arteriosus and branch pulmonary arteries are rooted in the development of the embryonic sixth aortic arches (see Chapter 30). The embryo has two dorsal aortas, which communicate with the ventrally located aortic sac via several pairs of branchial arch arteries. During development, there is an orderly appearance and regression of six pairs of primitive aortic arches. The fate of the fourth and sixth arches is most important to the topics covered in this chapter. The left fourth arch persists as the distal left aortic arch between the left common carotid and left subclavian arteries, and the left dorsal aorta persists to become the segment that extends between the left subclavian artery and the site of the entrance of the ductus arteriosus. The right fourth arch becomes the brachiocephalic trunk and proximal right subclavian artery, whereas the right dorsal aorta largely involutes. The proximal portions of the right and left sixth arches form the proximal right and left pulmonary arteries, respectively. The distal right sixth arch regresses, whereas the distal left sixth arch forms the ductus arteriosus [5].

### Anatomy

#### *PDA with left aortic arch*

In this anatomic configuration, the PDA represents a persistent vascular connection between the aortic isthmus and the superior aspect of the proximal left pulmonary artery (LPA). In the absence of right ventricular outflow obstruction, the configuration of the PDA is similar to that of the aortic arch but with the following distinguishing features: (i) the ductal arch is lower than the aortic arch; (ii) there is absence of head vessels; and (iii) in normal postnatal life with normal pulmonary vascular resistance, the direction of the ductal flow is from the aorta to the MPA, that is, direction is the reverse of flow in the aortic arch.

*Echocardiography in Pediatric and Congenital Heart Disease: From Fetus to Adult*
Edited by Wyman W. Lai, Luc L. Mertens, Meryl S. Cohen and Tal Geva
 ISBN: 978-1-405-17401-5

### *PDA with right aortic arch*

A right aortic arch is formed when the right dorsal aorta remains patent and either the left fourth arch or the left dorsal aorta fail to regress. Right aortic arch occurs in ~0.1% of the population and is common among patients with tetralogy of Fallot, tetralogy of Fallot with pulmonary atresia, truncus arteriosus, and tricuspid atresia [6–11]. In individuals with normal intracardiac anatomy, a right aortic arch is often associated with an aberrant origin of the left subclavian artery from the right descending aorta with a retroesophageal course [12]. In a right aortic arch, the ductus arteriosus can be either right-sided between the descending aorta and proximal right pulmonary artery (RPA), left-sided between the brachiocephalic trunk or proximal left subclavian artery and proximal LPA, or bilateral. The most common form of right aortic arch is with mirror image branching and a left ductus arteriosus from either the brachiocephalic trunk or the left subclavian artery [13,14]. The position of the arterial duct is especially important in the setting of right aortic arch, as it may cause a vascular ring (see Chapter 30).

### *Reverse-oriented PDA*

In the normal fetus, flow is directed from the right ventricular outflow tract through the PDA to the descending aorta. The anatomic configuration of the PDA assumes an arch with its concave aspect facing downward. In patients with low flow across the right ventricular outflow tract during fetal life, the ductus arteriosus is long and tortuous, and its connection to the aorta is oriented in a reverse fashion from the normal ductus. When flow in the ductus originates from the aorta in fetal life, the configuration of the PDA assumes an arch, with its initial course from the descending aorta having a concave aspect facing upward (Fig. 18.1). This ductal course is often referred to as a "reverse-oriented" ductus. Common examples of congenital heart lesions in which a reverse-oriented ductus arteriosus is present are tricuspid atresia, pulmonary atresia, and severe tetralogy of Fallot [15]. The presence of a reverse-oriented ductus is important, and may indicate a need for postnatal surgery to increase pulmonary blood flow. Reverse ductal orientation in patients with pulmonary valve abnormalities, conotruncal defects, or Ebstein malformation and an inferior angle <65°, is a specific indicator for early intervention to increase pulmonary blood flow [16].

### *Ductal aneurysm*

In this uncommon condition there is marked dilation of the ductus arteriosus. The reported incidence of ductal aneurysm varies from 0.8% in a neonatal autopsy study [17] to 1.5% in one prenatal series [18]. Another study in full-term neonates reported an incidence of 8.8% [19]. Inconsistent diagnostic criteria and variable age at examination explain some of the differences in the reported incidence [20]. A strong association with chromosomal abnormalities or syndromes (25%),

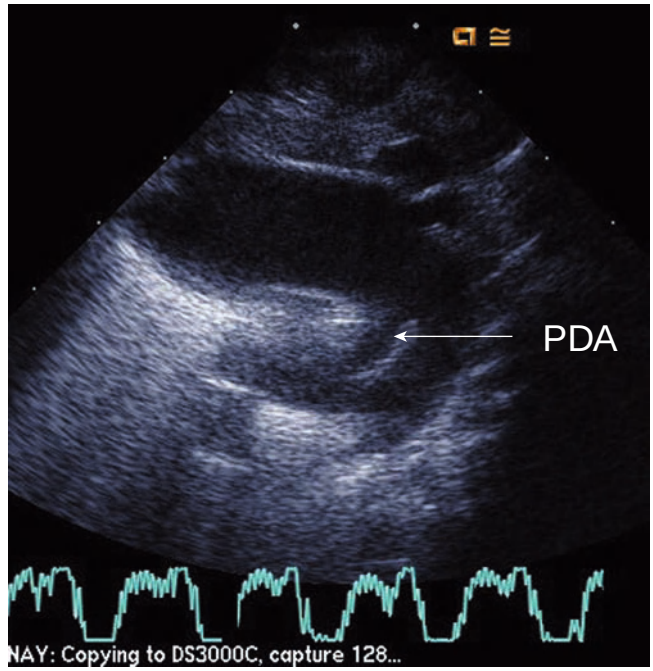


**Figure 18.1** Suprasternal notch view of reverse-oriented patent ductus arteriosus (PDA).

and a ~13% association with connective tissue disorders has been reported [18]. Other investigators have noted a higher incidence of ductal aneurysm in infants of diabetic mothers [19,21].

Most patients experience a benign course, with closure in about 70% after 3 days of age [19]. If symptoms occur, they are more likely due to compression of adjacent structures, erosion into airways or thrombus extension than from the large ductal aneurysm. Surgical resection may be indicated if the aneurysm persists beyond the neonatal period, or if complications develop [22].

## Pathophysiology

The pathophysiology of a persistent PDA depends on several factors, including patient age, associated congenital heart disease, and a complex interplay between multiple anatomic and hemodynamic factors. PDA is common in preterm infants and is associated with increased morbidity. In full-term infants and children, the flow pattern and hemodynamic sequelae of an isolated PDA depend on the smallest cross-sectional area and the length of the duct as well as the resistances of the pulmonary and systemic vascular beds. In the absence of elevated pulmonary vascular resistance, an isolated PDA is associated with left-to-right flow leading to increased pulmonary blood flow, and a volume load to the left heart. The left atrium and left ventricle are dilated, and ventricular systolic function is usually preserved through normal compensatory mechanisms. A large PDA causes a significant left-to-right shunt and, if untreated, leads to

pulmonary overcirculation, respiratory distress, growth failure and eventually pulmonary vascular disease. A small PDA is usually not associated with a significant hemodynamic burden but is associated with a risk of infective endarteritis. In patients with elevated pulmonary vascular resistance, ductal flow is either bidirectional (left-to-right during systole) or exclusively right-to-left. In patients with associated right heart obstructive lesions (e.g., tetralogy of Fallot, pulmonary atresia) a PDA provides an avenue for pulmonary blood flow. Conversely, in patients with obstructive left heart lesions (e.g., aortic atresia, coarctation of the aorta) a PDA allows systemic perfusion through the right heart. A congenital heart anomaly in which either the pulmonary or the systemic circulation depends on blood flow through a PDA for survival is called a "ductal-dependent lesion."

## Imaging

One of the most common indications for an echocardiogram early in life is to screen for PDA in a preterm infant. Echocardiography is required for early diagnosis in this age group due to the poor association between clinical findings and the presence of PDA [23].

### *Goals of the examination*

The objectives of echocardiographic examination in the setting of ductus arteriosus anomalies, particularly PDA, can be summarized as follows:

- Demonstrate the position, size and course of PDA using 2D and color Doppler.
- Measure the width of the PDA at the narrowest diameter on 2D and color Doppler images.
- Assess the velocity and direction of shunt flow by color and spectral Doppler.
- Estimate the peak systolic velocity of shunt flow (estimation of pulmonary artery pressure; record systemic blood pressure).
- Determine arch sidedness and branching order of brachiocephalic vessels.
- Evaluate for potential aortic coarctation, including transverse arch size and origin of the left subclavian artery.
- Evaluate branch pulmonary arteries and evaluate for LPA stenosis.
- Abdominal aorta Doppler – evaluate diastolic flow reversal.
- Evaluate left ventricular size and function.
- Evaluate left atrial size.
- Detect any associated lesions.

### *PDA with left aortic arch*

In most neonates with a PDA, ductal flow can be demonstrated by color Doppler from several acoustic windows, including subcostal, apical, parasternal and suprasternal notch.

*Parasternal views*

Ductal flow toward the transducer can be seen in the parasternal long-axis view with the transducer angled leftward and superiorly toward the distal right ventricular (RV) outflow tract and MPA. However, this view is not very sensitive as it relies on a relatively long extension of the jet from the PDA into the MPA. In the parasternal short-axis view, PDA flow is seen along the left lateral border of the MPA, and is usually directed toward the transducer. Cranial tilt of the transducer demonstrates the PDA (Fig. 18.2). By sliding the transducer superiorly into a high left parasternal window and rotating clockwise, the pulmonary artery (PA) bifurcation can be seen (Fig. 18.3 and Videoclip 18.1). In this view the LPA passes leftward of the descending aorta, and travels toward the left scapula. From this view of the branch pulmonary arteries, counterclockwise rotation of the transducer toward 12 o'clock demonstrates the long-axis of the PDA, which is located between the descending aorta and the LPA (Fig. 18.4 and Videoclips 18.2 and 18.3). This view is often referred to as the "ductal view."

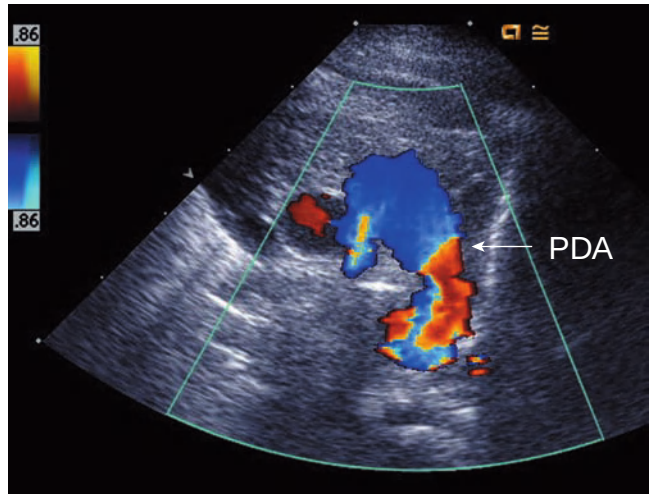


**Figure 18.2** High left parasternal short-axis view of the patent ductus arteriosus (PDA) in a patient with suprasystemic pulmonary hypertension. The direction of flow in the PDA is from the main pulmonary artery (MPA) to the descending aorta, which can be mistaken for a left pulmonary artery flow.

*Suprasternal window*

From a view of the aortic arch, a slight leftward tilt of the transducer reveals the LPA. To image the PDA, the transducer should then be rotated about 20° clockwise to image both the LPA and the descending aorta in the same plan. Once these two vessels are imaged simultaneously, a PDA, if present, will be visible in this plane.

*Doppler examination*

Although blood flow through a PDA can be seen from multiple windows, the most accurate Doppler signal is often obtained from the high left parasternal view, because at this site the transducer is closest to the PDA. The timing and direction of ductal flow provide valuable insight into the PA pressure. According to PA pressure and associated heart

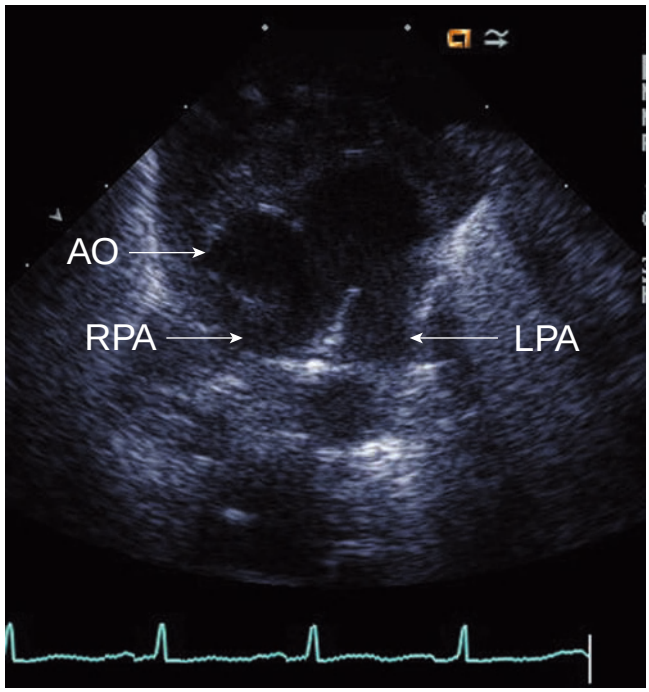


**Figure 18.3** Imaging of a patent ductus arteriosus (PDA) from a high left parasternal transverse view. The superior aspect of the right pulmonary artery (RPA) is seen coursing behind the ascending aorta (AO). LPA, left pulmonary artery.

lesions, three ductal shunting patterns predominate (Fig. 18.5):

**1** A dominant left-to-right shunt is observed in isolated PDA without significant PA hypertension, or in RV outflow tract obstruction. This shunt pattern is characterized by continuous flow with a peak velocity in late systole (Fig. 18.5a).

**2** A right-to-left shunt is observed when there is severe pulmonary hypertension associated with pulmonary vascular resistance at or above systemic vascular resistance (such as persistent fetal circulation). The flow profile is characterized by continuous or near continuous right-to-left flow with a peak velocity in early systole (Fig. 18.5b).

**3** In patients with a bidirectional ductal shunt, the right-to-left shunt (from the MPA to the descending aorta) occurs in systole and the left-to-right shunt (from the descending aorta to the MPA) begins in late systole and extends into diastole (Fig. 18.5c). A systolic right-to-left shunt always corresponds to the presence of significant pulmonary hypertension [24].

A large PDA with right-to-left flow might be difficult to identify because flow profile through the duct is similar to either the flow in the descending aorta or in the LPA (Fig. 18.2). Correct identification of the PDA is aided by the observations of severe PA hypertension and the lower arterial saturation in the lower extremities as compared with the upper extremities. If there is some restriction to the ductus, a signal resembling that seen in coarctation of the aorta may be present (Fig. 18.5b). A restrictive PDA can be distinguished from coarctation by:

- imaging an unobstructed aortic arch;
- normal lower extremity pulses and absence of upper-to-lower extremity blood pressure gradient on physical examination;
- clear imaging of the flow originating from the MPA and traveling via a PDA to the descending aorta;
- evidence of suprasystemic PA pressures (e.g., systolic septal configuration bowing toward the left ventricle);
- lower arterial oxygen saturation in lower extremities as compared with the upper extremities.

Rarely, infants with profound pulmonary vascular disease and low cardiac output as a result of low pulmonary blood flow will have reverse aortic arch flow (Fig. 18.6). In this circumstance, flow from the RV helps systemic perfusion through a PDA, indicating significantly decreased left ventricular output [25]. This finding may reverse quite easily

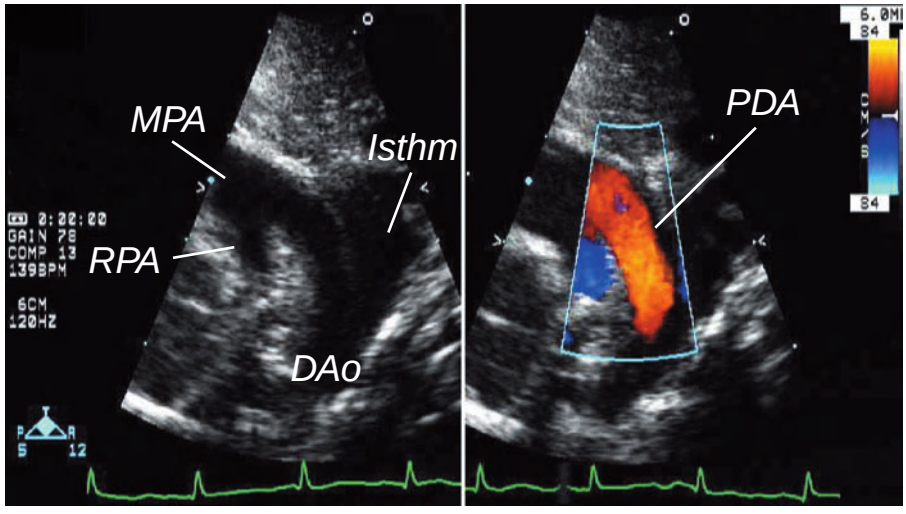


(a) (b)

**Figure 18.4** Imaging of a patent ductus arteriosus (PDA) from a high left parasternal sagittal view (also known as "ductal view"). This view is achieved by counterclockwise rotation of the transducer from the transverse view shown in Fig. 18.3. **(a)** Two-dimensional image of the PDA as it extends from the main pulmonary artery (MPA) to the descending aorta (DAo). **(b)** Color Doppler flow signal from the DAo to the MPA (left-to-right shunt). Isthm, isthmus; RPA, right pulmonary artery.

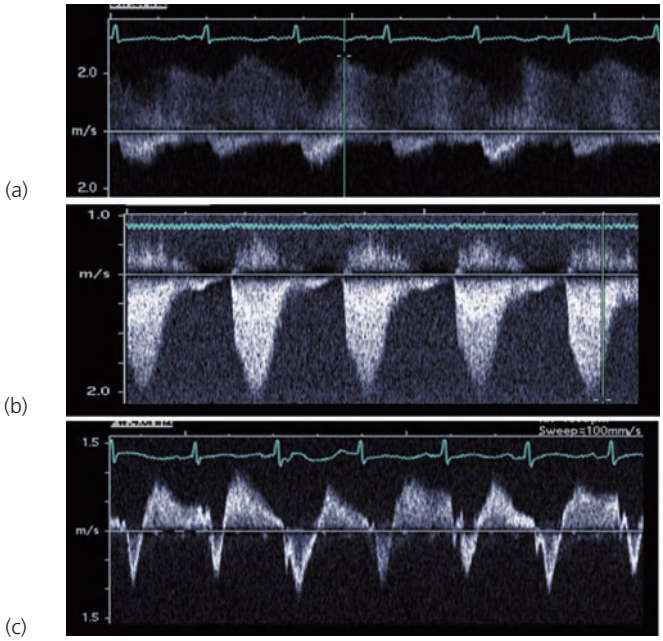


**Figure 18.5** Spectral Doppler flow patterns in a patent ductus arteriosus (PDA). **(a)** Continuous left-to-right flow in a patient with a small PDA and low pulmonary vascular resistance. **(b)** Right-to-left flow with ~15 mm Hg peak instantaneous pressure gradient from the main pulmonary artery to the descending aorta in a patient with markedly elevated pulmonary vascular resistance. **(c)** Bidirectional, low-velocity flow through a large PDA in an infant with pulmonary artery hypertension.

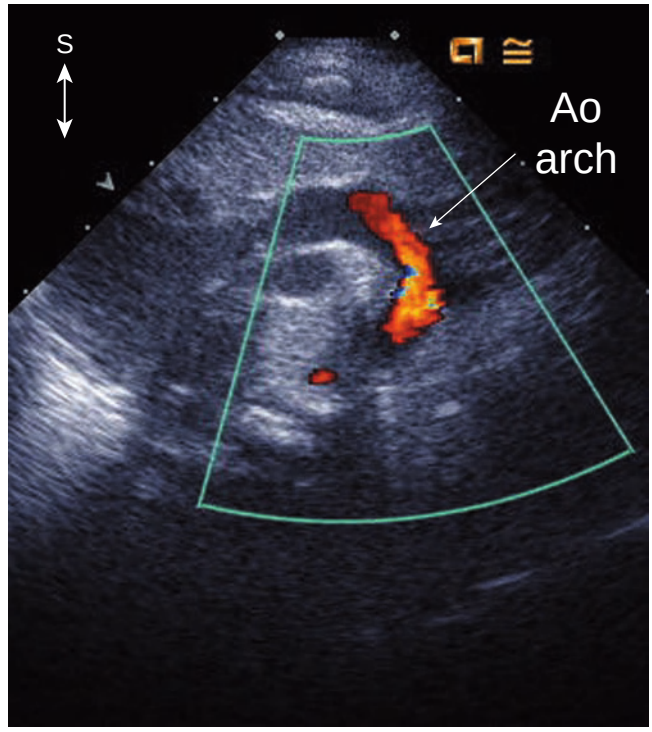


**Figure 18.6** Suprasternal notch view of the aortic arch (Ao arch) demonstrates retrograde flow in the transverse arch in a patient with severe pulmonary artery hypertension, a large patent ductus arteriosus with right-to-left shunt, and low left ventricular output.

with early and aggressive pulmonary vasodilator therapy (Fig. 18.7).

It is common to see a color Doppler flow pattern in normal patients that can be confused for PDA flow. In these cases, a patch of red signal, indicating flow toward the transducer, is seen along the medial border of the MPA artery in early systole (Fig. 18.8 and Videoclip 18.4). However, the medial location and the timing (in systole) of the flow distinguish this from typical left-to-right ductal flow. Most likely this normal flow pattern represents helical flow in the MPA, which is a consequence of flow in a curved tube [26].

*Assessment of the clinical significance of PDA with a left-to-right shunt*

Once the presence of a PDA has been identified, the next task of the echocardiographer is to determine whether this shunt is clinically significant. As the pulmonary vascular resistance decreases after birth, the left-to-right shunting of blood through the PDA increases, resulting in increased pulmonary venous return, and eventually left atrial and left ventricular enlargement. In preterm infants, a left atrium-to-aortic root diameter ratio ≥1.4 [27], a PDA diameter ≥1.4 mm per kg body weight, left ventricular enlargement, and holodiastolic flow reversal in the descending aorta indicate a significant PDA shunt. In the presence of a large left-to-right shunt, flow in the branch pulmonary arteries is increased, manifesting as abnormally high (≥0.5 m/s) antegrade diastolic flow [28]. The isovolumic relaxation time (IVRT) is shorter in neonates with PDA (mean 45 ms) compared with those with a closed duct (mean 55.3 ms), possibly due to elevated left atrial pressure [29].

*PDA with right aortic arch*

The identification of a PDA associated with a right aortic arch relies first on the identification of arch sidedness. This is best determined by imaging from the suprasternal window in the coronal plane with the specific goal of defining arch sidedness and branching order of the brachiocephalic vessels. With the transducer in a left–right orientation, imaging progresses from anterior–inferior to superior–posterior. First, the transducer is angled to visualize the ascending aorta in cross-section. The transducer is then angled superiorly, following the ascending aorta to the level of the transverse arch. The innominate vein is encountered anterior to the distal ascending aorta and, immediately beyond it, arises the first branch off the aortic arch. The direction of the first brachiocephalic vessel is opposite to the arch side. Once the side of the first brachiocephalic vessel has been determined, the next step is to identify whether this first head vessel bifurcates (Fig. 18.9). When the first branch does not

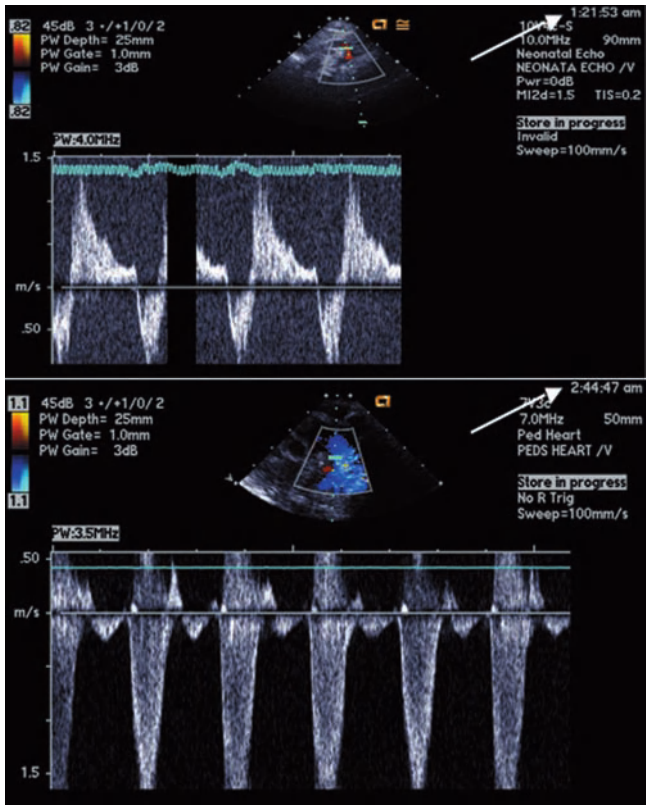


**Figure 18.7** Spectral Doppler evaluation of blood flow in the transverse aortic arch in the patient shown in Fig. 18.6. **(a)** At the time of initial evaluation systolic flow in the transverse arch is retrograde. **(b)** Approximately 1.5 hours later (see arrow indicating time), with the patient receiving inhaled nitric oxide, antegrade systolic flow is seen in the transverse arch. This is likely due to improved left ventricular output secondary to increased pulmonary blood flow and pulmonary venous return, in addition to a decrease in right-to-left ductal flow.

bifurcate, one can often see arterial flow from an anomalous vessel inferior to and separate from the carotid artery, consistent with aberrant origin of a subclavian artery (Fig. 18.10). An aberrant subclavian artery can also be seen in the coronal plane, from either the subcostal or suprasternal window, by imaging the descending aorta posteriorly using color Doppler to identify an artery heading superiorly from the thoracic descending aorta (Fig. 18.11).

Imaging a PDA in right aortic arch involves evaluation of the two potential sites from which the duct can originate: (i) the proximal descending aorta; and (ii) the base of the left subclavian artery. These locations are interrogated by color Doppler for arterial flow heading toward the pulmonary arteries. Pulsed Doppler then confirms the arterial nature of the flow. The PDA is followed by color Doppler from its origin to the pulmonary arteries – a right-sided PDA courses from the proximal descending aorta to the origin of the RPA, whereas a left-sided PDA courses from the base of the left subclavian artery to the origin of the LPA. The finding of a right aortic arch, aberrant left subclavian artery, and a left-sided PDA from the left subclavian artery to the LPA confirms the diagnosis of a vascular ring (see Chapter 30).

### *Reverse-oriented PDA*

The PDA arises from the underside of the aortic arch, and its tortuous course is best seen in the view of the aortic arch (Fig. 18.1). Often it is difficult to demonstrate the entire length of the PDA due to its tortuosity. Following the PDA with color Doppler demonstrates its entire course. The presence of a reverse-oriented ductus should prompt close evaluation for a PA coarctation, or discrete stenosis at or just distal to the site of ductal insertion into the PA (see "Congenital branch pulmonary artery stenosis").

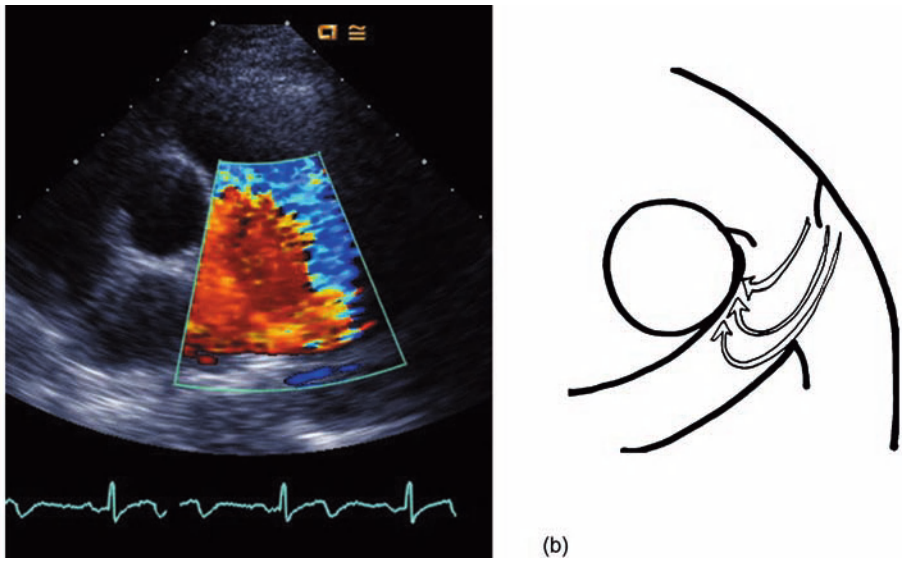


**Figure 18.8** Retrograde flow signal in the main pulmonary artery can be confused with patent ductus arteriosus (PDA) flow. **(a)** Parasternal short-axis view of the right ventricular outflow tract. Systolic flow reversal is indicated on the color Doppler pattern along the medial wall of the main pulmonary artery. **(b)** Diagram showing helical flow in the main pulmonary artery explaining the flow pattern seen in (a). This is distinguished from PDA flow by both its location (medial) and timing (systole).

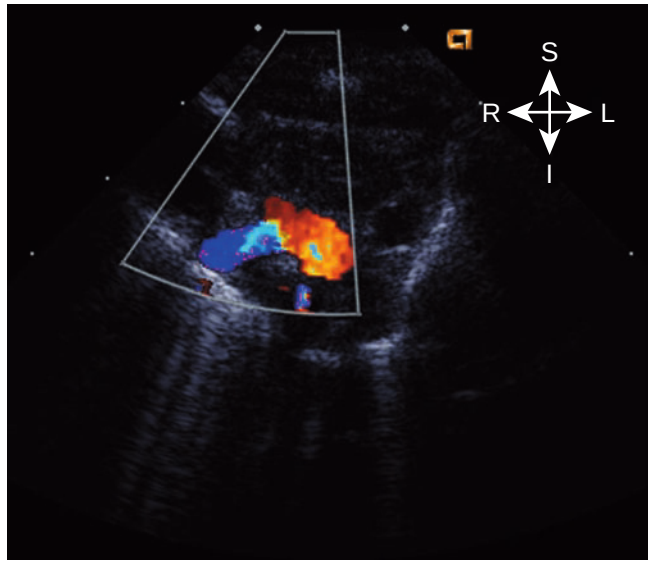


**Figure 18.9** Echocardiographic demonstration of aortic arch branching pattern. Suprasternal notch coronal view of the innominate artery showing a rightward course with bifurcation into right carotid and right subclavian arteries. This is consistent with a left aortic and normal branching order (see further discussion in Chapter 30).

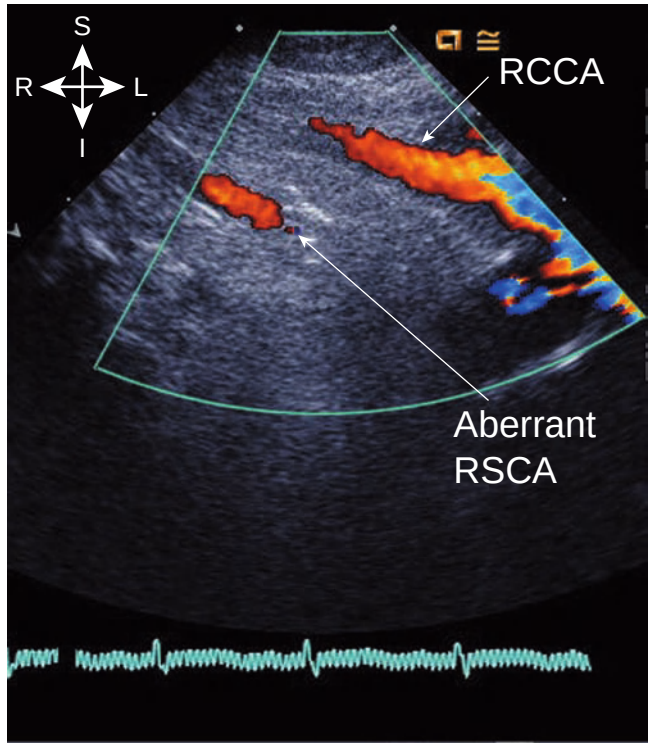


**Figure 18.10** Aberrant origin of the right subclavian artery from a left descending aorta. Note the separate, lower course of arterial flow in the right subclavian artery (Aberrant RSCA) and the separate, more superior flow in the right common carotid artery (RCCA), which arises from the transverse arch.

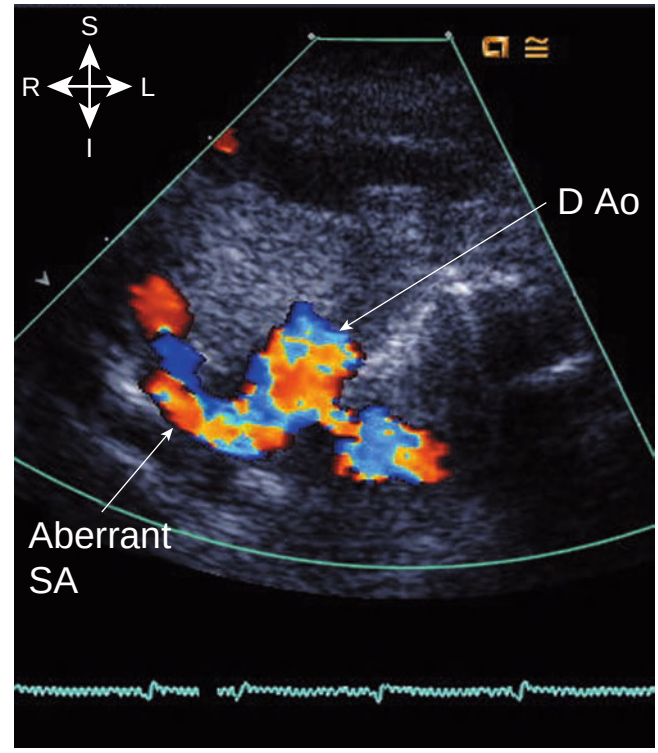


**Figure 18.11** Suprasternal coronal view of the descending aorta (D Ao) in same patient as shown in Fig. 18.10. The origin of the aberrant right subclavian artery (Aberrant SA) from the descending aorta is seen.

### *Ductal aneurysm*

Unusual direction of the ductal flow often provides the first clue to the presence of ductal aneurysm (Fig. 18.12 and Videoclip 18.5). In the high left parasternal short-axis view, a large vessel is seen to the left of the branch pulmonary arteries (Fig. 18.13 and Videoclip 18.6). The restricted part of the PDA is usually seen off the top of this ductal extension. Thus, in the high left parasternal short-axis view, three large vessels are seen from the medial to left lateral position – the ascending aorta, MPA, and ductal aneurysm. A characteristic image for ductal aneurysm is obtained from a suprasternal notch window in the coronal plane, when the transducer is angled posteriorly to image the descending aorta. This is the "rabbit-ear sign," consisting of the transverse aortic arch to the right, and the ductal aneurysm to the left, both joining inferiorly at the descending aorta (Fig. 18.14).

## Prenatal assessment

A PDA is a normal structure in the fetus (see detailed discussion in Chapter 42).

## Imaging of the adult

Patent ductus arteriosus is uncommon in adults. However, when present, PDA is associated with complications such

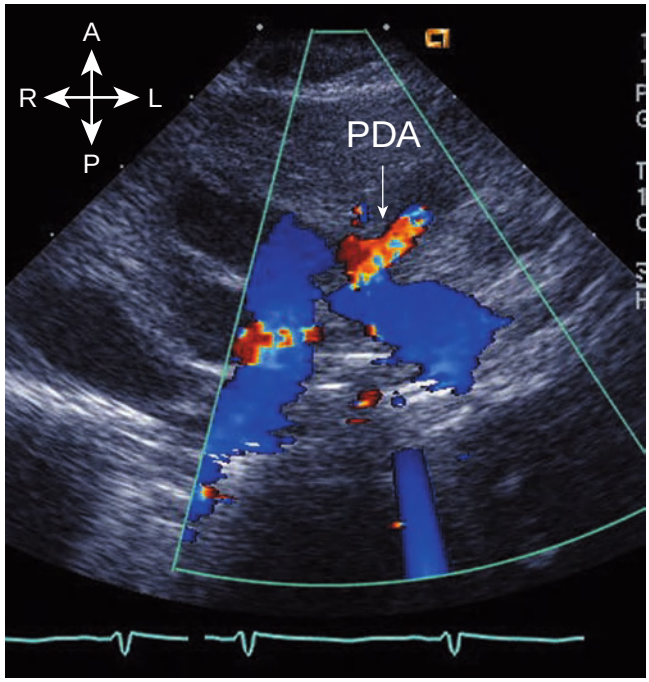


**Figure 18.12** High left parasternal short-axis view of the pulmonary arteries demonstrating acute angle of ductal entry into MPA (PDA), characteristic of a postnatal ductal aneurysm.

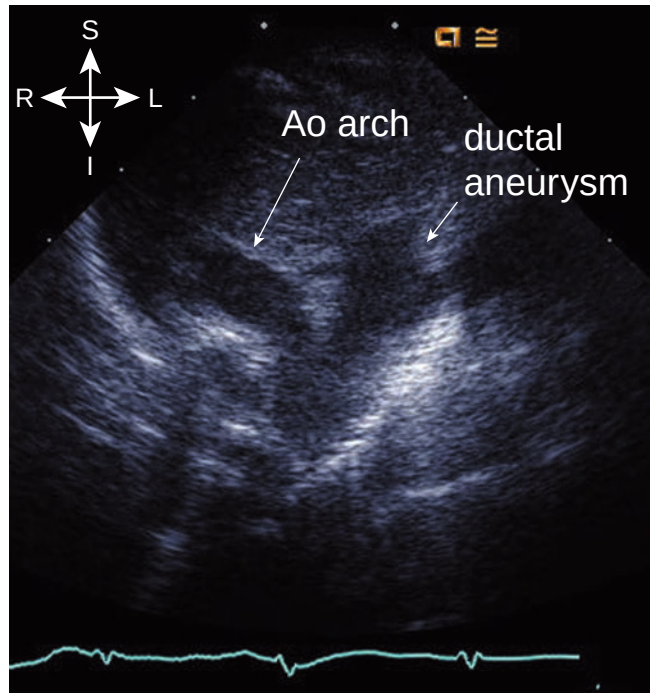


**Figure 18.14** Suprasternal notch view of descending aorta and ductal aneurysm in coronal plane demonstrating the "rabbit-ear" sign. Ao arch, aortic arch.

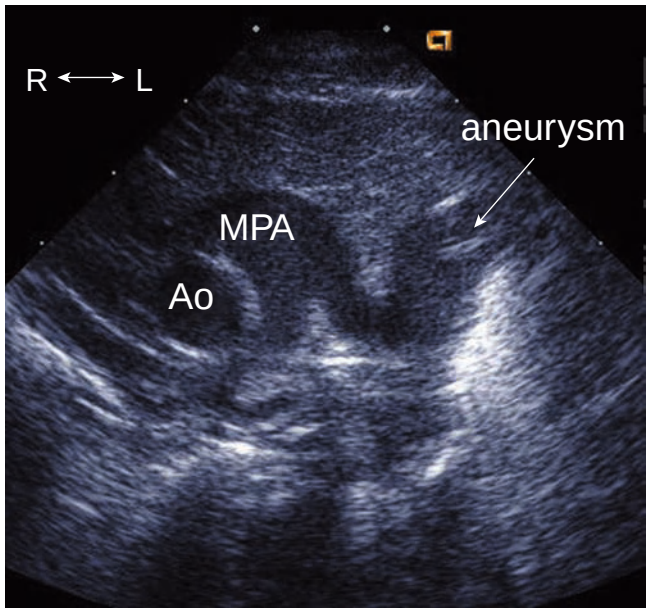


**Figure 18.13** High parasternal transverse view showing ductal aneurysm (aneurysm) to the left of the main pulmonary artery (MPA). Ao, aorta.

as endarteritis, aneurysm formation, dissection, rupture, left ventricular dilation, and pulmonary vascular disease. Echocardiographic imaging of PDA in adults can be challenging due to restricted acoustic windows. Imaging is best performed from the suprasternal notch using views and techniques similar to those described in younger patients. When the echocardiographic evaluation is inconclusive, cardiac magnetic resonance (CMR) imaging or computed tomography (CT) provide noninvasive alternatives. CMR is preferred due to its ability not only to image the PDA but also to assess the hemodynamic burden (measurement of the pulmonary-to-systemic flow ratio and biventricular size and function).

### Echocardiography during and after PDA closure

In a preterm infant PDA closure can be induced by pharmacologic means. When pharmacologic therapy fails or is contraindicated, surgical ligation and division is usually recommended if the PDA is deemed hemodynamically significant. Echocardiography is used to monitor the status of the duct before, during and after treatment. Recurrence of ductal flow can be encountered in preterm infants after initial functional closure of the duct. In older patients, closure of a PDA can be accomplished by surgical or by transcatheter techniques. Surgical options include PDA ligation and division through a lateral thoracotomy, or minimally invasive video-assisted thoracoscopic clipping. Transcatheter closure techniques are based on endoluminal placement of a coil or another occluding device. Intraoperative transesophageal echocardiography is used to monitor complete occlusion of the PDA during video-assisted thoracoscopic clipping [30]. After surgical or transcatheter PDA occlusion, echocardiography is used to

exclude residual ductal flow and to exclude inadvertent impingement or occlusion of the LPA or descending aorta.

## Pulmonary artery abnormalities

### Morphology

#### Congenital branch pulmonary artery stenosis

Congenital branch PA stenosis may be mild and transient, may be associated with syndromes, and may be associated with congenital heart disease, especially conotruncal anomalies. Physiologic branch PA stenosis in infants is characterized by a mild increase in branch PA flow velocity in the absence of discrete stenosis. The peak velocity in the branch PAs is usually less than 2 m/s [31]; however, flow velocity may be increased in the presence of anemia or high cardiac output for any reason. The most common syndromes associated with branch PA stenosis are Alagille (often a *JAG1* mutation) and Williams–Beuren syndromes (caused by a microdeletion at chromosome 7q11.23 [32]). In Alagille syndrome, branch PA stenosis is found in 76% of patients; 10% have tetralogy of Fallot [33]. About 50% of patients with Williams–Beuren syndrome have peripheral pulmonary stenosis, which can be progressive [34].

Congenital branch PA stenosis associated with cyanotic heart disease, especially conotruncal defects, is discussed in the respective chapters. An important cause of congenital unilateral branch PA stenosis, termed PA coarctation, is likely due to PDA tissue encircling the origin of a branch PA. This stenosis is discrete, and often there is proximal distortion of the affected PA. This anomaly is present in ~67% of patients with pulmonary atresia and in ~10% of cases with pulmonary stenosis [35]. It is important to identify this anomaly prior to any planned aortopulmonary shunt, as early correction (ideally at the time of aortopulmonary shunt placement) has a great impact on future PA development [36].

#### Discontinuous branch pulmonary arteries

Embryologically the proximal PA branches develop from the proximal sixth pharyngeal arches. Congenitally discontinuous branch pulmonary arteries may be due to regression of the sixth arch segment as part of a conotruncal anomaly. The incidence of chromosome 22q11 deletion in these patients is high [37]. In one series the incidence of 22q11 deletion in patients with discontinuous pulmonary arteries and/or right aortic arch was 45%, compared with 3% in patients with left aortic arch, normal arch branching pattern, and continuous branch pulmonary arteries [38]. In tetralogy of Fallot with discontinuous branch pulmonary arteries, bilateral ductus arteriosi are present in up to 16% of cases [39–43].

Rarely, one of the branch PAs is congenitally absent without associated congenital cardiovascular anomalies [44]. The absent mediastinal PA is usually contralateral to the side of the aortic arch. Before birth and in young infants the distal branches of the absent PA are supplied by a PDA. The duct usually arises from the base of the subclavian artery opposite to the side of the arch and terminates near or at the hilum of the lung on the side of the absent PA. When the PDA closes, a dimple is often seen at the base of the subclavian artery, and during surgery a ligament can be followed from the dimple to the peripheral branches of the absent mediastinal PA.

Anatomic variants of discontinuous pulmonary arteries include: (i) branch pulmonary arteries are discontinuous with each other and with the right ventricular outflow tract – each PA is supplied by either a PDA or a collateral vessel; and (ii) branch pulmonary arteries are discontinuous with each other; one PA is continuous with the RV outflow tract and the other PA is supplied by either a PDA or a collateral vessel [45]. Early diagnosis is imperative as successful recruitment of the PA is more successful with a staged surgical PA rehabilitation beginning early in life [37].

#### Crossed pulmonary arteries

Normally, the origin of the RPA from the MPA is lower than the origin of the LPA, and this discrepancy has been reported to be more pronounced in preterm infants [46]. In crossed PAs, the ostium of the LPA lies to the right and superior to the ostium of the RPA (Fig. 18.15). From their anomalous origins, the branch PAs course to their respective lungs, crossing one another proximally [47]. Another entity, which is a milder form of PA malposition, occurs when the LPA ostium is located directly superior to the RPA but without crossing of the proximal PAs. In one series, approximately 50% of patients with either crossed or malposed PAs had chromosome 22q11 deletion [47]. Care must be taken to distinguish crossed PAs from LPA sling. In the former the LPA does not course behind the trachea.

In crossed PAs the pulmonary trunk is short, which could make it difficult to perform a PA banding procedure [46]. Despite the abnormal course of the crossed PAs, a PDA tends to arise from its normal position, at the base of the LPA. When crossed PAs are associated with persistent truncus

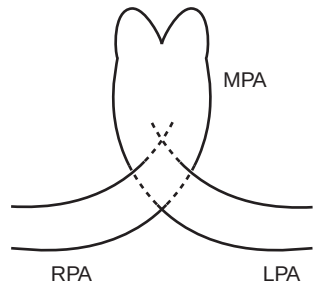


**Figure 18.15** Diagram showing crossed pulmonary arteries. The right pulmonary artery (RPA) is inferior and arises from the leftward aspect of the main pulmonary artery (MPA). The left pulmonary artery (LPA) is superior and arises from the rightward aspect of the MPA.

arteriosus, there tends to be an associated interruption of the aortic arch [48].

### Aortic origin of a branch pulmonary artery

There have been several dominant theories concerning the embryologic etiology of this entity. Edasery and colleagues proposed that an origin of the RPA from the aorta was a consequence of asymmetric division of the truncus arteriosus, resulting in the right sixth arch on the aortic side [49]. Other proposed theories include incomplete leftward migration of the RPA during its development [50] or failure of fusion of one of the sixth arches with the MPA, resulting in persistence of the aortic sac from which the sixth arches originate [51]. An association with chromosome 22q11 deletion has been suggested [52].

In the past, origin of the RPA and, less commonly, the LPA from the ascending aorta has been called "hemitruncus." However, these entities are quite distinct from truncus arteriosus, because they occur in the presence of separated aortic and pulmonary valves. This anomaly should be distinguished from other heart defects associated with an abnormal blood supply to the lungs, such as PDA, major collateral vessels between the systemic and pulmonary circulation, and truncus arteriosus.

Anomalous origin of the RPA from the ascending aorta is invariably associated with a left aortic arch and, less frequently, with a left PDA. Other cardiac malformations, including tetralogy of Fallot (TOF) and aortopulmonary window with interrupted aortic arch, have been reported. Anomalous origin of the LPA from the ascending aorta is rare and is usually associated with a right aortic arch and TOF [50]. The PDA in this anomaly is right-sided [51]. The origin of the branch PA from the ascending aorta can be proximal (close to the aortic valve; in ~85% of patients) or distal (close to the origin of the brachiocephalic artery; in ~15% of patients) [50,53].

Abnormal pulmonary vasculature in the lung supplied by the anomalous pulmonary branch has been reported [54,55]. When the anomalous origin of the RPA is not associated with intracardiac defects, there exist two separate nonparallel pulmonary circuits with independent flow and resistance [56]. High pressure in the LPA is common but the etiology of this finding is not well understood. Stenosis of either PA is unusual [57]. Coronary ischemia, presumably from either steal or low diastolic perfusion pressure, has been reported [58].

### Pulmonary artery sling

This anomaly is discussed in Chapter 30.

## Imaging

### Branch pulmonary artery stenosis

The branch PAs are imaged from multiple views with high-quality two-dimensional (2D) images and color Doppler. The parasternal long- and short-axis views are helpful, and the high left parasternal and suprasternal windows usually provide the best acoustic windows for imaging the branch PAs. In some patients branch PA stenosis can be subtle, and color Doppler can overestimate the caliber of the PA. Additionally, in unilateral branch PA stenosis, flow to the stenotic branch may be reduced as it is diverted toward the unobstructed PA. In this case, Doppler evaluation may underestimate the degree of obstruction due to reduced flow, whereas the unobstructed PA may demonstrate increased flow velocity due to high flow rate. For this reason, Doppler information about branch PA stenosis should be interpreted in the context of flow rate in each branch PA. Another pitfall in using Doppler velocimetry in this condition is that prediction of pressure gradient in the branch PAs by Doppler-derived peak tends to overestimation compared with catheter-based measures [59]. For these reasons, echocardiographic evaluation of branch PA stenosis severity is based on careful assessment of the PA anatomy, color and spectral Doppler, knowledge of flow rate in the branch PAs from lung perfusion scans, estimation of RV systolic pressure based on tricuspid regurgitation jet velocity and ventricular septal configuration in systole, and RV hypertrophy [60].

When imaging the branch PAs with color Doppler, any flow reversal should be noted, as this may indicate stenosis, increased stiffness or increased resistance. The systolic color flow signal may mask a discrete narrowing, which can manifest more clearly in diastole when looking at the diameter of reversed flow. If there is any pulmonary insufficiency with flow reversal in the branch pulmonary arteries, often the diameter of the reversed flow through the stenotic area will reveal more stenosis than suspected from forward color flow in systole (Fig. 18.16).

### Discontinuous pulmonary arteries

A heightened suspicion of the possibility of discontinuous PAs is key to accurate echocardiographic diagnosis, especially in patients with conotruncal anomalies such as TOF and pulmonary atresia. The imaging technique is similar to that described for PDA and for branch PA stenosis. Detailed 2D and color Doppler imaging of the RV outflow, MPA and each branch PA is done from multiple acoustic windows, with particular emphasis on imaging from the high left parasternal and suprasternal windows. In some patients a 2D image of the branch PAs from the high left parasternal window may look deceptively continuous because the vessels overlap each other in their course, and the walls that separate them may be difficult to see as they are in parallel with the ultrasound beam (Fig. 18.17 and Videoclip 18.7). Adjusting the transducer orientation to the bifurcation so that imaging is performed from a slight angle (by moving the transducer rightward) may help to identify any walls separating the two vessels. Regardless of PA discontinuity, it is important to scan for evidence of a PDA from each likely site of ductal origin as

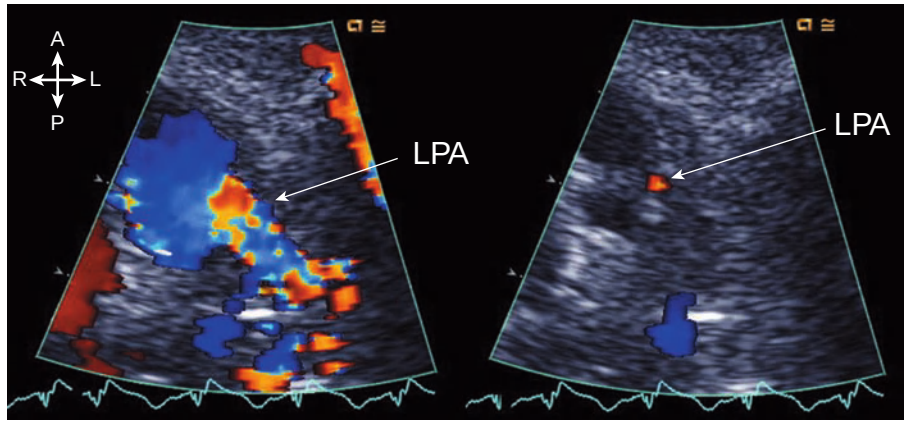


**Figure 18.16** Evaluation of left pulmonary artery (LPA) stenosis. Two subsequent color Doppler frames. **(a)** In systole, the LPA appears to have mild narrowing with flow acceleration. **(b)** In diastole, there is mild flow reversal, which in itself is not significant, but the narrow caliber of the flow jet is suggestive of more significant anatomic obstruction than previously suspected.

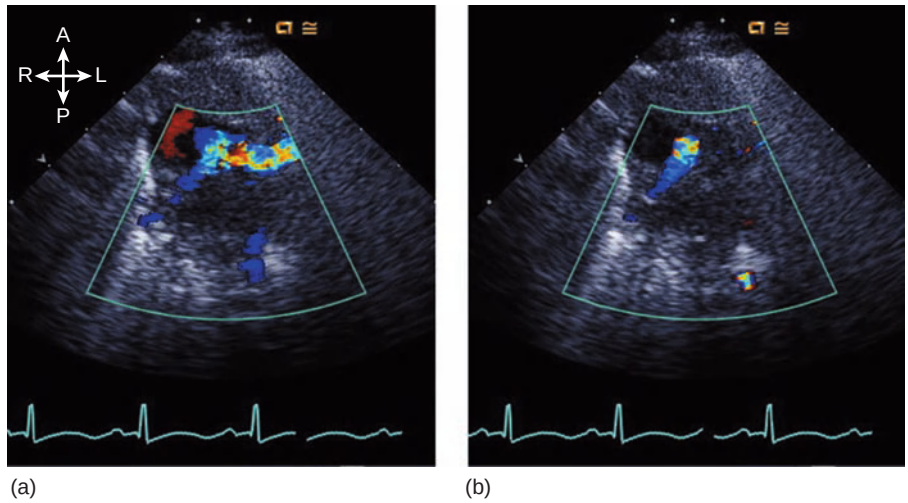


**Figure 18.17** Imaging of discontinuous branch pulmonary arteries from a high left parasternal view. In this patient the right pulmonary artery (RPA) is supplied by a patent ductus arteriosus and the left pulmonary artery (LPA) is continuous with the right ventricular outflow tract and main pulmonary artery. **(a)** In systole flow to both pulmonary arteries is seen, and, based on the color Doppler flow image alone, the pulmonary arteries appear to be contiguous. **(b)** In diastole, flow is demonstrated in the RPA but not in the LPA. The difference in flow pattern to the branch pulmonary arteries is an indication that the source of pulmonary blood flow to each branch pulmonary artery is different.

previously described. If a patient has bilateral ductus arteriosi and TOF with or without pulmonary atresia, then the likelihood of discontinuous PAs is high. When flow cannot be identified in each branch PA in a patient with TOF, administration of prostaglandin E may reveal discontinuity of the PAs by demonstrating the ductal source of flow after reopening [61].

The diagnosis of congenitally absent branch PA without associated congenital heart disease is suspected when either one of the branch PAs is not seen (Fig. 18.18 and Videoclip 18.8). The absent branch PA is usually on the opposite side of the aortic arch [44]. In young patients, a small PDA may be seen by color Doppler supplying the distal aspect of the discontinuous branch PA, usually near the hilum of the respective lung (Fig. 18.19 and Videoclip 18.9) [62]. Given that the absent branch PA is contralateral to the side of the descending aorta, the search for the PDA should begin at the base of the innominate artery (Fig. 18.20 and Videoclip 18.10). Pulsed Doppler demonstrates normal pulsatile flow in the branch PA that is in continuity with the RV outflow

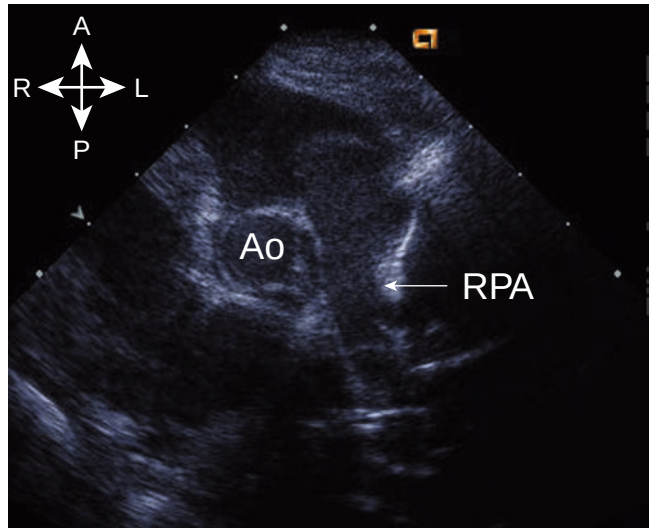


**Figure 18.18** Imaging of congenitally absent right pulmonary artery (RPA) from the high left parasternal view. Note the normally located main and left pulmonary arteries, absence of pulmonary artery bifurcation, and no right pulmonary artery coursing posterior to the ascending aorta. Ao, aorta.

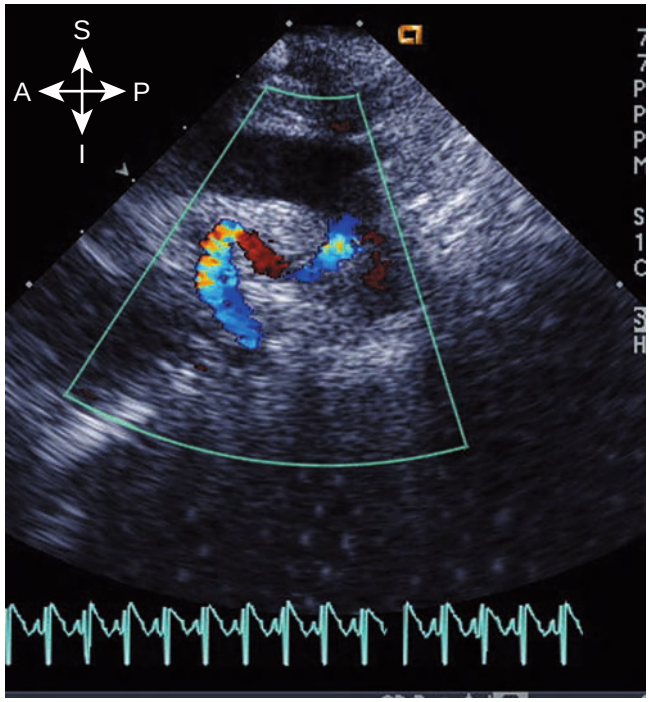


**Figure 18.19** Discontinuous branch pulmonary arteries with bilateral ductus arteriosi. The suprasternal notch view of the aortic arch demonstrates the left patent ductus arteriosus arising from the undersurface of the aortic isthmus and identifies it as the source of left pulmonary artery flow.

tract and continuous flow in the branch PA arising from the PDA.

### Crossed pulmonary arteries

The key to the diagnosis of crossed branch PAs is origin of the vessels at different heights without overlapping. In the high left parasternal short-axis view, the branching of both PAs cannot be seen simultaneously at the same plane. A sweep from inferior to superior from that view demonstrates the abnormal relations of the branch PA ostia. As the sweep begins inferiorly, the origin of the RPA from the MPA is seen first with the lateral wall of the MPA continuous with the posterior wall of the RPA. As the sweep progresses superiorly and the RPA is no longer seen, the LPA is seen with its posterior wall continuous with the medial wall of the MPA.

### Aortic origin of a branch pulmonary artery

Echocardiographic diagnosis is established by demonstrating two separate ventricular outflow tracts and semilunar valves, absence of the usual MPA bifurcation [63], origin of a branch PA from the ascending aorta, and continuity of the contralateral branch PA from the MPA. The abnormally connected branch PA is often seen as an abnormal vessel originating from the posterolateral aspect of the ascending aorta (Fig. 18.21 and Videoclip 18.11). When the branch PA arises from the distal aspect of the ascending aorta (~15% of cases) it should be differentiated from congenitally absent mediastinal PA with blood flow to the intrapulmonary branches via PDA. The key to differentiating these conditions is the origin of the anomalous vessel – from the distal ascending aorta proximal to the innominate artery takeoff in aortic origin of branch PA, and from the base of the subclavian artery in congenitally absent mediastinal PA. Furthermore, origin of branch PA from the ascending aorta should not be confused with aortopulmonary window, which demonstrates normal PA bifurcation in the high left parasternal window. In aortic origin of a branch PA the PAs are discontinuous and the normal bifurcation of the MPA is not seen from any angle. The arch sidedness and the PDA are usually contralateral to the anomalous PA [64]. The echocardiogram typically exhibits evidence of pulmonary hypertension.

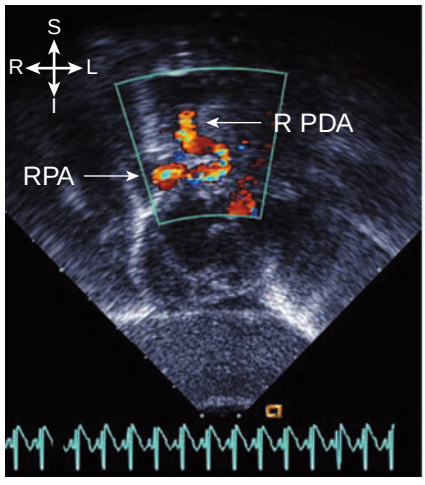


(a)

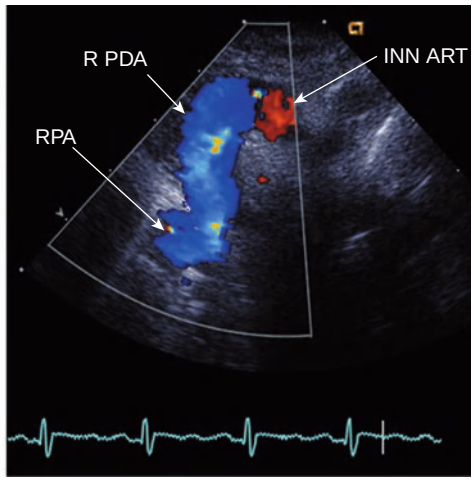


(b)

**Figure 18.20** Congenitally absent mediastinal right pulmonary artery (RPA) with no additional cardiac anomalies in a patient with a left aortic arch and a right patent ductus arteriosus (R PDA) from the innominate artery (INN ART) supplying the distal RPA. **(a)** Subcostal coronal view demonstrating the origin of a right PDA from the innominate artery supplying the distal RPA at the right lung hilum. **(b)** Suprasternal notch coronal view showing the origin of the right PDA from the right innominate artery.

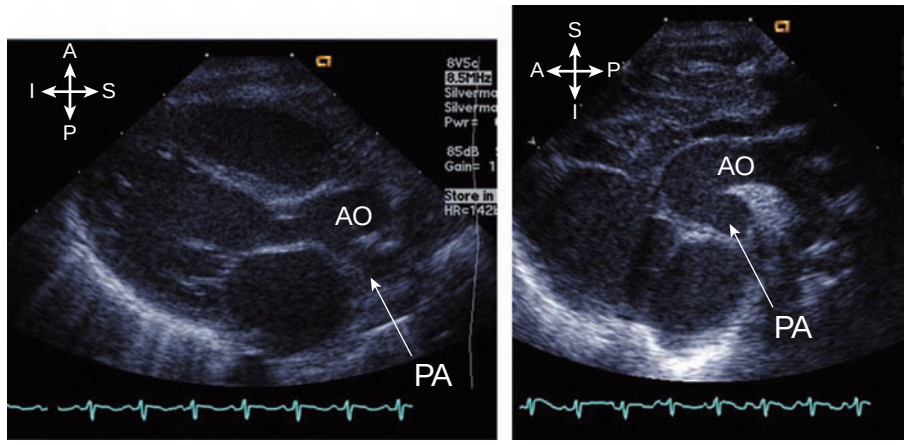


**Figure 18.21** Origin of the right pulmonary artery (PA) from the proximal ascending aorta. This patient has otherwise normal cardiac anatomy. **(a)** Parasternal long-axis view demonstrating the origin of the right PA from the posterior aspect of the ascending aorta. **(b)** Suprasternal notch view of arch demonstrating the origin of the right PA from the posterior aspect of the aorta. AO, aorta.

## References


1. Reller MD, Ziegler ML, Rice MJ et al. Duration of ductal shunting in healthy preterm infants: an echocardiographic color flow Doppler study. *J Pediatr* 1988;112:441–6.
2. Lim MK, Hanretty K, Houston AB et al. Intermittent ductal patency in healthy newborn infants: demonstration by colour Doppler flow mapping. *Arch Dis Child* 1992;67:1217–8.
3. Hoffman JI, Kaplan S. The incidence of congenital heart disease. *J Am Coll Cardiol* 2002;39:1890–900.
4. Kochilas L, Merscher-Gomez S, Lu MM et al. The role of neural crest during cardiac development in a mouse model of DiGeorge syndrome. *Dev Biol* 2002;251:157–66.
5. Moore K. The circulatory system. In: Moore K (ed.) *The Developing Human: Clinically Oriented Embryology*, 3rd edn. Philadelphia: WB Saunders, 1982;298–338.
6. Momma K, Matsuoka R, Takao A. Aortic arch anomalies associated with chromosome 22q11 deletion (CATCH 22). *Pediatr Cardiol* 1999;20:97–102.
7. Luetmer PH, Miller GM. Right aortic arch with isolation of the left subclavian artery: case report and review of the literature. *Mayo Clin Proc* 1990;65:407–13.
8. Knight L, Edwards JE. Right aortic arch. Types and associated cardiac anomalies. *Circulation* 1974;50:1047–51.
9. VanDyke CW, White RD. Congenital abnormalities of the thoracic aorta presenting in the adult. *J Thorac Imag* 1994;9:230–45.
10. McElhinney DB, Tworetzky W, Hanley FL, Rudolph AM. Congenital obstructive lesions of the right aortic arch. *Ann Thorac Surg* 1999;67:1194–202.
11. Hastreiter AR, D'Cruz IA, Cantez T et al. Right-sided aorta. I. Occurrence of right aortic arch in various types of congenital heart disease. II. Right aortic arch, right descending aorta, and associated anomalies. *Brit Heart J* 1966;28:722–39.
12. Stewart JR, Kincaid OW, Titus JL. Right aortic arch: plain film diagnosis and significance. *Amer J Roentgenol Ra* 1966;97:377–89.
13. Craatz S, Kunzel E, Spanel-Borowski K. Right-sided aortic arch and tetralogy of Fallot in humans – a morphological study of 10 cases. *Cardiovasc Pathol* 2003;12:226–32.
14. Rao PS, Wagman AJ, Chen SC. Coil occlusion of patent ductus arteriosus associated with right aortic arch. *Catheter Cardiovasc Interv* 2001;52:79–82.
15. Berning RA, Silverman NH, Villegas M et al. Reversed shunting across the ductus arteriosus or atrial septum in utero heralds severe congenital heart disease. *J Am Coll Cardiol* 1996;27:481–6.
16. Hinton R, Michelfelder E. Significance of reverse orientation of the ductus arteriosus in neonates with pulmonary outflow tract obstruction for early intervention. *Am J Cardiol* 2006;97:716–9.
17. Falcone MW, Perloff JK, Roberts WC. Aneurysm of the nonpatent ductus arteriosus. *Am J Cardiol* 1972;29:422–6.
18. Dyamenahalli U, Smallhorn JF, Geva T et al. Isolated ductus arteriosus aneurysm in the fetus and infant: a multi-institutional experience. *J Am Coll Cardiol* 2000;36:262–9.
19. Jan SL, Hwang B, Fu YC et al. Isolated neonatal ductus arteriosus aneurysm. *J Am Coll Cardiol* 2002;39:342–7.
20. Hornberger LK. Congenital ductus arteriosus aneurysm. *J Am Coll Cardiol* 2002;39:348–50.
21. Acherman RJ, Siassi B, Wells W et al. Aneurysm of the ductus arteriosus: a congenital lesion. *Am J Perinatol* 1998;15:653–9.
22. Jan SL, Hwang B, Fu YC, Chi CS. Initial clinical experience of real-time three-dimensional echocardiography in neonates with isolated congenital ductus arteriosus aneurysm. *Int J Cardiol* 2005;105:300–5.
23. Alagarsamy S, Chhabra M, Gudavalli M et al. Comparison of clinical criteria with echocardiographic findings in diagnosing PDA in preterm infants. *J Perinat Med* 2005;33:161–4.
24. Cloez JL, Isaaz K, Pernot C. Pulsed Doppler flow characteristics of ductus arteriosus in infants with associated congenital anomalies of the heart or great arteries. *Am J Cardiol* 1986;57:845–51.
25. Lane J, Acherman RJ, Khongphattanayothin A et al. Reverse aortic arch flow secondary to severe pulmonary hypertension in the neonate. *Am J Perinatol* 1999;16:143–9.
26. Naruse T, Tanishita K. Large curvature effect on pulsatile entrance flow in a curved tube: model experiment simulating blood flow in an aortic arch. *J Biomech Eng* 1996;118:180–6.
27. Silverman NH, Lewis AB, Heymann MA, Rudolph AM. Echocardiographic assessment of ductus arteriosus shunt in premature infants. *Circulation* 1974;50:821–5.
28. El Hajjar M, Vaksmann G, Rakza T et al. Severity of the ductal shunt: a comparison of different markers. *Arch Dis Child* 2005;90: F419–22.
29. Schmitz L, Stiller B, Koch H et al. Diastolic left ventricular function in preterm infants with a patent ductus arteriosus: a serial Doppler echocardiography study. *Early Hum Dev* 2004;76:91–100.

30. Lavoie J, Javorski JJ, Donahue K et al. Detection of residual flow by transesophageal echocardiography during video-assisted thoracoscopic patent ductus arteriosus interruption. *Anesth Analg* 1995;80:1071–5.
31. Rodriguez RJ, Riggs TW. Physiologic peripheral pulmonic stenosis in infancy. *Am J Cardiol* 1990;66:1478–81.
32. Wang CC, Hwu WL, Wu ET et al. Outcome of pulmonary and aortic stenosis in Williams–Beuren syndrome in an Asian cohort. *Acta Paediatr* 2007;96:906–9.
33. McElhinney DB, Krantz ID, Bason L et al. Analysis of cardiovascular phenotype and genotype–phenotype correlation in individuals with a JAG1 mutation and/or Alagille syndrome. *Circulation* 2002;106:2567–74.
34. Scheiber D, Fekete G, Urban Z et al. Echocardiographic findings in patients with Williams–Beuren syndrome. *Wiener klinische Wochenschrift* 2006;118:538–42.
35. Elzenga NJ, von Suylen RJ, Frohn-Mulder I et al. Juxtaductal pulmonary artery coarctation. An underestimated cause of branch pulmonary artery stenosis in patients with pulmonary atresia or stenosis and a ventricular septal defect. *J Thorac Cardiov Surg* 1990;100:416–24.
36. Shinkawa T, Yamagishi M, Shuntoh K et al. Pulmonary arterial reconstruction for pulmonary coarctation in early infancy. *Ann Thorac Surg* 2007;83:188–92.
37. Murphy D, Winlaw D, Cooper S, Nunn G. Successful early surgical recruitment of the congenitally disconnected pulmonary artery. *Ann Thorac Surg* 2004;77:29–35.
38. McElhinney DB, Driscoll DA, Levin ER et al. Chromosome 22q11 deletion in patients with ventricular septal defect: frequency and associated cardiovascular anomalies. *Pediatrics* 2003; 112:e472.
39. Robin E, Silberberg B, Ganguly SN, Magnisalis K. Aortic orgin of the left pulmonary artery. Variant of tetralogy of Fallot. *Am J Cardiol* 1975;35:324–9.
40. Shimazaki Y, Maehara T, Blackstone EH et al. The structure of the pulmonary circulation in tetralogy of Fallot with pulmonary atresia. A quantitative cineangiographic study. *J Thorac Cardiov Surg* 1988;95:1048–58.
41. Peirone A, Abdullah MM, Dicke F et al. Echocardiographic evaluation, management and outcomes of bilateral arterial ducts and complex congenital heart disease: 16 years' experience. *Cardiol Young* 2002;12:272–7.
42. Formigari R, Vairo U, de Zorzi A et al. Prevalence of bilateral patent ductus arteriosus in patients with pulmonic valve atresia and asplenia syndrome. *Am J Cardiol* 1992;70:1219–20.
43. Freedom RM, Moes CA, Pelech A et al. Bilateral ductus arteriosus (or remnant): an analysis of 27 patients. *Am J Cardiol* 1984;53:884–91.
44. Ten Harkel AD, Blom NA, Ottenkamp J. Isolated unilateral absence of a pulmonary artery: a case report and review of the literature. *Chest* 2002;122:1471–7.
45. Castaner E, Gallardo X, Rimola J et al. Congenital and acquired pulmonary artery anomalies in the adult: radiologic overview. *Radiographics* 2006;26:349–71.
46. Galinanes M, Stanley P, Guerin R et al. Pulmonary banding complicated by low origin of right pulmonary artery. *Tex Heart I J* 1993;20:238–40.
47. Recto MR, Parness IA, Gelb BD et al. Clinical implications and possible association of malposition of the branch pulmonary arteries with DiGeorge syndrome and microdeletion of chromosomal region 22q11. *Am J Cardiol* 1997;80:1624–7.
48. Becker AE, Becker MJ, Edwards JE. Malposition of pulmonary arteries (crossed pulmonary arteries) in persistent truncus arteriosus. *Amer J Roentgenol Ra* 1970;110:509–14.
49. Edasery B, Sharma M, Vaddigiri V, Santucci T Jr. Hemitruncus presenting in an adult. A case report. *Angiology* 1996;47:1023–6.
50. Kutsche LM, Van Mierop LH. Anomalous origin of a pulmonary artery from the ascending aorta: associated anomalies and pathogenesis. *Am J Cardiol* 1988;61:850–6.
51. Aru GM, English WP, Gaymes CH, Heath BJ. Origin of the left pulmonary artery from the aorta: embryologic considerations. *Ann Thorac Surg* 2001;71:1008–10.
52. Pahlajani DB, Pantvaidya SH, Pandit S et al. Anomalous origin of right pulmonary artery from ascending aorta with right ventricular endocardial fibroelastosis. *Pediatr Cardiol* 1985;6:47–9.
53. Nakamura Y, Yasui H, Kado H et al. Anomalous origin of the right pulmonary artery from the ascending aorta. *Ann Thorac Surg* 1991;52:1285–91.
54. Kuinose M, Tanemoto K, Murakami T et al. [Surgical treatment for a 16-year-old girl with anomalous origin of the right pulmonary artery from ascending aorta.] *Jpn J Thorac Cardiovasc Surg* 1998;46:380–4.
55. Fong LV, Anderson RH, Siewers RD et al. Anomalous origin of one pulmonary artery from the ascending aorta: a review of echocardiographic, catheter, and morphological features. *Brit Heart J* 1989;62:389–95.
56. Mair DD, Ritter DG, Danielson GK et al. Truncus arteriosus with unilateral absence of a pulmonary artery. Criteria for operability and surgical results. *Circulation* 1977;55:641–7.
57. Santos MA, Azevedo VM. Anomalous origin of a pulmonary artery from the ascending aorta: surgical repair resolving pulmonary arterial hypertension. *Arq Bras Cardiol* 2004;83:503–7; 498–502.
58. Peng EW, Shanmugam G, Macarthur KJ, Pollock JC. Ascending aortic origin of a branch pulmonary artery – surgical management and long-term outcome. *Eur J Cardiothorac Surg* 2004;26:762–6.
59. Frank DU, Minich LL, Shaddy RE, Tani LY. Is Doppler an accurate predictor of catheterization gradients for postoperative branch pulmonary stenosis? *J Am Soc Echocardiogr* 2002;15: 1140–4.
60. Roeleveld RJ, Marcus JT, Faes TJ et al. Interventricular septal configuration at MR imaging and pulmonary arterial pressure in pulmonary hypertension. *Radiology* 2005;234:710–7.
61. Patel JN, Lantin-Hermoso MR. Utility of prostaglandin in the identification of discontinuous pulmonary arteries by echocardiography. *Pediatr Cardiol* 2003;24:595–7.
62. Pfefferkorn J, Loser H, Pech G et al. Absent pulmonary artery. A hint to its embryogenesis. *Pediatr Cardiol* 1982;3:283–6.
63. Trapali CJ, Thanopoulos BD. Severe right ventricular dysfunction in a neonate with aortic origin of the RPA. *Pediatr Cardiol* 1998;19:425–7.
64. Prifti E, Bonacchi M, Murzi B et al. Anomalous origin of the right pulmonary artery from the ascending aorta. *J Cardiac Surg* 2004;19:103–12.

# 19 Anomalies of the Left Ventricular Outflow Tract and Aortic Valve

**John M. Simpson**
Evelina Children's Hospital, Guy's and St Thomas' NHS Foundation Trust, London, United Kingdom

This chapter deals with anomalies of the left ventricular outflow tract, with emphasis on echocardiographic evaluation. In general, lesions are divided into those causing obstruction of the left ventricular outflow tract and those involving the aortic root, such as sinus of Valsalva aneurysm, aortic valve cusp prolapse and aortico–left ventricular tunnel.

## Definitions

Obstruction of the left ventricular outflow tract may occur below the level of the aortic valve (*subaortic stenosis*), at the level of the aortic valve (*valvar aortic stenosis*), or above the aortic valve, typically at the level of the sinotubular junction (*supravalvar aortic stenosis*). When there is a ventricular septal defect immediately below the aortic valve there is the potential for one of the aortic cusps (usually the right coronary cusp) to prolapse into the ventricular septal defect, which can lead to regurgitation of the aortic valve. A sinus of Valsalva aneurysm refers to abnormal dilation of the aortic root wall or scalloped area of the cusps of the aortic valve. This condition can be complicated by rupture of the affected sinus into an adjacent area of the heart. An aortico–left ventricular tunnel is a lesion where there is abnormal communication between the ascending aorta and the left ventricle through an abnormal pathway ("tunnel"), which has the hemodynamic effect of severe aortic regurgitation.

## Incidence

The incidence of aortic valve stenosis in liveborn infants is around 0.4 per 1000 live births [1]. The incidence of bicuspid aortic valve is approximately 13.5 per 1000 live births [1]. In a cross-sectional study, Kitchiner et al. [2] described an incidence of subvalvar aortic stenosis of 0.09 per 1000, whereas that of supravalvar aortic stenosis was 0.05 per 1000. Sinus of Valsalva aneurysm and aortico–left ventricular tunnel are rare lesions without large reported numbers to give an accurate estimation of population incidence.

## Etiology

There is good evidence that cardiac defects causing left heart obstruction have a significant genetic component [3,4]. Aortic valve stenosis is seldom associated with major chromosomal abnormalities [5], but empiric studies of familial patterns of recurrence [3] suggest a significant genetic influence. Recent work has implicated the NOTCH pathway and genes such as *KCNJ2* and *NKX2*-5 [6]. Bicuspid aortic valve has a definite genetic component [7] and may coexist with other forms of left heart obstruction such as coarctation of the aorta. Supravalvar aortic stenosis is most characteristically associated with William syndrome, which is due to a deletion in the elastin gene on chromosome 7q11.23 [8]. Familial occurrence of supravalvar aortic stenosis has been observed without the characteristic phenotype or gene deletion found in William syndrome and may be due to other mutations in the elastin gene [9]. Subaortic stenosis may be familial [10] but in most cases is felt to be the result of the interaction of a number of factors. These factors include abnormal morphological findings such as ventricular septal defect, and abnormal aorto-septal angle producing increased septal shear stress, which in susceptible individuals leads to abnormal cellular proliferation causing subaortic obstruction [11,12].

## Subaortic stenosis

### Morphology and classification

Subaortic stenosis may occur in isolation or in association with other congenital heart defects such as ventricular septal defect, atrioventricular canal defect, bicuspid (bicommissural) aortic valve, aortic valve stenosis, coarctation of the aorta, interruption of the aortic arch, and double-chambered

*Echocardiography in Pediatric and Congenital Heart Disease: From Fetus to Adult*
Edited by Wyman W. Lai, Luc L. Mertens, Meryl S. Cohen and Tal Geva
 ISBN: 978-1-405-17401-5

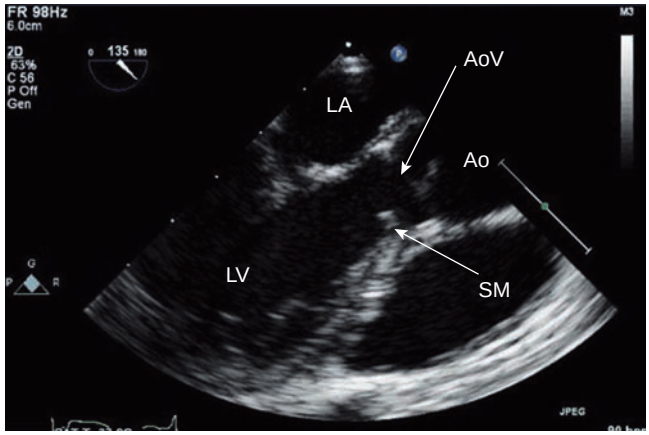


**Figure 19.1** Transesophageal echocardiogram of a patient with "membranous" subaortic stenosis. There is a discrete area of stenosis below the aortic valve. The aortic valve itself is of normal size. Ao, aorta; AoV, aortic valve; LA, left atrium; LV, left ventricle; SM, subaortic membrane.

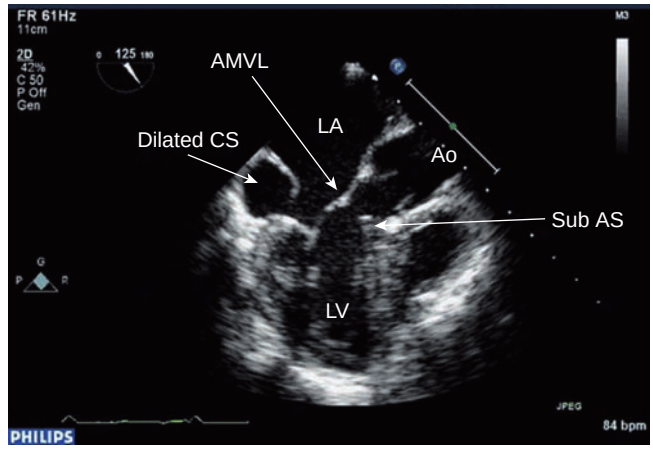


**Figure 19.2** Transesophageal echocardiogram of subaortic stenosis. This patient has a persisting left superior vena cava draining to the coronary sinus, which explains the dilated coronary sinus. The extension of the subaortic tissue onto the anterior leaflet of the mitral valve is well demonstrated. AMVL, anterior mitral valve leaflet; Ao, aorta; CS, coronary sinus; LA, left atrium; LV, left ventricle; Sub AS, subaortic stenosis.

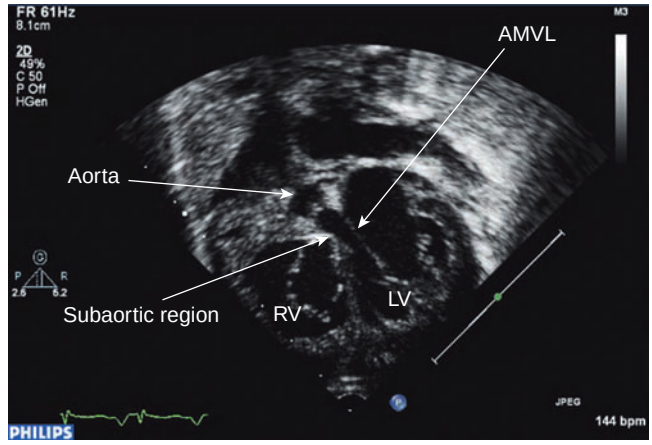


**Figure 19.3** Subcostal view of an infant with coarctation of the aorta and "tunnel"-type subaortic stenosis. There is no discrete "membrane" but the subaortic region is diffusely hypoplastic with the potential for a long segment of obstruction to the left ventricular outflow tract. AMVL, anterior mitral valve leaflet; LV, left ventricle; RV, right ventricle.

right ventricle [13–15]. In addition, subvalvar aortic stenosis may accompany conotruncal anomalies and complex anomalies, including transposition of the great arteries, double-outlet right ventricle and single ventricle. Abnormalities of the insertion of the mitral valve or accessory mitral valve tissue may also coexist [16]. Variation in the morphology of the left ventricular outflow tract obstruction can have several causes:

**1** Hypertrophic cardiomyopathy: hypertrophy of the ventricular septum can result in muscular obstruction of the left ventricular outflow tract. This may be accompanied by abnormal systolic anterior motion of the mitral valve. This is dealt with in more detail in Chapter 34.

**2** Discrete "membranous" subaortic stenosis (Figs 19.1 and 19.2; Videoclips 19.1 and 19.2): this form of subaortic stenosis usually manifests during childhood and is rare during infancy [17]. The morphology of the left ventricular outflow is characterized by a steeper angle between the plane of the ventricular septum and the aortic root (aorto-septal angle), elongation of the intervalvular fibrosa between the anterior mitral leaflet and the aortic valve, and an exaggerated aortic override above the ventricular septal crest [18]. There is a frequent association with a membranous ventricular septal defect, and abnormal shear stresses have been implicated, by causing abnormal proliferation of fibrous tissue. Although such discrete obstruction is amenable to surgical repair, regrowth of tissue may lead to recurrence of subaortic obstruction [19–22]. Note that the obstructive subaortic tissue does not exclusively involve the ventricular septum and may extend onto the anterior leaflet of the mitral valve (Fig. 19.2 and Videoclip 19.2).

**3** "Tunnel-type" subaortic stenosis (Fig. 19.3 and Videoclip 19.3): as the name implies, this form of subaortic stenosis involves a long segment of narrowing of the left ventricular outflow tract and is often caused by muscle. The muscular narrowing can involve an accessory anterolateral papillary muscle, septal hypertrophy, or a combination of the above. This form of obstruction frequently occurs early in life and is often associated with other forms of left heart obstruction. The clinical implication is that a more extensive type of surgical repair will be required compared with repair of the discrete fibrous form of obstruction [23,24].

**4** Posterior deviation of the outlet (infundibular) septum may cause subaortic obstruction [25]. This typically occurs in association with conditions such as type B interruption of the aortic arch or, less commonly, coarctation of the aorta with ventricular septal defect, where the aortic valve and ascending aorta may be hypoplastic.

## Pathophysiology

The development of subaortic stenosis is thought to be due to abnormal shear forces in the left ventricular outflow tract, leading to abnormal growth of fibrous tissue [11,26]. Such shear forces are increased in the presence of an abnormal aorto-septal angle and other lesions such as a ventricular septal defect. The obstruction to the left ventricular outflow tract leads to compensatory ventricular hypertrophy. Contractile function of the left ventricle is usually well maintained initially but may worsen with time if severe outflow tract obstruction is not relieved. The fibrous tissue below the aortic valve may extend onto the aortic valve leaflets and contribute to obstruction of the left ventricular outflow tract. The turbulent jet across the subaortic region may also interfere with optimal motion of the aortic valve and may contribute to aortic valve regurgitation. Consequently, some centers have advocated early surgical resection of the subaortic lesion to reduced aortic regurgitation [20,21], a strategy that has not been consistently adopted [27]. There is a clear indication for surgical intervention where there is severe left ventricular outflow tract obstruction. The indications for intervention in children with relatively mild outflow tract obstruction are less clear-cut. As a minimum, serial echocardiographic examination is required because rapid progression of subaortic stenosis may occur in infancy and early childhood [21]. For adults with relatively low Doppler gradients (<50 mm Hg) a conservative approach may be adopted although progression may occur during adult life, albeit more slowly than in infancy and early childhood [21,28].

## Imaging

The goals of echocardiography in subaortic stenosis include:

- Assessment of the severity of left ventricular outflow tract obstruction.
- Delineation of the morphology of the left ventricular outflow tract and the type of subaortic obstruction.
- Identification of associated abnormalities, particularly abnormalities of the aortic valve.

The assessment of severity of left ventricular outflow tract obstruction can be done in a manner analogous to that of aortic valve stenosis (see "Aortic valve stenosis" below). Muscular subaortic obstruction may be accompanied by an increase in the Doppler velocity in late systole leading to an asymmetric Doppler trace consistent with dynamic obstruction. To obtain optimal Doppler signals, imaging is undertaken from the apical and from the suprasternal notch views. Pulsed Doppler is helpful to localize flow acceleration and, in patients with several levels of obstruction, to determine the contribution of each location to the total estimated pressure drop. The maximum instantaneous and mean gradients across the left ventricular outflow are also recorded from both transducer positions by continuous-wave Doppler, with particular attention to optimization of the alignment between the ultrasound beam and the direction of flow. A detailed discussion of the principles of assessing stenosis by Doppler can be found in Chapter 6.

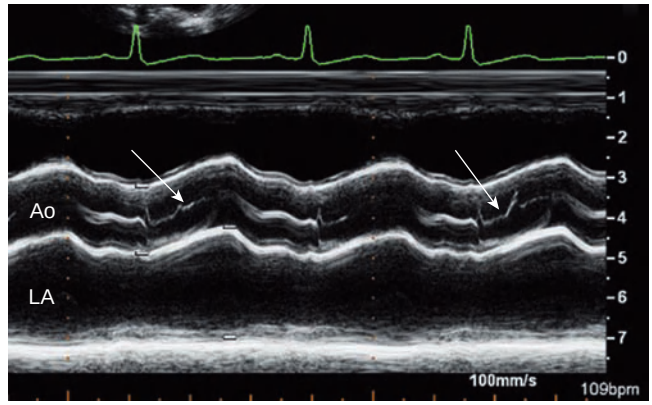


**Figure 19.4** M-mode echocardiogram of the long-axis aortic valve. "Fluttering" of the aortic valve leaflets is indicated by the arrows and is due to the turbulent subaortic jet striking the aortic valve leaflets. Ao, aorta; LA, left atrium.

Imaging of the morphology of the left ventricular outflow tract is crucial for planning management. In the membranous form of subaortic stenosis the full extent of the fibrous membrane should be defined, as such membranes vary in their distance from the aortic valve itself, and some extend circumferentially to involve the anterior leaflet of the mitral valve. This assessment is best achieved from the parasternal long- and short-axis views. Three-dimensional imaging allows en face views of the subaortic obstruction from the left ventricular cavity and through the aortic valve. In some patients, accessory tissue related to the mitral valve attaches to the subaortic septum, producing or contributing to subaortic stenosis [29]. The aortic valve may be intrinsically abnormal or be restricted in its motion due to encroachment of fibrous tissue onto the ventricular aspect of the leaflets. The aortic valve leaflets may "flutter" during systole as they are hit by the turbulent jet from the subaortic region (Fig. 19.4).

Comprehensive echocardiographic evaluation is crucial for planning subaortic stenosis surgery. Discrete "membranous" subaortic stenosis may be resected with preservation of the native aortic valve. However, "tunnel" forms of subaortic stenosis may not be able to be managed by resection of a localized area of tissue and may require a more extensive resection [19,23,24,30]. It is therefore essential to have all anatomic information before surgical repair. In the tunnel type of subaortic obstruction, the left ventricular outflow tract is often hypoplastic including the aortic valve annulus. In selected patients, extensive subaortic resection may have to be combined with insertion of the patient's pulmonary valve into the aortic position (Ross–Konno operation) [31,32]. In small infants, transthoracic echocardiographic imaging is usually all that is necessary to plan treatment, but in older children and adults, transesophageal echocardiography may be necessary to gain all relevant information. In

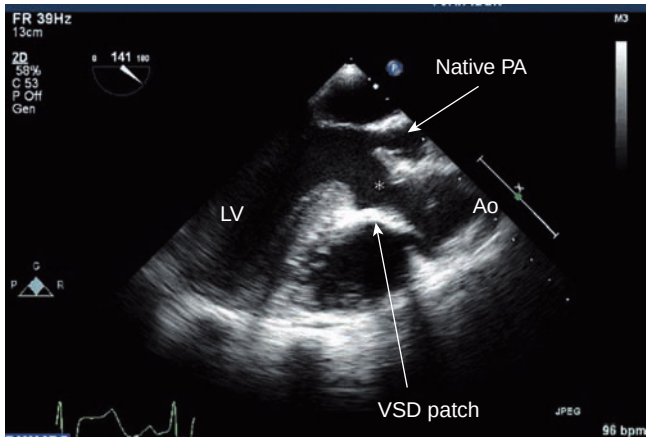


**Figure 19.5** Transesophageal echocardiogram of a patient with subaortic obstruction following a "Rastelli" repair of transposition of the great arteries with an associated ventricular septal defect (VSD) and pulmonary stenosis. The outflow of the left ventricle is across the ventricular septal defect. This leads to a tortuous subaortic area, and in this example there is stenosis between the native pulmonary artery and the VSD patch. The asterisk (*) denotes the area of subaortic narrowing. Ao, aorta; LV, left ventricle; PA, pulmonary artery; VSD, ventricular septal defect.

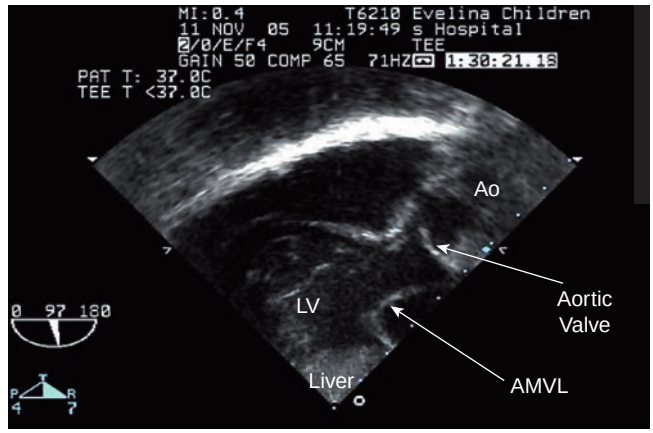


**Figure 19.6** Transgastric view of the left ventricular outflow tract on a transesophageal echocardiogram. This view provides the best means of aligning the Doppler cursor to the direction of blood flow, giving the most reliable estimate of blood flow velocity. AMVL, anterior mitral valve leaflet; Ao, aorta; LV, left ventricle.

some patients, subaortic obstruction follows repair of more complex forms of congenital heart disease [33]. An example of this would be subaortic obstruction following a "Rastelli" type of repair for conditions such as transposition of the great arteries with a ventricular septal defect and pulmonary stenosis. In this repair, the outflow from the left ventricle is baffled to the aorta across the ventricular septal defect, using a patch. The tortuous outflow tract is a substrate for subaortic obstruction (Fig. 19.5). Other examples include conditions such as double-inlet left ventricle with transposition of the great arteries, where the outlet of the left ventricle to the ascending aorta is through a bulboventricular foramen, which, if restrictive, effectively causes subaortic obstruction.

At this author's center, intraoperative imaging, either by an epicardial or transesophageal approach, is done in all cases of subaortic stenosis, whatever the anatomic substrate, to confirm adequacy of the surgical relief of obstruction. Alignment of the Doppler cursor to the direction of flow is typically best achieved by a transgastric transesophageal approach (Fig. 19.6) but this can be difficult or impossible when the chest is open during surgery. The severity of aortic regurgitation should be assessed because this can occasionally worsen following removal of fibrous subaortic obstruction, particularly in cases where fibrous tissue has extended onto the aortic valve leaflets themselves. The mitral valve should be imaged for evidence of mitral valve regurgitation as damage to the anterior leaflet may occur if a circumferential subaortic "membrane" has had to be surgically resected from the anterior mitral valve leaflet. Finally, it is necessary to guard against iatrogenic creation of a ventricular septal defect due to inadvertent perforation of the ventricular septum.

In the longer term, sequential echocardiography is indicated to exclude recurrence of subaortic stenosis, which can occur even after initial apparent complete resection of the obstructive tissue. The risk of recurrence is higher when the subaortic "membrane" is closer to the aortic valve and in patients with severe preoperative obstruction [22]. Aortic regurgitation should be assessed semiquantitatively and chamber dimensions, wall thickness, and contractile function should be measured.

## Aortic valve stenosis

### Morphology

Aortic valve stenosis in children is due to a congenitally abnormal aortic valve rather than degeneration of a morphologically normal valve as may occur in late adult life. Morphologically, the anomaly may be due to commissural underdevelopment, myxomatous thickening of the valve leaflets, annular hypoplasia, or a combination of these elements. As a result of commissural underdevelopment, the aortic valve may be unicuspid (when only one commissure, usually the left-noncoronary commissure, is well-formed), bicuspid (when one commissure is underdeveloped and the other two are well-formed), tricuspid (all three commissures are well-developed) or, rarely, quadricuspid (when an extra commissure is present) (Fig 19.7 and Videoclip 19.4). In some cases, particularly in infancy, it may be difficult to identify true separate cusps, with the appearance of a single central or eccentric orifice, which has been likened to a "volcano"-type orifice [34]. In some patients the valve may be incompetent and stenotic. Aortic regurgitation is invariably

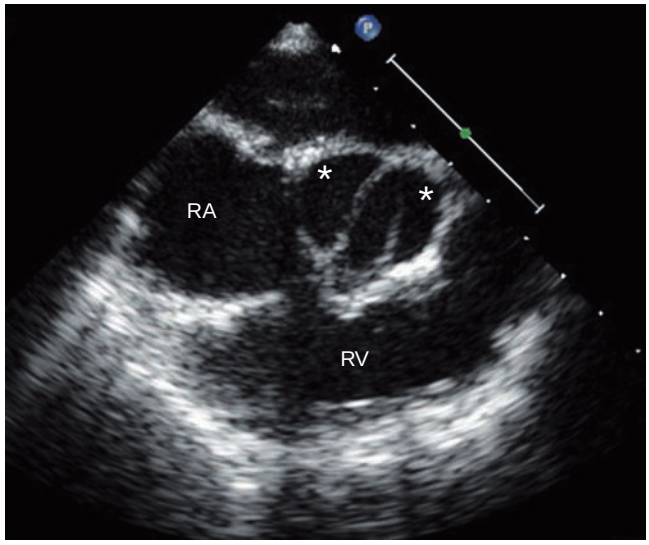


**Figure 19.7** Short-axis view of a bicuspid aortic valve on transesophageal echocardiography. This technique is ideal for assessing valve morphology in older patients in whom transthoracic images may be suboptimal. The asterisks (*) denote cusps of the aortic valve. RA, right atrium; RV, right ventricle.

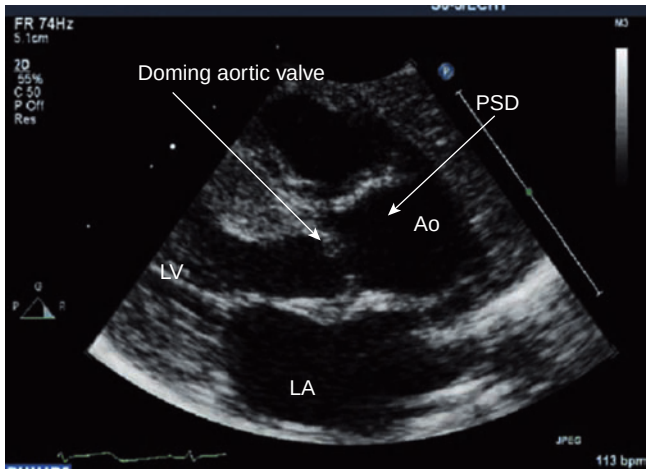


**Figure 19.8** Long-axis view of the left ventricle demonstrating poststenotic dilation of the ascending aorta in a patient with valvar aortic stenosis. Ao, aorta; LA, left atrium; LV, left ventricle; PSD, poststenotic dilation.

present following balloon valvuloplasty, either surgical or transcatheter. Post-stenotic dilation of the proximal ascending aorta also occurs due to the high-velocity, turbulent and often eccentric jet through the valve (Fig. 19.8).

## Pathophysiology

Obstruction to the left ventricular outflow tract results in an increased afterload on the left ventricle. The myocardial response to such an increase depends on the stage of development at which it occurs. During fetal life, mild stenosis of the aortic valve is usually well tolerated with good contraction of the left ventricle and normal development of left heart structures. In fetuses with severe aortic valve stenosis the left ventricle dilates, contractile function decreases and endocardial fibroelastosis often develops [35]. As gestational age advances, growth of the left ventricle and aorta is subnormal in the majority of cases so that, by term, the left ventricle and aorta are hypoplastic and postnatal management is more akin to that of hypoplastic left heart syndrome [35,36]. Such progression of aortic stenosis provides the rationale for intrauterine intervention to prevent progression of aortic valve stenosis to hypoplastic left heart syndrome, with the potential to improve the likelihood of a biventricular repair postnatally [37–39].

Following birth, once the arterial duct closes, the systemic arterial circulation has to be supported entirely by left heart structures. If there is severe aortic stenosis with significant left ventricular dysfunction and/or underdevelopment of left heart structures, then the left heart may be unable to support the circulation and the infant will present with cardiovascular collapse. In such circumstances, administration of prostaglandin E is life-saving, by reopening the arterial duct and permitting the right heart structures to support the systemic circulation. The term "critical" aortic stenosis is commonly applied to infants where the systemic circulation is dependent on the maintenance of ductal patency. In less severe cases, closure of the arterial duct does not lead to left ventricular failure because the left ventricle hypertrophies in response to left ventricular outflow tract obstruction and maintains an adequate cardiac output. Such infants and children may remain asymptomatic early in life and present for other reasons such as an incidental cardiac murmur, reduced exercise tolerance, or exercise-induced syncope. In adults, aortic valve stenosis may develop due to degeneration of an aortic valve that was not previously stenotic. Individuals with a congenitally bicuspid aortic valve have a higher risk of late degeneration of the valve than if the valve is tricuspid [40].

## Imaging

The aims of the echocardiographic examination of the patient with aortic valve stenosis include:

- Assessment of severity of aortic valve stenosis using Doppler echocardiography.
- Delineation of the morphology of the aortic valve.
- Assessment of aortic regurgitation, which frequently accompanies aortic stenosis.
- Comprehensive assessment of all left heart structures, including the mitral valve and aortic arch, to exclude associated abnormalities.
- Measurement of left ventricular dimensions, wall thickness and contractile function.

The severity of aortic valve stenosis is estimated by measurement of the Doppler-derived maximum instantaneous and mean pressure drop across the aortic valve. Classification by Doppler-derived pressure drop is only valid if left ventricular function is well preserved and cardiac output is normal. Assuming this to be the case, and beyond the neonatal age

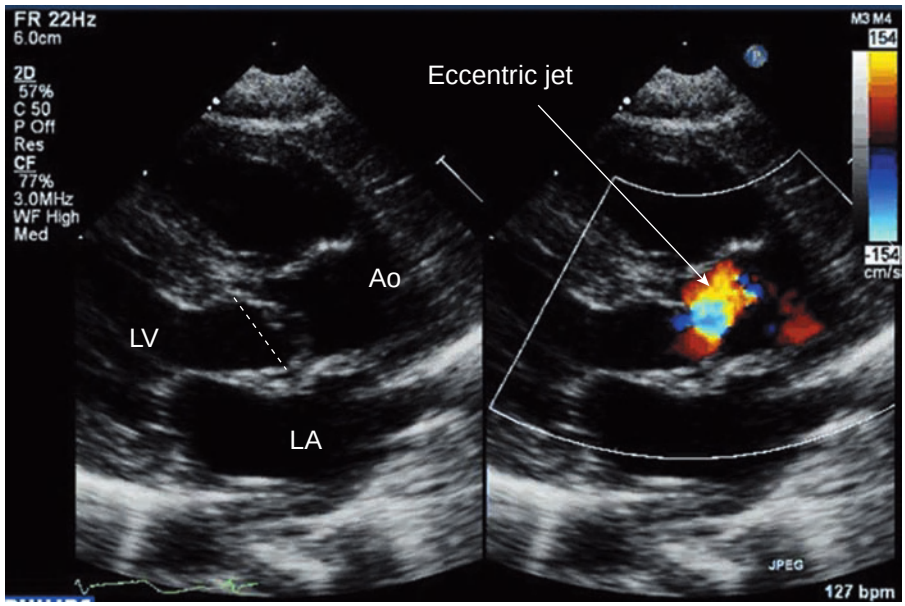


**Figure 19.9** Long-axis view of the left ventricle demonstrating aortic valve stenosis with an eccentric jet across the aortic valve. Use of color flow Doppler permits optimization of the angle of insonation to obtain the most accurate values of pressure drop across the valve. The dashed line represents the distance between the hinge points of the aortic valve, which is employed for balloon sizing for aortic valvuloplasty. Ao, aorta; LA, left atrium; LV, left ventricle.

range, mild aortic valve stenosis may be defined as a peak Doppler velocity of less than 3 m/s; moderate aortic valve stenosis has a peak velocity of 3–4 m/s, and severe aortic stenosis is characterized by a peak velocity of more than 4 m/s. Color Doppler flow mapping is extremely helpful to observe the direction of the flow jet, which may be eccentric, and allows optimal alignment of the Doppler cursor with the jet (Fig. 19.9 and Videoclip 19.5). Imaging from the suprasternal notch often has the best alignment with the direction of flow. Use of the low-frequency continuous-wave nonimaging Doppler probe is recommended as it provides optimal access to the suprasternal notch, particularly in smaller children. In infants and children an apical 2-chamber projection provides an excellent window for Doppler interrogation of the left ventricular outflow tract. Continuous-wave Doppler is optimal to determine the maximum instantaneous and mean Doppler-derived pressure drop, but pulsed-wave Doppler is extremely helpful in patients with multiple levels of left ventricular outflow tract obstruction because "step up" in velocity at different sites may be observed and allow determination of the relative contribution of the different levels of obstruction.

In older children and in young adults with congenital aortic valve stenosis, an assessment of valve area can be made by employing the continuity equation [41,42] or other formulas [43,44]. In mild aortic valve stenosis, the effective orifice area is >1.4 $cm^2$; in moderate aortic valve stenosis it is 1.0–1.4 $cm^2$, and in severe aortic valve stenosis it is <1.0 $cm^2$ [45]. One important group has relatively low "gradients" across the aortic valve due to reduced left ventricular ejection fraction resulting in a reduced cardiac output. In this group, severe aortic valve stenosis coexists with a relatively low Doppler velocity across the aortic valve. Dobutamine stress echocardiography examines for increases in effective orifice area, contractile function and pressure gradient under stress conditions, permitting stratification of risk for surgery [45].

The morphology of the aortic valve is best seen with a short-axis view of the aortic valve. The diameter of the aortic valve annulus is measured during systole from the parasternal long-axis view. If there is aortic regurgitation, the parasternal short-axis view is ideal for determining the site of regurgitation through the valve. Assessment of aortic regurgitation is discussed in detail in Chapter 6. Briefly, the severity can be assessed by the width of the vena contracta of the aortic regurgitation jet using color flow mapping from the parasternal long axis, relative to the aortic annulus diameter. Continuous-wave Doppler interrogation of the regurgitant jet can be used to estimate the pressure half-time, and the degree and duration of reversal of flow in the distal aortic arch or descending aorta during diastole can be helpful to give a semiquantitative assessment of the degree of aortic valve regurgitation.

In all cases of left ventricular outflow tract obstruction at any level, left ventricular dimensions and wall-thickness should be measured. These measurements can be obtained by M-mode echocardiography of the left ventricle at the level of the tips of the mitral valve in either a long- or a short-axis projection of the left ventricle. Alternatively, left ventricular volume, mass and systolic function can be measured by 2D or 3D techniques (see Chapter 7 for further details). It is essential that Doppler-derived pressure drop across a stenotic aortic valve is interpreted in light of left ventricular contractile function and blood flow rate. An example of this occurs in small infants with severe aortic stenosis in whom contractile function of the left ventricle may be so poor that only low-velocity jets are observed across a critically stenotic aortic valve.

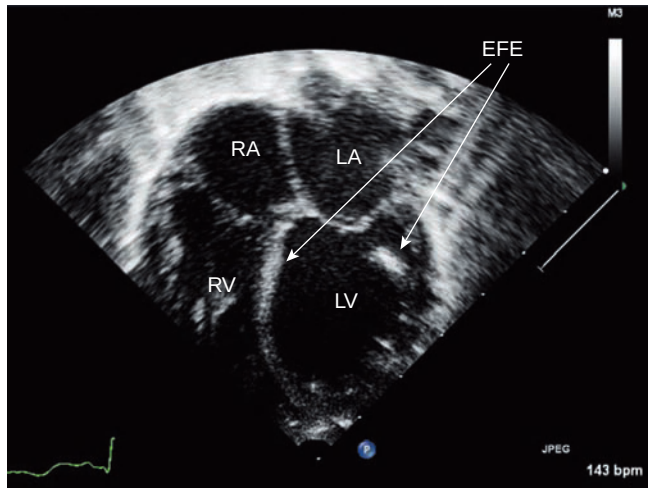


**Figure 19.10** Four-chamber view of a newborn with critical aortic stenosis. In this example the left ventricle is dilated and more globular than normal. There is endocardial fibroelastosis affecting mainly the papillary muscle apparatus and the ventricular septum. EFE, endocardial fibroelastosis; LA, left atrium; LV, left ventricle; RA, right atrium; RV, right ventricle.

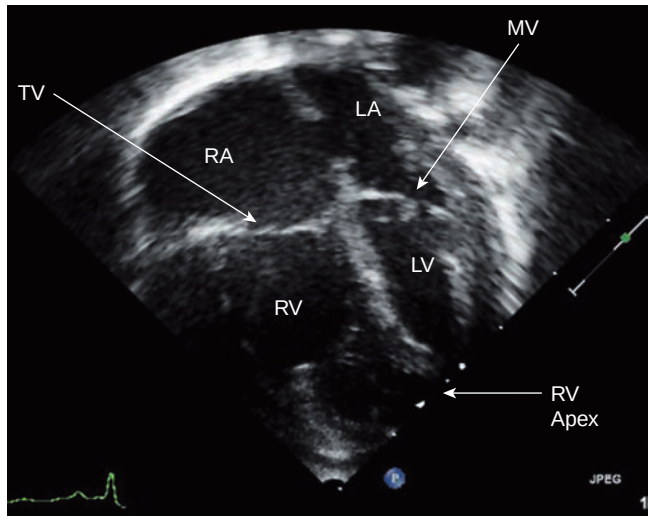


**Figure 19.11** Four-chamber view of a newborn with critical aortic stenosis with associated hypoplasia of the left ventricle and mitral valve. The left ventricle no longer forms the apex of the heart, which is now formed by the apex of the right ventricle. LA, left atrium; LV, left ventricle; MV, mitral valve; RA, right atrium; RV, right ventricle; TV, tricuspid valve.

A thorough examination of all left heart structures is essential when aortic valve stenosis is diagnosed. Aortic valve stenosis may coexist with other types of left heart obstruction including supramitral membrane, mitral valve stenosis, subaortic stenosis, and coarctation of the aorta. In infancy, critical aortic stenosis is frequently accompanied by hypoplasia of left heart structures including the mitral valve, left ventricle and aorta (Figs 19.10–19.12; Videoclips 19.6 and 19.7). Endocardial fibroelastosis is observed as a brightly

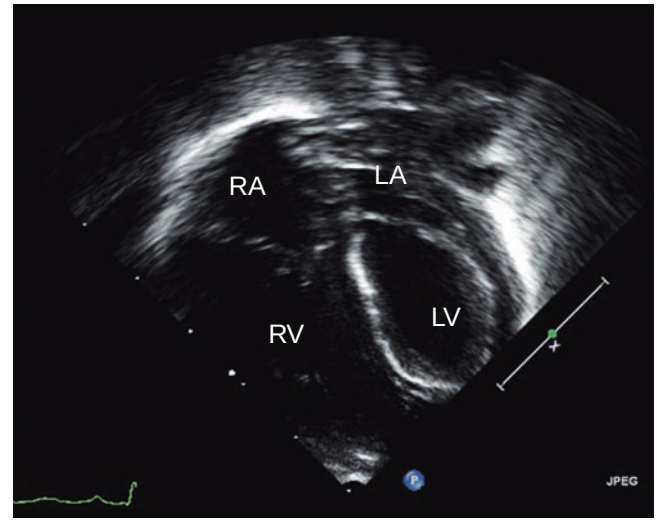


**Figure 19.12** An example of an infant with critical aortic stenosis and severe endocardial fibroelastosis accounting for the bright echogenicity of the entire left ventricle. Such extensive endocardial fibroelastosis is regarded as an adverse prognostic sign for a biventricular repair. LA, left atrium; LV, left ventricle; RA, right atrum; RV, right ventricle.

echogenic lining to the left ventricle; in its mildest form this may involve only the papillary muscles but in its severest form it may line the entire left ventricular cavity (Figs 19.11 and 19.12). In severely affected infants it may be difficult to judge whether left heart structures are capable of supporting the systemic arterial circulation or not. This poses a major challenge in terms of management because if left heart structures are judged adequate, an intervention to relieve the aortic valve stenosis may be attempted. However, if left heart structures are judged inadequate to support cardiac output a single-ventricle ("Norwood") palliation might be adopted. Echocardiographic criteria have been developed to aid in decision-making in this regard [46–48] and an online calculator developed by the Congenital Heart Surgeons Society is available (http://www.ctsnet.org/aortic_stenosis_calc/).

## Echocardiographic evaluation before, during and after intervention for aortic valve stenosis

In the preoperative assessment of the aortic valve, the echocardiographer should focus on the morphology of the aortic valve, noting the number of aortic valve leaflets, the morphology of the commissures and whether or not any leaflets are fused. An accurate measurement of the aortic valve at the hinge points of the aortic valve leaflets is essential for selection of the appropriate size of balloon for valvuloplasty (Fig. 19.9 and Videoclip 19.5). In addition, the degree of aortic regurgitation should be carefully documented as an increase in the degree of regurgitation may occur following intervention.

In most units, balloon aortic valvuloplasty is favored as the initial intervention to relieve critical aortic stenosis. Thus,

accurate measurement of the hinge points of the aortic valve is important to guide optimal balloon sizing. Echocardiography may be undertaken during the procedure if a complication is suspected, such as perforation of the left ventricle with a guidewire or damage to the aortic valve. At this author's center, echocardiography is not routinely performed during the interventional procedure unless a major complication is suspected but is performed shortly after the procedure to assess residual gradients across the aortic valve and to judge the severity of aortic valve regurgitation. Judging the severity of aortic valve regurgitation early after balloon valvuloplasty may be difficult because of reduced compliance of the left ventricle related to muscle hypertrophy or endocardial fibroelastosis, which may lead to underestimation of the degree of aortic regurgitation.

Follow-up echocardiography is indicated in all patients who have had intervention or surgery on the aortic valve. This is to evaluate restenosis of the aortic valve, particularly with growth, and to review the severity of aortic regurgitation, which is almost invariable following balloon aortic valvuloplasty or surgical valvotomy.

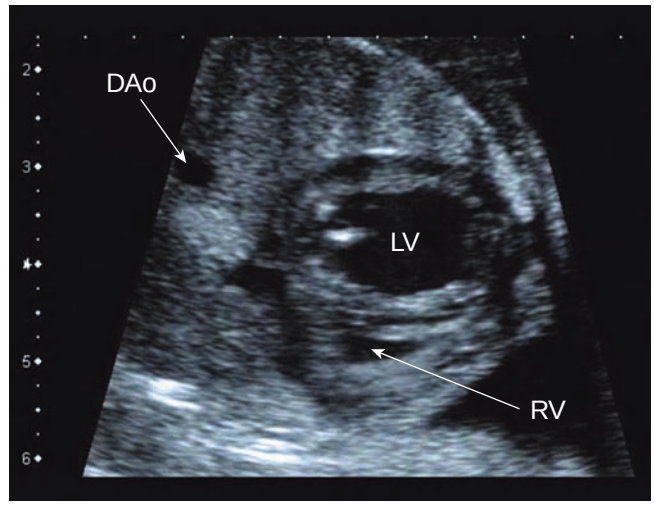


**Figure 19.13** Fetal echocardiogram of a fetus with severe aortic stenosis. The left ventricle is dilated and compresses the right ventricle. Growth of the left ventricle is subnormal in the majority of cases so that by late gestation the appearances are more akin to classical hypoplastic left heart syndrome. DAo, descending aorta; LV, left ventricle; RV, right ventricle.

## Aortic valve stenosis in the fetus

Aortic valve stenosis may be diagnosed accurately during fetal life and the echocardiographic findings have been reported [35–37]. In mild cases of aortic stenosis, there is an increased Doppler velocity across the aortic valve but with good left ventricular function and antegrade flow around the aortic arch. Growth of left heart structures is well maintained with advancing gestational age. Sequential echocardiography is indicated during fetal life to monitor for progression of aortic valve stenosis, as some fetuses will demonstrate progressively increased severity of left ventricular outflow tract obstruction.

In severe cases of aortic stenosis diagnosed during fetal life, the left ventricle is typically dilated early in gestation with reduced left ventricular function (Fig. 19.13). Endocardial fibroelastosis is a frequent association, although the severity may vary. This appears as a bright echogenic lining of the left ventricular cavity. Mitral valve regurgitation may occur and, if severe, is associated with a poor prognosis (Fig. 19.14 and Videoclip 19.8). The interatrial communication, which normally permits right-to-left flow of blood, may reverse due to left heart inflow obstruction. In some cases the atrial septum might be highly restrictive or even intact (Figs 19.15 and 19.16). Doppler interrogation of the pulmonary veins, with particular attention to the degree and duration of flow reversal during atrial contraction, is extremely helpful in determining the degree of restriction of the atrial septum (Fig. 19.17). With advancing gestational age, growth of left heart structures is almost always subnormal so that by term, the aorta, left ventricle and mitral valve are severely hypoplastic. Judging which fetuses will be managed toward a biventricular repair versus those that will be managed

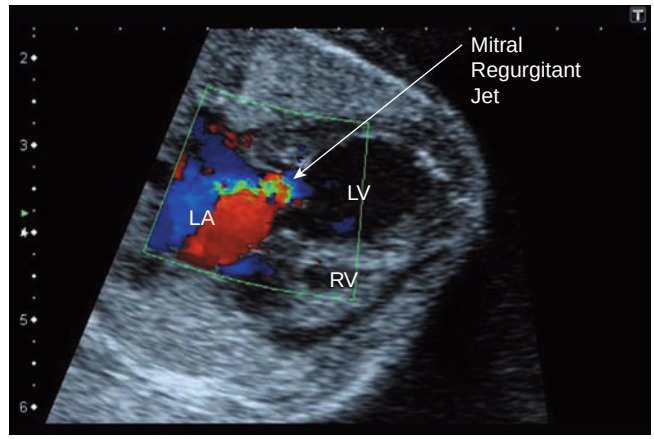


**Figure 19.14** Fetal echocardiogram demonstrating torrential mitral valve regurgitation in a fetus with critical aortic stenosis. There is a broad jet of mitral valve regurgitation, which fills a large portion of the dilated left atrium. LA, left atrium; LV, left ventricle; RA, right atrium.

toward a single ventricle circulation is often difficult. The relative diameters and lengths of the right and left ventricles, presence of endocardial fibroelastosis, degree of mitral valve regurgitation, hypoplasia of the aorta and direction of flow in the distal aortic arch may all help in prognostication [37]. Fetuses at this end of the spectrum will often require management with a single-ventricle palliation using a Norwood strategy rather than balloon dilation of the aortic valve or surgical valvotomy. It is the progression of aortic valve stenosis to a situation analogous to hypoplastic left heart syndrome that has led to prenatal intervention being considered for affected fetuses [37–39].

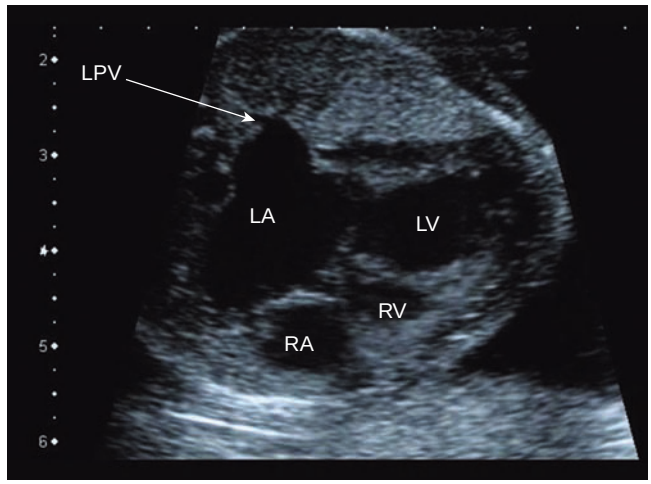


**Figure 19.15** Severe dilation of the left atrium in a fetus with critical aortic stenosis, severe mitral valve regurgitation and a restrictive interatrial communication. Note the pronounced dilation of the left pulmonary veins and bowing of the atrial septum from left to right. LA, left atrium; LPV, left pulmonary veins; LV, left ventricle; RA, right atrium; RV, right ventricle.

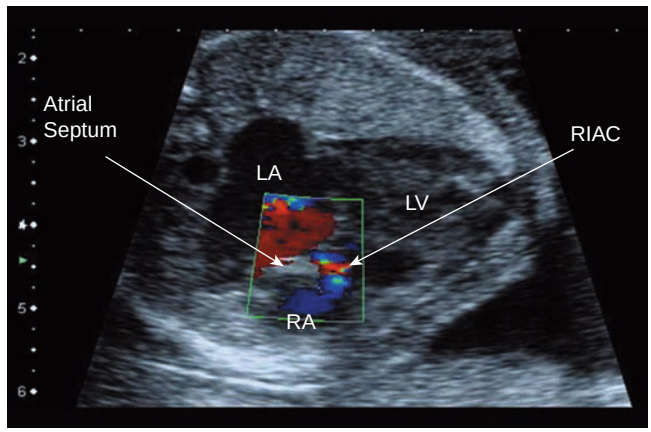


**Figure 19.16** Restriction interatrial communication in a fetus with criticial aortic stenosis. There is a narrow turbulent jet of blood from the left atrium to the right atrium representing the only point of decompression of the left atrium. LA, left atrium; LV, left ventricle; RA, right atrium; RIAC, restrictive interatrial communication.

The echocardiographic approach during fetal life should include all of the assessments listed above but in addition should also include:

- Diameters of left and right ventricles.
- Lengths of right and left ventricles.
- Diameters of the mitral and tricuspid annuli.
- Severity of mitral valve regurgitation.
- Diameters of aortic valve annulus and aortic arch.
- Direction of systolic flow in the distal aortic arch (antegrade versus retrograde).

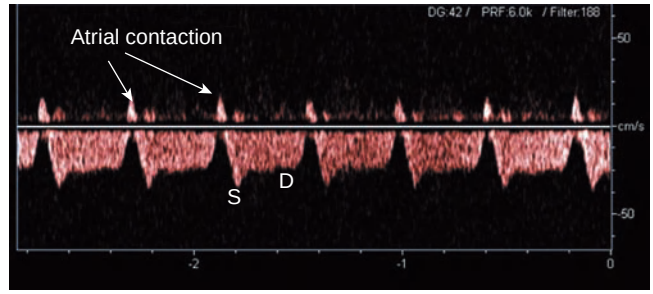


(a)

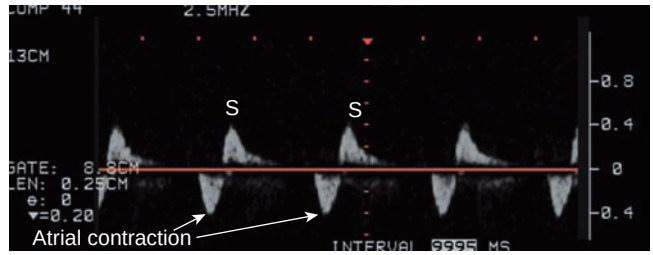


(b)

**Figure 19.17** Interrogation of the pulmonary veins can be helpful to assess the degree of restriction of the atrial septum in the context of severe left heart obstruction. In **(a)** there is flow into the left atrium during ventricular systole (S) and diastole (D) with only a short low-velocity period of flow reversal during atrial contraction. In **(b)** there is a short period of normal flow into the left atrium during early ventricular systole only, with major reversal of flow during atrial systole. This represents the findings where the atrial septum is highly restrictive.

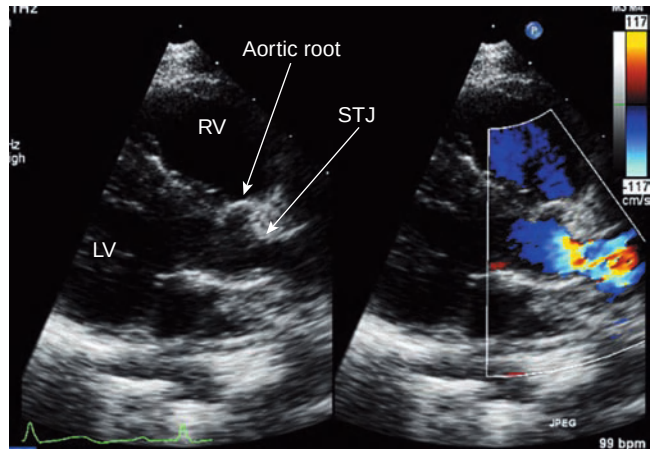


**Figure 19.18** Supravalvar aortic stenosis. Parasternal long-axis view demonstrating "pinching" of the aorta at the level of the sinotubular junction. Color flow mapping confirms that turbulence of blood flow originates in the supravalvar region. LV, left ventricle; RV, right ventricle; STJ, sinotubular junction.

## Supravalvar aortic stenosis

### Morphology

Supravalvar aortic stenosis typically occurs at the sinotubular junction and is characterized by discrete narrowing of the aortic lumen at this point (Figs 19.18 and 19.19;

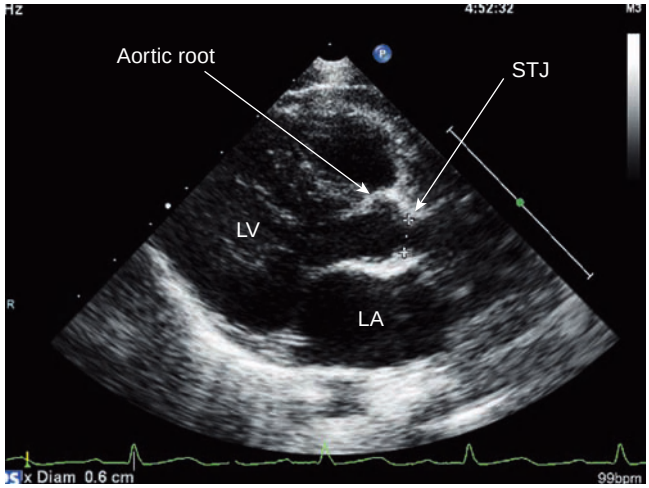


**Figure 19.19** Parasternal long-axis view of a patient with supravalvar aortic stenosis. The dashed line represents the dimension of the narrowest region of the aorta at the level of the sinotubular junction. LA, left atrium; LV, left ventricle; STJ, sinotubular junction.

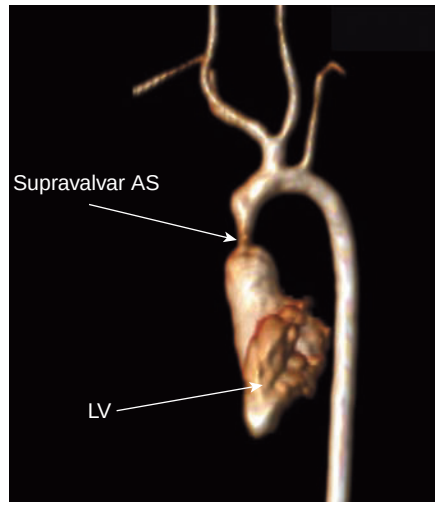


**Figure 19.20** Magnetic resonance imaging of the ascending aorta, aortic arch, and head and neck vessels. This form of imaging is extremely helpful in planning the surgical approach for repair of supravalvar aortic stenosis and to identify occult stenoses in other vessels. AS, aortic stenosis; LV, left ventricle.

Videoclip 19.9). This condition is most often seen due to defects in the elastin gene [49]. Marked thickening of the aortic media at the sinotubular junction produces the narrowing. The sinuses of Valsalva might be enlarged below the level of stenosis (Fig. 19.19), and tethering of the aortic valve leaflets and stenosis of the coronary ostia are frequent associations [50]. In addition to narrowing at the level of the sinotubular junction there may be varying degrees of hypoplasia of the ascending aorta, aortic arch and stenoses of head and neck vessels [51]. The extent of stenoses affecting other vessels or hypoplasia of the aortic arch may be assessed by magnetic resonance imaging (MRI; Fig. 19.20)) as well as echocardiography.

## Pathophysiology

Supravalvar aortic stenosis is extremely rare during fetal and early postnatal life but can become progressively more severe with age. It leads to increased afterload on the left ventricle and is associated with left ventricular hypertrophy when outflow tract obstruction is significant. In addition to the narrowing at the level of the sinotubular junction, the anomaly can involve the aortic valve with tethering and restricted leaflet motion. This can contribute further to the increased afterload on the left ventricle. Coronary ostial stenoses can occur in association with supravalvar aortic stenosis, which can lead to a precarious balance of coronary supply to the myocardium in the face of increased myocardial oxygen demand. Hypoplasia of the aortic arch and stenoses of the head and neck vessels can further increase the afterload on the left ventricle [50,51]. The abnormal composition of the vessel wall leads to increased medial hypertrophy and reduced elasticity of the vessel wall, which places further load on the left ventricle.

## Imaging

The aims of echocardiography in the assessment of supravalvar aortic stenosis include:

- Delineation of the aortic root, sinotubular junction and aortic valve morphology.
- Doppler evaluation of the severity of obstruction to blood flow.
- Assessment of the anatomy of the aortic arch and evaluation of flow around the aortic arch by Doppler.
- Visualization of the head and neck vessels to identify stenosis.
- Measurements of left ventricular size and function.

The imaging planes used to assess severity of obstruction are similar to those for aortic valve stenosis; imaging from the suprasternal notch is particularly helpful. Although obtaining good acoustic windows to evaluate the ascending aorta can be difficult, positioning the patient in a left or a right lateral decubitus can be helpful. Long-axis views of the left ventricle can be adapted to include the affected area at the sinotubular junction (Figs 19.18 and 19.19). Careful assessment of the aortic arch and head and neck vessels is essential because there may be generalized hypoplasia of the arch, coarctation of the aorta, and stenoses of the head and neck vessels, particularly at their origin from the aortic arch. If supravalvar aortic stenosis is considered severe enough to merit surgery, MRI is desirable to supplement echocardiography (Fig. 19.20). During surgery, transesophageal echocardiography or epicardial imaging is useful to confirm relief of obstruction and to image the aortic valve.

Follow-up echocardiography is important for any patient with supravalvar aortic stenosis. This is performed to evaluate progression of the severity of stenosis both before and after surgery. In some patients, the entire aortic arch is hypoplastic, and relief of supravalvar aortic stenosis at the

level of the sinotubular junction simply exposes pressure drops elsewhere in the aorta. The degree of aortic regurgitation should also be assessed because the aortic valve leaflets are frequently tethered at the level of the sinotubular junction and surgery occasionally results in worsening of the degree of aortic valve regurgitation.

## Bicuspid (bicommissural) aortic valve

### Morphology

In around 0.8–1.0% of individuals the aortic valve is made up of two rather than three cusps [1,52]. This is due to underdevelopment of one of the three commissures that define the aortic valve leaflets. The commissure can be absent, resulting in a truly bicuspid valve, or it may exhibit varying degrees of underdevelopment, a circumstance that has been described as "functionally bicuspid (or bicommissural) valve." It is worth noting that even when the commissure is absent, a raphe is typically present, marking the location of the commissure. One of the fused cusps is frequently hypoplastic. Although some bicuspid aortic valves may exhibit stenosis or, less frequently, regurgitation during infancy and childhood, many others function normally for decades. There is, however, an increased likelihood of degeneration with acquired stenosis later in life. Bicuspid aortic valve is more common in males (approximately 70%) and follows a genetic predisposition [7].

Dilation of the ascending aorta has been increasingly recognized as an accompaniment, which has been linked to structural abnormalities of the aortic wall similar to that seen in cystic medial necrosis associated with Marfan syndrome and other connective tissue disorders. This dilation has been linked to an increased risk of aortic dissection later in life [40,53,54]. Importantly, the sites of aortic dilation in bicuspid aortic valve and Marfan syndrome are different. The mid-ascending aorta is the site most involved in bicuspid aortic valve, whereas the sinuses of Valsalva (i.e., aortic root) are most commonly involved in Marfan syndrome. Recent data have confirmed a progressive increase in the aortic z-score of children followed sequentially because of a bicuspid aortic valve [55–57].

The morphology of the bicuspid aortic valve has clinical and prognostic implications. In ~60–70% of patients the intercoronary commissure is underdeveloped, leading to fusion of the left and right coronary cusps. In ~28–37% of patients the right noncoronary commissure is underdeveloped, leading to fusion of the right and noncoronary cusps. The left noncoronary commissure is underdeveloped in only 2–4% of cases with fusion of the left and noncoronary cusps [58,59]. Compared with other morphologies of the bicuspid aortic valve, underdevelopment of the intercoronary commissure is more often associated with coarctation of the aorta and other congenital heart disease, whereas underdevelopment of the right noncoronary commissure is more often associated with aortic valve dysfunction (stenosis and regurgitation) and with more severe dilation of the ascending aorta [58,60]. Associated congenital cardiac anomalies include, among others, coarctation of the aorta, interrupted aortic arch, hypoplastic left heart syndrome, atrioventricular canal defect, Ebstein anomaly, partially and totally anomalous pulmonary venous connection, tetralogy of Fallot, double-outlet right ventricle, and transposition of the great arteries.

### Imaging

Bicuspid aortic valves should be evaluated in a manner analogous to that used for aortic valve stenosis (Fig. 19.7 and Videoclip 19.4). In childhood there may be no evidence of obstruction at the valvar level, but bicuspid valves have a high likelihood of developing stenosis during adulthood. In some patients, the bicuspid valve exhibits mostly regurgitation. Thus, surveillance of aortic valve function is indicated in patients with bicuspid aortic valve. The evaluation should include measurements of the ascending aorta and root due to the risk of progressive aortic dilation. Quantitative measurements of left ventricular size and function are essential in patients with abnormal aortic valve function. Because the aortic valve is bicuspid in ~30% of children with coarctation of the aorta, the finding of a bicuspid valve should prompt a detailed assessment of the aortic arch. In young children, short-axis views by a transthoracic approach are adequate to image the aortic valve, but in older children and adults transesophageal echocardiography may be required to obtain adequate image quality, particularly if surgery is being considered.

## Aortic cusp prolapse

### Morphology

Aortic cusp prolapse occurs when one of the leaflets, usually the right coronary cusp, prolapses into a ventricular septal defect, which may be either a membranous or doubly committed subarterial (conal septal) defect [61,62]. Such prolapse of an aortic valve leaflet often leads to partial or complete occlusion of the ventricular septal defect and is associated with aortic regurgitation in most cases. The mechanism of prolapse is thought to be related to the flow dynamics across a restrictive ventricular septal defect. The high-velocity jet across the ventricular septum leads to a low-pressure area (known as the Venturi effect), which has the effect of drawing the coronary cusp into the ventricular septal defect [63]. The site of aortic regurgitation may be central or through a commissure between the aortic cusps, most commonly between the right and noncoronary cusps. If aortic regurgitation is moderate or worse, surgical intervention to restore aortic valve function is indicated. In cases with mild or no aortic regurgitation, serial echocardiography

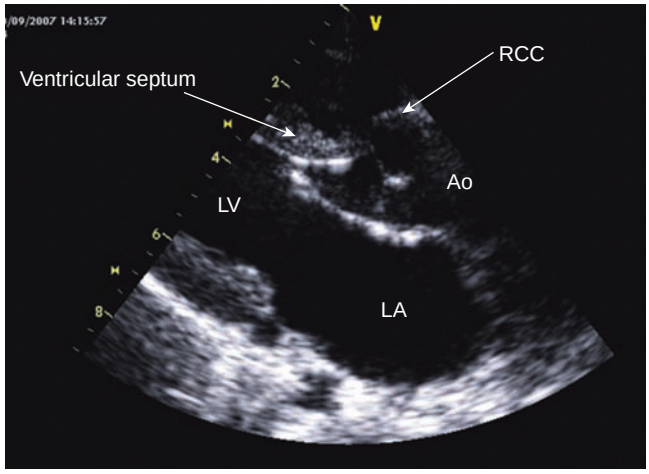


(a)

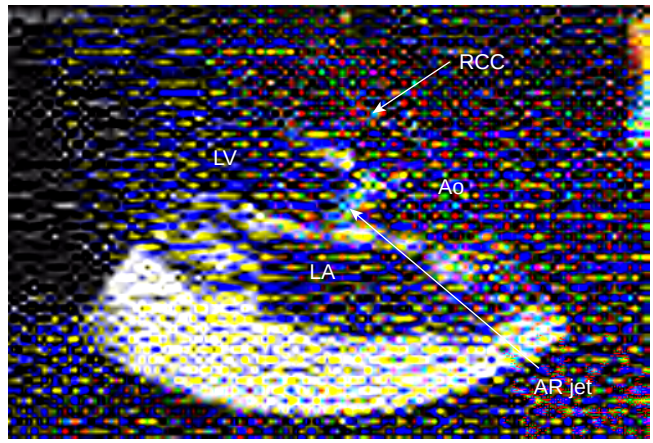


(b)

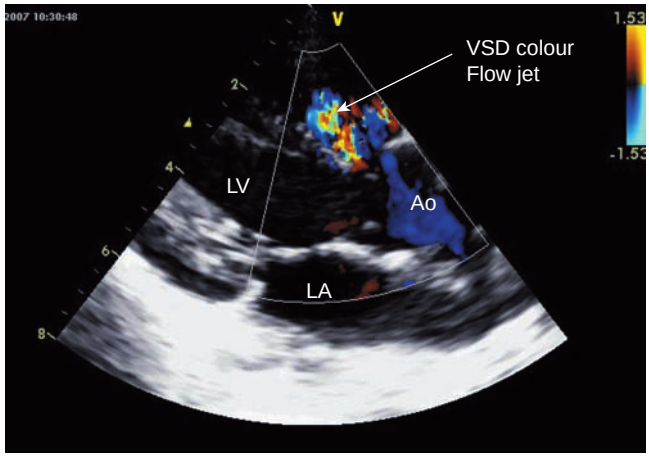


(c)

**Figure 19.21** Aortic cusp prolapse. **(a)** Parasternal long-axis view demonstrating prolapse of the right coronary cusp into a perimembranous ventricular septal defect (VSD). Note that the "belly" of the right coronary cusp is abnormally aligned to the crest of the ventricular septum. **(b)** The eccentric jet of aortic valve regurgitation is clearly seen, directed toward the anterior leaflet of the mitral valve. **(c)** The color flow jet of the restrictive perimembranous VSD can be readily visualized just below the right coronary cusp. Ao, aorta; AR, aortic regurgitation; LA, left atrium; LV, left ventricle; RCC, right coronary cusp.

is indicated to monitor for worsening aortic regurgitation [64–66]. Detailed visualization of the aortic valve is mandatory prior to surgical repair, with transesophageal echocardiography being the technique of choice [67].

### Imaging

Parasternal long-axis views show the prolapse of the cusp and the aortic regurgitant jet (Fig. 19.21a–c; Videoclip 19.10). The ventricular septum is aligned to the "belly" of the aortic valve leaflet rather than to the anterior wall of the aortic root. Short-axis views of the aortic valve demonstrate the location of any residual ventricular septal defect and the site of aortic regurgitation.

Transesophageal echocardiography is the technique of choice to document the anatomy when transthoracic imaging is insufficient. Surgical repair involves suspension of the affected aortic valve cusp and closure of the ventricular septal defect. Intraoperative transesophageal echocardiography is extremely helpful in monitoring the effectiveness of the repair and documenting aortic regurgitation, which may persist postoperatively. Follow-up echocardiography is mandatory, mainly to check for progression of aortic regurgitation following surgery. In some patients with aortic cusp prolapse, a conservative approach may be adopted if aortic regurgitation is absent or mild, without evidence of progression over sequential echocardiographic assessments.

## Sinus of Valsalva aneurysm

### Morphology

The aortic sinus of Valsalva is defined as the part of the aortic root that is delineated proximally by the attachments of the aortic valve leaflet and distally by the sinotubular ridge [68]. Aneurysms of the sinus of Valsalva may occur in isolation or in association with other cardiac lesions such as a ventricular septal defect, subaortic stenosis, tetralogy of Fallot or aortic valve abnormalities [69]. The aneurysm may originate from any one of the sinuses and the site of rupture may vary. Figure 19.22 shows a case where the aneurysm originated from the noncoronary sinus and ruptured to the right atrium (Videoclip 19.11). Most cases affect the right coronary sinus, with the most frequent site of rupture being the right ventricle (Fig. 19.23) [70]. Although such aneurysms may occur

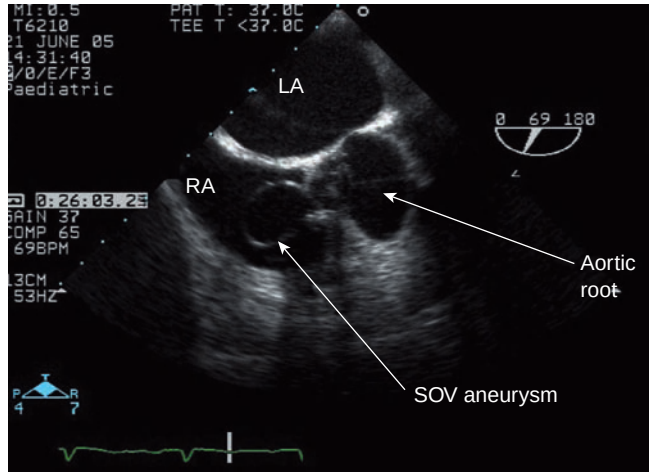


(a)

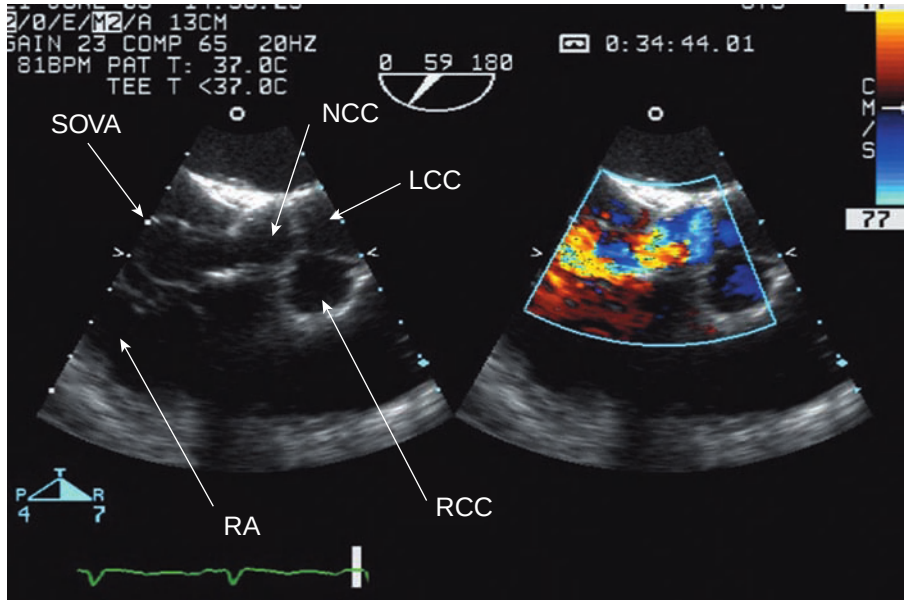


(b)

**Figure 19.22** Sinus of Valsalva aneurysm from noncoronary sinus to right atrium. **(a)** Transesophageal echocardiogram demonstrating the classic "windsock" appearance of a sinus of Valsalva aneurysm originating from the noncoronary cusp and entering the right atrium. **(b)** This dual projection image clearly shows the aneurysm of the sinus of Valsalva originating from the noncoronary sinus. The aneurysm has ruptured into the right atrium. LA, left atrium; LCC, left coronary cusp of the aortic valve; NCC, noncoronary cusp; RA, right atrium; RCC, right coronary cusp; SOVA, sinus of Valsalva aneurysm.

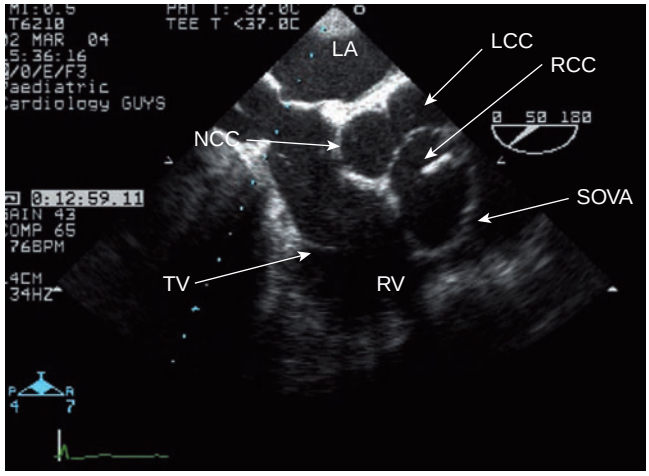


in the context of congenital heart disease, they may also occur in other conditions that weaken the wall of the aortic root, such as Marfan syndrome, syphilis, Behçet disease, endocarditis, and trauma [69]. Presentation is most commonly with shortness of breath during exercise, but chest pain, congestive cardiac failure, syncope, and an asymptomatic cardiac murmur are all recognized modes of presentation [69,70].

An aneurysm of the sinus of Valsalva may lead to aortic valve regurgitation, causing volume loading of the left ventricle. This may be asymptomatic while left ventricular

**Figure 19.23** (*left*) Sinus of Valsalva aneurysm from right coronary sinus to right ventricular outflow tract. There is a "windsock" of the sinus of Valsalva aneurysm extending into the right ventricular outflow tract. This is the most common site of origin and rupture of such aneurysms. LA, left atrium; LCC, left coronary cusp; NCC, noncoronary cusp; RCC, right coronary cusp; RV, right ventricle; SOVA, sinus of Valsalva aneurysm; TV, tricuspid valve.

function is maintained, but with increased volume loading symptoms such as exercise limitation and dyspnea may become more prominent. As mentioned above, the most frequent site of rupture of a sinus of Valsalva is from the right coronary cusp to the right ventricle [70]. This leads to a combination of regurgitation through the sinus and a left-to-right shunt as the blood flows from the systemic arterial circulation to the right ventricle and hence to the pulmonary circulation. In this clinical situation, symptoms of congestive cardiac failure are more pronounced, and urgent repair is indicated.

### Imaging

Sinus of Valsalva aneurysm occurs mainly in older children and adults. The aims of the echocardiographic study are to determine which sinus of Valsalva and aortic valve leaflet are affected and, if ruptured, to determine the site of rupture. The most common site of rupture is from the right coronary cusp to the right ventricle, followed in incidence by rupture of the right coronary cusp to the right atrium. The noncoronary cusp occasionally ruptures, but involvement of the left coronary cusp is rare. Associated findings include aortic valve regurgitation in almost half of patients, and around one-third of patients have an associated ventricular septal defect. Other associated anomalies include Marfan-like habitus, bicuspid aortic valve, coarctation of the aorta, tetralogy of Fallot, mitral valve regurgitation, tricuspid valve regurgitation, Ebstein anomaly, and atrial septal defect [70,71].

In patients with suboptimal transthoracic acoustic windows, transesophageal echocardiography provides excellent imaging of the aortic root to define the anatomy of the affected sinus of Valsalva and to determine where the ruptured sinus is draining. In a minority of cases, other techniques such as cardiac catheterization may be necessary to delineate the aneurysm, but MRI is proving increasingly helpful [71]. Intraoperative transesophageal echocardiography is helpful to confirm adequacy of surgical repair or to guide selected catheter intervention for device closure in selected cases [72].

## Aortico–left ventricular tunnel

### Morphology

Aortico–left ventricular tunnel is a rare congenital lesion characterized by an abnormal communication between the ascending aorta, at or above the level of the sinotubular junction, and the left ventricle [73]. The aortic origin of the tunnel is usually located above the right coronary ostium. The tunnel then passes in the tissue plane between the aorta and the posterior aspect of the subpulmonary infundibulum. The ventricular end of the tunnel occupies the same area as the fibrous triangle between the right and noncoronary leaflets of the aortic valve [74,75]. An aortico–left ventricular tunnel permits systemic arterial blood from the ascending aorta to regurgitate back into the left ventricle via the tunnel

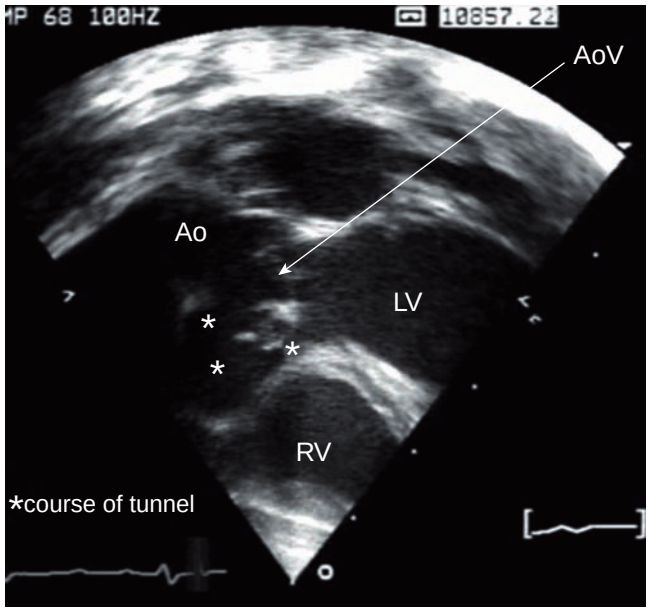


(a)

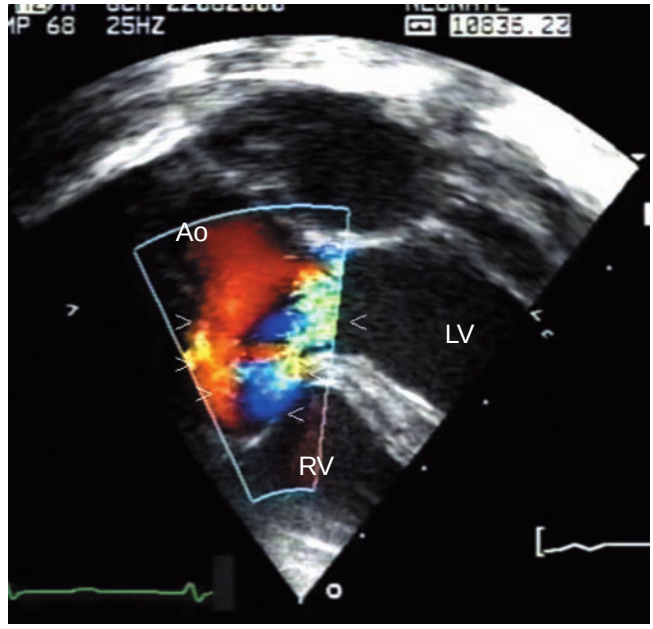


(b)

**Figure 19.24** Aortico–left ventricular tunnel. **(a)** Foreshortened apical view of an aortico–left ventricular tunnel in an infant in whom the lesion was identified prenatally. The course of the tunnel is shown by the asterisks. **(b)** Color flow Doppler mapping demonstrates the course of the tunnel and the free regurgitation of blood from the ascending aorta to the left ventricle. The asterisks (*) mark the course of the tunnel on the cross-sectional image. The arrowheads (< and >) mark the color flow jet through the tunnel. Ao, aorta; AoV, aortic valve; LV, left ventricle; RV, right ventricle.

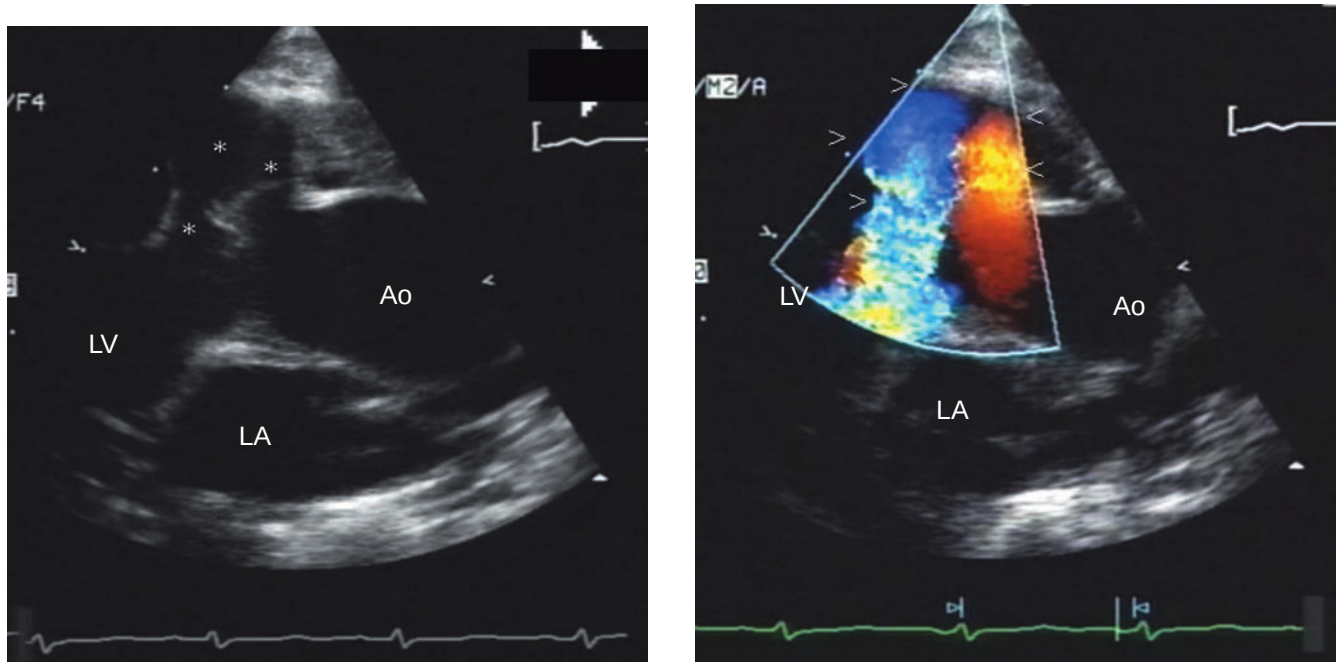


(a) (b)

**Figure 19.25** Aortico–left ventricular tunnel, long-axis views from the same infant as depicted in Fig. 19.24. **(a)** The tunnel can be seen to take a tortuous route from the aorta to the left ventricle. **(b)** Color flow Doppler mapping of the aortico–left ventricular tunnel with a broad jet passing from the aorta into the left ventricle; this has a hemodynamic effect analogous to that of severe aortic valve regurgitation. The asterisks (*) mark the course of the tunnel on the cross-sectional image. The arrowheads (< and >) mark the color flow jet through the tunnel. Ao, aorta; LV, left ventricle; RV, right ventricle.

(Figs 19.24 and 19.25). This has an identical physiologic effect to that of severe aortic valve regurgitation with volume loading and potential dysfunction of the left ventricle. Aortico–ventricular tunnels are thought to represent a developmental abnormality, having been described during fetal life [76,77]. The outcome for cases diagnosed early in fetal and neonatal life is guarded because of the effects on left ventricular function, but successful surgery has been reported [78].

### Imaging

The aims of echocardiographic evaluation of aortico–left ventricular tunnel are to delineate the anatomy of the tunnel and to assess the effect of severe volume loading on the left ventricle in terms of its size and contractile function. The aortic origin, the course, and the left ventricular exit site of the tunnel can be imaged from the parasternal window through a combination of long- and short-axis views. Color Doppler flow mapping is particularly helpful to delineate the tunnel, which is characterized by antegrade flow from the left ventricle to the ascending aorta during systole and retrograde flow through the tunnel during diastole. Spectral Doppler is helpful to determine the direction and timing of the to-and-fro flow through the tunnel [79]. In contrast to aortic regurgitation, the flow from the ascending aorta to the left ventricle during diastole does not cross the aortic valve. A fistula between the right coronary artery and the left ventricle is excluded based on imaging of an uninvolved proximal right coronary artery.

## False tendons

False tendons are occasionally observed within the cavity of the left ventricle and may run transversely or obliquely from the interventricular septum to the free wall (Fig. 19.26a,b). These relatively thin muscle bundles have been implicated in the causation of the innocent vibratory murmur prevalent during childhood, although recent data suggest that they are no more prevalent in children with murmurs than in a control group without murmurs [80]. Pathologic examination has confirmed that such "tendons" may involve the conduction system [81]. The possibility of a link to ventricular extrasystoles [82] and an association with ventricular tachycardia in a subgroup of patients has been reported [83,84].

## Acknowledgement

I would like to acknowledge the contribution of Ms Alexandra Savis (Chief Cardiac Physiologist) to the review and preparation of echocardiographic images used in this chapter.

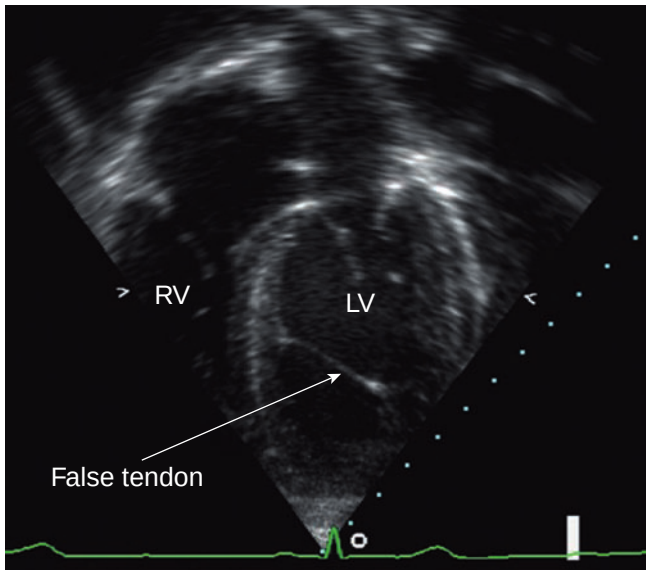


(a)

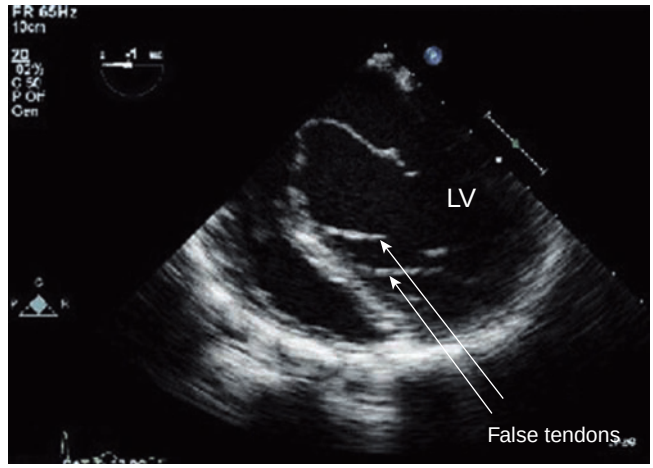


(b)

**Figure 19.26** **(a)** False tendon in the left ventricle of an asymptomatic child. **(b)** Transesophageal echocardiogram of a child with two false tendons. This child had a ventricular septal defect and aortic regurgitation, which prompted the examination. LV, left ventricle; RV, right ventricle.

## References


1. Hoffman JI, Kaplan S. The incidence of congenital heart disease. *J Am Coll Cardiol* 2002;39:1890–900.
2. Kitchiner D, Jackson M, Malaiya N et al. Incidence and prognosis of obstruction of the left ventricular outflow tract in Liverpool (1960–91): a study of 313 patients. *Br Heart J* 1994;71:588–95.
3. Gill HK, Splitt M, Sharland GK, Simpson JM. Patterns of recurrence of congenital heart disease: an analysis of 6,640 consecutive pregnancies evaluated by detailed fetal echocardiography. *J Am Coll Cardiol* 2003;42:923–9.
4. McBride KL, Pignatelli R, Lewin M et al. Inheritance analysis of congenital left ventricular outflow tract obstruction malformations: Segregation, multiplex relative risk, and heritability. *Am J Med Genet A* 2005;134:180–6.
5. Allan LD, Sharland GK, Milburn A et al. Prospective diagnosis of 1006 consecutive cases of congenital heart disease in the fetus. *J Am Coll Cardiol* 1994;23:1452–8.
6. Garg V. Molecular genetics of aortic valve disease. *Curr Opin Cardiol* 2006;21:180–4.
7. Cripe L, Andelfinger G, Martin LJ et al. Bicuspid aortic valve is heritable. *J Am Coll Cardiol* 2004;44:138–43.
8. Morris CA, Mervis CB. Williams syndrome and related disorders. *Annu Rev Genomics Hum Genet* 2000;1:461–84.
9. Park S, Seo EJ, Yoo HW, Kim Y. Novel mutations in the human elastin gene (ELN) causing isolated supravalvular aortic stenosis. *Int J Mol Med* 2006;18:329–32.
10. Richardson ME, Menahem S, Wilkinson JL. Familial fixed subaortic stenosis. *Int J Cardiol* 1991;30:351–3.
11. Cape EG, Vanauker MD, Sigfusson G et al. Potential role of mechanical stress in the etiology of pediatric heart disease: septal shear stress in subaortic stenosis. *J Am Coll Cardiol* 1997;30:247–54.
12. Sigfusson G, Tacy TA, Vanauker MD, Cape EG. Abnormalities of the left ventricular outflow tract associated with discrete subaortic stenosis in children: an echocardiographic study. *J Am Coll Cardiol* 1997;30:255–9.
13. Oztunc F, Ozme S, Ozkutlu S et al. Fixed subaortic stenosis in childhood. Medical and surgical course in 90 patients. *Jpn Heart J* 1992;33:327–35.
14. Reeder GS, Danielson GK, Seward JB et al. Fixed subaortic stenosis in atrioventricular canal defect: a Doppler echocardiographic study. *J Am Coll Cardiol* 1992;20:386–94.
15. Silverman NH, Gerlis LM, Ho SY, Anderson RH. Fibrous obstruction within the left ventricular outflow tract associated with ventricular septal defect: a pathologic study. *J Am Coll Cardiol.* 1995;25:475–81.
16. Marasini M, Zannini L, Ussia GP et al. Discrete subaortic stenosis: incidence, morphology and surgical impact of associated subaortic anomalies. *Ann Thorac Surg* 2003;75:1763–8.
17. Kleinert S, Ott DA, Geva T. Critical discrete subaortic stenosis in the newborn period. *Am Heart J* 1993;125:1187–9.
18. Kleinert S, Geva T. Echocardiographic morphometry and geometry of the left ventricular outflow tract in fixed subaortic stenosis. *J Am Coll Cardiol* 1993;22:1501–8.
19. van Son JA, Schaff HV, Danielson GK et al. Surgical treatment of discrete and tunnel subaortic stenosis. Late survival and risk of reoperation. *Circulation* 1993;88:II159–69.
20. Coleman DM, Smallhorn JF, McCrindle BW et al. Postoperative follow-up of fibromuscular subaortic stenosis. *J Am Coll Cardiol* 1994;24:1558–64.
21. Gersony WM. Natural history of discrete subvalvar aortic stenosis: management implications. *J Am Coll Cardiol* 2001;38:843–5.
22. Geva A, McMahon CJ, Gauvreau K et al. Risk factors for reoperation after repair of discrete subaortic stenosis in children. *J Am Coll Cardiol* 2007;50:1498–504.

23. Serraf A, Zoghby J, Lacour-Gayet F et al. Surgical treatment of subaortic stenosis: a seventeen-year experience. *J Thorac Cardiovasc Surg* 1999;117:669–78.
24. Caldarone CA. Left ventricular outflow tract obstruction: the role of the modified Konno procedure. *Semin Thorac Cardiovasc Surg Pediatr Card Surg Annu* 2003;6:98–107.
25. Choi JY, Sullivan ID. Fixed subaortic stenosis: anatomical spectrum and nature of progression. *Br Heart J* 1991;65:280–6.
26. Barkhordarian R, Wen-Hong D, Li W et al. Geometry of the left ventricular outflow tract in fixed subaortic stenosis and intact ventricular septum: an echocardiographic study in children and adults. *J Thorac Cardiovasc Surg* 2007;133:196–203.
27. McMahon CJ, Gauvreau K, Edwards JC, Geva T. Risk factors for aortic valve dysfunction in children with discrete subvalvar aortic stenosis. *Am J Cardiol* 2004;94:459–64.
28. Oliver JM, Gonzalez A, Gallego P et al. Discrete subaortic stenosis in adults: increased prevalence and slow rate of progression of the obstruction and aortic regurgitation. *J Am Coll Cardiol* 2001;38:835–42.
29. Bezold LI, Smith EO, Kelly K et al. Development and validation of an echocardiographic model for predicting progression of discrete subaortic stenosis in children. *Am J Cardiol* 1998;81: 314–20.
30. Gaynor JW, Elliott MJ. Congenital left ventricular outflow tract obstruction. *J Heart Valve Dis* 1993;2:80–93.
31. Jahangiri M, Nicholson IA, del Nido PJ et al. Surgical management of complex and tunnel-like subaortic stenosis. *Eur J Cardiothorac Surg* 2000;17:637–42.
32. Wilson WR, Greer GE, Durzinsky DS, Curtis JJ. Ross procedure for complex left ventricular outflow tract obstruction. *J Cardiovasc Surg (Torino)* 2000;41:387–92.
33. Belli E, Serraf A, Lacour-Gayet F et al. Biventricular repair for double-outlet right ventricle. Results and long-term follow-up. *Circulation* 1998;98:II360–5; discussion II5–7.
34. Anderson RH. Morphology of critically stenotic aortic valves. *J Thorac Cardiovasc Surg* 1995;110:565.
35. Simpson JM, Sharland GK. Natural history and outcome of aortic stenosis diagnosed prenatally. *Heart* 1997;77:205–10.
36. McCaffrey FM, Sherman FS. Prenatal diagnosis of severe aortic stenosis. *Pediatr Cardiol* 1997;18:276–81.
37. Makikallio K, McElhinney DB, Levine JC et al. Fetal aortic valve stenosis and the evolution of hypoplastic left heart syndrome: patient selection for fetal intervention. *Circulation* 2006;113: 1401–5.
38. Marshall AC, Tworetzky W, Bergersen L et al. Aortic valvuloplasty in the fetus: technical characteristics of successful balloon dilation. *J Pediatr* 2005;147:535–9.
39. Tworetzky W, Wilkins-Haug L, Jennings RW et al. Balloon dilation of severe aortic stenosis in the fetus: potential for prevention of hypoplastic left heart syndrome: candidate selection, technique, and results of successful intervention. *Circulation* 2004;110:2125–31.
40. Ward C. Clinical significance of the bicuspid aortic valve. *Heart* 2000;83:81–5.
41. Grayburn PA, Smith MD, Harrison MR et al. Pivotal role of aortic valve area calculation by the continuity equation for Doppler assessment of aortic stenosis in patients with combined aortic stenosis and regurgitation. *Am J Cardiol* 1988;61:376–81.
42. Zoghbi WA, Farmer KL, Soto JG et al. Accurate noninvasive quantification of stenotic aortic valve area by Doppler echocardiography. *Circulation* 1986;73:452–9.
43. Hakki AH, Iskandrian AS, Bemis CE et al. A simplified valve formula for the calculation of stenotic cardiac valve areas. *Circulation* 1981;63:1050–5.
44. Gorlin R, Gorlin SG. Hydraulic formula for calculation of the area of the stenotic mitral valve, other cardiac valves, and central circulatory shunts. I. *Am Heart J* 1951;41:1–29.
45. Chambers J. Low "gradient", low flow aortic stenosis. *Heart* 2006;92:554–8.
46. Rhodes LA, Colan SD, Perry SB et al. Predictors of survival in neonates with critical aortic stenosis. *Circulation* 1991;84:2325–35.
47. Colan SD, McElhinney DB, Crawford EC et al. Validation and re-evaluation of a discriminant model predicting anatomic suitability for biventricular repair in neonates with aortic stenosis. *J Am Coll Cardiol* 2006;47:1858–65.
48. Kovalchin JP, Brook MM, Rosenthal GL et al. Echocardiographic hemodynamic and morphometric predictors of survival after two-ventricle repair in infants with critical aortic stenosis. *J Am Coll Cardiol* 1998;32:237–44.
49. Smoot LB. Elastin gene deletions in Williams syndrome. *Curr Opin Pediatr* 1995;7:698–701.
50. Stamm C, Li J, Ho SY et al. The aortic root in supravalvular aortic stenosis: the potential surgical relevance of morphologic findings. *J Thorac Cardiovasc Surg* 1997;114:16–24.
51. Stamm C, Friehs I, Ho SY et al. Congenital supravalvar aortic stenosis: a simple lesion? *Eur J Cardiothorac Surg* 2001;19: 195–202.
52. Nistri S, Basso C, Marzari C et al. Frequency of bicuspid aortic valve in young male conscripts by echocardiogram. *Am J Cardiol* 2005;96:718–21.
53. Davies RR, Kaple RK, Mandapati D et al. Natural history of ascending aortic aneurysms in the setting of an unreplaced bicuspid aortic valve. *Ann Thorac Surg* 2007;83:1338–44.
54. Yap SC, Takkenberg JJ, Witsenburg M et al. Aortic stenosis at young adult age. *Expert Rev Cardiovasc Ther* 2005;3:1087–98.
55. Warren AE, Boyd ML, O'Connell C, Dodds L. Dilatation of the ascending aorta in paediatric patients with bicuspid aortic valve: frequency, rate of progression and risk factors. *Heart* 2006; 92:1496–500.
56. Holmes KW, Lehmann CU, Dalal D et al. Progressive dilation of the ascending aorta in children with isolated bicuspid aortic valve. *Am J Cardiol* 2007;99:978–83.
57. Beroukhim RS, Kruzick TL, Taylor AL et al. Progression of aortic dilation in children with a functionally normal bicuspid aortic valve. *Am J Cardiol* 2006;98:828–30.
58. Ciotti GR, Vlahos AP, Silverman NH. Morphology and function of the bicuspid aortic valve with and without coarctation of the aorta in the young. *Am J Cardiol* 2006;98:1096–102.
59. Fernandes SM, Sanders SP, Khairy P et al. Morphology of bicuspid aortic valve in children and adolescents. *J Am Coll Cardiol* 2004;44:1648–51.
60. Fernandes SM, Khairy P, Sanders SP, Colan SD. Bicuspid aortic valve morphology and interventions in the young. *J Am Coll Cardiol* 2007;49:2211–4.
61. Craig BG, Smallhorn JF, Burrows P et al. Cross-sectional echocardiography in the evaluation of aortic valve prolapse

associated with ventricular septal defect. *Am Heart J* 1986;112:800–7.
62. Menahem S, Johns JA, del Torso S et al. Evaluation of aortic valve prolapse in ventricular septal defect. *Br Heart J* 1986; 56:242–9.
63. Tweddell JS, Pelech AN, Frommelt PC. Ventricular septal defect and aortic valve regurgitation: pathophysiology and indications for surgery. *Semin Thorac Cardiovasc Surg Pediatr Card Surg Annu* 2006:147–52.
64. Tomita H, Fuse S, Chiba S. Is early surgery always necessary in patients with aortic valve prolapse complicating an Eisenmenger-type ventricular septal defect? *Acta Paediatr Jpn* 1998;40:232–5.
65. Tomita H, Yamada O, Kurosaki K et al. Eccentric aortic regurgitation in patients with right coronary cusp prolapse complicating a ventricular septal defect. *Circ J* 2003;67:672–5.
66. Butter A, Duncan W, Weatherdon D et al. Aortic cusp prolapse in ventricular septal defect and its association with aortic regurgitation – appropriate timing of surgical repair and outcomes. *Can J Cardiol* 1998;14:833–40.
67. de Waroux JB, Pouleur AC, Goffinet C et al. Functional anatomy of aortic regurgitation: accuracy, prediction of surgical repairability, and outcome implications of transesophageal echocardiography. *Circulation* 2007;116:I264–9.
68. Sutton JP 3rd, Ho SY, Anderson RH. The forgotten interleaflet triangles: a review of the surgical anatomy of the aortic valve. *Ann Thorac Surg* 1995;59:419–27.
69. Vural KM, Sener E, Tasdemir O, Bayazit K. Approach to sinus of Valsalva aneurysms: a review of 53 cases. *Eur J Cardiothorac Surg* 2001;20:71–6.
70. Moustafa S, Mookadam F, Cooper L et al. Sinus of Valsalva aneurysms – 47 years of a single center experience and systematic overview of published reports. *Am J Cardiol* 2007;99: 1159–64.
71. Feldman DN, Roman MJ. Aneurysms of the sinuses of Valsalva. *Cardiology* 2006;106:73–81.
72. Arora R, Trehan V, Rangasetty UM et al. Transcatheter closure of ruptured sinus of valsalva aneurysm. *J Interv Cardiol* 2004; 17:53–8.
73. Levy MJ, Schachner A, Blieden LC. Aortico-left ventricular tunnel: collective review. *J Thorac Cardiovasc Surg* 1982;84:102–9.
74. Ho SY, Muriago M, Cook AC et al. Surgical anatomy of aorto-left ventricular tunnel. *Ann Thorac Surg* 1998;65:509–14.
75. Cook AC, Fagg NL, Ho SY et al. Echocardiographic-anatomical correlations in aorto-left ventricular tunnel. *Br Heart J* 1995; 74:443–8.
76. Pascoli I, Cester M, Nanhorngue K, Paternoster DM. Aortico-left ventricular tunnel diagnosed prenatally: case report. *Prenat Diagn* 2007;27:1263–5.
77. Kenny D, Chen Q, Uzun O. Antenatal diagnosis of aortico-left ventricular tunnel. *Pediatr Cardiol* 2007;28:241–2.
78. Kolcz J, Januszewska K, Malec E. Successful repair of aorto-left ventricular tunnel diagnosed prenatally. *Cardiol Young* 2005; 15:219–22.
79. Humes RA, Hagler DJ, Julsrud PR et al. Aortico-left ventricular tunnel: diagnosis based on two-dimensional echocardiography, color flow Doppler imaging, and magnetic resonance imaging. *Mayo Clin Proc* 1986;61:901–7.
80. Van Oort A, Hopman J, De Boo T et al. The vibratory innocent heart murmur in schoolchildren: a case-control Doppler echocardiographic study. *Pediatr Cardiol* 1994;15:275–81.
81. Abdulla AK, Frustaci A, Martinez JE et al. Echocardiography and pathology of left ventricular "false tendons". *Chest* 1990; 98:129–32.
82. Suwa M, Hirota Y, Kaku K et al. Prevalence of the coexistence of left ventricular false tendons and premature ventricular complexes in apparently healthy subjects: a prospective study in the general population. *J Am Coll Cardiol* 1988;12:910–4.
83. Thakur RK, Klein GJ, Sivaram CA et al. Anatomic substrate for idiopathic left ventricular tachycardia. *Circulation* 1996;93: 497–501.
84. Suwa M, Yoneda Y, Nagao H et al. Surgical correction of idiopathic paroxysmal ventricular tachycardia possibly related to left ventricular false tendon. *Am J Cardiol* 1989;64:1217–20.

# 20 Hypoplastic Left Heart Syndrome

**David J. Goldberg[1] and Jack Rychik[1,2]**

[1]Pediatric Cardiology, The Children's Hospital of Philadelphia, Philadelphia, PA, USA;
[2]University of Pennsylvania School of Medicine

## Definition

Hypoplastic left heart syndrome (HLHS) describes a collection of heterogeneous congenital heart anomalies in which the left ventricle (LV), by virtue of structural abnormalities, is incapable of providing adequate systemic perfusion. HLHS may include abnormalities such as mitral stenosis or atresia, LV hypoplasia, aortic valve stenosis or atresia, and ascending aortic hypoplasia (Fig. 20.1 and Videoclip 20.1). The syndrome was first reported by Lev in 1952, and the term HLHS was first described by Noonan and Nadas [1,2]. It is one of the most severe forms of congenital anomalies and accounts for 20–25% of all mortality in infants born with congenital heart disease.

## Incidence and associated anomalies

The incidence of HLHS is 266 per 1 million live births, hence approximately 2000 affected infants are born each year in the USA [3]. The prevalence of HLHS in the population ranges from 0.02% to 0.08%, but is currently increasing as the accuracy of diagnosis and successful management strategies are increasing survival.

Autopsy series in patients with HLHS have described a prevalence of extracardiac anomalies or genetic/chromosomal syndromes of up to 28% [4]. In particular, Turner syndrome (XO) has been well described in association with HLHS and should be investigated in every female infant with this form of heart disease [5]. Other syndromes reported in association with HLHS include Smith–Lemli–Opitz, Holt–Oram, and Jacobsen.

Much attention has been focused on the relationship between the central nervous system and HLHS. Congenital brain anomalies that have been identified in association with HLHS include agenesis of the corpus callosum, holoprosencephaly and more subtle findings including abnormal appearance of the cortical mantle on autopsy examination [6]. Magnetic resonance imaging (MRI) of the brain in hemodynamically stable infants with HLHS prior to surgery demonstrates a high frequency of periventricular leukomalacia and an overall immature appearance to the brain [7,8]. The exact relationship between HLHS and these findings is unclear, but they may be a consequence of altered prenatal blood flow patterns inherent in HLHS or they may occur simply as an associated congenital malformation.

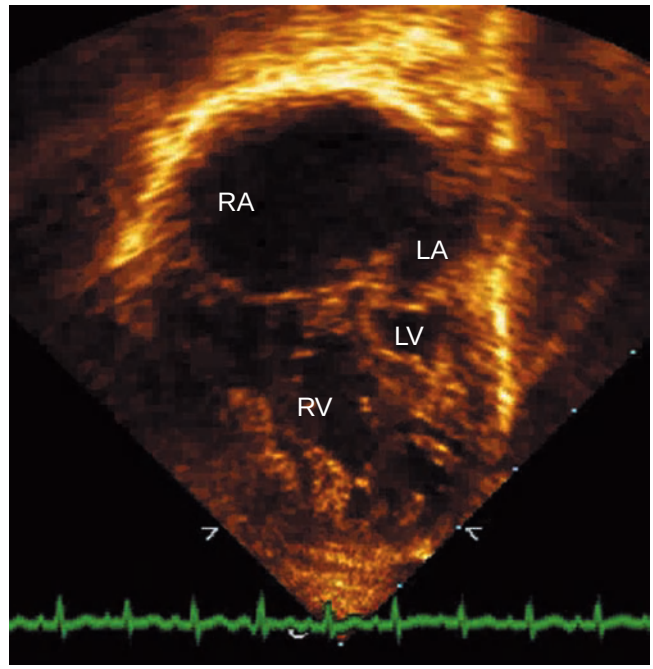


**Figure 20.1** An apical 4-chamber view of hypoplastic left heart syndrome (HLHS). The left-sided structures are small and incapable of contributing to systemic output. LA, left atrium; LV, left ventricle; RA, right atrium; RV, right ventricle.

## Etiology

The precise cause of HLHS is unknown. Because the disease phenotype is heterogeneous, there are probably a variety of

*Echocardiography in Pediatric and Congenital Heart Disease: From Fetus to Adult*
Edited by Wyman W. Lai, Luc L. Mertens, Meryl S. Cohen and Tal Geva
 ISBN: 978-1-405-17401-5

different developmental origins. Altered flow into the developing LV due to mitral or aortic valve stenosis and/or hypoplasia has been implicated as one explanation. Aortic stenosis with an initially dilated LV has been observed during fetal life to evolve into postnatal HLHS, presumably through the process of decreased transventricular blood flow and arrest of LV development [9]. Another hypothesis proposes that abnormalities of the atrial septum limit right-to-left flow early in gestation leading to reduced filling of the LV and resultant hypoplasia. Intrinsic abnormality of LV myocardial development may be another mechanism of HLHS.

Although the disease etiology is likely multifactorial, HLHS is clearly a heritable disorder with a strong genetic influence. Mutations associated with HLHS have been reported in the genes *NKX2-5*, connexin 43 and *NOTCH1* [10–12]. Studies have shown that anywhere from 5 to 19% of first-degree relatives of infants with HLHS have a congenital heart defect, with the dominant lesion being left-sided obstruction (bicuspid aortic valve or coarctation of the aorta) [13,14]. Research efforts are currently focused on family-based linkage analysis in order to identify loci harboring HLHS-causing genes [15].

## Morphology and classification

### Types

Hypoplastic left heart syndrome can be divided into the following major anatomic groups:

**1** mitral and aortic stenosis
**2** mitral stenosis and aortic atresia
**3** mitral and aortic atresia.

Other anatomic variations exist.

## Anatomy

### Systemic veins

In HLHS the right superior vena cava (RSVC) and the inferior vena cava (IVC) return to the right atrium normally. A review of pathology specimens with HLHS found that 5% had a left superior vena cava (LSVC) [16]. In the initial surgical management of HLHS, the presence of a LSVC can alter the technique of placement on cardiopulmonary bypass. In the second stage of palliation, the presence of a LSVC without a left innominate vein requires anastomosis of the LSVC to the left pulmonary artery. In the presence of a bridging left innominate vein, the LSVC may be ligated.

### Right atrium

The right atrium is generally unaffected in HLHS, although it may be dilated to accommodate both systemic and pulmonary blood flows.

### Left atrium

In patients with HLHS the left atrium is often small. However, if there is any restriction to flow across the atrial septum, the left atrium may become hypertensive and distended. Often, the finger-like left atrial appendage is easily visualized because of this distention.

### Atrial septum

Abnormalities of the atrial septum are common in HLHS and may include primum and secundum atrial septal defects or abnormal position and attachment of septum primum to the atrial wall [17,18] (Fig. 20.2 and Videoclip 20.2). However, it is those patients with an intact atrial septum (6% of all cases between 1990 and 1997 at our institution) who are at greatest risk of a poor outcome [19]. In a cohort review of 38 patients with a very restrictive or intact atrial septum,

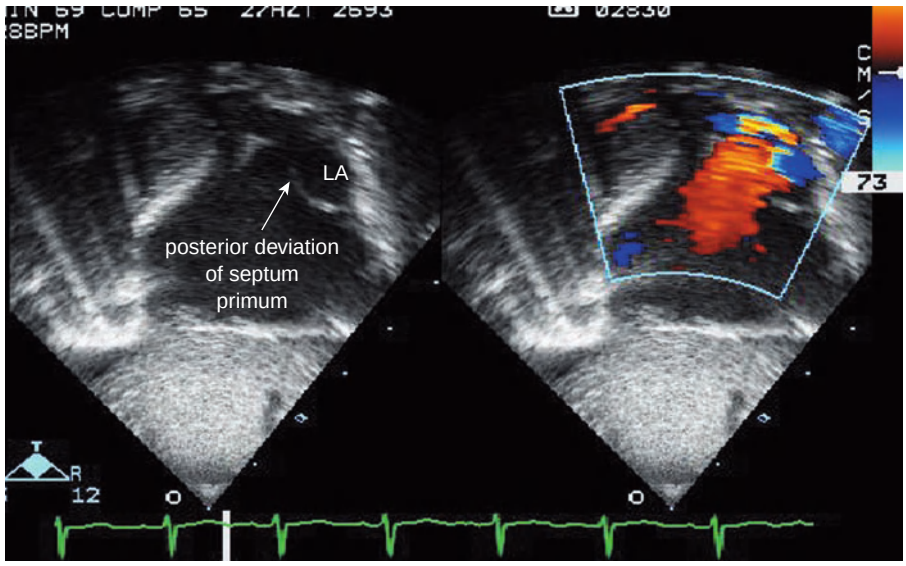


**Figure 20.2** Subcostal view demonstrating posterior deviation of septum primum (arrow). LA, left atrium.

there was only a 68% 30-day survival [19]. Survival decreased to 38% in those with a completely intact atrial septum and inadequate decompression [20], well below the survival numbers for HLHS as a whole.

### Pulmonary veins

The entry of the pulmonary veins into the left atrium is an important part of the overall characterization of HLHS and important for the purpose of surgical planning. Even when the veins seem to enter the left atrium normally, care should be taken to distinguish anomalous pulmonary venous *drainage* from anomalous pulmonary venous *connection* [21]. If the pulmonary veins enter the left atrium but there is a decompressing vein, this indicates anomalous drainage in the setting of normal venous connection. The decompressing vein, or "levoatriocardinal vein," is thought to be a remnant of the cardinal venous system that persists in the face of increased left atrial pressure [22,23]. This vein is distinct from a LSVC, which can be seen as a separate structure even in the presence of a decompressing vein [23].

### Mitral valve and left ventricle

The mitral valve in HLHS may be stenotic or atretic. This difference is important for a variety of reasons. First, the presence of a patent mitral valve implies the presence of an associated LV cavity. Such a cavity will be limited in its contribution to systemic perfusion, will contract poorly, may have endocardial fibroelastosis, will exist under high, perhaps suprasystemic pressure, and may adversely influence RV mechanics [24]. Second, investigators have reported on the possibility of an increased risk of mortality in patients falling within the HLHS subcategory of mitral stenosis, aortic atresia, particularly in those patients with left ventricular–coronary connections [25–27].

### Tricuspid valve and right ventricle

Morphologic abnormalities of the tricuspid valve are relatively common in HLHS and may play an important role in short- and long-term survival [28–30]. However, studies have not shown that tricuspid regurgitation (TR) is necessarily a risk factor [30–32]. In patients with HLHS, 7–12% may have a bileaflet tricuspid valve, and 35% may have significant tricuspid valve dysplasia (Fig. 20.3 and Videoclips 20.3 and 20.4) [16,33]. In patients with severely dysplastic and regurgitant tricuspid valves, a primary transplant strategy may be considered as an alternative to a high-risk staged reconstruction [34,35]. It is important to keep in mind that in the unoperated, neonatal state and following initial first-stage palliation there is a volume load on the RV as it supports both systemic and pulmonary blood flows. Such volume load may alter annular dimensions leading to incomplete leaflet coaptation. This, in combination with the anatomic variability of the tricuspid valve in HLHS, may influence the degree of regurgitation. However, when the volume load on the RV is reduced after the superior cavopulmonary anastomosis and Fontan completion operations, TR may improve [36–38].

### Aorta, coronary arteries and ductus arteriosus

In HLHS a patent ductus arteriosus (PDA) is necessary for survival. In the fetus with HLHS, the PDA is the predominant avenue for systemic flow, and the ductal arch consequently develops with a continuous, smooth transition into the descending aorta.

The ascending aorta in HLHS varies in size and is related to the degree of antegrade flow. In cases of aortic atresia, the ascending aorta may be markedly hypoplastic (diameter 1–2 mm) and may serve as a "common coronary artery" carrying blood in a retrograde manner from the PDA to the aortic root and into the left and right coronary arteries (Fig. 20.4; Videoclip 20.5). In cases of aortic stenosis, the ascending aorta may be larger depending on the ratio of antegrade flow from the LV to retrograde flow from the PDA. The transverse aortic arch often exhibits varying degrees of hypoplasia and elongation.

Coarctation of the aorta is common in HLHS [39]. Presumably this is related to flow dynamics as blood leaves the PDA and "branches" retrogradely through the aortic arch and antegradely through the descending aorta. Histologic studies have demonstrated ductal tissue in the juxtaductal area, tissue that may play a role in coarctation [40]. The extreme form of coarctation, interrupted aortic arch, has also been reported in HLHS [41]. In such cases, coronary perfusion and survival depend on sufficient antegrade flow across the aortic valve.

The descending aorta beyond the ductal arch is generally of normal caliber as it carries the normal systemic output to the lower half of the body.

The coronary arteries in HLHS typically have normal ostia, arise normally from the aortic root, and follow a normal course [42]. However, cases of anomalous origin of a coronary artery from the main and the right pulmonary arteries have been reported [43,44]. In the subset of HLHS characterized by mitral stenosis and aortic atresia, patients may be at risk of fistulous connections, with or without stenoses, from the left ventricle to the coronary arteries. These may place them at higher risk for morbidity and mortality than the HLHS population as a whole [27].

## Pathophysiology

Infants with HLHS typically manifest tachypnea and cyanosis at birth. Peripheral pulses may be weak, with cool extremities due to poor perfusion. Chest radiograph will usually reveal a large heart with increased pulmonary vascular markings. Postnatal survival depends upon patency of the PDA, which supplies the systemic circulation.

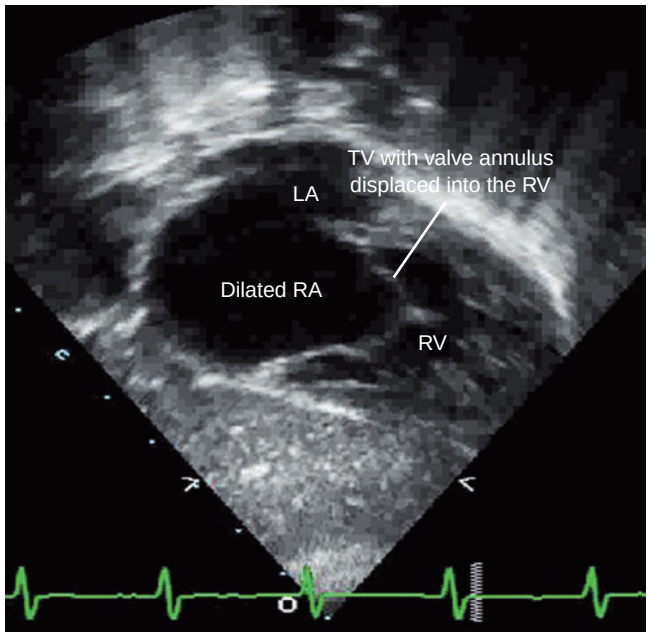


(a)

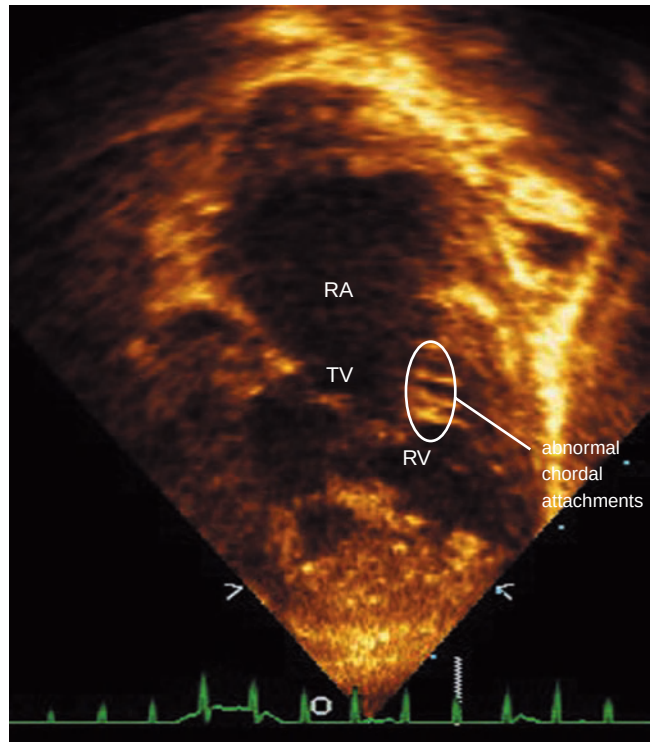


(b)

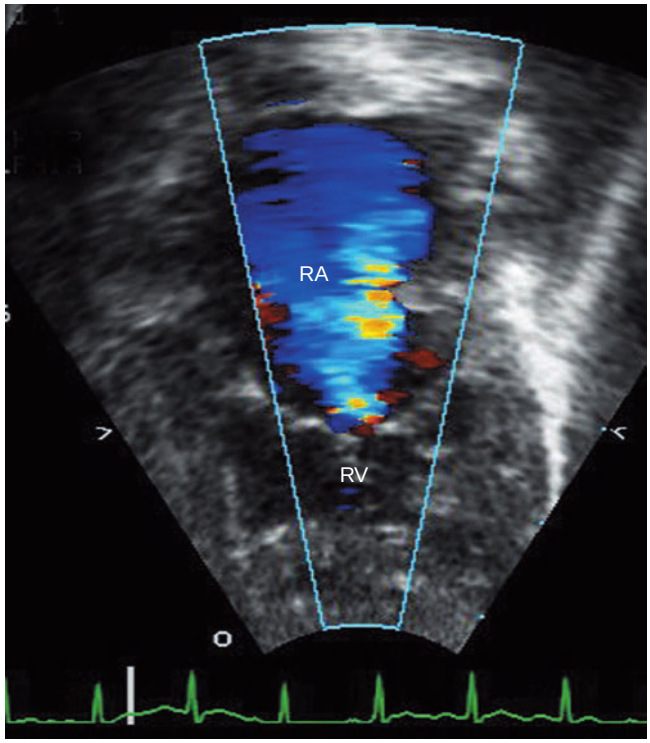


(c)

**Figure 20.3** The effective orifice of this tricuspid valve is displaced into the right ventricle. **(a)** The displacement from a subcostal frontal view. **(b)** An apical 4-chamber view showing abnormal chordal attachment of the septal leaflet "tethering" the leaflet to the ventricular septum and limiting excursion. **(c)** Severe tricuspid regurgitation due to the abnormal tricuspid valve. LA, left atrium; RA, right atrium; RV, right ventricle; TV, tricuspid valve.

Once the PDA begins to constrict, blood supply to the body decreases and an increasing amount of blood is driven into the pulmonary circulation, resulting in improved oxygenation but at the cost of hypotension and circulatory shock. When HLHS is identified, prostaglandin $E_1$ infusion should be initiated immediately in order to maintain patency of the PDA. Increasingly, prenatal diagnosis of HLHS and prompt initiation of prostaglandin $E_1$ infusion in the delivery room allows avoidance of neonatal shock as the presenting symptom.

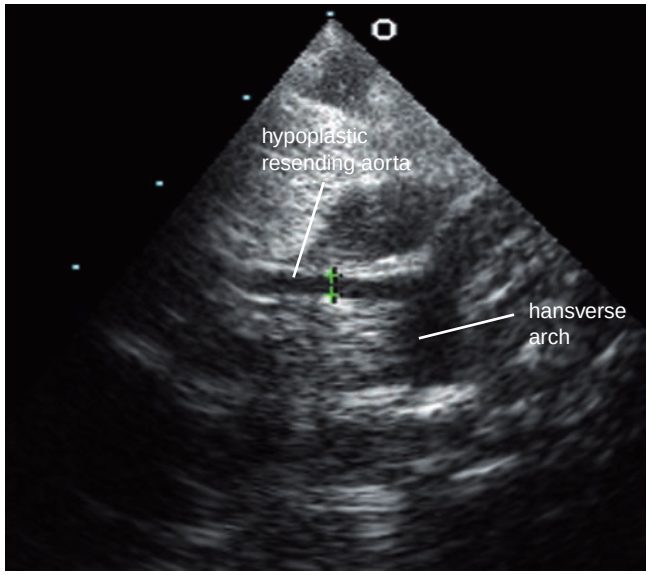


**Figure 20.4** Markedly hypoplastic ascending aorta in a newborn with aortic atresia. This vessel carries blood retrogradely from the aortic arch to the coronary arteries.

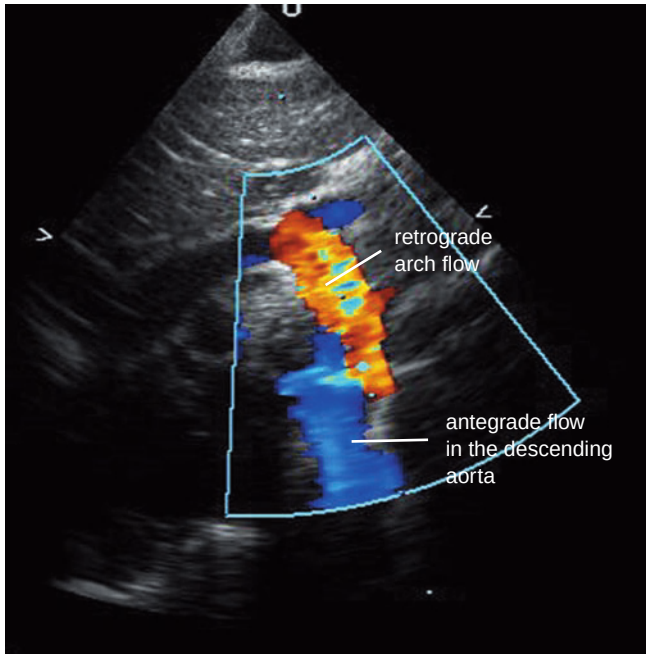


**Figure 20.5** Suprasternal sagittal view demonstrating retrograde flow in the aortic arch from the patent ductus arteriosus.

An open PDA supplies most, if not all, of the blood flow to the body. Depending on the anatomic type of HLHS, retrograde flow through the PDA into the aortic arch may also be the major or only source of blood supply to the upper extremities, head and coronary arteries (Fig. 20.5 and Videoclip 20.6). Because there is limited or no contribution to systemic blood flow from the LV, flow through the PDA will be from the pulmonary artery to the aorta during systole. However, during diastole it is the ratio of vascular resistances between the pulmonary and systemic circuits that dictates flow. With pulmonary vascular resistance normally lower than systemic vascular resistance following birth, diastolic flow across the PDA is typically left-to-right (aorta-to-pulmonary artery), creating a degree of systemic steal. In conditions in which the pulmonary vascular resistance is abnormally elevated – such as in the presence of a very restrictive or intact atrial septum, lung parenchymal disease, persistent pulmonary hypertension, or lung prematurity – the left-to-right shunt in diastole may be minimized or completely eliminated [45]. Such infants will manifest severe cyanosis. Alternatively, if pulmonary vascular resistance is very low relative to systemic vascular resistance, then diastolic flow from left to right may be substantial resulting in a significant systemic hypoperfusion.

## Management

The approach to palliation for HLHS is variable. Since Norwood's initial reports of successful palliation [46], substantial improvements in survival have taken place. Currently, there are a number of strategies available for the neonate with HLHS.

Primary cardiac transplantation is practiced at a small number of institutions in the USA, with good results [47]. However, limited donor availability has curtailed the widespread use of this practice as a primary means of therapy. As outcomes following staged reconstructive surgery have continued to improve, many centers have reserved primary transplantation for high-risk infants such as those with dysplasia of the tricuspid valve and severe regurgitation, and/or marked RV dysfunction.

Because mortality for neonatal Norwood reconstruction remains relatively high in comparison with surgery for other forms of congenital heart disease, some investigators have moved toward the development of strategies that avoid a major surgical operation in the neonatal period. By placing a stent in the PDA and banding the branch pulmonary arteries, it is possible to create a desirable physiologic situation in which the single RV supplies the systemic and pulmonary circulations with unimpeded flow to the descending aorta and in which pulmonary blood flow is limited and the pulmonary vasculature is protected (Figs 20.6 and 20.7; Videoclip 20.7) [48]. This "hybrid approach" involves both a cardiac catheter-driven procedure and surgical technique, and achieves physiologic goals that are similar to the Norwood first-stage reconstruction, but without the performance of a challenging neonatal operation [49]. Ultimately, arch reconstruction takes place in conjunction with a superior cavopulmonary anastomosis at a later time, typically at age 6 months. However, the precise role and the indications for a hybrid approach versus staged surgical reconstruction have not yet been established.

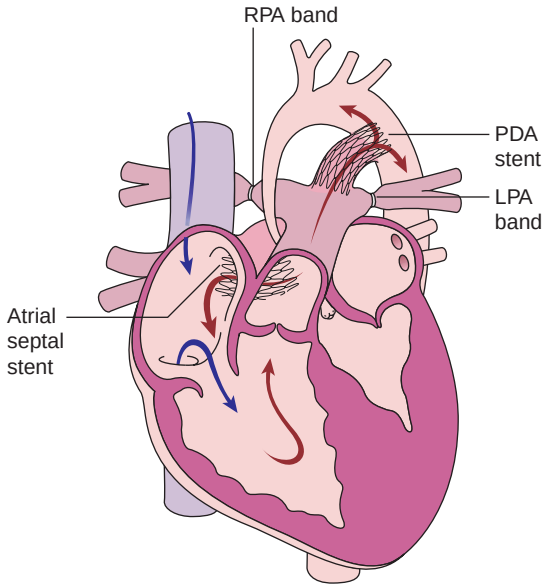


**Figure 20.6** Schematic representation of the "hybrid procedure." In this procedure stents are placed across the atrial septum and the ductus arteriosus and bands are placed across the branch pulmonary arteries. LPA, left pulmonary artery; PDA, patent ductus arteriosus; RPA, right pulmonary artery. Reproduced from Galantowicz M, Cheatham JP. Lessons learned from the development of a new hybrid strategy for the management of hypoplastic left heart syndrome. *Pediatric Cardiology* 2005;26(2):190–9, with kind permission of Springer Science and Business Media.

Although transplant and the "hybrid" approach are performed at some facilities, the most common palliation for HLHS continues to be the stage 1 reconstruction, also known as the Norwood procedure. This operation consists of an atrial septectomy, transection of the pulmonary artery with oversewing of the distal stump, construction of a neoaorta using the incised native aorta augmented with a homograft patch sewn to the native proximal pulmonary artery, ligation of the PDA, and the establishment of secure pulmonary blood flow using a modified Blalock–Taussig (BT) shunt [46]. More recently, the Sano modification, in which pulmonary blood flow is secured using a RV-to-pulmonary artery conduit, has emerged as an alternative to the BT shunt (Fig. 20.8) [50–52]. In high-volume centers, the outcome for this procedure can be quite good.

## Imaging

Once HLHS is suspected in the neonate, a detailed echocardiographic evaluation is undertaken, including 2D, color and spectral Doppler imaging. A segmental approach to analyzing this complex anomaly is performed in a systematic manner by the echocardiographer.

### Goals of the examination

In the setting of HLHS, echocardiographic examination has the following main objectives:

- Determination of the anatomic components of the HLHS: left atrium, mitral valve, left ventricular cavity, aortic valve, ascending aorta, aortic arch, and isthmus.
- Size of the interatrial communication and Doppler evaluation of flow restriction.
- Evaluation of the ductus arteriosus for size and flow characteristics.
- Assessment of tricuspid valve morphology and function.
- Evaluation of RV size and function.
- Imaging of the coronary arteries; note presence of LV–coronary fistulae.
- Detection of associated lesions (e.g., levoatrial cardinal vein).

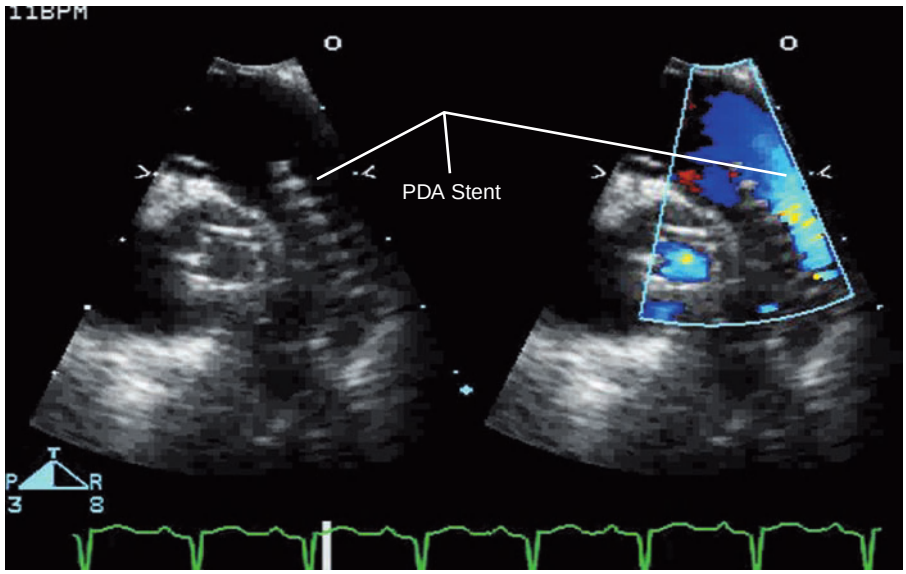


**Figure 20.7** In this example of the "hybrid procedure," the struts of the ductal stent can be seen. During systole, flow across the stent is from the pulmonary artery (PA) to the aorta. PDA, patent ductus arteriosus.

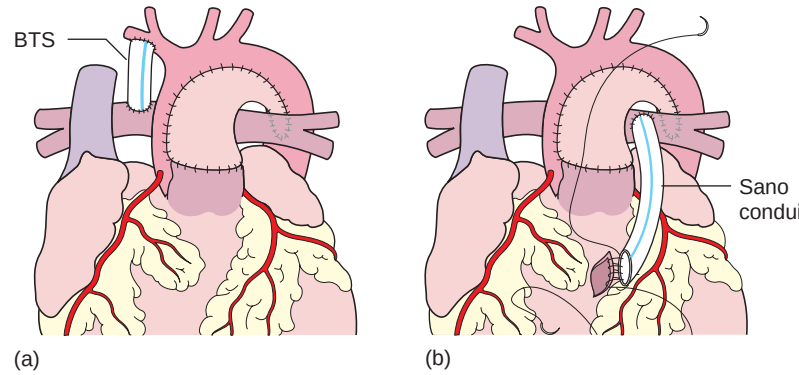


**Figure 20.8** Two common variations of the first-stage palliation for hypoplastic left heart syndrome. **(a)** Diagram of the Norwood procedure with a modified Blalock–Taussig shunt (BTS) connecting the systemic circulation to the pulmonary circulation. **(b)** Diagram of the Norwood procedure with the Sano modification: RV-to-PA conduit in place of the modified Blalock–Taussig shunt. Reproduced from Gardner TJ, Spray TL (eds) *Operative Cardiac Surgery*, 5th edn. London: Arnold Publishers, 2004, with permission.

## Preoperative imaging

### Right atrium and systemic veins

The right atrium is well seen from a variety of views. It is usually dilated and hypertrophied due to the volume load from obligate prenatal left-to-right shunting [16]. Subcostal long- and short-axis imaging delineates the systemic venous connections. In HLHS, the RSVC and the IVC typically have a normal course and entry into the right atrium, although an absent or underdeveloped Eustachian valve may be noted [53]. Anomalous systemic venous return has been reported and should be explicitly excluded [54].

Persistent LSVC to coronary sinus can be reliably identified by echocardiography. Visualization of a dilated coronary sinus from the subcostal, apical, and parasternal windows provides a clue that a LSVC is present. In the suprasternal view, the LSVC can be directly visualized and should course from superior to inferior, anterior to the left pulmonary artery. A LSVC should be distinguished from other venous structures such as a persistent levoatrial cardinal vein, which is a more posterior venous structure. Doppler interrogation demonstrating a low-velocity venous flow pattern confirms the presence of the LSVC and distinguishes it from other structures in the general vicinity, such as a branch pulmonary artery or the left atrial appendage. Whereas flow through a LSVC usually drains into the right atrium via the coronary sinus, there have been reports of coronary sinus ostial atresia with coronary venous decompression and retrograde flow through a LSVC to the innominate vein [55, 56]. The direction of flow through the LSVC can be confirmed using color and pulse-wave Doppler. If a cephalad direction of blood flow is noted through a LSVC, then further investigation of the nature of the coronary venous drainage should be undertaken as any manipulation of the LSVC in this circumstance could deleteriously impact coronary perfusion.

### Atrial septum

A rapid and accurate assessment of the atrial septum is crucial for decision-making about disposition in the immediate postnatal period. The specific anatomy of the atrial septum can be quickly and accurately diagnosed from subcostal imaging, particularly from long-axis, short-axis and in-between views. Acceleration across the atrial septum can be seen using color or pulsed-wave Doppler (Fig. 20.9).

### Levoatrial cardinal vein and other decompressing veins

The presence of a decompressing vein can be confirmed using color Doppler from the subcostal and suprasternal views, although other views may also be helpful to trace the entire course and anatomy of the vein. A levoatrial cardinal vein usually connects the left upper pulmonary vein to the left innominate vein, but other decompressing veins entering the RSVC, the IVC, or the azygous vein can be found. In the setting of a decompressing vein, obstruction may be seen anywhere along the course of the vein, hence a full view of its connection from the left atrium to the insertion into the systemic vein is important. A decompressing vein can be difficult to distinguish from the pulmonary arteries and other vascular structures coursing in the region above the heart but may be identified by the low-velocity continuous flow pattern seen by color or continuous wave Doppler.

### Pulmonary veins

The connections and drainage of all pulmonary veins must be visualized by 2D and color Doppler. Although the pulmonary veins can be seen from subcostal imaging, they are more reliably seen with color Doppler from the suprasternal frontal view. Spectral Doppler is important to assess for pulmonary vein stenosis, which manifests as high-velocity turbulent flow with diminished or absent phasic variations.

### Mitral valve and left ventricle

The mitral valve is evaluated for patency (stenosis versus atresia) and morphology. The dimensions of the mitral valve are measured in both the apical 4-chamber view (lateral diameter) and the parasternal long-axis view (antero-posterior diameter). The inflow pattern into the LV and the degree of mitral regurgitation should be documented using color and pulsed-wave Doppler. The presence of inflow into the LV, without evidence for mitral regurgitation, should alert the

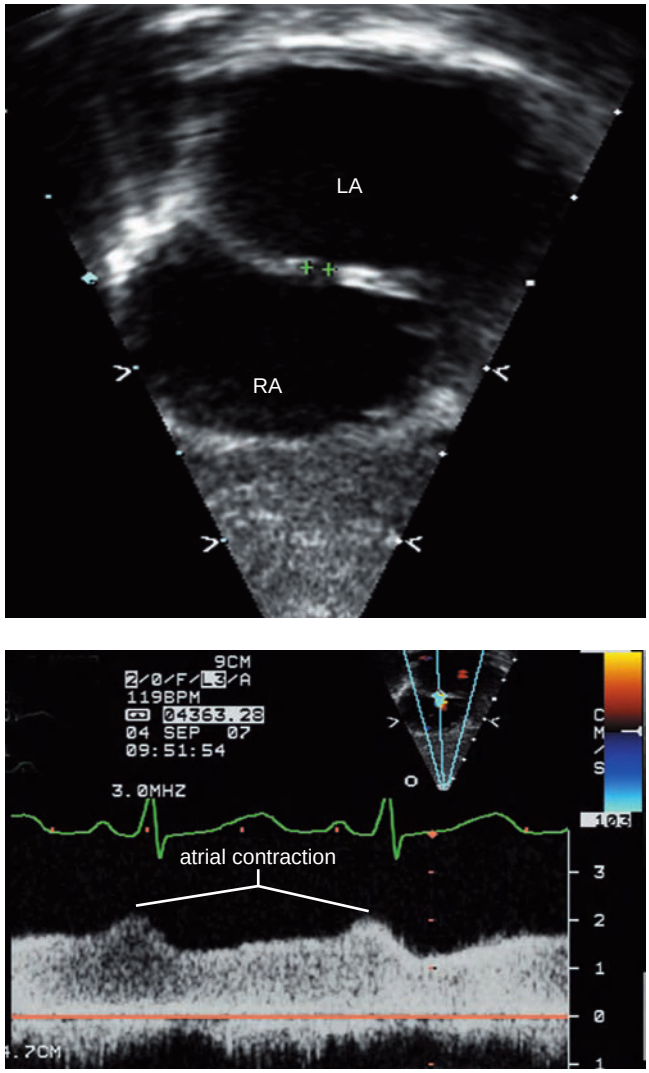


(a) (c)

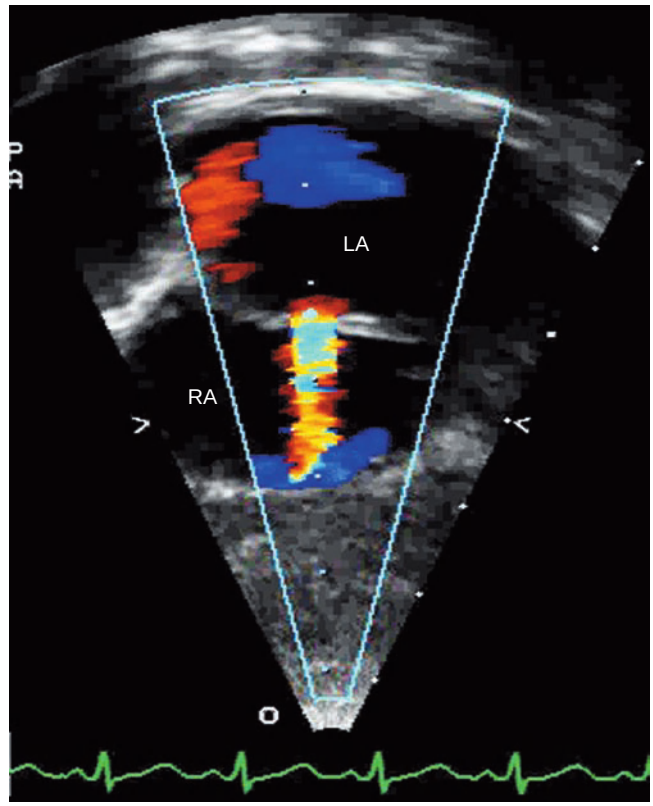


(b)

**Figure 20.9** Restrictive atrial septum in hypoplastic left heart syndrome. **(a)** 2D image from the subcostal view profiling a 2-mm atrial communication. **(b)** The flow jet from the left atrium (LA) to the right atrium (RA) is profiled. The jet is aliased and splays out on the back wall of the right atrium. **(c)** Continuous wave Doppler interrogation across the atrial communication. The velocity remains elevated throughout the cardiac cycle without the normal return to baseline.

echocardiographer to the likelihood of ventriculo-coronary connections as a means for decompressing the LV when there is aortic atresia. Color Doppler interrogation of the LV free wall, apex, and septum with a low Nyquist limit is performed in search of such connections.

Examination of the LV itself is best accomplished from the apical 4-chamber view, but imaging from the subxiphoid and parasternal windows is complementary. The presence of an echo-bright endocardium, which may represent endocardial fibroelastosis, should be noted. Rarely, the LV may contain calcifications, although these are not usually of hemodynamic significance.

### Tricuspid valve and right ventricle

The tricuspid valve is imaged from multiple views and angles. The subcostal oblique view demonstrates the tricuspid valve inflow and the pulmonary outflow in one plane. The apical 4-chamber and parasternal long-axis views are optimal for showing the morphology of the tricuspid valve and the subvalvar apparatus. Leaflet displacement and abnormal chordal or papillary attachments can be well seen from the apical view. It is important to identify and to quantify TR. This is best done from apical 4-chamber and parasternal windows using color Doppler interrogation.

### Aorta and ductus arteriosus

The aortic and ductal arches are well seen from suprasternal oblique sagittal imaging, and the ascending aorta by itself may be seen from parasternal long-axis views. The presence or absence of flow across the aortic valve can be seen by color Doppler interrogation in parasternal long- and short-axis views as well as the apical and high right parasternal views.

The full extent of the PDA is best evaluated from a high parasternal sagittal view. In the ideal "ductal view," the origin of both the right and left pulmonary arteries can be seen along with the insertion of the PDA (Fig. 20.10 and Videoclip 20.8). With very slight manipulations of the tail of the transducer, it is usually possible to see the full course of the ductus from the

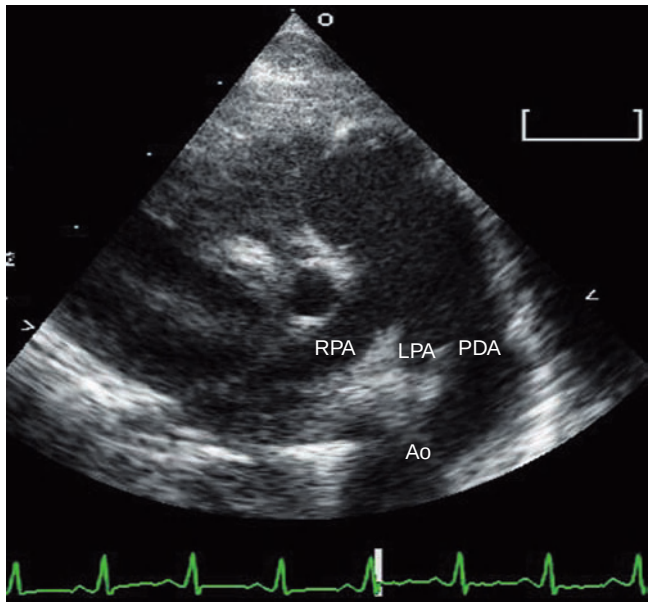


**Figure 20.10** Ductal view from the high parasternal window. This view delineates the branch pulmonary arteries as well as the course of the patent ductus arteriosus (PDA) from the main pulmonary artery to the aorta. Ao, aorta; LPA, left pulmonary artery; RPA, right pulmonary artery.

pulmonary artery to its insertion into the aorta. In HLHS, the PDA can be quite large and describes a smooth, curved trajectory with easy transition into the descending aorta. With the probe in the suprasternal sagittal position a similar image can be obtained and the ductal and aortic arches can be compared with mild left–right tilting. The aortic arch frequently has a more acute curve than normal and frequently appears as a "branch" off the larger ductal arch. The direction of flow in the ductus arteriosus is determined with color and pulsed-wave Doppler from the suprasternal or high left subclavicular sagittal views. Doppler sampling in the distal aspect of the aortic arch and aortic isthmus reveals the retrograde nature of the flow in systole up into the transverse aortic arch, with antegrade forward steal into the PDA and pulmonary vascular bed in diastole (Fig. 20.11). Placement of the Doppler cursor in the descending aorta distal to the PDA will reveal a flow pattern similar to that seen in the ductus arteriosus itself with antegrade flow in systole, and retrograde flow in diastole.

### Coronary arteries

The coronary arteries arise from the often small aortic root, and typically have a normal distribution. Their origins and course are best visualized in the parasternal short-axis view, with focus on the region of the aorta just above the level of the aortic valve. The right coronary artery may be more prominent than the left as it perfuses the systemic, dominant ventricle; however, if there are significant coronary-to-left ventricle fistulous connections, then the left coronary artery may appear enlarged. The right and left coronary artery distribution can also be appreciated from a modified apical view angled anteriorly and superiorly toward the outflow tract.

### Prenatal assessment

Hypoplastic left heart syndrome is readily diagnosed in the fetus and is one of the most frequently detected forms of congenital heart disease prior to birth. It can be easily identified by the abnormal chamber morphology at the time of screening prenatal ultrasound (Fig. 20.12). A detailed fetal echocardiographic examination delineates the anatomic details of HLHS, including the morphology of the left heart structures and associated cardiovascular anomalies. Because of the association with extracardiac anomalies and various syndromes, it is advisable for all fetuses with HLHS to have careful obstetrical ultrasound evaluation for other defects and amniocentesis for genetic/chromosomal abnormalities.

Blood flow patterns in the fetus with HLHS are different than normal. In HLHS the systemic and umbilical venous returns undergo mixing in the right atrium due to the hypoplastic left heart structures. The pulmonary venous return to the left atrium must traverse the atrial septum and drain to the right atrium. The presence of such a left-to-right atrial-level shunt is an important parameter, which defines the inadequacy of the left-sided structures. In addition to defining the direction of flow, the size of the interatrial communication is important. Patency of the interatrial communication is critical for normal lung development. A restrictive or intact atrial septum impairs pulmonary venous drainage and impacts pulmonary vascular development. Without an open atrial communication, blood returning from the lungs has no egress from the left atrium causing increased left atrial pressure. This increased pressure is transmitted back to the pulmonary vasculature, leading to smooth muscle proliferation in the walls of the pulmonary veins (Fig. 20.13) [19,57]. In some cases, severe restriction to atrial flow necessitates postnatal catheter-based intervention or open surgical septectomy to relieve left atrial obstruction [58,59] (Fig. 20.14; Videoclip 20.9). In these cases, prenatal identification of atrial-level restriction and immediate postnatal access to the cardiac catheterization laboratory or the operating room are essential.

The magnitude of atrial-level restriction is assessed by direct inspection of the atrial septum on 2D imaging as well as by color Doppler flow mapping. An apparently small interatrial communication should raise suspicion of a restrictive septum, even in the absence of increased flow velocity. Although of no immediate clinical consequences in utero, a restrictive or intact atrial septum complicates the postnatal course. Pulsed Doppler interrogation of the pulmonary veins is important for assessing the degree of restriction to left atrial egress and should be performed in every fetus with HLHS (Fig. 20.15) [60,61]. The greater

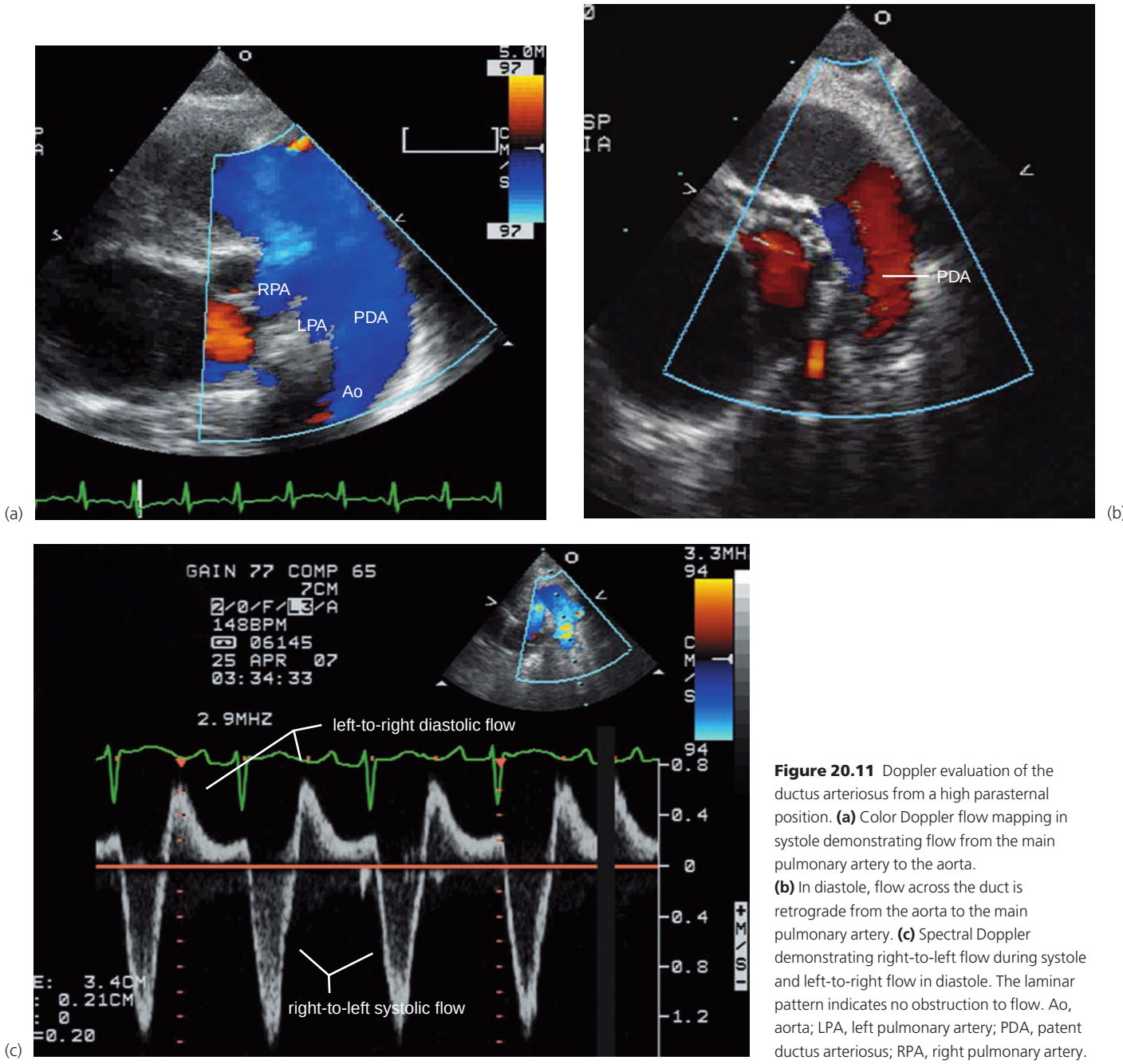


**Figure 20.11** Doppler evaluation of the ductus arteriosus from a high parasternal position. **(a)** Color Doppler flow mapping in systole demonstrating flow from the main pulmonary artery to the aorta. **(b)** In diastole, flow across the duct is retrograde from the aorta to the main pulmonary artery. **(c)** Spectral Doppler demonstrating right-to-left flow during systole and left-to-right flow in diastole. The laminar pattern indicates no obstruction to flow. Ao, aorta; LPA, left pulmonary artery; PDA, patent ductus arteriosus; RPA, right pulmonary artery.

the degree of reversal of pulmonary venous flow with atrial contraction, the greater is the degree of impediment to left atrial egress. The magnitude of flow reversal relates to the severity of pulmonary vascular disease and predicts the early postnatal course. The detection of important obstruction at the atrial level with significant pulmonary venous flow reversal should prompt consideration of prenatal intervention to open the atrial septum, which is technically possible [62]. The effectiveness and optimal timing for such intervention have not yet been determined. However, given the high mortality rates that currently exist despite timely postnatal intervention, such experimental endeavors should be pursued and may be of help to these patients. In the absence of fetal therapy, plans should be made for delivery at a site where immediate intervention at birth can take place to open the atrial septum either via catheter or surgical technique.

Other important variables to evaluate in the fetus with HLHS are the presence and degree of TR and RV function. Mild TR is common and is usually tolerated well. However,

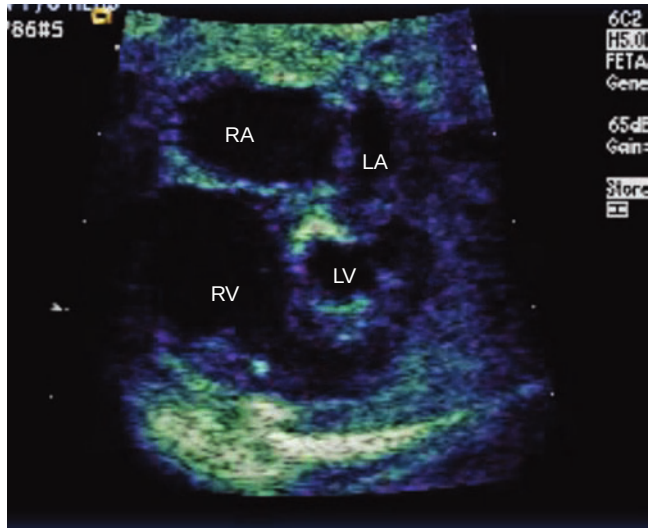


**Figure 20.12** A 4-chamber view of a fetus with hypoplastic left heart syndrome (HLHS). The small left ventricle (LV) is a typical feature of HLHS, although the LV may be normally sized early in gestation. LA, left atrium; RA, right atrium; RV, right ventricle.

moderate or severe TR may lead to fetal hydrops and indicate a poor prognosis (Fig. 20.16). Tricuspid valve incompetence may also worsen when transitioning from prenatal to postnatal life as RV afterload increases following separation from the low-resistance placental circuit and preload increases with the increase in pulmonary venous return to the heart once the lungs are expanded.

Serial echocardiographic evaluation during gestation is indicated in the fetus with HLHS as atrial level restriction or TR may newly develop or progress in later gestation, thereby affecting perinatal management. The evaluation includes Doppler sampling of flow in the ductus venosus, umbilical artery and middle cerebral artery, which provides useful information about the overall well-being of the fetus. Doppler analysis of normal flow in the ductus venosus demonstrates antegrade phasic flow throughout the cardiac cycle. Doppler evaluation of umbilical arterial flow demonstrates low systemic vascular resistance as evidenced by an abundance of diastolic flow, whereas evaluation of middle cerebral arterial flow demonstrates a relatively small amount of diastolic flow (Fig. 20.17). This reflects the normal healthy state of an increased cerebrovascular resistance relative to placental resistance. However, in some fetuses with HLHS, an increase in middle cerebral artery diastolic flow relative to umbilical artery diastolic flow may indicate a lower cerebrovascular resistance. It is hypothesized that lower cerebrovascular resistance is a compensatory mechanism to increase cerebral blood flow in fetuses with anatomic obstruction due to a small aorta.

## Postoperative assessment

### Assessment after stage 1 palliation for HLHS

In general, routine, non-question-directed echocardiography should be avoided in the early postoperative period after stage 1 reconstruction for HLHS as the stress of an unnecessary echocardiogram may disturb the fragile hemodynamics of the critically ill neonate. However, if specific targeted questions need to be answered, an echocardiogram can be a useful tool to help identify potential causes of acute decompensation.

If a mediastinal drain or chest tube suddenly stops draining, an urgent echocardiogram may be warranted to rule out a pericardial effusion. Build-up of pericardial blood can lead to tamponade physiology and cardiovascular collapse. Ventricular dysfunction and TR can also cause acute hemodynamic compromise and can be quickly assessed at the

(a)

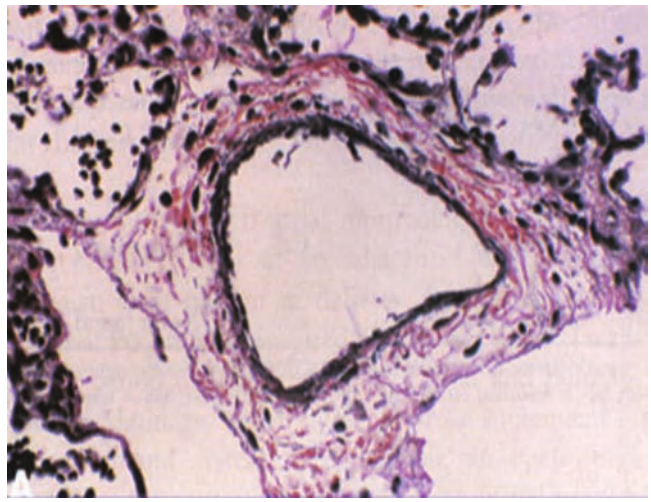

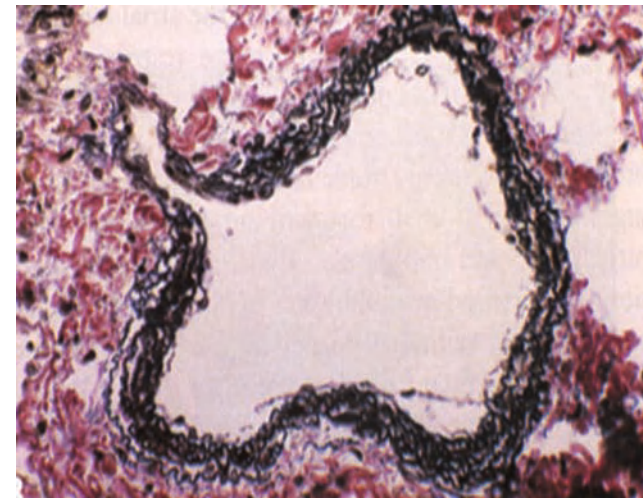

(b)

**Figure 20.13** Normal pulmonary venous histology has a relative paucity of smooth muscle **(a)**. Infants with hypoplastic left heart syndrome and an intact atrial septum have an increased presence of smooth muscle in the walls of the pulmonary veins **(b)**.

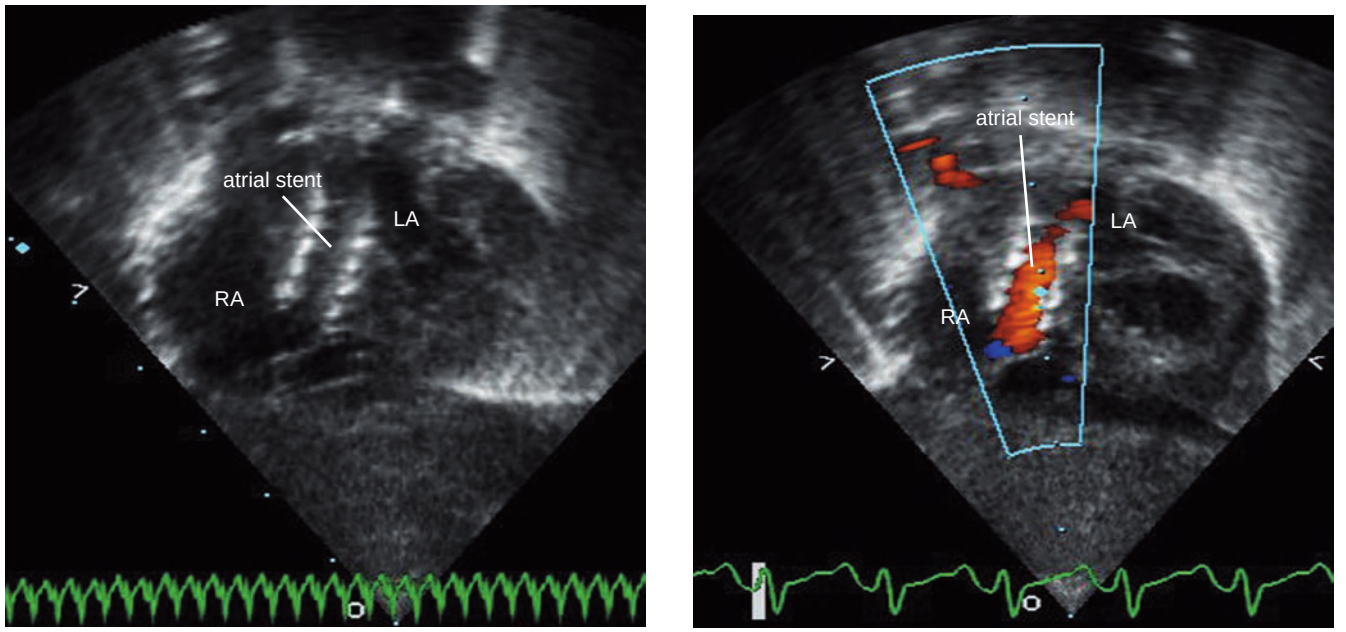


(a) (b)

**Figure 20.14** **(a)** Subcostal 2D image of a stent deployed across a restrictive atrial septum. The effective size of the atrial communication is equal to the diameter of the stent. **(b)** Color flow Doppler showing nonaliased flow through the atrial stent from the left atrium (LA) to the right atrium (RA).

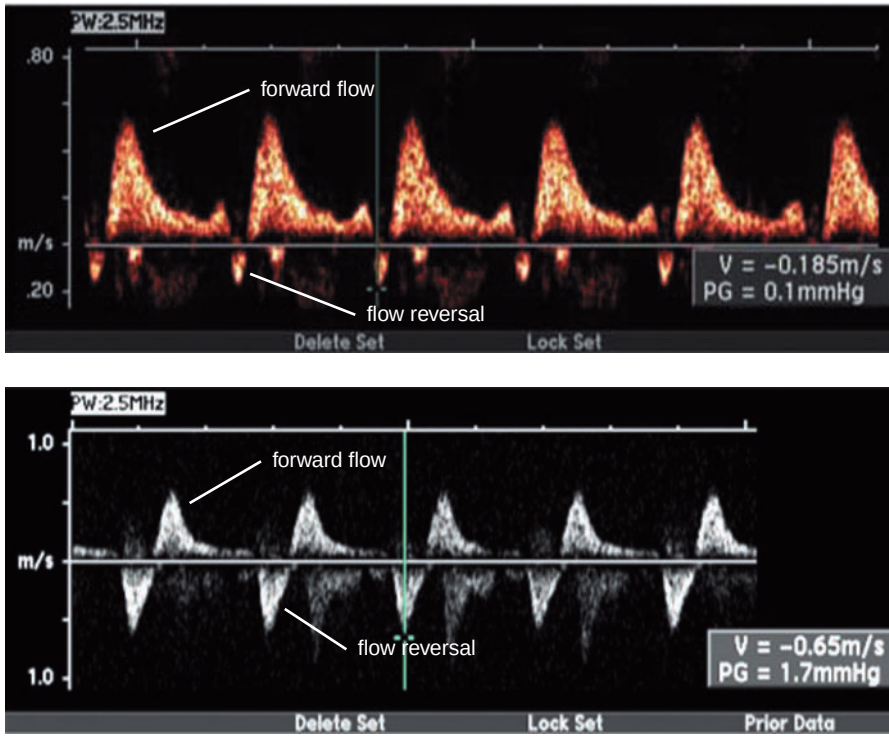


(a)

(b)

**Figure 20.15** Pulmonary venous Doppler pattern in the fetus. **(a)** Normal flow characterized by predominantly antegrade flow with only a small amount of retrograde flow during atrial contraction. **(b)** Hypoplastic left heart syndrome with a restrictive atrial septum. Note the much greater degree of retrograde flow implying impedance to flow across the atrial septum.

bedside with echocardiography. Postoperative pulmonary overcirculation is another potential cause of cardiovascular collapse [63]. A Doppler-derived aortic flow reversal ratio has been suggested as a means of assessing the ratio of pulmonary to systemic blood flow and may be clinically useful in some instances [64].

Unexpected cyanosis early after stage 1 reconstruction may be due to inadequate resection of the atrial septum or limited blood flow delivery to the pulmonary arteries due to shunt stenosis. Atrial septal anatomy and adequacy of the resection can be easily ascertained from subcostal imaging in the frontal or sagittal planes. A BT shunt can usually be seen

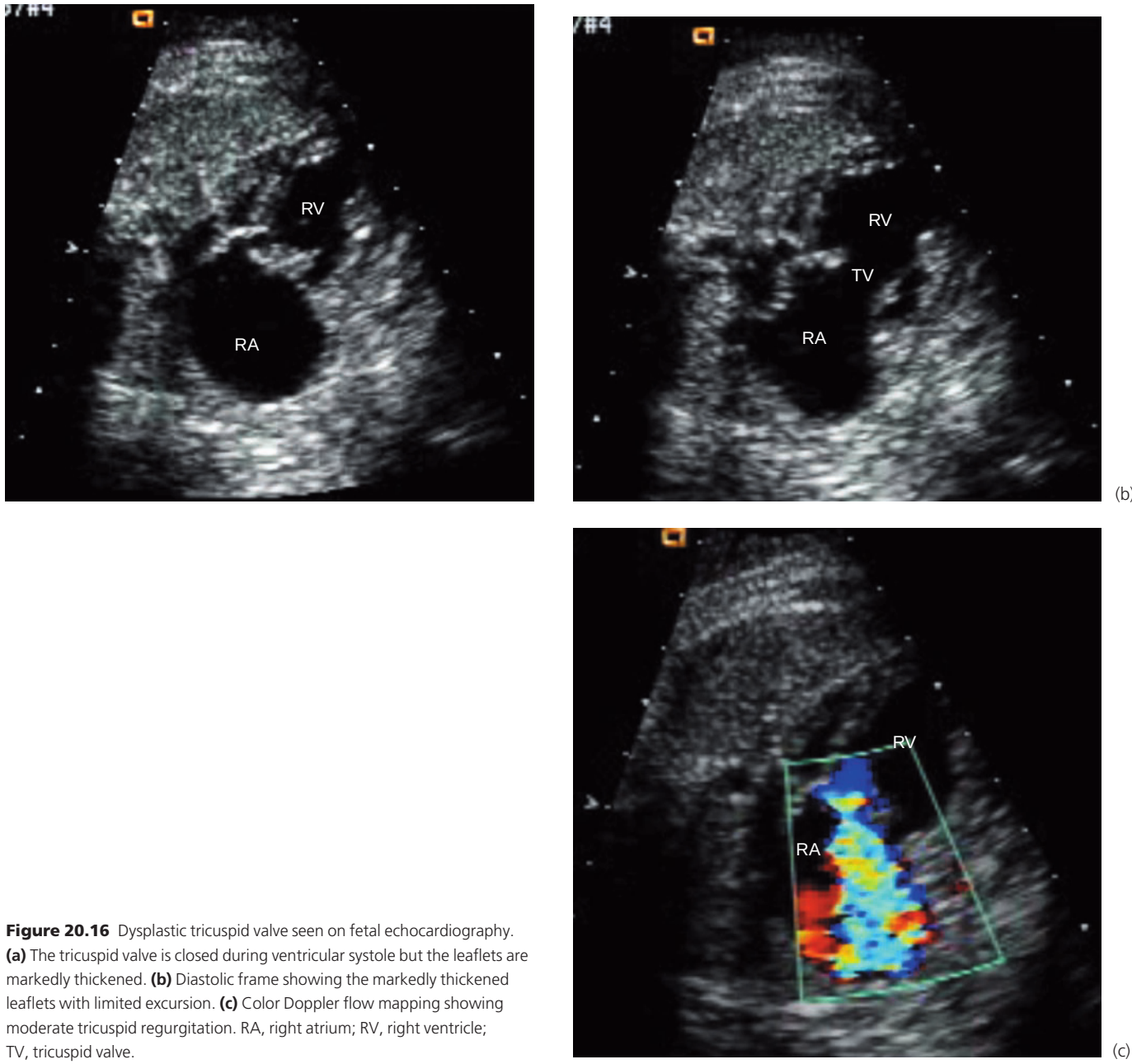


**Figure 20.16** Dysplastic tricuspid valve seen on fetal echocardiography. **(a)** The tricuspid valve is closed during ventricular systole but the leaflets are markedly thickened. **(b)** Diastolic frame showing the markedly thickened leaflets with limited excursion. **(c)** Color Doppler flow mapping showing moderate tricuspid regurgitation. RA, right atrium; RV, right ventricle; TV, tricuspid valve.

and traced from the suprasternal frontal view with angulation slightly toward the right (Fig. 20.18 and Videoclip 20.10). Flow through the shunt should be continuous throughout systole and diastole with a characteristic sawtooth Doppler spectral pattern, consistent with the continuous aortic to pulmonary pressure gradient present. Narrowing of the color jet through the shunt should raise concern for shunt narrowing or obstruction when clinical findings suggest decreased pulmonary blood flow. Shunt stenosis can be a challenging undertaking to confirm using echocardiography. Ultrasound scatter and artifact created by the shunt material itself may limit the ability to visualize directly the arterial origin, or pulmonary artery insertion site of the tube graft. In addition, Doppler interrogation and velocity data can underestimate the pressure gradient, as the modified Bernoulli equation is invalid in the case of a long-segment narrowing. Because the BT shunt originates from the innominate artery, one possible cause for limited pulmonary blood flow early after surgery may be torsion or kinking of the innominate artery itself. This can be identified on Doppler echocardiography by detection of turbulence and an increased velocity across the innominate artery at the site of shunt origin.

In patients with RV-to-PA conduit (Sano modification), postoperative cyanosis should prompt careful evaluation of

(a)

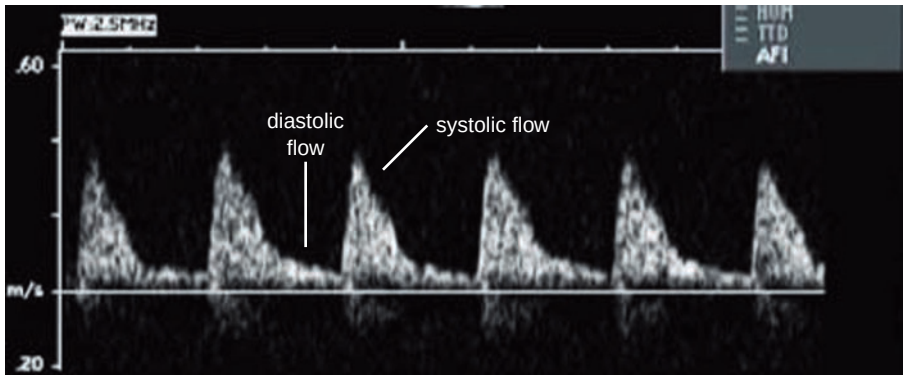


(b)

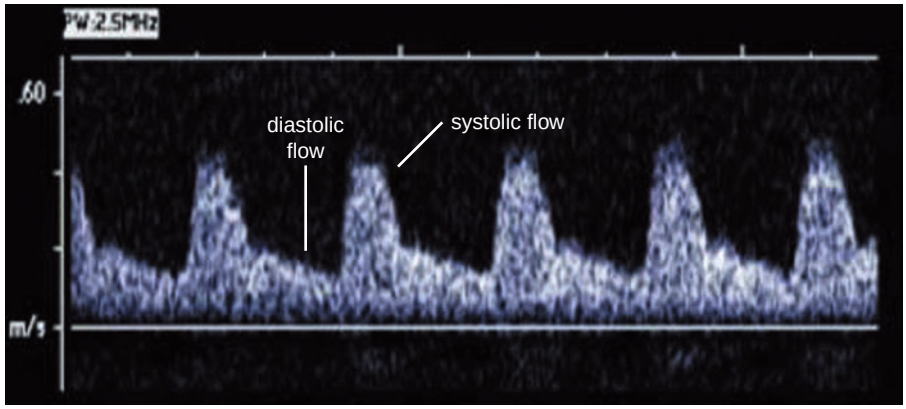


**Figure 20.17** Flow pattern in the middle cerebral artery. **(a)** Normal flow pattern characterized by little diastolic flow due to high cerebral vascular resistance. **(b)** Flow pattern in hypoplastic left heart syndrome. Note the marked increase in diastolic flow, probably due to diminished vascular tone as part of a neurohormonal feedback circuit that encourages cerebral blood flow from the ductus arteriosus retrogradely through the arch.

the conduit at its origin from the RV, along its course, and its insertion into the branch pulmonary arteries, as narrowing can occur at any site [65]. The conduit can usually be visualized in the subcostal sagittal view. In addition, an excellent view for examining the distal aspect of the conduit and the proximal branch pulmonary arteries can be achieved by a mid-left parasternal window angled superiorly (Figs 20.19 and 20.20; Videoclip 20.11). This view is obtained by starting at the standard apical view and moving medially and slightly cephalad toward the mid-sternum. Color and pulsed-wave Doppler sampling in the conduit and proximal branch pulmonary arteries demonstrate forward systolic flow and diastolic reversal back to the RV.

### Inter-stage assessment

Once outside the immediate postoperative period, routine echocardiographic evaluation becomes an important tool for assessing the outcome of the first-stage palliation and the progression of inter-stage physiology. Progressive obstruction can occur at the atrial septal level, weeks to months after initial surgery. In a review at The Children's Hospital of Philadelphia, 4% of patients had a pressure gradient of ≥5 mm Hg on routine echocardiography after stage 1 palliation. Severe restriction or an intact atrial septum before stage 1 surgery both correlated with the likelihood of postoperative obstruction [66]. As with the preoperative evaluation, pulsed-wave and color Doppler are used to demonstrate acceleration of flow across the atrial septum and determine the presence and degree of obstruction. However, velocity information alone is not sufficient to assess the clinical significance of atrial-level obstruction, as an increased rate of pulmonary venous return is seen in patients with pulmonary overcirculation.

Careful assessment of RV function is important and should be performed from a variety of angles and probe positions in order to assess global and regional performance of the RV. Apical and parasternal short-axis imaging are usually sufficient to evaluate RV wall shortening as these views provide orthogonal planes. Quantitative echocardiographic assessment of ventricular performance in HLHS is challenging due to the variable geometry of the systemic RV. For that reason, geometric formulae for measuring cavity volumes or myocardial mass are at best gross estimates and are frequently inaccurate compared with other imaging modalities. The role of 3D echocardiography and tissue Doppler imaging, a nongeometric technique, is the subject of ongoing research. Highly subjective but useful in experienced hands, qualitative assessment of ventricular performance remains the most commonly used means for evaluating RV function in HLHS.

Narrowing of the neoaorta following stage 1 palliation occurs primarily at the anastomosis of the reconstructed arch to the native pulmonary artery proximally or to the descending aorta distally (Fig. 20.21 and Videoclip 20.12).

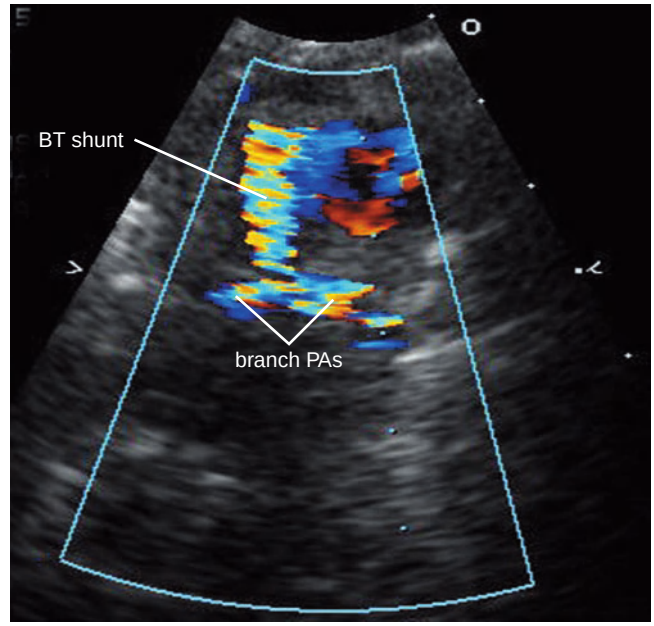


(a)

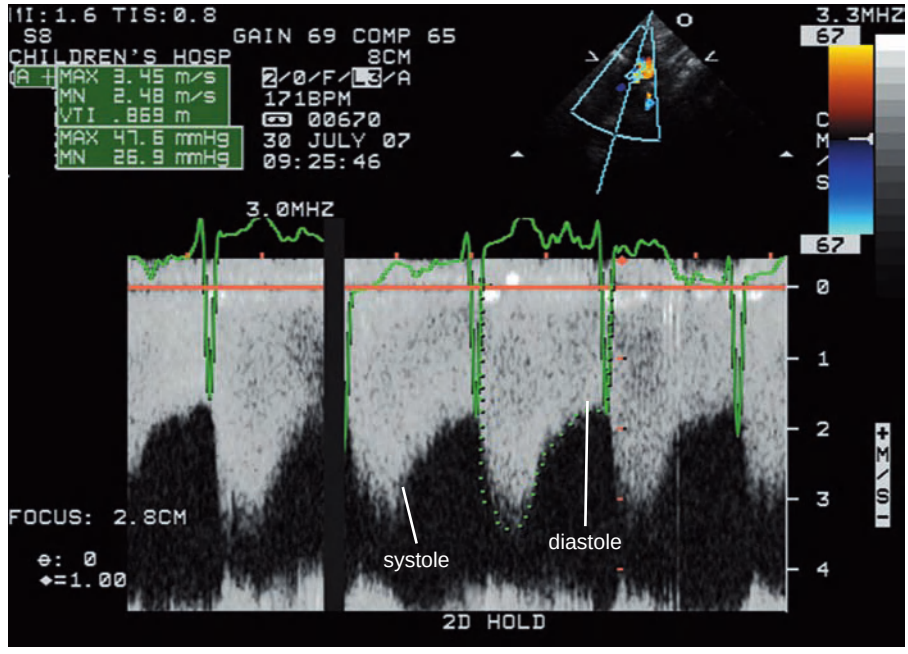


(b)

**Figure 20.18** Evaluation of a modified Blalock–Taussig (BT) shunt. **(a)** Suprasternal coronal image demonstrating the course of the BT shunt from the right innominate artery to the right pulmonary artery (PA). Note the aliased color Doppler flow pattern. **(b)** Continuous-wave Doppler across the shunt demonstrating high-velocity continuous flow.

Assessment of the proximal anastomosis is performed from subcostal, apical and parasternal imaging windows using color, pulsed-wave and continuous-wave Doppler. If there is obstruction, it usually occurs at the supravalvar region at the suture line. Assessment of the distal neoaortic anastomosis to the descending aorta is best done from the suprasternal sagittal view position. After stage 1 palliation, there is often an increase in velocity through the distal arch, particularly at the site of distal anastomosis, as the caliber of the vessel decreases from the large, augmented transverse arch to the native descending aorta in a funnel-like manner (Fig. 20.22). Whereas the altered geometry of the neoaorta creates unique flow patterns, the diminished distensibility of the homograft patch further complicates the diagnosis of coarctation [67,68]. In the absence of normal aortic distensibility, the diastolic runoff pattern typically seen in classic coarctation of the aorta will not be present. In addition, if present, the modified BT shunt will drain blood away from the descending aorta during diastole, further diminishing the appearance of forward diastolic runoff. In an attempt accurately to predict clinically significant arch narrowing, a "coarctation index" has been proposed, defined as the ratio of the narrowest portion of the descending aorta to the widest portion of the descending aorta. Investigators found that a coarctation

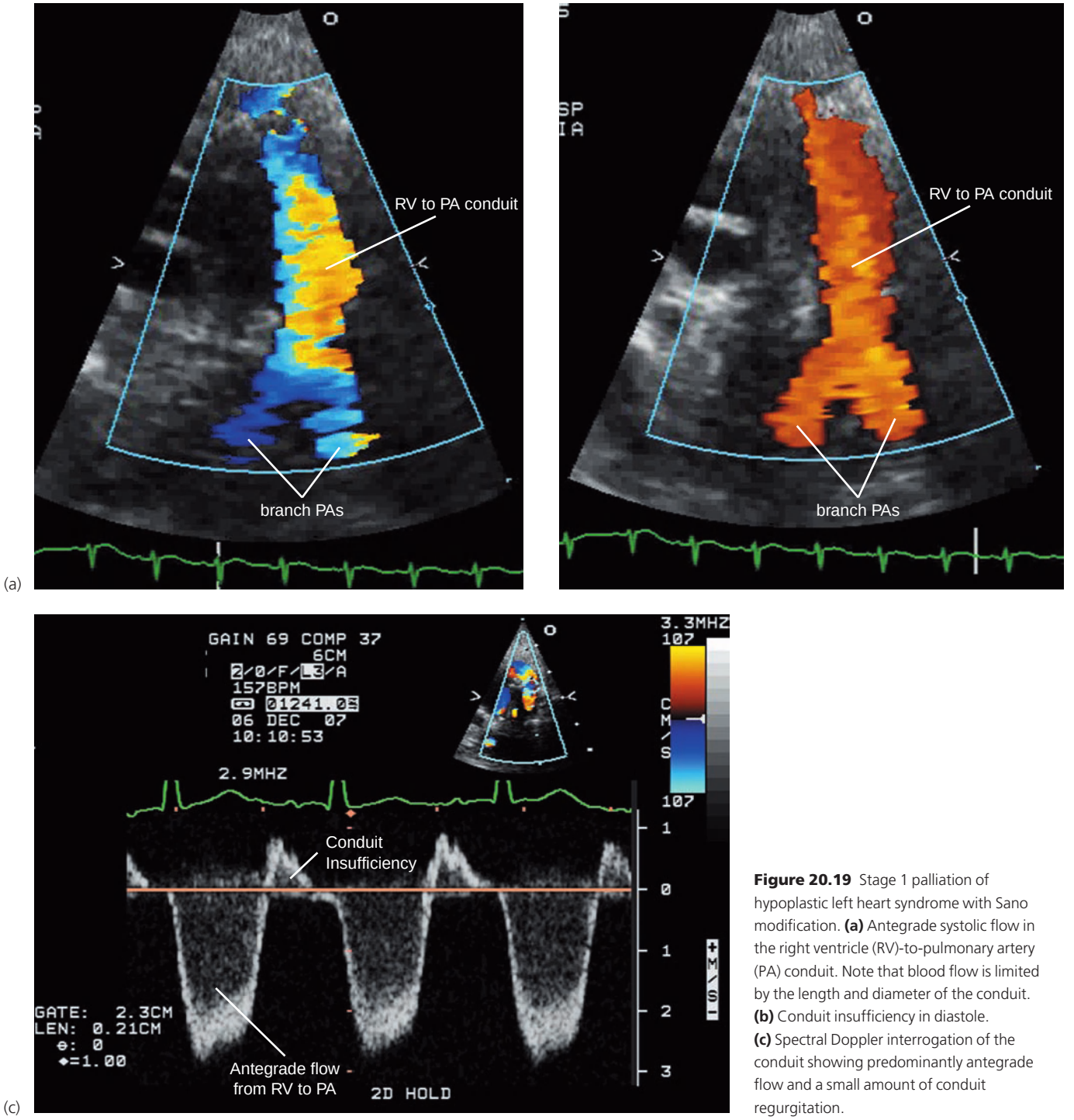


**Figure 20.19** Stage 1 palliation of hypoplastic left heart syndrome with Sano modification. **(a)** Antegrade systolic flow in the right ventricle (RV)-to-pulmonary artery (PA) conduit. Note that blood flow is limited by the length and diameter of the conduit. **(b)** Conduit insufficiency in diastole. **(c)** Spectral Doppler interrogation of the conduit showing predominantly antegrade flow and a small amount of conduit regurgitation.

index of <0.7 with a Doppler echocardiography-derived peak instantaneous gradient of >30 mm Hg correlated strongly with coarctation as identified on cardiac catheterization [69]. If imaging of the reconstructed arch from suprasternal imaging is technically difficult, an indirect estimate of the gradient across the aortic reconstruction can be made by comparing an estimate of RV pressure, based on the peak velocity of continuous-wave Doppler through the TR jet, with the blood pressure in the lower extremity. If TR is present, such estimates of RV pressure should always be made and compared with lower extremity blood pressure as a means of surveillance for the development of arch narrowing.

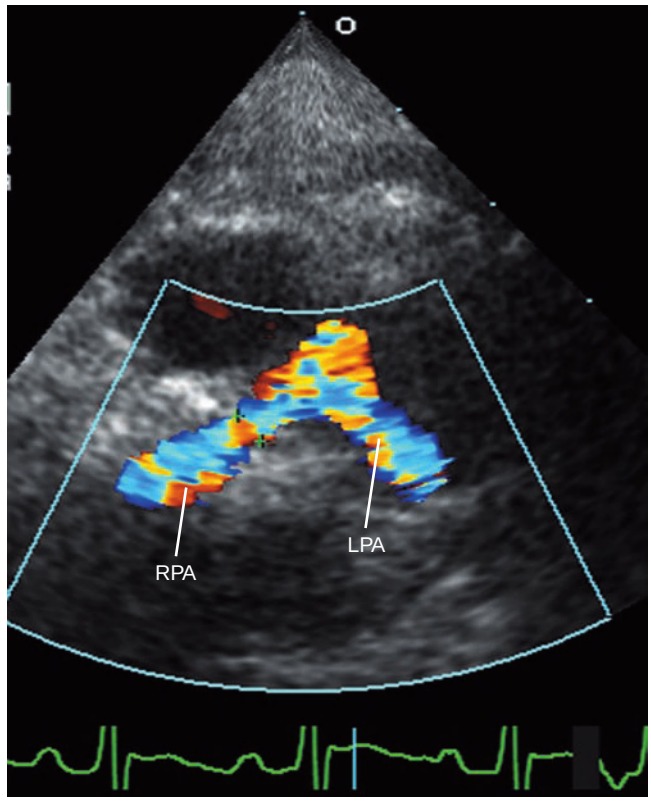


**Figure 20.20** Distal attachment of a Sano conduit to the branch pulmonary arteries. LPA, left pulmonary artery; RPA, right pulmonary artery.

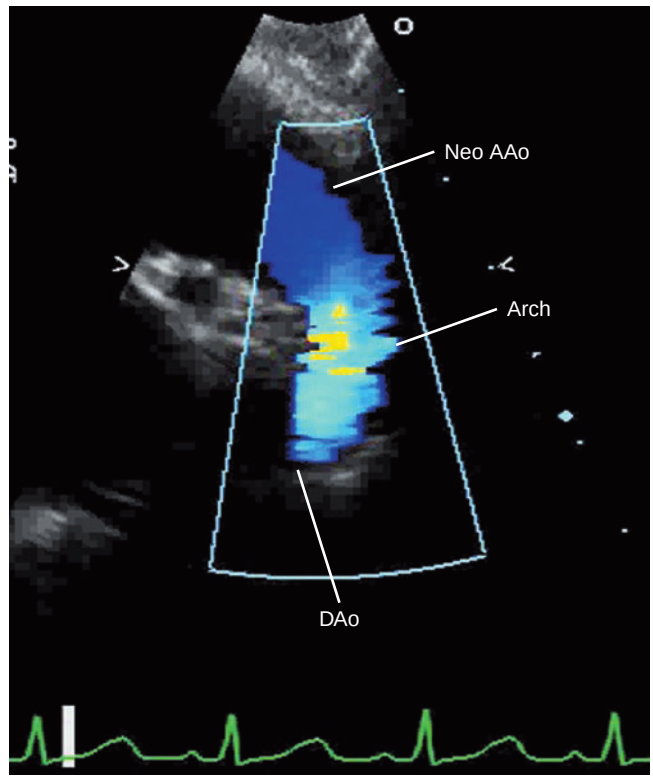


(a)

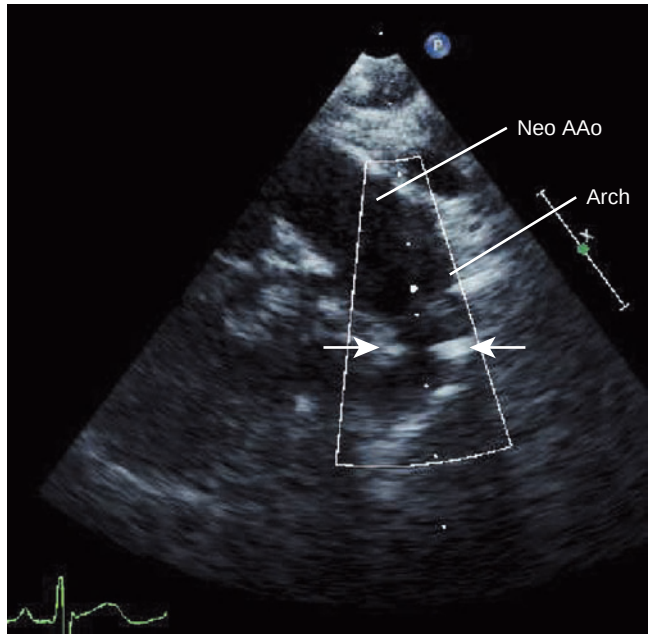


(b)

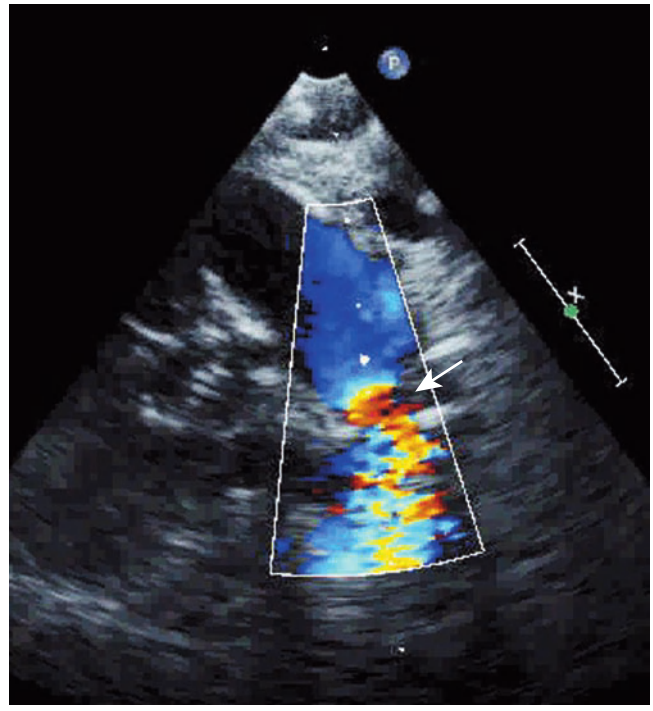

(c)

**Figure 20.21** Aortic arch reconstruction after stage 1 hypoplastic left heart syndrome palliation. **(a)** Suprasternal sagittal image showing an unobstructed reconstructed aorta. **(b)** Similar view showing coarctation (arrows). **(c)** Color Doppler flow mapping showing aliasing at the suture line (arrow).

(d)

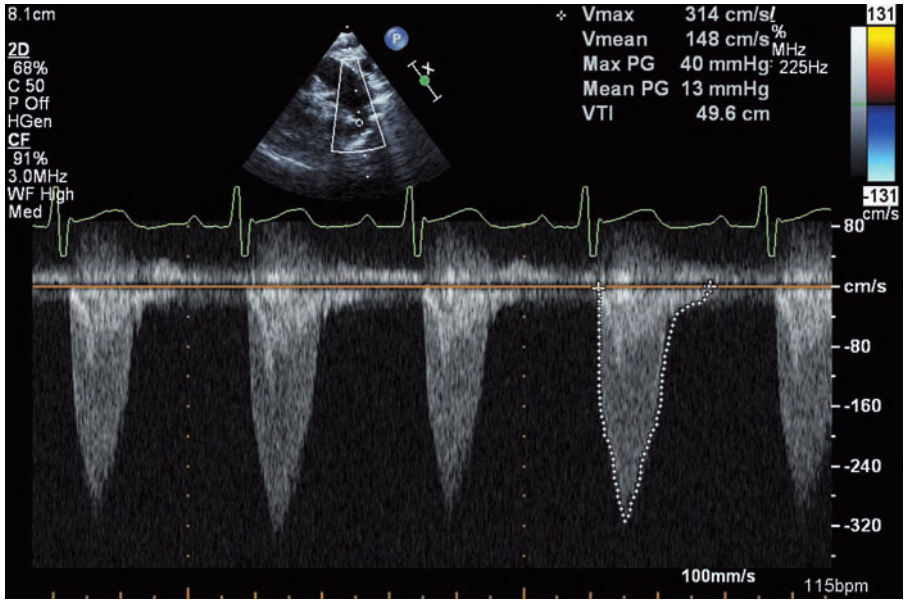


**Figure 20.21 (d)** Spectral Doppler across the coarctation. Note that the usual diastolic runoff pattern of a coarctation is not present as a result of competitive runoff through a Blalock–Taussig shunt. Neo-AAo, neo-ascending aorta; DAo, descending aorta.

(a)

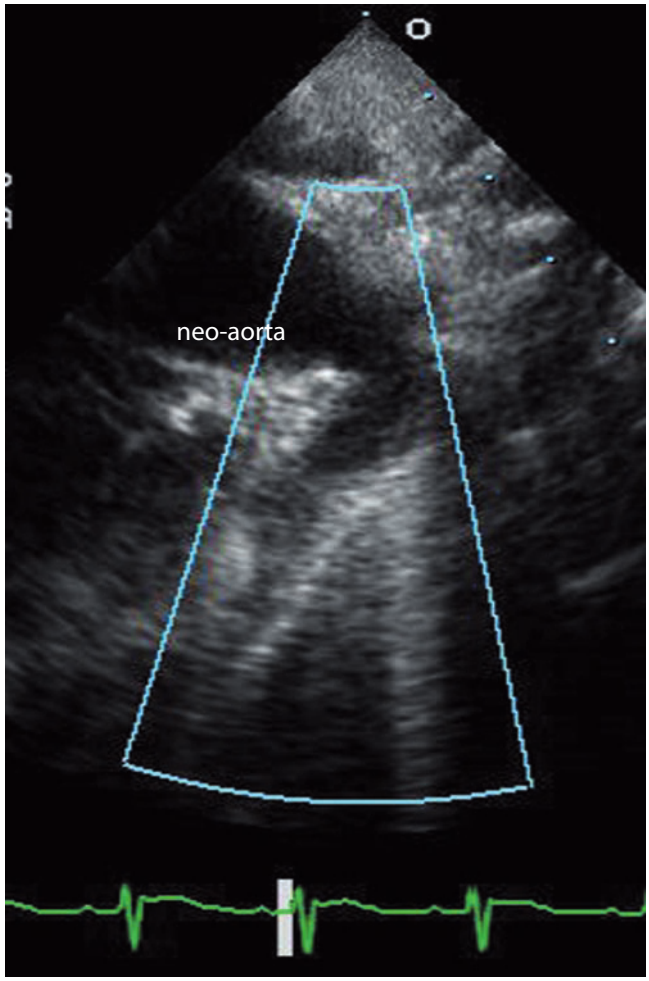


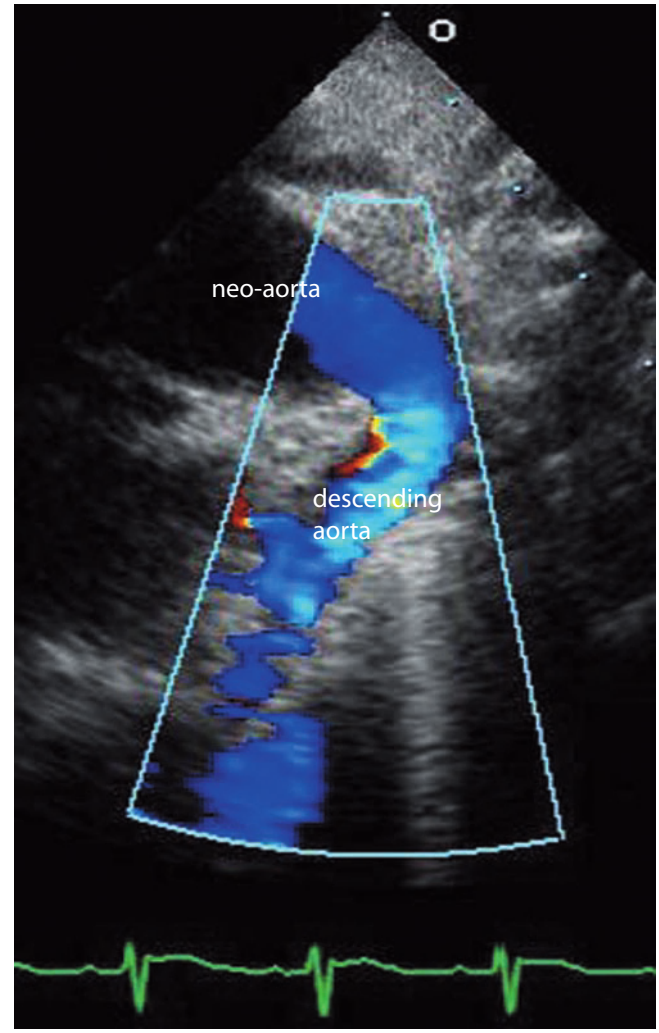


(b)

**Figure 20.22** Funnel-like tapering of the distal neoaorta often seen in patients after stage 1 reconstruction. **(a)** 2D imaging from the suprasternal notch. **(b)** Color Doppler shows no significant flow acceleration despite the narrowing seen by 2D imaging.

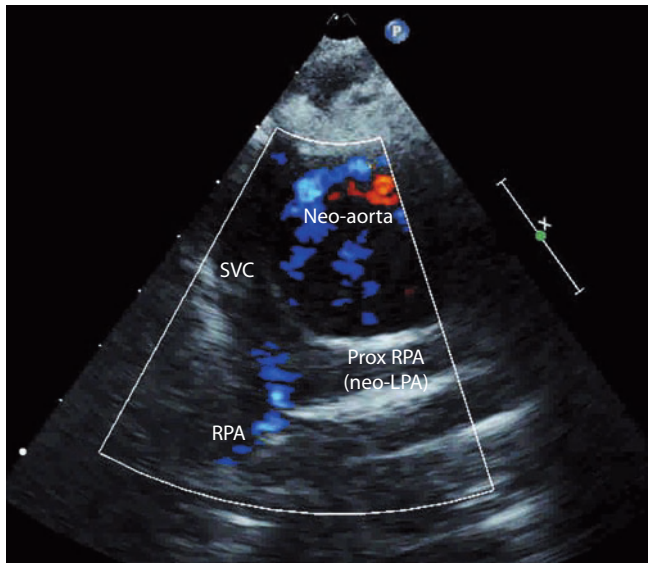


**Figure 20.23** Imaging of superior cavopulmonary anastomosis from the suprasternal frontal position. The superior vena cava (SVC) is seen coursing alongside the neoaorta. It has been transected and anastomosed to the right pulmonary artery (RPA). The portion of the RPA medial to the anastomosis is the neo-left pulmonary artery (neo-LPA). In this image the pulmonary arteries are widely patent. Prox RPA, proximal right pulmonary artery (= neo-LPA).

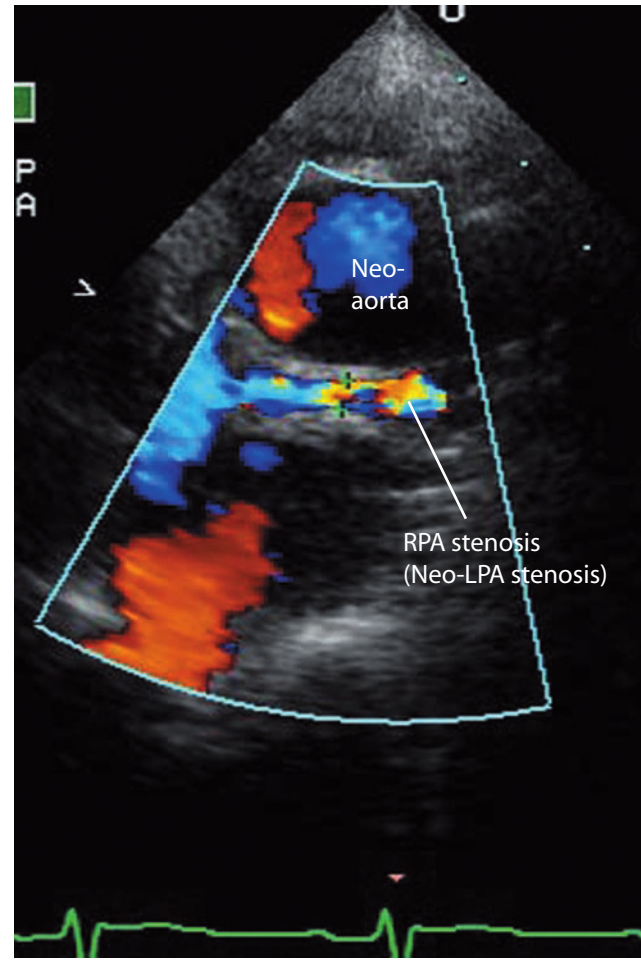


**Figure 20.24** Severe stenosis of the neo-left pulmonary artery (Neo-LPA) as it courses under the bulbous neoaorta. RPA, right pulmonary artery.

### Assessment before and after stage 2 of HLHS palliation

In the second stage of palliation for HLHS, superior caval blood is directed to the pulmonary arteries, either via a bidirectional Glenn [70] or a hemi-Fontan [71] procedure. In the bidirectional Glenn, the SVC is transected and the proximal portion is sewn directly into the superior aspect of the right pulmonary artery (Fig. 20.23 and Videoclip 20.13). In the hemi-Fontan, the posterior aspect of the superior vena cava is opened onto the anterior aspect of the right pulmonary artery. A patch is placed and then carried from the anastomosis out onto the proximal branch pulmonary artery to ensure wide patency. A dam is sewn into the entrance of the SVC into the RA, effectively separating the SVC from the heart. If a LSVC is present, the surgeon can elect to perform bilateral, bidirectional Glenn anastomoses or perform a hemi-Fontan on the right and a bidirectional Glenn on the left.

Echocardiography plays an important role in the diagnostic evaluation of patients prior to stage 2 surgery. RV function and TR should be assessed as a new, preoperative baseline. Examination of the atrial septum and pulmonary veins is helpful to rule out obstruction that may need to be addressed while in the operating room. The branch pulmonary arteries should be evaluated with echocardiography, although visualization may be limited to the proximal extraparenchymal portions. The portion of the pulmonary artery behind the reconstructed aorta is an important region for focus as a large bulbous reconstructed neoaorta may compress the pulmonary artery causing stenosis and distal hypoplasia (Fig. 20.24). The presence of a LSVC should be ascertained, as well as the presence and size of the innominate vein, as previously described. Even with optimal echocardiographic imaging, current practice in many institutions is to perform cardiac catheterization prior to the stage 2 surgery in order to determine safe candidacy for a cavopulmonary connection [72]. However, a randomized clinical trial found that a non-invasive approach utilizing echocardiography and cardiac MRI is a safe, effective and less costly alternative to routine catheterization in the evaluation of selected patients prior to bidirectional Glenn operation [73].

### Assessment before and after Fontan palliation

See the detailed discussion in Chapter 27. Cardiac catheterization is commonly performed as part of the evaluation prior to the Fontan operation; however, some centers have been moving toward a noninvasive imaging strategy in low-risk subgroups of patients. At The Children's Hospital of Philadelphia, we have identified a cohort of patients in

**Table 20.1** Criteria to forgo a cardiac catheterization prior to Fontan completion*

| **Clinical data** |
|---|
| Room air pulse oximetry ≥76% |
| Hemoglobin ≤18 g/dL |
| **Echocardiographic data** |
| Left pulmonary artery visualized without stenosis |
| No significant atrioventricular valve insufficiency (≤1+) |
| No significant ventricular dysfunction (qualitative) |
| No aortic coarctation |
| An unrestrictive atrial communication |
| No evidence of a decompressing vessel |

*If the above criteria are met, there is no benefit to performing a cardiac catheterization prior to Fontan completion [74].

whom cardiac catheterization is of no additional benefit above and beyond data derived from noninvasive imaging prior to the Fontan operation (Table 20.1) [74]. By applying these criteria we have been able to reduce substantially the number of patients undergoing invasive diagnostic testing and its associated potential complications. MRI techniques may advance our ability to reduce or possibly eliminate the need for diagnostic cardiac catheterization, relegating the role of catheterization to interventions once anatomic issues have been identified by noninvasive means [75].

## Imaging after the Fontan procedure

Serial echocardiographic assessment after Fontan completion is an important part of routine scheduled follow-up for patients with HLHS. Neoaortic dilation is a concern in many patients with congenital heart disease involving the great arteries. In the HLHS population, progressive dilation of the neoaortic annulus out of proportion to body mass index has been noted, and correlates with progressive neoaortic insufficiency [76]. This raises concerns for the long-term well-being of patients who have had the Fontan operation and merits close follow-up (Fig. 20.25).

Although pulmonary vascular resistance cannot be directly measured by echocardiography, the transpulmonary gradient, a surrogate of pulmonary vascular resistance, can be estimated based on the velocity of flow through an open Fontan baffle fenestration (Fig. 20.26 and Videoclip 20.14). In patients in whom the Fontan surgery did not include a fenestration, or in whom the fenestration closed with or without intervention, this evaluation is not an option.

Assessment of RV systolic and diastolic function is an important element of the echocardiographic evaluation in patients after Fontan palliation.

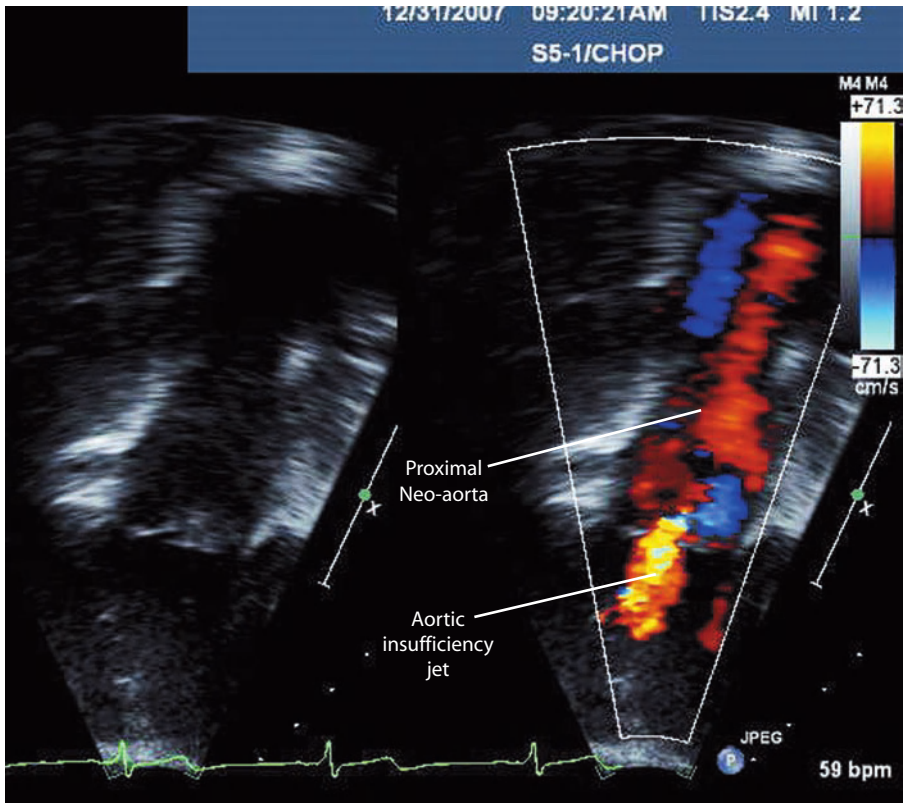


**Figure 20.25** Apical view showing an unobstructed proximal aortic anastomosis and central neoaortic insufficiency with retrograde flow through the visible portion of the ascending aorta.

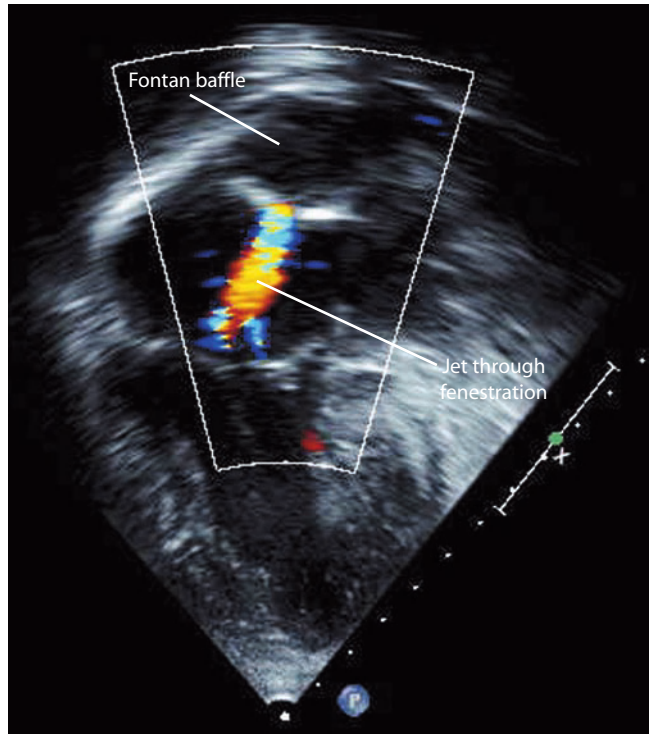


(a)

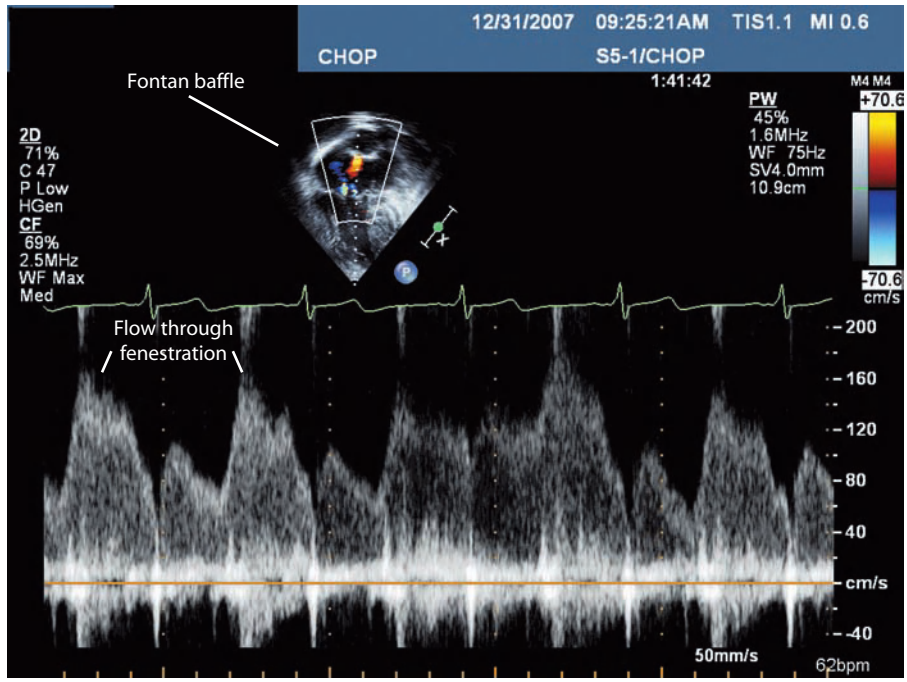


(b)

**Figure 20.26** Flow through a Fontan baffle fenestration. **(a)** Apical 4-chamber view showing turbulent right-to-left flow through the fenestration. **(b)** Spectral Doppler is used to determine the pressure gradient from the systemic veins to the pulmonary venous atrium. This pressure difference is the transpulmonary gradient.

## References


1. Lev M. Pathologic anatomy and interrelationship of hypoplasia of the aortic tract complexes. *Lab Invest* 1952;1:61–70.
2. Noonan JA, Nadas AS. The hypoplastic left heart syndrome; an analysis of 101 cases. *Pediatr Clin North Am* 1958;5:1029–56.
3. Hoffman JI, Kaplan S. The incidence of congenital heart disease. *J Am Coll Cardiol* 2002;39:1890–900.
4. Natowicz M, Chatten J, Clancy R et al. Genetic disorders and major extracardiac anomalies associated with the hypoplastic left heart syndrome. *Pediatrics* 1988;82:698–706.
5. Natowicz M, Kelley RI. Association of Turner syndrome with hypoplastic left-heart syndrome. *Am J Dis Child* 1987;141: 218–20.

6. Glauser TA, Rorke LB, Weinberg PM, Clancy RR. Congenital brain anomalies associated with the hypoplastic left heart syndrome. *Pediatrics* 1990;85:984–90.
7. Licht DJ, Wang J, Silvestre DW et al. Preoperative cerebral blood flow is diminished in neonates with severe congenital heart defects. *J Thorac Cardiovasc Surg* 2004;128:841–9.
8. Miller SP, McQuillen PS, Hamrick S et al. Abnormal brain development in newborns with congenital heart disease. *N Engl J Med* 2007;357:1928–38.
9. Hornberger LK, Sanders SP, Rein AJ et al. Left heart obstructive lesions and left ventricular growth in the midtrimester fetus. A longitudinal study. *Circulation* 1995;92:1531–8.
10. McElhinney DB, Geiger E, Blinder J et al. NKX2.5 mutations in patients with congenital heart disease. *J Am Coll Cardiol* 2003;42:1650–5.
11. Dasgupta C, Martinez AM, Zuppan CW et al. Identification of connexin43 (alpha1) gap junction gene mutations in patients with hypoplastic left heart syndrome by denaturing gradient gel electrophoresis (DGGE). *Mutat Res* 2001;479:173–86.
12. Garg V, Muth AN, Ransom JF et al. Mutations in NOTCH1 cause aortic valve disease. *Nature* 2005;437:270–4.
13. Lewin MB, McBride KL, Pignatelli R et al. Echocardiographic evaluation of asymptomatic parental and sibling cardiovascular anomalies associated with congenital left ventricular outflow tract lesions. *Pediatrics* 2004;114:691–6.
14. Loffredo CA, Chokkalingam A, Sill AM et al. Prevalence of congenital cardiovascular malformations among relatives of infants with hypoplastic left heart, coarctation of the aorta, and d-transposition of the great arteries. *Am J Med Genet A* 2004; 124:225–30.
15. Hinton RB Jr, Martin LJ, Tabangin ME et al. Hypoplastic left heart syndrome is heritable. *J Am Coll Cardiol* 2007;50:1590–5.
16. Bharati S, Lev M. The surgical anatomy of hypoplasia of aortic tract complex. *J Thorac Cardiovasc Surg* 1984;88:97–101.
17. Weinberg PM, Weindling S. Atrial septal anomalies differentiate types of hypoplastic left heart syndrome (abstr). *J Am Coll Cardiol* 1988;12(Suppl. A):136A.
18. Chin AJ, Weinberg PM, Barber G. Subcostal two-dimensional echocardiographic identification of anomalous attachment of septum primum in patients with left atrioventricular valve underdevelopment. *J Am Coll Cardiol* 1990;15:678–81.
19. Rychik J, Rome JJ, Collins MH et al. The hypoplastic left heart syndrome with intact atrial septum: atrial morphology, pulmonary vascular histopathology and outcome. *J Am Coll Cardiol* 1999;34:554–60.
20. Glatz JA, Tabbutt S, Gaynor JW et al. Hypoplastic left heart syndrome with atrial level restriction in the era of prenatal diagnosis. *Ann Thorac Surg* 2007;84:1633–8.
21. Seliem MA, Chin AJ, Norwood WI. Patterns of anomalous pulmonary venous connection/drainage in hypoplastic left heart syndrome: diagnostic role of Doppler color flow mapping and surgical implications. *J Am Coll Cardiol* 1992;19:135–41.
22. Edwards JE, Du SJ, Alcott DL, Burchell HB. Thoracic venous anomalies. III. Atresia of the common pulmonary vein, the pulmonary veins draining wholly into the superior vena cava. *AMA Arch Pathol* 1951;51:446–60.
23. Bernstein HS, Moore P, Stanger P, Silverman NH. The levoatriocardinal vein: morphology and echocardiographic identification of the pulmonary-systemic connection. *J Am Coll Cardiol* 1995; 26:995–1001.
24. Fogel MA, Weinberg PM, Fellows KE, Hoffman EA. A study in ventricular-ventricular interaction. Single right ventricles compared with systemic right ventricles in a dual-chamber circulation. *Circulation* 1995;92:219–30.
25. Jonas RA, Hansen DD, Cook N, Wessel D. Anatomic subtype and survival after reconstructive operation for hypoplastic left heart syndrome. *J Thorac Cardiovasc Surg* 1994;107:1121–7; discussion 7–8.
26. Patel CR, Lane JR, Spector ML et al. Prenatal diagnosis of ventriculocoronary arterial communication in fetuses with hypoplastic left heart syndrome. *J Ultrasound Med* 2006;25: 245–9.
27. Glatz JA, Fedderly RT, Ghanayem NS, Tweddell JS. Impact of mitral stenosis and aortic atresia on survival in hypoplastic left heart syndrome. *Ann Thorac Surg* 2008;85:2057–62.
28. Checchia PA, McGuire JK, Morrow S et al. A risk assessment scoring system predicts survival following the Norwood procedure. *Pediatr Cardiol* 2006;27:62–6.
29. Helton JG, Aglira BA, Chin AJ et al. Analysis of potential anatomic or physiologic determinants of outcome of palliative surgery for hypoplastic left heart syndrome. *Circulation* 1986; 74:I.70–6.
30. Barber G, Helton JG, Aglira BA et al. The significance of tricuspid regurgitation in hypoplastic left-heart syndrome. *Am Heart J* 1988;116:1563–7.
31. Gaynor JW, Mahle WT, Cohen MI et al. Risk factors for mortality after the Norwood procedure. *Eur J Cardiothorac Surg* 2002;22:82–9.
32. Stasik CN, Gelehrter S, Goldberg CS et al. Current outcomes and risk factors for the Norwood procedure. *J Thorac Cardiovasc Surg* 2006;131:412–7.
33. Stamm C, Anderson RH, Ho SY. The morphologically tricuspid valve in hypoplastic left heart syndrome. *Eur J Cardiothorac Surg* 1997;12:587–92.
34. Jenkins PC, Flanagan MF, Jenkins KJ et al. Survival analysis and risk factors for mortality in transplantation and staged surgery for hypoplastic left heart syndrome. *J Am Coll Cardiol* 2000;36:1178–85.
35. Jenkins PC, Flanagan MF, Sargent JD et al. A comparison of treatment strategies for hypoplastic left heart syndrome using decision analysis. *J Am Coll Cardiol* 2001;38:1181–7.
36. Mahle WT, Cohen MS, Spray TL, Rychik J. Atrioventricular valve regurgitation in patients with single ventricle: impact of the bidirectional cavopulmonary anastomosis. *Ann Thorac Surg* 2001;72:831–5.
37. Michelfelder EC, Kimball TR, Pearl JM et al. Effect of superior cavopulmonary anastomosis on the rate of tricuspid annulus dilation in hypoplastic left heart syndrome. *Am J Cardiol* 2002; 89:96–8.
38. Reyes A 2nd, Bove EL, Mosca RS et al. Tricuspid valve repair in children with hypoplastic left heart syndrome during staged surgical reconstruction. *Circulation* 1997;96(9 Suppl.):II.341–3; discussion II.4–5.
39. Hawkins JA, Doty DB. Aortic atresia: morphologic characteristics affecting survival and operative palliation. *J Thorac Cardiovasc Surg* 1984;88:620–6.

40. Machii M, Becker AE. Nature of coarctation in hypoplastic left heart syndrome. *Ann Thorac Surg* 1995;59:1491–4.
41. Devloo-Blancquaert A, Titus JL, Edwards JE et al. Interruption of aortic arch and hypoplastic left heart syndrome. *Pediatr Cardiol* 1995;16:304–8.
42. Lloyd TR, Evans TC, Marvin WJ Jr. Morphologic determinants of coronary blood flow in the hypoplastic left heart syndrome. *Am Heart J* 1986;112:666–71.
43. Ito T, Niino M, Ishikawa J et al. Hypoplastic left heart syndrome with a single coronary artery originating from the pulmonary artery. *Acta Paediatr Jpn* 1995;37:61–3.
44. Sarris GE, Drummond-Webb JJ, Ebeid MR et al. Anomalous origin of left coronary from right pulmonary artery in hypoplastic left heart syndrome. *Ann Thorac Surg* 1997;64:836–8.
45. Rychik J, Gullquist SD, Jacobs ML, Norwood WI. Doppler echocardiographic analysis of flow in the ductus arteriosus of infants with hypoplastic left heart syndrome: relationship of flow patterns to systemic oxygenation and size of interatrial communication. *J Am Soc Echocardiogr* 1996;9:166–73.
46. Norwood WI, Lang P, Hansen DD. Physiologic repair of aortic atresia-hypoplastic left heart syndrome. *N Engl J Med* 1983; 308:23–6.
47. Chrisant MR, Naftel DC, Drummond-Webb J et al. Fate of infants with hypoplastic left heart syndrome listed for cardiac transplantation: a multicenter study. *J Heart Lung Transplant* 2005;24:576–82.
48. Galantowicz M, Cheatham JP. Lessons learned from the development of a new hybrid strategy for the management of hypoplastic left heart syndrome. *Pediatr Cardiol* 2005;26: 190–9.
49. Akintuerk H, Michel-Behnke I, Valeske K et al. Stenting of the arterial duct and banding of the pulmonary arteries: basis for combined Norwood stage I and II repair in hypoplastic left heart. *Circulation* 2002;105:1099–103.
50. Sano S, Ishino K, Kado H et al. Outcome of right ventricle-to-pulmonary artery shunt in first-stage palliation of hypoplastic left heart syndrome: a multi-institutional study. *Ann Thorac Surg* 2004;78:1951–7; discussion 7–8.
51. Sano S, Ishino K, Kawada M et al. Right ventricle-pulmonary artery shunt in first-stage palliation of hypoplastic left heart syndrome. *J Thorac Cardiovasc Surg* 2003;126:504–9; discussion 9–10.
52. Sano S, Ishino K, Kawada M, Honjo O. Right ventricle-pulmonary artery shunt in first-stage palliation of hypoplastic left heart syndrome. *Semin Thorac Cardiovasc Surg Pediatr Card Surg Annu* 2004;7:22–31.
53. Remmell-Dow DR, Bharati S, Davis JT et al. Hypoplasia of the Eustachian valve and abnormal orientation of the limbus of the foramen ovale in hypoplastic left heart syndrome. *Am Heart J* 1995;130:148–52.
54. Kadletz M, Black MD, Smallhorn J et al. Total anomalous systemic venous drainage to the coronary sinus in association with hypoplastic left heart disease: more than a mere coincidence. *J Thorac Cardiovasc Surg* 1997;114:282–4.
55. Ohta N, Sakamoto K, Kado M et al. Surgical treatment of coronary sinus orifice atresia with hypoplastic left heart syndrome after total cavo-pulmonary connection. *Ann Thorac Surg* 2002;73:653–5.
56. Salminen JT, Hakala T, Pihkala J et al. Coronary sinus orifice atresia with left superior vena cava in patients with univentricular heart. *Ann Thorac Surg* 2006;81:e16–17.
57. Brann S, Brawn WJ, Raafat F, Sreeram N. Neonatal pulmonary vascular disease in hypoplastic left heart syndrome. *Ann Thorac Surg* 1995;60:433–4.
58. Vlahos AP, Lock JE, McElhinney DB, van der Velde ME. Hypoplastic left heart syndrome with intact or highly restrictive atrial septum: outcome after neonatal transcatheter atrial septostomy. *Circulation* 2004;109:2326–30.
59. Gossett JG, Rocchini AP, Lloyd TR, Graziano JN. Catheter-based decompression of the left atrium in patients with hypoplastic left heart syndrome and restrictive atrial septum is safe and effective. *Catheter Cardiovasc Interv* 2006;67:619–24.
60. Michelfelder E, Gomez C, Border W et al. Predictive value of fetal pulmonary venous flow patterns in identifying the need for atrial septoplasty in the newborn with hypoplastic left ventricle. *Circulation* 2005;112:2974–9.
61. Chintala K, Tian Z, Du W et al. Fetal pulmonary venous Doppler patterns in hypoplastic left heart syndrome: relationship to atrial septal restriction. *Heart* 2008;94:1446–9.
62. Marshall AC, van der Velde ME, Tworetzky W et al. Creation of an atrial septal defect in utero for fetuses with hypoplastic left heart syndrome and intact or highly restrictive atrial septum. *Circulation* 2004;110:253–8.
63. Murdison KA, Baffa JM, Farrell PE Jr et al. Hypoplastic left heart syndrome. Outcome after initial reconstruction and before modified Fontan procedure. *Circulation* 1990;82(5 Suppl.): IV199–207.
64. Rychik J, Bush DM, Spray TL et al. Assessment of pulmonary/systemic blood flow ratio after first-stage palliation for hypoplastic left heart syndrome: development of a new index with the use of doppler echocardiography. *J Thorac Cardiovasc Surg* 2000;120:81–7.
65. Cardis BM, Fyfe DA, Ketchum D, Mahle WT. Echocardiographic features and complications of the modified Norwood operation using the right ventricle to pulmonary artery conduit. *J Am Soc Echocardiogr* 2005;18:660–5.
66. Mahle WT, Rychik J, Gaynor JW et al. Restrictive interatrial communication after reconstructive surgery for hypoplastic left heart syndrome. *Am J Cardiol* 2001;88:1454–7, A9.
67. Fraisse A, Colan SD, Jonas RA et al. Accuracy of echocardiography for detection of aortic arch obstruction after stage I Norwood procedure. *Am Heart J* 1998;135:230–6.
68. Cardis BM, Fyfe DA, Mahle WT. Elastic properties of the reconstructed aorta in hypoplastic left heart syndrome. *Ann Thorac Surg* 2006;81:988–91.
69. Lemler MS, Zellers TM, Harris KA, Ramaciotti C. Coarctation index: identification of recurrent coarctation in infants with hypoplastic left heart syndrome after the Norwood procedure. *Am J Cardiol* 2000;86:697–9, A9.
70. Bridges ND, Jonas RA, Mayer JE et al. Bidirectional cavopulmonary anastomosis as interim palliation for high-risk Fontan candidates. Early results. *Circulation* 1990;82(5 Suppl.): IV170–6.
71. Douville EC, Sade RM, Fyfe DA. Hemi-Fontan operation in surgery for single ventricle: a preliminary report. *Ann Thorac Surg* 1991;51:893–9; discussion 900.

72. Brown DW, Gauvreau K, Moran AM et al. Clinical outcomes and utility of cardiac catheterization prior to superior cavopulmonary anastomosis. *J Thorac Cardiovasc Surg* 2003;126:272–81.
73. Brown DW, Gauvreau K, Powell AJ et al. Cardiac magnetic resonance versus routine cardiac catheterization before bidirectional Glenn anastomosis in infants with functional single ventricle: a prospective randomized trial. *Circulation* 2007;116: 2718–25.
74. Ro PS, Rychik J, Cohen MS et al. Diagnostic assessment before Fontan operation in patients with bidirectional cavopulmonary anastomosis: are noninvasive methods sufficient? *J Am Coll Cardiol* 2004;44:184–7.
75. Fogel MA. Is routine cardiac catheterization necessary in the management of patients with single ventricles across staged Fontan reconstruction? No! *Pediatr Cardiol* 2005;26:154–8.
76. Cohen MS, Marino BS, McElhinney DB et al. Neo-aortic root dilation and valve regurgitation up to 21 years after staged reconstruction for hypoplastic left heart syndrome. *J Am Coll Cardiol* 2003;42:533–40.

# 21 Aortic Arch Anomalies: Coarctation of the Aorta and Interrupted Aortic Arch

**Jan Marek[1,2], Matthew Fenton[2] and Sachin Khambadkone[1,2]**

[1]Institute of Child Health, University College London
[2]Great Ormond Street Hospital for Children, London, United Kingdom

## Coarctation of the aorta

### Definition

Coarctation of the aorta (COA) refers to narrowing of the aortic isthmus. Hypoplasia of the aortic arch and other associated cardiovascular anomalies are common. The term is also used to describe strictures of other segments of the thoracic or the abdominal aorta.

### Incidence

The incidence of COA is approximately 36 (range 29–49) per 100 000 live births, making it the seventh most common form of congenital heart disease (CHD), occurring in approximately 5–7% of CHD patients [1,2]. In about 64% of patients, COA manifests as the dominant CHD soon after birth, whereas in the remaining 36% it manifests at an older age. COA is 1.3–1.7 times more likely in males [3,4]. In prenatal series, COA constitutes 3–10% of all prenatal diagnoses of CHD [5].

### Etiology

No single cause of COA has been proven and evidence points to an interplay between genetic, environmental and hemodynamic factors [4–8]. Abnormal flow distribution during fetal life with decreased aortic flow has long been suspected. This is supported by the observation that 71% of cases of aortic atresia also have COA [6]. The role of genetic factors is increasingly recognized. For example, COA occurs in 12% of patients with Turner syndrome (XO), and the incidence of chromosome 22q11 microdeletion is increased in patients with coarctation or interruption of the aortic arch [7,8].

### Morphology and classification

COA usually results from narrowing of the aortic isthmus at its junction with the proximal descending aorta at the insertion of the arterial duct (juxtaductal coarctation). The anatomic spectrum is wide but different morphologic patterns can be distinguished based on age at diagnosis – before birth, early infancy, and in older children and adults. In the fetus and infant, the distal transverse aortic arch between the left common carotid and left subclavian arteries is often elongated and hypoplastic (tubular hypoplasia), the angle between the ascending aorta and transverse arch is acute, the aortic isthmus is diffusely hypoplastic, and the arterial duct is usually patent [5]. In neonates, gradual development of COA is reported during closure of the arterial duct, and histologic studies have demonstrated ductal tissue circumferentially surrounding the juxtaductal portion of the aorta [9]. Although the stenotic site is typically located at the distal isthmus, other locations or multiple sites can be found (e.g., opposite or proximal to the origin of the left subclavian or any other brachiocephalic artery). In older children and adults, aortic arch hypoplasia is less common, the coarctation segment is usually discrete, and collateral arteries bypassing the COA are common. These collateral vessels develop from increased flow through the internal mammary, intercostals, and scapular arteries.

Regardless of age at diagnosis, the coarctation segment is characterized by luminal narrowing due to thickening of the intima and media layers, hypoplasia and tortuosity. The endoluminal protrusion of the intimal–medial ridge (or "shelf") is typically circumferential but is often more prominent along the posterior and lateral wall of the aortic isthmus. The length of the stenotic segment varies from discrete (2–3 mm) to long-segment (7–20 mm). The proximal descending aorta immediately past the coarctation often exhibits poststenotic dilation, a feature more commonly found in older children and adults.

A high incidence (>50%) of associated cardiac abnormalities suggests that COA is a more complex defect than isolated narrowing of the aorta. COA is commonly associated with bicommissural aortic valve, ventricular septal defect (VSD), subvalvar and valvar aortic stenosis, common atrioventricular canal, transposition of the great arteries, double-outlet right ventricle (RV), secundum atrial septal defect (ASD), single ventricle, and tricuspid atresia with transposition of the great arteries. In fact, COA has been described in association with almost every type of CHD although its

*Echocardiography in Pediatric and Congenital Heart Disease: From Fetus to Adult*
Edited by Wyman W. Lai, Luc L. Mertens, Meryl S. Cohen and Tal Geva
 ISBN: 978-1-405-17401-5

association with right heart obstructive lesions is rare. COA is particularly common in patients with multiple left heart obstructive lesions, and it is part of Shone syndrome.

Rarely, COA affects other segments of the aorta. The morphology and pathophysiology of abdominal coarctation is different from coarctation of the aortic isthmus in that the involved segment is often long, the aortic media is markedly thickened, and involvement of the renal and mesenteric vessels is common. Involvement of the thoracic and abdominal aorta and branches has been reported in Takayasu aortitis, supravalvar aortic stenosis (Williams syndrome, familial aortic stenosis and sporadic supravalvar aortic stenosis) and mid-aortic syndrome.

"Pseudocoarctation" of the aorta refers to deformity of the aortic isthmus characterized by tortuosity but without luminal narrowing. The isthmus and part of the descending thoracic aorta are deformed, most frequently into the shape of the digit three ("3"). Internally, the caliber of the isthmus is not narrowed and blood flow is not obstructed.

## Pathophysiology

### Prenatal

The hemodynamic consequences of COA are usually tolerated well in the fetus because blood flow to the lower body and the placenta is supplied predominantly through the arterial duct with only ~10% of the combined cardiac output crossing the aortic isthmus. Narrowing of the aortic isthmus results in diversion of blood flow from the aorta to the pulmonary artery and the arterial duct. As a result, LV afterload increases and its output decreases, whereas RV output increases. Consequently, the RV dilates whereas the left ventricle (LV) is pressure loaded [10], resulting in the ventricular size disproportion observed when COA is present in the fetus.

### Neonatal

The pathophysiology of COA in the neonate depends on a complex interplay between the severity of aortic narrowing, the rate at which the COA progresses, patency of the arterial duct, pulmonary vascular resistance and associated cardiac anomalies. The hemodynamic burden imposed by severe COA manifests after birth as the foramen ovale closes and the arterial duct constricts and ultimately closes. As a result, the LV supplies the entire cardiac output and flow to the lower body must cross the narrow aortic segment(s). Under these conditions, the LV faces pressure overload and, as long as ventricular function is preserved, systolic blood pressure in the upper body is increased. In contrast, distal to the COA the systolic blood pressure is low, clinically manifesting as reduced pulse amplitude in the femoral arteries. When the coarctation occurs proximal to the left subclavian artery, decreased pulse amplitude is noted in the left arm. In the rare circumstance of COA proximal to the left subclavian artery associated with aberrant origin of the right subclavian artery, blood pressures and pulse volumes in the arms are similar to those in the lower extremities.

In neonates with severe COA, the increased impedance to LV emptying leads to elevated end-diastolic pressure and left atrial, pulmonary venous, and pulmonary arterial hypertension. A widely patent arterial duct allows right-to-left systolic flow from the main pulmonary artery to the descending aorta, providing adequate perfusion to the lower body and normal volume of the femoral pulse. In the absence of an atrial-level right-to-left shunt or associated cardiac lesions, oxygen saturation in the upper extremities (preductal) is greater than that in the lower extremities (postductal), a phenomenon called *differential cyanosis*.

Constriction and ultimate closure of the arterial duct in neonates with severe or rapidly progressing COA leads to LV dysfunction. Increased afterload due to the COA, decreased preload secondary to increased pulmonary vascular resistance and diastolic septal shift towards the LV, and decreased myocardial perfusion contribute to LV dysfunction. Failure of compensatory mechanisms ultimately leads to decreased cardiac output, hypoperfusion of the lower body, oliguria, acidosis, and shock. If the COA develops slowly and pulmonary vascular resistance normalizes, the left ventricular myocardium hypertrophies in response to the pressure load, wall stress is maintained and systolic function is preserved.

### Adult

Later in life coarctation is usually diagnosed either due to a heart murmur, low pulse amplitude in the lower extremities or systemic hypertension. The clinical course of this type of coarctation is often insidious. This is usually due to development of collateral vessels between the high-pressure aortic branches proximal to the COA and the low-pressure distal aorta. When the collateral vessels are extensive, the pulse volume and blood pressure in the lower extremities can be near normal. Left ventricular pressure overload is gradual in onset and myocardial failure usually develops over decades in response to systemic hypertension and coronary artery disease. Another complication seen in adults with COA is cerebral aneurysm(s).

## Imaging

Echocardiography provides adequate diagnostic information in most newborns, infants and young children. However, older children and adults often require other diagnostic modalities – e.g., magnetic resonance imaging (MRI) or computed tomography (CT) – as echocardiographic imaging of the aortic isthmus and proximal descending aorta is difficult because of increased distance from the transducer and intervening airways. It is imperative that comprehensive evaluation of the aortic arch, arch branches, isthmus, and descending aorta is performed before selecting a management plan. Two-dimensional (2D) echocardiographic imaging as well as color and spectral Doppler techniques are used from suprasternal, right and left infraclavicular approaches to evaluate the anatomy and to quantify the degree of obstruction.

### Goals of echocardiography

The goals of echocardiographic examination in the setting of coarctation of the aorta can be summarized as follows:

- Evaluation of heart situs and segmental cardiac anatomy.
- Doppler evaluation of flow profile in the descending aorta at or below the level of the diaphragm.
- Evaluation of aortic arch anatomy, origins of brachiocephalic vessels, aortic isthmus, and proximal descending aorta.
- Assessment of flow gradients in the transverse arch and at the COA site.
- Evaluation of flow in the arterial duct.
- Evaluation of morphology, size and function of the LV inflow and outflow, including the supramitral area, mitral valve, LV outflow, aortic valves, and sinotubular junction.
- Measurements of LV size (diameter, length, volume, thickness, and mass) and function.
- Evaluation of atrial communication(s), including direction of flow and measurement of mean pressure gradient.
- Estimation of the degree of pulmonary hypertension.
- Identification of associated anomalies.

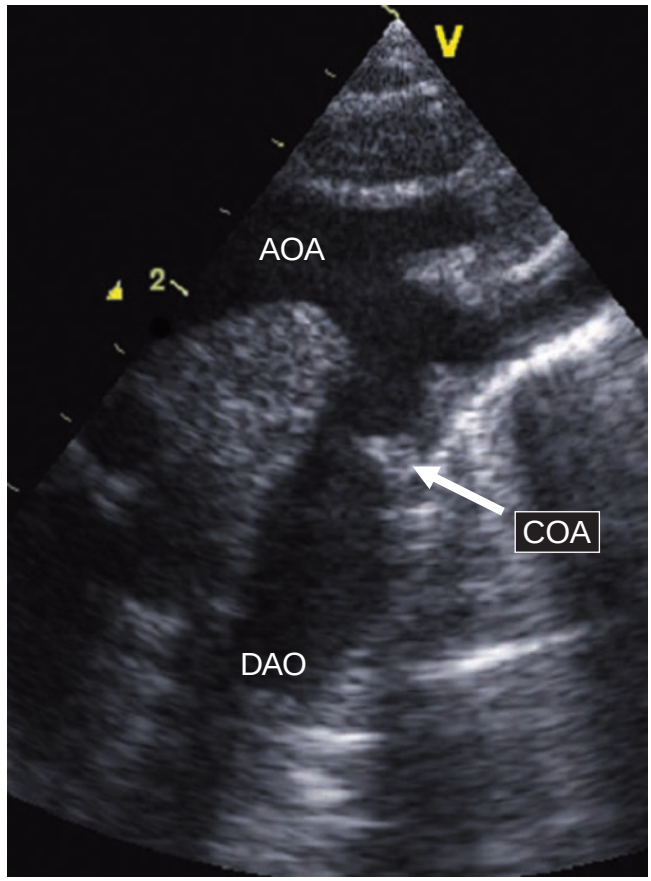


**Figure 21.1** Imaging of neonatal coarctation of the aorta from the suprasternal notch view. A coarctation ridge (COA) is located ~5 mm below the origin of left subclavian artery. Descending thoracic aorta (DAO) below the obstruction is dilated. AOA, aortic arch.

### Neonatal coarctation

#### *Imaging of the aortic arch and isthmus*

The entire aortic arch, isthmus, arterial duct, and descending aorta are imaged from the suprasternal notch and from the right and left infraclavicular windows. Extension of the neck and upper thorax by placing a rolled towel under the shoulders facilitates imaging. Because the distance between the transducer and the aorta is short, we recommend using a transducer with frequencies ranging from 7.5 to 12 MHz to provide high-resolution imaging.

Imaging is first performed in the transverse plane, following the ascending aorta cranially, demonstrating the arch branching pattern, and imaging the transverse arch. This view is essential to characterize the anatomy and sidedness of the aortic arch and to exclude associated abnormalities such as double aortic arch and aberrant origin of a subclavian artery. The oblique sagittal plane is then used to visualize the long axis of the ascending aorta, arch, isthmus, and proximal descending aorta (Fig. 21.1 and Videoclip 21.1). In neonates, the right infraclavicular area is particularly helpful for depicting most of the thoracic aorta in one plane. The distal aortic arch (between the left common carotid and left subclavian arteries) is often elongated and hypoplastic. The hypoplasia may extend from the origin of the brachiocephalic trunk or the left carotid artery up to the site of COA (Fig. 21.2 and

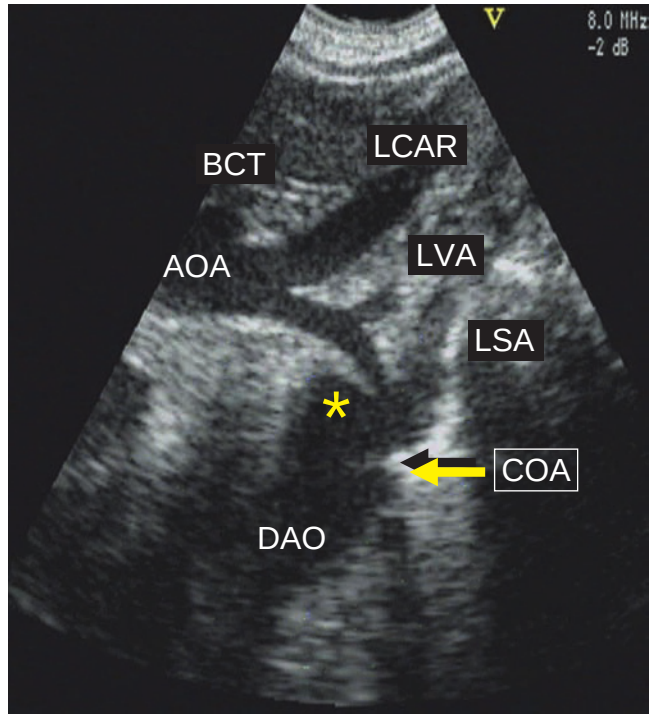


**Figure 21.2** Neonatal coarctation of the aorta (COA) with severe transverse aortic arch hypoplasia seen from the suprasternal view. It shows an elongated hypoplastic arch with maximal narrowing between the left carotid artery (LCAR), left vertebral artery (LVA) and left subclavian artery (LSA), which is predominantly supplied by arterial duct (asterisk).
AOA, aortic arch; BCT, brachiocephalic trunk; DAO, descending aorta.

Videoclips 21.2 and 21.3). The site of maximal narrowing is determined by 2-D imaging and color Doppler and the diameter of the narrowest aortic segment is then measured on a 2D image. Using body surface area-adjusted normal values (see Appendix 1), the z-score of the narrowest arch segment is calculated. The arch is defined as hypoplastic if its diameter z-score is less than –2.0.

The aortic isthmus, defined as the segment of the aorta distal to the origin of the left subclavian artery and the aortic end of the arterial duct, can be seen from the right subclavicular or suprasternal notch windows. When the isthmus is tortuous, imaging from the left subclavicular window in the sagittal plane often allows detailed imaging of the coarctation site. The degree of isthmus hypoplasia varies in both length and diameter. A protruding ridge is typically present at the site of COA but additional sites of obstruction can coexist due to the presence of another ridge, hypoplasia of the isthmus or both. The ridge is directed from the lateral and posterior aspects of the isthmus toward the aortic end of the arterial duct (Fig. 21.1 and Videoclip 21.1). When assessing flow through the aortic isthmus, the suprasternal or right subclavicular windows usually provide an optimal angle for Doppler interrogation. The sample volume is placed at the site of maximum narrowing to avoid overlap with ductal flow. Flow across the isthmus is forward and continuous throughout the cardiac cycle, producing the characteristic appearance of a diastolic tail (Figs 21.3 and 21.4). When the arterial duct is restrictive or closed and LV systolic function is preserved, the pressure difference across the coarctation is high. The Doppler flow tracing shows a characteristic "serrated" pattern with rapid acceleration and an early high-velocity systolic peak, followed by gradual deceleration throughout diastole (Fig. 21.4). Evaluation of the severity of coarctation with preserved LV systolic function is based on the peak and not the mean gradient because inclusion of the diastolic phase of the antegrade flow would not accurately reflect the systolic gradient. When multiple obstructions are present, usually in the context of associated aortic arch hypoplasia, the gradient measured by pulsed Doppler proximal to the isthmus should be subtracted from the total coarctation gradient measured by continuous-wave Doppler (Fig. 21.3).

Echocardiographic assessment in developing or mild COA may differ from results obtained in the more severe forms (Fig. 21.5). Instead of a typical coarctation ridge, 2D imaging demonstrates only mild isthmic narrowing. The Doppler signal in this situation shows only systolic acceleration rather than a typical "serrated" flow pattern.

Imaging of the arterial duct is performed from the left infraclavicular window, a position that provides an optimal angle for assessing ductal flow. When the COA is severe and pulmonary hypertension coexists, flow through the arterial duct is bidirectional – from the main pulmonary artery to the descending aorta during systole, and from the aorta to the pulmonary artery during diastole (Fig. 21.6; Videoclips 21.2 and 21.3). In patients without pulmonary hypertension, flow is from the aorta to the main pulmonary artery throughout the cardiac cycle. The optimal position of the pulsed Doppler sample is in the middle of the arterial duct. Repeat echocardiographic examination should be performed shortly after beginning prostaglandin administration to confirm ductal patency (Fig. 21.7).

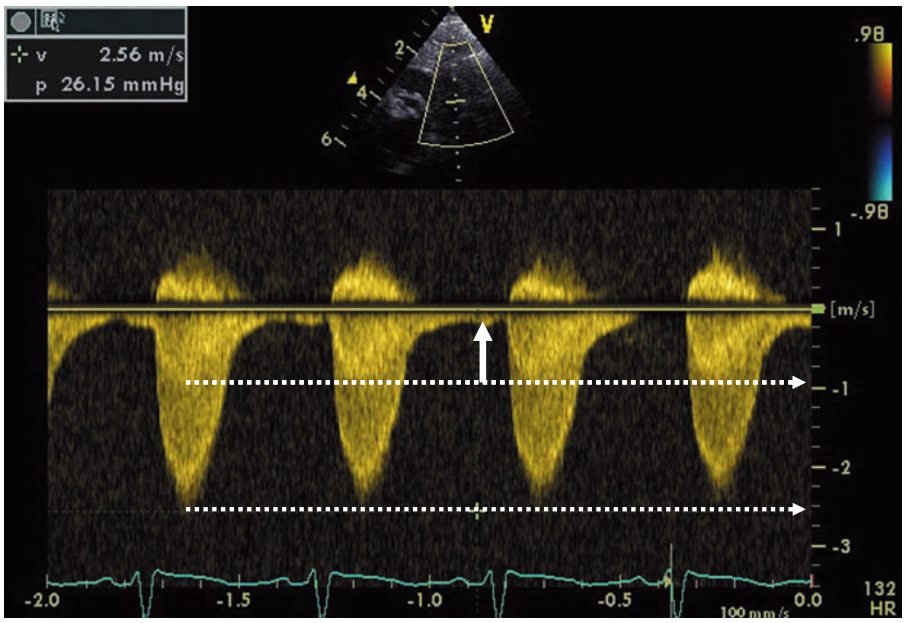


**Figure 21.3** Flow characteristics in aortic isthmus in neonatal coarctation. Summation of accelerated forward flow in systole across arterial duct (2.56 m/s) and lower velocity systolic flow (1 m/s) across aortic isthmus, and low-velocity diastolic flow (arrow) with respiratory variation through the aortic isthmus as a result of reduction in diastolic blood pressure in the pulmonary artery.

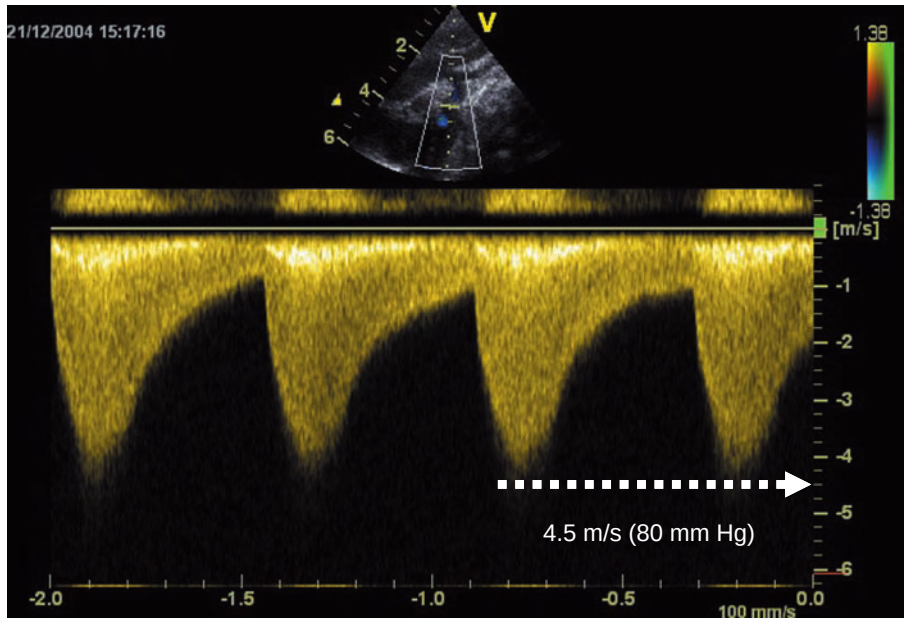


**Figure 21.4** Continuous-wave Doppler through the aortic isthmus of a patient with severe COA. Note the high-velocity systolic amplitude (4.5 m/s) with continuous antegrade flow throughout diastole.

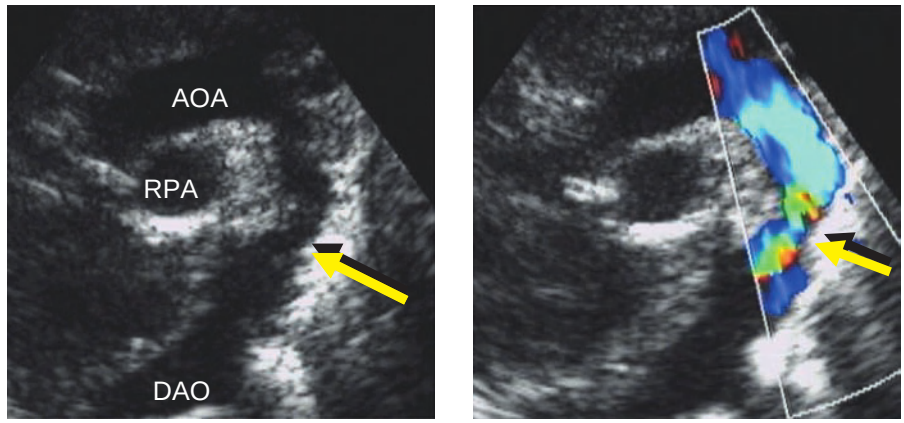


(a) (b)

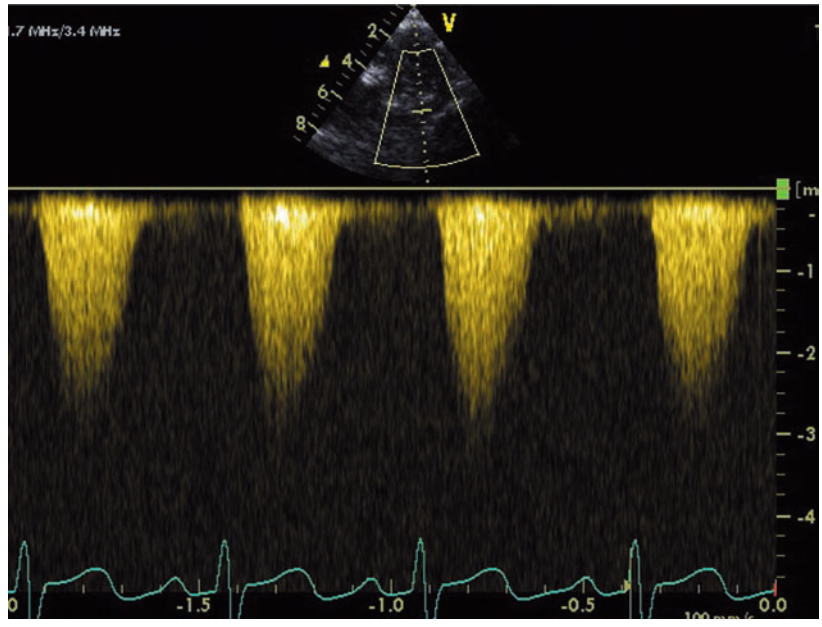


(c)

**Figure 21.5** Evolving coarctation (arrows) in a 6-week-old infant. **(a)** 2-D imaging; **(b)** color Doppler flow mapping; and **(c)** pulsed Doppler. Color aliasing indicates flow acceleration across mild isthmic narrowing in the absence of arterial duct. Pulsed Doppler technique indicated systolic acceleration (3 m/s) with no persistent diastolic flow. AOA, aortic arch; DAO, descending aorta; RPA, right pulmonary artery.

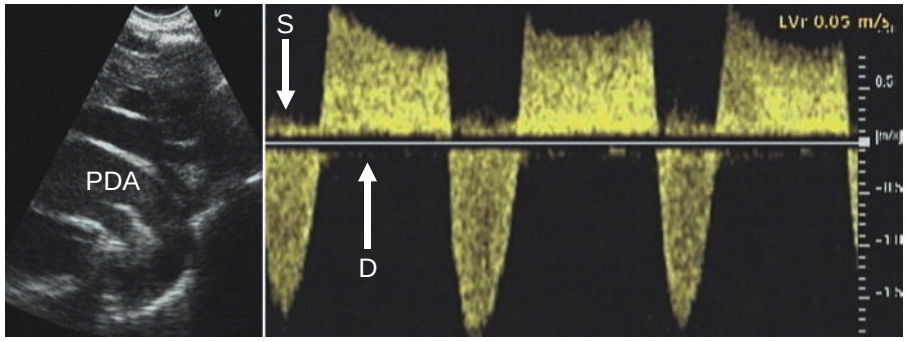


(a) (b)

**Figure 21.6** Ductal (PDA) flow patterns in severe neonatal coarctation. **(a)** The sample volume is placed in the middle of the arterial duct. **(b)** Bidirectional low-velocity flow with systolic right-to-left direction indicating high pulmonary arterial pressure. S, systolic right-to-left flow; D, diastolic left-to-right flow; PDA, patent ductus arteriosus.

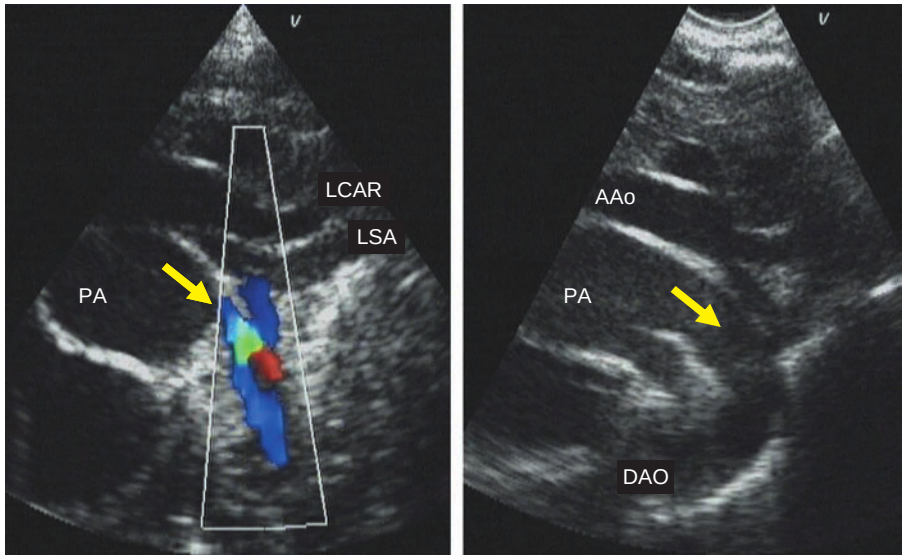


(a) (b)

**Figure 21.7** Serial echocardiograms in neonatal coarctation. **(a)** Restrictive arterial duct (arrow) demonstrated by color flow mapping prior to prostaglandin administration. **(b)** Significant ductal widening (arrow) after prostaglandin administration visualized by 2D imaging. AAo, ascending aorta; DAO, descending aorta; LCAR, left carotid artery; LSA, left subclavian artery; PA, pulmonary artery.

### *Subcostal views*

Following determination of abdominal situs, cardiac position and segmental evaluation of cardiac anatomy from the subcostal window, the characteristics of blood flow in the descending aorta at or below the level of the diaphragm are evaluated by pulsed Doppler. Care is taken to align the ultrasound beam with the long axis of the descending aorta. In neonates with severe COA, pulmonary hypertension and patent arterial duct, the amplitude of the pulse wave is usually slightly decreased or normal and the diastolic component is absent or slightly reversed. This essentially normal flow profile results from unimpeded systolic flow from the RV to the descending aorta through the arterial duct. The RV thus generates the pulse wave, and when systolic function is preserved, normal velocity is demonstrated in the aorta below the diaphragm (~20–40 cm/s; no angle correction). By contrast, in neonates with severe COA and a closing or a closed arterial duct, the flow profile in the abdominal aorta is strikingly different; it typically exhibits low-velocity systolic–diastolic flow with minimal phasic variations (Fig. 21.8). In addition to evaluation of the flow profile in the abdominal aorta, the entire aortic arch and the arterial duct can be viewed from the subcostal oblique sagittal plane.

Imaging of the atrial septum from the subcostal long- and short-axis views almost always demonstrates a patent foramen ovale. The direction of shunt is depicted by color flow mapping and by pulsed Doppler in the foramen ovale. In neonates with severe pulmonary hypertension and elevated right atrial pressure, flow across the foramen ovale is bidirectional. In neonates with less severe pulmonary hypertension flow is predominantly left-to-right with velocity proportional to the pressure gradient between the atria. Finally, the subcostal approach also provides excellent imaging of the size and function of the ventricles, the morphology and function of the atrioventricular (AV) valves, and the left and right ventricular outflow tracts. Table 21.1 summarizes key findings in infantile COA with and without pulmonary hypertension.

### *Apical views*

The apical 4-, 5- and 2-chamber views are important for assessment of LV inflow and outflow, measurements of LV volume and mass, and for determination of RV systolic

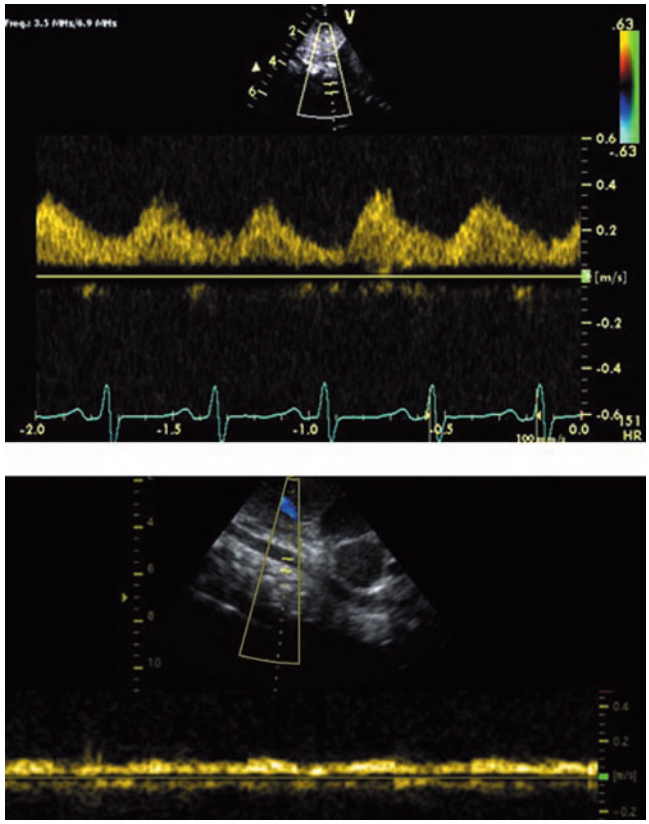


**Figure 21.8** Pulsed Doppler flow pattern in abdominal aorta from subcostal short-axis view. **(a)** Coarctation of the aorta (COA) with restrictive arterial duct and preserved systolic ventricular function in a 5-day-old neonate.The systolic waveform amplitude is low; antegrade diastolic flow indicates the obstruction proximal to sample volume. **(b)** COA with closed arterial duct and impaired systolic ventricular function in 10-day-old neonate. The abdominal aorta flow velocity is very low over the cardiac cycle indicating extremely low body perfusion.

pressure by the tricuspid regurgitation jet velocity. The mitral annulus in isolated neonatal COA may be small; however, mitral valve function is usually normal. Color and pulsed Doppler are used to evaluate the valve, with particular attention paid to restriction of blood flow at the level of the annulus, leaflets, chordae tendineae or at multiple levels (see Chapter 14 for further details). In an otherwise structurally normal mitral valve and nondilated LV with preserved systolic function, significant mitral regurgitation is uncommon.

Evaluation of the LV outflow from the apical window is particularly important due to the common association between COA and subvalvar and/or valvar aortic stenosis. The apical 4-, 5- and, in particular, the 2-chamber views are used to evaluate the morphology and flow characteristics across the LV outflow. Color, pulsed- and continuous-wave Doppler are used to determine the presence and severity of obstruction and/or regurgitation (see Chapter 19 for further details).

In neonates with severe pulmonary hypertension and a dilated RV, tricuspid regurgitation is often present due to annular dilation. Measurement of the peak tricuspid regurgitation jet velocity by Doppler provides an estimation of RV systolic pressure.

### *Parasternal views*

The parasternal long- and short-axis views are used to evaluate LV size and function; mitral valve morphology and function; LV outflow obstruction; aortic valve morphology, size and mechanism of stenosis or regurgitation; tricuspid regurgitation; and RV size and function. The RV outflow tract, pulmonary valve, and pulmonary arteries are also evaluated from the precordial windows. Measurement of the pulmonary regurgitation end-diastolic flow velocity provides information on the pulmonary artery diastolic pressure.

## Adult coarctation

COA in older children and adults is caused by slow progression of the aortic ridge into the lumen of the aortic isthmus (Fig. 21.9 and Videoclip 21.4). The presence of collateral arteries bypassing the COA is common. As mentioned earlier, suboptimal acoustic windows and a long distance from the transducer might hamper imaging of the distal aortic arch, isthmus and proximal descending aorta. Adjustment of

**Table 21.1** Echocardiographic features of coarctation of the aorta in infants with or without pulmonary hypertension

| Neonatal COA | PFO shunt | Left ventricle | | TR gradient | PDA | | COA gradient |
|---|---|---|---|---|---|---|---|
| | | Volume | Wall | | Dimension | Shunt | |
| **With pulmonary hypertension** | Right-to-left | Subnormal | Hypertrophy | >30 mm Hg | Patent | Bidirectional (low-velocity) | 0–20 mm Hg |
| **Without pulmonary hypertension** | Left-to-right | Normal or enlarged | Hypertrophy and dilation | <30 mm Hg | No (restrictive) | None or left-to-right (high-velocity) | 30–70 mm Hg (<30 mm Hg with LV dysfunction) |

The indicated values of gradients are approximate.
Abbreviations: COA, coarctation of aorta; LV, left ventricular; PDA, patent ductus arteriosus (patent arterial duct); PFO, patent foramen ovale; TR, tricuspid regurgitation.

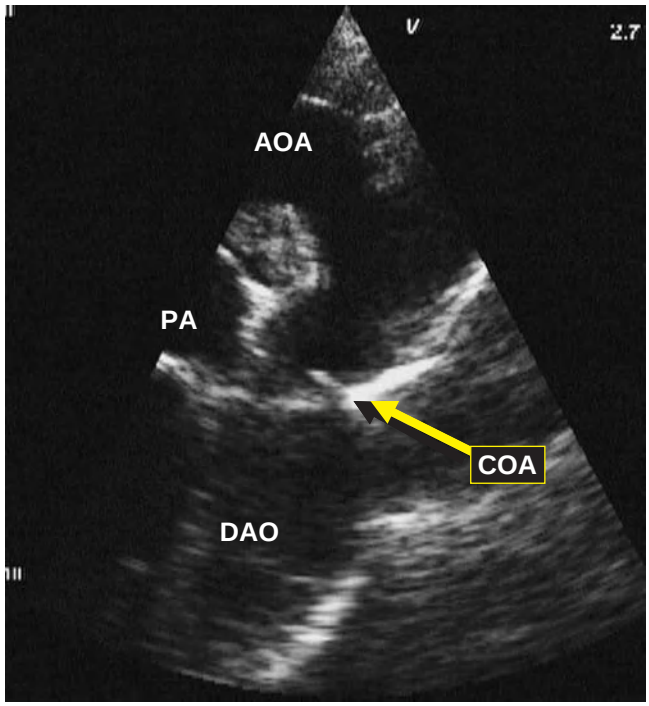


**Figure 21.9** Coarctation of the aorta (COA) in a 12-year-old boy. Note the discrete shelf partly occluding the aortic isthmus (COA) and marked poststenotic dilation of thoracic aorta. AOA, aortic arch; DAO, descending aorta; PA, pulmonary trunk.

patient position (e.g., extension of the neck), use of a low-frequency transducer and harmonic imaging are some of the tools that can aid in optimizing image quality. In addition, use of the left subclavicular window in the sagittal plane to visualize the aortic isthmus and the descending thoracic aorta is advised (Fig. 21.10 and Videoclip 21.5). Placing the patient in the left lateral decubitus position aids in obtaining this view. Doppler assessment of COA severity is similar to that in the neonate (Fig. 21.4). Optimal assessment of the velocity profile requires continuous-wave Doppler with a low-frequency filter to obtain a clear signal. As in neonatal COA, the gradient is estimated based on peak systolic velocity, not the mean gradient. When multiple obstructions of the aortic arch and isthmus coexist the contribution of each stenosis should be evaluated.

The Doppler flow profile of the abdominal aorta in adult COA is characterized by low-velocity systolic–diastolic flow, which can be visualized by pulsed Doppler and by color M-mode (Fig. 21.11). When significant collateral vessels are present the difference between the amplitudes of the systolic and diastolic components of the flow curve is inversely proportional to the size of arterial collaterals. The entire descending aorta (thoracic and abdominal) should also be imaged to exclude distal coarctation, which can involve the origins of the celiac, mesenteric and renal arteries (Fig. 21.12).

Similar to the assessment of neonatal COA, comprehensive echocardiographic evaluation of cardiac anatomy and function is crucial in older children and adults due to the high frequency of associated anomalies. Bicommissural aortic valve and dilation of the ascending aorta are common abnormalities in older children and adults with COA.

## Prenatal assessment

COA diagnosed in the fetus is characterized by narrowing of the aortic isthmus and by a frequently associated transverse arch hypoplasia [5]. The main pulmonary artery communicates with the descending aorta through a widely patent

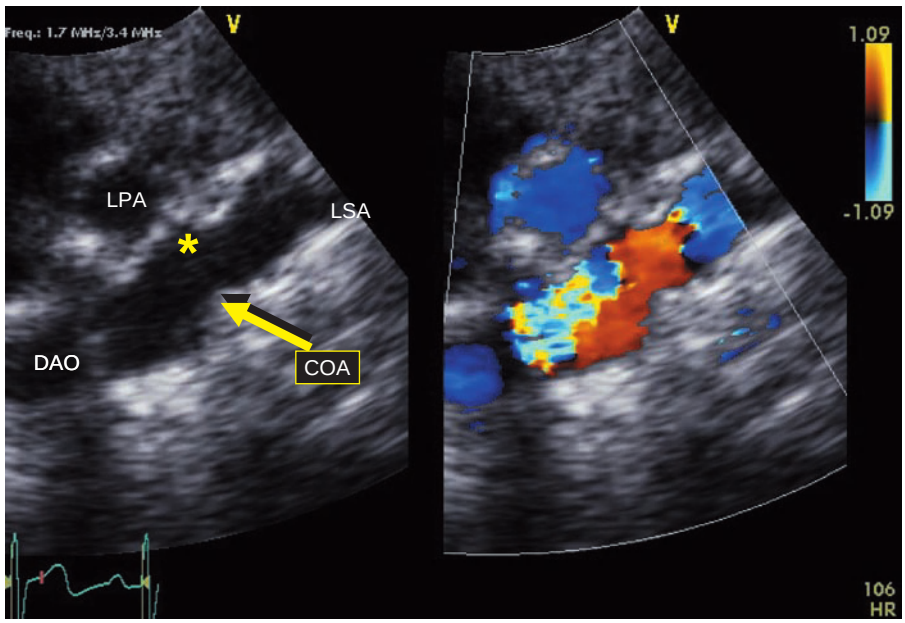


(a) (b)

**Figure 21.10** Left subclavicular view in the sagittal plane showing mild isthmic narrowing (arrow) in 7-year-old child. **(a)** A coarctation shelf (COA) is opposite to the aortic ampulla of the arterial duct (asterisk). **(b)** Flow acceleration across the aortic isthmus seen by color Doppler flow mapping. DAO, descending aorta; LPA, left pulmonary artery; LSA, left subclavian artery.

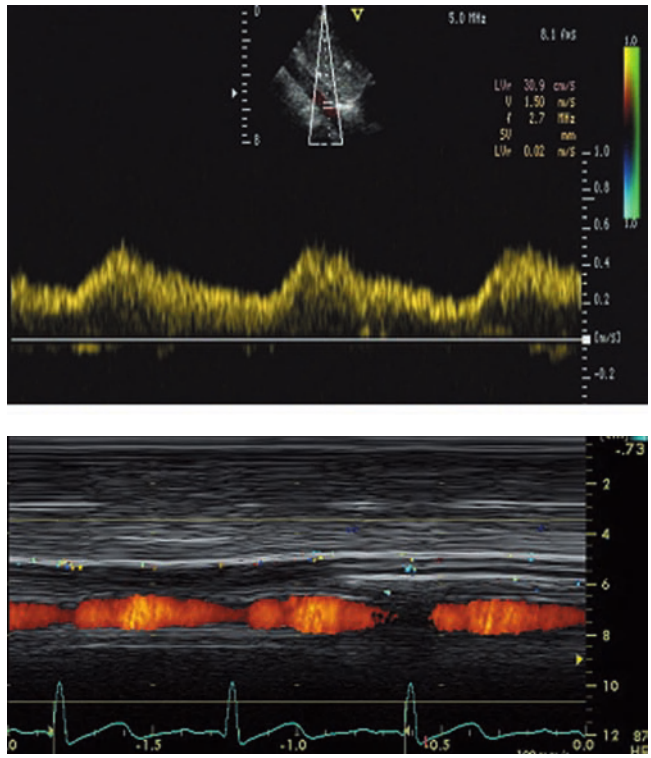

(a)

(b)

**Figure 21.11** Flow profile in the abdominal aorta of a 6-year-old child with coarctation of the aorta (COA). **(a)** Pulsed Doppler and **(b)** color M-mode. Systolic velocity does not exceed 50 cm/s, and antegrade diastolic flow of 25 cm/s indicates proximal obstruction with presence of collaterals. Continuous systolic–diastolic color flow Doppler superposed to 2D image in patient with COA and collaterals.

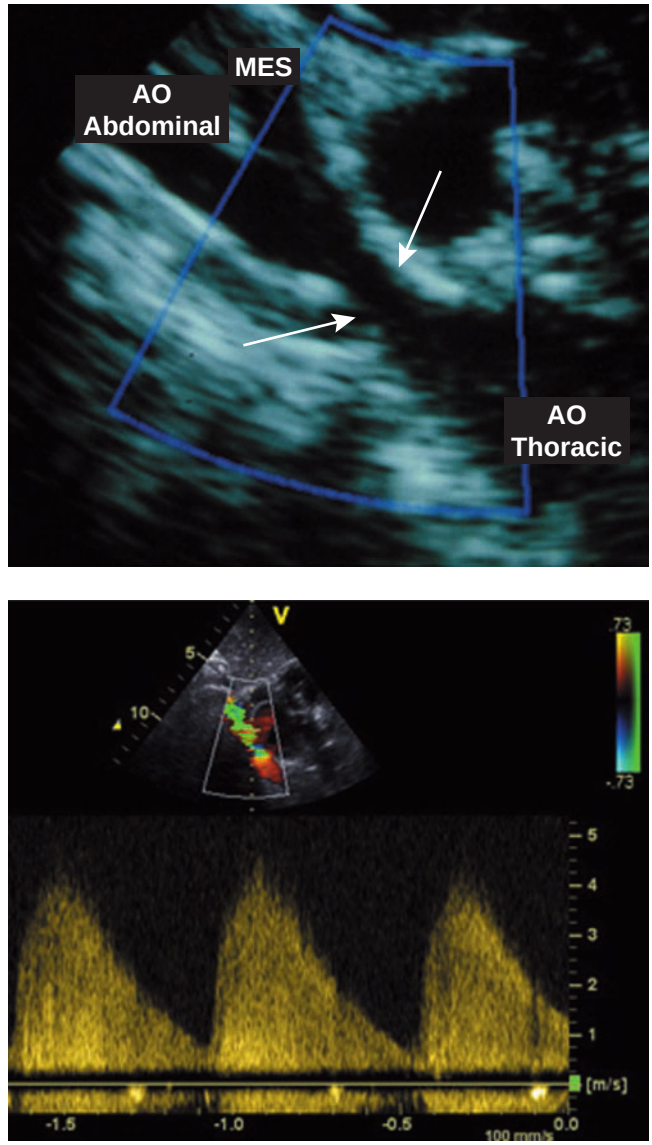


(a)

(b)

**Figure 21.12** **(a)** Coarctation (arrows) of suprarenal abdominal aorta in subcostal sagittal view. Narrowing was localized just above the origin of mesenteric artery (MES). **(b)** High-velocity (4.5 m/s) systolic–diastolic flow detected by continuous Doppler. AO, aorta.

arterial duct, creating a large ductal arch. Associated left heart obstructive lesions are also common.

Asymmetry of ventricular size (RV larger than LV) demonstrated in the 4-chamber view is frequently the first clue to prenatal diagnosis of COA (Fig. 21.13). The RV is enlarged and tricuspid regurgitation is frequently detected. RV dilation, however, is not specific for COA and is present in other forms of fetal cardiac and extracardiac anomalies. Ventricular function is usually normal and unlike other causes of RV enlargement no other signs of fetal–placental circulatory failure are present. Despite progress in fetal echocardiography and heightened awareness, prenatal diagnosis of COA continues to be challenging. Head and colleagues found that in only one-third of patients suspected by fetal echocardiography to have COA was the diagnosis ultimately confirmed after birth [11].

Diagnosis of COA in the fetus requires detailed imaging of the aortic arch and isthmus, and clear depiction of the aortic end of the arterial duct. The arch is visualized in the oblique sagittal plane either through the chest (Videoclip 21.6(a,b)) or through the back of the fetus. These views can depict the aorta along its entire length, including the root and ascending aorta, arch, origins of the brachiocephalic arteries, isthmus, and descending thoracic and abdominal aorta. The diameters of the aorta at different levels should be measured and compared with gestational age-adjusted normal values [12]. The ascending aorta is often smaller than the main pulmonary artery. Reliable diagnosis of COA can be made when aortic arch hypoplasia is present (Fig. 21.14). Demonstration of hypoplasia and/or tortuosity of the aortic isthmus are paramount for the diagnosis of COA in the fetus (Fig. 21.15). The width of the aortic isthmus is compared with the width of the aortic end of the arterial duct [13]. Color Doppler can be useful in assessing the width of both segments. It is

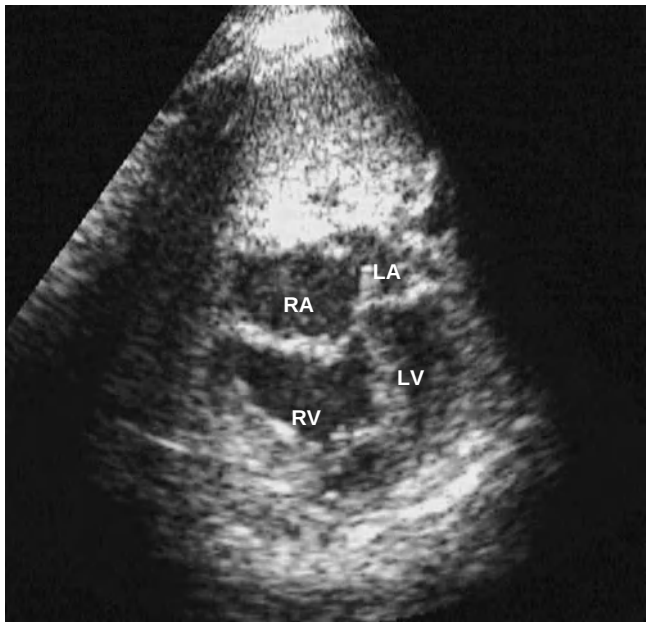


**Figure 21.13** Ventricular size disproportion seen in the 4-chamber view in a 26 weeks gestation fetus with coarctation of the aorta (COA). Right atrium (RA) and right ventricle (RV) are larger compared with left atrium (LA) and left ventricle (LV). The left ventricle is not hypoplastic and forms the apex of the heart.

important, however, to use appropriate color gain and velocity scale (Nyquist limit) to avoid "bleeding" of the flow signal. With optimum settings, stenotic flow can be seen at the site of the isthmus (Fig. 21.16 and Videoclip 21.7), and color flow mapping can be used to assess the diameters of the isthmus and arterial duct (Fig. 21.17).

### Therapeutic interventions and long-term follow-up

Treatment options for correction of COA include surgery, percutaneous balloon angioplasty and endovascular stent implantation. Although surgery is the dominant treatment choice for native COA in neonates, balloon angioplasty and/or stent implantation are commonly used for treatment of recurrent COA and native COA in older children and adults [14–17]. The treatment of choice among surgical techniques for COA repair is resection and end-to-end anastomosis. When patent, the arterial duct is ligated and divided. In patients with aortic arch hypoplasia, the arch is augmented either by an extended anastomosis between the undersurface of the arch and the descending aorta, or by reversed subclavian flap aortoplasty. Other less commonly used surgical techniques include subclavian flap aortoplasty, placement of a conduit bypassing the stenotic aortic segment, and patch plasty of the COA site. The latter technique has been associated with a high incidence of aneurysms at the repair site [18–20].

Echocardiographic evaluation after surgery or catheter-based treatment of COA is similar to that of native COA. Image quality is often hampered by postoperative changes and a larger body size, which restrict the acoustic windows available to image the distal arch, isthmus and descending aorta. The importance of detailed knowledge of the surgical or catheter procedure before the examination commences cannot be overemphasized. For example, following subclavian flap aortoplasty the proximal left subclavian artery is absent (Fig. 21.18). After balloon dilation of multilevel narrowing, restenosis between the brachiocephalic trunk and the left carotid artery, or between the left carotid and the left subclavian arteries can be seen. Visualization of a stent

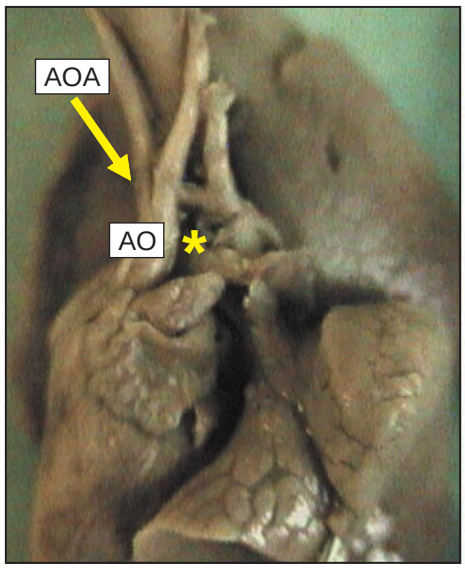


(a)

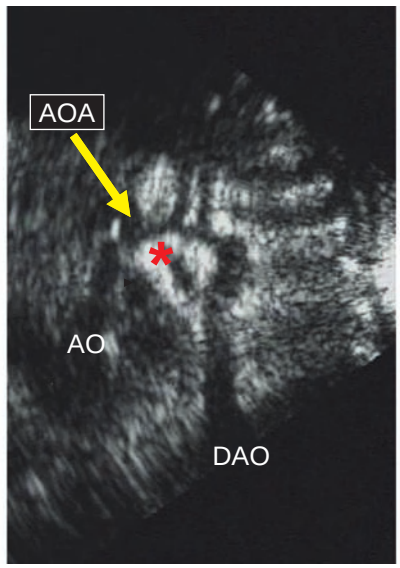


(b)

**Figure 21.14** Fetal coarctation with hypoplastic aortic arch (AOA). **(a)** Post-mortem; **(b)** prenatal echocardiogram. Hypoplastic transverse arch between left carotid and left subclavian artery (asterisks). AO, ascending aorta; DAO, descending aorta. Post-mortem specimen courtesy of Viera Povýšilová, Prague.

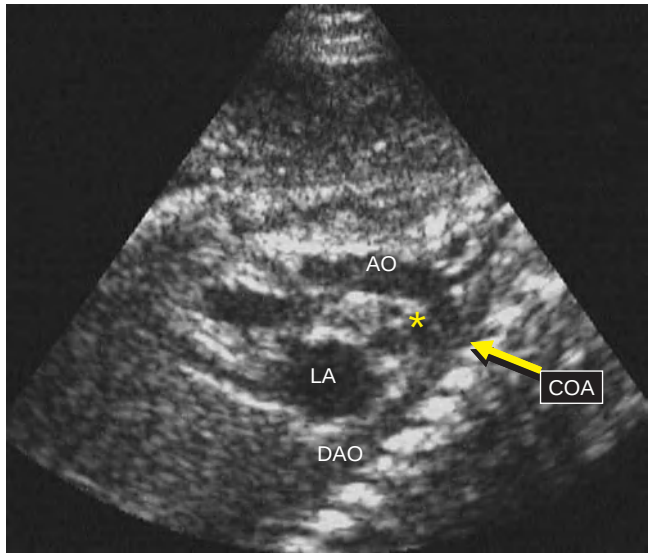


**Figure 21.15** Narrowing of the aortic isthmus (arrow) seen in the fetal sagittal view. The aortic ampulla of the arterial duct (asterisk) is connected to descending thoracic aorta (DAO). AO, aorta; COA, coarctation of the aorta; LA, left atrium. Reproduced from Marek J. *Pediatric and Prenatal Echocardiography*, 1st edn, 2003, with permission of Triton-books, Prague.

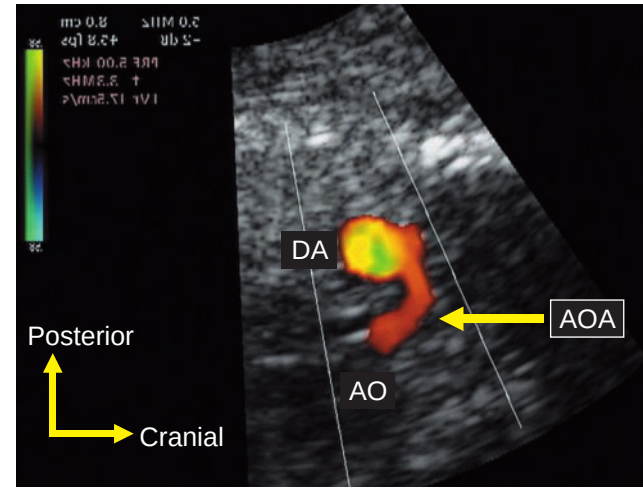


**Figure 21.17** Hypoplastic aortic arch seen in the sagittal plane with spine toward the transducer. Note difference in size between hypoplastic aortic arch (AOA) and wide arterial duct (DA). AO, ascending aorta. Reproduced from Marek J. *Pediatric and Prenatal Echocardiography*, 1st edn, 2003, with permission of Triton-books, Prague.

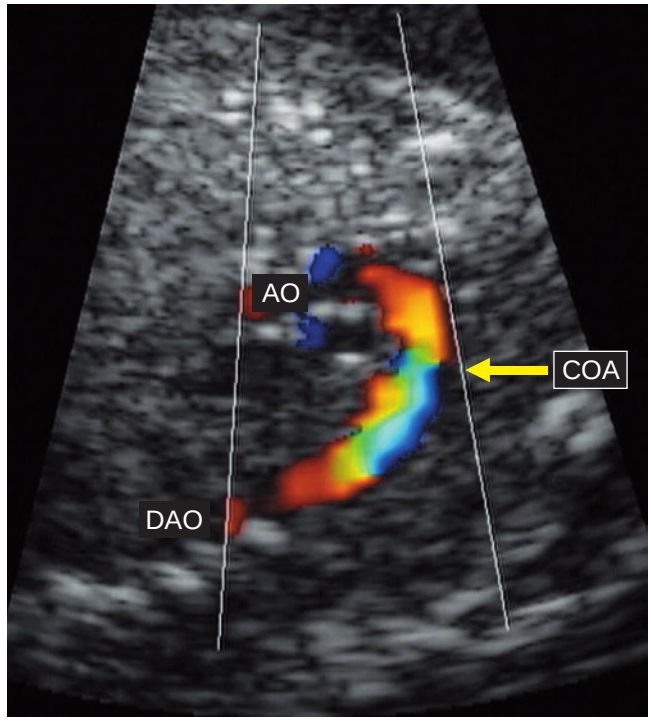


**Figure 21.16** Flow acceleration across a narrow aortic isthmus (arrow) in a 33 weeks gestation fetus with coarctation of the aorta (COA). Color Doppler flow mapping showing aliasing with Nyquist limit of 70 cm/s. AO, proximal aorta; DAO, distal aorta. Reproduced from Marek J. *Pediatric and Prenatal Echocardiography*, 1st edn, 2003, with permission of Triton-books, Prague.

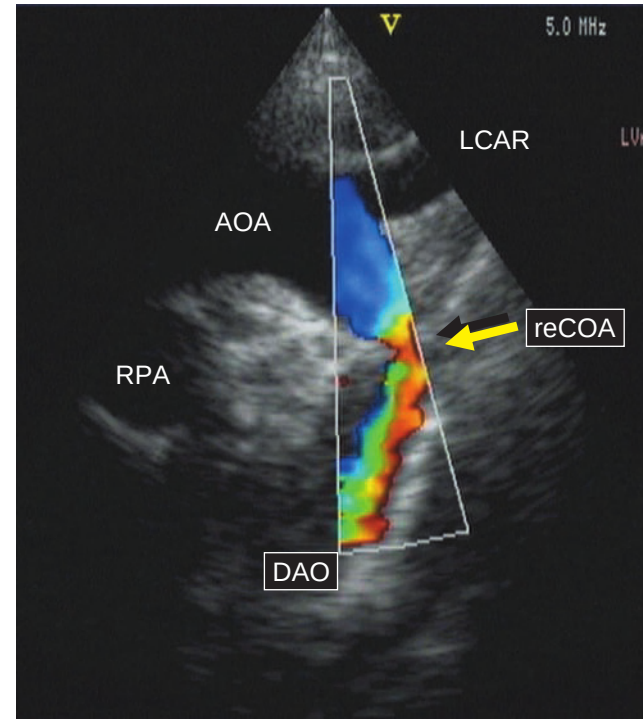


**Figure 21.18** Recurrent coarctation of the aorta (reCOA) in a patient after left subclavian flap aortoplasty (Waldhausen procedure). Narrowing with flow acceleration seen by color Doppler flow mapping at the level of origin of left subclavian artery, which was used to extend tubular aortic narrowing. AOA, aortic arch; DAO, descending aorta; LCAR, left carotid artery; RPA, right pulmonary artery.

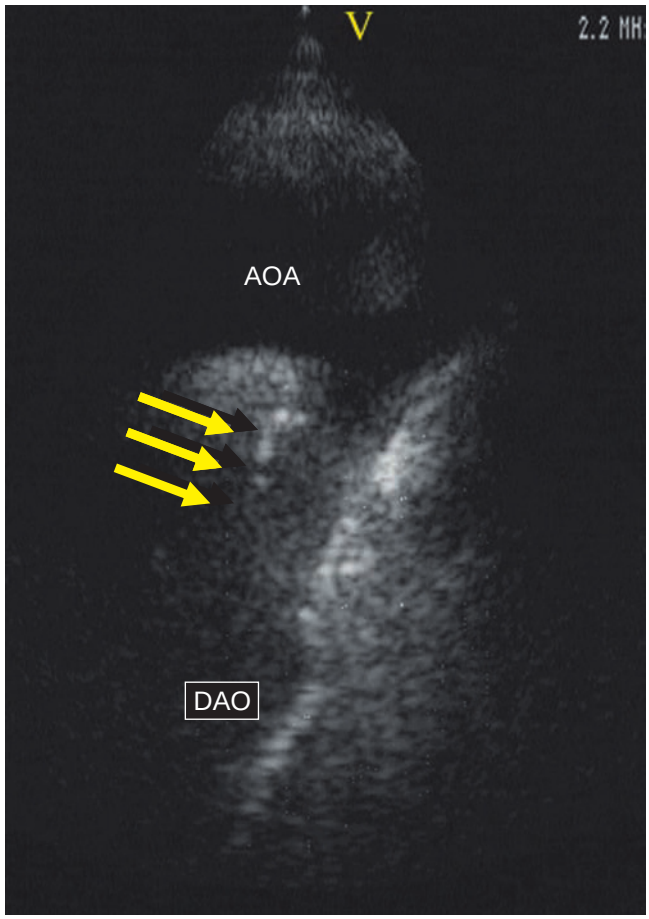


**Figure 21.19** Stent implantation at the level of residual narrowing in a patient with recurrent coarctation (arrows). AOA, aortic arch; DAO, descending aorta.

implanted in the aortic isthmus in adolescents and adults can be difficult due to artifacts produced by acoustic reflections from the stent, but is often adequate in younger patients (Fig. 21.19). Important potential complications after surgical or transcatheter treatment of COA that should be addressed by echocardiography include aneurysm formation and aortic dissection. Although vascular prostheses after extra-anatomic bypass are difficult to image in detail in most patients, efforts should be made to evaluate them (Fig. 21.20). As with evaluation of native COA, comprehensive assessment of LV inflow and outflow, mitral and aortic valve function, LV size and function, and diameters of the aortic root and ascending aorta is integral to echocardiographic follow-up after COA repair.

## Interrupted aortic arch

### Definition

Interruption of aortic arch (IAA) is a condition in which there is discontinuity between two adjacent segments of the aortic arch [21]. Aortic arch *interruption* should be

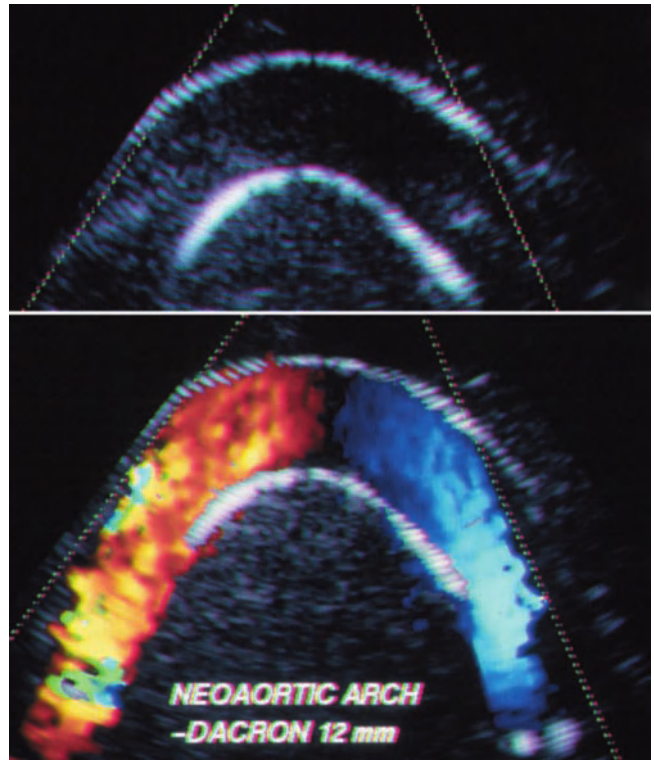


**Figure 21.20** Imaging of a Gore-Tex tube graft used to bypass tubular aortic arch hypoplasia from the left infraclavicular region. Color Doppler flow mapping demonstrates laminar flow from ascending to descending aorta. Reproduced from Marek J. *Pediatric and Prenatal Echocardiography*, 1st edn, 2003, with permission of Triton-books, Prague.

distinguished from aortic arch *atresia*, where there is anatomic continuity between the arch segments through a fibrous strand but the aortic lumen is completely obstructed. Because of their identical hemodynamic consequences, both conditions are discussed together in this chapter.

### Incidence

In the New England Regional Infant Cardiac Program, the incidence of IAA was 19 per million live births, or 1.3% of cases of severe CHD [22]. In the Pediatric Cardiac Care Consortium, a registry of CHD from 35 centers, the incidence of IAA in the first year of life was 262 of 9154 (2.9%) [23]. Isolated IAA is rare, and patency of the arterial duct and presence of VSD are common [24]. In the National Fetal Heart Screening Program of the Czech Republic (1986–2006), IAA accounted for 0.8% of all 1604 heart lesions detected in utero (J. Marek, personal communication).

### Etiology

The etiology of IAA remains incompletely understood. Based primarily on morphologic observations, several investigators proposed that interruption, atresia, or hypoplasia of the aortic arch are secondary to reduced flow in the ascending aorta during fetal life [25,26]. A growing body of evidence

suggests an important role for genetic anomalies, including chromosome 22q11 microdeletion, DiGeorge syndrome, velocardiofacial (Shprintzen) syndrome, conotruncal face anomaly syndrome and several other syndromes [27–30]. A particularly strong association between chromosome 22q11 microdeletion and type B IAA has been reported [30]. In mouse embryos deficient for the *Gbx2* gene, aberrant cardiac neural crest cell patterning and defects in pharyngeal arch-derived structures are seen with abnormal development of the fourth pharyngeal arch arteries, including type B IAA, right aortic arch, and retroesophageal right subclavian artery [31]. In mice, conditional inactivation of GATA-6 – a transcription factor regulating morphogenetic patterning of the cardiac outflow tract and aortic arch – has resulted in perinatal mortality from a spectrum of cardiovascular defects, including IAA and truncus arteriosus [32]. Finally, the role of exposure to teratogens in the etiology of IAA remains unknown but has been suggested in an experimental model of hamster embryos exposed to bis(dichloroacetyl)diamine [33].

## Morphology and classification

Celoria and Patton classified IAA into three types, A–C, according to the site of interruption in relation to the arch branches [34].

### Type A

Type A IAA involves interruption distal to the origin of the left subclavian artery (Fig. 21.21). This type accounts for 30–37% of cases. The arterial duct supplies the lower body and the ascending aorta supplies the upper body. From the standpoint of morphogenesis, type A IAA can be explained by involution of both dorsal aortas distal to the fourth arches and proximal to the persistent sixth aortic arch on the same side of the interruption. The anatomy is essentially identical to extreme coarctation and differs only in the absence of luminal continuity of the aortic isthmus (called *aortic isthmus atresia*). The atretic segment may be very short or, in case of a longer isthmus, the distance between both stumps can be several millimeters long. Aberrant origin of the right subclavian artery from the descending aorta occurs in ~5% of patients.

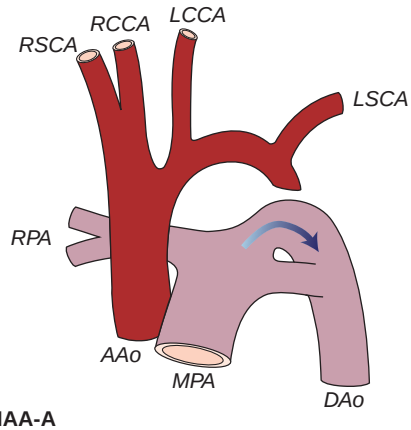


**Figure 21.21** Type A interrupted aortic arch, in which the interruption is situated distal to the left subclavian artery (LSCA). The descending aorta (DAo) is supplied via the arterial duct (arrow). The ascending aorta (AAo) gives rise to all brachiocephalic arteries. LCCA, left common carotid artery; MPA, pulmonary trunk; RCCA, right carotid artery; RPA, right pulmonary artery; RSCA, right subclavian artery.

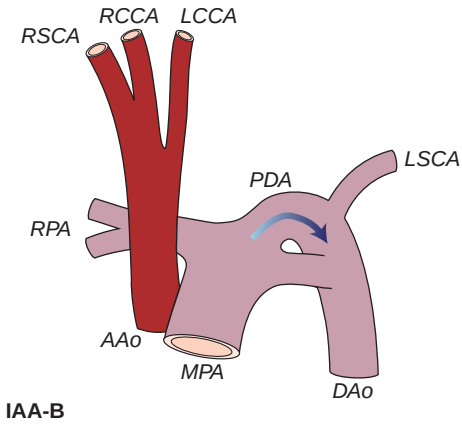


**Figure 21.22** Type B interrupted aortic arch, in which the interruption is sited between the left carotid artery (LCCA) and left subclavian artery (LSCA). The descending aorta (DAo) and LSCA are supplied via the arterial duct (arrow) and brachiocephalic trunk (RCCA, RSCA), and the LCCA is supplied from the ascending aorta (AO). LPA, left pulmonary artery; PA, pulmonary trunk; RCCA, right carotid artery; RPA, right pulmonary artery; RSCA, right subclavian artery; PDA, arterial duct.

### Type B

Type B IAA is defined by interruption between the left common carotid and left subclavian arteries (Fig. 21.22). This type accounts for 62–70% of cases. The arterial duct supplies the left subclavian artery and the lower body. In ~50% of cases the right subclavian artery arises aberrantly from the descending aorta distal to the interruption (Fig. 21.23). In these cases, the ascending aorta supplies only the head vessels. Type B IAA is likely due to involution or absence of the fourth aortic arch and of the dorsal aorta on the opposite side of the interruption. In cases with type B IAA and aberrant origin of the right subclavian artery, the morphology may be explained by involution of both fourth arches and the sixth arch on the side opposite to the interruption. The interruption is almost always complete, and fibrous continuity between the arch segments is rare. The distance between the interrupted arch segments varies and may exceed 10 mm.

In type B IAA, the VSD is considered an integral part of the anomaly, with an incidence of 94–100% [25,35]. It is described as a conoventricular defect with posterior malalignment of the conal (infundibular) septum. The term *conoventricular VSD* refers to its location between the conal septum superiorly and the Y of septal band inferiorly [36]. The designation *posterior malalignment* refers to the posterior, inferior and leftward deviation of the conal (infundibular,

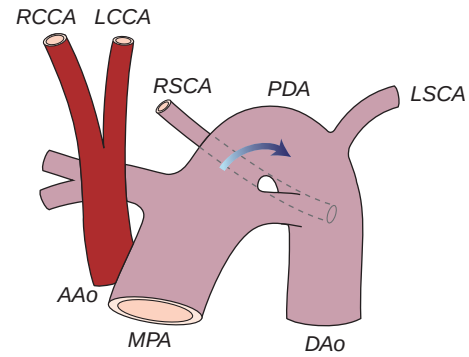


**Figure 21.23** Type B interrupted aortic arch with aberrant right subclavian artery. The interruption is between the left carotid artery (LCCA), and left subclavian artery (LSCA). The descending aorta (DAo), LSCA and aberrant right subclavian artery (RSCA) are supplied via the arterial duct (arrow); the aberrant right subclavian artery courses behind the trachea and esophagus. The ascending aorta (AAo) gives rise only to both carotid arteries. MPA, pulmonary trunk; RCCA, right carotid artery.

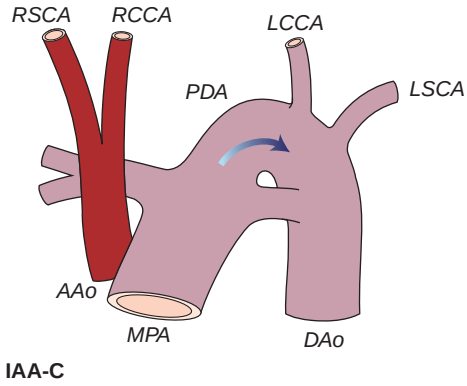


**Figure 21.24** Type C interrupted aortic arch, in which the interruption is between the right common carotid artery (RCCA) and left common carotid artery (LCCA). The descending aorta (DAo), LCCA and left subclavian artery (LSCA) are supplied by the arterial duct (arrow). The ascending aorta (AAo) supplies only the right subclavian artery (RSCA) and right carotid artery (RCCA). MPA, pulmonary trunk; PDA, arterial duct.

outlet) septum toward the LV outflow tract. When viewed from the RV aspect, the space between the superior and inferior limbs of the cranial termination of septal band, normally filled by the conal septum, is wide open. This leads to the subpulmonary location of the VSD when viewed from the RV. When viewed from the LV, the conal septum can be seen protruding into the subaortic area. The conal septum in type B IAA is often hypoplastic and short. The posterior, inferior, and leftward malalignment of the conal septum into the LV outflow tract leads to varying degrees of subaortic stenosis above the VSD [35]. Other anatomic variables that may contribute to subaortic stenosis in type B IAA include diffuse hypoplasia of the LV outflow tract, an accessory anterolateral papillary muscle of Moulaert [37] and a discrete subaortic ridge or "membrane." The aortic valve annulus is often hypoplastic. Bi- or unicommissural aortic valves with varying degrees of hypoplasia and/or stenosis have been reported in IAA [35,38].

### Type C

Type C IAA is defined as an interruption between the right and left common carotid arteries (Fig. 21.24). The arterial duct supplies the left common carotid artery, left subclavian artery and the descending aorta. This type accounts for 1% or less of cases [38–40].

### Association with other anomalies

IAA also occurs with other types of conotruncal anomalies, most commonly truncus arteriosus. In a series of 472 patients with IAA, 50 (11%) had truncus arteriosus [41]. The interruption was between the left common carotid and left subclavian arteries (type B) in 84% of the cases. IAA is also associated with transposition of the great arteries, double-outlet RV, tricuspid atresia, double-inlet LV, common atrioventricular canal, mitral stenosis or atresia, premature closure of the foramen ovale, multiple VSDs, heterotaxy syndrome, aorto-pulmonary window [42], interrupted right aortic arch [43,44], and interrupted cervical arch [45].

## Pathophysiology

Survival of newborns with IAA depends on a patent arterial duct. Spontaneous closure of the arterial duct leads to diminished perfusion of the systemic vascular bed distal to the interruption. Prompt initiation of prostaglandin infusion is life-saving. The pathophysiology is identical to critical COA with pulmonary hypertension. Most patients present within hours to days after birth, with lethargy, poor feeding, tachypnea, tachycardia, pulmonary congestion, diaphoresis, oliguria, cool and dusky skin, and sluggish capillary refill. In many patients, clinical deterioration with acute cardiovascular collapse progresses rapidly as the arterial duct closes and perfusion of major vascular beds rapidly decreases. Less commonly, patients with persistent arterial duct may present weeks or even months after birth with congestive heart failure, pulmonary overcirculation, and failure to grow. Without treatment, nearly 75% of patients die within the first month and almost 90% by the end of the first year. Rarely, interrupted aortic arch may present with systemic hypertension in adults [46].

## Imaging

Echocardiography allows comprehensive evaluation of the anatomy and hemodynamic manifestations of IAA and provides the information necessary for surgical planning in almost all patients [47–49]. Detailed descriptions of the aortic arch, site of interruption, location of origins of brachiocephalic

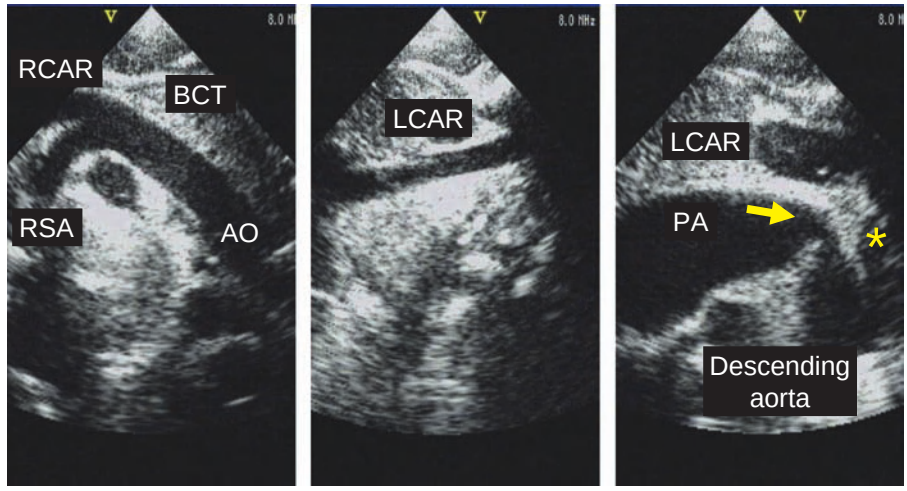


**Figure 21.25** Serial views to visualize aortic arch anatomy in a neonate with type B interrupted aortic arch. **(a)** Sagittal view oriented toward the right shoulder (transducer marker at 4–5 o'clock) demonstrates the brachiocephalic trunk (BCT) with normal branching patterns. **(b)** Sagittal view oriented toward the left shoulder (transducer marker at 1–2 o'clock) shows only left carotid artery (LCAR) with absent connection to distal aorta. **(c)** Ductal view showing the descending aorta (DAO) together with left subclavian artery (asterisk) connected to pulmonary trunk (PA) via restrictive arterial duct (arrow). AO, proximal aorta; RCAR, right carotid artery; RSA, right subclavian artery.

branches, distance between the interrupted aortic arch segments, status of the arterial duct, anatomy of the VSD, LV outflow, aortic valve and associated anomalies are important for planning surgical repair. The goals and imaging strategy of echocardiography in IAA are identical to those in COA (see above). Because of the frequent association between type B IAA and hypoplasia or agenesis of the thymus, particular attention is given to the presence and size of the thymus [50]. The thymus is best seen from the subclavicular or suprasternal notch views as solid tissue. Its absence or markedly reduced size increases the likelihood of chromosome 22q11 microdeletion.

The aortic arch, brachiocephalic vessels and arterial duct are imaged in the same way as in neonatal COA. Meticulous continuous sweeps of the transducer in the transverse plane (index mark points to the patient's left) demonstrate the ascending aorta in cross-section. From this view, the size of the ascending aorta (usually small) relative to the main pulmonary artery is determined. Further cranial angulations of the transducer demonstrate the origin of the first branch off the aortic arch (Fig. 21.25). This branch is then followed toward the neck to determine its identity – right brachiocephalic trunk or right common carotid artery. The caliber of the right brachiocephalic trunk is approximately twice that of the left common carotid artery and it bifurcates into a right subclavian and right common carotid arteries. The latter has the same caliber as the left common carotid artery and can be followed to the neck without bifurcation (Fig. 21.26). The site

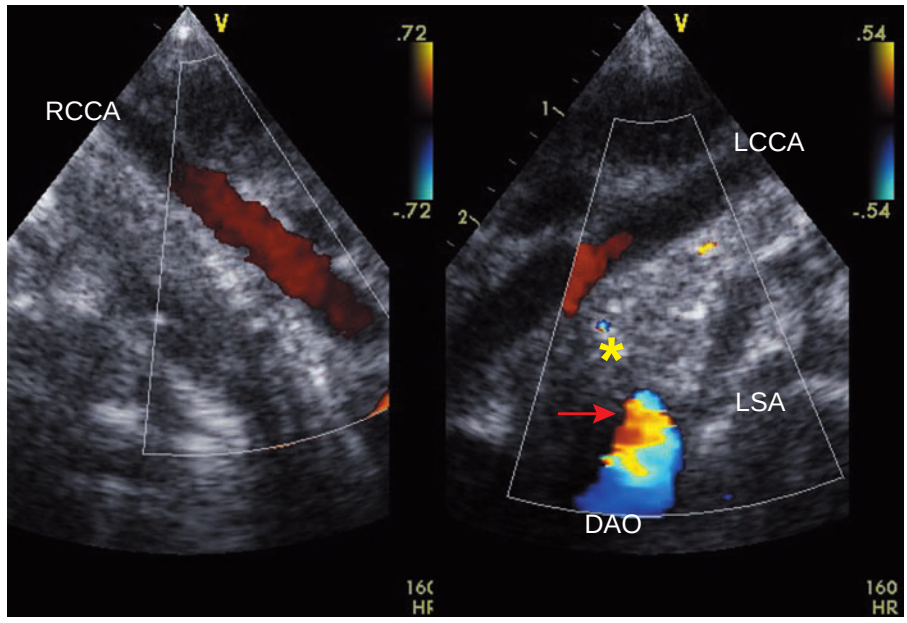


**Figure 21.26** Serial views in a neonate with type B interrupted aortic arch and aberrant right subclavian artery. **(a)** Rightward orientation of the transducer showing the proximal aorta giving rise to the right common carotid artery (RCCA). **(b)** Left common carotid artery (LCCA). Note the long-segment interruption (asterisk). Both subclavian arteries are connected to the descending aorta (DAO) (arrow) and supplied by the arterial duct. Image shows only left subclavian artery (LSA); the aberrant right subclavian artery is not documented here.

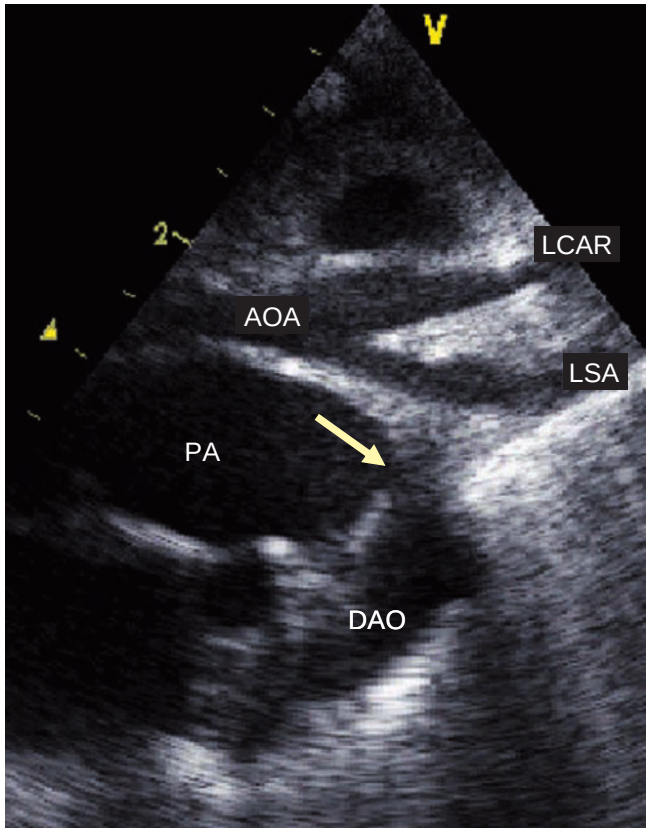


**Figure 21.27** Type A interrupted left aortic arch distal to left subclavian artery (LSA). The descending aorta (DAO) is supplied via the arterial duct (arrow). AOA, aortic arch; LCAR, left carotid artery; PA, pulmonary trunk.

of interruption is then determined as the arch ends with the brachiocephalic artery proximal to the interruption – distal to the left subclavian artery in type A (Fig. 21.27; Videoclip 21.8); distal to the left common carotid artery in type B (Fig. 21.28; Videoclips 21.9 and 21.10) [51]; and distal to the right common carotid artery in type C. The distance between the interrupted arch segments is measured at the origins of the corresponding brachiocephalic arteries. In the rare circumstance of an interrupted right aortic arch, the first branch is a left brachiocephalic or a left common carotid artery, followed by a right common carotid artery. The proximal descending aorta is to the right of the spine (Fig. 21.29) [44].

The arterial duct is imaged similarly to neonatal COA (see above). In IAA, the arterial duct forms an arch that should not be confused with the aortic arch (Videoclip 21.9). Careful imaging of the pulmonary origin and aortic termination confirms the anatomic identity of the arterial duct (Fig. 21.30). Color and pulsed Doppler are used to determine the direction of flow through the duct (Fig. 21.31 and Videoclip 21.9). Increased velocity of the right-to-left flow jet indicates restriction of the arterial duct.

The VSD in IAA is evaluated from the subcostal (Fig. 21.32), apical and parasternal windows. The posteriorly deviated infundibular septum can be seen in these views as a short ridge protruding into the LV outflow tract immediately below a hypoplastic aortic valve, leaving no infundibular septal tissue below the pulmonary valve. From an anteriorly angled apical view (5-chamber view), color Doppler demonstrates preferential flow from the LV to the RV (Fig. 21.33 and Videoclip 21.11). The flow velocity across the LV outflow

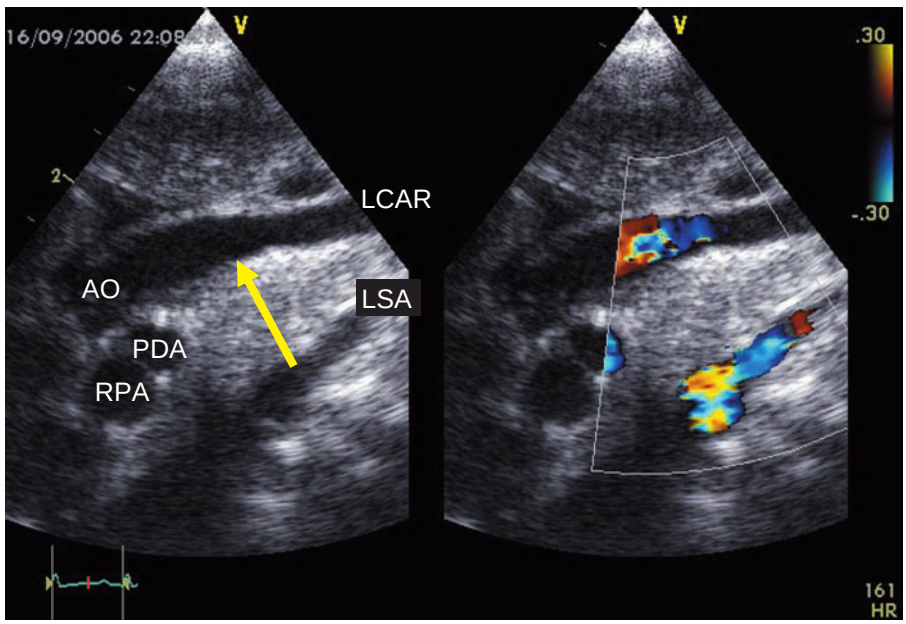


**Figure 21.28** Imaging of type B interrupted aortic arch from a leftward-oriented high right parasternal view. Note continuation between the proximal aorta (AO) and left carotid artery (LCAR) with long-segment discontinuity (arrow) between the left carotid artery and left subclavian artery (LSA). PDA, patent ductus arteriosus; RPA, right pulmonary artery.

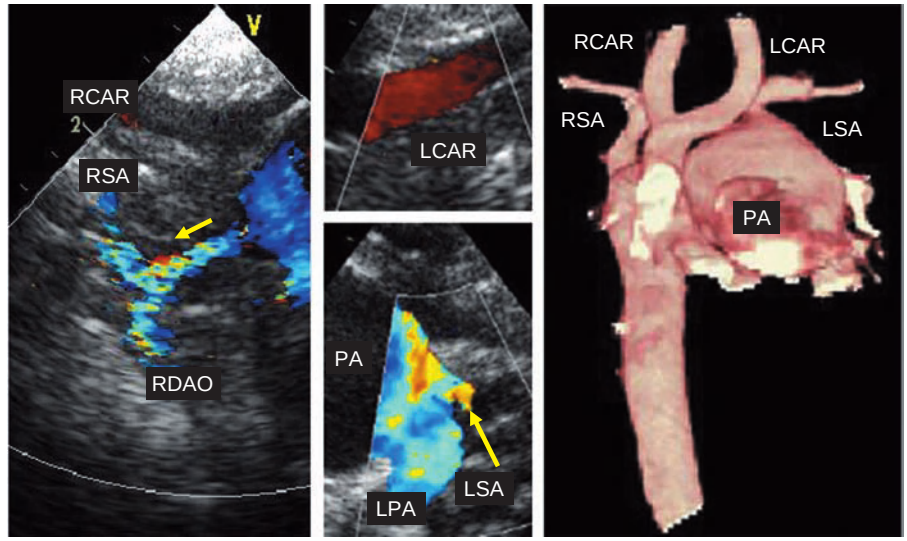


**Figure 21.29** Neonate with interruptions of the left and right aortic arches. **(a)** Echocardiography and **(b)** 3D volume rendered computed tomography (CT) angiogram. The proximal aorta gives rise to the right (RCAR) and left (LCAR) carotid arteries. The right subclavian artery (RSA) and right descending aorta (RDAO) are supplied by a restrictive right arterial duct (arrow); i.e., type B interruption of right aortic arch. The left subclavian artery (LSA) originates from the pulmonary trunk (PA) via a filiform left arterial duct responding to prostaglandin infusion. LPA, left pulmonary artery. The 3D CT image is reproduced courtesy of Cathy Owen and Andrew Taylor, Great Ormond Street Hospital, London.

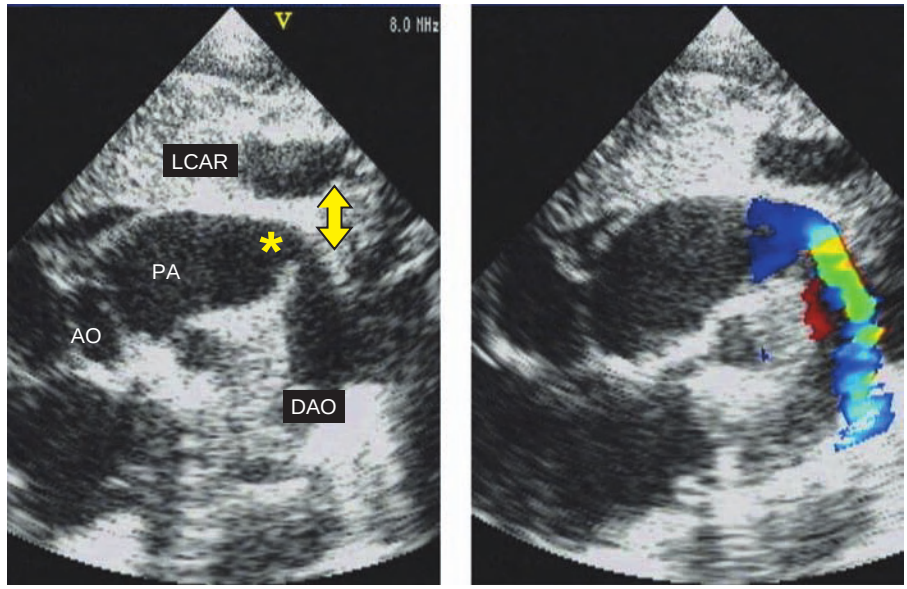


**Figure 21.30** Type B interrupted aortic arch viewed from a suprasternal projection. The ascending aorta gives rise to the brachiocephalic trunk and left carotid artery (LCAR); the left descending aorta (DAO) is supplied from the pulmonary trunk (PA) via a restrictive arterial duct (asterisk). The short distance between the left carotid artery and descending aorta suggests a possible direct end-to-side anastomosis (arrows). AO, ascending aorta.

is usually not significantly accelerated despite the often narrowed subaortic region and the hypoplastic aortic valve. The reasons for this include decreased flow rate across the LV outflow tract due to perfusion of only the head or head and right arm (depending on IAA location and origin of the right subclavian artery) and to ventricular dysfunction. The parasternal long-axis view is particularly helpful for depiction of the VSD and the LV outflow (Fig. 21.34 and Videoclip 21.12). The widths of the LV outflow and the aortic valve annulus are measured in this view. The preoperatively measured cross-sectional area of the LV outflow tract has been shown to be smaller in neonates with IAA who develop subaortic obstruction postoperatively, with a LV outflow tract (LVOT) area ≤0.7 $cm^2/m^2$ being a sensitive predictor [52]. A ratio of LVOT diameter to descending aorta diameter at the level of the diaphragm ≤1.0 is a determinant of infundibular resection to prevent postoperative subaortic stenosis (ratio in normal infants 1.3 ± 0.14) [53]. Real-time 3D echocardiography allows visualization of LV outflow obstruction (Fig. 21.35 and Videoclip 21.13(a,b)). This en face view can be useful when considering relief of obstruction either at the time of primary repair or before reoperation. Similar views can be obtained using a transesophageal approach [54]. Detailed imaging of the aortic valve from the parasternal short-axis view demonstrates its morphology.

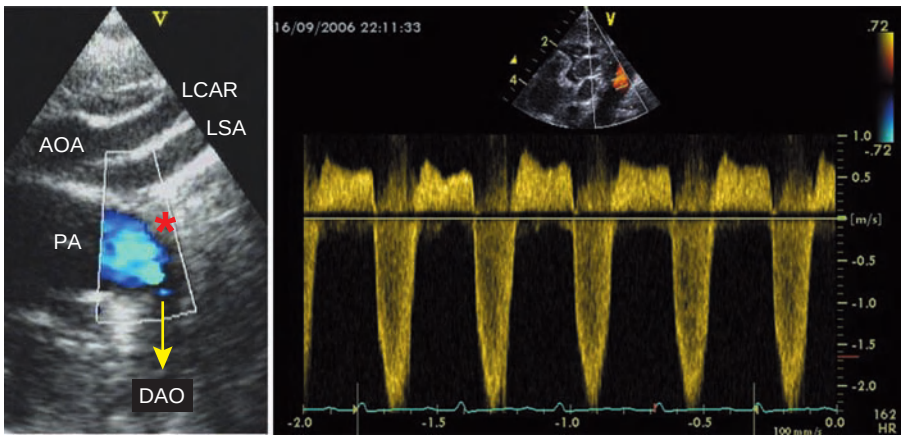


(a) (b)

**Figure 21.31** **(a)** A type A interrupted aortic arch with absent connection distal to the left subclavian artery (LSA, asterisk). Color flow mapping indicates laminar right-to-left flow across the arterial duct (arrow). **(b)** A pulsed Doppler tracing in the arterial duct shows a right-to-left shunt with peak velocity 2.3 m/s and a diastolic left-to-right shunt. AOA, aortic arch; LCAR, left carotid artery; DAO, descending aorta; PA, pulmonary trunk.

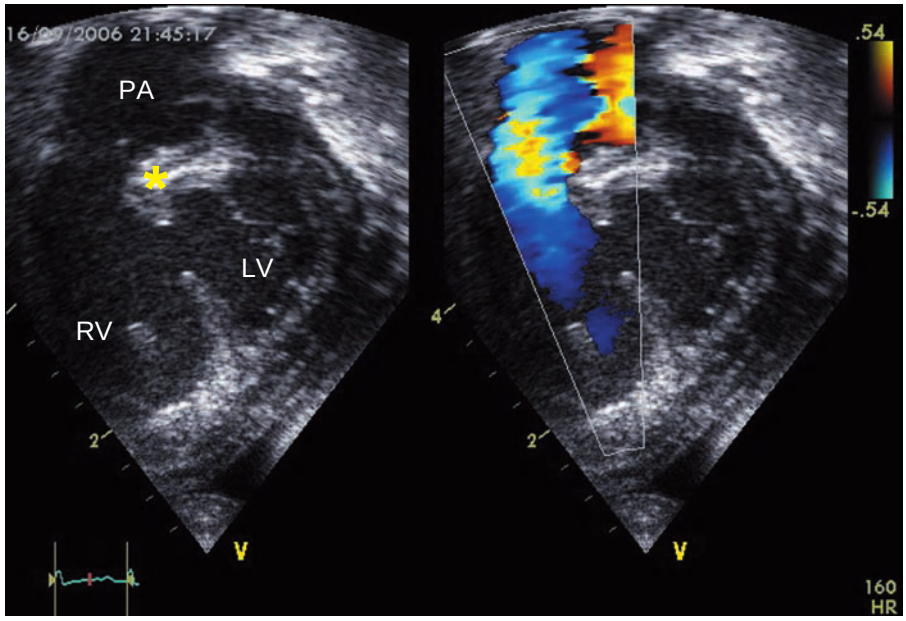


(a)

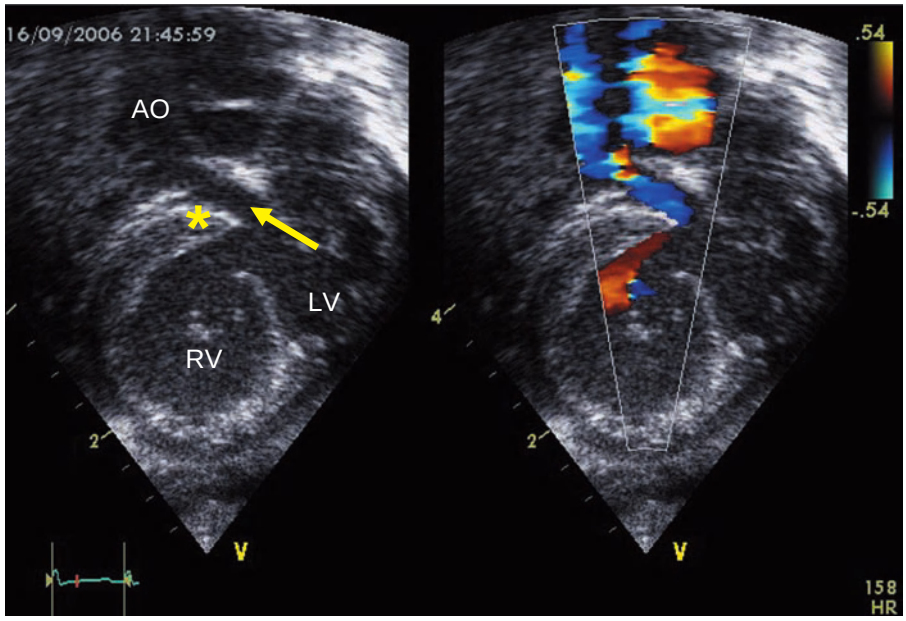


(b)

**Figure 21.32** Subcostal views of the right ventricular outflow **(a)** and the left ventricular outflow **(b)** in a neonate with interrupted aortic arch. The unrestrictive conoventricular septal defect has muscular margins; the infundibular septum (asterisk) is deviated posteriorly causing left ventricular outflow obstruction (arrow). AO, aorta; LV, left ventricle; PA, pulmonary trunk; RV, right ventricle.

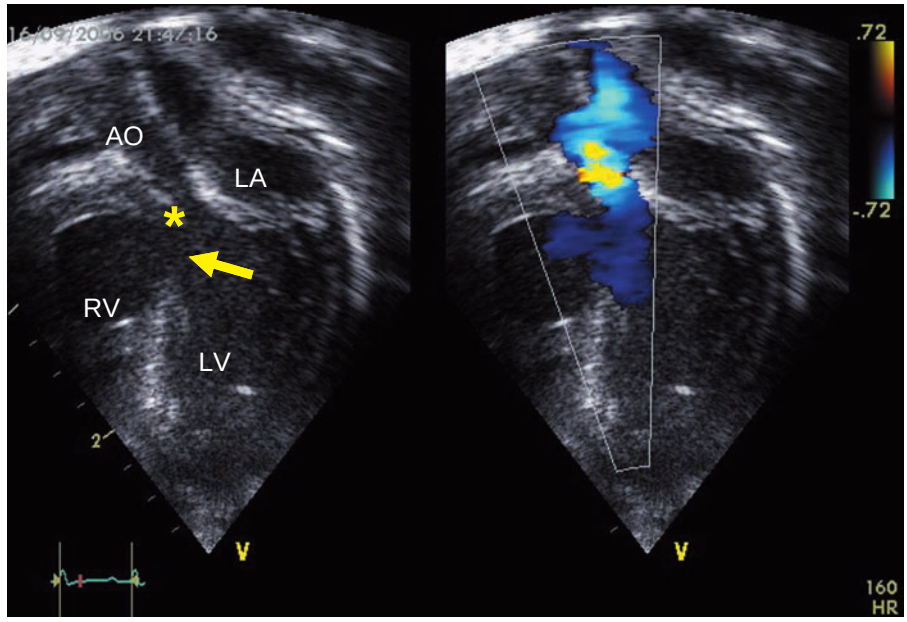


(a) (b)

**Figure 21.33 (a,b)** Apical 5-chamber view in a neonatal interrupted aortic arch demonstrating a large ventricular septal defect with unrestrictive left-to-right flow (arrow), posterior deviation of the infundibular septum (asterisk), and narrow left ventricular outflow tract. AO, ascending aorta; LA, left atrium; LV, left ventricle; RV, right ventricle.

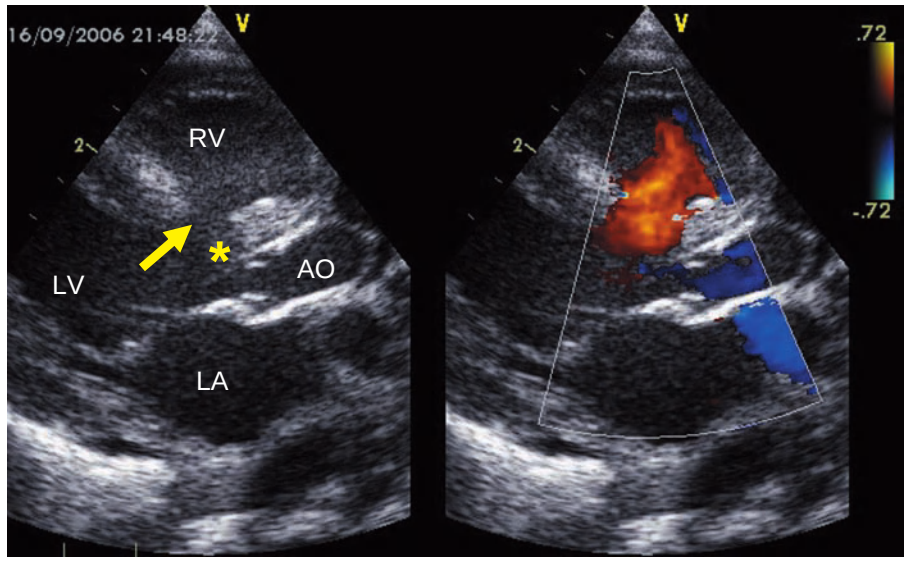


(a) (b)

**Figure 21.34 (a,b)** Parasternal long-axis view in neonatal interrupted aortic arch showing a large conoventricular septal defect (arrow) with unrestrictive left-to-right shunt seen by color Doppler flow mapping. The asterisk indicates posterior deviation of the infundibular septum. Incomplete opening of the aortic valve is consistent with bicuspid aortic valve. AO, aorta; LA, left atrium; LV, left ventricle; RV, right ventricle.

## Prenatal assessment

IAA does not usually adversely affect fetal physiology because the arterial duct bypasses the interruption. Prenatal echocardiographic examination of suspected IAA is conducted in the same way as in suspected COA (see details above). Similar to COA, however, prenatal diagnosis of IAA remains challenging (Fig. 21.36). When imaging in the sagittal plane of the fetus, it is important to distinguish between the ductal arch and the aortic arch, especially when the latter is interrupted (Figs 21.37 and 21.38; Videoclip 21.14). However, careful imaging of the aorta in the oblique sagittal and transverse planes can demonstrate the relevant anatomy. Presence of a typical posterior malalignment VSD is an important clue to the diagnosis of IAA. Color Doppler with the Nyquist limit at 60–100 cm/s without filtering low velocities displays the bidirectional flow through the VSD. The defect is usually larger than the diameter of the aortic annulus. Unlike COA, however, the 4-chamber view is often normal because the large VSD allows free communication between the ventricles. Imaging in the sagittal plane can show the VSD and the size discrepancy between the smaller ascending aorta and the larger main pulmonary artery.

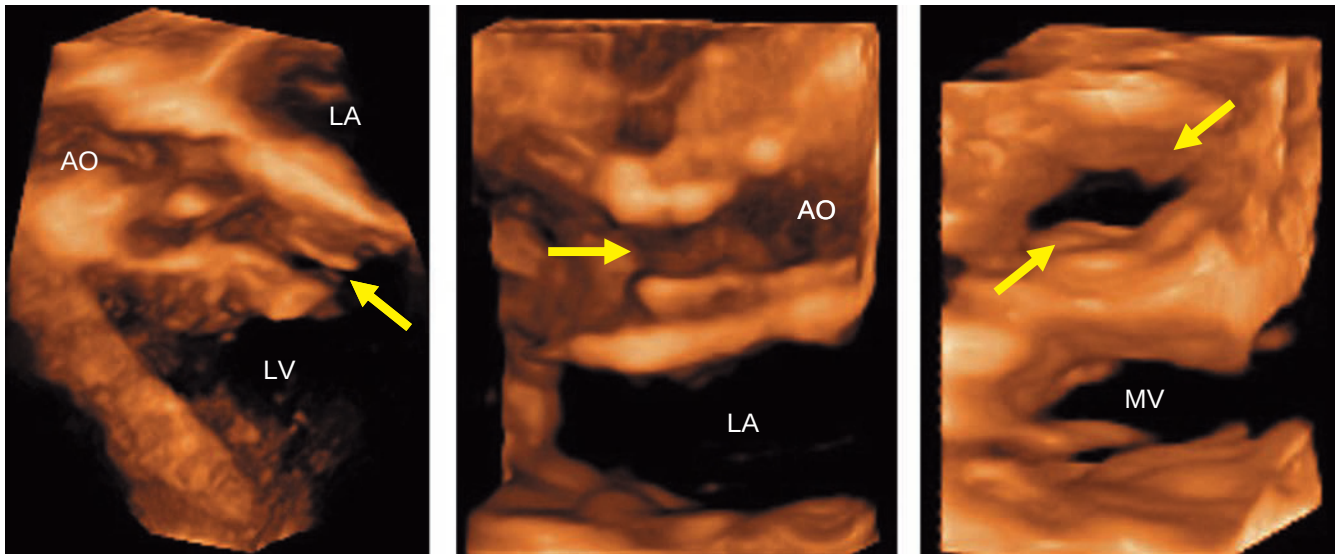


(a) (b) (c)

**Figure 21.35** Subcostal real-time 3D echocardiogram in a neonate with interrupted aortic arch. **(a)** Left ventricular outflow tract obstruction indicated by arrows in 5-chamber view. **(b)** Long-axis view. **(c)** En face view through the aortic valve as seen by the surgeon ("aortotomy view" from above). The obstruction is formed by complete subaortic conus with aorto-mitral discontinuity. AO, aorta; LA, left atrium; LV, left ventricle; MV, mitral valve.

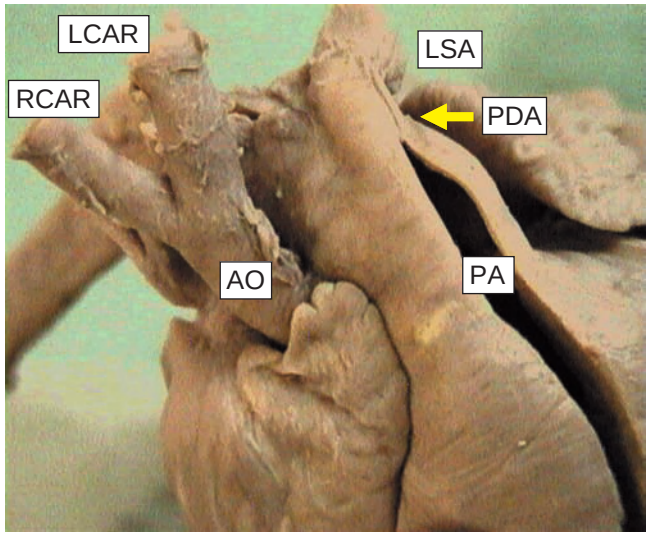


**Figure 21.36** Post-mortem finding in a 21-week-old fetus with type B interrupted aortic arch and aberrant right subclavian artery. The ascending aorta (AO) gives rise to the right (RCAR) and left (LCAR) carotid arteries; the left (LSA) and right subclavian arteries are connected to the junction of the large arterial duct and distal aorta (arrow). No connective tissue was found between the proximal and distal aorta. PA, pulmonary trunk; PDA, patent ductus arteriosus. Post-mortem specimen supplied courtesy of Viera Povýšilová, Prague.

### Therapeutic interventions and long-term follow-up

Surgery is the only treatment available for patients with IAA, and primary corrective surgery in the neonatal period is the preferred approach [21,41,55,56]. In most cases, primary anastomosis between the interrupted segments is possible after resection of ductal tissue and extensive mobilization of the arch and descending aorta. When the gap between the interrupted aortic segments cannot be fully closed, autologous pericardium or a prosthetic graft is used. However, every attempt is made to achieve connection between the proximal and distal segments through native tissue [57,58].

The goals and technique of the echocardiographic examination after IAA repair are identical to those after COA repair. The risk of postoperative LV outflow obstruction is high after type B IAA repair but it is also an important consideration after COA repair (Fig. 21.39). Detailed imaging of the reconstructed aortic arch can be hampered by postoperative changes and intervening airways. Alternative noninvasive imaging modalities (e.g., MRI, CT) should be considered when echocardiography does not provide adequate information.

## Acknowledgement

All images used in this chapter were taken from imaging archives of the Cardiothoracic Centre, Great Ormond Street Hospital, London, and Kardiocentrum, University Hospital Motol, Prague. Some echocardiographic images were reproduced from *Jan Marek: Paediatric and Prenatal Echocardiography*, with permission of Triton-books Ltd (Czech Republic).

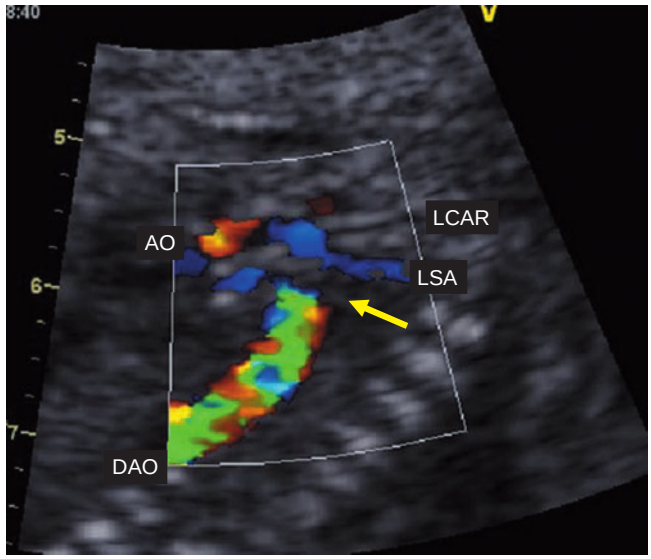


**Figure 21.37** Type A interruption of the aortic arch in a 22-week-old fetus: the interruption (arrow) is located between the left subclavian artery (LSA) and the descending aorta (DAO). AO, ascending aorta; LCAR, left common carotid artery. Reproduced from Marek J. *Pediatric and Prenatal Echocardiography*, 1st edn, 2003, with permission of Triton-books, Prague.

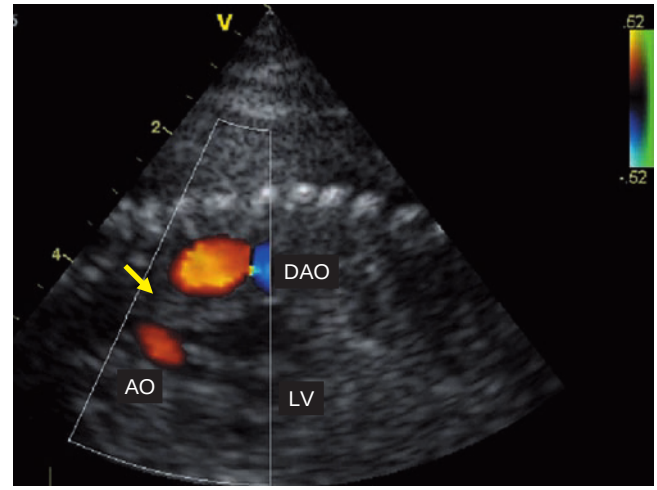


**Figure 21.38** Aortic arch viewed through the spine in a 23-week-old fetus showing type B interruption of the aortic arch. The arrow indicates no flow continuity between the proximal (AO) and distal aorta (DAO). LV, left ventricle. Reproduced from Marek J. *Pediatric and Prenatal Echocardiography*, 1st edn, 2003, with permission of Triton-books, Prague.

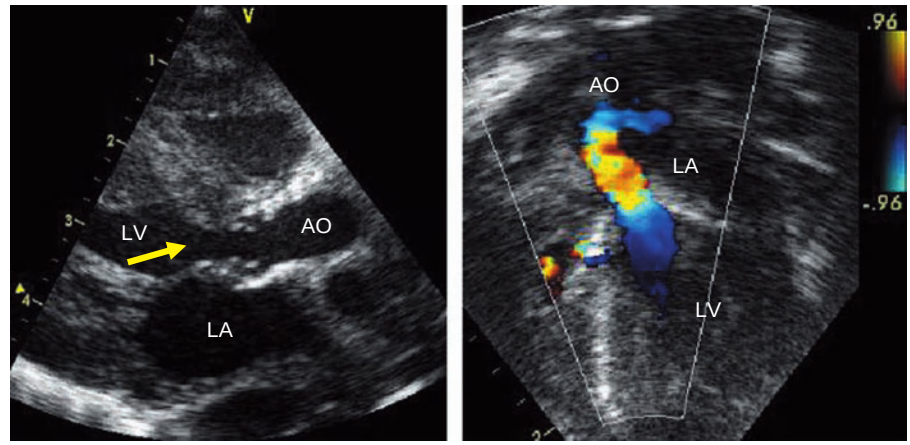


(a) (b)

**Figure 21.39** Left ventricular outflow tract obstruction (LVOTO) after repair of interruption of the aortic arch (IAA). **(a)** 2-D long-axis view. **(b)** Flow acceleration visualized by color Doppler flow mapping. The LVOTO formed as a result of a hypertrophied and posteriorly deviated infundibular septum (arrow). Incomplete systolic opening of the aortic valve suggests bicuspid valve. AO, aorta; LA, left atrium; LV, left ventricle.

## References


1. Hoffman JI, Kaplan S. The incidence of congenital heart disease. *J Am Coll Cardiol* 2002;39:1890–900.
2. Šamánek M, Voříšková M. Congenital heart disease among 815,569 children born between 1980 and 1990 and their 15-year survival: A prospective Bohemia survival study. *Pediatr Cardiol* 1999;20:411–41.
3. Bower C, Ramsay JM. Congenital heart disease: a 10 year cohort. *J Paediatr Child Health* 1994;30:414–18.
4. Campbell M, Polani PE. The aetiology of coarctation of the aorta. *Lancet* 1961;1:463–8.
5. Sharland GK, Chan KY, Allan LD. Coarctation of the aorta: difficulties in prenatal diagnosis. *Br Heart J* 1994;71:70–5.
6. Mahowald JM, Lucas RV Jr, Edwards JE. Aortic valvular atresia. Associated cardiovascular anomalies. *Pediatr Cardiol* 1982;2:99–105.
7. Ho VB, Bakalov VK, Cooley M et al. Major vascular anomalies in Turner syndrome: prevalence and magnetic resonance angiographic features. *Circulation* 2004;11:1694–700.
8. Goldmuntz E, Clark BJ, Mitchell LE et al. Frequency of 22q11 deletions in patients with conotruncal defects. *J Am Coll Cardiol* 1998;32:492–8.
9. Ho SY, Anderson RH. Coarctation, tubular hypoplasia, and the ductus arteriosus. Histological study of 35 specimens. *Br Heart J* 1979;41:268–74.

10. Rudolph A. *Congenital Diseases of the Heart.* Armonk, NY: Futura Publishing, 2001;378–393.
11. Head CE, Jowett VC, Sharland GK, Simpson JM. Timing of presentation and postnatal outcome of infants suspected of having coarctation of the aorta during fetal life. *Heart* 2005;91:1070–4.
12. Hornberger LK, Weintraub RG, Pesonen E et al. Echocardiographic study of the morphology and growth of the aortic arch in the human fetus. Observations related to the prenatal diagnosis of coarctation. *Circulation* 1992;86:741–7.
13. Pasquini L, Mellander M, Seale A et al. Z-scores of the fetal aortic isthmus and duct: an aid to assessing arch hypoplasia. *Ultrasound Obstet Gynecol* 2007;29:628–33.
14. Pfammatter JP, Ziemer G, Kaulitz R et al. Isolated aortic coarctation in neonates and infants: results of resection and end-to-end anastomosis. *Ann Thorac Surg* 1996;62:778–82.
15. Grinda JM, Mace L, Dervanian P et al. Bypass graft for complex forms of isthmic aortic coarctation in adults. *Ann Thorac Surg* 1995;60:1299–302.
16. Redington AN, Booth P, Shore DF, Rigby ML. Primary balloon dilatation of coarctation of the aorta in neonates. *Br Heart J* 1990;64:277–81.
17. Rodes-Cabau J, Miro J, Dancea A et al. Comparison of surgical and transcatheter treatment for native coarctation of the aorta in patients > or = 1 year old. The Quebec Native Coarctation of the Aorta Study. *Am Heart J* 2007;154:186–92.
18. Dietl CA, Torres AR, Favaloro RG et al. Risk of recoarctation in neonates and infants after repair with patch aortoplasty, subclavian flap, and the combined resection-flap procedure. *J Thorac Cardiovasc Surg* 1992;10:724–31.
19. Sciolaro C, Copeland J, Cork R et al. Long-term follow-up comparing subclavian flap angioplasty to resection with modified oblique end-to-end anastomosis. *J Thorac Cardiovasc Surg* 1991; 101:1–13.
20. Sweeney MS, Walker WE, Duncan JM et al. Reoperation for aortic coarctation: techniques, results, and indications for various approaches. *Ann Thorac Surg* 1985;40:46–9.
21. Tchervenkov CI, Jacobs JP, Sharma K, Ungerleider RM. Interrupted aortic arch: surgical decision making. *Semin Thorac Cardiovasc Surg Pediatr Card Surg Annu* 2005;92–102.
22. Fyler DC, Buckley DC, Hellenbrand WC, Cohn HE. Report of the New England Regional Infant Cardiac Program. *Pediatrics* 1980; 65:375–461.
23. Powell CB, Stone FM, Atkins DL et al. Operative mortality and frequency of coexistent anomalies in interruption of the aortic arch. *Am J Cardiol* 1997;79:1147–8.
24. Van Praagh R, Bernhard WF, Rosenthal A et al. Interrupted aortic arch: surgical treatment. *Am J Cardiol* 1971;27:200–11.
25. Van Mierop LHS, Kutsche LM. Interruption of the aortic arch and coarctation of the aorta: pathogenetic relations. *Am J Cardiol* 1984;54:829–34.
26. Rudolph AM, Heymann MA, Spitznas U. Hemodynamic considerations in the development of narrowing of the aorta. *Am J Cardiol* 1972;30:514–25.
27. Conley ME, Beckwith JB, Mancer JFK, Tenckhoff L. The spectrum of the DiGeorge syndrome. *J Pediatr* 1979;94:883–90.
28. Van Mierop LHS, Kutsche LM. Cardiovascular anomalies in DiGeorge syndrome and importance of neural crest as a possible pathogenetic factor. *Am J Cardiol* 1986;58:133–7.
29. Lewin MB, Lindsay EA, Jurecic V et al. A genetic etiology for interruption of the aortic arch type B. *Am. J Cardiol* 1997;80:493–7.
30. Goldmuntz E, Clark BJ, Mitchell LE et al. Frequency of 22q11 deletions in patients with conotruncal defects *J Am Coll Cardiol* 1998;32:492–8.
31. Byrd NA, Meyers EN. Loss of Gbx2 results in neural crest cell patterning and pharyngeal arch artery defects in the mouse embryo. *Dev Biol* 2005;284:233–45.
32. Lepore JJ, Mericko PA, Cheng L et al. GATA-6 regulates semaphorin 3C and is required in cardiac neural crest for cardiovascular morphogenesis. *J Clin Invest* 2006;116:929–39.
33. Binder M. The teratogenic effect of a bis(dichloroacetyl) diamine on hamster embryos. *Am J Pathol* 1985;118:179–93.
34. Celoria GC, Patton RB. Congenital absence of the aortic arch. *Am Heart J* 1959;58:407–13.
35. Kreutzer J, Van Praagh R. Comparison of left ventricular outflow tract obstruction in interruption of the aortic arch and in coarctation of the aorta, with diagnostic, developmental, and surgical implications. *Am J Cardiol* 2000;86:856–62.
36. Van Praagh R, Geva T, Kreutzer J. Ventricular septal defects: How should we describe, name and classify them? *J Am Coll Cardiol* 1989;14:1298–9.
37. Moulaert AJ, Oppenheimer-Dekker A. Anterolateral muscle bundle of the left ventricle, bulboventricular flange and subaortic stenosis. *Am J Cardiol* 1976;37:78–81.
38. McCrindle BW, Tchervenkov CI, Konstantinov IE et al. Risk factors associated with mortality and interventions in 472 neonates with interrupted aortic arch: a Congenital Heart Surgeons Society study. *J Thorac Cardiovasc Surg* 2005;129:343–50.
39. Sim MM, Chen CC. Transthoracic echocardiographic diagnosis of a type C interrupted aortic arch in an adult. *J Am Soc Echocardiogr* 2007;20:1418 e1–4.
40. Fujii I, Ueno Y, Kurano R, Goto Y. Interrupted aortic arch type C associated with DiGeorge syndrome in 22q11.2 deletion: first case detected in Japan. *Pediatr Int* 2005;47:698–700.
41. Konstantinov IE, Karamlou T, Blackstone EH et al. Truncus arteriosus associated with interrupted aortic arch in 50 neonates: a Congenital Heart Surgeons Society study. *Ann Thorac Surg* 2006;81:214–22.
42. Konstantinov IE, Karamlou T, Williams WG et al. Surgical management of aortopulmonary window associated with interrupted aortic arch: a Congenital Heart Surgeons Society study. *J Thorac Cardiovasc Surg* 2006;131:1136–41.
43. Pierpont MEM, Zollikofer CL, Moller JH, Edwards JE. Interruption of the aortic arch with right descending aorta: a rare condition and a cause of bronchial compression. *Pediatr Cardiol* 1982;2:153–9.
44. Geva T, Gajarski RJ. Echocardiographic diagnosis of type B interruption of a right aortic arch. *Am Heart J* 1995;129:1042–5.
45. Kutsche LM, Van Mierop LHS. Cervical origin of the right subclavian artery in aortic arch interruption: pathogenesis and significance. *Am J Cardiol* 1984;53:892–5.
46. Yildirim N, Aydin M, Hakimoglu K, Gungorduk A. Isolated interrupted aortic arch, a rare cause of hypertension in adults. *Int J Cardiol* 2008;127:e52–3.
47. Kaulitz R, Jonas RA, van der Velde ME. Echocardiographic assessment of interrupted aortic arch. *Cardiol Young* 1999;9: 562–71.

48. Tworetzky W, McElhinney DB, Brook MM et al. Echocardiographic diagnosis alone for the complete repair of major congenital heart defects. *J Am Coll Cardiol* 1999;33:228–33.
49. Riggs TW, Berry TE, Aziz KU, Paul MH. Two-dimensional echocardiographic features of interruption of the aortic arch. *Am J Cardiol* 1982;50:1385–90.
50. Moran AM, Colan SD, Mayer JE, Jr, van der Velde ME. Echocardiographic identification of thymic hypoplasia in tetralogy of fallot/tetralogy pulmonary atresia. *Am J Cardiol* 1999; 84:1268–71.
51. Smallhorn JF, Anderson RH, Macartney FJ. Cross-sectional echocardiographic recognition of interruption of aortic arch between left carotid and subclavian arteries. *Br Heart J* 1982; 48:229–35.
52. Geva T, Hornberger LK, Sanders SP et al. Echocardiographic predictors of left ventricular outflow tract obstruction after repair of interrupted aortic arch. *J Am Coll Cardiol* 1993;22:1953–60.
53. Minich LL, Snider AR, Bove EL, Lupinetti FM. Echocardiographic predictors of the need for infundibular wedge resection in infants with aortic arch obstruction, ventricular septal defect and subaortic stenosis. *Am J Cardiol* 1992;70:1626–7.
54. Ge S, Warner JG Jr, Fowle KM et al. Morphology and dynamic change of discrete subaortic stenosis can be imaged and quantified with three-dimensional transesophageal echocardiography. *J Am Soc Echocardiogr* 1997;10:713–6.
55. Brown JW, Ruzmetov M, Okada Y et al. Outcomes in patients with interrupted aortic arch and associated anomalies: a 20-year experience. *Eur J Cardiothorac Surg* 2006;29:666–73.
56. Schreiber C, Mazzitelli D, Haehnel JC et al. The interrupted aortic arch: an overview after 20 years of surgical treatment. *Eur J Cardiothorac Surg* 1997;12:466–9.
57. Oosterhof T, Azakie A, Freedom RM et al. Associated factors and trends in outcomes of interrupted aortic arch. *Ann Thorac Surg* 2004;78:1696–702.
58. Serraf A, Lacour-Gayet F, Robotin M et al. Repair of interrupted aortic arch: a ten-year experience. *J Thorac Cardiovasc Surg* 1996;112:1150–60.

# 22 Tetralogy of Fallot

**Shubhika Srivastava[1] and Ira A. Parness[2]**

[1]Echocardiography Laboratory, Mount Sinai Medical Center, New York, NY, USA
[2]Division of Pediatric Cardiology, Mount Sinai Medical Center, New York, NY, USA

## Definition

In 1671, Niels Stenson first described the pathology of the syndrome now known as tetralogy of Fallot (TOF). Fallot, in his seminal paper, was careful to point out the previous work and published cases of the same syndrome. However, it was not until his 1888 paper that Etienne-Louis Arthur Fallot debunked the prevailing theory that cardiac cyanosis ("la maladie bleue") was due to right-to-left foramen ovale shunting. Fallot was the first to appreciate that most patients with cyanotic heart disease had the complex of cardiac malformations that he coined a "tetralogy" consisting of pulmonary stenosis, ventricular septal defect (VSD), dextroposition of the aorta, and right ventricular (RV) hypertrophy [1–3]. Fallot postulated that the tetralogy was the consequence of an intrauterine malformation of the subpulmonary infundibulum and the pulmonary valve [2], and Fallot's assessment was later adopted by Abbott and Dawson [4] who, in 1924, named the malformation "tetralogy of Fallot." The nomenclature for TOF as recommended by the Congenital Heart Surgeons Society, to unify reporting and for multiinstitutional studies, classified TOF into three main groups:

**1** TOF with varying degrees of pulmonary stenosis
**2** TOF with common atrioventricular (AV) canal
**3** TOF with absent pulmonary valve.

TOF with pulmonary atresia was classified under the category of pulmonary atresia with VSD [5]. Nonetheless, in this chapter, we have categorized pulmonary atresia with VSD as the most severe morphologic variant of TOF.

## Incidence

Tetralogy of Fallot is the most common cyanotic heart defect, with an incidence of 32.6 per 100 000 live births [6,7]. Early neonatal complete repair was pioneered by Castaneda and colleagues [8] and was aimed at minimizing the exposure to cyanosis, as well as minimizing RV hypertrophy and promoting alveologenesis [9]. Initial medical and surgical mortality in the 1980s was reported to be as high as 28% [10], and subsequent improvement in diagnostic, surgical and anesthetic techniques has had a significant impact on the natural history of repaired TOF. There is now a large population of adults with repaired TOF, which has necessitated advances in diagnostic techniques and management [11].

## Embryology, genetics and molecular basis

The pathognomonic conotruncal abnormality of TOF has been attributed to arrest in neural crest cell migration [12]. Studies in chick and mouse embryos have demonstrated the key role of the secondary heart field (SHF) from the anterior mesoderm in cardiac embryogenesis [12–15], including a significant role in conotruncal and RV development in humans [16,17]. Following primary heart tube looping, committed precardiac cells from the SHF migrate to the anterior pole, where they are incorporated into the outflow tracts. Neural crest cells influence and modulate migration of the SHF. Ablation of the SHF and/or neural crest (NC) results in arrest of caudal migration of the committed precardiac cells toward the aortic sac [18–22]. The consequent short outflow tract [23], failure of normal rotation of the conotruncus, and abnormal coronary arteries are typical of TOF [24].

This embryologic theory supports the hypothesis proposed by Van Praagh and colleagues, who demonstrated that the primary morphologic abnormality in TOF is an underdeveloped subpulmonary infundibulum [3]. The secondary precardiac mesoderm expresses NKX2.5 and GATA 4 transcription factors [15,18,19]. Hence, gene defects affecting their expression may explain the resultant conotruncal abnormality in TOF. Microdeletion of chromosome 22q11, seen in DiGeorge or velocardiofacial phenotype syndromes, is a common example of a single gene defect causing

*Echocardiography in Pediatric and Congenital Heart Disease: From Fetus to Adult*
Edited by Wyman W. Lai, Luc L. Mertens, Meryl S. Cohen and Tal Geva
 ISBN: 978-1-405-17401-5

abnormal neural crest cell migration and resulting in TOF [17]. The prevalence of 22q11 deletions among patients with TOF is much higher in patients with associated pulmonary atresia than in patients with TOF alone [25].

The subpulmonary infundibulum derived from the SHF is highly sensitive to vascular endothelium growth factor (VEGF) signaling, which influences growth of the outflow tract cushions and RV myocardium. Hypoxia and other gene defects that cause upregulation of VEGF induce hyperplasia of the outflow tract cushions and apoptosis of the subpulmonary infundibulum. The resultant morphology is hypoplasia of the pulmonary trunk, right ventricular outflow tract (RVOT) obstruction and dextroposition of the aorta [26].

Approximately 50 syndromes associated with TOF have been identified [27]. Genetic syndromes have been shown to be an independent risk factor for mortality in TOF repair [28]. Known chromosomal anomalies, syndromes and single gene defects are associated with at least one-third of the cases with TOF (Table 22.1). In one study of 87 patients with TOF and associated common AV canal, 87.5% had a genetic syndrome and extracardiac abnormalities, 67% had Down syndrome, but none had 22q11 deletion [29].

### Environmental factors

Maternal diabetes, exposure to retinoic acid, maternal phenylketonuria, and trimethadione have been reported to be associated with TOF [46–48].

### Recurrence risk

The recurrence rate of TOF varies between 2.5% and 3% if one sibling is affected, and is 8% if more than one sibling is affected. The reported risk of recurrence is 1.4% from an affected father, and varies between 0.9% and 2.6% for an affected mother. The recurrence rate also depends upon associated syndromes and genetic or environmental factors [49–55].

## Morphology

### The conotruncus in TOF

Tetralogy of Fallot comprises conoventricular VSD, overriding aorta, RV outflow tract obstruction, and RV hypertrophy (Figs 22.1 and 22.2). However, the RV hypertrophy component is the consequence of prolonged systemic level RV pressures rather than being a primary morphologic feature. The principal developmental abnormality in TOF resulting in its components has been debated. There are two theories:

**1** The theory advocated by Van Praagh and colleagues [2,3,56]: The principal morphologic abnormality in TOF is hypoplasia of the subpulmonary infundibulum, the latter consisting of the parietal band and the muscle or conus subtended under the pulmonary valve [3]. The combination of a small subpulmonary infundibulum, or conus (they are synonyms), and absence of subaortic conus results in the antero-cephalad deviation of the infundibular septum. According to Van Praagh, the normal aortic overriding of the ventricular septum is exaggerated by the presence of a VSD in TOF and by the dilated aorta. The relationship between the aortic valve and pulmonary valve in severe TOF is often altered, with significant clockwise rotation of the conotruncus resulting in a rightward and more anteriorly located aortic valve, and a leftward and more posteriorly situated hypoplastic pulmonary valve [3].

**2** Becker et al. [1,57] and Anderson et al. [57,58], proposed that the principal abnormality in TOF is antero-superior deviation of the infundibular septum and not hypoplasia of the subpulmonary infundibulum. Because anterior deviation of

**Table 22.1** Genetic syndromes associated with tetralogy of Fallot (TOF)

| Anomaly | Known prevalence in TOF | Gene defect | Chromosome location | References |
|---|---|---|---|---|
| Trisomy 21 | 8% (14% in fetal series) | Not identified | | [27,30,31] |
| Trisomy 13 | 7% in fetal series | | | [31] |
| Trisomy 18 | 16% | | | [32] |
| Velocardiofacial | 20% (80% of those with RAA) | *TBX1* in 15% | 22q11 | [27] |
| Noonan | Rare | *PTNPII*, *KRAS*, *SOS1* | 12q24 | [33–36] |
| Alagille | 16% | *JAG1* | 20p12 | [37,38] |
| Holt–Oram | Rare | *TBX5* | | [39] |
| Goldenhar, or oculoauriculovertebral syndrome | 10% | | | [40] |
| DiGeorge | 8–35% | | 90% have 22q11 | [41–44] |
| Cardiac homeobox gene mutations | 4% | *NKX2.5* | 5q34-q35 | [5,27,42] |
| | ? | *ZFPM2/FOG2* | 8q23 | [17,24,45] |
| Cat-eye | Rare | | Duplication of 22pter22q11 | [27] |

RAA, right aortic arch.

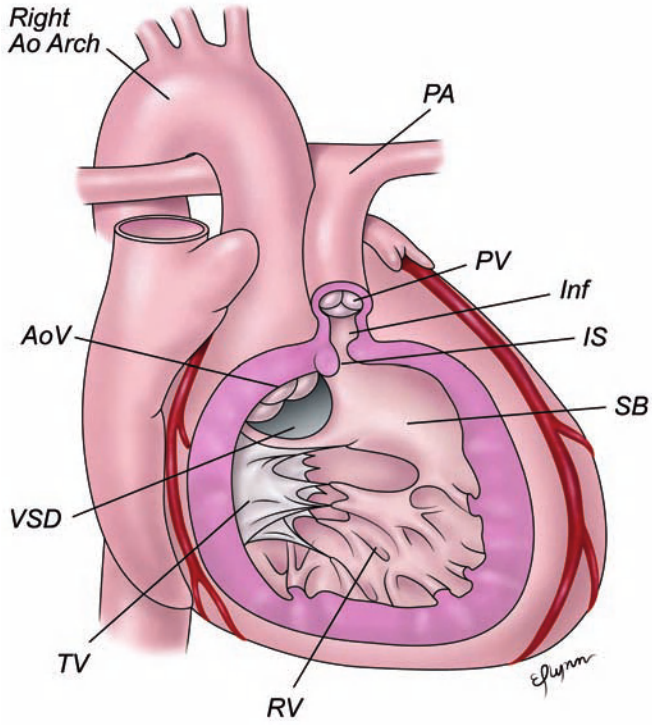


(a)

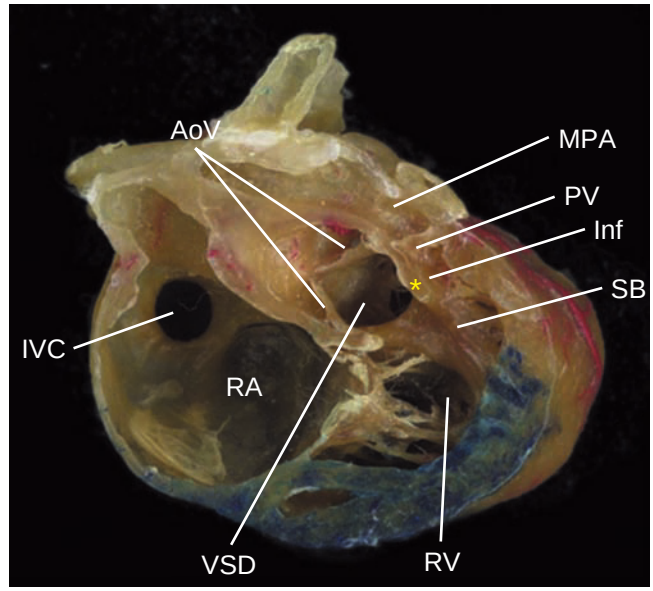


(b)

**Figure 22.1** Tetralogy of Fallot (TOF) with pulmonary stenosis. **(a)** Diagram showing anterior-leftward deviation of the infundibular septum (IS) relative to the muscular ventricular septum, narrowed subpulmonary infundibulum (Inf), pulmonary valve (PV) stenosis, right ventricular (RV) hypertrophy, aortic override, and right aortic arch. The ventricular septal defect (VSD) is enclosed anteriorly and postero-inferiorly between the limbs of the septal band (SB) and superiorly by infundibular septum and the junction of the anterior limb of septal band and RV free wall. This anterior malalignment type of conoventricular septal defect is typical of TOF. **(b)** Waxed heart specimen showing the right side of the heart of an infant TOF with pulmonary stenosis. Courtesy of Dr Paul Weinberg, Children's Hospital of Philadelphia. AoV, aortic valve; IVC, inferior vena cava; MPA, main pulmonary artery; PA, pulmonary artery; RA, right atrium; TV, tricuspid valve; asterisk (*) denotes the infundibular septum.

the conal septum may be present without RV outflow obstruction as in Eisenmenger type VSD [59–61], there must also be concomitant hypertrophy and/or hypoplasia of the subpulmonary infundibulum to produce TOF morphology. The infundibular septal deviation theory also does not easily explain the morphologic variant of TOF with doubly committed subarterial VSD, characterized by complete absence of the conal septum but hypoplasia of the pulmonary valve.

In either scheme, the embryonic morphologic abnormality of conal hypoplasia and/or conal septal malalignment results in failure of ventricular septation (VSD), subpulmonary and/or valvar pulmonary stenosis, and overriding of the aorta.

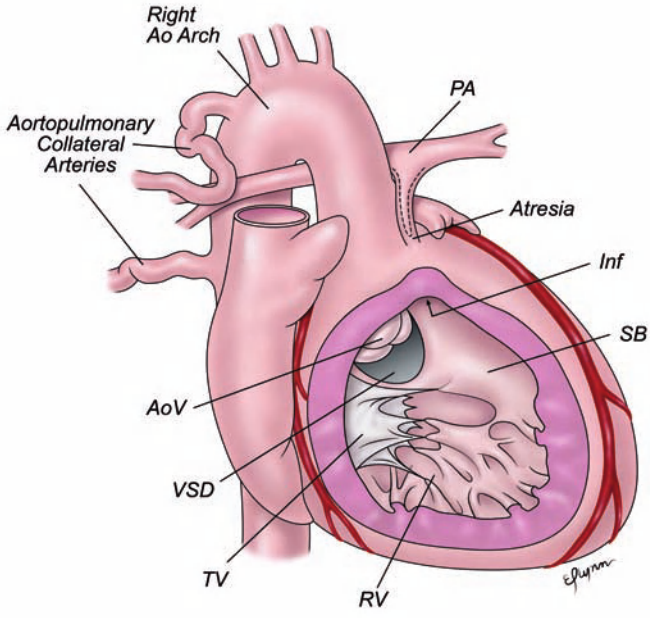


## Ventricular septal defect morphology

The anterior malalignment type of conoventricular septal defect is typical of TOF (Fig. 22.1) [2,62]. Some authors have classified these defects as paramembranous or perimembranous [63]. The defect results from anterior, superior

**Figure 22.2** (*left*) Diagram of tetralogy of Fallot (TOF) with pulmonary atresia. The subpulmonary infundibulum is obliterated by marked anterior-leftward malalignment of the conal septum. The pulmonary arteries are hypoplastic and aorto-pulmonary collateral vessels are shown. The anterior malalignment type of conoventricular septal defect is the same as in TOF with pulmonary stenosis. AoV, aortic valve; Inf, infundibulum; IVC, inferior vena cava; MPA, main pulmonary artery; PA, pulmonary artery; RV, right ventricle; SB, septal band; TV, tricuspid valve; VSD, ventricular septal defect.

and leftward deviation of the conal (infundibular or outlet) septum, which fails to align with the crest of the muscular septum. The malalignment of conal septum results in a wide communicating space between the ventricles rather than a deficiency, per se, in the "pars membranacea." The boundaries of the defect are formed by:

- Superiorly – the RV free wall and the aortic valve cusps, extending posteriorly to the tricuspid valve hinge point.
- Anteriorly – the parietal band of the crista supraventricularis.
- Inferiorly – the crest of the ventricular septum.
- Posteriorly – the muscle extending from septal band to the posterior muscular septum, also called the posterior limb of septal band. This muscle also separates the aortic valve from the tricuspid valve and is often referred to as the ventricular infundibular fold, which forms the inner heart curvature in a structurally normal heart. The width of this muscle is variable, at times being represented as a thin fibrous ridge allowing approximation of the tricuspid valve to the VSD [63].

The VSD is thus enclosed anteriorly and postero-inferiorly between the limbs of the septal band, and superiorly by the conal septum and the junction of the anterior limb of septal band and RV free wall [57]. Absence of the conal septum and associated hypoplasia of the subpulmonary infundibulum and hypertrophy of the septoparietal band results in a variant of TOF with doubly committed subarterial VSD, overriding aorta, and pulmonary annular hypoplasia and stenosis [64–67].

The VSD in TOF is typically large but a restrictive defect has been reported in 1.5% of cases [68,69]. The mechanism of obstruction in nearly all the cases results from overlying abnormal or accessory tissue associated with the tricuspid valve [69–72]. Rarely, myxomatous outpouching of the septal leaflet associated with Ebstein anomaly in TOF can result in a restrictive VSD [73]. Absolute small dimensions of the VSD caused by posterior deviation of the septal band and hypertrophy of the ventricular septum resulting in restriction to flow have rarely been described [68].

Tetralogy of Fallot can also be seen in association with common AV canal defects [57,74] characterized by an anteriorly malaligned conal septum in association with a predominantly Ratelli type C common AV valve [75]. In the setting of complete common AV canal and TOF, VSD morphology is that of a single defect with confluent inlet and outlet components along with the typically anteriorly deviated conal septum. TOF may also occur in association with a rare variant of common AV canal in which there is an absent or diminutive atrial septal defect component [76].

## Coronary arteries

Clockwise rotation of the aortic root (as viewed from the cardiac apex), and resultant rotated origins of the coronary arteries, are typical in TOF. Anomalies in the branching pattern of the coronary arteries are reported in approximately 5% of all cases (Fig. 22.3) [77]. The most common anomaly, occurring in 3%, is origin of the left anterior descending (LAD) coronary artery from the right coronary artery (RCA); this is followed by dual LAD in 1.8%, single RCA in 0.3%, single left coronary artery (LCA) in 0.2%, and coronary-to-pulmonary artery fistula in 0.2%. In an angiographic study, anomalies of coronary artery branching pattern were more prevalent in patients with the most prominent aorto-pulmonary rotation [78]. The extraordinarily rare "isolated infundibuloarterial inversion" in TOF is associated with the RCA crossing anteriorly across the subpulmonary infundibulum. Anomalous origin of the LCA from the pulmonary artery has been reported in patients with TOF [77, 79–82].

Coronary artery-to-pulmonary artery fistulae may rarely serve as a source of pulmonary blood flow in TOF with pulmonary valvar atresia or severe stenosis [83–85]. Isolated coronary ostial stenosis or obstruction has also been reported in the absence of any other coronary anomaly [81]. Acquired coronary cameral fistulae may be observed following surgery [86].

## Variants and associated lesions

### TOF and double-outlet right ventricle (DORV)

Some authorities have categorized extreme dextroposition or aortic overriding with more than 50% of the aortic annulus over the RV as DORV [57,58]. Nonetheless, according to Van Praagh et al., the maintenance of aortic-to-mitral valve fibrous continuity or normally related great arteries is pathognomonic for TOF irrespective of the degree of aortic override or dextroposition [2,57,87,88]. This approach recognizes a wide spectrum of aortic overriding within TOF without imposing an arbitrary dichotomous cutoff between TOF and DORV depending on the percentage of aortic override. Aortic–mitral fibrous continuity is also important in the prediction of postoperative left ventricular (LV) outflow tract obstruction: progressive subaortic obstruction following repair of typical TOF is rare [89]. However, progressive muscular hypertrophy causing subaortic obstruction may develop in cases of "TOF-like" DORV with retention of subaortic conus (see Chapter 25).

### TOF and double-chambered right ventricle (DCRV)

Double-chambered right ventricle is an anomaly characterized by obstruction within the RV with or without an associated VSD (see Chapter 16). It can also present as a progressive lesion following corrective surgery for TOF [90]. DCRV is often misdiagnosed as TOF because both lesions have a VSD and subpulmonary stenosis [90–96]. However, in DCRV, the primary morphologic abnormality resulting in subpulmonary stenosis is either marked hypertrophy of the septoparietal trabeculations or moderator band, and/or abnormal displacement of the moderator band resulting in narrowing of the proximal infundibular ostium. Unlike TOF, DCRV is typically associated with normal size and morphology of the pulmonary valve and main and branch pulmonary arteries. Additionally, the VSD seen in DCRV is typically

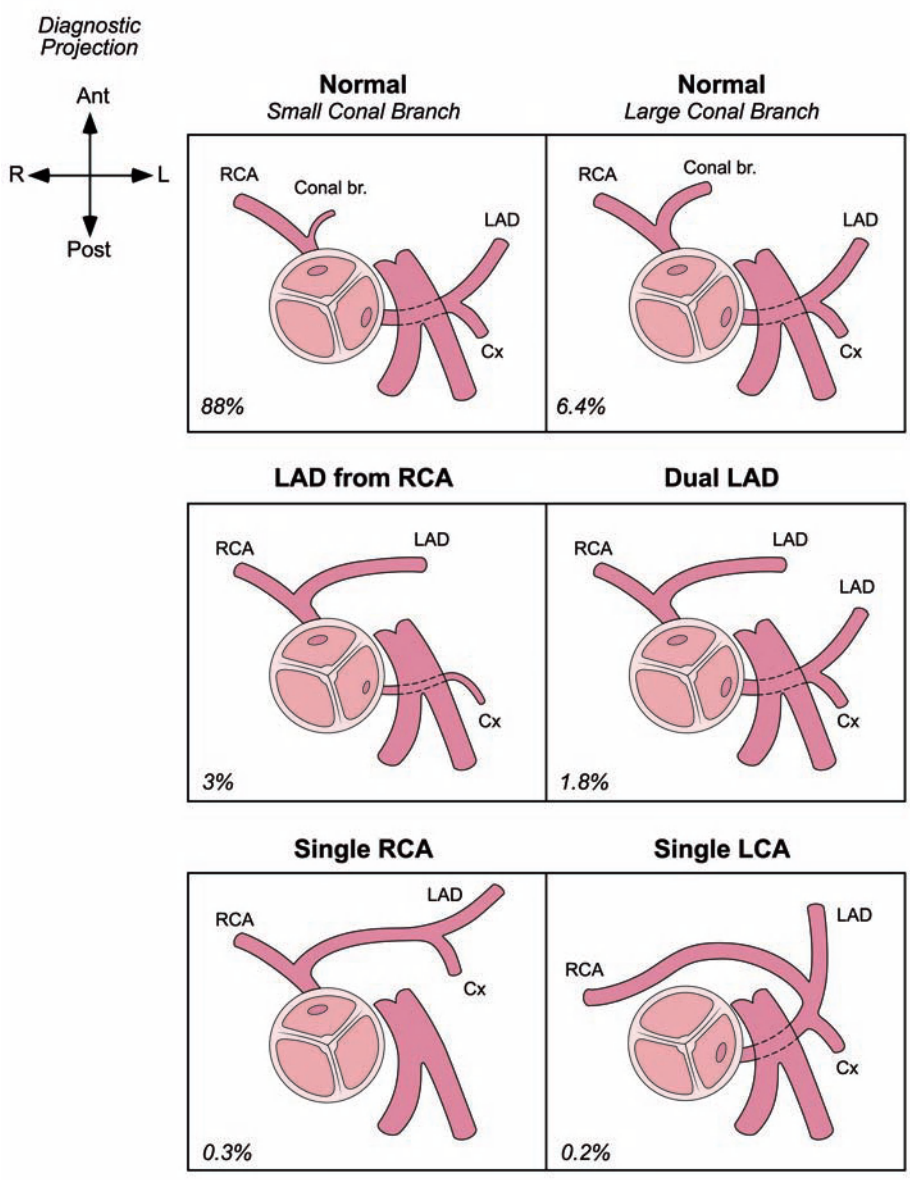


**Figure 22.3** Diagram of coronary artery patterns in tetralogy of Fallot. br., branch; Cx, circumflex artery; LAD, left anterior descending coronary artery; LCA, left coronary artery; RCA, right coronary artery.

membranous rather than the malalignment type typical of TOF. However, there are overlap syndromes that share features of DCRV and TOF, such as those with an anterior malalignment type of VSD and aortic overriding but with a morphologically normal pulmonary valve and a well-developed infundibulum; in these cases, the subpulmonary obstruction is limited to the proximal os infundibulum.

### TOF with pulmonary atresia and/or extreme pulmonary hypoplasia

Tetralogy of Fallot with pulmonary atresia is a severe form of TOF. In addition to valvar atresia (short-segment atresia) or valve and main pulmonary artery absence (long-segment atresia), this condition is characterized by marked variability in the degree of pulmonary artery hypoplasia or absence and/or the presence of abnormal pulmonary arterial supply. The intracardiac anatomy, like other forms of TOF, typically consists of an enlarged and overriding aorta and an anterior malalignment VSD. In addition, there is marked infundibular hypoplasia or subvalvar atresia due to extreme leftward deviation of the conal septum, which may merge with the septal parietal band and RV free wall.

This defect was initially misclassified as truncus arteriosus type IV in the classification of Collett and Edwards [97]. However, Van Praagh and Van Praagh correctly defined and classified this entity as TOF with pulmonary atresia [98]. This entity was also described as "pseudotruncus" by Bharati et al. [99]. The Congenital Heart Surgeons Society Nomenclature Committee classified TOF with pulmonary atresia under the umbrella of "Pulmonary atresia with VSD" [100]. The term "MAPCA(s)," or major aortopulmonary collateral artery, was coined by Macartney et al. [101].

Tetralogy of Fallot with pulmonary atresia can be further classified into three broad categories [100]:

**1** Native confluent branch pulmonary arteries are present, which supply all lung segments; patency of the ductus maintains pulmonary circulation. Interruption of antegrade pulmonary blood flow may be limited to the level of the valve, as in valvar atresia, or to the main pulmonary artery, as in long-segment pulmonary atresia.

**2** Both native pulmonary arteries and MAPCAs are present; lung segments can have dual blood supply and the native pulmonary arteries may be supplied by either a ductus and/or MAPCAs. The pulmonary atresia may be long-segment with confluent mediastinal branch pulmonary arteries or with discontinuous branch pulmonary arteries.

**3** Native mediastinal pulmonary arteries are absent and MAPCAs supply all lung segments. Bronchial and pleural vessels can also be alternative sources of pulmonary blood flow.

The size of the branch pulmonary arteries is inversely proportional to the extent of MAPCAs and presence of a ductus arteriosus [102–105]. The angiographically determined Nakata index predicts good outcomes of complete repair of TOF with pulmonary artery hypoplasia if the index is greater than 100 $mm^2$/body surface area (BSA) [106].

Other rare variations in the morphology of TOF with pulmonary atresia have been reported, such as restrictive VSD (68,107,108), coronary artery-to-pulmonary artery fistula [75], aortopulmonary window [109], retroaortic innominate vein [110], and a higher incidence of right aortic arch [99,111].

### TOF with atrioventricular canal defects

A common AV canal in association with TOF is a rare variant, seen in 1.7% of all cases of TOF and in 6.2% of cases with complete common AV canal defects [74,75]. A very high incidence (87.5%) of genetic and extracardiac abnormalities is seen in this morphologic variant [67].

Rastelli type C morphology of the common AV valve is the most common variant (85% of reported cases) [74]. The diagnosis of type A common AV valve morphology in TOF has been questioned by Suzuki et al., who argued that attachments of the superior bridging leaflet to the crest of a malalignment VSD are unlikely [75]. We have observed concomitant absence of conal septum in the setting of otherwise typical morphology for TOF with common atrioventricular canal (CAVC). A small or absent primum ASD component can also occur in this morphologic variant, which can increase the challenge of surgical correction of this lesion [74,112]. TOF may also exist in conjunction with a cleft mitral valve but with absent primum ASD [113].

### TOF with absent pulmonary valve syndrome

The incidence of TOF with absent pulmonary valve is reported to be between 3% and 6% of all TOF [88,114,115]. This TOF variant with typical anterior malalignment VSD and overriding aorta is differentiated by hypoplasia of the pulmonary valve annulus with rudimentary valve leaflets causing pulmonary stenosis and insufficiency. The main and/or one or both branch pulmonary arteries are typically aneurysmally enlarged [116,117]. This lesion is usually associated with absent patent ductus arteriosus, and prenatal absence of the ductus arteriosus has been demonstrated by fetal echocardiography [116,118]. Aneurysmal pulmonary artery dilation is associated with variable degrees of bronchial compression and intraparenchymal pulmonary arteriopathy, and may cause severe neonatal respiratory distress. In fetal life, severe forms may lead to hydrops fetalis and/or fetal demise.

### Aortic arch anomalies

Right aortic arch (RAA) is seen in approximately 25% of patients with TOF [119,120]. Double aortic arch and persistence of the fifth aortic arch and other morphologic variations of vascular rings may be seen in association with TOF [101, 121,122].

Right aortic arch with isolation of the subclavian artery or with aberrant origin of the left subclavian artery from the ascending aorta have been reported [123,124]. The isolated left subclavian artery can be supplied by the left vertebral artery (in which case the direction of blood flow is reversed) and may cause a subclavian steal phenomenon. Alternatively, the isolated left subclavian artery may be connected via a patent ductus arteriosus to the main pulmonary artery. In the latter case, the left vertebral artery supplies the main pulmonary artery resulting in a congenital pulmonary artery steal [123,125,126].

### Aortopulmonary defects and variations in pulmonary artery origin and bifurcation

Aortic origin of branch pulmonary artery [127,128], unilateral absence of branch pulmonary artery, crossed pulmonary arteries [80,129], aortopulmonary window [109,130,131], and pulmonary artery slings [132,133] have been described in association with TOF. Crossed pulmonary arteries may be a marker for 22q11 deletion [129,134–136].

### Left-sided lesions associated with TOF

Isolated reports of supravalvular mitral stenosis, LV outflow tract obstruction secondary to adherent anterior mitral valve leaflet, and cleft mitral valve have been described in patients with TOF [62,113,137]. Other left heart lesions reported in association with TOF include aortic valve abnormalities (bicommissural, stenosis, regurgitation) [138–141], coarctation of the aorta [139], LV diverticulum [142], and cor triatriatum [143,144].

### Rare segmental combinations in TOF

The usual segmental anatomy of TOF is {S,D,S}, with the rare occurrence of {I,L,I} in dextrocardia, the latter being

sometimes seen in association with the "polysplenia" type of heterotaxy syndrome [145]. Isolated infundibuloarterial inversion in the setting of atrial situs solitus, D-looped ventricles, and inversus normally related great arteries or {S,D,I} has been reported in TOF [146–148]. The presence of aortic-to-mitral valve fibrous continuity differentiates this rare conotruncus from that of anatomically corrected malposition.

### Systemic and pulmonary venous anomalies and atrial septal defects

In TOF, systemic and pulmonary venous anomalies may be seen independently or in association with heterotaxy syndrome [149–151]. Subaortic (retroaortic) position of the innominate vein is more commonly seen in TOF with pulmonary atresia [110]. Left superior vena cava to the coronary sinus (or rarely, to the left atrium) has been described in up to 11% of cases [114,152]. Left superior vena cava to left atrium without a connecting left innominate vein, if undiagnosed, can result in persistent hypoxemia following complete repair. Persistence of the levoatrial cardinal vein has also been reported [151]. Partially or totally anomalous pulmonary venous connection may be seen in association with TOF [153], rarely as part of scimitar syndrome [154]. Atrial septal defects, typically secundum type, are seen in 86% of cases [114]. Rarely, sinus venosus defects or coronary sinus septal defects occur in TOF [150,155].

### Other rare associated malformations

Ebstein anomaly and double-orifice tricuspid valve (TV) have been reported in TOF [73,156]. The association of TOF with ectopia cordis (often in combination with other midline defects and ventricular diverticulum) is known as "pentalogy of Cantrell" [157].

## Imaging

Detailed echocardiographic assessment has made diagnostic angiography nearly obsolete in the routine preoperative assessment of the anatomic details of TOF. However, angiography and cardiac magnetic resonance (CMR) serve an important complementary role in the assessment of rare aortic arch anomalies as well as MAPCAs and hypoplastic branch pulmonary arteries in the setting of associated pulmonary atresia and in absent pulmonary valve syndrome. CMR provides unique information about pulmonary vessels *and* airway architecture, both of which are important for surgical planning.

### Preoperative echocardiographic assessment of morphology

The goals of preoperative assessment can be summarized as follows:

- Cardiac position and presence or absence of thymus.
- Visceral and atrial situs and segmental diagnosis; conotruncal anatomy.
- Pulmonary and systemic venous connections and atrial septal defects.
- AV valve morphology and function.
- VSD morphology, differentiating between malalignment, doubly committed subarterial, and AV canal types [158]. Rule out additional muscular ventricular septal defects. Assess for rare restriction to flow and determine the direction of VSD shunting.
- Degree and morphology of RV outflow obstruction: assess infundibular septal size and position as well as additional muscular obstruction, as in DCRV.
- Assess pulmonary valve annular size and valve morphology.
- Determine main and branch pulmonary artery size and flow. Rule out anomalous origin or course of branch pulmonary arteries (e.g., left pulmonary artery [LPA] sling). Evaluate for branch pulmonary artery hypoplasia, discrete branch pulmonary artery stenosis, or discontinuous branch pulmonary arteries, especially following ductal closure.
- Subaortic and aortic valve morphology and function.
- Image PDA origin from the aortic arch or from the brachiocephalic arteries and rule out additional sources of pulmonary blood flow such as aorto-pulmonary collaterals. Distinguish PDA from MAPCA.
- Determine aortic arch sidedness and branching pattern. Assess for vascular rings and other arch malformations.
- Image coronary artery origin, branching, and flow; rule out anomalous origin of the LCA from the main pulmonary artery; anomalous origin of the LAD from the RCA or other large coronary branches crossing the RV outflow tract that may complicate transannular patch repair or conduit placement.

### Anatomic two-dimensional assessment

Organized, systematic, and detailed imaging starting with the subxiphoid long-axis window is our preferred approach for accurate diagnosis of congenital heart disease (see Chapter 4). At Mount Sinai Medical Center in New York, we routinely sedate infants with congenital heart disease using chloral hydrate. However, in TOF with moderate stenosis, sedation imposes an additional risk for a hypercyanotic spell due to the combination of intravascular volume depletion (from being kept NPO [nil per os] for sedation) and systemic vasodilation. Hence, whenever possible we aim at defining the details of branch pulmonary artery anatomy, arch morphology and coronary morphology early after diagnosis in the newborn period. Neonates will often sleep soundly after feeding, allowing a comprehensive and detailed examination without sedation.

#### Initial subxiphoid long-axis imaging

This view demonstrates visceral and atrial situs, systemic venous connections, coronary sinus and atrial septal morphology [159] (Videoclip 22.1). The descending aorta in

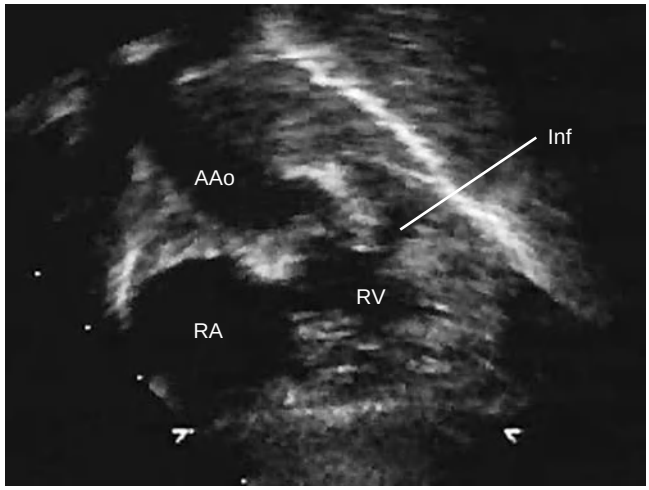


**Figure 22.4** Imaging of tetralogy of Fallot with pulmonary stenosis from the subxiphoid long-axis view. Anterior tilt of the transducer demonstrates the infundibular stenosis (Inf) and the ascending aorta (AAo). RA, right atrium; RV, right ventricle.

its cross-section may be visualized to the left of the spine, and through the course of the sweep it can be seen crossing over to the right of the thoracic spine. The VSD with overriding of the aorta may be seen as well as subpulmonary infundibular hypoplasia and stenosis (Fig. 22.4). Branch pulmonary arteries may also be identified from subxiphoid long-axis imaging (Fig. 22.5; Videoclip 22.2) as the RPA traverses from left to right above the atrial mass; the LPA and ductus are more difficult to image without color Doppler flow mapping.

### Subxiphoid short-axis imaging

This view defines the atrial septum, the entrance of the right upper pulmonary vein into the left atrium, VSD, RV hypertrophy, and muscle bundles within the RV that could result in additional intracavitary obstruction, as in the DCRV variant (Fig. 22.6). Cleft mitral valve and common AV valve are also well imaged in this plane (Fig. 22.7 and Videoclip 22.3).

### Anterior oblique subxiphoid view

This modified view is of exceptional benefit in viewing the subpulmonary infundibulum, inclusive of both the size of the conal septum and its displacement (Fig. 22.8 and Videoclip 22.4) [160]. This view is also useful for assessing additional muscle bundles contributing to RV outflow tract obstruction in the DCRV variant.

### Apical views

Apical views demonstrate the AV valves, VSD, aortic valve (Fig. 22.9 and Videoclip 22.5), and may identify other associated anomalies, such as left-sided obstructive lesions.

### Parasternal long-axis imaging

Parasternal imaging may be limited if the thymus, which usually provides a reliably good acoustic window, is absent. This view nicely demonstrates the overriding aorta, aortic-to-mitral valve fibrous continuity (distinguishing TOF from its related type of DORV) (Fig. 22.10a), VSD morphology, and pulmonary valve morphology as the transducer sweeps leftward and anteriorly (Fig. 22.10b and Videoclip 22.6).

### Parasternal short-axis imaging

This view further defines VSD morphology, subpulmonary obstruction, infundibular hypertrophy, and deviation of the conal septum (Fig. 22.11 and Videoclip 22.7). Extension of the edge of the VSD beyond the intercoronary commissure under the right and noncoronary cusps and bordering the pulmonary valve annulus in the absence of the conal septum defines a doubly committed subarterial defect in TOF [66].

(a)

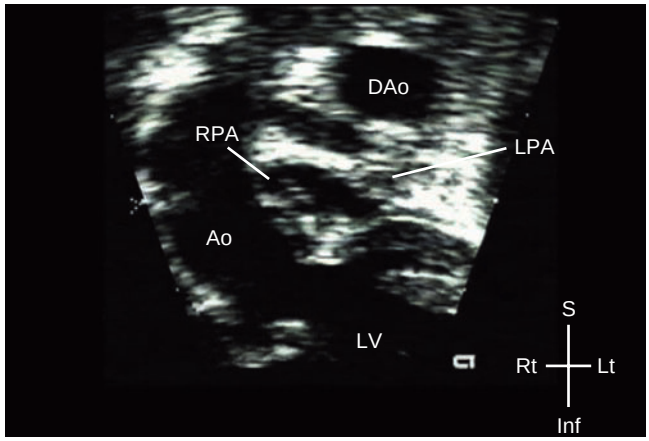


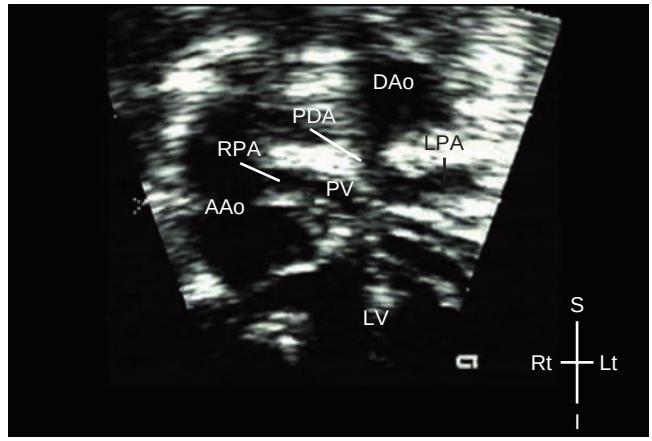


(b)

**Figure 22.5** Imaging branch pulmonary arteries from the subxiphoid long-axis view in tetralogy of Fallot. **(a)** Hypoplastic, continuous branch pulmonary arteries. **(b)** Discontinuous branch pulmonary arteries. The right pulmonary artery (RPA) is continuous with the main pulmonary artery, and the discontinuous left pulmonary artery (LPA) is supplied by a patent ductus arteriosus (PDA). AAo, ascending aorta; DAo, descending aorta; LV, left ventricle; PV, pulmonary valve; S, superior; I, inferior; Rt, right; Lt, left.

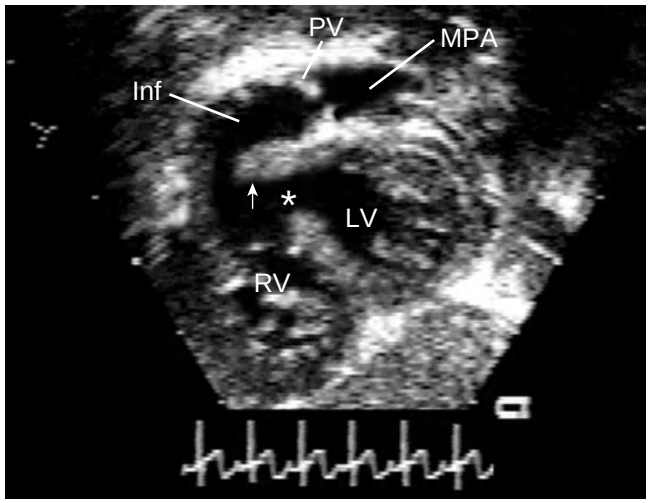


**Figure 22.6** Subxiphoid short-axis view in tetralogy of Fallot showing anterior-superior malalignment of the infundibular septum (arrow) resulting in infundibular stenosis. The anterior malalignment type of conoventricular septal defect (*) is bordered superiorly by the infundibular septum (arrow) and inferiorly by the muscular ventricular septum. Inf, infundibulum; LV, left ventricle; MPA, main pulmonary artery; PV, pulmonary valve; RV, right ventricle.

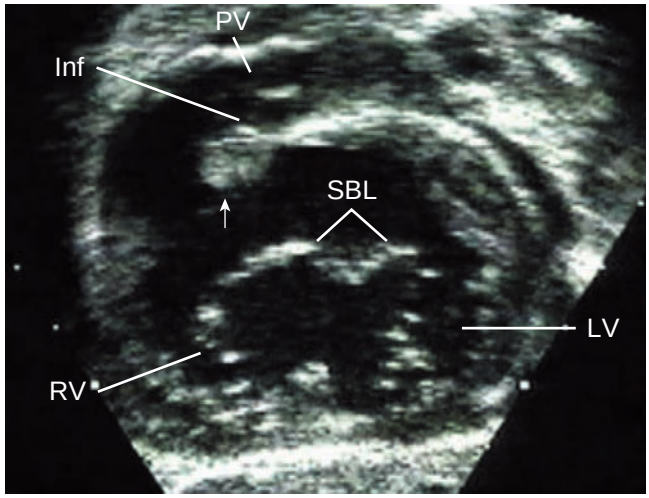


**Figure 22.7** Subxiphoid short-axis view showing tetralogy of Fallot with complete common atrioventricular (AV) canal defect. Note the undivided and unattached superior bridging leaflet (SBL), consistent with Rastelli type C morphology of the superior leaflet. The conal septum (arrow) is deviated anteriorly and superiorly and the subpulmonary infundibulum (Inf) is small. The conoventricular septal defect is confluent with AV canal (inlet) ventricular septal defect. LV, left ventricle; PV, pulmonary valve; RV, right ventricle.

## Imaging of the coronary arteries

The operator should employ the highest frequency transducers that will penetrate to achieve high-resolution coronary artery imaging. The Nyquist limit should be lowered on Doppler interrogation to accentuate low-velocity flow.

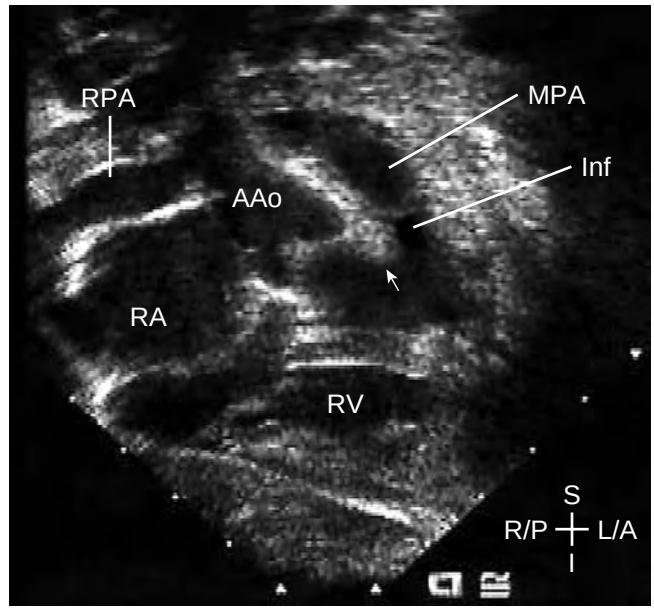


**Figure 22.8** Subxiphoid oblique coronal view demonstrating the anteriorly deviated infundibular septum (arrow), narrowed subpulmonary infundibulum (Inf), and main pulmonary artery (MPA). AAo, ascending aorta; RA, right atrium; RV, right ventricle; RPA, right pulmonary artery; S, superior; I, inferior; L/A, left-anterior; R/P, right-posterior.

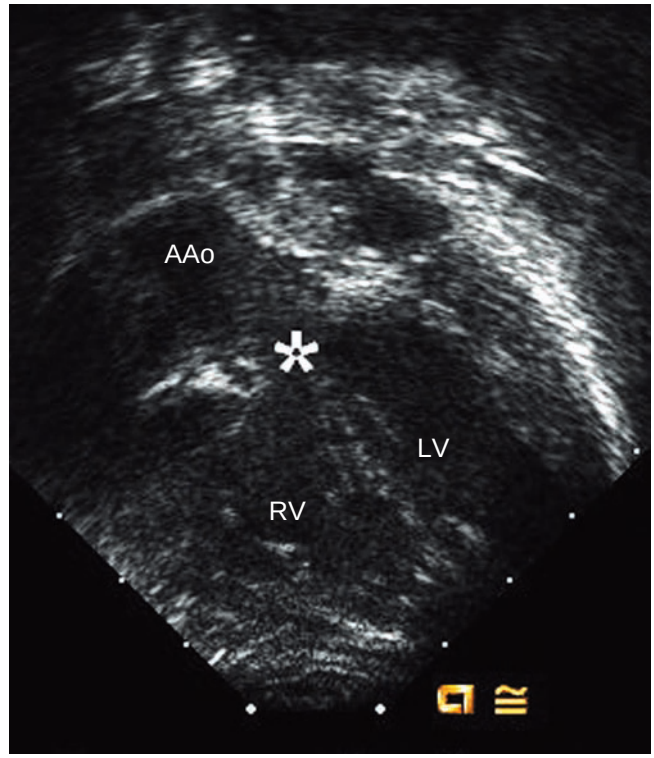


**Figure 22.9** Anteriorly angled apical view showing the ventricular septal defect (*) and the overriding aorta (AAo). LV, left ventricle; RV, right ventricle.

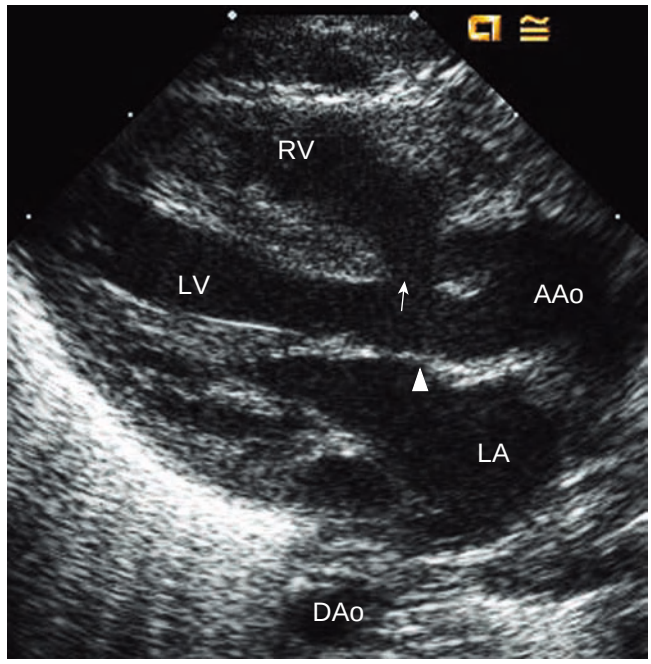


(a)

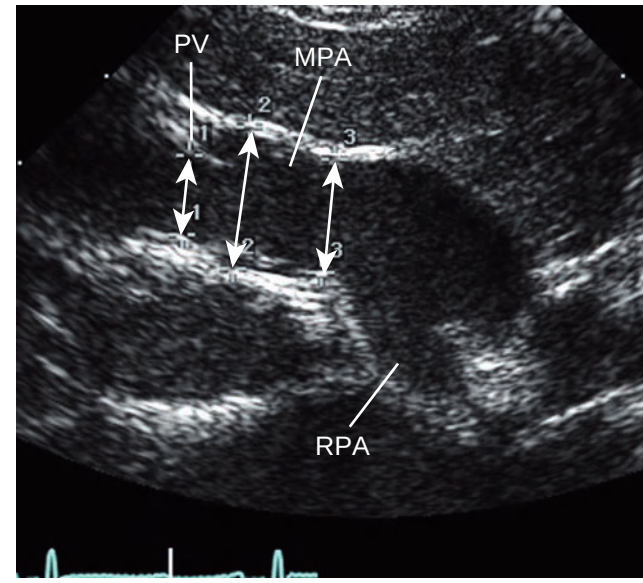


(b)

**Figure 22.10** Parasternal long-axis view. **(a)** Image of the large conoventricular septal defect (arrow) with the aortic valve overriding the ventricular septum. Note the fibrous continuity between the aortic and mitral valve (arrowhead). **(b)** Tilting the transducer toward the left shoulder demonstrates the pulmonary valve (PV), main pulmonary artery (MPA) and proximal right pulmonary artery (RPA). Measurements of the pulmonary valve annulus and MPA are shown. AAo, ascending aorta; DAo, descending aorta; LA, left atrium; LV, left ventricle; RV, right ventricle.

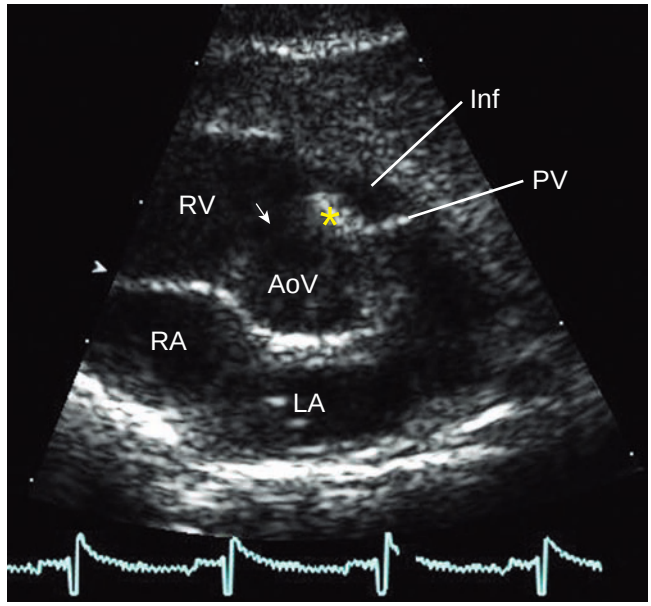


**Figure 22.11** Parasternal short-axis view showing anterior deviation of conal septum (*) and a hypoplastic infundibulum (Inf) with severe subpulmonary narrowing. The ventricular septal defect is clearly seen in this view (arrow). AoV, aortic valve; LA, left atrium; PV, pulmonary valve; RA, right atrium; RV, right ventricle.

The origin of the coronary arteries can be demonstrated from the short-axis image. Clockwise rotation of the origins as viewed from the apex, a common finding in TOF, may be appreciated in this view. The left main coronary artery and its bifurcation are elongated by clockwise rotation of the transducer from the short axis into a transverse plane. Evaluation for a LAD coronary artery origin from the RCA crossing the RV outflow tract requires a careful sweep from the standard reference view in the parasternal long axis, angling toward the left shoulder (Fig. 22.12). Additional views that may be helpful include a high left parasternal cut in a transverse plane (Videoclip 22.8) or a modified apical 4-chamber view angled anteriorly; the latter aims at "shaving" the anterior wall of the RV outflow tract. Prominent crossing conal branches or dual LAD may be diagnosed in these sweeps, or occasionally from the most coronal extent of subxiphoid long-axis sweeps. Rare single RCA or LCA and anomalous origin of the LCA from the pulmonary artery may also be diagnosed. However, the echocardiographer must recognize that the turbulent pulmonary artery flow jets that characterize TOF may obscure the retrograde coronary flow emptying into the pulmonary artery.

### Ductal views

Imaging is best performed from a high parasternal window in a parasagittal plane and/or from the suprasternal notch long-axis view. At times, differentiating between a ductus and aorto-pulmonary collateral is difficult because both may arise from the same location in the proximal descending thoracic aorta. However, the termination of the vessel at the proximal branch pulmonary artery origin is consistent with a ductus arteriosus, whereas aorto-pulmonary collaterals usually insert more distally into the branch pulmonary arteries

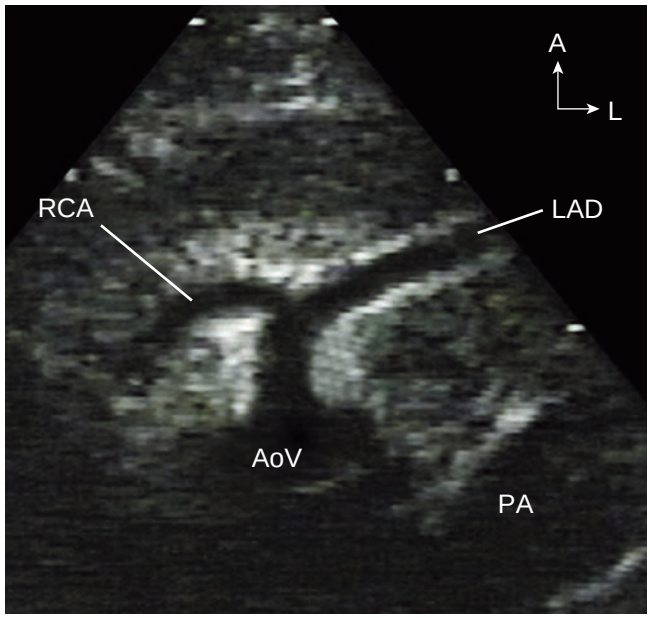


(a)

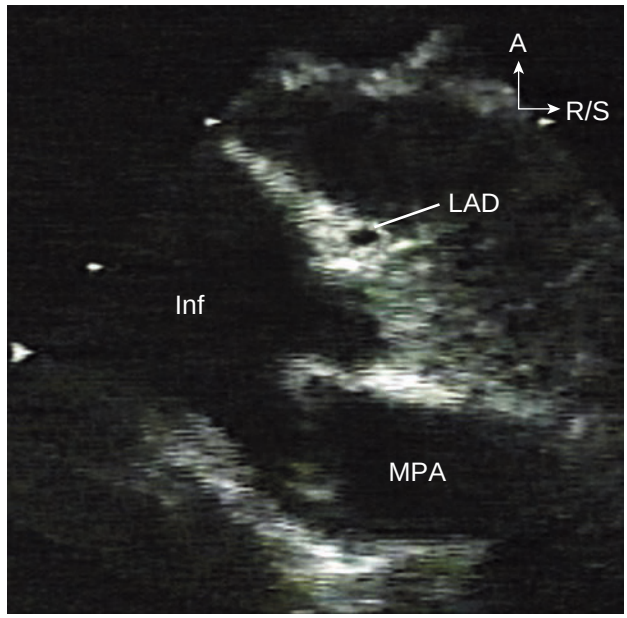


(b)

**Figure 22.12** Anomalous origin of the left anterior descending (LAD) coronary artery from the right coronary artery (RCA) in an infant with tetralogy of Fallot. **(a)** Modified parasternal short-axis view showing a prominent RCA arising from the right aortic sinus of Valsalva, which is rotated clockwise. The LAD arises from the proximal RCA and traverses the infundibular free wall. **(b)** Parasternal long-axis view with the transducer tilted toward the left shoulder demonstrates the LAD in cross-section in the infundibular free wall. AoV, aortic valve; Inf, infundibulum; MPA, main pulmonary artery; A, anterior; L, left; R/S, right-superior.

near the hilum. Additionally, orthogonal imaging in a coronal plane from a high left parasternal view will demonstrate the site of ductal insertion into the proximal branch pulmonary artery to evaluate the possibility for development of peripheral pulmonary artery stenosis or discontinuity consequent to ductal closure. Crossed pulmonary arteries are diagnosed when the RPA originates inferiorly from the left aspect of MPA and the LPA originates more superiorly from the right aspect of MPA.

### High left parasternal imaging

This view helps to evaluate the main and branch pulmonary arteries (Figs 22.13 and 22.14; Videoclip 22.9). It is important to align the beam perpendicularly to the pulmonary artery being interrogated by altering the window of interrogation for each pulmonary artery. High (subclavicular) left sternal border windows are best for the main and left pulmonary arteries. High (subclavicular) right sternal border windows are best for the RPA. Larger branch pulmonary arteries have a lesser likelihood of concomitant presence of aorto-pulmonary collaterals. A branch pulmonary artery diameter z-score of less than –2.5 had a sensitivity of 88% and specificity of 100% for the presence of one or more MAPCAs [103].

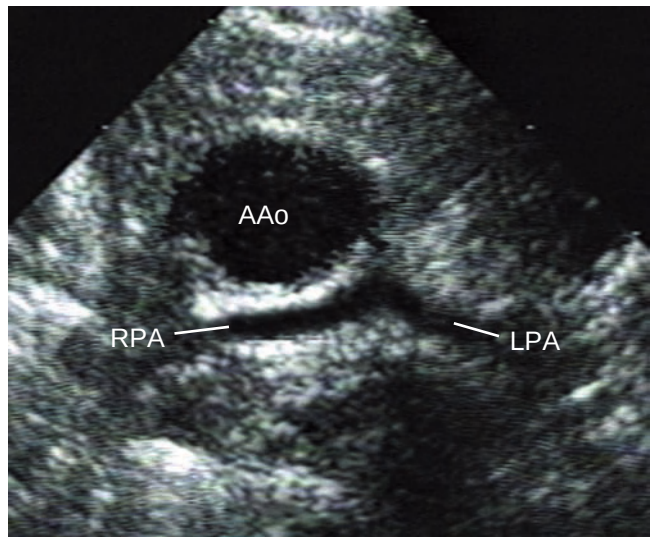


**Figure 22.13** Imaging of the branch pulmonary arteries from the high left parasternal window in an infant with tetralogy of Fallot and pulmonary atresia. Note the confluent, hypoplastic left (LPA) and right (RPA) pulmonary arteries. AAo, ascending aorta.

### Suprasternal notch imaging

Arch sidedness and branching pattern, retroaortic innominate vein (Fig. 22.15 and Videoclip 22.10), partially anomalous venous connections to a systemic vein, double aortic arch, and vascular rings can be evaluated from this view. Left superior vena cava to coronary sinus or directly to left atrium with an unroofed coronary sinus are best seen from this view or from a left parasternal window in the parasagittal plane.

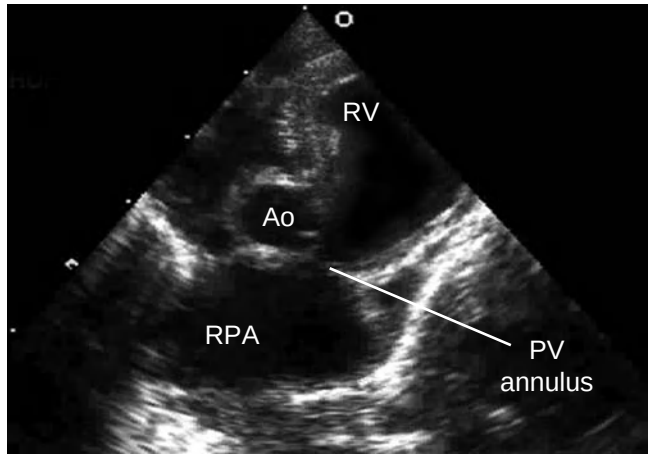


**Figure 22.14** Imaging of the branch pulmonary arteries from the left parasternal window in an infant with tetralogy of Fallot and absent pulmonary valve syndrome. Ao, aorta; PV, pulmonary valve; RPA, right pulmonary artery; RV, right ventricle.

### Right parasternal view

Imaging from this acoustic window is best performed with the patient in a right decubitus position. This window allows clear imaging of the atrial septum, right superior vena cava, and the right pulmonary veins in right parasternal short-axis, parasagittal and transverse imaging planes. "En face" common AV valve morphology in patients with TOF and common AV canal can also be seen well from this window in short-axis planes.

### Preoperative hemodynamic assessment

Color flow mapping and spectral Doppler are crucial in refining the diagnosis, screening for subtle structural abnormalities (e.g., coronary, arch and branch pulmonary artery) and, of course, in assessing the hemodynamics, as described in Chapter 6.

### Atrial septum

Color flow mapping of the atrial septum usually demonstrates the left-to-right shunting occurring in TOF even in the presence of severe pulmonary stenosis. Bidirectional or right-to-left shunting may be present in newborns.

### Ventricular septal defect

The flow across the large VSD is usually nonrestrictive and bidirectional; as noted above, only rarely is it restrictive. The degree of RV outflow tract obstruction determines the direction of flow across the VSD – less pulmonary stenosis allows predominantly left-to-right shunting, and the clinical scenario of "pink" TOF, even to the point of developing signs and/or symptoms of congestive heart failure. More severe pulmonary stenosis results in predominant right-to-left shunting and the more typical cyanosis. In the typical setting of a nonrestrictive VSD, RV peak pressures cannot exceed systemic levels; right-to-left shunting at the level of the VSD is not synonymous with suprasystemic RV pressures. Suprasystemic RV pressures in TOF can only occur in the setting of a restrictive VSD with pulmonary atresia or severe RV outflow tract obstruction [158]. Also, in the setting of a nonrestrictive malalignment VSD, additional muscular VSDs may be difficult to identify. Therefore, it is essential to interrogate the muscular septum by color flow mapping with a lowered Nyquist limit to identify low-velocity shunting across these small defects (Fig. 22.16 and Videoclip 22.11).

### Right ventricular outflow tract and pulmonary arteries

The level of obstruction can be determined by imaging and by sequential pulsed Doppler interrogation starting from within the RV cavity to the pulmonary valve annulus. In severe stenosis, antegrade flow may be demonstrated using a

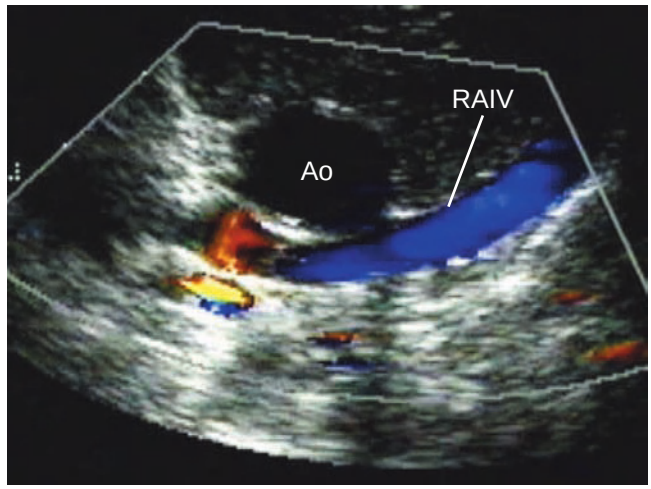


(a)

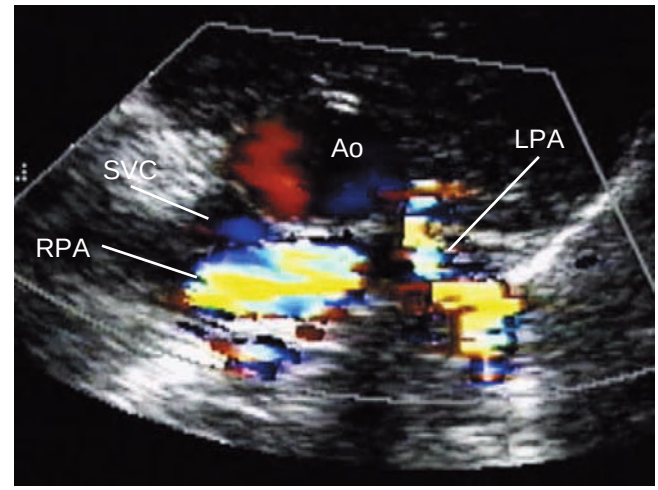


(b)

**Figure 22.15** Retroaortic innominate vein (RAIV). **(a)** Imaging from the high left parasternal window in the transverse plane. The left innominate vein is seen posterior to the distal ascending aorta (Ao). **(b)** Inferior tilt of the transducer demonstrates the left (LPA) and right (RPA) pulmonary arteries inferior to the RAIV. SVC, superior vena cava.

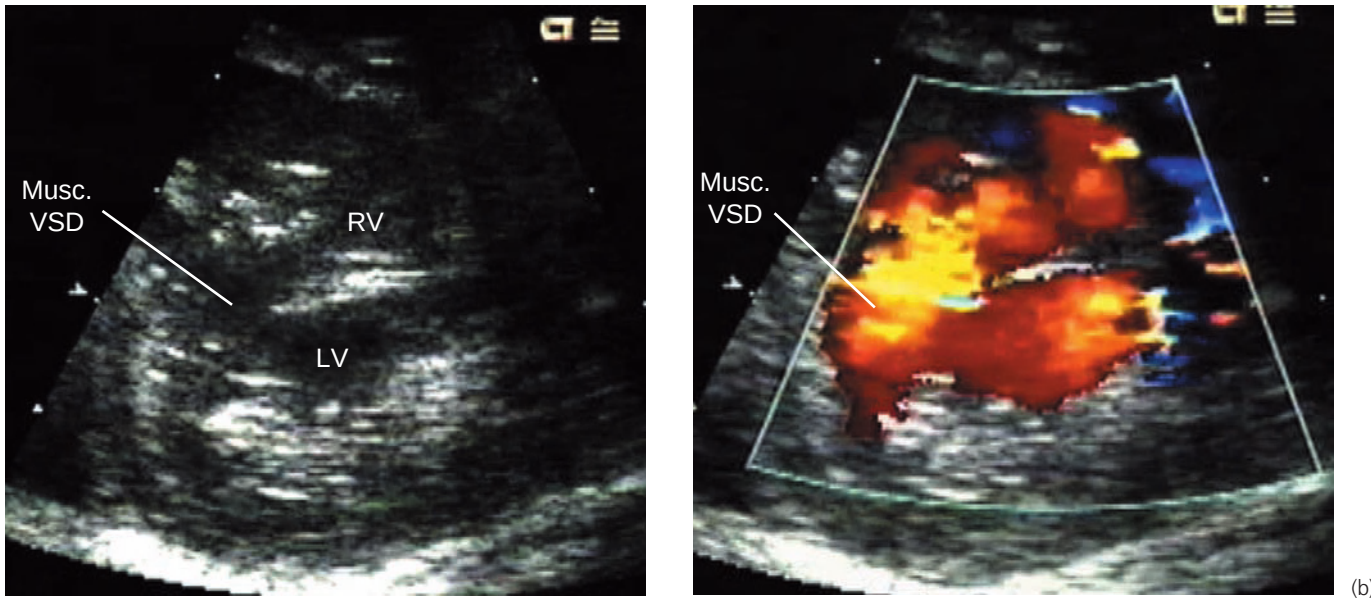


(a) (b)

**Figure 22.16** Additional posterior muscular ventricular septal defect (Musc. VSD) seen by 2D imaging **(a)** and by color Doppler with a low Nyquist limit **(b)**. LV, left ventricle; RV, right ventricle.

lower-frequency transducer that achieves a higher Nyquist limit; this allows less "aliasing" of the color flow map of the high-velocity flow across the stenotic outflow tract. Continuous-wave Doppler interrogation is essential to estimate the total maximal instantaneous gradient, but separation of the infundibular and valvar contributions to the total gradient is difficult with any Doppler interrogation technology (Fig. 22.17). The need for transannular patch repair may be predicted in infants weighing less than 10 kg with annular dimension of less than 7 mm [128].

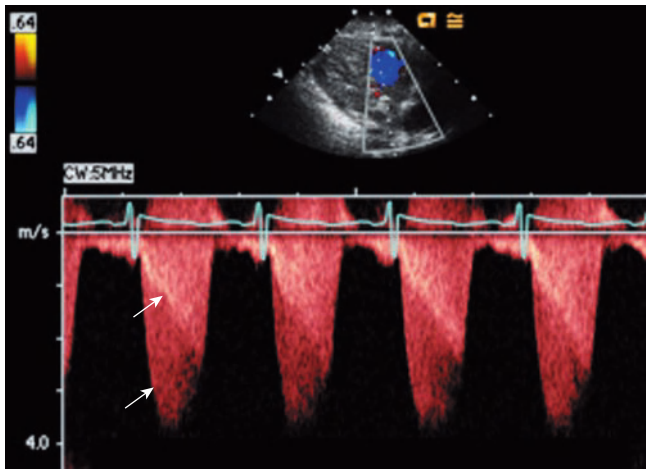


**Figure 22.17** Continuous-wave Doppler interrogation of the right ventricular outflow tract and pulmonary valve from the parasternal short-axis view demonstrates high-velocity flow with two velocity profiles. The first arrow points to a late-peaking, dagger-shaped lower-velocity flow profile consistent with dynamic infundibular obstruction, and the second arrow points to a higher velocity profile reflecting the total maximum instantaneous gradient.

In TOF with absent pulmonary valve syndrome, pulmonary insufficiency is easily demonstrated by color flow mapping (Fig. 22.18 and Videoclip 22.12) and may be associated with diastolic flow reversal in the branch pulmonary arteries. In patients with pulmonary atresia, color flow mapping and spectral Doppler interrogation help to identify mediastinal branch pulmonary arteries and collaterals, although color flow mapping may result in false positive diagnosis of aortopulmonary collateral (APC) [103]. In patients with long-segment pulmonary atresia the left atrial appendage can mimic the central main pulmonary artery segment (Videoclip 22.13); this can be further delineated by careful imaging and by demonstration of low velocity to-and-fro flow by color and pulsed-wave Doppler interrogation [161]. Because of its position under the aortic arch, the retroaortic innominate vein (also known as "anomalous brachiocephalic vein") may mimic central confluent branch pulmonary arteries in pulmonary atresia. Doppler interrogation demonstrates the connection of the retroaortic innominate vein to the internal jugular vein or superior vena cava; it can also differentiate the retroaortic innominate vein from a pulmonary artery, by identifying the typical multiphasic venous flow pattern in the innominate vein (Videoclip 22.10).

## Atrioventricular valves

Color flow mapping from the apical window is used to assess the AV valve regurgitation that is usually seen in patients with associated malformations of the AV valves (e.g., Ebstein, double-orifice TV and mitral valve [MV], common AV valve

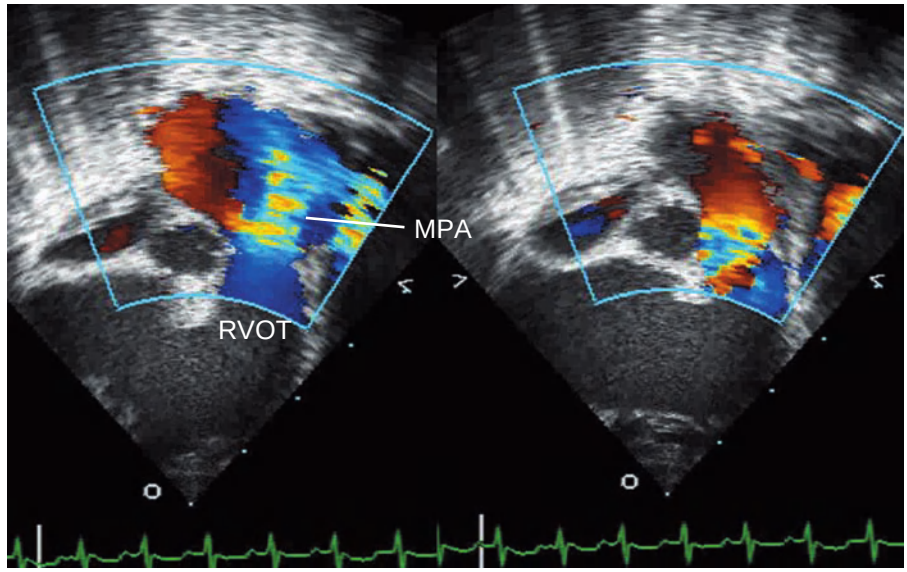


**Figure 22.18** Color Doppler flow mapping of the right ventricular outflow tract (RVOT) in an infant with tetralogy of Fallot and absent pulmonary valve syndrome. The left panel shows a systolic frame with antegrade flow from the RVOT to the main pulmonary artery (MPA). The right panel shows a diastolic frame with a wide jet of retrograde flow from the MPA into the RVOT.

and cleft MV). In the setting of significant mitral regurgitation without morphologic abnormalities and/or LV hypokinesis, associated anomalous origin of the LCA from the pulmonary artery must be excluded.

### Aortic root dilation and regurgitation

Standard measurements in parasternal views will identify root and ascending aortic dilation, commonly seen in TOF, and allow serial follow-up of aortic size. Aortic regurgitation is uncommon preoperatively; it is most often acquired postoperatively or secondary to endocarditis [141,162].

### Coronary arteries

Confirm the coronary origin and branching patterns by high-resolution parasternal imaging, with color flow mapping using a low Nyquist limit to exclude anomalous origin of the left coronary artery from the pulmonary artery. Depressed ventricular function is usually present in the setting of anomalous origin of the left coronary artery from the pulmonary artery (ALCAPA), but if there is associated pulmonary hypertension, as in cases of TOF with minimal pulmonary stenosis or with nonrestrictive patent ductus arteriosus, ventricular function may be normal. Coronary–cameral fistulae may also be detected by color flow mapping but coronary–pulmonary artery fistulae may be obscured by aliased pulmonary artery flow patterns due to the pulmonary stenosis.

## Intraoperative and postoperative assessment after TOF repair

Intraoperative echocardiographic assessment of TOF repair is almost always accomplished by using transesophageal echocardiography (TEE) or, in situations where esophageal access is not possible, utilizing an epicardial approach. The goal of the intraoperative TEE evaluation should be aimed at identification of hemodynamically significant lesions that can affect immediate postoperative management as well as long-term outcomes. Knowing the details of the surgical repair is essential to a successful intraoperative echocardiographic evaluation, and good communication between the surgeon and echocardiographer is paramount. Conventional echocardiography and TEE are important in the evaluation of the postoperative patient in the intensive care unit (ICU), especially to assess acute changes in clinical status. In addition to the TEE evaluation described below, conventional echocardiography enables assessment of diaphragmatic motion and pleural or pericardial effusions. Conventional windows are often superior to TEE for assessment of the aortic arch and branch pulmonary arteries.

Evaluation of surgical repair often begins with scanning for residual septal defects. The impact of residual atrial septal defects depends on the relative compliances of the right and left heart chambers. In the setting of RV dysfunction, which is common after TOF repair, right-to-left atrial-level shunting results in postoperative hypoxemia. In this setting, right-to-left diastolic shunting may also be noted across a residual VSD, even in the setting of left-to-right systolic shunting. Small residual VSDs with restrictive flow may have no impact on postoperative hemodynamics. However, intraoperative echocardiographic estimation of Qp:Qs can be challenging; the assessment of hemodynamic significance may be supplemented by direct intraoperative pressure and saturation data. Residual "intramural" VSDs occur when the VSD patch allows the blood to pursue a tortuous course within the myocardial trabeculae before exiting into the RV cavity [163]. These defects are often quite small or inapparent initially, but may enlarge progressively in mid- to long-term follow-up. Occasionally, surgical closure of the large malalignment VSD may unmask previously undiagnosed additional small muscular VSDs.

Evaluation for residual RV outflow tract obstruction can be achieved from deep transgastric longitudinal imaging planes. Pulmonary valve function and branch pulmonary arteries can be evaluated from the mid- and high esophageal imaging planes. Although RV pressures can be estimated from Doppler interrogation of tricuspid regurgitation, residual VSD jets or RV outflow tract gradients, the angle of interrogation is often suboptimal. When possible, such Doppler data should be confirmed by direct measurement of pressures.

It is important to assess tricuspid and aortic valve competence because either valve may be distorted by VSD patch closure. Postoperatively acquired small coronary fistulae are commonly seen following infundibular muscle resection; these hemodynamically insignificant fistulae often regress on follow-up exams but may persist in the long term [86].

Immediate postoperative TEE assessment of biventricular function following separation from cardiopulmonary bypass utilizes deep transgastric short-axis and mid-esophageal axial imaging planes. The functional assessment may be somewhat limited in the presence of arrhythmia or paced rhythm.

## Echocardiography in adults with TOF

Unrepaired TOF in adults is rare and adult surgical outcomes are generally good, with in-hospital mortality reported to be as low as 1.9% and significant functional improvement in the survivors [164]. Evaluation of adults is different only in so far as obtaining adequate acoustic access may be more challenging. Otherwise, assessment should proceed as described above.

Late echocardiographic assessment of adolescents and adults with repaired TOF involves additional issues, considered under the following three categories:

**1** Assessment of physiologic and hemodynamic parameters that influence outcome [165–168], including (i) RV and LV size and function; (ii) pulmonary regurgitation and/or stenosis; and (iii) tricuspid regurgitation. Similar to the electrophysiologic criteria of QRS duration >180 ms, serious derangements in the above categories have a significant impact on long-term outcomes, risk for ventricular arrhythmias and sudden death.

**2** Assessment of anatomic criteria of unknown significance on outcomes: RVOT aneurysm, DCRV, aortic dilation and aortic regurgitation.

**3** Assessment of suitability of RVOT morphology for transcatheter pulmonary valve implantation. Based on current criteria, RVOT diameter <22 mm and prior repair without a transannular patch is generally considered suitable for catheter deployment of a stented pulmonary valve [169–171]. However, patients with RVOT diameter somewhat larger than 22 mm have undergone successful percutaneous valve implantation [172].

### Assessment of RV function

#### *Systolic function*

Assessment of RV size and function is limited to qualitative estimates by 2D echocardiography. Quantitative evaluation by tissue Doppler-derived techniques correlates with CMR-measured RV size and function; CMR is the "gold standard" for RV size and function assessment. Indices derived from Doppler tissue imaging, such as systolic velocities and strain, have been shown to correlate well with CMR-derived RV ejection fraction and can be utilized as an interim follow-up tool [173–175]. Dobutamine stress echocardiography in combination with Doppler tissue indices (DTI) has been used to study RV functional reserve. Increasing the degree of pulmonary regurgitation (PR) has a negative impact on RV functional reserve [176,177]. Decreased systolic and annular E′ DTI velocities correlate with decreasing peak oxygen consumption during exercise. Importantly, RV systolic velocity is predictive of exercise capacity in repaired TOF [178].

Assessment of dyssynchrony may have a role in postoperative TOF evaluation. An increase in interventricular delay of >55 ms has been correlated with increased risk for arrhythmia [173]. Recently, three-dimensional (3D) echo measurements of RV size and function have been correlated with CMR, and this technology needs further evaluation and validation in order to become a reproducible and accurate method for serial assessment of RV size and function [179].

#### *Diastolic function*

The presence of antegrade late systolic (during atrial systole) pulmonary artery flow is posited as a sign of RV diastolic dysfunction or reduced compliance.

#### *Assessment of left ventricular function*

Accurate quantification of LV function is limited by traditional echocardiographic methods, again because of geometric issues in the postoperative patient. Conventionally derived shortening and ejection fractions are unreliable secondary to nearly universal diastolic septal flattening, which affects the geometric assumptions that underlie the methods used to calculate these ejection phase indices. Furthermore, RV dilation may interfere with apical windows, because the RV apex often replaces the LV apex as the acoustic window. Although theoretically septal flattening should similarly negatively affect LV cross-sectional area change fraction, we have found reasonable correlation between LV cross-sectional area fraction and CMR-derived LV ejection fraction (S. Srivastava and IA Parness, unpublished data). Again, 3D echocardiography, by measuring actual volumes without use of geometric assumptions, should provide accurate serial quantification of volumes and systolic function as long as acoustic windows are adequate. Diastolic LV function indices have not been systematically studied in TOF.

*Assessment of pulmonary regurgitation*

Echocardiographic evaluation of pulmonary regurgitation (PR) can be assessed by the following criteria:

**1** Jet width – PR may be graded according to the ratio of jet width/RV outflow diameter: mild ≤1/3; moderate 1/3–2/3; and severe ≥2/3.

**2** Ratio of duration of PR/duration of diastole >0.77 correlates with PR regurgitant fraction >24.5% by CMR [180].

**3** Pressure half-time <100 ms correlates with hemodynamically significant PR [172,181].

**4** Presence of diastolic flow reversal in branch pulmonary arteries is associated with hemodynamically significant PR [182].

*Assessment of pulmonary stenosis*

Doppler estimates of RV outflow tract obstruction or peripheral branch pulmonary artery stenosis may be limited by suboptimal angle of interrogation and/or overestimation due to pressure recovery. Appropriate alignment with LPA flow can be achieved from the high right parasternal or suprasternal notch windows; and with the RPA flow from the high left parasternal window. A pattern of continuous antegrade diastolic flow with a "sawtooth" configuration is consistent with branch pulmonary artery stenosis.

*Assessment of right atrial size*

Assessment of right atrial size is qualitative. Right atrial enlargement is considered a risk factor for arrhythmias, and its size should be evaluated in routine follow-up. Right atrial enlargement in the absence of significant tricuspid insufficiency may signal the presence of restrictive RV physiology.

*Assessment of tricuspid regurgitation*

Increased RV size due to PR can lead to annular dilation and an increase in tricuspid regurgitation that further aggravates RV volume overload [183]. Tricuspid regurgitation is infrequently a major contributor to RV dilation in postoperative TOF unless there is an associated congenital tricuspid valve anomaly or inadvertent tricuspid valve damage during surgical repair.

### Assessment of repaired TOF in pregnancy

Severe PR is associated with an increased incidence of low birth-weight babies, but does not affect maternal and infant morbidity and mortality [184].

## Prenatal assessment

Poon et al. reported their experience with fetal diagnosis of TOF at a mean gestational age of 20.6 weeks [31]. Increased nuchal translucency measurement >95th percentile was common (47%) but 19/37 fetuses had normal chromosomes. In their study cohort, 49% had chromosomal anomalies, including the 22q11 microdeletion in 15, with additional extracardiac malformations in 50% and additional cardiac malformations in 57%. In 70/129 (54%) cases, the parents chose termination of pregnancy.

Associated extracardiac anomalies can occur in up to approximately 30% of affected infants and children, and the incidence can be as high as 50–60% in fetal TOF. Important chromosomal and syndromic associations include microdeletion of chromosome 22q11, trisomies 21 and 18, pentalogy of Cantrell, VATER (vertebral anomalies, anal atresia, cardiac anomalies, tracheo-esophageal fistula, esophageal atresia, renal anomalies) or CHARGE (coloboma, heart defects, atresia of the choanae, retardation of growth, genital abnormalities, ear anomalies) association, tracheo-esophageal fistula, and omphalocele. Association with cleft palate may suggest velocardiofacial syndrome [31,185–187]. Appropriate prenatal evaluation and counseling for TOF requires careful high-level screening for noncardiac anomalies and chromosomal anomalies.

The diagnosis of TOF is often not obvious in the 4-chamber view. The LV outflow tract view or the 5-chamber view demonstrate aortic override (Fig. 22.19a and Videoclip 22.14), and on color flow mapping flow is directed from both ventricles into the aorta. The basal short-axis view demonstrates the deviation of the conal septum, malalignment VSD, and subpulmonary stenosis (Fig. 22.19b and Videoclip 22.15(a,b)). The 3-vessel view (high axial cut of the superior vena cava, aorta, and main pulmonary artery) can demonstrate vessel size discrepancy, with the aorta being larger than the pulmonary artery (Fig. 22.19c) [187]. The flow in the ductus arteriosus would be retrograde in case of severe pulmonic stenosis or atresia. Aortic arch sidedness and arch anomalies can be evaluated in the 3-vessel axial view, and the transmission qualities of the unexpanded fetal lungs can facilitate the prenatal diagnosis of vascular rings (Fig. 22.20). Serial prenatal echocardiography is recommended, primarily to reassess for progressive subpulmonary stenosis and/or progressive pulmonary artery hypoplasia.

### TOF with pulmonary atresia

Pulmonary atresia with TOF can be valvar, short-segment involving just the valve and proximal main pulmonary artery, or long-segment atresia in which the entire main pulmonary artery segment is missing. With long-segment atresia, it is prognostically essential to determine if there are central confluent mediastinal pulmonary arteries, and if present, their degree of hypoplasia. Pulmonary stenosis can be progressive and evolve prenatally into pulmonary atresia [188,189]. Pulmonary blood supply from multiple aortopulmonary collaterals can be seen prenatally [188,189]. With short-segment pulmonary atresia, hypoplastic branch pulmonary arteries may be supplied by a ductus.

Tetralogy of Fallot with pulmonary atresia may be mistaken for truncus arteriosus if the branch pulmonary artery origins are not clearly demonstrated. Both lesions share

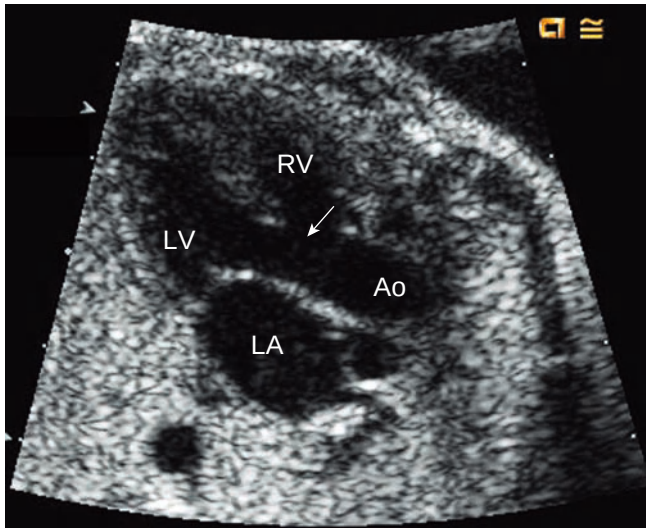


(a)

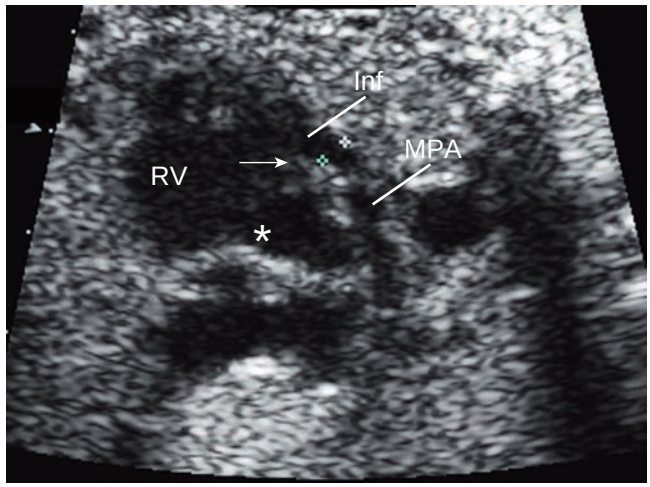


(b)

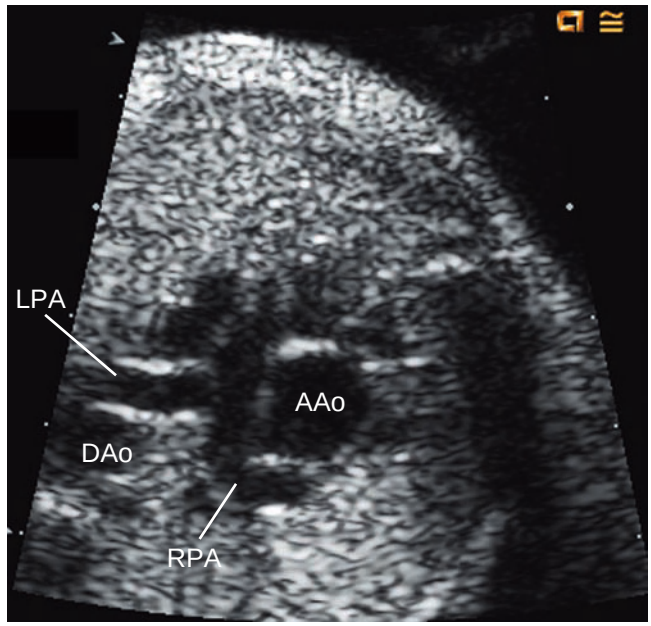


(c)

**Figure 22.19** Fetal echocardiography in tetralogy of Fallot with pulmonary stenosis. **(a)** Long-axis view of the left ventricular outflow demonstrates a large aortic root overriding a ventricular septal defect (arrow). **(b)** Imaging of the anteriorly deviated conal septum (arrow) and the conoventricular septal defect (*). Note the hypoplastic infundibulum (Inf) and main pulmonary artery (MPA). **(c)** Transverse view of the fetal chest demonstrating the relatively small branch pulmonary arteries in relation to the dilated ascending aorta (AAo). DAo, descending aorta; LA, left atrium; LPA, left pulmonary artery; LV, left ventricle; RPA, right pulmonary artery; RV, right ventricle.

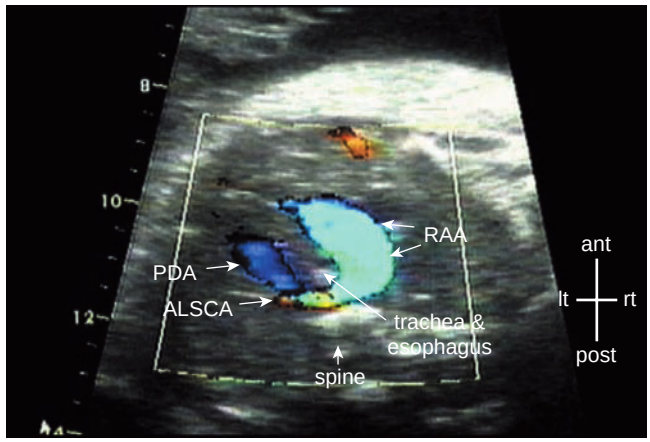


**Figure 22.20** Prenatal echocardiographic diagnosis of tetralogy of Fallot with vascular ring. The ring comprises a right aortic arch (RAA), aberrant origin of the left subclavian artery (ALSCA), and left patent ductus arteriosus (PDA). ant, anterior; post, posterior; lt, left; rt, right.

features of a large anterior malalignment VSD with overriding and enlarged semilunar root. Hence it is essential to image the origin or absence of branch pulmonary arteries when only one major vessel is seen overriding a malalignment VSD. It is also important to differentiate from truncus arteriosus the rare association of anomalous origin of a branch pulmonary artery from the ascending aorta with TOF (in the latter case, the contralateral branch pulmonary artery will be supplied by a separate, if small, pulmonary valve).

### TOF with absent pulmonary valve

This lesion is easily diagnosed in utero because its key features stand out: the dysplastic pulmonary valve with stenosis and regurgitation and the aneurysmal main and/or branch pulmonary arteries (Fig. 22.21 and Videoclip 22.16(a,b)). The ductus arteriosus is typically absent. Progressive RV and main pulmonary artery dilation may occur and result in hydrops fetalis due to RV dysfunction [118,190,191].

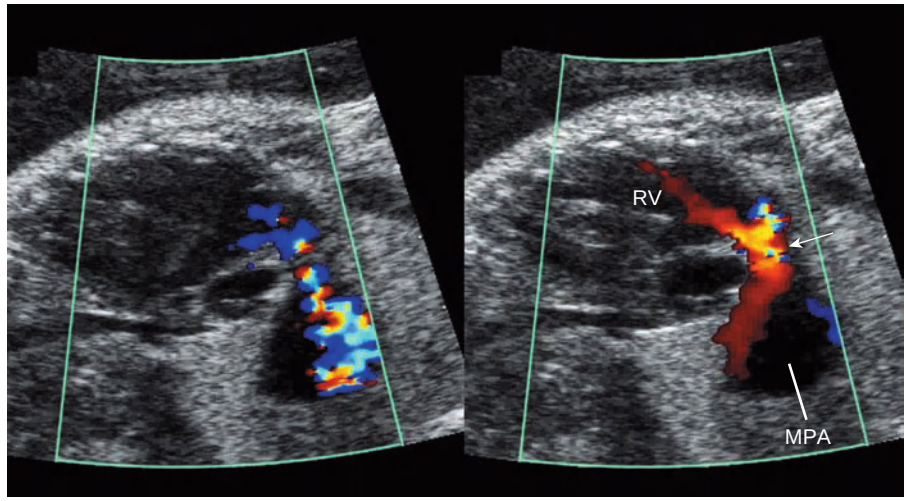


**Figure 22.21** Fetal echocardiogram in tetralogy of Fallot with absent pulmonary valve syndrome. The left panel shows a systolic frame with antegrade flow from the right ventricular outflow tract to a markedly dilated main pulmonary artery (MPA). The right panel shows a diastolic frame with pulmonary regurgitation jet into the right ventricle (RV). The arrow points to the location of the dysplastic pulmonary valve.

Neonatal outcome in published series was not predicted by the degree of pulmonary artery dilation but, as expected, outcome was poor in fetuses with fetal hydrops [118].

### TOF with complete atrioventricular canal

In this lesion, the 4-chamber view is abnormal because the VSD extends from the inlet to the outlet septum. It is important to determine whether there is a balanced versus unbalanced AV canal defect as well as the degree of any associated AV valve regurgitation.

Serial fetal echocardiographic evaluation is recommended to screen for progression of pulmonary stenosis and/or branch pulmonary artery hypoplasia. Mild pulmonary stenosis in the early second trimester may progress to severe stenosis or atresia by the late third trimester [192]. This impacts upon neonatal management and counseling of the parents. As mentioned above, amniocentesis for associated chromosomal anomalies and fluorescence in situ hybridization (FISH) for microdeletion should be suggested routinely as this also bears a significant impact on neonatal outcome. The association of intrauterine growth retardation, polyhydramnios, increased nuchal translucency, and aortic arch anomalies with TOF can predict 22q11 deletion with a sensitivity of 88% [185,193]. The postnatal prognosis of isolated TOF is good but outcomes of fetal diagnosis of conotruncal anomalies can be poor, mainly due to the frequent association with chromosomal and/or extracardiac anomalies, often leading to intrauterine or early neonatal death [31,194].

## References

1. Becker AE, Connor M, Anderson RH. Tetralogy of Fallot: a morphometric and geometric study. *Am J Cardiol* 1975;35:402–12.
2. Van Praagh R, Geva T, Kreutzer J. Ventricular septal defects: how shall we describe, name and classify them? *J Am Coll Cardiol* 1989;14:1298–9.
3. Van Praagh R, Van Praagh S, Nebesar RA et al. Tetralogy of Fallot: underdevelopment of the pulmonary infundibulum and its sequelae. *Am J Cardiol* 1970;26:25–33.
4. Abbott ME, Dawson WT. The clinical classification of congenital cardiac disease, with remarks upon its pathological anatomy, diagnosis and treatment. *Int Clin* 1924;4:156–88.
5. Jacobs ML. Congenital Heart Surgery Nomenclature and Database Project: tetralogy of Fallot. *Ann Thorac Surg* 2000;69 (4 Suppl.):S77–82.
6. Loffredo CA. Epidemiology of cardiovascular malformations: prevalence and risk factors. *Am J MedGenet* 2000;97:319–25.
7. Hoffman JI, Kaplan S. The incidence of congenital heart disease. *J Am Coll Cardiol* 2002;39:1890–900.
8. Castaneda AR, Freed MD, Williams RG, Norwood WI. Repair of tetralogy of Fallot in infancy. Early and late results. *J Thorac Cardiovasc Surg* 1977;74:372–81.
9. Rabinovitch M, Herrera-deLeon V, Castaneda AR, Reid L. Growth and development of the pulmonary vascular bed in patients with tetralogy of Fallot with or without pulmonary atresia. *Circulation* 1981;64:1234–49.
10. Karr SS, Brenner JI, Loffredo C et al. Tetralogy of Fallot. The spectrum of severity in a regional study, 1981–1985. *Am J Dis Child* 1992;146:121–4.
11. Marelli AJ, Mackie AS, Ionescu-Ittu R et al. Congenital heart disease in the general population: changing prevalence and age distribution. *Circulation* 2007;115:163–72.
12. de la Cruz MV, Sanchez Gomez C, Arteaga MM, Arguello C. Experimental study of the development of the truncus and the conus in the chick embryo. *J Anat* 1977;123:661–86.
13. Mjaatvedt CH, Nakaoka T, Moreno-Rodriguez R et al. The outflow tract of the heart is recruited from a novel heart-forming field. *Dev Biol* 2001;238:97–109.
14. Waldo KL, Kumiski DH, Wallis KT et al. Conotruncal myocardium arises from a secondary heart field. *Development* 2001;128:3179–88.
15. Kelly RG. Molecular inroads into the anterior heart field. *Trends Cardiovasc Med* 2005;15:51–6.
16. Ward C, Stadt H, Hutson M, Kirby ML. Ablation of the secondary heart field leads to tetralogy of Fallot and pulmonary atresia. *Dev Biol* 2005;284:72–83.

17. Towbin JA, Belmont J. Molecular determinants of left and right outflow tract obstruction. *Am J Med Genet* 2000;97:297–303.
18. Kelly RG, Brown NA, Buckingham ME. The arterial pole of the mouse heart forms from Fgf10-expressing cells in pharyngeal mesoderm. *Dev Cell* 2001;1:435–40.
19. Kelly RG, Buckingham ME. The anterior heart-forming field: voyage to the arterial pole of the heart. *Trends Genet* 2002; 18:210–16.
20. Bajolle F, Zaffran S, Kelly RG et al. Rotation of the myocardial wall of the outflow tract is implicated in the normal positioning of the great arteries. *Circ Res* 2006;98:421–8.
21. Kirby ML, Gale TF, Stewart DE. Neural crest cells contribute to normal aorticopulmonary septation. *Science* 1983;220:1059–61.
22. Restivo A, Piacentini G, Placidi S et al. Cardiac outflow tract: a review of some embryogenetic aspects of the conotruncal region of the heart. *Anat Rec A Discov Mol Cell Evol Biol* 2006; 288:936–43.
23. Yelbuz TM, Waldo KL, Kumiski DH et al. Shortened outflow tract leads to altered cardiac looping after neural crest ablation. *Circulation* 2002;106:504–10.
24. Tevosian SG, Deconinck AE, Tanaka M et al. FOG-2, a cofactor for GATA transcription factors, is essential for heart morphogenesis and development of coronary vessels from epicardium. *Cell* 2000;101:729–39.
25. Gelb BD. Molecular genetics of congenital heart disease. *Curr Opin Cardiol* 1997;12:321–8.
26. van den Akker NM, Molin DG, Peters PP et al. Tetralogy of Fallot and alterations in vascular endothelial growth factor-A signaling and notch signaling in mouse embryos solely expressing the VEGF120 isoform. *Circ Res* 2007;100:842–9.
27. Pierpont ME, Basson CT, Benson DW Jr et al. Genetic basis for congenital heart defects: current knowledge: a scientific statement from the American Heart Association Congenital Cardiac Defects Committee, Council on Cardiovascular Disease in the Young: endorsed by the American Academy of Pediatrics. *Circulation* 2007;115:3015–38.
28. Michielon G, Marino B, Formigari R et al. Genetic syndromes and outcome after surgical correction of tetralogy of Fallot. *Ann Thorac Surg* 2006;81:968–75.
29. Vergara P, Digilio MC, Zorzi AD et al. Genetic heterogeneity and phenotypic anomalies in children with atrioventricular canal defect and tetralogy of Fallot. *Clin Dysmorphol* 2006;15: 65–70.
30. Marino B, Digilio MC, Grazioli S et al. Associated cardiac anomalies in isolated and syndromic patients with tetralogy of Fallot. *Am J Cardiol* 1996;77:505–8.
31. Poon LC, Huggon IC, Zidere V, Allan LD. Tetralogy of Fallot in the fetus in the current era. *Ultrasound Obstet Gynecol* 2007; 29:625–7.
32. Van Praagh S, Truman T, Firpo A et al. Cardiac malformations in trisomy-18: a study of 41 postmortem cases. *J Am Coll Cardiol* 1989;13:1586–97.
33. Tartaglia M, Gelb BD. Noonan syndrome and related disorders: genetics and pathogenesis. *Annu Rev Genomics Hum Genet* 2005; 6:45–68.
34. Tartaglia M, Pennacchio LA, Zhao C et al. Gain-of-function SOS1 mutations cause a distinctive form of Noonan syndrome. *Nat Genet* 2007;39:75–9.
35. Schubbert S, Zenker M, Rowe SL et al. Germline KRAS mutations cause Noonan syndrome. *Nat Genet* 2006;38:331–6.
36. Roberts AE, Hult B, Rehm HL et al. The PTPN11 gene is not implicated in nonsyndromic hypertrophic cardiomyopathy. *Am J Med Genet A* 2005;132:333–4.
37. Krantz ID. Alagille syndrome: chipping away at the tip of the iceberg. *Am J Med Genet* 2002;112:160–2.
38. McElhinney DB, Krantz ID, Bason L et al. Analysis of cardiovascular phenotype and genotype–phenotype correlation in individuals with a JAG1 mutation and/or Alagille syndrome. *Circulation* 2002;106:2567–74.
39. Bruneau BG, Nemer G, Schmitt JP et al. A murine model of Holt–Oram syndrome defines roles of the T-box transcription factor Tbx5 in cardiogenesis and disease. *Cell* 2001;106: 709–21.
40. Kumar A, Friedman JM, Taylor GP, Patterson MW. Pattern of cardiac malformation in oculoauriculovertebral spectrum. *Am J Med Genet* 1993;46:423–6.
41. Goldmuntz E. DiGeorge syndrome: new insights. *Clin Perinatol* 2005;32:963–78, ix–x.
42. Goldmuntz E, Geiger E, Benson DW. NKX2.5 mutations in patients with tetralogy of fallot. *Circulation* 2001;104:2565–8.
43. McElhinney DB, Clark BJ 3rd, Weinberg PM et al. Association of chromosome 22q11 deletion with isolated anomalies of aortic arch laterality and branching. *J Am Coll Cardiol* 2001;37: 2114–9.
44. McElhinney DB, Geiger E, Blinder J et al. NKX2.5 mutations in patients with congenital heart disease. *J Am Coll Cardiol* 2003; 42:1650–5.
45. Pizzuti A, Sarkozy A, Newton AL et al. Mutations of ZFPM2/FOG2 gene in sporadic cases of tetralogy of Fallot. *Hum Mutat* 2003;22:372–7.
46. Koch R, Levy HL, Matalon R et al. The North American Collaborative Study of Maternal Phenylketonuria. Status report 1993. *Am J Dis Child* 1993;147:1224–30.
47. Levy HL, Guldberg P, Guttler F et al. Congenital heart disease in maternal phenylketonuria: report from the Maternal PKU Collaborative Study. *Pediatr Res* 2001;49:636–42.
48. Feldman GL, Weaver DD, Lovrien EW. The fetal trimethadione syndrome: report of an additional family and further delineation of this syndrome. *Am J Dis Child* 1977;131:1389–92.
49. Nora JJ, Nora AH. Familial risk of congenital heart defect. *Am J Med Genet* 1988;29:231–3.
50. Nora JJ, Nora AH. Update on counseling the family with a first-degree relative with a congenital heart defect. *Am J Med Genet* 1988;29:137–42.
51. Nora JJ, Nora AH. Maternal transmission of congenital heart diseases: new recurrence risk figures and the questions of cytoplasmic inheritance and vulnerability to teratogens. *Am J Cardiol* 1987;59:459–63.
52. Nora JJ, Nora AH. The evolution of specific genetic and environmental counseling in congenital heart diseases. *Circulation* 1978;57:205–13.
53. Nora JJ, Nora AH. Recurrence risks in children having one parent with a congenital heart disease. *Circulation* 1976;53:701–2.
54. Zellers TM, Driscoll DJ, Michels VV. Prevalence of significant congenital heart defects in children of parents with Fallot's tetralogy. *Am J Cardiol* 1990;65:523–6.

55. Calcagni G, Digilio MC, Sarkozy A et al. Familial recurrence of congenital heart disease: an overview and review of the literature. *Eur J Pediatr* 2007;166:111–6.
56. Geva T, Ayres NA, Pac FA, Pignatelli R. Quantitative morphometric analysis of progressive infundibular obstruction in tetralogy of Fallot. A prospective longitudinal echocardiographic study. *Circulation* 1995;92:886–92.
57. Anderson RH, Weinberg PM. The clinical anatomy of tetralogy of fallot. *Cardiol Young* 2005;15(Suppl. 1):38–47.
58. Anderson RH, Becker AE. Etienne-Louis Arthur Fallot and his tetralogy: a new translation of Fallot's summary and a modern reassessment of this anomaly. *Eur J Cardiothorac Surg* 1990;4: 229–32.
59. Oppenheimer-Dekker A, Gittenberger-de Groot AC, Bartelings MM et al. Abnormal architecture of the ventricles in hearts with an overriding aortic valve and a perimembranous ventricular septal defect ("Eisenmenger VSD"). *Int J Cardiol* 1985;9: 341–55.
60. Gatzoulis MA, Soukias N, Ho SY et al. Echocardiographic and morphological correlations in tetralogy of Fallot. *Eur Heart J* 1999;20:221–31.
61. Fukuda T, Suzuki T, Ito T. Clinical and morphologic features of perimembranous ventricular septal defect with overriding of the aorta – the so-called Eisenmenger ventricular septal defect. A study making comparisons with tetralogy of Fallot and perimembranous ventricular defect without aortic overriding. *Cardiol Young* 2000;10:343–52.
62. Van Praagh R, Corwin RD, Dahlquist EH Jr et al. Tetralogy of Fallot with severe left ventricular anomalous attachment of the mitral valve to the ventricular septum. *Am J Cardiol* 1970; 26:93–101.
63. Rosenquist GC, Sweeney LJ, Stemple DR et al. Ventricular septal defect in tetralogy of Fallot. *Am J Cardiol* 1973;31:749–54.
64. Ando M, Takahashi Y, Kikuchi T, Tatsuno K. Tetralogy of Fallot with subarterial ventricular septal defect. *Ann Thorac Surg* 2003;76:1059–64; discussion 1064–5.
65. Fu YC, Hwang B, Weng ZC et al. Influence of ventricular septal defect type on surgical results in children with tetralogy of Fallot. *Zhonghua Yi Xue Za Zhi (Taipei)* 2000;63:792–7.
66. Capelli H, Somerville J. Atypical Fallot's tetralogy with doubly committed subarterial ventricular septal defect. Diagnostic value of 2-dimensional echocardiography. *Am J Cardiol* 1983; 51:282–5.
67. Vargas FJ, Kreutzer GO, Pedrini M et al. Tetralogy of Fallot with subarterial ventricular septal defect. Diagnostic and surgical considerations. *J Thorac Cardiovasc Surg* 1986;92:908–12.
68. Flanagan MF, Foran RB, Van Praagh R et al. Tetralogy of Fallot with obstruction of the ventricular septal defect: spectrum of echocardiographic findings. *J Am Coll Cardiol* 1988;11:386–95.
69. Faggian G, Frescura C, Thiene G et al. Accessory tricuspid valve tissue causing obstruction of the ventricular septal defect in tetralogy of Fallot. *Br Heart J* 1983;49:324–27.
70. Kumar PR, Rakshak AD, Rajagopal P et al. Tetralogy of Fallot with flap valve ventricular septal defect producing suprasystemic right ventricular pressure: echocardiographic observations. *Indian Heart J* 1998;50:446–50.
71. Tewari P, Mittal P. Accessory tricuspid valve tissue in tetralogy of fallot causes hemodynamic changes during intermittent positive-pressure ventilation. *J Cardiothorac Vasc Anesth* 2006; 20:856–8.
72. van Meurs-van Woezik H, van Suylen RJ, Klein HW. A case of tetralogy of Fallot with pulmonary atresia and restrictive perimembranous ventricular septal defect. *Thorac Cardiovasc Surg* 1997;45:46–7.
73. Davido A, Maarek M, Jullien JL, Corone P. Ebstein's disease associated with Fallot's tetralogy. Apropos of a familial case, review of the literature, embryologic and genetic implications. *Arch Mal Coeur Vaiss* 1985;78:752–6.
74. Delius RE, Kumar RV, Elliott MJ et al. Atrioventricular septal defect and tetralogy of Fallot: a 15-year experience. *Eur J Cardiothorac Surg* 1997;12:171–6.
75. Suzuki K, Ho SY, Anderson RH et al. Morphometric analysis of atrioventricular septal defect with common valve orifice. *J Am Coll Cardiol* 1998;31:217–23.
76. Kaur A, Srivastava S, Lytrivi ID et al. Echocardiographic evaluation and surgical implications of common atrioventricular canal defects with absent or diminutive ostium primum defect. *Am J Cardiol* 2008;101:1648–51.
77. Need LR, Powell AJ, del Nido P, Geva T. Coronary echocardiography in tetralogy of fallot: diagnostic accuracy, resource utilization and surgical implications over 13 years. *J Am Coll Cardiol* 2000;36:1371–7.
78. Chiu IS, Wu CS, Wang JK et al. Influence of aortopulmonary rotation on the anomalous coronary artery pattern in tetralogy of Fallot. *Am J Cardiol* 2000;85:780–4, A9.
79. Johnston TA, Dyer K, Armstrong BA, Bengur AR. Anomalous origin of the left coronary artery in tetralogy of Fallot associated with abnormal mitral valve pathology. *Pediatr Cardiol* 1999;20: 438–40.
80. Carretero J, Rissech M, Mortera C et al. Aortic origin of the left pulmonary artery in an infant with Fallot's tetralogy. *Rev Esp Cardiol* 2005;58:1124–6.
81. Shiraishi I, Yamagishi M, Toiyama K et al. Coronary artery obstruction due to membranous ridge of the right sinus valsalva associated with tetralogy of Fallot: syncope mimics anoxic spell. *Ann Thorac Surg* 2004;77:321–2.
82. Meng CC, Eckner FA, Lev M. Coronary artery distribution in tetralogy of Fallot. *Arch Surg* 1965;90:363–6.
83. Krongrad E, Ritter DG, Hawe A et al. Pulmonary atresia or severe stenosis and coronary artery-to-pulmonary artery fistula. *Circulation* 1972;46:1005–12.
84. Suzuki K, Matsui M, Nakamura Y et al. A case of coronary artery-pulmonary artery fistula in tetralogy of Fallot with pulmonary atresia and major aortopulmonary collateral arteries (MAPCA). *Nippon Kyobu Geka Gakkai Zasshi* 1992;40:2252–7.
85. Sanders SP, Parness IA, Colan SD. Recognition of abnormal connections of coronary arteries with the use of Doppler color flow mapping. *J Am Coll Cardiol* 1989;13:922–6.
86. Chiu SN, Wu MH, Lin MT et al. Acquired coronary artery fistula after open heart surgery for congenital heart disease. *Int J Cardiol* 2005;103:187–92.
87. Edwards WD. Double-outlet right ventricle and tetralogy of Fallot. Two distinct but not mutually exclusive entities. *J Thorac Cardiovasc Surg* 1981;82:418–22.
88. Lev M, Eckner FA. The pathologic anatomy of tetralogy of Fallot and its variations. *Dis Chest* 1964;45:251–61.

89. Cicini MP, Giannico S, Marino B et al. "Acquired" subvalvular aortic stenosis after repair of a ventricular septal defect. *Chest* 1992;101:115–8.
90. Moran AM, Hornberger LK, Jonas RA, Keane JF. Development of a double-chambered right ventricle after repair of tetralogy of Fallot. *J Am Coll Cardiol* 1998;31:1127–33.
91. Wong PC, Sanders SP, Jonas RA et al. Pulmonary valve-moderator band distance and association with development of double-chambered right ventricle. *Am J Cardiol* 1991;68: 1681–6.
92. Galiuto L, O'Leary PW, Seward JB. Double-chambered right ventricle: echocardiographic features. *J Am Soc Echocardiogr* 1996;9:300–5.
93. Juffe Stein A, Kirklin JW. Double chambered right ventricle. Surgical results in 47 cases. *Rev Esp Cardiol* 1981;34:259–63.
94. McElhinney DB, Chatterjee KM, Reddy VM. Double-chambered right ventricle presenting in adulthood. *Ann Thorac Surg* 2000;70:124–7.
95. Morhy Borges Leal S, Andrade JL, de Souza M et al. Anomalous subaortic course of the left brachiocephalic (innominate) vein: echocardiographic diagnosis and report of an unusual association. *Cardiol Young* 2002;12:159–63.
96. Wang JK, Wu MH, Chang CI et al. Malalignment-type ventricular septal defect in double-chambered right ventricle. *Am J Cardiol* 1996;77:839–42.
97. Collett RW, Edwards JE. Persistent truncus arteriosus. A classification according to anatomic subtypes. *Surg Clin North Am* 1949;29:1245.
98. Van Praagh R, Van Praagh S. The anatomy of common aorticopulmonary trunk (truncus arteriosus communis) and its embryologic implications. A study of 57 necropsy cases. *Am J Cardiol* 1965;16:406–25.
99. Bharati S, Paul MH, Idriss FS et al. The surgical anatomy of pulmonary atresia with ventricular septal defect: pseudotruncus. *J Thorac Cardiovasc Surg* 1975;69:713–21.
100. Tchervenkov CI, Roy N. Congenital Heart Surgery Nomenclature and Database Project: pulmonary atresia – ventricular septal defect. *Ann Thorac Surg* 2000;69(4 Suppl.):S97–105.
101. Macartney F, Deverall P, Scott O. Haemodynamic characteristics of systemic arterial blood supply to the lungs. *Br Heart J* 1973;35:28–37.
102. Mackie AS, Gauvreau K, Perry SB et al. Echocardiographic predictors of aortopulmonary collaterals in infants with tetralogy of fallot and pulmonary atresia. *J Am Coll Cardiol* 2003;41:852–7.
103. Acherman RJ, Smallhorn JF, Freedom RM. Echocardiographic assessment of pulmonary blood supply in patients with pulmonary atresia and ventricular septal defect. *J Am Coll Cardiol* 1996;28:1308–13.
104. Hadjo A, Jimenez M, Baudet E et al. Review of the long-term course of 52 patients with pulmonary atresia and ventricular septal defect. Anatomical and surgical considerations. *Eur Heart J* 1995;16:1668–74.
105. Thiene G, Frescura C, Bortolotti U et al. The systemic pulmonary circulation in pulmonary atresia with ventricular septal defect: concept of reciprocal development of the fourth and sixth aortic arches. *Am Heart J* 1981;101:339–44.
106. Nakata S, Imai Y, Takanashi Y et al. A new method for the quantitative standardization of cross-sectional areas of the pulmonary arteries in congenital heart diseases with decreased pulmonary blood flow. *J Thorac Cardiovasc Surg* 1984;88:610–9.
107. Shinonaga M, Miyamura H, Watanabe H et al. Tetralogy of Fallot with a restrictive ventricular septal defect caused by a membranous flap. *Nippon Kyobu Geka Gakkai Zasshi* 1994;42:1378–81.
108. Padmanabhan J, Varghese PJ, Lloyd S, Haller JA Jr. Tetralogy of Fallot with suprasystemic pressure in the right ventricle. A case report and review of the literature. *Am Heart J* 1971;82: 805–11.
109. Alborino D, Guccione P, Di Donato R, Marino B. Aortopulmonary window coexisting with tetralogy of Fallot. *J Cardiovasc Surg (Torino)* 2001;42:197–9.
110. Ito M, Kikuchi S, Hachiro Y, Abe T. Anomalous subaortic position of the brachiocephalic vein associated with tetralogy of Fallot. *Ann Thorac Cardiovasc Surg* 2001;7:106–8.
111. Ramaswamy P, Lytrivi ID, Thanjan MT et al. Frequency of aberrant subclavian artery, arch laterality, and associated intracardiac anomalies detected by echocardiography. *Am J Cardiol* 2008;101:677–82.
112. Uretzky G, Puga FJ, Danielson GK et al. Complete atrioventricular canal associated with tetralogy of Fallot. Morphologic and surgical considerations. *J Thorac Cardiovasc Surg* 1984;87: 756–66.
113. Van Praagh S, Porras D, Oppido G et al. Cleft mitral valve without ostium primum defect: anatomic data and surgical considerations based on 41 cases. *Ann Thorac Surg* 2003;75:1752–62.
114. Rao BN, Anderson RC, Edwards JE. Anatomic variations in the tetralogy of Fallot. *Am Heart J* 1971;81:361–71.
115. Jekel L, Benatar A, Bennink GB et al. Tetralogy of Fallot with absent pulmonary valve. A continuing challenge. *Scand Cardiovasc J* 1998;32:213–7.
116. Emmanoulides GC, Thanopoulos B, Siassi B, Fishbein M. "Agenesis" of ductus arteriosus associated with the syndrome of tetralogy of Fallot and absent pulmonary valve. *Am J Cardiol* 1976;37:403–9.
117. Lakier JB, Stanger P, Heymann MA et al. Tetralogy of Fallot with absent pulmonary valve. Natural history and hemodynamic considerations. *Circulation* 1974;50:167–75.
118. Moon-Grady AJ, Tacy TA, Brook MM et al. Value of clinical and echocardiographic features in predicting outcome in the fetus, infant, and child with tetralogy of Fallot with absent pulmonary valve complex. *Am J Cardiol* 2002;89:1280–5.
119. Craatz S, Kunzel E, Spanel-Borowski K. Right-sided aortic arch and tetralogy of Fallot in humans – a morphological study of 10 cases. *Cardiovasc Pathol* 2003;12:226–32.
120. Allen HD, Adams FH, Moss AJ. *Moss and Adams' Heart Disease in Infants, Children, and Adolescents: Including the Fetus and Young Adult*, 6th edn. Philadelphia, PA/New York: Lippincott Williams & Wilkins, 2001.
121. Donti A, Soavi N, Sabbatani P, Picchio FM. Persistent left fifth aortic arch associated with tetralogy of Fallot. *Pediatr Cardiol* 1997;18:229–31.
122. Emmel M, Schmidt B, Schickendantz S. Double aortic arch in a patient with Fallot's tetralogy. *Cardiol Young* 2005;15:52–3.
123. Chen MR, Yu CH. Subclavian and pulmonary steal phenomenon in isolated left subclavian artery with left lung agenesis. *Jpn Heart J* 2002;43:429–32.
124. Krishnan KG, Theodore S, Kiran S, Neelakandhan KS. Embryologic and surgical considerations in tetralogy of Fallot

with right arch and aberrant left subclavian artery from the ascending aorta. *J Thorac Cardiovasc Surg* 2005;130:215–6.
125. Carano N, Piazza P, Agnetti A, Squarcia U. Congenital pulmonary steal phenomenon associated with tetralogy of Fallot, right aortic arch, and isolation of the left subclavian artery. *Pediatr Cardiol* 1997;18:57–60.
126. Yeh CN, Wang JN, Yao CT et al. Isolation of the left subclavian artery in a child with tetralogy of Fallot and right aortic arch. *J Formos Med Assoc* 2005;104:418–20.
127. Soylu M, Demir AD, Tikiz H et al. Left hemitruncus associated with tetralogy of fallot: a case report. *Catheter CardiovascInterv* 2000;51:58–60.
128. Calder AL, Barratt-Boyes BG, Brandt PW, Neutze JM. Postoperative evaluation of patients with tetralogy of Fallot repaired in infancy. Including criteria for use of outflow patching and radiologic assessment of pulmonary regurgitation. *J Thorac Cardiovasc Surg* 1979;77:704–20.
129. Chaturvedi R, Mikailian H, Freedom RM. Crossed pulmonary arteries in tetralogy of Fallot. *Cardiol Young* 2005;15:537.
130. Castaneda AR, Kirklin JW. Tetralogy of Fallot with aorticopulmonary window. Report of two surgical cases. *J Thorac Cardiovasc Surg* 1977;74:467–8.
131. Dipchand AI, Giuffre M, Freedom RM. Tetralogy of Fallot with non-confluent pulmonary arteries and aortopulmonary septal defect. *Cardiol Young* 1999;9:75–7.
132. Takeda Y, Asou T, Fakhri D et al. Pulmonary artery sling associated with tetralogy of fallot. *Asian Cardiovasc Thorac Ann* 2005;13:77–8.
133. Calder AL, Brandt PW, Barratt-Boyes BG, Neutze JM. Variant of tetralogy of fallot with absent pulmonary valve leaflets and origin of one pulmonary artery from the ascending aorta. *Am J Cardiol* 1980;46:106–16.
134. Recto MR, Parness IA, Gelb BD et al. Clinical implications and possible association of malposition of the branch pulmonary arteries with DiGeorge syndrome and microdeletion of chromosomal region 22q11. *Am J Cardiol* 1997;80:1624–7.
135. Zimmerman FJ, Berdusis K, Wright KL, Alboliras ET. Echocardiographic diagnosis of anomalous origins of the pulmonary arteries from the pulmonary trunk (crossed pulmonary arteries). *Am Heart J* 1997;133:257–60.
136. Siwik ES, Everman D, Morrison S. Images in cardiology: Crossed pulmonary arteries, ventricular septal defect, and chromosome 22q11 deletion. *Heart* 2002;88:88.
137. Hohn AR, Jain KK, Tamer DM. Supravalvular mitral stenosis in a patient with tetralogy of Fallot. *Am J Cardiol* 1968;22:733–7.
138. Aru GM, Juraszek A, Moskowitz I, Van Praagh R. Tetralogy of Fallot with congenital aortic valvar stenosis: the tetralogy-truncus interrelationship. *Pediatr Cardiol* 2006;27:354–9.
139. Freedom RM, Benson LN, Mikailian H. Aortic coarctation in an infant with tetralogy and pulmonary atresia. *Cardiol Young* 2005;15:667–8.
140. Ermis C, Gupta-Malhotra M, Titus JL. An obstructive bicuspid aortic valve in the setting of tetralogy of Fallot with pulmonary atresia: a rare combination. *Cardiol Young* 2004;14:99–101.
141. Capelli H, Ross D, Somerville J. Aortic regurgitation in tetrad of Fallot and pulmonary atresia. *Am J Cardiol* 1982;49:1979–83.
142. Alayunt A, Yagdi T, Alat I et al. Left ventricular diverticulum associated with Cantrell's syndrome and tetralogy of Fallot in an adult. *Scand Cardiovasc J* 2001;35:55–7.
143. Van Praagh R, Corsini I. Cor triatriatum: pathologic anatomy and a consideration of morphogenesis based on 13 postmortem cases and a study of normal development of the pulmonary vein and atrial septum in 83 human embryos. *Am Heart J* 1969;78:379–405.
144. Carroll SJ, Solowiejczyk D, Gersony WM. Preoperative diagnosis of co-existing divided left atrium and tetralogy of Fallot. *Cardiol Young* 2004;14:456–9.
145. Bittmann S, Ulus H, Springer A. Combined pentalogy of Cantrell with tetralogy of Fallot, gallbladder agenesis, and polysplenia: a case report. *J Pediatr Surg* 2004;39:107–9.
146. Santini F, Jonas RA, Sanders SP, Van Praagh R. Tetralogy of Fallot [S,D,I]: successful repair without a conduit. *Ann Thorac Surg* 1995;59:747–9.
147. Van Praagh R. Tetralogy of Fallot [S,D,I]: a recently discovered malformation and its surgical management. *Ann Thorac Surg* 1995;60:1163–5.
148. Foran RB, Belcourt C, Nanton MA et al. Isolated infundibuloarterial inversion (S,D,I): a newly recognized form of congenital heart disease. *Am Heart J* 1988;116:1337–50.
149. Ferrin LM, Atik E, Aiello V et al. Tetralogy of Fallot associated with left atrial isomerism. *Arq Bras Cardiol* 1996;67:249–53.
150. Da Cruz E, Milella L, Corno A. Left isomerism with tetralogy of Fallot and anomalous systemic and pulmonary venous connections. *Cardiol Young* 1998;8:131–3.
151. Fujiwara K, Naito Y, Komai H et al. Tetralogy of Fallot with levoatrial cardinal vein. *Pediatr Cardiol* 1999;20:136–8.
152. Brzezinski M, Keller R, Grichnik KP, Swaminathan M. Persistent left superior vena cava in a patient with a history of tetralogy of Fallot. *Anesth Analg* 2005;100:1269–70.
153. Redington AN, Raine J, Shinebourne EA, Rigby ML. Tetralogy of Fallot with anomalous pulmonary venous connections: a rare but clinically important association. *Br Heart J* 1990;64:325–8.
154. Azhari N, Al-Fadley F, Bulbul ZR. Tetralogy of Fallot associated with scimitar syndrome. *Cardiol Young* 2000;10:70–2.
155. Quaegebeur J, Kirklin JW, Pacifico AD, Bargeron LM Jr. Surgical experience with unroofed coronary sinus. *Ann Thorac Surg* 1979;27:418–25.
156. Oppido G, Napoleone CP, Ragni L et al. Double orifice tricuspid valve in an infant with tetralogy of Fallot. *Ann Thorac Surg* 2006;81:1121–3.
157. Cantrell JR, Haller JA, Ravitch MM. A syndrome of congenital defects involving the abdominal wall, sternum, diaphragm, pericardium, and heart. *Surg Gynecol Obstet* 1958;107:602–14.
158. Musewe NN, Smallhorn JF, Moes CA et al. Echocardiographic evaluation of obstructive mechanism of tetralogy of Fallot with restrictive ventricular septal defect. *Am J Cardiol* 1988;61:664–8.
159. Sanders SP, Bierman FZ, Williams RG. Conotruncal malformations: diagnosis in infancy using subxiphoid 2-dimensional echocardiography. *Am J Cardiol* 1982;50:1361–7.
160. Marino B, Ballerini L, Marcelletti C et al. Right oblique subxiphoid view for two-dimensional echocardiographic visualization of the right ventricle in congenital heart disease. *Am J Cardiol* 1984;54:1064–8.
161. Ramaswamy P, Lytrivi ID, Srivastava S et al. Left atrial appendage: variations in morphology and position causing pitfalls in pediatric echocardiographic diagnosis. *J Am Soc Echocardiogr* 2007;20:1011–6.

162. Niwa K. Aortic root dilatation in tetralogy of Fallot long-term after repair – histology of the aorta in tetralogy of Fallot: evidence of intrinsic aortopathy. *Int J Cardiol* 2005;103:117–9.
163. Preminger TJ, Sanders SP, van der Velde ME et al. "Intramural" residual interventricular defects after repair of conotruncal malformations. *Circulation* 1994;89:236–42.
164. Ghavidel AA, Javadpour H, Tabatabaei MB et al. Complete surgical repair of tetralogy of Fallot in adults, is it ever too late? *J Card Surg* 2008;23:23–6.
165. Gatzoulis MA, Elliott JT, Guru V et al. Right and left ventricular systolic function late after repair of tetralogy of Fallot. *Am J Cardiol* 2000;86:1352–7.
166. Geva T. Indications and timing of pulmonary valve replacement after tetralogy of Fallot repair. *Semin Thorac Cardiovasc Surg Pediatr Card Surg Annu* 2006:11–22.
167. Knauth AL, Gauvreau K, Powell A et al. Ventricular size and function assessed by cardiac MRI predict major adverse clinical outcomes late after tetralogy of Fallot repair. *Heart* 2008;94: 211–6.
168. Knauth AL, Gauvreau K, Powell AJ et al. Ventricular size and function assessed by cardiac MRI predict major adverse clinical outcomes late after tetralogy of Fallot repair. *Heart* 2008;94: 211–6.
169. Lurz P, Coats L, Khambadkone S et al. Percutaneous pulmonary valve implantation: impact of evolving technology and learning curve on clinical outcome. *Circulation* 2008;117: 1964–72.
170. Schievano S, Coats L, Migliavacca F et al. Variations in right ventricular outflow tract morphology following repair of congenital heart disease: implications for percutaneous pulmonary valve implantation. *J Cardiovasc Magn Reson* 2007;9:687–95.
171. Schievano S, Migliavacca F, Coats L et al. Percutaneous pulmonary valve implantation based on rapid prototyping of right ventricular outflow tract and pulmonary trunk from MR data. *Radiology* 2007;242:490–7.
172. Schreiber C, Horer J, Vogt M et al. A new treatment option for pulmonary valvar insufficiency: first experiences with implantation of a self-expanding stented valve without use of cardiopulmonary bypass. *Eur J Cardiothorac Surg* 2007;31:26–30.
173. D'Andrea A, Caso P, Sarubbi B et al. Right ventricular myocardial activation delay in adult patients with right bundle branch block late after repair of Tetralogy of Fallot. *Eur J Echocardiogr* 2004;5:123–31.
174. Lytrivi ID, Lai WW, Ko HH et al. Color Doppler tissue imaging for evaluation of right ventricular systolic function in patients with congenital heart disease. *J Am Soc Echocardiogr* 2005;18: 1099–104.
175. Abd El Rahman MY, Hui W, Yigitbasi M et al. Detection of left ventricular asynchrony in patients with right bundle branch block after repair of tetralogy of Fallot using tissue-Doppler imaging-derived strain. *J Am Coll Cardiol* 2005;45:915–21.
176. Baspinar O, Alehan D. Dobutamine stress echocardiography in the evaluation of cardiac haemodynamics after repair of tetralogy of Fallot in children: negative effects of pulmonary regurgitation. *Acta Cardiol* 2006;61:279–83.
177. Apostolopoulou SC, Laskari CV, Tsoutsinos A, Rammos S. Doppler tissue imaging evaluation of right ventricular function at rest and during dobutamine infusion in patients after repair of tetralogy of Fallot. *Int J Cardiovasc Imaging* 2007;23:25–31.
178. Sutton NJ, Peng L, Lock JE et al. Effect of pulmonary artery angioplasty on exercise function after repair of tetralogy of Fallot. *Am Heart J* 2008;155:182–6.
179. Niemann PS, Pinho L, Balbach T et al. Anatomically oriented right ventricular volume measurements with dynamic three-dimensional echocardiography validated by 3-Tesla magnetic resonance imaging. *J Am Coll Cardiol* 2007;50:1668–76.
180. Li W, Davlouros PA, Kilner PJ et al. Doppler-echocardiographic assessment of pulmonary regurgitation in adults with repaired tetralogy of Fallot: comparison with cardiovascular magnetic resonance imaging. *Am Heart J* 2004;147:165–72.
181. Silversides CK, Veldtman GR, Crossin J et al. Pressure half-time predicts hemodynamically significant pulmonary regurgitation in adult patients with repaired tetralogy of fallot. *J Am Soc Echocardiogr* 2003;16:1057–62.
182. Grothoff M, Spors B, Abdul-Khaliq H, Gutberlet M. Evaluation of postoperative pulmonary regurgitation after surgical repair of tetralogy of Fallot: comparison between Doppler echocardiography and MR velocity mapping. *Pediatr Radiol* 2008;38:186–91.
183. Mahle WT, Parks WJ, Fyfe DA, Sallee D. Tricuspid regurgitation in patients with repaired Tetralogy of Fallot and its relation to right ventricular dilatation. *Am J Cardiol* 2003;92:643–5.
184. Gelson E, Gatzoulis M, Steer PJ et al. Tetralogy of Fallot: maternal and neonatal outcomes. *BJOG-Int J Obstet Gy* 2008; 115:398–402.
185. Boudjemline Y, Fermont L, Le Bidois J et al. Can we predict 22q11 status of fetuses with tetralogy of Fallot? *Prenat Diagn* 2002;22:231–4.
186. Chaoui R, Kalache KD, Heling KS et al. Absent or hypoplastic thymus on ultrasound: a marker for deletion 22q11.2 in fetal cardiac defects. *Ultrasound Obstet Gynecol* 2002;20:546–52.
187. Yoo SJ, Lee YH, Kim ES et al. Three-vessel view of the fetal upper mediastinum: an easy means of detecting abnormalities of the ventricular outflow tracts and great arteries during obstetric screening. *Ultrasound Obstet Gynecol* 1997;9:173–82.
188. Miyashita S, Chiba Y. Prenatal demonstration of major aortopulmonary collateral arteries with tetralogy of Fallot and pulmonary atresia. *Fetal Diagn Ther* 2004;19:100–5.
189. Azancot A, Eydoux P, Vuillard E et al. Clinical spectrum of prenatal tetralogy of Fallot. *Arch Mal Coeur Vaiss* 2000;93:587–93.
190. Berg C, Thomsen Y, Geipel A et al. Reversed end-diastolic flow in the umbilical artery at 10–14 weeks of gestation is associated with absent pulmonary valve syndrome. *Ultrasound Obstet Gynecol* 2007;30:254–8.
191. Galindo A, Gutierrez-Larraya F, Martinez JM et al. Prenatal diagnosis and outcome for fetuses with congenital absence of the pulmonary valve. *Ultrasound Obstet Gynecol* 2006;28:32–9.
192. Hornberger LK, Sanders SP, Sahn DJ et al. In utero pulmonary artery and aortic growth and potential for progression of pulmonary outflow tract obstruction in tetralogy of Fallot. *J Am Coll Cardiol* 1995;25:739–45.
193. Boudjemline Y, Fermont L, Le Bidois J et al. Prenatal diagnosis of conotruncal heart diseases. Results in 337 cases. *Arch Mal Coeur Vaiss* 2000;93:583–6.
194. Paladini D, Rustico M, Todros T et al. Conotruncal anomalies in prenatal life. *Ultrasound Obstet Gynecol* 1996;8:241–6.

# 23 Truncus Arteriosus

**Mark B. Lewin and Jack C. Salerno**
Pediatric Cardiology and Echocardiography Laboratory, Seattle Children's Hospital, Seattle, WA, USA

In 1942 Lev and Saphir defined truncus arteriosus as the anomaly in which a single arterial trunk leaving the heart gives rise to the aorta, pulmonary arteries and coronary arteries [1]. This definition has persisted and is supported by other authors [2–5]. The earliest known descriptions of this defect were made by Wilson in 1798, as reported by Van Mierop et al. [6], and by Buchanan [7] in 1864. In recent years surgical repair in infants has been successful, and it is now the treatment of choice at presentation. We are now entering an era in which many patients who underwent neonatal repair of truncus arteriosus are becoming adults.

## Definition

Truncus arteriosus is defined as a congenital cardiac malformation in which a single arterial vessel gives rise to the aorta, the branch pulmonary arteries and the coronary arteries. Although not part of the definition, an associated subtruncal ventricular septal defect (VSD) is found in the majority of patients with truncus arteriosus.

## Incidence

Truncus arteriosus is a congenital heart anomaly occurring in approximately 1–4% of patients with congenital heart defects [2,3,5,8]. Without treatment truncus arteriosus is usually fatal; the mean age of death is 2.5 months [3], and 80% of children with this anomaly die during the first year of life [9].

## Etiology

Investigations using chick and mammalian embryos [10,11], as well as human studies, implicate a microdeletion at the 22q11.2 locus as at least one factor in the genetic etiology of truncus arteriosus. This deletion syndrome is associated with the DiGeorge and velocardiofacial syndromes. Unfortunately, the responsible gene within the 22q11.2 locus has not yet been definitively identified. Although the relationship between a chromosome 22q11 deletion and conotruncal lesions including truncus arteriosus is well established, preliminary studies suggest other putative mechanisms. The single tube that comprises the outflow tract in embryos undergoes septation into the aorta and the pulmonary trunk by means of a structure originating from the neural crest, the aortopulmonary septum. This structure is affected in the DiGeorge and velocardiofacial syndromes, resulting in truncus arteriosus. However, the remainder of the septation occurs by a different, less well understood mechanism, involving mesenchymal cells. Speculation has arisen that bone morphogenetic proteins (BMPs) may be involved in this process, and mouse embryo studies have demonstrated mutations in BMP as causing truncus arteriosus and type B interrupted aortic arch [11]. Clearly, disruption of multiple embryologic steps is required for truncus arteriosus to develop. As these mechanisms are further defined, we will have a better understanding of the genetics of this cardiac lesion.

Patients with conotruncal anomalies are at increased risk for a chromosome 22q11 microdeletion [12,13]. Fluorescence in situ hybridization (FISH) analysis for a chromosome 22q11 abnormality will detect a deletion in 35–40% of patients with truncus arteriosus [13–15]. Certain associated cardiac anomalies place these patients with truncus arteriosus at even higher risk, including the presence of a right aortic arch, abnormal aortic arch branching pattern, or a combination of these two features [15].

The phenotype of the patient with a 22q11 deletion is typically that of velocardiofacial or DiGeorge syndromes. DiGeorge syndrome occurs in approximately 33% of patients with truncus arteriosus and in 68% of patients with interrupted aortic arch type B [16]. In addition to the cardiac defects, DiGeorge syndrome is characterized by facial dysmorphism, thymic hypoplasia, parathyroid hypoplasia resulting in hypocalcemia, learning disabilities and psychiatric disorders later in life. Patients with a 22q11 deletion, and

*Echocardiography in Pediatric and Congenital Heart Disease: From Fetus to Adult*
Edited by Wyman W. Lai, Luc L. Mertens, Meryl S. Cohen and Tal Geva
 ISBN: 978-1-405-17401-5

features of either DiGeorge or velocardiofacial syndrome, have been grouped under the unifying acronym CATCH 22 syndrome to emphasize their phenotypic components (Cardiac defects, Abnormal face, Thymic hypoplasia, Cleft palate and Hypocalcemia) [17]. Facial features are often subtle, particularly in the newborn, and may include hypertelorism, micrognathia, short philtrum, bulbous nasal tip, and low-set posteriorly rotated ears. The phenotype is variable, and most patients are ascertained due to their cardiac findings, which subsequently prompt genetic testing. Due to the high prevalence of a chromosome 22q11 microdeletion in patients with truncus arteriosus, the current recommendations are to screen all patients identified with this cardiac lesion.

Other chromosomal abnormalities have also been identified in patients with truncus arteriosus, albeit at much lower frequencies. The possibility exists that these cumulative data may add useful information regarding the developmental derangements responsible for these complex cardiac lesions. For example, NKX2.5 is a transcription factor identified as important in the determination of myocardial cell fate, and thus of interest in understanding human cardiac development. NKX2.5 mutations have been implicated as a cause of various congenital cardiac defects, including truncus arteriosus [18]. Additionally, case reports have identified patients with truncus arteriosus manifesting a range of mutations, syndromes and modes of inheritance [19–21], which may provide insight into the etiology of this lesion. Finally, truncus arteriosus (as well as transposition of the great arteries and tricuspid atresia) has a higher prevalence in infants of diabetic mothers [22]. Whether this relationship is due to the teratogenic effect of circulating maternal glucose, or to an alternative mechanism for this associated disruption of organogenesis, remains speculative.

## Morphology and classification

### Developmental considerations

Two ridges that appear in the conotruncal segment of the 4–5-week embryo create the normal differentiation of the truncus into the aorta and pulmonary artery. These two ridges grow toward the midline and fuse to form the conotruncal septum, which divides the truncus into the aorta and pulmonary artery [23]. Ectomesenchymal cells derived from the cardiac neural crest contribute directly to aorticopulmonary septation [24]. The absence of conal cushion tissue, which during normal embryogenesis fuses with the muscular part of the interventricular septum to complete the separation of the ventricles, results in the typical infundibular or outlet VSD. Ablation of the cardiac neural crest in chick embryos results in truncus arteriosus, and partial ablation results in other conotruncal abnormalities, such as double-outlet right ventricle, transposition of the great arteries, and tetralogy of Fallot [25]. The ectomesenchymal cells also contribute to the development of the pharyngeal arches and thus to the thymus and parathyroid glands. Interestingly, the neural crest does not play a role in the development of the systemic and pulmonary veins, both of which are typically normal in truncus arteriosus. An alternative theory proposed by Van Praagh and Van Praagh [3] is that persistent truncus arteriosus is a form of tetralogy of Fallot combining pulmonary and infundibular atresia with failure of truncal separation – in essence an aortopulmonary window. Notably, neural crest abnormalities are found in tetralogy of Fallot, aortopulmonary window, and truncus arteriosus.

### Classification

Collett and Edwards classified truncus arteriosus into four major types based on the sources of pulmonary blood supply (Fig. 23.1, top panel) [2]:

**Type I**: short main pulmonary artery segment gives rise to both branch pulmonary arteries (Videoclips 23.1 and 23.2).

**Type II**: both branch pulmonary arteries arise from the common arterial trunk adjacent to one another with a rim of truncal tissue between them.

**Type III**: the branch pulmonary arteries arise from either side of the truncus and are somewhat remote from one another (Videoclip 23.3).

**Type IV** (previously termed pseudotruncus): the pulmonary circulation is supplied by collateral vessels from the descending aorta [2,4]. This anomaly is now considered a form of tetralogy of Fallot with pulmonary atresia rather than truncus arteriosus.

The classification of Van Praagh and Van Praagh [3] in 1965 (Fig. 23.1, bottom panel) modified the original classification of Collett and Edwards:

**Type I**: the branch pulmonary arteries arise from a short main pulmonary artery.

**Type II**: the branch pulmonary arteries arise directly from the arterial trunk through separate orifices.

**Type III**: only one branch pulmonary artery arises from the ascending segment of the arterial trunk. Collateral vessels usually supply the contralateral lung.

**Type IV**: truncus arteriosus with aortic arch hypoplasia, coarctation or interruption (usually type B interruption distal to the left common carotid artery). In this anatomic variant there is usually a well-formed main pulmonary artery and a small ascending aorta.

In each of the above types of truncus arteriosus, a modifier "A" (with VSD) or "B" (intact ventricular septum) is used.

### Morphology

#### Ventricular septal defect

In the majority of cases there is a subtruncal VSD over which the truncal valve sits, similar to tetralogy of Fallot (TOF). Rarely, the ventricular septum is intact [26,27]. The conal septum is usually absent and the truncal valve is in direct

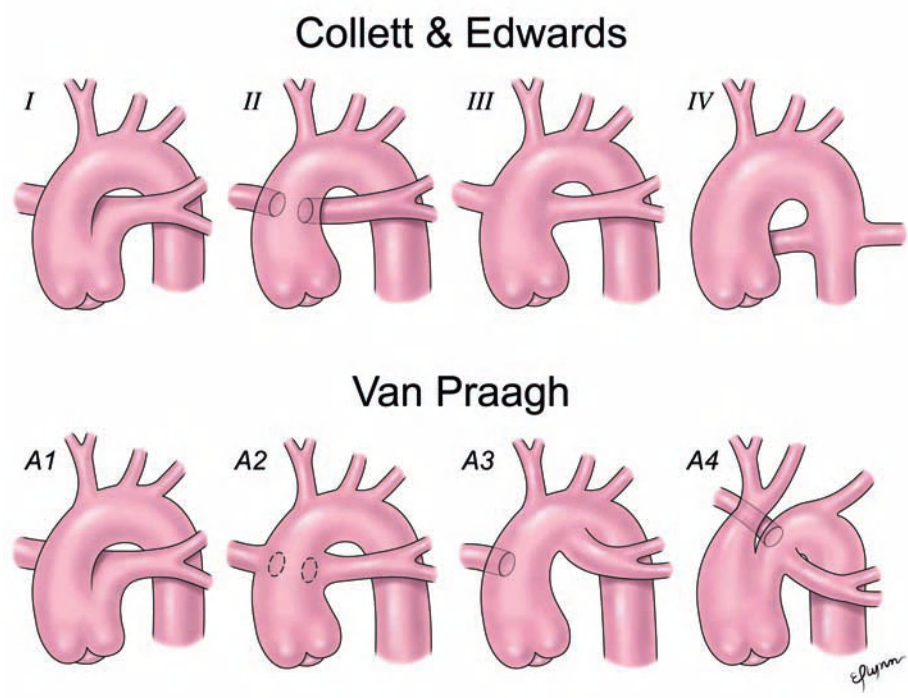


**Figure 23.1** Classification of truncus arteriosus. **Top panel:** Collett and Edwards. **Bottom panel:** Van Praagh and Van Praagh. See text for details.

fibrous continuity with the mitral valve. In rare circumstances, the truncal valve may be supported by a complete infundibulum and relates exclusively to the right ventricle.

### Truncal valve

The truncal valve leaflets are often thickened because of the expansion of the spongiosa and fibrosa layers, and the leaflets are often described as nodular [28–30]. The number and morphology of the leaflets are variable [2–5]: trileaflet valve in 65–70% of patients, quadricuspid in 9–24% (Fig. 23.2 and Videoclip 23.5) and bicuspid in 6–23%. Rarely, unicuspid [31] or pentacuspid valves are present. Truncal valve stenosis has been reported in ~33% of patients, and some degree of insufficiency is present in ~50% of patients (Videoclip 23.4) [32].

### Pulmonary arteries

In the majority of patients, the branch pulmonary arteries arise from the posterior-lateral aspect of the common trunk, either with a very short main pulmonary artery (type I; 48–68% of patients) or directly via two distinct orifices (type II; 29–48%) [2,4,5,31,33]. In ~6–10% of patients only one branch pulmonary artery arises from the ascending aspect of the common trunk (type III).

### Coronary arteries

The coronary artery pattern in truncus arteriosus is variable. The most common abnormality includes a higher and more posterior origin of the left coronary artery, which may result in the origin being in close proximity to the origin of the

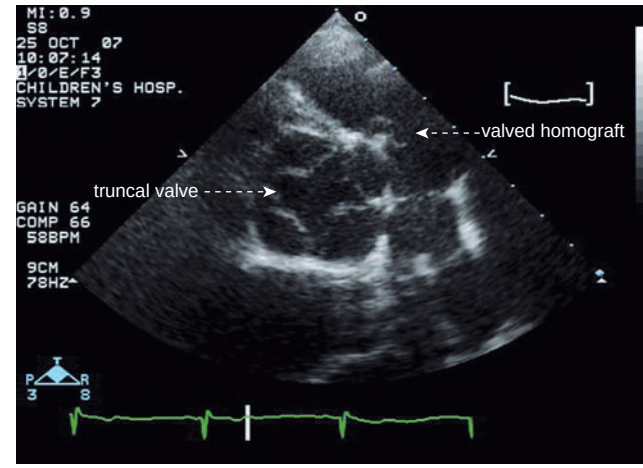


**Figure 23.2** Parasternal short-axis imaging plane demonstrating the quadricuspid morphology of the truncal valve.

pulmonary artery [34,35]. A single coronary artery has been reported in 13–18% of cases. Importantly, the coronary ostia may be narrowed or slit-like, resulting in significant coronary artery stenosis. Despite their highly variable origin, the distal coronary branches tend to follow a normal course [36]. There have also been reports of prominent diagonal branches off the right coronary artery; they parallel the course of the conus branch but are further down the anterior surface of the right ventricle. In addition, the conal branch off the right coronary artery may be prominent, distributing a network of vessels to the right ventricular outflow tract. The presence of coronary arteries in the infundibular free wall can

complicate placement of the right ventricle-to-pulmonary artery conduit as part of the surgical repair [37]. In addition to abnormalities of coronary ostial position, cases of multiple orifices of the right coronary artery and an intramural course opening into the pulmonary artery have also been reported [38].

### Associated cardiac lesions

The cardiac anomalies most frequently associated with truncus arteriosus are in the aortic arch. The aortic arch is right-sided in ~33% of patients [5]. Interrupted aortic arch occurs in approximately 19% of patients with truncus arteriosus (truncus type IV of Van Praagh) [16]. Conversely, approximately 12% of interrupted aortic arch anomalies have an associated truncus arteriosus. Type B interruption, between the left common carotid artery and the left subclavian artery, is the most common variant. Other forms of interrupted aortic arch occur only rarely. An aberrant origin of the left or right subclavian artery (depending on aortic side) is common in patients with truncus arteriosus.

Whereas a left superior vena cava is found in approximately 12% of patients with truncus arteriosus, other anomalies of systemic and pulmonary venous return are less common. Retro-aortic position of the left innominate vein is an anatomic variant of systemic venous anatomy associated with truncus arteriosus. Partially anomalous pulmonary venous return has been reported in approximately 1% of patients, and an associated totally anomalous pulmonary venous connection is rare [3,4,39]. Other anomalies rarely reported to accompany truncus arteriosus include: secundum atrial septal defect, tricuspid atresia, partial and complete atrioventricular canal defects, mitral atresia, mitral stenosis, aortic atresia, hypoplastic left ventricle, double-inlet left ventricle, tricuspid atresia, straddling tricuspid valve, Ebstein malformation, heterotaxy syndrome, and left pulmonary artery sling [40,41].

## Pathophysiology

The clinical presentation of truncus arteriosus is variable, but in most cases the dominant physiology is that of a large left-to-right shunt with pulmonary overcirculation. Typically, this left-to-right shunt physiology becomes clinically apparent over the first few weeks of life as the pulmonary vascular resistance decreases. The resistances in the pulmonary and systemic vascular beds determine the relative proportion of systemic and pulmonary blood flow. A widening pulse pressure accompanies the worsening pulmonary overcirculation as the pulmonary vascular resistance decreases, and the diastolic runoff into the pulmonary arteries results in reduction of diastolic arterial pressure.

The oxygen saturation in patients with truncus arteriosus depends on the amount of pulmonary blood flow. Because the pulmonary blood flow is generally excessive, most infants with truncus arteriosus have only mildly reduced systemic oxygen saturation (typically ≥90%). If severe congestive heart failure develops, intrapulmonary right-to-left shunt due to inefficient gas exchange can lead to cyanosis. If left unrepaired, cyanosis may ensue due to increased pulmonary vascular resistance associated with obstructive pulmonary vascular disease.

Abnormalities of the truncal valve, either insufficiency or stenosis, may play an important role in the clinical course and pathophysiology of infants with truncus arteriosus. In most patients, the stenosis and/or insufficiency are not severe enough to alter the presentation and initial clinical course. If severe truncal stenosis is present, the dominant physiology is that of biventricular outflow obstruction. In patients with moderate or severe truncal valve insufficiency, the combination of left-to-right shunt and retrograde flow through the incompetent truncal valve results in severe left ventricular volume load. A rapid fall in pulmonary vascular resistance in the newborn with truncal valve insufficiency may exacerbate the development of congestive heart failure.

The systemic circulation in infants with an interrupted aortic arch or severe coarctation depends on flow through a patent ductus arteriosus and, therefore, requires prompt diagnosis and administration of intravenous prostaglandin $E_1$. Closure of the arterial duct will lead to low cardiac output and development of symptoms of shock.

The management of truncus arteriosus consists of prompt surgical repair. Medical management is largely unsuccessful in controlling the symptoms of congestive heart failure, and mortality in the first year of life is exceedingly high [42]. Improvements in surgical techniques and perioperative management have enabled successful early repair, with a reported mortality of 5–11% [38,43–45]. Delayed surgical repair can result in development of pulmonary vascular obstructive disease and myocardial dysfunction. Surgical repair is performed under deep hypothermia with either low-flow continuous cardiopulmonary bypass or intermittent periods of circulatory arrest [46]. The pulmonary arteries are removed from the truncus, and the resultant opening is either closed primarily or with a patch. The VSD is closed with a patch. Continuity between the right ventricle and the pulmonary arteries is established using a cryopreserved homograft, or a valved heterograft conduit. When severe truncal valve insufficiency is present in infancy, most authors now advocate repair of the truncal valve [45–47], reserving replacement at the time of initial repair for only the most severe forms of regurgitation [45,48]. Additional associated anomalies that have been identified as independent risk factors for surgical mortality include interrupted aortic arch and coronary artery anomalies [44,49,50]. Progressive obstruction of the right ventricle-to-pulmonary artery conduit and truncal valve dysfunction are common

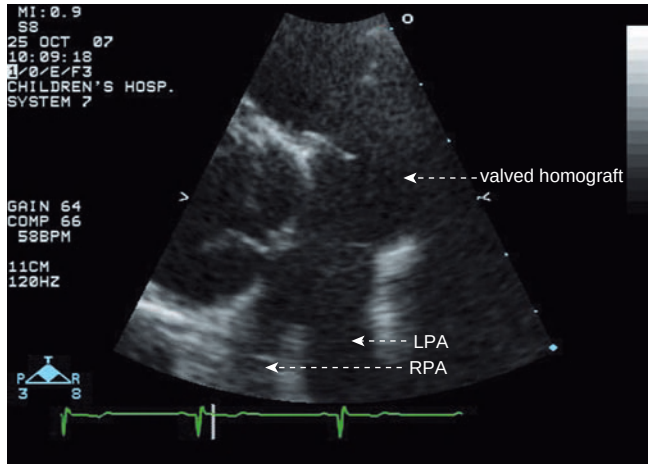


**Figure 23.3** Parasternal short-axis imaging plane demonstrating the valved pulmonary homograft, which appears echo-bright along its course secondary to calcification. The branch pulmonary arteries are seen arising without obvious pathology from the distal aspect of the conduit. LPA, left pulmonary artery; RPA, right pulmonary artery.

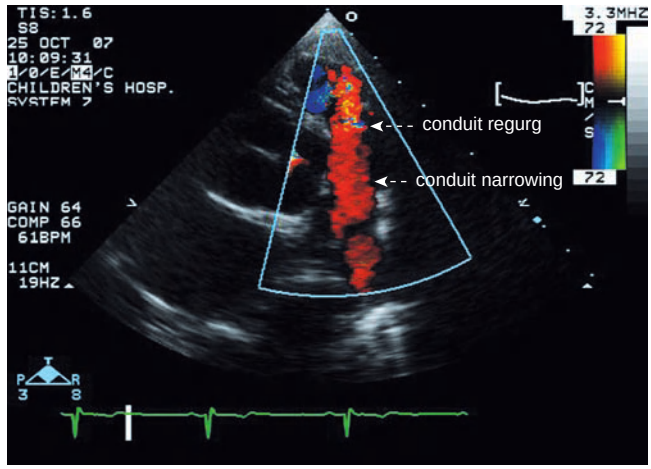


**Figure 23.4** Color Doppler interrogation from the parasternal short-axis imaging plane demonstrating pulmonary homograft regurgitation and flow reversal along the length of the conduit with associated conduit narrowing.

challenges in the follow-up of patients with repaired truncus arteriosus (Figs 23.3–23.5) [51–58].

## Echocardiographic imaging

### Goals of the examination

The goals of the echocardiographic evaluation of truncus arteriosus are dependent upon the patient's age, physiologic state and temporal relationship to surgical intervention. In general, the neonate requires a thorough evaluation of all components of the anatomic features. In addition, the examination must also assess any of the typical or unusual cardiac

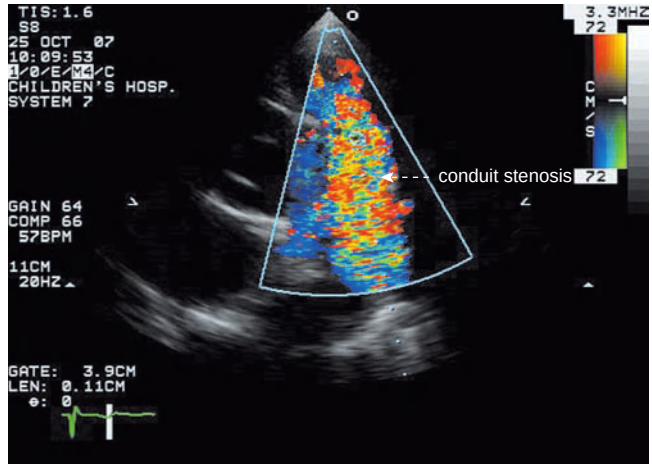


**Figure 23.5** Color Doppler interrogation from the parasternal short-axis imaging plane demonstrating pulmonary homograft stenosis along the length of the conduit. Flow is noted into the pulmonary artery branches.

anomalies associated with truncus arteriosus. The older child and adult will require evaluation of the underlying anatomy as well as the status of any surgical repair. In terms of the details of the components of each of these types of assessments, the following goals should be met:

### Neonatal echocardiographic exam

As part of a detailed, segment-by-segment evaluation of all aspects of cardiovascular anatomy and physiology, particular attention is focused on the following areas:

- Location and size of VSD; presence of additional VSDs (Videoclip 23.6).
- Presence of atrial communication.
- Atrioventricular valve anatomy and function; presence of straddling chordae or valve tissue across the VSD.
- Morphology and function of the truncal valve (Videoclip 23.7).
- Pulmonary artery anatomy, including presence or absence of a main pulmonary artery segment, pulmonary artery branch position and size (Videoclip 23.8).
- Sources of pulmonary blood flow other than branch pulmonary arteries, e.g., ductus arteriosus and aortopulmonary collateral vessels (especially important when one of the branch pulmonary arteries does not arise from the ascending aorta).
- Aortic arch anatomy (evaluation for arch sidedness, hypoplasia or interruption).
- Ventricular size and function.
- Coronary artery origin and proximal course; relationships between coronary ostia and origin(s) of pulmonary arteries and truncal valve leaflets.
- Associated lesions (e.g., persistent left superior vena cava, anomalous pulmonary venous connection, aberrant origin of the left or right subclavian arteries).

### Follow-up echocardiograms

Echocardiograms performed after the initial surgical intervention are typically focused upon those aspects of cardiac anatomy and physiology that raised concern early on, or might be expected to develop over time. Areas of particular interest include:

- Presence, size and flow velocity through residual VSD(s).
- Truncal valve function.
- Right ventricle-to-pulmonary artery conduit stenosis/insufficiency (Videoclips 23.9 and 23.10).
- Branch pulmonary artery stenosis.
- Assessment of right ventricular systolic pressure.
- Atrioventricular valve function.
- Ventricular size and function.
- Aortic arch (if obstruction or interruption noted at presentation).

### Imaging of truncus arteriosus

Truncus arteriosus can be accurately diagnosed using two-dimensional (2D) and Doppler echocardiography [59–62]. In most cases echocardiography is sufficient to provide a complete preoperative assessment. The goal of the echocardiographer should be to provide a detailed diagnosis based on (i) knowledge of the surgical questions, and (ii) the associated lesions. In assessing truncus arteriosus by echocardiography it is crucial to have a clear understanding of the data required from the study, but also the limitations of this diagnostic modality so that alternative testing can be employed when needed.

The echocardiographic examination should be systematic and organized so that details are not missed. The subcostal view provides an image of all aspects of the anatomy and is the preferred initial imaging approach in many centers. When the examination begins from the parasternal long-axis view, the presence of an overriding single semilunar valve and malalignment-type VSD provides an initial clue to the diagnosis of truncus arteriosus (Fig. 23.6). Often one can also image the pulmonary artery arising from the posterior aspect of the truncus (Figs 23.7 and 23.8). The truncal valve is well seen, and truncal insufficiency can be assessed with the use of color Doppler. In many instances truncal stenosis can be suggested by the anatomic appearance of the valve. When there is truncal stenosis, the valve appears thick and excursion is reduced. This view is inadequate for assessing the severity of truncal stenosis, because the Doppler cursor cannot be aligned parallel to the direction of flow across the valve. If there is an associated interruption of the aortic arch, the ascending aorta can be seen arising from the rightward aspect of the truncus. An enlarged coronary sinus may indicate a left superior vena cava. In the long-axis view the coronary sinus lies posteriorly just above the mitral valve within the pericardial shadow.

From the parasternal short-axis view with the transducer angled superiorly above the level of the truncal valve, the

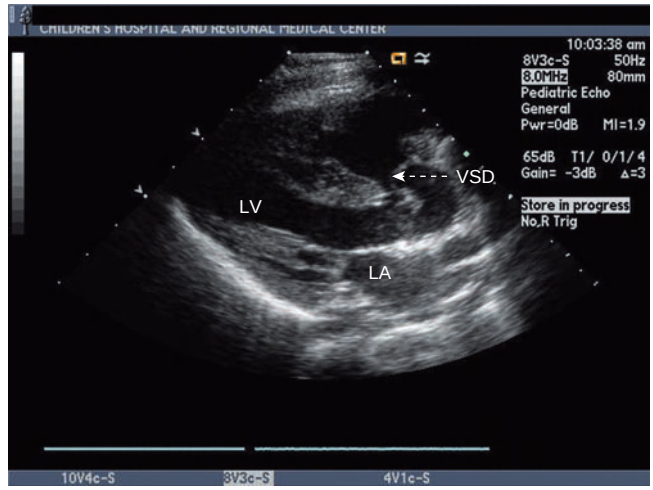


**Figure 23.6** Parasternal long-axis imaging plane demonstrating truncal override of the ventricular septal defect. LA, left atrium; LV, left ventricle; VSD, ventricular septal defect.

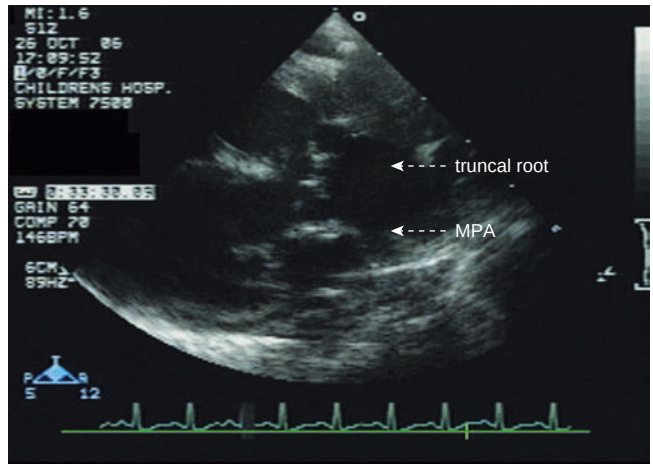


**Figure 23.7** Parasternal long-axis imaging plane demonstrating truncal override of the ventricular septal defect and the pulmonary artery origin from the truncal root. MPA, main pulmonary artery.

origin of the pulmonary arteries from the left-posterior aspect of the truncus can be readily seen (Figs 23.9 and 23.10). This view is also excellent to ascertain the type of truncus by imaging the branch pulmonary arteries (Figs 23.9–23.11). This view is also ideally suited for assessment of truncal valve morphology, including its commissures and leaflets. Three-dimensional echocardiography may be particularly helpful for assessment of truncal valve anatomy. At the level of the truncal valve, the location of the VSD can be determined. The VSD is usually within or superior to the Y of septal band, and when this is the case, a rim of muscle appears adjacent to the tricuspid valve in the short-axis view. If the VSD extends to the tricuspid valve in this view, it involves the membranous septum. The coronary arteries may be imaged in this view by rotating the transducer clockwise. To image the relationship

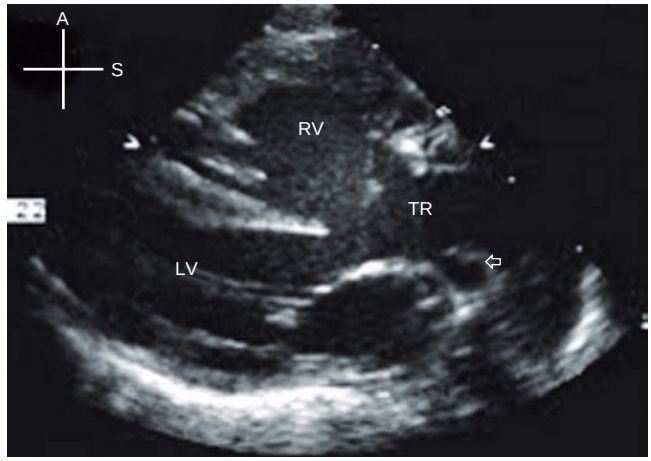


**Figure 23.8** Parasternal long-axis view demonstrating the pulmonary artery (arrow) arising from the truncus (TR). The truncal valve can be seen in the closed position. A, anterior; S, superior; LV, left ventricle; RV, right ventricle.

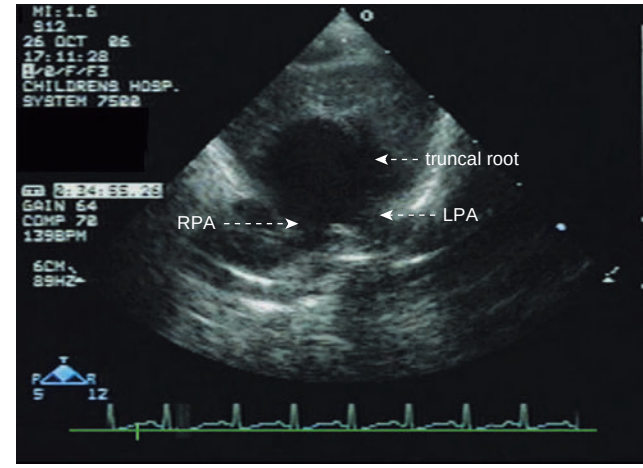


**Figure 23.10** Parasternal short-axis imaging plane demonstrating separate origins of the pulmonary artery branches from the truncal root (truncus arteriosus type II). RPA, right pulmonary artery; LPA, left pulmonary artery.

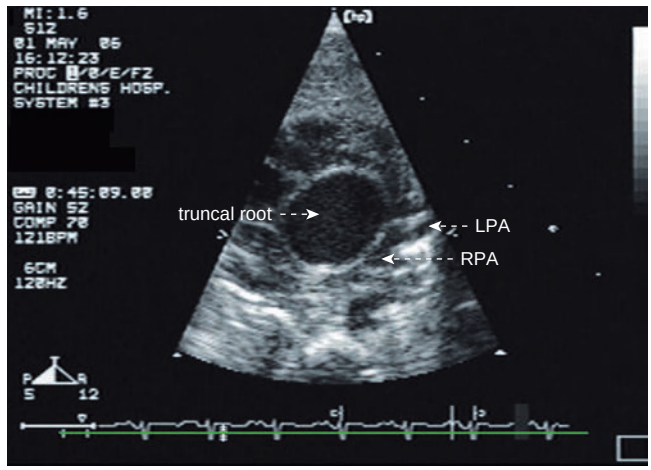


**Figure 23.9** Parasternal short-axis imaging plane demonstrating hypoplasia of the pulmonary artery branches. LPA, left pulmonary artery; RPA, right pulmonary artery.

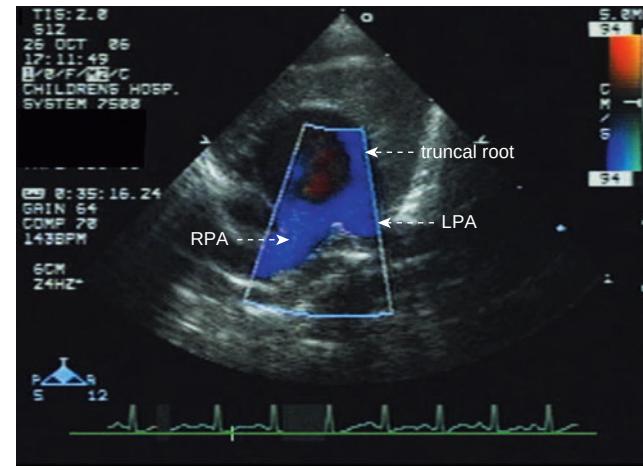


**Figure 23.11** Color Doppler interrogation from the parasternal short-axis imaging plane demonstrating unobstructed flow into the separate pulmonary artery branches as they originate from the truncal root (truncus arteriosus type II). LPA, left pulmonary artery; RPA, right pulmonary artery.

of the coronary artery to the pulmonary artery, one must angle the transducer superiorly and inferiorly such that the coronary artery and the pulmonary artery are imaged in the same plane. The parasternal long-axis view and the subcostal coronal view are also helpful in imaging the relationship of the coronary artery to the pulmonary artery, as they can often be seen in the same plane. Parasternal as well as suprasternal views allow assessment for the presence of a patent ductus arteriosus. Although there is typically a direct relationship between the presence of a patent ductus arteriosus and aortic arch hypoplasia/interruption, the patient rarely can have a normal aortic arch and a hemodynamically important ductus arteriosus [63].

The apical four-chamber view is most helpful in identifying additional muscular VSDs through the use of color Doppler. The typically large malalignment VSD is seen when the transducer is angled anteriorly toward the outflow tract (Fig. 23.12). This view is also particularly helpful for assessing truncal insufficiency and stenosis (Fig. 23.13). The Doppler beam can be aligned parallel to the flow from this view, and an accurate Doppler gradient can be measured when truncal stenosis is present. The relationship between the pulmonary artery origin and the truncal root can be imaged by angling anteriorly (Fig. 23.14).

The subcostal view provides an image of all aspects of the anatomy. At the atrial level the atrial septum can be imaged and the pulmonary veins can be seen entering the left atrium. As the transducer is swept superiorly, the truncal valve overriding the VSD can be imaged. In addition, the branch pulmonary arteries and their origin from the truncus

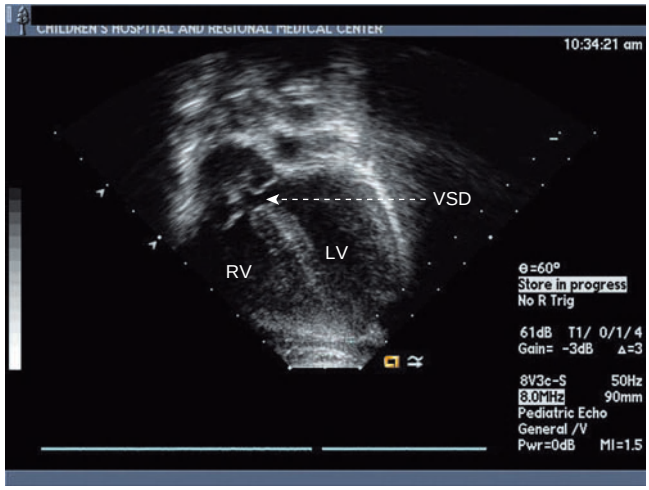


**Figure 23.12** Four-chamber imaging plane demonstrating truncal override of the ventricular septal defect. The truncal valve leaflets appear thickened. LV, left ventricle; RV, right ventricle; VSD, ventricular septal defect.

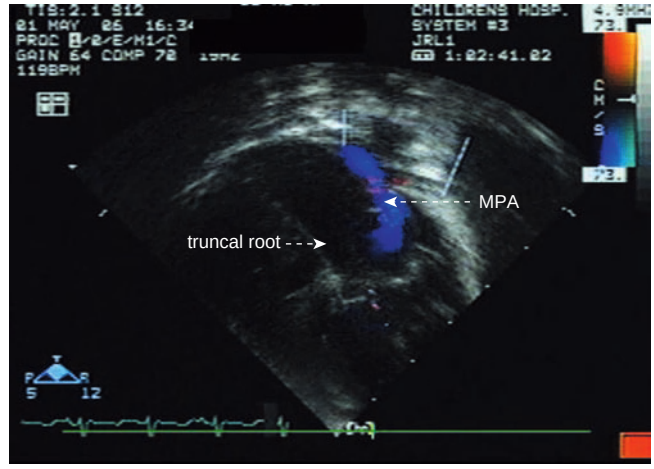


**Figure 23.14** Color Doppler interrogation from the 4-chamber imaging plane demonstrating flow into the main pulmonary artery originating from the truncal root. MPA, main pulmonary artery.

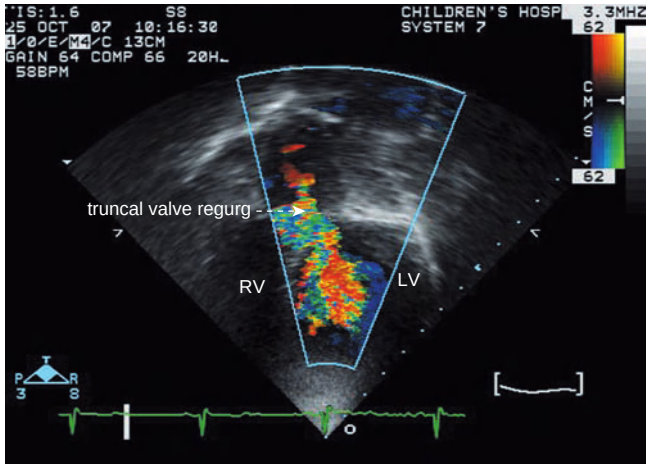


**Figure 23.13** Color Doppler interrogation from the 4-chamber imaging plane demonstrating truncal valve regurgitation and associated left ventricular dilation. LV, left ventricle; RV, right ventricle.

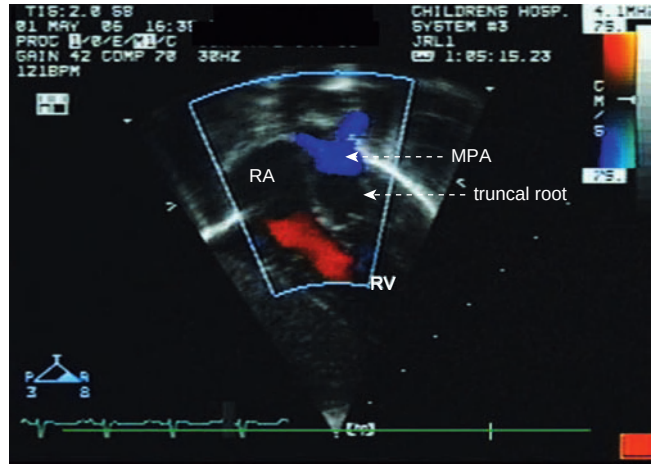


**Figure 23.15** Color Doppler interrogation from the subcostal long-axis imaging plane demonstrating flow into the pulmonary artery from its truncal root origin. MPA, main pulmonary artery; RA, right atrium; RV, right ventricle.

can be well seen (Figs 23.15 and 23.16). The right pulmonary artery can be imaged just inferior and posterior to the truncus. The main pulmonary artery segment and the branch pulmonary arteries can be seen arising from the truncus, and the coronary arteries can be imaged in this view. The subcostal view provides an image of the ascending aorta when the aortic arch is interrupted. The ascending aorta arises slightly rightward and superior to the truncal valve. If one tilts the transducer superiorly, the bifurcation of the ascending aorta into the innominate and left carotid arteries can be imaged. Imaging of the abdominal aorta is utilized to detect diastolic flow reversal by Doppler (Fig. 23.17).

The suprasternal notch view provides the best image of the aortic arch (Fig. 23.18). It is in this view that interruption of the aortic arch can be determined. When the aortic arch is interrupted, the descending aorta is supplied by the ductus arteriosus, which forms a ductal arch. Tilting the transducer to the left of the patient's sagittal plane can image the ductal arch. The ductal arch can be differentiated from the aortic arch by sweeping to the right and left and imaging the ascending aorta as a separate structure. In addition, the left subclavian artery arises from the descending aorta (typically being filled in a retrograde fashion via flow from the ductus arteriosus), and no carotid vessels can be seen to arise from the ductal arch. Doppler interrogation of the descending

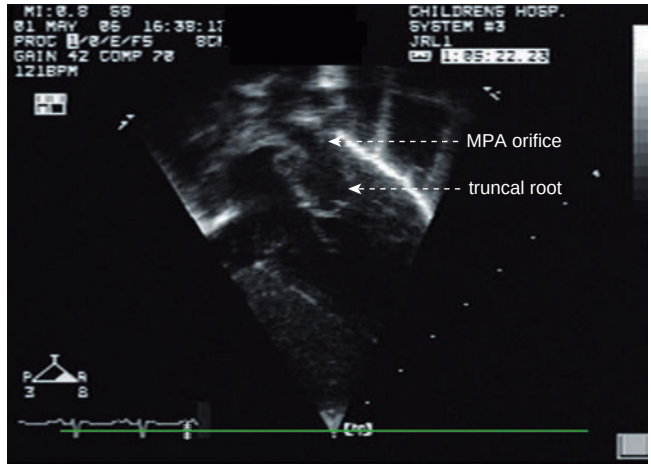


**Figure 23.16** Subcostal long-axis imaging plane demonstrating the origin of the pulmonary artery from the truncal root. MPA, main pulmonary artery.

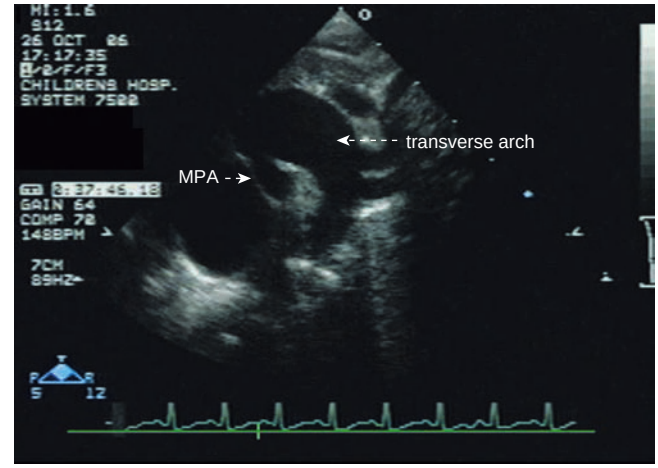


**Figure 23.18** Suprasternal notch long-axis imaging plane demonstrating the take-off of the pulmonary artery from the truncal root. MPA, main pulmonary artery.

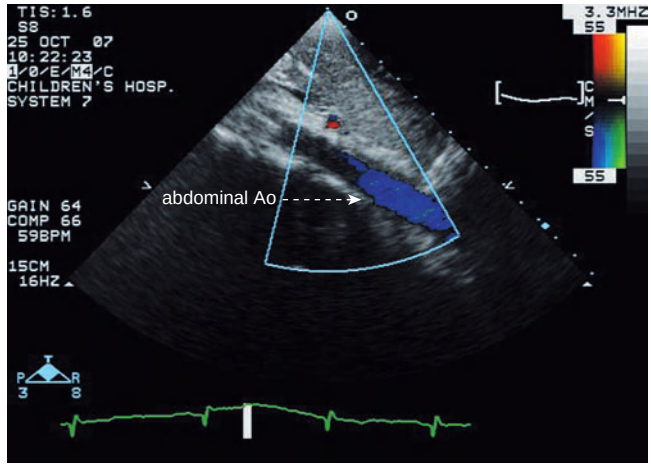


**Figure 23.17** Color Doppler interrogation from the subcostal imaging plane demonstrating flow reversal in the abdominal aorta secondary to truncal valve regurgitation. Ao, aorta.

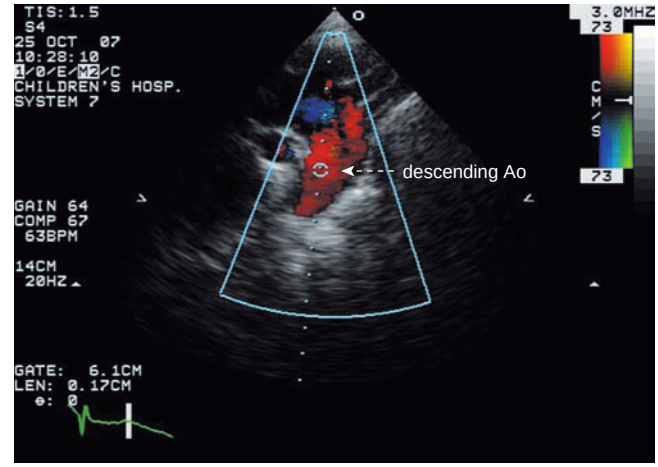


**Figure 23.19** Color Doppler interrogation from the suprasternal notch long-axis imaging plane demonstrating flow reversal in the proximal descending aorta secondary to truncal valve insufficiency. Ao, aorta.

aorta typically elicits diastolic flow reversal related to diastolic flow into the pulmonary arteries and/or presence of truncal valve insufficiency (Fig. 23.19).

## Prenatal assessment

Many cases of truncus arteriosus are now diagnosed prenatally by fetal echocardiography. The pregnant woman in whom the diagnosis of a fetus with truncus arteriosus is considered may come to attention because of: (i) a family history of congenital heart defect (typically a relative with a conotruncal defect); (ii) abnormal screening amniocentesis or chorionic villus sampling (often a 22q11 microdeletion by fluorescence in situ hybridization analysis); (iii) concern regarding a cardiac defect when the fetus is found on obstetrical ultrasound to have extracardiac anomalies (e.g., an abnormality of the palate in the patient with a 22q11 deletion); or (iv) the identification of a cardiac anomaly on routine obstetrical ultrasound screening.

The frequency of prenatal diagnostic screening has increased dramatically over the past decade, as obstetrical ultrasonic cardiac screening techniques have become more standardized [64]. The accuracy of the identification of complex fetal cardiac anatomy has been well established. Tometzki et al. [65] demonstrated their ability to define accurately a constellation of conotruncal defects, including fetuses with truncus arteriosus. Focused studies on the prenatal diagnosis of truncus arteriosus have also been performed, including the assessment of the associated cardiac anomalies [66,67]. These studies have shown a high degree of diagnostic accuracy for the overall identification of truncus arteriosus, including identification of VSD position, aortic arch anatomy, truncal valve pathology, and pulmonary

artery architecture. The differentiation between truncus arteriosus (origin of the branch pulmonary arteries from the truncus) and tetralogy of Fallot with pulmonary atresia (no pulmonary arteries arising from the ascending aorta) continues to be particularly challenging in the fetus. In addition, there are well-recognized variables in the accurate definition of fetal cardiac anatomy, including operator experience, fetal position, maternal body habitus, and gestational age. Nevertheless, the ability to provide accurate prenatal information to families and caregivers has greatly enhanced their options to make timely management decisions. The role of evolving technologies such as "real-time" 3D echocardiography [68] and fetal cardiac magnetic resonance imaging (MRI) [69] awaits further technological refinements and clinical validation.

The postnatal outcome of the prenatally diagnosed fetus with truncus arteriosus has been investigated. Although we can accurately diagnose truncus arteriosus before birth, the data regarding postnatal outcome are less encouraging. Duke and colleagues from the UK [66] reported that of 17 prenatal cases, pregnancy was terminated in 4 (24%), and 8 of the remaining 13 live births underwent neonatal surgery. Two newborns with severe truncal valve stenosis suffered preoperative sudden death. From this subset, 30-day surgical mortality was 25%.

## Intraoperative assessment

Miniaturization of transesophageal echocardiographic (TEE) probes allows intraoperative and postoperative assessment of truncus arteriosus repair before and after cardiopulmonary bypass [70]. TEE can be performed without entering the sterile field, and it allows a complete examination. In this way undetected anomalies may be clarified prior to cardiopulmonary bypass, and the adequacy of repair can be assessed for such lesions as residual VSDs, obstruction across the right ventricular-to-pulmonary artery conduit, and competency of the truncal valve [71]. As with other cardiac defects, TEE allows postoperative decision-making to be made in a timely fashion so that the need for further interventions can be determined in the operating room.

## Imaging of the adult

Echocardiographic imaging in the adult with repaired truncus arteriosus contains the essential components of the initial study with additional emphasis on evaluation of the truncal valve and pulmonary conduit (Fig. 23.20). In addition, by adulthood there will be many patients who have developed such severe truncal valve pathology that valve replacement is required (Figs 23.21 and 23.22). The adult with progressive

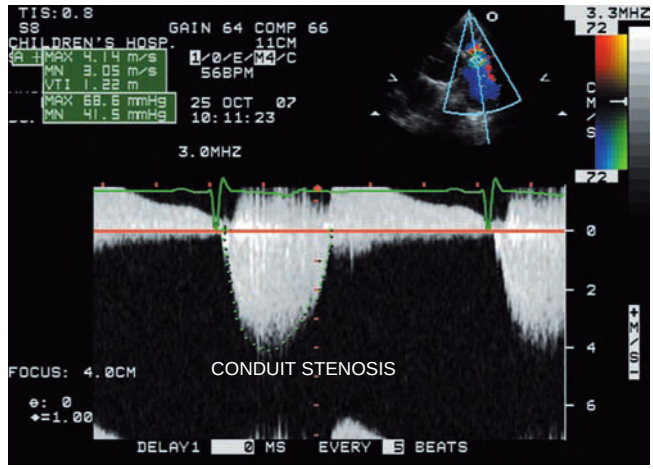


**Figure 23.21** Continuous-wave Doppler interrogation from the parasternal short-axis imaging plane demonstrating moderate to severe pulmonary conduit stenosis: peak velocity 4.1 m/s predicting a pressure gradient through the conduit of approximately 67 mm Hg.

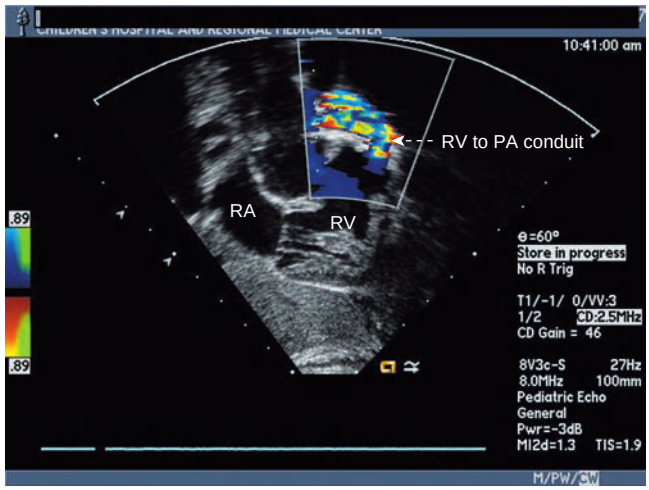


**Figure 23.20** Color Doppler interrogation from the subcostal long-axis imaging plane demonstrating turbulent flow into the pulmonary conduit from its right ventricular origin. PA, pulmonary artery; RA, right atrium; RV, right ventricle.

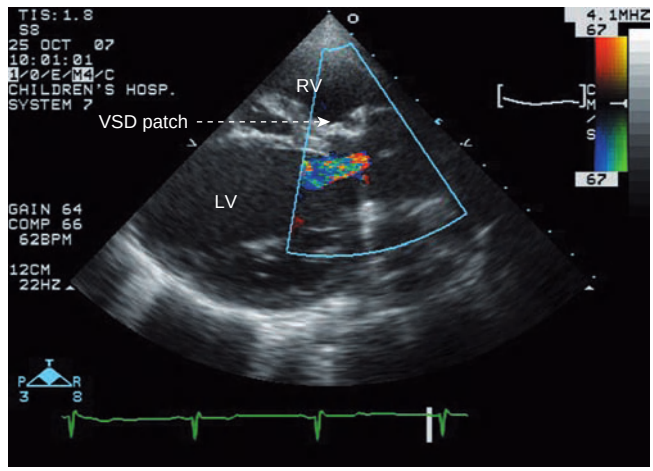


**Figure 23.22** Color Doppler interrogation from the parasternal long-axis imaging plane demonstrating truncal valve insufficiency and associated left ventricular dilation. In addition, the ventricular septal defect patch is seen. LV, left ventricle; RV, right ventricle.

truncal valve disease is assessed in a manner similar to the individual with isolated aortic valve pathology. This involves an evaluation of the severity of truncal insufficiency based upon color Doppler imaging, extent of diastolic flow reversal in the descending aorta, pressure half-time assessment, and left ventricular dilation and function. The assessment of truncal valve stenosis is similar to that of aortic valve stenosis, including Doppler assessment of peak and mean gradient, valve morphology, and left ventricular hypertrophy and function.

## Ancillary imaging modalities

There are instances in which additional diagnostic evaluation is necessary. As acoustic windows become restricted in older children and adults with repaired truncus arteriosus, cardiovascular MRI is the ideal alternative to echocardiography (Fig. 23.23). This modality allows comprehensive anatomic and functional assessments, including accurate quantification of truncal valve regurgitation and biventricular size and function as well as anatomic evaluation of the pulmonary arteries and aorta [72]. Computed tomography (CT) can be used as an alternative modality in patients with contraindications to MRI (e.g., pacemaker or implanted defibrillator). However, physicians recommending CT should carefully consider the risk of cancer due to ionizing radiation, which is considerably higher in young children [73]. In selected patients in whom noninvasive evaluation is inconclusive, cardiac catheterization may be required for hemodynamic assessment and for intervention to relieve conduit or branch pulmonary artery stenosis (Fig. 23.24) or to assess coronary artery anatomy.

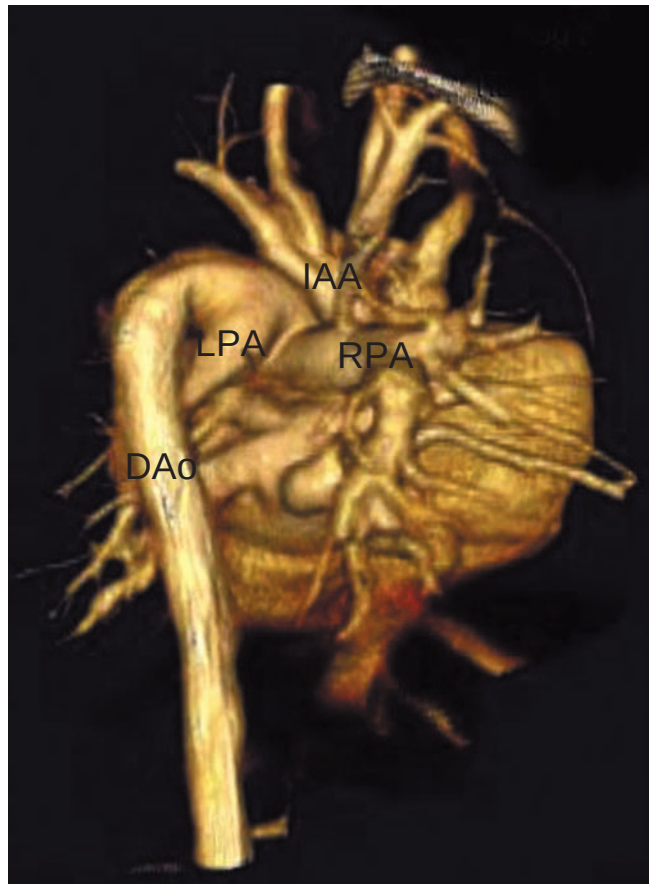


**Figure 23.23** Three-dimensional volume reconstruction of computed tomography angiogram in a patient with truncus arteriosus and interrupted aortic arch type A. View of carotid and subclavian arteries (IAA) arising from the ascending aorta, with pulmonary artery branches (LPA, RPA) slightly offset in position as they arise from the truncal root. DAo, descending aorta.

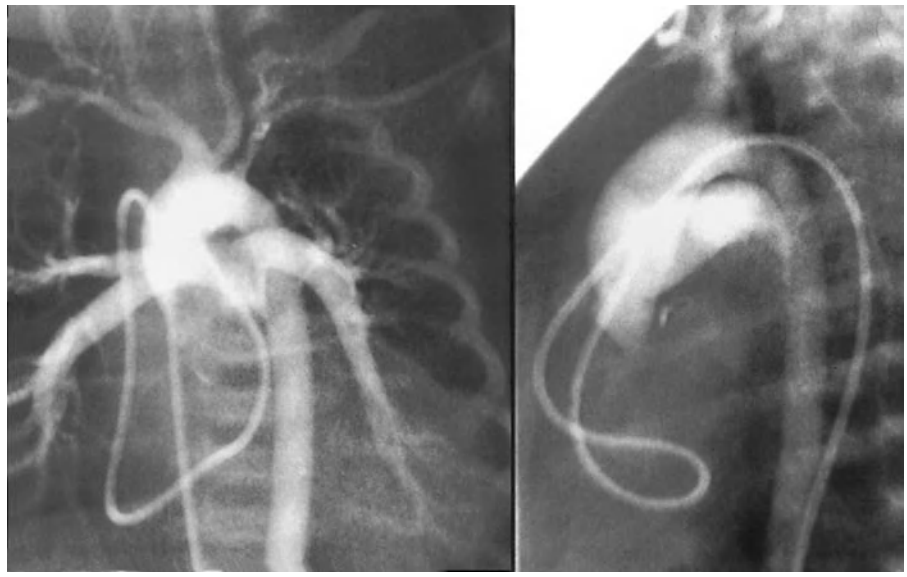

(a) (b)

**Figure 23.24 (a)** Antegrade truncal angiogram in the frontal view demonstrating the truncal root and, distally, the separation of the ascending aorta from the pulmonary arteries. **(b)** Prograde lateral view demonstrating the posterior relationship of the main pulmonary artery take off from the truncus with distal filling of aorta and pulmonary arteries. Reproduced by courtesy of Michael Nihill MD, Baylor College of Medicine.

## Follow-up

Although there have been significant trends toward improved survival in the current era, ongoing morbidity related to conduit obstruction and/or insufficiency, truncal valve abnormalities, and left and right ventricular dysfunction continue to dominate long-term outcomes. Interval echocardiographic imaging allows timely detection of progressive pathology prior to irreversible ventricular dysfunction, the development of a life-threatening hemodynamic state, or loss of opportunity to intervene via nonsurgical routes. As noted above, judicious use of other diagnostic modalities is particularly important during follow-up of patients with repaired truncus arteriosus.

## Acknowledgements

Cardiac catheterization images provided courtesy of Michael Nihill MD, Pediatric Cardiology, Texas Children's Hospital and Baylor College of Medicine, Houston, Texas. Intraoperative medical illustrations provided by Susan Russell Hall, Pediatric Cardiac Surgery, Mary Bridge Children's Hospital, Tacoma, Washington.

## References

1. Lev M, Saphir O. Truncus arteriosus communis persistens. *J Pediatr* 1942;20:74–88.
2. Collett RW, Edwards JE. Persistent truncus arteriosus: A classification according to anatomic types. *Surg Clin North Am* 1949;29:1245.
3. Van Praagh R, Van Praagh S. The anatomy of common aorticopulmonary trunk (truncus arteriosus communis) and its embryologic implications. *Am J Cardiol* 1965;16:406.
4. Crupi G, Macartney FJ, Anderson RH. Persistent truncus arteriosus: a study of 66 autopsy cases with special reference to definition and morphogenesis. *Am J Cardiol* 1977;40:569.
5. Calder L, Van Praagh R, Van Praagh S et al. Truncus arteriosus communis: clinical, angiographic and pathologic findings in 100 patients. *Am Heart J* 1976;92:23.
6. Van Mierop LHS, Patterson DF, Schnarr WR. Pathogenesis of persistent truncus arteriosus in light of observations made in dog embryo with the anomaly. *Am J Cardiol* 1978;41:755.
7. Buchanan G. Malformation of heart: undivided truncus arteriosus heart otherwise double. *Trans Pathol Soc London* 1864;15:89.
8. Tandon R, Hauck AJ, Nadas AS. Persistent truncus arteriosus: a clinical, hemodynamic, and autopsy study of nineteen cases. *Circulation* 1963;28:1050–60.
9. Locatelli G, Alfieri O, Villani M et al. Traitement chirurgical du truncus arteriosus dans la première année de la vie. *Chir Pediatr* 1980;21:89.
10. Kirby ML. Contribution of neural crest to heart and vessel morphology. In: Harvey R, Rosenthal N (eds) *Heart Development.* San Diego, CA: Academic Press, 1999;179–93.
11. Délot EC, Bahamonde ME, Zhao M, Lyons KM. BMP signaling is required for septation of the outflow tract of the mammalian heart. *Development* 2003;130:209–20.
12. Marino B, Digilio MC, Toscano A et al. Anatomic patterns of conotruncal defects associated with deletion 22q11. *Genet Med* 2001;3:45–8.
13. Goldmuntz E, Clark BJ, Mitchell LE et al. Frequency of 22q11 deletions in patients with conotruncal defects. *J Am Coll Cardiol* 1998;32:492–8.
14. Iserin L, de Lonlay P, Viot G et al. Prevalence of the microdeletion 22q11 in newborn infants with congenital conotruncal cardiac anomalies. *Eur J Pediatr* 1998;157:881–4.
15. McElhinney DB, Driscoll DA, Emanuel BS, Goldmuntz E. Chromosome 22q11 deletion in patients with truncus arteriosus. *Pediatr Cardiol* 2003;24:569–73.
16. Van Mierop LHS, Kutsche LM. Cardiovascular anomalies in DiGeorge syndrome and importance of neural crest as a possible pathogenetic factor. *Am J Cardiol* 1986;58:133.
17. Wilson DI, Burn J, Scambler P, Goodship J. DiGeorge syndrome: part of CATCH 22. *J Med Genet* 1993;30:852–6.
18. McElhinney DB, Geiger E, Blinder J et al. NKX2.5 mutations in patients with congenital heart disease. *J Am Coll Cardiol* 2003;42:1650–5.
19. Abushaban L, Uthaman B, Kumar AR, Selvan J. Familial truncus arteriosus: a possible autosomal-recessive trait. *Pediatr Cardiol* 2003;24:64–6.
20. Fan YS, Siu VM. Molecular cytogenetic characterization of a derivative chromosome 8 with an inverted duplication of 8p21.3→p23.3 and a rearranged duplication of 8q24.13→qter. *Am J Med Genet* 2001;102:266–71.
21. Farrell MJ, Stadt H, Wallis KT et al. HIRA, a DiGeorge syndrome candidate gene, is required for cardiac outflow tract septation. *Circ Res* 1999;84:127–35.
22. Wren C, Birrell G, Hawthorne G. Cardiovascular malformations in infants of diabetic mothers. *Heart* 2003;89:1217–20.
23. de la Cruz MV, Pio da Rocha J. An ontogenetic theory for the explanation of congenital malformations involving the truncus and conus. *Am Heart J* 1956;51:782.
24. Kirby ML. Cellular and molecular contributions of the cardiac neural crest to cardiovascular development. *Trends Cardiovasc Med* 1993;3:18–23.
25. Kirby ML, Waldo KL. Role of neural crest in congenital heart disease. *Circulation* 1990; 82:332–40.
26. Bain CWC, Parkinson J. Common aorto-pulmonary trunk: a rare congenital defect. *Br Heart J* 1943;5:97.
27. Carr I, Bharati S, Kusnoor VS, Lev M. Truncus arteriosus communis with intact ventricular septum. *Br Heart J* 1979;42:97.
28. Becker AE, Becker MJ, Edwards JE. Pathology of the semilunar valve in persistent truncus arteriosus. *J Thorac Cardiovasc Surg* 1971;62:16–26.
29. Gelband H, Meter SV, Gersony WM. Truncal valve abnormalities in infants with persistent truncus arteriosus: a clinicopathologic study. *Circulation* 1972;65:397–403.
30. Fuglestad SJ, Danielson GK, Puga FJ, Edwards WD. Surgical pathology of the truncal valve: a study of twelve cases. *Am J Cardiovasc Pathol* 1988;2:39–47.
31. Butto F, Lucas RV, Edwards JE. Persistent truncus arteriosus: pathologic anatomy in 54 cases. *Pediatr Cardiol* 1986;7:95–101.
32. Bengur AR. Truncus arteriosus. In: Garson A, Bricker JT, Fisher DJ, Neish SR (eds) *Science and Practice of Pediatric Cardiology*, Vol. 2. Philadelphia, PA: Lippincott Williams and Wilkins, 1998;1421.

33. Bharati S, McAllister HA Jr, Rosenquist GC et al. The surgical anatomy of truncus arteriosus communis. *J Thorac Cardiovasc Surg* 1974;67:501–10.
34. Suzuki A, Ho SY, Anderson RH, Deanfield JE. Coronary arterial and sinusoidal anatomy in hearts with a common arterial trunk. *Ann Thorac Surg* 1989;48: 792–7.
35. Shrivastava S, Edwards JE. Coronary arterial origin in persistent truncus arteriosus. *Circulation* 1977;55:551.
36. de la Cruz MV, Cayre R, Angelini P et al. Coronary arteries in truncus arteriosus. *Am J Cardiol* 1990;66:1482–6.
37. Anderson KR, McGoon MC. Surgical significance of the coronary arterial anatomy in truncus arteriosus communis. *Am J Cardiol* 1978;41:78–81.
38. Bove EL, Lupinetti FM, Pridjian AK et al. Results of a policy of primary repair of truncus arteriosus in the neonate. *J Thorac Cardiovasc Surg* 1993;105:1057–66.
39. Litovsky SH, Ostfeld I, Bjornstad PG et al. Truncus arteriosus with anomalous pulmonary venous connections. *Am J Cardiol* 1999;83:801–3.
40. Sharma D, Mehta AS, Bharati S, Lev M. Tricuspid atresia with persistent truncus arteriosus. *Chest* 1981;79:363.
41. Shapiro SR, Ruckman RB, Kapur S et al. Single ventricle with truncus arteriosus in siblings. *Am Heart J* 1981;102:456.
42. Marcelletti C, McGoon DC, Mair DD. The natural history of truncus arteriosus. *Circulation* 1976;54:108–11.
43. Pearl JM, Laks J, Drinkwater DC et al. Repair of truncus arteriosus in infancy. *Ann Thorac Surg* 1991;52:780–6.
44. Hanley FL, Heinemann MK, Jonas RA et al. Repair of truncus arteriosus in the neonate. *J Thorac Cardiovasc Surg* 1993;105:1047–56.
45. Thompson LD, McElhinney DB, Reddy MV et al. Neonatal repair of truncus arteriosus: continuing improvement in outcomes. *Ann Thorac Surg* 2001;72:391–5.
46. Imamura M, Drummond-Webb JJ, Sarris GE et al. Improving early and intermediate results of truncus arteriosus repair: a new technique of truncal valve repair. *Ann Thorac Surg* 1999;67:1142–6.
47. Jahangiri M, Zurakowski D, Mayer JE et al. Repair of truncal valve and associated interrupted arch in neonates with truncus arteriosus. *J Thorac Cardiovasc Surg* 2000;119:508–14.
48. McElhinney DB, Reddy VM, Rajasinghe HA et al. Trends in the management of truncal valve insufficiency. *Ann Thorac Surg* 1998;65:517–24.
49. Brown JW, Ruzmetov M, Okada Y et al. Truncus arteriosus repair: outcomes, risk factors, reoperation and management. *Eur J Cardiothorac Surg* 2001;20:221–7.
50. Pearl JM, Laks H, Drinkwater Jr DC et al. Repair of truncus arteriosus in infancy. *Ann Thorac Surg* 1991;52:780–6.
51. Yankah AC, Alexi-Meskhishvili V, Weng Y et al. Accelerated degeneration of allografts in the first two years of life. *Ann Thorac Surg* 1995;60:S71–S77.
52. Rajasinghe HA, McElhinney DB, Reddy VM et al. Long-term follow-up of truncus arteriosus repaired in infancy: a twenty-year experience. *J Thorac Cardiovasc Surg* 1997;113:869–78.
53. Dearani JA, Danielson GK, Puga FJ et al. Late follow-up of 1095 patients undergoing operation for complex congenital heart disease utilizing pulmonary ventricle to pulmonary artery conduits. *Ann Thorac Surg* 2003;75:399–410.
54. Lloyd TR, Marvin WJ, Mahoney LT, Lauer RM. Balloon dilation valvuloplasty of bioprosthetic valves in extracardiac conduits. *Am Heart J* 1987;114:268–74.
55. Ensing GJ, Hagler DJ, Seward JB et al. Caveats of balloon dilation of conduits and conduit valves. *J Am Coll Cardiol* 1989; 14:397–400.
56. Powell AJ, Lock JE, Keane JF et al. Prolongation of RV-PA conduit life span by percutaneous stent implantation. Intermediate term results. *Circulation* 1995;92:3282–8.
57. Bonhoeffer B, Boudjemline Y, Saliba Z et al. Transcatheter implantation of a bovine valve in the pulmonary position. *Circulation* 2000;102:813–16.
58. Hoerstrup SP, Sodian R, Daebritz S et al. Functional living trileaflet heart valves grown in vitro. *Circulation* 2000;102(19 Suppl 3):III44–9.
59. Rice MJ, Seward JB, Hagler DJ et al. Definitive diagnosis of truncus arteriosus by two dimensional echocardiography. *Mayo Clin Proc* 1982;57:476.
60. Smallhorn JF, Anderson RH, Macartney FJ. Two dimensional echocardiographic assessment of communications between ascending aorta and pulmonary trunk or individual pulmonary arteries. *Br Heart J* 1982;47:563.
61. Marin-Garcia J, Tonkin LD. Two dimensional echocardiographic evaluation of persistent truncus arteriosus. *Am J Cardiol* 1982; 50:1376.
62. Riggs TW, Paul MH. Two-dimensional echocardiographic prospective diagnosis of common truncus arteriosus in infants. *Am J Cardiol* 1982;50:1380.
63. Mello M, McElhinney DB, Parry AJ et al. Truncus arteriosus with patent ductus arteriosus and normal aortic arch. *Ann Thorac Surg* 1997;64:1808–10.
64. Copel JA, Pilu G, Green J et al. Fetal echocardiographic screening for congenital heart disease: the importance of the four-chamber view. *Am J Obstet Gynecol* 1987;157:648–55.
65. Tometzki AJ, Suda K, Kohl T et al. Accuracy of prenatal diagnosis and prognosis of fetuses with conotruncal anomalies. *J Am Coll Cardiol* 1999;33:1696–701.
66. Duke C, Sharland GK, Jones AM, Simpson JM. Echocardiographic features and outcome of truncus arteriosus diagnosed during fetal life. *Am J Cardiol* 2001;88:1379–84.
67. Volpe P, Paladini D, Marasini M et al. Common arterial trunk in the fetus: characteristics, associations, and outcome in a multicentre series of 23 cases. *Heart* 2003;89:1437–41.
68. Sklansky M. Advances in fetal cardiac imaging. *Pediatr Cardiol* 2004;25:307–21.
69. Muhler MR, Rake A, Schwabe M et al. Truncus arteriosus communis in a midtrimester fetus: comparison of prenatal ultrasound and MRI with postmortem MRI and autopsy. *Eur Radiol* 2004;14:2120–4.
70. Ungerleider RM, Kisslo J, Greeley WJ et al. Intraoperative echocardiography during congenital heart surgery: experience from 1000 cases. *Ann Thorac Surg* 1995;60:S539–42.
71. Muhiudeen IA, Roberson DA, Silverman NH et al. Intraoperative echocardiography in infants and children with congenital cardiac shunt lesions: transesophageal versus epicardial echocardiography. *J Am Coll Cardiol* 1990;16:1687–95.
72. Dorfman AL, Geva T. Magnetic resonance imaging evaluation of congenital heart disease: conotruncal anomalies. *J Cardiovasc Magn Reson* 2006;8:645–59.
73. Brenner D, Elliston C, Hall E, Berdon W. Estimated risks of radiation-induced fatal cancer from pediatric CT. *AJR Am J Roentgenol* 2001;176:289–96.

# 24 Transposition of the Great Arteries

**Luc L. Mertens[1], Manfred Otto Vogt[2], Jan Marek[3] and Meryl S. Cohen[4]**

[1]The Hospital for Sick Children, Toronto, Canada
[2]Clinic for Pediatric Cardiology and Congenital Heart Disease, German Heart Center Munich, Munich, Germany
[3]Great Ormond Street Hospital for Children, London, United Kingdom
[4]Department of Pediatrics, University of Pennsylvania School of Medicine, The Children's Hospital of Philadelphia, Philadelphia, PA, USA

## Definition

Transposition of the great arteries (TGA) is a conotruncal abnormality in which the aorta arises from the right ventricle (RV) and the pulmonary artery arises from the left ventricle (LV) resulting in ventriculo-arterial discordance. This anomaly can occur in isolation or in association with other cardiac defects. The most common intracardiac anomaly associated with TGA is a ventricular septal defect (VSD). In this chapter we focus on TGA with atrioventricular concordance. Congenitally corrected transposition (atrioventricular and ventriculo-arterial discordance) is discussed in Chapter 26. Transposition of the great arteries is also referred to as D-TGA. This is, however, a nonspecific term as the "D" might relate to the ventricular loop (D or L) or to the spatial position of the aortic and pulmonary valves. In the majority of patients with TGA, the aorta is malpositioned rightward and anterior to the pulmonary artery, but there is wide variability in the spatial relationships between the great vessels in the context of ventriculo-arterial discordance. Therefore the term D-TGA is better avoided; *D-loop TGA* is more specific, where the D-loop refers to the ventricular looping. In this chapter the term TGA is used to describe situs solitus, atrioventricular concordance, and ventriculo-arterial discordance. This anatomic type of TGA results in parallel systemic and pulmonary circulations in which the deoxygenated systemic venous blood returns to the aorta via the RV and the oxygenated pulmonary venous blood returns to the pulmonary arteries through the LV (Fig. 24.1). Clinical presentation occurs early in the neonatal period because of cyanosis.

## Incidence

The incidence of TGA is approximately 31.5 per 100 000 live births (range 23.1 to 38.8 per 100 000 live births). It is the 10th most common congenital heart defect and the second most common cyanotic lesion after tetralogy of Fallot [1]. The incidence is likely higher in the fetal population because termination of pregnancy is not included in most population studies. TGA affects males more commonly than females, with a ratio of over 2:1 [2]. Chromosomal anomalies in association with simple and complex forms of TGA are unusual. The incidence of TGA does not appear to be impacted by increased maternal age or increased parity [2].

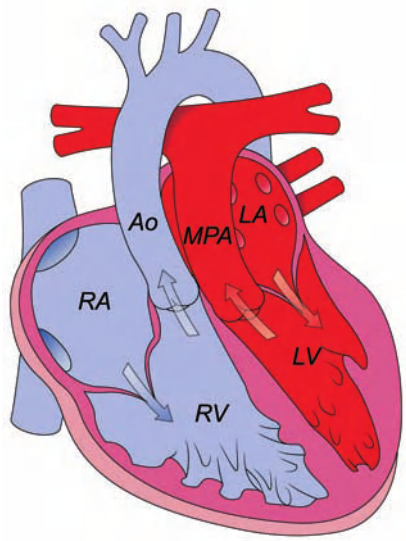


**Figure 24.1** Diagram of D-loop transposition of the great arteries with atrioventricular concordance and ventriculo-arterial discordance. Ao, aorta; LA, left atrium; LV, left ventricle; MPA, main pulmonary artery; RA, right atrium; RV, right ventricle.

*Echocardiography in Pediatric and Congenital Heart Disease: From Fetus to Adult*
Edited by Wyman W. Lai, Luc L. Mertens, Meryl S. Cohen and Tal Geva
 ISBN: 978-1-405-17401-5

## Etiology

The etiology of TGA remains unknown; however, a genetic cause is probable in most cases. Familial recurrence occurs in TGA; 10% of afflicted individuals have a relative with a congenital heart defect. Of those affected, TGA is the most common recurrent lesion [3]. Environmental factors have been implicated as well. Congenital heart disease is seen in infants of diabetic mothers, with TGA being the most common of these defects [4]. Exposure to the teratogen retinoic acid during gestation has also been associated with the development of TGA. Although 22q11 deletion is common in other conotruncal anomalies such as tetralogy of Fallot and truncus arteriosus, it is quite rare in TGA [5]; however, single-gene mutations such as *CFC1* have been reported [6].

## Morphology and classification

### Developmental considerations

The developmental mechanisms leading to TGA have not been fully elucidated. The cardiac outflow tract, including the muscular conus and the truncus arteriosus, develops with contributions from neural crest cells and from the anterior heart field, which also forms large portions of the RV. Mesenchymal cells derived from the neural crest contribute to the septum that divides the truncus arteriosus into the aorta and pulmonary artery. In the early developmental stages, the great vessels relate to each other in a way similar to TGA. Conotruncal rotation associated with septation and differential development of the infundibulum is required to align the aorta with the LV and the pulmonary artery with the RV. Abnormal conotruncal rotation as septation occurs probably results in TGA. This is suggested in the perlecan-deficient mouse embryo model that develops TGA with intact ventricular septum. Perlecan is a heparin-sulfate proteoglycan expressed in extracelluluar matrices. In this model, the mesenchyme of the outflow tract is disrupted. Outflow ridges normally twist in a counterclockwise pattern but in TGA this spiral likely does not occur, resulting in a "straight" outlet [7,8].

### Anatomy

#### TGA with intact ventricular septum

In the commonest form of TGA, the segmental anatomy is typically situs solitus with atrioventricular concordance and ventriculo-arterial discordance, with the aorta anterior and to the right of the pulmonary artery. This has also been described as {S,D,D}: the situs of the visceral organs and the atria is normal (solitus = S), the ventricles are D-looped (D), the atrioventricular alignment is concordant, and the ventriculo-arterial alignment is discordant with a rightward and anterior position of the aortic valve relative to the pulmonary valve (D, or dextro-malposition). The foramen ovale is usually patent; a true ostium secundum atrial septal defect is less common. In some cases, the aorta is directly anterior to the pulmonary artery and in others the great vessels are side by side, with the aortic valve to the right of the pulmonary valve. Rarely, the aorta can be leftward, in which case the segmental anatomy is {S,D,L}. This arrangement is typically associated with RV hypoplasia and superior-inferior ventricles. More rarely, the aortic valve can be located in a posterior and rightward position relative to the pulmonary valve (TGA with posterior aorta) [9]. For each patient the spatial relationship between the great vessels needs to be clearly defined on echocardiography.

The anatomy of the ventricular outflow tracts in TGA is important for surgical management. In almost 90% of cases of TGA there is a subaortic conus (infundibulum) separating the aortic valve from the tricuspid valve and absence of the subpulmonary conus, resulting in fibrous continuity between the mitral and pulmonary valves [9,10]. Abnormalities in the outflow tracts can result in outflow tract obstruction, which is important when considering surgical management. Variants of outflow tract or conal anatomy are seen in roughly 12% of patients – bilateral subarterial conus in ~7%, subpulmonary conus without subaortic conus in ~3%, and bilaterally absent conus in ~2% of patients with TGA [11]. Atypical outflow tract anatomy can be associated with outflow tract obstruction, VSD and unusual coronary anatomy.

In the setting of TGA with intact ventricular septum, a left aortic arch without obstruction is the norm. However, rare cases of coarctation of the aorta have been reported [12]. Systemic and pulmonary venous connections are usually normal. Dynamic LV outflow tract obstruction can be seen when LV pressure is subsystemic. This usually resolves after anatomic correction (see below). Fixed anatomic subpulmonary stenosis is rare. Most patients with TGA have a patent ductus arteriosus (PDA).

#### TGA with ventricular septal defect

Apart from patent foramen ovale and PDA, VSD is the most commonly associated defect, occurring in approximately 40–45% of cases. Similar to normally related great arteries, any type of VSD can be seen in association with TGA. Approximately 33% of patients have a perimembranous (membranous) defect, some 30% have a malalignment defect (often associated with obstruction of one of the outflow tracts), about 25% have a muscular defect, and roughly 5% each have an atrioventricular (AV) canal-type (inlet) or outlet septal (doubly committed subarterial or conal septal) defect (Fig. 24.2) [13]. Membranous defects may be large or restrictive and result in fibrous continuity between the tricuspid and the pulmonary valve leaflets. Spontaneous closure or restriction of the defect by tricuspid valve septal tissue is possible. Muscular defects can occur anywhere within the muscular septum (most commonly the mid-muscular

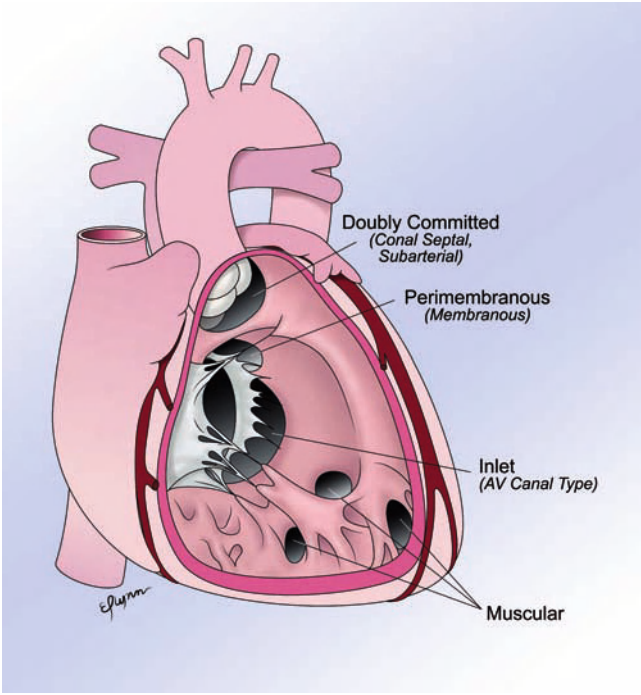


**Figure 24.2** Different types of ventricular septal defects in the setting of transposition. AV, atrioventricular.

region) and are often multiple. Muscular defects can also close or decrease in size spontaneously. In those with AV canal-type VSD, the tricuspid valve may straddle the ventricular septum, usually with associated RV hypoplasia. Outlet septal defects (doubly committed subarterial or conal septal defect) are characterized by deficiency or absence of the outlet (conal) septum with little or no muscular separation between the aortic and pulmonary valves. Surgical closure of this type of VSD can be challenging because the sutures must be anchored into the fibrous rim between the aortic and pulmonary valves, potentially distorting one or both semilunar valves.

Malalignment VSDs are of particular surgical importance. In the setting of anterior malalignment of the outlet (conal) septum the VSD is generally large and unrestrictive. This anatomy typically results in impingement on the RV outflow tract with multiple levels of obstruction. Subaortic stenosis and aortic annulus hypoplasia are common; distal obstruction can include aortic arch hypoplasia, coarctation of the aorta, or interruption of the aortic arch. By contrast, posterior malalignment of the outlet septum is often associated with LV outflow tract obstruction, including subvalvar and valvar pulmonary stenosis. In addition to posterior deviation of the outlet septum into the LV outflow tract, other potential mechanisms of pulmonary outflow obstruction include a discrete fibrous ring, muscular tunnel narrowing, abnormal mitral valve attachments, and redundant or straddling tricuspid valve tissue (Fig. 24.3). The pulmonary valve annulus may be hypoplastic and the pulmonary valve leaflets and commissures are often abnormal (e.g., bicuspid or unicuspid pulmonary valve).

## Coronary artery anatomy

Coronary artery anatomy is particularly important in TGA given that the majority of patients today undergo the arterial

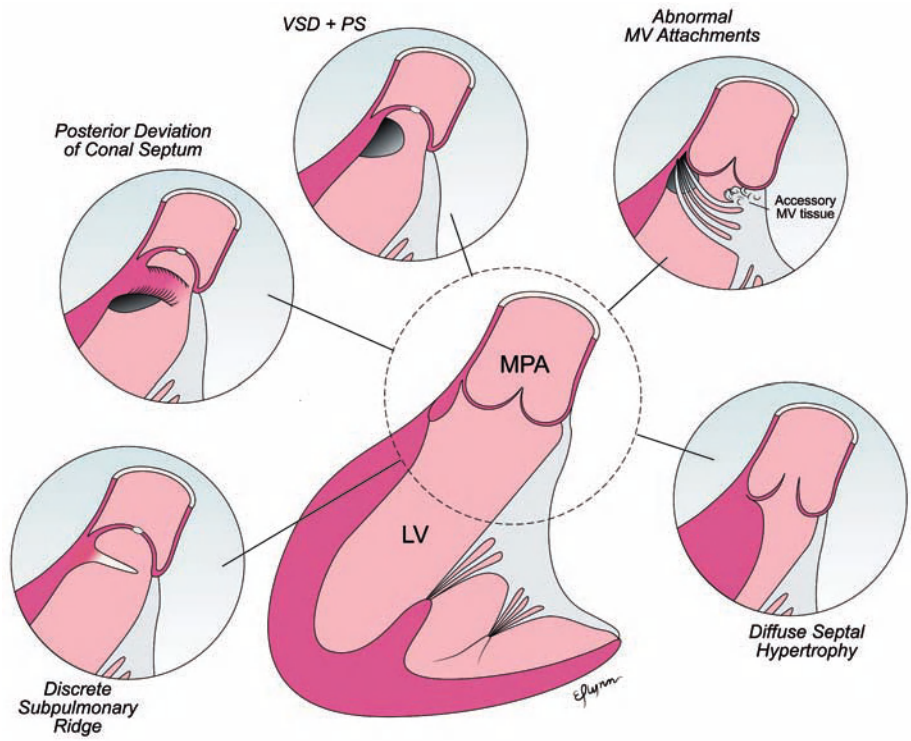


**Figure 24.3** Different mechanisms of left ventricular outflow obstruction in D-loop transposition of the great arteries (TGA). More than one mechanism can be present. LV, left ventricle; MPA, main pulmonary artery; MV, mitral valve; PS, pulmonary stenosis; VSD, ventricular septal defect.

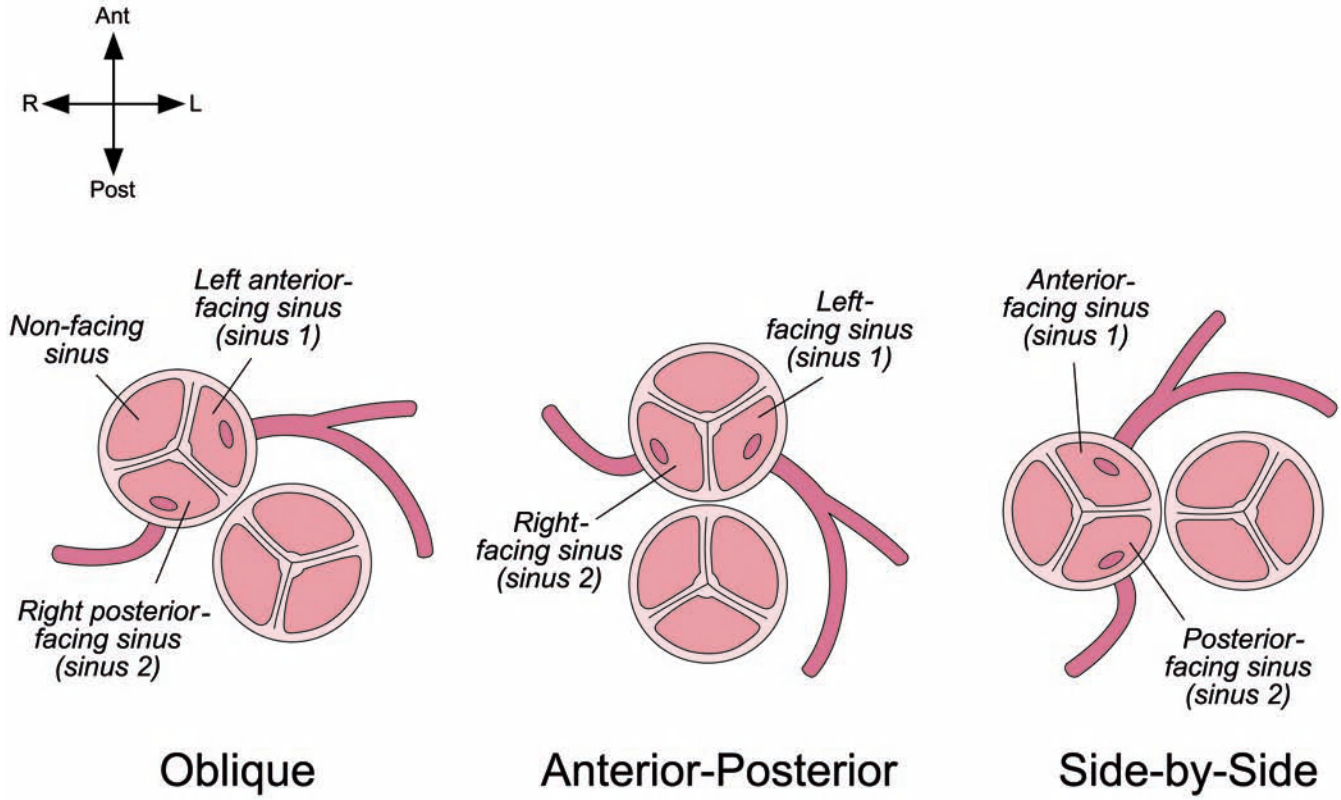


**Figure 24.4** Designations of the aortic sinuses of Valsalva when the spatial orientation of the aortic and pulmonary roots is oblique, anterior-posterior, and side-by-side. Ant, anterior; Post, posterior; R, right; L, left.

switch operation (ASO), which requires translocation of the coronary arteries to the neoaorta. Although the origin and proximal course of the coronary arteries is variable, in almost all cases these arteries originate from aortic sinuses facing the pulmonary valve. The aortic sinuses that face the pulmonary root are labeled according to their spatial location [14]. In the majority of patients, in whom the aortic valve is anterior and rightward relative to the pulmonary valve, the sinuses are termed right-posterior- and left-anterior-facing sinuses. When the aortic valve is directly anterior the sinuses are termed right- and left-facing sinuses, and when the great vessels are side by side the sinuses are termed posterior- and-anterior-facing sinuses (Fig. 24.4). Alternative taxonomies assign numbers or letters to the facing sinuses [15,16]. The Leiden terminology describes the origin of the coronary arteries from the facing aortic sinuses of Valsalva as viewed from the luminal aspect of the aorta. From this side, the observer takes a stance in the noncoronary sinus looking toward the pulmonary trunk (Fig. 24.4). Viewed from this position one sinus is always to the right of the observer (sinus 1) and the other sinus is always to the left of the observer (sinus 2). This definition holds irrespective of the relationship of the arterial trunks toward each other.

The eight major anatomic patterns of the coronary arteries in TGA are illustrated in Fig. 24.5. Based on three studies encompassing 533 patients [17–19], the most common or "usual" pattern of coronary artery origin – left anterior descending (LAD) and left circumflex (LCx) arising from the left-facing sinus (sinus 1) and the right coronary artery (RCA) arising from the right-facing sinus (sinus 2) – is present in 65% of patients. The second most common form – LAD from the left-facing sinus (sinus 1) and RCA and LCx from the right-facing sinus (sinus 2) – is present in 13.6% of patients. The LCx courses posterior to the pulmonary root before reaching the left atrioventricular groove. The third most common pattern seen in 7.5% of cases is a single RCA arising from the right-facing sinus (sinus 2) where the LCA passes posterior to the pulmonary root before bifurcating into the LAD and LCx branches. Other variations include a single LCA from the left-facing sinus (sinus 1) in 1.5% of cases, inverted coronary arteries (RCA from sinus 1 and LAD and LCx from sinus 2) in 2.6% of cases, and inverted RCA and LCx (RCA and LAD from sinus 1 and LCx from sinus 2) in 6% of cases. Intramural LCA and RCA are seen in 3% and 0.75% of patients, respectively. Based on analysis of nine studies from over two decades (total of 1942 patients),

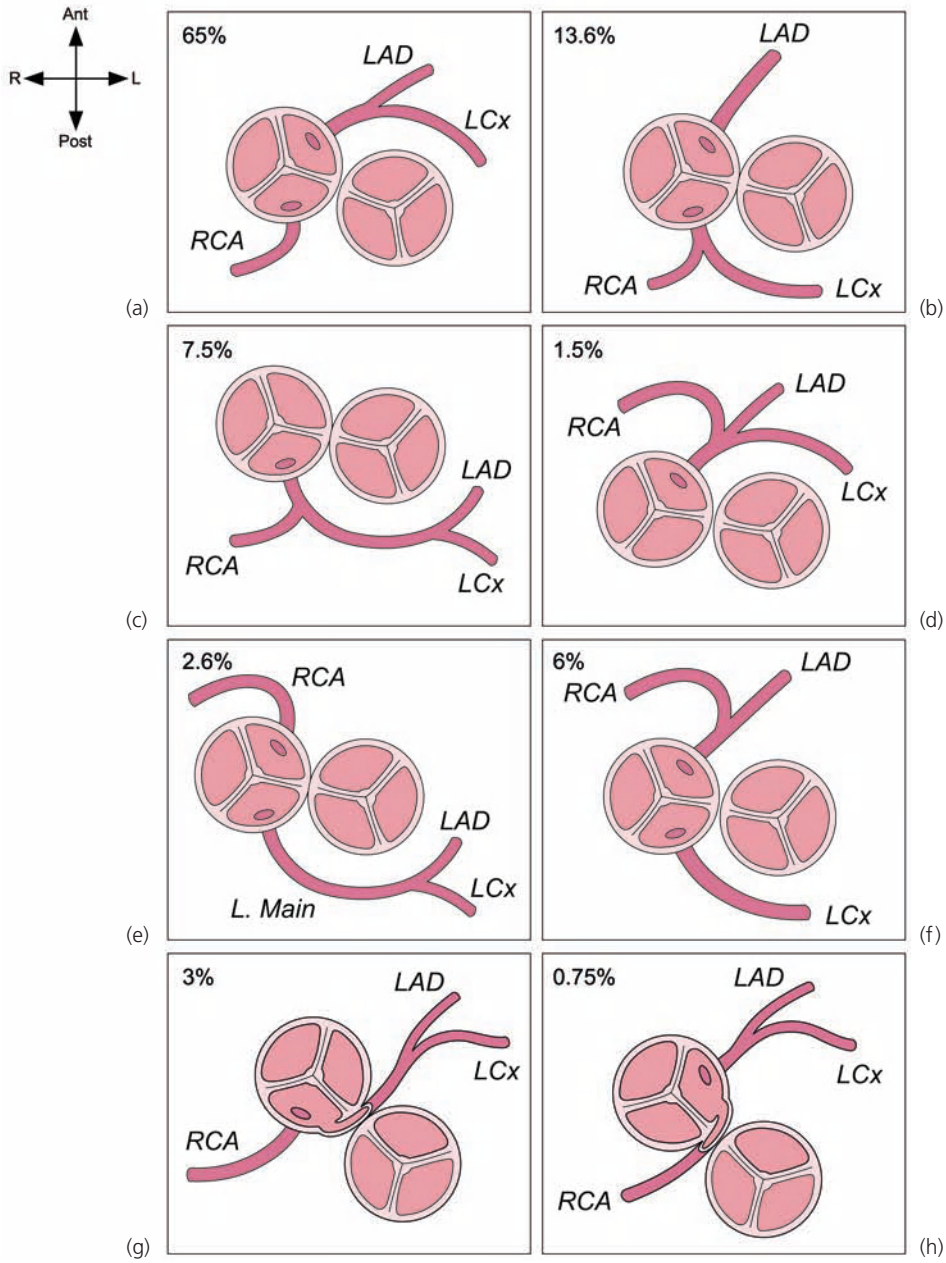


**Figure 24.5** The most common patterns of coronary anatomy in patients with D-loop transposition of the great arteries (TGA). **(a)** Usual coronary anatomy with left coronary artery (LCA) coming from sinus 1 and right coronary artery (RCA) coming from sinus 2. **(b)** Left circumflex (LCx) from RCA (sinus 2) and left anterior descending (LAD) coming from sinus 1. **(c)** Single coronary coming from sinus 2. **(d)** Single coronary artery coming from sinus 1. **(e)** Inverted origins with RCA coming from sinus 1 and LCA coming from sinus 2. **(f)** LAD and RCA coming from sinus 1 and LCx coming from sinus 2. **(g)** Intramural LCA with origin of LCA and RCA both from sinus 2 and intramural course of LCA. (h) Intramural RCA with origin of RCA and LCA from sinus 1 and intramural course of RCA.

Pasquali et al. found that intramural or single coronary artery patterns were associated with an increased risk of death in patients undergoing an ASO [20].

### Associated defects

In addition to patent foramen ovale, PDA, and VSD, TGA has been reported to be associated with a myriad of cardiovascular anomalies such as anomalies of the systemic (e.g., persistent left superior vena cava) and pulmonary veins (e.g., partially and totally anomalous pulmonary venous connections [21]), common AV canal, anomalies of the atrioventricular valves (e.g., stenosis, cleft, abnormal attachments, straddling [22]), left and right ventricular outflow tract abnormalities, and anomalies of the great vessels (e.g., aortic arch hypoplasia, interruption [23], coarctation, and double aortic arch [24]). Leftward juxtaposition of the atrial appendages occurs in approximately 2% of cases of TGA [25]. It is usually seen in association with other complex abnormalities such as dextrocardia and tricuspid atresia.

## Pathophysiology

The parallel arrangement of the systemic and pulmonary circulations in TGA is tolerated well before birth due to mixing of oxygenated and deoxygenated blood through the foramen

ovale and PDA. After birth, the decrease in pulmonary vascular resistance leads to increased pulmonary venous return to the left atrium, which is accentuated by flow from the aorta to the pulmonary artery through the PDA. If septum primum (valve of the fossa ovale) effectively seals off the intraatrial communication, severe hypoxia may occur within the first hours of life. In other cases, the foramen ovale remains open, allowing oxygenated blood returning to the left atrium to shunt from left to right, mixing with the deoxygenated blood returning from the systemic veins. When present, a VSD provides another opportunity for mixing of blood between the left and right sides of the heart, although it may not provide enough effective pulmonary blood flow.

The RV (systemic ventricle) is generally larger compared with the LV. The difference in size is not striking in the neonatal period because the LV is initially at systemic pressure. In the weeks after birth, pulmonary vascular resistance decreases and, in the absence of a large VSD or outflow tract obstruction, the afterload on the LV decreases. This causes the LV to remodel with a thinner free wall and a smaller short-axis diameter. The RV meanwhile remains hypertrophied and dilated. Ultimately, LV mass decreases (deconditioning) to a level that precludes its ability to sustain the systemic circulation after the ASO. Thus, in patients with TGA and intact ventricular septum or a small VSD, anatomic repair should be performed within the first weeks of life in order to avoid LV remodeling. For patients presenting after 2 months of life, careful preoperative assessment of LV size, wall thickness and mass is required. Other factors that should be taken into account include a large PDA or persistent pulmonary hypertension. This late presentation is rare as most infants with isolated TGA present early after birth with cyanosis.

## Imaging

Echocardiography is the imaging modality of choice in children with TGA, and currently most patients are referred for cardiac surgery based solely on echocardiographic diagnosis. Therefore, a comprehensive, detailed description of cardiovascular anatomy and suitability for surgical repair is paramount for successful management. In addition, echocardiography is often used as the primary imaging modality to guide balloon atrial septostomy.

### Goals of the preoperative examination

The goals of preoperative echocardiographic examination in the setting of TGA can be summarized as follows:

- Determine the segmental anatomy.
- Assess systemic and pulmonary venous connections to the heart.
- Evaluate the atrial septum for interatrial communication(s): location, size, and flow direction and velocity; measure mean transseptal flow gradient.
- Rule out juxtaposition of atrial appendages.
- Evaluate atrioventricular valve morphology (e.g., cleft, straddling, abnormal attachments) and function (e.g., stenosis, regurgitation).
- Determine biventricular size and function.
- Determine presence of VSD:
  - single or multiple defects;
  - location and size;
  - restriction to flow;
  - direction of flow.
- Demonstrate ventriculo-arterial connections:
  - position of aorta relative to the pulmonary artery at the level of the semilunar valves;
  - assessment of commissural alignment;
  - determination of presence and severity of outflow tract obstruction; if present, mechanism of obstruction;
  - semilunar valve anatomy and function (e.g., stenosis or regurgitation);
  - type of infundibulum (e.g., subaortic, bilateral, subpulmonary, bilaterally absent).
- Determine coronary artery anatomy.
- Establish presence, size and direction of flow through a PDA.
- Evaluate aortic arch sidedness; rule out aortic arch hypoplasia or coarctation.

### Imaging of TGA with intact ventricular septum

The subcostal acoustic window provides a wide-angle view of the heart and blood vessels and allows rapid diagnosis of TGA. After establishing the situs of the abdominal organs, a sweep of the transducer from the subcostal window in the oblique coronal plane demonstrates the systemic and venous connections to the heart, the atrial septum, atrioventricular and ventriculo-arterial connections and alignments, and the great vessels. As the transducer is swept from posterior-inferior to superior-anterior (Videoclip 24.1), the main pulmonary artery is seen originating directly from the LV bifurcating into the left and right pulmonary arteries (Fig. 24.6a). Further anterior tilt of the transducer demonstrates the origin of the aorta from the rightward and superior aspect of the RV, supported by infundibular muscle (Fig. 24.6b). Origin of the coronary arteries from the aortic root, often seen from the subcostal window, helps establish the identity of the aorta. Rotating the transducer clockwise roughly 90° to the ventricular short axis (oblique sagittal plane) demonstrates the superior-inferior and anterior-posterior relations of the cardiovascular structures. The transducer is swept from right to left, beginning at the bicaval view and ending at the level of the ventricular apex. This view is particularly helpful in demonstrating the connection of the right upper pulmonary vein to the left atrium, the atrial septum, the anatomy of the AV valves and their attachments, and the outflow tracts of both ventricles. In TGA, this view demonstrates the parallel course of the great arteries

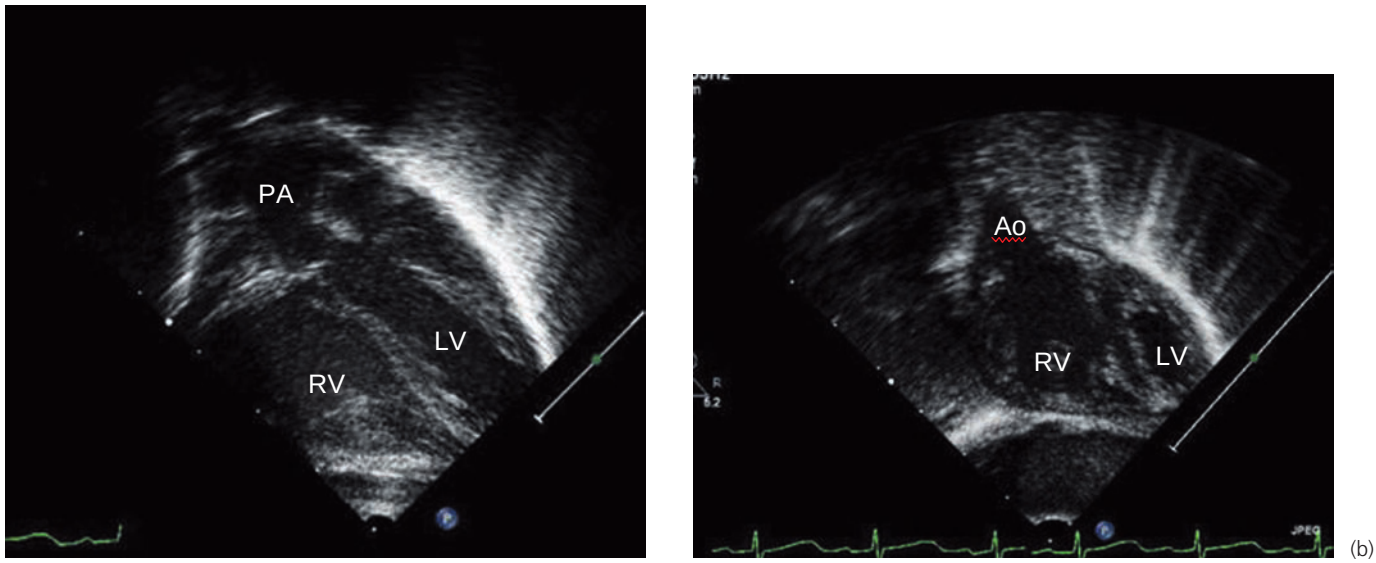


(a) (b)

**Figure 24.6** Subcostal long-axis views showing ventriculo-arterial discordance. **(a)** The main pulmonary artery (PA) is seen coming off the left ventricle (LV); **(b)** the aorta (Ao) is visible coming from the right ventricle (RV).

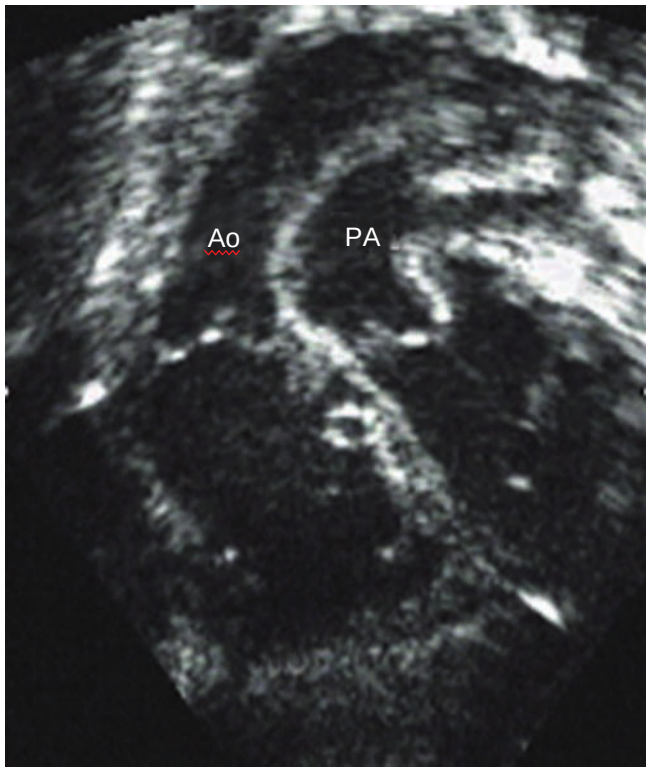


**Figure 24.7** Subcostal short-axis view showing parallel great arteries off each ventricle with the aorta (Ao) anterior to the pulmonary artery (PA).

(Fig. 24.7). Interrogation of blood flow by color Doppler provides essential information about atrial and ventricular septal defects, valve function, outflow tract obstruction, semilunar valve functions, and PDA. Evaluation of the atrial septum from the subcostal window includes determination of location and size of interatrial communications and assessment of the direction and velocity of blood flow. In most patients, atrial-level flow is from left to right. The mean gradient of the flow across the atrial septum should be measured by spectral Doppler.

The apical window allows evaluation of the ventricular inflow and outflow tracts and the ventricular septum. This view is ideal for assessment of the atrioventricular valves, by color and spectral Doppler, for stenosis or regurgitation. Careful interrogation of the ventricular septum with particular attention to the apex is important to exclude VSDs. In addition, the apical window provides an optimal angle of Doppler interrogation of the LV outflow tract for assessment of obstruction.

The parasternal window provides complementary anatomic and functional information. The parallel course of the great arteries is apparent in the parasternal long-axis view, in which both great vessels can be imaged longitudinally in the same plane (Fig. 24.8 and Videoclip 24.2). Although a parallel course of the aorta and main pulmonary artery in the same plane is not seen with normally related great vessels, it is important to recognize that it is not unique to TGA. For example, this anatomic arrangement is also seen in double-outlet right ventricle and congenitally corrected TGA. The parasternal long-axis view also demonstrates the fibrous continuity between the mitral and pulmonary valves in those with the typical subaortic conus. The aortic valve is seen anterior to the pulmonary valve and is supported by an infundibulum.

The parasternal short-axis plane is used to determine the spatial relationships between the semilunar valves and great

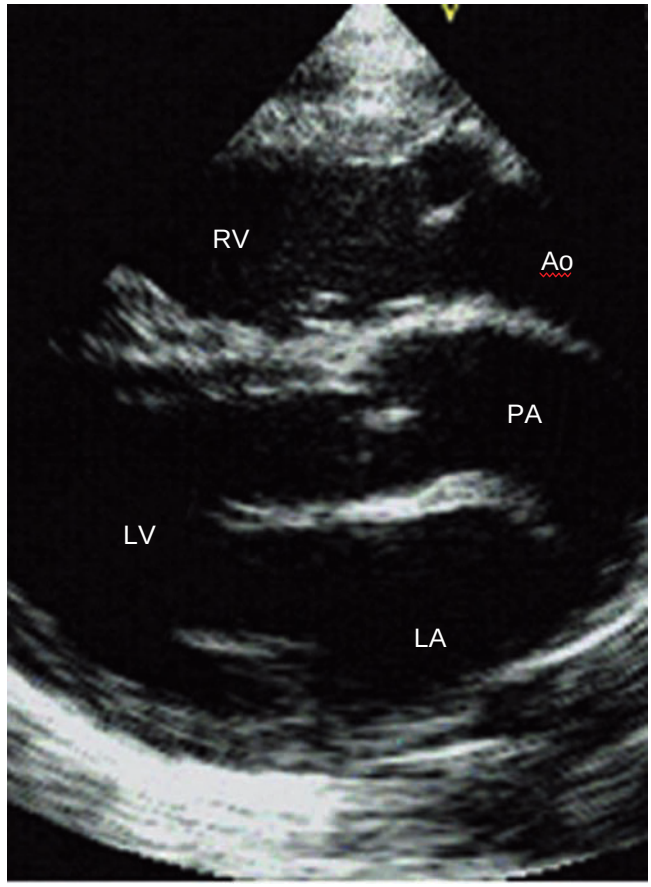


**Figure 24.8** Parasternal long-axis view showing parallel great artery orientation off each ventricle. Also the fibrous continuity between the mitral and the pulmonary valve can be seen. Ao, aorta; LA, left atrium; PA, pulmonary artery; RV, right ventricle; LV, left ventricle.

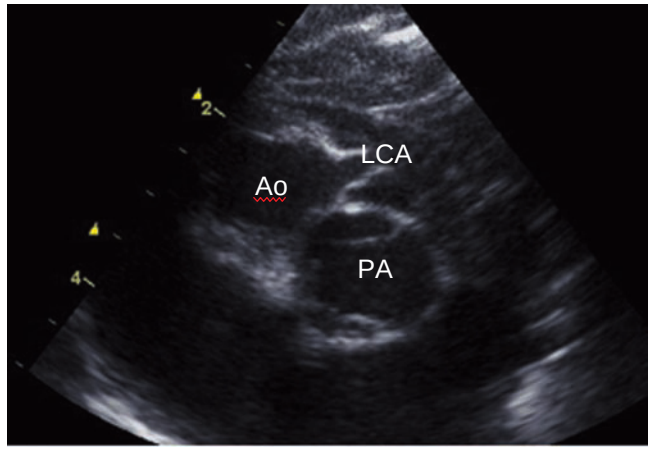


**Figure 24.9** Parasternal short-axis view demonstrating the spatial relationship between the great vessels. The aorta (Ao) is positioned anterior and to the right of the pulmonary artery (PA). The left coronary artery (LCA) is seen coming off the aorta anteriorly and leftwards.

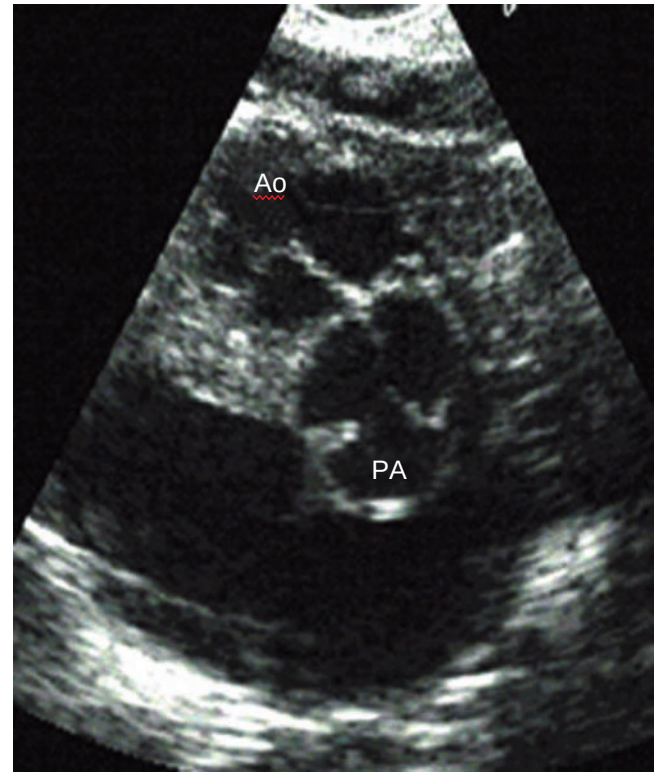


**Figure 24.10** Parasternal short-axis view demonstrating commissural alignment of the aortic (Ao) and pulmonary (PA) valves. The typical alignment of the commissures of the anterior aortic valve and the posterior pulmonary valve can be demonstrated.

vessels (Fig. 24.9 and Videoclip 24.3). The parallel orientation of the aorta and main pulmonary artery accounts for their simultaneous appearance in cross-section as two circles in a parasternal short-axis plane. Most commonly, the aortic valve is anterior and to the right of the pulmonary valve, but other relationships (e.g., side-by-side, anterior, leftward) are possible. In the majority of patients the aortic and pulmonary valves can be viewed simultaneously in the short-axis plane. Imaging from the high left parasternal position or through the manubrium sterni often optimizes this view. In most patients it is possible to obtain an image in which the commissures between aortic and pulmonary valve leaflets can be viewed simultaneously (Fig. 24.10). This is useful for assessing the commissural alignment between the valve leaflets, which is important for coronary transfer during the ASO (Videoclip 24.4). In some patients, this view cannot be obtained due to the superior position of the aortic valve relative to the pulmonary valve.

Assessment of biventricular size and function can be performed in multiple views. Assessment includes ventricular dimensions, wall thickness, and measures of systolic and diastolic performance. Biventricular systolic function is usually preserved in infants with TGA unless severe hypoxia and metabolic acidosis is present.

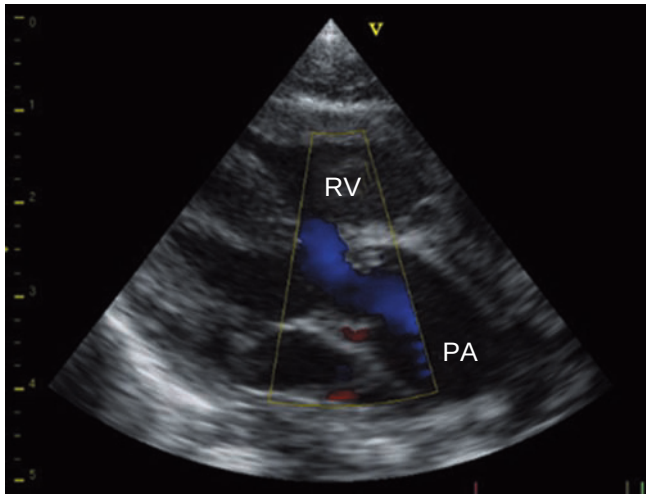


**Figure 24.11** Transposition of the great arteries with a perimembranous ventricular septal defect (VSD). On this slightly tilted parasternal long-axis view a perimembranous VSD with shunt from the right ventricle (RV) to the pulmonary artery (PA) is seen.

### Imaging of TGA with ventricular septal defect

Description of the location of VSDs in TGA is identical to that in patients with concordant ventriculo-arterial connections. A perimembranous VSD, the most common defect in TGA, is imaged from several imaging planes, including subcostal coronal (long-axis) and sagittal (short-axis), apical, parasternal short-axis, and tilted long-axis views (Fig. 24.11 and Videoclip 24.5(a,b)). In contrast to normally related great arteries, the parasternal short-axis view in TGA does not highlight membranous defects as well because of the relationship of the great arteries.

Muscular VSDs are identified by imaging in multiple cross-sectional planes. The location of these defects is variable and requires detailed interrogation of the entire septum by two-dimensional (2D) imaging and color Doppler. The apical 4-chamber view is particularly helpful for evaluation of the ventricular septum although the anterior-superior aspects of the septum are not seen optimally in this view. This view best depicts the basal (AV canal or inlet septum) and apical segments of the septum. The subcostal and parasternal short-axis views are helpful in evaluating the anterior-superior and posterior-inferior aspects of the septum as well as the mid-septum. Moderate–large defects can be easily detected using 2D imaging, whereas small defects are usually best visualized using color Doppler. Lowering the Nyquist limit of the color Doppler scale is important for delineating VSDs in TGA given the often equal or near-equal pressures in the left and right ventricles.

Malalignment defects (conoventricular septal defects) with anterior deviation of the outlet (conal) septum are readily seen in most imaging planes (Fig. 24.12 and Videoclip 24.6(a,b)). The subcostal sagittal view is particularly suitable to visualize the displaced outlet septum and associated RV outflow obstruction. This view is also used to measure the pressure gradient using pulsed-wave and continuous-wave Doppler. The presence of RV outflow tract narrowing should prompt careful assessment of the aortic arch and isthmus for obstruction.

Malalignment defects (conoventricular septal defects) with posterior deviation of the outlet (conal) septum are best viewed from the subcostal long- and short-axis views and from the parasternal long-axis view (Fig. 24.13(a,b)). Important

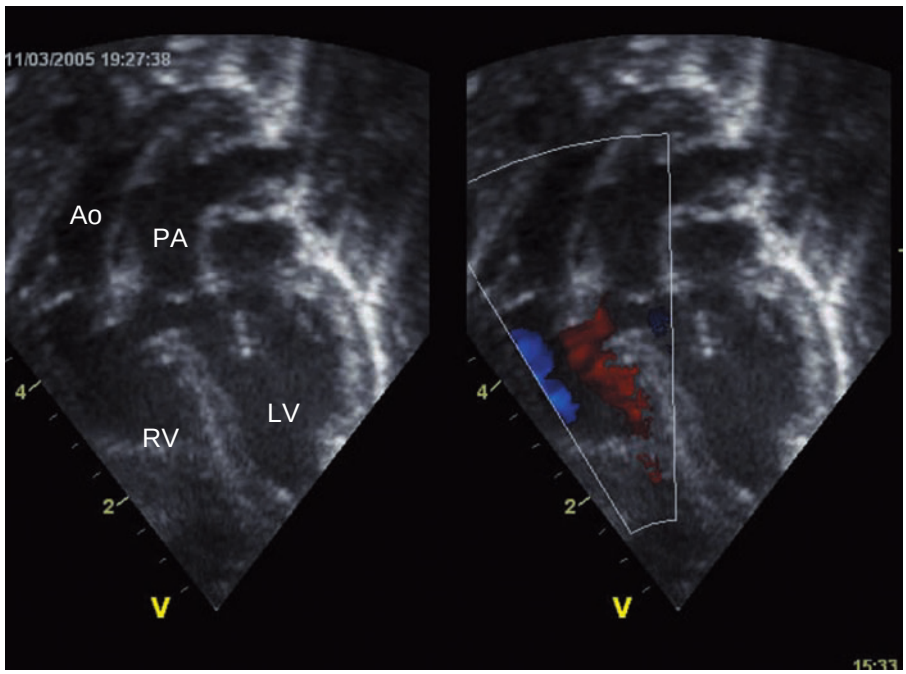


**Figure 24.12** Anterior malalignment type ventricular septal defect (VSD) in a patient with transposition of the great arteries. A subcostal long-axis view showing the parallel orientation of the great vessels. A malalignment VSD is seen with the infundibular part of the septum deviated anteriorly into the right ventricular outflow tract.

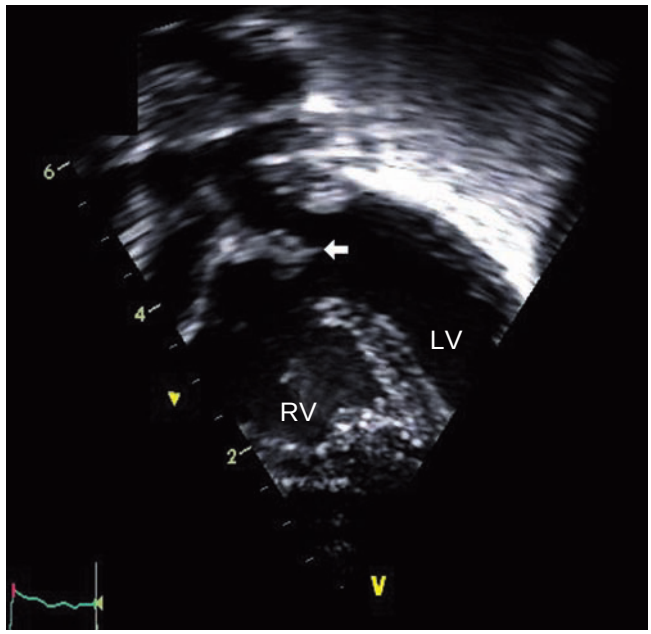


(a)

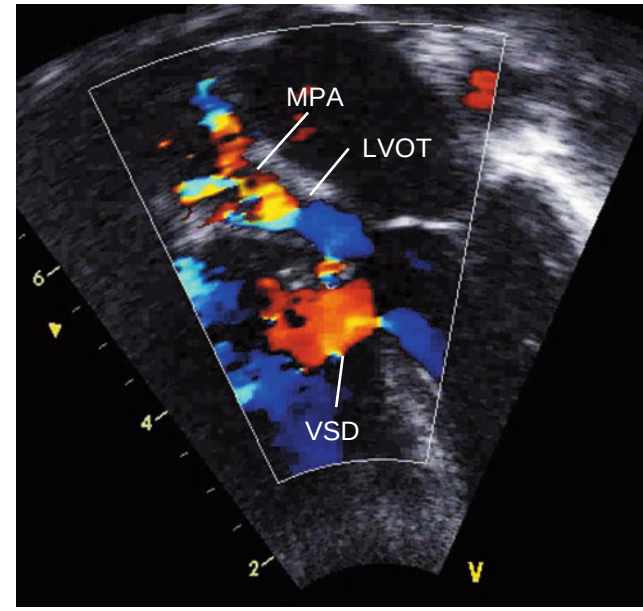


(b)

**Figure 24.13 (a)** Ventricular septal defect with posterior deviation of the outlet (conal) septum (white arrow) causing tunnel-like narrowing of the left ventricular outflow tract. **(b)** Colour Doppler interogation in the same patient shows flow across the ventricular septal defect (VSD) and acceleration of flow in the left ventricular outflow tract (LVOT) as a result of the posterior deviation of the outlet (conal) septum. MPA, main pulmonary artery.

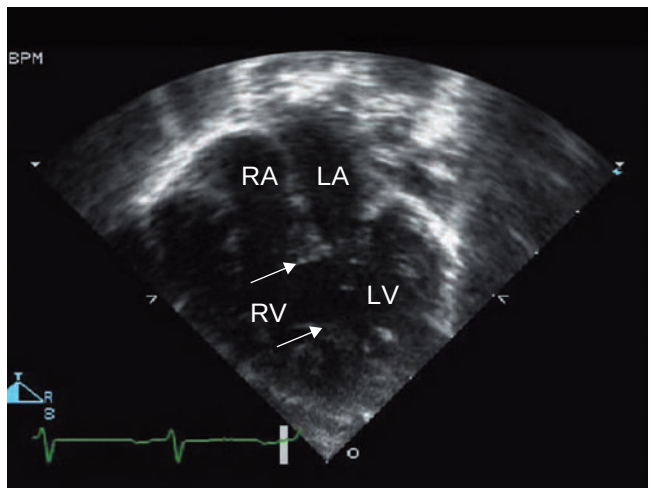


**Figure 24.14** Subcostal coronal view. A large ventricular septal defect (between arrows) extending to the inlet part of the septum can be seen.

elements of the echocardiographic evaluation include assessment of etiology and severity of LV outflow tract obstruction, which is commonly associated with this type of VSD. The gradient across the LV outflow tract can be measured by pulsed-wave and continuous-wave Doppler from the apical window. It should be noted, however, that as long as the PDA is large and pulmonary hypertension persists the gradient can be small despite significant obstruction.

Atrioventricular type (inlet) VSD can also be present in patients with TGA (Fig. 24.14). This type of defect is often associated with tricuspid valve anomalies, including abnormal chordal attachments to the crest of the ventricular septum, overriding, and straddling of the valve. Straddling tricuspid valve can complicate surgical closure of the VSD and requires precise preoperative imaging. This type of VSD is best imaged in the apical 4-chamber view but can also be seen from other acoustic windows. A posteriorly angled apical 4-chamber view shows the defect at the base of the ventricular septum with the AV valve annulus forming the superior-posterior border of the defect. Abnormal tricuspid valve attachments or accessory tissue related to the valve can prolapse through the VSD causing variable degrees of LV outflow tract obstruction.

Ventricular septal defect with hypoplasia or absence of the outlet or conal septum (doubly committed subarterial defect) is rarely seen in TGA. Subcostal and parasternal images demonstrate absence or hypoplasia of the outlet septum or conal muscle with typically fibrous continuity between the aortic and pulmonary valve leaflets (Fig. 24.15).

### Imaging of coronary arteries

Echocardiographic delineation of coronary artery anatomy in TGA can be challenging. Optimal imaging conditions, including proper position of the infant, removal of obstacles to imaging from the chest wall, and imaging when the patient is asleep are crucial for comprehensive evaluation of the origin and course of the coronary arteries. Imaging is performed predominantly from parasternal windows but complementary information is often gleaned from subcostal and apical views. The modified high parasternal short-axis view is used to image the origins of the coronary arteries

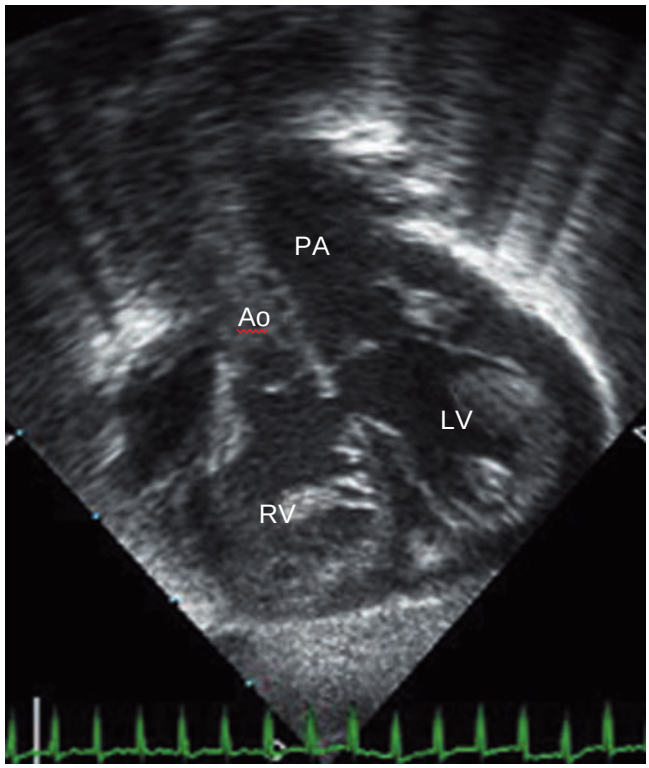


**Figure 24.15** Subcostal view in a patient with transposition of the great arteries (TGA) and a doubly committed ventricular septal defect (VSD). The VSD can be seen between both great vessels. The infundibular septum is hypoplastic in this setting and is sometimes absent.

(Fig. 24.16). For viewing the origin and proximal course of the LCA a slight clockwise rotation is used, reaching a transverse view with the transducer's index mark at roughly 3 o'clock. For viewing the origin and proximal course of RCA, a slight counterclockwise rotation of the transducer with the index mark at about 1 o'clock is helpful. In those with usual coronary anatomy, the parasternal long-axis view through the aortic root helps to visualize the origin of the RCA from the posterior sinus. When sweeping the transducer in the long-axis view toward the left shoulder the bifurcation of the LCA into the proximal LAD and LCx can be imaged. When the LCx originates from the right posterior-facing sinus (sinus 2), the posterior course of the coronary relative to the pulmonary trunk can be seen in the parasternal short-axis view and confirmed from the apical 4-chamber and subcostal views (Fig. 24.17). An anterior course of the coronary arteries, or combined anterior and posterior course relative to the aortic and pulmonary roots are present in cases of single coronary arteries arising from one sinus or in the inverted patterns (Videoclip 24.7(a,b)). Subcostal and apical views can also be helpful for delineating the relationship of the coronary arteries to the great vessels.

An intramural course of a coronary artery is associated with increased operative risk for the ASO and thus is important to identify preoperatively. An intramural coronary artery can generally be identified as a vessel originating from the opposite sinus of Valsalva in close proximity to the commissure that faces the pulmonary valve, with a parallel proximal course within the aortic wall. The origin of most intramural coronary arteries is tangential to the aortic wall. From the parasternal short-axis view, the intramural coronary artery will often be seen coursing between the aorta and the pulmonary artery (Fig. 24.18 and Videoclip 24.8). Every effort should be made to identify whether the origin of the intramural coronary artery is separate from the other coronary artery originating from the same aortic sinus of Valsalva (common orifice versus two separate orifices). Milder forms of intramural course are those coronary arteries that have a high takeoff relative to the sinotubular junction or when the artery has a proximal tangential course relative to the aortic wall. The origins of the coronary arteries should be imaged in detail because an intramural course can be missed when the artery does not cross the facing commissure in its proximal course.

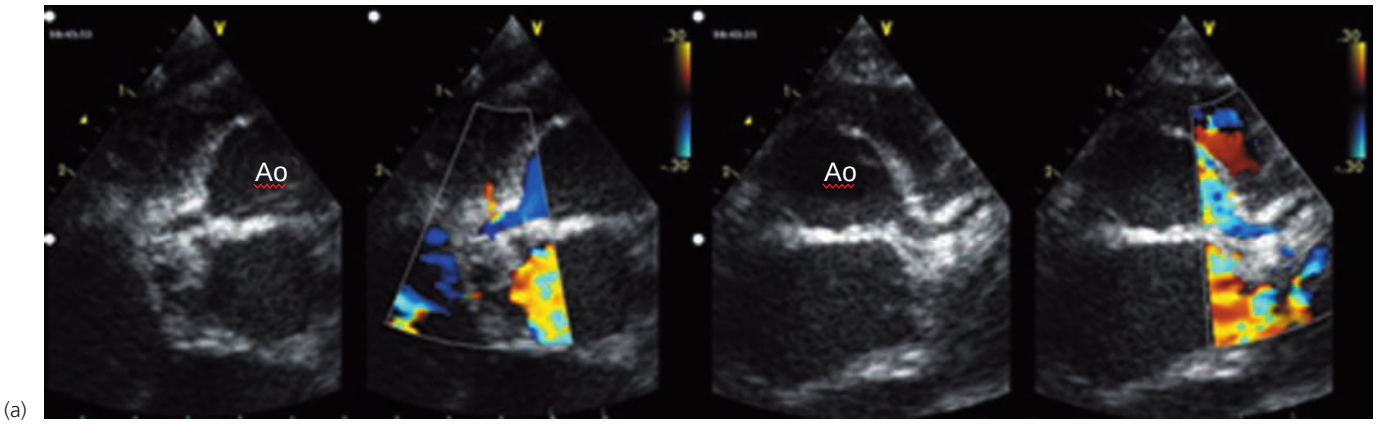


(a) (b)

**Figure 24.16** Parasternal short-axis views of the coronary arteries. **(a)** The origin of the right coronary artery (RCA) can be seen originating from sinus 2; **(b)** the left coronary artery (LCA) can be seen coming from sinus 1. Note that color Doppler is extremely helpful for identifying the coronary origins.

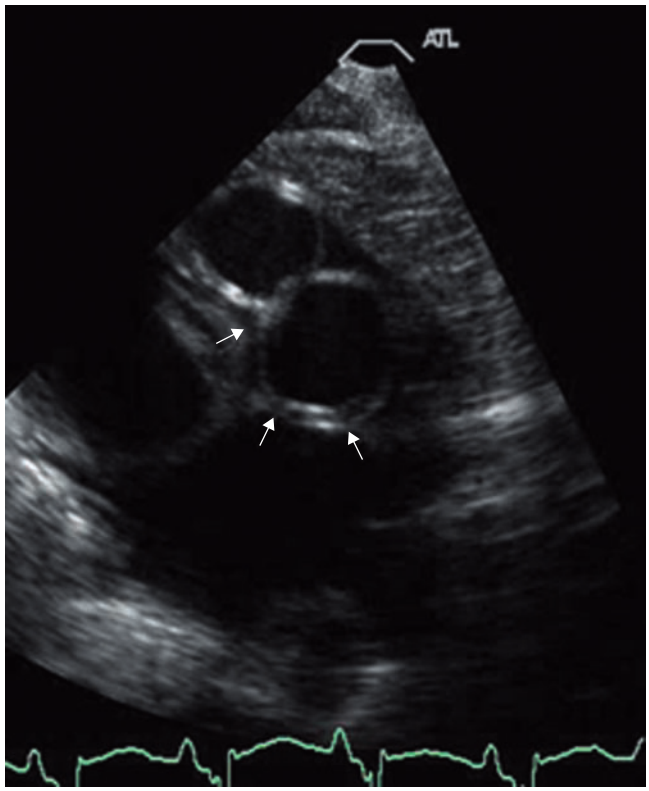


(a)

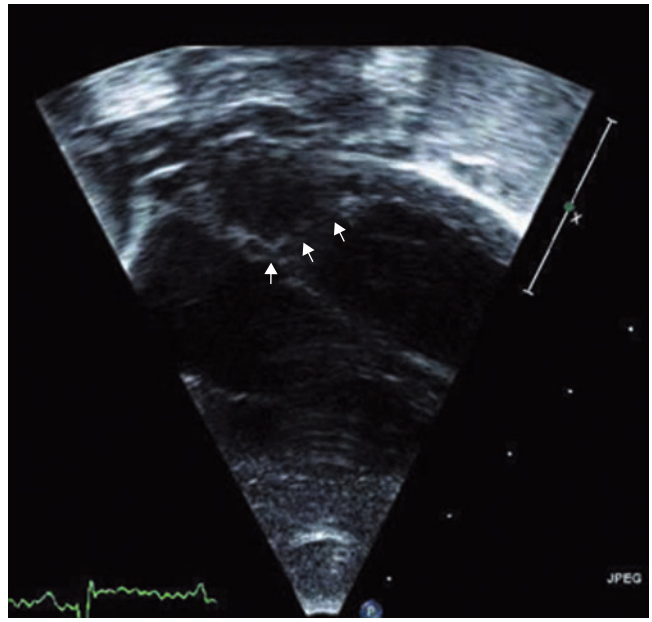


(b)

**Figure 24.17** Left circumflex from the right coronary artery (RCA) (from sinus 2). **(a)** Parasternal short-axis view shows the proximal part of the RCA coming from sinus 2 with the circumflex artery originating from the RCA, running posterior to the pulmonary artery (arrows). **(b)** On a subcostal 4-chamber view tilted posterior to the pulmonary artery the circumflex artery can be detected.

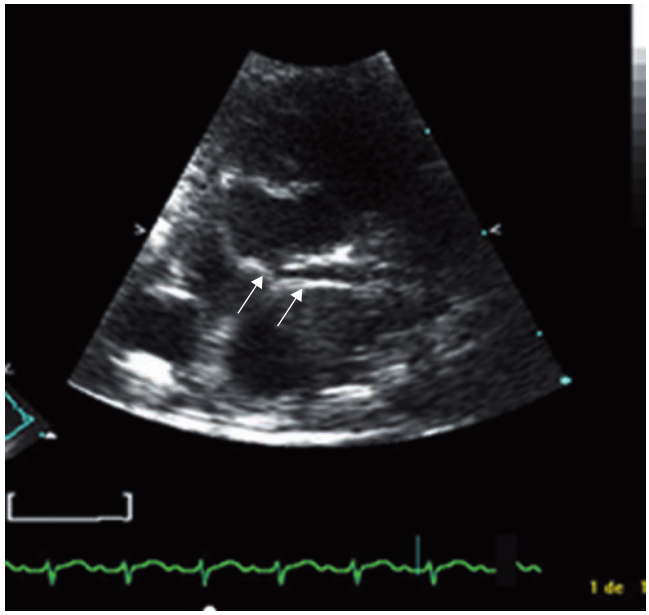

**Figure 24.18** Intramural course of the left coronary artery (LCA). Note the abnormal origin of the LCA from the right posterior sinus with a proximal intramural course (arrows).

### Imaging of the patent ductus arteriosus (arterial duct)

The presence of a PDA is important for mixing between the systemic and pulmonary circulations. In TGA, the orientation of the PDA is parallel to the long axis of the aortic arch and main pulmonary artery, allowing for imaging of all three vessels in one plane. The PDA is best seen from the suprasternal sagittal view, which demonstrates the connection of the aortic and pulmonary ends of the duct. Color and spectral Doppler demonstrate the direction of flow across the duct. In most patients flow is from the main pulmonary artery to the descending aorta during systole and from the aorta to the main pulmonary artery during diastole. In some patients pulmonary vascular resistance is increased due to abnormal development of the pulmonary vascular bed. In that circumstance flow through the PDA is predominantly right to left, which decreases effective pulmonary blood flow and results in severe cyanosis. Severe pulmonary hypertension can persist after the ASO and is associated with poor prognosis.

## Prenatal assessment

Prenatal diagnosis of TGA can be made during the second trimester of pregnancy. Several studies have demonstrated

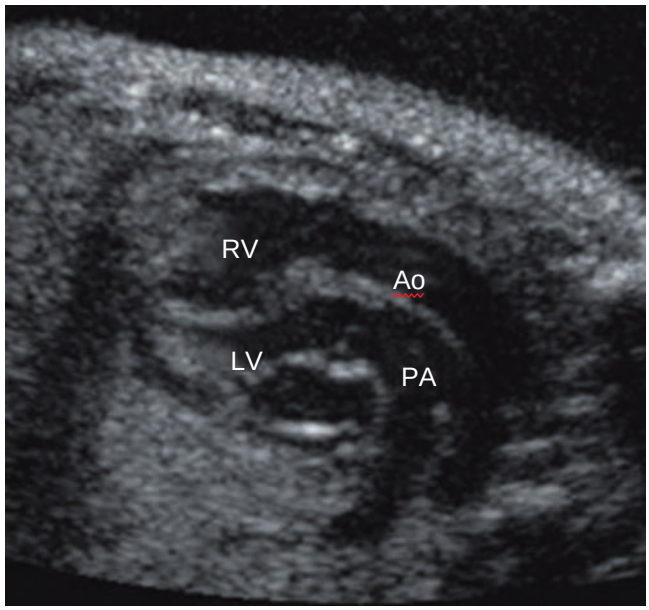


**Figure 24.19** Fetal diagnosis of transposition of the great arteries (TGA). Prenatal diagnosis of TGA relies on visualizing the outflow tracts where the parallel course of the great vessels is appreciated. The aorta (Ao) can be seen anterior to the pulmonary artery (PA).

that a screening ultrasound based solely on the 4-chamber view is inadequate for detection of conotruncal anomalies, including TGA [26–29]. In fact, the 4-chamber view may appear normal in a fetus with TGA unless there is a large VSD. More cephalad views that include the outflow tracts will readily identify the parallel orientation of the great vessels with origin of the main pulmonary artery from the LV and origin of the aorta from the anterior and rightward aspect of the RV (Fig. 24.19 and Videoclip 24.9). Associated VSDs can also be demonstrated but small defects might be missed, particularly if located in the muscular septum. Evaluation of the atrial septum is important for identification of a restrictive patent foramen ovale or intact atrial septum, conditions that may require balloon atrial septostomy immediately after birth. Significant atrioventricular or semilunar valve regurgitation is rare.

The data on the effects of prenatal diagnosis of TGA on postnatal morbidity and mortality rates are conflicting. Some studies suggest that prenatal diagnosis is associated with improved postnatal outcomes [30,31] whereas other studies have found no apparent benefit [32–34].

## Balloon atrial septostomy

When balloon atrial septostomy is required, echocardiography can guide the procedure and instantly evaluate the results. The subcostal long-axis (coronal) view is generally the best to monitor the entire procedure. The position of the balloon before pulling it across the atrial septum should be assessed to ensure it is free from the mitral valve, the left atrial appendage and the pulmonary veins (Fig. 24.20 and Videoclip 24.10). The pull-back through the atrial septum can be imaged although the heart might shift momentarily when pulling the catheter. After septostomy, subcostal imaging evaluates the size of the new atrial communication to determine whether the maneuver needs to be repeated and whether a pericardial effusion has developed from the procedure.

## Intraoperative assessment

Some centers perform transesophageal echocardiography (TEE) during surgery for TGA to evaluate the result immediately after coming off cardiopulmonary bypass. Epicardial

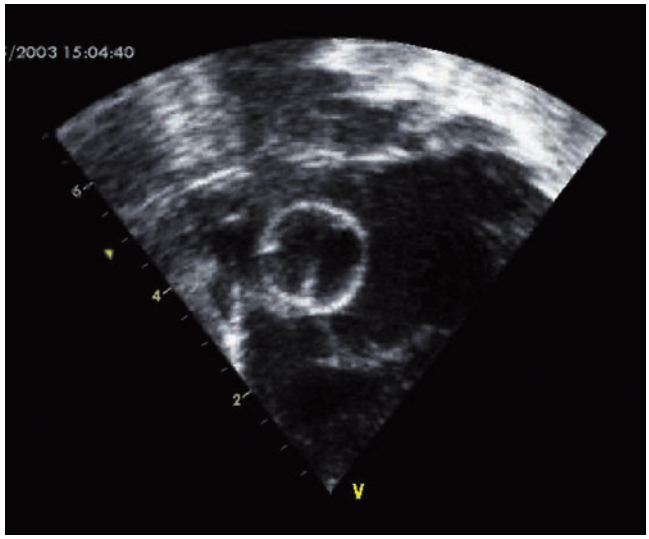


(a)

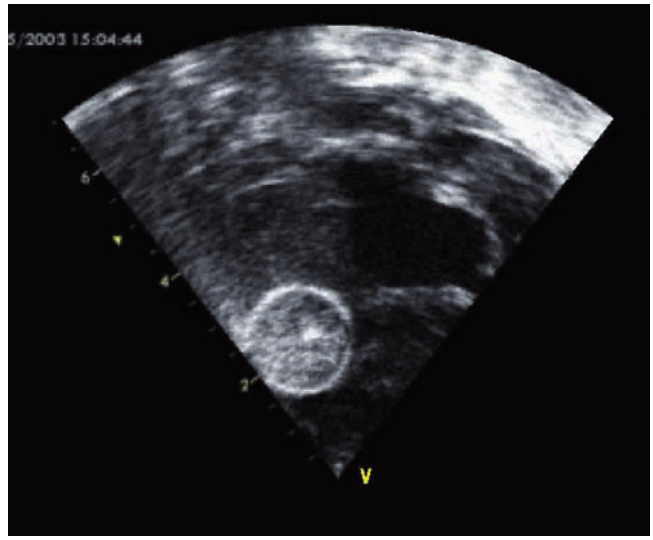


(b)

**Figure 24.20** Echocardiographic imaging of balloon septostomy under echocardiographic guidance. The subcostal long-axis views of the atria can be used to monitor the procedure. **(a)** The inflated balloon is seen in the left atrium. **(b)** The balloon is seen in the right atrium after having been pulled across the atrial septum.

echocardiography is an alternative approach preferred by some surgeons. Chapter 40 discusses the use of intraoperative TEE in detail. Here we summarize specific issues that the echocardiographer needs to address when using TEE after surgical procedures performed in patients with TGA.

### Arterial switch operation (ASO)

This operation is performed for TGA with intact ventricular septum as well as TGA with some types of VSD. In the operating room, particular attention is given to the following issues:

- Quantification of global and regional biventricular function as a determinant of coronary blood flow after translocation of the coronary arteries.
- Evaluation of the left and right ventricular outflow tracts for obstruction.
- Anatomy and functional assessment of the neoaorta, including evaluation of the neoaortic valve and neoaortic anastomosis.
- Anatomy and functional assessment of the neo-main pulmonary artery and proximal pulmonary arteries after the Lecompte maneuver.
- Assessment for residual VSD.

### Atrial switch operation

In the present era, the atrial switch operation is rarely performed for TGA. It is generally reserved for patients with congenitally corrected TGA undergoing a double (atrial and arterial) switch operation. However, intraoperative TEE may be requested on the rare occasion that an atrial switch operation is performed in a patient with TGA. Particular attention is given to the following issues:

- Assessment of the pulmonary venous pathway to the tricuspid valve.
- Assessment of the systemic venous pathway to the mitral valve.
- Evaluation of residual shunt or baffle leak(s) at the atrial level.
- Assessment of atrioventricular valve function.
- Evaluation of systolic performance of the systemic RV and the subpulmonary LV.
- Assessment for residual VSD.

### Rastelli operation

The procedure – LV-to-aortic valve baffle through the VSD and placement of a conduit from the RV to the pulmonary arteries – is performed for several cardiac anomalies, including TGA with posterior malalignment type VSD with pulmonary outflow tract obstruction. Particular attention is given to the following issues:

- Detection of residual VSD.
- Evaluation of the LV-to-aorta pathway.
- Evaluation of the RV-to-pulmonary artery pathway, including the proximal and distal conduit anastomoses.
- Assessment of atrioventricular valve function.
- Assessment of biventricular systolic performance.

## Follow-up assessment

Follow-up assessment for TGA is usually performed using transthoracic echocardiography. TEE can sometimes be required, especially in adult patients with poor transthoracic acoustic windows.

### After the arterial switch operation

Typical problems that require follow-up in the mid- and long-term after the ASO are generally related to the great vessels and the coronary arteries. Late complications after the ASO include dilation of the neoaortic root, neoaortic valve regurgitation, supravalvar pulmonary stenosis, and reduced coronary blood flow with or without impaired myocardial function.

#### *Coronary arteries*

Although early mortality after the ASO has decreased to ≤5% in experienced centers, rare instances of myocardial infarction or sudden death have been reported during follow-up [35–37]. Most events occur within the first postoperative year, and myocardial ischemia due to coronary insufficiency probably plays a major role. Careful monitoring of global and regional myocardial performance is important in the evaluation of patients after ASO. Identification of global or regional ventricular dysfunction on transthoracic echocardiography should prompt further investigation. Dobutamine stress echocardiography is an established method for detecting myocardial ischemia in adults with coronary artery disease. In patients who have undergone ASO, it can be used to identify stress-induced global and regional wall motion abnormalities that may not be detected at rest [38]. Intracoronary blood flow measurements and positron emission tomography have been used to detect coronary flow abnormalities, with variable results [39–40]. Both cardiac magnetic resonance (CMR) and computed tomography angiography (CTA) have been used successfully to image the coronary arteries after ASO [41,42]. However, the clinical significance of detecting coronary artery stenosis or occlusion by these and other diagnostic modalities remains controversial because some patients develop an extensive network of collateral coronary circulation and are asymptomatic. In the largest series looking at coronary lesions after ASO as many as 5% of all late survivors had coronary lesions [43]. Coronary angiography should be considered in patients in whom coronary stenosis or occlusion is strongly suspected.

#### *Neoaortic root and valve*

Long-term abnormalities of the neoaortic root include dilation [44–46] and neoaortic valve regurgitation [44–47]. Risk factors for neoaortic root dilation include previous pulmonary artery band, and risk factors for neoaortic regurgitation include previous pulmonary artery band, older age at ASO, and presence of VSD. The diameter of the aortic root is measured from the parasternal long axis during systole.

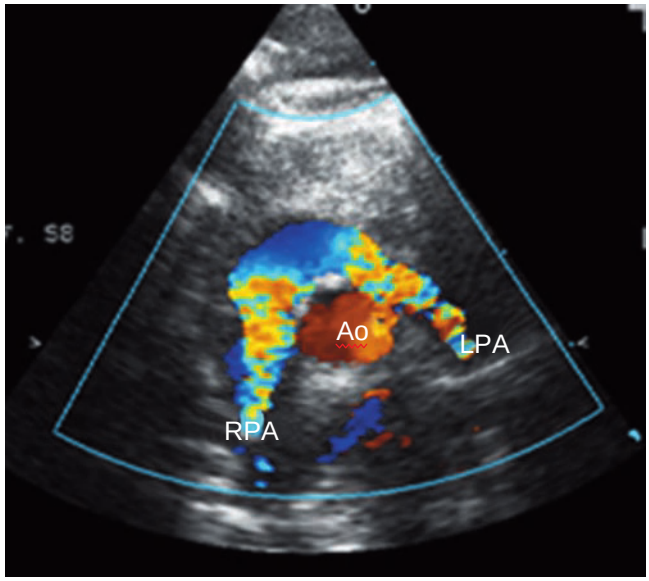


**Figure 24.21** The LeCompte maneuver: position of the pulmonary artery anterior to the aorta after the arterial switch procedure. High parasternal short-axis view demonstrates the branch pulmonary arteries after the arterial switch operation. Note that the pulmonary bifurcation is anterior to the aorta after the LeCompte maneuver. Ao, aorta; LPA, left pulmonary artery; RPA, right pulmonary artery.

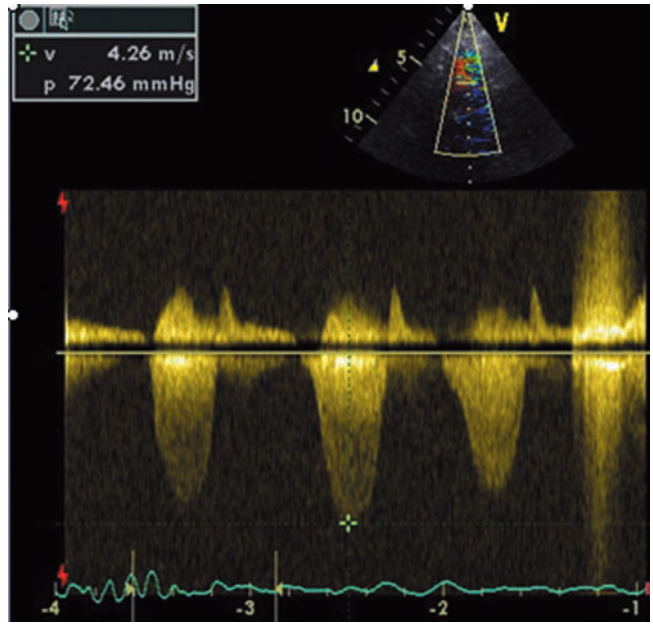


**Figure 24.22** Continuous wave (CW) Doppler of pulmonary artery branch stenosis after the arterial switch procedure. CW Doppler of the left pulmonary artery demonstrates a peak gradient of 72 mm Hg.

Importantly, z-scores of the aortic root are used to follow patients over time to determine whether the root is dilating out of proportion to somatic growth.

A mild degree of neoaortic valve regurgitation is common after the ASO, with or without aortic root dilation. Thus far, only 1–2% of patients after ASO have had evidence of hemodynamically important neoaortic regurgitation. Neoaortic incompetence can increase over time, with 98% freedom from at least moderate neoaortic regurgitation at 1 year, 96% at 5 years, and 93% at 10 years [45]. At present, surgical intervention for neoaortic regurgitation is rare (1.4%), accounting for only 11.6% of all reoperations after ASO [47]. The apical 3- and 5-chamber views and the parasternal long- and short-axis views are best to estimate the severity of the neoaortic regurgitation. The severity of the neoaortic regurgitation is graded based on the diameter of the jet's vena contracta and the degree of diastolic retrograde flow in the abdominal aorta. The degree of LV dilation and dysfunction are important factors in the decision to operate on the neoaortic valve for severe regurgitation.

### *Right ventricular outflow tract and pulmonary arteries*

Stenosis of the RV outflow tract at any level is the most common cause for late reoperation after ASO [35,37,47,49]. Losay et al. reported a 4% incidence of reoperation for RV outflow tract obstruction within 15 years [48, 49]. Obstruction can occur at any level but is most common at the suture line of the neo-main pulmonary arterial anastomosis. The subcostal oblique sagittal and the parasternal short-axis views best demonstrate this type of obstruction, and both views provide appropriate angles of interrogation for pulsed-wave and continuous-wave Doppler. The severity of neopulmonary regurgitation can also be estimated from these views. A high parasternal long-axis view demonstrates the RV outflow tract from the RV to the pulmonary artery bifurcation anterior to the ascending aorta. A left-to-right orientation of the transducer (index mark at 3 o'clock) from a high parasternal or suprasternal view demonstrates the pulmonary artery bifurcation with the proximal course of the branch pulmonary arteries anterior to the ascending aorta (LeCompte maneuver) (Figs 24.21 and 24.22). Peak velocities ≤2 m/s (predicted maximum instantaneous gradient ≤16 mm Hg) across the distal main pulmonary artery and branch pulmonary arteries are within normal limits after ASO [50]. Trivial (gradient between 17 and 24 mm Hg) supravalvar pulmonary stenosis is seen in up to 20% of patients, with less than 4% developing gradients of more than 30 mm Hg (Videoclip 24.11).

### *Ventricular size and function*

Given the potential for myocardial ischemia related to coronary artery abnormalities and neoaortic valve regurgitation after the ASO, long-term follow-up of left ventricular size and function is required. In the majority of patients, LV size and function continue to be within normal limits late after the ASO, with a rapid two-stage procedure early in life being a risk factor for LV dysfunction [49–51]. Methods for assessment of systolic and diastolic function are discussed in detail in Chapters 7 and 8 respectively.

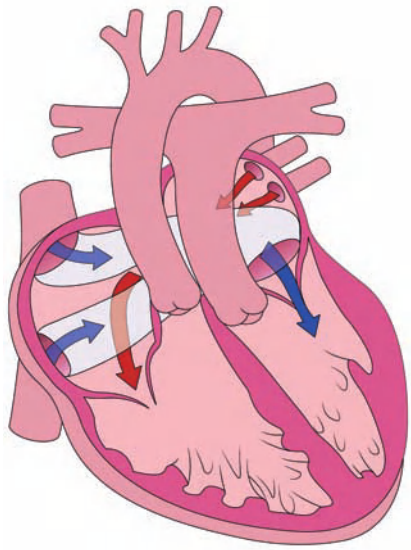

**Figure 24.23** Diagram showing the atrial baffles after the atrial switch procedure.

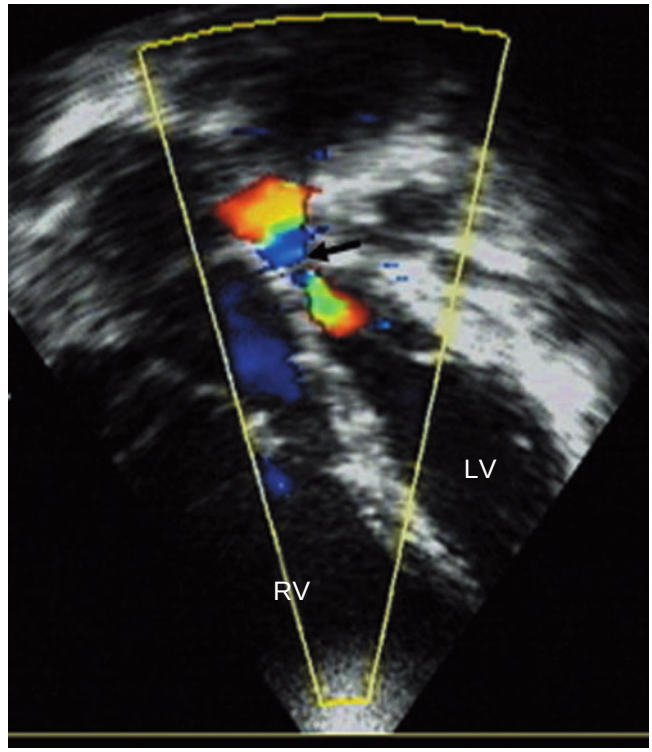


**Figure 24.24** Superior vena cava pathway obstruction after the atrial switch operation (arrow). An apical 4-chamber view demonstrating flow acceleration in the systemic venous baffle redirecting the blood toward the mitral valve. LV, left ventricle; RV, right ventricle.

### *Complications of the atrial switch operation*

Complications after an atrial switch operation include stenosis of the systemic and/or pulmonary venous pathways, baffle leak, atrial arrhythmias, tricuspid regurgitation, and systemic (RV) ventricular dysfunction. Baffle obstruction occurs in 11–31% of patients and is more common after the Mustard procedure [52,53]. Transthoracic echocardiography allows evaluation of the venous pathways in patients with good acoustic windows. However, alternative modalities are required in those with poor acoustic windows. TEE has been used extensively in atrial switch patients but its invasive nature and narrow field of view are relative weaknesses compared with CMR.

Transthoracic echocardiographic evaluation of the pulmonary and systemic venous pathways (Fig. 24.23) requires systematic imaging of each pathway from several views. Whenever possible, the subcostal window should be used. The apical window provides excellent views of the venous pathways even when other acoustic windows are suboptimal (Fig. 24.24 and Videoclip 24.12). Systematic sweeps of the transducer following each pathway with 2D and color Doppler can detect stenosis, and spectral Doppler can measure the mean gradient. Imaging from parasternal windows can be helpful, especially imaging of the pulmonary venous and superior limb of the systemic venous pathways, but suboptimal parasternal acoustic windows are common late after atrial switch procedure. TEE allows detailed imaging of the venous pathways and is the ideal method for detection of baffle leaks (Videoclip 24.15). Imaging is performed in multiple views, preferably using an omniplane probe (see Chapter 40 for details). Similar to transthoracic imaging, systematic sweeps of the transducer across each of the venous pathways using 2D and color Doppler allow detection of stenoses and leaks. TEE is also helpful for guidance of catheter-based treatment of pathway obstruction [54–56].

In detecting baffle leaks, the sensitivity of TEE is greater than that of transthoracic imaging because of the long distance from the transducer to the atrium with the latter approach. Contrast echocardiography with injection of agitated saline through a peripheral intravenous cannula can help to confirm the presence and extent of baffle leaks. The presence of LV dilation should raise suspicion of an atrial baffle leak.

The LV in atrial switch patients is typically low-pressure and wraps around the systemic RV (Videoclip 24.13). Significant mitral regurgitation and LV dysfunction are uncommon. In contrast, tricuspid regurgitation and systemic RV dysfunction are common late complications (Videoclip 24.14). Quantification of systemic RV function by echocardiography remains a challenge. In most clinical settings, assessment of global RV systolic function is qualitative. Quantitative methods include fractional area change [57] and tissue Doppler imaging. Meluzin et al. found that peak systolic tricuspid valve annular velocities <11.5 cm/s identified RV dysfunction with high sensitivity and specificity [58]. Isovolumic acceleration of the RV free wall is another measure that can be used for assessment of RV function after the atrial switch operation [59].

### After the Rastelli operation

In the long-term assessment after the Rastelli operation, obstruction of the RV-to-pulmonary artery conduit is essentially inevitable, requiring conduit revision or replacement. Echocardiographic evaluation of the conduit and branch pulmonary arteries requires 2D, color and spectral Doppler interrogations from several views. In infants and young children with good subcostal windows, the conduit can be imaged from short-axis views. Such views are particularly helpful for evaluation of the proximal conduit anastomosis. However, even when good subcostal windows are present, the distal conduit anastomosis and branch pulmonary arteries are better seen from parasternal and suprasternal views. Optimizing patient position (e.g., lateral decubitus) and flexible use of nonstandard transducer positions may allow visualization of the distal conduit and proximal pulmonary arteries even in patients with restricted transthoracic windows. Color Doppler is particularly helpful to identify flow through the conduit and to direct interrogation by spectral Doppler. Estimation of RV systolic pressure is based on the peak gradient across the conduit as well as the tricuspid regurgitation jet velocity and, when present, flow velocity across a VSD.

Obstruction of the LV-to-aortic valve pathway, aortic regurgitation and LV dysfunction are potential late complications after the Rastelli operation. Another potential complication is residual VSD, including intramural defects, which can develop years after surgery [60]. Detailed echocardiographic evaluation of these issues is integral to long-term follow-up of these patients.

### Imaging in the adult

Echocardiographic windows are often challenging in adults with TGA. Nevertheless, interval assessment of ventricular function, atrioventricular and semilunar valve function, venous pathways, and RV-to-pulmonary artery conduits is essential in the follow-up of the adult with TGA. Although transthoracic echocardiography is the first line of imaging in these patients, the importance of alternative diagnostic methods increases. Given the number of options available to practitioners caring for the adult with TGA (e.g., TEE, CMR, CTA, cardiac catheterization, single photon emission tomography, positron emission tomography, gated radionuclide angiography), judicious, patient-specific selection of techniques is paramount. TEE is ideally suited for evaluation of the venous pathways after the atrial switch operation [61] but is limited in its ability to assess the function of the systemic RV. Because of the high incidence of atrial arrhythmias, particularly atrial flutter and fibrillation after the atrial switch, TEE is often required prior to cardioversion to detect intraatrial thrombus. Limitations of TEE include sedation requirement and a small risk of complications.

Among the alternative imaging modalities, CMR is particularly helpful in adults after surgery for TGA due to its excellent ability to image all aspects of cardiovascular anatomy noninvasively, to measure biventricular size and function accurately, to measure blood flow (e.g., shunts, valve regurgitation), to image the proximal coronary arteries, and to assess myocardial viability. Freedom from exposure to ionizing radiation, with its attendant risk of cancer, renders CMR optimal for long-term follow-up in this patient group. CTA provides static images of cardiovascular anatomy with high spatial resolution, including the coronary arteries [41]. ECG-gated cine can be used to assess ventricular size and function in patients who cannot undergo a CMR examination (e.g., pacemaker) [62]. However, CTA exposes patients to relatively high doses of ionizing radiation and provides limited functional information. Cardiac catheterization is used selectively and its primary role is in catheter-based therapy. Radionuclide techniques have been used to address specific clinical or research questions in adults with TGA but they are not routinely employed.

## References


1. Hoffman JI, Kaplan S. The incidence of congenital heart disease. *J Am Coll Cardiol* 2002;39:1890–900.
2. Pradat P, Francannet C, Harris JA, Robert E. The epidemiology of cardiovascular defects, part I: a study based on data from three large registries of congenital malformations. *Pediatr Cardiol* 2003;24:195–221.
3. Digilio MC, Casey B, Toscano A et al. Complete transposition of the great arteries: patterns of congenital heart disease in familial precurrence. *Circulation* 2001;104:2809–14.
4. Wren C, Birrell G, Hawthorne G. Cardiovascular malformations in infants of diabetic mothers. *Heart* 2003;89:1217–20.
5. Goldmuntz E, Clark BJ, Mitchell LE et al. Frequency of 22q11 deletions in patients with conotruncal defects. *J Am Coll Cardiol* 1998;32:492–8.
6. Goldmuntz E, Bamford R, Karkera JD et al. CFC1 mutations in patients with transposition of the great arteries and double-outlet right ventricle. *Am J Hum Genet* 2002;70:776–80.
7. Costell M, Carmona R, Gustafsson E et al. Hyperplastic conotruncal endocardial cushions and transposition of great arteries in perlecan-null mice. *Circ Res* 2002;91:158–64.
8. Kirby ML. Embryogenesis of transposition of the great arteries: a lesson from the heart. *Circ Res* 2002;91:87–9.
9. Van Praagh R, Perez-Trevino C, Lopez-Cuellar M et al. Transposition of the great arteries with posterior aorta, anterior pulmonary artery, subpulmonary conus and fibrous continuity between aortic and atrioventricular valves. *Am J Cardiol* 1971; 28:621–31.
10. Wernovsky G. Transposition of the great arteries. In: Allen H, Driscoll D, Shaddy R, Feltes T (eds) Moss and Adams' Heart Disease in Infants, Children and Adolescents, Philadelphia, PA: Wolters Kluwer/Lippincott, Williams and Wilkins, 2007.
11. Pasquini L, Sanders SP, Parness IA et al. Conal anatomy in 119 patients with d-loop transposition of the great arteries and ventricular septal defect: an echocardiographic and pathologic study. *J Am Coll Cardiol* 1993;21:1712–21.

12. Kurisu K, Yonenaga K, Furusho N et al. [A case report of one-stage repair for transposition of the great arteries with intact ventricular septum and coarctation of the aorta in neonate]. *Nippon Kyobu Geka Gakkai Zasshi* 1997;45:1976–80.
13. Kirklin JW, Barratt Boyes B. Complete transposition of the great arteries. In: Kirklin JW, Barratt Boyes B (eds) Cardiac Surgery, New York: Churchill Livingstone, 1993.
14. Wernovsky G, Sanders SP. Coronary artery anatomy and transposition of the great arteries. *Coron Artery Dis* 1993;4: 148–57.
15. Planche C, Lacour-Gayet F, Serraf A. Arterial switch. *Pediatr Cardiol* 1998;19:297–307.
16. Yacoub MH, Radley-Smith R. Anatomy of the coronary arteries in transposition of the great arteries and methods for their transfer in anatomical correction. *Thorax* 1978;33:418–24.
17. Gremmels DB, Tacy TA, Brook MM, Silverman NH. Accuracy of coronary artery anatomy using two-dimensional echocardiography in d-transposition of great arteries using a two-reviewer method. *J Am Soc Echocardiogr* 2004;17:454–60.
18. Massoudy P, Baltalarli A, de Leval MR et al. Anatomic variability in coronary arterial distribution with regard to the arterial switch procedure. *Circulation* 2002;106:1980–4.
19. Blume ED, Altmann K, Mayer JE et al. Evolution of risk factors influencing early mortality of the arterial switch operation. *J Am Coll Cardiol* 1999;33:1702–9.
20. Pasquali SK, Hasselblad V, Li JS et al. Coronary artery pattern and outcome of arterial switch operation for transposition of the great arteries: a meta-analysis. *Circulation* 2002;106:2575–80.
21. Ueda Y, Miki S, Okita Y et al. Transposition of the great arteries associated with total anomalous pulmonary venous return. *Ann Thorac Surg* 1994;57:470–2.
22. Fraisse A, del Nido PJ, Gaudart J, Geva T. Echocardiographic characteristics and outcome of straddling mitral valve. *J Am Coll Cardiol* 2001;38:819–26.
23. Tlaskal T, Hucin B, Kostelka M, Marek J. Primary repair of transposition of the great arteries with interrupted aortic arch. *Eur J Cardiothorac Surg* 1998;13:310–2.
24. Shirali GS, Geva T, Ott DA, Bricker JT. Double aortic arch and bilateral patent ducti arteriosi associated with transposition of the great arteries: missing clinical link in an embryologic theory. *Am Heart J* 1994;127:451–3.
25. Van Praagh S, O'Sullivan J, Brili S, Van Praagh R. Juxtaposition of the morphologically right atrial appendage in solitus and inversus atria: a study of 35 postmortem cases. *Am Heart J* 1996;132:382–90.
26. Bakiler AR, Ozer EA, Kanik A et al. Accuracy of prenatal diagnosis of congenital heart disease with fetal echocardiography. *Fetal Diagn Ther* 2007;22:241–4.
27. Berghella V, Pagotto L, Kaufman M et al. Accuracy of prenatal diagnosis of congenital heart defects. *Fetal Diagn Ther* 2001; 16:407–12.
28. Rychik J, Ayres N, Cuneo B et al. American Society of Echocardiography guidelines and standards for performance of the fetal echocardiogram. *J Am Soc Echocardiogr* 2004;17: 803–10.
29. Randall P, Brealey S, Hahn S et al. Accuracy of fetal echocardiography in the routine detection of congenital heart disease among unselected and low risk populations: a systematic review. *BJOG-Int J Obstet Gy* 2005;112:24–30.
30. Bonnet D, Coltri A, Butera G et al. Detection of transposition of the great arteries in fetuses reduces neonatal morbidity and mortality. *Circulation* 1999;99:916–8.
31. Jouannic JM, Gavard L, Fermont L et al. Sensitivity and specificity of prenatal features of physiological shunts to predict neonatal clinical status in transposition of the great arteries. *Circulation* 2004;110:1743–6.
32. Blyth M, Howe D, Gnanapragasam J, Wellesley D. The hidden mortality of transposition of the great arteries and survival advantage provided by prenatal diagnosis. *BJOG-Int J Obstet Gy* 2008;115:1096–100.
33. Bartlett JM, Wypij D, Bellinger DC et al. Effect of prenatal diagnosis on outcomes in D-transposition of the great arteries. *Pediatrics* 2004;113:e335–40.
34. Kumar RK, Newburger JW, Gauvreau K et al. Comparison of outcome when hypoplastic left heart syndrome and transposition of the great arteries are diagnosed prenatally versus when diagnosis of these two conditions is made only postnatally. *Am J Cardiol* 1999;83:1649–53.
35. Brown JW, Park HJ, Turrentine MW. Arterial switch operation: factors impacting survival in the current era. *Ann Thorac Surg* 2001;71:1978–84.
36. Pretre R, Tamisier D, Bonhoeffer P et al. Results of the arterial switch operation in neonates with transposed great arteries. *Lancet* 2001;357:1826–30.
37. Daebritz SH, Nollert G, Sachweh JS et al. Anatomical risk factors for mortality and cardiac morbidity after arterial switch operation. *Ann Thorac Surg* 2000;69:1880–6.
38. Hui L, Chau AK, Leung MP et al. Assessment of left ventricular function long term after arterial switch operation for transposition of the great arteries by dobutamine stress echocardiography. *Heart* 2005;91:68–72.
39. Hauser M, Bengel FM, Kuhn A et al. Myocardial blood flow and flow reserve after coronary reimplantation in patients after arterial switch and Ross operation. *Circulation* 2001;103: 1875–80.
40. Oskarsson G, Pesonen E, Munkhammar P et al. Normal coronary flow reserve after arterial switch operation for transposition of the great arteries: an intracoronary Doppler guidewire study. *Circulation* 2002;106:1696–702.
41. Ou P, Mousseaux E, Azarine A et al. Detection of coronary complications after the arterial switch operation for transposition of the great arteries: first experience with multislice computed tomography in children. *J Thorac Cardiovasc Surg* 2006;131: 639–43.
42. Taylor AM, Dymarkowski S, Hamaekers P et al. MR coronary angiography and late-enhancement myocardial MR in children who underwent arterial switch surgery for transposition of great arteries. *Radiology* 2005;234:542–7.
43. Raisky O, Bergoend E, Agnoletti G et al. Late coronary artery lesions after neonatal arterial switch operation: results of surgical coronary revascularization. *Eur J Cardiothorac Surg* 2007; 31:894–8.
44. Hourihan M, Colan SD, Wernovsky G et al. Growth of the aortic anastomosis, annulus, and root after the arterial switch procedure performed in infancy. *Circulation* 1993;88:615–20.
45. Schwartz ML, Gauvreau K, del Nido P et al. Long-term predictors of aortic root dilation and aortic regurgitation after arterial switch operation. *Circulation* 2004;110:II128–32.

46. Hutter PA, Thomeer BJ, Jansen P et al. Fate of the aortic root after arterial switch operation. *Eur J Cardiothorac Surg* 2001;20: 82–8.
47. Losay J, Touchot A, Capderou A et al. Aortic valve regurgitation after arterial switch operation for transposition of the great arteries: incidence, risk factors, and outcome. *J Am Coll Cardiol* 2006;47:2057–62.
48. Losay J, Touchot A, Serraf A et al. Late outcome after arterial switch operation for transposition of the great arteries. *Circulation* 2001;104:I121–6.
49. Haas F, Wottke M, Poppert H, Meisner H. Long-term survival and functional follow-up in patients after the arterial switch operation. *Ann Thorac Surg* 1999;68:1692–7.
50. Hovels-Gurich HH, Seghaye MC, Dabritz S et al. Cardiological and general health status in preschool- and school-age children after neonatal arterial switch operation. *Eur J Cardiothorac Surg* 1997;12:593–601.
51. Colan SD, Boutin C, Castaneda AR, Wernovsky G. Status of the left ventricle after arterial switch operation for transposition of the great arteries. Hemodynamic and echocardiographic evaluation. *J Thorac Cardiovasc Surg* 1995;109:311–21.
52. Moons P, Gewillig M, Sluysmans T et al. Long term outcome up to 30 years after the Mustard or Senning operation: a nationwide multicentre study in Belgium. *Heart* 2004;90: 307–13.
53. Dos L, Teruel L, Ferreira IJ et al. Late outcome of Senning and Mustard procedures for correction of transposition of the great arteries. *Heart* 2005;91:652–6.
54. Asgar AW, Miro J, Ibrahim R. Recanalization of systemic venous baffles by radiofrequency perforation and stent implantation. *Catheter Cardiovasc Interv* 2007;70:591–4.
55. Mohsen AE, Rosenthal E, Qureshi SA, Tynan M. Stent implantation for superior vena cava occlusion after the Mustard operation. *Catheter Cardiovasc Interv* 2001;52:351–4.
56. Sharaf E, Waight DJ, Hijazi ZM. Simultaneous transcatheter occlusion of two atrial baffle leaks and stent implantation for SVC obstruction in a patient after Mustard repair. *Catheter Cardiovasc Interv* 2001;54:72–6.
57. Haddad F, Doyle R, Murphy DJ, Hunt SA. Right ventricular function in cardiovascular disease, part II: Pathophysiology, clinical importance, and management of right ventricular failure. *Circulation* 2008;117:1717–31.
58. Meluzin J, Spinarova L, Bakala J et al. Pulsed Doppler tissue imaging of the velocity of tricuspid annular systolic motion; a new, rapid, and non-invasive method of evaluating right ventricular systolic function. *Eur Heart J* 2001;22:340–8.
59. Vogel M, Derrick G, White PA et al. Systemic ventricular function in patients with transposition of the great arteries after atrial repair: a tissue Doppler and conductance catheter study. *J Am Coll Cardiol.*2004;43:100–6.
60. Preminger TJ, Sanders SP, van der Velde ME et al. "Intramural" residual interventricular defects after repair of conotruncal malformations. *Circulation* 1994;89:236–42.
61. Ge S, Shiota T, Rice MJ et al. Images in cardiovascular medicine. Transesophageal ultrasound imaging during stent implantation to relieve superior vena cava-to-intra-atrial baffle obstruction after Mustard repair of transposition of the great arteries. *Circulation* 1995;91:2679–80.
62. Raman SV, Cook SC, McCarthy B, Ferketich AK. Usefulness of multidetector row computed tomography to quantify right ventricular size and function in adults with either tetralogy of Fallot or transposition of the great arteries. *Am J Cardiol* 2005;95:683–6.

# 25 Double-Outlet Ventricle

**Leo Lopez**
The Children's Hospital at Montefiore, New York, NY, USA

Double-outlet ventricle exists when both great arteries are aligned with the right ventricle (RV: double-outlet right ventricle, or DORV), with the left ventricle (LV: double-outlet left ventricle, or DOLV), or with the infundibulum (double-outlet infundibulum). It is one type of ventriculo-arterial alignment within a classification system that describes the relationship of the semilunar valves and corresponding great arteries to the underlying ventricles (see Chapter 3). Other types of ventriculo-arterial alignments include concordant relationship, wherein the aorta arises from the LV and the pulmonary artery arises from the RV (such as normally related great arteries and anatomically corrected malposition of the great arteries); discordant relationship, wherein the aorta arises from the RV and the pulmonary artery arises from the LV (such as transposition of the great arteries, or TGA); and common outlet (such as truncus arteriosus). Because the spectrum of ventriculo-arterial alignments is in fact a continuum, any classification system must involve sharp borders between "discrete" groups within transition zones. As a result, some anatomic variations may straddle distinct categories at these transition zones. Nevertheless, classification is indispensable in the study of congenital heart diseases, especially in terms of natural history and treatment outcome.

## Double-outlet right ventricle

### Definition

DORV occurs when both great arteries are completely or nearly completely aligned with the RV. Although this definition appears straightforward at first glance, the approach to making the diagnosis has been fraught with controversy [1–5]. Over the past several decades, the diagnostic debate over this so-called "morphogenetic monster" [3] has focused primarily on whether the term DORV refers to a specific morphologic entity or to a broader group of defects with the same abnormal ventriculo-arterial alignment. In addition, the extent that one of the semilunar valves overrides the ventricular septal plane has contributed significantly to the confusion over this definition. Some argue that the "50% rule" should be utilized, defining origin of a great artery from a ventricle if more than half of the semilunar valve is related to that ventricle over a ventricular septal defect (VSD) [2,3]. Many others argue that the diagnosis should be reserved for cases where the great arteries are completely or nearly completely aligned with the RV (absent or minimal override) [6–9], an approach that minimizes overlap among the ventriculo-arterial alignment categories. Assigning a percentage to the degree of override can be arbitrary and imprecise, especially given the complex three-dimensional (3-D) relationship between the ventricles and great arteries, the curved geometry of the ventricular septum, and the rotational and translational motion of the heart during the cardiac and respiratory cycles. In addition, the "50% rule" classifies some patients with tetralogy of Fallot (TOF) or with a VSD and normally related great arteries as DORV, an approach that by itself contributes little to the clinical tasks of choosing appropriate intervention and predicting outcome. Regardless of the debates over definitions and classification systems, however, the primary task when caring for this heterogeneous group of patients is to obtain a precise morphologic and functional description of the heart in order to formulate a rational surgical approach [10–13].

### Historical perspective

In 1793, Abernathy provided one of the earliest descriptions of a heart in which both great arteries originated from the RV [14]. However, during the 19th and early 20th centuries, any abnormal relationship between the great arteries and ventricles was often considered as some form of TGA, and DORV was frequently classified as a subtype of TGA. Some early descriptions utilized the term "partial transposition" to describe a DORV because only the aorta and not the pulmonary artery was transposed [15,16]. In 1923, Spitzer reported a new classification system for TGA in which discordant ventriculo-arterial alignment was labeled "crossed transposition," and

*Echocardiography in Pediatric and Congenital Heart Disease: From Fetus to Adult*
Edited by Wyman W. Lai, Luc L. Mertens, Meryl S. Cohen and Tal Geva
 ISBN: 978-1-405-17401-5

DORV was labeled "simple transposition," again because only one great vessel was transposed [17]. In 1949, Taussig and Bing described their famous heart with "transposition of the aorta and levoposition of the pulmonary artery" [18], noted over a decade later to be a case of DORV with a subpulmonary VSD, bilateral conus and side-by-side great arteries [1,19]. Although in 1952 Braun et al. described a heart in which the RV served "as a double-outlet ventricle" [20], the specific term "double-outlet right ventricle" was actually introduced in 1957 by Witham [21]. Witham, however, still described DORV as a "partial transposition complex," and it was not until 1961 when McGoon utilized the term DORV on its own [9].

The role of the subarterial conus or infundibulum (outflow tract) in TGA and DORV has long been a focus of attention [1,5,18,22,23]. Van Praagh and colleagues highlighted the importance of abnormal conal development in the morphogenesis of abnormal great artery relationships [24]. They argued that DORV and TOF are separate clinical entities with mutually exclusive diagnostic criteria, an important distinction when reporting surgical results [5]. Moreover, they recognized that not all cases of DORV had bilateral conus, and emphasized that the diagnosis is based not on the conal morphology but on the ventriculo-arterial alignment. In 1972, Lev and colleagues proposed a classification system based on the anatomic position of the VSD relative to the great arteries, a system that is still widely used today [25]. In 1973, Kirklin et al. used the percentage by which a semilunar valve is related to each ventricle over a VSD to determine the ventriculo-arterial alignment in cases of anatomically corrected malposition of the great arteries with a VSD [26]. Anderson and colleagues subsequently proposed the "50% rule" in an effort to synthesize a nomenclature for the various ventriculo-arterial connections [2,3,27]. In 2000, the Congenital Heart Surgery Nomenclature and Database Committee of the Society of Thoracic Surgeons defined DORV as "a type of ventriculo-arterial connection in which both great vessels arise either entirely or predominantly from the RV" [28].

## Incidence

DORV is an uncommon congenital heart disease with an estimated incidence of 12.7 per 1000 live births, based on an analysis of 16 published articles spanning many decades [29]. However, the reported incidence has varied widely in individual reports: 3.2 in the New England Regional Infant Cardiac Program (1968–1974) [30]; 5.6 in the Baltimore-Washington Infant Study (1981–1982) [31]; 14.5 in the Alberta Heritage Pediatric Cardiology Program (1981–1984) [32]; and 22 in the Metropolitan Atlanta Congenital Defects Program (1995–1997) [33]. Among all the congenital heart lesions in the Baltimore-Washington Infant Study, DORV ranks 12th in frequency, representing 2% of all the cases [34]. Among all the cardiac diagnoses made at Children's Hospital Boston from 1988 to 2002, DORV ranks 16th in frequency [35].

## Etiology

The etiology of DORV is not known, and most cases are sporadic. A small number of familial cases have been reported [36]. Based on the Baltimore-Washington Infant Study, as many as 12% of patients with a DORV have an associated chromosomal abnormality [34], including trisomies 13 and 18 [37,38]. Although frequently associated with other conotruncal anomalies, chromosome 22q11 deletion occurs rarely with DORV [39]. Mutations that have been described in association with the DORV phenotype include genes related to the neural crest (*NF-1, Pax-3, RXRα*) [40–42], genes controlling laterality (*CFC1, Pitx2*) [43,44], genes controlling transcriptional factors (*GATA4*) [45], genes controlling cell proliferation and transformation from endothelial to mesenchymal cells (*TGFB2*) [46], genes controlling cell-to-cell communication (*Cx40*) [47], and genes controlling outflow tract myocardialization and polarization (*Vangl2* in the *Lp* mutant mouse) [48,49]. The large number of genetic defects associated with DORV suggests that multiple developmental abnormalities may result in this phenotype. In addition, DORV has been produced in several experimental models, including surgical ligature of the chick embryonic conus to prevent its incorporation onto the LV after conal division [50], and surgical ablation of "cardiac" neural crest cells in the chick embryo [51]. Finally, several maternal risk factors have been associated with the development of DORV, including nongestational diabetes [52], codeine use [53], and exposure to solvents [36].

## Morphology and classification

### Developmental considerations

Knowledge of the normal development of the ventricular outflow tracts helps to elucidate some of the factors involved in the morphogenesis of a DORV. A comprehensive review of cardiac embryology is beyond the scope of this chapter and can be found elsewhere [54–61]. At the conclusion of cardiac looping, the conotruncus relates exclusively to the developing RV. Shortly thereafter, pairs of internal ridges or cushions develop along the proximal and distal outflow tracts in a spiraling orientation. This is followed by migration of mesenchymal cells from the pharyngeal pouches into the distal outflow tract walls, contributing to their transformation from myocardial tissue to arterial tissue. At approximately the same time, there is also migration of cells derived from the neural crest into the developing cushions located in the distal segment of the conus and in the truncus arteriosus. The cushions with their neural crest-derived cells begin to fuse distally within the truncus arteriosus, separating the future proximal aorta from the future pulmonary artery. The arterial valve leaflets and sinuses also evolve from the developing cushions at the base of the truncus arteriosus. The proximal cushions now begin to fuse, separating the subpulmonary outflow tract from the subaortic outflow tract, both of which are still committed to the developing RV. At around

the same time, the endocardial cushion and muscular ventricular septum develop within the primordial ventricle. The fused proximal cushions eventually merge with the muscular ventricular septum, committing the RV to the pulmonary artery and the LV to the aorta. The subaortic outflow tract or conus is still intact at this time, and its regression with consequent fibrous continuity between the mitral and aortic valves does not occur until much later, at approximately 12 weeks of gestation.

Little is known about the morphogenesis of DORV in humans. Although the exact mechanisms are unknown at this time, studies suggest that a DORV can result from abnormalities in genetic and environmental signals for differentiation, proliferation and migration of cardiogenic cells in the primary and secondary heart fields as well as neural crest-derived cells. As discussed previously, the marked heterogeneity that characterizes DORV morphology strongly suggests that several developmental mechanisms are involved. Developmental arrest at the embryonic stage when the conotruncus relates exclusively to the RV, disruption in the development of the proximal cushions, and abnormal ventricular development (such as hypoplasia and malposition) with or without an abnormal conus are some of the proposed mechanisms.

## Anatomy

Given the morphologic and physiologic diversity of DORV, the following anatomic features are crucial in understanding each case and determining the optimal interventional approach:

- VSD location and size and its relationship to the semilunar valves;
- conal morphology;
- spatial relationship of the great arteries to each other;
- associated cardiac lesions, including outflow tract obstruction, atrioventricular (AV) valve anomalies, ventricular hypoplasia and malposition, and abnormal coronary artery patterns.

### *VSD location and size*

Description of the VSD location, especially in terms of its spatial relationship to the great arteries, has long been recognized as a clinically useful classification system for DORV [8,25,62–64]. When present, the VSD may fall into one of four categories [5,12,13,63,65–69]: subaortic, subpulmonary, doubly committed or noncommitted (remote) VSD. It is important to recognize that the VSD in most cases of DORV is usually located between the antero-superior and postero-inferior limbs of the septal band. The spatial relationship of the VSD to the semilunar valves is dictated by the presence, size and position of the subarterial conus and by deficiency of adjacent septal segments such as the conal septum and AV canal septum. The size of the VSD, the distance from the VSD to the semilunar valves, and the presence of AV valve attachments along the VSD margins or within the defect are important variables when planning surgical repair. Occasionally, there are multiple VSDs [12], and rarely, the ventricular septum is intact [63,70].

*Subaortic VSD (42–57% of cases)*

The defect is cradled between the limbs of the septal band below the aortic valve, located behind and to the right of the conal septum, and remote from the pulmonary valve. The postero-inferior margin may be in fibrous continuity with the tricuspid valve (confluent with the membranous septum), or it may consist of muscular extension of the posterior limb of the septal band [27,71]. This type of defect has been termed a malalignment VSD or conoventricular septal defect because the conal septum is not aligned with the underlying muscular septum. In DORV with D-malposition of the great arteries (aorta to the right of the pulmonary artery), the conal septum is rotated out of the plane of the ventricular septum and attached to the antero-superior limb of the septal band (Fig. 25.1) [71]. Right ventricular outflow tract obstruction is often present, and its severity is determined by the degree of anterior and leftward deviation of the conal septum and by associated pulmonary valve stenosis (Fig. 25.2). In DORV with L-malposition of the great arteries (aorta to the left of the pulmonary artery), the subaortic VSD is situated more anteriorly and superiorly within the limbs of the septal band [72]. In these cases, the aortic valve or subaortic conus represents the superior margin of the VSD.

*Subpulmonary VSD (24–37% of cases)*

The defect is also cradled between the limbs of the septal band. However, the conal septum is rotated out of the plane of the ventricular septum and attaches to the more posteriorly located ventriculo-infundibular fold rather than to the antero-superior limb of the septal band (Fig. 25.3) [71]. As a result, the conal septum shields the aortic valve from the defect with only a short distance from the defect to the pulmonary valve. In 60% of cases, the postero-inferior margin of the defect is in fibrous continuity with the AV valves (confluent with the membranous septum); a muscular inferior border representing continuity between the right ventriculo-infundibular fold and the postero-inferior limb of the septal band occurs in the other 40% [65]. The subaortic conus is usually well developed, and the aortic valve is rightward relative to the pulmonary valve with either side-by-side or slightly anterior position. The subpulmonary conus varies in size. In some cases the subpulmonary conus is incomplete, allowing fibrous continuity between the pulmonary and mitral valves. The distinction between DORV and TGA in this scenario is dictated by the alignment between the pulmonary valve and the underlying ventricles: DORV is present when the pulmonary valve relates nearly exclusively to the RV, and TGA is present when the pulmonary valve relates nearly exclusively to the LV. Categorization of intermediate cases with biventricular origin of the pulmonary

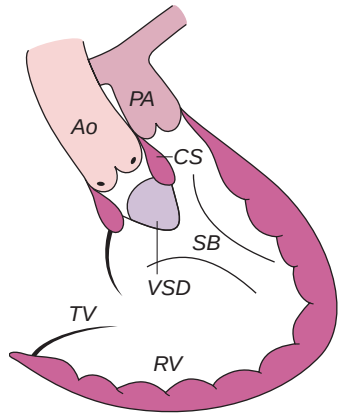


(a)

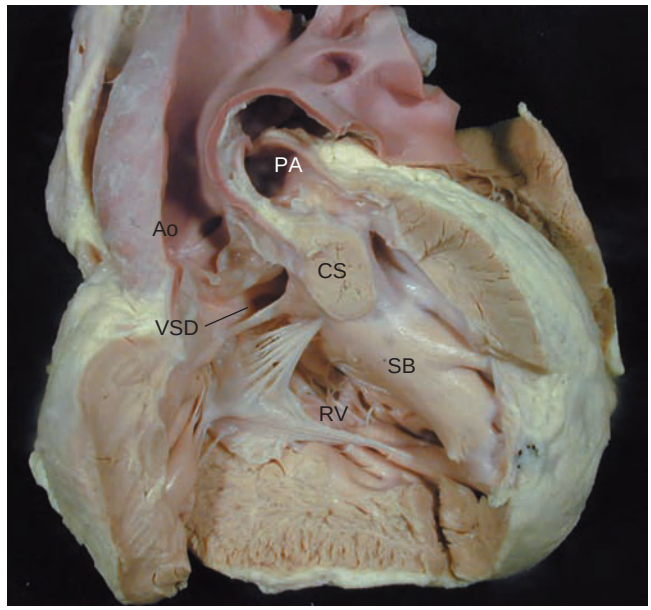


(b)

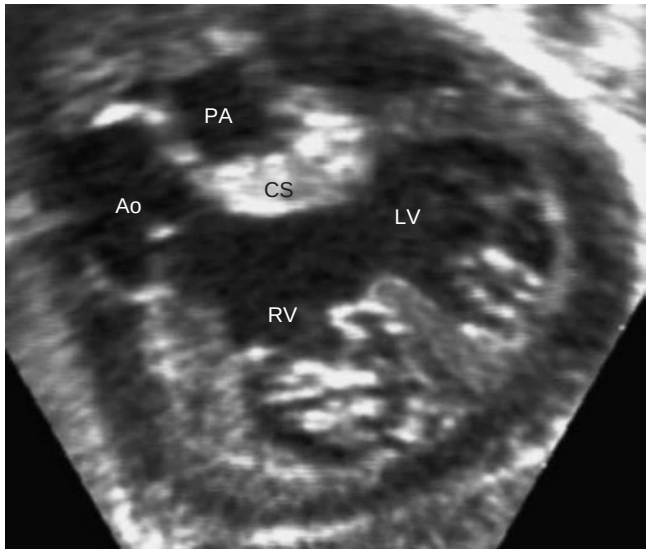


(c)

**Figure 25.1** Double-outlet right ventricle (DORV) with a subaortic ventricular septal defect (VSD) where the conal septum is attached to the antero-superior limb of the septal band: **(a)** an illustration; **(b)** a pathology specimen (reproduced with permission from Professor Robert H. Anderson, Institute of Child Health, London, UK); and **(c)** a modified subcostal short-axis view. Ao, aorta; CS, conal septum; LV, left ventricle; PA, pulmonary artery; RV, right ventricle; SB, septal band; TV, tricuspid valve.

artery is difficult and usually determined by the preferred approach of the diagnosing physician. Although many consider DORV with subpulmonary VSD synonymous with the Taussig–Bing anomaly, the original heart described by Taussig and Bing was a DORV case with a subpulmonary VSD, bilateral conus and side-by-side great arteries [18]. In patients with this anatomy, hypertrophy and rightward deviation of the conal septum as well as hypertrophy of the subaortic conal free wall can result in varying degrees of subaortic stenosis, which in turn is associated with coarctation or aortic arch interruption. In addition, the mitral valve may straddle the VSD with attachments to the subpulmonary conus.

*Doubly committed VSD (3–12% of cases)*

As a result of an absent or markedly deficient conal septum, the defect is in close proximity or even contiguous with both semilunar valves (Fig. 25.4). The VSD is located superiorly and is often large. The semilunar valves represent the antero-superior margin of the defect. Because the VSD is cradled between the limbs of the septal band, this part of the septal band along with the right ventriculo-infundibular fold form the entire postero-inferior margin of the defect; occasionally, however, the defect extends into the fibrous area of the membranous septum. Infrequently, these defects are associated with pulmonary or aortic outflow tract obstruction [73] (Fig. 25.4c,d).

*Noncommitted (remote) VSD (9–19% of cases)*

The defect is not cradled between the limbs of the septal band and thereby is considered noncommitted or remote because of the distance from the semilunar valves (Fig. 25.5). The defect can be located in the AV canal (inlet) septum, along the posterior aspect of the membranous septum, or within the muscular septum. It is important to recognize that some subaortic and subpulmonary VSDs cradled between the limbs of the septal band may appear remote because of elongated subarterial conus [71].

### *Conal morphology*

Conal morphology is important in the comprehensive description of DORV cases, but it is not a determining factor in

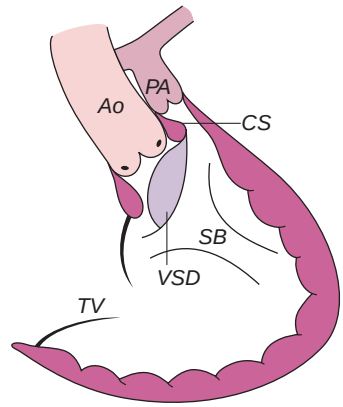


(a)

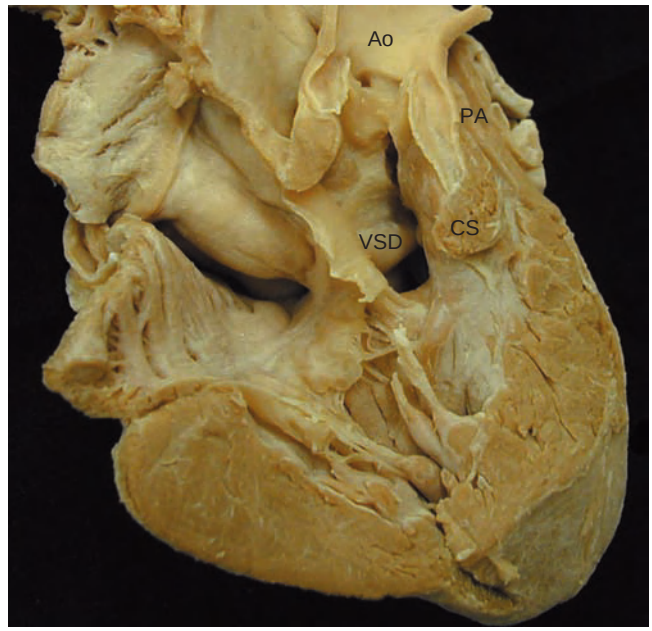


(b)

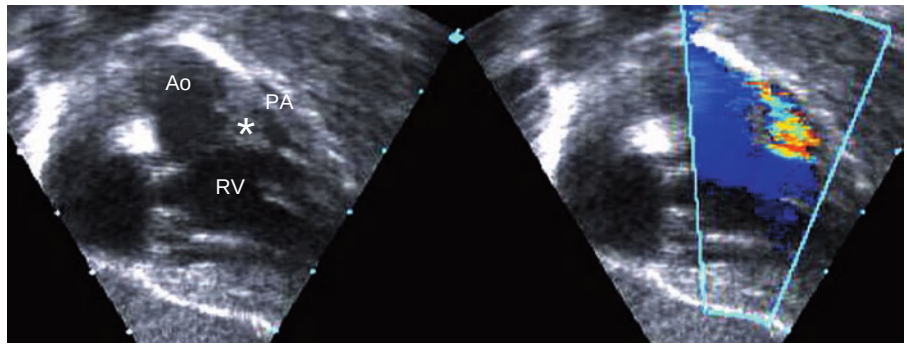


(c)

**Figure 25.2** Double-outlet right ventricle (DORV) with a subaortic ventricular septal defect (VSD) and pulmonary stenosis secondary to significant anterior attachment of the conal septum to the antero-superior limb of the septal band: **(a)** an illustration; **(b)** a pathology specimen (reproduced with permission from Professor Robert H. Anderson, Institute of Child Health, London, UK); and **(c)** a modified subcostal long-axis view (right axial oblique view) where the asterisk represents the conal septum. Ao, aorta; CS, conal septum; PA, pulmonary artery; RV, right ventricle; TV, tricuspid valve.

the definition of DORV [10,74]. Many configurations of conal morphology occur in DORV cases: bilateral conus, subpulmonary conus with absent subaortic conus, subaortic conus with absent subpulmonary conus, and bilaterally absent conus (Fig. 25.6). Van Praagh and colleagues [5,24] as well as Kirklin and Barratt-Boyes [68] have suggested that conal morphology is the primary determinant of the various patterns of great artery relationships seen in DORV. This view, however, has not been endorsed unanimously [10]. Other classification schemes of conal anatomy have been proposed as well [75].

An important aspect of the description of conal morphology is the distance from the VSD to each semilunar valve. This is particularly relevant in the setting of bilateral conus, where surgical repair likely involves a baffle from the LV through the VSD to the nearest semilunar valve (Fig. 25.7). In patients with a DORV and subaortic VSD, as the size of the subaortic conus increases, the distance from the tricuspid valve to the aortic valve increases and the distance from the tricuspid valve to the pulmonary valve decreases. Because the pathway from the LV to the aortic valve usually passes between the tricuspid and pulmonary valves, this measurement is crucial in determining the feasibility of intraventricular baffling (Fig. 25.8) [10,11,76]. Occasionally, surgical repair in a subpulmonary VSD involves baffling from the VSD to the distant aortic valve with resection of the conal septum [64,77]. Again the distance between the tricuspid and pulmonary valves can affect the feasibility of this repair.

Another important aspect is the morphology of the conal septum itself. The structure may be prominent with significant AV valve attachments, precluding an intraventricular baffle coursing from the VSD to the aortic valve with either a subaortic or a subpulmonary VSD. These attachments may also be problematic in cases where the semilunar valve adjacent to the VSD is hypoplastic and/or stenotic, and biventricular repair would require baffling from the VSD to the distant semilunar valve and resection of the conal septum. The conal septum may also deviate into one or the other subarterial outflow tract, resulting in some degree of subaortic or subpulmonary stenosis. In DORV with pulmonary stenosis, this deviation may or may not be associated with subpulmonary conal hypoplasia (Fig. 25.2). Often there

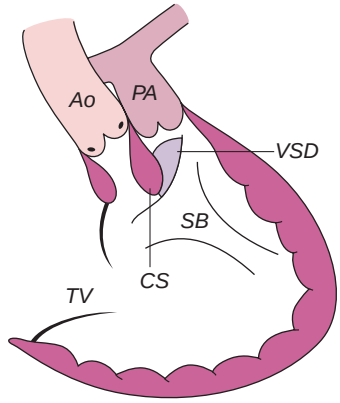


(a)

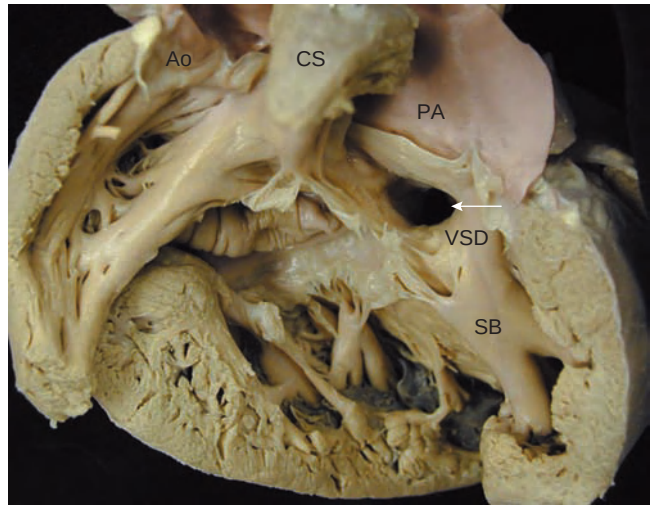


(b)

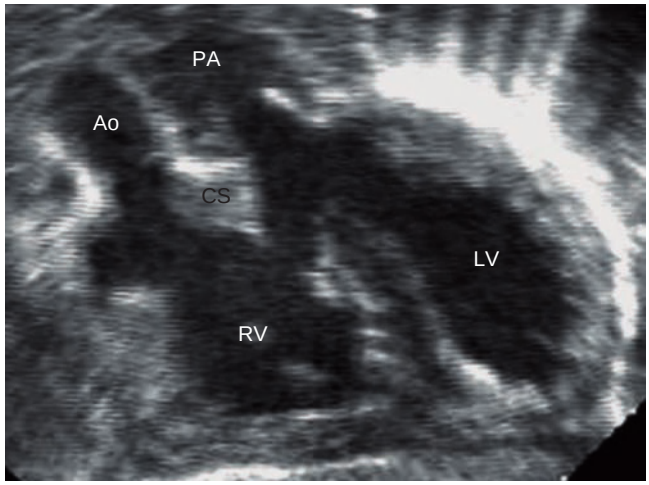


(c)

**Figure 25.3** Double-outlet right ventricle (DORV) with a subpulmonary ventricular septal defect (VSD) where the conal septum is attached to the right ventriculo-infundibular fold: **(a)** an illustration; **(b)** a pathology specimen (reproduced with permission from Professor Robert H. Anderson, Institute of Child Health, London, UK); and **(c)** a subcostal long-axis view. Ao, aorta; CS, conal septum; LV, left ventricle; PA, pulmonary artery; RV, right ventricle; SB, septal band; TV, tricuspid valve.

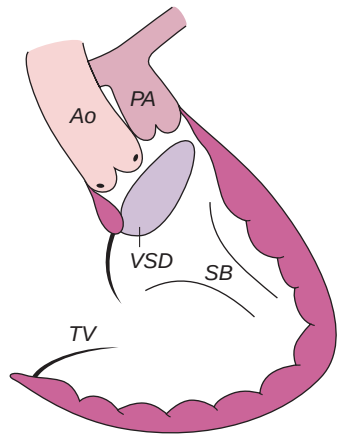


(a)

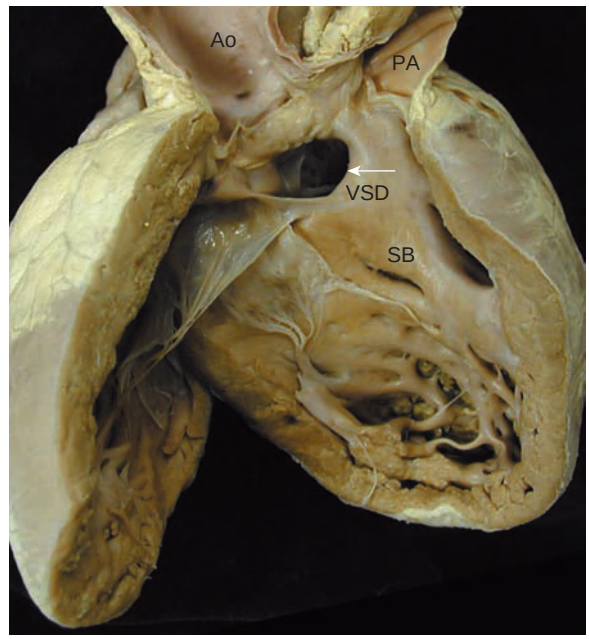


(b)

**Figure 25.4** Double-outlet right ventricle (DORV) with a doubly committed ventricular septal defect (VSD) and absent conal septum: **(a)** an illustration; **(b)** a pathology specimen (reproduced with permission from Professor Robert H. Anderson, Institute of Child Health, London, UK);

(c)

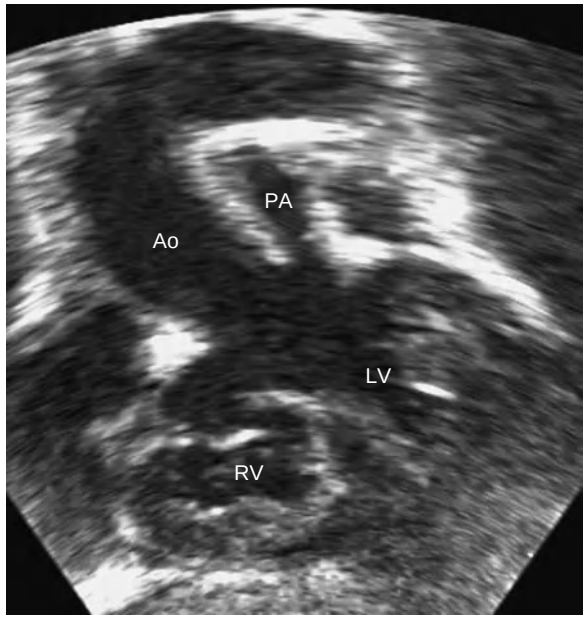


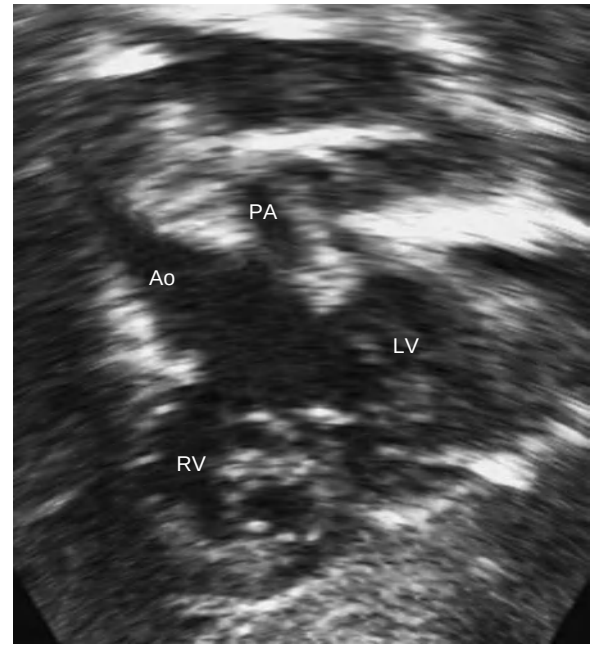


(d)

**Figure 25.4** (*continued*) **(c)** subcostal long-axis and **(d)** subcostal short-axis views, both of which also show the presence of pulmonary stenosis. Ao, aorta; LV, left ventricle; PA, pulmonary artery; RV, right ventricle; SB, septal band; TV, tricuspid valve.

is also pulmonary valve involvement with hypoplasia of the pulmonary annulus and pulmonary trunk as seen in TOF. In DORV with a subpulmonary VSD, the conal septum occasionally deviates into the subaortic region resulting in subaortic stenosis, coarctation or aortic arch interruption (Fig. 25.9).

### *Great artery relationships*

Possible positions of the semilunar valves relative to each other include: side-by-side; posterior and rightward aortic valve relative to the pulmonary valve (as in normally related great arteries); anterior and rightward aortic valve (D-malposition); aortic valve directly anterior to the pulmonary valve; posterior and leftward aortic valve (as in situs inversus totalis); and anterior and leftward aortic valve (L-malposition). The orientation of the great arteries relative to each other can be crossed or parallel. In the most common variant of DORV with subaortic VSD, the aorta is often rightward and slightly posterior or side-by-side relative to the main pulmonary artery. In DORV with subpulmonary VSD, the great arteries are generally side-by-side and parallel in their relationship, but the aorta can also be anterior and rightward relative to the pulmonary artery at the base of the heart (similar to {S,D,D} TGA). As stated previously, the spatial relationship of the great arteries does not always predict the VSD location [68] or the conal morphology [10].

### *Associated lesions*

Outflow tract obstruction occurs in up to 70% of DORV cases [12,13,65,68,78]. This usually requires some modification in the surgical approach and sometimes precludes biventricular repair. The most common variant involves pulmonary outflow tract obstruction at the subvalvar and/or valvar level, often seen in DORV with a subaortic VSD (Fig. 25.2). In the most severe cases, there is pulmonary atresia. Although the term DORV with pulmonary atresia can be problematic, the pulmonary trunk in most cases is clearly anchored to the RV such that the absence of connection is a functional phenomenon and not an anatomic one. Along the aortic outflow tract, subaortic stenosis and/or aortic arch obstruction (coarctation or aortic arch interruption) can occur in up to 50% of DORV cases with a subpulmonary VSD (Fig. 25.9) [75,79,80].

AV valve anomalies, including a common AV valve in the setting of an AV canal defect, occur in up to 35% of DORV cases [65,78]. An abnormal mitral valve is considered one of the significant risk factors for poor prognosis in these patients [13,67,81]. For example, a straddling mitral valve, which can occur in up to 20% of DORV cases with a subpulmonary VSD (Fig. 25.10) [65,80,82], may complicate a biventricular repair [83,84] or preclude it, thereby requiring single-ventricle palliation [85–87]. A parachute mitral valve or a supramitral ring with associated mitral stenosis can also

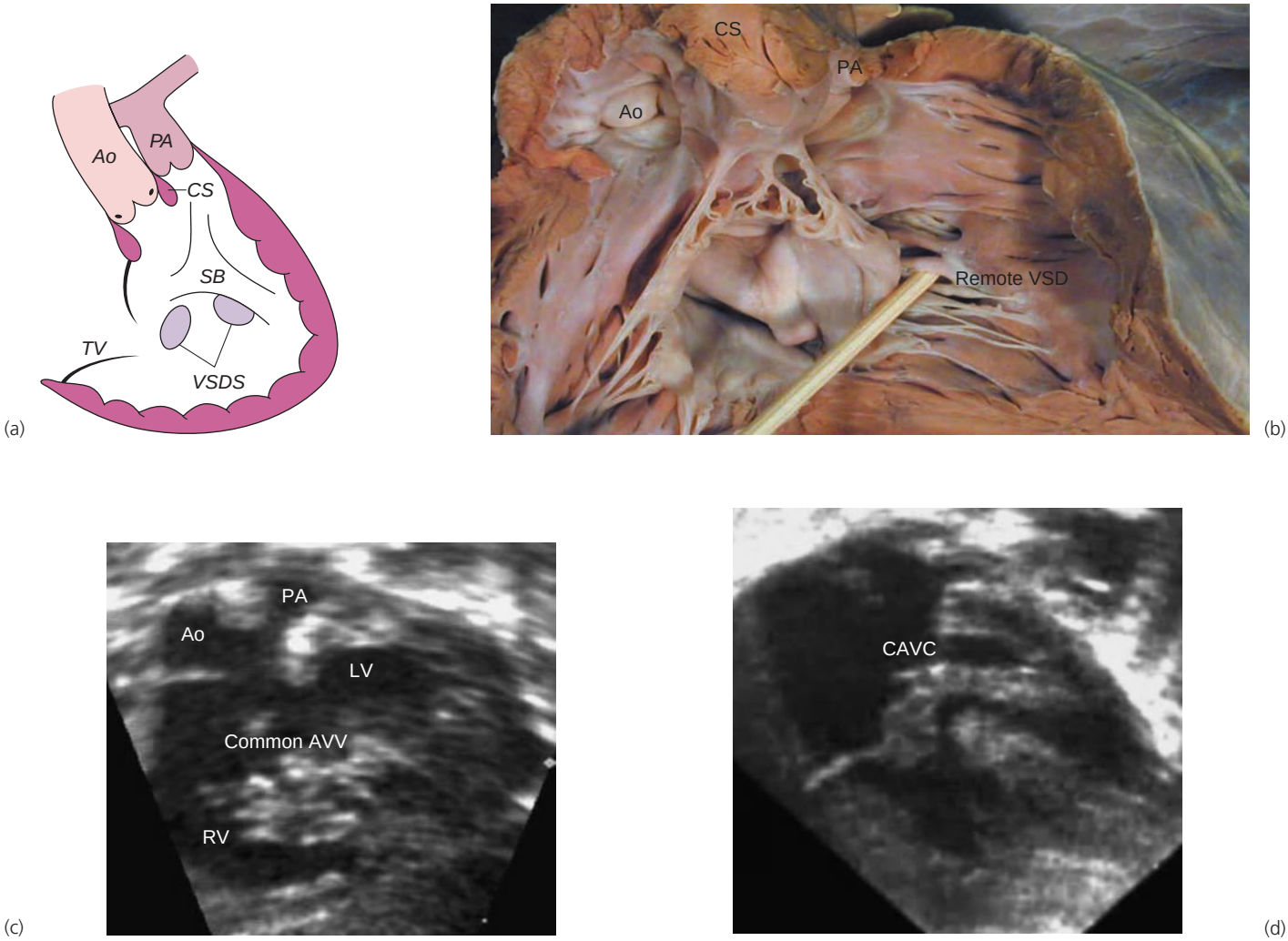


**Figure 25.5** Double-outlet right ventricle (DORV) with a remote ventricular septal defect (VSD): **(a)** an illustration; **(b)** a pathology specimen (reproduced with permission from Professor Robert H. Anderson, Institute of Child Health, London, UK); **(c)** a modified subcostal short-axis view showing the relationship of the great arteries to the VSD; and **(d)** an apical 4-chamber view showing the complete atrioventricular (AV) canal defect. Ao, aorta; AVV, atrioventricular valve; CAVC, complete atrioventricular canal defect; CS, conal septum; LV, left ventricle; PA, pulmonary artery; RV, right ventricle; SB, septal band; TV, tricuspid valve.

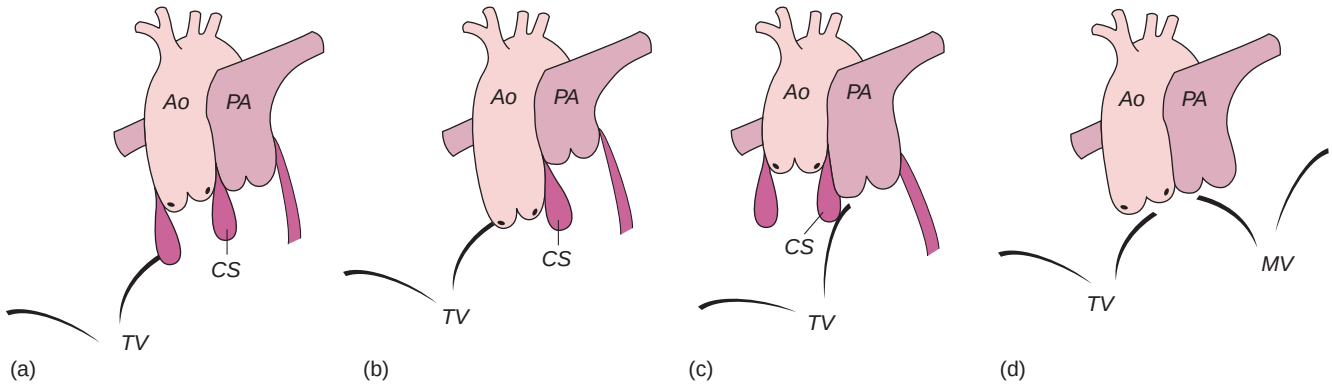


**Figure 25.6** Illustrations depicting the four categories of conal morphology: **(a)** bilateral conus, **(b)** absent subaortic conus, **(c)** absent subpulmonary conus and **(d)** bilaterally absent conus. Ao, aorta; CS, conal septum; MV, mitral valve; PA, pulmonary artery; TV, tricuspid valve.

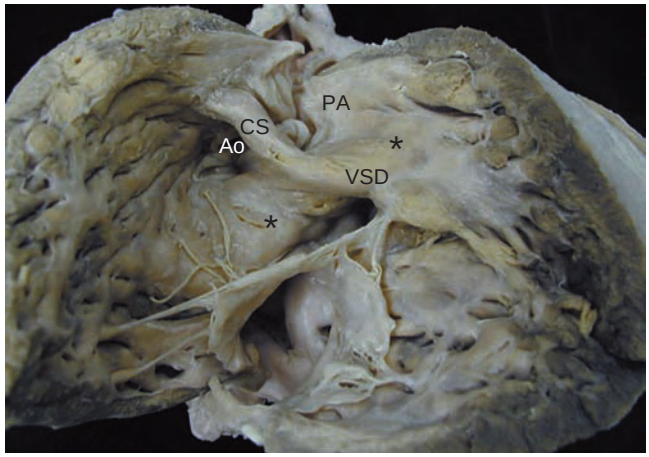


**Figure 25.7** Pathology specimen of a double-outlet right ventricle (DORV) with bilateral conus (indicated by the asterisks). Ao, aorta; CS, conal septum; PA, pulmonary artery; VSD, ventricular septal defect. Reproduced with permission from Professor Robert H. Anderson, Institute of Child Health, London, UK.

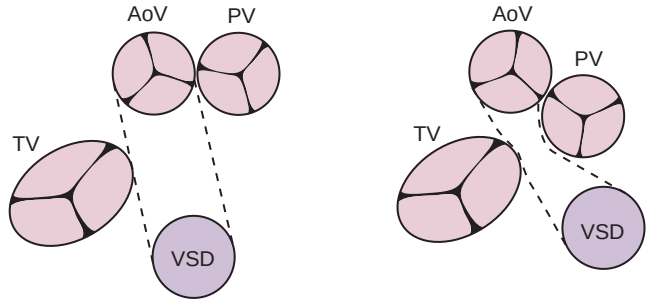


**Figure 25.8** Illustration of how the distance from the tricuspid valve (TV) to the pulmonary valve (PV) can affect the potential baffle pathway from the left ventricle (LV) to the aorta. AoV, aortic valve; VSD, ventricular septal defect.

(a)

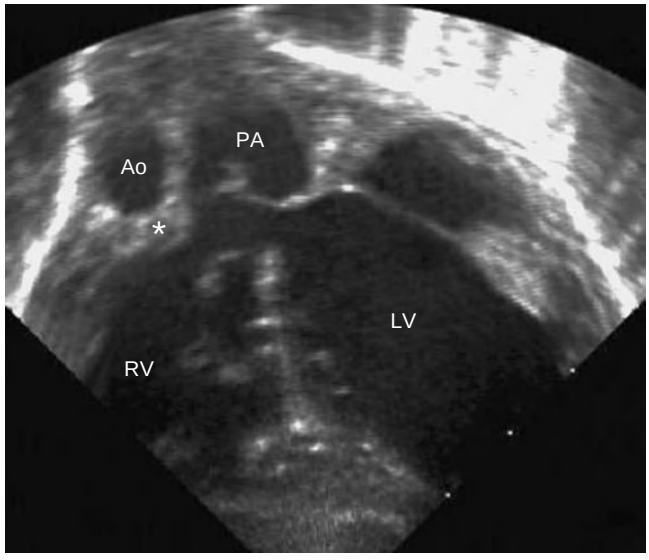


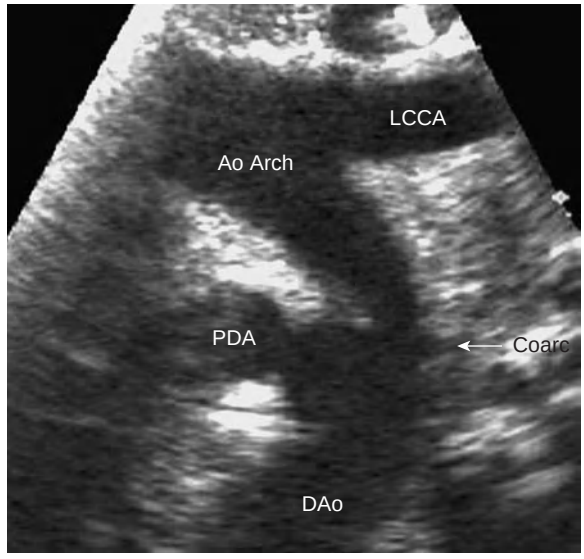


(b)

**Figure 25.9** Double-outlet right ventricle (DORV) with a subpulmonary ventricular septal defect (VSD), narrow subaortic region and coarctation: **(a)** subcostal long-axis view (the asterisk represents the conal septum); **(b)** suprasternal view. Ao, aorta; DAo, descending aorta; LCCA, left common carotid artery; LV, left ventricle; PA, pulmonary artery; PDA, patent ductus arteriosus; RV, right ventricle.

affect the long-term prognosis of biventricular repair and should be considered in planning the therapeutic approach. DORV with mitral atresia is a rare association that requires a single-ventricle palliation. A straddling tricuspid valve can also occur in DORV cases with a VSD in the AV canal septum. Rarely, the AV valves are situated in a criss-cross orientation, resulting in a complex relationship between the VSD and the great arteries (Fig. 25.11).

Other associated lesions include atrial septal defects, persistent left superior vena cava, and leftward juxtaposition of the atrial appendages (Fig. 25.12). DORV is common in patients with heterotaxy syndrome (usually of the asplenia type), often with associated systemic and pulmonary venous anomalies, common AV canal defects, and/or LV hypoplasia. Many heterotaxy cases cannot support a biventricular circulation and must therefore undergo single-ventricle palliation. A distinct constellation of cardiac anomalies involves a DORV with hypoplasia of the tricuspid valve and RV sinus, superior-inferior ventricles with criss-cross AV valves, and subvalvar and valvar pulmonary stenosis [5,88].

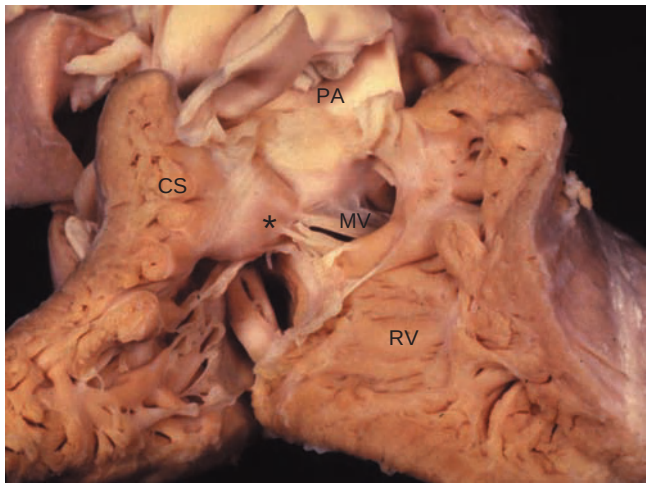


(a)

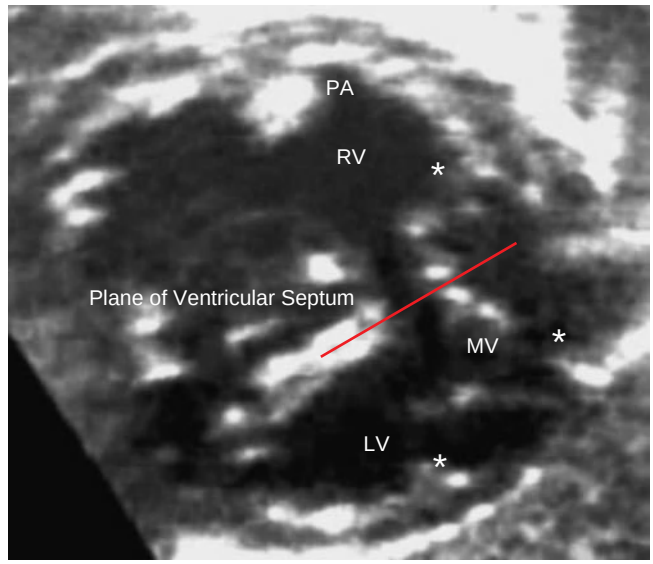


(b)

**Figure 25.10** Double-outlet right ventricle (DORV) with a subpulmonary ventricular septal defect (VSD) and straddling mitral valve: **(a)** pathology specimen (the aorta is located behind the conal septum) (reproduced with permission from Professor Robert H. Anderson, Institute of Child Health, London, UK); **(b)** subcostal short-axis view (the asterisks represent mitral valve attachments). CS, conal septum; LV, left ventricle; MV, mitral valve; PA, pulmonary artery; RV, right ventricle.

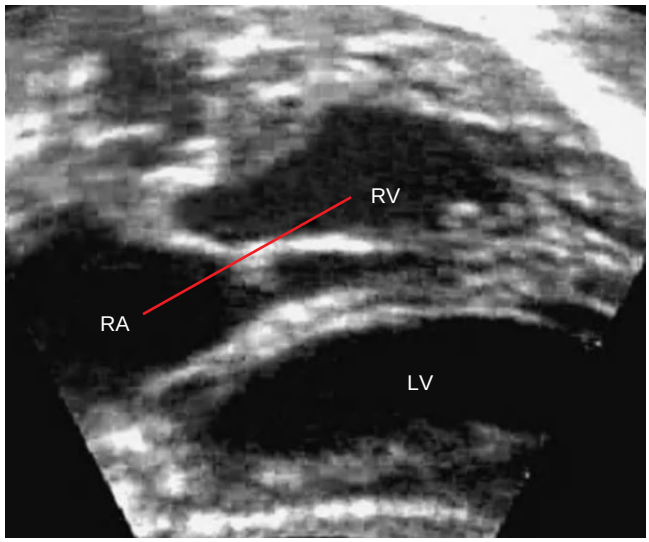


(a)

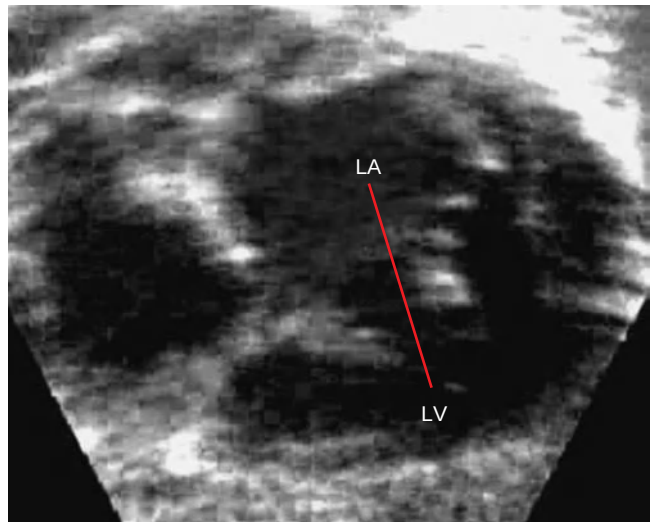


(b)

**Figure 25.11** Double-outlet right ventricle (DORV) with criss-cross atrioventricular (AV) valve orientation and superior–inferior ventricles in subcostal long-axis views showing **(a)** the right–left relationship of the right atrium to the superior right ventricle (RV), and **(b)** the postero-anterior relationship of the left atrium to the inferior left ventricle (LV). The red lines indicate the RA-to-RV and LA-to-LV inflow axes, respectively. LA, left atrium; RA, right atrium.

Coronary artery abnormalities occur in up to 30% of DORV cases [3], with an increased frequency in those with a subpulmonary or a remote VSD [12,89,90]. Side-by-side great arteries is another risk factor for an abnormal coronary arterial pattern [91]. The coronary artery pattern can be an important determinant of surgical management. For example, in DORV with a subpulmonary VSD requiring an arterial switch operation, an intramural coronary artery can potentially increase the operative risk. In DORV with a subaortic VSD and pulmonary stenosis, a coronary artery crossing the RV outflow tract can influence surgical repair of the pulmonary stenosis (Fig. 25.13).

## Pathophysiology

The variable clinical presentation and course of DORV patients reflect the anatomic and hemodynamic heterogeneity of this group. The pathophysiology is determined primarily by VSD size, VSD relationship to the great arteries and the consequent effects of blood flow streaming, presence of pulmonary or aortic outflow tract obstruction, pulmonary

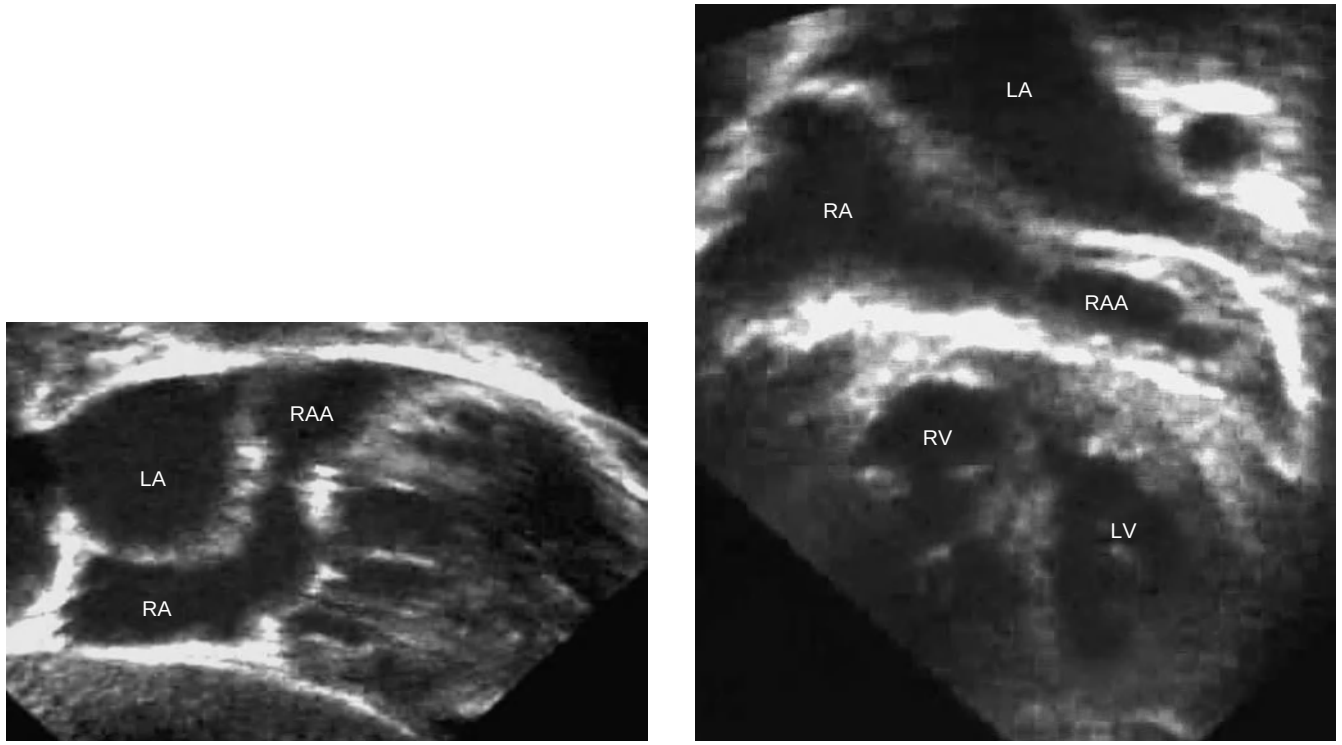


(a) (b)

**Figure 25.12** Double-outlet right ventricle (DORV) with leftward juxtaposition of the atrial appendages: **(a)** subcostal long-axis and **(b)** apical views. LA, left atrium; LV, left ventricle; RA, right atrium; RAA, right atrial appendage; RV, right ventricle.

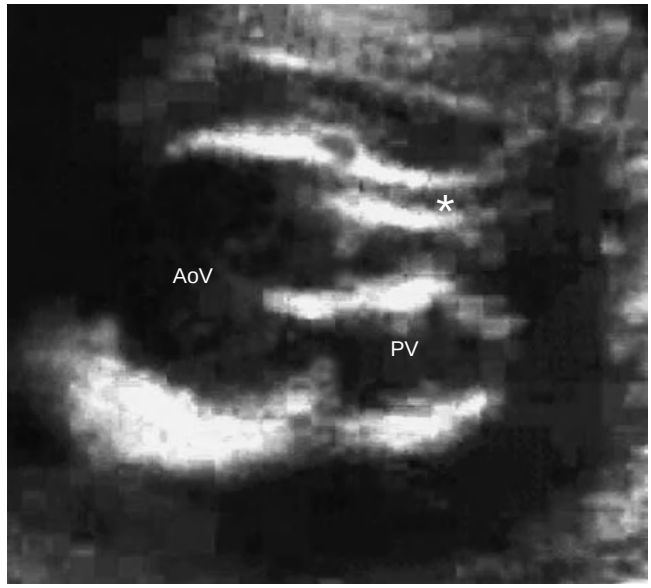


**Figure 25.13** Parasternal short-axis view of double-outlet right ventricle (DORV), subaortic ventricular septal defect and pulmonary stenosis where the right coronary artery conal branch (asterisk) crosses in front of the pulmonary outflow tract and supplies the anterior descending coronary artery. AoV, aortic valve; PV, pulmonary valve.

vascular resistance and associated cardiovascular anomalies. Some of the common pathophysiologic variants include:

- VSD physiology (DORV with a large VSD and no pulmonary stenosis);
- TOF physiology (DORV with a subaortic VSD and pulmonary stenosis);
- TGA physiology (DORV with a subpulmonary VSD ± aortic outflow obstruction);
- single-ventricle physiology (DORV with mitral atresia or significant ventricular hypoplasia, often in association with an unbalanced AV canal defect and/or heterotaxy syndrome).

## Imaging

### Goals of the examination and transthoracic imaging

The initial echocardiogram should establish the diagnosis and provide a comprehensive morphologic and physiologic description in order to determine the appropriate therapy. In addition to a detailed segmental approach [2,92–94], the evaluation should focus on the following features: VSD size and location; distance between the VSD and semilunar valves; presence of AV valve tissue between the VSD and semilunar valves; conal morphology (spatial relationship of the conal chambers, size and orientation of the conal septum, and presence and degree of outflow tract obstruction); spatial relationship of the great arteries and presence of associated cardiovascular anomalies.

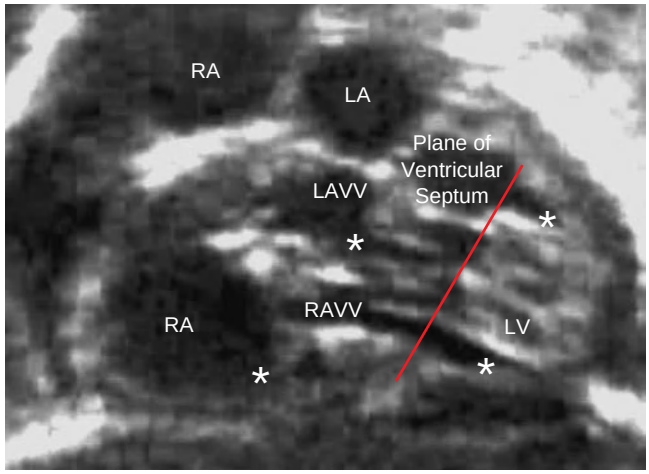


(a)

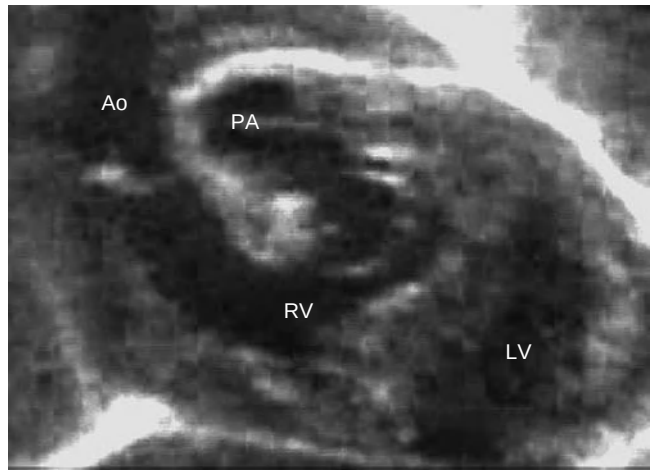


(b)

**Figure 25.14** Subcostal long-axis views of unusual double-outlet right ventricle (DORV) with mild left ventricular (LV) hypoplasia and bilateral straddling through a remote ventricular septal defect (VSD): **(a)** straddling of the right-sided and left-sided atrioventricular (AV) valves through the VSD where the asterisks represent the attachments of both AV valves to both ventricles; **(b)** both great arteries originating from the right ventricle (RV). Ao, aorta; LA, left atrium; LAVV, left atrioventricular valve; PA, pulmonary artery; RA, right atrium; RAVV, right atrioventricular valve.

Commitment of both great arteries to the RV can be displayed in standard long- and short-axis sweeps from subcostal, apical and parasternal views (Videoclip 25.1). Because of the 3-D relationship between the VSD and great arteries, determination of semilunar valve alignments relative to the ventricular septal plane must use multiple views, including subcostal short-axis, apical, and parasternal long-axis views. A parasternal short-axis sweep from the arterial roots toward the apex should quickly demonstrate the plane of the ventricular septum beyond the VSD. Upon returning to the short-axis view of the semilunar valves, an imaginary line representing the plane of the ventricular septum will transect the semilunar valves and help to delineate the degree of commitment to each ventricle. Real-time 3-D echocardiography is also helpful in the evaluation of ventriculoarterial alignment.

### *Systemic and pulmonary venous return and atrial morphology*

The systemic and pulmonary venous connections as well as the atrial morphology are best evaluated by imaging and color mapping sweeps in subcostal, parasternal short-axis, suprasternal, and right sternal border views. Systemic and pulmonary venous anomalies are particularly common in heterotaxy syndrome [95–97], but they can also occur in DORV without situs abnormalities. DORV is associated with leftward juxtaposition of the atrial appendages [98], particularly when the ascending aorta and pulmonary trunk are located along the extreme rightward aspect of the heart. Subcostal long-axis, apical, and parasternal short-axis sweeps will generally display the relationship of the atrial appendages to the great arteries (Fig. 25.12). During assessment of the atrial septum in these views, the septal plane may appear abnormally perpendicular to its usual location; this is because the perceived "atrial septum" is actually the plane of separation between the right atrial appendage and the left atrial chamber or appendage.

### *Atrioventricular canal*

The AV valves are best imaged from the subcostal, apical and parasternal views by 2-D and 3-D imaging. Identification of straddling chordae tendineae and leaflet tissue requires complete sweeps of the VSD in long- and short-axis planes from multiple views (Fig. 25.14; see also Fig. 25.10 and Videoclips 25.2 and 25.3). The mitral valve usually straddles an anterior conoventricular septal defect, whereas the tricuspid valve usually straddles a posterior AV canal-type (inlet) VSD. Other abnormalities of the mitral valve, such as parachute deformity, short chordae and supramitral ring, can be evaluated in subcostal short-axis, apical, and parasternal long- and short-axis views (Fig. 25.15). Criss-cross AV valves can be identified by visualizing the nearly perpendicular axes of mitral and tricuspid valve inflow along subcostal, apical and parasternal sweeps (Fig. 25.11; Videoclip 25.4).

### *Ventricular morphology and size*

Evaluation of ventricular morphology is described in Chapters 3 and 4. Ventricular size is an important determinant of biventricular repair versus single-ventricle palliation. Severe ventricular hypoplasia is usually obvious from standard subcostal and precordial views. Intermediate ventricular hypoplasia (moderate or less in degree) requires accurate measurements of volume and mass (see Chapter 5). Diastolic AV valve diameters are also informative.

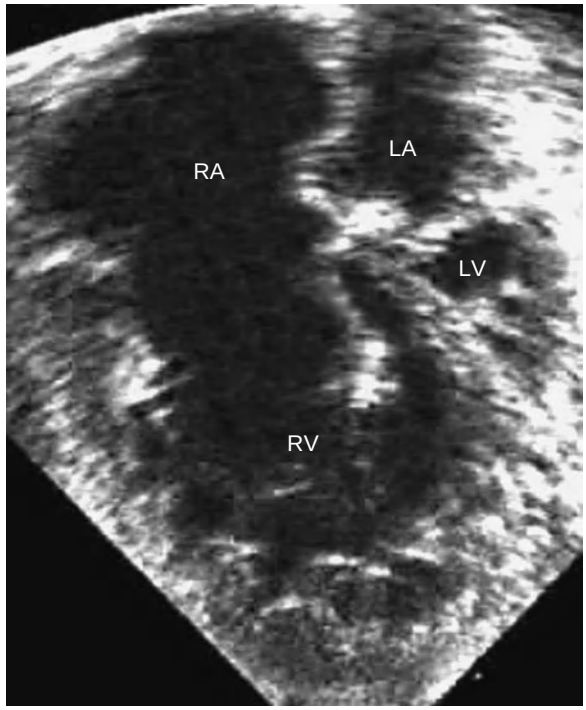


**Figure 25.15** Double-outlet right ventricle (DORV) with mitral stenosis and left ventricular (LV) hypoplasia in an apical 4-chamber view. LA, left atrium; RA, right atrium; RV, right ventricle.

### *VSD location and size*

As with the other segments of the heart, subcostal, apical and parasternal sweeps can delineate the location, extent and boundaries of a VSD and its spatial relationship to the great arteries (Figs 25.1, 25.3–25.5; Videoclips 25.5 and 25.6). For subaortic, subpulmonary and doubly committed VSDs, the inferior margin is usually the crest of the muscular septum between the limbs of septal band. The postero-inferior margin is usually the area of fibrous continuity between the tricuspid and mitral valves (when the defect is confluent with the membranous septum) or the muscular ventriculo-infundibular fold in continuity with the posterior limb of the septal band. The antero-superior margin is usually the adjacent semilunar valve or subarterial conus. These margins are easily delineated in subcostal, apical and parasternal long-axis (but not short-axis) views. These views can also be used to measure the distance from the VSD to the adjacent semilunar valve and to exclude potential obstacles to a baffle along this area (such as AV valve attachments and a short distance from the tricuspid valve to the other semilunar valve, as discussed previously). Remote VSDs are usually located in the AV canal (inlet) septum or within the apical muscular septum. These defects are best imaged in subcostal, apical and parasternal views. Evaluation should exclude straddling AV valves as well as complex muscular VSDs with multiple entrances and exits on either side of the ventricular septum.

### *Conal morphology and outflow tract obstruction*

In DORV with a subaortic VSD, subpulmonary stenosis can result from the same anatomic abnormalities seen in TOF (Fig. 25.2): leftward, anterior and superior deviation of the conal septum relative to the muscular septum; and hypertrophy of the conal free wall. The subpulmonary conus is hypoplastic, usually with significant obstruction and occasionally with valvar pulmonary atresia (Videoclip 25.7). The subpulmonary conus is best evaluated in subcostal, apical and parasternal views. The subaortic conus is best evaluated in parasternal long-axis views displaying the muscular separation between the mitral and aortic valves. When the subaortic conus is extensive with either anterior-posterior or side-by-side orientation of the conal chambers, subcostal long- and short-axis sweeps easily display its size. In DORV with a subpulmonary VSD, subaortic stenosis can result from the muscular tunnel produced by the conal septum (which is deviated to the right), a hypertrophied right ventriculo-infundibular fold, and the RV conal anterior free wall; subcostal long- and short-axis sweeps are useful in delineating these three components (Fig. 25.9a). Doppler interrogation in subcostal, apical, right sternal border and suprasternal views can evaluate the degree of obstruction.

In DORV with a subaortic VSD and bilateral conus, the distance from the tricuspid valve to the pulmonary valve can be measured in subcostal and parasternal views. As the subaortic conus becomes more elongated, the subpulmonary conus usually becomes attenuated. When the tricuspid-to-pulmonary valve distance is less than the aortic annular diameter, a baffle pathway from the LV to the aortic valve may become obstructed. In this situation, biventricular repair may involve resection of the conal septum, baffling from the LV to the aorta, and placement of a homograft or conduit from the RV to the pulmonary artery (Rastelli repair). Tricuspid valve attachments to the conal septum, as seen from the subcostal and parasternal views, may also obstruct a baffle pathway from the LV to the aortic valve.

### *Arterial roots*

Assessment of the spatial relationship between the great arteries can be accomplished in subcostal long-axis sweeps with a completely horizontal probe orientation. The appearance of each great artery is noted during the sweep in order to determine their relative positions. For example, side-by-side great arteries will appear simultaneously during the sweep, and great arteries in a direct anterior-posterior relationship will not be visible at the same time but should appear separately in the same area during the sweep. Parasternal imaging of the semilunar valves and arterial roots should be oriented along a transverse plane of the

thorax rather than a short-axis plane of the heart because the oblique views obtained with the latter can be misleading with regard to the spatial relationship of these structures.

### *Coronary arteries*

Identifying abnormalities in the coronary artery pattern is crucial in the preoperative assessment of all DORV patients. This is best achieved from parasternal short-axis views using a high-frequency transducer. In general, the coronary arteries originate from the two aortic sinuses facing the pulmonary valve. The bifurcation of the left main coronary artery into the anterior descending and circumflex coronary arteries should be identified. Absent bifurcation of the left coronary artery can indicate abnormal origin of one or more of the branches, which may course anterior or posterior to the great arteries in order to reach its/their usual distribution site(s) (such as inverted coronary arteries and origin of the anterior descending or circumflex coronary artery from the right coronary artery). An abnormal anterior coronary artery is usually seen in parasternal short-axis views (Fig. 25.13 and Videoclip 25.8). An abnormal posterior coronary artery is sometimes seen in subcostal long-axis or even apical sweeps (Fig. 25.16). The parasternal short-axis view can also display an intramural coronary artery.

### *Aortic arch*

Aortic arch abnormalities such as coarctation and aortic arch interruption are best evaluated in suprasternal views (Fig. 25.9b). The short-axis (transverse) view can determine the aortic arch branching pattern, and the long-axis view can quantify the degree of obstruction in coarctation or measure the length of separation in cases of interruption. A high left parasagittal view (also known as the ductal view), with the probe placed superiorly on the left chest in a vertical orientation, often provides excellent display of the aortic isthmus at the level of the coarctation. This is also the best location to evaluate a patent ductus arteriosus. Lastly, the abdominal aortic flow profile from subcostal views is usually abnormal in coarctation, with a blunted upstroke and delayed return to baseline.

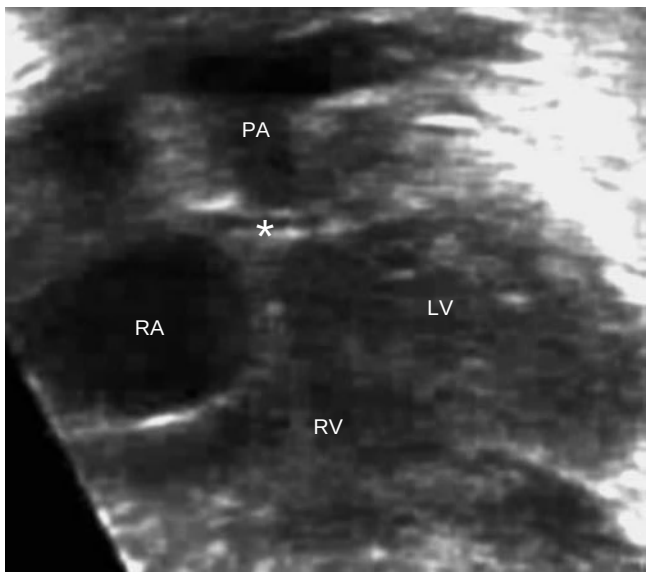


**Figure 25.16** Subcostal long-axis view of double-outlet right ventricle (DORV) with a subpulmonary ventricular septal defect and a circumflex coronary artery (asterisk) that originates from the right coronary artery and courses behind the pulmonary trunk. LV, left ventricle; PA, pulmonary artery; RA, right atrium; RV, right ventricle.

## Prenatal assessment

Similar to the postnatal data presented in the Baltimore-Washington Infant Study [34], DORV is the 12th most frequent diagnosis in a combined series of fetal cardiac malformations reported by Allan et al. [99], representing 62/2136 fetuses with congenital heart disease. In studies evaluating fetal detection of cardiac malformations [100,101], the prenatal incidence of DORV (1/6727 in low-risk and 1/3246 in high-risk pregnancies) is higher than the reported postnatal rates discussed previously [29–33]. This discrepancy may relate to high intrauterine and neonatal mortality rates [102], variations in diagnostic criteria, and selection bias.

DORV is often missed on routine obstetric ultrasound screening because the 4-chamber view is usually normal. Occasionally a ventricular or great arterial size discrepancy prompts performance of a fetal echocardiogram, during which the diagnosis can be made (Fig. 25.17). As in the postnatal assessment of DORV, the fetal study should evaluate the VSD, conal morphology, outflow tract obstruction, spatial relationship of the great arteries, anomalies of the aortic arch and associated malformations. Pulmonary outflow tract obstruction in the fetus may not be associated with a significant gradient by Doppler interrogation, but color mapping may reveal reversal of normal flow in the ductus arteriosus (from the aorta to the pulmonary arteries). Similarly, significant subaortic stenosis may be associated with reversal of flow in the aortic arch.

When a DORV is detected in utero, counseling should include discussion of the anatomic and functional findings, treatment options, mortality and morbidity statistics, and neurodevelopmental outcome data. It is also important to recognize that the fetal echocardiogram might not provide all the morphologic information needed to choose the appropriate surgical intervention. Amniocentesis should be recommended given the 12% frequency of chromosomal abnormalities associated with DORV [34].

## Intraoperative assessment

Surgical options for DORV include the following categories:

- Baffle from the LV to the aortic valve with or without resection of the conal septum while ensuring unobstructed intracardiac flow from the RV to the pulmonary arteries.

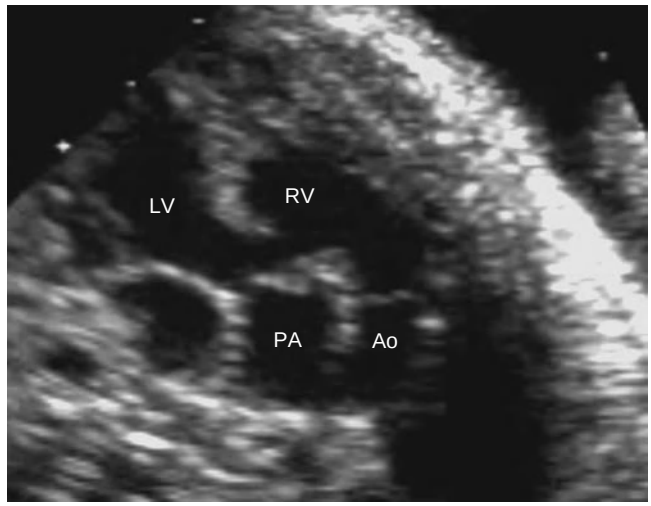


(a)

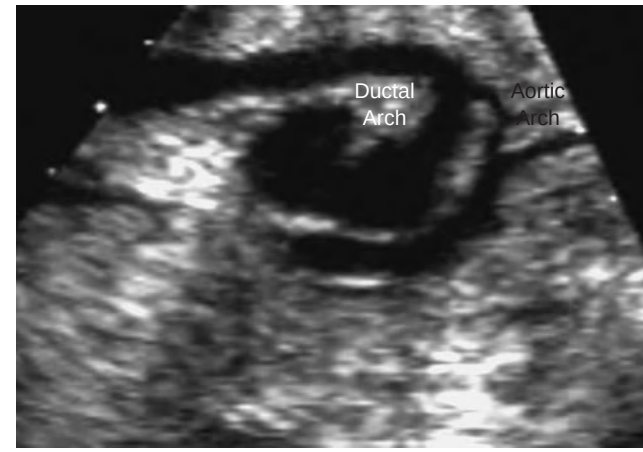


(b)

**Figure 25.17** Fetal echocardiogram of a double-outlet right ventricle (DORV) with a subpulmonary ventricular septal defect showing **(a)** the parallel great arteries originating from the right ventricle (RV), and **(b)** the small aortic arch inserting onto the ductal arch suggestive of aortic coarctation. Ao, aorta; LV, left ventricle; PA, pulmonary artery; RV, right ventricle. Reproduced courtesy of Dr Jack Rychik, Children's Hospital of Philadelphia.

- Baffle from the LV to the aortic valve with or without resection of the conal septum as well as placement of a homograft or conduit from the RV to the pulmonary artery (Rastelli procedure) or direct anastomosis of the pulmonary trunk to the RV free wall (réparation à l'étage ventriculaire, or REV procedure).
- Baffle from the LV to the pulmonary valve and arterial switch operation.
- Single ventricle palliation.

Because most patients with a DORV undergo surgical intervention within the first year of life, the information obtained by transthoracic imaging is usually adequate for surgical planning. Although new diagnostic information is rarely gleaned during the pre-bypass transesophageal echocardiogram (TEE), the study can confirm the preoperative diagnoses and provide the surgeon and cardiologist with another opportunity to review the planned surgical approach (Fig. 25.18). The goals of the pre-bypass TEE are the same as those of the transthoracic examination except for the aortic arch evaluation.

The post-bypass TEE in patients undergoing biventricular repair should exclude the following postoperative problems:

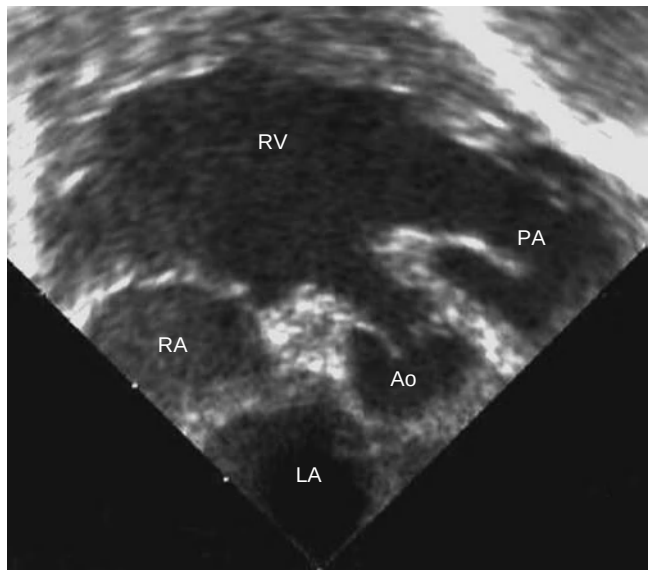


(a)

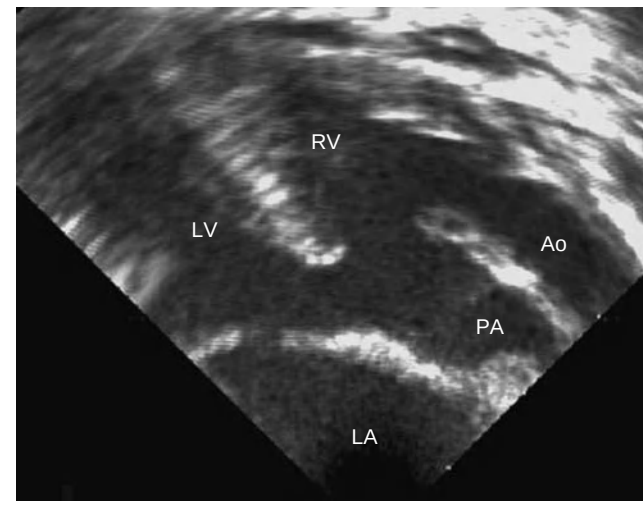


(b)

**Figure 25.18** Preoperative transesophageal echocardiogram in a vertical (longitudinal) plane of **(a)** a double-outlet right ventricle (DORV) with a subaortic ventricular septal defect (VSD), bilateral conus and prominent muscle bundles within the subaortic conus, and **(b)** a DORV with a subpulmonary VSD and mildly narrow subaortic region. Ao, aorta; LA, left atrium; LV, left ventricle; PA, pulmonary artery; RA, right atrium; RV, right ventricle.

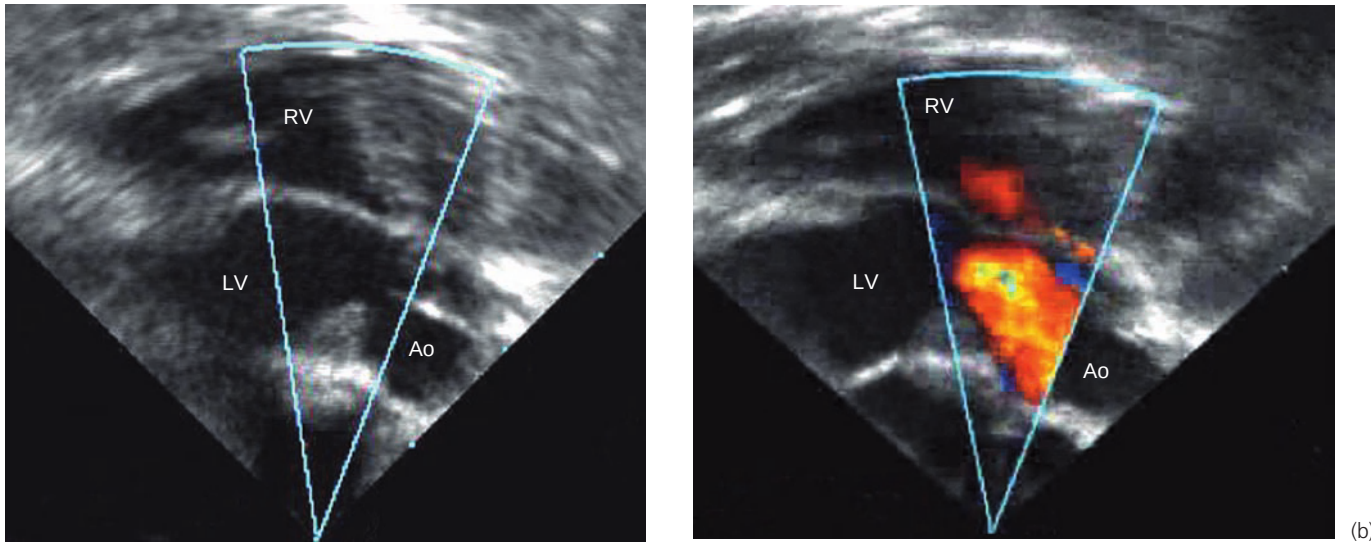


(a) (b)

**Figure 25.19** Postoperative transesophageal echocardiogram in a vertical (longitudinal) plane after biventricular repair of a double-outlet right ventricle (DORV) with a subaortic ventricular septal defect, bilateral conus and prominent muscle bundles in the subaortic conus now with **(a)** narrowing along the subaortic region and **(b)** turbulence in flow along this area, as revealed by color mapping. Ao, aorta; LV, left ventricle; RV, right ventricle.

- Residual VSD along the patch margins with the ventricular septum, along the patch margin at its attachment to the RV free wall (intramural VSD described by Preminger and colleagues [103]), or in the muscular septum.
- Aortic outflow tract obstruction (Fig. 25.19), especially if the preoperative anatomy involved a small VSD, an elongated subaortic conus or straddling AV valves.
- Pulmonary outflow tract obstruction.
- Pulmonary regurgitation, especially after a Rastelli or REV procedure.
- AV valve stenosis or regurgitation.
- Residual atrial septal defect or patent foramen ovale.
- Ventricular dysfunction.

## Follow-up assessment

The long-term sequelae of biventricular repair for DORV patients are as variable as the wide spectrum of morphologic features identified preoperatively. Some of the residual problems that may affect a patient's clinical status after biventricular repair include:

- VSD, including intramural defects, which are (i) located at the margin between the patch and the RV free wall, often just below the aortic valve; (ii) not always recognized because of their unusual location; and (iii) not always present in the early postoperative period until associated RV hypertrophy regresses (Fig. 25.20 and Videoclip 25.9) [103].
- Subaortic stenosis, particularly in patients who had a remote VSD or those whose VSD needed to be enlarged (Videoclip 25.10) [12,13].
- Neoaortic valve regurgitation, supravalvar aortic stenosis, or neoaortic root dilation after arterial switch operation.
- Aortic arch obstruction after coarctation repair or aortic arch reconstruction.
- Subvalvar pulmonary stenosis.
- Pulmonary stenosis, due to obstruction along the homograft or conduit after a Rastelli procedure or at the anastomosis of the pulmonary trunk to the RV in a REV procedure.
- Pulmonary regurgitation associated with a transannular RV outflow tract patch, pulmonary valvotomy or homograft valve.
- Supravalvar pulmonary stenosis or branch pulmonary artery obstruction after arterial switch operation.
- Mitral regurgitation or stenosis in patients after AV canal defect repair.
- RV or LV dysfunction.

Some of these issues may be relevant for DORV patients requiring single-ventricle palliation, but the long-term follow-up for this group of patients is discussed in other sections of this book.

## Imaging of the adult

Although most adults with DORV have undergone surgical intervention, few patients survive to adulthood without intervention. Examples include patients with pulmonary stenosis and optimal balance between systemic and pulmonary blood flow and those without pulmonary stenosis and pulmonary vascular obstructive disease. Transthoracic echocardiographic follow-up is challenging for adults because most do not have good subcostal windows, and parasternal views are limited in the setting of postoperative scarring and highly reflective structures such as calcified valves, patches and conduits. Although assessment of AV valve and LV function can usually be accomplished in apical

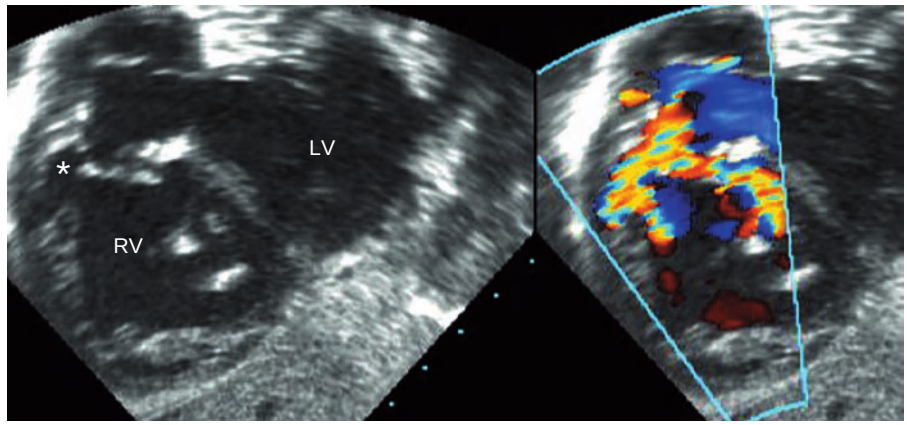


**Figure 25.20** Subcostal short-axis view after biventricular repair of a double-outlet right ventricle (DORV) with a subaortic conus showing a small residual intramural ventricular septal defect (asterisk) at the antero-superior patch margin where it is attached to the anterior free wall of the right ventricle (RV) below the aortic valve. LV, left ventricle.

and parasternal views, evaluation of complex baffle pathways in terms of residual outflow tract obstruction and intracardiac shunting remains difficult. Frequently, TEE, cardiovascular magnetic resonance (CMR) or cardiac catheterization is necessary to obtain adequate anatomic and physiologic data. CMR is a particularly useful adjunct to echocardiography in adolescent and adult patients with palliated DORV because this modality is not invasive, does not expose patients to ionizing radiation and the associated risk of cancer, and is capable of providing comprehensive morphologic and hemodynamic information irrespective of body size [104]. Computed tomography (CT) is a noninvasive alternative to CMR in patients with pacemakers or implanted defibrillators, although this modality provides little functional information.

## Double-outlet left ventricle

### Definition

Double-outlet left ventricle (DOLV) is a rare type of ventriculo-arterial alignment that can be defined as complete or nearly complete origin of both great arteries from the LV. Similar to DORV, the Congenital Heart Surgery Nomenclature and Database Committee of the Society of Thoracic Surgeons has defined DOLV as "a type of ventriculo-arterial connection in which both great arteries arise entirely or predominantly from the morphologic LV" [105].

### Historical perspective

Early reports suggested that DOLV is an embryologic improbability [106] or even an impossibility [107]. In 1967, Sakakibara and colleagues described the first DOLV patient undergoing surgical repair [108]. In 1970, Paul and colleagues published a report of an autopsy-proven case of DOLV with intact ventricular septum and bilaterally deficient conus [109]. Since the publication of these first cases over 40 years ago, nearly 200 cases of DOLV have been reported.

### Incidence

DOLV is such a rare anomaly that all of the previously discussed studies reporting the incidence rates of DORV do not include DOLV in their analyses [29–33]. Wilkinson suggested that DOLV probably accounts for only 5% of all biventricular hearts with double-outlet connections, corresponding to an incidence of 0.5 in 100 000 live births [65]. Among the 58 832 cases of congenital cardiac malformations diagnosed at Children's Hospital Boston from 1988 to 2002, only three patients had DOLV [35,78].

### Etiology

Similar to DORV, the etiology of DOLV is unknown but likely relates to several mechanisms. Paul and colleagues suggested that DOLV results from deficient conal growth beneath both semilunar valves (rather than the normal deficient conal growth beneath only the aortic valve) [109]. Anderson and colleagues, in their description of another case of DOLV in 1974, countered that errors in differential conal absorption or regression, rather than differential conal growth, provided a better explanation for the development of a DOLV [110]. Van Praagh and colleagues described the range of conal morphology found in 33 heart specimens with DOLV and speculated that a deficient subpulmonary conus associated with abnormal rotation of the outflow tract results in failure of normal alignment between the pulmonary valve and the RV [24]. Manner and colleagues used a chick embryo model to conclude that DOLV resulted not from errors in conal growth or absorption but from a malalignment between the conal septum and the posterior wall of the RV outflow tract, isolating the proximal part of the RV conus from the great arteries [111]. They emphasized the observation that the primordial conus and the primordial truncus arteriosus originate from different cardiogenic fields and that disruption in the normal development of the conal or proximal cushions might be the cause for this anterior malposition of the posterior RV conal wall.

## Morphology and classification

Several DOLV classification schemes have been proposed utilizing morphologic features to characterize the defect, determine the pathophysiology and provide a rationale for surgical intervention [112,113]. Almost 75% of cases have two well-developed ventricles [113], and most are amenable to biventricular repair. The remaining cases are associated with anomalies that preclude a biventricular outcome, such as tricuspid atresia and unbalanced common AV canal defect. Similar to the approach used for DORV variants, the distinguishing features include:

- segmental anatomy;
- location and size of the VSD and its relationship to the great arteries;
- conal morphology;
- spatial relationship of the great arteries;
- ventricular hypoplasia;
- associated lesions (such as AV valve anomalies and outflow tract obstruction).

### Segmental anatomy

An analysis of 109 DOLV cases by Van Praagh and colleagues [113] showed that patients with two well-developed ventricles presented with several distinct segmental patterns:

- The most common anatomic type (49% of cases) had {S,D,D} segmental anatomy with visceral and atrial situs solitus, ventricular D-loop, a rightward aortic valve and a subaortic VSD. Outflow tract obstruction occurred along the subpulmonary region (similar to TOF) in 27% and along the subaortic region in 3.7%; 1.8% had no outflow tract obstruction. DOLV {S,D,D} was associated with a subpulmonary VSD in 10.1% and with a doubly committed VSD in 6.4%.
- DOLV {S,D,L} with visceral and atrial situs solitus, ventricular D-loop, a leftward aortic valve, a subaortic VSD and pulmonary stenosis occurred in 16.5%.
- DOLV {S,L,L} with visceral and atrial situs solitus, ventricular L-loop and a leftward aortic valve occurred in 3.7%.
- DOLV {I,L,L} or {I,L,D} with visceral and atrial situs inversus, ventricular L-loop, and either leftward or rightward position of the aortic valve occurred in 2.8%. DOLV {I,D,D} with visceral and atrial situs inversus, ventricular D-loop and a rightward aortic valve occurred in 1.8%.

### VSD location and size

The following types of VSD morphology have been reported in DOLV [112,113]:

- subaortic (70–75%) (Fig. 25.21 and Videoclip 25.11);
- subpulmonary (15–17%);
- doubly committed (6–9%);
- noncommitted or remote (2%);
- intact ventricular septum (1–2%).

Similar to DORV, the subaortic, subpulmonary and doubly committed VSDs are located between the limbs of septal band. The defect may be contiguous with the tricuspid valve as it extends into the membranous septum, or it may be separated from the tricuspid valve by muscular tissue. Cases with a doubly committed VSD are often difficult to distinguish

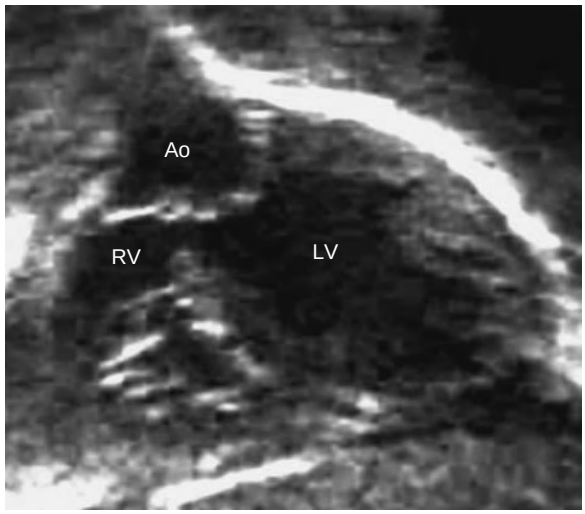


(a)

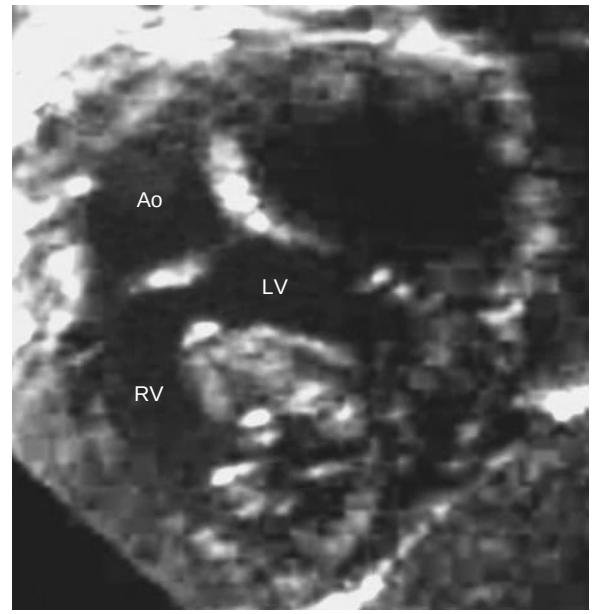


(b)

**Figure 25.21** Double-outlet left ventricle (DOLV) with a subaortic ventricular septal defect: **(a)** subcostal long-axis view, and **(b)** subcostal short-axis view. Ao, aorta; LV, left ventricle; RV, right ventricle.

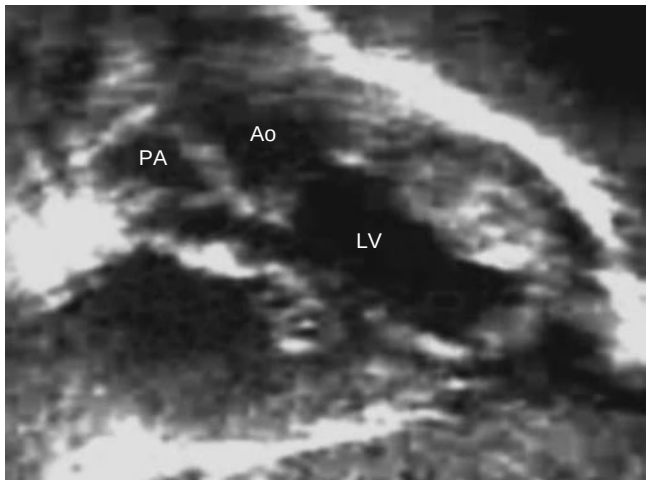


**Figure 25.22** Double-outlet left ventricle (DOLV) with a subpulmonary conus and pulmonary stenosis in a subcostal long-axis view. Ao, aorta; LV, left ventricle; PA, pulmonary artery.

from DORV, prompting some to label this diagnosis "double-outlet both ventricles" [114].

### Conal morphology

Among 33 DOLV specimens described by Van Praagh and colleagues in another report [24]:

- 16 (48%) had a subpulmonary conus only (Fig. 25.22 and Videoclip 25.11);
- 9 (27%) had a subaortic conus only;
- 4 (12%) had bilateral conus;
- 4 (12%) had bilaterally deficient conus.

### Spatial relationship of the great arteries

The spatial relationships of the great arteries are variable [75]. In more than half of DOLV cases, the aortic valve is to the right of and posterior, side-by-side or anterior to the pulmonary valve. Approximately 40% have a leftward aortic valve (Fig. 25.22 and Videoclip 25.11), and the aortic valve is directly anterior in another 8%.

### Associated anomalies

Among patients with biventricular hearts and a subaortic VSD, subvalvar and/or valvar pulmonary stenosis occurs in 90% (Fig. 25.22 and Videoclip 25.11) [113]. Aortic outflow tract obstruction occurs frequently in cases with a subpulmonary VSD, often accompanied by coarctation or aortic arch interruption. A hypoplastic ventricle occurs in 27%. Most are associated with a tricuspid valve anomaly (such as atresia, severe stenosis or Ebstein malformation), whereas others are associated with mitral atresia, double-inlet LV and heterotaxy syndrome.

### Pathophysiology

The primary determinants of the pathophysiology in DOLV patients include VSD location and size, and its relationship to the semilunar valves, conal morphology, conal septum orientation, outflow tract obstruction, ventricular hypoplasia, AV valve anomalies and segmental anatomy. In the absence of significant outflow tract obstruction, a patient with DOLV {S,D,D} and a subaortic VSD will present with the symptoms of a large VSD. Cyanosis may result from significant pulmonary outflow tract obstruction or streaming of blood from the RV to the aorta in the setting of a subaortic VSD. Patients with aortic outflow tract obstruction and significant coarctation or aortic arch interruption may present in a critical condition requiring persistent flow through the ductus arteriosus.

### Imaging

Because of the rarity of this defect, the few reports regarding surgical repair have generally included the following options [115, 116]:

- VSD closure and placement of a valved conduit from the RV to the pulmonary artery.
- VSD closure with translocation of the pulmonary root to the RV.
- Intraventricular baffling of the RV to the pulmonary artery with or without VSD enlargement.
- Single ventricle palliation.

The techniques for preoperative, intraoperative and postoperative imaging are similar to those outlined for DORV in the first section of this chapter. In addition, the long-term issues are also similar, and these need to be addressed using follow-up echocardiograms and/or other adjunct imaging modalities.

## References

1. Van Praagh R. What is the Taussig-Bing malformation? *Circulation* 1968;28:445–9.
2. Shinebourne EA, Macartney FJ, Anderson RH. Sequential chamber localization – logical approach to diagnosis in congenital heart disease. *Br Heart J* 1976;38:327–40.
3. Wilcox BR, Ho SY, Macartney FJ et al. Surgical anatomy of double-outlet right ventricle with situs solitus and atrioventricular concordance. *J Thorac Cardiov Surg* 1981;82:405–17.
4. Edwards WD. Double-outlet right ventricle and tetralogy of Fallot. Two distinct but not mutually exclusive entities. *J Thorac Cardiov Surg* 1981;82:418–22.
5. Van Praagh S, Davidoff A, Chin A et al. Double outlet right ventricle: Anatomic types and developmental implications based on a study of 101 autopsied cases. *Coeur* 1982;13: 389–440.
6. Neufeld HN, Dushane JW, Wood EH et al. Origin of both great vessels from the right ventricle. I. Without pulmonary stenosis. *Circulation* 1961;23:399–412.
7. Neufeld HN, Dushane JW, Edwards JE. Origin of both great vessels from the right ventricle. II. With pulmonary stenosis. *Circulation* 1961;23:603–12.
8. Neufeld HN, Lucas RV Jr, Lester RG et al. Origin of both great vessels from the right ventricle without pulmonary stenosis. *Br Heart J* 1962;24:393–408.

9. McGoon D. Origin of both great vessels from the right ventricle. *Surg Clin N Am* 1961;41:1113–20.
10. Lecompte Y, Batisse A, Di Carlo D. Double-outlet right ventricle: a surgical synthesis. *Adv Cardiac Surg* 1993;4:109–36.
11. Sakata R, Lecompte Y, Batisse A et al. Anatomic repair of anomalies of ventriculoarterial connection associated with ventricular septal defect. I. Criteria of surgical decision. *J Thorac Cardiov Surg* 1988;95:90–5.
12. Aoki M, Forbess JM, Jonas RA et al. Result of biventricular repair for double-outlet right ventricle. *J Thorac Cardiov Surg* 1994;107:338–49; discussion 49–50.
13. Belli E, Serraf A, Lacour-Gayet F et al. Biventricular repair for double-outlet right ventricle. Results and long-term follow-up. *Circulation* 1998;98(19 Suppl.):II360–5; discussion II5–7.
14. Abernathy J. *Surgical and Physiological Essays, Part II.* London: James Evans, 1793:162.
15. Peacock TB. *On Malformations of the Human Heart.* London: John Churchill and Sons 1866:32.
16. Vierordt H. Die angeborenen Herzkrankheiten. *Northnagel's Handb du spez Pathhol u Therap*. Wien: 1898:244.
17. Spitzer A. Uber den Bauplan des normalen und missbildeten Herzens. Versuch einer phylogenetischen theorie. *Virchows Arch F Path Anat* 1923;243:81–272.
18. Taussig HB, Bing RJ. Complete transposition of the aorta and levoposition of the pulmonary artery. *Am Heart J* 1949;37: 551–9.
19. Beuren A. Differential diagnosis of the Taussig–Bing heart from complete transposition of the great vessels with a posteriorly overriding pulmonary artery. *Circulation* 1960;21:1071–87.
20. Braun K, de Vries A, Feingold DS et al. Complete dextroposition of the aorta, pulmonary stenosis, interventricular septal defect, and patent foramen ovale. *Am Heart J* 1952;43:773–80.
21. Witham AC. Double outlet right ventricle. A partial transposition complex. *Am Heart J* 1957;53:928–39.
22. Baron MG. Radiologic notes in cardiology. Angiographic differentiation between tetralogy of Fallot and double-outlet right ventricle. Relationship of the mitral and aortic valves. *Circulation* 1971;43:451–5.
23. Sridaromont S, Ritter DG, Feldt RH et al. Double-outlet right ventricle. Anatomic and angiocardiographic correlations. *Mayo Clin Proc* 1978;53:555–77.
24. Van Praagh R, Layton WM, Van Praagh S. The morphogenesis of normal and abnormal relationships between the great arteries and the ventricles: pathologic and experimental data. In: Van Praagh R, Takao A (eds) *Etiology and Morphogenesis of Congenital Heart Disease*. Mount Kisco, NY: Futura, 1980; 271–316.
25. Lev M, Bharati S, Meng CC et al. A concept of double-outlet right ventricle. *J Thorac Cardiov Surg* 1972;64:271–81.
26. Kirklin JW, Pacifico AD, Bargeron LM Jr, Soto B. Cardiac repair in anatomically corrected malposition of the great arteries. *Circulation* 1973;48:153–9.
27. Howell CE, Ho SY, Anderson RH, Elliott MJ. Fibrous skeleton and ventricular outflow tracts in double-outlet right ventricle. *Ann Thorac Surg* 1991;51:394–400.
28. Walters HL 3rd, Mavroudis C, Tchervenkov CI et al. Congenital Heart Surgery Nomenclature and Database Project: double outlet right ventricle. *Ann Thorac Surg* 2000;69(4 Suppl.):S249–63.
29. Hoffman JI, Kaplan S. The incidence of congenital heart disease. *J Am Coll Cardiol* 2002;39:1890–900.
30. Fyler DC, Bucklet LP, Hellenbrand WE, Cohn HE. Report of the New England Regional Infant Cardiac Program. *Pediatrics* 1980;65(Suppl.):375–461.
31. Ferencz C, Rubin JD, McCarter RJ et al. Congenital heart disease: prevalence at livebirth. The Baltimore-Washington Infant Study. *Am J Epidemiol* 1985;121:31–6.
32. Grabitz RG, Joffres MR, Collins-Nakai RL. Congenital heart disease: incidence in the first year of life. The Alberta Heritage Pediatric Cardiology Program. *Am J Epidemiol* 1988;128:381–8.
33. Botto LD, Correa A, Erickson JD. Racial and temporal variations in the prevalence of heart defects. *Pediatrics* 2001;107: E32.
34. Perry LW, Neill CA, Ferencz C et al. Infants with congenital heart disease: the cases. In: Ferencz C, Rubin JD, Loffredo CA, Magee CA (eds) *Perspectives in Pediatric Cardiology Vol. 4: Epidemiology of Congenital Heart Disease The Baltimore-Washington Infant Study 1981–1989*. Mount Kisco, NY: Futura 1993;33–62.
35. Triedman JK. Methodological issues for database development: trends. In: Keane JF, Lock JE, Fyler DC (eds) *Nadas' Pediatric Cardiology*, 2nd edn. Philadelphia: Saunders Elsevier, 2006; 323–36.
36. Ferencz C, Correa-Villasenor A, Loffredo CA, Wilson PD. Malformations of the cardiac outflow tract. In: Ferencz C, Correa-Villasenor A, Loffredo CA, Wilson PD (eds) *Perspectives in Pediatric Cardiology Vol. 5: Genetic and Environmental Risk Factors of Major Cardiovascular Malformations The Baltimore–Washington Infant Study 1981–1989*. Armonk, NY: Futura, 1997: 59–102.
37. Vuillemin M, Pexieder T, Winking H. Pathogenesis of various forms of double outlet right ventricle in mouse fetal trisomy 13. *Int J Cardiol* 1991;33:281–304.
38. Van Praagh S, Truman T, Firpo A et al. Cardiac malformations in trisomy-18: a study of 41 postmortem cases. *J Am Coll Cardiol* 1989;13:1586–97.
39. Goldmuntz E, Clark BJ, Mitchell LE et al. Frequency of 22q11 deletions in patients with conotruncal defects. *J Am Coll Cardiol* 1998;32:492–8.
40. Brannan CI, Perkins AS, Vogel KS et al. Targeted disruption of the neurofibromatosis type-1 gene leads to developmental abnormalities in heart and various neural crest-derived tissues. *Gene Dev* 1994;8:1019–29.
41. Epstein JA. Pax3, neural crest and cardiovascular development. *Trends Cardiovas Med* 1996;6:255–60.
42. Gruber PJ, Kubalak SW, Pexieder T et al. RXR alpha deficiency confers genetic susceptibility for aortic sac, conotruncal, atrioventricular cushion, and ventricular muscle defects in mice. *J Clin Invest* 1996;98:1332–43.
43. Goldmuntz E, Bamford R, Karkera JD et al. CFC1 mutations in patients with transposition of the great arteries and double-outlet right ventricle. *Am J Hum Genet* 2002;70:776–80.
44. Franco D, Campione M. The role of Pitx2 during cardiac development. Linking left-right signaling and congenital heart diseases. *Trends Cardiovasc Med* 2003;13:157–63.
45. Pu WT, Ishiwata T, Juraszek AL et al. GATA4 is a dosage-sensitive regulator of cardiac morphogenesis. *Dev Biol* 2004; 275:235–44.

46. Bartram U, Molin DG, Wisse LJ et al. Double-outlet right ventricle and overriding tricuspid valve reflect disturbances of looping, myocardialization, endocardial cushion differentiation, and apoptosis in TGF-beta(2)-knockout mice. *Circulation* 2001;103:2745–52.
47. Gu H, Smith FC, Taffet SM, Delmar M. High incidence of cardiac malformations in connexin40-deficient mice. *Circ Res* 2003;93:201–6.
48. Henderson DJ, Phillips HM. Outflow tract remodeling – a role for tissue polarity? In: Artman M, Benson DW, Srivastava D, Nakazawa M (eds) *Cardiovascular Development and Congenital Malformations: Molecular and Genetic Mechanisms*. Malden, MA: Balckwell Futura, 2005;155–7.
49. Phillips HM, Murdoch JN, Chaudhry B et al. Vangl2 acts via RhoA signaling to regulate polarized cell movements during development of the proximal outflow tract. *Circ Res* 2005;96: 292–9.
50. Arteaga M, de la Cruz MV, Sanchez C, Diaz GF. Double outlet right ventricle: experimental morphogenesis in the chick embryo heart. *Pediatr Cardiol* 1982;3:219–27.
51. Kirby ML, Turnage KL 3rd, Hays BM. Characterization of conotruncal malformations following ablation of "cardiac" neural crest. *Anat Rec* 1985;213:87–93.
52. Ferencz C, Rubin JD, McCarter RJ, Clark EB. Maternal diabetes and cardiovascular malformations: predominance of double outlet right ventricle and truncus arteriosus. *Teratology* 1990; 41:319–26.
53. Zierler S, Rothman KJ. Congenital heart disease in relation to maternal use of Bendectin and other drugs in early pregnancy. *N Engl J Med* 1985;313:347–52.
54. Arey LB. The heart and circulation changes. In: *Developmental Anatomy: A Textbook and Laboratory Manual of Embryology,* revised 7th edn. Philadelphia: WB Saunders, 1974;375–95.
55. Moore KL. The circulatory system: the cardiovascular and lymphatic systems. In: *The Developing Human: Clinically Oriented Embryology*, 3rd edn. Philadelphia: WB Saunders, 1982;298–343.
56. Manner J. Cardiac looping in the chick embryo: a morphological review with special reference to terminological and biomechanical aspects of the looping process. *Anat Rec* 2000;259: 248–62.
57. de la Cruz MV, Markwald RR, Krug EL et al. Living morphogenesis of the ventricles and congenital pathology of their component parts. *Cardiol Young* 2001;11:588–600.
58. Moorman A, Webb S, Brown NA et al. Development of the heart: (1) formation of the cardiac chambers and arterial trunks. *Heart (British Cardiac Society)* 2003;89:806–14.
59. Anderson RH, Webb S, Brown NA et al. Development of the heart: (2) Septation of the atriums and ventricles. *Heart (British Cardiac Society)* 2003;89:949–58.
60. Anderson RH, Webb S, Brown NA et al. Development of the heart: (3) formation of the ventricular outflow tracts, arterial valves, and intrapericardial arterial trunks. *Heart (British Cardiac Society)* 2003;89:1110–8.
61. van den Hoff MJ, Moorman AF, Ruijter JM et al. Myocardialization of the cardiac outflow tract. *Dev Biol* 1999;212: 477–90.
62. Zamora R, Moller JH, Edwards JE. Double outlet right ventricle: anatomic types and associated anomalies. *Chest* 1975;68: 672–7.
63. Sridaromont S, Feldt RH, Ritter DG et al. Double outlet right ventricle: hemodynamic and anatomic correlations. *Am J Cardiol* 1976;38:85–94.
64. Patrick DL, McGoon DC. An operation for double-outlet right ventricle with transposition of the great arteries. *J Cardiovasc Surg* 1968;9:537–42.
65. Wilkinson JL. Double outlet ventricle. In: Anderson RH, Baker EJ, Macartney FJ et al. (eds) *Paediatric Cardiology*, 2nd edn. London: Churchill Livingstone, 2002;1353–81.
66. Takeuchi K, Del Nido PJ. Surgical management of double-outlet right ventricle with subaortic ventricular septal defect. *Semin Thorac Cardiovasc Surg Pediatr Card Surg Annu* 2000;3: 34–42.
67. Sondheimer HM, Freedom RM, Olley PM. Double outlet right ventricle: clinical spectrum and prognosis. *Am J Cardiol* 1977; 39:709–14.
68. Kirklin JW, Barratt-Boyes BG. Double-outlet right ventricle. In: *Cardiac Surgery,* 2nd edn. New York: Churchill Livingstone, 1993;1469–500.
69. Kleinert S, Sano T, Weintraub RG et al. Anatomic features and surgical strategies in double-outlet right ventricle. *Circulation* 1997;96:1233–9.
70. Troise DE, Ranieri L, Arciprete PM. Surgical repair for double outlet right ventricle and intact ventricular septum. *Ann Thorac Surg* 2001;71:1018–9.
71. Anderson RH, McCarthy K, Cook AC. Double outlet right ventricle. *Cardiol Young* 2001;11:329–44.
72. Van Praagh R, Perez-Trevino C, Reynolds JL et al. Double outlet right ventricle {S,D,L} with subaortic ventricular septal defect and pulmonary stenosis. *Am J Cardiol* 1975;35:42–53.
73. Uemura H, Yagihara T, Kadohama T et al. Repair of double outlet right ventricle with doubly committed ventricular septal defect. *Cardiol Young* 2001;11:415–9.
74. Pasquini L, Sanders SP, Parness IA et al. Conal anatomy in 119 patients with D-loop transposition of the great arteries and ventricular septal defect: an echocardiographic and pathologic study. *J Am Coll Cardiol* 1993;21:1712–21.
75. Snider AR, Serwer GA, Ritter SB. Double outlet right ventricle. In: *Echocardiography in Pediatric Heart Disease*, 2nd edn. St Louis, MO: Mosby, 1997;323–42.
76. Castaneda AR, Jonas RA, Mayer JE, Hanley FL. Double-outlet right ventricle. In: *Cardiac Surgery of the Neonate and Infant*. Philadelphia: WB Saunders, 1994;445–59.
77. Kawashima Y, Matsuda H, Yagihara T et al. Intraventricular repair for Taussig–Bing anomaly. *J Thorac Cardiov Surg* 1993;105:591–6; discussion 6–7.
78. Keane JF, Fyler DC. Double-outlet right ventricle. In: Keane JF, Lock JE, Fyler DC (eds) *Nadas' Pediatric Cardiology*, 2nd edn. Philadelphia: Saunders Elsevier, 2006;735–41.
79. Comas JV, Mignosa C, Cochrane AD, et al. Taussig–Bing anomaly and arterial switch: aortic arch obstruction does not influence outcome. *Eur J Cardiothorac Surg* 1996;10:1114–9.
80. Takeuchi K, McGowan FX Jr, Moran AM et al. Surgical outcome of double-outlet right ventricle with subpulmonary VSD. *Ann Thorac Surg* 2001;71:49–52; discussion 53–3.

81. Serraf A, Belli E, Lacour-Gayet F et al. Biventricular repair for double-outlet right ventricle. *Semin Thorac Cardiovasc Surg Pediatr Card Surg Annu* 2000;3:43–56.
82. Fraisse A, del Nido PJ, Gaudart J, Geva T. Echocardiographic characteristics and outcome of straddling mitral valve. *J Am Coll Cardiol* 2001;38:819–26.
83. Serraf A, Nakamura T, Lacour-Gayet F et al. Surgical approaches for double-outlet right ventricle or transposition of the great arteries associated with straddling atrioventricular valves. *J Thorac Cardiov Surg* 1996;111:527–35.
84. Aeba R, Katogi T, Takeuchi S, Kawada S. Surgical management of the straddling mitral valve in the biventricular heart. *Ann Thorac Surg* 2000;69:130–4.
85. Russo P, Danielson GK, Puga FJ et al. Modified Fontan procedure for biventricular hearts with complex forms of double-outlet right ventricle. *Circulation* 1988;78:III20–5.
86. Delius RE, Rademecker MA, de Leval MR et al. Is a high-risk biventricular repair always preferable to conversion to a single ventricle repair? *J Thorac Cardiov Surg* 1996;112:1561–8; discussion 8–9.
87. Serraf A, Jonas RA, Burke RP et al. Univentricular repair for complex double right ventricle and transposed great arteries. *Cardiol Young* 1997;7:207–14.
88. Geva T, Van Praagh S, Sanders SP et al. Straddling mitral valve with hypoplastic right ventricle, crisscross atrioventricular relations, double outlet right ventricle and dextrocardia: morphologic, diagnostic and surgical considerations. *J Am Coll Cardiol* 1991;17:1603–12.
89. Uemura H, Yagihara T, Kawashima Y et al. Coronary arterial anatomy in double-outlet right ventricle with subpulmonary VSD. *Ann Thorac Surg* 1995;59:591–7.
90. Lacour-Gayet F, Haun C, Ntalakoura K et al. Biventricular repair of double outlet right ventricle with noncommitted ventricular septal defect (VSD) by VSD rerouting to the pulmonary artery and arterial switch. *Eur J Cardiothorac Surg* 2002;21:1042–8.
91. Gordillo L, Faye-Petersen O, de la Cruz MV, Soto B. Coronary arterial patterns in double-outlet right ventricle. *Am J Cardiol* 1993;71:1108–10.
92. Tynan MJ, Becker AE, Macartney FJ et al. Nomenclature and classification of congenital heart disease. *Br Heart J* 1979; 41:544–53.
93. Smallhorn JF. Double-outlet right ventricle: An echocardiographic approach. *Semin Thorac Cardiovasc Surg Pediatr Card Surg Annu* 2000;3:20–33.
94. Sanders SP, Bierman FZ, Williams RG. Conotruncal malformations: diagnosis in infancy using subxiphoid 2-dimensional echocardiography. *Am J Cardiol* 1982;50:1361–7.
95. Van Praagh S. Cardiac malpositions and the heterotaxy syndromes. In: Keane JF, Lock JE, Fyler DC (eds) *Nadas' Pediatric Cardiology,* 2nd edn. Philadelphia: Saunders Elsevier, 2006; 675–95.
96. Rose V, Izukawa T, Moes CA. Syndromes of asplenia and polysplenia. A review of cardiac and non-cardiac malformations in 60 cases with special reference to diagnosis and prognosis. *Br Heart J* 1975;37:840–52.
97. Rubino M, Van Praagh S, Kadoba K et al. Systemic and pulmonary venous connections in visceral heterotaxy with asplenia. Diagnostic and surgical considerations based on seventy-two autopsied cases. *J Thorac Cardiov Surg* 1995;110: 641–50.
98. Lai WW, Ravishankar C, Gross RP et al. Juxtaposition of the atrial appendages: a clinical series of 22 patients. *Pediatr Cardiol* 2001;22:121–7.
99. Allan L, Hornberger LK, Sharland G. Appendix A.2. In: Allan L, Hornberger LK, Sharland G (eds) *Textbook of Fetal Cardiology* London: Greenwich Medical Media, 2000;581.
100. Hafner E, Scholler J, Schuchter K et al. Detection of fetal congenital heart disease in a low-risk population. *Prenatal Diag* 1998;18:808–15.
101. Buskens E, Stewart PA, Hess J et al. Efficacy of fetal echocardiography and yield by risk category. *Obstetr Gynecol* 1996;87: 423–8.
102. Kim N, Friedberg MK, Silverman NH. Diagnosis and prognosis of fetuses with double outlet right ventricle. *Prenatal Diag* 2006; 26:740–5.
103. Preminger TJ, Sanders SP, van der Velde ME et al. "Intramural" residual interventricular defects after repair of conotruncal malformations. *Circulation* 1994;89:236–42.
104. Dorfman AL, Geva T. Magnetic resonance imaging evaluation of congenital heart disease: conotruncal anomalies. *J Cardiovasc Magn Reson* 2006;8:645–59.
105. Tchervenkov CI, Walters HL 3rd, Chu VF. Congenital Heart Surgery Nomenclature and Database Project: double outlet left ventricle. *Ann Thorac Surg* 2000;69(4 Suppl.):S264–9.
106. Grant RP. The morphogenesis of transposition of the great vessels. *Circulation* 1962;26:819–40.
107. Van Mierop LHS, Wiglesworth FW. Pathogenesis of transposition complexes: II. Anomalies due to faulty transfer of the posterior great artery. *Am J Cardiol* 1963;12:226–32.
108. Sakakibara S, Arai T, Hashimoto A, Nogi M. Both great vessels arising from the left ventricle. *Bull Heart Inst Jpn* 1967:66–86.
109. Paul MH, Muster AJ, Sinha SN et al. Double-outlet left ventricle with an intact ventricular septum: clinical and autopsy diagnosis and developmental implications. *Circulation* 1970;41:129–39.
110. Anderson R, Galbraith R, Gibson R, Miller G. Double outlet left ventricle. *Br Heart J* 1974;36:554–8.
111. Manner J, Seidl W, Steding G. Embryological observations on the formal pathogenesis of double-outlet left ventricle with a right-ventricular infundibulum. *Thorac Cardiov Surg* 1997; 45:172–7.
112. Bharati S, Lev M, Stewart R et al. The morphologic spectrum of double outlet left ventricle and its surgical significance. *Circulation* 1978;58:558–65.
113. Van Praagh R, Weinberg PM, Srebro JP. Double outlet left ventricle. In: Adams FH, Emmanoulides GC, Riemenschneider TA (eds) *Moss's Heart Disease in Infants, Children, and Adolescents,* 4th edn. Baltimore: Williams & Wilkins, 1989;461–85.
114. Kirklin JW, Barratt-Boyes BG. Double outlet left ventricle. In: *Cardiac Surgery,* 2nd edn. New York: Churchill Livingstone, 1993:1501–9.
115. Freedom RM, Yoo S, Williams WG. Double-outlet ventricle. In: Freedom RM, You S, Makailian H, Williams WG (eds) *The Natural and Modified History of Congenital Heart Disease*. New York: Futura, 2004;370–80.
116. DeLeon SY, Ow EP, Chiemmongkoltip P et al. Alternatives in biventricular repair of double-outlet left ventricle. *Ann Thorac Surg* 1995;60:213–6.

# 26 Physiologically "Corrected" Transposition of the Great Arteries

**Erwin Oechslin**

Toronto Congenital Cardiac Centre for Adults, University Health Network, Toronto General Hospital, Toronto, Canada

## Definition

Physiologically "corrected" transposition of the great arteries is an uncommon congenital heart defect characterized by discordant atrioventricular (AV) and ventriculo-arterial (VA) connections (double discordance) (Fig. 26.1). The systemic veins join the right atrium (RA), which is connected by a mitral valve to the subpulmonary left ventricle (LV). The left atrium (LA) receives pulmonary venous blood from the pulmonary veins and is connected by a tricuspid valve to the subaortic right ventricle (RV). The VA connections are also discordant wherein the aorta arises from the morphologic RV and the pulmonary artery from the morphologic LV. Discordant AV and VA connections can occur in isolation; however, associated congenital cardiac anomalies are common.

## Incidence

Physiologically "corrected" transposition of the great arteries (TGA) is a very uncommon congenital heart defect – too infrequent to deserve separate mention in a large study reporting the incidence of congenital heart defects [1]. It comprises less than 0.5% of all forms of congenital heart defects. Several sources have reported incidences ranging from 2 to 7 per 100,000 live births [2]. The prospective Bohemia Survival Study yielded a prevalence of 3 per 100,000 live births; this accounted for 0.4% of all congenital heart defects in this study, which included more than 800 000 children born between 1980 and 1990 [3].

*Echocardiography in Pediatric and Congenital Heart Disease: From Fetus to Adult*
Edited by Wyman W. Lai, Luc L. Mertens, Meryl S. Cohen and Tal Geva
 ISBN: 978-1-405-17401-5

## Developmental considerations and etiology

The etiology of physiologically "corrected" TGA is unknown. The primitive heart tube with the sinus venosus and the atrium at one end and the conotruncus at the other end does not loop to the right (D-loop) as in the normal heart; instead, it loops to the left (L-loop). This leftward looping brings the future RV to the left and the LV to the right. This abnormal looping is associated with discordant connections between the ventricles and great arteries.

Both genetic and environmental factors have been implicated in the etiology of this congenital heart defect [4–6]. The recurrence of TGA (AV concordance/VA discordance, D-loop TGA) and physiologically "corrected" TGA (AV discordance/VA discordance, L-loop TGA) in the same family suggests a pathogenetic link between these two anatomically different malformations [5].

## Morphology and classification

### Common nomenclature

Rokitansky first described a cardiac malformation with inappropriate connections between the atria and ventricles and between the ventricles and great arteries, and noted the physiologic correction of this congenital heart defect [7]. Physiologically "corrected" TGA describes discordant AV and VA connections (i.e., double discordance): the atria connect to the inappropriate ventricles, which then connect to the inappropriate great arteries. There is a usual arrangement of the atria (atrial situs solitus) and L-transposition of the great arteries in the majority of patients (Fig. 26.1a). Throughout this chapter, LV and RV refer to the morphologic left and right ventricles, respectively, regardless of their spatial position or topology.

A mirror-image arrangement of the atria (atrial situs inversus) is present in approximately 5% of patients with physiologically "corrected" TGA. Importantly, patients with a mirror-image arrangement of the atria have a rightward

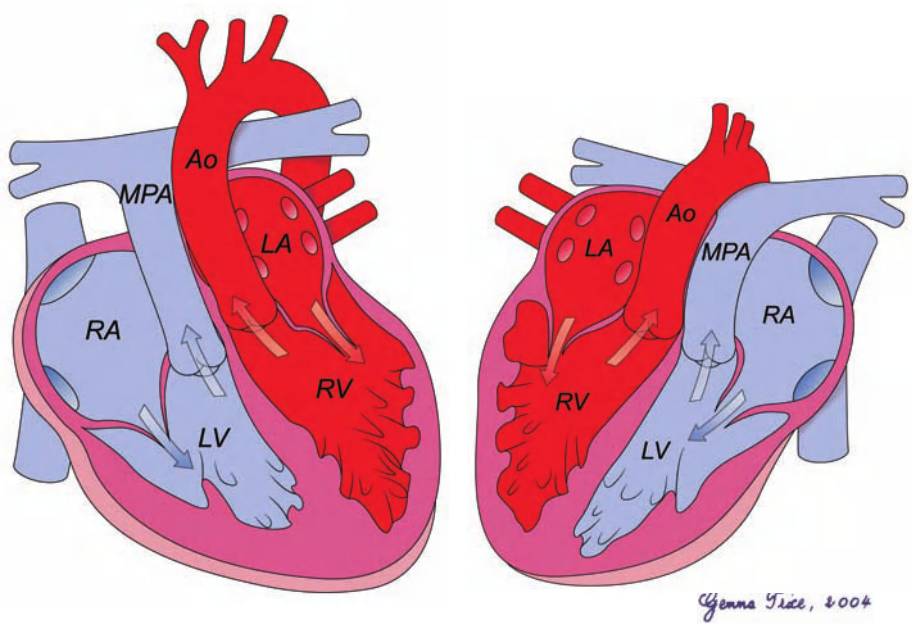


**Figure 26.1** Diagram showing physiologically "corrected" transposition of the great arteries or discordant atrioventricular and ventriculo-arterial connections (double discordance). **(a)** Usual arrangement of the atria (atrial situs solitus) with **L-**ventricular loop and **L-**transposition of the great arteries. **(b)** Mirror-image arrangement of the atria (atrial situs inversus) with **D-**ventricular loop and **D-**transposition of the great arteries. Ao, aorta; LA, left atrium; LV, left ventricle; MPA, main pulmonary artery; RA, right atrium; RV, right ventricle.

looping (D-ventricular loop) and not leftward looping of the primitive heart tube (Fig. 26.1b).

There are a number of synonyms for physiologically "corrected" TGA, including double discordance, discordant AV and VA connections, congenitally corrected TGA, and L-TGA. It should be noted that the phrase L-TGA is a non-specific term as the "L" might relate to the ventricular loop or to the spatial position of the great vessels [8]. Although in the majority of patients with physiologically "corrected" TGA in atrial situs solitus the aorta is positioned leftward and anterior to the pulmonary artery (L-malposition), there is wide variability in the spatial relationships between the great arteries in this condition. A minority of patients with physiologically "corrected" TGA in atrial situs solitus have an aorta that is anterior and to the right (D-malposition) of the pulmonary trunk [9]. Furthermore, leftward (L)-malposition of the aorta relative to the pulmonary trunk can be encountered in a variety of other complex congenital cardiac anomalies such as TGA with AV concordance and VA discordance, double-outlet right ventricle, crossed AV connections, univentricular hearts, and others [10,11]. Therefore, the term L-TGA is better avoided; *L-loop TGA* is more specific, where the L-loop refers to the ventricular looping [12].

Discordant AV and VA connections cannot be considered *anatomically* corrected because the RV is the subaortic ventricle supporting the systemic circulation and the LV is the subpulmonary ventricle giving rise to the pulmonary trunk [13,14]. The two discordant connections cancel each other with respect to the circulation; thus, *physiologically* "corrected" TGA is a more appropriate term indicating physiologic, but not anatomic, correction. However, the frequent association of other intracardiac defects makes physiologically "corrected" TGA far from being truly physiologically corrected. Other terms, such as ventricular inversion, dextroversion or L-TGA, were used in the past to describe combined abnormal segmental connections or discordant AV and VA connections. These terms are inappropriate and their use as a substitute for physiologically "corrected" TGA should be discouraged [9].

Discordant AV connections can only exist in the presence of discordant connection of the right and left atria to their inappropriate ventricles. Therefore, isomerism of the atrial appendages, atresia of an AV valve or univentricular atrioventricular connections (e.g., double-inlet left ventricle) exclude a discordant atrioventricular connection.

### Van Praagh's classification

Van Praagh describes three types of segmental sets: the viscera and atria, the ventricular loop, and the great arteries (see Chapter 3 for details) [15]. The viscero-arterial situs can be solitus (S), inversus (I) or ambiguous (A), as shown {S,–,–} or {I,–,–}. The ventricular arrangement is either a D-loop ventricle (D) or an L-loop (L) ventricle, as described in {–,D,–} or {–,L,–}. The great arterial situs is solitus in normally related great arteries {–,–,S} or inversus {–,–,L}. The right-sided aorta is symbolized as (D), the left-sided aorta as (L), and an anterior aorta as (A) in the setting of abnormal relation of the great arteries. According to the Van Praagh classification, physiologically "corrected" TGA is called {S,L,L} TGA in the presence of usual arrangement of the atria, or {I,D,D} TGA in the presence of a mirror-image arrangement of the atria. Other rare segmental combinations such as {S,L,D} and {I,D,L} TGA have been described.

## Anatomy

There may be usual arrangement of the viscera and atria (situs solitus) or a mirror-image arrangement (situs inversus);

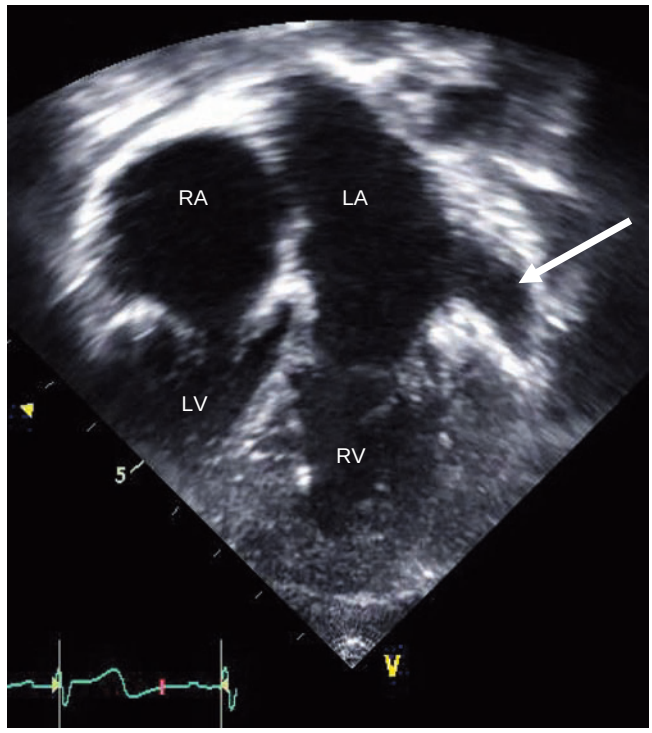


(a)

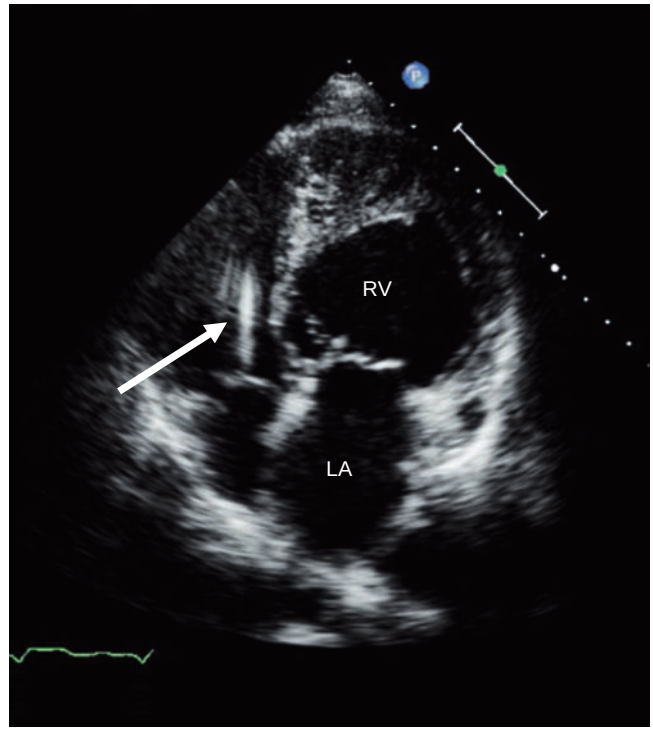


(b)

**Figure 26.2** Usual arrangement of the atria (atrial situs solitus). **(a)** Apical 4-chamber view in a 9-year-old boy showing discordant atrioventricular (AV) connection. Note the characteristic morphology of the left atrial appendage (arrow) identifying the location of the morphologic left atrium, which lies on the left of the morphologic right atrium. The inflow of the morphologic right ventricle lies on the left of the morphologic left ventricle, which indicates L-ventricular loop. **(b)** Usual arrangement of the atria (atrial situs solitus) with discordant atrioventricular connection in a 41-year-old man. Note eccentric hypertrophy and moderately reduced systolic function of the left-sided right ventricle and the presence of a pacemaker lead (arrow) in the right-sided left ventricle. LA, left atrium; LV, left ventricle; RA, right atrium; RV, right ventricle.

the cardiac orientation can be levocardia, dextrocardia, or mesocardia.

### Usual (solitus) arrangement of the atria

The majority (~95% of the patients) present with usual arrangement of the atria; that is, the right atrium lies to the right of the left atrium (Fig. 26.1a). The right-sided superior vena cava and inferior vena cava connect to the right-sided right atrium, which empties through the mitral valve into the LV, which gives rise to a right-sided pulmonary trunk. The LV is L-looped and lies to the right of the RV (Fig. 26.2a,b and Videoclip 26.1). The mitral valve has two papillary muscles and is in fibrous continuity with the cusps of the pulmonary valve (Fig. 26.3a,b and Videoclip 26.2). The pulmonary veins are connected to the left-sided left atrium, which in turn empties through the tricuspid valve into the subaortic RV, which lies on the left of the LV (Fig. 26.2a,b and Videoclip 26.1). In contrast to the normal heart, the left ventricular (pulmonary) and right ventricular (aortic) outflow tracts are in parallel, and the position of the ascending aorta is left and anterior (L-malposition) in relation to the pulmonary trunk (Figs 26.3c and 26.4; Videoclip 26.2).

### Mirror-image arrangement of the atria (atrial situs inversus)

Approximately 5% of patients with physiologically "corrected" TGA present with a mirror-image arrangement of the atria (Fig. 26.1b): the left-sided superior and inferior caval veins empty into the right atrium, which lies to the left of the left atrium (left-sided RA), and the pulmonary veins empty into the right-sided left atrium. As above, there are discordant AV and VA connections. However, the subaortic RV is not inverted and lies to the right of the subpulmonary LV (Figs 26.5 and 26.6; Videoclip 26.4). The aorta is right-sided and anteriorly located in relation to the pulmonary trunk (D-malposition of the great arteries). The subcostal long-axis and apical 4-chamber windows are the best views to differentiate between D- and L-ventricular loops: the inflow of the RV lies to the *right* of the LV in the presence of *D-ventricular loop* (Figs 26.5 and 26.6; Videoclip 26.4), whereas it lies to the *left* in the presence of *L-ventricular loop* (Fig. 26.2a,b and Videoclip 26.1).

### Cardiac orientation

The axis between the base of the heart and the apex can point to the left (levocardia) to the right (dextrocardia) or it

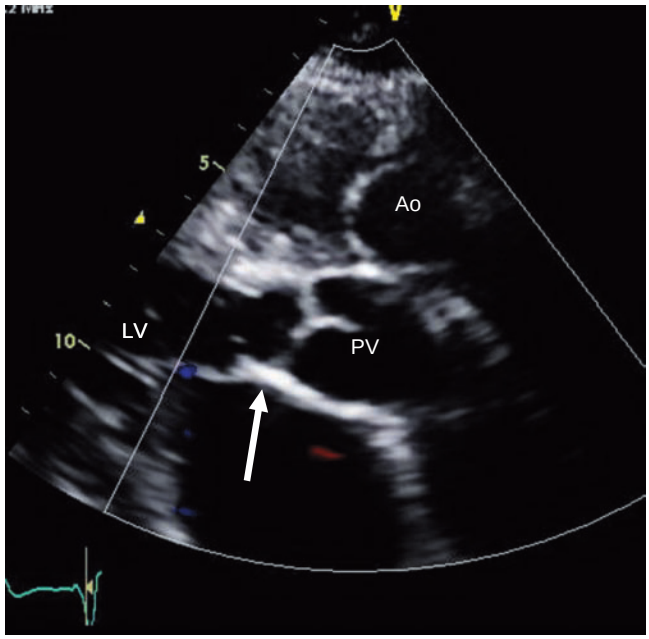


(a)

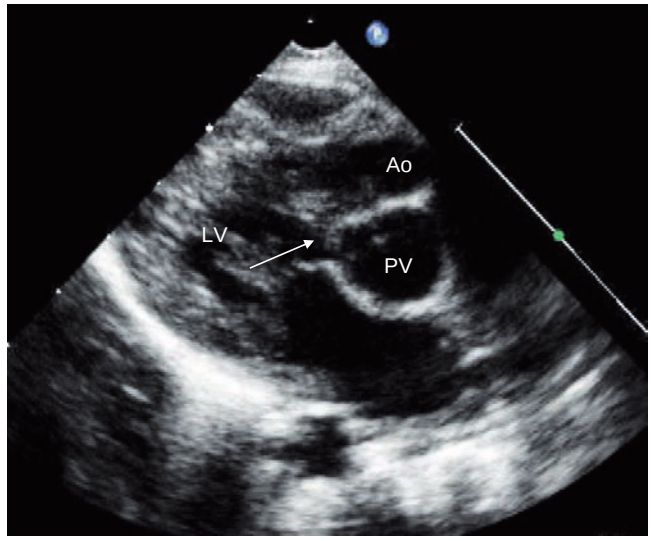


(b)

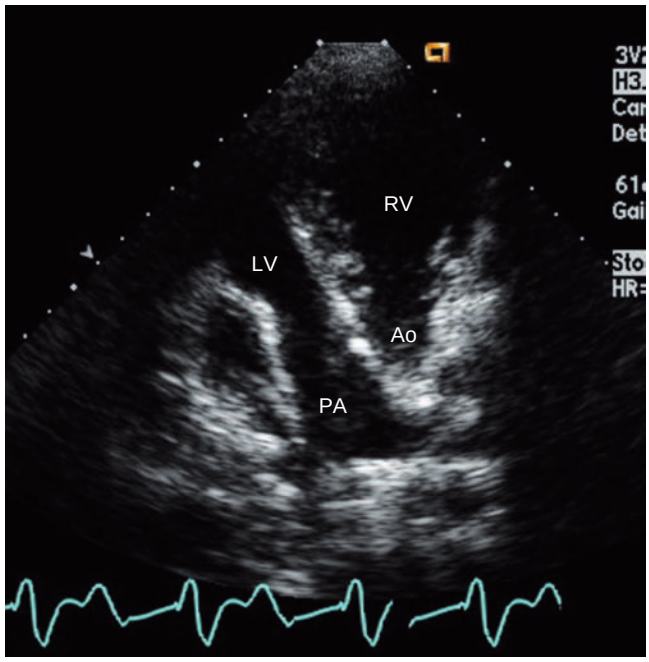


(c)

**Figure 26.3** Imaging the parallel position of the great arteries: the aorta is anterior and the pulmonary artery is posterior. **(a)** Parasternal long-axis view in a 41-year-old man without LV outflow tract obstruction. The arterial outflow tracts are parallel to each other. The AV valve is in fibrous continuity (long arrow) with the pulmonary valve. **(b)** Nine-month-old boy with subvalvular pulmonary stenosis (small arrow). **(c)** Apical position of the transducer with an anterior sweep to image the parallel position of the great arteries in an 18-year-old man. Note the leftward position of the aorta in relation to the pulmonary artery with its bifurcation. Ao, aorta; LV, left ventricle; PA, pulmonary artery; PV, pulmonary valve; RV, right ventricle.

can be in the midline (mesocardia). Approximately 75% of patients with physiologically "corrected" TGA present with levocardia.

### Ventricular topology

Ventricular topology describes the internal organization of the ventricle; it can be right- or left-handed. The abnormal looping (L-loop) results in a left-hand pattern [12]: the left hand must be used to place the palm of the hand against the RV septal surface in such a way that the thumb points to the inlet and the fingers point to the outlet of the RV (in contrast to a D-loop or a normal heart where the right hand must be used; see Chapter 3 for details).

### Atrioventricular valves

The mitral valve has two papillary muscles without insertion to the interventricular septum. However, one-fourth of the patients may present with abnormalities of the mitral valve

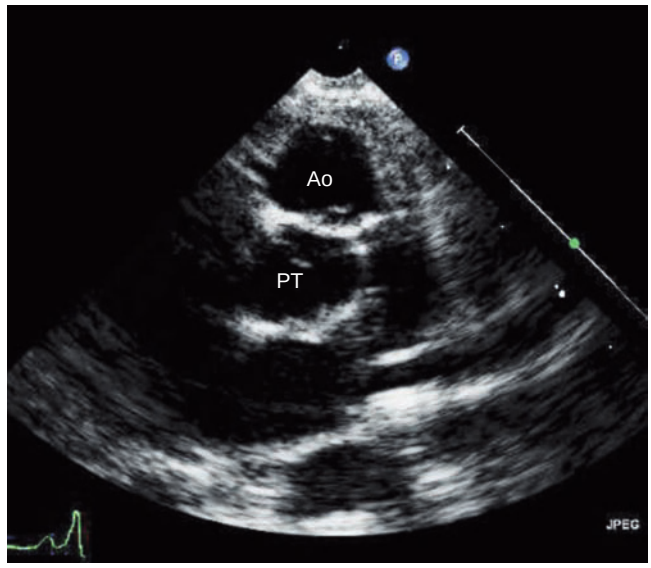


**Figure 26.4** Parasternal short-axis view of a 9-month-old boy showing the spatial relation of the aorta to the pulmonary trunk: the aorta (Ao) is anterior and leftward relative to the pulmonary trunk (PT) in atrial situs solitus.

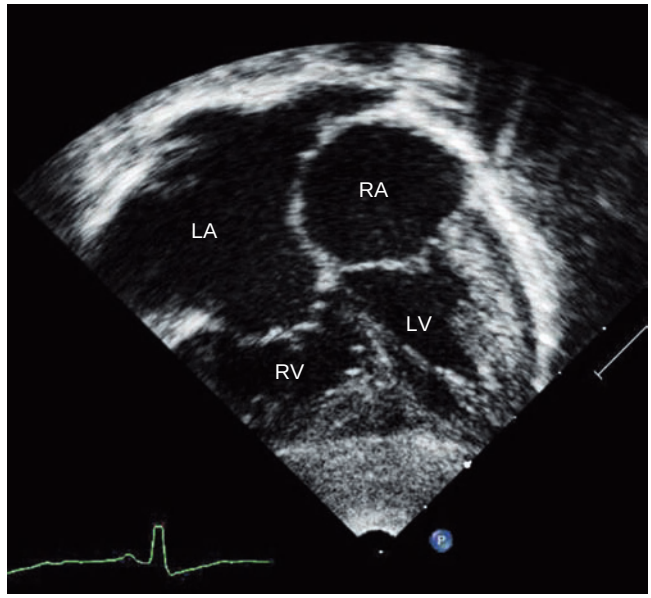


**Figure 26.5** Mirror-image arrangement of the atria (situs inversus). Apical 4-chamber view in an 8-month-old boy with situs inversus and dextrocardia. The right atrium is to the left of the left atrium and the right ventricle is right-sided. LA, left atrium; LV, left ventricle; RA, right atrium; RV, right ventricle.

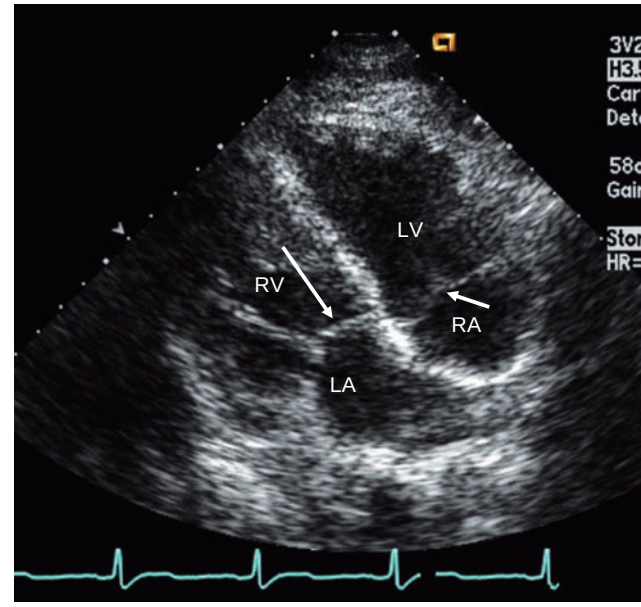


**Figure 26.6** Subcostal view in a 26-year-old man with situs inversus and dextrocardia. The short arrow indicates the mitral valve; the long arrow denotes the tricuspid valve. LA, left atrium; LV, left ventricle; RA, right atrium; RV, right ventricle.

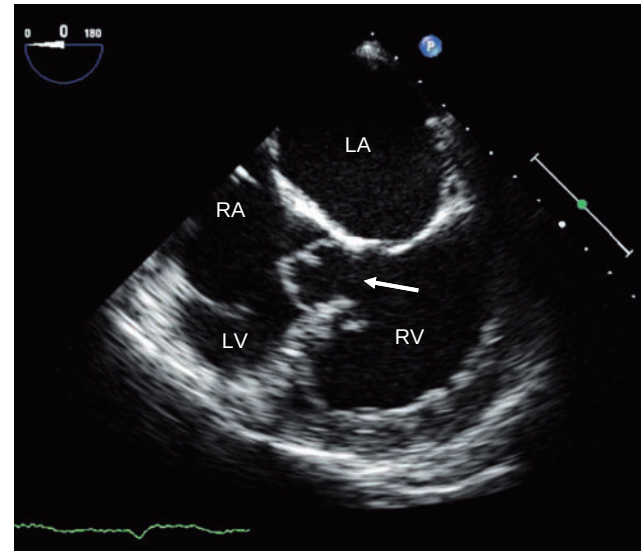


**Figure 26.7** Transesophageal echocardiogram in a 41-old-man with atrial situs solitus and septal malalignment. The gap between the atrial and ventricular septum is filled with a large, redundant membranous septum (arrow). LA, left atrium; LV, left ventricle; RA, right atrium; RV, right ventricle.

[16]. The tricuspid valve, which is left-sided in usual arrangement of the atria, is frequently dysplastic (see "Associated lesions" below).

### Septal malalignment

Malalignment between the atrial septum and the inlet part of the ventricular septum is a characteristic morphologic feature of discordant AV connection in patients with usual arrangement of the atria, and affects the position of the conduction system [17]. The AV septal malalignment results in a gap into which the subpulmonary LV outflow tract is wedged. This space is filled with a large membranous septum in patients without a ventricular septal defect (Fig. 26.7 and Videoclip 26.5). In the presence of a ventricular septal defect

(VSD), the septal malalignment has implications for the size and extent of the VSD, the severity of LV (pulmonary) outflow tract obstruction, and the position of the conduction system [18,19]. The degree of septal malalignment is less pronounced in hearts with a small or atretic pulmonary trunk or in patients with mirror-image arrangement of the atria than in those with severe left ventricular outflow tract obstruction or usual arrangement of the atria [19].

## Coronary arteries

Coronary artery anatomy and distribution have gained more attention because of the potential of a double switch procedure in the surgical management of physiologically "corrected" TGA. The coronary arteries reflect ventricular topology. In patients with usual arrangement of the atria, there is a mirror-image distribution of the coronary arteries, which follow the corresponding ventricles [20,21]: the epicardial distribution of the right-sided coronary artery is that of a morphologically left coronary artery (circumflex and anterior descending coronary arteries); the left-sided coronary artery follows the left AV groove and supplies the RV [20,22–25]. Although the origin and course of the coronary artery show frequent variation [20,22,25,26], the origin and proximal branching pattern in physiologically "corrected" TGA appear to be more consistent than in D-loop TGA (concordant AV and discordant VA connection, D-transposition) [25].

## Associated lesions

Physiologically "corrected" TGA occurs in isolation (rarely) or can be complicated by associated congenital heart defects. More than 90% of patients have associated defects [27–30] and the following triad of associated malformations is common: (i) VSD; (ii) LV (pulmonary) outflow tract obstruction; and (iii) anomalies of the tricuspid valve. Any combination of these anomalies can coexist.

### *Ventricular septal defect*

Ventricular septal defects are common, can occupy any position, and are described in the same way as in the normal heart and in D-loop TGA. The incidence ranges between 60% and 80% [21,27]. The VSD is frequently nonrestrictive and is the result of a malalignment between the atrial and ventricular septa. Perimembranous VSD is most common and is in fibrous continuity with the pulmonary and tricuspid valves. If the defect is located in the inlet (canal) septum, the offsetting of the attachment of both AV valves is lost; the moderator band and the ventricular crest allow identification of the RV (Fig. 26.8).

### *Left ventricular outflow tract obstruction*

Left ventricular outflow tract (subpulmonary) obstruction is observed in up to 50% of patients with usual arrangement of the atria and occurs at the subvalvar and/or valvar levels (Fig. 26.9 and Videoclips 26.6a–c and 26.7a,b; see also Fig. 26.3b). Isolated valvar pulmonary stenosis is rare whereas combined subvalvar and valvar obstruction is common [27,28]. The subvalvar stenosis can be muscular or caused by a fibrous shelf, fibrous tissue tags originating from any of the valves near the outflow tract, or a fibrous ridge from the membranous septum. LV outflow tract obstruction can also result from a large aneurysm of the membranous septum in the presence of severe septal malalignment or from systolic anterior motion (SAM) of the mitral valve leaflets due to abnormal geometry of the LV. LV outflow tract obstruction is commonly associated with a VSD, and tricuspid valve abnormalities are frequently associated as well.

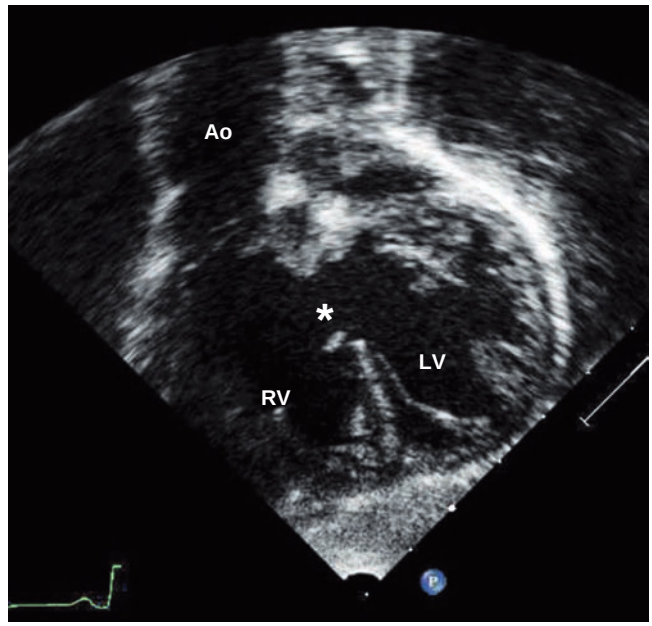


**Figure 26.8** Modified apical view in an 8-month-old boy with situs inversus showing a nonrestrictive ventricular septal defect extending from the inlet to the outlet septum (*). Ao, aorta; LV, left ventricle; RV, right ventricle.

### *Abnormalities of the tricuspid valve*

Abnormalities of the tricuspid valve are very common and occur in up to 90% in autopsy series; however, they are less frequently identified in the clinical setting [21,27,29–31]. The dysplastic tricuspid valve can occur without or with apical displacement of both the septal and posterior leaflets as in patients with concordant AV connection. Ebstein-like malformation of the tricuspid valve in physiologically "corrected" TGA is different from the classic Ebstein anomaly in patients with concordant connection (Figs 26.10 and 26.11; Videoclip 26.8a–d). In contrast to a classic Ebstein malformation, in discordant AV connections there is usually no rotational displacement of septal and posterior leaflets, neither is the inlet portion of the RV myocardium dilated and thinned. The anterior tricuspid leaflet is usually not

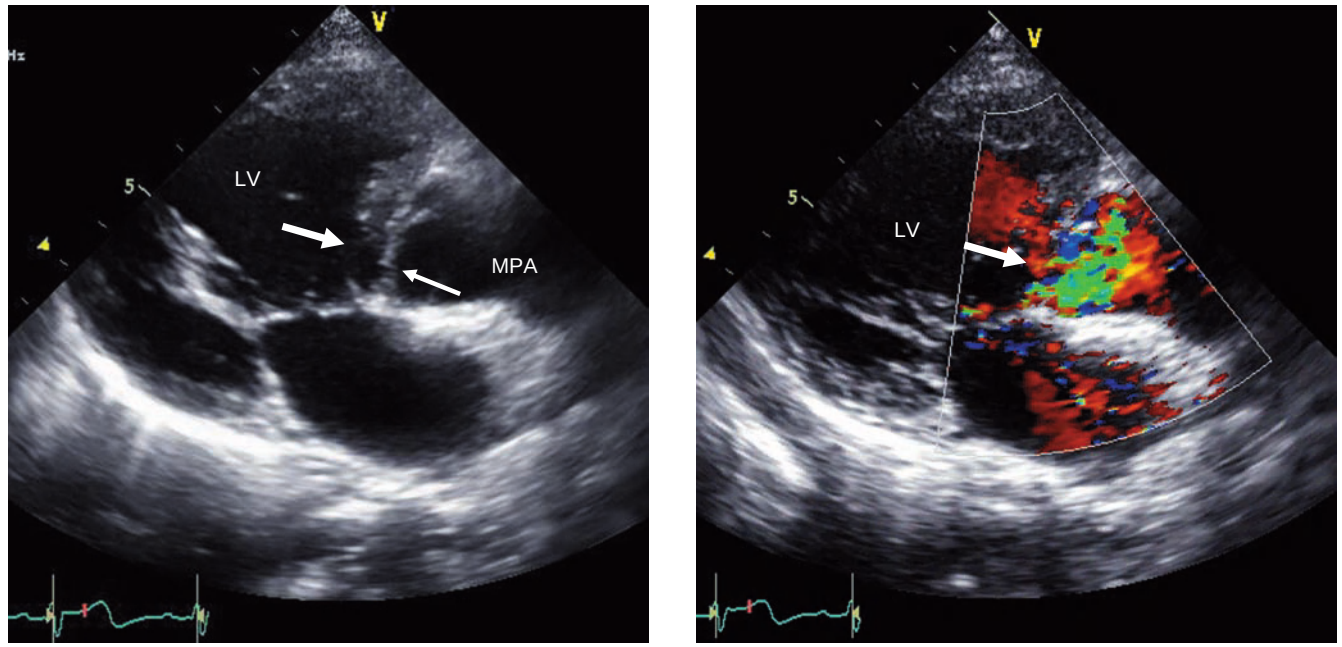


(a) (b)

**Figure 26.9** Modified parasternal long-axis views in a 9-year-old boy showing subvalvar pulmonary stenosis. **(a)** Two-dimensional image showing fibrous tissue in the left ventricular outflow (long arrow). The small arrow indicates pulmonary valve cusps. **(b)** Color Doppler flow mapping demonstrates flow acceleration (arrow) at the level of the subpulmonary left ventricular outflow.

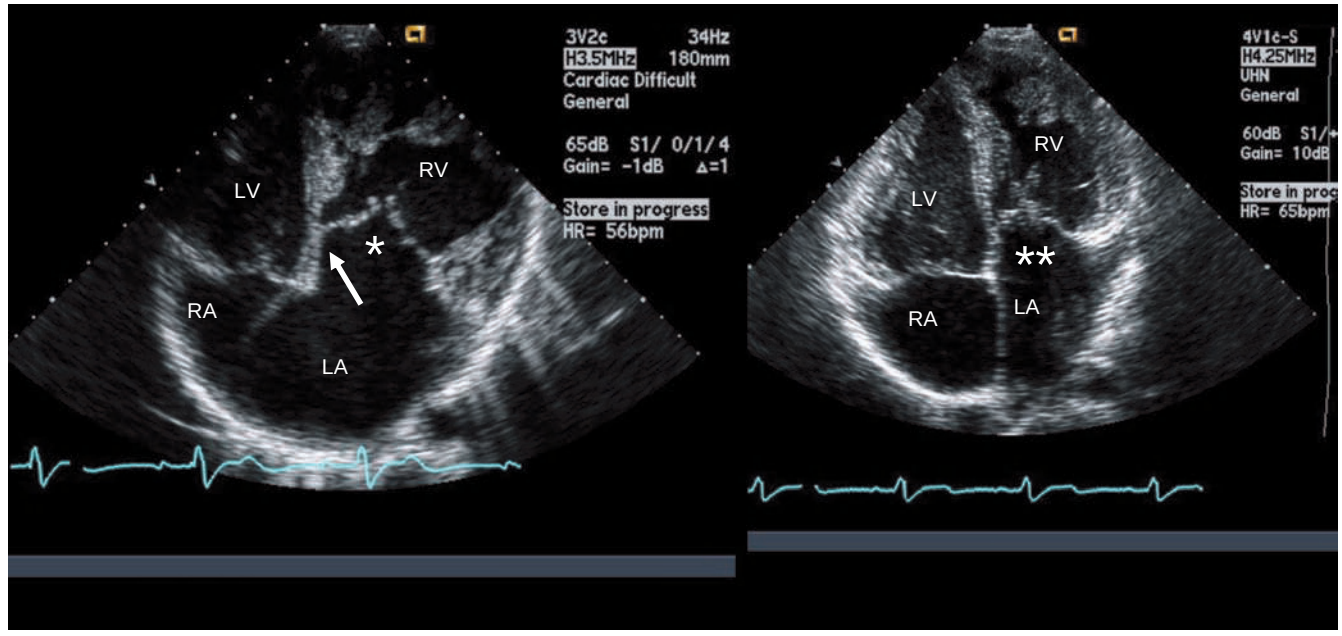


(a) (b)

**Figure 26.10** Two-dimensional imaging from the apical 4-chamber view in a 22-year-old man before **(a)** and after **(b)** banding of the main pulmonary artery for severe tricuspid regurgitation. Before banding (a), note the dysplastic tricuspid valve leaflets with Ebstein-like malformation (apical displacement of the septal leaflet, arrow). Note: the anterior leaflet is not large as in classic Ebstein patients. Incomplete coaptation (*) of the tricuspid valve leaflets is evident due to tricuspid annular dilation, abnormal geometry of the right ventricle, and shortened chordae tendineae secondary to severe dilation of the right ventricle. The interatrial septum shifts to the right, which reflects elevated pressure of the markedly enlarged left atrium due to severe tricuspid regurgitation. After the third banding (b), note the remodeling of both ventricles and atria. The first pulmonary artery banding was performed at the age of 19 and the third at the age of 21. The images were taken 3 years apart. The interventricular septum has shifted to the left, which results in better coaptation of the tricuspid valve leaflet (**) and less severe tricuspid regurgitation. The right atrium and left ventricle are larger, and the left atrium and right ventricle are significantly smaller. LA, left atrium; LV, left ventricle; RA, right atrium; RV, right ventricle.

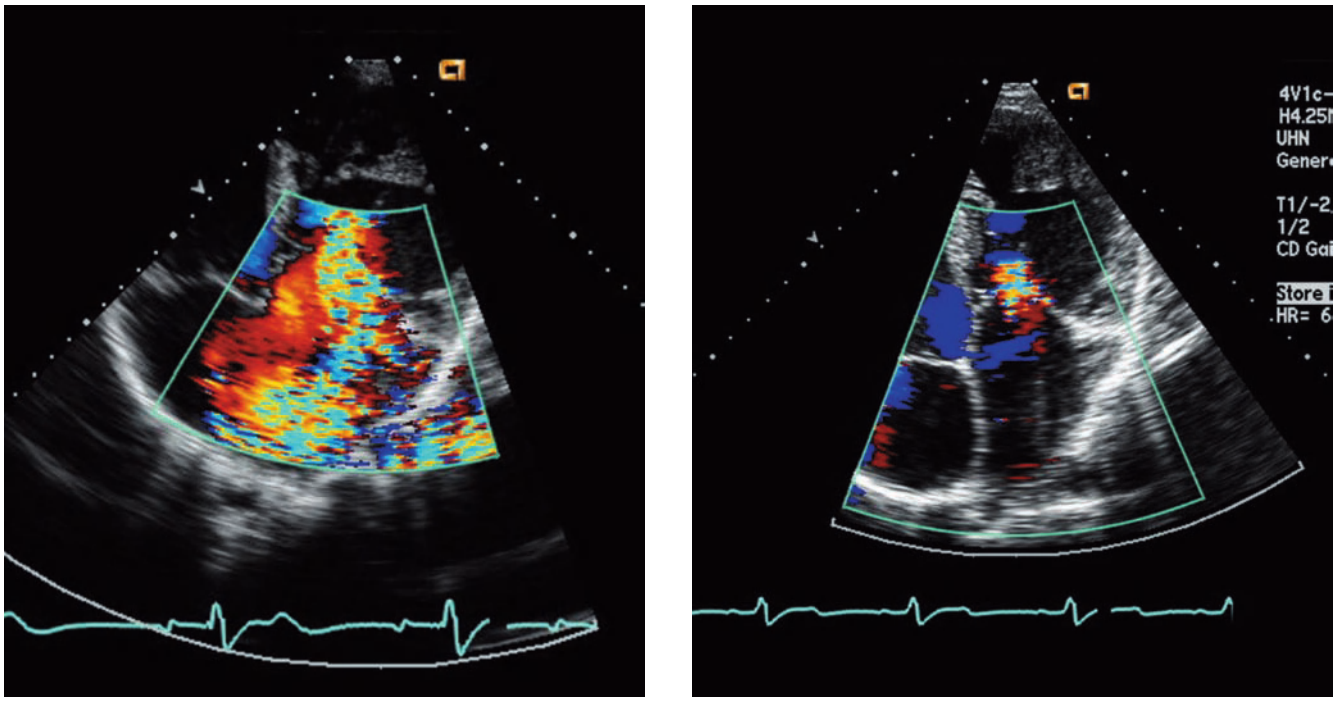


(a) (b)

**Figure 26.11** Color Doppler flow mapping in the apical 4-chamber view in the same patient as shown in Fig. 26.10. **(a)** Severe tricuspid regurgitation before pulmonary artery banding. **(b)** Significant improvement in tricuspid regurgitation after pulmonary artery banding and ventricular remodeling.

large and does not have a "sail-like" appearance, the adherence of the septal and posterior leaflets is limited, and the atrialized portion of the RV inflow is usually small.

Other rare associated defects of the AV valves include straddling or overriding, anomalies that can significantly complicate surgical treatment [32].

### *Other associated anomalies*

Aortic atresia can be observed in hearts with discordant segmental connections and an unguarded tricuspid valve [33,34]. Subaortic obstruction tends to coexist with aortic coarctation.

## Pathophysiology

The discordant AV and VA connections cancel each other with respect to the circulation. In visceral-atrial situs solitus, deoxygenated blood returning to the RA reaches the pulmonary circulation through the right-sided LV, whereas the oxygenated pulmonary venous blood returns to the LA and then, through the left-sided RV, reaches the systemic circulation (Fig. 26.1a). In visceral-atrial situs inversus, deoxygenated blood returning to the left-sided RA reaches the pulmonary circulation through the left-sided LV whereas the oxygenated pulmonary venous blood returns to the right-sided LA and then, through the right-sided RV, reaches the systemic circulation (Fig. 26.1b). Thus, patients with physiologically "corrected" TGA are acyanotic and the congenital heart defect can remain undiagnosed in the absence of any associated anomalies and murmurs. Both complexity and severity of the associated intracardiac defects determine the pathophysiology, and the natural and "unnatural" history [27,35–38]. The subaortic RV supporting the systemic circulation remodels and develops concentric and eccentric hypertrophy, respectively. As the myocardium is aging, the subaortic RV may fail, with subsequent dilation and development of hemodynamically relevant tricuspid regurgitation due to malcoaptation of the tricuspid valve leaflets secondary to annular dilation and abnormal geometry of the RV (Figs 26.10 and 26.11; Videoclip 26.8a–d) [27,35,37].

Associated intracardiac defects have different pathophysiologic effects on the subaortic RV and pulmonary blood flow. Volume load of the subaortic RV can be caused either by tricuspid regurgitation, or a nonrestrictive VSD, or both. Severe tricuspid regurgitation can be caused either by a pathology (dysplasia) of the tricuspid valve, or by malcoaptation of the tricuspid valve secondary to annular dilation and abnormal geometry of the RV as a consequence of a failing RV myocardium. Severe volume load of the RV can lead to heart failure symptoms during infancy or childhood.

Left ventricular outflow tract (pulmonary) obstruction reduces pulmonary blood flow, alters the pressure load on the subpulmonary LV, alters the volume load of the subaortic

RV, and modifies left and right ventricular interaction. Tricuspid regurgitation is usually less severe in the presence of significant LV outflow tract obstruction because the interventricular septum shifts to the left because of the increased LV systolic pressure. The leftward shift of the interventricular septum impacts RV geometry, improves coaptation of the tricuspid valve leaflets, and reduces the severity of tricuspid regurgitation. Leftward shift of the interventricular septum and remodeling of the RV are illustrated by pulmonary artery banding performed for "training" the LV in preparation for a double switch procedure. A higher LV systolic pressure is associated with less severe tricuspid regurgitation as a consequence of RV remodeling (Figs 26.10 and 26.11; Videoclip 26.8a–d). Hence, the presence of volume and/or pressure loads on both ventricles has an important impact on the interventricular interaction and on morbidity.

Complete heart block due to abnormal location and course of the AV node and the bundle of His may be the first symptom in children, adolescents or adults [17,27,39]. Thus, physiologically "corrected" TGA must be excluded in all patients who present with conduction abnormalities, such as second- or third-degree AV block.

## Imaging

Segmental analysis of cardiovascular anatomy (see Chapter 3) by echocardiography is crucial for comprehensive evaluation of patients with physiologically "corrected" TGA. A systematic, sequential approach helps in identifying the cardiac chambers, their connections and the associated anomalies. Once the morphologic assessment is completed and the diagnosis of physiologically "corrected" TGA is confirmed, hemodynamic evaluation and biventricular function assessment are performed.

### Goals of the examination

The main objectives of echocardiographic examination in the setting of physiologically "corrected" TGA can be summarized as follows:

- Determine the arrangement of the veins and atria (visceral-atrial situs): usual (situs solitus) or mirror-image arrangement (situs inversus).
- Cardiac orientation (base-to-apex axis) and position within the thorax: levocardia, mesocardia, dextrocardia.
- Determine the morphology of the ventricles.
- Determine the morphology of the great arteries.
- Determine the AV and VA connections.
- Determine the origin and proximal course of the coronary arteries (relevant for a double switch operation).
- Assess associated malformations:
  - tricuspid valve (dysplasia, Ebstein-like malformation).
  - straddling of the AV valves in the presence of a VSD.
  - ventricular septal defect(s).
  - presence, mechanism, and degree of LV (pulmonary) outflow tract obstruction; possible mechanisms include: (i) deviated outlet (conal) septum; (ii) accessory AV valve tissue; (iii) fibrous membrane; (iv) aneurysm of membranous septum; (v) hypoplastic pulmonary valve annulus; (vi) bicommissural pulmonary valve; (vii) narrowing of the pulmonary sinotubular junction; (viii) complex obstruction due to a combination of the above; and (ix) obstructed conduits between the LV and pulmonary artery.
  - aneurysm of the membranous septum (LV outflow obstruction?).
  - atrial septal defect.
  - patent ductus arteriosus.
  - persistent left superior vena cava.
  - aortic arch obstruction.

***Hemodynamic assessment:***

- Biventricular size and function: evidence of pressure and/or volume load.
- Severity of mitral and tricuspid valve regurgitation.
- Gradient across the LV outflow tract.
- Gradient across the VSD (restrictive versus nonrestrictive).
- Estimation of LV systolic pressure based on mitral regurgitation jet velocity.

### Transthoracic imaging

#### Subcostal views

The subcostal access provides the first view whereby the arrangement of the atria is defined. Usually, abdominal and atrial sidedness (situs) is concordant, which helps in determining the arrangement of the atria (atrial situs). The latter can be easily achieved by a cross-sectional view of the great vessels in the abdomen (see Chapters 3 and 4). In approximately 5% of patients with physiologically "corrected" TGA there is a mirror-image arrangement of the atria.

Moving from the cross-sectional view of the great vessels below the diaphragm to the subcostal view of the heart, the examiner can describe the connection of the great veins (inferior vena cava/hepatic veins and superior vena cava) to the atrium. If the inferior vena cava is present, it constantly connects to the morphologic RA. However, visualization of the connection between the inferior vena cava and the RA can be difficult or impossible in adults (Fig. 26.6). Injection of agitated saline into a vein of the right arm can help in identifying the systemic venous connection to the atria (Fig. 26.12).

Significant malalignment between the atrial and ventricular septum is common in patients with physiologically "corrected" TGA and can be the first hint of the presence of a discordant AV connection, as seen in the subcostal view or by transesophageal echocardiography (TEE) (Fig. 26.7 and Videoclip 26.5). The morphology of the ventricles can be easily described to identify the right and left ventricles by their intrinsic characteristic morphologic features (Figs 26.5

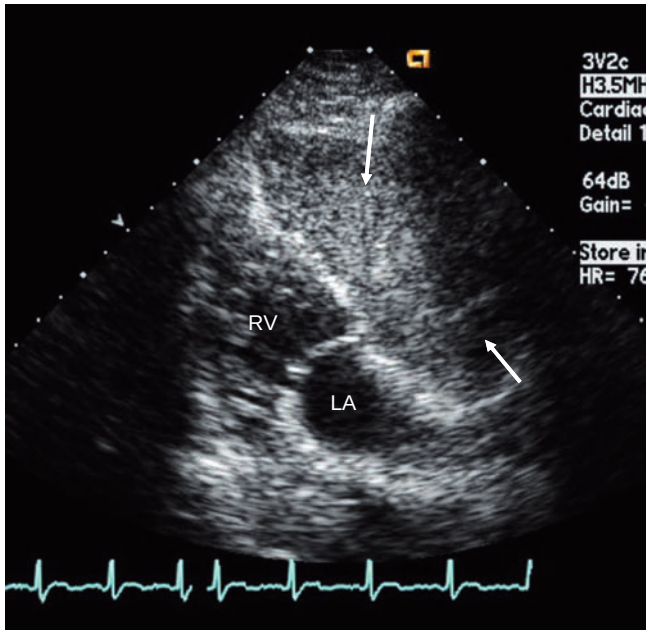


**Figure 26.12** Subcostal view of the same 26-year-old man as shown in Fig. 26.6. Agitated saline (arrows) appears in the left-sided chambers (right atrium [RA] and left ventricle [LV]) indicating situs inversus. The RV is to the right of the LV. Note: the base-apex axis points to the right (dextrocardia).

and 26.8; Videoclips 26.4 and 26.5). An anterior direction of the transducer allows good visualization of the right and left ventricular outflow tracts. When present, the location(s) and mechanism(s) of LV outflow tract obstruction are delineated by two- (2D) and three-dimensional (3D) imaging and by color Doppler (Fig. 26.13). The blood flow across the LV (pulmonary) outflow tract is usually well aligned (parallel) to the ultrasound beam, and the level of obstruction and gradients can be easily assessed by pulsed- and continuous-wave Doppler interrogation. LV-to-pulmonary artery conduits, which are implanted in some patients with complex LV (pulmonary) outflow tract obstruction, can be easily interrogated from the subcostal view with an anterior sweep of the transducer. The subaortic RV outflow tract can also be evaluated from the subcostal view (Fig. 26.14).

The subcostal view is also used to image the pulmonary veins, atrial septum and morphology of the AV valves, and to assess the ventricular septum for the presence of a VSD.

## Apical views

Apical views are obtained from the left lateral position (left chest) in patients with levocardia. However, acquisition of apical views may be challenging in the presence of dextrocardia, when the apical views are obtained in the right lateral position (right chest). Note that the transducer must be positioned on the chest according to standard guidelines to avoid any confusion or misinterpretation of the anatomy (Fig. 26.15). The transducer must always be positioned in such a fashion that it displays the patient's left side on the right side of the screen and the patient's right side on the left side of the screen (see Chapter 4).

The apical 4-chamber view is ideally suited to describe the morphology of the AV valves and to identify the morphologic right and left ventricles (Fig. 26.2; Videoclips 26.1 and 26.6). It is also a good view to describe ventricular looping (see Chapters 3 and 4). In L-ventricular loop the RV is positioned to the left of the LV.

An anterior position of the transducer in a modified apical 4- or 5-chamber view (the use of an "in-between" transducer angle) is encouraged to visualize the great arteries, which are usually arranged in parallel, and to identify the relation of the ascending aorta to the pulmonary artery. This is an appropriate view to describe L- or D-malposition (leftward or rightward position of ascending aorta in relation to the pulmonary artery).

Hemodynamic assessment of both AV valves is performed from the apical view: the severity of mitral and tricuspid valve regurgitation is evaluated by color Doppler (Fig. 26.11 and Videoclip 26.8), and LV (pulmonary) systolic pressure can be estimated by measurement of the mitral valve regurgitation jet velocity. The apical views are also important to identify and to describe the morphology of obstructions across the left and/or right ventricular outflow tracts, and to confirm or exclude VSDs. Alignment of the ultrasound beam parallel to the direction of blood flow across the LV (subpulmonary) outflow tract can be challenging, and accurate assessment of the gradients can be difficult in some patients.

## Parasternal views

A parallel position of the two great arteries in the parasternal long- and short-axis views confirms the diagnosis of TGA (Fig. 26.3). The parasternal long-axis view proves very useful for identifying an obstruction across the LV (subpulmonary) outflow tract and for describing the mechanism(s) of obstruction (Fig. 26.3b).

The parasternal short-axis view describes the relation of the ascending aorta to the pulmonary trunk. The ascending aorta is usually found leftward and anterior in relation to the pulmonary trunk (Fig. 26.4 and Videoclip 26.3). Although this relationship of the great arteries is typical, it is not uniform and cannot be used to describe ventricular looping.

The parasternal short-axis view also describes the orientation of the interventricular septum, the size and function of both ventricles, and the morphology of the mitral and tricuspid valves and their corresponding papillary muscles (Fig. 26.16). The VSD, when present, is usually located in the membranous septum and can be seen in the parasternal views. Muscular VSD(s) can be easily identified by color Doppler in parasternal short-axis views. When the pressure difference between the ventricles is low or absent (e.g.,

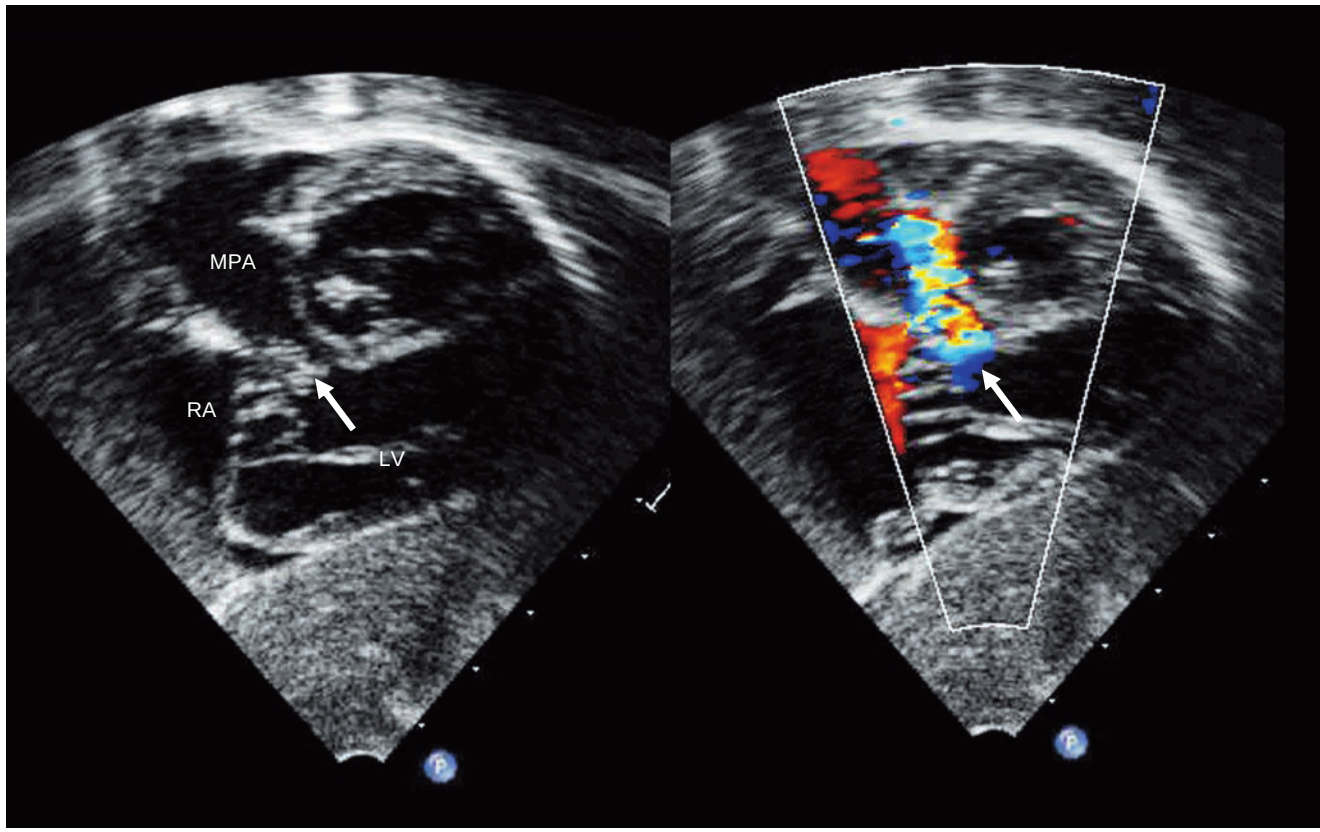


(a) (b)

**Figure 26.13** Imaging the left ventricular outflow tract from a subcostal view with an anterior sweep of the transducer in a 9-month-old boy with situs solitus and levocardia. **(a)** Two-dimensional imaging shows subpulmonary stenosis due to systolic anterior motion (SAM) of the mitral valve leaflets and ectopic fibrous tissue (arrow). **(b)** Color Doppler flow mapping shows the origin of the turbulent flow at the subvalvar area (arrow). LV, left ventricle; MPA, main pulmonary artery; RA, right atrium.

multiple VSDs, severe LV outflow obstruction), the Nyquist limit of the color Doppler velocity scale should be lowered to visualize low-velocity flow across the ventricular septum.

### Suprasternal views

These views are best suited to describe the presence or absence of a patent ductus arteriosus, aortic arch sidedness and morphology, and to image the branching pattern of the aortic arch. They are also best suited to exclude the occasional association of aortic coarctation.

### "In-between" views

Tailored "in-between" views or atypical views must frequently be obtained to complete a morphologic and hemodynamic assessment. In some patients LV outflow tract obstructions cannot be assessed by standard views, and a nonstandard transducer position and/or orientation should be employed. Atypical parasternal, apical or subcostal views help in visualizing the anatomy of the left and right ventricular outflow tracts and in aligning the ultrasound beam parallel to the direction of blood flow. VSDs and straddling AV valves are frequently seen in atypical parasternal and apical views. Modified parasternal views can also help to identify the ventricular septal crest (Fig. 26.17); this can be useful in the presence of an inlet (canal-type) VSD when the offset of the attachment of the AV valves is absent.

## Transesophageal echocardiography (TEE)

Seldom does TEE add to the description of the underlying anatomy and pathophysiology in the pediatric population as transthoracic echocardiography usually provides the necessary diagnostic information. However, in older patients with suboptimal transthoracic windows, TEE is valuable to visualize endocarditis-related intracardiac vegetations; to exclude thrombus formation in the atrial appendages in patients with sustained supraventricular arrhythmias; to describe atrial septal defects; and to determine the morphology of the AV valves, the inlet ventricular septum, LV outflow tract obstruction the membranous septum and associated aneurysm with or without LV outflow tract obstruction (Fig. 26.18 and Videoclip 26.10) [40]. The diagnosis by TEE of physiologically "corrected" TGA is aided by visualizing AV septal malalignment (Fig. 26.7 and Videoclip 26.5) and parallel position of the great arteries. Injection

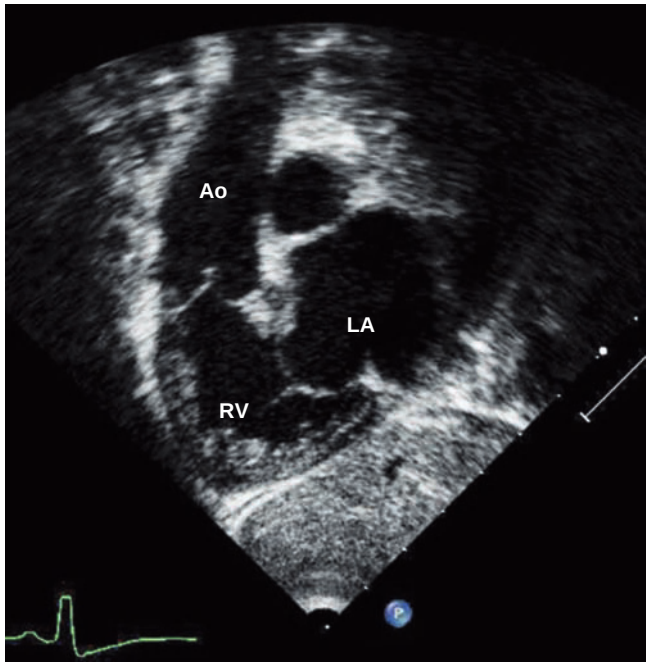


**Figure 26.14** Imaging the right ventricular (aortic) outflow tract from a modified subcostal view in an 8-month-old boy with situs inversus and dextrocardia. Ao, aorta; LA, left atrium; RV, right ventricle.

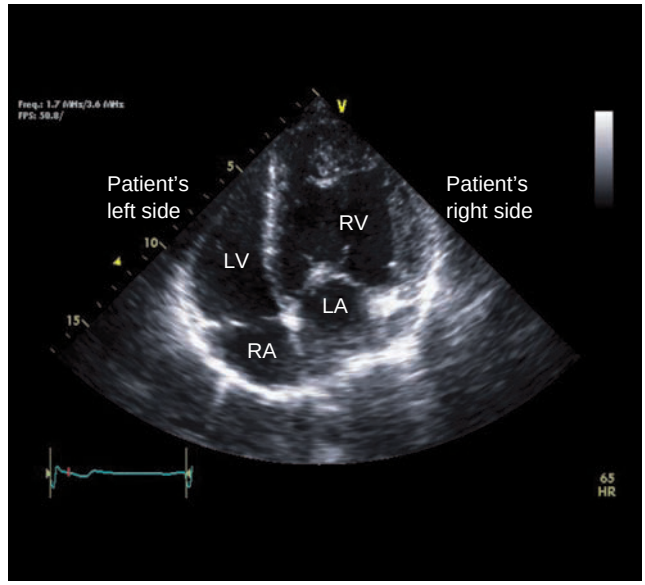


**Figure 26.15** Apical 4-chamber view in a 22-year-old patient with situs inversus and dextrocardia. As a result of inappropriate (left-right reversal) transducer orientation the heart is displayed in a way that suggests atrial situs solitus and L-ventricular loop, whereas in fact the patient has atrial situs inversus and D-ventricular loop. This mistake resulted from an attempt to orient the transducer in a way that "corrects" the anatomy as opposed to keeping the left-right orientation according to standard guidelines (the patient's left is displayed on the right side of the screen). LA, left atrium; LV, left ventricle; RA, right atrium; RV, right ventricle.

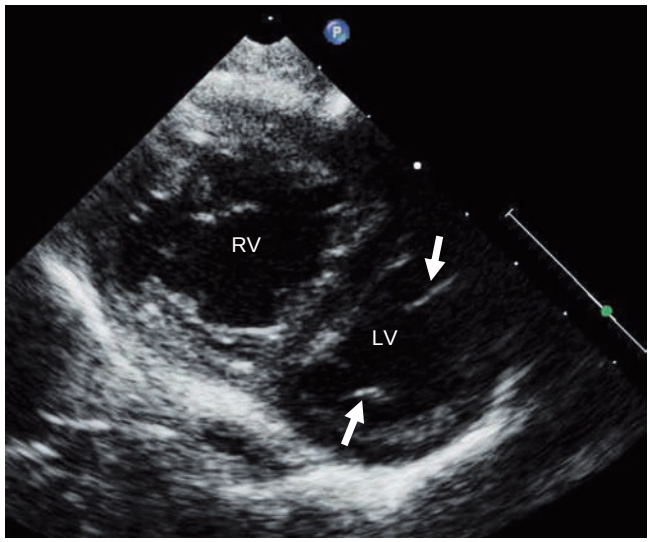


**Figure 26.16** Parasternal short-axis view of an 8-month-old boy with situs inversus, dextrocardia and D-ventricular loop. Two papillary muscles (arrows) help in identifying the posteriorly and leftwardly positioned left ventricle (LV). Note the eccentric hypertrophy of the anteriorly and rightwardly positioned right ventricle (RV) and flattening of the interventricular septum (D-shape).

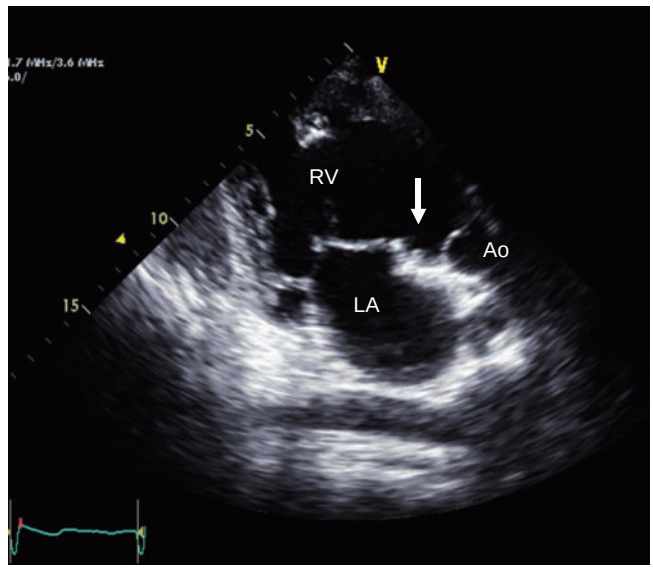


**Figure 26.17** Imaging the ventricular crest (arrow) using a modified parasternal long-axis view in a 22-year-old man with situs inversus and dextrocardia. Ao, aorta; LA, left atrium; RV, right ventricle.

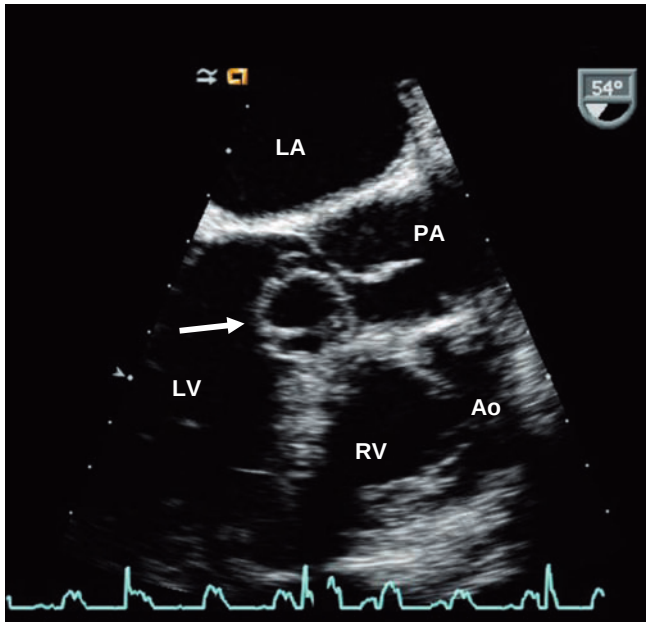


**Figure 26.18** Transesophageal echocardiogram in a 41-year-old man with situs solitus shows an aneurysm of the membranous septum protruding into the left ventricular outflow tract (arrow). Ao, aortic valve; LA, left atrium; LV, left ventricle; PA, pulmonary artery; RV, right ventricle.

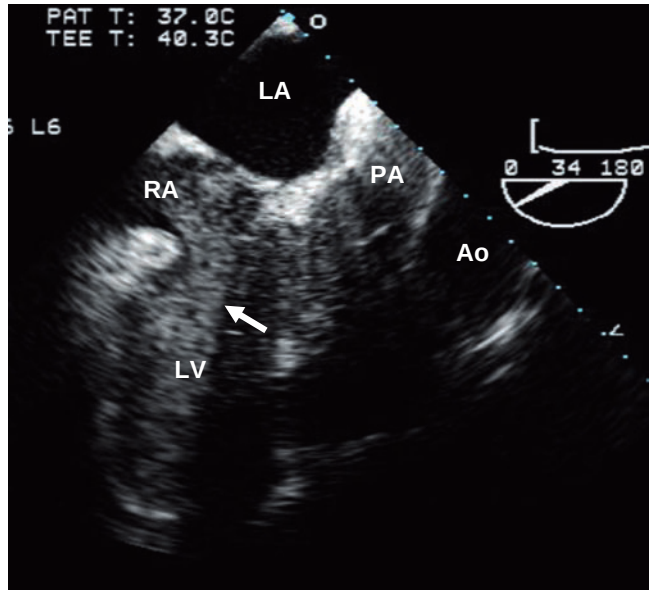


**Figure 26.19** Transesophageal echocardiogram in a 69-year-old man with situs solitus and levocardia (due to poor quality of the transthoracic echocardiogram). Agitated saline injected into a right arm vein is seen in the right-sided right atrium (RA), the right-sided left ventricle (LV) and in the posteriorly positioned pulmonary artery (PA). There is a shadow caused by the mechanical valve in the tricuspid position (arrow). Ao, aorta.

of agitated saline (bubble study) into a peripheral systemic vein is helpful in identifying the right atrium, the subpulmonary LV and the pulmonary arteries (Fig. 26.19). In addition, TEE is performed routinely during intraoperative repair to monitor ventricular function, to assess prosthetic tricuspid valves, and to detect residual atrial or ventricular defects. Assessment of conduits by TEE is usually difficult.

## Imaging of the fetus

Fetal diagnosis of physiologically "corrected" TGA is possible and depends on correct identification of the AV and VA connections (Fig. 26.20a–c and Videoclip 26.11). Diagnostic accuracy can be very high in specialized centers but the diagnosis may be more challenging in less experienced hands, especially during routine fetal screening. Associated lesions like Ebstein anomaly, VSD, septal malalignment, or an absent AV connection often give a clue for the diagnosis. There are a number of echocardiographic features that help in establishing the diagnosis of physiologically "corrected" TGA in the fetus [41,42]. First, there is the reversed differential septal insertion of the tricuspid and mitral valve, with the tricuspid valve identified as being on the left side of the heart. Correct use of this anatomic feature depends on accurately identifying the left and right sides of the fetus and requires careful identification of fetal position. The reversed offset might be more difficult to identify in cases with an inlet (canal-type) VSD. A second, generally more reliable sign is the presence of the moderator band in the left-sided ventricle. Identification of the moderator band is one of the most consistent echocardiographic signs for identifying the RV during fetal life and its abnormal position helps in diagnosing physiologically "corrected" TGA. A third echocardiographic sign is the parallel orientation of the great arteries. In this context the three-vessel view is very helpful to identify the abnormal spatial relationship of the great arteries. Also, a posterior-to-anterior sweep in a 4-chamber view can identify the first artery coming from the LV to be the pulmonary artery and the more anterior artery coming from the RV as being the aorta. Most fetuses with physiologically "corrected" TGA have associated lesions, the most common being tricuspid valve anomalies (Ebstein-like malformation), VSDs, and pulmonary artery stenosis or atresia. Severe tricuspid regurgitation, which can be present during fetal life, adversely affects fetal survival. Conduction abnormalities might already be present in fetal life, and cases with complete AV block have been reported [43,44]. In general, the short-term prognosis of the fetus with physiologically "corrected" TGA is good and is largely dependent on severity of associated lesions.

## Imaging the adult

Technical challenges due to restricted echocardiographic windows resulting in poor image quality are major limitations in the evaluation of adults, especially in those who have undergone previous surgery. The segmental approach to describe cardiovascular anatomy also applies to adults, as

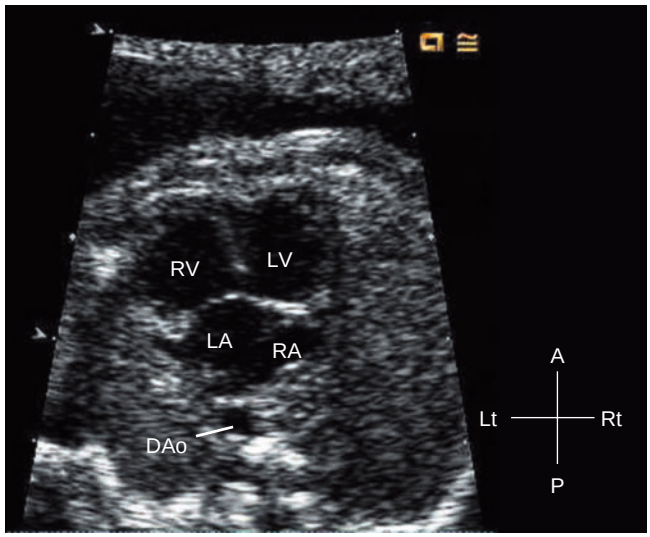


(a)

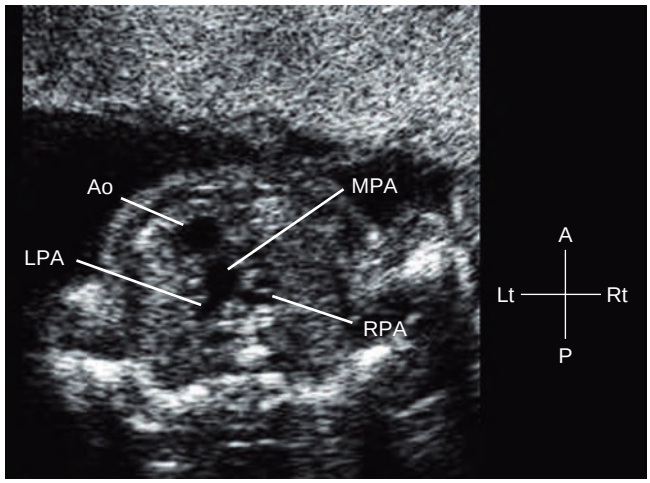


(b)

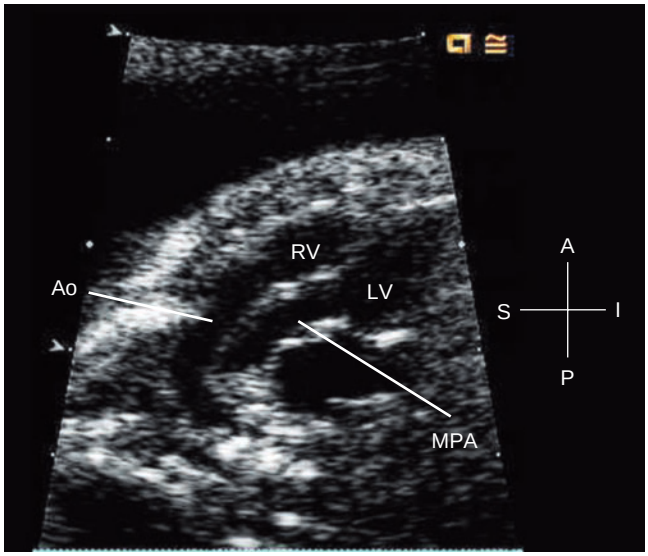


(c)

**Figure 26.20** Fetal echocardiogram at 20 weeks' gestation showing levocardia, situs solitus and physiologically "corrected" transposition of the great arteries (TGA) with intact ventricular septum. **(a)** Transverse view of the fetal thorax demonstrating a 4-chamber view with atrioventricular (AV) discordance. **(b)** Transverse view of the superior aspect of the fetal thorax showing the leftward and anterior ascending aorta (Ao) and the posterior and rightward main pulmonary artery (MPA). The branch pulmonary arteries are seen at this level. **(c)** Parasagittal view of the fetus showing the parallel course of the great arteries with an anterior aorta (Ao) and a posterior MPA. DAo, descending aorta; LA, left atrium; LPA, left pulmonary artery; LV, left ventricle; RA, right atrium; RPA, right pulmonary artery; RV, right ventricle; A, anterior; P, posterior; Lt, left; Rt, right; I, inferior; S, superior.

described above. TEE is an alternative to transthoracic echocardiography for delineating the intracardiac anatomy and the outflow tracts if the quality of the transthoracic images is inadequate [40,45]. Injection of agitated saline helps to identify the direction of blood flow and the chambers, as previously described.

Adults with physiologically "corrected" TGA and prior LV outflow tract obstruction can present with a conduit from the LV to the pulmonary artery (Videoclip 26.9). Heart block may be the first symptom of physiologically "corrected" TGA in adults as acquired complete AV block continues to develop at a rate of 2% per year [46]. Thus, physiologically "corrected" TGA in such a patient should be excluded by echocardiography.

Cardiac magnetic resonance (CMR) imaging provides an excellent noninvasive alternative to TEE in adults with inadequate echocardiographic windows, to describe the anatomy, to assess ventricular function, and to measure valve regurgitation and shunts [47,48]. Computed tomography or radionuclide angiography are alternatives in the presence of a pacemaker or claustrophobia [49,50]. Coronary angiography in patients at risk of coronary artery disease should be performed before any operative intervention if the patient is older than 40 years [51]. In addition, the coronary anatomy must be determined by any imaging modality in a patient who is considered for a double switch procedure.

## Perioperative assessment

Surgical management of physiologically "corrected" TGA can be divided into two broad categories:

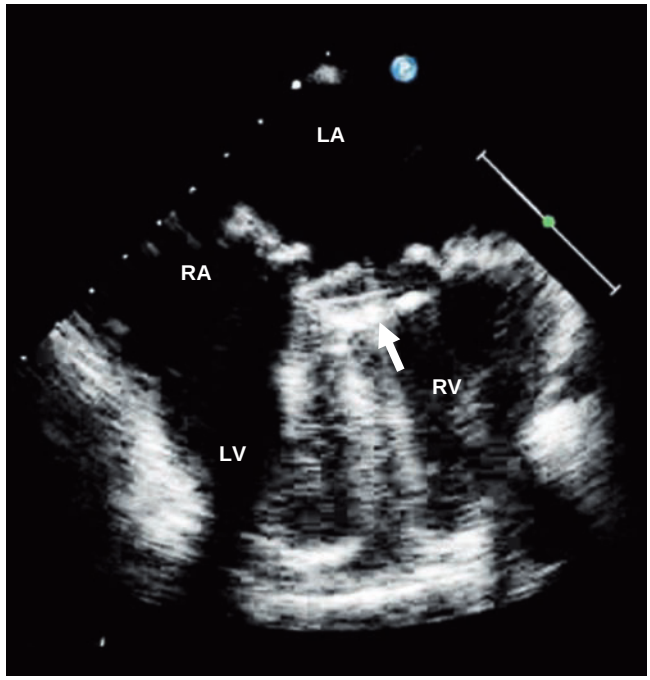


(a)

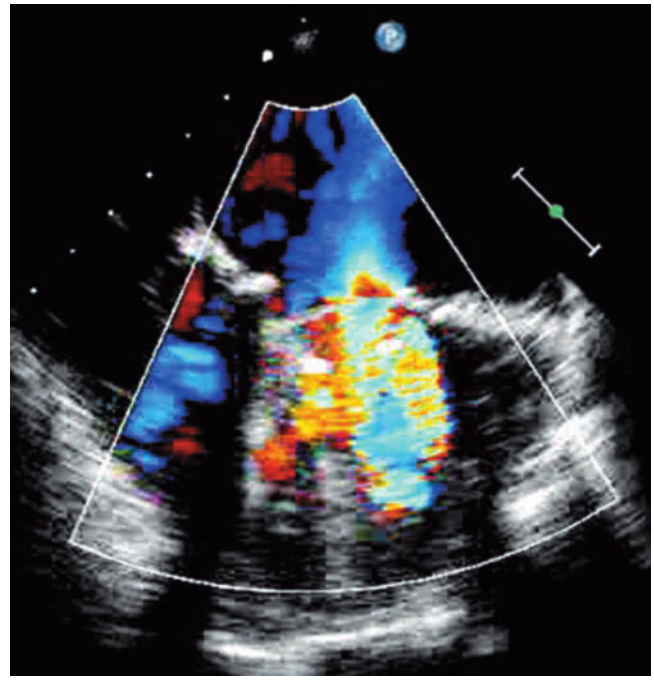

(b)

**Figure 26.21** Imaging a mechanical tricuspid valve in a 24-year-old woman at 12 weeks of pregnancy. **(a)** Transesophageal echocardiogram 4-chamber view reveals that the left atrium (LA) and right ventricle (RV) are both left-sided and dilated. The medial disk of the CarboMedics valve is immobile (arrow) due to pannus. There is no thrombus and the lateral leaflet opens normally. **(b)** Color Doppler flow mapping demonstrates turbulent flow across the tricuspid valve. Continuous-wave Doppler demonstrated a mean diastolic gradient of 14 mm Hg at a heart rate of 90 bpm. LV, left ventricle; RA, right atrium.

**1** A physiologic-palliative approach, including repair of associated lesions such as VSD closure, LV-to-pulmonary artery conduit, tricuspid valve plasty or replacement, pulmonary artery banding and pacemaker.
**2** Anatomic repair, including an atrial switch (Mustard or Senning) with either ventricular redirection (LV-to-aortic valve baffle and RV-to-PA conduit, also known as Rastelli procedure) or an arterial switch (also known as double switch operation). The first approach leaves the RV as the systemic ventricle whereas the second approach establishes the LV as the systemic ventricle.

Miniaturization of multiplane TEE probes allows routine intraoperative assessment by echocardiography not only in adults and adolescents but also in most infants weighing more than 3 kg [52]. The pre-cardiopulmonary bypass echocardiogram aims to confirm preoperative diagnoses and to refine surgical planning. Three-dimensional TEE can be particularly helpful in planning tricuspid valve repair in patients with Ebstein-like anomaly. Goals of the post-cardiopulmonary bypass echocardiogram depend on the type of surgery performed. In all cases, assessment of ventricular size, global and regional function, AV and semilunar valve function (stenosis and/or regurgitation), outflow tract obstruction, and exclusion of residual atrial or ventricular septal defects is performed. Special attention is given to evaluation of the systemic and pulmonary venous pathways for patency and leaks after an atrial switch procedure. The function of the semilunar valves and flow into the coronary arteries are evaluated after the arterial switch operation. Evaluation of conduits and prosthetic valves for a paravalvar leak or obstruction is performed when relevant.

## Pulmonary artery banding

Patients undergoing banding of the pulmonary artery in preparation for a double switch procedure are followed serially by echocardiography. Severe tricuspid regurgitation is present in the majority of patients before banding, and is caused by malcoaptation of the tricuspid valve leaflets secondary to tricuspid annular dilation and abnormal RV geometry, in addition to dysplasia or Ebstein-like malformation of the tricuspid valve (Figs 26.10 and 26.11; Videoclip 26.8d). Banding of the pulmonary artery leads to an increase in LV systolic pressure and to a shift of the interventricular septum toward the left-sided RV. The change in RV geometry improves the coaptation of the tricuspid valve leaflets and decreases the severity of tricuspid regurgitation. However, LV myocardial dysfunction can occur if the pulmonary artery banding is too tight and the procedure is not carefully monitored by pressure-volume loop analysis and by intraoperative echocardiographic assessment of the LV.

Echocardiographic assessment during and after pulmonary artery banding includes:

- evaluation of right and left ventricular systolic function;
- evaluation of tricuspid and mitral regurgitation;
- assessment of the gradient across the pulmonary artery and LV systolic pressure by Doppler echocardiography.

## Follow-up

Continued echocardiographic surveillance and periodic evaluations are integral to the long-term management of all patients with physiologically "corrected" TGA regardless of age [51,53,54]. These patients are at risk for late complications such as progressive tricuspid regurgitation, systemic RV dysfunction, LV outflow tract obstruction, AV block, endocarditis, mechanical tricuspid valve dysfunction (Fig. 26.21 and Videoclip 26.12a–d), conduit stenosis and/or insufficiency, and other abnormalities related to surgical procedures [27,35–38]. A detailed, lifelong echocardiographic assessment aims to detect these and other complications [53,55,56].

## References


1. Hoffman JI, Kaplan S. The incidence of congenital heart disease. *J Am Coll Cardiol* 2002;39:1890–900.
2. Keane JF, Fyler DC. Corrected transposition of the great arteries. In: Keane JF, Lock JE, Fyler DC (eds) *Nada's Pediatric Cardiology*, 2nd edn. Philadelphia: Saunders-Elsevier, 2006;791–7.
3. Samanek M, Voriskova M. Congenital heart disease among 815,569 children born between 1980 and 1990 and their 15-year survival: a prospective Bohemia survival study. *Pediatr Cardiol* 1999;20:411–7.
4. Kuehl KS, Loffredo CA. Population-based study of l-transposition of the great arteries: possible associations with environmental factors. *Birth Defects Res A Clin Mol Teratol* 2003;67:162–7.
5. Piacentini G, Digilio MC, Capolino R et al. Familial recurrence of heart defects in subjects with congenitally corrected transposition of the great arteries. *Am J Med Genet A* 2005;137:176–80.
6. McElhinney DB, Geiger E, Blinder J et al. NKX2.5 mutations in patients with congenital heart disease. *J Am Coll Cardiol* 2003;42:1650–5.
7. Rokitansky CF. Die Defecte der Scheidewande des Herzens. Wien: Wilhelm Braumuller, 1875:81–6.
8. Van Praagh R, Van Praagh S, Vlad P, Keith JD. Anatomic types of congenital dextrocardia: diagnostic and embryologic implications. *Am J Cardiol* 1964;13:510–31.
9. Wilkinson JL, Cochrane AD, Karl TR. Congenital Heart Surgery Nomenclature and Database Project: corrected (discordant) transposition of the great arteries (and related malformations). *Ann Thorac Surg* 2000;69:S236–48.
10. Freedom RM, Harrington DP, White RI, Jr. The differential diagnosis of levo-transposed or malposed aorta. An angiocardiographic study. *Circulation* 1974;50:1040–6.
11. Coto EO, Jimenez MQ, Cabrera A et al. Aortic levopositions without ventricular inversion. *Eur J Cardiol* 1978;8:523–41.
12. Van Praagh R. Diagnosis of complex congenital heart disease: morphologic-anatomic method and terminology. *Cardiovasc Intervent Radiol* 1984;7:115–20.
13. Van Praagh R. What is congenitally corrected transposition of the great arteries? *N Engl J Med* 1970;282:1097–8.
14. Warnes CA. Congenitally corrected transposition: the uncorrected misnomer. *J Am Coll Cardiol* 1996;27:1244–5.
15. Van Praagh R. Segmental approach to diagnosis. In: Keane JF, Lock JE, Fyler DC (eds) *Nada's Pediatric Cardiology*, 2nd edn. Philadelphia: Elsevier, 2006;39–46.
16. Penny DJ, Somerville J, Redington AN. Echocardiographic demonstration of important abnormalities of the mitral valve in congenitally corrected transposition. *Br Heart J* 1992;68:498–500.
17. Anderson RH, Becker AE, Arnold R, Wilkinson JL. The conducting tissues in congenitally corrected transposition. *Circulation* 1974;50:911–23.
18. Becker A, Anderson R. Conditions with discordant atrioventricular connections – anatomy and conducting tissues. In: Anderson RH, Macartney FJ, Shinebourne EA (eds) *Pediatric Cardiology*. Edinburgh: Churchill Livingstone, 1978;184–97.
19. Hosseinpour AR, McCarthy KP, Griselli M et al. Congenitally corrected transposition: size of the pulmonary trunk and septal malalignment. *Ann Thorac Surg* 2004;77:2163–6.
20. Dabizzi RP, Barletta GA, Caprioli G et al. Coronary artery anatomy in corrected transposition of the great arteries. *J Am Coll Cardiol* 1988;12:486–91.
21. Allwork SP, Bentall HH, Becker AE et al. Congenitally corrected transposition of the great arteries: morphologic study of 32 cases. *Am J Cardiol* 1976;38:910–23.
22. Chiu IS, Wu SJ, Chen SJ et al. Sequential diagnosis of coronary arterial anatomy in congenitally corrected transposition of the great arteries. *Ann Thorac Surg* 2003;75:422–9.
23. Van Praagh R, Papagiannis J, Grunenfelder J et al. Pathologic anatomy of corrected transposition of the great arteries: medical and surgical implications. *Am Heart J* 1998;135:772–85.
24. Shea PM, Lutz JF, Vieweg WV et al. Selective coronary arteriography in congenitally corrected transposition of the great arteries. *Am J Cardiol* 1979;44:1201–6.
25. McKay R, Anderson RH, Smith A. The coronary arteries in hearts with discordant atrioventricular connections. *J Thorac Cardiovasc Surg* 1996;111:988–97.
26. Ismat FA, Baldwin HS, Karl TR, Weinberg PM. Coronary anatomy in congenitally corrected transposition of the great arteries. *Int J Cardiol* 2002;86:207–16.
27. Graham TP Jr, Bernard YD, Mellen BG et al. Long-term outcome in congenitally corrected transposition of the great arteries: a multi-institutional study. *J Am Coll Cardiol* 2000;36:255–61.
28. Anderson RH, Becker AE, Gerlis LM. The pulmonary outflow tract in classically corrected transposition. *J Thorac Cardiovasc Surg* 1975;69:747–57.
29. Silverman NH, Gerlis LM, Horowitz ES et al. Pathologic elucidation of the echocardiographic features of Ebstein's malformation of the morphologically tricuspid valve in discordant atrioventricular connections. *Am J Cardiol* 1995;76:1277–83.

30. Anderson KR, Danielson GK, McGoon DC, Lie JT. Ebstein's anomaly of the left-sided tricuspid valve: pathological anatomy of the valvular malformation. *Circulation* 1978;58:I87–91.
31. Horvath P, Szufladowicz M, de Leval MR et al. Tricuspid valve abnormalities in patients with atrioventricular discordance: surgical implications. *Ann Thorac Surg* 1994;57:941–5.
32. Becker AE, Ho SY, Caruso G et al. Straddling right atrioventricular valves in atrioventricular discordance. *Circulation* 1980;61: 1133–41.
33. Celermajer DS, Cullen S, Deanfield JE, Sullivan ID. Congenitally corrected transposition and Ebstein's anomaly of the systemic atrioventricular valve: association with aortic arch obstruction. *J Am Coll Cardiol* 1991;18:1056–8.
34. Deanfield JE, Anderson RH, Macartney FJ. Aortic atresia with "corrected transposition of the great arteries" (atrioventricular and ventriculoarterial discordance). *Br Heart J* 1981;46:683–6.
35. Presbitero P, Somerville J, Rabajoli F et al. Corrected transposition of the great arteries without associated defects in adult patients: clinical profile and follow up. *Br Heart J* 1995;74:57–9.
36. Lundstrom U, Bull C, Wyse RK, Somerville J. The natural and "unnatural" history of congenitally corrected transposition. *Am J Cardiol* 1990;65:1222–9.
37. Connelly MS, Liu PP, Williams WG et al. Congenitally corrected transposition of the great arteries in the adult: functional status and complications. *J Am Coll Cardiol* 1996;27:1238–43.
38. Beauchesne LM, Warnes CA, Connolly HM et al. Outcome of the unoperated adult who presents with congenitally corrected transposition of the great arteries. *J Am Coll Cardiol* 2002;40:285–90.
39. Fischbach P, Law I, Serwer G. Congenitally corrected l-transposition of the great arteries: Abnormalities of atrioventricular conduction. *Prog Pediatric Cardiol* 1999;10:37–43.
40. Sreeram N, Stumper OF, Kaulitz R et al. Comparative value of transthoracic and transesophageal echocardiography in the assessment of congenital abnormalities of the atrioventricular junction. *J Am Coll Cardiol* 1990;16:1205–14.
41. Sharland G, Tingay R, Jones A, Simpson J. Atrioventricular and ventriculoarterial discordance (congenitally corrected transposition of the great arteries): echocardiographic features, associations, and outcome in 34 fetuses. *Heart* 2005;91:1453–8.
42. Chiappa E, Micheletti A, Sciarrone A et al. The prenatal diagnosis of, and short-term outcome for, patients with congenitally corrected transposition. *Cardiol Young* 2004;14:265–76.
43. Costa P, Monterroso J, Areias JC. Prenatal diagnosis of complete heart block and congenitally corrected transposition of the great arteries. *Pediatr Cardiol* 2007;28:414–5.
44. Jaeggi ET, Hornberger LK, Smallhorn JF, Fouron JC. Prenatal diagnosis of complete atrioventricular block associated with structural heart disease: combined experience of two tertiary care centers and review of the literature. *Ultrasound Obstet Gynecol* 2005;26:16–21.
45. Caso P, Ascione L, Lange A et al. Diagnostic value of transesophageal echocardiography in the assessment of congenitally corrected transposition of the great arteries in adult patients. *Am Heart J* 1998;135:43–50.
46. Huhta JC, Maloney JD, Ritter DG et al. Complete atrioventricular block in patients with atrioventricular discordance. *Circulation* 1983;67:1374–7.
47. Schmidt M, Theissen P, Deutsch HJ et al. Congenitally corrected transposition of the great arteries (L-TGA) with situs inversus totalis in adulthood: findings with magnetic resonance imaging. *Magn Reson Imaging* 2000;18:417–22.
48. Dodge-Khatami A, Tulevski II, Bennink GB et al. Comparable systemic ventricular function in healthy adults and patients with unoperated congenitally corrected transposition using MRI dobutamine stress testing. *Ann Thorac Surg* 2002;73:1759–64.
49. Leschka S, Oechslin E, Husmann L et al. Pre- and postoperative evaluation of congenital heart disease in children and adults with 64-section CT. *Radiographics* 2007;27:829–46.
50. Benson LN, Burns R, Schwaiger M et al. Radionuclide angiographic evaluation of ventricular function in isolated congenitally corrected transposition of the great arteries. *Am J Cardiol* 1986;58:319–24.
51. Therrien J, Warnes C, Daliento L et al. Canadian Cardiovascular Society Consensus Conference 2001 update: recommendations for the management of adults with congenital heart disease part III. *Can J Cardiol* 2001;17:1135–58.
52. Ayres NA, Miller-Hance W, Fyfe DA et al. Indications and guidelines for performance of transesophageal echocardiography in the patient with pediatric acquired or congenital heart disease: report from the task force of the Pediatric Council of the American Society of Echocardiography. *J Am Soc Echocardiogr* 2005;18:91–8.
53. Deanfield J, Thaulow E, Warnes C et al. Management of grown up congenital heart disease. *Eur Heart J* 2003;24:1035–84.
54. Warnes CA, Liberthson R, Danielson GK et al. Task force 1: the changing profile of congenital heart disease in adult life. *J Am Coll Cardiol* 2001;37:1170–5.
55. Child JS, Collins-Nakai RL, Alpert JS et al. Task force 3: workforce description and educational requirements for the care of adults with congenital heart disease. *J Am Coll Cardiol* 2001;37: 1183–7.
56. Therrien J, Dore A, Gersony W et al. CCS Consensus Conference 2001 update: recommendations for the management of adults with congenital heart disease. Part I. *Can J Cardiol* 2001;17: 940–59.

# 5 Miscellaneous Cardiovascular Lesions

*Echocardiography in Pediatric and Congenital Heart Disease: From Fetus to Adult*
Edited by Wyman W. Lai, Luc L. Mertens, Meryl S. Cohen and Tal Geva
 ISBN: 978-1-405-17401-5

# 27 Functionally Univentricular Heart

**Stéphane L.J. Moniotte and Catherine Barrea**
University of Louvain Medical School, Louvain; Pediatric Cardiology, Cliniques Universitaires St-Luc, Brussels, Belgium

## Introduction

The term "functionally univentricular heart" encompasses a group of cardiac malformations defined by the presence of a single ventricular chamber or a large dominant ventricle associated with a diminutive opposing ventricle [1–3]. The management of these malformations is designed to obtain fully saturated systemic arterial blood, achieved through a staged palliation and variants of total cavopulmonary anastomosis as the common final surgical procedure. Despite the increasing use of magnetic resonance imaging (MRI) to complement echocardiography (echo) and to provide unique information on cardiovascular anatomy, ventricular function and blood flow, 2D-echocardiography and Doppler ultrasound remain the primary diagnostic tools in patients with complex congenital heart diseases. This chapter reviews the various applications of echocardiography in patients with a single ventricle and their relevance before, during and after surgical or transcatheter management.

## Definition

Functionally single ventricle arrangements represent a heterogeneous group of anomalies sharing as a common feature a single functional cardiac chamber independently supporting either the systemic or pulmonary circulation. In most patients with functionally univentricular hearts (UVH) there are two morphologic ventricles, one of which is too small to sustain one of the circulations [1,2]. Different terminologies have been used to describe anatomic variants of single ventricle. Terms like "univentricular heart," "single ventricle" and "common ventricle" have all been used to describe the same anomalies. These terms are in fact misleading because from a pathologic point of view human hearts with a true single ventricle are extremely rare. In most cases there is a dominant ventricle with a second hypoplastic or rudimentary chamber. From the physiologic point of view this does not really matter as both the systemic and pulmonary circulations are supported by a single pumping chamber.

### Incidence

Because the terminology used to define UVH has been somewhat confusing, it is difficult to state the actual incidence. In different series of congenital heart disease patients, cases of UVH represent about 1–2% of the total [4].

## Etiology

Most cases of single ventricles are sporadic. However, several investigators have reported familial cases of tricuspid atresia [5–7]. Tricuspid atresia and other forms of functionally univentricular hearts have been associated with a variety of genetic syndromes, such as Holt–Oram [8,9], Noonan [10,11], velocardiofacial syndrome [12,13] and, rarely, trisomy 21 [14]. Most forms of UVH are considered to be polygenic in nature, with recurrence and transmission risks far below that expected from mendelian inheritance [15]. The risk to siblings and offspring of affected individuals is generally in the order of 2–5% [16–18]. Concordance rates may be higher in some specific subtypes of patients [19].

## Morphology and classification

### Developmental considerations

The embryologic cause of the UVH, as for most congenital cardiac defects, is not fully known. Two main theories exist. One states that the bulboventricular septum becomes realigned to form the interventricular septum, and that UVH is a consequence of failure of this realignment. The other states that bulboventricular and interventricular septa are different structures, and that the UVH results from failure of formation of the posterior interventricular septum.

*Echocardiography in Pediatric and Congenital Heart Disease: From Fetus to Adult*
Edited by Wyman W. Lai, Luc L. Mertens, Meryl S. Cohen and Tal Geva
 ISBN: 978-1-405-17401-5

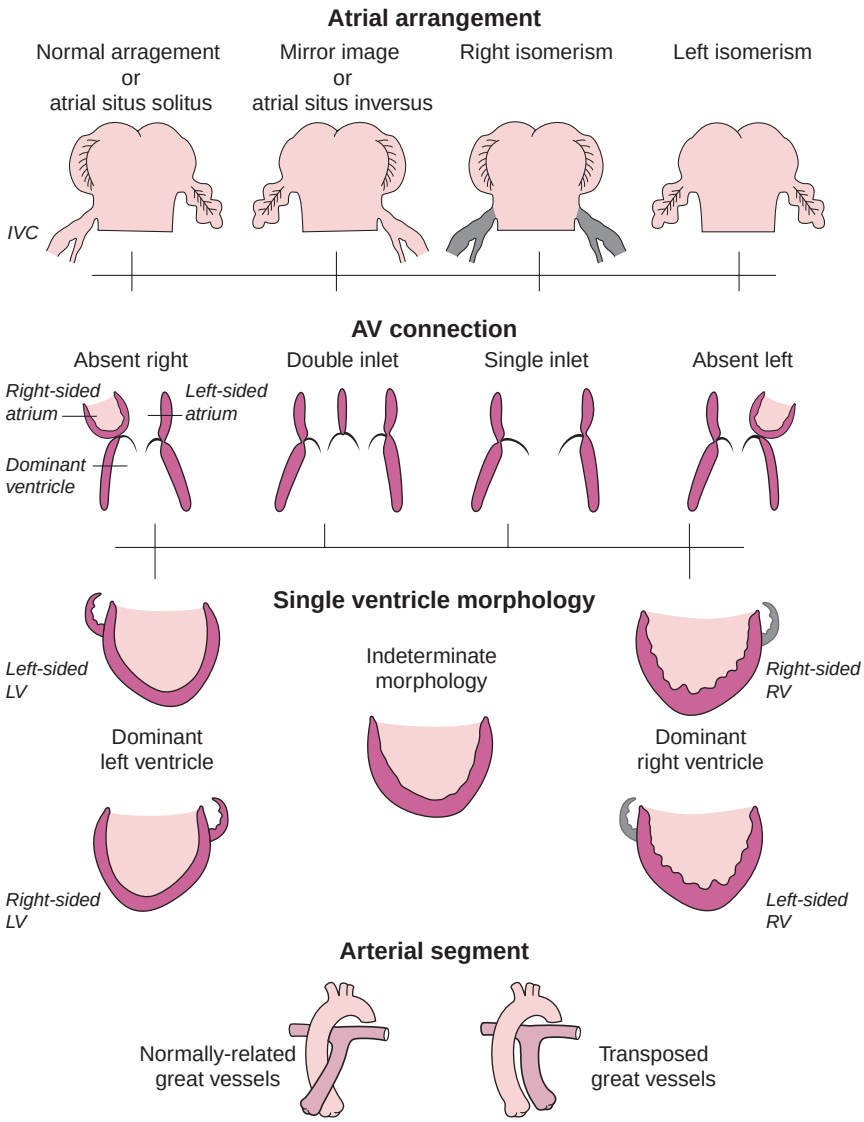


**Figure 27.1** Classification of univentricular hearts. Univentricular hearts are classified on the basis of their atrial arrangement (inferior vena caval [IVC] insertion and appendages morphology), type of atrioventricular (AV) connection (absent right, double-inlet or absent left), ventricular morphology (dominant left ventricle, dominant right ventricle or indeterminate single ventricle) and ventriculo-arterial connections (normally related vessels or transposed great arteries). IVC, inferior vena cava; LV, left ventricle; RV, right ventricle.

## Anatomy

The anatomy of complex congenital heart lesions is best approached in a systematic way. The segmental approach has generally been accepted as the standard method for analyzing and categorizing congenital heart malformations [5]. This method is based on describing the four primary segments of the heart (veins, atria, ventricles and arterial trunks) and the way they are joined together at the venoatrial, atrioventricular and ventriculo-arterial junctions. Central to the process is the use of constant "markers," which are constant morphologic characteristics of a certain segment. So, for instance, a constant feature of left atrial morphology is the presence of a left atrial appendage with the characteristic "finger-like" shape. For each chamber a certain number of unique "identifiers" have been established. Once the morphology of each chamber is defined, the connections can be studied. To describe precisely the type of UVH, the atrial arrangement, the pattern of atrioventricular connection, the ventricular morphology, the ventriculo-arterial connections and associated lesions should be accounted for (Fig. 27.1).

The atrial topological arrangement can be solitus (the usual pattern), inversus (mirror-image pattern), or ambiguous in case of left or right isomerism. Either type of atrioventricular connection can be associated with any of the four forms of atrial arrangement. The atrioventricular (AV) connection is, by definition, univentricular but there may be a double inlet, a common inlet, or an absent right or an absent left AV connection. In a double-inlet connection, there are two separate AV valves. Based on their morphologic characteristics, it is frequently not possible to define the valves as either mitral or tricuspid valves. Therefore it is better to refer to them as left and right AV valves on the basis of the anatomic position within the chest. In case of an absent AV connection, the absent valve can be on the right side or on the left side. The

remaining AV connection will usually be concordant with the main ventricle. This describes the classic forms of "tricuspid" and "mitral" atresia. In both the double-inlet connection or the absent AV connection, the dominant ventricle can be right, left or indeterminate.

*Overriding* refers to the commitment of an AV valve annulus to the nonconcordant ventricular chamber and results from malalignment of the atrial and ventricular septa. The percentage of annular commitment to a ventricular chamber relative to the position of the ventricular septum determines the AV valve connection to a ventricle. In the setting of an overriding AV valve, an atrium is considered to connect to the ventricle into which more than 50% of its valve empties. A univentricular AV connection would require more than 50% of both AV valves to be committed to one ventricular chamber. The remaining chamber would be considered an outlet or rudimentary chamber.

*Straddling* of the AV valve is a feature of the tensor apparatus (chordae and papillary muscles) and occurs if tensor insertions are present into the contralateral ventricle through a ventricular septal defect.

The identification of the ventricular myocardial morphology should be based on the most constant component of the ventricular anatomy, which is the trabecular component. From a descriptive point of view, a normal ventricle can be described as having an inlet, a trabecular and an outlet part. Sometimes an abnormal ventricle can lack both inlet and outlet. In those cases, the morphology of the ventricle can still be identified on the basis of the structure of the apical trabecular component. The left ventricular myocardium typically has a relatively smooth appearance with numerous fine oblique trabeculations, whereas the right ventricular myocardium has an irregular surface with relatively few coarse trabeculations. Based on these characteristics most ventricles can be recognized as being morphologically right or left. In rare situations there is only one ventricular chamber in the ventricular mass, with a trabecular pattern typical of neither left nor right ventricle (indeterminate or mixed ventricular morphology). The topology (relationship between the two ventricles in space) of the ventricle should also be determined. Chirality can be used to describe ventricular topology (Fig. 27.2). A ventricle is called a right-hand ventricle if the palmar surface of the right hand can be placed on the ventricular septum with the thumb pointing to the inlet and the fingers to the outlet, the wrist being in the apical component. In a normal heart the right ventricle is right-handed, reflecting the normal embryologic development with a D ventricular looping, whereas in AV and ventricular arterial discordance (also called congenitally corrected transposition), the right ventricle has a left-handed topology consistent with embryologic development with an L ventricular looping.

As a final part of the segmental approach, the ventriculo-arterial connections should be defined. This connection can be concordant, with the pulmonary artery arising from the right ventricle and the aorta from the left ventricle, or discordant, with transposed great artery relationships. Double-outlet ventricle (with both great arteries arising from one ventricle) and single-outlet ventricle (common arterial trunk or in pulmonary or aortic atresia) have also been described.

It is also important to describe associated anomalies like outflow obstructions. Associated subpulmonary, pulmonary or suprapulmonary stenosis, subaortic or aortic valve stenosis or associated coarctation of the aorta should be excluded. In some cases with outflow obstruction a persistent ductus arteriosus is mandatory to sustain the systemic circulation and should be systematically demonstrated. Anomalies of the pulmonary and systemic venous returns commonly occur in the context of isomerism and their detailed identification is extremely important. Also sidedness and branching pattern of the aorta and cranial vessels should be recognized. In absent AV connections, in hypoplasia of one AV valve, or in patients with transposition physiology, a restrictive atrial septal defect (ASD) must also be excluded.

## Specific lesions

### Tricuspid atresia

This is sometimes considered to be the "prototype" of hypoplastic right heart disease (Fig. 27.3; Videoclip 27.4). It encompasses a spectrum of anomalies with variability in the ventriculo-arterial (VA) connections as well as different sizes of interventricular septal defects, which will determine the physiology and clinical presentation. Tricuspid atresia has been classified based on the VA alignments and the degree of obstruction (Table 27.1) [20,21]. Type I is "simple" tricuspid atresia with concordant VA connections; type II is "simple" tricuspid atresia with discordant VA connections. Type III is "complex" tricuspid atresia with associated anomalies such as juxtaposition of the atrial appendages, incomplete AV canal defect, anomalous pulmonary venous connection and other associated anomalies. This classification has become obsolete and in most centers the segmental description will provide a detailed anatomic description of the lesion. The VA relationships and the size of the ventricular septal defect (VSD) will largely determine clinical presentation. In type I patients, a restrictive VSD will result in reduction of pulmonary blood flow, which can result in severe cyanosis and duct-dependent pulmonary blood flow. In type II patients a restrictive VSD will result in diminished systemic output and can be associated with aortic arch anomalies like aortic coarctation and interrupted aortic arch. The clinical presentation can be systemic hypoperfusion and shock, and there can be a duct-dependent systemic perfusion.

### Double-inlet left ventricle (DILV)

Double-inlet left ventricle is very similar to tricuspid atresia but two AV valves are present and connect both atria to the

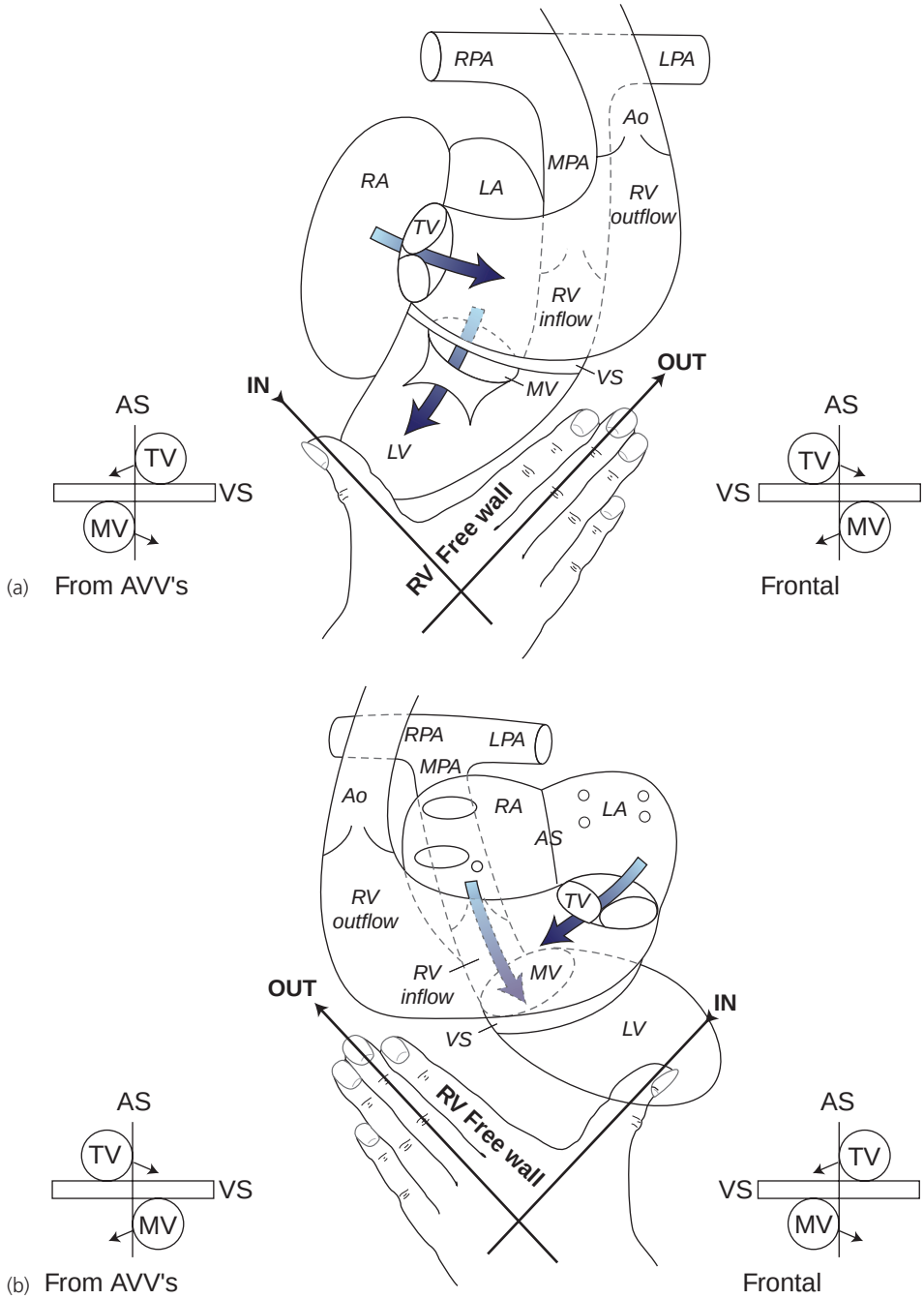


**Figure 27.2** The hand rule. **(a)** The D-loop, or solitus, right ventricle (RV), is right-handed. Figuratively speaking, the thumb of the right hand goes through the tricuspid valve (TV), indicating the RV inflow tract (IN). The fingers go into the RV outflow tract (OUT). The palm of the right hand faces the RV septal surface. The dorsum of the right hand is adjacent to the RV free wall. **(b)** The L-loop, or inverted, RV is left-handed. Figuratively speaking, the thumb of the left hand goes through the tricuspid valve, indicating the RV inflow tract (IN). The fingers of the left hand go into the RV outflow tract (OUT). The palm of the left hand faces the RV septal surface and the dorsum of the left hand is adjacent to the RV free wall. Ao, aorta; AS, atrial septum; AVVs, atrioventricular valves; LA, left atrium; LPA, left pulmonary artery; LV, left ventricle; MPA, main pulmonary artery; MV, mitral valve; RA, right atrium; RPA, right pulmonary artery; TV, tricuspid valve; VS, ventricular septum. Reproduced from Van Praagh S et al. Superoinferior ventricles, anatomic and angiocardiographic findings in 10 postmortem cases. In: Van Praagh R, Takao A (eds) *Etiology and Morphogenesis of Congenital Heart Disease*. Mt Kisco, NY: Futura, 1980;317–78, with permission from Blackwell Publishing.

dominant left ventricle (Fig. 27.4 and Videoclips 27.1–27.3). There is a hypoplastic right ventricle and there can be AV discordance (the most common form of DILV) or, more rarely, AV concordance. The hypoplastic right ventricle (RV) is anterior and leftward to the left ventricle (LV) in 63–74% of cases [22,23]. The topology of the RV will be left-handed in these cases.

The aorta arising from the outlet chamber is anterior and leftward to the pulmonary artery (also {S,L,L} segmental anatomy in the Van Praagh classification). In other cases, the hypoplastic RV will be anterior and to the right with right-hand topology (also called {S,D,D}). In that case, the great arteries are usually normally related, with the pulmonary artery anterior and rightward in relation to the aorta. This is also called the "Holmes heart" [24,25]. Each AV valve has its own chordae tendineae and papillary muscles. One of these valves may be abnormal with stenosis or atresia. When the two valves are patent, the right AV valve is closer to the septum and has chordal attachments to the septum or to the margin of the VSD. The left AV valve typically attaches to the free wall papillary muscles. Mostly it is not possible to define clearly the anatomy of the valves and it is better to

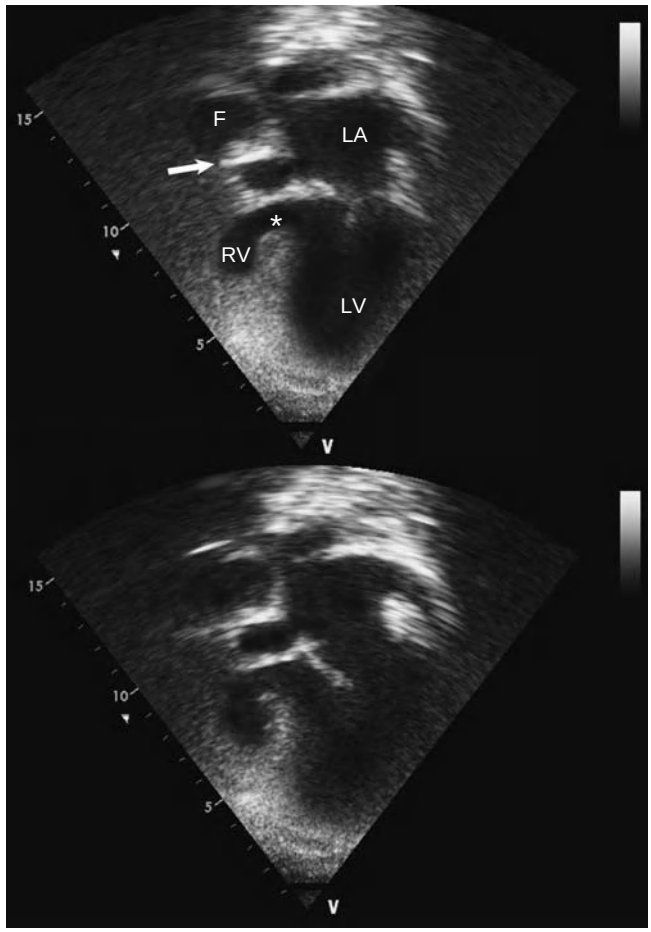


**Figure 27.3** Apical view in a patient with tricuspid atresia. Apical 4-chamber view in systole (top) and diastole (bottom) from a patient with tricuspid atresia, a medium-sized ventricular septal defect/bulboventricular foramen (asterisk) and a severely hypoplastic right ventricle (RV). Note the thick band of echoes arising from the fibrofatty tissue of the right atrioventricular sulcus as well as the echogenic device used for fenestration closure after a Fontan surgery (arrow). F, Fontan tunnel; LA, left atrium; LV, left ventricle; RV, right ventricle.

**Table 27.1** Tricuspid atresia subtypes

| |
|---|
| Type I |
| A No VSD, PA |
| B Small VSD, PS |
| C Large VSD, no PS |
| Type II (D-transposed great arteries) |
| A VSD, PA |
| B VSD, PS |
| C VSD, no PS |
| Type III: Complex |

PA, pulmonary atresia; PS, pulmonary stenosis; VSD, ventricular septal defect.

name them left and right AV valves. As in tricuspid atresia the relationship between the great vessels and the size of the VSD will determine the physiology. With VA discordance and a restrictive VSD, aortic arch anomalies (coarctation, hypoplastic arch, interrupted arch) are very often associated.

### Double-inlet and common-inlet right ventricles

Both types of single RV – double-inlet and common-inlet RV – are rare [26]. In double-inlet right ventricle (DIRV), both AV valves are exclusively committed to the RV, and both great arteries originate from it (double-inlet double-outlet RV) [27]. The AV valves are separate in approximately 35% of the cases [28]. When a single valve connects both atria with the RV, it often has the morphology of a tricuspid valve [29], although common-inlet single RV usually represents an extreme form of RV-dominant AV canal defect and is almost always associated with heterotaxy syndrome (right atrial isomerism).

### Criss-cross hearts and superior-inferior ventricles

Criss-cross hearts display the apparent crossing of tricuspid and mitral inflow at the AV level without mixing. Typically, the right-sided atrium connects to the left-sided ventricle and vice versa (Videoclip 27.11). The planes of the atrial and ventricular septae are nearly perpendicular to each other, and the ventricles have rotated around the long axis of the heart to produce the crossed inflows. This malformation is always associated with a VSD and frequently includes valvar stenoses or straddling valve chordae. The left ventricle is typically posterior, inferior and rightward. It is hypothesized that the inflow portion of the right ventricle is primarily abnormal, leading to abnormal spatial arrangements between the ventricles.

A different entity, sometimes confused with criss-cross AV connections, is superior-inferior ventricles, in which there is an abnormal spatial relationship between the ventricles, with the right ventricle being superior to the left ventricle instead of right anterior. In this condition the ventricular septum has a horizontal position, which can be identified easily echocardiographically using the subcostal short- and long-axis views. Superior-inferior ventricles is associated with criss-cross AV connections in about 60% of cases. Common associated lesions are VSDs (especially inlet defects), AV discordance, ventriculoarterial discordance, double-outlet right ventricle, AV valve anomalies (hypoplasia, atresia, straddling), and outflow tract obstruction. A systematic description of intersegmental connections and relative spatial positions is essential.

## Pathophysiology and treatment

Single ventricle physiology is characterized by obligatory mixing of the systemic and pulmonary venous returns, the aorta and pulmonary artery having mixed oxygen saturation. Depending on the exact anatomy, mixing of the pulmonary and systemic venous returns may not be complete,

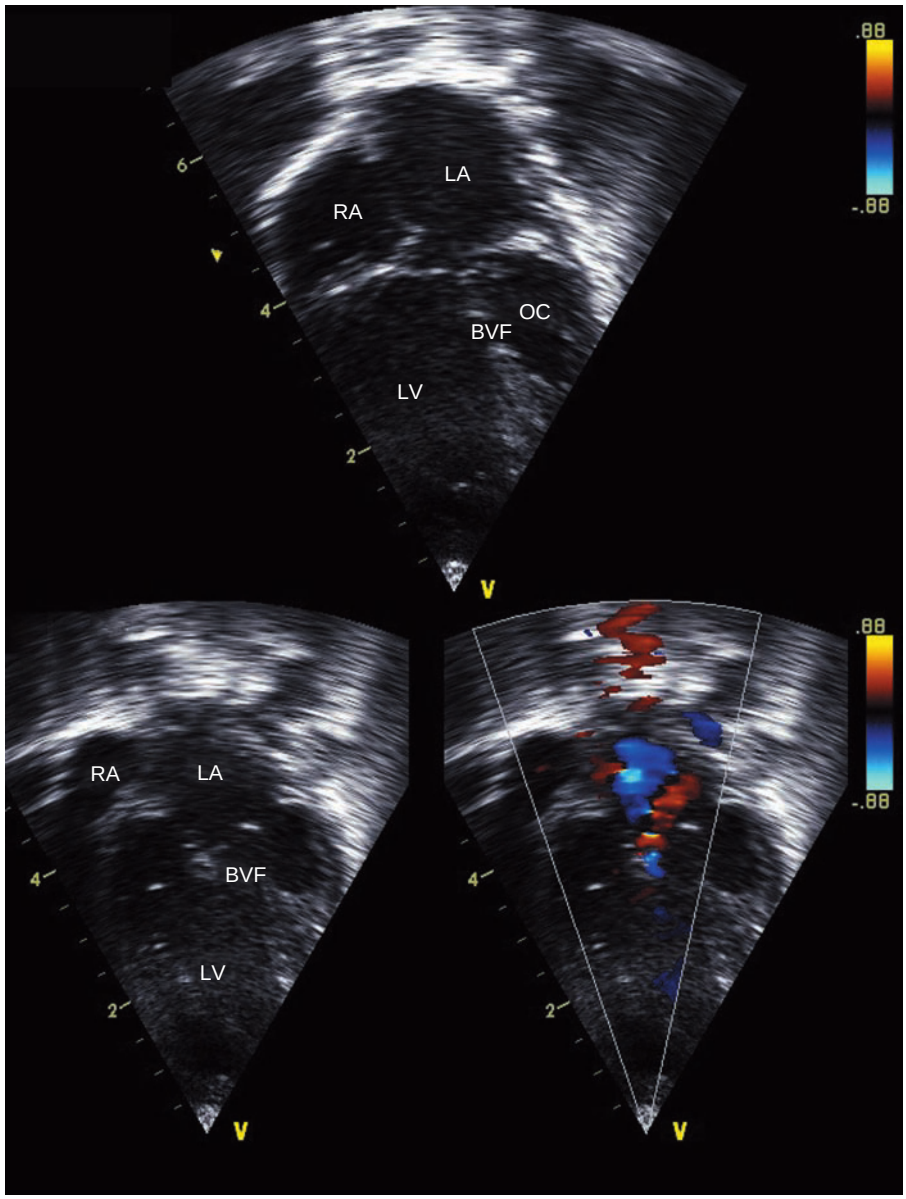


**Figure 27.4** Evaluation of the ventricular septal defect (VSD)/bulboventricular foramen (BVF) in a patient with double-inlet left ventricle (DILV), atresia of the right-sided atrioventricular (AV) valve and transposition of the great arteries. The apical view in systole (bottom) allows measurement of the apex-to-base dimension of the VSD. Combined with its transverse (short-axis) dimension, this measure allows determination of the cross-sectional area of the VSD by using the formula for a regular ellipse. This patient has a restrictive interventricular communication with echogenic signals below the aortic valve (not shown), and Doppler interrogation at the level of the AV valve revealed a mild AV valve regurgitation (bottom right, in blue). RA, right atrium; LA, left atrium; LV, left ventricle; OC, outlet chamber or right ventricle.

with preferential streaming of systemic or pulmonary blood flow toward one great artery. The combined ventricular output is distributed to both great vessels or to a single great artery connected to the other vascular bed through a patent ductus arteriosus and/or collateral vessel(s).

The systemic and pulmonary outputs are determined by the presence and degree of hypoplasia or narrowing of one of the great arteries and by the relative resistance in the pulmonary and systemic vascular beds. Pulmonary blood flow is determined by anatomic obstruction below, at or above the pulmonary valve, pulmonary arteriolar resistance, pulmonary venous obstruction and left atrial pressure. Similarly, anatomic obstruction at the aortic valve, aortic arch and isthmus, and systemic vascular resistance determine the systemic blood flow.

The respective amounts of pulmonary and systemic blood flow determine the clinical course of newborns with single ventricles. In the absence of pulmonary stenosis with regression of fetal pulmonary vascular resistance, the pulmonary blood flow gradually increases, ultimately causing congestive heart failure. Patients with pulmonary stenosis or atresia are cyanotic at birth, to a degree determined by the pulmonary flow supplied by the ductus arteriosus, aortopulmonary collaterals and bronchial circulation. If there is obstruction at any level of the systemic outflow tract, the neonate will present with signs of decreased systemic cardiac output.

Surgical palliation of anatomic and functional single ventricle usually requires a series of operative procedures. The final common surgical pathway for all these variants is one of several modifications of the Fontan procedure, in which the

systemic venous return is diverted directly to the pulmonary arteries and the pulmonary venous return crosses the AV valve(s) and is pumped by the "single ventricle" to the systemic vascular bed. Any type of outflow obstruction to the systemic circulation should be avoided. This usually requires a staged approach for each patient, and different types of intermediate procedures are performed depending on the patient's anatomy before the total cavopulmonary connection is finally performed.

During the first 2–3 months of life, it is not possible to create a "Fontan" circulation due to the neonatal increased pulmonary vascular resistance and the small size of the vessels. A progressive fall in pulmonary artery resistance occurring during the first weeks of life makes a total cavopulmonary connection feasible after 3–4 months of life. Currently, a staged approach is preferred, connecting the superior and inferior caval veins in two different steps. Such a staged approach allows optimization of the cardiac condition before the Fontan circulation is established, and reduces the overall operative morbidity and mortality.

In the neonatal period, the initial management must aim for (if not provided by nature):

- unrestricted flow from the heart to the aorta – if required: coarctectomy; Damus–Kaye–Stansel, Norwood repair;
- a well-balanced limited flow to the lungs – if required: pulmonary artery band; shunt – modified Blalock–Taussig shunt, central shunt or stent in the duct;
- unrestricted return of blood to the ventricle – if required: Rashkind balloon septostomy.

The infant is then allowed to grow for several months. During this time, the heart is submitted to a chronic volume overload, which allows the development of the pulmonary vasculature but, if excessive, negatively influences ventricular function. The infant will have mild desaturation, inversely related to cardiac failure. At the age of 4–12 months, most centers will perform a superior cavopulmonary connection or bidirectional Glenn shunt. This includes anastomosis of the cardiac end of the superior vena cava to the ipsilateral pulmonary artery leaving the pulmonary arteries confluent. Through this type of connection the systemic venous return from the upper part of the body is directed toward the pulmonary artery, bypassing the heart. This provides pulmonary blood flow with desatured blood while at the same time reducing the volume load on the single ventricle if other shunts are eliminated or reduced. Most patients will undergo Fontan completion at the age of 1–5 years, depending on center preference, growth of vascular structures, and cyanosis at rest and during exercise. The Fontan circuit is completed by connecting the inferior caval vein to the pulmonary artery, through an extracardiac conduit or a lateral tunnel.

Most centers advocate the use of a residual fenestration between the conduit and the atrium. Some studies have suggested that this further reduces early mortality and morbidity, especially in patients for whom the Fontan procedure is considered to be high-risk surgery. The fenestration decompresses the systemic veins by allowing right-to-left shunting and increases preload of the single ventricle, resulting in increased cardiac output at the expense of some degree of desaturation. It is possibly beneficial in helping the body adapt to the new circulation. This fenestration can later be closed percutaneously using various devices.

## Imaging

### Preoperative evaluation

The majority of patients with single ventricle present clinically during the neonatal period. The initial echocardiographic examination comprises a full segmental analysis and a detailed hemodynamic evaluation. The examination begins from the subcostal views, followed by the apical, parasternal, high parasternal, and suprasternal views. However, the echocardiographer should not be restricted to these standard transducer positions. Nonstandard views can be used to clarify specific anatomic issues or to optimize the angle of interrogation of the Doppler beam.

### General principles

First the basic anatomy of atrial and visceral situs and location of the cardiac apex must be defined. For this purpose, subcostal views and abdominal scans are particularly useful. The same subcostal scans can be used to define the systemic and pulmonary venous connections to the atria. Abnormalities in systemic venous return, like bilateral superior caval veins or interruption of the inferior caval vein with azygous continuation, can be diagnosed echocardiographically. Similarly abnormal pulmonary venous connections can be identified. This is very important especially if the pulmonary venous connection is obstructed. Effort should be made to identify all four pulmonary veins, because partial abnormal pulmonary venous connections can be present. The diagnostic echocardiographic features of the univentricular AV connection are best viewed from an apical view delineating the crux of the heart, such as the apical 4-chamber view. This view can be used to describe the AV connection as being double-inlet, atresia of one of the inlets, or a common AV valve. Additionally, parasternal and subcostal views are particularly helpful to detail the morphology of the dominant ventricle (right, left or indeterminate); the location of the rudimentary ventricles or outlet chambers (anterior or posterior, left or right); the location of the papillary muscles and chordal attachments within the ventricular chambers (straddling and/or overriding); the status of the AV valve leaflets; and the location, commitment and relationships of the great arteries (concordant or discordant). From the suprasternal notch the sidedness of the aortic arch and the presence and location of a patent ductus arteriosus can be imaged.

During the two-dimensional (2D) scan it is also important to assess the size of the interatrial and interventricular communications. A restrictive interatrial communication may produce pulmonary venous obstruction especially in left AV valve atresia or hypoplasia. In case of tricuspid atresia this will result in a reduced cardiac output. The size of the interatrial communication should be defined by 2D echocardiography, and the degree of restriction should be assessed by spectral and color flow Doppler. The size of the interventricular communication should be evaluated as well because it can indeed be (or become) restrictive. When the aorta originates from a small-outlet right ventricle (as in double-inlet left ventricle or right AV valve atresia with transposition), a restrictive VSD can cause severe systemic outlet obstruction. The initial size of the VSD is particularly predictive of subsequent development of subaortic stenosis. Patients with an initial ventricular septal area of <2 $cm^2/m^2$ are at high risk of having associated coarctation of the aorta or even interruption of the aortic arch, and are also at risk for subsequent development of subaortic stenosis [15].

Color flow imaging is particularly helpful to determine the exact location of pulmonary or systemic outflow tract obstruction. Subvalvar, valvar or supravalvar stenosis can be found. Also ductal, interventricular and interatrial shunting can be evaluated using color flow Doppler. Both the location and degree of shunting can be viewed. Finally, color flow imaging is extremely helpful in assessing AV valve function: stenosis and AV valve regurgitation should be recognized and evaluated with color flow mapping. Pulsed and continuous Doppler of the outflow tracts is useful to quantify outflow obstruction.

Two-dimensional echocardiography will assess global ventricular function. Wall motion abnormalities are common in single ventricle, limiting the usefulness of M-mode-derived measurements of shortening fraction or ejection fraction. Volumetric techniques such as biplane Simpson's volumes can provide useful estimates of ventricular volume and systolic function (ejection fraction, EF) but these techniques are all based on geometric assumptions of a normal left ventricle. This may limit their applicability to more complex single ventricles. The further development of three-dimensional (3D) echocardiography might provide better tools for evaluating systolic function of the single ventricle, but this needs more validation. Cardiac MRI currently offers a promising alternative.

### Tricuspid atresia

The atretic tricuspid valve is seen as a bright shelf or a plate at the floor of the right-sided atrium in D-ventricular loop, and at the floor of the left-sided atrium in L-ventricular loop. The atretic tricuspid valve is usually a muscular, and rarely a fibrous, plate [30]. From the apical and parasternal views, color Doppler imaging confirms the absence of antegrade flow across the atretic tricuspid valve (Fig. 27.3).

Abnormal systemic or pulmonary venous returns are uncommon in tricuspid atresia but need to be evaluated. The size of the atrial communication is assessed by 2-D imaging, and flow restriction is ruled out with color and spectral Doppler. The obligatory right-to-left flow usually crosses the atrial septum via a patent foramen ovale. Less commonly, there is a secundum-type ASD. Juxtaposition of the right atrial appendage may be present in cases of tricuspid atresia and transposition of the great arteries [31], and the left juxtaposed right atrial appendage is seen posterior to the great vessels and superior to the left atrium [32].

A VSD, also called *bulboventricular foramen* (BVF), is frequently seen in tricuspid atresia but its size varies considerably. The subcostal window offers an excellent view of the size and location of the VSD. It is typically a muscular VSD because the absence of the tricuspid valve is usually associated with an unrecognizable membranous septum. A small VSD is typically associated with malalignment of the outlet septum, and may result in subpulmonary or subaortic obstruction (see Fig. 27.4). As the restrictive nature of the VSD may not be apparent in early infancy, it is important to measure the size of the defect in two orthogonal views and to calculate its cross-sectional area [33,34]. This is calculated based on measurements of its major and minor diameters from long- and short-axis views. The VSD area = (major diameter × minor diameter × $\pi/4$). An area indexed to body surface area of <2 $cm^2/m^2$ was found to be predictive of subsequent obstruction.

The mitral valve is seen well from the subcostal, apical and parasternal views, and the presence and degree of regurgitation are evaluated based on the width of the vena contracta. The size of the LV, which may be dilated due to volume overload, is evaluated from long- and short-axis views.

Aortic arch sidedness and obstruction are best evaluated from the suprasternal notch. The branch pulmonary arteries are well seen from the parasternal short-axis view, and their size usually depends on pulmonary blood flow. The ductal view is performed to assess ductal patency.

### Double-inlet left ventricle (DILV)

Imaging DILV is very similar to imaging tricuspid atresia. When two normally functioning AV valves are present, the size of the interatrial communication is not important, unless one of the AV valves is stenotic or atretic. This immediately stresses the importance of evaluating AV valve morphology and function. The morphology and function of the AV valves are assessed from the subcostal, apical and parasternal windows (Figs 27.5 and 27.6). Measuring valve annulus size, leaflet morphology, and the architecture of the chordae tendineae and papillary muscles can all be performed from these acoustic windows. When the atrial septum is intact or in the presence of a restrictive atrial communication, AV valve stenosis is apparent by color and spectral Doppler assessment. In the setting of a nonrestrictive atrial communication, the flow profile across a stenotic AV valve will not reflect the

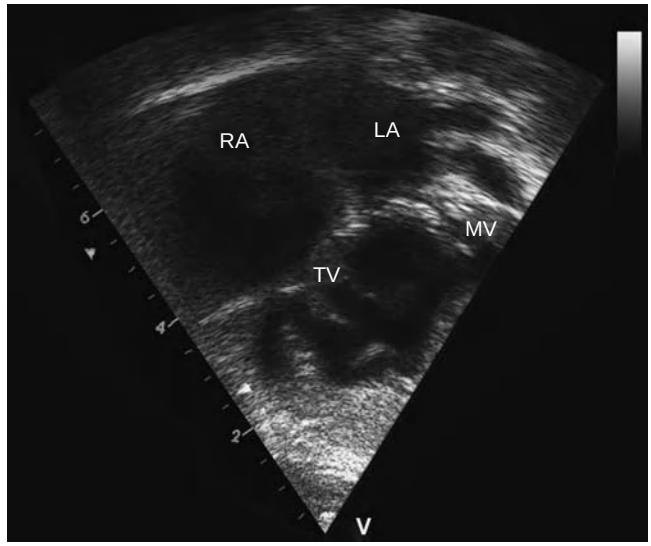


**Figure 27.5** Evaluation of the atrioventricular (AV) valves in a patient with double-inlet left ventricle (DILV). Apical 4-chamber view from a patient with DILV. Both right (RA) and left (LA) atria connect with the dominant left ventricle (LV) by way of two separate AV valves. This view is a posterior plane that passes through both AV valve inlets. Therefore, it lies posterior to the trabecular septum and rudimentary right ventricle. MV, mitral valve; TV, tricuspid valve.

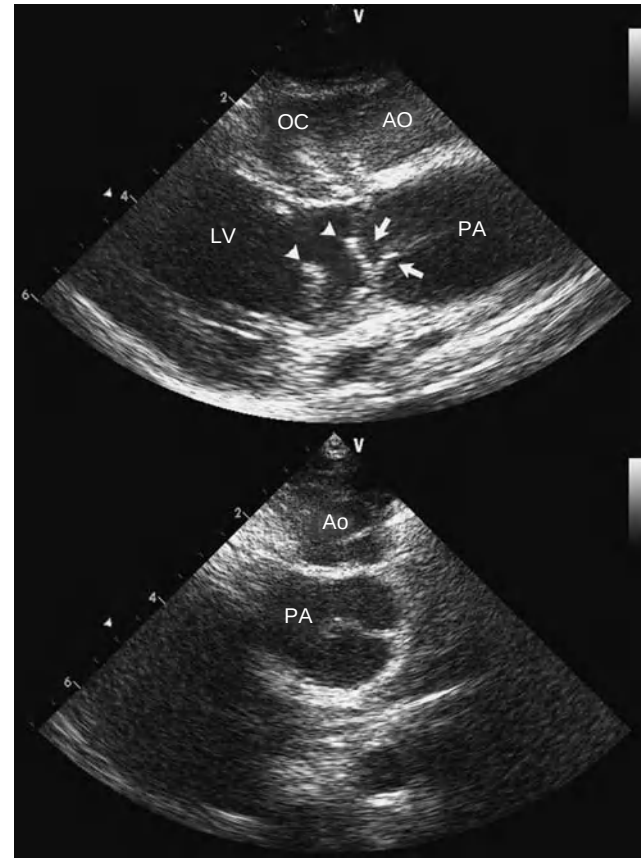


**Figure 27.6** Evaluation of the semilunar valves in a double-inlet left ventricle (DILV) with transposition of the great vessels. Parasternal long-axis (top) and short-axis (bottom) views from a patient with univentricular heart of the left ventricular type and discordant ventriculo-arterial connections. The main (left) ventricle (LV) is connected to a posterior pulmonary artery (PA). A small rightward and anterior outlet chamber gives rise to an anterior and rightward aorta (Ao). Many of the echographic features of transposition of the great vessels can be seen. In the parasternal long-axis view (top), the great vessels are in parallel and the posterior PA has a posterior sweep; in the parasternal short-axis view (bottom), both great vessels appear in cross-section as double circles. OC, outlet chamber.

degree of stenosis. In such circumstances, the assessment of AV valve stenosis relies mostly on 2D imaging. AV valve regurgitation is evaluated by color Doppler mapping. A qualitative or semiquantitative grading of AV valve regurgitation severity based on the width of the vena contracta can be used.

As in tricuspid atresia, VSD size assessment is essential in the initial echocardiographic examination in patients with DILV and transposition of the great arteries [35,36] and requires calculation of its cross-sectional area as described above.

## Postoperative evaluation

### Evaluation of patients after pulmonary artery banding

The goal of banding the pulmonary artery (PA) in children with functionally univentricular hearts is to reduce PA pressure and blood flow in order to relieve symptoms of heart failure and protect the pulmonary vascular circulation from developing obstructive pulmonary hypertension. Echocardiographic assessment includes evaluation of the position of and gradient through the PA band. By using 2-D echocardiography the position of the band can readily be assessed. The band sometimes migrates distally on the central pulmonary artery resulting in PA branch stenosis (generally the right PA). Color Doppler imaging can help to identify the position of the band relative to the origin of the pulmonary artery branches. To evaluate the gradient, continuous-wave Doppler flow velocities are used (Fig. 27.7).

The gradient measured through a PA band should be compared with systemic blood pressure to rule out pulmonary hypertension. Echocardiography is an important tool in evaluating PA band adequacy and facilitates the follow-up of patients after banding, including ones fitted with telemetric adjustable pulmonary artery banding [37] (Fig. 27.8). Apart from evaluating the band itself, AV valve function, ASD and VSD size, and ventricular function assessment are all essential when evaluating patients after banding of the pulmonary artery.

### Echocardiographic evaluation of stage I Norwood and Damus–Kaye–Stansel procedures

A complete echocardiographic evaluation is performed in all patients with single ventricle after the initial surgical procedure. This is discussed in detail in Chapter 20. The goals of the postoperative echocardiogram after Norwood, Sano or Damus–Kaye–Stansel procedures are to evaluate the

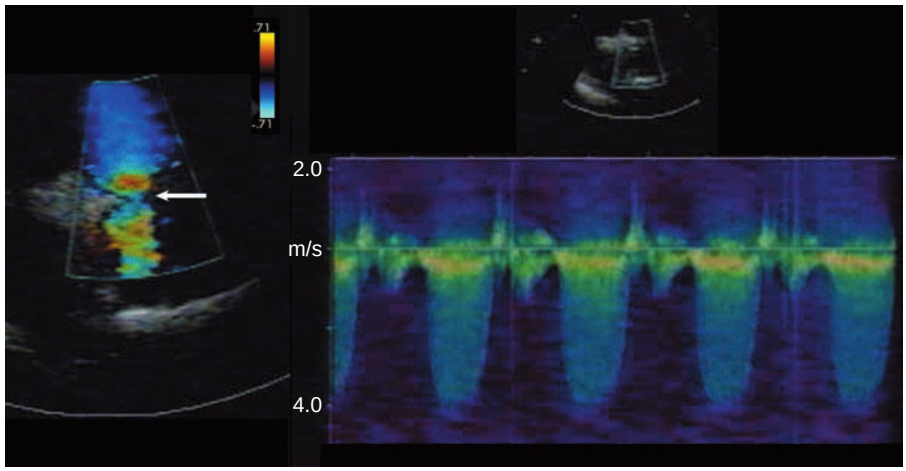


**Figure 27.7** Echocardiographic evaluation of a pulmonary artery banding. Viewed from the parasternal short axis, the flow velocity across the pulmonary artery banding (arrow) is measured by continuous-wave color Doppler (left). This Doppler velocity can be converted to a pressure gradient by using the modified Bernoulli equation. In the case illustrated, a flow velocity of 4 m/s corresponds to a pressure gradient of approximately 65 mm Hg.

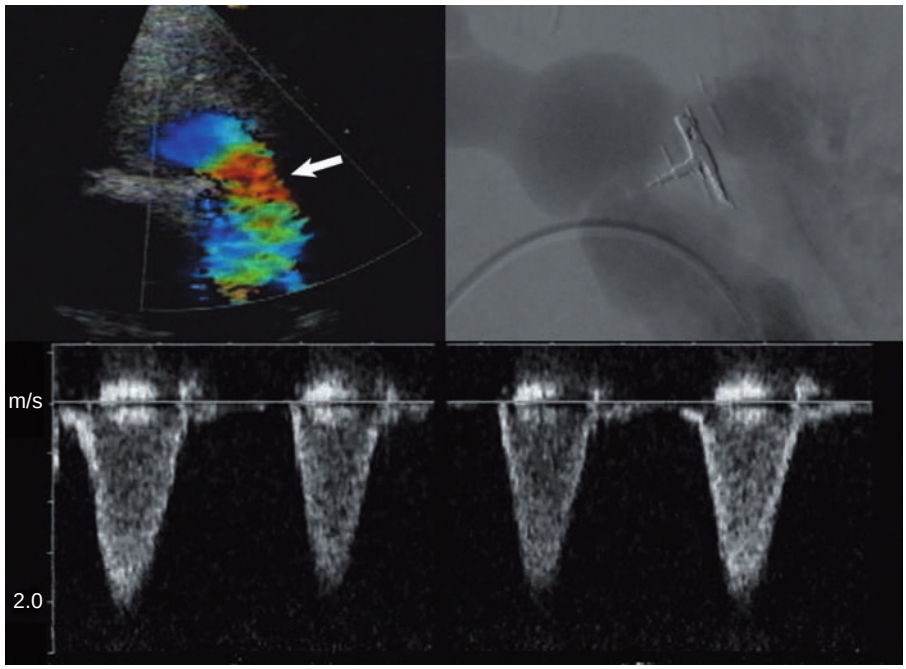


**Figure 27.8** Flow velocity across a telemetric pulmonary artery banding (arrow), as measured by continuous-wave Doppler from the parasternal short-axis view. The pulmonary artery angiogram shows the device in place below the pulmonary artery bifurcation (upper right). A pressure gradient of 16 mm Hg is demonstrated (peak velocity of 2 m/s) indicating the need for further tightening of the pulmonary artery banding.

following: (i) surgical anastomoses (Fig. 27.9); (ii) Blalock–Taussig shunt and branch pulmonary arteries or the RV-to-PA conduit; (iii) interatrial communication (Fig. 27.10); (iv) AV and semilunar valves; (v) ventricular function; and (vi) to rule out a pericardial effusion.

### The pre-Glenn echocardiogram

Prior to performing the bidirectional Glenn shunt, a complete echocardiographic examination is needed to evaluate the pulmonary veins and atrial septum for obstruction (see Fig. 27.10), the AV and semilunar valves for regurgitation, the branch pulmonary arteries for stenosis or distortion, the aortic arch to exclude obstruction, and the systemic ventricle for function. The systemic venous anatomy is assessed to rule out a persistent left superior vena cava (SVC) or an (hemi)azygos continuation in the setting of an interrupted inferior vena cava (IVC). The innominate vein and the coronary sinus are also imaged.

### After the bidirectional Glenn shunt

The bidirectional Glenn anastomosis is created by division of the SVC above its junction with the right atrium. The cardiac end of the SVC is suture-closed. The cephalic end of the SVC is anastomosed end-to-side to the ipsilateral branch pulmonary artery, allowing blood flow to both lungs. In the presence of bilateral SVC, bilateral bidirectional Glenn shunts are created, with each SVC connected to the ipsilateral branch pulmonary artery. A classic Glenn shunt – end-to-end anastomosis of the SVC and the ipsilateral pulmonary artery – was more frequently used in the past as a palliative

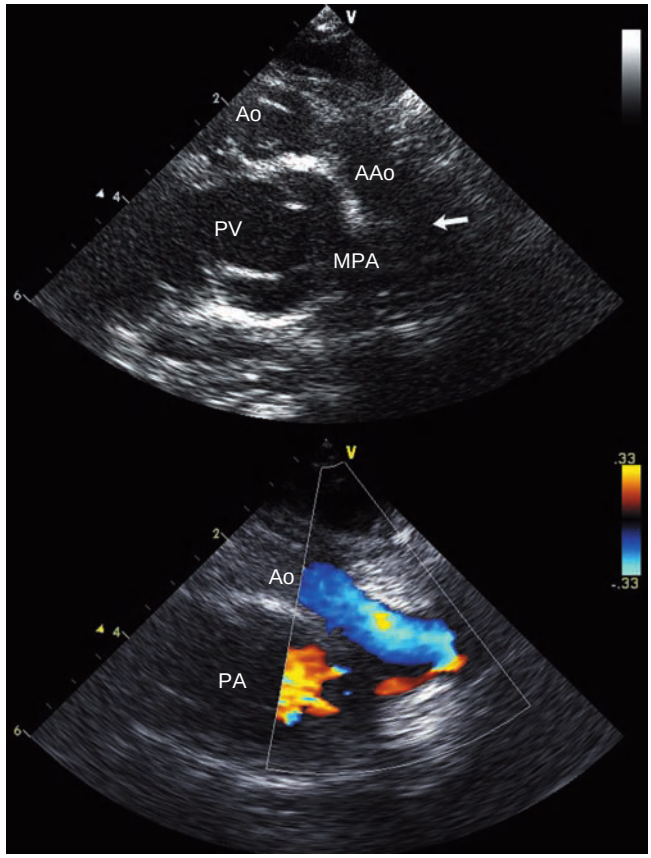


**Figure 27.9** The Damus–Kaye–Stansel anastomosis. Postoperative evaluation of a Damus–Kaye–Stansel anastomosis in the parasternal long-axis view of a patient with double-inlet left ventricle (DILV), transposition of the great vessels and ascending aortic hypoplasia. The anastomosis between the small anterior ascending aorta (AAo) and the posterior pulmonary artery trunk (MPA) can be seen (arrow), and there is laminar flow from the ascending aorta to the pulmonary artery. Ao, aortic valve; PA, pulmonary artery; PV, pulmonary valve.

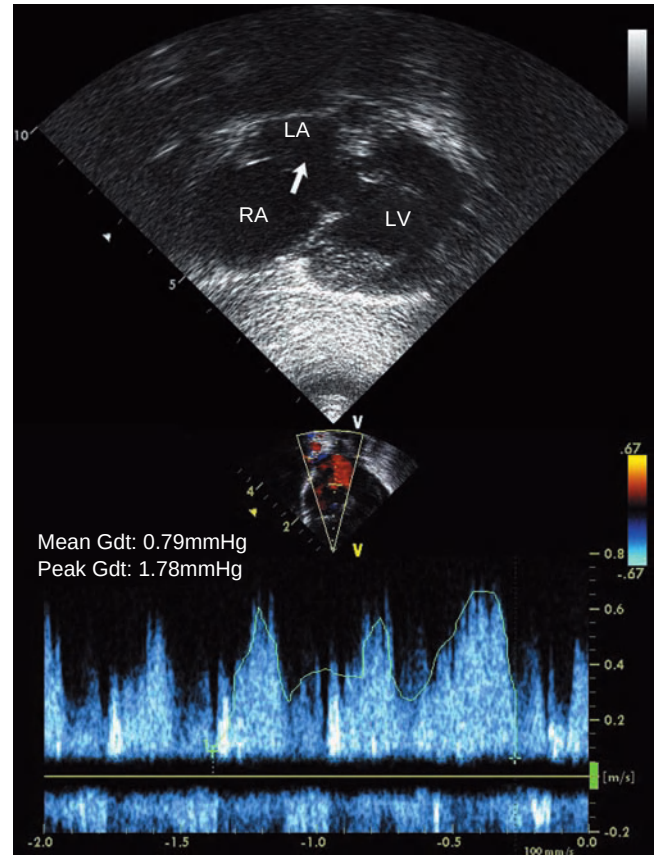


**Figure 27.10** Unrestrictive atrial septum in a patient with a single left ventricle. Subxiphoid view of the atrial septum in a patient with right ventricular hypoplasia. Because the atrial septum is perpendicular to the sound beam, this view is particularly useful to measure the atrial septal defect (arrow) and confirm unrestrictive blood flow across the atrial septum. Doppler imaging is routinely used to assess the mean gradient across the atrial septum. LA, left atrium; LV, left ventricle; RA, right atrium.

procedure. From the high parasternal view or the suprasternal view, the SVC and cavopulmonary anastomosis are assessed for obstruction and branch pulmonary arteries are imaged to rule out distortion or narrowing. Flow in the SVC and the pulmonary arteries is assessed by color and spectral Doppler and should be of low velocity, laminar and with phasic respiratory variations (Figs 27.11 and 27.12; Videoclip 27.6). The flow into the distal right and left pulmonary arteries should be viewed with color Doppler echocardiography (lowering the Nyquist limit) and, if possible, be measured using pulsed Doppler.

During a Glenn operation, very often the central pulmonary artery is oversewn just distal to the valve. Postoperatively it is important to look for residual antegrade flow from the ventricle to the pulmonary artery, and for thrombi in the pulmonary stump particularly when the valve leaflets have not been oversewn or resected [38]. The parasternal window often provides an excellent view of the pulmonary root

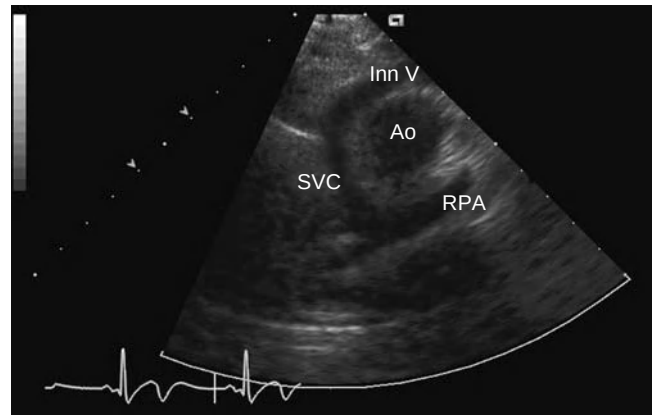


**Figure 27.11** Suprasternal short-axis view in a patient with a bidirectional Glenn shunt (BDG). The BDG is seen as an end-to-side anastomosis of the superior vena cava (SVC) to the right pulmonary artery (RPA). Ao, transverse aorta; Inn V, innominate vein.

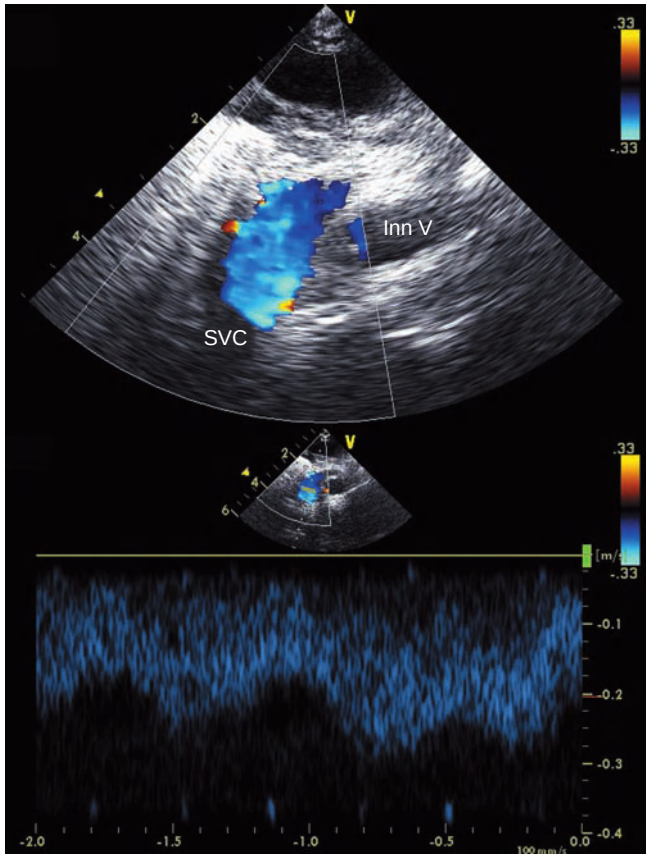


**Figure 27.12** Color Doppler examination in a patient with a bidirectional Glenn shunt showing low-velocity laminar flow in the superior vena cava (SVC) toward the right pulmonary artery. Inn V, innominate vein.

but this area can also be nicely imaged from an anteriorly angled apical view and from the subcostal window. The AV valve(s) and aortic and/or neoaortic valves are assessed for regurgitation as previously described. Volume load reduction of the systemic ventricle is one of the primary goals of the bidirectional Glenn shunt. Hence, assessment of ventricular dimensions and function is of major importance during the echocardiographic examination. In patients with a bidirectional cavopulmonary shunt, the arterial saturation will generally be superior to 80%, although older patients will be more likely to have lower saturations because SVC return represents progressively a smaller percentage of the total systemic venous return. More severe cyanosis may be secondary to the reopening of decompressing veins from the SVC into either the IVC (such as an azygous vein) or the atria (such as a left SVC), or multiple venovenous collaterals. These collateral vessels can be identified echocardiographically. Also aorta-to-pulmonary artery collaterals can develop and can be visualized from the suprasternal aortic windows.

## Echocardiography after the Fontan procedure

The Fontan procedure has undergone many modifications since the original description by Fontan and Baudet in 1971 [39]. The more recent modifications of the Fontan procedure are the total cavopulmonary connection with the lateral tunnel or the use of an extracardiac conduit [40]. A fenestration is often placed between the systemic venous pathway and the pulmonary venous atrium. The fenestration allows a right-to-left shunt that decompresses the systemic venous pathway and maintains adequate cardiac output. The resultant systemic desaturation is usually mild. This has resulted in improved immediate postoperative hemodynamics, reduced incidence and duration of pleural effusions, and shorter postoperative stay.

The echocardiographic examination in a postoperative Fontan patient should include all the previously described elements applying to patients after the bidirectional Glenn operation. However, specific attention should be given to:

**1** *The Fontan connections.* This includes evaluation of the superior cavopulmonary anastomosis as well as the whole IVC-to-PA connection. Flow in the IVC should be measured. In general there is low-velocity flow with increase in flow velocities on inspiration. Flow reversals are unusual or small in patients with total cavopulmonary connection. The connection between the IVC and the conduit can generally be imaged using the subcostal or apical windows (Videoclips 27.5 and 27.7). In infants and young children, subcostal imaging can demonstrate the IVC and hepatic veins, the IVC-to-PA pathway (an intra-atrial lateral tunnel or extracardiac

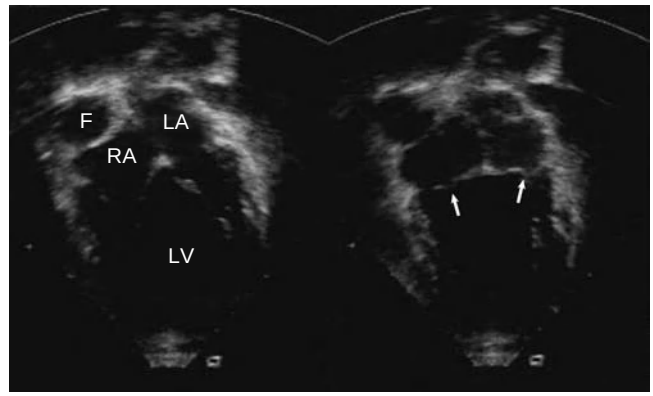


**Figure 27.13** Apical view of the Fontan pathway. Apical 4-chamber view of a patient with univentricular heart of the left ventricular type after a modified Fontan procedure using an intra-atrial conduit. The inferior vena cava flow is directed by way of a baffle (F) along the lateral wall of the right atrium (RA) to the undersurface of the right pulmonary artery. The conduit can usually be vizualized throughout most of its course using parasternal and apical views. This view is a posterior plane that passes through both atrioventricular valve inlets and the crux of the heart. Therefore, this plane lies posterior to the trabecular septum and rudimentary right ventricle. In diastole (right panel), the two atrioventricular valves (arrows) are opening in the single left ventricle (LV). LA, left atrium.

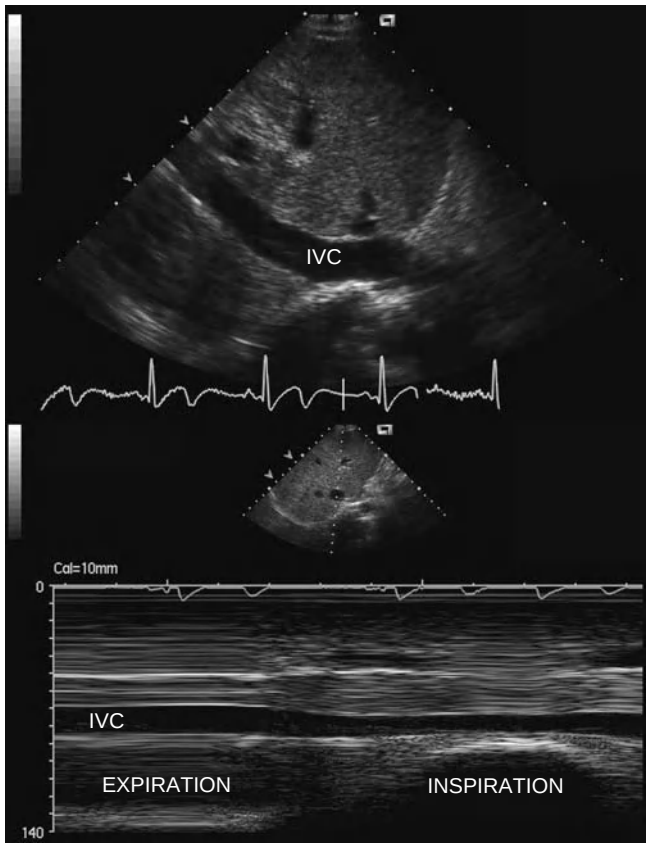


**Figure 27.14** Evaluation of the inferior vena cava (IVC) after the Fontan operation. Subcostal sagittal view of the IVC close to its junction with the right atrium in a patient with a modified Fontan operation. The IVC is not dilated and M-mode examination (bottom) reveals that it collapses with inspiration, suggesting a favorable drainage of the ICV flow to the pulmonary arteries.

conduit), the fenestration, the inferior IVC conduit and the superior conduit–PA anastomosis (Figs 27.13 and 27.14). In older children and adults with suboptimal subcostal windows, the apical, parasternal and suprasternal windows are used. The apical view provides an excellent assessment of the fenestration, if present (Videoclip 27.9). The patency and size of the fenestration can be most readily assessed with color Doppler imaging (Fig. 27.15). The mean gradient across the fenestration provides an estimate of the transpulmonary pressure gradient. It is measured by pulsed-wave Doppler over several cardiac cycles from an acoustic window that provides an optimal angle of interrogation. In case of an intracardiac-type of connection, additional baffle leaks should also be sought with color Doppler imaging. The entire venous circuit should also be assessed looking for thrombus (Videoclip 27.8). The high parasternal and/or suprasternal windows allow assessment of the bidirectional Glenn shunt and may also permit visualization of flow from the conduit into the pulmonary arteries. In older patients with difficult imaging windows visualization of the entire conduit might be extremely difficult and a transesophageal echocardiographic examination may be required. In patients with suboptimal transthoracic acoustic windows, MRI offers an excellent non-invasive alternative [41,42]. From the suprasternal views right and left proximal pulmonary arteries can be imaged and measured. Flow to both pulmonary arteries should be assessed using color Doppler and pulsed Doppler.

**2** *The pulmonary veins.* Obstructed pulmonary venous pathway was described as an early complication of the lateral tunnel cavopulmonary connection as a result of improper baffle creation and may be present in extracardiac conduits as they might compress the pulmonary veins [43]. Several reports [44–46] underlined the relative greater frequency of this complication in heterotaxy syndrome. In some instances, pulmonary venous obstruction developing a few months after device closure of the fenestration suggested that the additional scarring from device implantation contributes to the obstruction [47]. All four pulmonary veins should therefore be identified after the Fontan operation and pulmonary venous flow should be evaluated using color Doppler and pulsed Doppler techniques.

**3** *AV valve function.* AV valve stenosis but especially AV valve regurgitation should be evaluated.

**4** *Ventricular function assessment.* This is an important part of postoperative Fontan evaluation but due to the lack of quantitative techniques the approach adopted is largely a subjective qualitative approach. Also the evaluation of diastolic function is extremely difficult due to abnormal AV valve anatomy and abnormal pulmonary venous flow.

**5** *Detection of aortic-to-pulmonary collateral flow.* An estimated 80% of patients undergoing Fontan-type operations already have, or subsequently develop, systemic arterial-to-pulmonary arterial collaterals [48–52] as a consequence of preoperative, or continued, hypoxemia. Competitive flow from these aortopulmonary vessels can elevate right-sided pressures, thereby reducing systemic venous flow to the pulmonary arteries. These collaterals can be detected from the suprasternal aortic views but computed tomography (CT), MRI, and angiography are more sensitive noninvasive techniques for detecting collateral flow.

## Prenatal assessment

In high-risk fetuses, detailed study of the cardiac anatomy in the first trimester of pregnancy by means of ultrasound, transvaginally or transabdominally, is now feasible. Good-quality imaging of the four chambers and great arteries is possible as early as 11–14 weeks' gestation [53,54]. In experienced hands, first-trimester fetal echocardiography is accurate in detecting major structural cardiac abnormalities and yields a high negative predictive value. Such imaging of the fetal heart in the late first and early second trimester of pregnancy is technically more demanding than in mid-gestation because of the relatively smaller size of the fetus and cardiac structures (the semilunar valves are about 1.2 mm in

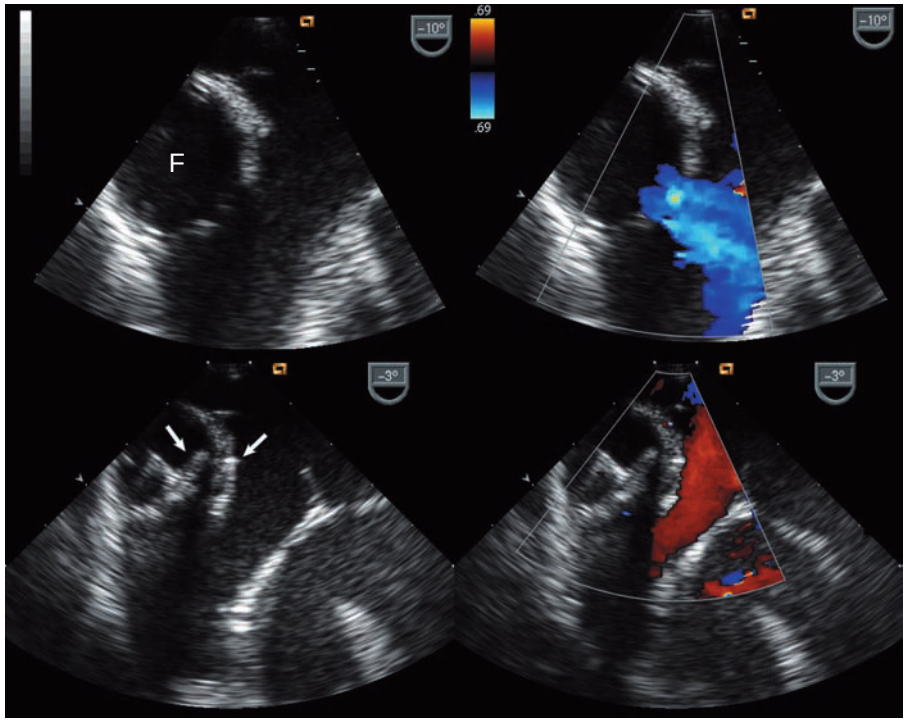


**Figure 27.15** Transesophageal echocardiography (TEE) guidance of fenestration device closure. Close-ups of transverse 4-chamber views and color Doppler examinations from a patient with tricuspid atresia at the time of fenestration closure in the cardiac catheterization laboratory. The Fontan tunnel (F) is connected to the atrium through a large fenestration, with a right-to-left shunt (upper right). After positioning of an Amplatzer device, the left and right disks are occluding the fenestration (lower left, arrows) and no residual shunt is appreciated (lower right).

diameter at 13 weeks). The accuracy of diagnosing structural heart disease varies between centers, depending on the level of experience and thoroughness, with reported rates of detection varying from 14 to 83% [55–5]. In the clinical setting, an early prenatal echocardiogram can be offered to families considered to be "at risk" for cardiac defects (mainly previous family history, increased fetal nuchal translucency, maternal disease, teratogenic drugs) and can be a powerful tool to reassure families regarding normality of major cardiac structures and connections. Because of the high prevalence of associated extracardiac defects and chromosomal abnormalities for many of the high-risk families, fetal heart scanning in the first trimester should be performed in conjunction with detailed first-trimester obstetric scanning and genetic workup when indicated.

In the low-risk population, although the imaging quality depends on maternal size and fetal position, single ventricle can be reliably screened prenatally [59–63]. Normally, the myocardium of both ventricles should reach the apex of the heart and both ventricles should be symmetric, with slight RV predominance during the third trimester. Imaging the short-axis of the ventricles is similarly important in assessing chamber size. Once a heart defect is suspected, a complete echocardiographic examination is mandatory.

The visceral situs as well as the systemic and pulmonary venous anatomy must be assessed. The atrial septum should be carefully examined with color and spectral Doppler in fetuses with suspected mitral/aortic atresia or hypoplasia, or

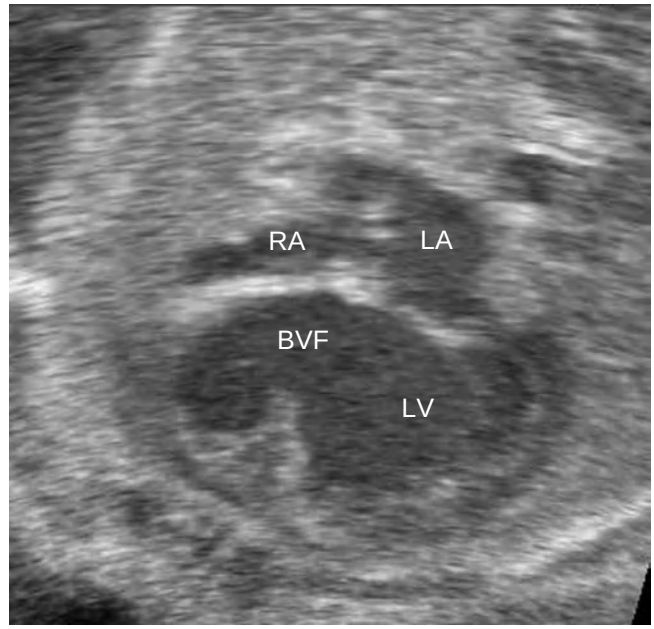


**Figure 27.16** Prenatal evaluation of a fetus with tricuspid atresia. Prenatal apical 4-chamber view in systole in a fetus with tricuspid atresia, normally related great arteries, a large ventricular septal defect and a hypoplastic right ventricle. Note the dense band of echo arising from the fibrofatty tissue of the right atrioventricular (AV) sulcus and the attachment of the anterior leaflet of the AV valve to the left side of the interatrial septum. BVF, bulboventricular foramen; LA, left atrium; LV, left ventricle; RA, right atrium.

tricuspid/pulmonary atresia or hypoplasia, or with transposed great vessels. Single ventricle anatomy or severe hypoplasia of one ventricle is usually suspected from the 4-chamber view (Fig. 27.16). These fetuses can also be further evaluated by 2D and 3D imaging when necessary [64,65] (Fig. 27.15).

Hypoplasia or atresia of the AV or semilunar valves is evaluated from multiple views. Valve diameters and ventricular sizes are measured and compared with normal values to determine z-scores [66,67]. AV valve function is assessed with color and spectral Doppler imaging.

The aortic arch is ideally imaged in its long axis. When this view cannot be obtained, the aortic arch can be imaged by a systematic inferior-to-superior sweep in axial views. By following the ascending and descending aorta and the main pulmonary artery, the transverse aortic arch and the ductal arch can be viewed. This transverse view of the fetal upper mediastinum shows the main pulmonary artery, ascending aorta and SVC arranged in a straight line and sized in decreasing order [68,69]. It provides important clues to the diagnosis of anomalies of the ventricular outflow tracts or the great arteries (or both) because most such anomalies show abnormal size, position or relationship between the ascending aorta and main pulmonary artery in major congenital heart diseases [70,71].

Following this protocol, single ventricles will be assessed with a high level of anatomic correlation between the prenatal and postnatal examinations, although hemodynamic concerns are different.

In accordance with published guidelines for performance of fetal echocardiograms [72,73], we recommend that all patients with anatomic or functional single ventricle be referred to a pediatric cardiologist with expertise in fetal echocardiography. This allows a comprehensive evaluation of cardiac anatomy and physiology as well as counseling on prognosis and perinatal care.

A multidisciplinary approach is essential in the management of fetuses with single ventricle. To achieve optimal outcome, pediatric cardiologists, pediatric cardiac surgeons, high-risk obstetricians, neonatologists, social workers, and specialized nurses must be involved. The opportunity to meet with a pediatric cardiac surgeon, to visit the cardiac intensive care unit, to meet with other members of the team, including nurses and social workers, and the opportunity to speak to families with children with similar heart disease should be part of the standard of care.

## References


1. Van Praagh R, David I, Van Praagh S. What is a ventricle? The single-ventricle trap. *Pediatr Cardiol* 1982;2:79–84.
2. Van Praagh R, Plett JA, Van Praagh S. Single ventricle. Pathology, embryology, terminology and classification. *Herz* 1979; 4:113–50.
3. Van Praagh R, Ongley PA, Swan HJ. Anatomic types of single or common ventricle in man. Morphologic and geometrc aspects of 60 necropsied cases. *Am J Cardiol* 1964;13:367–86.
4. Fyler DC, Buckley LP, Hellenbrand WE. Report of the New England Regional Infant Cardiac Program. *Pediatrics* 1980;65: 375–461.
5. Bonnet D, Fermont L, Kachaner J et al. Tricuspid atresia and conotruncal malformations in five families. *J Med Genet* 1999; 36:349–50.
6. Kumar A, Victorica BE, Gessner IH et al. Tricuspid atresia and annular hypoplasia: report of a familial occurrence. *Pediatr Cardiol* 1994;15:201–3.
7. Lin AE, Rosti L. Tricuspid atresia in sibs. *J Med Genet* 1998;35: 1055–6.
8. Sletten LJ, Pierpont ME. Variation in severity of cardiac disease in Holt–Oram syndrome. *Am J Med Genet* 1996;65:128–32.
9. Ruzic B, Bosnar B, Beleznay O. An unusual type of congenital heart disease associated with the Holt–Oram syndrome. *Radiologe* 1981;21:296–9.
10. Durairaj M, Chadha SK, Bhide M et al. Noonan's syndrome associated with single ventricle (a case report). *Indian Pediatr* 1979;16:927–9.
11. Antonelli D, Antonelli J, Rosenfeld T. Noonan's syndrome associated with hypoplastic left heart. *Cardiology* 1990;77:62–5.
12. Marino B, Digilio MC, Novelli G et al. Tricuspid atresia and 22q11 deletion. *Am J Med Genet* 1997;72:40–2.
13. Alva C, David F, Hernandez M et al. Tricuspid atresia associated with common arterial trunk and 22q11 chromosome deletion. *Arch Cardiol Mex* 2003;73:271–4.
14. Geva T, Ayres NA, Pignatelli RH et al. Echocardiographic evaluation of common atrioventricular canal defects: a study of 206 consecutive patients. *Echocardiography* 1996;13:387–400.
15. Weigel TJ, Driscoll DJ, Michels VV. Occurrence of congenital heart defects in siblings of patients with univentricular heart and tricuspid atresia. *Am J Cardiol* 1989;64:768–71.
16. Gill HK, Splitt M, Sharland GK et al. Patterns of recurrence of congenital heart disease: an analysis of 6,640 consecutive pregnancies evaluated by detailed fetal echocardiography. *J Am Coll Cardiol* 2003;42:923–9.
17. Weigel TJ, Driscoll DJ, Michels VV. Occurrence of congenital heart defects in siblings of patients with univentricular heart and tricuspid atresia. *Am J Cardiol* 1989;64:768–71.
18. Shapiro SR, Ruckman RN, Kapur S et al. single ventricle with truncus arteriosus in siblings. *Am Heart J*. 1981;102:456–9.
19. Whittemore R, Wells JA, Castellsague X. A second-generation study of 427 probands with congenital heart defects and their 837 children. *J Am Coll Cardiol* 1994;23:1459–67.
20. Tandon R, Edwards JE. Tricuspid atresia. A re-evaluation and classification. *J Thorac Cardiovasc Surg* 1974;67:530–42.
21. Van Praagh R, Ando M, Dungan WT. Anatomic types of tricuspid atresia: clinical and developmental implications. *Circulation* 1971;44:11.
22. Bevilacqua M, Sanders SP, Van Praagh S et al. Double-inlet single left ventricle: echocardiographic anatomy with emphasis on the morphology of the atrioventricular valves and ventricular septal defect. *J Am Coll Cardiol* 1991;18:559–68.
23. Shiraishi H, Silverman NH. Echocardiographic spectrum of double inlet ventricle: evaluation of the interventricular communication. *J Am Coll Cardiol* 1990;15:1401–8.

24. Dobell AR, Van Praagh R. The Holmes heart: historic associations and pathologic anatomy. *Am Heart J* 1996;132:437–45.
25. Holmes WT. Case of malformation of the heart. *Trans Med Chir Soc Edin* 1824;1:252–9.
26. Van Praagh R, Ongley PA, Swan HJ. Anatomic types of single or common ventricle in man. Morphologic and geometrc aspects of 60 necropsied cases. *Am J Cardiol* 1964;13:367–86.
27. Keeton BR, Macartney FJ, Hunter S et al. Univentricular heart of right ventricular type with double or common inlet. *Circulation* 1979;59:403–11.
28. Keeton BR, Macartney FJ, Hunter S et al. Univentricular heart of right ventricular type with double or common inlet. *Circulation* 1979;59:403–11.
29. Van Praagh R, Plett JA, Van Praagh S. Single ventricle. Pathology, embryology, terminology and classification. *Herz* 1979;4:113–50.
30. Orie JD, Anderson C, Ettedgui JA et al. Echocardiographic-morphologic correlations in tricuspid atresia. *J Am Coll Cardiol* 1995;26:750–8.
31. Van Praagh S, O'Sullivan J, Brili S et al. Juxtaposition of the morphologically right atrial appendage in solitus and inversus atria: a study of 35 postmortem cases. *Am Heart J* 1996;132: 382–90.
32. Rice MJ, Seward JB, Hagler DJ et al. Left juxtaposed atrial appendages: diagnostic two-dimensional echocardiographic features. *J Am Coll Cardiol* 1983;1:1330–6.
33. Shiraishi H, Silverman NH. Echocardiographic spectrum of double inlet ventricle: evaluation of the interventricular communication. *J Am Coll Cardiol* 1990;15:1401–8.
34. Matitiau A, Geva T, Colan SD et al. Bulboventricular foramen size in infants with double-inlet left ventricle or tricuspid atresia with transposed great arteries: influence on initial palliative operation and rate of growth. *J Am Coll Cardiol* 1992;19: 142–8.
35. Matitiau A, Geva T, Colan SD et al. Bulboventricular foramen size in infants with double-inlet left ventricle or tricuspid atresia with transposed great arteries: influence on initial palliative operation and rate of growth. *J Am Coll Cardiol* 1992;19:142–8.
36. Shiraishi H, Silverman NH. Echocardiographic spectrum of double inlet ventricle: evaluation of the interventricular communication. *J Am Coll Cardiol* 1990;15:1401–8.
37. Bonnet D, Corno AF, Sidi D et al. Early clinical results of the telemetric adjustable pulmonary artery banding FloWatch-PAB. *Circulation* 2004;110:II158–II163.
38. Rosenthal DN, Bulbul ZR, Friedman AH et al. Thrombosis of the pulmonary artery stump after distal ligation. *J Thorac Cardiovasc Surg* 1995;110:1563–5.
39. Fontan F, Baudet E. Surgical repair of tricuspid atresia. *Thorax* 1971;26:240–8.
40. van Son JA, Reddy M, Hanley FL. Extracardiac modification of the Fontan operation without use of prosthetic material. *J Thorac Cardiovasc Surg* 1995;110:1766–8.
41. Fogel MA. Cardiac magnetic resonance of single ventricles. *J Cardiovasc Magn Reson* 2006;8:661–70.
42. Marx GR, Geva T. MRI and echocardiography in children: how do they compare? *Semin Roentgenol* 1998;33:281–92.
43. Fogel MA, Chin AJ. Imaging of pulmonary venous pathway obstruction in patients after the modified Fontan procedure. *J Am Coll Cardiol* 1992;20:181–90.
44. Uchida T, Uemura H, Yagihara T et al. Pulmonary venous obstruction after total cavopulmonary connection in heterotaxy. *Ann Thorac Surg* 2002;73:273–4.
45. Berman W Jr, Fripp RR, Yabek SM. Late-onset pulmonary v-enous pathway obstruction after Fontan operation: presentation masquerading as intra-atrial baffle leakage. *Pediatr Cardiol* 1997;18:49–51.
46. Padalino MA, Saiki Y, Tworetzky W et al. Pulmonary venous pathway obstruction from recurrent restriction at atrial septum late after Fontan procedure. *J Thorac Cardiovasc Surg* 2004; 127:281–3.
47. Padalino MA, Saiki Y, Tworetzky W et al. Pulmonary venous pathway obstruction from recurrent restriction at atrial septum late after Fontan procedure. *J Thorac Cardiovasc Surg* 2004;127: 281–3.
48. Ichikawa H, Yagihara T, Kishimoto H et al. Extent of aortopulmonary collateral blood flow as a risk factor for Fontan operations. *Ann Thorac Surg* 1995;59:433–7.
49. Kanter KR, Vincent RN, Raviele AA. Importance of acquired systemic-to-pulmonary collaterals in the Fontan operation. *Ann Thorac Surg* 1999;68:969–74.
50. Spicer RL, Uzark KC, Moore JW et al. Aortopulmonary collateral vessels and prolonged pleural effusions after modified Fontan procedures. *Am Heart J* 1996;131:1164–8.
51. Triedman JK, Bridges ND, Mayer JE Jr et al. Prevalence and risk factors for aortopulmonary collateral vessels after Fontan and bidirectional Glenn procedures. *J Am Coll Cardiol* 1993;22: 207–15.
52. McElhinney DB, Reddy VM, Tworetzky W et al. Incidence and implications of systemic to pulmonary collaterals after bidirectional cavopulmonary anastomosis. *Ann Thorac Surg* 2000;69: 1222–8.
53. Yagel S, Cohen SM, Messing B. First and early second trimester fetal heart screening. *Curr Opin Obstet Gynecol* 2007;19:183–90.
54. Huggon IC, Ghi T, Cook AC et al. Fetal cardiac abnormalities identified prior to 14 weeks' gestation. *Ultrasound Obstet Gynecol* 2002;20:22–9.
55. Bromley B, Estroff JA, Sanders SP et al. Fetal echocardiography: accuracy and limitations in a population at high and low risk for heart defects. *Am J Obstet Gynecol* 1992;166:1473–81.
56. Hafner E, Scholler J, Schuchter K et al. Detection of fetal congenital heart disease in a low-risk population. *Prenat Diagn* 1998;18:808–15.
57. Stumpflen I, Stumpflen A, Wimmer M et al. Effect of detailed fetal echocardiography as part of routine prenatal ultrasonographic screening on detection of congenital heart disease. *Lancet* 1996;348:854–7.
58. Stoll C, Alembik Y, Dott B et al. Evaluation of prenatal diagnosis of congenital heart disease. *Prenat Diagn* 1998;18:801–7.
59. Sinclair BG, Sandor GG, Farquharson DF. Effectiveness of primary level antenatal screening for severe congenital heart disease: a population-based assessment. *J Perinatol* 1996;16:336–40.
60. Daubeney PE, Sharland GK, Cook AC et al. Pulmonary atresia with intact ventricular septum: impact of fetal echocardiography on incidence at birth and postnatal outcome. UK and Eire Collaborative Study of Pulmonary Atresia with Intact Ventricular Septum. *Circulation* 1998;98:562–6.
61. Maeno YV, Boutin C, Hornberger LK et al. Prenatal diagnosis of right ventricular outflow tract obstruction with intact

ventricular septum, and detection of ventriculocoronary connections. *Heart* 1999;81:661–8.
62. Blake DM, Copel JA, Kleinman CS. Hypoplastic left heart syndrome: prenatal diagnosis, clinical profile, and management. *Am J Obstet Gynecol* 1991;165:529–34.
63. Wald RM, Tham EB, McCrindle BW et al. Outcome after prenatal diagnosis of tricuspid atresia: a multicenter experience. *Am Heart J*. 2007;153:772–8.
64. Herberg U, Goldberg H, Breuer J. Three- and four-dimensional freehand fetal echocardiography: a feasibility study using a hand-held Doppler probe for cardiac gating. *Ultrasound Obstet Gynecol* 2005;25:362–71.
65. Yagel S, Cohen SM, Shapiro I et al. 3D and 4D ultrasound in fetal cardiac scanning: a new look at the fetal heart. *Ultrasound Obstet Gynecol* 2007;29:81–95.
66. Sanders SP. Echocardiography and related techniques in the diagnosis of congenital heart disease. I. Veins, atria and interatrial septum. *Echocardiography* 1984;1:185–217.
67. Schneider C, McCrindle BW, Carvalho JS et al. Development of Z-scores for fetal cardiac dimensions from echocardiography. *Ultrasound Obstet Gynecol* 2005;26:599–605.
68. Yoo SJ, Lee YH, Kim ES et al. Three-vessel view of the fetal upper mediastinum: an easy means of detecting abnormalities of the ventricular outflow tracts and great arteries during obstetric screening. *Ultrasound Obstet Gynecol* 1997;9:173–82.
69. Yoo SJ, Lee YH, Cho KS. Abnormal three-vessel view on sonography: a clue to the diagnosis of congenital heart disease in the fetus. *AJR Am J Roentgenol* 1999;172:825–30.
70. Yoo SJ, Lee YH, Kim ES et al. Three-vessel view of the fetal upper mediastinum: an easy means of detecting abnormalities of the ventricular outflow tracts and great arteries during obstetric screening. *Ultrasound Obstet Gynecol* 1997;9:173–82.
71. Yoo SJ, Lee YH, Cho KS. Abnormal three-vessel view on sonography: a clue to the diagnosis of congenital heart disease in the fetus. *AJR Am J Roentgenol* 1999;172:825–30.
72. Rychik J, Ayres N, Cuneo B et al. American Society of Echocardiography guidelines and standards for performance of the fetal echocardiogram. *J Am Soc Echocardiogr* 2004;17:803–10.
73. Allan L, Dangel J, Fesslova V et al. Recommendations for the practice of fetal cardiology in Europe. *Cardiol Young* 2004;14: 109–14.

# 28 Cardiac Malpositions and Heterotaxy Syndrome

**Irene D. Lytrivi[1] and Wyman W. Lai[2]**

[1]Pediatric Cardiology, Mount Sinai Medical Center, New York, NY, USA; Maimonides Medical Center, Brooklyn, New York, NY, USA

[2]Columbia University; Noninvasive Cardiology Imaging Laboratory, Division of Pediatric Cardiology, Morgan Stanley Children's Hospital of New York Presbyterian, New York, NY, USA

## Cardiac malpositions

### Definitions

Cardiac malposition may be defined as any heart other than a left-sided heart in a situs solitus individual [1]. The term is also used to describe abnormal spatial arrangements of the individual cardiac segments – atria, ventricles and the great arteries – and thus encompasses a much wider range of anomalies. This section on cardiac malpositions covers malposition of the heart as a whole (dextro-/mesocardia) and selected malpositions of individual cardiac segments (juxtaposition of the atrial appendages, isolated ventricular inversion and anatomically corrected malposition). Heterotaxy syndromes, the complexity of which arises from abnormal spatial organization of the thoraco-abdominal organs and the associated anomalies of multiple cardiac segments, are discussed separately. Cardiac malposition due to ectopia cordis is not addressed in this chapter.

*Dextrocardia* and *mesocardia* are terms indicating the position of the heart and the direction of its major axis: base-to-apex axis pointing to the right in dextrocardia, caudally in mesocardia [2]. *Situs inversus* refers to the mirror-image reversal of the normal thoraco-abdominal visceral arrangement (see Chapter 3). Situs inversus is generally associated with dextrocardia, referred to as *situs inversus totalis*, but may be rarely seen with levocardia. *Dextroposition* refers to cardiac displacement to the right hemithorax by extracardiac factors such as a hypoplastic right lung, and does not imply any intracardiac anomalies. Another term commonly used in the literature is *dextroversion*, or pivotal dextrocardia. It usually describes dextrocardia with situs solitus, where the cardiac apex appears as having been rotated from the left hemithorax to the right.

*Juxtaposition of the atrial appendages* (JAA) refers to malposition of either of the two atrial appendages. In situs solitus, juxtaposition of the morphologically left atrial appendage places both atrial appendages on the right side of the great arteries (commonly referred to as right JAA); in situs inversus, juxtaposition of the morphologically left atrial appendage places both atrial appendages to the left side of the great arteries [3]. Similar terminology applies to juxtaposition of the morphologically right atrial appendage [4].

*Isolated ventricular inversion* is a term first used in 1966 [5] to describe a rare situation where ventricular inversion is not associated with transposition of the great arteries as in the usual case of "corrected" transposition. Instead, the case originally presented displayed thoraco-abdominal situs solitus, L-loop ventricles and normally related great arteries with normal ventriculo-arterial alignment. The definition also applies to atrial situs inversus with D-loop ventricles and inversely normally related great arteries (segmental set: {I,D,I}) [6]. Strictly speaking, cases of atrial isomerism should be excluded, although there are reports of "isolated" ventricular inversion in the setting of heterotaxy syndrome [7,8].

*Anatomically corrected malposition of the great arteries* (ACM), a term introduced by Van Praagh et al. [9] in 1971, is an equally rare anomaly with similarities to isolated ventricular inversion. In ACM, the great arteries arise from the appropriate ventricles despite an abnormal spatial interrelationship, resulting in arterial trunks situated in parallel instead of spiraling around each other [10]. Thus, in D-loop ventricles, the aorta is positioned leftward and anterior to the pulmonary artery; in L-loop ventricles, the aorta is rightward and anterior to the pulmonary artery. Other spatial arrangements of the great arteries have also been described, and, currently, the diagnostic criteria include ventriculo-arterial concordance and parallel arrangement of the arterial trunks even in cases of rightward and posterior aortic position [10]. The presence of bilateral conus, initially considered an integral part of the diagnosis, was later found to be nonessential, and rare cases have been described with only subaortic [11], bilaterally absent [12], or even only subpulmonary [10] conus.

### Incidences

The incidence of fetal dextrocardia is reported as 220 to 830 per 100 000 fetuses referred for echocardiography [13,14].

*Echocardiography in Pediatric and Congenital Heart Disease: From Fetus to Adult*
Edited by Wyman W. Lai, Luc L. Mertens, Meryl S. Cohen and Tal Geva
 ISBN: 978-1-405-17401-5

Postnatally, dextrocardia is reported in 2.8% of cyanotic congenital heart disease and 0.4% of acyanotic heart disease [15]. The most common type of dextrocardia in the general population is associated with situs inversus totalis. The prevalence of situs inversus is approximately 1 in 10 000 for situs inversus totalis [16] and 1 in 22 000 for situs inversus with levocardia [17]. Situs solitus or situs ambiguus in the setting of dextrocardia are associated with cardiovascular malformations at a higher frequency. Situs inversus with levocardia, which incorporates heterotaxy syndrome patients in some series, is also associated with a very high rate of cardiovascular malformations. In contrast, situs inversus totalis is found with normal intracardiac anatomy in up to 89% of cases [14].

The incidence of juxtaposition of the atrial appendages was 280 per 100 000 cases in a clinical echocardiographic series [18] and 760 per 100 000 in an autopsy series [19]. Isolated ventricular inversion and ACM are very rare anomalies and only case reports or small case series exist in the literature.

## Etiology

Unlike the genetics of situs inversus and heterotaxy syndrome, which have been extensively studied (see "Heterotaxy syndrome" below), the genetic basis of dextrocardia and the rare forms of cardiac malposition described here is not precisely known. Mutations affecting laterality and left–right asymmetry affect ventricular looping and frequently result in complex congenital heart disease [20].

## Morphology and classification

### Developmental considerations

Dextrocardia in D-loop ventricles is probably related to arrested migration of the cardiac apex to the left hemithorax, a process that normally occurs between 23 and 35 days of gestation. L-loop ventricles, however, have a natural tendency to migrate to the right hemithorax, which explains the high incidence of dextrocardia in this type of looping.

During the early period of cardiac morphogenesis (at and prior to 23 days of gestation), left-sided JAA is normal. Between 23 and 27 days of gestation, the conotruncus migrates to the left of the right atrial appendage, as the ventricular D-loop slowly swings from right to left during the fourth and fifth weeks of fetal development. Failure of this leftward movement of the ventricular apex results in left juxtaposition of the right atrial appendage (JRAA) and dextrocardia, and explains the high rate of concurrence of these two anomalies.

The embryogenesis of both isolated ventricular inversion [5] and ACM [21] is believed to be twisting of the ventricles and great arteries in different directions during early cardiovascular development. Isolated ventricular inversion typically occurs with normal conotruncal development in the setting of a ventricular L-loop. In contrast, ACM occurs most commonly with leftward twisting of the conotruncus with a normal ventricular D-loop.

### Anatomy

As mentioned before, a broad spectrum of cardiac anomalies can accompany dextrocardia, especially in the setting of atrial situs solitus and ambiguus, ranging from an isolated ventricular septal defect (VSD) to the most complex forms of cyanotic heart disease. In the case of situs inversus totalis (segmental set: {I,L,I}), the most commonly reported congenital heart defects are tetralogy of Fallot and VSD [22], but rarer conditions such as single coronary ostium and hypoplastic left heart syndrome have been reported [23,24]. The aortic arch is usually right-sided [25].

Juxtaposition of the right atrial appendage (to the left in situs solitus, to the right in situs inversus) is a syndrome of major congenital heart disease, the salient features of which are tricuspid atresia or extreme stenosis in 40–60%, right ventricular (RV) hypoplasia or absence in 71–74%, subaortic or bilateral conus in 71–100%, pulmonary outflow tract obstruction in 52%, VSD in 88%, and secundum atrial septal defect (ASD) in 71% [4,26]. Transposition of the great arteries is particularly common, having been reported in up to two-thirds of the cases of JRAA [27]. Dextrocardia is another common association, occurring twice as commonly in JRAA as in a control series without JRAA [26,28].

Juxtaposition of the left atrial appendage (JLAA; to the right in situs solitus, to the left in situs inversus) is more commonly associated with normal conus, but major cardiovascular malformations are typically present: stenosis or atresia of the mitral valve or a left-sided tricuspid valve in 69%, aortic outflow obstruction or atresia in 39%, common atrioventricular valve in 28%, and heterotaxy syndrome in 28% [3].

Isolated ventricular inversion is an example of heart disease with ventriculo-arterial concordance but atrioventricular discordance [29]. The great arteries, which have a normal spatial interrelationship, arise lower than usual from the ventricular cavities and have normal ventriculo-arterial alignments. The segmental sets applicable to this entity are {S,L,S}, the most commonly recognized form, and {I,D,I}, which is exceedingly rare [6]. Additional intracardiac defects, such as VSD, hypoplastic tricuspid valve with RV hypoplasia, and coarctation of the aorta, have been described [30].

In ACM, the ventriculo-arterial alignments are also concordant but the ventriculo-arterial connections are markedly abnormal [28]. As a rule, the great arteries are not normally interrelated (i.e., parallel arterial trunks). The circulation is potentially normal, depending on the atrioventricular alignments, but most described cases have additional intracardiac defects. Deficient ventricular septation has been described in the majority of them. JRAA, abnormal right atrioventricular junction with right heart hypoplasia, and obstruction of the subpulmonary or subaortic outflow tracts are frequent associations. Another interesting observation is the high frequency of anomalies of coronary origin (single coronary artery or both coronary arteries arising from the right sinus of Valsalva) in this group of patients [10,31].

## Pathophysiology

The presentation of dextrocardia can vary from incidental discovery after a chest X-ray is taken for unrelated reasons, to presentation with critical symptoms of cyanotic heart disease when dextrocardia is part of a complex cardiovascular malformation. In the case of situs inversus totalis, the majority of cases have no associated congenital heart disease and should have a normal life span.

Juxtaposition of the atrial appendages does not cause any hemodynamic disturbance, yet it is frequently associated with complex cardiovascular anatomy requiring intervention [18]. Because of the association of JAA with transposition of the great arteries, balloon atrial septostomy is a common procedure. In such cases, diagnosis of JAA prior to the procedure is important in order to avoid the potential rupture of the juxtaposed appendage during balloon inflation and pull-back [26,32].

Isolated ventricular inversion is associated with transposition physiology, and profound cyanosis in the neonatal period is usually present. The opposite is true for ACM, where, in the absence of other anomalies, the circulation is normal. The pathophysiology in ACM is usually the result of associated intracardiac lesions, which are frequently present.

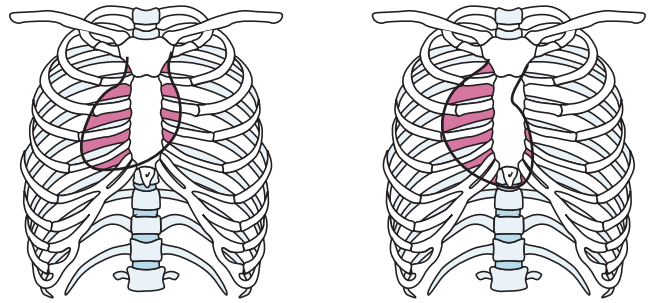

(a) *Dextrocardia* (b) *Dextroposition*

**Figure 28.1** Dextrocardia **(a)** versus dextroposition **(b)**.

## Imaging

### *General goals of the examination*

The main objectives of echocardiographic examination in the setting of cardiac malposition can be summarized as follows:

- Determination of the location of the heart in the thorax and direction of the cardiac apex.
- Identification of individual cardiac segments and careful attention to their alignments and connections.
- In JAA, particular attention to the atrial outlet and ventricle associated with the juxtaposed appendage and examination for conotruncal abnormalities, which are more commonly seen in JRAA.
- Identification of associated intracardiac anomalies.

### *Dextrocardia*

When the heart is in the right chest, a distinction should be made between a rightward and a leftward apex (true dextrocardia versus dextroposition) (Fig. 28.1a,b). During all imaging,

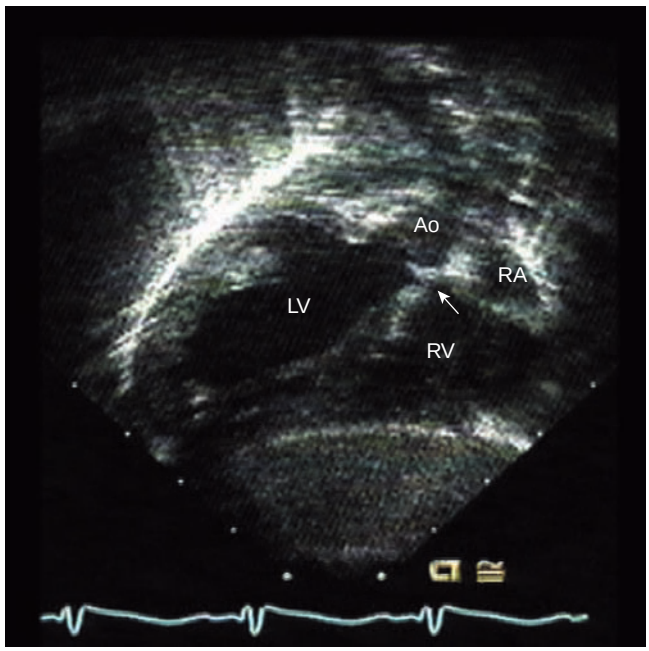


(a)

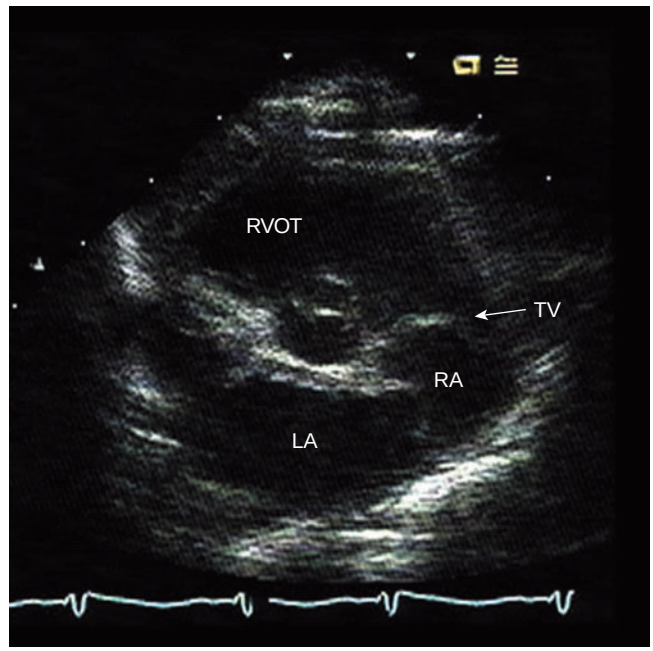


(b)

**Figure 28.2** Situs inversus totalis. **(a)** Subxiphoid long-axis image of situs inversus totalis {I,L,I} with a membranous ventricular septal defect (arrowhead). **(b)** Right parasternal short-axis image of situs inversus totalis with a membranous ventricular septal defect (not shown). Ao, aorta; LA, left atrium; LV, left ventricle; RA, right atrium; RV, right ventricle; RVOT, right ventricular outflow tract; TV, tricuspid valve.

care should be taken to maintain true right–left orientation. In the subxiphoid long-axis view, dextrocardia is, thus, displayed with the apex to the left of the videoscreen (Fig. 28.2a and Videoclip 28.1). The normal short-axis orientation, however, is maintained, but sweeping occurs from left to right (base to apex). In the apical 4-chamber view the probe is placed on the right chest with the notch pointing to the left, resulting in normal orientation on the display screen. For the parasternal long-axis view the probe is placed on the right chest with the notch, by convention, pointing to the left shoulder. This results in the normal display of the cardiac apex on the left of the videoscreen. To obtain the parasternal short-axis view, the probe is rotated clockwise from the parasternal long axis, with the notch now pointing to the left hip (Fig. 28.2b). Left parasternal long- and short-axis views can also be utilized and have been found helpful in delineating great artery relationships [2]. Any type of heart malformation can occur in dextrocardia, so the same segmental approach should apply for right-sided hearts as left-sided hearts.

### *Juxtaposition of the atrial appendages*

Juxtaposition is best visualized from subxiphoid long- and short-axis views (Fig. 28.3 and Videoclip 28.2) and the parasternal short-axis view (Fig. 28.4 and Videoclip 28.3) [18]. The juxtaposed atrial appendage is always superior to

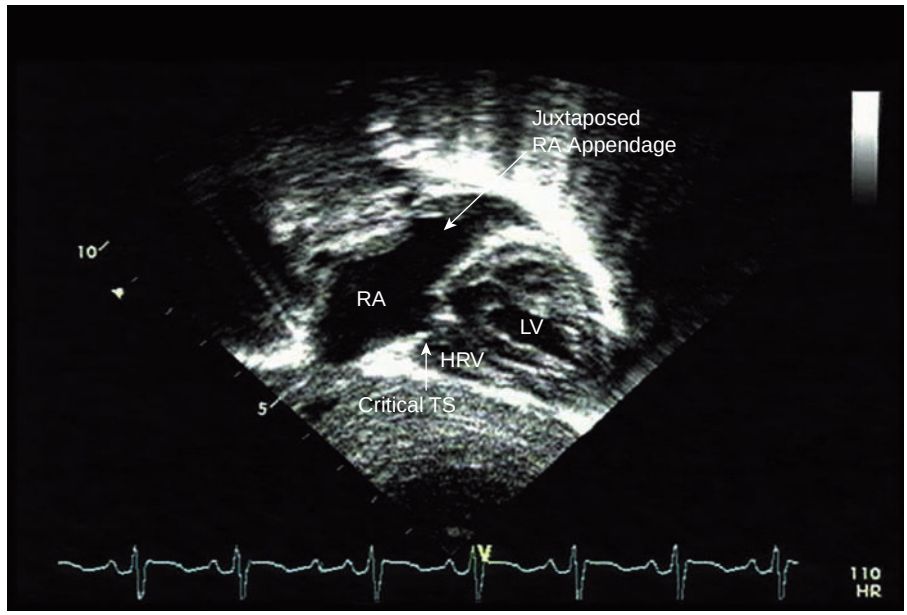


**Figure 28.3** Subxiphoid image of leftward juxtaposition of the right atrial appendage in the setting of critical tricuspid stenosis (TS) and severely hypoplastic right ventricle (HRV). RA, right atrium; LV, left ventricle.

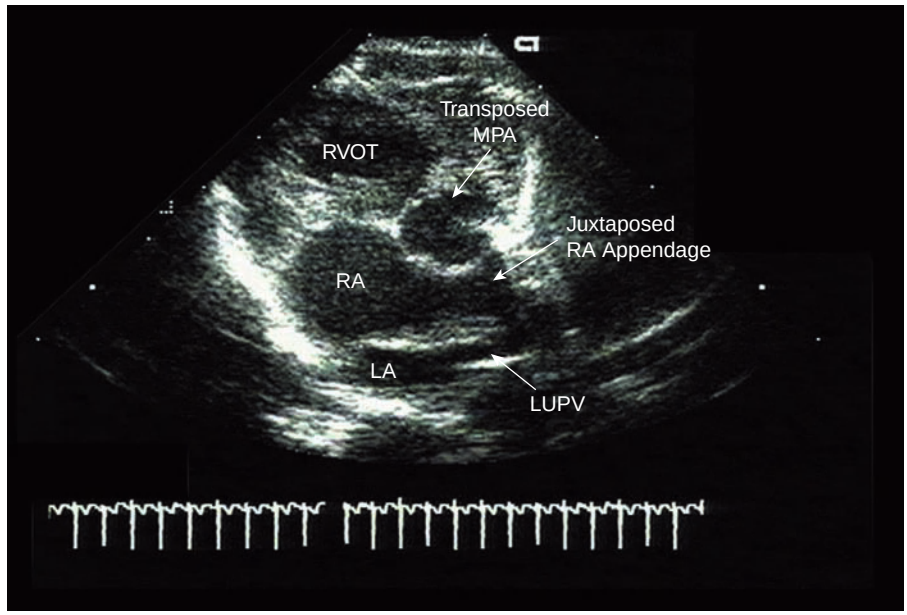


**Figure 28.4** Parasternal image of leftward juxtaposition of the right atrial appendage (LJRAA). Horizontal orientation of the atrial septum is typically seen with the juxtaposed atrial appendages. In this case there is juxtaposition of the right atrial (RA) appendage in the setting of transposition of the great arteries. LA, left atrium; LUPV, left upper pulmonary vein; MPA, main pulmonary artery; RA, right atrium; RVOT, right ventricular outflow tract.

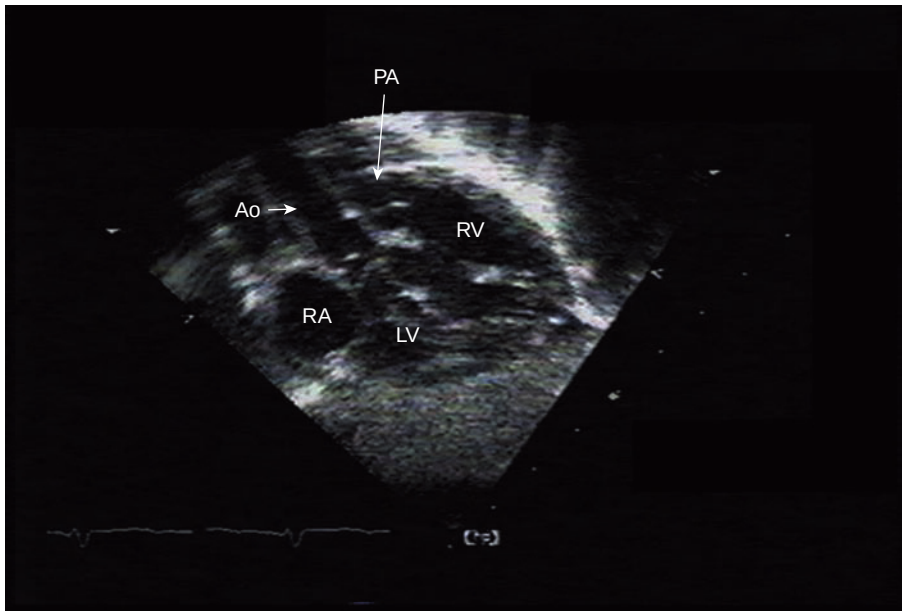


**Figure 28.5** Subxiphoid long-axis image of isolated ventricular inversion with solitus atria, L-loop ventricles, and normally related great arteries with subpulmonary conus. Ao, aorta; LV, left ventricle; PA, pulmonary artery; RA, right atrium; RV, right ventricle.

the normally positioned appendage and adjacent to the great arteries. Abnormal spatial orientation of the atrial septum is frequently, but not universally, present [27,32]. Isolated imaging of the juxtaposed atrial appendage is best in a nearly coronal plane from a high thoracic or suprasternal window [18]. Transesophageal imaging is also readily diagnostic of JAA, especially in the adult patient. Features include lateral deviation of the mid-portion of the atrial septum on the midesophageal 4-chamber view and a frontal orientation of the antero-superior portion with more cranial imaging [33]. The extension of the venous component of the atrial cavity to the juxtaposed atrial appendage may also be well demonstrated.

### *Isolated ventricular inversion and ACM*

As always, imaging is dictated by the segmental approach to diagnosis. Observations unique to isolated ventricular inversion, as described by Pasquini et al. [29], are as follows:

- The ventriculo-arterial alignments *and* connections are normal with aortic-mitral valve fibrous continuity and subpulmonary conus.
- The infundibulum runs more vertical than in the solitus normal heart and the great arteries appear to run parallel from subxiphoid long-axis views but they appear to cross from parasternal long-axis views (Figs 28.5 and 28.6a,b; Videoclip 28.4).
- Interrogation of the atrial septum often reveals a sealed foramen ovale or a very restrictive secundum atrial septal defect (ASD) [34], contributing to the severe cyanosis that is usually the presenting feature.

Detection of ACM is based on morphologic analysis of the individual cardiac segments and detailed imaging of the conotruncal region. Malposition of the great arteries is identified by the abnormal ventriculo-arterial connections. ACM is recognized as the presence of concordant ventriculo-arterial alignments despite abnormal ventriculo-arterial connections (Fig. 28.7a,b and Videoclip 28.5).

## Prenatal assessment

Identification of abnormal position of the heart in the thorax is easily accomplished in the obstetrical ultrasound exam, and is a major reason for referral for detailed fetal echocardiography. Differentiation between true dextrocardia and secondary dextroposition is the first important step of the fetal echocardiogram. Although intrathoracic pathology, including diaphragmatic hernia, cystic adenomatoid malformation of the lung, bronchogenic cysts, and pericardial and pulmonary tumors, is the main reason for dextroposition, there are also reported cases of dextroposition without intrathoracic space-occupying lesions [35]. These cases are associated with right lung hypoplasia and diminutive right pulmonary artery, and the most common cardiac defect encountered is scimitar syndrome.

Fetal diagnosis of JAA is almost always made in the setting of complex heart disease. The atrial appendages should be carefully examined in cases of dextrocardia, tricuspid atresia, transposition of the great arteries, and double-outlet right ventricle – the diagnoses most commonly associated with JAA [18]. JAA is often first suspected on the 3-vessel view, where abnormal vascular spaces are seen to the left or right of the cross-section of the arterial trunks [36] (Fig. 28.8).

Isolated ventricular inversion and ACM have rarely been diagnosed in utero [37], but the diagnosis can be accomplished by detailed sequential segmental analysis of the cardiac anatomy.

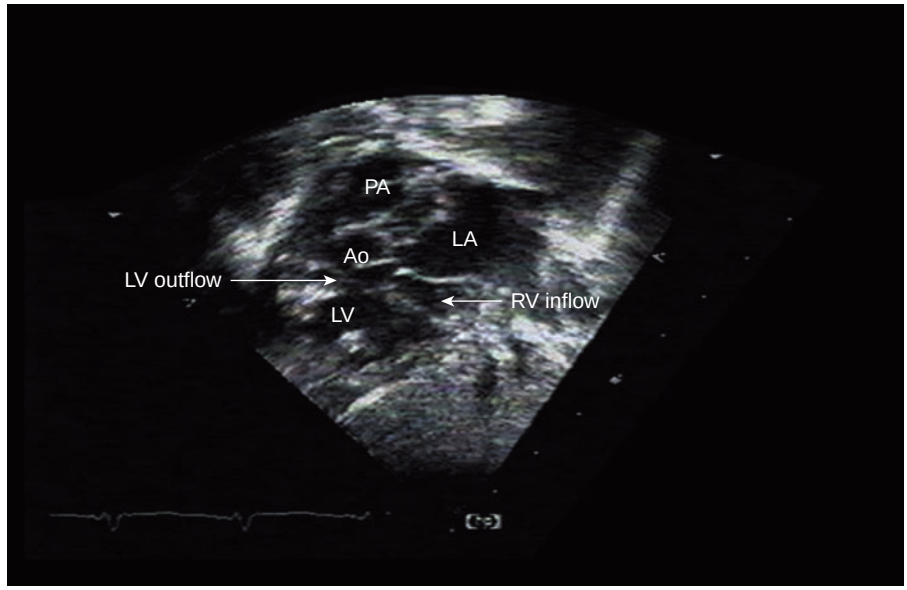


(a)

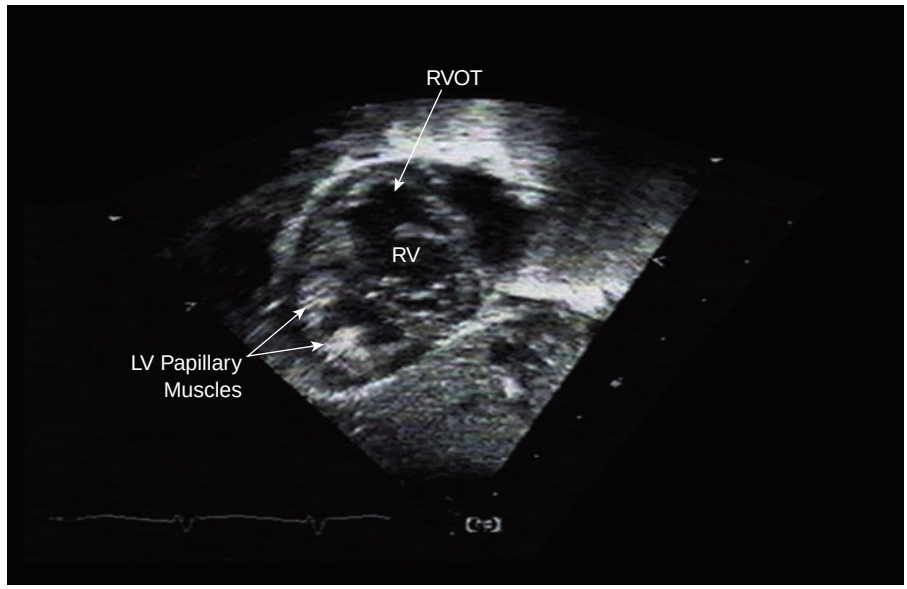


(b)

**Figure 28.6** Subxiphoid short-axis images of isolated ventricular inversion at the level of the great arteries **(a)** and of the ventricles **(b)**, showing the abnormal spatial relationship of the L-looped ventricles with normally positioned great arteries. Ao, aorta; LA, left atrium; LV, left ventricle; PA, pulmonary artery; RV, right ventricle; RVOT, right ventricular outflow tract.

### Preoperative and postoperative assessment

All the above-described cardiac malpositions have a tendency to coexist. The careful search for – and identification of – all associated anomalies is of paramount importance prior to surgical correction. The objectives of postoperative assessment are dictated by the procedures performed.

The importance of accurate diagnosis of JAA prior to balloon atrial septostomy has been stressed. In addition, identification of the juxtaposed appendages before intra-atrial baffle procedures is important because such juxtaposition may require revision of the surgical technique of atrial baffle procedures [38].

Isolated ventricular inversion can be managed surgically with an atrial switch procedure that corrects the transposition physiology and maintains the left ventricle on the systemic side of the circulation. Associated intracardiac defects need to be accurately diagnosed preoperatively and repaired at the same time. The most common associated defect is a VSD, and correct diagnosis of the ventricular inversion is important prior to patch closure of the defect so that complete heart block can be avoided. In these cases the conduction system runs on the right-sided left ventricular side of the septum so the patch needs to be placed on the left side [39].

In cases of ACM, the atrioventricular connections should be ascertained first. The majority of reported cases have concordant atrioventricular connections and, thus, normal physiology of the circulation. However, almost all have VSDs, and JAA and obstruction of the subpulmonary or subaortic outflow tracts

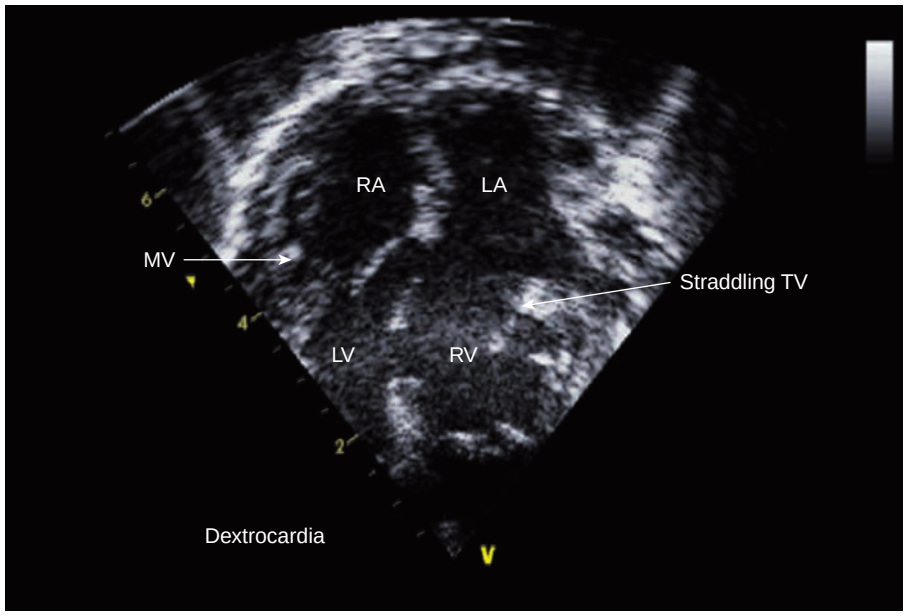


(a)

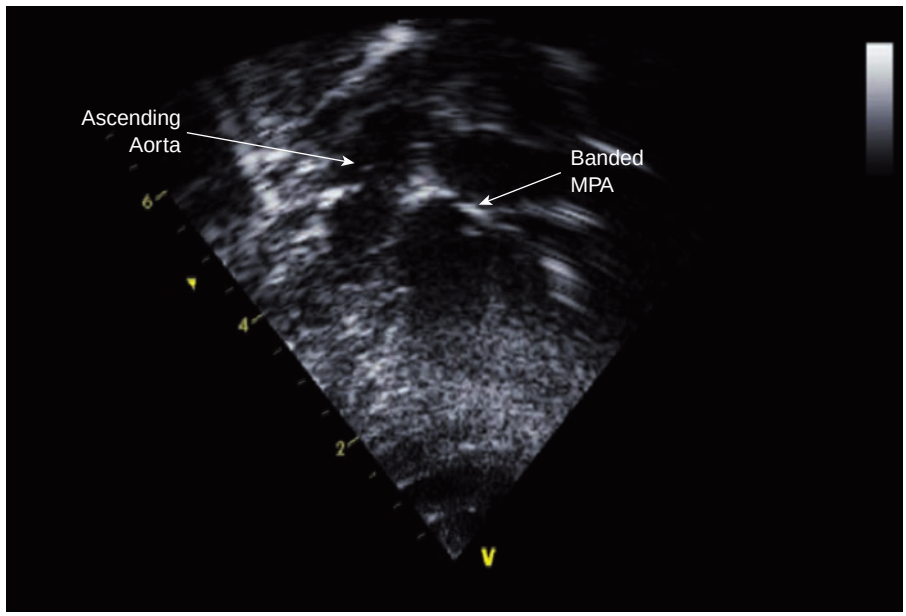


(b)

**Figure 28.7** Anatomically corrected malposition of the great arteries: apical 4-chamber views showing atrial situs solitus with atrioventricular discordance and ventriculo-arterial concordance in the setting of dextrocardia. There is a large ventricular septal defect, and the left-sided tricuspid valve (TV) is straddling over the defect **(a)**. Angled anteriorly the rightward and anterior aorta is shown to be aligned with the right-sided left ventricle, whereas the leftward and posterior main pulmonary artery (MPA) is aligned with the left-sided right ventricle. **(b)**. The segmental set is {S,L,D}, and the aorta is supported by a subaortic conus. LA, left atrium; LV, left ventricle; MV, mitral valve; RA, right atrium; RV, right ventricle.

are frequent associations. A significant percentage of cases also have solitary coronary arteries. Less commonly, the atrioventricular connections are discordant and the patients present as having physiologically uncorrected transposition. In those cases, the appendages are typically not malposed, but the ventricular septum is again almost always deficient and subaortic obstruction is frequent. A smaller percentage of the reported cases of ACM also have atresia of the right ventricular (RV) inflow or double-inlet left ventricle (LV). The commonly associated anomalies in this subgroup are JAA, obstruction of the subpulmonary outflow tract and abnormal coronary arterial pattern [31].

## Heterotaxy syndrome

### Definitions

In contrast to the remarkable external symmetry of all vertebrates, including humans, the internal organs normally are asymmetrically positioned along the left–right axis [40]. This asymmetry refers to both lateralization of unpaired organs (e.g., heart, liver, spleen, and stomach) as well as morphologic differences of paired organs (lungs, bronchi, atrial appendages) that do not allow them to be mirror images of each other. The term heterotaxy refers to the failure to generate

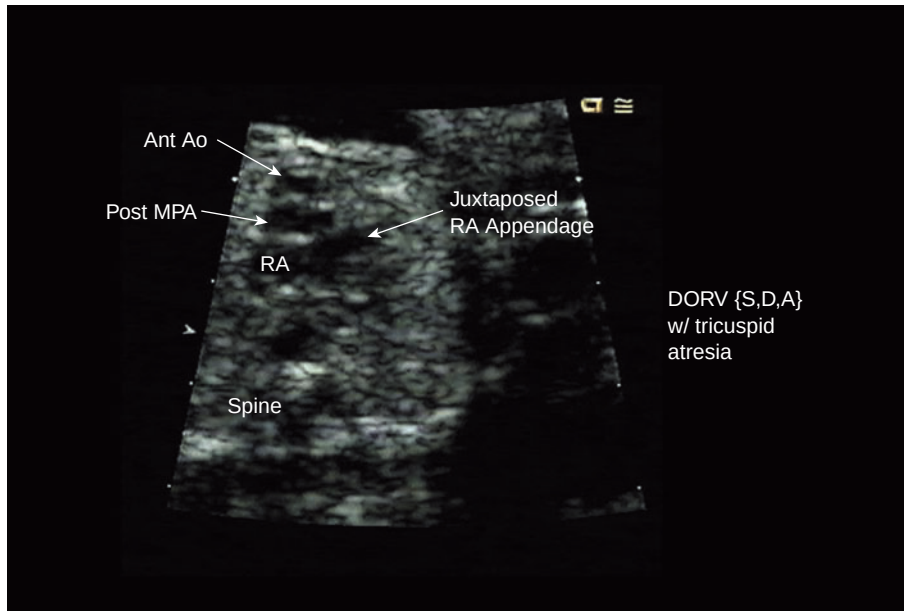


**Figure 28.8** Fetal 4-chamber view of leftward juxtaposition of the right atrial appendage (LJRAA), angled anteriorly showing the abnormal spatial relationship of the great arteries – aorta rightward and anterior, pulmonary artery leftward and posterior. The juxtaposed right atrial appendage is seen traversing behind the pulmonary trunk to the left of the great vessels. Ant Ao, anterior aorta; DORV, double-outlet right ventricle; MPA, main pulmonary artery; RA, right atrium.

normal left–right asymmetry, and it is defined as the presence of a pattern of spatial organization of the thoracic and abdominal viscera that is neither that of situs solitus nor that of complete situs inversus (mirror image of normal) [41]. The situs inconsistency extends to the cardiac segments (atria, ventricles, and great arteries) and, in combination with the abnormalities of the systemic and pulmonary veins, forms the basis for the complexity of the cardiac defects found in heterotaxy syndrome patients.

The encountered anomalies are conventionally grouped in two categories: (i) asplenia syndrome, also known as right atrial isomerism, and (ii) polysplenia syndrome, also known as left atrial isomerism. The distinction between the two groups is based on the common concurrence of different anomalies, although there is a wide variation of the abnormalities found in any given patient. There is also a smaller group with single right-sided spleen in which the cardiovascular malformations are very similar to the asplenia syndrome group [41]. As a rule, the cardiac lesions in asplenia syndrome are more complex and the prognosis is poorer. It is important to emphasize that in heterotaxy syndrome, the splenic malformations are not the fundamental abnormality, and they probably represent one of the effects of the teratogenic process rather than the cause of it. In the literature, the terms asplenia and polysplenia versus right and left atrial isomerism, respectively, are used almost interchangeably. It is generally acknowledged that no system of nomenclature for heterotaxy syndrome is entirely accurate in terms of anatomic definition or etiologic classification. To the fullest extent possible, the thoraco-abdominal visceral situs, all cardiovascular malformations and any identified associated anomaly should be described separately for each patient utilizing a systematic, that is, a segmental, approach.

## Incidence

Despite the continuing problems with classification and terminology that make most series difficult to interpret, the majority of the published studies estimate the incidence of heterotaxy at 10–14 per 100 000 livebirths [42–46]. The relative frequency of heterotaxy syndrome is reported as 2.3–4.2% of congenital heart disease [42,44].

## Etiology

Heterotaxy is due to a lack of regulation of left–right asymmetry and it appears to be highly heterogeneous genetically. Studies in humans and the *iv/iv* and *inv* mouse models suggest an autosomal recessive pattern of inheritance with variable penetrance, but polygenic or multifactorial causes have also been implicated, and familial cases [47–49], autosomal dominant, recessive and X-linked inheritance have all been described. In terms of environmental factors, vertebrate studies have shown a role for maternal diabetes [45] and retinoic acid [50] exposure in utero.

A link between ciliary motility and the regulation of left–right asymmetry was proposed when it was observed that a significant number of individuals with primary ciliary dyskinesia also have situs inversus. The malfunctioning monocilia of afflicted humans result in random generation of asymmetry or even abnormal symmetry as observed in heterotaxy [51]. How cilia affect lateralization goes back to the fetal node, a transient midline structure that is covered with specialized monocilia. The prevailing model to explain how fluid flow directed by ciliary movement in the early embryonic stages confers left–right asymmetry proposes that signaling proteins such as sonic hedgehog (Shh), fibroblast growth factor, or Nodal are swept to the left side of the embryonic node where they initiate downstream signaling

pathways [52]. Disruption of the midline barrier separating left from right may permit a mixing of molecules that are normally asymmetrically distributed in early embryos, resulting in abnormal organ sidedness later in development. Nine genes have so far been linked to nonsyndromic human laterality disorders [40]. Despite these advances, the determinants of laterality are still not completely understood, and the correlation of genotype with phenotype remains at an early stage.

## Morphology and classification

### Developmental considerations

The major events in normal cardiac development that appear to be arrested or absent in heterotaxy syndrome occur largely during the fifth week of gestation [53], and the hearts of many patients with heterotaxy syndrome bear a remarkable resemblance to the heart of a normal embryo at 35 days of gestation. More specifically, the growth of the endocardial cushions, septation of the conotruncus, lobation of the lungs and rotation of the gut begin between days 28 and 35 of gestation [54] whereas the spleen is present at about 32 days and is well demarcated by 35–36 days [53].

### Anatomy

According to Van Praagh et al. [41] the fulfillment of at least 4 of the 12 criteria outlined in Table 28.1 correctly identifies patients with heterotaxy syndrome. The atrial appendages merit special mention as a diagnostic criterion, because they have been considered by many [55,56] to be the unifying link in the definition and classification of patients with heterotaxy syndrome. Whether isomerism accurately applies to the heart or not, it is true that the appendages frequently share characteristics of a right atrial appendage in asplenia syndrome and of a left atrial appendage in polysplenia syndrome. It has been suggested that the extent of the pectinate muscles relative to the muscular atrioventricular vestibule can reliably distinguish between left and right atrial appendages. In hearts with isomeric appendages, there is either bilateral extension of the pectinate muscles in cases of right atrial isomerism, or continuity between the vestibule of the atrioventricular junction and the smooth-walled venous component of the atrium without interposition of pectinate muscles in cases of left atrial isomerism [57]. Because the identification of internal anatomy, size and location of the appendages is not always feasible by echocardiography, we propose the combination of multiple criteria in order to classify correctly patients with heterotaxy.

**Table 28.1** Criteria for visceral heterotaxy and abnormal visceral symmetry

| | |
|---|---|
| 1 | Thoraco-abdominal situs inconsistency |
| 2 | Abnormally symmetric lung lobes |
| 3 | Abnormally symmetric bronchial branching pattern |
| 4 | Abnormal symmetry of the liver |
| 5 | Unusual or abnormal systemic venous connections |
| 6 | Unroofed coronary sinus |
| 7 | Abnormal pulmonary venous connections or drainage |
| 8 | Similarities in the shape and morphology of the atrial appendages |
| 9 | Abnormal mesenteric attachments |
| 10 | Abnormal bowel location +/– malrotation |
| 11 | Asplenia, polysplenia or single right-sided spleen |
| 12 | Abnormal position and/or size of the pancreas |

The usual constellation of symptoms in asplenia syndrome includes: total anomalous pulmonary venous connection, usually to a systemic vein; bilateral superior venae cavae; unroofed coronary sinus; common atrium; complete common atrioventricular canal (CCAVC); a high incidence of single ventricle, usually of right morphology; pulmonary stenosis or atresia; and transposition of the great arteries (Fig. 28.9a–d and Videoclip 28.6). In polysplenia syndrome,

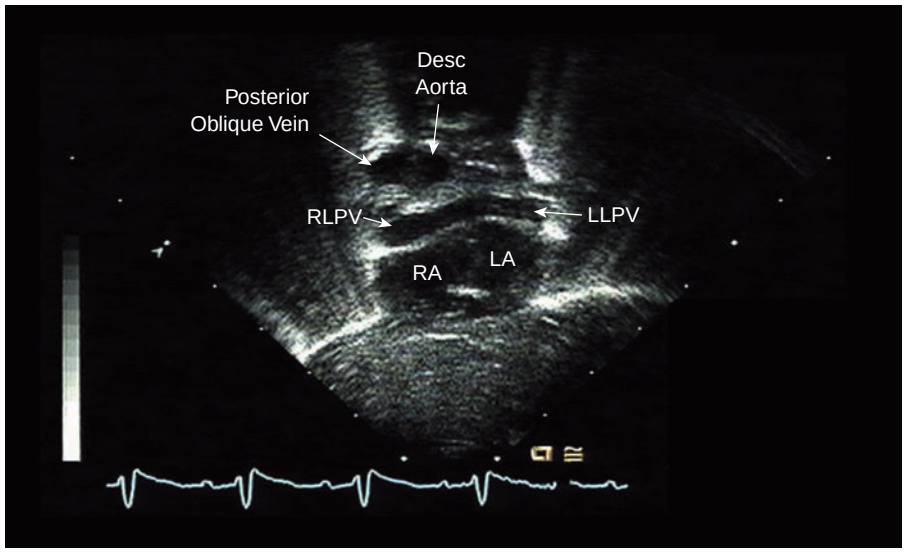


(a)

**Figure 28.9** Heterotaxy syndrome most consistent with asplenia. **(a–d)** Sequential subxiphoid long-axis images from posterior/inferior to anterior/superior showing the typical constellation of findings in asplenia syndrome in a patient with double-outlet right ventricle {A,L,L}: bilateral superior venae cavae, totally anomalous pulmonary venous connections, nearly common atrium, complete common atrioventricular canal, and severe subpulmonary stenosis with bilateral conus. Asc, ascending; AV, atrioventricular; Desc, descending; LA, left atrium; LLPV, left lower pulmonary vein; LPA, left pulmonary artery; LV, left ventricle; MPA, main pulmonary artery; PV, pulmonary valve; RA, right atrium; RLPV, right lower pulmonary vein; RPA, right pulmonary artery; RV, right ventricle; SVC, superior vena cava.

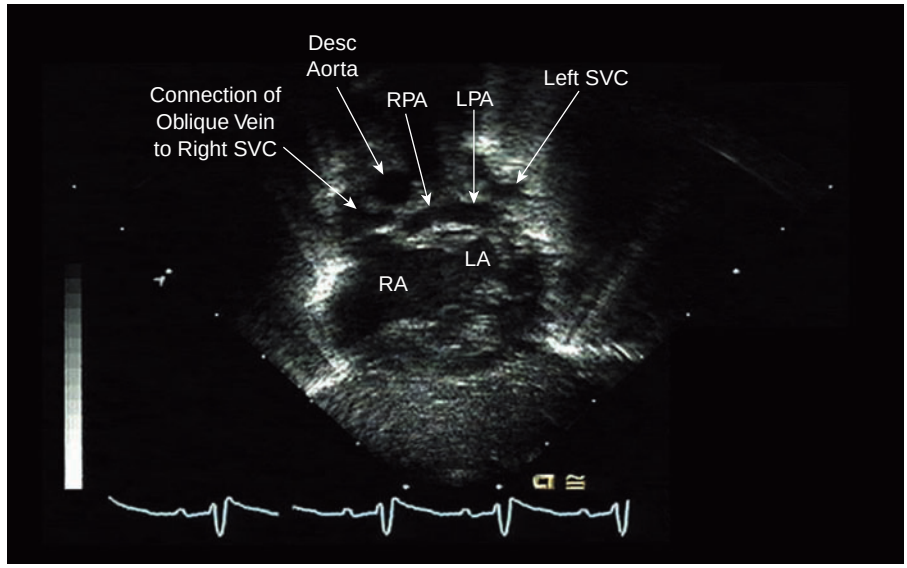


(b)

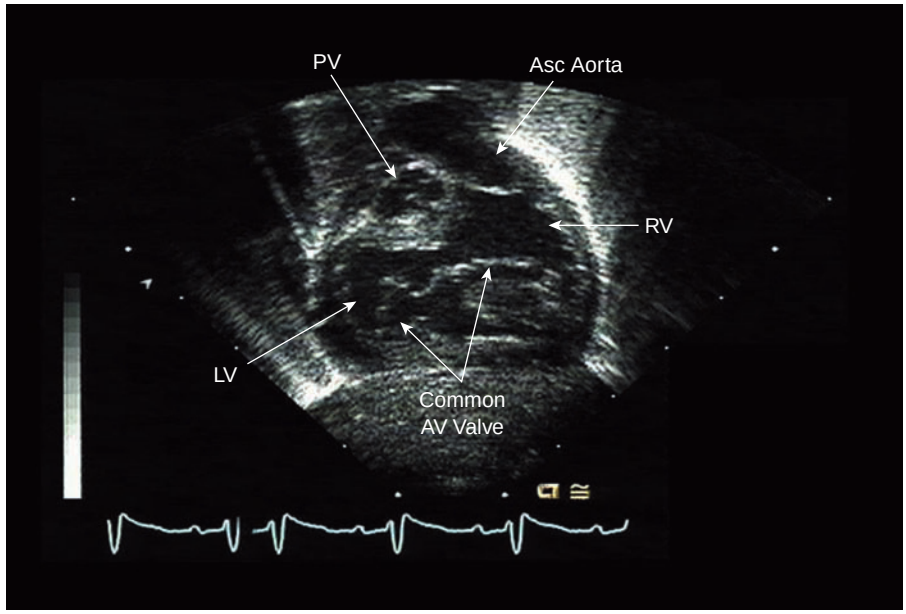


(c)

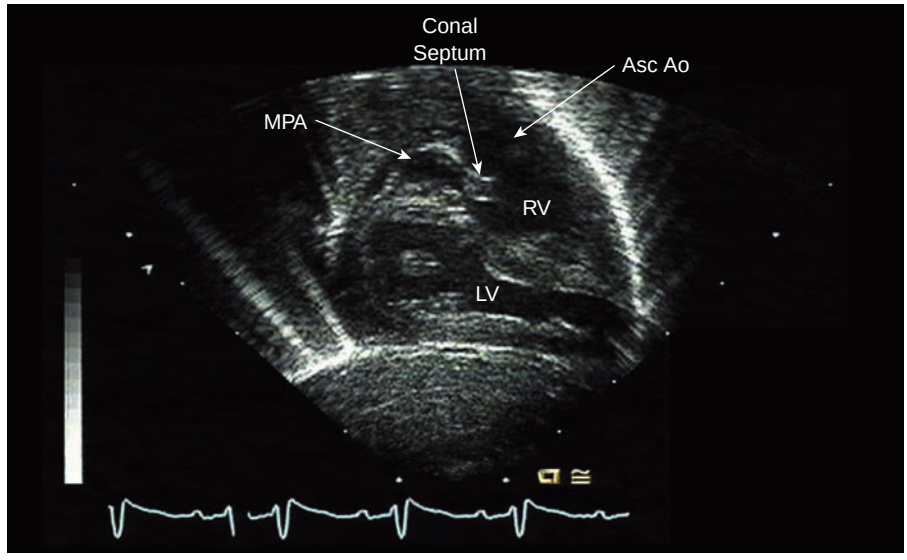


(d)

**Figure 28.9** (*continued*)

as a rule, the cardiovascular anomalies are not as severe and usually consist of: interrupted inferior vena cava with azygos continuation; bilateral superior venae cavae; pulmonary veins draining to ipsilateral atria; CAVC in 50%; left ventricular outflow tract obstruction; rarely, transposition of the great arteries; and, uncommonly, pulmonary stenosis (Fig. 28.10a,b and Videoclip 28.7). The various cardiac anomalies frequently encountered in the heterotaxy syndrome and their incidences in reported series are listed in Table 28.2. Additional details of the encountered anomalies are given below.

### *Systemic venous connections*

Interrupted inferior vena cava used to be considered pathognomonic for polysplenia syndrome, but recent case reports have shown that it can rarely be associated with asplenia syndrome as well [47,58]. In cases with interrupted inferior vena cava, the hepatic veins connect with the anatomic right atrium directly, either as a single trunk or separate connections of the left and right hepatic veins. When the inferior vena cava is intact, the hepatic veins join it in the majority of the cases, although in about one-third of cases, the hepatic veins draining the lobe of the liver opposite to the inferior vena cava connect with the atrium directly (Fig. 28.11).

### *Pulmonary venous connections*

Pulmonary venous obstruction can be due to extracardiac obstruction or pulmonary venous hypoplasia [59]. In asplenia syndrome totally anomalous pulmonary venous connection

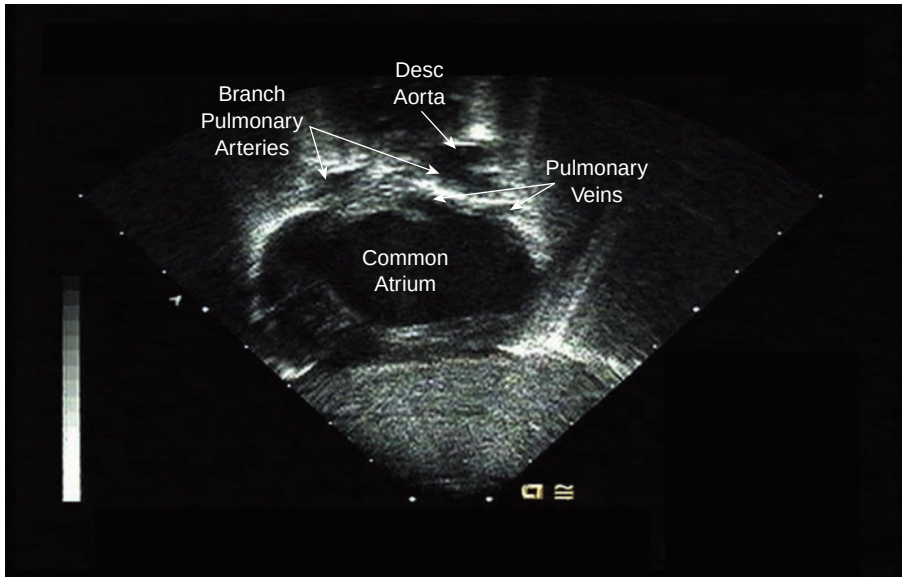


(a)

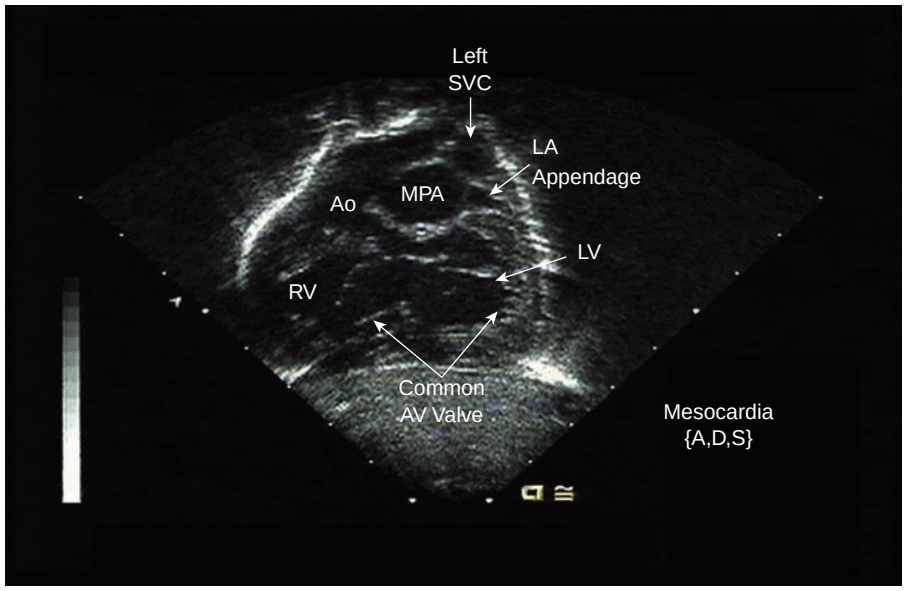


(b)

**Figure 28.10 (a,b)** Heterotaxy syndrome most consistent with polysplenia. Constellation of findings most consistent with polysplenia syndrome in a patient with mesocardia and abdominal visceral situs ambiguus (segmental set {A,D,S}): interrupted inferior vena cava with left azygos continuation to the left superior vena cava (SVC), common atrium, partial atrioventricular (AV) canal with a common AV valve, and normally related great arteries. Ao, aorta; Desc, descending; LA, left atrial; LV, left ventricle; MPA, main pulmonary artery; RV, right ventricle.

**Table 28.2** Incidence of cardiac anomalies in heterotaxy syndrome

| | Asplenia syndrome (%) | Single right-sided spleen (%) | Polysplenia syndrome (%) |
|---|---|---|---|
| Dextrocardia | 27–41 [41,54,57,62,68,104,105] | 0 [41] | 27–45 [41,43,57,62,104–106] |
| Interrupted IVC | 0–3 [41,54,57,62,68,104,105] | 0 [41] | 65–92 [41,43,57,62,104–106] |
| Continuous IVC entering the RA | 48–77 [41,57,68,104] | 80 [41] | 0–34 [41,57,104,106] |
| Continuous IVC entering the LA | 20–52 [41,57,68,104] | 20 [41] | 0–16 [41,57,104,106] |
| Hepatic veins entering the atria directly | 16–38 [41,54,57,62,68,104,105] | 0 [41] | 84–96 [41,43,57,62,104,105] |
| Unroofed coronary sinus | 32–100 [41,54,57,62,104,105] | 80 [41] | 26–46 [41,43,57,62,104–106] |
| Bilateral superior venae cavae | 38–71 [41,54,57,62,68,104,105] | 40 [41] | 33–50 [41,43,57,62,104–106] |
| TAPVC to a systemic vein | 31–87 [41,54,57,62,68,104,105] | 60 [41] | 0–13 [41,43,57,104,106] |
| Pulmonary veins to RA (partial or total) | 2 –19 [41,57] | 0 [41] | 37–74 [41,43,57,104,106] |
| Common atrium | 40–84 [54,57,62,68,105] | 0 [41] | 30–53 [41,43,57] |
| Atrial situs solitus | 50 [41] | 40 [41] | 78 [41] |
| Atrial situs inversus | 31 [41] | 60 [41] | 22 [41] |
| Atrial situs ambiguus | 19 [41] | 0 [41] | 0 [41] |
| CAVC | 69–92 [41,54,57,62,68,104,105] | 40 [41] | 16–66 [41,43,57,104,106] |
| Pulmonary stenosis/atresia | 78–96 [41,54,57,62,68,104,105] | 100 [41] | 28–43 [41,43,57,104,106] |
| Aortic valve hypoplasia/LVOT obstruction/coarctation | 2–12 [41,54,57,62,68,105] | 0 [41] | 17–25 [41,43,62,106] |
| Single ventricle | 29–73 [41,54,57,62,68,104,105] | 60 [41] | 26–43 [41,43,62,104] |
| TGA -D, -L/DORV | 47–91 [41,54,57,62,68,104,105] | 100 [41] | 16–48 [41,43,62,104,106] |
| Abnormal coronary pattern | 10–64 [54,57,62,104,105] | NS | 8–24 [62,106] |
| Aortic arch laterality: | | NS | |
| Left | 56 [104] | | 33 [104] |
| Right | 32–49 [54,68,104] | | 67 [104] |

CAVC, complete common atrioventricular canal; DORV, double-outlet right ventricle; IVC, inferior vena cava; LA, left atrium; LVOT, left ventricular outflow tract; RA, right atrium, TAPVC, totally anomalous pulmonary venous connection; TGA, transposition of the great arteries.

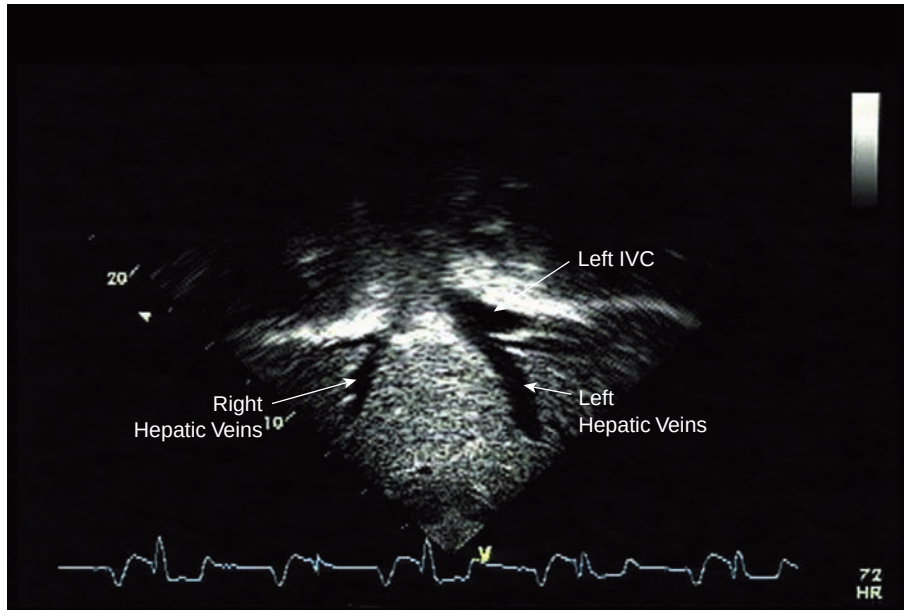


**Figure 28.11** Ipsilateral hepatic veins. Subxiphoid long-axis view at the level of the diaphragm showing the left hepatic veins joining the left-sided intact inferior vena cava (IVC) and the right hepatic veins draining separately.

is most commonly to a systemic vein and frequently obstructed, whereas in polysplenia syndrome the pulmonary veins connect normally but drain anomalously due to malposition of the septum primum toward the anatomic left atrium (see below).

### *Atrial septum*

Common atrium is frequently seen in both asplenia and polysplenia syndromes. Especially in asplenia syndrome, both septum secundum and septum primum may be absent, and only remnants of atrial septal tissue are recognized in these patients, such as a fibromuscular strand that crosses the inferior aspect of the common atrium (inferior limbic band of the fossa ovale) or remnants of venous valve tissue.

In polysplenia syndrome, it has been proposed that the partially or totally anomalous pulmonary venous connection to the contralateral atrium is due to malposition of septum primum, probably secondary to the absence of septum secundum [60]. The pulmonary veins appear to be connected normally to the left atrial wall externally but drain to the right atrium anomalously because of the malpositioned septum primum. There is usually an interatrial communication of variable size between the septum primum and the posterior atrial wall, which strictly speaking is not a foramen ovale [53]. A sinoseptal defect, frequently in the form of complete unroofing of the coronary sinus, is a common association, especially in patients with asplenia syndrome.

### *Atrioventricular valves*

A partial or complete common atrioventricular (AV) canal is the most common cardiac malformation in both asplenia and polysplenia syndromes. A strong association between an unroofed coronary sinus and partial or complete AV canal has been reported [61] regardless of the status of the spleen.

### *Ventricles*

L-looped ventricles are encountered in 22–38% of patients with asplenia syndrome and in 12–30% of cases with polysplenia syndrome [61,62]. Preoperative recognition of ventricular looping is important because it can predict the location of the specialized conduction tissue. L-looped ventricles, irrespective of heterotaxy subgroup, usually have dual AV nodes, one situated anterolaterally and the other postero-inferiorly, occasionally with a "sling" of conduction tissue connecting them [63]. D-looped ventricles in the setting of polysplenia syndrome usually possess a solitary AV node, situated where the ventricular septum meets the atrioventricular junction postero-inferiorly; the AV conduction axis is often discontinuous, providing the substrate for AV block.

The morphologic left ventricle in cases of asplenia syndrome with CAVC is reported to have morphologic variations of the AV valve apparatus that may contribute to the valve insufficiency and ventricular dysfunction known to complicate surgical repair. More specifically, a study concentrating on cases of balanced CAVC in the setting of heterotaxy syndrome reports a higher frequency of solitary papillary muscles (Fig. 28.12), shorter and deviated dual papillary muscles, and a smaller circumference of the mural leaflet of the morphologic left ventricle in asplenia syndrome compared with cases of CAVC in polysplenia syndrome or absence of heterotaxy [64].

### *Ventriculo-arterial alignment*

The rule in cases of asplenia syndrome is the presence of subaortic or bilateral conus with double-outlet right ventricle or transposition of the great arteries. In contrast, polysplenia syndrome is characterized by the absence of

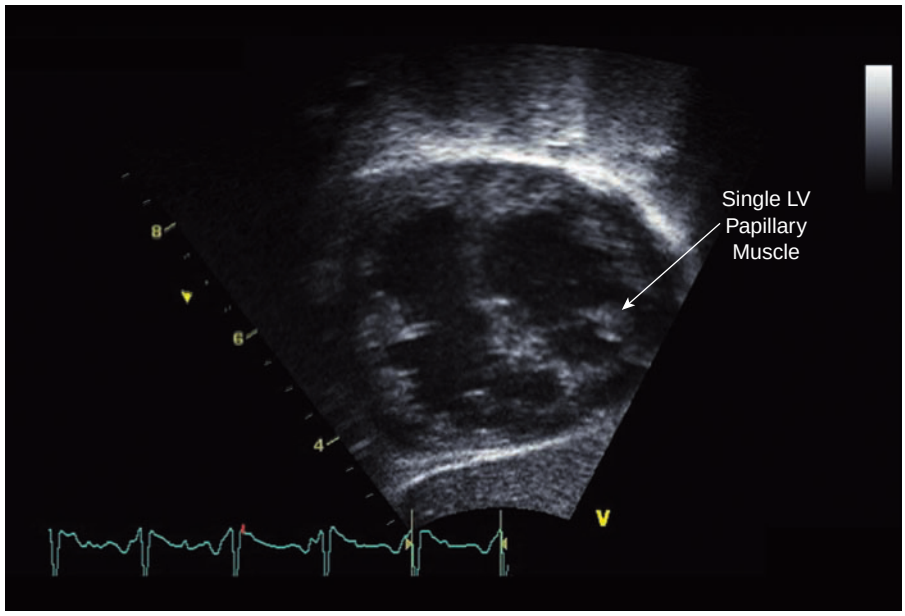


**Figure 28.12** Single left ventricular papillary muscle. Subxiphoid short-axis image showing the well-balanced common atrioventricular valve and a single left ventricular (LV) posteromedial papillary muscle.

subaortic conus, even in cases of transposition [61]. Abnormal connection of the pulmonary veins to a systemic vein, irrespective of the heterotaxy subgroup, is almost always associated with abnormal infundibulum (either subaortic or bilateral) [61].

### *Pulmonary outflow tract obstruction*

Pulmonary stenosis or atresia is very common, especially in asplenia syndrome, and, together with pulmonary venous obstruction, constitutes one of the most severe problems in the newborn period. A study of 72 post-mortem cases of asplenia syndrome [60] reported an interesting association between these two problems. Specifically, when the pulmonary artery branches were severely hypoplastic, stenotic or discontinuous, anomalous pulmonary venous connections were more probable (86% versus 51% with pulmonary arteries that were only mildly hypoplastic or normal). Pulmonary venous obstruction was also more common (57% versus 24%).

### *Aortic outflow tract obstruction*

In post-mortem studies [62,65], subaortic obstruction was seen in 4–10% of patients with asplenia syndrome, and in 28–33% of patients with polysplenia syndrome. Van Praagh et al. described in detail the pathologic findings and clarified the anatomic basis of the malformation [65]. More specifically, there was no subaortic conus in any of their cases, and the obstruction was caused by the following lesions (Fig. 28.13):

- redundant leaflet of the tricuspid valve;
- aneurysm of the membranous septum;
- excessive fibrous tissue from the mitral or common AV valve;
- hypoplasia of the mitral valve and left ventricle;
- malposition of the conal septum.

### *Aortic arch, brachiocephalic vessels and patent ductus arteriosus*

Coarctation of the aorta and interrupted aortic arch are relatively uncommon, especially in asplenia syndrome (Fig. 28.14a,b). The incidence of right aortic arch is given in Table 28.2. In our database, out of 56 cases with heterotaxy syndrome, right aortic arch was diagnosed in 39% (all with mirror-image branching). Isolated left innominate artery has also rarely been described (three cases), with both asplenia and polysplenia syndromes. Two of these three cases had associated aortic atresia [66]. Another reported association is the presence of bilateral ductus arteriosus in 25% of cases with pulmonary atresia and asplenia syndrome [67].

### *Noncardiac anomalies*

In asplenia syndrome, in addition to the frequently encountered bronchial symmetry with bilateral trilobed lungs and eparterial bronchi, a midline liver is present in the majority of the cases whereas gastrointestinal and genitourinary anomalies are present in one-third and one-tenth of patients, respectively [68]. The most common gastrointestinal abnormality is intestinal malrotation.

In polysplenia syndrome, the incidence of extracardiac anomalies is higher, with these occurring in 36% of patients in the largest clinical series to date [43]. Gastrointestinal anomalies are common, with biliary atresia and intestinal malrotation occurring in 11% and 13% of patients,

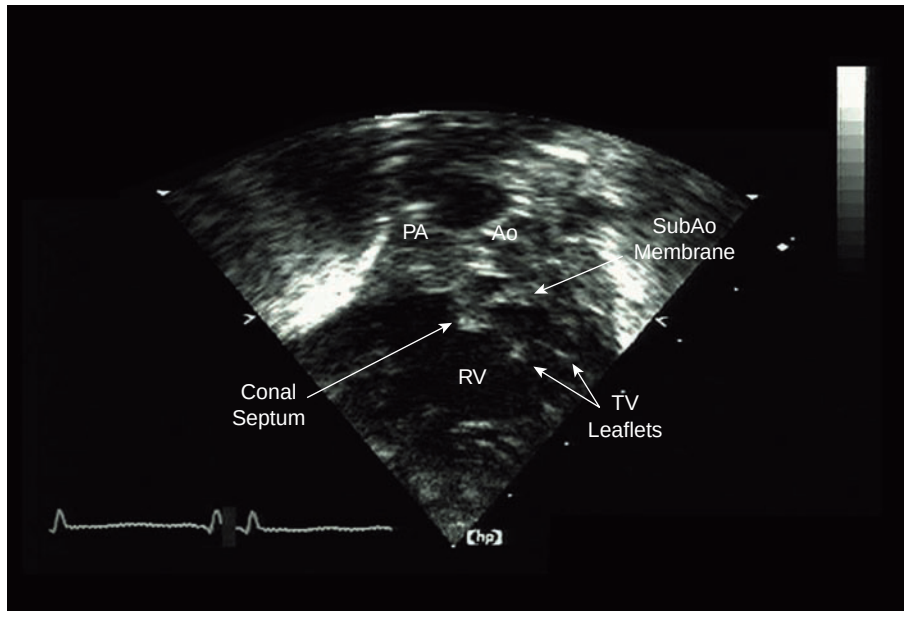


**Figure 28.13** Mechanisms of ventricular outflow tract obstruction. Subxiphoid long-axis image angled anteriorly showing the different mechanisms of obstruction of the systemic outflow in heterotaxy syndrome, with critical obstruction in the systemic outflow due to posterior malalignment of conal septum, discrete subaortic membrane, tricuspid valve attachments and aortic valve hypoplasia. Ao, aorta; PA, pulmonary artery; RV, right ventricle; SubAo, subaortic; TV, tricuspid valve.

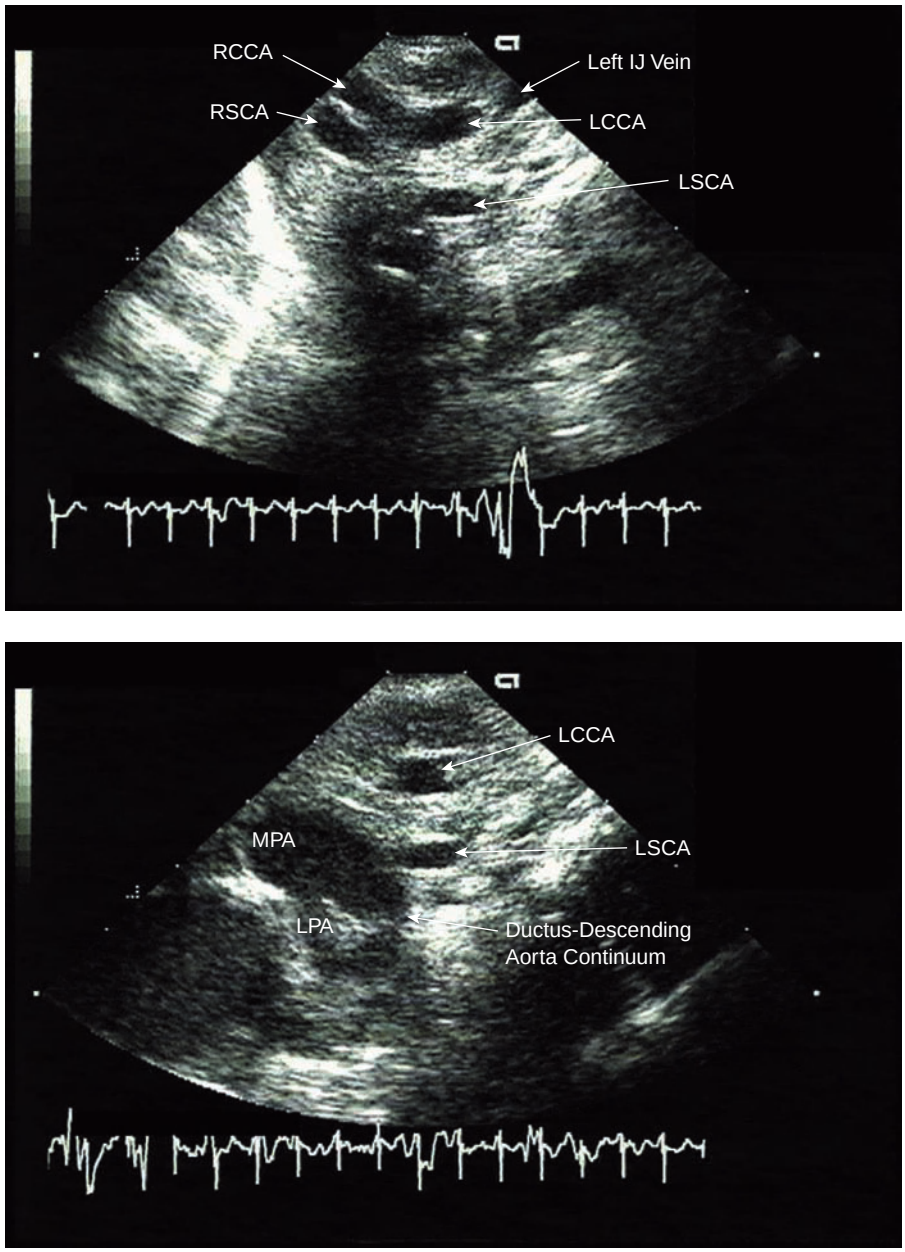


**Figure 28.14 (a,b)** Complex interrupted aortic arch type A in polysplenia syndrome. Short- and long-axis suprasternal notch images reveal a very unusual branching pattern of a probably left aortic arch: the first vessel is the left subclavian artery (LSCA), which arises from the ascending aorta, 15 mm above the level of the aortic annulus. The ascending aorta continues for another 8 mm before it trifurcates to the right subclavian (RSCA), right common carotid (RCCA) and left common carotid (LCCA) arteries. The distance between the distal ascending aorta and the descending aorta is measured at about 1 cm. IJ, internal jugular; LPA, left pulmonary artery; MPA, main pulmonary artery.

respectively, whereas genitourinary and neurologic abnormalities occur in 6% and 4% of patients, respectively.

## Pathophysiology

Cyanosis in the newborn period is the presenting symptom in many patients with asplenia syndrome, due to the frequent presence of pulmonary stenosis or atresia, as well as common atrium and transposition physiology. In polysplenia syndrome, pulmonary stenosis or atresia and transposition physiology are relatively uncommon, making symptoms of congestive heart failure from large left-to-right shunts the predominant presenting picture.

Conduction abnormalities are common in both groups of heterotaxy syndrome. There are dual sinus nodes in the majority of asplenia syndrome cases, whereas in polysplenia syndrome the sinus node tends to be hypoplastic and malpositioned [63]. Congenital complete atrioventricular block mainly affects patients with polysplenia syndrome and is responsible for fetal loss. It has been attributed to discontinuity between the AV node and the ventricular conduction axis [69]. Postnatally, it has been described in 7% of patients with polysplenia syndrome [43]; additionally, there is a small percentage of patients who develop complete AV block postoperatively.

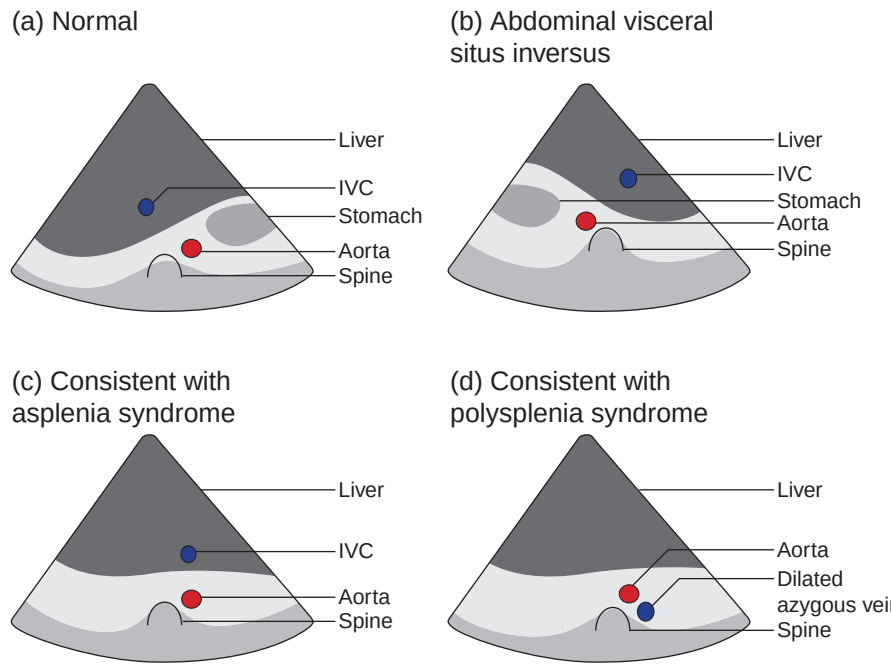


**Figure 28.15** Abdominal visceral situs. **(a)** Normal. **(b)** Abdominal visceral situs inversus: left-sided liver with inferior vena cava (IVC), right-sided stomach and right-sided descending aorta. **(c)** Abdominal visceral situs ambiguus consistent with asplenia syndrome: midline liver with IVC and descending aorta on the same side. **(d)** Abdominal visceral situs ambiguus consistent with polysplenia syndrome: midline liver with interrupted IVC and dilated azygos vein.

The splenic abnormalities that accompany heterotaxy syndrome contribute significantly to morbidity and mortality due to fulminant sepsis and should be promptly diagnosed with a liver spleen scan in all patients. Howell–Jolly bodies can be found irrespective of the anatomic status of the spleen and are occasionally encountered in normal neonates. Because functional asplenia can develop with age [70] it is recommended that patients with heterotaxy syndrome, even with documented multiple or solitary spleens, are monitored regularly for Howell–Jolly bodies. Due to the risk of developing functional asplenia at a later stage, all patients should be vaccinated against the pneumococcus, and once Howell–Jolly bodies are detected, prophylaxis with penicillin should be initiated immediately.

## Imaging

The highly variable and often complex anatomy of heterotaxy requires an organized approach and an exhaustive checklist of structures to be examined in order to determine the diagnosis accurately, both pre- and postnatally.

### *Goals of the examination*

Our proposed checklist, as follows, involves determination of:

- abdominal visceral situs;
- mesocardia or dextrocardia;
- systemic venous connections, including hepatic veins;
- coronary sinus septum;
- anatomy and drainage of pulmonary veins;
- atrial septum and atrial appendages;
- atrioventricular valve anatomy and function;
- ventricular size, morphology, looping and function;
- size and location of ventricular septal defect(s), potential LV-to-aorta or -pulmonary artery baffle pathway in cases of transposition of the great arteries with VSD or double-outlet right ventricle;
- sources of pulmonary blood flow (including branch pulmonary arteries, patent ductus arteriosus, and aortopulmonary collaterals);
- systemic ventricular outflow tract for presence and type of obstruction;
- aortic arch sidedness and branching pattern.

The examination begins with subxiphoid imaging to evaluate the abdominal viscera and establish the sidedness of the abdominal aorta and inferior vena cava (Fig. 28.15a–d). Subsequently, the location of the heart in the chest and the direction of the cardiac apex are determined. The same principles as described above for imaging dextrocardia should be applied. Following these initial steps, the cardiac segments (atria, ventricles, and great arteries) and their connections (AV junction and conotruncus) need to be analyzed independently and characterized in terms of situs and alignments following the principles of the segmental approach to diagnosis [71–73]. Starting with the atrial situs, the right atrium is identified based on the following characteristics:

**1** the chamber receives a normal coronary sinus (not unroofed);

**2** the chamber receives the venae cavae (the suprahepatic segment of the inferior vena cava, in cases of interruption);

**3** the chamber has a larger, more anterior, broad-based and triangular atrial appendage;

**4** the septal surface comprises the septum secundum;

**5** the chamber has an identifiable crista terminalis.

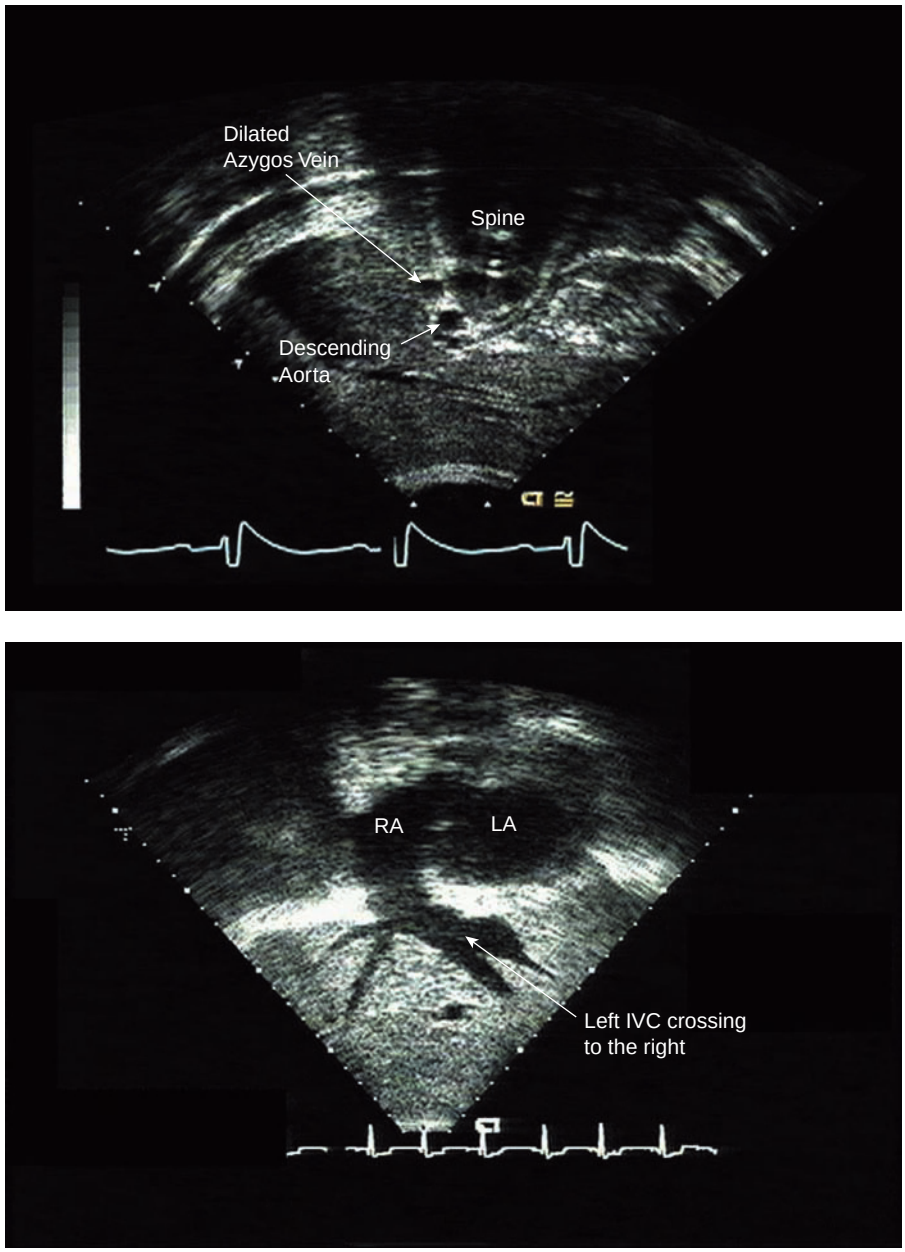


**Figure 28.16** Systemic venous anomalies in heterotaxy. **(a)** Subxiphoid short-axis image at the level of the diaphragm showing the dilated azygos vein located posterior to the aorta in the setting of interrupted inferior vena cava in polysplenia syndrome. **(b)** Subxiphoid short-axis image showing a left-sided inferior vena cava (IVC) crossing to the right and receiving all hepatic veins. This is a case of asplenia syndrome with a single right ventricle and severe pulmonary stenosis, status post-Fontan takedown. LA, left atrium; RA, right atrium.

Based on the above criteria, Van Praagh and Van Praagh were able correctly to diagnose atrial situs in 100% of their post-mortem cases of polysplenia syndrome, 100% of cases of right-sided spleen, and 81% of cases of asplenia syndrome [74]. In the remaining cases of asplenia syndrome, the inferior vena cava and the larger and more anterior appendage were contralateral; the diagnosis of situs ambiguus was made in those cases.

The inferior vena cava, hepatic veins, and their atrial connections as well as the abdominal aorta and the azygos vein termination to the superior vena cava are best seen from subxiphoid long- and short-axis views (Fig. 28.16a,b) [75]. The hepatic vein connections can also be imaged from apical views angled inferiorly toward the abdomen. The superior vena cava on either side can be imaged using subxiphoid, suprasternal, and high parasternal views [76]. Subxiphoid views are also good for the imaging of pulmonary venous connections below the diaphragm (Fig. 28.17a). Due to the high frequency of pulmonary venous obstruction, especially in asplenia syndrome, Doppler assessment of pulmonary venous flow is of paramount importance. To increase the sensitivity of the interrogation, filter settings should be low, and each vein should be interrogated by color flow mapping distal to the orifice for turbulent or high-velocity flow. In cases of pulmonary vein stenosis the Doppler flow pattern is no longer laminar and triphasic; instead it becomes

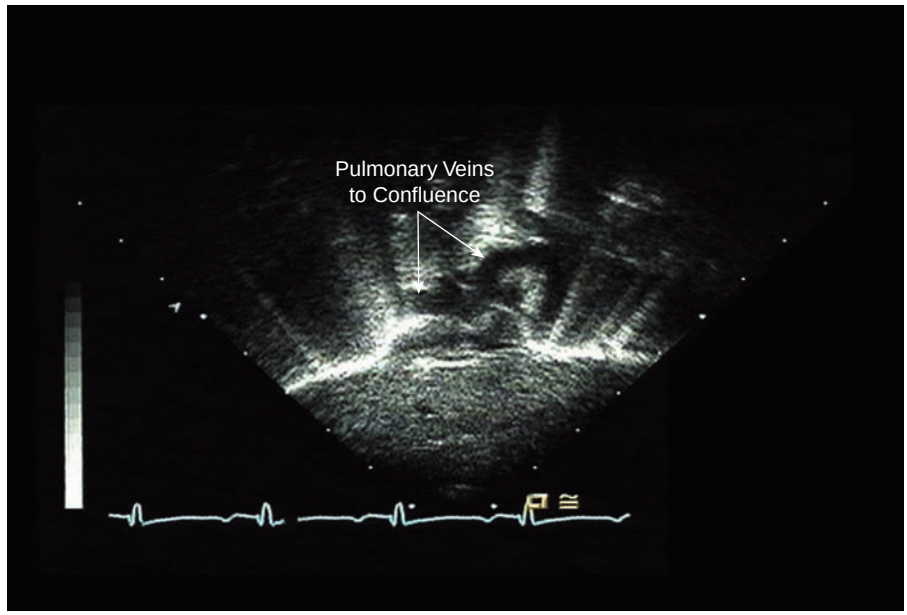


(a)

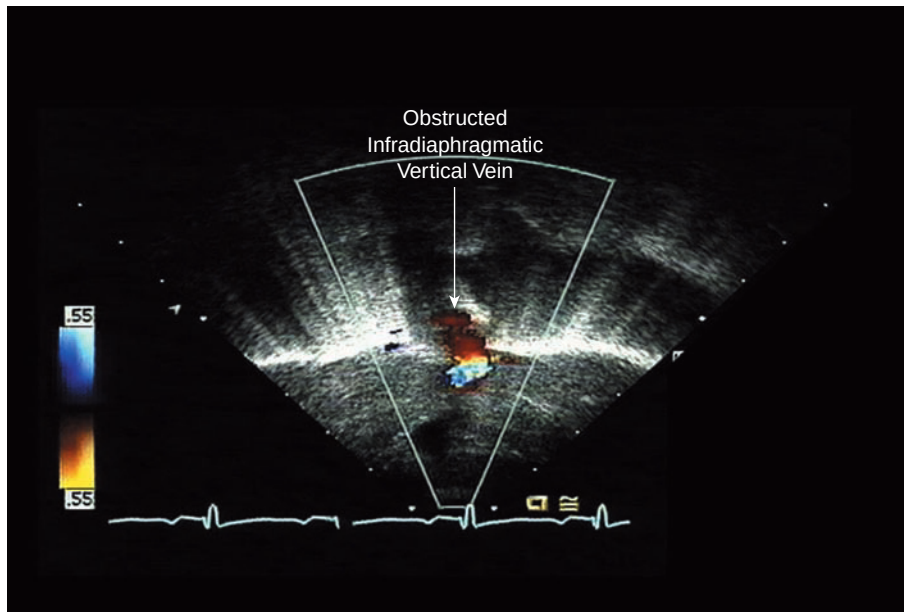


(b)

**Figure 28.17** Infradiaphragmatic total anomalous pulmonary venous connections. **(a)** Subxiphoid long-axis 2D. **(b)** color Doppler images of a vertical vein that accepts all pulmonary veins and is directed below the diaphragm into the hepatic portal venous system with mild flow acceleration (mean gradient of 4–5 mm Hg).

turbulent and continuous (Fig. 28.17b) with a pattern reminiscent of a patent ductus arteriosus [77,78].

Imaging of the atrial appendages to determine their size and location can be attempted from subxiphoid and parasternal short-axis views, but the internal anatomy is difficult to ascertain. The malpositioned septum primum is seen well from subxiphoid long-axis and apical 4-chamber views [53].

Imaging of the AV canal area is described in detail in Chapter 15. The valve apparatus should be carefully evaluated for abnormalities of the number, size and location of the papillary muscles, especially in asplenia syndrome [64]. Ventricular size and morphology need to be evaluated from all available views; the method for determining the identity of the ventricles and the ventricular looping has been described earlier (see Chapter 3). The outflow tracts can be imaged from subxiphoid views, apical views angled anteriorly and high parasternal views. The main pulmonary and branch pulmonary arteries should all be measured. If aortic outflow tract obstruction is present, coarctation should be suspected.

In cases with suboptimal transthoracic windows and an inconclusive diagnosis, transesophageal echocardiography is recommended [79,80]. In such cases, cardiac magnetic resonance imaging can also be considered as a noninvasive alternative [81,82] with the additional capability of delineation of the splenic status and the bronchial tree anatomy.

### Prenatal assessment

The most common reasons for referral in cases of fetal heterotaxy syndrome are abnormal position of the stomach and/or heart, identified by obstetrical ultrasound examination, and fetal bradycardia. Prenatal diagnosis of heterotaxy syndrome has greatly improved over the last few years, although the diagnosis of hepatic venous and inferior vena caval connections is still not as accurate, with correct diagnosis achieved in 62–67% of cases [83]. With respect to clinical outcomes, prenatal diagnosis does not appear to confer any survival advantage in either asplenia or polysplenia syndromes [83], but it offers prospective parents valuable time to reach an informed decision when they are faced with the diagnosis of severe cardiac anomalies.

In cases of polysplenia syndrome, heart block and extracardiac anomalies (biliary atresia, gastric volvulus, bowel malrotation) are risk factors for fetal and neonatal loss, and long-term survival is reported at 14–52% [46,83,84]. It is known that heterotaxy syndrome patients with heart block have significantly lower ventricular and atrial rates compared with those with other structural lesions or no structural heart disease, and low ventricular rate appears to be a primary risk factor for perinatal loss [85]. In rare cases of association of polysplenia syndrome with ventricular noncompaction, described both pre- [86] and postnatally [87,88], the prognosis is dismal, especially when heart block is also present. In asplenia syndrome diagnosed prenatally, long-term survival is reported at

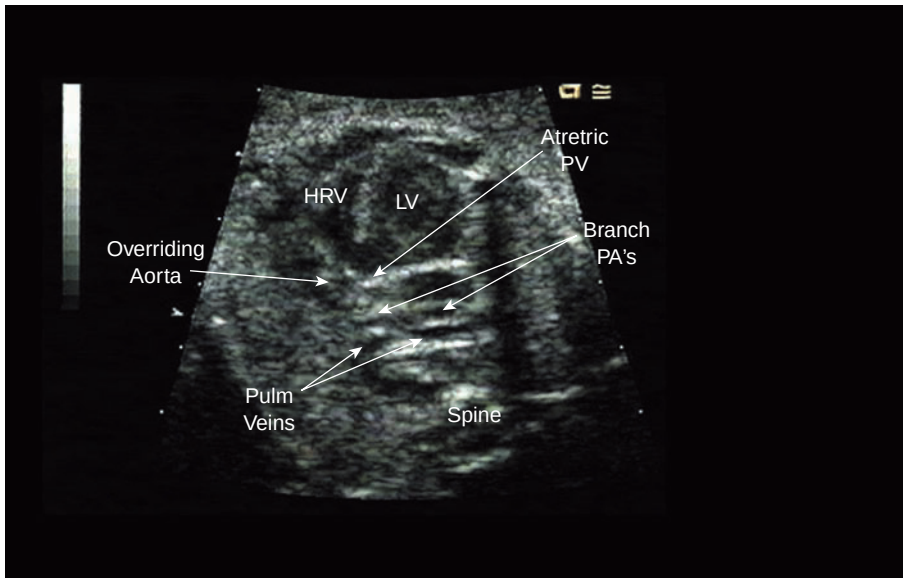


(a)

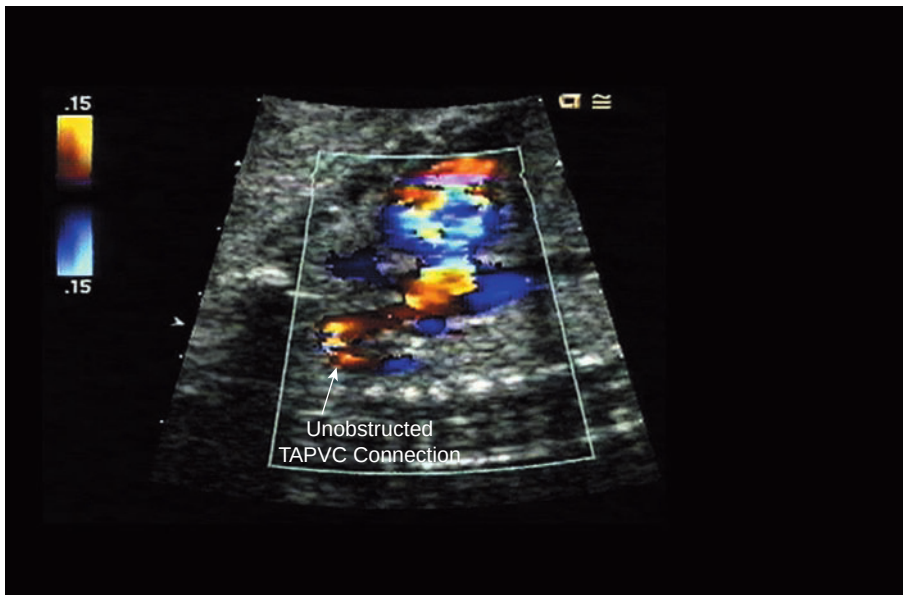


(b)

**Figure 28.18** Fetal heterotaxy syndrome with total anomalous pulmonary venous connections (TAPVC). Fetal echocardiogram at 26 weeks' gestation with **(a)** 4-chamber. **(b)** long-axis images demonstrating unobstructed TAPVC. The individual pulmonary veins form a confluence behind the left atrium and drain via a vertical vein to the left superior vena cava. In addition to TAPVC, this fetus was diagnosed as having levocardia with abdominal situs inversus, tricuspid atresia (segmental set {I,D,D}), pulmonary atresia, hypoplastic right ventricle (HRV) and systemic venous anomalies (left-sided intact inferior vena cava and bilateral superior venae cavae). PA, pulmonary artery; PV, pulmonary valve.

13–16% [83,89], mainly due to the complex intracardiac anomalies and the high surgical mortality of neonatal repair.

In evaluating the fetus for possible heterotaxy syndrome, it is essential to follow the same comprehensive approach as for postnatal imaging. The first step is to determine the fetal lie and position and, thus, distinguish the left and right side of the fetus and the relative position of the thoracic and abdominal organs. Dextrocardia is relatively common in heterotaxy syndrome and should be ruled in or out early in the examination. Identification of atrial appendage morphology as well as the systemic venous connections will aid in differentiating between the two subgroups of heterotaxy syndrome. The atrial appendages [90] can be visualized from the 4-chamber view angled cranially. In polysplenia syndrome, the inferior vena cava is usually interrupted, and the dilated azygos can be identified posterior to the aorta; in asplenia syndrome the inferior vena is intact and typically on the same side of the spine as the aorta. Anomalous pulmonary venous connections, more commonly seen with asplenia syndrome, may be difficult to detect in utero, especially in cases with pulmonary stenosis or atresia (Fig. 28.18a,b and Videoclip 28.8). That being said, with the color scale appropriately set to detect low flow rates and a narrowed sector to increase the frame rate, it is feasible to arrive at an accurate diagnosis (Fig. 28.19) of even the most complex forms of pulmonary venous return [91]. The intracardiac anomalies associated with heterotaxy syndrome are easy to identify

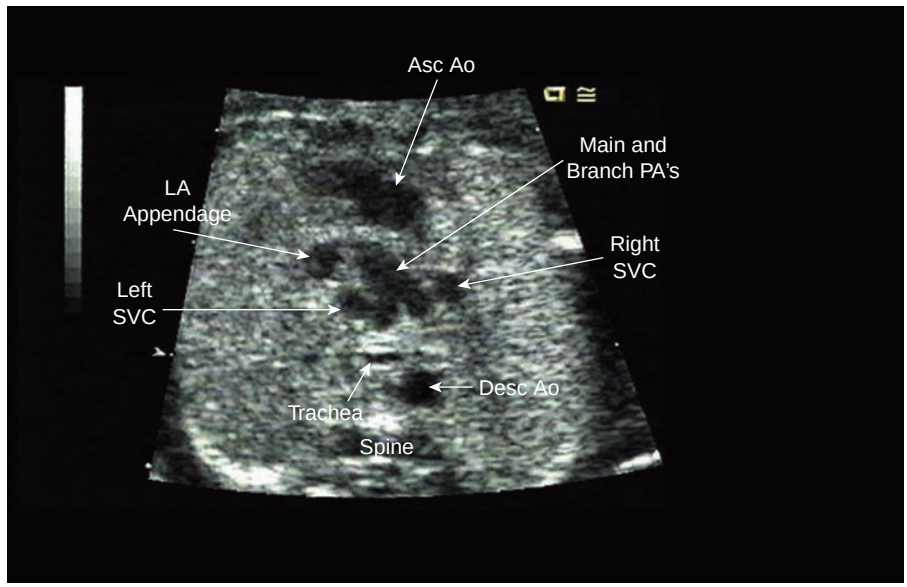


(a)

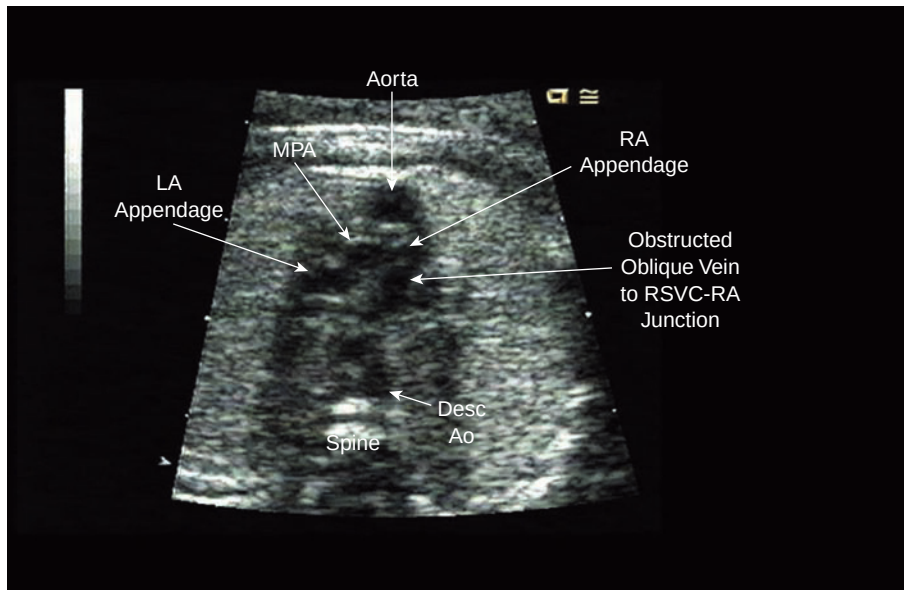


(b)

**Figure 28.19** Fetal obstructed total anomalous pulmonary venous connections. **(a)** Fetal echocardiogram at 22 weeks' gestation with an axial image showing bilateral superior venae cavae, an anterior aorta, and a right-sided thoracic descending aorta. **(b)** Slight modification of the previous image reveals the obstructed oblique vein that drains the pulmonary veins to the right superior vena cava (RSVC)–right atrial (RA) junction.

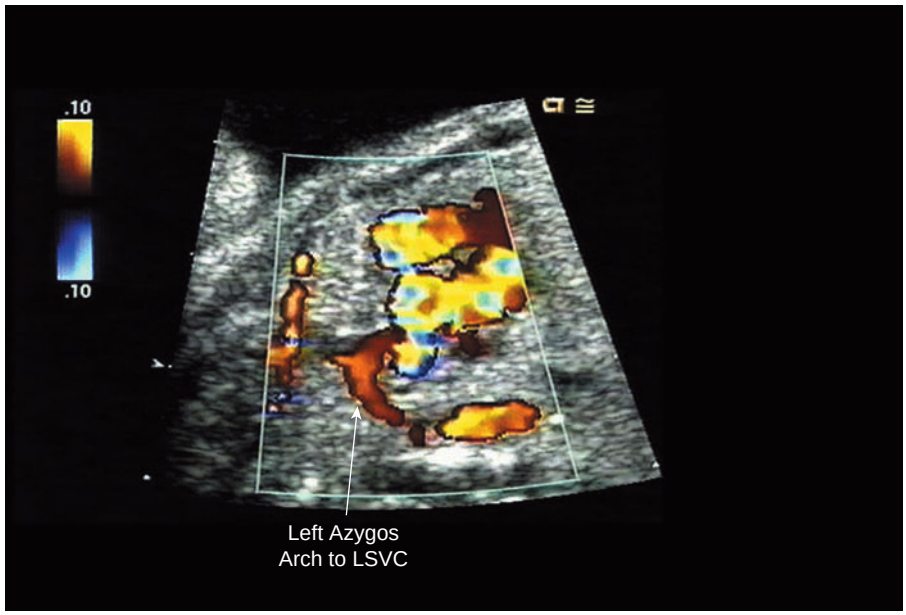


(c)

**Figure 28.19 (c)** Long-axis image shows a prominent azygos arch draining into the left superor vena cava (LSVC). The inferior vena cava was intact and left-sided. The diagnosis also included double-outlet right ventricle {I,D,D}, complete common atrioventricular canal and pulmonary stenosis. Ao, aorta; Asc, ascending; Desc, descending; LA, left atrial; MPA, main pulmonary artery; PA, pulmonary artery.

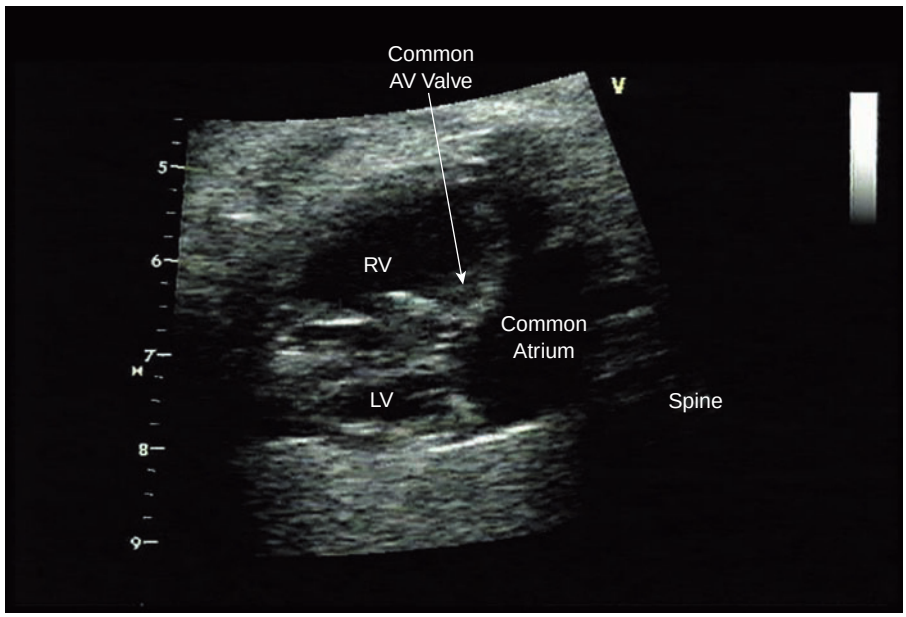


(a)

**Figure 28.20** Fetal heterotaxy syndrome with severe pulmonary stenosis. **(a)** Fetal echocardiogram at 27 weeks' gestation with a 4-chamber view showing levocardia, common atrium and complete common atrioventricular canal.

(Fig. 28.20), and ductal dependency can be accurately predicted. Complete heart block is readily identified in the fetus because of the fetal bradycardia; the methods of assessment of fetal rhythm disturbances are described in Chapter 42.

Detailed prenatal diagnosis allows for appropriate family counseling. Because asplenia syndrome, in particular, is currently considered one of the worst forms of congenital heart disease [92], it is very important to arrive at an accurate diagnosis in a timely manner and to be able to delineate all management options for the families.

## Preoperative assessment

In the majority of cases, asplenia syndrome is best suited for a single ventricle palliation due to the complex cardiovascular anatomy [93,94]. Biventricular repair is only feasible in the rare cases with two balanced ventricles and anatomy suitable for a two-ventricle repair. In cases of borderline ventricular hypoplasia, calculation of ventricular volumes is very important preoperatively, and a systemic–pulmonary shunt can be placed for the purpose of increasing the ventricular volume to facilitate intraventricular rerouting in addition to providing a stable source of pulmonary blood flow [95].

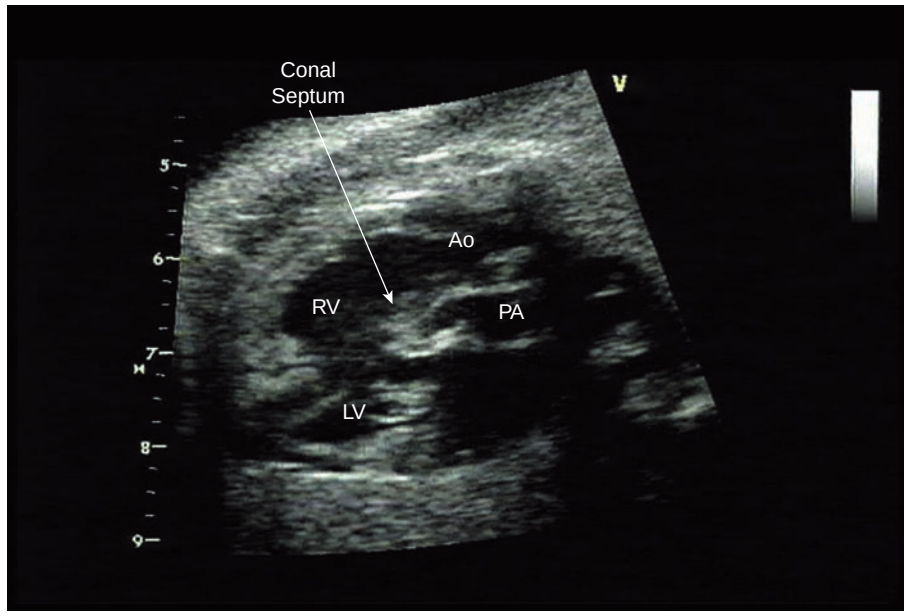


(b)

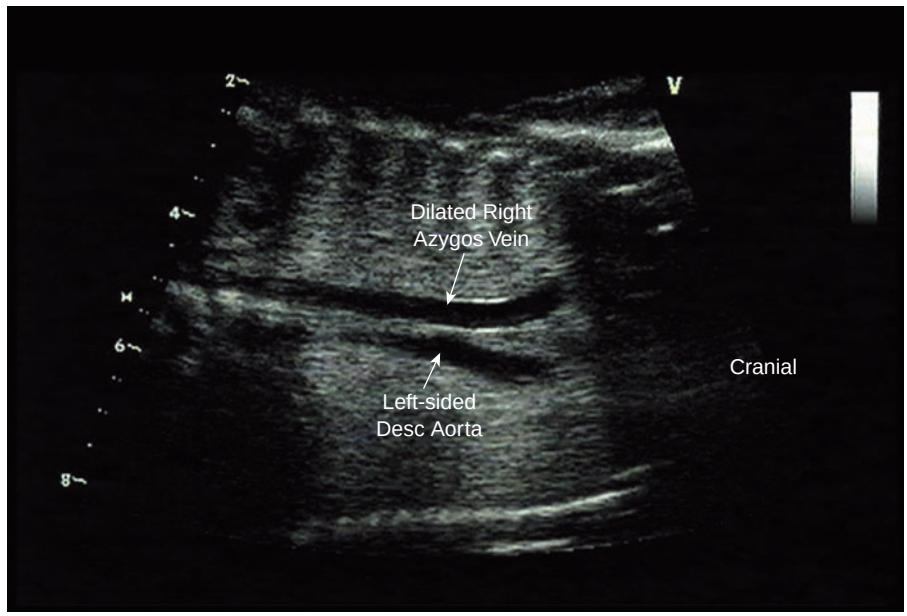


(c)

**Figure 28.20 (b)** Imaging of the ventricular outflows indicates the additional diagnoses of double-outlet right ventricle {A,D,D}, anterior aorta, and severe subvalvar and valvar pulmonary stenosis. **(c)** Coronal image demonstrates a dilated right azygos vein in the setting of an interrupted inferior vena cava. The cardiovascular findings in this fetus are most consistent with polysplenia syndrome. Ao, aorta; LV, left ventricle; RV, right ventricle; PA, pulmonary artery.

The systemic venous anatomy requires special attention in preoperative patients with heterotaxy syndrome. An intact inferior vena cava with a dilated azygos needs to be differentiated from interrupted inferior vena cava with azygos continuation in order to decide whether the azygos should be ligated [60]. An interconnecting venous sinus between the inferior vena cava and the hepatic veins below their separate entry to the heart needs to be ruled out prior to the Kawashima procedure [60,96]. It is also critically important to evaluate for bilateral superior venae cavae, and the presence of an interconnecting vein should be determined before deciding whether to perform a bilateral bidirectional or cavopulmonary (i.e., Glenn) anastomosis. The exact location of the entrance of the systemic veins to the heart needs to be determined in cases where a biventricular repair will be attempted and atrial septation for separation of the pulmonary and systemic venous flow is necessary [97].

Totally anomalous pulmonary venous connection in asplenia syndrome often presents with obstruction and may warrant emergency operation in the newborn period, with a high mortality risk [59,94,98,99]. The techniques for diagnosis of pulmonary venous obstruction have been described earlier. Additionally, based on a study of totally anomalous pulmonary venous connection cases, 44% of which were

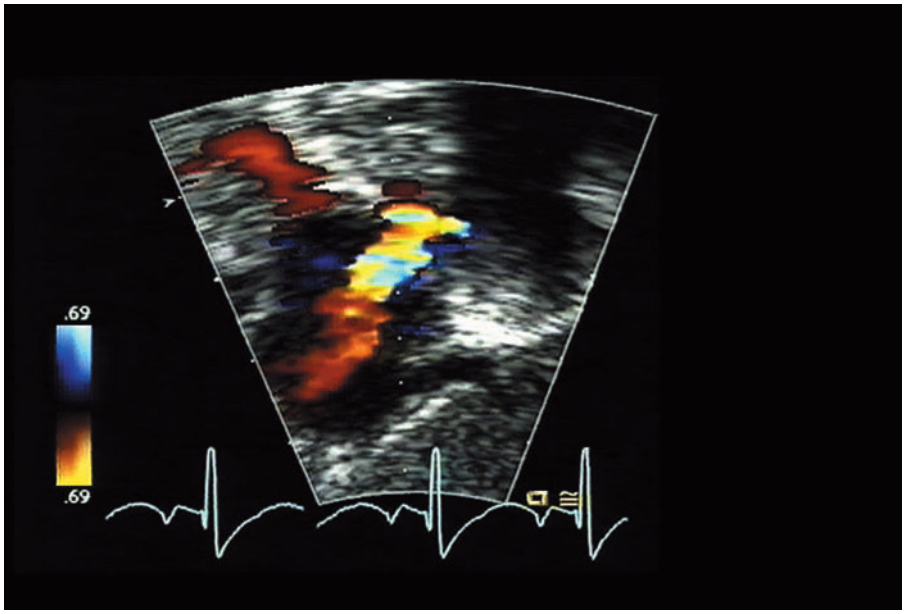


**Figure 28.21** Postoperative obstructed totally anomalous pulmonary venous connections (TAPVC). Subxiphoid short-axis image showing moderate to severe obstruction at the pulmonary venous anastomosis after infradiaphragmatic TAPVC repair. A Doppler cursor is positioned at the anastomotic site.

in the setting of heterotaxy syndrome, the measurement of individual pulmonary vein size and use of the indexed pulmonary vein sum can predict long-term survival and the probability of intrinsic pulmonary vein abnormalities preoperatively [100]. In cases of obstruction, the need for simultaneous shunt placement may be underestimated. The reverse is also true: the relief of critical obstruction of pulmonary blood flow may unmask obstructed total pulmonary venous connections in heterotaxy syndrome [101].

Before performing the Fontan operation, the degree of AV valve regurgitation needs to be assessed [102] because it affects surgical outcome. The ventricular septum should also be thoroughly interrogated and the type of VSD determined, especially in cases of double-outlet right ventricle, where the relation of the VSD to the aorta will determine the feasibility of an LV-aorta baffle repair.

### Postoperative assessment and imaging in the adult

The main focus of the postoperative and follow-up examinations in patients with heterotaxy syndrome depends on the type of procedure performed. Because the majority of heterotaxy syndrome patients require staged single-ventricle palliation, the follow-up is as described in Chapter 27. After correction of totally anomalous pulmonary venous connection, the individual pulmonary veins require special attention for evidence of stenosis, both at the anastomotic site (Fig. 28.21) and more distally in the lumen of the veins. Transesophageal echocardiography may be necessary for pulmonary venous imaging in the adult. Ventricular function and AV valve regurgitation need to be carefully assessed and followed longitudinally to determine the timing and feasibility of surgical repair. Despite the improved success rate of corrective and palliative surgeries in recent years, mortality remains high [43,68]. In case of severe AV valve regurgitation and/or ventricular dysfunction, cardiac transplantation may be the only surgical option, and results have been encouraging with reported 5-year survival that favorably compares with results of palliative procedures [103].

## References

1. Stanger P, Rudolph AM, Edwards JE. Cardiac malpositions. An overview based on study of sixty-five necropsy specimens. *Circulation* 1977;56:159–72.
2. Huhta JC, Hagler DJ, Seward JB et al. Two-dimensional echocardiographic assessment of dextrocardia: a segmental approach. *Am J Cardiol* 1982;50:1351–60.
3. Van Praagh S, O'Sullivan J, Brili S, Van Praagh R. Juxtaposition of the morphologically left atrial appendage in solitus and inversus atria: a study of 18 postmortem cases. *Am Heart J* 1996;132:391–402.
4. Van Praagh S, O'Sullivan J, Brili S, Van Praagh R. Juxtaposition of the morphologically right atrial appendage in solitus and inversus atria: A study of 35 postmortem cases. *Am Heart J* 1996;132:382–90.
5. Van Praagh R, Van Praagh S. Isolated ventricular inversion. A consideration of the morphogenesis, definition and diagnosis of nontransposed and transposed great arteries. *Am J Cardiol* 1966;17:395–406.
6. Espino-Vela J, De la Cruz MV, Munoz-Castellanos L et al. Ventricular inversion without transposition of the great vessels in situs inversus. *Br Heart J* 1970;32:292–303.
7. McElhinney DB, Reddy VM, Silverman NH, Hanley FL. Intraatrial baffle repair of isolated ventricular inversion with left atrial isomerism. *Ann Thorac Surg* 1996;62:1529–32.

8. Park SC, Siewers RD, Neches WH et al. Ventricular inversion with normal ventriculoarterial connection and left atrial isomerism: correction by the Mustard operation. *J Am Coll Cardiol* 1984;4:136–40.
9. Van Praagh R, Perez Trevino C, Lopez Cuellar M et al. Transposition of the great arteries with posterior aorta, anterior pulmonary artery, subpulmonary conus and fibrous continuity between aortic and atrioventricular valves. *Am J Cardiol* 1971; 28:621–31.
10. Cavalle-Garrido T, Bernasconi A, Perrin D, Anderson RH. Hearts with concordant ventriculoarterial connections but parallel arterial trunks. *Heart* 2007;93:100–6.
11. Van Praagh R, Durnin RE, Jockin H et al. Anatomically corrected malposition of the great arteries {S, D, L}. *Circulation* 1975;51:20–31.
12. Loya YS, Desai AG, Sharma S. "Anatomically corrected malposition": a rare case with bilateral absence of a complete subarterial muscular infundibulum. *Int J Cardiol* 1991;30:131–4.
13. Bernasconi A, Azancot A, Simpson JM et al. Fetal dextrocardia: diagnosis and outcome in two tertiary centres. *Heart* 2005;91: 1590–4.
14. Walmsley R, Hishitani T, Sandor GGS et al. Diagnosis and outcome of dextrocardia diagnosed in the fetus. *Am J Cardiol* 2004; 94:141–3.
15. Campbell M, Deuchar DC. Dextrocardia and isolated laevocardia. II. Situs inversus and isolated dextrocardia. *Br Heart J* 1966; 28:472–87.
16. Splitt MP, Burn J, Goodship J. Defects in determination of left-right asymmetry. *J Med Genet* 1996;33:498–503.
17. Campbell M, Deuchar DC. Dextrocardia and isolated laevocardia I: isolated laevocardia. *Br Heart J* 1965;27:69–82.
18. Lai WW, Ravishankar C, Gross RP et al. Juxtaposition of the atrial appendages: a clinical series of 22 patients. *Pediatr Cardiol* 2001;22:121–7.
19. Sharma S, Devine W, Anderson RH, Zuberbuhler JR. The determination of atrial arrangement by examination of the appendage morphology in 1842 heart specimens. *Br Heart J* 1988;60:227–31.
20. Kathiriya IS, Srivastava D. Left-right asymmetry and cardiac looping: implications for cardiac development and congenital heart disease. *Am J Med Genet* 2000;97:271–9.
21. Zakheim R, Mattioli L, Vaseenon T, Edwards W. Anatomically corrected malposition of the great arteries (S, L, D). *Chest* 1976; 69:101–4.
22. Merklin RJ, Varano NR. Situs inversus and cardiac defects. A study of 111 cases of reversed asymmetry. *J Thorac Cardiovasc Surg* 1963;45:334–42
23. Turchin A, Radentz SS, Burke A. Situs inversus totalis and single coronary ostium: A coincidence or a pattern? *Cardiovasc Pathol* 2000;9:127–9.
24. Oppido G, Napoleone CP, Martano S, Gargiulo G. Hypoplastic left heart syndrome in situs inversus totalis. *Eur J Cardiothorac Surg* 2004;26:1052–4.
25. Gutgesell HP. Cardiac malposition and heterotaxy. In: Garson A, Bricker JT, Fisher DJ, Neish SR (eds) *The Science and Practice of Pediatric Cardiology*, 2nd edn. Baltimore, MD: Williams and Wilkins, 1998;1539–61.
26. Melhuish BP, Van Praagh R. Juxtaposition of the atrial appendages: a sign of severe cyanotic congenital heart disease. *Br Heart J* 1968;30:269–84.
27. Chin AJ, Bierman FZ, Williams RG et al. Two-dimensional echocardiographic appearance of complete left-sided juxtaposition of the atrial appendages. *Am J Cardiol* 1983;52:346–8.
28. Van Praagh R, Weinberg PM, Smith SD et al. Malpositions of the heart. In: Adams FH, Emmanouilides GC, Riemenschneider TA (eds) *Moss' Heart Disease in Infants, Children, and Adolescents,* 4th edn. Baltimore, MD: Williams and Wilkins, 1989;530–80.
29. Pasquini L, Sanders SP, Parness I et al. Echocardiographic and anatomic findings in atrioventricular discordance with ventriculoarterial concordance. *Am J Cardiol* 1988;62:1256–62.
30. Quero-Jimenez M, Raposo-Sonnenfeld I. Isolated ventricular inversion with situs solitus. *Br Heart J* 1975;37:293–304.
31. Bernasconi A, Cavalle-Garrido T, Perrin DG, Anderson RH. What is anatomically corrected malposition? *Cardiol Young* 2007;17:26–34.
32. Rice MJ, Seward JB, Hagler DJ et al. Left juxtaposed atrial appendages: diagnostic two-dimensional echocardiographic features. *J Am Coll Cardiol* 1983;1:1330–6.
33. Stumper O, Rijlaarsdam M, Vargas-Barron J et al. The assessment of juxtaposed atrial appendages by transesophageal echocardiography. *Int J Cardiol* 1990;29:365–71.
34. Snider AR, Enderlein MA, Teitel DF et al. Isolated ventricular inversion: two-dimensional echocardiographic findings and a review of the literature. *Pediatr Cardiol* 1984;5:27–33.
35. Abdullah MM, Lacro RV, Smallhorn J et al. Fetal cardiac dextroposition in the absence of intrathoracic mass: sign of significant right lung hypoplasia. *J Ultrasound Med* 2000;19: 669–76.
36. Abdullah M, Yoo SJ, Lee YH et al. Diagnosis of left juxtaposition of the atrial appendages in the fetus. *Cardiol Young* 2000; 10:220–4.
37. Williams IA, Sharma J, Kleinman CS. Discordant anatomically corrected malposition of the great vessels and Ebstein's malformation: fetal and neonatal findings.*Ultrasound Obstet Gynecol* 2006;28:103–5.
38. Wood AE, Freedom RM, Williams WG, Trusler GA. The Mustard procedure in transposition of the great arteries associated with juxtaposition of the atrial appendages with and without dextrocardia. *J Thorac Cardiovasc Surg* 1983;85:451–6.
39. Baudet EM, Hafez A, Choussat A, Roques X. Isolated ventricular inversion with situs solitus: successful surgical repair. *Ann Thorac Surg* 1986;41:91–4.
40. Peeters H, Devriendt K. Human laterality disorders. *Eur J Med Genet* 2006;49:349–62.
41. Van Praagh S, Kreutzer J, Alday L, Van Praagh R. Systemic and pulmonary venous connections in visceral heterotaxy, with emphasis on the diagnosis of the atrial situs: A study of 109 postmortem cases. In: Clark EB, Takao A (eds) *Developmental Cardiology: Morphogenesis and Function*. Mount Kisko, NY: Futura Publishing Co, 1990;671–727.
42. Fyler DC, Buckley LP, Hellenbrand WE, Cohn HE. Report of the New England Regional Infant Cardiac Program. *Pediatrics* 1980;65(Suppl.):375–461.

43. Gilljam T, McCrindle BW, Smallhorn JF et al. Outcomes of left atrial isomerism over a 28-year period at a single institution. *J Am Coll Cardiol* 2000;36:908–16.
44. Ferencz C, Rubin JD, McCarter RJ et al. Congenital heart disease: Prevalence at livebirth. The Baltimore-Washington Infant Study. *Am J Epidemiol* 1985;121:31–6.
45. Lin AE, Ticho BS, Houde K et al. Heterotaxy: Associated conditions and hospital-based prevalence in newborns. *Genet Med* 2000;2:157–72.
46. Lim JS, McCrindle BW, Smallhorn JF et al. Clinical features, management, and outcome of children with fetal and postnatal diagnoses of isomerism syndromes. *Circulation* 2005;112:2454–61.
47. Ruscazio M, Van Praagh S, Marass AR et al. Interrupted inferior vena cava in asplenia syndrome and a review of the hereditary patterns of visceral situs abnormalities. *Am J Cardiol* 1998; 81:111–16.
48. Chen SC, Monteleone PL. Familial splenic anomaly syndrome. *J Pediatr* 1977;91:160–1.
49. Katcher AL. Familial asplenia, other malformations, and sudden death. *Pediatrics* 1980;65:633–5.
50. Colbert MC. Retinoids and cardiovascular developmental defects. *Cardiovasc Toxicol* 2002;2:25–39.
51. Kennedy MP, Omran H, Leigh MW et al. Congenital heart disease and other heterotaxic defects in a large cohort of patients with primary ciliary dyskinesia. *Circulation* 2007;115: 2814–21.
52. Bisgrove BW, Yost HJ. The roles of cilia in developmental disorders and disease. *Development* 2006;133:4131–43.
53. Van Praagh S, Carrera ME, Sanders S et al. Partial or total direct pulmonary venous drainage to right atrium due to malposition of septum primum. Anatomic and echocardiographic findings and surgical treatment: a study based on 36 cases. *Chest* 1995; 107:1488–98.
54. Phoon CK, Neill CA. Asplenia syndrome: Insight into embryology through an analysis of cardiac and extracardiac anomalies. *Am J Cardiol* 1994;73:581–7.
55. Sapire DW, Ho SY, Anderson RH, Rigby ML. Diagnosis and significance of atrial isomerism. *Am J Cardiol* 1986;58:342–6.
56. Macartney FJ, Zuberbuhler JR, Anderson RH. Morphological considerations pertaining to recognition of atrial isomerism. Consequences for sequential chamber localisation. *Br Heart J* 1980;44:657–67.
57. Uemura H, Ho SY, Devine WA et al. Atrial appendages and venoatrial connections in hearts from patients with visceral heterotaxy. *Ann Thorac Surg* 1995;60:561–9.
58. Anderson C, Devine WA, Anderson RH et al. Abnormalities of the spleen in relation to congenital malformations of the heart: a survey of necropsy findings in children. *Br Heart J* 1990;63: 122–8.
59. Heinemann MK, Hanley FL, Van Praagh S et al. Total anomalous pulmonary venous drainage in newborns with visceral heterotaxy. *Ann Thorac Surg* 1994;57:88–91.
60. Rubino M, Van Praagh S, Kadoba K et al. Systemic and pulmonary venous connections in visceral heterotaxy with asplenia. Diagnostic and surgical considerations based on seventy-two autopsied cases. *J Thorac Cardiovasc Surg* 1995;110: 641–50.
61. Van Praagh S. Cardiac malpositions and the heterotaxy syndromes. In: Keany JF, Lock JE, Fyler DC (eds) *Nadas' Pediatric Cardiology*, 2nd edn. Philadelphia, PA: Saunders Elsevier, 2006; 675–95.
62. Uemura H, Ho SY, Anderson RH, Yagihara T. Ventricular morphology and coronary arterial anatomy in hearts with isomeric atrial appendages. *Ann Thorac Surg* 1999;67:1403–11.
63. Smith A, Ho SY, Anderson RH et al. The diverse cardiac morphology seen in hearts with isomerism of the atrial appendages with reference to the disposition of the specialized conduction system. *Cardiol Young* 2006;16:437–54.
64. Uemura H, Anderson RH, Ho SY et al. Left ventricular structures in atrioventricular septal defect associated with isomerism of atrial appendages compared with similar features with usual atrial arrangement. *J Thorac Cardiovasc Surg* 1995; 110:445–52.
65. Van Praagh S, Geva T, Friedberg DZ et al. Aortic outflow obstruction in visceral heterotaxy: A study based on twenty postmortem cases. *Am Heart J* 1997;133:558–68.
66. Papagiannis J, Kanter RJ, Vander Heide RS et al. Isolated innominate artery in asplenia syndrome with aortic atresia: Newly recognized cardiovascular complex. *Am Heart J* 1996; 131:1042–4.
67. Formigari R, Vairo U, de Zorzi A et al. Prevalence of bilateral patent ductus arteriosus in patients with pulmonic valve atresia and asplenia syndrome. *Am J Cardiol* 1992;70: 1219–20.
68. Hashmi A, Abu-Sulaiman R, McCrindle BW et al. Management and outcome of right atrial isomerism: a 26-year experience. *J Am Coll Cardiol* 1998;31:1120–6.
69. Ho SY, Fagg N, Anderson RH et al. Disposition of the atrioventricular conduction tissues in the heart with isomerism of the atrial appendages: its relation to congenital complete heart block. *J Am Coll Cardiol* 1992;20:904–10.
70. Nagel BH, Williams H, Stewart L et al. Splenic state in surviving patients with visceral heterotaxy. *Cardiol Young* 2005;15: 469–73.
71. Van Praagh R, Van Praagh S, Vlad P, Keith JD. Anatomic types of congenital dextrocardia. Diagnostic and embryologic implications. *Am J Cardiol* 1964;13:510–31.
72. Van Praagh R. The segmental approach to diagnosis of congenital heart disease. In: *Birth Defects: Original Article Series*, vol. 8. Baltimore: Williams & Wilkins, 1972;4–23.
73. Anderson RH, Becker AE, Freedom RM et al. Sequential segmental analysis of congenital heart disease. *Pediatr Cardiol* 1984;5:281–8.
74. Van Praagh R, Van Praagh S. Atrial isomerism in the heterotaxy syndromes with asplenia, or polysplenia, or normally formed spleen: an erroneous concept. *Am J Cardiol* 1990;66: 1504–6.
75. Huhta JC, Smallhorn JF, Macartney FJ. Two dimensional echocardiographic diagnosis of situs. *Br Heart J* 1982;48:97–108.
76. Huhta JC, Smallhorn JF, Macartney FJ et al. Cross-sectional echocardiographic diagnosis of systemic venous return. *Br Heart J* 1982;48:388–403.
77. Smallhorn JF, Freedom RM, Olley PM. Pulsed Doppler echocardiographic assessment of extraparenchymal pulmonary vein flow. *J Am Coll Cardiol* 1987;9:573–9.

78. Smallhorn JF, Pauperio H, Benson L et al. Pulsed Doppler assessment of pulmonary vein obstruction. *Am Heart J* 1985; 110:483–6.
79. Stumper OF, Sreeram N, Elzenga NJ, Sutherland GR. Diagnosis of atrial situs by transesophageal echocardiography. *J Am Coll Cardiol* 1990;16:442–6.
80. Stumper O, Vargas-Barron J, Rijlaarsdam M et al. Assessment of anomalous systemic and pulmonary venous connections by transesophageal echocardiography in infants and children. *Br Heart J* 1991;66:411–8.
81. Geva T, Vick W III, Wendt RE, Rokey R. Role of spin echo and cine magnetic resonance imaging in presurgical planning of heterotaxy syndrome. Comparison with echocardiography and catheterization. *Circulation* 1994;90:348–56.
82. Niwa K, Uchishiba M, Aotsuka H et al. Magnetic resonance imaging of heterotaxia in infants. *J Am Coll Cardiol* 1994;23: 177–83.
83. Taketazu M, Lougheed J, Yoo S-J et al. Spectrum of cardiovascular disease, accuracy of diagnosis, and outcome in fetal heterotaxy syndrome. *Am J Cardiol* 2006;97:720–4.
84. Jaeggi ET, Hornberger LK, Smallhorn JF, Fouron JC. Prenatal diagnosis of complete atrioventricular block associated with structural heart disease: combined experience of two tertiary care centers and review of the literature. *Ultrasound Obstet Gynecol* 2005;26:16–21.
85. Schmidt KG, Ulmer HE, Silverman NH et al. Perinatal outcome of fetal complete atrioventricular block: a multicenter experience. *J Am Coll Cardiol* 1991;91:1360–6.
86. Friedberg MK, Ursell PL, Silverman NH. Isomerism of the left atrial appendage associated with ventricular noncompaction. *Am J Cardiol* 2005;96:985–90.
87. Ozkutlu S, Ayabakan C, Celiker A, Elshershari H. Noncompaction of ventricular myocardium: a study of twelve patients. *J Am Soc Echocardiogr* 2002;15:1523–8.
88. Feldt RH, Rahimtoola SH, Davis GD et al. Anomalous ventricular myocardial patterns in a child with complex congenital heart disease. *Am J Cardiol* 1969;23:732–4.
89. Lin JH, Chang CI, Wang JK et al. Intrauterine diagnosis of heterotaxy syndrome. *Am Heart J* 2002;143:1002–8.
90. Berg C, Geipel A, Kohl T et al. Fetal echocardiographic evaluation of atrial morphology and the prediction of laterality in cases of heterotaxy syndromes. *Ultrasound Obstet Gynecol* 2005; 26:538–45.
91. Yeager SB, Parness IA, Spevak PJ et al. Prenatal echocardiographic diagnosis of pulmonary and systemic venous anomalies. *Am Heart J* 1984;128:397–405.
92. Freedom RM, Jaeggi ET, Lim JS, Anderson RH. Hearts with isomerism of the right atrial appendages – one of the worst forms of disease in 2005. *Cardiol Young* 2005;15:554–67.
93. Hirooka K, Yagihara T, Kishimoto H et al. Biventricular repair in cardiac isomerism. Report of seventeen cases. *J Thorac Cardiovasc Surg* 1995;109:530–5.
94. Yun T-J, Al-Radi OO, Adatia I et al. Contemporary management of right atrial isomerism: Effect of evolving therapeutic strategies. *J Thorac Cardiovasc Surg* 2006;131:1108–13.
95. Koh M, Yagihara T, Uemura H et al. Biventricular repair for right atrial isomerism. *Ann Thorac Surg* 2006;81:1808–16.
96. Kawashima Y, Kitamura S, Matsuda H et al. Total cavopulmonary shunt operation in complex cardiac anomalies. A new operation. *J Thorac Cardiovasc Surg* 1984;7:74–81.
97. Vargas FJ, Mayer JE, Jonas RA, Castaneda AR. Anomalous systemic and pulmonary venous connections in conjunction with atriopulmonary anastomosis (Fontan-Kreutzer). Technical considerations. *J Thorac Cardiovasc Surg* 1987;93:523–32.
98. Sadiq M, Stumper O, De Giovanni JV et al. Management and outcome of infants and children with right atrial isomerism. *Heart* 1996;75:314–19.
99. Cheung YF, Cheng VYW, Chau AKT et al. Outcome of infants with right atrial isomerism: is prognosis better with normal pulmonary venous drainage? *Heart* 2002;87:146–52.
100. Jenkins KJ, Sanders SP, Orav EJ et al. Individual pulmonary vein size and survival in infants with totally anomalous pulmonary venous connection. *J Am Coll Cardiol* 1993;22:201–6.
101. Freedom RM, Olley PM, Coceani F, Rowe RD. The prostaglandin challenge. Test to unmask obstructed total anomalous pulmonary venous connections in asplenia syndrome. *Br Heart J* 1978;40:91–4.
102. Zoghbi WA, Enriquez-Sarano M, Foster E et al. American Society of Echocardiography. Recommendations for evaluation of the severity of native valvular regurgitation with two-dimensional and Doppler echocardiography. *J Am Soc Echocardiog* 2003;16:777–802.
103. Larsen RL, Eguchi JH, Mulla NF et al. Usefulness of cardiac transplantation in children with visceral heterotaxy (asplenic and polysplenic syndromes and single right-sided spleen with levocardia) and comparison of results with cardiac transplantation in children with dilated cardiomyopathy. *Am J Cardiol* 2002;89:1275–9.
104. Rose V, Izukawa T, Moes CAF. Syndromes of asplenia and polysplenia. A review of cardiac and non-cardiac malformations in 60 cases with special reference to diagnosis and prognosis. *Br Heart J* 1975;37:840–52.
105. Uemura H, Ho SY, Devine WA, Anderson RH. Analysis of visceral heterotaxy according to splenic status, appendage morphology, or both. *Am J Cardiol* 1995;76:846–9.
106. Peoples WM, Moller JH, Edwards JE. Polysplenia: Review of 146 cases. *Pediatr Cardiol* 1983;4:129–37.

# 29 Congenital Anomalies of the Coronary Arteries

**J. René Herlong**
Duke University School of Medicine, Durham, NC, USA

## Definition

The term *coronary* derives from the Latin root *coronarius*, which means crown. Indeed, the coronary arteries sit on the heart as a crown, and they are the "crowning subject" of adult cardiology due to the prevalence of acquired coronary artery disease. Although less of a preeminent subject in pediatric cardiology, coronary artery anomalies, with and without concomitant structural congenital heart disease, are an important topic for the pediatric cardiologist. This chapter reviews echocardiography of congenital coronary artery anomalies of importance to the pediatric cardiologist. Material pertinent to all congenital coronary artery anomalies is presented first, followed by material particular to each important anomaly.

## Developmental considerations

Before the development of the coronary arteries, the loosely packed myocardium of the embryonic heart is nourished by sinusoids throughout the heart cavities. As the myocardium becomes more compact, veins, arteries and capillaries develop from these primitive sinusoids. Then, at around 32 days of gestation, subepicardial vascular networks develop; shortly thereafter, endothelial buds appear at the base of the truncus arteriosus. These two anlagen join to one another by around 45 days of gestation, and the definitive coronary arterial circulation is thus established.

Controversy exists regarding the number of endothelial buds present at the base of the truncus arteriosus and the manner in which the two coronary anlagen (subepicardial vascular networks and endothelial buds) connect with one another. Abrikossoff originally described two endothelial buds that were "allotted" to the aorta by division of the truncus into aorta and pulmonary artery [1]. Hackensellner later suggested that there are endothelial buds in each of the six sinuses of Valsalva of the great arteries and that all but two of these ultimately involute [2]. The latter theory has better withstood subsequent investigation [3], but either theory may readily explain the multitude of coronary artery anomalies that exist. The method of involution and induction of the appropriate sinuses of Valsalva remains speculative [4].

## Normal coronary anatomy

There are normally two major coronary arteries, which originate from the right and left aortic sinuses of Valsalva. These sinuses are small outpouchings of the aorta between the sinotubular junction and the aortic valve leaflets. There are normally three such sinuses; the third, or posterior, sinus of Valsalva, is usually devoid of a coronary artery orifice. It is thus called the noncoronary sinus of Valsalva.

### The left coronary artery

The left main coronary artery arises from the left sinus of Valsalva and courses only a short distance (<4 cm in the adult) before dividing into the left circumflex and left anterior descending coronary arteries (Fig. 29.1). The left circumflex coronary artery varies considerably in size depending on whether the posterior descending coronary artery is a branch of the right coronary artery (right-dominant coronary system) or a branch of the circumflex coronary artery (left-dominant coronary system). If the posterior descending coronary artery originates from the circumflex coronary artery (this occurs in about 10% of patients), the circumflex coronary artery is large. In some patients with a dominant right coronary artery, the circumflex coronary artery may be quite small. The circumflex coronary artery travels under the left atrial appendage and along the groove of the left atrioventricular valve. In 50% of cases, the sinus node artery arises from the left circumflex coronary artery. The sinus node artery courses under the left atrial appendage, penetrates the interatrial septum, encircles the base of the superior vena cava, and supplies the sinus node. When the sinus node artery is

*Echocardiography in Pediatric and Congenital Heart Disease: From Fetus to Adult*
Edited by Wyman W. Lai, Luc L. Mertens, Meryl S. Cohen and Tal Geva
 ISBN: 978-1-405-17401-5

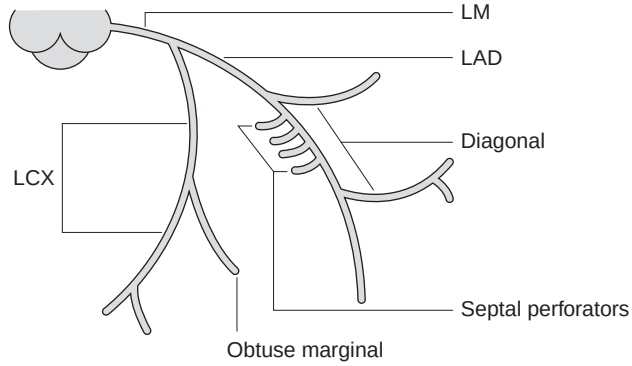


**Figure 29.1** The normal left coronary artery system. LCX, left circumflex; LM, left main coronary artery; LAD, left anterior descending coronary arteries.

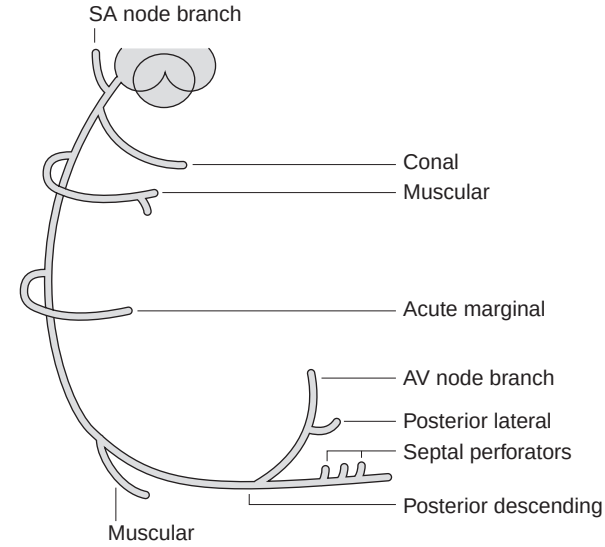


**Figure 29.2** The normal right coronary artery system. SA, sinoatrial; AV, atrioventricular.

not a branch of the left circumflex coronary artery, it is a branch of the right coronary artery. Kugel's artery may arise from the left circumflex coronary artery (alternatively, it may arise from the right or left main coronary artery) and courses through the interatrial septum, anastomosing with the artery to the atrioventricular node. Marginal branches arise from the left circumflex coronary artery and supply areas of the lateral wall of the left ventricle. These are called obtuse marginal branches. The left atrial circumflex artery may arise from the left circumflex coronary artery and supply the left posterior atrial wall. Occasionally, the sinus node artery can arise from the left atrial circumflex coronary artery.

The left anterior descending coronary artery appears to be a direct continuation of the left main coronary artery rather than a branch of it. The left anterior descending coronary artery travels along the interventricular sulcus and may continue around the apex of the heart onto the posterior interventricular sulcus to anastomose with the posterior descending coronary artery. The left conus artery is the first branch of the left anterior descending coronary artery and may anastomose with the conal branch of the right coronary artery, forming the circle of Vieussens. Four to six septal branches of the left anterior descending coronary artery penetrate the ventricular septum and anastomose with posterior septal branches arising from the posterior descending coronary artery. The left anterior descending coronary artery gives rise to diagonal branches that supply the anterior surface of the right and left ventricles and the right ventricular infundibulum.

## The right coronary artery

The right coronary artery arises from the right aortic sinus of Valsalva and courses behind the pulmonary artery beneath the right atrial appendage and along the right atrioventricular groove (Fig. 29.2). At the acute margin of the heart, it turns posteriorly and caudally over the diaphragmatic surface of the heart. The branches of the right coronary artery include the right conal branch, the sinus node artery, an atrial branch, right ventricular muscle branches (acute marginal branches), posterior descending coronary artery, atrioventricular node artery and septal branches. The right conus artery is the first branch of the right coronary artery in about 50% of cases; in the others, it arises directly from the right aortic sinus of Valsalva. The sinus node artery arises from the right coronary artery in 50% of cases and from the left circumflex artery in the remainder. The right ventricular free wall is supplied by several branches of the right coronary artery. The largest of these branches is the acute marginal branch of the right coronary artery.

Ninety percent of people have a dominant right coronary artery system; that is, the posterior descending coronary artery is a branch of the right coronary artery. In the remainder, the posterior descending coronary artery originates from the left coronary artery. The term "dominant right coronary artery system" refers only to the origin of the posterior descending coronary artery, not to the coronary artery that supplies most of the myocardium. Indeed, except in unusual circumstances, the majority of the myocardium is supplied by the left coronary artery regardless of the "dominance" of the coronary artery system.

The posterior descending coronary artery supplies the lower portion of the ventricular septum. The septal branches of the posterior descending coronary artery anastomose with the septal branches of the left anterior descending coronary artery. Muscular branches supplying the diaphragmatic portions of the right and left ventricles also arise from the posterior descending coronary artery. The artery to the atrioventricular node originates from the posterior descending coronary artery at or near the crux of the heart and travels cephalad to reach the atrioventricular node.

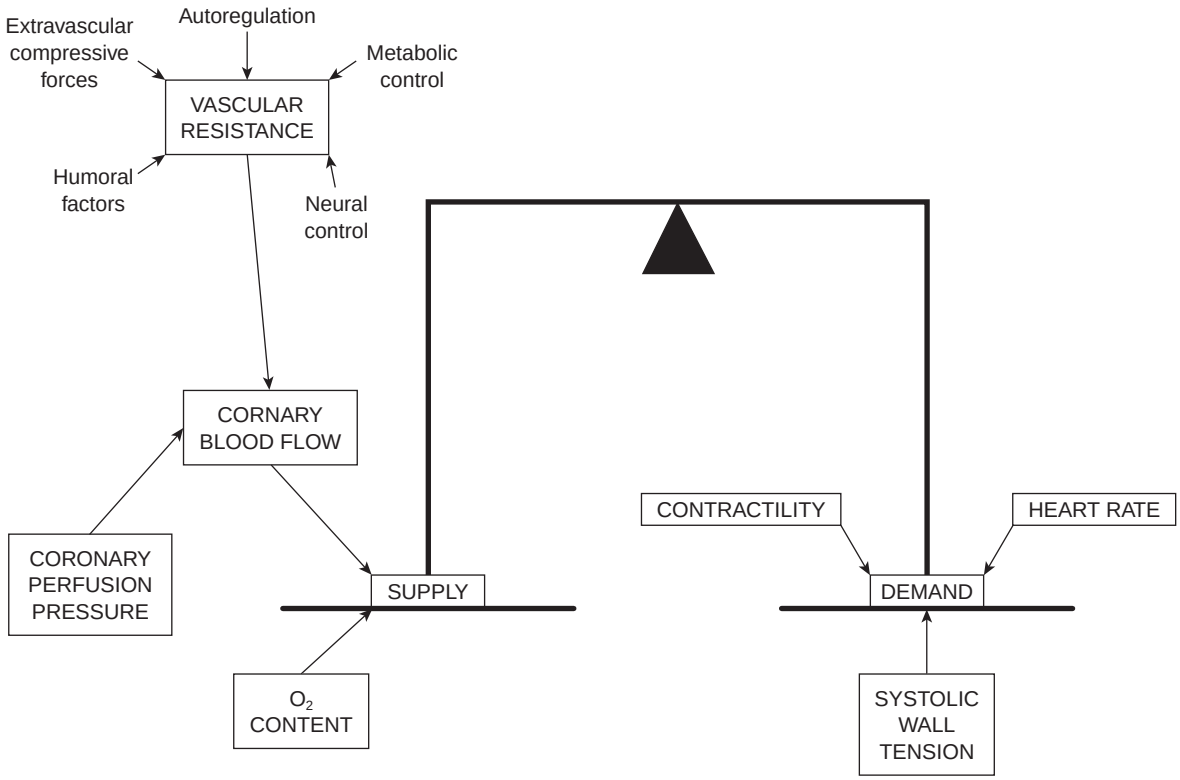


**Figure 29.3** The delicate balance between myocardial oxygen supply and demand and the factors that influence this balance. Adapted from Ardehali A, Ports TA. Myocardial oxygen supply and demand. *Chest* 1990;98:699–705, with permission from The American College of Chest Physicians.

## Physiology

The purpose of the coronary arteries is to provide a flow of oxygenated blood to the almost exclusively aerobic myocardium, and a delicate balance is maintained between myocardial oxygen supply and demand (Fig. 29.3). Upsetting this balance produces myocardial ischemia and thus impaired ventricular contraction. The three primary determinants of myocardial oxygen demand are systolic wall tension, contractility and heart rate. Pressure work increases myocardial oxygen consumption to a greater degree than does volume work. Myocardial oxygen supply is determined by the oxygen content of the blood and the coronary blood flow. Coronary blood flow is in turn determined by coronary perfusion pressure and by coronary vascular resistance.

Coronary perfusion pressure equals coronary artery pressure minus downstream pressure, and is different for different regions of the myocardium. In the absence of a fixed or dynamic obstruction in the coronary circulation, coronary artery pressure equals aortic pressure. Distal to such an obstruction, coronary artery pressure and coronary perfusion pressure are reduced. Coronary vascular resistance is influenced by metabolic, humoral, and neural factors as well as by autoregulation and by extravascular compressive forces.

The importance of extravascular compressive forces as determinants of vascular resistance is unique to the myocardium. Myocardial wall tension is so great in the left ventricle during systole that sufficient extrinsic compression is placed on the coronary arteries to cause coronary vascular resistance to approach infinity and coronary blood flow to approach zero. Thus, the vast preponderance of coronary blood flow to the left ventricle occurs during diastole. Compressive forces exerted by the right ventricle are ordinarily far less than those of the left ventricle; therefore, coronary blood flow to the right ventricle is not interrupted during ventricular systole. However, such flow interruption may occur with right ventricular hypertension [5].

Normally, coronary blood flow far exceeds the metabolic demands of the myocardium; there is thus a large safety margin to protect the heart from ischemia. This concept has been expressed as coronary flow reserve, which is the difference between resting and maximal coronary blood flow at any given perfusion pressure. When coronary flow reserve is absent, ischemia ensues. Coronary flow reserve may be decreased if resting coronary blood flow increases or if maximal coronary blood flow decreases. Causes of an increase in resting coronary blood flow include exercise, anemia, hypoxemia, tachycardia, thyrotoxicosis, and ventricular hypertrophy. Causes of a decrease in maximal coronary blood flow include disease or occlusion of the large or small

coronary arteries, an increase in left ventricular pressure without a corresponding increase in perfusion pressure, tachycardia, and polycythemia. All of these factors reduce coronary flow reserve and thereby increase the potential for myocardial ischemia [6].

The subendocardium is particularly susceptible to ischemia. This is due to this region's limited reserve for vasodilation, increased extrinsic compression from the higher wall stress to which it is subjected, and its resultant higher metabolic demands. This region is therefore often the first to manifest ischemic changes.

## Echocardiographic features pertinent to all anomalies

### Goals of the examination and transthoracic imaging

Two-dimensional echocardiography with color Doppler has become an important tool in the diagnosis and functional evaluation of infants and children with suspected anomalies of the coronary arteries. In experienced hands, both transthoracic and transesophageal echocardiography can reliably image the proximal coronary arteries. Generally, coronary artery branches cannot be delineated well by echocardiography. Because transesophageal echocardiographic imaging of the coronaries is seldom required in the pediatric population, the remainder of this discussion focuses on transthoracic imaging.

The goals of the examination are:

- Identify the origin of each major coronary artery (left anterior descending, circumflex and right).
- Identify the proximal course of each major coronary artery.
- Demonstrate direction of flow in each major coronary artery by color Doppler.
- Evaluate global and regional left ventricular function.
- Evaluate for mitral regurgitation.
- Identify associated defects.

Every echocardiographic examination should include evaluation of the origins and proximal courses of the coronary arteries [7]. Routine imaging of the coronary arteries in the course of an echocardiographic examination is important because coronary artery anomalies may be asymptomatic, they may be surgically important, and prospectively identifying them may save lives. Decreasing the log compression of the instrument often allows more distinct identification of the coronary arteries. Most modern echocardiography machines have a factory preset that accomplishes this. The highest frequency probe that allows adequate penetration should be used. Often this will be a higher frequency probe than would typically be used for a particular view, as the coronary arteries are often in the near-field of the sector.

The proximal coronary arteries may be best imaged in the parasternal long- and short-axis views and from subcostal coronal images. The origins and proximal courses of the vessels may be reliably seen; thus, abnormalities of branching may be appreciated. In the parasternal short-axis view at the base of the heart, both main coronary artery origins, often simultaneously, may be seen to arise from their respective sinuses of Valsalva (Figs 29.4 and 29.5). Clockwise rotation of the probe is often necessary for optimal imaging of the left coronary artery, and either clockwise or counterclockwise rotation may be necessary for optimal imaging of the right coronary artery. These movements are very subtle.

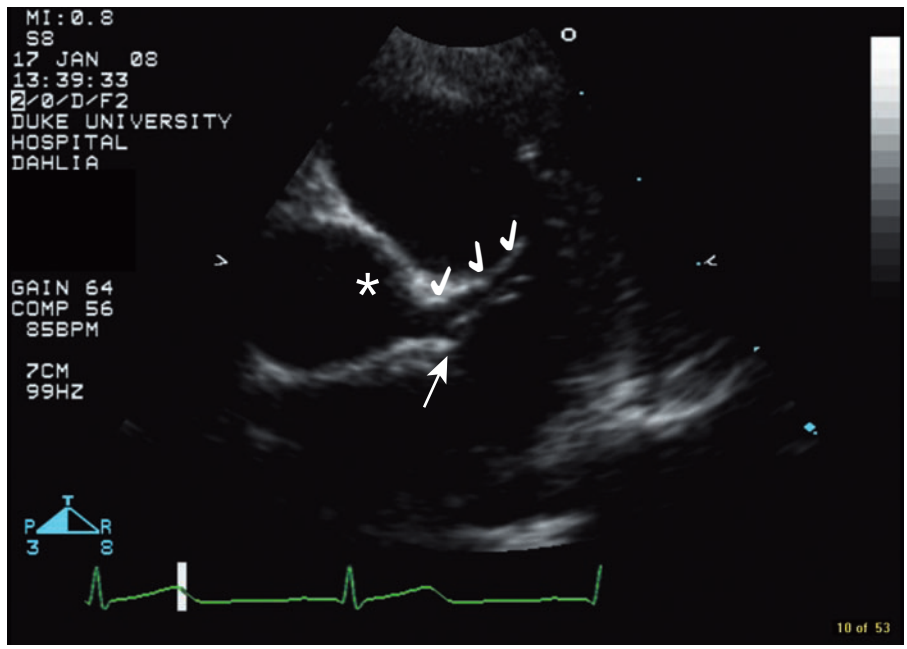


**Figure 29.4** Parasternal short-axis image at the base of the heart. The left main coronary artery is seen arising from the aorta at the left sinus of Valsalva. The left anterior descending coronary artery (carat marks) and most proximal portion of the left circumflex coronary artery (arrow) are seen to arise from the left main coronary artery. The asterisk (*) marks the position of the intercoronary commissure of the aortic valve.

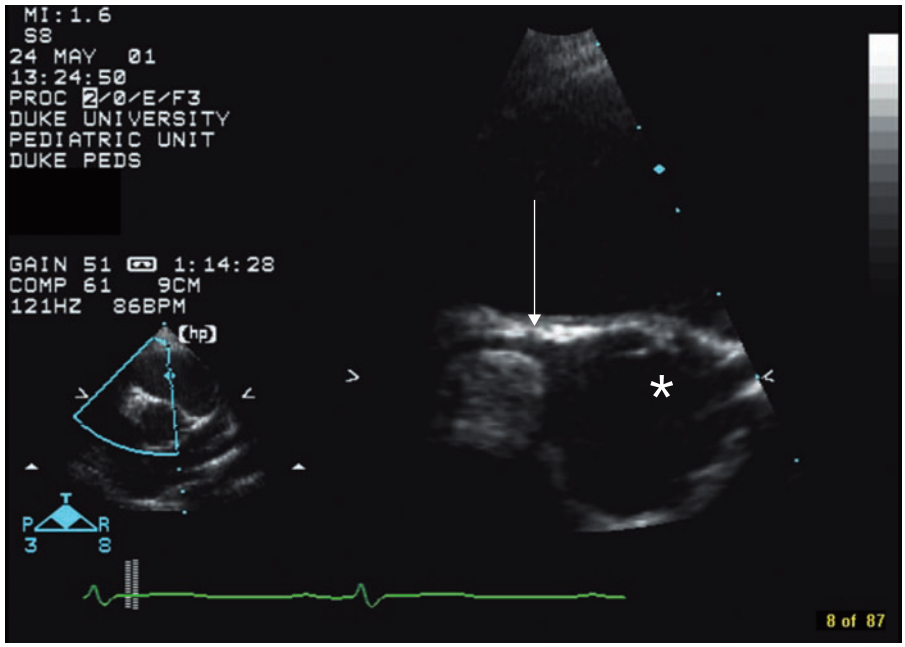


**Figure 29.5** Parasternal short-axis image at the base of the heart. The proximal right coronary artery (arrow) is seen arising from the aorta at the right sinus of Valsalva. The asterisk (*) marks the position of the intercoronary commissure of the aortic valve.

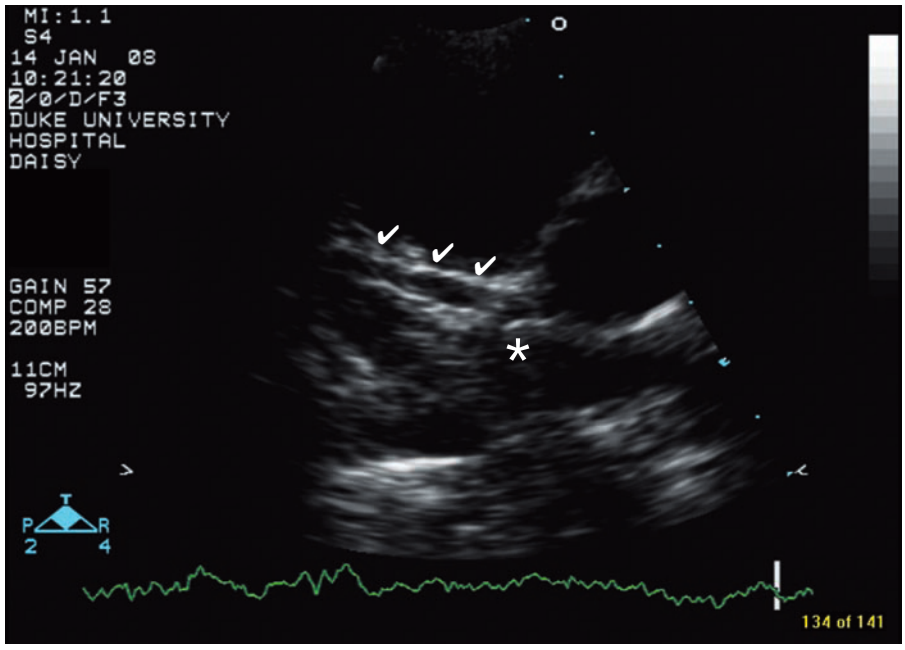


**Figure 29.6** Parasternal long-axis image angled leftwardly and superiorly toward the right ventricular outflow tract. The left main coronary artery is seen to arise from the aorta and branch into left anterior descending (carats) and left circumflex (*) coronary arteries.

From the parasternal long-axis view, leftward angulation of the probe allows visualization of the bifurcation of the left coronary artery as well as a long length of the left anterior descending coronary artery in its epicardial course down the interventricular septum (Fig. 29.6). From the subcostal coronal (long-axis) view at the level of the aortic root, the proximal left and right coronary arteries may be visualized also (Fig. 29.7).

The distal portions of the coronary arteries may also be visualized from several views. The distal right coronary artery may be seen in the posterior right atrioventricular groove from an apical 4-chamber view (Fig. 29.8), whereas the distal circumflex coronary artery may be seen in the same view in the posterior left atrioventricular groove. The posterior descending coronary artery is often best seen from an inferiorly angled parasternal long-axis view (Fig. 29.9).

In addition to the anatomic information discussed above, echocardiography may provide important functional information about the coronary arteries. The direction of flow in the coronary arteries may be demonstrated with color

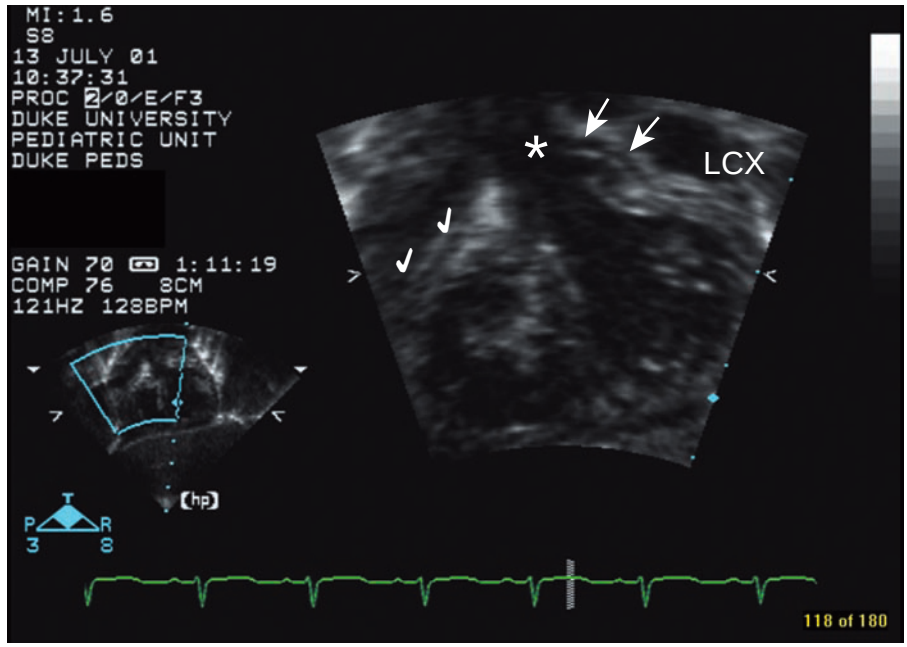


**Figure 29.7** Subcostal long-axis image with some counterclockwise rotation at the level of the left ventricular outflow showing a high origin (*) (just above the sinotubular junction) of the left main coronary artery (arrows) and a segment of the proximal right coronary artery in the anterior right atrioventricular groove (carats). The left circumflex coronary artery (LCx) is seen as a continuation of the left main coronary artery in the left atrioventricular groove.

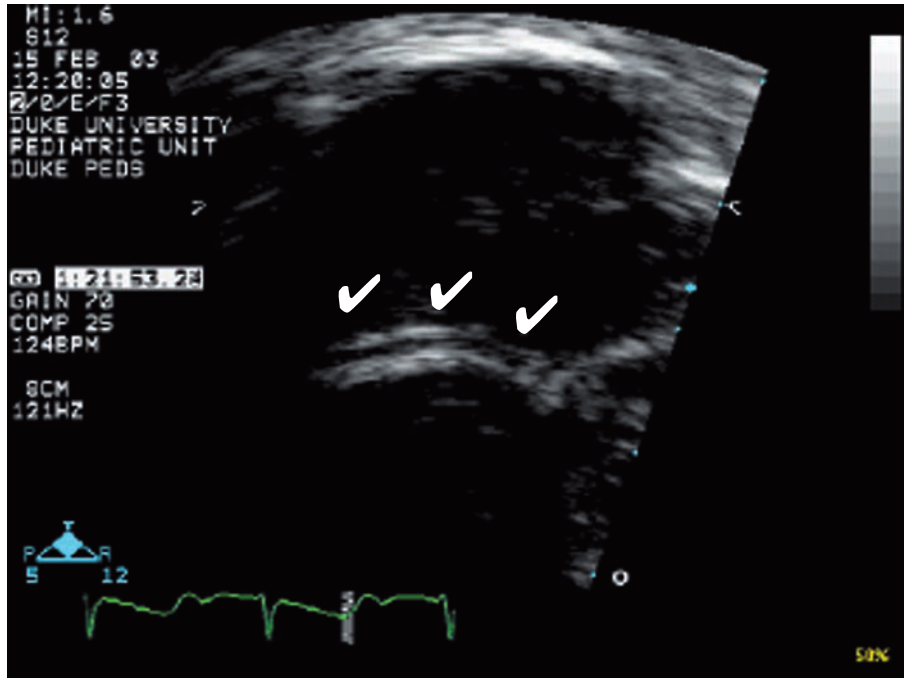


**Figure 29.8** Apical 4-chamber view of the anterior right atrioventricular groove showing a long length of the proximal right coronary artery (carats).

Doppler; this may provide pivotal information regarding anomalies of coronary artery origin from the pulmonary artery, as described below. Both systolic and diastolic function may be altered in certain forms of congenital coronary artery anomalies, and these parameters may be readily evaluated with echocardiography. Finally, regional wall motion abnormalities may be appreciated and thereby point to a specific area of perfusion deficit.

## Prenatal assessment

Rarely can the coronary arteries be seen well in fetal imaging. The exception would be congenital coronary artery anomalies that lead to significant dilation of the coronary arteries and/or lead to abnormal flow from the coronary arteries into a cardiac chamber or great vessel. These situations hold in cases of coronary–cameral fistulae, and these abnormalities have occasionally been noted on prenatal echocardiograms [8,9].

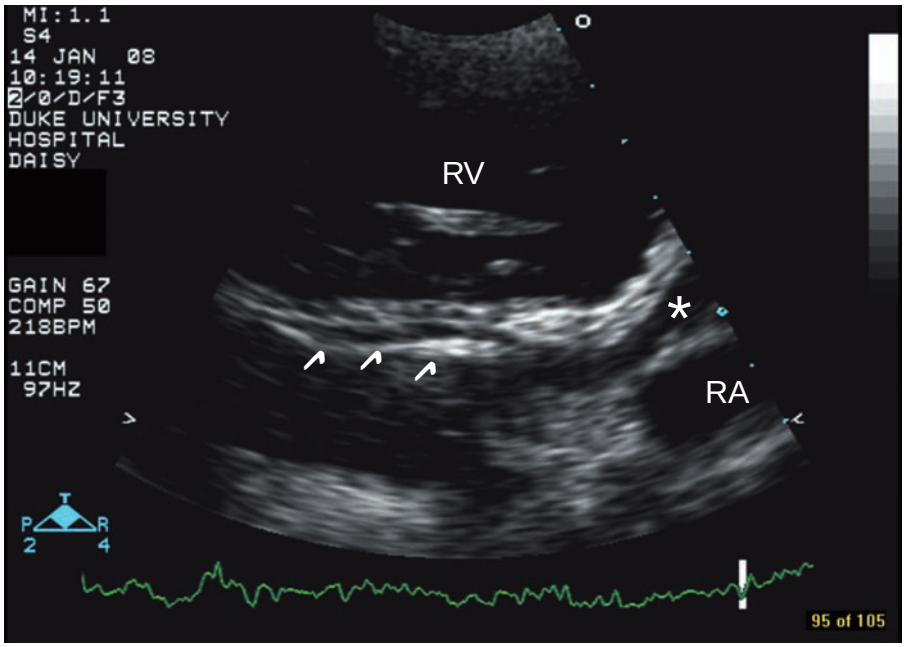


**Figure 29.9** Parasternal long-axis view angled inferiorly to show the posterior descending coronary artery (carats). Asterisk (*) denotes the coronary sinus. RA, right atrium; RV, right ventricle.

### Imaging of the adult and alternative imaging techniques

Cardiac catheterization with aortic root angiography or selective coronary arteriography represents the gold standard in the diagnosis of many congenital coronary artery anomalies. Magnetic resonance coronary angiography and multislice computed tomographic imaging of the coronary arteries have shown considerable promise in the imaging of adult coronary arteries. Both techniques have also been used in the diagnosis of congenital coronary artery anomalies in the adult population [10–12]. However, these techniques currently require a relatively motionless, cooperative patient with a slow heart rate for proper gating of the images. In the younger pediatric population these techniques require further technologic advances to achieve their full potential usefulness.

## Congenital coronary artery anomalies

A classification of congenital coronary artery anomalies is provided in Table 29.1. Many other classifications are available [13]. One of the more extensive of these has been proposed by the Society of Thoracic Surgeons [14]. These anomalies are numerous. Some are minor, and some are life-threatening. Some are present in otherwise normal hearts, and some are often associated with specific congenital heart lesions. Some are extremely rare, whereas others are relatively common. The remainder of this chapter discusses the congenital coronary artery anomalies that are most important to the pediatric cardiologist.

### Minor variations in coronary artery anatomy

Minor variations in coronary artery anatomy are those that are hemodynamically insignificant and not associated with an increased risk of sudden death. Their presence must nonetheless be recognized to interpret coronary arteriograms and echocardiograms properly, to avoid inadequate myocardial protection when cardioplegia is given selectively into the coronary orifices, and to avoid injury to these anomalous arteries at the time of surgery.

The most common minor variation in coronary artery anatomy is origin of the left circumflex coronary artery from the right aortic sinus. After its aberrant origin, this artery courses posterior to the aorta to reach its normal area of distribution. This anomaly occurs in about 0.5% of individuals undergoing coronary arteriography and is completely compatible with normal life. This anomaly is most often recognized echocardiographically by seeing a horizontal linear lucency (the proximal aberrant circumflex coronary artery) coursing posterior to the aorta from the apical 4-chamber view (Fig. 29.10).

Variations in the number of coronary artery ostia are common. In approximately 50% of cases, the right conus artery originates from a separate orifice in the right coronary sinus. Less commonly, the left circumflex coronary artery has a separate orifice in the left coronary sinus. Very rarely, these two anomalies occur together, and produce four coronary ostia.

Finally, variations in the position of the coronary artery ostia are also common. Normally, in adults, the coronary artery ostia are located just below the junction of the sinus and tubular portions of the aorta or within 1 cm above this

**Table 29.1** A classification of congenital coronary artery anomalies

**I. Anomalies of coronary artery origin**

A. Origin of one or more coronary arteries from the pulmonary artery (PA)
1. Left main coronary artery (LMCA) from PA
2. Right coronary artery (RCA) from PA
3. Left circumflex coronary artery (LC) from PA
4. Accessory coronary from PA
5. RCA and LMCA from PA
6. Single coronary artery from PA
7. Origin of a coronary artery from a branch pulmonary artery

B. Anomalous origin of one or more coronary arteries from the aorta
1. LMCA and RCA from right aortic sinus
2. LMCA and RCA from left aortic sinus
3. LMCA and RCA from posterior aortic sinus
4. RCA and LC from right aortic sinus (or LC from RCA) and left anterior descending coronary artery (LAD) from left aortic sinus
5. RCA and LAD from right aortic sinus (or LAD from RCA) and LC from left aortic sinus
6. RCA from posterior aortic sinus and LMCA from left aortic sinus
7. LMCA from posterior aortic sinus and RCA from right aortic sinus
8. LAD and LC from a separate ostium in the left aortic sinus (absence of LMCA) and RCA from right aortic sinus

C. Origin of only one coronary artery from the aorta without origin of a coronary artery from the PA (single coronary ostium)
1. From the right aortic sinus
2. From the left aortic sinus
3. From the posterior aortic sinus

D. Ostial anomalies
1. Abnormal number of ostia
2. Abnormal position of the ostia relative to the sinotubular junction
3. Intramural coronary artery

**II. Anomalies of coronary artery course or distribution or anomalies intrinsic to the artery**

A. Congenital coronary artery aneurysms
B. Congenital coronary artery stenosis
C. Congenital coronary artery hypoplasia
D. Coronary arterial loops
E. Myocardial bridges

**III. Anomalies of coronary artery termination**

A. Congenital coronary arteriovenous fistulae
B. Congenital coronary–cameral fistulae

**IV. Coronary artery anomalies associated with congenital heart disease**

A. Tetralogy of Fallot
B. D-transposition of the great arteries
C. L-transposition of the great arteries
D. Double-inlet left ventricle or univentricular heart
E. Double-outlet right ventricle
F. Truncus arteriosus
G. Pulmonary atresia with intact ventricular septum
H. Hypoplastic left heart syndrome

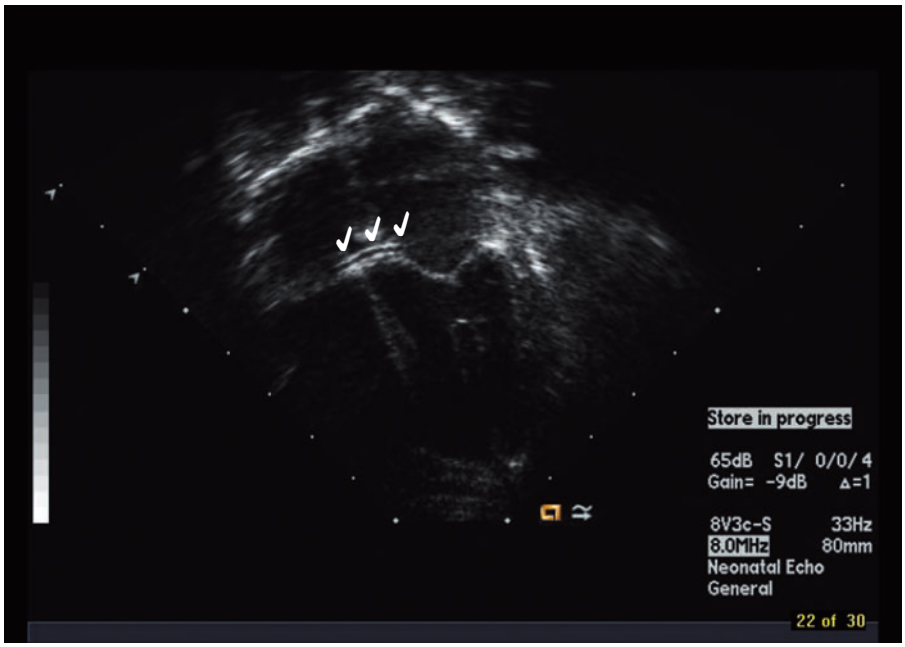


**Figure 29.10** Apical 4-chamber view just posterior to the aortic root. An anomalous circumflex coronary artery arising from the right coronary sinus of Valsalva is seen crossing posterior to the aortic root (carats).

point. But ostial positions above or below this occur in up to 40% of individuals undergoing coronary arteriography. Such variations appear to be benign [13].

## Anomalies of coronary arterial origin

### Anomalous left main coronary artery from the pulmonary artery

#### *History, incidence, anatomy and embryology*

Anomalous left main coronary artery from the pulmonary artery (ALCAPA) is one of the most important congenital coronary artery anomalies for the pediatric cardiologist. Pulmonary artery origin of coronary arteries was first described by Brooks in 1886 [15] and was further discussed by Abbott in 1908 [16]. The first clinical description of this anomaly, however, was given eloquently by Bland, White and Garland in 1933 [17], and the ALCAPA syndrome often bears the eponym *Bland–White–Garland syndrome*.

This anomaly is rather rare. It occurs approximately once per 300 000 live births and represents 0.5% of cases of congenital heart disease [18]. It generally occurs as an isolated anomaly but has been associated with patent ductus arteriosus, ventricular septal defects, atrioventricular canal defects, tetralogy of Fallot, coarctation of the aorta, and truncus arteriosus [19–25].

The left main coronary artery usually originates from either the left or the posterior sinus of the pulmonary artery. It then branches and distributes in a manner analogous to a normally arising left coronary artery. It is thus only the origin of the coronary artery that is abnormal. The etiology of this abnormal origin may be explained embryologically in one of two ways. Following Abrikossoff's theory, the pulmonary arterial origin is secondary to abnormal aorticopulmonary septation; following Hackensellner's theory, the abnormal origin is due to persistence of a pulmonary endothelial bud and its attachment to the developing left main coronary artery [26].

#### *Physiology*

The physiology of this anomaly depends on the status of blood flow in the left coronary artery (Fig. 29.11). Classically, four hemodynamic stages have been described [27–29]. In the first phase, pulmonary vascular resistance and pulmonary arterial pressure are high, and the anomalous coronary artery is supplied by blood from the pulmonary artery. This occurs in the newborn period and does not produce myocardial ischemia. The second phase is the transitional period during which pulmonary vascular resistance and pulmonary arterial pressure fall. During this time, flow into the left coronary artery begins to be retrograde, that is, from right coronary artery to left coronary artery via collaterals, and left coronary perfusion pressure falls. Unless there is an extensive collateral circulation, signs and symptoms of myocardial ischemia occur during this time. The third, or adult, phase is one in which there is an extensive collateral circulation and adequate perfusion of the myocardium supplied by the left coronary artery. Blood flows from the right coronary artery into the left coronary circulation and then into the pulmonary artery. There are no signs of myocardial ischemia in this phase. In the fourth phase, the left coronary artery no longer functions as a "feeding vessel" to the left ventricular myocardium but rather as a conduit from the right coronary artery to the pulmonary artery. That is, there is "steal" of oxygenated blood from the arteriolar and capillary vessels of the left coronary circulation. Myocardial ischemia is thus produced.

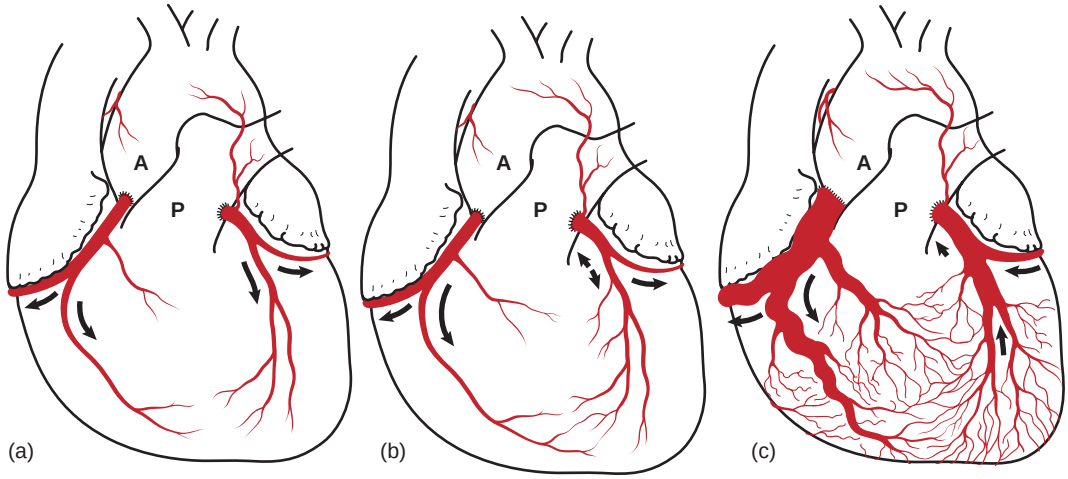


**Figure 29.11** Diagrammatic portrayal of varying functional states in anomalous origin of the left coronary artery from the pulmonary trunk. **(a)** During fetal life aortic (A) and pulmonary arterial (P) pressures are essentially equal. Flow in the anomalous artery is from the pulmonary trunk into the myocardium. **(b)** In early postnatal life pulmonary pressure has fallen below levels that pertain during fetal life. Rich intercoronary collateral channels have not yet developed. In this phase, flow through the anomalous coronary artery is probably at a low level. The anomalous vessel may be perfused either from the pulmonary trunk or from the right coronary artery through developing collateral systems. **(c)** In the final phase a rich collateral system has developed between the two coronary arteries. Characteristics of an arteriovenous fistula now pertain, with the major contribution to fistulous flow coming from the right coronary artery. Mediastinal arteries, which make communication with the coronary arterial system, may also contribute to such flow. Adapted from Edwards JE. The direction of blood flow in coronary arteries arising from the pulmonary trunk. *Circulation* 1964;29:164, with permission from The American Heart Association.

Not all patients pass consecutively through each of these phases. Indeed, most patients present in infancy during the transitional phase and never progress beyond this. A few patients have numerous collateral vessels between the right and left coronary arteries and pass unscathed through infancy to present in adulthood in phase three or four. The above schema nonetheless presents a useful framework for the description of the varied physiologies with which these patients may present.

### *Clinical features*

The majority of patients present in early infancy with failure to thrive, tachypnea, dyspnea, wheezing, diaphoresis, or angina-like episodes. Classically, infantile angina is brought on by feeding and consists of "paroxysmal attacks of acute discomfort precipitated by the exertion of nursing" [17]. Examination of such infants shows the signs of congestive heart failure. Either no systolic murmur or a very short grade 1–2 systolic murmur is heard. Occasionally, the murmur of mitral insufficiency may be the only presenting sign. The etiology of the mitral insufficiency is some combination of ischemia or infarction of the mitral valve papillary muscles and stretching of the mitral valve annulus due to the dilated cardiomyopathy that ensues from ischemia.

Occasionally, patients escape symptomatology in the infantile period. These are patients who have extensive collateral coronary arteries, and they present either with a continuous murmur or with sudden cardiac death in later childhood or adulthood [30]. Another group of patients who escape symptomatology in the infantile period are those with ALCAPA syndrome and a concomitant congenital heart defect that preserves pulmonary hypertension. These patients may present with catastrophic left ventricular dysfunction following repair of the associated lesion if the anomalous left coronary goes unrecognized.

### *Imaging preoperatively*

Echocardiographically, the findings comprise a dilated, hypocontractile left ventricle and a dilated left atrium. There is left ventricular hypertrophy, but the ratio of myocardial volume to end-diastolic volume in the left ventricle is low; that is, the degree of volume expansion is out of proportion to the degree of hypertrophy. The left ventricular dysfunction is global. There is no specific regional wall motion abnormality [31]. All of these findings may be seen with myocarditis and dilated cardiomyopathy in addition to the ALCAPA syndrome. Thus, the coronary arteries must be diligently evaluated in any patient who presents with the above 2D echocardiographic findings.

Two-dimensional imaging of the coronary arteries alone is inadequate to distinguish ALCAPA from these other conditions. Although the right coronary artery is often dilated in the ALCAPA syndrome [32], this is not always appreciated; the left coronary artery may so closely approach the left aortic sinus of Valsalva that this coronary artery may appear to take its origin from the aorta even when ALCAPA is clearly

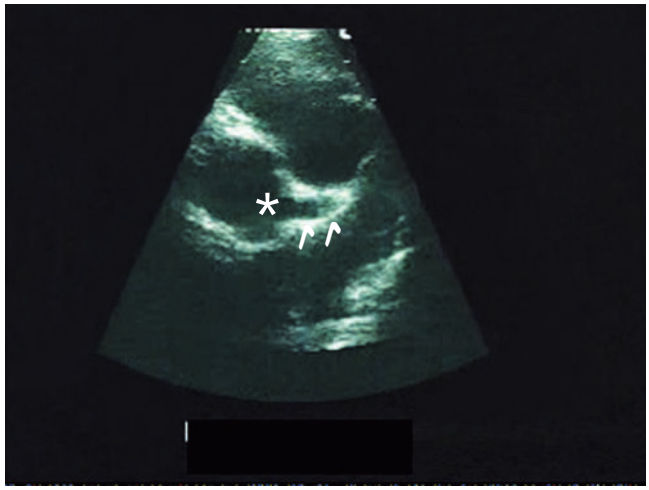

**Figure 29.12** Parasternal short-axis view at the base of the heart in a patient with anomalous left coronary artery from the pulmonary artery. Note how closely the left main coronary artery (carats) approaches the left aortic sinus of Valsalva (*).

present. Color flow mapping of the coronary arteries, however, adds diagnostic certainty to the echocardiographic examination in these conditions (Fig. 29.12). The direction of flow in the various segments of the left coronary artery is the differentiating feature and must be evaluated in any patient with the findings of a dilated, hypocontractile left ventricle (Videoclip 29.1). Demonstration of an abnormal flow jet into the pulmonary artery combined with detection of retrograde flow in at least two of the three segments of the left coronary artery is highly reliable for diagnosing the ALCAPA syndrome (Fig. 29.13 and Videoclip 29.2). Furthermore, demonstration of antegrade flow in at least one segment of the left coronary artery is useful for excluding ALCAPA syndrome in patients with dilated cardiomyopathy [33]. Flow in the septal perforators is often prominent and represents one source of collateral coronary circulation (Fig. 29.14).

***Imaging intraoperatively and postoperatively***

Intraoperatively, transesophageal echocardiography is used to evaluate left ventricular function and mitral regurgitation. The anatomy is confirmed, and the coronary artery origin is identified and the direction of coronary artery flow is demonstrated. Postoperatively, prograde flow from the aorta into the left main coronary artery is affirmed. Recovery of left ventricular function and improvement of mitral regurgitation are followed with serial examinations [31].

## Other anomalies of pulmonary arterial origin of coronary arteries

The right coronary artery may rarely arise from the pulmonary artery. Most patients with this anomaly are asymptomatic, although symptoms relating to myocardial ischemia have been reported [34]. The diagnosis is made by echocardiography or angiography or incidentally at autopsy [13,35–37] (Fig. 29.15 and Videoclip 29.3)

Either the left anterior descending coronary artery or the circumflex coronary artery may take its origin from the pulmonary artery. Both anomalies are extremely rare but may be associated with signs of myocardial ischemia. An accessory coronary artery, most commonly a conus coronary artery, may also arise from the pulmonary artery; this is of no functional significance [38].

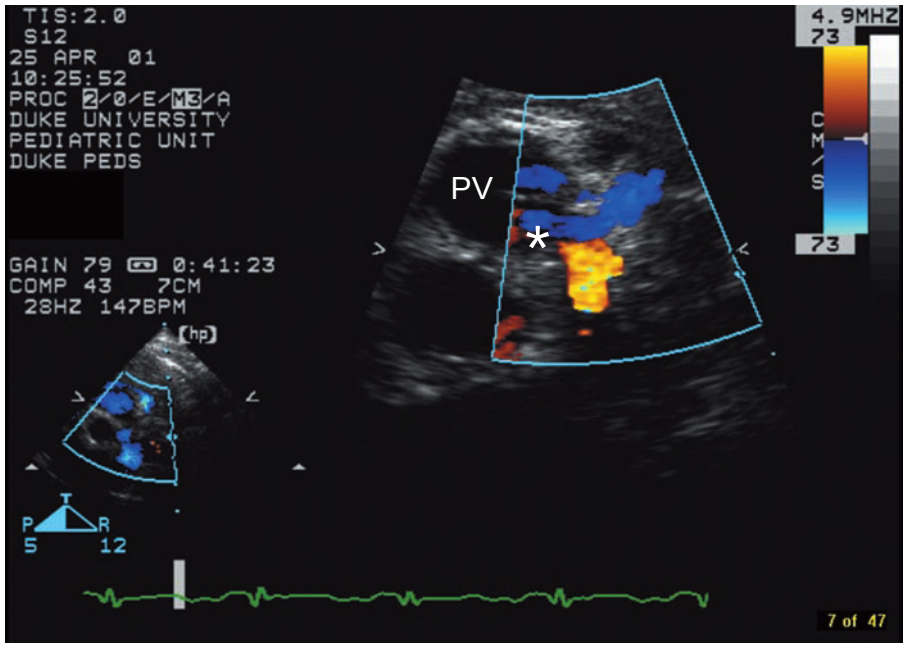


**Figure 29.13** High parasternal axial image of the pulmonary valve (PV) and sinuses in a patient with anomalous left coronary artery from the pulmonary artery. Retrograde flow is seen in the left anterior descending coronary artery (blue) and in the left circumflex coronary artery (red), and flow is seen entering the left-facing pulmonary sinus (*).

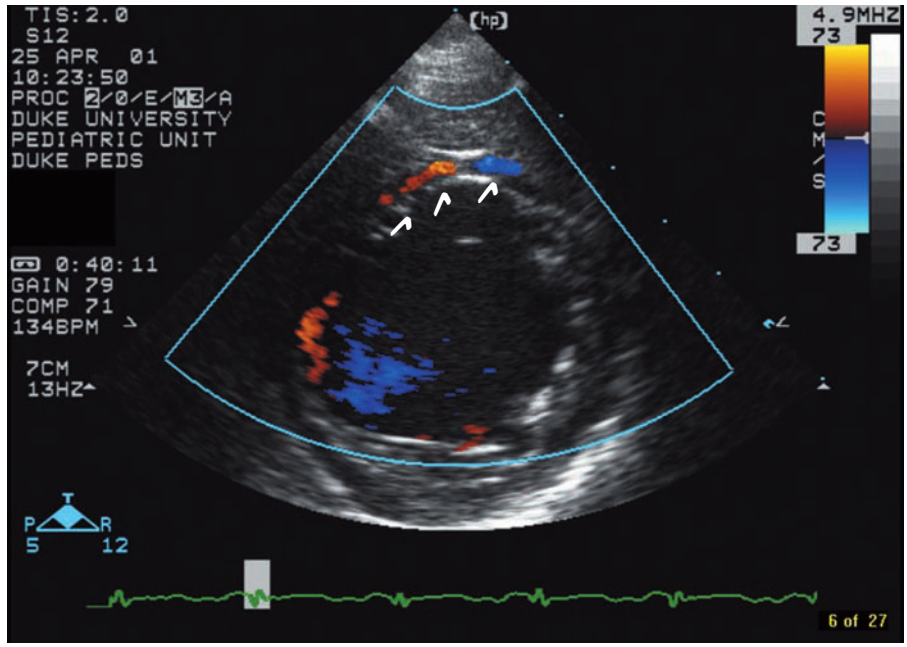


**Figure 29.14** Parasternal short-axis view at mid-ventricular level in a patient with anomalous left coronary artery from the pulmonary artery and a dilated left ventricle. Note the prominent retrograde flow in the septal perforator coronary arteries (carats).

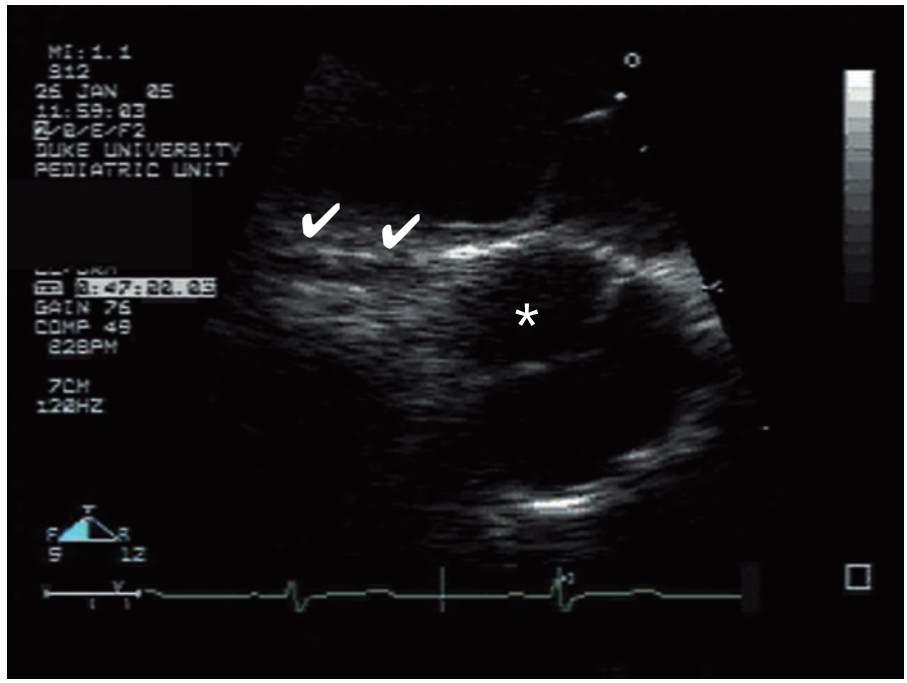


**Figure 29.15** **(a)** Parasternal short-axis view at the base of the heart in a patient with anomalous origin of the right coronary artery from the pulmonary artery. Note how closely the right coronary artery (carats) approaches the right aortic sinus of Valsalva (*).

(a)

Origin of both coronary arteries from the pulmonary artery, either from separate orifices or as a single coronary artery, is another rare anomaly. Most of these infants present in the early neonatal period with profound heart failure and quickly succumb to this. Longer survival has been described in infants with concomitant congenital heart disease associated with elevations in pulmonary artery pressure, oxygen saturation or both [26]. Until recently, this anomaly has been uniformly lethal. Urcelay et al. report successful repair in two infants by direct reimplantation of the coronary arteries into the aortic root [39].

The left main coronary artery has also been found to originate from a branch pulmonary artery, and this has been successfully repaired [40].

(b)

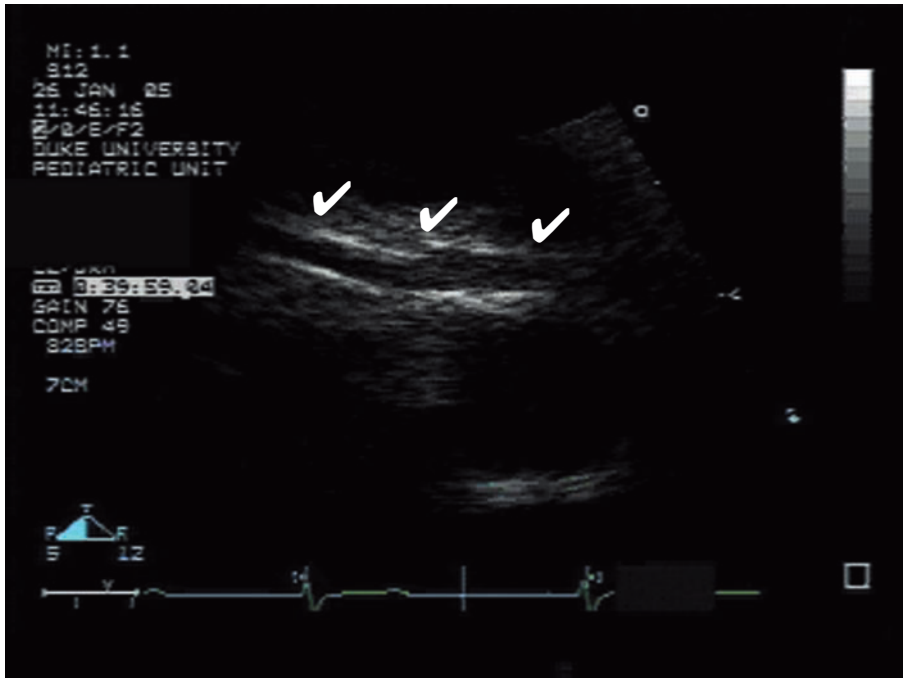


(c)

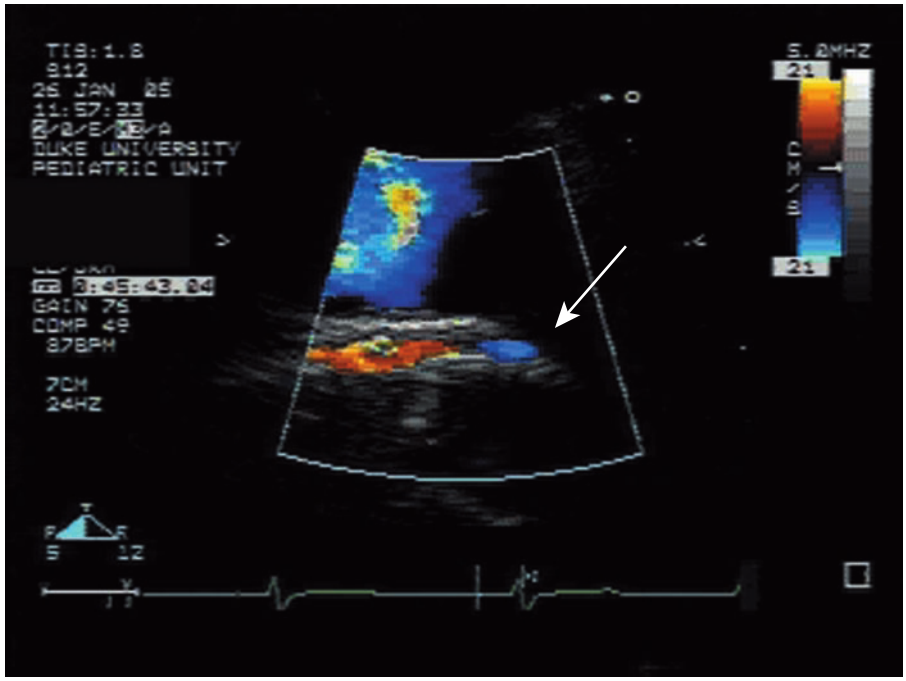


**Figure 29.15** **(b)** Slightly more superior angulation shows that the right coronary artery (carats) bypasses the right aortic sinus of Valsalva to enter the pulmonary sinus of Valsalva. **(c)** Color Doppler in the right coronary artery shows retrograde flow in the coronary artery and flow entering the pulmonary artery (arrow).

### Origin of the left coronary artery from the right coronary sinus

Anomalous origin of the left main coronary artery from the right coronary sinus or from the proximal right coronary artery is a rare lesion, but one of great clinical importance because it has been associated with sudden cardiac death in children and adolescents [38,41–43]. After its anomalous origin, the left main coronary artery may take one of four different routes:

- anterior to the pulmonary artery
- posterior to the aorta
- in the interventricular septum beneath the right ventricular infundibulum
- between the aorta and pulmonary artery.

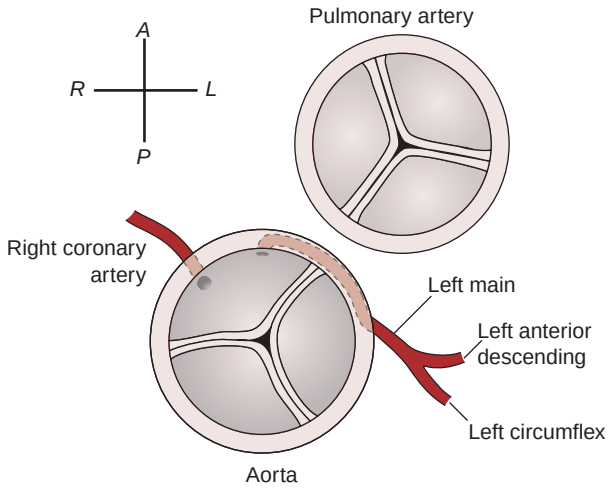


**Figure 29.16** Anomalous origin of the left main coronary artery from the right aortic sinus of Valsalva with an intramural and interarterial course. Note the slit-like orifice of the left main coronary artery. A, anterior; P, posterior; R, right; L, left.

Even rarer is anomalous origin of only the left anterior descending coronary artery from the right coronary artery or from the right sinus of Valsalva, but this anomaly probably has similar clinical behavior to anomalous origin of the entire left coronary artery system from the right coronary artery or the right sinus of Valsalva.

Patients in whom the anomalous left main coronary artery takes a course between the aorta and the pulmonary artery appear to be at greatest risk for sudden death (Fig. 29.16). The mechanism of such sudden death is acute myocardial ischemia, which is produced by embarrassment of flow in the left main coronary artery. This occurs most often during exercise, when myocardial oxygen demand is at its highest and the increased stroke volume causes outward expansion of the roots of both great vessels. The mechanism of obstruction to flow seems to be a combination of compression of the intramural portion of the left main coronary artery, compression of the left main coronary artery between the aorta and the pulmonary trunk, and worsening of the intrinsic narrowing or kinking at the anomalous ostium [38].

The most common presenting symptoms of individuals with anomalous left main coronary artery arising from the right coronary sinus are syncope, presyncope, or chest pain associated with exercise. However, many patients with this anomaly are asymptomatic until sudden death occurs. In fact, coronary artery anomalies including anomalous left main coronary artery arising from the right coronary sinus join hypertrophic cardiomyopathy as the most common cardiac anomalies associated with sudden cardiac death in adolescents and young adults. Exercise stress testing of patients with this anomaly may show myocardial ischemia but also may be completely normal. Thus, any evaluation of exercise-related syncope, presyncope or chest pain must include definition of coronary arterial anatomy, and echocardiography is most often the imaging modality of choice [44].

### *Imaging*

Excellent definition of the origins and proximal courses of the anomalous coronary artery may most often be achieved with echocardiography. The parasternal short-axis view at the base of the heart is the best view to appreciate both the relationship of the origin of the left coronary artery to the intercoronary commissure and its often intramural course as well as its relationship to the right ventricular outflow (Fig. 29.17). Because of the extreme translation of the coronary artery origins during the cardiac cycle, the excellent temporal resolution of echocardiography (compared with that of other noninvasive techniques) makes this the diagnostic technique of choice in most cases. The extreme translation of the coronary artery makes diagnosis in real time often difficult. Obtaining a loop that is one to several heartbeats in duration and then playing this back slowly is often of great help in visualizing the anomalous coronary artery as well as discerning its relationship to the intercoronary commissure (Videoclip 29.4). Color Doppler should be made to write in the intramural segment of the left main coronary artery. The interarterial course of the anomalous left main coronary artery can often be seen to advantage in the leftwardly angled parasternal long-axis view (Fig. 29.18 and Videoclip 29.5).

In older patients with slower heart rates, both magnetic resonance imaging and multislice computed tomography have proven useful as well [45,46]. If any question remains, coronary angiography is often recommended, although this technique does not allow for completely nonambiguous delineation of the proximal course of the coronary artery.

## Origin of the right coronary artery from the left coronary sinus

Until recently, origin of the right coronary artery from the left coronary sinus was considered a benign variant. It is reported less often than anomalous origin of the left main coronary artery from the right coronary sinus, but its true incidence is probably greater than this better-recognized anomaly [38,47]. It is common for the anomalous right coronary artery to pass between the great vessels, although other courses are possible. Such a course provides the anatomic substrate for myocardial ischemia in an identical manner to that with anomalous origin of the left coronary artery from the right sinus. Although presentation with sudden cardiac death not preceded by other symptoms is less likely with this anomaly than with anomalous origin of the left coronary artery from the right sinus of Valsalva, up to one-fourth of individuals with an anomalous right coronary artery found at autopsy died suddenly and unexpectedly, and almost one-third of them died of cardiac causes [48]. Operative intervention for anomalous origin of the right coronary artery from

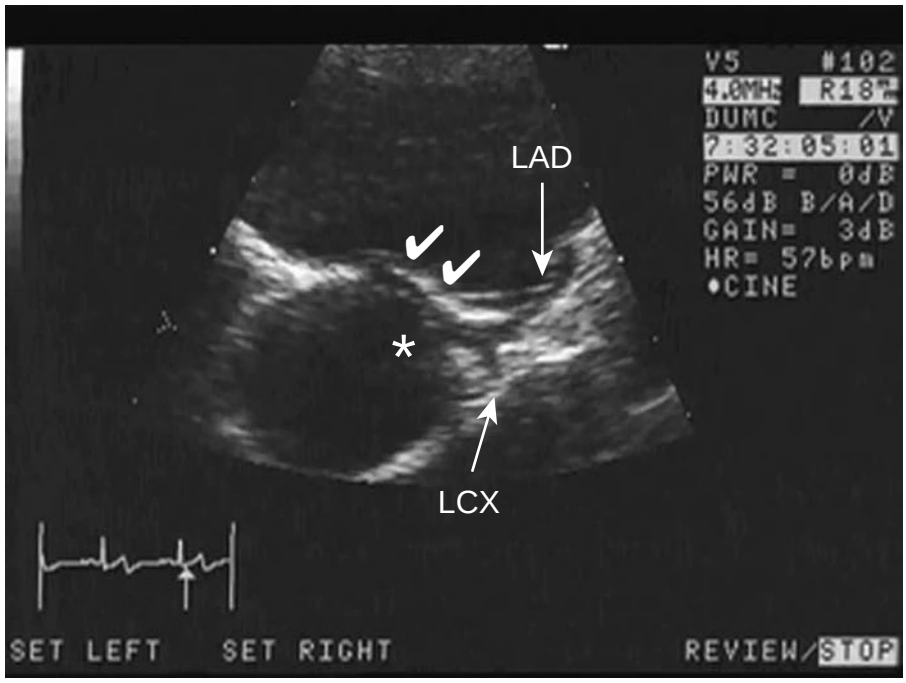


**Figure 29.17** Parasternal short-axis view at the base of the heart in a patient with anomalous origin of the left main coronary artery from the right aortic sinus of Valsalva. The intramural and interarterial course of the left main coronary artery is apparent (carats). The asterisk (*) marks the location of the intercoronary commissure. LAD, left anterior descending coronary artery; LCx, left circumflex coronary artery.

(a)

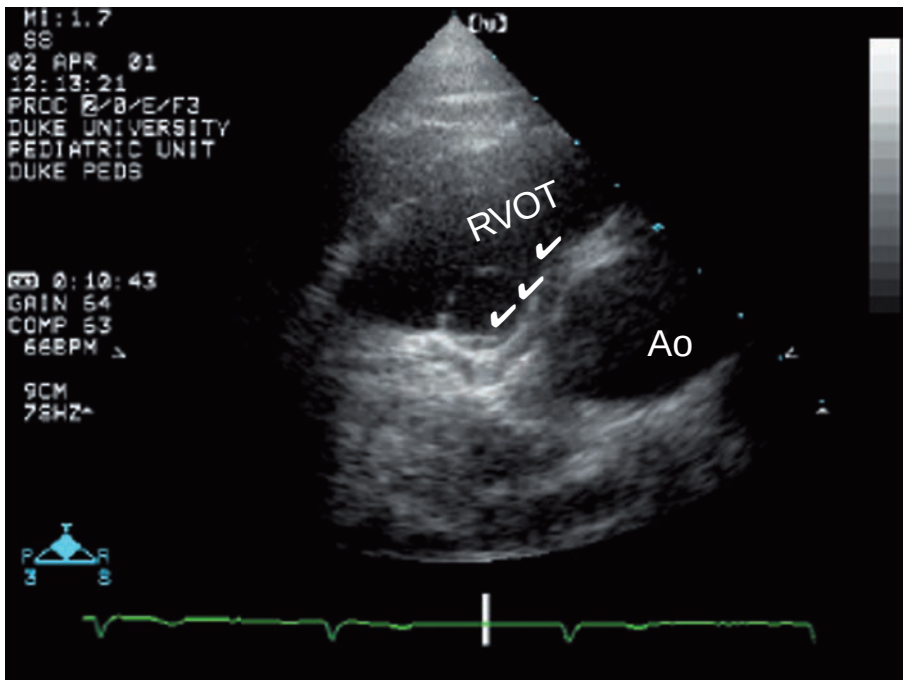


**Figure 29.18** **(a)** Leftwardly angled parasternal long-axis view of the left coronary artery in a patient with anomalous origin of the left main coronary artery from the right aortic sinus of Valsalva. The interarterial course is demonstrated (carats). RVOT, right ventricular outflow tract.

the left sinus in asymptomatic patients is controversial but is performed in a number of institutions [49].

### *Imaging*

This anomaly is most often diagnosed by echocardiography either as an unexpected finding or as part of an evaluation for a patient with chest pain or exercised-induced syncope. It is found using the same principles as for anomalous left coronary artery from the right coronary sinus of Valsalva in that the parasternal short-axis view allows determination of the anomalous origin and proximal course of the right coronary artery. In this entity, an unusually high origin of the anomalous right coronary artery (at or slightly above the sinotubular junction) is common. When the origin is high, takedown of the intercoronary commissure during an unroofing procedure is usually not necessary; thus this

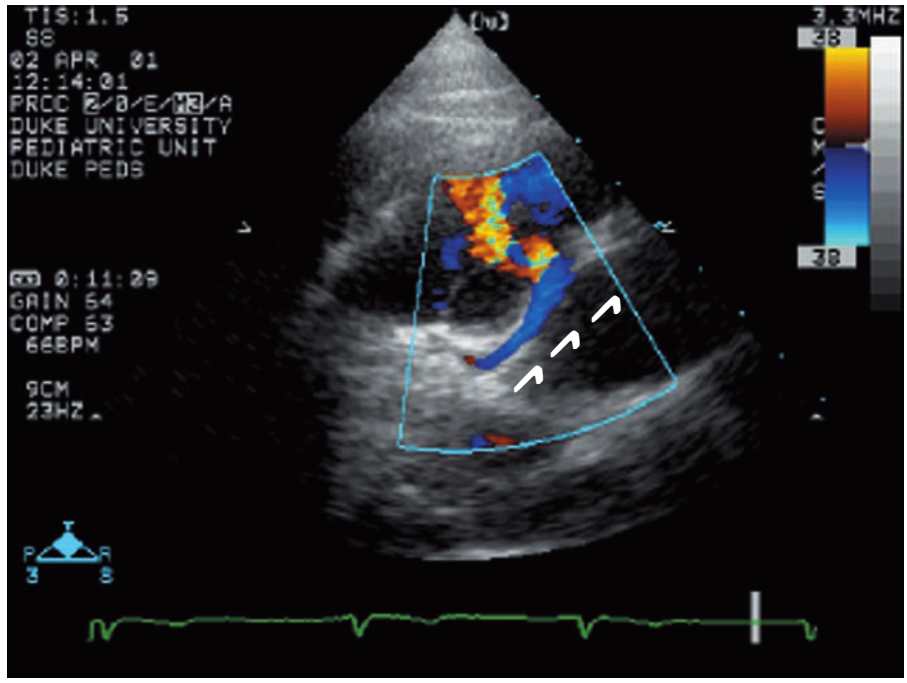


(b)

**Figure 29.18 (b)** Color Doppler demonstrates prograde flow in the interarterial segment of the left main coronary artery (carats). Ao, aortic root; RVOT, right ventricular outflow tract.

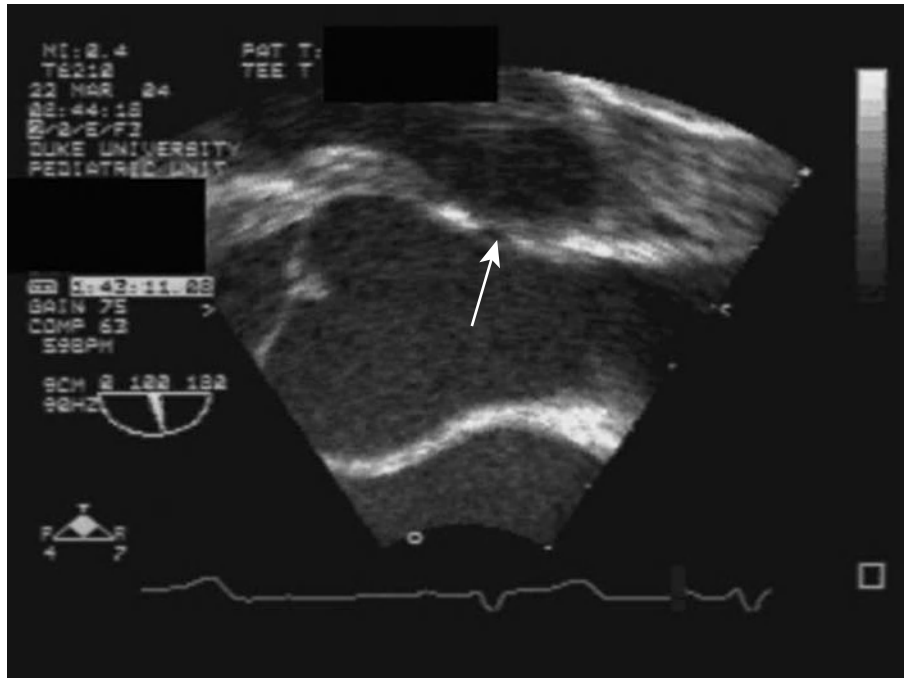


**Figure 29.19** Long-axis transesophageal echocardiogram at the level of the ascending aorta in a patient with anomalous origin of the right coronary artery from the left aortic sinus of Valsalva. The origin of the right coronary artery (arrow) is seen just at the sinotubular junction.

identification is surgically important [50]. Identifying the origin in relation to the sinotubular junction is best accomplished in the parasternal long-axis view or in a long-axis transesophageal echocardiographic view (Fig. 29.19 and Videoclip 29.6). We have found transesophageal echocardiography to be the imaging procedure of choice if anomalous aortic origin of a coronary artery is suspected but not definitively diagnosed by transthoracic imaging.

### *Postoperative imaging of anomalous aortic origin of a coronary artery*

In patients who have had an unroofing procedure for repair of anomalous aortic origin of a coronary artery, it is necessary postoperatively to evaluate for aortic insufficiency due to potential distortion of the aortic valve. One should also demonstrate flow from the appropriate aortic sinus into the coronary artery (Fig. 29.20).

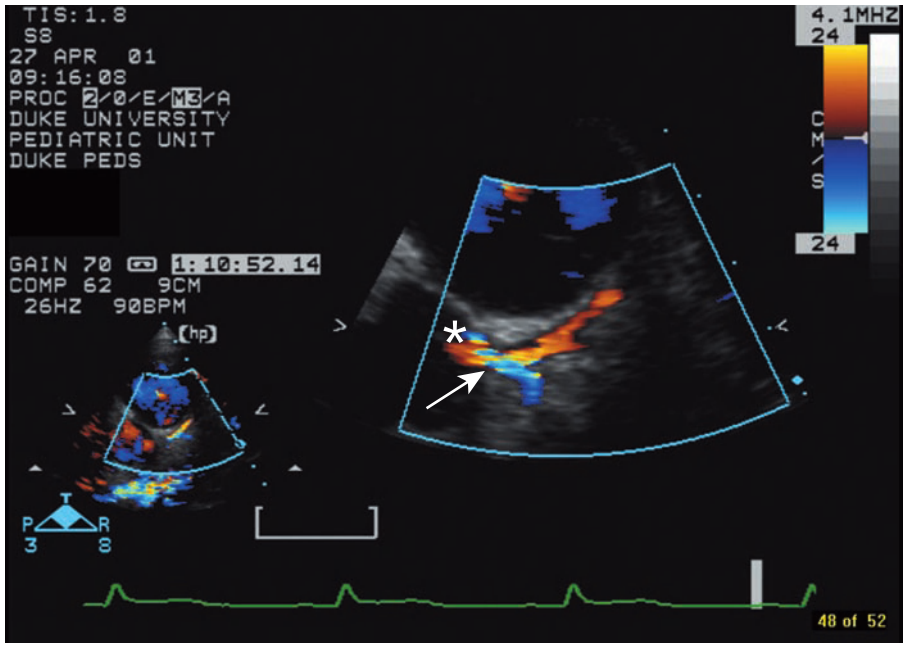


**Figure 29.20** Parasternal short-axis view at the base of the heart in a patient who has undergone an unroofing procedure for repair of anomalous origin of the left main coronary artery from the right sinus of Valsalva. Color Doppler demonstrates prograde flow into the left main coronary artery from the left aortic sinus of Valsalva (arrow). The asterisk (*) denotes the position of the intercoronary commissure.

### Single coronary artery

This anomaly may be defined as one in which a single coronary artery arises from a single ostium in one of the aortic sinuses of Valsalva and follows the peripheral course and distribution of one or both right and left coronary arteries or follows an abnormal distribution [13]. This is a rare anomaly in individuals with an otherwise normal heart but was made publicly well known by the untimely death of "Pistol" Pete Maravich due to sudden cardiac death related to a single right coronary artery [51]. Classification schemes for single coronary artery have been proposed by Smith [52], Ogden and Goodyer [53], and Shirani and Roberts [54]. The latter scheme is most complete and describes three features of the coronary circulation: the sinus of origin of the single coronary artery, the presence or absence of an aberrantly coursing coronary artery, and the course of the aberrantly coursing coronary artery if present.

The majority of patients with this anomaly are asymptomatic. Indeed, the anomaly is compatible with a normal life. Whether people with this anomaly are particularly prone to atherosclerotic disease is controversial [55]. Clearly, however, the consequences of atherosclerotic occlusion of a single coronary artery are dire. Patients with a single right coronary artery with an aberrant left coronary artery (or branch of the left coronary artery) that courses between the great vessels seem to be at particular risk for sudden cardiac death. The pathophysiology of this phenomenon is probably the same as that for sudden death related to anomalous left coronary artery from the right coronary artery, as discussed above.

A single coronary artery in a patient with an otherwise structurally normal heart is almost always an incidental finding. The origin and proximal course of each of the three major coronary arteries should be confirmed in multiple views when a single coronary artery is suspected.

### Anomalies of coronary artery course or distribution and anomalies intrinsic to the artery

This heading encompasses a diverse group of coronary artery anomalies, each of which is rare, but all of which deserve mention because of their potential importance to the pediatric cardiologist.

### Congenital coronary artery aneurysm

Congenital aneurysm of a coronary artery accounts for roughly 17% of all coronary artery aneurysms [56]. The majority of coronary artery aneurysms are secondary to atherosclerotic disease, associated with congenital coronary–cameral fistulae, associated with Kawasaki disease, or of infectious or traumatic etiology. Congenital coronary artery aneurysm is thus a diagnosis of exclusion that may be made after these other more common etiologies are ruled out.

Congenital coronary artery aneurysms are felt to be caused by a deficiency of the elastic elements in the media of the coronary arteries [57]. Patients with this anomaly present with signs and symptoms of myocardial ischemia, particularly during exercise. The diagnosis may be suggested on chest radiography by an abnormal bulge on the cardiac silhouette or by the presence of calcific rings along the distribution of the coronary arteries. Definitive diagnosis is made by coronary arteriography.

Complications of congenital coronary artery aneurysms include rupture of the aneurysm, myocardial infarction from embolization of clots from the aneurysm to the more

distal coronary artery, and infective endocarditis. Such complications may be prevented by surgical therapy [13,58–61].

Echocardiographic evaluation of congenital coronary aneurysms is accomplished just as it is in the evaluation of coronary aneurysms associated with Kawasaki disease. This is covered in Chapter 37.

## Anomalies of coronary artery termination

### Congenital coronary–cameral and coronary–arteriovenous fistulae

These lesions have the same physiology and are therefore discussed together. A coronary–cameral fistula involves an abnormal fistulous connection between a coronary artery and a cardiac chamber, whereas a coronary–arteriovenous fistula involves such a connection between a coronary artery and one of the great veins entering the heart. Not strictly included under this nominal rubric but in the same category of lesions is a coronary artery-to-pulmonary artery fistula. Hereafter in this chapter, all of the above entities are called simply coronary arteriovenous fistulae (CAVFs).

#### *History, incidence, anatomy and embryology*

Krause provided the first description of this anomaly in 1865 [62]. Although it is uncommon, CAVF is one of the more common congenital anomalies of the coronary arteries. This entity accounts for 0.2–0.4% of congenital cardiac anomalies and roughly half of congenital anomalies of the coronary arteries [63–65].

About 60% of CAVFs originate from the right coronary artery and 40% originate from the left coronary artery; rarely, such a fistula may take its origin from both coronary arteries [13,63,66]. In the vast majority of cases (about 90%), the CAVF terminates in the right side of the heart. The right ventricle is the most common site of termination, but the right atrium and the pulmonary artery are often seen as sites of termination. The left side of the heart rarely receives a coronary artery fistulous communication. The site of termination of the fistula may be a single entry site, multiple entry sites, a plexiform communication between the coronary artery and a cardiac chamber, or a side-to-side communication between the coronary artery and a cardiac chamber. The embryologic basis for CAVFs is postulated to be persistence of portions of the embryonic coronary sinusoids that connect the primitive coronary arteries to the cardiac chambers [13].

#### *Physiology*

The physiology of a coronary arteriovenous fistula varies with the chamber or vessel in which the fistula terminates. Coronary arteriovenous fistulae that terminate in the right atrium have the physiology of a pretricuspid left-to-right shunt, whereas those that terminate in the right ventricle or pulmonary artery have the physiology of a posttricuspid left-to-right shunt. Those that terminate in the left atrium have a physiology similar to mitral regurgitation, and those that terminate in the left ventricle have a physiology similar to aortic regurgitation.

In addition to the above varied physiologies of CAVFs, each such fistula has the potential to produce a coronary artery steal. That is, blood is stolen from the coronary arterial bed distal to the insertion of the fistula because of the runoff of coronary arterial blood into the chamber or vessel of termination. Such steal may cause myocardial ischemia or rarely infarction [67].

#### *Imaging*

Two-dimensional echocardiography shows dilation of the proximal portion of the coronary artery that feeds the fistula and chamber dilation consistent with the physiology of the particular fistula (Fig. 29.21). Occasionally, the fistulous connection itself may be imaged, but fistula detection is greatly aided by color Doppler imaging [68] (Fig. 29.22 and Videoclip 29.7) Often small CAVFs are first detected by abnormal diastolic flow into a right heart chamber or into the main or branch pulmonary arteries. These small fistulae are usually unexpected findings in an asymptomatic patient with no murmur and without dilation of any cardiac chamber or of the proximal coronary artery. Occasionally, coronary-to-right ventricle fistulae are acquired following operative muscle resection, typically for surgery to relieve right ventricular outflow obstruction.

Intervention upon CAVFs requires detailed definition of the distal coronary artery anatomy, and this is not possible by echocardiography. Rather, angiography (most often selective coronary angiography) is necessary. Transesophageal or intracardiac echocardiography may be used during or after transcatheter occlusion of a CAVF to document occlusion and to evaluate for potential wall-motion abnormalities related to ischemia as a complication of the occlusion [69].

## Coronary artery anomalies associated with congenital heart disease

Anomalies of coronary arteries are surgically important in numerous types of congenital heart disease, and these associations are discussed in the chapters on each individual lesion. It is worth emphasizing, though, that accurate delineation of the coronary artery anatomy is required in any patient who is to undergo surgery for congenital heart disease. It is necessary to make certain that a coronary artery anomaly does not place a major epicardial coronary artery in the region of surgical repair. Perhaps most important is the need to ensure that there is no abnormal origin of a coronary artery from the pulmonary artery [70], because the repair may change the physiology by decreasing the pulmonary artery pressure and thereby causing coronary steal and myocardial ischemia or infarction in the vulnerable period immediately upon weaning from cardiopulmonary bypass. One can avoid this catastrophic outcome by assiduous attention to coronary arterial anatomy in the preoperative echocardiogram.

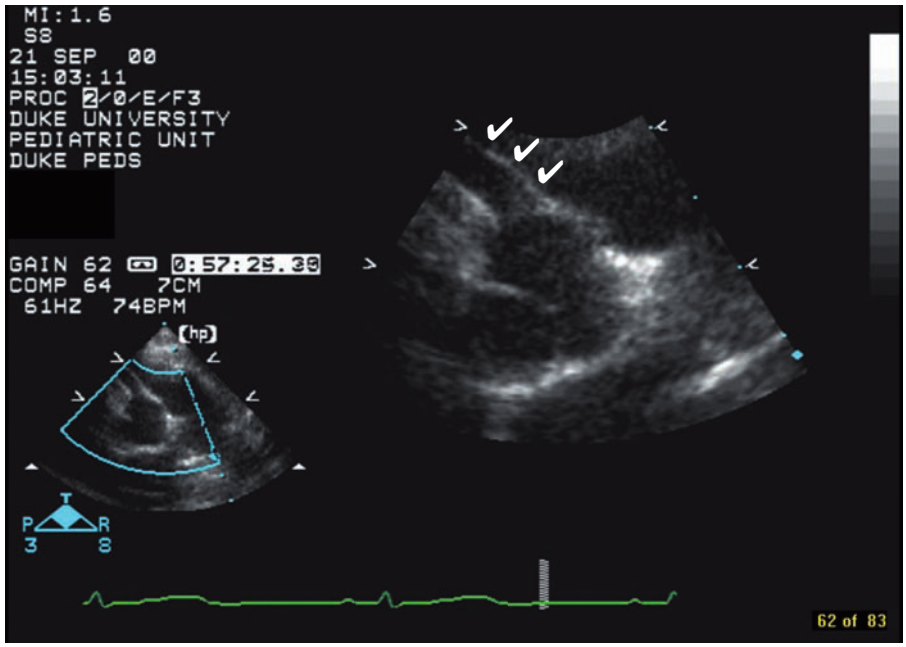


**Figure 29.21** Parasternal short-axis view at the base of the heart in a patient with a coronary–cameral fistula from the right coronary artery to the right ventricle. The right main coronary artery (carats) is very dilated.

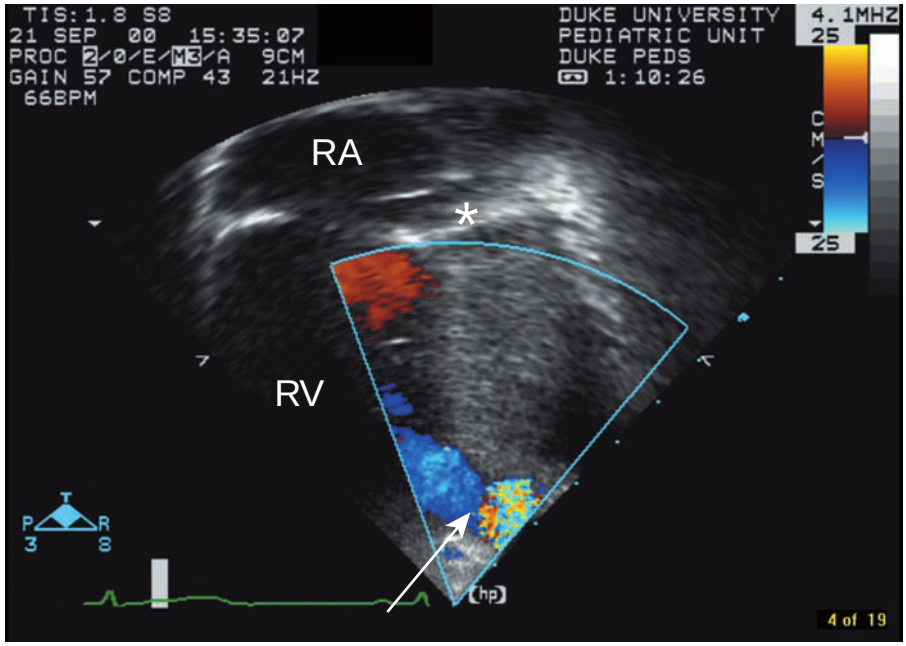


**Figure 29.22** Apical 4-chamber view posteriorly at the level of the coronary sinus. Fistulous flow enters the right ventricular apex near the interventricular septum (arrow). The asterisk (*) indicates the coronary sinus. RA, right atrium; RV, right ventricle.

## References

1. Abrikossoff A. Aneurysma des linken Herzeventrikels mit abnormer Abgangsstelle der linker Karonararterie von der Pulmonalis bei einem funfmonatichen Kinde. *Virchows Arch (Pathol Anat)* 1911;203:413–20.
2. Hackensellner HA. Uber akgessorische, von der Arteria pulmonalis abgehende Herzgfaesse und ihre Bedentung für das Verstaendnis der formalen Genese des Ursprunges einer oder beider Coronararterien von der Lungenschlagader. *Frankf Z Path* 1955;66:463–70.
3. Conte G, Pellegrini A. On the development of the coronary arteries in human embryos, stages 14–19. *Anat Embryol* 1984; 169:209–18.
4. Hutchins GM, Kessler-Hanna A, Moore GW. Development of the coronary arteries in the embryonic human heart. *Circulation* 1988;77:1250–7.
5. Braunwald E, Sobel BE. Coronary blood flow and myocardial ischemia. In: Braunwald E (ed.) *Heart Disease: a Textbook of*

*Cardiovascular Medicine*, 4th edn. Philadelphia: Saunders; 1992; 1161–99.
6. Hoffman JIE. Maximal coronary flow and the concept of coronary vascular reserve. *Circulation* 1984;70:153–9.
7. Lai WW, Geva T, Shirali GS et al. Guidelines and standards for performance of a pediatric echocardiogram: a report from the Task Force of the Pediatric Council of the American Society of Echocardiography. *J Am Soc Echocardiogr* 2006;19:1413–30.
8. Cotton JL. Diagnosis of a left coronary artery to right ventricular fistula with progression to spontaneous closure. *J Am Soc Echocardiogr* 2000;13:225–8.
9. Khan MD, Sivasubramonian S, Simpson JM. Prenatal diagnosis of tetralogy of Fallot associated with a fistula from the left coronary artery to the left atrium. *Cardiol Young* 2003;13:194–6.
10. Flamm SD, Muthupillai R. Coronary artery magnetic resonance angiography. *J Magn Reson Imaging* 2004;19:686–709.
11. Pannu HK, Flohr TG, Corl FM, Fishman EK. Current concepts in multi-detector row CT evaluation of the coronary arteries: principles, techniques, and anatomy. *Radiographics* 2003;23(Spec. No.):S111–25.
12. Dodd JD, Ferencik M, Liberthson RR et al. Congenital anomalies of coronary artery origin in adults: 64-MDCT appearance. *Am J Roentgenol* 2007;188:W138–46.
13. Neufeld HN, Schneeweiss A. *Coronary Artery Disease in Infants and Children.* Philadelphia: Lea and Febiger, 1983.
14. Dodge-Khatami A, Mavroudis C, Backer CL. Congenital Heart Surgery Nomenclature and Database Project: anomalies of the coronary arteries. *Ann Thorac Surg* 2000;69(4 Suppl.): S270–97.
15. Brooks HS. Two cases of an abnormal coronary artery of the heart arising from the pulmonary artery: with some remarks upon the effect of this anomaly in producing cirsoid dilatation of the vessels. *J Anat Physiol* 1886;20:26–9.
16. Abbott M. Congenital cardiac disease. In: Osler W (ed.) *Modern Medicine: its Theories and Practices*. Philadelphia: Lea and Febiger, 1908;323–425.
17. Bland EF, White PD, Garland J. Congenital anomalies of the coronary arteries: report of an unusual case associated with cardiac hypertrophy. *Am Heart J* 1933;8:787–801.
18. Keith JD. The anomalous origin of the left coronary artery from the pulmonary artery. *Br Heart J* 1959;21:149–61.
19. Rao BN, Lucas RV Jr, Edwards JE. Anomalous origin of the left coronary artery from the right pulmonary artery associated with ventricular septal defect. *Chest* 1970;58:616–20.
20. Pinsky WW, Gillette PC, Duff DF et al. Anomalous origin of left coronary artery from the pulmonary artery with ventricular septal defect. *Circulation* 1978;57:1026–30.
21. Hallman GL, Cooley DA, Singer DB. Congenital anomalies of the coronary arteries: anatomy, pathology, and surgical treatment. *Surgery* 1966;59:133–44.
22. Wilcox WD, Hagler DJ, Lie JT et al. Anomalous origin of left coronary artery from pulmonary artery in association with intracardiac lesions. Report of two cases. *J Thorac Cardiovasc Surg* 1979;78:12–20.
23. Driscoll DJ, Garson A Jr, McNamara DG. Anomalous origin of the left coronary artery from the right pulmonary artery associated with complex congenital heart disease. *Cathet Cardiovasc Diagn* 1982;8:55–61.
24. Arciniegas E, Farooki ZQ, Hakimi M, Green EW. Management of anomalous left coronary artery from the pulmonary artery. *Circulation* 1980;62:I180–9.
25. Nehgme RA, Dewar ML, Lutin WA et al. Anomalous left coronary artery from the main pulmonary trunk: physiologic and clinical importance of its association with persistent ductus arteriosus. *Pediatr Cardiol* 1992;13:97–9.
26. Heifetz SA, Robinowitz M, Mueller KH, Virmani R. Total anomalous origin of the coronary arteries from the pulmonary artery. *Pediatr Cardiol* 1986;7:11–8.
27. Edwards JE. The direction of blood flow in coronary arteries arising from the pulmonary trunk. *Circulation* 1964;29:163–6.
28. Askenazi J, Nadas AS. Anomalous left coronary artery originating from the pulmonary artery. Report on 15 cases. *Circulation* 1975;51:976–87.
29. Wright NL, Baue AE, Baum S et al. Coronary artery steal due to an anomalous left coronary artery originating from the pulmonary artery. *J Thorac Cardiovasc Surg* 1970;59:461–7.
30. Wesselhoeft H, Fawcett JS, Johnson AL. Anomalous origin of the left coronary artery from the pulmonary trunk. Its clinical spectrum, pathology, and pathophysiology, based on a review of 140 cases with seven further cases. *Circulation* 1968;38: 403–25.
31. Rein AJ, Colan SD, Parness IA, Sanders SP. Regional and global left ventricular function in infants with anomalous origin of the left coronary artery from the pulmonary trunk: preoperative and postoperative assessment. *Circulation* 1987;75:115–23.
32. Schmidt KG, Cooper MJ, Silverman NH, Stanger P. Pulmonary artery origin of the left coronary artery: diagnosis by two-dimensional echocardiography, pulsed Doppler ultrasound and color flow mapping. *J Am Coll Cardiol* 1988;11:396–402.
33. Karr SS, Parness IA, Spevak PJ et al. Diagnosis of anomalous left coronary artery by Doppler color flow mapping: distinction from other causes of dilated cardiomyopathy. *J Am Coll Cardiol* 1992;19:1271–5.
34. Williams IA, Gersony WM, Hellenbrand WE. Anomalous right coronary artery arising from the pulmonary artery: a report of 7 cases and a review of the literature. *Am Heart J* 2006;152: 1004.e9–.e17.
35. Tingelstad JB, Lower RR, Eldredge WJ. Anomalous origin of the right coronary artery from the main pulmonary artery. *Am J Cardiol* 1972;30:670–3.
36. Bregman D, Brennan FJ, Singer A et al. Anomalous origin of the right coronary artery from the pulmonary artery. *J Thorac Cardiovasc Surg* 1976;72:626–30.
37. Lerberg DB, Ogden JA, Zuberbuhler JR, Bahnson HT. Anomalous origin of the right coronary artery from the pulmonary artery. *Ann Thorac Surg* 1979;27:87–94.
38. Roberts WC. Major anomalies of coronary arterial origin seen in adulthood. *Am Heart J* 1986;111:941–63.
39. Urcelay GE, Iannettoni MD, Ludomirsky A et al. Origin of both coronary arteries from the pulmonary artery. *Circulation* 1994; 90:2379–84.
40. Tanaka SA, Takanashi Y, Nagatsu M et al. Origin of the left coronary artery from the right pulmonary artery. *Ann Thorac Surg* 1996;61:986–8.
41. Cheitlin MD, De Castro CM, McAllister HA. Sudden death as a complication of anomalous left coronary origin from the

anterior sinus of Valsalva, A not-so-minor congenital anomaly. *Circulation* 1974;50:780–7.
42. Davia JE, Green DC, Cheitlin MD et al. Anomalous left coronary artery origin from the right coronary sinus. *Am Heart J* 1984; 108:165–6.
43. Barth CW 3rd, Roberts WC. Left main coronary artery originating from the right sinus of Valsalva and coursing between the aorta and pulmonary trunk. *J Am Coll Cardiol* 1986;7:366–73.
44. Chu E, Cheitlin MD. Diagnostic considerations in patients with suspected coronary artery anomalies. *Am Heart J* 1993;126: 1427–38.
45. Bunce NH, Lorenz CH, Keegan J et al. Coronary artery anomalies: assessment with free-breathing three-dimensional coronary MR angiography. *Radiology* 2003;227:201–8.
46. Deibler AR, Kuzo RS, Vohringer M et al. Imaging of congenital coronary anomalies with multislice computed tomography. *Mayo Clin Proc* 2004;79:1017–23.
47. Brandt B 3rd, Martins JB, Marcus ML. Anomalous origin of the right coronary artery from the left sinus of Valsalva. *N Engl J Med* 1983;309:596–8.
48. Taylor AJ, Rogan KM, Virmani R. Sudden cardiac death associated with isolated congenital coronary artery anomalies. *J Am Coll Cardiol* 1992;20:640–7.
49. Frommelt PC, Frommelt MA, Tweddell JS, Jaquiss RD. Prospective echocardiographic diagnosis and surgical repair of anomalous origin of a coronary artery from the opposite sinus with an interarterial course. *J Am Coll Cardiol* 2003;42:148–54.
50. Jaggers J, Lodge AJ. Surgical therapy for anomalous aortic origin of the coronary arteries. *Semin Thorac Cardiovasc Surg Pediatr Card Surg Annu* 2005:122–7.
51. Choi JH, Kornblum RN. Pete Maravich's incredible heart. *J Forensic Sci* 1990;35:981–6.
52. Smith JC. Review of single coronary artery with report of 2 cases. *Circulation* 1950;1:1168–75.
53. Ogden JA, Goodyer AV. Patterns of distribution of the single coronary artery. *Yale J Biol Med* 1970;43:11–21.
54. Shirani J, Roberts WC. Solitary coronary ostium in the aorta in the absence of other major congenital cardiovascular anomalies. *J Am Coll Cardiol* 1993;21:137–43.
55. Click RL, Holmes DR Jr, Vlietstra RE et al. Anomalous coronary arteries: location, degree of atherosclerosis and effect on survival – a report from the Coronary Artery Surgery Study. *J Am Coll Cardiol* 1989;13:531–7.
56. Daoud AS, Pankin D, Tulgan H, Florentin RA. Aneurysms of the coronary artery. Report of ten cases and review of literature. *Am J Cardiol* 1963;11:228–37.
57. Harris PN. Aneurysmal dilatation of the cardiac coronary arteries: review of the literature and report of a case. *Am J Pathol* 1937;13:89–98.
58. Dawson JE Jr, Ellison RG. Isolated aneurysm of the anterior descending coronary artery. Surgical treatment. *Am J Cardiol* 1972;29:868–71.
59. Ebert PA, Peter RH, Gunnells JC, Sabiston DC Jr. Resecting and grafting of coronary artery aneurysm. *Circulation* 1971;43: 593–8.
60. Ghahramani A, Iyengar R, Cunha D et al. Myocardial infarction due to congenital coronary arterial aneurysm (with successful saphenous vein bypass graft). *Am J Cardiol* 1972;29:863–7.
61. Gray LA Jr, McMartin DE. Surgical treatment of coronary artery aneurysm with rupture into the right atrium. *J Thorac Cardiovasc Surg* 1977;74:455–60.
62. Krause W. Uber den Ursprung einer Accessorischen A. Coronaria Cordis aus der A pulmonalis. *Z Rationalle Med* 1865;24: 225–7.
63. McNamara JJ, Gross RE. Congenital coronary artery fistula. *Surgery* 1969;65:59–69.
64. Fernandes ED, Kadivar H, Hallman GL et al. Congenital malformations of the coronary arteries: the Texas Heart Institute experience. *Ann Thorac Surg* 1992;54:732–40.
65. Luo L, Kebede S, Wu S, Stouffer GA. Coronary artery fistulae. *Am J Med Sci* 2006;332:79–84.
66. Neufeld HN, Lester RG, Adams PJ et al. Congenital communication of a coronary artery with a cardiac chamber or the pulmonary trunk ("coronary artery fistula"). *Circulation* 1961;24:171–9.
67. Bishop JO, Mathur VS, Guinn GA. Letter: Congenital coronary artery fistula with myocardial infarction. *Chest* 1974;65:233–4.
68. Velvis H, Schmidt KG, Silverman NH, Turley K. Diagnosis of coronary artery fistula by two-dimensional echocardiography, pulsed Doppler ultrasound and color flow imaging. *J Am Coll Cardiol* 1989;14:968–76.
69. Fischer G, Apostolopoulou SC, Rammos S et al. Transcatheter closure of coronary arterial fistulas using the new Amplatzer vascular plug. *Cardiol Young* 2007;17:283–7.
70. Bafani E, Shukla AC, DiNardo JA. Unrecognized anomalous origin of the left coronary artery from the pulmonary artery as a cause of ventricular fibrillation after patent ductus arteriosus ligation in an infant. *Anesth Analg* 2007;104:81–3.

# 30 Vascular Rings and Slings

**Andrew J. Powell**
Cardiovascular MRI, Children's Hospital Boston, Boston, MA, USA

Airway obstruction in children and its accompanying symptoms of stridor and respiratory distress can be caused by intrinsic abnormalities of the tracheobronchial tree and/or extrinsic compression of the airway. Among the causes of the latter are selected abnormalities in the embryologic development of the aorta or pulmonary arteries, which may be grouped together as vascular rings and slings.

## Vascular rings

### Definition

A vascular ring is an anomaly of aortic arch development that results in complete encirclement of the trachea and the esophagus by vascular structures. Some of the vascular components of the ring may not be patent but rather consist of fibrous remnants such as the ductal ligament or an atretic segment of the aorta [1].

### Incidence

Because some vascular rings may not cause symptoms, the true prevalence of vascular rings is difficult to ascertain. They are clearly a rare anomaly and most evidence indicates that they represent approximately 1–3% of congenital cardiovascular anomalies [2]. Based on surgical case series, a double aortic arch is the most common vascular ring, followed by a right aortic arch with an aberrant left subclavian artery and a left ductal ligament [3–7]. Usually vascular rings are isolated abnormalities, although they may occur with other congenital heart disease, most commonly ventricular septal defect and tetralogy of Fallot [6].

### Etiology

The etiology of most vascular rings is unknown. Chromosome 22q11 deletions are associated with isolated aortic arch anomalies including vascular rings, as well as with conotruncal cardiac defects and noncardiac abnormalities [8].

### Morphology and classification

#### Developmental considerations

Knowledge of the morphogenesis of the aortic arch system provides a framework for understanding and classifying the wide variety of vascular rings [9,10]. In the early embryo, six paired arches form to connect the truncus arteriosus of the embryonic heart tube to the paired dorsal aortas, which fuse to form the descending aorta (Fig. 30.1). In humans, the arches develop sequentially, and persist or regress but are never all present simultaneously. In normal development, the first arches contribute to the external carotid arteries (Table 30.1). The second arches regress rapidly and only a portion remains to form the stapedial and hyoid arteries. The third arches become the common carotid arteries and the proximal portion of the internal carotid arteries. The left fourth arch forms that part of the definitive left aortic arch between the left carotid and left subclavian arteries. The right fourth arch is incorporated into the proximal right subclavian artery. The fifth arches regress. For the sixth arches, the proximal parts form the branch pulmonary arteries, and the distal portions join the pulmonary vascular tree to the descending aorta via bilateral ductus, with the right usually regressing completely to leave a left ductus arteriosus. Between the sixth arches (the ductus) and the descending aorta are the paired dorsal aortas, which connect to the descending aorta. The seventh intersegmental arteries arise from the dorsal aortas and become the left subclavian and the distal right subclavian arteries. When the right dorsal aorta regresses, as is usual, the definitive left aortic arch is formed.

In conjunction with embryologic anatomy, the hypothetical double-arch model, originally introduced by Edwards [11] and modified, simplified and redrawn many times since, helps in understanding various arch anomalies (Fig. 30.2). In this model, the ascending aorta divides into two arches, one passing to the right of the trachea and esophagus and the other to the left. These arches join posteriorly to form the descending aorta. From each arch there is a segment that gives rise to the right and left common carotids as the first

*Echocardiography in Pediatric and Congenital Heart Disease: From Fetus to Adult*
Edited by Wyman W. Lai, Luc L. Mertens, Meryl S. Cohen and Tal Geva
 ISBN: 978-1-405-17401-5

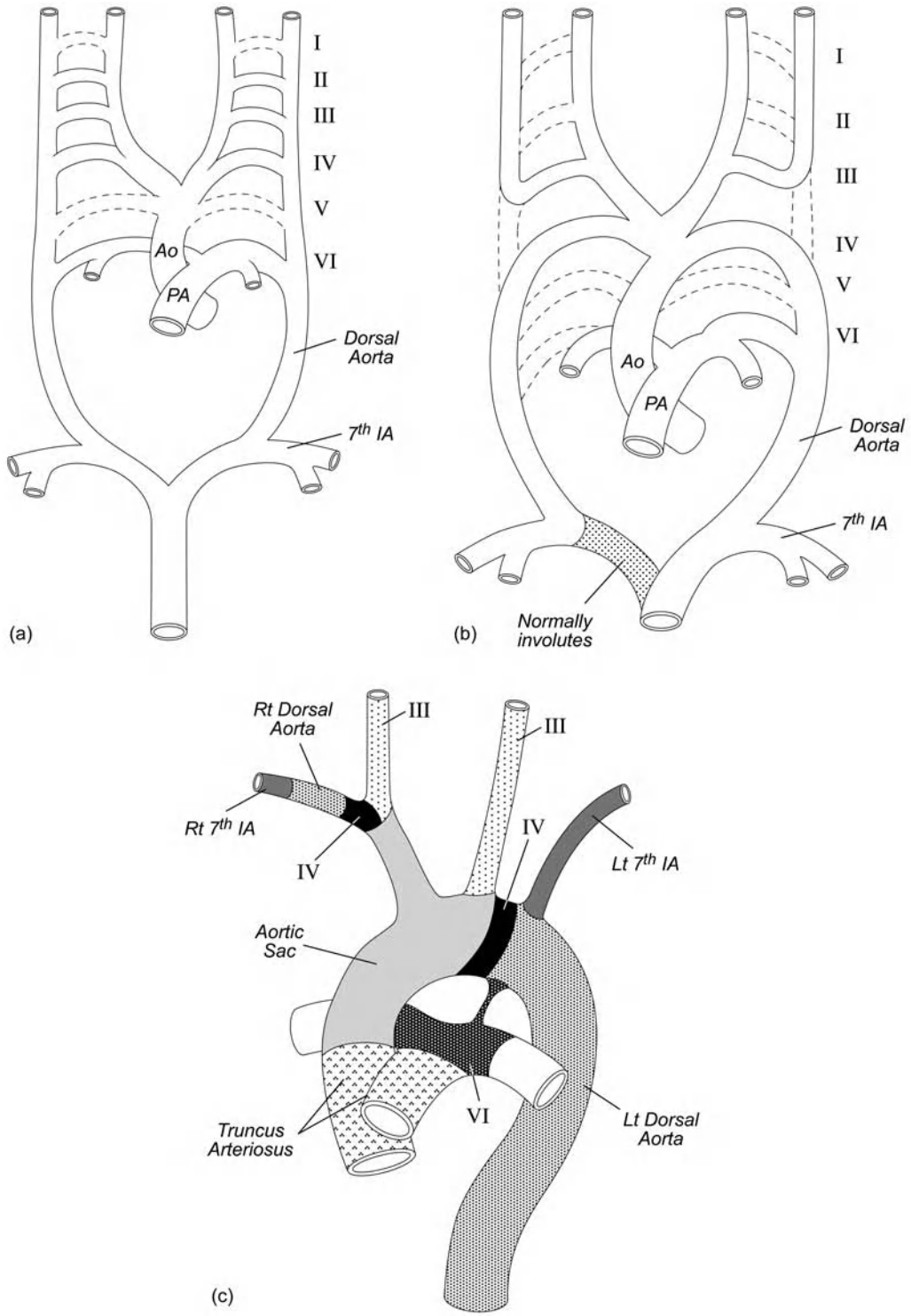


**Figure 30.1** Diagrammatic representation of normal aortic arch development at **(a)** 5 weeks, **(b)** 7 weeks and **(c)** maturity. Roman numerals enumerate the embryonic aortic arches. Ao, ascending aorta; Lt, left; PA, main pulmonary artery; Rt, right; 7th IA, seventh intersegmental artery.

branches on either side, and the right and left subclavian arteries as the second branches on either side. A ductus arises from the proximal aspect of each subclavian segment. This model allows anomalies of the aortic arch to be conceptualized as variations in regression of segments of the hypothetical double arch. A further simplified line drawing is easily sketched and can be used in daily practice to conceptualize almost every known arch anomaly (Fig. 30.3).

**Table 30.1** Normal development of the embryonic aortic arches

| Embryonic structure | Outcome |
|---|---|
| Truncus arteriosus | Proximal ascending aorta and pulmonary root |
| Aortic sac | Distal ascending aorta, innominate artery, and arch to the origin of the left common carotid artery (proximal aortic arch) |
| 1st arch | Portion of the external carotid artery |
| 2nd arch | Portions of the hyoid and stapedial arteries |
| 3rd arch | Common carotid artery and proximal internal carotid artery |
| 4th arch | |
| Left | Aortic arch segments between the left common carotid and left subclavian arteries (distal aortic arch) |
| Right | Proximal right subclavian artery |
| 5th arch | Complete involution |
| 6th arch | |
| Left | Proximal portion becomes the proximal left pulmonary artery; distal portion becomes the ductus arteriosus |
| Right | Proximal portion becomes the proximal right pulmonary artery; distal portion involutes |
| Left dorsal aorta | Aortic isthmus distal to the left subclavian artery |
| Right dorsal aorta | Cranial portion becomes the right subclavian artery distal to the contribution from the right 4th arch; distal portion involutes |
| Left 7th intersegmental artery | Left subclavian artery |
| Right 7th intersegmental artery | Distal right subclavian artery |

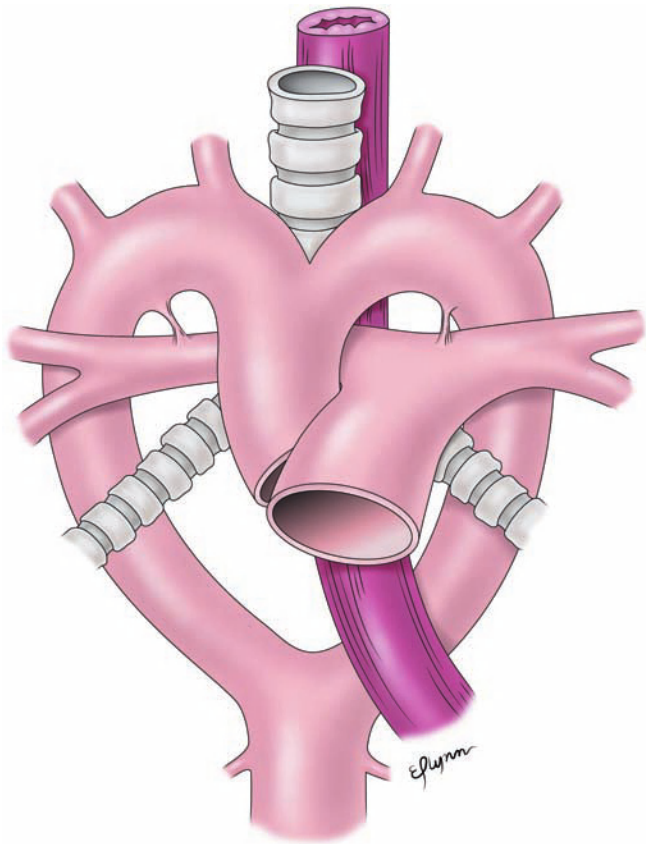

**Figure 30.2** Edwards' hypothetical double aortic arch with bilateral ductus.

## Anatomy

### *Double aortic arch*

In a double aortic arch, both of the embryonic right and left arches persist, arising from the ascending aorta, passing on both sides of the trachea and esophagus, and joining posteriorly to form the descending aorta, thereby completely encircling the trachea and esophagus (Figs 30.4 and 30.5; Fig. 30.3a and Videoclips 30.1 and 30.2). A ductal ligament usually contributes to the ring and is most often left-sided. The carotid and subclavian arteries arise separately from each arch and are usually symmetrically positioned around the trachea. The right arch is larger than the left in approximately 75% of cases, and typically higher as well [12]. Occasionally, a segment of an arch (usually the left) may be atretic with a fibrous cord either between the carotid and subclavian arteries, or distal to the left subclavian artery. In such cases, the aortic arch branching pattern evident on imaging studies may mimic other aortic anomalies.

### *Right aortic arch with an aberrant left subclavian artery*

In the hypothetical double arch paradigm, a right aortic arch with an aberrant left subclavian artery is the result of regression of the left aortic arch segment between the left common carotid and subclavian segments (Fig. 30.3e). As a result, the left subclavian artery originates as the last branch from the aortic arch, at a relatively posterior location, coursing behind the esophagus to the left arm. A left ductal ligament originates from a bulbous dilation at the base of the left subclavian artery (termed diverticulum of Kommerell) and attaches to the proximal left pulmonary artery, effectively pulling the aorta and the diverticulum forward, compressing

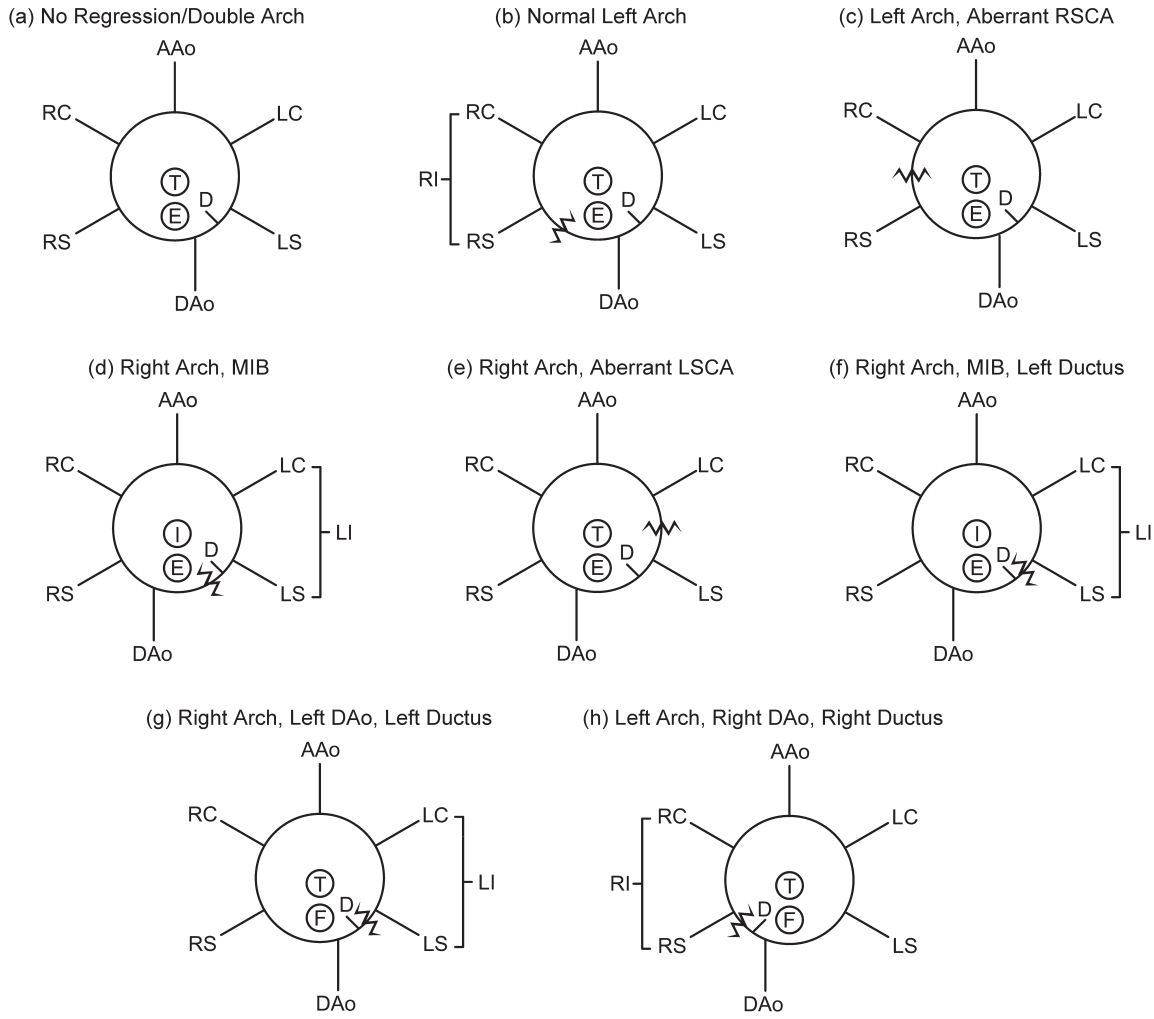


**Figure 30.3 (a–h)** Simple line drawings illustrating how anomalies of the aortic arch can be conceptualized as variations in regression of segments of the hypothetical double arch. The jagged line indicates regression of that arch segment. AAo, ascending aorta; D, ductus; DAo, descending aorta; E, esophagus; LC, left carotid; LI, left innominate artery; LS, left subclavian; LSCA, left subclavian artery; MIB, mirror-image branching; RC, right carotid; RI, right innominate artery; RS, right subclavian; RSCA, right subclavian artery; T, trachea.

the esophagus and trachea, and forming a vascular ring (Fig. 30.6 and Videoclips 30.3 and 30.4). Rarely, the ductus arteriosus is right-sided and connects the right pulmonary artery to the right-sided aortic arch, and thus no vascular ring is formed. In such cases, there is no diverticulum of Kommerell and the caliber of the left subclavian artery is uniform throughout.

### *Right aortic arch with mirror-image branching and a left ductus arteriosus*

A right aortic arch with mirror-image branching has the first branch off the arch as the innominate artery followed by the right carotid and the right subclavian arteries (Fig. 30.3d). Typically, this is the end to the mirror-image symmetry of the normal left aortic arch as the ductus arteriosus usually is left-sided, arising anteriorly from the base of the innominate artery rather than posteriorly from the descending aorta (Videoclips 30.5 and 30.6). Less frequently, the ductus arises from the descending aorta and connects to the proximal right pulmonary artery, yielding the true mirror image of the normal left aortic arch. Because in both of these cases there is no left-sided encirclement of the trachea and esophagus, neither forms a vascular ring. On occasion, however, the ductus or ligament arises from the right-sided descending aorta, stemming from a retroesophageal diverticulum, courses leftward and then connects to the proximal left pulmonary artery. A vascular ring is thereby formed from the right aortic arch, retroesophageal ductal diverticulum, and left-sided ductal ligament (Fig. 30.7). Embryologically, this ring results from regression of a segment of left dorsal aorta between the left seventh intersegmental artery (destined to become the subclavian artery) and the left sixth arch

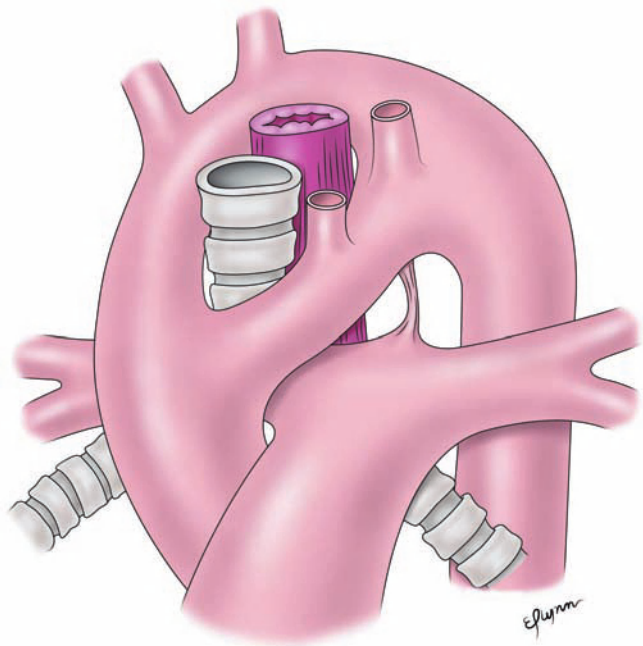

**Figure 30.4** Drawing of a double aortic arch. The ring encircling the trachea and esophagus comprises the right and left aortic arches, and the ductal ligament.

(destined to become the ductus arteriosus as well as the right sixth arch) (Fig. 30.3f).

### *Right aortic arch with a left descending aorta and a left ductus arteriosus*

In this type of vascular ring there is a right aortic arch that curves leftward to pass posterior to the esophagus and trachea and then joins a left-sided descending aorta. A left ductus arteriosus or ductal ligament connects the descending aorta and the proximal left pulmonary artery completing the vascular ring (Fig. 30.8 and Videoclips 30.7 and 30.8). Note that unlike the more common type of right aortic arch, in which the aorta descends to the right of the spine for some distance before gradually crossing to the left of the spine at about the level of the diaphragm, in this anomaly, the aortic arch itself crosses to the left and is posterior to the esophagus, after which it gives rise to the ductus arteriosus. Because of the course of the aorta, some authors have called this a "circumflex retroesophageal right aortic arch." The arch vessel branching pattern may be either the left carotid artery followed by the right carotid, right subclavian and left subclavian arteries, or the left innominate followed by the right carotid and right subclavian arteries. Developmentally, depending on the branching pattern, this anomaly results from either regression of the left fourth arch or left dorsal aorta distal to the left subclavian artery (Fig. 30.3g). The distal arch is composed of the retroesophageal right-sided dorsal aorta, and the persistent left sixth arch (ductus) completes the ring.

### *Left aortic arch with a right descending aorta and right ductus arteriosus*

This anomaly is nearly a mirror-image version of the right aortic arch with a left descending aorta and left ductus arteriosus mentioned above, but is less common. A left aortic arch courses posterior to the esophagus and trachea and to the right leading to a right-sided descending aorta. A ductus or ductal ligament connects the descending aorta and the proximal right pulmonary artery completing the vascular ring (Fig. 30.9). Developmentally, this anomaly results from the regression of the right fourth arch (segment between the right common carotid and right subclavian segments), persistence of the left dorsal aorta passing retroesophageally to a descending aorta beginning to the right of the spine, and persistence of the right sixth arch (Fig. 30.3h).

## Pathophysiology

Vascular rings can cause varying degrees of compression of the trachea and esophagus. Mild tracheal compression may be asymptomatic. More significant involvement in younger patients may manifest as stridor, dyspnea and a barking cough, all of which are worse during feeding or exertion [4–7]. "Reflex" apnea lasting seconds or even minutes may be triggered by feeding. Older children may have a history of chronic cough or wheezing misdiagnosed as asthma. Symptoms related to esophageal compression are less frequent and less well defined. They include vomiting, choking and nonspecific feeding difficulties in infants, and dysphagia and slow eating in older children.

## Imaging

The diagnosis of vascular rings requires a high index of suspicion because of the relative infrequency of this entity compared with other conditions that cause respiratory distress in children such as asthma, respiratory infection, and gastroesophageal reflux. Once suspected, diagnostic imaging studies should be obtained with the goals of (1) identifying the cause of a patient's symptoms by demonstrating the relevant vascular and airway anatomy, and (2) preoperative planning. If video-assisted thoracoscopic surgery is available, it is important to determine whether the ring can be released by dividing ligamentous (nonpatent) or hypoplastic portions. This requires the diagnostician to have a high level of certainty regarding vessel caliber and patency throughout the ring. For both thoracoscopic and open surgery, the diagnosis must be established confidently enough to determine whether a right, left, or midline approach is appropriate.

Many imaging modalities are in use to evaluate vascular rings including chest radiographs, barium contrast esophagrams, bronchoscopy, X-ray angiography, transthoracic echocardiography, computed tomography, and magnetic resonance imaging. Development of a single universal diagnostic imaging algorithm is complicated by varying ages and modes of presentation and the numerous specialists involved in such

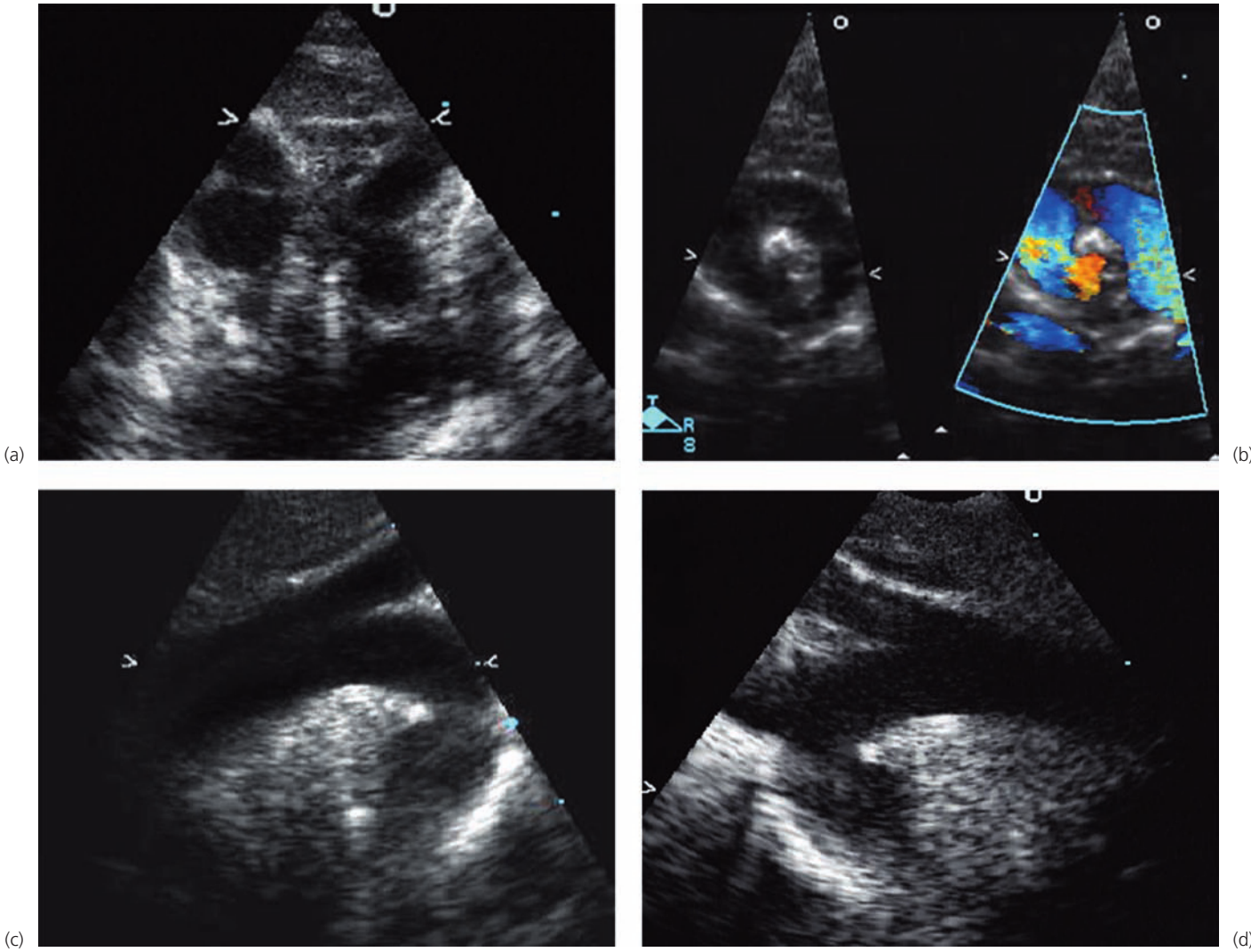


**Figure 30.5** Double aortic arch. Echocardiogram using a suprasternal notch window. **(a)** Transverse view superior to the arch level illustrating the symmetric origins of the right and left carotid and subclavian arteries from their respective arches. **(b)** Transverse view demonstrating the right and left aortic arches with 2D and color Doppler imaging. **(c)** Long-axis view of the unobstructed left aortic arch. **(d)** Long-axis view of the unobstructed right aortic arch. Note that by convention right aortic arches are displayed with the right–left screen orientation inverted so that superior structures are positioned to the left on the screen.

cases. There are no reported studies that rigorously compare different imaging strategies with respect to accuracy, patient safety and cost-effectiveness. In practice, a center's diagnostic testing algorithm is tailored to fit local expertise, experience, costs, and available technology. The approach is then individualized to the patient, taking into account severity of symptoms, previous findings, age, and other medical conditions. It is important to note that no imaging modality except direct visualization can show ligamentous or atretic structures. Their presence is typically inferred based on anatomic patterns, the position of vessels, and the presence of a diverticulum or dimple.

Echocardiography can provide a good depiction of the relevant vasculature and in many cases is sufficient for diagnosis and surgical planning [13,14]. It has the additional advantage of being able to define associated cardiovascular anomalies. Its principal weakness is poor visualization of the airway and esophagus. In addition, not infrequently portions of the dorsal aortic arch may be obscured by the trachea, and posterior vessels such as aberrant subclavian arteries may be difficult to visualize in their entirety. Because of these limitations, the evaluation for a vascular ring with echocardiography may be incomplete and additional imaging with computed tomography or magnetic resonance imaging may be indicated (Fig. 30.10).

In practice, if a left aortic arch with a normal branching pattern is clearly demonstrated by echocardiography, a vascular ring is excluded. Note, however, that simply demonstrating

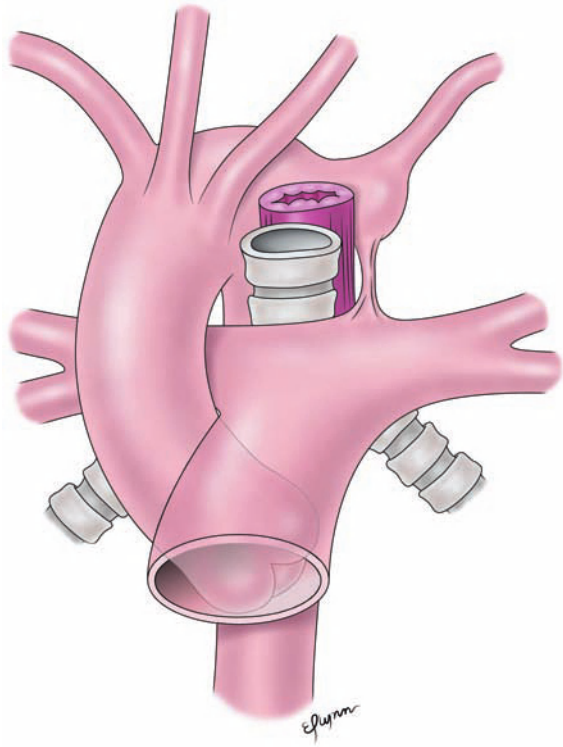

**Figure 30.6** Drawing of a right aortic arch with an aberrant origin of the left subclavian artery. The ring encircling the trachea and esophagus comprises the right aortic arch, base of the left subclavian artery (diverticulum of Kommerell) and the left-sided ductal ligament.

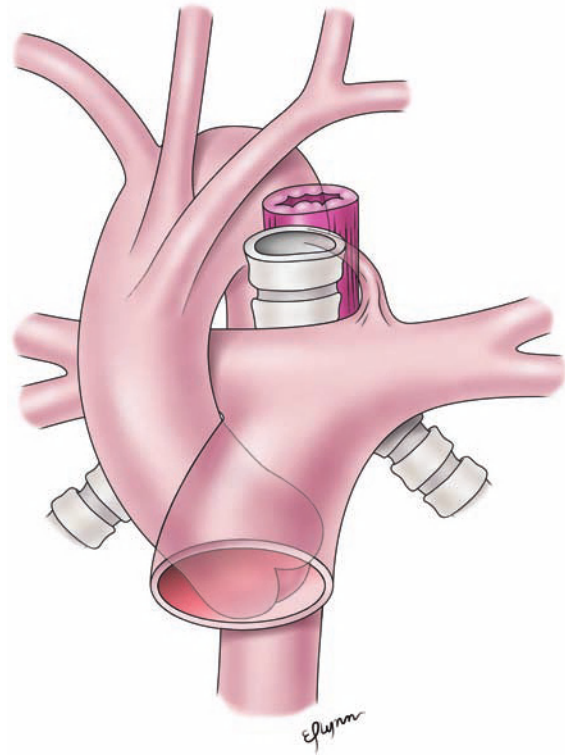

**Figure 30.7** Drawing of a right aortic arch with mirror-image branching and a left ductal ligament. The ring encircling the trachea and esophagus comprises the right aortic arch, retroesophageal ductal diverticulum and left-sided ductal ligament.

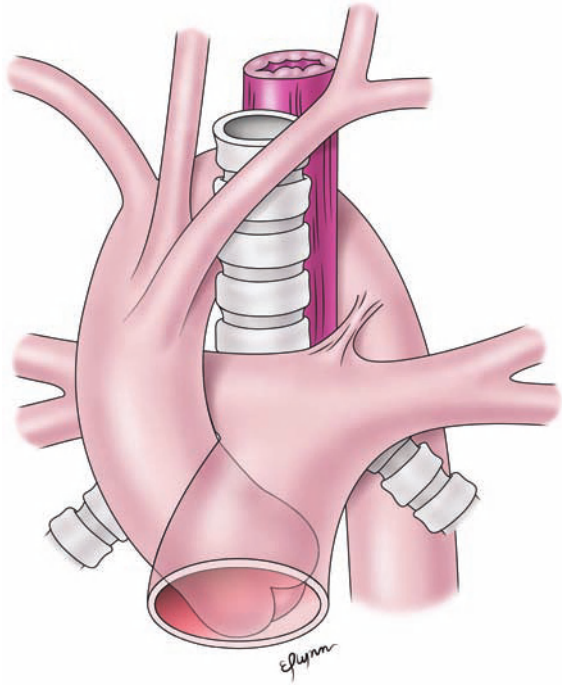

**Figure 30.8** Drawing of a right aortic arch with mirror-image branching, a left descending aorta and a left ductal ligament. The ring encircling the trachea and esophagus comprises the right aortic arch, retroesophageal right-sided dorsal aorta, and left-sided ductal ligament.

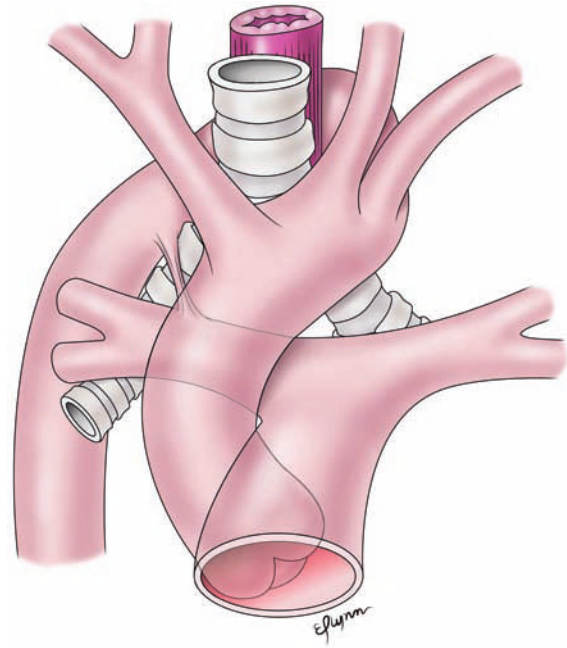

**Figure 30.9** Drawing of a left aortic arch with normal branching, a right descending aorta and a right ductal ligament. The ring encircling the trachea and esophagus comprises the left aortic arch, retroesophageal left-sided dorsal aorta, and right-sided ductal ligament.

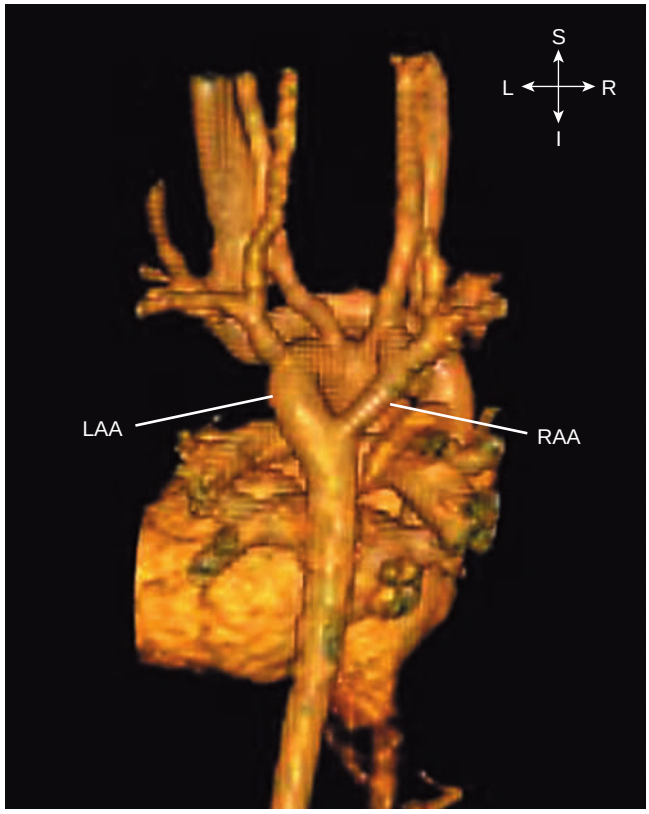


(a)

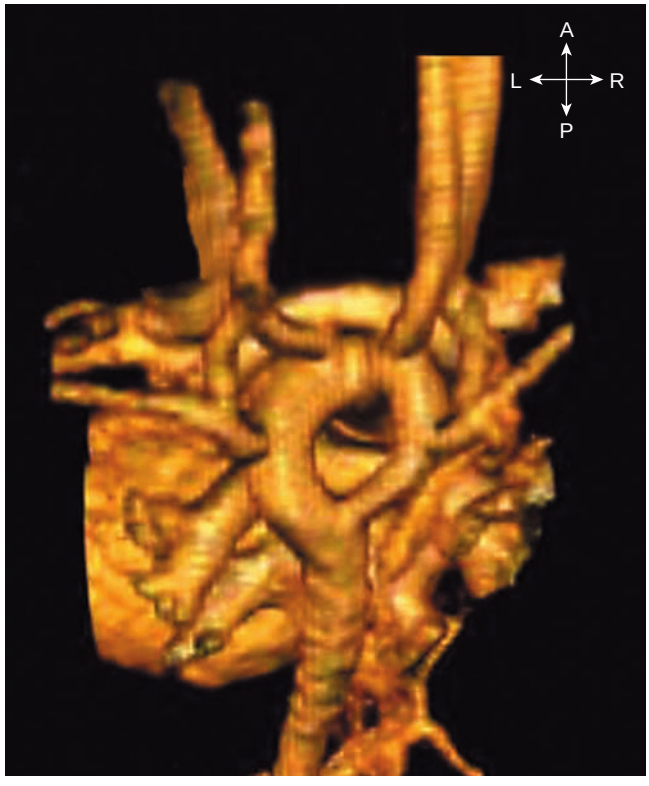


(b)

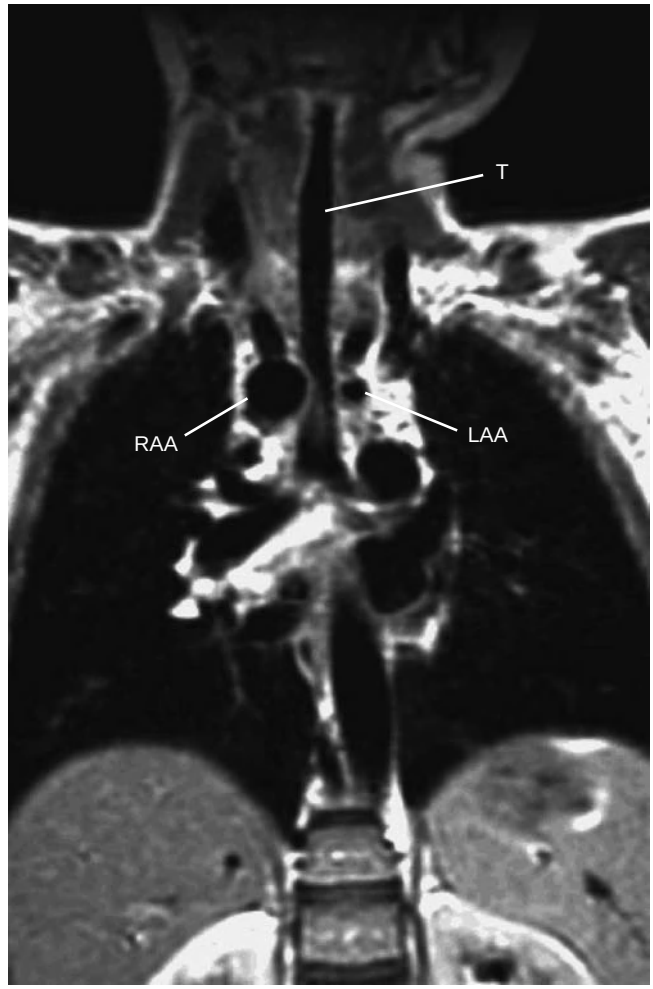


(c)

**Figure 30.10** Double aortic arch with both arches patent. Volume-rendered 3D magnetic resonance angiogram viewed from **(a)** posterior and **(b)** superior vantage points. **(c)** Magnetic resonance imaging using fast spin-echo imaging and blood signal suppression in an oblique coronal plane illustrating tracheal compression by the right and left aortic arches, which are seen in cross-section. LAA, left aortic arch; RAA, right aortic arch; T, trachea.

the presence of a right aortic arch with mirror-image branching does not always exclude a vascular ring. This pattern may be seen in rings such as right aortic arch with mirror-image branching and a left ductus, or a double aortic arch with an atretic left arch segment distal to the left subclavian artery. Features that can help identify these uncommon vascular rings, such as tracheal narrowing and the presence of a dimple or diverticulum, are difficult or impossible to detect by echocardiography.

### Echocardiography imaging protocol

As with all medical procedures, proper preparation is paramount and will maximize the likelihood of success. The

medical history and prior imaging studies should be reviewed. Sedation with appropriate monitoring should be used in those patients who are unable to cooperate for a comprehensive echocardiogram, and is well tolerated even in patients with moderate degrees of stridor [13]. The suprasternal notch and high parasternal windows are the most useful for examining the aortic arch, and, typically, imaging is optimized by elevating the patient's shoulders with a cushion so that the neck is extended approximately 30°. From either of these windows, it is useful to begin this portion of the examination with an axial (transverse) sweep of the transducer (i.e., marker directed to the patient's left). The sweep begins inferiorly showing the ascending aorta and superior vena cava in cross-section, passing superiorly through the pulmonary arteries and continuing through the aortic arch and its branches. It is often necessary to reposition the transducer to best follow the branching of the vessels arising from the aortic arch. From these images, arch sidedness can be determined based on whether the transverse arch courses to the left (left arch) or right (right arch) of the trachea. The trachea is identified as an echo-bright structure (because it is air-filled) that runs vertically in the midline (Fig. 30.11). A left aortic arch will curve to the left as it is followed distally to a descending aorta that is positioned left of the spine. However, because the ascending aorta is positioned relatively rightward to start, a right aortic arch will be primarily directed straight posteriorly, rather than rightward, as it is followed distally to a descending aorta that is usually positioned to the right of the spine (Fig. 30.11 and Videoclips 30.3 and 30.5). In a double aortic arch, the ascending aorta is seen to split into two arch vessels, which course to the right and left of the trachea (Fig. 30.5 and Videoclips 30.1 and 30.2). As the trachea can sometimes be difficult to identify, some echocardiographers have found it helpful to highlight the esophagus by having the patient drink a liquid (preferably carbonated) and then use this as a midline landmark and substitute for the trachea to determine whether the arch passes to the left or right.

The branching pattern of the aortic arch vessels should also be defined from the axial sweeps and can be of some help in identifying arch sidedness. One can begin by determining whether the first (i.e., most proximal) vessel off the arch is an innominate artery by following it superiorly and laterally and demonstrating that it bifurcates into two vessels of nearly equal caliber – a common carotid artery that continues into the neck and a subclavian artery that courses toward the shoulder. To demonstrate bifurcation, it may be helpful to rotate the transducer to image the suspected innominate artery and branches in the long-axis view. The innominate artery is also typically larger at its origin than the other vessels off the arch. One must be careful not to mistake the bifurcation of the superior vena cava into the subclavian and jugular veins for the innominate artery bifurcation. Demonstration of an arterial flow pattern in the vessels by pulsed wave or color Doppler will help avoid this error. Note also that some patients, particularly those with a chromosome 22q11 deletion, may have an unusually distal bifurcation. If bifurcation of the first branch off the arch cannot be demonstrated (i.e., it is not an innominate artery), the branch is usually a carotid artery and the echocardiographer should suspect the presence of an aberrant origin of the subclavian artery from the descending aorta. Other possibilities in this situation include double aortic arch and isolation of the subclavian artery. Efforts should be made to visualize

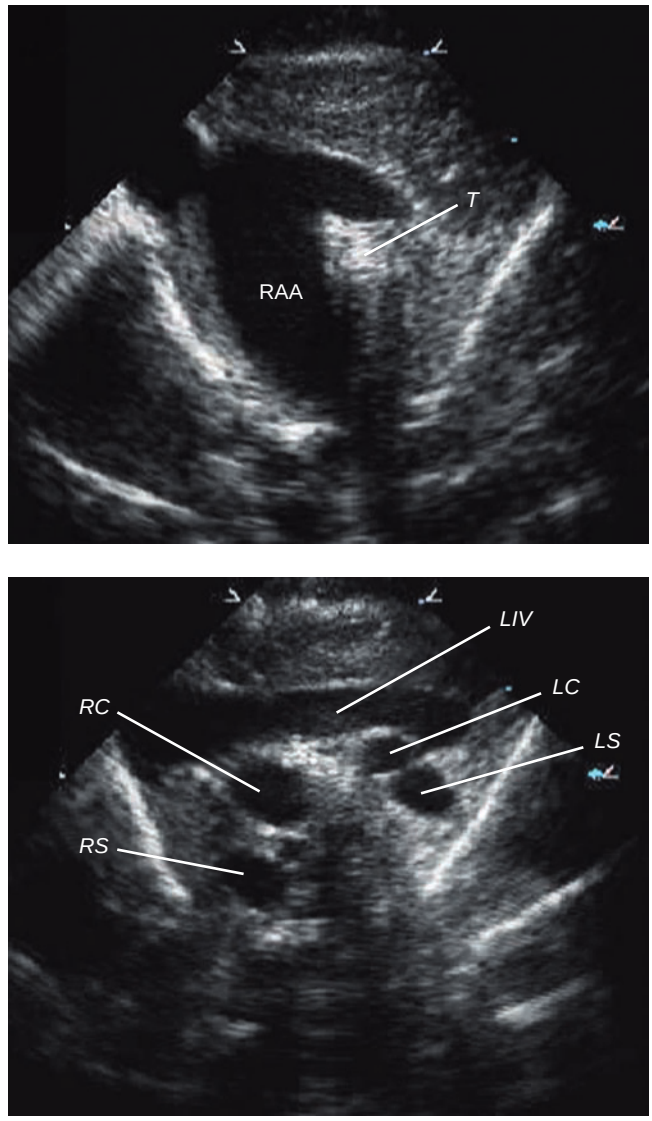


**Figure 30.11** Right aortic arch and mirror-image branching. Echocardiogram using a suprasternal notch window. **(a)** Transverse view showing the transverse aortic arch (RAA) positioned to the right of the echo-bright trachea (T). **(b)** Transverse view superior to the aortic arch showing the arch vessel branching pattern. LC, left carotid artery; LIV, left innominate vein; LS, left subclavian artery; RC, right carotid artery; RS, right subclavian artery.

the aberrant subclavian artery by imaging the proximal descending aorta from a suprasternal notch window, aiming the transducer toward the feet in an oblique coronal imaging plane (Videoclips 30.4 and 30.9). The aberrant subclavian arises from the medial aspect of the descending aorta and crosses the midline and courses superiorly. Color Doppler imaging is useful in highlighting the vessel; blood flow in it will usually be toward the transducer (i.e., red).

After demonstrating the bifurcation of the first arch branch, the other arch vessels and the location of the proximal descending aorta should be identified. Echocardiographers should be familiar with two frequent normal variants of the left aortic arch. One is the common brachiocephalic trunk (also known as a bovine, or ovine trunk) in which the innominate and left carotid arteries arise from a single origin [15]. The second is a separate origin of the left vertebral artery from the aortic arch proximal to the left subclavian artery rather than from the subclavian artery. Once the branching pattern of the aortic arch vessels is known, it can help confirm the sidedness of the arch. In all cases, except the very rare isolated or aberrant innominate artery, the first arch vessel contains a carotid artery opposite to the side of the aortic arch [1]. Thus in a right aortic arch, the first (i.e., most proximal) branch should course to the left and either bifurcate into left carotid and subclavian arteries as in mirror-image branching or continue without bifurcating as the left carotid artery, as in an aberrant origin of the left subclavian artery (Videoclip 30.3). In a double aortic arch, the carotid and subclavian arteries arise separately from their respective arches. As a result, the initial axial sweeps often reveal a view of the aorta and its vessels with right–left symmetry, which is quite characteristic of a double aortic arch (Fig. 30.5a and Videoclip 30.1).

Having established the basic anatomy of the aorta, long-axis imaging of the arch is then performed in oblique sagittal planes with particular attention to the caliber of the various arch segments and identifying obstruction. Some echocardiography laboratories by convention display long-axis images of right arches with the right–left orientation inverted so that superior structures are positioned to the left on the screen (Figs 30.5c,d). This presentation may be accomplished by rotating the transducer 180° or by selecting a right–left inversion option on the echocardiography machine. Assessment of the arch from long-axis views should be complemented by spectral and color Doppler imaging. In patients with a double aortic arch, it is important to completely interrogate both arches for obstruction as one will frequently be smaller or have an atretic portion. Differentiation of the right from left arch may be facilitated by careful sweeps from side to side. An active effort should also be made to identify arterial ducts keeping in mind the variety of potential locations and that they may be bilateral. Finally, subcostal imaging may be useful in identifying the position of the descending aorta relative to the spine.

#### Prenatal assessment

There are a few reports describing the diagnosis of vascular rings by fetal echocardiography [16–20]. The overall approach to imaging is similar to postnatal echocardiography. Because the lumen of the trachea in the fetus is filled with fluid, it appears echo-dark and is often quite distinct. Another relative advantage in assessing the fetus is that the ductus arteriosus is patent rather than ligamentous and therefore this component of the ring is easily visualized. A particularly careful assessment for a vascular ring should be made in any fetus with congenital heart disease or with a diagnosis of 22q11 deletion. Moreover, any fetus who has a vessel coursing posterior to the trachea has a high likelihood of a vascular ring [20].

#### Intraoperative assessment

Once the diagnosis has been established, echocardiography has little role in intraoperative assessment during surgical division of vascular rings.

#### Follow-up assessment

Complications related to vascular ring division are rare, and those that do occur, such as nerve damage, chylothorax or incomplete ring division, are difficult to assess by echocardiography. Similarly, clinical issues in follow-up usually relate to airway and swallowing symptoms and echocardiography is rarely helpful.

## Pulmonary artery sling

### Definition

Pulmonary artery sling, also known as anomalous left pulmonary artery from the right pulmonary artery, is a vascular anomaly in which the left pulmonary artery arises aberrantly from the proximal part of the right pulmonary artery and courses over the right mainstem bronchus, posterior to the trachea and anterior to the esophagus, to reach the left hilum (Fig. 30.12). This arrangement creates a vascular "sling" surrounding and compressing the trachea but not the esophagus.

### Incidence

Pulmonary artery sling is a very rare congenital malformation; reliable data on its prevalence are not published.

### Etiology

Pulmonary artery sling is a developmental malformation. A genetic association (Mowat–Wilson syndrome) has recently been identified [21–24].

### Morphology and classification

#### Developmental considerations and anatomy

Normally, the distal pulmonary arteries arise from their respective lung buds and join the proximal pulmonary arteries, which have formed from the sixth aortic arch [9].

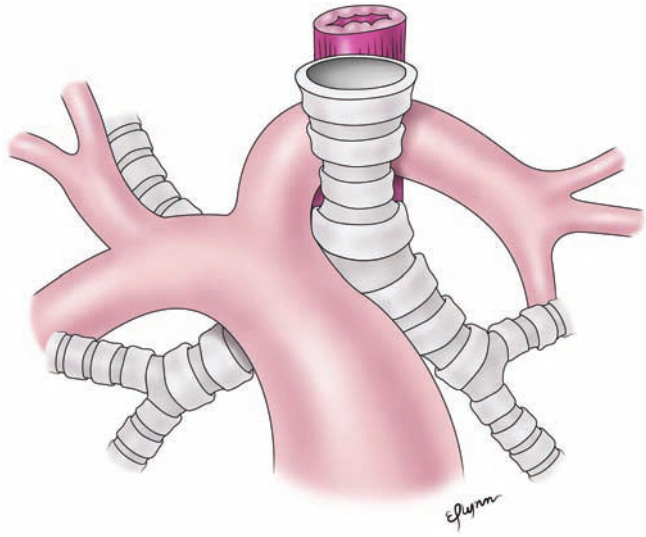

**Figure 30.12** Drawing of a left pulmonary artery sling. The left pulmonary artery arises aberrantly from the proximal right pulmonary artery and courses posterior to the trachea and anterior to the esophagus toward the left hilum.

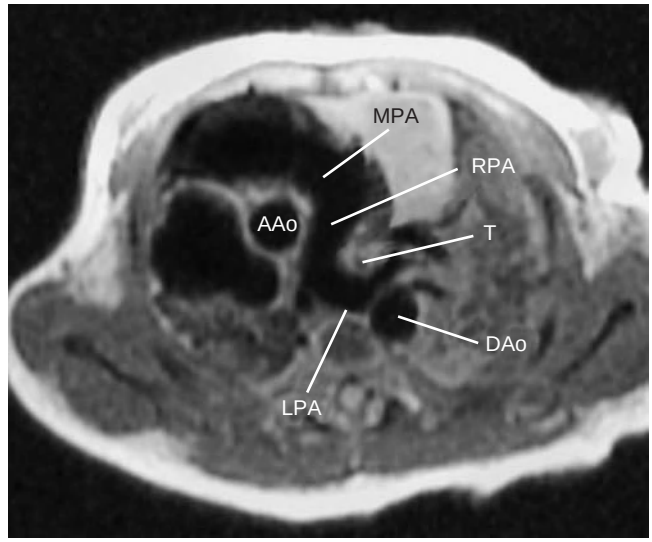


**Figure 30.13** Left pulmonary artery sling. Magnetic resonance imaging (MRI) using fast spin-echo and blood signal suppression in an axial plane, illustrating the left pulmonary artery arising from the right pulmonary artery and coursing posterior to the narrowed trachea. Note also the right lung hypoplasia and secondary dextrocardia. AAo, ascending aorta; DAo, descending aorta; LPA, left pulmonary artery; MPA, main pulmonary artery; RPA, right pulmonary artery; T, trachea.

The embryology of the pulmonary artery sling has not been definitively identified. It has been hypothesized to occur when the proximal part of the left sixth arch regresses or fails to develop its normal connections to the left lung bud and a "collateral" vessel to the left lung develops. This vessel originates from the transverse portion of the right pulmonary artery, just to the right of the trachea, and then curves posteriorly and sharply to the left, superior and posterior to the right main bronchus and trachea, but anterior to the esophagus in its course to the left hilum and lung. The ductal ligament is positioned to the left of the trachea and connects the descending aorta to the distal main pulmonary artery. This anatomic arrangement causes constriction of the right main bronchus, the trachea or both. In at least half of the cases, there are associated complete cartilaginous tracheal rings in which the posterior membranous portion of the trachea and proximal bronchi is absent and the tracheal cartilage is circumferential, the so-called "ring-sling" complex [25]. The complete cartilaginous rings may be localized to the area adjacent to the sling or extend throughout the trachea. Complete cartilaginous rings are often but not always associated with significant airway narrowing and may be an important source of airway symptoms in addition to the sling itself. Other abnormalities associated with left pulmonary artery sling include a tracheal origin of the right upper lobe bronchus (also known as bronchus suis), hypoplastic left pulmonary artery, right lung agenesis, and atrial and ventricular septal defects [26,27].

## Pathophysiology

The airway narrowing associated with left pulmonary artery sling leads to respiratory stridor and distress, which often are severe and typically manifest in the newborn period. In addition, right pulmonary artery hypoplasia can lead to decreased right lung perfusion and pulmonary hypertension.

## Imaging

Echocardiography can usually demonstrate the abnormal origin of the left pulmonary artery, and is sufficient to establish the diagnosis [13,14,28]. Because of the high incidence of tracheal anomalies other than simple compression by the sling, bronchoscopy is also warranted in most cases. This may be supplemented by computed tomography or magnetic resonance imaging as needed to ensure that the trachea, bronchi and pulmonary arteries have been completely assessed (Fig. 30.13) [29–31]. Angiography and bronchography are rarely indicated.

### Echocardiography imaging protocol

Echocardiography for diagnosing pulmonary artery sling focuses on imaging of the pulmonary arteries. The suprasternal notch and high parasternal windows are the most useful; positioning the patient on his/her left side or elevating the shoulders with a cushion may improve visualization. The abnormal origin of the left pulmonary artery is best appreciated by imaging in an axial (transverse) orientation (i.e., marker directed to the patient's left). The origin of the left pulmonary artery is displaced to the right, and appears as a vessel arising from the posterior aspect of the right pulmonary artery (Fig. 30.14 and Videoclip 30.10). The left

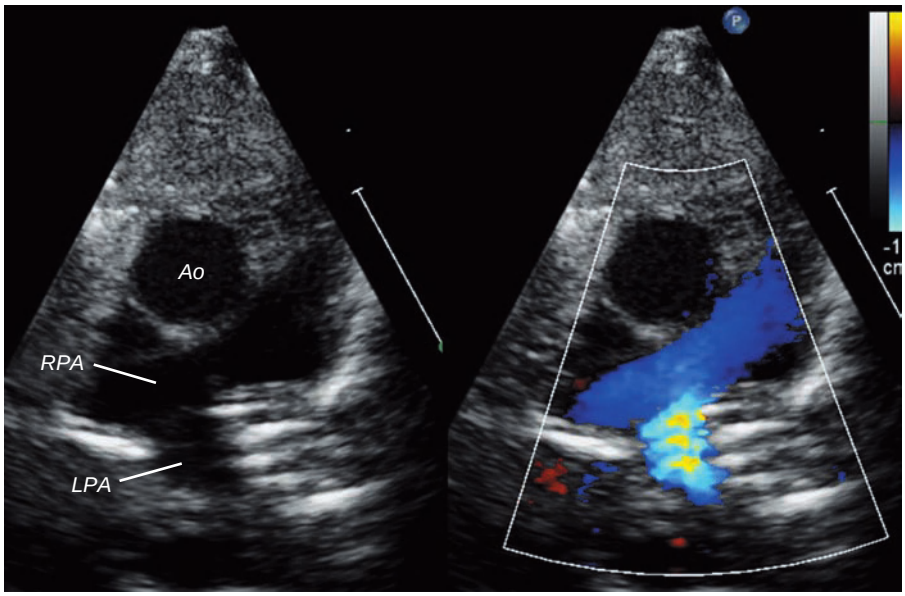


**Figure 30.14** Left pulmonary artery sling. Echocardiogram using a high parasternal window, a transverse orientation, and 2D and color Doppler imaging. Note that the left pulmonary artery (LPA) arises from the right pulmonary artery (RPA) and courses leftward and posterior to the faintly seen echo-bright trachea.

pulmonary artery then curves leftward and posterior to the echo-bright distal trachea and continues toward the left hilum. Suspicion for this lesion should be aroused when the proximal left pulmonary artery does not have its typical course, in which it travels primarily posteriorly and only slightly leftward, appearing nearly as a continuation of the main pulmonary artery. Alternatively, a left pulmonary artery sling can be missed by mistaking the left atrial appendage or a patent ductus arteriosus for a normal left pulmonary artery [28]. Imaging from a subcostal window in the coronal plane may also be used to demonstrate the course of the pulmonary arteries. Once the diagnosis is established, the size of the pulmonary arteries should be measured from 2D images. Color Doppler is often useful in delineating the course of the pulmonary arteries, and spectral Doppler assessment should be performed to estimate the degree of obstruction. Note that the maximal instantaneous gradient may be low in the setting of significant anatomic obstruction if most of the flow is into the right pulmonary artery.

### Prenatal assessment

Prenatal diagnosis of a left pulmonary artery sling is extremely rare. In principle, the same strategy as is applied to postnatal assessment should be employed. Every effort should be made to visualize the main and branch pulmonary arteries in fetuses with pulmonary abnormalities.

### Intraoperative assessment

Transesophageal echocardiography can be used intraoperatively to assess the branch pulmonary arteries. Particular attention should be paid postoperatively to evaluating the left pulmonary artery for obstruction.

### Follow-up assessment

Patients who have undergone repair of a left pulmonary artery sling have a high incidence of left pulmonary artery stenosis. Accordingly, the branch pulmonary arteries should be assessed with 2D imaging and Doppler techniques, and the right ventricular pressure estimated using the tricuspid regurgitation jet velocity and ventricular septal position.

## Innominate artery compression syndrome

### Definition and etiology

Innominate artery compression syndrome refers to children with symptoms of airway obstruction who are found to have significant tracheal narrowing where the innominate artery passes anteriorly to the trachea [32]. Typically, localized tracheomalacia with dynamic airway narrowing is found, but it remains controversial whether this is primarily an intrinsic airway problem. Some reports have attributed the tracheal narrowing to a more distal, posterior and leftward origin of the innominate artery from the aortic arch; however, careful studies have not found this to be a consistent finding [33–35]. Others have proposed that mediastinal crowding and an enlarged thymus gland contribute to the pathology. Innominate artery compression syndrome is rarely associated with congenital heart disease.

### Pathophysiology

Presentation is in infancy with stridor, which may be sufficiently severe to cause apnea or syncope. Feeding difficulties (e.g., poor weight gain, gastroesophageal reflux) as well as a history of esophageal atresia and tracheoesophageal fistual are common.

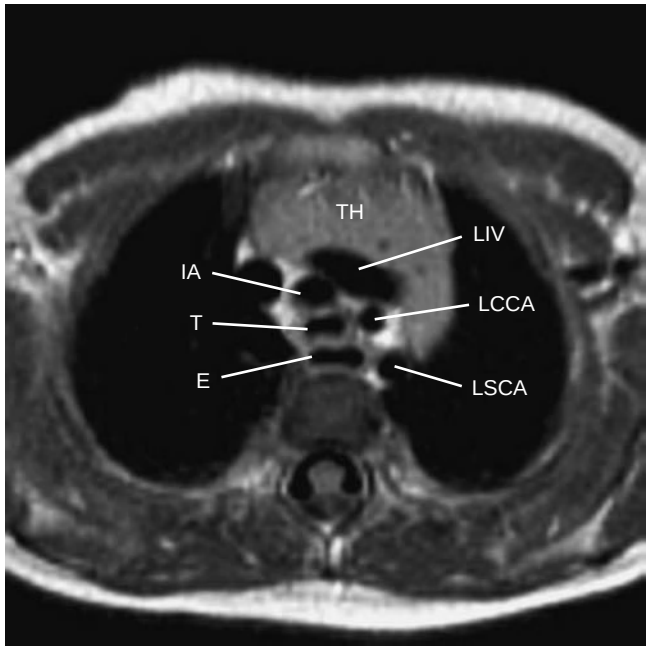


**Figure 30.15** Innominate artery compression syndrome. Magnetic resonance imaging (MRI) using fast spin-echo and blood signal suppression in an axial plane illustrating a narrow trachea with the innominate artery located anteriorly. E, esophagus; IA, innominate artery; LCCA, left common carotid artery; LIV, left innominate vein; LSCA, left subclavian artery; T, trachea; TH, thymus.

## Imaging

Because echocardiography is poorly suited for evaluating the trachea, it has little role in establishing a diagnosis of innominate artery compression syndrome. Rather, this condition is best identified through a combination of bronchoscopy and computed tomography or magnetic resonance imaging. On bronchoscopy, there is a characteristic anterior pulsatile indentation of the trachea 1–2 cm above the carina. The trachea should be narrowed at least 50–75% during spontaneous respiration to attribute symptoms to this diagnosis. The tomographic imaging studies demonstrate the relationship of the aorta, innominate artery and thymus to the trachea (Fig. 30.15).

## References

1. Weinberg PM. Aortic arch anomalies. In: Allen HD, Gutgesell HP, Clark EB, Driscoll DJ (eds) *Moss and Adams' Heart Disease in Infants, Children, and Adolescents*, 6th edn. Philadelphia: Lippincott Williams & Wilkins, 2001;707–35.
2. Marmon LM, Bye MR, Haas JM et al. Vascular rings and slings: long-term follow-up of pulmonary function. *J Pediatr Surg* 1984;19:683–92.
3. Dodge-Khatami A, Tulevski II, Hitchcock JF et al. Vascular rings and pulmonary arterial sling: from respiratory collapse to surgical cure, with emphasis on judicious imaging in the hi-tech era. *Cardiol Young* 2002;12:96–104.
4. van Son JA, Julsrud PR, Hagler DJ et al. Surgical treatment of vascular rings: the Mayo Clinic experience. *Mayo Clin Proc* 1993; 68:1056–63.
5. Bonnard A, Auber F, Fourcade L et al. Vascular ring abnormalities: a retrospective study of 62 cases. *J Pediatr Surg* 2003;38: 539–43.
6. Woods RK, Sharp RJ, Holcomb GW III et al. Vascular anomalies and tracheoesophageal compression: a single institution's 25-year experience. *Ann Thorac Surg* 2001;72:434–8.
7. Backer CL, Ilbawi MN, Idriss FS et al. Vascular anomalies causing tracheoesophageal compression. Review of experience in children. *J Thorac Cardiovasc Surg* 1989;97:725–31.
8. McElhinney DB, Clark BJ III, Weinberg PM et al. Association of chromosome 22q11 deletion with isolated anomalies of aortic arch laterality and branching. *J Am Coll Cardiol* 2001;37:2114–19.
9. Larsen WJ. *Human Embryology*. New York: Churchill Livingstone, 1997.
10. Barry A. The aortic arch derivatives in the human adult. *Anat Rec* 1951;111:221–38.
11. Edwards JE. Anomalies of the derivatives of the aortic arch system. *Med Clin North Am* 1948;32:925–49.
12. Moes CAF. Vascular rings and related conditions. In: Freedom RM, Mawson JB, Yoo SJ, Benson LN (eds) *Congenital Heart Disease: Textbook of Angiocardiography*, 1st edn. Armonk, NY: Futura Publishing Company, 1997;947–83.
13. Murdison KA, Andrews BA, Chin AJ. Ultrasonographic display of complex vascular rings. *J Am Coll Cardiol* 1990;15:1645–53.
14. Lillehei CW, Colan S. Echocardiography in the preoperative evaluation of vascular rings. *J Pediatr Surg* 1992;27:1118–20.
15. Katz JC, Chakravarti S, Ko HH et al. Common origin of the innominate and carotid arteries: prevalence, nomenclature, and surgical implications. *J Am Soc. Echocardiogr* 2006;19:1446–8.
16. Achiron R, Rotstein Z, Heggesh J et al. Anomalies of the fetal aortic arch: a novel sonographic approach to in-utero diagnosis. *Ultrasound Obstet Gynecol* 2002;20:553–7.
17. Bronshtein M, Lorber A, Berant M et al. Sonographic diagnosis of fetal vascular rings in early pregnancy. *Am J Cardiol* 1998; 81:101–3.
18. Yoo SJ, Min JY, Lee YH et al. Fetal sonographic diagnosis of aortic arch anomalies. *Ultrasound Obstet Gynecol* 2003;22:535–46.
19. Chaoui R, Schneider MB, Kalache KD. Right aortic arch with vascular ring and aberrant left subclavian artery: prenatal diagnosis assisted by three-dimensional power Doppler ultrasound. *Ultrasound Obstet Gynecol* 2003;22:661–3.
20. Patel CR, Lane JR, Spector ML et al. Fetal echocardiographic diagnosis of vascular rings. *J Ultrasound Med* 2006;25:251–7.
21. Adam MP, Schelley S, Gallagher R et al. Clinical features and management issues in Mowat–Wilson syndrome. *Am J Med Genet A* 2006;140:2730–41.
22. Ishihara N, Yamada K, Yamada Y et al. Clinical and molecular analysis of Mowat–Wilson syndrome associated with ZFHX1B mutations and deletions at 2q22-q24.1. *J Med Genet* 2004;41: 387–93.
23. Zweier C, Thiel CT, Dufke A et al. Clinical and mutational spectrum of Mowat–Wilson syndrome. *Eur J Med Genet* 2005;48: 97–111.

24. Strenge S, Heinritz W, Zweier C et al. Pulmonary artery sling and congenital tracheal stenosis in another patient with Mowat–Wilson syndrome. *Am J Med Gene A* 2007;143:1528–30.
25. Berdon WE, Baker DH, Wung JT et al. Complete cartilage-ring tracheal stenosis associated with anomalous left pulmonary artery: the ring-sling complex. *Radiology* 1984;152:57–64.
26. Tesler UF, Balsara RH, Niguidula FN. Aberrant left pulmonary artery (vascular sling): report of five cases. *Chest* 1974;66: 402–7.
27. Pu WT, Chung T, Hoffer FA et al. Diagnosis and management of agenesis of the right lung and left pulmonary artery sling. *Am J Cardiol* 1996;78:723–7.
28. Yeager SB, Chin AJ, Sanders SP. Two-dimensional echocardiographic diagnosis of pulmonary artery sling in infancy. *J Am Coll Cardiol* 1986;7:625–9.
29. van Son JA, Julsrud PR, Hagler DJ et al. Imaging strategies for vascular rings. *Ann Thorac Surg* 1994;57:604–10.
30. Newman B, Meza MP, Towbin RB et al. Left pulmonary artery sling: diagnosis and delineation of associated tracheobronchial anomalies with MR. *Pediatr Radiol* 1996;26:661–8.
31. Beekman RP, Hazekamp MG, Sobotka MA et al. A new diagnostic approach to vascular rings and pulmonary slings: the role of MRI. *Magn Reson Imaging* 1998;16:137–45.
32. Gross RE, Neuhauser EB. Compression of the trachea by an anomalous innominate artery. An operation for its relief. *Am J Dis Child* 1948;75:570–4.
33. Fletcher BD, Cohn RC. Tracheal compression and the innominate artery: MR evaluation in infants. *Radiology* 1989;170: 103–7.
34. Ardito JM, Ossoff RH, Tucker GF Jr et al. Innominate artery compression of the trachea in infants with reflex apnea. *Ann Oto Rhinol Laryngol* 1980;89:401–5.
35. Mustard WT, Bayliss CE, Fearon B et al. Tracheal compression by the innominate artery in children. *Ann Thorac Surg* 1969;8: 312–19.

# 31 Connective Tissue Disorders

**Julie De Backer[1], Ann De Paepe[2], Bart Loeys[2] and Harry C. Dietz[3]**

[1]Department of Cardiology, University Hospital Ghent, Ghent, Belgium
[2]Department of Medical Genetics, University Hospital Ghent, Belgium
[3]Institute of Genetic Medicine, Department of paediatrics, Medicine and Molecular Biology and Genetics; Howard Hughes Medical Institute, John Hopkins University School of Medicine, Baltimore, MD, USA

## Introduction

Heritable connective tissue disorders are associated with cardiovascular anomalies like aortic dilation and aneurysm formation, aortic dissection and atrioventricular (AV) valve prolapse. Echocardiography plays an important role in the diagnosis of the cardiovascular manifestations. This chapter specifically summarizes echocardiographic findings in heritable connective tissue disorders.

### Definition of connective tissue disorders

#### Connective tissue

"Connective tissue" refers to a complex structure or network, composed of a cellular component (fibroblasts, smooth muscle cells) and the extracellular matrix (ECM). The ECM is made up of many different components, which provide specific environmental signals involved in controlling cell morphology, migration, differentiation, proliferation and metabolism. The ECM includes both structural proteins (collagen, fibrillin, and fibronectin) and ground substance (proteoglycans). Together they form a network that provides resistance to mechanical forces while allowing diffusion of small molecules.

#### Connective tissue in the cardiovascular system

Extracellular matrix molecules are widely distributed in the heart and can be found in the endocardial layer and in the interstitial spaces between cardiomyocytes, but the major sites of deposition of cardiac connective tissue are at the insertions of the aorta and pulmonary artery, continuing in the AV rings to form a network for the attachment of the valves. The valves themselves (both AV valves and semilunar valves) are composed of different layers of connective tissue, covered with endothelial cells. As an example, the adult human aortic valve cusps are composed of about 10–15% elastin and 45–55% collagen [1]. The composition of the ECM in blood vessels depends on the type and subtype of vessel (elastic or muscular arteries; small, medium, or large veins). Within the blood vessels, the ECM is composed of different molecules according to the layer (i.e., tunica intima, media, or adventitia).

#### Classification of connective tissue disorders with cardiovascular involvement

Although historical accounts consistent with the heritability of connective tissue disorders date back over 100 years, only in the past two decades has definite proof with molecular diagnosis been possible. By now it has become clear that these disorders represent generalized single-gene-determined defects of some element of connective tissue [2]. Based on the identification of these underlying genetic defects, the different clinical entities are now becoming more clearly delineated and interesting new insights have emerged concerning the pathophysiologic basis of cardiovascular lesions in connective tissue disorders.

A proper understanding of this molecular background is important for the correct diagnosis, treatment and follow-up of patients. For example, the selection of specific imaging studies in patients with connective tissue disorders will be influenced by genetic diagnosis.

Molecular genetics has not only allowed us to improve diagnostic accuracy, but also has altered our insights into the pathophysiology of connective tissue disorders. One of the most intriguing recent findings was the observation of the importance of the transforming growth factor-β (TGF-β) pathway in several connective tissue disorders. The first such disorder found to be related to the TGF-β pathway was Marfan syndrome (MFS). MFS is an autosomal dominant connective tissue disorder caused by mutations in the fibrillin-1 gene (*FBN1*) [3]. Until recently, the underlying pathogenesis of aneurysm formation in MFS was considered to be a consequence of structurally abnormal fibrillin-1 fibers. Recent developments have changed this view and it is now recognized that fibrillin-1 fibers play an important functional role in the complex TGF-β pathway. Sakai and colleagues demonstrated that fibrillin was homologous with

*Echocardiography in Pediatric and Congenital Heart Disease: From Fetus to Adult*
Edited by Wyman W. Lai, Luc L. Mertens, Meryl S. Cohen and Tal Geva
 ISBN: 978-1-405-17401-5

the family of latent TGF-β binding proteins (LTBPs), which serve to hold TGF-β in an inactive complex in various tissues, including the ECM. Researchers showed that fibrillin-1 can bind TGF-β and LTBPs [4–7].

Dietz and colleagues hypothesized that abnormal fibrillin-1, or reduced levels of fibrillin-1, in connective tissue might result in an excess of active TGF-β [8]. The current hypothesis is that fibrillin-1 participates in the regulation of TGF-β signaling through direct interaction between the large latent complex and the matrix. Because the large latent complex binds TGF-β, abnormal fibrillin-1 fibers will lead to failed matrix sequestration of the latent TGF-β complex and hence to increased amounts of active TGF-β, which underlies the pleiotropic manifestations in MFS [8]. The TGF-β pathway is involved in cardiovascular abnormalities such as mitral valve prolapse and aortic root aneurysm. In accordance with these observations, very similar findings have been observed for other hereditary connective tissue disorders, implying an important role for the TGF-β pathway in the pathogenesis of aneurysm formation.

An overview of the different clinical entities and their underlying genetic defect is provided in Table 31.1.

Although there is substantial overlap with regards to the cardiovascular findings between these disease entities there are some important differences, which will be addressed below. Imaging studies need to be guided by the primary location and the extent of the lesions occurring in these different conditions.

## Cardiovascular lesions

### Marfan syndrome

Marfan syndrome (MFS) is an autosomal dominant connective tissue disorder caused by mutations in the fibrillin-1 (*FBN1*) gene. The diagnosis is based on the identification of major and minor diagnostic criteria in the skeletal, ocular, cardiovascular, and central nervous organ systems. Major criteria include a combination of four out of eight skeletal features, lens dislocation, dural ectasia, and aortic root dilation/dissection [9]. Minor cardiovascular criteria include mitral valve prolapse and pulmonary artery dilation. Clinical manifestations in MFS vary widely both within and between families. Severe cardiovascular phenotypes exist, with significant AV valve dysfunction and/or rapidly progressive aortic root dilation, so called "neonatal MFS" [10–12]. In the more common, so-called "classic MFS," cardiovascular manifestations tend to develop in adolescence, although absence of manifestations until later in life has also been reported [13,14].

**Table 31.1** Overview of the different connective tissue disorders and their respective main cardiovascular findings

| | Connective tissue disorder | | | | | | | |
|---|---|---|---|---|---|---|---|---|
| | **MFS** | **LDS** | **Vascular EDS** | **ATS** | **TAAD** | **TAA with PDA** | **TAAD with BAV** | **TAA with cutis laxa** |
| Gene | *FBN1* | *TGFBR1/2* | *COL3A1* | *SLC2A10* | * | *MYH11* | ? | Elastin<br>Fibulin-4 |
| Inheritance | AD | AD | AD | AR | AD | AD | AD | AD |
| Median life expectancy (years) | 45 | 26 | 48 | | ? | ? | ? | ? |
| Aortic root aneurysm | +++ | +++ | + | + | ++ | +++ | ++ | +++ |
| Arterial tortuosity | + | +++ | – | +++ | ++ | ? | – | ? |
| Aortic/arterial dissection | + | ++ | +++ | – | + | ++ | + | ++ |
| Descending aortic aneurysm/dissection | + | ++ | + | – | ? | – | – | – |
| Main pulmonary artery dilation | ++ | ++ | – | + | – | ? | + | – |
| Pulmonary artery stenosis | – | – | – | ++ | ? | – | – | + (Fbln4) |
| LV dilation | + | + | – | – | | ? | – | |

AD, autosomal dominant; AR, autosomal recessive; ATS, arterial tortuosity syndrome; BAV, bicuspid aortic valve; EDS, Ehlers–Danlos syndrome; Fbn, fibulin; MFS, Marfan syndrome; LDS, Loeys–Dietz syndrome; LV, left ventricle; PDA, patent ductus arteriosus; TAAD, thoracic aortic aneurysms and dissections.

*Familial TAAD is genetically heterogeneous with two loci and three genes being identified so far: TAAD1 at 5q13-14, FAA1 at 11q23.20-24, *TGFBR2*, *MYH11* and *ACTA2*.

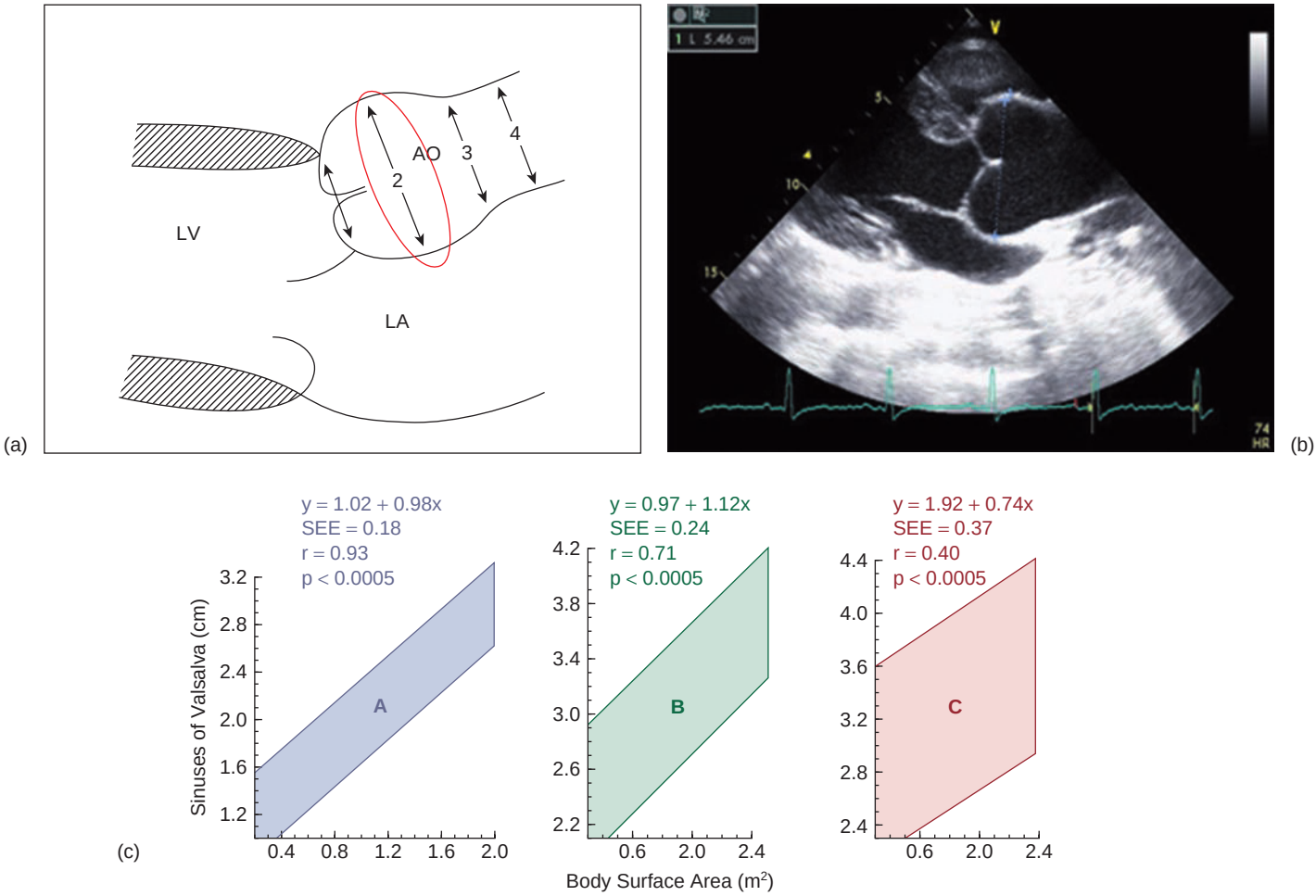


**Figure 31.1** Illustration **(a)** and echocardiographic image **(b)** of ascending aortic aneurysm at the level of the sinus of Valsalva in Marfan syndrome. Measurement has to be done at end-diastole using the "leading edge to leading edge" principle. LA, left atrium; LV, left ventricle. **(c)** Graphs showing nomograms for three different age groups with the corresponding regression equation for the age range (A: <18 years; B: 18–40 years; C: ≥40 years). Reproduced from Roman MJ, Devereux RB, Kramer-Fox R, O'Loughlin J. Two-dimensional echocardiographic aortic root dimensions in normal children and adults. *Am J Cardiol* 1989;64:507–12, with permission from Weill Cornell Medical College.

Echocardiography plays a key role in the diagnostic workup of cardiovascular manifestations as well as in follow-up and guidance of treatment.

### Dilation of the ascending aorta

The primary cardiovascular manifestation in MFS is progressive dilation of the aortic root, eventually leading to aortic dissection or rupture. It is estimated that aortic root dilation is present in more than 80% of adult MFS patients [15]. Echocardiographic recordings should be obtained from the parasternal long-axis window to visualize the aortic root and proximal ascending aorta. Two-dimensional (2D) images should be used to visualize the left ventricular (LV) outflow tract, and the aortic root should be recorded in different views in various intercostal spaces and at different distances from the left sternal border. Measurements are usually taken at: (i) aortic valve annulus (hinge point of aortic leaflets); (ii) the maximal diameter at the sinuses of Valsalva; (iii) sinotubular junction (transition between the sinuses of Valsalva and the tubular portion of the ascending aorta); and (iv) the more distal aorta.

When measuring the aortic diameter, it is particularly important to use the maximum diameter measured perpendicularly to the long axis of the vessel in that view. Some sonographers (especially the pediatric group) favor measurement from inner edge to inner edge at end-systole to match measurements obtained by other methods of imaging the aorta, such as magnetic resonance imaging (MRI) and computed tomography (CT) scanning. However, the normative data for echocardiography as well as the most recent guidelines from the American Society of Echocardiography were obtained at end-diastole using the leading edge to leading edge technique (Fig. 31.1) [16,17]. Absolute differences between the techniques are small, and further improvements in image

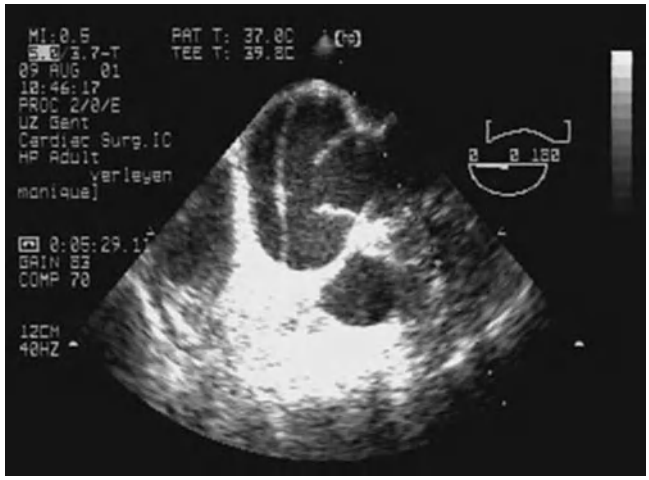


**Figure 31.2** Transesophageal echocardiographic image of dissection of the ascending aorta at the level of the sinuses of Valsalva. There is a flap within the ascending aorta, which is typical for a dissection of the aorta.

resolution should minimize the difference between these measurement methods.

Two-dimensional aortic diameter measurements are preferable to M-mode measurements, as cyclic motion of the heart and resultant changes in M-mode cursor location relative to the maximum diameter of the sinuses of Valsalva result in systematic underestimation (by up to 2 mm) of aortic diameter by M-mode compared with the 2D aortic diameter [18].

Aortic root dilation in MFS occurs typically at the sinuses of Valsalva and is defined as an aortic root diameter above the upper limit of the 95% confidence interval of the distribution in a large reference population. Aortic dilation can be easily detected by plotting observed aortic root diameter versus body surface area (BSA) on previously published nomograms [16]. Another possibility is the use of z-scores derived from the regression equation on the nomogram. A z-score ≥2 indicates a value exceeding 2 SD (i.e., the 95% confidence interval).

In some Marfan patients, aortic root dilation is asymmetric and, therefore, measurement in the transverse plane of the aorta (parasternal short-axis view) may be important. One study by Meijboom et al. using MRI revealed that the largest aortic root diameter was between the right and left coronary cusps. For a given noncoronary to right coronary cusp diameter – which is the diameter assessed in the parasternal long-axis (PSLAX) view – 95% confidence intervals revealed a variation of –20 to +20% in the aortic root area [19]. So far, no echocardiographic study has been performed to confirm these results.

The predilection for the ascending aorta to dilate is a result of both structural and local hemodynamic factors. Both the aortic root and the proximal part of the pulmonary artery (which also dilates in MFS, see below) are derived from the neural crest, whereas the more distal arterial structures stem from the mesoderm. It has been demonstrated that the elastic fiber content is higher in the ascending aorta than in any other region of the arterial tree [20]. Diseases such as MFS that affect elastic fiber integrity will therefore manifest more easily in this region. Furthermore, it is primarily the ascending portion of the aorta that is subjected to the repetitive stress of left ventricular ejection, eventually resulting in progressive dilation [21,22]. Because pressures in the aorta are significantly higher than in the pulmonary artery, dilation will be more pronounced at the aortic root.

In order to define indications for surgical intervention, absolute growth of the aortic root should be reported in addition to the diameter. Annual growth of rates exceeding 1 cm/year are considered as a risk factor for dissection.

### Dissection of the ascending aorta

Progressive dilation of the ascending aorta can lead to its dissection or rupture (Videoclip 31.1). Echocardiography is a very important tool in the setting of aortic dissection, not only for confirmation of the diagnosis but also for evaluation of complications such as pericardial tamponade or acute myocardial ischemia due to coronary artery obstruction or dissection. Transesophageal echocardiography (TEE) is preferred in this setting because it allows better visualization of the ascending aorta and aortic arch as well as the descending aorta.

The arch itself and origins of two of the great vessels can be seen in most patients. There is a blind spot in the upper ascending aorta and the proximal arch that is not seen by TEE because of the interposed tracheal bifurcation.

In patients with aortic aneurysms not associated with connective tissue disorders, the degree of aortic dilation is well correlated with the risk of aortic rupture or dissection [23]. The risk rises substantially when the diameter exceeds 55 mm (Fig. 31.2). In patients with MFS, however, the risk of aortic rupture or dissection does depend solely on the degree of aortic dilation [24]. Some patients develop aortic dissection at diameters below 55 mm [25,26]. Silverman and colleagues demonstrated that a family history of severe cardiovascular disease in MFS is associated with increased aortic diameter and decreased survival [27].

Other possible risk factors have been studied such as central pulse pressure (pressure difference between systolic and diastolic pressure in the ascending aorta) [28] and aortic stiffness [29–32], but none of these have a higher predictive value than the absolute aortic diameter. Aortic stiffness appeared to have a diagnostic value in young patients in one study [33]. In daily clinical practice, these parameters are not easy to apply because no accurate cut-off values are available.

### Mitral valve prolapse (MVP)

Two-dimensional echocardiography is currently the recommended tool for the identification of MVP. Both parasternal long-axis and apical 4-chamber views may be used [34,35] (Videoclips 31.2 and 31.3).

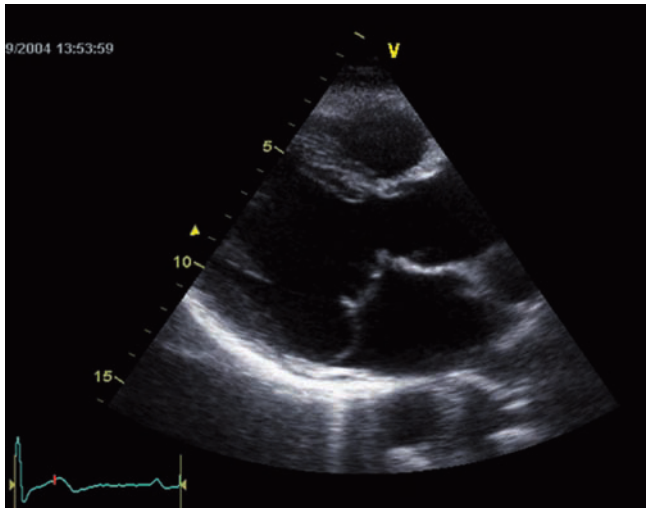


**Figure 31.3** Parasternal long-axis view of anterior mitral valve leaflet prolapse.

Prolapse is defined as leaflet displacement in systole exceeding the mitral valve annular plane by ≥2 mm, with leaflet thickening exceeding 5 mm. Nonclassic prolapse refers to leaflet displacement without valve thickening. An example of mitral valve prolapse is illustrated in Fig. 31.3. In a survey of 166 MFS patients, more than 50% were identified with clinical or echocardiographic evidence of MVP [36]. In our own series, we observed MVP using echocardiography in 66% of MFS patients – 35% of whom had classic MVP [37].

### Main pulmonary artery dilation

Guidelines for the assessment of main pulmonary artery (MPA) dilation are scarce in the literature. Nollen and colleagues clearly demonstrated increased diameters assessed with MRI [38]. Using a cut-off value of 28 mm at the level of the MPA root, they reported a prevalence of MPA dilation of 74%. In our own series with echocardiography, we proposed a cut-off value of 23 mm to define main pulmonary artery dilation in adult MFS patients [37]. The MPA is best viewed in the parasternal short-axis view – the largest diameter distal to the valve insertion should be measured. Complications arising from MPA dilation are mild. Pulmonary regurgitation is reported in many MFS patients [39]. However, pulmonary artery dissection is very rare.

### Dilation or dissection of the descending aorta

Complications in the descending aorta occur in a minority of MFS patients [40,41]. There are a few case reports of Marfan syndrome patients presenting with thoraco-abdominal aortic aneurysm/dissection [42,43]. Other reports on the descending aorta in MFS patients are mainly limited to surgical data describing the occurrence of primary or secondary complications in the descending aorta necessitating surgical intervention. Finkbohner and colleagues reported that 15% of their patients had a first surgical intervention involving portions of the descending aorta [44]. Nollen and colleagues reported on increased growth (defined as >1 mm/year) in a small subset of patients (6% in the descending thoracic aorta and 7% in the abdominal aorta). They also demonstrated that aortic stiffness is an independent predictor of progressive abdominal aortic dilation [45]. Kawamoto and colleagues studied the progression of thoraco-abdominal aortic diameters in MFS patients after surgical repair, and defined a subgroup of patients showing progressive dilation of the distal aorta (>3 mm/year) [46].

Guidelines for the assessment of descending aortic dilation are lacking in the literature. To view the descending aorta, TEE may be used although CT scan or MRI are more convenient and informative techniques. In our own series of 29 MFS patients studied with MRI, we noted increased diameters at different levels of the descending aorta. However, there was too much overlap with normal controls to define cut-off values. We found no significant correlations with the proximal aortic diameter, although dilation occurred more frequently in patients with previous aortic root surgery [37].

With our current knowledge of the existence of Marfan-like conditions, such as Loeys–Dietz syndrome (see below), it is important to note that some Loeys–Dietz syndrome patients may have been included in older reports on MFS: patients with widespread vascular involvement should be especially carefully reconsidered.

Interestingly, abnormal elastic properties of the aorta are not confined to the ascending aorta, but are also detected in the normally sized, more distal parts of the vessel [30]; these alterations may be observed in patients who have previously undergone aortic root surgery as well in unoperated MFS patients [47]. Local distensibility of the descending thoracic aorta appears to be an independent predictor of progressive descending aortic dilation [45].

### Left ventricular dysfunction

Although not included in the diagnostic criteria for MFS, dilated cardiomyopathy beyond that explained by aortic or mitral valve regurgitation, seems to occur with greater prevalence in patients with MFS, perhaps implying a role of the extracellular matrix protein fibrillin-1 in the cardiac ventricles [15].

Left ventricular dysfunction in MFS may occur as a consequence of valvular heart disease. However, there is recent evidence suggesting that LV function may be impaired irrespective of the presence of valvular heart disease, as indicated by increased LV dimensions in a subset of patients [48]. In addition it has been demonstrated in a few small studies that left ventricular diastolic function is also impaired in MFS [49–51].

We performed a detailed study of left ventricular systolic and diastolic function and observed significant impairment in MFS patients using dedicated techniques such as tissue Doppler imaging and MRI [52].

## Loeys–Dietz syndrome (LDS)

Loeys–Dietz syndrome is an autosomal dominant disorder caused by mutations in either of the transforming growth factor-β receptor genes (*TGFBR1* or *TGFBR2*). It is characterized clinically by aortic aneurysms and dissections, widespread arterial tortuosity/aneurysms, bifid uvula and hypertelorism [53]. The expression of the disease is variable between and within families. When compared with MFS, the natural history of LDS patients is significantly worse, mainly related to cardiovascular complications. The mean age at the first major cardiovascular complication is 27 years [54]. The cardiovascular lesions in LDS have a more aggressive course than in MFS. The annual increase in aortic root diameter is greater in LDS patients. In 22 cases for which we had serial data, we found an annual increase of at least 8% per year (J. De Backer et al., unpublished data). Another illustration of the more aggressive course of the arterial disease is the documentation of ascending aortic dissection at root diameters of 40–45 mm in several patients, which is well below classic surgical limits applied in MFS, where dissection of the aortic root commonly occurs at diameters >55 mm.

In addition to the increased disease progression, the lesions are also more widespread in LDS when compared with MFS. Aortic aneurysms and dissections in more distal parts of the aorta are more common in LDS (30% in our series versus estimates of 7–17% in MFS) [44,45]. In LDS, aneurysms may also develop outside the aorta in large and middle-sized arteries, whereas aneurysm formation in MFS is generally confined to the aorta.

Finally, additional congenital cardiac anomalies including patent ductus arteriosus, bicuspid aortic valve, mitral valve prolapse, and atrial septal defect (ASD) are more prevalent in LDS patients [54]. Williams et al. demonstrated that surgical outcome in LDS patients is good [55], which contrasts strongly with vascular Ehlers–Danlos syndrome, known as a "surgical nightmare" due to the extreme fragility of the vasculature and skin [56]. Many LDS patients in the study by Williams underwent repeated interventions, usually in different parts of the aorta, with good outcomes.

In view of the extent of cardiovascular lesions in LDS, multiple imaging techniques are required. Echocardiography is essential for assessment of aortic root dimensions as well as for identification of associated lesions. Vascular studies such as MR angiography or CT scanning with three-dimensional (3D) reconstruction from head to pelvis are required for the detection of distal aortic/arterial complications.

Figure 31.4 illustrates an MR study in a patient with LDS.

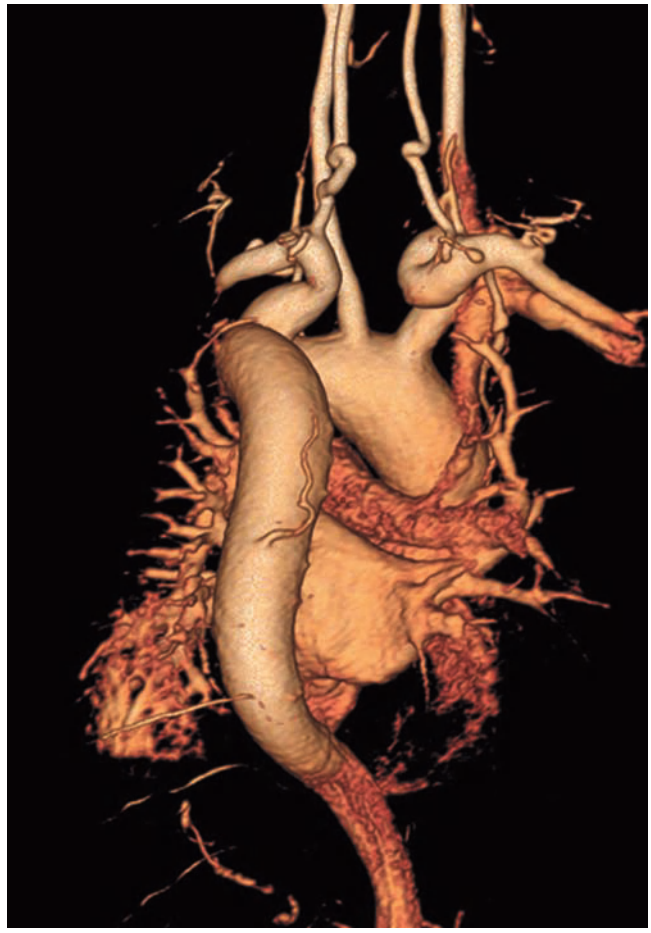

**Figure 31.4** Magnetic resonance 3D reconstruction of the thoracic aorta and side branches in a patient with Loeys–Dietz syndrome. Note the dilated aortic root, the tortuous aorta, and the tortuous and ectatic subclavian arteries.

## Vascular Ehlers–Danlos syndrome (EDS)

Vascular EDS is an autosomal dominant connective tissue disorder caused by mutations in the collagen type 3 gene (*COL3A1*). It is clinically characterized by joint hypermobility, skin abnormalities (cigarette paper scars, easy bruising, soft velvety skin), fragility of intestinal and genitourinary organs, and vascular fragility leading to dissection or rupture of medium to large muscular arteries.

Typically in vascular EDS, dissections often occur without preceding dilation/aneurysm formation. In vascular EDS patients, complications in early childhood are rare. The average age at the time of a first complication in the large series reported by Pepin and colleagues was 23.5 years, with rupture of the gastrointestinal tract likely to occur at an earlier age than arterial rupture [56]. About half of the arterial complications in vascular EDS involved the thoracic or abdominal arteries and the rest were divided equally between the head, neck and limbs [56].

In vascular EDS, the reported incidence of fatal complications during or immediately after vascular surgery is around 45% [56,57].

Clinical features in LDS and vascular EDS may be indistinguishable in some patients. So called LDS type 2 patients have the same skin lesions as vascular EDS patients (easy bruising, wide and atrophic scars, translucent skin, velvety

skin) and may also present visceral rupture. Cardiovascular lesions (arterial tortuosity and/or aortic root aneurysm) are generally more pronounced in LDS patients. In some cases genetic testing may be the only way to distinguish the two diseases.

It is very difficult to establish useful guidelines for cardiovascular imaging in vascular EDS because complications may occur unannounced and no specific treatment is currently available. Some authors advise against pursuing additional investigation or surveillance, both to avoid undue anxiety and because a conservative approach will be adopted irrespective of the results of such pursuits [58]. Others recommend noninvasive cardiovascular imaging with echocardiography and vascular CT/MRI [57].

### Arterial tortuosity syndrome (ATS)

Arterial tortuosity syndrome is an autosomal recessive disorder caused by mutations in a glucose transporter gene (the *SLC2A10* gene) [59].

In ATS arterial tortuosity is the most prominent clinical feature, along with large artery stenosis. Aneurysms form in the aorta and large arteries, although to a lesser extent than in LDS.

Patients with ATS require imaging studies of the entire vascular tree such as CT or MRI. Echocardiography is helpful to identify pulmonary artery stenoses and aortic dilation or stenosis.

### Thoracic aortic aneurysms and dissections (TAAD)

Familial TAAD is genetically heterogeneous, with two loci (TAAD1 at 5q13-14 and *FAA1* [familial aortic aneurysms 1] at 11q23.24) and three genes (*TGFBR2, MYH11* and *ACTA2*) being identified so far.

By definition, the entity of TAAD is restricted to those cases presenting with "isolated" TAAD – as opposed to the known syndromes such as MFS and LDS. In practice, most reported families also exhibit some additional clinical features.

Pannu and colleagues reported the presence of *TGFBR2* mutations in four unrelated families with TAAD [60]. Imaging studies were limited to echocardiographic examination of the ascending aorta. Nevertheless, some patients included in the study did have vascular anomalies outside the aorta (two carotid artery aneurysms, three cerebral aneurysms, and two abdominal artery/popliteal artery aneurysms) or in the descending aorta (four patients with a type B dissection), and one patient had enlargement of the pulmonary artery, further raising the suspicion for LDS.

Guo et al. reported on a family with TAAD whether or not in combination with livedo reticularis and iris flocculi, associated with mutations in the smooth muscle alpha-actin (*ACTA2*) gene. The patients reported by Zhu and colleagues [61] with mutations in the *MYH11* gene, had a clear association with patent ductus arteriosus. In their patients there also appears to be a clear association with intracranial dissections and aneurysms whereas manifestations in the distal aorta appear less common. The major cardiovascular imaging study in TAAD is echocardiography for assessment of the proximal aortic diameters.

### Thoracic aortic aneurysms and dissections associated with bicuspid aortic valve

Bicuspid aortic valve (BAV) affects 1–2% of the population and is associated with abnormalities of the aortic wall such as coarctation of the aorta, aortic dissection and aortic aneurysm [62]. Aortic wall abnormalities associated with BAV are characterized by cystic medial necrosis [63,64], the same process observed in the aorta of patients with Marfan syndrome. Cystic medial necrosis in BAV patients has been demonstrated in the aortic wall of patients with BAV, even without significant aneurysm formation.

In patients with BAV there is a ninefold increase in the risk of developing acute dissections when compared with patients with normal aortic valves. Aortic aneurysms and dissections occur irrespective of altered hemodynamics or age [65]. In contrast to Marfan syndrome, aortic root dilation in BAV patients is generally located in the ascending aorta, above the sinuses of Valsalva [66]. Even young children with BAV have aortic root dilation when compared with controls [67,68]. Notably, the process of progressive dilation of the ascending aorta continues after valve replacement. Patients with BAV require continuous surveillance to treat associated lesions and prevent complications.

Bicuspid aortic valve may occur sporadically or in a familial manner. Familial cases account for a minimum frequency of between 9.1 and 17.1% [69,70]. Analysis of these families indicated that the condition is inherited in an autosomal dominant manner with reduced penetrance.

Dietz and colleagues performed a comprehensive evaluation of multiple pedigrees segregating BAV with ascending aortic aneurysm, which revealed a high incidence of individuals with ascending aneurysm alone, suggesting that BAV and ascending aortic aneurysm are both primary manifestations of a single gene defect with variable expression [71]. Similar observations of isolated aortic aneurysm formation in family members of patients with BAV were reported by Loscalzo et al. [72]. Based on these findings, it is recommended that all family members, including those without BAV, require follow-up using imaging protocols that specifically assess aortic segments beyond the sinotubular junction.

Echocardiographic evaluation is done in the parasternal long-axis view for assessment of the aortic root dimensions as described above. The ascending aorta may be visualized from the high parasternal long-axis view (one intercostal space more cranially), at the crossing of the right pulmonary artery. The aortic arch is visualized from the suprasternal notch view.

### Aortic aneurysms with cutis laxa

Cutis laxa is an acquired or inherited condition characterized by redundant, pendulous and inelastic skin. Both autosomal

**Table 31.2** Recommended diagnostic and follow-up examinations and the anomalies to be sought for each connective tissue disorder

| | Diagnostic examination | | Follow-up examination | |
|---|---|---|---|---|
| **Disorder** | **Method** | **Anomalies** | **Method** | **Anomalies** |
| Marfan | Echocardiography | ARD, MVP, MPAdil | Echocardiography | ARD |
| | | | CT/MRI | Descending aortic dilation |
| Loeys–Dietz | Echocardiography | ARD, ASD, BAV, MVP | Echocardiography | ARD |
| | CT/MRI | Aortic/arterial tortuosity/dilation | CT/MRI | Aortic/arterial tortuosity/dilation |
| Vascular Ehlers–Danlos | Echocardiography? | ARD | Echocardiography? | ARD |
| | CT/MRI? | Aortic/arterial dilation | CT/MRI? | Aortic/arterial dilation |
| Arterial tortuosity | Echocardiography | ARD, PS | Echocardiography | ARD, PS |
| | CT/MRI | Arterial tortuosity/stenosis/dilation | CT/MRI | Arterial tortuosity/stenosis/dilation |
| Thoracic aortic aneurysm | Echocardiography | ARD, PDA | Echocardiography | ARD |
| Bicuspid aortic valve | Echocardiography | ARD, valvular morphology and function, coarctation | Echocardiography | ARD, valvular function |
| | CT/MRI | Ascending aortic dilation, coarctation | CT/MRI | Ascending aortic dilation |

ARD, aortic root dilation; ASD, atrial septal defect; BAV, bicuspid aortic valve; CT, computed tomography; MPAdil, main pulmonary artery dilation; MRI, magnetic resonance imaging; MVP, mitral valve prolapse; PDA, patent ductus arteriosus; PS, pulmonary stenosis.

dominant and autosomal recessive forms have been described. Underlying genetic defects are found in the elastin gene (*ELN*) and the fibulin-5 gene. Until recently, it was believed that the dominant form was free of grave systemic lesions and was associated with a normal lifespan [73]. However, recent observations by Szabo et al. revealed the presence of an aortic aneurysmal phenotype ranging from mild dilation to severe aortic root aneurysm or aortic rupture in a family and a young girl with sporadic cutis laxa due to a mutation in the *ELN* gene [74]. Aortic aneurysms were located at the sinuses of Valsalva.

## Practical guidelines for cardiovascular imaging in connective tissue disorders

Table 31.2 provides a overview of the recommended examinations and the anomalies to be looked for in the diagnostic setting and in follow-up, for each connective tissue disorder.

## References


1. Schoen FJ. Aortic valve structure-function correlations: role of elastic fibers no longer a stretch of the imagination. *J Heart Valve Dis* 1997;6:1–6.
2. McKusick VA. Heritable disorders of connective tissue: a personal account of the origins, evolution, validation, and expansion of a concept. In: Royce PM, Steinman B (eds) *Connective Tissue and its Heritable Disorders*, 1st edn. New York: Wiley-Liss Inc, 2002;13–8.
3. Dietz HC, Cutting GR, Pyeritz RE et al. Marfan syndrome caused by a recurrent de novo missense mutation in the fibrillin gene. *Nature* 1991;352:337–9.
4. Dallas SL, Keene DR, Bruder SP et al. Role of the latent transforming growth factor beta binding protein 1 in fibrillin-containing microfibrils in bone cells in vitro and in vivo. *J Bone Miner Res* 2000;15:68–81.
5. Dallas SL, Miyazono K, Skerry TM et al. Dual role for the latent transforming growth factor-beta binding protein in storage of latent TGF-beta in the extracellular matrix and as a structural matrix protein. *J Cell Biol* 1995;131:539–49.
6. Saharinen J, Hyytiainen M, Taipale J, Keski-Oja J. Latent transforming growth factor-beta binding proteins (LTBPs) – structural extracellular matrix proteins for targeting TGF-beta action. *Cytokine and Growth Factor Reviews* 1999;10:99–117.
7. Isogai Z, Ono RN, Ushiro S et al. Latent transforming growth factor beta-binding protein 1 interacts with fibrillin and is a microfibril-associated protein. *J Biol Chem* 2003;278:2750–7.
8. Neptune ER, Frischmeyer PA, Arking DE et al. Dysregulation of TGF-beta activation contributes to pathogenesis in Marfan syndrome. *Nat Genet* 2003;33:407–11.
9. De Paepe A, Devereux RB, Dietz HC et al. Revised diagnostic criteria for the Marfan syndrome. *Am J Med Genet* 1996;62:417–26.
10. Tiecke F, Katzke S, Booms P et al. Classic, atypically severe and neonatal Marfan syndrome: twelve mutations and genotype–phenotype correlations in FBN1 exons 24–40. *Eur J Hum Genet* 2001;9:13–21.
11. Kainulainen K, Karttunen L, Puhakka L et al. Mutations in the fibrillin gene responsible for dominant ectopia lentis and neonatal Marfan syndrome. *Nat Genet* 1994;6:64–9.
12. Putnam EA, Cho M, Zinn AB et al. Delineation of the Marfan phenotype associated with mutations in exons 23–32 of the FBN1 gene. *Am J Med Genet* 1996;62:233–42.

13. Black C, Withers AP, Gray JR et al. Correlation of a recurrent FBN1 mutation (R122C) with an atypical familial Marfan syndrome phenotype. *Hum Mutat* 1998(Suppl. 1):S198–200.
14. De Backer J, Loeys B, Leroy B et al. Utility of molecular analyses in the exploration of extreme intrafamilial variability in the Marfan syndrome. *Clin Genet* 2007;72:188–98.
15. Judge DP, Dietz HC. Marfan's syndrome. *Lancet* 2005;366: 1965–76.
16. Roman MJ, Devereux RB, Kramer-Fox R, O'Loughlin J. Two-dimensional echocardiographic aortic root dimensions in normal children and adults. *Am J Cardiol* 1989;64:507–12.
17. Lang RM, Bierig M, Devereux RB et al. Recommendations for chamber quantification: a report from the American Society of Echocardiography's Guidelines and Standards Committee and the Chamber Quantification Writing Group, developed in conjunction with the European Association of Echocardiography, a branch of the European Society of Cardiology. *J Am Soc Echocardiogr* 2005;18:1440–63.
18. Roman MJ, Devereux RB, Kramer-Fox R, Spitzer MC. Comparison of cardiovascular and skeletal features of primary mitral valve prolapse and Marfan syndrome. *Am J Cardiol* 1989;63: 317–21.
19. Meijboom LJ, Groenink M, van der Wall EE et al. Aortic root asymmetry in Marfan patients; evaluation by magnetic resonance imaging and comparison with standard echocardiography. *Int J Card Imaging* 2000;16:161–8.
20. Apter JT. Correlation of visco-elastic properties with microscopic structure of large arteries. IV. Thermal responses of collagen, elastin, smooth muscle, and intact arteries. *Circ Res* 1967;21: 901–18.
21. Pyeritz RE. Marfan syndrome: current and future clinical and genetic management of cardiovascular manifestations. *Semin Thorac Cardiovasc Surg* 1993;5:11–6.
22. Roman MJ, Rosen SE, Kramer-Fox R, Devereux RB. Prognostic significance of the pattern of aortic root dilation in the Marfan syndrome. *J Am Coll Cardiol* 1993;22:1470–6.
23. Dapunt OE, Galla JD, Sadeghi AM et al. The natural history of thoracic aortic aneurysms. *J Thorac Cardiovasc Surg* 1994;107: 1323–32; discussion 32–3.
24. Pyeritz RE. Genetics and cardiovascular disease. In: Braunwald E (ed.) *Cardiovascular Disease*. Philadelphia: Saunders, 1992; 1641–3.
25. Groenink M, Lohuis TA, Tijssen JG et al. Survival and complication free survival in Marfan's syndrome: implications of current guidelines. *Heart* 1999;82:499–504.
26. Legget ME, Unger TA, O'Sullivan CK et al. Aortic root complications in Marfan's syndrome: identification of a lower risk group. *Heart* 1996;75:389–95.
27. Silverman DI, Gray J, Roman MJ et al. Family history of severe cardiovascular disease in Marfan syndrome is associated with increased aortic diameter and decreased survival. *J Am Coll Cardiol* 1995;26:1062–7.
28. Jondeau G, Boutouyrie P, Lacolley P et al. Central pulse pressure is a major determinant of ascending aorta dilation in Marfan syndrome. *Circulation* 1999;99:2677–81.
29. Adams JN, Brooks M, Redpath TW et al. Aortic distensibility and stiffness index measured by magnetic resonance imaging in patients with Marfan's syndrome. *Br Heart J* 1995;73:265–9.
30. Groenink M, de Roos A, Mulder BJ et al. Biophysical properties of the normal-sized aorta in patients with Marfan syndrome: evaluation with MR flow mapping. *Radiology* 2001;219:535–40.
31. Hirata K, Triposkiadis F, Sparks E et al. The Marfan syndrome: cardiovascular physical findings and diagnostic correlates. *Am Heart J* 1992;123:743–52.
32. Jeremy RW, Huang H, Hwa J et al. Relation between age, arterial distensibility, and aortic dilatation in the Marfan syndrome. *Am J Cardiol* 1994;74:369–73.
33. Baumgartner D, Baumgartner C, Matyas G et al. Diagnostic power of aortic elastic properties in young patients with Marfan syndrome. *J Thorac Cardiovasc Surg* 2005;129:730–9.
34. Freed LA, Levy D, Levine RA et al. Prevalence and clinical outcome of mitral-valve prolapse. *N Engl J Med* 1999;341:1–7.
35. Levine R, Handschumacher M, Sanfilippo A et al. Three-dimensional echocardiographic reconstruction of the mitral valve, with implications for the diagnosis of mitral valve prolapse. *Circulation* 1989;80:589–98.
36. Pyeritz RE, Wappel MA. Mitral valve dysfunction in the Marfan syndrome. Clinical and echocardiographic study of prevalence and natural history. *Am J Med* 1983;74:797–807.
37. De Backer J, Loeys B, Devos D et al. A critical analysis of minor cardiovascular criteria in the diagnostic evaluation of patients with Marfan syndrome. *Genet Med* 2006;8:401–8.
38. Nollen GJ, van Schijndel KE, Timmermans J et al. Pulmonary artery root dilatation in Marfan syndrome: quantitative assessment of an unknown criterion. *Heart* 2002;87:470–1.
39. Dietz HC, Pyeritz RE. Marfan syndrome and related disorders. In: Scriver CRBA, Sly WS, Valle D (eds) *The Metabolic and Molecular Bases of Inherited Diseases.* New York: McGraw-Hill, 1995;5287–311.
40. Finkbohner R, Johnston D, Crawford ES et al. Marfan syndrome: long-term survival and complications after aortic aneurysm repair. *Circulation* 1995;91:728–33.
41. Engelfriet PM, Boersma E, Tijssen JG et al. Beyond the root: dilatation of the distal aorta in the marfan syndrome. *Heart* 2006;92:1238–43.
42. van Ooijen B. Marfan's syndrome and isolated aneurysm of the abdominal aorta. *Br Heart J* 1988;59:81–4.
43. Pruzinsky MS, Katz NM, Green CE, Satler LF. Isolated descending thoracic aortic aneurysm in Marfan's syndrome. *Am J Cardiol* 1988;61:1159–60.
44. Finkbohner R, Johnston D, Crawford ES et al. Marfan syndrome. Long-term survival and complications after aortic aneurysm repair. *Circulation* 1995;91:728–33.
45. Nollen GJ, Groenink M, Tijssen JG et al. Aortic stiffness and diameter predict progressive aortic dilatation in patients with Marfan syndrome. *Eur Heart J* 2004;25:1146–52.
46. Kawamoto S, Bluemke DA, Traill TA, Zerhouni EA. Thoracoabdominal aorta in Marfan syndrome: MR imaging findings of progression of vasculopathy after surgical repair. *Radiology* 1997; 203:727–32.
47. Nollen GJ, Meijboom LJ, Groenink M et al. Comparison of aortic elasticity in patients with the marfan syndrome with and without aortic root replacement. *Am J Cardiol* 2003;91:637–40.
48. Chatrath R, Beauchesne LM, Connolly HM et al. Left ventricular function in the Marfan syndrome without significant valvular regurgitation. *Am J Cardiol* 2003;91:914–6.

49. Savolainen A, Nisula L, Keto P et al. Left ventricular function in children with the Marfan syndrome. *Eur Heart J* 1994;15: 625–30.
50. Porciani MC, Giurlani L, Chelucci A et al. Diastolic subclinical primary alterations in Marfan syndrome and Marfan-related disorders. *Clin Cardiol* 2002;25:416–20.
51. Das BB, Taylor AL, Yetman AT. Left ventricular diastolic dysfunction in children and young adults with Marfan syndrome. *Pediatr Cardiol* 2006;27:256–8.
52. De Backer JF, Devos D, Segers P et al. Primary impairment of left ventricular function in Marfan syndrome. *Int J Cardiol* 2006; 112:353–8.
53. Loeys BL, Chen J, Neptune ER et al. A syndrome of altered cardiovascular, craniofacial, neurocognitive and skeletal development caused by mutations in TGFBR1 or TGFBR2. *Nat Genet* 2005;37:275–81.
54. Loeys BL, Schwarze U, Holm T et al. Aneurysm syndromes caused by mutations in the TGF-beta receptor. *N Engl J Med* 2006;355:788–98.
55. Williams JA, Loeys BL, Nwakanma LU et al. Early surgical experience with Loeys–Dietz: a new syndrome of aggressive thoracic aortic aneurysm disease. *Ann Thorac Surg* 2007;83:S757–63; discussion S85–90.
56. Pepin M, Schwarze U, Superti-Furga A, Byers PH. Clinical and genetic features of Ehlers–Danlos syndrome type IV, the vascular type. *N Engl J Med* 2000;342:673–80.
57. Oderich GS, Panneton JM, Bower TC et al. The spectrum, management and clinical outcome of Ehlers–Danlos syndrome type IV: a 30-year experience. *J Vasc Surg* 2005;42:98–106.
58. Bergqvist D. Ehlers–Danlos type IV syndrome. A review from a vascular surgical point of view. *Eur J Surg (Acta Chirurgica)* 1996;162:163–70.
59. Coucke PJ, Willaert A, Wessels MW et al. Mutations in the facilitative glucose transporter GLUT10 alter angiogenesis and cause arterial tortuosity syndrome. *Nat Genet* 2006;38:452–7.
60. Pannu H, Fadulu VT, Chang J et al. Mutations in transforming growth factor-{beta} receptor type II cause familial thoracic aortic aneurysms and dissections. *Circulation* 2005;112:513–20.
61. Zhu L, Vranckx R, Van Kien PK et al. Mutations in myosin heavy chain 11 cause a syndrome associating thoracic aortic aneurysm/aortic dissection and patent ductus arteriosus. *Nat Genet* 2006; 38:343–9.
62. Mills P, Leech G, Davies M, Leathan A. The natural history of a non-stenotic bicuspid aortic valve. *Br Heart J* 1978;40:951–7.
63. de Sa M, Moshkovitz Y, Butany J, David TE. Histologic abnormalities of the ascending aorta and pulmonary trunk in patients with bicuspid aortic valve disease: clinical relevance to the ross procedure. *J Thorac Cardiovasc Surg* 1999;118:588–94.
64. Fedak PW, Verma S, David TE et al. Clinical and pathophysiological implications of a bicuspid aortic valve. *Circulation* 2002; 106:900–4.
65. Hahn RT, Roman MJ, Mogtader AH, Devereux RB. Association of aortic dilation with regurgitant, stenotic and functionally normal bicuspid aortic valves. *J Am Coll Cardiol* 1992;19:283–8.
66. Cecconi M, Manfrin M, Moraca A et al. Aortic dimensions in patients with bicuspid aortic valve without significant valve dysfunction. *Am J Cardiol* 2005;95:292–4.
67. Gurvitz M, Chang RK, Drant S, Allada V. Frequency of aortic root dilation in children with a bicuspid aortic valve. *Am J Cardiol* 2004;94:1337–40.
68. Basso C, Boschello M, Perrone C et al. An echocardiographic survey of primary school children for bicuspid aortic valve. *Am J Cardiol* 2004;93:661–3.
69. Huntington K, Hunter AG, Chan KL. A prospective study to assess the frequency of familial clustering of congenital bicuspid aortic valve. *J Am Coll Cardiol* 1997;30:1809–12.
70. Emanuel R, Withers R, O'Brien K et al. Congenitally bicuspid aortic valves. Clinicogenetic study of 41 families. *Br Heart J* 1978;40:1402–7.
71. Goh D, Han L, Judge DP, Dietz H. Linkage of familial bicuspid aortic valve with aortic aneurysm to chromosome 15q. *Am J Hum Genet* 2002; 2002. 71 (suppl.): 211.
72. Loscalzo M, Goh D, Spevak PJea. A prospective analysis of the inheritance, pathogenesis and natural history of bicuspid aortic valve with thoracic aortic aneurysm. American Society of Human Genetics; 2004; 2004.
73. Beighton P. The dominant and recessive forms of cutis laxa. *J Med Genet* 1972;9:216–21.
74. Szabo Z, Crepeau MW, Mitchell AL et al. Aortic aneurysmal disease and cutis laxa caused by defects in the elastin gene. *J Med Genet* 2006;43:255–8.

# 32 Cardiac Tumors

**Michele A. Frommelt**
Division of Pediatric Cardiology, Medical College of Wisconsin, Children's Hospital of Wisconsin, Milwaukee, WI, USA

## Introduction

Tumors of the heart in the pediatric age group are typically characterized by a proliferation of tissue normally present at the site of origin. Cardiac tumors can comprise muscle (rhabdomyoma), fibrous tissue (fibroma), vascular tissue (hemangioma), mixed tissue (teratoma), fatty tissue (lipoma) and, rarely, metastatic tissue. Tumors of the heart can be defined as primary or secondary to other disease processes, as well as benign or malignant. Primary cardiac tumors are much more common in children, with almost all being histologically benign. This is in contrast to adults, where most cardiac tumors are secondary and related to metastatic disease.

## Incidence

Cardiac tumors are rare in children, with an estimated incidence of 0.03–0.4%. In a review of 11 000 pediatric autopsies from the Boston Children's Hospital, reported by Nadas and Ellison in 1968, cardiac tumors were present in 0.027% [1]. In the New England regional study of more than 2000 infants with congenital heart disease, nine had primary cardiac tumors (0.4%) [2]. In an 8-year review of more than 14 000 fetal echocardiograms, cardiac tumors were present in 19 pregnancies, an incidence of 0.14% [3]. The majority of cardiac tumors in all of these studies were benign, with the most common being rhabdomyoma.

Over the past few decades, the recognition of cardiac tumors has increased. This is likely not related to a true increase in their prevalence, but can be explained by the widespread availability and increased sensitivity of two-dimensional (2D) echocardiography. This is nicely demonstrated in a study by Beghetti et al., a 15-year review of more than 27 000 pediatric patients with cardiac disease [4]. The overall incidence of a primary cardiac tumor was 0.2%, with an increase in incidence over each successive 5-year period (from 0.06% in the first period to 0.32% in the last). More than half of the patients were less than 1 year old at the time of diagnosis, and 12 of the 56 patients were diagnosed prenatally. 2D echocardiography was the imaging modality of choice in 55/56 patients.

Rhabdomyoma is the most common primary pediatric cardiac tumor, comprising about 60–80% of all tumors (Table 32.1). Cardiac fibromas have the second highest incidence (6–25%), followed closely by the teratoma. Hemangiomas and lipomas are much less common. The cardiac myxoma is rarely seen in the pediatric population, despite being the most common primary cardiac tumor in adults [5–8].

## Rhabdomyoma

### Classification

Rhabdomyomas, also known as hamartomas, are defined as an anomalous, benign proliferation of primitive myocardial tissue displaying typical "spider cells" on histopathology [9]. They are the most common benign congenital tumor, and are frequently associated with the tuberous sclerosis complex (50–86%). The genetic mutation in the tuberous sclerosis complex leads to proliferation of embryonal myoblasts, most commonly yielding multiple solid masses, which may arise anywhere in the atrial or ventricular myocardium [10]. Of importance, spontaneous regression of these cardiac tumors after birth is the rule [11–14].

### Echocardiography

Perhaps the most defining echocardiographic feature of the cardiac rhabdomyoma is the presence of multiple tumors (Fig. 32.1 and Videoclip 32.1). The tumors appear nodular and embedded in the myocardium, but often protrude into the involved cardiac chamber (Fig. 32.2). They are typically homogeneous and hyperechoic compared with normal myocardium (Fig. 32.3). Cardiac rhabdomyomas also have a distinct preference for the ventricles. In a study by Nir et al.,

*Echocardiography in Pediatric and Congenital Heart Disease: From Fetus to Adult*
Edited by Wyman W. Lai, Luc L. Mertens, Meryl S. Cohen and Tal Geva
 ISBN: 978-1-405-17401-5

**Table 32.1** Characteristics of primary cardiac tumors in childhood

| Type | Rhabdomyoma | Fibroma | Teratoma | Hemangioma | Myxoma |
|---|---|---|---|---|---|
| **Percent** | 60–80 | 6–25 | 6–25 | <10 | <1 |
| **Location** | Ventricles | Ventricles | Pericardium | Right atrium | Left atrium |
| **Appearance** | Multiple<br>Hyperechoic<br>Homogeneous | Large, solitary<br>Hyperechoic<br>Heterogeneous (areas of calcification) | Solitary<br>Mixed echogenicity<br>Solid/multicystic | Solitary<br>Mixed echogenicity<br>Color Doppler signals | Solitary<br>Pedunculated<br>Mixed echogenicity |
| **Age** | Fetal/infancy | Any age | Fetal/infancy | Neonatal | Adolescence |
| **Regression** | Yes | No | No | Yes, in infancy | No |
| **Associations** | Tuberous sclerosis | Outflow obstruction | Pericardial effusion | Pericardial effusion | Emboli |

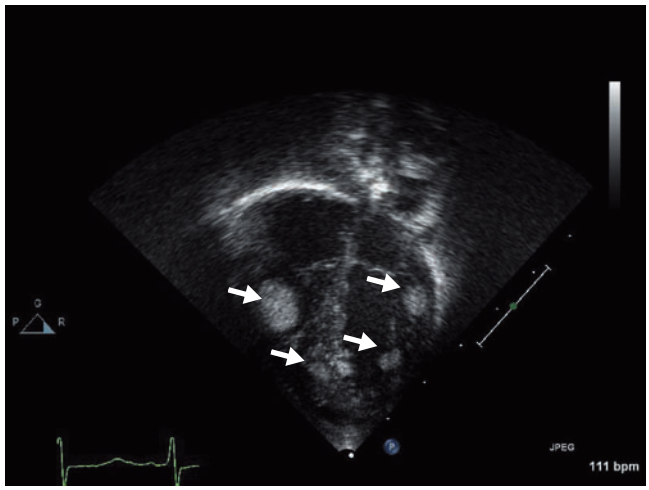


**Figure 32.1** Apical 4-chamber view in a patient with tuberous sclerosis and rhabdomyomas. Multiple hyperechoic masses (arrows) are seen in the left and right ventricular free wall, as well as the ventricular septum.

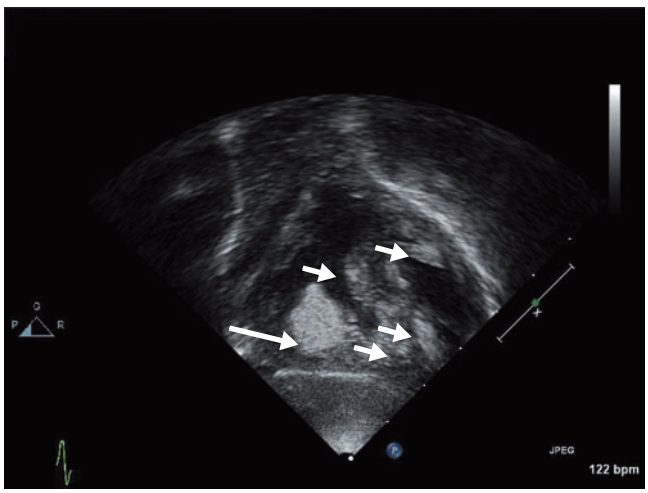


**Figure 32.2** Subcostal 4-chamber view of the right ventricular outflow tract in a patient with tuberous sclerosis and rhabdomyomas. A large hyperechoic mass is seen just below the infundibulum (large arrow); multiple smaller masses are seen in the anterior muscular ventricular septum (small arrows).

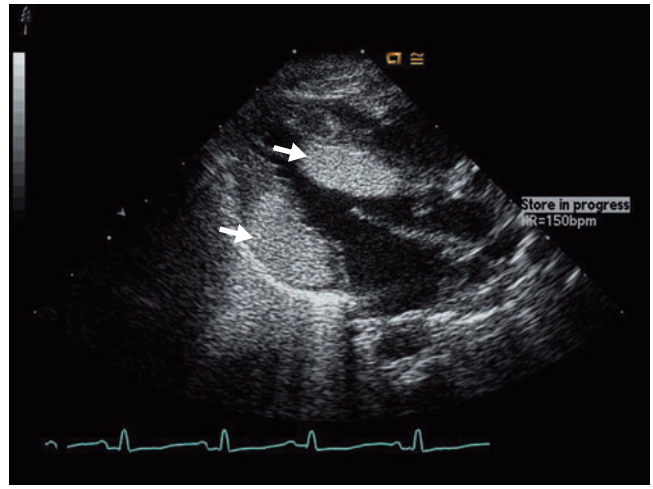


**Figure 32.3** Parasternal long-axis view in a patient with tuberous sclerosis who presented with supraventricular tachycardia. Two large rhabdomyomas are seen in the left ventricular free wall and septum (arrows). The tumors appear embedded in the myocardium, and are hyperechoic and homogeneous.

109 patients with the diagnosis of tuberous sclerosis underwent a comprehensive 2D echocardiogram. Of these patients, 47 (43%) had cardiac rhabdomyoma. The tumors were most commonly located in the left and right ventricles (68% and 66% respectively); only three patients (6%) were found to have right atrial tumors. None were found in the left atrium [15].

Two-dimensional imaging as well as color and pulsed Doppler from standard acoustic windows should be performed. The goals of the examination should include determination of tumor size, location, and number. Hemodynamic abnormalities associated with the tumor should also be sought, with quantification of inflow or outflow tract obstruction, as well as valvar insufficiency. Evaluation of ventricular function is also critical, as replacement of the ventricular muscle by noncontractile tumor tissue may mimic a cardiomyopathy [16]. In the fetus, it is also important to evaluate cardiac rhythm, and to investigate the serous cavities for effusions.

Serial echocardiographic evaluation of these patients is critical, both prenatally and postnatally. Several studies have reported significant growth of cardiac rhabdomyoma in mid-gestation, suggesting that hormonal stimulation in utero plays a role in the growth process [3,17]. If there is a family history of tuberous sclerosis, it is important to remember that prenatal ultrasound rarely detects tumors prior to 20 weeks' gestation [18]. Therefore, an early screening ultrasound may be falsely reassuring. After birth, most cardiac rhabdomyomas will undergo spontaneous regression. This phenomenon has been extensively studied, and, indeed, is one of the hallmarks of these tumors [11–14]. Surgery is recommended only for those patients with severe hemodynamic compromise or refractory arrhythmias. Of note, rapid tumor growth has been reported postnatally when the patient is treated with corticosteroids. The size of the cardiac rhabdomyoma should be followed carefully in those patients receiving this type of drug therapy [19].

### Clinical course

The clinical course is generally benign and largely determined by tumor size and the presence of inflow or outflow tract obstruction. Rarely, global ventricular function may be depressed if there is significant tumor replacement of normal myocardium. Cardiac arrhythmias are well reported, and may be related to interruption of the normal conduction pathways. In several studies, the presence of Wolff–Parkinson–White syndrome was more frequent in patients with tuberous sclerosis compared with the normal population. Incessant ventricular arrhythmias, although rare, can be life-threatening [20–22].

The timing of presentation also influences clinical course. In the older child referred to the echocardiography laboratory with a new diagnosis of tuberous sclerosis, it would be unusual to find a cardiac rhabdomyoma of clinical significance. However, when the diagnosis of tuberous sclerosis is suspected prenatally, the fetus may present with demise secondary to severe outflow tract obstruction or sustained arrhythmias. In a retrospective 7-year review by Geipel et al., 12 cases of cardiac tumors were observed prenatally. Eleven of the 12 were ultimately found to be rhabdomyomas, with one fibroma. Presenting symptoms were common in this age group, and included hydrops fetalis in five patients and arrhythmias in four patients. There were three elective terminations of pregnancy, one intrauterine demise related to severe left ventricular outflow tract (LVOT) obstruction, and three neonatal deaths, all related to massive tumor infiltration of the ventricular septum [23].

## Fibroma

### Classification

The cardiac fibroma is a benign connective tissue tumor derived from fibroblasts. It is the second most common type of primary cardiac tumor occurring in the pediatric age group. Cardiac fibromas are generally large tumors, averaging 5 cm in diameter, with the larger lesions able to obstruct outflow tracts and compress cardiac chambers. Their growth is typically within the myocardial mass itself, and they occur much more frequently within the anterior free wall of the left ventricle or the interventricular septum than in the posterior left ventricular wall or right ventricle. Although less common than the rhabdomyoma, fibromas are more often associated with symptoms, and more often require surgery. In contrast to the behavior of rhabdomyomas, spontaneous regression of fibromas is unusual [4–6,16].

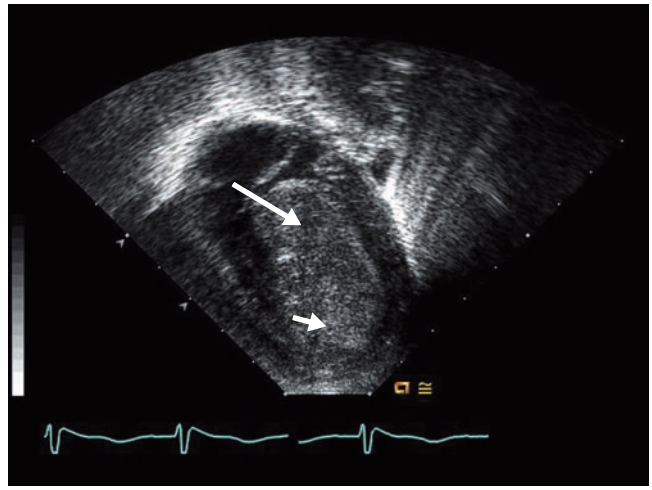

**Figure 32.4** Apical 4-chamber view in a patient with a septal fibroma who presented with low cardiac output. A large hyperechoic mass is seen arising from the ventricular septum (large arrows), limiting mitral inflow and aortic outflow. The mass is heterogeneous, with areas of calcification (small arrow).

### Echocardiography

Cardiac fibromas are solitary lesions that arise from the ventricular septum or the free wall of the left or right ventricle (Fig. 32.4). They often appear circumscribed, and are typically hyperechoic compared with normal myocardium. Calcification is frequent and an important diagnostic imaging feature. Areas of focal necrosis and cystic degeneration are common in the larger tumors. It is important to remember that a large septal fibroma may have the appearance of a hypertrophic obstructive cardiomyopathy. The absence of thickening/hypertrophy of other cardiac walls may suggest the diagnosis of fibroma. Also, calcification does not occur in hypertrophic cardiomyopathy. Fibromas can be massive, markedly distorting the cardiac muscle (Figs 32.5 and 32.6, Videoclip 32.2(a,b)). This irregular appearance is also unusual for hypertrophic cardiomyopathy.

Two-dimensional imaging as well as color and pulsed Doppler interrogation from standard acoustic windows is important. In the symptomatic patient, severe LVOT obstruction may be profound and can mimic hypertrophic

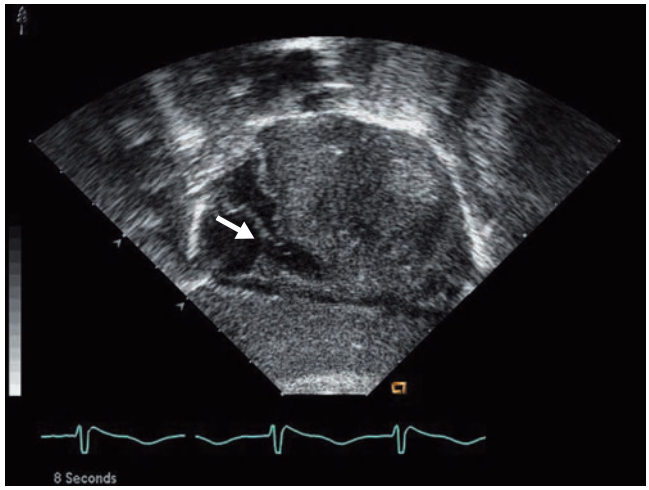


**Figure 32.5** Subcostal 4-chamber view of the mitral inflow in a patient with a massive septal fibroma. The mass is irregular and heterogeneous, markedly distorting the cardiac architecture. Mitral inflow is compromised (small arrow).

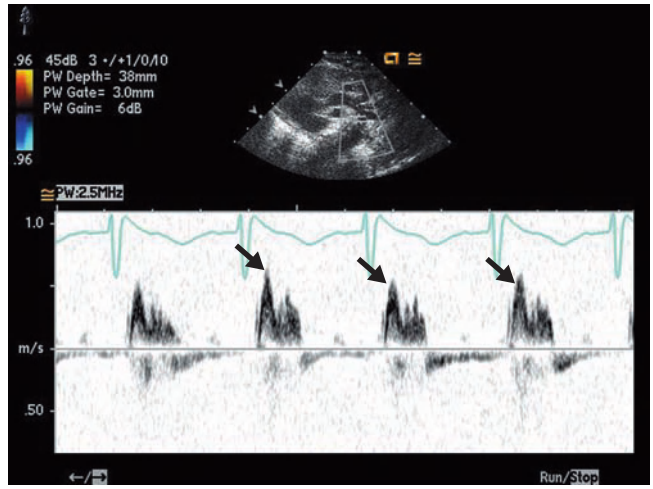


**Figure 32.7** Suprasternal notch Doppler recording of the distal transverse arch in a newborn with a massive septal fibroma. There is no significant antegrade flow around the arch, with predominant retrograde systolic supply (arrow) of the arch from a patent ductus arteriosus. The patient presented with low cardiac output, but stabilized on prostaglandin therapy.

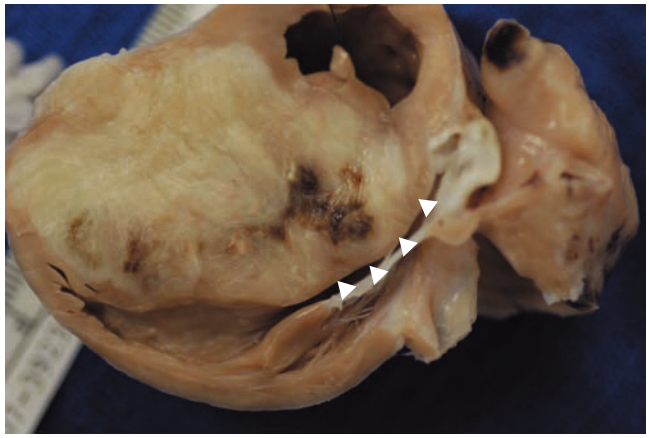

**Figure 32.6** Pathologic specimen of the explanted heart in a patient with a massive septal fibroma who underwent cardiac transplantation. The fibrous mass occupies almost the entire ventricular septum, covered only by a thin rim of myocardium (arrows). The left ventricular cavity is small, with marked narrowing of the left ventricular outflow tract.

obstructive cardiomyopathy, with limited ventricular filling and dynamic outflow obstruction. In fact, the neonate who presents with severe LVOT obstruction may have ductal-dependent systemic blood flow. Doppler interrogation of the transverse arch should be performed to look for retrograde ductal supply of the transverse arch (Fig. 32.7).

### Clinical course

The age at presentation is variable, and often dependent on the presence of obstruction. Burke and colleagues identified 23 cases of cardiac fibroma from the files of the Armed Forces Institute of Pathology. The mean age at the time of diagnosis was 13 years; more than one-third of the patients were younger than 1 year of age [24]. Presentation in infancy heralds severe disease, with symptoms related to severe left or right ventricular outflow tract obstruction. The older child may be asymptomatic, but life-threatening arrhythmias and sudden cardiac death are well reported.

Spontaneous regression of the cardiac fibroma is rare. Therefore, in the patient with symptoms, surgical resection or palliation is often considered. Reports suggest that many ventricular fibromas can be completely resected with excellent early and late results [25,26]. However, cardiac transplantation may be a better option, especially in those patients with massive obstructive tumors [27]. Another approach has involved partial resection of a massive right ventricular fibroma with the addition of a bidirectional cavopulmonary shunt to provide a stable source of pulmonary blood flow [28].

## Teratoma

### Classification

Cardiac teratomas appear to be the third most common tumor type encountered in infants and children [4–7]. Nearly two-thirds are found in infants, and many more are detected antenatally than postnatally [29]. Cardiac teratomas most commonly originate in the pericardial cavity attached to the great vessels; pericardial effusion is present in almost all cases and may be significant. The tumor has a smooth external surface; cut sections reveal multiloculated cysts and solid areas (Fig. 32.8). The tumor contains derivatives of all three germ layers, similar to the extrapericardial (i.e., sacrococcygeal) teratomas seen in the pediatric age group.

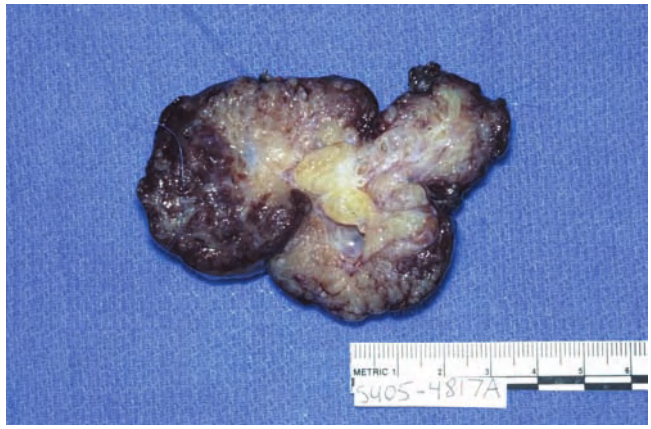


**Figure 32.8** Pathologic specimen of a surgically removed pericardial teratoma. The teratoma has a predominantly solid surface with multiple microcysts filled with serous fluid. Microscopically, the tumor contained derivatives of all three germ layers, including elements of skin, gastrointestinal tract, respiratory tract, cartilage, liver, pancreas, and neural tissue.

### Echocardiography

Intrapericardial teratomas are attached to the root of the pulmonary artery or aorta, with both solid and multicystic areas (Fig. 32.9a and Videoclip 32.3(a,b)). Foci of calcification are also common. The presence of a pericardial effusion in association with a pericardial mass is almost diagnostic of a teratoma. The effusions can be large and hemodynamically important (Fig. 32.9b). Intrapericardial teratoma in the fetus has also been well reported. Nonimmune hydrops is not uncommon, and may be related to cardiac tamponade or obstruction of systemic venous return from the tumor itself. In a literature review published by Bader et al., 31 cases of prenatal intrapericardial teratoma were identified. The diagnosis was typically suspected because of the presence of a pericardial effusion in the second or third trimester. Most tumors were located at the base of the heart. More than 75% of the fetuses developed hydrops. Fetal pericardial drainage was performed in 11 of the 31 reported cases with technical success, although reaccumulation of fluid was common [29].

Echocardiographic assessment of cardiac tamponade is critical in the patient with a large pericardial effusion. This should include 2D assessment of right atrial and right ventricular diastolic collapse, as well as Doppler interrogation of respiratory variable cardiac filling and cardiac output.

### Clinical course

Regression of teratomas is unusual. The majority of patients are symptomatic, either secondary to the large pericardial effusion or compression of the cardiac chambers and great vessels. Early recognition is important, as surgical resection is curative and can be accomplished with an excellent survival rate (4–7).

## Myxoma

### Classification

The cardiac myxoma is a benign tumor derived from cardiac multipotential mesenchymal cells [30]. It is the most common primary tumor of the heart in adults but is very rare in the pediatric age group [4–8]. Myxomas arise from the endocardium and form exophytic intracavitary masses. There are two distinct morphologies of myxoma; the solid myxoma appears firm and smooth whereas the papillary

(a)

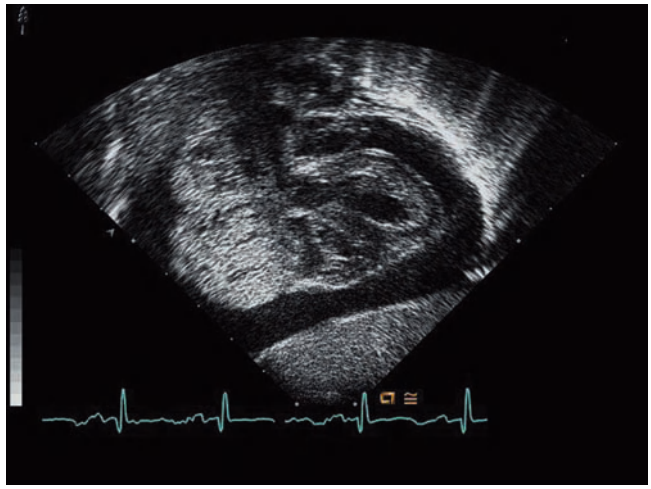

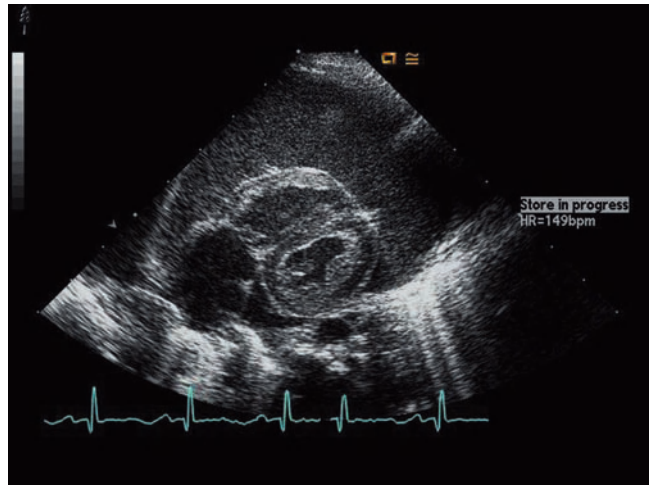


(b)

**Figure 32.9** **(a)** Subcostal 4-chamber view of the left ventricular outflow tract in a patient with a pericardial teratoma. The teratoma is heterogeneous, with multiple cystic areas. It appears to arise from the base of the heart, with an associated pericardial effusion. **(b)** Parasternal short-axis view in the same patient demonstrating the massive pericardial effusion. The 3-week-old infant presented with tachycardia and severe cardiomegaly on chest radiograph.

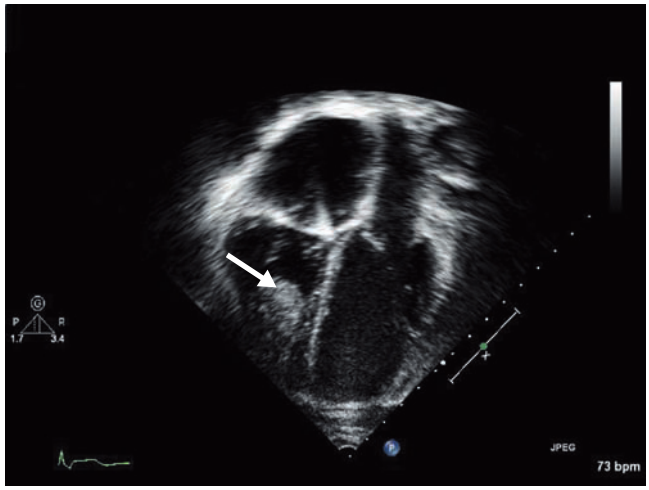


**Figure 32.10** Apical 4-chamber view in a patient with a recurrent right ventricular myxoma (arrow). The myxoma is hyperechoic and appears to be involved with the tricuspid valve apparatus. The patient also had tricuspid valve repair at the time of the initial myxoma removal; a Carpentier ring is identified in the tricuspid annulus.

myxoma has a more cauliflower-like appearance [31,32]. The site of origin is usually the left atrium (Videoclip 32.4) [33]. Presenting symptoms are common and include congestive heart failure, systemic emboli, and neurologic symptoms [8]. There are few reports in the literature describing myxomas in children. Interestingly, most myxomas described in the pediatric age group have occurred on the right side of the heart [34–36].

### Echocardiography

Tumor location, size, attachment and mobility can be assessed by echocardiography [37–40]. Approximately 75% of myxomas are found in the left atrium, with 20% in the right atrium and the remaining 5% equally distributed between the left and right ventricles (Fig. 32.10). Typically myxomas are isolated, pedunculated tumors in the left atrium attached to the area of the foramen ovale by a stalk. If the tumor does not arise from the lower part of the interatrial septum, the diagnosis of myxoma should be questioned. Both hypoechoic and hyperechoic foci may be seen, reflecting areas of hemorrhage and calcification, respectively. Depending on the size, the tumor may prolapse through the mitral orifice in diastole, occasionally producing a tumor "plop" and accounting for the common misdiagnosis of mitral stenosis. Doppler echocardiography should be used to quantitate the degree of mitral stenosis or mitral insufficiency.

An atrial myxoma must be differentiated from a left atrial thrombus. A thrombus is usually situated in the posterior portion of the atrium, has a layered appearance, and extends into the left atrial appendage. Also, the formation of atrial thrombi is unusual in the pediatric setting, unless there is associated ventricular dysfunction or a history of atrial arrhythmias. Transthoracic echocardiography is usually sufficient to make the diagnosis, but if imaging is suboptimal, transesophageal echocardiography should be employed [41].

### Clinical course

Symptoms of left heart inflow obstruction and/or embolic phenomena are almost inevitable in the setting of an atrial myxoma. In a study by Swartz et al., only 8% of patients were asymptomatic at the time of diagnosis [42]. Regression is atypical, and, in fact, recurrence is likely if the tumor is not completely resected. Surgery has been successful, with little operative mortality and minimal morbidity [43–45].

## Hemangioma

### Classification

Hemangiomas are common benign congenital vascular lesions. They most commonly occur in the skin , but are occasionally found in internal organs. Cardiac hemangiomas comprise about 2.8% of all primary cardiac tumors and most are diagnosed in the neonatal period [46,47]. Cardiac hemangiomas are composed of endothelial cells that line interconnecting vascular channels. The main histologic types are based on the size of the vascular lumen. The cavernous hemangioma consists of large vascular channels, whereas the capillary hemangioma is composed of smaller vessels resembling capillaries. There are also mixed varieties.

Age at diagnosis appears to be predictive of histologic type, tumor location and clinical presentation. The fetus or young infant is much more likely to have a cavernous-type hemangioma located within the right atrium. Symptoms are common in this age group, generally related to the presence of a large pericardial effusion. The infantile tumor is more likely to regress spontaneously, and is responsive to antiangiogenic therapy. The older child with a vascular tumor is rarely symptomatic and much more likely to have a capillary-type hemangioma. Spontaneous regression is unusual in this setting [48].

### Echocardiography

Cardiac hemangiomas can occur at any location in the heart, including the epicardial surface and pericardium (Fig. 32.11). In the fetus and infant, the right atrium is the major primary site. The tumors are usually of mixed echogenicity. Cystic spaces can be identified, and have been attributed to both cavernous lakes and degeneration. Associated pericardial effusions are seen in most patients. Identification of color Doppler blood flow signals in the mass helps make the diagnosis, although the absence of these signals is not uncommon. Unlike hemangiomas in other organs, such as the liver, significant blood flow is unusual; cardiac chamber enlargement and high-output congestive heart failure are rare.

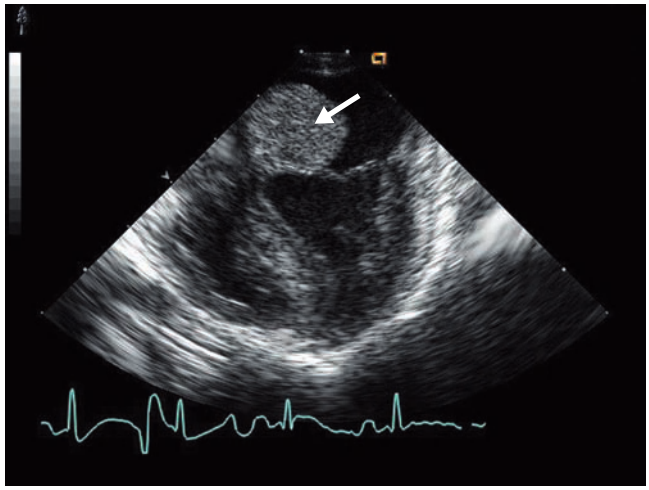

**Figure 32.11** A transverse transesophageal image in a patient with a left atrial hemangioma. The absence of a stalk and a wide base of attachment to the anterior mitral valve leaflet helps to differentiate this from a left atrial myxoma.

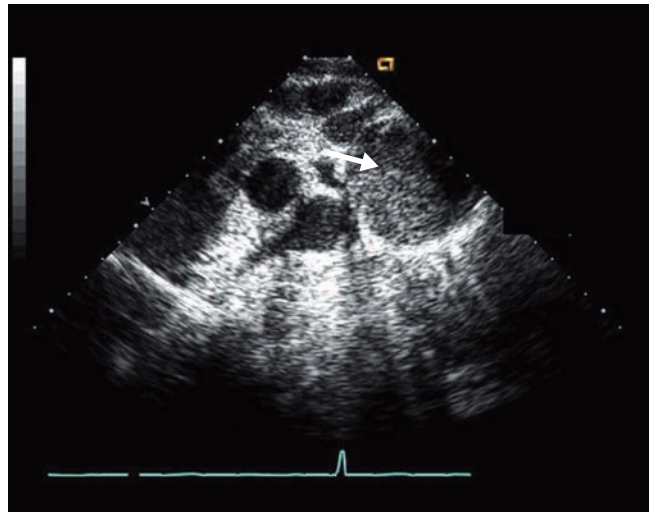

**Figure 32.12** High left parasternal view of the branch pulmonary arteries in a patient with Hodgkin disease. The right pulmonary artery is of good size; the left pulmonary artery is compressed by a large, solid mediastinal mass (arrow).

### Clinical course

Generally, vascular tumors have an excellent prognosis. The cavernous-type hemangioma has a tendency to regress spontaneously, but is also responsive to antiangiogenic therapy. In the older child, surgical resection can be accomplished with minimal morbidity/mortality.

## Malignant cardiac tumors

Primary malignant cardiac tumors in children are rare. When they occur, they are almost exclusively sarcomas [4–7]. Rhabdomyosarcoma is the leading malignancy in the infant, whereas angiosarcoma is more common in the older child. The prognosis is bleak in all patients [49].

Secondary tumor involvement of the heart, either by distant metastasis or direct tumor extension, occurs in less than 2% of children with malignant solid tumors [50]. The tumors with the highest rate of cardiac metastasis include lymphoma and neuroblastoma, whereas direct tumor extension has been most often reported in patients with Wilms tumor [51,52]. External compression of cardiac structures can be seen with Hodgkin disease (Fig. 32.12).

### Echocardiography

The echocardiographic characteristics of primary malignant cardiac tumors are not substantially different from those of the benign tumors. The tumors behave more aggressively, and there are extensive metastases at the time of presentation. The cardiac angiosarcoma should be suspected when a hemorrhagic pericardial effusion is present, and the pericardium appears markedly thickened, with an irregular surface (Fig. 32.13a,b).

## Association with syndromes

It is important to remember that primary cardiac tumors in children can be associated with hereditary syndromes [53]. Perhaps the best-recognized association is that of cardiac rhabdomyoma and the tuberous sclerosis complex [4–7, 10–17]. Tuberous sclerosis is a genetic disorder that affects cellular differentiation and proliferation, resulting in hamartoma formation in many organs, including the heart. Although it has an autosomal dominant inheritance pattern, more than half of the cases have been attributed to spontaneous mutations. There are two known genetic loci, one mapping to chromosome 9 and the other to chromosome 16 (also termed *TSC1* and *TSC2*). Defects in the affected proteins (tuberin and hamartin) lead to unregulated cellular growth and differentiation. It is currently thought that the majority of children with cardiac rhabdomyomas have tuberous sclerosis [54].

Although most cardiac fibromas in children occur as an isolated defect, approximately 3–5% of children with cardiac fibromas will have the nevoid basal cell carcinoma syndrome (Gorlin syndrome) [55]. Gorlin syndrome is an autosomal dominant disorder characterized by the development of basal cell carcinomas at an early age, jaw keratocysts, and palmar or plantar pits. Cardiac tumors that have been described in Gorlin syndrome include cardiac fibromas and fibrous histiocytomas. Of note, it is not unusual to have multiple cardiac fibromas in the patient with Gorlin syndrome (Fig. 32.14). The syndrome results from mutations in the *PTCH1* (patched) gene, which has been mapped to chromosome 9. This gene is thought to function primarily as a tumor suppressor. Cardiac myxomas are rare in children; however, they can be

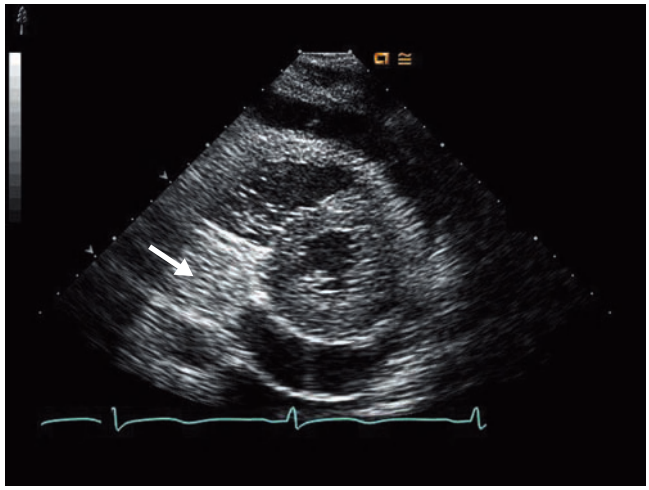

(a)

**Figure 32.13 (a)** Parasternal short-axis view in a patient with a cardiac angiosarcoma. A hyperechoic circumscribed mass is seen in the pericardial sac (arrow); there is an associated moderate pericardial effusion.

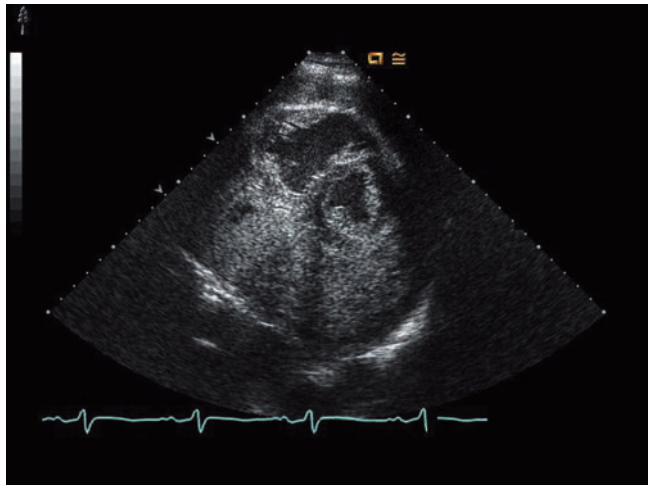

(b)

**(b)** Parasternal short-axis view in the same patient one month later. The pericardial sac now appears completely occupied by the angiosarcoma.

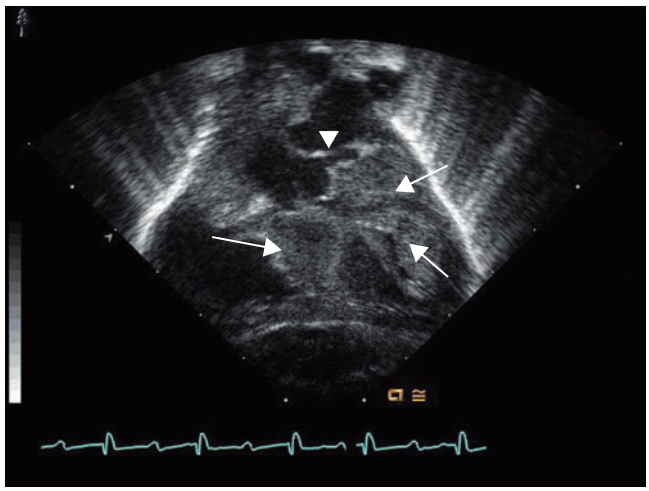

**Figure 32.14** Subcostal 4-chamber view of the left ventricular outflow tract in a patient with Gorlin syndrome. Multiple fibromas are seen in the ventricular septum and left ventricular free wall (large arrows). The left main coronary artery appears dilated and is displaced by the mass (small arrow).

associated with Carney syndrome. Carney syndrome is characterized by cardiac myxomas, spotty pigmentation of the skin, and endocrine overactivity [56]. Although myxomas typically occur as an isolated lesion, there can be multiple tumors in patient with Carney syndrome. Several mutations have been identified in the PRK (protein kinase) gene on chromosome 17; this gene also functions as a tumor suppressor.

## References


1. Nadas AS, Ellison RC. Cardiac tumors in infancy. *Am J Cardiol* 1968;21:363–6.
2. Talner CN. Report of the New England Regional Infant Cardiac Program, by Donald C. Fyler, MD. *Pediatrics* 1980;65(Suppl.): 375–461.
3. Holley DG, Martin GR, Brenner JI et al. Diagnosis and management of fetal cardiac tumors: a multicenter experience and review of published reports [see comment]. *J Am Coll Cardiol* 1996;28:1080.
4. Beghetti M, Gow RM, Haney I et al. Pediatric primary benign cardiac tumors: a 15-year review. *Am Heart J* 1997;134:1107–14.
5. Van der Hauwaert LG. Cardiac tumors in infancy and childhood. *Br Heart J* 1971;33:125–32.
6. Arciniegas E, Hakimi M, Farooki ZQ et al. Primary cardiac tumors in children. *J Thorac Cardiovasc Surg* 1980;79:582–91.
7. Freedom RM, Lee KJ, MacDonald C, Taylor G. Selected aspects of cardiac tumors in infancy and childhood. *Pediatr Cardiol* 2000; 21:299–316.
8. Reynen K. Cardiac myxomas [see comment]. *N Engl J Med* 1995; 333:1610–7.
9. Fenoglio JJ Jr, McAllister HA Jr, Ferrans VJ. Cardiac rhabdomyoma: a clinicopathologic and electron microscopic study. *Am J Cardiol* 1976;38:241–51.
10. Jowiak S, Kotulska K, Kasprzyk-Obara J et al. Clinical and genotype studies of cardiac tumors in 154 patients with tuberous sclerosis complex. *Pediatrics* 2006;118:e1146–51.
11. Farooki ZQ, Ross RD, Paridon SM et al. Spontaneous regression of cardiac rhabdomyoma. *Am J Cardiol* 1991;67:897–9.
12. Alkalay AL, Ferry DA, Lin B et al. Spontaneous regession of cardiac rhabdomyoma in tuberous sclerosis. *Clin Pediatr* 1987;26: 532–5.
13. Smythe JF, Dyck JD, Smallhorn JF, Freedom RM. Natural history of cardiac rhabdomyoma in infancy and childhood [see comment]. *Am J Cardiol* 1990;66:1247–9.

14. Bosi G, Lintermans JP, Pellegrino PA et al. The natural history of cardiac rhabdomyoma with and without tuberous sclerosis. *Acta Paediatr* 1996;85:928–31.
15. Nir A, Tajik AJ, Freeman WK et al. Tuberous sclerosis and cardiac rhabdomyoma. *Am J Cardiol* 1995;76:419–21.
16. Isaacs H Jr. Fetal and neonatal cardiac tumors. *Pediatr Cardiol* 2004;25:252–73.
17. Nir A, Ekstein S, Nadjari M et al. Rhabdomyoma in the fetus: illustration of tumor growth during the second half of gestation. *Pediatr Cardiol* 2001;22:515–8.
18. Achiron R, Weissman A, Rotstein Z et al. Transvaginal echocardiographic examination of the fetal heart between 13 and 15 weeks' gestation in a low-risk population. *J Ultras Med* 1994;13: 783–9.
19. Hishitani T, Hoshino K, Ogawa K et al. Rapid enlargement of cardiac rhabdomyoma during corticotrophin therapy for infantile spasms. *Can J Cardiol* 1997;13:72–4.
20. Wu CT, Chen MR, Hou SH. Neonatal tuberous sclerosis with cardiac rhabdomyomas presenting as fetal supraventricular tachycardia. *Jpn Heart J* 1997;38:133–7.
21. Case CL, Gillette PC, Crawford FA. Cardiac rhabdomyomas causing supraventricular and lethal ventricular arrhythmias in an infant. *Am Heart J* 1991;122:1484–6.
22. O'Callaghan FJ, Clarke AC, Joffe H et al. Tuberous sclerosis complex and Wolff–Parkinson–White syndrome. *Arch Dis Child* 1998;78:159–62.
23. Geipel A, Krapp M, Germer U et al. Perinatal diagnosis of cardiac tumors. *Ultrasound Obstet Gynecol* 2001;17:17–21.
24. Burke AP, Rosado-de-Christenson M, Templeton PA, Virmani R. Cardiac fibroma: clinicopathologic correlates and surgical treatment. *J Thorac Cardiovasc Surg* 1994;108:862–70.
25. Cho JM, Danielson GK, Puga FJ et al. Surgical resection of ventricular cardiac fibromas: early and late results. *Ann Thorac Surg* 2003;76:1929–34.
26. Davies B, Oppido G, Brizard CP. Surgical management of symptomatic cardiac fibromas in children. *J Thorac Cardiovasc Surg* 2007;133:254–5.
27. Waller BR, Bradley SM, Crumbley AJ 3rd et al. Cardiac fibroma in an infant: single ventricle palliation as a bridge to heart transplantation. *Ann Thorac Surg* 2003;75:1306–8.
28. Beghetti M, Haney I, Williams WG et al. Massive right ventricular fibroma treated with partial resection and a cavopulmonary shunt. *Ann Thorac Surg* 1996;62:882–4.
29. Bader R, Hornberger LK, Nijmeh LJ et al. Fetal pericardial teratoma: presentation of two cases and review of literature. *Am J Perinatol* 2006;23:53–8.
30. Johansson L. Histogenesis of cardiac myxomas. An immunohistochemical study of 19 cases, including one with glandular structures, and review of the literature. *Arch Pathol Lab Med* 1989;113:735–41.
31. Heath D. Pathology of cardiac tumors. *Am J Cardiol* 1968;21:315–27.
32. St John Sutton MG, Mercier LA, Giuliani ER, Lie JT. Atrial myxomas: a review of clinical experience in 40 patients. *Mayo Clin Proc* 1980;55:371–6.
33. Schaff HV, Mullany CJ. Surgery for cardiac myxomas. *Semin Thorac Cardiovasc Surg* 2000;12:77–88.
34. George KM, Przygodzki RM, Jonas RA, Di Russo GB. Resection of an obstructive neonatal cardiac myxoma of the infundibulum. *Pediatr Cardiol* 2006;27:369–71.
35. Balsara RK, Pelias AJ. Myxoma of right ventricle presenting as pulmonic stenosis in a neonate. *Chest* 1983;83:145–6.
36. Paladini D, Tartaglione A, Vassallo M, Martinelli P. Prenatal ultrasonographic findings of a cardiac myxoma. *Obstet Gynecol* 2003;102:1174–6.
37. Goswami KC, Shrivastava S, Bahl VK et al. Cardiac myxomas: clinical and echocardiographic profile. *Int J Cardiol* 1998;63: 251–9.
38. Jelic J, Milici D, Alfirevi I et al. Cardiac myxoma: diagnostic approach, surgical treatment and follow-up. A twenty year experience. *J Cardiovasc Surg (Torino)* 1996;37(6 Suppl. 1):113–7.
39. Liu HY, Cheng KZ, Yang WY et al. Diagnosis of intracardiac myxomas by echocardiography. *Chin Med J* 1983;96:421–8.
40. Tansel T, Harmandar B, Ugurlucan M et al. Over 14 years of experience with cardiac myxomas. *Acta Cardiologica* 2006;61: 285–8.
41. Perez de Isla L, de Castro R, Zamorano JL et al. Diagnosis and treatment of cardiac myxomas by transesophageal echocardiography. *Am J Cardiol* 2002;90:1419–21.
42. Swartz MF, Lutz CJ, Chandan VS et al. Atrial myxomas: pathologic types, tumor location, and presenting symptoms. *J Cardiac Surg* 2006;21:435–40.
43. Bastos P, Barreiros F, Casanova J, Gomes MR. Cardiac myxomas: surgical treatment and long-term results. *Cardiovasc Surg* 1995;3:595–7.
44. Bortolotti U, Maraglino G, Rubino M et al. Surgical excision of intracardiac myxomas: a 20-year follow-up. *Ann Thorac Surg* 1990;49:449–53.
45. Bortolotti U, Maraglino G, Rubino M et al. Surgical excision of intracardiac myxomas: a 20-year follow-up. *Ann Thorac Surg* 1990;49:449–53.
46. Laga S, Gewillig MH, Van Schoubroeck D, Daenen W. Imminent fetal cardiac tamponade by right atrial hemangioma. *Pediatr Cardiol* 2006;27:633–5.
47. Tsend JJ, Chou MM, Lee YH, Ho ES. In utero diagnosis of cardiac hemangioma. *Ultrasound Obstet Gynecol* 1999;13:363–5.
48. Mackie AS, Kozakewich HP, Geva T et al. Vascular tumors of the heart in infants and children: case series and review of the literature. *Pediatr Cardiol* 2005;26:344–9.
49. Booth AM, LeGallo RD, Stoler MH et al. Pediatric angiosarcoma of the heart: a unique presentation and metastatic pattern. *Pediatr Dev Pathol* 2001;4:490–5.
50. Huh J, Noh CI, Kim YW et al. Secondary cardiac tumor in children. *Pediatr Cardiol* 1999;20:400–3.
51. Szymik-Kontorowicz S, Urbanowicz W, Malec E, Kordon Z. Right atrial extension of Wilms' tumor. *Med Sci Monitor* 2003;9:CS13–7.
52. Shamberger RC, Ritchey ML, Haase G et al. Intravascular extension of Wilms' tumor. *Ann Surg* 2001;234:116–21.
53. Vidaillet HJ Jr. Cardiac tumors associated with hereditary syndromes. *Am J Cardiol* 1988;61:1355.
54. Rosser T, Panigraphy A, McClintock W. The diverse clinical manifestations of tuberous sclerosis complex: a review. *Semin Pediatr Neurol* 2006;13:27–36.
55. Bossert T, Walther T, Vondrys D et al. Cardiac fibroma as an inherited manifestation of nevoid basal-cell carcinoma syndrome. *Tex Heart Inst J* 2006;33:88–90.
56. Goldstein MM, Casey M, Carney JA, Basson CT. Molecular genetic diagnosis of the familial myxoma syndrome (Carney complex). *Am J Med Genet* 1999;85:62–5.

# 6 Anomalies of Ventricular Myocardium

*Echocardiography in Pediatric and Congenital Heart Disease: From Fetus to Adult*
Edited by Wyman W. Lai, Luc L. Mertens, Meryl S. Cohen and Tal Geva
 ISBN: 978-1-405-17401-5

# 33 Dilated Cardiomyopathy and Myocarditis

**Carolyn T. Spencer**
Department of Cardiology, Harvard Medical School; Children's Hospital Boston, Boston, MA, USA

## Definition

In 1995, the World Health Organization (WHO) defined cardiomyopathies as "diseases of the myocardium associated with cardiac dysfunction," and classified them according to morphology into four distinct types: dilated cardiomyopathy (DCM), hypertrophic cardiomyopathy, restrictive cardiomyopathy, and arrhythmogenic right ventricular dysplasia [1]. Specifically, DCM was defined as "dilation and impaired contraction of the left ventricle or both ventricles" [1]. Today, cardiomyopathies are considered to be more heterogeneous and complex, especially as molecular genetics has emerged as an important tool in the diagnosis and recognition of cardiovascular disease, shedding new light on these conditions.

Current debate exists as to the method of classification of cardiomyopathies, with traditional classification adopting a phenotypic approach and a new proposed classification recommending a primarily genetics-based approach. In the genetic-based classification, cardiomyopathy has been defined as "a heterogeneous group of diseases of the myocardium associated with mechanical and/or electrical dysfunction that usually (but not invariably) exhibit inappropriate ventricular hypertrophy or dilation and are due to various causes (frequently genetic). Cardiomyopathies are either confined to the heart muscle (primary) or are part of generalized systemic disorders (secondary); these processes often lead to cardiovascular death or progressive heart failure-related disability" [2]. The primary cardiomyopathies are subcategorized as genetic, mixed (genetic and nongenetic) and acquired [2]. The DCM phenotype is typically characterized by progressive dilation and impaired systolic function of the left or both ventricles, usually with normal wall thickness [2]. Phenotypic classification systems have evolved from the WHO definition of cardiomyopathy as well [3], allowing inclusion of genotypic information into a phenotypically organized classification scheme. One recent modification to this classification includes the category of "hypocontractile-hypertrophic cardiomyopathy" separately to categorize cardiomyopathy (CM) associated with left ventricle (LV) dilation, increased mass-to-volume ratio and decreased systolic function that is often seen in association with mitochondrial myopathy.

Inflammatory myocardial disease is involved in the pathogenesis of some forms of DCM and other cardiomyopathies. Specifically, myocarditis is defined as an inflammatory disease of the myocardium diagnosed by established histologic, immunologic, and immunohistochemical criteria. Idiopathic, autoimmune, and infectious forms of inflammatory cardiomyopathy are recognized [1]. These inflammatory forms of cardiomyopathy are typically acquired, although some people may be genetically predisposed to these diseases. Myocarditis may be triggered by an infectious process, usually of viral etiology, but it can also be associated with bacterial, fungal, rickettsial and parasitic disease or with hypersensitivity reactions. The Dallas criteria [4], which require histopathologic evidence of inflammatory infiltrate and myocardial cell damage, have been used to diagnose myocarditis. However, these criteria underestimate the incidence because of issues with sampling error, variation in interpretation, immune modulation in the heart, variable host immunologic response, and differences in patient selection for cardiac biopsy. Identification of viral DNA or evidence of systemic immune activation can aid in the diagnosis of myocarditis in the appropriate clinical setting. Clinical pathologic classification of myocarditis includes fulminant (onset within 2 weeks of presentation with marked LV dysfunction), chronic persistent (less distinct onset of LV dysfunction), giant cell (characteristic giant cells on myocardial biopsy), and eosinophilic type [5]. In myocarditis, diagnostic echocardiographic findings are nonspecific; the distinction between DCM and myocarditis is often not possible. Cardiac magnetic resonance imaging (CMR) may be more sensitive and specific [6,7] in confirming the inflammatory nature of the disease.

*Echocardiography in Pediatric and Congenital Heart Disease: From Fetus to Adult*
Edited by Wyman W. Lai, Luc L. Mertens, Meryl S. Cohen and Tal Geva
 ISBN: 978-1-405-17401-5

**Table 33.1** Incidence of cardiomyopathy per 100 000 children

| Source | Primary CM (all types) | DCM | DCM in infants <1 year of age |
|---|---|---|---|
| PCMR, age <18 years [8,10] | 1.13 | 0.57 | 4.4 |
| Australia, age <10 years [9] | 1.24 | 0.73 | 4.76 |

CM, cardiomyopathy; DCM, dilated cardiomyopathy; PCMR, Pediatric Cardiomyopathy Registry.

## Incidence

The true incidence of CM has been difficult to ascertain, and may vary by geography, race/ethnicity and socioeconomic status. Data from the Pediatric Cardiomyopathy Registry (PCMR) and Australia indicate the annual incidence of all forms of primary pediatric cardiomyopathy is 1.13–1.24 cases per 100 000, with DCM accounting for approximately 50–60% of these cases [8,9] (Table 33.1). These reports exclude those with DCM due to congenital heart disease, arrhythmia, and/or chemotherapy exposure. Presentation with DCM is most common in children under 1 year of age. PCMR data indicate that in children with primary DCM, 66% of cases are idiopathic in nature, with myocarditis and neuromuscular diseases predominating among those with known causal etiology [10]. The annual incidence of nonischemic DCM in the adult population is 6 to 7 cases per 100 000 [11,12].

Myocarditis as a separate entity is typically sporadic and its incidence has been even more difficult to ascertain. Clinical manifestations are variable, the ability to confirm active or preceding viral infection is limited, and the initial presentation may be clinically silent. In a retrospective study, biopsy-proven myocarditis in children occurred at a rate of 2.5 cases per year in a population of 3 million people [13].

## Etiology

Most cases of pediatric DCM are idiopathic in nature, with known causes identified 32% to 44% of the time [9,10,14]. Specific etiologies include genetic, metabolic, infectious, immune-mediated, mitochondrial and environmental toxins (Table 33.2) [2]. Data analysis from the PCMR indicates that myocarditis is the largest single cause of DCM in those under 18 years of age, accounting for 16–18% of all cases. However, in cases of DCM in which a specific cause can be identified, myocarditis accounts for approximately 50% of the cases with known etiologies [10,14]. The true incidence of myocarditis as a cause of DCM may be higher, as it cannot be formally diagnosed without histologic criteria or demonstration of viral DNA. Other causes of DCM in the pediatric or adolescent population include neuromuscular disorders (such as Duchenne or Becker muscular dystrophy), familial DCM, and inborn errors of metabolism, accounting for 9%, 5% and 4% of cases, respectively [10]. Additional etiologies include congenital heart disease, valvular heart disease, postpartum cardiomyopathy, pacemaker-induced DCM, arrhythmia-induced DCM, and coronary artery/ischemic disease, but these will not be discussed in this chapter.

In familial DCM, most of the known mutations are associated with autosomal dominant inheritance, although some forms of X-linked (Barth syndrome, Duchenne muscular dystrophy) and mitochondrial inheritance are reported. Familial cases of DCM are probably underestimated, as not all families undergo extended evaluations or mutation analysis, some mutations may manifest incomplete penetrance, or the index case represents a new mutation. Mutations associated with autosomal dominant inheritance include those involving cytoskeletal proteins such as β- and δ-sarcoglycan, and sarcomere proteins such as actin and cardiac troponin T. Interestingly, several of these mutations are also associated with development of hypertrophic cardiomyopathy [2,15]. In addition, several genetic forms of DCM are associated with skeletal myopathy, including Duchenne/Becker muscular dystrophy (dystrophin mutations), Barth syndrome (G4.5 mutations), Emery–Dreifuss muscular dystrophy (lamin A/C mutations), and limb-girdle muscular dystrophy (sarcoglycan mutations).

Although myocarditis (or inflammatory cardiomyopathy) can be infectious or noninfectious, its primary etiology in the pediatric population is viral or postviral. Viruses implicated include coxsackie B, adenovirus, cytomegalovirus, enterovirus, influenza A and B, varicella, picornavirus, parvovirus, HIV, and Epstein–Barr virus [12,16]. Myocarditis associated with bacterial disease includes group A streptococcus (rheumatic fever), meningococcus, and salmonellae [17]. Other infectious agents associated with myocarditis include rickettsial disease, fungal infections, and parasitic disease. Giant cell myocarditis is an aggressive inflammatory myocarditis that is rare in children and associated with severe ventricular arrhythmia. Eosinophilic myocarditis is also rare and associated with hypersensitivity reactions. Chronic myocarditis can be due to chronic viral infection and autoimmune conditions.

**Table 33.2** Classification of the dilated cardiomyopathies (modified phenotype-based classification)

**Primary**
- Peripartum cardiomyopathy
- Post-myocarditis
- Primary familial dilated cardiomyopathy
- Stress cardiomyopathy ("tako-tsubo")
- X-linked cardiomyopathy (dystrophinopathy)

**Secondary**
- Cardiovascular
- Congenital heart disease
- Tachycardia induced
- Valvar heart disease

**Connective tissue disorders**
- Juvenile rheumatoid arthritis
- Lupus erythematosis
- Osteogenesis imperfecta
- Polyarteritis nodosa
- Reye syndrome
- Sarcoidosis
- Systemic sclerosis

**Inflammatory (myocarditis)**
- Infectious:
  - Bacterial
  - Fungal
  - Parasitic
  - Protozoal
  - Rickettsial
  - Spirochetal
  - Viral
- Kawasaki

**Ischemic**
- Congenital coronary artery malformation
- Acquired coronary artery disease

**Metabolic**
- Endocrine
- Fatty acid oxidation
- Glycogenoses
- Mucopolysaccharidoses
- Sphingolipidoses

**Mitochondrial**
- Kearns–Sayre
- Mitochondrial myopathy, encephalopathy, lactic acidosis and stroke (MELAS)
- Myoclonic epilepsy associated with ragged-red fibers (MERRF)
- NADH–coenzyme Q reductase deficiency
- Cytochrome C oxidase deficiency

**Nutritional**
- Selenium deficiency (Keshan disease)
- Thiamine deficiency (beri-beri)

**Neuromuscular**
- Dystrophinopathies (Duchenne, Becker dystrophies)
- Emery–Dreifuss muscular dystrophy
- Myotonic dystrophy
- Polymyositis
- Roussy–Lévy polyneuropathy
- Scapulohumeral muscular dystrophy
- Spinal muscular atrophy

**Toxic**
- Alcoholic
- Anthracyclines
- Arsenic
- Chloramphenicol
- Cobalt
- Iron (hemochromatosis)
- Lead

Reprinted from Colan SD. Classification of the cardiomyopathies. *Prog Pediatr Cardiol* 2007;23:5–15, with permission from Elsevier.

## Pathophysiology

Myocardial damage and reduced cardiac function lead to decreased cardiac output and consequently a complex cascade of neurohormonal and vascular changes that result in both increased preload and afterload, triggering a cycle of continued myocardial damage and remodeling. Stimulation of the sympathetic and renin–angiotensin systems leads to vasoconstriction, increased circulating catecholamines, stimulation of aldosterone secretion, and salt and water retention. Both the primary myocardial insult and the secondary effects of vascular and neurohormonal alterations result in myocardial cellular changes, including necrosis, apoptosis, and fibrosis. These changes lead to myocardial remodeling, with alterations in LV geometry and compliance.

The immunopathogenesis of inflammatory cardiomyopathy has been primarily studied in animal models, predominantly mice [18]. Host factors that play a role in susceptibility to infection and development of myocarditis include genetic factors (i.e., major histocompatibility complex), age, gender, and nutritional state [18]. Myocardial damage can result directly from infection or through immune-modulated mechanisms. In murine myocarditis, the acute phase (days 0–3) consists of myocyte necrosis without inflammatory cell infiltrate, and the subacute phase (days 4–14) consists of cellular infiltrate (natural killer cells followed by T- and B-cell lymphocytes), cytokine production, development of antibodies (viral-neutralizing antibodies and autoantibodies), and elimination of culturable virus from cardiomyocytes. Evidence indicates that the development and severity of myocarditis is related to cellular-mediated immune function,

primarily associated with T-cell lymphocyte activity [18]. Additionally, cytokines that mediate inflammatory proteins and cellular function probably play a major role in the inflammatory response in myocarditis [18,19]. In the chronic phase of myocarditis (days 15–90), the inflammatory cell infiltrate has typically resolved, and fibrosis and heart enlargement develop. Viral RNA can be detected using molecular techniques such as polymerase chain reaction (PCR), and viral persistence in the myocardium may play a role in chronic myocarditis [17]. Viral myocarditis is also associated with the development of autoantibodies, which may contribute to its pathophysiology [19]. There is also evidence that viral myocarditis could be a trigger for apoptotic cell death [18].

## Treatment and outcome

Current therapeutic strategies for treatment of cardiomyopathy are aimed at improving symptoms as well as reversing the negative effects of maladaptive ventricular remodeling (e.g., LV dilation and myocyte hypertrophy). This phenomenon of improving cardiac geometry and function with various therapies is known as "reverse remodeling" and occurs at the molecular, cellular, tissue, and chamber levels. These therapies may include decreasing afterload (usually through angiotensin-converting enzyme inhibitors or receptor blockers), decreasing preload (diuretics) and altering the neurohormonal profile (usually through beta-blocker therapy aimed at decreasing the effects of sympathetic system activation and counteracting the negative effects of increased catecholamines). Intravenous therapies using agents such as milrinone and dobutamine further decrease afterload and increase myocardial contractility. Additional medical therapies may include anticoagulation, nutritional support, and use of antiarrhythmic medication. Failure of maximal medical therapies necessitates other forms of support, including biventricular pacing (cardiac resynchronization therapy, CRT), mechanical support (ventricular assist device, VAD), extracorporeal membrane oxygenation (ECMO), or cardiac transplantation.

Aside from supportive treatment, there is no consistent approach or recommendation for immune-modulated therapy for myocarditis. Some pediatric centers use intravenous gamma-globulin and/or steroids in the clinical setting of suspected or proven myocarditis, and some patients with fulminant myocarditis require mechanical support with ECMO or VAD. There are some data to suggest that those with biopsy-proven myocarditis may have a better outcome than those with idiopathic disease [10,20,21].

The clinical course of DCM in the pediatric population is variable, and a comprehensive risk stratification algorithm does not exist. Recent data suggest that the 1- and 5-year risks of death or transplantation in pediatric DCM are 28–31% (1-year risk) and 37–46% (5-year risk) [10,20]. In a systematic review of outcome predictors in pediatric DCM [21], younger age at diagnosis, higher LV shortening fraction (SF) and ejection fraction (EF), and the presence of myocarditis have been associated with better prognosis. Poor prognostic factors inconsistently identified in smaller studies have included the presence of a more spherically shaped LV (higher sphericity index), endocardial fibroelastosis, lack of improvement in cardiac function over time, arrhythmia, intracardiac thrombus, thinning of the posterior wall and significant mitral regurgitation [10,20,22–25]. Data also suggest that measures of myocardial velocities and RV function may be predictive [26].

## Imaging

Echocardiography is instrumental in the diagnosis, management and follow-up of myocarditis and DCM. However, it is usually not helpful in determining the etiology of the disease process.

### Goals of the examination

The goals of echocardiographic examination in the setting of DCM and myocarditis can be summarized as follows:

- assessment of systolic left and right ventricular performance;
- assessment of diastolic left and right ventricular performance;
- structural assessment to rule out structural heart disease as cause of dysfunction;
- assessment for presence and severity of mitral and aortic valve regurgitation;
- measurement of RV pressure estimate to assess for elevated pulmonary vascular resistance;
- assessment of coronary artery origins and courses from aorta – color flow direction in the coronary arteries.

The presence of a dilated, poorly contractile ventricle is easily recognized with transthoracic imaging (Fig. 33.1; Videoclips

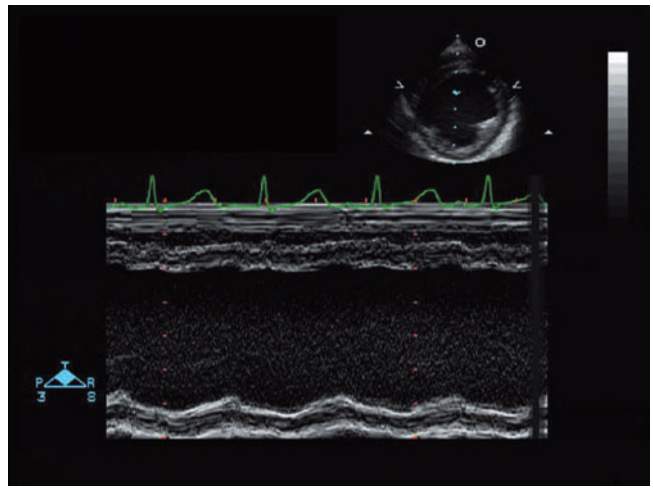

**Figure 33.1** M-mode demonstrating poor left ventricular shortening with dilated cardiomyopathy.

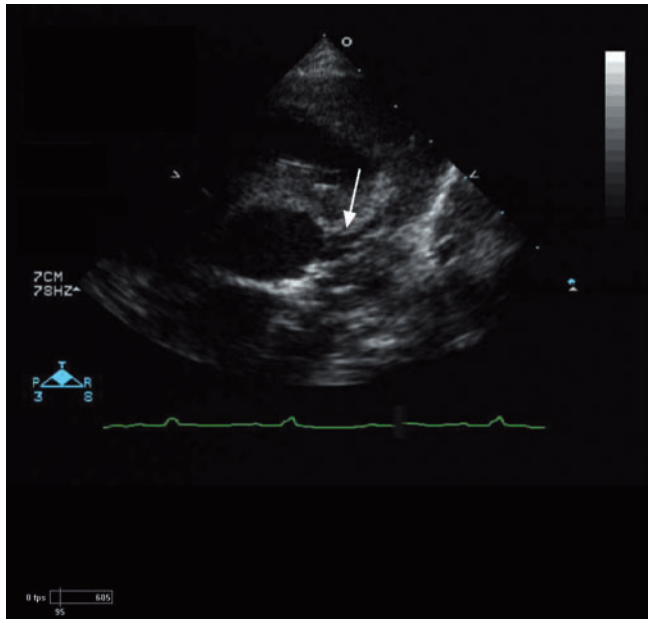


(a)

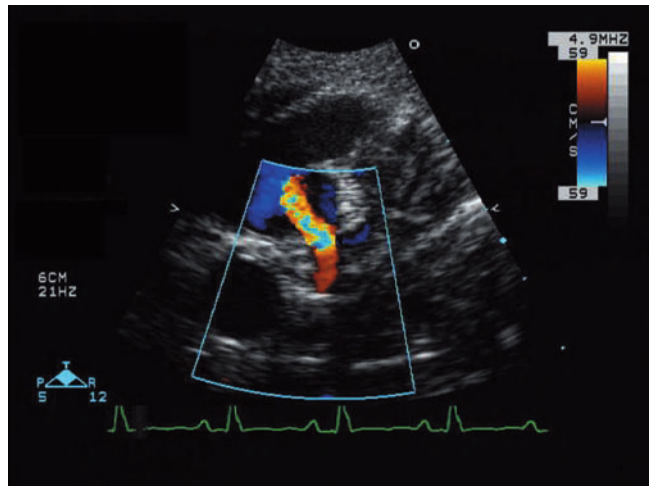


(b)

**Figure 33.2** Anomalous origin of the left coronary artery (arrow) from the pulmonary artery (ALCAPA). By two-dimensional imaging alone the left coronary artery may appear to be normal **(a)**, but with color Doppler **(b)**, flow from the left coronary artery can be seen entering the pulmonary artery. In this patient, the pulmonary vascular resistance has dropped and there is coronary "steal" into the pulmonary artery.

33.1 and 33.2). Factors including afterload, preload and contractility affect overall cardiac performance. Therefore at the time of initial presentation, volume- and/or pressure-loading lesions must be excluded (e.g., aortic stenosis or regurgitation, coarctation, mitral regurgitation). It is also imperative to exclude other surgically correctable lesions, the most common being anomalous origin of the left coronary artery from the pulmonary artery (ALCAPA) (Fig. 33.2). In any patient presenting with features of DCM, the origin of the coronary arteries should be demonstrated and confirmed by color Doppler in multiple views. Two-dimensional imaging of the coronary arteries alone is not confirmatory. However, dilation of the right coronary suggests that ALCAPA may be present. If the coronary artery origins are not demonstrated conclusively by color Doppler, then alternative imaging (i.e., angiography) is recommended. Additionally, congenital coronary ostial stenosis may also be associated with development of LV dilation and dysfunction.

Useful echocardiographic assessment in the patient with DCM or myocarditis includes data regarding flow, pressures, volumes, and fiber shortening. Left ventricular dimensions, wall thickness, volumes, mass, wall stress, rate-corrected velocity of circumferential fiber shortening (VcFc), shortening fraction (SF), ejection fraction (EF), and sphericity are the echocardiographic variables typically used to evaluate cardiac size and performance and thus the presence and severity of DCM.

More recently, other echocardiographic modalities including measurement of myocardial velocities with tissue Doppler imaging (TDI), measurement of strain rate, myocardial performance index (MPI, or Tei index), and three-dimensional (3D) imaging have added to the ability to evaluate ventricular size and morphology and cardiac performance. Other associated findings that can be present with DCM and/or myocarditis include pericardial effusion, left atrial (LA) enlargement, mitral regurgitation, LV dyssynchrony, pulmonary artery hypertension, and intracardiac thrombi.

Most measures of LV size and function in the pediatric population are based on normal values derived from age- and body-surface-area-adjusted variables. Reporting these data as z-scores (number of standard deviations from the mean value) allows standardization of variables that change with age and growth (see Chapter 5). Thus, accurate recording of the patient height and weight is crucial for appropriate interpretation of numeric data.

### Left ventricular size

Measures of LV size typically include the LV end-diastolic and systolic dimensions from M-mode or two-dimensional (2D) imaging, and the LV end-diastolic and systolic volumes from 2D or 3D imaging. In children, values derived from 2D imaging are adjusted for body surface area (BSA) to determine the z-score and to trend LV size over time. Often in DCM the heart is so large that the LV apex is difficult to image, and care must be taken not to foreshorten the ventricle. From 2D imaging, common methods of determining LV volume include both the 5/6 area–length method and Simpson's biplane method. It is critical that the specific method of determining ventricular volumes for patients in clinical practice be the same method used to determine

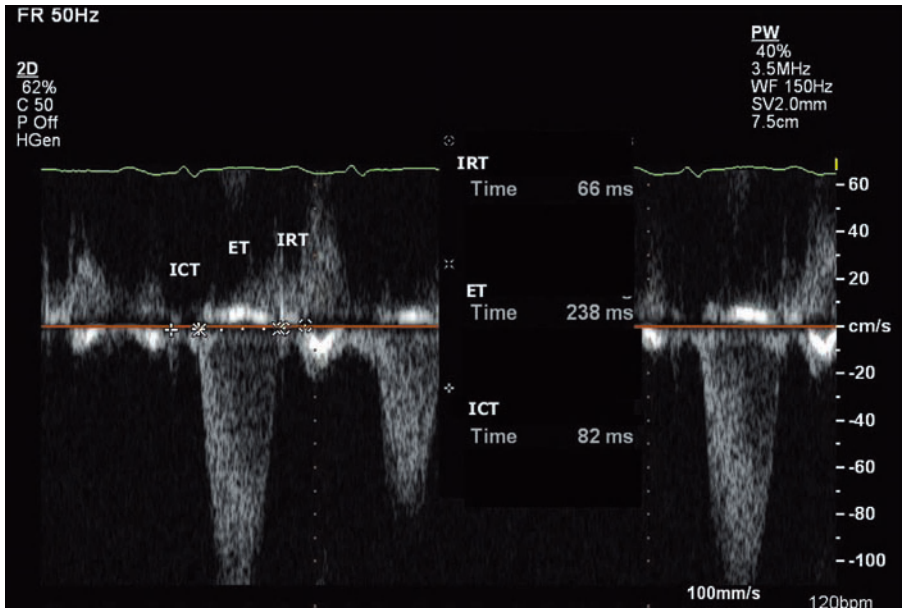


**Figure 33.3** Measurement of the myocardial performance index (MPI, or Tei index) in a patient with dilated cardiomyopathy. ET, ejection time; ICT, isovolumetric contraction tme; IRT, isovolumetric relaxation time (ms). The MPI is 0.62 (elevated).

ventricular volumes for the normal database and z-scores that are referenced because these methods yield different values.

### Shortening fraction and ejection fraction

Measures of ventricular systolic function that are most commonly used in clinical practice include SF and EF. M-mode or 2D-derived LV dimensions are used to determine SF, as well as VcFc. Two-dimensional imaging and determination of ventricular volumes provides values for EF. An important concept is that VcFc, SF and EF are sensitive to loading conditions and are not always a true reflection of underlying myocardial contractility. Despite these limitations, SF and EF are relatively easy to measure and are useful for comparing systolic function in the same patient over time.

### Wall stress and measurement of afterload

Left ventricular wall stress can be calculated as a measure of afterload. It is possible to determine peak, mean, total, and end-systolic stress and thus determine afterload at different phases of the cardiac cycle. Afterload is an important determinant of overall cardiac performance, and end-systolic stress is the most relevant measurement with regard to systolic function [27]. The stress-adjusted shortening (relationship of wall stress to SF, also dependent on preload) and stress-adjusted velocity (relationship of wall stress to VcFc, but not dependent on preload) can then be used to determine the combined effects of preload and afterload and thus determine true contractility. The method of measuring end-systolic wall stress is reported in Chapter 7. The utility of end-systolic wall stress and the stress-adjusted velocity in pediatric patients has been demonstrated in those with sickle-cell anemia, anthracycline exposure, and various forms of congenital heart disease and arrhythmia [28–30]. LV end-systolic wall stress is predictive of outcome in adult patients with DCM [31].

### Myocardial performance index (MPI)

The MPI, or Tei index, is a Doppler method that assesses global ventricular systolic and diastolic function [32]. It can be measured by both pulsed-wave Doppler and tissue Doppler imaging (TDI) by determining the sum of the isovolumetric contraction and isovolumetric relaxation times divided by the ejection time (Fig, 33.3). With progressive LV dysfunction, the LV ejection time is decreased and the MPI becomes prolonged. The MPI in pediatric patients with dilated cardiomyopathy ($0.78 \pm 0.28$) has been shown to be significantly increased compared with that in normal subjects ($0.36 \pm 0.07$) [33], although it is not a strong predictor of death, transplantation, need for hospitalization or intravenous ionotropic support [26]. It is sensitive but not specific, and can reflect abnormalities in preload, afterload, contractility, diastolic function, and conduction. The MPI has had some success in predicting outcome in DCM and heart failure in adults [34,35].

### Tissue Doppler imaging (TDI)

Direct myocardial velocities can be measured using TDI. This technique allows quantitative measurement of regional myocardial function and is less load dependent than other function parameters. Myocardial velocities at the level of the mitral or tricuspid valve annulus are indicative of longitudinal left or right ventricular function, respectively (Fig. 33.4). The systolic myocardial peak ($S_a$), the early diastolic velocity ($E_a$) and the late diastolic velocity ($A_a$) are typically measured. Normal values for children have been published [36–38].

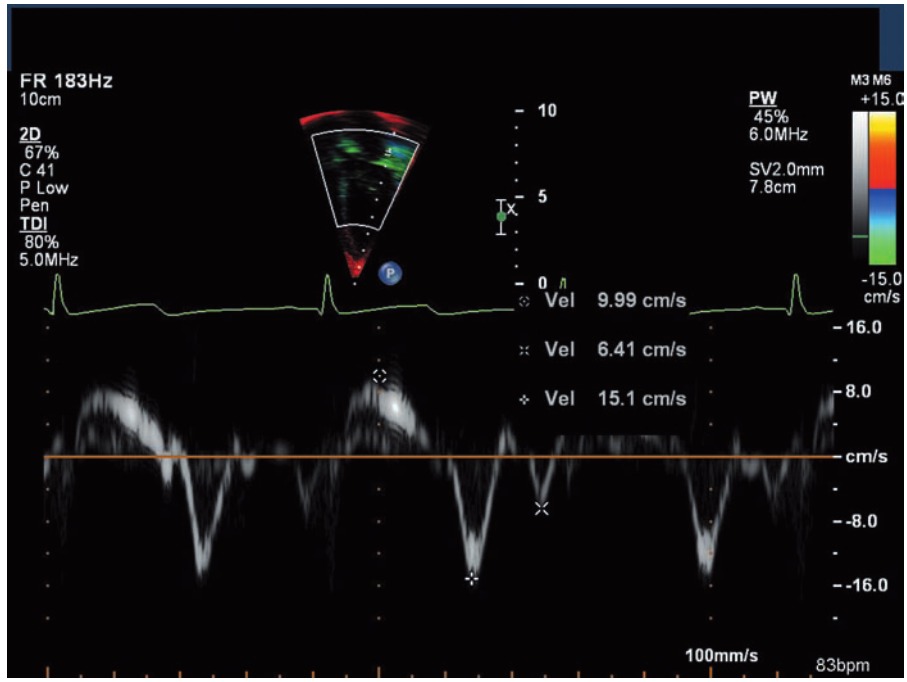


(a)

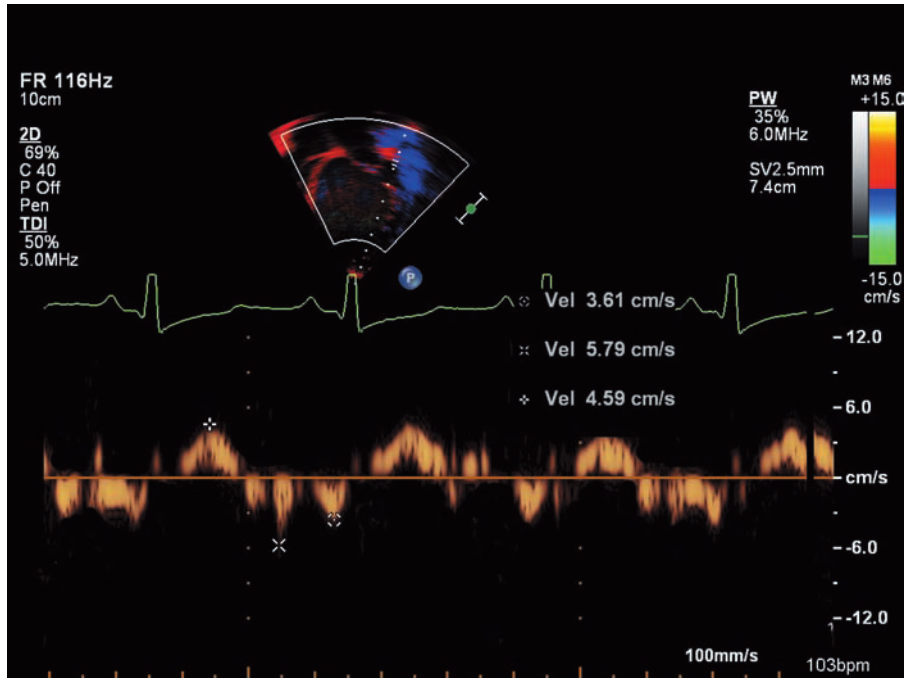


(b)

**Figure 33.4** Tissue Doppler imaging with myocardial velocities from the lateral mitral annulus in a normal subject **(a)** with normal myocardial velocities, and in a patient with severe DCM. **(b)**, demonstrating significantly lower myocardial velocities.

In the absence of significant wall motion abnormalities, measurement of myocardial velocities at the lateral mitral valve annulus is the most informative with regard to global LV function. Mitral annular velocities are decreased in adult [39] and pediatric [26,40] patients with DCM compared with healthy subjects (Table 33.3). Additional findings in DCM include increased pulsed-wave E to TDI $E_a$ ratio ($E/E_a$) compared with controls [40], and an indication that lower early diastolic mitral and tricuspid annular velocities may be predictive of worse outcome in pediatric DCM [26]. The $E_a/A_a$ ratio is easy to measure and can be used serially to follow patients with DCM.

### Three-dimensional echocardiography

Ventricular volumes as measured by 3D echocardiography and volumetric methods are more accurate than those measured by 2D (biplane) methods, including evaluation of cardiomyopathy associated with altered ventricular geometry

**Table 33.3** Myocardial performance index (MPI) and Doppler tissue imaging (DTI) data in patients with dilated cardiomyopathy and in control subjects

| | Dilated cardiomyopathy | Control subjects |
|---|---|---|
| *N* | 80 | 80 |
| Age (years) | 7.2 ± 6.1 | 7.1 ± 5.7 |
| LV SF (%) | 21.6 ± 6.6** | 38.1 ± 4.0 |
| LV MPI | 0.67 ± 0.20** | 0.33 ± 0.06 |
| **Mitral DTI**§ | | |
| MV-$E_a$ | 11.8 ± 4.8*** | 16.8 ± 4.7 |
| MV-$A_a$ | 5.6 ± 3.0* | 6.4 ± 1.9 |
| MV-$S_a$ | 6.5 ± 2.2*** | 9.1 ± 3.0 |
| **Septal DTI**§ | | |
| IVS-$E_a$ | 8.5 ± 2.9*** | 12.8 ± 2.7 |
| IVS-$A_a$ | 5.6 ± 1.8 | 5.9 ± 1.2 |
| IVS-$S_a$ | 5.7 ± 2.0*** | 7.8 ± 1.9 |
| **Tricuspid DTI**§ | | |
| TV-$E_a$ | 12.7 ± 3.9*** | 15.9 ± 3.2 |
| TV-$A_a$ | 9.2 ± 3.3* | 10.3 ± 2.5 |
| TV-$S_a$ | 10.6 ± 2.9*** | 12.9 ± 2.2 |
| Mitral $E/E_a$ ratio | 9.4 ± 6.5*** | 6.1 ± 2.1 |
| Septal $E/E_a$ ratio | 11.7 ± 4.2*** | 7.8 ± 2.1 |
| Tricuspid $E/E_a$ ratio | 4.5 ± 1.7* | 3.9 ± 0.9 |

$A_a$, Late diastolic velocity as measured by DTI; DTI, Doppler tissue imaging; E, early diastolic velocity; $E_a$, early diastolic velocity as measured by DTI; IVS, septal annulus; LV, left ventricle; MV, lateral mitral annulus; $S_a$, systolic velocity as measured by DTI; SF, shortening fraction; TV, lateral tricuspid annulus.

Data expressed as mean ± SD.

§Doppler velocity data expressed in cm/s.

*$P < 0.05$ compared with control subjects.

**$P < 0.01$ compared with control subjects.

***$P < 0.001$ compared with control subjects.

Reprinted from Eidem BW, McMahon CJ, Ayres NA, et al. Impact of chronic left ventricular preload and afterload on Doppler tissue imaging velocities: a study in congenital heart disease. *J Am Soc Echocardiogr* 2005;18:830–8, with permission from Elsevier.

and morphology [41,42]. In very large ventricles, 3D echocardiography may still underestimate volumes compared with CMR [42,43]. Additionally, 3D echocardiography can be used to evaluate and quantify other cardiac chambers, including RV size and function as well as LA volumes, both of which may be important in patients with cardiomyopathy [44,45].

### Change in LV pressure over time (d*P*/d*t*)

Doppler echocardiography can also be useful in evaluating cardiac performance. If mitral regurgitation is present, d*P*/d*t* (change in LV pressure over time) can be calculated. With significant LV dysfunction, the peak velocity of mitral regurgitation will not occur in early systole but rather in mid-to-late systole, as there is a slower rate of rise in LV pressure seen in the presence of poor contractility. As with other measures of LV systolic function, d*P*/d*t* is both preload and afterload dependent. In addition, an adequate amount of mitral regurgitation must be present to make this measure.

### LV geometry and sphericity index

Remodeling of the LV geometry in the presence of LV dysfunction is characterized by change from an ellipsoid shape to more of a spherical shape. This process is associated with increased thinning of the ventricular wall, increased end-systolic wall stress, decreased contractility and increased mitral regurgitation [46,47]. The sphericity index (SI) is a measure of the LV geometry and is calculated as the LV diastolic short-axis dimension divided by the LV diastolic long-axis dimension; the SI approaches unity as the LV becomes more spherical (Fig. 33.5). It is useful only in structurally normal hearts. In a small group of children and adolescents, the mean SI was reported as 0.66 ± 0.07 in healthy patients and 0.89 ± 0.10 in those with LV dysfunction [46]. This same study demonstrated a significant negative correlation between SI and measures of LV systolic function (SF and EF), as well as an improvement in the SI in the subset of children with LV dysfunction whose LV function improved.

### Stress echocardiography

Stress echocardiography is an additional useful technique in the evaluation of contractile function in dilated cardiomyopathy. Most published studies focus on adults, although stress echocardiography data have been published for healthy children [48,49], childhood cancer survivors [48], patients with Kawasaki disease [50], cardiac transplant recipients [51], and patients with congenital heart disease [52]. "Stress" is typically induced pharmacologically or with exercise. Pharmacologic methods most commonly use dobutamine. There is no consensus regarding which protocol, method of stress, infusion rate of dobutamine, or measure of contractile reserve to use. Measures of contractile reserve include SF, EF, posterior wall thickening, wall-motion score index [53,54], change in end-systolic volume [54,55], end-systolic stress and VcFc [56,57], cardiac power [12,56,58], and changes in SI [53,57]. Studies using dobutamine stress echocardiography in adults with nonischemic DCM have demonstrated that measures of contractile reserve may correlate with functional capacity and peak oxygen consumption ($Vo_2$) [55,57], as well as prognosis and recovery of LV function [59,60], and survival [54,58,61].

Few studies are published in the pediatric population regarding stress echocardiography and assessment of myocardial contractile reserve, with most studies focused on pediatric patients with anthracycline exposure [62,63]. In one study of normal children and adolescents using a maximum of 5 μg/kg/min of dobutamine, the SF increased from 34 ± 7% to 50 ± 9%, EF increased from 64 ± 9% to 80 ± 14%, LV posterior wall thickening percent from 86 ± 42% to

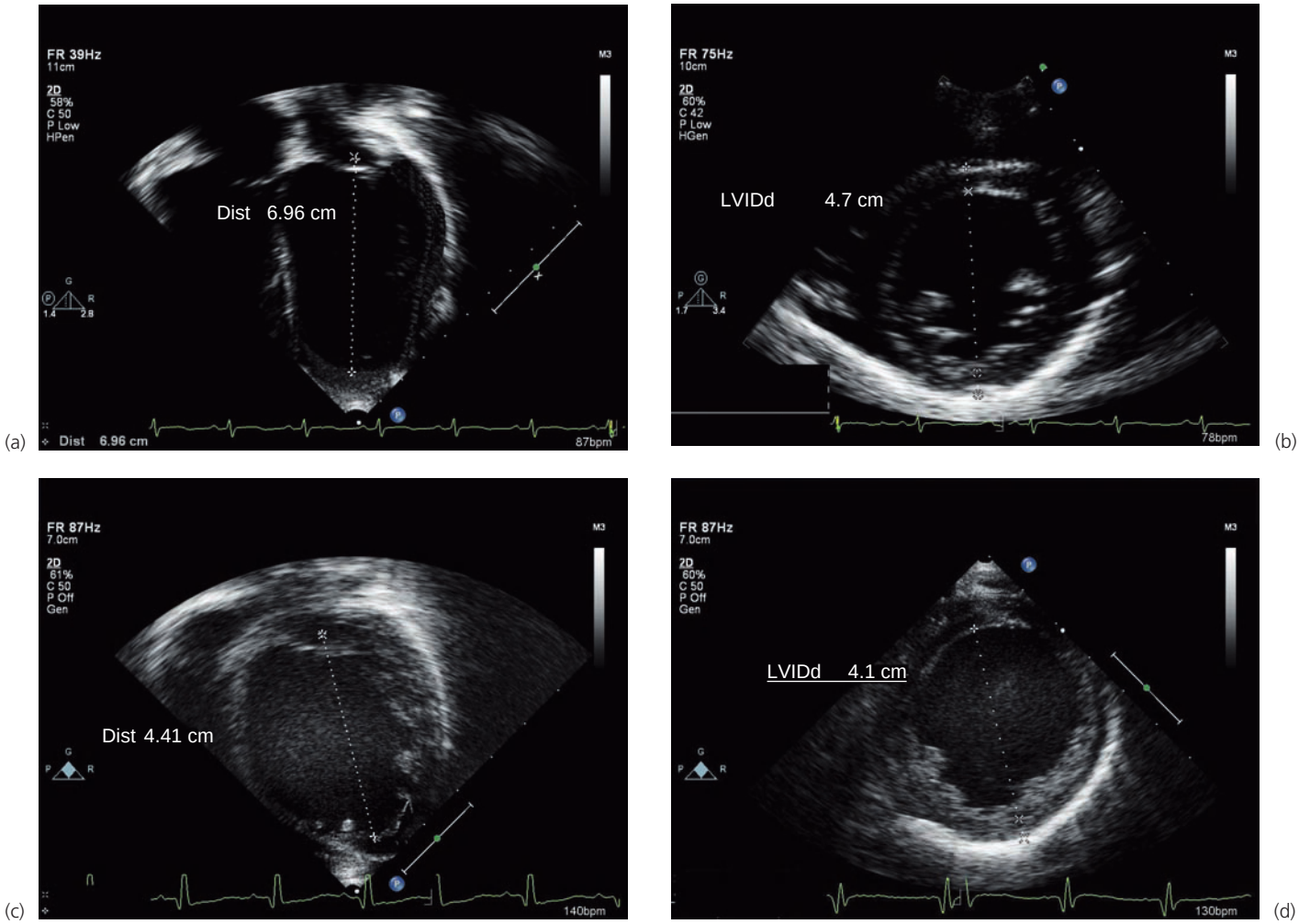


**Figure 33.5** Sphericity index in a normal patient **(a,b)** and a patient with dilated cardiomyopathy (DCM) **(c,d)**. The sphericity indexes are 0.67 for the healthy patient and 0.93 for the patient with DCM, respectively. Dist, distance; LVIDd, left ventricular end-diastolic dimension.

154 ± 60%, and VcFc (circ/s) from 1.1 ± 0.2 to 1.8 ± 0.6 from baseline to peak dobutamine [48]. An additional study in children, using a protocol that included atropine and sedation in most patients, demonstrated that changes indicative of contractile reserve could be seen up to, but not beyond, 20 μg/kg/min of dobutamine [49]. Data indicate that dobutamine stress echocardiography has prognostic significance in adolescent patients with DCM, and may be of added benefit in clinical decision-making in conjunction with metabolic exercise testing in this group of patients [64].

## Fetal dilated cardiomyopathy and myocarditis

Fetal CM is rare and accounts for a very small portion of heart disease discovered during fetal ultrasonography. In one center, fetal DCM accounted for 0.2% of all fetal echocardiograms performed in a high-risk fetal cardiology center over a 20-year period, and 1.8% of all diagnosed fetal cardiac abnormalities (excluding arrhythmia) [65]. Etiologies of dilated CM in the fetus are typically the same as in the neonate and include metabolic disease, myocarditis, tachycardia, familial/genetic and idiopathic. Other causes that may be seen predominantly in fetal life include anemia (related to maternal factors, inherited anemias or parvovirus B19 infection) and endocardial fibroelastosis related to maternal anti-Ro/La antibodies. Etiologies may be classified as familial, secondary or idiopathic, and most of these causes affect both the right and left ventricles. Importantly, cardiac dysfunction secondary to structural heart disease (such as LV outflow tract obstruction) must be excluded. Fetal cardiac function may appear normal early in pregnancy, with evidence of DCM developing after 23 weeks [66]. Overall prognosis of DCM diagnosed in fetal life is poor, although fetuses with DCM secondary to treatable causes may have a better outcome [66]. In one series of 50 cases of fetal DCM, 30% died during fetal life, 20% died during the neonatal period or infancy, and 30% survived, including one transplant recipient (with the remaining pregnancies terminating) [65]. Another study reported a fetal/neonatal mortality of

**Table 33.4** Fetal cardiovascular score

| | NORMAL | -1 POINT | -2 POINT |
|---|---|---|---|
| Hydrops | None (2 Pts) | Ascites or pleural effusion or Pericardial effusion | Skin edema |
| Venous Doppler (Umbilical (vein) (Ductus venosus) | 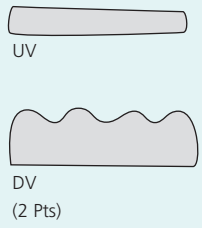 UV DV (2 Pts) | 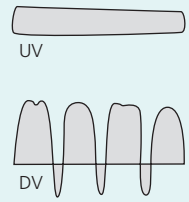 UV DV | 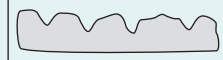 UV Pulsations |
| Heart Size (Heart Area/ Chest Area) | >0.20 and <0.35 (2 Pts) | 0.35–0.50 | >0.50 or <0.20 |
| Cardiac Function | Normal TV & MV RV/LV SF >0.28 Biphasic diastolic filling (2 Pts) | Holosystolic TR or RV/LV SF <0.28 | Holosystolic MR or TR dP/dt <400 or Monophasic filling |
| Arterial Doppler (Umbilical artery) | 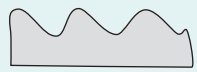 UA (2 Pts) |  UA (AEDV) |  UA (REDV) |

AEDV, absent end-diastolic velocity; dPdt, change in pressure over time; DV, ductus venosus; LV, left ventricle; MR, mitral regurgitation; MV, mitral valve; REDV, reversed end-diastolic velocity; RV, right ventricle; SF, shortening fraction; TR, tricuspid regurgitation; TV, tricuspid valve; UA, umbilical artery; UV, umbilical vein.

Reproduced courtesy of James C. Huhta, University of South Florida College of Medicine.

80% in fetuses diagnosed prenatally with DCM [67]. Survival is less than 20% in fetuses with DCM and hydrops, and approximately 50% in nonhydropic fetuses with DCM [65].

Fetal echocardiography for evaluation of cardiac function should include evaluation of both the RV and LV, including systolic and diastolic function, as both ventricles are pumping to the systemic circulation. Evaluation can include measurement of cardiac output for both ventricles, LV SF and EF, mitral and tricuspid inflow Doppler patterns, and evaluation of Doppler flow patterns in the vena cava, ductus venosus and umbilical vein. Newer methods still being investigated in the fetus include determination of the MPI, and use of TDI to evaluate myocardial velocities in the fetus. Although the MPI can be used for both the RV and LV, there is no consistent agreement on the precise Doppler method or the normal values for MPI in the fetus [68–70]. Studies of TDI in the fetus may prove useful, especially for evaluation of fetal diastolic function. Myocardial velocities in normal fetuses increase throughout gestation, as does the $E_a$:$A_a$ ratio [71]. Measurement of myocardial velocities and TDI-derived MPI may also be useful in assessment of fetal RV function [72]. Additionally, a fetal cardiovascular profile score has been developed to assess overall fetal cardiac well-being [72–74] (Table 33.4). For fetuses at increased risk of DCM (family history, anemia, etc.), serial fetal echocardiograms may be useful given the evolving nature of the disease and its potential for late gestational presentation.

## Preoperative and postoperative assessment

Interventional procedures and institution of mechanical support for DCM may consist of pacemaker/resynchronization therapy, mechanical support with ECMO or VAD, or cardiac transplantation. In myocarditis, mechanical support

can be used while awaiting recovery of cardiac function or as a bridge to cardiac transplantation. Echocardiographic assessment in the preoperative and postoperative setting is valuable when considering and/or managing these patients. Therapies such as pacing/CRT, mechanical support and cardiac transplantation are being used with increasing frequency.

## Echocardiography in pacemaker therapy for cardiomyopathy

Ventricular dyssynchrony may be present in patients with DCM, and can be either "electrical" or "mechanical." Electrical dyssynchrony refers to abnormal electrical propagation through the heart resulting in prolonged QRS duration, usually due to bundle branch block. Mechanical dyssynchrony can either be interventricular, referring to discordant timing of contraction between the LV and RV, or intraventricular, referring to delayed activation of one region of a ventricle relative to another region in the same ventricle. Intraventricular dyssynchrony results in regional delays in peak contraction, including regions of the ventricle in the systolic phase with other regions in the relaxation phase. With ventricular dyssynchrony, the end result is reduced cardiac efficiency and stroke volume. Pacemaker therapies with CRT have been shown to reduce morbidity and mortality in selected adults with heart failure [75–78]. Echocardiography can be used to guide patient selection and pacing parameters in CRT, although there is no consensus on the best parameters and measures to predict response or follow patients undergoing CRT.

In adults with heart failure, methods and parameters used to evaluate ventricular dyssynchrony have included the following:

*Intraventricular dyssynchrony*

**1** *Septal-to-posterior wall motion delay.* This is determined using parasternal short-axis M-mode by measuring the time from the maximal posterior displacement of the anterior septum to the maximum thickening of the posterior wall, with >130 ms being significant in adults [75,77,79].

**2** *LV pre-ejection interval.* This is measured using pulsed-wave Doppler of the LV outflow tract as the time from QRS onset to start of Doppler flow in that region, with >140 ms considered prolonged in adults (Fig. 33.6) [75;79].

**3** *Left lateral wall contraction.* This describes the overlap of lateral wall contraction and onset of diastolic filling, using M-mode and transmitral Doppler, respectively [78,79]. Intraventricular dyssynchrony measures can also include duration of left lateral wall contraction (interval between QRS onset and end of left lateral wall contraction on TDI).

**4** *Tissue Doppler imaging.* TDI methods of CRT are gaining popularity and are currently most often used in the adult heart failure population. TDI can be used to measure regional electromechanical delays, by measuring the time interval from QRS onset to the beginning, peak or end of the S-wave in different basal and mid-LV segments [78–80]. Evaluating more segments will provide a better determination of LV dyssynchrony, with the differences in time to peak systolic contraction between segments being the primary determinant of LV dyssynchrony with this method. However, TDI does not distinguish between active and passive myocardial motion. Methods using strain rate imaging (measuring the rate of regional myocardial deformation) can be used to determine true regional myocardial shortening. Delayed longitudinal contraction (postsystolic shortening) can be measured in this way [75].

*Interventricular dyssynchrony*

**1** *Interventricular mechanical delay.* This is the difference between the left ventricle pre-ejection interval and the right ventricle pre-ejection interval (measured from QRS to onset of flow in the right ventricle outflow tract), with a difference between the right and left ventricular ejection periods of >40 ms being considered abnormal in the adult population (Fig. 33.6) [78,79].

**2** *TDI lateral-to-lateral delay.* Interventricular delay can be evaluated by the difference in timing interval between onset of the QRS to S-wave at the lateral mitral valve and tricuspid valve annuli.

Additional measures used to evaluate pacemaker therapy and CRT can include diastolic filling time (left ventricular filling time, LVFT). This is measured by transmitral pulsed-wave Doppler from onset of mitral inflow (E-wave) to end of atrial contraction (A-wave) and is used as a measure of atrioventricular (AV) synchrony. In adults, an LV filling time of <40% of the cardiac cycle (RR interval) is evidence of AV dyssynchrony [75,78], although no such parameters currently exist for children. These parameters are also used to optimize pacemaker settings in heart failure patients.

Experience with CRT therapy in children with cardiomyopathy and heart failure is limited compared with adults. Preliminary evidence indicates that CRT is beneficial in children who have heart failure due to congenital heart disease and cardiomyopathy, but detailed methods or protocols of evaluation have not been fully described [81]. Most pediatric patients do not have left bundle-branch block and do not meet criteria for CRT by current adult standards (QRS ≥120 ms, New York Heart Association class III, IV with EF ≤35% [82–84]). Likewise, predictors of response to CRT are very limited in children. Pediatric patients with cardiomyopathy tend not to have electrical dyssynchrony but have evidence of mechanical dyssynchrony [85]. Interventricular dyssynchrony is more common in children given the higher incidence of right ventricular surgery. QRS duration in children has not been shown to be predictive of response to CRT [81].

## Echocardiography in cardiac mechanical support

Mechanical support for patients with cardiomyopathy and heart failure can be used both as a bridge to transplantation

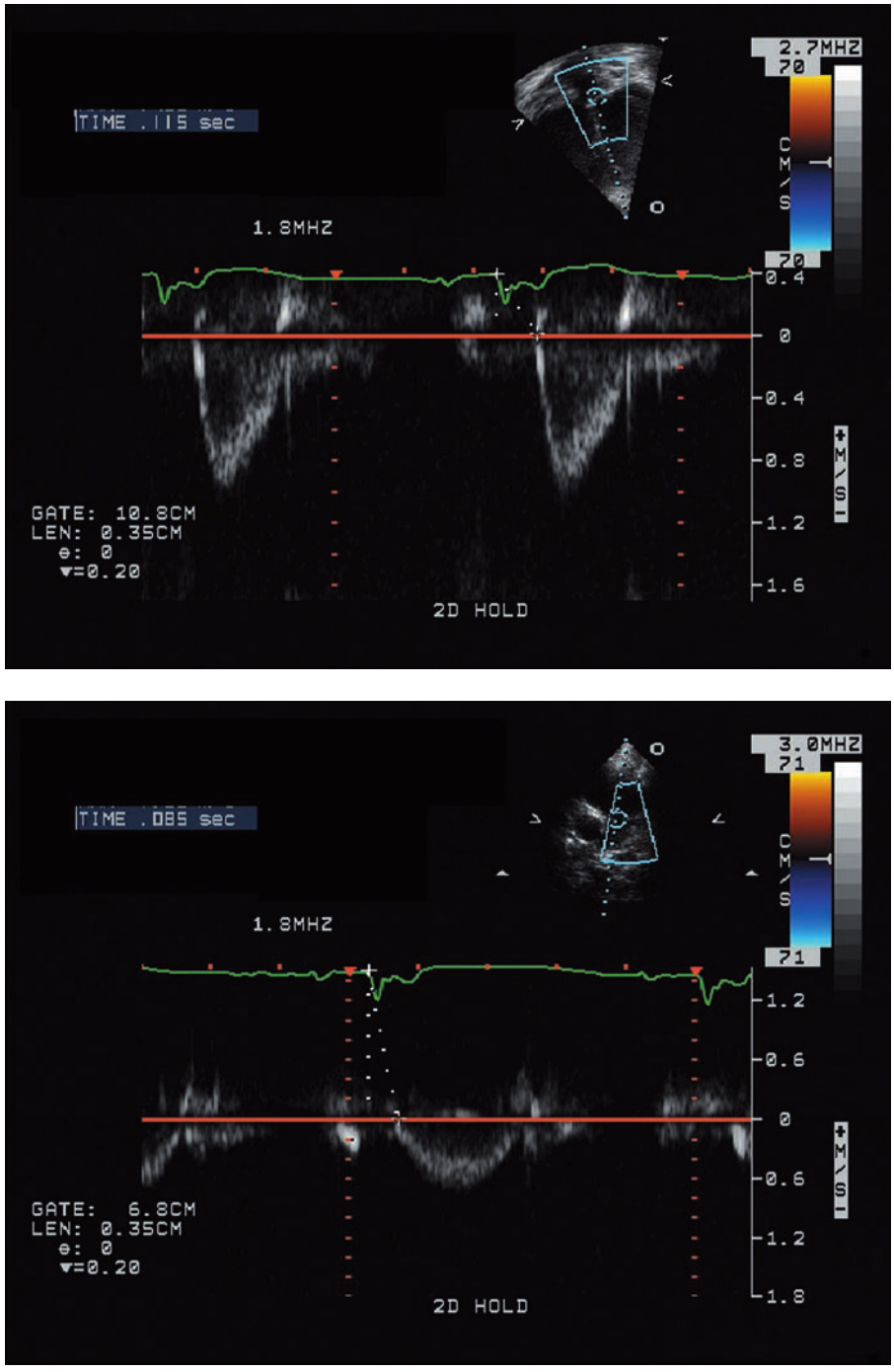


**Figure 33.6** **(a)** Left ventricular (LV) and **(b)** right ventricular (RV) pre-ejection intervals (PEIs), demonstrating a difference between the LV-PEI and RV-PEI of 30 ms.

as well as during recovery for myocarditis or other forms of acute heart failure. Mechanical support typically includes ECMO or use of a VAD. Although most of the experience with VAD support is in adults, experience in children and adolescents is increasing [86].

A ventricular assist device is used either for isolated LV support (LVAD) or biventricular support (BiVAD). For LVAD support, typically a cannula is placed in the LV apex (inlet cannula), with unidirectional flow from the LV apical cannula into the blood chamber and then expulsion of blood into the ascending aorta through a long outlet cannula and graft (Fig. 33.7). The VAD pump rate is usually completely dissociated from the ventricular rhythm.

Preoperative or intraoperative echocardiography findings can greatly influence surgical and medical management in these patients. Such important findings can include the presence of a patent foramen ovale (PFO), aortic regurgitation, intracavitary thrombus and assessment of right

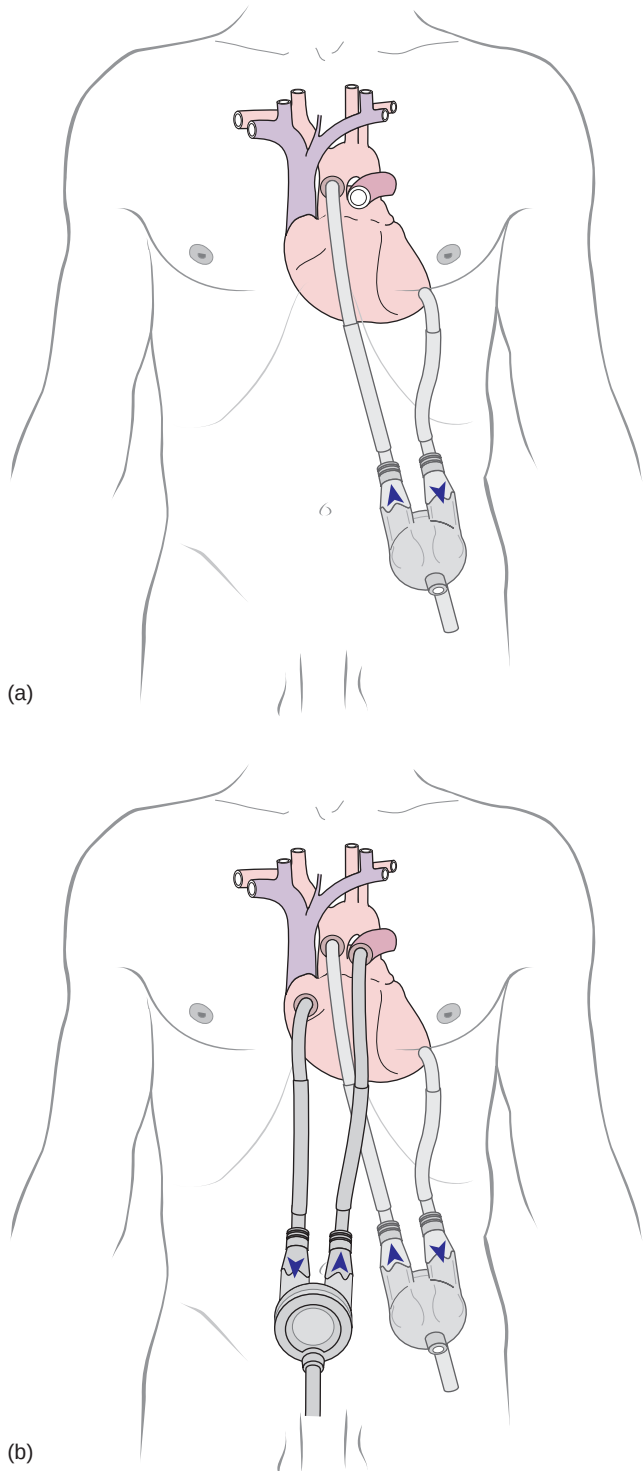


**Figure 33.7** Placement of left ventricular assist device with apical cannulation **(a)** and biventricular assist device **(b)**. Reproduced courtesy of Berlin Heart, Berlin, Germany.

ventricular function [87]. As the LV and LA pressures fall with initiation of VAD flow, right-to-left shunting at the PFO with associated systemic arterial desaturation and risk of embolus can occur [87,88]. The PFO is typically closed surgically or with a device in this setting. Aortic regurgitation can become an important phenomenon, as with normal VAD function the ventricular pressure is low and the aortic valve may remain closed (Videoclip 33.3). The regurgitation creates a circulatory loop and thus increases VAD preload, decreases effective forward output, and alters the pump function. The practice in some adult centers is to repair, replace, or oversew the aortic valve in the presence of aortic regurgitation [87,89,90]. Preoperative and intraoperative evaluation should also include careful evaluation for intracardiac thrombus. The most common locations for thrombus are in the LA appendage, as well as the LV apex (which is typically the site of the inlet cannula placement).

Right ventricular function is assessed preoperatively and intraoperatively by both transthoracic and transesophageal echocardiography (TEE). Evaluation of RV function is often qualitative, although RV fractional area of change (FAC) may be used to quantitate RV systolic function. Those with an RV FAC of less than 20% may develop progressive RV failure with initiation of LVAD therapy [87]. Dilation of the RV with progressive tricuspid regurgitation as seen on intraoperative TEE is an indication of RV failure. This may lead to a sequence of decreased pulmonary venous return, collapse of the LA and LV, potential obstruction of the inflow cannula, and air in the aorta associated with continued VAD pumping [87]. Evidence of RV failure can be an indication for other ionotropic or pulmonary vasodilator therapy or additional use of RV mechanical support. Additionally, both tricuspid regurgitation and mitral regurgitation may be present at the time of preoperative evaluation, but both may improve with VAD therapy.

Intraoperative assessment during VAD placement also includes evaluation for air in the outflow cannula and assessment of inlet cannula position [87]. Significant angulation of the inlet cannula can create inflow obstruction. Inlet cannula obstruction can be evaluated by color and spectral Doppler, with flow being laminar and unidirectional in the setting of normal inlet cannula function (Videoclip 33.4(a,b).

Postoperative evaluation of the patient with a VAD includes evaluation of LV decompression (Fig. 33.8). Additionally, images should include documentation of cannula position by 2D imaging, color flow and spectral Doppler flow (Fig. 33.9 and Videoclip 33.4a). Additional assessment includes RV function and evaluation for pericardial effusion/tamponade (Videoclip 32.5(a,b). The most common types of VAD malfunction that can be identified by echocardiography are development of inlet cannula valve regurgitation, inlet cannula obstruction, obstruction/kinking of the outflow cannula, and/or new or progressive aortic

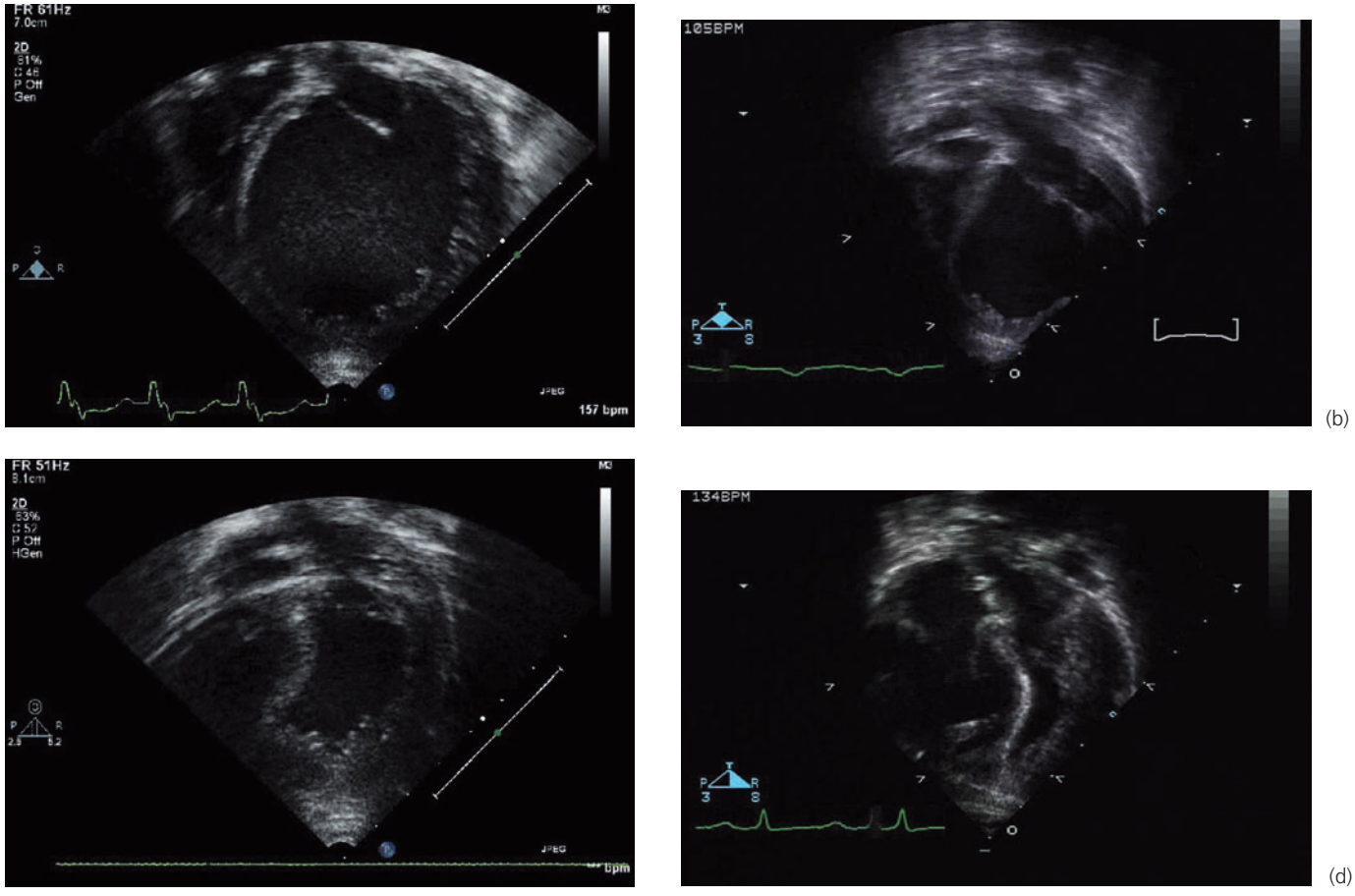


(a) (b) (c) (d)

**Figure 33.8** Ventricular geometry prior to and after left ventricular assist device (LVAD) placement; images taken within 36 hours in the same patient. These images demonstrate progressive decompression of the left ventricle (LV) with proper LVAD function. **(a)** Severe dilated cardiomyopathy (DCM) prior to LVAD placement. **(b)** Just after LVAD placement without significant LV decompression. **(c)** Some evidence of LV decompression. **(d)** Significant decompression of the LV.

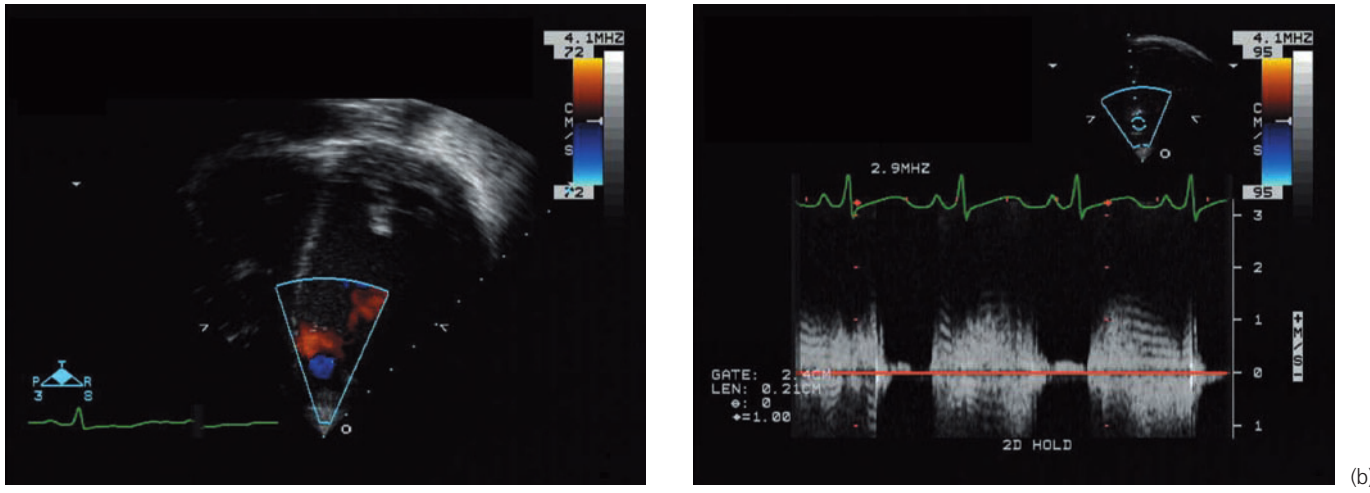


(a) (b)

**Figure 33.9** Transthoracic imaging of left ventricular assist device (LVAD) **(a,b)** and right ventricular assist device (RVAD).

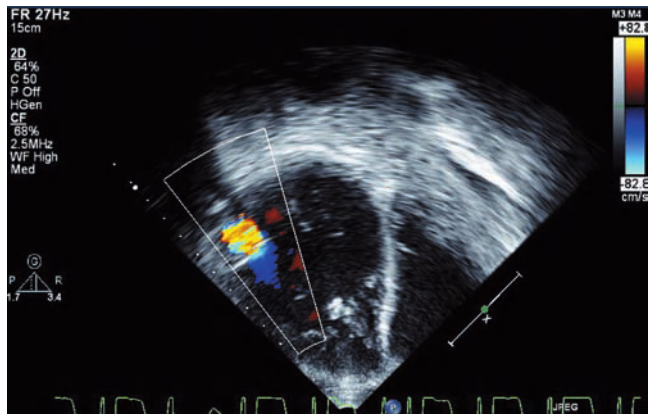


(c)

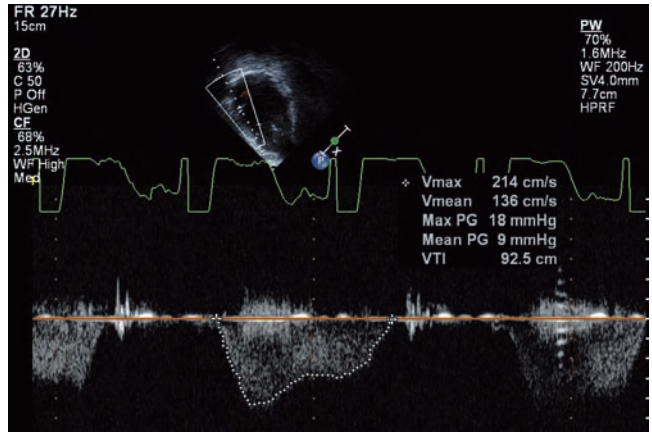


(d)

**Figure 33.9 (c,d)**, with flow seen in the LV apical inlet cannula by color Doppler (a) and spectral Doppler (b). In (c) the inlet cannula of the RVAD is seen with blood flowing out of the ventricle and into the inlet cannula toward the VAD chamber; (d) demonstrates the gradient by spectral Doppler.

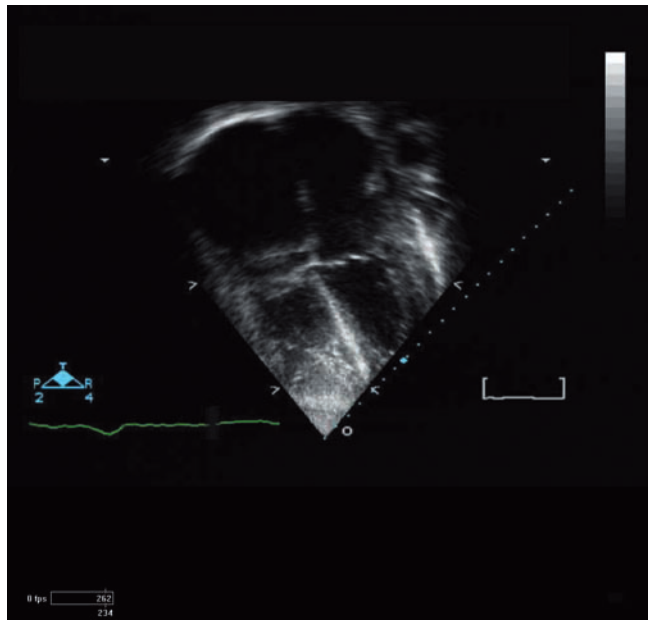

**Figure 33.10** The appearance of biatrial enlargement in a patient status post-heart transplant with a biatrial anastomosis.

regurgitation [91]. In some circumstances, regurgitation of the inlet or outlet valves of the VAD pump can also contribute to decreased VAD flow rates. This can be evaluated by spectral Doppler interrogation of the pump valves, which should have unidirectional flow [87,91].

### Echocardiography after cardiac transplantation

Postoperative evaluation in cardiac transplantation requires knowledge of the type of surgical procedure used to perform the transplant. Although all cardiac transplants have anastomotic sites at the pulmonary artery and aorta, the venous anastomoses can either be biatrial or bicaval with pulmonary venous anastomoses. Biatrial anastomoses typically give the atria a significantly enlarged appearance (Fig. 33.10). Each anastomotic site has the potential to become obstructed. TEE and transthoracic echo can demonstrate obstruction at the inferior vena cava–RA junction [92], superior vena cava [93] (Fig. 33.11), and within the left atrium leading to pulmonary venous obstruction [94,95]. Additionally, there is a higher incidence of left atrial thrombi in biatrial cardiac transplant as diagnosed by TEE [96,97], including 15% with evidence of acute arterial embolic events [97]. Other significant findings at the time of transplantation can include a PFO in the donor organ (which would likely be closed at the time of transplant) and clinically significant RV dysfunction and tricuspid regurgitation in the allograft due to increased pulmonary vascular resistance in the recipient [98,99]. The severity of tricuspid regurgitation on postoperative TEE at the time of cardiac transplantation has been shown to predict poor late survival in adult cardiac transplant recipients [99].

In the first year after transplantation, rejection (both cellular and humoral) is the most common cardiac complication. As endomyocardial biopsy is currently the gold-standard for diagnosis of rejection, other methods of identifying rejection, including serologic markers and echocardiographic predictors, have been aggressively pursued. Although measures demonstrating a decrease in cardiac performance may have good specificity in predicting rejection in pediatric heart transplant patients, sensitivity is limited [100]. However, some investigators have used a 2D-guided M-mode-based multiparametric scoring algorithm with good reported sensitivity and specificity, especially when used in a modified algorithm that accounts for patient-specific changes from baseline [101].

Recently, investigators have used techniques including TDI, isovolumic contraction acceleration (IVA) and MPI to evaluate myocardial function in transplant patients.

(a)

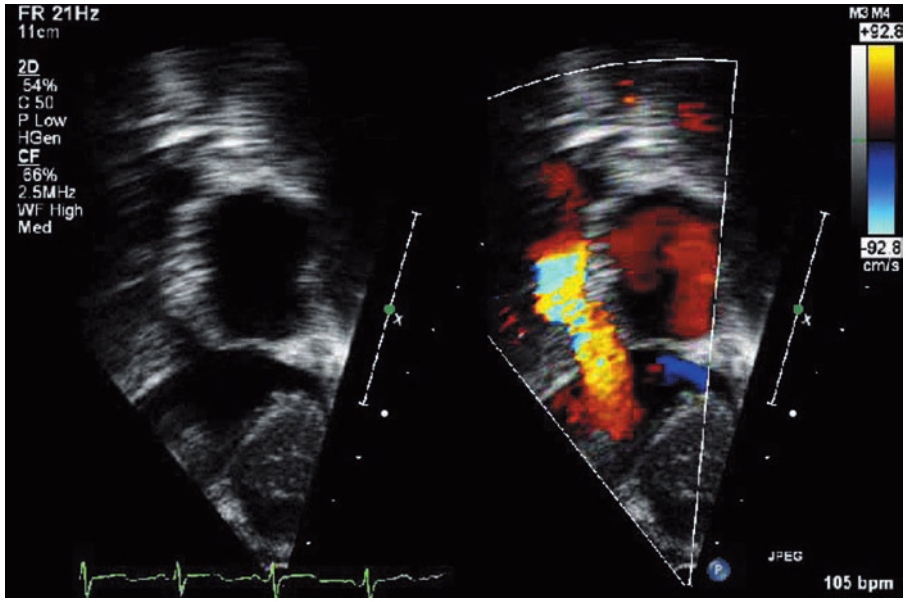


(b)

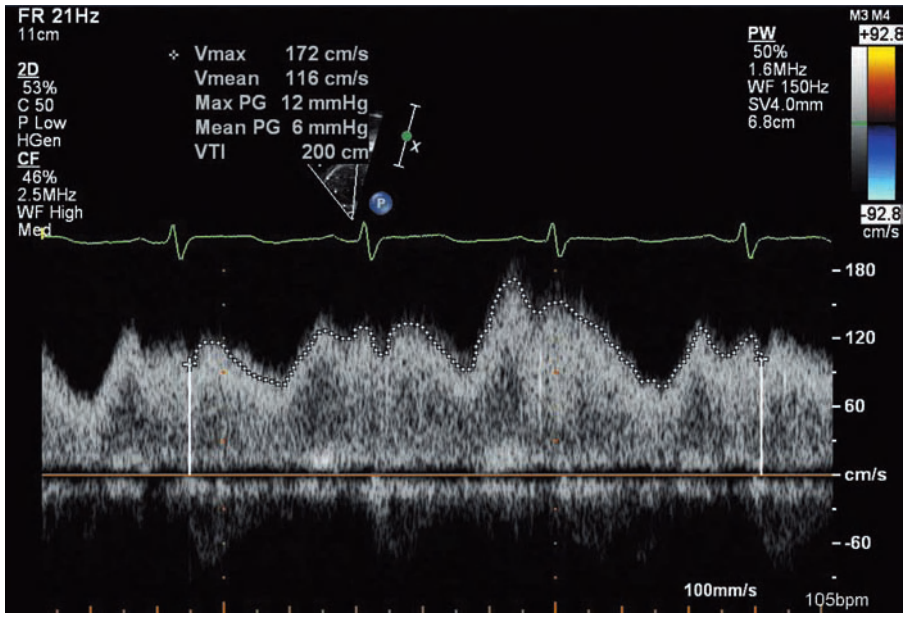


**Figure 33.11** Superior vena caval (SVC) obstruction in a patient status post-heart transplant. **(a)** Narrowing at the SVC anastomosis is demonstrated by 2D and color Doppler imaging; **(b)** spectral Doppler evaluation of the gradient.

Early after pediatric transplant, both systolic and diastolic longitudinal myocardial velocities, as assessed by TDI, are depressed. Velocities improve over the first 6 months after transplant but remain below controls [102]. In those pediatric patients without any history of rejection, longitudinal LV and RV myocardial velocities determined by TDI are lower than in healthy controls, the LV MPI is more prolonged, and wall motion abnormalities are common [103], although LV IVA is preserved [103,104]. In rejection, TDI velocities are further reduced (Fig. 33.12) and IVA and MPI are prolonged [104, 105]. Importantly, many echocardiographic measures have very good negative predictive value for rejection [100,101]. Therefore, echocardiography may be more useful in excluding rejection as a diagnosis and potentially limiting the number of invasive myocardial biopsies.

Echocardiography in the post-transplant patient should also include evaluation for RV dysfunction, pericardial effusion and tricuspid regurgitation as these are common findings in the postoperative period. The development of clinically significant tricuspid regurgitation in children with heart transplants is associated with graft failure [106]. Tricuspid regurgitation may also develop as a result of injury to the valve during myocardial biopsy. Some clinicians have used real-time 2D and 3D echocardiography for echo-guided myocardial biopsies [107,108].

In long-term follow-up of the child who has undergone cardiac transplantation, the most common causes of death are

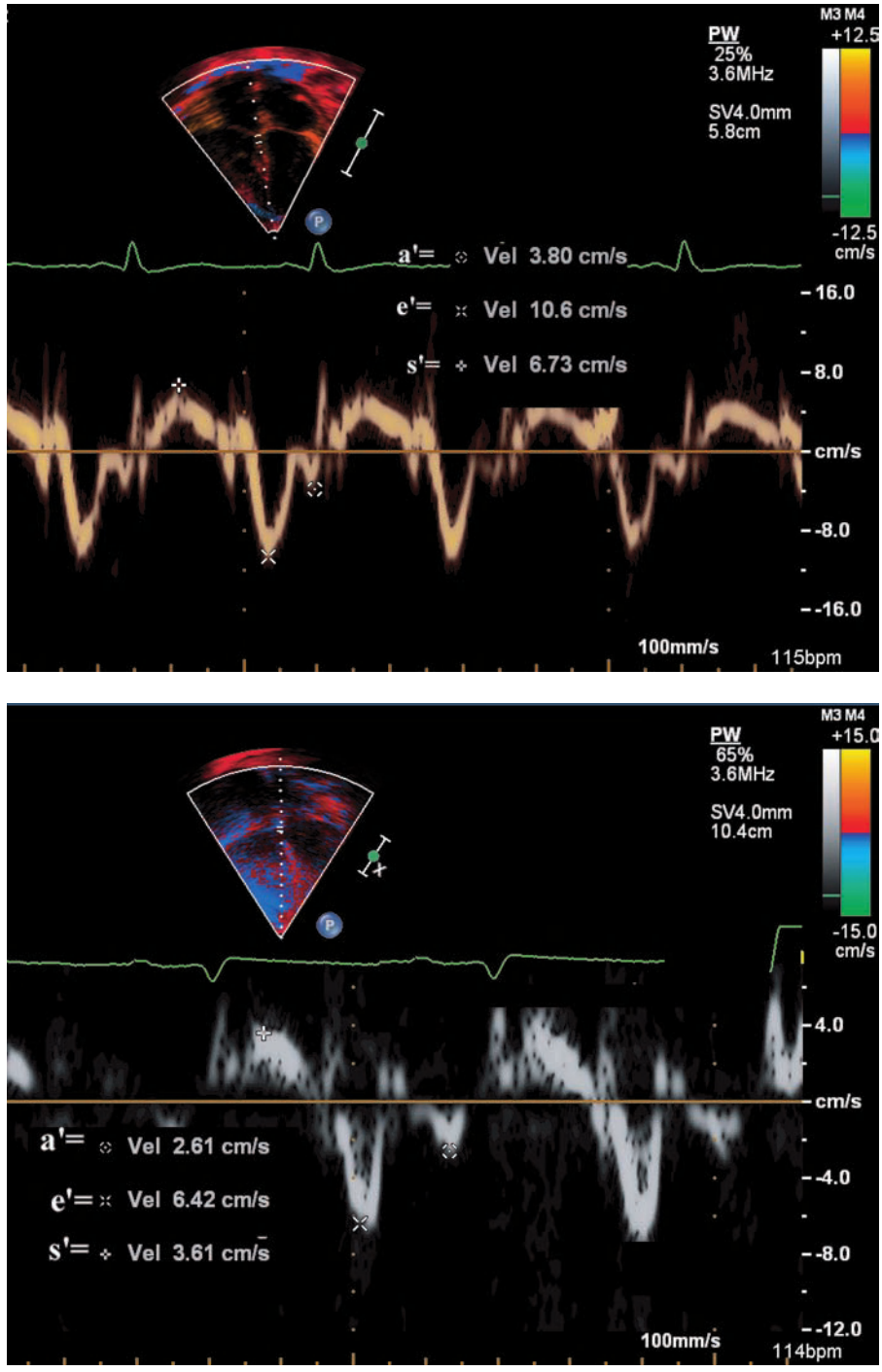


**Figure 33.12** **(a)** Septal myocardial velocities 1 month prior to severe rejection. **(b)** Further decreased myocardial velocities in the same patient with severe, acute rejection.

coronary artery vasculopathy and graft failure [109]. Clinical manifestations and symptoms of coronary vasculopathy may be subtle due to the diffuse, multifocal nature of the vascular changes and denervation of the heart. Current methods used to detect graft vascular disease include angiography in combination with exercise or dobutamine stress echocardiography (DSE) [110,111], intravascular ultrasound (IVUS) [112], cardiac computed tomography (CT) angiography [113], positron emission tomography (PET), and nuclear perfusion techniques [114]. Although angiography is the most commonly used screening tool, it may not correlate with either pathologic findings or functional significance of the vasculopathy. IVUS is more sensitive than angiography, predicts morbidity and mortality in adult transplant patients [115,116] (Fig. 33.13), and can be safely and effectively performed in pediatric patients [117,118]. There are also data in both children and

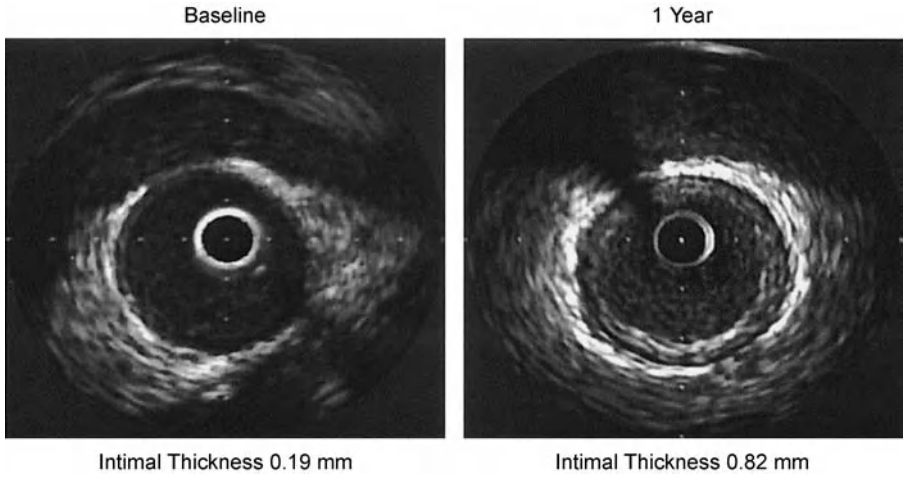


**Figure 33.13** Intravascular ultrasound (IVUS) images showing a >0.5 mm difference between the intimal thickness observed at baseline and 1 year post-transplant, demonstrating rapidly progressive transplant vasculopathy. Reproduced from Tuzcu EM, Kapadia SR, Sachar R et al. Intravascular ultrasound evidence of angiographically silent progression in coronary atherosclerosis predicts long-term morbidity and mortality after cardiac transplantation. *J Am Coll Cardiol* 2005;45:1538–42, with permission from Elsevier.

adults indicating that conventional DSE [51,112] is useful in detection of graft coronary vasculopathy, and quantitative DSE using strain rate imaging may additive [119].

## Outlook

Echocardiography remains the most commonly used modality to evaluate ventricular size and function. Advances in technology allow more information to be gained regarding cardiac performance in patients with DCM and myocarditis. Even with advances in technology, it remains imperative to collect data on individual patients and the cardiomyopathy population as a whole in an organized, reproducible and meticulous manner. Attention to detail in terms of technical considerations, image quality, measurements and acquisition of quantitative data is critically important. Sonographers and cardiologists alike should strive to acquire information in a way that allows confidence in both clinical decision-making and research data analysis.

## References

1 Richardson P, McKenna W, Bristow M et al. Report of the 1995 World Health Organization/International Society and Federation of Cardiology Task Force on the Definition and Classification of Cardiomyopathies. *Circulation* 1996;93:841–2.
2 Maron BJ, Towbin JA, Thiene G et al. Contemporary definitions and classification of the cardiomyopathies: an American Heart Association Scientific Statement from the Council on Clinical Cardiology, Heart Failure and Transplantation Committee; Quality of Care and Outcomes Research and Functional Genomics and Translational Biology Interdisciplinary Working Groups; and Council on Epidemiology and Prevention. *Circulation* 2006;113:1807–16.
3 Colan SD. Classification of the cardiomyopathies. *Prog Pediatr Cardiol* 2007;23:5–15.
4 Aretz HT, Billingham ME, Edwards WD et al. Myocarditis. A histopathologic definition and classification. *Am J Cardiovasc Pathol* 1987;1:3–14.
5 Baughman KL. Diagnosis of myocarditis: death of Dallas criteria. *Circulation* 2006;113:593–5.
6 Mahrholdt H, Goedecke C, Wagner A et al. Cardiovascular magnetic resonance assessment of human myocarditis: a comparison to histology and molecular pathology. *Circulation* 2004;109:1250–8.
7 Skouri HN, Dec GW, Friedrich MG, Cooper LT. Noninvasive imaging in myocarditis. *J Am Coll Cardiol* 2006;48:2085–93.
8 Lipshultz SE, Sleeper LA, Towbin JA et al. The incidence of pediatric cardiomyopathy in two regions of the United States. *N Engl J Med* 2003;348:1647–55.
9 Nugent AW, Daubeney PE, Chondros P et al. The epidemiology of childhood cardiomyopathy in Australia. *N Engl J Med* 2003;348:1639–46.
10 Towbin JA, Lowe AM, Colan SD et al. Incidence, causes, and outcomes of dilated cardiomyopathy in children. *JAMA* 2006;296:1867–76.
11 Rakar S, Sinagra G, Di Lenarda A et al. Epidemiology of dilated cardiomyopathy. A prospective post-mortem study of 5252 necropsies. The Heart Muscle Disease Study Group. *Eur Heart J* 1997;18:117–23.
12 Codd MB, Sugrue DD, Gersh BJ, Melton LJ III. Epidemiology of idiopathic dilated and hypertrophic cardiomyopathy. A population-based study in Olmsted County, Minnesota, 1975–1984. *Circulation* 1989;80:564–72.
13 English RF, Janosky JE, Ettedgui JA, Webber SA. Outcomes for children with acute myocarditis. *Cardiol Young* 2004;14:488–93.
14 Cox GF, Sleeper LA, Lowe AM et al. Factors associated with establishing a causal diagnosis for children with cardiomyopathy. *Pediatrics* 2006;118:1519–31.
15 Towbin JA, Bowles NE. The failing heart. *Nature* 2002;415:227–33.
16 Amabile N, Fraisse A, Bouvenot J et al. Outcome of acute fulminant myocarditis in children. *Heart* 2006;92:1269–73.
17 Calabrese F, Thiene G. Myocarditis and inflammatory cardiomyopathy: microbiological and molecular biological aspects. *Cardiovasc Res* 2003;60:11–25.

18 Kawai C. From myocarditis to cardiomyopathy: mechanisms of inflammation and cell death: learning from the past for the future. *Circulation* 1999;99:1091–100.
19 Pankuweit S, Portig I, Maisch B. Pathophysiology of cardiac inflammation: molecular mechanisms. *Herz* 2002;27:669–76.
20 Daubeney PE, Nugent AW, Chondros P et al. Clinical features and outcomes of childhood dilated cardiomyopathy: results from a national population-based study. *Circulation* 2006;114: 2671–8.
21 Alvarez JA, Wilkinson JD, Lipshultz SE. Outcome predictors for pediatric dilated cardiomyopathy: A systematic review. *Prog Pediatr Cardiol* 2007;23:25–32.
22 Burch M, Siddiqi SA, Celermajer DS et al. Dilated cardiomyopathy in children: determinants of outcome. *Br Heart J* 1994;72: 246–50.
23 Matitiau A, Perez-Atayde A, Sanders SP et al. Infantile dilated cardiomyopathy. Relation of outcome to left ventricular mechanics, hemodynamics, and histology at the time of presentation. *Circulation* 1994;90:1310–18.
24 Wiles HB, McArthur PD, Taylor AB et al. Prognostic features of children with idiopathic dilated cardiomyopathy. *Am J Cardiol* 1991;68:1372–6.
25 Azevedo VM, Santos MA, Albanesi Filho FM et al. Outcome factors of idiopathic dilated cardiomyopathy in children – a long-term follow-up review. *Cardiol Young* 2007;17:175–84.
26 McMahon CJ, Nagueh SF, Eapen RS et al. Echocardiographic predictors of adverse clinical events in children with dilated cardiomyopathy: a prospective clinical study. *Heart* 2004;90:908–15.
27 Colan SD, Borow KM, Neumann A. Left ventricular end-systolic wall stress-velocity of fiber shortening relation: a load-independent index of myocardial contractility. *J Am Coll Cardiol* 1984;4:715–24.
28 Colan SD, Boutin C, Castaneda AR, Wernovsky G. Status of the left ventricle after arterial switch operation for transposition of the great arteries. Hemodynamic and echocardiographic evaluation. *J Thorac Cardiovasc Surg* 1995;109:311–21.
29 Fishberger SB, Colan SD, Saul JP et al. Myocardial mechanics before and after ablation of chronic tachycardia. *Pacing Clin Electrophysiol* 1996;19:42–9.
30 Kertesz NJ, Friedman RA, Colan SD et al. Left ventricular mechanics and geometry in patients with congenital complete atrioventricular block. *Circulation* 1997;96:3430–5.
31 Hara Y, Hamada M, Hiwada K. Left ventricular end-systolic wall stress is a potent prognostic variable in patients with dilated cardiomyopathy. *Jpn Circ J* 1999;63:196–200.
32 Tei C, Ling LH, Hodge DO et al. New index of combined systolic and diastolic myocardial performance: a simple and reproducible measure of cardiac function – a study in normals and dilated cardiomyopathy. *J Cardiol* 1995;26:357–66.
33 Eto G, Ishii M, Tei C et al. Assessment of global left ventricular function in normal children and in children with dilated cardiomyopathy. *J Am Soc Echocardiogr* 1999;12:1058–64.
34 Dujardin KS, Tei C, Yeo TC et al. Prognostic value of a Doppler index combining systolic and diastolic performance in idiopathic-dilated cardiomyopathy. *Am J Cardiol* 1998;82:1071–6.
35 Harjai KJ, Scott L, Vivekananthan K et al. The Tei index: a new prognostic index for patients with symptomatic heart failure. *J Am Soc Echocardiogr* 2002;15:864–8.
36 Eidem BW, McMahon CJ, Cohen RR et al. Impact of cardiac growth on Doppler tissue imaging velocities: a study in healthy children. *J Am Soc Echocardiogr* 2004;17:212–21.
37 Mori K, Hayabuchi Y, Kuroda Y et al. Left ventricular wall motion velocities in healthy children measured by pulsed wave Doppler tissue echocardiography: normal values and relation to age and heart rate. *J Am Soc Echocardiogr* 2000;13:1002–11.
38 Rychik J, Tian ZY. Quantitative assessment of myocardial tissue velocities in normal children with Doppler tissue imaging. *Am J Cardiol* 1996;77:1254–7.
39 Mishiro Y, Oki T, Yamada H et al. Evaluation of left ventricular contraction abnormalities in patients with dilated cardiomyopathy with the use of pulsed tissue Doppler imaging. *J Am Soc Echocardiogr* 1999;12:913–20.
40 Eidem BW, McMahon CJ, Ayres NA et al. Impact of chronic left ventricular preload and afterload on Doppler tissue imaging velocities: a study in congenital heart disease. *J Am Soc Echocardiogr* 2005;18:830–8.
41 Gutierrez-Chico JL, Zamorano JL, Perez DI et al. Comparison of left ventricular volumes and ejection fractions measured by three-dimensional echocardiography versus by two-dimensional echocardiography and cardiac magnetic resonance in patients with various cardiomyopathies. *Am J Cardiol* 2005;95:809–13.
42 Shiota T, McCarthy PM, White RD et al. Initial clinical experience of real-time three-dimensional echocardiography in patients with ischemic and idiopathic dilated cardiomyopathy. *Am J Cardiol* 1999;84:1068–73.
43 Chuang ML, Hibberd MG, Salton CJ et al. Importance of imaging method over imaging modality in noninvasive determination of left ventricular volumes and ejection fraction: assessment by two- and three-dimensional echocardiography and magnetic resonance imaging. *J Am Coll Cardiol* 2000;35: 477–84.
44 Papavassiliou DP, Parks WJ, Hopkins KL, Fyfe DA. Three-dimensional echocardiographic measurement of right ventricular volume in children with congenital heart disease validated by magnetic resonance imaging. *J Am Soc Echocardiogr* 1998;11: 770–7.
45 Poutanen T, Jokinen E, Sairanen H, Tikanoja T. Left atrial and left ventricular function in healthy children and young adults assessed by three dimensional echocardiography. *Heart* 2003; 89:544–9.
46 Tani LY, Minich LL, Williams RV, Shaddy RE. Ventricular remodeling in children with left ventricular dysfunction secondary to various cardiomyopathies. *Am J Cardiol* 2005;96: 1157–61.
47 Cohn JN, Ferrari R, Sharpe N. Cardiac remodeling – concepts and clinical implications: a consensus paper from an international forum on cardiac remodeling. Behalf of an International Forum on Cardiac Remodeling. *J Am Coll Cardiol* 2000;35: 569–82.
48 De Wolf D, Suys B, Verhaaren H, Matthys D, Taeymans Y. Low-dose dobutamine stress echocardiography in children and young adults. *Am J Cardiol* 1998;81:895–901.
49 Michelfelder EC, Witt SA, Khoury P, Kimball TR. Moderate-dose dobutamine maximizes left ventricular contractile response during dobutamine stress echocardiography in children. *J Am Soc Echocardiogr* 2003;16:140–6.

50 Zilberman MV, Goya G, Witt SA et al. Dobutamine stress echocardiography in the evaluation of young patients with Kawasaki disease. *Pediatr Cardiol* 2003;24:338–43.

51 Pahl E, Crawford SE, Swenson JM et al. Dobutamine stress echocardiography: experience in pediatric heart transplant recipients. *J Heart Lung Transplant* 1999;18:725–32.

52 Kimball TR. Pediatric stress echocardiography. *Pediatr Cardiol* 2002;23:347–57.

53 Wu WC, Bhavsar JH, Aziz GF, Sadaniantz A. An overview of stress echocardiography in the study of patients with dilated or hypertrophic cardiomyopathy. *Echocardiography* 2004;21: 467–75.

54 Otasevic P, Popovic ZB, Vasiljevic JD et al. Head-to-head comparison of indices of left ventricular contractile reserve assessed by high-dose dobutamine stress echocardiography in idiopathic dilated cardiomyopathy: five-year follow up. *Heart* 2006;92: 1253–8.

55 Scrutinio D, Napoli V, Passantino A et al. Low-dose dobutamine responsiveness in idiopathic dilated cardiomyopathy: relation to exercise capacity and clinical outcome. *Eur Heart J* 2000; 21:927–34.

56 Avramides D, Perakis A, Voudris V, Gezerlis P. Noninvasive assessment of left ventricular systolic function by stress-shortening relation, rate of change of power, preload-adjusted maximal power, and ejection force in idiopathic dilated cardiomyopathy: prognostic implications. *J Am Soc Echocardiogr* 2000;13:87–95.

57 Paraskevaidis IA, Dodouras T, Adamopoulos S, Kremastinos DT. Effects of dobutamine on left ventricular shape and geometry: an easy way to detect the functional status of chronic heart failure in patients with dilated cardiomyopathy. *J Am Soc Echocardiogr* 2003;16:132–9.

58 Marmor A, Schneeweiss A. Prognostic value of noninvasively obtained left ventricular contractile reserve in patients with severe heart failure. *J Am Coll Cardiol* 1997;29:422–8.

59 Naqvi TZ, Goel RK, Forrester JS, Siegel RJ. Myocardial contractile reserve on dobutamine echocardiography predicts late spontaneous improvement in cardiac function in patients with recent onset idiopathic dilated cardiomyopathy. *J Am Coll Cardiol* 1999;34:1537–44.

60 Kitaoka H, Takata J, Yabe T et al. Low dose dobutamine stress echocardiography predicts the improvement of left ventricular systolic function in dilated cardiomyopathy. *Heart* 1999;81: 523–7.

61 Pratali L, Picano E, Otasevic P et al. Prognostic significance of the dobutamine echocardiography test in idiopathic dilated cardiomyopathy. *Am J Cardiol* 2001;88:1374–8.

62 Hamada H, Ohkubo T, Maeda M, Ogawa S. Evaluation of cardiac reserved function by high-dose dobutamine-stress echocardiography in asymptomatic anthracycline-treated survivors of childhood cancer. *Pediatr Int* 2006;48:313–20.

63 De Wolf D, Suys B, Maurus R et al. Dobutamine stress echocardiography in the evaluation of late anthracycline cardiotoxicity in childhood cancer survivors. *Pediatr Res* 1996;39: 504–12.

64 Paraskevaidis IA, Adamopoulos S, Tsiapras D et al. Prognostic usefulness of echocardiographic dobutamine in younger (14 to 25 years) and older (40 to 55 years) patients with idiopathic dilated cardiomyopathy. *Am J Cardiol* 2004;93:251–5.

65 Sivasankaran S, Sharland GK, Simpson JM. Dilated cardiomyopathy presenting during fetal life. *Cardiol Young* 2005;15: 409–16.

66 Yinon Y, Yagel S, Hegesh J et al. Fetal cardiomyopathy – in utero evaluation and clinical significance. *Prenat Diagn* 2007; 27:23–8.

67 Pedra SR, Smallhorn JF, Ryan G et al. Fetal cardiomyopathies: pathogenic mechanisms, hemodynamic findings, and clinical outcome. *Circulation* 2002;106:585–91.

68 Hernandez-Andrade E, Lopez-Tenorio J, Figueroa-Diesel H et al. A modified myocardial performance (Tei) index based on the use of valve clicks improves reproducibility of fetal left cardiac function assessment. *Ultrasound Obstet Gynecol* 2005;26: 227–32.

69 Eidem BW, Edwards JM, Cetta F. Quantitative assessment of fetal ventricular function: establishing normal values of the myocardial performance index in the fetus. *Echocardiography* 2001;18:9–13.

70 Friedman D, Buyon J, Kim M, Glickstein JS. Fetal cardiac function assessed by Doppler myocardial performance index (Tei Index). *Ultrasound Obstet Gynecol* 2003;21:33–6.

71 Chan LY, Fok WY, Wong JT et al. Reference charts of gestation-specific tissue Doppler imaging indices of systolic and diastolic functions in the normal fetal heart. *Am Heart J* 2005;150:750–5.

72 Aoki M, Harada K, Ogawa M, Tanaka T. Quantitative assessment of right ventricular function using doppler tissue imaging in fetuses with and without heart failure. *J Am Soc Echocardiogr* 2004;17:28–35.

73 Falkensammer CB, Paul J, Huhta JC. Fetal congestive heart failure: correlation of Tei-index and Cardiovascular-score. *J Perinat Med* 2001;29:390–8.

74 Huhta JC. Guidelines for the evaluation of heart failure in the fetus with or without hydrops. *Pediatr Cardiol* 2004;25:274–86.

75 Vitarelli A, Franciosa P, Conde Y et al. Echocardiographic assessment of ventricular asynchrony in dilated cardiomyopathy and congenital heart disease: tools and hopes. *J Am Soc Echocardiogr* 2005;18:1424–39.

76 Bristow MR, Saxon LA, Boehmer J et al. Cardiac-resynchronization therapy with or without an implantable defibrillator in advanced chronic heart failure. *N Engl J Med* 2004;350: 2140–50.

77 Pitzalis MV, Iacoviello M, Romito R et al. Cardiac resynchronization therapy tailored by echocardiographic evaluation of ventricular asynchrony. *J Am Coll Cardiol* 2002;40:1615–22.

78 Cazeau S, Bordachar P, Jauvert G et al. Echocardiographic modeling of cardiac dyssynchrony before and during multisite stimulation: a prospective study. *Pacing Clin Electrophysiol* 2003; 26:137–43.

79 Hawkins NM, Petrie MC, Macdonald MR et al. Selecting patients for cardiac resynchronization therapy: electrical or mechanical dyssynchrony? *Eur Heart J* 2006;27:1270–81.

80 Yu CM, Fung WH, Lin H et al. Predictors of left ventricular reverse remodeling after cardiac resynchronization therapy for heart failure secondary to idiopathic dilated or ischemic cardiomyopathy. *Am J Cardiol* 2003;91:684–8.

81 Dubin AM, Janousek J, Rhee E et al. Resynchronization therapy in pediatric and congenital heart disease patients: an

international multicenter study. *J Am Coll Cardiol* 2005;46: 2277–83.

82 McAlister FA, Ezekowitz J, Hooton N et al. Cardiac resynchronization therapy for patients with left ventricular systolic dysfunction: a systematic review. *JAMA* 2007;297:2502–14.

83 McAlister FA, Tu JV, Newman A et al. How many patients with heart failure are eligible for cardiac resynchronization? Insights from two prospective cohorts. *Eur Heart J* 2006;27: 323–9.

84 Swedberg K, Cleland J, Dargie H et al. Guidelines for the diagnosis and treatment of chronic heart failure: executive summary (update 2005): The Task Force for the Diagnosis and Treatment of Chronic Heart Failure of the European Society of Cardiology. *Eur Heart J* 2005;26:1115–40.

85 Friedberg MK, Silverman NH, Dubin AM, Rosenthal DN. Mechanical dyssynchrony in children with systolic dysfunction secondary to cardiomyopathy: a Doppler tissue and vector velocity imaging study. *J Am Soc Echocardiogr* 2007;20: 756–63.

86 Blume ED, Naftel DC, Bastardi HJ et al. Outcomes of children bridged to heart transplantation with ventricular assist devices: a multi-institutional study. *Circulation* 2006;113:2313–19.

87 Scalia GM, McCarthy PM, Savage RM et al. Clinical utility of echocardiography in the management of implantable ventricular assist devices. *J Am Soc Echocardiogr* 2000;13:754–63.

88 Liao KK, Miller L, Toher C et al. Timing of transesophageal echocardiography in diagnosing patent foramen ovale in patients supported with left ventricular assist device. *Ann Thorac Surg* 2003;75:1624–6.

89 Feldman CM, Silver MA, Sobieski MA, Slaughter MS. Management of aortic insufficiency with continuous flow left ventricular assist devices: bioprosthetic valve replacement. *J Heart Lung Transplant* 2006;25:1410–12.

90 Rao V, Slater JP, Edwards NM et al. Surgical management of valvular disease in patients requiring left ventricular assist device support. *Ann Thorac Surg* 2001;71:1448–53.

91 Horton SC, Khodaverdian R, Chatelain P et al. Left ventricular assist device malfunction: an approach to diagnosis by echocardiography. *J Am Coll Cardiol* 2005;45:1435–40.

92 Jacobsohn E, Avidan MS, Hantler CB et al. Case report: inferior vena cava-right atrial anastomotic stenosis after bicaval orthotopic heart transplantation. *Can J Anaesth* 2006;53:1039–43.

93 Shah M, Anderson AS, Jayakar D et al. Balloon-expandable stent placement for superior vena cava-right atrial stenosis after heart transplantation. *J Heart Lung Transplant* 2000;19:705–9.

94 Canivet JL, Defraigne JO, Demoulin JC, Limet R. Mechanical flow obstruction after heart transplantation diagnosed by TEE. *Ann Thorac Surg* 1994;58:890–1.

95 Law Y, Belassario A, West L et al. Supramitral valve obstruction from hypertrophied native atrial tissue as a complication of orthotopic heart transplantation. *J Heart Lung Transplant* 1997; 16:922–5.

96 Bouchart F, Derumeaux G, Mouton-Schleifer D et al. Conventional and total orthotopic cardiac transplantation: a comparative clinical and echocardiographical study. *Eur J Cardiothorac Surg* 1997;12:555–9.

97 Derumeaux G, Habib G, Schleifer DM et al. Standard orthotopic heart transplantation versus total orthotopic heart transplantation. A transesophageal echocardiography study of the incidence of left atrial thrombosis. *Circulation* 1995;92(9 Suppl.): II196–II201.

98 Romano P, Mangion JM. The role of intraoperative transesophageal echocardiography in heart transplantation. *Echocardiography* 2002;19:599–604.

99 Anderson CA, Shernan SK, Leacche M et al. Severity of intraoperative tricuspid regurgitation predicts poor late survival following cardiac transplantation. *Ann Thorac Surg* 2004;78: 1635–42.

100 Moran AM, Lipshultz SE, Rifai N et al. Non-invasive assessment of rejection in pediatric transplant patients: serologic and echocardiographic prediction of biopsy-proven myocardial rejection. *J Heart Lung Transpl* 2000;19:756–64.

101 Putzer GJB, Cooper D, Keehn C et al. An improved echocardiographic rejection-surveillance strategy following pediatric heart transplantation. *J Heart Lung Transpl* 2000;19:1166–74.

102 Mahle WT, Cardis BM, Ketchum D et al. Reduction in initial ventricular systolic and diastolic velocities after heart transplantation in children: improvement over time identified by tissue Doppler imaging. *J Heart Lung Transpl* 2006;25:1290–6.

103 Pauliks LB, Pietra BA, Kirby S et al. Altered ventricular mechanics in cardiac allografts: a tissue Doppler study in 30 children without prior rejection events. *J Heart Lung Transpl* 2005;24: 1804–13.

104 Pauliks LB, Pietra BA, DeGroff CG et al. Non-invasive detection of acute allograft rejection in children by tissue Doppler imaging: myocardial velocities and myocardial acceleration during isovolumic contraction. *J Heart Lung Transpl* 2005;24(7 Suppl.): S239–S248.

105 Leonard GT Jr, Fricker FJ, Pruett D et al. Increased myocardial performance index correlates with biopsy-proven rejection in pediatric heart transplant recipients. *J Heart Lung Transpl* 2006; 25:61–6.

106 Sivarajan VB, Chrisant MR, Ittenbach RF et al. Prevalence and risk factors for tricuspid valve regurgitation after pediatric heart transplantation. *J Heart Lung Transpl* 2008;27:494–500.

107 Scheurer M, Bandisode V, Ruff P et al. Early experience with real-time three-dimensional echocardiographic guidance of right ventricular biopsy in children. *Echocardiography* 2006; 23:45–9.

108 Bedanova H, Necas J, Petrikovits E et al. Echo-guided endomyocardial biopsy in heart transplant recipients. *Transpl Int* 2004;17:622–5.

109 Boucek MM, Aurora P, Edwards LB et al. Registry of the International Society for Heart and Lung Transplantation: tenth official pediatric heart transplantation report – 2007. *J Heart Lung Transpl* 2007;26:796–807.

110 Di FS, Semiond B, Roriz R et al. Non-invasive detection of coronary artery disease by dobutamine-stress echocardiography in children after heart transplantation. *J Heart Lung Transpl* 2003;22:876–82.

111 Kimball TR, Witt SA, Daniels SR. Dobutamine stress echocardiography in the assessment of suspected myocardial ischemia in children and young adults. *Am J Cardiol* 1997;79:380–4.

112 Spes CH, Klauss V, Mudra H et al. Diagnostic and prognostic value of serial dobutamine stress echocardiography for noninvasive assessment of cardiac allograft vasculopathy: a comparison with coronary angiography and intravascular ultrasound. *Circulation* 1999;100:509–15.

113 Gregory SA, Ferencik M, Achenbach S et al. Comparison of sixty-four-slice multidetector computed tomographic coronary angiography to coronary angiography with intravascular ultrasound for the detection of transplant vasculopathy. *Am J Cardiol* 2006;98:877–84.

114 Maiers J, Hurwitz R. Identification of coronary artery disease in the pediatric cardiac transplant patient. *Pediatr Cardiol* 2008;29:19–23.

115 Tuzcu EM, Kapadia SR, Sachar R et al. Intravascular ultrasound evidence of angiographically silent progression in coronary atherosclerosis predicts long-term morbidity and mortality after cardiac transplantation. *J Am Coll Cardiol* 2005;45:1538–42.

116 Kobashigawa JA, Tobis JM, Starling RC et al. Multicenter intravascular ultrasound validation study among heart transplant recipients: outcomes after five years. *J Am Coll Cardiol* 2005; 45:1532–7.

117 Dent CL, Canter CE, Hirsch R, Balzer DT. Transplant coronary artery disease in pediatric heart transplant recipients. *J Heart Lung Transplant* 2000;19:240–8.

118 Nicolas RT, Kort HW, Balzer DT et al. Surveillance for transplant coronary artery disease in infant, child and adolescent heart transplant recipients: an intravascular ultrasound study. *J Heart Lung Transpl* 2006;25:921–7.

119 Eroglu E, D'hooge J, Sutherland GR et al. Quantitative dobutamine stress echocardiography for the early detection of cardiac allograft vasculopathy in heart transplant recipients. *Heart* 2008;94:e3.

# 34 Hypertrophic Cardiomyopathy

**Colin J. McMahon**[1] **and Javier Ganame**[2]

[1]Department of Paediatric Cardiology, Our Lady's Hospital for Sick Children, Crumlin, Ireland
[2]Department of Pediatric Cardiology, University Hospitals Leuven, Leuven, Belgium

## Introduction

Hypertrophic cardiomyopathy (HCM) is defined as myocardial hypertrophy without an identifiable cause. It is the second most common cardiomyopathy in children and may occur in either sporadic or familial forms [1,2]. HCM is one of the most important cardiac diagnoses because it is the most common cause of cardiac death in children and young adults [3]. In 1958 Teare first reported "asymmetrical hypertrophy of the heart," what we now recognize as HCM [4]. Histologic assessment of the myocardium revealed muscle bundles in different orientations separated by connective tissue. Since its initial description, there have been significant advances in the diagnosis of HCM, in our understanding of its complex pathophysiology, and in its outcome and management. Echocardiography has played a crucial role in these advances. HCM represents a challenging condition given the marked heterogeneity in clinical manifestations and specifically the difficulty in assessing children at highest risk of sudden cardiac death.

## Incidence

The estimated incidence of HCM among adults is reported to be 0.2% of the population [5]. The incidence is likely higher as this disease may go unrecognized in a person's lifetime, particularly in those with no symptoms. There is a genetic predisposition and family clusters have been reported.

## Etiology

### Primary hypertrophic cardiomyopathy

Familial HCM is a genetic disease with an autosomal dominant pattern of inheritance, and characterized by hypertrophy of the ventricular septum and left ventricle with occasional right ventricular involvement [5,6]. The first gene for familial HCM was localized to chromosome 14q11.2-q12 [7]. Since then over 100 specific mutations in 11 different genes have been discovered for this disease [8–15]. Most mutations code for sarcomere proteins, including β-myosin heavy chain, myosin essential light chain 1, myosin regulatory light chain 2, cardiac actin, cardiac troponin T, cardiac troponin I, alpha-tropomyosin and cardiac myosin binding protein. Genotype–phenotype correlations, although only performed for a limited number of mutations, show a high correlation with prognosis [3,16].

Performing molecular techniques to detect these mutations is a challenging task. Moreover, no abnormal genotype can be identified in nearly one-third of patients with HCM and a definite family history of HCM [17]. These facts have limited the widespread use of genetic tests to diagnose and stratify risk of patients with HCM.

### Secondary hypertrophic cardiomyopathy

Specific metabolic, mitochondrial, and syndromic diseases (i.e., Noonan, Leopard syndromes) may manifest in HCM. These are called "secondary HCM." Cases of secondary HCM usually present in infancy (up to 15% of infants with HCM) and have a poor outcome. Typically, patients with secondary HCM develop concentric HCM, often accompanied by involvement of the right ventricle [18,19]. Metabolic screening and, in certain cases, muscle biopsy will help delineate the etiology.

Fabry disease is an X-linked recessive disease that accounts for 4% of cases of unexplained left ventricular (LV) hypertrophy in young men [20]. Symptoms usually start in the first decade of life, with acroparesthesiae, heat intolerance and development of cutaneous angiokeratomas. From the second decade onwards patients develop proteinuria and neurologic manifestations, including vestibular and hearing disturbance and autonomic dysfunction. Cardiac involvement is present early in life but is usually not detected clinically until the third or fourth decade [21]. Early cardiomyopathy is characterized by concentric remodeling, progressing later to concentric biventricular hypertrophy, which causes diastolic

*Echocardiography in Pediatric and Congenital Heart Disease: From Fetus to Adult*
Edited by Wyman W. Lai, Luc L. Mertens, Meryl S. Cohen and Tal Geva
 ISBN: 978-1-405-17401-5

dysfunction. Asymmetric septal hypertrophy and dynamic left ventricle outflow tract (LVOT) obstruction are rare (5–10% of cases), but do occur [22]. The mitral and aortic valves are thickened and distorted, resulting in regurgitation. The diagnosis can readily be made by measuring serum levels of the enzyme alpha-galactosidase A. This is of particular relevance because two recombinant enzyme preparations are approved for the treatment of Fabry disease.

Danon disease is an X-linked deficiency of lysosome-associated membrane protein type 2. It can present at variable ages as multisystemic disease with skeletal myopathy, mental retardation and cardiomyopathy. Cardiac involvement is characterized by massive hypertrophy, ventricular preexcitation and heart failure. Disease clinically confined to the heart is described in some cases with later onset [23,24].

Pompe disease (acid-maltase deficiency) is an autosomal recessive disorder that may also result in HCM in infancy. It is associated with severe skeletal muscle hypotonia, progressive weakness, hepatomegaly and macroglossia. The electrocardiogram (ECG) typically shows broad, high-voltage QRS complexes and the concentric left ventricular hypertrophy is typically severe.

Mitochondrial diseases may also result in HCM [25]. Friedreich ataxia, a progressive form of spinocerebellar degeneration due to lack of the mitochondrial protein frataxin, may also give rise to HCM, and all young adults with this condition should undergo routine screening [26].

Left ventricular noncompaction cardiomyopathy may result in an undulating phenotype, which may alternate between dilated and hypertrophic phenotypes [27].

## Classification: anatomy

In HCM, the LV myocardium is abnormally thick with a typically nondilated LV cavity. This can occur with or without LV outflow tract (LVOT) obstruction. The hypertrophy can develop early in life or in childhood or adolescence depending on the etiology. The mitral valve can be abnormal and thickened. The development of septal hypertrophy and anterior displacement of the mitral apparatus frequently leads to narrowing of the LVOT and creation of a dynamic pressure gradient across the LVOT. Although this pressure gradient was initially attributed to a muscular sphincter action in the subaortic region, it is now considered to be related to further narrowing of an already small outflow tract by systolic anterior motion of the often elongated mitral valve leaflets against the hypertrophied septum [28].

## Pathophysiology

There continues to be considerable controversy about the cause and the significance of the LVOT gradient in HCM. Whether there is true obstruction to LV ejection or whether the gradient is simply the consequence of vigorous LV emptying remains a matter of debate. Most now favor the view that a true mechanical impediment to LV ejection occurs when outflow tract gradients are present, and that the gradients result from anterior displacement of the mitral valve apparatus contacting the interventricular septum in mid-systole [29,30].

Most patients with HCM also demonstrate abnormalities of diastolic function. These abnormalities of diastolic filling are largely independent of the extent and distribution of myocardial hypertrophy. Even patients with mild localized hypertrophy may show marked diastolic dysfunction suggesting that the myopathic process occurs in ventricular regions that are not macroscopically hypertrophied. Diastolic dysfunction leads to increased filling pressures despite a normal or small LV cavity and appears to be related to abnormalities of LV relaxation and distensibility [1]. Early diastolic filling is impaired when relaxation is prolonged; this impairment is thought to be related to a number of factors including abnormal handling of calcium, subendocardial ischemia, nonuniformity of load, activation among different myocardial regions and abnormal loading conditions secondary to LVOT obstruction [31]. Late diastolic filling is altered when LV distensibility is impaired; as a consequence, filling pressures rise. HCM may cause abnormal distensibility because of fibrosis or cellular disarray.

Myocardial ischemia may occur in patients with HCM. Proposed causes include: impaired vasodilator reserve, perhaps related to the thickened and narrowed intramural coronary arteries; increased oxygen demand, especially in patients with LVOT obstruction; and elevated LV diastolic pressures with resultant subendocardial ischemia [32]. In children in particular, compression of intramyocardial segments of the left anterior descending artery (so-called myocardial bridging) may predispose to myocardial ischemia and sudden death [33].

### Clinical manifestations

Most patients with HCM are asymptomatic or only mildly symptomatic and are often identified during screening of relatives of a patient with HCM. Unfortunately, the first clinical manifestation in such individuals may be sudden cardiac death even before significant LV hypertrophy develops [2]. For this reason, it is crucial to identify the disease in childhood at the earliest possible time because mortality rate is higher in younger individuals (1–2% per year); death is often sudden and unexpected. Syncope and sudden death are associated with competitive sport in patients with HCM, therefore it is important to diagnose this condition so affected subjects can be excluded from these activities. Syncope can result from inadequate LV output in the presence of LVOT gradient or from cardiac arrhythmias.

The most common symptom in patients with HCM is dyspnea, which is secondary to elevated LV (and consequently

left atrial and pulmonary venous) diastolic pressure. Congestive heart failure and failure to thrive are frequently the first manifestations of infants with HCM [19]. Angina pectoris with exercise is present in 50% of symptomatic patients. A variety of mechanisms may contribute to the production of angina and myocardial ischemia as described above.

## Differential diagnosis

A fundamental step in the evaluation of a child with suspected HCM is to rule out underlying conditions that may masquerade as HCM. Left ventricular outflow tract obstruction secondary to subaortic, valvar or supravalvar aortic stenosis, and coarctation of the aorta must always be excluded. Differentiation between HCM and a fixed subaortic stenosis can be particularly challenging. Fixed subaortic stenosis may be due to a discrete fibrous membrane or to a muscular narrowing leading to LVOT obstruction and subsequent development of hypertrophy. The absence of a muscular (tunnel-like) or membranous subaortic narrowing adjacent to the aortic valve should be sought in multiple views [29,34]. In patients with fixed subaortic obstruction, Doppler echocardiography shows an early peak gradient generally associated with some degree of aortic regurgitation. Occasionally transesophegeal echocardiography (TEE) is needed to delineate the LVOT anatomy adequately.

Systemic hypertension may cause concentric left ventricular hypertrophy and should be differentiated from HCM. There are other conditions that may mimic asymmetric septal HCM in children. Left ventricular false tendons are normal structures that run parallel to the septum. Prominent false tendons may lead to overestimation of septal wall thickness, especially when performing measurements with M-mode echocardiography. Disproportionate asymmetric septal hypertrophy may be present in 10–15% of children with pulmonary hypertension secondary to congenital heart disease [35,36].

## Athlete's heart

Diagnosis of HCM in athletes is particularly important given the high propensity to sudden death in affected individuals engaging in competitive sports. Athletic heart is characterized by left ventricular hypertrophy, which may be difficult to differentiate from HCM. Typically, maximal end-diastolic septal thickness in adolescent male athletes is <12 mm (<11 mm in females) and <16 mm in grown-up elite athletes (Videoclip 34.1) [36,37]. Additionally, the left ventricular cavity is dilated in athletes (>55 mm). Importantly, reduced systolic and early diastolic myocardial velocities (<9 cm/s) are seen in patients with HCM but are normal or supranormal in athletes [38]. Exercise testing may be important in differentiating HCM from cardiovascular adaptation to training. Athletes frequently have a peak oxygen consumption >120% of predicted whereas 98% of patients with HCM have abnormal indices. Finally, in athletes periods of deconditioning (3–6 months) result in resolution of left ventricular hypertrophy.

## Family screening and preclinical diagnosis

All first-degree relatives of patients with HCM should be screened for this condition, with detailed family history, 12-lead electrocardiogram and echocardiography. The development of hypertrophy generally occurs during puberty, so repeat imaging at yearly intervals during childhood and adolescence is warranted in relatives of affected individuals. In adults repeat imaging can be performed at longer time intervals of 5 years because of the possibility of later development of hypertrophy [39]. Patients with HCM secondary to mutations in myosin-binding protein C generally develop hypertrophy in their fourth or fifth decade.

The diagnosis of familial HCM is made in three circumstances:

**1** When maximal wall thickness is two standard deviations above the mean for age and body surface area.

**2** When septal thickness is >15 mm or posterior wall thickness is >13 mm.

**3** When electrocardiographic abnormalities and a septal thickness >14 mm or posterior thickness >12 mm are present [40].

Patients with HCM resulting from mutations in troponin T often manifest with only mild left ventricular hypertrophy but are at high risk of sudden death. Strict adherence to previous criteria would not permit the diagnosis of HCM in these individuals. Thus, care should be taken to assess the morphologic findings in the context of the family history. The electrocardiogram is usually abnormal in this setting [41].

Studies with cardiac magnetic resonance imaging (CMR) have shown increased sensitivity of this technique over echocardiography for the preclinical diagnosis of HCM, especially when there is localized hypertrophy and for apical forms [42].

## Prognostic factors in children with HCM

The most important challenge in the management of HCM is the identification of those patients at increased risk for sudden death. Several parameters have been reported as risk factors for cardiac death in children with HCM, including young age at presentation, previous aborted sudden cardiac death, a malignant family history of HCM, a history of syncope, and ventricular tachycardia on ambulatory monitoring [43]. Echocardiographic risk factors include marked and diffuse left ventricular hypertrophy defined as maximal end-diastolic wall thickness >30 mm [44,45]. An elevated transmitral early filling velocity/myocardial early filling velocity ($E/E_a$) ratio has been found to correlate with ventricular tachycardia, cardiac arrest or death in a study of 80 consecutive children with HCM [46]. Left ventricular dilation and decreased ejection fraction are associated with both symptoms of heart failure and reduced survival.

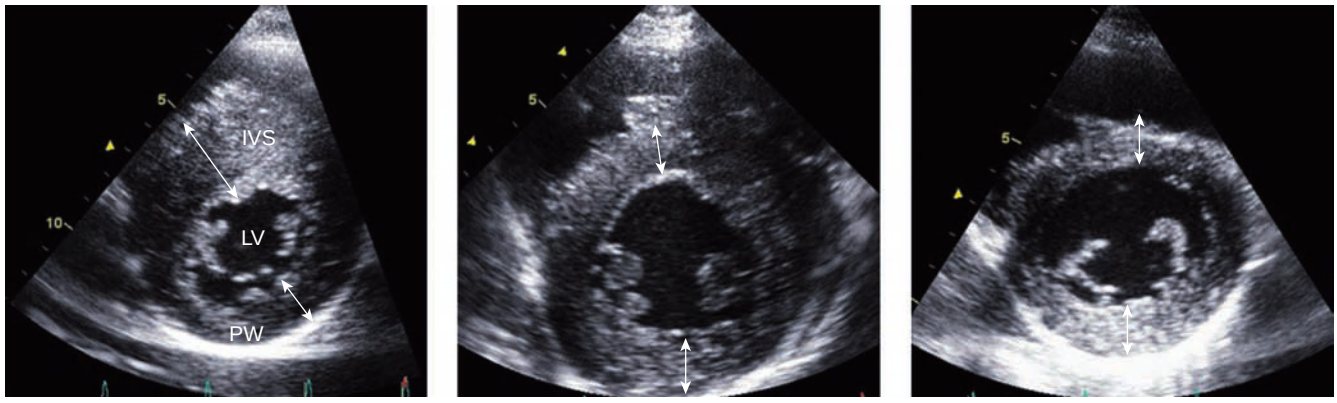


(a) (b) (c)

**Figure 34.1** Two-dimensional echocardiograms from short-axis views of three patients with different forms of hypertrophic cardiomyopathy. **(a)** Asymmetric septal hypertrophy, with hypertrophy limited to the interventricular septum; the posterior wall is of normal thickness. **(b)** Diffuse concentric hypertrophy. **(c)** Hypertrophy confined to the posterior wall. Double arrows denote thickness of myocardial wall. IVS, interventricular septum; LV, left ventricle; PW, posterior wall.

In the pediatric population, age less than 1 year at presentation, presence of massive hypertrophy HCM of a metabolic cause, troponin T mutations or an abnormal response of blood pressure with exercise carry a poor prognosis [18,19,47,48].

## Imaging

Complete evaluation of the child with HCM includes M-mode and two-dimensional (2D) imaging, Doppler evaluation of the mitral inflow and LVOT, tissue Doppler imaging (TDI) and, in some cases, strain rate imaging. Serial echocardiographic evaluation is important to assess for progression of disease. CMR and cardiac catheterization offer important additional methods of evaluation in particular clinical settings [49,50].

### Goals of the examination

The goals of echocardiographic examination in the setting of HCM can be summarized as follows:

- Assessment for structural heart disease that may cause ventricular hypertrophy.
- Accurate assessment of ventricular septal and free wall thickness.
- Assessment for right ventricular hypertrophy.
- Determination of etiology of LVOT obstruction, if present.
- Assessment of presence and severity of mitral regurgitation.
- Doppler interrogation of the entire LVOT from apex to above the aortic valve.
- Assessment of the presence and severity of aortic insufficiency.
- Assessment of LV systolic performance.
- Assessment of diastolic function.

### M-mode and 2D echocardiography

Two-dimensional echocardiography provides the primary screening tool to rule out the presence of HCM and allows a comprehensive assessment of cardiac structure and function. Pediatric HCM may manifest increased left ventricular wall thickness as asymmetric septal hypertrophy with predominant involvement of the basal septum (70% of cases), concentric hypertrophy (25%), posterior left ventricular hypertrophy (3–5%) or apical HCM (2%) (Fig. 34.1) [18,51]. The echocardiographic finding of a septal-to-posterior wall thickness ratio >1.3 is strongly suggestive of HCM. Each of these forms of hypertrophy may be associated with an obstructive LVOT gradient. Using echocardiography, LVOT obstruction is manifest in only 25% of patients with HCM at rest [52,53]. The presence, magnitude and distribution of left ventricular hypertrophy should be first determined using 2D imaging in the parasternal long-axis view, serial parasternal short-axis sweeps from the mitral valve level down to the most apical segments, multiple apical views and subcostal views (Figs 34.2–34.4; Videoclip 34.2). The suprasternal views typically add little diagnostic information in the evaluation of HCM but must be performed to rule out arch obstruction as the cause of the LV hypertrophy.

Two-dimensional or M-mode methods are used for accurate measurements of the interventricular septum and LV posterior wall thickness. Measurements should be taken at end-diastole; they are indexed to body surface area and z-score measurements are obtained. M-mode is typically performed in the parasternal long-axis or short-axis views [54]. Care should be taken to obtain correct alignment of the ultrasound beam with the orthogonal planes of the heart to avoid oblique transections of the left ventricle, which lead to overestimation of wall thickness. In addition to M-mode measurements, direct 2D measurements of the

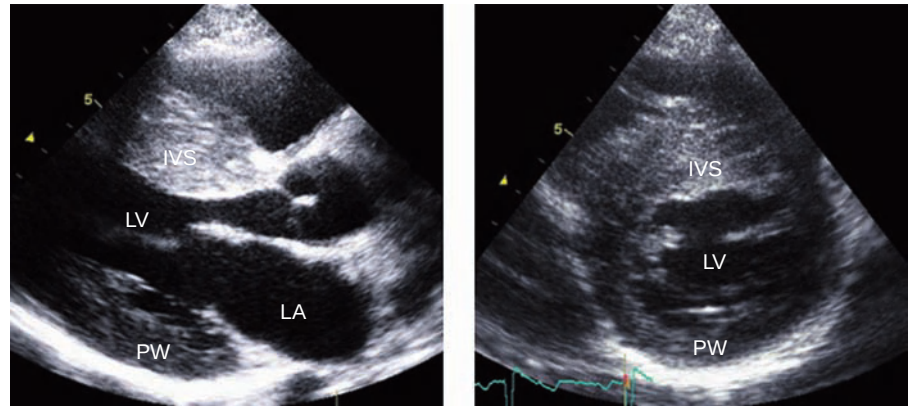


(a) (b)

**Figure 34.2** Two-dimensional echocardiograms of asymmetric septal hypertrophy from parasternal long-axis **(a)** and short-axis **(b)** views at end-diastole. The interventricular septum is thickened and has increased reflectivity. IVS, interventricular septum; LA, left atrium; LV, left ventricle; PW, posterior wall.

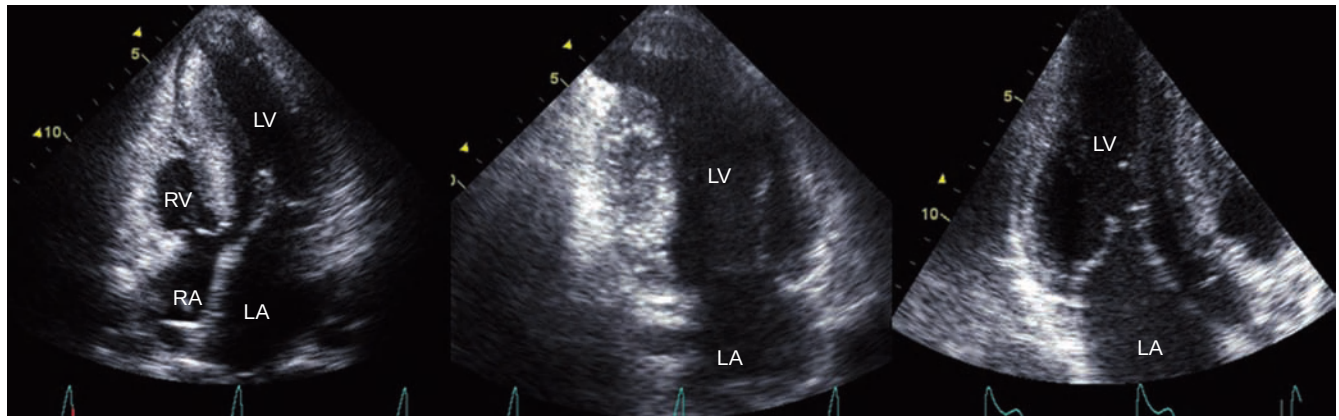


(a) (b) (c)

**Figure 34.3** Optimal evaluation of patients with hypertrophic cardiomyopathy includes the use of apical 4-chamber **(a)**, 2-chamber **(b)** and long-axis **(c)** views to determine the degree, extent, and distribution of hypertrophy. Considerable (25-mm) hypertrophy of the entire interventricular septum with extension onto the inferior wall is noted. In the 4-chamber view a dilated left atrium can be seen. The hypertrophied myocardium has increased reflectivity. LA, left atrium; LV, left ventricle; RV, right ventricle; RA, right atrium.

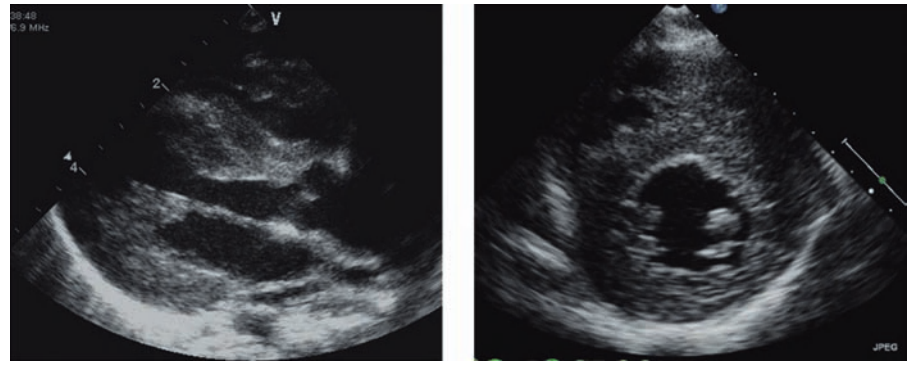

(a) (b)

**Figure 34.4** Hypertrophic cardiomyopathy secondary to metabolic diseases usually presents in infancy showing diffuse concentric biventricular hypertrophy and involvement of the papillary muscles, as can be seen in these two-dimensional echocardiograms from long- **(a)** and short-axis **(b)** views.

maximal septal thickness can be obtained in the parasternal long-axis and short-axis views. These often provide additional crucial data where there is an uneven distribution of septal hypertrophy. Direct 2D measurements also avoid oblique transections of the interventricular septum and inclusion of myocardium of the right ventricle as part of septal thickness.

Quantification of left ventricular mass is important but challenging given the inhomogeneous distribution of hypertrophy in patients with HCM. Alternatives include semiquantitative scores. A 10-point scoring system has been proposed to quantify the extent of left ventricular hypertrophy (Table 34.1) [1,55]. This score incorporates the degree of septal hypertrophy at the basal septum, the length of septal

**Table 34.1** Extent of left ventricular hypertrophy according to echocardiographic point score

| Extent of hypertrophy | Points |
|---|---|
| Basal septal thickness: | |
| 15–19 mm | 1 |
| 20–24 mm | 2 |
| 25–29 mm | 3 |
| >30 mm | 4 |
| Extension to papillary muscles (basal 2/3 of septum) | 2 |
| Extension to apex (all septum involved) | 2 |
| Anterolateral wall involvement | 2 |
| **Total** | 10 |

Reproduced from Wigle ED, Sasson Z, Henderson MA et al. Hypertrophic cardiomyopathy. The importance of the site and extent of hypertrophy. *Prog Cardiovasc Dis* 1985;28:1–83, with permission from Elsevier.

hypertrophy, and the extension of hypertrophy to the anterolateral wall. Another score reports the sum of maximal wall thickness from the septal, anterior, lateral, and posterior walls in the short-axis view at the mitral and papillary muscle levels [56].

M-mode findings in HCM include systolic anterior motion of the anterior mitral leaflet (SAM) and mid-systolic closure or notching of the aortic valve (Figs 34.5 and 34.6) [57,58]. However, these findings are not pathognomonic for HCM as they have been detected in other conditions (Table 34.2).

## Assessment of systolic performance

Assessment of systolic function is routinely performed by measuring left ventricular dimensions, shortening fraction (SF) and ejection fraction (EF). Most patients with HCM have small left ventricular cavity dimensions and supranormal EF or SF. In fact, the development of left ventricular dilation and depressed EF or SF are signs of poor prognosis that require institution of treatment for heart failure. It is important to note that in HCM a normal EF or SF does not exclude myocardial dysfunction, which can be detected with more sensitive techniques such as myocardial velocities, or strain rate imaging [59,60].

## Assessment of diastolic performance

Diastolic filling is impaired in HCM; this may result in dyspnea on exertion, elevated filling pressures and left atrial enlargement [61,62]. Left atrial volume reflects chronic left atrial hemodynamic burden from left ventricular diastolic dysfunction and mitral regurgitation. Relaxation is further impaired by the nonuniformity of load and inactivation in different myocardial segments of the left ventricle [63].

The transmitral inflow pattern should be carefully assessed with spectral Doppler performed at the tips of the mitral leaflets in the apical 4-chamber view [61]. The mitral E- and A-wave pattern typically represents marked perturbations in diastolic relaxation, with a reduced E-wave velocity, increased A-wave velocity (decreased E/A-wave ratio), prolonged E-wave deceleration time and prolonged isovolumetric relaxation time (Fig. 34.7). Pulmonary vein Doppler recordings demonstrate a progressive decrease in systolic flow and an increase in A-wave reversal with increasing diastolic dysfunction [64]. In cases of elevated left ventricular end-diastolic pressure, the diastolic (D-wave) flow time–velocity integral exceeds the systolic flow (S-wave) (Fig. 34.8).

A reduction in ventricular compliance is believed to account for the increased diastolic distribution of flow. In adult patients the left ventricular filling pressure may be estimated by comparing the time duration between the pulmonary venous A-wave and the mitral A-wave. Late diastolic left atrial contraction results in antegrade flow of blood through the mitral valve and retrograde flow into the pulmonary

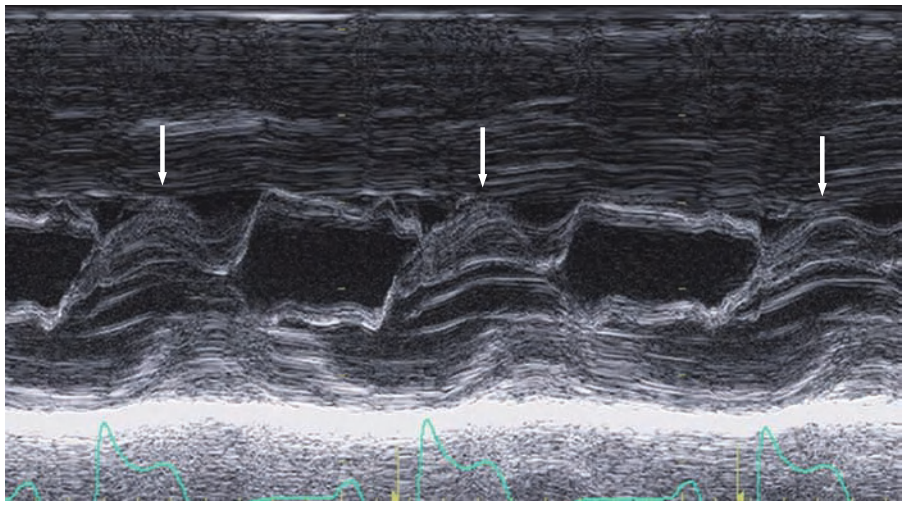

**Figure 34.5** M-mode echocardiogram from the parasternal long-axis view showing systolic anterior motion of the anterior mitral leaflet and septal contact (arrows) during mid- and late systole contributing to left ventricular outflow obstruction.

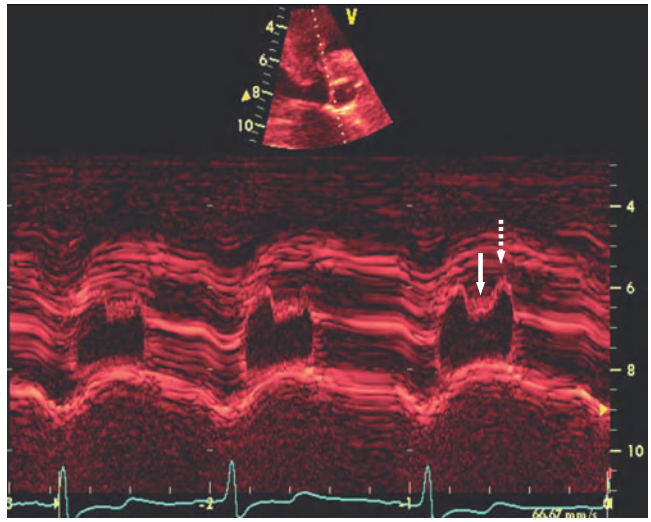

**Figure 34.6** M-mode echocardiogram from the parasternal long-axis view showing premature closure of the aortic valve (solid arrow) secondary to systolic anterior motion and left ventricular outflow tract obstruction occurring in mid-systole. Reopening of the aortic valve (dotted arrow) occurs in late systole when systolic anterior motion ceases.

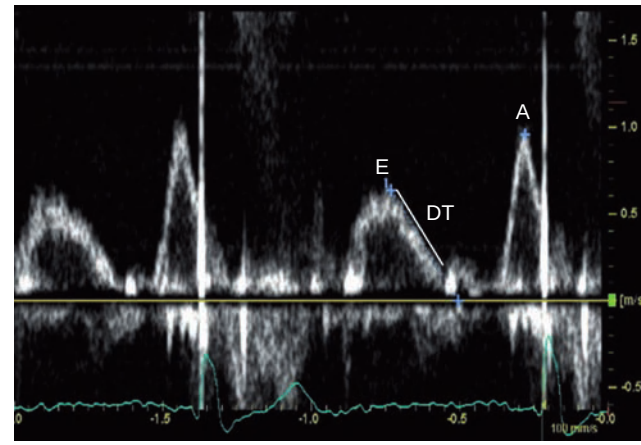


**Figure 34.7** Mitral inflow pulsed wave Doppler recording of a patient with HCM. The Doppler pattern shows abnormal relaxation. The early rapid filling velocity (E) is decreased (60 cm/s), there is prolonged deceleration time (DT) of the E wave (230 ms) and prominent atrial filling (A) velocity (94 cm/s).

**Table 34.2** Causes of systolic anterior motion and dynamic left ventricular outflow obstruction

| |
|---|
| Basal septal hypertrophy |
| Anomalous papillary muscle |
| After aortic valve replacement with LVH and hyperdynamic EF |
| After mitral valve repair |
| Apical ballooning |
| Apical myocardial infarction with hyperdynamic function of basal myocardial segments |
| Massive mitral annular calcification |
| Hypovolemia in patients with small LV cavity |

EF, ejection fraction; LVH, left ventricular hypertrophy.

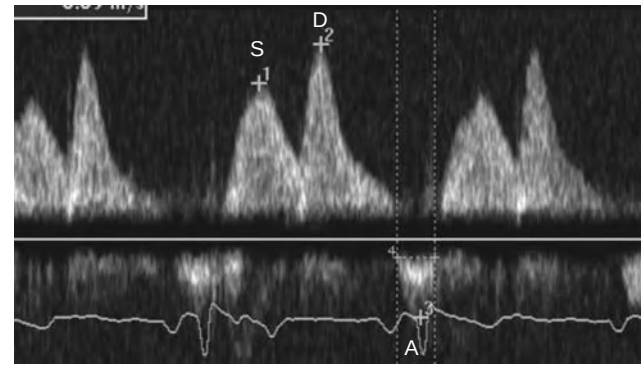


**Figure 34.8** Pulmonary venous pulsed-wave Doppler recording from the same patient as in Fig. 34.7. There is a blunted systolic component (S) and a prominent and prolonged atrial flow reversal component (A). This is suggestive of increased left ventricular end-diastolic pressure.

veins. In cases of elevated left heart filling pressures the pulmonary venous A-wave duration exceeds the mitral A-wave duration [65]. In such cases this predicts a left ventricular end-diastolic pressure >15 mm Hg, with 85% sensitivity and 79% specificity. This can be difficult to measure in children, however, because of increased heart rates and the small differences that may exist between these two measurements.

Pseudonormalization may occur with intermediate degrees of diastolic dysfunction when the mitral E/A-wave ratio appears normal; however, the pulmonary venous A-wave reversal will be increased, lateral mitral tissue Doppler velocities will be diminished, and during the Valsalva maneuver there is a reduction of flow into the left heart. Advanced degree of diastolic dysfunction manifests in restrictive physiology. There is an increase in E-wave velocity, decrease in A-wave velocity (increased E/A-wave ratio), and decreased E-wave deceleration time and isovolumetric relaxation time. The duration of the atrial contraction signal recorded in the pulmonary veins has a significant correlation with left ventricular end-diastolic pressure [65].

## Mitral valve function

In HCM, septal hypertrophy and anterior displacement of the mitral apparatus and papillary muscles lead to LVOT narrowing and obstruction, which in turn generates eddy currents in the subaortic region (Fig. 34.9) [66]. This hemodynamic abnormality results in anterior displacement of the distal portion of the anterior leaflet of the mitral valve leaflet, known as "systolic anterior motion" (SAM) of the mitral valve [67].

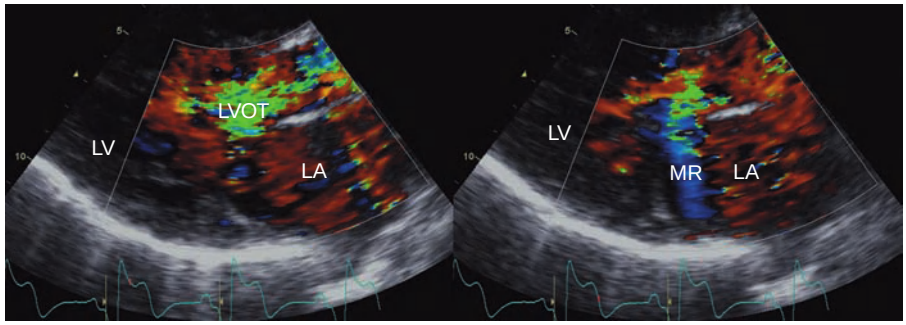


**Figure 34.9** Parasternal long-axis view with color flow mapping showing the temporal relationship between left ventricular outflow tract (LVOT) obstruction and occurrence of mitral regurgitation. Obstruction to flow occurs first, and mitral regurgitation ensues. LA, left atrium; LV, left ventricle; MR, mitral regurgitation.

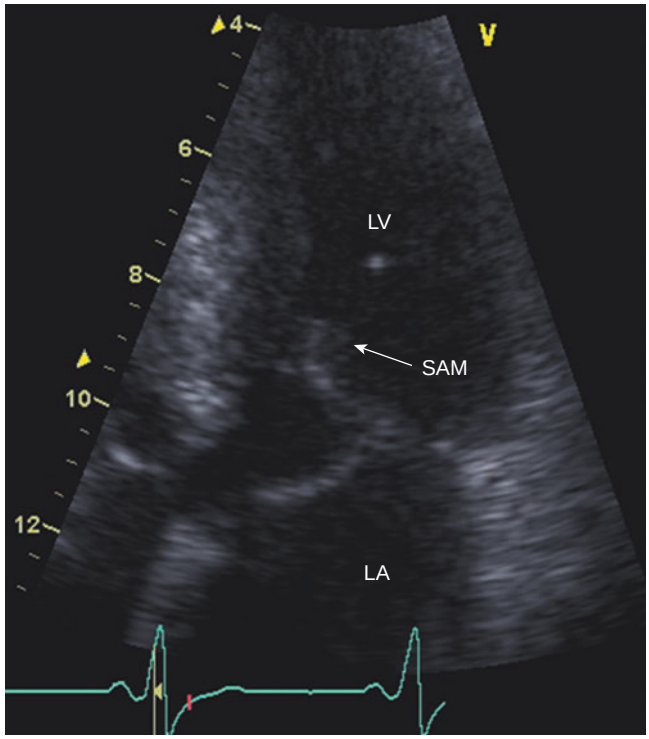


**Figure 34.10** Apical 4-chamber view showing systolic anterior motion (SAM) of the anterior and posterior mitral leaflets producing septal contact. This contributes to left ventricular outflow tract obstruction. LA, left atrium; LV, left ventricle.

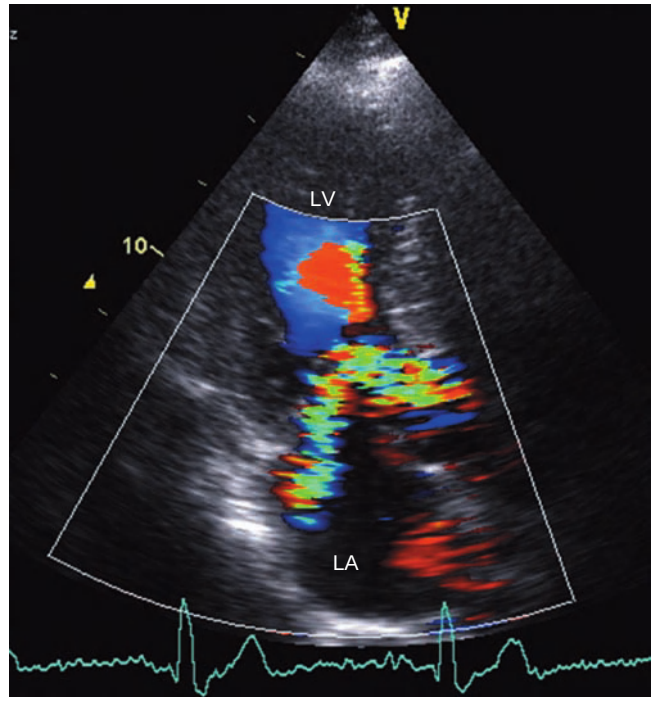


**Figure 34.11** Color flow mapping apical long-axis view showing left ventricular outflow tract obstruction and eccentric, posteriorly directed mitral regurgitation occurring at mid-systole. LA, left atrium; LV, left ventricle.

SAM is not pathognomonic of HCM, and has been observed in other conditions listed in Table 34.2. The parasternal long-axis view demonstrates SAM very well. Two-dimensional imaging and M-mode can also be used to assess the motion of the anterior leaflet of the mitral valve (Fig. 34.10 and Videoclip 34.3). SAM often results in noncoaptation of the mitral valve leaflets during mid- and end-systole, with a jet of mitral regurgitation directed posteriorly along the lateral wall of the left atrium (Fig. 34.11 and Videoclip 34.4). The degree of mitral regurgitation can range from mild to severe [67]. Severe mitral regurgitation may result in retrograde flow into the pulmonary veins, contributing to pulmonary venous and arterial hypertension. Given the high left ventricular systolic pressures, the mitral regurgitant jet velocity is usually very high (5–7 m/s).

Mitral regurgitation in patients with HCM can also be secondary to intrinsic mitral valve disease, with enlarged mitral leaflets being particularly common. The presence of a non-posteriorly directed jet in apical or parasternal long-axis views suggests primary leaflet pathology independent of SAM [68].

## Doppler imaging of LVOT

The presence of SAM usually indicates some form of LVOT obstruction, particularly when it persists for >40% of systole [66]. The pattern of LVOT obstruction in HCM is typically in mid- to late systole with no significant obstruction in early

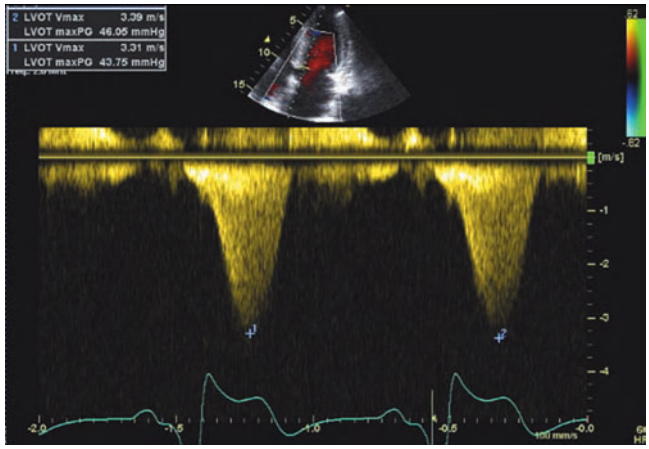


**Figure 34.12** Continuous-wave Doppler spectra from the apex showing dynamic left ventricular outflow tract obstruction. Note the typical start after the QRS complex, which is preceded by a low-velocity presystolic signal and the late-peaking configuration similar to a dagger. Peak velocity is 3.3 m/s, corresponding to a peak gradient of 44 mm Hg (= $4 \times 3.3^2$).

systole [29]. Left ventricular ejection typically diminishes during mid- to late systole resulting in partial closure of the aortic valve, often with reopening with final ejection. This can be identified using M-mode through the aortic valve in the parasternal long-axis view (Fig. 34.6).

The degree of LVOT obstruction is measured using Doppler imaging. The angle of interrogation is typically best in the apical 5-chamber view. Doppler provides a quantitative evaluation of the gradient across the outflow tract. In addition, the degree of dynamic obstruction can be elucidated from the appearance of the Doppler envelope. A dagger shape to the spectral wave pattern indicates a dynamic form of obstruction (Fig. 34.12) [29,69].

Pulsed-wave Doppler can be recorded sequentially from the left ventricular apex to the outflow tract. The peak velocity increases as the sample volume approaches the site of obstruction. Pulsed-wave Doppler is, however, often inadequate to measure the true gradient, and continuous-wave velocity may be necessary to measure a true gradient [69]. In those patients with SAM the location of the obstruction is clear and hence the use of continuous-wave analysis is appropriate. However, a true estimate of the degree of LVOT obstruction may be difficult as the majority of the stroke volume may have been ejected before late systole. In patients with a noncompliant left ventricle there may be evidence of presystolic forward flow in the LVOT secondary to atrial contraction with the A-wave transmitted to the LVOT. This is akin to the appearance of antegrade diastolic flow in the pulmonary arteries in patients with restrictive right ventricular (RV) physiology.

Color Doppler imaging of the LVOT often demonstrates aliasing due to the outflow tract gradient exceeding the Nyquist limit [70]. This is often helpful in identifying the exact location of outflow obstruction (Fig. 34.11 and Videoclip 34.5).

SAM of the mitral leaflet and LVOT obstruction are rather labile phenomena. Therefore a patient can have a pronounced gradient in one study and essentially none during the next. Several physiologic manipulations may provoke or unmask an LVOT gradient. These include squatting to standing, the strain phase of the Valsalva maneuver, administering amylnitrate, or any manipulation that increases contractility such as stress echocardiography with exercise or dobutamine administration [71,72]. Significant (>50 mm Hg) LVOT obstruction is present in only 25–30% of HCM patients under resting conditions but in up to 70% of HCM patients when they undergo exercise echocardiography. These high gradients are associated with heart failure symptoms [52].

There can be technical challenges to using Doppler in HCM. It may be difficult, albeit very important, to distinguish the high-velocity signal coming from the LVOT from the signal of mitral regurgitation. The spectral signal of mitral regurgitation is characterized by an earlier onset, higher velocity (>6 m/s) and a more abrupt initial increase in velocity. Differentiation can also be accomplished by orienting the transducer more medially and anteriorly away from the mitral jet [29,55]. The mitral regurgitation may be useful when the angle of interrogation in the LVOT is poor. An estimation of the LV pressure by the mitral regurgitation jet along with a simultaneous systolic blood pressure measurement can give an estimation of the LVOT gradient.

## Left ventricular mid-cavitary obstruction

In some patients the most prominent location of septal hypertrophy is mid-septal. Consequently during systole there may be mid-cavitary obstruction with formation of a distinct (sometimes aneurysmal) apical chamber, and a marked decrease in stroke volume leading to syncope and sudden death (Videoclip 34.6) [73]. The combination of color flow mapping with pulsed- and continuous-wave Doppler techniques is helpful in localizing the site and severity of obstruction (Fig. 34.13).

## Apical hypertrophic cardiomyopathy

This unusual form of HCM is characterized by electrocardiograms with giant negative T-waves in the precordial leads. Apical HCM is associated with a good prognosis. Echocardiography in the apical and parasternal views shows increased wall thickness of one or more apical segments (Fig. 34.14). The diagnosis may be missed if the true left ventricular apex is not visualized (because of foreshortening) or if endocardial definition is limited due to poor acoustic windows [74]. Contrast echocardiography may be useful in enhancing endocardial definition for identification of apical HCM. Long-term complications of apical HCM include the development of diastolic dysfunction, apical aneurysms, or mid-cavitary obstruction.

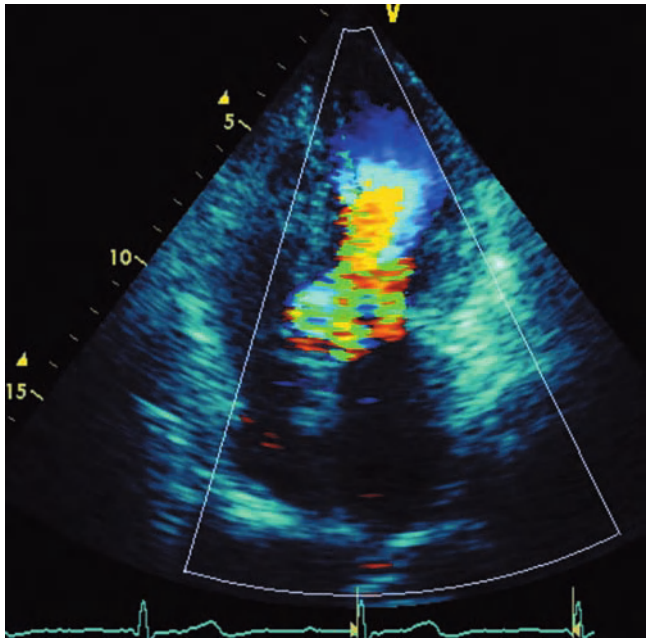


**Figure 34.13** Mid-cavitary obstruction is characterized by prominent mid-septal hypertrophy, formation of a distinct apical chamber during systole, and appearance of a mosaic color jet at the mid-ventricular level in mid-systole.

## Tissue Doppler imaging (TDI)

Tissue Doppler imaging employs spectral Doppler analysis to measure the velocity of myocardial tissue contraction or relaxation, specifically early systolic ($S_a$), early diastolic ($E_a$) and late diastolic velocities ($A_a$) [75]. Annular TDI velocities can be measured from the apical 4-chamber view. With the sample volume located at the junction of the myocardium and the annulus, using small sample volumes with the gains and filters set low, the early diastolic relaxation velocity can be measured. With increasing left ventricular filling pressures the transmitral E velocity increases and the early diastolic relaxation velocity ($E_a$) reduces (Fig. 34.15) [76]. The relationship between the transmitral E velocity and $E_a$ velocity ($E/E_a$ ratio) provides an estimation of the left ventricular filling pressure (atrial pressure). In adults the normal $E/E_a$ ratio is <10. An $E/E_a$ ratio >15 has been reported to predict a filling pressure exceeding 15 mm Hg [77]. In a study of 100 patients undergoing simultaneous catheterization and invasive hemodynamic measurements there was a strong correlation between pulmonary capillary wedge pressure and $E/E_a$ ($r = 0.86$) [78]. In a study of 80 consecutive children and adolescents with hypertrophic cardiomyopathy, the transmitral $E/E_a$ ratio was most sensitive and specific in predicting children at risk of sudden cardiac death, arrhythmia or need for transplantation [46].

Experimental data show that myocardial dysfunction occurs before the development of left ventricular hypertrophy in HCM. Reports suggest that in individuals carrying mutations that cause HCM, TDI velocities are reduced before the hypertrophy arises. An additional study shows that hypertrophy eventually develops in those subjects with diminished myocardial velocities [79]. Additional data are needed to determine the ideal cut-off value and the prognostic significance of these findings.

## Myocardial performance index (MPI)

In the 1990s a combined measure of systolic and diastolic ventricular function was derived, termed the MPI [80]. MPI measures the isovolumetric relaxation and isovolumetric contraction time as a function of left ventricular ejection time to produce a ratio. This has been of contentious clinical utility given the combination of both systolic and diastolic parameters within one measure. In patients with HCM, MPI values have been demonstrated to be abnormal. However, when tested against other echocardiographic indices in predicting clinical outcomes in children, MPI appears to have limited value.

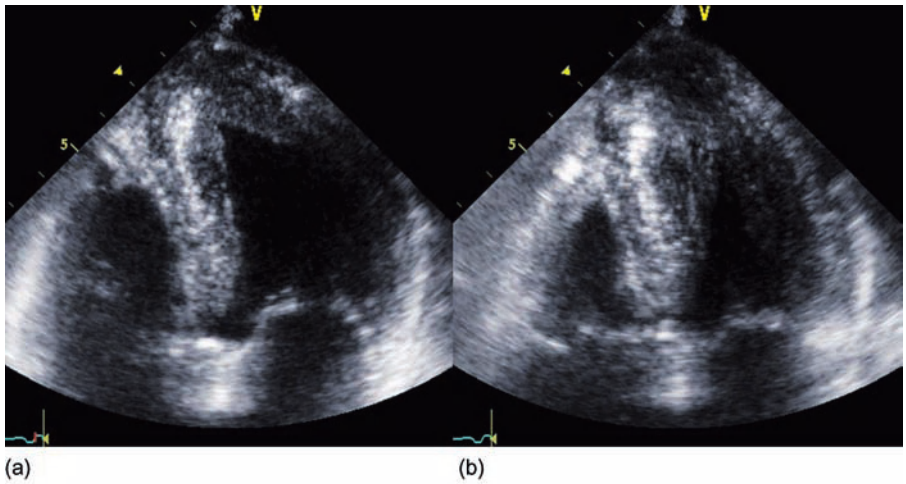


**Figure 34.14** End-diastolic **(a)** and end-systolic **(b)** transthoracic echocardiogram from apical 4-chamber view of a patient with apical hypertrophic cardiomyopathy showing increased thickness of all apical myocardial segments. Note obliteration of the apical cavity at end-systole.

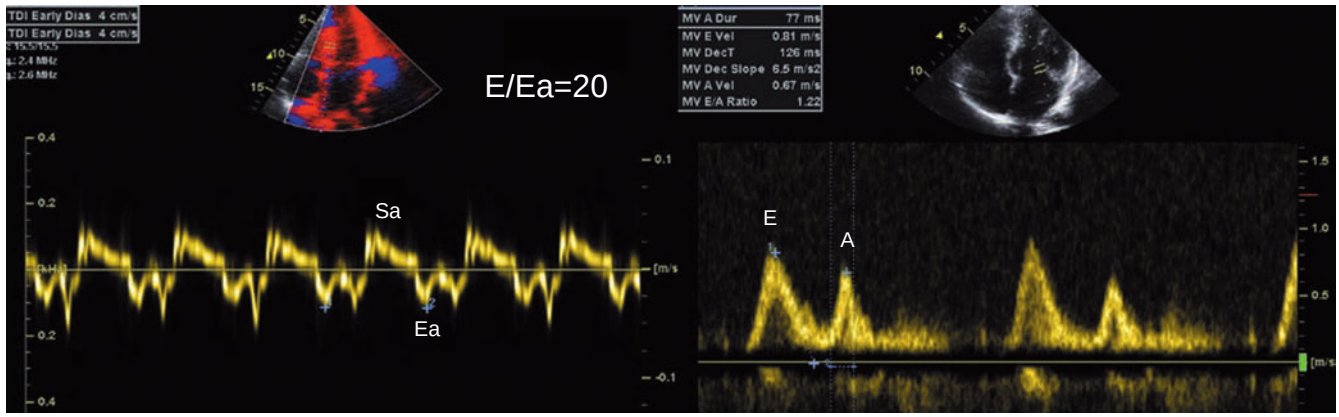


**Figure 34.15** Tissue Doppler recording of the septal mitral annulus and pulsed wave Doppler recording of the mitral inflow of a 12-year-old with hypertrophic cardiomyopathy. Peak systolic ($S_a$) and early diastolic ($E_a$) myocardial velocities are reduced. The mitral $E/E_a = 20$. This suggests elevated left atrial pressure.

## Strain rate imaging (SRI) and three-dimensional (3D) imaging

Newer, more sensitive techniques might improve diagnostic accuracy in HCM. HCM is a disease with marked nonuniformity in myocardial thickness and function. SRI allows the calculation of regional myocardial deformation. SRI studies have shown there is regional myocardial dysfunction with systolic lengthening instead of shortening in up to 50% of basal and mid-septal myocardial segments of patients with HCM (Fig. 34.16) [81]. Also, severely reduced systolic deformation and asymmetric septal hypertrophy distinguish patients with HCM from those with hypertension and left ventricular hypertrophy [60]. The noninvasive study of radial, longitudinal and circumferential myocardial deformation with SRI detects early abnormalities in myocardial function in patients with preserved global ventricular function [82].

Intraventricular mechanical dyssynchrony, whereby activation and relaxation of the different myocardial segments occur at different time intervals, can contribute to worsening of symptoms in patients with HCM. TDI and SRI can help identify mechanical dyssynchrony and guide cardiac resynchronization therapy [83].

Three-dimensional echocardiography renders full-volume dynamic pyramidal datasets that encompass the entire heart

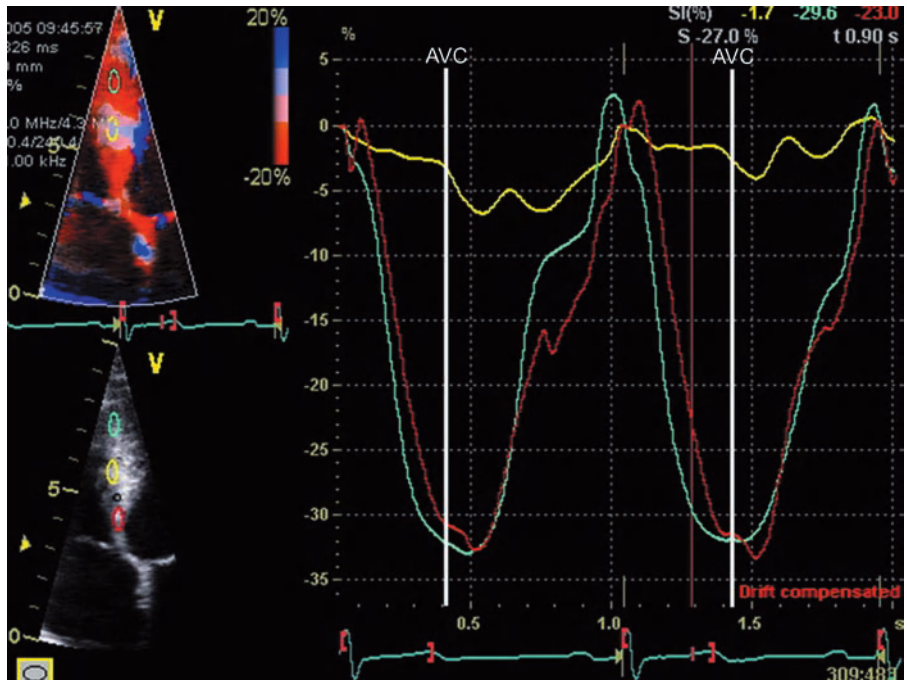


**Figure 34.16** Myocardial deformation (strain) in asymmetric septal hypertrophic cardiomyopathy. The hypertrophied midseptum (yellow line) shows reduced and delayed deformation persisting after aortic valve closure (AVC, white line). The other septal myocardial segments (green and red lines) do not exhibit any significant degree of hypertrophy and have preserved myocardial deformation. This technique may help detect mild and localized forms of hypertrophic cardiomyopathy.

and are obtained from a single acoustic window. Biventricular dimensions, wall thickness in all myocardial segments and ejection fraction can be calculated without relying on geometric assumptions of uniform chamber size and shape [84]. This leads to higher accuracy in the measurements. Additionally, the heart can be visualized from any point of view. In HCM, this is particularly helpful in defining mitral valve and LVOT anatomy before surgical or catheter-directed interventions [85]. The main current limitation of 3D systems is their limited spatial and temporal resolution.

## Echocardiography in the management of HCM

Management in HCM is optimized by monitoring the response to therapy with serial echocardiographic and Doppler studies. Symptomatic patients are treated with three classes of pharmacologic agents: beta-blockers, disopyramide, and calcium channel blockers [45,55]. These agents produce a decrease in contractility that results in decreased ejection velocity, delayed onset of SAM, and consequently decreased LVOT obstruction and mitral regurgitation. This may indirectly improve left ventricular diastolic filling and improve symptoms.

Dual-chamber pacing alleviates LVOT obstruction by reducing the inward motion of the interventricular septum during systole. Early observational studies in adults reported significant improvement in symptoms. However, subsequent blinded and controlled studies have not substantiated these initial findings but instead have suggested a placebo effect [86].

### Surgical myectomy and septal catheter ablation

Septal reduction therapy is feasible with surgical myectomy or intracoronary alcohol ablation. Patients with a dynamic gradient exceeding 30–50 mm Hg at rest or exceeding 60 mm Hg with exercise and a septal thickness greater than 15 mm may benefit from either procedure. It is important to determine the exact site of obstruction as patients with mid- or distal ventricular obstruction generally do not benefit from basal septal reduction [87].

Septal myectomy has been performed for four decades in patients who have significant LVOT obstruction and are symptomatic despite maximal medical therapy. This procedure consists of direct excision of the hypertrophied basal septum, which ideally results in widening of the LVOT, decreased dynamic obstruction of the LVOT and decreased SAM. Perioperative complications of surgery include aortic regurgitation, ventricular septal defects and atrioventricular block requiring permanent pacemaker implantation.

Echocardiography is useful in defining patients suitable for surgical myectomy. The preoperative characteristics of patients who benefit from surgical myectomy include asymmetric hypertrophy, severe and prolonged SAM, and a high LVOT gradient at rest or provoked with exercise [88]. Preoperative echocardiographic evaluation also includes the assessment of intrinsic mitral valve disease that warrants surgery, and concomitant aortic valve disease as well as the detection of additional sites of obstruction (mid-ventricular, or right ventricular outflow tract). Some patients undergoing myectomy will also require mitral valve replacement for severe mitral regurgitation.

Surgical myectomy performed via a transaortic approach gives limited exposure of the ventricular septum. Intraoperative TEE improves visualization of the surgical area allowing for delineation of the required myectomy. The adequacy of septal resection can be assessed and residual SAM or mitral regurgitation requiring further correction can be detected (Fig. 34.17) [89]. Surgical complications like ventricular septal defects, aortic regurgitation, left ventricular dysfunction or pericardial tamponade can be excluded with TEE. Echocardiographic studies performed at rest and with provocative maneuvers are important in the follow-up of patients after surgical myectomy (Fig. 34.18).

Septal catheter ablation consists of the selective injection of ethanol into the first septal perforator branch of the left anterior descending artery. This leads to occlusion of the septal branch and a localized infarction of the hypertrophied basal septum. The infarction results in thinning of the infarcted myocardial segment, decreased SAM, and immediate (generally modest) relief of the LVOT obstruction in the majority of patients. Chronic ventricular remodeling with further decrease in septal thickness, SAM and enlargement of the LVOT leads to further decrease in LVOT obstruction over time [90].

Transesophageal echocardiography is used during septal ablation procedures. The intraarterial injection of contrast agents allows the localization of the vascular beds perfused by individual septal perforators. After the injection of the contrast agent, the myocardial segments supplied by the septal branch become opacified (Fig. 34.19). The extent of myocardial opacification can be evaluated from multiple apical views. The vascular territory targeted by the procedure is the region of anterior mitral leaflet–septal contact adjacent to the zone of flow acceleration in the LVOT. If contrast opacification is seen in areas remote from the site of mitral leaflet–septal contact, this necessitates selection of another vessel to be targeted. The injection of ethanol has the same distribution as that of the contrast agent and results in increased reflectivity of the targeted myocardial area [91].

It has been shown that the use of intraprocedural contrast echocardiography improves outcome after septal catheter ablation because it limits the number of vessels injected, lowers the volume of ethanol used and causes fewer cases of atrioventricular block [92].

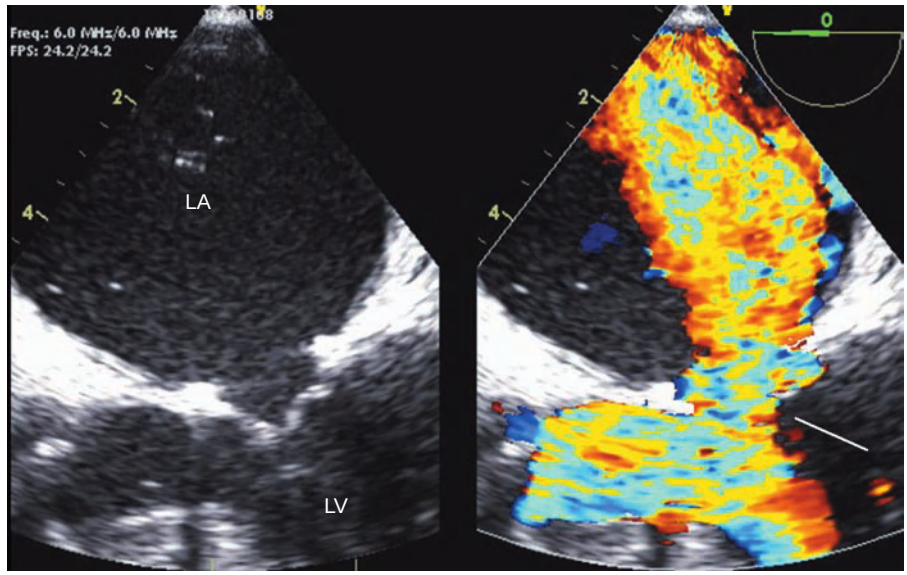


**Figure 34.17** Systolic anterior motion (SAM) is not exclusive of patients with hypertrophic cardiomyopathy. It can also occur after repair of the anterior mitral leaflet. This intraoperative transesophageal echocardiogram performed to assess the success of mitral repair shows chordal and anterior leaflet SAM leading to left ventricular outflow tract obstruction, malcoaptation of the mitral valve leaflets (white line), and severe, posteriorly directed eccentric mitral regurgitation. LA, left atrium; LV, left ventricle.

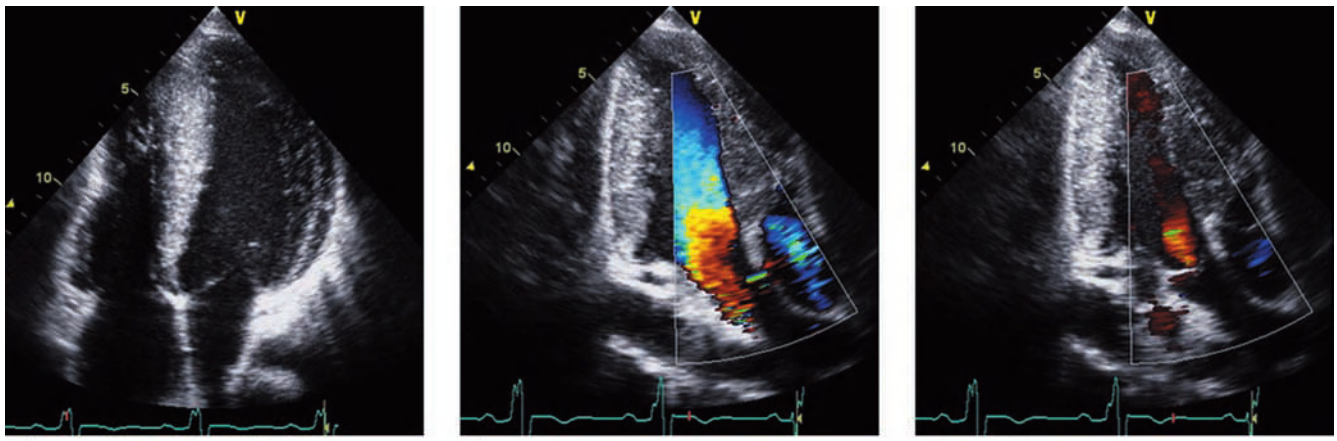

(a) (b) (c)

**Figure 34.18** Transthoracic echocardiogram taken 3 months after surgical myectomy. There is thinning of the basal septum **(a)**. Color flow mapping shows no significant left ventricular outflow tract obstruction **(b)**. Mild to moderate aortic regurgitation is present **(c)**.

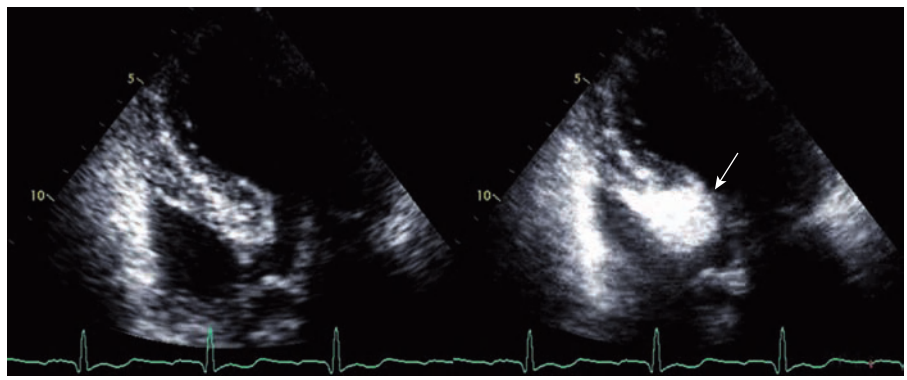

(a) (b)

**Figure 34.19** Transthoracic echocardiogram to guide ethanol septal ablation procedure. End-diastolic septal thickness was 18 mm, peak left ventricular outflow tract gradient was 65 mm Hg. **(a)** Basal septal hypertrophy. **(b)** Myocardial perfusion imaging after administration of contrast agent into the first septal perforator branch. Contrast opacifies only the hypertrophied basal septum (arrow) where there is mitral leaflet–septal contact. These findings make the patients eligible for ethanol septal ablation.

### Tissue Doppler imaging velocities following interventions for HCM

In adult patients with HCM, studies have demonstrated an improvement in diastolic relaxation and a reduction in left heart filling pressures subsequent to ethanol septal ablation [93,94]. This has provided some of the first evidence that infarction of septal tissue results in an improvement in hemodynamics and left ventricular diastolic function. This is more difficult to prove following surgical myomectomy given the potential deleterious effects of cardiopulmonary bypass on ventricular function.

## References


1. Wigle ED, Sasson Z, Henderson MA et al. Hypertrophic cardiomyopathy. The importance of the site and extent of hypertrophy. *Prog Cardiovasc Dis* 1985;28:1–83.
2. Maron BJ. Hypertrophic cardiomyopathy. Lancet 1997;350: 127–33.
3. Marian AJ. On predictors of sudden cardiac death in hypertrophic cardiomyopathy. *J Am Coll Cardiol* 2003;41:1887–96.
4. Teare D. Asymmetrical hypertrophy of the heart in young adults. *Br Heart J* 1958;20:1–8.
5. Maron BJ, Peterson EE, Maron MS et al. Prevalence of hypertrophic cardiomyopathy in an outpatient population referred for echocardiographic study. *Am J Cardiol* 1994;73:577–80.
6. Chang AC, Towbin JA. Heart failure in children and young adults: from molecular mechanisms to medical and surgical strategies. Philadelphia: Saunders/Elsevier, 2006;278–97.
7. Jarcho JA, McKenna W, Pare JA et al. Mapping a gene for familial hypertrophic cardiomyopathy to chromosome 14q1. *N Engl J Med* 1989;321:1372–8.
8. Watkins H, McKenna WJ, Thierfelder L et al. Mutations in the genes for cardiac troponin T and alpha-tropomyosin in hypertrophic cardiomyopathy. *N Engl J Med* 1995;332:1058–64.
9. Niimura H, Bachinski LL, Sangwatanaroj S et al. Mutations in the gene for human cardiac myosin-binding protein C and late-onset familial hypertrophic cardiomyopathy. *N Engl J Med* 1998;338:1248–57.
10. Thierfelder L, Watkins H, MacRae C et al. Alpha-tropomyosin and cardiac troponin T mutations cause familial hypertrophic cardiomyopathy: a disease of the sarcomere. *Cell* 1994;77:701–2.
11. Mogensen J, Klausen IC, Pedersen AK et al. Alpha-cardiac actin is a novel disease gene in familial hypertrophic cardiomyopathy. *J Clin Invest* 1999;103:R39–R43.
12. Arad M, Penas-Lado M, Monserrat L et al. Gene mutations in apical hypertrophic cardiomyopathy. *Circulation* 2005;112: 2805–11.
13. Geier C, Perrot A, Ozcelik C et al. Mutations in the human muscle LIM protein gene in families with hypertrophic cardiomyopathy. *Circulation* 2003;107:1390–5.
14. Towbin J. Pediatric myocardial disease. *Pediatr Clin North Am* 1999;46:289–312.
15. MacRae CA, Ghaisas N, Kass S et al. Familial hypertrophic cardiomyopathy with Wolff–Parkinson–White syndrome maps to a locus on chromosome 7q3. *J Clin Invest* 1995;96:1216–20.
16. Spirito P, Seidman CE, McKenna WJ, Maron BJ. The management of hypertrophic cardiomyopathy. *N Engl J Med* 1997;336:775–85.
17. Van Driest SL, Ommen SR, Tajik AJ et al. Sarcomeric genotyping in hypertrophic cardiomyopathy. *Mayo Clin Proc* 2005;80:463–9.
18. Nugent AW, Daubeney PE, Chondros P et al. Clinical features and outcomes of childhood hypertrophic cardiomyopathy: results from a national population-based study. *Circulation* 2005;112: 1332–8.
19. Colan SD, Lipshultz SE, Lowe AM et al. Epidemiology and cause-specific outcome of hypertrophic cardiomyopathy in children: findings from the Pediatric Cardiomyopathy Registry. *Circulation* 2007;115:773–81.
20. Sachdev B, Takenaka T, Teraguchi H et al. Prevalence of Anderson–Fabry disease in male patients with late onset hypertrophic cardiomyopathy. *Circulation* 2002;105:1407–11.
21. Linhart A, Elliott PM. The heart in Anderson–Fabry disease and other lysosomal storage disorders. *Heart* 2007;93:528–35.
22. Nakao S, Takenaka T, Maeda M et al. An atypical variant of Fabry's disease in men with left ventricular hypertrophy. *N Engl J Med* 1995;333:288–93.
23. Arad M, Maron BJ, Gorham JM et al. Glycogen storage diseases presenting as hypertrophic cardiomyopathy. *N Engl J Med* 2005; 352:362–72.
24. Yang Z, McMahon CJ, Smith LR et al. Danon disease as an underrecognized cause of hypertrophic cardiomyopathy in children. *Circulation* 2005;112:1612–17.
25. Wallace DC. Mitochondrial defects in cardiomyopathy and neuromuscular disease. *Am Heart J* 2000;139:S70–85.
26. Dutka DB, Donnelly JE, Palka P et al. Echocardiographic characterization of cardiomyopathy in Friedreich's ataxia with tissue Doppler echocardiographically derived myocardial velocity gradients. *Circulation* 2000;102:1276–82.
27. Pignatelli RH, McMahon CJ, Dreyer WJ et al. Clinical characterization of left ventricular noncompaction in children: a relatively common form of cardiomyopathy. *Circulation* 2003;108:2672–8.
28. Wigle ED, Rakowski H, Kimball BP, Williams WG. Hypertrophic cardiomyopathy. Clinical spectrum and treatment. *Circulation* 1995;92:1680–92.
29. Rakowski H, Sasson Z, Wigle ED. Echocardiographic and Doppler assessment of hypertrophic cardiomyopathy. *J Am Soc Echocardiogr* 1988;1:31–47.
30. Sherrid MV, Chu CK, Delia E et al. An echocardiographic study of the fluid mechanics of obstruction in hypertrophic cardiomyopathy. *J Am Coll Cardiol* 1993;22:816–25.
31. Betocchi S, Hess OM, Losi MA et al. Regional left ventricular mechanics in hypertrophic cardiomyopathy. *Circulation* 1993; 88:2206–14.
32. Perrone-Filardi P, Bacharach SL, Dilsizian V et al. Regional systolic function, myocardial blood flow and glucose uptake at rest in hypertrophic cardiomyopathy. *Am J Cardiol* 1993;72: 199–204.
33. Yetman AT, McCrindle BW, MacDonald C et al. Myocardial bridging in children with hypertrophic cardiomyopathy – a risk factor for sudden death. *N Engl J Med* 1998;339:1201–9.
34. Prasad K, Atherton J, Smith GC et al. Echocardiographic pitfalls in the diagnosis of hypertrophic cardiomyopathy. *Heart* 1999; 82(Suppl. 3):III8–III15.

35. Maron BJ, Clark CE, Henry WL et al. Prevalence and characteristics of disproportionate ventricular septal thickening in patients with acquired or congenital heart diseases: echocardiographic and morphologic findings. *Circulation* 1977;55:489–96.
36. Sharma S, Maron BJ, Whyte G et al. Physiologic limits of left ventricular hypertrophy in elite junior athletes: relevance to differential diagnosis of athlete's heart and hypertrophic cardiomyopathy. *J Am Coll Cardiol* 2002;40:1431–6.
37. Pelliccia A, Maron BJ, Spataro A et al. The upper limit of physiologic cardiac hypertrophy in highly trained elite athletes. *N Engl J Med* 1991;324:295–301.
38. Vinereanu D, Florescu N, Sculthorpe N et al. Differentiation between pathologic and physiologic left ventricular hypertrophy by tissue Doppler assessment of long-axis function in patients with hypertrophic cardiomyopathy or systemic hypertension and in athletes. *Am J Cardiol* 2001;88:53–8.
39. Maron BJ, Seidman JG, Seidman CE. Proposal for contemporary screening strategies in families with hypertrophic cardiomyopathy. *J Am Coll Cardiol* 2004;44:2125–32.
40. McKenna WJ, Spirito P, Desnos M et al. Experience from clinical genetics in hypertrophic cardiomyopathy: proposal for new diagnostic criteria in adult members of affected families. *Heart* 1997;77:130–2.
41. Moolman JC, Corfield VA, Posen B et al. Sudden death due to troponin T mutations. *J Am Coll Cardiol* 1997;29:549–55.
42. Moon JC, Fisher NG, McKenna WJ, Pennell DJ. Detection of apical hypertrophic cardiomyopathy by cardiovascular magnetic resonance in patients with non-diagnostic echocardiography. *Heart* 2004;90:645–9.
43. Spirito P, Chiarella F, Carratino L et al. Clinical course and prognosis of hypertrophic cardiomyopathy in an outpatient population. *N Engl J Med* 1989;320:749–55.
44. Spirito P, Maron BJ. Relation between extent of left ventricular hypertrophy and occurrence of sudden cardiac death in hypertrophic cardiomyopathy. *J Am Coll Cardiol* 1990;15: 1521–6.
45. Spirito P, Seidman CE, McKenna WJ, Maron BJ. The management of hypertrophic cardiomyopathy. *N Engl J Med* 1997;336: 775–85.
46. McMahon CJ, Nagueh SF, Pignatelli RH et al. Characterization of left ventricular diastolic function by tissue Doppler imaging and clinical status in children with hypertrophic cardiomyopathy. *Circulation* 2004;109:1756–62.
47. Suda K, Kohl T, Kovalchin JP, Silverman NH. Echocardiographic predictors of poor outcome in children with hypertrophic cardiomyopathy. *Am J Cardiol* 1997;80:595–60.
48. Moolman JC, Corfield VA, Posen B et al. Sudden death due to troponin T mutations. *J Am Coll Cardiol* 1997;29:549–55.
49. Moon JC, Mogensen J, Elliot PM et al. Myocardial late gadolinium enhancement cardiovascular magnetic resonance in hypertrophic cardiomyopathy caused by mutations in troponin I. *Heart* 2005;91:1036–40.
50. Redwood DR, Scherer JL, Epstein SE. Biventricular cineangiography in the evaluation of patients with asymmetric septal hypertrophy. *Circulation* 1974;49:1116–21.
51. Shapiro LM, McKenna WJ. Distribution of left ventricular hypertrophy in hypertrophic cardiomyopathy: a two-dimensional echocardiographic study. *J Am Coll Cardiol* 1983;2:437–44.
52. Maron MS, Olivotto I, Zenovich AG et al. Hypertrophic cardiomyopathy is predominantly a disease of left ventricular outflow tract obstruction. *Circulation* 2006;114:2232–9.
53. Watkins H, McKenna WJ. The prognostic impact of septal myectomy in obstructive hypertrophic cardiomyopathy. *J Am Coll Cardiol* 2005;46:477–9.
54. Feigenbaum H (ed.) *Feigenbaum's Echocardiography*, 6th edn. Philadelphia: Lippincott, Williams and Wilkins, 2004;171–5.
55. Woo A, Wigle ED, Rakowski H. Echocardiography in the evaluation and management of patients with hypertrophic cardiomyopathy. In: Otto C (ed.) *The Practice of Clinical Echocardiography*, 2nd edn. Philadelphia: W.B. Saunders, 2002;588–610.
56. Maron BJ, Gottdiener JS, Epstein SE. Patterns and significance of distribution of left ventricular hypertrophy in hypertrophic cardiomyopathy. A wide angle, two dimensional echocardiographic study of 125 patients. *Am J Cardiol* 1981;48:418–28.
57. Gilbert BW, Pollick C, Adelman AG, Wigle ED. Hypertrophic cardiomyopathy: subclassification by m mode echocardiography. *Am J Cardiol* 1980;45:861–72.
58. Nagueh SF, Mahmarian JJ. Noninvasive cardiac imaging in patients with hypertrophic cardiomyopathy. *J Am Coll Cardiol* 2006;48:2410–22.
59. Carabello BA. Evolution of the study of left ventricular function: everything old is new again. *Circulation* 2002;105:2701–3.
60. Kato TS, Noda A, Izawa H et al. Discrimination of nonobstructive hypertrophic cardiomyopathy from hypertensive left ventricular hypertrophy on the basis of strain rate imaging by tissue Doppler ultrasonography. *Circulation* 2004;110:3808–14.
61. Maron BJ, Spirito P, Green KJ et al. Noninvasive assessment of left ventricular diastolic function by pulsed Doppler echocardiography in patients with hypertrophic cardiomyopathy. *J Am Coll Cardiol* 1987;10:733–42.
62. Nihoyannopoulos P, Karatasakis G, Frenneaux M et al. Diastolic function in hypertrophic cardiomyopathy: relation to exercise capacity. *J Am Coll Cardiol* 199;19:536–40.
63. Bonow RO, Vitale DF, Maron BJ et al. Regional left ventricular asynchrony and impaired global left ventricular filling in hypertrophic cardiomyopathy: effect of verapamil. *J Am Coll Cardiol* 1987;9:1108–16.
64. Kuecherer HF, Muhiudeen IA, Kusumoto FM et al. Estimation of mean left atrial pressure from transoesophageal pulsed Doppler echocardiography of pulmonary venous flow. *Circulation* 1990;82:1127–39.
65. Rossvoll O, Hatle LK. Pulmonary venous flow velocities recorded by transthoracic Doppler ultrasound: relation to left ventricular diastolic pressures. *J Am Coll Cardiol* 1993;21: 1687–96.
66. Pollick C, Rakowski H, Wigle ED. Muscular subaortic stenosis: the quantitative relationship between systolic anterior motion and pressure gradient. *Circulation* 1984;69:43–9.
67. Schwammenthal E, Nakatani S, He S et al. Mechanism of mitral regurgitation in hypertrophic cardiomyopathy: mismatch of posterior to anterior leaflet length and mobility. *Circulation* 1998;98:856–65.
68. Panza JA, Petrone RK, Fananapazir L, Maron BJ. Coexistence of mitral valve prolapse in a consecutive group of 528 patients with hypertrophic cardiomyopathy assessed with echocardiography. *J Am Coll Cardiol* 1992;20:55–61.

69. Panza JA, Petrone RK, Fananapazir L, Maron BJ. Utility of continuous wave Doppler in noninvasive assessment of the left ventricular outflow tract pressure gradient in patients with hypertrophic cardiomyopathy. *J Am Coll Cardiol* 1992;19:91–9.
70. Hoit BD, Penonen E, Dalton N, Sahn DJ. Doppler color flow mapping studies of jet formation and spatial orientation in obstructive hypertrophic cardiomyopathy. *Am Heart J* 1989;117: 1119–26.
71. Nellen M, Gotsman MS, Vogelpoel L et al. Effects of prompt squatting on the murmur in idiopathic hypertrophic obstructive cardiomyopathy. *Br Heart J* 1967;3:140–3.
72. Marwick TH, Nakatani S, Haluska B et al. Provocation of latent left ventricular outflow tract gradients with amyl nitrite and exercise in hypertrophic cardiomyopathy. *Am J Cardiol* 1995;75: 805–9.
73. Shen AY, Gupta N, Napoor G. Severe intraventricular diastolic gradient due to hypertrophic cardiomyopathy and systolic left ventricular midcavitary obstruction. *Echocardiography* 2005;22: 47–8.
74. Webb JG, Sasson Z, Rakowski H et al. Apical hypertrophic cardiomyopathy: clinical follow-up and diagnostic correlates. *J Am Coll Cardiol* 1990;15:83–90.
75. McMahon CJ, Nagueh SF, Eapen RS et al. Echocardiographic predictor of adverse clinical events in children with dilated cardiomyopathy: a prospective clinical study. *Heart* 2004;90: 908–15.
76. Nagueh SF, Middleton KJ, Kopelen HA et al. Doppler tissue imaging: a noninvasive technique for evaluation of left ventricular relaxation and estimation of filling pressures. *J Am Coll Cardiol* 1997;30:1527–33.
77. Nagueh SF, Lakkis NM, Middleton KJ et al. Doppler estimation of left ventricular filling pressures in patients with hypertrophic cardiomyopathy. *Circulation* 1999;99:254–61.
78. Ommen SR, Nishimura RA, Appleton CP et al. Clinical utility of Doppler echocardiography and tissue Doppler imaging in the estimation of left ventricular filling pressures: A comparative simultaneous Doppler-catheterization study. *Circulation* 2000; 102:1788–94.
79. Nagueh SF, McFalls J, Meyer D et al. Tissue Doppler imaging predicts the development of hypertrophic cardiomyopathy in subjects with subclinical disease. *Circulation* 2003;108:395–8.
80. Tei C, Ling LH, Hodge DO et al. New index of combined systolic and diastolic myocardial performance: a simple and reproducible measure of cardiac function – a study in normal and dilated cardiomyopathy. *J Cardiol* 1995;26:357–66.
81. Ganame J, Mertens L, Eidem BW et al. Regional myocardial deformation in children with hypertrophic cardiomyopathy: morphological and clinical correlations. *Eur Heart J* 2007;8: 2886–94.
82. Serri K, Reant P, Lafitte M et al. Global and regional myocardial function quantification by two-dimensional strain: application in hypertrophic cardiomyopathy. *J Am Coll Cardiol* 2006;47: 1175–81.
83. D'Andrea A, Caso P, Severino S et al. Prognostic value of intraleft ventricular electromechanical asynchrony in patients with hypertrophic cardiomyopathy. *Eur Heart J* 2006;27:1311–8.
84. Caiani EG, Corsi C, Sugeng L et al. Improved quantification of left ventricular mass based on endocardial and epicardial surface detection with real time three dimensional echocardiography. *Heart* 2006;92:213–9.
85. Franke A, Schondube FA, Kuhl HP et al. Quantitative assessment of the operative results after extended myectomy and surgical reconstruction of the subvalvular mitral apparatus in hypertrophic obstructive cardiomyopathy using dynamic three-dimensional transesophageal echocardiography. *J Am Coll Cardiol* 1998;31:1641–9.
86. Sorajja P, Elliott PM, McKenna WJ. Pacing in hypertrophic cardiomyopathy. *Cardiol Clin* 2000;18:67–79.
87. Roberts R, Sigwart U. Current concepts of the pathogenesis and treatment of hypertrophic cardiomyopathy. *Circulation* 2005; 112:293–6.
88. McCully RB, Nishimura RA, Bailey KR et al. Hypertrophic obstructive cardiomyopathy: preoperative echocardiographic predictors of outcome after septal myectomy. *J Am Coll Cardiol* 1996;27:1491–6.
89. Ommen SR, Park SH, Click RL et al. Impact of intraoperative transesophageal echocardiography in the surgical management of hypertrophic cardiomyopathy. *Am J Cardiol* 2002;90:1022–4.
90. Flores-Ramirez R, Lakkis NM, Middleton KJ et al. Echocardiographic insights into the mechanisms of relief of left ventricular outflow tract obstruction after nonsurgical septal reduction therapy in patients with hypertrophic obstructive cardiomyopathy. *J Am Coll Cardiol* 2001;37:208–14.
91. Lakkis NM, Nagueh SF, Kleiman NS et al. Echocardiography-guided ethanol septal reduction for hypertrophic obstructive cardiomyopathy. *Circulation* 1998;98:1750–5.
92. Faber L, Seggewiss H, Gleichmann U. Percutaneous transluminal septal myocardial ablation in hypertrophic obstructive cardiomyopathy: results with respect to intraprocedural myocardial contrast echocardiography. *Circulation* 1998;98:2415–21.
93. Nagueh SF, Lakkis NM, Middleton KJ et al. Changes in left ventricular diastolic function 6 months after nonsurgical septal reduction therapy for hypertrophic cardiomyopathy. *Circulation* 1999;99:344–7.
94. Lakkis NM, Nagueh SF, Dunn JK et al. Nonsurgical septal reduction therapy for hypertrophic obstructive cardiomyopathy: one year follow-up. *J Am Coll Cardiol* 2000;36:852–5.

# 35 Restrictive Cardiomyopathy and Pericardial Disease

**Cecile Tissot[1,2], Christina Phelps[1] and Adel K. Younoszai[1]**

[1]The Children's Hospital, University of Colorado Health Sciences Center at Denver, Aurora, Co, USA
[2]The Children's Hospital, Geneva, Switzerland

## Restrictive cardiomyopathy

### Introduction

Restrictive cardiomyopathy is a rare disorder in children characterized by abnormal diastolic filling or compliance with normal or decreased diastolic volume of the ventricular chamber, in the setting of normal or near-normal systolic function [1]. The natural history is variable and at least partially depends on the etiology. Once symptoms develop, the morbidity and mortality are high and the prognosis is poor. The probability of survival at 1, 2 and 5 years is 80.5%, 39% and 20%, respectively [2]. The degree of hemodynamic abnormality and the risk of sudden death are significant [3], and heart transplantation is the treatment of choice once symptoms are present [4–6].

### Incidence and etiology

Although its exact incidence is unknown, restrictive cardiomyopathy is the least common of all pediatric cardiomyopathies, representing approximately 5% of cases. No known racial predilection exists. Restrictive cardiomyopathy may be slightly more common in girls than in boys [7,8]. Idiopathic restrictive cardiomyopathy represents the majority of cases in children. In patients with a familial component to their restrictive cardiomyopathy, the mode of inheritance is predominantly autosomal recessive [9]. Additionally, patients with hypertrophic cardiomyopathy and diabetic cardiomyopathy can also present with a restrictive component to their disease process. Restrictive cardiomyopathy is also seen with rare diseases, as summarized in Table 35.1 [10].

### Pathophysiology

The physiology of restrictive cardiomyopathy is characterized by impaired myocardial relaxation and ventricular compliance leading to atrial dilation and dysfunction. As a result, ventricular filling is primarily limited to early diastole. Typical hemodynamic characteristics include increased ventricular end-diastolic pressures with equalization of diastolic pressure between the atrial and ventricular chambers.

Anatomic findings include atrial enlargement, normal ventricular size with normal wall thickness or concentric hypertrophy. Histology reveals endocardial and interstitial fibrosis with increased collagen deposition, and myocyte hypertrophy without myofiber necrosis or disarray and without inflammatory infiltration. In children, endomyocardial biopsies are usually not helpful in the diagnosis, unless amyloidosis or hemochromatosis is the cause [11,12].

### Imaging

Echocardiography is uniquely suited as a diagnostic tool to detect the anatomic and functional abnormalities associated with restrictive cardiomyopathy and remains the major noninvasive imaging modality employed in the initial assessment of restrictive and constrictive physiology [13,14]. A complete

**Table 35.1** Etiologies of restrictive cardiomyopathy

| |
|---|
| Idiopathic |
| Amyloidosis |
| Hemosiderosis |
| Hemochromatosis |
| Hypereosinophilia: |
| Loeffler syndrome |
| Carcinoid syndrome |
| Endocardial fibroelastosis |
| Metabolic diseases: |
| Gaucher's disease |
| Fabry's disease |
| Hurler syndrome |
| Glycogen storage disease |
| Secondary to radiation therapy |
| Secondary to anthracycline administration |

*Echocardiography in Pediatric and Congenital Heart Disease: From Fetus to Adult*
Edited by Wyman W. Lai, Luc L. Mertens, Meryl S. Cohen and Tal Geva
 ISBN: 978-1-405-17401-5

study consisting of two-dimensional (2D) imaging, M-mode and Doppler interrogation of both cardiac systolic and diastolic function allows the examiner to identify specific features of restrictive physiology, to correlate with left-sided and right-sided filling pressures, and, importantly, to differentiate and distinguish from constrictive physiology.

### *Goals of the examination*

The goals of echocardiographic examination in the setting of restrictive cardiomyopathy can be summarized as follows:

- Measurement of left and right atrial size.
- Assessment of left ventricular performance and wall thickness.
- Estimation of right ventricular pressure by tricuspid regurgitation jet.
- Assessment of atrioventricular valve function.
- Determination of dilation of the inferior vena cava.
- Assessment of diastolic function and tissue Doppler imaging: distinction of restrictive from constrictive patterns.
- Assessment for pericardial disease.

### *Two-dimensional echocardiography*

In restrictive cardiomyopathy, both ventricular cavities are typically small with decreased end-diastolic dimensions. Marked biatrial enlargement is pathognomonic (Fig. 35.1a and Videoclip 35.1), with the atrial dimension in adults usually measuring more than 45 mm in an apical 4-chamber view. A left atrial dimension greater than 60 mm has been associated with a poor prognosis [15]. Atrial thrombi may be seen, especially in the appendages. Concentric left ventricular hypertrophy with normal or slightly decreased systolic function is usual [16]. Thickening of the atrial septum and cardiac valves is also common. Valvular dysfunction is often present, especially atrioventricular regurgitation (Fig. 35.1b). In most cases there is evidence of pulmonary hypertension (Fig. 35.1c) including flattened ventricular septum in the parasternal short-axis view and an elevated right ventricular pressure estimate as measured by the tricuspid regurgitation jet (in 4-chamber view). It is important to realize that the right ventricular pressure may be underestimated using this method because the right atrial pressure (which must be included in the equation) is often quite high. Subxiphoid imaging often reveals that the inferior vena cava is dilated and does not collapse with inspiration (plethora), reflecting increased right atrial pressure (Fig. 35.2). A pericardial effusion may be present. Myocardial reflectance is usually increased. In case of amyloidosis, the ventricular walls are thickened with a granular or sparkling myocardium on echocardiography reflecting amyloid deposits. M-mode echocardiography provides basic assessment of cardiac structure and dimensional changes during the cardiac cycle [17]. When examined with this imaging modality, the ventricular chambers are typically small and mild concentric hypertrophy is usually seen.

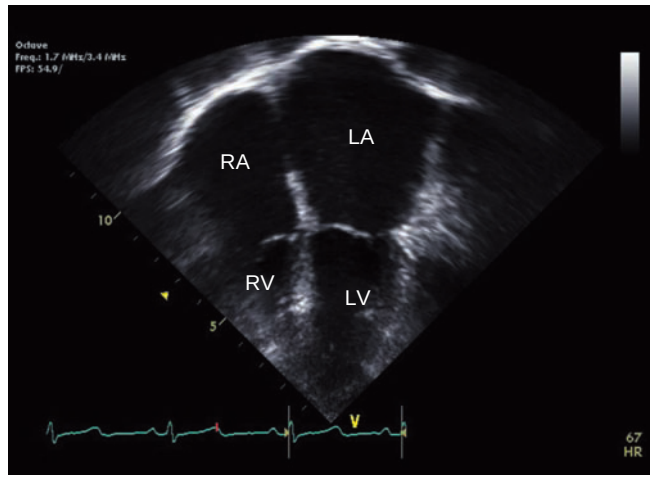


(a)

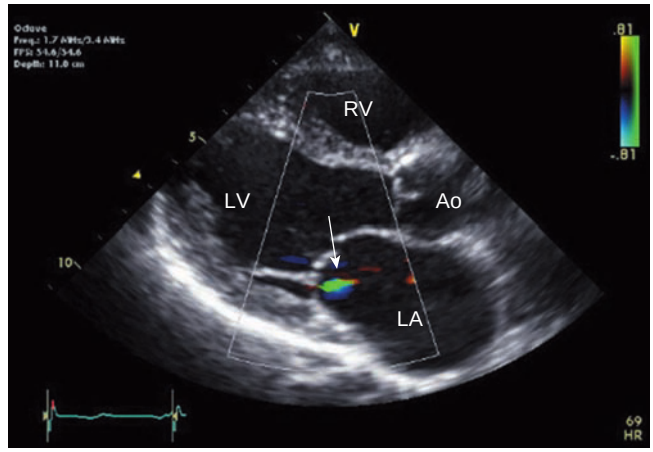


(b)

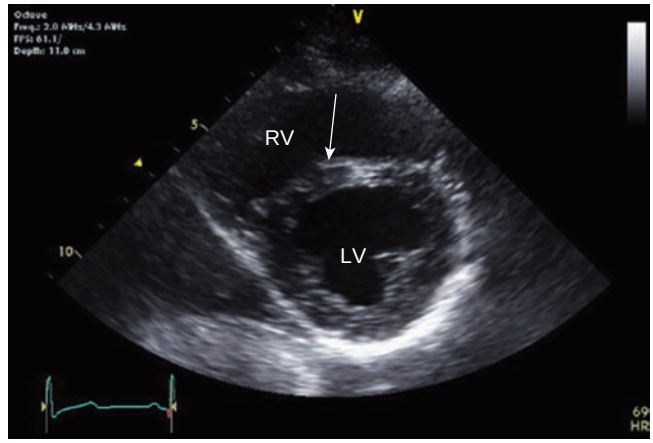


(c)

**Figure 35.1** **(a)** Apical 4-chamber view of a patient with restrictive physiology. Both ventricular cavities are small with decreased end-diastolic dimensions. The marked atrial enlargement ("ice-cream cone heart") is pathognomonic. **(b)** Parasternal long-axis view of a patient with restrictive cardiomyopathy demonstrating markedly dilated left atrium and minimal mitral valve regurgitation (arrow). **(c)** Parasternal short-axis view demonstrating flattening of the interventricular septum (arrow) indicative of pulmonary hypertension. Ao, aorta; LA, left atrium; LV, left ventricle; RA, right atrium; RV, right ventricle.

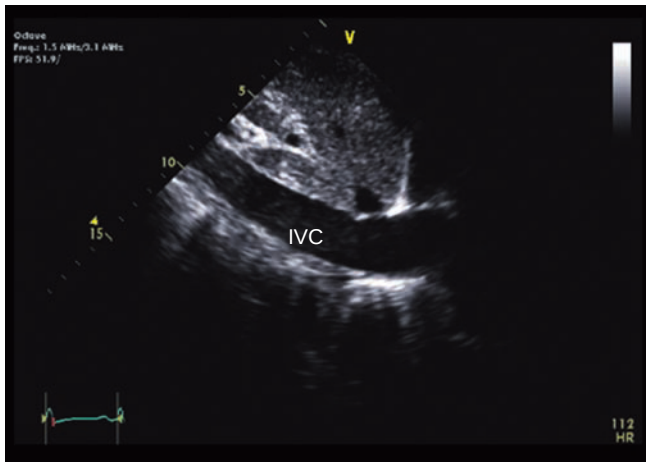


**Figure 35.2** Subcostal sagittal view of a markedly dilated inferior vena cava (IVC), reflecting increased right atrial pressure.

**Table 35.2** Stages of diastolic dysfunction

| | |
|---|---|
| Grade I | Impaired relaxation |
| Grade II | Pseudonormalization |
| Grade III | Restrictive reversible |
| Grade IV | Restrictive irreversible |

### *Flow characteristics*

Doppler echocardiography remains the primary clinical tool for providing a reliable assessment of diastolic function. In the preliminary stages of restriction, an impaired relaxation pattern may be present before the onset of abnormal compliance. Determination of severity of diastolic dysfunction is important not only for diagnostic but also for prognostic reasons, as mortality rate is strongly associated with a markedly restrictive pattern [18].

Evaluation of diastolic function routinely comprises measurement of mitral early (E-wave) and late (A-wave) diastolic inflow, and pulmonary vein systolic (S-wave), diastolic (D-wave) and atrial reversal (AR-wave) flow with the corresponding right-sided tricuspid and hepatic vein flow waves. Progressive impairment of diastolic function leads to a different pattern of transmitral, pulmonary venous Doppler and mitral annular tissue Doppler velocities. Using these parameters, four stages of diastolic dysfunction may be determined (Table 35.2) [19].

The classic Doppler pattern of impaired relaxation is characterized by [20–22]:

**1** *Mitral inflow.* In the initial phase of delayed relaxation, reversal of the normal transmitral E- and A-waves, with E < A, is noted (Fig. 35.3a). When restriction is present, a large E-wave and small A-wave with a E/A ratio >2 [23,24], a short deceleration time (DT) <150 ms, and a short isovolumetric relaxation time (IVRT) <60 ms are noted (Fig. 35.3b). In contrast to constrictive pericarditis, there is no significant change in mitral E-wave, DT or IVRT with respiration (Fig. 35.3c).

**2** *Pulmonary veins.* The initial phase of delayed relaxation is characterized by reversal of the normal S- and D-waves. Restriction is defined as a D-predominant flow pattern with a small S-wave and large D-wave, with an S/D ratio <0.5. In

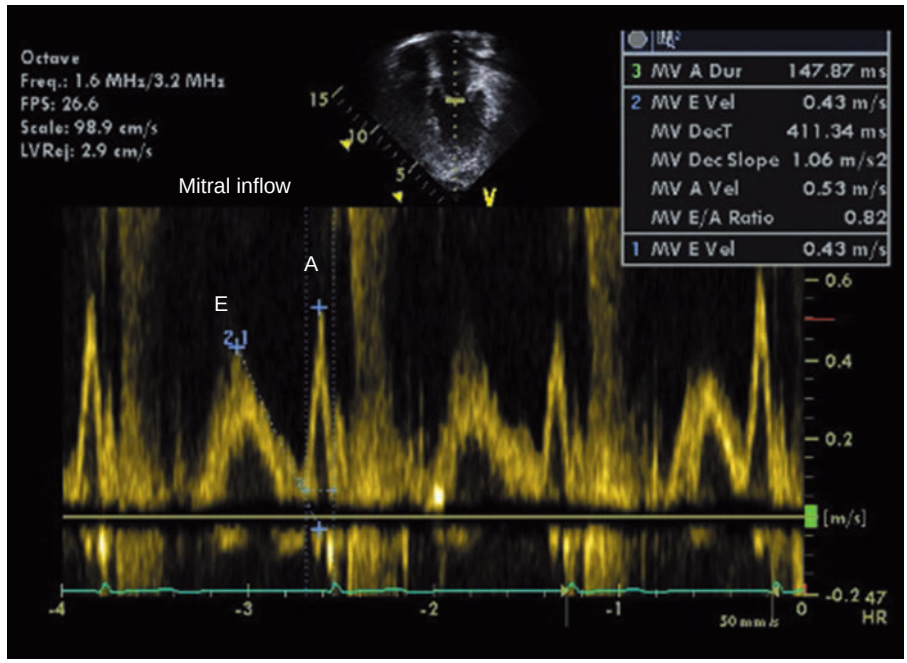


(a)

**Figure 35.3 (a)** Mitral valve inflow Doppler showing predominantly late diastolic filling of the left ventricle, with E/A wave reversal (E < A).

(b)

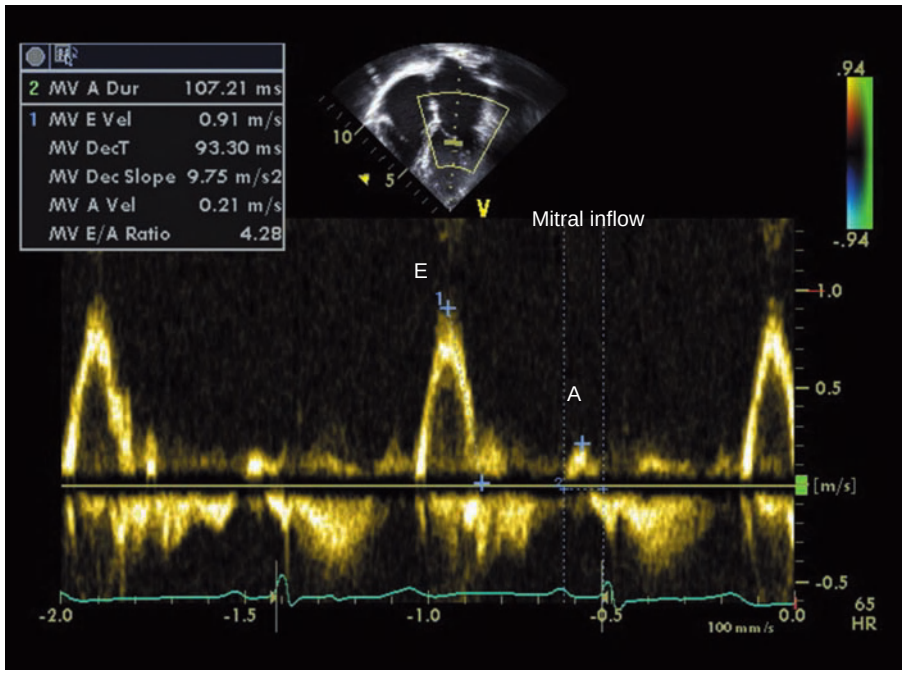


(c)

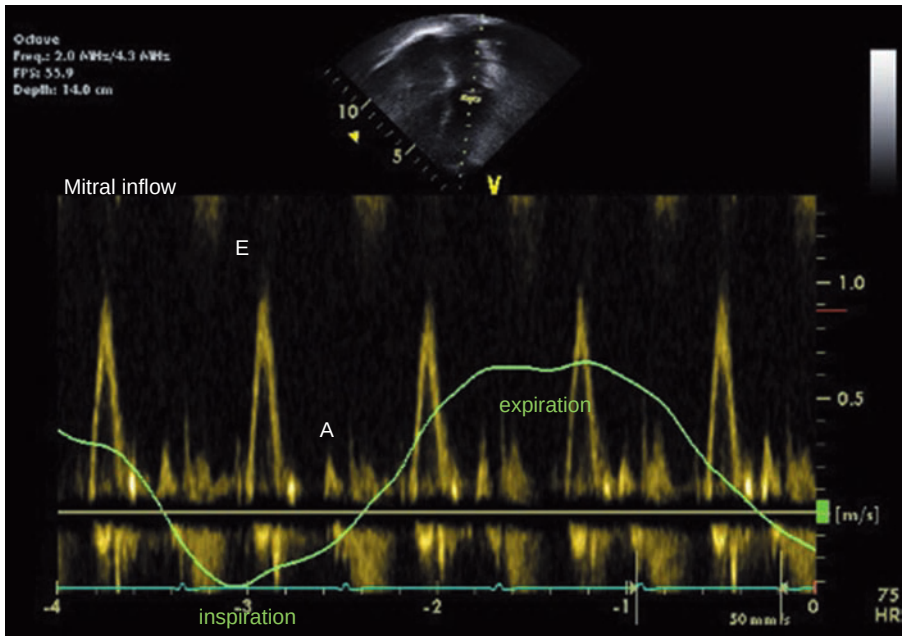


**Figure 35.3** **(b)** Mitral valve inflow Doppler of a patient with restrictive physiology. The large E-wave and a small A-wave with an E/A ratio >4 and a short deceleration time (DT) of 93 ms are characteristic of a restrictive physiology. **(c)** Mitral inflow Doppler showing no respiratory variation in peak inflow velocities, which is characteristic of restrictive physiology, and distinct from constrictive physiology.

young children in whom a dominant D-wave is normally seen, evaluation of the S- and D-wave pattern is of little value. Prominent A-reversal with both increased amplitude and prolongation is seen, with an A-reversal width greater than the mitral A-wave duration (Fig. 35.4). In contrast to a constrictive pattern, there is no significant respiratory variation of the D-wave in restrictive cardiomyopathy.

**3** *Tricuspid inflow.* The patterns are similar to mitral inflow with restriction characterized by an increased E/A ratio and a short DT (Fig. 35.5). Further shortening of the DT is noted with respiration, with minimal change in the E/A ratio.

**4** *Hepatic veins.* The patterns are similar to those of pulmonary vein flow. An S/D ratio <0.5 with prominent atrial and ventricular reversal is noted with restriction (Fig. 35.6). There is increased prominence of reversal waves with respiration.

It is important to remember that these measurements are dependent on loading conditions and assume that the patient is in sinus rhythm. As noted previously, and as opposed to constriction, there is no respiratory variation in mitral and

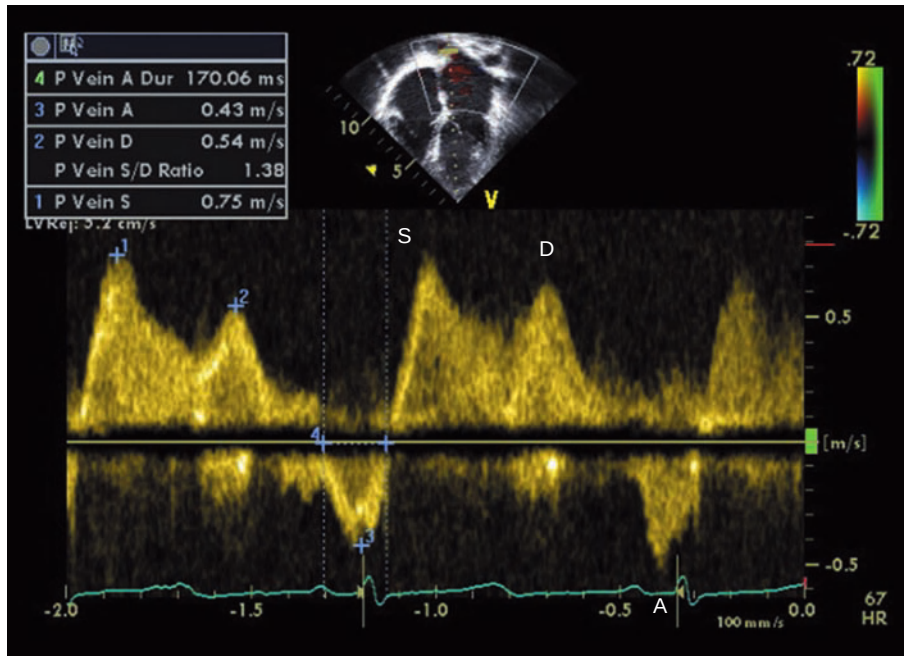


**Figure 35.4** Pulmonary vein Doppler interrogation demonstrates prominent A-wave reversal with both increased amplitude and prolongation (corresponding to the numbers 3 and 4 respectively). The A-reversal width is greater than the mitral A-wave duration in the same patient (see Fig. 35.3a,b). D, D-wave maximal velocity; S, S-wave maximal velocity.

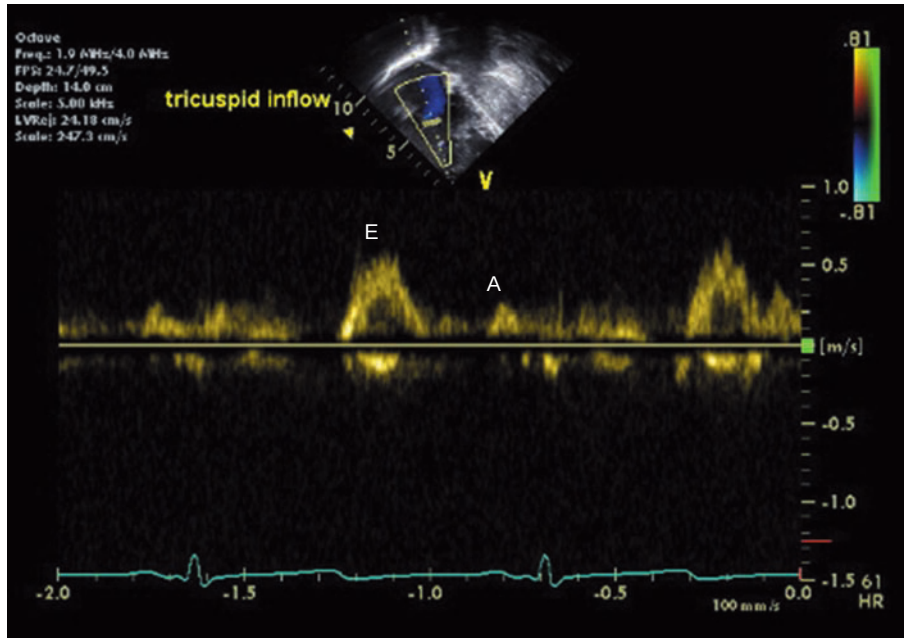


**Figure 35.5** Tricuspid inflow of a patient with restrictive cardiomyopathy showing a large E-wave (E) and a small A-wave (A).

tricuspid E-waves and in left ventricular IVRT in restrictive physiology [25]. Unfortunately, Doppler echocardiographic findings still show overlap between restrictive and constrictive patterns. Intravascular volume expansion has been shown to be safe and effective in augmenting the diastolic impairment of restrictive physiology [26].

### *Color M-mode*

Color M-mode offers a unique view into the fluid dynamics of left ventricular inflow. It assesses the flow propagation from the mitral valve into the left ventricle, which depends on the development of intraventricular pressure gradients. The velocity of propagation (*V*p), assessed by the slope of the color aliasing velocity at the leading edge of the E-wave, is enhanced with rapid normal ventricular relaxation [27,28]. The flow propagation velocity provides a relatively preload-independent determination of relaxation and can be used in conjunction with the mitral inflow E-wave to estimate pulmonary capillary wedge pressure [29]. In restrictive cardiomyopathy, the *V*p is decreased, compared with constrictive

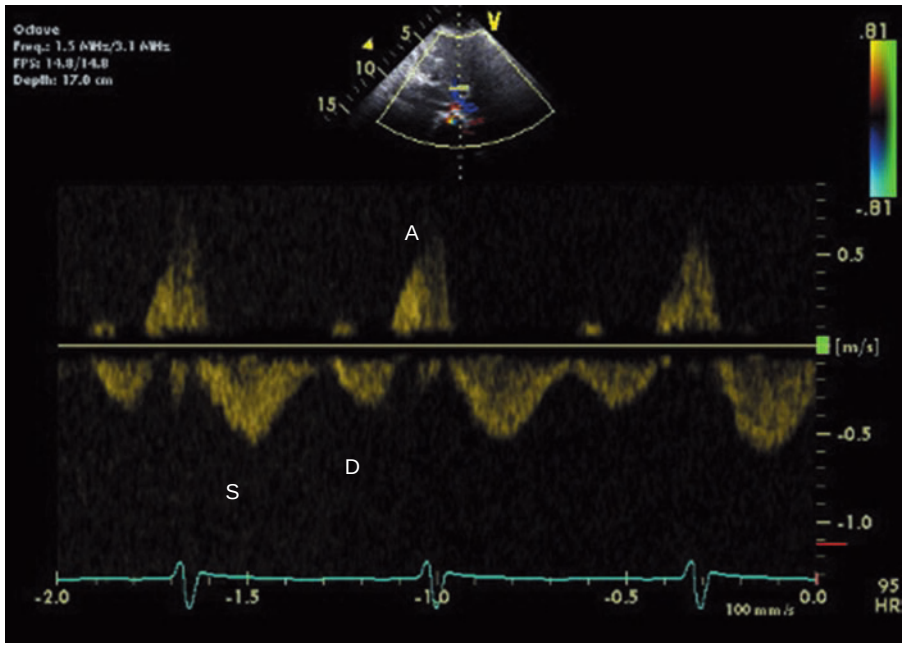


**Figure 35.6** Doppler interrogation of the hepatic vein in restrictive cardiomyopathy demonstrating prominent A-wave reversal. D, D-wave maximal velocity; S, S-wave maximal velocity.

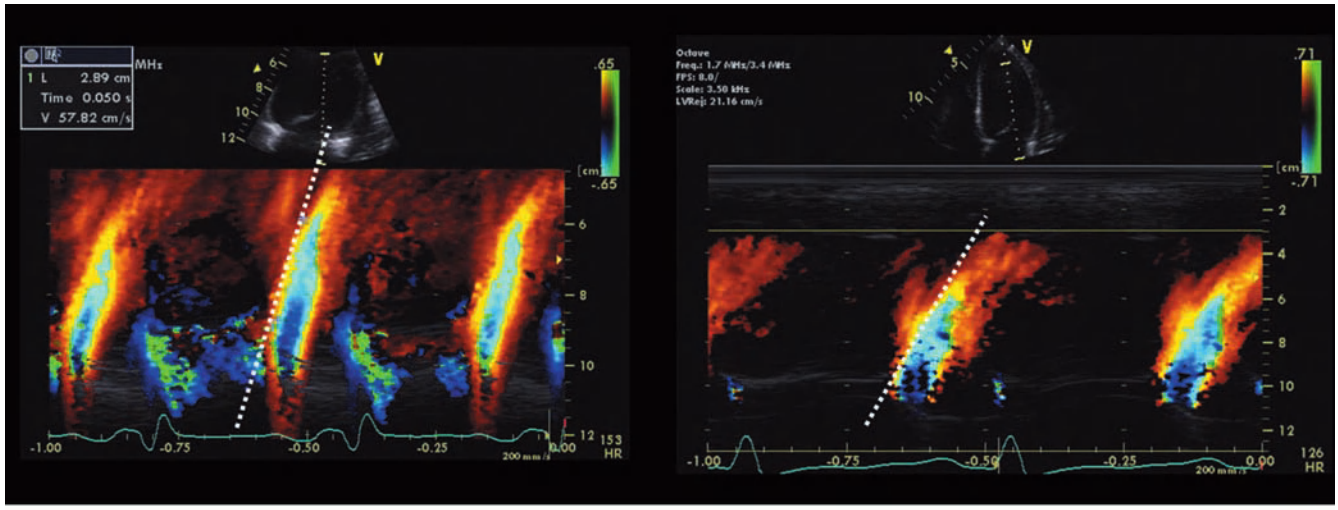


(a) (b)

**Figure 35.7** Color M-mode of a patient with restrictive cardiomyopathy **(b)**, demonstrating decreased flow propagation velocity (*V*p), as illustrated by the slope of the dotted line, compared with a normal color M-mode and *V*p **(a)**.

pericarditis, where the *V*p is normal or increased (Fig. 35.7) [30–32].

### *Tissue mechanics*

Using either Doppler principles or tissue tracking technology the movement of the myocardium can be evaluated as well. Tissue motion as measured by tissue Doppler imaging (TDI) is less load sensitive than blood flow. This is useful in distinguishing constrictive from restrictive physiology. Patients with restrictive cardiomyopathy have an abnormality of both relaxation and compliance, whereas those with constrictive pericarditis have normal relaxation but impaired compliance. The early mitral annular velocity ($E_a$-wave) is usually reduced in restriction (Fig. 35.8a), whereas it is normal or increased in constrictive pericarditis [32]. As with Doppler evaluation of mitral inflow in the initial phase of delayed relaxation, TDI of the mitral annulus reveals a similar reversal of the $E_a$ and $A_a$ pattern with $E_a < A_a$ (Fig. 35.8b) and velocities less than the normal 8 cm/s. However, with progressive diastolic dysfunction, early myocardial velocities remain depressed without the pseudonormalized pattern that confounds evaluation with transmitral flow. Measurement of the ratio of the Doppler transmitral E-wave to the tissue Doppler mitral $E_a$-wave ($E/E_a$ ratio) is useful in assessing left ventricular filling pressure. An $E/E_a$ ratio >15 indicates elevated left ventricular pressure [33–36].

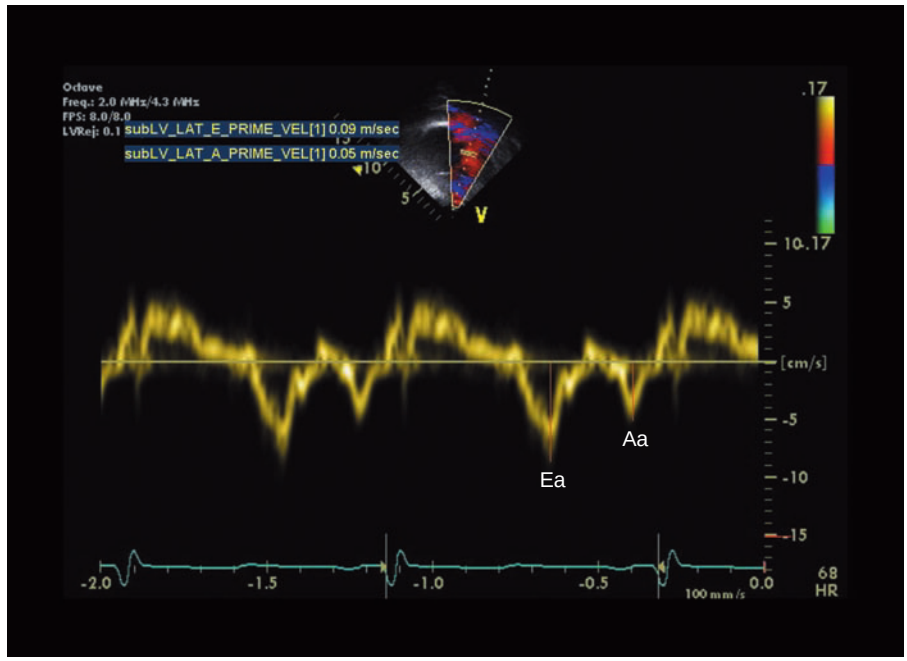


(a)

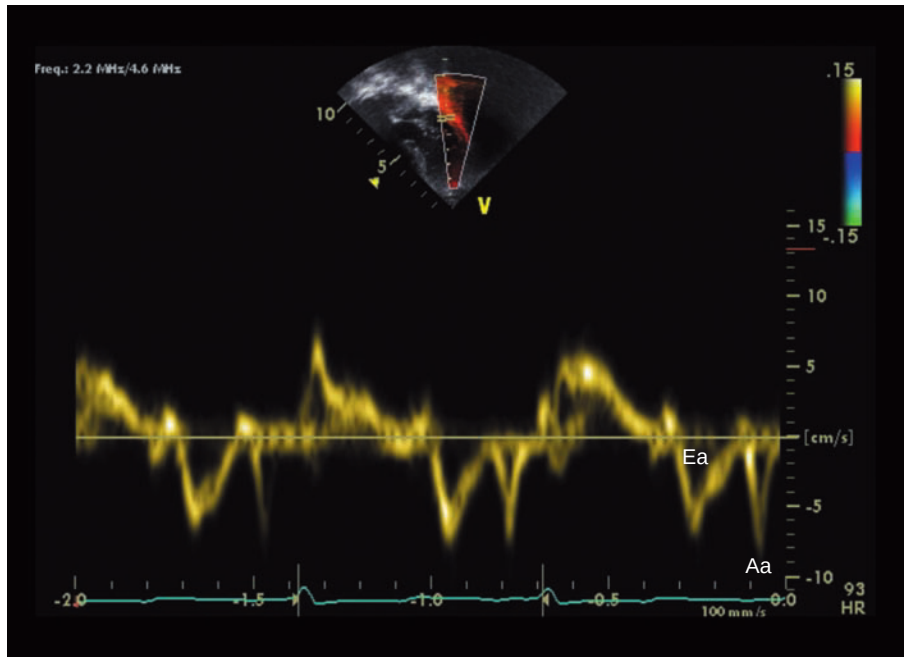


(b)

**Figure 35.8** **(a)** Reduced $E_a$ and small $A_a$ waves by tissue Doppler imaging of a patient with restrictive cardiomyopathy obtained from the mitral annulus. **(b)** Tissue Doppler imaging in severe restrictive cardiomyopathy showing reversal of $E_a$ and $A_a$, with $E_a < A_a$.

Additional methods of diagnosing abnormal myocardial mechanics in restrictive cardiomyopathy include strain and strain rate. Strain represents the relative deformation of myocardium, and strain rate is defined as the speed of deformation of myocardium [37]. Strain is a dimensionless quantity and is produced by the application of stress. It represents the percentage of change from the original or unstressed dimension and includes both lengthening or expansion (positive strain) and shortening or compression (negative strain). Compared with tissue velocities, these parameters are less influenced by cardiac motion and allow more accurate assessment of segmental myocardial function. Strain correlates with both pulmonary arterial wedge pressure and end-diastolic pressure [22]. This is useful to demonstrate early impairment in systolic function at a time when fractional shortening remains normal [38]. In patients with impaired relaxation, the subendocardial fibers demonstrate slower times for relaxation in early diastole. Recently, tissue tracking techniques have been developed to eliminate the inherent angle dependency of conventional Doppler

**Table 35.3** Echocardiographic parameters of diastolic dysfunction in the adult

| | |
|---|---|
| Mitral inflow | E/A >1.5<br>DT <150 ms<br>IVRT <60 ms<br>MVA duration/Pv AR duration <0.9 |
| Pulmonary venous flow | S/D <0.4<br>AR peak velocity >35 cm/s<br>PV AR duration or MVA duration >30 ms |
| Hepatic venous flow | Blunted S-wave<br>Deep AR |
| Color M-mode | *Vp* <45 cm/s |
| TDI | $E_a$ <8 cm/s<br>$E/E_a$ >15 |

A, MV A (late diastolic) wave peak velocity; AR, atrial reversal wave; D, Pv D (diastolic) wave peak velocity; E, MV E (early diastolic) wave peak velocity; Ea, tissue Doppler early mitral annular peak velocity; IVRT, isovolumetric relaxation time; MV, mitral valve; Pv, pulmonary vein; S, Pv S (systolic) wave peak velocity; TDI, Tissue Doppler Imaging; Vp, left ventricle velocity of propagation (color M-mode).
Adapted from Tam JW, Shaikh N, Sutherland E. Echocardiographic assessment of patients with hypertrophic and restrictive cardiomyopathy: imaging and echocardiography. *Curr Opin Cardiol* 2002;17:470–7.

echocardiography. Tissue tracking of the myocardium has been used to evaluate both tissue velocities and deformation [39]. These novel applications should play an increasing role in future evaluation of restrictive physiology.

The different echocardiographic parameters of diastolic dysfunction in adults are summarized in Tables 35.3 and 35.4, and in Fig. 35.9. It is important to remember that in young children, especially infants, the mature Doppler patterns of blood flow are not established, making the confident evaluation of diastolic function more challenging than in adults. Despite these limitations, with our growing understanding of myocardial mechanics, diastole should not be ignored in children. Evaluation of relaxation using all of our available tools is important to help identify isolated diastolic dysfunction – such as in restrictive cardiomyopathy – and monitor the patient's disease state. Further work to develop clear measures of diastolic function in children is ongoing.

### *Transesophageal echocardiography*

Transesophageal echocardiography (TEE) affords improved imaging windows in the older patient, and a superior angle of interrogation for analysis of the pulmonary vein flow. Additionally, the transgastric view offers a direct visualization of the pericardium. As described above, volume expansion has been shown to be effective in augmenting the diastolic impairment of restrictive physiology, increasing the likelihood of a positive diagnosis by TEE [40].

### *Additional modalities*

Cardiac computed tomography (CT) and magnetic resonance imaging (MRI) are useful for helping to differentiate restrictive cardiomyopathy from constrictive pericarditis by

**Table 35.4** Parameters and echocardiographic measures of diastolic function in children and adults

| Parameters | Normal for youngsters | Normal for adults | Mild diastolic dysfunction (grade I) | Pseudonormal (grade II) | Restrictive pattern (grade III–IV) |
|---|---|---|---|---|---|
| LV relaxation | Normal | Normal | ↓ | ↓↓ | ↓↓↓ |
| LV stiffness | Normal | Normal | ↑ | ↑↑ | ↑↑↑ |
| LA contractility | Normal | Normal | ↑ | Normal | ↓ |
| Preload | Normal | Normal | Normal | ↑ | ↑↑ |
| E/A | >1 | >1 | <1 | 1–2 | >2 |
| DT (ms) | <220 | <220 | >220 | 150–200 | <150 |
| IVRT (ms) | <100 | <100 | >100 | 60–100 | <60 |
| S/D | <1 | ≥1 | ≥1 | <1 | <1 |
| AR (cm/s) | <35 | <35 | <35 | ≥35 | ≥25 |
| *Vp* (cm/s) | >55 | >45 | <45 | <45 | <45 |
| $E_a$ (cm/s) | >10 | >8 | <8 | <8 | <8 |

A, A (late diastolic) wave peak velocity; AR, Pv atrial reversal velocity; D, Pv D (diastolic) wave peak velocity; E, MV E (early diastolic) wave peak velocity; $E_a$, tissue Doppler early mitral annular peak velocity; IVRT, isovolumetric relaxation time; LA, left atrium; LV, left ventricle; LVH, left ventricular hypertrophy; MV, mitral valve; PAP, pulmonary arterial pressure; Pv, pulmonary vein; S, Pv S (systolic) wave peak velocity; RAP, right atrial pressure; RVSP, right ventricular systolic pressure, TDI, Tissue Doppler Imaging; TR, tricuspid regurgitation; Vp, left ventricle velocity of propagation (color M-mode). Adapted with permission from Garcia MJ, Thomas JD, Klein AL, New Doppler echocardiographic application for the study of diastolic function, JACC 1998 32:4:866–75..

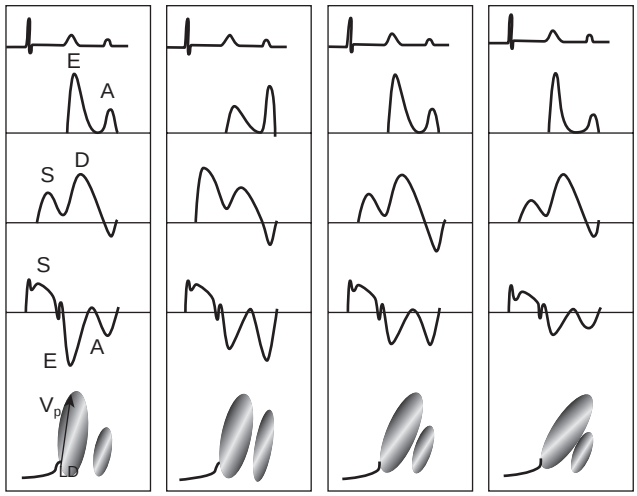


**Figure 35.9** Comparison of the changes in mitral inflow Doppler (first line, A: MV A (late diastolic) wave peak velocity; E: MV E (early diastolic) wave peak velocity), pulmonary vein Doppler (second line, D: Pv D (diastolic) wave peak velocity; AR: Pv atrial reversal velocity; D: Pv D (diastolic) wave peak velocity), tissue Dopler (third line, A: late diastolic mitral annular peak velocity; E: early diastolic mitral annular peak velocity; S: systolic mitral annular peak velocity) and left ventricular propagation velocity (fourth line, Vp: velocity of propagation). Adapted with permission from Garcia MJ, Thomas JD, Klein AL, New Doppler echocardiographic application for the study of diastolic function, JACC 1998 32:4:866-75 and Asher CR, Diastolic Heart Failure: restrictive cardiomyopathy, constrictive pericarditis and cardiac tamponade: clinical and echocardiographic evalution, Cardiology in Review 2002 10;4:218-229.

assessing pericardial thickness. Cardiac catheterization can help in the distinction as well.

## Pericardial disease

### Constrictive pericarditis

#### Introduction

Constrictive pericarditis is defined as inflammation, thickening and fusion of the thin and easily distensible parietal and visceral pericardium, resulting in impaired venous return and ventricular filling of the heart [41]. The process is typically indolent and slowly progressive, with clinical manifestation usually appearing months or even years after the initial inflammatory insult.

#### Incidence and etiology

Constrictive pericarditis is very rare and sporadic in the pediatric population [42]. The disease is most commonly a complication of acute pericarditis, either a single intense episode or multiple recurrent flares [43]. The underlying inciting event frequently varies with the ethnicity and country of origin of the patient. Tuberculous pericarditis is the most frequent known cause of chronic constrictive pericarditis worldwide. Overall prevalence is increased among patients who have undergone cardiac surgery, with mediastinal irradiation and cardiac surgery the most common causes of constriction in Europe and North America [44]. The diagnosis of constrictive pericarditis is often made after an extensive diagnostic workup in the setting of failure of conventional medical therapy for congestive heart failure. Life expectancy is reduced in untreated children and in patients with relatively acute onset of symptoms [45]. There is no statistical difference between race and gender in the frequency of the disease.

**Table 35.5** Causes of constrictive pericarditis

| |
|---|
| Idiopathic |
| Post-acute pericarditis |
| Tuberculosis |
| Infectious: |
| Viral |
| Bacterial: staphylococci, streptococci |
| Fungal: histoplasmosis |
| Rheumatoid disease |
| Sarcoidosis |
| Mediastinal radiation (Hodgkin lymphoma) |
| Trauma (hemopericardium) |
| Status post-cardiac surgery (postpericardiotomy syndrome) |
| Uremia |
| Neoplasia with pericardial infiltration |
| Metabolic and genetic disorders |

Different etiologies can produce variable clinical findings, depending on the rapidity and severity of development (Table 35.5). Chronic constrictive pericarditis develops insidiously and frequently no etiology is found.

#### Pathophysiology

In constrictive pericarditis, the size of the heart is usually normal. The pericardium typically shows inflammation, fibrosis, thickening and obliteration of the space between the visceral and parietal layers. Adhesions occur between the pericardium and myocardium. The pericardial thickening and adhesions may be focal or diffuse. Calcifications may also be present. Myocardial histologic findings include fibrotic thickening, chronic inflammation, granulomas, and calcification.

Conditions that lead to constrictive pericarditis result in decreased cardiac compliance. This leads to diminished ventricular distensibility, inability to maintain adequate preload, and biventricular diastolic dysfunction. In contrast to pericardial effusion, early ventricular filling is not altered in constrictive pericarditis. However, as the ventricles fill, they meet the inelastic resistance of the stiff, often calcified pericardium, at which time filling pressure rises rapidly to an elevated plateau. This late diastolic phenomenon is due to a change in the volume–elasticity curve, a small increase in volume resulting in a considerable increase in end-diastolic pressure. Atrial filling pressures are elevated, reflecting both ventricular noncompliance and atrial constraint by the thick

(a)

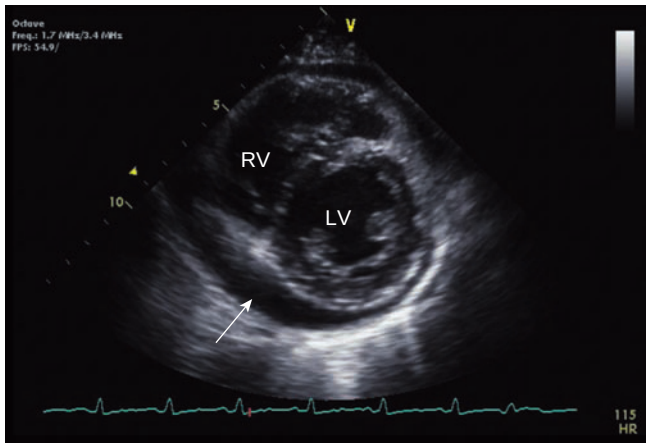


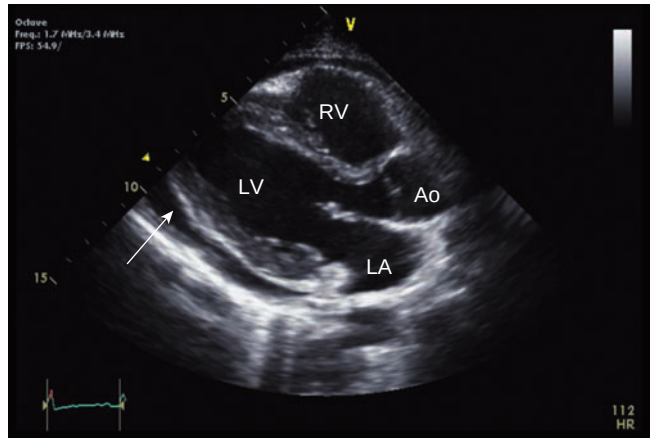


(b)

**Figure 35.10** **(a)** Parasternal short-axis view of a small pericardial effusion consistent with constrictive pericarditis (arrow). **(b)** Long-axis view of the same patient with constrictive pericarditis and a small circumferential pericardial effusion (arrow), known as the halo sign. Ao, aorta; LA, left atrium; LV, left ventricle; RV, right ventricle.

pericardium. Because there is isolated encasement of the pericardium but not of the systemic veins or lungs, there is dissociation between intrathoracic and intracardiac pressures, with marked interventricular dependence, respiratory variation and discordance in right and left heart filling [46–48].

## Imaging

Echocardiography remains the best tool in the initial assessment of constrictive pericarditis [49]. A combination of 2D imaging, M-mode and Doppler information is capable of diagnosing the anatomic and pathophysiologic features of constrictive pericarditis in most patients.

### *Goals of the examination*

The goals of echocardiographic examination in the setting of constrictive pericarditis can be summarized as follows:

- Assessment for fluid in pericardial space.
- Determination of dilation of the inferior vena cava.
- Assessment for "septal bounce".
- Assessment of atrial and ventricular size.
- Assurance that ventricular systolic performance is normal.
- Determination of reciprocal respiratory variation of right and left heart flows.
- Assessment of diastolic function and tissue Doppler imaging: distinction of restrictive from constrictive patterns.

### *Two-dimensional echocardiography*

A thickened pericardium with some degree of pericardial effusion may be observed in various echocardiographic views [50]. However, 2D echocardiography can be insensitive, as mildly increased pericardial thickening can be missed and a false positive finding can be obtained if the gains are set too high. Pericardial calcifications with localized tethering of atrial or ventricular cavities may be noted. Separation of the entire pericardium by a small fixed space is known as the "halo sign" (Fig. 35.10a,b). An abnormal echo contour at the reflection of the pericardium to the posterior left atrial wall may be seen. In subxiphoid imaging, the systemic veins are usually dilated, with the inferior vena cava exhibiting absent collapse with inspiration (plethora) (Fig. 35.2).

Abnormal motion of the myocardium relative to the pericardium is best seen anterior to the right ventricular outflow tract or at the lateral apex in the 4-chamber view, with the myocardium appearing to pull the pericardium without altering the small echo-free separation of these two layers. Septal "bounce" is typical, defined as abrupt posterior movement of the interventricular septum in early diastole during inspiration; this is caused by underfilling of the left ventricle and redistribution of blood from the left to the right ventricle. The finding of septal "bounce" may represent the first and best clue for the presence of constriction [51]. The left ventricular posterior wall may show the same "bouncing" pattern.

In addition to these findings, most echocardiographic views will show that the right and left ventricular chamber sizes are decreased, and both atria are mildly enlarged, related to the compliance abnormality of the ventricles. The ventricles often have an elongated appearance, giving the heart a tubular shape. The inspiratory increase in chamber size is larger in patients with constrictive pericarditis than in those with restrictive cardiomyopathy. The biventricular systolic function is usually normal. A typical feature of constrictive pericarditis is parallel motion of the epicardium and the parietal pericardium, as occurs in the normal state, in contrast to the dampening pattern of pericardial effusion. Interventricular septal motion may be paradoxical or flat as a sign of ventricular interdependence (Videoclip 35.2). Using M-mode, a characteristic septal notch has been

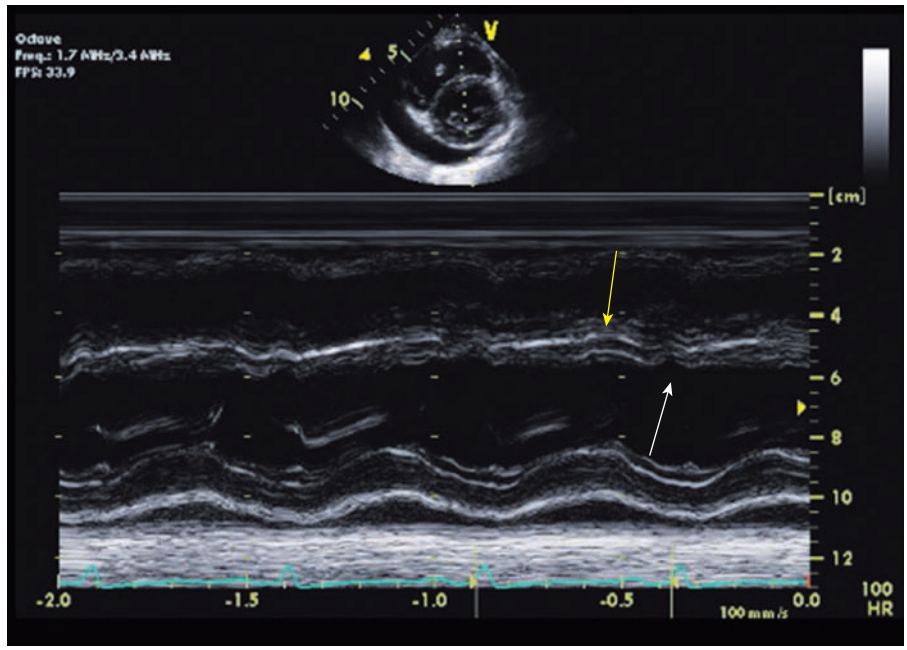


**Figure 35.11** M-mode demonstrating paradoxical septal motion (yellow arrow) and septal notch (white arrow) in early diastole in constrictive pericarditis.

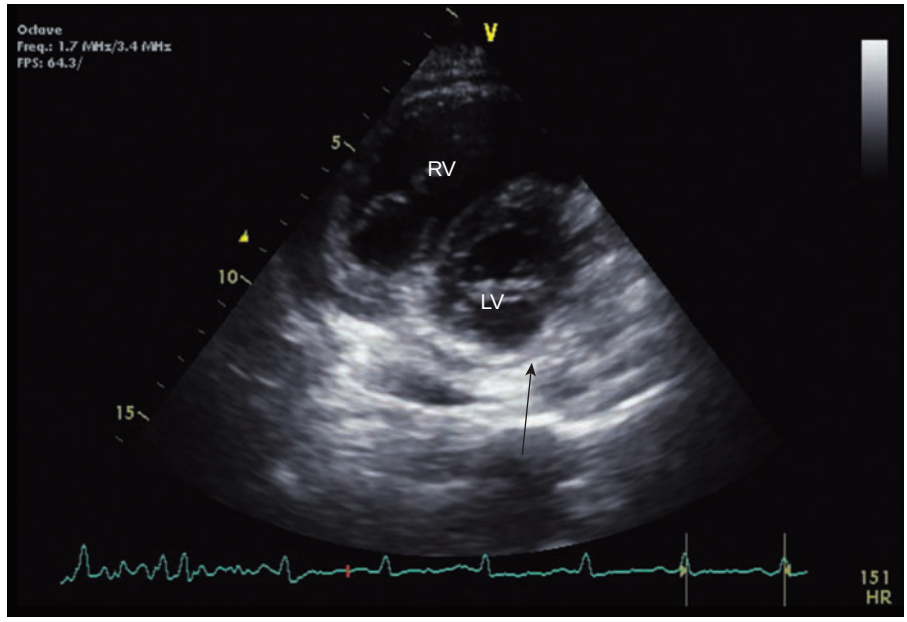


**Figure 35.12** Parasternal short-axis view of a patient with constrictive pericarditis showing thickening of the posterior pericardium (black arrow). LV, left ventricle; RV, right ventricle.

described in early diastole (Fig. 35.11), corresponding to the pericardial knob, which occurs between the second and third heart sounds, and to the septal bounce seen by 2D echocardiography [52,53]. M-mode and 2D can also show extensive areas of adhesions seen posteriorly to provide evidence for generalized pericardial thickening and constriction (Fig. 35.12).

### *Flow characteristics*

The hallmark of Doppler examination in constrictive pericarditis is reciprocal respiratory variation of right and left heart flows caused by interventricular dependence. The classic Doppler pattern consists of the following [22,54,55]:

**1** *Mitral inflow.* During inspiration, a smaller E-wave, longer IVRT and shorter DT are noted. During expiration, there is a larger E-wave, shorter IVRT and usually a longer DT. The E-wave is typically increased more than 25% with expiration, and the IVRT increases more than 25% with inspiration.

**2** *Pulmonary veins.* During inspiration, S- and D-waves are near equal in size. During expiration, larger S- and D-waves are noted.

**3** *Tricuspid inflow.* This shows the same pattern, with reciprocal changes compared to the mitral inflow. During expiration, a smaller E-wave, longer IVRT and shorter DT are noted. During inspiration, there is a larger E-wave, shorter IVRT and usually a longer DT. The E-wave is typically increased more than 40% with inspiration.
**4** *Hepatic veins.* During inspiration, the S-wave is greater than the D-wave, with a small A-reversal and ventricular reversal. During expiration, the S-wave is greater than the D-wave, with a small or absent D-wave and a larger A-reversal and ventricular reversal.

Also described in constrictive pericarditis are inspiratory increases in the tricuspid regurgitant jet velocity and duration of the signal [56].

In contrast to restrictive cardiomyopathy, constrictive pericarditis shows more pronounced respiratory variation in the filling phases. It is important to note that no single Doppler measurement can fully characterize left ventricular diastolic function. Most of the parameters are dependent on load, heart rate, and age.

### *Color M-mode*

The propagation velocity (*V*p) of early diastolic transmitral flow on color M-mode is normal or increased in constrictive pericarditis, in contrast to restrictive cardiomyopathy, in which the *V*p is decreased (Fig. 35.7) [33].

### *Tissue mechanics*

Early mitral annular velocity ($E_a$-wave) is usually normal or high in constrictive pericarditis, whereas it is reduced in restrictive cardiomyopathy [57]. The usually positive linear relation between mitral Doppler E-wave velocity and tissue Doppler $E_a$-wave velocity ($E/E_a$), is useful to assess left atrial pressure and is found to be reversed (annular paradox) in constrictive pericarditis [58].

### *Transesophageal echocardiography*

Although typically not performed in this setting in children, TEE offers a unique view of the pericardium particularly from the transgastric window [59,60]. Rapid volume expansion during TEE can be used to broaden the distinction between constrictive pericarditis and restrictive cardiomyopathy; in the former it significantly enhances the respiratory variation of the pulmonary vein diastolic flow velocity [61]. Measurement of pericardial thickness by TEE correlates strongly with data obtained by CT scan.

### *Additional studies*

The chest X-ray may be unremarkable. Heart size is not enlarged but pericardial calcifications are present in 40–50% of patients, giving an eggshell appearance to the cardiac silhouette (Fig. 35.13a) [62]. The right superior mediastinum may appear enlarged due to dilation of the superior vena

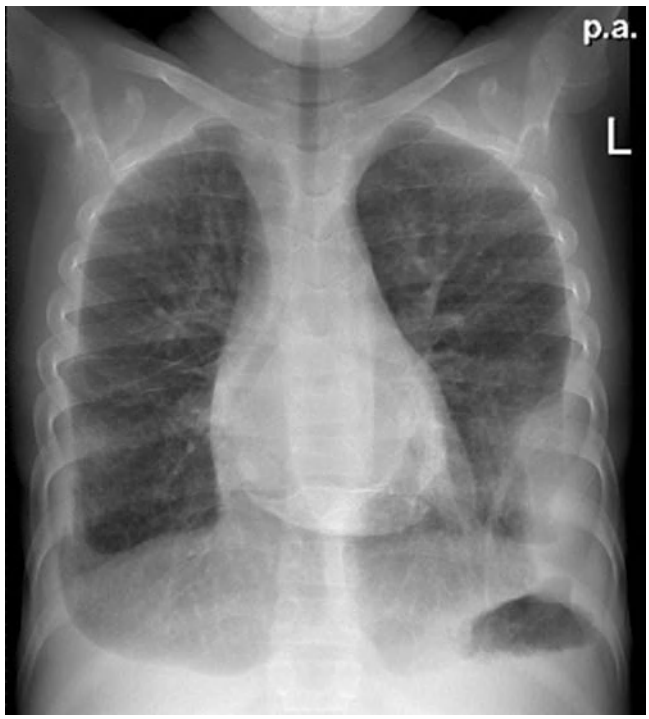


(a)

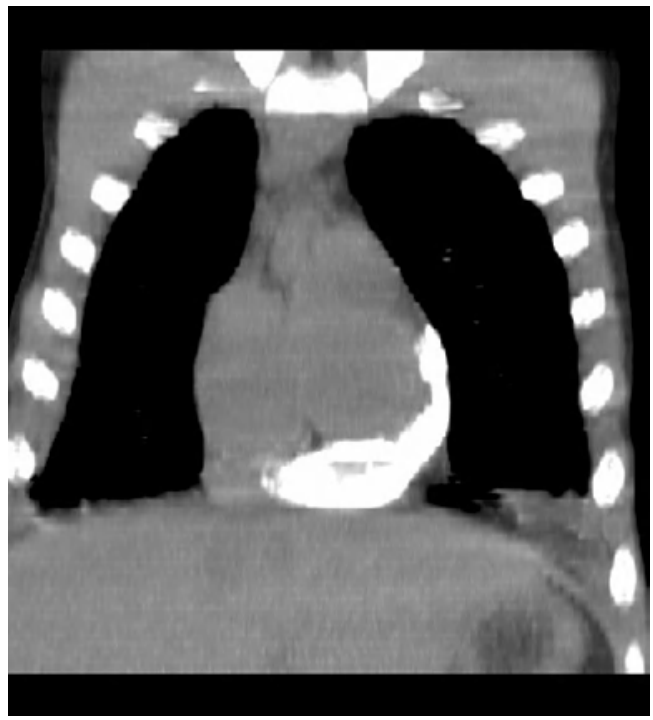

(b)

**Figure 35.13 (a)** Chest X-ray demonstrating pericardial calcifications and an eggshell appearance of the cardiac silhouette. Calcifications are present in 40–50% of patients with constrictive pericarditis. **(b)** CT scan of the chest of the same patient demonstrating pericardial calcification. Both CT and MRI can detect a thickened pericardium (≥4 mm); however, an advantage of CT is its ability to detect calcification, indicative of constrictive pericarditis.

cava. Pleural effusions may be present, reflecting chronic right heart failure. Pulmonary infiltrates are uncommon.

Cardiac MRI may demonstrate pericardial thickening, right atrial dilation, and a characteristic intraventricular septal "bounce" in early diastole, characterized by early diastolic septal inversion occurring at the onset of inspiration [63]. Both CT and MRI can detect a thickened pericardium (≥4 mm), but this is an insensitive finding. An advantage of CT is the ability to detect calcification (Fig. 35.13b), indicative of constrictive pericarditis [64]. However, CT may have difficulty in differentiating pericardial fluid from thickened pericardium. The absence of pericardial thickening does not rule out hemodynamically significant constrictive pericarditis.

## Pericardial effusion and cardiac tamponade

### Introduction

The pericardial space normally contains a small amount of fluid, which serves as lubrication between the visceral and parietal layers of the pericardium. This fluid is produced by the visceral pericardium and is essentially an ultrafiltrate of plasma. Pericardial effusion defines the presence of more than a physiologic amount of fluid in the pericardial space, usually as a result of inflammation. Cardiac tamponade (compression of the heart) results from rapid or excessive pericardial fluid accumulation, with subsequent restricted ventricular filling and hemodynamic compromise. Cardiac tamponade is a medical emergency with a rapidly and universally fatal course if untreated. A chest X-ray will often identify a markedly enlarged cardiac silhouette in patients with large pericardial effusions and tamponade (Fig. 35.14). This must be distinguished from cardiomegaly associated with cardiomyopathy or myocarditis.

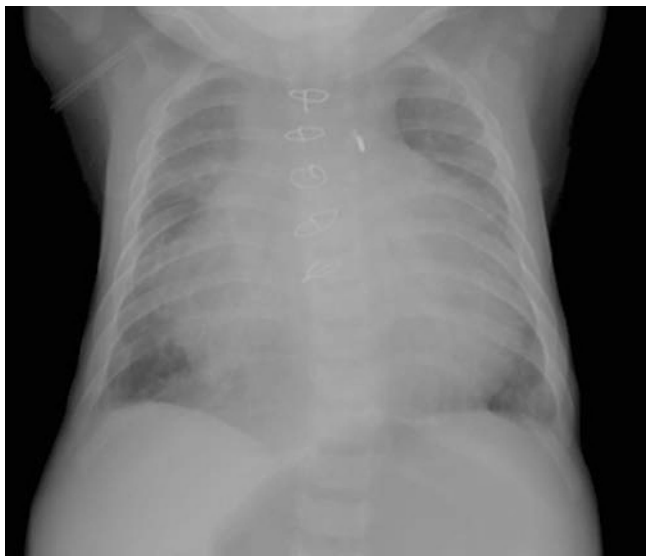

**Figure 35.14** Chest X-ray revealing an enlarged cardiac silhouette in a patient with a large pericardial effusion (so-called water-bottle heart).

### Incidence and etiology

Acute pericarditis is the most common cause of pericardial effusion. The true incidence of pericardial effusion is unknown because it may go unrecognized in mild cases. Some of the most common causes of pericardial effusions are summarized in Table 35.6 [65]. Up to 5–10% of children who have had cardiac surgery may develop postpericardiotomy syndrome, a pericardial fluid accumulation that occurs in the weeks after the repair. In children, cardiac tamponade is more common in boys than in girls, with a male-to-female ratio of 7:3.

### Pathophysiology

Abnormal pericardial fluid production is usually secondary to injury or inflammation. Transudative fluid results from obstruction of fluid drainage, whereas exudative fluid is secondary to inflammatory, infectious, malignant, or autoimmune processes. Significant fluid accumulation can result in marked increases in pericardial pressure, leading to decreased cardiac output and hypotension (cardiac tamponade). The clinical manifestations of pericardial effusion are highly dependent upon the rate of accumulation of fluid in the pericardial sac. Rapid accumulation of pericardial fluid causes sudden increased intrapericardial pressure with hemodynamic compromise. Slowly progressing effusions can be asymptomatic even when large fluid volumes are present [66].

The underlying pathophysiologic process for the development of tamponade is markedly diminished diastolic filling because transmural distending pressures are insufficient to overcome the elevated intrapericardial pressures. In tamponade, inspiration augments inflow to the right ventricle, causing an abrupt expansion of the right ventricle during diastole at the expense of the left ventricle [67]. The opposite happens during expiration, with left ventricular expansion causing right ventricular and atrial diastolic collapse. The reciprocating behavior of the ventricles during respiration is responsible for the physical exam finding of a pulsus paradoxus (an exaggerated decrease in systolic blood pressure during inspiration) [68].

### Imaging

Echocardiography is the primary screening tool for the diagnosis of pericardial effusion. If a chest X-ray shows an enlarged cardiac silhouette, then echocardiography can distinguish between a dilated cardiomyopathy and a pericardial effusion.

#### *Goals of the examination*

In the setting of pericardial effusion and tamponade, echocardiographic examination has the following main objectives:

- Measurement of size of effusion in multiple views.
- Assessment for right-sided collapse.
- Assessment for inferior vena cava dilation.
- Respiratory variation in transvalvular flow.

**Table 35.6** Causes of pericardial effusion and acute pericarditis

| | |
|---|---|
| Idiopathic | |
| Infectious | Viral (coxsackievirus, echovirus, mumps, varicella, Epstein–Barr, adenovirus, influenza, human immunodeficiency virus) |
| | Bacterial (streptococcus, pneumococcus, staphylococcus, *Neisseria* species, mycoplasmas, *Haemophilus influenzae* type b, *E. coli*, *Listeria*, *Legionella* species, *Pseudomonas*) |
| | Fungal (candidiasis, histoplasmosis, actinomycosis) |
| | Parasitic (toxoplasmosis, coccidiomycosis *Echinococcus*, *Entamoeba histolytica*, rickettsias) |
| | Tuberculosis |
| Uremia | |
| Hypothyroidism | |
| Neoplasia | Metastases |
| | Leukemia |
| | Lymphoma |
| Post-surgery (post-pericardiotomy syndrome) | |
| Acute myocardial infarction | |
| Aortic dissection | |
| Post-irradiation | |
| Rheumatic fever | |
| Collagen vascular disease and inflammatory | Rheumatoid arthritis |
| | Systemic lupus erythematosus |
| | Sarcoidosis |
| | Dermatomyositis |
| | Familial Mediterranean fever |
| Trauma | |
| Hypercholesterolemia | |
| Chylopericardium | |
| Whipple disease | |
| Drug-induced | Hydralazine, isoniazid, procainamide |

### *Two-dimensional echocardiography*

Pericardial effusion appears as an "echo-free" space between the visceral and parietal pericardium [69]. Early effusions tend to accumulate posterior and inferior to the left ventricle, owing to an expandable posterolateral pericardium. Accumulation of fluid above the right atrium in the 4-chamber view is the most sensitive indication as it is the first place where a pericardial effusion is seen. Moderate effusions extend toward the apex of the heart, and large effusions circumscribe the heart (Fig. 35.15a,b; Videoclip 35.3) [70].

- *Small effusion:* seen along the length of the posterior wall, not anteriorly, and is defined as <10 mm in a mature heart.
- *Moderate effusion:* usually seen circumferentially. Weitzman criteria define a moderate effusion as 10–20 mm during diastole.
- *Large effusion:* seen circumferentially. Weitzman criteria define a large effusion as >20 mm [71].

The presence of a pericardial effusion does not necessarily cause hemodynamic compromise to the patient. The effects of the effusion must be evaluated by echocardiographic parameters of cardiac filling and transvalvular flow. The rapidity of fluid accumulation and the compliance of the pericardium influence the pressure elevation for any given fluid volume. As pericardial fluid accumulates, intrapericardial pressure increases until it exceeds normal filling pressure of the heart, leading to tamponade.

The first sign of hemodynamic significance is expiratory right ventricular free wall collapse early in diastole (Fig. 35.16a), reflecting the brief period when intrapericardial pressure is greater than the right ventricular transmural distending pressure [72,73]. The echocardiogram shows flattening or even dynamic reversal of the concave outward curvature of the right ventricle. The right ventricle is the first to collapse, related to its lowest intracardiac pressure compared with the left ventricle. Although right ventricular collapse is generally a specific indicator of tamponade, the sensitivity can be reduced in conditions that have increased right ventricular pressure such as pulmonary hypertension or unrepaired tetralogy of Fallot [74].

Expiratory right atrial collapse occurs in late diastole, seen by echocardiography as an indentation of the normally rounded anterosuperior right atrial wall (Fig. 35.16b and Videoclip 35.4). The sensitivity of expiratory right atrial collapse for diagnosing tamponade is low (55%), but the specificity is high (90%). Extension of collapse to greater than one-third of the cardiac cycle increases the sensitivity of this finding to more than 90% [75,76]. Therefore, absence of expiratory right atrial collapse virtually excludes tamponade.

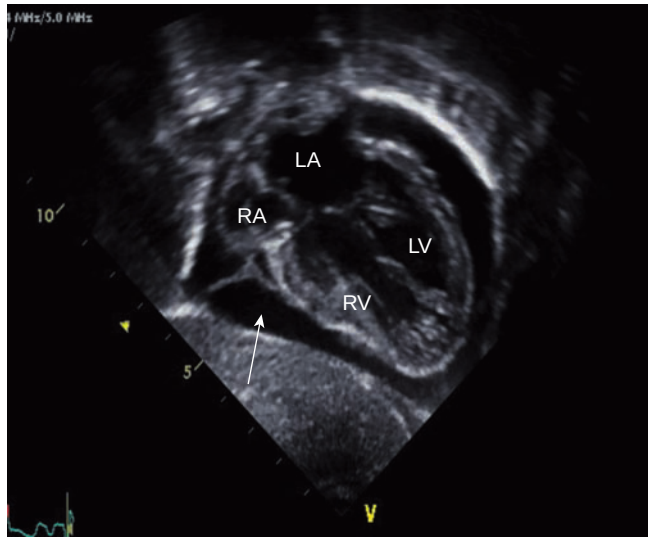


(a)

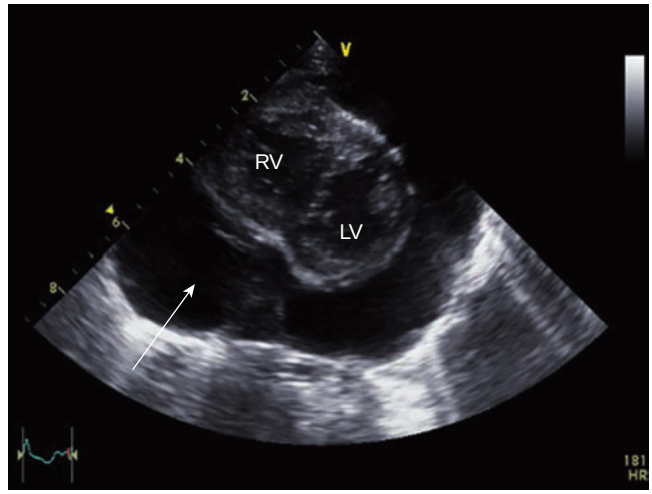


(b)

**Figure 35.15 (a)** Subcostal echocardiographic image demonstrating a large circumferential pericardial effusion (arrow). **(b)** Parasternal short-axis view of a large pericardial effusion (arrow). LA, left atrium; LV, left ventricle; RA, right atrium; RV, right ventricle.

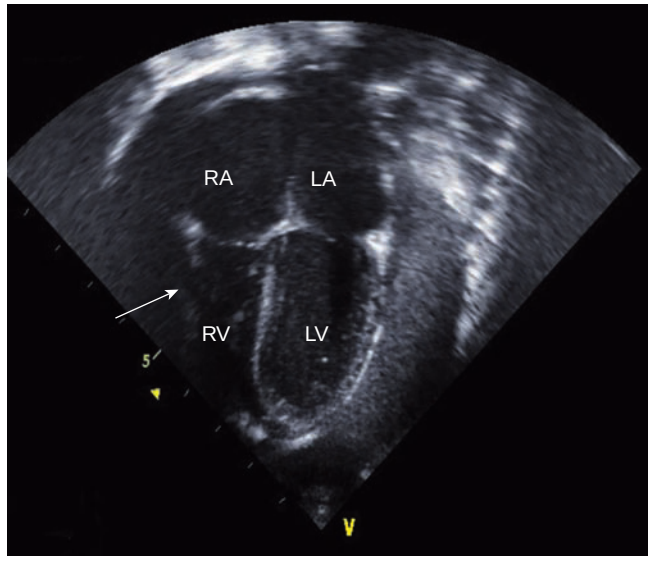


(a)

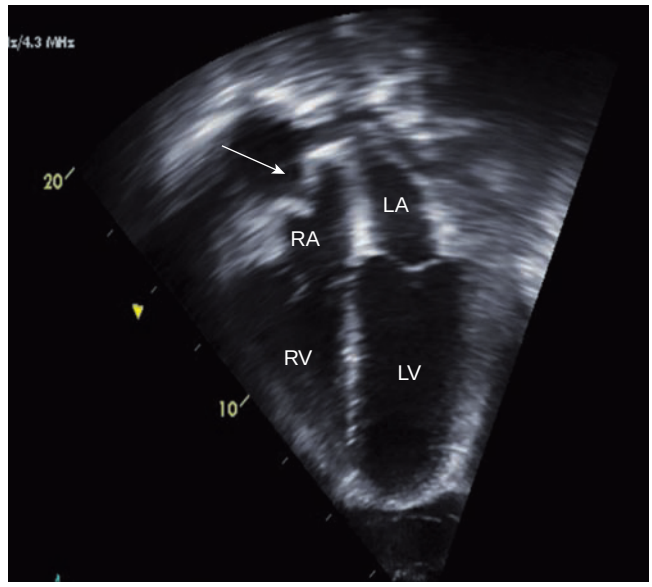


(b)

**Figure 35.16 (a)** Four-chamber view demonstrating right ventricular collapse (arrow) as a finding of tamponade physiology. **(b)** Four-chamber view demonstrating right atrial collapse (arrow) seen in tamponade. LA, left atrium; LV, left ventricle; RA, right atrium; RV, right ventricle.

As intrapericardial pressure increases further, the right-sided chamber volumes become markedly reduced. In adults, the inferior vena cava becomes dilated (Fig. 35.2), exceeding 20 mm in diameter, and shows no inspiratory collapse (plethora), assessed by a <5-mm decrease in diameter during inspiration [77]. The sensitivity of inferior vena cava plethora is high (97%), but the specificity is low (66%), as seen in other conditions like right heart failure, pericardial constriction and mechanical ventilation. The cardiac chambers become small as a result of impaired filling. Decreased diastolic volume of the left atrium and left ventricle may occur during inspiration, related to the increased right heart inflow and abrupt expansion of the right ventricle. Nevertheless, left ventricular collapse is rarely seen as the left ventricle is thicker walled and less compliant. It usually shows signs of preload reduction but not frank free wall compression.

In cardiac tamponade, the heart is swinging in the pericardial fluid on a beat-to-beat basis (Videoclip 35.3), a finding that correlates with electrical alternans on the electrocardiogram. This swinging is characterized as counterclockwise rotational movement, which occurs in addition

to the triangular movement of the heart, producing a dance-like motion. The parietal pericardium shows "damping" (loss of parallel motion with the myocardium) and flattening, whereas the motion of the visceral layer and the heart is exaggerated. When the effusion is large, it can be seen anterior to the right ventricle. In tense pericardial effusion, fluid can also be seen behind the left atrium. When assessed by M-mode echocardiography, a phasic decrease in right ventricular diameter to less than 1 cm (with the patient in the supine position) synchronous with expiration is strongly suggestive of tamponade. M-mode can be used for assessment of expiratory right ventricular diastolic collapse, timing with the opening of the mitral valve or posterior wall motion. Changes in leaflet separation and in the E to F slope of the mitral valve during diastole are also useful, with the leaflet separation decreasing and the slope being reduced during inspiration, reflecting a decrease in mitral inflow.

### *Flow mechanics*

The mitral and tricuspid inflow, the aortic and pulmonary outflow, and the hepatic vein flow show large swings in amplitude. Exaggerated respiratory variation in transvalvular flow is an important indicator of significant hemodynamic effusion. Normally, there is no more than 10% variation in the amplitude of inflow and outflow signal, but this exceeds 30% in tamponade.

The classic Doppler pattern of cardiac tamponade includes the following [78,79]:

**1** *Mitral inflow*. During inspiration, the E-wave decreases and IVRT increases by more than 30% compared with expiration (Fig. 35.17a).

**2** *Pulmonary veins.* During inspiration, the D-wave decreases compared with expiration.

**3** *Tricuspid inflow.* During inspiration, the E-wave increases by more than 50% compared with expiration (Fig. 35.17b).

**4** *Hepatic veins.* During inspiration, the S-wave is greater than the D-wave. During expiration, there is a very limited or absent D-wave with prominent reversals.

These flow variations may precede chamber collapse.

### *Echocardiographically guided pericardiocentesis*

The approach to pericardiocentesis is to assess the distribution of the effusion as well as the ideal needle entry site and trajectory. The transducer is placed approximately 3–5 cm from the parasternal border and the area of maximal pericardial fluid accumulation. The needle trajectory is established by the angle of the transducer. Echo-guided pericardiocentesis has been proven to be a safe and effective procedure (Fig. 35.18a). Whenever required, a pericardial drain can be left in place (Fig. 35.18b). Confirmation of diminished effusion is performed at the end of the case. This echo-guided procedure can be performed at a monitored bedside or in the cardiac catheterization laboratory. Frequently pericardiocentesis is accompanied by insertion of a drainage catheter to reduce the rate of recurrence, which may complicate simple needle drainage. This technique is often considered the primary and definitive therapy for patients with clinically significant effusions [80,81].

### *Additional studies*

Chest X-rays may demonstrate an enlarged cardiac silhouette (Fig. 35.14) with a water bottle-shaped heart when excessive pericardial fluid accumulation is present [82]. Another finding is pericardial fat stripe. The lung fields are usually oligemic, and a pleural effusion is often associated. CT can potentially determine composition of fluid and may detect as little as 50 mL. MRI can detect as little as 30 mL of pericardial fluid, and may be able to distinguish hemorrhagic and nonhemorrhagic effusions. Both MRI and CT scan may be superior to echocardiography in detecting loculated pericardial effusions and pericardial thickening

## Differentiating restriction, constriction and tamponade

Both restrictive cardiomyopathy and constrictive pericarditis are characterized by abnormal diastolic ventricular filling and elevated ventricular end-diastolic pressures. Distinguishing between the two diagnoses can be difficult, particularly in cancer patients who have received anthracycline chemotherapy as well as in those who have received thoracic radiation. As described above, Doppler echocardiography is generally helpful in distinguishing between the two. In restrictive cardiomyopathy ventricular end-diastolic pressures are generally discordant, with left ventricular end-diastolic pressure being higher than right ventricular end-diastolic pressure, as opposed to the situation in constrictive pericarditis. Echocardiographically there is evidence of significant respiratory variation in Doppler ventricular inflow signals in constrictive pericarditis, compared with minimal respiratory variation in restrictive cardiomyopathy. The different characteristics of echocardiographic findings between restrictive cardiomyopathy, constrictive pericarditis, and tamponade are summarized in Table 35.7.

## Acute pericarditis

Pericarditis is inflammation of the pericardium. When the pericardium becomes inflamed, the amount of fluid between the two layers usually increases, leading to pericardial effusion. Pericarditis may be serous, fibrinous, purulent, hemorrhagic, or chylous.

### Incidence and etiology

Most of the time, the cause is unknown and presumed to be a result of a viral infection [83,84]. The identified causes are summarized in Table 35.6. Because there are so many causes of acute pericarditis, and it may go undiagnosed, the true incidence is unknown.

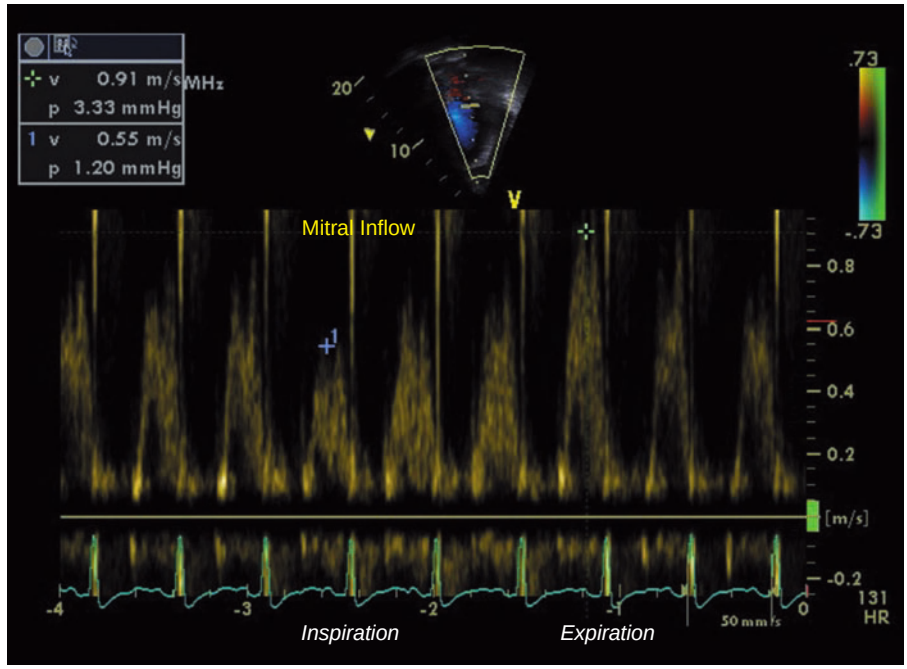


(a)

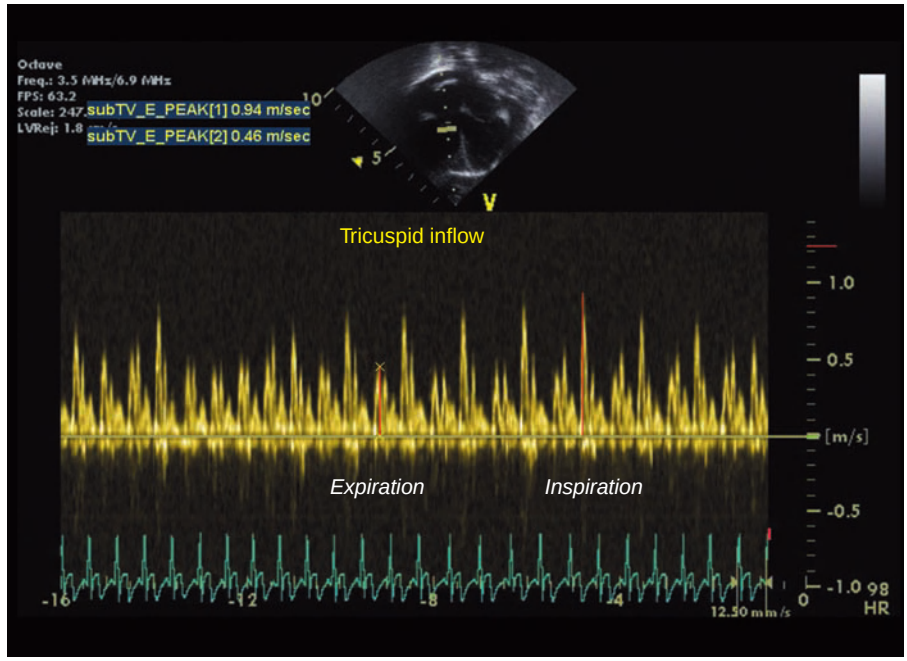


(b)

**Figure 35.17** **(a)** Pulsed-wave Doppler demonstrates respiratory changes in the mitral E-wave Doppler patterns consistent with tamponade physiology. During inspiration, the mitral valve inflow E-wave decreases by more than 30% compared with expiration. **(b)** Pulsed-wave Doppler demonstrates respiratory changes in the tricuspid E-wave Doppler. The tricuspid valve E-wave inflow demonstrates the opposite of the mitral valve and increases by more than 50% during inspiration compared with expiration.

The pericardium serves as a protective barrier against the spread of infection or inflammation from adjacent structures and contains a physiologic amount of fluid. In case of inflammation or infection, effusion can accumulate in the pericardial space. The pericardium shows inflammation with infiltration of polymorphonuclear leukocytes and pericardial vascularization. Often, the pericardium manifests a fibrinous reaction with exudates and adhesions. A granulomatous pericarditis occurs with tuberculosis, fungal infections, rheumatoid arthritis and sarcoidosis.

## Imaging

### *Two-dimensional echocardiography*

The echocardiogram is often normal, unless acute pericarditis is associated with pericardial effusion (Videoclip 35.5). Although the finding of a pericardial effusion supports the

diagnosis of acute pericarditis, its absence does not exclude it. In pericarditis, the pericardium may have a normal appearance.

### *Additional studies*

The normal thickness of the pericardium as measured by CT scanning is less than 2 mm, and it is less than 4 mm by MRI. The limitation of a CT scan is the difficulty in differentiating fluid from thickened pericardium. An increase in cardiac troponin I levels has been described as detectable in about 30% of patients with acute pericarditis, with a level beyond the acute myocardial infarction threshold in about 8% of patients, especially in young patients, when ECG ST segment and a pericardial effusion are present [85].

## Miscellaneous diseases of the pericardium

### Absence of the pericardium

Absence of the pericardium can result from complete or partial deficiency of the pericardium, which can be a congenital anomaly or a consequence of surgical removal. The normal pericardium exerts considerable influence on cardiac motion, provides stability of the heart in the chest, limits dilation of the chambers and provides a barrier to the spread of infection.

Complete absence of the pericardium leads to enlargement of the right ventricle, excessive motion of the posterior left ventricular wall, paradoxical motion of the interventricular septum, and a shift of the heart to the left resulting in more of the right ventricle being seen on the left parasternal long-axis view. All of these findings mimic right ventricular volume overload and thus this diagnosis should be excluded [86].

Partial absence of the pericardium sometimes results in herniation of a chamber through the defect, with the false appearance of wall motion abnormality. True wall motion abnormality is seen if a coronary artery is compressed.

### Pericardial cyst

Pericardial cysts are rare, with an estimated incidence of 1 per 100 000 in the general population [87]. Approximately 20 reported cases have presented before the age of 18 years [88]. Pericardial cysts most often occur at the right atrial border and are difficult to detect with transthoracic echocardiography [89]. They present as an echo-free space that is more localized and spherical than a pericardial effusion [90].

Thoracic MRI and contrast CT scan are preferred methods to confirm a suspected diagnosis of pericardial cyst [91]. On CT scan pericardial cysts are thin-walled, sharply defined, oval homogeneous masses. Their attenuation is slightly

(a)

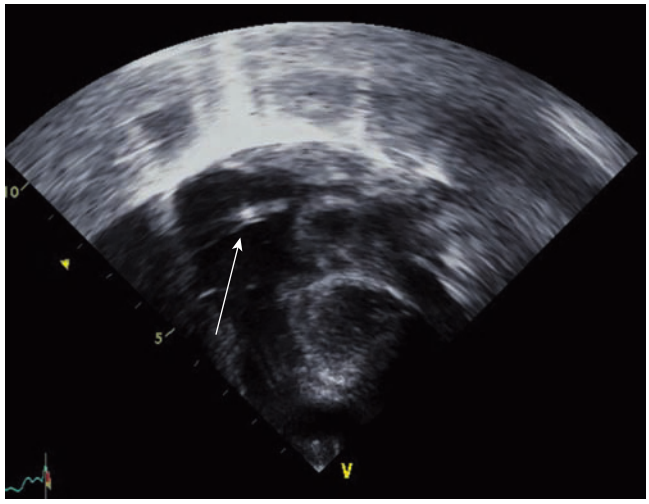

(b)

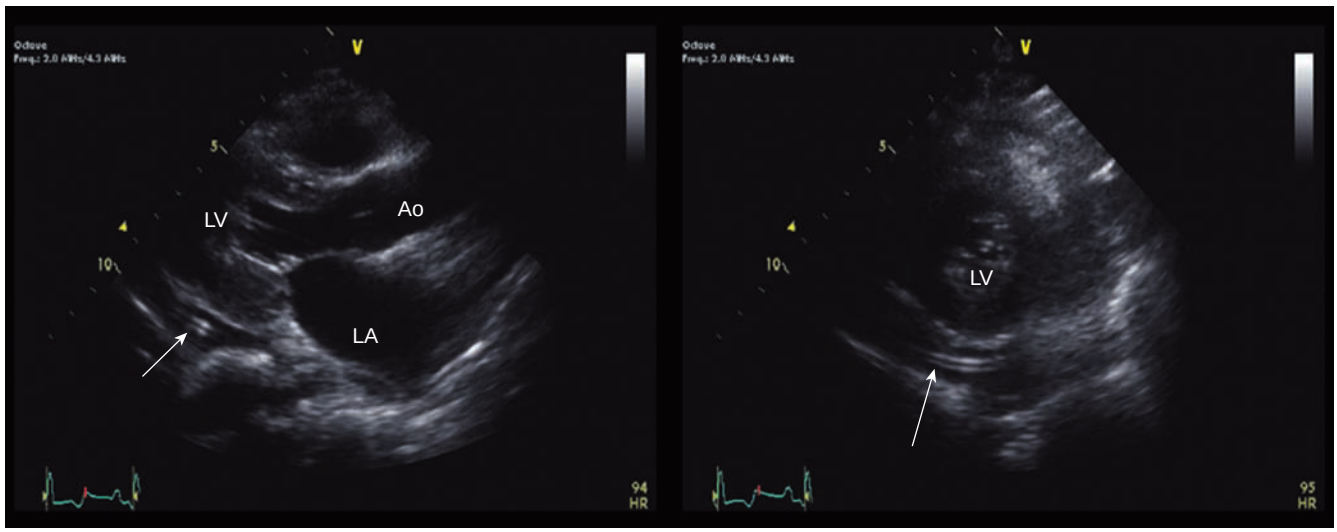


**Figure 35.18** **(a)** Echo-guided pericardiocentesis. The arrow is pointing to the needle, which has been advanced into the pericardial space to drain the fluid collection. **(b)** Arrow showing the drain in place (left: parasternal long-axis view; right: parasternal short-axis view). Ao, aorta; LA, left atrium; LV, left ventricle.

**Table 35.7** Echocardiographic parameters to distinguish between restriction, constriction and tamponade

| Parameter | Tamponade | Constrictive pericarditis | Restrictive cardiomyopathy |
|---|---|---|---|
| RAP | ↑ | ↑ | ↑ |
| RV and LV filling pressures | ↑<br>RV = LV | ↑<br>RV = LV | ↑<br>LV > RV |
| PAP | Normal | Mild↑<br>RVSP <40 mm Hg | Moderate–severe↑<br>RVSP >40 mm Hg |
| RV diastolic pressure plateau | | >1/3 peak RV pressure | <1/3 RV pressure |
| 2D echo | Pericardial effusion | Pericardial thickening<br>Septal shudder<br>Interventricular dependence: IVS diastolic shift toward LV during inspiration and toward RV during expiration | LVH<br><br>No interventricular dependence |
| M-mode | | Septal notch | No septal notch |
| Doppler MV and TV | Reciprocal respiratory changes in RV and LV filling<br>↑TV E during inspiration<br>↑MV E during expiration | Respiratory variation (>10%) in RV and LV filling<br>↑MV E during expiration | No respiratory variation in RV and LV filling |
| | | Respiratory variation in IVRT | No respiratory variation in IVRT |
| | LV inflow: E > A | LV inflow: E > A | LV inflow:<br>early: E < A<br>late: E >> A with ↓A velocity |
| | | ↑TR peak velocity, VTI and duration during inspiration | No respiratory variation in TR jet |
| Doppler Pv | | Respiratory variation in Pv flow: ↑D during expiration | No respiratory variation in Pv flow |
| | | Pv flow:<br>↑AR<br>↓S | Pv flow:<br>↑AR velocity and duration<br>Early: ↑S and ↓D<br>Late: normal S and ↑D |
| | | S/D >0.65 during inspiration | S/D <0.4 |
| TDI | | $E_a$ >8 cm/s<br>$E/E_a$ <15 | $E_a$ <8 cm/s<br>$E/E_a$ >15 |
| Color M-mode | | *V*p >100 cm/s | *V*p <45 cm/s |

A, MV A (late diastolic) wave peak velocity; AR, Pv atrial reversal velocity; D, Pv D (diastolic) wave peak velocity; E, MV E (early diastolic) wave peak velocity; Em, tissue Doppler early mitral annular peak velocity; IVRT, isovolumetric relaxation time; IVS, interventricular septum; LA, left atrium; LV, left ventricle; LVH, left ventricular hypertrophy; MV, mitral valve; PAP, pulmonary artery pressure; Pv, pulmonary vein; S, Pv S (systolic) wave peak velocity; RAP, right atrial pressure; RVSP, right ventricular systolic pressure; TDI, Tissue Doppler Imaging; TR, tricuspid regurgitation; TV, tricuspid valve; Vp, left ventricle velocity of propagation (color M-mode). Adapted with permission from Otto CM. textbook of clinical echocardiography, 3rd edition, Table 10-3, p273, Pericardial disease Chapter, Elsevier Saunders, Philadelphia, PA, USA and from Tam JW, Shaikh N, Sutherland E, Echocardiographic assessment of patients with hypertrophic and restrictive cardiomyopathy: imaging and echocardiography, Curr Opinion in Cardiology 2002 17:470–7.

higher than water density – 30 to 40 Hounsfield units – and the cyst fails to enhance with intravenous contrast [92].

## References


1. Richardson P, McKenna W, Bristow M et al. Report of the 1995 World Health Organization/International Society and Federation of Cardiology Task Force on the Definition and Classification of Cardiomyopathies. *Circulation* 1996;93:841–2.
2. Kimberling MT, Balzer DT, Hirsch R et al. Cardiac transplantation for pediatric restrictive cardiomyopathy: presentation, evaluation, and short-term outcome. *J Heart Lung Transplant* 2002;21:455–9.
3. Weller RJ, Weintraub R, Addonizio LJ et al. Outcome of idiopathic restrictive cardiomyopathy in children. *Am J Cardiol* 2002; 90:501–6.
4. Lewis AB. Clinical profile and outcome of restrictive cardiomyopathy in children. *Am Heart J* 1992;123:1589–93.
5. Cetta F, O'Leary PW, Seward JB, Driscoll DJ. Idiopathic restrictive cardiomyopathy in childhood: diagnostic features and clinical course. *Mayo Clin Proc* 1995;70:634–40.

6. Russo LM, Webber SA. Idiopathic restrictive cardiomyopathy in children. *Heart* 2005;91:1199–202.
7. Denfield SW, Rosenthal G, Gajarski RJ et al. Restrictive cardiomyopathies in childhood. Etiologies and natural history. *Tex Heart Inst J* 1997;24:38–44.
8. Rivenes SM, Kearney DL, Smith EO et al. Sudden death and cardiovascular collapse in children with restrictive cardiomyopathy. *Circulation* 2000;102:876–82.
9. Fitzpatrick AP, Shapiro LM, Rickards AF, Poole-Wilson PA. Familial restrictive cardiomyopathy with atrioventricular block and skeletal myopathy. *Br Heart J* 1990;63:114–8.
10. Kushwaha SS, Fallon JT, Fuster V. Restrictive cardiomyopathy. *N Engl J Med* 1997;336:267–76.
11. Angelini A, Calzolari V, Thiene G et al. Morphologic spectrum of primary restrictive cardiomyopathy. *Am J Cardiol* 1997;80: 1046–50.
12. Yoshizato T, Edwards WD, Alboliras ET et al. Safety and utility of endomyocardial biopsy in infants, children and adolescents: a review of 66 procedures in 53 patients. *J Am Coll Cardiol* 1990; 15:436–42.
13. Asher CR, Klein AL. Diastolic heart failure: restrictive cardiomyopathy, constrictive pericarditis, and cardiac tamponade: clinical and echocardiographic evaluation. *Cardiol Rev* 2002;10:218–29.
14. Vaitkus PT, Kussmaul WG. Constrictive pericarditis versus restrictive cardiomyopathy: a reappraisal and update of diagnostic criteria. *Am Heart J* 1991;122:1431–41.
15. Ammash NM, Seward JB, Bailey KR et al. Clinical profile and outcome of idiopathic restrictive cardiomyopathy. *Circulation* 2000;101:2490–6.
16. Gewillig M, Mertens L, Moerman P, Dumoulin M. Idiopathic restrictive cardiomyopathy in childhood. A diastolic disorder characterized by delayed relaxation. *Eur Heart J* 1996;17:1413–20.
17. Mehta AV, Ferrer PL, Pickoff AS et al. M-mode echocardiographic findings in children with idiopathic restrictive cardiomyopathy. *Pediatr Cardiol* 1984;5:273–9.
18. Klein AL, Hatle LK, Taliercio CP et al. Prognostic significance of Doppler measures of diastolic function in cardiac amyloidosis. A Doppler echocardiography study. *Circulation* 1991;83:808–16.
19. Zile MR, Brutsaert DL. New concepts in diastolic dysfunction and diastolic heart failure: Part I: diagnosis, prognosis, and measurements of diastolic function. *Circulation* 2002;105:1387–93.
20. Klein AL, Hatle LK, Burstow DJ et al. Doppler characterization of left ventricular diastolic function in cardiac amyloidosis. *J Am Coll Cardiol* 1989;13:1017–26.
21. Asher CR, Klein AL. Diastolic heart failure: restrictive cardiomyopathy, constrictive pericarditis, and cardiac tamponade: clinical and echocardiographic evaluation. *Cardiol Rev* 2002;10:218–29.
22. Fowler SJ, Narula J, Gurudevan SV. Review of noninvasive imaging for hypertrophic cardiac syndromes and restrictive physiology. *Heart Fail Clin* 2006;2:215–30.
23. Appleton CP, Hatle LK, Popp RL. Relation of transmitral flow velocity patterns to left ventricular diastolic function: new insights from a combined hemodynamic and Doppler echocardiographic study. *J Am Coll Cardiol* 1988;12:426–40.
24. Giannuzzi P, Imparato A, Temporelli PL et al. Doppler-derived mitral deceleration time of early filling as a strong predictor of pulmonary capillary wedge pressure in postinfarction patients with left ventricular systolic dysfunction. *J Am Coll Cardiol* 1994; 23:1630–7.
25. Hatle LK, Appleton CP, Popp RL. Differentiation of constrictive pericarditis and restrictive cardiomyopathy by Doppler echocardiography. *Circulation* 1989;79:357–70.
26. Abdalla IA, Murray RD, Lee JC et al. Does rapid volume loading during transesophageal echocardiography differentiate constrictive pericarditis from restrictive cardiomyopathy? *Echocardiography* 2002;19:125–34.
27. Rakowski H, Appleton C, Chan KL et al. Canadian consensus recommendations for the measurement and reporting of diastolic dysfunction by echocardiography: from the Investigators of Consensus on Diastolic Dysfunction by Echocardiography. *J Am Soc Echocardiogr.* 1996;9:736–60.
28. Garcia MJ, Palac RT, Malenka DJ et al. Color M-mode Doppler flow propagation velocity is a relatively preload-independent index of left ventricular filling. *J Am Soc Echocardiogr* 1999;12: 129–37.
29. Garcia MJ, Ares MA, Asher C et al. An index of early left ventricular filling that combined with pulsed Doppler peak E velocity may estimate capillary wedge pressure. *J Am Coll Cardiol* 1997; 29:448–54.
30. Garcia MJ, Thomas JD, Klein AL. New Doppler echocardiographic applications for the study of diastolic function. *J Am Coll Cardiol* 1998;32:865–75.
31. Rajagopalan N, Garcia MJ, Rodriguez L et al. Comparison of new Doppler echocardiographic methods to differentiate constrictive pericardial heart disease and restrictive cardiomyopathy. *Am J Cardiol* 2001;87:86–94.
32. Garcia MJ, Rodriguez L, Ares M et al. Differentiation of constrictive pericarditis from restrictive cardiomyopathy: assessment of left ventricular diastolic velocities in longitudinal axis by Doppler tissue imaging. *J Am Coll Cardiol* 1996;27:108–14.
33. Garcia MJ, Thomas JD, Klein AL. New Doppler echocardiographic applications for the study of diastolic function. *J Am Coll Cardiol* 1998;32:865–75.
34. Nagueh SF, Middleton KJ, Kopelen HA et al. Doppler tissue imaging: a noninvasive technique for evaluation of left ventricular relaxation and estimation of filling pressures. *J Am Coll Cardiol* 1997;30:1527–33.
35. Nagueh SF, Mikati I, Kopelen HA et al. Doppler estimation of left ventricular filling pressure in sinus tachycardia. A new application of tissue doppler imaging. *Circulation* 1998;98:1644–50.
36. McMahon CJ, Nagueh SF, Pignatelli RH et al. Characterization of left ventricular diastolic function by tissue Doppler imaging and clinical status in children with hypertrophic cardiomyopathy. *Circulation* 2004;109:1756–62.
37. Sutherland GR, Di Salvo G, Claus P et al. Strain and strain rate imaging: a new clinical approach to quantifying regional myocardial function. *J Am Soc Echocardiogr* 2004;17:788–802.
38. Koyama J, Ray-Sequin PA, Falk RH. Longitudinal myocardial function assessed by tissue velocity, strain, and strain rate tissue Doppler echocardiography in patients with AL (primary) cardiac amyloidosis. *Circulation* 2003;107:2446–52.
39. Helle-Valle T, Crosby J, Edvardsen T et al. New noninvasive method for assessment of left ventricular rotation: speckle tracking echocardiography. *Circulation* 2005;112:3149–56.

40. Abdalla IA, Murray RD, Lee JC et al. Does rapid volume loading during transesophageal echocardiography differentiate constrictive pericarditis from restrictive cardiomyopathy? *Echocardiography* 2002;19:125–34.
41. Myers RB, Spodick DH. Constrictive pericarditis: clinical and pathophysiologic characteristics. *Am Heart J* 1999;138:219–32.
42. Gomes Ferreira SM, Gomes Ferreira A Jr et al. Constrictive chronic pericarditis in children. *Cardiol Young* 2001;11:210–3.
43. Troughton RW, Asher CR, Klein AL. Pericarditis. *Lancet* 2004;363:717–27.
44. Haley JH, Tajik AJ, Danielson GK et al. Transient constrictive pericarditis: causes and natural history. *J Am Coll Cardiol* 2004; 43:271–5.
45. Chen CA, Lin MT, Wu ET et al. Clinical manifestations and outcomes of constrictive pericarditis in children. *J Formos Med Assoc* 2005;104:402–7.
46. Hatle LK, Appleton CP, Popp RL. Differentiation of constrictive pericarditis and restrictive cardiomyopathy by Doppler echocardiography. *Circulation* 1989;79:357–70.
47. Myers RB, Spodick DH. Constrictive pericarditis: clinical and pathophysiologic characteristics. *Am Heart J* 1999;138:219–32.
48. Shabetai R, Fowler NO, Guntheroth WG. The hemodynamics of cardiac tamponade and constrictive pericarditis. *Am J Cardiol* 1970;26:480–9.
49. Asher CR, Klein AL. Diastolic heart failure: restrictive cardiomyopathy, constrictive pericarditis, and cardiac tamponade: clinical and echocardiographic evaluation. *Cardiol Rev* 2002;10: 218–29.
50. Schnittger I, Bowden RE, Abrams J, Popp RL. Echocardiography: pericardial thickening and constrictive pericarditis. *Am J Cardiol* 1978;42:388–95.
51. Himelman RB, Lee E, Schiller NB. Septal bounce, vena cava plethora, and pericardial adhesion: informative two-dimensional echocardiographic signs in the diagnosis of pericardial constriction. *J Am Soc Echocardiogr* 1988;1:333–40.
52. Tei C, Child JS, Tanaka H, Shah PM. Atrial systolic notch on the interventricular septal echogram: an echocardiographic sign of constrictive pericarditis. *J Am Coll Cardiol* 1983;1:907–12.
53. Gibson TC, Grossman W, McLaurin LP et al. An echocardiographic study of the interventricular septum in constrictive pericarditis. *Br Heart J* 1976;38:738–43.
54. Mehta A, Mehta M, Jain AC. Constrictive pericarditis. *Clin Cardiol* 1999;22:334–44.
55. Agatston AS, Rao A, Price RJ, Kinney EL. Diagnosis of constrictive pericarditis by pulsed Doppler echocardiography. *Am J Cardiol* 1984;54:929–30.
56. Klodas E, Nishimura RA, Appleton CP et al. Doppler evaluation of patients with constrictive pericarditis: use of tricuspid regurgitation velocity curves to determine enhanced ventricular interaction. *J Am Coll Cardiol* 1996;28:652–7.
57. Rajagopalan N, Garcia MJ, Rodriguez L et al. Comparison of new Doppler echocardiographic methods to differentiate constrictive pericardial heart disease and restrictive cardiomyopathy. *Am J Cardiol* 2001;87:86–94.
58. Ha JW, Oh JK, Ling LH et al. Annulus paradoxus: transmitral flow velocity to mitral annular velocity ratio is inversely proportional to pulmonary capillary wedge pressure in patients with constrictive pericarditis. *Circulation* 2001;104:976–8.
59. Kronzon I, Tunick PA, Freedberg RS. Transesophageal echocardiography in pericardial disease and tamponade. *Echocardiography* 1994;11:493–505.
60. Ling LH, Oh JK, Tei C et al. Pericardial thickness measured with transesophageal echocardiography: feasibility and potential clinical usefulness. *J Am Coll Cardiol* 1997;29:1317–23.
61. Abdalla IA, Murray RD, Lee JC et al. Does rapid volume loading during transesophageal echocardiography differentiate constrictive pericarditis from restrictive cardiomyopathy? *Echocardiography* 2002;19:125–34.
62. Kameda Y, Funabashi N, Kawakubo M et al. Heart in an eggshell – eggshell appearance calcified constrictive pericarditis demonstrated by three-dimensional images of multislice computed tomography. *Int J Cardiol* 2007;120:269–72.
63. Francone M, Dymarkowski S, Kalantzi M et al. Assessment of ventricular coupling with real-time cine MRI and its value to differentiate constrictive pericarditis from restrictive cardiomyopathy. *Eur Radiol* 2006;16:944–51.
64. Chen SJ, Li YW, Wu MH et al. CT and MRI findings in a child with constrictive pericarditis. *Pediatr Cardiol* 1998;19:259–62.
65. Ilan Y, Oren R, Ben-Chetrit E. Etiology, treatment, and prognosis of large pericardial effusions. A study of 34 patients. *Chest* 1991;100:985–7.
66. Spodick DH. Acute cardiac tamponade. *N Engl J Med* 2003;349: 684–90.
67. Little WC, Freeman GL. Pericardial disease. *Circulation* 2006;113: 1622–32.
68. Guntheroth WG, Morgan BC, Mullins GL. Effect of respiration on venous return and stroke volume in cardiac tamponade. Mechanism of pulsus parodoxus. *Circ Res* 1967;20:381–90.
69. Horowitz MS, Schultz CS, Stinson EB et al. Sensitivity and specificity of echocardiographic diagnosis of pericardial effusion. *Circulation* 1974;50:239–47.
70. Pepi M, Muratori M. Echocardiography in the diagnosis and management of pericardial disease. *J Cardiovasc Med (Hagerstown)* 2006;7:533–44.
71. Weitzman LB, Tinker WP, Kronzon I et al. The incidence and natural history of pericardial effusion after cardiac surgery – an echocardiographic study. *Circulation* 1984;69:506–11.
72. Schiller NB, Botvinick EH. Right ventricular compression as a sign of cardiac tamponade: an analysis of echocardiographic ventricular dimensions and their clinical implications. *Circulation* 1977;56:774–9.
73. Armstrong WF, Schilt BF, Helper DJ et al. Diastolic collapse of the right ventricle with cardiac tamponade: an echocardiographic study. *Circulation* 1982;65:1491–6.
74. Singh S, Wann LS, Schuchard GH et al. Right ventricular and right atrial collapse in patients with cardiac tamponade – a combined echocardiographic and hemodynamic study. *Circulation* 1984;70:966–71.
75. Gillam LD, Guyer DE, Gibson TC et al. Hydrodynamic compression of the right atrium: a new echocardiographic sign of cardiac tamponade. *Circulation* 1983;68:294–301.
76. Kronzon I, Cohen ML, Winer HE. Diastolic atrial compression: a sensitive echocardiographic sign of cardiac tamponade. *J Am Coll Cardiol* 1983;2:770–5.
77. Himelman RB, Kircher B, Rockey DC, Schiller NB. Inferior vena cava plethora with blunted respiratory response: a sensitive

echocardiographic sign of cardiac tamponade. *J Am Coll Cardiol* 1988;12:1470–7.
78. Klein AL, Cohen GI. Doppler echocardiographic assessment of constrictive pericarditis, cardiac amyloidosis, and cardiac tamponade. *Cleve Clin J Med* 1992;59:278–90.
79. Appleton CP, Hatle LK, Popp RL. Cardiac tamponade and pericardial effusion: respiratory variation in transvalvular flow velocities studied by Doppler echocardiography. *J Am Coll Cardiol* 1988;11:1020–30.
80. Tsang T, El-Najdawi E, Seward JB, et al. Percutaneous echocardiographically guided pericardiocentesis in pediatric patients: evaluation of safety and efficacy. *J Am Soc Echocardiogr* 1998;11: 1072–7.
81. Tsang TS, Freeman WK, Sinak LJ, Seward JB. Echocardiographically guided pericardiocentesis: evolution and state-of-the-art technique. *Mayo Clin Proc* 1998;73:647–52.
82. Eisenberg MJ, de Romeral LM, Heidenreich PA et al. The diagnosis of pericardial effusion and cardiac tamponade by 12-lead ECG. A technology assessment. *Chest* 1996;110:318–24.
83. Troughton RW, Asher CR, Klein AL. Pericarditis. *Lancet* 2004; 363:717–27.
84. Lange RA, Hillis LD. Clinical practice. Acute pericarditis. *N Engl J Med* 2004;351:2195–202.
85. Imazio M, Demichelis B, Cecchi E et al. Cardiac troponin I in acute pericarditis. *J Am Coll Cardiol* 2003;42:2144–8.
86. Payvandi MN, Kerber RE. Echocardiography in congenital and acquired absence of the pericardium. An echocardiographic mimic of right ventricular volume overload. *Circulation* 1976; 53:86–92.
87. Patel J, Park C, Michaels J et al. Pericardial cyst: case reports and a literature review. *Echocardiography* 2004;21:269–72.
88. Noyes BE, Weber T, Vogler C. Pericardial cysts in children: surgical or conservative approach? *J Pediat Surg* 2003;38:1263–5.
89. Patel J, Park C, Michaels J et al. Pericardial cyst: case reports and a literature review. *Echocardiography* 2004;21:269–72.
90. Hynes JK, Tajik AJ, Osborn MJ et al. Two-dimensional echocardiographic diagnosis of pericardial cyst. *Mayo Clin Proc* 1983;58: 60–3.
91. Lau CL, Davis RD. The mediastinum. In: Townsend CM, Beauchamp RD, Evers BM, Mattox KL (eds) *Sabiston's Textbook of Surgery*, 17th edn. Philadelphia: Elsevier, 2004;1738–9, 1758.
92. Demos TC, Budorick NE, Posniak HV. Benign mediastinal cysts: pointed appearance on CT. *J Comput Assist Tomog* 1989;13: 132–3.

# 36 Other Anomalies of the Ventricular Myocardium

**Mary Etta E. King**
Massachusetts General Hospital, Boston, MA, USA

## Introduction

A number of uncommon but important disorders that affect the left and right ventricular myocardium will be reviewed in this chapter. It is important that they be considered during echocardiographic evaluation of patients with ventricular dysfunction, arrhythmia, syncope, or thromboembolism. The echocardiographic findings may be subtle and easily missed if the examiner does not intentionally consider them in the differential diagnosis.

## Left ventricular noncompaction

### Definition

Left ventricular noncompaction (LVNC) is classified as a primary genetic cardiomyopathy [1] characterized by "spongy" myocardium with prominent trabeculae separated by deep intertrabecular recesses affecting the left ventricular apex and mid-ventricle (Fig. 36.1a,b; Videoclips 36.1 and 36.2). The intertrabecular recesses are lined with endothelium and communicate with the ventricular cavity, which distinguishes this feature from myocardial sinusoids. Although this anomaly typically affects the left ventricle, involvement of the right ventricle is also described [2,3] (Fig. 36.2). Left ventricular noncompaction can occur as an isolated anomaly (iLVNC) or in association with other structural heart defects (nonisolated, or ni-LVNC) such as ventricular septal defects, and left or right heart outflow obstruction.

### Incidence

Although it is recognized as a rare form of cardiomyopathy, the true incidence of LVNC is unknown because there have been no prospective randomized clinical trials to date. Incidence figures are also clouded by the fact that the diagnosis is frequently missed because of incomplete evaluation by echocardiography or due to lack of awareness of LVNC as a distinct cardiomyopathy – it is often subsumed in the category of hypertrophic cardiomyopathy or dilated cardiomyopathy with trabeculations. It is also difficult to know if LVNC can be diagnosed in children and adults who have noncompacted-appearing myocardium without evidence of ventricular dysfunction or cardiac symptoms. Studies in adult populations suggest that LVNC is quite rare, with a prevalence of 0.014% [4]; however, these data may be confounded by technical imaging limitations in adult studies. A somewhat higher prevalence has been noted in pediatric populations, with a prospective study showing LVNC in 1.26% of all children referred for echocardiography at a single center over a $2^1/_2$-year period [5]. LVNC has been identified as the third most frequent cause of cardiomyopathy in children, representing about 9% of cardiomyopathies seen in a large retrospective single-center study and a large epidemiologic survey [3,6].

### Etiology

Left ventricular noncompaction is a genetically heterogeneous myopathy occurring both sporadically and in familial forms. Many of the identified genetic mutations involve proteins in the common pathway that connects the extracellular matrix to the sarcolemma, sarcomere and nuclear membrane. Isolated LVNC has been clearly associated with mutations in the Xq28 region of the X chromosome, and specifically for the *G4.5* gene encoding tafazzin in infants and children with X-linked familial LVNC. Mutations of this same locus are associated with Barth syndrome and other X-linked infantile cardiomyopathies [7,8]. A variety of mutations in the *CYPHER/ZASP* gene have been described in patients with isolated LVNC and in families with both dilated cardiomyopathy and LVNC [9]. Autosomal dominant familial LVNC in adulthood has been mapped to a locus on chromosome 11p15 [10]. In families with nonisolated LVNC associated with congenital heart disease, mutations in α-dystrobrevin and transcription factor NKX2.5 have been demonstrated [11]. Associations have been noted with a variety of other genetic conditions such as Roifman syndrome, MIDAS

*Echocardiography in Pediatric and Congenital Heart Disease: From Fetus to Adult*
Edited by Wyman W. Lai, Luc L. Mertens, Meryl S. Cohen and Tal Geva
 ISBN: 978-1-405-17401-5

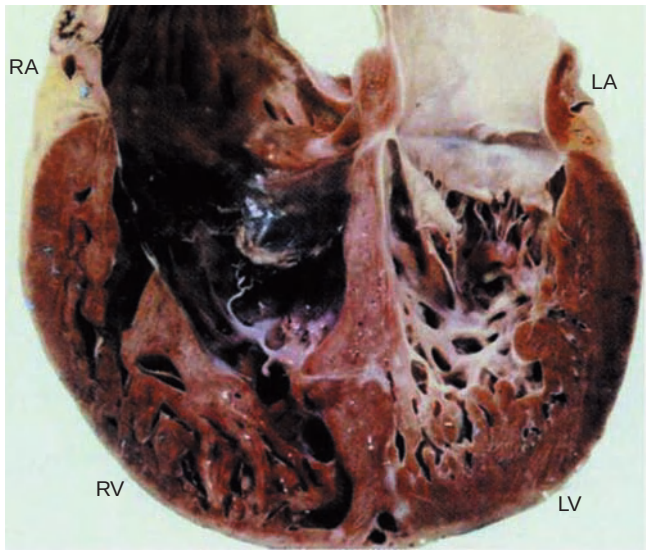


(a)

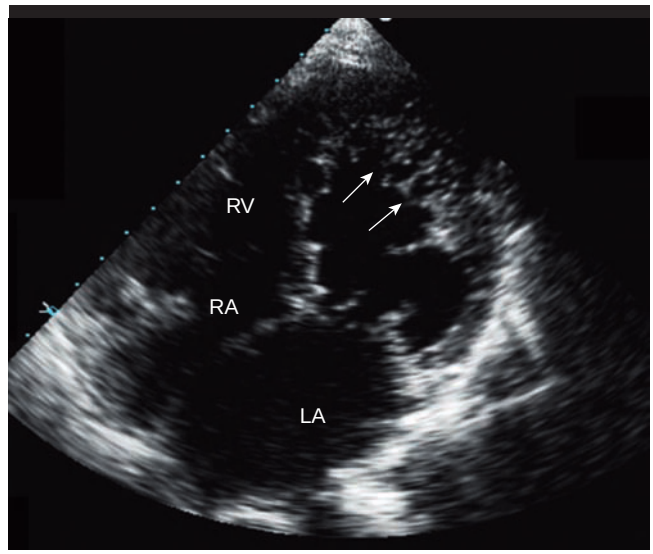


(b)

**Figure 36.1 (a)** A pathologic specimen of a heart with left ventricular (LV) noncompaction showing the dense trabeculations and deep recesses in the LV apex and mid-ventricle. Reproduced from Oechslin E, Attenhofer C, Jost C et al. Long-term follow-up of 34 adults with isolated left ventricular noncompaction: a distinct cardiomyopathy with poor prognosis. *J Am Coll Cardiol* 2000:36:495, with permission from Elsevier Inc. **(b)** The echocardiographic appearance of apical trabeculations (arrows) in an apical view from a patient with LV noncompaction. LA, left atrium; LV, left ventricle; RA, right atrium; RV, right ventricle.

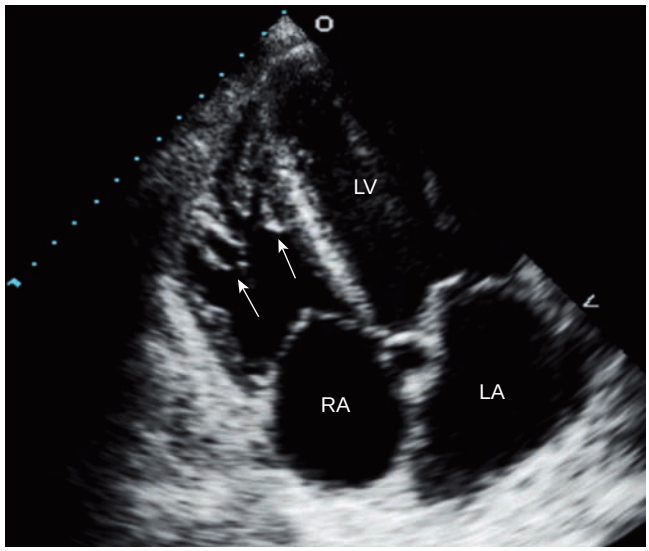


**Figure 36.2** Prominent trabeculations (arrows) fill the right ventricular apex in this apical 4-chamber echocardiographic image. LA, left atrium; LV, left ventricle; RA, right atrium.

syndrome, Melnick–Needles syndrome, nail-patella syndrome, DiGeorge syndrome and trisomy 13 [3,12–16]

## Morphology and classification

### Developmental considerations

During normal cardiac development, the ventricular myocardium begins as a spongy meshwork of myocardial fibers with intertrabecular recesses supplied from the ventricular cavity. Compaction of the myocardium then progresses from epicardium toward endocardium and from base to apex, with the vascular recesses becoming capillaries that eventually connect with the epicardial coronary artery system [17]. Arrest in this normal embryologic process of myocardial compaction is thought to be responsible for the findings in LVNC. This assumption would appear to be supported by the similarity in the appearance of the left ventricular (LV) myocardium in LVNC with that of embryonic myocardium, and by reports of prenatal diagnosis [18,19] as well as symptomatic cases described in patients from infancy through adulthood. Countering this pathogenetic assumption are several documented cases in which LVNC was diagnosed but evidence of normal myocardial architecture had been demonstrated in previous echo studies [8,20]. It is possible, therefore, that the features of LVNC can be either a persistence of embryonic myocardial structure or a developmental pattern in a genetically impaired myocardium. As more family and population screening studies are being reported, a larger number of asymptomatic individuals with LVNC have been identified and a considerable variability in natural history is being recognized, perhaps related to the genetic heterogeneity of the disorder.

### Anatomy

The anatomic features of LVNC include multiple trabeculations affecting the apex and the inferior and lateral walls at the mid-ventricle, with deep intertrabecular recesses that communicate with the cavity of the left ventricle (LV) and are lined with endocardial endothelium. The epicardial layer of the myocardium is thin and compact. There are often

histologic areas of ischemia within the noncompacted endocardial layer, and subendocardial fibrosis and endocardial fibroelastosis have been described in autopsied hearts [4,21] Electron microscopy has been inconsistent in findings related to myofiber and mitochondrial morphology. Trabeculation also affects the right ventricle (RV) in less than 50% of cases, but differentiation of pathologic from normal degrees of RV trabeculation can be difficult.

Nonisolated LVNC occurs in association with ventricular septal defects (predominantly muscular), and with left or right ventricular outflow obstruction. Lesions affecting the left heart may include subaortic stenosis, valvar aortic stenosis, coarctation of the aorta, and hypoplastic left heart syndrome. Right heart obstructions described include valvar pulmonary stenosis, tetralogy of Fallot, pulmonary atresia and hypoplastic right heart syndrome [5].

## Pathophysiology

The classic description of the clinical course in LVNC has included progressive heart failure, arrhythmia and thromboembolism with a poor long-term prognosis. The segments of the left ventricle with noncompacted myocardium usually exhibit decreased systolic function as a result of hypoperfusion, ischemia and fibrosis, which has been confirmed by thallium imaging, positron emission tomography (PET) scanning and myocardial biopsy [2,22]. Impaired diastolic filling with restrictive physiology is also noted due to the hypertrabeculated myocardium [3]. Patients may present with clinical symptoms of heart failure during fetal life, infancy, childhood or in adult years. Although there can be some improvement in function with aggressive medical management of heart failure, progression of the cardiomyopathic process usually leads to cardiac transplantation or death from heart failure, arrhythmia or stroke. A series of adult LVNC patients described by Ritter et al., showed a 47% mortality rate over a 6-year follow-up period [23]. A retrospective review of a large series of children with both i-LVNC and ni-LVNC showed a 14% mortality over a 0.5–12-year follow-up, with 83% of the cases showing depressed systolic function [3]. Understanding of the natural history of LVNC is being further elucidated by the detection of asymptomatic cases during family or population screening studies. These more prospective investigations suggest that there may be a long preclinical phase with a much less dire natural history in asymptomatic cases [2,24].

Electrocardiographic abnormalities are frequently observed in patients with LVNC, and may include left and right bundle branch block, ST- and T-wave abnormalities, pathologic Q-waves or poor R-wave progression, biventricular hypertrophy, and Wolff–Parkinson–White syndrome. Arrhythmias are a common feature, with atrial fibrillation, supraventricular tachycardia and ventricular tachycardia being noted on baseline electrocardiogram (ECG) or Holter monitoring [3,23]. Sudden death from presumed ventricular arrhythmia is a recognized complication in LVNC, and aggressive management of ventricular arrhythmia with pharmacologic therapy or an implantable defibrillator is often warranted.

Thrombus formation within the deep intertrabecular recesses and associated arrhythmia is a likely explanation for the frequent occurrence of thromboembolic events in patients with LVNC. Adult series have reported up to 24% of patients suffering from transient ischemic attack (TIA), stroke or peripheral emboli [4]. The frequency in pediatric series is somewhat lower, but still a serious complication. Anticoagulation is recommended in patients with proven thromboembolic episodes or with thrombus visualized by echocardiography, and antiplatelet agents are often recommended as a prophylactic measure at the time of initial diagnosis of LVNC.

## Imaging

### Goals of the examination

The goals of echocardiographic examination in the setting of LVNC can be summarized as follows:

- Determine the presence and location of myocardial trabeculation.
- Quantify the thickness and ratio of noncompacted to compacted myocardium.
- Verify communication of the intertrabecular recesses with the ventricular blood pool by color Doppler or contrast.
- Evaluate the recesses for thrombus.
- Assess the segmental and global ventricular systolic function.
- Measure the diastolic transmitral flows and annular velocities to assess diastolic function.
- Evaluate associated structural heart disease.

Two-dimensional echocardiography is the primary method of diagnosis for LVNC. Because trabeculations can often be seen in normal hearts and in pressure- or volume-overloaded ventricles, the following specific criteria have been recommended for establishing the diagnosis of LVNC [25]:

**1** A two-layer appearance with a thinner compacted layer and a thicker trabecular layer, with a ratio of noncompacted to compacted myocardium of >2 (measured in systole) (Fig. 36.3).

**2** Segmental involvement of the apex and the inferior and lateral walls at the mid-ventricular level.

**3** Color flow Doppler demonstrating blood flow from the LV cavity perfusing the trabecular recesses (Fig. 36.4a).

When all three criteria are met, LVNC can be accurately distinguished from other disorders that cause increased LV trabeculation, such as hypertensive or valvular heart disease and dilated cardiomyopathy [26].

### Prenatal assessment

Prenatal diagnosis of LVNC is possible but the criteria can sometimes be more difficult to use. It should be suspected in any fetus with poor ventricular systolic performance

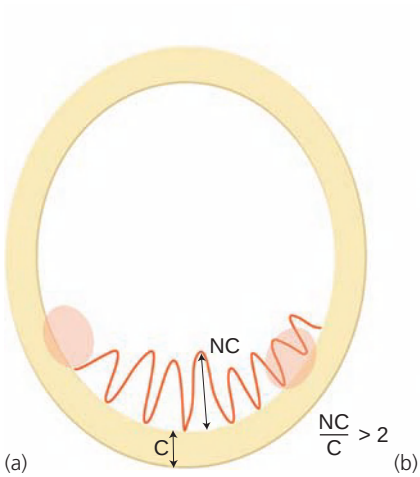


(a)

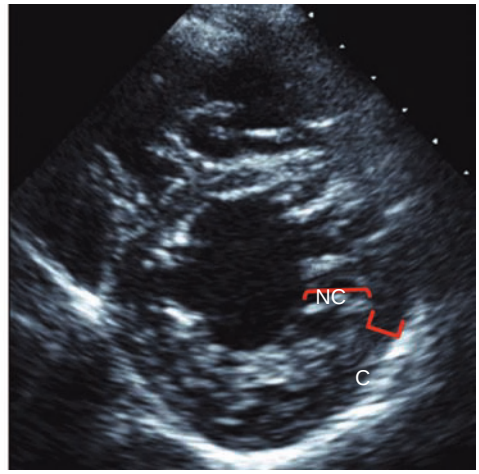


(b)

**Figure 36.3** **(a)** Diagrammatic representation of the left ventricle in cross-section demonstrating the compacted (C) and noncompacted (NC) layers of myocardium found in left ventricular noncompaction (LVNC). A ratio of noncompacted wall thickness to compacted wall thickness of >2:1 is consistent with a diagnosis of LVNC. **(b)** Echocardiographic image of the left ventricle at the mid-ventricular level from a patient with LVNC, depicting prominent trabeculations and a thinner compacted layer.

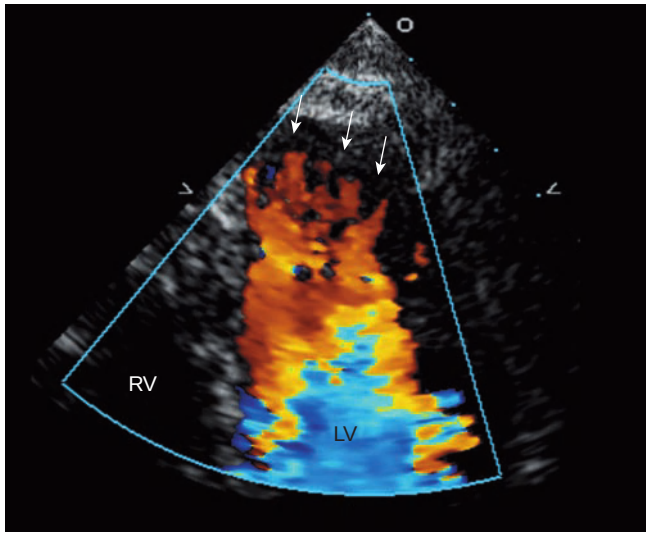


(a)

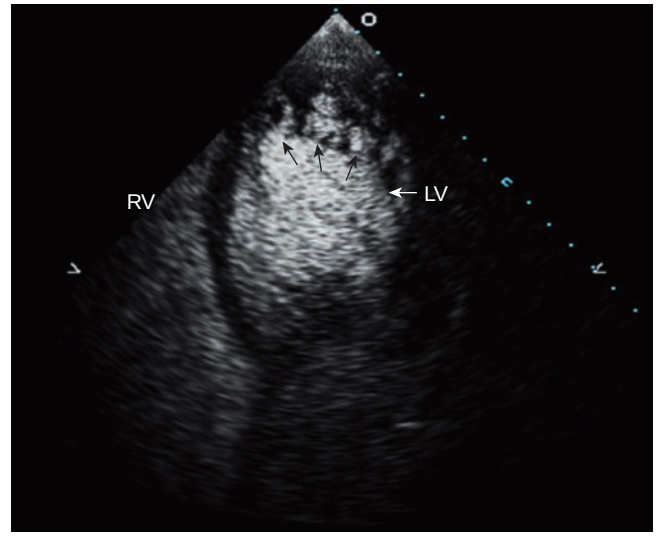


(b)

**Figure 36.4** **(a)** Color Doppler image demonstrating communication of the deep intertrabecular recesses (arrows) with the blood pool within the left ventricular cavity in an apical view. **(b)** Contrast echocardiography is used to define the deep trabecular spaces (arrows) in a similar view. LV, left ventricle; RV, right ventricle.

although ventricular performance may be preserved. Some fetuses suspected of having LVNC will have chromosomal or noncardiac abnormalities in association. Other abnormalities may be seen, such as complete heart block. This association carries a very poor prognosis (Fig. 36.5 and Videoclip 36.3) [27]. If ventricular function is poor, hydrops fetalis may develop as well. Similar to the assessment of a child with LVNC, color Doppler can be helpful to assess for flow within the trabecular recesses.

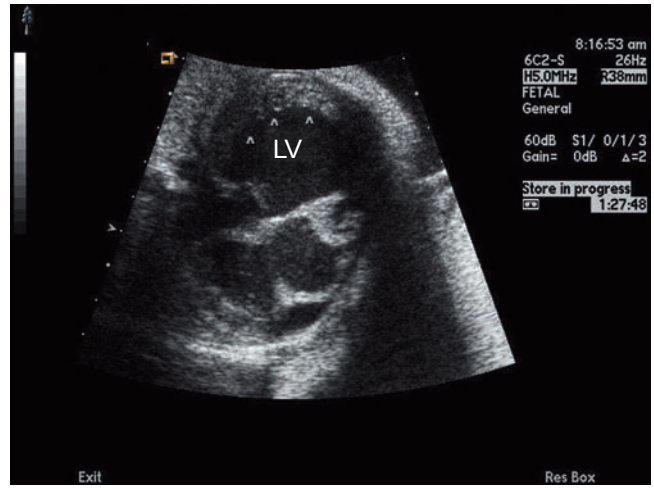


**Figure 36.5** Fetal echocardiogram in the 4-chamber view demonstrating noncompaction of the left ventricle (LV, arrowheads). This fetus also had tricuspid atresia and complete heart block.

### Imaging of children and adults

Contrast echocardiography is helpful in defining the continuity of the left ventricular cavity with the trabecular spaces, particularly when the quality of standard imaging is limited [28] (Fig. 36.4b). Exquisite detail of myocardial trabeculation can be obtained by cardiac magnetic resonance imaging, and a study comparing patients with LVNC with other

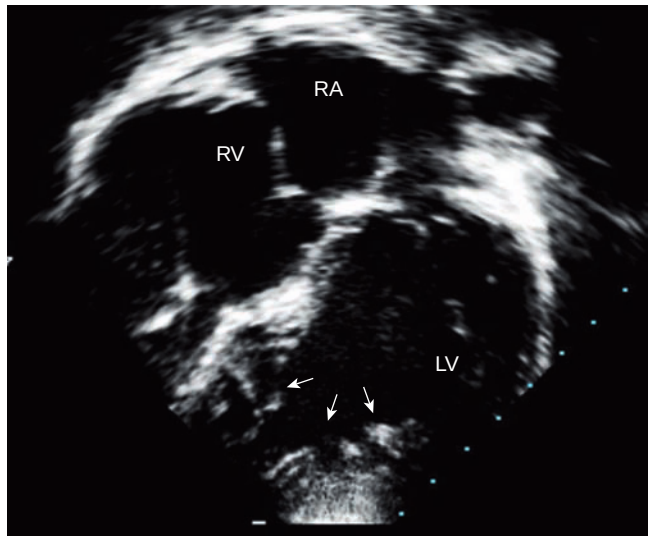


(a)

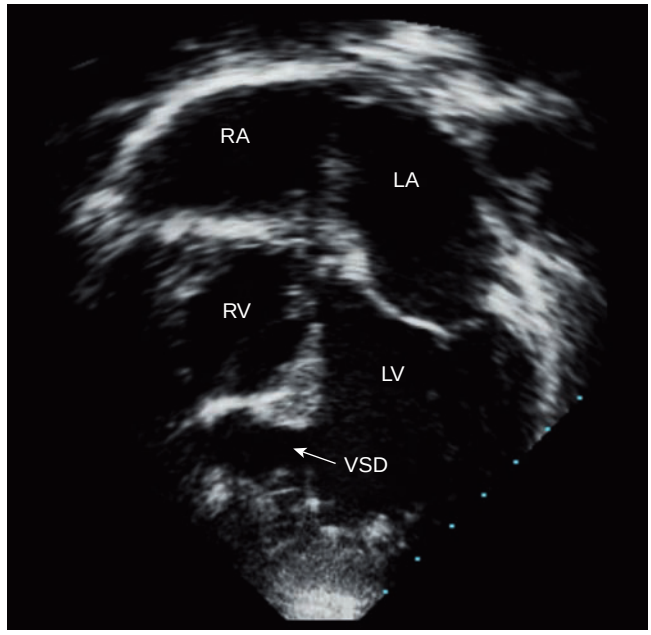


(b)

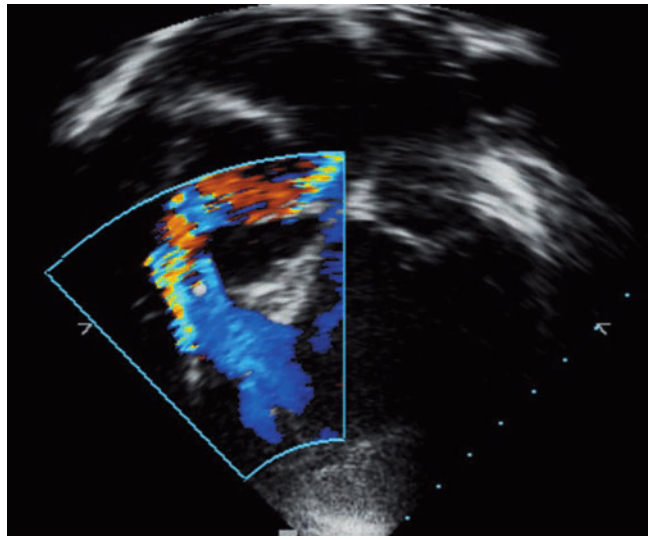

(c)

populations with LV trabeculation suggested that a noncompaction-to-compaction ratio of >2.3 (measured in diastole) is highly specific for the diagnosis of LVNC [29].

When myocardial dysfunction is present, careful cross-sectional and apical imaging assessment of LV segmental function will detect hypokinesis of the noncompacted regions, and standard methods for quantifying LV chamber size and ejection fraction should be used to measure global LV performance. In asymptomatic patients who have been identified through family screening studies, left ventricular function may be normal and decisions regarding management and prognosis may be difficult. A method of predicting those patients with LVNC most at risk for adverse clinical outcome has been proposed, utilizing tissue Doppler-derived measures of LV diastolic relaxation. In a study comparing 56 children with LVNC with normal controls, the lateral mitral annular early diastolic tissue Doppler velocity ($E_a$) was most predictive of hospitalization for congestive heart failure, need for transplantation or death. A lateral mitral annular $E_a$ <7.8 cm/s had an 87% sensitivity and 79% specificity for predicting death or need for transplant [30].

In patients with ni-LVNC, echocardiographic evaluation of associated lesions should be performed in the usual manner. Conversely, when assessing patients with ventricular septal defect and left or right heart outflow obstructions, careful evaluation of trabeculated myocardium against the criteria of LVNC is important as the presence of this myopathic disorder may significantly alter the overall prognosis (Fig. 36.6a–c).

## Left ventricular aneurysm and diverticula

### Definition

Congenital LV aneurysms and diverticula have often been mentioned interchangeably in discussion of protrusions from the LV cavity lacking any other etiologic explanation. As Van Praagh and colleagues point out [31], the two are distinct entities, beginning with the origin of their names: *aneurysm* is derived from the Greek root *eurys*, meaning "wide", whereas diverticulum is from the Latin word meaning a "byroad" with the connotation of a narrow, meandering pathway. Although both are uncommon, they are potentially lethal abnormalities. LV aneurysms are characterized as a protrusion

**Figure 36.6** (*left*) **(a)** Apical echocardiographic view depicting increased trabeculations in the left ventricular apex (arrows) in a 5-year-old child with nonisolated left ventricular noncompaction (LVNC). **(b,c)** Images from the same patient, with the apical view angled slightly more anteriorly to demonstrate a large, complex muscular ventricular septal defect (arrow). Doppler color flow mapping (c) portrays flow through the VSD. LA, left atrium; LV, left ventricle; RA, right atrium; RV, right ventricle; VSD, ventricular septal defect.

from the myocardium with a wide mouth and consisting of thinned or abnormal myocardium or fibrous tissue that expands in systole. LV diverticula have a narrow communication with the functional ventricle and are composed of endocardium, myocardium and epicardium with contractile function. Diverticula of the right ventricle (RV) have also been reported, arising either from the conal region, the base or the apex [32–34,]

## Incidence

Left ventricular aneurysm and diverticula are both rare anomalies, mostly described in case reports and small case series. A frequency of 0.12% was reported for congenital LV aneurysm from a large cardiac pathology registry [30]. LV diverticulum was noted in 0.4% of an autopsy series of cardiac deaths and in 0.26% of nonselected patients undergoing cardiac catheterization [35,36].

## Etiology

Congenital LV aneurysm and diverticula are presumed to be an idiopathic developmental abnormality of the endomyocardium [30]. They are not associated with abnormalities of the coronary arteries or coronary insufficiency, and should be distinguished from aneurysms or pseudoaneurysms caused by ischemic, infective, or traumatic processes. A particular subtype of LV aneurysm, the submitral aneurysm, seen most often in patients from sub-Saharan Africa, is thought to result from a congenital deficiency in the fusion of myocardium with the cardiac fibrous skeleton [37]. Both aneurysms and diverticula have been described in utero, some resulting in fetal demise [38], and they occur in children and adults either as incidental findings or associated with clinical symptoms of arrhythmia, heart failure, mitral insufficiency or thromboembolism. There is one report of the occurrence of LV diverticulum in siblings [39] but no genetic markers have yet been described. Apical LV diverticula occur in patients with Cantrell syndrome, a defect in the ventral mesoderm that results in abnormalities of the abdominal wall, sternum, anterior diaphragm, pericardium and intracardiac anatomy. It has been postulated that the diverticulum in this syndrome may be caused by an abnormal attachment of the heart tube to the yolk sac, causing the myocardium to be drawn out as the yolk sac recedes [40].

## Morphology and classification

### Anatomy

Congenital ventricular aneurysms are wide-mouthed protrusions from the ventricle that expand dyskinetically during systole. The aneurysm consists of thinned or dysplastic myocardium and fibrous tissue [30]. Whereas aneurysms are seen most often at the LV apex, they may involve the LV free wall, the septum, or the submitral and subaortic annular regions. Subannular aneurysms may have one or more smaller entry sites from the left ventricle around the mitral and aortic annuli, and the aneurysmal chamber either conforms to the shape of the annulus with multiple internal septations or extends significantly anteriorly, posteriorly or laterally. The extent of the aneurysm and its involvement of mitral supporting structures influences the degree of clinical symptoms.

Ventricular diverticula classically have a narrow orifice from the ventricle, are composed of endocardium, myocardium and epicardium, and demonstrate intrinsic contractility. They may occur as single or multiple small protrusions from the left or right ventricle, or as a large meandering channel extending into the extracardiac thoracic cavity or passing through the diaphragm in patients with Cantrell syndrome.

## Pathophysiology

Small aneurysms and diverticula are usually asymptomatic and found incidentally by echocardiography or angiography. Larger abnormalities may present as a deformity of the cardiac silhouette on chest X-ray. Systolic clicks or murmurs on auscultation have been described in patients with aneurysms and diverticula due to expansion of the lesion in systole or because of flow across the narrow diverticular neck. Mitral regurgitation may be the initial clinical feature in patients with submitral aneurysms or basilar congenital aneurysms that undermine the mitral support apparatus. Coronary compression with changes of ischemia or infarction has been reported with large aneurysms in the region of the left anterior descending or circumflex coronary arteries [36,41]. The ECG is frequently abnormal in patients with diverticula or other forms of congenital aneurysm, and includes findings of premature ventricular beats, ventricular tachycardia, left axis deviation and left bundle branch block [42].

The natural history of these disorders is variable. Cases described in utero have suffered fetal or perinatal death from heart failure with hydrops, or from leaking and rupture of the aneurysm or diverticulum, presaged by fetal pericardial effusion. In other prenatal cases, the size of the diverticulum remains unchanged or decreases with growth of the surrounding myocardium. LV aneurysms often continue to expand during gestation, with outcome related to the volume of the aneurysm relative to the ventricular cavity [30,43,44]. Postnatally, patients can present with symptoms of arrhythmias or thromboembolism resulting from clots that form in the aneurysmal chamber or diverticulum. Rupture of a thin-walled aneurysm or a high-pressure diverticulum can also result in tamponade and sudden death. Alternatively, some patients remain asymptomatic with no change in the size of the abnormal chamber over long-term follow-up [45]. Management of these rare anomalies must be individualized depending upon size and location of the defect and associated symptoms. Successful surgical repair with simple excision or modified Dor procedure has been reported [46,47]. Anticoagulation to prevent embolic complications should be considered if surgical resection is not feasible.

## Imaging

### Goals of the examination

In the setting of LV aneurysm or diverticula, echocardiographic examination has the following objectives:

- Detection of distortion, deformity or protrusion of ventricular cavities or subannular regions.
- Determination of the size of the communication between the cardiac chamber and the aneurysm or diverticulum.
- Assessment of the wall of the aneurysm or diverticulum for the presence of myocardium and contractility.
- Evaluation of the aneurysm or diverticulum for the presence of thrombus.
- Quantification of global ventricular function.
- Investigation for associated structural cardiac anomalies and valvular function.

### Prenatal assessment

Left ventricular aneurysm or diverticulum should be considered in the prenatal assessment of cardiomegaly, fetal hydrops, arrhythmia and pericardial effusion, as well as in the complete evaluation of fetuses with midline thoracoabdominal defects. Sizable aneurysms are easily detected during fetal echocardiography as distortions of the normal ventricular contour (Videoclips 36.4 and 36.5). Attention should be directed to the width of the connection to the chamber of origin, the presence of contractility or expansion of the aneurysmal region, and the presence of thrombus within the abnormal segment. Diverticula may be more elusive, but investigation of the apical and submitral areas for irregular sonolucent regions may lead to the diagnosis. In some cases of large diverticula, hydrops fetalis may be present (Fig. 36.7 and Videoclip 36.6).

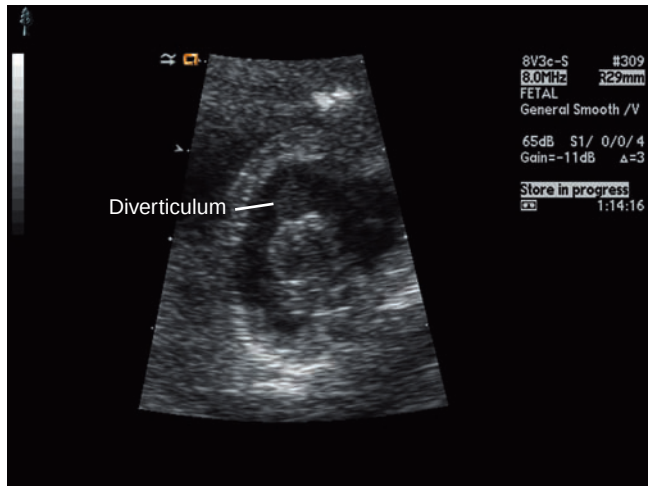


**Figure 36.7** Fetal echocardiogram demonstrating a large protrusion from the cardiac apex consistent with a congenital diverticulum.

### Imaging of children and adults

In children and adults, two-dimensional (2D) echocardiography detects outpouching of the ventricular cavity at the apex, from the LV free wall, the submitral region, or rarely from the RV free wall (Figs 36.8 and 36.9; Videoclip 36.7). The distinction between aneurysm and diverticulum is

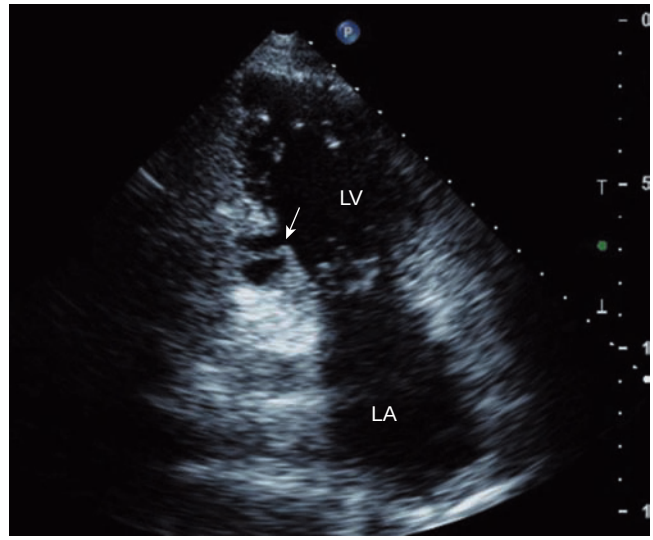


**Figure 36.8** Apical 2-chamber view from a 56-year-old female demonstrating a small left ventricular (LV) diverticulum arising from the inferior wall at the mid-ventricular level. The arrow designates the narrow neck of the diverticulum. LA, left atrium.

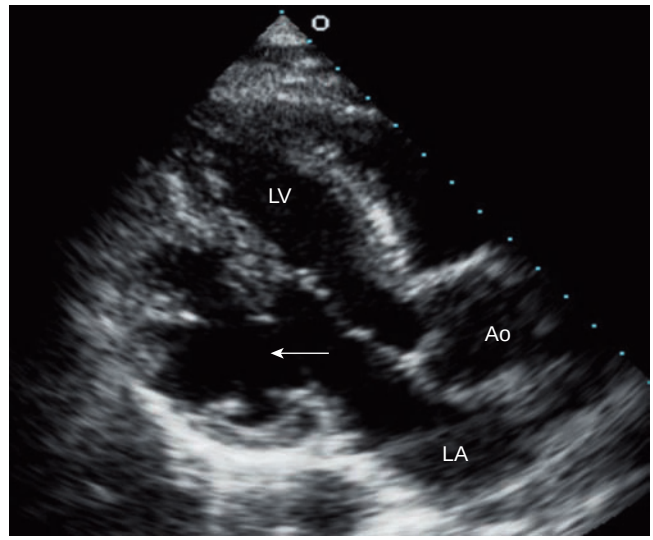


**Figure 36.9** Parasternal long-axis echocardiographic view from a 38-year-old male demonstrating a congenital left ventricular aneurysm arising from the posterobasal aspect of the ventricle. The arrow demonstrates the wide mouth of this aneurysmal chamber. No evidence of coronary artery disease was found in this patient by coronary angiography. Ao, aorta; LA, left atrium; LV, left ventricle.

determined by the width of the neck, the components of the wall and the contractility of the abnormal region. In some cases, a diverticulum may paradoxically appear to be a large extracardiac chamber but the entrance from the ventricle is covered by a thin membrane with a small orifice for entry and exit of flow (Fig. 36.10a–c and Videoclip 36.8). Submitral and subaortic aneurysms will appear as spaces in the vicinity of the mitral annulus or intervalvular fibrosa that communicate with the ventricular cavity (Fig. 36.11a,b). Mitral and aortic regurgitation will be present when there is significant undermining of the valvular support or perforation of the aneurysmal space into the left atrium (Videoclip 36.9). Segmental LV function should be assessed if coronary compromise is suspected from the location of the aneurysm. Thrombus may be present in the aneurysm and should be identified (Fig. 36.12). Contrast echocardiography may be helpful to define further the extent of the aneurysm or to demonstrate better the extracardiac extent of a diverticulum. This technique also permits differentiation of pooled blood from thrombus within the aneurysm (Fig. 36.13) [48].

When defects in the anterior abdominal wall are present, LV diverticula should be sought in addition to structural cardiac anomalies including dextrocardia, atrial septal defect, ventricular septal defect and tetralogy of Fallot. Less frequently, truncus arteriosus, tricuspid atresia, endocardial cushion defect, and anomalous pulmonary and systemic venous return have also been described in this complex anomaly [49].

### Postoperative assessment

Evaluation following repair of congenital aneurysm or diverticulum should include assessment of the effectiveness of the resection or exclusion method. Global and segmental ventricular function as well as mitral valve competence

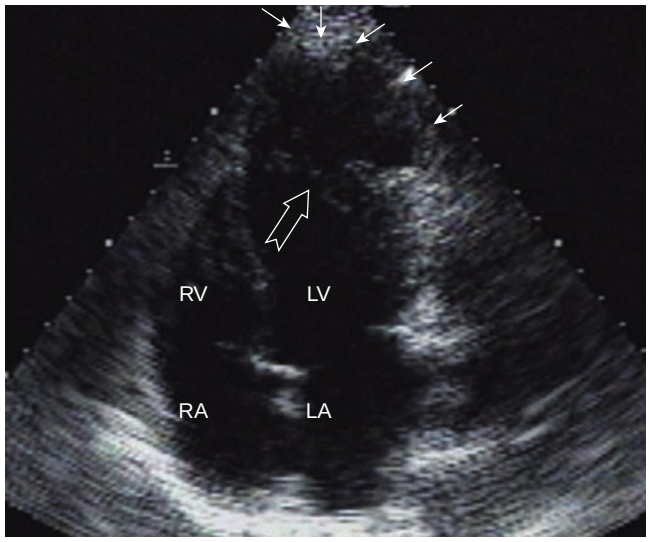


(a)

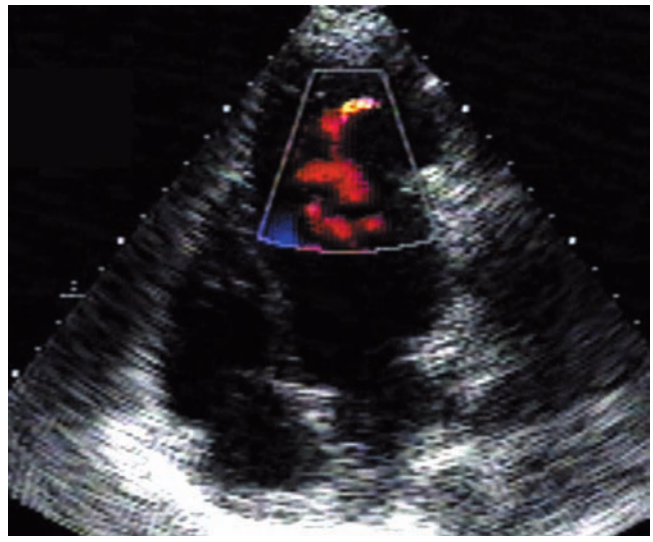

(b)

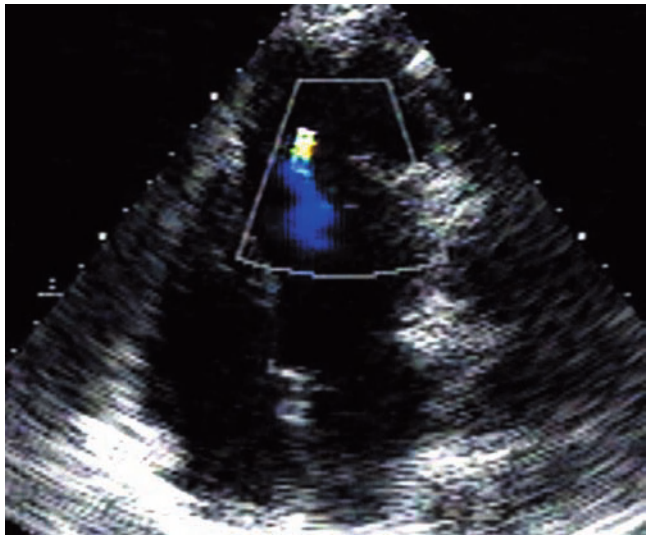

(c)

**Figure 36.10** **(a)** Apical echocardiographic view from a 7-year-old child with a large multilobulated apical diverticulum (white arrows). A linear fibromuscular structure demarcates the entrance to the diverticulum from the left ventricular (LV) cavity (open arrow). **(b)** Doppler color flow mapping depicting flow entering the diverticulum through the narrow neck (red flow stream). **(c)** Flow enters the LV cavity from the diverticulum (blue flow stream) indicating contractile function within the diverticulum. LA, left atrium; LV, left ventricle; RA, right atrium; RV, right ventricle.

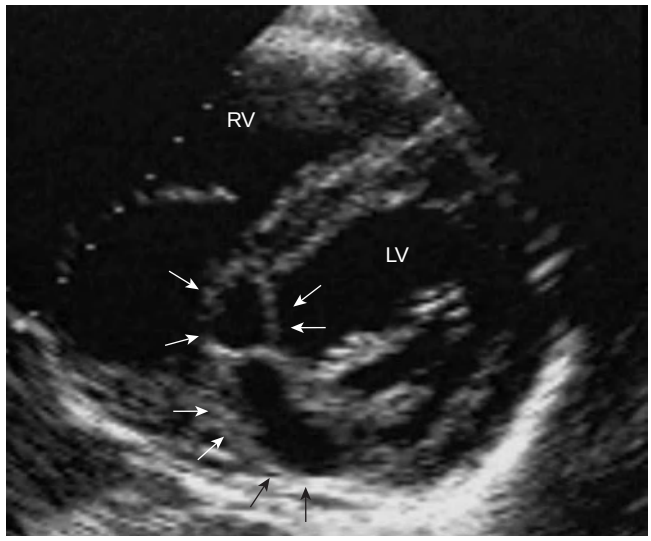


(a)

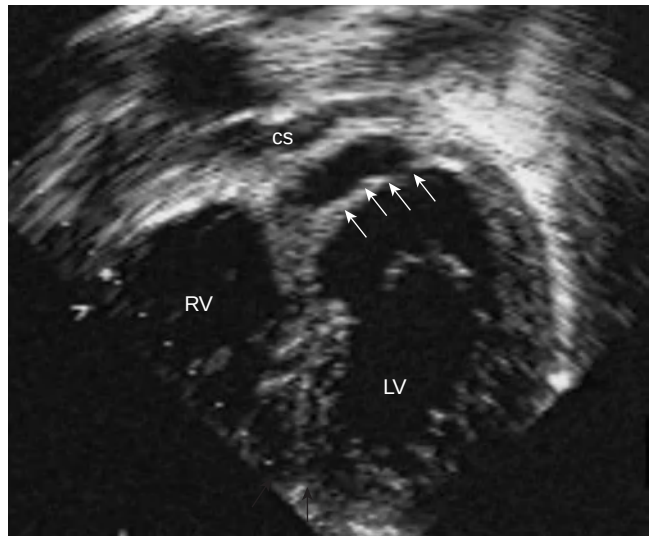


(b)

**Figure 36.11 (a)** Parasternal short-axis echocardiographic view from a 44-year-old Nigerian male. Multiple arrows delineate the septated sonolucent areas in the subaortic and mitral annular region indicative of a submitral aneurysm. **(b)** Apical echocardiographic view that has been posteriorly angulated to show the extent of the submitral aneurysm along the posterior aspect of the mitral annulus (arrows). The coronary sinus (cs) can be seen superior to the submitral aneurysm. LV, left ventricle; RV, right ventricle.

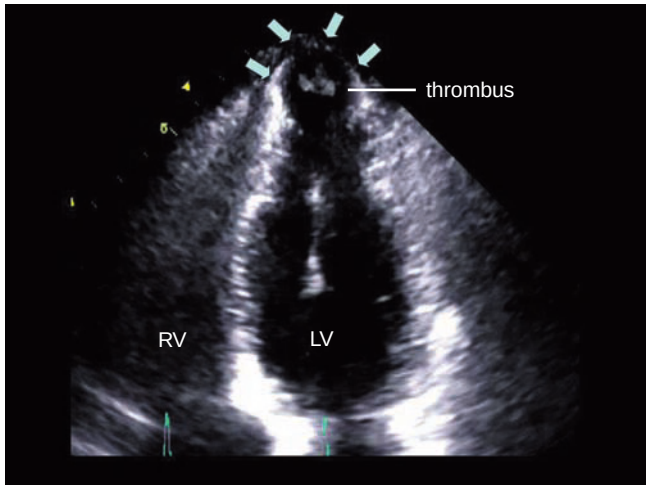


**Figure 36.12** Apical echocardiographic view in a 32-year-old female. A small apical aneurysm is shown (arrows) containing a thrombus. The patient had no history of coronary artery disease or ischemia, and left ventricular segmental function was otherwise normal. LV, left ventricle; RV, right ventricle.

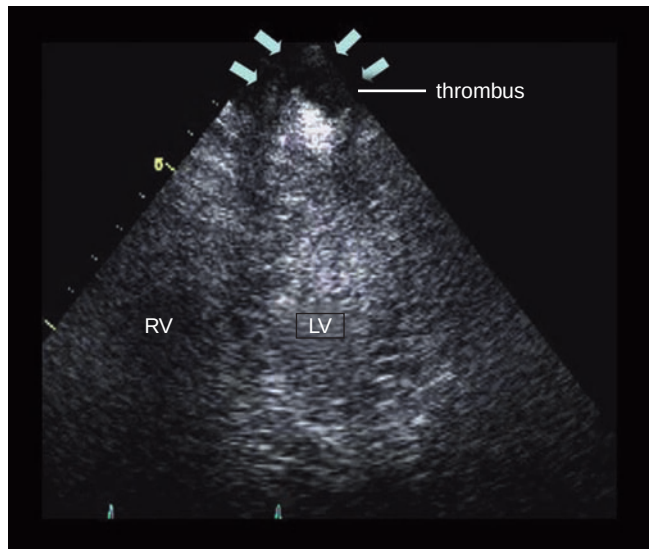


**Figure 36.13** Echocardiographic contrast study with left ventricular opacification showing filling of the apical aneurysm (arrows) with a filling defect corresponding to the thrombus noted in Fig. 36.12. LV, left ventricle; RV, right ventricle.

should be documented and followed over time. Patients with repair of associated structural congenital defects should be evaluated postoperatively as is lesion-appropriate and discussed in other sections of the text.

## Arrhythmogenic right ventricular dysplasia

### Definition

Arrhythmogenic right ventricular dysplasia (ARVD) is an uncommon disorder classified as a primary genetic cardiomyopathy [1]. It predominantly affects the right ventricle and is characterized by fibrofatty replacement of myocardium leading to progressive myocardial dysfunction and potentially lethal ventricular arrhythmias. To provide standardization of diagnosis of affected individuals and family members, a set of diagnostic criteria has been proposed by a task force of the European Society of Cardiology [50] (Box 36.1). These guidelines employ a series of major and minor criteria, which include structural and functional changes in the right

### Box 36.1 Criteria for diagnosis of arrhythmogenic right ventricular dysplasia

I. Global and/or regional dysfunction and structural alterations*

*Major*:

- Severe dilation and reduction of right ventricular ejection fraction with no (or only mild) left ventricular impairment.
- Localized right ventricular aneurysms (akinetic or dyskinetic areas with diastolic bulging).
- Severe segmental dilation of the right ventricle.

*Minor*:

- Mild global right ventricular dilation and/or ejection fraction reduction with normal left ventricle.
- Mild segmental dilation of the right ventricle.
- Regional right ventricular hypokinesia.

II. Tissue characterization of wall

*Major*:

- Fibrofatty replacement of myocardium on endomyocardial biopsy.

III. Repolarization abnormalities

*Minor*:

- Inverted T-waves in right precordial leads ($V_2$ and $V_3$) in people aged >12 years, in absence of right bundle branch block.

IV. Depolarization/conduction abnormalities

*Major*:

- Epsilon waves or localized prolongation (>110 ms) of the QRS complex in right precordial leads ($V_1$–$V_3$).

*Minor*:

- Late potentials (signal-averaged ECG).

V. Arrhythmias

*Minor*:

- Left bundle branch block type ventricular tachycardia (sustained and nonsustained) by ECG, Holter monitor or exercise testing.
- Frequent ventricular extrasystoles (>1000/24 hours) (Holter).

VI. Family history

*Major*:

- Familial disease confirmed at necropsy or surgery.

*Minor*:

- Family history of premature sudden death (<35 years) due to suspected right ventricular dysplasia.
- Familial history (clinical diagnosis based on present criteria).

*Criteria for diagnosis of arrhythmogenic right ventricular dysplasia*: The presence of two major criteria or one major and two minor criteria, or four minor criteria allows a diagnosis of ARVD.

Adapted from McKenna WJ, Thiene G, Nava A et al. Diagnosis of arrhythmogenic right ventricular dysplasia/cardiomyopathy. Task Force of the Working Group Myocardial and Pericardial Disease of the European Society of Cardiology and of the Scientific Council on Cardiomyopathies of the International Society and Federation of Cardiology. *Br Heart J* 1994;71:215–8.

ventricle, electrocardiographic abnormalities and arrhythmia, family history, and tissue characterization of the myocardium by biopsy. A combination of two major, one major plus two minor, or four minor criteria is considered diagnostic of ARVD.

## Incidence

Reports of the clinical description of ARVD appeared in the early 1980s, and since then the disorder has been recognized in Europe, Asia and the USA, with a prevalence of about 1 in 5000 persons [51–53]. The majority of cases manifest clinical symptoms between the ages of 15 and 40 years, with a male preponderance. ARVD is found in up to 20% of patients presenting with sudden death, and is a well recognized cause of sudden death in young athletes [54,55].

## Etiology

A familial occurrence of ARVD is reported, characterized by an autosomal dominant pattern of inheritance with

incomplete penetrance, and accounting for about 30% of cases. ARVD has been described in association with Naxos disease (palmoplantar keratoderma and woolly hair) and with Carvajal syndrome, both of which demonstrate autosomal recessive modes of inheritance [56]. Recent genetic studies have identified ARVD to be a genetically heterogeneous disorder of desmosomal dysfunction, with mutations discovered in genes encoding desmoplakin, plakophilin-2, plakoglobin, desmoglein-2, desmocollin-2, the cardiac ryanodine receptor RyR2, and regulatory sequences of transforming growth factor-β (TGF-β) [1,57,58].

Some sporadic cases of ARVD are isolated genetic mutations, but an association with infection by cardiotropic viral agents has also been reported, including coxsackievirus B3, enterovirus and adenovirus. The significance of this association is uncertain. It has been speculated that the disruption in myocardial function caused by ARVD may increase susceptibility to viral infection. Alternatively, the consequences of myocardial infection and inflammation may result in disruption of myocardial cellular junctions and ion channels, which leads to the clinical signs of ARVD [59].

## Morphology and classification

### Developmental considerations

Although ARVD classically makes its clinical appearance during adolescence and young adulthood, it has been diagnosed in utero, and there are a few case reports of younger children with ventricular tachycardia and evidence of RV and LV involvement with fibrofatty replacement [60–62]. The appearance of clinical symptoms usually later in life may be because it takes years of contractions and stress gradually to disrupt the myocardium, which is inherently flawed in its cellular structure. The added stress of vigorous exercise, particularly on the thinner-walled RV, may account for an earlier appearance of symptoms in individuals with ARVD who perform regular intensive sporting activities [63,64].

### Anatomy

The hallmark of ARVD is fibrofatty replacement of myocardial cells in the right ventricle. This abnormality results in thinning, localized aneurysmal bulging and eventually RV dilation with global dysfunction. Specific areas of involvement of the RV are commonly seen and have been termed the "triangle of dysplasia" [51]: the RV apex, RV outflow tract and subtricuspid area. LV involvement also occurs and may be more frequent than previously recognized. When assessed by sensitive techniques such as cardiac magnetic resonance, 84% of patients with ARVD were found to have evidence of LV involvement, including LV enlargement, decreased LV ejection fraction, LV intramyocardial fat, LV wall motion abnormalities, or late enhancement in a nonischemic pattern [57]. Microscopic study of the bundle of His and its branches has shown fibrous and fibrofatty infiltration in 68% of a series of ARVD patients with sudden death [54].

## Pathophysiology

Patients with ARVD most commonly present with syncope, palpitations or sudden death. ECG findings include frequent premature ventricular contractions, epsilon waves, inverted T-waves, prolongation of the QRS, and delayed S-wave upstroke in the right precordial leads. Ventricular tachycardia with left bundle branch morphology can be detected on Holter monitoring or exercise testing, and is often the proximate cause of sudden death. With progressive involvement of the RV myocardium, dysfunction may eventuate with signs of right heart failure. The development of LV involvement with biventricular failure is a poor prognostic sign.

The natural history reported for patients with symptomatic ARVD from a European population includes a high mortality from sudden death and progressive heart failure [65]. However, studies from populations including symptomatic probands and asymptomatic patients detected by family screening show a much more favorable long-term outcome with medical therapy and implantable cardiac defibrillator treatment for those at high risk for sudden death [66].

## Imaging

### Goals of the examination and transthoracic imaging

The goals of echocardiographic examination in the setting of ARVD can be summarized as follows:

- Detection of RV wall thinning, saccular aneurysms and segmental dysfunction in the "triangle of dysplasia."
- Quantification of RV chamber enlargement, particularly RV outflow tract diameter.
- Evaluation of RV trabecular disarray.
- Detection of a highly reflective moderator band.
- Assessment of global RV and LV function.

### Prenatal assessment

Although ARVD is extremely rare in the fetus, infant and younger child, it should be considered in the evaluation of fetal arrhythmia or unexplained right heart enlargement and dysfunction. Localized areas of thinning and segmental dysfunction of the right ventricle may be apparent [59].

### Imaging of children and adults

Although it is an uncommon disorder, ARVD should be considered in the differential diagnosis of all children, adolescents and adults presenting with syncope or palpitations. Two-dimensional echocardiographic study should focus carefully on RV wall thickness, and segmental and global RV function. RV wall definition is often limited in standard 2D echo exams, and the examiner should be intentional about specifically focusing on the RV outflow tract thickness and contractility, the subtricuspid annular region of the RV lateral wall, the inferior RV wall in short-axis views, and the apex. Subxiphoid views often provide optimal resolution of the subannular and diaphragmatic surface of the RV,

whereas the best imaging of the lateral wall and apex may require off-axis apical views. It may be helpful to employ a high-frequency probe specifically to scan the RV free wall and apical myocardium.

Morphologic abnormalities that have been described in echocardiographic study of patients with ARVD include: trabecular disarray of the RV, hyperreflectivity of the moderator band, and areas of focal RV wall thinning with saccular aneurysms [67,68] (Figs 36.14–36.17; Videoclip 36.10).

Assessment of RV size and function is an important aspect of the evaluation of patients for ARVD. In a review of echocardiograms of patients from a multicenter registry for ARVD, the most common and readily quantified abnormality was dilation of the RV outflow tract, which was present in all

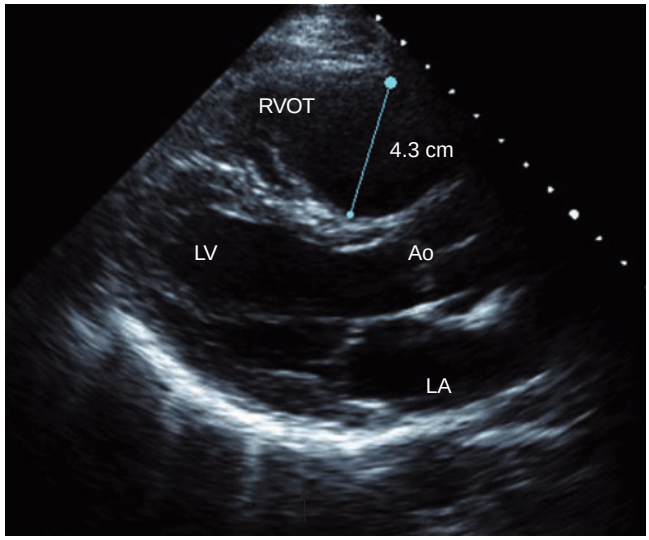


**Figure 36.14** Parasternal long-axis echocardiographic view from a patient with arrhythmogenic right ventricular dysplasia (ARVD) demonstrating the dilation of the right ventricular outflow tract. Ao, aorta; LA, left atrium; LV, left ventricle; RVOT, right ventricular outflow tract.

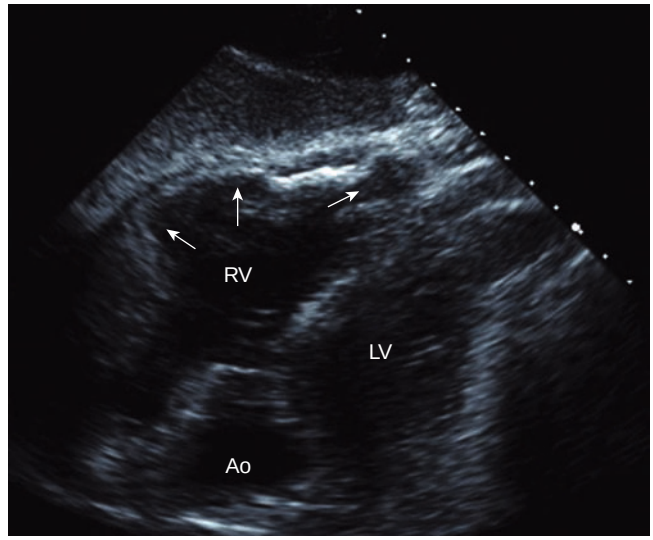


**Figure 36.16** Subcostal echocardiographic image demonstrating thinning and aneurysmal deformation of the right ventricular (RV) free wall (arrows) near the tricuspid annulus and at the apex of the RV, which is typical of changes seen in arrhythmogenic right ventricular dysplasia (ARVD). Ao, aorta; LV, left ventricle.

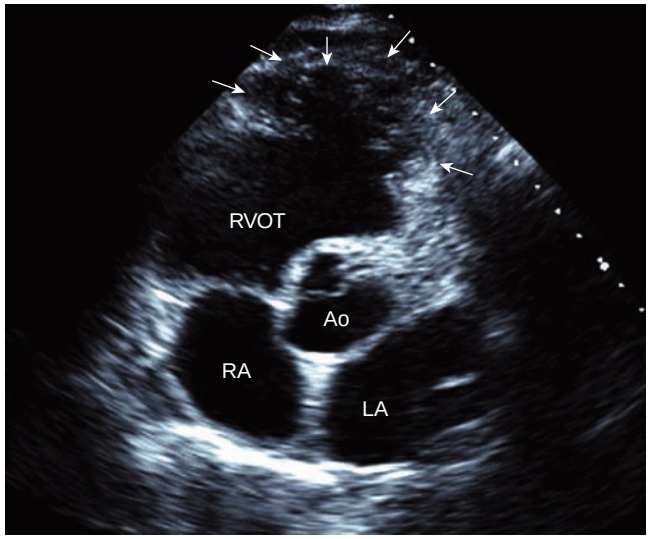


**Figure 36.15** Parasternal short-axis echocardiographic view at the base of the heart in a patient with thinning and aneurysmal changes in the free wall of the right ventricular outflow tract (RVOT, arrows). Ao, aorta; LA, left atrium; RA, right atrium.

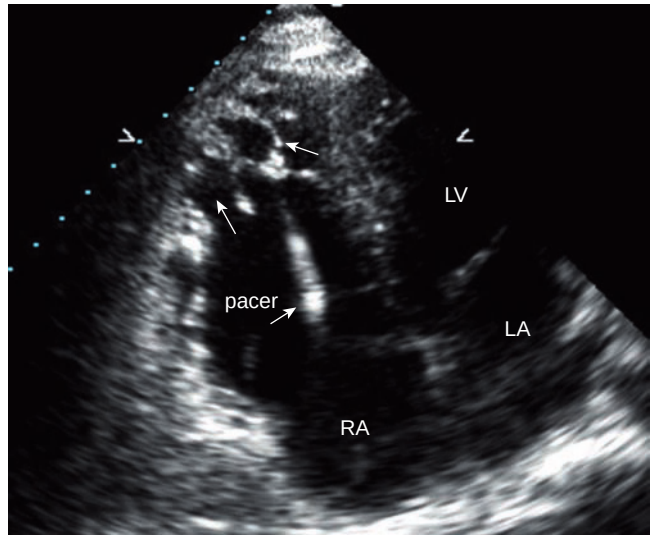


**Figure 36.17** Apical echocardiographic view in a patient with arrhythmogenic right ventricular dysplasia (ARVD) demonstrating prominent trabeculations in a somewhat disordered pattern (arrows). LA, left atrium; LV, left ventricle; RA, right atrium; pacer, pacing wire.

patients who met Task Force criteria. An RVOT dimension of >30 mm for adult subjects, measured in diastole in the parasternal long-axis view, was a strong indicator of RV enlargement (see Fig. 36.14). Dimensional measurements of the RV sinus may also be abnormal but because of the segmental nature of the myocardial process, dilation of the RV body is often a late feature in the course of the disease, accompanying global RV dysfunction. Methods to quantify RV systolic function by echocardiography have traditionally been problematic. However, RV fractional area change (FAC) from the 4-chamber view, myocardial performance index (MPI), and tricuspid annular tissue Doppler imaging (TDI) measurements have all been utilized as measures of RV dysfunction in patients with ARVD [67,69,70]. In the multicenter registry study, an RV FAC >32% was considered normal RV function, FAC 27–32% was mildly impaired, and FAC <27% was severely impaired [67]. Cardiac magnetic resonance imaging is often recommended for patients with suspected ARVD for quantification of RV volume and segmental and global function, and for the ability to detect fatty replacement [71].

Contrast echocardiography may play a role in facilitating the definition of RV myocardial borders and chamber size, and assisting in the detection of regional wall motion abnormalities. One report has suggested that this technique can also detect altered areas of perfusion in regions where fatty replacement of myocardium has occurred [72,73].

Left ventricular chamber size and function should be measured, as LV involvement does occur with ARVD. Rarely, regions of thinning and segmental dysfunction may be found in the left ventricle as well.

## References


1. Maron BJ, Towbin JA, Thiene G et al. Contemporary definitions and classification of the cardiomyopathies: An American Heart Association scientific statement from the Council on Clinical Cardiology, Heart Failure and Transplantation Committee; Quality of Care and Outcomes Research and Functional Genomics and Translational Biology Interdisciplinary Working Groups; and Council on Epidemiology and Prevention. *Circulation* 2006;113: 1807–1816.
2. Ichida F, Hamamichi Y, Miyawaki T et al. Clinical features of isolated noncompaction of the ventricular myocardium. *J Am Coll Cardiol* 1999;34:233–40.
3. Pignatelli RH, McMahon CJ, Dreyer WJ et al. Clinical characterization of left ventricular noncompaction in children: a relatively common form of cardiomyopathy. *Circulation* 2003;108:2672–8.
4. Oechslin E, Attenhofer C, Jost C et al. Long-term follow-up of 34 adults with isolated left ventricular noncompaction: a distinct cardiomyopathy with poor prognosis. *J Am Coll Cardiol* 2000;36: 493–500.
5. Lilje C, Razek V, Joyce JJ et al. Complications of noncompaction of the left ventricular myocardium in a paediatric population: a prospective study. *Eur Heart J* 2006;27:1855–60.
6. Nugent AW, Daubeney PEF, Chondros P et al. The epidemiology of childhood cardiomyopathy in Australia. *New Engl J Med* 2003;348:1639–46.
7. Bione S, D'Adamo P, Maestrini E et al. A novel X-linked gene, G4.5, is responsible for Barth syndrome. *Nat Genet* 1996;12:385–9.
8. Bleyl SB, Mumford BR, Brown-Harrison M-C et al. Xq28-linked noncompaction of the left ventricular myocardium: prenatal diagnosis and pathologic analysis of affected individuals. *Am J Med Genetics* 1997;72:257–65.
9. Vatta M, Mohapatra B, Jimenez S et al. Mutations in *Cypher/* ZASP in patients with dilated cardiomyopathy and left ventricular non-compaction. *J Am Coll Cardiol* 2003;42:2014–27.
10. Sasse-Klaassen S, Probst S, Gerull B et al. Novel gene locus for autosomal dominant left ventricular noncompaction maps to chromosome 11p15. *Circulation* 2004:109;2720–3.
11. Ichida F, Tsubata S, Bowles KR et al. Novel gene mutations in patients with left ventricular noncompaction or Barth syndrome. *Circulation* 2001:103;1256–63.
12. Mandel K, Gruenebaum E, Benson L. Noncompaction of the myocardium associated with Roifman syndrome. *Cardiol Young* 2001:11;240–3.
13. Happle R, Daniels O, Koopman RJJ. MIDAS syndrome (microphthalmia, dermal aplasia, and sclerocornea): an X-linked phenotype distinct from Goltz syndrome. *Am J Med Genet* 1993; 47:710–3.
14. Finsterer J, Stollberger C, Wanschitz J et al. Nail-patella syndrome associated with respiratory chain disorder. *Eur Neurol* 2001;46:92–5.
15. Wong JA, Bofinger MK. Noncompaction of the ventricular myocardium in Melnick–Needles syndrome. *Am J Med Genet* 1997;71:72–5.
16. McMahon CJ, Chang AC, Pignatelli RH et al. Left ventricular noncompaction cardiomyopathy in association with trisomy 13. *Pediatr Cardiol* 2005;26:477–9.
17. Sedmera D, Pexieder T, Vuillemin M et al. Developmental patterning of the myocardium. *Anat Rec* 2000;258:319–37.
18. Winer N, Lefevre M, Nomballais MF et al. Persisting spongy myocardium. A case indicating the difficulty of antenatal diagnosis. *Fetal Diagn Ther* 1998;13:227–32.
19. Moura C, Hillion Y, Daikha-Dahmane F et al. Isolated noncompaction of the myocardium diagnosed in the fetus: two sporadic and two familial cases. *Cardiol Young* 2002;12:278–83.
20. Finsterer J, Stollberger C, Blazek G, Spahits E. Cardiac involvement in myotonic dystrophy, Becker muscular dystrophy and mitochondrial myopathy: a five-year follow-up. *Can J Cardiol* 2001;17:1061–9.
21. Burke A, Mont E, Kutys R, Virmani R. Left ventricular noncompaction: a pathological study of 14 cases. Hum Pathol 2005;36: 403–11.
22. Jenni R, Wyss CA, Oechslin EN, Kaufmann PA. Isolated ventricular noncompaction is associated with coronary microcirculatory dysfunction. *J Am Coll Cardiol* 2002;39:450–4.
23. Ritter M, Oechslin E, Sutsch G et al. Isolated noncompaction of the myocardium in adults. *Mayo Clin Proc* 1997;72:26–31.
24. Murphy RT, Thaman R, Blanes JG et al. Natural history and familial characteristics of isolated left ventricular noncompaction. *Eur Heart J* 2005;26:187–92.
25. Jenni R, Oechslin E, Schneider J et al. Echocardiographic and pathoanatomical characteristics of isolated left ventricular

non-compaction: a step towards classification as a distinct cardiomyopathy. *Heart* 2001;86:666–71.
26. Frischknecht BS, Attenhofer Jost CH, Oechslin EN et al. *J Am Soc Echocardiogr* 2005;18:865–72.
27. Karatza AA, Holder SE, Gardiner HM. Isolated non-compaction of the ventricular myocardium: prenatal diagnosis and natural history. *Ultrasound Obstet Gynecol* 2003;21:75–80.
28. Lowery MH, Martel JA, Zambrano JP et al. Noncompaction of the ventricular myocardium: the use of contrast-enhanced echocardiography in diagnosis. *J Am Soc Echocardiogr* 2003;16:94–6.
29. Petersen SE, Selvanayagam JB, Wiesmann F et al. Left ventricular non-compaction: insights from cardiovascular magnetic resonance imaging. *J Am Coll Cardiol* 2005;46:101–5.
30. McMahon CJ, Pignatelli RH, Nagueh SF et al. Left ventricular non-compaction cardiomyopathy in children: characterization of clinical status using tissue Doppler-derived indices of left ventricular diastolic relaxation. *Heart* 2007;93:676–81.
31. Papagiannis J, Van Praagh R, Schwint O et al. Congenital left ventricular aneurysm: clinical, imaging, pathologic, and surgical findings in seven new cases. *Am Heart J* 2001;141:491–9.
32. Cumming GR. Congenital diverticulum of the right ventricle. *Am J Cardiol* 1969;23:294–7.
33. Higgins CB, Hayden WG, Copeland J, Stinson EB. Congenital diverticulum of the right ventricle: clinical and angiographic features. *Br J Radiol* 1976;49:188–90.
34. Congenital diverticula of the left and right ventricles: 3 cases. *Am J Cardiol* 1984;53:342–4.
35. Mardini MK. Congenital diverticulum of the left ventricle: report of two unusual cases. *Br Heart J* 1984;51:321–6.
36. Baltaxe HA, Wilson WJ, Amiel M. Diverticulosis of the left ventricle. *Am J Radiol* 1979;133:257–61.
37. Chesler E, Joffe N, Schamroth L, Meyers A. Annular subvalvular left ventricular aneurysms in the South African Bantu. *Circulation* 1965;32:43–51.
38. Tsujimoto H, Takeshita S, Kawamura Y et al. Isolated congenital left ventricular diverticulum with perinatal dysrhythmia: a case report and review of the literature. *Pediatr Cardiol* 2000;21:175–9.
39. Shizukuda Y, Murakami H. Iwakura M et al. Siblings with left ventricular diverticulum and hypertrophic cardiomyopathy *J. Cardiol* (Japan) 1988;18:867–74.
40. Cantrell JR, Haller JA, Ravitch MM. A syndrome of congenital defects involving the abdominal wall, sternum, diaphragm, pericardium and heart. *Surg Gynecol Obstet* 1958;107:602–13.
41. Simpson L, Duncan JM, Stainback RF. Perforated submitral left ventricular aneurysm resulting in severe mitral annular regurgitation. *Tex Heart Inst J* 2006;33:492–4.
42. Hamaoka K, Onaka M, Tanaka T, Onuchi Z. Congenital ventricular aneurysm and diverticulum in children. *Pediatr Cardiol* 1987;8:169–75.
43. Bernasconi A, Delezoide AL, Menez F et al. Prenatal rupture of a left ventricular diverticulum: a case report and review of the literature. *Prenat Diagn* 2004;24:504–7.
44. McElhinney DB, Silverman NH. Left ventricular aneurysm in the fetus: a diagnosis with a mixed prognosis. *Cardiol Young* 1999;9:123–6.
45. Archbold RA, Robinson NM, Mills PG. Long-term follow-up of a true contractile left ventricular diverticulum. *Am J Cardiol* 1999;83:810–3.
46. Pome G, Vignati G, Mauri L et al. Isolated congenital left ventricular diverticulum. *Eur J Cardiothorac Surg* 1995;9:709–12.
47. Yoshizumi K, Ishino K, Kawada M et al. Dor procedure for left ventricular diverticulum with mitral regurgitation in an infant. *Ann Thorac Surg* 2005;80:332–3.
48. Yalonetsky S, Agmon Y, Lessick J. Contrast echocardiographic imaging of left ventricular diverticulum in adult patients. *J Am Soc Echo* 2007;20:198.e1–e3.
49. Nicod P, Laird WP, Firth BG et al. Congenital diverticula of the left and right ventricles: 3 cases. *Am J Cardiol* 1984;53:342–4.
50. McKenna WJ, Thiene G, Nava A et al. Diagnosis of arrhythmogenic right ventricular dysplasia/cardiomyopathy: Task Force of the Working Group Myocardial and Pericardial Disease of the European Society of Cardiology and of the Scientific Council on Cardiomyopathies of the International Society and Federation of Cardiology. *Br Heart J* 1994;71:215–8.
51. Duncan WT, Garson A Jr, Gilette DC. Arrhythmogenic right ventricular dysplasia: A cause of ventricular tachycardia in children with apparently normal hearts. *Am Heart J* 1981;102:745.
52. Marcus FI, Fontaine GH, Guiraudon G et al. Right ventricular dysplasia: a report of 24 adult cases. *Circulation* 1982;65:384–98.
53. Peters S, Trummel M, Meyners W. Prevalence of right ventricular dysplasia: cardiomyopathy in a non-referral hospital. *Int J Cardiol* 2004;97:499–501.
54. Thiene G, Nava A, Corrado D et al. Right ventricular cardiomyopathy and sudden death in young people. *N Engl J Med* 1988;318:129–133.
55. Tabib A, Loire R, Chalabreysse L et al. Circumstances of death and gross and microscopic observations in a series of 200 cases of sudden death associated with arrhythmogenic right ventricular cardiomyopathy and/or dysplasia. *Circulation* 2003;108:3000–5.
56. Protonotarios N, Tsatsopoulou A. Naxos disease and Carvajal syndrome: cardiocutaneous disorders that highlight the pathogenesis and broaden the spectrum of arrhythmogenic right ventricular cardiomyopathy. *Cardiacvasc Pathol* 2004;13:185.
57. Van Tintelen JP, Entius MM, Bhuiyan ZA et al. Plakophilin-2 mutations are the major determinant of familial arrhythmogenic right ventricular dysplasia/cardiomyopathy. *Circulation* 2006;113:1650–8.
58. Sen-Chowdhry S, Syrris P, Ward D et al. Clinical and genetic characterization of families with arrhythmogenic right ventricular dysplasia/cardiomyopathy provides novel insights into patterns of disease expression. *Circulation* 2007;115:1710–20.
59. Bowles NE, NiJ, Marcus F, Towbin JA. The detection of cardiotropic viruses in the myocardium of patients with arrhythmogenic right ventricular dysplasia/cardiomyopathy. *J Am Coll Cardiol* 2002;39:892–5.
60. Rustico MA, Benettoni A, Fontaliran F, Fontaine G. Prenatal echocardiographic appearance of arrhythmogenic right ventricle dysplasia: a case report. *Fetal Diagn Ther* 2001;16:433–6.
61. Dungan WT, Garson A Jr, Gilette DC. Arrythmogenic right ventricular dysplasia: A cause of ventricular tachycardia in children with apparently normal hearts. *Am Heart J* 1981;102:745–750.
62. Atalay S, Imamoglu A, Gumus H et al. Value of the echocardiographic findings of arrhythmogenic right ventricular dysplasia with left ventricular involvement in a child. *Pediatr Cardiol* 1996;17:40–2.

63. Marcus F, Towbin JA. The mystery of arrhythmogenic right ventricular dysplasia/cardiomyopathy: from observation to mechanistic explanation. *Circulation* 2006;114:1794–5.
64. Daubert C, Vauthier M, Carre F et al. Influence of exercise and sport activity on functional symptoms and ventricular arrhythmias in arrhythmogenic right ventricular disease. *J Am Coll Cardiol* 1994;23(Suppl.):34A.
65. Hulot J-S, Jouven X, Empana J-P et al. Natural history and risk stratification of arrhythmogenic right ventricular dysplasia/cardiomyopathy. *Circulation* 2004;110:1879–84.
66. Dalal D, Khurram N, Bomma C et al. Arrhythmogenic right ventricular dysplasia: a United States experience. *Circulation* 2005;112:3823–32.
67. Scognamiglio R, Rasoli G, Nava A et al. Contribution of cross-sectional echocardiography to the diagnosis of right ventricular dysplasia at the asymptomatic stage. *Eur Heart J* 1989;10:538–42.
68. Yoerger DM, Marcus F, Sherrill D et al. Echocardiographic findings in patients meeting Task Force criteria for arrhythmogenic right ventricular dysplasia: new insights from the multidisciplinary study of right ventricular dysplasia. *J Am Coll Cardiol* 2005;45:860–5.
69. Yoerger DM, Marcus F, Sherrill D et al. Right ventricular myocardial performance index in probands from the multicenter study of arrhythmogenic right ventricular dysplasia. *J Am Coll Cardiol* 2005;45:147A.
70. Lindstrom L, Wilkenshoff UM, Larsson H, Wranne B. Echocardiographic assessment of arrhythmogenic right ventricular cardiomyopathy. *Heart* 2001;86:31–8.
71. Tandri H, Castillo E, Ferrari VA et al. Magnetic resonance imaging of arrhythmogenic right ventricular dysplasia. *J Am Coll Cardiol* 2006;48:2277–84.
72. Lopez-Fernandez T, Garcia-Fernandez MA, Perez DE, Moreno YM. Usefulness of contrast echocardiography in arrhythmogenic right ventricular dysplasia. *J Am Soc Echocardiogr* 2004;17:391–3.
73. Nemes A, Vletter WB, Scholten MG, enCate FJ. Contrast echocardiography for perfusion in right ventricular cardiomyopathy. *Eur J Echocardiogr* 2005;6:470–2.

# 7 Acquired Pediatric Heart Disease

*Echocardiography in Pediatric and Congenital Heart Disease: From Fetus to Adult*
Edited by Wyman W. Lai, Luc L. Mertens, Meryl S. Cohen and Tal Geva
 ISBN: 978-1-405-17401-5

# 37 Kawasaki Disease

**Erik C. Michelfelder**
Fetal Heart Program, Cincinnati Children's Hospital Medical Center, Cincinnati, OH, USA

## Definition

Kawasaki disease is an acute systemic vasculitis of as yet unknown cause, first described in Japanese by Tomisaku Kawasaki in 1967 [1], and subsequently in English in 1974 [2]. Since its original description, mucocutaneous lymph node syndrome – or Kawasaki disease – has come to be recognized as a common form of acquired heart disease in the pediatric population, with a worldwide distribution and affecting children of all races. Kawasaki disease is diagnosed by recognition of its principal signs and symptoms (Box 37.1), which characteristically include fever, changes in the extremities, polymorphous skin exanthema, nonexudative conjunctivitis, changes in the lips and mucous membranes, and cervical lymphadenopathy. In addition to the "classic" clinical findings, there are multiple associated features that can be recognized, including (but not limited to) cardiac involvement, arthritis/arthralgia, vomiting, diarrhea, gallbladder hydrops, and irritability. Recent recommendations have addressed the diagnosis of "incomplete" Kawasaki disease, where persistent fever is identified in patients with only two or three classic clinical findings. In this setting, incomplete Kawasaki disease may be diagnosed when additional laboratory data and/or echocardiographic findings support the diagnosis [3].

**Box 37.1 "Classic" clinical features of Kawasaki disease [3]**

- Fever persisting ≥5 days
- Presence of *at least* four principal clinical features:
  - Changes in extremities:
    Acute: erythema of palms and/or soles, edema of hands and/or feet
    Subacute: periungual desquamation of fingers and toes
  - Polymorphous exanthema
  - Bilateral nonexudative conjunctival injection
  - Changes in lips and oral mucosa: erythema, cracked lips, strawberry tongue, diffuse injection of oral/pharyngeal mucosa
  - Cervical lymphadenopathy (>1.5 cm node), usually unilateral
- Exclusion of diseases with similar findings

## Incidence

Kawasaki disease primarily affects young children, with 80% of cases reported in children under 5 years of age, and 90% of cases occurring in children under 8 years of age [4]. In Japan, where the incidence of Kawasaki disease is greatest, the disease occurs in 134 per 100 000 children aged under 5 years. Outside of Japan, the incidence ranges from 8 to 67 per 100 000 children under 5 years, depending on the ethnicity of the population being studied [5]. The disease occurs with highest frequency in children of Asian descent, followed by African–Americans, Hispanics and Caucasians [6]. Males are affected more frequently than females, in a ratio of 1.5 to 1.

## Etiology

The etiology of Kawasaki disease is unknown, although an infectious cause is likely given the clinical and epidemiologic characteristics of the disease. In addition to its classic clinical characteristics, Kawasaki disease also features winter-spring predominance, a characteristic age distribution, evidence of community outbreaks, and evidence of prior epidemic periods. Laboratory data obtained during the illness also support an infectious agent as the cause of Kawasaki disease. Prior theories, such as toxic exposures or bacterial superantigen-mediated inflammation, have not gained widespread acceptance. The pathogen responsible for Kawasaki disease, however, remains unidentified.

*Echocardiography in Pediatric and Congenital Heart Disease: From Fetus to Adult*
Edited by Wyman W. Lai, Luc L. Mertens, Meryl S. Cohen and Tal Geva
 ISBN: 978-1-405-17401-5

## Pathophysiology

The acute febrile phase of the illness features a diffuse microvascular angiitis, with endarteritis and perivascular inflammation of the coronary arteries [7]. In addition, the inflammatory process may involve pericarditis, myocarditis [8] and/or endocarditis. The acute phase of the disease, therefore, can be associated with pericardial effusion, acute myocardial dysfunction and valvar regurgitation. In the subacute phase – clinically following resolution of fever – there is a persistent panvasculitis of the coronary arteries, which may be associated with ectasia, aneurysm, and/or thrombosis of these vessels. Pericarditis, myocarditis and endocarditis are also frequently seen in this phase.

In the convalescent and chronic phases of the disease, resolution of the microvascular angiitis is replaced by granulation and intimal thickening of the coronary arteries. Coronary artery scarring, stenosis and calcification are typically seen in later phases of the illness. Thrombosis of the coronary arteries can be observed in all phases of the disease. Approximately 50–60% of coronary artery aneurysms will demonstrate evidence of regression over the first 3–5 years following acute Kawasaki disease [9,10]; however, the mechanism for regression of aneurysms can consist of either myointimal proliferation with narrowing of the vessel lumen, or organization of endovascular thrombus [11]. Mitral regurgitation and myocardial dysfunction seen in later phases of the disease are usually due to myocardial and papillary muscle ischemia from coronary disease. In addition to these anatomic abnormalities, the coronary endothelial function has been shown to be abnormal in patients in the chronic phases of Kawasaki disease, with reduced coronary artery flow reserve and vascular reactivity [12–14].

## Imaging

### General principles

Because Kawasaki disease usually presents acutely (and subacutely) as a pancarditis, echocardiographic assessment must focus on the endocardium, myocardium and pericardium in addition to assessment for coronary artery abnormalities. Identification of pericardial effusion, mitral regurgitation or myocardial dysfunction may in fact be associated with an elevated risk of coronary artery changes [15]. These findings may also increase clinical suspicion of Kawasaki disease when clinical criteria are incomplete [3]. In patients with coronary artery abnormalities who are followed chronically, the focus of the echocardiographic assessment shifts to assessment of coronary artery insufficiency, regional and global myocardial function, and ischemia-related atrioventricular valve dysfunction. Children with Kawasaki disease tend to be extremely irritable, making transthoracic imaging a challenge, particularly when the focus is on the coronary arteries. Sedation in young children is recommended for performance of the study.

### Goals of the examination

Although the pathophysiology may change in acute, subacute and chronic phases of the disease, echocardiography must focus on coronary artery abnormalities, valvar dysfunction, and myocardial function in all phases of the illness:

- Identification of coronary artery abnormalities:
  - evidence of perivascular inflammation;
  - ectasia;
  - aneurysm;
  - localization of coronary artery abnormalities;
  - classification of severity of coronary artery abnormalities;
  - identification of coronary artery thrombus;
  - identification of coronary artery stenosis.
- Identification of valvar involvement:
  - mitral and tricuspid valve regurgitation;
  - aortic regurgitation;
  - aortic root dilation.
- Identification of myocardial involvement:
  - global myocardial dysfunction;
  - regional myocardial dysfunction.
- Identification of pericardial involvement:
  - pericardial effusion.

### Consensus recommendations

The pathophysiology of Kawasaki disease dictates that the cardiovascular sequelae of the disease appear with variable frequency during both the acute and subacute phases, which encompass the first 6–8 weeks of the illness. During these phases, consensus recommendations published by the American Heart Association [3,16] recommend echocardiographic imaging at diagnosis, at 2 weeks and again at 6–8 weeks after diagnosis. During this period of time, acute changes in valvar or myocardial function, pericardial effusion, or acute coronary artery changes should be noted. In addition, imaging in the first 6–8 weeks of illness includes the period during which transient changes in coronary artery dilation and ectasia will often resolve. Alternatively, it is during this same time period that coronary artery aneurysms obtain their maximum size [17]. In complex cases where coronary artery aneurysms and/or thrombosis, significant valvar regurgitation, effusion or myocardial dysfunction occur, echocardiography during the acute and subacute phases should be performed as indicated by clinical circumstances. For patients with chronic – primarily coronary – abnormalities, annual follow-up with echocardiography is recommended. These evaluations are aimed at identification of resolution of coronary artery abnormalities and evidence of coronary artery thrombosis/stenosis, valvar dysfunction or myocardial dysfunction/ischemia. The proposed algorithm

**Table 37.1** Consensus recommendations for follow-up imaging in Kawasaki disease

| Risk level | Diagnostic imaging | Invasive testing |
|---|---|---|
| **I** (No CA changes at any stage of illness) | None | None |
| **II** (Transient CA ectasia resolving within first 6–8 weeks) | None | None |
| **III** (1 small–medium CA aneurysm) | Echocardiogram, ECG yearly; biennial stress test, perfusion imaging | Angiography, if noninvasive imaging suggests ischemia |
| **IV** (≥1 large or giant CA aneurysm, or multiple/complex aneurysms in same CA, no stenosis) | Echocardiogram, ECG twice yearly; annual stress test, perfusion imaging | Angiography at 6–12 months after diagnosis or as clinically indicated; repeated angiography if noninvasive testing suggests ischemia |
| **V** (CA obstruction) | Echocardiogram, ECG twice yearly; annual stress test, perfusion imaging | Angiography to evaluate therapeutic options |

CA, coronary artery; ECG, electrocardiogram.
Adapted from Newburger JW, Takahashi M, Gerber MA et al. Diagnosis, treatment, and long-term management of Kawasaki disease: a statement for health professionals from the Committee on Rheumatic Fever, Endocarditis and Kawasaki Disease, Council on Cardiovascular Disease in the Young, American Heart Association. *Circulation* 2004;110:2747–71.

for long-term follow-up echocardiography, myocardial perfusion imaging and angiography is summarized in Table 37.1.

## General principles for coronary artery assessment

Coronary artery abnormalities are the most significant short- and long-term sequelae of Kawasaki disease. Echocardiography is a highly sensitive, specific and noninvasive means of assessing the proximal coronary arterial system, and thus occupies a central role in the diagnostic workup of children with Kawasaki disease.

In general, coronary artery imaging should be performed at the highest feasible transducer frequency. Reducing two-dimensional (2D) gain and dynamic range (i.e., compression) settings will often improve demonstration of the endovascular lumen and thereby improve coronary artery imaging. Too much gain will produce an image with false evidence of perivascular brightness in the lining of the coronary arteries. Imaging at a greater depth will also enhance anatomic visualization.

### Imaging of the left coronary artery (LCA) system

The left coronary artery (LCA) is best imaged in the parasternal and apical windows. The left main coronary artery is most readily imaged in the parasternal short-axis window at the level of the aortic root. In the parasternal short axis, the left anterior descending (LAD) and proximal left circumflex (LCx) arteries can also be demonstrated. Often, a slight clockwise rotation of the transducer from the standard parasternal short axis will increase visualization of a greater length of both LAD and LCx (Fig. 37.1). In the parasternal long axis, sweeping the plane of sound between aorta and pulmonary artery – from right to left – will often demonstrate the proximal LCA, LAD and LCx (Fig. 37.2 and Videoclip 37.1). In the apical 4-chamber view, anterior angulation of the plane of sound will demonstrate the more distal LCx in the anterior atrioventricular groove (Fig. 37.3). Although technically more challenging, subcostal views can also be used to demonstrate the LCx, particularly when aneurysms are present (Fig. 37.4).

### The right coronary artery (RCA) system

The RCA can be visualized in several imaging windows. In the parasternal short axis at the aortic root, the proximal

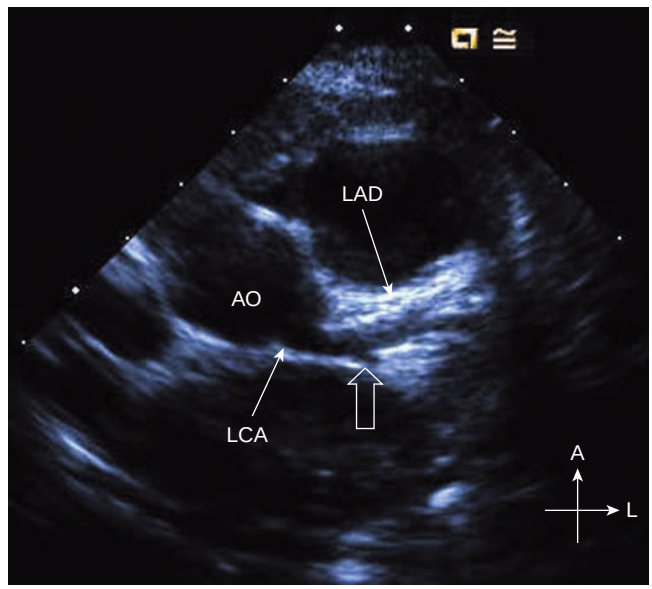


**Figure 37.1** Parasternal short-axis image with slight clockwise rotation, demonstrating the left main coronary artery (LCA), the proximal left anterior descending (LAD) coronary artery, and the proximal left circumflex coronary artery (open arrow). Note the diffuse enlargement of the LCA and LAD in this child with Kawasaki disease. A, anterior; Ao, aorta; L, left.

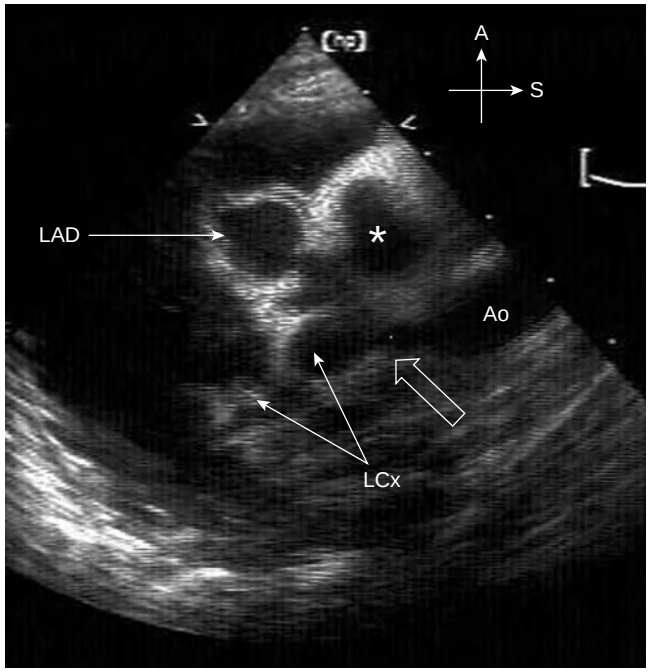


**Figure 37.2** Parasternal long-axis image, with leftward angulation from standard view, of aorta and left ventricular outflow tract. The left main coronary artery (open arrow), left anterior descending coronary artery (LAD) and left circumflex (LCx) coronary artery are seen; note the multiple saccular aneurysms involving both coronary arteries. Note also the relationship of the aorta (Ao), LAD and pulmonary artery (asterisk) in this view. A, anterior; S, superior.

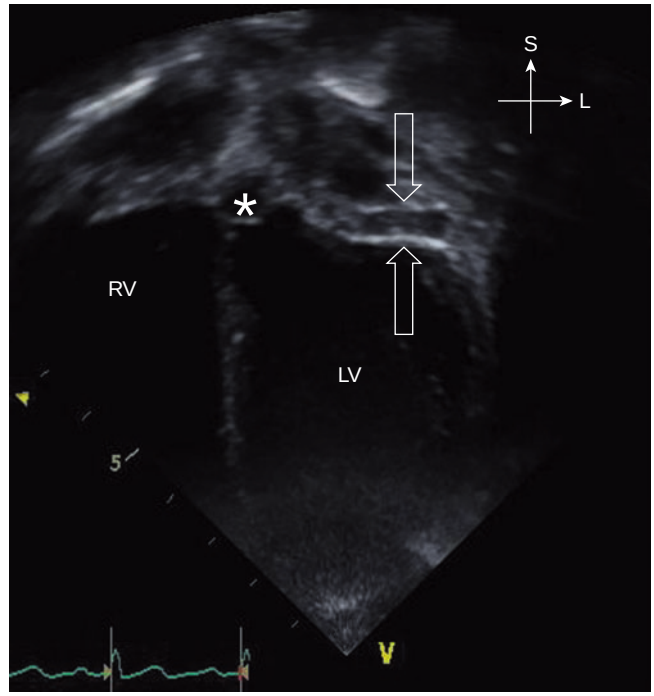


**Figure 37.3** With anterior angulation of the plane of sound from the standard apical 4-chamber view, the left circumflex coronary artery can be demonstrated in the left anterior atrioventricular groove (open arrows). The aorta (asterisk) can also be seen on this image. Note the diffuse enlargement of the left circumflex artery and the increased perivascular echogenicity in a child with acute Kawasaki disease. L, left; LV left ventricle; RV, right ventricle; S, superior.

RCA is usually well seen (Fig. 37.5). Again, a slight clockwise rotation of the plane of sound in this view will usually result in better visualization of a longer length of the proximal RCA. The proximal RCA can also be visualized in the anterior atrioventricular groove using either apical imaging (with anterior angulation of the plane of sound: Fig. 37.6), or in the subcostal frontal (coronal) view (Fig. 37.7). The middle portion of the RCA can be visualized in cross-section in parasternal long-axis views, angulated toward the tricuspid valve and lateral atrioventricular groove; it may also be visualized in the subcostal sagittal view by angulation rightward into the lateral atrioventricular groove. The distal RCA and the junction of the RCA with the posterior descending coronary artery can be imaged in the apical window with posterior angulation into the posterior right atrioventricular groove, and similarly in the subcostal frontal view with posterior angulation.

It is important to make every effort to image each segment of the left and right coronary artery system, to determine the sites involved when coronary artery aneurysms occur. The most common sites for coronary artery aneurysms are the proximal LAD and proximal RCA, followed in descending frequency by the left main coronary artery, LCx, distal RCA, and proximal posterior descending artery. Isolated RCA or

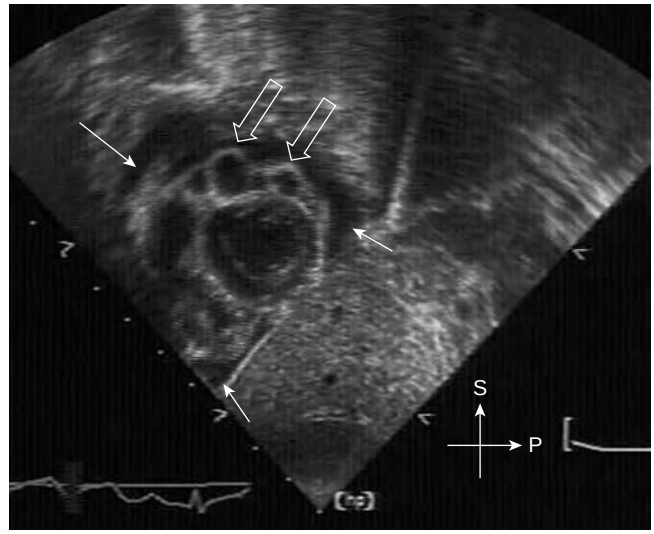


**Figure 37.4** Multiple, saccular left circumflex artery aneurysms (open arrows) seen on subcostal sagittal imaging at the level of the left atrioventricular groove. Note also the modest pericardial effusion (white arrows) seen in a patient with acute-phase disease. P, posterior; S, superior.

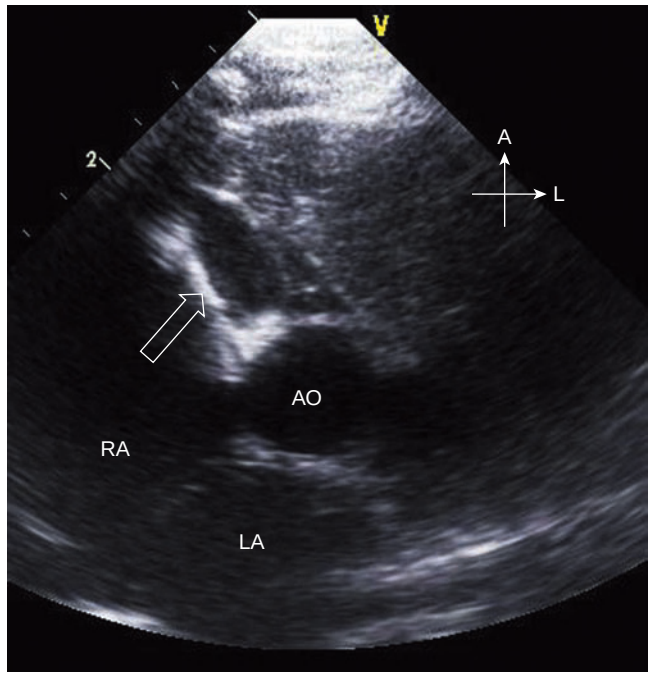


**Figure 37.5** Parasternal short-axis view demonstrating a large fusiform aneurysm of the proximal right coronary artery (open arrow). A, anterior; AO, aorta; L, left; LA, left atrium; RA, right atrium.

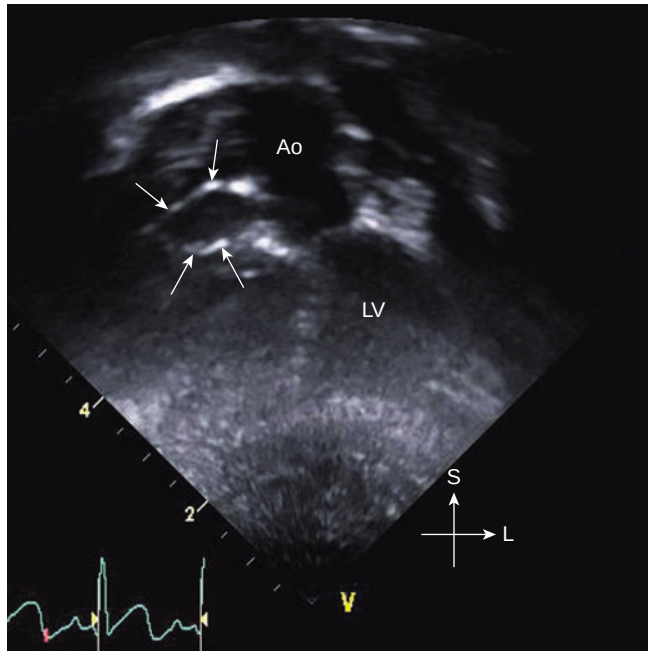


**Figure 37.6** With anterior angulation of the plane of sound from the standard apical 4-chamber into the apical 5-chamber view, the proximal right coronary artery can be demonstrated in the right anterior atrioventricular groove (arrows). Note the large fusiform right coronary artery aneurysm in this image, which tapers proximally at the right coronary artery ostium. Ao, aorta; L, left; LV, left ventricle; S, superior.

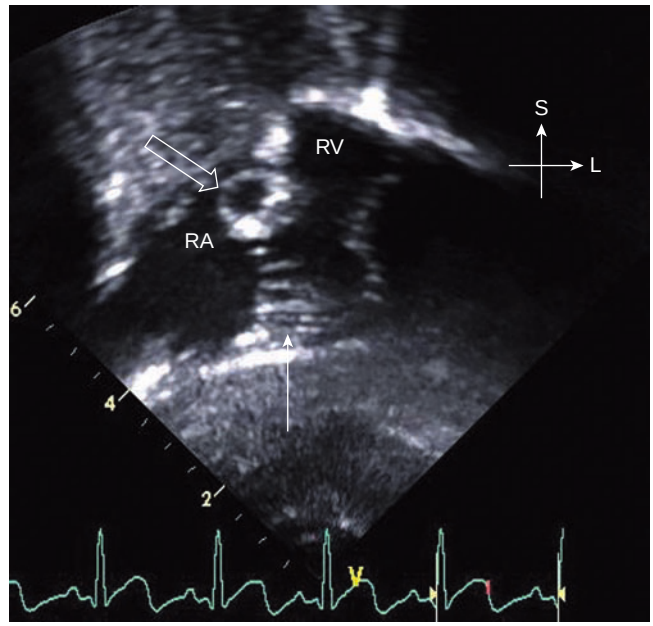


**Figure 37.7** Right coronary artery aneurysm demonstrated in the anterosuperior portion of the right atrioventricular groove in the subcostal frontal (coronal) window. The right atrium (RA), tricuspid valve (white arrow), and right ventricle are also demonstrated. L, left; S, superior.

LAD aneurysms are relatively uncommon, and isolated LCx lesions are rare. More commonly, multiple lesions involving both right and left coronary systems – particularly involving the LAD, RCA and left main coronary – are seen [18].

## Characterization of coronary artery abnormalities

Coronary aneurysms should be characterized both qualitatively and quantitatively by 2D echocardiography. Coronary *ectasia* is defined as coronary artery enlargement without aneurysm (Fig. 37.8). Coronary aneurysms are described as *saccular* when the axial and longitudinal dimensions are nearly equal (Fig. 37.9; see also Fig. 37.7), or *fusiform* when the axial dimension is less than the longitudinal dimension, and the aneurysm tapers at its ends (Figs 37.5 and 37.6). Characterization of aneurysm type is of prognostic importance, as fusiform aneurysms are more likely to regress over time than saccular aneurysms [19]. In addition to frank coronary artery aneurysms, other more subtle changes have been reported in the acute phase of the illness, including perivascular echogenicity or brightness seen in the coronary arterial wall (Fig. 37.3) and mild, diffuse coronary artery enlargement [5].

Quantitative coronary artery assessment should be performed in all patients being evaluated for Kawasaki disease. In addition to having prognostic importance, recent management guidelines [3,16] are based on aneurysm size, number, and location. Internal vessel diameters should be measured on 2D echocardiographic images from inner edge to inner edge (Fig. 37.10). The American Heart Association previously

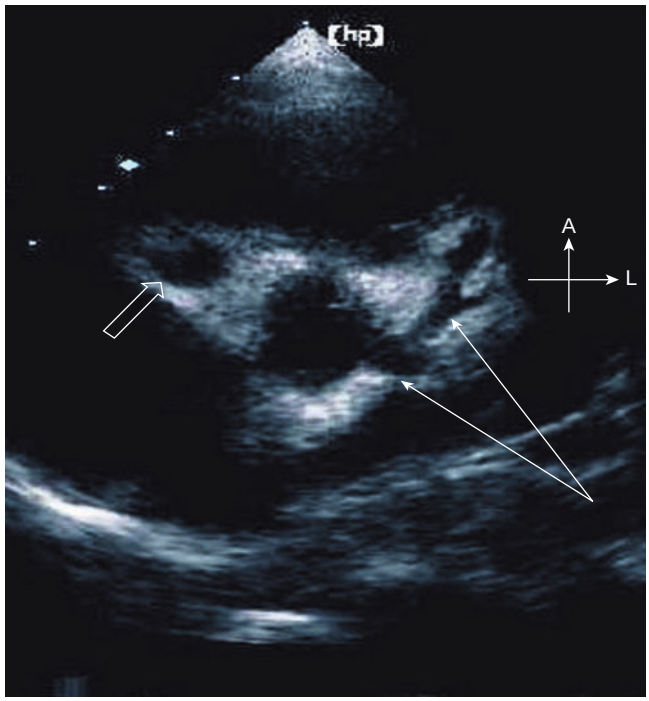


**Figure 37.8** Parasternal short-axis image demonstrating diffuse ectasia of the left main and left anterior descending coronary arteries (white arrows). Note the moderate saccular aneurysm of the right coronary artery (open arrow). A, anterior; L, left.

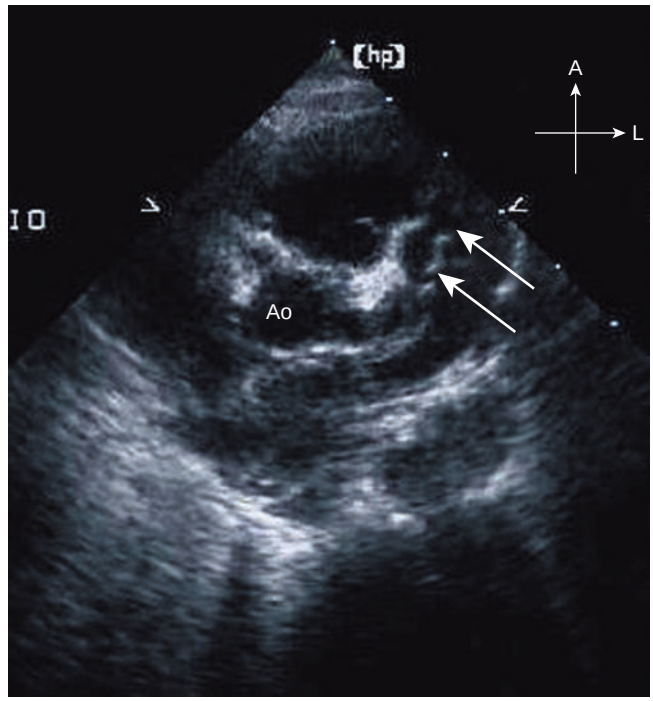


**Figure 37.9** Parasternal short-axis image demonstrating two saccular aneurysms involving the left anterior descending coronary artery (arrows). A, anterior; Ao, aorta; L, left.

classified aneurysms by internal diameter as either small (<5 mm), medium (5–8 mm), or giant (>8 mm) [16]. Most recently, however, aneurysms have been reclassified as small–medium (>3 mm but <6 mm, coronary z-score of +3 to +7), large (≥6 mm), or giant (>8 mm), to reflect consensus suggestions for cardiovascular risk assessment [3]. Alternatively, the Japanese Ministry of Health has defined coronary artery dilation if: (i) the internal diameter is >3 mm in children aged under 5 years; (ii) the internal diameter is >4 mm in children aged 5 years or above; (iii) the internal diameter is at least 1.5 times the diameter of an adjacent coronary segment; or (iv) the coronary artery lumen is clearly irregular [20]. In addition to these criteria, It is important also to assess coronary artery dimensions relative to published normal values (z-scores) (Fig. 37.11) [21,22]. Understanding, however, that published normal values exist only for the RCA, left main coronary artery and LAD, it is also important to assess other coronary segments relative to their adjacent segments, as described above, using Japanese Ministry of Health criteria.

The location, number and distribution of coronary artery aneurysms should also be noted, as the presence of multiple aneurysms (Fig. 37.12) in one or more coronary arteries results in higher risk stratification, more aggressive pharmacologic therapy, and the need for additional testing, such as coronary angiography and perfusion assessment.

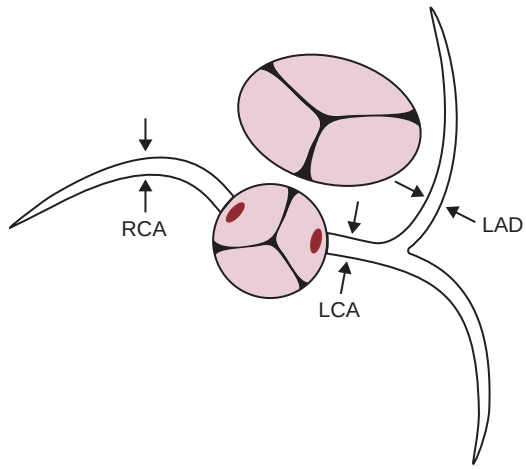


**Figure 37.10** Standard locations for making quantitative measurements of left main coronary artery (LCA), left anterior descending coronary artery (LAD) and right main coronary artery (RCA) dimensions. Note that the LCA dimension should be measured distal to its ostium, and prior to its bifurcation into LAD and left circumflex arteries. The RCA is measured after its initial turn rightward from the aortic sinus. The LAD is measured distal to its bifurcation from the LCA and prior to the takeoff of the first marginal branch. Adapted from de Zorzi A, Colan SD, Gauvreau K et al. Coronary artery dimensions may be misclassified as normal in Kawasaki disease. *J Pediatr* 1998;133:254–8, with permission from Elsevier.

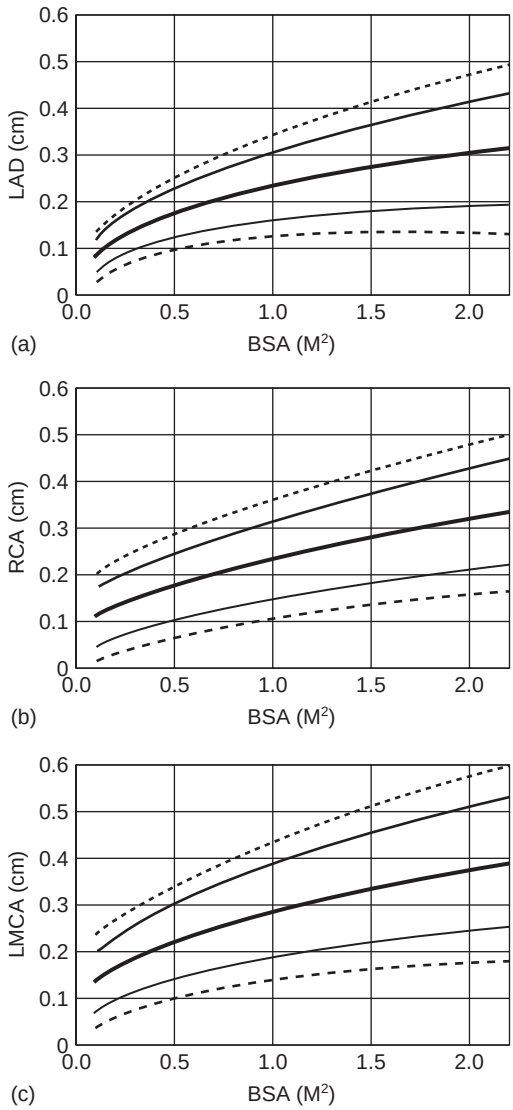


**Figure 37.11** Graphs demonstrating normal dimensions for **(a)** left anterior descending (LAD) coronary artery; **(b)** right main coronary artery (RCA); and **(c)** left main coronary artery (LMCA) relative to body surface area (BSA) in children under 18 years of age. Curves indicate the mean expected dimension and prediction limits for both two and three standard deviations. Reproduced from Newburger JW, Takahashi M, Gerber MA et al. Diagnosis, treatment, and long-term management of Kawasaki disease: a statement for health professionals from the Committee on Rheumatic Fever, Endocarditis and Kawasaki Disease, Council on Cardiovascular Disease in the Young, American Heart Association. *Circulation* 2004;110:2755, with permission from Lippincott Williams & Wilkins.

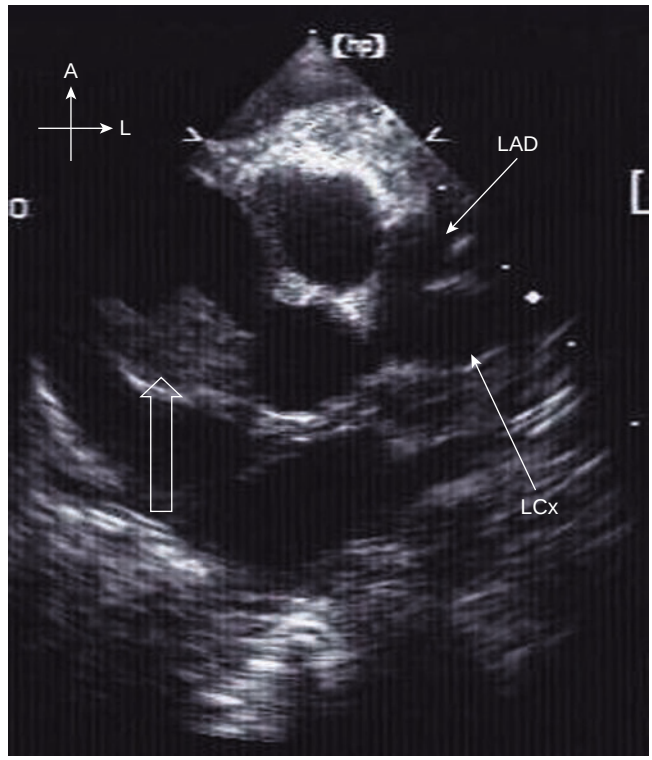


**Figure 37.12** Parasternal short-axis view in a patient with multiple complex coronary artery aneurysms. Large saccular aneurysms involving the left anterior descending (LAD) coronary artery and left circumflex (LCx) coronary artery are present (white arrows); note also the giant right coronary artery aneurysm with thrombus formation (open arrow). A, anterior; L, left.

The presence of thrombus formation within coronary artery aneurysms, particularly in giant aneurysms, should be identified (Fig. 37.13 and Videoclip 37.2). Attempts should also be made to determine the presence of stenoses or obstruction of the coronary arteries due to acute thrombosis or to chronic fibrosis and thickening of the vessel wall, although this may be difficult by 2D echocardiography alone [23]. Color flow Doppler can aid in this diagnosis because color will be visualized going around the thrombus and acceleration of flow in the coronary artery may be seen when obstruction occurs. Identification of coronary artery stenoses may be improved by functional assessment of coronary artery perfusion, as discussed below.

## Valvar involvement

In the acute phase of Kawasaki disease, color flow Doppler evaluation can often identify tricuspid and mitral regurgitation. Atrioventricular valve regurgitation in acute Kawasaki disease is usually mild and transient, and felt to be related to either valvulitis or myocarditis [24,25]. In one report, the presence of mitral regurgitation was associated with a reduced left ventricular ejection fraction in the acute phase of the illness [24]. Acute mitral regurgitation can be severe, particularly if associated with myocardial ischemia and papillary muscle dysfunction [25–27].

Aortic regurgitation can also occur, and is felt to be secondary to valvulitis and/or aortitis. Aortic regurgitation during the acute phase is also typically mild and transient

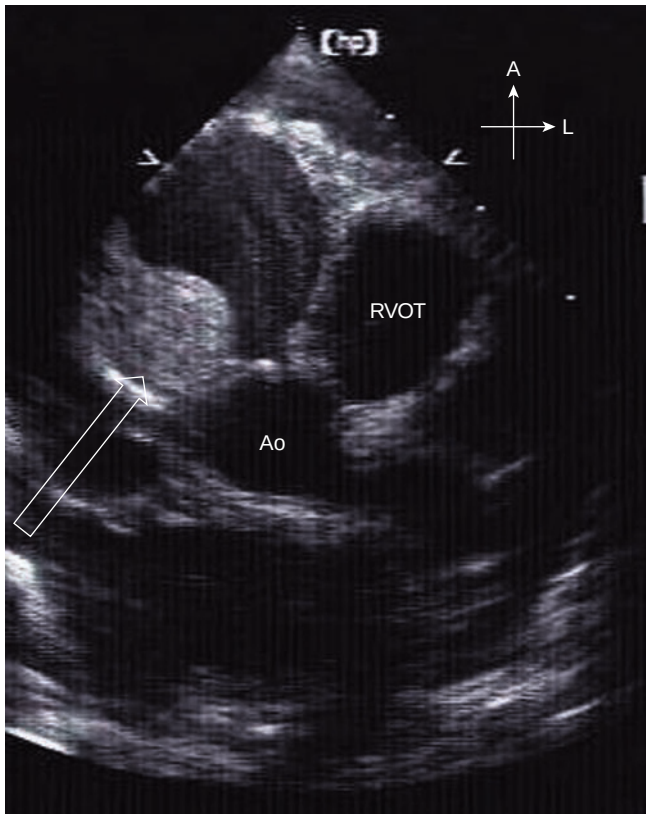


**Figure 37.13** Parasternal short-axis view in a patient with a large thrombus (arrow) within a giant right coronary artery aneurysm. Spontaneous contrast can also been seen within the aneurysm. A, anterior; Ao, aorta; L, left; RVOT, right ventricular outflow tract.

[27,28]. Aortic root dilation has been noted in Kawasaki disease [29], and may account in part for development of aortic regurgitation. Aortic regurgitation may persist chronically and in rare cases requires surgical intervention [30,31].

## Myocardial involvement

Histologic evidence of myocarditis in the acute phase of Kawasaki disease is present in virtually all cases [7,8,32,33]. Echocardiographic assessment of ventricular function during the acute phase of Kawasaki disease is therefore an important component of initial and follow-up evaluations. Quantitative methods of assessing global ventricular chamber size and function are discussed in detail in Chapters 7 and 8. Because coronary involvement is the primary concern, evaluation of regional wall motion abnormalities should also be performed. This can be achieved by imaging in the parasternal long- and short-axis, and apical 4- and 2-chamber views. These windows allow the examiner to assess 16 standard myocardial segments [34] and determine the specific coronary artery territory affected when segmental wall motion abnormalities are identified (Fig. 37.14). Long-term imaging in patients with severe coronary artery involvement may reveal significant myocardial dysfunction, scarring and mitral regurgitation related to papillary muscle ischemia (Videoclip 37.3).

## Pericardial involvement

In the acute phase of Kawasaki disease, pericardial inflammation can produce modest pericardial effusions. Although such effusions are rarely of hemodynamic significance, there have been reports of pericardial tamponade in association with severe acute Kawasaki disease [35,36]. Identification of pericardial effusion may also be of value in assessing the risk of coronary artery changes [15] or in providing supportive diagnostic data in "incomplete" Kawasaki disease.

## Noninvasive assessment of coronary perfusion

In addition to anatomic imaging and identification of coronary artery abnormalities, *functional* imaging of the coronary arterial tree is important in Kawasaki disease, specifically in patients with known coronary artery aneurysms. In patients with severe coronary artery aneurysms, the ability of 2D echocardiography to demonstrate anatomic coronary artery stenoses is limited. If stenoses are suspected, stress echocardiography is an important tool that can be used to evaluate coronary artery function. Stress echocardiography is based on the presumption that a *stressor* – either dynamic, such as exercise, or pharmacologic, such as dobutamine – will induce relative ischemia in myocardial segments with inadequate coronary arterial blood supply. By increasing myocardial oxygen demand, stress echocardiography can produce, and subsequently demonstrate, ischemia-induced wall motion abnormalities – not present during resting imaging – in myocardial segments supplied by stenotic coronary artery branches. Stress echocardiography has the additional diagnostic advantage of focusing on regional wall motion abnormalities, which appear earlier during myocardial ischemia than either electrocardiographic changes or elevation of cardiac enzymes.

In the pediatric population exercise stress echocardiography, performed either immediately after or during exercise, has several disadvantages, which are largely technical in nature. Exercise is usually performed in a graded, stepwise fashion on either a treadmill or bicycle ergometer. Although the degree of physiologic stress, typically expressed as peak heart rate multiplied by peak systolic blood pressure – the rate–pressure product – is excellent, many children are unable to perform adequately the exercise itself for complete assessment. Imaging either during or immediately after exercise can be technically challenging, due either to movement during exercise or hyperpnea. Nonetheless, exercise stress echocardiography has successfully demonstrated angiographically confirmed coronary stenoses in patients following Kawasaki disease [37].

Pharmacologic stress echocardiography, in contrast, has several advantages in the pediatric patient with Kawasaki

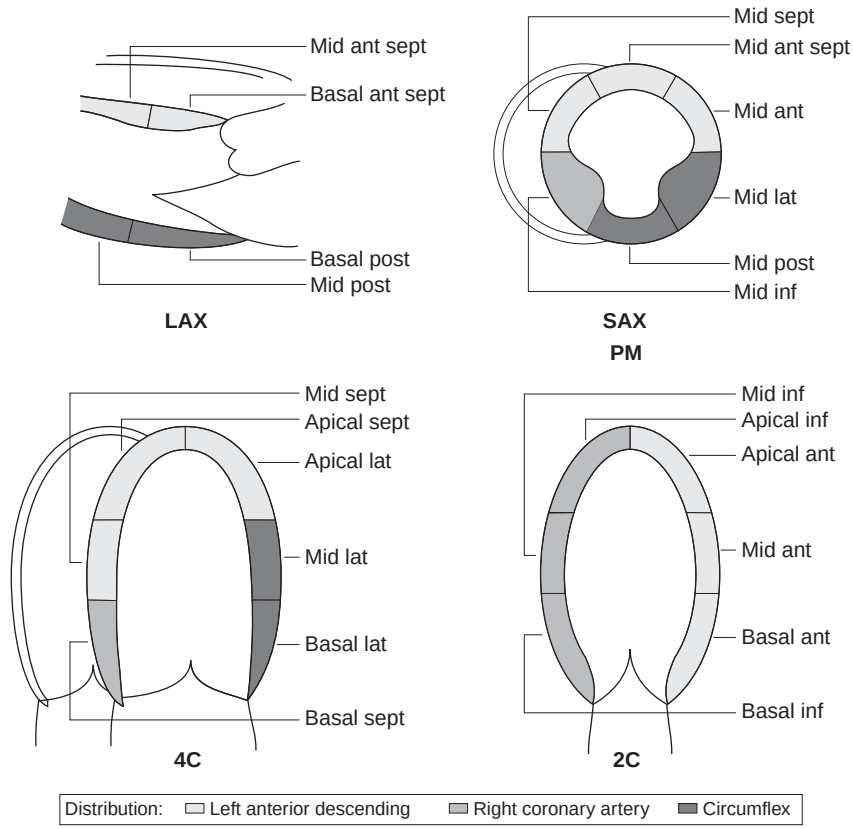


**Figure 37.14** Sixteen myocardial segments demonstrated on parasternal and apical imaging of the left ventricle. Note the coronary artery supply to each specific segment. ANT, anterior; INF, inferior; LAT, lateral; LAX, long axis; PM, papillary muscles; POST, posterior; SAX, short axis; SEPT, septum; 2C, 2-chamber; 4C, 4-chamber. Reproduced from Segar DS, Brown SE, Sawada SG et al. Dobutamine stress echocardiography: correlation with coronary lesion severity as determined by quantitative angiography. *J Am Coll Cardiol* 1992;19:1197–202, with permission from Elsevier.

disease. Pharmacologic stressors obviate the need for children to perform graded exercise to determine wall segment abnormalities. This is particularly important when assessing children who are less than 7 or 8 years of age, or for the physically or developmentally disabled. Dobutamine, the most widely reported agent used in pediatric pharmacologic stress studies [38–42], is safe [38,40], and has been associated with a very low frequency of significant side effects. During dobutamine stress echocardiography, baseline images are obtained in the parasternal long and short axes, and in the apical 4- and 2-chamber views, in order to evaluate all 16 standard myocardial segments (Fig. 37.14) [34]. Continuous dobutamine infusion is then administered in 3–5-minutes stages, at infusion rates of 10, 20, 30, 40 and 50 μg/kg/min (some laboratories will also infuse at 5 μg/kg/min, and some limit maximum dosing to 30 μg/kg/min). Continuous electrocardiographic and vital sign monitoring is performed, and image acquisition is repeated at the end of each infusion stage. Current echocardiographic systems allow digital display of images in quad-screen format, which allows side-by-side comparison of either single views at multiple infusion rates, or multiple views at a single infusion rate. Most laboratory protocols compare resting, low-dose and high-dose, and recovery images for evidence of regional wall motion abnormalities. High (maximum) dose is typically reached either when target heart rate is attained or when maximum dose (30–50 μg/kg/min) is reached. Maximum heart rate is defined as 85% of predicted maximum heart rate, which is in turn estimated as 220 bpm minus patient age (in years). Atropine is administered in some laboratories in order to increase the heart rate response in subjects with inadequate heart rate elevations on high-dose dobutamine.

Data regarding the use of dobutamine stress echocardiography in children with Kawasaki disease suggest that the technique can be used safely to identify coronary artery stenosis [38,40,42]. In the largest such study, Noto et al. [40] demonstrated that dobutamine stress echocardiography identified coronary artery stenoses with a sensitivity of 90%, and a specificity of 100%. Side effects during dobutamine stress echocardiography are generally mild and resolve rapidly with termination of the dobutamine infusion; common side effects include headache, nausea, hypertension, and atrial/ventricular ectopy [40,42]. Serious arrhythmias and hypotension have been described, but are rare in the pediatric age group.

## Alternative imaging modalities

Echocardiography has a central role in the noninvasive assessment of the sequelae of Kawasaki disease. However, when significant coronary artery abnormalities are suspected, cardiac catheterization with coronary angiography has

generally been performed to evaluate fully the extent and distribution of coronary artery aneurysms (Table 37.1). Angiography can fully delineate coronary artery anatomy, particularly in the distal vessels, but is invasive and not without clinical risk. Noninvasive alternatives to cineangiography are now available in the form of both magnetic resonance imaging (MRI) and computed tomography (CT). Reports describing the use of both MRI [43–46] and multidetector/ultrafast CT [47,48] have established the accuracy of both modalities in identifying and characterizing coronary artery abnormalities in Kawasaki disease. Both MRI and CT may provide a noninvasive means of assessing coronary artery anatomy in the course of long-term follow-up of Kawasaki disease, particularly in patients with high-risk coronary artery abnormalities or patients with limited echocardiographic imaging windows.

For assessment of coronary artery perfusion, alternatives to stress echocardiography include stress nuclear perfusion studies [49–51], and stress MRI with regional perfusion assessment [52]. The method of assessing coronary artery perfusion in Kawasaki disease is likely to be determined largely by local experience, available resources and clinical familiarity.

## Acknowledgement

The author would like to acknowledge Stacy Meredith RDCS, for her help and assistance in preparing images and figures for this chapter.

## References

1. Kawasaki T. [Acute febrile mucocutaneous syndrome with lymphoid involvement with specific desquamation of the fingers and toes in children] [see comment]. *Arerugi – Japanese Journal of Allergology* 1967;16:178–222.
2. Kawasaki T, Kosaki F, Okawa S et al. A new infantile acute febrile mucocutaneous lymph node syndrome (MLNS) prevailing in Japan. *Pediatrics* 1974;54:271–6.
3. Newburger JW, Takahashi M, Gerber MA et al. Diagnosis, treatment, and long-term management of Kawasaki disease: a statement for health professionals from the Committee on Rheumatic Fever, Endocarditis and Kawasaki Disease, Council on Cardiovascular Disease in the Young, American Heart Association. *Circulation* 2004;110:2747–71.
4. Bell DM, Morens DM, Holman RC et al. Kawasaki syndrome in the United States 1976 to 1980. *Am J Dis Child* 1983;137:211–4.
5. Newburger JW, Taubert KA, Shulman ST et al. Summary and abstracts of the Seventh International Kawasaki Disease Symposium: December 4–7, 2001, Hakone, Japan. *Pediatr Res* 2003;53:153–7.
6. Holman RC, Curns AT, Belay ED et al. Kawasaki syndrome hospitalizations in the United States, 1997 and 2000. *Pediatrics* 2003;112:495–501.
7. Fujiwara H, Hamashima Y. Pathology of the heart in Kawasaki disease. *Pediatrics* 1978;61:100–7.
8. Yutani C, Go S, Kamiya T et al. Cardiac biopsy of Kawasaki disease. *Arch Pathol Lab Med* 1981;105:470–3.
9. Akagi T, Rose V, Benson LN et al. Outcome of coronary artery aneurysms after Kawasaki disease. *J Pediatr* 1992;121:689–94.
10. Kato H, Ichinose E, Yoshioka F et al. Fate of coronary aneurysms in Kawasaki disease: serial coronary angiography and long-term follow-up study. *Am J Cardiol* 1982;49:1758–66.
11. Sasaguri Y, Kato H. Regression of aneurysms in Kawasaki disease: a pathological study. *J Pediatr* 1982;100:225–31.
12. Shinohara M, Sone K, Tomomasa T. Morphologic and functional assessment of coronary aneurysm after Kawasaki disease by repeated dipyridamole-loading coronary angiography. *Am J Cardiol* 1998;82:387–9.
13. Sugimura T, Kato H, Inoue O et al. Vasodilatory response of the coronary arteries after Kawasaki disease: evaluation by intracoronary injection of isosorbide dinitrate. *J Pediatr* 1992;121:684–8.
14. Yamakawa R, Ishii M, Sugimura T et al. Coronary endothelial dysfunction after Kawasaki disease: evaluation by intracoronary injection of acetylcholine. *J Am Coll Cardiol* 1998;31:1074–80.
15. Gidding SS, Duffy CE, Pajcic S et al. Usefulness of echocardiographic evidence of pericardial effusion and mitral regurgitation during the acute stage in predicting development of coronary arterial aneurysms in the late stage of Kawasaki disease. *Am J Cardiol* 1987;60:76–9.
16. Dajani AS, Taubert KA, Takahashi M et al. Guidelines for long-term management of patients with Kawasaki disease. Report from the Committee on Rheumatic Fever, Endocarditis, and Kawasaki Disease, Council on Cardiovascular Disease in the Young, American Heart Association. *Circulation* 1994;89:916–22.
17. Yanagisawa M, Yano S, Shiraishi H et al. Coronary aneurysms in Kawasaki disease: follow-up observation by two-dimensional echocardiography. *Pediatr Cardiol* 1985;6:11–16.
18. Onouchi Z, Shimazu S, Kiyosawa N et al. Aneurysms of the coronary arteries in Kawasaki disease. An angiographic study of 30 cases. *Circulation* 1982;66:6–13.
19. Takahashi M, Mason W, Lewis AB. Regression of coronary aneurysms in patients with Kawasaki syndrome. *Circulation* 1987;75:387–94.
20. Research Committee on Kawasaki Disease. *Report of Subcommittee on Standardization of Diagnostic Criteria and Reporting of Coronary Artery Lesions in Kawasaki Disease*. Tokyo: Ministry of Health and Welfare, 1984.
21. de Zorzi A, Colan SD, Gauvreau K et al. Coronary artery dimensions may be misclassified as normal in Kawasaki disease. *J Pediatr* 1998;133:254–8.
22. Kurotobi S, Nagai T, Kawakami N, Sano T. Coronary diameter in normal infants, children and patients with Kawasaki disease. *Pediatr Int* 2002;44:1–4.
23. Fujiwara T, Fujiwara H, Ueda T et al. Comparison of macroscopic, postmortem, angiographic and two-dimensional echocardiographic findings of coronary aneurysms in children with Kawasaki disease. *Am J Cardiol* 1986;57:761–4.
24. Suzuki A, Kamiya T, Tsuchiya K et al. Tricuspid and mitral regurgitation detected by color flow Doppler in the acute phase of Kawasaki disease. *Am J Cardiol* 1988;61:386–90.

25. Takao A, Niwa K, Kondo C et al. Mitral regurgitation in Kawasaki disease. *Prog Clin Biol Res* 1987;250:311–23.
26. Tomita H, Sawada Y, Higashidate Y et al. Mitral regurgitation with gross deformity of a mitral leaflet due to Kawasaki disease. *Pediatr Cardiol* 1990;11:153–5.
27. Akagi T, Kato H, Inoue O et al. Valvular heart disease in Kawasaki syndrome: incidence and natural history. *Am Heart J* 1990;120:366–72.
28. Nakano H, Nojima K, Saito A, Ueda K. High incidence of aortic regurgitation following Kawasaki disease. *J Pediatr* 1985;107: 59–63.
29. Ravekes WJ, Colan SD, Gauvreau K et al. Aortic root dilation in Kawasaki disease. *Am J Cardiol* 2001;87:919–22.
30. Fukunaga S, Egashira A, Arinaga K et al. Aortic valve replacement for aortic regurgitation due to Kawasaki disease. Report of two cases. *J Heart Valve Dis* 1996;5:231–4.
31. Takahashi T, Taniguchi K, Matsuda H. Surgical treatment for aortic regurgitation and left ventricular dysfunction caused by Kawasaki disease. *Cardiol Young* 1998;8:123–5.
32. Amano S, Hazama F, Kubagawa H et al. General pathology of Kawasaki disease. On the morphological alterations corresponding to the clinical manifestations. *Acta Pathol Jpn* 1980;30: 681–94.
33. Landing BH, Larson EJ. Pathological features of Kawasaki disease (mucocutaneous lymph node syndrome). *Am J Cardiovasc Pathol* 1987;1:218–29.
34. Cerqueira MD, Weissman NJ, Dilsizian V et al. Standardized myocardial segmentation and nomenclature for tomographic imaging of the heart: a statement for healthcare professionals from the Cardiac Imaging Committee of the Council on Clinical Cardiology of the American Heart Association. *Circulation* 2002;105:539–42.
35. Dahlem PG, von Rosenstiel IA, Lam J, Kuijpers TW. Pulse methylprednisolone therapy for impending cardiac tamponade in immunoglobulin-resistant Kawasaki disease. *Intensive Care Med* 1999;25:1137–9.
36. Ozdogu H, Boga C. Fatal cardiac tamponade in a patient with Kawasaki disease. *Heart Lung* 2005;34:257–9.
37. Pahl E, Sehgal R, Chrystof D et al. Feasibility of exercise stress echocardiography for the follow-up of children with coronary involvement secondary to Kawasaki disease. *Circulation* 1995; 91:122–8.
38. Kimball TR, Witt SA, Daniels SR. Dobutamine stress echocardiography in the assessment of suspected myocardial ischemia in children and young adults. *Am J Cardiol* 1997;79:380–4.
39. Larsen RL, Applegate PM, Dyar DA et al. Dobutamine stress echocardiography for assessing coronary artery disease after transplantation in children. *J Am Coll Cardiol* 1998;32:515–20.
40. Noto N, Ayusawa M, Karasawa K et al. Dobutamine stress echocardiography for detection of coronary artery stenosis in children with Kawasaki disease. *J Am Coll Cardiol* 1996;27: 1251–6.
41. Pahl E, Crawford SE, Swenson JM et al. Dobutamine stress echocardiography: experience in pediatric heart transplant recipients. *J Heart Lung Transplant* 1999;18:725–32.
42. Zilberman MV, Goya G, Witt SA et al. Dobutamine stress echocardiography in the evaluation of young patients with Kawasaki disease. *Pediatr Cardiol* 2003;24:338–43.
43. Greil GF, Seeger A, Miller S et al. Coronary magnetic resonance angiography and vessel wall imaging in children with Kawasaki disease. *Pediatr Radiol* 2007;37:666–73.
44. Greil GF, Stuber M, Botnar RM et al. Coronary magnetic resonance angiography in adolescents and young adults with Kawasaki disease. *Circulation* 2002;105:908–11.
45. Mavrogeni S, Papadopoulos G, Douskou M et al. Magnetic resonance angiography is equivalent to X-ray coronary angiography for the evaluation of coronary arteries in Kawasaki disease. *J Am Coll Cardiol* 2004;43:649–52.
46. Takemura A, Suzuki A, Inaba R et al. Utility of coronary MR angiography in children with Kawasaki disease. *AJR Am J Roentgenol* 2007;188:W534–9.
47. Chu WC, Mok GC, Lam WW et al. Assessment of coronary artery aneurysms in paediatric patients with Kawasaki disease by multidetector row CT angiography: feasibility and comparison with 2D echocardiography. *Pediatr Radiol* 2006;36:1148–53.
48. Frey EE, Matherne GP, Mahoney LT et al. Coronary artery aneurysms due to Kawasaki disease: diagnosis with ultrafast CT. *Radiology* 1988;167:725–6.
49. Fukuda T, Akagi T, Ishibashi M et al. Noninvasive evaluation of myocardial ischemia in Kawasaki disease: comparison between dipyridamole stress thallium imaging and exercise stress testing. *Am Heart J* 1998;135:482–7.
50. Fukuda T, Ishibashi M, Yokoyama T et al. Myocardial ischemia in Kawasaki disease: evaluation with dipyridamole stress technetium 99 m tetrofosmin scintigraphy. *J Nucl Cardiol* 2002;9: 632–7.
51. Kondo C, Hiroe M, Nakanishi T, Takao A. Detection of coronary artery stenosis in children with Kawasaki disease. Usefulness of pharmacologic stress 201Tl myocardial tomography. *Circulation* 1989;80:615–24.
52. Muhling O, Jerosch-Herold M, Nabauer M, Wilke N. Assessment of ischemic heart disease using magnetic resonance first-pass perfusion imaging. *Herz* 2003;28:82–9.
53. Segar DS, Brown SE, Sawada SG et al. Dobutamine stress echocardiography: correlation with coronary lesion severity as determined by quantitative angiography. *J Am Coll Cardiol* 1992;19:1197–202.

# 38 Rheumatic Fever

**Luciana T. Young**
Children's Memorial Hospital, Chicago, USA

## Definition

Rheumatic fever is an acute inflammatory illness that occurs following an upper respiratory infection with group A β-hemolytic streptococci [1,2]. Although rheumatic fever may affect several organ systems, including the joints and central nervous system, its adverse effects on the cardiovascular system and the development of rheumatic heart disease account for its significant long-term morbidity and mortality.

## Incidence

Rheumatic heart disease is the most common form of acquired heart disease in children and young adults throughout the world. Its highest incidence is in developing countries, presumably due to lower socioeconomic environments and crowded living conditions. In the USA, rheumatic fever had become a rare entity until the mid-1980s, when several outbreaks were reported in certain geographic areas [3]. However, these outbreaks were not associated with an overall national increase in rheumatic fever.

Rheumatic fever afflicts 0.1% to 3% of the general population and appears to follow a seasonal pattern, paralleling that of streptococcal pharyngitis [4]. Occurring most commonly in children aged 6 to 15 years, acute rheumatic fever rarely presents in patients before the age of 5 years. There is no gender predilection. Rheumatic fever has been associated with a strong genetic predisposition and heterogeneous presentation in certain families [5,6].

## Pathophysiology

The currently accepted theory regarding the pathogenicity of rheumatic fever is that following an apparent recovery from pharyngitis due to group A β-hemolytic streptococci, breakdown products from the streptococcal organisms, which have molecular similarity to certain human tissues, are recognized by the immune system and initiate a humoral and cellular autoimmune response, resulting in tissue damage [1,7,8]. Tissues with antigenic similarity to the streptococcal organism include the heart, nerve tissue and cartilage, thus explaining their involvement in the setting of acute rheumatic fever.

Approximately 2 to 5 weeks following an upper respiratory infection, the clinical symptoms of rheumatic fever become apparent. These may involve one or more systems including the skin, musculoskeletal system, central nervous system and the cardiovascular system.

The diagnosis of rheumatic fever relies on the identification of major and minor manifestations known as the Jones criteria (Box 38.1) [9]. The diagnosis is established when two

**Box 38.1 Jones criteria, updated 1992**

MAJOR criteria:
- Carditis
- Polyarthritis
- Chorea
- Erythema marginatum
- Subcutaneous nodules

MINOR criteria:
- Arthralgia
- Fever
- Elevated acute phase reactants:
  - Erythrocyte sedimentation rate
  - C-reactive protein
- Prologed PR interval

PLUS supporting evidence of an antecedent group A streptococcal infection:
Positive throat culture or rapid strep test
Elevated or rising streptococcal antibody titers

*Echocardiography in Pediatric and Congenital Heart Disease: From Fetus to Adult*
Edited by Wyman W. Lai, Luc L. Mertens, Meryl S. Cohen and Tal Geva
 ISBN: 978-1-405-17401-5

major or one major and two minor criteria are present. In addition, evidence of a preceding streptococcal infection is necessary. Echocardiographic evidence of subclinical carditis has been proposed as an additional criterion for the diagnosis of acute rheumatic fever, but to date has not been included in the Jones criteria [10].

Rheumatic carditis occurs in 40–50% of cases of rheumatic fever and may last for 4 weeks to 6 months [2,11]. The degree to which the heart is involved is variable, with the presentation ranging from mild valvar regurgitation with no symptoms to severe disease with acute congestive failure due to decreased ventricular function and ventricular arrhythmias. Mitral and aortic regurgitation are the principal echocardiographic features, with mitral regurgitation being the more common [11,12]. Although most patients recover, residual involvement of the cardiac valves may lead to chronic regurgitation or stenosis. Myocarditis without associated valvulitis is likely not due to rheumatic fever. Pericarditis may occasionally occur, and is typically associated with moderate to severe valvar regurgitation [13,14].

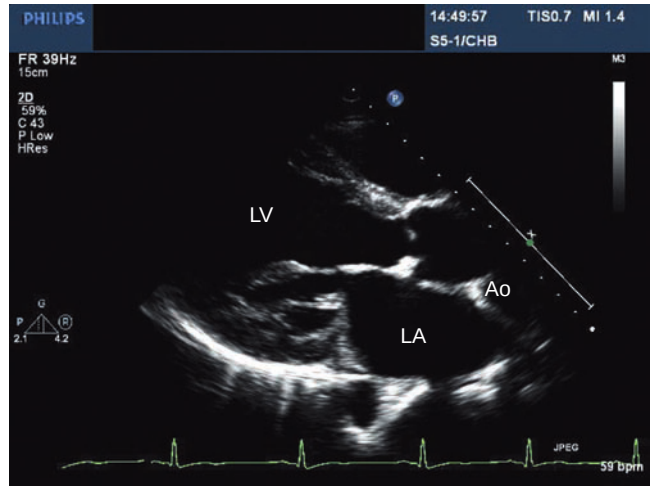


**Figure 38.1** Parasternal long-axis view of a patient with acute rheumatic fever demonstrating thickening of the mitral and aortic valves. Ao, aorta; LA, left atrium; LV, left ventricle.

## Imaging

Echocardiography is important for confirming the clinical findings in acute rheumatic fever. It also enhances our understanding of the critical role of valve regurgitation in the development of rheumatic heart failure and the long-term consequences of rheumatic heart disease. This noninvasive technique is helpful for assessing valve morphology and function, chamber size, ventricular function, and the presence and size of pericardial effusions. Furthermore, serial echocardiographic evaluation is essential for guiding management in patients with evolving rheumatic heart disease.

### Rheumatic mitral disease

#### Mitral valvulitis

The mitral valve is the predominant valve affected during acute rheumatic carditis. Characteristic changes occur to the valve, which include annular dilation and chordal elongation, leading to prolapse of the anterior leaflet (Fig. 38.1). As a result, the leaflets no longer coapt appropriately and there is formation of a regurgitant orifice (Videoclips 38.1 and 38.2) [14–16]. In rheumatic carditis, the regurgitant jet is typically directed toward the posterolateral wall of the left atrium, causing thickening and calcification of the endocardium (otherwise known as MacCallum's patch) [17].

It is important to differentiate rheumatic mitral prolapse from the mitral prolapse seen in Barlow syndrome. In rheumatic mitral carditis, only the coapting portion of the anterior leaflet prolapses and there is no billowing of the medial portion (Videoclip 38.3). In contrast, billowing of the posterior or both leaflets of the mitral valve occurs in Barlow syndrome (mitral valve prolapse) (Videoclip 38.4). Another differentiating feature is that chordal rupture frequently occurs with Barlow syndrome, but is rarely seen in patients with rheumatic mitral valve disease [18,19].

##### *Goals of the examination for acute rheumatic mitral valvulitis*

The goals of echocardiographic examination in this setting can be summarized as follows:

- Define mitral valve anatomy.
- Measure mitral annular dimensions and compare with normal z-score measurements.
- Perform a hemodynamic assessment of mitral regurgitation:
  - assess regurgitant flow (by color and spectral Doppler).
  - quantitate mitral regurgitation:
    - determine size and extent of the regurgitant jet;
    - determine proximal flow convergence;
    - assess the regurgitant volume;
    - determine the regurgitant fraction;
    - measure the effective regurgitant orifice area;
    - perform pulmonary venous Doppler and assess the intensity of the continuous-wave jet.
  - assess for evidence of hemodynamic overload (left atrial and left ventricular enlargement).
- Estimate right ventricular systolic pressure based on tricuspid regurgitant jet velocity and/or the systolic configuration of the ventricular septum.
- Evaluate left ventricular size and function.
- Identify associated lesions.
- Perform serial evaluations to assess for progression.

Two-dimensional (2D) and M-mode echocardiography techniques provide important information regarding the

severity and hemodynamic consequences of mitral regurgitation. As the degree of mitral regurgitation increases, the left atrium and left ventricle dilate to accommodate the increase in volume. Similarly, the mitral annulus may dilate as a result of chamber enlargement. Left ventricular end-diastolic dimensions should be measured by 2D or M-mode and followed longitudinally for progressive chamber enlargement. Serial evaluation of left ventricular end-diastolic volume by 2D imaging may also be helpful in clinical management. Early detection of deteriorating ventricular function is crucial to appropriate clinical management and, therefore, serial assessment of ejection phase indices such as shortening fraction and ejection fraction should be included in the examination.

Doppler echocardiography is a very sensitive tool for diagnosing subclinical carditis that might otherwise not be detectable by clinical exam (i.e., "silent" mitral regurgitation). The presence of trivial or physiologic mitral regurgitation must be differentiated from pathologic regurgitation in order to avoid rendering a false diagnosis. Pathologic mitral regurgitation may be distinguished from physiologic mitral regurgitation by the following Doppler characteristics:

**1** The color jet must be confirmed in at least two views;
**2** The color jet is directed posterolaterally and should extend at least 1 cm into the left atrium;
**3** Color aliasing should indicate higher-velocity turbulent flow and
**4** The regurgitant jet should be holosystolic by pulsed-wave and continuous wave Doppler [20].

Several indirect Doppler indices are also of value in determining the degree of mitral regurgitation. These include signal intensity of the continuous-wave regurgitant jet, size and extent of the jet into the left atrium, and abnormal pulmonary venous flow patterns. [21–27]. A clear, easily recordable mitral regurgitant continuous waveform is indicative of severe mitral regurgitation. The regurgitant jet width (vena contracta) measured from the parasternal long-axis or apical 4-chamber view has been shown to be predictive of the size of the regurgitant jet orifice. In adult studies, a proximal jet area of ≥4 $cm^2/m^2$ has been shown to correlate with a regurgitant fraction of ≥30%. The ratio of regurgitant jet area to left atrial area (RJA/LAA) is easily determined by color Doppler and can be used to discriminate between mild (<30%), moderate (30–50%), and severe (>50%) regurgitation [23]. Regurgitant jet area indexed to body surface area (RJA/BSA) has likewise been reported to correlate with the angiographic gradient of regurgitation.

The degree of mitral regurgitation may also be reflected by the pulmonary venous waveform. As the amount of regurgitation increases, the peak diastolic velocity and diastolic velocity–time integral increase, whereas the peak systolic velocity and systolic velocity–time integral decrease. Systolic flow reversal is seen in the presence of severe mitral regurgitation. Increased left atrial pressure may limit this technique. Additional methods for determining the degree of mitral regurgitation include flow convergence and proximal isovelocity surface area (PISA); however, these methods have not gained widespread use in the pediatric population.

Direct calculation of mitral regurgitation severity can be accomplished by using a combination of 2D and Doppler techniques [22]. Total stroke volume (TSV) is calculated by subtracting left ventricular end-systolic volume from the end-diastolic volume. Forward stroke volume (FSV) is obtained using pulsed Doppler to determine mean velocity across the aortic valve, and multiplying this value by the vessel cross-sectional area. Mitral regurgitant volume (RV) can then be calculated as TSV – FSV, and the regurgitant fraction can be calculated as RV/TSV. The regurgitant fraction can be calculated by obtaining the stroke volume across the mitral valve and cardiac output across the aortic valve; however, this technique may be limited by difficulty in measuring mitral annular dimensions accurately [24,26]. Recent studies have shown a correlation between real-time three-dimensional (3D) color flow Doppler assessment of mitral regurgitation and regurgitant/atrial volume ratios and 2D techniques [28].

### Chronic mitral valve disease

The natural history of rheumatic mitral valve disease has been described as a pendulum swinging from regurgitation, to complete resolution of the regurgitation without evidence of heart disease, and then on to later development of stenosis for some patients (Fig. 38.2) [29]. The pendulum may stop at any point on this continuum, such that some patients may present with subclinical, or "silent," mitral regurgitation, but still end up with clinically significant mitral stenosis and/or regurgitation when they reach adulthood. In children, isolated pure mitral regurgitation is the most common form of chronic rheumatic heart disease and occurs by the same mechanism as it does in the acute phase of rheumatic fever. The echocardiographic evaluation and quantification of mitral regurgitation is performed in the same manner as described previously for acute mitral valvulits.

Rheumatic fever is the predominant cause of mitral stenosis in adults [19]. Characteristic changes occur to the mitral valve apparatus in rheumatic fever, including thickening and scarring of the valve leaflets, commissures and chordae tendineae. Fusion of the mitral valve cusps and chordae tendineae leads to thickening and shortening of these structures, resulting in a mitral orifice that is restricted in size and shaped like a funnel (Videoclip 38.5) [25,26]. Approximately 25% of adult patients with rheumatic heart disease have pure mitral stenosis, whereas an additional 40% have combined mitral stenosis and regurgitation, resulting from abnormal leaflet coaptation during systole and restricted opening during diastole [19].

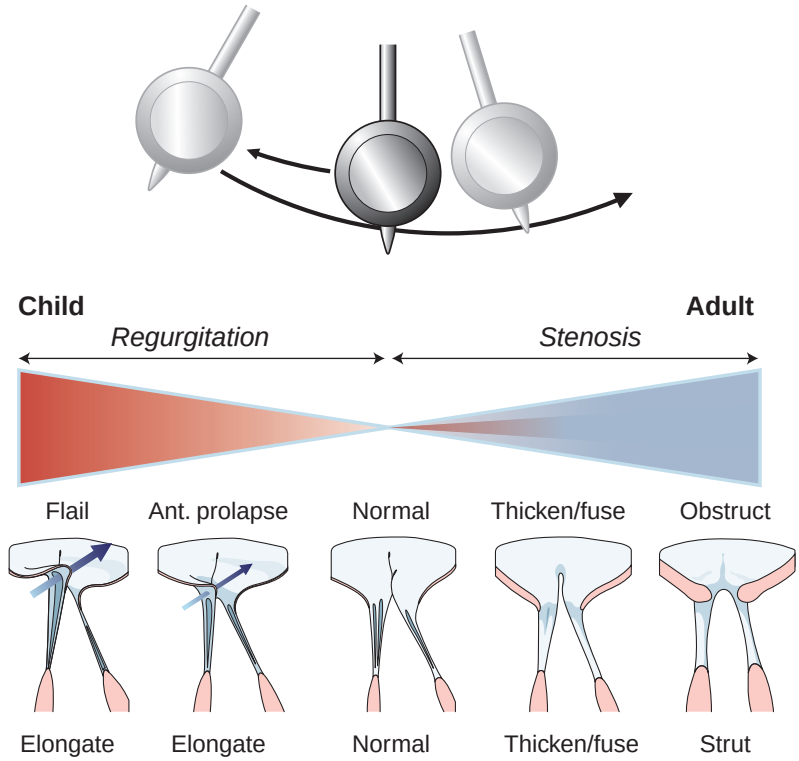


**Figure 38.2** **Top:** Schematic representation of the natural history of rheumatic mitral valve disease. The swing of the pendulum may stop at any point in its arc. **Bottom:** Schematic representation of the pathologic changes to the mitral valve chordae and leaflets that correspond with the degree of mitral stenosis or regurgitation demonstrated above. Reproduced from Minich LL et al. Role of echocardiography in the diagnosis and follow-up of rheumatic carditis. In: Jagat N, Virmani R, Reddy KS, Tandon R (eds) *Rheumatic Fever*. Washington DC: American Registry of Pathology Press, 1999;308, with permission from American Registry of Pathology Press.

### *Goals of the examination for chronic rheumatic mitral valve disease*

The goals of echocardiographic examination in this setting can be summarized as follows:

- Define mitral valve anatomy.
- Measure mitral annular dimensions and compare with normal.
- Perform a hemodynamic assessment:
  - measure peak and mean diastolic gradients across the valve;
  - calculate mitral valve area by planimetry, proximal flow convergence, pressure half-time, and the continuity equation;
  - assess for evidence of increased left atrial pressure (left atrial enlargement, abnormal pulmonary venous Doppler);
  - estimate right ventricular systolic pressure based on tricuspid regurgitant jet velocity and/or the systolic configuration of the ventricular septum.
- Evaluate biventricular function.
- Identify associated lesions.
- Perform serial evaluations to assess for progression.

Two-dimensional imaging demonstrates characteristic changes in the mitral valve due to chronic rheumatic disease. The anterior and posterior leaflets become progressively thickened and calcified. Commissural fusion results in decreased leaflet excursion and poor separation during ventricular diastole, thus restricting valve flow area [19,25,26]. In mild mitral stenosis, some leaflet mobility may be preserved, resulting in diastolic doming of the anterior leaflet. This creates a characteristic "hockey stick" appearance of the leaflet (Videoclip 38.6). As thickening and fibrosis of the leaflets progresses, the valve orifice becomes smaller and even more echo-dense in appearance. Calcification occurs at the leaflet tips, with later extension to the annulus. Over time, the leaflets become less pliable and more restricted in their mobility. As the degree of mitral stenosis progresses, the left atrium enlarges and left atrial pressure increases in order to maintain transmitral flow. Pulmonary hypertension and right heart failure eventually develop.

Typical M-mode features of rheumatic mitral stenosis include thickening of the leaflets and decrease of the E–F slope (Fig. 38.3). 2D imaging in the parasternal short-axis view provides "en face" visualization of the valve orifice (Fig. 38.4). The smallest orifice area during maximal diastolic leaflet separation may be traced by planimetry to estimate mitral valve area. The advantage of this method is that it is not significantly affected by heart rate or cardiac output. However, the technique is largely operator-dependent, and some limitations include improper alignment of the imaging plane, incorrect timing of the measurement during the cardiac cycle, and low resolution of the image due to inappropriate gain settings [22].

The severity of mitral stenosis can be determined by noninvasive means using Doppler echocardiography. Several methods are used for quantification of mitral stenosis, including conversion of Doppler velocities to instantaneous

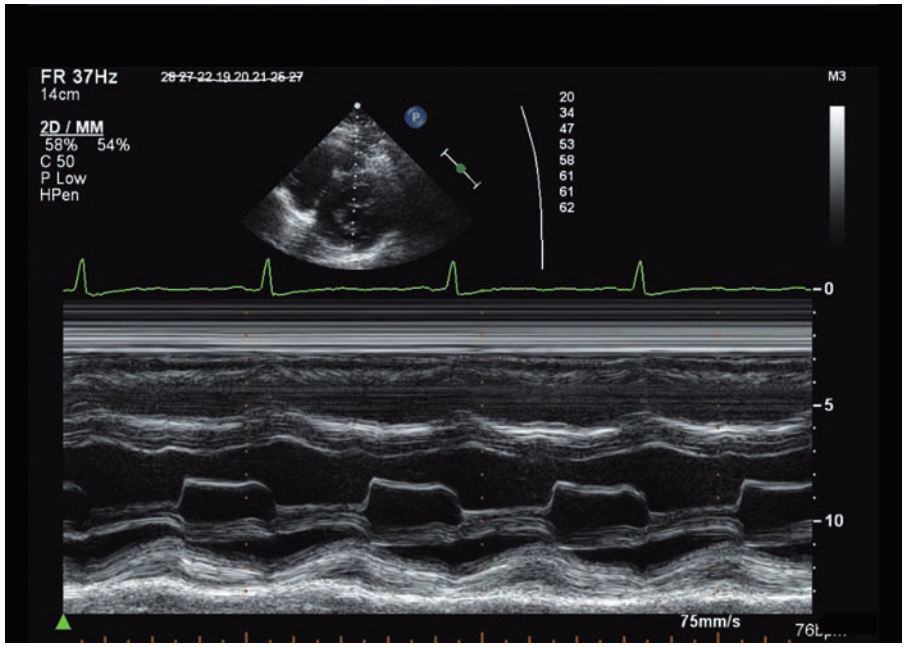


**Figure 38.3** M-mode echocardiogram of a patient with rheumatic mitral stenosis. The mitral leaflets are thickened and the E–F slope is prolonged.

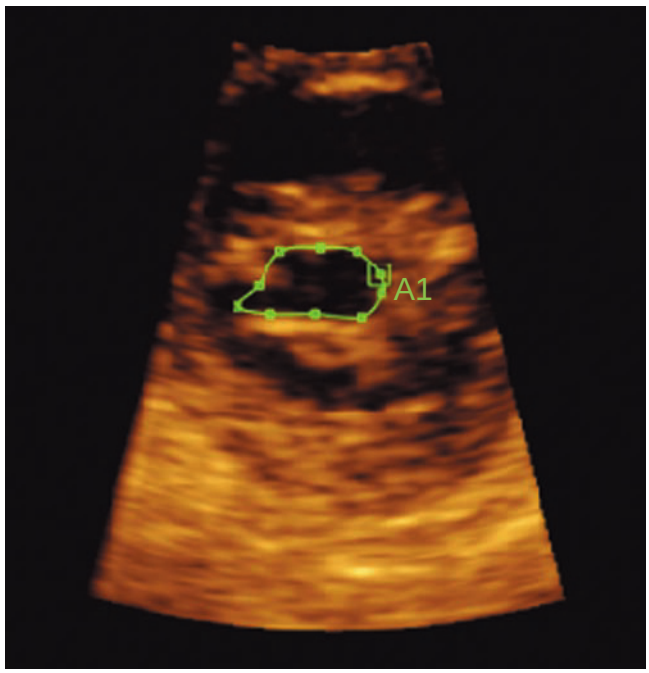


**Figure 38.4** Parasternal short-axis view showing manual tracing of the mitral valve orifice area in a patient with rheumatic mitral stenosis.

and mean pressure gradients across the valve, calculation of mitral valve area by pressure half-time or flow convergence, the continuity equation and PISA. These are discussed in further detail in Chapter 6 [28]. Doppler flow patterns may vary according to severity of obstruction, presence of atrial fibrillation, and coexistence of mitral regurgitation. Continuous-wave Doppler can be applied to estimate pulmonary arterial pressure from the tricuspid regurgitant velocity. Color flow imaging can determine whether mitral regurgitation, aortic regurgitation and other valve abnormalities exist. Real-time 3D echocardiography is also a feasible method for assessing mitral valve area in patients with rheumatic mitral valve stenosis, and has been shown to correlate well with invasive testing [30].

## Rheumatic aortic disease

### Aortic valvulitis

The aortic valve is involved to a lesser degree in acute rheumatic fever, with involvement occurring in approximately 20% of patients (Fig. 38.5) [31]. When present, aortic regurgitation is usually seen in association with mitral regurgitation. Because aortic regurgitation is rarely seen in normal children, inaudible aortic regurgitation detected by Doppler echocardiography suggests the presence of subclinical carditis.

#### *Goals of examination for acute aortic valvulitis*

The goals of echocardiographic examination in this setting can be summarized as follows:

- Assess aortic valve anatomy.
- Perform a hemodynamic assessment:
  - quantitate aortic regurgitation:
    - measure jet width and cross-sectional area;
    - determine the regurgitant volume;
    - estimate the regurgitant fraction;
    - determine the slope and pressure half-time;
    - measure the proximal flow convergence and
    - calculate the regurgitant orifice area.
  - assess for flow reversal in the abdominal aorta.
  - assess for evidence of left ventricular overload (left ventricular size).

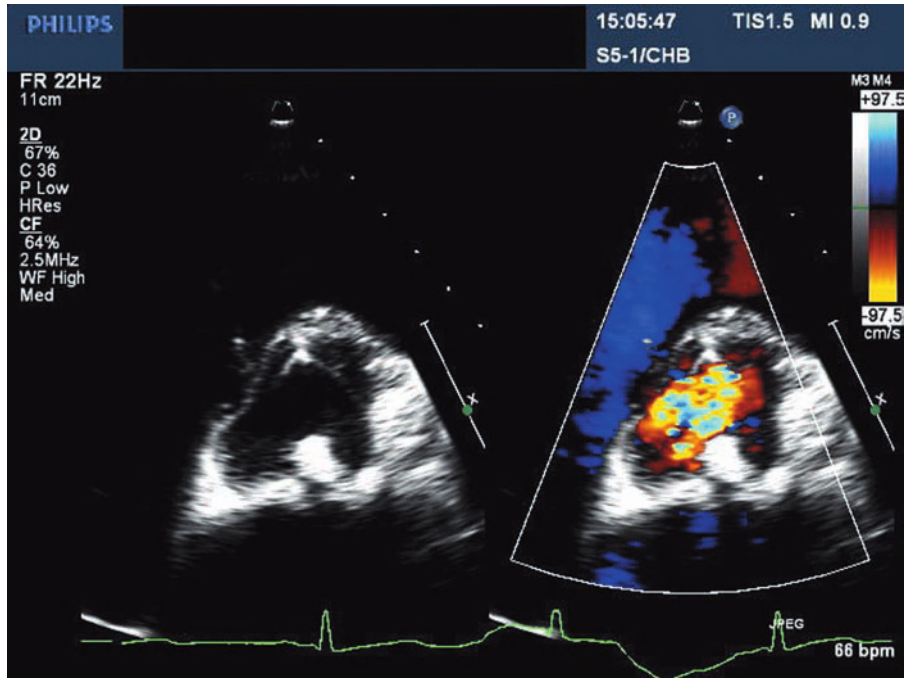


**Figure 38.5** Dual image in parasternal short-axis view demonstrating chronic rheumatic aortic valve disease. The aortic valve is seen "en face" with thickened leaflets and evidence of calcification. Color Doppler demonstrates a significant central jet of aortic regurgitation.

- Assess left ventricular function.
- Identify associated lesions.

The aortic valve should be examined carefully by 2D imaging to exclude the possibility of a congenital bicuspid valve, which may result in incomplete closure and/or prolapse of the leaflets. In rheumatic carditis, the aortic valve usually appears structurally normal. M-mode echocardiography may demonstrate premature mitral valve closure or diastolic opening of the aortic valve when left ventricular diastolic pressure is markedly increased. Significant aortic regurgitation may cause a quivering motion of the anterior leaflet of the mitral valve (Videoclip 38.7). Increased left ventricular dimensions reflect left ventricular volume overload due to significant aortic regurgitation. M-mode is also helpful for assessing left ventricular function.

Doppler assessment of the aortic valve in the parasternal long-axis view reveals high-velocity turbulent flow below the aortic valve immediately after valve closure and throughout diastole (Fig. 38.6). As with mitral regurgitation, several echocardiographic methods may be used to quantitate aortic regurgitation [32]. Although the regurgitant jet width and length in the parasternal long-axis view may grossly correlate with angiographic grading of aortic regurgitation, the size of the jet may be influenced by hemodynamic conditions, eccentricity of the jet, and Nyquist settings. In addition, jet eccentricity and spreading may contribute further to the variability in jet width, making this measurement inaccurate for grading the severity of aortic regurgitation.

Reliable predictors of aortic regurgitation severity include Doppler jet width normalized to left ventricular outflow tract (LVOT) width in the parasternal long-axis view, jet area normalized to LVOT area in the short-axis view, and holodiastolic abdominal aortic flow reversal [33]. A jet width/LVOT width ratio of 0–0.26 is consistent with mild (1+) aortic regurgitation angiographically, whereas a ratio of ≥0.71 correlates with severe (4+) aortic regurgitation. Similar values may be used for jet area normalized to LVOT area in the short-axis view.

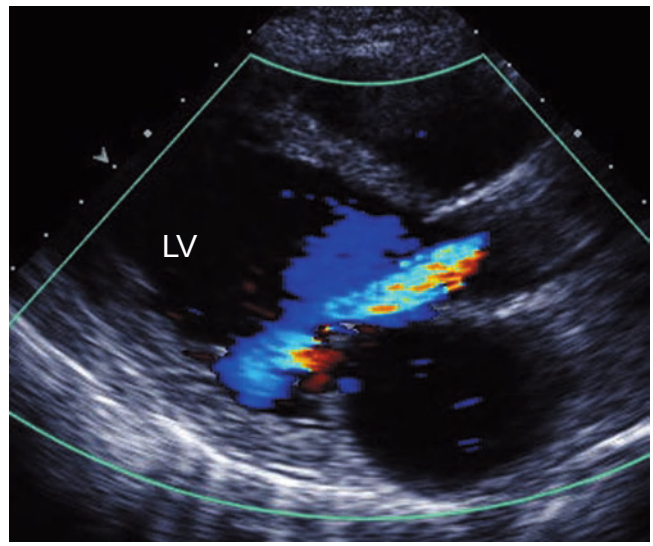


**Figure 38.6** Color Doppler tracing in the parasternal long-axis view demonstrating high-velocity turbulent flow below the aortic valve immediately after valve closure, in a patient with rheumatic aortic valvulitis.

Regurgitant volume can be quantified by using the volumetric or PISA methods, as described in Chapter 6. Regurgitant fraction (RF) is calculated by the following equation:

RF = aortic regurgitant volume/LVOT stroke volume × 100%

The effective regurgitant orifice area may be obtained by dividing the regurgitant volume by the aortic regurgitant time–velocity integral or by using the PISA method. Additional modalities for determining aortic regurgitation severity include pressure half-time (PHT) of the regurgitant jet and deceleration time (DT) of the mitral flow E velocity. As the severity of aortic regurgitation progressively worsens, PHT and DT shorten due to a decreased pressure difference between the aorta and left ventricle. As left ventricular diastolic pressure increases, the mitral inflow pattern changes to reflect restrictive diastolic filling [22,28].

## Chronic aortic valve disease

Over time, the aortic valve cusps may become infiltrated with fibrous tissue, resulting in retraction and loss of apposition during diastole (Fig. 38.5). The end result of these changes is the creation of a regurgitant orifice. The valve commissures may also fuse, leading to restricted opening of the valve during systole (Videoclip 38.8). In most cases, all commissures are equally affected, producing a central stenotic opening [19,26]. These changes are easily apparent by 2D imaging. Additional calcification of the aortic leaflets may worsen the severity of the stenosis. Rheumatic aortic stenosis is commonly seen in association with mitral stenosis, and therefore both valves should be assessed in detail during the echocardiographic exam.

### *Goals of examination for chronic aortic valve disease*

The goals of echocardiographic examination in this setting can be summarized as follows:

- Assess aortic valve anatomy.
- Perform a hemodynamic assessment:
  - quantitate aortic regurgitation (as described).
  - quantitate aortic stenosis:
    - measure the peak aortic flow velocity;
    - measure the mean pressure gradient;
    - determine the aortic valve area and
    - measure the LVOT-to-aortic valve time–velocity integral ratio.
  - Look for evidence of left ventricular overload (left ventricular size).
- Undertake a serial assessment of left ventricular function.
- Identify associated lesions.

The severity of aortic stenosis can be determined by noninvasive means using Doppler echocardiography. Several methods are used for quantification of aortic stenosis, including peak aortic flow velocity, mean pressure gradient, calculation of aortic valve area, and the LVOT/aortic valve time–velocity integral ratio. These are discussed in further detail in Chapter 6. Measurement of LVOT velocity is performed from the apical 5-chamber view. When performing the exam, it is important to differentiate the aortic stenosis jet from other Doppler-associated findings, such as mitral regurgitation or sites of additional LVOT obstruction. Changes in left ventricular function and cardiac output may affect aortic peak velocity and mean aortic pressure gradient, such that the severity of aortic stenosis may be underestimated or overestimated. In this case, the LVOT/aortic valve time–velocity integral (TVI) ratio and aortic valve area may be more helpful in predicting the severity of aortic stenosis. In the presence of significant aortic regurgitation, flow across the aortic valve increases, as does the pressure gradient. Because the increased flow is reflected in the LVOT and aortic valve proportionally; the TVI ratio remains the same for a given aortic valve area [22].

## Chronic rheumatic right heart involvement

Rheumatic tricuspid stenosis occurs in up to 10% of adults with rheumatic heart disease and is always seen in association with mitral stenosis. The anterior valve leaflet domes during diastole, and all the leaflets demonstrate a decrease in mobility (Fig. 38.7). Unlike the rheumatic mitral valve, the tricuspid valve rarely calcifies. Tricuspid regurgitation may also be present [25]. Doppler assessment of the tricuspid valve is similar to that performed for the mitral valve. Undiagnosed tricuspid involvement may complicate the postoperative course of patients undergoing surgical repair of left-sided obstructive lesions, and therefore careful evaluation of the right heart should be included for all patients with rheumatic heart disease.

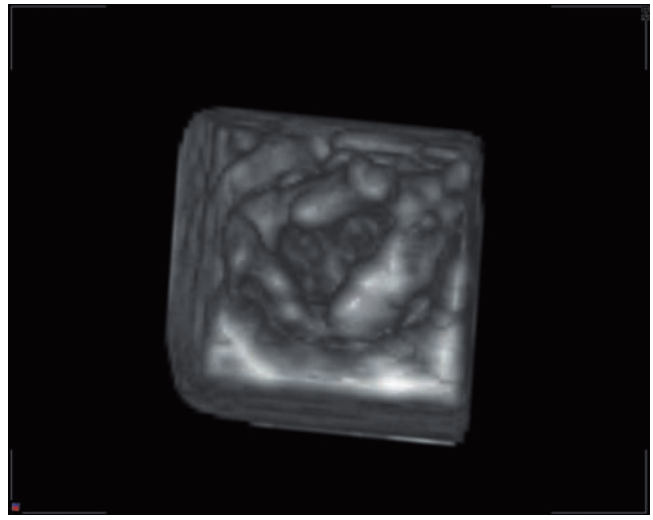

**Figure 38.7** Three-dimensional en face view of the tricuspid valve in a patient with rheumatic tricuspid stenosis. Note thickened leaflets with "rolled" edges.

Chronic and significant mitral valve disease can lead to secondary changes in the right heart. Increased left atrial, pulmonary venous and pulmonary arterial pressure may lead to the development of right ventricular enlargement, hypertrophy and dysfunction. When seen in combination with tricuspid regurgitation and/or stenosis, right heart failure may occur.

### Role of echocardiography in transcatheter and surgical intervention

Echocardiography is helpful in predicting which patients with rheumatic mitral stenosis will benefit from balloon valvotomy. 2D imaging is used to create a score based on valve thickness, calcification and mobility and subvalvar thickening. Each item is graded on increasing severity from 0 to 4, with 0 being normal and 4 being the most abnormal. A score of 8 or less predicts a good result from mitral balloon valvotomy. When combined with peak gradient, the score can also be used to predict the rate of progression of mitral stenosis [22].

Additional echocardiographic techniques that can be used to provide even more detailed information regarding valve anatomy prior to intervention include transesophageal and 3D imaging. Transesophageal imaging is necessary to exclude the possibility of an associated left atrial thrombus prior to balloon valvotomy. During the valvotomy procedure, transesophageal imaging is helpful in guiding transeptal puncture and provides information regarding balloon position, adequacy of the balloon dilation, and potential complications of the procedure. Transesophageal and 3D imaging also provide improved resolution of valve morphology, which may impact valvotomy or surgery. Intraoperative use of these imaging modalities is likewise helpful for determining whether valvuloplasty versus valve replacement is indicated and for guiding postoperative care [34].

## Acknowledgements

The author wishes to acknowledge the contributions of her colleagues to this chapter, namely Dr Lloyd Y. Tani (University of Utah School of Medicine) and Dr Lissa Sugeng (University of Chicago Medical Center).

## References

1. Bisno AL. Group A streptococcal infections and acute rheumatic fever. *N Engl J Med* 1991;325:783–93.
2. Alsaeid K, Majeed HA. Acute rheumatic fever: diagnosis and treatment. *Pediatr Ann* 1998;27:295–300.
3. Veasy LG, Tani LY, Hill HR. Persistence of acute rheumatic fever in the intermountain area of the United States. *J Pediatr* 1994; 124:9–16.
4. Martins TB, Veasy LG, Hill HR. Antibody responses to Group A streptococcal infections in acute rheumatic fever. *Pediatr Infect Dis J* 2006;25:832–7.
5. Khanna, AK, Buskirk DR, Williams RC et al. Presence of non-HLAB cell antigen in rheumatic fever patients and their families as defined by a monoclonal antibody. *J Clin Invest* 1989;83:1710.
6. Harrington A, Visvanathan K, Skinner NA et al. B-cell antigen D8/17 is a marker of rheumatic fever susceptibility in Aboriginal Australians and can be tested in remote settings. *Med J Aust* 2006;184:507.
7. Cairns LM. The immunology of rheumatic fever. *N Z Med J* 1988;101:388–91.
8. Bisno AL, Brito MO, Collins CM. Molecular basis of group A streptococcal virulence. *Lancet Infect Dis* 2003;3:191–200.
9. Dajani As, Ayoub E, Burman FZ et al. Special Writing Group of the Committee on Rheumatic Fever, Endocarditis, and Kawasaki Disease of the Council on Cardiovascular Disease in the Young of the American Heart Association. Guidelines for the diagnosis of rheumatic fever. Jones Criteria, 1992 update. *JAMA* 1992;268:2069–73.
10. Ferrieri P. Jones Criteria Working Group. Proceedings of the Jones Criteria Workshop. *Circulation* 2002;106:2521–3.
11. Veasy LG, Hill HR. Immunological and clinical correlations in rheumatic fever and rheumatic heart disease. *Pediatr Infect Dis* J 1997;16:400–7.
12. Roberts S, Kosanke S, Terrence Dunn S et al. Pathogenic mechanisms in rheumatic carditis: focus on valvular endothelium. *J Infect Dis* 2001;183:507–11.
13. Essop MR, Wisenbaugh T, Sareli P. Evidence against a myocardial factor as the cause of left ventricular dilation in acute rheumatic carditis. *J Am Coll Cardiol* 1993;22:826–9.
14. Veasy GL, Tani LY. A new look at acute rheumatic mitral regurgitation. *Cardiol Young* 2005;15:568–77.
15. Kalangos A, Behetti M, Vala D et al. Anterior mitral leaflet prolapse as a primary cause of pure rheumatic mitral insufficiency. *Ann Thorac Surg* 2000;69:755–61.
16. Marcus RH, Sareli P, Pocock WA et al. Functional anatomy of severe mitral regurgitation in active rheumatic carditis. *Am J Cardiol* 1989;63:577–84.
17. MacCallum WG. Rheumatic lesions of the left auricle of the heart. *Bull Johns Hopkins Hospital* 1924;35:341.
18. Barlow JB. Epilogue. In: Barlow JB (ed.) *Perspectives on the Mitral Valve*. Philadelphia, PA: FA Davis and Co., 1987;361.
19. Braunwald E. *Braunwald's Heart Disease: A Textbook of Cardiovascular Medicine*, 8th edn. Philadelphia, PA: WB Saunders Co., 2007.
20. Minich LL, Tani LY, Pagotto LT et al. Doppler echocardiography distinguishes between physiologic and pathologic "silent" mitral regurgitation in patients with rheumatic fever. *Clinic Cardiol* 1997;20:924–6.
21. Snider AR. Methods for obtaining quantitative information from the echocardiographic examination. In: Snider AR, Serwer GA, Ritter SB (eds) *Echocardiography in Pediatric Heart Disease*. St Louis: Mosby-Year Book, 1997;186–9.
22. Oh JK, Seward JB, Tajik AF. *The Echo Manual*, 2nd edn. Philadelphia: Lippincott Williams & Wilkins, 1999.
23. Wu YT, Chang AC, Chin AJ. Semi quantitative assessment of mitral regurgitation by Doppler color flow imaging in patients aged <30 years. *Am J Cardiol* 1993;71:7727–32.

24. Aotsuka H, Tobita K, Hamada H et al. Validation of the proximal isovelocity surface area method for assessing mitral regurgitation in children. *Pediatr Cardiol* 1996;17:351–9.
25. Maniet R, de Guise M, St John Sutton MG. Mitral and tricuspid valve disease. In: St John Sutton MG, Odershaw PJ, Kotler MN (eds) *Textbook of Echocardiography and Doppler in Adults and Children*. Oxford: Blackwell Science, 1996;142–91.
26. Otto CM. Valvular regurgitation: diagnosis, quantitation, and clinical approach. In: *Textbook of Clinical Echocardiography*, 3rd edn. Philadelphia: Elsevier-Saunders, 2004;339–41.
27. Zoghbi WA, Enriquez-Sarano M, Foster E et al. Recommendations for evaluation of the severity of native valvular regurgitation with two-dimensional and Doppler echocardiography. *J Am Soc Echocardiogr* 2003;16:777–802.
28. Sugeng L, Weinert L, Lang RM. Real-time 3-dimensional color Doppler flow of mitral and tricuspid regurgitation: feasibility and initial quantitative comparison with 2-dimensional methods. *J Am Soc Echocardiogr* 2007;20:1050–7.
29. Virmani R. Farb A, Burke AP, Narula J. Pathology of acute rheumatic carditis. In: Narula J, Virmani R, Reddy KS, Tandon R (eds) *Rheumatic Fever*. Washington, DC: American Registry of Pathology Press, 1999;221.
30. Zamorano J, Cordeiro P, Sugeng L et al. Real-time three-dimensional echocardiography for rheumatic mitral valve stenosis evaluation. *J Am Coll Cardiol* 2004;43:2091–6.
31. Ayoub EM. Acute rheumatic fever. In: Emmanouilides GC, Riemenschneider TA, Allen HD, Gutgesell HP (eds) *Moss and Adams' Heart Disease in Infants, Children, and Adolescents: including the Fetus and Young Adult*, 5th edn. Baltimore, MD: Williams &Wilkins, 1995;1406–7.
32. Tribouilloy CM, Enriquez-Sarano M, Bailey KR et al. Assessment of severity of aortic regurgitation using the width of the vena contracta: A clinical color Doppler imaging study. *Circulation* 2000;102:558–64.
33. Tani LY, Minich LL, Day RW et al. Doppler evaluation of aortic regurgitation in children. *Am J Cardiol* 1997;80:927–31.
34. Sugeng L, Coon P, Weinert L et al. Use of real-time 3-dimensional transthoracic echocardiography in the evaluation of mitral valve disease. *J Am Soc Echocardiogr* 2006;19:413–21.

# 39 Infective Endocarditis

**Manfred Otto Vogt**
Clinic for Pediatric Cardiology and Congenital Heart Disease, German Heart Center Munich, Munich, Germany

## Definition

Infective endocarditis (IE) is a subacute infectious disease of the heart and its surrounding vessels that carries a very high risk of morbidity and mortality. Unfortunately, a clear-cut diagnosis of IE is rare in patients with congenital heart disease (CHD) and is reserved for those who fulfill the classic Oslerian manifestations: bacteremia or fungemia, evidence of active vasculitis, and/or peripheral emboli (Fig. 39.1) and immunologic vascular phenomena. In most cases the clinical presentation is quite variable and therefore the diagnosis is related to an evidence-based scoring system that includes clinical, microbiological and echocardiographic findings (Tables 39.1 and 39.2). The Duke criteria [1] and their modification in 2000 [2] have been validated not only in adults but also in children [3,4]. It should be kept in mind that the Duke criteria were developed primarily to facilitate epidemiologic and clinical research efforts so that data could be compared between different centers and countries. In present clinical practice these criteria serve as a guide for diagnosing IE but can never replace final clinical judgment.

## Incidence

The incidence of IE in infancy and childhood is unknown as no data exist from a population-based cohort. Overall, the incidence of IE appears to be increasing but in absolute terms it is relatively rare in children. CHD now constitutes the predominant underlying condition for IE in children over the age of 2 years in developed countries [5]. Some of the cases in this age group are due to the complexity of neonatal and pediatric intensive care and may be related to indwelling catheters and instrumentation in this population (Videoclip 39.1).

In pediatric hospitals, IE accounts for about 1 in 1280 pediatric admissions per year [6]. In patients with CHD, ventricular septal defect, patent ductus arteriosus, aortic valve abnormalities (e.g., bicuspid aortic valve), and tetralogy of Fallot are the most common underlying conditions in which IE occurs. IE may afflict such patients before surgical intervention, but an increasing proportion of patients have had previous corrective or palliative surgery [7–10].

Corrective surgery with no residual defects eliminates the increased risk of IE, within 6 months of surgery, in children with ventricular and atrial septal defects and/or patent ductus arteriosus. The highest annual risk for IE has been found in children with repaired or palliated cyanotic CHD [10]. Palliative shunt procedures (Videoclip 39.2) or complex intracardiac repairs increase the risk for postoperative IE [8]. The risk is highest among patients who have had prosthetic aortic valve replacement (Fig. 39.2 and Videoclip 39.3) or operations performed because of reduced pulmonary blood flow. In those patients with prosthetic valves or conduits the risk for IE is high even in the immediate postoperative period (first 2 weeks after surgery) whereas for all other patients with residual defects the risk increases with time after surgery [11].

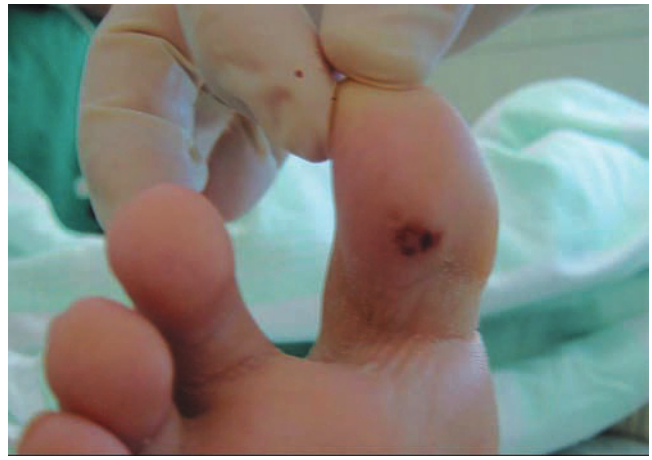

**Figure 39.1** An Osler node of the first toe as a typical dermatologic sign of bacterial infective endocarditis.

*Echocardiography in Pediatric and Congenital Heart Disease: From Fetus to Adult*
Edited by Wyman W. Lai, Luc L. Mertens, Meryl S. Cohen and Tal Geva
 ISBN: 978-1-405-17401-5

**Table 39.1** Definition of terms used in the Duke criteria for the diagnosis of infective endocarditis (IE)*

**Major criteria**

**1** Positive blood culture for IE
- Typical microorganism consistent with IE from two separate blood cultures: viridans streptococci, *Streptococcus bovis*, HACEK group, *Staphylococcus aureus*, or community-acquired enterococci in the absence of a primary focus† *OR*
- Microorganisms consistent with IE from persistently positive blood cultures defined as follows: at least two positive cultures of blood samples drawn >12 h apart, or all of three or a majority of four or more separate cultures of blood (with first and last samples drawn at least 1 h apart)
- **Single positive blood culture for *Coxiella burnetii* or anti-phase 1 IgG antibody titer >1:800**

**2** Evidence of endocardial involvement
- Echocardiogram positive for IE defined as:
  **(TEE is recommended for patients with: (i) prosthetic valves; (ii) at least "possible IE" by clinical criteria; or (iii) complicated IE [paravalvular abscess]; TTE as first test in other patients)**
  - Oscillating intracardiac mass on valve or supporting structures in the path of regurgitant jets, or on implanted material in the absence of an alternative anatomic explanation; *OR*
  - Presence of an abscess, *OR*
  - New partial dehiscence of prosthetic valve, *OR*
  - New valvular regurgitation (worsening or changing or preexisting murmur not sufficient)

**Minor criteria**

**1** Predisposition, predisposing heart condition, or intravenous drug use

**2** Fever, temperature >38°C

**3** Vascular phenomena including major arterial emboli, septic pulmonary infarcts, mycotic aneurysm, intracranial hemorrhage, conjunctival hemorrhages, and Janeway lesions

**4** Immunologic phenomena: glomerulonephritis, Osler nodes, Roth spots, and rheumatoid factor

**5** Microbiologic evidence: positive blood culture but does not meet a major criterion as noted above or serologic evidence of active infection with organism consistent with IE

**6 Echocardiographic minor criteria eliminated**

TEE, transesophageal echocardiography; TTE, transthoracic echocardiography.
*Modifications shown in bold typeface.
†Excludes single positive cultures for coagulase-negative staphylococci and organisms that do not cause endocarditis.
Reprinted from Li JS, Sexton DJ, Mick N et al. Proposed modifications to the Duke criteria for the diagnosis of infective endocarditis. *Clin Infect Dis* 2000;30:633–8, with permission from The University of Chicago Press.

Children with congenital or acquired immunodeficiencies but without identifiable risk factors for IE (such as central venous catheters) do not appear to be at increased risk for IE compared with the general population [5]. Intravenous (i.v.) drug use is infrequent in childhood but the incidence is rising in adolescence and adulthood. The exact incidence of IE in i.v. drug users is unknown [12] but 1.5 to 3.3 cases per 1000 person-years [13,14] is a conservative estimate. IE is more frequent in HIV-seropositive i.v. drug users than in HIV-seronegative patients [15]. It may be difficult to diagnose IE correctly in febrile i.v. drug users because 35% do not present with a heart murmur on admission [16]. The predilective site of infection in this group is typically the tricuspid valve even in structurally normal hearts (Fig. 39.3).

In the adult population, the incidence of IE is approximately five episodes/100 000 person-years if i.v. drug users are excluded [17]. Apart from preexisting structural heart disease, which accounts for three-quarters of all cases of IE, an increasing number of invasive instrumentation procedures, such as pacemaker and defibrillator implantations (Fig. 39.4), play a major role [18]. For most devices used to occlude atrial or ventricular septal defects, IE in the follow-up period is rare but has been reported [19].

A population that is especially at risk for IE is the increasing number of adults with CHD. IE accounted for 4% of hospital admissions of these patients in specialized centers [20]. In this study, adults with unoperated or palliated CHD presented with IE at the site of a ventricular septal defect, left ventricular outflow tract or mitral valve. In those with repaired CHD, IE was most commonly seen after surgery for tetralogy of Fallot or atrioventricular (AV) canal defects (Fig. 39.5 and Videoclip 39.4) [21]. An atrial septal defect alone (unrepaired or later than 6 months after operation/catheter intervention) was not associated with an increased risk for IE in any age group.

## Etiology and pathogenesis

The pathogenesis of IE is characterized by the triad of endothelial damage, platelet adhesion and microbial adherence

**Table 39.2** Definition of infective endocarditis (IE) according to modified Duke criteria*

**Definitive IE**

**1** Pathological criteria
- Microorganisms demonstrated by culture or histologic examination of a vegetation, a vegetation that has embolized, or an intracardiac abscess specimen, *OR*
- Pathologic lesions: vegetation or intracardiac abscess present, confirmed by histology showing active endocarditis

**2** Clinical criteria
- Two major criteria, or
- One major criterion and three minor criteria, or
- Five minor criteria

**Possible IE**

**1 One major criterion and one minor criterion**

**2 Three minor criteria**

**Rejected**

**1** Firm alternative diagnosis explaining evidence of IE, *OR*

**2** Resolution of IE syndrome with antibiotic therapy for <4 days, *OR*

**3** No pathologic evidence of IE at surgery or autopsy, with antibiotic therapy for <4 days, *OR*

**4** Does not meet criteria for possible IE as above

*Modifications shown in bold typeface.

Reprinted from Li JS, Sexton DJ, Mick N et al. Proposed modifications to the Duke criteria for the diagnosis of infective endocarditis. *Clin Infect Dis* 2000;30:633–8, with permission from The University of Chicago Press.

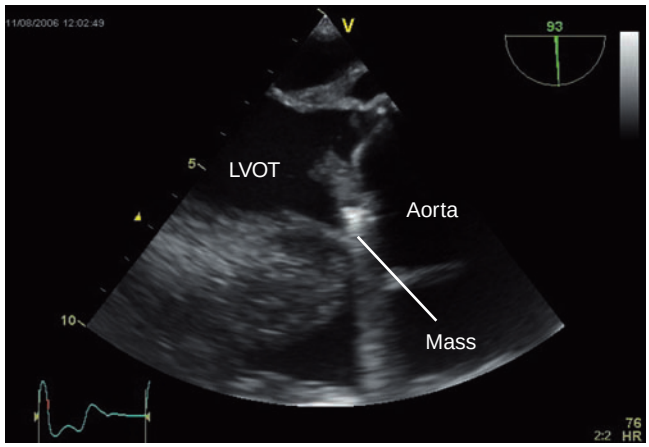


**Figure 39.2** Transesophageal echocardiographic view of the left ventricular outflow tract (LVOT) after mechanical valve replacement, showing a subvalvular echogenic mass from the anterior portion of the valve ring indicating infective endocarditis.

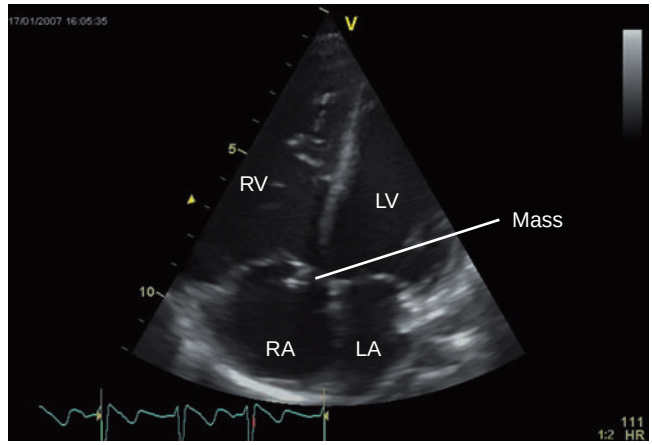


**Figure 39.3** Transthoracic echocardiographic apical 4-chamber view showing an oscillating mass fixed to the atrial aspect of the septal leaflet of the tricuspid valve, as is typical in intravenous drug users. LA, left atrium; LV, left ventricle; RA, right atrium; RV, right ventricle.

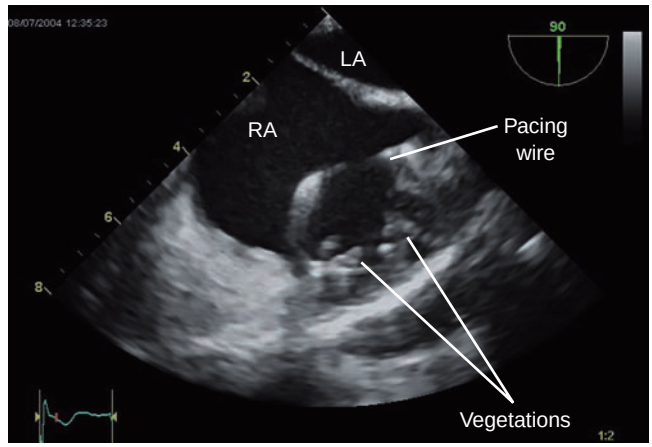


**Figure 39.4** Transesophageal echocardiogram in the sagittal plane of an atrial pacemaker lead with fixation to the anterior wall of the right atrium. Multiple mobile vegetations can be seen adherent to the lead. LA, left atrium; RA, right atrium.

to the vegetation or intact valvular tissue [22]. An intact endothelium within the heart is generally a poor stimulator of blood coagulation and therefore not predestined for bacterial attachment [5]. However, in children with CHD, abnormal high-velocity jet streams of blood (as seen in such lesions as ventricular septal defect, patent ductus arteriosus, aortic or pulmonary valve stenosis, or regurgitant AV valves) lead to damage of the endothelium due to shear stress forces and activation of the prothrombotic cascade in the circulating blood. Subsequently, a sterile platelet–fibrin deposition on the endothelial lesion provides a milieu for bacterial colonization. In addition to CHD, the administration of indwelling intravenous catheters into the right side of a structurally normal heart may traumatize the endocardium or valvular endothelium by exposing the subendothelial collagen [23]. This is one of the major mechanisms resulting in IE of the newborn.

Once the inciting lesion has been formed, bacteremia must be present to colonize the vegetation. Even in the presence of

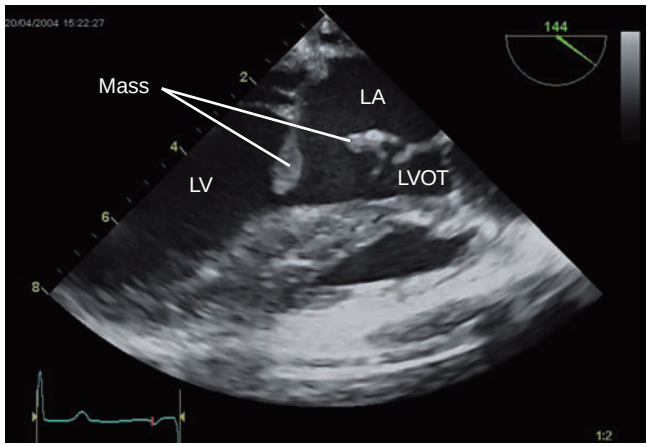


**Figure 39.5** Transesophageal echocardiogram in a patient after repair of atrioventricular canal defect demonstrating a large echogenic mass adherent to the "posterior" leaflet of the left atrioventricular valve mitral leaflet and another smaller mass fixed to the "anterior" leaflet. LA, left atrium; LV, left ventricle; LVOT, left ventricular outflow tract.

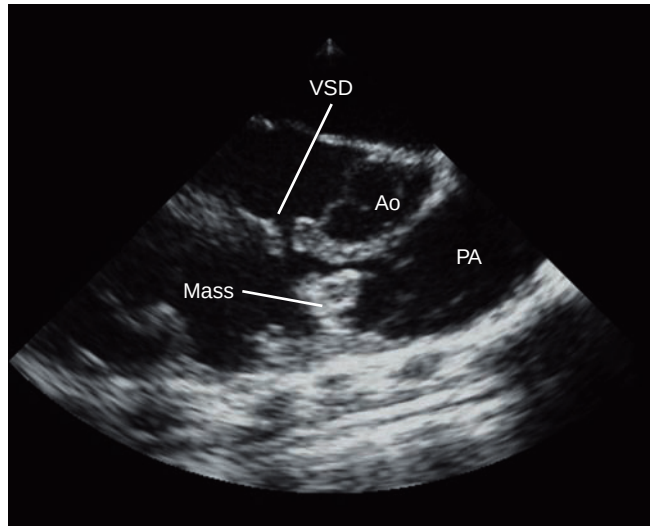


**Figure 39.6** Transesophageal echocardiogram in a patient with a small restrictive ventricular septal defect (VSD) under the aortic valve. A large vegetation is seen at the site of the jet-lesion on the anterior right ventricular wall just below the pulmonary artery (PA). Ao, aorta.

an endothelial lesion and a sterile thrombus formation, not every bacteremia event leads to IE. Bacteria must be able to survive in the bloodstream in sufficient numbers and adhere to the platelet–fibrin–fibrinectin complex on the lesion. Organisms such as *Staphylococcus aureus*, *Streptococcus viridans*, *Streptococcus pneumoniae*, HACEK organisms and group A, C and G streptococci as well as *Candida albicans* are known to have specific surface receptors for fibronectin that promote the adhesion of bacteria to the thrombus formation [24]. After adhesion, the microorganisms are trapped within the vegetation and thus protected from phagocytic cells and other host defense mechanisms [5].) Within the growing vegetation, proliferation is possible up to a maximum bacterial density of $10^7$ to $10^{10}$ colony-forming units per gram of tissue [25,26].

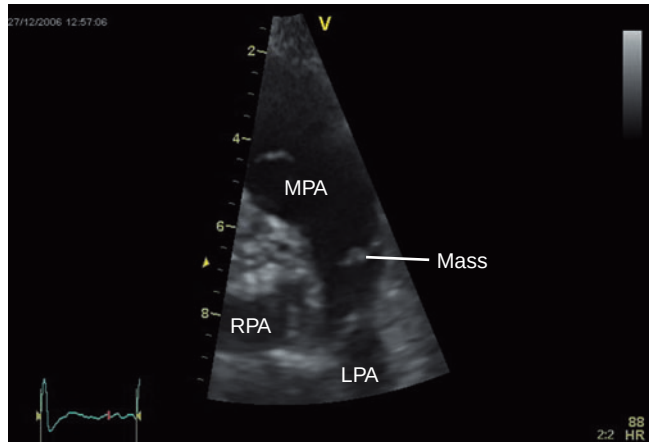


**Figure 39.7** Transthoracic echocardiogram in the parasternal short-axis view demonstrating a very mobile thin vegetation originating from a small persistent ductus arteriosus. The mass oscillates toward the main pulmonary artery (MPA) similar to the direction of blood flow. LPA, left pulmonary artery; RPA, right pulmonary artery.

## Morphology and classification

The morphology of IE vegetations is dependent on the location of the endothelial lesion and always follows the "pathologic" bloodstream. When IE occurs in association with a ventricular septal defect, the vegetation is typically visualized on the right ventricular aspect of the septum and/or on the site where the high-velocity jet strikes the right ventricular free wall (Fig. 39.6). In the case of patent ductus arteriosus, the vegetation may float through the pulmonary opening of the ductus into the main pulmonary artery (Fig. 39.7 and Videoclip 39.5). With regurgitant AV valves, the lesion is located on the atrial side (Fig. 39.8 and Videoclip 39.6). Vegetations may cause valve perforation (Fig. 39.9 and Videoclip 39.7), chordal rupture, and can also extend to the outside of the valve (Fig. 39.10) into surrounding structures. When semilunar valves are affected, the primary vegetation is typically on the ventricular surface of the valve (Fig. 39.11) but may also extend more proximally through the valve into the supravalvar region in systole (Videoclip 39.8). When the aortic valve is affected, perforation through the annulus into the myocardium or into either atria is possible. Newly acquired AV block (Fig. 39.12) together with clinical suspicion of IE may be a strong indicator for the presence of para-aortic ring abscess (Fig. 39.13) [27].

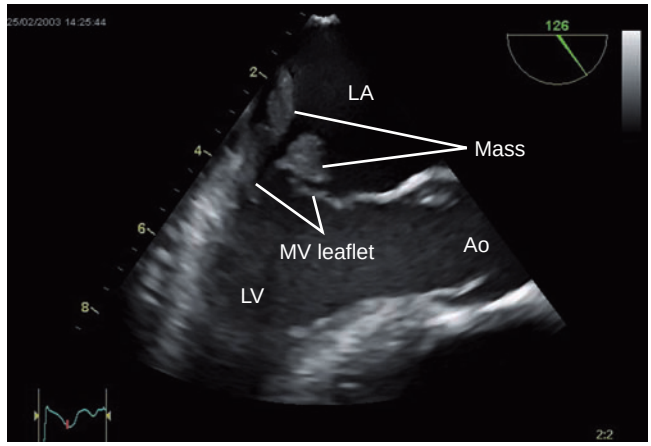


**Figure 39.8** Transesophageal echocardiogram in the left ventricular outflow view demonstrating multiple echogenic masses attached to the atrial side of the mitral valve leaflets. Ao, aorta; LA, left atrium; LV, left ventricle; MV, mitral valve.

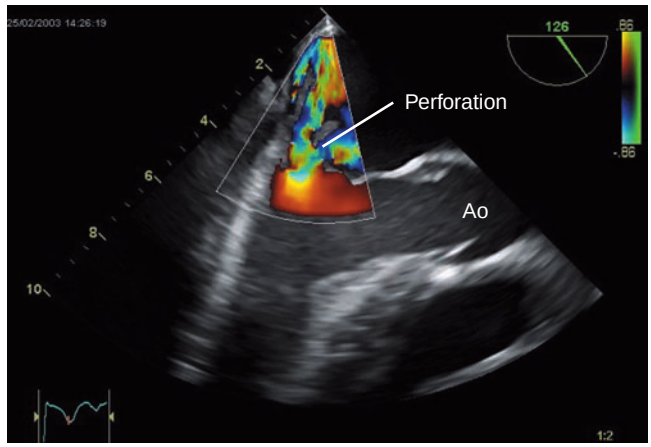


**Figure 39.9** Transesophageal echocardiogram of the same patient as in Fig. 39.8. Color Doppler shows newly acquired mitral regurgitation through a perforation in the posterior leaflet of the mitral valve. Ao, aorta.

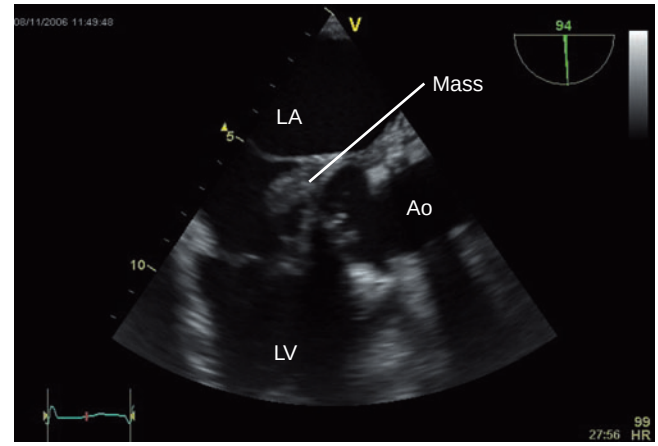


**Figure 39.10** Transesophageal echocardiogram demonstrating an aortic ring abscess with perforation into the left atrium (LA). The underlying heart disease was a calcified stenotic aortic valve. Ao, aorta; LV, left ventricle.

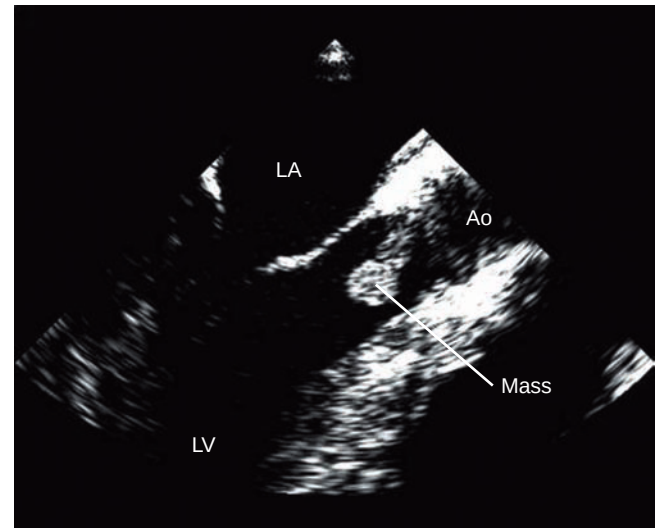


**Figure 39.11** Transesophageal echocardiogram in the left ventricular outflow tract view demonstrating native aortic valve endocarditis with a large globular vegetation on the ventricular side of the semilunar valve. Ao, aorta; LA, left atrium; LV, left ventricle.

In a series of 153 patients [28], the major underlying cardiac lesion associated with IE in childhood was the unoperated ventricular septal defect (30%) (Fig. 39.6) followed by mitral regurgitation (15%) (Fig. 39.14) and bicuspid aortic valve (9%) (Fig. 39.15 and Videoclip 39.9). In patients who undergo palliative surgery, infected aorto-pulmonary shunts (80%) predominate. In those who have corrective surgery, the most common sites for development of IE include right ventricle-to-pulmonary artery valved conduits (27%) (Fig. 39.16; Videoclip 39.10), prosthetic valves (22%) and ventricular septal defect patch closure (22%) (Table 39.3 and Fig. 39.17). [28,29]

Endocarditis on prosthetic valves usually initiates on the valvular cuff (Fig. 39.2 and Videoclip 39.3) and often extends outside the annulus, causing dehiscence (Fig. 39.18 and Videoclip 39.11) and myocardial involvement [22]. Mechanical prosthetic valves appear to have greater risk for endocarditis in the early period after surgery whereas the risk with bioprosthetic valves is greater later on [30,31]. Implantable rings have the least risk for endocarditis [32].

## Pathophysiology

The pathophysiologic consequences of IE are primarily defined by the underlying CHD and the complications that arise from the insult, such as valvular obstruction, regurgitation and/or

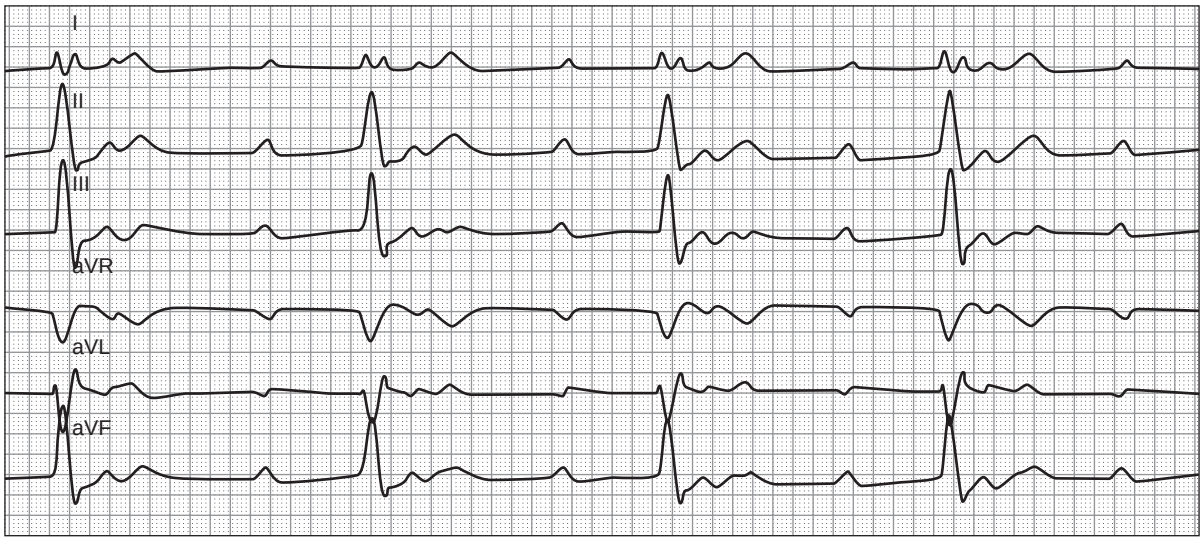


**Figure 39.12** Electrocardiogram demonstrating newly acquired atrioventricular block in a patient with aortic valve replacement who developed a paravalvular abscess. A transesophageal echocardiogram of this patient is shown in Fig. 39.13 and Videoclip 39.14.

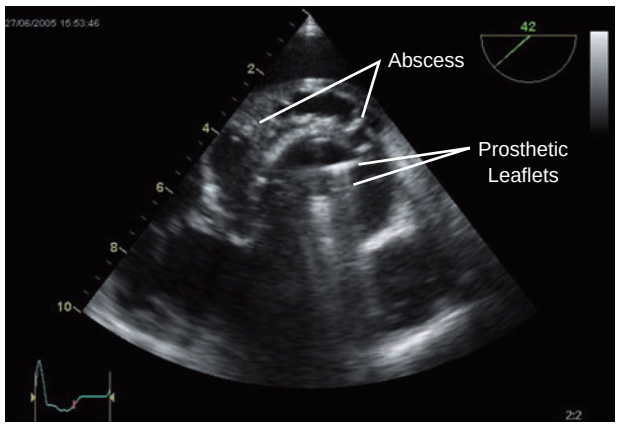


**Figure 39.13** Transesophageal echocardiogram demonstrating a large paravalvular ring abscess years after aortic valve replacement with a mechanical St Jude Medical valve.

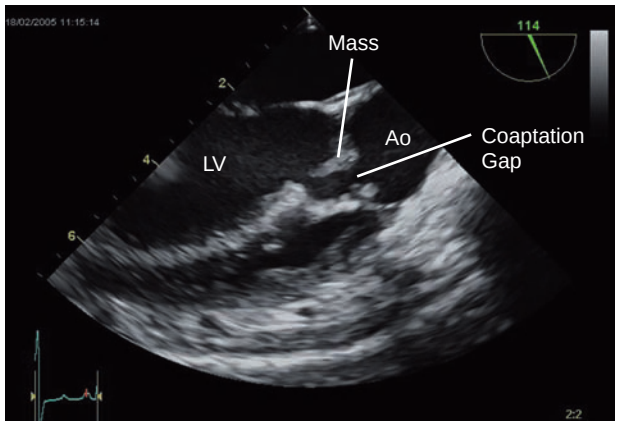


**Figure 39.15** Transesophageal echocardiogram demonstrating a bicuspid aortic valve with a mobile vegetation on the posterior cusp and an immobile lesion on the anterior cusp such that the leaflets have a significant coaptation gap when closed. Ao, aorta; LV, left ventricle.

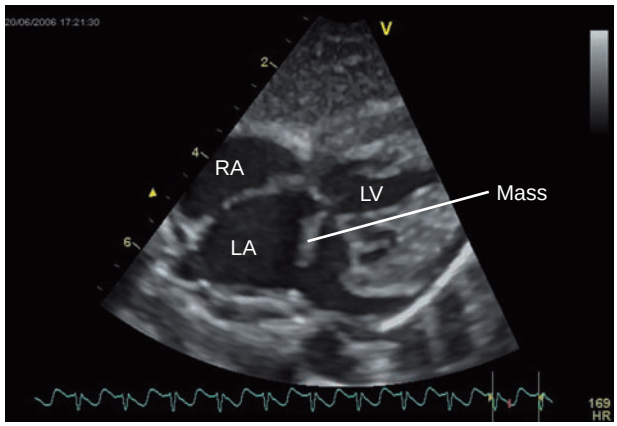


**Figure 39.14** Transthoracic echocardiogram in the subcostal frontal view of a single mobile vegetation on the left atrial side of the anterior mitral leaflet. LA, left atrium; LV, left ventricle; RA, right atrium.

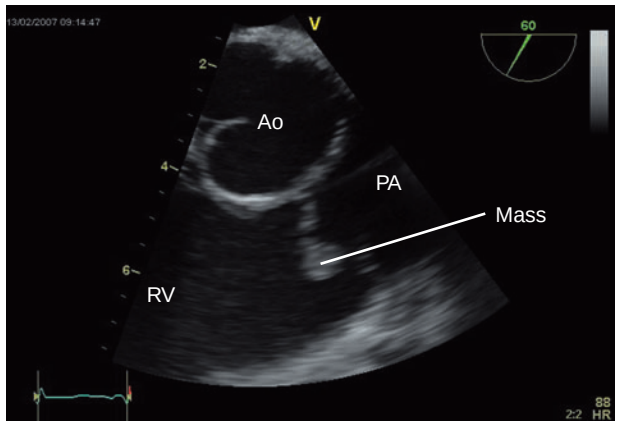


**Figure 39.16** Transesophageal echocardiogram in a patient after the Ross operation with right ventricle (RV)-to-pulmonary artery (PA) conduit using a valved pulmonary homograft. There is a large vegetation attached to the homograft valve. Ao, aorta.

**Table 39.3** Patients with congenital heart disease (CHD) at risk for infective endocarditis

| |
|---|
| **Patients without surgery** |
| Ventricular septal defect, patent ductus arteriosus, atrioventricular septal defect, tetralogy of Fallot, mitral valve prolapse, bicuspid aortic valve, aortic valve stenosis, mitral valve regurgitation, pulmonary valve stenosis, complex CHD |
| **Patients with previous palliation** |
| Aorto-pulmonary shunt, pulmonary banding, aortic/pulmonary conduit |
| **Patients with corrective surgery – increasing risk with residual lesion** |
| Ventricular septal defect patch (simple and complex), tetralogy of Fallot repair, prosthetic valve implantation, atrioventricular canal repair, aortic/mitral valve surgery, coarctectomy, complex CHD, pacemaker implantation |

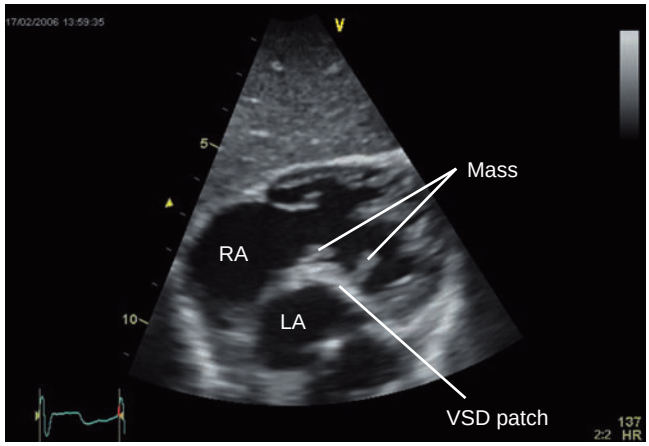


**Figure 39.17** Transthoracic echocardiogram in a subcostal frontal view demonstrating a ventricular septal defect (VSD) that has been closed with a GORE-TEX patch. On the right ventricular surface, several finger-shaped vegetations can be seen. LA, left atrium; RA, right atrium.

perforation; ventricular dysfunction; embolic phenomena and conduction disturbances. Age at presentation and location of IE (right-sided versus left-sided) also play a pivotal role. In newborns, symptoms are generally related to septicemia rather than cardiac failure [33,34]. In children with systemic–pulmonary artery shunts, increasing cyanosis may be the primary symptom together with pulmonary findings related to septic pulmonary embolization [35].

In adult patients with left-sided IE, congestive heart failure is one of the complications with greatest impact on prognosis [36–38]. Moderate to severe heart failure is identified as one of five independent risk factors for 6-month mortality [36]. The severity of symptoms is not influenced by appropriate antibiotic therapy. Compensation of heart failure is dependent on the valve affected, with acute aortic regurgitation being tolerated the least and acute tricuspid regurgitation being tolerated the best. Congestive heart failure will develop acutely when there is perforation of a native or bioprosthetic valve leaflet, acute valve dehiscence, rupture of an infected mitral chorda, obstruction to outflow from a bulky vegetation, or sudden intracardiac shunt from a fistulous tract [12].

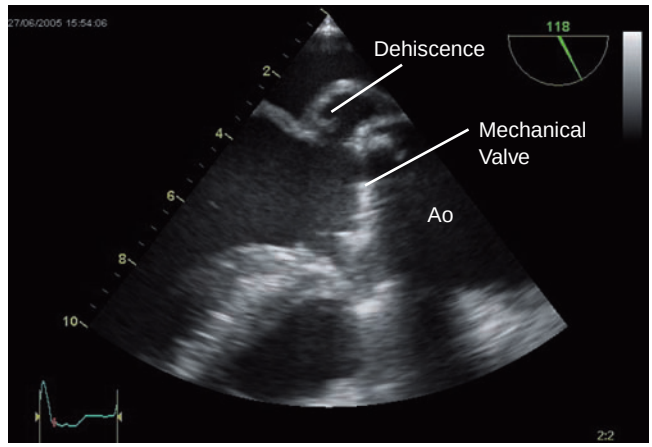


**Figure 39.18** Transesophageal echocardiogram just prior to surgery for infective endocarditis of a mechanical valve prosthesis with aortic ring abscess and incomplete dissection of the valve. Intraoperatively the valve was found to be held in place by only the last two stitches. Ao, aorta.

## Imaging

### Transthoracic versus transesophageal imaging

Echocardiography is the gold standard of imaging in cases of suspected IE in any age group. However, echocardiography is not an appropriate screening test in the evaluation of patients with fever or a positive blood culture when IE is not suspected by any other clinical criteria. The classic echocardiographic findings of IE described in the Duke criteria include an oscillating mobile intracardiac mass or vegetation attached to valve leaflets or the endocardium, an annular abscess or prosthetic valve dehiscence, and/or new valvular regurgitation [12]. The first-line diagnostic tool should be a transthoracic echocardiogram (TTE) regardless of age. When the acoustic window is inadequate or the suspicion of IE is high but TTE does not demonstrate a lesion, then transesophageal echocardiography (TEE) should be performed without delay (Table 39.4 and Fig. 39.19) [39]. TTE can often visualize even small vegetations [40] but its sensitivity is estimated to be 81% [41]. In a small pediatric series of patients with IE, TTE was compared with TEE, and a sensitivity of 86% was found for detection of all events [42]. However, one of three patients with abscess formation and one of 14 with an intracardiac vegetation was missed on TTE. Even when TTE findings are positive, TEE may be required to assess a paravalvular abscess or any patient with suspected IE who has a prosthetic valve.

**Table 39.4** Cardiac conditions associated with the highest risk of adverse outcome from infective endocarditis (IE)

| |
|---|
| Prosthetic cardiac valve |
| Previous IE |
| Congenital heart disease (CHD):<br>• Unrepaired cyanotic CHD, including palliative shunts and conduits<br>• Repaired CHD with prosthetic material or device, whether placed by surgery or by catheter intervention, during first 6 months after the procedure<br>• Repaired CHD with residual defects at the site or adjacent to the site of a prosthetic patch or prosthetic device (which inhibit endothelialization) |

Modified from Wilson W, Taubert KA, Gewitz M et al. Prevention of Infective Endocarditis. Guidelines From the American Heart Association. A Guideline From the American Heart Association Rheumatic Fever, Endocarditis, and Kawasaki Disease Committee, Council on Cardiovascular Disease in the Young, and the Council on Clinical Cardiology, Council on Cardiovascular Surgery and Anesthesia, and the Quality of Care and Outcomes Research Interdisciplinary Working Group. *Circulation* 2007;116:1736–54.

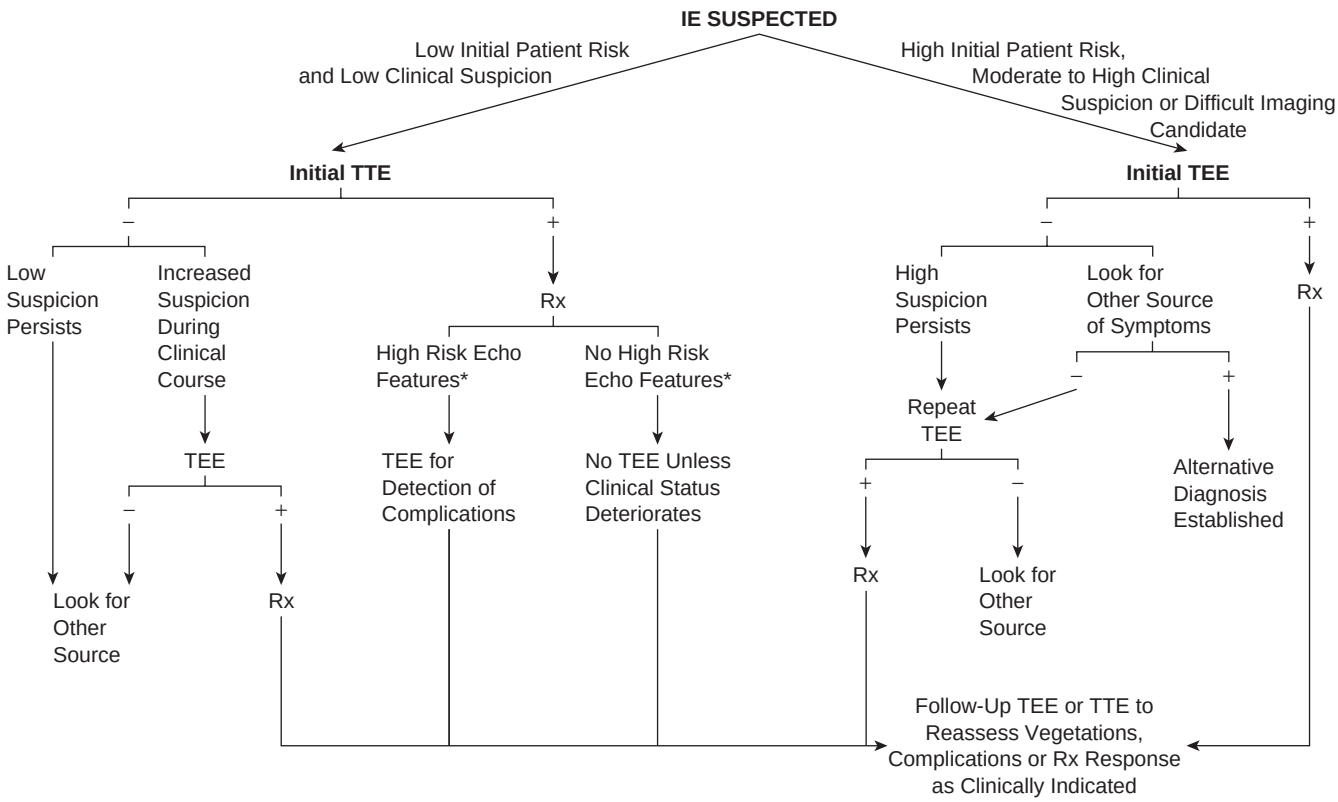


**Figure 39.19** Guidelines for transthoracic echocardiography (TTE) versus transesophageal echocardiography (TEE) when infective endocarditis is suspected. Reproduced from Wilson W, Taubert KA, Gewitz M. Prevention of infective Endocarditis. Circulation 2005;111:394–434 Baddour et al., adopted form Circulation 1998;98:2936–2948 Bayer AS et al., with permission from American Heart Association.

In adults, TEE is superior in detecting vegetations measuring less than 5 mm, with a sensitivity of more than 90% [43]. It is also the best modality to diagnose prosthetic valve endocarditis and paravalvular abscesses [44,45]. In patients with a high probability of IE but an initially negative TEE, a repeat TEE after an interval of 7–10 days may be indicated when clinical suspicion persists [46]. Some findings, like tricuspid vegetations (Videoclip 39.12) or abnormalities of the right ventricular outflow tract may occasionally be better visualized with TTE than with TEE [47].

## Goals of the examination

The objectives of echocardiographic examination in the setting of infective endocarditis can be summarized as follows:

- Identify masses/vegetation within the heart and/or its surrounding vessels.
- Determine the location, size, extent and number of IE lesions.
- Assess the severity of intracardiac damage as a result of the vegetation:
  - severity of valvular regurgitation;
  - perforation of valve leaflets;

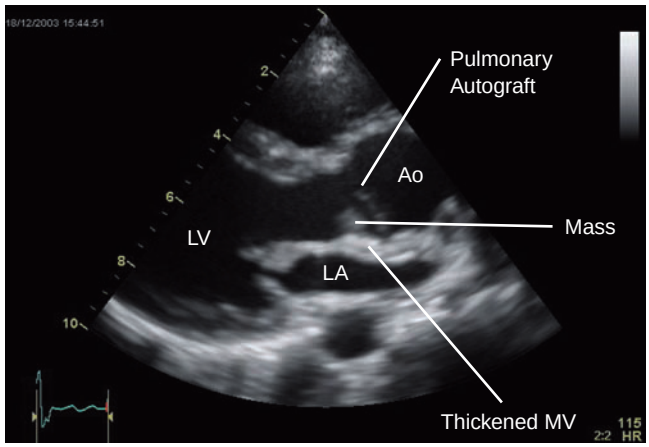


**Figure 39.20** Parasternal long-axis view in a patient after the Ross operation demonstrating an echogenic mass on the ventricular side of the neoaorta. There is also thickening of the mitral valve in the region of the mitral–aortic fibrous continuity as an indicator of infiltration. Ao, aorta; LA, left atrium; LV, left ventricle; MV, mitral valve.

**Table 39.5** Goals of echocardiography for infective endocarditis (IE) in congenital heart disease

| |
|---|
| **Diagnosis of IE** |
| Site and extent of vegetation |
| Description of valvular function |
| Monitoring of hemodynamic consequences |
| Monitoring of cardiac function – ventricular performance |
| Detection of pericardial effusion – myocardial abscess |
| **Therapeutic decision** |
| Indication for surgery – based on vegetation size/location |
| Prediction of embolic events |
| **Monitoring of treatment** |
| Monitoring of conservative therapy |
| Intraoperative echocardiography |
| Post-treatment echocardiography |

- development of paravalvular abscess or fistula formation;
- for prosthetic valves, determine if dehiscence has occurred.

- Assess whether the vegetation is mobile or adherent.

Initial screening by TTE in patients with CHD should be focused on the underlying heart defect and the knowledge that IE is primarily located on the site of the endothelial jet lesion. Using the 2D modality, any unknown echogenic mass that moves faster than the surrounding cardiac structures is highly suspicious for IE (Fig. 39.20 and Videoclip 39.13). In some patients with resolving IE, the vegetation may become calcified. New vegetations will typically move with a high frequency (i.e., an oscillating mass) whereas calcifications will usually have the same motion as the valve itself. Color Doppler is a sensitive modality for detecting pathologic flow patterns at the ventricular, valvular or vessel level, and is helpful in discriminating the site of a possible endothelial lesion.

Once the diagnosis is established and the site of the infection located, TTE/TEE is mandatory to describe the extent of valvular damage and to monitor cardiac function and the possible hemodynamic consequences of IE, such as pulmonary hypertension due to mitral regurgitation or acute volume load of the left ventricle due to aortic perforation (Table 39.5).

## Imaging of the adult

Adults with CHD often present with limited TTE windows. Therefore, TEE is indicated as a first-line imaging modality when IE is suspected (see Table 39.4 and Fig. 39.19) [48,49]. A rare localization of IE in the adult that may be easily missed on TTE is the Eustachian valve (Fig. 39.21 and Videoclip 39.14) [50]. Pulmonary embolism may be the first clinical sign in this right-sided endocarditis; TEE is often performed in order to detect thrombus formation once pulmonary embolism is diagnosed.

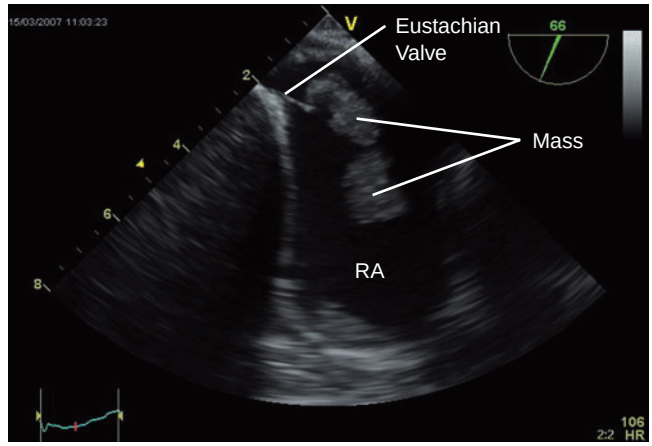


**Figure 39.21** Transesophageal echocardiogram in the sagittal view of the inferior vena cava–right atrium (RA) junction showing two large vegetations attached to the Eustachian valve.

## Preoperative assessment

Echocardiography may identify patients at high risk for complications such as systemic embolism (Fig. 39.22), abscess cavities (Fig. 39.23), pseudoaneurysms, valvular perforation or dehiscence, and reveals evidence of decompensated heart failure with a potential need for surgery (Table 39.6). [51]. The incidence of systemic embolism in IE ranges from 13% to 49% and may greatly influence mortality rate. In a prospective study, vegetation length exceeding 15 mm was an independent predictor of 1-year mortality [52].

Vegetation size and mobility must be taken into account, as well as bacteriologic and other clinical factors, when considering early surgery to avoid embolization [53]. Despite the wide acceptance of echocardiography for the diagnosis

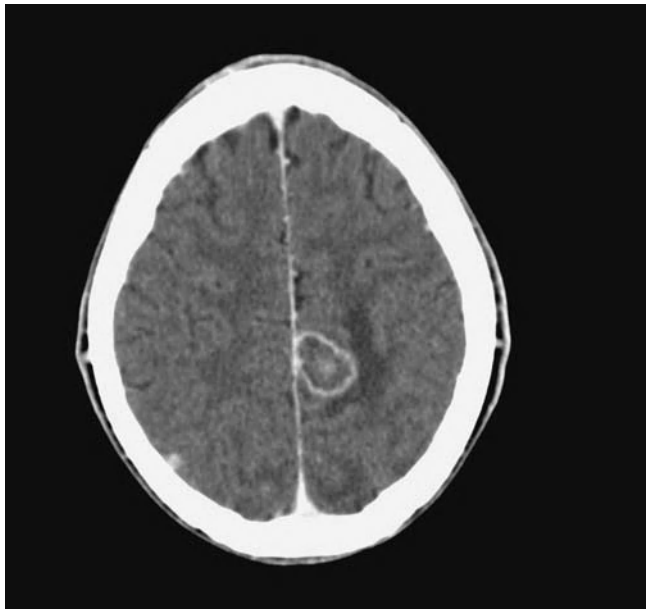

**Figure 39.22** Cranial computed tomogram of a patient with *Staphylococcus aureus* endocarditis after mechanical aortic valve replacement. After contrast enhancement a 2-cm abscess is seen in the left parasagittal parietal region.

**Table 39.6** Echocardiographic findings in infective endocarditis (IE) that suggest a potential need for surgical intervention

| |
|---|
| **Vegetation** |
| Vegetation size >15 mm in left-sided IE |
| Highly mobile vegetation |
| Persistent vegetation after systemic embolization |
| More than one embolic events during first 2 weeks of antimicrobial therapy |
| An increase in vegetation size despite appropriate antimicrobial therapy |
| **Valvular dysfunction** |
| Acute aortic or mitral insufficiency with signs of ventricular failure |
| Heart failure unresponsive to medical therapy |
| Valve perforation or rupture |
| **Perivalvular extension** |
| Valvular dehiscence, rupture or fistulous formation |
| New onset of heart block |
| Large abscess or extension of abscess despite appropriate antimicrobial therapy |

Adapted from Baddour LM, Wilson WR, Bayer AS. Infective endocarditis: diagnosis, antimicrobial therapy and management of complications. *Circulation* 2005;111:394–434.

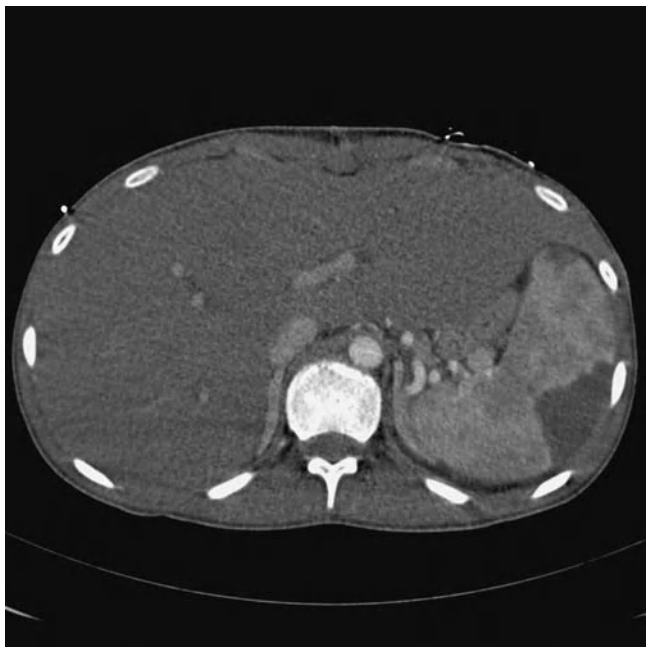

**Figure 39.23** Computed tomogram of the abdomen of the same patient as in Fig. 39.22 showing a triangular zone of infarction in the lateral portion of the spleen with another focus more caudal. Infarction was also demonstrated in both kidneys.

and management of IE, few published data support its use as a risk-stratification tool. A study has compared standard indications for surgery (such as heart failure, recurrent embolic events, severe valvular regurgitation and persistent bacteremia) with echocardiography-guided indications (such as vegetations >10 mm in length) [54]. The echocardiographic-based strategy reduced the risk for embolic stroke and death and was cost-effective [55].

## Echocardiographic guidance of surgical treatment and postoperative assessment

Prior to actual surgery, intraoperative TEE is helpful in determining the mechanism, localization and degree of valvular dysfunction and/or region of myocardial disruption. It is also useful for excluding contamination of other valves and cardiac structures. The surgeon can then save time on cardiopulmonary bypass if he or she is sure that only right-sided or left-sided structures of the heart are infected. In cases where valves have to be replaced, preoperative determination of valve annulus size is mandatory.

Postoperative TEE should confirm the adequacy of the repair or valve replacement and document the successful closure of fistulous tracts [12]. Patients with previous IE are at high risk for a second bout of IE; thus surgical therapy should correct any residual defects, including paravalvular leaks, residual ventricular septal defect and/or residual fistulae. Postoperative TEE should also monitor hemodynamic changes after repair and assess ventricular performance, although alterations may occur once the patient is awake and extubated. In smaller children with an adequate acoustic window, a follow-up TTE may be sufficient; in all other cases a TEE prior to completion of medical therapy is indicated.

### Nonbacterial thrombotic endocarditis

The pathognomonic feature of nonbacterial thrombotic endocarditis (NBTE) is a vegetation consisting of a mesh of fibrin and platelets without an identified microorganism [56]. The primary pathogenetic mechanisms of this disorder are damage to the valvular endothelium and hypercoagulability. Both cancer and autoimmune diseases, such as systemic lupus erythematosus (i.e., Libman–Sacks endocarditis) are known to be associated with NBTE. The diagnosis, however, may be difficult in patients in whom the underlying disease is associated with fever. IE in this setting has to be ruled out carefully. NBTE is usually a postmortem diagnosis, with an incidence of 1.2% in autopsy patients. It has been reported to occur in all age groups but predominantly between the fourth and eighth decades of life [57]. Echocardiography cannot reliably distinguish between NBTE and IE. The NBTE vegetation usually grows on the atrial surface of the atrioventricular valves and the ventricular surface of the semilunar valves [58]. Although all valves may be affected, the mitral valve is most often involved [59].

Typically, NBTE has an indolent course, but systemic emboli may occur in 50% of the patients [58]. In very rare cases, surgical therapy is indicated due to major valvular involvement with hemodynamic compromise [60].

## References


1. Durack DT, Lukes AS, Bright DK. New criteria for diagnosis of infective endocarditis: utilization of specific echocardiographic findings. Duke Endocarditis Service. *Am J Med* 1994;96: 200–9.
2. Li JS, Sexton DJ, Mick N et al. Proposed modifications to the Duke criteria for the diagnosis of infective endocarditis. *Clin Infect Dis* 2000;30:633–8.
3. Stockheim JA, Chadwick EG, Kessler S et al. Are the Duke criteria superior to Beth Israel criteria for diagnosis of infective endocarditis in children. *Clin Infect Dis* 1998;27:1451–6.
4. Del Pont JM, De Cicco LT, Vartalitis C et al. Infective endocarditis in children: clinical analyses and evaluation of two diagnostic criteria. *Pediatr Infect Dis J* 1995;14:1079–86.
5. Ferrieri P, Gewitz MH, Gerber MA et al., Committee on Rheumatic Fever, Endocarditis, and Kawasaki Disease of the American Heart Association Council on Cardiovascular Disease in the Young. Unique features of infective endocarditis in childhood. *Circulation* 2002;105:2115–27.
6. Van Hare GF, Ben-Shachar G, Liebman J et al. Infective endocarditis in infants and children during the past 10 years: a decade of change. *Am Heart J* 1984;107:1235–40.
7. Stull TL, LiPuma JJ. Endocarditis in children. In: Kaye D (ed.) *Infective Endocarditis,* 2nd edn. New York, NY: Raven Press, 1992; 313–27.
8. Saiman L, Prince A, Gersony WM. Pediatric infective endocarditis in the modern era. *J Pediatr* 1993;122:847–53.
9. Martin JM, Neches WH, Wald ER. Infective endocarditis: 35 years of experience at a children's hospital. *Clin Infect Dis* 1997; 24:669–75.
10. Morris CD, Reller MD, Menashe VD. Thirty-year incidence of infective endocarditis after surgery for congenital heart defect. *JAMA* 1998:279:599–603.
11. Karl T, Wensley D, Stark J et al. Infective endocarditis in children with congenital heart disease: comparison of selected features in patients with surgical correction or palliation and those without. *Br Heart J* 1987;58:57–65.
12. Baddour LM, Wilson WR, Bayer AS et al., Committee on Rheumatic Fever, Endocarditis, and Kawasaki Disease; Council on Cardiovascular Disease in the Young; Councils on Clinical Cardiology, Stroke, and Cardiovascular Surgery and Anesthesia; American Heart Association; Infectious Diseases Society of America. Infective endocarditis: diagnosis, antimicrobial therapy, and management of complications: a statement for healthcare professionals from the Committee on Rheumatic Fever, Endocarditis, and Kawasaki Disease, Council on Cardiovascular Disease in the Young, and the Councils on Clinical Cardiology, Stroke, and Cardiovascular Surgery and Anesthesia, American Heart Association: endorsed by the Infectious Diseases Society of America. *Circulation* 2005;111:394–434.
13. Wilson LE, Thomas DL, Astemborski J et al. Prospective study of infective endocarditis among injection drug users. *J Infect Dis* 2002;185:1761–6.
14. Reisberg BE. Infective endocarditis in the narcotic addict. *Prog Cardiovasc Dis* 1979;22:193–204.
15. Sklaver AR, Hoffman TA, Greenman RL. Staphylococcal endocarditis in addicts. *South Med J* 1978;71:638–43.
16. Levine DP, Crane LR, Zervos MJ. Bacteremia in narcotic addicts at the Detroit Medical Center, II: infectious endocarditis. A prospective comparative study. *Rev Infect Dis* 1986;8:374–96.
17. Berlin JA, Abrutyn E, Strom BL et al. Incidence of infective endocarditis in the Delaware Valley, 1988–1990. *Am J Cardiol* 1995;76:933–6.
18. Sohail MR, Uslan DZ, Khan AH et al. Management and outcome of permanent pacemaker and implantable cardioverter-defibrillator infections. *J Am Coll Cardiol* 2007;49:1851–9.
19. Sievert H, Babic UU, Hausdorf G et al. Transcatheter closure of atrial septal defect and patent foramen ovale with ASDOS device (a multi-institutional European trial). *Am J Cardiol* 1998;82: 1405–13.
20. Borghi A, Ciuffreda M, Quattrociocchi M, Preda L. The grown-up congenital cardiac patient. *J Cardiovasc Med* 2007;8:78–82.
21. Li W, Somerville J. Infective endocarditis in the grown-up congenital heart (GUCH) population. *Eur Heart J* 1998;19:166–73.
22. Bashore TM, Cabell Ch, Fowler V. Update on infective endocarditis. *Curr Probl Cardiol* 2006;31:274–352.
23. Noel GJ, O'Loughlin JE, Edelson PJ. Neonatal *Staphylococcus epidermidis* right-sided endocarditis: description on five catheterized infants. *Pediatrics* 1988;82:234–9.
24. Moreillon P, Que YA, Bayer AS. Pathogenesis of streptococcal and staphylococcal endocarditis. *Infect Dis Clin North Am* 2002; 16:297–318.
25. Durack DT, Beeson PB. Experimental bacterial endocarditis. I. Colonization of a sterile vegetation. *Br J Exp Pathol* 1972;53: 44–9.
26. Durack DT, Beeson PB. Experimental bacterial endocarditis. II. Survival of bacteria in endocardial vegetation. *Br J Exp Pathol* 1972;53:50–3.

27. Graupner C, Vilacosta I, SanRoman J et al. Periannular extension of infective endocarditis. *J Am Coll Cardiol* 2002;39: 1204–11.
28. Filippo SD, Delahaye F, Semiond B et al. Current patterns of infective endocarditis in congenital heart disease. *Heart* 2006;92: 1490–5.
29. Awadallah SM, Kavey RE, Byrum CJ et al. The changing pattern of infective endocarditis in childhood. *Am J Cardiol* 1991;68: 90–4.
30. Karchmer A. Infective endocarditis. In: Zipes DP, Libby P, Bonow RO (eds) *Heart Disease*. Philadelphia: Elsevier Saunders, 2005;1633–56.
31. Sexton DJ, Bashore TM. Infective endocarditis. In: Topol EJ (ed.) *Textbook of Cardiovascular Medicine*. Philadelphia: Lippincott Williams & Wilkins, 2002;569–93.
32. Gordon SM, Serkey JM, Longworth DL et al. Early onset prosthetic valve endocarditis: the Cleveland Clinic experience 1992–1997. *Ann Thorac Surg* 2000:69:1388–92.
33. Oelberg DG, Fisher DJ, Gross DM et al. Endocarditis in high-risk neonates. *Pediatrics* 1983;71:392–7.
34. Syndych PS, Krauss AN, Winchester P. Endocarditis following intracardiac placement of umbilical venous catheters in neonates. *J Pediatr* 1977;90:287–9.
35. Nucifora G, Badano L, Hysko F et al. Pulmonary embolism and fever: When should right-sided infective endocarditis be considered? *Circulation* 2007;115:173–6.
36. Hasbun R, Vikram HR, Barakat LA et al. Complicated left-sided native valve endocarditis in adults. *JAMA* 2003;289:1933–40.
37. Vikram HR, Buenconsejo J, Hasbun R, Quagliarello VJ. Impact of valve surgery on 6-month mortality in adults with complicated left-sided native valve endocarditis *JAMA* 2003;290:3207–14.
38. Mills J, Utley J, Abbott J. Heart failure in infective endocarditis: predisposing factors, course and treatment. *Chest* 1974;66: 151–7.
39. Wilson W, Taubert KA, Gewitz M et al. Prevention of Infective Endocarditis. Guidelines From the American Heart Association. A Guideline From the American Heart Association Rheumatic Fever, Endocarditis, and Kawasaki Disease Committee, Council on Cardiovascular Disease in the Young, and the Council on Clinical Cardiology, Council on Cardiovascular Surgery and Anesthesia, and the Quality of Care and Outcomes Research Interdisciplinary Working Group. *Circulation* 2007;116:1736–54.
40. Roy P, Tajik AJ, Giuliani ER et al. Spectrum of echocardiographic findings in bacterial endocarditis. *Circulation* 1976;53: 474–82.
41. Kavey RE, Frank DM, Byrum CJ et al. Two-dimensional echocardiographic assessment of infective endocarditis in children. *Am J Dis Child* 1983;137:851–6.
42. Humpl T, McCrindle BW, Smallhorn JF. The relative roles of transthoracic compared with transesophageal echocardiography in children with suspected infective endocarditis. *J Am Coll Cardiol* 2003;41:2068–71.
43. Erbel R, Rohmann S, Drexler M et al. Improved diagnostic value of echocardiography in patients with infective endocarditis by transesophageal approach. A prospective study. *Eur Heart J* 1988;9:43–53.
44. Daniel WG, Mugge A, Grote J et al. Comparison of transthoracic and transesophageal echocardiography for detection of abnormalities of prosthetic and bioprosthetic valves in the mitral and aortic positions. *Am J Cardiol* 1993;71:210–5.
45. Daniel WG, Mugge A, Martin RP et al. Improvement in the diagnosis of abscesses associated with endocarditis by transesophageal echocardiography. *N Engl J Med* 1991;324:795–800.
46. Rohmann S, Erbel R, Darius H et al. Prediction of rapid versus prolonged healing of infective endocarditis by monitoring vegetation size. *J Am Soc Echocardiogr* 1991;4:465–74.
47. San Roman JA, Vilacosta I, Zamorano JL et al. Transesophageal echocardiography in right-sided endocarditis. *J Am Coll Cardiol* 1993;21:1226–30.
48. Miller-Hance WC, Silverman NH. Transesophageal echocardiography (TEE) in congenital heart disease with focus on the adult. *Cardiol Clin* 2000;18:861–92.
49. Gersony WM, Hayes CJ, Deiscoll DJ et al. Bacterial endocarditis in patients with aortic stenosis, pulmonary stenosis, or ventricular septal defect. *Circulation* 1993;87(Suppl.):I121–6.
50. Pellicelli AM, Pino P, Terranova A et al. Eustachian valve endocarditis: a rare localization of right side endocarditis. A case report and review of the literature *Cardiovasc Ultrasound* 2005;3:30–5.
51. Bayer AS, Bolger AF, Taubert KA et al. Diagnosis and management of infective endocarditis and its complications. *Circulation* 1998;98:2936–48.
52. Thuny F, Di Salvo G, Belliard O et al. Risk of embolism and death in infective endocarditis: prognostic value of echocardiography: a prospective multicenter study. *Circulation* 2005;112:69–75.
53. Erbel R, Rohmann S, Drexler M et al. Improved diagnostic value of echocardiography in patients with infective endocarditis by transoesophageal approach: a prospective study. *Eur Heart J* 1988;9:43–53.
54. Olaison L, Pettersson G. Current best practices and guidelines. Indications for surgical intervention in infective endocarditis. *Cardiol Clin* 2003;21:235–51.
55. Liao L, Kong DF, Samad Z et al. Echocardiographic risk stratification for early surgery with endocarditis: a cost-effectiveness analysis. *Heart* 2008;94:e18.
56. Eftychiou Ch, Fanourgiakis P, Vryonis E et al. Factors associated with non-bacterial thrombotic endocarditis: case report and literature review. *J Heart Valve Dis* 2005;14:859–62.
57. Salem DN, Stein PD, Al-Ahmad A et al. Antithrombotic therapy in valvular heart disease – native and prosthetic. The Seventh ACCP conference on antithrombotic and thrombolytic therapy. *Chest* 2004;126:457S–82S.
58. Lopez JA, Ross RS, Fishbein MC, Siegel RJ. Nonbacterial thrombotic endocarditis: A review. *Am Heart J* 1987;113:773–83.
59. Hesselink DA, Van Der Klooster JM, Schelfhout LJDM, Scheffer MG. Non-bacterial thrombotic (marantic) endocarditis associated with giant-cell arteritis. *Eur J Int Med* 2001;12:454–8.
60. Einav E, Gitig A, Marinescu M et al. Valvulitis requiring triple valve surgery as an initial presentation of systemic lupus erythematosus. *J Am Soc Echocardiogr* 2007;20:1315.el–3.

# 8 Special Techniques and Topics

*Echocardiography in Pediatric and Congenital Heart Disease: From Fetus to Adult*
Edited by Wyman W. Lai, Luc L. Mertens, Meryl S. Cohen and Tal Geva
 ISBN: 978-1-405-17401-5

# 40 Transesophageal Echocardiography

**J. Geoffrey Stevenson**
University of Washington School of Medicine, Seattle, WA, USA

## Introduction

Transesophageal echocardiography (TEE) has been performed in adult patients for many years, but its use in small children was delayed until the development of smaller pediatric probes in the early 1990s [1–28]. Since that time, use of pediatric TEE has become widespread. Guidelines for its use in pediatric patients [29] have been recently updated by the American Society of Echocardiography [30]. Adherence to such guidelines has been associated with improved performance and outcome during intraoperative TEE [31]. For adult patients, appropriateness criteria for transthoracic echocardiography (TTE) and TEE examinations have recently been published [32]. Many of the adult clinical applications are also encountered in the pediatric population. This chapter will focus on the performance of TEE examination in infants and children, and demonstrate the findings available from standard TEE imaging on annotated videoclips. The specific anatomic and diagnostic features of congenital and acquired lesions are discussed in the preceding chapters.

## Indications

Diagnostic indications for pediatric TEE include:
- an inadequate transthoracic echocardiogram in a patient with known, suspected or repaired congenital heart disease;
- evaluation for possible right-to-left shunting in a patient evaluated for stroke or being considered for transvenous pacemaker implantation;
- examination for vegetation, abscess or central line infection;
- examination to evaluate for thrombus prior to cardioversion [30].

Perioperative indications include preoperative evaluation of cardiac anatomy, function and hemodynamics when surface echocardiography is unclear, and evaluation of intraoperative and postoperative surgical results and hemodynamics. In addition, TEE evaluation of volume status has proven superior to central venous pressure monitoring during scoliosis surgery [33], and has been advocated for monitoring function during solid organ transplantation [34,35] and during oncologic surgery [36,37].

Transesophageal echocardiography is also indicated during a variety of interventional catheterization procedures, as discussed below. Anesthesiologists have reported significant utility in assessing volume status, and response to anesthetic, pressor or volume management, during a variety of procedures [38,39].

## Contraindications

Absolute contraindications include the presence of unrepaired tracheo-esophageal fistula, esophageal obstruction or stricture, perforated hollow viscus, poor airway control, severe respiratory depression and the presence of an uncooperative unsedated patient [30]. Relative contraindications that need to be considered or evaluated further prior to TEE include a history of previous esophageal surgery and possible residual obstruction or diverticulum, amount and severity of esophageal varices, amount and location of gastric or esophageal bleeding, known vascular ring, aortic arch anomaly that could produce airway compromise, significant oropharyngeal pathology, severe coagulopathy and cervical spine injury or instability [30]. As with any procedure, the benefit of the procedure should outweigh the risks.

## Equipment

Pediatric TEE examinations are currently performed with a complete ultrasound system offering capabilities for two-dimensional (2D) imaging, color and spectral pulsed Doppler, and continuous-wave Doppler. Pediatric TEE probes are available for most of these contemporary cardiac ultrasound instruments. A mechanism for recording the examination is

*Echocardiography in Pediatric and Congenital Heart Disease: From Fetus to Adult*
Edited by Wyman W. Lai, Luc L. Mertens, Meryl S. Cohen and Tal Geva
 ISBN: 978-1-405-17401-5

necessary, usually videotape or digital storage. Appropriate equipment and staff for sedation, airway management and patient comfort and safety should be available where TEE is performed.

## Personnel

Those performing pediatric TEE should conform to established guidelines and currency of TEE caseload [30]. They must be proficient in obtaining standard TEE images, and in the assessment and interpretation of hemodynamics. Awareness of the limitations of TEE imaging is also important.

## Probe size

The proper probe size depends on a number of issues [40–42]. Over the years, probes generally have become smaller, and provide greater penetration and resolution. In general, one should select the smallest probe that can provide adequate imaging. Although there are reports of TEE use in patients weighing 2.4 kg and below, caution has also been urged in using TEE probes in patients weighing under 3 kg [41,42]. Regardless of patient size, TEE probes should pass easily. Force should not be applied to the TEE probe during insertion. If the probe does not easily pass, it may be useful to insert a laryngoscope to confirm probe entry into the esophagus, and to confirm that probe tip flexion is aligned with the lumen of the esophagus. There have been rare occurrences of esophageal perforation. One clue to perforation having occurred is the inability to obtain the usual retrocardiac and gastric imaging planes.

## Probe care

The probes used in TEE are fragile. The cable system for probe flexion must not be stressed by undue flexion force. The transducer tip itself is vulnerable to physical trauma if the probe is held only by the handle, allowing the tip to whip about. The shaft and tip are subject to scraping by teeth. Each probe should be carefully inspected for cracks or other damage prior to each insertion; visibly damaged probes should not be used. Cracks in the TEE probe surface may expose patients to electrical current. Furthermore, cracks may contain residual disinfectant, which could damage oropharyngeal, esophageal or gastric mucosae.

The use of a latex TEE probe cover sheath has been advocated by Fritz et al., as an alternative to disinfection in adult patients [43]. Although the standard in the USA is for disinfection after each use of a TEE probe, it has been our practice to place the disinfected TEE probe in a latex-free sheath (Civco Medical Solutions, Kalowna, IA) as an added measure for mucosal protection. The use of sheaths has not altered image quality. Sheath use further guards against infection, and places a barrier between the probe and the mucosa. Further, some TEE probes themselves contain latex, thus exposing patients to the latex; use of a latex-free sheath avoids this exposure. Upon completion of the TEE, the sheath is removed by gloved hands, allowing free touching of the unsheathed TEE probe, preventing transmission of esophageal and gastric secretions to the operating room environment and staff. Further, sheath use obviates the need for removal of mucus from the probe, facilitating cleaning prior to disinfection. A standard regimen for disinfection has been a 20-minute soak in Cidex, followed by a thorough rinsing in warm water.

## TEE outside the operating room

In adults, TEE is frequently requested because of inadequate TTE imaging. In infants and small children, this is a less frequent indication for TEE, but is encountered more often in larger subjects. Thus, in many infants and children who are undergoing surface echocardiography for evaluation of possible endocarditis, many of these TTE examinations will be sufficient. Occasionally, TEE will be considered to resolve questionable TTE images. We have utilized TEE for ultrasound examination of ventilated patients in the intensive care unit (ICU) whose pulmonary disease significantly compromises TTE.

### TEE during interventions

Transesophageal echocardiography is commonly utilized in the catheterization laboratory to aid in interventional catheterization, and device closure of shunt lesions such as atrial septal defect, ventricular septal defect and patent ductus arteriosus [44–55]. Limitations include the inability to be sure of the position of the most distal aspect of guidewires or catheters, as the image may appear to show the tip, when in reality the structure has just passed out of the plane of ultrasound. In evaluation of patients with atrial septal defect, the pliability of the atrial septum often leads to a much larger defect size by balloon sizing than the unstretched size of the noninstrumented defect seen on 2D echo. Differences of at least 50% between balloon and 2D are commonly encountered. The use of color Doppler to confirm that balloon inflation has abolished the shunt at time of sizing is useful confirmatory information. TEE has been useful in device closure of muscular and multiple ventricular septal defects, in confirming the distance between defects, and proper placement of devices in the defect(s) selected for closure. After device closure, imaging for device encroachment upon adjacent structures, and confirming absence of development of new flow disturbances, is routine. Given the limitations in TEE imaging of branch pulmonary

arteries, TEE is less commonly used during these right-sided interventions.

### Arrhythmia and thrombus

In patients with atrial arrhythmias, TEE is often requested to evaluate for thrombus prior to cardioversion [56]. It is important to be aware that atrial appendage location and morphology may be altered with some congenital defects, or from previous use for cannulation during surgery. A thorough examination for masses is indicated, not only in the atria but also in other locations such as the oversewn pulmonary artery stump in patients who have had single ventricle management. TEE has been shown by Fyfe et al. to be superior to TTE in detection of thrombus in Fontan pathways [57,58].

### Anesthesia, sedation and airway concerns

It has been our practice to perform pediatric TEE examinations under anesthesia and tracheal intubation in most pediatric subjects. Larger subjects may be safely managed using propofol anesthesia without intubation, but with use of a bite-block [59]. Advantages of controlling the airway in smaller pediatric subjects include a smoother TEE examination, reduced patient movement, and greater comfort and safety for the patient. This presumes the availability of experienced pediatric anesthesiologists for assistance with anesthesia.

Alternatively, Heard et al. report the use of topical lidocaine, midazolam and propofol in spontaneously breathing pediatric patients [60]. They caution that this regimen may be unsuitable for patients who cannot tolerate the associated reductions in blood pressure, cardiac output and systemic vascular resistance, or who may be intolerant of the associated mild increase in $P_aCO_2$ (arterial partial pressure of $CO_2$). Mart et al. have also demonstrated safety and efficacy of deep sedation with propofol for outpatient TEE in pediatric cardiac subjects over 2 years of age, without intubation [61].

### Location of the TEE examination

Choosing the location in which the TEE examination is to be performed is a joint decision made by the cardiologist, anesthesiologist and others involved, such as the ICU attending physician. As TEE is very portable, it can be performed at the bedside in the ICU, in induction or recovery rooms, or in other specialized facilities having the capability for anesthesia with its requisite equipment and staff.

The utility of TEE in the ICU setting for evaluation of hemodynamics and fluid status has been evaluated by Tibby et al. [62]. In patients returning from the operating room with an open chest, TEE may provide the only route for comprehensive postoperative ultrasound examination [63]. The restricted transthoracic windows that may be associated with disease processes in patients requiring extracorporeal membrane oxygenation or other assist devices, make TEE advantageous for echocardiographic evaluation [64].

## Intraoperative TEE

Performance of intraoperative echocardiography to document the success of repairs of congenital heart disease was begun by Ungerleider and associates at Duke University [65–69]. In the pre-transesophageal era, they utilized echocardiography by the epicardial approach, and demonstrated the need for pre- and post-bypass examinations, and the utility of echocardiography in intraoperative decision-making. In addition, they confirmed the effect of intraoperative echocardiography on outcome, and the effect of the learning curve for the procedure. With the development of small pediatric probes, virtually all centers performing intraoperative echocardiography now utilize TEE [70]. By far the most frequent utilization of pediatric TEE is as an adjunct to the intraoperative care of infants and children undergoing surgical procedures. Most of these procedures are cardiac, but monitoring of function in patients with repaired congenital heart defects during repair of scoliosis, for example [33], can be used to monitor function and evaluate volume status and responses to anesthetic management. Similar applications have been described for patients undergoing liver transplantation or tumor resection [34–37].

### Who should perform intraoperative TEE?

There has been considerable debate concerning who should perform intraoperative TEE [71,72]. Most would agree that the individual performing intraoperative TEE should meet established experience and training guidelines for pediatric TEE [30,73,74]. Although most examinations are performed by cardiologists, a number of pediatric cardiac anesthesiologists have been important contributors, advocates and performers of intraoperative pediatric TEE [75–78]. Sloth et al. reported a series of 532 children in whom intraoperative TEE examinations were performed by anesthesiologists [75]. There was but a single complication, one extubation. TEE was used to guide volume replacement and inotropes in 45% of cases. In another study in which TEE examinations were performed by anesthesiologists [76], Bettex et al. showed a return to bypass rate of 7.3%, and changes in medical management in 19.4% of 865 cases. Miller et al. demonstrated that experienced cardiac anesthesiologists can obtain and correctly interpret most basic intraoperative transesophageal echocardiograms [78].

It has been my observation that trained pediatric cardiac anesthesiologists can readily perform intraoperative TEE well during uneventful routine cases. Moreover, having an additional individual performing TEE during difficult times can be invaluable because it ensures continuous availability of TEE information regarding problems and responses to their treatment. It is recommended that pediatric cardiac anesthesiologists performing intraoperative TEE have a TEE-qualified pediatric cardiologist readily available for

consultation or for performing the remainder of the TEE examination should patient management require the full attention of the anesthesiologist. In our institution, TEE has been the responsibility of cardiology, with welcome input and assistance from our pediatric cardiac anesthesia colleagues. Other centers may implement different utilization plans on an effective basis as well.

## Should TEE be performed on every intraoperative case?

There has been considerable debate regarding the best utilization of intraoperative TEE during repair of congenital cardiac defects [39,79–84]. In a 1999 survey of North American centers doing surgery for congenital heart disease, 65 centers submitted responses [70]. Thirty-two percent of centers indicated that TEE was being performed on all cases, open and closed. In 38% of institutions, TEE was being performed on all open-heart cases, except secundum atrial defects. In 29%, TEE was being performed on selected cases only. It has been our practice to utilize TEE during nearly all open-heart cases, and selected closed cases. Indications for the latter may be in patients with ventricular dysfunction or significant regurgitation undergoing closed procedures. TEE monitoring of function and response to anesthetic management has occasionally been of lifesaving importance. Utilization of TEE for those cases expected to have the greatest yield – "selected cases" – presumes the team's ability correctly to predict the finding that would need to be evaluated by TEE. In my experience, some of the most useful applications have been in those patients who have had an unexpected intraoperative TEE finding [85]. It is reasonable that each center determines a policy for intraoperative TEE utilization.

## Pre- and post-bypass TEE examinations

It is important to perform a complete TEE examination prior to surgery, and not just a postsurgical examination [86]. The importance lies in several areas. First, the pre-bypass TEE examination allows a final check of the anatomy and physiology that was found on the TTE. Surgeons often like a last minute "update" of the anatomy and physiology prior to beginning surgery. Another important consideration is that a number of things may change under anesthesia. With intubation and ventilation with added oxygen, it is common to find smaller tricuspid regurgitation jet color displays, at lower peak velocity, due to lower pulmonary resistance in the anesthetized state. Cardiac output may be lowered under anesthesia, giving lower peak velocities through obstructions. Lack of knowledge of pre-bypass findings may lead to misinterpretation of post-repair findings and their management.

## Recommended TEE procedure

Following induction of anesthesia and placement of all monitoring lines, the patient is ready for insertion of the TEE probe. If a nasogastric or feeding tube is in place, it is removed. The airway pressure, minute ventilation and end-tidal carbon dioxide level, along with heart rate, saturation and arterial line pressure, are reviewed prior to probe insertion, as changes may occur upon insertion of the TEE probe. A rise in end-tidal carbon dioxide level may indicate either TEE probe-induced advancement of the endotracheal tube into the mainstem bronchus or inadvertent tracheal extubation. Heart rate increases may indicate a lighter-than-desired level of anesthesia. Compression of pulmonary venous drainage in infants with total anomalous pulmonary venous return has been reported, heralded by falling systemic saturation [87]. In patients with aberrant origin of a subclavian artery, TEE probe compression of that aberrant artery may lead to dampening of the arterial waveform from an involved radial artery [88] (Fig. 40.1). It is important to recognize that dampening of the arterial waveform does not reflect systemic hypotension. When the presence of an aberrant subclavian artery is known preoperatively, it is advisable to place the arterial monitoring line in the other radial artery.

Most TEE probe insertions can be performed manually, without a laryngoscope [41]. For insertion, the head is placed in the midline. A small amount of lubricating gel is placed on the distal aspect of the sheathed probe. A gloved index finger is inserted into the mouth, for manual location of the esophagus. Insertion of the TEE probe alongside the gloved finger allows manual guidance into the esophagus. Tactile sensation provides information as to whether neck extension, or changes in TEE probe flexion are needed to follow the path of the index finger.

There should be little resistance to further advancement of the probe to the retrocardiac and gastric positions. If the probe does not easily pass, review of adequacy of sedation, anesthesia and muscle relaxation is required. If there is a question about the position of the probe, inspection via a laryngoscope may be helpful. If resistance to probe passage is encountered, no force should be applied, and the probe should be removed. Such inability to pass the probe, if unrelated to degree of muscle relaxation and depth of anesthesia, could indicate the presence of unknown esophageal pathology, unrecognized arch anomalies, or other of the relative contraindications mentioned above [30]. During the TEE examination, unexpected changes in airway pressure, ventilation, saturation or hemodynamic changes should prompt consideration of probe removal. The echocardiographer must be alert to audible changes in oximetry and heart rate throughout the examination.

Following placement of the TEE probe, a complete TEE examination is performed. An initial evaluation of the defect being repaired is reasonable, such as an evaluation of the location, number and velocity of flow through a ventricular septal defect. A complete examination of remaining structures and flows should be undertaken as well, to screen for unsuspected or previously undetected defects. In this regard, it is important to be aware of a limitation of TEE examination

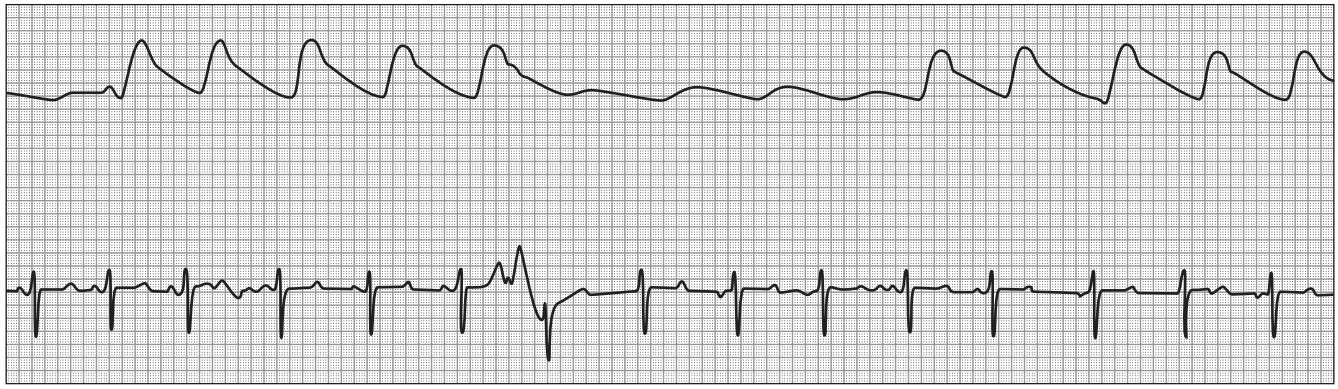

**Figure 40.1** Dampening of a right radial artery waveform in a patient with aberrant right subclavian artery. Upon passing the transesophageal echocardiography probe, the right radial artery pressure waveform dampens as the probe is manipulated in the esophagus. At times, this may be noted just upon passing the unflexed probe to the retrocardiac position, and at other times, dampening may occur when the probe is flexed.

for the potential for atrial shunting. Although color Doppler is sensitive for the display of atrial shunting, shunting may not be present through a foramen ovale that is closed to flow as long as left atrial pressure exceeds right atrial pressure. Should pressure or volume relationships change, a potential shunt pathway may open. This has particular importance during planned open repair of defects in certain situations. An example is replacement of a right ventricle-to-pulmonary artery conduit, on bypass, but without cross-clamping of the aorta or administration of cardioplegia. An important contribution by Cassorla et al. [89] calls attention to the prevalence of potential atrial shunts through the fossa ovalis, which may show no evidence of shunt during baseline conditions. At surgery, the surgeon evaluated the atrial septum. In those having negative color Doppler and contrast echocardiograms, a 20% prevalence of probe-patent foramen ovale was found. Although we still perform saline contrast echocardiography during a Valsalva maneuver prior to bypass cases such as mentioned, a negative study does not entirely exclude the potential for occult air entry into the left atrium.

Once the pre-bypass TEE examination has been completed, it is recommended that the findings be reviewed with the anesthesiology and surgical teams. An important educational activity is, when possible, for the echocardiographer to return to the operating room to view the surgical anatomy. This allows the echocardiographer to compare anatomic and echocardiographic information, to know what anatomic features are important to the surgeons, and gain a perspective from which to review the post-repair TEE findings.

When cardioplegia is administered to arrest the heart for surgery, it has been reported that TEE may show regurgitation of cardioplegic solution as a contrast effect, through valves that were competent prior to cross-clamping. In a subjective assessment [90], it was found that the degree of cardioplegia regurgitation corresponded to reduced duration of the effect of cardioplegia.

## Post-repair TEE

During rewarming, an important component of the TEE examination is screening for chamber and myocardial air. Left-sided chamber air should be removed, if possible, prior to resumption of ejection. Chamber air usually rises to the most anterior aspect of the chamber, and can be trapped in the atrial appendage and along the atrial and ventricular septa, requiring specific directed imaging for its detection or exclusion (Videoclips 40.7 and 40.8). It is remarkable that chamber air does not usually flow along with blood flow, but may remain retained in recesses or along chamber walls. It is distinguished from sludged blood (sedimentation during the period of no flow during cardiopulmonary bypass) by its location and by its motion within the chamber. Intramyocardial air is commonly encountered when the left side of the heart has been entered during surgery directly, or in the presence of intracardiac shunts. It is manifest by regional myocardial echogenicity and usually dysfunction of the affected distribution [91]. As the right coronary origin is anterior on the aortic root, myocardial air is more commonly encountered in the distribution of the right coronary artery. Intramyocardial air may be mobilized by epicardial coronary massage by the surgeon, or by proceeding through the coronary circulation. The latter may be augmented by raising the blood pressure, the driving force for flow through the coronary circulation. Air will clear from epicardium to endocardium, in that order. Retained intramyocardial air during weaning from bypass may predispose to arrhythmia, dysfunction and possible fibrillation, so it is advisable not to wean from bypass until air has cleared.

## Evaluation of the repair

During rewarming, one often can determine whether there are areas of concern, such as residual shunt flow or valve regurgitation [92]. Color Doppler is very useful for determining the adequacy of septal defect repair, valve repairs, patency of systemic-to-pulmonary shunts, or residual obstruction(s)

[93–111]. It is recommended that a thorough examination be performed of all aspects of a given repair, followed by a complete examination of chambers, valves and vessels for unexpected findings. The majority of TEE imaging usually centers upon the repair. TEE may be utilized for serial evaluation of attempts at repair, and revision of those repairs. For example, Lim et al. have demonstrated the use of TEE to guide, evaluate and revise surgical repairs of aortic insufficiency in congenial heart disease [111]. The downside of return(s) to bypass and readministration of cardioplegia must be weighed against the likelihood of successful surgical revision.

During the TEE evaluation of a surgical repair, it is important to remember that the size of the color Doppler display of imaged blood flow is under the control of the echocardiographer and instrument settings, and that color Doppler alone does not indicate the severity of a finding. Low Nyquist settings may be required to image blood flow at low velocity or at an unfavorable intercept angle (Videoclips 40.15 and 40.16). Furthermore, one must consider the pressure (systemic or pulmonic) that is driving the color Doppler flow display [86,112,113]. Regurgitant jets may appear substantially larger at higher pressures, and residual shunts may not be evident if there is little pressure difference between chambers. Similarly, systemic-to-pulmonary shunt flows may be minimally turbulent during lower systemic pressures, or elevated pulmonary resistance.

Intracardiac volume status can greatly affect TEE findings. Recognition of this is one of the most important aspects of intraoperative TEE implementation. An underfilled ventricle may appear to have poor systolic function, even a regional wall motion abnormality, only to normalize with appropriate filling [114]. Acute reduction in filling may induce regional wall motion abnormalities that are not related to ischemia [114]. TEE findings of intracavitary obliteration may suggest hypovolemia [115]. Underfilled ventricles may also be associated with intracavitary flow acceleration, which may resolve with appropriate filling [116]. Experience has shown that TEE may show findings that could be expected to improve following surgery. Kaushal et al. recommend revision of *fixed* right ventricular outflow tract obstructions following tetralogy repair, but observed that patients with *dynamic* outflow tract obstructions uniformly had significant reduction in those gradients over time [117].

Given these factors, the echocardiographer must be eager to suggest and contribute to direct pressure measurements, and drawing of saturations if it is possible that these alternative tests could confirm, refine or draw into question the apparent TEE findings. These should always be considered in a team discussion about whether to return to bypass for further surgery [118]. Some defects are so trivial that revision is not appropriate. Examples are tiny suture line ventricular septal defect patch shunts. Others may be significant, but not considered amenable to revision. In that situation, the TEE findings may guide and assess the response to hemodynamic and anesthetic management. The final decision of whether to return to bypass is one made by the surgeon, upon consideration of the full information available from the intraoperative team. TEE has been reported to identify problems needing a return to bypass for further surgery in about 3–8% of bypass cases [6–8,12,13,17,18,20,21,23–25,27,66–70,75,94,99,101,110,118,119]. With a return to bypass rate in this range, the routine use of TEE during repair of congenital heart malformations is cost-effective [82,83,100,101,120,121].

It is important to realize that the TEE findings only reflect the status of the repair, and the hemodynamics present during the post-bypass TEE examination. They are not predictive of future echocardiographic findings. Lee et al. compared intraoperative TEE findings of mitral regurgitation after repair of atrioventricular septal defect with the degree of regurgitation present at follow-up with TTE [107]. They found that in 45% of patients, the degree of regurgitation increased on the follow-up echocardiogram. Similar results were found by Kim et al. for left-sided regurgitation following repair of atrioventricular septal defect: 29% showed an increase in regurgitation at follow-up [108], whereas Honjo et al. reported an increase in atrioventricular valve regurgitation in 63% [109]. The apparent increases in regurgitation may be due to durability of repair, changes in blood pressure, volume status and afterload between study conditions. In patients with ventricular septal defect repair, larger degrees of suture line shunts on predischarge transthoracic echocardiography may result from remodeling of the patch and sutures, or sutures working through surgically manipulated septal tissue.

## Evaluation of function, filling and response to interventions

In contrast to most transthoracic examinations, intraoperative TEE examinations are enhanced by the display of monitored filling pressures and systemic blood pressure. Thus, it is relatively easy and quick to see the response to various interventions such as volume administration or augmented inotropic support. The operator's impression of filling is based on experience with imaging of normally sized atria, recognition of dilated atria, and subjective assessment of relative ventricular size. A small right atrium and low central venous pressure suggest the need for volume; atrial size and central venous pressure should improve with volume administration. Overly distended atria and ventricles are usually associated with significant atrioventricular valve regurgitation, even though the valves are known to be structurally normal. Reich et al. demonstrated that experienced anesthesiologists and echocardiographers could reliably and accurately measure changes in left ventricular end-diastolic area that occurred upon transfusion or removal of a volume of blood that changed arterial blood pressure by 5–10 mm Hg [121].

The interatrial septal contour responds to the pressure difference between the atria. For example, the atrial septum may bow far to the right with conditions where left atrial pressure is high, such as with left-sided volume loads or severe dysfunction. Conversely, it is common to observe a leftward septal contour shift with elevated central venous pressure, for example following tetralogy repair.

The Tei myocardial performance index can be used as a gauge of combined systolic and diastolic function [122–126]. Required measurements of ejection time and atrioventricular valve filling intervals are easy to obtain, and the index may be used for right and/or left ventricular function. Other methods occasionally employed are the determination of d*P*/dT from regurgitant atrioventricular valve Doppler waveforms as an index of ventricular function [127]. Tibby et al. describe a method for determination of changes in cardiac output by measuring changes in minute distance (heart rate × velocity–time integral, or VTI) from descending aortic Doppler waveforms. Correlation with measured femoral artery thermodilution was very good [128]. Alternatively, we commonly utilize serial assessment of the aortic or pulmonary VTIs as indicators of changes in cardiac output (in the absence of semilunar valve stenosis).

Tissue Doppler velocity measurements can be readily made during TEE from the retrocardiac 4-chamber view. This view is also well suited for measurement of atrioventricular valve inflow velocities and velocity of waveform propagation. These methods are useful adjuncts to assessment of both filling and function.

In large part, however, the assessment of function post-bypass is subjective. An important exception is the discovery of post-bypass regional wall motion abnormalities. Whereas it is common to observe hypokinesis adjacent to surgical sites (right ventricular anterior wall in the region of the origin of a Sano shunt, ventricular septum near a ventricular septal defect patch), regional changes suggesting coronary artery insufficiency must be carefully evaluated. From short-axis images of the aortic valve, the origin of right and left coronary arteries can be visualized (Videoclip 40.17). Lowering of the color Doppler pulse repetition frequency (Nyquist limit), along with greatly reducing the size of the color display box, allows for color Doppler examination of coronary artery flow (Videoclips 40.15 and 40.16). This is an important component of the post-bypass TEE examination when surgery has involved the coronaries, such as with arterial switch operation, Bentall aortic root replacement or Ross repair. Demonstration of a color flow signal within the proximal coronary means just that, and does not determine the adequacy of the volume flow downstream. Inability to demonstrate a color Doppler lumen signal is highly suggestive of absence of flow, especially if associated with a regional wall motion abnormality. Occasionally, turbulent signals are found, which could suggest obstruction, begging incorporation of that finding into the other aspects of the post-bypass state.

### Effect of rhythm: atrioventricular synchrony

For a number of cardiac defects, the presence of atrioventricular synchrony is important to cardiac performance. It is not uncommon to see marked improvement in indices of output, and reduction in atrioventricular valve regurgitation upon establishment of synchrony with epicardial pacing. Adjustment of pacing parameters is also important to allow for appropriate filling, and in the case of semilunar valve regurgitation, to reduce (within reason) the diastolic interval for regurgitation.

## Imaging

Transesophageal echocardiographic images are obtained from retrocardiac and transgastric transducer positions, and positions in between (Figs 40.2–40.10). From each, a variety of imaging planes with resulting images are obtained; a number of representative images are displayed in the videoclips for this chapter. Because of the limited imaging planes, there is less flexibility in TEE imaging than in transthoracic imaging. Omniplane probes allow the echocardiographer to rotate the imaging plane or plane of sound, to yield desired images at angles from zero through 180 degrees. As anatomic features vary between patients, use of specific angles to guide the examination is unwise. Rather, varying the angle of imaging plane, and observing the resulting image, is far preferable. In general, transverse images are obtained close to zero degrees, and longitudinal images at

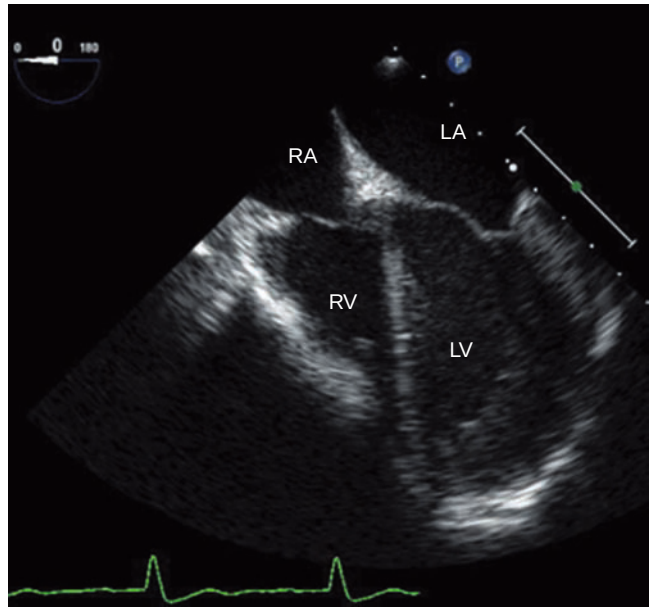


**Figure 40.2** Mid-oesophageal 4-chamber view. This transoesophageal four-chamber view is obtained from a mid-oesophageal position. The left atrium (LA), left ventricle (LV), right atrium (RA) and right ventricle are all imaged in this projection.

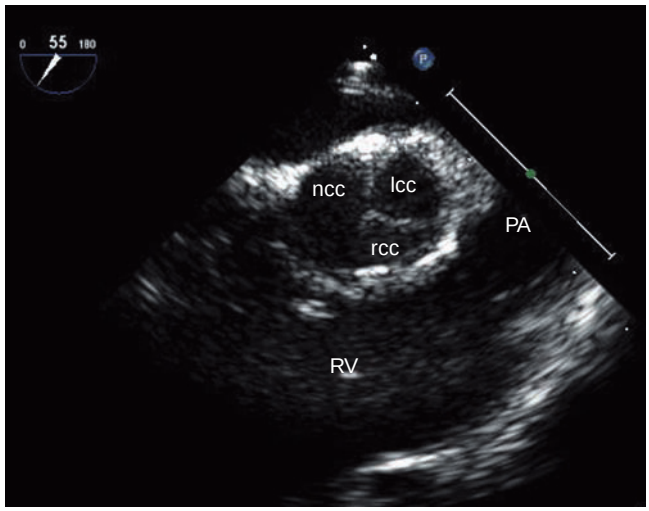


**Figure 40.3** Short axis view at aortic valve level. This transoesophageal short axis view is taken at the level of the aortic valve, showing the leaflets of the aortic valve. lcc, left coronary cusp; rcc, right coronary cusp; ncc, non-coronary cusp; RV, right ventricle; PT, pulmonary trunk.

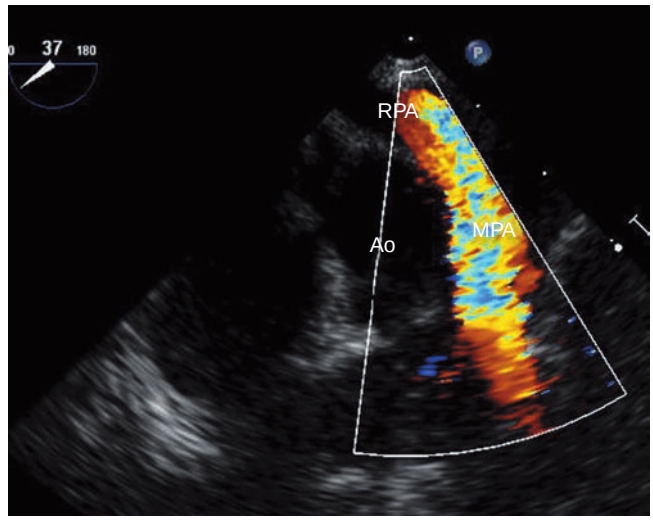


**Figure 40.5** Color Doppler of RVOT view. This transoespohageal short axis view shows the main pulmonary artery (PT) and the right pulmonary artery (RPA). The proximal part of the right pulmonary artery runs posterior to the aorta (Ao). Note that the proximal left pulmonary artery cannot be seen on this view.

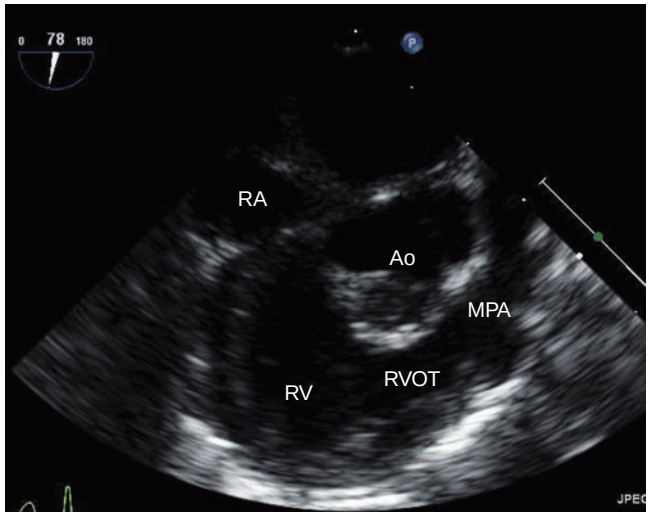


**Figure 40.4** RVOT view. This transoespohageal short axis view shows the right ventricular outflow tract (RVOT), revealing the infundibulum, the pulmonary valve, and the main pulmonary artery (MPA). RV, right ventricle; RA, right atrium; Ao, aorta.

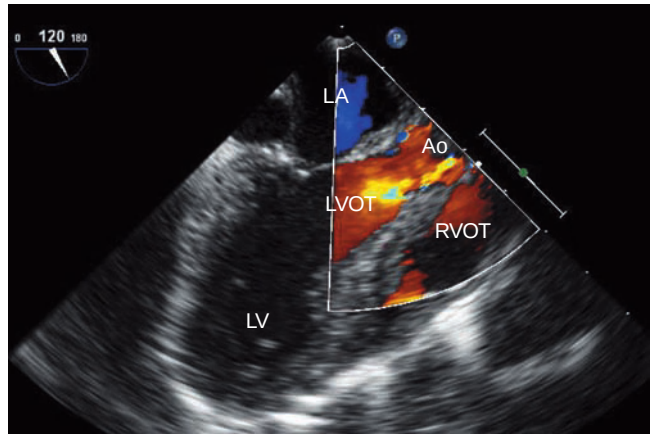


**Figure 40.6** Long-axis view of LVOT. The colour-Doppler transoesophageal long-axis view shows the left ventricle and left ventricular outflow tract (LVOT). This view is used to look for obstruction in the outflow tract and aortic insufficiency. LV, left ventricle; Ao, aorta; RVOT, right ventricular outflow tract; LA, left atrium.

around 90°, with individual adjustment as needed. Images should correspond to the guidelines for image orientation published by the American Society of Echocardiography.

## Retrocardiac 4-chamber images

The retrocardiac 4-chamber image, transverse plane, is useful for demonstration of a standard 4-chamber view, imaging of the crux of the heart, the atrial and ventricular septa, atrioventricular connections and valves (Videoclip 40.1). It is a view that is useful for imaging intracardiac masses. TEE during tumor resection, to evaluate for retained tumor or to screen for tumor-fragment embolization, has been recommended [36,37].

From the retrocardiac 4-chamber view, rotation to the right may provide right-sided pulmonary venous inflow signals (Videoclip 40.5), whereas rotation to the left can provided left-sided pulmonary venous inflow signals (Videoclip 40.6).

As shown in Videoclip 40.2, flow through the atrial septum is easily demonstrated by color Doppler. Careful examination of the various portions of the atrial septum

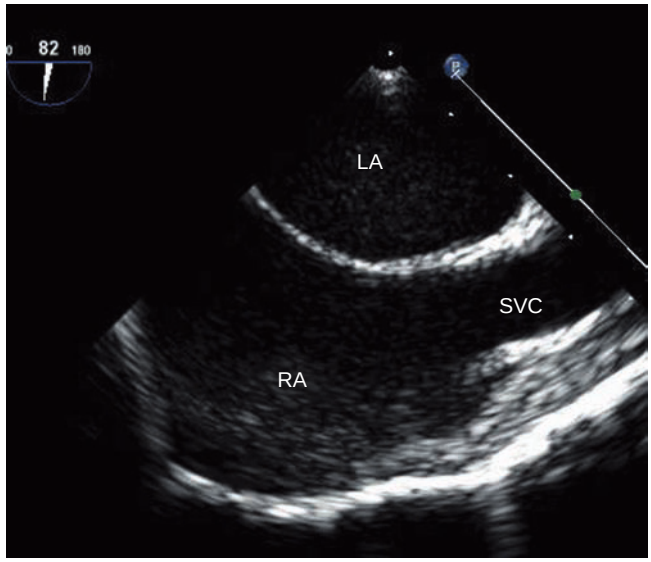


**Figure 40.7** Long-axis view of the atrial septum. This transoesophageal long-axis view is taken at the level of the atrial septum, showing the long axis of the atrial septum separating the left (LA) from the right atrium (RA). The superior caval vein (SVC) is seen entering the right atrium.

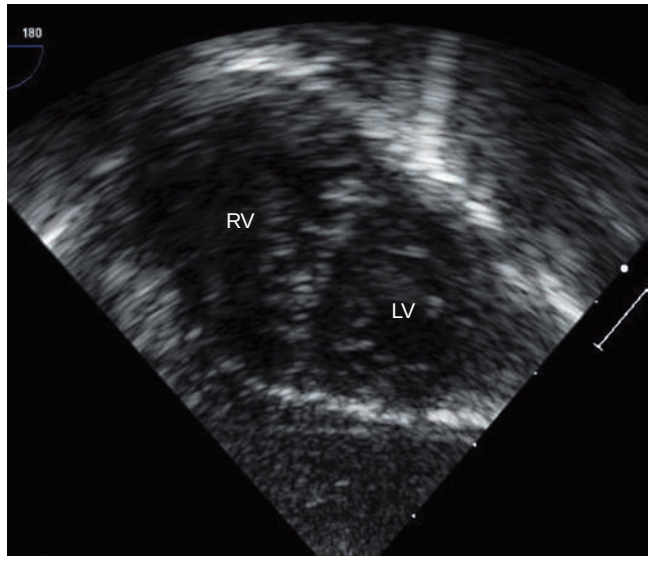


**Figure 40.8** Transgastric short-axis view. The transgastric short-axis view cuts through both the left (LV) and the right ventricle (RV). This view is used for assessing biventricular function.

allows determination of the type of defect: secundum (Videoclip 40.2), primum or sinus venosus, as in earlier chapters.

Color Doppler imaging of flow through the atrial septum is useful when present, but the absence of a shunt by color Doppler does not exclude the possibility of a nonshunting, closed foramen flap that could be probed open, or opened widely, if interatrial pressure relationships change (see above).

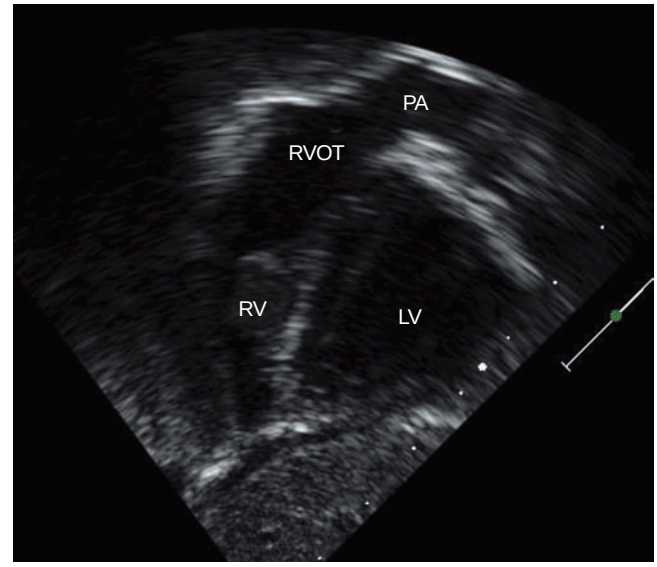


**Figure 40.9** Transgastric right ventricular outflow tract. The transgastric view provided a more longitudinal image of the right ventricular outflow tract. From this window, it is often possible to obtain good Doppler alignment to assess any obstruction within the outflow tract. RV, right ventricle; LV, left ventricle; RVOT, right ventricular outflow tract; PA, pulmonary trunk.

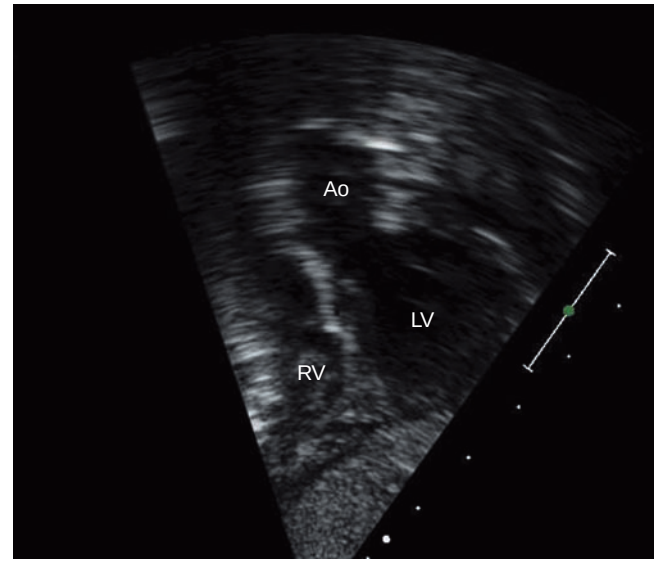


**Figure 40.10** From transgastric position, it is also possible to cut longitudinally along the left ventricular outflow tract. From this window, it is often possible to obtain good Doppler interrogation of obstructions within the outflow tract. RV, right ventricle; LV, left ventricle; Ao, aorta.

The retrocardiac 4-chamber image is especially well suited to evaluation of ventricular septal defects, as shown in Videoclips 40.9 and 40.10. Alignment with membranous defect jets provides good evaluation of ventricular septal defect (VSD) jet velocity, and estimation of the interventricular pressure drop. This view is of VSDs.

The 4-chamber view is good for evaluation of atrioventricular valve regurgitation as in surface echocardiography. It is the best view for evaluation of straddle or overriding of the atrioventricular valves. Special intraoperative applications may require image adjustment to align for peak tricuspid regurgitation velocity and estimation of right ventricular systolic pressure, and for determination of d*P*/d*t* as an index of function. Development of significant atrioventricular valve regurgitation, or increases in existing breadth and extent of color regurgitant signals, may indicate an overfilled heart with chamber distension. It is important to monitor for this as patients are weaned from cardiopulmonary bypass.

From the retrocardiac 4-chamber view, probe flexion, and some withdrawal, provides imaging of the pulmonary valve, the opportunity to image the bifurcation and screen for patent ductus arteriosus flow, and to image the right pulmonary artery and cross-section of the superior vena cava (Videoclips 40.11–40.13).

### Retrocardiac long-axis image

The retrocardiac long-axis image is obtained by rotating the plane of sound to around 90°, with small adjustments to produce the desired image. This view is excellent for demonstration of the left ventricular outflow tract, aortic valve and supravalvar aorta. It is also used to image the superior and inferior caval vein entering the right atrium (Videoclips 40.3 and 40.4). For intraoperative examinations, routine imaging of the aortic root is advised as it is possible to produce supravalvar aortic stenosis upon tying down of the root cannulation pursestring suture, especially if the aorta is small. Further withdrawal and rotation of the probe may provide images of the upper root and arch, rotating in the direction of the descending arch, be it right or left. The caliber of the arch is easily demonstrated. This view is useful in arch reconstructions. Rotating the omniplane plane of sound to the side of the descending aorta gives a long-axis view of the descending aorta (Videoclip 40.12). Normal pulsatility can be confirmed. In addition, it is usually possible to image the mid- and distal portions of the left pulmonary artery as it crosses the descending aorta, as described by Phoon and Rutkowski [129]. This is useful, as the left mainstem bronchus frequently interferes with retrocardiac imaging of the origin of the left pulmonary artery (LPA) from the retrocardiac position. Notation of continuous turbulence in the distal LPA from the aortic long-axis approach could confirm the patency of systemic-to-pulmonary artery shunt flow on into the LPA. Alternatively, intense systolic turbulence in the distal LPA, associated with normal flow in the main pulmonary artery (MPA) and right (RPA) pulmonary arteries from the retrocardiac view, suggests LPA stenosis.

The retrocardiac long-axis imaging plane may reveal subpulmonary stenosis at the entrance to the right ventricular outflow tract. Such obstructions may occur in isolation, or in association with tetralogy of Fallot.

Lesser degrees of flexion provide images of the aortic valve in cross-section and provide for evaluation of anatomic features of the aortic valve, as shown in Videoclip 40.14. Slight withdrawal of the probe to the level of the coronary artery origins may show important abnormalities, such as depicted in Videoclip 40.17. Reduction of the color pulse repetition frequency or the Nyquist limit (velocity range) may confirm color Doppler flow signals within the coronaries themselves – especially useful if there is concern over the coronary flow, as in switch repaired transposition (Videoclips 40.15 and 40.16).

### Retrocardiac short-axis images

Retrocardiac short-axis images across the plane of the atrioventricular valves may be obtained by advancing the probe a little from the standard 4-chamber view, and flexing the probe to image across the atrioventricular valves. From this view, it is possible to assess the number of atrioventricular valve leaflets, and thereby determine the anatomy of the atrioventricular valve and its ventricle (Videoclip 40.21). This view is especially valuable in patients with balanced or unbalanced atrioventricular septal defect, as shown in Videoclip 40.20. From these images, the surgeon may inspect the size, mobility and adequacy of the various scallops in an assessment for intraoperative repair.

### Transgastric images

The transgastric approach to TEE imaging is very useful [15,16]. It can usually be obtained in most patients, but it has been our practice to avoid transgastric imaging in patients with gastrostomy tubes or buttons. To obtain these images, the probe is advanced into the stomach, flexed, and withdrawn in the flexed position to abut the fundus of the stomach, much in the orientation of a surface echo from the subcostal window. If the degree of flexion is mild, a relatively anterior plane of sound may result, giving images of anterior structures such as the right ventricular outflow tract, pulmonary valve and main pulmonary artery (Videoclips 40.22 and 40.23). More flexion will draw the plane of sound posteriorly into the left ventricular outflow tract, for imaging of the levels of the left ventricular outflow tract, aortic valve and aortic root (Videoclips 40.22 and 40.23). Rotation of the omniplane angle may bring into view mitral inflow. The transgastric short-axis image of the mid- and apical portions of the left ventricle gives a global assessment of regional function (Videoclips 40.18 and 40.19). The transgastric short-axis image of the mid- and apical portions of the left ventricle may be suitable for automatic edge detection techniques for monitoring area change and filling rates.

## Limitations of TEE imaging

It is readily accepted that TEE images are usually of better quality than TTE images, even in pediatric subjects.

However, the limited imaging windows and planes encountered with TEE do restrict both imaging and alignment for Doppler velocity recording. Whereas TTE has multiple imaging approaches, TEE is restricted to retrocardiac and transgastric windows. Furthermore, important structures, such as the pulmonary veins, may be so close to the TEE probe as to complicate imaging or flow evaluation of them. Also, some instruments have such high Nyquist settings for pediatrics that the atrial portion of the heart may not display color flow signals unless the Nyquist setting is lowered. This can be important in evaluation of pulmonary veins and atrial shunts, especially following repair of total anomalous pulmonary venous return. The difficulty in imaging the left pulmonary artery from a retrocardiac approach has been mentioned earlier.

Imaging and flow evaluation of the superior vena cava (SVC) is a routine component of a complete TEE examination. The SVC–right atrial junction is readily imaged, and the portion of the SVC between the right atrium and the level of the right pulmonary artery. If pulmonary venous inflow signals to the SVC are demonstrable, this may be a useful technique for diagnosis of partial anomalous pulmonary venous return (PAPVR). However, PAPVR often involves pulmonary venous connections above the level of the right pulmonary artery, to a portion of the SVC that is uncommonly imaged by TEE. When performing TEE for evaluation of central line thrombus and vegetation, it is important to realize that a substantial portion of central lines are not imaged by TEE. Most thrombi and vegetations occur toward the ends of the lines, but some can occur in locations not amenable to TEE imaging.

Transesophageal echocardiographic measurement of peak blood flow velocity is limited due to restrictions preventing alignment with some lesions. However, TEE is excellent for measurement of peak atrioventricular valve velocity, and calculation of estimated ventricular pressures, or of $dP/dt$, as jets are usually well aligned with the Doppler beam. VSD jets may or may not be aligned with retrocardiac or gastric imaging planes. Retrocardiac windows are poorly suited for aortic and left ventricular outflow tract velocities, with the caveat that the velocity is at least as high as registered. Gastric imaging is well suited for outflow tract velocity measurement, closely approximating the subcostal window of TTE. Given these limitations, it is prudent for the echocardiographer to ask for direct intraoperative needle pressure measurements when needed.

## Complications

A procedural complication may be considered to be an unintended consequence that is encountered during the procedure [119,130]. Thus, we have considered the inability to insert the TEE probe to be a complication of TEE. Inability to insert the probe may result from inadequate sedation or anesthesia, prompting a review of anesthetic administration. Use of a laryngoscope to ensure probe entry into the upper esophagus may be useful. Failure to insert may result from unknown esophageal abnormalities, arch anomalies or unclear reasons. If the probe insertion does not proceed smoothly, force must never be applied to the probe. In our experience, inability to insert the probe occurs in fewer than 1% of TEE attempts.

Complications related to the airway occur in about 1.5% of our cases. Airway complications are reported in association with arch anomalies [30,131]. Inadvertent tracheal extubation may occur if the endotracheal tube is inadequately secured, with less chance for extubation with the use of nasotracheal intubation. Similarly, advancement of the endotracheal tube into the right mainstem bronchus is more likely with poorly secured tubes, and with greater probe-to-tube contact with orotracheal intubation. Airway obstruction – manifest by an increase in airway pressure, increased end-tidal carbon dioxide level and decreased minute ventilation – has occurred in fewer than 1% of our cases [130], and has also been reported by Ho et al. [132] and Gilbert et al. [133]. In our experience, patients at risk for obstruction are those weighing between 5 and 10 kg. It is postulated that the TEE probe impinges on the membranous trachea in this weight group [134]. Airway obstruction is an indication for probe removal. In patients with an aberrant retroesophageal subclavian artery there may be compression of that artery upon TEE probe passage or manipulation [88], as discussed earlier and shown in Fig. 40.1. Actual hypotension has been reported [135], and in infants this may be noted upon probe flexion during gastric imaging with the TEE probe compressing the abdominal aorta. Transgastric imaging should be avoided during performance of the median sternotomy incision, to avoid pushing the fundus of the stomach into the lower portion of the operative field [130]. Cases of esophageal injury have been reported, albeit infrequently.

Esophageal erythema was observed in 64% of subjects following removal of TEE probes [136]. This is likely common, and due to mucosal reaction to the probe. In that series, no long-term feeding or swallowing difficulties were noted in any of the surviving patients. The occurrence of dysphagia has also been reported following intraoperative TEE, with a prevalence of 18% [137]. Risk factors for dysphagia included age less than 3 years, intubation prior to operation, length of intubation, and size of TEE probe in relation to body weight. It is unclear which of these risk factors is most important. Feeding difficulties are commonly observed in small infants undergoing surgery without TEE. The benefit of performing intraoperative TEE must be weighed against the possible but uncommon adverse effects, many of which may be more common in smaller infants.

## References


1. Kyo S, Koike K, Takanawa E et al. Impact of transesophageal Doppler echocardiography on pediatric cardiac surgery. *Int J Cardiac Imaging* 1989;4:41–2.
2. Stumper OF, Elzenga NJ, Hess J, Sutherland GR. Transesophageal echocardiography in children with congenital heart disease: An initial experience. *J Am Coll Cardiol* 1990;16:433–41.
3. Kyo S, Omoto R, Matsumura M et al. Intraoperative transesophageal echocardiography in pediatric patients. *J Thorac Cardiovasc Surg* 1990;99:373–5.
4. Stumper O, Kraulitz R, Sreeram N et al. Intraoperative transesophageal vs epicardial ultrasound in surgery for congenital heart disease. *J Am Soc Echocardiogr* 1990;3:392–401.
5. Ritter SB. Transesophageal real-time echocardiography in infants and children with congenital heart disease. *J Am Coll Cardiol* 1991;18:569–80.
6. Cyran SE, Myers JL, Gleason MM et al. Application of intraoperative transesophageal echocardiography in infants and small children. *J Cardiovasc Surg (Torino)* 1991;32:318–21.
7. Fyfe DA, Kline CH. Transesophageal echocardiography for congenital heart disease. *Echocardiography* 1991;8:573–86.
8. Stumper O, Kaulitz R, Elzenga NJ et al. The value of transesophageal echocardiography in children with congenital heart disease. *J Am Soc Echocardiogr* 1991;4:164–76.
9. Lam J, Neirotti RA, Nijveld A et al. Transesophageal echocardiography in pediatric patients: Preliminary results. *J Am Soc Echocardiogr* 1991;4:43–50.
10. Weintraub R, Shiota T, Elkadi T et al. Transesophageal echocardiography in infants and children with congenital heart disease. *Circulation* 1992;86:711–22.
11. Shah PM, Stewart S III, Calalang CC, Alexson C. Transesophageal echocardiography and the intraoperative management of pediatric congenital heart disease: Initial experience with a pediatric esophageal 2D color flow echocardiographic probe. *J Cardiothorac Vasc Anesth* 1992;6:8–14.
12. Muhiudeen I, Silverman NH. Intraoperative transesophageal echocardiography using high resolution imaging in infants and children with congenital heart disease. *Echocardiography* 1993;10:599–608.
13. Lam J, Neirotti RA, Lubbers WJ et al. Usefulness of biplane transesophageal echocardiography in neonates, infants and children with congenital heart disease. *Am J Cardiol* 1993;72:699–706.
14. Sutherland GR, Stumper OF. Transthoracic vs transesophageal echocardiography in the pediatric patient. *Curr Opin Pediatr* 1993;5:598–605.
15. Hoffman P, Stumper O, Rydelwska-Sadowska W. Transgastric imaging: A valuable addition to the assessment of congenital heart disease by transverse plane transesophageal imaging. *J Am Soc Echocardiogr* 1993;6:35–44.
16. Muhiudeen IA, Silverman NH, Anderson RH. Transesophageal transgastric echocardiography in infants and children: The subcostal view equivalent. *J Am Soc Echocardiogr* 1995;8:231–44.
17. O'Leary PW, Hagler DJ, Seward JB et al. Biplane intraoperative transesophageal echocardiography in congenital heart disease. *Mayo Clin Proc* 1995;70:317–26.
18. Stevenson JG. Role of intraoperative transesophageal echocardiography during repair of congenital cardiac defects. *Acta Ped Scand* 1995;S410:23–33.
19. Cromme-Dijkhuis AH, Djoa KK, Bom N, Hess J. Pediatric transesophageal echocardiography by means of a miniature 5-MHz multiplane transducer. *Echocardiography* 1996;13:685.
20. Gentles TL, Rosenfeld HM, Sanders SP et al. Pediatric biplane transesophageal echocardiography: Preliminary experience. *Am Heart J* 1994;128:1225–33.
21. Bezold LI, Pignatelli R, Altman CA et al. Intraoperative transesophageal echocardiography in congenital heart surgery: The Texas Children's Hospital experience. *Tex Heart Inst J* 1996;23:108–15.
22. Lam J, Neirotti RA, Hardjowijono R et al. Transesophageal echocardiography with the use of a four-millimeter probe. *J Am Soc Echocardiogr* 1997;10:499–504.
23. Muhiudeen-Russell IA, Miller-Hance WC, Silverman NH. Intraoperative transesophageal echocardiography for pediatric patients with congenital heart disease. *Anesth Analg* 1998;87:1058–76.
24. Kavanaugh-McHugh A, Tobias JD, Doyle T et al. Transesophageal echocardiography in pediatric congenital heart disease. *Cardiol Rev* 2000;8:288–306.
25. Kececioglu D, Kehl HG, Schmid C et al. Morphologic characterization and assessment of mitral regurgitation after repair of atrioventricular defects in children. *Thorac Cardiovasc Surg* 1997;45:70–4.
26. Chaliki HP, Click RL, Abel MD. Comparison of intraoperative transesophageal echocardiographic examinations with the operative findings: A prospective review of 1918 cases. *J Am Soc Echocardiogr* 1999;12:237–40.
27. Singh GK, Shiota T, Cobanoglu A et al. Diagnostic accuracy and role of intraoperative biplane transesophageal echocardiography in pediatric patients with left ventricle outflow tract lesions. *J Am Soc Echocardiogr* 1998;11:47–56.
28. Kavanaugh McHugh A, Tobias JD, Doyle T et al. Transesophageal echocardiography in pediatric congenital heart disease. *Cardiol Rev* 2000;8:288–306.
29. Fyfe DA, Ritter SB, Snider AR et al. Guidelines for transesophageal echocardiography in children. *J Am Soc Echocardiogr* 1992;5:640–4.
30. Ayres NA, Miller-Hance W, Fyfe DA et al. Indications and guidelines for performance of transesophageal echocardiography in the patient with pediatric acquired or congenital heart disease: Report from the Task Force of the Pediatric Council of the American Society of Echocardiography. *J Am Soc Echocardiogr* 2005;18:91–8.
31. Stevenson JG. Adherence to physician training guidelines for pediatric transesophageal echocardiography affects the outcome of patients undergoing repair of congenital cardiac defects. *J Am Soc Echocardiogr* 1999;12:165–72.
32. Douglas PS, Stainback RF, Weissman NJ et al. ACCF/ASE.ACEP/SCAI/SCCT/SCMR 2007 appropriateness criteria for transthoracic and transesophageal echocardiography. *J Am Soc Echocardiogr* 2007;20:787–805.
33. Soliman DE, Maslow AD, Bokesch PM et al. Transesophageal echocardiography during scoliosis repair: Comparison with CVP monitoring. *Can J Anesth* 1998;45:925–32.

34. Suriani RJ, Cutrone A, Feierman D, Konstadt S. Intraoperative transesophageal echocardiography during liver transplantation. *J Cardiothorac Vasc Anes* 1996;10:699–701.
35. Schumann R. Intraoperative resource utilization in anesthesia for liver transplantation in the United States: A survey. *Anesth Analg* 2003;97:21–8.
36. Poortmans G, Schupfer G, Roosens C, Poelaert J. Perioperative transesophageal echocardiography as a diagnostic and monitoring tool in pediatric oncologic surgery. *J Cardiothorac Vasc Anesth* 2001;15:118–20.
37. O'Keefe PA, Jin XY, Jenkins M. Unidentified retained left atrial myxoma: Intraoperative detection by transesophageal echocardiography. *Eur J Cardiothorac Surg* 1995;9:599–601.
38. Beique FA, Lavoie J. TEE monitoring. *Can J Anaesth* 1998;45: 919–24.
39. Ramamoorthy C, Lynn A, Williams GD et al. Utility of transesophageal echocardiography as assessed by anesthesiologists during surgery for congenital heart disease. *J Am Soc Echocardiogr* 1999;12:420.
40. Stevenson JG, Sorensen GK. Proper probe size for pediatric transesophageal echocardiography. *Am J Cardiol* 1993;72: 491–2.
41. Bruce CJ, Packer DL, O'Leary PW, Seward JB. Feasibility study: transesophageal echocardiography with a 10F (3.2 mm) multifrequency (5.5–10 mHz) ultrasound catheter in a rabbit model. *J Am Soc Echocardiogr* 1999;12:596–600.
42. Stevenson JG. Pediatric TEE probe size. *J Am Soc Echocardiogr* 2000;13:254.
43. Fritz S, Hust MH, Ochs C et al. Use of a latex cover sheath for transesophageal echocardiography instead of regular disinfection of the echoscope? *Clin Cardiol* 1993;16:737–40.
44. Masura J, Gavora P, Formanek A, Hijazi ZM. Transcatheter closure of secundum atrial septal defects using the new self-centering Amplatzer septal occluder: Initial human experience. *Cathet Cardiovasc Diagn* 1997;42:388–93.
45. Omeish A, Hijazi ZM. Transcatheter closure of atrial septal defects in children and adults using the Amplatzer septal occluder. *J Interv Cardiol* 2001;14:37–44.
46. Van der Velde ME, Perry SB. Transesophageal echocardiography during interventional catheterization in congenital heart disease. *Echocardiography* 1997;14:513–28.
47. Murzi B, Bonanomi GL, Giusti S et al. Surgical closure of muscular ventricular septal defects using double umbrella devices. *Eur J Cardiothoracic Surg* 1997;12:450–4.
48. Thanopoulos BD, Tsaousis GS, Konstadopoulou GN, Zarayelyan AG. Transcatheter closure of muscular ventricular septal defects with the Amplatzer ventricular septal defect occluder; initial clinical applications in children. *J Am Coll Cardiol* 1999; 33:1395–9.
49. Lam J, Tanke RB, van Oort A et al. The use of transesophageal echocardiography monitoring of transcatheter closure of a persistent ductus arteriosus. *Echocardiography* 2001;18:197–202.
50. McElhinney DB, Burch GH, Kung GC et al. Echocardiographic guidance for transcatheter coil embolization of congenital coronary arterial fistulas in children. *Pediatr Cardiol* 2000;21: 253–8.
51. Hahn K, Gal R, Sarnoski J. Transesophageal echocardiographically guided atrial transeptal catheterization in patients with normal sized atria: Incidence of complications. *J Clin Cardiol* 1994;18:217–20.
52. Komai H, Naito Y, Fujiwara K, Uemura S. The benefits of surgical atrial septostomy guided by transesophageal echocardiography in pediatric patients. *J Thorac Cardiovasc Surg* 1999;118: 758–9.
53. Ho AC, Chen CK, Yang MW et al. Usefulness of intraoperative transesophageal echocardiography in the assessment of surgical repair of pediatric ventricular septal defects with video-assisted endoscopic techniques in children. *Chang Gung Med J* 2004;27:646–53.
54. Vitarelli A, DeCurtis G, Conde Y et al. Assessment of congenital coronary artery fistulas by transesophageal color Doppler echocardiography. *Am J Med* 2002;113:127–33.
55. Figueroa MI, Balaguru D, McClure C et al. Experience with the use of multiplane transesophageal echocardiography to guide closure of atrial septal defects using the Amplatzer device. *Pediatr Cardiol* 2002;23:430.
56. Klein AL, Grimm RA, Murray RD et al. Assessment of cardioversion using transesophageal echocardiography. *N Engl J Med* 2001;344:1411–20.
57. Fyfe DA, Kline CH, Sade RM, Gillette PC. Transesophageal echocardiography detects thrombus formation not identified by transthoracic echocardiography after the Fontan operation. *J Am Coll Cardiol* 1991;18:1733–7.
58. Fyfe DA, Kline CH, Sade RM et al. The utility of transesophageal echocardiography during and after Fontan operations in small children. *Am Heart J* 1991;122:1403–15.
59. Marcus B, Steward DJ, Khan NR et al. Outpatient transesophageal echocardiography with intravenous propofol anesthesia in children and adolescents. *J Am Soc Echocardiogr* 1993;6:205–9.
60. Heard CMB, Gunnarsson B, Heard AMB et al. Anaesthetic technique for transoesophageal echocardiography in children. *Pediatr Anesth* 2001;11:181–4.
61. Mart CR, Parrish M, Rosen KL et al. Safety and efficacy of sedation with propofol for transesophageal echocardiography in children in an outpatient setting. *Cardiol Young* 2006;16:152–6.
62. Tibby SM, Hatherill M, Durward A, Murdoch IA. Are transesophageal Doppler parameters a reliable guide to paediatric haemodynamic status and fluid management? *Intens Care Med* 2001;27:201–5.
63. Marcus B, Wong PC, Wells WJ et al. Transesophageal echocardiography in the postoperative child with an open sternum. *Ann Thorac Surg* 1994;58:235–6.
64. Kececioglu D, Galal O, Halees Z et al. Transesophageal echocardiography in children with cardiac assist. *Thorac Cardiovasc Surg* 1994;42:21–4.
65. Ungerleider RM, Greeley WJ, Kisslo J. Intraoperative echocardiography in congenital heart disease surgery: Preliminary report on a current study. *Am J Cardiol* 1989;63:3F–8F.
66. Ungerleider R, Kisslo JA, Greeley WJ et al. Intraoperative pre bypass and post bypass epicardial color flow imaging of atrioventricular septal defects. *J Thorac Cardiovasc Surg* 1989; 98:90–9.
67. Ungerleider R. Decision making in pediatric cardiac surgery using intraoperative echocardiography. *Int J Cardiac Imag* 1989; 4:33–5.

68. Ungerleider RM, Greeley WJ, Sheikh KH et al. The use of intraoperative echo with Doppler color flow imaging to predict outcome after repair of congenital cardiac defects. *Ann Surg* 1989;210:526–34.
69. Ungerleider RM, Greeley WJ, Kanter RJ, Kisslo JA. The learning curve for intraoperative echocardiography during congenital heart surgery. *Ann Thorac Surg* 1992;54:691–8.
70. Stevenson JG. Utilization of intraoperative transesophageal echocardiography during repair of congenital cardiac defects: A survey of seventy North American centers. *Clin Cardiol* 2003; 26:132–4.
71. Sangwan S, Au C, Mahajan A. Pro: Pediatric anesthesiologists should be the primary echocardiographers for pediatric patients undergoing cardiac surgical procedures. *J Cardiothorac Vasc Anesth* 2001;15:388–90.
72. Moran AM, Geva T. Con: Pediatric anesthesiologists should not be the primary echocardiographers for pediatric patients undergoing cardiac surgical procedures. *J Cardiothorac Vasc Anesth* 2001;15:391–3.
73. Quinones MA, Douglas PS, Foster E et al. ACC/AHA clinical competence statement on echocardiography: A report of the American College of Cardiology, American Heart Association, American College of Physicians, American Society of Internal Medicine Task Force on Clinical Competence. *J Am Coll Cardiol* 2003;41:687–708.
74. Cahalan MK, Stewart W, Pearlman AS et al. American Society of Echocardiography and Society of Cardiovascular Anesthesiologists task force guidelines for training in perioperative echocardiography. *J Am Soc Echocardiogr* 2002;15:647–52.
75. Sloth E, Pedersen J, Olsen KH et al. Transesophageal echocardiographic monitoring during paediatric cardiac surgery: Obtainable information and feasibility in 532 children. *Pediatr Anesth* 2001;11:657–62.
76. Bettex D, Schmidlin D, Bernath M-A et al. Intraoperative transesophageal echocardiography in pediatric congenital cardiac surgery: A two center observational study. *Anesth Analg* 2003;97:1275–82.
77. Russell IM, Silverman NH, Miller-Hance WC et al. Intraoperative transesophageal echocardiography for infants and children undergoing congenital heart surgery: The role of the anesthesiologist. *J Am Soc Echocardiogr* 1999;12:1009–14.
78. Miller JP, Lambert AS, Shapiro WA et al. The adequacy of basic intraoperative transesophageal echocardiography performed by experienced anesthesiologists. *Anesth Analg* 2001;92:1103–10.
79. Ramamoorthy C, Lynn AM, Stevenson JG. Pro: Transesophageal echocardiography should be routinely used during pediatric open cardiac surgery. *J Cardiothorac Vasc Anesth* 1999;13:629–31.
80. McGowan FX Jr, Laussen PC. Con: Transesophageal echocardiography should be routinely used during pediatric open cardiac surgery. *J Cardiovasc Thorac Surg* 1999;13:629–31.
81. Oberhansli I, Rouge JC, Friedli B. Transesophageal echocardiography: Is it indicated for children undergoing heart surgery? *Helv Chir Acta* 1992;58:465–71.
82. Stevenson JG, Sorensen GK, Hall DG, Rittenhouse EA. Is routine use of intraoperative transesophageal echocardiography cost-effective? *J Am Soc Echocardiogr* 1994;7:S5.
83. Siwik ES, Spector ML, Patel CR, Zahka KG. Costs and cost-effectiveness of routine transesophageal echocardiography in congenital heart surgery. *Am Heart J* 1999;138:771–6.
84. Randolph GR, Hagler DJ, Connolly HM et al. Intraoperative transesophageal echocardiography during surgery for congenital heart defects. *J Thorac Cardiovasc Surg* 2002;124:1176–82.
85. Ulma G, Stevenson JG, Lupinetti FM, Morray JP. Transesophageal echocardiographic diagnosis of iatrogenic coronary sinus ligation. *J Thorac Cardiovasc Surg* 1997;114:493–5.
86. Stevenson JG, Sorensen GK. Significant reduction in intraoperative color Doppler tricuspid regurgitation jet area from effects of anesthesia, prior to actual surgical repair. *J Am Coll Cardiol* 1991;17:19.
87. Frommelt PC, Stuth EA. Transesophageal echocardiography in total anomalous pulmonary venous drainage: Hypotension caused by compression of the pulmonary venous confluence during probe passage. *J Am Soc Echocardiogr* 1994;7:652–4.
88. Pontus SP Jr, Frommelt PC. Detection of a previously undiagnosed anomalous subclavian artery during insertion of a transesophageal echocardiography probe. *Anesth Analg* 1994;78: 805–7.
89. Cassorla L, Miller-Hance WC, Rouine-Rapp K et al. Reliability of intraoperative contrast transesophageal echocardiography for detecting interatrial communications in patients with other cardiovascular malformations. *Am J Cardiol* 2003;91:1027–31.
90. Stevenson JG, Sorensen GK, Oakes RL et al. Regurgitation of cardioplegic solution through normal aortic valves reduces effective cardioplegia effect: An additional application of intraoperative transesophageal echocardiography. *J Am Soc Echocardiogr* 1994;7:S47.
91. Greeley WJ, Kern FH, Ungerleider RM. Intramyocardial air causes right ventricular dysfunction after repair of a congenital heart defect. *Anesthesiology* 1990;73:1042–6.
92. Ninomiya J, Yamauchi H, Hosaka H et al. Continuous transesophageal echocardiography monitoring during weaning from cardiopulmonary bypass in children. *Cardiovasc Surg* 1997;5:129–33.
93. Stevenson JG, Sorensen GK, Gartman DM et al. Left ventricular outflow tract obstruction: An indication for intraoperative transesophageal echocardiography. *J Am Soc Echocardiogr* 1993; 6:525–35.
94. Tee SD, Shiota T, Weintraub R et al. Evaluation of ventricular septal defect by transesophageal echocardiography: Intraoperative assessment. *Am Heart J* 1994;127:585–92.
95. Wienecke M, Fyfe DA, Kline CH et al. Comparison of intraoperative transesophageal echocardiography to epicardial imaging in children undergoing ventricular septal defect repair. *J Am Soc Echocardiogr* 1991;4:607–14.
96. Kececioglu D, Kehl HG, Schmid C et al. Morphologic characterization and assessment of mitral regurgitation after repair of atrioventricular defects in children. *Thorac Cardiovasc Surg* 1997;45:70–4.
97. Roberson DA, Muhiudeen IA, Silverman NH. Intraoperative transesophageal echocardiography of atrioventricular septal defect. *J Am Coll Cardiol* 1991;18:537–45.
98. Joyce JJ, Hwang EY, Wiles HB et al. Reliability of intraoperative transesophageal echocardiography during tetralogy of Fallot repair. *Echocardiography* 2000;17:319–27.

99. Singh GK, Shiota T, Cobanglu A et al. Diagnostic accuracy of intraoperative biplane transesophageal echocardiography in pediatric patients with left ventricle outflow tract lesions. *J Am Soc Echocardiogr* 1998;11:47–56.
100. Ius P, Salandin V, Zussa C, Valfre C. Surgical treatment of left ventricular outflow tract obstruction guided by intraoperative transesophageal echocardiography. *Thorac Cardiovasc Surg* 1991;39:205–7.
101. Movsowitz C, Jacobs LE, Eisenberg S et al. Discrete subaortic valvular stenosis: The clinical utility and limitations of transesophageal echocardiography. *Echocardiography* 1993;10:485–7.
102. Eriksson H, Midgley FM, Karr SS, Martin GR. Role of echocardiography in the diagnosis and surgical management of accessory mitral valve tissue causing left ventricular outflow tract obstruction. *J Am Soc Echocardiogr* 1995;8:105–7.
103. Alboliras ET, Gotteiner NL, Berdusis K, Webb CL. Transesophageal echocardiographic imaging for congenital lesions of the left ventricular outflow tract and aorta. *Echocardiography* 1996;13:439–46.
104. Frommelt PC, Lewis DA, Pelech AN. Intraoperative transgastric echo assessment during left ventricular outflow tract surgery: A reliable predictor of residual obstruction. *Echocardiography* 1998;15:581–5.
105. Stevenson JG, Sorensen GK, Stamm SJ et al. Intraoperative transesophageal echocardiography of coronary artery fistulae. *Ann Thorac Surg* 1994;57:1217–21.
106. Joyce JJ, Hwang EY, Wiles HB et al. Reliability of intraoperative transesophageal echocardiography during tetralogy of Fallot repair. *Echocardiography* 2000;17:319–27.
107. Lee HR, Montenegro LM, Nicholson SC et al. Usefulness of intraoperative transesophageal echocardiography in predicting the degree of mitral regurgitation secondary to atrioventricular septal defect in children. *Am J Cardiol* 1999;83:750–3.
108. Kim HK, Kim WH, Hwang SW et al. Predictive value of intraoperative transesophageal echocardiography in complete atrioventricular septal defect. *Ann Thorac Surg* 2005;80:56–9.
109. Honjo O, Kotani Y, Osaki S et al. Discrepancy between intraoperative transesophageal echocardiography and postoperative transthoracic echocardiography in assessing congenital valve surgery. *Ann Thorac Surg* 2006;82:2240–6.
110. Balmer C, Barron D, Wright JG et al. Experience with intraoperative ultrasound in pediatric cardiac surgery. *Cardiol Young* 2006;16:455–62.
111. Lim DS, Dent JM, Gutgesell HP et al. Transesophageal echocardiographic guidance for surgical repair of aortic insufficiency in congenital heart disease. *J Am Soc Echocardiogr* 2007;20: 1080–85.
112. Stevenson JG. Two-dimensional color Doppler estimation of the severity of atrioventricular valve regurgitation: Important effects of instrument gain setting, pulse repetition frequency and carrier frequency. *J Am Soc Echocardiogr* 1989;2:1–10.
113. Stevenson JG, Otto CM. Impact of color flow Doppler physics on clinical assessment of flow abnormalities. In: Otto CM (ed.) *The Practice of Clinical Echocardiography*. Philadelphia: WB Saunders, 1997;291–306.
114. Seeberger MD, Cahalan MK, Rouine-Rapp K et al. Acute hypovolemia may cause segmental wall motion abnormalities in the absence of myocardial ischemia. *Anesth Analg* 1997;85:1252–7.
115. Leung JM, Levine EH. Left ventricular end-systolic cavity obliteration as an estimate of intraoperative hypovolemia. *Anesthesiology* 1994;81:1102–9.
116. Pass RH, Solowiejczyk DE, Quaegebeur JM et al. Bulboventricular foramen resection: Hemodynamic and electrophysiologic results. *Ann Thorac Surg* 2001;71:1251–4.
117. Kaushal SK, Radhakrishanan S, Dagar KS et al. Significant intraoperative right ventricular outflow gradients after repair of tetralogy of Fallot: to revise or not to revise? *Ann Thorac Surg* 1999;68:1705–12.
118. Stevenson JG, Sorensen GK, Gartman DM et al. Transesophageal echocardiography during repair of congenital cardiac defects: Identification of residual problems necessitating reoperation. *J Am Soc Echocardiogr* 1993;6:356–65.
119. Sheil ML, Baines DB. Intraoperative transesophageal echocardiography for paediatric cardiac surgery: an audit of 200 cases. *Anes Int Care* 1999;27:591–5.
120. Bettex D, Pretre R, Jenni R, Schmid ER. Cost-effectiveness of routine intraoperative transesophageal echocardiography in pediatric cardiac surgery: A 10 year experience. *Anesth Analg* 2005;100:1271–5.
121. Reich DL, Konstadt SN, Nejat M et al. Intraoperative transesophageal echocardiography for the detection of cardiac preload changes induced by transfusion and phlebotomy in pediatric patients. *Anesthesiology* 1993;79:10–15.
122. Tei C. New noninvasive index for combined systolic and diastolic ventricular function. *J Cardiol* 1995;26:135–6.
123. Tei C, Ling LH, Hodge DO et al. New index of combined systolic and diastolic myocardial performance: A simple and reproducible measure of cardiac function – a study of normals and dilated cardiomyopathy. *J Cardiol* 1995;26:357–66.
124. Tei C, Nishimura RA, Seward JB, Tajik AJ. Noninvasive Doppler derived myocardial performance index: Correlation with simultaneous measurements of cardiac catheterization. *J Am Soc Echocardiogr* 1997;10:168–78.
125. Eidem BW, Tei C, O'Leary PW et al. Nongeometric quantitative assessment of right and left ventricular function: Myocardial performance index in normal children and patients with Ebstein anomaly. *J Am Soc Echocardiogr* 1998;11:849–56.
126. Stevenson JG, French JW, Wright S et al. New Doppler index of combined systolic and diastolic left ventricular function: Normal values in 300 children. *J Am Soc Echocardiogr* 1997;10: 447.
127. Rhodes J, Marx GR, Tardiff JC et al. Evaluation of ventricular dp/dt before and after open heart surgery using transesophageal echocardiography. *Echocardiography* 1997;14:15–22.
128. Tibby SM, Hatherill M, Murdoch IA. Use of transesophageal Doppler ultrasonography in ventilated pediatric patients: Derivation of cardiac output. *Crit Care Med* 2000;28:2045–50.
129. Phoon CK, Rutkowski M. Transesophageal imaging of the mid to distal left pulmonary artery in congenital heart disease. *J Am Soc Echocardiogr* 1999;12:663–8.
130. Stevenson JG. Incidence of complications in pediatric transesophageal echocardiography: Experience in 1650 cases. *J Am Soc Echocardiogr* 1999;12:527–32.
131. Phoon CK, Bhardwaj N. Airway obstruction caused by transesophageal echocardiography in a patient with double aortic arch and truncus arteriosus. *J Am Soc Echocardiogr* 1999;12:540.

132. Ho AC, Tan PP, Yang MW et al. Airway compression by biplane pediatric transesophageal echocardiography probe: Case report. *Changgene Yi Xue Za Zhi* 1998;21:333–7.
133. Gilbert TB, Panico FG, McGill WA et al. Bronchial obstruction by transesophageal echocardiography probe in a pediatric cardiac patient. Anesth Analg 1992;74:156–8.
134. Sorensen GK, Stevenson JG, Siebert J, Mulroy J Jr. The mechanism of airway obstruction during intraoperative transesophageal echocardiography in infants. *J Am Coll Cardiol* 1992;19:237A.
135. Lunn RJ, Oliver WC, Hagler DJ. Aortic compression by transesophageal echocardiographic probe in infants and children undergoing cardiac surgery. *Anesthesiology* 1992;77:587–90.
136. Greene MA, Alexander JA, Knauf DG et al. Endoscopic evaluation of the esophagus in infants and children immediately following intraoperative use of transesophageal echocardiography. *Chest* 1999;116:1247–50.
137. Kohr LM, Dargan M, Hague A et al. The incidence of dysphagia in pediatric patients after open heart procedures with transesophageal echocardiography. *Ann Thorac Surg* 2003;76:1450–6.

# 41 3D Echocardiography

**Folkert Jan Meijboom[1], Annemien van den Bosch[2] and Jackie McGhie[3]**

[1]Department of Pediatrics and Cardiology, Academic Medical Centre Utrecht, Utrecht, The Netherlands
[2]Department of Cardiology, Erasmus University Rotterdam, Rotterdam, The Netherlands
[3]Erasmus University Medical Center Rotterdam, Rotterdam, The Netherlands

## Introduction

### Why 3D echo?

About 30 years ago, clinical echocardiography started with B-mode. The dot jumping up and down on the monitor was difficult to interpret. M-mode was the next step, with a time axis added to the B-mode. Two-dimensional (2D) echocardiography was the next leap forward in noninvasive cardiac assessment. Currently 2D imaging is the core of every echocardiographic examination, together with M-mode, pulsed Doppler, continuous-wave Doppler and color Doppler. In pediatric cardiology, the assessment of sometimes complex anatomy is the major task for the echocardiographer. Using current 2D imaging techniques, an experienced cardiologist can accurately diagnose most congenital malformations. However, 2D imaging has several limitations. Firstly, the quantification of ventricular volumes and function requires geometrical assumptions that are reasonable for normal left ventricles but are often inaccurate for dilated and structurally abnormal hearts. 3D echo could obviate the need for these assumptions, as the entire ventricle can be visualized during the cardiac cycle and ventricular volumes can be measured. The first manuscript on this application of 3D echocardiography was published in 1974 [1]. Secondly the anatomy of congenital heart defects is often so complex that conceptualization of the true "surgical" anatomy out of a series of 2D cut-planes through the heart is often difficult. Transesophageal echo (TEE) can sometimes lead to a better understanding of the intracardiac anatomy due to better image resolution and the possibility of paraplane imaging (cutting through intracardiac structures at different levels) and anyplane imaging (cutting through intracardiac structures at different angles), but it remains essentially a 2D technique. A clear presentation of true anatomy, instead of a conceptualized 3D image in each operator's head, would make discussion about the interpretation of echocardiographic studies more objective. 3D echocardiography allows visualization of 3D relationships instead of having to conceptualize them mentally. These two reasons explain why so much effort was put into developing 3D imaging techniques [2].

### History of 3D imaging techniques

In the early phase of 3D echo, a 3D dataset was created by merging individual 2D cross-sections, obtained at different levels or from different angles [3,4]. The first technique was "freehand scanning:" multiple 2D scanning planes were obtained manually, with the help of an external reference system for the transducer position. The transducer position could be determined with a mechanical arm or with sensors (optical or electrical). In experimental settings the results were promising regarding volumetric data, but the procedure was very time-consuming, suffered from many artifacts and had poor resolution. The second technique used internal reference systems for the acquisition of the cut-planes, and systematic image acquisition was achieved by means of a predetermined transducer motion. This preprogrammed motion of the transducer was linear, fanlike or rotational. It was done transthoracically and by TEE (Fig. 41.1). Many studies showed that not only could volumetric data be produced, but also complex intracardiac structures could be displayed in a 3D way. The "en face" view of intracardiac structures such as valves, impossible to obtain with 2D echo, was greatly appreciated. This transthoracic approach never reached clinical use because of many artifacts and poor image quality. The transesophageal approach, with a stepwise rotation of the echo beam, had a much better image quality, and some echocardiographers integrated 3D TEE into their clinical practice, although the entire procedure remained very time-consuming and was not real-time.

In the early 1990s von Ramm and colleagues developed the first real-time 3D (RT3D) matrix phased-array transducer, containing 512 elements, with a frame rate high enough to depict cardiac motion (Fig. 41.2) [5]. The rapid progression of computer technology, with better calculating power and microprocessor technology, allowed further improvements of this design. Commercially available RT3D echo systems

*Echocardiography in Pediatric and Congenital Heart Disease: From Fetus to Adult*
Edited by Wyman W. Lai, Luc L. Mertens, Meryl S. Cohen and Tal Geva
 ISBN: 978-1-405-17401-5

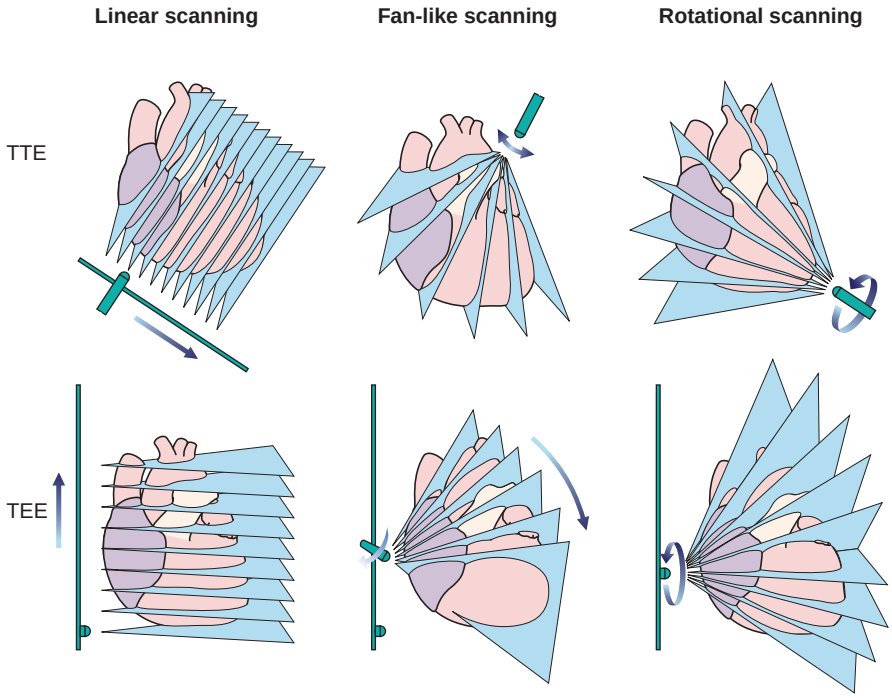


**Figure 41.1** Scanning modes used before the matrix transducer became available. Multiple two-dimensional (2D) scanning planes could be merged to create a three-dimensional (3D) volume. TEE, transesophageal echocardiography; TTE, transthoracic echocardiography.

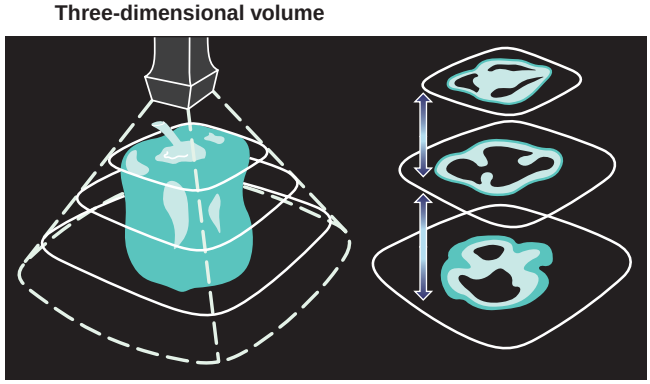


**Figure 41.2** Cross-sections at different levels of a green pepper, used by the pioneers of matrix transducers to illustrate the concept of 3D volumetrics.

now have transducers based on complex matrix-array technology, containing around 3000 elements, all connected with a microbeam former, within the transducer head. The combination of a multidirectional ultrasound beam that is emitted at a high frame rate and very powerful microchips allows the creation of a real-time pyramidal volume. In the current generation of RT3D ultrasound machines, this real-time pyramid has an angle of approximately 30° × 60°. This is actual real-time 3D, but the angle of the pyramid is generally not wide enough to include the entire left ventricle or an anatomic structure – like an atrial septal defect – in relation to other intracardiac structures. To obtain this, a pyramid with wider angles is needed. This can be constructed by "stitching" together several consecutively obtained narrow pyramids (electrocardiogram [ECG]-gated) to form one wider pyramid, with angles of 90° × 90° or 110° × 110°. This is no longer a real-time 3D dataset, and analysis can only be performed after the acquisition is completed. A regular heart rhythm is necessary. If this is not the case, the component segments of the composite volume will represent different stages of the cardiac cycle, and hence be "out of phase," which will be apparent at the "stitching" lines as "stitching artifacts." Stitching artifacts can also occur due to respiration and motion artifacts. 3D color Doppler is now integrated in ultrasound systems and combines presentation of blood flow velocity (Doppler data) with cardiac morphology. Currently, color Doppler is not available in real-time, and quantification of color Doppler-derived flow measurements is still experimental. Recently the first RT3D TEE probe was launched, but no reports on its performance have been published yet.

## Clinical application of real-time 3D echocardiography

In clinical practice, RT3D echo has been shown to have advantages over the existing echo modalities for the following indications:

- chamber quantification (mass and volumes);
- valve morphology and function;
- congenital heart disease;
- guidance of catheter interventions.

Real-time 3D echo can easily be integrated into a normal echocardiographic examination. The learning curve in the acquisition phase mainly concerns learning how to use the different 3D echo modalities for different clinical questions: real-time with narrow sector, zoom mode or full-volume. A clinical question should be translated into a defined region of interest to be evaluated with RT3D echo. Currently it is not possible to obtain a full analysis of the entire heart with one dataset acquired from a single view. It should be realized that 3D echo is an ultrasound technique and that all the limitations of ultrasound also hold for 3D echo, namely: penetration limits (a probe adequate for the size of the patient must be chosen); and the lower lateral resolution compared with the in-depth resolution. As a consequence, a morphologic structure is best visualized when perpendicular to the central part of the ultrasound beam, not too distally from the transducer. In order to answer all the clinical questions, different 3D acquisitions are necessary, often from different transducer positions, depending on the structure of interest.

Due to new crystal technology built into the latest pediatric matrix transducer, the 2D image quality acquired with these probes is good, so that the entire echo examination – 2D, 3D and nearly all Doppler modalities (except continuous-wave Doppler) – can be done using a single transducer [6]. The 2D image quality of the transducers available for adult use, however, is still substantially less than that of conventional 2D transducers. Hence, several transducers are required during a single examination to perform a full 2D and 3D study. After image acquisition, the 3D analysis is performed off-line. When starting out with 3D echo analysis one can spend hours navigating through a single dataset [7], but after some training and experience almost always a specific region of interest can be analyzed within 10 minutes. The essential "cropped views" and cross-section can be stored as "bookmarks" and included in the structured echo report [8].

## Examination protocol

Now that RT3D echo is increasingly being used in clinical practice, there is a need for an examination protocol, as proposed by some experts in the field [9]. The following is a summary of our recommendations.

### Image acquisition

For a good 3D volume dataset, several points have to be taken into consideration at the time of acquisition:

**1** Choosing the optimal transducer frequency. In adults, penetration is important and lower-frequency transducers are used. In pediatric patients, penetration is less important and higher-frequency transducers produce a superior spatial resolution.

**2** Regular heart rate. This is required for full-volume datasets as stitching the pyramids together is ECG-based. Although it is now possible to obtain time-gated volume datasets, an optimal full-volume dataset will exist of a series of four or seven ECG-gated narrow data pyramids that are stitched together to form a full-volume data pyramid.

**3** Optimal 2D image with a distinct blood–tissue border (minimal noise). When an optimal 2D image is obtained, the overall gain is increased. This ensures visualization of any structures in the planes that are not represented on the bi-plane mode. Switching back and forth between 2D and RT3D gives the operator an idea of the 3D quality.

**4** The region of interest must be 5–15 cm (in adults) from the transducer and perpendicular to the transducer.

**5** The region of interest must lie in the center and between the dotted lines in the bi-plane mode.

**6** Choose the smallest angle that will fit your whole region of interest (the smaller the angle, the greater the line density, the greater the resolution).

**7** Acquisition during breath-hold reduces breathing artifacts.

### Image rendering

Once an optimal 3D dataset has been obtained – that is, one without ECG, breathing or motion artifacts – you can proceed to the image-rendering phase. This can be done using one of the commercially available computer software analysis systems; these have several tools for the display of and navigation through an acquired 3D dataset. Using the rendering technique enables the operator to cut the heart in multiple sections and visualize the cardiac structures of interest from any desired angle. The exact mode of navigating the datasets differs for the various systems. We discuss one such approach.

Once the dataset is read into the analyzing system your full-volume pyramid dataset will be presented encased in a cube. This cube we call the "crop box" (Fig. 41.3). This gives the operator the possibility of "walking through" the dataset from all six sides of the cube, moving from the outer edge to the center, or even crossing the center to the opposite side. So, in terms of cutting planes, we have a sagittal (right–left), coronal (anterior–posterior) and transverse (superior–inferior) orientation, giving us several cross-sections along each plane. The crop box can also be rotated in its entirety, and the 3D dataset can be displayed in any orientation.

Multiplane reconstruction (MPR), or "quad tiling" mode, is another way of looking at a 3D volume dataset. This features a quad screen display with three 2D cut-planes (sagittal, coronal, transverse) and a 3D volume dataset cube. In MPR mode, the maximum or minimum size/opening of a region of interest can be located by using two of the three 2D planes. Some simple distance calculations are also possible. The accuracy of the calculation, of course, is dependent on the image quality and operator skills. Some systems allow the placing of landmarks in the 2D images in MPR mode that will also appear in the 3D dataset, thereby helping the operator to identify different structures in complex hearts. A more detailed description of the analysis software and modes

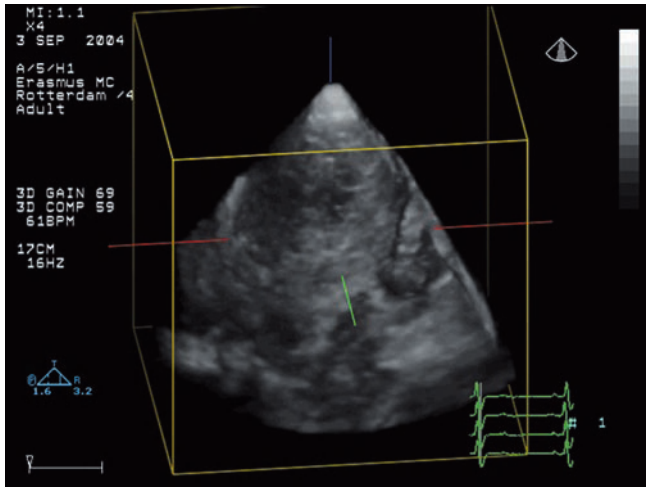


**Figure 41.3** A full-volume 3D dataset in a crop box.

is beyond the scope of this chapter. Moreover, it is expected that these systems will develop considerably in the future to make them more user friendly.

## Volumetric quantification

### Background

In clinical practice, the most widely used method of assessing left ventricular volumes and function in the past decades has been 2D echocardiography. Several factors influence its accuracy: foreshortened views, geometric assumptions and poor endocardial border detection. Because left ventricular (LV) ejection fraction is important in clinical decision-making, a more reliable assessment of LV ejection fraction is required. Radionuclide angiography was regarded for a long time as the gold standard for determining LV ejection fraction, but it meant an invasive study and exposure to radiation. Magnetic resonance imaging (MRI)-based volumetry has been developed as a good alternative with acceptable inter- and intra-observer variability. It is, however, not readily available. Multislice computed tomography (CT) has become another alternative technique providing very high-resolution images of the beating heart within a very short acquisition time. It can be used for coronary artery imaging as well as for the quantification of cardiac volumes, especially LV volumes. The disadvantage of cardiac CT is that it involves exposure to radiation, which is an important drawback, especially for children. Moreover, volumetry using CT still needs further validation.

Differences in volumetric measurements between CT and MRI were noted, and RT3D echocardiography produces significantly different LV volumes compared with MRI and CT [10,11]. The differences between 3D echo and MRI might be explained by the different techniques used for quantification – disk-summation versus a rotational approach – but even if the same approaches are used, a systematic difference remains. This could be related to differences in border detection, but it certainly requires further study.

### Real-time 3D echocardiography for LV functional analysis

In the few years since RT3D echo became commercially available, it has been used clinically for the assessment of LV function because of the relative ease of acquisition of volumetric data as well as the proven superiority of 3D echo for volumetric quantification [12–19]. Both in terms of correlation with MRI-derived volumes and in terms of intra- and inter-observer variation, RT3D echo is superior to M-mode or 2D echo for assessing LV volumes and function. With a transducer in a position comparable to that of an apical 4-chamber view, a full-volume 3D data pyramid must be acquired, with a volume of approximately 90° × 90°. This will normally comprise the entire left ventricle, except in case of dilated left ventricles. The newer transducers have a smaller footprint, thus fitting better in the intercostal space, and have wider angles – now up to 110° × 110° – to image larger ventricles.

Left ventricular volumes can be calculated online on the echo machine, or offline using the software installed on a workstation or personal computer. Different analysis software packages are available, which vary slightly in the way the analysis is performed. The first step is imaging the heart in two of the three orthogonal planes – the sagittal (apical 2-chamber) and the coronal (apical 4-chamber) – in order to find the true maximum longitudinal diameter of the LV, avoiding a foreshortened view of the LV cavity [20]. A short-axis view of the LV, perpendicular to the two long-axis planes, often at the level of the papillary muscles, can be viewed to check that no substantial area of the left ventricle is missed and that oblique imaging planes are avoided. When the true long axis is found, the volumetric analysis can be continued. The most commonly used analysis algorithm is a centroid-based rotational algorithm. This produces multiple (or actually an infinite number of) long-axis views. Theoretically, the more cross-sections that are analyzed, the less dependent the technique will be on assumptions about shape and contours and the more reliable it will be. However, the advantage of continuous endocardial border detection versus analysis of eight evenly spaced cross-sections will probably be very small [21].

A few anatomic landmarks must be indicated, such as basal septum, and lateral and anterior wall at the level of the mitral valve and apex in the coronal and sagittal views (Figs 41.4 and 41.5). A semiautomated algorithm developed for detection of the blood–endocardium difference will allow instantaneous calculations of the cavity contours, that is, LV volume. These automated systems seem to be the most logical choice for the follow-up of individual patients with structurally normal hearts.

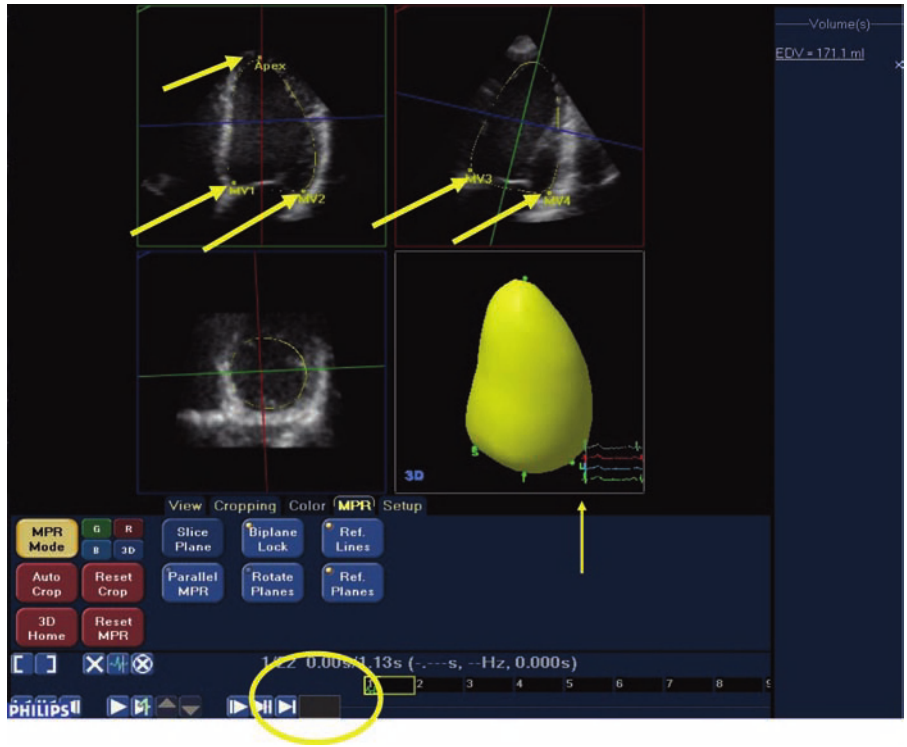


**Figure 41.4** Left ventricular analysis: end-diastolic tracing and calculation of end-diastolic volume (EDV). MV, mitral valve.

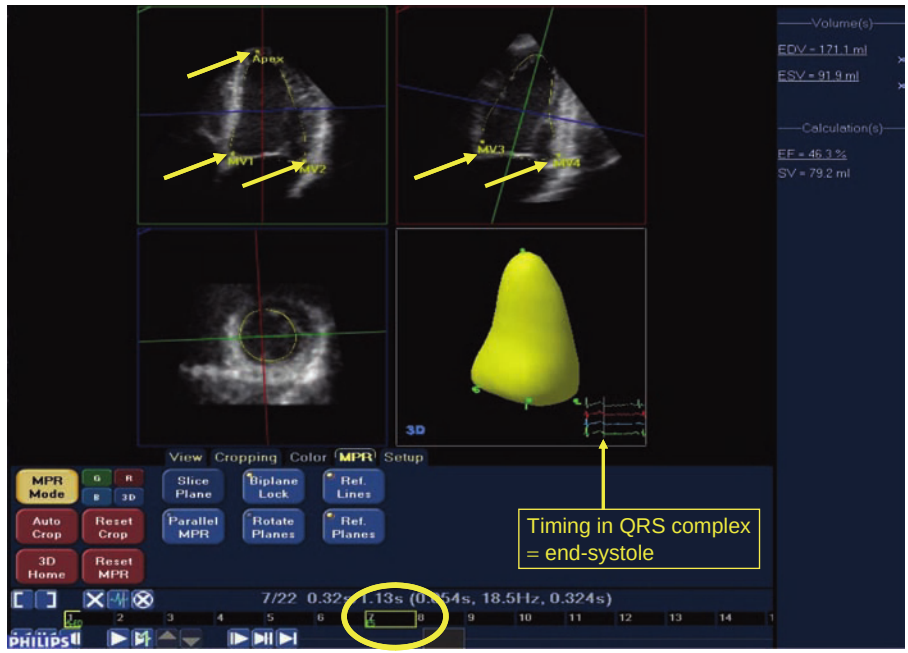


**Figure 41.5** Left ventricular analysis: end-systolic tracing and calculation of end-systolic volume (ESV). EF, ejection fraction; MV, mitral valve; SV, stroke volume.

In congenital heart disease, with often abnormally shaped left ventricles due to intrinsically abnormal geometry or as a result of deformity on the right side of the heart, fully automated border detection seems to be less reliable than fully manual border detection or the automatic mode with the use of manual override [22]. The most likely explanation for the inexact function and unreliable results of the fully automated mode in these hearts is the markedly different shape of the ventricles in such hearts compared with the (hundreds of) left ventricles on which the algorithms are based. This also implies that these systems need to be used with caution in patients with abnormal anatomy; more manual border tracking throughout the cardiac cycle is required.

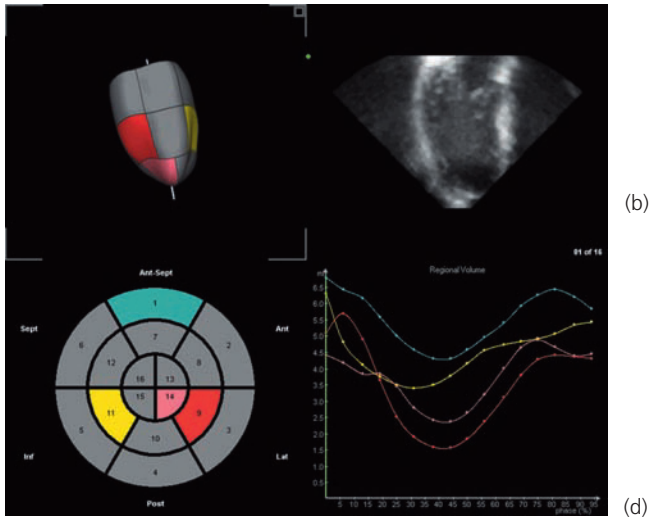


**Figure 41.6** Regional volume curves. **(a)** shows the location of the different segments in the model of the left ventricle **(b)** shows a grey-scale 2-D cut through the left ventricle **(c)** shows the highlighted segments which are compared for regional volume analysis. Turquoise is the basal anterior septum, yellow is the mid inferior wall segment, red is the mid lateral wall segment and pink is the apical lateral segment. **(d)** shows the regional volume curves in the four regional segments. The mid inferior segment (yellow) is hypocontractile and out of phase of the three other segments. Ant, anterior; Inf, inferior; Lat, lateral; Post, posterior; Sept, septal.

## Real-time 3D echocardiography and stress echocardiography

The capability to show two or three orthogonal planes simultaneously can shorten the acquisition time that is needed for stress echocardiography [23]. The major advantage of RT3D echo over 2D stress is that the 2-chamber and 4-chamber views can be recorded simultaneously, and data from the different walls can be obtained during the same cardiac cycle without having to move the probe. This allows a more accurate evaluation of regional functional changes throughout the test.

## Real-time 3D echocardiography and cardiac resynchronization therapy

Not only can general LV volumes be generated, but by dividing the LV into 17 or 16 segments, regional LV volumes can also be assessed. The volume of each segment relative to the LV center-line can be calculated. Changes in regional volumes can be visualized graphically and differences in timing of volume changes between different segments can be evaluated using a volume–time curve (Fig. 41.6). In a normally functioning heart, all segments reach their minimum volume (= maximum contraction) approximately at the same time. When there is ventricular dyssynchrony, differences in time intervals to reach the regional minimum volumes between the different segments can be recorded. This can be visualized in an intuitive way and has proven to be a helpful tool in guiding cardiac resynchronization therapy (CRT) (Fig. 41.7). The dyssynchrony index seems to give a good indication of

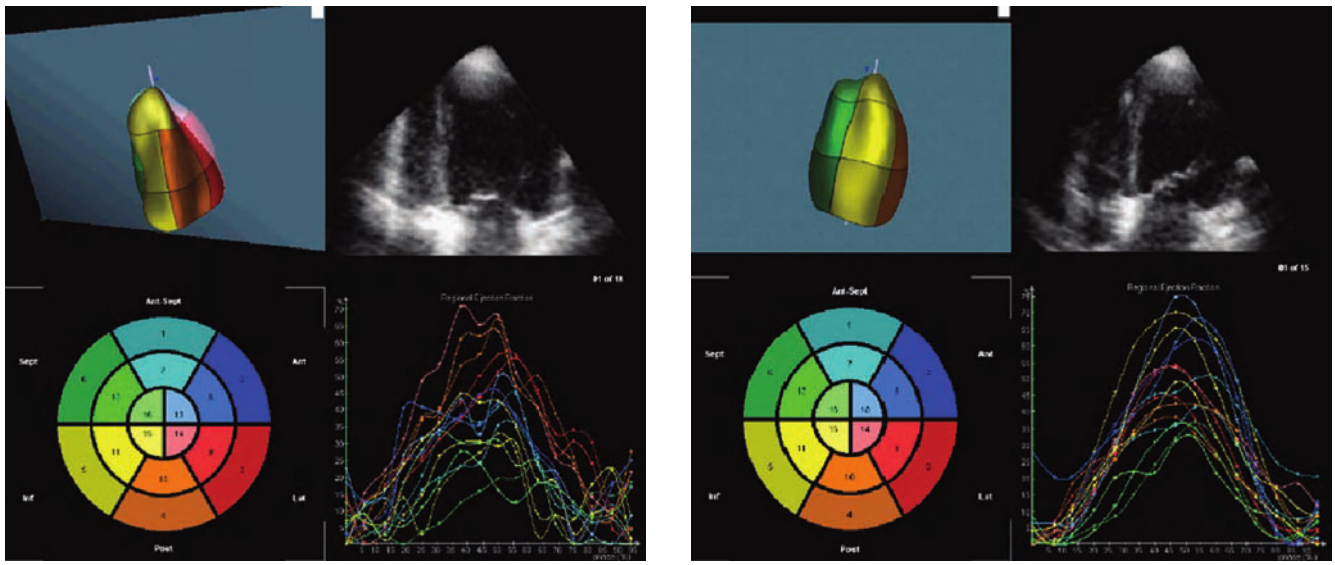


(a) Patient with a LBBB

(b) Same patient after CRT

**Figure 41.7** Three-dimensional volumes and cardiac resynchronization therapy (CRT). **(a)** Regional volume analysis as it appears on the screen of the echo machine or during off-line analysis. Regional volumes are color coded and shown in a left ventricle (LV) cast in frame 1 and as a bull's eye presentation in frame 3. Frame 2 shows the moving images of the LV. Frame 4 shows the percentage of volume change of each segment versus a horizontal time axis. The differences of timing of maximal contraction of each segment are clearly visible. **(b)** The same patient after CRT: frame 4 shows that the regional volumes contract much more in phase than before CRT. Ant, anterior; Inf, inferior; Lat, lateral; LBBB, left bundle branch block; Post, posterior; Sept, septal.

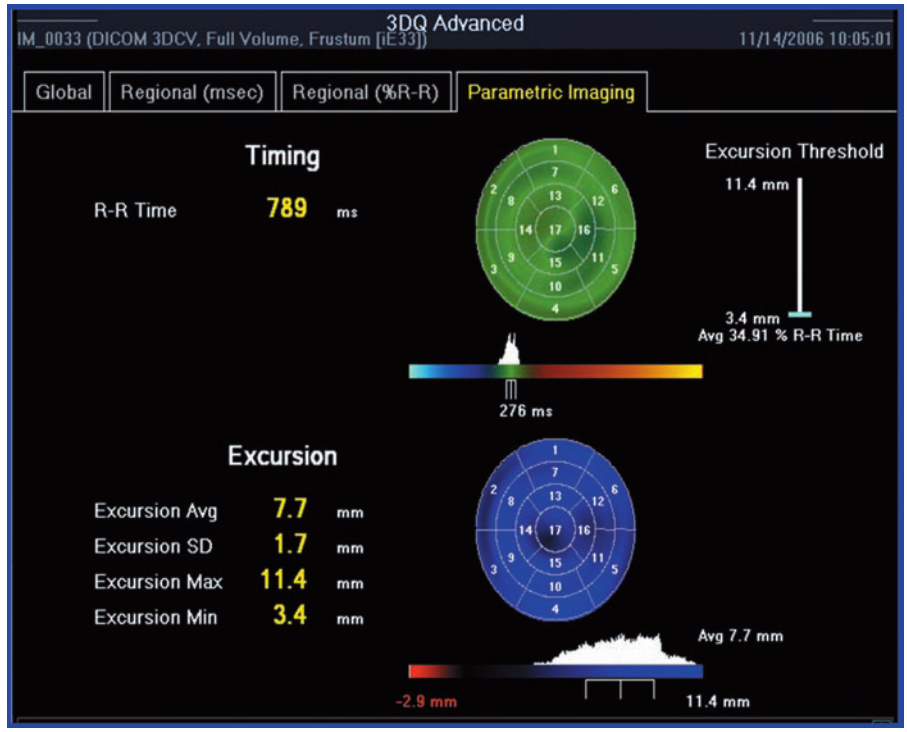


**Figure 41.8** With parametric imaging, both the degree of excursion and timing of regional volumes can be visualized. In the upper part of the figure the time axis is color coded; in the lower part the differences in color represent different degrees of excursion.

whether or not a patient will improve after CRT [24–28]. Parametric imaging is another way to look at regional wall motion abnormalities. Using this method the left ventricle is divided into more than 100 segments. Either the timing or the extent of segmental volume changes can be represented in color. This offers an intuitive representation of dyssynchrony or regional wall motion abnormalities (Figs 41.8–41.11).

## Quantification of left ventricular mass

Left ventricular mass can be calculated using 3D echocardiography. As during acquisition of RT3D echo data for LV volumes and function, the transducer position is that of the apical 4-chamber view. During the analysis care must be taken to correct for foreshortening, which is an important potential source of error in LV mass assessment [13,20,29–31].

In contrast to the large number of reported studies on the feasibility and reliability of determining LV volumes, there are only a few studies correlating RT3D echo and MRI LV mass calculations [32,33]. Compared with 2D measurements, 3D mass calculations correlate better with MRI-derived LV mass, with lower inter- and intra-observer variability (Fig. 41.12). Although the mean differences between MRI and RT3D echo-derived values of LV mass are within acceptable limits, the standard deviation (SD) of the measurements is substantial in the different published studies. This means that the confidence limits of LV mass measurements are wide, much wider compared with LV volume measurements. This is understandable, as a small error in, for example, endocardial border identification, will have relatively

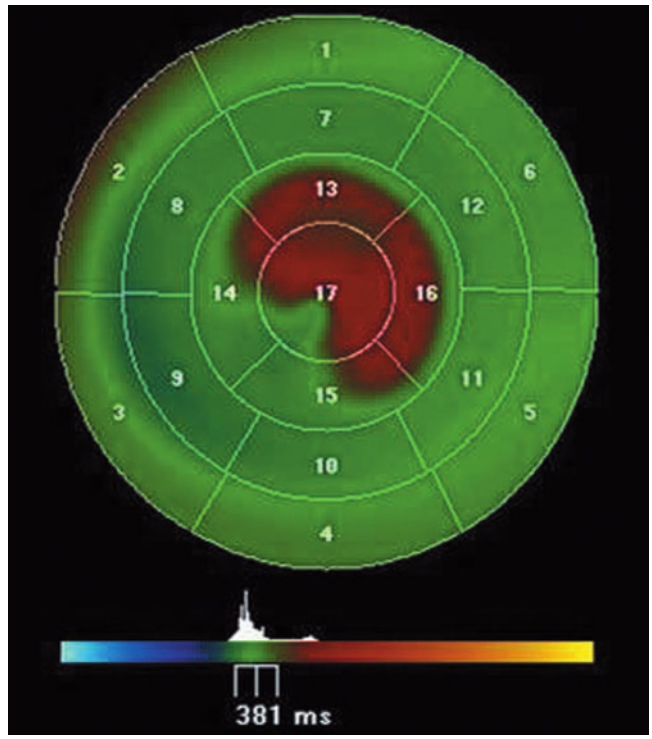


**Figure 41.9** Regional left ventricular volumes and the timing of their maximum-to-minimum volume changes. Regions of delayed contraction can be visualized so that they can be understood by non-experts in echo or electrophysiologic studies. The red coded areas are areas of late contraction, out of phase with the other myocardial segments.

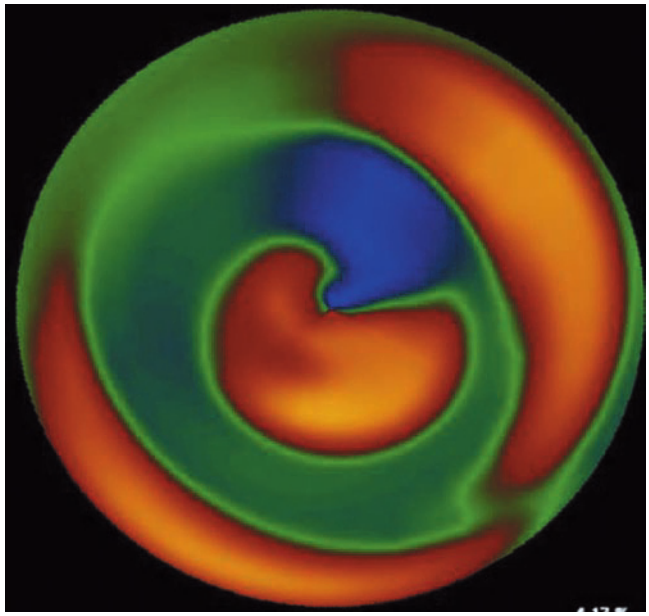

**Figure 41.10** Different timing of activation of the left ventricle can be color-coded and represented as color pictures like this one. This is where esthetics, ultrasound imaging and electrophysiology meet. Blue represents early activation, green normal activation and red are segments activated late.

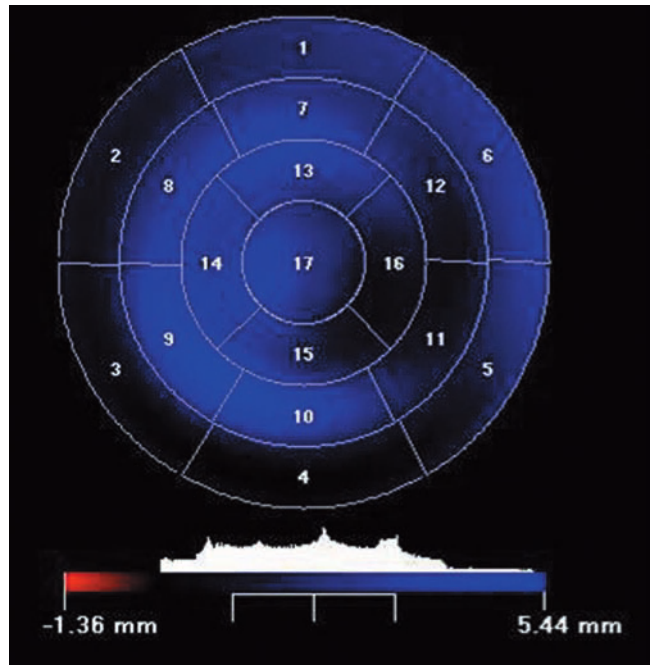


**Figure 41.11** This bull's eye representation of regional left ventricular volumes, in this case divided into 17 segments, depicts the excursion (in millimeters) of individual segments, represented by a color code. Decreased excursions of one or several segments might indicate ischemia.

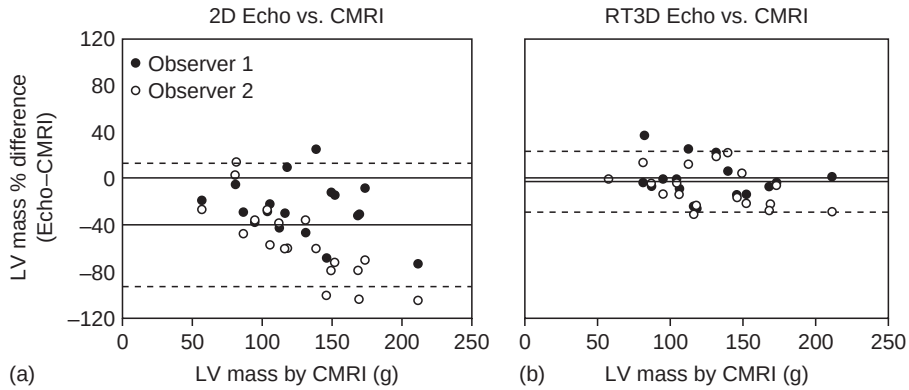


**Figure 41.12** Left ventricular (LV) mass: comparison of interobserver variability between **(a)** 2D echo versus cardiac magnetic resonance imaging (CMRI) and **(b)** real-time 3D (RT3D) echo versus MRI. Because the inter-observer difference with RT3D echo is less, it is a better, more robust way to assess LV mass than 2D echo.

more impact when measuring a "smaller" structure like the myocardial wall compared with the much greater LV volume. In our experience, when the image quality of the RT3D echo is less than optimal, both reproducibility and degree of agreement with MRI-derived values become unacceptably low. This means that the applicability of this technique for use in clinical practice remains to be established.

## Quantitative assessment of right ventricular size and function

The right ventricle (RV) is difficult to assess with conventional 2D echocardiography because of its complex shape and geometry. A lot of mental reconstruction is needed to get an image of the complex anatomy of the RV based on different 2D echo views. Also 2D quantification of RV function is difficult and clinically rarely used. Probably the best correlation of 2D echo images with MRI results is best achieved by visual appraisal of the images by an experienced echocardiographer. 3D imaging of the anatomy of the entire RV and quantitative functional assessment would be very useful clinically. Some authors have reported that transthoracic evaluation of RV function with 3D echo is feasible, not only in experimental studies [34] but also in humans [35,36]. There is now a commercially available dedicated software package developed specifically for quantitative RV analysis (Fig. 41.13). The initial results are promising, but its applicability in clinical practice remains to be established (Fig. 41.14). However, its potential use for congenital heart disease will be important.

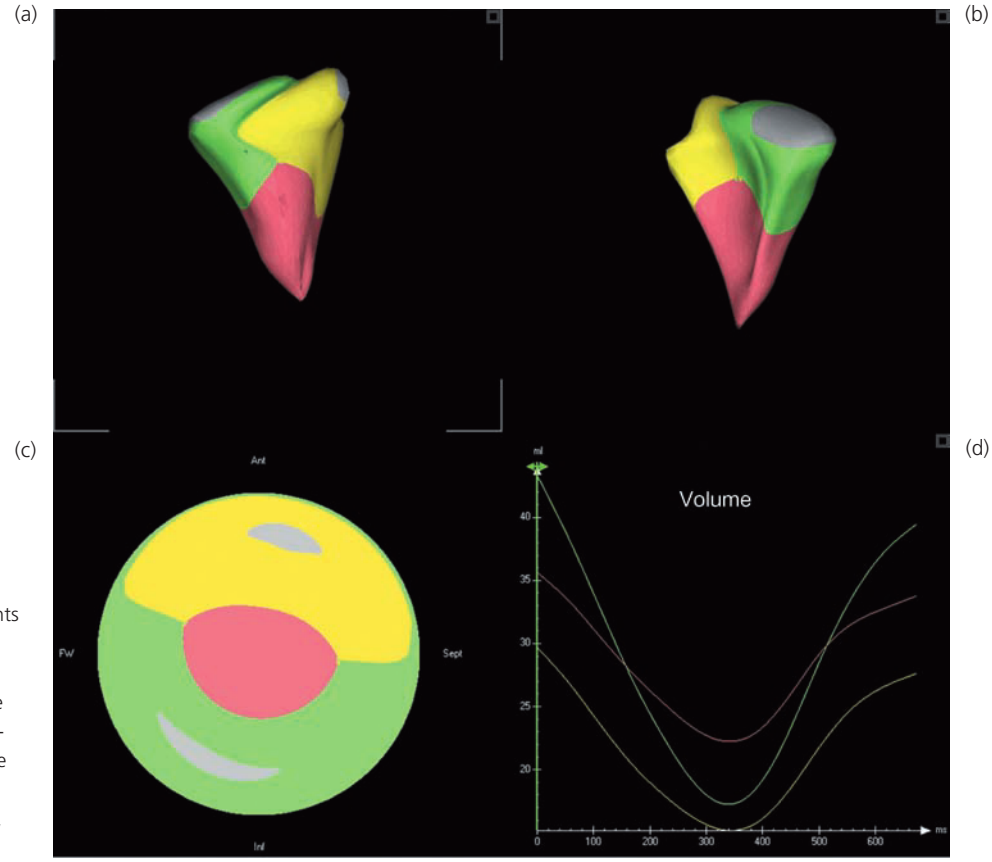


**Figure 41.13** Right ventricular (RV) segments can be presented as segments with different colors, as 3D pictures **(a,b)** or as a bull's eye presentation **(c)**. In **(d)** the changes in volume during the cardiac cycle of the different color-coded segments are represented. For the time being this technique remains a research tool. Ant, anterior; Fw, free wall; Inf, inferior; Sept, septal.

### Quantification of atrial volumes

There are a few reports on the feasibility of assessing left atrial volumes with RT3D echo, correlating the measurements with 2D echocardiography or MRI. Also, right atrial volumes can be assessed using 3D echocardiography. Further work is necessary before RT3D echo can play a clinical role in quantification of atrial volumes [37–41].

## Valve morphology and function

### Mitral valve

The mitral valve (MV) is the cardiac structure that has been most extensively studied using 3D echocardiography [42]. Because of its nonplanar, saddle-shaped form, it serves as the ideal example of the advantages of 3D visualization. The entire structure, including annulus, leaflets and subvalvar apparatus, can now be imaged in one view. From the apex, the MV annulus can be visualized together with the posterior and anterior leaflets. RT3D echo measurements of the MV annulus correlate better with MRI measurements than 2D measurements [43,44]. The narrow sector of the real-time 3D mode is mostly wide enough to visualize the entire annulus and movement of the leaflets, but the papillary muscles are not always within the data pyramid. An alternative strategy is full-volume acquisition from either the apex or the parasternal long axis. In their closed position, both leaflets are largely perpendicular to the ultrasound beam from the apex and can be visualized very well in the "en face" view. The closure line can be seen and the segments of the mitral valve, according to the Carpentier classification, can be visualized in a single view. By rotating the dataset through 180°, the MV can also be seen "en face" from the left atrial side. This view simulates the surgical view during MV repair. In combination with color Doppler, the mitral regurgitation (MR) jet can be visualized and the regurgitant orifice can be traced [45,46]. Using 3D color for assessment of mitral regurgitant flow, Yosefy et al. [47] found that the proximal flow convergence region (PFCR), or proximal isovelocity surface area (PISA), was not hemispheric but biconcave. This implies that the PISA utilized in 2D is an unreliable tool for quantitative assessment of severity of mitral regurgitation [48]. Direct measurement of the orifice area of the MR with RT3D Doppler echocardiography is a promising alternative method for assessing the severity of MR.

In MV stenosis, the "en face" view obtained from a dataset acquired from the apex is also very valuable (Fig. 41.15) [49]. The size and shape of the orifice can be seen from the atrial or the ventricular side. Planimetry of the orifice can be performed as its exact localization and orientation can be determined (Fig. 41.16) [50–52]. Some studies report a good

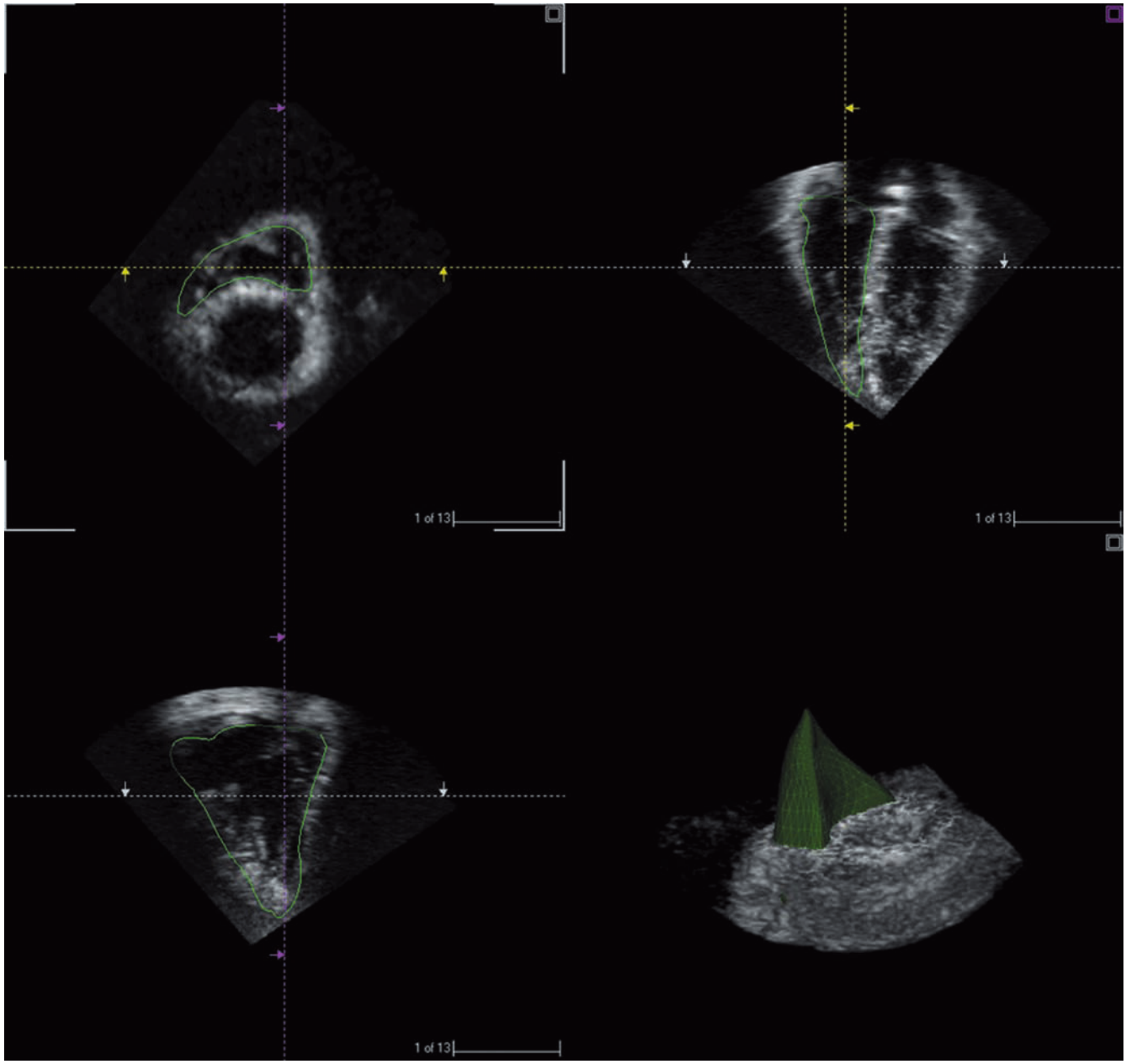


**Figure 41.14** Example of RV 3-D volume assessment. Contouring is performed in three different perpendicular planes through the RV cavity and based on this semi-automatic contouring, the right ventricular volume is calculated and represented in a three-dimensional model of the right ventricle. Based on this RV end-diastolic and end-systolic volumes and ejection fraction are calculated.

correlation of 3D planimetry with invasive studies and orifices calculated on the basis of echo Doppler-derived flow velocities and pressure half-time.

If the movement of the MV leaflets during the cardiac cycle is studied from a dataset acquired from the apex, it can happen that (especially) the anterior leaflet is poorly visible during diastole. The explanation is that during diastole – in opened position – this thin, delicate structure is parallel to the ultrasound beam. With the transducer in the position of a parasternal view, or of a foreshortened 4-chamber view, the anterior leaflet is often better visualized. Although the posterior leaflet is less visible from this position, this view is rewarding when imaging a cleft in the anterior mitral valve leaflet [53]. In congenital heart disease, in case of an atrioventricular septal defect, the septal commissure, between the anterior and posterior bridging leaflet, can be imaged very well using this view.

## Aortic valve

In an adult heart, assessment of the aortic valve from apical views is often difficult, due to the poor resolution in the far field of a 3D dataset. In the pediatric population, the same

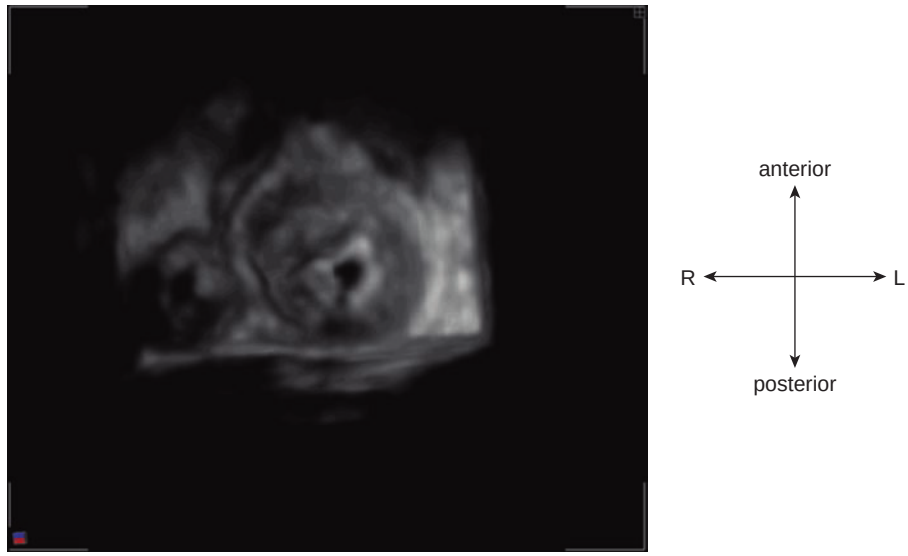


**Figure 41.15** En face view of mitral valve and tricuspid valve, both stenosed. Planimetry of the effective orifice is possible and probably reliable. The problem is validation of these measurements, because there is no gold standard.

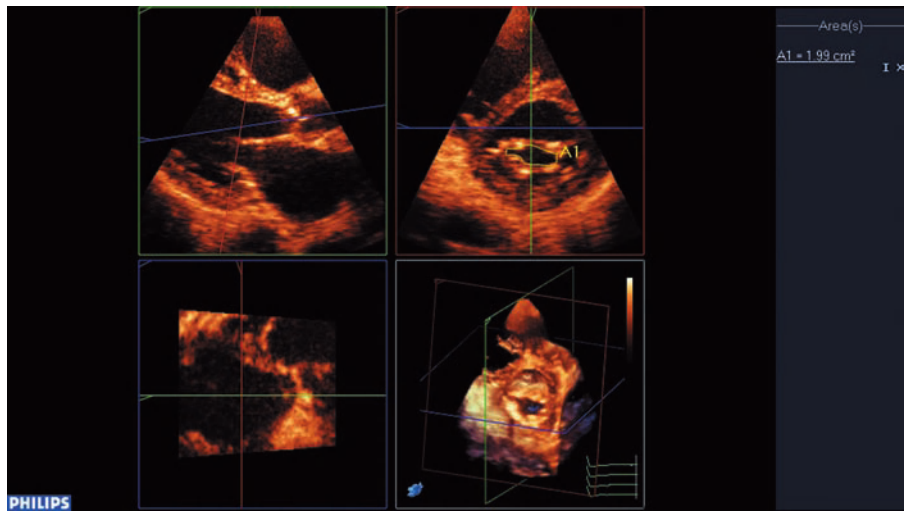


**Figure 41.16** Tile presentation. In the 3D dataset, the focus is on the mitral valve. In frame 1, a 2D parasternal long-axis view is shown. In this plane, the red line represents the level and orientation of the cross-section that is represented in frame 3 by the red plane. By visualizing the exact level at which planimetry is done, the orifice is probably measured more reliably than with 2D echo alone. Frame 2 represents a coronal plane corresponding to the blue line in the other frames. Frame 4 represents the 3-D volume set.

problem occurs as the high-frequency transducers have a better resolution but lower penetration. In the parasternal long-axis view the leaflets have a course parallel to the ultrasound beam when the valve is closed and so cannot be seen. Closure lines are visible, but the cusps often appear as black holes, and it is not possible to discriminate between a real perforation and dropout (Fig. 41.17). Color Doppler can be used to rule out severe aortic regurgitation, but because the blood flow is also perpendicular to the ultrasound beam, this is not very reliable either. In systole, the leaflets are more visible, allowing better assessment of valve anatomy. In our experience, a view obtained from the high right parasternal window is a better approach for viewing the aortic valve (Fig. 41.18).

Planimetry for aortic stenosis is often done on the basis of 2D echo images, but the results are not very reliable [54,55]. 3D planimetry is believed to give more reliable results than 2D planimetry because the smallest opening, its shape (round or slitlike) and precise orientation (anterior–posterior orientation or medial–lateral orientation) can be better assessed (Fig. 41.19). It is surprising how irregular the shapes of the narrowed orifices often are [56]. Some investigators report a good correlation between planimetry and operative anatomy [57] as well as with values for the aortic valve orifice calculated using the continuity equation [58]. Doddamani et al. [59] recently reported that the left ventricular outflow tract (LVOT) is often oval instead of circular. This has important consequences for the reliability of the continuity equation. When the LVOT is not circular, the surface of the LVOT calculated with $\pi r^2$ (with $r = {}^1/_2$ cross-section of the LVOT, measured with 2D or M-mode) does not represent the surface of the LVOT. Theoretically, tracing the LVOT area in a 3D echo dataset would provide a more reliable value for this area

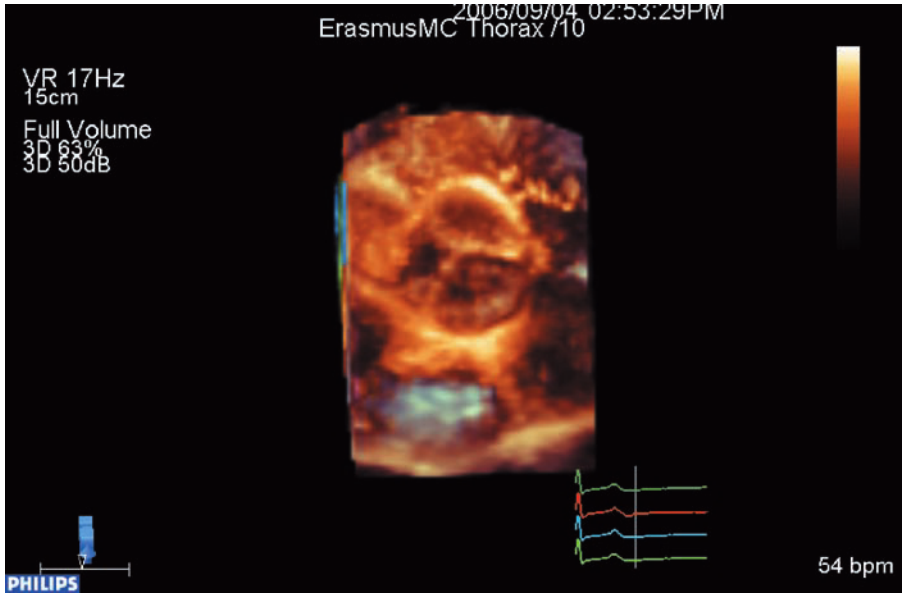


**Figure 41.17** Sometimes it can be difficult to distinguish between artefacts or artificial dropouts or real perforations within a valve leaflet. In this picture dropouts can be noted in the right and left coronary leaflets but it is unclear whether there represent artefacts or perforations. Adding color Doppler to the picture can help to differentiate.

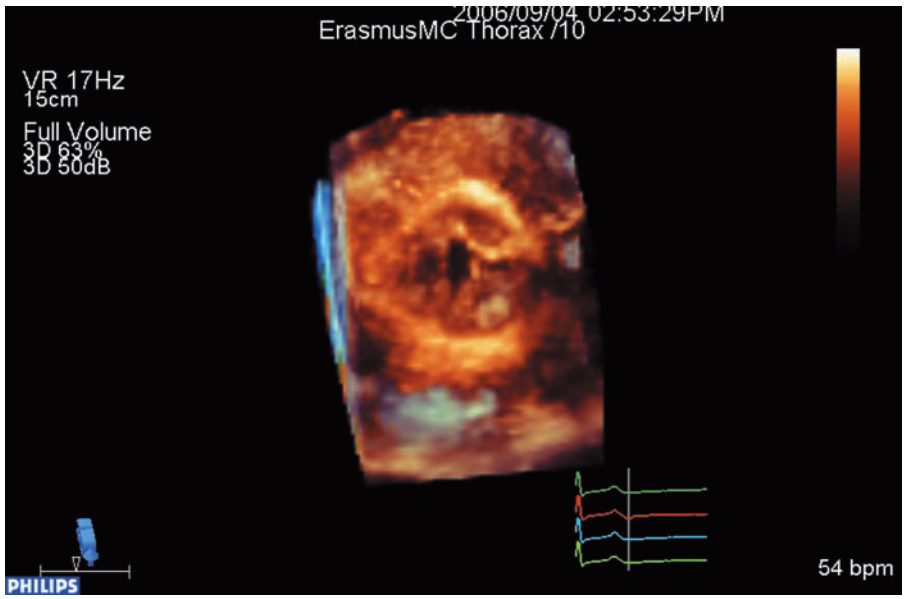


**Figure 41.18** En face view looking from the aorta onto the end-systolic frame of a bicuspid aortic valve with raphe. Dataset acquired from the third intercostal space, right.

compared with a calculated area, but this needs further validation.

In case of aortic regurgitation, the combination of RT3D echo and color Doppler can be helpful for the quantification of the regurgitant orifice [60,61]. As the regurgitant orifice can differ substantially in shape, it is not surprising that 2D color Doppler techniques for the assessment of severity of aortic regurgitation, like measurement of the vena contracta, are not very reliable.

## Tricuspid valve

There are three possible ways to acquire images of the tricuspid valve (TV) with RT3D: the apical 4-chamber position; the rightward-tilted parasternal long-axis position; and the subcostal views. In all these views, the right ventricular inflow, the TV and the right atrium can be seen. All three acquisitions enable visualization of the three leaflets [62]. The oval shape of the tricuspid annulus can be assessed (Fig. 41.20). With 2D echo it can be difficult to assess all three leaflets. From the apical 4-chamber view the two leaflets that are seen are invariably the septal and the anterior-superior leaflet. In the parasternal long-axis view it is always the anterior-superior leaflet at the free wall side, but on the septal side it is sometimes the septal leaflet, sometimes the mural leaflet (Fig. 41.21) [63]. RT3D echo allows identification of all three leaflets (Fig. 41.22), including their

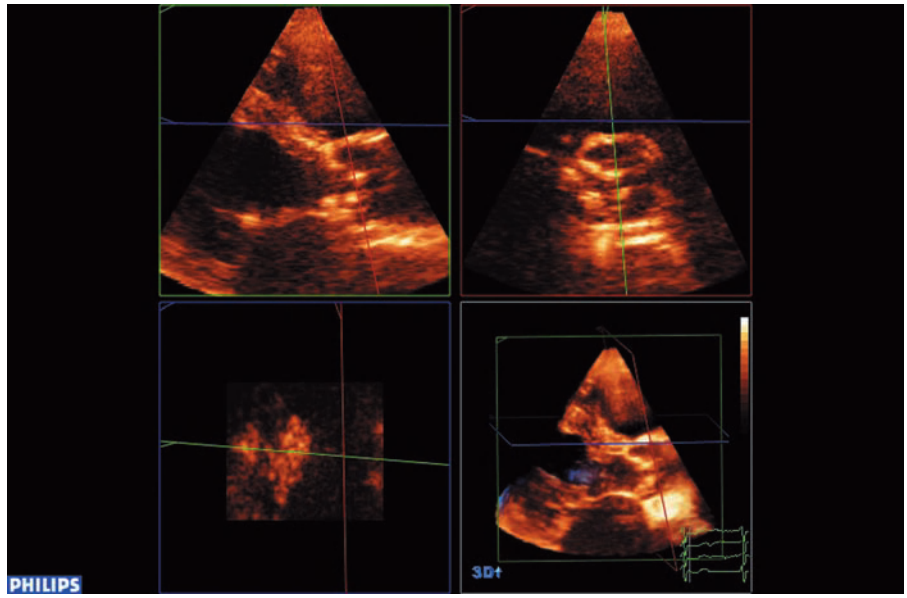


**Figure 41.19** Tile presentation with three cutting planes adjusted to the aortic valve. Using the longitudinal plane, the short axis view of the aortic valve can be optimised so the the planimetry in short axis can be performed at the level where the orifice be optimally visualised. Frames 1 is thus sed to optimise frame 2, frame 3 is in a perpendicular plane that is not really useful for this purpose.

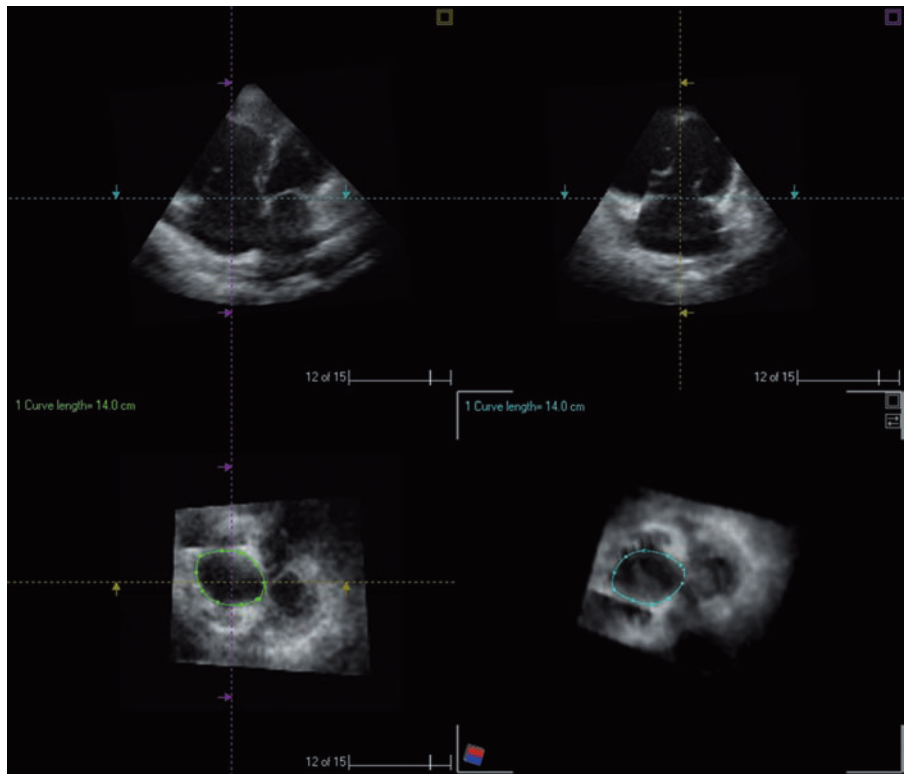


**Figure 41.20** Planimetry of the tricuspid annulus in a patient with transposition of the great arteries after a Mustard operation. "Tile" presentation of three orthogonal planes and a 3D sagittal view (bottom right frame). Dataset acquired from a foreshortened 4-chamber view. Frame 1 is the apical four-chamber, frame 2 the apical two-chamber and frame 3 the short axis view of the tricuspid valve. Planimetry is performed on the short axis view and the result is represented in frame 4.

motion throughout the cardiac cycle. In combination with color Doppler the regurgitant orifice can be measured. Tethering of a leaflet, for example, attachment to a pacemaker wire or to a central venous line, can be viewed and the identity of the affected leaflet can be ascertained. An "en face" view of the TV will allow planimetry for measurement of the orifice (Fig. 41.23). Assessment of TV annulus size is important in clinical decision-making before TV surgery is considered in case of isolated tricuspid regurgitation or associated with MV regurgitation. Nonstandardized measurements done using TTE or TEE often do not represent the true maximum diameter of the annulus [63]. RT3D echo has the potential to improve diagnostic accuracy in this respect.

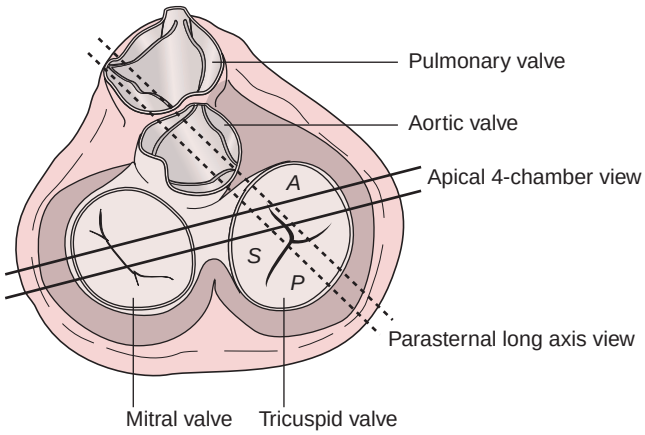


**Figure 41.21** Schematic drawing of a cross-section of the heart at the level of the mitral valve (MV) and tricuspid valve (TV) annulus. The common 2D scanning planes from the apical 4-chamber view are found between the two solid lines: the leaflets from the TV that are cross-sectioned are invariably the septal and the anterior-superior leaflets. Between the dotted lines is shown the range of the cross-sections from the parasternal long-axis view. It is evident that sometimes antero-superior and postero-inferior leaflets are cross-sectioned, and sometimes septal and postero-inferior leaflets. A, anterior; P, posterior; S, septal.

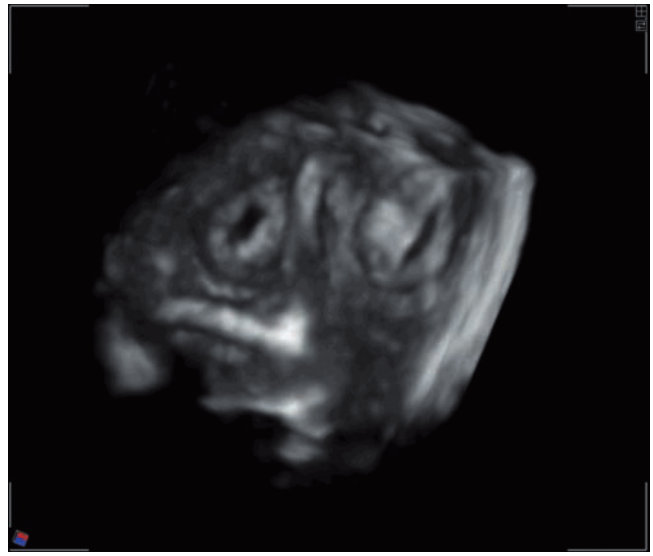

**Figure 41.23** Rheumatic heart disease. En face view from the apex showing thickened leaflets from the mitral and tricuspid valves.

For congenital heart disease, the visualization of the TV in relation to the MV and LVOT is often important, not only in complex congenital cardiac malformations, but also, for example, in case of a ventricular septal defect.

## Pulmonary valve

In our experience this is the most difficult valve for 3D visualization [44]. The very thin leaflets, together with their position in the near field, often result in suboptimal RT3D assessment of the pulmonary valve (PV). In children this can be resolved by subcostal imaging. In adults, a 3D dataset acquired from a parasternal view with the transducer positioned a little more inferior and lateral from the standard parasternal view can give better results. In children, with a dataset acquired from the subcostal view, the PV can be centered in the ultrasound pyramid. In diastole, in closed

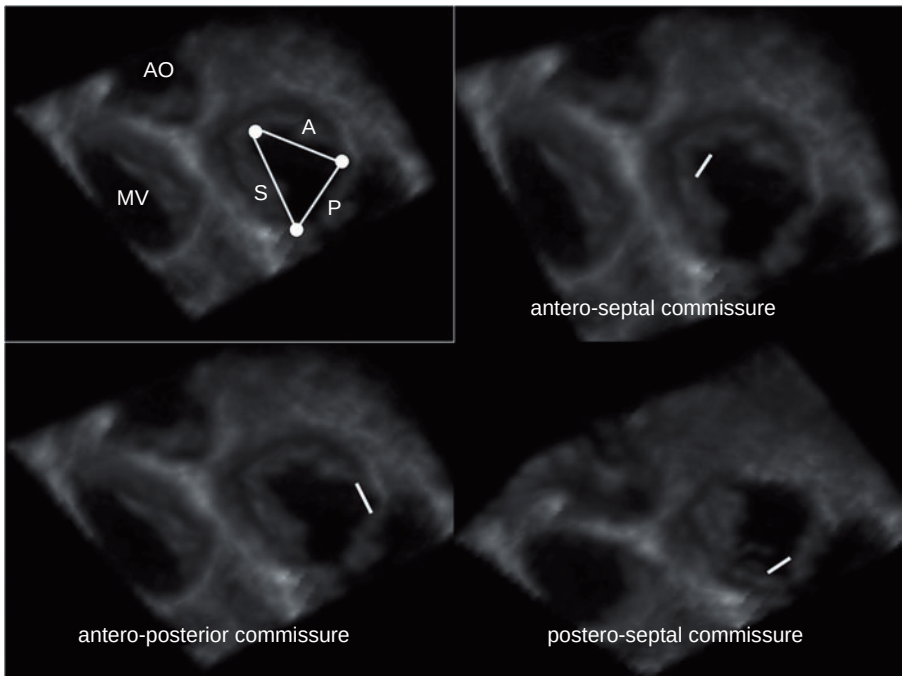


**Figure 41.22** View from the right atrium down toward a normal tricuspid valve. The leaflets are visible in **(a)**, and the commissures are indicated in **(b–d)** by a white bar. AO, aorta; MV, mitral valve; A, anterior; P, posterior; S, septal.

position, the surface of the leaflets are perpendicular to the ultrasound beam and these can be visualized. As a rule, only the closing line and the pulmonary annulus can be assessed.

### Normal values

For RT3D echo to become an integral part of clinical echocardiography, normal values of all intracardiac structures, for both genders and for all age groups – or corrected for height/length/body surface area – will be needed. Very few such values are available thus far [64,65], and it is obvious that more are needed.

## Congenital heart disease

In experienced hands, a 2D echo examination of a patient with congenital heart disease is almost always diagnostic. Ever since the introduction of 3D echo, the image resolution has been good enough for analysis of LV volumes and function. However, in its earlier stages of development, 3D echo spatial resolution was not good enough for analysis of structural heart disease. The "en face" view of valves and the theoretical possibility of visualizing spatial relationships in complex congenital heart disease were recognized as promising, but as a rule the image quality was insufficient for actual diagnosis. Only after improvement of the image resolution, realized when RT3D echo platforms became commercially available and especially after the introduction of the pediatric high-frequency probe, did interest in the application of this technique to clinical practice in congenital heart disease grow substantially. Its exact role in the diagnosis and treatment of pediatric and congenital heart disease still remains to be established.

Here we illustrate some examples of 3D echo images of different congenital cardiac malformations, with remarks on the acquisition and potential use for diagnostic purposes.

### Atrial septal defect (ASD)

The size of ASDs and their exact position has become more important since transcatheter closure of ASDs was introduced [66–68]. Not all defects are suitable for transcatheter closure; they should not be too large relative to septal size, the rims should be sufficient to provide "anchoring" of the device, and the defects should not be too close to important intracardiac structures (mitral and tricuspid valves or orifices of systemic/pulmonary veins). In children, transthoracic 2D echocardiography is often diagnostic. The intraatrial septum can be visualized from several transducer positions (especially subcostal views). The ASD, with its rims and distances to important intracardiac structures, can be measured. The optimal 3D dataset is acquired from the subcostal position, which is almost always feasible in infants and children, but rarely in adults. For these patients, a foreshortened 4-chamber position or a parasternal long-axis view angulated to the right, with the ASD between the dotted lines and no further than 15 cm from the transducer, is next best. The advantage that RT3D echo has for analysis of an ASD is the possibility to create an "en face" view that looks at the interatrial septum [69]. The entire interatrial septum can be seen, with the defect within it (Fig. 41.24). It can be viewed and measured, both from the left and right atrial sides, and the rims around the defect can be seen in one view. From the right-sided view, distances to important anatomic landmarks, such as the tricuspid valve, the ostium of the coronary sinus and the ostia of the caval veins, can be measured (Fig. 41.25). Mathewson et al. proposed a standardized

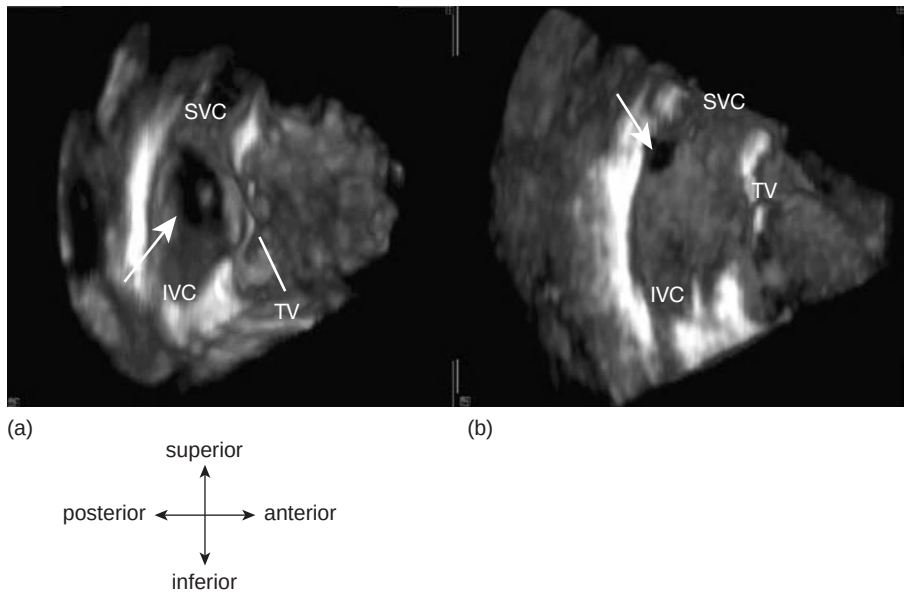


**Figure 41.24** Right lateral view, looking on the right side of the interventricular and interatrial septum. The en face view allows assessment of size and localization of atrial septal defects (ASDs) (arrows). **(a)** A large secundum ASD is seen with good rims surrounding the defect. **(b)** A small secundum ASD is seen high in the interatrial septum, without a posterior rim. IVC, inferior vena cava; SVC, superior vena cava; TV, tricuspid valve.

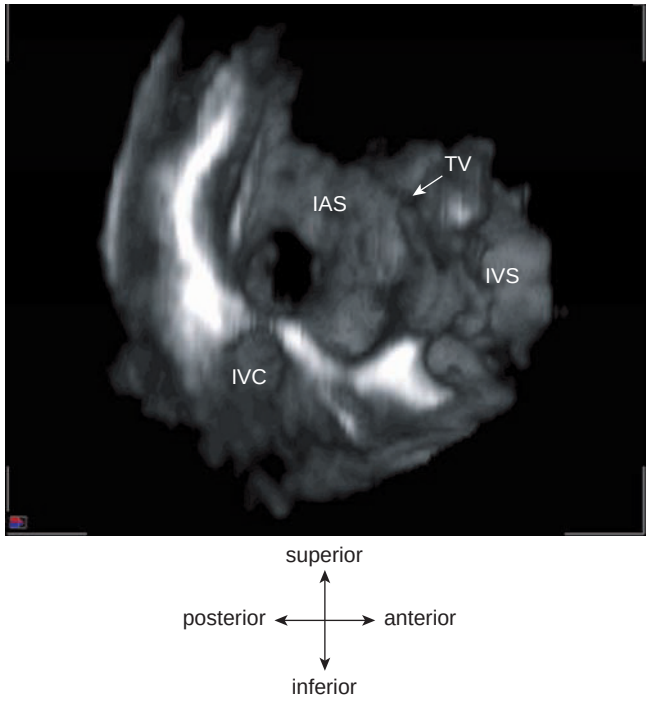


**Figure 41.25** Right lateral view of the heart, providing an en face view of the interatrial septum. A large postero-inferiorly located secundum atrial septal defect is seen. With only narrow inferior and posterior rims, it is unlikely that this defect can be closed with a device. IAS, interatrial septum; IVC, inferior vena cava; IVS, interventricular septum; TV, tricuspid valve.

orientation and nomenclature for the rims (Fig. 41.26). If the dataset is cropped from the left lateral side, the distance to the right pulmonary veins and mitral valve can be assessed. What cannot be imaged in these "en face" views is the extent of the aortic rim, at the antero-superior side of the ASD. It is impossible to discriminate between the aortic rim and the antero-superior part of the roof of the right atrium directly adjacent to the aortic root. This can be done in a transthoracic 3D dataset by scrolling back and forth through the dataset, from right to left, with a plane in the correct angle to visualize this. This plane must be found in the "any plane" module. More elegantly it can be shown in a transverse plane of the heart at the level of the aortic root and the interatrial septum: it actually mimics a TEE cross-section at ±45° rotation, a standard view to assess the aortic rim (Fig. 41.27). A good correlation between RT3D echo and surgical measurements and between RT3D echo and TEE is reported regarding measurements of the rim. In all patients who have sufficient transthoracic echo image quality, a RT3D echo study provides all the answers to the questions about the feasibility of transcatheter closure and a TEE can be omitted. Van den Bosch et al. showed not only that transthoracic RT3D echo could replace TEE in a large proportion of patients with an ASD, but also that the size of an ASD was assessed more reliably with RT3D echo than with transthoracic 2D echo [70]. Most ASDs are not round but have an oval or slitlike shape. This can be (mentally) reconstructed by the integration of multiple 2D

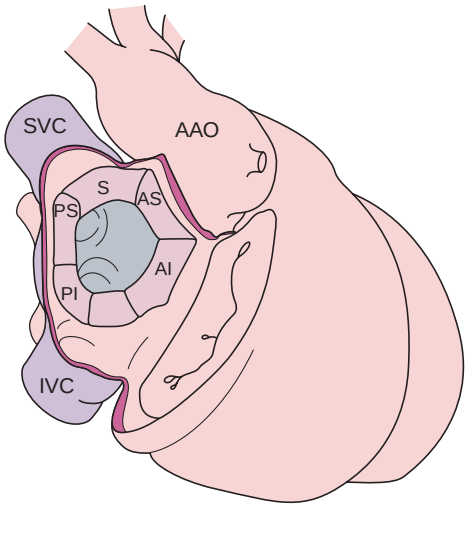


(a)

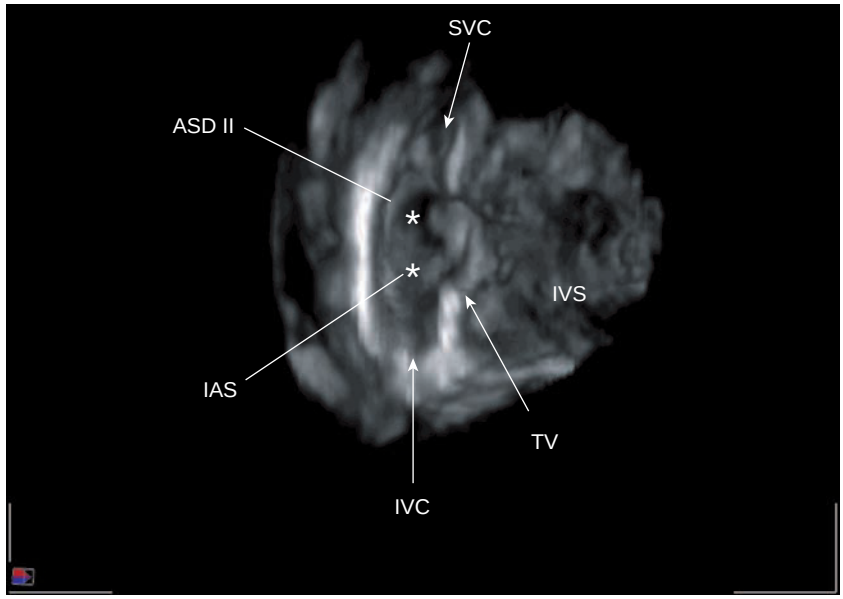


(b)

**Figure 41.26** **(a)** A schematic presentation of the interatrial septum, the atrial septal defect (ASD) and surrounding rims, as proposed by Mathewson et al. AAO, ascending aorta; AI, antero-inferior; AS, antero-superior; IVC, inferior vena cava; PI, postero-inferior; PS, postero-superior; SVC, superior vena cava; S, superior. Mathewson JW, Bichell D, Rothman A, Ing FF. Absent posteroinferior and anterosuperior atrial septal defect rims: Factors affecting nonsurgical closure of large secundum defects using the Amplatzer occluder. J Am Soc Echocardiogr. 2004 Jan;17(1):62–9. **(b)** A right lateral view of the interatrial and interventricular septum. The upper asterisk shows the atrial septal defect. The inferior asterisk shows the inferior-posterior rim. ASD II, atrial septal defect; IAS, interatrial septum; IVC, inferior vena cava; IVS, interventricular septum; SVC, superior vena cava; TV, tricuspid valve.

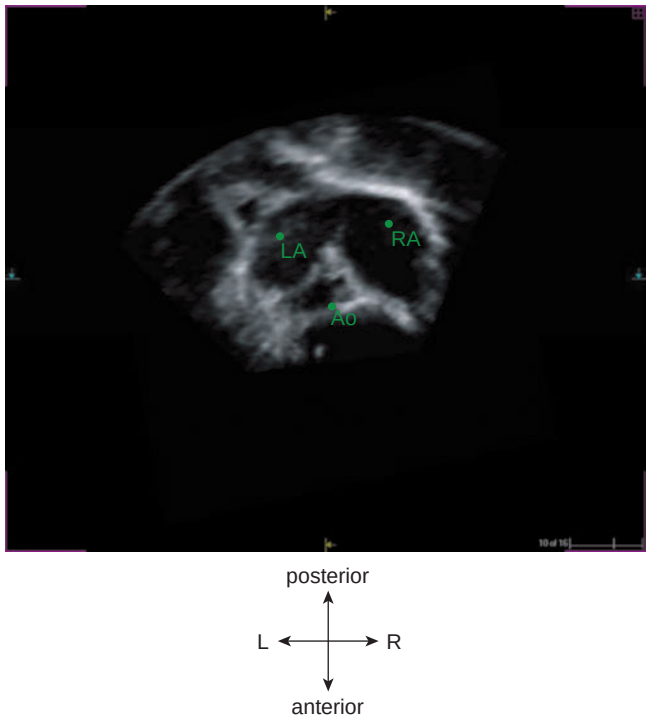


**Figure 41.27** Transesophageal echocardiography (TEE)-like cross-section, derived from a 3D dataset obtained from a foreshortened 4-chamber position, to visualize the aortic rim of a secundum atrial septal defect. Ao, aorta; LA, left atrium; RA, right atrium.

echo views, but it can actually be visualized with RT3D. A good correlation between RT3D and balloon sizing was reported regarding the size of ASD [71]. Something difficult to appreciate with 2D echo is the size change of the ASD during the cardiac cycle, but this is easy to see in the "en face" view using RT3D echo [72–78]. The area of the defect is largest during atrial relaxation, coinciding with ventricular systole, and smallest during atrial contraction. During this period, the area was reported to be 51 ± 15% smaller than during atrial relaxation. This information is important for the interventional cardiologist, who depends on these anatomic details when deciding on transcatheter closure [79].

## Ventricular septal defect (VSD)

The interventricular septum has a complex, spherical shape, which cannot be visualized in a 2D plane. VSDs change in size during the cardiac cycle. Muscular defects can even close entirely during ventricular systole. In perimembranous defects the size change is less striking, which can probably be explained by the fact that such a defect is not entirely surrounded by contracting muscular tissue. It is again the "en face" view of the interventricular septum that brings the benefit, by showing the curved interventricular septum, the VSD within it and the relationship with other intracardiac structures (Fig. 41.28). The spatial relation of the VSD to other parts of the intracardiac anatomy can be assessed – directly, during the data acquisition, or off-line – in one 3D dataset (Fig. 41.29) [80–83].

From the left side, image quality is often better, with sharper contours of the VSD compared with views from the right side. In general, the size and position of the VSD can reliably be assessed also from the right side. Perimembranous VSDs are often partially covered by tricuspid valve leaftlet tissue, blocking the view from the right lateral view to the VSD. This tissue can be "cut away" electronically, thus exposing the entire VSD. This view is valuable because it mimics a surgical view used for VSD closure. Several authors have reported a better correlation between RT3D echo assessments of VSDs

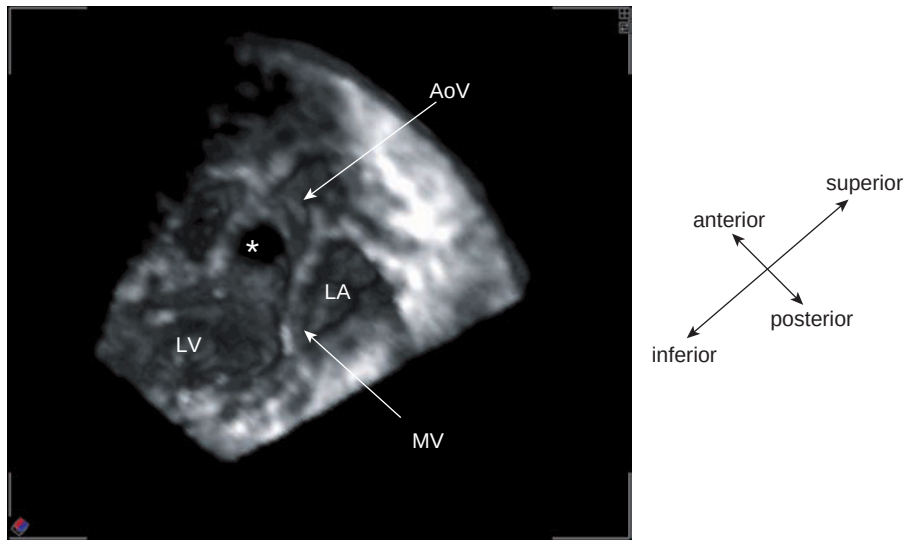


**Figure 41.28** Left lateral view. En face view of the interventricular septum showing a perimembranous ventricular septum defect, denoted by the asterisk (*). AoV, aortic valve; LA, left atrium; LV, left ventricle; MV, mitral valve.

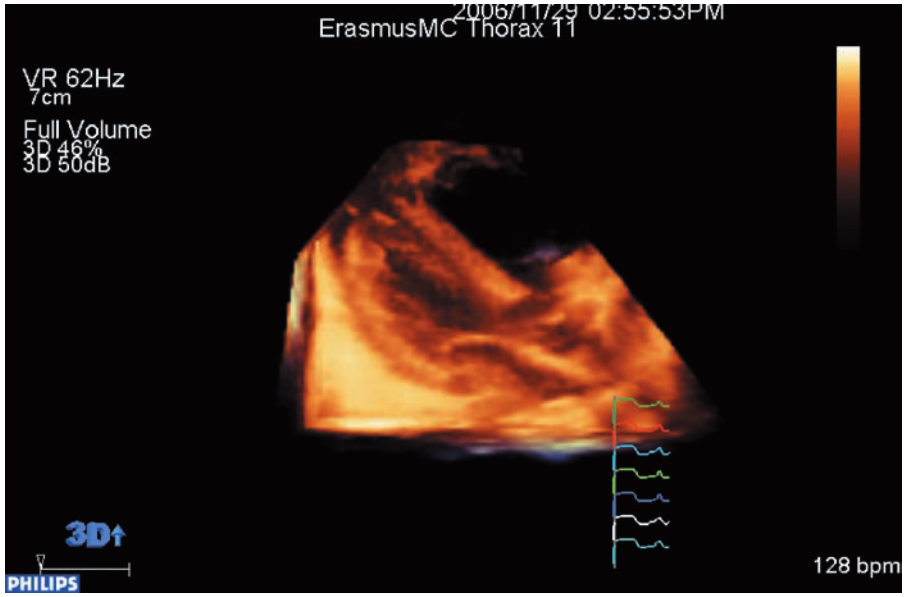


**Figure 41.29** Three-dimensional dataset from a patient with tetralogy of Fallot. This shows the presence of a ventricular septal defect in the outlet part of the septum with overriding of the aorta. The right ventricle is dilated and hypertrophied.

and surgical anatomy compared with 2D imaging [77,84]. This is crucial for the interventional cardiologist considering transcatheter closure of the VSD. Although TEE will guide the cardiologist during the catheter closure, it is a poor substitute for the possibility of direct visualization that the surgeon has [85].

Datasets are acquired from the apical 4-chamber position and from the parasternal long-axis view. In pediatric patients, the subcostal view is very rewarding. If cropped from the left side, the left-lateral view also reveals its relation (or distance) to the mitral and aortic valves. If the same dataset is viewed from the right side, the VSD can be seen in relation to the tricuspid and pulmonary valves.

## Atrioventricular septal defect (AVSD)

Scrolling through the dataset of an AVSD is extremely rewarding. If the effort is made – during the acquisition – to position the region of interest between the dotted lines, it will appear in the middle of the dataset when cropping starts (auto-crop mode). Scrolling from anterior to posterior in a 4-chamber view, the anterior and posterior bridging leaflets can readily be seen, crossing the midline and extending on both left and right sides of the cardiac cavity (Fig. 41.30). These leaflets can be seen in relation with the atrial and ventricular defect. A left lateral view will give images comparable with those of the 2D parasternal long-axis view, but the depth that is added will provide an "en face" view of the interatrial and interventricular septa. By adding depth to an image that has an inferior–superior orientation, the extent of the defect in the posterior–anterior axis is shown also. From all

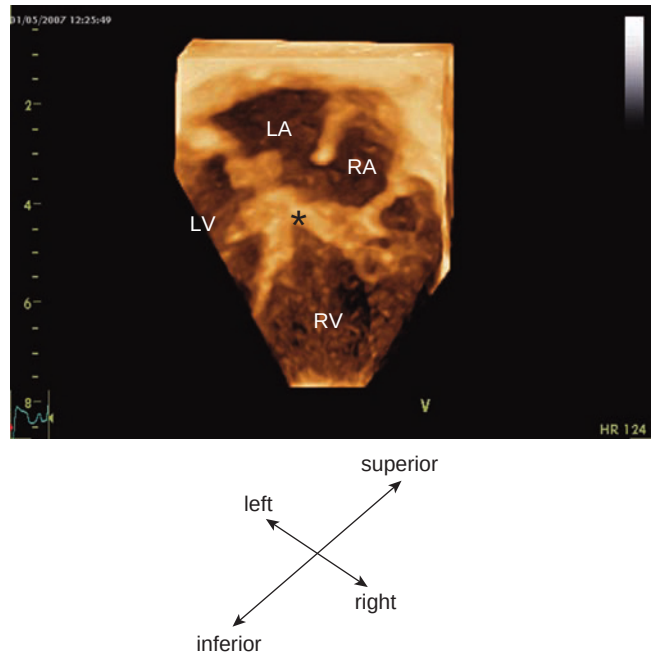


**Figure 41.30** Incomplete atrioventricular septal defect in diastole. The anterior bridging leaflet (denoted by the asterisk) is seen "folded over" the cranial end of the interventricular septum. Left and right mural leaflets are seen as well. The size of the defect at the atrial level, both in the superior-inferior direction and in the anterior-posterior direction, is clearly visible. LA, left atrium; LV, left ventricle; RA, right atrium; RV, right ventricle. Reproduced with courtesy of Dr Jan Marek, Great Ormond Street Hospital for Children, London.

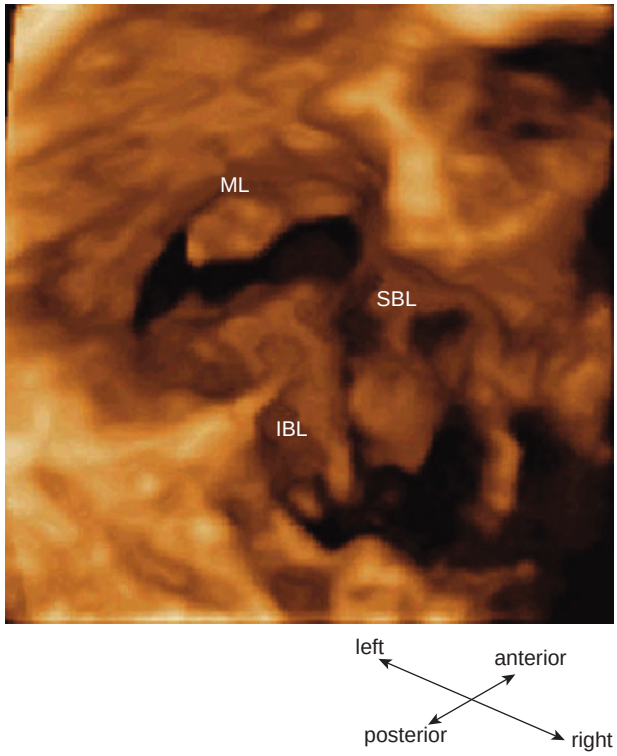


**Figure 41.31** View from the atrial side down toward the common atrioventricular junction of a patient with a complete atrioventricular septal defect. In the single orifice, the superior and inferior bridging leaflets are visible in an en face view, as is the left mural leaflet. IBL, inferior bridging leaflet; ML, mural leaflet; SBL, superior bridging leaflet. Reproduced courtesy of Dr Jan Marek, Great Ormond Street Hospital for Children, London.

the possible views, the "en face" view of the atrioventricular valve is probably the most valuable (Fig. 41.31). This can be done from the posterior, atrial side – the surgical view – and from the ventricular side, often with a better image quality. This "en face" view has contributed a lot to our understanding of the functioning of these abnormal valves [86–92]. The anatomy of the AVSD is described in detail elsewhere (see Chapter 15). The anatomic hallmark of an AVSD is the presence of one common atrioventricular(AV) junction guarded by a common AV valve, most often consisting of five leaflets (Fig. 41.32). A complete AVSD has a single, undivided orifice. In a partial AVSD, both the anterior and posterior bridging leaflets are attached to each other and to the interventricular septum. This results in two orifices. The AV annulus is not a flat, 2D structure,which is why the entire annulus and its leaflets can rarely be depicted in one plane by 2D echo. RT3D echo adds depth to a 2D plane, and the annulus, although it is a curved, saddle-shaped structure, can be visualized this way. The resolution of the 3 and 4 MHz transducers is often not good enough to visualize the individual leaflets properly, whereas the higher-frequency pediatric probes can do so. In a full-volume 3D dataset obtained from an apical 4-chamber position, the entire valve can actually be visualized in the "en face" view.

Assessment of the size of the individual leaflets and their movements, combined with assessment of the localization and degree of regurgitation by means of color Doppler, will allow a better preoperative estimation of the amount of valve tissue that is available for valve reconstruction. This is crucial in assessing the chances of a successful repair versus the likely outcome of valve replacement or other therapeutic strategies. In infants and young children, both the subcostal and the apical 4-chamber views will provide good datasets that include the AV annulus. In adults, only the apical and foreshortened 4-chamber views can be used. The sector of the full-volume dataset is almost always wide enough to include the entire annulus. Epicardial RT3D echo directly after surgical repair, on a beating heart and before closing the sternum, is reported as being very helpful in the immediate post-bypass assessment [93].

In adults, the most common presentation is either an unoperated patient who – most likely – will have a previously undetected incomplete AVSD, or a patient who has undergone surgical repair in the past and now has residual left-sided AV valve regurgitation [94]. In a dataset of an adult patient, unavoidably obtained from an apical or foreshortened 4-chamber position, the atrial "en face" view is often disappointing (when compared with this view in children) because of the limited resolution in the far-field. The "en face" view from the ventricular side is, however, very useful. The cleft (actually the septal commissure between anterior and posterior bridging leaflet) is seen over its entire course from the tip of the leaflets, toward the interventricular septum (Fig. 41.33). With 2D echocardiography, it is sometimes difficult to distinguish left-sided and right-sided AV valves in an AVSD from normal mitral and tricuspid valves. With RT3D this confusion is more unlikely, because the marked difference of these AV valves from the normal anatomy can be readily visualized.

## Ebstein malformation

Echocardiographic analysis of the tricuspid valve (TV) is difficult. In the standard 2D echo views only two leaflets are visible, and it can be difficult to differentiate between the septal and the postero-inferior leaflets [63]. TEE is sometimes very helpful in the evaluation of the TV, but because the TV is positioned anteriorly, away from the transducer located in the esophagus, the results can be disappointing, especially in adults. This is also true in case of Ebstein malformation, the most common congenital malformation of the TV. The anatomy and 2D echo workup of Ebstein's disease (Chapter 13) is discussed extensively elsewhere in this book.

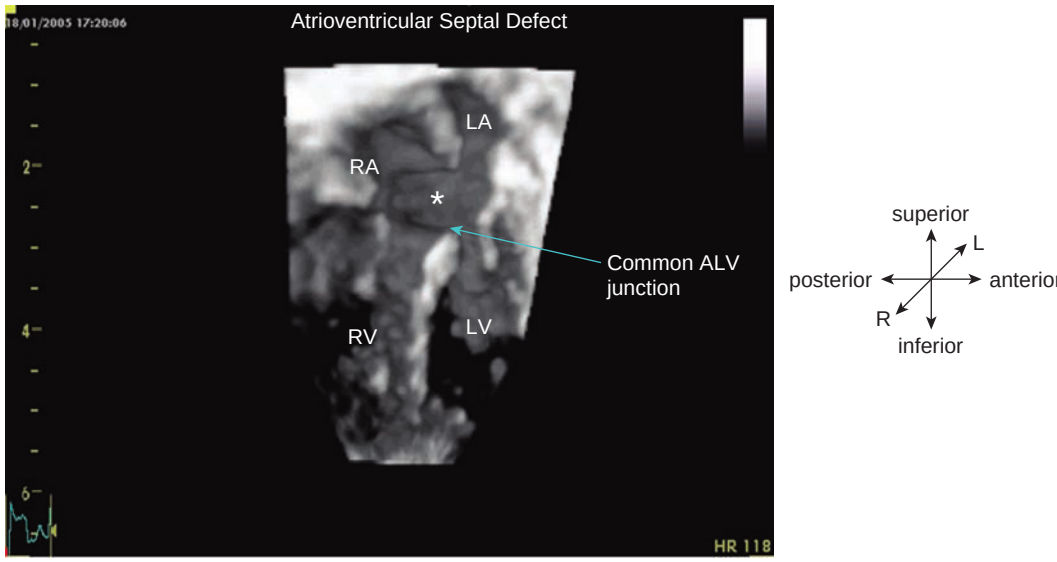


**Figure 41.32** Systolic frame of a patient with an atrioventricular septal defect (AVSD). The anterior part of the heart is cut away and we can see one bridging leaflet extending on both sides of the interventricular septum. The asterisk (*) denotes an atrial septal defect (primum type). LA, left atrium; LV, left ventricle; RA, right atrium; RV, right ventricle. Reproduced courtesy of Dr Jan Marek, Great Ormond Street Hospital for Children, London.

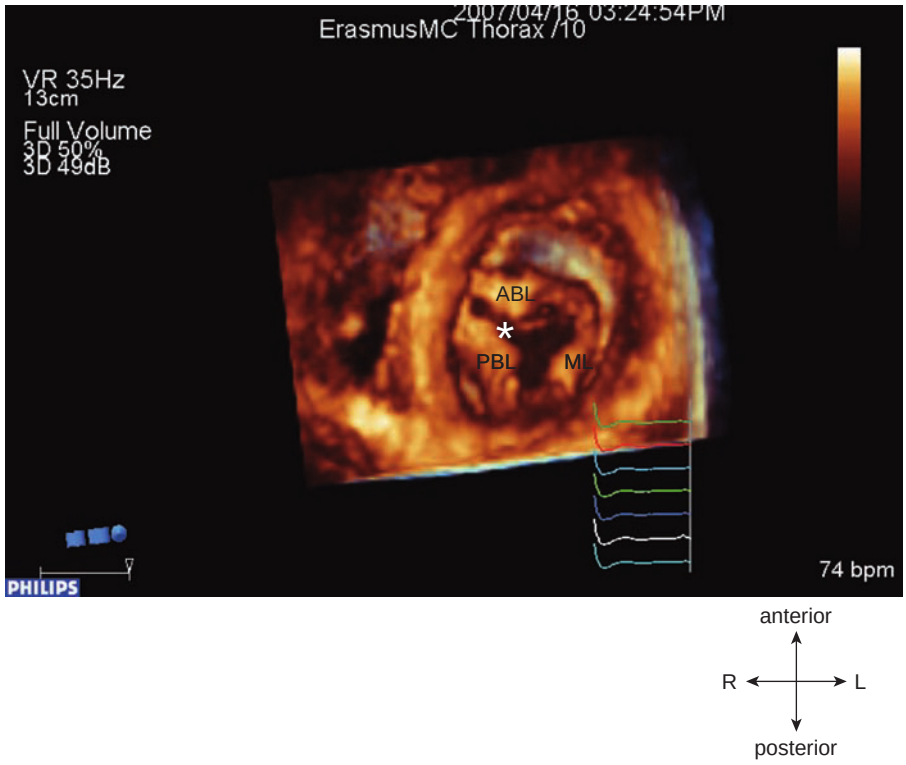


**Figure 41.33** En face view from the apex of the left ventricle toward a left atrioventricular valve in a patient with a partial atrioventricular septal defect (AVSD). The "septal commissure" between the anterior and posterior bridging leaflets is clearly seen (denoted by the asterisk). ABL, anterior bridging leaflet; ML, mural leaflet; PBL, posterior bridging leaflet.

An RT3D dataset acquired from the subcostal view in children or from the apical or foreshortened 4-chamber position in adults will encompass the whole TV. A parasternal long-axis view, with the transducer angulated to the right, toward the right hip, can also provide a good 3D dataset. A right lateral view, by cutting away the right ventricular free wall, will show the tricuspid annulus, the leaflets, their attachment to the septum and to the anterior wall, and the degree of displacement of the functional TV orifice toward the pulmonary valve or the apex (Fig. 41.34).

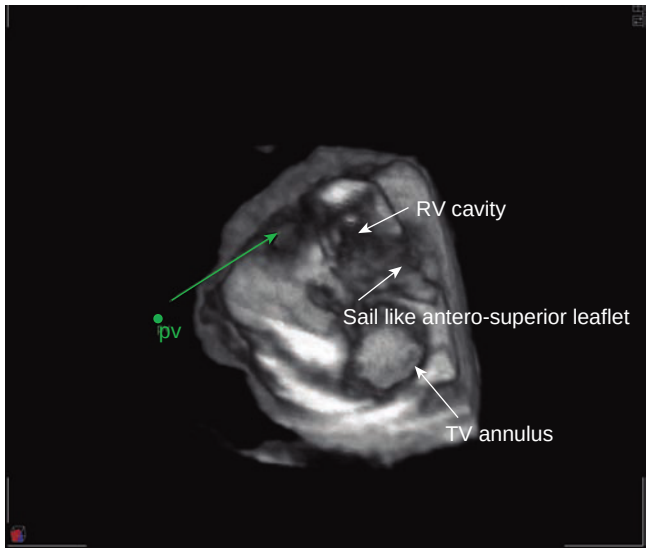


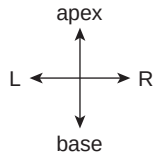


**Figure 41.34** Ebstein's anomaly. View from the apex toward the mitral (MV) and tricuspid valves (TV). The entire TV annulus is sharply defined, without interference of TV leaflets (which are not visible). The view of the MV annulus is "blocked" by the two leaflets of the MV. RV, right ventricle.

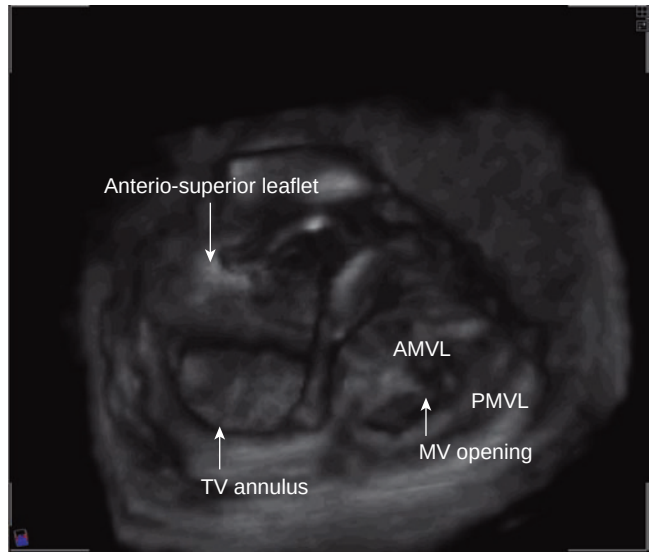


**Figure 41.35** Ebstein anomaly, right lateral view. The right ventricular (RV) free wall is digitally cut away so that one looks into the RV cavity. The entire circumference of the tricuspid valve (TV) annulus is seen. The antero-superior leaflet is big, sail-like and extends toward the right ventricular outflow tract. AMVL. anterior mitral valve leaflets; MV, mitral valve; PMVL, posterior mitral valve leaflets.

In order to assess the size and (often very irregular) shape of the TV orifice, an "en face" view is necessary. It can be a challenge to obtain a good "en face" view because of the wide variety of degree and direction of displacement of the TV opening. It can rarely be visualized adequately in one of the three preprogrammed orthogonal planes, and the anyplane module will almost always be necessary for this.

Once a good "en face" view is obtained, not only can the orifice be seen but also how sail-like the anterior-superior leaflet really is can be appreciated; moreover, the same view shows the right ventricular anterior wall (Fig. 41.35). This allows assessment of perforations of the antero-superior leaflet and degree of tethering (attachment) to the right ventricular free wall. In case of TV stenosis, the "en-face" view can be used for planimetry of the orifice. Both the "en face" view and the right lateral view will provide extra anatomic information on top of the 2D analysis. Combination of RT3D with color Doppler will provide more insight in the mechanism of tricuspid regurgitation.

## Transposition of the great arteries (TGA)

In the anatomic diagnosis of simple transposition of the great arteries, RT3D echo gives no special advantage over and above 2D echo. With 2D echo the anatomy is depicted reliably, and 3D "en face" views generally do not yield much extra information. In the case of complex transposition, 3D visualization of the spatial relation of septal defects to other cardiac structures may be very useful.

In adult congenital heart disease, many patients with simple transposition of the great arteries have undergone either a Mustard or a Senning atrial switch procedure. The right ventricle (RV) sustains the systemic circulation and is subject to systemic ventricular pressures, causing the ventricular septum to bulge to the left (Fig. 41.36). Assessment of LV function by 2D echo is less reliable because the assumptions underlying Simpson's 2D planimetry method are not valid in abnormally shaped LVs. It has been repeatedly reported that RT3D can measure LV function reliably in these abnormal ventricles [22]. Assessment of RV function remains difficult. The systemic RV lies anteriorly in the chest and is, almost always, dilated. From an apical 4-chamber position an attempt can be made to image the entire RV in a 3D dataset, but we have rarely been successful in this. Further improvements in the technique are needed.

Real-time 3D echo is very helpful for imaging atrial baffles, whose anatomy is sometimes difficult to understand. Figure 41.37 is a schematic drawing intended to help understanding of this aspect of the anatomy. Multiplane reconstruction ("quad tiling") is the first very helpful step in the analysis of a transposition after atrial switch. By scrolling

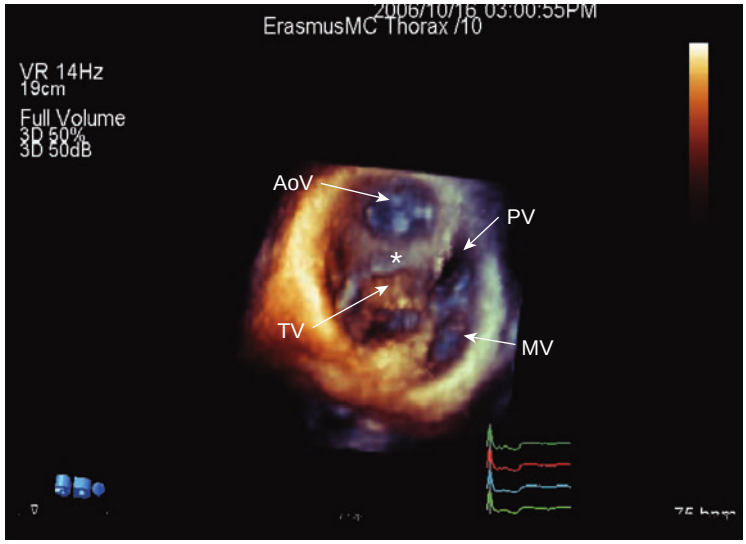


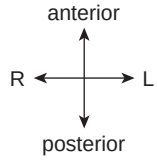


**Figure 41.36** Transposition of the great arteries. Note the muscular band between tricuspid valve and aortic valve. View from the apex toward the atrioventricular and ventriculo-arterial valves. The aorta is anterior and to the right of the pulmonary valve. The asterisk (*) denotes the muscle band separating aortic valve (AoV) and tricuspid valve (TV). The left ventricle is flattened behind and to the left of the highly pressured right ventricle. MV, mitral valve; PV, pulmonary valve.

(a)

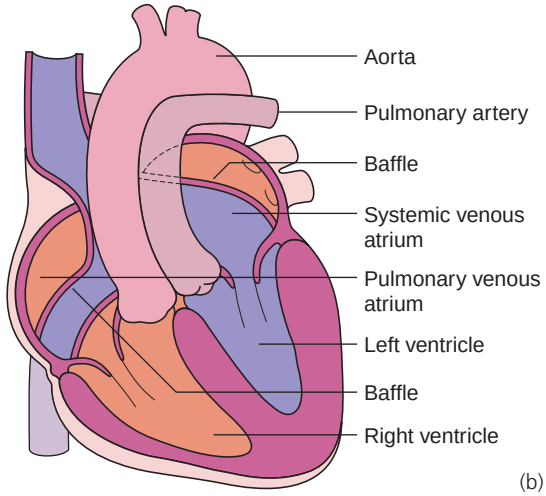


(b)

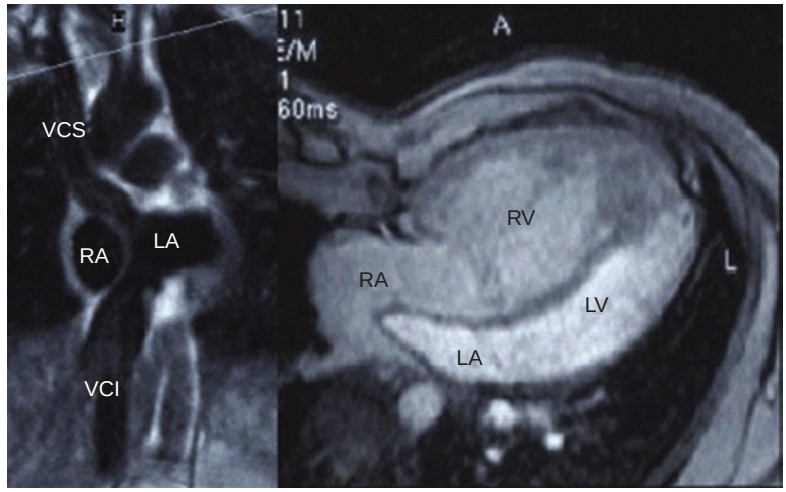


(c)

**Figure 41.37 (a)** Schematic drawing that does justice to both physiology and anatomy. Note that the superior and inferior baffles enter the anterior part of the left atrium (the posterior part is left free for drainage of the pulmonary veins) at an almost acute angle. This is also visible in **(b)**, a magnetic resonance image (MRI) with a coronal view of the heart. Image **(c)** is an axial cross section of the heart showing that the pulmonary veins in the posterior wall of the left atrium drain into the right atrium. The inferior baffle runs beneath this level from left to right; the superior baffle runs above the level of this cutting plane from inferior to superior. LA, left atrium; LV, left ventricle; RA, right atrium; RV, right ventricle; VCI, vena cava inferior; VCS, vena cava superior.

through the oblique coronal plane from posterior to anterior, the inferior baffle is seen first, with its course almost exclusively from right to left (Fig. 41.38a–c). At this level, the pulmonary venous atrium is seen, posterior from this inferior baffle, with the left pulmonary veins draining from the left-lateral side into this compartment (Fig. 41.39). On scrolling more anteriorly, the inferior baffle disappears from this plane and the right pulmonary veins can now be seen entering the pulmonary venous atrium as well as the connection between pulmonary venous atrium and the right atrium, approximately at the level of the former interatrial septum (which has been removed during surgery). Going further anteriorly, the pulmonary venous atrium disappears from view and the superior baffle is visualized, with a predominant superior-to-inferior course. Most of these 2D cross-sections can be acquired during the standard 2D echo workup, and it can therefore be argued that RT3D echo gives no real benefit. However, in our experience, the benefit consists of the possibility to show, off-line, the exact place and orientation of these cross-sections in space in the intracardiac anatomy. Moreover, there is an

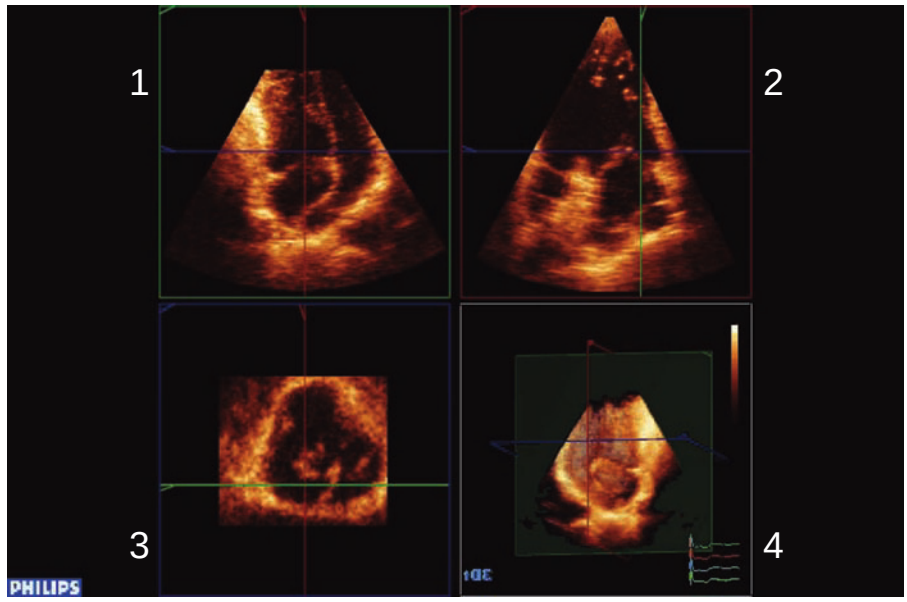


(a)

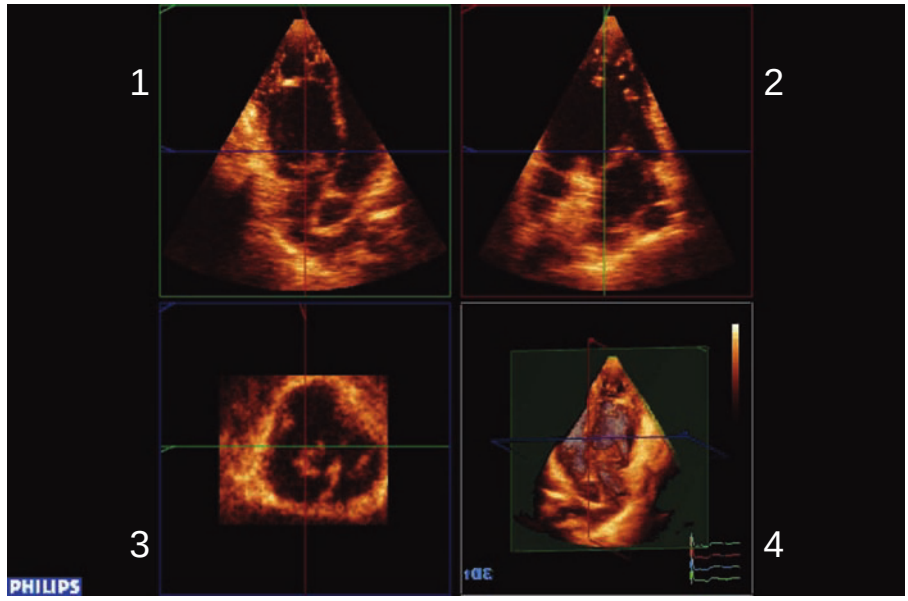


(b)

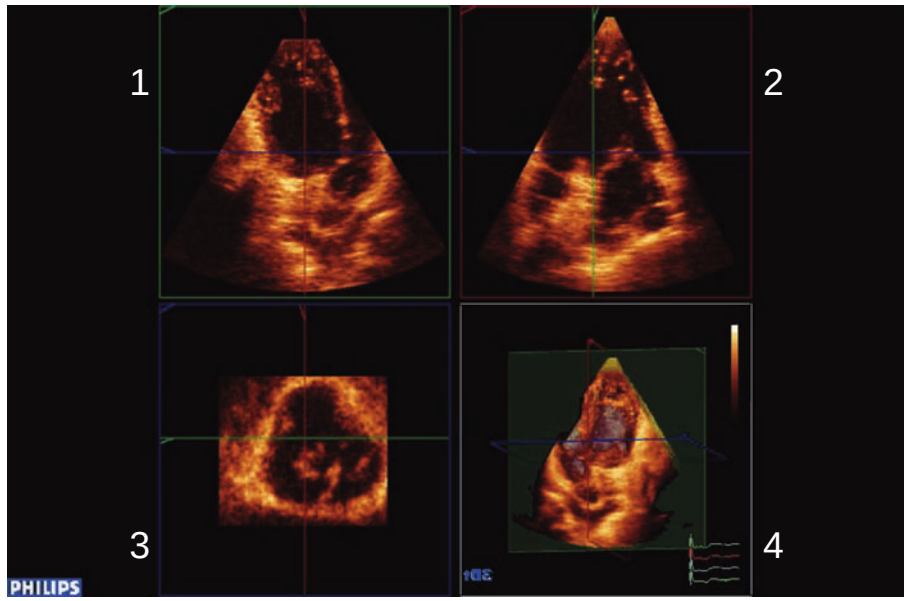


(c)

**Figure 41.38** Three tile presentations each of a 3D image and three orthogonal 2D cross-sections. The images differ in the level of the cross-section through the 3D dataset, indicated in each case by the green plane in tile 4 (bottom right). The representation of the green section is shown in tile 1; the levels of the cross-sections are seen in tiles 2 and 3. The first level of the cross-section **(a)** is quite posterior and the connection with the inferior baffle is shown. Moving a bit more anteriorly. **(b)**, the inferior baffle is out of this plane, but the connection of the pulmonary veins and pulmonary venous atrium to the right atrium can be seen. Moving even further anteriorly. **(c)**, the pulmonary venous atrium disappears and the first part of the superior baffle is visible.

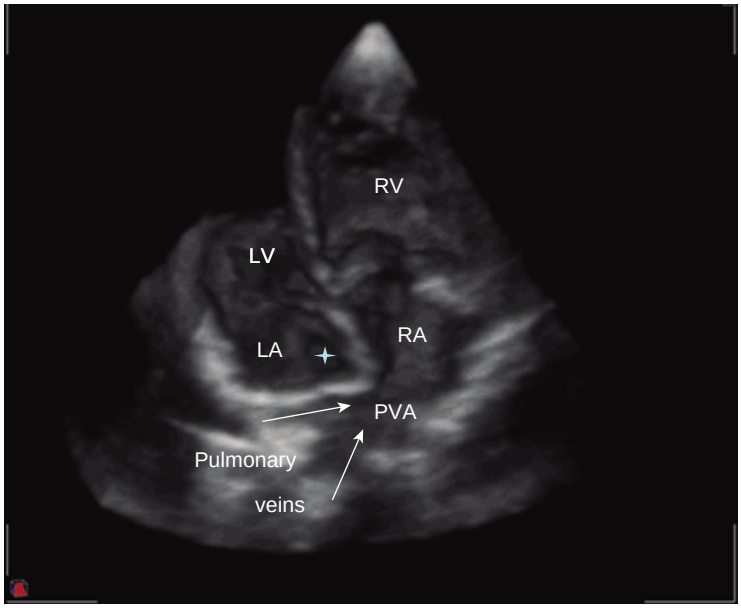


✦ = orifice of inferior baffle

**Figure 41.39** The anterior wall of the heart is cut away to give a view parallel to the interventricular septum in the heart. The "orifice" where the inferior baffle enters into the left atrium can be seen and is indicated with a star. Pulmonary veins from left and right can be seen entering the pulmonary vein atrium (PVA), which is connected without obstruction with the right atrium (RA). LA, left atrium; LV, left ventricle; RV, right ventricle.

excellent "en face" view of both superior and inferior baffles, and their course from the caval veins to their entrance in the remnants of the original left atrium can be followed (Figs 41.40–41.42). If a baffle stenosis is present, the area and length of a narrowed segment in the baffle can be seen. A previously placed stent can also be assessed this way. When embarking for the first time on 3D analysis of patients with TGA after a Mustard- or Senning-type repair, it is helpful to start with a patient who has an endocardial pacemaker. The superior vena cava and the superior baffle are identified easily because they contain a pacemaker wire. A stent can be helpful as well: if a patient has a stent in a superior or inferior baffle, recognition of the anatomic structure that contains the stent makes orientation in the difficult 3D anatomy easier.

Once an investigator becomes more experienced in cropping, he or she will find that the anyplane analysis mode will usually provide the optimal cutting plane through the 3D dataset and that this will rarely be one of the predefined orthogonal planes.

For patients with a complex transposition and a Rastelli-type repair, the intracardiac conduit from the left ventricle

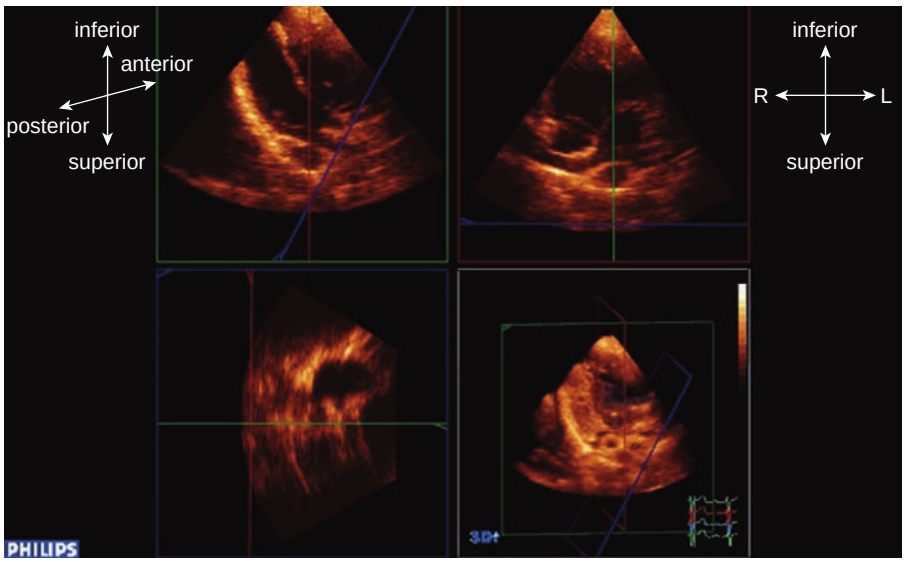


✦ = orifice of inferior baffle

**Figure 41.40** Tile presentation of a 3D dataset with three planes of cross-section. The red and green planes are perpendicular to each other, and the blue plane is modified to produce a good cross-section of the superior baffle. This plane can be moved from inferior to superior providing cross-sections of the superior baffle along its course. The diameter and circumference of the baffle can be measured reliably with planimetry in this way. The entire superior baffle is visualized within the green plane, and the entire inferior baffle is seen in the red plane. This demonstrates that the baffles have a course perpendicular to each other and enter the remains of the left atrium with separate orifices. This patient has a stent in the inferior baffle, making the entrance of the inferior baffle clearly visible.

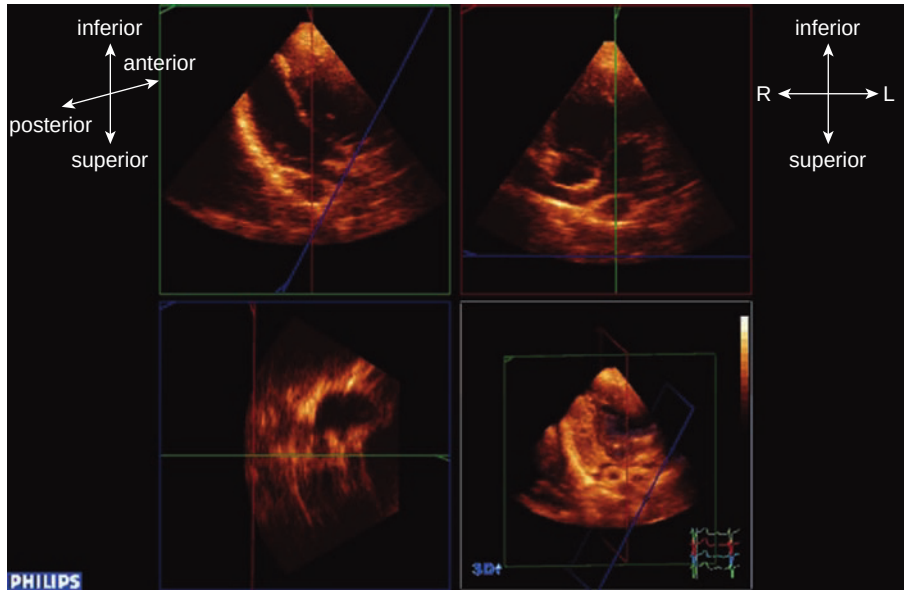


**Figure 41.41** The same patient as in Fig. 41.40. Now the green plane is adjusted in such a way that it gives a cross-section of the inferior baffle. The blue plane still represents the plane perpendicular to the course of the superior baffle.

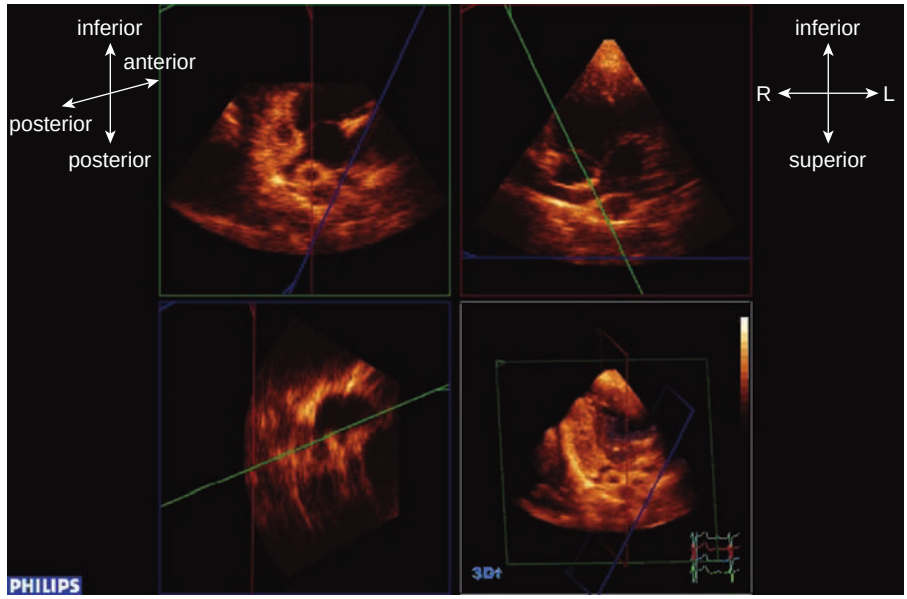


**Figure 41.42** Again the same patient as in the previous figures. The green plane is adjusted to follow the course of the inferior baffle more to the right in the direction of the inferior caval vein. The inferior baffle can be followed this way along its course and planimetry can be done to measure surface and circumference.

toward the anteriorly positioned aortic valve can be visualized and shown in relation to the adjacent structures. It is difficult, just as in 2D echo, to assess the anteriorly positioned conduit from right ventricle to pulmonary artery.

## Tetralogy of Fallot

In infants, a dataset acquired from the subcostal position can contain the entire heart with tetralogy of Fallot. The whole anatomy, with the relation between the VSD, the aortic valve, the interventricular septum and the narrowed right ventricular outflow tract and pulmonary valve, can be shown nicely (Fig. 41.43). If the VSD has an uncommon shape or extension, for example, also toward the perimembranous or inlet part, this can be appreciated from both left lateral and right lateral views. The fact that the entire defect and its bordering structures can be visualized in one view is the most important benefit of 3D echo. Planimetry of the pulmonary annulus is sometimes feasible, but the outcomes rarely differ from what is known from 2D echo.

The biggest challenge for the sonographer in tetralogy of Fallot after surgical correction is not morphology but assessment of ventricular volumes and function. As stated before, LV function can be assessed more reliably with RT3D echo than with 2D echo [22], and assessment of RV volumes

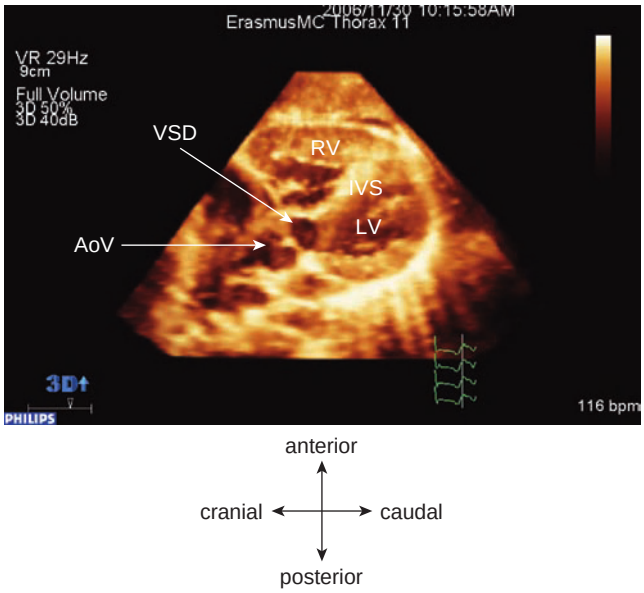


**Figure 41.43** "Anyplane" cross-section in a patient with tetralogy of Fallot, showing left ventricle (LV), hypertrophic right ventricle (RV), ventricular septal defect (VSD) and overriding aorta. AoV, aortic valve; IVS, interventricular septum.

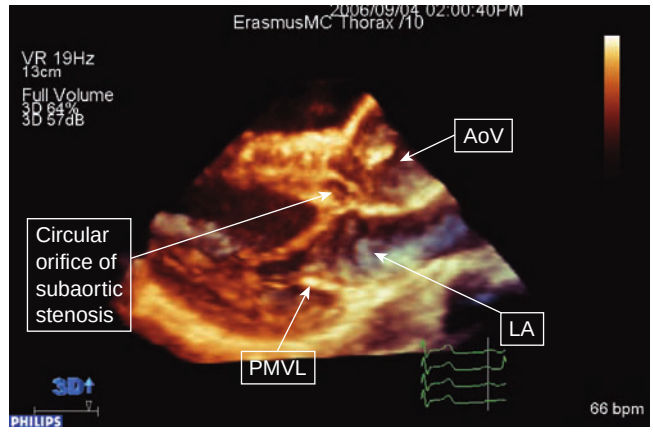


**Figure 41.44** Left lateral view from a dataset acquired from a parasternal position. The left lateral wall of left atrium, left ventricle and ascending aorta are cut away. The circular opening of the subaortic stenosis is clearly visible. AoV, aortic valve; LA, left atrium; PMVL, posterior mitral valve leaflet.

and ejection fraction is "work in progress." The first commercially available software system designed exclusively for analysis of RV volumes has recently been introduced. No data on tetralogy patients have been published yet.

### Real-time 3D echo in other congenital cardiac malformations

There is very little experience published so far about the benefits of RT3D echo in malformations other than the few described above. There have been case reports about subaortic stenosis [95] (Fig. 41.44), double aortic arch [96], right atrial aneurysm [97], and infective endocarditis of a patent foramen ovale [98]. These are examples of the growing awareness of the potential of RT3D echo for use in congenital heart disease, but more experience is needed and the exact role of RT3D echo in the analysis of these complex congenital cardiac lesions remains to be established. The "en face" view on septa or valves and the possibilities for imaging abnormalities in relation to the surrounding anatomy are the most important aspects by which RT3D echo differs from 2D echo. The extent of the benefits that these views will have will differ for each abnormality, probably from virtually nothing to extremely helpful.

## Future applications

A serious limitation of the current 3D imaging modes – echo, MRI or CT alike – is the fact that 3D data are represented as holograms on a flat, 2D screen. We have demonstrated that if RT3D echocardiographic data are displayed in a real 3D environment, physicians without specific echo knowledge but with a good understanding of cardiac anatomy, were able to navigate through a 3D dataset and make sensible cross-sections within 10 minutes [99,100] (Fig. 41.45). However, it is our experience [7] that it takes at least one day of training before people who already are echo experts to navigate reasonably well through a 3D dataset. 3D representation of 3D data will be a big step forward. The technique will then be less dependent on echo expertise.

Reliable color flow quantification by RT3D echocardiography would represent another big step forward. The idea alone has been an inspiration for a lot of research, and some have reported some successes in this respect [101]. We think that more research is necessary before 3D color flow quantification can be considered a clinically useful tool.

Multiparametric imaging is probably the next step in 3D echocardiography: the visualization of several parameters of cardiac function integrated in one imaging modality. Parameters that could be displayed simultaneously could be regional wall motion – in terms of change of volume and in timing of the wall motion – and possibly myocardial perfusion. Integration of speckle tracking or vector velocity imaging into RT3D echocardiography has recently been introduced.

A better temporal resolution will be needed to study ventricular kinetics. The short history of the 2D tissue Doppler studies has taught us that high frame rates are necessary to monitor the rapid succession of events and motions that occur in the ventricular wall. To achieve the goal of imaging the integral, complex 3D movement of the left ventricle, with longitudinal shortening, circumferential shortening

**Figure 41.45** It is possible to view data in a 3D way. In a virtual reality "3D hologram" navigating through the intracardiac anatomy is much more intuitive (and therefore easier) than in a 3D dataset represented on a flat screen.

and twist – clockwise rotation at the base of the heart and counterclockwise rotation at the apex – a frame rate of at least 150 images per second (possibly even higher) is probably needed. The assessment of right ventricular kinetics, not in a simplified 2D way but doing justice to its complex 3D geometry, has hardly ever been studied in detail so far; it is very important for assessing congenital heart disease, and remains a big challenge for us all in the coming years.

## Acknowledgements

We owe a lot to Willeke van de Bent-Tomasouw, our research assistant and secretary. Without her secretarial support and relentless efforts to keep us going, this manuscript, figures and legends never would have been finished.

## References

1. Dekker DL, Piziali RL, Dong E Jr. A system for ultrasonically imaging the human heart in three dimensions. *Comput Biomed Res* 1974;7:544–53.
2. Lang RM, Mor-Avi V, Sugeng L et al. Three-dimensional echocardiography: the benefits of the additional dimension. *J Am Coll Cardiol* 2006;48:2053–69.
3. Salgo IS. Three-dimensional echocardiographic technology. *Cardiol Clin* 2007;25:231–9.
4. Gill EA, Klas B. Three-dimensional echocardiography: an historical perspective. *Cardiol Clin* 2007;25:221–9.
5. von Ramm OT, Smith SW. Real time volumetric ultrasound imaging system. *J Digit Imaging* 1990;3:261–6.
6. Acar P, Abadir S, Paranon S et al. Live 3D echocardiography with the pediatric matrix probe. *Echocardiography* 2007;24:750–5.
7. Jenkins C, Monaghan M, Shirali G et al. An intensive interactive course for 3D echocardiography: Is "Crop Till You Drop" an effective learning strategy? *Eur J Echocardiogr* 2007;9:373.
8. Hare JL, Jenkins C, Nakatani S et al. Feasibility and clinical decision-making with 3D echocardiography in routine practice. *Heart* 2008;94(4):440–5.
9. Nanda NC, Kisslo J, Lang R et al. Examination protocol for three-dimensional echocardiography. *Echocardiography* 2004;21:763–8.
10. Sugeng L, Mor-Avi V, Weinert L et al. Quantitative assessment of left ventricular size and function: side-by-side comparison of real-time three-dimensional echocardiography and computed tomography with magnetic resonance reference. *Circulation* 2006;114:654–61.
11. Iino M, Shiraishi H, Ichihashi K et al. Volume measurement of the left ventricle in children using real-time three-dimensional echocardiography: comparison with ventriculography. *J Cardiol* 2007;49:221–9.
12. Monaghan MJ. Role of real time 3D echocardiography in evaluating the left ventricle. *Heart* 2006;92:131–6.
13. Caiani EG, Corsi C, Zamorano J et al. Improved semiautomated quantification of left ventricular volumes and ejection fraction using 3-dimensional echocardiography with a full matrix-array transducer: comparison with magnetic resonance imaging. *J Am Soc Echocardiogr* 2005;18:779–88.
14. Gutierrez-Chico JL, Zamorano JL, Perez de Isla L et al. Comparison of left ventricular volumes and ejection fractions measured by three-dimensional echocardiography versus by two-dimensional echocardiography and cardiac magnetic resonance in patients with various cardiomyopathies. *Am J Cardiol* 2005;95:809–13.
15. Jenkins C, Bricknell K, Hanekom L, Marwick TH. Reproducibility and accuracy of echocardiographic measurements of left ventricular parameters using real-time three-dimensional echocardiography. *J Am Coll Cardiol* 2004;44:878–86.
16. Nosir YF, Fioretti PM, Vletter WB et al. Accurate measurement of left ventricular ejection fraction by three-dimensional echocardiography. A comparison with radionuclide angiography. *Circulation* 1996;94:460–6.
17. Iwase M, Kondo T, Hasegawa K et al. Three-dimensional echocardiography by semi-automatic border detection in

assessment of left ventricular volume and ejection fraction: comparison with magnetic resonance imaging. *J Cardiol* 1997; 30:97–105.
18. Buck T, Hunold P, Wentz KU et al. Tomographic three-dimensional echocardiographic determination of chamber size and systolic function in patients with left ventricular aneurysm: comparison to magnetic resonance imaging, cineventriculography, and two-dimensional echocardiography. *Circulation* 1997; 96:4286–97.
19. Altmann K, Shen Z, Boxt LM et al. Comparison of three-dimensional echocardiographic assessment of volume, mass, and function in children with functionally single left ventricles with two-dimensional echocardiography and magnetic resonance imaging. *Am J Cardiol* 1997;80:1060–5.
20. Mor-Avi V, Sugeng L, Weinert L et al. Fast measurement of left ventricular mass with real-time three-dimensional echocardiography: comparison with magnetic resonance imaging. *Circulation* 2004;110:1814–8.
21. Voormolen MM, Krenning BJ, van Geuns RJ et al. Efficient quantification of the left ventricular volume using 3-dimensional echocardiography: the minimal number of equiangular long-axis images for accurate quantification of the left ventricular volume. *J Am Soc Echocardiogr* 2007;20:373–80.
22. van den Bosch AE, Robbers-Visser D, Krenning BJ et al. Real-time transthoracic three-dimensional echocardiographic assessment of left ventricular volume and ejection fraction in congenital heart disease. *J Am Soc Echocardiogr* 2006;19:1–6.
23. Franke A. Real-time three-dimensional echocardiography in stress testing: bi- and triplane imaging for enhanced image acquisition. *Cardiol Clin* 2007;25:261–5.
24. Krenning BJ, Szili-Torok T, Voormolen MM et al. Guiding and optimization of resynchronization therapy with dynamic three-dimensional echocardiography and segmental volume–time curves: a feasibility study. *Eur J Heart Fail* 2004;6:619–25.
25. Horstman JA, Monaghan MJ, Gill EA. Intraventricular dyssynchrony assessment by real-time three-dimensional echocardiography. *Cardiol Clin* 2007;25:253–60.
26. Zhang Q, Yu CM, Fung JW et al. Assessment of the effect of cardiac resynchronization therapy on intraventricular mechanical synchronicity by regional volumetric changes. *Am J Cardiol* 2005;95:126–9.
27. Yu CM, Bax JJ, Monaghan M, Nihoyannopoulos P. Echocardiographic evaluation of cardiac dyssynchrony for predicting a favourable response to cardiac resynchronisation therapy. *Heart* 2004;90(Suppl. 6):vi17–22.
28. Zamorano J, Perez de Isla L, Roque C, Khanhderia B. The role of echocardiography in the assessment of mechanical dyssynchrony and its importance in predicting response to prognosis after cardiac resynchronization therapy. *J Am Soc Echocardiogr* 2007;20:91–9.
29. Qin JX, Shiota T, Thomas JD. Determination of left ventricular volume, ejection fraction, and myocardial mass by real-time three-dimensional echocardiography. *Echocardiography* 2000; 17:781–6.
30. Oe H, Hozumi T, Arai K et al. Comparison of accurate measurement of left ventricular mass in patients with hypertrophied hearts by real-time three-dimensional echocardiography versus magnetic resonance imaging. *Am J Cardiol* 2005;95: 1263–7.
31. Chuang ML, Beaudin RA, Riley MF et al. Three-dimensional echocardiographic measurement of left ventricular mass: comparison with magnetic resonance imaging and two-dimensional echocardiographic determinations in man. *Int J Card Imaging* 2000;16:347–57.
32. van den Bosch AE, Robbers-Visser D, Krenning BJ et al. Comparison of real-time three-dimensional echocardiography to magnetic resonance imaging for assessment of left ventricular mass. *Am J Cardiol* 2006;97:113–17.
33. Yap SC, van Geuns RJ, Nemes A et al. Rapid and accurate measurement of LV mass by biplane real-time 3D echocardiography in patients with concentric LV hypertrophy: Comparison to CMR. *Eur J Echocardiogr* 2008;9(2):255–60.
34. Hoch M, Vasilyev NV, Soriano B et al. Variables influencing the accuracy of right ventricular volume assessment by real-time 3-dimensional echocardiography: an in vitro validation study. *J Am Soc Echocardiogr* 2007;20:456–61.
35. Jenkins C, Chan J, Bricknell K et al. Reproducibility of right ventricular volumes and ejection fraction using real-time three-dimensional echocardiography: comparison with cardiac MRI. *Chest* 2007;131:1844–51.
36. Kjaergaard J, Sogaard P, Hassager C. Quantitative echocardiographic analysis of the right ventricle in healthy individuals. *J Am Soc Echocardiogr* 2006;19:1365–72.
37. Anwar AM, Soliman OI, Geleijnse ML et al. Assessment of left atrial volume and function by real-time three-dimensional echocardiography. *Int J Cardiol* 2008;123(2):155–61.
38. Anwar AM, Geleijnse ML, Soliman OI et al. Left atrial Frank Starling law assessed by real-time three-dimensional echocardiographic left atrial volume changes. *Heart* 2007;93:1393–97.
39. Keller AM, Gopal AS, King DL. Left and right atrial volume by freehand three-dimensional echocardiography: in vivo validation using magnetic resonance imaging. *Eur J Echocardiogr* 2000;1:55–65.
40. Jenkins C, Bricknell K, Marwick TH. Use of real-time three-dimensional echocardiography to measure left atrial volume: comparison with other echocardiographic techniques. *J Am Soc Echocardiogr* 2005;18:991–7.
41. Poutanen T, Ikonen A, Vainio P et al. Left atrial volume assessed by transthoracic three dimensional echocardiography and magnetic resonance imaging: dynamic changes during the heart cycle in children. *Heart* 2000;83:537–42.
42. Mumm B, Baumann R, Hyca M. Three-dimensional echo for the assessment of valvular heart disease. *Cardiol Clin* 2007;25: 283–95.
43. Anwar AM, Soliman OI, Nemes A et al. Assessment of mitral annulus size and function by real-time 3-dimensional echocardiography in cardiomyopathy: comparison with magnetic resonance imaging. *J Am Soc Echocardiogr* 2007;20:941–8.
44. Anwar AM, Soliman O, van den Bosch AE et al. Assessment of pulmonary valve and right ventricular outflow tract with real-time three-dimensional echocardiography. *Int J Cardiovasc Imaging* 2007;23:167–75.
45. Agricola E, Oppizzi M, Pisani M et al. Accuracy of real-time 3D echocardiography in the evaluation of functional anatomy of mitral regurgitation. *Int J Cardiol* 2008;127(3):342–9.

46. Mihalatos DG, Joseph S, Gopal A et al. Mitral annular remodeling with varying degrees and mechanisms of chronic mitral regurgitation. *J Am Soc Echocardiogr* 2007;20:397–404.
47. Yosefy C, Levine RA, Solis J et al. Proximal flow convergence region as assessed by real-time 3-dimensional echocardiography: challenging the hemispheric assumption. *J Am Soc Echocardiogr* 2007;20:389–96.
48. Iwakura K, Ito H, Kawano S et al. Comparison of orifice area by transthoracic three-dimensional Doppler echocardiography versus proximal isovelocity surface area (PISA) method for assessment of mitral regurgitation. *Am J Cardiol* 2006;97:1630–7.
49. de Agustin JA, Nanda NC, Gill EA et al. The use of three-dimensional echocardiography for the evaluation of and treatment of mitral stenosis. *Cardiol Clin* 2007;25:311–8.
50. Xie MX, Wang XF, Cheng TO et al. Comparison of accuracy of mitral valve area in mitral stenosis by real-time, three-dimensional echocardiography versus two-dimensional echocardiography versus Doppler pressure half-time. *Am J Cardiol* 2005;95:1496–9.
51. Mannaerts HF, Kamp O, Visser CA. Should mitral valve area assessment in patients with mitral stenosis be based on anatomical or on functional evaluation? A plea for 3D echocardiography as the new clinical standard. *Eur Heart J* 2004;25: 2073–4.
52. Messika-Zeitoun D, Brochet E, Holmin C et al. Three-dimensional evaluation of the mitral valve area and commissural opening before and after percutaneous mitral commissurotomy in patients with mitral stenosis. *Eur Heart J* 2007;28:72–9.
53. Sugeng L, Coon P, Weinert L et al. Use of real-time 3-dimensional transthoracic echocardiography in the evaluation of mitral valve disease. *J Am Soc Echocardiogr* 2006;19:413–21.
54. Donal E, Novaro GM, Deserrano D et al. Planimetric assessment of anatomic valve area overestimates effective orifice area in bicuspid aortic stenosis. *J Am Soc Echocardiogr* 2005; 18:1392–8.
55. Brasch AV, Luo H, Khan SS et al. Effect of harmonic imaging for planimetry on transthoracic echocardiography on visualization of the aortic valve. *Am J Cardiol* 2001;88:1047–9.
56. Handke M, Heinrichs G, Beyersdorf F et al. In vivo analysis of aortic valve dynamics by transesophageal 3-dimensional echocardiography with high temporal resolution. *J Thorac Cardiovasc Surg* 2003;125:1412–19.
57. Sadagopan SN, Veldtman GR, Sivaprakasam MC et al. Correlations with operative anatomy of real time three-dimensional echocardiographic imaging of congenital aortic valvar stenosis. *Cardiol Young* 2006;16:490–4.
58. Goland S, Trento A, Iida K et al. Assessment of aortic stenosis by three-dimensional echocardiography: an accurate and novel approach. *Heart* 2007;93:801–7.
59. Doddamani S, Bello R, Friedman MA et al. Demonstration of left ventricular outflow tract eccentricity by real time 3D echocardiography: Implications for the determination of aortic valve area. *Echocardiography* 2007;24:860–6.
60. Acar P, Jones M, Shiota T et al. Quantitative assessment of chronic aortic regurgitation with 3-dimensional echocardiographic reconstruction: comparison with electromagnetic flowmeter measurements. *J Am Soc Echocardiogr* 1999;12:138–48.
61. Shiota T, Jones M, Tsujino H et al. Quantitative analysis of aortic regurgitation: real-time 3-dimensional and 2-dimensional color Doppler echocardiographic method – a clinical and a chronic animal study. *J Am Soc Echocardiogr* 2002;15:966–71.
62. Ahlgrim AA, Nanda NC, Berther E, Gill EA. Three-dimensional echocardiography: an alternative imaging choice for evaluation of tricuspid valve disorders. *Cardiol Clin* 2007;25:305–9.
63. Anwar AM, Geleijnse ML, Ten Cate FJ, Meijboom FJ. Assessment of tricuspid valve annulus size, shape and function using real-time three-dimensional echocardiography. *Interact Cardiovasc Thorac Surg* 2006;5:683–7.
64. Poutanen T, Tikanoja T, Sairanen H, Jokinen E. Normal mitral and aortic valve areas assessed by three- and two-dimensional echocardiography in 168 children and young adults. *Pediatr Cardiol* 2006;27:217–25.
65. Nii M, Roman KS, Macgowan CK, Smallhorn JF. Insight into normal mitral and tricuspid annular dynamics in pediatrics: a real-time three-dimensional echocardiographic study. *J Am Soc Echocardiogr* 2005;18:805–14.
66. McMahon CJ, Feltes TF, Fraley JK et al. Natural history of growth of secundum atrial septal defects and implications for transcatheter closure. *Heart* 2002;87:256–9.
67. Cooke JC, Gelman JS, Harper RW. Echocardiologists' role in the deployment of the Amplatzer atrial septal occluder device in adults. *J Am Soc Echocardiogr* 2001;14:588–94.
68. Reddy SC, Rao PS, Ewenko J et al. Echocardiographic predictors of success of catheter closure of atrial septal defect with the buttoned device. *Am Heart J* 1995;129:76–82.
69. Marx GR, Sherwood MC, Fleishman C, Van Praagh R. Three-dimensional echocardiography of the atrial septum. *Echocardiography* 2001;18:433–43.
70. van den Bosch AE, Ten Harkel DJ, McGhie JS et al. Characterization of atrial septal defect assessed by real-time 3-dimensional echocardiography. *J Am Soc Echocardiogr* 2006;19:815–21.
71. Zhu W, Cao QL, Rhodes J, Hijazi ZM. Measurement of atrial septal defect size: a comparative study between three-dimensional transesophageal echocardiography and the standard balloon sizing methods. *Pediatr Cardiol* 2000;21:465–9.
72. Marx GR, Fulton DR, Pandian NG et al. Delineation of site, relative size and dynamic geometry of atrial septal defects by real-time three-dimensional echocardiography. *J Am Coll Cardiol* 1995;25:482–90.
73. Handke M, Schafer DM, Muller G et al. Dynamic changes of atrial septal defect area: new insights by three-dimensional volume-rendered echocardiography with high temporal resolution. *Eur J Echocardiogr* 2001;2:46–51.
74. Acar P. Three-dimensional echocardiography in children with atrial septal defect. *Minerva Pediatr* 2004;56:29–40.
75. Lange A, Walayat M, Turnbull CM et al. Assessment of atrial septal defect morphology by transthoracic three dimensional echocardiography using standard grey scale and Doppler myocardial imaging techniques: comparison with magnetic resonance imaging and intraoperative findings. *Heart* 1997;78:382–9.
76. Xie MX, Fang LY, Wang XF et al. Assessment of atrial septal defect area changes during cardiac cycle by live three-dimensional echocardiography. *J Cardiol* 2006;47:181–7.
77. Chen FL, Hsiung MC, Nanda N et al. Real time three-dimensional echocardiography in assessing ventricular septal

defects: an echocardiographic-surgical correlative study. *Echocardiography* 2006;23:562–8.
78. Mehmood F, Vengala S, Nanda NC et al. Usefulness of live three-dimensional transthoracic echocardiography in the characterization of atrial septal defects in adults. *Echocardiography* 2004;21:707–13.
79. Acar P, Roux D, Dulac Y et al. Transthoracic three-dimensional echocardiography prior to closure of atrial septal defects in children. *Cardiol Young* 2003;13:58–63.
80. Mehmood F, Miller AP, Nanda NC et al. Usefulness of live/real time three-dimensional transthoracic echocardiography in the characterization of ventricular septal defects in adults. *Echocardiography* 2006;23:421–7.
81. Cheng TO, Xie MX, Wang XF et al. Real-time 3-dimensional echocardiography in assessing atrial and ventricular septal defects: an echocardiographic-surgical correlative study. *Am Heart J* 2004;148:1091–5.
82. Hsu JH, Wu JR, Dai ZK, Lee MH. Real-time three-dimensional echocardiography provides novel and useful anatomic insights of perimembranous ventricular septal aneurysm. *Int J Cardiol* 2007;118:326–31.
83. Dall'Agata A, Cromme-Dijkhuis AH, Meijboom FJ et al. Three-dimensional echocardiography enhances the assessment of ventricular septal defect. *Am J Cardiol* 1999;83:1576–9, A1578.
84. van den Bosch AE, Ten Harkel DJ, McGhie JS et al. Feasibility and accuracy of real-time 3-dimensional echocardiographic assessment of ventricular septal defects. *J Am Soc Echocardiogr* 2006;19:7–13.
85. Mercer-Rosa L, Seliem MA, Fedec A et al. Illustration of the additional value of real-time 3-dimensional echocardiography to conventional transthoracic and transesophageal 2-dimensional echocardiography in imaging muscular ventricular septal defects: does this have any impact on individual patient treatment? *J Am Soc Echocardiogr* 2006;19:1511–19.
86. Barrea C, Levasseur S, Roman K et al. Three-dimensional echocardiography improves the understanding of left atrioventricular valve morphology and function in atrioventricular septal defects undergoing patch augmentation. *J Thorac Cardiovasc Surg* 2005;129:746–53.
87. Seliem MA, Fedec A, Szwast A et al. Atrioventricular valve morphology and dynamics in congenital heart disease as imaged with real-time 3-dimensional matrix-array echocardiography: comparison with 2-dimensional imaging and surgical findings. *J Am Soc Echocardiogr* 2007;20:869–76.
88. van den Bosch AE, Ten Harkel DJ, McGhie JS et al. Surgical validation of real-time transthoracic 3D echocardiographic assessment of atrioventricular septal defects. *Int J Cardiol* 2006;112:213–18.
89. van den Bosch AE, van Dijk VF, McGhie JS et al. Real-time transthoracic three-dimensional echocardiography provides additional information on left-sided AV valve morphology after AVSD repair. *Int J Cardiol* 2006;106:360–4.
90. Hlavacek AM, Crawford FA Jr, Chessa KS, Shirali GS. Real-time three-dimensional echocardiography is useful in the evaluation of patients with atrioventricular septal defects. *Echocardiography* 2006;23:225–31.
91. Takahashi K, Guerra V, Roman KS et al. Three-dimensional echocardiography improves the understanding of the mechanisms and site of left atrioventricular valve regurgitation in atrioventricular septal defect. *J Am Soc Echocardiogr* 2006;19:1502–10.
92. Singh A, Romp RL, Nanda NC et al. Usefulness of live/real time three-dimensional transthoracic echocardiography in the assessment of atrioventricular septal defects. *Echocardiography* 2006;23:598–608.
93. Rawlins DB, Austin C, Simpson JM. Live three-dimensional paediatric intraoperative epicardial echocardiography as a guide to surgical repair of atrioventricular valves. *Cardiol Young* 2006;16:34–9.
94. Roman KS, Nii M, Macgowan CK et al. The impact of patch augmentation on left atrioventricular valve dynamics in patients with atrioventricular septal defects: early and midterm follow-up. *J Am Soc Echocardiogr* 2006;19:1382–92.
95. Miyamoto K, Nakatani S, Kanzaki H et al. Detection of discrete subaortic stenosis by 3-dimensional transesophageal echocardiography. *Echocardiography* 2005;22:783–4.
96. Sivaprakasam MC, Vettukattil JJ. 3-D echocardiographic imaging of double aortic arch. *Eur J Echocardiogr* 2006;7:476–7.
97. Guerra VC, Coles J, Smallhorn JF. Aneurysm of right atrium diagnosed by 3-dimensional real-time echocardiogram. *J Am Soc Echocardiogr* 2005;18:1221.
98. Acar P, Abadir S, Bassil R. Images in congenital heart disease. Infective endocarditis of the patent oval fossa assessed by three-dimensional echocardiography. *Cardiol Young* 2007;17:113.
99. van den Bosch AE, Koning AH, Meijboom FJ et al. Dynamic 3D echocardiography in virtual reality. *Cardiovasc Ultrasound* 2005;3:37.
100. Bol Raap G, Koning AH, Scohy TV et al. Virtual reality 3D echocardiography in the assessment of tricuspid valve function after surgical closure of ventricular septal defect. *Cardiovasc Ultrasound* 2007;5:8.
101. Sugeng L, Weinert L, Lang RM. Real-time 3-dimensional color Doppler flow of mitral and tricuspid regurgitation: feasibility and initial quantitative comparison with 2-dimensional methods. *J Am Soc Echocardiogr* 2007;20:1050–7.

# 42 Fetal Echocardiography

**Lisa K. Hornberger**

Department of Pediatrics, Division of Pediatric Cardiology, Department of Obstetrics and Gynecology, University of Alberta, Alberta, AB, Canada

## Introduction

Fetal cardiology has evolved over the past two decades into a highly specialized clinical field that merges fetal-perinatal medicine and pediatric cardiology. At the center of this field is the fetal echocardiogram, which permits the evaluation of fetal cardiovascular anatomy, function and rhythm. Over the past two to three decades, fetal echocardiography has provided insights into normal human fetal cardiovascular growth and physiology, an area previously understood only through fetal animal models. Improvements in ultrasound technology have led to the capability not only to detect most forms of congenital heart disease (CHD), but to evaluate cardiac pathology with significant detail. The technology has contributed significantly to our understanding of the prenatal and perinatal pathophysiology of structural and functional cardiovascular lesions. Serial observations have provided insights into the evolution and etiologies of the postnatal spectrum of CHD, improved prenatal counseling regarding prognosis, and even prompted development of fetal and perinatal interventions to alter the course of disease and thus improve outcome. Fetal echocardiography has provided a means of evaluating fetal arrhythmias, which has led to the development of successful therapeutic strategies to prevent or reverse associated fetal heart failure. Finally, our ability to evaluate fetal heart function and to predict the potential for evolution of heart failure in primary cardiovascular lesions and in lesions that secondarily influence the fetal heart has continued to improve. Fetal echocardiography will continue to play a crucial role in the management of a large spectrum of primary cardiac and noncardiac fetal pathologies.

*Echocardiography in Pediatric and Congenital Heart Disease: From Fetus to Adult*
Edited by Wyman W. Lai, Luc L. Mertens, Meryl S. Cohen and Tal Geva
 ISBN: 978-1-405-17401-5

## Indications and timing of fetal echocardiography

Currently there are many indications for fetal echocardiography, as listed in Table 42.1. Knowledge of the types and incidence of lesions associated with a given risk factor, and the likelihood of diagnosis at a given gestational age, is important in determining the approach to examination, counseling and follow-up of the pregnancy.

The most common reasons for referral for fetal echocardiography include maternal disease, maternal teratogen exposure, and a family history of CHD or syndromes associated with CHD [1–2]. The indications for referral with the greatest yield of fetal cardiac pathology (>85%), however, include an obstetrical ultrasound suggesting a fetal cardiac or extracardiac abnormality including chromosomal abnormality. As such, routine obstetrical ultrasound screening plays a critical role in the detection of fetal CHD and the ultimate impact of fetal echocardiography.

The timing of the fetal echocardiogram, in part, depends upon the reason for referral. Most are performed in the second trimester, between 17 and 23 weeks. This is typically the gestational age at which routine obstetrical ultrasounds are performed, and prior to the gestational age limit for pregnancy termination if fetal pathology is identified. Occasionally, referral occurs in the late second or third trimesters, for instance, when a repeat sonogram suggests a change in fetal anatomy, rhythm or the evolution of fetal hydrops. Finally, with the advent of endovaginal transducers and high-resolution curvilinear probes, over the past decade there has grown an interest in late first and early second trimester fetal echocardiography beginning at 10 weeks. The latter has been prompted partly as a consequence of the development of nuchal translucency screening at 10–14 weeks, which identifies the fetus at risk for aneuploidy [3–5] and CHD in the absence of aneuploidy [6–10].

## Technical considerations

Diagnostic imaging of the fetal heart requires a different technical approach from that used in routine obstetrical

**Table 42.1** Indications for fetal echocardiography

| |
|---|
| **Maternal** |
| Metabolic disorders: |
| Diabetes mellitus |
| Gestational diabetes |
| Phenylketonuria |
| Autoimmune disease: |
| Sjögren syndrome |
| Systemic lupus erythematosus |
| Teratogen exposure: |
| Alcohol |
| Lithium |
| Vitamin A derivatives |
| Anticonvulsants |
| SSRI antidepressants |
| Maternal/intrauterine infection |
| Maternal CHD |
| **Fetal** |
| Suspected fetal heart abnormality by ultrasound |
| Extracardiac structural abnormalities: |
| Central nervous system |
| Renal pathology |
| Abdominal wall defects |
| Gastrointestinal abnormalities |
| Diaphragmatic hernia |
| Skeletal anomalies |
| Cystic adenomatous malformation |
| Arteriovenous malformations |
| Increased nuchal translucency |
| Cystic hygroma |
| Single umbilical artery |
| Chromosomal abnormalities – confirmed or suspected |
| Fetal arrhythmia |
| Monochorionic twin gestation: |
| Twin–twin transfusion syndrome |
| Acardiac twin gestation |
| Conjoined twins |
| Fetal nonimmune hydrops |
| **Familial** |
| Previously affected child |
| Paternal CHD |
| Consanguinity |
| Mendelian syndromes (examples): |
| DiGeorge syndrome |
| Tuberous sclerosis |
| William syndrome |
| Ellis–van Creveld syndrome |

CHD, congenital heart disease; SSRI, selective serotonin reuptake inhibitors.

ultrasound, one more akin to postnatal imaging of the heart. The dynamic nature and complexity of the heart requires high frame rates and optimal resolution. To obtain details of the diminutive fetal cardiovascular structures, a high-frequency transducer in the 6–10-MHz range with dynamic focusing capabilities is required in most cases. The highest frequency transducer that provides the required penetration should be chosen. The frame averaging option or persistence is set to off or low. A compress setting allowing for a narrow dynamic range (grayscale) has better sensitivity and defines the blood–tissue interfaces. The maternal abdominal wall – which may be thick and may have echogenic areas from adipose or scar tissue, lotions and oils used on the skin, and fetal bone all contribute to reduced image quality and limit planes of imaging. Amniotic fluid provides a very useful interface between the maternal abdomen and the fetal chest. Changing to a lower frequency transducer and use of harmonic imaging can facilitate the evaluation of third trimester patients or if the fetus is a great distance from the transducer. Finally, in late first trimester pregnancies, use of high-frequency, high-resolution endovaginal transducers (if available) may be necessary in some patients for even a basic evaluation of the fetal heart [10–12].

## The screening fetal echocardiogram

A complete fetal echocardiogram should include: two-dimensional (2D) imaging of the fetal cardiac anatomy; spectral and color Doppler interrogation of intracardiac, great arteries/arches, and systemic and pulmonary venous blood flow; and a basic assessment of fetal heart function and rhythm (Table 42.2).

Fetal heart assessment has several unique features compared with echocardiographic evaluation of patients after birth. The echocardiographer must understand the fetal position within the mother. The fetus is active and may shift many times during an exam, particularly earlier in pregnancy, requiring reorientation to the fetal position. The standard planes of imaging through the heart that are frequently used in postnatal assessments are not available, and hence the examiner must be creative in deciphering particularly complex fetal structural heart disease. The unique aspects of the fetal circulation, including the parallel circulation and the presence of the foramen ovale and ductus arteriosus with equalization of pressures and redistribution of flow, must be taken into consideration, and this frequently results in the need to use indirect observations, such as discrepancy in ventricular or great artery size, to determine the severity of a condition. Finally, the details gleaned must immediately be processed in order to provide accurate counseling for a usually very stressed patient and her partner.

### Two-dimensional imaging

Fetal echocardiographic assessment requires an approach that is just as systematic and uniform as a typical postnatal examination, with determination of segmental anatomy, atrioventricular and ventriculo-arterial connections, and

**Table 42.2** Components of a complete fetal echocardiogram

**Two-dimensional imaging**
Orientation to fetal position

Exclude obvious fetal hydrops:
- Pleural effusions
- Pericardial effusion
- Ascites
- Skin edema

Visceral and atrial situs evaluation

Cross-sectional images:
- Four-chamber view sweeps:
  - Cardiac axis
  - Cardiac size/cardiothoracic ratio
  - Cardiac position
  - Left and right atria
  - Atrial septal anatomy
  - Pulmonary veins (at least one right and one left)
  - Tricuspid valve
  - Mitral valve
  - Right ventricular morphology
  - Left ventricular morphology
  - Ventricular septal anatomy
  - Left ventricular outflow–aorta–pulmonary artery
  - Right ventricular outflow
- Three-vessel view sweeps:
  - Three-vessel view –normal great artery position and size relationship
  - Branch pulmonary arteries
  - Ductus arteriosus orientation and size
  - Aortic arch orientation and size
  - Trachea
  - Left innominate vein
- Sagittal sweeps:
  - Right superior vena cava
  - Right inferior vena cava
  - Left and right atria
  - Atrial septal anatomy
  - Aortic arch
  - Ductal arch
  - Tricuspid and mitral valve en face
  - Right and left ventricular morphology
  - Aortic and pulmonary outflow tracts
  - Basic RV and LV systolic function assessment
  - Ductus venosus and umbilical artery and vein anatomy

**Color Doppler interrogation**
- Tricuspid and mitral valves
- Ventricular outflows
- Pulmonary veins
- Aortic arch
- Ductal arch
- Inferior vena cava
- Ductus venosus
- Umbilical artery and vein

**Pulsed Doppler interrogation**
- Ventricular inflows
- Ventricular outflows
- Ductus arteriosus
- Aortic arch/isthmus
- Pulmonary veins
- Inferior vena cava or hepatic vein
- Ductus venosus
- Umbilical vein
- Umbilical artery

**Rhythm assessment**
- Fetal heart rate
- Relationship between atrial and ventricular contractions

aortic and ductal arch morphology and position. Cross-sectional, sagittal and coronal images through the fetal chest, and short- and long-axis imaging of the fetal heart are valuable in the evaluation of both normal and abnormal anatomy. The fetal heart and vascular structures are surrounded by fluid-filled lung, which provides a unique opportunity to appreciate the normal and abnormal relationship of these structures to each other and their position within the thorax itself.

Delineation of visceral and atrial situs requires an orientation to the fetal position. This is probably the most challenging task of the pediatric echocardiographer as there are innumerable potential fetal positions (e.g., supine, prone, transverse, vertex). It becomes exponentially more difficult in multiple pregnancies. Techniques have been described to facilitate orientation, but none is without potential for error. Orientation of the transducer along the fetal sagittal plane (long axis), with imaging of the spine, head and legs at lower magnification, provides information regarding the fetal position within the uterus. Use of a doll or model can facilitate recognition of the fetal position, including left and right sides and planes of imaging. In one published technique, when the fetus is supine or prone, whether vertex or breech, orientation of the transducer groove toward the fetal head along the long axis of the fetal body and 90° clockwise rotation results in a cross-sectional image that displays the fetal left to the right of the screen when supine, and the reverse when prone [13]. This technique becomes more difficult to use when the fetus is in a transverse lie. Irrespective of the technique employed, if there is fetal cardiovascular pathology, the responsible clinician should put his or her hands on the transducer, as the potential for error in determining the fetal left and right is significant and impossible to recognize with solely a review of images.

Once the fetal position is determined, cross-sectional images beginning at the level of the fetal abdomen with sweeps to the fetal chest provide information regarding

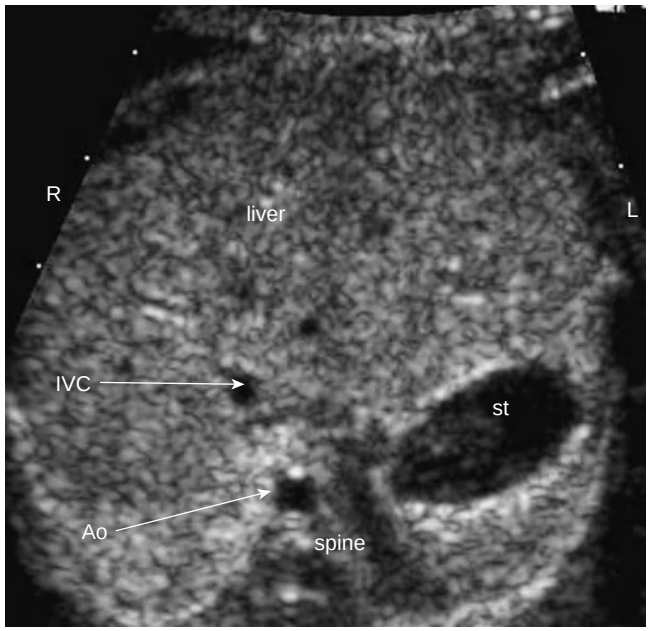


**Figure 42.1** Cross-sectional image through the normal fetal abdomen. Ao, descending aorta; IVC, inferior vena cava; st, stomach; L, left; R, right.

visceral and atrial situs. A right-dominant liver, and left-sided stomach and spleen as well as a right-sided inferior vena cava suggests visceral situs solitus (Fig. 42.1). Sweeping to the fetal chest, the inferior vena cava moves anteriorly to connect ultimately with the floor of the right atrium, just beneath septum primum and the pathway to the foramen ovale. A cross-sectional image through the fetal chest provides images of the four chambers of the heart (Fig. 42.2 and Videoclip 42.1). The heart should be roughly a third the size of the fetal chest. The cardiac axis – the axis of the ventricular septum relative to the midline of the fetal chest – shows little variation in normal fetuses, at 43 ± 7° [14]. The right atrium and a portion of the right ventricle are to the right of the midline, whereas the left ventricle, left atrium and a portion of the right ventricle are to the left. Any change in cardiac axis or position of the four chambers relative to the midline should prompt a search for either intracardiac or intrathoracic extracardiac pathology, the latter including unilateral lung hypoplasia [15,16], diaphragmatic hernia, pulmonary sequestrations and cystic adenomatous malformations.

The left atrium is the most posterior of the four cardiac chambers, positioned just anterior to the descending aorta in the normal heart. At least one left and one right pulmonary vein should be demonstrated at this level connecting with the left atrium, with the left pulmonary veins coursing closest to the left descending aorta, using color and pulsed Doppler for confirmation (Fig. 42.3).

Evaluation of the fetal atrial and ventricular septa is best accomplished from planes of imaging perpendicular to the septum, thus preventing dropout of thinner structures including septum primum and the membranous ventricular septum. Atrial septum assessment should include imaging of septum secundum and primum and the foramen ovale (Fig. 42.4). Sweeping posteriorly and inferiorly from the

(a)

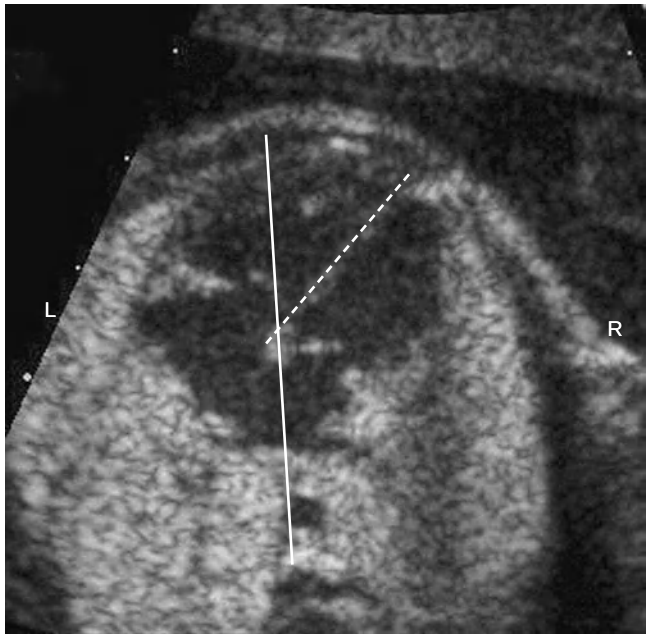


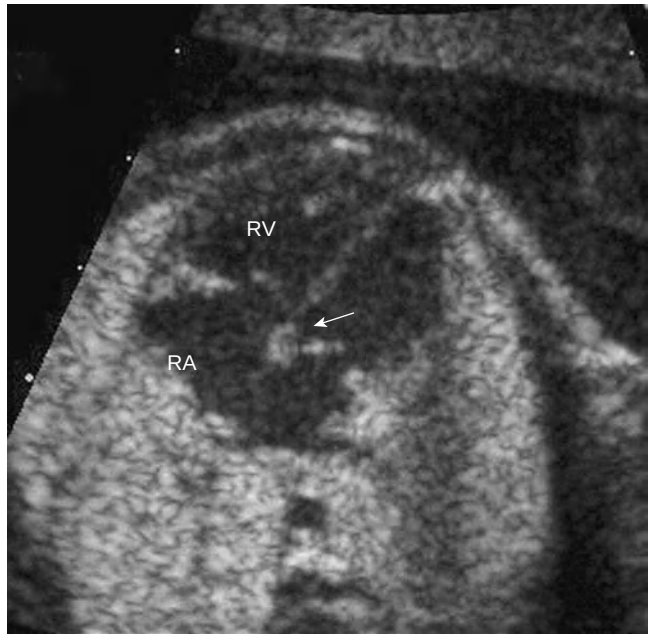


(b)

**Figure 42.2** Cross-sectional image through the fetal thorax demonstrating **(a)** the cardiac axis – angle of the septum (dashed line) from the midline (solid line) – and **(b)** the 4-chamber view (the arrow demonstrates the offset of the atrioventricular valves). RA, right atrium; RV, right ventricle; L, left; R, right.

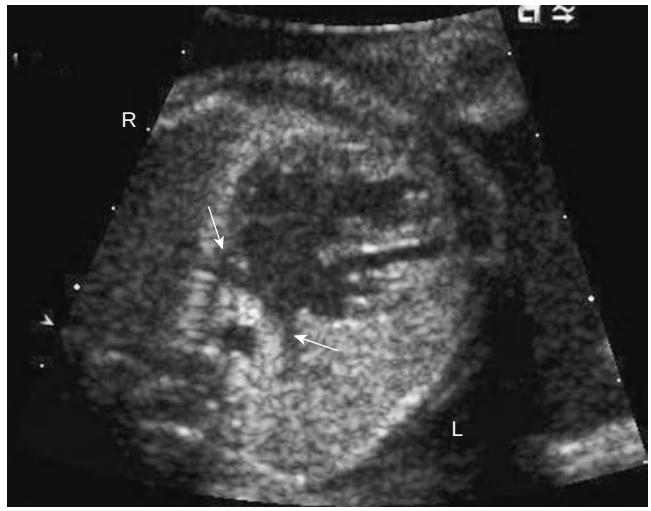


(a)

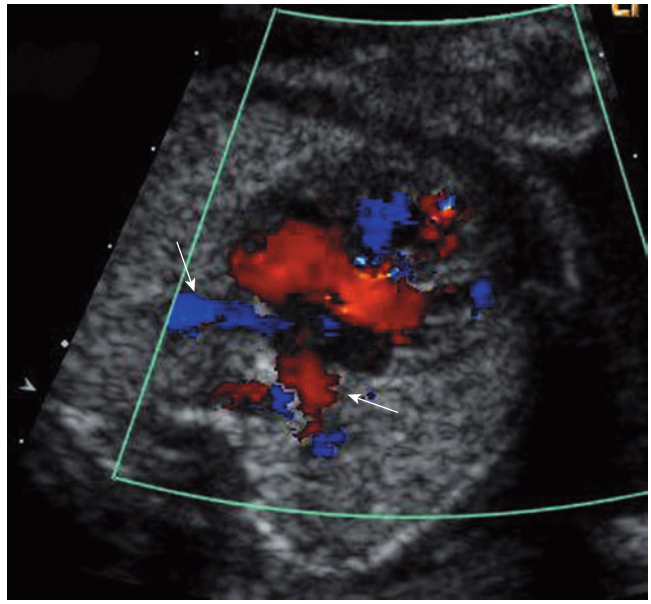

(b)

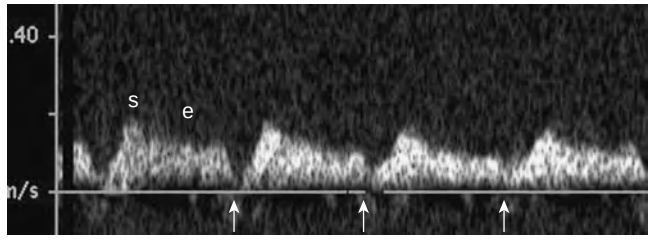


(c)

**Figure 42.3** **(a)** Four-chamber view demonstrating left and right pulmonary veins. **(b)** Color Doppler confirms the connection of left and right pulmonary veins with the left atrium. **(c)** Normal pulmonary vein flow is of low velocity with peaks in ventricular systole (s) and early diastole (e) and decreased flow during atrial systole (arrows). L, left; R, right.

4-chamber view, the thin coronary sinus is visualized as it courses within the left atrium just behind the inferior-posterior ring of the mitral valve. Dilation of the coronary sinus, which may be misinterpreted as an atrial septal defect at its mouth into the right atrium, suggests the presence of a persistent left superior vena cava.

The mitral and tricuspid valves should be evaluated in both 4-chamber and short-axis planes. In the normal heart, there is a subtle offset of the valves, with a more apically displaced septal leaflet of the tricuspid relative to the anterior leaflet of the mitral valve (see Fig. 42.2). A short-axis image through the inflow portion of the ventricles further delineates the atrioventricular (AV) valve morphology, with the anterior leaflet of the mitral valve shown pulling away from the ventricular septum (Fig. 42.5).

Whereas postnatally the trabeculation pattern may help in distinguishing the ventricles, prenatally this finding is less

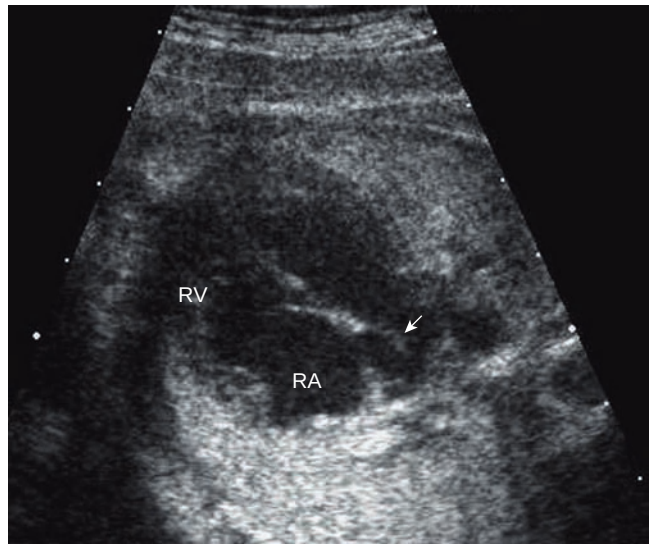


(a)

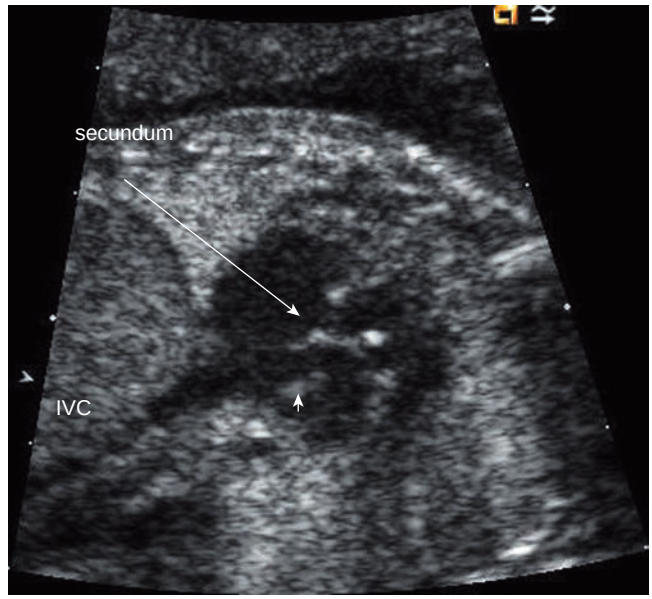


(b)

**Figure 42.4** Atrial septal anatomy from the **(a)** 4-chamber and **(b)** sagittal views. The short arrow points to septum primum or the flap of the foramen ovale in both images. RA, right atrium; RV, right ventricle; IVC, interior vena cava.

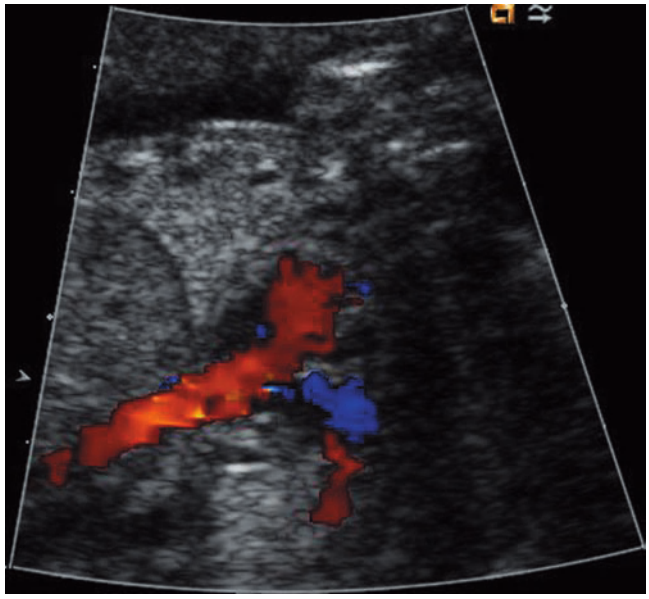

(c)

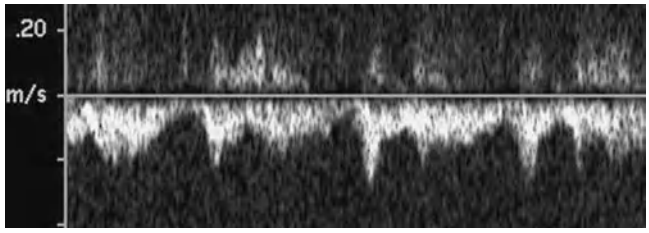


(d)

**Figure 42.4 (c)** Color Doppler demonstrates the path of the foramen ovale from right to left atrium. **(d)** Pulsed Doppler demonstrates the pulsatile flow pattern. IVC, inferior vena cava; RA, right atrium; RV, right ventricle; L, left; R, right.

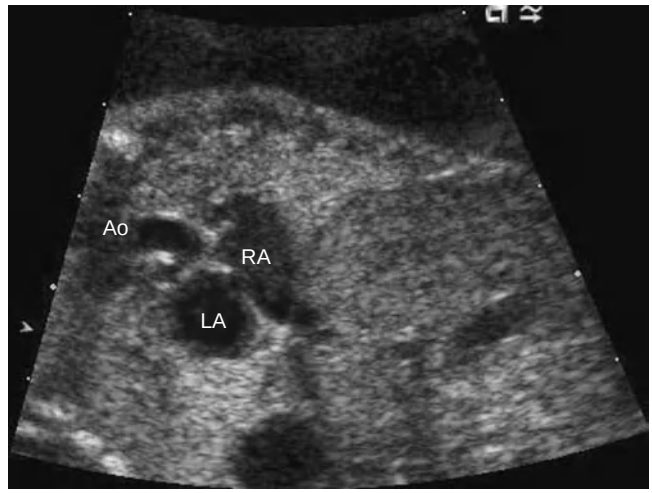


(b)

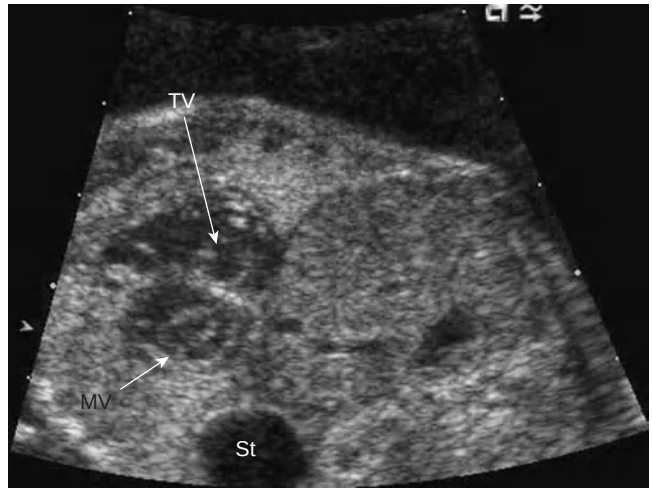


(c)

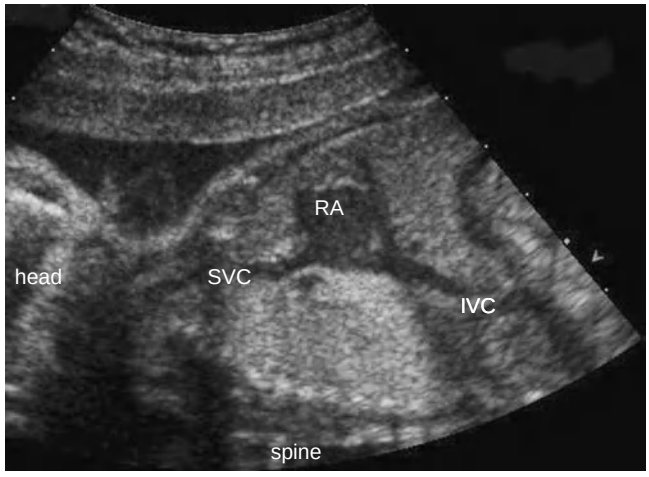


(a)

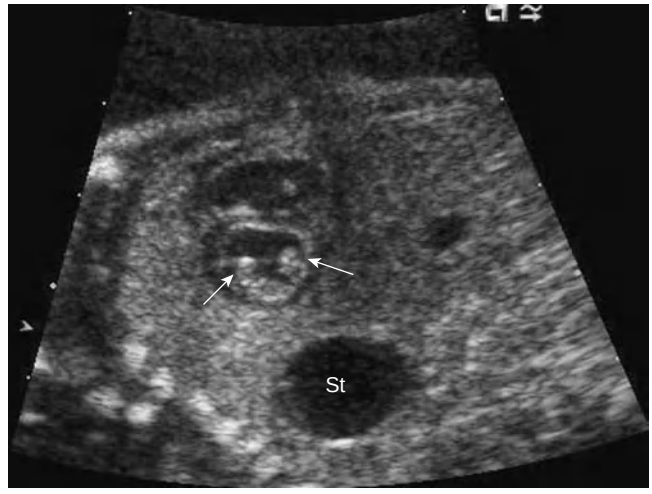


(d)

**Figure 42.5 (a–d)** Sagittal sweeps through the fetal thorax. Ao, ascending aorta; IVC, inferior vena cava; LA, left atrium; MV, mitral valve; RA, right atrium; St, stomach; SVC, superior vena cava; TV, tricuspid valve; arrows denote left ventricular papillary muscles.

distinct, and thus other criteria must be used. The AV valves, when of normal morphology, can assist in defining the ventricles. The right ventricle has a more pyramidal shape, with an inflow portion, a body, and an outflow (or infundibulum) from which one or both great arteries arise. Identification of the moderator band, best recognized in a 4-chamber image, is also useful. In contrast, the more bullet-shaped left ventricle has two papillary muscles, best visualized in a short-axis or sagittal sweep through the heart (Fig. 42.5), and continuity between the anterior mitral valve leaflet and the semilunar valve (usually aorta) can be demonstrated.

The ventricular septal anatomy, including the inlet, membranous, trabecular and outlet (conal septum) portions, can be evaluated using cross-sectional sweeps through the fetal chest from the crux of heart just above the diaphragm to the ventricular outlets, or a sagittal sweep from a more rightward aspect of the fetal heart leftward to the ventricular apex. Slow sweeps with color Doppler at low velocity can permit detection of even smaller ventricular septal defects.

When sweeping to the fetal head from a 4-chamber image, the ventricular outflow tracts and great arteries can be demonstrated (Fig. 42.6). The left ventricular outflow tract begins more posterior and leftward relative to the right ventricular outflow, and courses toward the right. The right ventricular outflow tract begins more anterior and courses leftward, wrapping around the left ventricular outflow and ultimately meeting the pulmonary artery, which lies to the left of the midline. The "three vessel view" facilitates recognition of normal and abnormal anatomy of the great arteries, arches and airways [17]. It is a cross-sectional image obtained through the superior mediastinum that in normal fetuses consistently demonstrates the relationship of the right superior vena cava, ascending aorta and main pulmonary artery to each other and to other structures within the fetal chest (Fig. 42.6c and Videoclip 42.2). The main pulmonary artery is seen in this view in its long axis as the most anterior and leftward vessel. The ascending aorta, in its short axis, is rightward and slightly more posterior. Finally, the right superior vena cava seen in its short axis is more rightward and most posterior and usually has the smallest diameter. Demonstration of a normal three-vessel view quickly establishes the presence of normally related great arteries. The size relationship of the structures assists in identifying altered flow through or growth of any of the three vessels as may occur in left or right heart obstruction, the presence of semilunar valve insufficiency, and interrupted inferior vena cava with azygous continuation or vein of Galen aneurysm (dilated superior vena cava). In the three-vessel view the right pulmonary artery courses in its long axis behind the ascending aorta and superior vena cava. Visualization of the left pulmonary artery often requires a slight rotation of the transducer from a straight cross-sectional plane as it courses under the ductus arteriosus.

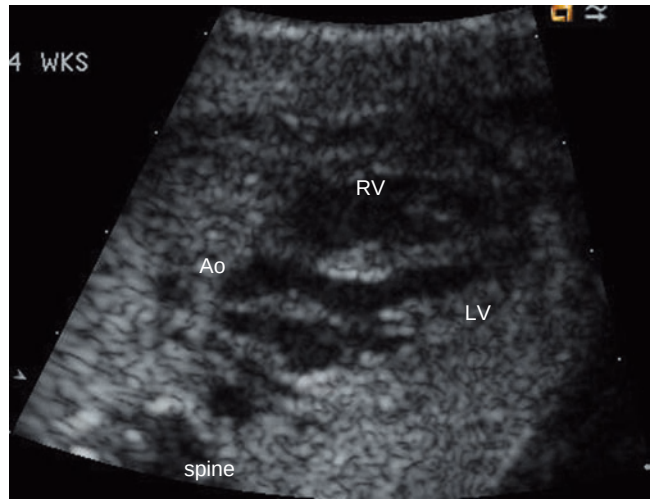


(a)

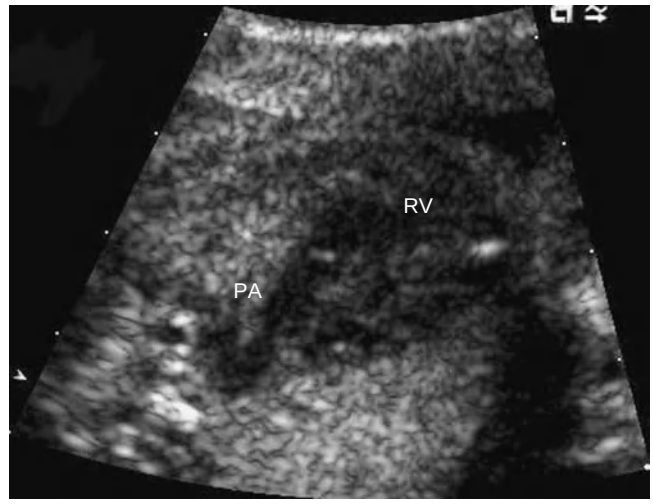


(b)

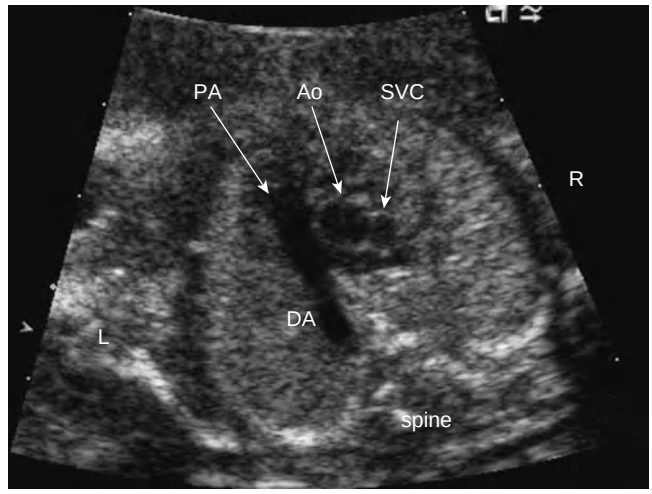


(c)

**Figure 42.6 (a,b)** Long-axis images through the fetal heart demonstrating crossing of the ventricular outlets and great arteries. **(c)** The normal three-vessel view. Ao, ascending aorta; DA, ductus arteriosus; L, left; LV, left ventricle; PA, main pulmonary artery; R, right; RV, right ventricle; SVC, superior vena cava.

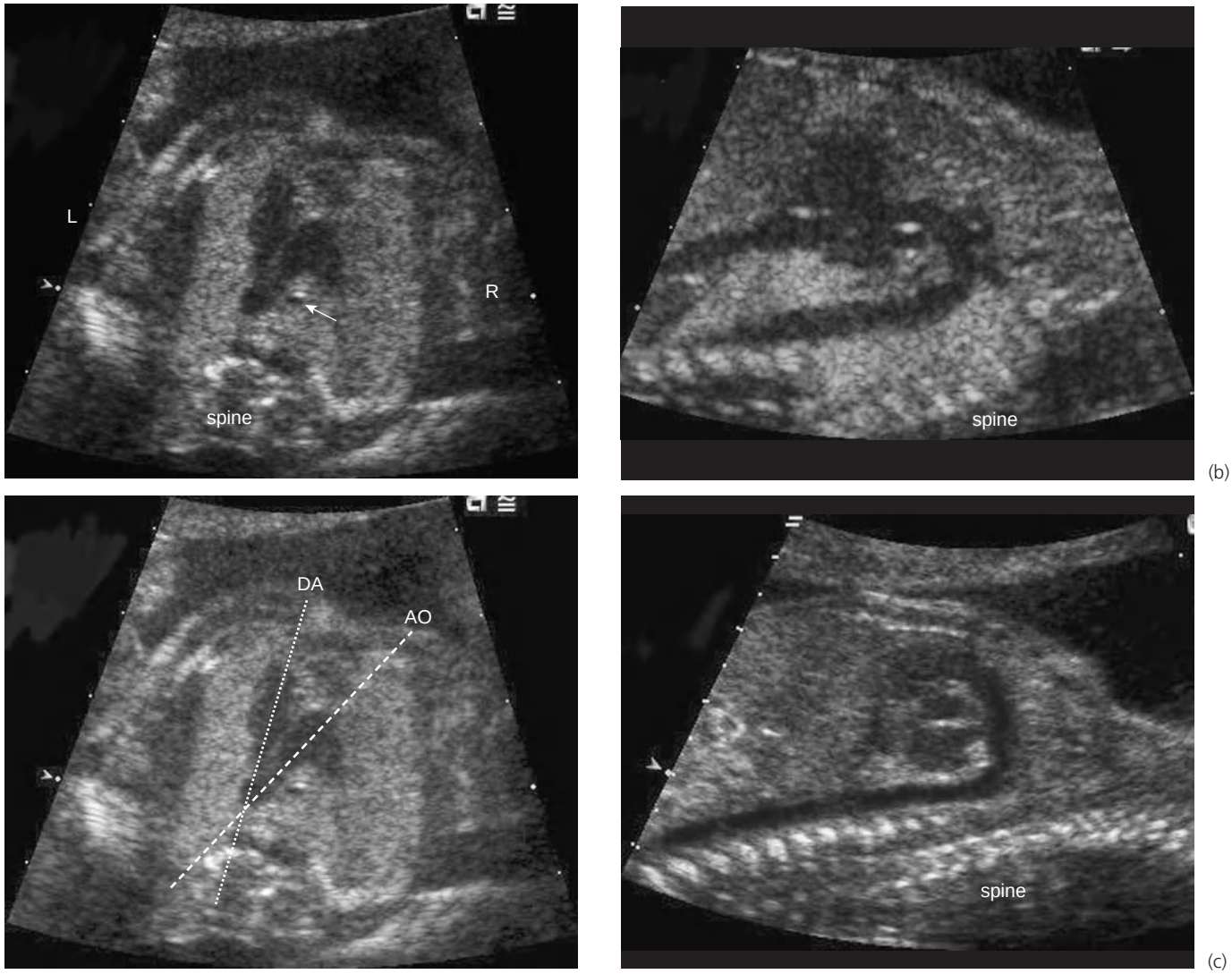


(a) (b) (c)

**Figure 42.7** **(a)** A slightly rotated (clockwise) three-vessel view demonstrating aortic and ductal arches. This view can help in obtaining long-axis views of the aortic **(b)** and ductal **(c)** arches. The arrow in **(a)** points to the trachea which, in the normal fetus, is to the right of both aortic and ductal arches. AO, aorta; DA, ductus arteriosus; L, left; R, right.

In the three-vessel view, the main pulmonary artery joins the ductus arteriosus (Fig. 42.7; see also Fig. 42.6), which dives straight back just to the left of the midline to meet the left-sided descending aorta. Sweeping toward the fetal head, the aortic arch can be seen coursing from right-anterior to left-posterior, crossing the midline toward the left of the trachea and ultimately joining the descending aorta (Fig. 42.7). This confirms the presence of left-sided aortic and ductal arches. From the three-vessel sweeps, one can immediately orient the transducer to obtain a long axis of the arches. For instance, when the fetus is supine, rotating the transducer 90° along the plane of the ascending aorta (from right-anterior to left-posterior) produces a long-axis image of the fetal aortic arch. The ascending aorta begins slightly more centrally, courses anteriorly and curves posteriorly to meet the descending aorta, giving rise to the three brachiocephalic arteries. Its classic "cane-handle" appearance is readily distinguishable from the more hockey-stick shape of the ductus arteriosus, with its nearly 90° angle with the descending aorta.

Early in gestation, in the normal fetus, the left and right sides of the heart are usually symmetric or nearly symmetric, particularly prior to 16 weeks. Later in gestation, however, the right atrium, right ventricle, main pulmonary artery and even the ductus arteriosus may be slightly larger than the left-sided structures [18,19]. More exaggerated or reverse asymmetry (the former particularly earlier in pregnancy) may be a clue to subtle left and right heart obstructive lesions including coarctation of the aorta [20]. Many of these can progress to more severe disease later in gestation. Use of normograms for fetal cardiac dimensions with generation of z-scores can be helpful in establishing the size of structures relative to normal and in following growth [21].

## Doppler interrogation

Spectral Doppler interrogation of the fetal heart requires the use of narrowed sample volumes and low velocity settings. Although Doppler assessment is important, in fact much of the pathology can be detected or surmised from careful 2D imaging of the fetal cardiovascular anatomy, with Doppler providing confirmation. Occasionally, though, new information or early pathology may be identified that warrants more detailed and ongoing assessment of the pregnancy. Color and pulsed Doppler may assist in the detection of certain aspects of normal anatomy where the image resolution is not sufficient. This is particularly true in very early pregnancy. Color Doppler identifies abnormal flows, including valve insufficiency and obstruction, ventricular septal defects, and altered ductal and arch flow, as observed in critical pulmonary or systemic outflow obstruction, respectively. Routine pulsed Doppler interrogation of both ventricular inflows and outflows, pulmonary venous, aortic and ductal arches, inferior vena cava, ductus venosus and umbilical arterial and vein flow is not only useful in confirming normal flows and function, but also helps with the recognition of abnormal flows and altered fetal heart function (Figs 42.8 and 42.9).

## Fetal heart function

Evaluation of fetal heart function requires basic knowledge of normal fetal cardiovascular physiology and the developmental changes that occur during gestation. It should consist of an evaluation of general features, as well as systolic and diastolic function parameters. Evaluation of fetal heart size or cardiothoracic ratio, wall thickness, inferior vena cava diameter, fetal heart rate, and the presence or absence of hydrops can provide initial clues to the presence of normal or abnormal fetal heart function. Basic systolic function may be assessed through the measurement of ventricular shortening fraction using either 2D images or M-mode interrogation. In the normal fetus, the left and right ventricular shortening fraction is 34 ± 3% and it does not change from 17 weeks to term [22]. Although fetal ventricular ejection fractions have also been documented using biplane Simpson techniques [23], the reproducibility of these volumetric measurements

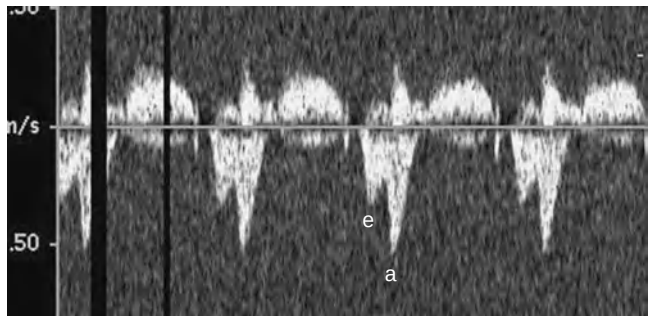


(a)

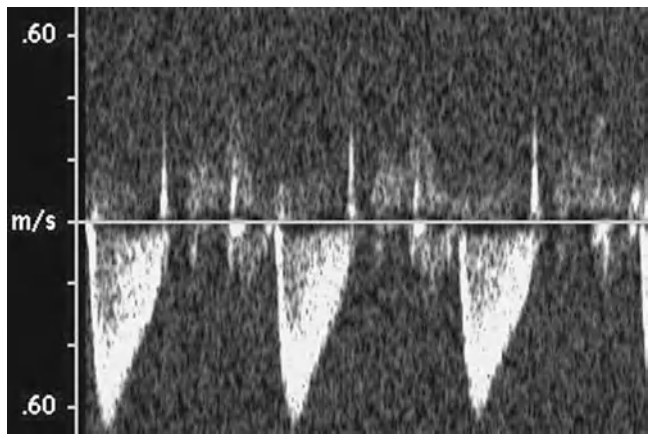


(b)

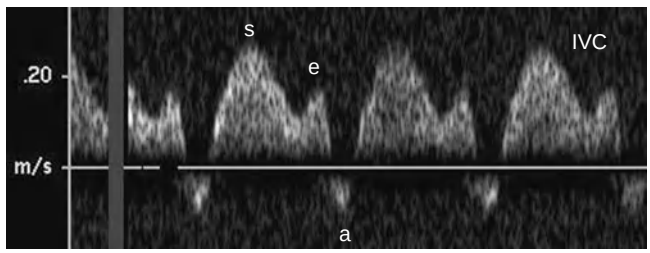


(c)

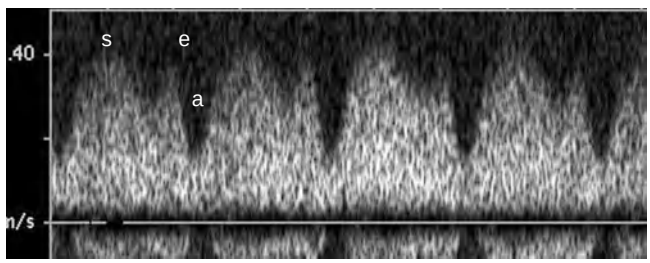


(d)

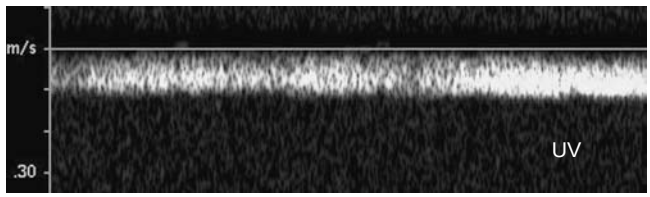


(e)

**Figure 42.8** Pulsed Doppler spectra of **(a)** the right ventricular inflow and **(b)** outflow; **(c)** the inferior vena cava; **(d)** the ductus venosus; and **(e)** the umbilical vein. Inflow Doppler spectra are characterized from 12 weeks' gestation as biphasic and A-wave (atrial systole) dominant, with increasing E-wave (early ventricular diastole) velocities through gestation. Outflow velocities progressively increase during gestation as cardiac output increases. Inferior vena caval (IVC) **(c)** and ductus venosus (DV) **(d)** flows are phasic, with forward flow in ventricular systole (s) and early diastole (e), and flow reversal (IVC) or reduced velocities (DV) in atrial systole (a). **(e)** Umbilical vein (UV) flow is continuous and of low velocity and displays mild undulations during fetal breathing.

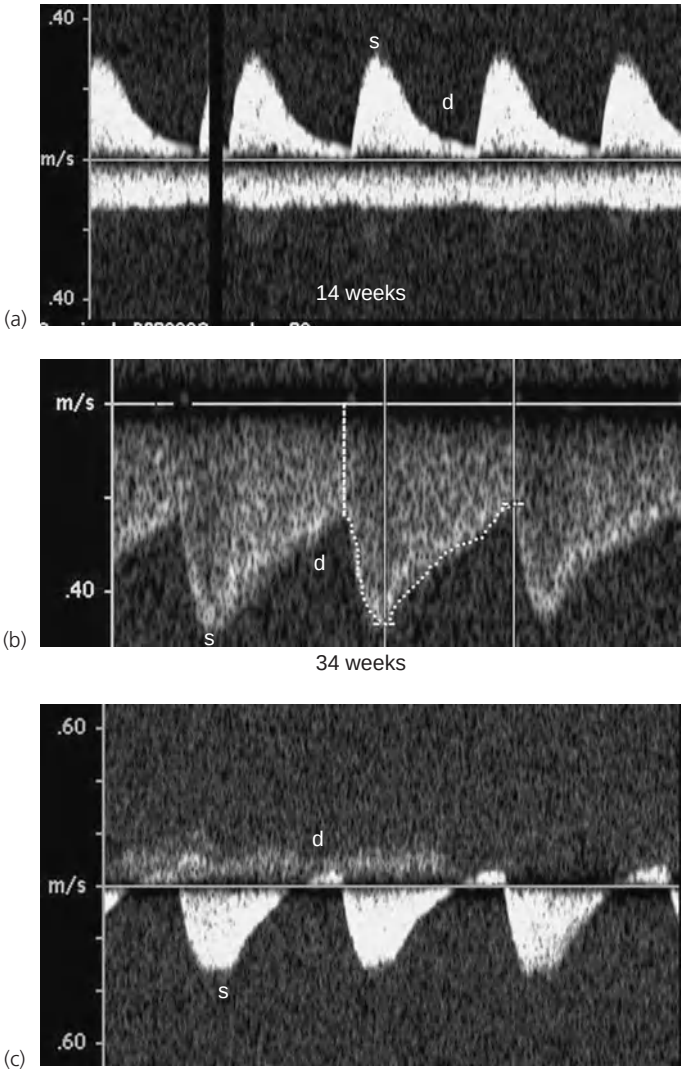


**Figure 42.9** Umbilical arterial flow from **(a)** 14 weeks' gestation consists of systolic and diastolic flows, which increase with gestation. **(b)** The more dramatic increase in diastolic flow later in gestation reflects decreasing placental resistance. **(c)** Reversed flow in diastole is never normal and may be seen where there is severe placental insufficiency. S, systole; d, diastole.

is poor [24]. Three-dimensional (3D) and four-dimensional (4D) echocardiography may ultimately provide the most accurate means of volumetric and mass assessment of the fetal heart [25–27].

Stroke volume and cardiac output can also be assessed. The normal fetal left ventricular stroke volume and cardiac output are less than those of the right ventricle from the second-trimester to term [28]. Documentation of fetal ventricular stroke volume and output is very useful in fetuses with hydrops fetalis, with or without a known etiology, to determine if increased output is contributing to the clinical picture; or in a fetus at risk to document the evolution of disease. Increasing cardiac output has been demonstrated, for instance, in such conditions as anemia, AV malformations, acardiac twin gestations and agenesis of the ductus venosus [29–31].

There has been growing interest in the evaluation of fetal diastolic function in health and disease. Pulsed Doppler assessment of ventricular inflow, inferior vena cava, ductus venosus, and umbilical vein flow patterns and velocities has been useful in recognizing changes in diastolic or filling function that may place the fetus at greatest risk of heart failure and compromised umbilical flow through altered central venous pressures [32,33]. Changes that occur in left and right ventricular inflow Doppler flow patterns with increasing E-wave velocities during early ventricular diastole and minimal change in the A-wave velocity, reflect developmental changes in the diastolic properties of the fetal myocardium, which may include both progressively more efficient relaxation and greater compliance [34,35]. Simultaneous assessment of left ventricular inflow and outflow velocities permits measurement of the left ventricular isovolumic relaxation time, which in the normal fetus is 43 ± 8 milliseconds (heart rate corrected) from 20 weeks' gestation to term [36]. Finally, the so-called Tei index, or myocardial performance index, has been used to define global fetal myocardial function [37]. The Tei index equals the sum of the isovolumic relaxation and isovolumic contraction times divided by the ejection time. It can be calculated for either the left or right ventricle using the offset of ventricular inflow to the onset of the next inflow (a) minus the ejection period (b) over b. In the normal second- or third-trimester fetus, the Tei index decreases with gestational age, with the left ventricular index showing a greater decline than the right ventricular index [38].

The use of tissue Doppler imaging in the assessment of fetal heart function has only relatively recently been reported, with documentation of peak tissue velocities, strain and strain rate in normal pregnancies [39–41], and in pregnancies complicated by fetal and maternal disease [42]. Myocardial tissue velocities in the normal fetal heart increase with gestational age, but strain and strain rate do not change and all appear independent of heart rate.

## Fetal rhythm assessment

Finally, a complete screening fetal echocardiogram should include a limited assessment of fetal heart rate and rhythm. This can be accomplished routinely through the use of either M-mode or pulsed Doppler techniques [43,44], which demonstrate the mechanical events of atrial and ventricular contraction (wall motion or flow) from which electrophysiologic events are surmised. Figures 42.10 and 42.11 demonstrate techniques that are routinely used. Several pulsed Doppler techniques have been developed to assess flow

(a)

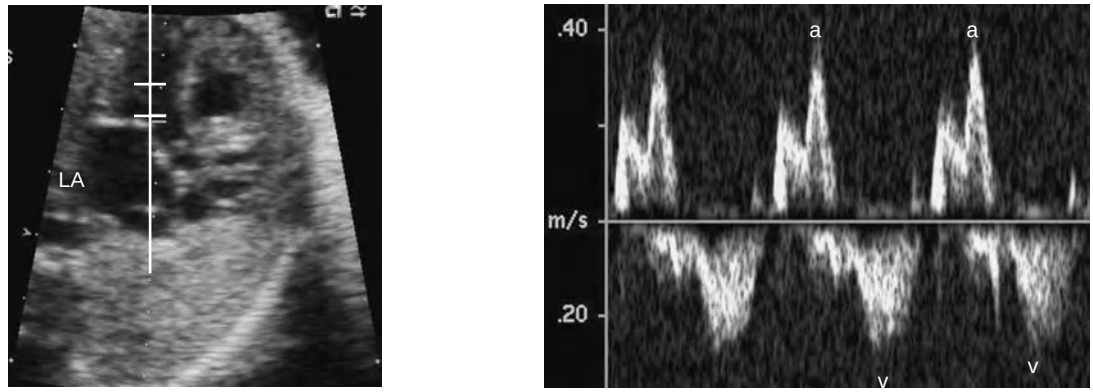


(b)

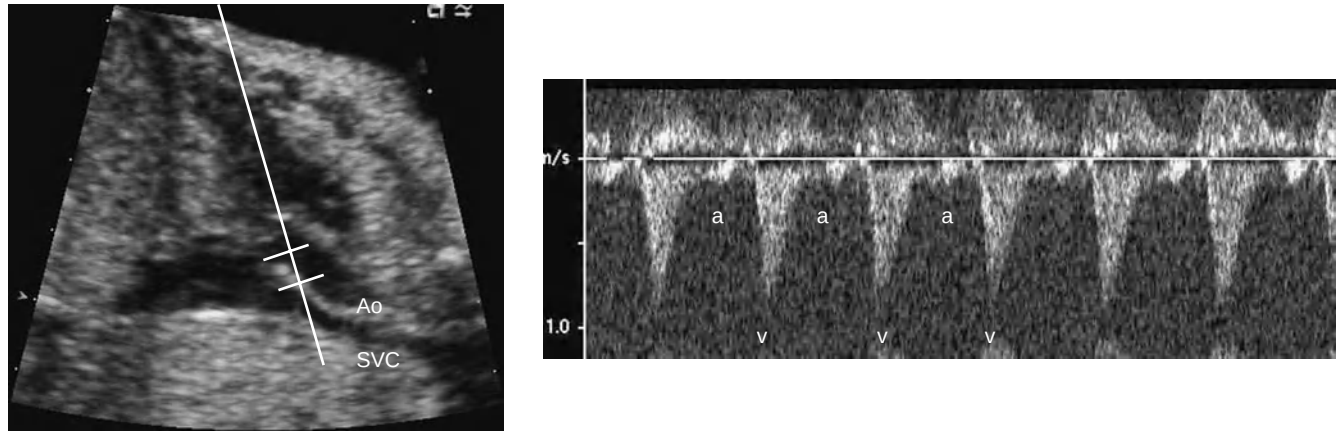


**Figure 42.10** Rhythm assessment using simultaneous **(a)** left ventricular inflow and outflow, and **(b)** superior vena caval and ascending aortic pulsed Doppler interrogation. Doppler atrioventricular (A–V) intervals provide a rough estimate of the P–R interval. a, atrial systole; v, ventricular systole. Ao, aorta; LA, left atrium; SVC, superior vena cava.

during atrial and ventricular contraction, including simultaneous left ventricular inflow and outflow, pulmonary artery and pulmonary vein [45], and superior vena cava and ascending aortic interrogation [46]. All of these techniques are limited to some extent by image resolution and fetal position. In addition they require experience in interpreting the tracings. Tissue Doppler imaging with simultaneous evaluation of atrial and ventricular wall movement at multiple sites may

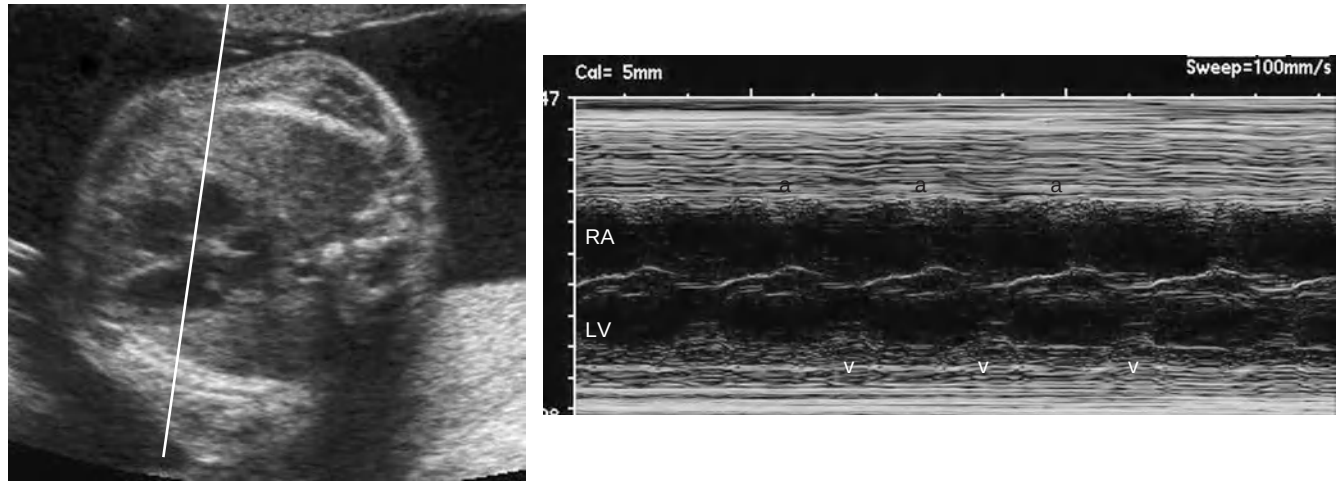


**Figure 42.11** Fetal rhythm assessment using M-mode echocardiography. The M-mode cursor is directed through the right atrium and left ventricle to obtain the tracing. RA, right atrium; LV, left ventricle.

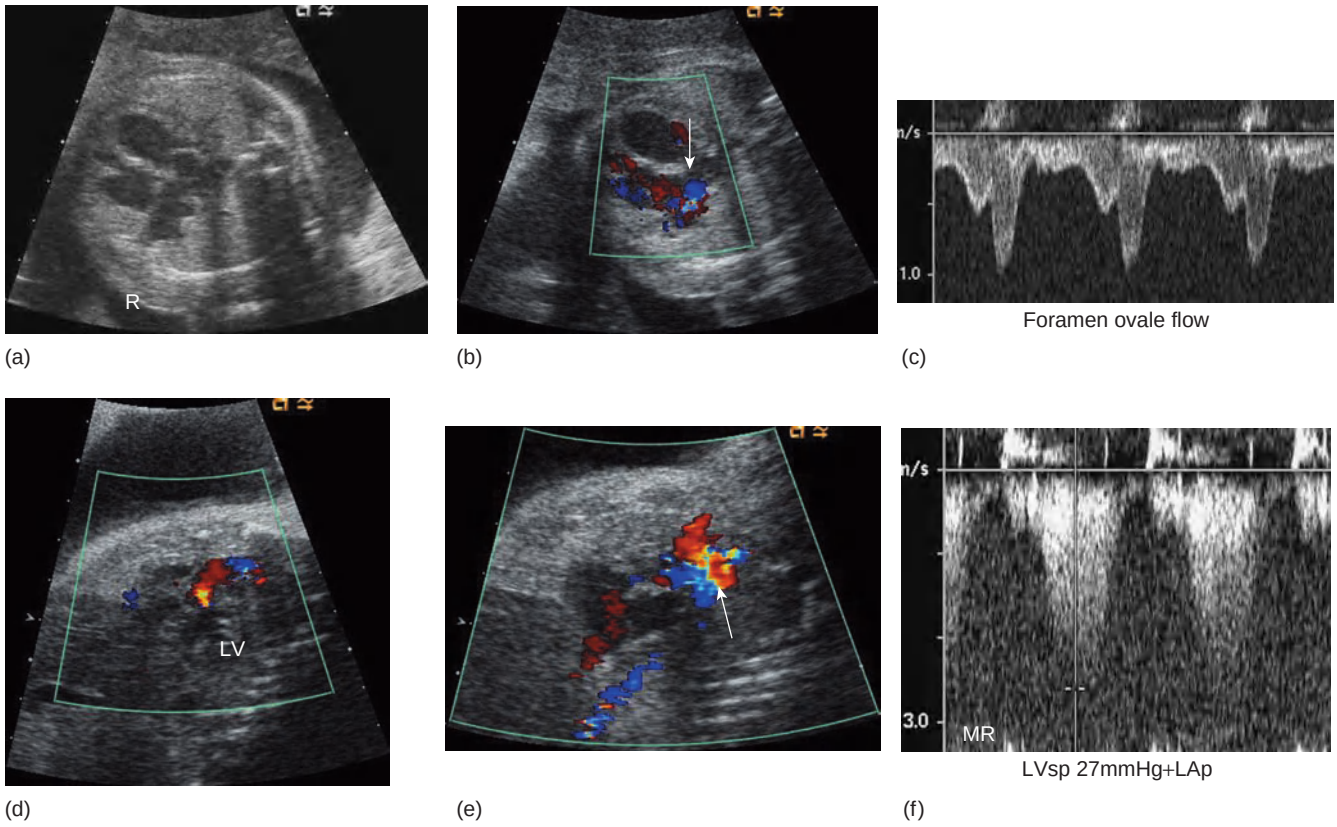


**Figure 42.12** Critical aortic stenosis at 23 weeks' gestation. **(a)** Four-chamber view with dilated left ventricle. **(b,c)** Foramen ovale flow from left to right with mild restriction. **(d)** Forward flow (red) through the aortic valve. **(e)** Retrograde aortic arch flow in keeping with critical left heart obstruction. **(f)** Estimated left ventricular (LV) systolic pressure is 27 mm Hg + left atrial pressure (LAp) by the mitral regurgitation (MR) jet (high for the systemic systolic blood pressure at 23 weeks). This lesion will progress to hypoplastic left heart syndrome over the next several weeks in utero.

prove to be the most effective echocardiographic technique for assessment of arrhythmias as it is less limited by image resolution and fetal position, and may be easier to interpret [47]. Programs for simultaneous assessment of atrial and ventricular wall motion are, however, universally clinically available at this time.

## Fetal cardiovascular pathology

### Fetal structural heart disease

Definition of the segmental anatomy, beginning with visceral and atrial situs, the atrioventricular (AV) and ventriculo-arterial (VA) connections, and aortic and ductal arch position, morphology and flow, becomes critically important when there is fetal cardiovascular pathology, particularly of a complex nature. Detailed assessment for associated cardiac pathology that can complicate the prenatal and postnatal outcome, with consideration of what can and cannot be confirmed, and knowledge of the potential for progression of fetal heart disease, is critical for accurate counseling in an affected pregnancy and for perinatal management planning.

The cardiovascular pathology most often encountered prenatally tends to represent a more severe spectrum of pathology than is encountered after birth. This is due at least in part to referral bias, with pathology most recognizable in the 4-chamber view (e.g., hypoplastic left heart syndrome) more likely to be detected at routine obstetrical ultrasound [48]. Cardiovascular lesions associated with extracardiac pathology including aneuploidy are also more often detected [2,48]. Reviews of the prenatal features of specific forms of CHD are provided in the individual chapters devoted to the lesions. Additional examples of approaches to the evaluation of structural CHD in utero are provided in Figs 42.12–42.17.

Fetal echocardiography permits the diagnosis of all forms of CHD before birth [49–51]. The accuracy of fetal diagnosis in the context of more complex structural heart disease has been best demonstrated in heterotaxy syndrome, where associated cardiac pathology includes abnormalities of visceral and atrial situs, systemic and pulmonary venous connections, AV and VA connections, abnormalities of the AV valves and outflows, abnormalities of the arches and even abnormalities of rhythm. In a large, single-center series of fetal heterotaxy,

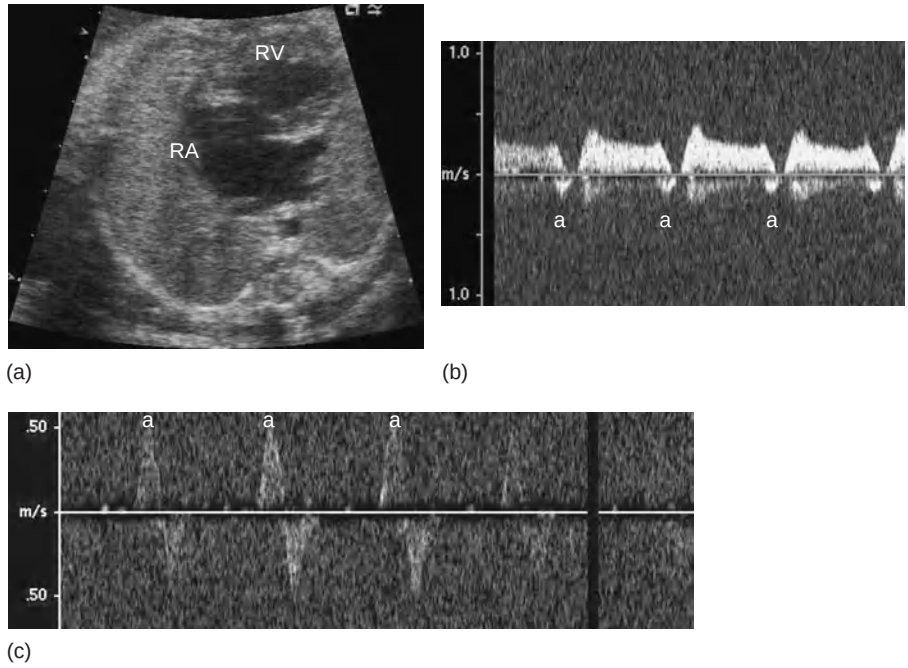


**Figure 42.13** **(a)** Hypoplastic left heart syndrome and assessment of left atrial pressure through pulmonary venous flow pattern. **(b)** Pulmonary venous flow pattern showing low-velocity retrograde flow in atrial systole (a). **(c)** With severe left atrial hypertension, there is loss of forward flow in early diastole and reduced flow in ventricular systole with increased retrograde flow in atrial systole. The fetus with the pulmonary vein flow depicted in (c) had a maximum $P_{a}O_{2}$ of 17 mm Hg after birth. RA, right atrium; RV, right ventricle.

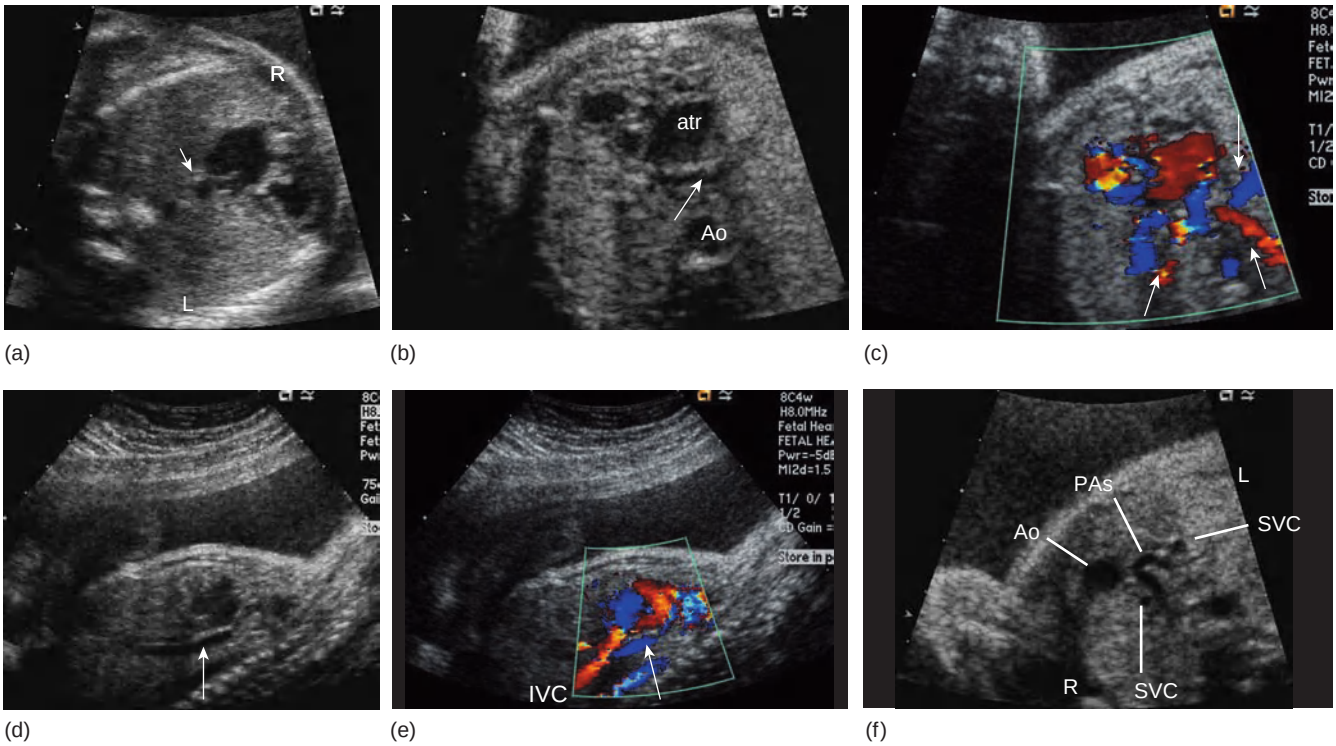


**Figure 42.14** Fetal echocardiogram in a 27-week fetus with right atrial isomerism/asplenia syndrome – segmental anatomy {A,D,D}. **(a)** Four-chamber image demonstrating levocardia, an unbalanced atrioventricular (AV) septal defect and dominant D-looped right ventricle. **(b)** Pulmonary vein confluence (arrow) is behind the posterior aspect of the atrium, and **(c)** color Doppler confirms pulmonary venous flow. **(d,e)** The pulmonary vein confluence joins a vertical vein (also seen in (a) behind the atrium) that descends through the diaphragm to join the portal venous system (arrow). **(f)** The "three-vessel view" demonstrating bilateral superior vena cava, a large anterior aorta and pulmonary atresia; the latter is confirmed by retrograde ductus arteriosus flow. Ao, aorta; atr, atrium; IVC, inferior vena cava; L, left; PAs, pulmonary arteries; R, right; SVC, superior vena cava.

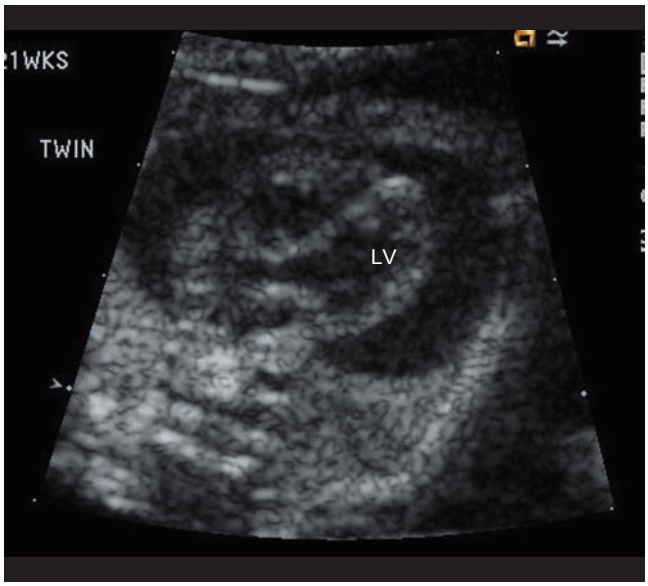


(a)

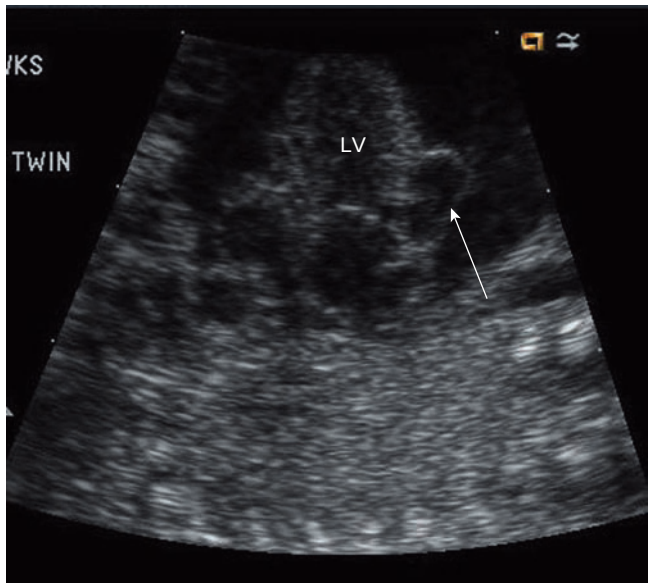


(b)

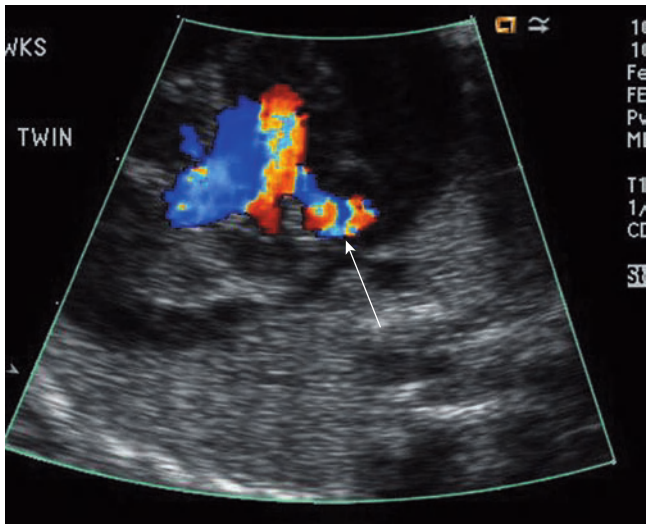


(c)

**Figure 42.15** Echocardiogram findings in a 20-week fetus with a left ventricular (LV) free wall diverticulum. **(a)** Associated large pericardial effusion without other signs of hydrops. **(b)** Two-dimensional imaging of a thin-walled protrusion from the LV free wall that communicates through a narrow neck with the LV cavity; **(c)** color Doppler of same feature.

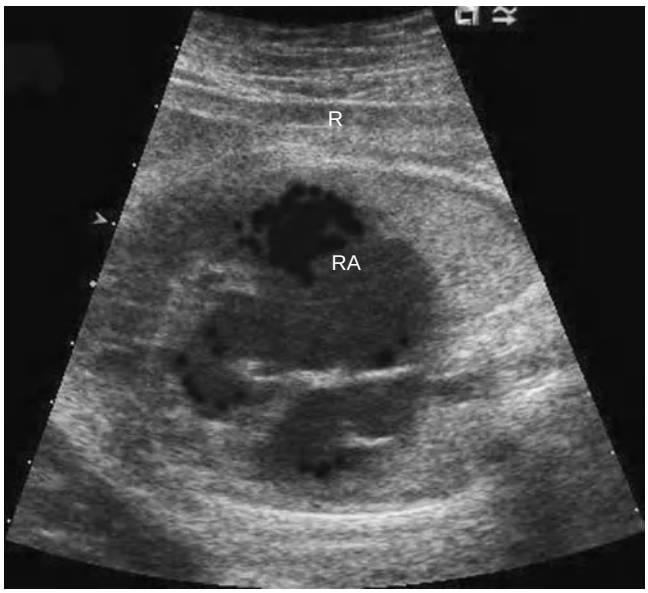


(a)

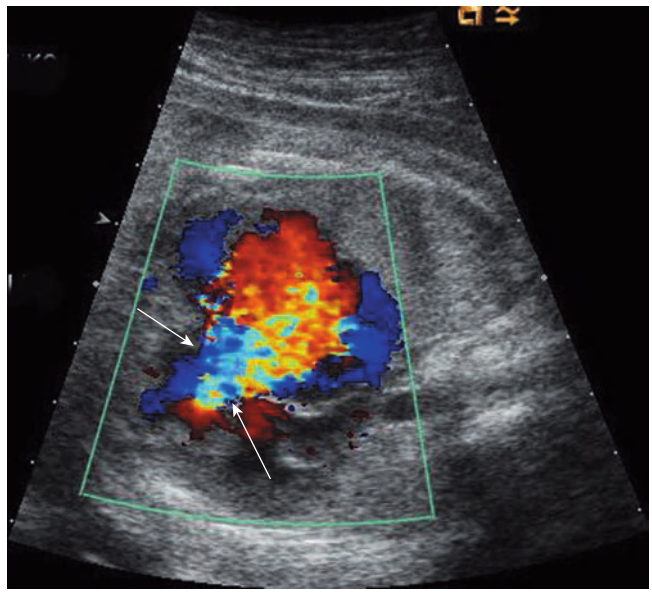

(b)

**Figure 42.16** Ebstein anomaly of the tricuspid valve with severe tricuspid regurgitation in a 33-week fetus. **(a)** Significant cardiomegaly in the 4-chamber view. **(b)** Color Doppler confirms the presence of severe tricuspid insufficiency with failure of the leaflets to coapt in systole (arrows).

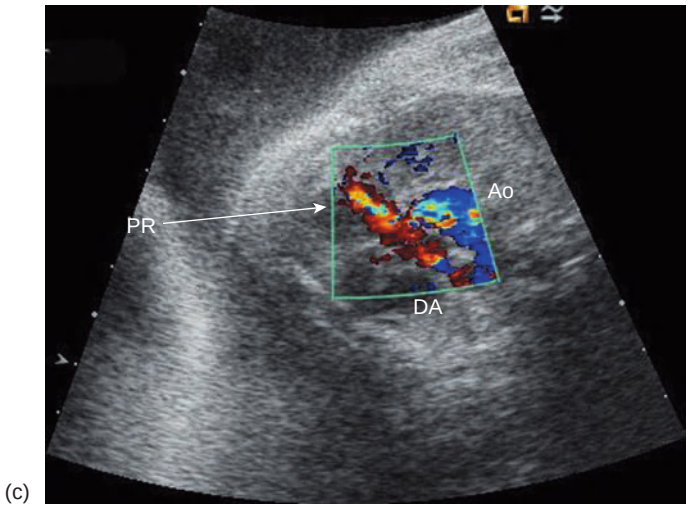


(c)

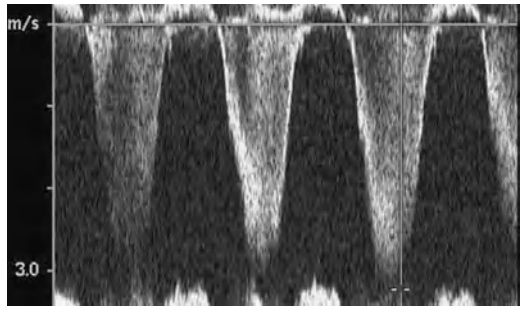


(d)

RVsp 40mmHg+RAp

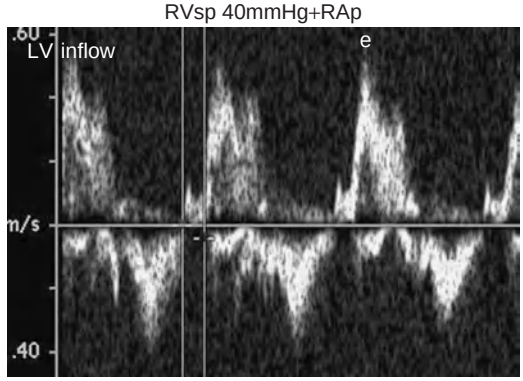


(e)

**Figure 42.16** **(c)** Pulmonary regurgitation in systole (confirming patency of the pulmonary valve) with retrograde ductus arteriosus flow. **(d)** Although the right ventricle (RV) cannot eject into the main pulmonary artery, the pressure generated is very close to that of normal systemic systolic blood pressure and greater than half the systolic pulmonary pressure of a normal newborn. **(e)** Left ventricular (LV) inflow with dominant E-wave. Ao, aorta; DA, ductus arteriosus; PR, pulmonary regurgitation; RA, right atrium; RAp, right atrial pressure; RVsp, right ventricular systolic pressure.

Taketazu et al. [51] demonstrated that, at least in more recent years, the majority of the cardiac pathology can be accurately defined when compared with observations at autopsy or postnatal echocardiography (Table 42.3). There are some limitations, however, in fetal echocardiography, and the following features may still be missed or underappreciated: small to moderate-sized ventricular and atrial septal defects; minor valve abnormalities; complex apical muscular defects; partial anomalous pulmonary veins; and coronary anomalies and cardiac lesions that evolve after birth (e.g., juxtaductal coarctation, subaortic membrane).

Although most CHD is present after 5–7 weeks of gestation, there are many ways in which structural heart disease can evolve in utero, as listed in Box 42.1 [52]. This is at least

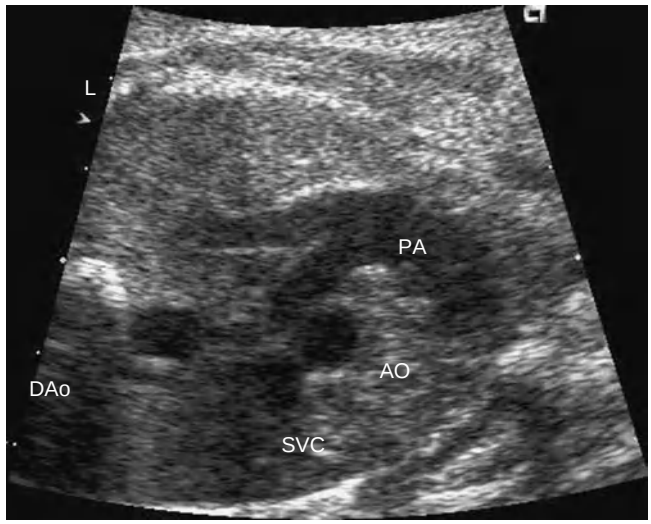


(a)

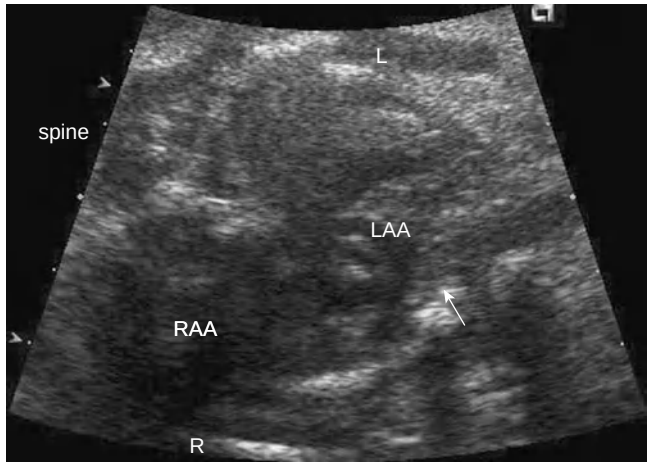


(b)

**Figure 42.17** Echocardiogram in a 28-week fetus with a double aortic arch. **(a)** The three-vessel view suggests the presence of a right arch. **(b)** Sweeping toward the fetal head, the smaller left arch and left ductus arteriosus course to the left of the trachea (arrow), thereby completing the ring;

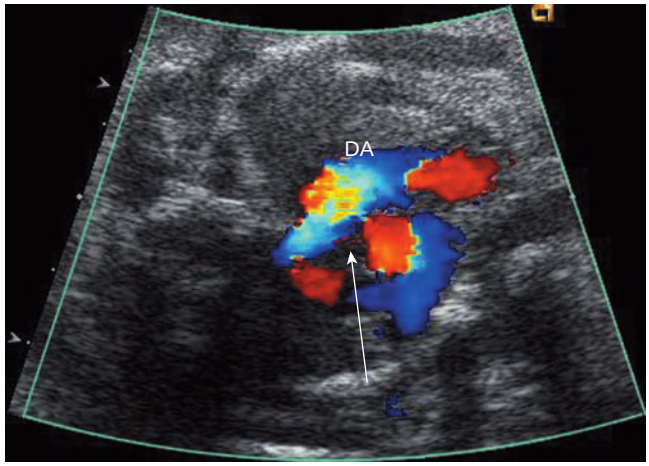


(c)

**Figure 42.17 (c)** color Doppler showing the same features. AO, ascending aorta; DA, ductus arteriosus; DAo, descending aorta; L, left; LAA, left aortic arch; PA, main pulmonary artery; RAA, right aortic arch; SVC, superior vena cava.

## Box 42.1 Mechanisms of evolution of fetal heart disease

- Development/progression of ventricular inflow, outflow and arch obstruction [53–56,98–104]
- Development/progression of structural hypoplasia [53–56,105–110]
- Development/progression of valvular regurgitation [98]
- Development/progression of dysrhythmia [51,75–77,98,111,112]
- Development of foramen ovale restriction [66,113]
- Diminution and closure of ventricular septal defect [114]
- Development of ductus arteriosus aneurysm or spontaneous constriction [67,115]
- Development of primary myocardial disease [31,116–119]
- Development of congestive heart failure [120–124]
- Development of, progression or regression of cardiac tumors [125–127]

**Table 42.3** Accuracy of specific structural pathology at diagnosis of fetal heterotaxy and its evolution with study era

| Variable | Total (*n* = 45) | 1991–1996 (*n* = 18) | 1997–2002 (*n* = 27) | *P* |
|---|---|---|---|---|
| IVC connection in RAI* | 5/9 (56%) | 1/2 (50%) | 4/7 (62%) | >0.99 |
| Interrupted IVC in LAI | 30/32 (94%) | 11/12 (91%) | 19/20 (95%) | >0.99 |
| SVC anatomy† | 37/43 (86%) | 12/17 (71%) | 25/26 (96%) | 0.03 |
| Intracardiac lesions | 42/45 (93%) | 15/18 (83%) | 27/27 (100%) | 0.06 |
| Ventriculo-arterial connection | 42/45 (93%) | 16/18 (89%) | 25/27 (93%) | >0.99 |
| Outflow obstruction‡ | 39/44 (89%) | 16/17 (94%) | 23/27 (85%) | 0.63 |
| Pulmonary vein connection§ | 30/39 (77%) | 4/12 (33%) | 26/27 (93%) | <0.0001 |
| Hepatic vein connection** | 20/31 (65%) | 6/10 (60%) | 14/21 (67%) | >0.99 |
| Splenic lesion†† | 18/24(75%) | 5/7 (71%) | 13/17 (76%) | >0.99 |

The numerator/denominator indicates the number of lesions accurately diagnosed before birth/the number of lesions identified after birth or at postmortem. Accurate diagnosis ratio is showed as percent.
IVC, inferior vena cava; LAI, left atrial isomerism; RAI, right atrial isomerism; SVC, superior vena cava (includes bilateral cava, unilateral SVC, and left or right SVC to coronary sinus).
*Includes inferior vena cava to the left side of the atrium or left-sided atrium, inferior vena cava to the right side of the atrium or right-sided atrium.
†Includes isolated right or left superior vena cava to the atrium or coronary sinus, or bilateral superior vena cava.
‡Aortic, pulmonary or bilateral outflow obstruction.
§Normal pulmonary venous connection or totally anomalous connection with details regarding specific location of return.
**Connection of all hepatic veins to the inferior vena cava, separate connection and to which atrium.
††No spleen, single left or right spleen or multilobed spleen.
Data from Taketazu M, Lougheed J, Yoo SJ, Hornberger LK. Fetal heterotaxy syndrome: spectrum of heart disease, accuracy of diagnosis and clinical outcome. *Am J Cardiol* 2006:97:720–4.

partly a consequence of the unique features of the fetal circulation, which permit a redistribution of blood flow. The potential for progression should prompt serial evaluation of most pregnancies with fetal CHD.

Left and right heart obstructive lesions are among those of greatest interest given their risk of progression. More subtle abnormalities may be missed. Mild and moderate obstruction of either AV or semilunar valves may be associated with subtle ventricular or great artery size discrepancy. If mild or moderate semilunar valve obstruction is present early in gestation, there may be progressive obstruction that leads to more severe disease at birth. More severe obstruction of either semilunar valve may result in progressive hypertrophy of the ipsilateral ventricle and the development of tricuspid or mitral valve insufficiency with increasing flow velocities demonstrated by continuous-wave Doppler, suggesting increasing ventricular systolic pressures [53–56]. Eventually, when there is more critical obstruction, retrograde ductal or aortic arch flow confirms the diagnosis and the need for prostaglandin therapy after delivery [57]. If severe obstruction occurs early in gestation, eventual failure of the ipsilateral ventricle or evolution of endocardial fibroelastosis observed in critical aortic valve stenosis may result in a redistribution of flow toward the contralateral heart as a consequence of the foramen ovale (Fig. 42.12 and Videoclip 42.3). As long as the contralateral ventricle can sustain the equivalent of a biventricular output, the fetus can thrive but there is typically progressive hypoplasia of the ipsilateral ventricle, AV valve and great artery [53–56].

In severe left heart obstruction, progressive restriction of the foramen ovale may lead to severe left atrial hypertension, cyanosis and pulmonary edema at birth. Foramen ovale restriction may be suggested by the presence of a thickened atrial septum, a small atrial septal communication and turbulent flow through the atrial septum. It can be confirmed by the use of pulmonary venous Doppler [58] (Fig. 42.13). As the left atrial pressure increases, increasing flow reversal in atrial systole and decreasing early diastolic forward flow occur, leading eventually to only to-and-fro flow. The evolution of more severe secondary pathology, including a hypoplastic left or right ventricle in the presence of severe semilunar valve obstruction and restriction of the foramen ovale, has prompted the development of invasive procedures to ameliorate the obstruction prenatally. To date, balloon aortic and pulmonary valvuloplasty [59–61] and atrial septoplasty and stent placement have been described, with moderate success [62].

Some cardiovascular lesions are identified uniquely or more frequently before birth. Cardiovascular disease incompatible with the fetal circulation or associated with lethal extracardiac pathology leading to fetal demise may be encountered. Ventricular aneurysms or diverticulum may be more common in prenatal series partly because more severe pathology is not tolerated by the fetal circulation, and more subtle lesions not associated with symptoms may go unrecognized after birth [63–65] (Fig. 42.15). There are abnormalities of the fetal circulation, including restriction of the foramen ovale [66], ductus arteriosus constriction [67] and agenesis of the ductus venosus [30], that can cause cardiovascular compromise, for which the treatment is often delivery at a viable age.

## Fetal heart failure

Umbilical venous return, which provides oxygenated blood from the placenta directed largely through the ductus venosus and across the foramen ovale, requires low downstream systemic venous, atrial and ventricular filling pressures. Any pathology that influences central venous pressures can adversely affect the fetal circulation and lead to the evolution of hydrops, compromised umbilical flow with hypoxemia and demise. The fetal circulation requires at least one patent and competent AV and semilunar valve, a normally filling and ejecting ventricle, and a well-functioning placenta. Many conditions can lead to the evolution of fetal heart failure, which manifests in its worst state as hydrops with pleural and pericardial effusions, ascites and skin edema. It occurs as a consequence of primary myocardial or structural heart disease that influences the function of both ventricles, fetal bradyarrhythmias or tachyarrhythmias that affect ven tricular filling or ejection, and extracardiac abnormalities that affect the fetal cardiac output (Table 42.4). In the presence of primary myocardial disease, systolic and diastolic function may be affected, the latter of which is most associated with the evolution of fetal heart failure [31]. Pulsed Doppler evaluation of the fetal ventricular inflows, inferior vena cava (IVC), ductus venosus and umbilical venous flow patterns can help to define the severity of altered central venous pressures and the likelihood of evolution of fetal hydrops (Fig. 42.18). Abnormalities of systemic venous Doppler echocardiograms have been used to distinguish cardiovascular from noncardiovascular etiologies of hydrops. Figure 42.19 provides an example of fetal cardiomyopathy with evolution of hydrops (Videoclips 42.4 and 42.5).

An example of CHD that is among those least tolerated by the fetal circulation is that of severe tricuspid valve insufficiency (Fig. 42.16; Videoclips 42.6 and 42.7). In this condition, the right atrium and right ventricle become progressively dilated, which worsens the severity of tricuspid insufficiency further. Eventually, the right ventricle is unable to generate sufficient pressure to open the pulmonary valve in systole. If the pulmonary valve is patent there may be pulmonary insufficiency (Videoclip 42.7), which only worsens the right ventricular volume load. Although initially there is a redistribution of flow toward the left heart through the foramen ovale, with the left ventricle sustaining the equivalent of a biventricular output, the right ventricular loading ultimately influences left heart function, particularly filling

**Table 42.4** Primary and secondary causes of fetal heart failure

**Primary cardiac causes**

*Myocardial disease*
- Intrinsic
  - Cardiomyopathies
    - Autosomal recessive
    - Autosomal dominant
    - X-linked
    - Mitochondrial
  - Aneuploidy
- Extrinsic
  - Infectious – myocarditis
  - Maternal anti-Ro/anti-La-mediated

*Primary structural heart disease*
- Severe atrioventricular (AV) valve insufficiency
  - Ebstein anomaly of the tricuspid valve
  - Tricuspid valve dysplasias
  - Severe aortic stenosis
  - Severe pulmonary stenosis
  - Atrioventricular septal defect
- Severe semilunar valve insufficiency
  - Truncus arteriosus
  - Tetralogy of Fallot/absent pulmonary valve syndrome
- Inflow obstruction
  - Severe right heart obstruction with foramen ovale restriction
  - Cardiac tumors
- Outflow obstruction
  - Truncus arteriosus with truncal valve obstruction
  - Severe pulmonary outflow obstruction*
  - Severe aortic outflow obstruction*
  - Ductus arteriosus constriction
  - Cardiac tumors
- Other
  - Ventricular aneurysm with biventricular dysfunction

*Arrhythmias*
- Tachyarrhythmias
  - Supraventricular tachycardia (incessant, <32 weeks, structural disease)
    - Atrial flutter
    - AV accessory pathway
    - Long V–A tachycardias
    - Junctional ectopic tachycardia
  - Ventricular tachycardia
- Bradycardias
  - Fetal AV block (structural heart disease, myocardial dysfunction)

**Secondary causes**

*High-output states*
- Anemia
- Acute twin–twin or fetal–maternal hemorrhage
- Arteriovenous malformations
- Agenesis of the ductus venosus
- Acardiac twin gestation

*High afterload*
- Twin–twin transfusion syndrome
- Placental insufficiency

*Reduced preload*
- Extracardiac/intrathoracic mass
  - Congenital cystic adenomatous malformation
  - Diaphragmatic hernia
  - Cystic hygroma
- Pericardial effusion – teratoma

*Usually with severe atrioventricular valve insufficiency or dysfunction of the contralateral ventricle (at times from compression).

[68]. This can lead to increasing central venous pressures and eventual hydrops. In addition, altered left ventricular filling and consequent reduced output [69] probably impact critically the ability of the fetus to respond to acute physiologic changes resulting in an increased risk of sudden demise, particularly in the early third trimester. Associated supraventricular tachyarrhythmias compromise the fetal heart further by reducing the filling time of the left ventricle. Other volume

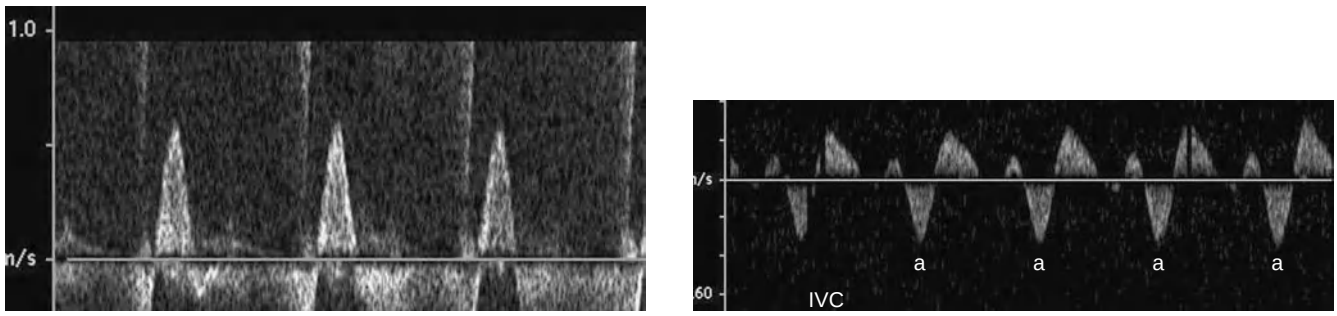


(a) (b)

**Figure 42.18** Pulsed Doppler flow patterns with increased atrial and ventricular filling pressures and high central venous pressures. **(a)** Uniphasic (atrial systole), short-duration ventricular inflow pattern seen in severe fetal myocardial disease. **(b)** Inferior vena caval flow (IVC) with increased A-wave reversal.

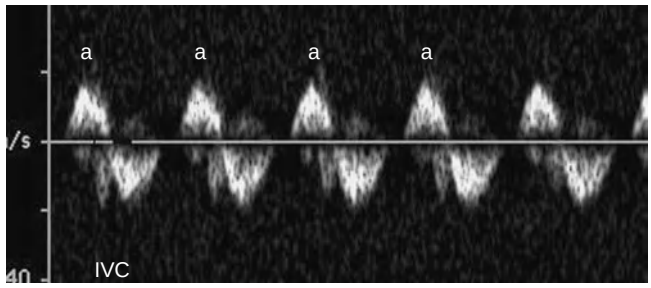


(c)

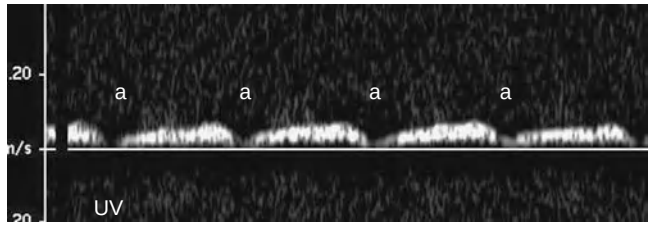


(e)

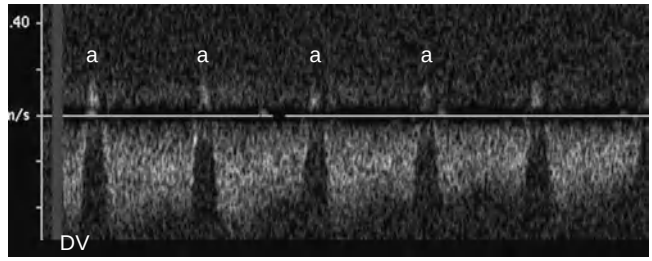


(d)

**Figure 42.18** **(c)** With higher atrial and ventricular filling and central venous pressures, there is loss of flow in early ventricular diastole. **(d)** In the ductus venosus (DV) there is cessation of forward flow in atrial systole and eventual A-wave reversal. **(e)** Eventually, umbilical venous (UV) pulsations develop with cessation of flow in atrial systole (a).

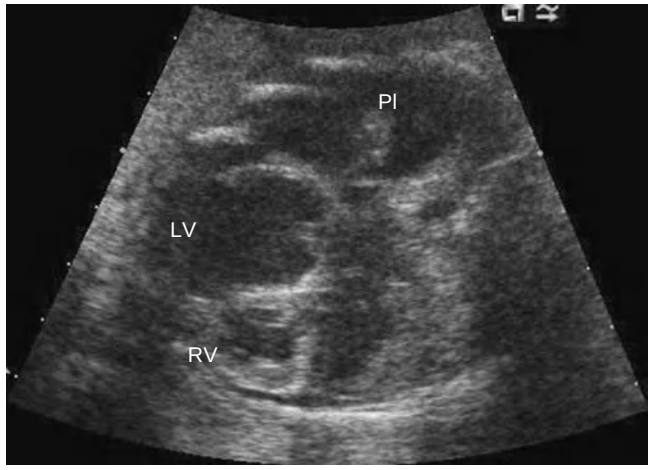


(a)

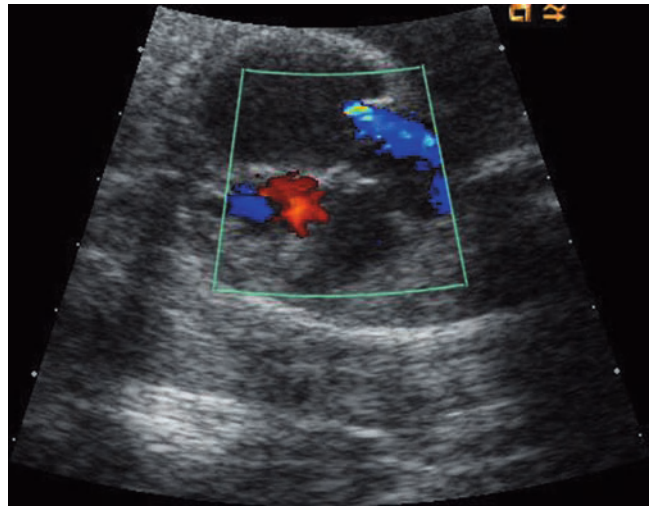

(b)

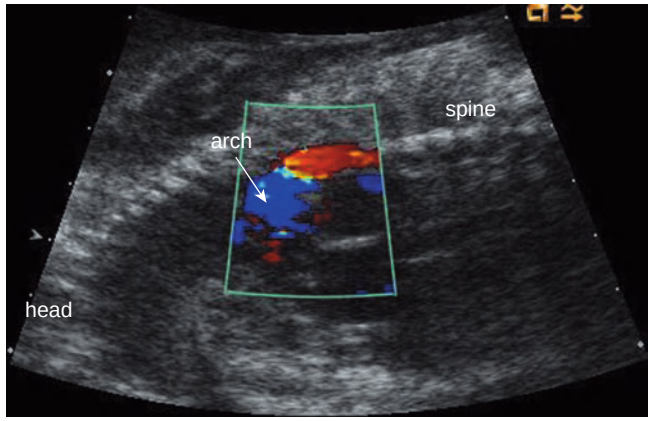


(c)

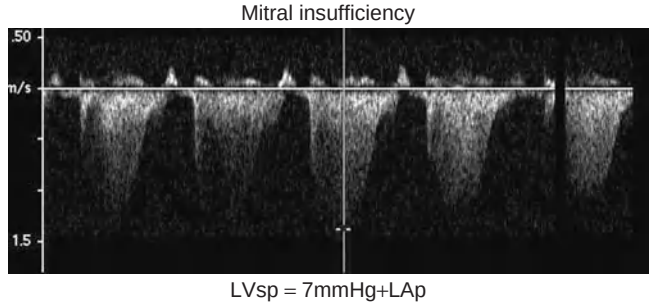


(d)

**Figure 42.19** Fetal primary left ventricular (LV) cardiomyopathy at 25 weeks' gestation. **(a)** Dilated LV with severe systolic dysfunction. A large right pleural effusion (Pl) was present at diagnosis, as was ascites. **(b)** Color Doppler revealed mitral insufficiency and no forward flow or regurgitation through the aortic valve. **(c)** Retrograde aortic arch flow suggested inadequate LV output. **(d)** Very low calculated LV systolic pressures based on the mitral regurgitation was in keeping with primary myocardial disease and not aortic outflow obstruction. LVsp, left ventricular systolic pressure; LAp, left atrial pressure; RV, right ventricle.

loading conditions are similarly less tolerated by the fetal circulation, including tetralogy of Fallot with absent pulmonary valve syndrome [70].

The ability to assess the evolution of fetal heart failure and to define better the etiology of nonimmune fetal hydrops with an inclusion or exclusion of a cardiovascular cause, has increased the importance of fetal echocardiography in the evaluation and noninvasive and invasive management of many fetal conditions that alter cardiac function. For instance, fetal echocardiography has been increasingly used in the care of monochorionic twin pregnancies complicated by twin–twin transfusion syndrome [71–73].

## Evaluation of fetal arrhythmias

More than 90% of pregnancies referred for fetal arrhythmia are either found to have no arrhythmia at the time of fetal echocardiography or premature atrial beats [74]. Rarely, more important tachyarrhythmias or bradyarrhythmias may be identified that have the potential to lead to cardiovascular compromise and hydrops. Table 42.5 summarizes the fetal arrhythmias detected before birth and the echocardiographic features that distinguish each mechanism. Figure 42.20 provides an example of Doppler and M-mode findings in a case of premature atrial beats with AV block. If these occur frequently, as in a bigeminal pattern, fetal bradycardia may

**Table 42.5** Echocardiographic features of fetal arrhythmias

| Rhythm | Atrial and ventricular rates | Atrial and ventricular intervals | Onset/offset | Associated lesions |
|---|---|---|---|---|
| Sinus rhythm | 120–160 bpm | Normal A–V relationship | Gradual | Normal |
| Premature atrial contraction (PAC) | Variable | Short A–A from sinus to PAC but normal A–A interval from PAC to next sinus beat | Acute | Cardiac tumors, atrial dilation, redundant septum primum |
| Premature ventricular contraction (PVC) | Variable | Short V–V from preceding sinus beat to PVC | Acute | Cardiac tumors, myocardial disease, aneurysms, LAI |
| Sinus tachycardia | A and V rates 170–210 bpm | Long V–A relative to A–V | Gradual with beat–beat variability | Maternal thyrotoxicosis |
| Ectopic atrial tachycardia | A and V rates 170–240 bpm | Long V–A relative to A–V | Gradual with beat–beat variability | Cardiac tumors, atrial dilation |
| PJRT | A and V rates 220–230 bpm | Long V–A relative to A–V | Typically incessant | None |
| SVT with VA accessory pathway | A and V rates 220–300 bpm | Short V–A relative to A–V | Acute onset without beat–beat variability | Ebstein anomaly |
| Atrial flutter | A-rates 300–500 bpm and variable V-rates | Often 2:1 or 3:1 A–V conduction | Acute onset without atrial beat–beat variability | Cardiac tumors, atrial dilation |
| Junctional tachycardia | V-rates 180–270 bpm | Usual V–A dissociation | Gradual or acute | Cardiomyopathy<br>Maternal autoantibodies |
| Ventricular tachycardia | V-rates 150–300 bpm | Usually A–V dissociation, rarely V–A conduction | Usually acute | Cardiac tumors<br>Maternal autoantibodies anti-Ro and anti-La |
| Sinus bradycardia | A and V rates <110 bpm | Normal A–V relationship | Gradual | Fetal distress, umbilical cord compression |
| Second-degree AVB | A-rates 120–160 bpm<br>V-rates 60–80 bpm | A–V synchrony present with conducted beats; often 2:1 A–V ratio | Intermittent or incessant | LAI, L-ventricular looping, maternal autoantibodies anti-Ro and anti-La, fetal cardiomyopathy with EFE |
| Third-degree AVB | A-rates 120–160 bpm<br>V-rates 30–120 bpm | A–V dissociation | Usually incessant | LAI, L-ventricular looping, maternal autoantibodies anti-Ro and anti-La, fetal cardiomyopathy with EFE |

A, atrial; AVB, atrioventricular block; bpm, beats per minute; EFE, endocardiofibroelastosis; LAI, left atrial isomerism or polysplenia syndrome; PJRT, permanent junctional reciprocating tachycardia; SVT, supraventricular tachycardia; V, ventricular; VA, ventriculoatrial.

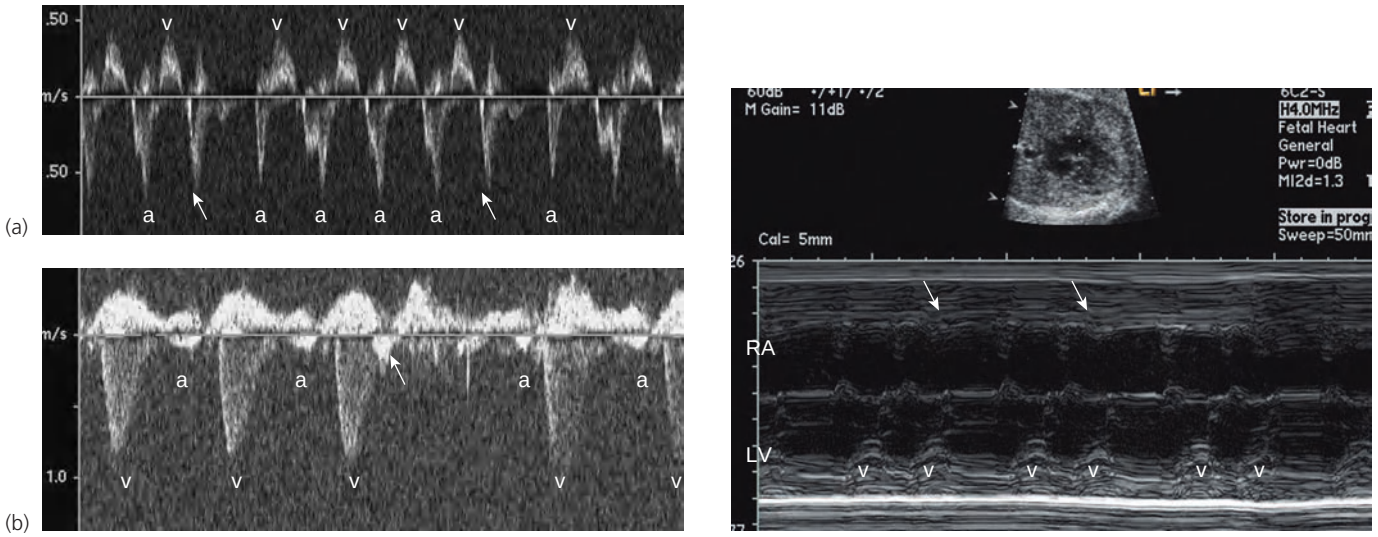


**Figure 42.20** Premature atrial beats (arrows) with atrioventricular (AV) block demonstrated by **(a)** simultaneous left ventricular (LV) inflow and outflow Doppler; **(b)** superior vena cava–aortic Doppler and **(c)** in a trigeminal pattern by M-mode. a, normal atrial systole; RA, right atrium; v, ventricular systole.

be the referring diagnosis as a result of either blocked AV conduction with the atrial extrasystoles or lack of detection by clinically applied Doppler devices of the lower stroke volumes with extrasystoles.

Tachyarrhythmias encountered before birth include supraventricular tachycardia (SVT), atrial flutter, junctional ectopic tachycardia and ventricular tachycardia. Accurate delineation of the tachyarrhythmia mechanism is important in the management of affected pregnancies and counseling of the parents [44,46]. The relationship of the atrial and ventricular contractions, mode of onset and offset, and the atrial and ventricular rates all provide clues to the diagnosis. The most common fetal tachyarrhythmia is that of SVT in which there is 1:1 A–V contraction. SVT can be divided into short and long V–A types. With simultaneous Doppler interrogation of superior vena caval and ascending aortic flows, Fouron et al. showed that the relationship of the atrial and ventricular contractions can be demonstrated with measurement of A–V and V–A time intervals [46]. When the A–V interval is longer than the V–A interval, a short V–A SVT is present, whereas, a short A–V interval suggests the diagnosis of a long V–A tachycardia (Fig. 42.21). As is true after birth, short V–A SVTs include reentrant tachycardias associated with an accessory AV pathway. Long V–A tachycardias include sinus tachycardia, ectopic atrial tachycardia and permanent junctional reciprocating tachycardia. In atrial flutter, the second most common fetal tachyarrhythmia, atrial rates may range from 350 to 500 bpm, with usually variable AV

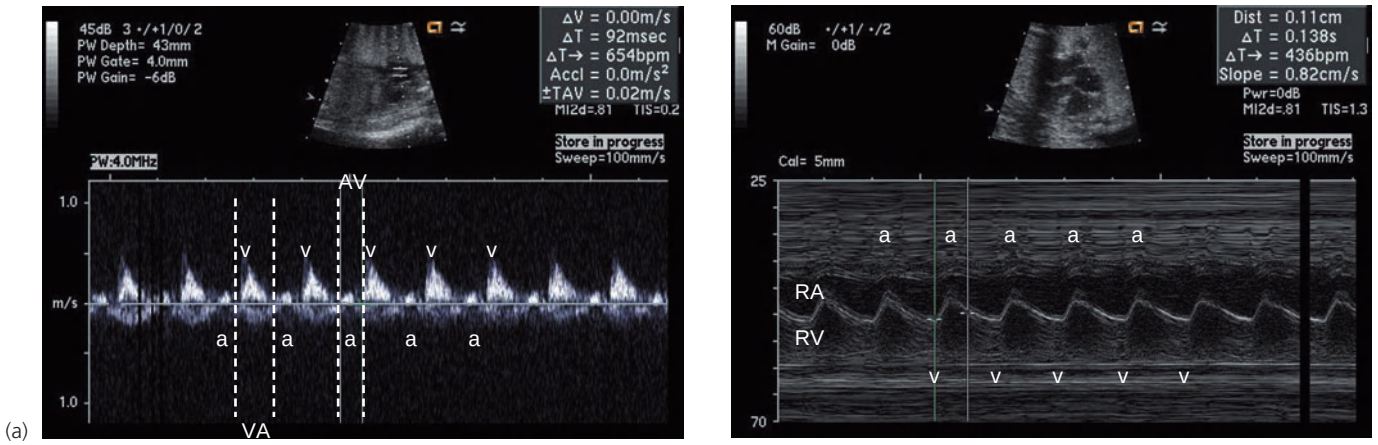


**Figure 42.21** Long V–A (ventriculoatrial) tachyarrhythmia at a rate of 230 bpm in a 35-week fetus diagnosed after birth with permanent reciprocating junctional tachycardia. **(a)** The superior vena cava–aortic Doppler demonstrates a shorter A–V interval relative to the V–A interval. **(b)** M-mode also shows the 1:1 AV relationship. a, atrial systole; RA, right atrium; RV, right ventricle; v, ventricular systole.

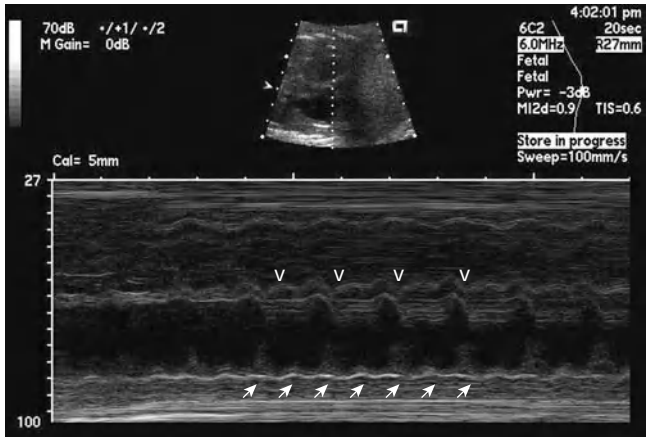


**Figure 42.22** M-mode echocardiogram obtained in a 32-week fetus with atrial flutter. Atrial contractions (arrows) occurred at a rate of 450 bpm and ventricular contractions (v) at a rate of 225 bpm, consistent with 2:1 A–V (atrioventricular) conduction.

conduction (Fig. 42.22 and Videoclip 42.8). In both ventricular and junctional ectopic tachycardia, rapid ventricular rates, often with lack of V–A synchrony, suggest these diagnoses. Given the inability to assess the QRS wave morphology, however, delineation between these two arrhythmias can be difficult. In any arrhythmia, exclusion of important structural and primary functional cardiac abnormalities is important for counseling regarding prognosis, and planning treatment strategies and perinatal management.

Fetal bradycardia is diagnosed when the ventricular rates are less than 110 bpm. The most common cause is sinus bradycardia, which may occur in a healthy fetus intermittently during an exam and should rapidly resolve. Persistent fetal sinus bradycardia suggests more diffuse systemic disease and fetal distress. Persistent fetal bradycardia with ventricular rates of 35–120 bpm may also be caused by second- or third-degree AV block (Fig. 42.23). AV block may be observed in the presence of structural heart disease (e.g., left atrial isomerism or polysplenia syndrome and lesions associated with L-ventricular looping; see Videoclip 42.9) [75,76] or in isolation, the latter of which is largely due to the influence of the maternal autoantibodies anti-Ro and anti-La [75,77]. With the development of normal AV time intervals in fetuses from 17 weeks to term using both pulsed-wave and tissue Doppler techniques [78,79], even first-degree AV block can be diagnosed prenatally.

## Evolving and future directions in fetal echocardiography

Although there has been significant progress in fetal echocardiography over the past two or three decades, the future holds even more promise. Technological advances and ongoing experience will continue to enhance our ability to evaluate all forms of fetal heart disease. Endovaginal ultrasound transducers have been used in first-trimester fetal imaging since the mid-1980s, however, very few centers have documented their use in late first- and early second-trimester fetal echocardiography [10–12,80–83] (Figs 42.24 and 42.25; Videoclips 42.10 and 42.11). This has been in part due to the reluctance of fetal and pediatric cardiologists to use the technology. However, over the past decade some groups have demonstrated successful imaging of the fetal heart using a transabdominal approach from 13–14 weeks [12,84]. Earlier diagnoses, although a natural evolution of fetal echocardiography, are not without important limitations. The extremely small size of the fetal heart in the first trimester means that cardiovascular structures cannot be resolved before 10 weeks' gestation, and only limited resolution

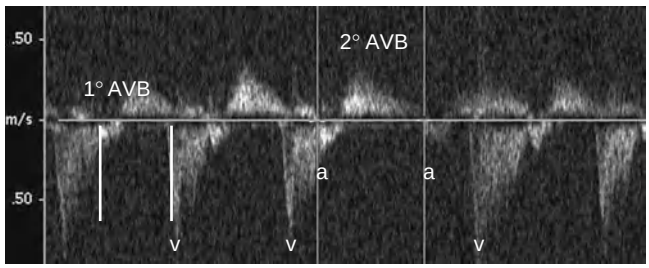


(a)

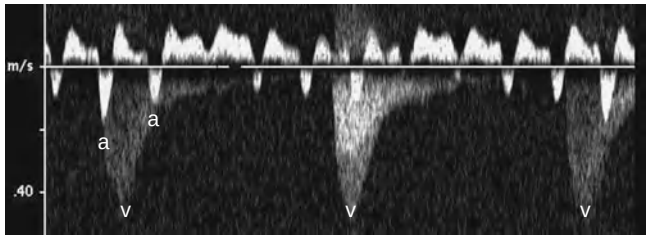


(b)

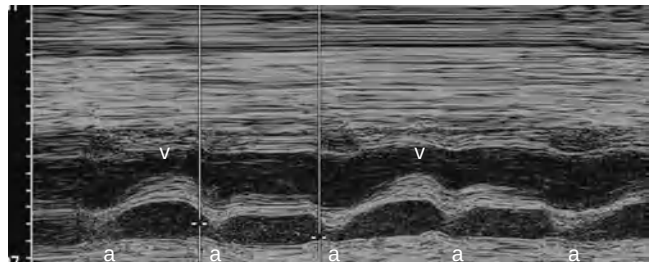


(c)

**Figure 42.23** Doppler and M-mode methods demonstrating varying degrees of atrioventricular block (AVB). **(a)** superior vena cava–aortic Doppler in a fetus with first-degree AVB (1° AVB) (A–V time interval 280 ms) and occasional episodes of second-degree AVB (2° AVB). **(b)** Simultaneous azygous and descending aortic flows in a fetus with complete AVB associated with polysplenia and a ventricular rate of 30–40 bpm. **(c)** Complete AVB demonstrated by M-mode. a, atrial systole; v, ventricular systole.

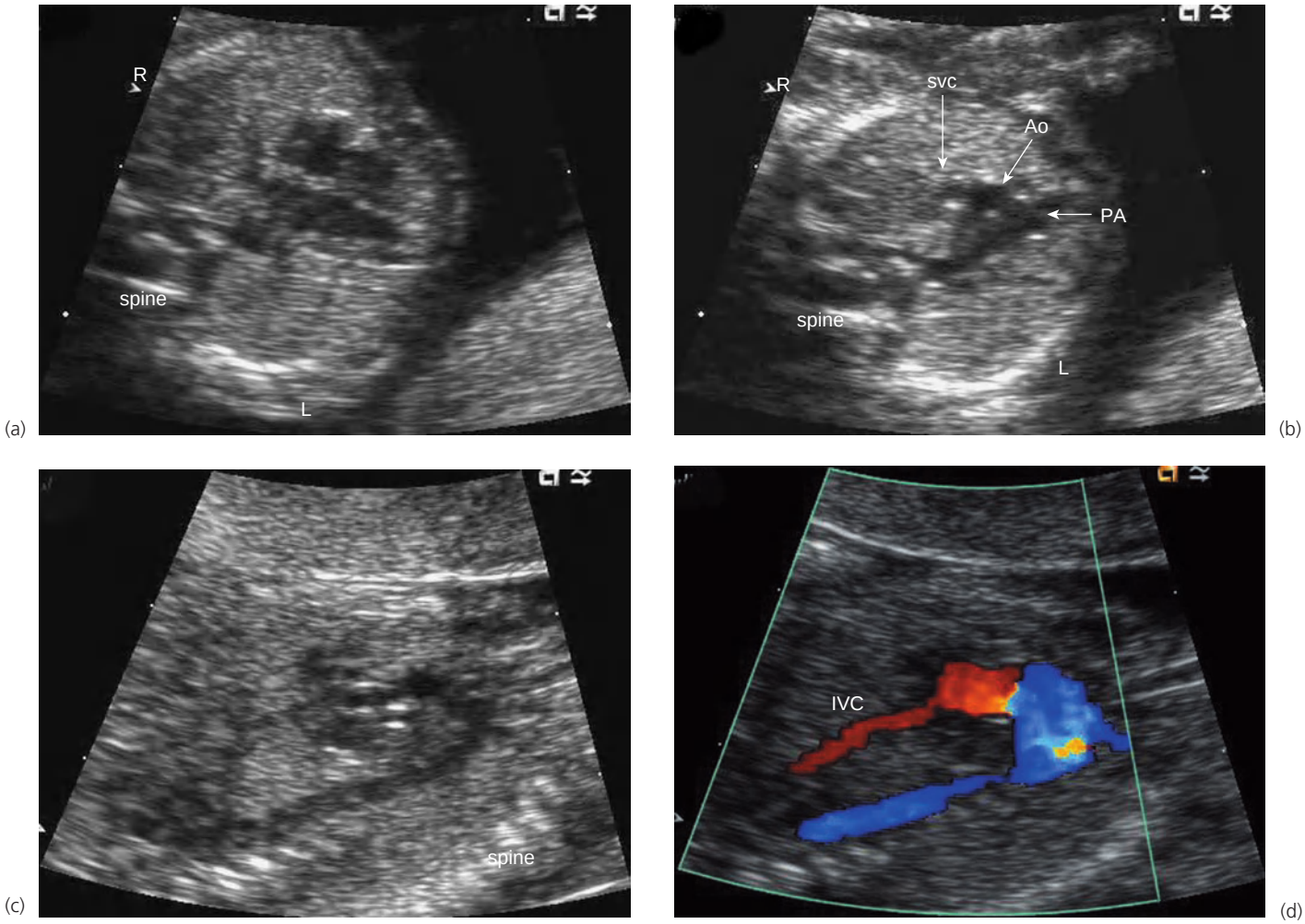


**Figure 42.24** Echocardiographic assessment of a 14-week fetus with no heart disease. **(a)** Four-chamber view; **(b)** three-vessel view; **(c)** aortic arch. **(d)** Color Doppler confirms the presence of an intact inferior vena cava (IVC). Ao, aorta; L, left; PA, main pulmonary artery; R, right; SVC, superior vena cava.

of basic fetal cardiac anatomy is possible from 10 to 14 weeks. More subtle pathology and associated cardiovascular lesions can be missed [11,84]. Still, the details in diagnosis are not unlike those experienced in the earlier era of fetal echocardiography. The development of high-frequency, high-resolution endovaginal transducers in the future as an adjunct tool for fetal cardiovascular assessment prior to 14 weeks, and the education of fetal cardiologists in their use, in conjunction with the use of more objective screening tools such as nuchal translucency evaluation, should promote attempts at earlier diagnosis at least among the highest risk pregnancies. Furthermore, as the genes responsible for the development of a spectrum of cardiovascular pathologies are identified, earlier diagnosis is inevitable. Serial observations from the first and early second trimesters will provide further insight into the evolution of fetal cardiovascular disease during this period of very rapid fetal cardiovascular and general somatic growth. Already underway, first-trimester observations of fetal heart function may help us better to understand the role of myocardial function in the viability of pregnancies [85,86]

In addition to first-trimester fetal echocardiography, the development of high resolution 3D and 4D fetal echocardiography will likely revolutionize prenatal detection through a reduction in scanning time, decrease in operator and window dependence, improved comprehension of the pathology and more accurate volumetric data [87].

Earlier prenatal detection, further delineation of the evolution of fetal heart disease and its etiologies, and ongoing experience should promote the development of more timely and effective fetal cardiovascular interventions. Fetal echocardiography will play an increasingly more crucial role in patient selection, planning of fetal cardiovascular and noncardiovascular interventions, directing therapy and evaluating the success of the therapy (Fig. 42.26). Fetal echocardiography, for instance, has already been used to

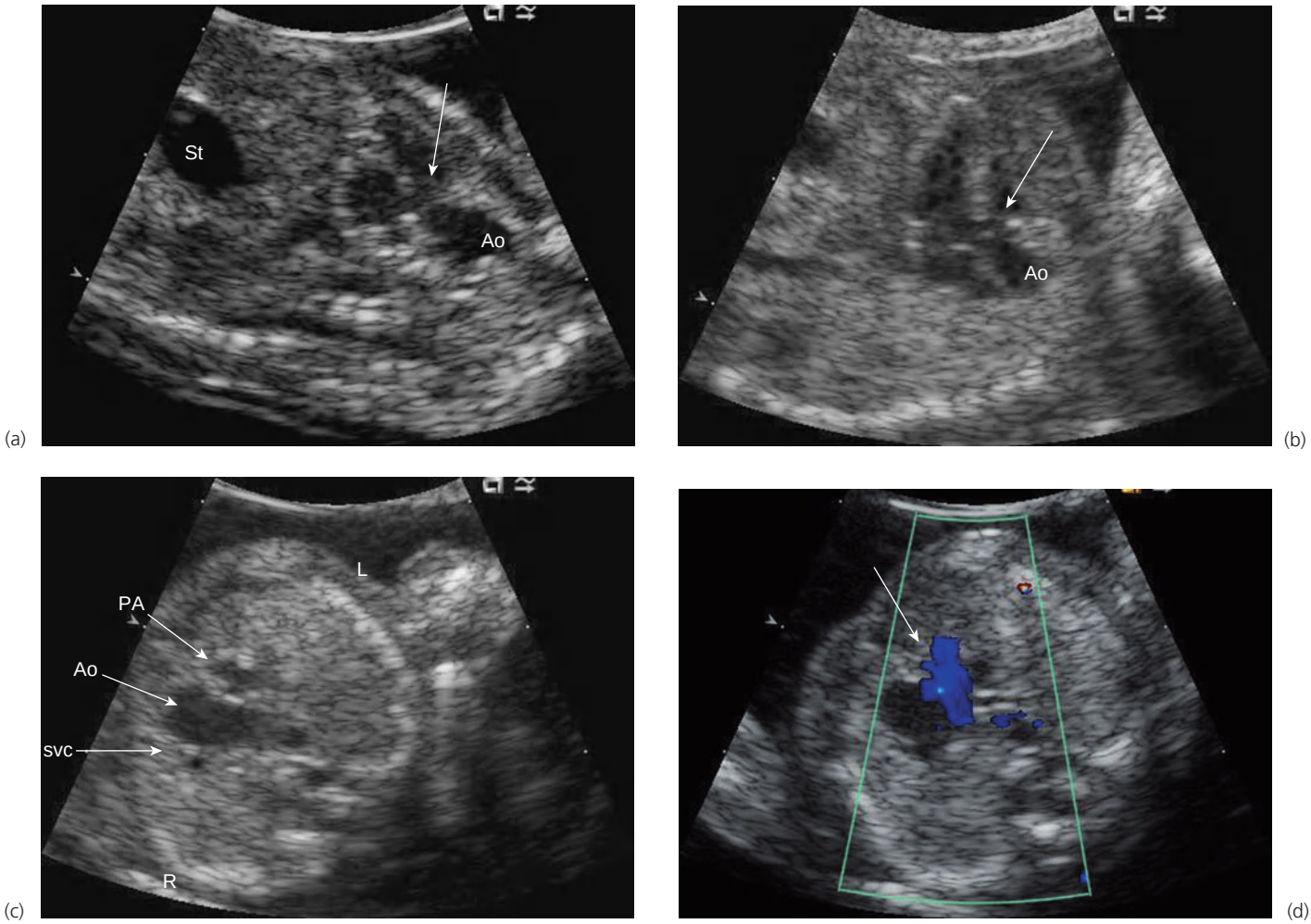


(a) (b) (c) (d)

**Figure 42.25** Echocardiogram in a 14-week fetus with tetralogy of Fallot referred for increased nuchal translucency. **(a)** Sagittal and **(b)** long-axis views demonstrate the ventricular septal defect (arrow) and aortic override. **(c)** The three-vessel view shows a large and anterior aorta and a smaller main pulmonary artery. **(d)** Patency of the pulmonary outflow tract was confirmed by color Doppler (arrow). Ao, aorta; L, left; PA, main pulmonary artery; R, right; St, stomach; SVC, superior vena cava.

evaluate lung growth through the measurement of branch pulmonary artery diameters, which correlate with lung mass [88]. With the evolution of less invasive strategies to promote lung growth in such conditions as diaphragmatic hernia, the additional parameters of pulmonary vascular growth and resistance will no doubt enhance patient selection and be used in determining the subsequent success. Fetal echocardiography has already been employed in the evaluation and management of fetal conditions with potential for fetal hydrops and during fetal procedures [89].

Finally, fetal echocardiography and the prenatal diagnosis of fetal heart disease significantly impacts the outcome of affected pregnancies in many ways. It has led to improved perinatal and neonatal outcomes of critical neonatal heart disease and heart disease associated with cardiovascular compromise before birth [90–93]. It has provided insight into the spectrum of postnatally encountered heart disease. Prenatal diagnosis provides time for the affected family members to understand better and prepare for the delivery of their infant. Also importantly, it has begun to impact on the prevalence of more severe heart disease after birth [94]. Unfortunately, however, the impact of fetal echocardiography and prenatal diagnosis is severely limited by the generally low rates of detection of fetal heart disease at routine obstetrical ultrasound internationally [95–98]. This is despite the fact that the vast majority of major fetal heart disease is detectable before birth and that, in the USA and most other countries, most pregnant women undergo at least one obstetrical ultrasound at 16 weeks' gestation or later. For fetal echocardiography to reach its full potential, ongoing education, the development of more objective screening tools for fetal heart disease and greater regulation of the practices governing routine screening are critical.

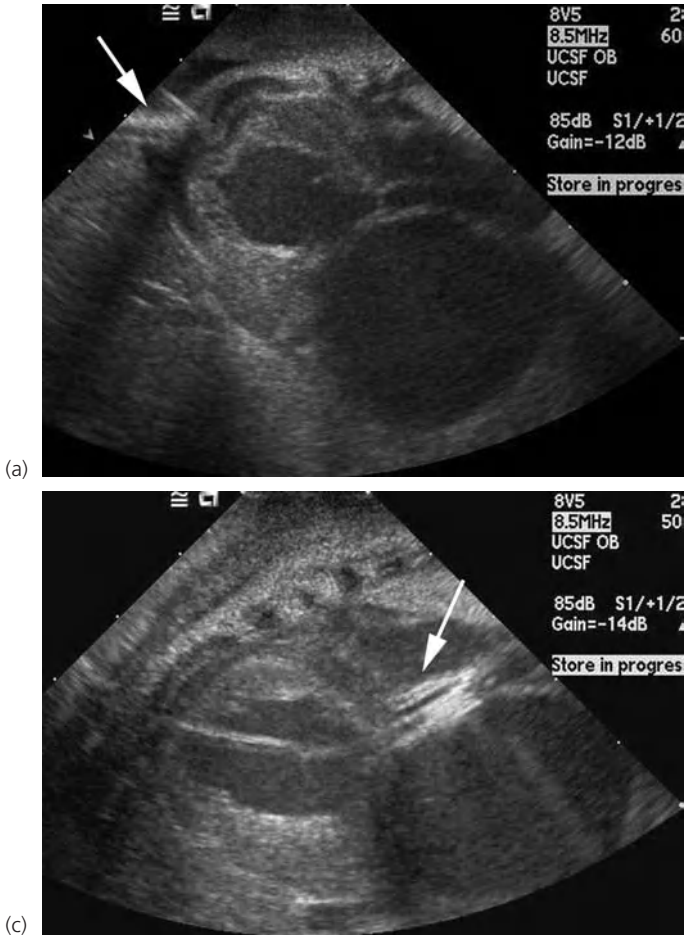


(a)

(c)

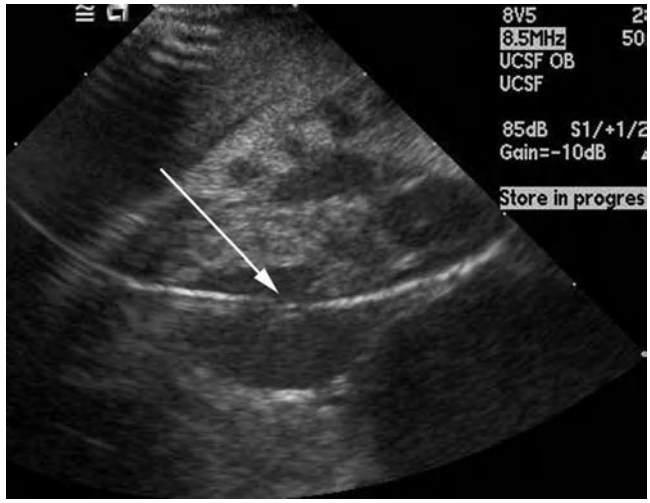


(b)

**Figure 42.26** Balloon aortic valvuloplasty in a 27-week fetus with hydrops associated with critical aortic stenosis. The procedure is performed using a transuterine (maternal), transthoracic (fetal) approach following maternal laparotomy. **(a)** The introducing needle (arrow) can be seen indenting the left ventricular (LV) apex. **(b)** With the needle in the LV cavity, a wire (arrow) is passed through the needle and across the aortic valve. **(c)** The balloon is positioned through the aortic valve (arrow) and expanded. LA, left atrium.

## References


1. Sharland GK, Lockhart SM, Chita SK, Allan LD. Factors influencing the outcome of congenital heart disease detected prenatally. *Arch Dis Child* 1991;66:284–7.
2. Friedberg M, Silverman NH. Changing indications for fetal echocardiography in a University Center population. *Prenatal Diagn* 2004;24:781–6.
3. Ville Y, Lalondrelle C, Doumere S, Nicolaides KH. First-trimester diagnosis of nuchal anomalies: significance and fetal outcome. *Ultrasound Obstet Gynecol* 1992;2:314–16.
4. Nicolaides KH, Brizot ML, Snijders RJM. Fetal nuchal translucency thickness: ultrasound screening for fetal trisomy in the first trimester of pregnancy. *Br J Obstet Gynaecol* 1994;101:782–6.
5. Pandya PP, Brizot ML, Khun P et al. First-trimester fetal nuchal translucency thickness and risk for trisomies. *Obstet Gynecol* 1994;84:420–3.
6. Hyett J, Perdu M, Sharland G et al. Using fetal nuchal translucency to screen for major congenital cardiac defects at 10–14 weeks of gestation: population based cohort study. *Br Med J* 1999;318:81–5.
7. Souka AP, Krampl E, Bakalis S et al. Outcome of pregnancy in chromosomally normal fetuses with increased nuchal translucency in the first trimester. *Ultrasound Obstet Gynecol* 2001;18:9–17.
8. Hyett JA, Perdu M, Sharland GK et al. Increased nuchal translucency at 10–14 weeks of gestation as a marker for major cardiac defects. *Ultrasound Obstet Gynecol* 1997;10:242–6.
9. Mavrides E, Cobian F, Tekay A et al. Fetal nuchal translucency measurements in screening for major congenital cardiac defects in chromosomally normal fetuses [abstract]. *Cardiol Young* 2000;10(Suppl. 2):9.
10. Mcauliffe FM, Trines T, Nield LE et al. Early fetal echocardiography – a reliable prenatal diagnosis tool. *Am J Obstet Gynecol* 2005:193:1253–9.
11. Carvalho JS, Moscoso G, Tekay A et al. Clinical impact of first and early second trimester fetal echocardiography on high risk pregnancies. *Heart* 2004;90:921–6.
12. Vimpelli T, Huhtala H, Acharya G. Fetal echocardiography during routine first-trimester screening: a feasibility study in an unselected population. *Prenat Diagn* 2006;26:475–82.
13. Cordes TM, O'Leary PW, Seward JB, Hagler DJ. Distinguishing right from left: A standard technique for fetal echocardiography. *J Am Soc Echocardiogr* 1994;7:47–54.
14. Shipp TD, Bromley B, Hornberger LK et al. Levorotation of the fetal cardiac axis: a clue for the presence of congenital heart disease. *Obstet Gynecol* 1995;85:97–102.
15. Bromley B, Benacerraf BR. Unilateral lung hypoplasia: Report of three cases. *J Ultrasound Med* 1997;16:599.
16. Abdullah MM, Lacro RV, Smallhorn J et al. Fetal cardiac dextroposition in the absence of an intrathoracic mass: sign of significant right lung hypoplasia. *J Ultrasound Med* 2000;19:669–76.

17. Yoo SJ, Lee YH, Cho KS. Abnormal three-vessel view on sonography: a clue to the diagnosis of congenital heart disease in the fetus. *AJR Am J Roentgenol* 1999;172:825–30.
18. Sharland GK, Allan LD. Normal fetal cardiac measurements derived by cross-sectional echocardiography. *Ultrasound Obstet Gynecol* 1992;2:175–81.
19. Tan J, Silverman NH, Hoffman JI et al. Cardiac dimensions determined by cross-sectional echocardiography in the normal human fetus from 18 weeks to term. *Am J Cardiol* 1992;70:1459–67.
20. Brown DL, Durfee SM, Hornberger LK. Ventricular discrepancy as a sonographic sign of coarctation of the fetal aorta: How reliable is it? *J Ultrasound Med* 1997;16:95–9.
21. Schneider C, McCrindle BW, Carvalho JS et al. Development of Z scores for fetal cardiac dimensions from echocardiography. *Ultrasound Obstet Gynecol* 2005;26:599–605.
22. Schmidt KG, Birk E, Silverman NH et al. Echocardiographic evaluation of dilated cardiomyopathy in the human fetus. *Am J Cardiol* 1989;63:599–605.
23. Schmidt KG, Silverman NH, Hoffman JI. Determination of ventricular volumes in human fetal hearts by two-dimensional echocardiography. *Am J Cardiol* 1995;76:1313–16.
24. Simpson JM, Cook A. Repeatability of echocardiographic measurements in the human fetus. *Ultrasound Obstet Gynecol* 2002;20:332–9.
25. Gonçalves LF, Espinoza J, Romero R et al. Four-dimensional fetal echocardiography with spatiotemporal image correlation (STIC): a systematic study of standard cardiac views assessed by different observers. *J Matern Fetal Neonatal Med* 2005;17:323–31.
26. Bhat AH, Corbett V, Carpenter N et al. Fetal ventricular mass determination on three-dimensional echocardiography: studies in normal fetuses and validation experiments. *Circulation* 2004;110:1054–60.
27. Esh-Broder E, Ushakov FB, Imbar T, Yagel S. Application of free-hand three-dimensional echocardiography in the evaluation of fetal cardiac ejection fraction: a preliminary study. *Ultrasound Obstet Gynecol* 2004;23:546–51.
28. Mielke G, Benda N. Cardiac output and central distribution of blood flow in the human fetus. *Circulation* 2001;103:1662–8.
29. Barss VA, Doubilet PM, St John-Sutton M et al. Cardiac output in a fetus with erythroblastosis fetalis: assessment using pulsed Doppler. *Obstet Gynecol* 1987;70:442–4.
30. Brassard M, Fouron JC, Leduc L et al. Prognostic markers in twin pregnancies with an acardiac fetus. *Obstet Gynecol* 1999;94:409–14.
31. Jaeggi ET, Fouron J-C, Hornberger LK et al. Agenesis of the ductus venosus associated with extrahepatic umbilical vein drainage: Clinical presentation, echocardiographic features and fetal outcome. *Am J Obstet Gynecol* 2002:187:1031–7.
32. Gudmundsson S, Huhta JC, Wood DC et al. Venous Doppler ultrasonography in the fetus with nonimmune hydrops. *Am J Obstet Gynecol* 1991;164:33–7.
33. Fontes-Pedra SRF, Smallhorn J, Ryan G et al. Fetal cardiomyopathies: etiologies, hemodynamic findings and clinical outcome. *Circulation* 2002;106:585–91.
34. Reed KL, Meijboom EJ, Sahn DJ et al. Cardiac Doppler flow velocities in human fetuses. *Circulation* 1986;73:41–6.
35. Carceller-Blanchard AM, Fouron JC. Determinants of the Doppler flow velocity profile through the mitral valve of the normal fetus. *Br Heart J* 1993;70:457–60.
36. Mori Y, Rice MJ, McDonald RW et al. Evaluation of systolic and diastolic ventricular performance of the right ventricle in fetuses with ductal constriction using the Doppler Tei index. *Am J Cardiol* 2001;88:1173–8.
37. Tei C. New non-invasive index for combined systolic and diastolic ventricular function. *J Cardiol* 1995;26:135–6.
38. Tsutsumi T, Ishii M, Eto G et al. Serial evaluation for myocardial performance in fetuses and neonates using a new Doppler index. *Pediatr Int.* 1999;41:722–7.
39. Perles Z, Nir A, Gavri S, Rein AJ. Assessment of fetal myocardial performance using myocardial deformation analysis. *Am J Cardiol* 2007;99:993–6.
40. Nii M, Roman KS, Kingdom J et al. Assessment of the evolution of normal fetal diastolic function during mid and late gestation by spectral Doppler tissue echocardiography. *J Am Soc Echocardiogr* 2006;19:1431–7.
41. Gardiner HM, Pasquini L, Wolfenden J et al. Myocardial tissue Doppler and long axis function in the fetal heart. *Int J Cardiol* 2006;113:39–47.
42. Gardiner HM, Pasquini L, Wolfenden J et al. Increased periconceptual maternal glycated haemoglobin in diabetic mothers reduces fetal long axis cardiac function. *Heart* 2006;91:1125–30.
43. Hornberger LK. Echocardiographic assessment of fetal arrhythmias. *Heart* 2007;93:1331–3.
44. Hornberger LK, Sahn DJ. Rhythm abnormalities in the fetus. *Heart* 2007;93:1294–1300.
45. Carvalho JS, Prefumo F, Ciardelli V et al. Evaluation of fetal arrhythmias from simultaneous pulsed wave Doppler in pulmonary artery and vein. *Heart* 2007;93:1448–53.
46. Fouron JC. Fetal arrhythmias: the Sainte-Justine hospital experience. *Prenatal Diagn* 2004;24:1068–80.
47. Rein AJ, O'Donnell C, Geva T et al. Use of tissue velocity imaging in the diagnosis of fetal cardiac arrhythmias. *Circulation* 2002;106:1827–33.
48. Allan LD, Sharland GK, Milburn A et al. Prospetive diagnosis of 1006 consecutive cases of CHD in the fetus. *J Am Coll Cardiol* 1994;23:1452–8.
49. Tometzki AJ, Suda K, Kohl T et al. Accuracy of prenatal echocardiographic diagnosis and prognosis of fetuses with conotruncal anomalies. *J Am Coll Cardiol* 1999;33:1696–701.
50. Gottliebson WM, Border WL, Franklin CM et al. Accuracy of fetal echocardiography: a cardiac segment specific analysis. *Ultrasound Obstet Gynecol* 2006;28:15–21.
51. Taketazu M, Lougheed J, Yoo SJ, Hornberger LK. Fetal heterotaxy syndrome: spectrum of heart disease, accuracy of diagnosis and clinical outcome. *Am J Cardiol* 2006:97:720–4.
52. Hornberger LK, Trines J. Evolution of congenital heart disease in utero. *Pediatr Cardiol* 2004;25:287–98.
53. Hornberger L, Sanders SP, Rein AJJT et al. Left heart obstructive lesions and left ventricular growth in the midtrimester fetus. A longitudinal study. *Circulation* 1995;92:1531–8.
54. Simpson JM, Sharland GK. Natural history and outcome of aortic stenosis diagnosed prenatally. *Heart* 1997;77:205–10.
55. Hornberger LK, Need L, Benacerraf BR. Development of significant left and right ventricular hypoplasia in the second and third trimester fetus. *J Ultrasound Med* 1996;15:60–5.
56. Mäkikallio K, McElhinney DB, Levine JC et al. Fetal aortic valve stenosis and the evolution of hypoplastic left heart syndrome:

patient selection for fetal intervention. *Circulation* 2006;113: 1401–5.
57. Berning RA, Silverman NH, Villegas M et al. Reversed shunting across the ductus arteriosus or atrial septum in utero heralds severe congenital heart disease. *J Am Coll Cardiol* 1996;27:481–6.
58. Taketazu M, Barrea C, Smallhorn J, Hornberger LK. Pulmonary vein flow in fetal hypoplastic left heart syndrome. *J Am Coll Cardiol* 2004;43:1902–7.
59. Kohl T. Fetal echocardiography: new grounds to explore during fetal cardiac intervention. *Pediatr Cardiol* 2002;23:334–46.
60. Tworetzky W, Wilkins-Haug L, Jennings RW et al. Balloon dilation of severe aortic stenosis in the fetus: potential for prevention of hypoplastic left heart syndrome: candidate selection, technique, and results of successful intervention. *Circulation* 2004;110:2125–31.
61. Viesca R, Huhta JC. Update in fetal cardiac intervention. *Curr Treat Options Cardiovasc Med* 2006;8:379–86.
62. Marshall AC, van der Velde ME, Tworetzky W et al. Creation of an atrial septal defect in utero for fetuses with hypoplastic left heart syndrome and intact or highly restrictive atrial septum. *Circulation* 2004;110:253–8.
63. Hornberger LK, Dalvi B, Benacerraf BR: Prenatal sonographic detection of cardiac aneurysms and diverticula. *J Ultrasound Med* 1994;13:967–70.
64. Cavallé-Garrido T, Cloutier A, Harder J et al. Evolution of fetal ventricular aneurysms and diverticula of the heart: an echocardiographic study. *Am J Perinatol* 1997;14:393–400.
65. McAuliffe FM, Hornberger LK, Johnson J et al. Cardiac diverticulum with pericardial effusion: report of two new cases treated by in-utero pericardiocentesis and a review of the literature. *Ultrasound Obstet Gynecol* 2005;25:401–4.
66. Chobot V, Hornberger LK, Hagen-Ansert S, Sahn DJ. Prenatal detection of restrictive foramen ovale. *J Am Soc Echocardiogr* 1990;3:15–19.
67. Hofstadler G, Tulzer G, Altmann R et al. Spontaneous closure of the human fetal ductus arteriosus – A cause of fetal congestive heart failure. *J Obstet Gynecol* 1996;174:879–83.
68. Inamura N, Taketasu M, Smallhorn JF, Hornberger LK. Left ventricular myocardial performance in the fetus with severe tricuspid valve disease and tricuspid insufficiency. *Am J Perinatol* 2005;22:91–7.
69. Pavlova M, Fouron JC, Drblik SP et al. Factors affecting the prognosis of Ebstein's anomaly during fetal life. *Am Heart J* 1998;135:1081–5.
70. Inamura N, Kado Y, Nakajima T, Kayatani F. Left and right ventricular function in fetal tetralogy of Fallot with absent pulmonary valve. *Am J Perinatol* 2005;22:199–204.
71. Barrea C, Hornberger LK, Alkazaleh F et al. Impact of selective laser ablation of placental anastomoses in twin-to-twin transfusion syndrome on the cardiovascular pathology of the recipient twin. *Am J Obstet Gynecol* 2006;195:1388–95.
72. Michelfelder E, Gottliebson W, Border W et al. Early manifestations and spectrum of recipient twin cardiomyopathy in twin-twin transfusion syndrome: relation to Quintero stage. *Ultrasound Obstet Gynecol* 2007;30:965–71.
73. Rychik J, Tian Z, Bebbington M et al. The twin-twin transfusion syndrome: spectrum of cardiovascular abnormality and development of a cardiovascular score to assess severity of disease. *Am J Obstet Gynecol* 2007;197:39.
74. Kleinman CS, Nehgme RA. Cardiac arrhythmias in the fetus. *Pediatr Cardiol* 2004;25:234–51.
75. Schmidt KG, Ulmer HE, Silverman NH et al. Perinatal outcome of fetal complete atrioventricular block: a multicenter experience. *J Am Coll Cardiol* 1991;17:1360–6.
76. Jaeggi ET, Hornberger LK, Smallhorn JF, Fouron J-C. Prenatal diagnosis of complete atrio-ventricular block associated with structural heart disease since 1990: combined experience of 2 tertiary care centers and review of the literature. *Ultrasound Obstet Gynecol* 2005;26:16–21.
77. Jaeggi ET, Hamilton RM, Silverman ED et al. Outcome of children with fetal, neonatal or childhood diagnosis of isolated congenital atrioventricular block. A single institution's 30 year experience. *J Am Coll Cardiol* 2002;39:130–7.
78. Van Bergen AH, Cuneo BF, Davis N. Prospective echocardiographic evaluation of atrioventricular conduction in fetuses with maternal Sjögren's antibodies. *Am J Obstet Gynecol* 2004; 191:1014–18.
79. Nii M, Hamilton RM, Fenwick L et al. Assessment of fetal atrioventricular time intervals by tissue Doppler and pulse Doppler echocardiography: normal values and correlation with fetal electrocardiography. *Heart* 2006;92:1831–7.
80. Gembruch U, Bald R, Hansmann M. Early diagnosis of fetal congenital heart disease by transvaginal echocardiography. *Ultrasound Obstet Gynecol* 1993;3:310–17.
81. Yagel S, Weissman A, Rotstein Z et al. Congenital heart defects: natural course and in utero development. *Circulation* 1997;96: 550–5.
82. Rustico MA, Benettoni A, D'Ottavio G et al. Early screening for fetal cardiac anomalies by transvaginal echocardiography in an unselected population: role of operator experience. *Ultrasound Obstet Gynecol* 2000;16:614–19.
83. Gabriel CC, Galindo A, Martinez JM, Carrera JM et al. Early prenatal diagnosis of major cardiac anomalies in a high risk population. *Prenat Diagn* 2002;22:586–93.
84. Huggon IC, Ghi T, Cook AC et al. Fetal cardiac abnormalities identified prior to 14 weeks' gestation. *Ultrasound Obstet Gynecol* 2002;20:22–9.
85. Leiva MC, Tolosa JE, Binotto CN et al. Fetal cardiac development and hemodynamics in the first trimester. *Ultrasound Obstet Gynecol* 1999;14:169–74.
86. Włoch A, Rozmus-Warcholinska W, Czuba B et al. Doppler study of the embryonic heart in normal pregnant women. *J Matern Fetal Neonatal Med* 2007;20:533–9.
87. Sklansky MS, DeVore GR, Wong PC. Real-time 3-dimensional fetal echocardiography with an instantaneous volume-rendered display: early description and pictorial essay. *J Ultrasound Med* 2004;23:283–9.
88. Sokol J, Bohn D, Lacro RV et al. Fetal pulmonary artery diameters and their association with pulmonary hypoplasia and postnatal outcome in congenital diaphragmatic hernia. *Am J Obstet Gynecol* 2002:186:1085–90.
89. Keswani SG, Crombleholme TM, Rychik J et al. Impact of continuous intraoperative monitoring on outcomes in open fetal surgery. *Fetal Diagn Ther* 2005;20:316–20.
90. Eapen RS, Rowland DG, Franklin WH. Effect of prenatal diagnosis of critical left heart obstruction on perinatal morbidity and mortality. *Am J Perinatol* 1998;15:237–42.

91. Krishna K, Newburger JW, Gauvreau K, et al. Comparison of the outcome when hypoplastic left heart syndrome and transposition of the great arteries are diagnosed prenatally versus when diagnosis of these two conditions is made only postnatally. *Am J Cardiol* 1999;83:1649–53.
92. Bonnet D, Coltri A, Butera G et al. Prenatal diagnosis of transposition of the great vessels reduces neonatal morbidity and mortality. *Arch Mal Coeur Vaiss* 1999;92:637–40.
93. Tworetzsky W, McElhinney DB, Reddy VM et al. Improved surgical outcome after fetal diagnosis of hypoplastic left heart syndrome. *Circulation* 2001;103:1269–73.
94. Allan LD, Cook A, Sullivan I, Sharland GK. Hypoplastic left heart syndrome: effects of fetal echocardiography on birth prevalence. *Lancet* 1991;337:959–61.
95. Garne E, Loane M, Dolk H et al. Prenatal diagnosis of severe structural congenital malformations in Europe. *Ultrasound Obstet Gynecol* 2005;25:6–11.
96. Wong SF, Chan FY, Cincotta RB et al. Factors influencing the prenatal detection of structural congenital heart diseases. *Ultrasound Obstet Gynecol* 2003;21:19–25.
97. Shima Y, Shindoh F, Nakajima M et al. Prenatal diagnosis of congenital heart disease: clinical experience and analysis. *J Nippon Med Sch* 2004;71:328–32.
98. Hornberger LK, Sahn DJ, Kleinman CS et al. Tricuspid valve disease with significant tricuspid insufficiency in the fetus: diagnosis and outcome. *J Am Coll Cardiol* 1991;17:167–73.
99. Hornberger LK, Benacerraf BR, Bromley BS et al. Prenatal detection of severe right ventricular outflow tract obstruction: pulmonary stenosis and pulmonary atresia. *J Ultrasound Med* 1994;13:743–50.
100. Hornberger LK, Shan DJ, Kleinman CS et al. Antenatal diagnosis of coarctation of the aorta: a multicenter experience. *J Am Coll Cardiol* 1994;23:417–23.
101. Hornberger LK, Sanders SP, Sahn DJ et al. In utero pulmonary artery and aortic growth and potential for progression of pulmonary outflow tract obstruction in tetralogy of Fallot. *J Am Coll Cardiol* 1995;23:739–45.
102. Lougheed J, Sinclair BG, Fung Kee Fung K et al. Acquired right ventricular outflow tract obstruction in the recipient twin in twin-twin transfusion syndrome. *J Am Coll Cardiol* 2001;38:1533–8.
103. McCaffrey FM, Sherman FS. Prenatal diagnosis of severe aortic stenosis. *Pediatr Cardiol* 1997;18:276–81.
104. Rici MJ, McDonald RW, Peller MD. Progressive pulmonary stenosis in the fetus: two case reports. *Am J Perinatol* 1993;10:424–7.
105. Allan LD, Sharland GK, Tynan MJ. The natural history of the hypoplastic left heart syndrome. *Int J Cardiol.* 1989;25:343–6.
106. Danford DA, Cronican P. Hypoplastic left heart syndrome: progression of left ventricular dilation and dysfunction to left ventricular hypoplasia in utero. *Am Heart J* 1992;123:1712–13.
107. Hornberger LK, Benacerraf BR, Bromley BS et al. Prenatal detection of severe right ventricular outflow tract obstruction: pulmonary stenosis and pulmonary atresia. *J Ultrasound Med* 1994;13:743–50.
108. Maeno YV, Boutin C, Hornberger LK et al. Prenatal diagnosis of right ventricular outflow tract obstruction with intact ventricular septum, and detection of ventriculocoronary connections. *Heart* 1999;81:661–8.
109. Scott RJ, Sullivan ID. Hypoplastic left heart syndrome in the second trimester. *Pediatr Pathol Lab Med* 1996;16:543–8.
110. Sharland GK, Chita SK, Fagg NLK et al. Left ventricular dysfunction in the fetus: relation to aortic valve anomalies and endocardial fibroelastosis *Br Heart J* 1999;66:419–24.
111. Simpson JM, Sharland GK. Fetal tachycardia: management and outcome of 127 consecutive cases. *Heart* 1998;79:576–81.
112. Van Engelen AD, Weijtens O, Brenner JI et al. Management outcome and follow-up of fetal tachycardia. *Am Coll Cardiol* 1994;24:1371–5.
113. Bharati S, Patel AG, Varga P et al. In utero echocardiographic diagnosis of premature closure of the foramen ovale with mitral regurgitation and large left atrium. *Am Heart J* 1991;122:597–600.
114. Paladini D, Palmieri S, Lamberti A et al. Characterization and natural history of ventricular septal defects in the fetus. *Ultrasound Obstet Gynecol* 2000;16:118–22.
115. Dyamenahalli U, Smallhorn JF, Geva T et al. Isolated ductus arteriosus aneurysm in the fetus and infant: a multi-institutional experience. *J Am Coll Cardiol* 2000;36:262–9.
116. Barrea C, Alkazaleh F, Ryan G et al. Prenatal cardiovascular manifestations in twin-to-twin transfusion syndrome (TTTS) and the impact of therapeutic amnioreduction. *Am J Obstet Gynecol* 2005;192:892–902.
117. Fesslova V, Villa L, Nava S et al. Fetal and neonatal echocardiographic findings in twin-twin transfusion syndrome. *Am J Obstet Gynecol* 1998;179:1056–62.
118. Nield LE, Silverman ED, Taylor GP et al. Maternal anti-Ro and anti-La antibody-associated endocardial fibroelastosis. *Circulation* 2002;105:843–8.
119. Sivasankaran S, Sharland GK, Simpson JM. Dilated cardiomyopathy presenting during fetal life. *Cardiol Young* 2005;15:409–16.
120. Allan LD, Crawford DC, Sheridan R, Chapman MG. Aetiology of non-immune hydrops: the value of echocardiography. *Br J Obstet Gynaecol* 1986;93:223–5.
121. Kleinman CS, Donnerstein RL, DeVore GR et al. Fetal echocardiography for evaluation of in utero congestive heart failure. *N Engl J Med* 1982;306:568–75.
122. Tsang W, van der Velde Mary, Windrim R et al. Hydrops fetalis: primary cardiovascular etiologies and clinical outcome in 98 affected pregnancies. *J Am Coll Cardiol* 2002;39,415A.
123. Naheed ZJ, Strasburger JF, Deal BJ et al. Fetal tachycardia: mechanisms and predictors of hydrops fetalis. *J Am Coll Cardiol* 1996;27:1736–40.
124. Silverman NH, Kleinman CS, Rudolph AM et al. Fetal atrioventricular valve insufficiency associated with nonimmune hydrops: a two-dimensional echocardiographic and pulsed Doppler ultrasound study. *Circulation* 1985;72:825–32.
125. Bader RS, Chitayat D, Kelly E et al. Fetal rhabdomyoma: prenatal diagnosis, clinical outcome and incidence of associated tuberous sclerosis complex. *J Pediatr* 2003;143:620–4.
126. Holley DG, Martin GR, Brenner JI et al. Diagnosis and management of fetal cardiac tumors: a multicenter experience and review of published reports. *J Am Coll Cardiol* 1995;26:516–20.
127. Nir A, Ekstein S, Nadjari M et al. Rhabdomyoma in the fetus: illustration of tumor growth during the second half of gestation. *Pediatr Cardiol* 2001;22:515–18.

# 43 Vascular Ultrasound Imaging in Children

**Elif Seda Selamet Tierney[1] and Tajinder P. Singh[2]**

[1]Department of Cardiology, Children's Hospital Boston, Boston, MA, USA
[2]Department of Pediatrics, Harvard Medical School; Pediatric Cardiology, Children's Hospital Boston, Boston, MA, USA

## Introduction

Vascular ultrasound imaging is used for anatomic and physiologic assessment of central and peripheral blood vessels. It is an important clinical tool in adult patients with suspected atherosclerotic disease of the central (carotid) or peripheral (extremity) conduit arteries, used to detect arterial stenosis or occlusion. Thus, it is of great utility for diagnostic assessment of the femoral artery system in an adult presenting with limb claudication and of the carotid artery system for stroke. Symptomatic atherosclerosis does not occur in children except in patients with rare metabolic disorders such as homozygous hypercholesterolemia or progeria. The clinical role of vascular ultrasound imaging in pediatrics has therefore been limited and is most useful in patients with suspected vascular thrombosis secondary to indwelling catheters or suspected peripheral embolism from a central source.

Atherosclerosis has its origins during childhood and progresses subclinically for decades before manifesting itself clinically as stroke, myocardial infarction or peripheral arterial disease, usually during the middle and later parts of adult life. It was first recognized by the detection of fatty streaks and fibrous plaques in autopsy studies of children and young adults dying of unrelated causes [1]. The last 25 years have seen an exponential increase in our understanding of the origins of atherosclerosis. Vascular ultrasound imaging has played a key role in advancing this understanding by providing access to arteries for studying vascular physiology and anatomic changes during the natural history of atherosclerosis. The focus of research using vascular ultrasound has not been to search for and develop a summary of all atherosclerotic plaques in the body but instead to develop a brief and reproducible approach that provides an assessment of the global vascular health (and atherosclerosis burden) in a subject or a cohort. This application of vascular ultrasound in the research laboratory in adults and children has played a key role in improving our understanding of the pathogenesis of atherosclerosis.

## Vascular function and atherosclerosis

It is now well accepted that the single cell layer lining the vascular lumen (endothelium) plays a pivotal role in maintaining vascular health. The role of endothelium in vascular health and disease has been a focus of much scientific work [2,3]. In addition to being a barrier between the vascular lumen and the vessel wall, endothelium has active antiatherosclerotic functions such as inhibition of leukocyte adhesion, platelet–vessel wall interaction, platelet aggregation and vascular smooth muscle proliferation [2]. Endothelium also produces several vasoactive molecules such as endothelin (vasoconstrictor), prostacyclin (vasodilator) and endothelium-dependent hyperpolarizing factor (vasodilator). The most important mediator of endothelial function, however, is believed to be nitric oxide (NO) [4,5]. NO stimulates the enzyme soluble guanylate cyclase in vascular smooth muscle resulting in increased production of tissue cyclic GMP. This results in muscle relaxation and vasodilation.

Several lines of evidence support the concept that the physiologic perturbation described as "endothelial dysfunction" is a precursor of anatomic changes of atherosclerosis [3,6,7]. Inhibition of NO synthase in animal models causes accelerated atherosclerosis [8]. Endothelial dysfunction has been demonstrated in nonatherosclerotic blood vessels of adults with established atherosclerotic disease. Furthermore, both adults and children with risk factors for atherosclerosis, such as smoking, hypercholesterolemia and diabetes, have impaired endothelial function compared with controls [9–16]. Endothelial dysfunction appears to have a prognostic value in patients with atherosclerotic vascular disease, as suggested by its association with a higher risk of clinical events on follow-up [17,18].

Endothelial function has been assessed directly by measuring vascular responses to intraarterial infusion of

*Echocardiography in Pediatric and Congenital Heart Disease: From Fetus to Adult*
Edited by Wyman W. Lai, Luc L. Mertens, Meryl S. Cohen and Tal Geva
 ISBN: 978-1-405-17401-5

acetylcholine or substance P in the brachial artery or the coronary artery [6,7,19]. Although elegant and precise, these methods are invasive with a significant potential for complications. A noninvasive method, assessment of flow-mediated dilation (FMD) using high-resolution vascular ultrasound, has evolved into a standard method for evaluation of endothelial function in the peripheral circulation [10,20]. This method assesses the degree of arterial dilation during reactive hyperemia following the inflation and release of a proximal or distal sphygmomanometer cuff. When assessed using the protocol described below (distal cuff inflation for 4–5 minutes), FMD is mediated primarily by endothelial release of NO [21,22]. The absolute and percent change in vessel diameter in response to increased flow through the vessel is used as an index of conductance vessel function. Assessment of endothelium-independent dilation is often performed using sublingual nitroglycerin and measures nonspecific smooth muscle relaxation.

The change in arterial diameter during the cardiac cycle evaluated by high-resolution ultrasound can be related to the distending pressure, providing a series of direct measures of stiffness or elasticity. The relationship of atherosclerosis to mechanical properties of the central and peripheral arterial walls has been closely examined in recent years, and atherosclerosis has been found to be associated with an increase in arterial stiffness [23–26]. Increased stiffness of the common carotid artery is a significant and independent predictor of cardiovascular complications [27–29]. The elastic properties of the common carotid artery wall can be estimated by calculating the pressure-strain elastic modulus (Ep) and stiffness index (β) using ultrasound imaging [30]. Peterson's (elastic) modulus is the pressure step required for (theoretical) 100% stretch from resting diameter at fixed vessel length whereas stiffness index is the ratio of the logarithm of the difference in systolic and diastolic pressures to the relative change in vessel diameter.

## Early anatomic changes in atherosclerosis

Vascular ultrasound imaging is often used to diagnose the presence of carotid atherosclerosis in patients being evaluated for stroke. This evaluation is focused on detecting carotid luminal narrowing and the presence and stability of plaques. The pathophysiologic mechanism responsible for the earliest plaque deposition has been a subject of much controversy. Previously, plaque was thought to be deposited at sites of increased shear rates, but it is now believed to form first at sites of relative stagnation or slow blood flow, such as the far wall of the proximal internal carotid artery. The prolonged residence time of small lipid particles favors their transport into the artery wall [31].

Several population-based longitudinal studies have examined the relationship between baseline measurements of carotid intima–media thickness (IMT; i.e., the thickness of the intima and media combined) and/or presence of discrete plaques and subsequent cardiovascular disease events [32–36]. Carotid IMT thus began to be investigated as an anatomic marker of the atherosclerosis burden in adults [37]. A large body of work has confirmed that the increase in carotid IMT is detectable as early as the teenage years in children exposed to conventional risk factors [15,24,38–49]. Similarly, several studies have demonstrated an association between the presence of known cardiovascular risk factors during childhood and raised values of carotid IMT during childhood or early adulthood [49]. Specifically, a greater carotid IMT compared with age-matched controls occurs in children with hypercholesterolemia, family history of premature myocardial infarction, obesity, hypertension, type 1 diabetes mellitus, history of Kawasaki disease, HIV infection, Williams syndrome, beta-thalassemia major and congenital adrenal hyperplasia [15,24,38–48]. Table 43.1 shows reported IMT measurements in control populations published in recent years.

**Table 43.1** Intima–media thickness (IMT) in children (recent published control data)

| IMT (mm) | Age (years) | *N* | Publication |
|---|---|---|---|
| 0.51 ± 0.02 | 9 ± 2 | 21 | Aggoun et al., 2000 [47] |
| 0.53 ± 0.06 | 12.1 ± 0.9 | 33 | Sorof et al., 2003 [40] |
| 0.53 ± 0.03 | 14.9 ± 2.8 | 44 | de Groot et al., 2004 [76] |
| 0.39 ± 0.05 | 14.7 ± 2.15 | 20 | Meyer et al., 2006 [68] |
| 0.424 ± 0.010 | 12 ± 3.1 | 28 | Dalla Pozza et al., 2007 [77] |

## Imaging

### General principles

The arterial wall consists of three layers [50]. The outermost layer (*tunica externa*) is composed of connective tissue. The middle layer (*tunica media*) is made up of smooth muscle cells and elastic tissue; and the innermost layer (*tunica intima*) consists mostly of endothelial cells. Vascular images are usually obtained along the longitudinal axis of the artery of interest. A segment of the artery that has a clearly defined intimal–luminal interface with anterior and posterior wall is imaged continuously with two-dimensional (2D) grayscale imaging (Fig. 43.1). The ultrasound beam should be perpendicular to the vessel of interest. Machine settings such as gain, compression, depth and focal zone placement should be adjusted to improve the quality of the images. The blood flow through the vessel is assessed using pulse Doppler images. The position and the orientation of the cursor are important for accurate estimation of flow through the artery

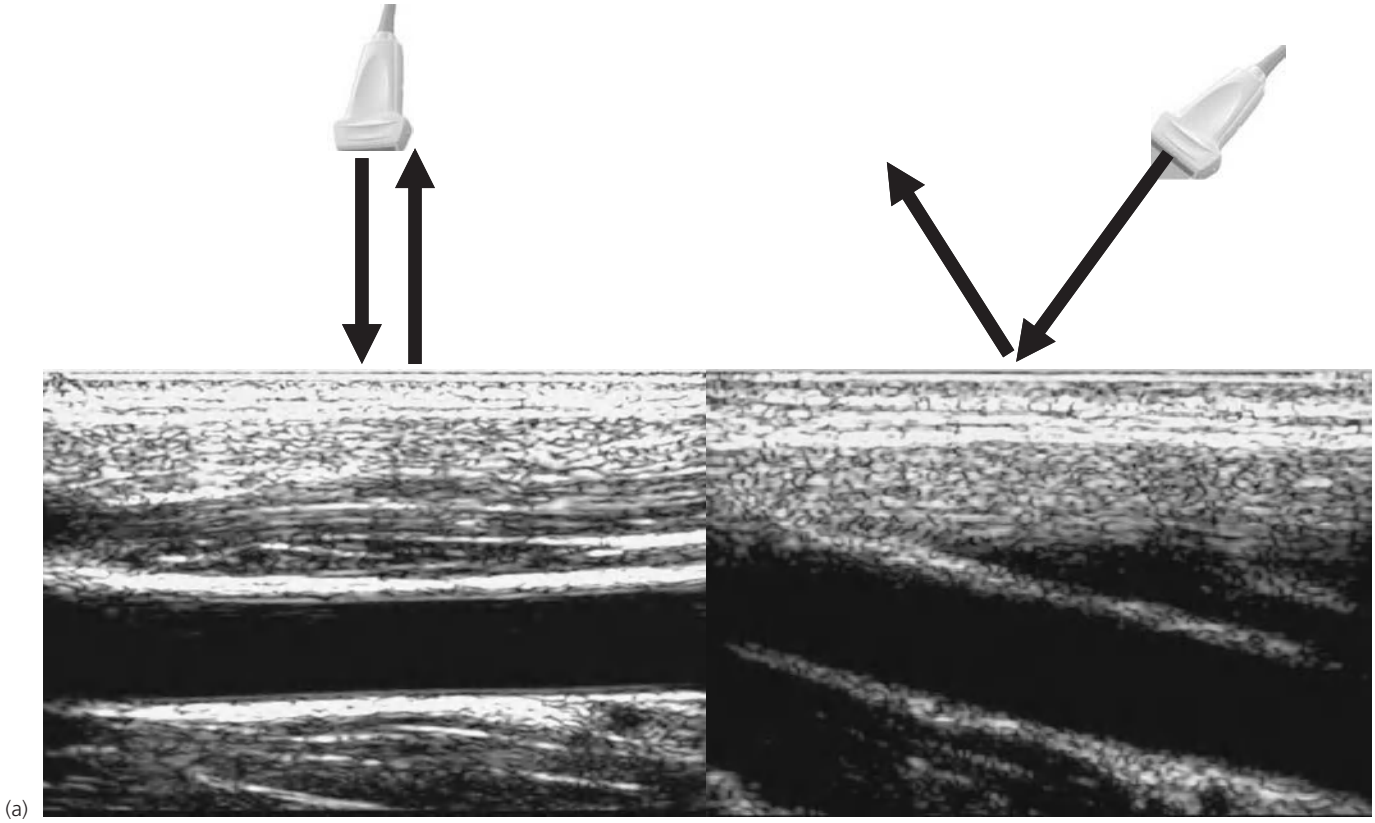

(a) (b)

**Figure 43.1** The vessel of interest should be perpendicular to the ultrasound beam. **(a)** Correct positioning of the ultrasound probe with clearly defined intimal–luminal interface. **(b)** Poorly defined wall structure with incorrect positioning of the ultrasound probe. Reproduced from Gerhard-Herman M, Gardin JM, Jaff M et al. American Society of Echocardiography; Society for Vascular Medicine and Biology. Guidelines for noninvasive vascular laboratory testing: a report from the American Society of Echocardiography and the Society for Vascular Medicine and Biology. *J Am Soc Echocardiogr* 2006;19:955–72, with permission from Elsevier.

(Fig. 43.2). For accurate Doppler velocity spectral waveforms, it is important to have an angle of 60° of insonation relative to the vessel axis.

## Physiologic imaging of brachial artery

Despite widespread use of FMD, the procedural details for assessing brachial artery FMD are not consistent across research laboratories. These variations were addressed in an International Brachial Artery Reactivity Task Force Guidelines statement for assessing brachial artery vascular function [20]. The method described in this chapter is consistent with these guidelines and takes into account additional, more recently published work.

### Subject preparation

Vascular function should be assessed in a quiet, temperature-controlled room by a trained vascular sonographer. Factors such as a fatty meal, smoking, exercise and sympathetic stimulation can cause acute changes in endothelial function that may persist for 4–6 hours [51]. Patients should be therefore instructed to avoid these exposures on the day of their vascular study. The study is best performed after 6 hours of fasting. All vasoactive medications, including caffeine, should be withheld for four half-lives.

### Equipment and image acquisition

The ultrasound equipment should be equipped with vascular imaging software – vascular probes of frequency 7.5 MHz and higher – and an internal electrocardiogram system that allows time for imaging with regard to the cardiac cycle. The subject should lie supine with his or her arm in a comfortable position. The brachial artery images are obtained along its longitudinal axis just above the antecubital fossa. A segment of brachial artery that has a clearly defined intimal–luminal interface with anterior and posterior wall is imaged continuously with 2D grayscale imaging (Fig. 43.3).

### Flow-mediated (endothelium-dependent) dilation

A blood pressure (sphygmomanometer) cuff is placed around the forearm at the start of the study. A baseline image of the brachial artery is recorded along its long axis and a pulsed-wave Doppler signal is obtained from a mid-artery sample volume to estimate baseline flow.

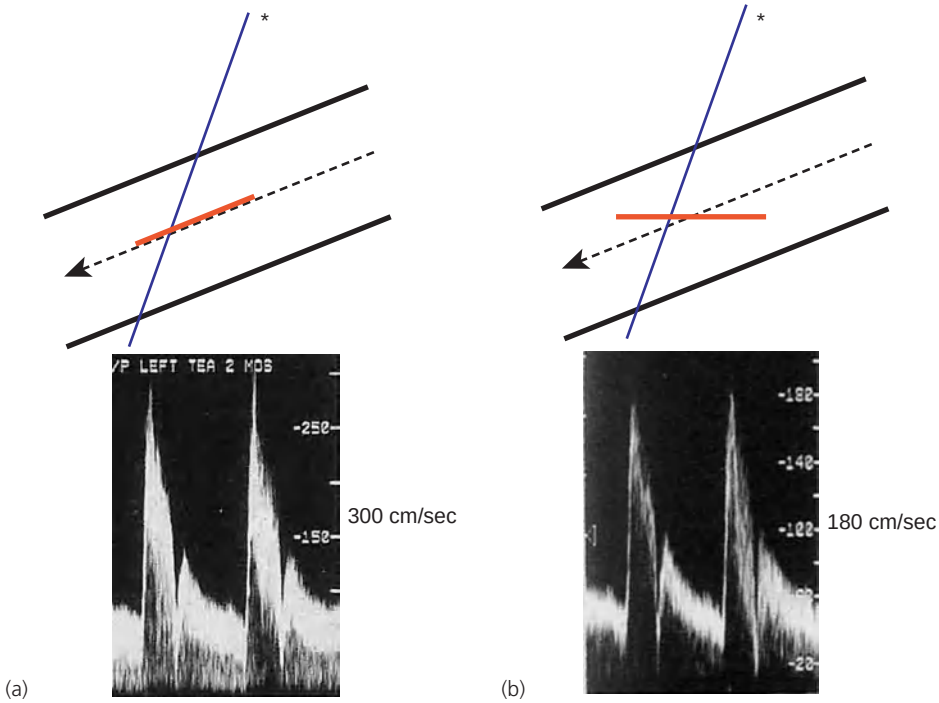


**Figure 43.2** An angle of 60° of Doppler insonation relative to the vessel axis provides the most accurate Doppler velocities. **(a)** Appropriate alignment of Doppler beam. **(b)** Inaccurate Doppler angle. Pulsed-wave Doppler images obtained from same internal carotid artery demonstrate underestimation of peak systolic velocity with an inaccurate Doppler angle (b). Reproduced from Gerhard-Herman M, Gardin JM, Jaff M, et al. American Society of Echocardiography; Society for Vascular Medicine and Biology. Guidelines for noninvasive vascular laboratory testing: a report from the American Society of Echocardiography and the Society for Vascular Medicine and Biology. *J Am Soc Echocardiogr* 2006;19:955–72, with permission from Elsevier.

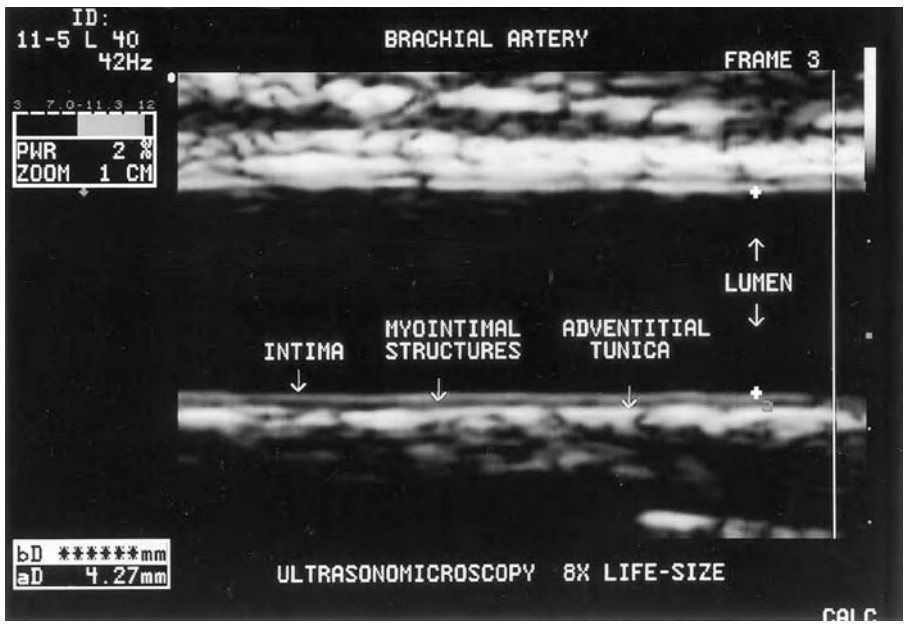


**Figure 43.3** A two-dimensional image of the brachial artery in longitudinal axis (8× magnification) with identification of vessel wall structures. The lumen diameter is usually measured from intima to intima. Reproduced from Corretti MC, Anderson TJ, Benjamin EJ et al. Guidelines for the ultrasound assessment of endothelial-dependent flow-mediated vasodilation of the brachial artery: a report of the International Brachial Artery Reactivity Task Force. *J Am Coll Cardiol* 2002;39:257–65, with permission of the American College of Cardiology Foundation.

The forearm cuff is now inflated to 50–100 mm Hg above the systolic blood pressure and left in the inflated position for 4–5 minutes. Complete occlusion of blood flow to the distal forearm induces dilation of distal forearm resistance vessels. When the cuff is deflated, there is an increased flow through the brachial artery (reactive hyperemia). The shear stress induced by increased flow results in brachial artery dilation, which is primarily mediated by endothelial release of NO. The brachial artery is imaged continuously from 30 seconds before to about 2 minutes after the release of the distal cuff.

A pulsed Doppler sample volume within 15 s of cuff release allows estimation of hyperemic flow through the artery. Peak brachial artery vasodilation occurs approximately 60 s after cuff deflation. The flow stimulus (site and duration of vessel occlusion) should be standardized and be consistent across subjects for the laboratory.

In some laboratories, the cuff is placed proximal to the imaging site around the upper arm. This is associated with a larger ischemic stimulus and more brachial artery dilation than that following release of a cuff placed distally. Other laboratories have used a cuff occlusion duration of longer than 5 minutes to elicit more ischemia. We do not recommend these modifications because the resulting brachial artery dilation is mediated by multiple mechanisms (metabolic and ischemic) instead of being a functional response to endothelial release of NO [52].

### Endothelium-independent dilation

After the FMD study is completed, the subject rests for approximately 15 minutes (at least 10 minutes). A second baseline image of the brachial artery and assessment of flow through the artery with pulsed Doppler is obtained. A sublingual spray or tablet of nitroglycerine (400 μg) is then administered and a brachial artery image obtained 3–4 minutes later when maximum vascular dilation occurs. The vasodilation observed is endothelium-independent and is a measure of vascular smooth muscle function.

### Image analysis

Images are analyzed off-line. A longitudinal segment of the artery with clear delineation of anterior and posterior walls of the intimal–lumen interface is selected. The diameter is measured either manually using electronic calipers or by using automated edge-detection software. Typically, multiple measurements of the luminal diameter are averaged. The timing of measurements should be consistent with regards to the cardiac cycle. This is facilitated by ECG gating of the images. Measurements usually reported include lumen diameter at baseline, and the absolute and percent change in diameter with flow (endothelium-dependent) and with nitroglycerine (endothelium-independent).

### Quality control

Vascular imaging for physiologic evaluation is technically challenging with a significant learning curve. The Task Force recommended that a sonographer should perform at least 100 studies under supervision before performing them independently. At least 100 studies per year should be performed to maintain skills.

## Anatomic imaging of carotid artery

Recent reports from the American Society of Echocardiography and the Society of Vascular Medicine and Biology have described detailed guidelines for carotid artery imaging [53,54]. The technique described here is in agreement with these guidelines and also takes into account additional published work.

### Anatomy

The head and the neck are supplied by two common carotid arteries (CCA), which ascend on either side of the neck. Each CCA divides into two branches: the external (ECA) and the internal carotid arteries (ICA). The right CCA begins at the bifurcation of the innominate artery behind the sternoclavicular joint and is confined to the neck. The left CCA springs from the highest part of the arch of the aorta to the left of and in a plane posterior to the innominate artery and therefore consists of a thoracic and a cervical portion. Each vessel travels obliquely upward, from behind the sternoclavicular articulation, to the level of the upper border of the thyroid cartilage, where it divides into the external and internal carotid arteries [50].

### Image acquisition

The equipment and software used for anatomic imaging are similar to those used for physiologic imaging. Carotid ultrasound imaging includes (i) 2D imaging of structure and motion, and (ii) color flow and pulsed-wave Doppler analysis.

The patient should be supine with slight hyperextension and rotation of the neck away from the probe. Two-dimensional imaging is used to identify the location and the course of the CCA. A slow transverse scan is performed from the lowest portion of the CCA, at the level just superior to the clavicle, to where it bifurcates, near the angle of the jaw. Transverse images are displayed with their orientation on the monitor so that the patient's right side is on the right side of the screen. This scan helps to determine the course of the carotid artery and detect plaques. The transducer is then rotated longitudinally. The longitudinal images are displayed with the more distal (toward the head) segment of the carotid on the left side of the screen (Fig. 43.4). The transducer is oriented as parallel to the vessel wall as possible.

The thickness of the intima–media complex (i.e., IMT) of the carotid artery wall is measured using high-resolution B-mode imaging (Fig. 43.4). IMT is measured at end-diastole for the CCA, the bifurcation (bulb) and one or both branch vessels (usually the ICA). Measurement yield and reproducibility of IMT are greater for the CCA than for the ICA or the bulb [55–58]. Measurement reproducibility for the near and the far walls is comparable, but the measurement yield of the near wall is lower and its accuracy may be less than that of the far wall because of technical considerations [43,46].

The internal and external carotid artery branches are distinguished from each other using standard anatomic and Doppler features. The ICA is usually larger, more lateral and posterior. The Doppler velocity spectral waveform in the ICA has a monophasic flow pattern with strong systolic and

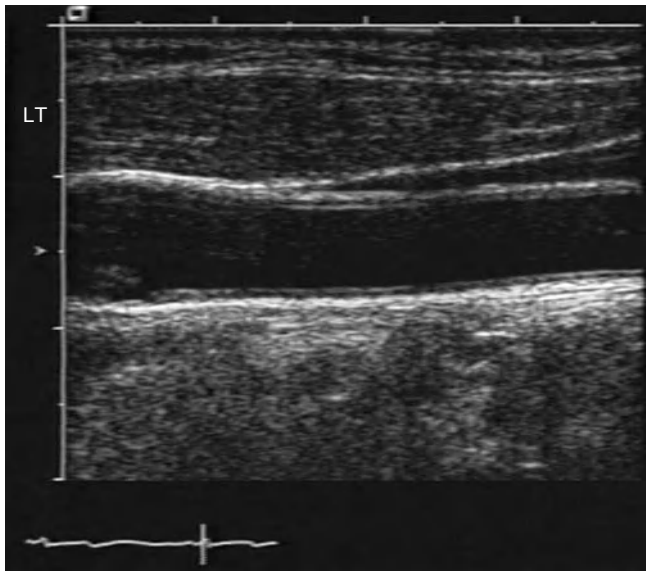


**Figure 43.4** B-mode image of the distal common carotid artery. The distal common carotid artery is depicted on the right side of the screen. Modified from Roman MJ, Naqvi Z., Gardin JM *et al*. Clinical Application of Noninvasive Vascular Ultrasound in Cardiovascular Risk Stratification: A Report from the American Society of Echocardiography and the Society of Vascular Medicine and Biology. J Am Soc of Echocardiogr 2006;19:943–54, with permission from Elsevier.

diastolic flow due to low vascular resistance of the intracerebral branches. The ECA flow is more pulsatile due to greater resistance of the branches supplying the neck and the face (Fig. 43.5) [31].

The systolic and diastolic diameters of the CCA are measured between the intimal–luminal interface of the near and the far walls. These measurements are used to calculate mechanical indices of CCA, such as pressure-strain elastic modulus (Ep) and stiffness index (β), indirect measures of arterial stiffness [30,59]. Blood pressure measurements are obtained using a sphygmomanometer.

$$Ep = K \times (P_{syst} - P_{diast}) \\ (D_{syst} - D_{diast})/D_{diast}$$

$$\beta = \ln(P_{syst} - P_{diast}) \\ (D_{syst} - D_{diast})/D_{diast}$$

$P_{syst}$ and $P_{diast}$ are the systolic and diastolic blood pressures (mm Hg). $D_{syst}$ and $D_{diast}$ are the corresponding vessel diameters (mm). Ep is measured in newtons/$m^2$ ($N/m^2$). The constant K (= 133.3) allows conversion of mm Hg to newtons/$m^2$.

## Imaging pitfalls

The pitfalls of vascular ultrasound imaging include poor image quality, improper machine settings and difficult patient anatomy or body habitus.


**Figure 43.5** **(a)** The pulsatile Doppler velocity spectral waveform in the external carotid artery. **(b)** The internal carotid artery Doppler velocity spectral waveform has a low-resistance pattern with higher velocity diastolic flow.

## Definition of abnormal IMT

Intima–media thickness increases with age, beginning in childhood and, on average, is greater in men than women [56,60–62]. Racial differences have been reported; African Americans have greater CCA IMT values than age-matched Caucasians or non-Hispanic whites [63]. Finally, systolic blood pressure is an important determinant of IMT, presumably as a result of medial hypertrophy [56,60,61,64].

## Definition of stenosis by pulsed-wave Doppler

Several velocity criteria used to detect the presence and severity of carotid artery disease have been published [54, 65]. Table 43.2 summarizes absolute velocities and velocity ratios that are useful in diagnosing significant ICA stenosis.

**Table 43.2** Criteria for classification of internal carotid artery disease

| Degree of stenosis (%) | ICA PSV (cm/s) | Plaque estimate (%) | ICA EDV (cm/s) | ICA CCA PSV ratio |
|---|---|---|---|---|
| Normal | <125 | 0 | <40 | <2 |
| <50 | <125 | <50 | <40 | <2 |
| 50–69 | 125–230 | >50 | 40–100 | 2–4 |
| >70 | >230 | >50 narrow lumen | >100 | >4 |
| Subtotal occlusion | 0 | >50 | 0 | Variable |
| Total occlusion | 0 | >50 | 0 | <1 |

CCA, common carotid artery; EDV, end-diastolic velocity; ICA, internal carotid artery; PSV, peak systolic velocity.
Reproduced from Gerhard-Herman M, Gardin JM, Jaff M, et al. American Society of Echocardiography; Society for Vascular Medicine and Biology. Guidelines for noninvasive vascular laboratory testing: a report from the American Society of Echocardiography and the Society for Vascular Medicine and Biology. *J Am Soc Echocardiogr* 2006;19:955–72, with permission from Elsevier.

## Role of vascular imaging in children

Vascular imaging is currently being used as a research tool in children. The physiologic and anatomic components assess, in theory, the total atherosclerotic burden of a subject at a preclinical stage. Physiologic vascular imaging has been used extensively to study populations (including children) exposed to traditional atherosclerosis risk factors and to study the effect of large-scale interventions. Children with low birthweight and those with diabetes, hypercholesterolemia, obesity or exposure to smoking (passive smokers) have all been demonstrated to have endothelial dysfunction [15,16,66–68]. In ongoing longitudinal studies in large cohorts of children, the effect of risk-factor interventions on endothelial function and atherosclerosis is being examined [69,70]. It is important to recognize, however, that a multitude of factors affect FMD, some of them acting for a very brief duration [51]. This makes it unclear whether the biologic variability of FMD can be low enough and its reproducibility high enough for it to be used as a reliable clinical tool [71].

Similarly, several studies have demonstrated an association between the presence of known cardiovascular risk factors during childhood and elevated values of carotid IMT during childhood or early adulthood [49]. Specifically, a greater thickness of carotid IMT compared with age-matched controls occurs in children with hypercholesterolemia, family history of premature myocardial infarction, obesity, hypertension, type 1 diabetes mellitus, history of Kawasaki disease, HIV infection, Williams syndrome, beta-thalassemia major, and congenital adrenal hyperplasia [15,24,38–48].

The Cardiovascular Risk in Young Finns Study assessed mechanical properties of the carotid artery in 2255 adults who had risk factor data available since childhood. They found that cardiovascular risk factors identified in childhood and adolescence predict decreased carotid artery elasticity in adulthood [72]. Increased carotid artery stiffness has been reported in children with a history of Kawasaki disease, beta-thalassemia major, hypercholesterolemia, end-stage renal disease and in children on parenteral nutrition [44,45,73–75].

Vascular imaging will likely continue to provide insights into vascular physiology in health and disease. Whether the data obtained will be used to guide an individual's care during decades of preclinical changes is difficult to predict. It is possible to envision the role of serial vascular imaging performed every few years in individuals (including children) with known exposure to risk factors, to measure the effectiveness of interventions, a role similar to that of glycosylated hemoglobin (HbA1C) in measuring the effectiveness of glucose control in diabetics. For this role to be a reality, studies will need to refine further and establish "normal" values of these measurements in different populations, interstudy variability of measurements, normal rates of progression, effect of interventions on various measurements in large populations and cost-effectiveness of such monitoring in individuals. For now, this role of vascular imaging for monitoring atherosclerosis in clinical practice appears distant in adults and unlikely in children.

## References


1. Berenson GS, Srinivasan SR, Bao W et al. Association between multiple cardiovascular risk factors and atherosclerosis in children and young adults. The Bogalusa Heart Study. *N Engl J Med* 1998;338:1650–6.
2. Vane JR, Anggard EE, Botting RM. Regulatory functions of the vascular endothelium. *N Engl J Med* 1990;323:27–36.
3. Ross R. The pathogenesis of atherosclerosis: a perspective for the 1990s. *Nature* 1993;362:801–9.
4. Furchgott RF, Zawadzki JV. The obligatory role of endothelial cells in the relaxation of arterial smooth muscle by acetylcholine. *Nature* 1980;288:373–6.
5. Palmer RM, Ferrige AG, Moncada S. Nitric oxide release accounts for the biological activity of endothelium-derived relaxing factor. *Nature* 1987;327:524–6.
6. Ludmer PL, Selwyn AP, Shook TL et al. Paradoxical vasoconstriction induced by acetylcholine in atherosclerotic coronary arteries. *N Engl J Med* 1986;315:1046–51.
7. Cox DA, Vita JA, Treasure CB et al. Atherosclerosis impairs flow-mediated dilation of coronary arteries in humans. *Circulation* 1989;80:458–65.
8. Cayatte AJ, Palacino JJ, Horten K, Cohen RA. Chronic inhibition of nitric oxide production accelerates neointima formation and impairs endothelial function in hypercholesterolemic rabbits. *Arterioscler Thromb* 1994;14:753–9.
9. Vita JA, Treasure CB, Nabel EG et al. Coronary vasomotor response to acetylcholine relates to risk factors for coronary artery disease. *Circulation* 1990;81:491–7.

10. Celermajer DS, Sorensen KE, Gooch VM et al. Non-invasive detection of endothelial dysfunction in children and adults at risk of atherosclerosis. *Lancet* 1992;340:1111–5.
11. Celermajer DS, Sorensen K, Ryalls M et al. Impaired endothelial function occurs in the systemic arteries of children with homozygous homocystinuria but not in their heterozygous parents. *J Am Coll Cardiol* 1993;22:854–8.
12. Seiler C, Hess OM, Buechi M et al. Influence of serum cholesterol and other coronary risk factors on vasomotion of angiographically normal coronary arteries. *Circulation* 1993;88:2139–48.
13. Celermajer DS, Sorensen KE, Bull C et al. Endothelium-dependent dilation in the systemic arteries of asymptomatic subjects relates to coronary risk factors and their interaction. *J Am Coll Cardiol* 1994;24:1468–74.
14. Reddy KG, Nair RN, Sheehan HM, Hodgson JM. Evidence that selective endothelial dysfunction may occur in the absence of angiographic or ultrasound atherosclerosis in patients with risk factors for atherosclerosis. *J Am Coll Cardiol* 1994;23:833–43.
15. de Jongh S, Lilien MR, Bakker HD et al. Family history of cardiovascular events and endothelial dysfunction in children with familial hypercholesterolemia. *Atherosclerosis* 2002;163:193–7.
16. Singh TP, Groehn H, Kazmers A. Vascular function and carotid intimal-medial thickness in children with insulin-dependent diabetes mellitus. *J Am Coll Cardiol* 2003;41:661–5.
17. Suwaidi JA, Hamasaki S, Higano ST et al. Long-term follow-up of patients with mild coronary artery disease and endothelial dysfunction. *Circulation* 2000;101:948–54.
18. Yeboah J, Crouse JR, Hsu FC et al. Brachial flow-mediated dilation predicts incident cardiovascular events in older adults: the Cardiovascular Health Study. *Circulation* 2007;115:2390–7.
19. Anderson TJ, Uehata A, Gerhard MD et al. Close relation of endothelial function in the human coronary and peripheral circulations. *J Am Coll Cardiol* 1995;26:1235–41.
20. Corretti MC, Anderson TJ, Benjamin EJ et al. Guidelines for the ultrasound assessment of endothelial-dependent flow-mediated vasodilation of the brachial artery: a report of the International Brachial Artery Reactivity Task Force. *J Am Coll Cardiol* 2002;39:257–65.
21. Joannides R, Haefeli WE, Linder L et al. Nitric oxide is responsible for flow-dependent dilatation of human peripheral conduit arteries in vivo. *Circulation* 1995;91:1314–19.
22. Green D. Point: Flow-mediated dilation does reflect nitric oxide-mediated endothelial function. *J Appl Physiol* 2005;99:1233–4; discussion 7–8.
23. Cheung YF, Chan GC, Ha SY. Arterial stiffness and endothelial function in patients with beta-thalassemia major. *Circulation* 2002;106:2561–6.
24. Cheung YF, Chow PC, Chan GC, Ha SY. Carotid intima-media thickness is increased and related to arterial stiffening in patients with beta-thalassaemia major. *Br J Haematol* 2006;135:732–4.
25. van Popele NM, Grobbee DE, Bots ML et al. Association between arterial stiffness and atherosclerosis: the Rotterdam Study. *Stroke* 2001;32:454–60.
26. Wada T, Kodaira K, Fujishiro K et al. Correlation of ultrasound-measured common carotid artery stiffness with pathological findings. *Arterioscler Thromb* 1994;14:479–82.
27. Simons PC, Algra A, Bots ML et al. Common carotid intima-media thickness in patients with peripheral arterial disease or abdominal aortic aneurysm: the SMART study. Second Manifestations of ARTerial disease. *Atherosclerosis* 1999;146:243–8.
28. Blacher J, Pannier B, Guerin AP et al. Carotid arterial stiffness as a predictor of cardiovascular and all-cause mortality in end-stage renal disease. *Hypertension* 1998;32:570–4.
29. Franklin SS, Sutton-Tyrrell K, Belle SH et al. The importance of pulsatile components of hypertension in predicting carotid stenosis in older adults. *J Hypertens* 1997;15:1143–50.
30. Kawasaki T, Sasayama S, Yagi S et al. Non-invasive assessment of the age related changes in stiffness of major branches of the human arteries. *Cardiovasc Res* 1987;21:678–87.
31. Polak JF. *Peripheral Vascular Sonography*, 2nd edn. Philadelphia: Lippincott Williams & Wilkins, 2004.
32. Salonen JT, Salonen R. Ultrasound B-mode imaging in observational studies of atherosclerotic progression. *Circulation* 1993;87 (3 Suppl.):II56–65.
33. O'Leary DH, Polak JF, Kronmal RA et al. Carotid-artery intima and media thickness as a risk factor for myocardial infarction and stroke in older adults. Cardiovascular Health Study Collaborative Research Group. *N Engl J Med* 1999;340:14–22.
34. Belcaro G, Nicolaides AN, Laurora G et al. Ultrasound morphology classification of the arterial wall and cardiovascular events in a 6-year follow-up study. *Arterioscler Thromb Vasc Biol* 1996;16:851–6.
35. Chambless LE, Heiss G, Folsom AR et al. Association of coronary heart disease incidence with carotid arterial wall thickness and major risk factors: the Atherosclerosis Risk in Communities (ARIC) Study, 1987–1993. *Am J Epidemiol* 1997;146:483–94.
36. Cerne A, Kranjec I. Atherosclerotic burden in coronary and peripheral arteries in patients with first clinical manifestation of coronary artery disease. *Heart Vessels* 2002;16:217–26.
37. Greenland P, Abrams J, Aurigemma GP et al. Prevention Conference V: Beyond secondary prevention: identifying the high-risk patient for primary prevention: noninvasive tests of atherosclerotic burden: Writing Group III. *Circulation* 2000;101:E16–22.
38. Pauciullo P, Iannuzzi A, Sartorio R et al. Increased intima-media thickness of the common carotid artery in hypercholesterolemic children. *Arterioscler Thromb* 1994;14:1075–9.
39. Cuomo S, Guarini P, Gaeta G et al. Increased carotid intima-media thickness in children-adolescents, and young adults with a parental history of premature myocardial infarction. *Eur Heart J* 2002;23:1345–50.
40. Sorof JM, Alexandrov AV, Garami Z et al. Carotid ultrasonography for detection of vascular abnormalities in hypertensive children. *Pediatr Nephrol* 2003;18:1020–4.
41. Jarvisalo MJ, Putto-Laurila A, Jartti L et al. Carotid artery intima-media thickness in children with type 1 diabetes. *Diabetes* 2002;51:493–8.
42. Tounian P, Aggoun Y, Dubern B et al. Presence of increased stiffness of the common carotid artery and endothelial dysfunction in severely obese children: a prospective study. *Lancet* 2001;358:1400–4.
43. Krantz JS, Mack WJ, Hodis HN et al. Early onset of subclinical atherosclerosis in young persons with type 1 diabetes. *J Pediatr* 2004;145:452–7.
44. Noto N, Okada T, Yamasuge M et al. Noninvasive assessment of the early progression of atherosclerosis in adolescents with

Kawasaki disease and coronary artery lesions. *Pediatrics* 2001; 107:1095–9.
45. Cheung YF, Wong SJ, Ho MH. Relationship between carotid intima-media thickness and arterial stiffness in children after Kawasaki disease. *Arch Dis Child* 2007;92:43–7.
46. McComsey GA, O'Riordan M, Hazen SL et al. Increased carotid intima media thickness and cardiac biomarkers in HIV infected children. *AIDS* 2007;21:921–7.
47. Aggoun Y, Sidi D, Levy BI et al. Mechanical properties of the common carotid artery in Williams syndrome. *Heart* 2000;84: 290–3.
48. Sartorato P, Zulian E, Benedini S et al. Cardiovascular risk factors and ultrasound evaluation of intima-media thickness at common carotids, carotid bulbs, and femoral and abdominal aorta arteries in patients with classic congenital adrenal hyperplasia due to 21-hydroxylase deficiency. *J Clin Endocrinol Metab* 2007;92:1015–18.
49. Davis PH, Dawson JD, Riley WA, Lauer RM. Carotid intimal-medial thickness is related to cardiovascular risk factors measured from childhood through middle age: The Muscatine Study. *Circulation* 2001;104:2815–19.
50. Lewis W (ed.) *Gray's Anatomy of the Human Body*, 20th edn. New York: Bartleby, 2000.
51. Vogel RA, Corretti MC, Plotnick GD. Effect of a single high-fat meal on endothelial function in healthy subjects. *Am J Cardiol* 1997;79:350–4.
52. Pyke KE, Tschakovsky ME. The relationship between shear stress and flow-mediated dilatation: implications for the assessment of endothelial function. *J Physiol* 2005;568:357–69.
53. Roman MJ, Naqvi TZ, Gardin JM et al. Clinical application of noninvasive vascular ultrasound in cardiovascular risk stratification: a report from the American Society of Echocardiography and the Society of Vascular Medicine and Biology. *J Am Soc Echocardiogr* 2006;19:943–54.
54. Gerhard-Herman M, Gardin JM, Jaff M et al. Guidelines for noninvasive vascular laboratory testing: a report from the American Society of Echocardiography and the Society of Vascular Medicine and Biology. *J Am Soc Echocardiogr* 2006;19:955–72.
55. Crouse JR 3rd, Craven TE, Hagaman AP, Bond MG. Association of coronary disease with segment-specific intimal-medial thickening of the extracranial carotid artery. *Circulation* 1995;92: 1141–7.
56. Howard G, Sharrett AR, Heiss G et al. Carotid artery intimal-medial thickness distribution in general populations as evaluated by B-mode ultrasound. ARIC Investigators. *Stroke* 1993;24: 1297–304.
57. O'Leary DH, Polak JF, Wolfson SK Jr et al. Use of sonography to evaluate carotid atherosclerosis in the elderly. The Cardiovascular Health Study. CHS Collaborative Research Group. *Stroke* 1991;22:1155–63.
58. Stensland-Bugge E, Bonaa KH, Joakimsen O. Reproducibility of ultrasonographically determined intima-media thickness is dependent on arterial wall thickness. The Tromso Study. *Stroke* 1997;28:1972–80.
59. Peterson LH. Regulation of blood vessels. *Circulation* 1960;21: 749–59.
60. Ebrahim S, Papacosta O, Whincup P et al. Carotid plaque, intima media thickness, cardiovascular risk factors, and prevalent cardiovascular disease in men and women: the British Regional Heart Study. *Stroke* 1999;30:841–50.
61. Roman MJ, Pickering TG, Pini R et al. Prevalence and determinants of cardiac and vascular hypertrophy in hypertension. *Hypertension* 1995;26:369–73.
62. Urbina EM, Srinivasan SR, Tang R et al. Impact of multiple coronary risk factors on the intima-media thickness of different segments of carotid artery in healthy young adults (The Bogalusa Heart Study). *Am J Cardiol* 2002;90:953–8.
63. D'Agostino RB Jr, Burke G, O'Leary D et al. Ethnic differences in carotid wall thickness. The Insulin Resistance Atherosclerosis Study. *Stroke* 1996;27:1744–9.
64. Roman MJ, Saba PS, Pini R et al. Parallel cardiac and vascular adaptation in hypertension. *Circulation* 1992;86:1909–18.
65. Grant EG, Benson CB, Moneta GL et al. Carotid artery stenosis: gray-scale and Doppler US diagnosis – Society of Radiologists in Ultrasound Consensus Conference. *Radiology* 2003;229:340–6.
66. Kallio K, Jokinen E, Raitakari OT et al. Tobacco smoke exposure is associated with attenuated endothelial function in 11-year-old healthy children. *Circulation* 2007;115:3205–12.
67. Jarvisalo MJ, Raitakari M, Toikka JO et al. Endothelial dysfunction and increased arterial intima-media thickness in children with type 1 diabetes. *Circulation* 2004;109:1750–5.
68. Meyer AA, Kundt G, Steiner M et al. Impaired flow-mediated vasodilation, carotid artery intima-media thickening, and elevated endothelial plasma markers in obese children: the impact of cardiovascular risk factors. *Pediatrics* 2006;117:1560–7.
69. Raitakari OT, Ronnemaa T, Jarvisalo MJ et al. Endothelial function in healthy 11-year-old children after dietary intervention with onset in infancy: the Special Turku Coronary Risk Factor Intervention Project for children (STRIP). *Circulation* 2005;112: 3786–94.
70. Woo KS, Chook P, Yu CW et al. Effects of diet and exercise on obesity-related vascular dysfunction in children. *Circulation* 2004;109:1981–6.
71. Deanfield JE, Halcox JP, Rabelink TJ. Endothelial function and dysfunction: testing and clinical relevance. *Circulation* 2007;115: 1285–95.
72. Juonala M, Jarvisalo MJ, Maki-Torkko N et al. Risk factors identified in childhood and decreased carotid artery elasticity in adulthood: the Cardiovascular Risk in Young Finns Study. *Circulation* 2005;112:1486–93.
73. Aggoun Y, Bonnet D, Sidi D et al. Arterial mechanical changes in children with familial hypercholesterolemia. *Arterioscler Thromb Vasc Biol* 2000;20:2070–5.
74. Aggoun Y, Niaudet P, Laffont A et al. [Cardiovascular impact of end-stage renal insufficiency in children undergoing hemodialysis]. *Arch Mal Coeur Vaiss* 2000;93:1009–13.
75. Aggoun Y, Colomb V, Turanlahti M et al. Endothelial function and mechanical properties of the common carotid artery in children on parenteral nutrition. *Pediatr Res* 2004;55:789–93.
76. de Groot E, Hovingh GK, Wiegman A et al. Measurement of arterial wall thickness as a surrogate marker for atherosclerosis. *Circulation* 2004;109(23 Suppl. 1):III33–III38.
77. Dalla Pozza R, Bechtold S, Urschel S et al. Subclinical atherosclerosis, but normal autonomic function after Kawasaki disease. *J Pediatr* 2007;151:239–43.

# 44 The Echocardiographic Assessment of Pulmonary Arterial Hypertension

**Jeffrey F. Smallhorn**
Division of Pediatric Cardiology, Stollery Children's Hospital, University of Alberta, Edmonton, Alberta, AB, Canada

## Introduction

Pulmonary hypertension is defined as a mean pulmonary artery pressure of >25 mm Hg at rest, or >30 mm Hg with exercise in the absence of increased left-sided pressures. Pulmonary endothelial dysfunction promotes a triad of vasoconstriction, cell proliferation and thrombosis through the action of mediators such as thromboxane $A_2$, endothelin I and serotonin. Under normal circumstances these are counterbalanced by prostacyclin, nitric oxide and vasoactive intestinal peptide. The end result is irreversible vascular changes with intimal fibrosis, pulmonary arteriolar occlusion and plexiform lesions [1].

## Definition of pulmonary arterial hypertension

Different classifications of pulmonary hypertension have been proposed, the most recent one being the Evian–Venice classification. In this approach the term "primary" in the descriptor "primary pulmonary arterial hypertension" has been replaced with "idiopathic" when no cause is found, and with "familial" when there is a genetic component to the disease. Idiopathic pulmonary hypertension is a rare disorder in children. More commonly, secondary forms of pulmonary hypertension are diagnosed.

## Secondary pulmonary hypertension

Patients with pulmonary hypertension associated with congenital heart disease represent a heterogeneous population, including:

**1** Congenital heart disease with an associated large ventricular septal defect and an unobstructed pulmonary outflow tract and shunts at great vessel level, i.e., patent ductus arteriosus, aortopulmonary window and truncus arteriosus.

**2** Congenital pulmonary venous abnormalities – encountered either in the newborn period with total anomalous pulmonary venous drainage, or in the form of congenital pulmonary vein stenosis, either in isolation or associated with other forms of congenital heart disease. Rarely, pulmonary hypertension may be seen with partial anomalous pulmonary venous drainage, usually in association with scimitar syndrome and invariably associated with an intracardia or extracardiac left-to-right shunt. Acquired pulmonary vein stenosis is most commonly seen post repair of total anomalous pulmonary venous drainage, particularly when there is an associated small pulmonary venous confluence or hypoplastic pulmonary veins.

**3** Absence of a mediastinal left or right pulmonary artery may be associated with pulmonary hypertension, particularly when the other lung is exposed to an intracardiac or extracardiac shunt. In this setting the pulmonary arterial hypertension is often out of keeping with the magnitude of the left-to-right shunt.

**4** Pulmonary arterial hypertension may be secondary to upper airway obstruction in cases with Down syndrome, sleep apnea and/or obesity. Also, interstitial fibrosis, prior severe hyaline membrane disease, diaphragmatic hernia and chronic exposure to high altitudes may be associated with pulmonary arterial hypertension.

**5** Pulmonary arterial hypertension in the newborn period in the absence of associated structural heart disease.

**6** Less commonly encountered is pulmonary arterial hypertension secondary to systemic atrioventricular valve regurgitation, or left ventricular systolic and/or diastolic dysfunction.

**7** Pulmonary arterial hypertension secondary to left-sided obstructive lesions such as coarctation of the aorta, cortriatrium, mitral stenosis or relative hypoplasia of the systemic left ventricle is seen in the newborn period.

**8** Pulmonary embolic disease is uncommon in pediatrics, but may be encountered in infants with chronic venous lines. Other embolic sources, such as infected vegetations, or thrombi secondary to acute myeloid leukemia, may be rarely encountered.

*Echocardiography in Pediatric and Congenital Heart Disease: From Fetus to Adult*
Edited by Wyman W. Lai, Luc L. Mertens, Meryl S. Cohen and Tal Geva
 ISBN: 978-1-405-17401-5

**9** Finally, the echocardiographer is often asked to assess the pulmonary artery pressure during the early postoperative period, in newborns and infants with structural heart disease who have undergone repair of a large intracardiac left-to-right shunt.

## Technique and pitfalls of assessing the pediatric patient with suspected pulmonary arterial hypertension

In the pediatric population the diagnosis of idiopathic pulmonary arterial hypertension is made only after an exhaustive search for an underlying associated defect. Therefore, the exclusion of an associated intracardiac or extracardiac shunt lesion is essential. Whereas an associated perimembranous ventricular septal defect, atrial septal defect or patent ductus arteriosus is rarely overlooked, this is not the case with an aortopulmonary window. Frequent "dropout" in the area where the aorta and pulmonary artery cross may give the impression of an aortopulmonary window. However, inadequate interrogation of this region may result in the defect being missed, particularly in the child with a poor ultrasound window. As the majority of aortopulmonary windows are large, color Doppler interrogation may not be of great value, particularly as the direction of flow is invariably at right angles to the Doppler beam. Moreover, early pulmonary arterial hypertension that limits the degree of left-to-right shunting may remove the secondary clues of left-sided chamber enlargement. Therefore attention should be paid to the right-sided structures, such as secondary dilation of the main pulmonary artery and right ventricle.

A similar situation arises in cases where there is absence of a branch pulmonary artery and an associated intracardiac or extracardiac shunt, or in the setting of anomalous origin of a branch pulmonary artery from the aorta. In the latter case, the abnormally arising pulmonary artery may lie in close proximity to its counterpart, giving the impression that they are connected. It is therefore imperative to be sure that the branch pulmonary arteries and their origins are clearly defined in such cases. Also, when the mediastinal component of the right pulmonary artery is absent, there may be an echo-free space in its place that gives the appearance of the artery. In this setting, the clue is the absence of flow in this echo-free space.

## Exclusion of pulmonary venous obstruction

Doppler interrogation of the pulmonary veins is an important component of the evaluation of any new referral with suspected congenital heart disease, even more so in the patient with suspected pulmonary arterial hypertension. This is readily achieved with the use of color Doppler in the apical and subcostal coronal views, with supplementary interrogation from the suprasternal coronal view in smaller patients. The normal pattern is that of low-velocity phasic flow [2–4], which is in marked contrast to an obstructive pattern of higher-velocity turbulent flow. It must be remembered that in some cases there is total occlusion of an extraparenchymal pulmonary vein, which is difficult to diagnose unless there is an excellent ultrasound window as seen in the newborn and small infant. Although the amount of pulmonary blood flow to the obstructed side of a pulmonary artery is reduced, it is usually still possible to detect the turbulent velocity pattern in the affected pulmonary vein.

Interpretation of pulmonary venous velocity profiles may be difficult in cases with an associated large left-to-right shunt and associated mild pulmonary vein stenosis. In this setting, the left-to-right shunt increases the peak systolic and diastolic velocities, making interpretation difficult. It is therefore important for all such cases to undergo pulmonary vein interrogation after surgical repair, or following occlusion with an interventional device. Another area of confusion relates to the increased pulmonary venous Doppler velocity that is frequently observed in the left lower pulmonary vein. This profile is due to mild compression by the descending aorta (with a left aortic arch).

## Echocardiographic techniques to evaluate the pulmonary vascular bed

- Indirect assessment of pulmonary arterial hypertension.
- Measurement of pulmonary artery systolic pressure from tricuspid valve regurgitation and end-diastolic pressure from pulmonary regurgitation.
- The use of a ventricular septal defect to measure systolic right ventricular and subsequently pulmonary artery systolic pressure in the absence of associated right ventricular outflow tract obstruction.
- Doppler interrogation of a patent arterial duct for the assessment of systolic, diastolic and mean pulmonary artery pressure.
- Doppler interrogation of systemic-to-pulmonary artery shunts.
- Measurements of pulmonary capacitance and compliance by combining Doppler interrogation techniques.

### Indirect measurement of pulmonary artery pressure

#### Interventricular septal shape

In addition to systolic afterload, pressure develops and is maintained by factors that influence ventricular function, namely geometry, stroke volume, rate of contraction and inotropic state of the ventricles. Also, left–right ventricular interaction and continuity between the pulmonary and systemic circuits contribute to the function of both ventricles. This interaction is seen in transposition where a Mustard

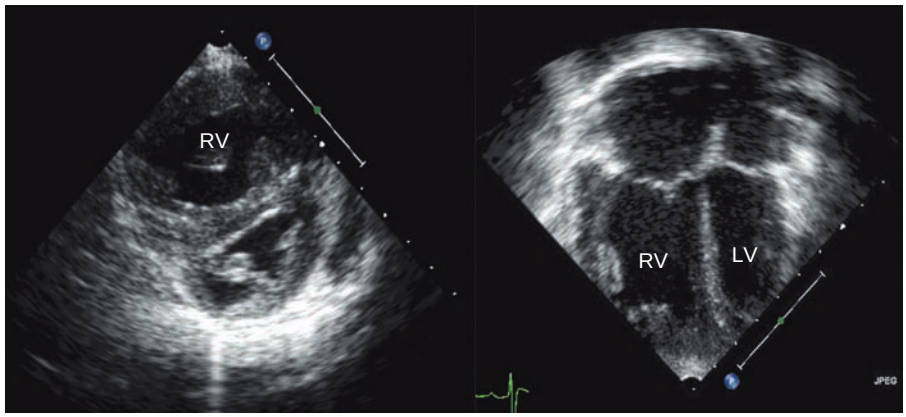


**Figure 44.1** Montage from a case with pulmonary hypertension and systemic right ventricular pressure. Note the flat interventricular septum, as seen in systole. The right-hand panel shows dilation of the right ventricle. LV, left ventricle; RV, right ventricle.

procedure has been performed with a low-pressure left ventricle and an interventricular septum that bows into its cavity. This pattern is reversed when an arterial switch procedure is performed. This observation is also seen in cases with normal intracardiac anatomy and pulmonary arterial hypertension, where a suprasystemic right ventricle results in the interventricular septum bowing into the left ventricle. Indeed, this observation has been used for a long time to provide an indirect assessment of right ventricular and pulmonary artery pressure. Normally the interventricular septum rounds in systole; however, as right ventricular pressure increases it becomes flat and eventually inverts toward the left ventricular cavity (Fig. 44.1). Although these parameters have provided indirect evidence of increased pulmonary artery pressure, they do not yield absolute values.

Indirect parameters are still of importance, as indicated by a study that used echocardiographic parameters to predict outcome in adult patients with pulmonary hypertension, with an end-point of death or transplantation [5]. In this study right atrial size, which is a reflection of right ventricular function and right atrial pressure, was the best independent predictor of outcome ($P$ <0.0004).

## Systolic time intervals

These were used to obtain an indirect assessment of pulmonary artery pressure prior to the application of continuous-wave Doppler to measure absolute pressure [6]. Most studies have been in adults, with slower and relatively stable heart rates, unlike those encountered in the pediatric population, where the various time intervals are affected by heart rate. Despite these limitations it is important to understand the physiologic variables that affect these intervals.

*Pre-ejection period (PEP):* This is measured from the onset of the "q" wave to the beginning of the pulmonary artery acceleration. The duration of the PEEP is inversely proportional to contractility and directly related to the pulmonary artery pressure and impedance.

*Ejection time (ET):* At a given heart rate, ejection time is directly related to stroke volume and inversely related to contractility.

*Acceleration time (AT):* This is the time interval measured from the onset to the peak of ejection, and is directly related to inertial and resistive properties, as well as contractility, and is inversely related to vascular compliance.

All of these parameters, namely PEP, ET and AT, assess the interaction between pressure and flow. Despite an overall good correlation in adult studies, there has been a considerable scatter when comparing individual values. In an attempt to overcome this limitation it has been suggested that the relationship between the pulmonary and systemic measurements be used, which takes into account the interaction between the two circulations [7].

## Pulmonary valve motion

Patterns of pulmonary valve motion also provide a clue to the pulmonary artery pressure. In those with normal pulmonary artery pressures the M-mode of the anterior leaflet of the pulmonary valve has a prominent "a" wave with uninterrupted motion. This "a" wave is absent in pulmonary hypertension; also, there is mid-systolic closure.

## Tricuspid and pulmonary valve time intervals

The time interval between pulmonary valve closure and tricuspid valve opening has been used to predict indirectly systolic right ventricular pressure [8–10]. This period is not truly isovolumic, because in most cases with pulmonary hypertension, tricuspid regurgitation is present. As pulmonary artery pressure increases this time period is prolonged. A similar technique can be used in cases where the duration of the tricuspid regurgitant (TR) jet can be measured, but not the peak. In cases with pulmonary hypertension and good systolic right ventricular function, there is a strong correlation between the time between pulmonary valve closure and the end of the tricuspid regurgitant jet and the right ventricular systolic pressure. As with most interval measurements this would be affected by heart rates that lie outside the normal range. Indeed, in the adult study that reported this technique, the heart rates were between 70 and 110 bpm [8]. Of note, this correlation did not appear to hold in cases with cardiomyopathy [8].

Using a similar technique, another group overcame this problem in patients with heart failure, by using the relationship between pulmonary valve opening and tricuspid regurgitation to assess pulmonary artery diastolic pressure [11]. This was achieved by measuring the time between the R-wave on the electrocardiogram (ECG) and the opening of the pulmonary valve and superimposing this on the tricuspid regurgitant velocity profile. Measurement of the tricuspid regurgitant velocity at the superimposed time has been shown to correlate with the pulmonary artery diastolic pressure.

## Tricuspid valve regurgitation

Tricuspid valve regurgitation provides the most consistent means for measuring right ventricular and subsequently pulmonary artery systolic pressure, in the absence of right ventricular outflow tract obstruction [12]. To achieve this, an adequate spectral trace is essential to avoid underestimation of the maximum Doppler gradient. Color Doppler is helpful in ensuring that the Doppler interrogation is parallel to the regurgitant jet. It is important to interrogate the regurgitant jet from multiple views to ensure that the maximum velocity has been recorded (Fig. 44.2). Also, in patients with an associated ventricular septal defect an obligatory left ventricle-to-right atrial shunt may contaminate the tricuspid regurgitant jet, providing an apparently artificially high tricuspid regurgitant velocity.

To provide an absolute value of systolic right ventricular pressure (RVP), determination of right atrial pressure (RAP) is necessary, given that:

$$RVP = 4(TR)^2 + RAP$$

However, in the absence of an absolute measurement, an indirect assessment from the inferior vena cava can be obtained. In general, the inferior vena cava should collapse during inspiration by more than 50% if the right atrial pressure is less than 10 mm Hg [13]. The absence of such a collapse indicates that the pressure is greater than 10 mm Hg, and if the inferior vena cava is dilated then the pressure probably exceeds 20 mm Hg. It should be noted that if a patient is receiving positive-pressure ventilation then this cannot be used as an indirect assessment of right atrial pressure.

## Pulmonary regurgitation for pulmonary artery end-diastolic pressure

Physiologic pulmonary regurgitation is present in a large number of normal individuals and provides a measure of end-diastolic pulmonary artery pressure. As with tricuspid valve regurgitation, it is important to pay attention to technical details to obtain a reliable measurement. First and foremost is the need to obtain a parallel angle to the regurgitant jet. This is usually possible, as the majority of jets are central and not entrained (Fig. 44.3). Frequently, a Doppler signal can be obtained; however, if the signal is weak then it may be difficult to detect the end-diastolic velocity. To overcome this, the signal may be enhanced with the use of contrast agents; in one series enhancement of weak signals was possible in 96% of cases [14]. Of note, as with tricuspid valve regurgitation, an indirect measure of right atrial pressure is necessary to obtain a reliable measurement.

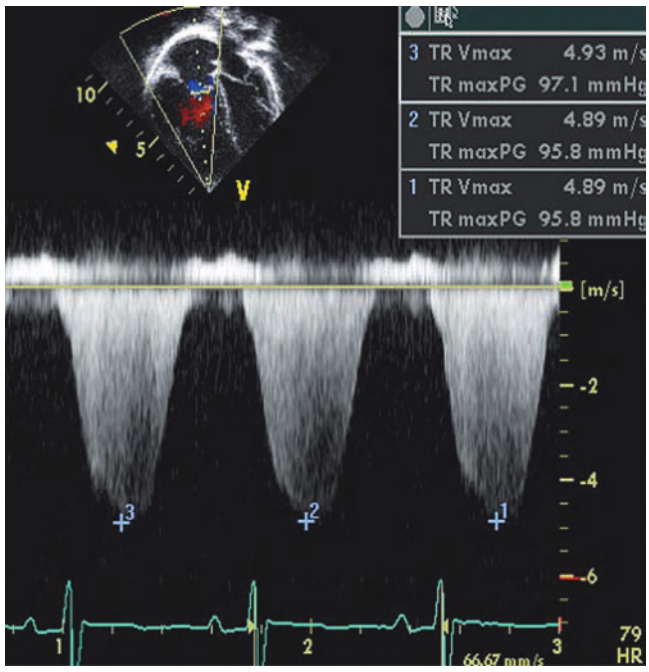


**Figure 44.2** Doppler trace of tricuspid valve regurgitation indicating elevated right ventricular pressure.

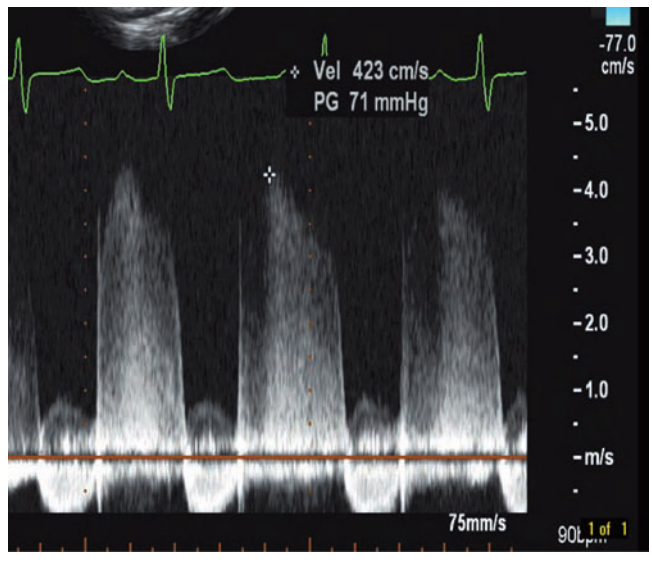


**Figure 44.3** Pulmonary regurgitation Doppler trace in a patient with pulmonary hypertension. Note the peak Doppler velocity is 71 mm Hg, with an associated high end-diastolic velocity.

It has also been shown that there is a good correlation between measured mean pulmonary artery pressure and the peak diastolic velocity from pulmonary regurgitation [15]. This is a fortuitous relationship, as mean pulmonary artery pressure is a calculation, rather than a physiologic event. Despite this nonphysiologic relationship, the measurement is of value, as mean pulmonary artery pressure is an important component of calculated pulmonary vascular resistance.

## Indirect measurement of pulmonary artery pressure

There is an excellent correlation between invasively measured systolic, diastolic and mean pulmonary artery pressures. Using this relationship and the systolic right ventricular pressure as assessed from tricuspid valve regurgitation, it has been possible to measure mean and diastolic pulmonary artery pressure with reliability using Doppler echocardiography [16]. Using a regression equation, diastolic pulmonary artery (PA) pressure can be measured from the peak tricuspid regurgitant jet using the following formula:

$$\text{PA diastolic pressure} = 0.49 \times \text{PA systolic pressure (from peak TR gradient)}$$

There are few data to support the application of all these techniques to predict outcome in patients with pulmonary hypertension. One study used echocardiographic parameters to predict outcome in adult patients with pulmonary hypertension, with an end-point of death or transplantation [17]. The right atrial size, which is a reflection of right ventricular function and right atrial pressure, was the best independent predictor of outcome in this group ($P < 0.0004$). Furthermore, right ventricular ejection time (RVET) and severity of TR also were predictors, but with less statistical significance ($P < 0.02$).

## Ventricular septal defect and right ventricular systolic pressure measurement

Ventricular septal defects (VSDs) provide a window to the pulmonary vascular bed, either in the presence or absence of associated pulmonary outflow tract obstruction. Continuous-wave Doppler techniques have been shown to provide an accurate assessment of right ventricular and systolic pulmonary artery pressures. Certain technical and theoretical considerations must be appreciated when using this approach. Maintaining a parallel angle between the ventricular septal defect jet and Doppler beam is important to prevent underestimation of the true pressure drop. This is aided by using color Doppler and multiple views to obtain the maximum velocity. Although this is possible in the majority of cases, it can be somewhat challenging in those with a perimembranouus inlet defect, where the color jet skirts the undersurface of the tricuspid valve in a lateral direction. Likewise, in a perimembranous inlet ventricular septal defect there may be an associated obligatory left ventricular-to-right atrial shunt that contaminates the continuous wave signal (Fig. 44.4).

Although the correlation between Doppler assessment and absolute pressure differences between a fluid-filled catheter in the left and right ventricles has been very satisfactory in moderately sized defects, this has not been the case when the defect is small [18,19]. In this setting, there may be an underestimation of the true pressure drop between the left and right ventricles due to jets that are often at a large angle with the Doppler beam. Also, in small defects the maximum velocity can overestimate the true pressure drop across the ventricular septal defect.

Large ventricular septal defects with increased right ventricular and pulmonary artery pressures pose another problem. Some authors have reported an overestimation of the actual measured pressure drop across the ventricular septal defect in this setting. It has been suggested that the proximal

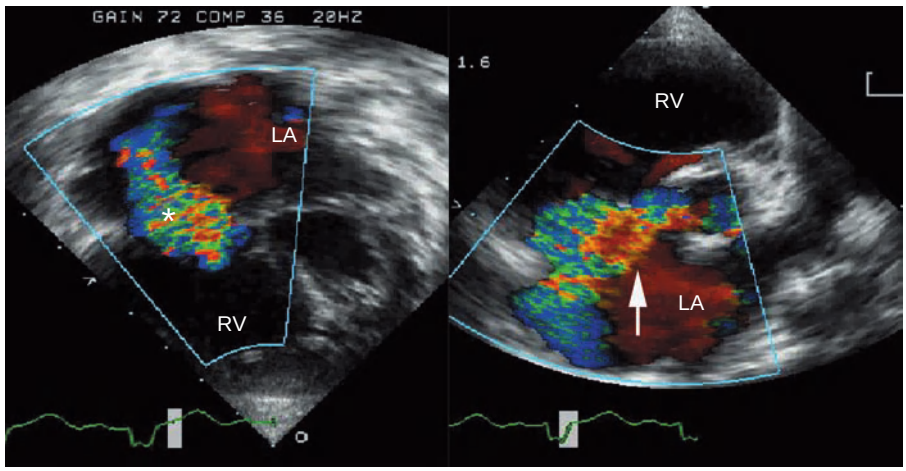


**Figure 44.4** Ventricular septal defect with tricuspid valve regurgitation and a left ventricle (LV)-to-right atrium (RA) shunt, as indicated by the arrow in the right-hand panel. LA, left atrium; RV, right ventricle.

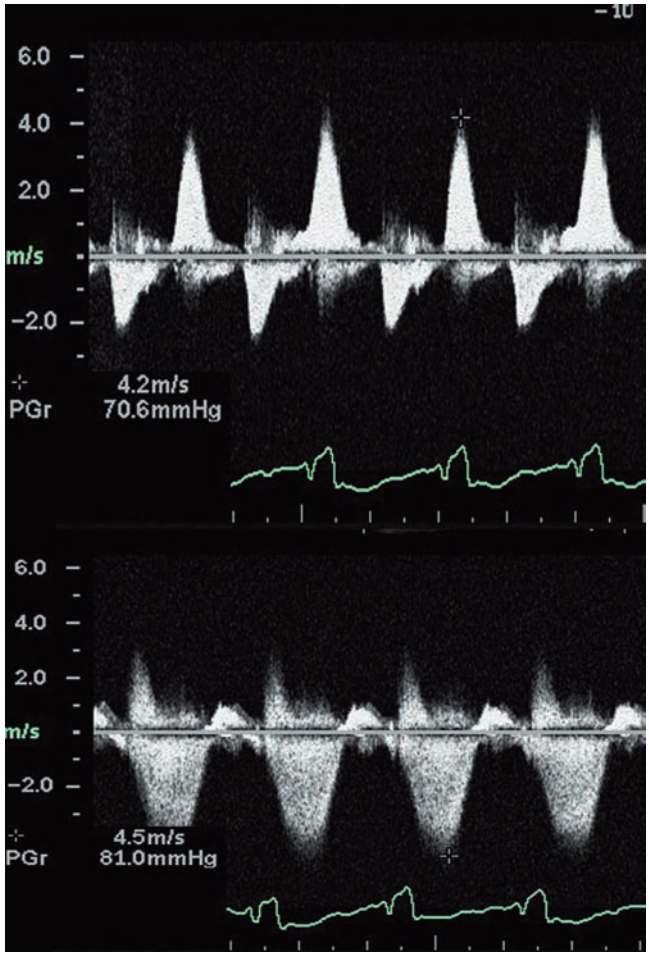


**Figure 44.5** Doppler traces from an anterior ventricular septal defect. Note that the tricuspid valve regurgitation jet demonstrates a right ventricular (RV) pressure of 81 mm Hg + right atrial pressure (RAP), whereas there is a 70 mm Hg pressure drop across the ventricular septal defect. Note there is complete right bundle branch block, which probably accounts for the difference. In this case there was no obligatory left ventricle-to-right atrium shunt.

velocity be taken into consideration using the formula pressure gradient, $4(V_2 - V_1)^2$, to measure the absolute pressure drop across a large defect. Moreover, it must be remembered that Doppler provides true peak instantaneous pressure gradients, whereas hemodynamic measurements represent peak-to-peak differences between the right and left ventricles. The contraction of the left and right ventricles also occurs at a slightly different time, which is exacerbated when there is complete right bundle branch block (Fig. 44.5).

When using this technique to predict systolic right ventricular or pulmonary artery pressure an accurate systolic blood pressure measurement is also necessary. The pressure drop across the defect is then subtracted from the systolic blood pressure to provide an absolute value. Although this works in practice, it must be remembered that distal peripheral systolic blood pressure is higher than that measured centrally.

Muscular ventricular septal defects frequently pose a challenge, as it may be difficult to obtain a Doppler beam parallel to the jet, resulting in underestimation. Also, muscular defects are frequently long and irregular, making measurements potentially inaccurate. Unlike perimembranous and subarterial defects, where the diameter remains fairly constant throughout systole, those in the muscular septum frequently become smaller throughout the cardiac cycle, which will affect the velocity measurements.

## Ventricular septal defect and right ventricular outflow tract obstruction

In the presence of a ventricular septal defect and associated right ventricular outflow tract obstruction, a combination of the systolic blood pressure and velocity across the ventricular septal defect and right ventricular outflow tract permits an assessment of systolic pulmonary artery pressure. This is of particular importance in those cases where it is felt appropriate to delay complete repair beyond the first 6 months of life. When the ventricular septal defect is restrictive, it is sometimes difficult to separate a left-to-right jet directed toward the right ventricular outflow tract, from that across the obstruction, particularly when imaging from the precordium. If the child is young enough, a right anterior oblique view may help in separating the two jets, permitting a parallel angle between the Doppler beam and the right ventricular outflow tract.

In the presence of tetralogy of Fallot with a long tunnel-like obstruction, there may be a problem with either overestimating the true pressure drop, or underestimating it if there is significantly reduced pulmonary blood flow.

## Patent arterial duct and pulmonary artery pressure measurement

The patent arterial duct provides a valuable method for measuring pulmonary artery pressure, particularly in the younger patient where it is more likely to be encountered. Simultaneous hemodynamic and Doppler measurements have demonstrated that this is one of the few techniques that provide a measurement of mean pulmonary artery pressure [20] (Fig. 44.6). As a result of jet entrainment, the majority of ductal left-to-right shunting hugs the anterior wall of the main pulmonary artery, providing a parallel angle for Doppler interrogation. If the mean and systolic blood pressures are obtained, then mean and systolic pulmonary artery pressures can be measured by subtracting the mean and peak pressure drop across the patent arterial duct from these measurements of blood pressure. The mean Doppler gradient across the patent arterial duct is obtained by planimetry of the spectral recording between two R–R intervals (Fig. 44.7).

This technique may not be applicable in several settings. Firstly, if the jet is very eccentric then parallel interrogation is

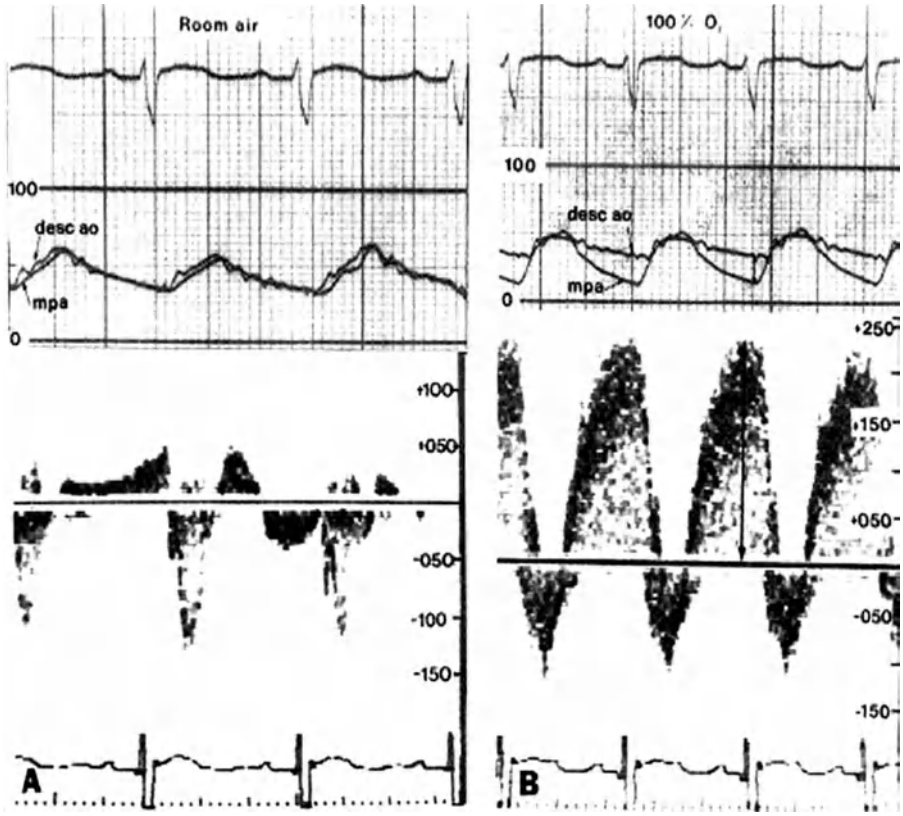


**Figure 44.6** Demonstration of the use of the patent ductus arteriosus in the evaluation of pulmonary artery reactivity. The right-hand panel shows the drop in pulmonary artery pressure following the administration of oxygen.

difficult, resulting in an underestimation of the true pressure drop across the patent arterial duct. Secondly, if the patent arterial duct is very small only abbreviated left-to-right shunting can be detected, thus making measurements unreliable. Thirdly, if the patent arterial duct is tortuous, as seen in cases with severe right ventricular outflow tract obstruction, then parallel Doppler interrogation is difficult.

What about those cases with bidirectional shunting across the patent ductus arteriosus? In these there is usually left-to-right shunting in diastole, with right-to-left in systole, making planimetry difficult. The very presence of bidirectional shunting indicates a high pulmonary artery pressure and, more importantly, the duration of right-to-left shunting provides important insight into the pulmonary vascular bed. In general, a greater degree of right-to-left shunting in systole and into diastole indicates suprasystemic pulmonary artery pressure. This observation is seen more frequently in cases with pulmonary hypertension in the newborn period

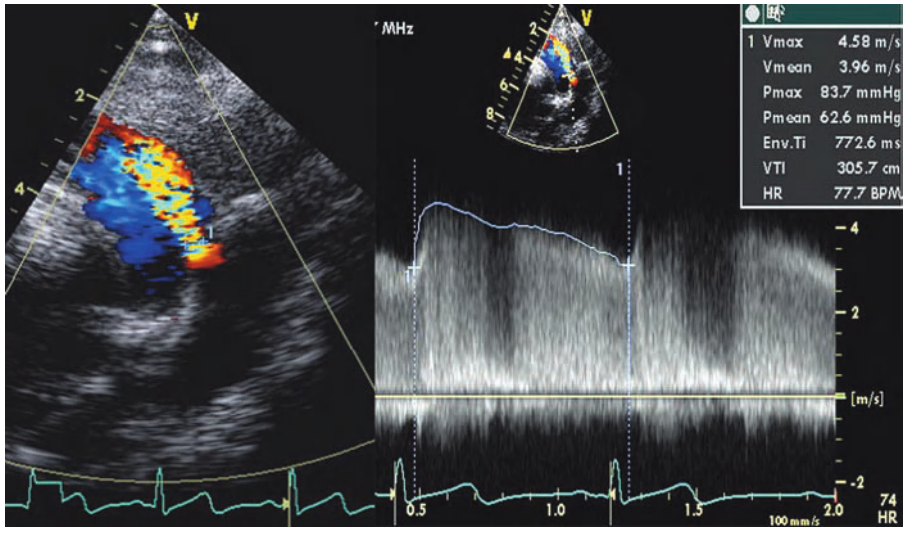


**Figure 44.7** Doppler echocardiogram of a patent arterial duct. Note in the left-hand picture the entrainment of the jet toward the anterior wall of the main pulmonary artery. The right-hand panel demonstrates the calculation of mean and peak pulmonary systolic artery pressures.

with a normal heart [21], hypoplastic left heart syndrome and a restrictive atrial septal defect or obstructed total anomalous pulmonary venous drainage.

## Measurement of pulmonary artery pressure from systemic-to-pulmonary artery shunts

Another technique for assessing pulmonary artery pressure has been the use of Doppler gradients across systemic-to-pulmonary artery shunts, which are still a common occurrence in the small child with congenital heart disease. Although this is relatively simple to do, its validity has been called into question using the simplified modified Bernoulli equation [22].

## Measurements of pulmonary artery capacitance by Doppler

### Background

Pulmonary vascular resistance is the resistance in the small vessels and the pulmonary vascular cross-sectional area, but does not account for the large and medium vessels, nor the pulsatile elements in the pulmonary circulation. Pulmonary vascular capacitance is a measure of workload on the right ventricle. When the capacitance is high all of the forward blood goes to the peripheral vessels, whereas when it is low the blood is initially stored in the large-capacitance vessels, which increases the load on the heart. This also results in a wide pulse pressure, which is a known risk factor on the left side of the heart [23].

The workload on a pump is proportional to forward output and the impedance of the vascular bed. Impedance is proportional to resistance and inversely proportional to capacitance. Pulmonary compliance represents the stretch of the vessel walls and how much they will increase in volume for a given pressure.

Pulmonary vascular capacitance measures how much the vascular tree dilates with each contraction of the right ventricle. Therefore, capacitance = stroke volume (mL)/pulse pressure (mm Hg). By echocardiography the stroke volume can be calculated from the left or right ventricular outflow tracts, for example:

right ventricular stroke volume (mL)
= pulmonary valve diameter $(cm/2)^2 \times \pi \times$ VT I (cm)

VTI = velocity-time integrate

The pulse pressure is the peak systolic gradient from tricuspid valve regurgitation (TR) minus the end-diastolic pressure from pulmonary regurgitation (PR), that is:

Pulmonary compliance
= RV stroke volume (mL)/$4 \times (TR^2 - PR^2)$.

This noninvasive measurement of pulmonary vascular capacitance was found to be the best predictor of adverse events in a group of adults with pulmonary hypertension, with a risk ratio of 3:1 [23]. This measurement also was a better predictor of adverse events than systolic, diastolic and mean pulmonary artery pressures; however, in a multivariate model pulmonary vascular resistance added to prognostic value. The measurement of pulmonary vascular capacitance is probably a strong predictor of adverse events, as it takes into consideration the load on the right side of the heart and the status of the lung parenchyma.

To measure pulmonary vascular capacitance it is necessary to have a measurement of pulmonary diastolic pressure from pulmonary regurgitation. As not all patients have pulmonary valve regurgitation, other authors have used invasive techniques based on the relationship between pulmonary artery diastolic and systolic pressures [24]:

pulmonary artery diastolic pressure
= 0.49 × pulmonary artery systolic pressure.

There appears to be a reasonable correlation using this technique between indexed right ventricular anterior wall thickness and pulmonary artery capacitance.

### Pulmonary artery compliance and Doppler

Pulmonary vascular resistance is a steady-state parameter and measures opposition to continuous flow. However, this ignores the very nature of pulmonary flow, which is pulsatile in nature. Flow into the pulmonary vascular bed requires a coordinated effort from the right ventricular pump in systole and the pulmonary vascular bed in diastole. In an attempt to measure this variation throughout the cardiac cycle, a combination of change in pulmonary artery wall diameter throughout the cardiac cycle using color M-mode Doppler tissue imaging, coupled with systolic pressure as measured from tricuspid valve regurgitation, has been used [25]. Color M-mode Doppler tissue imaging has high spatial (1.6–1.9 mm) and temporal resolution (5 ms) and overcomes some of the limitations of other techniques used to detect instantaneous changes in the vessel diameter over time. There appears to be a very good correlation between the changes in diameter of the pulmonary artery as measured by this technique compared with intravascular ultrasound:

compliance (dynes) = $[(D(s) - D(d))/(D(d) \times P(s))] \times 10(4)$

where D(s) = systolic diameter, D(d) = diastolic diameter and P(s) = systolic pressure.

This technique might play a role in evaluating treatment regimes for pulmonary hypertension. For example, increased pulmonary artery pressure may produce a stiffer vessel on the basis of the strain-stiffness effect, rather than being secondary to abnormalities of the vessel wall. With vasodilator

therapy, if it is a strain-stiffness effect then the response to treatment will be different than if there is a true abnormality in the vessel wall. In one study it was found that a >40% change in right pulmonary artery diameter per 100 mm Hg was consistent with a compliant vessel, whereas a value of <40% indicated a stiffer vessel [25]. This technique is not applicable if there is significant pulmonary regurgitation. Of note, the authors commented that the 40% cut-off value may change through further studies in which a wider variation of pressures could be assessed. Also, the technique required further validation through challenging with high pressure-high flow and high pressure-low flow situations.

## The impact of pulmonary arterial hypertension on the right ventricle

### Myocardial performance index (Tei index)

The Tei index, which measures global ventricular function, has been used to assess the impact of increased pulmonary artery pressure in a pediatric population [26]. Its relative independence of heart rate makes it theoretically attractive in the pediatric population. It has been used to assess the response to pulmonary vasodilator therapy both in children and adults. Compared with controls, the right ventricular Tei index was higher in those with pulmonary arterial hypertension, with a reduction in the value following a fall in pulmonary artery pressure [26]. Despite this, the Tei index appeared to be only a weak predictor of adverse events in adults with pulmonary hypertension [23]. Other groups have used the right ventricular isovolumic relaxation time to provide an indirect assessment of pulmonary artery pressure [27].

Although it is appealing to relate this change in the Tei index to a lowering of pulmonary artery pressure, it could be that the change is due to an alteration of afterload on the right ventricle. Indeed, experimental evidence in animals where the loading conditions are altered suggests that this index may be afterload sensitive [28].

### The use of tissue Doppler imaging and right ventricular function in pulmonary hypertension

Tricuspid annular tissue Doppler imaging has been used to assess the Tei index in combination with peak early mitral inflow velocity to calculate a M-index (mitral inflow velocity/Tei) in patients with idiopathic and secondary pulmonary arterial hypertension due to an embolus [29]. Those with an embolus had a lower M-index compared with controls or those with primary pulmonary hypertension. This effect could be due to a sudden high afterload on the right ventricle (RV) resulting in diastolic dysfunction. By combining the Tei index with mitral inflow velocity there was a better receiver–operator curve than with the Tei index alone.

Other groups have compared two-dimensional (2D) strain and strain rate and similar measurements from the same site using tissue Doppler imaging in adult patients with pulmonary hypertension [30]. There appears to be a good correlation between 2D strain and strain rate and pulmonary artery pressure and ejection fraction. Notably, there appeared to be an acceptable inter- and intra-observer variability for 2D strain, which has been a concern with tissue Doppler imaging.

Armed with this new technique, an evaluation before and after treatment with the pulmonary vasodilators bosentan and inhaled or oral prostanoid has been undertaken [31]. In this study the basal segment of the right ventricle had a strain of $-8.8 \pm 4.1$ prior to treatment, compared with a normal value of $-24.3 \pm 4.7$ ($P < 0.001$). After treatment, the RV basal strain increased to $-13.3 \pm 6.2$ ($P < 0.001$). There was a weaker correlation with tissue Doppler-derived strain in the same segment ($P < 0.2$), and also a weak correlation with isovolumic acceleration, pre- and post-treatment ($P < 0.2$). The Tei index was also evaluated, and in a similar fashion to tissue Doppler had a weaker correlation with treatment of the pulmonary hypertension. There was a significant drop in pulmonary vascular resistance ($P < 0.001$) with an increase in the 6-minute walk ($P < 0.002$) pre- and post-treatment. Two-dimensional strain ($P < 0.03$) and tricuspid annular excursion ($P < 0.02$) had a weak correlation with the 6-minute walk.

## The impact of pulmonary hypertension on the left ventricle

Left–right ventricular interaction in patients with pulmonary hypertension with an intact ventricular septum may result in an abnormal left ventricular diastolic inflow pattern. This was initially felt to be related to abnormal diastolic function, but more recently has been attributed to altered left ventricular preload. This latter view has been supported by alterations in the mitral E/A pattern, pulmonary venous flow and mitral annular tissue Doppler [32]. In this study, an observed increase in the mitral E/A ratio and pulmonary venous Doppler velocity, with relatively normal mitral tissue Doppler parameters, was observed post-thromboendarctorectomy in adults with secondary pulmonary arterial hypertension and preserved right ventricular systolic ventricular function. A similar finding of decreased left ventricular filling rate and stroke volume has also been observed by magnetic resonance imaging (MRI) in adults with primary pulmonary hypertension [33].

The role of pericardial constraint, as a cause for abnormal left–right ventricular interaction in pulmonary arterial hypertension, is somewhat controversial. In an acute model of pulmonary hypertension secondary to pulmonary embolus, the observed decrease in left ventricular stroke

volume can be reversed by opening the pericardium. However, in a similar chronic model this increase has not been observed, thus calling into question the role of pericardial constraint.

## References


1. Fox DJ, Khatter RS. Pulmonary arterial hypertension: classification, diagnosis and contemporary management. *Postgrad Med J* 2006;82:717–22.
2. Keren G, Sherez J, Megidish R et al. Pulmonary venous flow pattern – its relationship to cardiac dynamics. A pulsed Doppler echocardiographic study. *Circulation* 1985;71:1105–12.
3. Smallhorn JF, Freedom RM, Olley PM. Pulsed Doppler echocardiographic assessment of extraparenchymal pulmonary vein flow. *J Am Coll Cardiol* 1987;9:573–9.
4. Smallhorn JF, Burrows P, Wilson G et al. Two-dimensional and pulsed Doppler echocardiography in the postoperative evaluation of total anomalous pulmonary venous connection. *Circulation* 1987;76:298–305.
5. Bustamante-Labarta M, Perrone S, Leon de la Fuente R et al. Right atrial size and tricuspid regurgitation severity predict mortality or transplantation in primary pulmonary hypertension. *J Am Soc Echocardiogr* 2002;15:1160–4.
6. Morera J, Hoadley SD, Roland JM et al. Estimation of the ratio to systemic pressures by pulsed-wave Doppler echocardiography for assessment of pulmonary arterial pressure. *Am J Cardiol* 1989;63:862–6.
7. Sorrell VL, Reeves WC. Non invasive right and left heart catheterization: taking the echo lab beyond an image-only aboratory. *Echocardiography* 2001;18:31–41.
8. Brecker SJD, Xiao HB, Maissouroum M, Gibson DG. Assessment of the peak tricuspid regurgitant velocity from the dynamics of retrograde flow. *Int J Cardiol* 1992;34:267–71.
9. Burstin L. Determination of pressure in the pulmonary artery by external graphic recordings. *Br Heart J* 1967;29:396–404.
10. Hatle L, Angelsen BAJ, Tromsdal A. Non-invasive estimation of pulmonary artery systolic pressure with Doppler ultrasound. *Br Heart J* 1982;45:157–65.
11. Lanzarini L, Fontana A, Campana A, Kletsy C. Two simple echo-Doppler measurements can accurately identify pulmonary hypertension in the large majority of patients with chronic heart failure. *J Heart Lung Transplant* 2005;24:745–54.
12. Yock PG, Popp RL. Noninvasive estimation of right ventricular systolic pressure by Doppler ultrasound in patients with tricuspid regurgitation. *Circulation* 1984;70:657–62.
13. Kircher BJ, Himelman RB, Schiller NB. Noninvasive estimation of right atrial pressure from the inspiratory collapse of the inferior vena cava. *Am J Cardiol* 1990;66:493–6.
14. Tanabe K, Asanuma T, Yoshitomi H et al. Doppler estimation of pulmonary artery end-diastolic pressure using contrast enhancement of pulmonary regurgitant signals. *Am J Cardiol* 1996;78:1145–8.
15. Masuyama T, Kodama K, Kitabatake A et al. Continuous-wave Doppler echocardiographic detection of pulmonary regurgitation and its application to noninvasive estimation of pulmonary artery pressure. *Circulation* 1986;74:484–92.
16. Friedberg MK, Feinstein JA, Rosenthal DN. A novel echocardiographic Doppler method for estimation of pulmonary arterial pressures. *J Am Soc Echocardiogr* 2006;19:559–62.
17. Bustamante-Labarta M, Perrone S, Leon de la Fuente R et al. Right atrial size and tricuspid regurgitation severity predict mortality or transplantation in primary pulmonary hypertension. *J Am Soc Echocardiogr* 2002;15:1160–4.
18. Zhiming G, Yun Z, Weiqiang K et al. Noninvasive evaluation of interventricular pressure gradient across ventricular septal defect: A simultaneous study of Doppler echo cardiography and cardiac catheterization. *Am Heart J* 1992;124:176–82.
19. Zhiming G, Yun Zhang, Weiqiang Kang et al. Non invasive evaluation of right ventricular and pulmonary artery systolic pressures in patients with ventricular septal defects: Simultaneous study of Doppler and catheterization data. *Am Heart J* 1993;125:1073–81.
20. Musewe NN, Smallhorn JF, Benson LN et al. Validation of Doppler-derived pulmonary arterial pressure in patients with ductus arteriosus under different hemodynamic states. *Circulation* 1987;76:1081–91.
21. Musewe NN, Poppe D, Smallhorn JF et al. Doppler echocardiographic measurement of pulmonary artery pressure from ductal Doppler velocities in the newborn. *J Am Coll Cardiol* 1990;15:446–56.
22. DeGroff CG, Shandas R, Kwon J, Valdes-Cruz L. Accuracy of the Bernoulli equation for estimation of pressure gradient across stenotic Blalock–Taussig shunts: an in vitro and numerical study. *Pediatr Cardiol* 2000;21:439–47.
23. Mahapatra S, Nishimura RA, Oh JK, McGoon MD. The prognostic value of pulmonary vascular capacitance determined by Doppler echocardiography in patients with pulmonary arterial hypertension. *J Am Soc Echocardiogr* 2006;19:1045–50.
24. Friedberg MK, Feinstein JA, Rosenthal DN. Non invasive assessment of pulmonary arterial capacitance by echocardiography. *J Am Soc Echocardiogr* 2007;20:186–90.
25. Dyer K, Lanning C, Das B et al. Noninvasive Doppler tissue measurement of pulmonary artery compliance in children with pulmonary hypertension. *J Am Soc Echocardiogr* 2006;19:403–12.
26. Dyer KL, Paulkis LB, Das Bibhuti et al. Use of myocardial performance index in pediatric patients with idiopathic pulmonary hypertension. *J Am Soc Echocardiogr* 2006;19:21–7.
27. Dambrauskaite V, Delcrois M, Claus P et al. The evaluation of pulmonary hypertension using right ventricular myocardial isovolumic relaxation time. *J Am Soc Echocardiogr* 2005;18:1113–20.
28. Cheung MM, Smallhorn JF, Redington AN, Vogel M. The effects of changes in loading conditions and modulation of inotropic state on the myocardial performance index: comparison with conductance catheter measurements. *Eur Heart J* 2004;25:2238–42.
29. Shih-Hung Hsiao, Shu-Mei Chang, Chiu-Yen Lee et al. Usefulness of tissue Doppler parameters for identifying pulmonary embolism in patients with signs of pulmonary hypertension. *Am J Cardiol* 2006;98:685–90.
30. Pirat B, McCulloch ML, Zoghbi WA. Evaluation of global and regional right ventricular systolic function in patients with pulmonary hypertension using a novel speckle tracking method. *Am J Cardiol* 2006;98:699–704.

31. Borges AC, Knebel F, Eddicks S et al. Right ventricle function assessed by two-dimensional strain and tissue Doppler echocardiography in patients with pulmonary arterial hypertension and effect of vasodilator therapy. *Am J Cardiol* 2006;98:530–4.
32. Gurudevan SV, Malouf PJ, Auger WR et al. Abnormal left ventricular diastolic filling in chronic thromboemblic pulmonary hypertension – true diastolic dysfunction or left ventricular underfilling? *J Am Coll Cardiol* 2007;49:1334–9.
33. Gan Tji-Joong, Lankhaar Jan-Willem, Marcus JT et al. Impaired left ventricular filling due to right to left ventricular interaction in patients with pulmonary arterial hypertension. *Am J Physiol Heart Circ Physiol* 2006;290:H1528–33.

# Appendix 1: Normal Values for Cardiovascular Structures

Variation in imaging modalities and methods of measurements contributes to differences in the values obtained for the measurement of the same cardiovascular structure. Multiple prior reports have documented significant differences in the normative data that have been derived from various measuring modalities (autopsy, angiography, echocardiography, magnetic resonance imaging) and methods of measurements (inner–inner edge, outer–inner edge, area, circumference), as summarized in Sluysmans and Colan [1]. The issue of using comparable methods to some extent supersedes the issue of correctness, that is, using the method that provides the value that is closest to the "truth." Ultimately, the reproducibility and predictive value of a measurement relative to response to treatment or to outcome is more important than an independently verifiable standard of "truth." Although one can presume that the "true" value will have the greatest predictive value, this is currently impossible to prove because none of the available measurement methods is capable of achieving this degree of veracity.

With regard to measurements performed on M-mode and two-dimensional (2D) echocardiographic images, there are several identifiable technical factors that contribute to measurement error and variability (intra- and inter-observer) of these measurements. These technical issues are discussed in detail elsewhere in this textbook and are simply summarized here:

**1** Resolution is greatly influenced by the frequency of the transducer; the highest-frequency transducer allowing adequate penetration should be used. Similarly, when available, harmonics should be used and the focal point of the transducer should be close to the center of the structure measured to optimize resolution.

**2** Optimized gain settings are those that balance artifact while avoiding echocardiographic dropout of cardiovascular borders. Because of the need to prioritize visualization of endocardial borders for purposes of measurement, higher gain settings are often required for measurements compared with images used for anatomic diagnosis.

**3** The limited size of the pixel matrix that is used to encode and display echocardiographic images creates a need to adjust image size to maximize the number of pixels devoted to the structure that is being measured and also to allow higher frame rates to maximize time resolution. This invariably requires adjustment of the depth setting and use of zoom mode.

**4** Calibration may be required for offline measurements to correct for potential difference in the vertical and horizontal display formats and for depth setting at which the measurements were made. Newer image recording methods, such as the Digital Imaging and Communications in Medicine (DICOM) standard, overcome this source of error.

**5** Conversion of the digital images produced by modern ultrasound equipment to analog video recordings is associated with a nearly 50% loss of information due to reduction in resolution. Therefore, accurate measurement requires either digital storage of the image data or online data analysis.

**6** Timing of the point in the cardiac cycle at which measurements are obtained is critical to reproducibility. Numerous methods have been used to define the fiducial points of interest. Adequate definition of the method of frame selected is essential and is often insufficiently specified.

The measurements that are reported in this appendix consist of M-mode linear measurements of the left ventricle (LV), 2D linear and area measurements of the LV, 2D linear measurements of valves and vessels, and a number of calculated variables that were derived from these measurements. The methods for each of these measurements are detailed here.

## M-mode methods

The method of recording the M-mode normative data that are reported here is presented in detail in Colan et al. [2]. The M-mode tracing of the LV was obtained using parasternal short-axis views and was recorded on a high-resolution strip chart recorder at maximum paper speed (100 mm/s) along with the electrocardiogram, a phonocardiographic recording at the position that optimized the resolution of the second heart sound, and an indirect carotid pulse tracing using a tonometer. Three successive cardiac cycles from the M-mode

*Echocardiography in Pediatric and Congenital Heart Disease: From Fetus to Adult*
Edited by Wyman W. Lai, Luc L. Mertens, Meryl S. Cohen and Tal Geva
 ISBN: 978-1-405-17401-5

echocardiogram of the LV were then hand digitized to a microcomputer using custom software, including the right ventricular septal surface, the septal and free wall endocardial surfaces of the LV, and the epicardial surface of the posterior wall. The septal and free wall thickness and left ventricular short-axis dimension were thereby obtained as continuous measurements over the course of the cardiac cycle. The following fiducial points were obtained for each cycle:

- the q-wave on the electrocardiogram;
- the timing of the aortic valve closure (the first high-frequency component of the second heart sound);
- the onset of the systolic upstroke of the carotid pulse tracing;
- the dicrotic notch on the carotid pulse tracing.

End-diastole was defined as the time of the maximum left ventricular dimension, and end-systole was defined as the time of aortic valve closure. The end-diastolic and end-systolic septal (EDSTh, ESSTh) and posterior wall thicknesses (EDPWTh, ESPWTh) and left ventricular end-diastolic and end-systolic dimensions (EDD, ESD) were taken from the continuous tracings. The ejection time was measured as the time interval from the upstroke to the dicrotic notch of the carotid pulse tracing. The end-systolic blood pressure was obtained by interpolation of the position of the dicrotic notch on the carotid pulse tracing [3–5].

Evolution of the ultrasound equipment now makes exact reproduction of these methods impossible, primarily because the ultrasound manufacturers no longer support high-resolution strip chart recorders. The primary advantage of the strip chart recorders was the production of output at higher resolution than could be obtained from the video recording. Currently available hard copy devices print at video image resolution, so this advantage has been lost. Continuous manual digitizing of the endocardial and epicardial M-mode recording is time consuming and not supported in most laboratories, and the phonocardiographic and tonometric instrumentation has become increasingly unavailable.

There are practical alternatives that yield similar results for the above M-mode values. Measuring three successive beats and averaging the values is a practical and useful method of reducing measurement error in addition to eliminating the effect of respiratory variation in ventricular filling. Maximum dimension is usually easily identifiable within or just after the QRS complex on the electrocardiogram. The published standard of using the q-wave as the time of end-diastole [6] fails to represent the maximum dimension, particularly in children, as can be easily verified on tracings of the mitral valve inflow, which invariably demonstrate continued filling of the LV until well after the q-wave. End-systole can be taken as the minimum dimension, although there is frequently an identifiable septal notch at the time of aortic valve closure that can also be used. Ejection time can be measured from the aortic valve Doppler tracing. The mean blood pressure taken from an automated oscillometric blood pressure device provides a reasonable estimate of end-systolic pressure [7,8].

The derived M-mode variables are obtained using standard methods. Fractional shortening (FS) is calculated as:

$$FS = (EDD - ESD)/EDD$$

The rate-corrected velocity of circumferential fiber shortening (VCFc) was calculated as FS/ETc, where ETc is ejection time divided by the square root of the Q–Q interval on the electrocardiogram. Left ventricular meridional end-systolic wall stress was calculated according to the formula of Grossman [9] as:

$$(0.34 \times ESP \times ESD)/(ESSTh\ (1 + (ESSTh/ESD)))$$

where ESP is end-systolic pressure.

## Vascular and valvar dimensions and areas

The dimensions of all vascular and valvar structures were measured from inner surface to inner surface at the moment of maximal expansion during the cardiac cycle. The dimensions of the aortic valve anulus (AoV), aortic root (AoRoot), sinotubular junction and ascending aorta were measured on parasternal long-axis views at mid-systole. The measurements of distal transverse aorta, left subclavian and left carotid arteries at their origin and of the aortic isthmus were obtained from high parasternal long-axis or suprasternal notch views at mid-systole [10,11]. The lateral dimensions of mitral and tricuspid valves were measured in early diastole on 4-chamber apical views ($MV_{4CH}$ and $TV_{4CH}$, respectively), and the antero-posterior dimension from the left parasternal long-axis view ($MV_{2CH}$ and $TV_{2CH}$, respectively), at the proximal attachment of the leaflets at each side of the anulus [11,12]. The diameters of the pulmonary valve, main pulmonary artery, pulmonary arteries at their origin [13,14] and of the proximal left main (LCA), anterior descending (LAD) and proximal right (RCA) coronary arteries were obtained on short-axis parasternal views [15]. The left upper and lower (LUPV, LLPV) and the right upper and lower (RUPV, RLPV) pulmonary veins were measured from subcostal, apical, high parasternal long-axis or suprasternal notch short-axis views at their point of junction with the left atrium. Mitral and tricuspid valve areas were calculated as ellipses from 2-chamber and 4-chamber view diameters; for example:

$$\text{mitral valve area} = (\pi/4) \times (MV_{2CH}) \times (MV_{4CH}).$$

## Left ventricular mass and volume measurements

The end-diastolic endocardial and epicardial, and the end-systolic endocardial short-axis cross-sectional area values of

the LV were measured from parasternal short-axis images. The end-diastolic endocardial and epicardial, and the end-systolic endocardial long-axis lengths of the LV were measured on 4-chamber apical views [11,16]. End-diastole for these measurements was defined as the frame following mitral valve closure, and end-systole was defined as the frame preceding mitral valve opening. The end-diastolic endocardial (EDV) and epicardial volumes, and the end-systolic endocardial (ESV) volume were then calculated from their respective lengths and areas using the formula [6]:

$$\text{volume} = 5/6 \times \text{area} \times \text{length}.$$

Left ventricular mass (LVM) was calculated as the difference between the epicardial and endocardial volumes multiplied by the specific gravity of the myocardium (1.05). Ejection fraction was calculated as (EDV – ESV)/EDV.

## References


1. Sluysmans T, Colan SD. Theoretical and empirical derivation of cardiovascular allometric relationships in children. *J Appl Physiol* 2005;99:445–57.
2. Colan SD, Parness IA, Spevak PJ et al. Developmental modulation of myocardial mechanics: age- and growth-related alterations in afterload and contractility. *J Am Coll Cardiol* 1992; 19:619–29.
3. Colan SD, Fujii A, Borow KM et al. Noninvasive determination of systolic, diastolic and end-systolic blood pressure in neonates, infants and young children: comparison with central aortic pressure measurements. *Am J Cardiol* 1983;52:867–70.
4. Colan SD, Borow KM, Neumann A. Use of the calibrated carotid pulse tracing for calculation of left ventricular pressure and wall stress throughout ejection. *Am Heart J* 1985;109: 1306–10.
5. Colan SD, Borow KM, MacPherson D et al. Use of the indirect axillary pulse tracing for noninvasive determination of ejection time, upstroke time, and left ventricular wall stress throughout ejection in infants and young children. *Am J Cardiol* 1984; 53:1154–8.
6. Lang RM, Bierig M, Devereux RB et al. Recommendations for chamber quantification: a report from the American Society of Echocardiography's Guidelines and Standards Committee and the Chamber Quantification Writing Group, developed in conjunction with the European Association of Echocardiography, a branch of the European Society of Cardiology. *J Am Soc Echocardiogr* 2005;18:1440–63.
7. Aggarwal S, Pettersen MD, Gurckzynski J et al. Measuring stress velocity index using mean blood pressure: simple yet accurate? *Pediatr Cardiol* 2008;29:108–12.
8. Karr SS, Martin GR. A simplified method for calculating wall stress in infants and children. *J Am Soc Echocardiogr* 1994;7: 646–51.
9. Grossman W, Jones D, McLaurin LP. Wall stress and patterns of hypertrophy in the human left ventricle. *J Clin Invest* 1975;56: 56–64.
10. Snider AR, Enderlein MA, Teitel DF et al. Two-dimensional echocardiographic determination of aortic and pulmonary artery sizes from infancy to adulthood in normal subjects. *Am J Cardiol* 1984;53:218–24.
11. Hanseus K, Bjorkhem G, Lundstrom NR. Dimensions of cardiac chambers and great vessels by cross-sectional echocardiography in infants and children. *Pediatr Cardiol* 1988;9:7–16.
12. King DH, Smith EO, Huhta JC et al. Mitral and tricuspid valve annular diameter in normal children determined by two-dimensional echocardiography. *Am J Cardiol* 1985;55:787–9.
13. Lappen RS, Riggs TW, Lapin GD et al. Two-dimensional echocardiographic measurement of right pulmonary artery diameter in infants and children. *J Am Coll Cardiol* 1983;2:121–6.
14. Benjamin IJ, Jalil JE, Tan LB et al. Isoproterenol-induced myocardial fibrosis in relation to myocyte necrosis. *Circ Res* 1989;65:657–70.
15. Pasquini L, Sanders SP, Parness IA et al. Diagnosis of coronary artery anatomy by two-dimensional echocardiography in patients with transposition of the great arteries. *Circulation* 1987; 75:557–64.
16. Nidorf SM, Picard MH, Triulzi MO et al. New perspectives in the assessment of cardiac chamber dimensions during development and adulthood. *J Am Coll Cardiol* 1992;19:983–8.

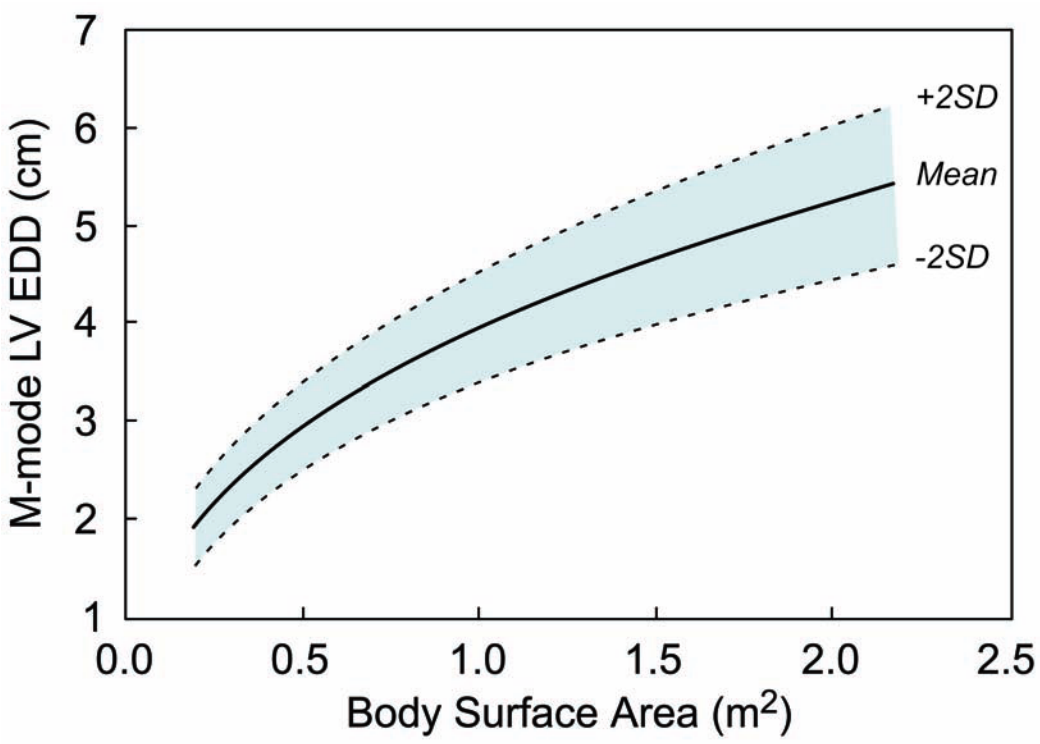


**Figure 1** M-mode left ventricular (LV) end-diastolic dimension (EDD) versus body surface area.

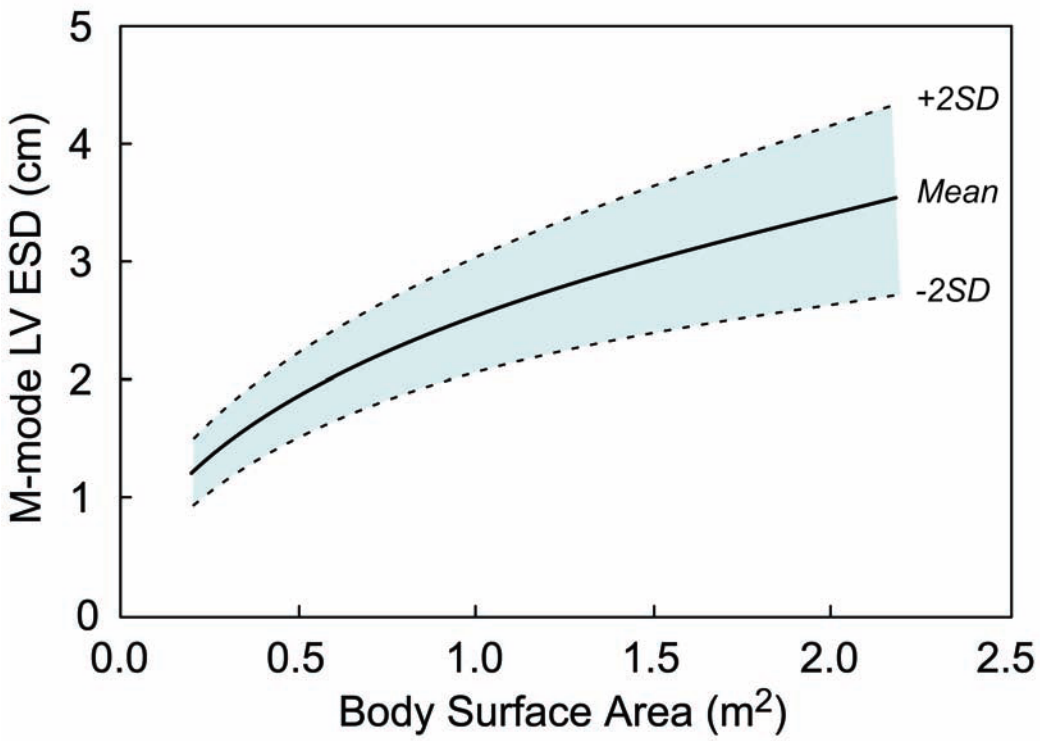


**Figure 2** M-mode left ventricular (LV) end-systolic dimension (ESD) versus body surface area.

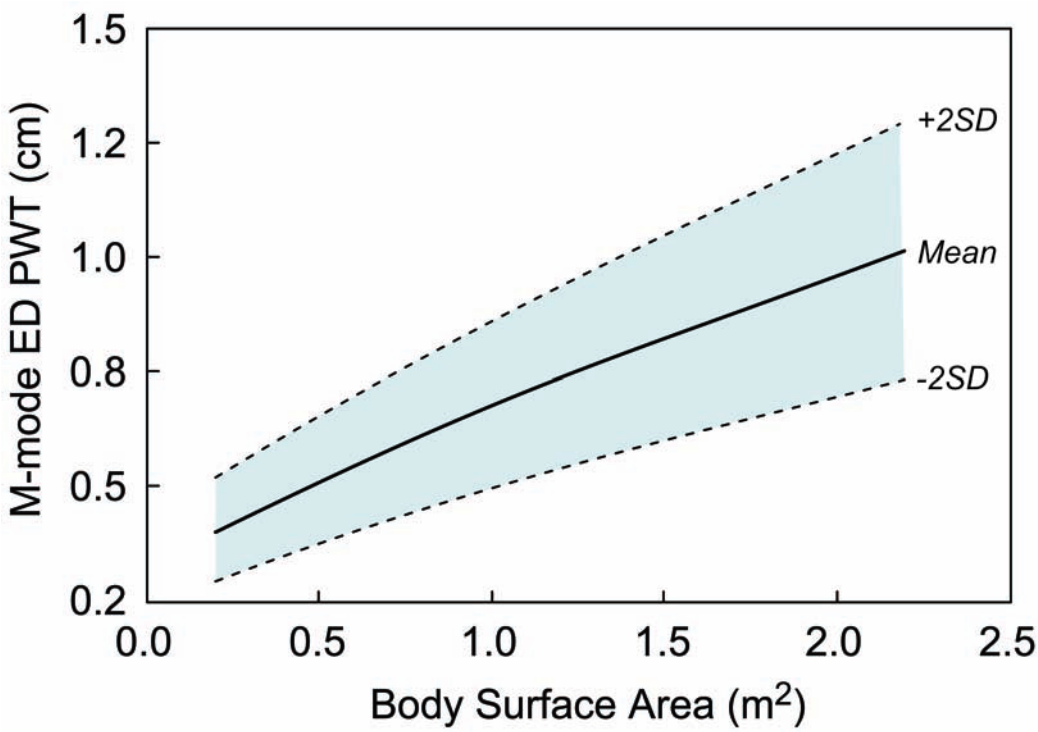


**Figure 3** M-mode left ventricular (LV) end-diastolic (ED) posterior wall thickness (PWT) versus body surface area.

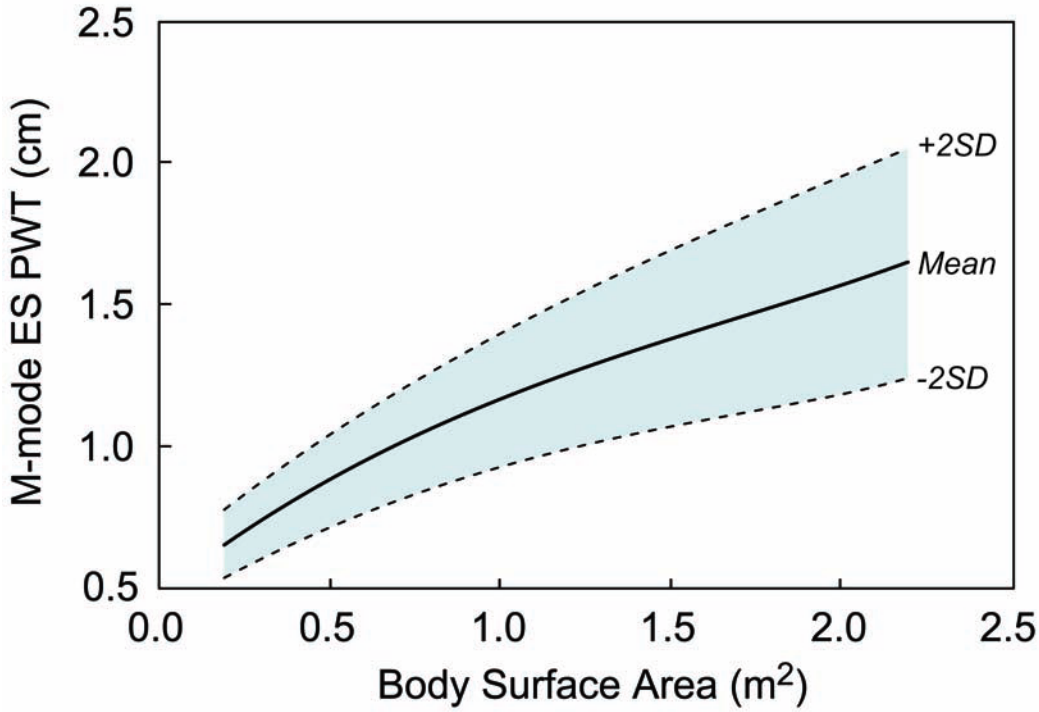


**Figure 4** M-mode left ventricular (LV) end-systolic (ES) posterior wall thickness (PWT) versus body surface area.

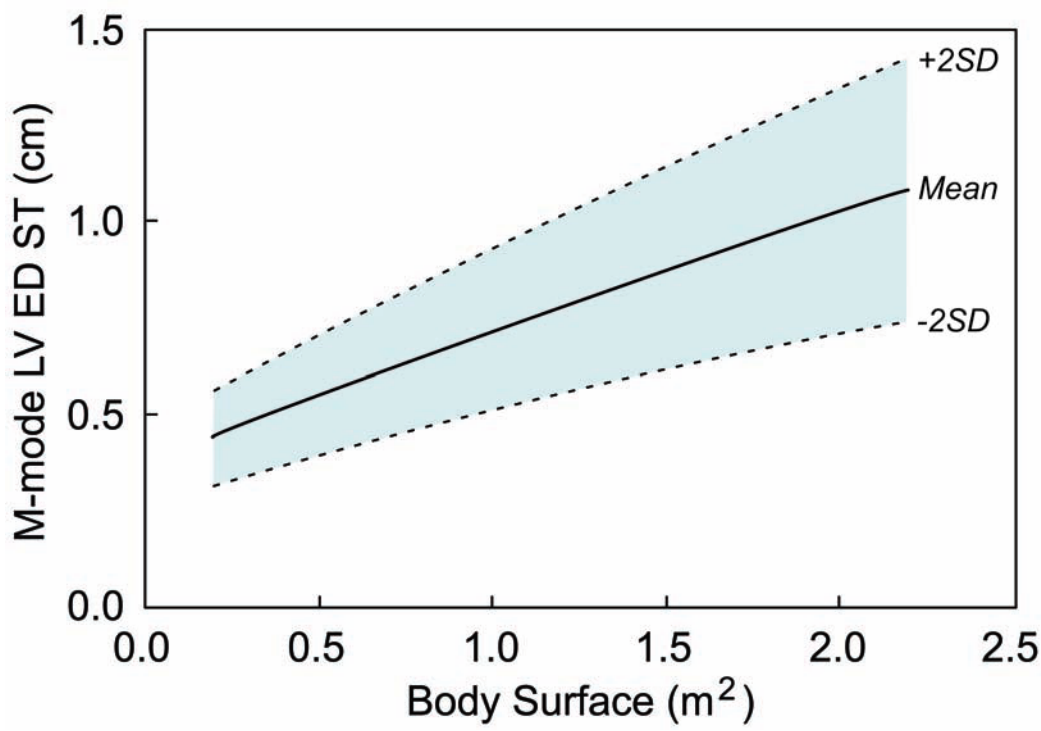


**Figure 5** M-mode left ventricular (LV) end-diastolic (ED) septal thickness (ST) versus body surface area.

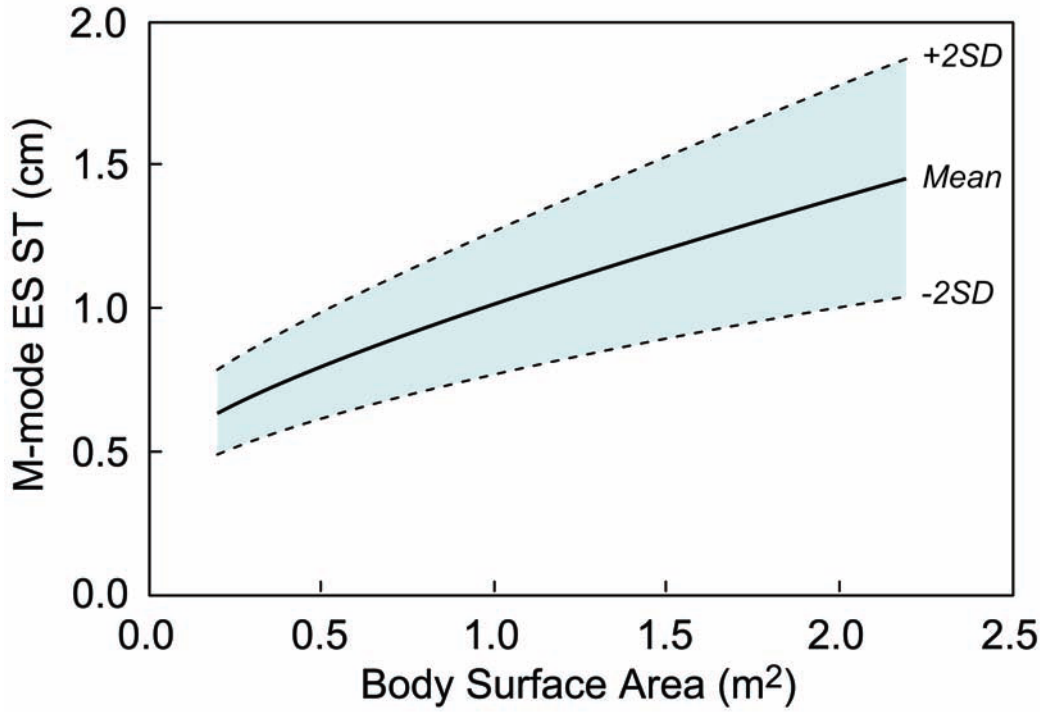


**Figure 6** M-mode left ventricular (LV) end-systolic (ES) septal thickness (ST) versus body surface area.

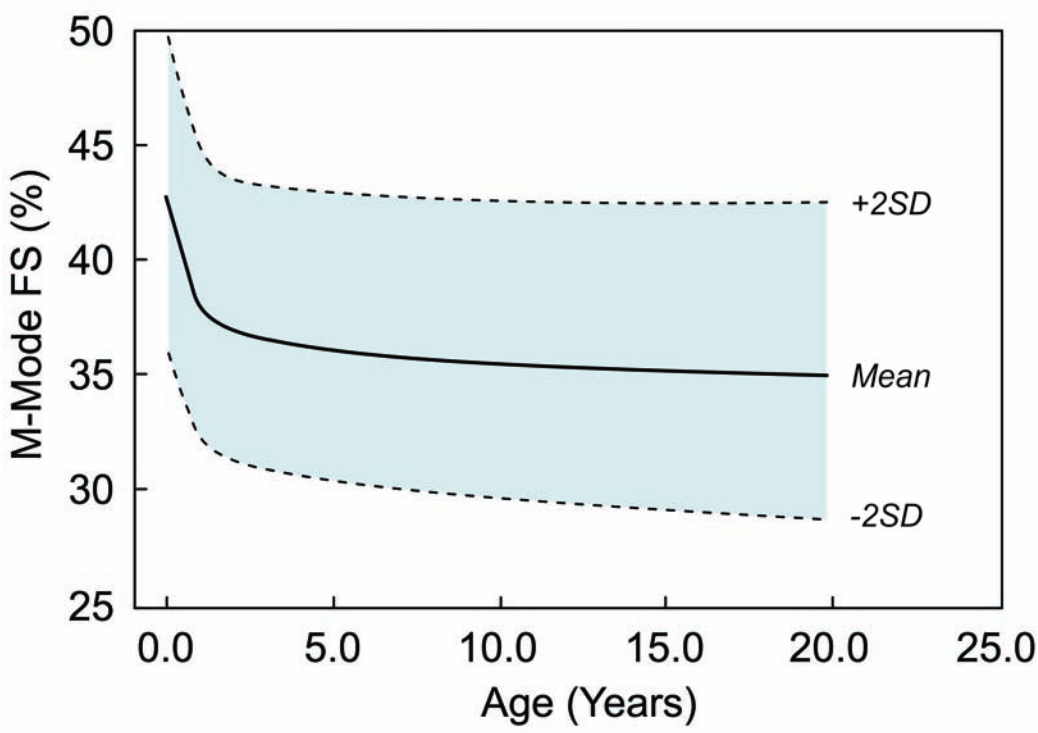


**Figure 7** M-mode left ventricular (LV) endocardial percent fractional shortening (FS) versus age.

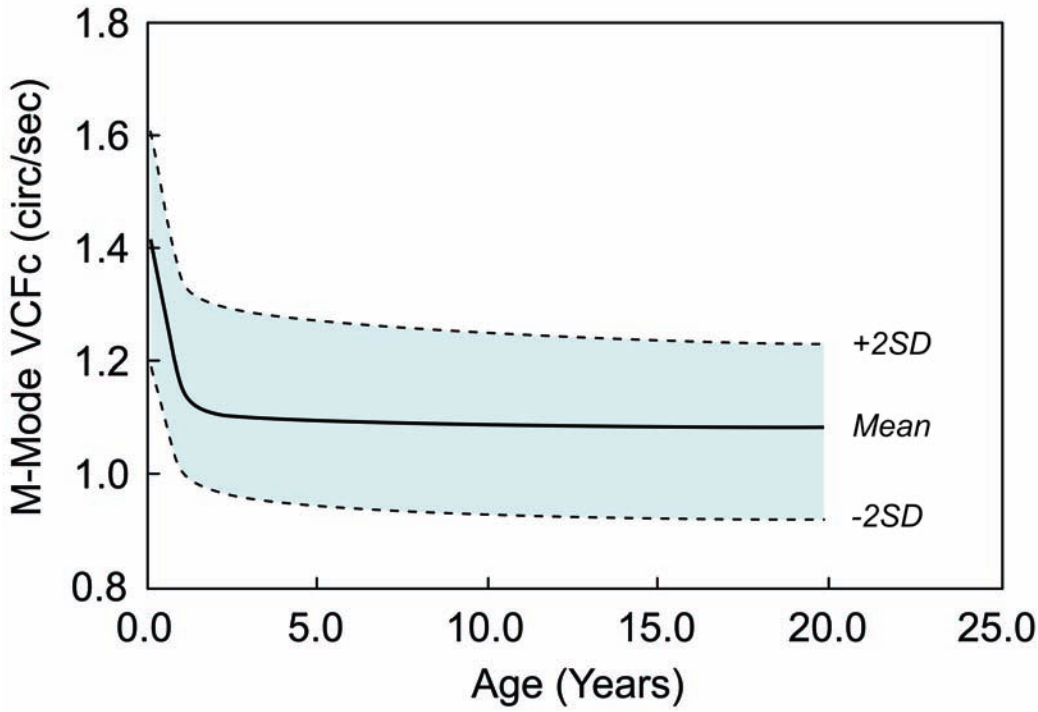


**Figure 8** M-mode left ventricular (LV) endocardial rate-corrected velocity of circumferential fiber shortening (VCFc) versus age.

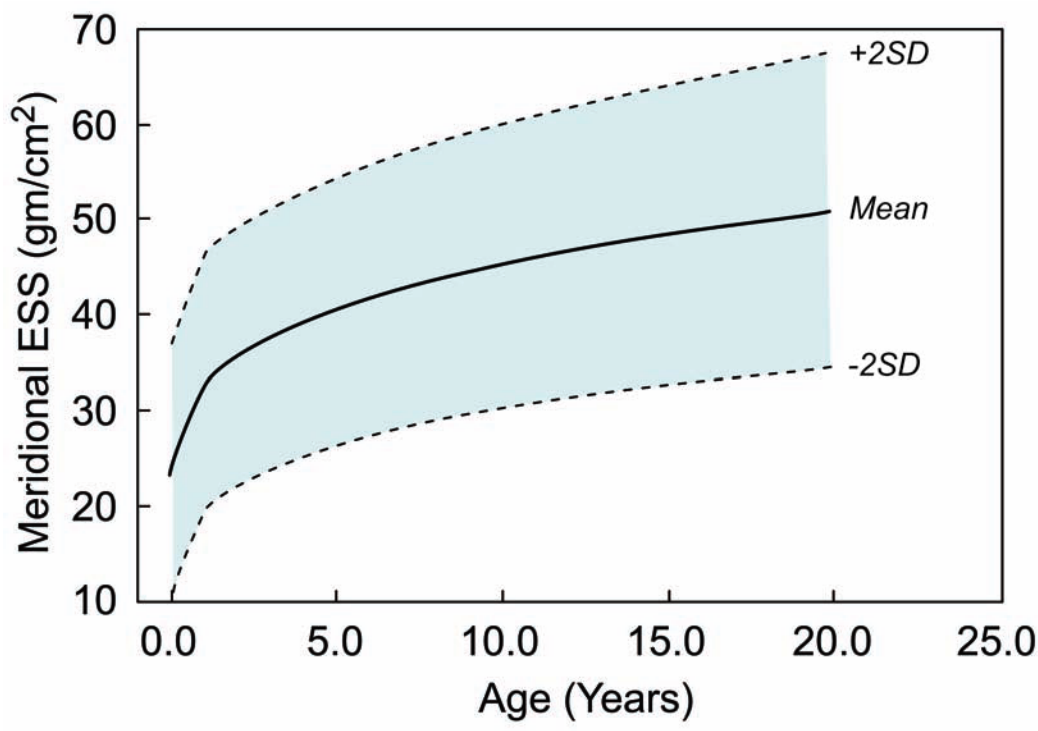


**Figure 9** Left ventricular meridional end-systolic stress (ESS) versus age.

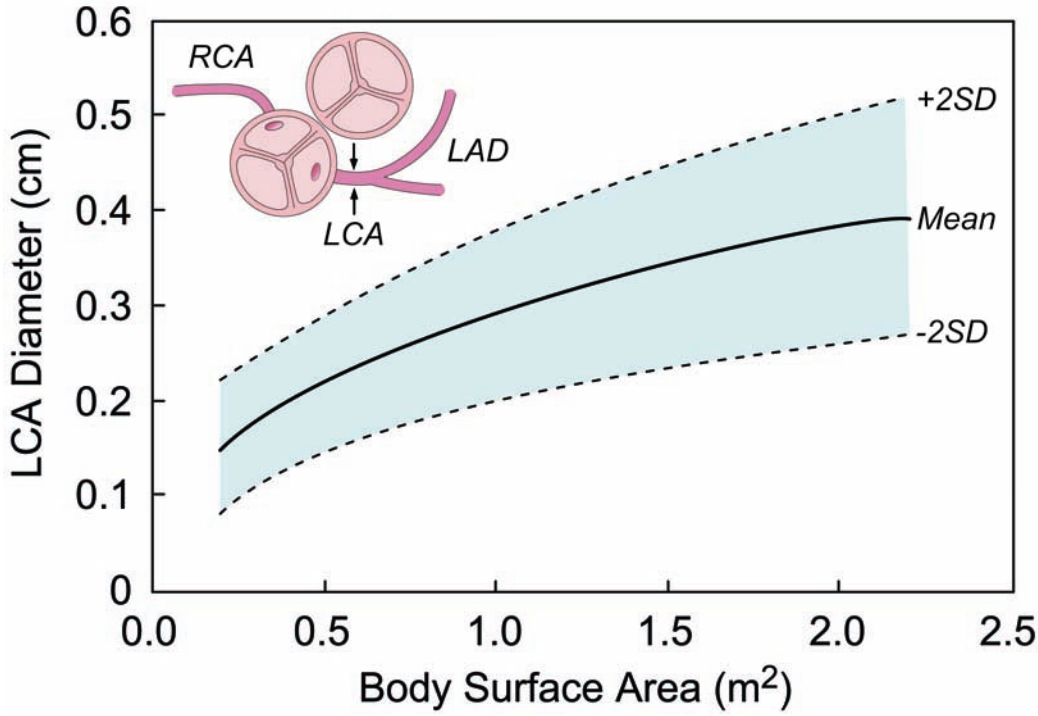


**Figure 10** Left main coronary artery (LCA) diameter versus body surface area. LAD, left anterior descending coronary artery; RCA, right coronary artery.

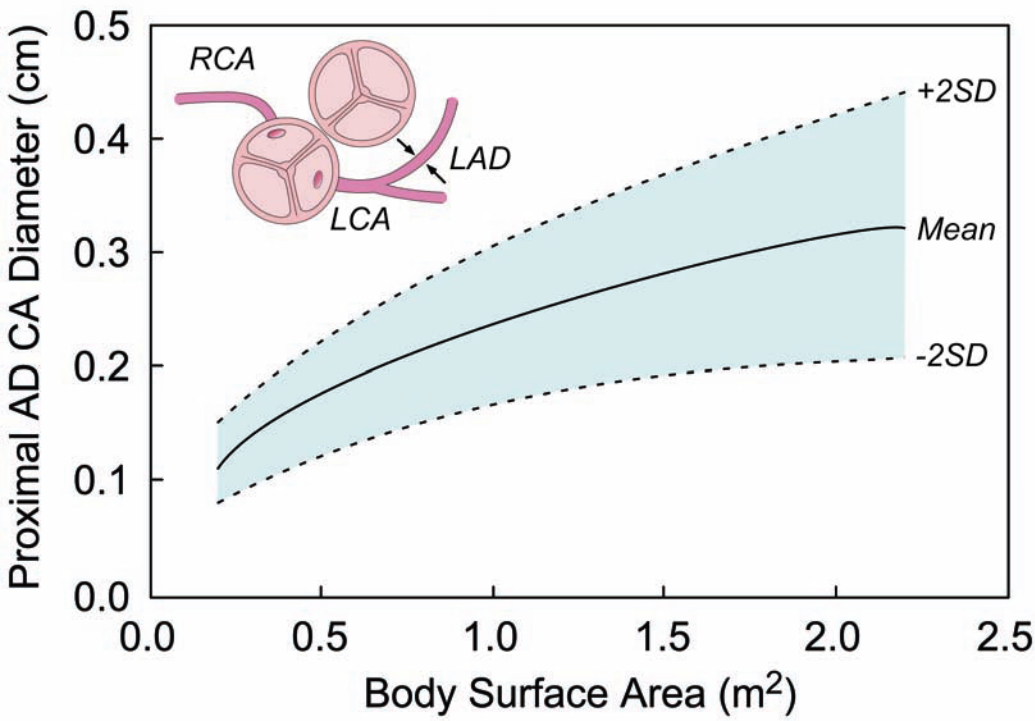


**Figure 11** Proximal anterior descending (AD) coronary artery (CA) diameter versus body surface area. LAD, left anterior descending coronary artery; LCA, left main coronary artery; RCA, right coronary artery.

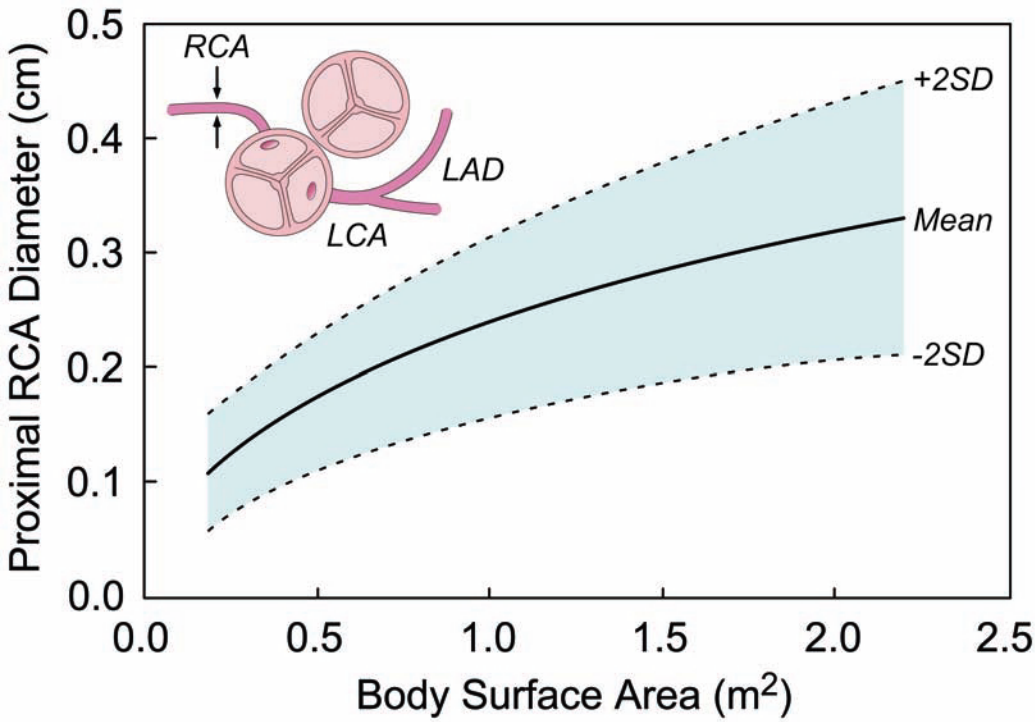


**Figure 12** Proximal right coronary artery (RCA) diameter versus body surface area. LAD, left anterior descending coronary artery; LCA, left coronary artery.

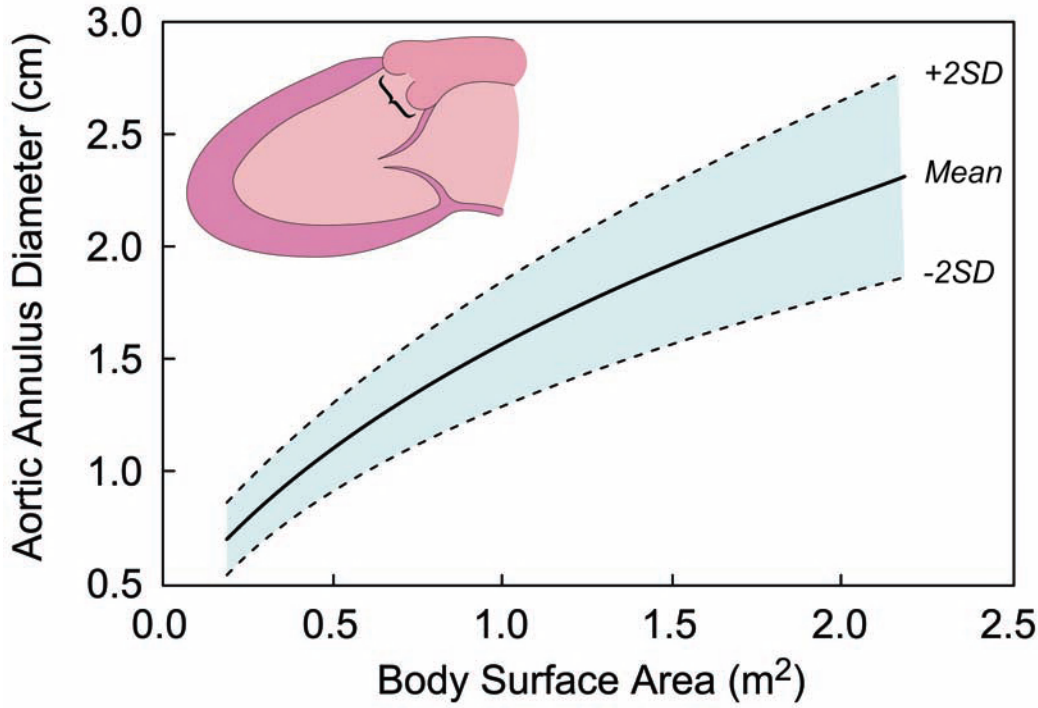


**Figure 13** Aortic valve annulus diameter versus body surface area.

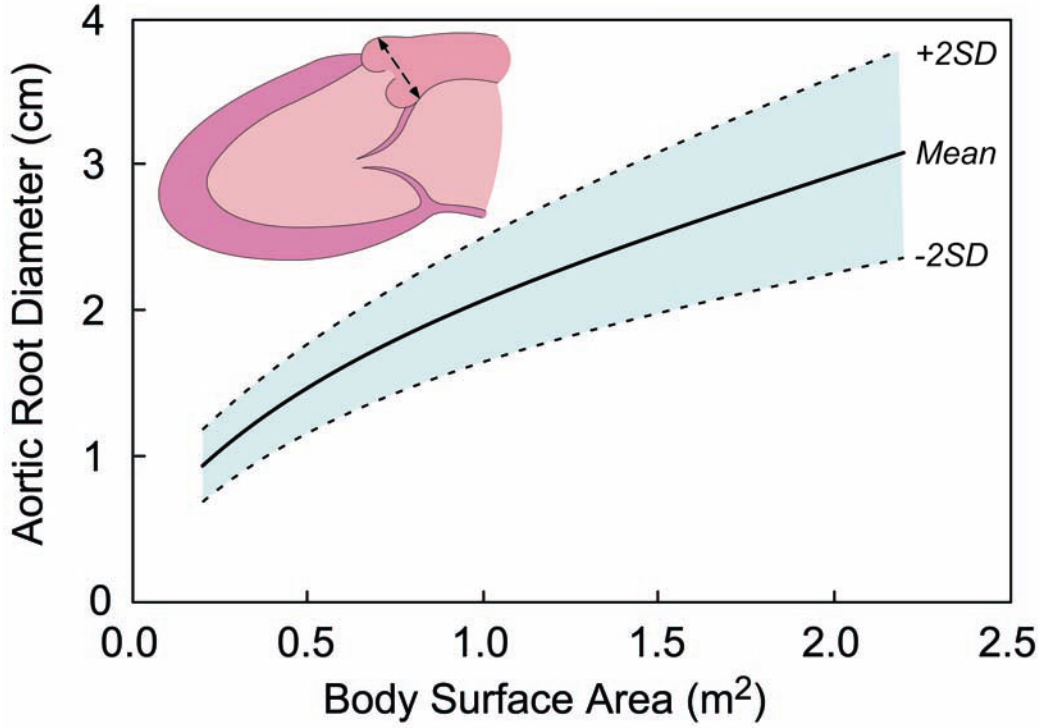


**Figure 14** Aortic root diameter versus body surface area.

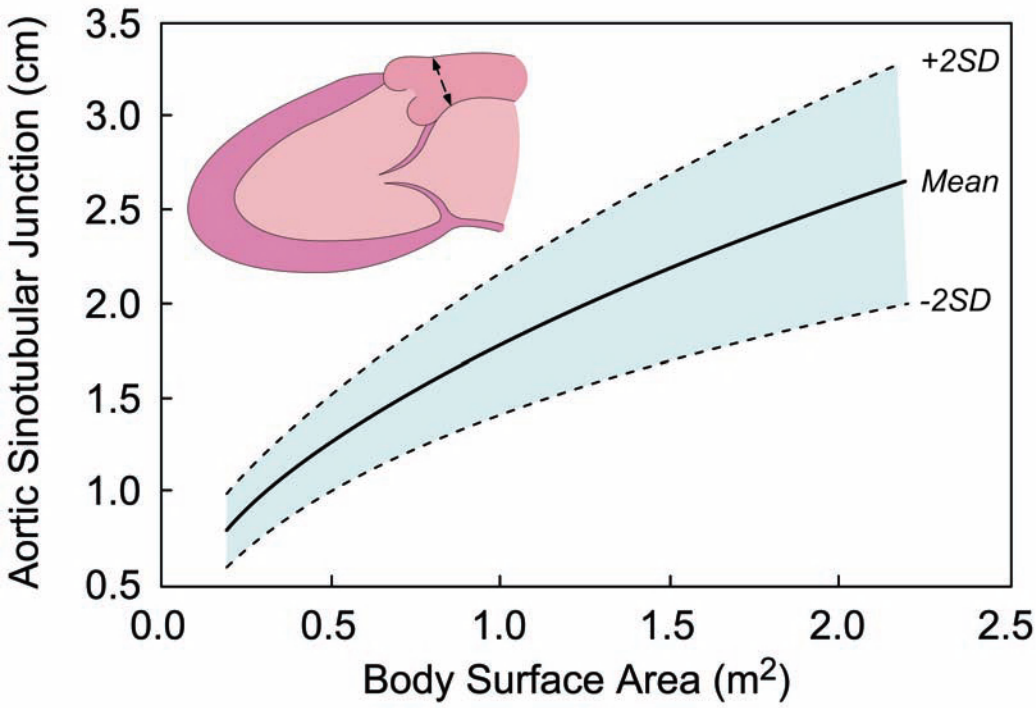


**Figure 15** Aortic sinotubular junction diameter versus body surface area.

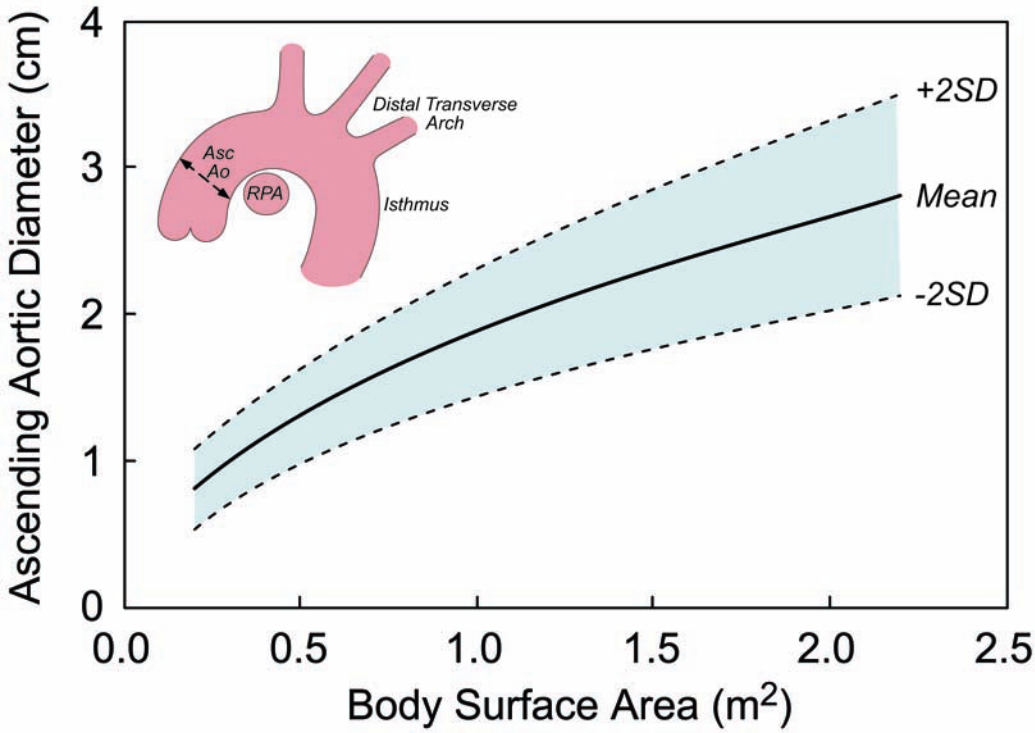


**Figure 16** Ascending aortic diameter versus body surface area, measured directly anterior to the crossing of the right pulmonary artery. AscAo, ascending aorta; RPA, right pulmonary artery.

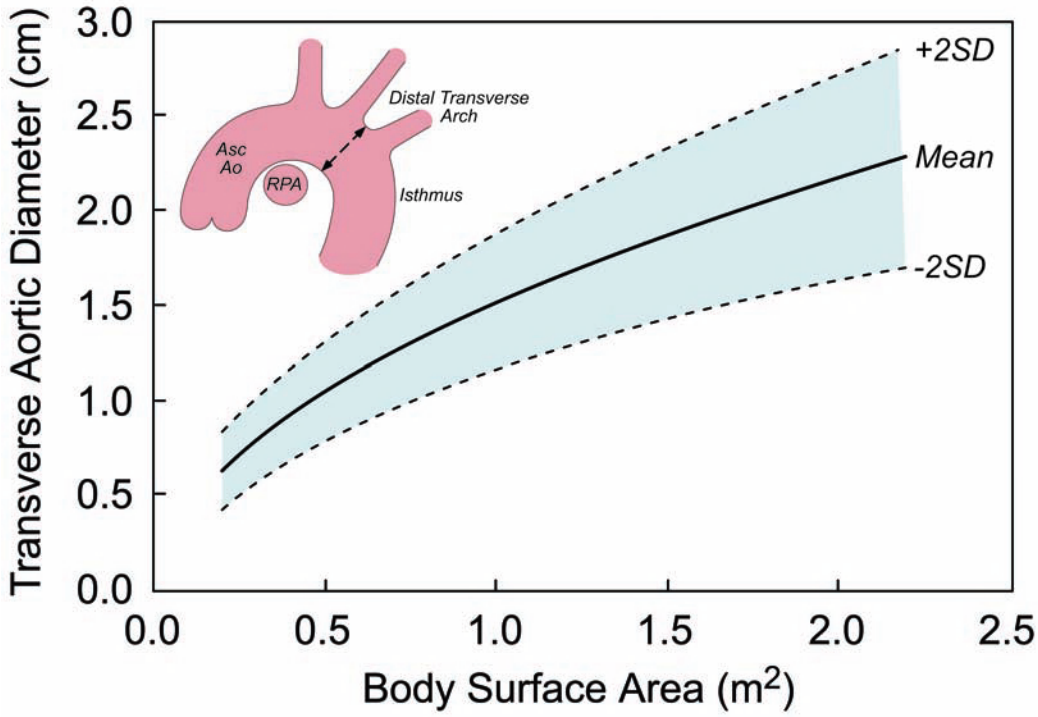


**Figure 17** Distal transverse aortic diameter versus body surface area, measured at the mid-point between the origin of the left carotid and left subclavian arteries. AscAo, ascending aorta; RPA, right pulmonary artery.

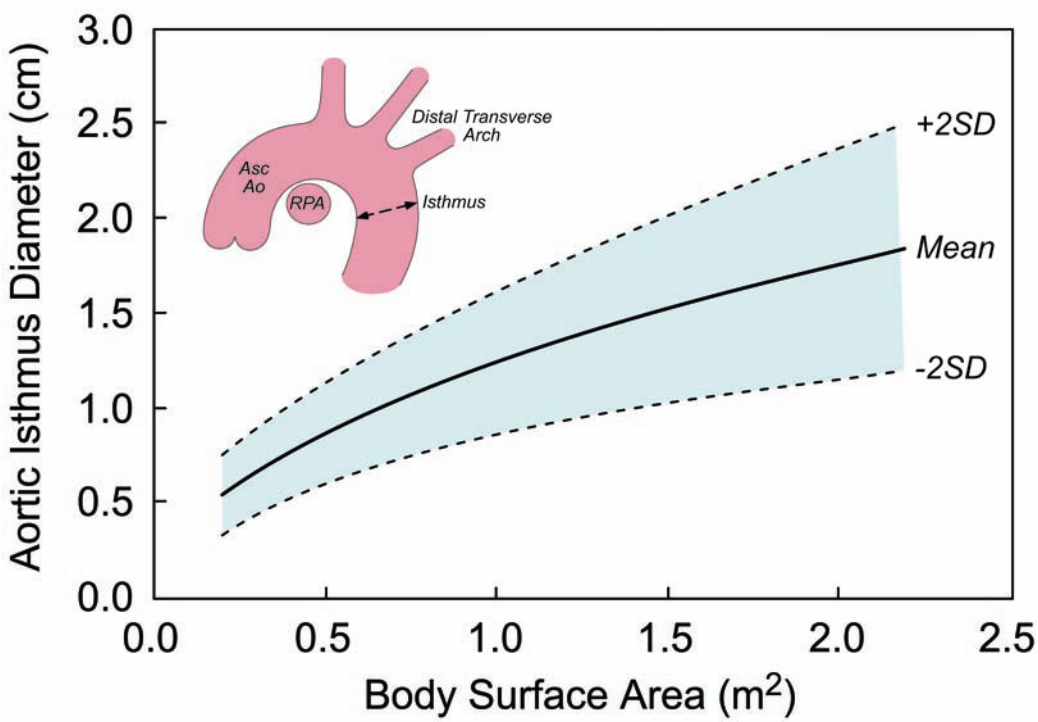


**Figure 18** Aortic isthmus diameter versus body surface area, measured just distal to the origin of the left subclavian artery. AscAo, ascending aorta; RPA, right pulmonary artery.

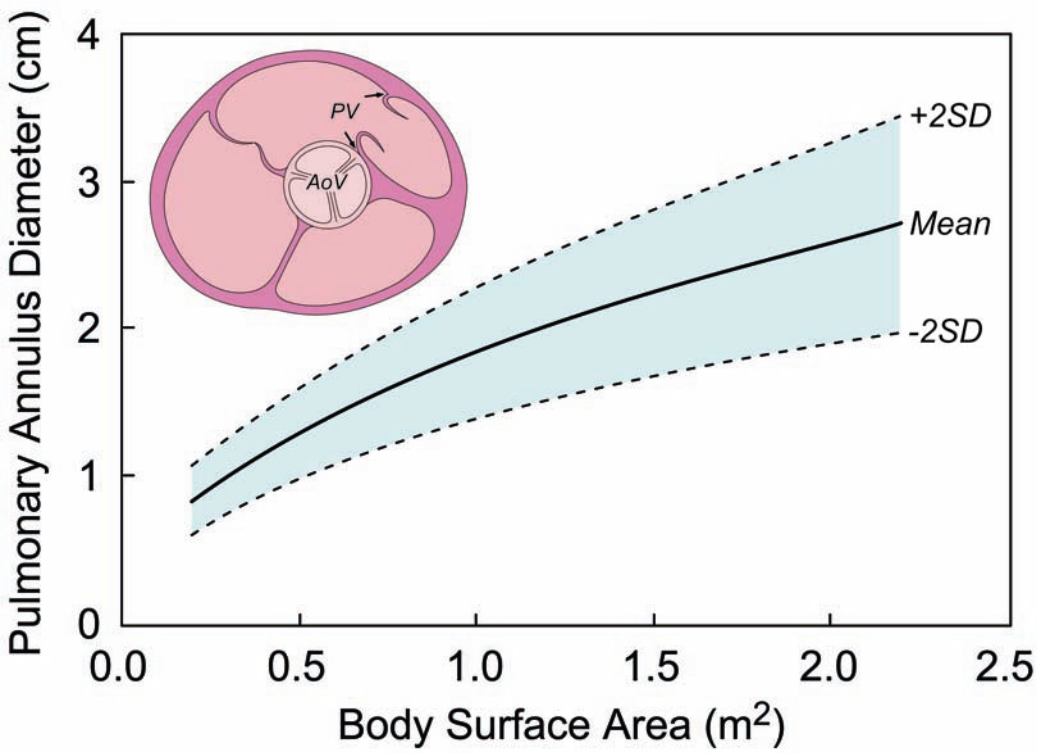


**Figure 19** Pulmonary valve annulus diameter versus body surface area. AoV, aortic valve; PV, pulmonary valve.

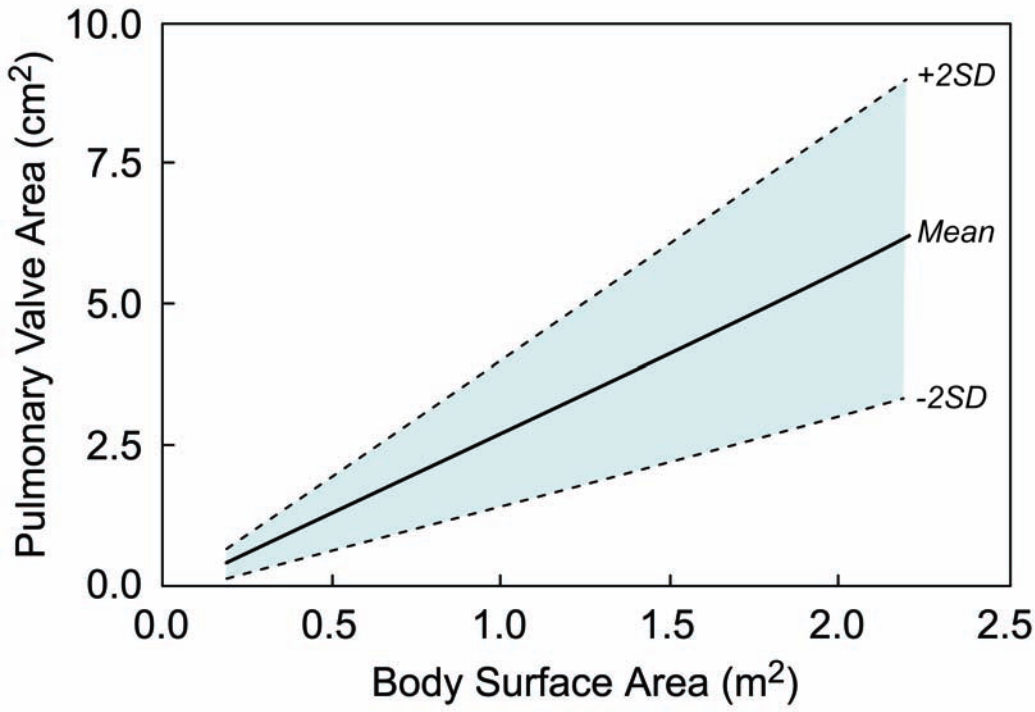


**Figure 20** Pulmonary valve annulus cross-sectional area versus body surface area.

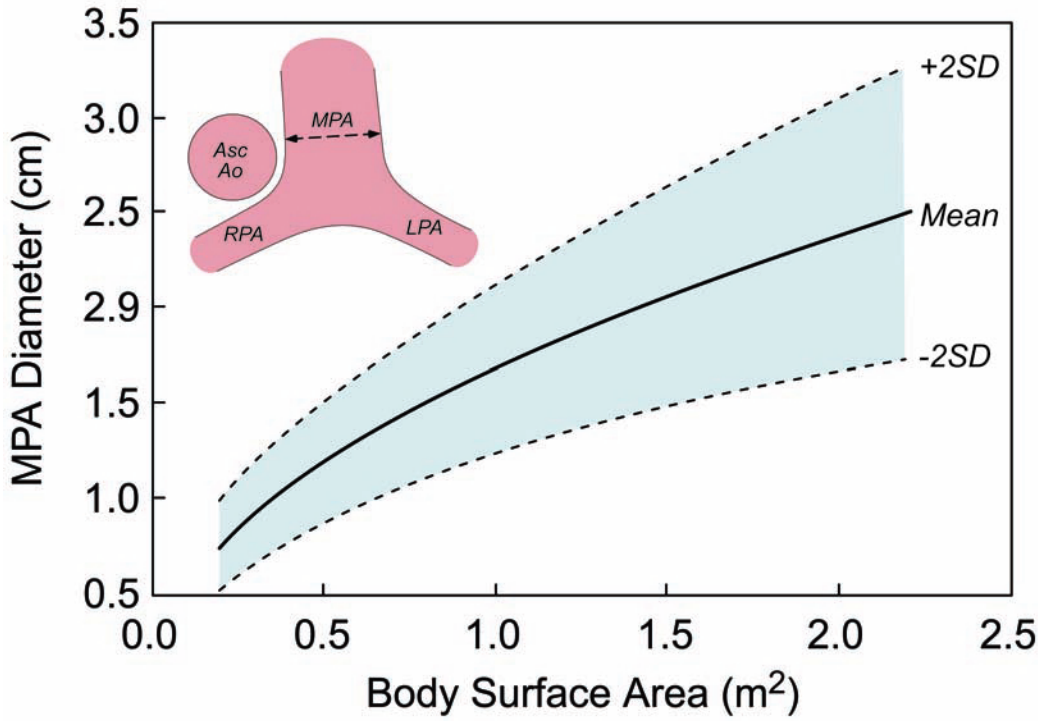


**Figure 21** Main pulmonary artery (MPA) diameter versus body surface area. AscAo, ascending aorta; LPA, left pulmonary artery; RPA, right pulmonary artery.

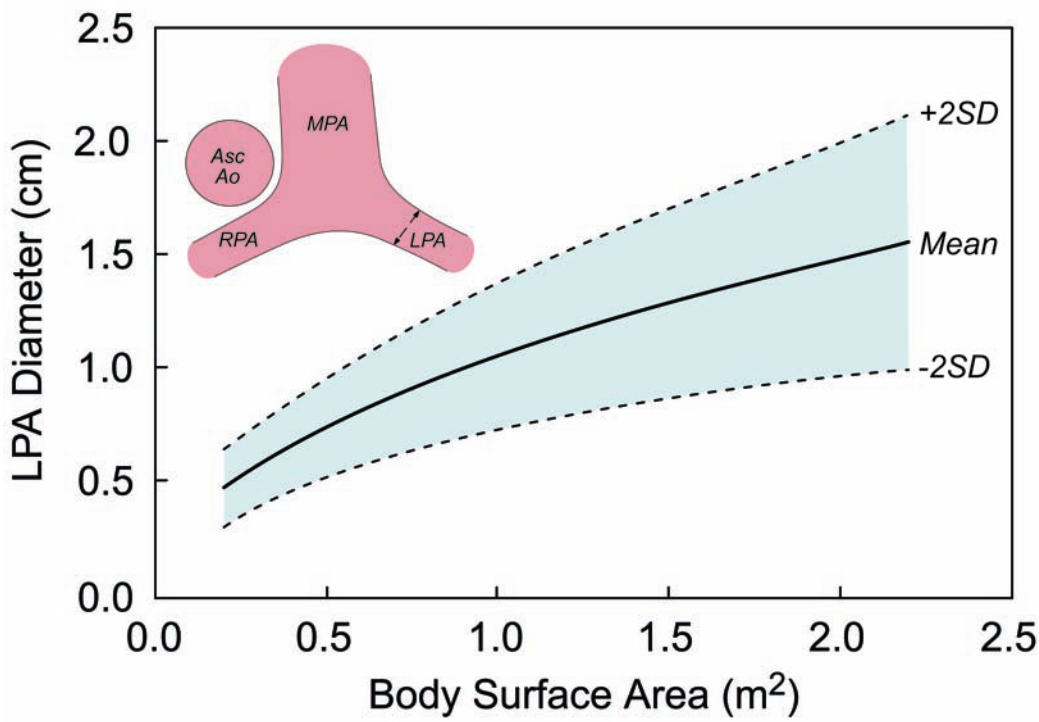


**Figure 22** Left pulmonary artery (LPA) diameter versus body surface area. AscAo, ascending aorta; MPA, main pulmonary artery; RPA, right pulmonary artery.

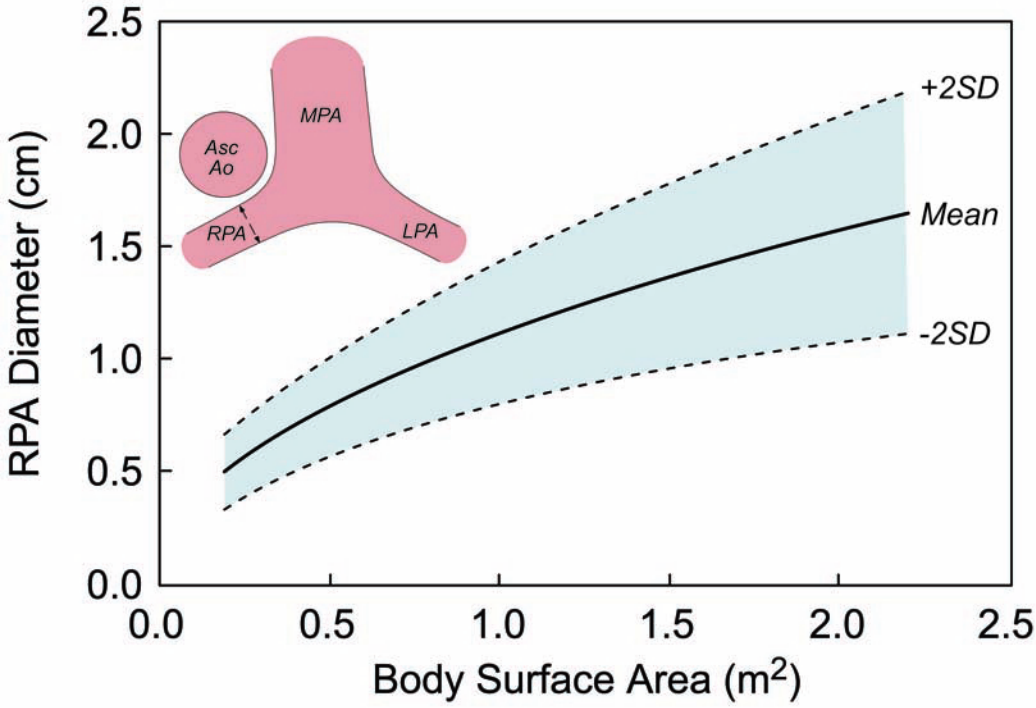


**Figure 23** Right pulmonary artery (RPA) diameter versus body surface area. AscAo, ascending aorta; LPA, left pulmonary artery; MPA, main pulmonary artery.

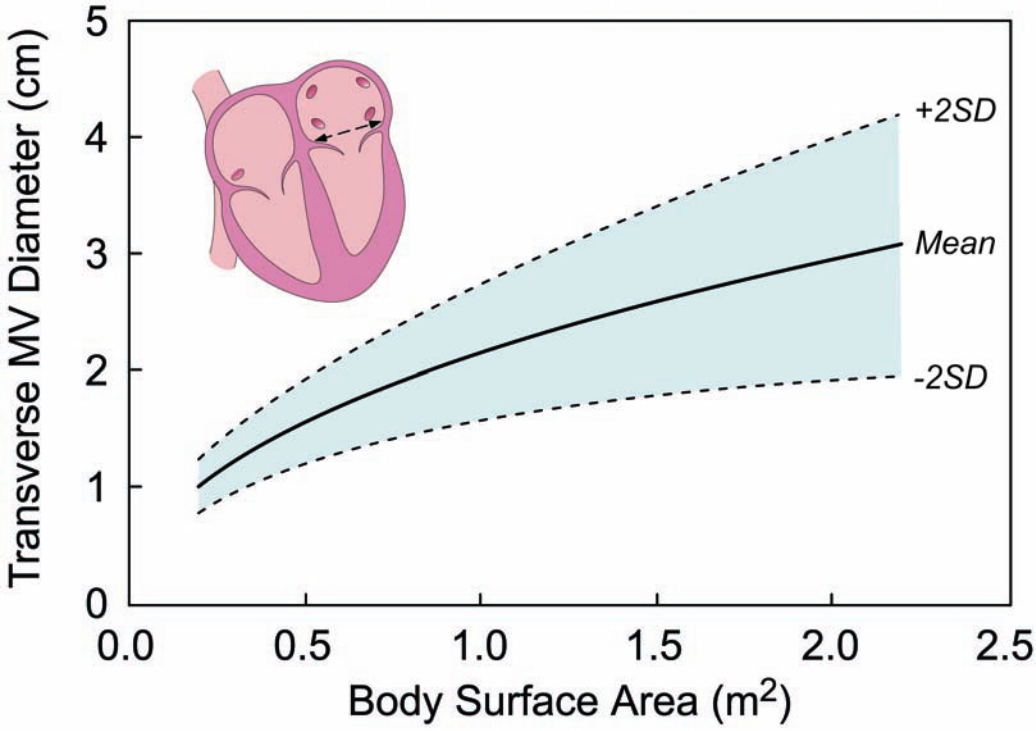


**Figure 24** Transverse mitral valve (MV) annulus diameter versus body surface area, measured from the apical 4-chamber view.

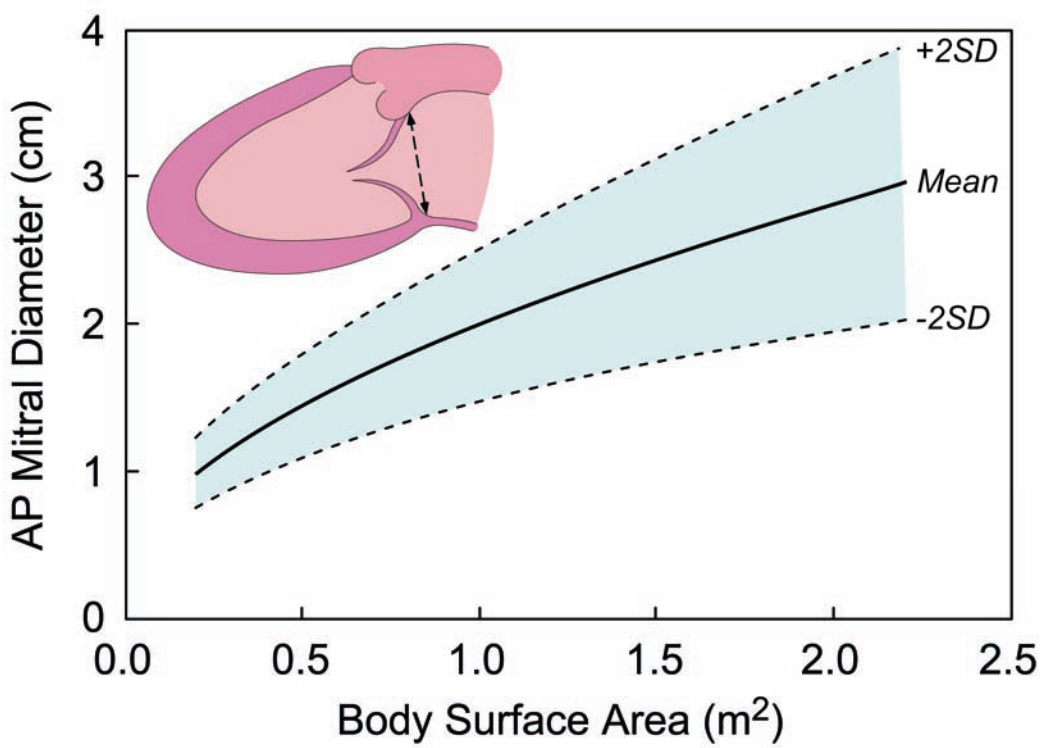


**Figure 25** Antero-posterior (AP) mitral valve (MV) annulus diameter versus body surface area, measured from the parasternal long-axis view.

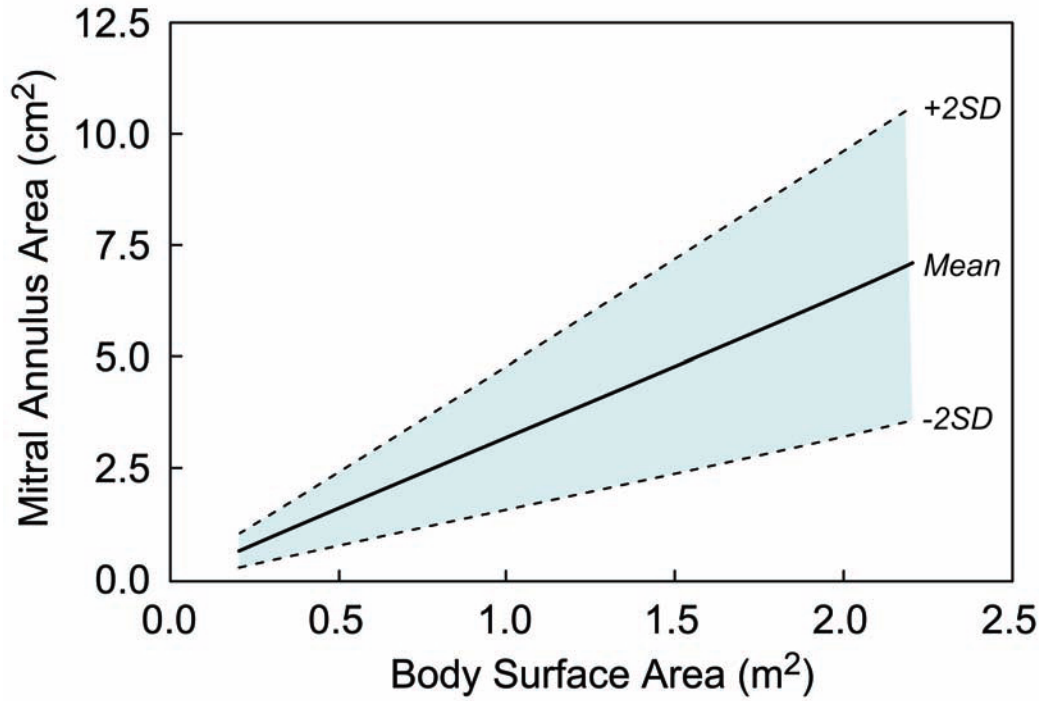


**Figure 26** Mitral valve annulus cross-sectional area versus body surface area, calculated as an ellipse from the transverse and antero-posterior annulus dimensions.

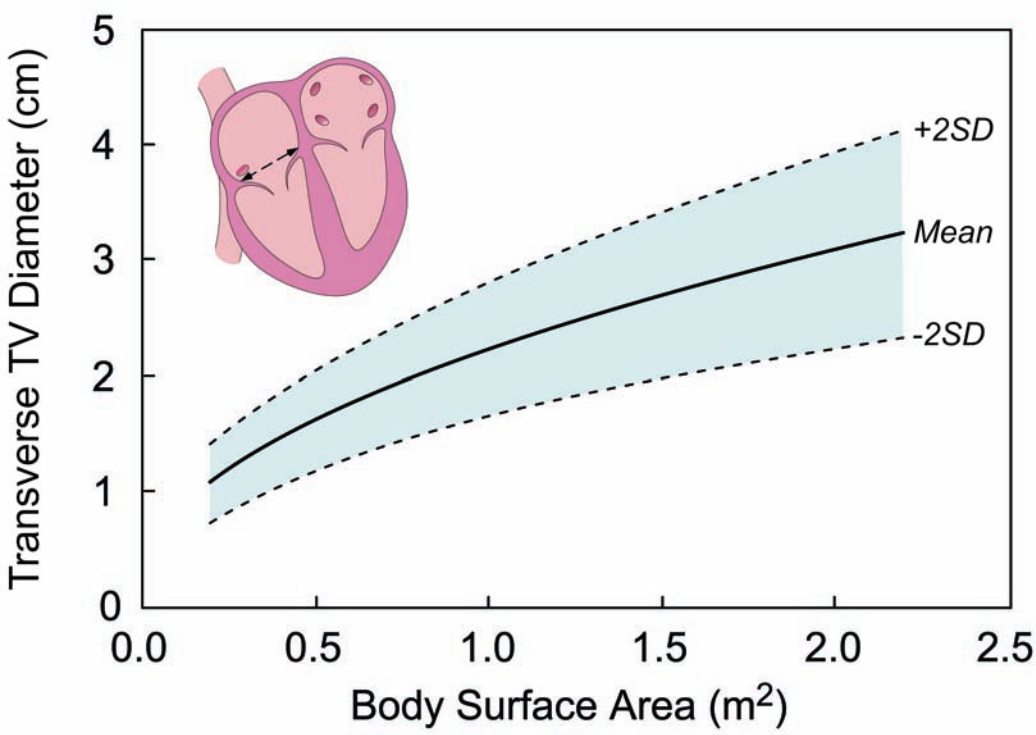


**Figure 27** Transverse tricuspid valve (TV) annulus diameter versus body surface area, measured from the apical 4-chamber view.

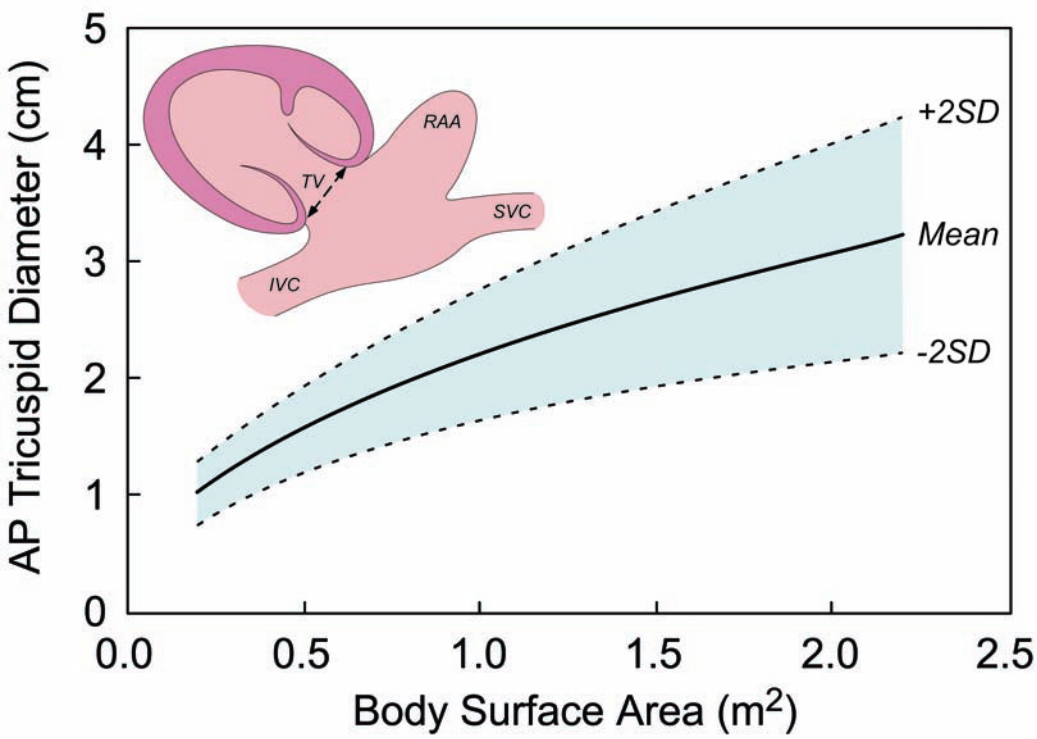


**Figure 28** Antero-posterior (AP) tricuspid valve (TV) annulus diameter versus body surface area, measured from the parasternal long-axis view. IVC, inferior vena cava; RAA, right atrial appendage; SVC. superior vena cava.

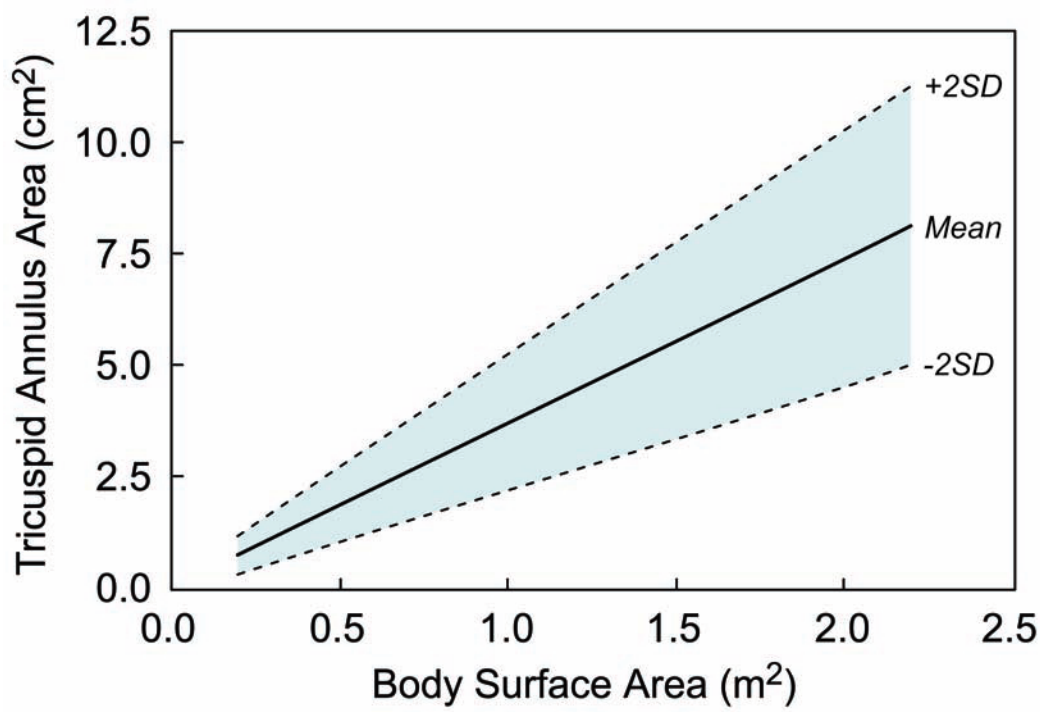


**Figure 29** Tricuspid valve annulus cross-sectional area versus body surface area, calculated as an ellipse from the transverse and antero-posterior annulus dimensions.

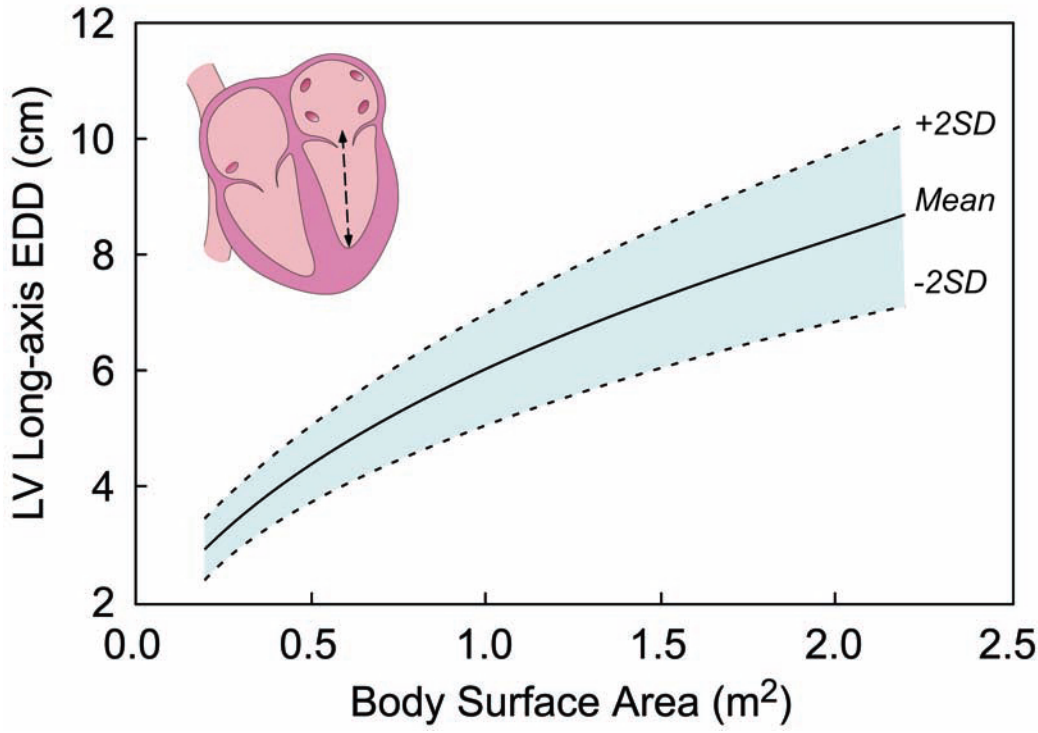


**Figure 30** Left ventricular (LV) long-axis end-diastolic dimension (EDD) versus body surface area.

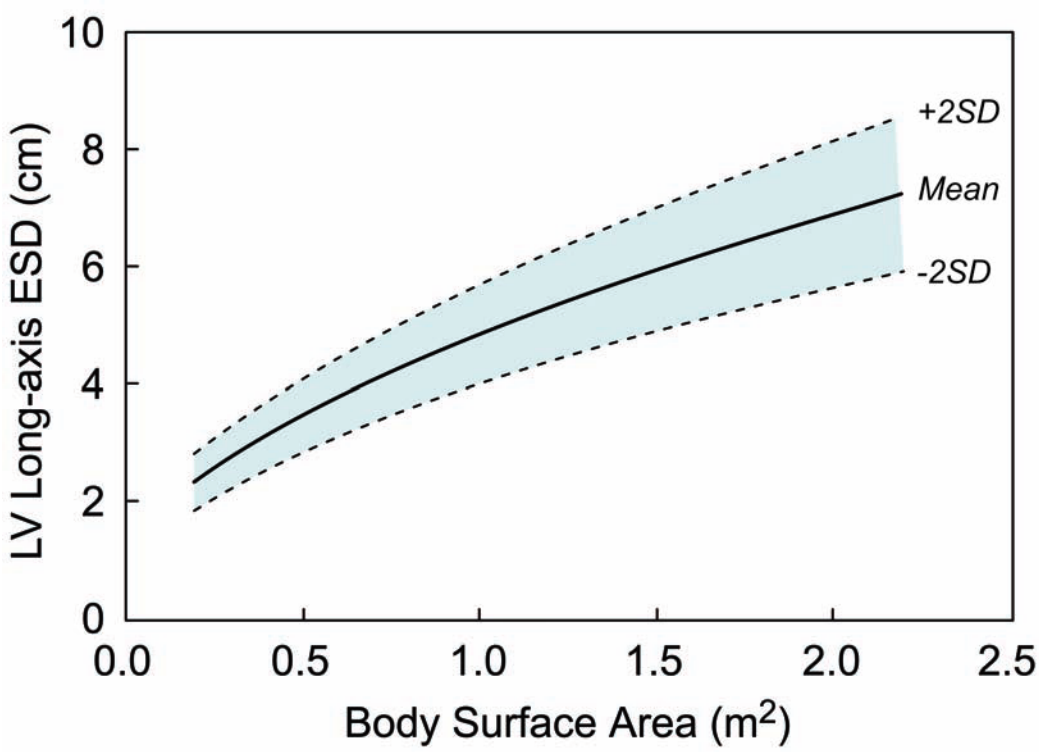


**Figure 31** Left ventricular (LV) long-axis end-systolic dimension (ESD) versus body surface area.

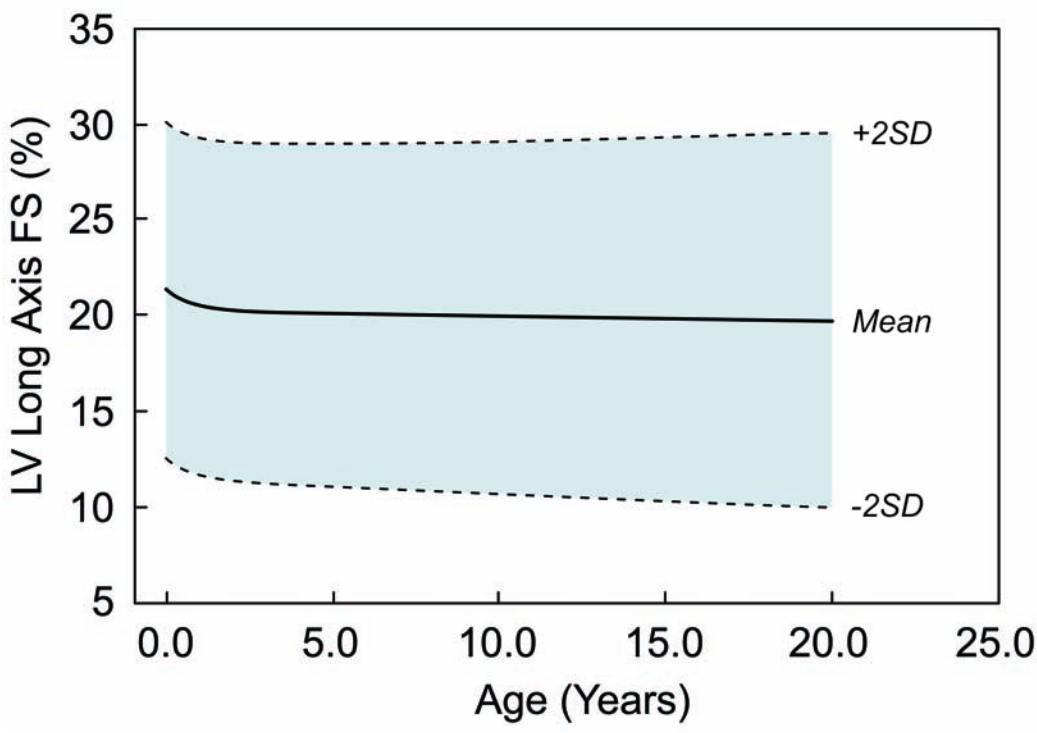


**Figure 32** Left ventricular (LV) endocardial long-axis percent fractional shortening (FS) versus age.

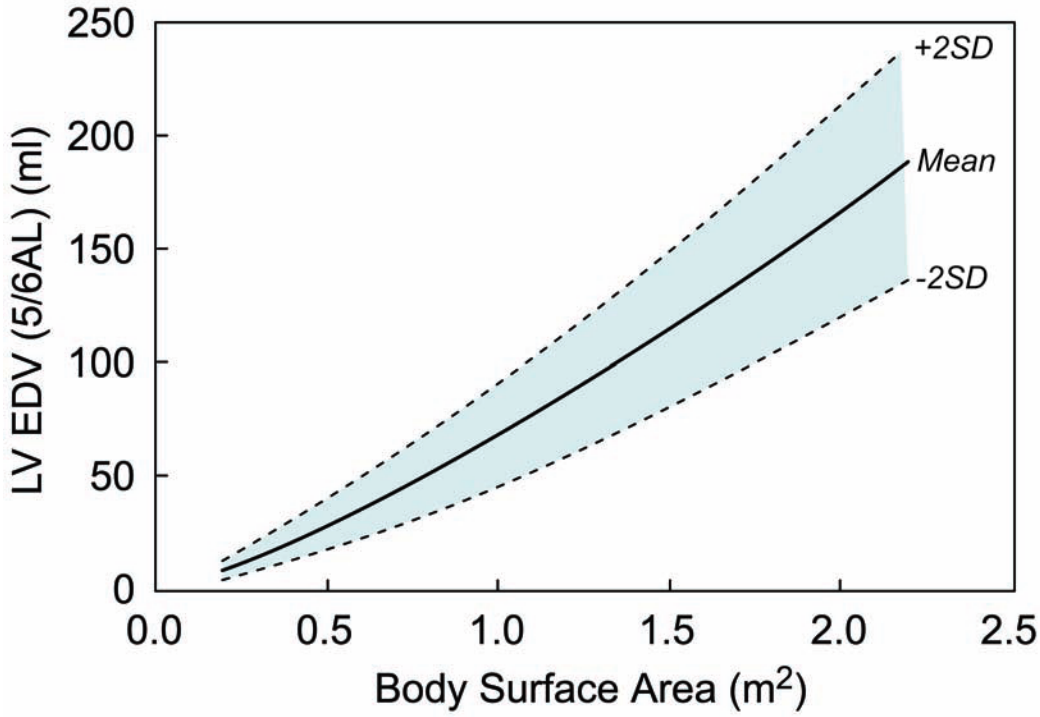


**Figure 33** Left ventricular (LV) end-diastolic volume (EDV) using the 5/6 × area × length algorithm (5/6AL) versus body surface area.

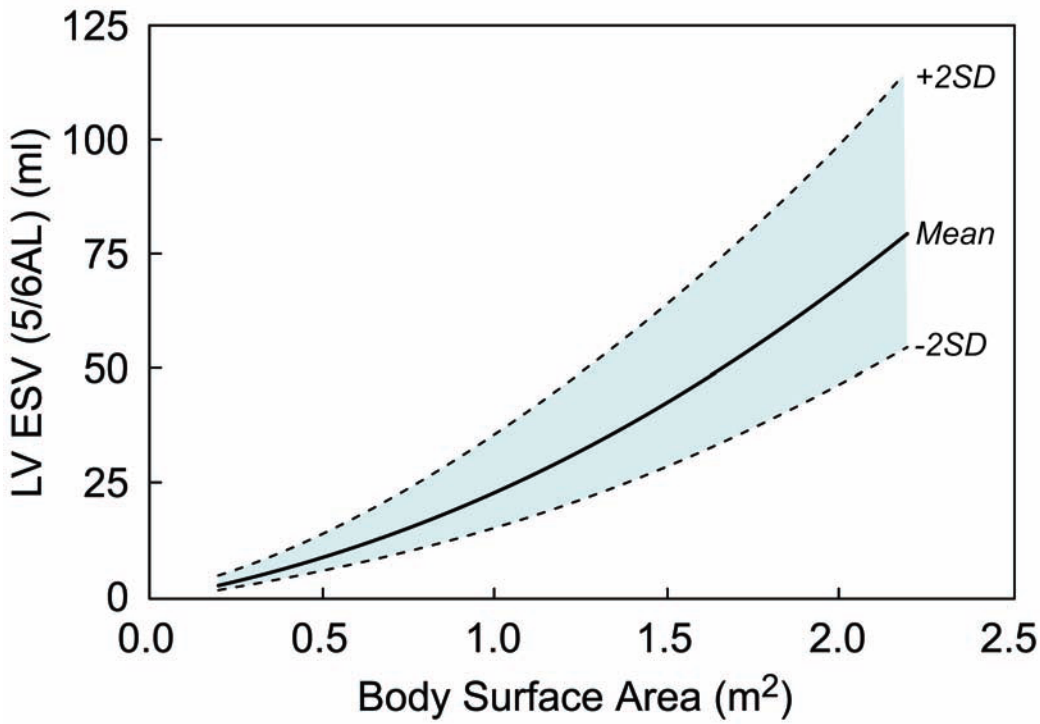


**Figure 34** Left ventricular (LV) end-systolic volume (ESV) using the 5/6 × area × length algorithm (5/6AL) versus body surface area.

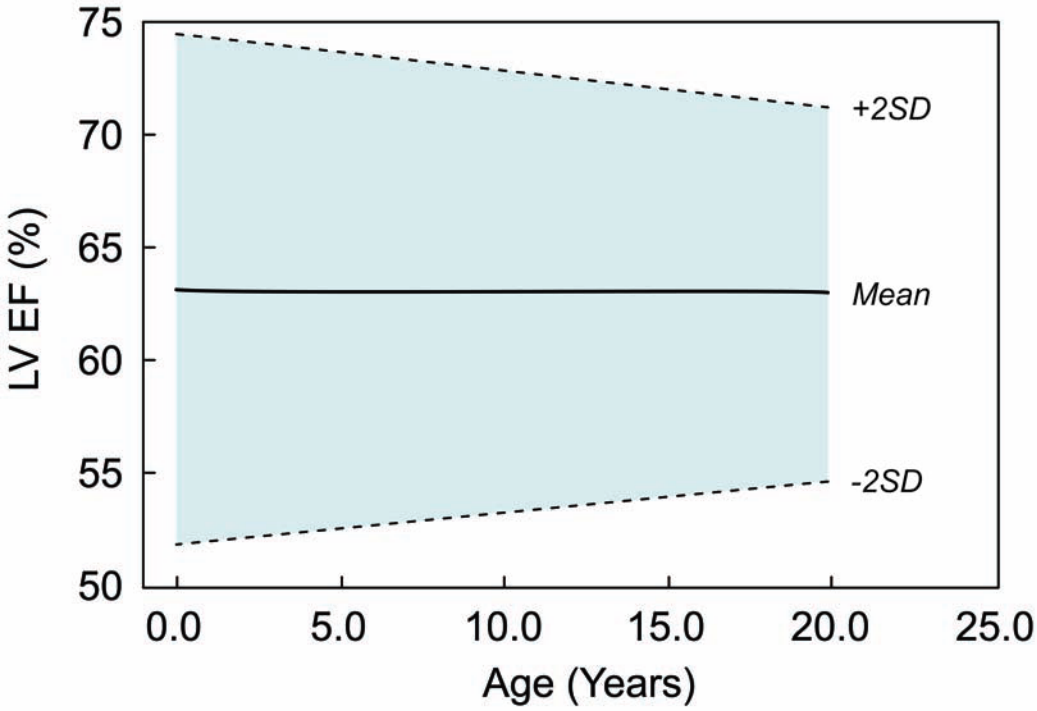


**Figure 35** Left ventricular (LV) percent ejection fraction (EF) using the 5/6 × area × length algorithm (5/6AL) versus age.

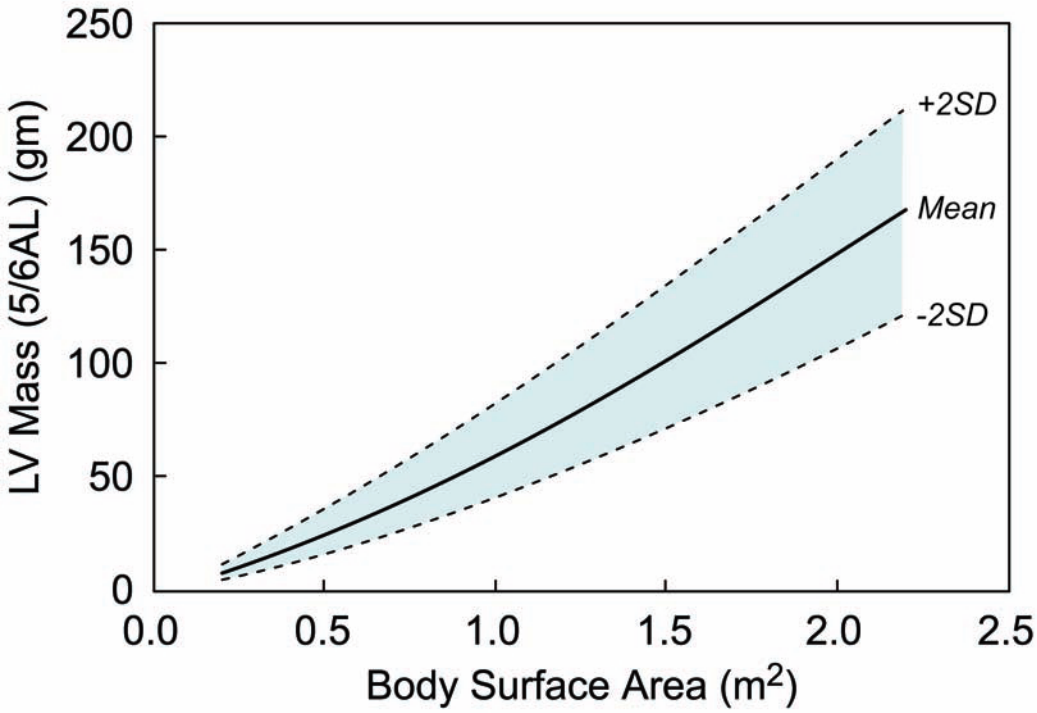


**Figure 36** Left ventricular (LV) mass using the 5/6 × area × length algorithm (5/6AL) versus body surface area.

# Index

Page numbers in *italics* represent figures; those in **bold** represent tables.




 ISBN: 978-1-405-17401-5